

中草藥研究中心

2019 年 9 月 1 日~2020 年 12 月 31 日

(中)論文集



CHANG GUNG UNIVERSITY OF SCIENCE AND TECHNOLOGY

長庚科技大學
中草藥研究中心
2019年9月1日~2020年12月31日
論文集
目 錄

序號	期刊論文	學校主要 負責教師	頁碼
1.	Hsieh, H.-L., Tsai, M.-M. Tumor progression-dependent angiogenesis in gastric cancer and its potential application. World Journal of Gastrointestinal Oncology 11(9): 686-704; 2019.	蔡明明、 謝喜龍	1
2.	Liu, C.-H., Liu, Y.-X., Kumari, M., Wu, W.-C. Multivariate analysis of metabolic parameters and optimization of antibody production using high cell density hybridoma in hollow fiber bioreactors. Biotechnology Letters 41(8-9): 963-977; 2019.	劉繼賢	20
3.	Lee, C.-W., Chi, M.-C., Peng, K.-T., Chiang, Y.-C., Hsu, L.-F., Yan, Y.-L., Li, H.-Y., Chen, M.-C., Lee, I.-T., Lai, C.-H. Water-soluble fullereneol C60(OH)36 toward effective anti-air pollution induced by urban particulate matter in HaCaT cell. International Journal of Molecular Sciences 20(17): 259; 2019.	李江文	35
4.	Chang, Z.-Y., Chen, C.-C., Liu, H.-M., Yeh, Y.-C., Lin, T.-Y., Lee, T.-Y., Huang, T.-H. Positive effects of Ger-Gen-Chyn-Lian-Tang on cholestatic liver fibrosis in bile duct ligation-challenged mice. International Journal of Molecular Sciences 20(17): 4181; 2019.	黃澤宏	55
5.	Liu, F.-C., Yu, H.-P., Chen, P.-J., Yang, H.-W., Chang, S.-H., Tzeng, C.-C., Cheng, W.-J., Chen, Y.-R., Chen, Y.-L., Hwang, T.-L. A novel NOX2 inhibitor attenuates human neutrophil oxidative stress and ameliorates inflammatory arthritis in mice. Redox Biology 26: 101273; 2019.	黃聰龍	67
6.	Kao, H.-H., Kuo, C.-Y., Chen, K.-S., Chen, J.-P. Preparation of gelatin and gelatin/hyaluronic acid cryogel scaffolds for the 3D culture of mesothelial cells and mesothelium tissue regeneration. International Journal of Molecular Sciences 20(18): 4527; 2019.	陳志平	84
7.	Hsiao, C.-Y., Yang, S.-C., Alalaiwe, A., Fang, J.-Y. Laser ablation and topical drug delivery: a review of recent advances. Expert Opinion on Drug Delivery 16(9): 937-952; 2019.	蕭千祐、 方嘉佑	104
8.	Wang, P.-W., Lin, T.-Y., Hung, Y.-C., Chang, W.-N., Yang, P.-M., Chen, M.-H., Yeh, C.-T., Pan, T.-L. Characterization of fibrinogen as a key modulator in patients with wilson's diseases with functional proteomic tools. International Journal of Molecular Sciences 20(18): 4528; 2019.	潘台龍	120
9.	Lin, J.-Y., Kung, Y.-A., Shih, S.-R. Antivirals and vaccines for Enterovirus A71. Journal of Biomedical Science 26(1): 65; 2019.	施信如	137

10.	Huang, S.-Y., Huang, C.-H., Chen, C.-J., Chen, T.-W., Lin, C.-Y., Lin, Y.-T., Kuo, S.-M., Huang, C.-G., Lee, L.-A., Chen, Y.-H., Chen, M.-F., Kuo, R.-L., Shih, S.-R. Novel Role for miR-1290 in Host Species Specificity of Influenza A Virus. <i>Molecular Therapy - Nucleic Acids</i> 17: 10-23; 2019.	施信如	147
11.	Yang, H.-C., Wu, Y.-H., Yen, W.-C., Liu, H.-Y., Hwang, T.-L., Stern, A., Chiu, D.T.-Y. The Redox Role of G6PD in Cell Growth, Cell Death, and Cancer. <i>Cells</i> 8(9); 2019.	吳依璇、 黃聰龍、 趙崇義	161
12.	Chen, M.-H., Hsu, J.-W., Huang, K.-L., Su, T.-P., Li, C.-T.a,b, Lin, W.-C., Tsai, S.-J., Cheng, C.-M., Chang, W.-H., Pan, T.-L., Chen, T.-J., Bai, Y.-M. Risk and coaggregation of major psychiatric disorders among first-degree relatives of patients with bipolar disorder: a nationwide population-based study. <i>Psychological Medicine</i> 49(14): 2397-2404; 2019.	潘台龍	190
13.	Chen, Y.-F., Chen, W.-F., Wen, Z.-H., Hwang, T.-L., Zhang, Z.-J., Sung, P.-J. New bioactive $\Delta 11(17)$ -furanoeunicellins from an octocoral <i>Cladiella</i> sp. <i>Phytochemistry Letters</i> 33: 31-35, 2019.	黃聰龍	198
14.	Wang, P.-W., Wu, T.-H., Lin, T.-Y., Chen, M.-H., Yeh, C.-T., Pan, T.-L. Characterization of the Roles of Vimentin in Regulating the Proliferation and Migration of HSCs during Hepatic Fibrogenesis. <i>Cells</i> 8(10); 2019.	潘台龍	203
15.	Lu, Y.-J., Chuang, E.-Y., Cheng, Y.-H., Anilkumar, T.S., Chen, H.-A., Chen, J.-P. Thermosensitive magnetic liposomes for alternating magnetic field-inducible drug delivery in dual targeted brain tumor chemotherapy. <i>Chemical Engineering Journal</i> 373: 720-733; 2019.	陳志平	223
16.	Huang, P.-S., Wang, C.-S., Yeh, C.-T., Lin, K.-H. Roles of thyroid hormone-associated microRNAs affecting oxidative stress in human hepatocellular carcinoma. <i>International Journal of Molecular Sciences</i> 20(20): 5220; 2019.	林光輝	237
17.	Chen, C.-T., Chen, C.-H., Sheu, C., Chen, J.-P. Ibuprofen-loaded hyaluronic acid nanofibrous membranes for prevention of postoperative tendon adhesion through reduction of inflammation. <i>International Journal of Molecular Sciences</i> 20(20): 5038; 2019.	陳志平	261
18.	Liu, Y.-C., Yeh, C.-T., Lin, K.-H. Molecular functions of thyroid hormone signaling in regulation of cancer progression and anti-apoptosis. <i>International Journal of Molecular Sciences</i> 20(20): 4986; 2019.	林光輝	280
19.	Chiang, C.-C., Cheng, W.-J., Korinek, M., Lin, C.-Y., Hwang, T.-L. Neutrophils in Psoriasis. <i>Frontiers in Immunology</i> 10: 2376; 2019.	黃聰龍	307
20.	Chen, P.-Y., Wu, C.Y.-J., Fang, J.-H., Chen, H.-C., Feng, L.-Y., Huang, C.-Y., Wei, K.-C., Fang, J.-Y., Lin, C.-Y. Functional Change of Effector Tumor-Infiltrating CCR5+CD38+HLA-DR+CD8+ T Cells in Glioma Microenvironment. <i>Frontiers in Immunology</i> 10: 2395; 2019.	方嘉佑	319

21. Wang, T.-H., Chen, C.-C., Huang, K.-Y., Shih, Y.-M., Chen, C.-Y. High levels of EGFR prevent sulforaphane-induced reactive oxygen species-mediated apoptosis in non-small-cell lung cancer cells. *Phytomedicine* 64: 152926; 2019. 陳琦媛 333
22. Liou, C.-J., Dai, Y.-W., Wang, C.-L., Fang, L.-W., Huang, W.-C. Maslinic acid protects against obesity-induced nonalcoholic fatty liver disease in mice through regulation of the Sirt1/AMPK signaling pathway. *FASEB Journal* 33(11): 11791-11803; 2019. 劉倩君、黃文忠 340
23. Shalumon, K.T., Liao, H.-T., Kuo, C.-Y., Wong, C.-B., Li, C.-J., Mini, P.A., Chen, J.-P. Rational design of gelatin/nanohydroxyapatite cryogel scaffolds for bone regeneration by introducing chemical and physical cues to enhance osteogenesis of bone marrow mesenchymal stem cells. *Materials Science and Engineering C* 104: 109855; 2019. 陳志平 353
24. Weng, J.-R., Huang, T.-H., Lin, Z.-C., Alalaiwe, A., Fang, J.-Y. Cutaneous delivery of [1-(4-chloro-3-nitrobenzenesulfonyl)-1H-indol-3-yl]-methanol, an indole-3-carbinol derivative, mitigates psoriasiform lesion by blocking MAPK/NF- κ B/AP-1 activation. *Biomedicine and Pharmacotherapy* 119: 109398; 2019. 方嘉佑 372
25. Lee, K.-F., Tsai, M.-M., Tsai, C.-Y., Huang, C.-G., Ou, Y.-H., Hsieh, C.-C., Hsieh, H.-L., Wang, C.-S., Lin, K.-H. DEK is a potential biomarker associated with malignant phenotype in gastric cancer tissues and plasma. *International Journal of Molecular Sciences* 20(22): 5689; 2019. 林光輝 384
26. Wang, T.-H., Leu, Y.-L., Chen, C.-C., Shieh, T.-M., Lian, J.-H., Chen, C.-Y. Psorachromene Suppresses Oral Squamous Cell Carcinoma Progression by Inhibiting Long Non-coding RNA GAS5 Mediated Epithelial-Mesenchymal Transition. *Frontiers in Oncology* 9: 1168; 2019. 陳琦媛 403
27. Tsai, Y.-F., Chen, C.-Y., Chang, W.-Y., Syu, Y.-T., Hwang, T.-L. Resveratrol suppresses neutrophil activation via inhibition of Src family kinases to attenuate lung injury. *Free Radical Biology and Medicine* 145: 67-77; 2019. 黃聰龍 415
28. Wu, M.-F., Shu, C.-C., Wang, J.-Y., Yan, B.-S., Lai, H.-C., Chiang, B.-L., Wu, L.S.-H., Yu, C.-J. NLRP3 inflammasome is attenuated in patients with Mycobacterium avium complex lung disease and correlated with decreased interleukin-1 β response and host susceptibility. *Scientific Reports* 9(1): 12534; 2019. 賴信志 426
29. Huang, T.-H., Wu, A.T.H., Cheng, T.-S., Lin, K.-T., Lai, C.-J., Hsieh, H.-W., Chang, P.M.-H., Wu, C.-W., Huang, C.-Y.F., Chen, K.-Y. In silico identification of thiostrepton as an inhibitor of cancer stem cell growth and an enhancer for chemotherapy in non-small-cell lung cancer. *Journal of Cellular and Molecular Medicine* 23(12): 8184-8195; 2019. 黃澤宏 436
30. Wang, I.-L., Hsiao, C.-Y., Shen, J., Wang, Y., Huang, C.-C., Chen, Y.-M. The effects of Jilin sika Deer's (Cervus dybowski) tendon liquid supplementation on endurance drop jumps performance, biochemistry profile of free boxing players. *Journal*

of Ethnopharmacology 245: 112119; 2019.

31. Zhang, Z.-J., Wang, Y.-H., Chen, S.-R., Peng, B.-R., Yang, S.-N., Hu, C.-C., Fang, L.-S., Hwang, T.-L., Sung, P.-J. Novel secoeunicellins produced by an octocoral *Cladiella* sp. *Tetrahedron Letters* 60(49): 151300; 2019. 黃聰龍 458
32. Lu, C.W., Lin, T.Y., Wang, S.J., Huang, S.K. Asiatic acid, an active substance of *Centella asiatica*, presynaptically depresses glutamate release in the rat hippocampus. *European Journal of Pharmacology* 865:172781; 2019. 王素珍 462
33. Huang, W.-C., Ting, N.-C., Huang, Y.-L., Chen, L.-C., Lin, C.-F., Liou, C.-J. *Helminthostachys zeylanica* water extract ameliorates airway hyperresponsiveness and eosinophil infiltration by reducing oxidative stress and Th2 cytokine production in a mouse asthma model. *Mediators of Inflammation* 2020: 1702935; 2020. 黃文忠、林傳福、劉倩君 470
34. Wu, L.-C., Chen, C.-C., Lin, C.-H. Synthesis and thermal characteristic of liquid crystalline polyoxetane containing trans-stilbene side group. *Polymers* 12(1): 185; 2020. 林志鴻 485
35. Huang, W.-C., Liou, C.-J., Shen, S.-C., Hu, S., Hsiao, C.-Y., Wu, S.-J. Luteolin Attenuates IL-1 β -Induced THP-1 Adhesion to ARPE-19 Cells via Suppression of NF- κ B and MAPK Pathways. *Mediators of Inflammation* 2020: 9421340; 2020. 黃文忠、劉倩君、蕭千祐、吳淑如 496
36. Kumari, M., Liu, C.-H., Wu, W.-C. Oligochitosan modified albumin as plasmid DNA delivery vector: Endocytic trafficking, polyplex fate, in vivo compatibility. *International Journal of Biological Macromolecules* 142: 492-502; 2020. 劉繼賢 511
37. Yang, S.-C., Tsai, Y.-F., Pan, Y.-L., Hwang, T.-L. Understanding the role of neutrophils in acute respiratory distress syndrome. *Biomedical Journal*; 2020. in press 黃聰龍 522
38. Li, Y.-C., Tanapichatsakul, C., Pripdeevech, P., Hwang, T.L., Kuo, P.-C., Tzen, J.T.C. Characterisation of teaghrein-like principles from Assam tea cultivated in Thailand. *Natural Product Research*; 2020. in press 黃聰龍 530
39. Hsieh, H.-L., Liu, S.-H., Chen, Y.-L., Huang, C.-Y., Wu, S.-J. Astragaloside IV suppresses inflammatory response via suppression of NF- κ B, and MAPK signalling in human bronchial epithelial cells. *Archives of Physiology and Biochemistry*; 2020. in press 謝喜龍、吳淑如 537
40. Jose, G., Shalumon, K.T., Chen, J.-P. Natural polymers based hydrogels for cell culture applications. *Current Medicinal Chemistry* 27(16): 2734-2776; 2020. 陳志平 547
41. Yang, H.-C., Stern, A., Chiu, D.T.-Y. G6PD: A hub for metabolic reprogramming and redox signaling in cancer. *Biomedical Journal*; 2020. in press 趙崇義 590
42. Liao, H.T., Lai, Y.-T., Kuo, C.-Y., Chen, J.-P. A bioactive multi-functional heparin-grafted aligned poly(lactide-co-

- glycolide)/curcumin nanofiber membrane to accelerate diabetic wound healing. *Materials Science and Engineering C*: 111689; 2020.
43. Hung, Y.-C., Wang, P.-W., Lin, T.-Y., Yang, P.-M., You, J.-S., Pan, T.-L. Functional Redox Proteomics Reveal That *Salvia miltiorrhiza* Aqueous Extract Alleviates Adriamycin-Induced Cardiomyopathy via Inhibiting ROS-Dependent Apoptosis. *Oxidative Medicine and Cellular Longevity* 2020: 5136934; 2020. 潘台龍 613
 44. Kuo, P.-C., Tai, S.-H., Hung, C.-C., Hwang, T.-L., Kuo, L.-M., Lam, S.H., Cheng, K.-C., Kuo, D.-H., Hung, H.-Y., Wu, T.-S. Antiinflammatory triterpenoids from the fruiting bodies of *Fomitopsis pinicola*. *Bioorganic Chemistry*: 104562; 2020. 黃聰龍 628
 45. Ma, J., Chan, C.-C., Huang, W.-C., Kuo, M.-L. Berberine inhibits pro-inflammatory cytokine-induced IL-6 and ccl11 production via modulation of stat6 pathway in human bronchial epithelial cells. *International Journal of Medical Sciences* 17(10): 1464-1473; 2020. 黃文忠、郭敏玲 639
 46. Chung, H.-M., Chang, Y.-M., Wang, W.-H., Chen, J.-J., Hwang, T.-L., Sung, P.-J. Rumphellolide K, a novel C-3/8 ether linkage caryophyllane from *rumphella antipathes*. *Heterocycles* 100(9); 2020. 黃聰龍 649
 47. Chan, C.-M., Hsiao, C.-Y., Li, H.-J., Fang, J.-Y., Chang, D.-C., Hung, C.-F. The inhibitory effects of gold nanoparticles on VEGF-A-induced cell migration in choroid-retina endothelial cells. *International Journal of Molecular Sciences* 21(1):109; 2020. 蕭千祐、方嘉佑 655
 48. Chen, Y.-H., Chin, H.-K., Peng, B.-R., Chen, Y.-Y., Hu, C.-C., Zheng, L.-G., Huynh, T.-H., Su, T.-P., Zhang, Y.-L., Wen, Z.-H., Hwang, T.-L., Wu, Y.-C., Sung, P.-J. Survey of briarane-type diterpenoids – Part VII. *Heterocycles* 100(6): 857-870; 2020. 黃聰龍 666
 49. Su, T.-P., Kuo, T.-J., Yang, S.-N., Lee, G.-H., Lee, Y.-T., Wang, Y.-C., Chen, J.-J., Wen, Z.-H., Hwang, T.-L., Sung, P.-J. 11 β ,20 β -Epoxybriaranes from the gorgonian coral *Junceella fragilis* (Ellisellidae). *Marine Drugs* 18(4): 18040183; 2020. 黃聰龍 678
 50. Lan, M.-Y., Hsu, Y.-B., Lan, M.-C., Chen, J.-P., Lu, Y.-J. Polyethylene Glycol-Coated Graphene Oxide Loaded with Erlotinib as an Effective Therapeutic Agent for Treating Nasopharyngeal Cancer Cells. *International journal of nanomedicine* 15: 7569-7582; 2020. 陳志平 688
 51. Khan, M., Huang, Y.-A., Kuo, C.-Y., Lin, T., Lu, C.-H., Chen, L.-C., Kuo, M.-L. Blocking pannexin1 reduces airway inflammation in a murine model of asthma. *American Journal of Translational Research* 12(7): 4074-4083; 2020. 郭敏玲 702
 52. Huang, P.-S., Chang, C.-C., Wang, C.-S., Lin, K.-H. Functional roles of non-coding RNAs regulated by thyroid hormones in liver cancer. *Biomedical Journal*; 2020. in press 林光輝 713

53. Wang, T.-H., Chen, C.-C., Leu, Y.-L., Lee, Y.-S., Lian, J.-H., Hsieh, H.-L., Chen, C.-Y. Palbociclib induces DNA damage and inhibits DNA repair to induce cellular senescence and apoptosis in oral squamous cell carcinoma. *Journal of the Formosan Medical Association*; 2020. in press 謝喜龍、陳琦媛 726
54. Vo, T.T.T., Lee, C.-W., Wu, C.-Z., Liu, J.-F., Lin, W.-N., Chen, Y.-L., Hsu, L.-F., Tsai, M.-H., Lee, I.T. Surfactin from *Bacillus subtilis* attenuates ambient air particulate matter-promoted human oral cancer cells metastatic potential. *Journal of Cancer* 11(20): 6038-6049; 2020. 李江文 737
55. Lin, T.-L., Lu, C.-C., Lai, W.-F., Wu, T.-S., Lu, J.-J., Chen, Y.-M., Tzeng, C.-M., Liu, H.-T., Wei, H., Lai, H.-C. Role of gut microbiota in identification of novel TCM-derived active metabolites. *Protein and Cell*; 2020. in press 賴信志 749
56. Gong, Y.-N., Tsao, K.-C., Hsiao, M.-J., Huang, C.-G., Huang, P.-N., Huang, P.-W., Lee, K.-M., Liu, Y.-C., Yang, S.-L., Kuo, R.-L., Chen, K.-F., Liu, Y.-C., Huang, S.-Y., Huang, H.-I., Liu, M.-T., Yang, J.-R., Chiu, C.-H., Yang, C.-T., Chen, G.-W., Shih, S.-R. SARS-CoV-2 genomic surveillance in Taiwan revealed novel ORF8-deletion mutant and clade possibly associated with infections in Middle East. *Emerging Microbes and Infections* 9(1): 1457-1466; 2020. 施信如 766
57. Yen, W.-C., Wu, Y.-H., Wu, C.-C., Lin, H.-R., Stern, A., Chen, S.-H., Shu, J.-C., Tsun-Yee Chiu, D. Impaired inflammasome activation and bacterial clearance in G6PD deficiency due to defective NOX/p38 MAPK/AP-1 redox signaling. *Redox Biology* 28: 101363; 2020. 吳依璇、趙崇義 776
58. Hsu, C.-C., Fu, T.-C., Huang, S.-C., Chen, C.P.-C., Wang, J.-S. Increased serum brain-derived neurotrophic factor with high-intensity interval training in stroke patients: A randomized controlled trial. *Annals of Physical and Rehabilitation Medicine*; 2020. in press 王素珍 787
59. Senghore, T., Wang, W.-C., Chien, H.-T., Chen, Y.-X., Young, C.-K., Huang, S.-F., Yeh, C.-C. Association of XRCC2 rs2040639 with the survival of patients with oral squamous cell carcinoma undergoing concurrent chemoradiotherapy. *Gene* 145283; 2020. 簡暉慈 795
60. Tseng, C.-P., Huang, Y.-L., Chang, Y.-W., Liao, H.-R., Chen, Y.-L., Hsieh, P.-W. Polysaccharide-containing fraction from *Artemisia argyi* inhibits tumor cell-induced platelet aggregation by blocking interaction of podoplanin with C-type lectin-like receptor 2. *Journal of Food and Drug Analysis* 28(1): 115-123; 2020. 謝佩文 802
61. Peng, B.-R., Lai, K.-H., Chang, Y.-C., Chen, Y.-Y., Su, J.-H., Huang, Y.M., Chen, P.-J., Yu, S.S.-F., Duh, C.-Y., Sung, P.-J. Sponge-Derived 24-Homoscleranes as Potent Anti-Inflammatory Agents. *Marine Drugs* 18(9): 434; 2020. 張祐嘉 811
62. Jose, G., Shalumon, K.T., Liao, H.-T., Kuo, C.-Y., Chen, J.-P. Preparation and characterization of surface heat sintered nanohydroxyapatite and nanowhitlockite embedded poly (Lactic-

co-glycolic acid) microsphere bone graft scaffolds: In vitro and in vivo studies. *International Journal of Molecular Sciences* 21(2): 528; 2020.

63. Chiang, C.-C., Cheng, W.-J., Lin, C.-Y., Lai, K.-H., Ju, S.-C., Lee, C., Yang, S.-H., Hwang, T.-L. Kan-Lu-Hsiao-Tu-Tan, a traditional Chinese medicine formula, inhibits human neutrophil activation and ameliorates imiquimod-induced psoriasis-like skin inflammation. *Journal of Ethnopharmacology* 246: 112246; 2020. 黃聰龍 843
64. Kamel, N.M., Helmy, M.W., Abdelfattah, E.-Z., Khattab, S.N., Ragab, D., Samaha, M.W., Fang, J.-Y., Elzoghby, A.O. Inhalable Dual-Targeted Hybrid Lipid Nanocore-Protein Shell Composites for Combined Delivery of Genistein and All-Trans Retinoic Acid to Lung Cancer Cells. *ACS Biomaterials Science and Engineering* 6(1): 71-87; 2020. 方嘉佑 857
65. Chi, L.-M., Hsiao, Y.-C., Chien, K.-Y., Chen, S.-F., Chuang, Y.-N., Lin, S.-Y., Wang, W.-S., Chang, I.Y.-F., Yang, C., Chu, L.J., Chiang, W.-F., Chien, C.-Y., Chang, Y.-S., Chang, K.-P., Yu, J.-S. Assessment of candidate biomarkers in paired saliva and plasma samples from oral cancer patients by targeted mass spectrometry. *Journal of Proteomics* 211: 103571; 2020. 余兆松 874
66. Peng, B.-R., Lai, K.-H., Chen, Y.-Y., Su, J.-H., Huang, Y.M., Chen, Y.-H., Lu, M.-C., Yu, S.S.-F., Duh, C.-Y., Sung, P.-J. Probing anti-proliferative 24-homoscalaranes from a sponge *Lendenfeldia* sp. *Marine Drugs* 18(2): 76; 2020. 賴奎宏 885
67. Yu, H.-P., F.-C.a,b, Umoro, A., Lin, Z.-C., Elzoghby, A.O., Hwang, T.-L., Fang, J.-Y. Oleic acid-based nanosystems for mitigating acute respiratory distress syndrome in mice through neutrophil suppression: How the particulate size affects therapeutic efficiency. *Journal of Nanobiotechnology* 18(1): 25; 2020. 黃聰龍、方嘉佑 895
68. Hu, C.-C., Lin, N.-C., Peng, B.-R., Chen, Y.-Y., Wen, Z.-H., Chang, Y.-C., Lee, G.-H., Wu, Y.-C., Sung, P.-J. New trihydroxybriarane diterpenoids from an octocoral *Briareum* sp. *Phytochemistry Letters* 35: 23-27; 2020. 張祐嘉 911
69. Liu, C.-H., Lee, G.-W., Wu, W.-C., Wang, C.-C. Encapsulating curcumin in ethylene diamine- β -cyclodextrin nanoparticle improves topical cornea delivery. *Colloids and Surfaces B: Biointerfaces* 186: 110726; 2020. 劉繼賢 916
70. Chao, C.-C., Lee, C.-W., Chang, T.-M., Chen, P.-C., Liu, J.-F. CXCL1/CXCR2 paracrine axis contributes to lung metastasis in osteosarcoma. *Cancers* 12(2): 459; 2020. 李江文 925
71. Wang, C.C., Ho, Y.H., Hung, C.F., Kuo, J.R., Wang, S.J. Xanthohumol, an active constituent from hop, affords protection against kainic acid-induced excitotoxicity in rats. *Neurochemistry International* 133: 104629; 2020. 王素珍 941
72. Liu, C.-C., Chou, Y.-S., Chen, C.-Y., Liu, K.-L., Huang, G.-J., Yu, J.-S., Wu, C.-J., Liaw, G.-W., Hsieh, C.-H., Chen, C.-K. 余兆松 950

- Pathogenesis of local necrosis induced by *Naja atra* venom: Assessment of the neutralization ability of Taiwanese freeze-dried neurotoxic antivenom in animal models. *PLoS Neglected Tropical Diseases* 14(2): e0008054; 2020.
73. Abdelaziz, H.M., Elzoghby, A.O., Helmy, M.W., Abdelfattah, E.-Z.A., Fang, J.-Y., Samaha, M.W., Freag, M.S. Inhalable Lactoferrin/Chondroitin-Functionalized Monoolein Nanocomposites for Localized Lung Cancer Targeting. *ACS Biomaterials Science and Engineering* 6(2): 1030-1042; 2020. 方嘉佑 970
 74. Leu, Y.-L., Wang, T.-H., Wu, C.-C., Huang, K.-Y., Jiang, Y.-W., Hsu, Y.-C., Chen, C.-Y. Hydroxygenkwanin suppresses non-small cell lung cancer progression by enhancing EGFR degradation. *Molecules* 25(4): 941; 2020. 陳琦媛 983
 75. Chen, B.-S., Lee, H.-C., Lee, K.-M., Gong, Y.-N., Shih, S.-R. Enterovirus and Encephalitis. *Frontiers in Microbiology* 11: 261; 2020. 施信如 995
 76. Yu-Ju Wu, C., Chen, C.-H., Lin, C.-Y., Feng, L.-Y., Lin, Y.-C., Wei, K.-C., Huang, C.-Y., Fang, J.-Y., Chen, P.-Y. CCL5 of glioma-associated microglia/macrophages regulates glioma migration and invasion via calcium-dependent matrix metalloproteinase 2. *Neuro-Oncology* 22(2): 253-266; 2020. 方嘉佑 1010
 77. Chen, C.-Y., Chen, C.-C., Chuang, W.-Y., Leu, Y.-L., Ueng, S.-H., Hsueh, C., Yeh, C.-T., Wang, T.-H. Hydroxygenkwanin Inhibits Class I HDAC Expression and Synergistically Enhances the Antitumor Activity of Sorafenib in Liver Cancer Cells. *Frontiers in Oncology* 10: 216; 2020. 陳琦媛 1024
 78. Wu, C.-H., Chen, C.-Y., Yeh, C.-T., Lin, K.-H. Radiosensitization of hepatocellular carcinoma through targeting radio-associated microRNA. *International Journal of Molecular Sciences* 21(5): 1859; 2020. 林光輝 1037
 79. Hsu, C.-C., Fu, T.-C., Huang, S.-C., Wang, J.-S. High-intensity interval training recuperates capacity of endogenous thrombin generation in heart failure patients with reduced ejection fraction. *Thrombosis Research* 187: 159-165; 2020. 王鐘賢 1051
 80. Hsiao, Y.-C., Lin, S.-Y., Chien, K.-Y., Chen, S.-F., Wu, C.-C., Chang, Y.-T., Chi, L.-M., Chu, L.J., Chiang, W.-F., Chien, C.-Y., Chang, K.-P., Chang, Y.-S., Yu, J.-S. An immuno-MALDI mass spectrometry assay for the oral cancer biomarker, matrix metalloproteinase-1, in dried saliva spot samples. *Analytica Chimica Acta* 1100: 118-130; 2020. 余兆松 1058
 81. Lee, W.-R., Lin, Y.-K., Alalaiwe, A., Wang, P.-W., Liu, P.-Y., Fang, J.-Y. Fractional Laser-Mediated siRNA Delivery for Mitigating Psoriasis-like Lesions via IL-6 Silencing. *Molecular Therapy - Nucleic Acids* 19: 240-251; 2020. 方嘉佑 1071
 82. Yeh, J.-Y., Shyu, Y.-C., Lee, S.-Y., Yuan, S.-S., Yang, C.-J., Yang, K.-C., Lee, T.-L., Sun, C.-C., Wang, L.-J. Comorbidity of Narcolepsy and Psychotic Disorders: A Nationwide Population-Based Study in Taiwan. *Frontiers in Psychiatry* 11: 205; 2020. 徐于喬 1083

83. Liou, C.-J., Chen, Y.-L., Yu, M.-C., Yeh, K.-W., Shen, S.-C., Huang, W.-C. Sesamol alleviates airway hyperresponsiveness and oxidative stress in asthmatic mice. *Antioxidants* 9(4): 295; 2020. 劉倩君、黃文忠 1092
84. Chen, Y.-M., Chiu, W.-C., Chiu, Y.-S., Li, T., Sung, H.-C., Hsiao, C.-Y. Supplementation of nano-bubble curcumin extract improves gut microbiota composition and exercise performance in mice. *Food and Function* 11(4): 3574-3584; 2020. 蕭千祐 1109
85. Chang, C.-H., Ahmed, A.F., Yang, T.-S., Lin, Y.-C., Huang, C.-Y., Hwang, T.-L., Sheu, J.-H. Isolation of Lobane and Prenyleudesmane Diterpenoids from the Soft Coral *Lobophytum varium*. *Marine Drugs* 18(4): 223; 2020. 黃聰龍 1120
86. Ho, S.-Y., Chiu, C.-H., Huang, Y.-C., Chen, C.-J., Lien, R., Chu, S.-M., Huang, C.-G., Tsao, K.-C., Shih, S.-R., Hsu, J.-F. Investigation and successful control of an echovirus 11 outbreak in neonatal intensive care units. *Pediatrics and Neonatology* 61(2): 180-187; 2020. 施信如 1137
87. Lee, C.-W., Su, Y.-H., Chiang, Y.-C., Lee, I.-T., Li, S.-Y., Lee, H.-C., Hsu, L.-F., Yan, Y.-L., Li, H.-Y., Chen, M.-C., Peng, K.-T., Lai, C.-H. Glycofullerenes inhibit particulate matter induced inflammation and loss of barrier proteins in HaCaT human keratinocytes. *Biomolecules* 10(4): 514; 2020. 李江文 1145
88. Lu, C.W., Lin, T.Y., Wang, S.J. 11-Keto- β -Boswellic Acid Attenuates Glutamate Release and Kainic Acid-Induced Excitotoxicity in the Rat Hippocampus. *Planta Medica* 86(6): 434-441; 2020. 王素珍 1168
89. Wang, T.-H., Wu, C.-C., Huang, K.-Y., Chuang, W.-Y., Hsueh, C., Li, H.-J., Chen, C.-Y. Profiling of subcellular EGFR interactome reveals hnRNP A3 modulates nuclear EGFR localization. *Oncogenesis* 9(4): 40; 2020. 陳琦媛 1176
90. Yu, H.-P., Liu, F.-C., Lin, C.-Y., Umoro, A., Trousil, J., Hwang, T.-L., Fang, J.-Y. Suppression of neutrophilic inflammation can be modulated by the droplet size of anti-inflammatory nanoemulsions. *Nanomedicine* 15(8): 773-791; 2020. 黃聰龍、方嘉佑 1190
91. Chen, H.-A., Ma, Y.-H., Hsu, T.-Y., Chen, J.-P. Preparation of peptide and recombinant tissue plasminogen activator conjugated poly(Lactic-co-glycolic acid) (PLGA) magnetic nanoparticles for dual targeted thrombolytic therapy. *International Journal of Molecular Sciences* 21(8): 2690; 2020. 陳志平 1209
92. Huang, P.-S., Lin, Y.-H., Chi, H.-C., Tseng, Y.-H., Chen, C.Y., Lin, T.-K., Yeh, C.-T., Lin, K.-H. Dysregulated FAM215A Stimulates LAMP2 Expression to Confer Drug-Resistant and Malignant in Human Liver Cancer. *Cells* 9(4); 2020. 林光輝 1232
93. Yeh, Y.-C., Huang, T.-H., Yang, S.-C., Chen, C.-C., Fang, J.-Y. Nano-Based Drug Delivery or Targeting to Eradicate Bacteria for Infection Mitigation: A Review of Recent Advances. *Frontiers in Chemistry* 8: 286; 2020. 方嘉佑 1252

94. Lin, T.-L., Shu, C.-C., Chen, Y.-M., Lu, J.-J., Wu, T.-S., Lai, W.-F., Tzeng, C.-M., Lai, H.-C., Lu, C.-C. Like Cures Like: Pharmacological Activity of Anti-Inflammatory Lipopolysaccharides From Gut Microbiome. *Frontiers in Pharmacology* 11: 554; 2020. 賴信志 1274
95. Yang, S.-C., Wang, Y.-H., Tsai, Y.-F., Chang, Y.-W., Wu, T.-S., Ho, C.-M., Hwang, T.-L. A synthesized heterocyclic chalcone inhibits neutrophilic inflammation through K⁺-dependent pH regulation. *FASEB Journal* 34(5): 7127-7143; 2020. 黃聰龍 1283
96. Lai, Y.-W., Wang, S.-W., Hu, Y.-Y., Hwang, T.-L., Cheng, M.-J., Chen, I.-S., Sung, P.-J., Chen, J.-J. Anti-inflammatory alkaloids from the root bark of *Hernandia nymphaeifolia*. *Phytochemistry* 173: 112326; 2020. 黃聰龍 1300
97. Chang, Y.-C., Lai, K.-H., Kumar, S., Chen, P.-J., Wu, Y.-H., Lai, C.-L., Hsieh, H.-L., Sung, P.-J., Hwang, T.-L. 1H NMR-based isolation of anti-inflammatory 9,11-secoosteroids from the octocoral *sinularia leptoclados*. *Marine Drugs* 18(5): 271; 2020. 張祐嘉、
吳依璇、
謝喜龍、
黃聰龍 1307
98. Lin, Y.-C., Lin, J.-J., Chen, S.-R., Hwang, T.-L., Fang, S.-Y., Korinek, M., Chen, C.-Y., Lin, Y.-S., Wu, T.-Y., Yen, M.-H., Wang, C.-H., Cheng, Y.-B. Clerodane diterpenoids from *callicarpa hypoleucophylla* and their anti-inflammatory activity. *Molecules* 25(10): 2288; 2020. 黃聰龍 1317
99. Alalaiwe, A., Lin, C.-F., Hsiao, C.-Y., Chen, E.-L., Lin, C.-Y., Lien, W.-C., Fang, J.-Y. Development of flavanone and its derivatives as topical agents against psoriasis: The prediction of therapeutic efficiency through skin permeation evaluation and cell-based assay. *International Journal of Pharmaceutics* 581: 119256; 2020. 蕭千祐、
方嘉佑 1327
100. Al-Sayed, E., Ke, T.-Y., Hwang, T.-L., Chen, S.-R., Korinek, M., Chen, S.-L., Cheng, Y.-B. Cytotoxic and anti-inflammatory effects of lignans and diterpenes from *Cupressus macrocarpa*. *Bioorganic and Medicinal Chemistry Letters* 30(10): 127127; 2020. 黃聰龍 1339
101. Li, C.-Y., Chang, C.-C., Tsai, Y.-H., El-Shazly, M., Wu, C.-C., Wang, S.-W., Hwang, T.-L., Wei, C.-K., Hohmann, J., Yang, Z.-J., Cheng, Y.-B., Wu, Y.-C., Chang, F.-R. Anti-inflammatory, Antiplatelet Aggregation, and Antiangiogenesis Polyketides from *Epicoccum sorghinum*: Toward an Understating of Its Biological Activities and Potential Applications. *ACS Omega* 5(19): 11092-11099; 2020. 黃聰龍 1344
102. Liu, Y.-C., Yeh, C.-T., Lin, K.-H. Cancer Stem Cell Functions in Hepatocellular Carcinoma and Comprehensive Therapeutic Strategies. *Cells* 9(6); 2020. 林光輝 1352
103. Cheng, C.-Y., Haque, A., Hsieh, M.-F., Hassan, S.I., Faizi, M.S.H., Dege, N., Khan, M.S. 1,4-disubstituted 1h-1,2,3-triazoles for renal diseases: Studies of viability, anti-inflammatory, and antioxidant activities. *International Journal of*

104. Lee, T.-H., Chen, J.-L., Liu, P.-S., Tsai, M.-M., Wang, S.-J., Hsieh, H.-L. Rottlerin, a natural polyphenol compound, inhibits upregulation of matrix metalloproteinase-9 and brain astrocytic migration by reducing PKC- δ -dependent ROS signal. *Journal of Neuroinflammation* 17(1): 177; 2020. 蔡明明、王素珍、謝喜龍 1398
105. Lin, S.-L., Lin, Y.-H., Chi, H.-C., Lin, T.-K., Chen, W.-J., Yeh, C.-T., Lin, K.-H. A Novel Long Non-Coding RNA-01488 Suppressed Metastasis and Tumorigenesis by Inducing miRNAs That Reduce Vimentin Expression and Ubiquitination of Cyclin E. *Cells* 9(6); 2020. 林光輝 1411
106. Huang, S.-S., Chen, T.-Y., Deng, J.-S., Pao, L.-H., Cheng, Y.-C., Chao, J. An Ethnobotanical Study on Qīng-Cǎo-Chá Tea in Taiwan. *Frontiers in Pharmacology* 11: 931; 2020. 鮑力恆 1428
107. Kuo, P.-C., Wu, Y.-H., Hung, H.-Y., Lam, S.-H., Ma, G.-H., Kuo, L.-M., Hwang, T.-L., Kuo, D.-H., Wu, T.-S. Anti-inflammatory principles from *Lindera aggregata*. *Bioorganic and Medicinal Chemistry Letters* 30(13): 127224; 2020. 黃聰龍 1441
108. Huang, S.-L., Chang, T.-C., Chao, C.C.K., Sun, N.-K. Role of the TLR4-androgen receptor axis and genistein in taxol-resistant ovarian cancer cells. *Biochemical Pharmacology* 177: 113965; 2020. 孫念康 1445
109. Kuei Huang, S., Lin, T.-Y., Wang, S.-J. Tapentadol Suppresses Glutamatergic Transmission and Neuronal Firing in Rat Hippocampal CA3 Pyramidal Neurons. *Pharmacology* 105(7-8): 445-453; 2020. 王素珍 1457
110. Zhang, Y.-L., Chiang, C.-C., Lee, Y.-T., Wen, Z.-H., Wu, Y.-C., Wu, Y.-J., Hwang, T.-L., Wu, T.-Y., Chang, C.-Y., Sung, P.-J. Briarenols Q-T: Briaranes from a cultured octocoral *Briareum stechei* (Kükenthal, 1908). *Marine Drugs* 18(8): 383; 2020. 黃聰龍 1466
111. Lu, C.-H., Chen, C.-M., Ma, J., Wu, C.-J., Chen, L.-C., Kuo, M.-L. DNA methyltransferase inhibitor alleviates bleomycin-induced pulmonary inflammation. *International Immunopharmacology* 84: 106542; 2020. 郭敏玲 1476
112. Cheng, C.-Y., Lin, Y.-K., Yang, S.-C., Alalaiwe, A., Lin, C.-J., Fang, J.-Y., Lin, C.-F. Percutaneous absorption of resveratrol and its oligomers to relieve psoriasiform lesions: In silico, in vitro and in vivo evaluations. *International Journal of Pharmaceutics* 585: 119507; 2020. 鄭靜宜、方嘉佑、林傳福 1483
113. Yang, C.-L., Wu, H.-C., Hwang, T.-L., Lin, C.-H., Cheng, Y.-H., Wang, C.-C., Kan, H.-L., Kuo, Y.-H., Chen, I.-S., Chang, H.-S., Lin, Y.-C. Anti-inflammatory and antibacterial activity constituents from the stem of *Cinnamomum validinerve*. *Molecules* 25(15): 3382; 2020. 黃聰龍 1497
114. Chen, M.M., Chiu, C.-H., Yuan, C.-P., Liao, Y.-C., Guo, S.-E. Influence of environmental tobacco smoke and air pollution on fetal growth: A prospective study. *International Journal of*

115. Huang, C.-G., Lee, K.-M., Hsiao, M.-J., Yang, S.-L., Huang, P.-N., Gong, Y.-N., Hsieh, T.-H., Huang, P.-W., Lin, Y.-J., Liu, Y.-C., Tsao, K.-C., Shih, S.-R. Culture-based virus isolation to evaluate potential infectivity of clinical specimens tested for COVID-19. *Journal of Clinical Microbiology* 58(8): e01068-20; 2020. 施信如 1519
116. Liu, Y.-C., Kuo, R.-L., Shih, S.-R. COVID-19: The first documented coronavirus pandemic in history. *Biomedical Journal* 43(4): 328-333; 2020. 施信如 1527
117. Huang, H.-I., Lin, J.-Y., Chiang, H.-C., Huang, P.-N., Lin, Q.-D., Shih, S.-R. Exosomes facilitate transmission of enterovirus A71. *Journal of Infectious Diseases* 222(3): 456-469; 2020. 施信如 1533
118. Anilkumar, T.S., Lu, Y.-J., Chen, J.-P. Optimization of the preparation of magnetic liposomes for the combined use of magnetic hyperthermia and photothermia in dual magneto-photothermal cancer therapy. *International Journal of Molecular Sciences* 21(15): 5187; 2020. 陳志平 1547
119. Gaber, M., Elhasany, K.A., Sabra, S., Helmy, M.W., Fang, J.-Y., Khattab, S.N., Bekhit, A.A., Teleb, M., Elkodairy, K.A., Elzoghby, A.O. Co-Administration of Tretinoin Enhances the Anti-Cancer Efficacy of Etoposide via Tumor-Targeted Green Nano-Micelles. *Colloids and Surfaces B: Biointerfaces* 192: 110997; 2020. 方嘉佑 1570
120. Tang, K.-W., Lin, Z.-C., Wang, P.-W., Alalaiwe, A., Tseng, C.-H., Fang, J.-Y. Facile skin targeting of a thalidomide analog containing benzyl chloride moiety alleviates experimental psoriasis via the suppression of MAPK/NF- κ B/AP-1 phosphorylation in keratinocytes. *Journal of Dermatological Science* 99(2): 90-99; 2020. 方嘉佑 1581
121. Chen, C.-Y., Fang, J.-Y., Chen, C.-C., Chuang, W.-Y., Leu, Y.-L., Ueng, S.-H., Wei, L.-S., Cheng, S.-F., Hsueh, C., Wang, T.-H. 2-O-Methylmagnolol, a Magnolol Derivative, Suppresses Hepatocellular Carcinoma Progression via Inhibiting Class I Histone Deacetylase Expression. *Frontiers in Oncology* 10: 1319; 2020. 方嘉佑 1591
122. Hu, H.-C., Li, C.-Y., Tsai, Y.-H., Yang, D.-Y., Wu, Y.-C., Hwang, T.-L., Chen, S.-L., Fülöp, F., Hunyadi, A., Yen, C.-H., Cheng, Y.-B., Chang, F.-R. Secondary metabolites and bioactivities of *aspergillus ochraceopetaliformis* isolated from *anthurium brownii*. *ACS Omega* 5(33): 20991-20999; 2020. 黃聰龍 1604
123. Fang, J.-Y., Tang, K.-W., Yang, S.-H., Alalaiwe, A., Yang, Y.-C., Tseng, C.-H., Yang, S.-C. Synthetic Naphthofuranquinone Derivatives Are Effective in Eliminating Drug-Resistant *Candida albicans* in Hyphal, Biofilm, and Intracellular Forms: An Application for Skin-Infection Treatment. *Frontiers in Microbiology* 11: 2053; 2020. 方嘉佑 1613

124. Chiang, M.-H., Liang, C.-J., Lin, L.-C., Yang, Y.-F., Huang, C.-C., Chen, Y.-H., Kao, H.-L., Chen, Y.-C., Ke, S.-R., Lee, C.-W., Lin, M.-S., Chen, Y.-L. miR-26a attenuates cardiac apoptosis and fibrosis by targeting ataxia–telangiectasia mutated in myocardial infarction. *Journal of Cellular Physiology* 235(9): 6085-6102; 2020. 李江文 1626
125. Li, S.-L., Wu, H.-C., Hwang, T.-L., Lin, C.-H., Yang, S.-S., Chang, H.-S. Phytochemical investigation and anti-inflammatory activity of the leaves of *Machilus japonica* var. *kusanoi*. *Molecules* 25(18): 4149; 2020. 黃聰龍 1644
126. Cheng, C.-Y., Vo, T.T.T., Lin, W.-N., Huang, H.-W., Chuang, C.-C., Chu, P.-M., Lee, I.-T. Nrf2/HO-1 partially regulates cytoprotective effects of carbon monoxide against urban particulate matter-induced inflammatory responses in oral keratinocytes. *Cytokine* 133: 155185; 2020. 鄭靜宜 1658
127. Lin, T.-Y., Wang, P.-W., Huang, C.-H., Yang, P.-M., Pan, T.-L. Characterizing the relapse potential in different luminal subtypes of breast cancers with functional proteomics. *International Journal of Molecular Sciences* 21(17): 6077; 2020. 潘台龍 1668
128. Chen, P., Kuo, L., Wu, Y., Chang, Y., Lai, K., Hwang, T. BAY 41-2272 attenuates CTGF expression via sGC/cGMP-independent pathway in TGFβ1-activated hepatic stellate cells. *Biomedicines* 8(9): 330; 2020. 張祐嘉、黃聰龍 1684
129. Alalaiwe, A., Lin, Y.-K., Lin, C.-H., Wang, P.-W., Lin, J.-Y., Fang, J.-Y. The absorption of polycyclic aromatic hydrocarbons into the skin to elicit cutaneous inflammation: The establishment of structure–permeation and in silico–in vitro–in vivo relationships. *Chemosphere* 255: 126955; 2020. 方嘉佑 1699
130. Al-Sayed, E., Korinek, M., Esmat, A., Chen, G.-Y., Cheng, Y.-B., Hsieh, P.-W., Chen, B.-H., Hwang, T.-L. Anti-inflammatory, hepatoprotective and antioxidant activity of ellagitannin isolated from *Melaleuca styphelioides*. *Phytochemistry* 177: 112429; 2020. 謝佩文、黃聰龍 1713
131. Liu, J.-F., Lee, C.-W., Lin, C.-Y., Chao, C.-C., Chang, T.-M., Han, C.-K., Huang, Y.-L., Fong, Y.-C., Tang, C.-H. CXCL13/CXCR5 interaction facilitates VCAM-1-dependent migration in human osteosarcoma. *International Journal of Molecular Sciences* 21(17): 6095; 2020. 李江文 1723
132. Lu, Y.-J., Wang, Y.-H., Sahu, R.S., Chen, J.-P., Dash, B.S., Chung, P.-J., Yang, H.-W., Chuang, E.-Y., Hwang, T.-L. Mechanism of nanoformulated graphene oxide-mediated human neutrophil activation. *ACS Applied Materials and Interfaces* 12(36): 40141-40152; 2020. 黃聰龍 1736
133. Chi, H.-C., Tsai, C.-Y., Wang, C.-S., Yang, H.-Y., Lo, C.-H., Wang, W.-J., Lee, K.-F., Lai, L.-Y., Hong, J.-H., Chang, Y.-F., Tsai, M.-M., Yeh, C.-T., Wu, C.H., Hsieh, C.-C., Wang, L.-H., Chen, W.-J., Lin, K.-H. DOCK6 promotes chemo- and radioresistance of gastric cancer by modulating WNT/β-catenin signaling and cancer stem cell traits. *Oncogene* 39(37): 5933- 蔡明明、林光輝 1748

5949; 2020.

- | | | | |
|------|---|---------------------|------|
| 134. | Liou, C.-J., Wu, S.-J., Shen, S.-C., Chen, L.-C., Chen, Y.-L., Huang, W.-C. Phloretin ameliorates hepatic steatosis through regulation of lipogenesis and Sirt1/AMPK signaling in obese mice. <i>Cell and Bioscience</i> 10(1): 114; 2020. | 劉倩君、
吳淑如、
黃文忠 | 1765 |
| 135. | Wu, C.-H., Yeh, C.-T., Lin, K.-H. Thyroid hormones suppress FOXM1 expression to reduce liver cancer progression. <i>Oncology Reports</i> 44(4): 1686-1698; 2020. | 林光輝 | 1779 |
| 136. | Lu, Y.-J., Lan, Y.-H., Chuang, C.-C., Lu, W.-T., Chan, L.-Y., Hsu, P.-W., Chen, J.-P. Injectable thermo-sensitive chitosan hydrogel containing CPT-11-loaded EGFR-targeted graphene oxide and SLP2 shRNA for localized drug/gene delivery in glioblastoma therapy. <i>International Journal of Molecular Sciences</i> 21(19): 7111; 2020. | 陳志平 | 1792 |
| 137. | Liu, Z.-H., Huang, Y.-C., Kuo, C.-Y., Kuo, C.-Y., Chin, C.-Y., Yip, P.K., Chen, J.-P. Docosahexaenoic acid-loaded polylactic acid core-shell nanofiber membranes for regenerative medicine after spinal cord injury: In vitro and in vivo study. <i>International Journal of Molecular Sciences</i> 21(19): 7031; 2020. | 陳志平 | 1820 |
| 138. | Mykhailenko, O., Korinek, M., Ivanauskas, L., Bezruk, I., Myhal, A., Petrikaite, V., El-Shazly, M., Lin, G.-H., Lin, C.-Y., Yen, C.-H., Chen, B.-H., Georgiyants, V., Hwang, T.-L. Qualitative and quantitative analysis of Ukrainian iris species: A fresh look on their antioxidant content and biological activities. <i>Molecules</i> 25(19): A4; 2020. | 黃聰龍 | 1839 |
| 139. | Chiang, C.-C., Korinek, M., Cheng, W.-J., Hwang, T.-L. Targeting Neutrophils to Treat Acute Respiratory Distress Syndrome in Coronavirus Disease. <i>Frontiers in Pharmacology</i> 11: 572009; 2020. | 黃聰龍 | 1863 |
| 140. | Ebada, S.S., Al-Jawabri, N.A., Youssef, F.S., El-Kashef, D.H., Knedel, T.-O., Albohy, A., Korinek, M., Hwang, T.-L., Chen, B.-H., Lin, G.-H., Lin, C.-Y., Aldalaen, S.M., Disi, A.M., Janiak, C., Proksch, P. Anti-inflammatory, antiallergic and COVID-19 protease inhibitory activities of phytochemicals from the Jordanian hawksbeard: Identification, structure-Activity relationships, molecular modeling and impact on its folk medicinal uses. <i>RSC Advances</i> 10(62): 38128-38141; 2020. | 黃聰龍 | 1877 |
| 141. | Virly, Chiu, C.-H., Tsai, T.-Y., Yeh, Y.-C., Wang, R. Encapsulation of β -Glucosidase within PVA Fibers by CCD-RSM-Guided Coelectrospinning: A Novel Approach for Specific Mogroside Sweetener Production. <i>Journal of Agricultural and Food Chemistry</i> 68(42): 11790-11801; 2020. | 邱群惠 | 1891 |
| 142. | Lee, K.-M., Gong, Y.-N., Shih, S.-R. Methods for detection and study of virus-derived small RNAs produced from the intramolecular base-pairing region of the picornavirus genome. <i>Methods</i> 183: 4-12; 2020. | 施信如 | 1903 |
| 143. | Jose, G., Lu, Y.-J., Hung, J.-T., Yu, A.L., Chen, J.-P. Co-delivery of cpt-11 and panobinostat with anti-gd2 antibody conjugated | 陳志平 | 1912 |

immunoliposomes for targeted combination chemotherapy. *Cancers* 12(11): 3211; 2020.

144. Hsu, S.K., Hung, C.F., Yang, H.C., Weng, J.R., Wang, S.J. TCD, a triterpenoid isolated from wild bitter gourd, reduces synaptosomal release of glutamate and protects against kainic acid-induced neuronal death. *Food and Function* 11(11): 9858-9867; 2020. 王素珍 1937
145. Lu, C.-W., Lin, T.-Y., Chiu, K.-M., Lee, M.-Y., Huang, J.-H., Wang, S.-J. Silymarin inhibits glutamate release and prevents against kainic acid-induced excitotoxic injury in rats. *Biomedicines* 8(11): 486; 2020. 王素珍 1947
146. Lu, C.W., Lin, T.-Y., Yang, H.C., Hung, C.F., Weng, J.R., Chang, D.C., Wang, S.J. [1-(4-chloro-3-nitrobenzenesulfonyl)-1H-indol-3-yl]-methanol, an indole-3-carbinol derivative, inhibits glutamate release in rat cerebrocortical nerve terminals by suppressing the P/Q-type Ca^{2+} channels and Ca^{2+} /calmodulin/protein kinase A pathway. *Neurochemistry International* 140: 104845; 2020. 王素珍 1969
147. Yang, H.-C., Yu, H., Ma, T.-H., Tjong, W.-Y., Stern, A., Chiu, D.T.-Y. Tert-butyl hydroperoxide (Tbhp)-induced lipid peroxidation and embryonic defects resemble glucose-6-phosphate dehydrogenase (g6pd) deficiency in *c. elegans*. *International Journal of Molecular Sciences* 21(22): 8688; 2020. 趙崇義 1977
148. Chang, Y.-C., Chiang, C.-C., Chang, Y.-S., Chen, J.-J., Wang, W.-H., Fang, L.-S., Chung, H.-M., Hwang, T.-L., Sung, P.-J. Novel Caryophyllane-Related Sesquiterpenoids with Anti-Inflammatory Activity from *Rumphella antipathes* (Linnaeus, 1758). *Marine drugs* 18(11); 2020. 張祐嘉、黃聰龍 1988
149. Li, M.-L., Chen, B.-S., Shih, S.-R. Editorial: Viral Encephalitis. *Frontiers in Microbiology* 11: 599257; 2020. 施信如 1998
150. Nguyen, D.D., Lai, J.-Y. Advancing the stimuli response of polymer-based drug delivery systems for ocular disease treatment. *Polymer Chemistry* 11(44): 6988-7008; 2020. 賴瑞陽 2000
151. Lee, T.-H., Liu, P.-S., Tsai, M.-M., Chen, J.-L., Wang, S.-J., Hsieh, H.-L. The COX-2-derived PGE2 autocrine contributes to bradykinin-induced matrix metalloproteinase-9 expression and astrocytic migration via STAT3 signaling. *Cell Communication and Signaling* 18(1): 185; 2020. 蔡明明、王素珍、謝喜龍 2021
152. Chiang, C.-C., Li, Y.-R., Lai, K.-H., Cheng, W.-J., Lin, S.-C., Wang, Y.-H., Chen, P.-J., Yang, S.-H., Lin, C.-C., Hwang, T.-L. Aqueous extract of kan-lu-hsiao-tu-tan ameliorates collagen-induced arthritis in mice by inhibiting oxidative stress and inflammatory responses. *Life* 10(12): 313; 2020. 黃聰龍 2034
153. Li, H.-J., Wu, N.-L., Pu, C.-M., Hsiao, C.-Y., Chang, D.-C., Hung, C.-F. Chrysin alleviates imiquimod-induced psoriasis-like skin inflammation and reduces the release of CCL20 and antimicrobial peptides. *Scientific Reports* 10(1): 2932; 2020. 蕭千祐 2051

154. Elzoghby, A.O., Abdelmoneem, M.A., Hassanin, I.A., Abd Elwakil, M.M., Elnaggar, M.A., Mokhtar, S., Fang, J.-Y., Elkhodairy, K.A. Lactoferrin, a multi-functional glycoprotein: Active therapeutic, drug nanocarrier & targeting ligand. *Biomaterials* 263: 120355; 2020. 方嘉佑 2064
155. Yang, S.-C., Hsu, C.-Y., Chou, W.-L., Fang, J.-Y., Chuang, S.-Y. Bioactive Agent Discovery from the Natural Compounds for the Treatment of Type 2 Diabetes Rat Model. *Molecules (Basel, Switzerland)* 25(23); 2020. 方嘉佑 2085
156. Lee, T.-L., Lee, M.-H., Chen, Y.-C., Lee, Y.-C., Lai, T.-C., Lin, H.Y.-H., Hsu, L.-F., Sung, H.-C., Lee, C.-W., Chen, Y.-L. Vitamin D Attenuates Ischemia/Reperfusion-Induced Cardiac Injury by Reducing Mitochondrial Fission and Mitophagy. *Frontiers in Pharmacology* 11: 604700; 2020. 李江文 2103
157. Yeh, K.C., Hung, C.F., Lin, Y.F., Chang, D.C., Pai, M.S., Wang, S.J. Neferine, a bisbenzylisoquinoline alkaloid of *Nelumbo nucifera*, inhibits glutamate release in rat cerebrocortical nerve terminals through 5-HT_{1A} receptors. *European Journal of Pharmacology* 889: 173589; 2020. 王素珍 2120
158. Chen, Y.-H., Chang, Y.-C., Chen, Y.-H., Zheng, L.-G., Huang, P.-C., Huynh, T.-H., Peng, B.-R., Chen, Y.-Y., Wu, Y.-J., Fang, L.-S., Su, J.-H., Hsu, C.-M., Sung, P.-J. Natural Products from Octocorals of the Genus *Dendronephthya* (Family Nephtheidae). *Molecules (Basel, Switzerland)* 25(24); 2020. 張祐嘉 2130
159. 蔡書憲(Shu-Hsien Tsai)；鄭潔穎(Jie-Ying Zheng)；簡全基(Chuan-Chi Chien)；李士畦(Shih-Chi Lee)；鄭俊昇(Chun-Shen Cheng)；范植軒(Chin-Hsuan Fan)；李明怡(Ming-Yi Lee)。在農業循環經濟浪潮下柑橘類檸檬皮渣之再利用技術現況及展望(Current Status and Prospects on Reuse Technology of Citrus Limon Waste in The Agricultural Circular Economy)。長庚科技學刊 32 期: 125 - 137; 2020. 李明怡 2156

Original Article

Blocking pannexin1 reduces airway inflammation in a murine model of asthma

Matarr Khan^{1*}, Yung-An Huang¹, Chieh-Ying Kuo¹, Tong Lin¹, Chun-Hao Lu^{1,2,3}, Li-Chen Chen⁴, Ming-Ling Kuo^{1,4,5}

¹Department of Microbiology and Immunology, Graduate Institute of Biomedical Sciences, College of Medicine, Chang Gung University, Taoyuan, Taiwan; ²Department of Fundamental Oncology, University of Lausanne, Lausanne, Switzerland; ³Ludwig Institute for Cancer Research, University of Lausanne, Épalinges, Switzerland; ⁴Division of Allergy, Asthma, and Rheumatology, Department of Pediatrics, Chang Gung Memorial Hospital, Taoyuan, Taiwan; ⁵Research Center for Chinese Herbal Medicine, College of Human Ecology, Chang Gung University of Science and Technology, Taoyuan, Taiwan; *Current address: Division of Immunobiology, Institute of Immunology, Center for Pathophysiology, Infectiology and Immunology, Medical University of Vienna, Vienna, Austria.

Received February 13, 2020; Accepted May 31, 2020; Epub July 15, 2020; Published July 30, 2020

Abstract: Stressed or injured cells release ATP into the extracellular milieu via the pannexin1 (Pannx1) channels, which is the basis of inflammation in a variety of conditions, including allergic lung inflammation. Although the role of Pannx1 in mediating inflammation has been well established, the role of its mimetic peptide, ¹⁰Pannx1, which inhibits ATP release from Pannx1 channels, in allergic asthma remains understudied. The aim of this study was to evaluate the effects of using ¹⁰Pannx1 to inhibit Pannx1 channel in a murine model of ovalbumin (OVA)-induced asthma. We demonstrate that blockade of Pannx1 significantly attenuated goblet cell hyperplasia and inflammatory cell infiltration into the lungs of OVA-sensitized mice. Inhibition of Pannx1 also reduced the total and eosinophil cell numbers in the bronchoalveolar lavage fluid (BALF) and reduced expression of CCL11 and CCL2 in lung tissues from mice. Moreover, we detected lower levels of IL-5 and IL-13 in the culture supernatant of OVA-restimulated splenocytes from ¹⁰Pannx1-treated mice. Collectively, our findings suggest that Pannx1 inhibition of allergen-mediated lung inflammation has the potential to suppress allergic responses in asthma.

Keywords: Extracellular ATP, pannexin1, ¹⁰Pannx1, chemokine, lung inflammation, asthma

Introduction

Asthma is a complex, chronic inflammatory disease of the airways that affects about approximately 300 million people worldwide. It is characterized by airway inflammation, reversible airway obstruction, airway hyperreactivity, and airway remodeling, which are facilitated by the synergistic interaction of the innate and adaptive immune cells with airway epithelial cells [1, 2]. Cytokines of T-helper type 2 (Th2) cells and chemokines of innate immune cells, including CCL2 and CCL11, work together in the pathophysiological process of asthma and become the focus of targeted asthma therapy [2, 3].

Although Th2 immunity plays a crucial role in the pathophysiology of asthma, there is increasing evidence that airway epithelial cells release

danger signals (such as ATP, HMGB1, and uric acid) against inhaled allergen that can promote the induction of allergic responses [4]. Among the danger signals, ATP has been identified as a mediator of lung inflammation in asthma and has been shown to accumulate in the airways of asthmatic patients and mice [5, 6]. ATP is released into the extracellular space by stressed, injured, or apoptotic cells during tissue stress or damage, causing the recruitment of inflammatory cells to the inflammatory sites by binding to purinergic receptors [7, 8].

Various mechanisms mediate the extracellular release of ATP; however, the pannexin (Pannx) channels are important for ATP release [9]. The Pannx channels are non-junctional plasma membrane hemichannels whose opening is induced by various mechanisms during innate and adap-

tive immune responses [10]. In vertebrates, the Panx family comprises three subtypes, Panx1, 2, and 3 [9, 10]. Among the subtypes, Panx1 is the most ubiquitously expressed and is present in a variety of tissues and cell types, including the airway epithelium and cells of the immune system [10, 11]. Panx1-mediated ATP release can drive inflammation through activation of T cells, production of proinflammatory cytokines, and the activation and chemotaxis of innate immune cells [12, 13]. Panx1 has been implicated in the pathogenesis of diseases such as inflammatory bowel diseases, pulmonary fibrosis, and chronic obstructive pulmonary disease [9-13]. ATP release from the Panx1 channels can be inhibited using the mimetic peptide, ¹⁰Panx1, which mimics the loop-to-loop interaction between two hemichannels [9, 11].

Multiple lines of evidence suggest that targeting Panx1 may be beneficial in the treatment of inflammatory diseases [14-16]. Thus, Panx1 may be a target for alleviating the inflammatory responses in asthma. We investigated the therapeutic potential of targeting Panx1 in a murine model of ovalbumin (OVA)-induced asthma using the Panx1-mimetic peptide ¹⁰Panx1.

Materials and methods

Animals

Female BALB/c mice were purchased from the National Laboratory Animal Center, Taiwan. The mice were housed and maintained by the animal care facility of Chang Gung University. The housing, care, and experimental procedure were carried out in accordance with the guidelines of Chang Gung University Institutional Animal Care and Use Committee (IACUC Approval number 106-029).

Allergen sensitization, challenge, and drug treatment

Mice were sensitized intraperitoneally (I.P.) on days 0 and 7 with 100 µg OVA (Sigma-Aldrich, St. Louis, MO, USA) together with 2 mg aluminum hydroxide (Alum, Thermo Fisher Scientific, Rockford, IL, USA) in 200 µl normal saline. On days 19, 22, 26, 29, and 33, the mice were challenged by intratracheally (I.T.) with 10 µg OVA. For peptide treatments, 1.5 mg/kg and 3 mg/kg of ¹⁰Panx1 (synthesized by Kelowna Int'l Scientific, New Taipei City, Taiwan) or 3 mg/kg of scrambled (SCR) peptide (Kelowna Int'l

Scientific) were I.T. administered to mice together with the 10 µg OVA in 50 µl of PBS on days 19, 22, 26, 29, and 33. On day 34, mice were sacrificed to analyze cell infiltration, ATP levels, and cytokine, or chemokine production.

Histological analysis

At sacrifice, the lungs were collected without lavage and fixed with 4% formaldehyde, embedded in paraffin and sectioned. Lung sections were stained with hematoxylin and eosin (H&E) for lung eosinophilia analysis or with periodic acid-Schiff (PAS) for goblet cell hyperplasia and mucus evaluation. Digital images were obtained at 200 × magnification using an Olympus 1X71 microscope with DP controller software (Olympus America Inc, Melville, NY, USA) and the quantitation of digital images was performed by MetaMorph software (Molecular Devices, San Jose, CA, USA).

Collection of bronchoalveolar lavage fluid and counting of cells

Twenty-four hours after the final OVA challenged, mice were sacrificed, lungs were lavaged with 1.5 ml PBS, bronchoalveolar lavage fluid (BALF) was collected, and cell counts were performed using a hemocytometer. Cells were also smeared on frosted slides using Cytospin 4 (Thermo Fisher Scientific, Pittsburgh, PA, USA) and stained with Wright-Giemsa stain for differential cell counting. Two hundred cells were examined for each sample.

Extracellular ATP measurement

To detect extracellular ATP levels, the lungs of mice were lavaged with PBS containing 5 mM EDTA to minimize catabolism of ATP. The BALF samples were supplemented with 5 mM MgCl₂, and ATP levels were measured with an ATPlite detection kit (PerkinElmer, Waltham, MA, USA) and luminescence was detected using a luminometer (GloMax, Promega, Madison, WI, USA). The concentration of ATP in each BALF sample was determined using a known concentration of the ATP standard according to the manufacturer's instructions.

In vitro OVA restimulation of splenocytes

Splenocytes were isolated from all groups of mice. Suspended single splenocytes were seeded in a 24 well plate at a concentration of

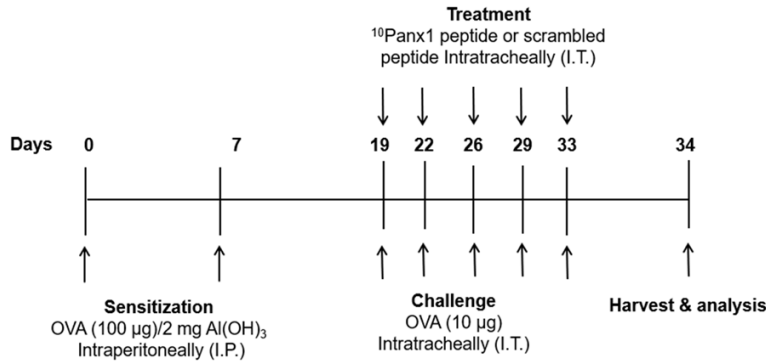


Figure 1. Sensitization model of ovalbumin (OVA)-induced allergic airway inflammation. This diagram depicts the OVA-induced airway inflammation model used in the study. On days 0 and 7, mice were sensitized by intraperitoneal injection (I.P.) with 100 µg OVA with 2 mg Alum in 200 µl normal saline. On days 19, 22, 26, 29, and 33, mice were challenged with 10 µg of OVA intratracheally (I.T.) together with 1.5 or 3 mg/kg ¹⁰Panx1 for the treatment groups and 3 mg/kg of scrambled Panx1 peptide for the control group. Twenty four hours after the last challenge, mice were sacrificed and analyzed.

5×10^6 cells/ml in RPMI 1640 medium and stimulated with 100 µg/ml OVA. The stimulation lasted for 6 days, and the levels of Th2-related cytokines in the supernatants were measured by ELISA.

Detection of antibodies, chemokines, and cytokines

The levels of OVA-specific IgG1 and IgE, CCL2, CCL11, IL-4, IL-5, and IL-13 were assayed by ELISA according to the manufacture's instruction. The ELISA kits for OVA-specific antibodies and IL-5 were purchased from BD Biosciences (San Jose, CA, USA) and ELISA kits for CCL2, CCL11, IL-4, and IL-13 were purchased from R&D Systems (Minneapolis, MN, USA).

Gene expression analysis

RNA from lung tissues was isolated using TRIzol reagent (Carlsbad, CA, USA). The MMLV Reverse Transcription Kit (PROTECH, Taipei, Taiwan) was used to synthesize cDNA. The expression of CCL2 (5'-TTAAAAACCTGGATCGGAACCAA, 3'-GCATTAGCTTCAGATTTACGGGT) and CCL11 (5'-GAATCACCAACAACAGATGCAC, 3'-ATCCTGGAC-CCACTTCTTCTT) were measured with iQTM SYBR Green Supermix (Bio-Rad, Hercules, CA, USA). Primers were synthesized by Tri-biotech (Taipei, Taiwan).

Statistical analysis

All data are presented as mean \pm SEM and analyzed using Prism software (GraphPad Soft-

ware, La Jolla, CA, USA). Statistical significance between groups was calculated by the Kruskal-Wallis test and then by uncorrected Dunn's test. A *P*-value of < 0.05 was considered significant between groups and expressed as **P* < 0.05 , ***P* < 0.01 , ****P* < 0.001 .

Results

Blocking Panx1 suppresses airway inflammation

To investigate whether Panx1 blockade treatment alleviates airway inflammation, we used a murine model of OVA-induced asthma (**Figure 1**).

Twenty-four hours after the last OVA challenge, lung tissues were collected to assess airway inflammation. Hematoxylin and eosin (H&E)-stained lung sections were evaluated. Histological analysis of lung sections revealed increased accumulation of eosinophils in the peribronchial region of OVA-sensitized mice compared with healthy controls. The administration of 3 mg/kg of ¹⁰Panx1 (P3 group) reduced the infiltration of eosinophils in the peribronchial region (**Figure 2A** top panel and **2B**). We further evaluated goblet cell hyperplasia and mucus secretion using periodic acid-Schiff (PAS) staining. Mice in the P3 group had significantly less goblet cell hyperplasia, and mucus secretion compared to OVA-sensitized and scrambled peptide-treated (SCR) control groups (**Figure 2A** bottom panel and **2C**).

Inhibiting Panx1 reduces the number of cells and ATP levels in the bronchoalveolar lavage fluid of mice

Next, we examined whether Panx1 blockade affects eosinophilic infiltration and extracellular ATP release in BALF. Total and differential population cell numbers were counted. The total number of infiltrating cells in BALF was reduced in mice treated with 3 mg/kg of ¹⁰Panx1 compared to OVA-sensitized mice (**Figure 3A**). Blocking Panx1 also reduced the number (**Figure 3B**) and the percentage of eosinophils in BALF (**Figure 3C**). To assess the role of Panx1 channels in the extracellular

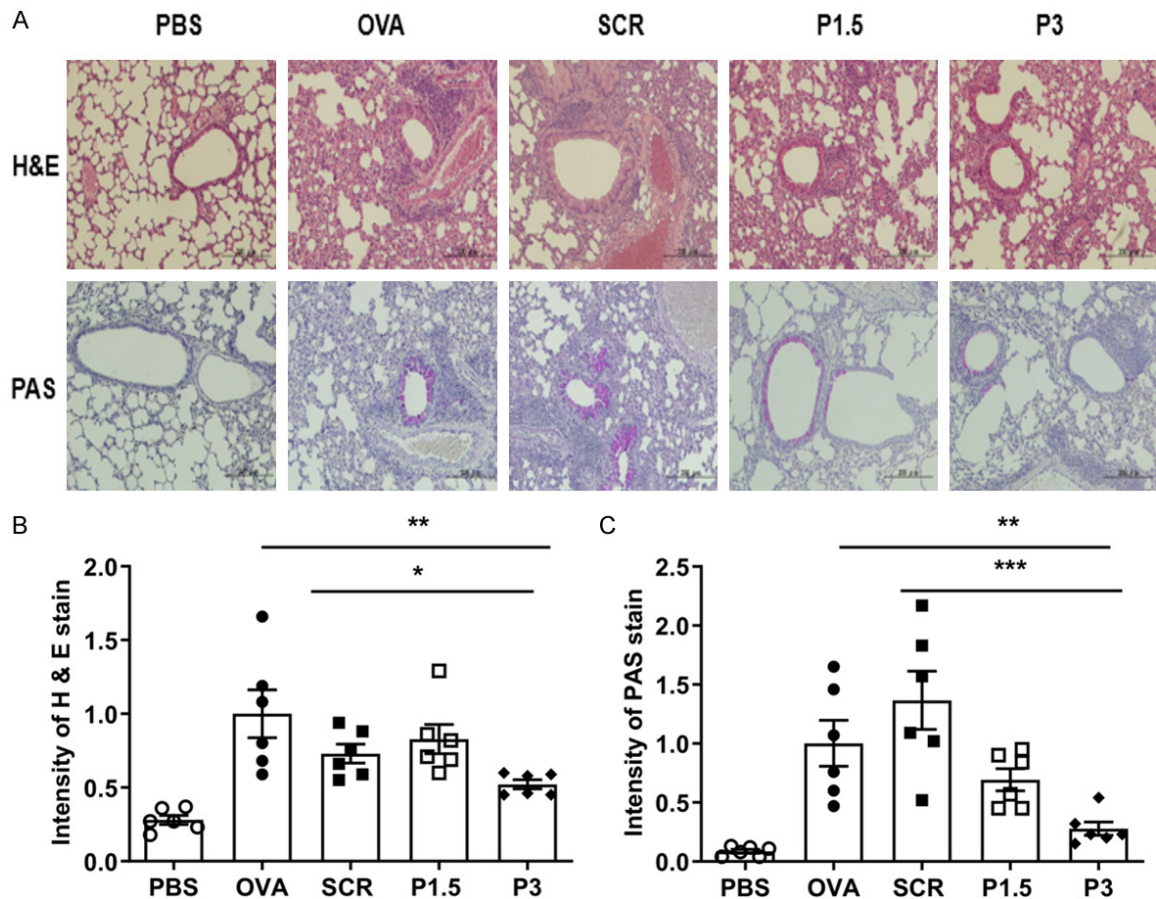


Figure 2. Blockade of Panx1 suppresses airway inflammation and goblet cell hyperplasia in the lungs of OVA-sensitized mice. A. Representative micrographs of hematoxylin and eosin (H&E) stained lung sections to determine eosinophil infiltration (top panel) and periodic acid-Schiff (PAS) stained lung sections to determine goblet cell hyperplasia (bottom panel) (original magnification; 200 ×). Digital images obtained from histological sections were quantified using MetaMorph software. The integrated intensity of H&E and PAS-positive cells was obtained. B. Quantification of H&E-stained cells per bronchia showing airway inflammation. C. Quantification of PAS-stained cells per bronchia showing mucus production. Intensity fold changes were calculated from the average values of the OVA group. PBS, normal control mice; OVA, OVA-sensitized and challenged mice; SCR, 3 mg/kg (scrambled Panx1 peptide) treatment + OVA-sensitized and challenged mice; P1.5 and P3 (1.5 or 3 mg/kg ¹⁰Panx1, respectively) treatment + OVA-sensitized and challenged mice. All data are expressed as the mean ± SEM. *P < 0.05, **P < 0.01, ***P < 0.001.

release of ATP during allergen challenge, we measured ATP levels in mouse BALF. An increase in ATP levels was observed in OVA-sensitized mice compared to PBS control mice. Administration of ¹⁰Panx1 reduced the ATP levels in BALF (**Figure 3D**).

Inhibition of Panx1 suppresses the mRNA expression and serum levels of chemokines

Given that we observed reduced numbers of inflammatory cells in the airways of mice treated with ¹⁰Panx1, we hypothesized that Panx1 inhibition might impair the expression of key

chemokines that promote airway inflammation. Therefore, we analyzed the mRNA expression of CCL11 (eotaxin 1) in lung tissues and serum. Blocking Panx1 with 3 mg/kg of ¹⁰Panx1 significantly reduced CCL11 expression in lung tissues (**Figure 4A**) and serum (**Figure 4B**). We also examined whether inhibition of Panx1-mediated ATP release affects CCL2 expression in allergic airway inflammation. Increased mRNA expression of CCL2 was detected in lung tissues and serum from OVA-sensitized mice (**Figure 4C** and **4D**). Blockade of Panx1 significantly reduced the mRNA expression of CCL2 in lung tissues, compared to the SCR con-

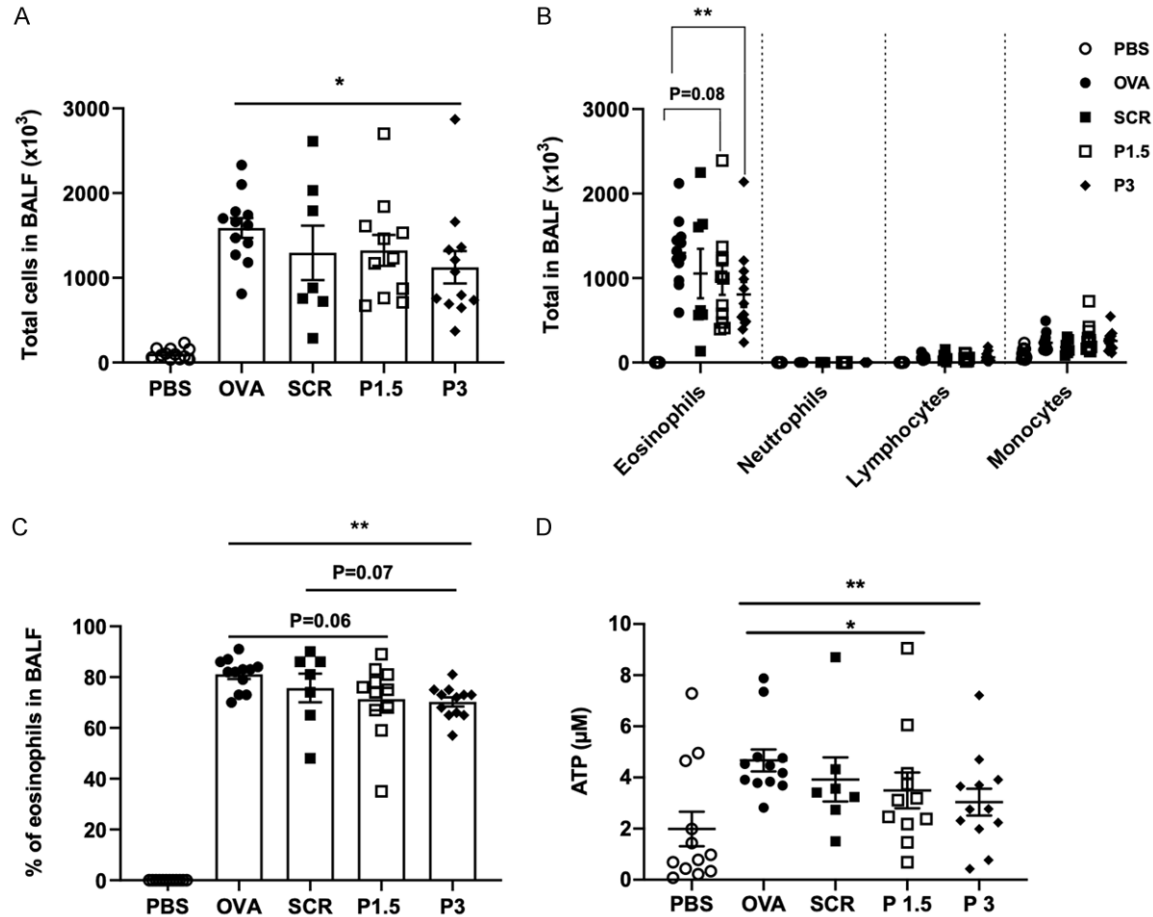


Figure 3. Intratracheal administration of ¹⁰Panx1 reduced cell numbers and ATP levels in bronchoalveolar lavage fluid (BALF) of mice. BALF from each mouse was collected to assess cell infiltration in the airways and the accumulation of ATP. A. Total cell counts in BALF were determined using a hemocytometer. B. Differential cell counts were performed according to the morphological characteristics of the cells. C. The percentage of eosinophils in each mouse was determined. D. The level of ATP in each BALF sample was measured by a luminometer. PBS, normal control mice; OVA, OVA-sensitized and challenged mice; SCR, 3 mg/kg (scrambled Panx1 peptide) treatment + OVA-sensitized and challenged mice; P1.5 and P3 (1.5 or 3 mg/kg ¹⁰Panx1, respectively) treatment + OVA-sensitized and challenged mice. All data are expressed as the mean ± SEM. *P < 0.05, **P < 0.01.

trol group (Figure 4C), but not in serum (Figure 4D).

Reduced levels of IL-5 and IL-13 from splenocytes

Because Th2-type cytokines play a critical role in coordinating allergic airway inflammation, we examined the levels of Th2 cytokines in the splenocyte supernatants that were restimulated with OVA for 6 days. Levels of IL-5 and IL-13, but not IL-4, were markedly reduced in P3 group mice (Figure 5A-C). Furthermore, we observed a decrease in OVA-specific IgG1 (Figure 5D), whereas the level of OVA-specific IgE remained unchanged (Figure 5E) in the serum from ¹⁰Panx1-treated mice.

Discussion

Extracellular ATP is an important mediator of inflammation in many diseases [17]. For example, airway cells release ATP into the extracellular space upon exposure to allergens [18, 19]. Many cells, including immune cells, airway epithelial cells, alveolar epithelial cells, and airway smooth muscle cells, release ATP into the extracellular milieu [20] under stimuli such as tissue stress or injury [21], leading to recruitment and activation of immune cells [22], such as DCs that are important in allergic responses found in BALF of asthmatic mice [5, 23].

The pannexin1 (Panx1) channel is recognized to be a major conduit for ATP release [24, 25]. A

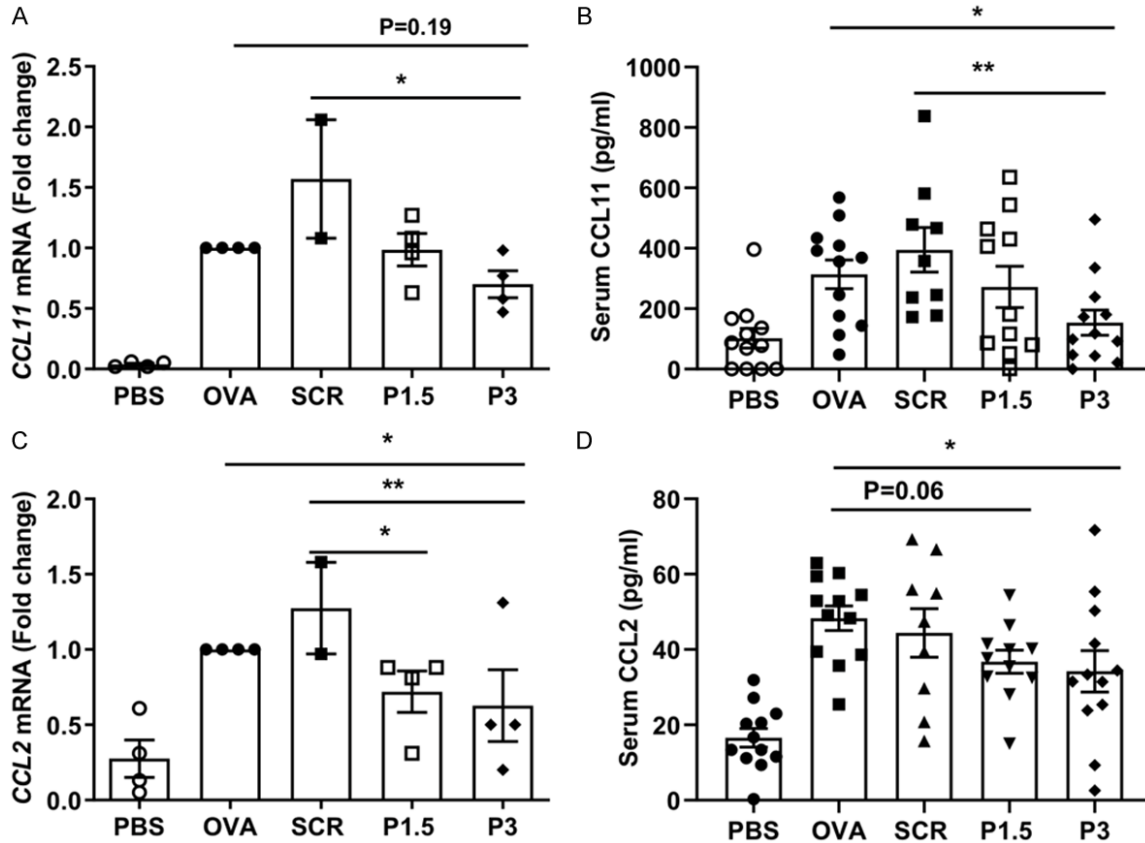


Figure 4. Inhibition of Panx1 suppresses chemokine expression. The mRNA expression of (A) CCL11 and (C) CCL2 was analyzed by real-time PCR. Both genes were normalized to β -actin, and their fold changes were normalized to the OVA-sensitized group. (B) Serum levels of CCL11 and (D) CCL2 were also determined by ELISA (9-12 mice per group). PBS, normal control mice; OVA, OVA-sensitized and challenged mice; SCR, 3 mg/kg (scrambled panx1 peptide) treatment + OVA-sensitized and challenged mice; P1.5 and P3 (1.5 or 3 mg/kg 10 Panx1, respectively) treatment + OVA-sensitized and challenged mice. All data are expressed as the mean \pm SEM. *P < 0.05, **P < 0.01.

diminished inflammatory response can be induced by targeting extracellular ATP either by hydrolyzing it with apyrase or blocking its release from Panx1 channels with 10 Panx1 [5, 23, 26, 27]. Inhibition of ATP signaling by apyrase, blockade, or deletion of P2 receptors leads to lower eosinophil infiltration in lung tissues of murine asthma models [5, 18, 28]. The inhibition of Panx1-mediated ATP release has been shown to attenuate the severity of various pathological and physiological conditions [26, 29-31].

To investigate the potential of Panx1 for targeted treatment of asthma, we used a murine model of OVA-induced asthma. The results showed that inhibition of Panx1 prevented the accumulation of ATP in BALF of asthmatic mice. It significantly reduced eosinophilia and goblet cell hyperplasia and CCL11 and CCL2 mRNA in the lungs of 10 Panx1-treated mice.

Furthermore, lower levels of IL-5 and IL-13 were detected from splenocytes of 10 Panx1-treated mice when restimulated with OVA. Overall, these data support ATP as a key mediator of allergic airway inflammation, and targeting Panx1-mediated ATP release can suppress airway inflammation.

Activation of Panx1 can be mediated by the inflammatory cytokine TNF- α [32]. TNF- α plays a crucial role in regulating Panx1 channel opening and leukocyte emigration through the venous endothelium [32], so we also confirmed that the gene expression levels of TNF- α were comparable in the lungs of mice treated without or with 10 Panx1 (data not shown). We hypothesized that extracellular ATP exerted its effect via signaling of P2 receptors expressed on immune cells, inducing their activation and chemotaxis toward inflammatory sites [7, 33].

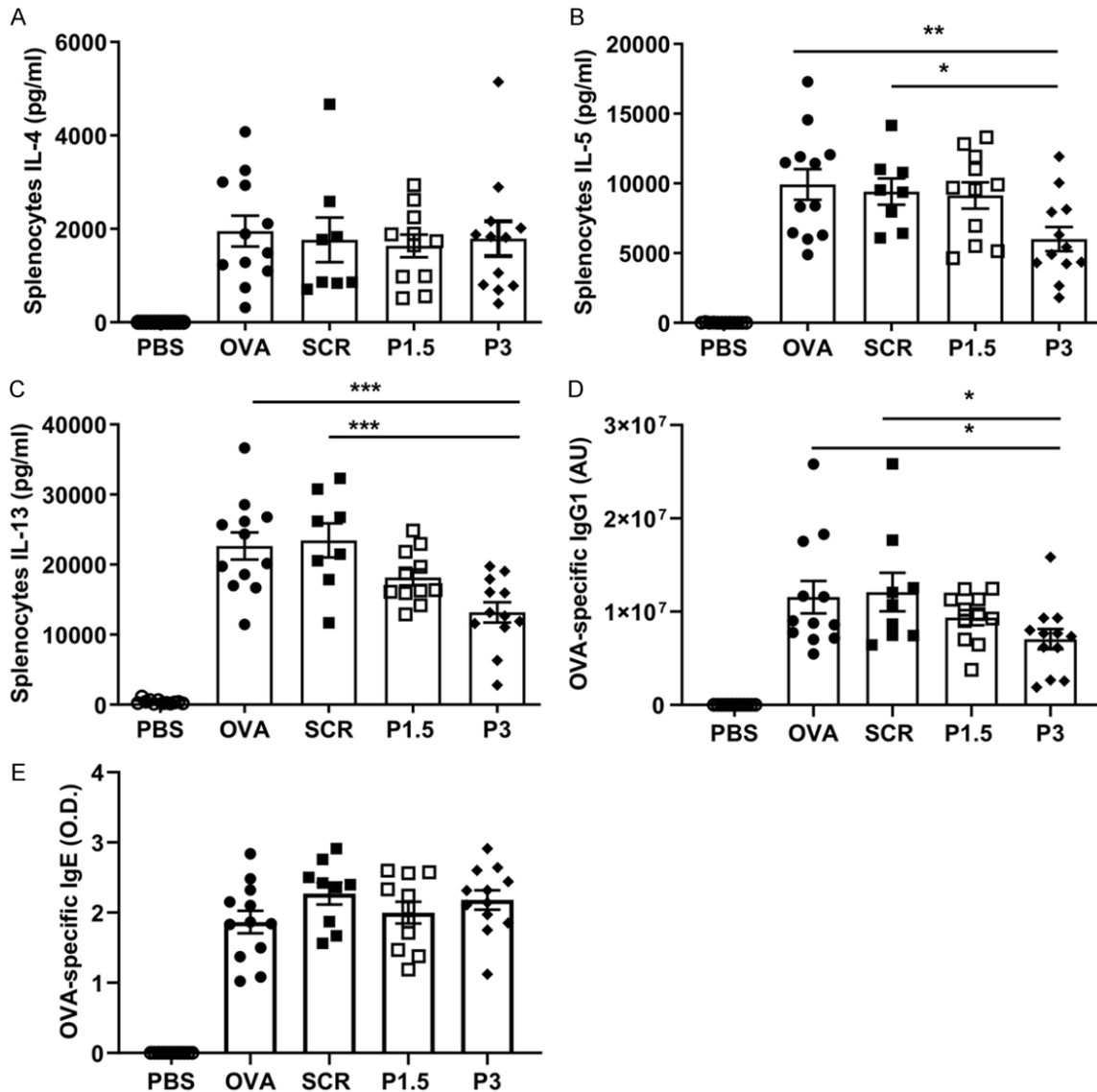


Figure 5. ¹⁰Panx1 administration influences Th2 responses in mice. At sacrifice, splenic cells were isolated and restimulated with 100 µg/ml OVA for six days without ¹⁰Panx1 or scrambled peptide to detect the level of Th2 cytokines. (A) There was no change in IL-4 levels. (B) IL-5 and (C) IL-13 levels were lower in mice after ¹⁰Panx1 administration. The level of OVA-specific antibodies was also determined by ELISA. (D) OVA-specific IgG1 levels were lower in mice treated with ¹⁰Panx1. (E) No change in OVA-specific IgE. PBS, normal control mice; OVA, OVA-sensitized and challenged mice; SCR, 3 mg/kg (scrambled Panx1 peptide) treatment + OVA-sensitized and challenged mice; P1.5 and P3 (1.5 or 3 mg/kg ¹⁰Panx1, respectively) treatment + OVA-sensitized and challenged mice. All data are expressed as the mean ± SEM. *P < 0.05, **P < 0.01, ***P < 0.001.

Given that we observed a decrease in lung eosinophilia, the accumulation of ATP during allergen exposure may induce the release of chemokines that promote the recruitment of inflammatory cells into the airways [3]. Our data suggest that inhibition of Panx1 reduces mRNA expression and levels of CCL11 and CCL2 in lung tissues. Moreover, *in vitro* stimulation of MLE-12 by exogenous ATP induc-

ed CCL2 expression and cellular secretion (Supplementary Figure 1). These findings suggest that ATP may promote airway inflammation through chemokine-mediated recruitment of inflammatory cells into the airways. Studies have demonstrated that CCL2 plays an essential role in asthma by recruiting cells into the airways, and that blocking CCL2 release or signaling reduces airway inflammation, airway re-

modeling, and airway hyperreactivity [34-38]. Thus, a potential mechanism associated with ¹⁰Panx1 treatment is that it abolishes Panx1-mediated ATP release and downregulates CCL2 production. However, whether reduced airway inflammation and goblet cell hyperplasia are directly associated with reduced CCL2 levels require further study.

Type 2 immune responses play an important role in the pathophysiology of asthma. They are orchestrated by Th2 cells and innate immune cells by releasing the canonical type 2 cytokines IL-4, IL-5, and IL-13. Among them, IL-4 induces Th2 cell differentiation and promotes antibody gene class switching in B cells, IL-5 promotes eosinophil infiltration, and IL-13 promotes airway remodeling and inflammation [1-3]. Previous studies have found that activation of CD4⁺ T cells can be prevented by blocking the channel or inhibiting Panx1-mediated P₂X receptor activation [39-41], suggesting that targeting Panx1 may alleviate Th2-mediated allergic responses. We observed decreased levels of IL-5 and IL-13 in the supernatants of splenocytes from ¹⁰Panx1-treated mice restimulated with OVA. These observations suggest that treatment with ¹⁰Panx1 suppresses cytokines secretion and type 2 immune response, resulting in reduced cellular infiltration of BALF and goblet cell hyperplasia.

Taken together, the results of this study highlight the critical role of Panx1-mediated ATP release in promoting allergic asthma and suggest that inhibition of these channels may serve as a target for reducing inflammatory responses in asthma.

Acknowledgements

This work was supported, in part, by grants from the Ministry of Science and Technology (MOST105-2320-B-182-019-MY3 and MOST 107-2320-B-182-005-MY3) of the Republic of China, as well as from Chang Gung Memorial Hospital (CMRPD1I0081~2, CORPD1F00-21~3, CMRPD160333, and BMRP362). We are grateful to Dr. Albert Ko for English editorial assistance.

Disclosure of conflict of interest

None.

Address correspondence to: Dr. Ming-Ling Kuo, Department of Microbiology and Immunology, Graduate Institute of Biomedical Sciences, College of Medicine, Chang Gung University, No. 259, Wen-Hua 1st Road, Kwei-Shan District, Taoyuan 33303, Taiwan. Tel: 886-3-2118800 Ext. 3319; Fax: 886-3-2118293; E-mail: mingling@mail.cgu.edu.tw

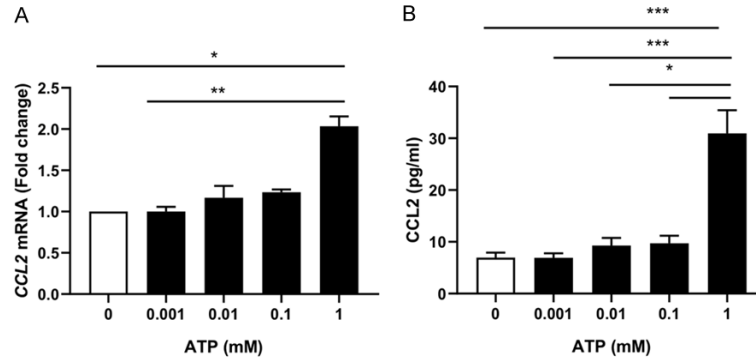
References

- [1] Fahy JV. Type 2 inflammation in asthma—present in most, absent in many. *Nat Rev Immunol* 2015; 15: 57-65.
- [2] Lambrecht BN, Hammad H and Fahy JV. The cytokines of asthma. *Immunity* 2019; 50: 975-991.
- [3] Barnes PJ. The cytokine network in asthma and chronic obstructive pulmonary disease. *J Clin Invest* 2008; 118: 3546-3556.
- [4] Lambrecht BN and Hammad H. The immunology of asthma. *Nat Immunol* 2015; 16: 45-56.
- [5] Idzko M, Hammad H, van Nimwegen M, Kool M, Willart MA, Muskens F, Hoogsteden HC, Luttmann W, Ferrari D, Di Virgilio F, Virchow JC Jr and Lambrecht BN. Extracellular ATP triggers and maintains asthmatic airway inflammation by activating dendritic cells. *Nat Med* 2007; 13: 913-919.
- [6] Kouzaki H, Iijima K, Kobayashi T, O'Grady SM and Kita H. The danger signal, extracellular ATP, is a sensor for an airborne allergen and triggers IL-33 release and innate Th2-type responses. *J Immunol* 2011; 186: 4375-4387.
- [7] Cekic C and Linden J. Purinergic regulation of the immune system. *Nat Rev Immunol* 2016; 16: 177-192.
- [8] Walton EL. Perturbing purinergic signaling: a pathogen's guidebook to counteracting inflammatory responses. *Biomed J* 2016; 39: 229-233.
- [9] Velasquez S and Eugenini EA. Role of pannexin-1 hemichannels and purinergic receptors in the pathogenesis of human diseases. *Front Physiol* 2014; 5: 96.
- [10] Makarenkova HP and Shestopalov VI. The role of pannexin hemichannels in inflammation and regeneration. *Front Physiol* 2014; 5: 63.
- [11] Xu J, Chen L and Li L. Pannexin hemichannels: a novel promising therapy target for oxidative stress related diseases. *J Cell Physiol* 2018; 233: 2075-2090.
- [12] Crespo Yanguas S, Willebrords J, Johnstone SR, Maes M, Decrock E, De Bock M, Leybaert L, Cogliati B and Vinken M. Pannexin1 as mediator of inflammation and cell death. *Biochim Biophys Acta Mol Cell Res* 2017; 1864: 51-61.
- [13] Adamson SE and Leitinger N. The role of pannexin1 in the induction and resolution of inflammation. *FEBS Lett* 2014; 588: 1416-1422.

- [14] Jankowski J, Perry HM, Medina CB, Huang L, Yao J, Bajwa A, Lorenz UM, Rosin DL, Ravichandran KS, Isakson BE and Okusa MD. Epithelial and endothelial pannexin1 channels mediate AKI. *J Am Soc Nephrol* 2018; 29: 1887-1899.
- [15] Good ME, Eucker SA, Li J, Bacon HM, Lang SM, Butcher JT, Johnson TJ, Gaykema RP, Patel MK, Zuo Z and Isakson BE. Endothelial cell pannexin1 modulates severity of ischemic stroke by regulating cerebral inflammation and myogenic tone. *JCI Insight* 2018; 3: e96272.
- [16] Diezmos EF, Markus I, Perera DS, Gan S, Zhang L, Sandow SL, Bertrand PP and Liu L. Blockade of pannexin-1 channels and purinergic P2X7 receptors shows protective effects against cytokines-induced colitis of human colonic mucosa. *Front Pharmacol* 2018; 9: 865.
- [17] Antoniolli L, Blandizzi C, Pacher P and Hasko G. The purinergic system as a pharmacological target for the treatment of immune-mediated inflammatory diseases. *Pharmacol Rev* 2019; 71: 345-382.
- [18] Muller T, Robaye B, Vieira RP, Ferrari D, Grimm M, Jakob T, Martin SF, Di Virgilio F, Boeynaems JM, Virchow JC and Idzko M. The purinergic receptor P2Y2 receptor mediates chemotaxis of dendritic cells and eosinophils in allergic lung inflammation. *Allergy* 2010; 65: 1545-1553.
- [19] Lambrecht BN and Hammad H. Allergens and the airway epithelium response: gateway to allergic sensitization. *J Allergy Clin Immunol* 2014; 134: 499-507.
- [20] Ito S, Furuya K, Sokabe M and Hasegawa Y. Cellular ATP release in the lung and airway. *AIMS Biophysics* 2016; 3: 571-584.
- [21] Vitiello L, Gorini S, Rosano G and la Sala A. Immunoregulation through extracellular nucleotides. *Blood* 2012; 120: 511-518.
- [22] Kurashima Y, Kiyono H and Kunisawa J. Pathophysiological role of extracellular purinergic mediators in the control of intestinal inflammation. *Mediators Inflamm* 2015; 2015: 427125.
- [23] Zhang F, Su X, Huang G, Xin XF, Cao EH, Shi Y and Song Y. Adenosine triphosphate promotes allergen-induced airway inflammation and Th17 cell polarization in neutrophilic asthma. *J Immunol Res* 2017; 2017: 5358647.
- [24] Dosch M, Gerber J, Jebbawi F and Beldi G. Mechanisms of ATP release by inflammatory cells. *Int J Mol Sci* 2018; 19: 1222.
- [25] Bao L, Locovei S and Dahl G. Pannexin membrane channels are mechanosensitive conduits for ATP. *FEBS Lett* 2004; 572: 65-68.
- [26] Maes M, McGill MR, da Silva TC, Abels C, Leb-
ofsky M, Weemhoff JL, Tiburcio T, Veloso Alves
Pereira I, Willebrords J, Crespo Yanguas S, Far-
hood A, Beschin A, Van Ginderachter JA, Penu-
ela S, Jaeschke H, Cogliati B and Vinken M. In-
hibition of pannexin1 channels alleviates
acetaminophen-induced hepatotoxicity. *Arch
Toxicol* 2017; 91: 2245-2261.
- [27] Riteau N, Gasse P, Fauconner L, Gombault A, Couegnat M, Fick L, Kanellopoulos J, Ques-
niaux VF, Marchand-Adam S, Crestani B, Ryffel B
and Couillin I. Extracellular ATP is a danger sig-
nal activating P2X7 receptor in lung inflamma-
tion and fibrosis. *Am J Respir Crit Care Med*
2010; 182: 774-783.
- [28] Muller T, Vieira RP, Grimm M, Durk T, Cicko S,
Zeiser R, Jakob T, Martin SF, Blumenthal B,
Sorichter S, Ferrari D, Di Virgilio F and Idzko M.
A potential role for P2X7R in allergic airway in-
flammation in mice and humans. *Am J Respir
Cell Mol Biol* 2011; 44: 456-464.
- [29] Xiong XX, Gu LJ, Shen J, Kang XH, Zheng YY,
Yue SB and Zhu SM. Probenecid protects
against transient focal cerebral ischemic injury
by inhibiting HMGB1 release and attenuating
AQP4 expression in mice. *Neurochem Res*
2014; 39: 216-224.
- [30] Burma NE, Bonin RP, Leduc-Pessah H, Baimel
C, Cairncross ZF, Mousseau M, Shankara JV,
Stemkowski PL, Baimoukhametova D, Bains
JS, Antle MC, Zamponi GW, Cahill CM, Bor-
gland SL, De Koninck Y and Trang T. Blocking
microglial pannexin-1 channels alleviates mor-
phine withdrawal in rodents. *Nat Med* 2017;
23: 355-360.
- [31] Freeman TJ, Sayedyahosseini S, Johnston D,
Sanchez-Pupo RE, O'Donnell B, Huang K,
Lakhani Z, Nouri-Nejad D, Barr KJ, Harland L,
Latosinsky S, Grant A, Dagnino L and Penuela
S. Inhibition of pannexin1 reduces the tumori-
genic properties of human melanoma cells.
Cancers (Basel) 2019; 11: 102.
- [32] Lohman AW, Leskov IL, Butcher JT, Johnstone
SR, Stokes TA, Begandt D, DeLalio LJ, Best AK,
Penuela S, Leitingner N, Ravichandran KS,
Stokes KY and Isakson BE. Pannexin1 chan-
nels regulate leukocyte emigration through the
venous endothelium during acute inflamma-
tion. *Nat Commun* 2015; 6: 7965.
- [33] Saez PJ, Vargas P, Shoji KF, Harcha PA, Lennon-
Dumenil AM and Saez JC. ATP promotes the
fast migration of dendritic cells through the ac-
tivity of pannexin1 channels and P2X7 recep-
tors. *Sci Signal* 2017; 10: eaah7107.
- [34] Roy RM, Wuthrich M and Klein BS. Chitin elicits
CCL2 from airway epithelial cells and induces
CCR2-dependent innate allergic inflammation
in the lung. *J Immunol* 2012; 189: 2545-2552.
- [35] Schneider D, Hong JY, Bowman ER, Chung Y,
Nagarkar DR, McHenry CL, Goldsmith AM,
Bentley JK, Lewis TC and Hershenson MB.
Macrophage/epithelial cell CCL2 contributes
to rhinovirus-induced hyperresponsiveness
and inflammation in a mouse model of allergic
airways disease. *Am J Physiol Lung Cell Mol
Physiol* 2013; 304: L162-169.

- [36] Zhao L, Yang W, Yang X, Lin Y, Lv J, Dou X, Luo Q, Dong J, Chen Z, Chu Y and He R. Chemerin suppresses murine allergic asthma by inhibiting CCL2 production and subsequent airway recruitment of inflammatory dendritic cells. *Allergy* 2014; 69: 763-774.
- [37] Lee YG, Jeong JJ, Nyenhuis S, Berdyshev E, Chung S, Ranjan R, Karpurapu M, Deng J, Qian F, Kelly EA, Jarjour NN, Ackerman SJ, Natarajan V, Christman JW and Park GY. Recruited alveolar macrophages, in response to airway epithelial-derived monocyte chemoattractant protein 1/CCl2, regulate airway inflammation and remodeling in allergic asthma. *Am J Respir Cell Mol Biol* 2015; 52: 772-784.
- [38] Singh SR, Sutcliffe A, Kaur D, Gupta S, Desai D, Saunders R and Brightling CE. CCL2 release by airway smooth muscle is increased in asthma and promotes fibrocyte migration. *Allergy* 2014; 69: 1189-1197.
- [39] Schenk U, Westendorf AM, Radaelli E, Casati A, Ferro M, Fumagalli M, Verderio C, Buer J, Scanziani E and Grassi F. Purinergic control of T cell activation by ATP released through pannexin-1 hemichannels. *Sci Signal* 2008; 1: ra6.
- [40] Woehrle T, Yip L, Elkhail A, Sumi Y, Chen Y, Yao Y, Insel PA and Junger WG. Pannexin-1 hemichannel-mediated ATP release together with P2X1 and P2X4 receptors regulate T-cell activation at the immune synapse. *Blood* 2010; 116: 3475-3484.
- [41] Ledderose C, Liu K, Kondo Y, Slubowski CJ, Dertnig T, Denicolo S, Arbab M, Hubner J, Konrad K, Fakhari M, Lederer JA, Robson SC, Visner GA and Junger WG. Purinergic P2X4 receptors and mitochondrial ATP production regulate T cell migration. *J Clin Invest* 2018; 128: 3583-3594.

Pannexin1 blockade reduces asthmatic inflammation



Supplementary Figure 1. Extracellular ATP is a trigger to the production of CCL2. Mouse lung epithelial cell line (MLE-12) was used to determine the cellular response to various concentration of extracellular ATP (0, 0.001, 0.01, 0.1, 1 mM) for 24 hours. CCL2 was upregulated in (A) mRNA and (B) protein levels in a dose-dependent manner. The concentration of CCL2 was assessed by ELISA and the fold change of *cc12* was performed by real-time PCR. All data are expressed as the mean \pm SEM. * $P < 0.05$.

Available online at www.sciencedirect.com

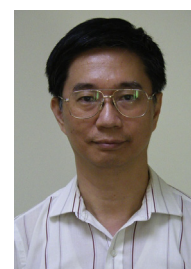
ScienceDirect

Biomedical Journal

journal homepage: www.elsevier.com/locate/bj

Review Article

Functional roles of non-coding RNAs regulated by thyroid hormones in liver cancer

Po-Shuan Huang^{a,b}, Cheng-Chih Chang^c, Chia-Siu Wang^c,
Kwang-Huei Lin^{a,b,d,e,*}^a Department of Biochemistry, College of Medicine, Chang Gung University, Taoyuan, Taiwan^b Graduate Institute of Biomedical Sciences, College of Medicine, Chang Gung University, Taoyuan, Taiwan^c Department of General Surgery, Chang Gung Memorial Hospital at Chia yi, Chia yi, Taiwan^d Liver Research Center, Chang Gung Memorial Hospital, Linkou, Taoyuan, Taiwan^e Research Center for Chinese Herbal Medicine, College of Human Ecology, Chang Gung University of Science and Technology, Taoyuan, Taiwan

ARTICLE INFO

Article history:

Received 8 July 2020

Accepted 24 August 2020

Available online xxx

Keywords:

Non-coding RNA

Thyroid

Receptors

Hepatocellular carcinoma

ABSTRACT

Recent reports have shown the important role of the non-coding part of human genome RNA (ncRNA) in cancer formation and progression. Among several kinds of ncRNAs, microRNAs (miRNA) play a pivotal role in cancer biology. Accumulating researches have been focused on the importance of non-coding genes in various diseases. In addition to miRNAs, long non-coding RNAs (lncRNAs) have also been extensively documented. Recently, the study of human liver cancer has gradually shifted to these non-coding RNAs that were originally considered “junk”. Notably, dysregulated ncRNAs maybe influence on cell proliferation, angiogenesis, anti-apoptosis, and metastasis. Thyroid hormones play critical roles in human development and abnormalities in thyroid hormone levels are associated with various diseases, such as liver cancer. Thyroid hormone receptors (TR) act as ligand-activated nuclear transcription factors to affect multiple functions through the gene-level regulation in the cells and several studies have revealed that thyroid hormone associated with ncRNAs expression. TR actions are complex and tissue- and time-specific, aberrant expression of the various TR isoforms have different effects and are associated with different types of tumor or stages of development. In this review, we discuss various aspects of the research on the thyroid hormones modulated ncRNAs to affect the functions of human liver cells.

Thyroid hormones (TH) play critical roles in human growth and development and abnormalities in TH levels are associated with various human diseases, such as cancer. Thyroid

hormones in the human body affect multiple functions predominantly through gene-level regulation and act as ligand-activated nuclear transcription factors that interact with

* Corresponding author. Department of Biochemistry, College of Medicine, Chang Gung University, 259, Wenhua 1st Rd., Gueishan, Taoyuan 333, Taiwan.

E-mail address: khlin@mail.cgu.edu.tw (K.-H. Lin).

Peer review under responsibility of Chang Gung University.

<https://doi.org/10.1016/j.bj.2020.08.009>

2319-4170/© 2020 Chang Gung University. Publishing services by Elsevier B.V. This is an open access article under the CC BY-NC-ND license (<http://creativecommons.org/licenses/by-nc-nd/4.0/>).

Please cite this article as: Huang P-S et al., Functional roles of non-coding RNAs regulated by thyroid hormones in liver cancer, Biomedical Journal, <https://doi.org/10.1016/j.bj.2020.08.009>

their cognate hormone response elements (TRE) in the promoters of different genes to induce positive or negative regulation. In recent years, accumulating research has focused on the importance of non-coding genes in various diseases. In addition to the originally identified microRNAs (miRNA), the physiological relevance of frequently fragmented long non-coding RNAs (lncRNA) has been extensively documented. MiRNAs exert their specific effects via direct interactions with three prime untranslated regions (3'-UTR) of various target genes, leading to decreased mRNA expression. The molecular mechanisms of lncRNAs in cells are relatively more complex, with different modes of action in the nucleus and cytoplasm. More and more studies, including therapeutic strategies and biomarkers, have been focused on the non-coding RNAs. For example, compared with coding genes, miRNA has the characteristics to affect different target genes' expression and potentially alter several carcinogenic or tumor suppressor pathways at the same time. Besides, the design and implementation of inhibitors or drugs formulated for nucleic acids are easier than those for proteins. Thus, non-coding RNAs have been considered as the most potential targets in cancer treatment. Further, several studies have revealed that the thyroid hormone acts as a transcription factor in association with non-coding genes. The application of thyroid hormones in cancer has long been recognized. Therefore, to understand the relationship between thyroid hormone and non-coding RNAs is an urgent need for clinical application. In the current review, we specifically focus on the miRNAs and lncRNAs affected by thyroid hormones in liver cancer, along with their roles and mechanisms of action in tumor development.

Thyroid hormone in human liver cancer

Hepatocellular carcinoma (HCC)

Hepatocellular carcinoma (HCC) is a common primary malignant tumor of the liver and one of the leading causes of cancer-related death worldwide. The incidence of HCC increases progressively with advancing age in all populations and global cases have continued to rise over the last decade [1]. The burden of liver cancer varies considerably by geographic region and sex due to the distribution of underlying diseases, genetic factors and variable exposure to environmental and behavioral risk factors. Globally, hepatitis B virus (HBV) is the leading cause of liver cancer death, accounting for 33% mortality, followed by alcohol and hepatitis C virus (HCV) infection [2]. While prognosis of patients with HCC is generally poor, the 5-year survival rate is >70% in patients diagnosed at an early stage. However, early diagnosis of HCC is complicated by the coexistence of inflammation and cirrhosis, highlighting the urgent requirement for novel biomarkers of early-stage HCC. Currently, diagnosis of HCC without pathological correlation is achieved by analysis of serum α -fetoprotein (AFP) levels combined with imaging techniques. Advances in genomics and proteomics platforms and biomarker assay techniques over the last decade have resulted in the identification of numerous novel biomarkers

and improved diagnosis of HCC. These biomarkers are not only useful for early diagnosis of HCC but also provide insights into the mechanisms driving oncogenesis that could facilitate the development of effective treatment strategies [3]. For instance, Sorafenib is an oral multikinase (receptor tyrosine kinase, RTK) inhibitor that suppresses tumor cell proliferation and angiogenesis and promotes apoptosis. The drug was approved by FDA as a unique target for advanced hepatocellular carcinoma (HCC) in 2007 [4,5] as one of the therapeutic options based on in-depth understanding of the carcinogenic mechanisms underlying liver cancer in recent years. Regrettably, sorafenib prolongs life expectancy by only about 3 months. One of the possible factors is that HCC is a complex disease with multiple signaling pathways involved in its pathogenesis. As a result, the targeted treatment of liver cancer is not effective. Combining the use of a variety of drugs with different mechanisms of action is a new clinical treatment strategy. For example, Sorafenib is combined with a MEK kinase inhibitor. The effect has also been validated to be helpful to patients [6]. The development of different technologies to identify genes with important roles in liver cancer remains a significant focus of scientific and clinical research. To date, several biotechnological methods, including next-generation sequencing and multiple "omics" data analyses including genomics, epigenomics, transcriptomics, proteomics, metabolomics, and metagenomics, have been developed and applied for HCC diagnostic biomarker screening [7].

Thyroid hormone and receptor

The thyroid hormone system starts from the hypothalamus, where thyrotropin-releasing hormone (TRH) is synthesized and released from the periventricular nucleus (PVN). TRH binding to its receptor on the thyrotroph of the anterior pituitary gland stimulates proliferation, synthesis and secretion of thyroid stimulating hormone (TSH). TSH subsequently interacts with the TSH receptor (TSHR) on individual thyroid follicular cells of the thyroid gland to stimulate synthesis and release of the two major thyroid hormone forms, tetraiodothyronine (T_4) and 3,3',5-tri-iodo-L-thyronine (T_3). T_3 is the active form of thyroid hormone and T_4 the prohormone activated by deiodinases at the cellular and circulatory levels [8]. The actions of T_3 are mediated by nuclear thyroid hormone receptors (TR) located on human chromosomes 17 and 3, which primarily serve as T_3 -inducible transcription factors. Two major isoforms of TRs exist, specifically, THRA (TR α) and THRB (TR β). Different TRs are composed of similar domains, including an amino-terminal A/B domain to recruit regulatory proteins, a central DNA-binding domain (DBD) or C region displaying high affinity for DNA sequences of TREs, a linker D region necessary for nuclear translocation of the receptor, and a carboxy-terminal ligand-binding domain (LBD) that interacts with thyroid hormones [9]. Expression of TR isoforms is tissue-dependent. TR α is predominantly expressed in bone and heart and TR β in liver and kidney. Within cells, TR forms a heterodimer with the retinoid X receptor (RXR) that interacts with thyroid hormone response elements (TRE) in regulatory regions of target genes [10].

Role of thyroid hormone and receptor in human liver cancer

Thyroid hormone plays a critical regulatory role in cellular homeostasis and its imbalance in the body is significantly associated with multiple chronic diseases, including obesity, diabetes, cardiovascular, and liver disorders [9]. Under physiological conditions, thyroid hormones control tumor cell development, differentiation, metabolism, and growth pathways. Evidence of TR involvement in human carcinogenesis is based on the discovery of TR mutations in hepatocellular carcinoma, renal clear cell carcinoma, breast cancer, pituitary tumor, and thyroid cancer. Loss of normal expression of *THRB* located on chromosome 3p due to truncation or deletion has been additionally reported in several malignancies including lung, melanoma, breast, head-and-neck, renal cell, uterine cervical, ovarian, and testicular tumors [11]. In liver, the effects of thyroid hormones appear to be particularly important. The liver has regenerative capacity but is subject to molecular pathologies that may lead to cancer, such as fibrosis, cirrhosis, and non-alcoholic fatty liver disease. In addition, cancer cells undergo reprogramming of their metabolism that results in drastic changes, such as aerobic glycolysis in lieu of oxidative phosphorylation [12]. Hypothyroidism is associated with poorer overall and recurrence-free survival of HCC patients receiving liver transplantation [13]. T_3 or its analogs, in particular, agonists of TR β , may serve as useful tools in HCC therapy. The T_3 /TR β axis has been shown to cause a shift in the global expression profile of the most aggressive preneoplastic nodules towards that of normal liver [14].

Thyroid hormone regulates non-coding RNAs in human liver cancer

Non-coding RNAs

Traditionally, the central dogma of molecular biology explaining the destiny of genes is stated as “DNA makes RNA and RNA makes protein”, which subsequently performs the physiological function of its encoded gene. Over the years, the focus of research has gradually shifted to other non-coding RNAs that were originally considered “junk” [15]. These nucleic acids that do not encode proteins not only store and transmit genetic information but also perform vital intracellular functions as regulators of gene expression. Non-coding RNAs are defined by inability to code for peptide chains long enough to constitute proteins (amino acids encoded within the open reading frame (ORF) are <100) and classified based on length of the nucleic acid chain [16]. Typically, microRNAs (miRNA), long non-coding RNAs (lncRNA) and circular RNAs (circRNA) play crucial roles in regulating vital biological processes, especially in malignant diseases [17]. Among these molecules, miRNAs and lncRNAs have been a considerable focus of tumor-related research in recent years. MiRNAs are non-coding RNAs about 21–23 nucleotides in size. Compared with other non-coding RNAs with longer fragment sizes, miRNAs perform simple functions and were discovered at an early stage of research. These RNA molecules undergo a series of biogenesis steps that convert primary miRNA transcripts into mature miRNAs, which are subsequently loaded into the

RNA-induced silencing complex (RISC) targeting the 3'-untranslated regions (3' UTR) of target genes, eventually leading to translational repression or target mRNA degradation [18]. In contrast, long non-coding RNAs (>200 nucleotides transcribed by RNA polymerase II) contain introns and present a 7-methylguanosine cap at the 5' end and a poly(A) chain at the 3' end, similar to mRNAs.

Compared with miRNA, the mechanisms of action of lncRNAs are complex. LncRNAs can interact with protein, DNA or RNA (RNA-protein, RNA-DNA or RNA-RNA) to perform their functions and are distributed in both nucleus and cytoplasm. In the nucleus, lncRNAs affect downstream gene transcription via multiple roles (enhancer, guide, and decoy or chromatin architect). In the cytoplasm, lncRNAs serve as miRNA/protein sponges or micropeptide templates to affect mRNA translation and stability. Indicating lncRNAs participate many process (epigenetic modification, transcriptional regulation and post-transcriptional regulation) in the cells [19,20].

Non-coding RNAs in liver cancer

Non-coding RNAs have been reported to participate in cancer hallmarks, including uncontrolled cell growth, invasion and metastasis, angiogenesis, resistance to cell death, and evasion of immune destruction [21,22]. MicroRNAs participate in cell proliferation, apoptosis, and transformation, as they can regulate gene expression and intracellular signal transduction for various physiological processes [23]. The tumor-suppressive effects that binding specificities, target genes, and regulated pathways of the miRNA-449 family (miR-449a, miR-449b, and miR-449c) are slightly different in HCC. They inhibited cell proliferation and migration, induced apoptosis, and reduced tumor growth to different extents by directly target to SRY-Box Transcription Factor 4 (SOX4), which codes for a transcription factor involved in epithelial–mesenchymal transition (EMT) and HCC metastasis, and thereby inhibited TGF- β mediated cell migration [24]. MiRNA-196a has been reported to be overexpressed in many types of cancers, including HCC. A mouse model demonstrated that down-regulation of miR-196a inhibited human liver cancer cell migration and invasion in vivo through direct targeting Forkhead box protein O1 (FOXO1) and could benefit the clinical therapy of HCC in the future [25]. MiR-122 and miR-22 are known to be related to the occurrence and progression of HBV related HCC. MiR-122 and miR-22 were downregulated in HBV related HCC patients and were related to tumor size, lymph node metastasis, TNM stage, pathological type, differentiation grade, liver cirrhosis, AFP and HBV DNA in clinical [23].

LncRNAs are a kind of non-coding RNAs [26]. Dysregulated lncRNAs are gradually considered to be closely related to the growth, metastasis, and deterioration of liver cancer [20]. LncRNA Highly Up-regulated in Liver Cancer (HULC) is highly upregulated in HCC and negatively associated with the expression of Phosphatase and Tensin Homolog (PTEN) and miR15a. Further, HULC is related to highly specific upregulation characterized in HCC tissues and associated with intrahepatic metastases, TNM stage, and HCC recurrence [20,27]. In addition to the miR-449 mentioned above, HOXD cluster antisense RNA 1 (HOXD-AS1) also interacts

with SOX4. HOXD-AS1 is significantly upregulated in HCC tissues and associated with poor prognosis and high tumor node metastasis stage of HCC patients. HOXD-AS1 competitively binds to miR-130a-3p that prevented SOX4 from miRNA mediated degradation, thus activates the expression of the Enhancer of zeste homolog 2 (EZH2), Matrix Metalloproteinase-2 (MMP-2), and facilitated HCC metastasis [28]. lncRNAs play emerging EMT regulators to regulate different types (1–3) of EMT, such as Tripartite Motif Containing (TRIM) 71 interacting long non-coding RNA (Trincr)1 that can promote embryonic stem cells self-renewal and suppress ERK target genes through inhibiting TRIM71. Besides, lncRNAs have been found to target EMT-related genes and signaling pathways to increase epithelial plasticity [29]. Moreover, some evidence indicates that lncRNAs are aberrantly expressed in diverse cancer stem cell (CSC)s and regulate CSC properties at different molecular levels. As an example, Differentiation Antagonizing Non-protein Coding RNA (DANCR) can interact with CTNNB1 mRNA and significantly promotes stemness features in HCC [30].

Non-coding RNAs as biomarker/therapeutic targets for liver cancer

Serum Alpha-fetoprotein (AFP) is the most used biomarkers for HCC. But, AFP lacks the specificity for use as the standard diagnostic tool for HCC in clinical. Also other biomarkers, such as Desgamma Carboxyprothrombin (DCP) and fucosylated AFP, have been investigated for their clinical usefulness as well but showed equally low accuracy as AFP. Thus, non-coding RNA based assays could be considered as an alternative diagnostic tool for HCC, since most protein-based assays lack the desired accuracy [31]. Many reports suggest that non-coding RNAs alone or in combinations act as candidate biomarkers for HCC diagnosis. The lncRNA Urothelial Carcinoma Associated-1 (UCA1) is an example of lncRNA based HCC diagnostic biomarker. And the simultaneous detection of JUN mRNA was more accurate than the single detection of UCA1 (the sensitivity and specificity were 97.1% and 80%) [32]. Similarly, several miRNAs show their value in clinical diagnosis. For example, miR-26a was identified as a promising biomarker for the diagnosis of early HCC. Even further, the expression levels of miR-221 and miR-101-1 could be used as non-invasive biomarkers for the diagnosis of early HCC from HCV patients [33]. In the choice of biomarker, in addition to the specificity and accuracy of the test, the method of obtaining the specimen is also a very important consideration. Therefore, non-invasive sample acquisition has become the most common consideration. Among them, in the serum of patients, detecting non-coding RNAs in exosomes secreted by cells is a way to obtain higher quality targets to be tested, and it has attracted attention in clinical development [34]. Like circulating exosomal miRNA-21 and lncRNA Activated By TGF- β (ATB) were related to the TNM stage and other prognostic factors, including the T stage and portal vein thrombosis that can novel prognostic markers and therapeutic targets for HCC [35]. These values underline the utility of RNA based detection methods for early HCC diagnostic.

The application of non-coding RNAs in the HCC therapeutic strategy has great potential. Based on the action

characteristics of lncRNA, its function similar to the miRNA plays the role of sponge. Therefore, lncRNAs with different tumor suppressor roles can be designed to inhibit oncogenic miRNAs with the abnormal performance for treatment [36]. Further, lncRNA targeting approaches hold some advantages than protein targeting methods in terms of base pairing principle is much more straightforward than designing a specific protein-binding inhibitor, such as antisense oligonucleotides (ASOs) and RNA interference (RNAi) [37]. For example, linc00210 is highly expressed along with liver tumorigenesis and linc00210 drives the self-renewal and propagation of liver tumor-initiating cells (TICs) through activating Wnt/ β -catenin signaling. Also, ASO-mediated linc00210 silence has been shown to repress the self-renewal and invasion of HCC cells [38]. Besides, knockdown of oncogenic lncRNA cancer susceptibility 9 (CASC9) by RNAi also significantly reduced the tumor formation in an HCC mouse model [39]. Nucleic acid inhibitors can inhibit endogenous miRNAs or piRNAs that exhibit tumor-promoting functions in cancer. Thus, miR-122 inhibitor has been tested in phase 2a clinical trials for treating patients with HCV infection [40].

Thyroid hormone regulates microRNA expression in liver cancer

Recent studies have highlighted that thyroid hormone as a transcription factor is closely associated with various non-coding RNAs, including microRNAs (miRNAs) and long non-coding RNAs (lncRNAs). In liver cancer, thyroid hormone affects tumor progression through effects on multiple non-coding genes. Our group has extensively investigated miRNAs and lncRNAs with potential clinical value in diagnosis and treatment of liver cancer. As a result, several miRNAs and lncRNAs clearly affected by thyroid hormones and receptors have been identified [9,41].

MiR-214 is reported to act as either a tumor suppressor or oncogene in various malignancies [42]. The miRNA has been characterized as a tumor suppressor in HCC. Interactions of miR-214 with different target genes exert a range of effects on different cells in HCC. Hepatoma-derived growth factor (HDGF) is a heparin binding protein purified from conditioned medium of HuH-7 hepatoma cells and expressed in a range of tissues, such as liver and lung. Overexpression of HDGF has been reported in multiple cancer types and the HDGF level is correlated with poor prognosis in breast, colorectal, pancreatic, non-small cell lung and gallbladder cancers as well as HCC [43]. Dysregulated miR-214 contributes to the unusual hypervascularity of HCC via direct activation of target genes in the HDGF paracrine pathway of angiogenesis [44,45]. MiR-214 additionally suppresses cell proliferation, migration and metabolism by targeting Flotillin 1 (FLOT1), pyruvate dehydrogenase kinase 2 (PDK2), and plant homeodomain finger protein 6 (PHF6) in hepatocellular carcinoma [42,46]. Previous studies suggest that T₃ induces miR-214 expression and suppresses cell proliferation through interactions with the target proto-oncogene, the serine/threonine-protein kinase PIM-1, thus contributing to inhibition of HCC tumor formation [47].

An miRNA cluster is a set of two or more miRNAs transcribed from physically adjacent miRNA genes. In common cognition processes, miRNA clusters are located in similar

chromosomes under the same circumstances and therefore often subject to the same regulation mechanisms or play a consistent role [48]. For instance, the miR-106b-25 cluster regulates atherosclerosis by influencing clearance of VLDL and LDL from the plasma and dysregulation of the miR-183 cluster causes defects in differentiation of photoreceptors and other retinal neurons through effects on target gene expression patterns [49,50]. The miR-199a/miR-214 cluster has additionally been identified as two miRNAs with the similar effects in a number of studies. Both miR-199a and miR-214 are significantly downregulated during differentiation and induce expression of a series of genes correlated with differentiation (COX-2, NF- κ B p50/p65, and CREB1) [51]. In addition, miR199/miR214 play roles in the differentiation of mammalian skeletal precursor cells into osteoblasts or chondrocytes, function in the development of muscle and heart, and regulate the development and progression of various cancer types [52]. The transcription factor, Twist-1, drives the expression of a 7.9 kb non-coding RNA transcript (from the Dynamin-3 gene intron) encoding the miR-199a/miR-214 cluster [53].

MiR-199 family members are downregulated in HCC tumors and cell lines in association with poor overall survival. MiR-199a overexpression in HCC cell lines has been shown to inhibit cell proliferation, migration and invasion by targeting Rho-associated coiled-coil kinase 1 (ROCK1), Regulators of G-protein signaling (RGS) and X-box binding protein 1 (XBP1) [54–56]. Interestingly, the miR-199a/miR-214 cluster is subject to the same regulation processes, which seems not so complete. In terms of the effects of thyroid hormones on these miRNAs, the results were unexpected. Earlier studies by our group revealed an interesting regulatory mechanism whereby thyroid hormones exert opposite effects on miR-199a and miR-214. Notably, miR-199a is downregulated by T₃/TR while miR-214 is upregulated. The differential regulatory effects on miR-199a and miR-214 are attributed to different TREs in the region between the two miRNAs [47]. Analogous to this finding, miR-17-92 clusters [play distinct roles in lymphomas and solid tumors [57].

MiR-130b acts as an oncogene in HCC, showing significantly higher expression in tumor tissues compared to matched normal tumor-adjacent tissues. Clinical analyses disclosed that high expression of miR-130b is significantly correlated with venous infiltration, high Edmondson-Steiner grade and advanced tumor-node-metastasis (TNM) stage [58]. The serum miR-130b level may present an ideal marker for monitoring the recurrence and prognosis of primary hepatocellular carcinoma (PHC) after radiofrequency ablation (RFA) treatment [59]. The miR-130b gene inhibits protein expression of Notch-Dll1 to promote proliferation, invasion and metastasis of liver cancer cells [60]. Negative regulation of miR-130b by T₃/TR has been reported with the identification of a novel pathway interlinking T₃/TR, miR-130b and its target gene, interferon regulatory factor 1 (IRF1), which affects the EMT-related genes, p-mTOR, p-STAT3, and the p-AKT cascade, in turn, regulating motility and invasion of hepatoma cells [61].

In addition to miR-130b, miR-21 is a potential tumor biomarker of liver cancer, and combined detection of miR-130b and miR-21 in serum is suggested to aid in diagnosis of HCC [62]. Another study confirmed an oncogenic role of miR-21 and its utility as a potential diagnostic biomarker for

early diagnosis of HCC [63]. MiR-21 expression in exosomes is positively correlated with that in cells and negatively correlated with expression of its target genes, such as PTEN, PTENp1 and TETs, to affect HCC cell growth [64]. Serum visfatin is associated with histology and metastasis of HCC. Serum levels of both visfatin and miR-21 were shown to be significantly higher in HCC patients. Visfatin promoted miR-21 expression and migration of HepG2 cells, suggesting that visfatin-induced HCC cell migration is attributable to upregulation of miR-21 [65]. In addition to visfatin, thyroid hormone affects the performance of miR-21 in HCC. MiR-21 is activated by T₃ through its binding to a native T₃ response element in the primary promoter region. Stimulation of miR-21 by T₃ and subsequent suppression of T-cell lymphoma invasion and metastasis 1 (TIAM1) promotes hepatoma cell migration and invasion [66].

Reports on the role of miR-17 in HCC are controversial and the issue of whether this miRNA plays a carcinogenic or tumor suppressor role is yet to be established. Several studies have shown that miR-17 is highly expressed in HCC, especially in patients with higher risk of metastasis, supporting its utility as a novel prognostic marker [67,68]. The p38 MAPK pathway plays a crucial role in miR-17-induced phosphorylation of HSP27 and enhances HCC cell migration [69]. MiR-17 affects cell growth through direct targeting of SMAD family member 3 (SMAD3) in HCC cells. Downregulation of SMAD3 was shown to be consistently associated with high miR-17 levels in HCC tissues of patients, compared with normal liver tissues [70]. However, a few studies put forward the opposite view that miR-17 has the ability to inhibit tumor spread in liver cancer patients with a higher risk of metastasis. In one of these studies, HCC patients with lower miR-17 and higher ERBB3 levels had significantly shorter overall survival (OS) and progression-free survival (PFS) rates after surgical resection [71]. In another study, miR-17 suppressed postoperative metastasis of hepatocellular carcinoma through blocking the HGF/ERBB3-NF- κ B positive feedback loop [71]. Global gene expression profiling data from another investigation indicate that miR-17 targets and inhibits MYC to affect cell cycle progression, supporting the potential of anti-miR-17 as a therapeutic strategy for MYC-driven HCC [72]. T₃/TR negatively regulates miR-17 expression in HCC. MiR-17 expression was significantly negatively associated with TR α 1 and matrix metalloproteinase-3 (MMP-3) in HCC, suggesting that T₃/TR, miR-17 and MMP3 activities are interlinked in the regulation of metastasis [73].

MiR-206 plays an important regulatory role in cell growth in multiple cancer types. Reduced expression of miR-206 has been reported in HCC [74,75]. MiR-206 directly targets the 3' UTRs of cyclin-dependent kinase 9 (CDK9), cMET and protein tyrosine phosphatase 1B (PTP1B) genes for silencing, in turn, inhibiting HCC proliferation and invasion and simultaneously promoting apoptosis [74–76]. Liver cancer stem cells (CSC) are involved in tumor progression, drug resistance and recurrence of HCC. MiR-206 was reduced in patients with chemoresistant and recurrent HCC and shown to suppress HCC cell dedifferentiation and liver CSC expansion by targeting the epidermal growth factor receptor (EGFR) signaling pathway [77]. The action of thyroid hormone on lipid metabolism in liver is associated with a number of genes involved in lipogenesis and

lipid metabolism. Serum miR-206 expression is reduced in patients with hyperthyroidism. In addition, miR-206 is involved in T₃-mediated regulation of lipid metabolism in HCC cells, indicating a role in thyroid hormone-induced disorders of lipid metabolism in liver [78].

Hepatic lipid droplets (LD) are associated with metabolic syndrome, type 2 diabetes, hepatitis C, and both alcoholic and non-alcoholic fatty liver disease. The novel miRNA, miR-181d, has been identified as an inhibitor that decreases LD levels by about 60%. Data from biochemical assays showed that miRNA-181d reduces cellular triglyceride and cholesterol ester levels that may be relevant in hepatic diseases arising from obesity and alcohol abuse [79]. Thyroid hormone regulates the transcription of numerous metabolic genes in the liver through interactions with its nuclear receptors. MiRNA-181d is regulated by thyroid hormone in hepatic cells and functions in negative regulation of key metabolic genes through effects on two novel thyroid hormone-regulated target genes, caudal type homeobox 2 (CDX2) and sterol O-acyltransferase 2 (SOAT2 or ACAT2) [80].

Thyroid hormone regulates long non-coding RNA expression in liver cancer

In addition to miRNAs, several studies have revealed increasingly important roles of lncRNAs that also belong to the non-coding RNA family. The mechanism of action of lncRNAs is relatively complex, compared to that of miRNAs. Emerging evidence suggests a crucial role of lncRNAs in tumor progression of HCC. Various HCC-related lncRNAs have been shown to display aberrant expression patterns and participate in cancerous phenotypes, such as proliferation, evasion of apoptosis, promotion of vessel formation, and metastasis capability [37]. The most typical lncRNA in HCC associated with the thyroid hormone is brain cytoplasmic RNA 1 (BCYRN1/BC200), a 200-nucleotide ncRNA originally identified as a neuron-specific transcript that is abnormally overexpressed in several tumor types, such as colorectal, breast, lung and liver cancer [81–83]. A number of recent studies have focused on the mechanisms by which abnormal expression of BC200 RNA contributes to cancer development. BC200 expression is reported to be significantly higher in HCC tissues and effective as an independent prognostic marker. Moreover, BC200 affects cell proliferation and migration through influencing c-Myc, Bax and Bcl-xL expression [84] and induces cell growth and tumor sphere formation via regulation of cell cycle-related genes and stemness markers (CD133, CD44, Nanog and Sox2). Simultaneously, BC200 protects cyclin E2 mRNA from degradation via direct interactions and promotes CDK2–cyclin E2 complex formation [85]. Using the Human Disease-Related lncRNA Profiler to identify the lncRNAs regulated by thyroid hormone in HepG2 cells overexpressing thyroid hormone receptor $\alpha 1$ (HepG2-TR $\alpha 1$), BC200 was identified as an lncRNA downregulated by the thyroid hormone. The results support the existence of a novel pathway involving thyroid hormone-mediated regulation of BC200, cyclin E2 and CDK2, which, in turn, modulates proliferation and tumor sphere formation of hepatoma cells, highlighting the potential of therapeutic strategies targeting BC200 and associated molecules for treatment of HCC [85].

Our group used microarray analysis for profiling of other important lncRNAs in HepG2-TR $\alpha 1$ cells treated with/without T₃ and HCC specimens. These oncogenic lncRNAs were identified through random sampling verification and down-regulated by thyroid hormones [Table 1] [86].

Taurine up-regulated gene 1 (TUG1) is an lncRNA shown to play an oncogenic role in various cancers. TUG1 is highly expressed in HCC tissues and contributes to proliferation, metastasis and apoptosis via activation of distal-less homeobox 2 (DLX2) in HCC [94]. In view of the finding that TUG1 can be easily detected in patient samples and has clinical significance, this lncRNA may serve as a novel potential biomarker in HCC, as determined with a valid non-invasive technique [95]. The majority of research to date suggests that TUG1 predominantly acts as a miRNA sponge in HCC, exerting effects on miR-216b-5p, miR-142-3p, miR-144 and miR-132. Interactions of TUG1 with multiple miRNAs lead to its participation in various tumor processes in HCC [94,96–98]. Cancer cells can alter their glucose metabolism and activate aerobic glycolysis [99]. TUG1 is reported to induce cell migration, invasion, and glycolysis through suppression of miR-455-3p. MiR-455-3p directly interacts with the 3'UTR of adenosine monophosphate-activated protein kinase subunit beta 2 (AMPK $\beta 2$). The TUG1/miR-455-3p/AMPK $\beta 2$ axis regulates cell growth, metastasis, and glycolysis through modulation of hexokinase 2 (HK2) in HCC [100]. Hypothyroidism in patients is associated with high risk of HCC and levels of the glycoprotein, alpha-fetoprotein (AFP), are increased in the majority of patients with HCC. Despite the controversy regarding the utility of AFP, it still presents a useful diagnostic biomarker. TUG1 is regulated by thyroid hormone to affect AFP. Specifically, thyroid hormone suppresses TUG1 expression, leading

Table 1 lncRNAs negatively associated with thyroid hormones in the HepG2 liver cancer cell line.

lncRNAs Negatively Affected by Thyroid Hormones			
lncRNA	In HCC (Fold)	T ₃ /48 h (Fold)	In HCC Ref.
FAM215A	7.23	0.42	[87]
ANKRD20A8P	2.20	0.43	
HCG18	2.23	0.43	
PVT1	7.47	0.44	[88]
SNHG1	4.69	0.45	[89]
SNHG3	3.2	0.46	[90]
UNK	3.49	0.46	
TUG1	3.25	0.47	[86]
SNHG7	3.30	0.47	[91]
DDX11-AS1	10.20	0.47	[92]
DUSP5P	9.46	0.48	
AGSK1	2.79	0.49	
MF12-AS1	5.07	0.49	[93]

Microarray analysis of long non-coding RNA (lncRNA) expression in two pairs of HCC specimens. Data are presented as average tumor/adjacent normal (T/N ratio) of the two specimen pairs. The specified lncRNAs were highly expressed (>2-fold) in HCC specimens. HepG2 cell lines overexpressing TR $\alpha 1$ were treated with thyroid hormone (10 nM) and subjected to microarray analysis of lncRNA expression after 48 h. Notably, the above lncRNAs were negatively affected (<0.5-fold) upon thyroid hormone stimulation. The references pertain to studies on the roles of these lncRNAs in liver cancer.

to downregulation of AFP. AFP is positively correlated with TUG1 levels and unfavorable prognosis in patients with non-hepatitis B/non-hepatitis C (NBNC) HCC [86].

While correlations of thyroid hormone with other lncRNAs have only been observed in our preliminary research, their oncogenic roles in HCC are clear-cut. Family with sequence similarity 215 member A (FAM215A) is a tissue-specific lncRNA with different roles in ovarian cancer and HCC. High expression of FAM215A in low-grade ovarian cancer and early-stage disease has been reported, compared to high-grade ovarian cancer and late-stage disease [101]. In HCC, overexpression of FAM215A is positively correlated with tumor size, vascular invasion, and pathology stage [87]. Overexpression of FAM215A accelerates proliferation and metastasis of HCC cells. FAM215A additionally increases doxorubicin (DOX) resistance in HCC in association with enhanced expression of lysosome-associated membrane protein 2 (LAMP2). Furthermore, FAM215A interacts with and stabilizes LAMP2 to increase tumor progression along with decreasing doxorubicin sensitivity [87].

Long non-coding small nucleolar RNA host genes (SNHG) are abnormally expressed in multiple cancers, including urologic neoplasms, respiratory tumors, and digestive cancers, and crucial for tumor progression [102]. SNHGs, including SNHG1, SNHG3, SNHG6, SNHG16, and SNHG20, are reported to play variable roles in HCC via multiple regulatory mechanisms, with both promotory and inhibitory effects on tumorigenesis [90,103]. SNHG1 is an oncogenic lncRNA highly expressed in different tumor types, including colorectal, liver, lung, prostate and gastric cancer. Expression of SNHG1 is significantly positively associated with advanced tumor stage, tumor size, TNM stage, and decreased overall survival in liver cancer. Furthermore, aberrant expression of SNHG1 contributes to cell proliferation, metastasis, migration and invasion of HCC cancer cells [104]. Mechanistically, SNHG1 is proposed to act as an miRNA sponge (miR-195-5p and miR-21) and enhance tumor cell proliferation and invasion ability through targeting and inhibition of p53 by binding DNA methyltransferase 1 (DNMT1) [105–107]. Another member of the SNHG family, SNHG3, is highly expressed in HCC tissues and positively correlated with tumor size, portal vein tumor thrombus (PVTT), and relapse. Additionally, high expression of SNHG3 is correlated with OS, recurrence-free survival (RFS), and disease-free survival (DFS) [108]. Simultaneously, SNHG3 is suggested to promote tumor invasion and sorafenib resistance by affecting MET via the miR-128/CD151/Akt/PI3K [109] and miR-326/Sma and Mad Related Family 3 (SMAD3)/zinc finger E-box binding homeobox 1 (ZEB1) signaling pathways [90].

DDX11-AS1 expression is markedly higher in HCC tissues and cell lines and associated with poor predicted overall survival [110]. DDX11-AS1 promotes cell proliferation in gastric cancer through inhibiting miR-30-5p and miR-145-5p [111]. Proliferation, cell cycle progression, migration, and invasion of HCC cells are reduced upon DDX11-AS1 silencing. RNA immunoprecipitation (RIP) and chromatin immunoprecipitation (ChIP) findings suggest that DDX11-AS1 reduces expression of large tumor suppressor kinase 2 (LATS2) by interacting with Enhancer of zeste homolog 2 (EZH2) and DNA (cytosine-5)-methyltransferase 1 (DNMT1) in HCC cells [92].

Discussion

The majority of the human genome is not translatable into protein but can be transcribed into RNA. While non-coding RNAs do not encode proteins, aberrations in these molecules contribute to several disorders, such as Alzheimer's disease (AD), Parkinson's disease (PD), amyotrophic lateral sclerosis (ALS), spinal muscular atrophy (SMA), Huntington's disease (HD) and various cancer types [112]. These findings are mainly attributable to the development of high-throughput RNA sequencing technology over the years that has facilitated the discovery of thousands of non-coding RNA genes. A simple sub-classification system is generally used, with ncRNAs divided into short (sncRNAs) and long ncRNAs (lncRNAs) based on a size cut-off of >200 bases. The sncRNA group comprises microRNAs (miRNAs) with small fragment sizes of 21–23 bases [113]. Non-coding RNAs have been shown to be involved in liver cancer progression. For instance, miR-296-5p attenuates the epithelial–mesenchymal transition (EMT) program through Neuregulin (1NRG1)/erb-b2 receptor tyrosine kinase 2 (ERBB2)/ERBB3 signaling. Moreover, miR-296-5p exerts an inhibitory effect on the stemness potency of HCC cells via direct targeting of the Brahma-related gene-1 (BRG1)/Sal-like protein 4 (SALL4) axis [114]. MiR-486-3p is downregulated in sorafenib-resistant HCC cell lines and tumor tissue relative to adjacent normal tissue in HCC patients and could induce apoptosis by targeting fibroblast growth factor receptor 4 (FGFR4) and EGFR [115]. Golgin A2 pseudogene 10 (GOLGA2P10) is frequently upregulated in HCC tissues as well as hepatoma cells subjected to endoplasmic reticulum (ER) stress inducers. Higher GOLGA2P10 levels are correlated with shorter recurrence-free survival of HCC patients. GOLGA2P10 enhances Bcl-xL protein levels and BAD phosphorylation, and confers resistance to ER stress-induced apoptosis in tumor cells [116]. Expression of cancer susceptibility candidate 15 (CASC15) is elevated in HCC tissues and positively correlated with tumor size, TNM stage and metastasis. CASC15 activates the Wnt/ β -catenin pathway via enhancing expression of SRY-Box Transcription Factor 4 (SOX4), thus promoting tumor progression [117]. While several non-coding RNAs with different sizes, functions and significance have been identified over the years, this review has mainly focused on the miRNAs and lncRNAs involved in liver cancer and their correlations with the thyroid hormone pathway.

A number of molecular mechanisms have been proposed to explain the involvement of the thyroid hormone and effects on non-coding RNAs in liver cancer [Fig. 1], and thyroid hormone-associated non-coding RNAs including their roles and expression patterns in liver cancer [Table 2] are listed.

Thyroid hormones, a transcription factor affect the expression of various non-coding RNAs (miRNAs and lncRNAs). This leads to several regulatory pathways in liver cells.

Previously, from ours or other reports indicate that the thyroid hormone is involved in various mechanisms underlying the growth and development of liver cells, inevitably resulting in different roles. An earlier study reported hypothyroidism over ten years in female patients with

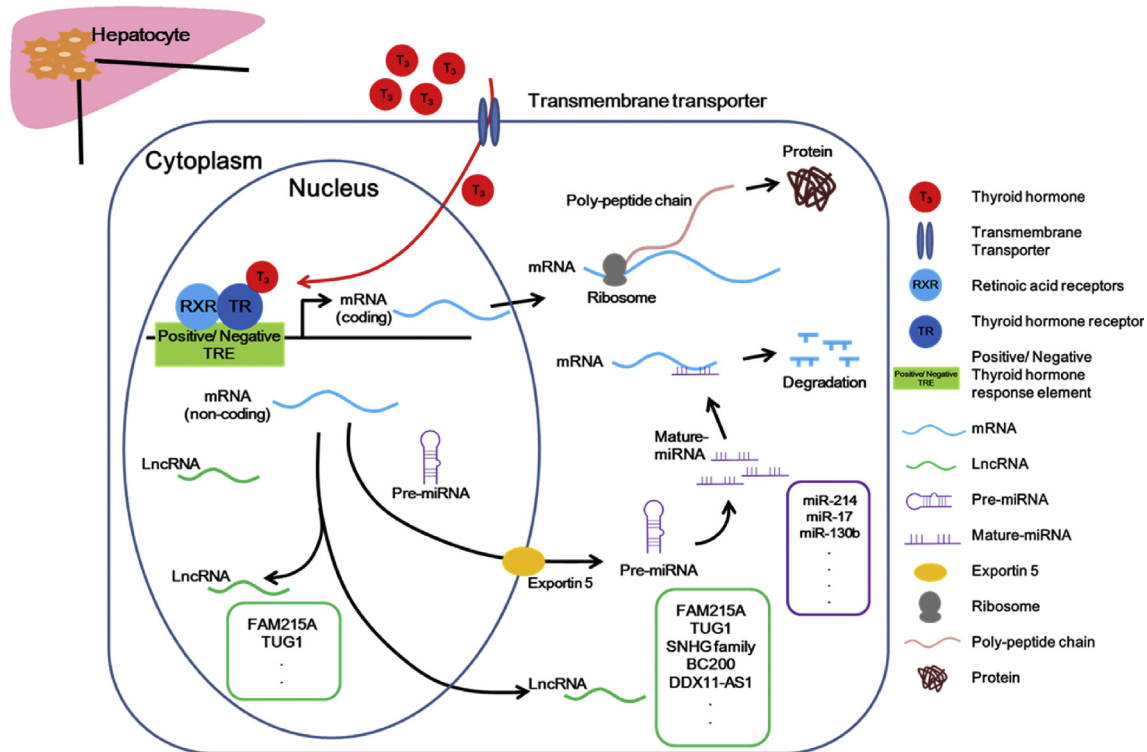


Fig. 1 Thyroid hormones regulate various non-coding RNAs in liver.

hepatocellular carcinoma, indicating a significant association of hypothyroidism with high risk of HCC in females independent of known risk factors [118]. In clinical samples of liver cancer patients, thyroid-stimulating hormone receptor (TSHR) is overexpressed, indicative of a hypothyroid state [119]. At the same time that in terms of therapeutic strategies, thyroid

hormones and/or thyromimetics may be useful for treatment of patients with HCC [14]. Thus, thyroid hormone acts as a transcription factor and its role as a tumor suppressor has been confirmed at the genomic level. We also found that thyroid hormone suppresses HCC development through protecting hepatocytes from HBx-induced damage in transgenic

Table 2 Differential effects of thyroid hormone via regulation of multiple non-coding RNAs in liver cancer.

Gene	Role	Target	Function	T ₃ /TR	Ref.
Thyroid hormone as a tumor suppressor					
miR-214	Suppressor	HDGF FLOT1 PDK2 PHF6	Angiogenesis Proliferation Metastasis Metabolism	Up	[44] [46] [42]
miR-17	Dual role	PIM-1 MAPK SMAD3 MYC MMP3	Proliferation Metastasis	Down	[47] [69] [70] [72] [73]
miR-130b	Oncogene	Notch-Dll1 AP-1 IRF1	Proliferation Metastasis	Down	[60] [61]
BC200	Oncogene	c-Myc Bax Bcl-xL CD133 CD44 Nanog Sox2 Cyclin E2	Proliferation Sphere formation	Down	[84] [85]

Table 2 – (continued)

Gene	Role	Target	Function	T ₃ /TR	Ref.
Thyroid hormone as a tumor suppressor					
TUG1	Oncogene	miR-216b-5p	Proliferation	Down	[94]
		miR-142-3p	Metastasis		[96]
		miR-144	Apoptosis		[97]
		miR-132			[98]
		AFP			[86]
FAM215A	Oncogene	LAMP2	Proliferation	Down	[87]
			Metastasis		
SNHG family	Oncogene	miR-195-5p miR-21	Drug resistance	Down	
		miR-128	Proliferation		[105]
		miR-326	Metastasis		[106]
		SMAD3	Drug resistance		[109]
DDX11-AS1	Oncogene	LATS2	Proliferation	Down	[90]
		EZH2	Metastasis		[92]
Thyroid hormone as an oncogene					
Gene	Role	Target	Function	T ₃ /TR	Ref.
miR-199	Suppressor	ROCK1	Proliferation	Down	[56]
		RGS	Metastasis		[55]
		XBP1			[54]
miR-21	Oncogene	PTEN	Proliferation	Up	[64]
		PTENp1	Metastasis		
		TETs			
		TIAM1			[66]
miR-206	Suppressor	CDK9	Proliferation	Down	[74]
		cMET	Metastasis Apoptosis		[75]
		PTP1B	Drug resistance		[76]
		EGFR	Metabolism		
Potential roles of thyroid hormone-related non-coding RNAs.					

mice via activation of PTEN-induced kinase 1 (PINK1) [120]. And in a murine model of diethylnitrosamine (DEN)-induced HCC, thyroid hormone suppresses the carcinogenic process via activation of death-associated protein kinase 2 (DAPK2), a serine/threonine protein kinase, which enhances phosphorylation of sequestosome 1 (SQSTM1) to promote selective autophagic clearance of protein aggregates [121]. The oncogene, Stathmin (STMN1), is downregulated by thyroid hormone in liver. Thyroid hormone-mediated suppression of STMN1 additionally supports its role as an inhibitor of HCC tumor growth and suggests that lack of normal THR function leads to elevated STMN1 expression and promotes malignancy [122]. As discussed, thyroid hormones play a suppressive role by repressing non-coding RNAs such as miR-214, miR-130b, TUG1 and BC200 to protect liver cells from damage and disease.

Taken together, based on the pathological and clinical analyses and data from different animal models, we propose that thyroid hormone acts as a tumor suppressor to repress several non-coding RNAs as well as coding-genes. In view of the finding that thyroid hormone and its receptor inhibit liver cancer progression, thyroid hormone receptor- β agonists, such as GC-1, MB07344 and KB2115, have been developed as treatment strategies that induce a good response in terms of hepatic metabolism and damage in various animal models. Results from a recent phase II trial consistently showed preventive effects on NAFLD accompanied by improved metabolism (decreased serum levels of LDL cholesterol and TG)

[123]. Thus, therapeutic strategies involving modulation of thyroid hormone-regulated non-coding RNAs are feasible for treatment or diagnosis of liver diseases.

Funding

This research was funded by grants from Chang Gung Memorial Hospital, Taoyuan, Taiwan (CMRPG6K0031 to C.-C.C., and C.-S.W) and from the Ministry of Science and Technology of the Republic of China (MOST 106-2314-B-182A-130- to C.-S.W). We would like to thank the Taiwan Liver Cancer Network (TLCN) for providing the hepatoma tissue samples and related clinical data (all anonymous).

Conflict of interest

The authors declare no competing financial interests.

REFERENCES

- [1] Chiew Woon L, Joycelyn Jie Xin L, Su Pin C. Nivolumab for the treatment of hepatocellular carcinoma. *Expert Opin Biol Ther* 2020;20:687–93.

- [2] Lange N, Dufour JF. Changing epidemiology of HCC: how to screen and identify patients at risk? *Dig Dis Sci* 2019;64:903–9.
- [3] Tsuchiya N, Sawada Y, Endo I, Saito K, Uemura Y, Nakatsura T. Biomarkers for the early diagnosis of hepatocellular carcinoma. *World J Gastroenterol* 2015;21:10573–83.
- [4] Keating GM. Sorafenib: a review in hepatocellular carcinoma. *Targeted Oncol* 2017;12:243–53.
- [5] Zhu YJ, Zheng B, Wang HY, Chen L. New knowledge of the mechanisms of sorafenib resistance in liver cancer. *Acta Pharmacol Sin* 2017;38:614–22.
- [6] Swamy SG, Kameshwar VH, Shubha PB, Looi CY, Shanmugam MK, Arfuso F, et al. Targeting multiple oncogenic pathways for the treatment of hepatocellular carcinoma. *Targeted Oncol* 2017;12:1–10.
- [7] Liu XN, Cui DN, Li YF, Liu YH, Liu G, Liu L. Multiple "Omics" data-based biomarker screening for hepatocellular carcinoma diagnosis. *World J Gastroenterol* 2019;25:4199–212.
- [8] Liu YC, Yeh CT, Lin KH. Molecular functions of thyroid hormone signaling in regulation of cancer progression and anti-apoptosis. *Int J Mol Sci* 2019;20:4986.
- [9] Huang PS, Wang CS, Yeh CT, Lin KH. Roles of thyroid hormone-associated microRNAs affecting oxidative stress in human hepatocellular carcinoma. *Int J Mol Sci* 2019;20:5220.
- [10] Ritter MJ, Amano I, Hollenberg AN. Thyroid hormone signaling and the liver. *Hepatology* 2020;72:742–52.
- [11] Park JW, Zhao L, Cheng SY. Inhibition of estrogen-dependent tumorigenesis by the thyroid hormone receptor beta in xenograft models. *Am J Canc Res* 2013;3:302–11.
- [12] Gionfra F, De Vito P, Pallottini V, Lin HY, Davis PJ, Pedersen JZ, et al. The role of thyroid hormones in hepatocyte proliferation and liver cancer. *Front Endocrinol* 2019;10:532.
- [13] Zhang N, Jin W, Zhou S, Yang JD, Harmsen WS, Giana NH, et al. Hypothyroidism is associated with worse outcomes of hepatocellular carcinoma patients after liver transplantation. *Canc Med* 2018;7:5870–8.
- [14] Kowalik MA, Puliga E, Cabras L, Sulas P, Petrelli A, Perra A, et al. Thyroid hormone inhibits hepatocellular carcinoma progression via induction of differentiation and metabolic reprogramming. *J Hepatol* 2020;72:1159–69.
- [15] Vicentini C, Galuppini F, Corbo V, Fassan M. Current role of non-coding RNAs in the clinical setting. *Non-coding RNA Res* 2019;4:82–5.
- [16] Niazi F, Valadkhan S. Computational analysis of functional long noncoding RNAs reveals lack of peptide-coding capacity and parallels with 3' UTRs. *RNA* 2012;18:825–43.
- [17] Zhang S, Zhou Y, Wang Y, Wang Z, Xiao Q, Zhang Y, et al. The mechanistic, diagnostic and therapeutic novel nucleic acids for hepatocellular carcinoma emerging in past score years. *Brief Bioinform* 2020;6:bbaa023.
- [18] Hammond SM. An overview of microRNAs. *Adv Drug Deliv Rev* 2015;87:3–14.
- [19] Cipriano A, Ballarino M. The ever-evolving concept of the gene: the use of RNA/protein experimental techniques to understand genome functions. *Front Mole Biosci* 2018;5:20.
- [20] Chen X, Tang FR, Arfuso F, Cai WQ, Ma Z, Yang J, et al. The emerging role of long non-coding RNAs in the metastasis of hepatocellular carcinoma. *Biomolecules* 2020;10:66.
- [21] Gutschner T, Diederichs S. The hallmarks of cancer: a long non-coding RNA point of view. *RNA Biol* 2012;9:703–19.
- [22] Van Roosbroeck K, Calin GA. Cancer hallmarks and MicroRNAs: the therapeutic connection. *Adv Canc Res* 2017;135:119–49.
- [23] Qiao DD, Yang J, Lei XF, Mi GL, Li SL, Li K, et al. Expression of microRNA-122 and microRNA-22 in HBV-related liver cancer and the correlation with clinical features. *Eur Rev Med Pharmacol Sci* 2017;21:742–7.
- [24] Sandbothe M, Buurman R, Reich N, Greiwe L, Vajen B, Gurlevik E, et al. The microRNA-449 family inhibits TGF-beta-mediated liver cancer cell migration by targeting SOX4. *J Hepatol* 2017;66:1012–21.
- [25] Yang L, Peng F, Qin J, Zhou H, Wang B. Downregulation of microRNA-196a inhibits human liver cancer cell proliferation and invasion by targeting FOXO1. *Oncol Rep* 2017;38:2148–54.
- [26] Lim LJ, Wong SYS, Huang F, Lim S, Chong SS, Ooi LL, et al. Roles and regulation of long noncoding RNAs in hepatocellular carcinoma. *Canc Res* 2019;79:5131–9.
- [27] Xin X, Wu M, Meng Q, Wang C, Lu Y, Yang Y, et al. Long noncoding RNA HULC accelerates liver cancer by inhibiting PTEN via autophagy cooperation to miR15a. *Mol Canc* 2018;17:94.
- [28] Wang H, Huo X, Yang XR, He J, Cheng L, Wang N, et al. STAT3-mediated upregulation of lncRNA HOXD-AS1 as a ceRNA facilitates liver cancer metastasis by regulating SOX4. *Mol Canc* 2017;16:136.
- [29] Cheng JT, Wang L, Wang H, Tang FR, Cai WQ, Sethi G, et al. Insights into biological role of lncRNAs in epithelial-mesenchymal transition. *Cells* 2019;8:1178.
- [30] Ma Z, Wang YY, Xin HW, Wang L, Arfuso F, Dharmarajan A, et al. The expanding roles of long non-coding RNAs in the regulation of cancer stem cells. *Int J Biochem Cell Biol* 2019;108:17–20.
- [31] Klingenberg M, Matsuda A, Diederichs S, Patel T. Non-coding RNA in hepatocellular carcinoma: mechanisms, biomarkers and therapeutic targets. *J Hepatol* 2017;67:603–18.
- [32] El-Tawdi AH, Matboli M, El-Nakeep S, Azazy AE, Abdel-Rahman O. Association of long noncoding RNA and c-JUN expression in hepatocellular carcinoma. *Exp Rev Gastroenterol Hepatol* 2016;10:869–77.
- [33] Jiang Y, He J, Li Y, Guo Y, Tao H. The diagnostic value of MicroRNAs as a biomarker for hepatocellular carcinoma: a meta-analysis. *BioMed Res Int* 2019;5179048.
- [34] Kelemen E, Danis J, Goblos A, Bata-Csorgo Z, Szell M. Exosomal long non-coding RNAs as biomarkers in human diseases. *Ejifcc* 2019;30:224–36.
- [35] Lee YR, Kim G, Tak WY, Jang SY, Kweon YO, Park JG, et al. Circulating exosomal noncoding RNAs as prognostic biomarkers in human hepatocellular carcinoma. *Int J Canc* 2019;144:1444–52.
- [36] Xu F, Zha G, Wu Y, Cai W, Ao J. Overexpressing lncRNA SNHG16 inhibited HCC proliferation and chemoresistance by functionally sponging hsa-miR-93. *Oncotargets Ther* 2018;11:8855–63.
- [37] Huang Z, Zhou JK, Peng Y, He W, Huang C. The role of long noncoding RNAs in hepatocellular carcinoma. *Mol Canc* 2020;19:77.
- [38] Fu X, Zhu X, Qin F, Zhang Y, Lin J, Ding Y, et al. Linc00210 drives Wnt/beta-catenin signaling activation and liver tumor progression through CTNNBIP1-dependent manner. *Mol Canc* 2018;17:73.
- [39] Klingenberg M, Gross M, Goyal A, Polycarpou-Schwarz M, Miersch T, Ernst AS, et al. The long noncoding RNA cancer susceptibility 9 and RNA binding protein heterogeneous nuclear ribonucleoprotein L form a complex and coregulate genes linked to AKT signaling. *Hepatology* 2018;68:1817–32.
- [40] Janssen HL, Reesink HW, Lawitz EJ, Zeuzem S, Rodriguez-Torres M, Patel K, et al. Treatment of HCV infection by targeting microRNA. *N Engl J Med* 2013;368:1685–94.
- [41] Dong H, Paquette M, Williams A, Zoeller RT, Wade M, Yauk C. Thyroid hormone may regulate mRNA abundance in liver by acting on microRNAs. *PLoS One* 2010;5:e12136.

- [42] Yu Q, Zhou J, Jian Y, Xiu Z, Xiang L, Yang D, et al. MicroRNA-214 suppresses cell proliferation and migration and cell metabolism by targeting PDK2 and PHF6 in hepatocellular carcinoma. *Cell Biol Int* 2020;44:117–26.
- [43] Yang GY, Zhang AQ, Wang J, Li CH, Wang XQ, Pan K, et al. Hepatoma-derived growth factor promotes growth and metastasis of hepatocellular carcinoma cells. *Cell Biochem Funct* 2016;34:274–85.
- [44] Shih TC, Tien YJ, Wen CJ, Yeh TS, Yu MC, Huang CH, et al. MicroRNA-214 downregulation contributes to tumor angiogenesis by inducing secretion of the hepatoma-derived growth factor in human hepatoma. *J Hepatol* 2012;57:584–91.
- [45] Liu Y, Wang J, Dong L, Xia L, Zhu H, Li Z, et al. Long noncoding RNA HCP5 regulates pancreatic cancer gemcitabine (GEM) resistance by sponging hsa-miR-214-3p to target HDGF. *Oncotargets Ther* 2019;12:8207–16.
- [46] Liu C, Shang Z, Ma Y, Ma J, Song J. HOTAIR/miR-214-3p/FLOT1 axis plays an essential role in the proliferation, migration, and invasion of hepatocellular carcinoma. *Int J Clin Exp Pathol* 2019;12:50–63.
- [47] Huang PS, Lin YH, Chi HC, Chen PY, Huang YH, Yeh CT, et al. Thyroid hormone inhibits growth of hepatoma cells through induction of miR-214. *Sci Rep* 2017;7:14868.
- [48] Cantini L, Bertoli G, Cava C, Dubois T, Zinovyev A, Caselle M, et al. Identification of microRNA clusters cooperatively acting on epithelial to mesenchymal transition in triple negative breast cancer. *Nucleic Acids Res* 2019;47:2205–15.
- [49] Semo J, Chernin G, Jonas M, Shimon S, George J. Deletion of the Mir-106b~ 25 MicroRNA cluster attenuates atherosclerosis in Apolipoprotein E knockout mice. *Lipids Health Dis* 2019;18:208.
- [50] Amini-Farsani Z, Asgharzade S. The impact of miR-183/182/96 gene regulation on the maturation, survival, and function of photoreceptor cells in the retina. *J Comp Neurol* 2020;528:1616–25.
- [51] Mishra R, Benhabib H, Guo W, Lerma Cervantes CB, Mendelson CR. Developmental decline in the MicroRNA 199a (miR-199a)/miR-214 cluster in human fetal lung promotes type II cell differentiation by upregulating key transcription factors. *Mol Cell Biol* 2018;38:e00037–18.
- [52] Desvignes T, Contreras A, Postlethwait JH. Evolution of the miR199-214 cluster and vertebrate skeletal development. *RNA Biol* 2014;11:281–94.
- [53] Lee YB, Bantounas I, Lee DY, Phylactou L, Caldwell MA, Uney JB. Twist-1 regulates the miR-199a/214 cluster during development. *Nucleic Acids Res* 2009;37:123–8.
- [54] Lou Z, Gong YQ, Zhou X, Hu GH. Low expression of miR-199 in hepatocellular carcinoma contributes to tumor cell hyper-proliferation by negatively suppressing XBP1. *Oncol Lett* 2018;16:6531–9.
- [55] Zhang W, Qian S, Yang G, Zhu L, Zhou B, Wang J, et al. MicroRNA-199 suppresses cell proliferation, migration and invasion by downregulating RGS17 in hepatocellular carcinoma. *Gene* 2018;659:22–8.
- [56] Zhan Y, Zheng N, Teng F, Bao L, Liu F, Zhang M, et al. MiR-199a/b-5p inhibits hepatocellular carcinoma progression by post-transcriptionally suppressing ROCK1. *Oncotarget* 2017;8:67169–80.
- [57] Ji M, Rao E, Ramachandradeddy H, Shen Y, Jiang C, Chen J, et al. The miR-17-92 microRNA cluster is regulated by multiple mechanisms in B-cell malignancies. *Am J Pathol* 2011;179:1645–56.
- [58] Xu Q, Cai W, Zhang M, Liu Q, Liu X. The expression and clinicopathological significance of miR-130b in human hepatocellular carcinoma. *Xi bao yu fen zi mian yi xue za zhi = Chinese journal of cellular and molecular immunology* 2016;32:387–92.
- [59] Hu XY, Li L, Wu HT, Liu Y, Wang BD, Tang Y. Serum miR-130b level, an ideal marker for monitoring the recurrence and prognosis of primary hepatocellular carcinoma after radiofrequency ablation treatment. *Pathol Res Pract* 2018;214:1655–60.
- [60] Ou C, Peng NF, Li H, Peng YC, Li LQ. The potential mechanism of miR-130b on promotion of the invasion and metastasis of hepatocellular carcinoma by inhibiting Notch-Dll1. *J Recept Signal Transduct Res* 2020;40:157–65.
- [61] Lin YH, Wu MH, Liao CJ, Huang YH, Chi HC, Wu SM, et al. Repression of microRNA-130b by thyroid hormone enhances cell motility. *J Hepatol* 2015;62:1328–40.
- [62] Zhang N, Hu Z, Qiang Y, Zhu X. Circulating miR-130b- and miR-21-based diagnostic markers and therapeutic targets for hepatocellular carcinoma. *Mole Gen Genom Med* 2019;7:e1012.
- [63] Qu J, Yang J, Chen M, Cui L, Wang T, Gao W, et al. MicroRNA-21 as a diagnostic marker for hepatocellular carcinoma: a systematic review and meta-analysis. *Pak J Med Sci* 2019;35:1466–71.
- [64] Cao LQ, Yang XW, Chen YB, Zhang DW, Jiang XF, Xue P. Exosomal miR-21 regulates the TETs/PTENp1/PTEN pathway to promote hepatocellular carcinoma growth. *Mol Canc* 2019;18:148.
- [65] Liang N, Chen Y, Yang L, He S, Liu T. Visfatin increases miR-21 to promote migration in HCC. *Cell Mol Biol* 2018;64:48–52.
- [66] Huang YH, Lin YH, Chi HC, Liao CH, Liao CJ, Wu SM, et al. Thyroid hormone regulation of miR-21 enhances migration and invasion of hepatoma. *Canc Res* 2013;73:2505–17.
- [67] Zheng J, Dong P, Gao S, Wang N, Yu F. High expression of serum miR-17-5p associated with poor prognosis in patients with hepatocellular carcinoma. *Hepato-Gastroenterology* 2013;60:549–52.
- [68] Chen L, Jiang M, Yuan W, Tang H. miR-17-5p as a novel prognostic marker for hepatocellular carcinoma. *J Invest Surg* 2012;25:156–61.
- [69] Yang F, Yin Y, Wang F, Wang Y, Zhang L, Tang Y, et al. miR-17-5p Promotes migration of human hepatocellular carcinoma cells through the p38 mitogen-activated protein kinase-heat shock protein 27 pathway. *Hepatology* 2010;51:1614–23.
- [70] Lu Z, Li X, Xu Y, Chen M, Chen W, Chen T, et al. microRNA-17 functions as an oncogene by downregulating Smad3 expression in hepatocellular carcinoma. *Cell Death Dis* 2019;10:723.
- [71] Liu DL, Lu LL, Dong LL, Liu Y, Bian XY, Lian BF, et al. miR-17-5p and miR-20a-5p suppress postoperative metastasis of hepatocellular carcinoma via blocking HGF/ERBB3-NF-kappaB positive feedback loop. *Theranostics* 2020;10:3668–83.
- [72] Dhanasekaran R, Gabay-Ryan M, Baylot V, Lai I, Mosley A, Huang X, et al. Anti-miR-17 therapy delays tumorigenesis in MYC-driven hepatocellular carcinoma (HCC). *Oncotarget* 2018;9:5517–28.
- [73] Lin YH, Liao CJ, Huang YH, Wu MH, Chi HC, Wu SM, et al. Thyroid hormone receptor represses miR-17 expression to enhance tumor metastasis in human hepatoma cells. *Oncogene* 2013;32:4509–18.
- [74] Pang C, Huang G, Luo K, Dong Y, He F, Du G, et al. miR-206 inhibits the growth of hepatocellular carcinoma cells via targeting CDK9. *Canc Med* 2017;6:2398–409.
- [75] Wang Y, Tai Q, Zhang J, Kang J, Gao F, Zhong F, et al. MiRNA-206 inhibits hepatocellular carcinoma cell proliferation and migration but promotes apoptosis by modulating cMET expression. *Acta Biochim Biophys Sin* 2019;51:243–53.
- [76] Yang Q, Zhang L, Zhong Y, Lai L, Li X. miR-206 inhibits cell proliferation, invasion, and migration by down-regulating

- PTP1B in hepatocellular carcinoma. *Biosci Rep* 2019;39:BSR20181823.
- [77] Liu C, Li J, Wang W, Zhong X, Xu F, Lu J. miR-206 inhibits liver cancer stem cell expansion by regulating EGFR expression. *Cell Cycle* 2020;19:1077–88.
- [78] Zheng Y, Zhao C, Zhang N, Kang W, Lu R, Wu H, et al. Serum microRNA miR-206 is decreased in hyperthyroidism and mediates thyroid hormone regulation of lipid metabolism in HepG2 human hepatoblastoma cells. *Mol Med Rep* 2018;17:5635–41.
- [79] Whittaker R, Loy PA, Sisman E, Suyama E, Aza-Blanc P, Ingemann RS, et al. Identification of MicroRNAs that control lipid droplet formation and growth in hepatocytes via high-content screening. *J Biomol Screen* 2010;15:798–805.
- [80] Yap CS, Sinha RA, Ota S, Katsuki M, Yen PM. Thyroid hormone negatively regulates CDX2 and SOAT2 mRNA expression via induction of miRNA-181d in hepatic cells. *Biochem Biophys Res Commun* 2013;440:635–9.
- [81] Shin H, Kim Y, Kim M, Lee Y. BC200 RNA: an emerging therapeutic target and diagnostic marker for human cancer. *Mol Cell* 2018;41:993–9.
- [82] Booy EP, McRae EK, Koul A, Lin F, McKenna SA. The long non-coding RNA BC200 (BCYRN1) is critical for cancer cell survival and proliferation. *Mol Canc* 2017;16:109.
- [83] Gu L, Lu L, Zhou D, Liu Z. Long noncoding RNA BCYRN1 promotes the proliferation of colorectal cancer cells via up-regulating NPR3 expression. *Cell Physiol Biochem : Int J Exp Cell Phys Biochem Pharm* 2018;48:2337–49.
- [84] Tan N, Zhu B, Shu H, Tao YF, Wu JR, Fang M, et al. Effect of lncRNABC200 on proliferation and migration of liver cancer cells in vitro and in vivo. *Oncol Rep* 2020;43:461–70.
- [85] Lin YH, Wu MH, Huang YH, Yeh CT, Chi HC, Tsai CY, et al. Thyroid hormone negatively regulates tumorigenesis through suppression of BC200. *Endocr Relat Canc* 2018;25:967–79.
- [86] Lin YH, Wu MH, Huang YH, Yeh CT, Lin KH. TUG1 is a regulator of AFP and serves as prognostic marker in non-hepatitis B non-hepatitis C hepatocellular carcinoma. *Cells* 2020;9:262.
- [87] Huang PS, Lin YH, Chi HC, Tseng YH, Chen CY, Lin TK, et al. Dysregulated FAM215A stimulates LAMP2 expression to confer drug-resistant and malignant in human liver cancer. *Cells* 2020;9:961.
- [88] Jiang B, Yang B, Wang Q, Zheng X, Guo Y, Lu W. lncRNA PVT1 promotes hepatitis B virus-positive liver cancer progression by disturbing histone methylation on the cMyc promoter. *Oncol Rep* 2020;43:718–26.
- [89] Qu A, Yang Q. lncRNA SNHG1 promotes cell progression and metastasis via sponging miR-377-3p in hepatocellular carcinoma. *Neoplasia* 2020;67:557–66.
- [90] Zhao Q, Wu C, Wang J, Li X, Fan Y, Gao S, et al. lncRNA SNHG3 promotes hepatocellular tumorigenesis by targeting miR-326. *Tohoku J Exp Med* 2019;249:43–56.
- [91] Yang X, Sun L, Wang L, Yao B, Mo H, Yang W. lncRNA SNHG7 accelerates the proliferation, migration and invasion of hepatocellular carcinoma cells via regulating miR-122-5p and RPL4. *Biomedicine & pharmacotherapy = Biomedicine & pharmacotherapie* 2019;118:109386.
- [92] Li Y, Zhuang W, Huang M, Li X. Long noncoding RNA DDX11-AS1 epigenetically represses LATS2 by interacting with EZH2 and DNMT1 in hepatocellular carcinoma. *Biochem Biophys Res Commun* 2019;514:1051–7.
- [93] Wei Y, Wang Z, Zong Y, Deng D, Chen P, Lu J. lncRNA MFI2-AS1 promotes HCC progression and metastasis by acting as a competing endogenous RNA of miR-134 to upregulate FOXM1 expression. *Biomed Pharmacother* 2020;125:109890.
- [94] Dai Q, Deng J, Zhou J, Wang Z, Yuan XF, Pan S, et al. Long non-coding RNA TUG1 promotes cell progression in hepatocellular carcinoma via regulating miR-216b-5p/DLX2 axis. *Canc Cell Int* 2020;20:8.
- [95] Refai NS, Louka ML, Halim HY, Montasser I. Long non-coding RNAs (CASC2 and TUG1) in hepatocellular carcinoma: clinical significance. *J Gene Med* 2019;21:e3112.
- [96] He C, Liu Z, Jin L, Zhang F, Peng X, Xiao Y, et al. lncRNA TUG1-mediated Mir-142-3p downregulation contributes to metastasis and the epithelial-to-mesenchymal transition of hepatocellular carcinoma by targeting ZEB1. *Cell Physiol Biochem : Int J Exp Cell Phys Biochem Pharm* 2018;48:1928–41.
- [97] Lv J, Kong Y, Gao Z, Liu Y, Zhu P, Yu Z. lncRNA TUG1 interacting with miR-144 contributes to proliferation, migration and tumorigenesis through activating the JAK2/STAT3 pathway in hepatocellular carcinoma. *Int J Biochem Cell Biol* 2018;101:19–28.
- [98] Li J, Zhang Q, Fan X, Mo W, Dai W, Feng J, et al. The long noncoding RNA TUG1 acts as a competing endogenous RNA to regulate the Hedgehog pathway by targeting miR-132 in hepatocellular carcinoma. *Oncotarget* 2017;8:65932–45.
- [99] Zhao Y, Butler EB, Tan M. Targeting cellular metabolism to improve cancer therapeutics. *Cell Death Dis* 2013;4:e532.
- [100] Lin YH, Wu MH, Huang YH, Yeh CT, Cheng ML, Chi HC, et al. Taurine up-regulated gene 1 functions as a master regulator to coordinate glycolysis and metastasis in hepatocellular carcinoma. *Hepatology* 2018;67:188–203.
- [101] Fu Y, Biglia N, Wang Z, Shen Y, Risch HA, Lu L, et al. Long non-coding RNAs, ASAP1-IT1, FAM215A, and LINC00472, in epithelial ovarian cancer. *Gynecol Oncol* 2016;143:642–9.
- [102] Yang H, Jiang Z, Wang S, Zhao Y, Song X, Xiao Y, et al. Long non-coding small nucleolar RNA host genes in digestive cancers. *Canc Med* 2019;8:7693–704.
- [103] Shuwen H, Xi Y, Quan Q, Yin J, Miao D. Can small nucleolar RNA be a novel molecular target for hepatocellular carcinoma? *Gene* 2020;733:144384.
- [104] Thin KZ, Tu JC, Raveendran S. Long non-coding SNHG1 in cancer. *Clinica chimica acta. Int J Clin Chem* 2019;494:38–47.
- [105] Li SJ, Wang L, Sun ZX, Sun SJ, Gao J, Ma RL. lncRNA SNHG1 promotes liver cancer development through inhibiting p53 expression via binding to DNMT1. *Eur Rev Med Pharmacol Sci* 2019;23:2768–76.
- [106] Li W, Dong X, He C, Tan G, Li Z, Zhai B, et al. lncRNA SNHG1 contributes to sorafenib resistance by activating the Akt pathway and is positively regulated by miR-21 in hepatocellular carcinoma cells. *J Exp Clin Canc Res* 2019;38:183.
- [107] Huang D, Wei Y, Zhu J, Wang F. Long non-coding RNA SNHG1 functions as a competitive endogenous RNA to regulate PDCD4 expression by sponging miR-195-5p in hepatocellular carcinoma. *Gene* 2019;714:143994.
- [108] Zhang T, Cao C, Wu D, Liu L. SNHG3 correlates with malignant status and poor prognosis in hepatocellular carcinoma. *Tumour Biol* 2016;37:2379–85.
- [109] Zhang PF, Wang F, Wu J, Wu Y, Huang W, Liu D, et al. lncRNA SNHG3 induces EMT and sorafenib resistance by modulating the miR-128/CD151 pathway in hepatocellular carcinoma. *J Cell Physiol* 2019;234:2788–94.
- [110] Shi M, Zhang XY, Yu H, Xiang SH, Xu L, Wei J, et al. DDX11-AS1 as potential therapy targets for human hepatocellular carcinoma. *Oncotarget* 2017;8:44195–202.
- [111] Liu H, Zhang Z, Wu N, Guo H, Zhang H, Fan D, et al. Integrative analysis of dysregulated lncRNA-associated ceRNA Network reveals functional lncRNAs in gastric cancer. *Genes* 2018;9:303.

- [112] Lekka E, Hall J. Noncoding RNAs in disease. *FEBS Lett* 2018;592:2884–900.
- [113] Hombach S, Kretz M. Non-coding RNAs: classification, biology and functioning. *Adv Exp Med Biol* 2016;937:3–17.
- [114] Shi DM, Shi XL, Xing KL, Zhou HX, Lu LL, Wu WZ. miR-296-5p suppresses stem cell potency of hepatocellular carcinoma cells via regulating Brg1/Sall4 axis. *Cell Signal* 2020;72:109650.
- [115] Ji L, Lin Z, Wan Z, Xia S, Jiang S, Cen D, et al. miR-486-3p mediates hepatocellular carcinoma sorafenib resistance by targeting FGFR4 and EGFR. *Cell Death Dis* 2020;11:250.
- [116] Wu MZ, Fu T, Chen JX, Lin YY, Yang JE, Zhuang SM. LncRNA GOLGA2P10 is induced by PERK/ATF4/CHOP signaling and protects tumor cells from ER stress-induced apoptosis by regulating Bcl-2 family members. *Cell Death Dis* 2020;11:276.
- [117] Wang C, Zi H, Wang Y, Li B, Ge Z, Ren X. LncRNA CASC15 promotes tumour progression through SOX4/Wnt/beta-catenin signalling pathway in hepatocellular carcinoma. *Artif Cells Nanomed Biotechnol* 2020;48:763–9.
- [118] Hassan MM, Kaseb A, Li D, Patt YZ, Vauthey JN, Thomas MB, et al. Association between hypothyroidism and hepatocellular carcinoma: a case-control study in the United States. *Hepatology* 2009;49:1563–70.
- [119] Shih YL, Huang YH, Lin KH, Chu YD, Yeh CT. Identification of functional thyroid stimulating hormone receptor and TSHR gene mutations in hepatocellular carcinoma. *Anticancer Res* 2018;38:2793–802.
- [120] Chi HC, Chen SL, Lin SL, Tsai CY, Chuang WY, Lin YH, et al. Thyroid hormone protects hepatocytes from HBx-induced carcinogenesis by enhancing mitochondrial turnover. *Oncogene* 2017;36:5274–84.
- [121] Chi HC, Chen SL, Tsai CY, Chuang WY, Huang YH, Tsai MM, et al. Thyroid hormone suppresses hepatocarcinogenesis via DAPK2 and SQSTM1-dependent selective autophagy. *Autophagy* 2016;12:2271–85.
- [122] Tseng YH, Huang YH, Lin TK, Wu SM, Chi HC, Tsai CY, et al. Thyroid hormone suppresses expression of stathmin and associated tumor growth in hepatocellular carcinoma. *Sci Rep* 2016;6:38756.
- [123] Chi HC, Tsai CY, Tsai MM, Yeh CT, Lin KH. Molecular functions and clinical impact of thyroid hormone-triggered autophagy in liver-related diseases. *J Biomed Sci* 2019;26:24.

Available online at www.sciencedirect.com

ScienceDirect

journal homepage: www.jfma-online.com

Original Article

Palbociclib induces DNA damage and inhibits DNA repair to induce cellular senescence and apoptosis in oral squamous cell carcinoma

Tong-Hong Wang^{a,b,c,1}, Chin-Chuan Chen^{a,d,1}, Yann-Lii Leu^{a,d},
Yun-Shien Lee^{e,f}, Jang-Hau Lian^f, Hsi-Lung Hsieh^{b,g,**},
Chi-Yuan Chen^{a,b,*}

^a Tissue Bank, Chang Gung Memorial Hospital, Tao-Yuan 33305, Taiwan

^b Graduate Institute of Health Industry Technology and Research Center for Chinese Herbal Medicine, College of Human Ecology, Chang Gung University of Science and Technology, Tao-Yuan 33303, Taiwan

^c Liver Research Center, Department of Hepato-Gastroenterology, Chang Gung Memorial Hospital, Tao-Yuan 33305, Taiwan

^d Graduate Institute of Natural Products, Chang Gung University, Tao-Yuan 33303, Taiwan

^e Department of Biotechnology, Ming Chuan University, 5 De Ming Rd., Taoyuan City 333, Taiwan

^f Genomic Medicine Research Core Laboratory, Chang Gung Memorial Hospital, Tao-Yuan 33305, Taiwan

^g Department of Neurology, Chang Gung Memorial Hospital, Tao-Yuan 33305, Taiwan

Received 7 August 2020; received in revised form 24 November 2020; accepted 2 December 2020

KEYWORDS

Palbociclib;
DNA damage;
DNA repair;
Senescence;
Oral squamous cell
carcinoma

Background/purpose: Palbociclib is an FDA-approved cyclin-dependent kinase (CDK) 4/6 inhibitor that has been clinically proven to be effective in breast cancer. However, its use in oral cancer is not well researched. In this study, we investigated the inhibitory activity of palbociclib against oral squamous cell carcinoma (OSCC) cells and explored the mechanism of inhibition.

Methods: The effects of palbociclib on the cytotoxicity of OSCC cells were determined by MTT and colony formation assays. β -Galactosidase staining and cell-cycle analysis were used to determine palbociclib-induced cellular senescence and apoptosis of OSCC cells. Wound healing and transwell assays were performed to assess the effects of palbociclib treatment on migration and invasion ability of OSCC cells. Whole transcriptome sequencing was conducted to show the relationship between DNA damage repair of OSCC cells and palbociclib treatment.

* Corresponding author. Tissue Bank, Chang Gung Memorial Hospital, Tao-Yuan, 33305 Taiwan. Fax: +886 3 4226062.

** Corresponding author. Graduate Institute of Health Industry Technology and Research Center for Chinese Herbal Medicine, College of Human Ecology, Chang Gung University of Science and Technology, Tao-Yuan 33303, Taiwan. Fax: +886 3 4226062.

E-mail addresses: hlhsieh@mail.cgu.edu.tw (H.-L. Hsieh), d49417002@gmail.com (C.-Y. Chen).

¹ These authors contributed equally to this work.

<https://doi.org/10.1016/j.jfma.2020.12.009>

0929-6646/Copyright © 2020, Formosan Medical Association. Published by Elsevier Taiwan LLC. This is an open access article under the CC BY-NC-ND license (<http://creativecommons.org/licenses/by-nc-nd/4.0/>).

Please cite this article as: Wang T-H et al., Palbociclib induces DNA damage and inhibits DNA repair to induce cellular senescence and apoptosis in oral squamous cell carcinoma, Journal of the Formosan Medical Association, <https://doi.org/10.1016/j.jfma.2020.12.009>

Palbociclib-induced DNA damage and repair capacity of OSCC cells were confirmed by comet assay and immunofluorescence confocal microscopy. Western blotting was used to verify the palbociclib-mediated changes in the CDK/pRB/c-Myc/CDC25A pathway. Finally, in vitro findings were tested in a mouse xenograft model.

Results: Our results showed that palbociclib can significantly inhibit the growth, migration, and invasive ability of OSCC cells and can accelerate cellular senescence and apoptosis. We found that palbociclib induced DNA damage and p21 expression through the p53-independent pathway, thereby downregulating c-Myc and CDC25A expression to inhibit cell cycle progression. In addition, palbociclib downregulated RAD51 expression to inhibit DNA damage repair ability of OSCC cell.

Conclusion: Palbociclib was found to have anti-oral squamous cell carcinoma activity and to simultaneously induce DNA damage and inhibit its repair, and to accelerated cellular senescence and apoptosis.

Copyright © 2020, Formosan Medical Association. Published by Elsevier Taiwan LLC. This is an open access article under the CC BY-NC-ND license (<http://creativecommons.org/licenses/by-nc-nd/4.0/>).

Introduction

According to the World Health Organization (WHO), in 2018, oral cancer ranked fourth highest in incidence worldwide. Approximately 300,000 people worldwide are diagnosed with oral cancer each year, of which, around 90% are diagnosed with oral squamous cell carcinoma (OSCC).¹ Currently, the main treatment for OSCC is surgical resection combined with radiotherapy or chemotherapy with drugs such as 5-Fu, doxorubicin, and cisplatin.^{2–4} Due to the high metastatic ability of OSCC, the treatment outcome remains unsatisfactory with 5-year survival rate of advanced OSCC patients lower than 30%.^{5,6} Moreover, the side effects of chemotherapeutic drugs greatly reduce the quality of life of patients. Therefore, there is an urgent need to develop new drugs or treatment strategies to improve the treatment of oral cancer.

The risk factors for OSCC include smoking, drinking, chewing tobacco or betel nuts, as well as viral infections and genetic mutations that lead to cancerous cells.^{7,8} Previous studies found that about 70% of OSCC tissues overexpress EGFR (EGFR/ErbB1/HER1), and that the EGFR expression level is significantly positively correlated with the malignancy of OSCC.^{9–11} Many EGFR inhibitors consist of anti-EGFR antibodies (cetuximab and panitumumab) or small-molecule tyrosine kinase inhibitors (gefitinib and erlotinib), which have been developed and tested for their efficacy in OSCC.^{12–15} Among them, cetuximab has been approved by the FDA for the treatment of OSCC because it can markedly inhibit the progression of OSCC and prolong the survival of patients.¹⁶ However, only about 50% of patients respond to cetuximab.^{17,18} Immune checkpoint inhibitors including pembrolizumab and nivolumab have also been approved for the treatment of OSCC, but they are only effective in less than 20% of patients, signaling a need to develop more effective treatment strategies.^{19,20}

In addition to EGFR overexpression, the overexpression of cyclin D1 and the deletion of p16 are also commonly observed in OSCC.^{21,22} The abnormal expression of these

cell cycle checkpoint regulators leads to uncontrolled cell cycle, resulting in aberrant cell proliferation and carcinogenesis. Therefore, inhibiting the activation or expression of cell cycle regulators is one of the main treatment strategies for oral cancer. As an FDA approved CDK4/6 inhibitor, palbociclib can specifically inhibit the activity of CDK4/6, and therefore inhibit the phosphorylation of retinoblastoma protein (Rb).²³ This reduces the expression of E2F-dependent genes, blocks the G1 to S phase of the cell cycle and inhibits the proliferation of tumor.^{24–27} It has been clinically proven that palbociclib is effective in breast cancer and can significantly prolong the survival of patients^{28,29}; however, its efficacy in OSCC and mechanism of action have been scarcely discussed. In this study, we tested the inhibitory activity of palbociclib against oral cancer and explored its mechanism of action to determine its therapeutic potential for oral cancer.

Materials and methods

Cell lines

SAS is a high-grade human tongue squamous cell carcinoma from the Japanese Collection of Research Bioresources (Tokyo, Japan). OEM1 is a non-tumorigenic Taiwanese human gingival squamous carcinoma cell, derivative according to previous study. Both cell lines were cultured in Dulbecco's modified Eagle's medium (DMEM) containing 10% fetal bovine serum (FBS), 1.2 g/L sodium bicarbonate, 0.5 mM sodium pyruvate, and 2.5 mM L-glutamine. Culture media, FBS, and chemical compounds were purchased from Life Technologies (Grand Island, NY, USA). Cells were grown at 37 °C in a humidified 5% CO₂ incubator.

Reagents and antibodies

Palbociclib was purchased from Sigma–Aldrich (St. Louis, MO, USA). Polyclonal antibodies against p21, RB, phospho-

RB, c-Myc, CDC25A, γ -H2AX, β -actin were purchased from Genetex (Irvine, CA) and Cell Signaling Technology (Beverly, MA). Secondary antibodies were purchased from Santa Cruz Biotechnology (Santa Cruz, CA). Gel electrophoresis reagents were purchased from Bio-Rad (Berkeley, CA, USA).

Assay for cell viability and clonogenic formation ability

Cell viability was carried out by seeding 3000 cells/well into 96-well plates. After 24 h, the cells were treated with different concentrations of palbociclib and then incubated for 48 h. Cell viability was detected using the MTT assay as described previously.³⁰ For clonogenic formation ability, the cells were seeded into six-well plates (500 cells/well), and treated with various concentrations of palbociclib for 24 h. The treated cells were then incubated in the absence of palbociclib for eight days, stained with crystal violet, and the number of foci formation was measured.

Phenotypic analysis for migration and invasion ability by wound healing assay and transwell assay

The migration and invasion assays were performed as described previously.³¹

Senescence β -galactosidase staining

Cells were fixed and then incubated at 37 °C for 18 h with a staining solution (40 mmol/L citric acid, sodium phosphate, pH 6.0, 1 mg/mL 5-bromo-4-chloro-3-isolyl- β -D-galactoside (X-gal, sigma), 5 mmol/L potassium ferrocyanide, 5 mmol/L potassium ferricyanide, 150 mmol/L NaCl, and 2 mmol/L MgCl₂). Senescence-associated- β -gal- positive cells were observed by microscopy, and over 100 cells were counted in five independent fields.

Comet assay

SAS and OECM1 cells were seeded to 24-well plates (4×10^4 cells per well), incubated for 16 h, and treated with 200 μ M etoposide for 1 h. The etoposide was then washed out with PBS, and the cells were treated with different concentrations of palbociclib or DMSO in etoposide-free medium for 4 h. The cells were trypsinized, washed with ice-cold PBS, and subjected to comet assay as described previously. Comet images were obtained using a fluorescence microscope (Nikon ECLIPSE Ni-U plus), and the tail moment was calculated using Open comet software.

Immunofluorescence confocal microscopy

Immunofluorescence staining of target proteins was performed as described previously [46]. Briefly, cells on slides were fixed in 4% paraformaldehyde, permeabilized, and stained with anti- γ H2AX antibodies. After washing three times with phosphate buffer saline (PBS) containing 0.1% Triton X-100, cells were incubated with fluorescein isothiocyanate (FITC)-conjugated secondary antibodies (Molecular Probes, Eugene, OR, USA). Immunofluorescence

analyses were carried out under a confocal microscope (LSM 700; Carl Zeiss, Jena, Germany) and images were processed using Zen 2009 software (Carl Zeiss).

Real-time reverse transcription-polymerase chain reaction (RT-PCR) analysis

Total RNA from SAS and OECM1 cells was extracted using TOOLS[®] RNA extractor (BIOTOOLS, new Taipei city, Taiwan) and RNeasy Mini Kit (QIAGEN, Gaithersburg, MD, USA) according to the manufacturer's instructions. Complementary DNA (cDNA) was synthesized using a ToolScript MMLV RT Kit (BIOTOOLS Co., Ltd., Taiwan). The expression of CDC25A, RAD51, and p21 was analyzed using the following primer set: CDC25A: 5'-GAGGAGTCTCCACCTG-GAAGTACA-3' (forward) and 5'-GCCATTCAAACAGATGCCA-TAA-3' (reverse); RAD51: 5'-TGGCCCAACCCATTTCAC-3' (forward) and 5'-TCAATGTACATGGCCTTCCTTCAC-3' (reverse); p21: 5'-TGAGCCGCGACTGTGATG-3' (forward) and 5'-GTCTCGGTGACAAAGTCGAAGTT-3' (reverse). TOOLS 2x SYBR qPCR Mix (BIOTOOLS Co., Ltd., Taiwan) and an ABI StepOnePlus[™] System (Applied Biosystems, Foster City, CA, USA) were used. Glyceraldehyde-3-phosphate dehydrogenase (GAPDH) was used as an internal control.

Western blotting

Cells were washed twice with phosphate-buffered saline (PBS) and lysed in 200 μ L of RIPA lysis buffer (BIOTOOLS CO., LTD., Taiwan) containing protease inhibitors, and incubated on ice for 10 min. The samples were centrifuged at 12,000 rpm for 30 min at 4 °C, and the protein-containing supernatants were collected. Protein concentrations were determined using the Bio-Rad protein assay, and Western blotting was performed as described previously.³²

Cell-cycle analysis

Cells were trypsinized, washed twice, and fixed with pre-cooled 70% ethanol at -20 °C for 1 h. The fixed cells were subsequently incubated in phosphate-buffered saline (PBS) containing 0.12% Triton X-100, 0.12 mmol/L EDTA, and 100 mg/mL ribonuclease A. Propidium iodide (50 μ g/mL) was then added to each sample for 20 min at 4 °C. Cell cycle distribution was analyzed by flow cytometry (Beckman Coulter Epics Elite, Beckman, Inc.).

Whole-transcriptome sequencing

RNA from cells was isolated using a RNeasy mini kit (QIAGEN, Gaithersburg, MD, USA), according to the manufacturer's instructions. The whole-transcriptome sequencing was performed as previously described.³²

In vivo xenograft experiments

SAS cells (5×10^5) were injected subcutaneously into the back of six-week-old male Balb/c nude mice (NARLabs, Taipei, Taiwan) on day 0. Seven days post-implantation, mice were randomized into two experimental groups (n = 5 per group):

vehicle control (0.05 N lactic acid) and palbociclib treatment (120 mg/kg body weight). Treatment was administered daily by oral gavage, and tumor volumes (V) were calculated as $V = 0.5 \times (\text{length} \times \text{width}^2)$ twice weekly. After 16 days, the mice were sacrificed, and tumors were harvested and weighed. All animal experiments were performed under an approved protocol in accordance with the guidelines for the Animal Care Ethics Commission of Chang Gung University (IACUC approval no.: CGU106-168, approval date: 2020/1/17).

Immunohistochemistry

The tumors from the mice were fixed in formalin and embedded in paraffin. Consecutive 2- μm -thick sections were cut from the paraffin-embedded tissue blocks and floated onto glass slides. The slide-mounted tissue sections were subjected to immunohistochemical staining as described previously.³²

Statistics

Comparisons between groups were analyzed using Student's t-tests. The results were expressed as the mean values \pm standard deviation. All statistical analyses were performed using the Statistical Package for the Social Sciences version 16.0 and Excel 2007 software. All p values were two-sided, with $p < 0.05$ considered to indicate a statistically significant difference.

Results

Palbociclib inhibits OSCC cell growth and accelerates cellular senescence and apoptosis

To determine if palbociclib inhibits OSCC cell proliferation, we treated OSCC cells and human fibroblast cells with

various concentrations of palbociclib and analyzed cell proliferation ability using the MTT assay. The results showed that compared to the vehicle control group, palbociclib inhibited the growth of SAS and OECM1 cells starting at 2 μM . The inhibitory effect became more pronounced as the drug concentration increased (Fig. 1A). In addition, palbociclib had a significantly stronger inhibitory effect on SAS cells than on OECM1 cells, with the half maximal inhibitory concentration (IC_{50}) being 7.94 μM and 11.64 μM , respectively. However, we did not observe growth inhibition of the human fibroblast cell line, HFB treated with palbociclib (Fig. 1A). The results indicate that palbociclib can selectively inhibit the growth of OSCC cells without significant toxicity to normal cells. We also examined the effect of palbociclib on OSCC colony formation. The results show that palbociclib significantly inhibited the colony formation of OSCC cell lines in a dose-dependent manner. Below 2 μM palbociclib, the colony formation ability of OSCC cells was suppressed by over 70% (Fig. 1B–C), and palbociclib showed a larger inhibitory effect on the highly malignant SAS cells than on the non-tumorigenic OECM1 cells. These results confirm the anti-OSCC activity of palbociclib.

To understand the mechanism by which palbociclib inhibits cell growth, we further analyzed the cell cycle changes in OSCC cells treated with palbociclib. The results show that compared with the control group, palbociclib-treated cells mostly remained in the G1 phase, and that the number of cells in the sub-G1 phase increased dramatically (Fig. 2A–B), showing that palbociclib can inhibit cell cycle progression as well as induce apoptosis. Using a cellular senescence assay, we found that the expression level of senescence-associated beta-galactosidase (SA- βgal) in SAS and OECM1 cells significantly increased after treatment with palbociclib compared to control, showing that palbociclib can accelerate cellular senescence (Fig. 2C–D).

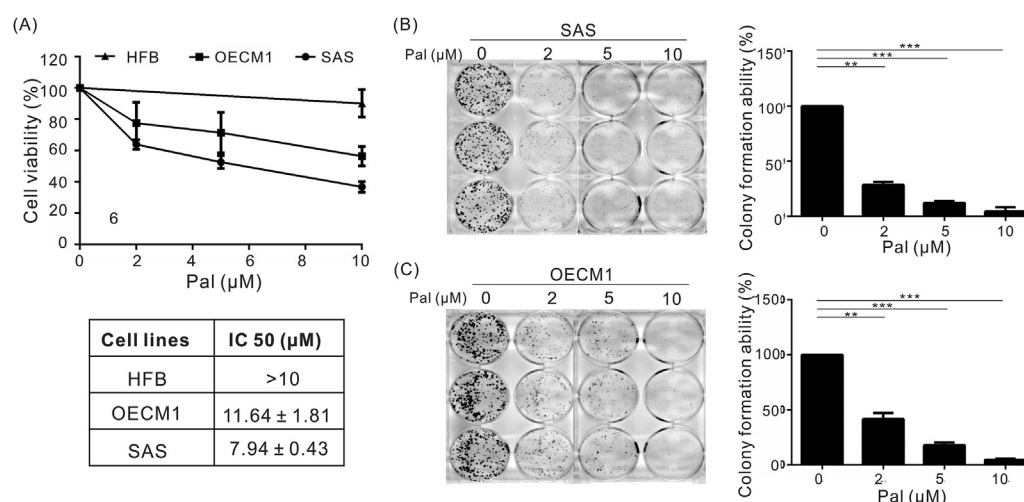


Figure 1 Palbociclib inhibits OSCC cell growth and colony formation. (A) Human skin fibroblast, SAS, and OECM1 cells were treated with different concentrations of palbociclib for 48 h. The viability of treated cells was determined by MTT assay. (B–C) SAS and OECM1 cells were treated with different concentrations of palbociclib for 24 h, and then culture for an additional eight days without palbociclib. Colonies were fixed with methanol and stained with 0.1% crystal violet (Sigma–Aldrich, St. Louis, MO, USA). Visible colonies were imaged and manually quantified (right panel). Data are expressed as mean \pm SD of three independent experiments. ** $p < 0.01$; and *** $p < 0.001$, as analyzed with the unpaired t-test.

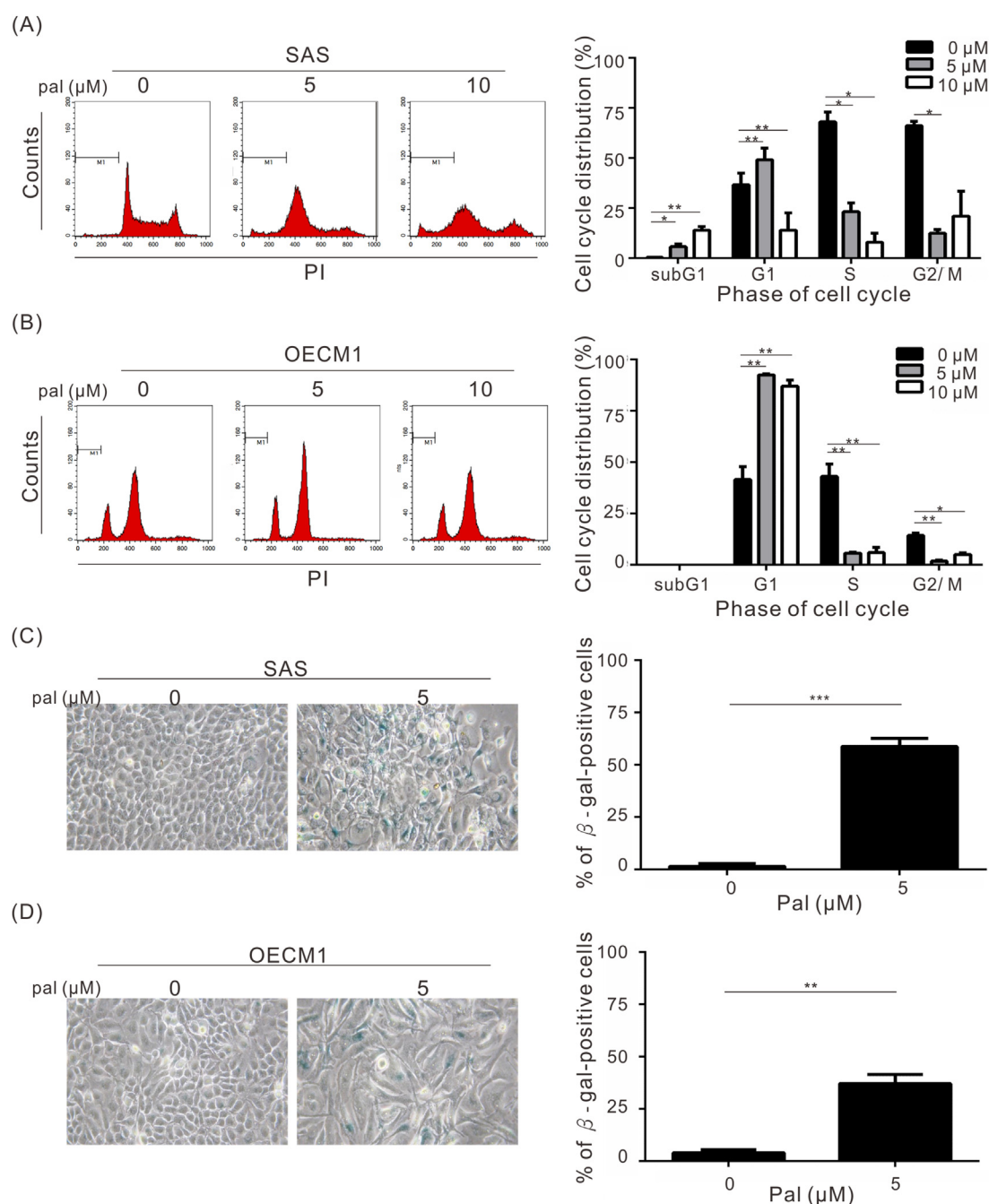


Figure 2 Palbociclib inhibits cell cycle progression and accelerates OSCC cellular senescence and apoptosis. (A, B) SAS and OECM1 cells were treated with stated concentrations of palbociclib for 48 h. The cell cycle distribution was measured by propidium iodide staining and quantified by flow cytometry. The quantitative results are shown in the right panels. (C, D) Cells were treated with palbociclib for 48 h, and the cellular senescence were determined by β -galactosidase staining. The β -gal positive cells were quantified and shown in the right panel. The data shown are expressed as the mean \pm SD of three independent experiments. * $p < 0.05$, ** $p < 0.01$, and *** $p < 0.001$, as analyzed by unpaired t-tests.

Palbociclib inhibits the migration and invasion ability of OSCC cells

Previous studies have revealed that oral cancer cells are highly invasive and metastatic, which in turn make them difficult to treat.³³ To determine if palbociclib can inhibit the migration and invasion ability of OSCC cells, we used

wound healing assays, transwell migration, and invasion assays to examine the effect of palbociclib on cell migration and invasion ability. The results show that 5 μ M palbociclib remarkably inhibited the migration ability of SAS cells, but did not affect the migration of non-tumorigenic OECM1 cells (Fig. 3A–B). Similar results were obtained with the transwell migration and invasion assay. Fig. 3C–D

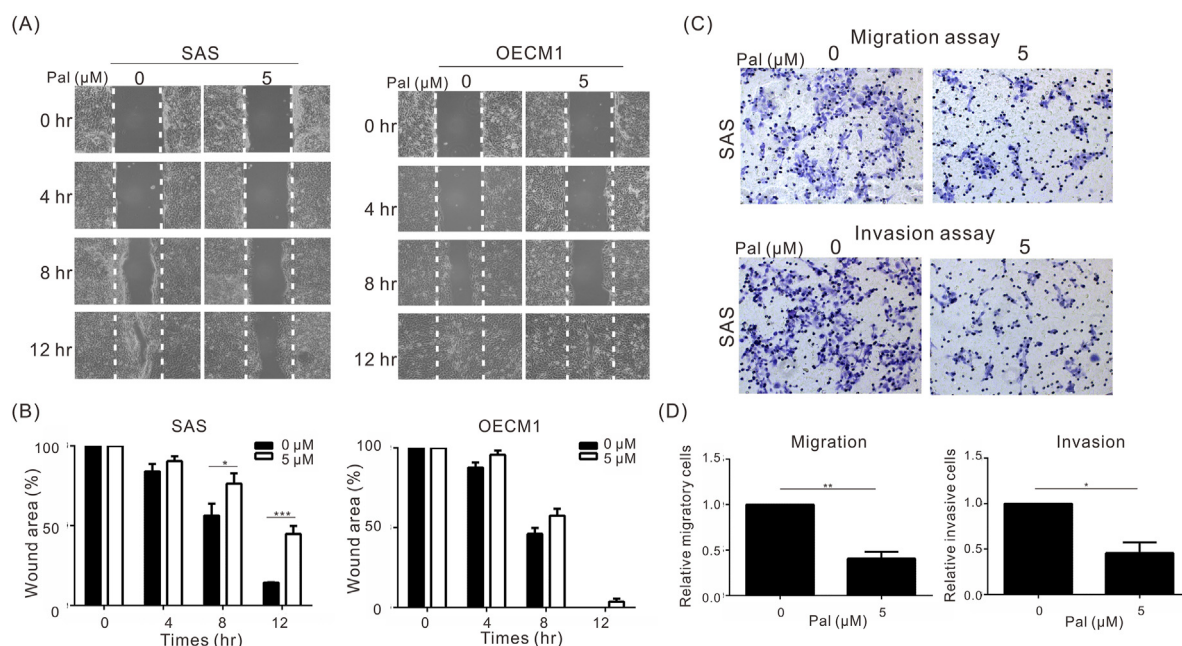


Figure 3 Palbociclib inhibits the migration and invasion abilities of OSCC cells. (A) The effect of palbociclib on the wound-healing ability of SAS and OECM1 cells. The quantitative results are shown in (B). (C) The effect of palbociclib on the transwell migration and invasiveness of SAS cells. Quantitative results are shown in (D). All data are expressed as the means \pm standard deviations of 3 independent experiments. * $p < 0.05$ and ** $p < 0.01$, and *** $p < 0.001$.

shows that palbociclib at a concentration of 5 μM , can inhibit cell migration and invasion by approximately 60%.

Palbociclib regulates cell cycle and signaling pathways related to DNA damage repair

In order to understand the anti-OSCC mechanism of palbociclib, we treated the SAS and OECM1 cell lines with palbociclib followed by whole transcriptome sequencing to analyze genes and signaling pathways. Fig. 4A shows that the gene expression pattern of palbociclib-treated cells is significantly different from that of the control group. We further performed ingenuity pathway analysis which revealed that palbociclib primarily regulated cell cycle, DNA replication, cellular senescence, and DNA repair mechanisms, such as base excision repair, mismatch repair, and homologous recombination (Fig. 4B–C), suggesting that palbociclib may inhibit cell growth and accelerate cellular senescence by inhibiting cell cycle progression and DNA repair.

Palbociclib induces DNA damage and inhibits DNA repair thereby accelerating apoptosis and cellular senescence

To confirm that palbociclib affects the ability of OSCC cells to repair DNA damage, we first treated the OSCC cells with the chemotherapeutic drug etoposide to induce DNA damage. This was followed by the comet assay to examine the effect of palbociclib on DNA damage repair. The results show that palbociclib-treated cells repaired DNA damage at a slower rate than the control cells (vehicle only) and in a

dose-dependent manner (Fig. 5A–B). Moreover, quantitative real-time RT-PCR and Western blot results also revealed that RNA and protein expression levels of the DNA repair regulatory protein RAD51 decreased substantially in the cell line treated with palbociclib (Fig. 5C–D), suggesting that palbociclib can inhibit RAD51 and consequently the progress of DNA repair.

We also detected DNA damage in OSCC cells treated with palbociclib alone using the comet assay (Fig. 5E–F). The results show that palbociclib treatment alone induced DNA damage in both OSCC cells. In addition, the expression of $\gamma\text{-H2AX}$, a DNA damage response marker, was analyzed by Western blot and immunofluorescence assay. As shown in Fig. 5D and 5G–J, palbociclib induced the expression of $\gamma\text{-H2AX}$ in both SAS and OECM1 cells in a dose-dependent manner, and SAS cells exhibited higher DNA damage response to palbociclib than OECM1 cells. Therefore, palbociclib can induce DNA damage and inhibit the DNA repair ability of cells, thus accelerating the senescence and apoptosis of OSCC cells.

Palbociclib can induce p21 expression through the p53-independent pathway to inhibit the CDK/pRB/c-Myc/CDC25A pathway

p21, a CDK inhibitor, plays an important role in the regulation of cell cycle and is closely associated with the regulation of cell differentiation, cellular senescence, and apoptosis.³⁴ Past studies have shown that DNA damage can induce p21 expression through a p53-dependent or p53-independent pathway, which in turn inhibits CDK4/6 activation and leads to cell cycle arrest.^{35,36} To determine if palbociclib inhibits cell growth through the above

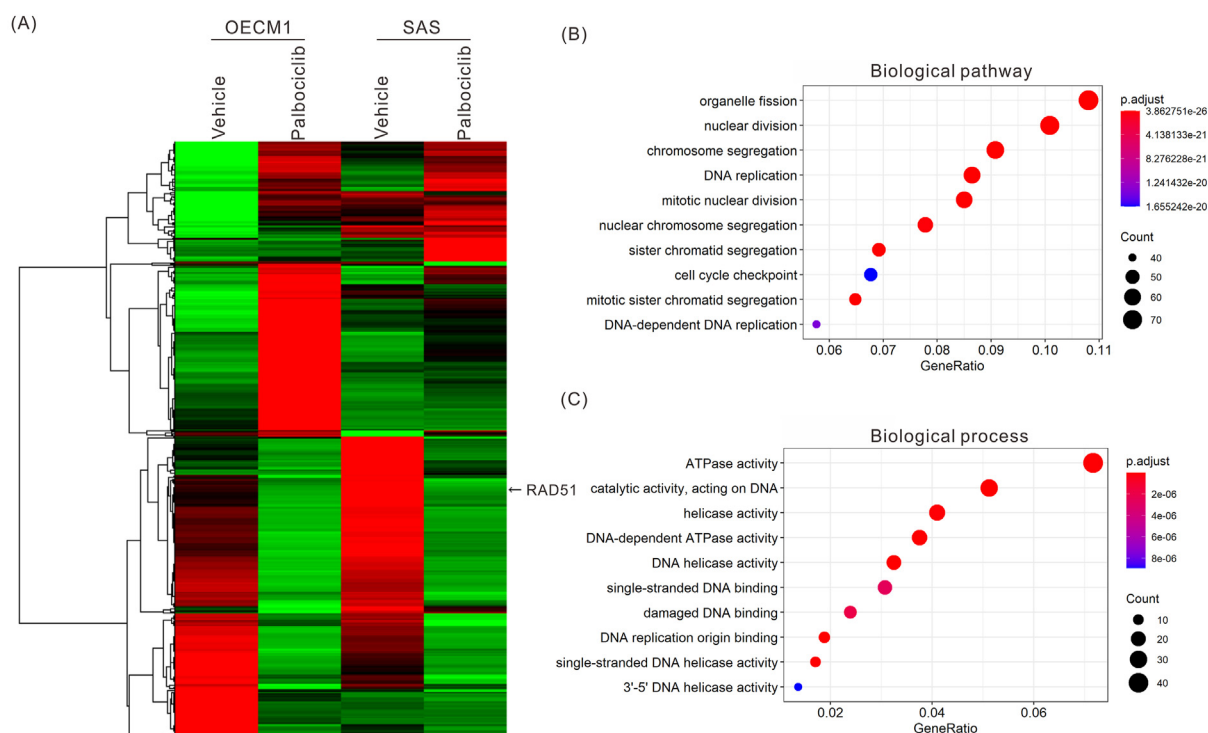


Figure 4 Palbociclib regulates cell cycle and signaling pathways related to DNA damage repair. (A) A heatmap showed the gene expression profile in SAS and OECM1 cells with or without palbociclib treatment (red and green indicate higher and lower expression, respectively). Bar charts represent the enriched biological pathways (B) and biological processes (C) associated with the differentially expressed genes after palbociclib treatment.

mechanism, we treated OECM1 (a point mutation at codon 173 of the p53) and SAS (p53 deficient) cell lines with palbociclib, and examined the effects on p21 and downstream cell cycle regulatory protein expression. We found that the expression levels of p21 mRNA and protein significantly increased in both cell lines treated with palbociclib, which inhibited activation of CDK and the phosphorylation of Retinoblastoma protein (Rb), thereby inhibiting the expression of E2F-regulated, c-Myc, and c-Myc-regulated, CDC25A. Consequently, palbociclib induced p21 expression through a p53-independent pathway and inhibited the activation and expression of downstream regulatory proteins in the cell cycle, thereby inhibiting the growth of OSCC cells (Fig. 6A–E).

Palbociclib suppresses tumor growth in mice

To verify the anti-OSCC effects of palbociclib, a mouse xenograft model was used to analyze the effects of palbociclib on tumor growth in mice. Compared with the control group, the tumor growth was significantly inhibited in the palbociclib treated group (Fig. 7A–D). This result indicated that palbociclib exhibited anti-OSCC activity *in vivo*.

Mouse tumor tissues were sectioned and subjected to immunohistochemical staining to analyze the expression of p21, phospho-Rb, c-Myc, CDC25A, and RAD51 genes. Our results were consistent with those from *in vitro* experiments which showed that palbociclib induced p21 expression, which inhibited the phosphorylation of Rb, thereby

downregulating c-Myc and CDC25A expression to inhibit OSCC growth (Fig. 7E–F).

Discussion

Palbociclib is a FDA approved CDK4/6 specific inhibitor that inhibits the phosphorylation of Rb and blocks cell cycle progression. Palbociclib has been clinically proven to be effective in breast cancer,^{37–39} but its use in oral cancer has rarely been explored. In this study, in addition to confirming the inhibitory activity of palbociclib on OSCC, we showed that palbociclib can induce DNA damage and inhibit CDK4/6 activity by inducing p21 expression through a p53-independent pathway, which in turn downregulates the expression of c-Myc and CDC25A and results in cell cycle arrest. Moreover, palbociclib can inhibit RAD51 expression and inhibit the ability of cells to repair DNA damage. To the best of our knowledge, this is the first demonstration that palbociclib can simultaneously induce DNA damage and inhibit its repair to accelerate cellular senescence and apoptosis.

To elucidate the tumor suppressor pathway regulated by palbociclib, we adopted whole transcriptome sequencing analysis to analyze the gene expression profile of OSCC cell lines treated with palbociclib. Through Kyoto Encyclopedia of Genes and Genomes (KEGG) pathway analysis, we found that palbociclib not only regulates cell cycle-related genes, but also cellular senescence and DNA damage repair pathways including base excision repair, mismatch repair, and homologous recombination. In this

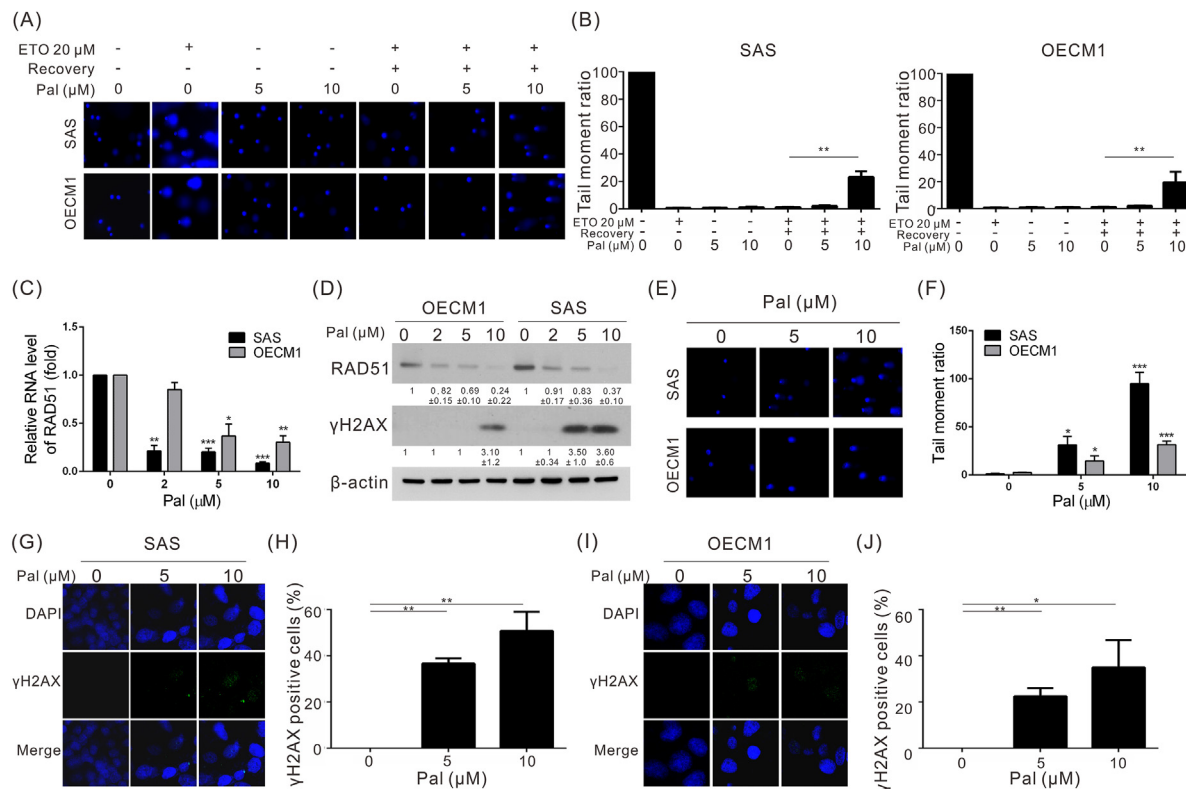


Figure 5 Palbociclib simultaneously induces DNA damage and inhibits DNA repair. (A) Comet assays represented the activity of DNA damage repair after treatment with different concentrations of palbociclib. SAS and OECM1 cells were treated with 20 μ M etoposide (ETO) for 1 h, followed by treatment with different concentrations of palbociclib in etoposide-free medium for 4 h. The cells were harvested and subjected to comet assays to detect the DNA repair activity. The quantitative DNA damage repair activity results are shown in (B). $p < 0.01$ (**). (C) SAS and OECM1 cells were treated with different concentrations of palbociclib for 48 h. The RNA levels of RAD51 were analyzed using quantitative real-time RT-PCR. GAPDH was used as an internal control. Cell lysates were subjected to western blotting to detect the level of RAD 51 and γ H2AX (D). β -Actin served as an internal control. (E) SAS and OECM1 cells were treated with different concentrations of palbociclib for 24h. The cells were harvested and subjected to comet assays. The quantitative DNA damage results are shown in (F). * $p < 0.05$ and *** $p < 0.001$. (G, I) SAS and OECM1 cells were treated with different concentrations of palbociclib for 48 h. Cells were fixed and immunostained for γ H2AX (green), and nuclei was counterstained with DAPI (blue). The percentage of γ H2AX cells were measured and shown in (H, J). Data shown are mean \pm SD from three independent experiments. * $p < 0.05$ and ** $p < 0.01$.

study, we also demonstrated that palbociclib can induce DNA damage and upregulate p21 expression to inhibit cell cycle progression. Palbociclib can also inhibit RAD51 expression to inhibit DNA repair. This leads to accelerated cellular senescence and apoptosis.

c-Myc is known to regulate the transcription of genes related to cellular senescence, including hTERT, p16, p53, Bmi-1, and p27.^{40–42} Nevertheless, there are related reports on its positive and negative regulation of senescence. Previous studies showed that c-Myc inactivation reduces histone H4 acetylation and increases histone H3 K9 methylation, thus inducing the senescence of untransformed cells (such as human fibroblasts) and various tumor cells.^{43,44} However, some studies imply that c-Myc can induce p14ARF transcription and p14ARF can bind to MDM2 to prevent p53 ubiquitination and degradation and accelerate cellular senescence and apoptosis.^{45,46} We speculated that palbociclib induces cellular senescence in part due to its inhibition of c-myc. However, as c-Myc regulates a wide

range of genes, its complex regulatory mechanism of senescence needs to be studied in depth.

Cell based assays suggested that palbociclib had a stronger inhibitory effect on SAS cells compared to OECM1 cells, whereas the comet assay and immunofluorescence staining showed that palbociclib was more effective in producing DNA damage in SAS cells compared to OECM1 cells (Fig. 5C, F-I). Furthermore, palbociclib exerted a markedly stronger inhibitory effect on RAD51 expression in SAS cells compared to OECM1 cells (Fig. 5C). One reason may be that SAS cells show better sensitivity to palbociclib, and another possibility is that the two strains differ in genetic background and produce varied responses to palbociclib. More work is required in the future to confirm this hypothesis and mechanism.

In conclusion, palbociclib was found to have anti-oral cancer activity and to simultaneously induce DNA damage and inhibit its repair, and to accelerate cellular senescence and apoptosis. The findings suggest that palbociclib has good potential for the clinical treatment of oral cancer.

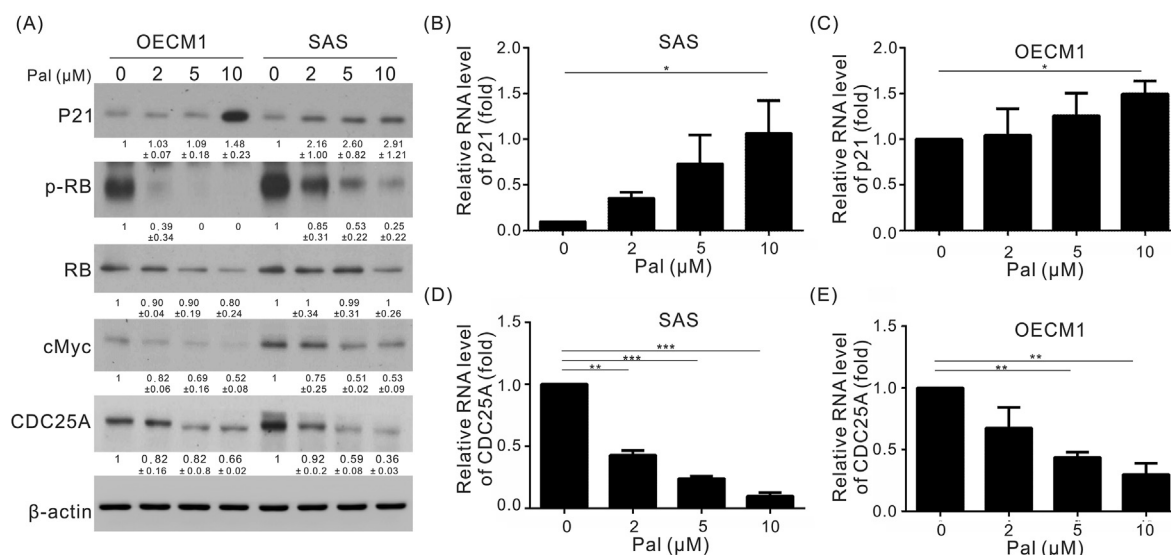


Figure 6 Palbociclib induces p21 expression through the p53-independent pathway and inhibits the activation of downstream cell cycle regulatory proteins. (A) SAS and OECM1 cells were treated with stated concentrations of palbociclib for 48 h. The expression levels of RB, phospho-RB (pRB), p21, CDC25A, and c-Myc were determined by Western blot. β -Actin served as an internal control. (B–E) SAS and OECM1 cells were treated with stated concentrations of palbociclib for 48 h. The RNA levels of p21 and CDC25A were analyzed using quantitative real-time RT-PCR. Error bars represent mean \pm standard deviation from three independent experiments. $p < 0.05$ (*), $p < 0.01$ (**), $p < 0.001$ (***).

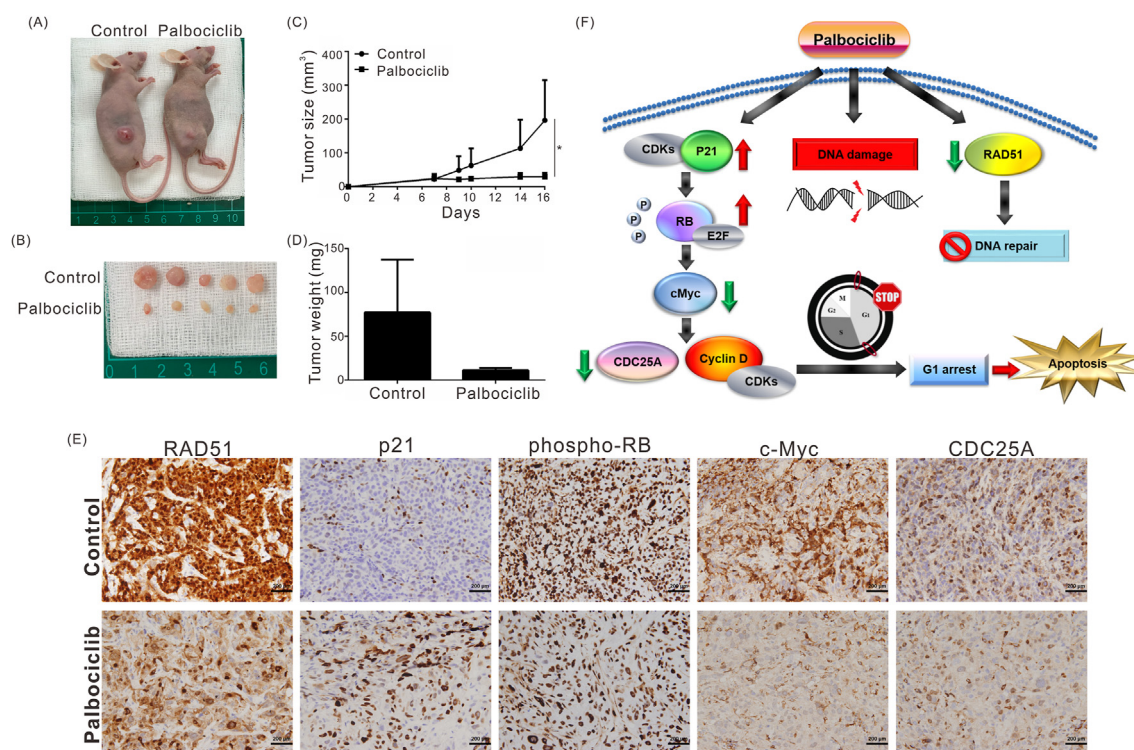


Figure 7 Palbociclib suppresses tumor growth in mice. (A–B) SAS cells (5×10^5) were injected into the back of nude mice ($n = 5$ per group) to induce tumor formation. Subsequently, the mice received palbociclib (120 mg/kg body weight) or vehicle (0.05N lactic acid) daily by oral gavage. Representative images show the tumor xenografts at 16 days after implantation. (C) Tumor volumes were calculated twice weekly after the injection of SAS cells. The volume of each tumor was calculated as follows: $0.5 \times (\text{length} \times \text{width}^2)$. Bars indicate S.D. * $p < 0.05$. (D) Tumor weights at the end point. (E) Immunohistochemical staining representing the effect of palbociclib on p21, phospho-Rb, c-Myc, CDC25A, and RAD51 expression in mice xenograft tumors. Magnification: $400 \times$. (F) Schematic representation summarizing the anti-OSCC mechanism of palbociclib.

Funding

This research was partially supported by the Ministry of Science and Technology of Taiwan (grant MOST 107-2320-B255-0), the Chang Gung Medical Research Program, Taiwan (CMRPF1H0013 and CMRPG3J0862), and Chang Gung University of Science and Technology (grant ZRRPF3K0111).

Declaration of competing interest

The authors have no conflicts of interest relevant to this article.

Acknowledgments

We thank the Tissue Bank at the Chang Gung Memorial Hospital, Lin-Kou, Taiwan for tissue processing and Yu-Han Lin, Chieh-Wen Chan, Ya-Min Shih, Fang-Ching Chuang, and Li-Shan Wei for their technical assistance in this project.

References

1. Bagan J, Sarrion G, Jimenez Y. Oral cancer: clinical features. *Oral Oncol* 2010;46(6):414–7.
2. Gau M, Karabajakian A, Reverdy T, Neidhardt EM, Fayette J. Induction chemotherapy in head and neck cancers: results and controversies. *Oral Oncol* 2019;95:164–9.
3. Li CC, Shen Z, Bavarian R, Yang F, Bhattacharya A. Oral cancer: genetics and the role of precision medicine. *Surg Oncol Clin* 2020;29(1):127–44.
4. Pons-Fuster Lopez E, Gomez Garcia F, Lopez Jornet P. Combination of 5-Fluorouracil and polyphenol EGCG exerts suppressive effects on oral cancer cells exposed to radiation. *Arch Oral Biol* 2019;101:8–12.
5. Marcazzan S, Varoni EM, Blanco E, Lodi G, Ferrari M. Nanomedicine, an emerging therapeutic strategy for oral cancer therapy. *Oral Oncol* 2018;76:1–7.
6. Wang B, Zhang S, Yue K, Wang XD. The recurrence and survival of oral squamous cell carcinoma: a report of 275 cases. *Chin J Canc* 2013;32(11):614–8.
7. Hashim D, Genden E, Posner M, Hashibe M, Boffetta P. Head and neck cancer prevention: from primary prevention to impact of clinicians on reducing burden. *Ann Oncol* 2019;30(5):744–56.
8. Rivera C. Essentials of oral cancer. *Int J Clin Exp Pathol* 2015;8(9):11884–94.
9. Xie X, Wang Z, Chen F, Yuan Y, Wang J, Liu R, et al. Roles of FGFR in oral carcinogenesis. *Cell Prolif* 2016;49(3):261–9.
10. Huang SF, Chien HT, Cheng SD, Chuang WY, Liao CT, Wang HM. EGFR copy number alterations in primary tumors, metastatic lymph nodes, and recurrent and multiple primary tumors in oral cavity squamous cell carcinoma. *BMC Canc* 2017;17(1):592.
11. Kimura I, Kitahara H, Ooi K, Kato K, Noguchi N, Yoshizawa K, et al. Loss of epidermal growth factor receptor expression in oral squamous cell carcinoma is associated with invasiveness and epithelial-mesenchymal transition. *Oncol Lett* 2016;11(1):201–7.
12. Cohen RB. Current challenges and clinical investigations of epidermal growth factor receptor (EGFR)- and ErbB family-targeted agents in the treatment of head and neck squamous cell carcinoma (HNSCC). *Canc Treat Rev* 2014;40(4):567–77.
13. Cripps C, Winquist E, Devries MC, Stys-Norman D, Gilbert R, Head, et al. Epidermal growth factor receptor targeted therapy in stages III and IV head and neck cancer. *Curr Oncol* 2010;17(3):37–48.
14. Shahoumi LA, Yeudall WA. Targeted therapies for non-HPV-related head and neck cancer: challenges and opportunities in the context of predictive, preventive, and personalized medicine. *EPMA J* 2019;10(3):291–305.
15. Khalil A, Jameson MJ. The EGFR inhibitor gefitinib enhanced the response of human oral squamous cell carcinoma to cisplatin in vitro. *Drugs R* 2017;17(4):545–55.
16. Yamamoto VN, Thylur DS, Bauschard M, Schmale I, Sinha UK. Overcoming radioresistance in head and neck squamous cell carcinoma. *Oral Oncol* 2016;63:44–51.
17. Naruse T, Yanamoto S, Matsushita Y, Sakamoto Y, Morishita K, Ohba S, et al. Cetuximab for the treatment of locally advanced and recurrent/metastatic oral cancer: an investigation of distant metastasis. *Mol Clin Oncol* 2016;5(2):246–52.
18. Yanamoto S, Umeda M, Kioi M, Kirita T, Yamashita T, Hiratsuka H, et al. Multicenter retrospective study of cetuximab plus platinum-based chemotherapy for recurrent or metastatic oral squamous cell carcinoma. *Canc Chemother Pharmacol* 2018;81(3):549–54.
19. Cramer JD, Burtneess B, Ferris RL. Immunotherapy for head and neck cancer: recent advances and future directions. *Oral Oncol* 2019;99:104460.
20. Kujan O, van Schaijik B, Farah CS. Immune checkpoint inhibitors in oral cavity squamous cell carcinoma and oral potentially malignant disorders: a systematic review. *Cancers* 2020;12(7).
21. Zainal NS, Lee BKB, Wong ZW, Chin IS, Yee PS, Gan CP, et al. Effects of palbociclib on oral squamous cell carcinoma and the role of PIK3CA in conferring resistance. *Canc Biol Med* 2019;16(2):264–75.
22. Chuerduangphui J, Pientong C, Patarapadungkit N, Chotiyan A, Vatanasapt P, Kongyingyoes B, et al. Amplification of EGFR and cyclin D1 genes associated with human papillomavirus infection in oral squamous cell carcinoma. *Med Oncol* 2017;34(9):148.
23. Clark AS, Karasic TB, DeMichele A, Vaughn DJ, O'Hara M, Perini R, et al. Palbociclib (PD0332991)-a selective and potent cyclin-dependent kinase inhibitor: a review of pharmacodynamics and clinical development. *JAMA Oncol* 2016;2(2):253–60.
24. Schoninger SF, Blain SW. The ongoing search for biomarkers of CDK4/6 inhibitor responsiveness in breast cancer. *Mol Canc Therapeut* 2020;19(1):3–12.
25. Bonelli M, La Monica S, Fumarola C, Alfieri R. Multiple effects of CDK4/6 inhibition in cancer: from cell cycle arrest to immunomodulation. *Biochem Pharmacol* 2019;170:113676.
26. Schettini F, De Santo I, Rea CG, De Placido P, Formisano L, Giuliano M, et al. CDK 4/6 inhibitors as single agent in advanced solid tumors. *Front Oncol* 2018;8:608.
27. Chen L, Pan J. Dual cyclin-dependent kinase 4/6 inhibition by PD-0332991 induces apoptosis and senescence in oesophageal squamous cell carcinoma cells. *Br J Pharmacol* 2017;174(15):2427–43.
28. Spring LM, Wander SA, Andre F, Moy B, Turner NC, Bardia A. Cyclin-dependent kinase 4 and 6 inhibitors for hormone receptor-positive breast cancer: past, present, and future. *Lancet* 2020;395(10226):817–27.
29. Pandey K, An HJ, Kim SK, Lee SA, Kim S, Lim SM, et al. Molecular mechanisms of resistance to CDK4/6 inhibitors in breast cancer: a review. *Int J Canc* 2019;145(5):1179–88.
30. Leu YL, Wang TH, Wu CC, Huang KY, Jiang YW, Hsu YC, et al. Hydroxygenkwanin suppresses non-small cell lung cancer progression by enhancing EGFR degradation. *Molecules* 2020;25(4).

31. Chen CY, Chiou SH, Huang CY, Jan CI, Lin SC, Hu WY, et al. Tid1 functions as a tumour suppressor in head and neck squamous cell carcinoma. *J Pathol* 2009;**219**(3):347–55.
32. Chen CY, Chen CC, Shieh TM, Hsueh C, Wang SH, Leu YL, et al. Corylin suppresses hepatocellular carcinoma progression via the inhibition of epithelial-mesenchymal transition, mediated by long noncoding RNA GAS5. *Int J Mol Sci* 2018;**19**(2).
33. Noguti J, De Moura CF, De Jesus GP, Da Silva VH, Hossaka TA, Oshima CT, et al. Metastasis from oral cancer: an overview. *CANCER GENOMICS PROTEOMICS* 2012;**9**(5):329–35.
34. Shamloo B, Usluer S. p21 in cancer research. *Cancers* 2019;**11**(8).
35. Jung SY, Kho S, Song KH, Ahn J, Park IC, Nam KY, et al. Novel focal adhesion kinase 1 inhibitor sensitizes lung cancer cells to radiation in a p53-independent manner. *Int J Oncol* 2017;**51**(5): 1583–9.
36. Park HY, Park SH, Jeong JW, Yoon D, Han MH, Lee DS, et al. Induction of p53-independent apoptosis and G1 cell cycle arrest by fucoidan in HCT116 human colorectal carcinoma cells. *Mar Drugs* 2017;**15**(6).
37. Murphy CG, Dickler MN. The role of CDK4/6 inhibition in breast cancer. *Oncol* 2015;**20**(5):483–90.
38. Morikawa A, Henry NL. Palbociclib for the treatment of estrogen receptor-positive, HER2-negative metastatic breast cancer. *Clin Canc Res* 2015;**21**(16):3591–6.
39. Zhou J, Zhang S, Chen X, Zheng X, Yao Y, Lu G, et al. Palbociclib, a selective CDK4/6 inhibitor, enhances the effect of selumetinib in RAS-driven non-small cell lung cancer. *Canc Lett* 2017;**408**:130–7.
40. Yetil A, Anchang B, Gouw AM, Adam SJ, Zabuawala T, Parameswaran R, et al. p19ARF is a critical mediator of both cellular senescence and an innate immune response associated with MYC inactivation in mouse model of acute leukemia. *Oncotarget* 2015;**6**(6):3563–77.
41. Campaner S, Doni M, Verrecchia A, Faga G, Bianchi L, Amati B. Myc, Cdk2 and cellular senescence: old players, new game. *Cell Cycle* 2010;**9**(18):3655–61.
42. Hydbring P, Bahram F, Su Y, Tronnorsjo S, Hogstrand K, von der Lehr N, et al. Phosphorylation by Cdk2 is required for Myc to repress Ras-induced senescence in cotransformation. *Proc Natl Acad Sci U S A* 2010;**107**(1):58–63.
43. Wu CH, van Riggelen J, Yetil A, Fan AC, Bachireddy P, Felsner DW. Cellular senescence is an important mechanism of tumor regression upon c-Myc inactivation. *Proc Natl Acad Sci U S A* 2007;**104**(32):13028–33.
44. Poole CJ, van Riggelen J. MYC-master regulator of the cancer epigenome and transcriptome. *Genes* 2017;**8**(5).
45. Ko A, Han SY, Song J. Dynamics of ARF regulation that control senescence and cancer. *BMB Rep* 2016;**49**(11):598–606.
46. Ko A, Han SY, Choi CH, Cho H, Lee MS, Kim SY, et al. Oncogene-induced senescence mediated by c-Myc requires USP10 dependent deubiquitination and stabilization of p14ARF. *Cell Death Differ* 2018;**25**(6):1050–62.

Research Paper

Surfactin from *Bacillus subtilis* attenuates ambient air particulate matter-promoted human oral cancer cells metastatic potential

Thi Thuy Tien Vo^{1#}, Chiang-Wen Lee^{2,3,4,5#}, Ching-Zong Wu¹, Ju-Fang Liu⁶, Wei-Ning Lin⁷, Yuh-Lien Chen⁸, Lee-Fen Hsu^{9,10}, Ming-Horng Tsai^{11,12}, I-Ta Lee¹✉

1. School of Dentistry, College of Oral Medicine, Taipei Medical University, Taipei, Taiwan.
2. Department of Orthopaedic Surgery, Chang Gung Memorial Hospital, Puzi City, Chiayi County 61363, Taiwan.
3. Department of Nursing, Division of Basic Medical Sciences, and Chronic Diseases and Health Promotion Research Center, and Research Center for Chinese Herbal Medicine, Chang Gung University of Science and Technology, Puzi City, Chiayi County 61363, Taiwan.
4. Department of Safety Health and Environmental Engineering, Ming Chi University of Technology, New Taipei City 24301, Taiwan.
5. College of Medicine, Chang Gung University, Guishan Dist., Taoyuan City 33303, Taiwan.
6. School of Oral Hygiene, College of Oral Medicine, Taipei Medical University, Taipei, Taiwan.
7. Graduate Institute of Biomedical and Pharmaceutical Science, Fu Jen Catholic University, New Taipei City, Taiwan.
8. Department of Anatomy and Cell Biology, College of Medicine, National Taiwan University, Taipei, Taiwan.
9. Department of Respiratory Care, Chang Gung University of Science and Technology, Puzi City, Chiayi County 613, Taiwan.
10. Division of Neurosurgery, Department of Surgery, Chang Gung Memorial Hospital, Puzi City, Chiayi County 613, Taiwan.
11. Department of Pediatrics, Division of Pediatric Hematology/Oncology and Neonatology, Yunlin Chang Gung Memorial Hospital, Yunlin, Taiwan.
12. College of Medicine, Chang Gung University, Taoyuan, Taiwan.

#These authors contributed equally to this work.

✉ Corresponding author: I-Ta Lee, School of Dentistry, College of Oral Medicine, Taipei Medical University, Taipei, Taiwan, 250 Wuxing St. Taipei 11031, Taiwan. Tel.: +886-2-27361661 ext. 5162; Fax: +886-2-27362295; E-mail addresses: itlee0128@tmu.edu.tw.

© The author(s). This is an open access article distributed under the terms of the Creative Commons Attribution License (<https://creativecommons.org/licenses/by/4.0/>). See <http://ivyspring.com/terms> for full terms and conditions.

Received: 2020.05.17; Accepted: 2020.08.06; Published: 2020.08.18

Abstract

Recently, many studies have indicated that ambient air particulate matter (PM) can increase the risk of oral cancer. The most common malignant tumor in the oral cavity is oral squamous cell carcinoma (OSCC). Usually, cancer cell migration/invasion is the most important cause of cancer mortality. Matrix metalloproteinase-2 (MMP-2) and MMP-9 have been shown to play important roles in regulating metastasis and the tumor microenvironment. Here, we studied the anti-cancer effects of surfactin, a cyclic lipopeptide generated by *Bacillus subtilis*, on cancer cell migration and invasion. Surfactin suppressed PM-promoted cell migration and invasion and colony formation of SCC4 and SCC25 human oral squamous cell carcinoma cell lines. We observed that PM induced MMP-2 and MMP-9 expression, which was inhibited by surfactin. Transfection with p65, p50, c-Jun, c-Fos, p85, p110, Akt, mammalian target of rapamycin (mTOR), or interleukin-6 (IL-6) siRNA markedly inhibited PM-induced MMP-2 and MMP-9 expression. Moreover, surfactin could reduce Akt, mTOR, p65, and c-Jun activation and IL-6 secretion induced by PM. Finally, we proved that transfection with Akt, p65, or c-Jun siRNA significantly inhibited PM-induced IL-6 release. Taken together, these results suggest that surfactin functions as a suppressor of PM-induced MMP2/9-dependent oral cancer cell migration and invasion by inhibiting the activation of phosphoinositide 3-kinase (PI3K)/Akt/mTOR and PI3K/Akt/nuclear factor- κ B (NF- κ B) and activator protein-1 (AP-1)/IL-6 signaling pathways.

Key words: Surfactin, Invasion, Particulate matter, Oral cancer, Matrix metalloproteinase

Introduction

In many parts of the world, new cases of oral cancer and deaths are increasing. Known risk factors include smoking, drinking, human papillomavirus

(HPV), and betel quid chewing [1]. It is also believed that exposure to heavy metals and emissions from petroleum and chemical plants is also related to the

development of oral cancer, and it is well known that air pollution, especially ambient air particulate matter (PM), is harmful to the respiratory and cardiovascular system [2]. The combined effects of household and ambient air pollution cause approximately 7 million premature deaths every year, mainly due to heart disease, stroke, lung cancer, chronic obstructive pulmonary disease, and acute respiratory infections leading to increased mortality [3, 4]. The composition of PM is very complicated including nitrate, sulfate, ammonia, and so on. Compared to PM₁₀, PM_{2.5} can cause greater harm to human health. PM_{2.5} generally penetrates the lung barrier and enters the blood system. Most studies in the past have explored the relationship between betel nuts, cigarettes, or alcohol and oral cancer, but few studies have studied the relationship between air pollution and oral cancer. The most common malignant tumor in the oral cavity is oral squamous cell carcinoma (OSCC). Moreover, cancer cell migration/invasion is the most important cause of cancer mortality [5]. Matrix metalloproteinases (MMPs) belong to a family of zinc-dependent endopeptidases [6]. Members of the MMP family include collagenase, gelatinase, stromalysin, stromelysin, and membrane-type MMP [6]. Moreover, MMP-9 can mediate extracellular matrix (ECM) remodeling by cleaving many ECM proteins. MMP-2 or MMP-9 has been shown to play an important role in regulating metastasis including oral cancer [5, 7]. PM_{2.5} also has been shown to induce MMP-2 and MMP-9 expression in keratinocytes [6]. Therefore, reducing the expression of MMP-2 and MMP-9 or its upstream regulatory signaling pathways is essential for the treatment of malignant tumors. Up-regulation of MMP-2 and MMP-9 expression was mediated through various signaling pathways [8, 9]. Here, we studied the novel pathways involved in PM-mediated MMP-2 and MMP-9 expression in the SCC4 and SCC25 human oral squamous cell carcinoma cell lines.

Surfactin is a bacterial cyclic lipopeptide generated by *Bacillus subtilis* [10]. Surfactin has been shown to possess some properties including anti-cancer, anti-bacterial, and anti-viral activities [11]. Even though surfactin has been regarded as a potential anti-cancer agent, its specific effects on cancer cells and the detailed mechanisms involved are still unknown. Park et al. indicated that surfactin reduced TPA-mediated breast cancer cell migration/invasion via the inhibition of MMP-9 levels [10]. In addition, Wang et al. also proved that surfactin could promote apoptosis of HepG2 cells via the reactive oxygen species (ROS) signaling [12]. Here, we studied the anti-cancer effects of surfactin on PM-induced human oral squamous cell carcinoma cell migration and invasion and the novel mechanisms underlying

these processes. The present study proved that PM induces MMP-2/9-dependent cell migration and invasion via the phosphoinositide 3-kinase (PI3K)/Akt/mammalian target of rapamycin (mTOR) and PI3K/Akt/NF- κ B and activator protein-1 (AP-1)/interleukin-6 (IL-6) signaling pathways. Moreover, surfactin can inhibit MMP-2/9 expression via inhibition of the activation of these two pathways induced by PM and then reduce cell migration and invasion.

Methods

Materials

We purchased anti-Akt, anti-phospho-Akt, anti-mTOR, anti-phospho-mTOR, anti-MMP-2, anti-MMP-9, anti-GAPDH, anti-tissue inhibitor of matrix metalloproteinase (TIMP)-1, anti-TIMP-2, anti-phospho-c-Jun, and anti-phospho-p65 antibodies from Santa Cruz Biotechnology Inc (Santa Cruz, CA, USA). Surfactin and urban PM (SRM 1648a) were purchased from Sigma (St. Louis, MO, USA).

Cell culture

SCC4 and SCC25 human oral squamous cell carcinoma cell lines were kindly provided by Dr. J. F. Liu (School of Oral Hygiene, College of Oral Medicine, Taipei Medical University, Taipei, Taiwan). SCC4 and SCC25 cells were grown in DMEM/F12 supplemented with 10% FBS, 2 mM glutamine and 0.4 μ g/ml hydrocortisone. Cells were maintained as monolayer cultures in a humidified atmosphere of 5% CO₂ at 37°C.

Cell viability

The cell viability of SCC4 and SCC25 cells in response to PM or surfactin was assessed using PrestoBlue Cell Viability Reagent (Invitrogen, CA, USA) according to the manufacturer's protocol.

Western blot

Cells were incubated with PM under various experimental design conditions at 37°C. Western blot was then performed based on previously published literature in our laboratory [13]. At last, membranes were incubated with the anti-Akt, anti-phospho-Akt, anti-mTOR, anti-phospho-mTOR, anti-MMP-2, anti-MMP-9, anti-GAPDH, anti-TIMP-1, anti-TIMP-2, anti-phospho-c-Jun, or anti-phospho-p65 antibody for 24 h and then incubated with the anti-mouse or anti-rabbit horseradish peroxidase antibody for 1 h. We used enhanced chemiluminescence (ECL) reagents to observe immunoreactive bands.

Real-Time PCR

Total RNA was extracted by using TRIzol reagent. We further reverse-transcribed mRNA into cDNA and analyzed by real-time PCR using SYBR Green PCR reagents (Applied Biosystems, Branchburg, NJ, USA) based on previously published literature in our laboratory [14].

Transient transfection with siRNAs

Human scrambled, MMP-2, MMP-9, p65, p50, c-Jun, c-Fos, p85, p110, Akt, mTOR, and IL-6 siRNAs were from Sigma (St. Louis, MO). Transient transfection of siRNAs was performed using a Lipofectamine 2000 Transfection Reagent according to the manufacturer's instructions.

Analysis of luciferase reporter gene activity

Human MMP-2, MMP-9, AP-1, and NF- κ B promoter-luciferase constructs were kindly provided by Dr. C. W. Lee (Department of Nursing, Chang Gung University of Science and Technology, Puzi City, Chiayi County, Taiwan). The luciferase activity was quantitatively assessed as previously described [15] using a luciferase assay system (Promega, Madison, Wis.). Firefly luciferase activities were standardized for β -gal activity.

Gelatin zymography

Cells were seeded onto 6-well culture plates and made quiescent at confluence by incubation in serum-free DMEM/F12 for 24 h. Growth-arrested cells were treated with PM under various experimental design conditions at 37°C. The culture medium was collected and centrifuged at $10000 \times g$ for 5 min at 4°C to remove cell debris. The expression of MMP-2 and MMP-9 was determined as previously published literature in our laboratory [15].

Measurement of IL-6 secretion

Cells were incubated with PM under various experimental design conditions and then the media were collected. The levels of IL-6 were assayed by using an IL-6 ELISA kit (BioSource International, Camarillo, CA) according to the manufacturer's instructions.

Migration assay

Cells were cultured in respective 10-cm cell culture dishes and grown for 80% confluence, then starved for 24 h by using serum-free DMEM/F12. Next, a sterile scalpel blade was manually utilized to generate identically wide scratches through the center of the cellular monolayer of both cell lines under aseptic conditions. The cell debris was washed once by PBS for totally removal. Serum-free DMEM/F12

with or without PM at concentration of 50 $\mu\text{g}/\text{cm}^2$ was then added into designated dishes after 1 h preincubation with 10 μM surfactin containing DNA synthesis inhibitor hydroxyurea. The cellular migration from the cell wound boundary was monitored by taking pictures using digital camera under light microscope (Olympus, Japan) at baseline and 24 h time point. The number of migratory cells was counted based on the resulting 4 phase images of each time point, and the mean value was calculated. The data was obtained from independently triplicate experiments.

Invasion assay

For cell invasion assay, BioCoat® Matrigel™ Invasion Chambers with 8.0 μm PET Membrane in two 24 well inserts that simulate the cell invasion through the extracellular matrix were utilized following the manufacturer's instructions. SCC4 and SCC25 cells were re-suspended in serum-free DMEM/F12, then loaded onto respective Matrigel-coated cell culture inserts and incubated for 24 h. After incubation, the remaining cells on the upper side of the membrane were carefully removed using cotton swabs. The invaded cells that attached on the lower side of the membrane were fixed with 70% ethanol for 10 min and stained with 2% ethanol containing 0.2% crystal violet. The number of invaded cells was then enumerated in four randomly different observatory fields under light microscope with $\times 10$ objective to calculate the average sum of cells that had invaded through the membrane.

Chromatin immunoprecipitation (ChIP) assay

The protocol was modified based on previous study [10]. Cells were cultured in respective 10-cm dishes at density of 2×10^7 cells per dish. Next, 1% formaldehyde as a cross-linking agent was added into the medium in the cell culture dishes for 10 min at room temperature. The cross-linking reaction was quenched by using 0.125 M glycine. For chromatin fragmentation, the sample was aliquoted and subjected to sonication, followed by nuclease digestion with 10 U of MNase at 37°C for 15 min to produce chromatin at primarily mononucleosome size. Next, fragmented chromatin was bound to specific antibodies for 3 h at 4°C for immunoprecipitation. Protein-DNA complexes were recovered by using protein A agarose beads, then washed and eluted with elution buffer. The eluted complexes were incubated in 0.25 M NaCl at 65°C overnight to reverse the formaldehyde-caused-crosslinks, followed by digested with proteinase K for 2 h at 50°C to digest the protein. The immunoprecipitated DNAs were subsequently isolated and used for PCR experiments.

Colony formation assay

After incubating SCC4 and SCC25 cells with PM with or without surfactin, these cells were seeded in complete media at a density of 2×10^4 cells in 60-mm dishes containing a top layer of 0.7% agar and a bottom layer of 1% agar. The plates were incubated at 37°C for 14 days and then stained with 0.2% crystal violet. Colonies of greater than 20 cells were counted manually.

Statistical analysis

We analyzed the data with the GraphPad Prism program (GraphPad, San Diego, CA, USA). Quantitative data were expressed as the mean \pm S.E.M. and analyzed with one-way ANOVA followed with Tukey's post-hoc test. We considered $P < 0.05$ as a significant difference.

Results

The effects of PM and surfactin on the cell viability of SCC4 and SCC25 cells

We explored the cell viability of SCC4 and SCC25 cells in response to PM and surfactin. We found that 5, 10, 25, and 50 $\mu\text{g}/\text{cm}^2$ PM had no significant effects on the cell viability of SCC4 and SCC25 cells (Fig. 1A). In addition, the cell viability of

SCC4 and SCC25 cells was not affected in response to 1, 5, and 10 μM surfactin (Fig. 1B). Therefore, 50 $\mu\text{g}/\text{cm}^2$ PM and 10 μM surfactin were applied in all the subsequent experiments.

Surfactin reduces PM-induced migration, invasion, and colony formation of SCC4 and SCC25 cells

Cancer cell migration/invasion is the most important cause of cancer mortality [5]. Surfactin has been shown to possess some properties including anti-cancer, anti-bacterial, and anti-viral activities [11]. We investigated whether surfactin could inhibit PM-induced cell migration and invasion. SCC4 and SCC25 cells were treated with PM for 24 h in the presence or absence of surfactin. As shown in Figs. 2A and B, PM could induce cell migration and invasion, which was inhibited by surfactin. The process of tumor metastasis is very complicated including the proteolytic digestion of ECM, cell migration to the circulatory system and colonization at the site of metastasis [16]. Thus, we observed the effects of surfactin on colony-forming ability in response to PM in SCC4 and SCC25 cells. As shown in Fig. 2C, we proved that surfactin could suppress PM-mediated colony-forming ability in these cells.

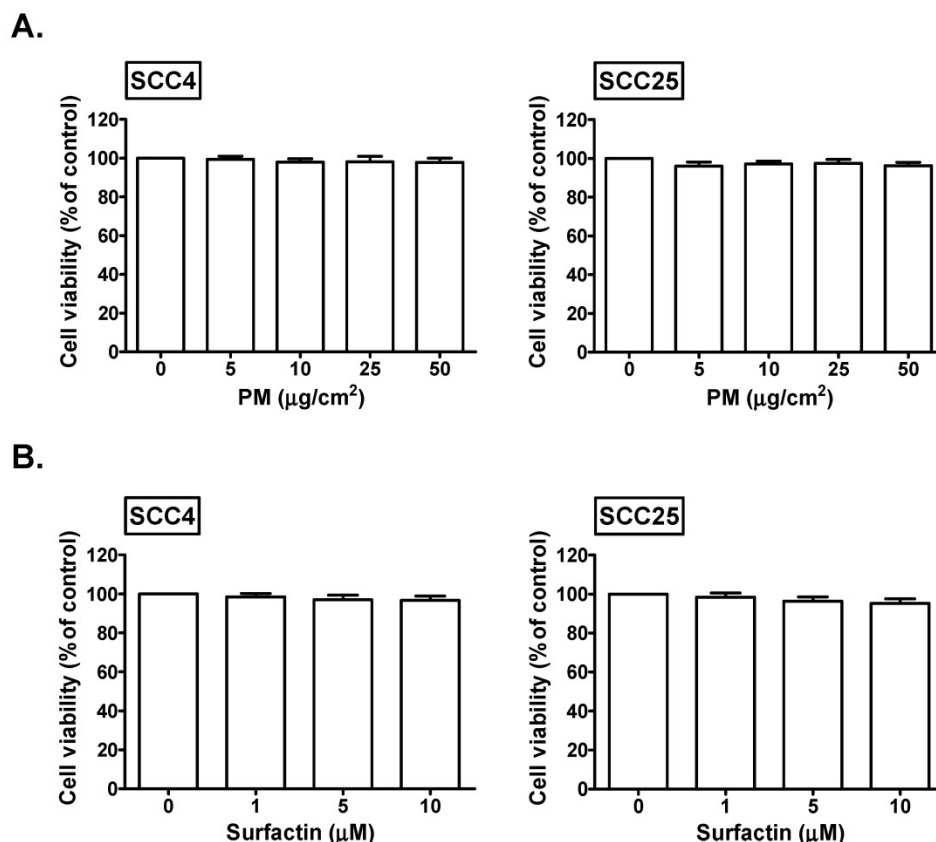


Figure 1. The effects of PM and surfactin on SCC4 and SCC25 cell viability. Cells were treated with the indicated concentrations of (A) PM or (B) surfactin for 24 h. The cell viabilities were then measured.

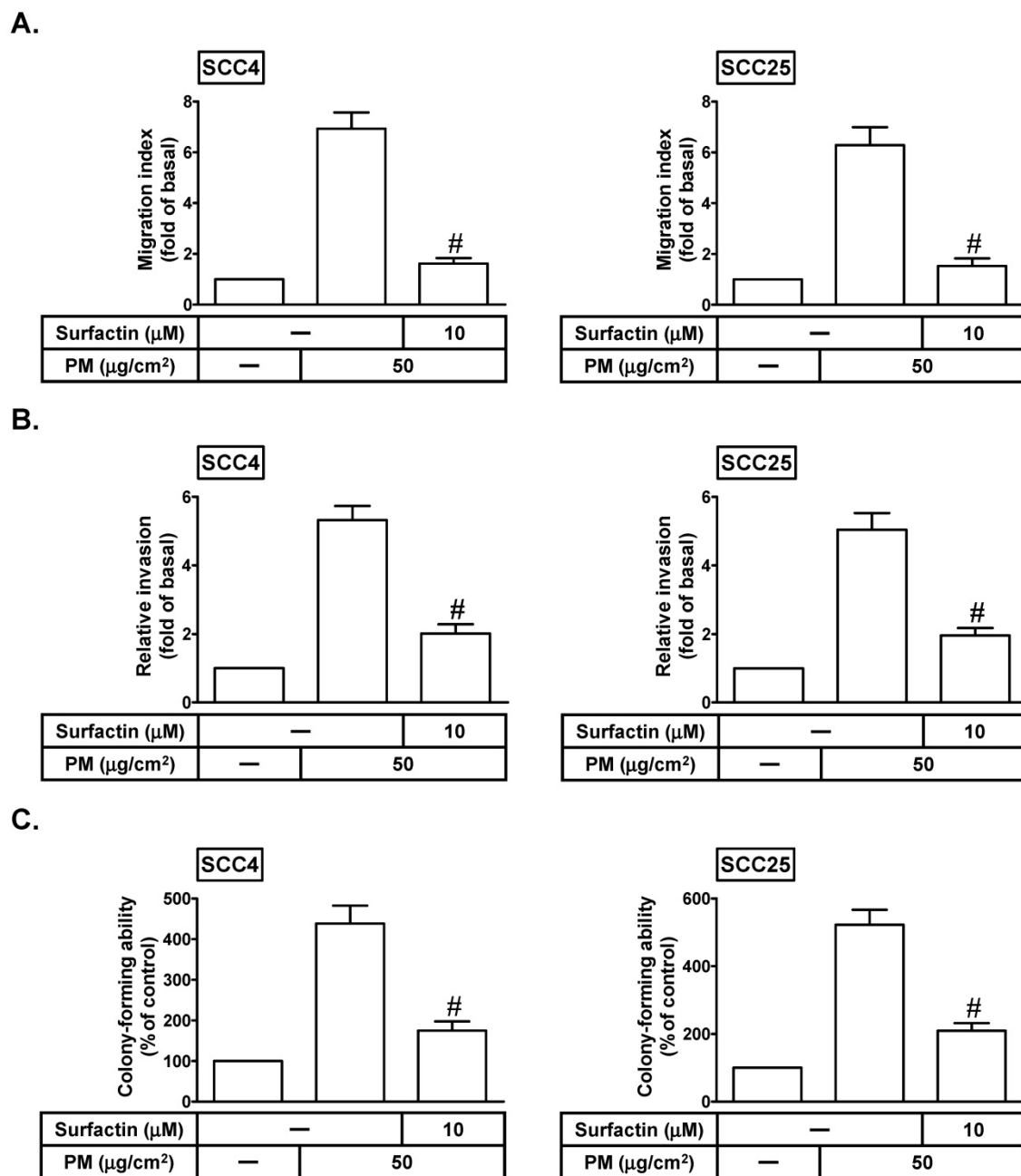


Figure 2. Surfactin decreases PM-induced migration, invasion, and colony-forming ability of SCC4 and SCC25 cells. Cells were pretreated with surfactin for 1 h and then incubated with PM for 24 h. The cell migration assay and matrigel invasion assay were performed and then the (A) migrating cells and (B) invaded cells were counted. (C) Cells were cultured in soft agar gel with PM for 14 days in the absence or presence of surfactin. The colonies were counted. Data are expressed as mean \pm S.E.M. of three independent experiments. [#] $P < 0.01$, as compared with the cells exposed to PM alone.

Surfactin inhibits PM-induced MMP-2 and MMP-9 expression and enzyme activity

MMP-9 or MMP-2 has been shown to play an important role in regulating metastasis [17]. We studied whether MMP-2 and MMP-9 were involved in PM-induced cell migration and invasion. As shown in Fig. 3A, we proved that transfection with MMP-2 or MMP-9 siRNA markedly inhibited PM-induced cell migration and invasion in SCC4 cells. We further investigated whether surfactin could reduce PM-induced MMP-9 and MMP-2 expression and activity.

As shown in Figs. 3B-D, we found that PM could enhance MMP-2 and MMP-9 protein expression, enzyme activity, mRNA levels, or promoter activity, which was inhibited by surfactin in SCC4 cells. Surfactin had similar inhibitory effects on MMP-9 expression induced by PM in SCC25 cells (data not shown). TIMP is the endogenous inhibitor of most secreted MMPs [18]. Finally, we studied the effects of surfactin on TIMP-1 and TIMP-2 expression. As shown in Fig. 3E, surfactin had no effects on TIMP-1 and TIMP-2 protein levels in SCC4 cells.

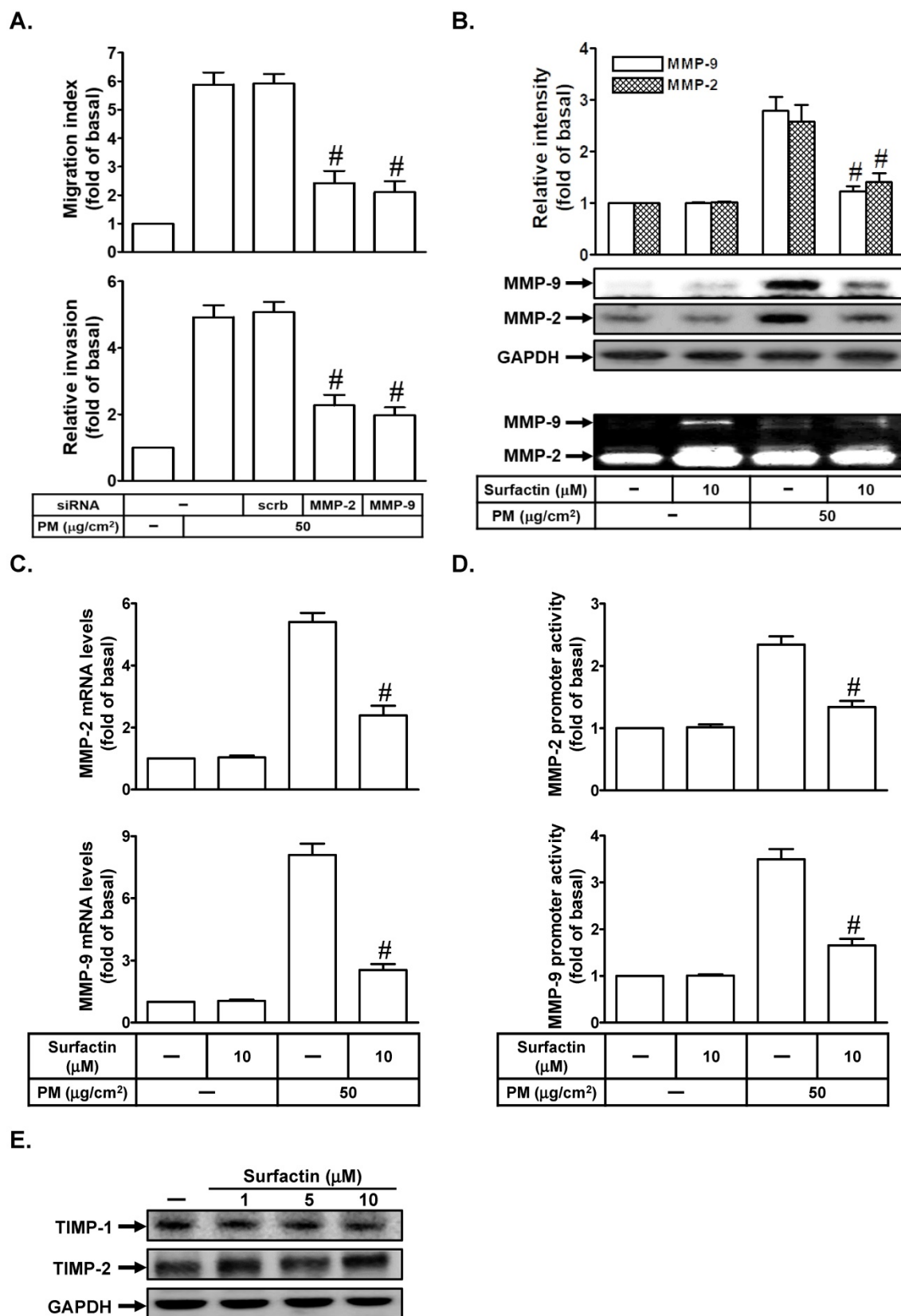


Figure 3. Surfactin suppresses MMP-2 and MMP-9 expression and enzyme activity induced by PM. (A) SCC4 cells were transfected with siRNA of scrambled (scrb), MMP-2, or MMP-9 and then treated with PM for 24 h. The cell migration assay and matrigel invasion assay were performed and then the migrating cells and invaded cells were counted. (B) SCC4 cells were pretreated with surfactin for 1 h and then incubated with PM for 24 h. Culture supernatant was analyzed by gelatin zymography. The cellular extract was analyzed by Western blot. SCC4 cells were pretreated with surfactin for 1 h and then incubated with PM for 6 h. The (C) mRNA levels and (D) promoter activity of MMP-2 and MMP-9 were determined. (E) SCC4 cells were treated with the indicated concentrations of surfactin for 24 h. The protein levels of TIMP-1 and TIMP-2 were determined by Western blot. Data are expressed as mean±S.E.M. of three independent experiments. #P < 0.01, as compared with the cells exposed to PM + scrambled siRNA (A). #P < 0.01, as compared with the cells exposed to PM alone (B-D).

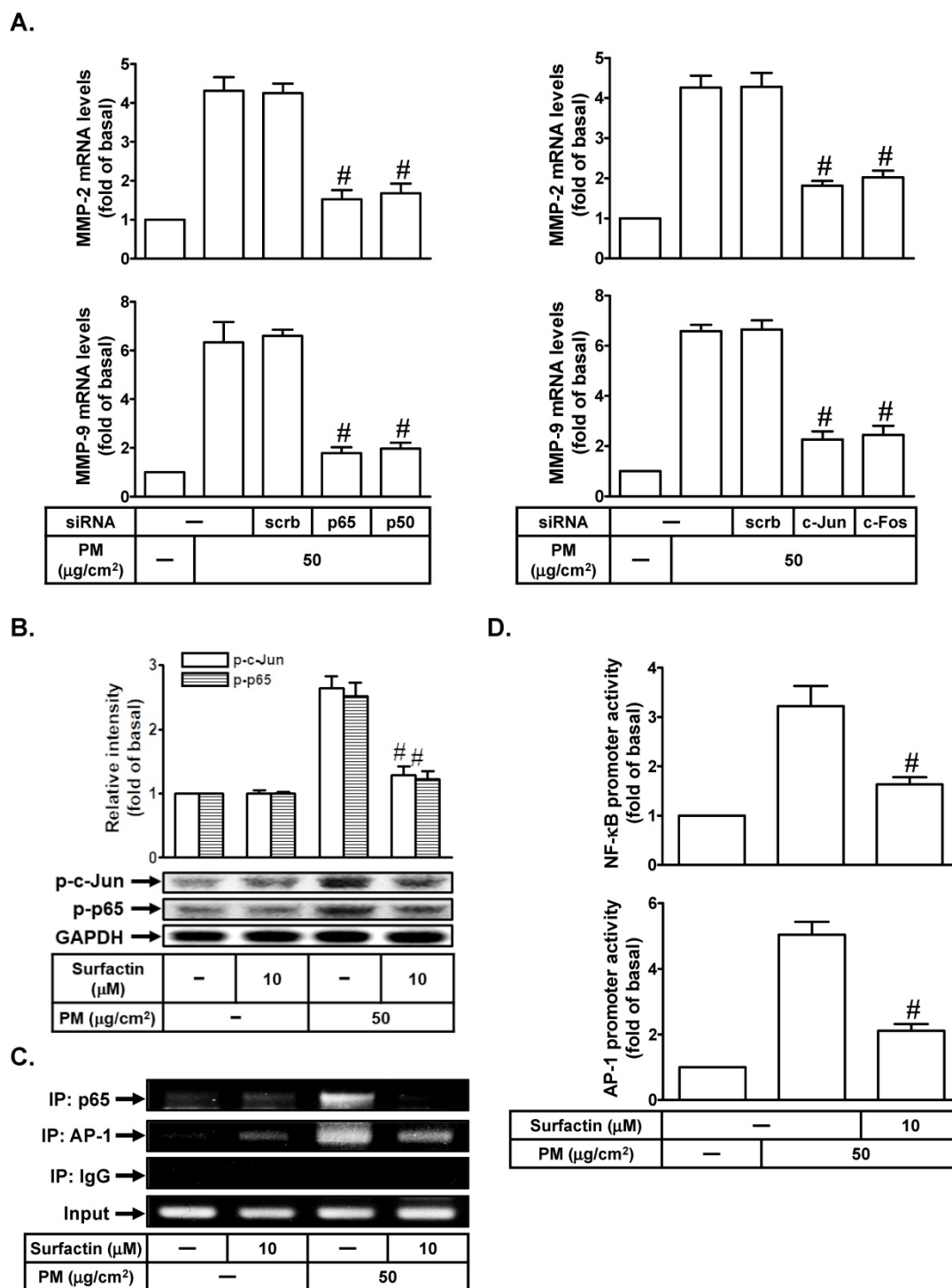


Figure 4. Surfactin suppresses PM-induced NF-κB and AP-1 activation. (A) SCC4 cells were transfected with siRNA of scrambled (scrub), p65, p50, c-Jun, or c-Fos and then treated with PM for 6 h. The mRNA levels of MMP-2 and MMP-9 were determined. (B) SCC4 cells were pretreated with surfactin for 1 h and then incubated with PM for 1 h. The protein levels of phospho-c-Jun (p-c-Jun) and phospho-p65 (p-p65) were determined by Western blot. (C) SCC4 cells were pretreated with surfactin for 1 h and then incubated with PM for 4 h. A ChIP assay was performed with anti-NF-κB p65 or anti-AP-1 antibodies. (D) SCC4 cells were pretreated with surfactin for 1 h and then incubated with PM for 1 h. The promoter activity of NF-κB and AP-1 were determined. Data are expressed as mean±S.E.M. of three independent experiments. #P < 0.01, as compared with the cells exposed to PM + scrambled siRNA (A). #P < 0.01, as compared with the cells exposed to PM alone (B, D).

Surfactin suppresses PM-induced MMP-2 and MMP-9 expression via inhibition of the activation of NF-κB and AP-1

Up-regulation of MMP-2 and MMP-9 expression

was mediated through various signaling pathways including AP-1 and NF-κB [19, 20]. We studied whether AP-1 and NF-κB were involved in PM-induced MMP-2 and MMP-9 expression in SCC4 cells. As shown in Fig. 4A, transfection with p65, p50, c-Jun,

or c-Fos siRNA markedly reduced PM-mediated MMP-2 and MMP-9 mRNA levels in SCC4 cells. We further investigated whether surfactin could inhibit PM-induced AP-1 and NF- κ B activation. As shown in Fig. 4B, we showed that PM could induce c-Jun and p65 phosphorylation, which was reduced by surfactin in SCC4 cells. Surfactin had similar inhibitory effects on c-Jun and p65 phosphorylation induced by PM in SCC25 cells (data not shown). We used a ChIP assay to observe the effects of surfactin on the binding activities of NF- κ B and AP-1 with the MMP-9 promoter. As shown in Fig. 4C, we proved that PM could increase the *in vivo* binding of NF- κ B and AP-1 to the MMP-9 promoter, which was reduced by surfactin. Finally, we showed that PM enhanced NF- κ B and AP-1 promoter activity, which was also inhibited by surfactin (Fig. 4D).

Surfactin decreases PM-enhanced MMP-2 and MMP-9 expression through the inhibition of activation of PI3K/Akt/mTOR signaling pathway

The PI3K/Akt/mTOR signaling is a frequently hyperactivated pathway in cancer and is critical for the growth and survival of tumor cells [21]. We also studied whether the PI3K/Akt/mTOR signaling pathway was involved in PM-induced cell migration and invasion. At first, we proved that transfection with p85, p110, Akt, or mTOR siRNA markedly inhibited PM-induced MMP-2 and MMP-9 mRNA levels in SCC4 cells (Fig. 5A). Moreover, we also found that PM could induce Akt and mTOR phosphorylation in SCC4 cells (Fig. 5B). We then studied whether surfactin could inhibit Akt and mTOR activation induced by PM. As shown in Fig. 5C, we found that surfactin significantly reduced PM-caused Akt and mTOR activation in SCC4 cells. Surfactin had similar inhibitory effects on Akt and mTOR phosphorylation induced by PM in SCC25 cells (data not shown). AP-1 and NF- κ B activation was regulated through many signaling pathways, such as PI3K/Akt [22, 23]. In our study, we proved that transfection with Akt siRNA inhibited PM-induced NF- κ B and AP-1 promoter activity in SCC4 cells (Fig. 5D). Finally, we showed that transfection with Akt, mTOR, p65, or c-Jun siRNA reduced PM-promoted cell migration and invasion (Fig. 5E).

IL-6 is involved in PM-induced MMP-2 and MMP-9 expression

Many reports indicated that IL-6 can promote tumor growth and metastasis [24, 25]. IL-6 also has been shown to regulate MMP-9 expression [26]. Here, we found that transfection with IL-6 siRNA could markedly inhibit PM-induced MMP-2 and MMP-9

mRNA expression and promoter activity (Fig. 6A). On the other hand, we studied whether surfactin could reduce PM-induced IL-6 release in SCC4 and SCC25 cells. As shown in Fig. 6B, we proved that PM could enhance IL-6 secretion, which was reduced by surfactin in these cells. Finally, we investigated the pathways involved in PM-induced IL-6 release in SCC4 and SCC25 cells. As shown in Fig. 6C, we showed that transfection with siRNA of Akt, p65, or c-Jun significantly inhibited IL-6 secretion in response to PM. Therefore, these data suggest that PM can induce MMP-2 and MMP-9 expression via the PI3K/Akt/NF- κ B and AP-1/IL-6 pathway, which was inhibited by surfactin.

Discussion

PM exposure causes various inflammatory diseases. Chu et al. proved that Taiwanese men exposed to higher concentrations of PM_{2.5} have an increased risk of oral cancer [2]. The seventh most common cancer in the world is OSCC [27]. A very important step in tumor metastasis is that cancer cells invade the surrounding tissues and vasculature. However, the chemotactic migration of cancer cells is required in this process, which is controlled by protrusive activity of the cell membrane and its attachment to the ECM [28]. MMP-2 and MMP-9 expression is known to promote the migration/invasion and metastasis of cancer cells [29]. Surfactin has been shown to suppress cancer progression by cell cycle arrest, apoptosis, growth inhibition, and metastasis arrest [30]. The potential mechanisms by which surfactin inhibits oral cancer cell migration and invasion in response to PM still unclear. Here, we proved that PM induces MMP-2/9-dependent cell migration and invasion via the PI3K/Akt/mTOR and PI3K/Akt/NF- κ B and AP-1/IL-6 signaling pathways. Moreover, surfactin can inhibit MMP-2/9 expression via inhibition of the activation of these two pathways induced by PM and then reduce cell migration and invasion.

Most studies have explored the relationship between betel nuts, cigarettes, or alcohol and oral cancer, but few studies have studied the relationship between air pollution and oral cancer. PM is typically a representative indicator of air pollution [2, 4]. Compared to PM₁₀, PM_{2.5} can cause greater harm to human health [4]. PM_{2.5} generally penetrates the lung barrier and enters the blood system. Zhang and Li indicated that PM_{2.5} could induce the cell proliferation, migration, and invasion of human hepatocellular carcinoma (HCC) cell line SMMC-7721 [31]. This is confirmed by our observation that PM could induce cell migration and invasion and colony-forming ability of SCC4 and SCC25 cells. *Bacillus*

subtilis generates the cyclic lipopeptide surfactin. Its heptapeptide head has two negatively charged amino acid residues, and its tail consists of fatty acid residues [30]. Surfactin has been shown to possess some properties including anti-cancer, anti-bacterial, and

anti-viral activities [11]. Moreover, we found that surfactin has the anti-oral cancer effects by our observation that surfactin inhibited PM-induced cell migration and invasion and colony-forming ability of SCC4 and SCC25 cells.

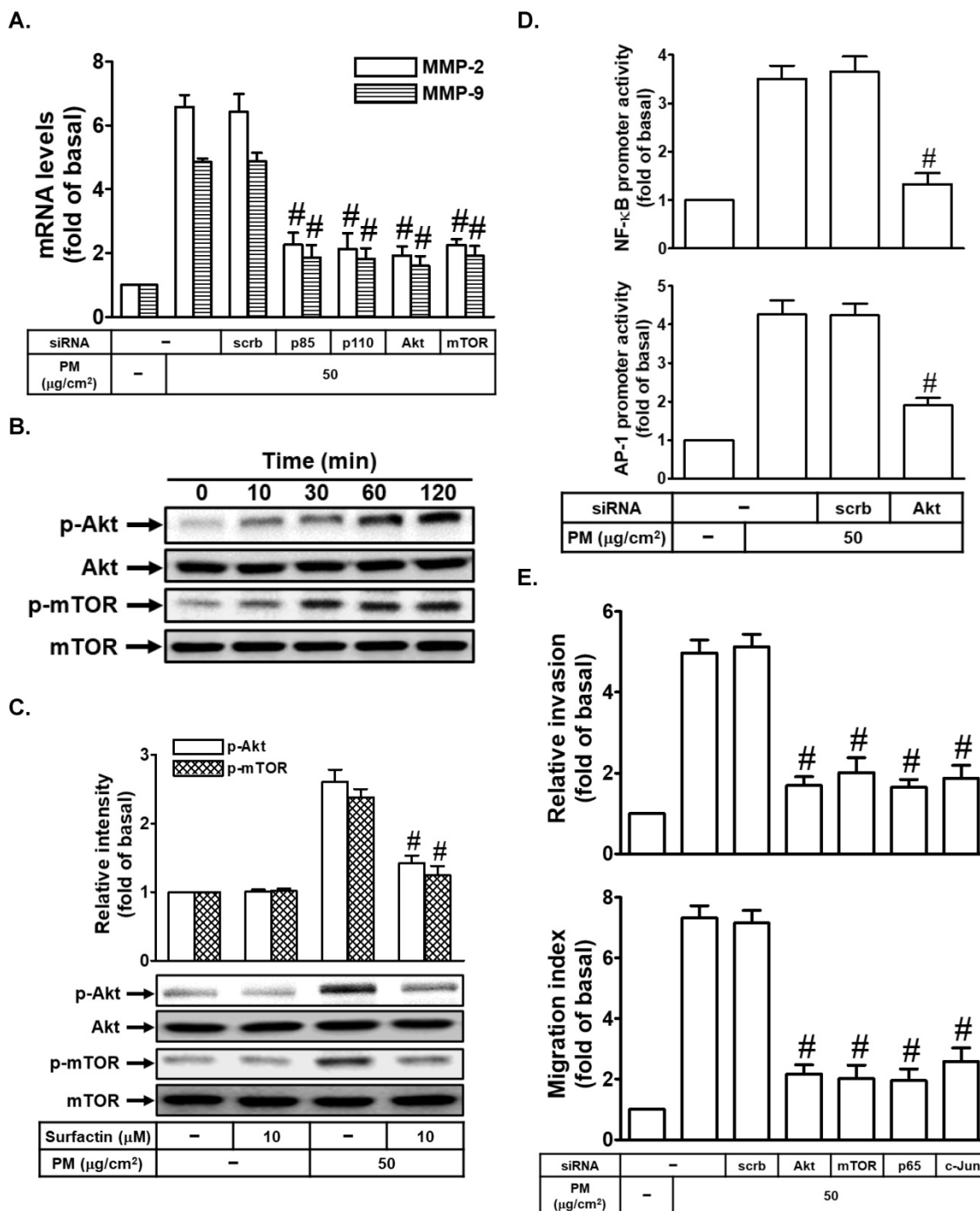


Figure 5. Surfactin decreases PM-regulated PI3K/Akt/mTOR signaling pathway activation. (A) SCC4 cells were transfected with siRNA of scrambled (scr), p85, p110, Akt, or mTOR and then treated with PM for 6 h. The mRNA levels of MMP-2 and MMP-9 were determined. (B) SCC4 cells were treated with 50 µg/cm² PM for the indicated times and then the protein levels of phospho-Akt and phospho-mTOR were determined by Western blot. (C) SCC4 cells were pretreated with surfactin for 1 h and then incubated with PM for 1 h. The protein levels of phospho-Akt and phospho-mTOR were determined. (D) SCC4 cells were transfected with siRNA of scrambled (scr) or Akt and then treated with PM for 1 h. The promoter activity of NF-κB and AP-1 were determined. (E) SCC4 cells were transfected with siRNA of scrambled (scr), Akt, mTOR, p65, or c-Jun and then treated with PM for 24 h. The cell migration assay and matrigel invasion assay were performed and then the migrating cells and invaded cells were counted. Data are expressed as mean ± S.E.M. of three independent experiments. #P < 0.01, as compared with the cells exposed to PM + scrambled siRNA (A, D, E). ##P < 0.01, as compared with the cells exposed to PM alone (C).

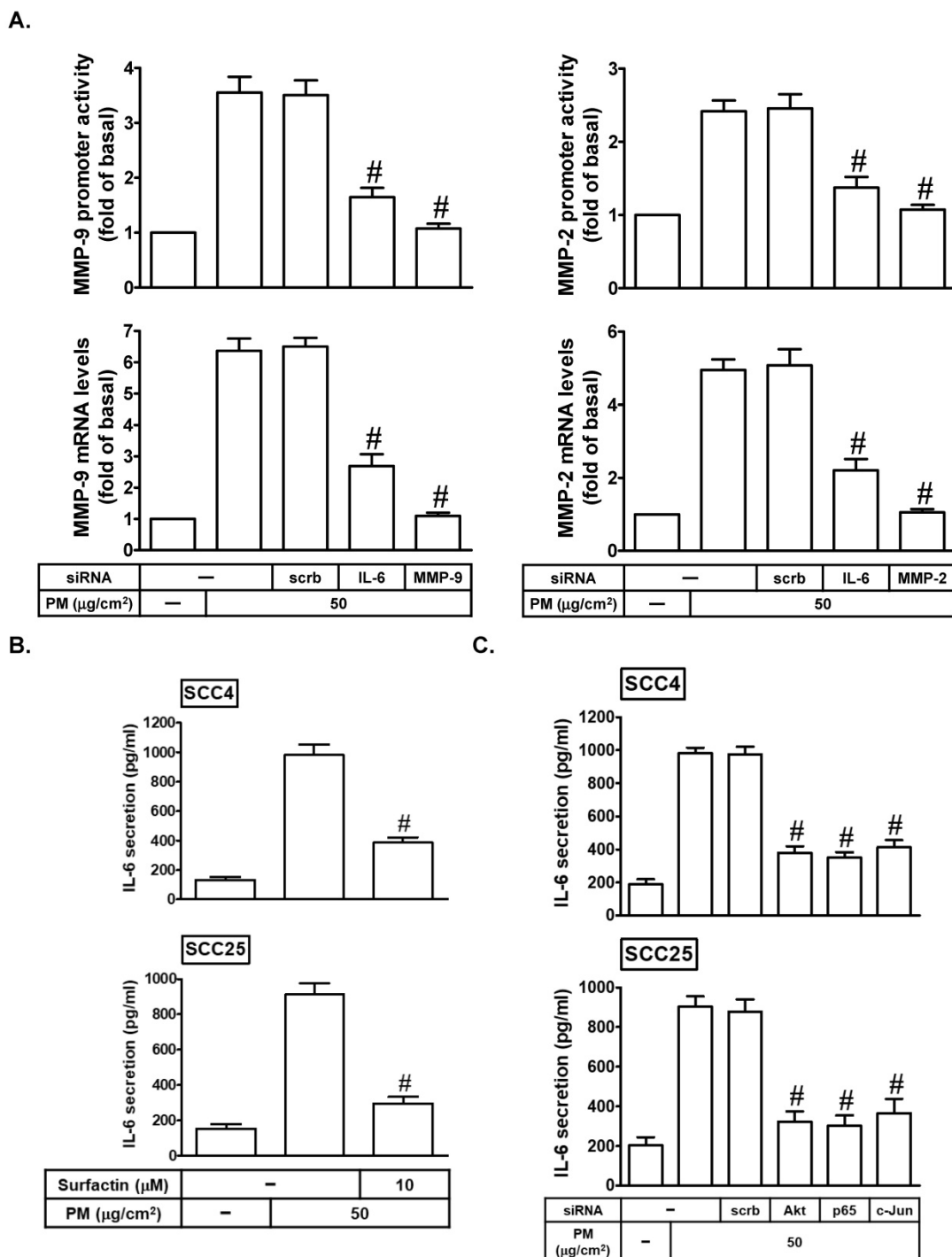


Figure 6. PM induces MMP-2 and MMP-9 expression via IL-6. (A) SCC4 cells were transfected with siRNA of scrambled (scrb), IL-6, MMP-2, or MMP-9 and then treated with PM for 6 h. The mRNA levels and promoter activity of MMP-2 and MMP-9 were determined. **(B)** SCC4 cells were pretreated with surfactin for 1 h and then incubated with PM for 24 h. The secretion of IL-6 was measured. **(C)** SCC4 cells were transfected with siRNA of scrambled (scrb), Akt, p65, or c-Jun and then treated with PM for 24 h. The secretion of IL-6 was measured. Data are expressed as mean±S.E.M. of three independent experiments. [#]*P* < 0.01, as compared with the cells exposed to PM + scrambled siRNA (A, C). [#]*P* < 0.01, as compared with the cells exposed to PM alone (B).

Degradation of the ECM is an important step in tumor cell invasion. Although various proteases are involved in ECM degradation, MMPs, a family of zinc and calcium-dependent proteolytic enzymes, digest many components of ECM [32]. MMPs are important to cell migration/invasion and metastasis [32]. At least more than 20 different MMPs work on multiple

substrates including collagen types I, II, III, IV and stromelylin [32, 33]. Among these MMPs, gelatinases, especially MMP-2 and MMP-9, are considered to play an important role in the degradation of type IV collagen and gelatin. The release of MMP-2 and MMP-9 is increased in various types of cancers including oral cancer and their increased levels are

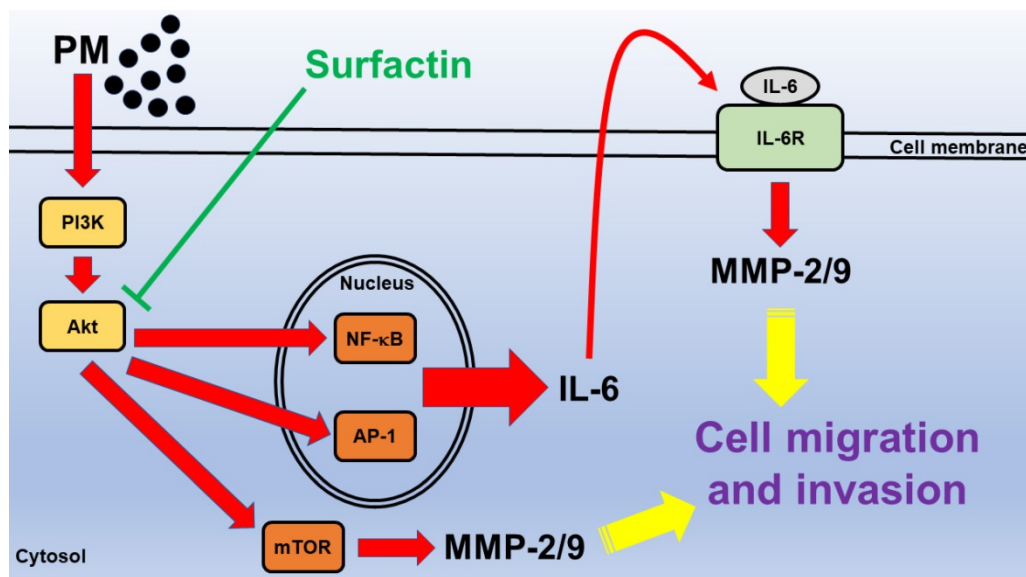


Figure 7. Schematic diagram illustrating the signaling pathway involved in surfactin-inhibited PM-induced human oral squamous cell carcinoma cell line migration and invasion. PM induces MMP-2/9-dependent cell migration and invasion via the PI3K/Akt/mTOR and PI3K/Akt/NF-κB and AP-1/IL-6 signaling pathways. Moreover, surfactin from *Bacillus subtilis* can inhibit MMP-2/9 expression via inhibition of the activation of these two pathways induced by PM and then reduce cell migration and invasion.

associated with poor prognosis [33]. In the present study, we proved that PM could induce MMP-2 and MMP-9 activity and expression in SCC4 and SCC25 cells. On the other hand, PM_{2.5} has been shown to induce MMP-2 and MMP-9 expression in human keratinocytes and cause skin aging [6]. Indeed, we also found that the levels of MMP-2 and MMP-9 in oral cancer cells or breast cancer cells are higher than in human gingival fibroblasts under the stimulation of PM (Supplementary Fig. 1). Moreover, surfactin can markedly reduce PM-induced MMP-2 and MMP-9 mRNA levels in these cells. These results suggest that in addition to inflammation, MMP-2 and MMP-9 may also contribute to the migration and invasion of cancer cells. Moreover, surfactin can inhibit PM-induced cell migration and invasion via inhibition of MMP-2 and MMP-9 expression in various cancer cells including oral cancer cells and breast cancer cells. TIMP is the endogenous inhibitor of most secreted MMPs [18]. In our study, we proved that surfactin could not inhibit cell migration and invasion through induction of these endogenous inhibitors including TIMP-1 and TIMP-2. Thus, we suggest that surfactin has the anti-cancer effects by directly inhibiting MMP-2 and MMP-9 levels in response to PM.

Up-regulation of MMP-2 and MMP-9 expression was mediated through various signaling pathways including AP-1 and NF-κB [19, 20]. NF-κB is the main mediator and can regulate the crosstalk between inflammation and cancer at multiple levels [34]. AP-1 is composed of a Jun-Jun homodimer or a Jun-Fos heterodimer [35]. *AP-1* is involved in the control of many cancer cells [35]. The PI3K/Akt/mTOR signaling is a frequently hyperactivated pathway in

cancer and is critical for the growth and survival of tumor cells [21]. AP-1 and NF-κB activation was regulated via many signaling pathways, such as Akt [22, 23]. We proved that PM induced MMP-2 and MMP-9 expression via these signaling pathways by using siRNA of p65, c-Jun, p50, c-Fos, p85, p110, Akt, or mTOR. PM also caused p65, c-Jun, Akt, and mTOR activation in these cells. However, surfactin could inhibit MMP-2 and MMP-9-dependent cell migration/invasion via inhibition of the activation of NF-κB, AP-1, Akt, and mTOR in response to PM. Although many studies have showed that surfactin has anti-cancer function, our research team first pointed out that surfactin can inhibit oral cancer migration and invasion induced by PM. In the future, we will investigate other novel signaling pathways involved in surfactin-inhibited MMP-2 and MMP-9 expression and activity in response to PM.

IL-6 is one of the cytokines in the tumour micro-environment. In addition, IL-6 is a critical factor which is detected at high levels and shown to be deregulated in cancer. Many reports indicated that IL-6 can promote tumor growth and metastasis [24, 25]. IL-6 also has been shown to regulate MMP-9 expression [26]. This is confirmed by our observation that IL-6 siRNA suppressed PM-induced MMP-2 and MMP-9 expression. As we expected, surfactin decreased IL-6 secretion induced by PM. In the future, we will investigate other cytokines involved in PM-caused cell migration and invasion. However, surfactin can achieve anti-cancer effects by inhibiting these cytokines induced by PM.

In Fig. 7, we prove that in SCC4 and SCC25 cells, PM induces MMP-2/9-dependent cell migration and

invasion via the PI3K/Akt/mTOR and PI3K/Akt/NF- κ B and AP-1/IL-6 signaling pathways. Surfactin from *Bacillus subtilis* can inhibit MMP-2/9 expression via inhibition of the activation of these two pathways induced by PM and then reduce cell migration and invasion. These experimental data also give us a new direction for the prevention and treatment of oral cancer.

Supplementary Material

Supplementary figure S1.

<http://www.jcancer.org/v11p6038s1.pdf>

Acknowledgments

This work was supported by the Taipei Medical University, grant number TMU108-AE1-B10; the Taipei Medical University Hospital, grant number 109TMU-TMUH-16; Chang Gung University of Science Foundation, grant number ZRRPF6K0011; Chang Gung Medical Research Program Foundation, grant number CMRPF6H0101, CMRPF6J0051, and CMRPF6K0041.

Competing Interests

The authors have declared that no competing interest exists.

References

- Myers D, Allen E, Essa A, Gbadamosi-Akindele M. Rapidly growing squamous cell carcinoma of the tongue. *Cureus*. 2020; 12: e7164-7.
- Chu YH, Kao SW, Tantoh DM, Ko PC, Lan SJ, Liaw YP. Association between fine particulate matter and oral cancer among Taiwanese men. *J Investig Med*. 2019; 67: 34-8.
- Hwang J, Bae H, Choi S, Yi H, Ko B, Kim N. Impact of air pollution on breast cancer incidence and mortality: a nationwide analysis in South Korea. *Sci Rep*. 2020; 10: 5392-8.
- Zhang Z, Zhu D, Cui B, Ding R, Shi X, He P. Association between particulate matter air pollution and lung cancer. *Thorax*. 2020; 75: 85-7.
- Xie H, Ma Y, Li J, Chen H, Xie Y, Chen M, et al. WNT7A promotes EGF-induced migration of oral squamous cell carcinoma cells by activating β -catenin/MMP9-mediated signaling. *Front Pharmacol*. 2020; 11: 98-113.
- Hyun YJ, Piao MJ, Kang KA, Zhen AX, Madushan Fernando PDS, Kang HK, et al. Effect of fermented fish oil on fine particulate matter-induced skin aging. *Mar Drugs*. 2019; 17: 61-71.
- Chen BH, Hsieh CH, Tsai SY, Wang CY, Wang CC. Anticancer effects of epigallocatechin-3-gallate nanoemulsion on lung cancer cells through the activation of AMP-activated protein kinase signaling pathway. *Sci Rep*. 2020; 10: 5163-73.
- Wang Q, Xu H, Zhao X. Baicalin inhibits human cervical cancer cells by suppressing protein kinase C/signal transducer and activator of transcription (PKC/STAT3) signaling pathway. *Med Sci Monit*. 2018; 24: 1955-61.
- Li H, Chen C. Quercetin has antimetastatic effects on gastric cancer cells via the interruption of uPA/uPAR function by modulating NF- κ B, PKC- δ , ERK1/2, and AMPK α . *Integr Cancer Ther*. 2018; 17: 511-23.
- Park SY, Kim JH, Lee YJ, Lee SJ, Kim Y. Surfactin suppresses TPA-induced breast cancer cell invasion through the inhibition of MMP-9 expression. *Int J Oncol*. 2013; 42: 287-96.
- Cao X, Wang AH, Jiao RZ, Wang CL, Mao DZ, Yan L, et al. Surfactin induces apoptosis and G₂/M arrest in human breast cancer MCF-7 cells through cell cycle factor regulation. *Cell Biochem Biophys*. 2009; 55: 163-71.
- Wang CL, Liu C, Niu LL, Wang LR, Hou LH, Cao XH. Surfactin-induced apoptosis through ROS-ERS-Ca²⁺-ERK pathways in HepG2 cells. *Cell Biochem Biophys*. 2013; 67: 1433-9.
- Lee IT, Lin CC, Yang CC, Hsiao LD, Wu MY, Yang CM. Resveratrol attenuates *Staphylococcus aureus*-induced monocyte adhesion through downregulating PDGFR/AP-1 activation in human lung epithelial cells. *Int J Mol Sci*. 2018; 19: 3058-73.
- Lee CW, Wu CH, Chiang YC, Chen YL, Chang KT, Chuang CC, et al. Carbon monoxide releasing molecule-2 attenuates *Pseudomonas aeruginosa*-induced ROS-dependent ICAM-1 expression in human pulmonary alveolar epithelial cells. *Redox Biol*. 2018; 18: 93-103.
- Yang CM, Lee IT, Hsu RC, Chi PL, Hsiao LD. NADPH oxidase/ROS-dependent PYK2 activation is involved in TNF- α -induced matrix metalloproteinase-9 expression in rat heart-derived H9c2 cells. *Toxicol Appl Pharmacol*. 2013; 272: 431-42.
- Payne SL, Levin M, Oudin MJ. Bioelectric control of metastasis in solid tumors. *Bioelectricity*. 2019; 1: 114-30.
- Yu W, Wang Y, Liu L, Li S, Zhu K. LOC101060264 silencing suppresses invasion and metastasis of human colon cancer. *Med Sci Monit*. 2020; 26: e920270-9.
- Li J, Xu X, Jiang Y, Hansbro NG, Hansbro PM, Xu J, et al. Elastin is a key factor of tumor development in colorectal cancer. *BMC Cancer*. 2020; 20: 217-28.
- Yang CC, Lin CC, Jou MJ, Hsiao LD, Yang CM. RTA 408 inhibits interleukin-1 β -induced MMP-9 expression via suppressing protein kinase-dependent NF- κ B and AP-1 activation in rat brain astrocytes. *Int J Mol Sci*. 2019; 20: 2826-44.
- Hsieh MJ, Chen JC, Yang WE, Chien SY, Chen MK, Lo YS, et al. Dehydroandrographolide inhibits oral cancer cell migration and invasion through NF- κ B, AP-1, and SP-1-modulated matrix metalloproteinase-2 inhibition. *Biochem Pharmacol*. 2017; 130: 10-20.
- Zhang J, Xie T. Ghrelin inhibits cisplatin-induced MDA-MB-231 breast cancer cell apoptosis via PI3K/Akt/mTOR signaling. *Exp Ther Med*. 2020; 19: 1633-40.
- Lian J, Zou Y, Huang L, Cheng H, Huang K, Zeng J, et al. Hepatitis B virus upregulates cellular inhibitor of apoptosis protein 2 expression via the PI3K/AKT/NF- κ B signaling pathway in liver cancer. *Oncol Lett*. 2020; 19: 2043-52.
- Chiu YC, Lin CY, Chen CP, Huang KC, Tong KM, Tzeng CY, et al. Peptidoglycan enhances IL-6 production in human synovial fibroblasts via TLR2 receptor, focal adhesion kinase, Akt, and AP-1 dependent pathway. *J Immunol*. 2009; 183: 2785-92.
- Zeng J, Chen S, Li C, Ye Z, Lin B, Liang Y, et al. Mesenchymal stem/stromal cells-derived IL-6 promotes nasopharyngeal carcinoma growth and resistance to cisplatin via upregulating CD73 expression. *J Cancer*. 2020; 11: 2068-79.
- Wu Y, Xu M, He R, Xu K, Ma Y. ARHGAP6 regulates the proliferation, migration and invasion of lung cancer cells. *Oncol Rep*. 2019; 41: 2281-8.
- Zhu M, Yang M, Yang Q, Liu W, Geng H, Pan L, et al. Chronic hypoxia-induced microvessel proliferation and basal membrane degradation in the bone marrow of rats regulated through the IL-6/JAK2/STAT3/MMP-9 pathway. *Biomed Res Int*. 2020; 2020: 9204708-17.
- Oh LJ, Phan K, Kim SW, Low TH, Gupta R, Clark JR. Elective neck dissection versus observation for early-stage oral squamous cell carcinoma: Systematic review and meta-analysis. *Oral Oncol*. 2020; 105: 104661-5.
- Yamaguchi H, Wyckoff J, Condeelis J. Cell migration in tumors. *Curr Opin Cell Biol*. 2005; 17: 559-64.
- Xu D, McKee CM, Cao Y, Ding Y, Kessler BM, Muschel RJ. Matrix metalloproteinase-9 regulates tumor cell invasion through cleavage of protease nexin-1. *Cancer Res*. 2010; 70: 6988-98.
- Wu YS, Ngai SC, Goh BH, Chan KG, Lee LH, Chuah LH. Anticancer activities of surfactin and potential application of nanotechnology assisted surfactin delivery. *Front Pharmacol*. 2017; 8: 761-82.
- Zhang H, Li Z. microRNA-16 via Twist1 inhibits EMT induced by PM2.5 exposure in human hepatocellular carcinoma. *Open Med*. 2019; 14: 673-82.
- Roomi MW, Kalinovsky T, Niedzwiecki A, Rath M. Modulation of MMP-2 and -9 secretion by cytokines, inducers and inhibitors in human melanoma A-2058 cells. *Oncol Rep*. 2017; 37: 3681-7.
- Roomi MW, Monterrey JC, Kalinovsky T, Rath M, Niedzwiecki A. Patterns of MMP-2 and MMP-9 expression in human cancer cell lines. *Oncol Rep*. 2009; 21: 1323-33.
- Kaltschmidt B, Greiner JFW, Kadhim HM, Kaltschmidt C. Subunit-specific role of NF- κ B in cancer. *Biomedicines*. 2018; 6: 44-55.
- Jochum W, Passequé E, Wagner EF. AP-1 in mouse development and tumorigenesis. *Oncogene*. 2001; 20: 2401-12.



REVIEW

Role of gut microbiota in identification of novel TCM-derived active metabolites

Tzu-Lung Lin¹, Chia-Chen Lu^{2,3}, Wei-Fan Lai⁴, Ting-Shu Wu^{4,5,6}, Jang-Jih Lu^{5,6}, Young-Mao Chen⁷, Chi-Meng Tzeng⁸, Hong-Tao Liu⁹, Hong Wei¹⁰, Hsin-Chih Lai^{1,5,6,11,12}✉

¹ Department of Medical Biotechnology and Laboratory Science, College of Medicine, Chang Gung University, Gueishan, Taoyuan 33302, Taiwan, China

² Department of Respiratory Therapy, Fu Jen Catholic University, New Taipei City 24205, Taiwan, China

³ Department of Chest Medicine, Internal Medicine, Fu Jen Catholic University Hospital, Fu Jen Catholic University, New Taipei City 24205, Taiwan, China

⁴ Department of Medicine, Chang Gung University, Taoyuan 33302, Taiwan, China

⁵ Department of Laboratory Medicine and Internal Medicine, Linkou Chang Gung Memorial Hospital, Taoyuan 33305, Taiwan, China

⁶ Central Research Laboratory, Xiamen Chang Gung Hospital, Xiamen 361026, China

⁷ Bachelor Degree Program in Marine Biotechnology, College of Life Sciences, National Taiwan Ocean University, Keelung 20224, Taiwan, China

⁸ School of Pharmaceutical Sciences, Xiamen University, Xiamen 361005, China

⁹ College of Basic Medicine, Hubei University of Chinese Medicine, Wuhan 430065, China

¹⁰ Central Laboratory, Clinical Medicine Scientific and Technical Innovation Park, Shanghai Tenth People's Hospital, Tongji University, Shanghai 200435, China

¹¹ Microbiota Research Center and Emerging Viral Infections Research Center, Chang Gung University, Taoyuan 33302, Taiwan, China

¹² Research Center for Chinese Herbal Medicine and Research Center for Food and Cosmetic Safety, College of Human Ecology, Chang Gung University of Science and Technology, Gueishan, Taoyuan 33303, Taiwan, China

✉ Correspondence: hclai@mail.cgu.edu.tw (H.-C. Lai)

Received March 13, 2020 Accepted May 29, 2020

ABSTRACT

Traditional Chinese Medicine (TCM) has been extensively used to ameliorate diseases in Asia for over thousands of years. However, owing to a lack of formal scientific validation, the absence of information regarding the mechanisms underlying TCMs restricts their application. After oral administration, TCM herbal ingredients frequently are not directly absorbed by the host, but rather enter the intestine to be transformed by gut microbiota. The gut microbiota is a microbial community living in animal intestines, and functions to maintain host homeostasis and health. Increasing evidences indicate that TCM herbs closely affect gut microbiota composition, which is associated with the conversion of herbal components into active metabolites. These may significantly affect the therapeutic

activity of TCMs. Microbiota analyses, in conjunction with modern multiomics platforms, can together identify novel functional metabolites and form the basis of future TCM research.

KEYWORDS Traditional Chinese Medicine, herbs, microbiota, transformation, multiomics

INTRODUCTION

TCM and herbal formulae

TCM has been used for centuries in China to alleviate symptoms, treat disease, and promote well-being in Chinese patients (Zhao et al., 2014). In contrast to modern Western medicine, research progress made in TCM is often inhibited because of the inherent complexity of herbs as medicine and a comparative lack of modern scientific validation.

Tzu-Lung Lin and Chia-Chen Lu have contributed equally.

Accordingly, TCM research must be modernized by meeting the scientific method.

Historically, recordings that emerged from functional TCM herbal ingredients and aimed at treating specific diseases, eventually evolved into the creating of specific formulae. These formulae were further revised and assembled to create the TCM version of the “Materia Medica”. These manuals established a solid basis and references of TCM for clinical treatment. Among these references, the “*Shennong Bencao Jing*” (literally, *Shennong’s Classic of Materia Medica*) (Jin et al., 2013), “*HuangDi NeiJing*” (literally *The Yellow Emperor’s Classic of Medicine*) (Ni, 1995), and “*Compendium of “Materia Medica”*” (Li et al., 2014; Hao and Jiang, 2015; Gao et al., 2016; Ding et al., 2020) were featured. TCM-derived materia medicas have been rapidly developed and created complicated herbal networks for clinical applications. Each materia medica contained many formulae, with each formula comprising a combination of herbal drugs. Among these, complex components including carbohydrates/polysaccharides (PS), proteins/peptides, glycolipids/glycoproteins, lipids, together with their metabolic derivatives such as glycosides, amines, fatty acids, flavonoids, terpenoids, phenols, and alkaloids intimately interacted with each other and modulated biological responses of immune cells and the hosts (Li and Kan, 2017; Yu et al., 2018b; Zhang et al., 2020c). Differential agonistic, compatible, or antagonistic interactions occur among TCM herbal ingredients. For instance, the Fuzheng Huayu (FZHY) is mainly composed of *Radix Salvia Miltiorrhizae*, *Cordyceps*, *Semen Persicae*, *Gynostemma Pentaphyllum*, *Pollen Pini*, and *Fructus Schisandrae Chinensis*. It is widely administered to ameliorate chronic liver diseases and functions through modulation of multiple signaling pathways in a number of organs (Chen et al., 2019). FZHY effectively regulates immune functions, optimizes systematic amino acid metabolism and endocrine function, and reduces portal vein hypertension (Chen et al., 2019). These alterations lead to improved liver function and antifibrotic effects. Additionally, FZHY also has no serious adverse reactions (Chen et al., 2019). Further, Gegen Qinlian decoction (GQD), composed of four herbs: Gegen (*Radix Puerariae*), Huangqin (*Radix Scutellariae*), Huanglian (*Rhizoma Coptidis*) and Gancao (Honey-fried Licorice Root) is frequently used in TCM for alleviation of type 2 diabetes (Xu et al., 2015). The Qushi Huayu Decoction (QHD), made up of *Herba Artemisiae capillaris*, *Rhizoma Polygoni cuspidati*, *Herba Hyperici Japonici*, *Rhizoma Curcumae longae*, and *Gardenia jasminoides* ameliorates non-alcoholic fatty liver disease (NAFLD) in patients (Feng et al., 2013).

Current advances in identification of active components from TCM herbs

The basic principle of scientific exploration in Western medicine has been the discovery of functional compounds

and their corresponding targets in specific signaling pathways within cells. To achieve this understanding, standardized phytochemistry, pharmacology, pharmacokinetics (PK, absorption/distribution/metabolism/excretion, ADME), pharmacodynamics (PD, effects/action/mechanism), and toxicology research procedures are performed (Chen et al., 2020). Currently, platforms for high throughput screening of compounds, together with stringent functional and safety validations are used to better understand the mechanisms of action of functional compounds. Concordantly, for the development of novel therapeutic drugs from TCM-derived herbs, a similar approach was established (Martel et al., 2017a; Jiang et al., 2020). Through this method, many active components in TCM herbs were identified. One famous example was the discovery of artemisinin, a plant-derived compound with anti-malaria and anti-cancer functions (Zhang et al., 2007; Carqueijeiro et al., 2019). Other examples included berberine purified from berberis, capsaicin from chili peppers, caffeine from coffee beans, ephedrine from Ephedra, chitosan from mushrooms, genistein from soybeans, celastrol from thunder god vine, epigallocatechin gallate from green tea, glycyrrhizin from licorice roots, quercetin from various plants, and curcumin from turmeric (Martel et al., 2017b). Besides small chemicals, functional polysaccharides (PS) derived from TCM herbs have also been characterized, such as those from *Ganoderma lucidum* mycelium (Chang et al., 2015), *Hirsutella sinensis* mycelium (Chang et al., 2015; Wu et al., 2019), and *Poria cocos* (Sun et al., 2019).

To improve the efficiency of screening for novel functional TCM herbal components, new approaches using modern technology have been explored. For example, a luciferase-based high-throughput screening (HTS) assay has been used to integrate multiple chemical messages derived from effective TCM healing formulae. This pipeline can expedite the active ingredient discovery process by reducing replicated leads (Yu et al., 2019a). Beyond this screen, a TCM System Pharmacology Database and Analysis Platform (TCMSP) had been established. The TCMSP is a systematic pharmacology database which compiles drug discovery results from previous herbal medicine experiments. This database contains pharmacochemistry, ADME and toxicity properties, drug likeness and targets, associated diseases, and interaction networks. Importantly, this database can be used to unravel active components in TCM herbs and their targeted cellular pathways (Ru et al., 2014; Li et al., 2020). Exploration of this database can be combined with other systems, such as Gene Ontology (GO) predictions and Kyoto Encyclopedia of Genes and Genomes (KEGG) pathway enrichment analyses to identify potential ameliorative mechanisms of key molecules (Yu et al., 2019a). Additionally, interactions between active molecules and their predicted target proteins may be further predicted by “molecular docking” and protein-protein interaction networks, which may enhance understanding of underlying potential interactions. Finally, the TCMSP database enables the linking of identified

compounds to their corresponding targets/pathways involved in disease amelioration. Therefore, through these analyses, axis of component-target-disease (C-T-D) and the corresponding target-pathway (T-P) networks could be established, to further dissect the active compounds, potential targets, and core pathways in treatment of diseases by a specific TCM formula (Li et al., 2020). Subsequently, LC and/or GC-MS/MS can be used to practically monitor the active ingredients of TCMs. This style of pipeline may provide a new, standardized approach to systematically screen TCM herbal components for treatment of diseases (Li et al., 2020). Accordingly, functional molecules in TCMs can be assessed in the context of heterogeneous cell signaling pathways to predict their effects on diseases at immunological, metabolic, and molecular levels (Zhang et al., 2016; Li and Kan, 2017).

Even though many *in vitro* assay-based screening systems are available for high throughput screening, most purified small chemical components directly derived from herbs still suffer from marginal potency, adverse effects, and low bioavailability in animal or clinical studies (Belcher et al., 2019; Liu et al., 2019a; Teijaro et al., 2019). For example, the compound rhein showed beneficial effects on diabetic nephropathy, which is related to reduced levels of TGF- β_1 , renal fibrosis, metabolism, and oxidative stress status (Hu et al., 2019). However, its adverse effects, such as hepatotoxicity, nephrotoxicity, and embryonic toxicity were also highlighted (Yuan et al., 2016). Further, chemical compounds derived from *Polygonum multiflorum* (also known as Heshouwu) showed ameliorative effects on hair-blackening, liver and kidney-tonifying, anti-aging, as well as neuronal disease treatment (Lin et al., 2015). However, these compounds could induce hepatotoxicity, nephrotoxicity and embryonic toxicity (Lin et al., 2015). Comparatively, the PS purified from TCM herbs showed less toxicity and were frequently modified in the host (Chen et al., 2016). So far the underlying molecular mechanism of PS effects remains poorly understood.

GUT MICROBIOTA MAINTAINS INTESTINAL HOMEOSTASIS AND PROMOTE HEALTH

The gut microbiota is a collection of microbes colonizing the intestine (Lin et al., 2014; Tsai et al., 2019; Zmora et al., 2019). More than 100 trillion (10^{14}) microbes inhabit the human gastrointestinal (GI) tract, which included about 10 times more bacterial cells than the number of human cells, and over 100 times the amount of genetic contents (microbiome) in contrast to the human genome (Thursby and Juge, 2017). Bacteria at the number between 10^2 – 10^4 colony-forming units (CFU)/mL are found in the first section of the small intestine, the duodenum. Generally, the Lactobacilli, Streptococci, Veillonellae, Staphylococci, Actinobacilli and yeasts dominate the duodenum and jejunum (Lin et al., 2014). The GI microbiota changes markedly from the

duodenum to the ileum, with an according increase in bacterial load, reaching up to 10^6 – 10^8 CFU/mL. In the large intestine, commensal bacteria reach high numbers (10^7 – 10^{12} CFU/mL) and are extremely diverse. At the same time, the environment of colon is strictly anaerobic. This means that obligate anaerobes that obtain their energy from fermentation dominate. More than 1,500 bacterial species have been identified in the colon of humans (Lin et al., 2014; Chang et al., 2019). However, a large proportion of the GI microbiota bacteria cannot be easily isolated and cultured *in vitro*, necessitating the use of culturomics (Lagier et al., 2018).

Under homeostasis situation, the intestinal microenvironment provides a barrier to prevent the translocation of pathogens or harmful agents (such as the endotoxin LPS) across the intestinal epithelial cells (IECs) into the surrounding lymphoid system and blood (Boyapati et al., 2016). Gut microbiota bacteria maintain host integrity and regulate many important physiological functions, including homeostasis of energy and metabolism, modification of xenobiotics, modulation of intestinal homeostasis, regulation of immunity and protection against pathogens, and even normal host neuronal behavior and cognitive functions (Clemente et al., 2012; Schachter et al., 2018; Lin et al., 2019).

In aberrant physical, chemical, or biological conditions, such as long-term high fat diet, antibiotic treatment, or increased oxidative stress, the composition of gut microbiota changes, lead to GI dysbiosis and disruption of the intestinal mucosa. This dysbiosis results in a damaged intestinal barrier and increased intestinal permeability. Proinflammatory elements, such as pathogen-associated molecular pattern molecules (PAMPS) (mainly the endotoxin, LPS) or damage-associated molecular pattern molecules (DAMPS) (Tang et al., 2012), are increased in intestines and blood, resulting in both local intestinal injury and systemic chronic inflammation (Yan, 2018; Alexandrov et al., 2019). This “leaky gut” phenomenon is closely related to development of chronic inflammation-related diseases. In a broad sense, the gut microbiota appears to be critical in maintaining host homeostasis and health (Lin et al., 2014; Wang et al., 2017a; Gentile and Weir, 2018).

CLOSE INTERACTION BETWEEN TCM HERBS AND GUT MICROBIOTA IN DISEASES AMELIORATION

TCM herbs closely interact with gut microbiota and affect their composition (Peng et al., 2020). Reciprocally, the gut microbiota also plays essential roles in the conversion of carbohydrates, proteins, lipids, and non-nutritive small chemical compounds from TCM herbs into chemical metabolites that may show beneficial or adverse effects on human health (Blaut and Clavel, 2007; Wang et al., 2013; Yu et al., 2018a; Feng et al., 2019; Lu et al., 2019; Qu et al., 2019; Yue et al., 2019; Zhang et al., 2019a, b, 2020c) (Fig. 1

and Table 1). These results indicated that modulation of gut microbiota composition may contribute to the effects of disease amelioration by TCM treatment. For oral treatment, TCM herbs have mostly been prepared by soaking the ingredients in boiling/hot water to generate a water extract that contains a mixture of chemical components, which was generally named as “decoction” (Zhou et al., 2016; Chi et al., 2019; Deng et al., 2019). While some TCM nutraceuticals may directly affect epithelial and immune cells of the digestive tract; others, such as indigestible PS, polyphenols, and alkaloids, etc., may pass through the stomach and reach small and large intestine. Many herbal ingredients are frequently fermented or converted by local gut microbiota to form bioactive, bioavailable, or even toxic metabolites (Lyu et al., 2017; Liu et al., 2018b; Dey, 2019; Wu and Tan, 2019; Yang and Lao, 2019). Depending on use of different formulae, some transformed metabolites may be functionally novel and not clearly defined (Fig. 1). Both changed microbiota bacteria and transformed TCM metabolites may contribute to control of progression of diseases development. Take the TCM effects on amelioration of diabetes as an example: while almost all bacterial phyla seemed to be affected by

TCM herbs administration, Bacteroidetes, Firmicutes (and therefore the Firmicutes/Bacteroidetes (F/B) ratio), Proteobacteria, Verrucomicrobia, Cyanobacteria, Deferribacteres, and Actinobacteria were mostly reported (Dey, 2019; Zhang et al., 2019a). Further detailed analyses indicated the abundance of potentially beneficial (such as anti-inflammatory, or SCFAs producers) and harmful (proinflammatory and pathogenic) bacteria could be differentially affected by ingestion of different TCM herbs (Chang et al., 2015; Lyu et al., 2017; Tong et al., 2018; Lin et al., 2019; Nie et al., 2019; Wu et al., 2019). Alteration of the gut microbiota composition is therefore closely related to development of differential immune and metabolic activities in the hosts. Roles of these bacteria on health or disease development are species or even strain dependent under different disease situations, which is under intensive study (Lin et al., 2019).

Recent studies have shown a variety of TCM herbal components influence microbial abundance and diversity, which reciprocally is closely related to the efficacy of TCM herbs (Table 1). Among these, effects from PS treatment on obesity, diabetes and related metabolic syndromes seemed to be most intensively studied. For example, treatment with

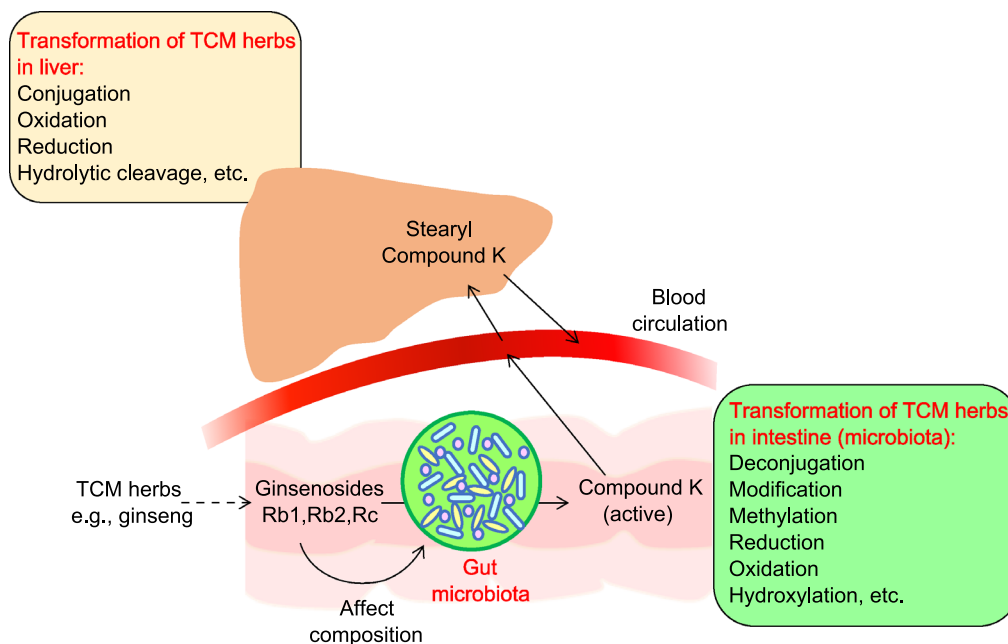


Figure 1. The transformation of TCM herbal ingredients (ginseng extracts as an example). Transformation of TCM herbal ingredients into active metabolites in host was contributed both by gut microbiota and liver. Understanding ginseng's pharmacokinetics is important for better medication in patients. After oral administration of ginseng, the bioavailability of ginsenosides is low, and the metabolites transformed by gut microbiota may become biologically active. For example, ginsenosides Rb1, Rb2 and Rc were transformed by gut microbiota to form compound K, followed by absorption into the blood (Qi et al., 2011). Compound K showed higher potency and activity compared with ginsenoside Rb1. Compound K adsorbed into blood metabolized again in liver to form stearyl compound K (Kim, 2018). On the other hand, ginsenoside Rb1 also could modulate the composition of gut microbiota (Wan et al., 2017). Therefore, gut microbiota produces active metabolites and plays an important role in the pharmacological action of orally administered ginseng.

Table 1. Relationship between TCM herbal ingredients, gut microbiota composition, metabolites produced and targeted diseases. ND, not clearly defined.

TCM herbal ingredients	Microbiota affected	Metabolites produced	Target diseases	References
Main component: Decoction or Tang				
Daesi ho Tang (DSHT)	Bacteroidetes, Bacteroidetes/Firmicutes ratio	ND	Obesity	(Hussain et al., 2016)
Gegen Qinlian Decoction (GQD)	<i>Faecalibacterium prausnitzii</i>	ND	Type 2 diabetes	(Xu et al., 2015)
Qushi Huayu Decocti (QHD)	Generally affects gut microbiota composition. Does not affect identified Gram-negative bacteria.	ND	NAFLD	(Leng et al., 2020)
Xiexin Tang (XXT)	Adlercreutzia, Alloprevotella, Barnesiella, Ventriosum group, Blautia, Lachnospiraceae UCG-001, Papillibacter, Prevotellaceae NK3B31 group	SCFAs	Type 2 diabetes	(Wei et al., 2018)
Metformin and a specifically designed herbal formula, AMC	Blautia spp., <i>Faecalibacterium</i> spp.	ND	Type 2 diabetes	(Tong et al., 2018)
Huang-Lian-Jie-Du decoction (HLJDD)	Parabacteroides, Blautia, Akkermansia, Aerococcus, Staphylococcus-Corynebacterium	SCFAs	Hyperglycemia and insulin resistance	(Chen et al., 2018b)
Qijian mixture	Mainly Bacteroidetes	55 proteins and related metabolism of galactose, valine, leucine, isoleucine, alanine, aspartate and glutamate. Biosynthesis of aminoacyl-tRNA.	Type 2 diabetes	(Gao et al., 2018)
Main component: TCM polysaccharide				
<i>G. lucidum</i>	Parabacteroides, Roseburia, Eubacterium, Clostridium	ND	Obesity, NAFLD, diabetes mellitus	(Chang et al., 2015)
<i>H. sinensis</i> mycelium	<i>P. goldsteinii</i>	ND	Obesity, NAFLD, diabetes mellitus	(Wu et al., 2019)
Mulberry fruit	Bacteroidales, Lactobacillus, Allobaculum, Bacteroides, Akkermansia	ND	Obesity	(Chen et al., 2018a)
<i>Ganoderma atrum</i>	ND	SCFAs	Intestinal mucosal dysfunction, type 2 diabetes	(Zhu et al., 2016) (Ying et al., 2020)
Stigma maydis	Lactobacillus, Bacteroides			(Wang et al., 2016)

Table 1. continued

TCM herbal ingredients	Microbiota affected	Metabolites produced	Target diseases	References
Main component: Proteins/amino acids				
A variety of different herbs	Multiple phyla in microbiota bacteria	-ammonia -amines -gases (methane, hydrogen gas, H ₂ S) -catecholamines and phenols (<i>p</i> -cresol, <i>p</i> -nitrosophenol, <i>p</i> -diazquinone, indoxyl sulfate, hippuric acid, phenyl sulfate, pyrocatechol sulfate, 4-ethylphenyl sulfate, <i>p</i> -cresol glucuronide, and equol 7-glucuronide) -neuro-active metabolites, such as serotonin, melatonin, kynurenine, quinolinine, indole, IAA, IPA, and tryptamine	Chronic inflammation related diseases	(Baumann and Bisping, 1995; Magee et al., 2000; Blachier et al., 2007; Neis et al., 2015; Liu et al., 2016; Mazzoli and Pessione, 2016; Portune et al., 2016; Velenosi et al., 2016; Lin et al., 2017; Ma et al., 2017; Kaur et al., 2019)
Main component: Lipids/fatty acids				
A variety of different herbs	Multiple phyla in microbiota bacteria	-conjugated essential fatty acids (conjugated linoleic acid) -trimethyl amine (TMA)	Chronic inflammation related diseases	(Devillard et al., 2007; Marques et al., 2015; Rath et al., 2017; Janeiro et al., 2018; Schoeler and Caesar, 2019; Yu et al., 2019b)
Main component: Chemicals and related				
A variety of different herbs	Multiple phyla in microbiota bacteria	-secondary glycosides and/or aglycones -CPT-11 related SN-38-glucuronide -secondary bile acids	Chronic inflammation related diseases	(Dabek et al., 2008; Yang et al., 2011; Yan et al., 2013; Chen et al., 2015; Wahlstrom et al., 2016; Ramirez-Perez et al., 2017; Jia et al., 2018)
Ginsenosides in Du-Shen-Tang (DST)	Enhance the growth of <i>Lactobacillus</i> spp. and <i>Bacteroides</i> spp.	ND	Fatigue, acute cold stress	(Zhou et al., 2016)
Banxia Xiexin decoction (BXD)	ND	Baicalin, baicalin, wogonoside-wogonin, scutellarin, berberine, coptisine, ginsenoside Rb1, ginsenoside Re	Diabetic gastroparesis	(Xu et al., 2018)
Melformin and <i>Houttuynia cordata</i> extract (HCE)	<i>Roseburia</i> , <i>Akkermansia</i> , Gram-negative bacteria including <i>Escherichia coli</i> , <i>Bacteroidetes fragilis</i> .	ND	Insulin resistance and metabolic syndromes	(Wang et al., 2017b; Wang et al., 2018a)
Berberine derived from <i>Coptis chinensis</i>	<i>Bifidobacterium</i> , <i>Escherichia coli</i>	ND	Glucolipid metabolism and insulin resistance in diabetic mice	(Han et al., 2016; Liu et al., 2018b)
Rhein	<i>Bacteroidetes</i>	ND	Antidiabetic effects	(Wang et al., 2018b)

PS purified from *G. lucidum* and *H. sinensis* mycelium significantly reduced obesity through enhancement of a consortium of commensal bacteria, including *Parabacteroides goldsteinii*, *Roseburia*, *Eubacterium* and *Clostridium* spp. (Chang et al., 2015; Wu et al., 2019). Mulberry fruit PS also influenced obesity and modulated gut microbiota (Chen et al., 2018a), while PS from *Ganoderma atrum* ameliorated intestinal mucosal dysfunction and improved liver function in type 2 diabetes (Zhu et al., 2016), and *stigma maydis* PS ameliorated type-2 diabetes (Wang et al., 2016) by changing gut microbial populations and related fermentation functions. Further, the PS and ginsenosides contained in decoction of ginseng, the Du-Shen-Tang (DST), restored fatigue and acute cold stress, and modulates the gut microbiota composition (Zhou et al., 2016). There were many other examples highlighting the microbial change during the treatment of obesity, diabetes and metabolic syndromes (Table 1). These examples include Daesih-Tang (DSHT) that attenuated obesity and significantly increased the relative abundance of Bacteroidetes, B/F ratio, Akkermansia, Bifidobacterium, Lactobacillus, and decreased the level of Firmicutes (Hussain et al., 2016), Gegen Qinlian Decoction (GQD) alleviated Type 2 diabetes and significantly increased *Faecalibacterium prausnitzii* (Xu et al., 2015), while Qushi Huayu Decoction (QHD) reduced HFD-induced non-alcoholic fatty liver disease (NAFLD), and significantly increased the abundance of Parabacteroides and decreased the abundance of Odoribacter, Rikenella, Tyzzerella, Intestini-bacter, Romboutsia and 2 members in Lachnospiraceae (Leng et al., 2020). Other examples related to gut microbiota changes included (Table 1): 20% *Folium Mori* amelioration of diabetes (Zhang et al., 2019a), Xiexin Tang-mediated improvement of type 2 diabetes (Wei et al., 2018), amelioration of human type 2 diabetes by metformin and a traditional Chinese herbal formula, AMC (Tong et al., 2018), Huang-Lian-Jie-Du decoction-mediated treatment of hyperglycemia and insulin resistance (Chen et al., 2018b), improvement of type 2 diabetes by treatment with Qijian (Gao et al., 2018), Banxia Xiexin decoction on diabetic gastroparesis rats (Xu et al., 2018), *Houttuynia cordata* facilitation of metformin on reducing insulin resistance (Wang et al., 2017b), berberine, the main bioactive alkaloid of *Coptis chinensis*, on glucolipid metabolism and insulin resistance in diabetic mice (Han et al., 2016; Liu et al., 2018a), and rhein's role in antidiabetic effects (Wang et al., 2018b). Evidently, efficacy of TCM herbal treatment is closely related to their influence on gut microbiota composition. Therefore, the ingredients of TCM herbs may not only directly regulate host cells activity, but also be metabolized by gut microbiota and affect their structures. Close interaction between TCM and gut microbiota contributes to modulating the host immune and metabolic activities. New research approaches based on gut microbiota-related characterization of clinically applicable TCM components have to be developed (Zhao et al., 2014).

ROLE OF GUT MICROBIOTA IN FERMENTATION OF TCM PS

TCM PS as well as other plant-derived PS such as vegetables, fruits, and whole grains etc. were shown to play important functions in immune-modulation and disease amelioration (Chang, 2002; Yang et al., 2009; Li et al., 2013; Yu et al., 2018b; Sun et al., 2019). For example, both high (>100 kDa.) and low (<100 kDa.) molecular weight, and neutral and acidic PS prepared from *Panax ginseng* that displayed differential functions affecting cellular and host physiology (Sun, 2011; Kim et al., 2020) were among the many examples. Owing to the limited digestive enzymes encoded by the human genome, PS are frequently undigested until they reach the colon (Baumann and Bisping, 1995). In the colon, fermentable PS, such as β -glucans, were broken down by gut microbes via their saccharolytic machinery to produce important groups of natural bioactive products. Serial digestion of PS resulted in production of a number of short-chain oligosaccharides, comprising varying chain lengths, structural conformations, and number of branches (Tzianabos, 2000; Santa et al., 2014). These varied oligosaccharides may function to enhance growth of probiotics, such as *Bifidobacterium* spp. and *Bacteroides* spp. (Bouhnik et al., 2004). The shorter PS may be further digested to form either monosugars such as mannose (Man), glucose (Glc), galactose (Gal), rhamnose (Rha), arabinose (Ara), and fucose (Fuc) which enhance bacterial growth (Koropatkin et al., 2012; Tremaroli and Backhed, 2012). Monosugars can continuously be catabolized to form metabolites such as short chain fatty acids (SCFAs) (formate, acetate, propionate, butyrate), lactate, hydrogen, and carbon dioxide, which may directly affect host physiology (Schwartz et al., 2010; Simpson and Campbell, 2015; Burokas et al., 2017; Martel et al., 2017a). On the other hand, degraded products such as D-mannose may act as signaling molecules which show differential immunomodulatory effects and functions towards host cells and tissues (Zhang et al., 2017; Zhang et al., 2018).

A consortium of gut bacteria participates in the degradation of TCM-derived PS. For example, a host of bacterial species are involved in butyrate production, including *F. prausnitzii*, *Eubacterium rectale*, *Roseburia* spp. *Clostridium* spp. and many others belonging to Bacteroidetes (Zhang et al., 2018). These functional bacteria were characterized by their displays of several to dozens of enzymes used to degrade PS by targeting specific glycosidic linkages or chemical substituents (Martens et al., 2011). Genetic clusters involved in binding, degradation and importation of various PS include miscellaneous polysaccharide utilization loci (PULs), or starch utilization system (Sus)-like systems in Bacteroidetes (Bayer et al., 2008; Ravcheev et al., 2013). Comparatively, with respect to carbohydrate active enzymes (CAZymes), Bacteroidetes degrade a relatively wide range of polysaccharides, while Firmicutes prefer to catabolize selected polysaccharides (Cockburn and Koropatkin, 2016;

Zhang et al., 2018). Many different bacterial species may involve sequential catabolism of PS, and the functional metagenomics of consortium of bacteria that participate in PS metabolism are currently under intensive study.

TCM AFFECTS GUT MICROBIOTA THAT PRODUCES FUNCTIONAL AMINO ACIDS METABOLITES

Dietary proteins including those derived from TCM herbs, dietary foods, and other nutraceuticals can be digested by both hosts and gut microbiota, which may further affect gut microbiota structure (Conlon and Bird, 2014; Madsen et al., 2017; Amaretti et al., 2019). At the same time, certain gut bacteria in the distal colon also metabolize amino acids to form unique functional metabolites through specific biochemical pathways (Baumann and Bisping, 1995; Neis et al., 2015; Liu et al., 2016). The metabolic intermediates produced may involve either optimal modulation of energy homeostasis, nutrition metabolism, intestinal health and immunity, or cause inflammation and diseases (Neis et al., 2015; Portune et al., 2016; Lin et al., 2017). Basically, deamination of amino acids results in the production of ammonia, whereas decarboxylation leads to amine production (Baumann and Bisping, 1995). Depending on the amount of proteins up taken, the concentrations of ammonia, trace amines, and gases (methane, hydrogen, H₂S) related to cytotoxins, genotoxins, and carcinogens produced in colon are altered (Ma et al., 2017). These harmful metabolites may translocate across the intestinal barrier and enter the blood for systematic circulation, resulting diseases development.

Anaerobic fermentation of cysteine and methionine by bacteria results in H₂S formation. Long term increased sulfide and ammonia concentrations in the colon were shown to promote colitis and tumorigenesis (Baumann and Bisping, 1995; Magee et al., 2000). Also, metabolism of aromatic amino acids may produce a group of uremic toxins, including indoxyl sulfate, *p*-cresyl sulfate, hippuric acid, phenyl sulfate, pyrocatechol sulfate, 4-ethylphenyl sulfate, *p*-cresol glucuronide, and equol 7-glucuronide (Velenosi et al., 2016). These compounds are closely related to the development of chronic kidney disease (CKD), where the gut-plasma-kidney metabolic axis is established (Mishima et al., 2017; Liu et al., 2018b). Furthermore, degradation of “tyrosine” gives rise to catecholamines and phenols, where *p*-cresol, *p*-nitrosophenol and *p*-diazquinone are proposed to show carcinogenic effects (Bone et al., 1976; Kikugawa and Kato, 1988), tyramine is related to hypertension, and DOPA, dopamine and nor-adrenaline can modulate multiple physiological functions (Mazzoli and Pessione, 2016). On the other hand, the anaerobic conversion of “tryptophan” also produces functional metabolites related to the gut-brain axis (GBA). These include neuro-active metabolites, such as serotonin, melatonin, kynurenine, quinolinic acid, indole, IAA, IPA, and tryptamine (Mazzoli and Pessione, 2016; Kaur et al., 2019). Other

neuroactive molecules including histamine, glutamate, and GABA are also synthesized owing to the close interaction between the host and the microbiota (Sharon et al., 2014; Mazzoli and Pessione, 2016). The gut bacteria involved in such metabolism processes were widely categorized into five phyla including Actinobacteria, Firmicutes, Bacteroidetes, Proteobacteria, and Fusobacteria, in which *Clostridium*, *Burkholderia*, *Streptomyces*, *Pseudomonas*, and *Bacillus* were further enriched to be involved in the many tryptophan metabolism pathways (Kaur et al., 2019).

Branched chain amino acids (BCAAs), such as leucine (Leu), isoleucine (Ile), and valine (Val), work both as the substrates for anabolism of nitrogenous compounds and as signaling molecules regulating energy homeostasis via multiple signaling networks, including the phosphoinositide 3-kinase/protein kinase B/mammalian target of rapamycin (PI3K/AKT/mTOR) pathway (Nie et al., 2018). Gut microbiota also participates in fermentation of BCAA and generates a complex mixture of metabolites, including ammonia, SCFAs, and branched-chain fatty acids (valerate, isobutyrate, and isovalerate). These bacterial metabolites have been shown to influence normal mucosal immunity of the host (Blachier et al., 2007).

Generally, the abundance of gut microbiota bacteria that are involved in amino acids metabolism are frequently affected by TCM herbs administration (Chang et al., 2015; Lyu et al., 2017; Tong et al., 2018; Feng et al., 2019; Lin et al., 2019; Nie et al., 2019; Wu et al., 2019; Yue et al., 2019; Zhang et al., 2019a). These included the *Clostridium* clusters, *Bacillus*, *Lactobacillus*, *Streptococcus*, and *Proteobacteria* in human small intestine, and the *Clostridia* and *Peptostreptococci* in large intestine of healthy humans (Neis et al., 2015). More and more bacterial species are expected to be unraveled to be involved in protein metabolism. Therefore, advances with regard to unraveling the protein/amino acid fermentation pathways, the potential novel corresponding metabolites produced by gut microbiota, and modulation of microbiota composition by TCM herbs are essential (Zhang et al., 2019b).

TCM-AFFECTED GUT MICROBIOTA PRODUCES FUNCTIONAL METABOLITES IN LIPID METABOLISM

Lipids and their derived functional metabolites play multiple physiological roles in the host. Lipids from TCM herbs and daily foods intake have also been shown to affect gut microbial growth and composition, while gut microbiota bacteria are also important players in lipid metabolism in hosts (Marques et al., 2015; Di et al., 2019; Schoeler and Caesar, 2019; Yu et al., 2019b) (Table 1). Besides SCFAs, many other functional metabolites derived from lipid metabolism are also produced by bacteria in the gut. For example, commensal bacteria, including *Roseburia*, *Lactobacillus*, *Butyrivibrio*, and *Megasphaera* participate in fatty acid metabolism to produce an array of conjugated essential fatty

acids (e.g., conjugated linoleic acid) that intricately influence host physiology (Devillard et al., 2007). On the other hand, milk fat increases taurine-conjugation of bile acids, which leads to the further growth of *Bilophila wadsworthia* that then uses the increased availability of amino acid-derived sulfur to produce H_2S closely related to the incidence rates of colitis (Devkota et al., 2012).

Using key enzyme components of the trimethylamine (TMA)-synthesis pathways such as the choline TMA-lyase (CutC) pathway and carnitine oxygenase (CntA) pathway, gut bacteria such as *Clostridium* XIVa strains and *Eubacterium* spp. catabolize choline and L-carnitine to produce TMA. TMA is converted to trimethylamine-N-oxide (TMAO) in the liver (Rath et al., 2017; Janeiro et al., 2018). Many studies have indicated a close association between TMAO plasma levels and the risk of atherothrombotic cardiovascular disease (CVD) (Canyelles et al., 2018).

Previous studies have highlighted the roles of gut bacteria, such as Akkermansia, Butyrivibrio, Christensenellaceae, Eggerthella, Tenericutes, and Pasteurellaceae, on affecting specific aspects of lipid metabolism and/or distinct classes of lipoproteins (Ghazalpour et al., 2016). At the same time, rapid progresses have been made in unraveling the underlying mechanisms of TCM-mediated regulation of lipid metabolism and amelioration of disease. For instance, TCMs have been shown to inhibit intestinal absorption, reduce de novo biosynthesis, increase catabolism, and enhance secretion in lipids (Bei et al., 2012). The changed gut microbiota composition by TCM herbs administration may contribute to the ameliorative effects on abnormal lipids metabolism (Huang et al., 2019; Zhang et al., 2019a). On the other hand, ginseng extract can enrich *Enterococcus faecalis* that produces an unsaturated long chain fatty acid, myristoleic acid (MA), leading to reducing adiposity by activation of brown adipose tissue (BAT) and formation of beige fat (Quan et al., 2019). Therefore, modulation of gut microbiota bacteria by TCM herbs may produce optimal amounts of beneficial lipid metabolites, which is an effective strategy for promotion of well-being in hosts.

TRANSFORMATION OF TCM SMALL CHEMICAL MOLECULES BY GUT MICROBIOTA

Different TCM formulae contain an array of small chemical molecules with a number biological functions, including flavonoids, saponins, alkaloids, and anthraquinones, etc. (Xu et al., 2013; Yan et al., 2013; Chen et al., 2015; Zhang et al., 2020b) (Table 1). Both gut microbiota and the liver involve conversion of the xenobiotics ingredients into subsequent metabolites (Fig. 1). In the intestines, these components can be modified/deconjugated by gut microbiota. Alternatively, they can also be absorbed and transported to the liver, where they are also modified/conjugated to increase their water solubility and facilitate excretion. After excretion into the intestinal tract from liver, these metabolites may further

undergo modification/deconjugation by gut microbiota to form secondary metabolites (Wahlstrom et al., 2016; Kim, 2018). Many of the transformed metabolites frequently act as functional compounds directly influencing the curative effects of TCM treatment. For example, herbal glycosides such as saponins, geniposide, iridoid glycosides, and flavone glycosides frequently identified in TCM ingredients are metabolized into secondary glycosides or aglycones by bacterial β -glucosidase (GUS) (Dabek et al., 2008; Yang et al., 2011) (Fig. 1). Such transformation may affect the bioavailability and bioactivity of these molecules (Yang et al., 2011). Additionally, the gut microbial GUS enzymes encoded by a variety of gut bacteria belonging to Firmicutes (60%) and Bacteroidetes (21%) (Humblot et al., 2007; Creekmore et al., 2019) also catalyze hydrolysis of β -D-glucuronic acid from their conjugated compounds and influence drug potency and toxicity. The transformation of ginseng extracts is taken as an example (Fig. 1). After oral administration, ginsenosides such as Rb1, Rb2 and Rc from ginseng extracts were transformed by gut microbiota to form 20-O- β -D-glucopyranosyl-20(S)-protopanaxadiol (compound K) which was absorbed into the blood to achieve the pharmacological functions. Compound K showed more potent anti-tumor, anti-inflammatory, and anti-allergic activities more than ginsenoside Rb1 (Wang et al., 2011; Kim et al., 2013). Therefore, the gut microbiota plays an important role in the pharmacological action of orally administered ginseng.

Another example is the CPT-11 which is a potent anti-cancer agent metabolized to the active compound, SN-38 *in vivo*. A balanced SN-38 concentration in patients is essential to maintain optimal efficacy of cancer treatment while reducing toxicity. Intriguingly, both TCM components and gut microbiota are involved in modulation of SN-38 activity. For detoxification, SN-38 is conjugated to SN-38-glucuronide by UDP-glucuronosyltransferase (UGT). However, purified herbal aglycons where the glycosyl group of a glycoside was removed inhibited UGT activity (Yokoi et al., 1995; Ramesh et al., 2010; Bailly, 2019), leading to an increase in toxic SN-38 concentration in the enterohepatic circulation. On the other hand, gut microbiota bacteria also use the *gus* encoded β -glucuronidase for deconjugation of the SN-38-glucuronide. Therefore, the underlying regulatory activities formed a complicated regulatory network (Dabek et al., 2008). How to achieve a balanced SN-38 activity in patients with maximal efficacy of cancer treatment while reducing toxicity is an important issue.

Gut microbiota also transform bile acids and cholesterol, producing a variety of functional metabolites (Gerard, 2013). Among these, primary bile acids are produced in the liver as glycine, taurine, or sulfate conjugates, and after secretion into the intestine, are deconjugated and modified by intestinal bacteria. Through interaction with bile acid farnesoid X receptor (FXR) and G protein-coupled bile acid receptor 1 (TGR5), bile acids signaling controls multiple important physiological behaviors and maintains intestinal homeostasis and a healthy environment (Jia et al., 2018). Bacteria such as

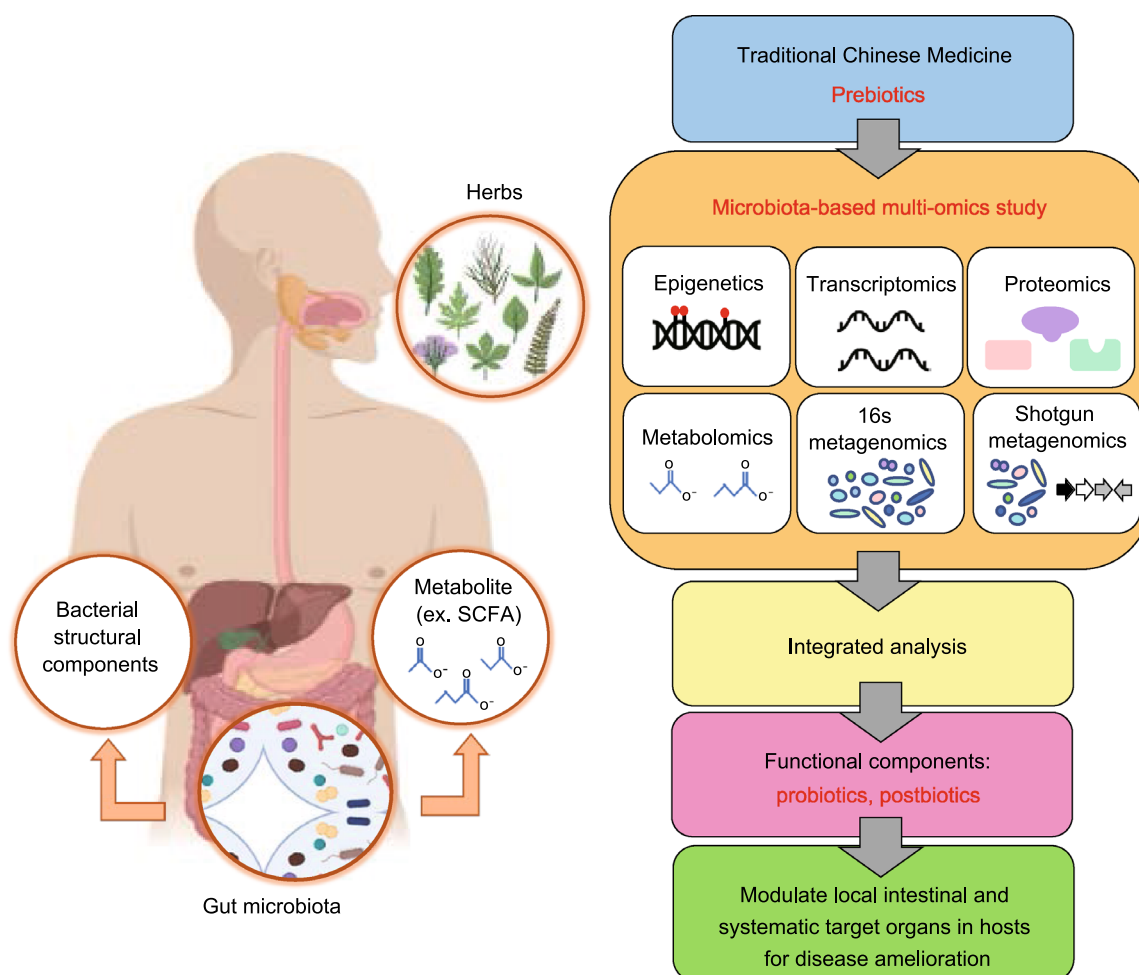


Figure 2. Microbiota-based integrated multi-omics platforms for TCM-derived herb study. The basic rationale is to identify TCM herbs related active components after transformation by gut microbiota fermentation. The multiomics platforms such as, epigenetics, 16s metagenomics, shotgun metagenomics, transcriptomics, proteomics, and metabolomics are to be used, followed by the integrated analysis. Such strategy may identify novel TCM prebiotics, bacteria (probiotics) and metabolites (postbiotics) as well as bacterial structural components (paraprobiotics) to modulate local intestine and systematic target organs in hosts for disease amelioration.

Bacteroides, Bifidobacterium, Clostridium, Egghertella, Escherichia, Eubacterium, Fusobacterium, Lactobacillus, Listeria, Peptococcus, Peptostreptococcus, Pseudomonas, and Ruminococcus, use their enzymes in deconjugation, oxidation and epimerization, 7-dehydroxylation, esterification, and desulfatation of the bile acids (Gerard, 2013). Secondary bile acids that might work as tumor promoters are therefore produced after bacterial fermentation in intestine (Wahlstrom et al., 2016; Ramirez-Perez et al., 2017; Jia et al., 2018). Accordingly, the development of disease-treatment strategies using TCM herbs, or use of metabolically engineered bacteria to modify chemicals for maintaining health are warranted (van Duynhoven et al., 2011; Lee et al., 2012; Anlu et al., 2019).

MICROBIOTA-BASED INTEGRATED MULTIOMICS STUDY-THE NEXT GENERATION TCM HERBAL RESEARCH

Owing to the difficulties encountered in TCM research, one must consider developing novel strategy to characterize TCM herbs related active components. For future TCM-derived herbal studies, use of microbiota-based integrated multiomics platforms seems critical (Fig. 2). The underlying basic rationale is as follows: instead of directly screening functional components from herbal extracts, identifying functional components after transformation by gut microbiota fermentation using multiomics approaches (Fig. 2). Prepared TCM herbal products (such as crude extracts/decoctions or powders), are first fed to animals to evaluate their efficacy of

disease amelioration. If positive results are obtained, the classification and abundance of bacteria in intestine/feces, and their derived metabolites (including bacterial structural components containing potential paraprobiotics) in intestine/feces/blood samples are subsequently quantified. Bacteria and metabolites that show statistical differences between control and experimental groups may be involved in treatment efficacy of the disease in question, and accordingly will be targets of interest. These bacteria (potential probiotics) or compounds (potential postbiotics or paraprobiotics), either singly or in a consortium, will then be systematically assessed for their function and mechanism. To achieve this, cutting-edge analyses platforms, such as next generation sequencing (NGS), proteomics, and metabolomics are to be used.

The experimental design of microbiota-based TCM multiomics research is described as follows (Fig. 2): (i) In preparing TCM herbal products such as decoction, strictly follow the instructions for consistency. (ii) Optimally grouping the animals and humans, followed by observing disease progression and development, and finally evaluating the results by statistics. (iii) The composition of gut microbiota and/or their predicted functions of gut microbiome are analyzed by 16S rRNA gene sequencing, or shotgun sequencing, respectively, followed by bioinformatics analyses on operational taxonomic units (OTUs), and other functional DNA fragments. (iv) Metabolites will be analyzed by metabolomics combined with other analyses such as metatranscriptomics (for gut microbiota), and epigenetics, transcriptomics/single cell RNA sequencing (scRNA seq), and proteomics (for host). This multiomics approach will work in concert with traditional immunological, physiological, and pathological analyses for holistic results. (v) Associations between and among datasets obtained from control and experimental groups are analyzed to identify parameters with significant differences. Potential enriched or decreased biochemical pathways are established by GO and KEGG pathway analyses. Besides, some databases related to TCM and gut microbiota research including the TCM-Mesh, TCMSp, Traditional Chinese Medicines Integrated Database (TCMID), Compound Reference Database (CRD) and HIT, as well as pathogen-host databases (PHI-base and EHFPI) can be used as references of analytical systems for TCM pharmacology network analysis (Zhang et al., 2020a, b). (v) Isolate selected microbiota bacteria and purify or synthesize novel functional metabolites for further evaluation or validation of their safety and efficacy. (vii) Based on the results obtained, evaluate the possibility of further clinical trials.

Critically, after fermentation of TCM ingredients by microbiota, only important elements involved in the regulation of signaling pathways and diseases amelioration are highlighted. These elements are then selected to develop new treatment strategies. Currently, there are many multiomics-based templates that can be recruited as references for use in TCM and microbiota related studies. For instance,

a functional analysis of the gut microbiota ecosystem for better understanding inflammatory bowel disease (IBD) (Lloyd-Price et al., 2019), while the modified ColPortal platform (Esteban-Gil et al., 2019) integrates multiomics studies to understand the relationship between the microbiota and metabolomics in inflammatory bowel disease (IBS) disease model (Liu et al., 2019b). The pipelines described here have the potential to identify novel TCM-based herbal prebiotics, probiotics, and postbiotics for treatment of disease.

PERSPECTIVE

Recent studies have demonstrated that gut microbiota participate in the metabolism of foods and nutrients and play central roles in the transformation of original TCM herbal components into functional metabolites. Under increasing studies on characterizing the metabolites after administration of various TCM herbs and gut microbiota transformation, together with the help from cutting-edge multiomics research tools, such as the NGS and metabolomics platforms, as well as the advanced bioinformatics analyses, databases, and algorithms, the identification of novel and effective metabolites for safe treatments is possible. Ultimately, a better understanding of the molecular mechanisms TCM function will make great contributions to the effective treatment of the chronic inflammation related diseases.

ACKNOWLEDGEMENTS

We would like to express our thankfulness for funding provided from CORPD1F0013 and CORPD1J0052 from Chang Gung Memorial Hospital, Microbiota Research Center from Chang Gung University, and the Research Center for Emerging Viral Infections from The Featured Areas Research Center Program within the framework of the Higher Education Sprout Project (MOST109-2634-F-182-001, 109-2320-B-030-010, 109-2327-B-182-001).

ABBREVIATIONS

ADME, absorption/distribution/metabolism/excretion; Ara, arabinose; BAT, brown adipose tissue; BCAAs, branched chain amino acids; CAZymes, carbohydrate active enzymes; CFU, colony-forming units; CKD, chronic kidney disease; CRD, compound Reference Database; C-T-D, component-target-disease; CVD, cardiovascular disease; DAMPS, damage-associated molecular pattern molecules; DSHT, Daesiho-Tang; DST, Du-Shen-Tang; F/B, Firmicutes/Bacteroidetes; Fuc, Fucose; FZHY, Fuzheng Huayu; Gal, galactose; GI, gastrointestinal; Glc, glucose; GO, Gene Ontology; GQD, Gegen Qinlian decoction; GUS, β -glucosidase; HTS, high-throughput screening; IBD, inflammatory bowel disease; IECs, intestinal epithelial cells; Ile, isoleucine; KEGG, Kyoto Encyclopedia of Genes and Genomes; Leu, leucine; MA, myristoleic acid; Man, mannose; NAFLD, non-alcoholic fatty liver disease; NGS, next generation sequencing; OTUs, operational taxonomic units; PAMPS, pathogen-associated molecular pattern molecules; PD, pharmacodynamics; PK, pharmacokinetics; PS, polysaccharides; PULs, polysaccharide utilization loci; QHD, Qushi Huayu Decoction; Rha, rhamnose;

SCFAs, short chain fatty acids; scRNA seq, single cell RNA sequencing; Sus, starch utilization system; TCM, Traditional Chinese Medicine; TCMID, Traditional Chinese Medicines Integrated Database; TCMSP, TCM System Pharmacology Database and Analysis Platform; TMA, trimethylamine; TMAO, trimethylamine-*N*-oxide; T-P, target-pathway; UGT, UDP-glucuronosyltransferase; Val, valine.

COMPLIANCE WITH ETHICS GUIDELINES

Tzu-Lung Lin, Chia-Chen Lu, Wei-Fan Lai, Ting-Shu Wu, Jang-Jih Lu, Young-Mao Chen, Chi-Meng Tzeng, Hong-Tao Liu, Hong Wei, and Hsin-Chih Lai declare that they have no conflict of interest.

OPEN ACCESS

This article is licensed under a Creative Commons Attribution 4.0 International License, which permits use, sharing, adaptation, distribution and reproduction in any medium or format, as long as you give appropriate credit to the original author(s) and the source, provide a link to the Creative Commons licence, and indicate if changes were made. The images or other third party material in this article are included in the article's Creative Commons licence, unless indicated otherwise in a credit line to the material. If material is not included in the article's Creative Commons licence and your intended use is not permitted by statutory regulation or exceeds the permitted use, you will need to obtain permission directly from the copyright holder. To view a copy of this licence, visit <http://creativecommons.org/licenses/by/4.0/>.

REFERENCES

- Alexandrov P, Zhai Y, Li W, Lukiw W (2019) Lipopolysaccharide-stimulated, NF- κ B-, miRNA-146a- and miRNA-155-mediated molecular-genetic communication between the human gastrointestinal tract microbiome and the brain. *Folia Neuropathol* 57:211–219
- Amaretti A, Gozzoli C, Simone M, Raimondi S, Righini L, Perez-Brocal V, Garcia-Lopez R, Moya A, Rossi M (2019) Profiling of protein degraders in cultures of human gut microbiota. *Front Microbiol* 10:2614
- Anlu W, Dongcheng C, He Z, Qiuyi L, Yan Z, Yu Q, Hao X, Keji C (2019) Using herbal medicine to target the “microbiota-metabolism-immunity” axis as possible therapy for cardiovascular disease. *Pharmacol Res* 142:205–222
- Bailey C (2019) Irinotecan: 25 years of cancer treatment. *Pharmacol Res* 148:104398
- Baumann U, Bisping B (1995) Proteolysis during tempe fermentation. *Food Microbiol* 12:39–47
- Bayer EA, Lamed R, White BA, Flint HJ (2008) From cellulosomes to cellulosomes. *Chem Rec* 8:364–377
- Bei WJ, Guo J, Wu HY, Cao Y (2012) Lipid-regulating effect of traditional chinese medicine: mechanisms of actions. *Evid Based Complement Altern Med* 2012:970635
- Belcher SM, Cline JM, Conley J, Groeters S, Jefferson WN, Law M, Mackey E, Suen AA, Williams CJ, Dixon D et al (2019) Endocrine disruption and reproductive pathology. *Toxicol Pathol* 47:1049–1071
- Blachier F, Mariotti F, Huneau JF, Tome D (2007) Effects of amino acid-derived luminal metabolites on the colonic epithelium and physiopathological consequences. *Amino Acids* 33:547–562
- Blaut M, Clavel T (2007) Metabolic diversity of the intestinal microbiota: implications for health and disease. *J Nutr* 137:751S–755S
- Bone E, Tamm A, Hill M (1976) The production of urinary phenols by gut bacteria and their possible role in the causation of large bowel cancer. *Am J Clin Nutr* 29:1448–1454
- Bouhnik Y, Raskine L, Simoneau G, Vicaud E, Neut C, Flourie B, Brouns F, Bornet FR (2004) The capacity of nondigestible carbohydrates to stimulate fecal bifidobacteria in healthy humans: a double-blind, randomized, placebo-controlled, parallel-group, dose-response relation study. *Am J Clin Nutr* 80:1658–1664
- Boyapati RK, Rossi AG, Satsangi J, Ho GT (2016) Gut mucosal DAMPs in IBD: from mechanisms to therapeutic implications. *Mucosal Immunol* 9:567–582
- Burokas A, Arbolea S, Moloney RD, Peterson VL, Murphy K, Clarke G, Stanton C, Dinan TG, Cryan JF (2017) Targeting the microbiota-gut-brain axis: prebiotics have anxiolytic and antidepressant-like effects and reverse the impact of chronic stress in mice. *Biol Psychiatry* 82:472–487
- Canyelles M, Tondo M, Cedo L, Farras M, Escola-Gil JC, Blanco-Vaca F (2018) Trimethylamine N-Oxide: a link among diet, gut microbiota, gene regulation of liver and intestine cholesterol homeostasis and HDL function. *Int J Mol Sci* 19(10):3228
- Carqueijeiro I, Langley C, Grzech D, Koudounas K, Papon N, O'Connor SE, Courdavault V (2019) Beyond the semi-synthetic artemisinin: metabolic engineering of plant-derived anti-cancer drugs. *Curr Opin Biotechnol* 65:17–24
- Chang CJ, Lin CS, Lu CC, Martel J, Ko YF, Ojcius DM, Tseng SF, Wu TR, Chen YY, Young JD et al (2015) *Ganoderma lucidum* reduces obesity in mice by modulating the composition of the gut microbiota. *Nat Commun* 6:7489
- Chang CJ, Lin TL, Tsai YL, Wu TR, Lai WF, Lu CC, Lai HC (2019) Next generation probiotics in disease amelioration. *J Food Drug Anal* 27:615–622
- Chang R (2002) Bioactive polysaccharides from traditional Chinese medicine herbs as anticancer adjuvants. *J Altern Complement Med* 8:559–565
- Chen C, You LJ, Huang Q, Fu X, Zhang B, Liu RH, Li C (2018a) Modulation of gut microbiota by mulberry fruit polysaccharide treatment of obese diabetic db/db mice. *Food Funct* 9:3732–3742
- Chen J, Hu Y, Chen L, Liu W, Mu Y, Liu P (2019) The effect and mechanisms of Fuzheng Huayu formula against chronic liver diseases. *Biomed Pharmacother* 114:108846
- Chen L, Kerkels EHJ, Verweij PE, Buil JB, Knibbe CAJ, Bruggemann RJM (2020) Pharmacokinetics and pharmacodynamics of posaconazole. *Drugs* 80:671–695
- Chen M, Liao Z, Lu B, Wang M, Lin L, Zhang S, Li Y, Liu D, Liao Q, Xie Z (2018b) Huang-Lian-Jie-Du-Decoction ameliorates hyperglycemia and insulin resistant in association with gut microbiota modulation. *Front Microbiol* 9:2380

- Chen Q, Xiao S, Li Z, Ai N, Fan X (2015) Chemical and metabolic profiling of Si-Ni decoction analogous formulae by high performance liquid chromatography-mass spectrometry. *Sci Rep* 5:11638
- Chen Y, Yao F, Ming K, Wang D, Hu Y, Liu J (2016) Polysaccharides from traditional Chinese medicines: extraction, purification, modification, and biological activity. *Molecules* 21:1705
- Chi X, Wang S, Baloch Z, Zhang H, Li X, Zhang Z, Zhang H, Dong Z, Lu Y, Yu H et al (2019) Research progress on classical traditional Chinese medicine formula Lily Bulb and Rehmannia Decoction in the treatment of depression. *Biomed Pharmacother* 112:108616
- Clemente JC, Ursell LK, Parfrey LW, Knight R (2012) The impact of the gut microbiota on human health: an integrative view. *Cell* 148:1258–1270
- Cockburn DW, Koropatkin NM (2016) Polysaccharide degradation by the intestinal microbiota and its influence on human health and disease. *J Mol Biol* 428:3230–3252
- Conlon MA, Bird AR (2014) The impact of diet and lifestyle on gut microbiota and human health. *Nutrients* 7:17–44
- Creekmore BC, Gray JH, Walton WG, Biernat KA, Little MS, Xu Y, Liu J, Gharaibeh RZ, Redinbo MR (2019) Mouse gut microbiome-encoded beta-glucuronidases identified using metagenome analysis guided by protein structure. *Systems* 4:e00452-19
- Dabek M, McCrae SI, Stevens VJ, Duncan SH, Louis P (2008) Distribution of beta-glucosidase and beta-glucuronidase activity and of beta-glucuronidase gene gus in human colonic bacteria. *FEMS Microbiol Ecol* 66:487–495
- Deng Z, Jing WG, Wang SH, Jiao MJ, Zhang Q, Zhou HY, Zhang J, Liu A (2019) Discussion and research progress in standard decoction of medicinal slices. *Zhongguo Zhong Yao Za Zhi* 44:242–248
- Devillard E, McIntosh FM, Duncan SH, Wallace RJ (2007) Metabolism of linoleic acid by human gut bacteria: different routes for biosynthesis of conjugated linoleic acid. *J Bacteriol* 189:2566–2570
- Devkota S, Wang Y, Musch MW, Leone V, Fehlner-Peach H, Nadimpalli A, Antonopoulos DA, Jabri B, Chang EB (2012) Dietary-fat-induced taurocholic acid promotes pathobiont expansion and colitis in IL10^{-/-} mice. *Nature* 487:104–108
- Dey P (2019) Gut microbiota in phytopharmacology: a comprehensive overview of concepts, reciprocal interactions, biotransformations and mode of actions. *Pharmacol Res* 147:104367
- Di S, Wang Y, Han L, Bao Q, Gao Z, Wang Q, Yang Y, Zhao L, Tong X (2019) The intervention effect of traditional Chinese medicine on the intestinal flora and its metabolites in glycolipid metabolic disorders. *Evid Based Complement Alternat Med* 2019:2958920
- Ding Z, Zhong R, Xia T, Yang Y, Xing N, Wang W, Wang Y, Yang B, Sun X, Shu Z (2020) Advances in research into the mechanisms of Chinese Materia Medica against acute lung injury. *Biomed Pharmacother* 122:109706
- Esteban-Gil A, Perez-Sanz F, Garcia-Solano J, Albuquerque-Gonzalez B, Parreno-Gonzalez MA, Legaz-Garcia MDC, Fernandez-Breis JT, Rodriguez-Braun E, Pimentel P, Tuomisto A et al (2019) ColPortal, an integrative multiomic platform for analysing epigenetic interactions in colorectal cancer. *Sci Data* 6:255
- Feng Q, Gou X-J, Meng S-X, Huang C, Zhang Y-Q, Tang Y-J, Wang W-J, Xu L, Peng J, Hu Y-Y (2013) Qushi Huayu decoction inhibits hepatic lipid accumulation by activating AMP-activated protein kinase in vivo and in vitro. *Evid-Based Complement Alternat Med: eCAM* 2013:184358
- Feng W, Ao H, Peng C, Yan D (2019) Gut microbiota, a new frontier to understand traditional Chinese medicines. *Pharmacol Res* 142:176–191
- Gao K, Yang R, Zhang J, Wang Z, Jia C, Zhang F, Li S, Wang J, Murtaza G, Xie H et al (2018) Effects of Qijian mixture on type 2 diabetes assessed by metabolomics, gut microbiota and network pharmacology. *Pharmacol Res* 130:93–109
- Gao W, Guo SZ, Han LW, Zhang FZ (2016) Analysis of projects funded by NSFC in field of Chinese material medica resource in recent three years. *Zhongguo Zhong Yao Za Zhi* 41:3696–3701
- Gentile CL, Weir TL (2018) The gut microbiota at the intersection of diet and human health. *Science* 362:776–780
- Gerard P (2013) Metabolism of cholesterol and bile acids by the gut microbiota. *Pathogens* 3:14–24
- Ghazalpour A, Cespedes I, Bennett BJ, Allayee H (2016) Expanding role of gut microbiota in lipid metabolism. *Curr Opin Lipidol* 27:141–147
- Han Y, Li C, Huan Y, Sun S, Mu Y, Shen Z (2016) Effects of berberine compatible with stachyose on glucolipid metabolism and gut microbiota in diabetic mice. *Chin J Clin Pharmacol* 32:1121–1124
- Hao YF, Jiang JG (2015) Origin and evolution of China Pharmacopoeia and its implication for traditional medicines. *Mini Rev Med Chem* 15:595–603
- Hu HC, Zheng LT, Yin HY, Tao Y, Luo XQ, Wei KS, Yin LP (2019) A significant association between rhein and diabetic nephropathy in animals: a systematic review and meta-analysis. *Front Pharmacol* 10:1473
- Huang X, Chen W, Yan C, Yang R, Chen Q, Xu H, Huang Y (2019) Gypenosides improve the intestinal microbiota of non-alcoholic fatty liver in mice and alleviate its progression. *Biomed Pharmacother* 118:109258
- Humblot C, Murkovic M, Rigottier-Gois L, Bensaada M, Bouclet A, Andrieux C, Anba J, Rabot S (2007) Beta-glucuronidase in human intestinal microbiota is necessary for the colonic genotoxicity of the food-borne carcinogen 2-amino-3-methylimidazo [4,5-f]quinoline in rats. *Carcinogenesis* 28:2419–2425
- Hussain A, Yadav MK, Bose S, Wang JH, Lim D, Song YK, Ko SG, Kim H (2016) Daesihotang is an effective herbal formulation in attenuation of obesity in mice through alteration of gene expression and modulation of intestinal microbiota. *PLoS ONE* 11:e0165483
- Janeiro MH, Ramirez MJ, Milagro FI, Martinez JA, Solas M (2018) Implication of trimethylamine N-Oxide (TMAO) in disease: potential biomarker or new therapeutic target. *Nutrients* 10(10):1398
- Jia W, Xie G, Jia W (2018) Bile acid-microbiota crosstalk in gastrointestinal inflammation and carcinogenesis. *Nat Rev Gastroenterol Hepatol* 15:111–128
- Jiang Y, Liu M, Liu H, Liu S (2020) A critical review: traditional uses, phytochemistry, pharmacology and toxicology of *Stephania tetrandra* S. Moore (Fen Fang Ji). *Phytochem Rev* 19:449–489
- Jin R, Lin ZJ, Xue CM, Zhang B (2013) An improved association-mining research for exploring Chinese herbal property theory:

- based on data of the Shennong's Classic of Materia Medica. *J Integr Med* 11:352–365
- Kaur H, Bose C, Mande SS (2019) Tryptophan metabolism by gut microbiome and gut-brain-axis: an in silico analysis. *Front Neurosci* 13:1365
- Kikugawa K, Kato T (1988) Formation of a mutagenic diazoquinone by interaction of phenol with nitrite. *Food and Chemical Toxicology* 26:209–214
- Kim DH (2018) Gut microbiota-mediated pharmacokinetics of ginseng saponins. *J Ginseng Res* 42:255–263
- Kim HM, Song Y, Hyun GH, Long NP, Park JH, Hsieh YSY, Kwon SW (2020) Characterization and Antioxidant Activity Determination of Neutral and Acidic Polysaccharides from *Panax Ginseng* C.A. Meyer. *Molecules* 25:791
- Kim KA, Jung IH, Park SH, Ahn YT, Huh CS, Kim DH (2013) Comparative analysis of the gut microbiota in people with different levels of ginsenoside Rb1 degradation to compound K. *PLoS One* 8:e62409
- Koropatkin NM, Cameron EA, Martens EC (2012) How glycan metabolism shapes the human gut microbiota. *Nat Rev Microbiol* 10:323–335
- Lagier JC, Dubourg G, Million M, Cadoret F, Bilen M, Fenollar F, Levasseur A, Rolain JM, Fournier PE, Raoult D (2018) Culturing the human microbiota and culturomics. *Nat Rev Microbiol* 16:540–550
- Lee JW, Na D, Park JM, Lee J, Choi S, Lee SY (2012) Systems metabolic engineering of microorganisms for natural and non-natural chemicals. *Nat Chem Biol* 8:536–546
- Leng J, Huang F, Hai Y, Tian H, Liu W, Fang Y, Hu Y, Peng J (2020) Amelioration of non-alcoholic steatohepatitis by Qushi Huayu decoction is associated with inhibition of the intestinal mitogen-activated protein kinase pathway. *Phytomedicine* 66:153135
- Li C, Du X, Liu Y, Liu QQ, Zhi WB, Wang CL, Zhou J, Li Y, Zhang H (2020) A systems pharmacology approach for identifying the multiple mechanisms of action for the Rougui-Fuzi Herb pair in the treatment of cardiocerebral vascular diseases. *Evid Based Complement Alternat Med* 2020:5196302
- Li G, Wang D, Fang S, Xu M (2014) Textual research on *Costus root* (*Aucklandia lappa* Decne) in the *Sheng nong ben cao jing* (Shennong's Classic of Materia Medica). *Zhonghua Yi Shi Za Zhi* 44:135–137
- Li LC, Kan LD (2017) Traditional Chinese medicine for pulmonary fibrosis therapy: Progress and future prospects. *J Ethnopharmacol* 198:45–63
- Li SP, Wu D-T, Lv G-P, Zhao J (2013) Carbohydrates analysis in herbal glycomics. *TrAC Trends Anal Chem* 52:155–169
- Lin CS, Chang CJ, Lu CC, Martel J, Ojcius DM, Ko YF, Young JD, Lai HC (2014) Impact of the gut microbiota, prebiotics, and probiotics on human health and disease. *Biomed J* 37:259–268
- Lin L, Ni B, Lin H, Zhang M, Li X, Yin X, Qu C, Ni J (2015) Traditional usages, botany, phytochemistry, pharmacology and toxicology of *Polygonum multiflorum* Thunb.: a review. *J Ethnopharmacol* 159:158–183
- Lin R, Liu W, Piao M, Zhu H (2017) A review of the relationship between the gut microbiota and amino acid metabolism. *Amino Acids* 49:2083–2090
- Lin T-L, Shu C-C, Lai W-F, Tzeng C-M, Lai H-C, Lu C-C (2019) Investiture of next generation probiotics on amelioration of diseases—strains do matter. *Med Microecol* 1–2:100002
- Liu C, Li S, Zhang Q, Guo F, Tong M, Martinez M, Wang HH, Zhao Y, Shang D (2019a) Emerging role of chinese herbal medicines in the treatment of pancreatic fibrosis. *Am J Chin Med* 47:709–726
- Liu D, Zhang Y, Liu Y, Hou L, Li S, Tian H, Zhao T (2018a) Berberine modulates gut microbiota and reduces insulin resistance via the TLR4 signaling pathway. *Exp Clin Endocrinol Diabetes* 126:513–520
- Liu M, Wang Y, Liu Y, Ruan R (2016) Bioactive peptides derived from traditional Chinese medicine and traditional Chinese food: a review. *Food Res Int* 89:63–73
- Liu S, Si C, Yu Y, Zhao G, Chen L, Zhao Y, Zhang Z, Li H, Chen Y, Min L et al (2019b) Multi-omics analysis of gut microbiota and metabolites in rats with irritable bowel syndrome. *Front Cell Infect Microbiol* 9:178
- Liu Y, Li J, Yu J, Wang Y, Lu J, Shang EX, Zhu Z, Guo J, Duan J (2018b) Disorder of gut amino acids metabolism during CKD progression is related with gut microbiota dysbiosis and metagenome change. *J Pharm Biomed Anal* 149:425–435
- Lloyd-Price J, Arze C, Ananthakrishnan AN, Schirmer M, Avila-Pacheco J, Poon TW, Andrews E, Ajami NJ, Bonham KS, Brislawn CJ et al (2019) Multi-omics of the gut microbial ecosystem in inflammatory bowel diseases. *Nature* 569:655–662
- Lu Y-M, Xie J-J, Peng C-G, Wang B-H, Wang K-C, Li L-J (2019) Enhancing clinical efficacy through the gut microbiota: a new field of traditional Chinese medicine. *Engineering* 5:40–49
- Lyu M, Wang YF, Fan GW, Wang XY, Xu SY, Zhu Y (2017) Balancing herbal medicine and functional food for prevention and treatment of cardiometabolic diseases through modulating gut microbiota. *Front Microbiol* 8:2146
- Ma N, Tian Y, Wu Y, Ma X (2017) Contributions of the interaction between dietary protein and gut microbiota to intestinal health. *Curr Protein Pept Sci* 18:795–808
- Madsen L, Myrmet LS, Fjaere E, Liaset B, Kristiansen K (2017) Links between dietary protein sources, the gut microbiota, and obesity. *Front Physiol* 8:1047
- Magee EA, Richardson CJ, Hughes R, Cummings JH (2000) Contribution of dietary protein to sulfide production in the large intestine: an in vitro and a controlled feeding study in humans. *Am J Clin Nutr* 72:1488–1494
- Marques TM, Wall R, O'Sullivan O, Fitzgerald GF, Shanahan F, Quigley EM, Cotter PD, Cryan JF, Dinan TG, Ross RP et al (2015) Dietary trans-10, cis-12-conjugated linoleic acid alters fatty acid metabolism and microbiota composition in mice. *Br J Nutr* 113:728–738
- Martel J, Ko YF, Ojcius DM, Lu CC, Chang CJ, Lin CS, Lai HC, Young JD (2017a) Immunomodulatory properties of plants and mushrooms. *Trends Pharmacol Sci* 38:967–981
- Martel J, Ojcius DM, Chang CJ, Lin CS, Lu CC, Ko YF, Tseng SF, Lai HC, Young JD (2017b) Anti-obesogenic and antidiabetic effects of plants and mushrooms. *Nat Rev Endocrinol* 13:149–160
- Martens EC, Lowe EC, Chiang H, Pudlo NA, Wu M, McNulty NP, Abbott DW, Henrissat B, Gilbert HJ, Bolam DN et al (2011) Recognition and degradation of plant cell wall polysaccharides by two human gut symbionts. *PLoS Biol* 9:e1001221

- Mazzoli R, Pessione E (2016) The neuro-endocrinological role of microbial glutamate and GABA signaling. *Front Microbiol* 7:1934
- Mishima E, Fukuda S, Mukawa C, Yuri A, Kanemitsu Y, Matsumoto Y, Akiyama Y, Fukuda NN, Tsukamoto H, Asaji K et al (2017) Evaluation of the impact of gut microbiota on uremic solute accumulation by a CE-TOFMS-based metabolomics approach. *Kidney Int* 92:634–645
- Neis EP, Dejong CH, Rensen SS (2015) The role of microbial amino acid metabolism in host metabolism. *Nutrients* 7:2930–2946
- Ni M (1995) The yellow emperor's classic of medicine: a new translation of the Neijing Suwen with commentary. Shambhala, Boston and London
- Nie C, He T, Zhang W, Zhang G, Ma X (2018) Branched chain amino acids: beyond nutrition metabolism. *Int J Mol Sci.* 1:1. <https://doi.org/10.1136/gutjnl-2019-319114>
- Nie Q, Chen H, Hu J, Fan S, Nie S (2019) Dietary compounds and traditional Chinese medicine ameliorate type 2 diabetes by modulating gut microbiota. *Crit Rev Food Sci Nutr* 59:848–863
- Peng Y, Li X, Zhang S, Liu Z, Ji J, Wu C, Yang J (2020) Gut microbiota and Chinese medicine syndrome: altered fecal microbiotas in spleen (Pi)-deficient patients. *J Tradit Chin Med* 40:137–143
- Portune KJ, Beaumont M, Davila A-M, Tomé D, Blachier F, Sanz Y (2016) Gut microbiota role in dietary protein metabolism and health-related outcomes: the two sides of the coin. *Trends Food Sci Technol* 57:213–232
- Qi LW, Wang CZ, Du GJ, Zhang ZY, Calway T, Yuan CS (2011) Metabolism of ginseng and its interactions with drugs. *Curr Drug Metab* 12:818–822
- Qu W, Liu S, Zhang W, Zhu H, Tao Q, Wang H, Yan H (2019) Impact of traditional Chinese medicine treatment on chronic unpredictable mild stress-induced depression-like behaviors: intestinal microbiota and gut microbiome function. *Food Funct* 10:5886–5897
- Quan LH, Zhang C, Dong M, Jiang J, Xu H, Yan C, Liu X, Zhou H, Zhang H, Chen L et al (2019) Myristoleic acid produced by enterococci reduces obesity through brown adipose tissue activation. *Gut*. 69(7):1239–1247
- Ramesh M, Ahlawat P, Srinivas NR (2010) Irinotecan and its active metabolite, SN-38: review of bioanalytical methods and recent update from clinical pharmacology perspectives. *Biomed Chromatogr* 24:104–123
- Ramirez-Perez O, Cruz-Ramon V, Chinchilla-Lopez P, Mendez-Sanchez N (2017) The role of the gut microbiota in bile acid metabolism. *Ann Hepatol* 16:s15–s20
- Rath S, Heidrich B, Pieper DH, Vital M (2017) Uncovering the trimethylamine-producing bacteria of the human gut microbiota. *Microbiome* 5:54
- Ravcheev DA, Godzik A, Osterman AL, Rodionov DA (2013) Polysaccharides utilization in human gut bacterium *Bacteroides thetaiotaomicron*: comparative genomics reconstruction of metabolic and regulatory networks. *BMC Genomics* 14:873
- Ru J, Li P, Wang J, Zhou W, Li B, Huang C, Li P, Guo Z, Tao W, Yang Y et al (2014) TCMSp: a database of systems pharmacology for drug discovery from herbal medicines. *J Cheminform* 6:13
- Santa HSD, Romão PRT, Sovrani V, Oliveira FR, Peres A, Monteiro MC (2014) Dietary polysaccharides and Immune Modulation. In: Ramawat KG, Mérillon J-M (eds) *Polysaccharides: bioactivity and biotechnology*. Springer International Publishing, Cham, pp 1–24
- Schachter J, Martel J, Lin CS, Chang CJ, Wu TR, Lu CC, Ko YF, Lai HC, Ojcius DM, Young JD (2018) Effects of obesity on depression: a role for inflammation and the gut microbiota. *Brain Behav Immun* 69:1–8
- Schoeler M, Caesar R (2019) Dietary lipids, gut microbiota and lipid metabolism. *Rev Endocr Metab Disord* 20:461–472
- Schwiertz A, Taras D, Schafer K, Beijer S, Bos NA, Donus C, Hardt PD (2010) Microbiota and SCFA in lean and overweight healthy subjects. *Obesity (Silver Spring)* 18:190–195
- Sharon G, Garg N, Debelius J, Knight R, Dorrestein PC, Mazmanian SK (2014) Specialized metabolites from the microbiome in health and disease. *Cell Metab* 20:719–730
- Simpson HL, Campbell BJ (2015) Review article: dietary fibre-microbiota interactions. *Aliment Pharmacol Ther* 42:158–179
- Sun SS, Wang K, Ma K, Bao L, Liu HW (2019) An insoluble polysaccharide from the sclerotium of *Poria cocos* improves hyperglycemia, hyperlipidemia and hepatic steatosis in ob/ob mice via modulation of gut microbiota. *Chin J Nat Med* 17:3–14
- Sun Y (2011) Structure and biological activities of the polysaccharides from the leaves, roots and fruits of *Panax ginseng* C.A. Meyer: an overview. *Carbohydrate Polymers - CARBOHYD POLYM* 85:490–499
- Tang D, Kang R, Coyne CB, Zeh HJ, Lotze MT (2012) PAMPs and DAMPs: signal 0s that spur autophagy and immunity. *Immunol Rev* 249:158–175
- Tejaro CN, Adhikari A, Shen B (2019) Challenges and opportunities for natural product discovery, production, and engineering in native producers versus heterologous hosts. *J Ind Microbiol Biotechnol* 46:433–444
- Thursby E, Juge N (2017) Introduction to the human gut microbiota. *Biochem J* 474:1823–1836
- Tong X, Xu J, Lian F, Yu X, Zhao Y, Xu L, Zhang M, Zhao X, Shen J, Wu S et al (2018) Structural alteration of gut microbiota during the amelioration of human type 2 diabetes with hyperlipidemia by metformin and a traditional Chinese herbal formula: a multicenter, randomized, Open label clinical trial. *mBio*. 9(3):e02392-17
- Tremaroli V, Backhed F (2012) Functional interactions between the gut microbiota and host metabolism. *Nature* 489:242–249
- Tsai YL, Lin TL, Chang CJ, Wu TR, Lai WF, Lu CC, Lai HC (2019) Probiotics, prebiotics and amelioration of diseases. *J Biomed Sci* 26:3
- Tzianabos AO (2000) Polysaccharide immunomodulators as therapeutic agents: structural aspects and biologic function. *Clin Microbiol Rev* 13:523–533
- van Duynhoven J, Vaughan EE, Jacobs DM, Kemperman RA, van Velzen EJ, Gross G, Roger LC, Possemiers S, Smilde AK, Dore J et al (2011) Metabolic fate of polyphenols in the human superorganism. *Proc Natl Acad Sci USA* 108(Suppl 1):4531–4538
- Velenosi TJ, Hennop A, Feere DA, Tieu A, Kucey AS, Kyriacou P, McCuaig LE, Nevison SE, Kerr MA, Urquhart BL (2016) Untargeted plasma and tissue metabolomics in rats with chronic kidney disease given AST-120. *Sci Rep* 6:22526
- Wahlstrom A, Sayin SI, Marschall HU, Backhed F (2016) Intestinal crosstalk between bile acids and microbiota and its impact on host metabolism. *Cell Metab* 24:41–50

- Wan JY, Wang CZ, Zhang QH, Liu Z, Musch MW, Bissonnette M, Chang EB, Li P, Qi LW, Yuan CS (2017) Significant difference in active metabolite levels of ginseng in humans consuming Asian or Western diet: the link with enteric microbiota. *Biomed Chromatogr*. <https://doi.org/10.1002/bmc.3851>
- Wang B, Yao M, Lv L, Ling Z, Li L (2017a) The human microbiota in health and disease. *Engineering* 3:71–82
- Wang C, Yin Y, Cao X, Li X (2016) Effects of Maydis stigma polysaccharide on the intestinal microflora in type-2 diabetes. *Pharm Biol* 54:3086–3092
- Wang JH, Bose S, Lim SK, Ansari A, Chin YW, Choi HS, Kim H (2017b) *Houttuynia cordata* facilitates metformin on ameliorating insulin resistance associated with gut microbiota alteration in OLETF rats. *Genes (Basel)* 8:239
- Wang JH, Bose S, Shin NR, Chin YW, Choi YH, Kim H (2018a) Pharmaceutical impact of *houltuynia cordata* and metformin combination on high-fat-diet-induced metabolic disorders: link to intestinal microbiota and metabolic endotoxemia. *Front Endocrinol (Lausanne)* 9:620
- Wang L, Liu QM, Sung BH, An DS, Lee HG, Kim SG, Kim SC, Lee ST, Im WT (2011) Bioconversion of ginsenosides Rb(1), Rb(2), Rc and Rd by novel beta-glucosidase hydrolyzing outer 3-O glycoside from *Sphingomonas* sp. 2F2: cloning, expression, and enzyme characterization. *J Biotechnol* 156:125–133
- Wang Q, Kuang H, Su Y, Sun Y, Feng J, Guo R, Chan K (2013) Naturally derived anti-inflammatory compounds from Chinese medicinal plants. *J Ethnopharmacol* 146:9–39
- Wang R, Zang P, Chen J, Wu F, Zheng Z, Ma J, Yang C, Du H (2018b) Gut microbiota play an essential role in the antidiabetic effects of rhein. *Evid Based Complement Alternat Med* 2018:6093282
- Wei X, Tao J, Xiao S, Jiang S, Shang E, Zhu Z, Qian D, Duan J (2018) Xiexin Tang improves the symptom of type 2 diabetic rats by modulation of the gut microbiota. *Sci Rep* 8:3685
- Wu TR, Lin CS, Chang CJ, Lin TL, Martel J, Ko YF, Ojcius DM, Lu CC, Young JD, Lai HC (2019) Gut commensal *Parabacteroides goldsteinii* plays a predominant role in the anti-obesity effects of polysaccharides isolated from *Hirsutella sinensis*. *Gut* 68:248–262
- Wu XM, Tan RX (2019) Interaction between gut microbiota and ethnomedicine constituents. *Nat Prod Rep* 36:788–809
- Xu J, Lian F, Zhao L, Zhao Y, Chen X, Zhang X, Guo Y, Zhang C, Zhou Q, Xue Z et al (2015) Structural modulation of gut microbiota during alleviation of type 2 diabetes with a Chinese herbal formula. *ISME J* 9:552–562
- Xu JD, Mao Q, Shen H, Zhu LY, Li SL, Yan R (2013) Ultra-high performance liquid chromatography coupled with photo-diode array and quadrupole/time-of-flight mass spectrometry based chemical profiling approach to evaluate the influence of preparation methods on the holistic quality of Qiong-Yu-Gao, a traditional complex herbal medicine. *J Chromatogr A* 1304:154–168
- Xu M, Yue RS, Yang MY, Yang X, Wu TC, Li JN (2018) Effects of Banxia Xiexin Decoction on intestinal flora and inflammatory factors of diabetic gastroparesis rats. *Chinese Traditional and Herbal Drugs* 49:3056–3061
- Yan Q (2018) Neuroimmune imbalances and Yin-Yang dynamics in stress, anxiety, and depression. *Methods Mol Biol* 1781:77–85
- Yan Y, Chai CZ, Wang DW, Yue XY, Zhu DN, Yu BY (2013) HPLC-DAD-Q-TOF-MS/MS analysis and HPLC quantitation of chemical constituents in traditional Chinese medicinal formula Ge-Gen Decoction. *J Pharm Biomed Anal* 80:192–202
- Yang M, Lao L (2019) Emerging applications of metabolomics in traditional Chinese medicine treating hypertension: biomarkers. *Pathways and More. Front Pharmacol* 10:158
- Yang M, Sun J, Lu Z, Chen G, Guan S, Liu X, Jiang B, Ye M, Guo DA (2009) Phytochemical analysis of traditional Chinese medicine using liquid chromatography coupled with mass spectrometry. *J Chromatogr A* 1216:2045–2062
- Yang YS, Zhang T, Yu SC, Ding Y, Zhang LY, Qiu C, Jin D (2011) Transformation of geniposide into genipin by immobilized beta-glucosidase in a two-phase aqueous-organic system. *Molecules* 16:4295–4304
- Ying M, Zheng B, Yu Q, Hou K, Wang H, Zhao M, Chen Y, Xie J, Nie S, Xie M (2020) *Ganoderma atrum* polysaccharide ameliorates intestinal mucosal dysfunction associated with autophagy in immunosuppressed mice. *Food Chem Toxicol* 138:111244
- Yokoi T, Narita M, Nagai E, Hagiwara H, Aburada M, Kamataki T (1995) Inhibition of UDP-glucuronosyltransferase by aglycons of natural glucuronides in kampo medicines using SN-38 as a substrate. *Jpn J Cancer Res* 86:985–989
- Yu J, Guo J, Tao W, Liu P, Shang E, Zhu Z, Fan X, Shen J, Hua Y, Zhu KY et al (2018a) Gancao-Gansui combination impacts gut microbiota diversity and related metabolic functions. *J Ethnopharmacol* 214:71–82
- Yu Y, Li Z, Guo R, Qian J, Zhang H, Zhang J, Zhao X, Wang S, Wang Y (2019a) Ononin, sec-O-beta-d-glucosylhamadul and astragaloside I: antiviral lead compounds identified via high throughput screening and biological validation from traditional Chinese medicine Zhongjing formulary. *Pharmacol Res* 145:104248
- Yu Y, Raka F, Adeli K (2019b) The role of the gut microbiota in lipid and lipoprotein metabolism. *J Clin Med* 8(12):2227
- Yu Y, Shen M, Song Q, Xie J (2018b) Biological activities and pharmaceutical applications of polysaccharide from natural resources: a review. *Carbohydr Polym* 183:91–101
- Yuan Y, Zheng J, Wang M, Li Y, Ruan J, Zhang H (2016) Metabolic activation of rhein: insights into the potential toxicity induced by rhein-containing herbs. *J Agric Food Chem* 64:5742–5750
- Yue SJ, Wang WX, Yu JG, Chen YY, Shi XQ, Yan D, Zhou GS, Zhang L, Wang CY, Duan JA et al (2019) Gut microbiota modulation with traditional Chinese medicine: a system biology-driven approach. *Pharmacol Res* 148:104453
- Zhang B, Yue R, Chen Y, Yang M, Huang X, Shui J, Peng Y, Chin J (2019a) Gut microbiota, a potential new target for Chinese herbal medicines in treating diabetes mellitus. *Evid Based Complement Alternat Med* 2019:2634898
- Zhang D, Chia C, Jiao X, Jin W, Kasagi S, Wu R, Konkel JE, Nakatsukasa H, Zanvit P, Goldberg N et al (2017) D-mannose induces regulatory T cells and suppresses immunopathology. *Nat Med* 23:1036–1045
- Zhang D, Yang L, Yang LX, Wang MY, Tu YY (2007) Determination of artemisinin, arteannuin B and artemisinic acid in *Herba*

- Artemisiae Annuae by HPLC-UV-ELSD. Yao Xue Xue Bao 42:978–981
- Zhang D, Zhang Y, Gao Y, Chai X, Pi R, Chan G, Hu Y (2020a) Translating traditional herbal formulas into modern drugs: a network-based analysis of Xiaoyao decoction. Chin Med 15:25
- Zhang ND, Han T, Huang BK, Rahman K, Jiang YP, Xu HT, Qin LP, Xin HL, Zhang QY, Li YM (2016) Traditional Chinese medicine formulas for the treatment of osteoporosis: Implication for antiosteoporotic drug discovery. J Ethnopharmacol 189:61–80
- Zhang R, Gao X, Bai H, Ning K (2020b) Traditional Chinese medicine and gut microbiome: their respective and concert effects on healthcare. Front Pharmacol 1:1. <https://doi.org/10.3389/fphar.2020.00538>
- Zhang T, Yang Y, Liang Y, Jiao X, Zhao C (2018) Beneficial effect of intestinal fermentation of natural polysaccharides. Nutrients 10 (8):55
- Zhang WJ, Wang S, Kang CZ, Lv CG, Zhou L, Huang LQ, Guo LP (2020c) Pharmacodynamic material basis of traditional Chinese medicine based on biomacromolecules: a review. Plant Methods 16:26
- Zhang YL, Cai LT, Qi JY, Lin YZ, Dai YC, Jiao N, Chen YL, Zheng L, Wang BB, Zhu LX et al (2019b) Gut microbiota contributes to the distinction between two traditional Chinese medicine syndromes of ulcerative colitis. World J Gastroenterol 25:3242–3255
- Zhao CQ, Zhou Y, Ping J, Xu LM (2014) Traditional Chinese medicine for treatment of liver diseases: progress, challenges and opportunities. J Integr Med 12:401–408
- Zhou SS, Xu J, Zhu H, Wu J, Xu JD, Yan R, Li XY, Liu HH, Duan SM, Wang Z et al (2016) Gut microbiota-involved mechanisms in enhancing systemic exposure of ginsenosides by coexisting polysaccharides in ginseng decoction. Sci Rep 6:22474
- Zhu KX, Nie SP, Tan LH, Li C, Gong DM, Xie MY (2016) A polysaccharide from ganoderma atrum improves liver function in type 2 diabetic rats via antioxidant action and short-chain fatty acids excretion. J Agric Food Chem 64:1938–1944
- Zmora N, Suez J, Elinav E (2019) You are what you eat: diet, health and the gut microbiota. Nat Rev Gastroenterol Hepatol 16:35–56



SARS-CoV-2 genomic surveillance in Taiwan revealed novel ORF8-deletion mutant and clade possibly associated with infections in Middle East¹

Yu-Nong Gong^{a,b,*}, Kuo-Chien Tsao^{a,b,c,*}, Mei-Jen Hsiao^b, Chung-Guei Huang^{b,c}, Peng-Nien Huang^{a,d}, Po-Wei Huang^b, Kuo-Ming Lee^b, Yi-Chun Liu^b, Shu-Li Yang^{b,c}, Rei-Lin Kuo^{a,c,e,f}, Kuan-Fu Chen^{g,h,i}, Yen-Chin Liu^a, Sheng-Yu Huang^a, Hsing-I. Huang^{a,c,e,j}, Ming-Tsan Liu^k, Ji-Rong Yang^k, Cheng-Hsun Chiu^{l,m}, Cheng-Ta Yang^{n,o}, Guang-Wu Chen^{b,p} and Shin-Ru Shih^{b,q}

^aResearch Center for Emerging Viral Infections, College of Medicine, Chang Gung University, Taoyuan, Taiwan; ^bDepartment of Laboratory Medicine, Linkou Chang Gung Memorial Hospital, Taoyuan, Taiwan; ^cDepartment of Medical Biotechnology and Laboratory Science, College of Medicine, Chang Gung University, Taoyuan, Taiwan; ^dDivision of Infectious Diseases, Department of Pediatrics, Linkou Chang Gung Memorial Hospital, Taoyuan, Taiwan; ^eGraduate Institute of Biomedical Sciences, College of Medicine, Chang Gung University, Taoyuan, Taiwan; ^fDivision of Asthma, Allergy, and Rheumatology, Department of Pediatrics, Linkou Chang Gung Memorial Hospital, Taoyuan, Taiwan; ^gDepartment of Emergency Medicine, Chang Gung Memorial Hospital, Keelung, Taiwan; ^hClinical Informatics and Medical Statistics Research Center, Chang Gung University, Taoyuan, Taiwan; ⁱCommunity Medicine Research Center, Chang Gung Memorial Hospital, Keelung, Taiwan; ^jDepartment of Pediatrics, Linkou Chang Gung Memorial Hospital, Taoyuan, Taiwan; ^kCenters for Disease Control, Taipei, Taiwan; ^lDivision of Pediatric Infectious Diseases, Department of Pediatrics, Chang Gung Memorial Hospital, Chang Gung University College of Medicine, Taoyuan, Taiwan; ^mMolecular Infectious Disease Research Center, Chang Gung Memorial Hospital, Chang Gung University College of Medicine, Taoyuan, Taiwan; ⁿDepartment of Respiratory Therapy, College of Medicine, Chang Gung University, Taoyuan, Taiwan; ^oDepartment of Thoracic Medicine, Linkou Chang Gung Memorial Hospital, Taoyuan, Taiwan; ^pDepartment of Computer Science and Information Engineering, School of Electrical and Computer Engineering, College of Engineering, Chang Gung University, Taoyuan, Taiwan; ^qResearch Center for Chinese Herbal Medicine, Research Center for Food and Cosmetic Safety, and Graduate Institute of Health Industry Technology, College of Human Ecology, Chang Gung University of Science and Technology, Taoyuan, Taiwan

ABSTRACT

Taiwan experienced two waves of imported infections with Coronavirus Disease 2019 (COVID-19). This study aimed at investigating the genomic variation of severe acute respiratory syndrome coronavirus 2 (SARS-CoV-2) in Taiwan and compared their evolutionary trajectories with the global strains. We performed culture and full-genome sequencing of SARS-CoV-2 strains followed by phylogenetic analysis. A 382-nucleotides deletion in open reading frame 8 (ORF8) was found in a Taiwanese strain isolated from a patient on February 4, 2020 who had a travel history to Wuhan. Patients in the first wave also included several sporadic, local transmission cases. Genomes of 5 strains sequenced from clustered infections were classified into a new clade with ORF1ab-V378I mutation, in addition to 3 dominant clades ORF8-L84S, ORF3a-G251V and S-D614G. This highlighted clade also included some strains isolated from patients who had a travel history to Turkey and Iran. The second wave mostly resulted from patients who had a travel history to Europe and Americas. All Taiwanese viruses were classified into various clades. Genomic surveillance of SARS-CoV-2 in Taiwan revealed a new ORF8-deletion mutant and a virus clade that may be associated with infections in the Middle East, which contributed to a better understanding of the global SARS-CoV-2 transmission dynamics.

ARTICLE HISTORY Received 30 April 2020; Revised 8 June 2020; Accepted 9 June 2020

KEYWORDS COVID-19; SARS-CoV-2; genome sequencing; Phylogeny; ORF8 deletion

Introduction

Coronaviruses (CoVs) are classified into four genera, including *Alphacoronavirus*, *Betacoronavirus*, *Gamma-coronavirus*, and *Deltacoronavirus* [1]. Prior to 2019, six CoVs were known to infect human, including human CoV 229E and NL63 belonging to the genera *Alphacoronavirus*, and human CoV OC43, HKU1, Severe Acute Respiratory Syndrome-related CoV (SARSr-CoV), and Middle East Respiratory Syndrome CoV (MERS-CoV) belonging to the genera *Betacoronavirus* [2–5]. The

seventh and novel coronavirus emerged from Wuhan, Hubei province in China, in December 2019 [6]. This virus belongs to the genera *Betacoronavirus* and has been designated as Severe Acute Respiratory Syndrome Coronavirus 2 (SARS-CoV-2), and the disease is named as Coronavirus Disease 2019 (COVID-19) [7]. The World Health Organization declared this disease a pandemic on March 11, 2020.

As of April 14, 2020, the outbreak of COVID-19 has resulted in 1,844,863 confirmed cases and 117,021

CONTACT Guang-Wu Chen ✉ gwchen@mail.cgu.edu.tw; Shin-Ru Shih ✉ srshih@mail.cgu.edu.tw Research Center for Emerging Viral Infections, College of Medicine, Chang Gung University, No.259, Wenhua 1st Rd., Guishan Dist., Taoyuan, Taiwan

*These authors contributed equally to this work.

¹ Supplemental data for this article can be accessed <https://doi.org/10.1080/22221751.2020.1782271>

© 2020 The Author(s). Published by Informa UK Limited, trading as Taylor & Francis Group, on behalf of Shanghai Shangyixun Cultural Communication Co., Ltd
This is an Open Access article distributed under the terms of the Creative Commons Attribution License (<http://creativecommons.org/licenses/by/4.0/>), which permits unrestricted use, distribution, and reproduction in any medium, provided the original work is properly cited.

deaths worldwide [8], among which 393 confirmed cases and 6 deaths were reported in Taiwan [9]. With rapidly increasing number of infections, the Global Initiative on Sharing All Influenza Data (GISAID) [10] provides a platform for sharing SARS-CoV-2 sequences and their metadata. Three major clades, including clade G (with G variant at position 614 within the spike protein, as S-D614G), clade S (ORF8-L84S), and clade V (ORF3a-G251V), were designated by the GISAID (<https://www.gisaid.org/hcov-19-analysis-update/>). However, the imbalance of genome information contributed to this platform could prevent us from comprehensively understand the viral transmission and epidemiology of this pandemic. In particular that none or very few sequences have been reported from some countries. With more virus genomes become available, we would be able to better address the diversification and evolution of this virus.

There have been two waves of COVID-19 cases in Taiwan. The first occurred from late January to the end of February, with most infections originating from China either by Chinese tourists or Taiwanese businessmen returning to Taiwan from China for celebrating Chinese New Year. The second and bigger wave started in early March, during which the infections were largely caused by Taiwanese tourists, business travellers, or students returning from other countries. Although most of these cases were traced to their foreign origins, some small and clustered infections were suspected to have been resulted from local transmission.

In this study, we performed culture and full-genome sequencing of SARS-CoV-2 isolates, and further investigated the viral genome polymorphism within individual human clinical specimens through their metagenomic data. We compared the genomes of Taiwanese strains to those of global strains to describe their genetic variations and evolutionary trajectory. Strikingly, an open reading frame 8 (ORF8) deletion was found in one Taiwanese strain. Moreover, a highlighted clade with ORF1ab-V378I mutation was observed in addition to the three major clades designated by the GISAID. Interestingly, included in this clade were some strains isolated from patients with travel history to Turkey and Iran, where few viral genomes have yet been reported in the Middle East region.

Materials and Methods

Ethics statement

This study was approved by the Institutional Review Board of Chang Gung Medical Foundation, Linkou Medical Center, Taoyuan, Taiwan (approval no. 202000468B0B1).

Specimen collection

SARS-CoV-2 infection in patients was confirmed by real-time reverse-transcriptase–polymerase chain reaction (RT-PCR) according to the guidelines of the Taiwan Centers for Disease Control (CDC; <https://www.cdc.gov.tw/En>) [11]. All nasopharyngeal swab, throat swab, and sputum samples were maintained in viral transport medium for further analysis.

Cell culture and virus isolation

Vero-E6 (ATCC, Manassas, VA, USA), MK-2 (ATCC), and Calu-3 (ATCC) cells were maintained in Minimum Essential Medium (MEM, Thermo Fisher Scientific, Waltham, MA, USA) supplemented with 10% fetal bovine serum and 1x penicillin-streptomycin at 37°C in the presence of 5% CO₂. To isolate the virus, all procedures were performed in accordance with the laboratory biosafety guidelines of the Taiwan CDC in a biosafety level-3 facility. Cells grown to 80–90% confluency in standard screw-up culture tubes (16 × 125 mm) were inoculated with 500 µL of the virus solution. The virus solution was prepared by diluting 100 µL of the specimen samples with 1.5 mL of sample pre-treatment medium consisting of MEM, 2% fetal bovine serum, and 2x penicillin-streptomycin solution, followed by incubation at 37°C for 1 h. Virus absorption process was allowed at 37°C for 1 h, after which 2 mL of the virus culture medium composed of MEM, 2% fetal bovine serum, and 1x penicillin-streptomycin solution was added, and the culture mixture was maintained at 37°C. Infected cells were observed daily to determine the cytopathic effect of the virus on the cells. Additionally, RT-PCR analysis using the RNA extracted from part of the culture supernatant every 2 days after inoculation was performed to monitor viral growth. We continuously observed the infected cells until the cytopathic effect was noticed in more than 75% of the cells, after which the culture supernatant was harvested and stored at –70°C. Viral titer was determined by Vero-E6 cells with medium consisting of DMEM, 2% fetal bovine serum and 0.4% agarose, followed by incubation at 37°C for 3 days.

Whole-Genome sequencing

Twenty samples (CGMH-CGU No. 1–20) were collected (Table 1). RNA was extracted either from the culture supernatant or directly from the specimens using a QIAmp viral RNA mini Kit (Qiagen, Hilden, Germany) according to the manufacturer's instructions, except that the carrier RNA was replaced with linear acrylamide (Thermo Fisher Scientific) as the co-precipitant. The amount of viral RNA was evaluated by quantitative RT-PCR to examine the Ct value of the viral E gene (Table 1). For RNAs showing a high Ct value, we

Table 1. Specimen collection, culture, and sequencing.

CGMH-CGU ID / Strain name	Accession number	Collection date	Viral culture (day)	Source* (Ct value of E gene)	Coverage and avg. depth of SARS-CoV-2
1	EPI_ISL_411915	2020-01-25	–	SP (17.01)	99.9%; 1157.4
2	EPI_ISL_417518	2020-02-04	14	MK2 (10.0)	100.0%; 5891.8
3	EPI_ISL_415741	2020-02-26	10	MK2 (14.25)	100.0%; 18,300.8
4	EPI_ISL_415742	2020-02-27	4	Vero E6 (26.15)	99.2%; 449.6
5	EPI_ISL_415743	2020-02-27	4	MK2 (12.78)	100.0%; 26,521.5
6	EPI_ISL_417519	2020-03-05	5	MK2 (12.82)	100.0%; 13,718.5
7	EPI_ISL_417520	2020-03-09	–	SP (22.98)	100.0%; 53.1
8	EPI_ISL_417521	2020-03-10	–	NP (23.18)	100.0%; 11,499.4
9	EPI_ISL_417522	2020-03-13	3	MK2 (10.89)	100.0%; 30,044.7
10	EPI_ISL_417523	2020-03-13	3	MK2 (10.45)	100.0%; 29,572.7
11	EPI_ISL_417524	2020-03-14	3	Vero E6 (11.08)	100.0%; 24,326.9
12	EPI_ISL_417525	2020-03-14	3	MK2 (10.11)	100.0%; 34,422.0
13	EPI_ISL_424969	2020-03-17	7	MK2 (9.12)	100.0%; 10,227.7
14	EPI_ISL_424970	2020-03-17	7	MK2 (9.92)	100.0%; 15,863.1
15	EPI_ISL_424971	2020-03-17	7	MK2 (10.94)	100.0%; 14,292.3
16	EPI_ISL_424972	2020-03-16	7	MK2 (12.37)	100.0%; 11,611.7
17	EPI_ISL_424973	2020-03-17	7	MK2 (11.57)	100.0%; 21,393.0
18	EPI_ISL_424974	2020-03-18	7	MK2 (10.02)	100.0%; 15,382.4
19	EPI_ISL_424975	2020-03-18	7	Vero E6 (11.93)	100.0%; 9395.7
20	EPI_ISL_424978	2020-03-18	7	Vero E6 (11.50)	100.0%; 13,364.3
Taiwan/2	EPI_ISL_406031	2020-01-23	–	–	–
Taiwan/3	EPI_ISL_411926	2020-01-24	–	–	–
Taiwan/125	EPI_ISL_420082	2020-03-19	–	–	–
Taiwan/128	EPI_ISL_420083	2020-03-18	–	–	–
Taiwan/170	EPI_ISL_420084	2020-03-21	–	–	–
Taiwan/107	EPI_ISL_420085	2020-03-20	–	–	–

*Sources are sputum (SP) and nasopharyngeal swab (NP) specimens, or supernatants of cultured MK2 and Vero E6 cells.

used the Ovation RNA-Seq System V2 (Nugen Technologies, San Carlos, CA, USA) to synthesize cDNA that was further processed into a library using the Celero DNA-Seq System (Nugen Technologies). Other samples with lower Ct values were used for library preparation by using the Trio RNA-Seq kit (Nugen Technologies). Next-generation sequencing (NGS) was performed on an Illumina MiSeq System (San Diego, CA, USA) with paired-end reads. More than 0.75 and 2.5 Gb of raw data per sample were generated from viral isolates and clinical specimens, respectively.

Next-generation sequencing data analysis pipeline

We first trimmed the raw data by removing low-quality and short reads using Trimmomatic (version 0.39) [12]. Next, quality reads were mapped to the human reference genome to remove host sequences using HISAT2 (version 2.1.0) [13]. SPAdes (version 3.14.0) [14] was then used to perform *de novo* assembly for constructing contig sequences, and BLASTN was used to query the assembled contigs by searching the nucleotide sequence (NT) database of the National Center for Biotechnology Information (NCBI). Viral and bacterial candidates were identified using the top reported BLASTN hits for each of the queried contig sequences, followed by mapping NGS reads onto these candidates to reveal the metagenome. To specifically determine the SARS-CoV-2 genome of interest, on the other hand, we used a reference strain Wuhan-1 (accession number MN908947.3) as the mapping template and used an iterative mapping approach [15] to increase the read

depth and coverage. Reads mapping to the obtained viral genome from iterative mapping was used for assembling again by SPAdes to re-confirm the genomic context. Distributions of read coverages were generated by R package ggplot2 [16].

Phylogenetic and sequence analysis

Out of the 20 whole genomes assembled in this study, 17 were obtained from the virus isolates and three were directly from specimens (Table 1; with additional six genomes provided by Taiwan CDC). In total, genomic data of 26 strains were deposited in the GISAID with accession numbers also given in Table 1. We also downloaded all complete and high-coverage genomes of SARS-CoV-2 from GISAID as of March 14, 2020 and obtained 332 sequences after removing those with sequence gaps or ambiguous nucleotides. The reference strain MN908947.3 from GenBank (NCBI) was also included. As the result, a total of 359 sequences were aligned using MAFFT (version 7.427) [17]. The phylogenetic tree was inferred using RAXML (version 8.2.12) [18] under the GTRGAMMA model with 1000 bootstrap replicates to investigate the genomic relationships between virus strains.

RT-PCR and viral growth analyses for the ORF8-deletion mutant

The ORF8 deletion found in one Taiwanese CGMH-CGU-02 isolate was verified by NGS directly from the specimen, as well as amplifying and re-sequencing the concerned region using Sanger method. Briefly,

cDNA preparation was also performed using the MMLV Reverse Transcription kit (Protech, Taiwan) according to the manufacturer's instructions. The primer sequences used to amplify ORF8 containing region or E gene are as follows: SARS-CoV-2-E-For: 5'-ATG-TACTCATTTCGTTTCGGAAGAGAC-3', SARS-CoV-2-E-Rev: 5'-TTAGACCAGAAGATCAGGAAGCTC-TAG-3', SARS-CoV-2-27760-For: 5'-TTGAACTTT-CATTAATTGACTTCTATTTGTG-3', and SARS-CoV-2-N-Rev: 5'-TTAGGCCTGAGTTGAGTCAG-CACTGCTC-3'.

To examine the effect of ORF8 deletion on viral growth, 4×10^5 Calu-3 cells grown in a 12-well plate were infected with either CGMH-CGU-01 or CGMH-CGU-02 at an MOI of 0.05. Total RNA was extracted from infected cells using TRIzol reagent (Thermo Fisher Scientific) at 24 and 48 h post-infection, according to the manufacturer's instructions. RT-PCR was performed to examine the viral growth, and primers and probes used were described by Corman et al. [11]. Genome copies were converted from Ct by using in vitro transcribed RNA of RNA-dependent RNA polymerase (RdRp, also named nsp12) and Envelope (E) genes as the standard RNA. Normalization was based on the Ct of β -actin using primers as follows: β -actin-For: 5'-CTACAATGAGCTGCGTGTGG-3'; β -actin-Rev: 5'-GCTCATTGCCAATGGTGATG-3'.

Results

ORF8 deletion revealed by NGS data analysis

Complete genomic data of 20 SARS-CoV-2 strains obtained in this study were derived from 3 specimens (CGMH-CGU-01, -07, and -08) and 17 isolates (-02 to -06 and -09 to -20), and have been uploaded in GISAID. Table 1 shows their NGS coverage and depth. The average depths for all the 17 isolates were greater than 9000X, except that CGMH-CGU-02 and -04 have 5892X and 450X respectively. Among the three genomes derived directly from the specimens, one (CGMH-CGU-08) has comparably high depth as virus isolate genomes did, whereas two (CGMH-CGU-01 and -07) showed a lower depth of 1157.4 and 53.1, respectively. Table 1 also includes the 6 strains previously submitted by Taiwan CDC. Figure 1A shows the NGS coverage and depth distribution of CGMH-CGU-01, which has an identical genome as the Wuhan-1 strain (accession number MN908947.3). Notably, we detected a deletion in a 382-nucleotide (nt) sequence at the genomic positions 27,848–28,229 in one Taiwanese genome (CGMH-CGU-02) as shown in Figure 1B. This deletion mostly overlaps with the ORF8 of 366-nt (27,894–28,259) according to the CGMH-CGU-01 or Wuhan-1 strain (Figure 1C). Since the CGMH-CGU-02 genome was determined from a virus isolate, we further performed

NGS using a specimen directly from the same patient for verifying this deletion. Reads yielding the same 382-nt deletion were confirmed in the original specimen, although only a partial genome was assembled with a coverage and average depth of 80.0% and 4.2, respectively. RT-PCR was also performed to verify the NGS data, wherein we designed the primers pairing with the end of ORF7 and N gene, respectively. Sanger sequence (bottom of Figure 1C) shows the evidence of this ORF8 deletion, which reduced the amplicon size from 1774 to 1329 nt (Figure 1D, CGMH-CGU-02).

CGMH-CGU-02 was isolated from a patient with a travel history to Wuhan and who returned to Taiwan on February 3, 2020. Clinical specimen from this patient was collected on February 4, indicating that this ORF8-deletion has already occurred in China. Four nucleotide substitutions were found in this strain when compared to the genome of the Wuhan-1 strain. Two were located at the ORF1ab position 8517 changing from C to T (as C8517T) and position 16577 from A to G (A16577G). The latter was a non-synonymous mutation resulting in an amino acid change at position 5526 from K to R (K5526R). The other two mutations in CGMH-CGU-02 were also non-synonymous, located in the S gene at C145T (H49Y) and C2651T (S884F). Nevertheless, 3 strains isolated from Singapore have shown the same 382-nt ORF8 deletion as of April 14, 2020. Mutations from these ORF8-deletion genomes by comparing to the reference strain were summarized in Table 2. One strain hCoV-19/Singapore/14/2020 showed only one synonymous mutation ORF1ab-C8517T, which was also found in CGMH-CGU-02. The other two (hCoV-19/Singapore/12/2020 and hCoV-19/Singapore/13/2020) each additionally showed two different non-synonymous mutations S-T2449C (F817L) and ORF3a-C176A (A59D), and ORF1ab-T17459C (V5820A) and N-C595T (P199S), respectively. These Singapore strains were collected from clustered infections from February 13–18, 2020, and apparently had different mutations compared with those in CGMH-CGU-02.

Since we successfully isolated the strain containing ORF8-deletion, we further investigated the impact of this deletion on viral replication. Human Calu-3 cells were infected with CGMH-CGU-01 and -02 at an MOI of 0.05 for 24 and 48 h. We measured RNA expression levels of RdRp and E gene using RT-qPCR, and found no significant difference in RdRp and in E gene with CGMH-CGU-02 infected cells at 48 h compared with CGMH-CGU-01 (Supplementary Figure S1), indicating that the ORF8 deletion does not affect viral RNA replication in cultured human cells.

Co-existence with *Haemophilus parainfluenzae*

Three out of 20 CGMH-CGU samples (-01, -07, and -08) were obtained from clinical specimens.

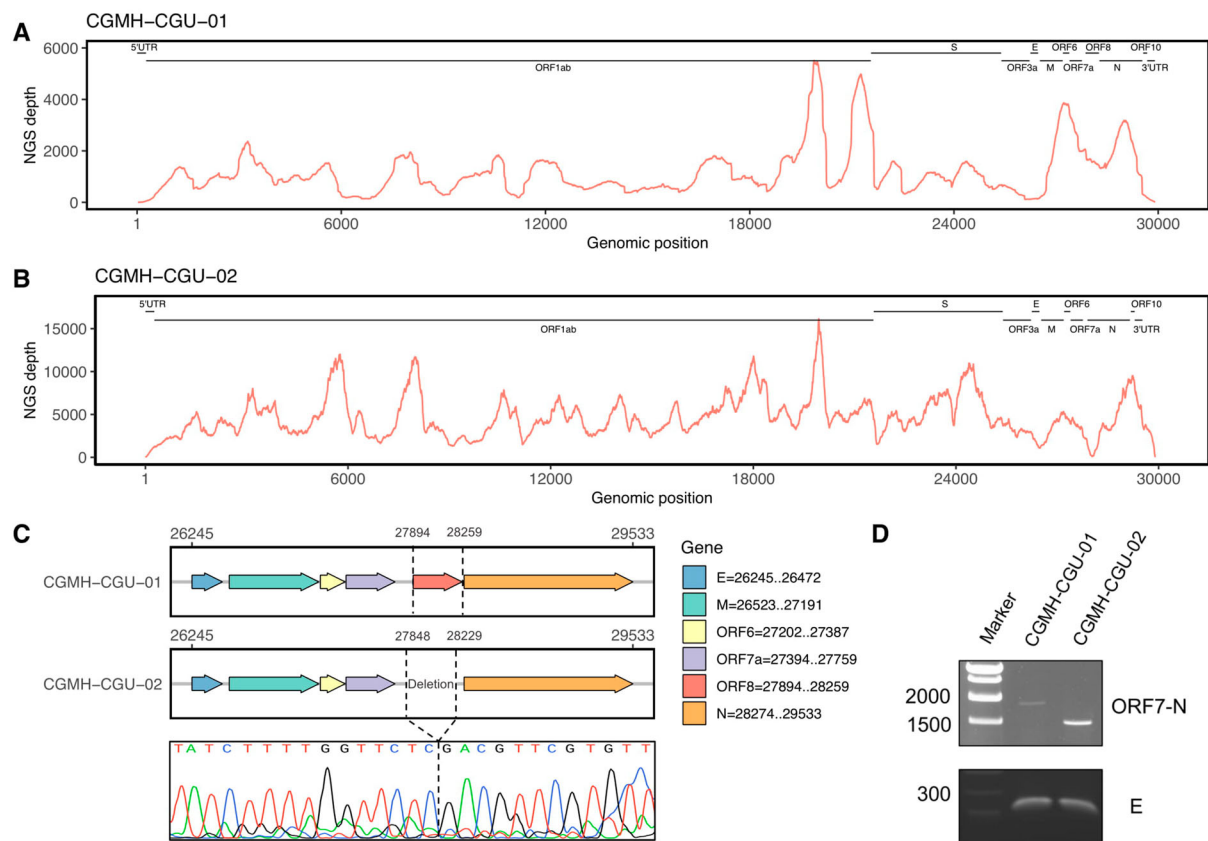


Figure 1. ORF8 deletion in SARS-CoV-2 genome. (A and B) NGS depths of CGMH-CGU-01 and CGMH-CGU-02. (C) Genomic regions of ORF8 and deletion according to the genomic positions of reference strain Wuhan-1 (MN908947.3), and Sanger sequence of this deletion in CGMH-CGU-02. (D) ORF8 deletion was further verified by RT-PCR showing a reduced amplicon size.

Haemophilus parainfluenzae (accession number CP035368.2, a genome that is 2,067,650-bp long) was the dominant population in metagenomic contigs of CGMH-CGU-07 and -08, having a read coverage of 62.6% and 62.5% and an average depth of 53.5 and 53.5, respectively. On the other hand, metagenomic reads of CGMH-CGU-01 mapping to the same bacterial genome resulted in a less yet still sizable coverage of 21.6% and an average depth of 75.4. Particularly, some peaked NGS depths were found approaching or were over 20,000 (Supplementary Figure S2), covering 16S (approximately 1550-nt long) or 23S (2900-nt) ribosomal RNA, signalling the co-existence of *Haemophilus parainfluenzae* in these 3 Taiwanese COVID-19 patients.

Table 2. Genomic mutations of Taiwanese and Singapore strains with the ORF8-deletion.

Strain name	Nucleotide (amino acid) mutation
CGMH-CGU-02	ORF1ab-C8517T, ORF1ab-A16577G (K5526R), S-C145T (H49Y), S-C2651T (S884F)
hCoV-19/Singapore/12/2020	ORF1ab-C8517T, S-T2449C (F817L), ORF3a-C176A (A59D)
hCoV-19/Singapore/13/2020	ORF1ab-C8517T, ORF1ab-T17459C (V5820A), N-C595T (P199S)
hCoV-19/Singapore/14/2020	ORF1ab-C8517T

*Nucleotide or amino acid position was based on gene position of the reference strain (Wuhan-1).

Phylogenetic tree of Taiwanese and global strains

Taiwan experienced two waves of imported cases, first from China in January to late February, followed another wave from other countries starting in early March. The phylogenetic tree of Taiwanese and global strains was constructed to infer the evolutionary relationships among the strains under consideration (Figure 2). To better illustrate phylogenetic clades, we designated and numbered yellow clade as IV harbouring ORF1ab-V378I mutation in this study and three others (blue clade I of ORF8-L84S, gray clade II of ORF3a-G251V, and pink clade III of S-D614G) identified based on previous GISAID annotations of clades S, V, and G, respectively. Figure 3 supports Figure 2 in further illustrating the SARS-CoV-2 genome variations in each of the phylogenetic clades from the 26 investigated Taiwanese genomes.

In the first wave, most Taiwanese strains identified originated from China. CGMH-CGU-01 was isolated on January 25, 2020 from a patient with a travel history to Wuhan, which has been included at the root of Figure 2 (bottom-left) together with Chinese strains in the early stage of the outbreak. Two first-wave strains (CGMH-CGU-02 and Taiwan/3) were grouped in clade I (Figure 2B). Although the CGMH-CGU-02 strain did not carry the ORF8-L84S mutation due to

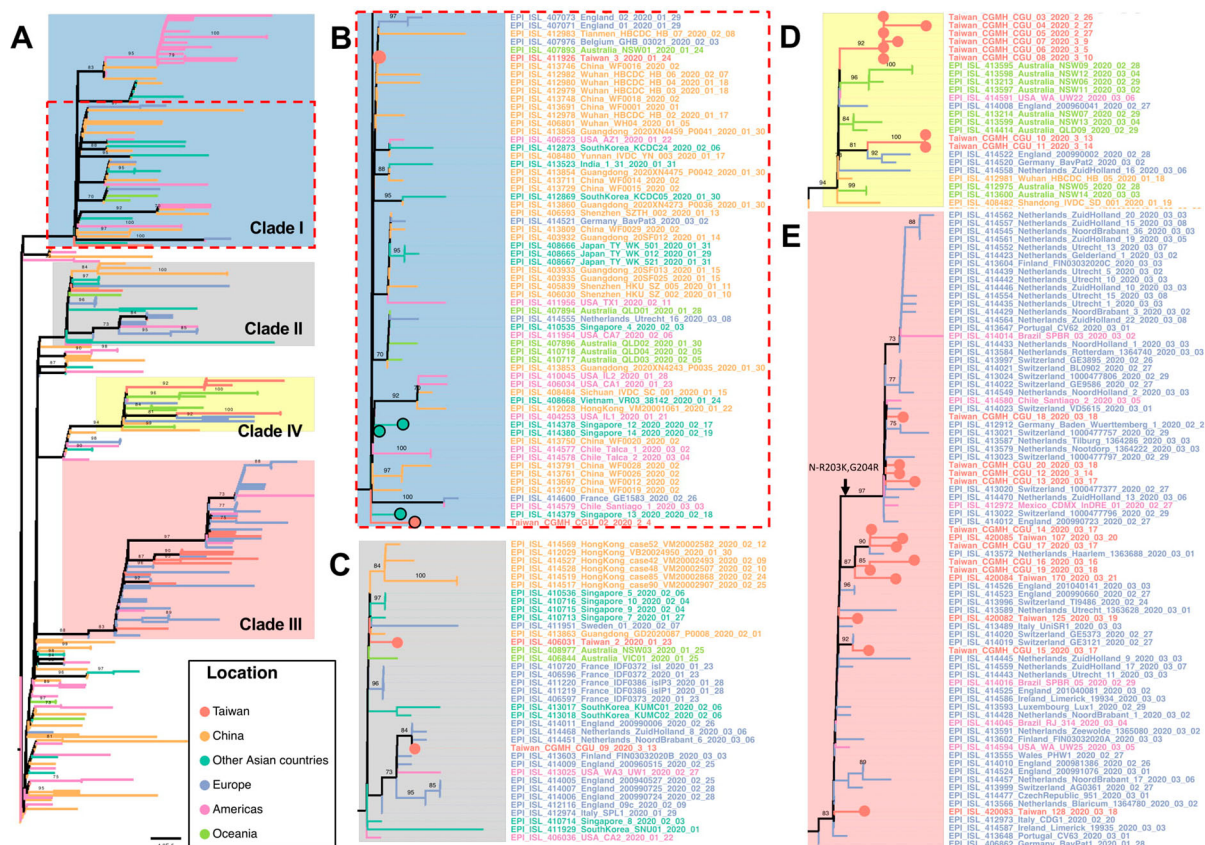


Figure 2. Phylogenetic tree of Taiwanese and global strains. (A) Phylogenetic analysis was performed using the maximum likelihood approach. Significant bootstrap support values greater than 70% are shown. Strains isolated from different locations and clades with specific variations are marked in different colours. Taiwanese strains are located in 4 different clades I, II, III and IV, including (B) and clade I with ORF8-L84S, (C) clade II with ORF3a-G251V, (D) clade IV with ORF1ab-V378I, and (E) clade III with S-D614G. In addition, CGMH-CGU-02 and three Singapore strains with the ORF8-deletion mutation in clade I were marked by light red and cyan solid circle, respectively.

the aforementioned ORF8 deletion, it shared the ORF1ab-C8517T mutation with Taiwan/2 and other strains in this clade (Figures 2B and 3B). Two Taiwanese strains (Taiwan/2 from the first wave and CGMH-CGU-09 from the second wave) were grouped in clade II (Figure 2C). CGMH-CGU-09 was isolated from a patient who had a travel history to Germany, and has been clustered with other European strains. In addition to the signature mutation ORF3a-G251V of clade II, CGMH-CGU-09 also has 3 more mutations in ORF1ab (Figure 3C).

Locally clustered and global transmission in the new ORF1ab-V378I clade

Viral genomes of CGMH-CGU-03 to -07 were determined from clustered infection samples (-03 was the index patient), together with -08 (a case originating from the United Kingdom), and -10 and -11 (having travel history to Turkey) were shown in clade IV of ORF1ab-V378I (Figure 2D). Five Australian strains (NSW05, NSW06, NSW11, NSW12, and NSW13) [19] and one German strain (BavPat2, according to the metadata from the GISAID) from patients having a travel history to Iran were also grouped in this

clade. While the two earliest sequences classified in clade IV were dated mid-January and originated in Wuhan and Shandong in China, respectively, CGMH-CGU-03 was obtained from a patient who had no travel history and the specimen was collected nearly 6 weeks after the two Chinese isolates. All the other viruses in this clade were also dated after February 26. This long time gap in the identification of the two Chinese strains isolated in mid-January suggests that it is unlikely that the later strains were directly linked to the Wuhan strains. Some patients (e.g. CGMH-CGU-10 and -11) infected with virus strains belonging to this clade had a travel history to Middle East, suggesting a possible transmission route via these countries for the occurrence of clustered infections in Taiwan.

COVID-19 can be transmitted via close contact with infected patients. Regardless of whether the infected individuals are symptomatic, their family members and co-workers are at risk of infection. Viral genomes CGMH-CGU-4 to -7 were obtained from patients who had made contact with an index patient who was infected with the CGMH-CGU-03 strain. CGMH-CGU-03, -05, and -06 genomes were identical and served as the baseline for assessing

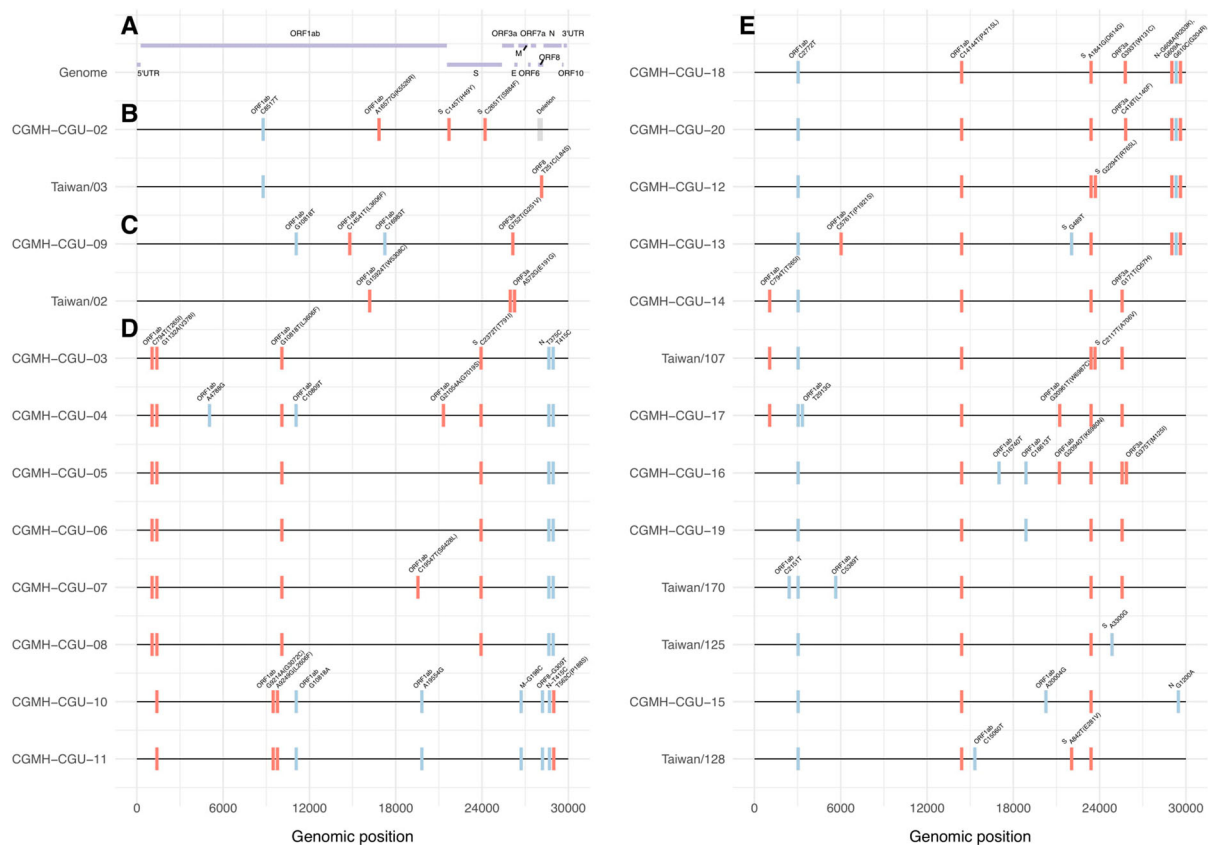


Figure 3. Nucleotide and amino acid variations in SARS-CoV-2 genomes. (A) SARS-CoV-2 genome is illustrated. CGMH-CGU-01 genome was identical to the reference genome, and nucleotide and amino acid variations in the SARS-CoV-2 genomes from the other 25 Taiwanese strains are shown. In line with the phylogenetic clade designation in sub-figures 2B to 2E, mutations in these 25 Taiwanese genomes are shown from (B to E), respectively. Synonymous and non-synonymous mutations were marked by blue and red bars, respectively. Amino acid changes are annotated in parentheses. ORF8 deletion in CGMH-CGU-02 genome is marked in gray.

pairwise genetic distances to the other two cluster members. CGMH-CGU-04 was found to have 3 ORF1ab nucleotide substitutions (A4788G, C10809T, and G21055A); the third position was a non-synonymous change with a G7019S amino acid substitution (Figure 3D). On the other hand, CGMH-CGU-07 showed only one non-synonymous substitution from the baseline at a different ORF1ab position C19547T (S6248L) (Figure 3D). These results suggest that only up to 4 nucleotide changes occurred between CGMH-CGU-04 and -07 genomes within these five Taiwanese clustered infection cases.

Second wave initiated from infections in European countries

Taiwanese genomes in the second wave were majorly located in clade III (Figure 2E), including CGMH-CGU-12 to -20, Taiwan/107, Taiwan/125, Taiwan/128 and Taiwan/170. These strains were isolated from patients who had a travel history to European countries, except CGMH-CGU-14, -16, and -19, which is in line with the observation that many European strains were grouped to this clade. In addition to the signature mutation S-D614G annotated by GISAID in clade III, all the Taiwanese genomes

shared two ORF1ab mutations C2772T and C14144T (P4715L) (Figure 3E). The most divergent genomes among the Taiwanese cases in this clade were CGMH-CGU-13 and -16, each with 8 nucleotide substitutions (resulting in 5 amino acid changes) in the coding region compared to the reference. We further found 4 Taiwanese strains (CGMH-CGU-12, -13, -18, and -20, top four in Figure 3E) shared the same N gene mutations R203K and G204R resulting from 3 nucleotide mutations G608A, G609A, and G610C.

Taken together, Figure 2(B–E) show that Taiwanese isolates were distributed in distinct lineages, indicating that no single dominant strain has been circulating in Taiwan. Figure 3 shows how all the 26 Taiwanese genomes were different from Wuhan-1 (except CGMH-CGU-01 which was identical to Wuhan-1), among which the most divergent strain was CGMH-CGU-04 that showed 9 nucleotide changes (resulting in 5 amino acid changes) in the coding region. Moreover, 8 Taiwanese genomes (including 5 determined from samples obtained from clustered infection cases in the first wave) exhibited the mutation ORF1ab-V378I that was not mentioned before; these strains have now been included in the new genetic clade IV (Figure 2D) along with some foreign strains identified from

patients who had a travel history to Europe and the Middle East.

Discussion

Timely sharing of full genomic data of SARS-CoV-2 strains with the required chronological information pertaining to different geographical locations is important for monitoring the genetic changes in the virus that may be associated with viral spreading and clinical manifestations. Clade IV featuring the ORF1ab-V378I mutation was highlighted, in which some infections may be associated with infections caused in the Middle East, including two Taiwanese (CGMH-CGU-10 and -11) strains having a travel history to Turkey, and some strains from Australia and Germany having a travel history to Iran. Currently, there are abundant viral genomic data from Asia, Europe, and America but very few from the Middle East. Our findings may contribute to developing a better understanding of the global SARS-CoV-2 transmission dynamics.

We detected a 382-nt deletion covering nearly the entire ORF8 of the genome of the CGMH-CGU-02 isolate obtained from a patient who returned from Wuhan in February 2020. A similar observation was found in Singapore strains [20]. These observations suggest the possible circulation of this strain in Wuhan in the first few months of the outbreak, as well as transmission to other geographical regions. Deletions in ORF8 were also observed during the SARS-CoV outbreak in 2003, which were associated with a reduced ability for virus replication in human cells [21]. The SARS-CoV-2 strains with this ORF8 deletion are believed to be still evolving and might have different evolutionary paths compared with those having no such deletion.

Despite the overall high sequence similarity, different clusters of SARS-CoV-2 strains identified in several countries can be distinguished based on phylogenetic analysis, and each cluster has been characterized by its conserved and unique mutations (Figure 3). It is not unusual to have viral mutations during an outbreak, especially for RNA viruses, but mutations that might affect virulence or pathogenicity are of concern. The second-wave strains circulating in Taiwan (Figure 2E and 3E) are characterized by Asp to Gly mutation at position 614 of the S gene that encodes the spike protein required for viral entrance. SARS-CoV-2 spike protein is divided into S1 and S2 subunits that function in receptor binding and membrane fusion, respectively [22]. Biochemical and structural studies have indicated several unique residues of SARS-CoV-2 that greatly improve the receptor-binding activity [23–26]. In addition, a four amino acid, Pro-Arg-Arg-Ala, inserted immediately upstream of the S1/S2 cleavage site generates a polybasic cleavage site of ubiquitous furin-like proteases that might affect the tissue

tropism and/or transmissibility [22]. Lau et al. further used a Vero-E6 culture system to detect an attenuated variant with S1/S2 junction deletions [27]. Whether the receptor-binding activity or furin cleavage might be altered by D614G mutation remains to be investigated. Moreover, its nearby region contains several glycosylations as determined from the glycosylation shield structures [28]. Whether the mutation might change the glycosylation status and eventually change antigenicity awaits further analysis.

RNA viruses show variations in their genomes due to nucleotide substitutions generated by the low fidelity of RNA-dependent RNA polymerase during replication. Such genomic variations are believed to facilitate the successful adaption of the virus to various hosts. Previous studies show that the mutation rates of RNA viruses vary in different viruses and depend on the viral transmission modes [29]. Sequence analysis of SARS-CoV-2 isolated from 5 clustered infections between February 26 to March 9, 2020 in Taiwan revealed only 4 mutations in their 29,903-nt genomic RNA, suggesting that the nucleotide substitution rate was limited during viral RNA replication. The nsp14 exoribonuclease encoded by several coronaviruses plays a crucial role in proofreading during genome replication [30,31]. Investigation of the function of SARS-CoV-2 nsp14 and its replication fidelity is required to be undertaken in the future.

Metagenomic sequencing can help in rapidly exploring the genomic content of targeted viruses in a sample. It also helps in detecting any other pathogens in the microenvironment. *Haemophilus* are common and representative bacterial species found in the upper respiratory tract samples of patients, and play an important role between the host and the environment [32,33]. Molyneaux et al. and Hofstra et al. found a significant outgrowth of *Haemophilus influenzae* and *Haemophilus parainfluenzae* from the pre-existing upper respiratory tract after a rhinovirus infection in subjects with chronic obstructive pulmonary disease and healthy volunteers, respectively [34,35]. Kosikowska et al. further demonstrated that *Haemophilus parainfluenzae* could be a marker of microbiota changes in the upper respiratory tract caused by antibiotics [36]. Ou et al. recently detected *Haemophilus parainfluenzae* and *Moraxella catarrhalis* from sputum samples collected from a severe COVID-19 case [37]. Although the prevalence and clinical impact of *Haemophilus parainfluenzae* in SARS-CoV-2-positive cases remain unclear, we demonstrated the advantage and capacity of metagenomic NGS in identifying co-existence with *Haemophilus parainfluenzae*. It suggested that further NGS studies are required to determine the respiratory microbiota composition and detect the co-infection/existence with other respiratory pathogens, providing new insights to the association between the virus with other pathogens.

In summary, two waves of the COVID-19 pandemic were documented in Taiwan. The first wave mostly included patients who had returned from China and the second one mostly included those who had travelled to Europe and Americas. We found a 382-nucleotide deletion in open reading frame 8 (ORF8) in one isolate in the first wave, as well as 5 clustered cases failed to trace to any imported ones and were hence considered sporadic local transmission cases. Moreover, these 5 genomes were phylogenetically designated to a clade harbouring the ORF1ab-V378I mutation, which is different from the 3 previously reported clades ORF8-L84S, ORF3a-G251V and S-D614G. Also included in this clade were some strains obtained from patients who had a travel history to Turkey and Iran. Highlighting this clade may provide important viral genome information regarding the COVID-19 outbreaks in the Middle East.

Disclosure statement

No potential conflict of interest was reported by the author(s).

Funding

This work was financially supported by the Research Center for Emerging Viral Infections from The Featured Areas Research Center Program within the framework of the Higher Education Sprout Project by the Ministry of Education (MOE) in Taiwan, the Ministry of Science and Technology (MOST), Taiwan (MOST 109-2634-F-182-001, MOST 107-2221-E-182-064-MY2, and MOST 106-2320-B-182A-013-MY3), Linkou Chang Gung Memorial Hospital Taiwan (No. CLRP3B0048 and CMRPD1H0231-3), and Johns Hopkins CEIRS, United States (No. HHSN272201400007C).

ORCID

Yu-Nong Gong  <http://orcid.org/0000-0002-6799-1561>
Kuo-Ming Lee  <http://orcid.org/0000-0002-3215-8342>
Guang-Wu Chen  <http://orcid.org/0000-0002-5322-4839>
Shin-Ru Shih  <http://orcid.org/0000-0003-4874-401X>

References

- [1] Lefkowitz EJ, Dempsey DM, Hendrickson RC, et al. Virus taxonomy: the database of the International Committee on Taxonomy of viruses (ICTV). *Nucleic Acids Res.* 2018 Jan 4;46(D1):D708–D717.
- [2] Drosten C, Gunther S, Preiser W, et al. Identification of a novel coronavirus in patients with severe acute respiratory syndrome. *N Engl J Med.* 2003 May 15;348(20):1967–1976.
- [3] van der Hoek L, Pyrc K, Jebbink MF, et al. Identification of a new human coronavirus. *Nat Med.* 2004 Apr;10(4):368–373.
- [4] Woo PC, Lau SK, Chu CM, et al. Characterization and complete genome sequence of a novel coronavirus, coronavirus HKU1, from patients with pneumonia. *J Virol.* 2005 Jan;79(2):884–895.
- [5] de Groot RJ, Baker SC, Baric RS, et al. Middle East respiratory syndrome coronavirus (MERS-CoV): announcement of the Coronavirus study Group. *J Virol.* 2013 Jul;87(14):7790–7792.
- [6] Zhu N, Zhang D, Wang W, et al. A novel Coronavirus from patients with Pneumonia in China, 2019. *N Engl J Med.* 2020 Feb 20;382(8):727–733.
- [7] Coronaviridae Study Group of the International Committee on Taxonomy of V. The species severe acute respiratory syndrome-related coronavirus: classifying 2019-nCoV and naming it SARS-CoV-2. *Nat Microbiol.* 2020 Apr;5(4):536–544.
- [8] Coronavirus disease 2019 (COVID-19) situation reports: World Health Organization; [cited 2020 April 14]. Available from: <https://www.who.int/emergencies/diseases/novel-coronavirus-2019/situation-reports>.
- [9] Number of Confirmed Cases of COVID-19 in Taiwan: Taiwan Centers for Disease Control; [cited 2020 April 14]. Available from: <https://sites.google.com/cdc.gov.tw/2019-ncov/taiwan>.
- [10] Shu Y, McCauley J. GISAID: global initiative on sharing all influenza data - from vision to reality. *Euro Surveill.* 2017 Mar 30;22(13):30494.
- [11] Corman VM, Landt O, Kaiser M, et al. Detection of 2019 novel coronavirus (2019-nCoV) by real-time RT-PCR. *Euro Surveill.* 2020 Jan;25(3):2000045.
- [12] Bolger AM, Lohse M, Usadel B. Trimmomatic: a flexible trimmer for Illumina sequence data. *Bioinformatics.* 2014 Aug 1;30(15):2114–2120.
- [13] Kim D, Langmead B, Salzberg SL. HISAT: a fast spliced aligner with low memory requirements. *Nat Methods.* 2015 Apr;12(4):357–360.
- [14] Bankevich A, Nurk S, Antipov D, et al. SPAdes: a new genome assembly algorithm and its applications to single-cell sequencing. *J Comput Biol.* 2012 May;19(5):455–477.
- [15] Gong YN, Chen GW, Yang SL, et al. A next-generation sequencing data analysis pipeline for detecting unknown pathogens from mixed clinical samples and revealing their genetic diversity. *PLoS One.* 2016;11(3):e0151495.
- [16] Wickham H. Ggplot2: Elegant graphics for data analysis. New York: Springer-Verlag; 2016.
- [17] Kuraku S, Zmasek CM, Nishimura O, et al. Aleaves facilitates on-demand exploration of metazoan gene family trees on MAFFT sequence alignment server with enhanced interactivity. *Nucleic Acids Res.* 2013 Jul;41(Web Server issue):W22–W28.
- [18] Stamatakis A. RAXML version 8: a tool for phylogenetic analysis and post-analysis of large phylogenies. *Bioinformatics.* 2014 May 1;30(9):1312–1313.
- [19] Eden JS, Rockett R, Carter I, et al. An emergent clade of SARS-CoV-2 linked to returned travellers from Iran. *Virus Evol.* 2020 Jan;6(1):veaa027.
- [20] Su YCF, Anderson DE, Young BE, et al. Discovery of a 382-nt deletion during the early evolution of SARS-CoV-2. *bioRxiv.* 2020;2020.03.11.987222.
- [21] Muth D, Corman VM, Roth H, et al. Attenuation of replication by a 29 nucleotide deletion in SARS-coronavirus acquired during the early stages of human-to-human transmission. *Sci Rep.* 2018 Oct 11;8(1):15177.
- [22] Walls AC, Park YJ, Tortorici MA, et al. Structure, function, and antigenicity of the SARS-CoV-2 spike Glycoprotein. *Cell.* 2020 Apr 16;181(2):281–292.e6.

- [23] Shang J, Ye G, Shi K, et al. Structural basis of receptor recognition by SARS-CoV-2. *Nature*. 2020 May;581(7807):221–224.
- [24] Letko M, Marzi A, Munster V. Functional assessment of cell entry and receptor usage for SARS-CoV-2 and other lineage B betacoronaviruses. *Nat Microbiol*. 2020 Apr;5(4):562–569.
- [25] Lan J, Ge J, Yu J, et al. Structure of the SARS-CoV-2 spike receptor-binding domain bound to the ACE2 receptor. *Nature*. 2020 May;581(7807):215–220.
- [26] Wrapp D, Wang N, Corbett KS, et al. Cryo-EM structure of the 2019-nCoV spike in the prefusion conformation. *Science*. 2020 Mar 13;367(6483):1260–1263.
- [27] Lau SY, Wang P, Mok BW, et al. Attenuated SARS-CoV-2 variants with deletions at the S1/S2 junction. *Emerg Microbes Infect*. 2020 Dec;9(1):837–842.
- [28] Vankadari N, Wilce JA. Emerging WuHan (COVID-19) coronavirus: glycan shield and structure prediction of spike glycoprotein and its interaction with human CD26. *Emerg Microbes Infect*. 2020;9(1):601–604.
- [29] Hanada K, Suzuki Y, Gojobori T. A large variation in the rates of synonymous substitution for RNA viruses and its relationship to a diversity of viral infection and transmission modes. *Mol Biol Evol*. 2004 Jun;21(6):1074–1080.
- [30] Eckerle LD, Lu X, Sperry SM, et al. High fidelity of murine hepatitis virus replication is decreased in nsp14 exoribonuclease mutants. *J Virol*. 2007 Nov;81(22):12135–12144.
- [31] Denison MR, Graham RL, Donaldson EF, et al. Coronaviruses: an RNA proofreading machine regulates replication fidelity and diversity. *RNA Biol*. 2011 Mar-Apr;8(2):270–279.
- [32] Dickson RP, Huang YJ, Martinez FJ, et al. The lung microbiome and viral-induced exacerbations of chronic obstructive pulmonary disease: new observations, novel approaches. *Am J Respir Crit Care Med*. 2013 Nov 15;188(10):1185–1186.
- [33] Nørskov-Lauritsen N. Classification, identification, and clinical significance of *Haemophilus* and *Aggregatibacter* species with host specificity for humans. *Clin Microbiol Rev*. 2014 Apr;27(2):214–240.
- [34] Molyneux PL, Mallia P, Cox MJ, et al. Outgrowth of the bacterial airway microbiome after rhinovirus exacerbation of chronic obstructive pulmonary disease. *Am J Respir Crit Care Med*. 2013 Nov 15;188(10):1224–1231.
- [35] Hofstra JJ, Matamoros S, van de Pol MA, et al. Changes in microbiota during experimental human Rhinovirus infection. *BMC Infect Dis*. 2015 Aug 14;15:336.
- [36] Kosikowska U, Biernasiuk A, Rybojad P, et al. *Haemophilus parainfluenzae* as a marker of the upper respiratory tract microbiota changes under the influence of preoperative prophylaxis with or without postoperative treatment in patients with lung cancer. *BMC Microbiol*. 2016 Apr 6;16:62.
- [37] Ou X, Zhou L, Huang H, et al. A severe case with co-infection of SARS-CoV-2 and common respiratory pathogens. *Travel Med Infect Dis*. 2020 Apr 16;35:101672.



Impaired inflammasome activation and bacterial clearance in G6PD deficiency due to defective NOX/p38 MAPK/AP-1 redox signaling

Wei-Chen Yen^{a,b,1}, Yi-Hsuan Wu^{c,1}, Chih-Ching Wu^{b,d,e,1}, Hsin-Ru Lin^b, Arnold Stern^f, Shih-Hsiang Chen^g, Jwu-Ching Shu^b, Daniel Tsun-Yee Chiu^{b,c,g,*}

^a Graduate Institute of Biomedical Sciences, College of Medicine, Chang Gung University, Taoyuan, Taiwan

^b Department of Medical Biotechnology and Laboratory Sciences, College of Medicine, Chang Gung University, Taoyuan, Taiwan

^c Research Center for Chinese Herbal Medicine, College of Human Ecology, Chang Gung University of Science and Technology, Taoyuan, Taiwan

^d Molecular Medicine Research Center, Chang Gung University, Tao-Yuan, Taiwan

^e Department of Otolaryngology - Head & Neck Surgery, Chang Gung Memorial Hospital, Tao-Yuan, Taiwan

^f New York University School of Medicine, New York, NY, USA

^g Department of Pediatric Hematology/Oncology, Linkou Chang Gung Memorial Hospital, Taoyuan, Taiwan

ARTICLE INFO

Keywords:

G6PD
Inflammasome
NADPH oxidase
IL-1 β
Bactericidal response
Redox homeostasis

ABSTRACT

Glucose-6-phosphate dehydrogenase (G6PD) is the rate-limiting enzyme of the pentose phosphate pathway that modulates cellular redox homeostasis via the regeneration of NADPH. G6PD-deficient cells have a reduced ability to induce the innate immune response, thus increasing host susceptibility to pathogen infections. An important part of the immune response is the activation of the inflammasome. G6PD-deficient peripheral blood mononuclear cells (PBMCs) from patients and human monocytic (THP-1) cells were used as models to investigate whether G6PD modulates inflammasome activation. A decreased expression of IL-1 β was observed in both G6PD-deficient PBMCs and PMA-primed *G6PD*-knockdown (*G6PD*-kd) THP-1 cells upon lipopolysaccharide (LPS)/adenosine triphosphate (ATP) or LPS/nigericin stimulation. The pro-IL-1 β expression of THP-1 cells was decreased by *G6PD* knockdown at the transcriptional and translational levels in an investigation of the expression of the inflammasome subunits. The phosphorylation of p38 MAPK and downstream c-Fos expression were decreased upon *G6PD* knockdown, accompanied by decreased AP-1 translocation into the nucleus. Impaired inflammasome activation in *G6PD*-kd THP-1 cells was mediated by a decrease in the production of reactive oxygen species (ROS) by NOX signaling, while treatment with hydrogen peroxide (H₂O₂) enhanced inflammasome activation in *G6PD*-kd THP-1 cells. *G6PD* knockdown decreased *Staphylococcus aureus* and *Escherichia coli* clearance in *G6PD*-kd THP-1 cells and G6PD-deficient PBMCs following inflammasome activation. These findings support the notion that enhanced pathogen susceptibility in G6PD deficiency is, in part, due to an altered redox signaling, which adversely affects inflammasome activation and the bactericidal response.

1. Introduction

Although glucose-6-phosphate dehydrogenase (G6PD) deficiency is perhaps the most common sex-linked enzymopathy on earth [1], the biochemical and physiologic roles of this housekeeping enzyme have not been fully explored [2]. Biochemically, G6PD is well known as the

rate-limiting enzyme of the pentose phosphate pathway for regenerating nicotinamide adenine dinucleotide phosphate (NADPH) [3–6]. NADPH, an essential cofactor in the redox system, maintains a proper level of reducing equivalence such as reduced glutathione (GSH) and acts as a substrate for NADPH oxidase (NOX) and nitric oxide synthase (NOS), which generate reactive oxygen species (ROS) and

Abbreviations: G6PD, glucose-6-phosphate dehydrogenase; NADPH, reduced form of nicotinamide adenine dinucleotide phosphate; NOX, NADPH oxidase; NO, nitric oxide; NOS, nitric oxide synthase; UP-LPS, ultrapure lipopolysaccharide; PMA, phorbol 12-myristate 13-acetate; ATP, adenosine triphosphate; MAPK, mitogen-activated protein kinases; AP-1, activator protein 1; ROS, reactive oxygen species; PBMC, peripheral blood mononuclear cells; H₂O₂, hydrogen peroxide; THP-1, human monocytic cells; *G6PD*-kd, *G6PD* knockdown

* Corresponding author. Department of Medical Biotechnology and Laboratory Science; Chang Gung University, 259 Wen-Hwa 1st Road, Guishan Dist, Tao-Yuan, Taiwan.

E-mail address: dtychiu@mail.cgu.edu.tw (D. Tsun-Yee Chiu).

¹ These authors contributed equally to this work.

<https://doi.org/10.1016/j.redox.2019.101363>

Received 23 August 2019; Received in revised form 18 October 2019; Accepted 25 October 2019

Available online 02 November 2019

2213-2317/ © 2019 The Authors. Published by Elsevier B.V. This is an open access article under the CC BY-NC-ND license (<http://creativecommons.org/licenses/by-nc-nd/4.0/>).

nitric oxide (NO), respectively, for a subsequent role in signal transduction [1,7,8]. Physiologically, evidence has been emerging to indicate that G6PD deficiency affects glucose metabolism [9], cell growth, embryonic development, lethality [10,11] and susceptibility to infections by modulating redox homeostasis [12,13].

How G6PD deficiency can disrupt immune responses has not been clearly delineated. Since G6PD plays a vital role in cellular redox homeostasis [14], this enzyme can influence the redox microenvironment in cells leading to modulation of physiological functions [15]. NOXs are a major source of ROS [16–18] and are involved in the initiation of cell signaling to modulate inflammatory response and the antimicrobial defense in phagocytes [14,19]. Some transcription factors, such as NF- κ B and AP-1, and certain signal transduction pathway proteins, such as MAPKs, are activated by intracellular ROS to induce inflammatory signaling [20–22]. Patients with G6PD deficiency or G6PD knockdown cells are more susceptible to pathogen infections [13,23,24], indicating that the immune response is affected by G6PD status.

A key physiological function of the innate immune response is the activation of the inflammasome [25,26]. This mainly leads to the production of pro-inflammatory cytokines, especially interleukin-1 β (IL-1 β) and IL-18, in response to invading pathogens [27]. The most common inflammasomes include NLRP1, AIM2, NLRP3, and NLRP4, and are classified by their oligomer composition and different stimuli [25]. Among the inflammasomes, NLRP3 is stimulated by environmental- and pathogen/host-derived factors. The processes mediated by inflammasomes are critical during microbial infections, including the regulation of metabolic processes and mucosal immune responses [28]. The activation of the inflammasome requires strict regulation; otherwise, it leads to many diseases [29–32]. How G6PD is involved in the activation of the inflammasome has not been clearly defined.

The activation of the NLRP3 inflammasome is ROS dependent [33,34] and is mediated by the NOX pathway [35]. Decreased ROS production is observed in G6PD-deficient granulocytes upon lipopolysaccharide (LPS) or phorbol 12-myristate 13-acetate (PMA) stimulation and such abnormality has been attributed to impaired NOX signaling [14,36,37]. Increased susceptibility to pathogen infections in G6PD-deficient cells is due to an insufficient ROS-triggered inflammatory response [13]. These findings provide support for the notion that G6PD deficiency impairs ROS production via the NOX signaling pathway. The effect of G6PD on NLRP3 inflammasome activation deserves further attention. In the current study, a decrease in IL-1 β was observed in the PBMCs of patients with G6PD deficiency and in G6PD-kd THP-1 cells. This led to an investigation of the role of G6PD in inflammasome activation and its association with the bactericidal effect in phagocytes. Mechanistically, G6PD deficiency provides less NADPH as a substrate for NOX, causing less ROS generation to activate the inflammasome.

2. Materials and methods

2.1. Reagents

Ficoll-Paque was purchased from GE Healthcare (Little Halfont, Buckinghamshire, UK). Ultrapure LPS was purchased from InvivoGen (California, USA). Anti-IL-1 β , anti-p65, anti-phospho-p65, anti-p38, anti-phospho-p38, anti-ERK, anti-phospho-ERK, anti-JNK, anti-phospho-JNK, anti-c-Jun, anti-phospho-c-Jun, anti-phospho-c-Fos and anti-c-Fos were all purchased from Cell Signaling Technology (Beverly, MA, USA). Anti-G6PD was purchased from Genesis Biotech (Taiwan). ATP, nigericin, PMA, hydrogen peroxide, DPI, NADPH, and anti- β -Actin were purchased from Sigma-Aldrich (St. Louis, MO, USA). Anti-NLRP3 was purchased from AdipoGen Life Sciences (San Diego, CA, USA), and anti-ASC was purchased from Medical & Biological Laboratories (Japan). The anti-caspase-1, anti-pro-IL-1 β , anti-mouse and anti-rabbit antibodies were purchased from Santa Cruz Biotechnology (Dallas, TX, USA). Anti- α -tubulin was purchased from Merck Millipore (Burlington,

Table 1

Partial characteristics of patients with G6PD deficiency and normal subjects.

No. ^a	G6PD status	Sex (Male/ Female)	Age	Point mutation site of <i>G6PD</i> gene
1	Normal	Male	22	–
2	Normal	Female	24	–
3	Normal	Female	21	–
4	Normal	Male	22	–
5	Normal	Female	24	–
6	Normal	Male	22	–
7	Normal	Male	21	–
8	Normal	Female	40	–
9	Normal	Male	21	–
10	Normal	Male	21	–
11	Deficiency	Male	22	1376
12	Deficiency	Female	21	1376
13	Deficiency	Female	21	1388
14	Deficiency	Male	22	1376
15	Deficiency	Female	21	1376
16	Deficiency	Male	20	1376
17	Deficiency	Female	21	1376
18	Deficiency	Male	21	1376
19	Deficiency	Male	21	1376
20	Deficiency	Male	70	1376

^a All volunteers are non-smokers and have no medical background.

USA). Anti-lamin B1 was purchased from Proteintech (Illinois, USA). Polyvinylidene difluoride (PVDF) membranes and Immobilon Western Chemiluminescent HRP Substrate (ECL) were purchased from Millipore Corporation (Billerica, MA, USA).

2.2. PBMCs isolation and cell culture

This study was approved by the Institutional Review Board at Chang Gung Memorial Hospital, and written informed consent was acquired from every volunteer. Human whole blood was taken from healthy volunteers and G6PD-deficient patients, which are non-smokers and have no medical background. PBMCs were isolated from whole blood using Ficoll-Paque density gradient centrifugation.

THP-1 was a kind gift from Dr. Hsing-I Huang (Chang Gung University) and was cultured in RPMI 1640 (Gibco, USA) supplemented with 10% FBS (Biological Industries, USA), 100 units/mL penicillin and 100 μ g/mL streptomycin (Gibco, USA) at 37 °C in a humidified atmosphere of 5% CO₂.

The human embryonic kidney cell line (293T) was purchased from the American Type Culture Collection (Rockville, MD, USA) and was cultured in Dulbecco's Modified Eagle's Medium (Gibco, USA) supplemented with 10% FBS, 100 units/mL penicillin, and 100 μ g/mL streptomycin at 37 °C in a humidified atmosphere of 5% CO₂.

2.3. Transfection of siRNAs

Specific sets of human siRNA for *G6PD* and a universal negative control were obtained from Dharmacon RNA Technologies (Lafayette, CO, USA). Transfection of the target siRNA (50 nM per 10⁶ cells) was performed by using Lipofectamine 3000 reagent (Invitrogen, CA, USA) based on the manufacturer's instructions. On the next day, the cells were treated with stimuli as described below.

2.4. Cell stimulation

PBMCs isolated from whole blood were incubated with LPS (1 μ g/mL) for 3 h and ATP (5 mM) for another 3 h. The supernatants were collected for IL-1 β determination by an ELISA kit.

THP-1 cells were cultured in the presence of 150 ng/ml PMA to allow for differentiation into macrophage-like cells. After incubation for 24 h, the cells were incubated with fresh RPMI 1640 for another 24 h, followed by 0.1 μ g/ml LPS treatment and 20 μ M nigericin treatment.

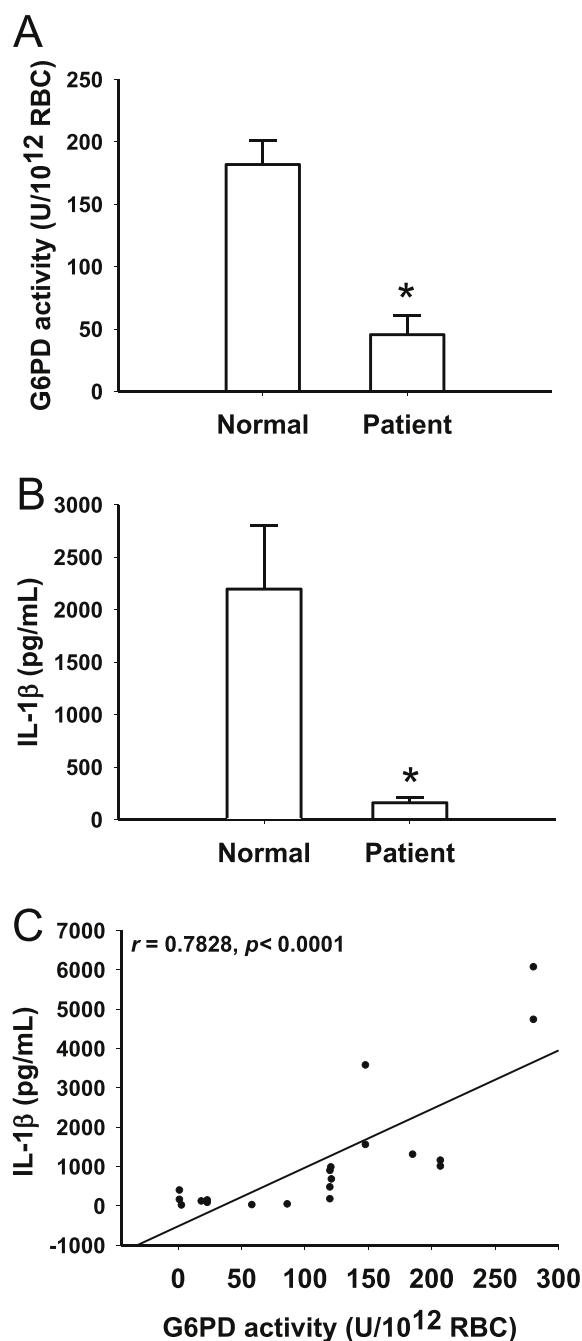


Fig. 1. IL-1 β secretion in G6PD-deficient PBMCs. (A) G6PD activity of whole blood from patients with G6PD deficiency and normal subjects. (B) IL-1 β concentration in the supernatant determined by ELISA ($n = 10$ and 10 for normal and G6PD deficiency subjects, respectively, $*p < 0.05$). (C) The correlation of G6PD activity and IL-1 β secretion ($n = 20$, $p < 0.0001$).

The cell lysate and supernatant were collected for the indicated experiments.

2.5. ELISA

Cell supernatants were harvested for human IL-1 β quantification using an ELISA kit (R&D Systems, Minneapolis, MN) according to the manufacturer's instructions.

2.6. G6PD activity

The G6PD activity of whole blood was measured using a G6PD quantitative kit (Trinity Biotech) according to the manufacturer's instructions. In brief, 500 μ l assay reagent and 5 μ l whole blood were added to the cuvette and incubated for 5 min at room temperature. Then, 1 ml of the substrate solution was added to the cuvette and incubated for 2 min at 37 $^{\circ}$ C. The reduction of NADP $^{+}$ was measured spectrophotometrically at 340 nm. The activity of G6PD is expressed as U/10¹² erythrocytes (RBCs).

G6PD activity was measured spectrophotometrically at 340 nm by the reduction of NADP $^{+}$ in the presence of glucose-6-phosphate as previously described [38]. In brief, the cells were lysed in lysis buffer (50 mM Tris-HCl, 150 mM NaCl₂, 1 mM EDTA, 0.05% SDS, 1 mM NaF, 1% Triton-X 100, pH 7.5). After centrifugation, the cell lysate was reacted with G6PD assay buffer (50 mM Tris-HCl (pH 8), 50 mM MgCl₂, 4 mM NADP $^{+}$, and 4 mM glucose 6-phosphate). The G6PD activity was analyzed at 340 nm by spectrophotometry (Beckman Coulter, USA).

2.7. Western blot analysis

The total protein in lysates and supernatants was analyzed by a Western blot. The cells were collected using lysis buffer (50 mM Tris-HCl, 150 mM NaCl₂, 1 mM EDTA, 0.05% SDS, 1 mM NaF, 1% Triton-X 100, pH 7.5), and the protein concentration was determined by the Bradford assay. The protein in supernatants was concentrated by trichloroacetic acid (TCA) precipitation [39]. Samples were denatured, electrophoresed on SDS-polyacrylamide gel, and transferred onto PVDF membranes. The membranes were incubated overnight at 4 $^{\circ}$ C with an appropriate dilution of a primary antibody (1:1000). The membranes were then incubated with an appropriate dilution of an HRP-conjugated secondary antibody for 1.5 h. The immunoreactive bands were visualized by ECL reagents. ImageJ software was used to analyze the intensity. β -Actin was used as a loading control.

2.8. qRT-PCR

The total RNA was extracted using TRIzol Reagent (Life Technologies, CA, USA). RNA was reverse transcribed into cDNA by oligo-dT (Biomart Scientific, Taipei, Taiwan) as the primer in the presence of reverse transcriptase (Superscript III, Invitrogen). qRT-PCR was conducted using a SsoFast[™] EvaGreen[®] Supermix reagent (Bio-Rad, CA, USA) with an iQ5 real-time thermal cycler (Bio-Rad, CA, USA). The expression levels were normalized to those of endogenous *ACTB*, and the data were analyzed using the $2^{-\Delta\Delta C_t}$ method. The sequences of the primers used in qRT-PCR are as follows: *IL1B*: 5'-TGTCTGGTCCATATGAACGTG-3' and 5'-GCTGTAGAGTGGGCTTATC-3'; *ACTB*: 5'-TCCACCTTCCAGCAGATG-3' and 5'-GTGTAACGCAACTAAGTCATAG-3'.

2.9. Dual-luciferase promoter assay

The human IL-1 β promoter plasmid was a kind gift from Dr. Ben-Kuen Chen (National Cheng Kung University) [40]. The deletion sequence of the AP-1 binding site bearing the luciferase plasmid was constructed using site-directed mutagenesis. The 293FT cells cultured in 24-well plates were transfected with 600 ng of pLKO-scramble or pLKO-G6PD [38] together with 300 ng of the IL-1 β promoter plasmid (wild-type or deletion) and 100 ng of pRL-TK vector by Lipofectamine[®] 2000 (Thermo Fisher Scientific, MA, USA). Forty-eight hours after transfection, the luciferase activity was measured by using the Dual-Luciferase Assay (Promega, MA, USA) with a GLOMAX luminometer (Promega, MA, USA). The cellular extracts were assayed for luciferase activity and normalized to the Renilla luciferase levels. The data are presented relative to the pLKO-scramble levels (relative light unit; RLU).

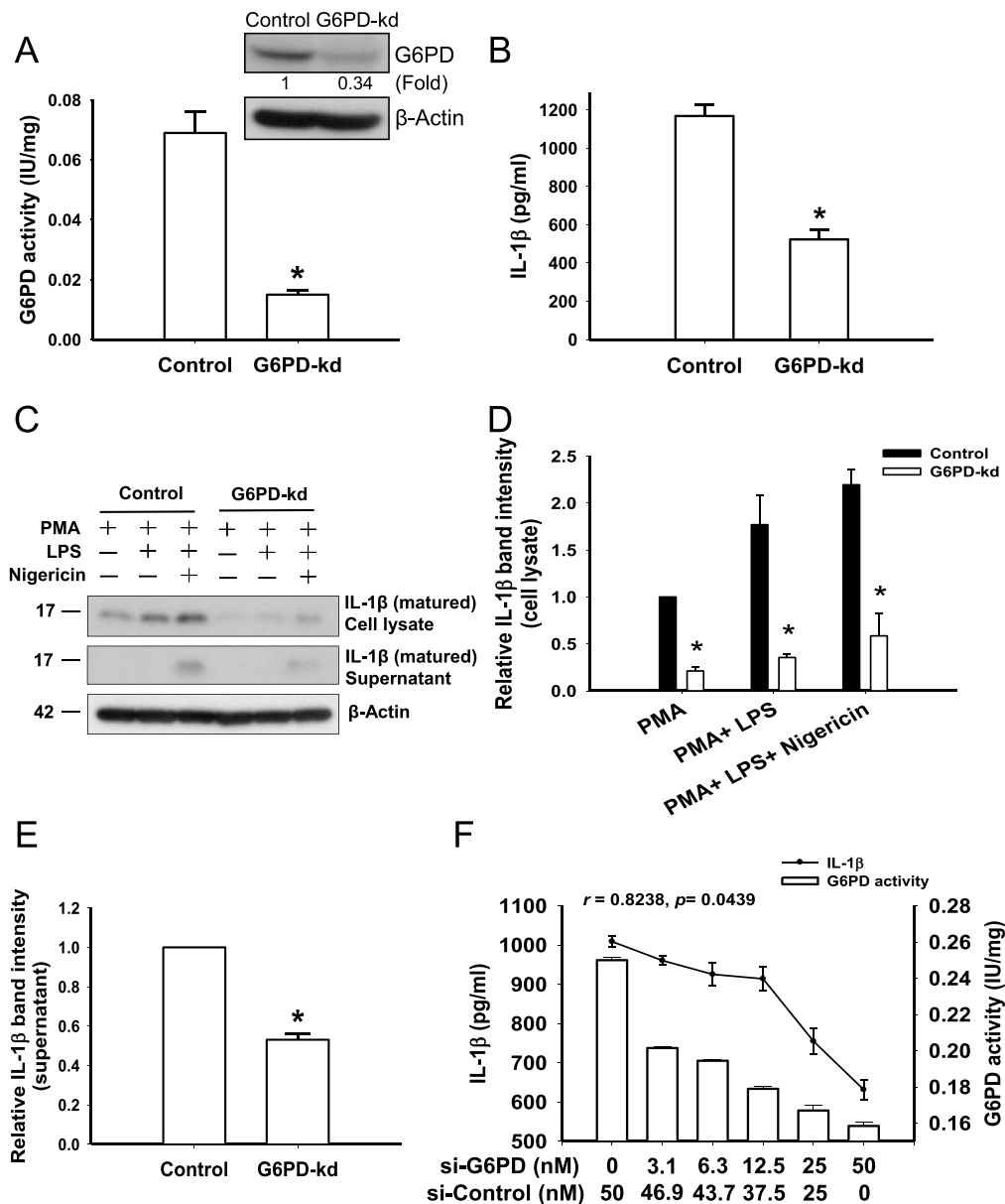


Fig. 2. Inflammation activation in G6PD-kd THP-1 cells. (A) Western blot and spectrophotometry assays of G6PD protein expression and activity in G6PD-kd THP-1 cells ($n = 3$, $*p < 0.05$). (B) ELISA and (C) Western blot analyses of IL-1 β in the supernatant and cell lysate. (D), (E) IL-1 β quantitative level in cell lysate and supernatant of (C). β -Actin was used as a normalized loading control of the cell lysate. (F) The correlation of G6PD activity and IL-1 β secretion. THP-1 cells were transfected with G6PD siRNA (0, 3.1, 6.3, 12.5, 25 or 50 nM). PMA-differentiated THP-1 were treated with LPS and nigericin, cell lysate and supernatant were collected for G6PD activity and IL-1 β analysis. These data are representative of three independent experiments ($n = 3$, $p < 0.05$).

2.10. Detection of ROS production

Cells were incubated for 30 min with 10 μ M CM-H₂DCFDA (Thermo Fisher Scientific, MA, USA) at 37 °C. The cells were detached from the wells by a 5 min incubation with PBS (containing 50 mM EDTA) and a 5 min incubation with Trypsin-EDTA at 37 °C. The cells were washed twice and re-suspended in PBS (containing 1% FBS) before flow cytometry (FCM) analysis. FCM data are presented as the mean fluorescence intensity (MFI) for all cells.

2.11. Superoxide measurement by cytochrome c reduction

Superoxide production was measured using cytochrome c reduction according to the previous study [41]. Since cytochrome c cannot enter into cells, this assay exclusively determine superoxide produced from NOX in extracellular medium. In brief, 200 μ l PMA-treated cells (10^6 /ml) were seeded in 96 well plate to allow for differentiation into macrophage-like cells. After incubation for 24 h, the cells were incubated with fresh RPMI 1640 for another 24 h. Cells were incubated in pre-warmed HBSS containing 100 μ M cytochrome c and stimulated

0.1 μ g/ml LPS. Absorbance at 550 nm was recorded for 20 min with 1 measurement per 5 min at 37 °C with gentle shaking. The production of superoxide was calculated using an absorption coefficient of 21 $\text{mM}^{-1}\text{cm}^{-1}$ for cytochrome c.

2.12. Gentamicin protection assay

Staphylococcus aureus and *Escherichia coli* OP50 were incubated in Luria-Bertani (LB) media at 37 °C with shaking one day before the experiment. The density of bacteria was measured at 670 nm in a DU 800 spectrophotometer after washing three times with PBS. LPS-primed THP-1 cells and PBMCs from subjects were infected with bacteria at an MOI (multiplicity of infection) of 10 and were incubated for 2 h at 37 °C in a humidified atmosphere of 5% CO₂. After being infected, the cells were washed three times with HBSS and were incubated with gentamicin (200 μ g/ml) containing RPMI 1640 for 30 min to kill extracellular bacteria. After replacing the medium with fresh medium, the cells were incubated with 20 μ M nigericin for 30 min to induce inflammasome activation. The cells were washed once by HBSS, followed by lysis with 1% Triton X-100. The cell lysate was serially diluted and spread onto

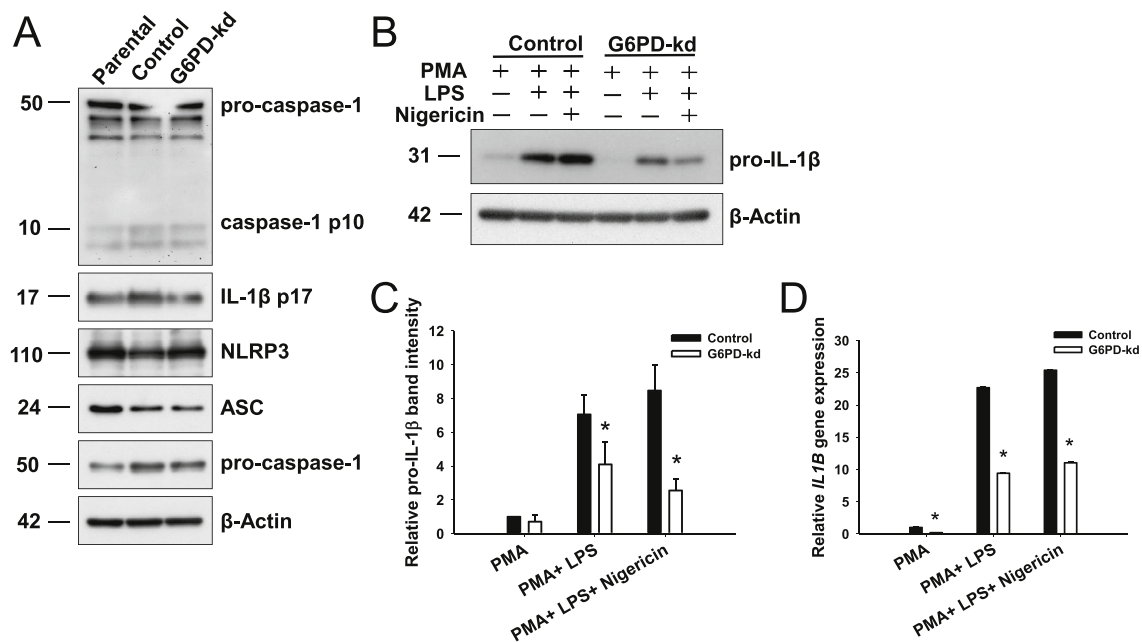


Fig. 3. NLRP3 inflammasome activation in *G6PD*-kd THP-1 cells. (A) Cells were treated with LPS (0.1 μ g/mL) for 180 min and with nigericin (20 μ M) for 30 min. Western blot of cell lysate and supernatant protein expression of the inflammasome complex. (B) Cells were treated with LPS (0.1 μ g/mL) for 180 min with or without nigericin (20 μ M) for 30 min. Western blot of the protein expression of pro-IL-1 β . (C) pro-IL-1 β quantitative level of (B). β -Actin was used as a normalized loading control of the cell lysate in (A) and (B). (D) Gene expression of *IL1B* analyzed by qRT-PCR, where *ACTB* was used as the normalized control. These data are representative of three independent experiments ($n = 3$, $*p < 0.05$).

agar plates. The next day, the efficiency of bacterial clearance was determined by counting the colony forming units (CFUs) on agar plates [42].

2.13. Statistical analysis

The significance of the G6PD activity, the IL-1 β concentration and the activity of intracellular bacterial clearance from normal and G6PD-deficient patients was evaluated by the Mann-Whitney test. These data were expressed as the mean \pm SEM from replicate determinations. The significance of the correlation of G6PD activity and IL-1 β was assessed by the Pearson Correlation. Student's *t*-test was used to compare the mean values from the control and *G6PD*-kd THP-1 cells, and for the comparing of superoxide production (expression as the mean \pm SEM from replicate determinations). These data are expressed as the mean \pm standard deviation of at least three separate experiments. The difference was regarded as significant when the *p* value was < 0.05 .

3. Results

3.1. Reduced IL-1 β secretion in *G6PD*-deficient PBMCs

Ten patients with G6PD deficiency and 10 healthy controls were recruited for this study (Table 1). Of the patients with G6PD deficiency and the normal controls, all subjects were within an age range of 20–70. The point mutation sites of the *G6PD* gene from patients with G6PD deficiency are 1376 and 1388 (Table 1). The G6PD activity of whole blood from patients with G6PD deficiency was much lower than that of the normal controls (Fig. 1A). IL-1 β secretion was significantly decreased in G6PD-deficient human PBMCs (Fig. 1B) compared to that in normal control PBMCs, indicating that G6PD deficiency is associated with lower IL-1 β production. The activity of G6PD was positively correlated with the secretion of IL-1 β (Fig. 1C).

3.2. Decreased IL-1 β secretion in *G6PD*-knockdown THP-1 cells

G6PD-kd THP-1 cells expressed approximately 21.7% of the G6PD levels in the control THP-1 cells (Fig. 2A). According to the results of MTT assay and the Cell Counting Kit-8 (CCK8), cell viability was similar between control and *G6PD*-kd THP-1 cells (Fig. S1). Similar to that observed in PBMCs from G6PD-deficient patients (Fig. 1B), *G6PD*-kd THP-1 cells had decreased IL-1 β secretion upon inflammasome activation (Fig. 2B), and the pattern of protein expression in the cell lysates and supernatants was the same as that found by ELISA (Fig. 2C). The quantitative intensity of IL-1 β in the cell lysate and supernatant is shown in Fig. 2D and E, respectively. The activity of G6PD was positively correlated with the secretion of IL-1 β (Fig. 2F).

3.3. Decreased pro-IL-1 β expression in *G6PD*-kd THP-1 cells upon inflammasome activation

G6PD knockdown reduced the expression of mature IL-1 β , but not the expression of caspase-1 or the components of the inflammasome (NLRP3, ASC and pro-Caspase-1) (Fig. 3A). A decrease in the translational level of pro-IL-1 β upon inflammasome activation was detected by a Western blot (Fig. 3B) in *G6PD*-kd THP-1 cells compared to the level in the controls. The quantitative intensity of pro-IL-1 β is shown in Fig. 3C. The mRNA level of IL-1 β also decreased in *G6PD*-kd THP-1 cells (Fig. 3D).

3.4. Decreased phosphorylation of p38 MAPK signaling in *G6PD*-kd THP-1 cells upon inflammasome activation

The phosphorylation of p38 at different time points upon inflammasome activation was decreased in *G6PD*-kd THP-1 cells compared to that in the control cells without a change in the phosphorylation levels of p65, ERK and JNK (Fig. 4A). The quantitative intensity of p-p38 is shown in Fig. 4B. Control and *G6PD*-kd THP-1 cells treated with SB203580 (an inhibitor of p38 MAPK) resulted in p38 inhibition (Fig. 4C). Cells were reacted with LPS, which resulted in impaired pro-

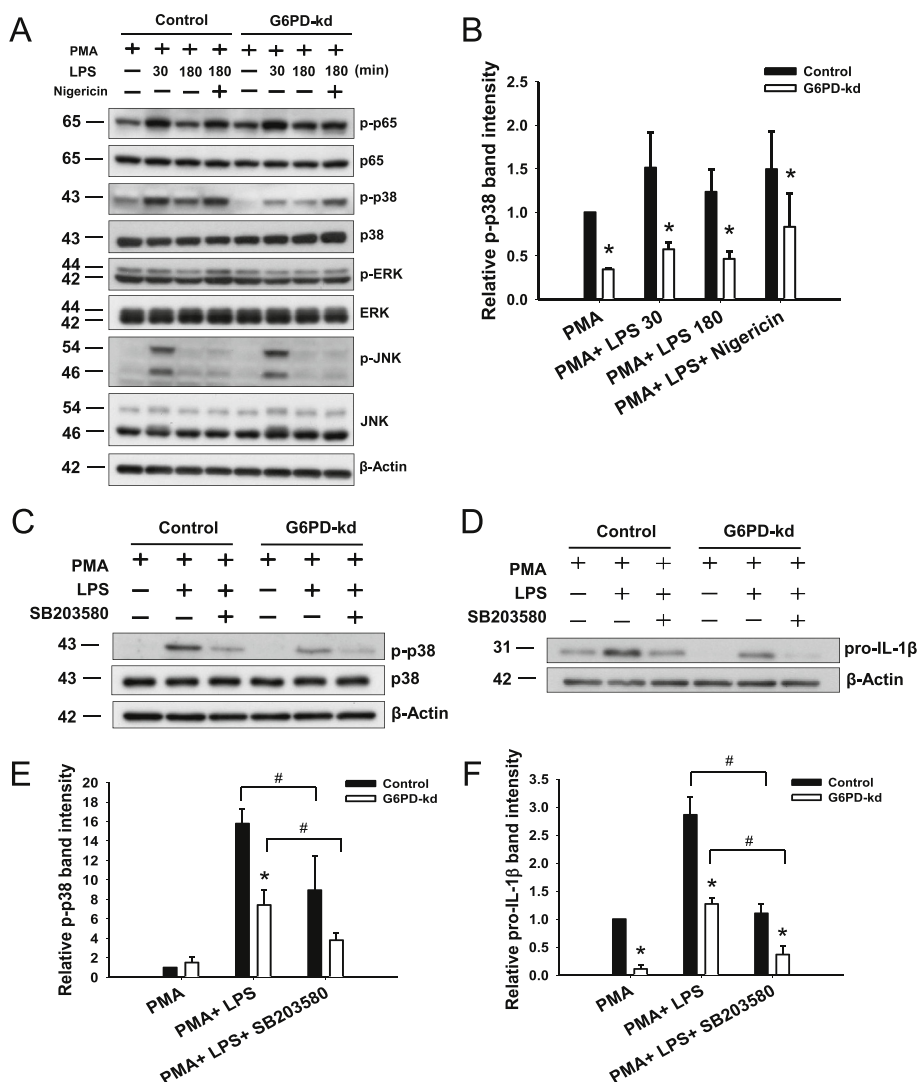


Fig. 4. P38/MAPK pathway in *G6PD*-kd THP-1 cells. (A) Western blot of the expression of p-p65, p65, p-p38, p38, p-ERK, ERK, p-JNK and JNK. PMA differentiated control and *G6PD*-kd THP-1 cells were treated with LPS for 30 or 180 min then with nigericin for 30 min. (B) P-p38 quantitative level of (A). (C), (D) Western blot of the expression of p-p38, p38 and pro-IL-1β. PMA-differentiated control and *G6PD*-kd THP-1 cells were treated with SB203580 for 30 min prior LPS treatment for 30 min for p38 detection or 180 min for pro-IL-1β detection. (E), (F) p-p38, p38 and pro-IL-1β quantitative levels of (C) and (D). β-Actin was used as a normalized loading control. The results are representative of three independent experiments ($n = 3$, $*p < 0.05$).

IL-1β expression (Fig. 4D). The quantitative intensity of p-p38 and pro-IL-1β is shown in Fig. 4E and F, respectively.

3.5. Inhibition of pro-IL-1β expression through AP-1 signaling in *G6PD*-kd THP-1 cells

The total and phosphorylated form of c-Fos, but not c-Jun, decreased with or without LPS treatment in *G6PD*-kd THP-1 cells (Fig. 5A). The quantitative intensities of p-c-Fos and c-Fos are shown in Fig. 5B and C, respectively. AP-1 signaling, which is the heterodimer of c-Fos and c-Jun and is downstream of p38, decreased after treatment with SB203580 in both control and *G6PD*-kd THP-1 cells (Fig. 5D). The quantitative intensity of c-Fos is shown in Fig. 5E. LPS treatment promoted the translocation of c-Jun, c-Fos and p65 from the cytoplasm to the nucleus in control and *G6PD*-kd THP-1 cells (Fig. 5F). The translocation of c-Fos was reduced in *G6PD*-kd THP-1 cells, although c-Jun translocation was increased upon *G6PD* knockdown compared with that in the scrambled control cells. No significant difference was observed in the translocation of NF-κB. The quantification of nuclear c-Fos is shown in Fig. 5G. The *IL1B* reporter plasmid construction is shown in Fig. 5H, upper panel. 293FT cells were chosen to measure the binding activity of AP-1 because of the ease of transfection of these cells compared to that of THP-1 cells. The binding activity of AP-1 was lower in 293FT pLKO-*G6PD*-kd cells compared to the binding activity of 293FT pLKO-scrambled cells (Fig. 5H).

3.6. Impaired p38 MAPK/AP-1 signaling by *G6PD* knockdown in the presence of decreasing ROS production in THP-1 cells

The treatment of differentiated control and *G6PD*-kd THP-1 cells with LPS and nigericin increased ROS production, which was less than that in *G6PD*-kd THP-1 cells (Fig. 6A). The production of superoxide was lower in *G6PD*-kd THP-1 cells than that in control cells upon LPS incubation for 20 min (Fig. 6B). The pretreatment of *G6PD*-kd and control THP-1 cells with DPI, an inhibitor of NADPH oxidase, decreased the expression of p-p38 and pro-IL-1β in both cells (Fig. 6C and E). The quantitative intensity of p-p38 and pro-IL-1β is shown in Fig. 6D and F, respectively. *G6PD*-kd THP-1 cells treated with H₂O₂ (100 μM) and NADPH (100 μM) increased the expression of p-p38 and pro-IL-1β (Fig. 6G and I). The quantitative intensity of p-p38 and pro-IL-1β is shown in Fig. 6H and J, respectively. The expression of IL-1β was improved by overexpress IDH1 in THP-1-LG and *G6PD*-kd cells (Fig. S2). Variable ROS level has different effects on cellular physiology. In Fig. S3, the expression of IL-1β was only induced in high concentrated H₂O₂-treated THP-1 cells. This suggests that *G6PD* deficiency decreases ROS level by only affecting inflammasome signal 1 pathway but not signal 2.

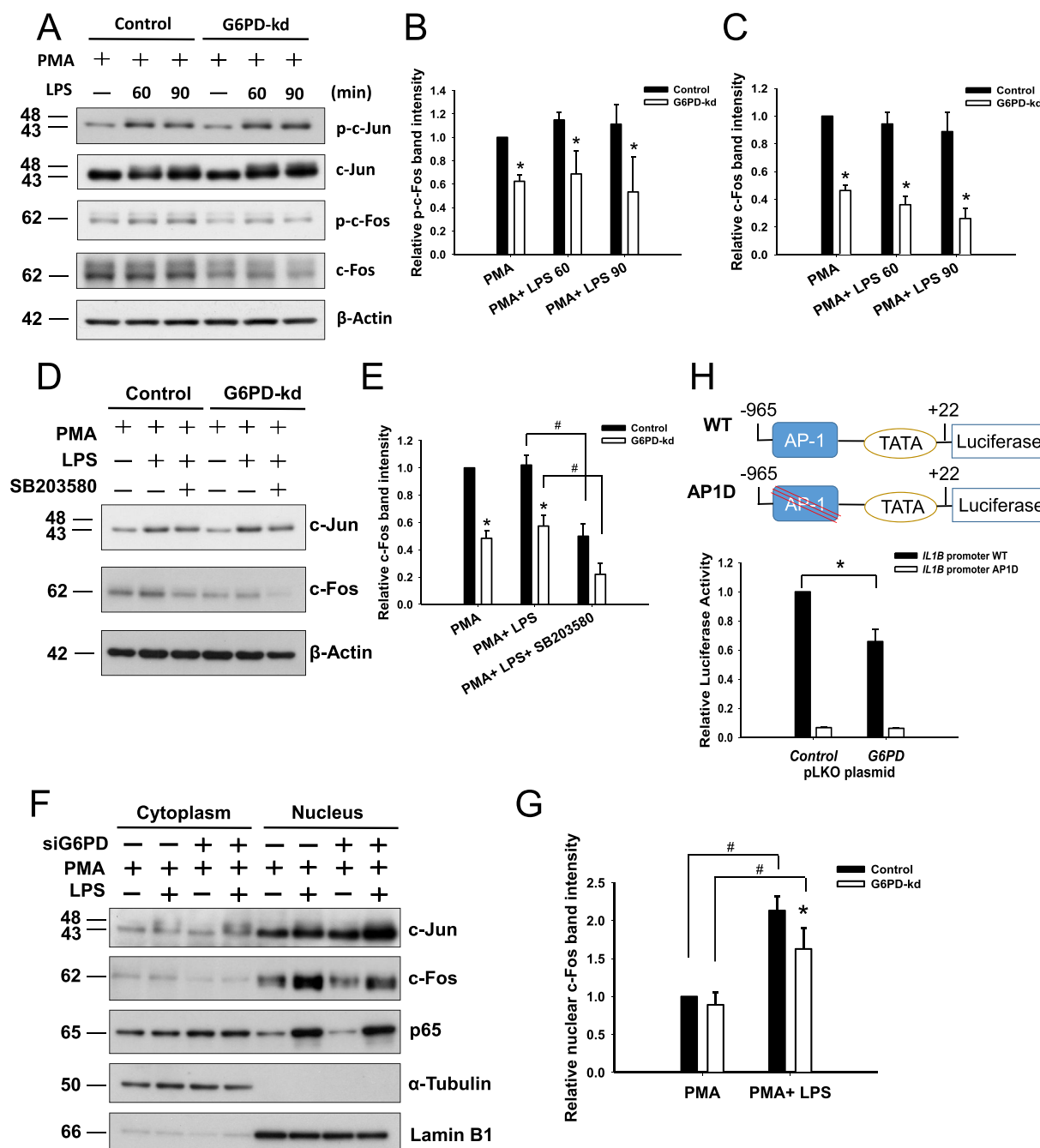


Fig. 5. AP-1 signaling in G6PD-kd THP-1 cells. (A) Western blot of the expression of c-Jun and c-Fos. Cells were treated with LPS for 60 or 90 min. (B), (C) p-c-Fos and c-Fos quantitative level of (A). (D) Western blot of the expression of c-Jun and c-Fos. Cells were treated with SB203580 for 30 min prior to LPS treatment for 60 min. (E) c-Fos quantitative level of (D). β -Actin was used as a normalized loading control in (A) and (D). The results are representative of three independent experiments ($n = 3$, $*p < 0.05$). (F) Western blot of cytoplasmic and nuclear proteins. Cells were treated with LPS for 60 min. α -Tubulin and lamin B1 were used as cytoplasmic and nuclear loading controls. (G) c-Fos quantitative level of (F). The results are representative of three independent experiments ($n = 3$, $*p < 0.05$). (H) Luciferase activity assay of 293T cells transfected with a firefly luciferase reporter plasmid containing a partial sequence with the putative AP-1 binding site (WT) or the deleted mutation (AP1D). This assay was standardized by Renilla activity after transfection for 48 h ($*p < 0.05$ compared to basal conditions).

3.7. Decreased activity of intracellular bacterial clearance in G6PD-kd THP-1 cells

Gram-positive *S. aureus* (Fig. 7A and B) and gram-negative *E. coli* (Fig. 7C and D) were analyzed for the bacterial clearance activity in G6PD-kd THP-1 and PBMCs from patients with G6PD deficiency. The CFU number was higher in G6PD-kd THP-1 cells and PBMCs from patients with G6PD deficiency compared to the CFU number in the scrambled control THP-1 cells and PBMCs from normal controls with both pathogens. The impairment of the bactericidal effect due to G6PD

deficiency could be improved by adding IL-1 β .

4. Discussion

Certain chronic and infectious diseases are associated with G6PD deficiency [13,24,43]. The impact of G6PD status on innate immunity, especially upon inflammasome activation, is unknown. The present study is the first to show that G6PD-kd THP-1 cells and PBMCs from patients with G6PD deficiency with different mutations of the enzyme have a decrease in IL-1 β expression and NLRP3 inflammasome

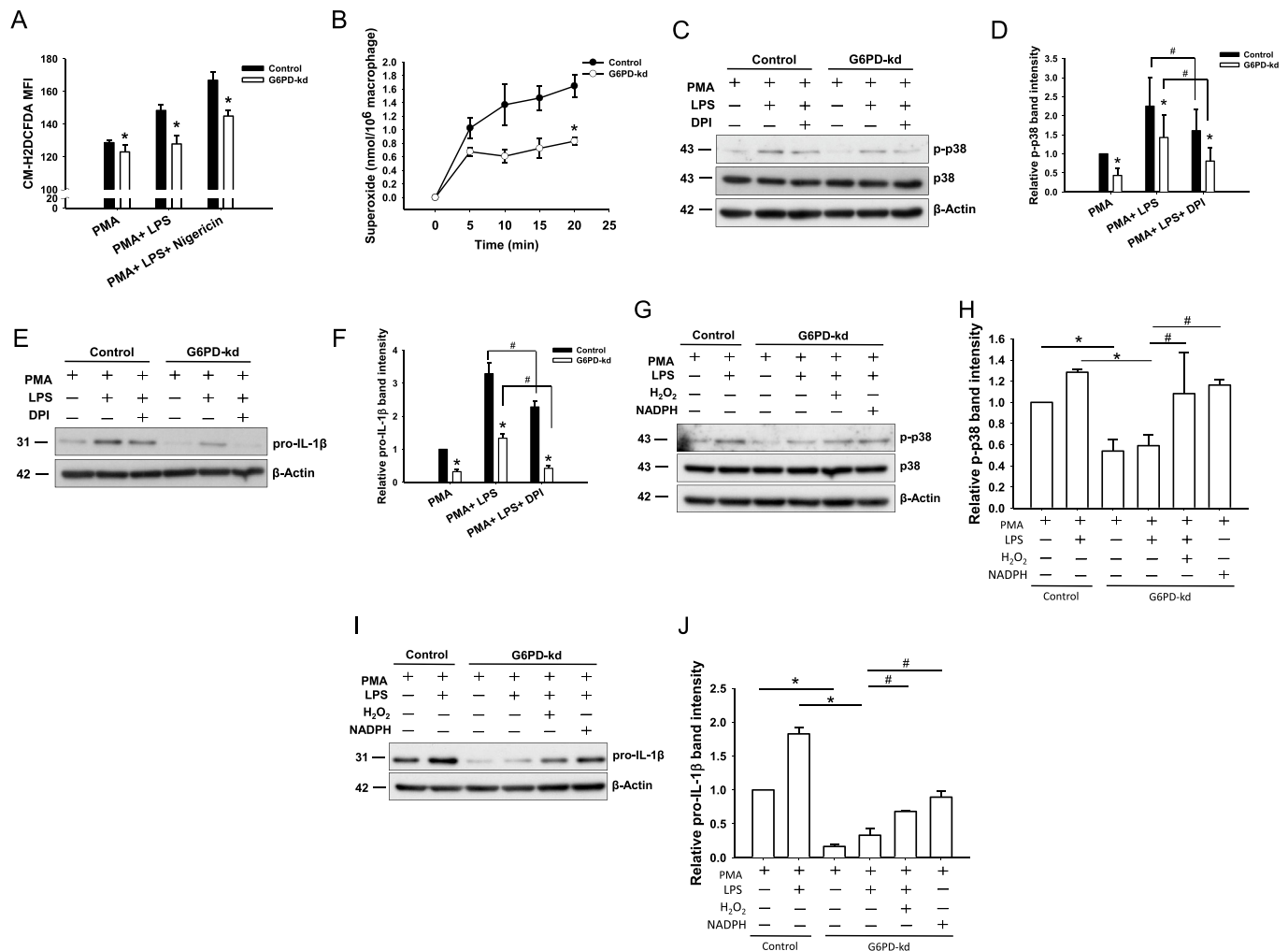


Fig. 6. Signaling of p38 MAPK/AP-1 modulated by the ROS level in *G6PD*-kd THP-1 cells. (A) Flow cytometry for determining the ROS production in PMA-differentiated control THP-1 cells and *G6PD*-kd THP-1 cells. Cells were treated with LPS for 30 min. Cells were stained with 10 μ M CM-H₂DCFDA for 30 min. (B) Superoxide production was measured by cytochrome c reduction. The PMA-differentiated control and *G6PD*-kd THP-1 cells were incubated in cytochrome c containing HBSS with 0.1 μ g/ml LPS. The production of superoxide was measured spectrophotometrically at 550 nm. The PMA-differentiated control and *G6PD*-kd THP-1 cells were treated with (C, E) DPI, (G, I) H₂O₂ or NADPH for 60 min prior to LPS treatment for 30 min for p38 detection or 180 min for pro-IL-1 β detection. The expression of p-p38, p38 and pro-IL-1 β was determined by a Western blot. (D), (F) p-p38 and pro-IL-1 β quantitative levels of (C) and (E). (H), (J) p-p38 and pro-IL-1 β quantitative levels of (G) and (I). β -Actin was used as a loading control. The results are representative of three independent experiments (n = 3, *p < 0.05).

activation. Such defect in NLRP3 inflammasome activation could be attributed to the inhibition of p38-MAPK and AP-1 signaling upon LPS stimulation. The underlying mechanism is due to decreased superoxide production by NOX, as found in *G6PD*-kd THP-1 cells. Together, these results indicate that G6PD deficiency impairs the cellular innate immune response by a disturbance in redox homeostasis, which can have clinical implications in G6PD-deficient individuals with infectious diseases.

G6PD is important in maintaining cellular redox homeostasis by regenerating NADPH, the substrate of NOX and NOS. The formation of superoxide by NOX is dependent on the electrons are transferred from cytoplasmic NADPH to extracellular oxygen. Superoxide can be reduced by extracellular superoxide dismutase (SOD1) to produce H₂O₂, which transfer into cells through aquaporin channels, or influx into cytoplasm through the chloride channel-3 to initiate intracellular signaling [44]. Since the activity of NOX is modulated by G6PD status, the pathway-mediated inflammatory response is impaired by G6PD deficiency [12]. G6PD deficiency increases the cellular susceptibility to a variety of pathogen-induced viral and bacterial infections [13,23,24]. Compared to the levels in normal phagocytes, G6PD-deficient phagocytes have

lower levels of superoxide and other ROS needed for effective microbial killing [36,45]. Such susceptibility to microbial infections in patients with G6PD deficiency may be due to an impaired response, the absence of NETosis [46], and a still unknown defense mechanism. The present study shows that the inflammasome response is modulated by G6PD status and provides an additional mechanism for why G6PD deficiency increases susceptibility to infections as proposed in Fig. 8.

The level of ROS can have significant consequence on various cellular function [8,12–14,36,38,47–49]. Cytotoxic level of ROS, such as oxidative burst in phagocytic cells, participates in host defense by direct killing of foreign pathogen [48]. On the other hand, cyto regulatory level of ROS mediates intracellular signaling that maintain proper redox environment and regulate many cellular signaling pathways [14,49,50]. In the present study, we provide evidence to support the notion that cyto regulatory level of ROS influenced p38/MAPK/AP-1 pathway and bactericidal effect in G6PD deficient cells. The pathway of inflammasome activation involves two signals, including priming (signal 1) and activation (signal 2) [25]. Our results indicate that G6PD deficiency can influence p38/MAPK/AP-1 pathway (signal 1), but not the expression of inflammasome subunit influenced by signal 2

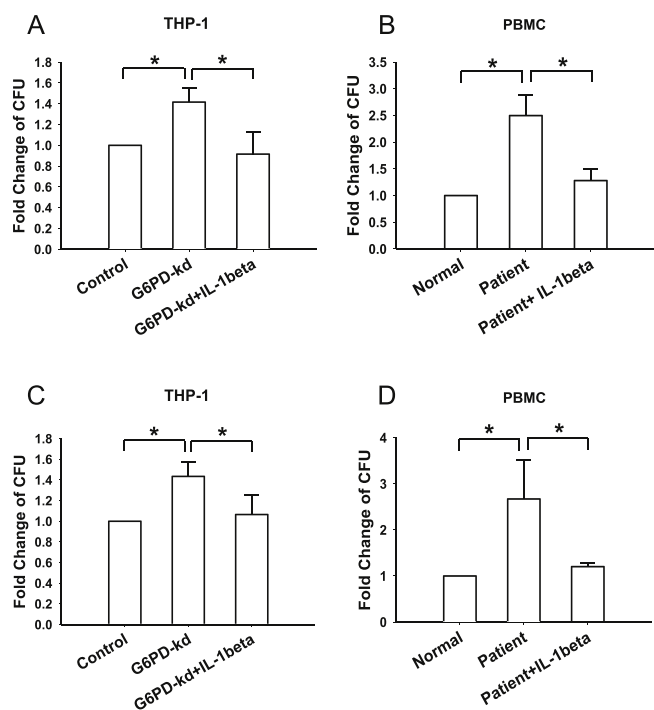


Fig. 7. Bacterial clearance activity in *G6PD*-kd THP-1 cells and PBMCs from patients with *G6PD* deficiency. LPS-primed THP-1 cells and PBMCs were infected by a bacterial MOI of 10: (A, B) *S. aureus* and (C, D) *E. coli*. The results are representative of three independent experiments ($n = 4$, $*p < 0.05$).

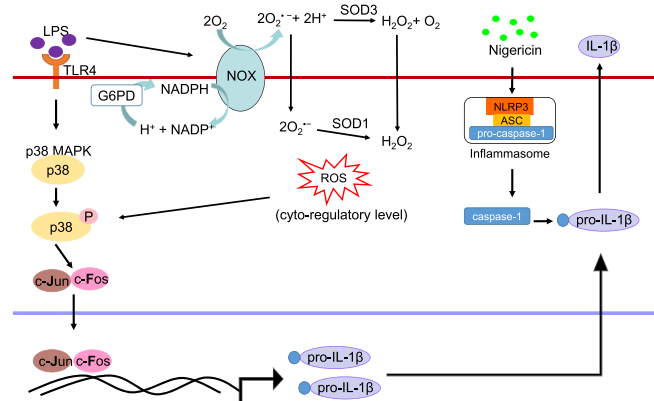


Fig. 8. Proposed schematic representation of the signaling pathways involved in the redox regulation of inflammasome activation in *G6PD*-deficient cells. *G6PD* knockdown results in the reduced generation of pro-IL-1 β and an impairment of the LPS-induced p38/MAPK-AP-1 pathway. IL-1 β secretion is also reduced in *G6PD*-knockdown cells.

suggesting that low concentration of ROS in *G6PD* deficiency can affect signal 1 but not signal 2. Furthermore, the expression of phospho-p38 and pro-IL-1 β has been found to be improved in low-dose (0.1 mM) H_2O_2 treated cells (Fig. 6G–J). In contrast, IL-1 β secretion has been detected under high level of H_2O_2 stimulation (Fig. S3). High concentration of ROS leads cells undergo apoptosis or pyroptosis, which is the common programmed cell death upon inflammasome activation. In contrast, cyto-regulatory level of ROS is important for cells to regulate cellular signaling transduction [50]. All in all, ROS can affect inflammasome activation via both signals 1 and 2 at high concentration (cytotoxic level), whereas low concentration of ROS is involved in regulating only signal 1 of inflammasome activation.

Cells need to maintain redox homeostasis for regulating proper functioning. Redox pathways have been identified in and between cells

for broad functions to relay and generate cellular signals. Since *G6PD* plays a role in the production of NADPH as the substrate of NOX, it is anticipated that *G6PD* may be involved in modulating redox-sensitive signaling [49]. When NADPH is decreased, superoxide production is reduced by NOX. This may cause an impaired Nrf2 antioxidant response [51] and a decrease in NF- κ B [13,52] and SP-1/HIF-1 α signaling [53–55]. AP-1 signaling is a part of the *G6PD*-regulated redox pathway, thereby contributing to the activity of redox networks. The transcription factor AP-1 is a heterodimer composed of the proteins c-Fos, c-Jun and those from the ATF families [56]. The stability of the Jun-Fos heterodimer allows for higher DNA-binding activity [57]. *G6PD* knockdown decreased p38 phosphorylation and c-Fos expression, which reduced *IL1B* expression. The terminal differentiation of THP-1 cells is associated with the induction of c-Fos, implying that this could be the growth arrest signal in the differentiation of monocytes [58].

A number of redox-related transcription factors are modulated by *G6PD* status, indicating the importance of *G6PD* in cellular redox homeostasis. Hemolytic crisis, diabetes [59], hypertension [6], infectious diseases [46,60] and protection against malaria are associated with *G6PD* deficiency. That patients with *G6PD* deficiency are susceptible to infection may involve a novel mechanism that includes impaired inflammasome activation. Moreover, NADPH is also the substrate for many protective enzymes. Antioxidant defences may play a role in *G6PD*-regulated inflammasome activation. NAD(P)H:quinone oxidoreductase-1 (NQO-1) is a major quinone reductases, which requires NADPH as electron donor to catalyze quinones to hydroquinone. The enzyme also plays an antioxidant enzyme in cellular redox homeostasis [61]. The induction of NQO-1 can be mediated by Nrf2-mediated mechanism under a variety of stress responses presumably as a cellular protective system [62,63]. In terms of inflammatory response, NQO-1 as an inhibitor in immune response by promoting I κ B- ζ degradation leading to impaired TLR-mediated the production of cytokines [64]. Glutathione is also as antioxidant and plays critical role in many metabolic processes. Our previous metabolomics studies have shown that alteration of *G6PD* status affects cellular metabolic pathway [9,65]. Abnormal glycerophospholipid metabolism in *G6PD* deficient embryos leads to defective embryonic development [65]. *G6PD* deficient cells are unable to regenerate enough NADPH under a stressful situation then rapid switch to GSH biosynthetic supply, which causes energy crisis and ineffective AMPK activation [9]. However, whether *G6PD* deficiency affected the inflammasome activation via the change of antioxidants or metabolites needs to be further investigated. Since infectious and metabolic diseases in patients with *G6PD* deficiency may be more severe than in patients with a normal level of *G6PD*, we concur with the notion that an escalating diagnostic algorithm should include a determination of *G6PD* activity in these patients [46].

Although the induction of the NLRP3 inflammasome contributes to host defenses against infections, dysregulated inflammasomes are associated with many human diseases, such as cancer, autoimmune diseases, and inflammatory disorders [29–32,66]. Our findings that *G6PD* inhibition can attenuate inflammasome activation suggest a new approach for therapeutic intervention of inflammasome-associated diseases [67,68] with inflammasome as a target. Hence, a *G6PD* inhibitor such as Polydatin, might be considered as a therapeutic agent to attenuate inflammasome-associated diseases [67,68].

In conclusion, impaired inflammasome activation by *G6PD* deficiency can present a phenomenon of increased susceptibility to bacterial infections. Mechanistically, defective bacterial clearance found in *G6PD*-kd THP-1 cells is due to impaired NOX/p38 MAPK/AP-1 signaling and may appear in patients with *G6PD* deficiency. The change in *G6PD* status contributes to an imbalance in cellular redox homeostasis that affects inflammatory-associated signal transduction to influence cellular infectivity. The care of patients with *G6PD* deficiency to prevent infection might include appropriate antibiotic prophylaxis and the modulation of inflammasome activity.

Author contributions

All authors co-designed the experiments. The experiments were performed by Wei-Chen Yen, Yi-Hsuan Wu and Hsin-Ru Lin. All authors analyzed the results, wrote the manuscript, contributed substantially to the present work, and then read and approved the final manuscript.

Declaration of competing interest

The authors declare that there are no conflicts of interest.

Acknowledgments

This work is made possible by grants from the Ministry of Science and Technology of Taiwan (MOST105-2320-B-182-031-MY2, MOST107-2320-B-182-013 and MOST108-2320-B-182-001 to DTYC, MOST108-2320-B-182-030-MY3 to CCW), from the Ministry of Education of Taiwan (EMRPD1G0181 to CGU), from Chang Gung Memorial Hospital (BMRP098 and CMRPD110121 to DTYC, CLRPD190018 and BMRP077 to CCW), and from Featured Areas Research Center Program within the Framework of Higher Education Sprout Project by Ministry of Education and Ministry of Science and Technology, Taiwan (MOST 107-3017-F-182-001). This manuscript was edited by American Journal Experts.

Appendix A. Supplementary data

Supplementary data to this article can be found online at <https://doi.org/10.1016/j.redox.2019.101363>.

References

- G. Manganelli, U. Masullo, S. Passarelli, S. Filosa, Glucose-6-phosphate dehydrogenase deficiency: disadvantages and possible benefits, *Cardiovasc. Haematol. Disord. - Drug Targets* 13 (1) (2013) 73–82.
- H.C. Yang, Y.H. Wu, W.C. Yen, H.Y. Liu, T.L. Hwang, A. Stern, D.T. Chiu, The redox role of G6PD in cell growth, cell death, and cancer, *Cells* 8 (9) (2019).
- M.D. Cappellini, G. Fiorelli, Glucose-6-phosphate dehydrogenase deficiency, *Lancet* 371 (9606) (2008) 64–74.
- L. Luzzatto, E. Seneca, G6PD deficiency: a classic example of pharmacogenetics with on-going clinical implications, *Br. J. Haematol.* 164 (4) (2014) 469–480.
- G.H. Wan, S.C. Tsai, D.T. Chiu, Decreased blood activity of glucose-6-phosphate dehydrogenase associates with increased risk for diabetes mellitus, *Endocrine* 19 (2) (2002) 191–195.
- R.S. Gaskin, D. Estwick, R. Peddi, G6PD deficiency: its role in the high prevalence of hypertension and diabetes mellitus, *Ethn. Dis.* 11 (4) (2001) 749–754.
- R.C. Stanton, Glucose-6-phosphate dehydrogenase, NADPH, and cell survival, *IUBMB Life* 64 (5) (2012) 362–369.
- H.Y. Ho, M.L. Cheng, D.T. Chiu, Glucose-6-phosphate dehydrogenase—beyond the realm of red cell biology, *Free Radic. Res.* 48 (9) (2014) 1028–1048.
- H.Y. Tang, H.Y. Ho, P.R. Wu, S.H. Chen, F.A. Kuypers, M.L. Cheng, D.T. Chiu, Inability to maintain GSH pool in G6PD-deficient red cells causes futile AMPK activation and irreversible metabolic disturbance, *Antioxidants Redox Signal.* 22 (9) (2015) 744–759.
- L. Longo, O.C. Vanegas, M. Patel, V. Rosti, H. Li, J. Waka, T. Merghoub, P.P. Pandolfi, R. Notaro, K. Manova, L. Luzzatto, Maternally transmitted severe glucose 6-phosphate dehydrogenase deficiency is an embryonic lethal, *EMBO J.* 21 (16) (2002) 4229–4239.
- H.C. Yang, T.L. Chen, Y.H. Wu, K.P. Cheng, Y.H. Lin, M.L. Cheng, H.Y. Ho, S.J. Lo, D.T. Chiu, Glucose 6-phosphate dehydrogenase deficiency enhances germ cell apoptosis and causes defective embryogenesis in *Caenorhabditis elegans*, *Cell Death Dis.* 4 (2013) e616.
- H.R. Lin, Y.H. Wu, W.C. Yen, C.M. Yang, D.T. Chiu, Diminished COX-2/PGE2-mediated antiviral response due to impaired NOX/MAPK signaling in G6PD-knockdown lung epithelial cells, *PLoS One* 11 (4) (2016) e0153462.
- Y.H. Wu, D.T. Chiu, H.R. Lin, H.Y. Tang, M.L. Cheng, H.Y. Ho, Glucose-6-Phosphate dehydrogenase enhances antiviral response through downregulation of NADPH sensor HSCARG and upregulation of NF-kappaB signaling, *Viruses* 7 (12) (2015) 6689–6706.
- H.C. Yang, M.L. Cheng, H.Y. Ho, D.T. Chiu, The microbicidal and cytoprotective roles of NADPH oxidases, *Microb. Infect.* 13 (2) (2011) 109–120.
- K.M. Holmstrom, T. Finkel, Cellular mechanisms and physiological consequences of redox-dependent signalling, *Nat. Rev. Mol. Cell Biol.* 15 (6) (2014) 411–421.
- H.Y. Ho, M.L. Cheng, D.T. Chiu, Glucose-6-phosphate dehydrogenase—from oxidative stress to cellular functions and degenerative diseases, *Redox Rep.* 12 (3) (2007) 109–118.
- T.L. Leto, S. Morand, D. Hurt, T. Ueyama, Targeting and regulation of reactive oxygen species generation by Nox family NADPH oxidases, *Antioxidants Redox Signal.* 11 (10) (2009) 2607–2619.
- B.M. Babior, NADPH oxidase: an update, *Blood* 93 (5) (1999) 1464–1476.
- K.L. Singel, B.H. Segal, NOX2-dependent regulation of inflammation, *Clin. Sci. (Lond.)* 130 (7) (2016) 479–490.
- J.A. McCubrey, M.M. Lahair, R.A. Franklin, Reactive oxygen species-induced activation of the MAP kinase signaling pathways, *Antioxidants Redox Signal.* 8 (9–10) (2006) 1775–1789.
- Y. Son, Y.K. Cheong, N.H. Kim, H.T. Chung, D.G. Kang, H.O. Pae, Mitogen-activated protein kinases and reactive oxygen species: how can ROS activate MAPK pathways? *J. Signal Transduct.* 2011 (2011) 792639.
- Y. Liang, Y. Zhou, P. Shen, NF-kappaB and its regulation on the immune system, *Cell. Mol. Immunol.* 1 (5) (2004) 343–350.
- H.Y. Ho, M.L. Cheng, S.F. Weng, L. Chang, T.T. Yeh, S.R. Shih, D.T. Chiu, Glucose-6-phosphate dehydrogenase deficiency enhances enterovirus 71 infection, *J. Gen. Virol.* 89 (Pt 9) (2008) 2080–2089.
- Y.H. Wu, C.P. Tseng, M.L. Cheng, H.Y. Ho, S.R. Shih, D.T. Chiu, Glucose-6-phosphate dehydrogenase deficiency enhances human coronavirus 229E infection, *J. Infect. Dis.* 197 (6) (2008) 812–816.
- V.A. Rathinam, S.K. Vanaja, K.A. Fitzgerald, Regulation of inflammasome signaling, *Nat. Immunol.* 13 (4) (2012) 333–342.
- A. Abderrazak, T. Syrovets, D. Couchie, K. El Hadri, B. Friguet, T. Simmet, M. Rouis, NLRP3 inflammasome: from a danger signal sensor to a regulatory node of oxidative stress and inflammatory diseases, *Redox Biol.* 4 (2015) 296–307.
- T. Yamazaki, T. Ichinohe, Inflammasomes in antiviral immunity: clues for influenza vaccine development, *Clin. Exp. Vaccine Res.* 3 (1) (2014) 5–11.
- K.W. Chen, C.J. Gross, F.V. Sotomayor, K.J. Stacey, J. Tschopp, M.J. Sweet, K. Schroder, The neutrophil NLR4 inflammasome selectively promotes IL-1beta maturation without pyroptosis during acute Salmonella challenge, *Cell Rep.* 8 (2) (2014) 570–582.
- M. Lamkanfi, L. Vande Walle, T.D. Kanneganti, Deregulated inflammasome signaling in disease, *Immunol. Rev.* 243 (1) (2011) 163–173.
- X. He, Z. Wei, J. Wang, J. Kou, W. Liu, Y. Fu, Z. Yang, Alpinetin attenuates inflammation responses by suppressing TLR4 and NLRP3 signaling pathways in DSS-induced acute colitis, *Sci. Rep.* 6 (2016) 28370.
- T. Gicquel, S. Robert, T. Victorini, V. Lagente, [The NLRP3 inflammasome: physiology and therapeutic application], *Presse Med.* 45 (4 Pt 1) (2016) 438–446.
- H.M. Lee, J.J. Kim, H.J. Kim, M. Shong, B.J. Ku, E.K. Jo, Upregulated NLRP3 inflammasome activation in patients with type 2 diabetes, *Diabetes* 62 (1) (2013) 194–204.
- O. Gross, C.J. Thomas, G. Guarda, J. Tschopp, The inflammasome: an integrated view, *Immunol. Rev.* 243 (1) (2011) 136–151.
- J. Lugin, N. Rosenblatt-Velin, R. Parapanov, L. Liaudet, The role of oxidative stress during inflammatory processes, *Biol. Chem.* 395 (2) (2014) 203–230.
- A. Sokolovska, C.E. Becker, W.K. Ip, V.A. Rathinam, M. Brudner, N. Paquette, A. Tanne, S.K. Vanaja, K.J. Moore, K.A. Fitzgerald, A. Lacy-Hulbert, L.M. Stuart, Activation of caspase-1 by the NLRP3 inflammasome regulates the NADPH oxidase NOX2 to control phagosome function, *Nat. Immunol.* 14 (6) (2013) 543–553.
- K.J. Tsai, I.J. Hung, C.K. Chow, A. Stern, S.S. Chao, D.T. Chiu, Impaired production of nitric oxide, superoxide, and hydrogen peroxide in glucose 6-phosphate dehydrogenase-deficient granulocytes, *FEBS Lett.* 436 (3) (1998) 411–414.
- S. Brechard, S. Plancon, E.J. Tschirhart, New insights into the regulation of neutrophil NADPH oxidase activity in the phagosome: a focus on the role of lipid and Ca(2+) signaling, *Antioxidants Redox Signal.* 18 (6) (2013) 661–676.
- Y.H. Wu, Y.H. Lee, H.Y. Shih, S.H. Chen, Y.C. Cheng, D. Tsun-Yee Chiu, Glucose-6-phosphate dehydrogenase is indispensable in embryonic development by modulation of epithelial-mesenchymal transition via the NOX/Smad3/miR-200b axis, *Cell Death Dis.* 9 (1) (2018) 10.
- L. Koontz, TCA precipitation, *Methods Enzymol.* 541 (2014) 3–10.
- S.C. Ko, C.R. Huang, J.M. Shieh, J.H. Yang, W.C. Chang, B.K. Chen, Epidermal growth factor protects squamous cell carcinoma against cisplatin-induced cytotoxicity through increased interleukin-1beta expression, *PLoS One* 8 (2) (2013) e55795.
- Z. Khan, X.Z. Shen, E.A. Bernstein, J.F. Giani, M. Eriguchi, T.V. Zhao, R.A. Gonzalez-Villalobos, S. Fuchs, G.Y. Liu, K.E. Bernstein, Angiotensin-converting enzyme enhances the oxidative response and bactericidal activity of neutrophils, *Blood* 130 (3) (2017) 328–339.
- C.Y. Chen, C.H. Yang, Y.F. Tsai, C.C. Liaw, W.Y. Chang, T.L. Hwang, Ugonin U stimulates NLRP3 inflammasome activation and enhances inflammasome-mediated pathogen clearance, *Redox Biol.* 11 (2017) 263–274.
- Y.T. Hsieh, M.H. Lin, H.Y. Ho, L.C. Chen, C.C. Chen, J.C. Shu, Glucose-6-phosphate dehydrogenase (G6PD)-deficient epithelial cells are less tolerant to infection by *Staphylococcus aureus*, *PLoS One* 8 (11) (2013) e79566.
- A.B. Fisher, Redox signaling across cell membranes, *Antioxidants Redox Signal.* 11 (6) (2009) 1349–1356.
- B.K. Rada, M. Geiszt, K. Kaldi, C. Timar, E. Ligeti, Dual role of phagocytic NADPH oxidase in bacterial killing, *Blood* 104 (9) (2004) 2947–2953.
- U. Siler, S. Romao, E. Tejera, O. Pastukhov, E. Kuzmenko, R.G. Valencia, V. Meda Spaccamela, B.H. Belohradsky, O. Speer, M. Schmugge, E. Kohne, M. Hoenig, J. Freiherst, A.S. Schulz, J. Reichenbach, Severe glucose-6-phosphate dehydrogenase deficiency leads to susceptibility to infection and absent NETosis, *J. Allergy Clin. Immunol.* 139 (1) (2017) 212–219 e3.
- M. Schieber, N.S. Chandel, ROS function in redox signaling and oxidative stress, *Curr. Biol.* 24 (10) (2014) R453–R462.
- R. Spooner, O. Yilmaz, The role of reactive-oxygen-species in microbial persistence

- and inflammation, *Int. J. Mol. Sci.* 12 (1) (2011) 334–352.
- [49] H.C. Yang, Y.H. Wu, H.Y. Liu, A. Stern, D.T. Chiu, What has passed is prolog: new cellular and physiological roles of G6PD, *Free Radic. Res.* 50 (10) (2016) 1047–1064.
- [50] I. Silva, T. Peccerella, S. Mueller, V. Rausch, IL-1 beta-mediated macrophage-hepatocyte crosstalk upregulates hepcidin under physiological low oxygen levels, *Redox Biol.* 24 (2019) 101209.
- [51] B.M. Hybertson, B. Gao, S.K. Bose, J.M. McCord, Oxidative stress in health and disease: the therapeutic potential of Nrf2 activation, *Mol. Asp. Med.* 32 (4–6) (2011) 234–246.
- [52] M. Ham, J.W. Lee, A.H. Choi, H. Jang, G. Choi, J. Park, C. Kozuka, D.D. Sears, H. Masuzaki, J.B. Kim, Macrophage glucose-6-phosphate dehydrogenase stimulates proinflammatory responses with oxidative stress, *Mol. Cell. Biol.* 33 (12) (2013) 2425–2435.
- [53] M. Philippe, Y. Larondelle, F. Lemaigre, B. Mariame, H. Delhez, P. Mason, L. Luzzatto, G.G. Rousseau, Promoter function of the human glucose-6-phosphate dehydrogenase gene depends on two GC boxes that are cell specifically controlled, *Eur. J. Biochem.* 226 (2) (1994) 377–384.
- [54] A. Franze, M.I. Ferrante, F. Fusco, A. Santoro, E. Sanzari, G. Martini, M.V. Ursini, Molecular anatomy of the human glucose 6-phosphate dehydrogenase core promoter, *FEBS Lett.* 437 (3) (1998) 313–318.
- [55] G.P. Laliotis, I. Bizelis, A. Argyrokastritis, E. Rogdakis, Cloning, characterization and computational analysis of the 5' regulatory region of ovine glucose 6-phosphate dehydrogenase gene, *Comp. Biochem. Physiol. B Biochem. Mol. Biol.* 147 (4) (2007) 627–634.
- [56] M. Karin, Z. Liu, E. Zandi, AP-1 function and regulation, *Curr. Opin. Cell Biol.* 9 (2) (1997) 240–246.
- [57] T. Kouzarides, E. Ziff, The role of the leucine zipper in the fos-jun interaction, *Nature* 336 (6200) (1988) 646–651.
- [58] J. Lee, K. Mehta, M.B. Blick, J.U. Gutterman, G. Lopez-Berestein, Expression of c-fos, c-myc, and c-myc in human monocytes: correlation with monocytic differentiation, *Blood* 69 (5) (1987) 1542–1545.
- [59] N.Y. Spencer, R.C. Stanton, Glucose 6-phosphate dehydrogenase and the kidney, *Curr. Opin. Nephrol. Hypertens.* 26 (1) (2017) 43–49.
- [60] S. Zamani, A.Z. Hoseini, A.M. Namin, Glucose-6-phosphate dehydrogenase (G6PD) activity can modulate macrophage response to *Leishmania major* infection, *Int. Immunopharmacol.* 69 (2019) 178–183.
- [61] J.M. Park, D.H. Kim, H.K. Na, Y.J. Surh, Methylseleninic acid induces NAD(P)H:quinone oxidoreductase-1 expression through activation of NF-E2-related factor 2 in Chang liver cells, *Oncotarget* 9 (3) (2018) 3014–3028.
- [62] C.H. Song, N. Kim, S.M. Lee, R.H. Nam, S.I. Choi, S.R. Kang, E. Shin, D.H. Lee, H.N. Lee, Y.J. Surh, Effects of 17beta-estradiol on colorectal cancer development after azoxymethane/dextran sulfate sodium treatment of ovariectomized mice, *Biochem. Pharmacol.* 164 (2019) 139–151.
- [63] D. Ross, D. Siegel, Functions of NQO1 in cellular protection and CoQ10 metabolism and its potential role as a redox sensitive molecular switch, *Front. Physiol.* 8 (2017) 595.
- [64] A. Kimura, M. Kitajima, K. Nishida, S. Serada, M. Fujimoto, T. Naka, Y. Fujii-Kuriyama, S. Sakamoto, T. Ito, H. Handa, T. Tanaka, A. Yoshimura, H. Suzuki, NQO1 inhibits the TLR-dependent production of selective cytokines by promoting IkappaB-zeta degradation, *J. Exp. Med.* 215 (8) (2018) 2197–2209.
- [65] T.L. Chen, H.C. Yang, C.Y. Hung, M.H. Ou, Y.Y. Pan, M.L. Cheng, A. Stern, S.J. Lo, D.T. Chiu, Impaired embryonic development in glucose-6-phosphate dehydrogenase-deficient *Caenorhabditis elegans* due to abnormal redox homeostasis induced activation of calcium-independent phospholipase and alteration of glycerophospholipid metabolism, *Cell Death Dis.* 8 (1) (2017) e2545.
- [66] S. Tarte, T.D. Kanneganti, Differential role of the NLRP3 inflammasome in infection and tumorigenesis, *Immunology* 156 (4) (2019) 329–338.
- [67] R. Lv, L. Du, X. Liu, F. Zhou, Z. Zhang, L. Zhang, Polydatin alleviates traumatic spinal cord injury by reducing microglial inflammation via regulation of iNOS and NLRP3 inflammasome pathway, *Int. Immunopharmacol.* 70 (2019) 28–36.
- [68] J. Tang, Y. Li, J. Wang, Q. Wu, H. Yan, Polydatin suppresses the development of lung inflammation and fibrosis by inhibiting activation of the NACHT domain-, leucine-rich repeat-, and pyd-containing protein 3 inflammasome and the nuclear factor-kappaB pathway after *Mycoplasma pneumoniae* infection, *J. Cell. Biochem.* 120 (6) (2019) 10137–10144.

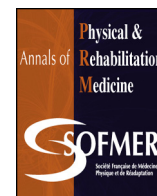


Available online at

ScienceDirect
www.sciencedirect.com

Elsevier Masson France

EM|consulte
www.em-consulte.com



Original article

Increased serum brain-derived neurotrophic factor with high-intensity interval training in stroke patients: A randomized controlled trial

Chih-Chin Hsu^{a,b,c}, Tieh-Cheng Fu^{a,d}, Shu-Chun Huang^e, Carl Pai-Chu Chen^e, Jong-Shyan Wang^{a,f,g,*}

^a Department of Physical Medicine and Rehabilitation, Keelung Chang Gung Memorial Hospital, 204 Keelung, Taiwan

^b School of Medicine, College of Medicine, Chang Gung University, 333 Taoyuan, Taiwan

^c Community Research Center, Keelung Chang Gung Memorial Hospital, 204 Keelung, Taiwan

^d Heart Failure Research Center, Keelung Chang Gung Memorial Hospital, 204 Keelung, Taiwan

^e Department of Physical Medicine and Rehabilitation, Linkou Chang Gung Memorial Hospital, 333 Taoyuan, Taiwan

^f Department of Physical Therapy, College of Medicine, Graduate Institute of Rehabilitation Science, Chang Gung University, 333 Taoyuan, Taiwan

^g Research Center for Chinese Herbal Medicine, College of Human Ecology, Chang Gung University of Science and Technology, 333 Taoyuan, Taiwan

ARTICLE INFO

Article history:

Received 12 February 2020

Accepted 24 March 2020

Keywords:

Stroke

Aerobic exercise

BDNF

Oxygen consumption

Cerebrovascular circulation

ABSTRACT

Background: Physiological adaptations of stroke patients after high-intensity interval training (HIIT) and moderate-intensity continuous training (MICT) remain unclear.

Objective: This study determined the HIIT and MICT effects on aerobic capacity, cerebral oxygenation, peak cardiac output (CO), and serum brain-derived neurotrophic factor (BDNF) in stroke patients.

Methods: We included 23 stroke patients with age about 55 years and stroke duration > 24 months; participants completed 36 sessions of exercise training for 30 min; 13 were randomly assigned to perform MICT at 60% of peak oxygen consumption (VO_{2peak}) and 10 to perform HIIT at alternating 80% (3 min) and 40% (3 min) VO_{2peak} . Before and after interventions, we evaluated VO_{2peak} , peak CO, arteriovenous oxygen difference (AV O_{2diff}), bilateral frontal cortex oxygenation (relative changes of oxyhemoglobin $\Delta[O_2Hb]$, deoxyhemoglobin $\Delta[HHb]$, and total hemoglobin $\Delta[THb]$ levels), serum brain-derived neurotrophic factor (BDNF) level, and fluorescent cell staining for neuron morphology and percentage of cell-bearing neurites (% neurites).

Results: HIIT induced significant increases in VO_{2peak} ($P = 0.008$), CO ($P = 0.038$), $\Delta[HHb]$ ($P = 0.046$), $\Delta[THb]$ ($P = 0.046$), and serum BDNF level ($P = 0.012$). The improvement in VO_{2peak} was significantly greater with HIIT than MICT (20.7% vs. 9.8%, $P = 0.031$), as was AV O_{2diff} ($P = 0.041$), $\Delta[HHb]$ ($P = 0.027$), and serum BDNF level ($P < 0.001$). HIIT facilitated neuron dendritic protrusions (greater % neurites, $P = 0.012$) with prominent redistribution of mitochondria.

Conclusion: As compared with MICT, HIIT-improved aerobic capacity by increasing systemic tissue O_2 extraction in stroke patients. Increased cerebral O_2 utilization in the involved hemisphere was also identified after HIIT. These physiological adaptations may be associated with increased serum BDNF level. In vitro dendritic growth in neurons treated with serum from HIIT participants may imply significant effects on neuron activities as compared with MICT.

ClinicalTrials.gov identifier: NCT04135391.

© 2020 The Author(s). Published by Elsevier Masson SAS. This is an open access article under the CC BY-NC-ND license (<http://creativecommons.org/licenses/by-nc-nd/4.0/>).

* Corresponding author. College of Medicine, Graduate Institute of Rehabilitation Science, Chang Gung University, 259, Wen-Hwa 1st Road, 333 Kwei-Shan, Taoyuan, Taiwan.

E-mail addresses: steele0618@gmail.com (C.-C. Hsu), fic6481@gmail.com (T.-C. Fu), h0711@ms13.hinet.net (S.-C. Huang), s120011676@gmail.com (J.-S. Wang).

<https://doi.org/10.1016/j.rehab.2020.03.010>

1877-0657/© 2020 The Author(s). Published by Elsevier Masson SAS. This is an open access article under the CC BY-NC-ND license (<http://creativecommons.org/licenses/by-nc-nd/4.0/>).

1. Introduction

Stroke is characterized as a focal neurological deficit caused by interrupted blood supply to the brain [1]. Its related medical complications have a substantial effect on the final outcome of stroke patients and often impede the neurological recovery [2]. Among the post-stroke complications, cognitive impairment occurs in 30% to

40% of stroke patients [3]. The clinical consequence was associated with 116.4 million disability-adjusted life-years worldwide in 2016 [4]. The evidence suggests that stroke is the leading cause of long-term disability and has enormous socioeconomic impacts on patients, their families, and modern health services.

At 30 days after stroke onset, the peak oxygen consumption ($\text{VO}_{2\text{peak}}$) was found reduced to as much as 50% of that in a healthy population of the same age [5]. Direct assessment of the cardiac output (CO) non-invasively during exercise tests provides valuable information on the exercise physiology in tested subjects and has been incorporated into traditional cardiopulmonary exercise tests (CPETs) [6]. Lowered serum brain-derived neurotrophic factor (BDNF) level has also been reported in stroke patients [7]. BDNF, identified in neurons of most brain areas, is essential for maintaining neurogenesis and synaptic plasticity [8]. The increase in serum BDNF level, significantly correlated with enhanced brain oxygenation [9], may be the key mechanism in exercising improving brain function [10]. Although previous studies showed that aerobic exercise improved $\text{VO}_{2\text{peak}}$ [11] and promoted BDNF secretion [12], the associations among aerobic capacity, brain oxygenation, and serum BDNF level have not been fully explored.

A few randomized controlled trials (RCTs) of aerobic exercise training showed that high-intensity exercise ($\geq 70\%$ VO_2 reserve) was associated with a significantly increased circulating BDNF level and cognitive function in healthy individuals of different ages [13,14]. High-intensity interval training (HIIT) has been used as a therapeutic strategy to improve aerobic capacity in recent clinical practice [15] and is characterized by alternating periods of exercise at $\geq 80\%$ of one's $\text{VO}_{2\text{peak}}$ with less intense recovery periods (40–50% of $\text{VO}_{2\text{peak}}$) [16]. Evidence from RCTs showed that aerobic capacity and serum BDNF level improved quickly after a single HIIT bout in stroke survivors [17]. However, the effect of optimal exercise parameters on serum BDNF level in stroke patients requires further investigation.

Moderate-intensity continuous training (MICT) was found significantly associated with improved aerobic capacity as well as platelet mitochondria activities [18] and selected cognitive domains related to motor learning in stroke patients [19]. In addition to the above findings, 8 weeks of bicycle ergometer training improved serum BDNF level in ischemic stroke patients [12]. Therefore, we hypothesized that HIIT may be the most effective training modality to improve cardiopulmonary function. At this training regimen, the O_2 delivery as well as utilization system is maximally stressed [20], which may provide the most effective stimulus to enhance aerobic capacity, cerebral oxygenation, and serum BDNF level in stroke patients.

The present work was designed to compare changes in serum BDNF level and related physiological adaptations for stroke patients who underwent 36 sessions of HIIT and MICT over 3 months. Because we could not directly assess different exercise training effects on living cerebral tissues in stroke patients, findings from an in vitro morphology study of neurons treated with serum from participants before and after the exercise regimens could imply different exercise effects on neuron biology.

2. Materials and methods

2.1. Design

The Institutional Review Board of a tertiary care hospital approved the study (IRB No. 201600576A3) and the study was registered at ClinicalTrials.gov (NCT04135391). We performed a clinical trial of the effects of different aerobic exercise regimens on chronic stroke patients with assessor and subject blinding from August 2016 to June 2018. Before inclusion, we surveyed stroke

patients still under 6 sessions/month of maintenance traditional rehabilitation programs, consisting of balance, range of motion, or therapeutic exercise for 30 to 45 min in each session. All participants provided informed consent after the experimental procedures were explained. A computer-generated, concealed allocation schedule was used to randomly allocate participants to 30 min of in-hospital supervised MICT or HIIT for 36 sessions. Data were collected by a blinded assessor before randomization and after completing the exercise training.

2.2. Participants

Neurologists determined the hemorrhagic or ischemic stroke based on the brain CT, and the ischemic stroke subtype was determined according to the TOAST classification system [18]. The inclusion criteria were:

- ≥ 20 years old;
- stroke events with stable clinical status > 3 months;
- Mini-Mental State Examination score > 24 and;
- no acute coronary syndrome in the past month.

Baseline demographic characteristics and clinical information, including motor status assessed by Brunnstrom recovery stage and modified Rankin scale, were also recorded in all participants. We excluded individuals with absolute contraindications for CPET, aerobic activities, and unstable clinical presentations, suggested by the American College of Sports Medicine (ACSM) [21].

2.3. Cardiopulmonary exercise test

2.3.1. Graded exercise test

Participants underwent an incremental exercise test on a bicycle ergometer (Ergoselect 150P, ergoline GmbH, Bitz, Germany) at an increased work-rate of 10 W/min with continuous monitoring of heart rate (HR), brachial blood pressure, and arterial oxygen saturation, until the stop conditions described previously [15]. This examination was performed 2 days before exercise training and 2 days after completing exercise training [15]. Oxygen consumption (VO_2) was measured by a cardiopulmonary measurement device (MasterScreen CPX, CareFusion Corp., Hoechst, Germany). $\text{VO}_{2\text{peak}}$ was defined by:

- level of VO_2 increased < 2 mL/kg/min over least 2 min;
- $\text{HR} > 85\%$ of predicted maximal value;
- respiratory exchange ratio > 1.15 or;
- some other symptom/sign limitations, as per the ACSM guideline for exercise testing [21].

2.3.2. Cardiac hemodynamic measurements

A non-invasive continuous cardiac output monitoring system (NICOM, Cheetah Medical, Wilmington, DE, USA) was used to measure peak CO during exercise tests. Arteriovenous O_2 difference ($\text{AV O}_{2\text{diff}}$) was then estimated by the Fick equation: $\text{VO}_{2\text{peak}} = \text{CO} \times \text{AV O}_{2\text{diff}}$.

2.3.3. Cerebral hemodynamic measurements

Each pair of near infrared (NIR) probes (Oxymon, Artinis, The Netherlands) was separately placed over the involved and uninvolved frontal cortex (FC) regions to monitor the absorption of light across cerebral tissues during CPET. The space (range 2.5–3.5 cm) between each pair of optodes was adjusted to ensure proper signal strength (10–30%) on each participant. The modified Beer-Lambert law was applied to measure relative micromolar (μM) changes in cerebral tissue oxyhemoglobin ($\Delta[\text{O}_2\text{Hb}]$) and

deoxyhemoglobin ($\Delta[\text{HHb}]$) concentrations by using received optical densities from 2 continuous NIR wavelengths (780 and 850 nm) at a sampling frequency of 10 Hz. The relative change in total Hb concentration ($\Delta[\text{THb}]$), calculated as the sum of $\Delta[\text{O}_2\text{Hb}]$ and $\Delta[\text{HHb}]$, was an index of the blood volume change in the FC. Differences in brain oxygenation and regional blood volume between the involved and uninvolved (involved-uninvolved) FC were used to estimate the exercise effects on the involved hemisphere [6,22]. The integrated CPET setting detail is shown in Appendix 1.

2.4. Health-related quality of life and cognitive function

Health-related quality of life (QoL) was measured by the Medical Outcomes Study Short Form-36 (SF-36), and the Mini-Mental State Examination was used to assess cognitive function.

2.5. Exercise training protocols

Participants underwent 36 sessions of supervised MICT or HIIT (2 to 3 sessions/week) on a bicycle ergometer. The training comprised a warm-up at 30% of $\text{VO}_{2\text{peak}}$ for 3 min, followed by MICT (60% $\text{VO}_{2\text{peak}}$) or HIIT (five 3-min intervals at 80% $\text{VO}_{2\text{peak}}$, each interval separated by 3 min of exercise at 40% of $\text{VO}_{2\text{peak}}$) for 30 min, then a cool-down at 30% $\text{VO}_{2\text{peak}}$ for 3 min. The 2 protocols have been found to be isocaloric at the same exercise duration [15]. We increased exercise intensity during the exercise training by approximately 10% HR reserve every 2 weeks as the participant could tolerate. The training was terminated when participants had symptoms/signs suggested by the ACSM guidelines [21].

2.6. Serum preparation

An amount of 20 mL fresh blood was collected immediately before CPET from all participants before and after exercise training. Samples were centrifuged at 2500 rpm for 5 min at room temperature, and the upper serum was preserved for cell culture and measurement of serum BDNF level.

2.6.1. Measurement of serum BDNF level

An amount of 100 μL prepared serum was used for measuring BDNF level by an Elisa kit (BioVision Inc., Milpitas, CA, USA) before and after aerobic exercise training.

2.6.2. Cell culture and neurite growth assay

Rat neuroblastic cells (PC-12 cell line, Bioresource Collection and Research Center, Hsinchu, Taiwan) at 10^5 were grown in Dulbecco's modified Eagle's medium (DMEM), then supplemented with 50 ng/mL nerve growth factor (Promega Corp., Madison, WI, USA), 7.5% patient serum (before and after exercise training), 7.5% horse serum, and 100 units/mL penicillin + 100 mg/L streptomycin for 7 days. Morphological changes were observed by Leica TCS SP8 confocal microscopy (Leica TCS SP8, Leica Microsystems Inc., Buffalo Grove, IL, USA). The proportion of cells with neurites of at least one cell body diameter long was determined in 5 independent fields in every plate [23].

2.6.3. Fluorescent staining

PC-12 cells at 10^5 were inoculated in each well of the eight-chamber slide (Millicell EZ slide, Millipore Corp., Billerica, MA, USA) and were incubated in pre- and post-MICT or -HIIT serum for 12 hr. Staining with Vivid Mitotracker (Invitrogen Corp., Carlsbad, CA, USA) was used to observe mitochondria in live cells treated with serum from pre- and post-exercise status. Cells were stained with primary rabbit monoclonal anti- α -tubulin antibodies (Vector

Laboratories Inc., Burlingame, CA, USA). The fluorescein isothiocyanate-conjugated AffiniPure goat anti-rabbit IgG (Jackson ImmunoResearch Laboratories, West Grove, PA, USA) was used as the secondary antibody. Nuclei were counterstained with mounting medium (Vector Laboratories Inc., Burlingame, CA, USA) containing 40,6-diamidino-2-phenylindole. Stained cells were examined by confocal microscopy.

2.7. Statistical methods

The primary outcome measure was the change in BDNF measured after the different exercise regimens. With a mean (SD) value of the main criterion of 0.2, statistical power ($1 - \beta$) 80% and α value of 0.05 in a bilateral hypothesis, we hypothesized that to obtain a 20% change in BDNF level with HIIT vs. MICT, we needed at least 10 participants in each group.

Data are presented as mean with (95% CI) or number (%). Exercise-induced changes in parameters were normalized to compare exercise effects on different individuals by using the equation $[(\text{PostEx} - \text{PreEx}) / \text{PreEx}]$, where Post/PreEx represents parameters measured after/before exercise training. Chi² test was used to compare differences in non-parametric parameters and Mann-Whitney U test to compare differences in baseline demographic characteristics and parameters. Within-group changes were assessed by Wilcoxon matched-pair signed-rank test. The correlation between demographic characteristics and all clinical parameters after exercise training was analyzed by Pearson correlation. $P < 0.05$ was considered statistically significant.

3. Results

3.1. Participant characteristics

We surveyed 43 stroke patients and enrolled 36 but excluded 8 on the basis of our exclusion criteria. Participants were randomly assigned to the HIIT ($n = 13$) or MICT ($n = 15$) group. Three HIIT and 2 MICT participants were lost during follow-up. Therefore, all 10 HIIT and 13 MICT participants completed the 36 sessions of exercise training (Fig. 1). The mean age was 58.5 (49.8–67.2) and 53.1 (46.2–60.0) years in the HIIT and MICT groups. The mean time since stroke was > 2 years in both groups. Baseline clinical information was similar in both groups (Table 1).

3.2. Effect of exercise training on aerobic capacity and hemodynamics

Stroke patients in both groups showed significantly improved $\text{VO}_{2\text{peak}}$ after exercise training, with a greater degree of improvement ($P = 0.031$) in the HIIT than MICT group (median 20.7% vs. 9.8%). HIIT participants showed a significant improvement in peak cardiac output (CO) after exercise training (median pre- vs. post-HIIT = 8.35 vs. 9.80 L/min), but the degree of improvement was similar ($P = 0.095$) between the 2 groups (HIIT vs. MICT = median 15.0% vs. 10.1%). Although HIIT and MICT could not significantly increase $\text{AV O}_{2\text{diff}}$ (Table 2), the normalized change of $\text{AV O}_{2\text{diff}}$ was significantly greater with HIIT than MICT (median 7.9% vs. –18.6%, $P = 0.041$) (Fig. 2).

3.3. Effect of exercise training on cerebral oxygenation in involved hemispheres

Despite a non-significant improvement of $\Delta[\text{O}_2\text{Hb}]$ in both groups, $\Delta[\text{HHb}]$ and $\Delta[\text{THb}]$ were significantly increased in the involved frontal cortex after HIIT (Table 2). HIIT participants showed a significant increase in normalized change of $\Delta[\text{HHb}]$ in the involved hemispheres as compared with MICT participants

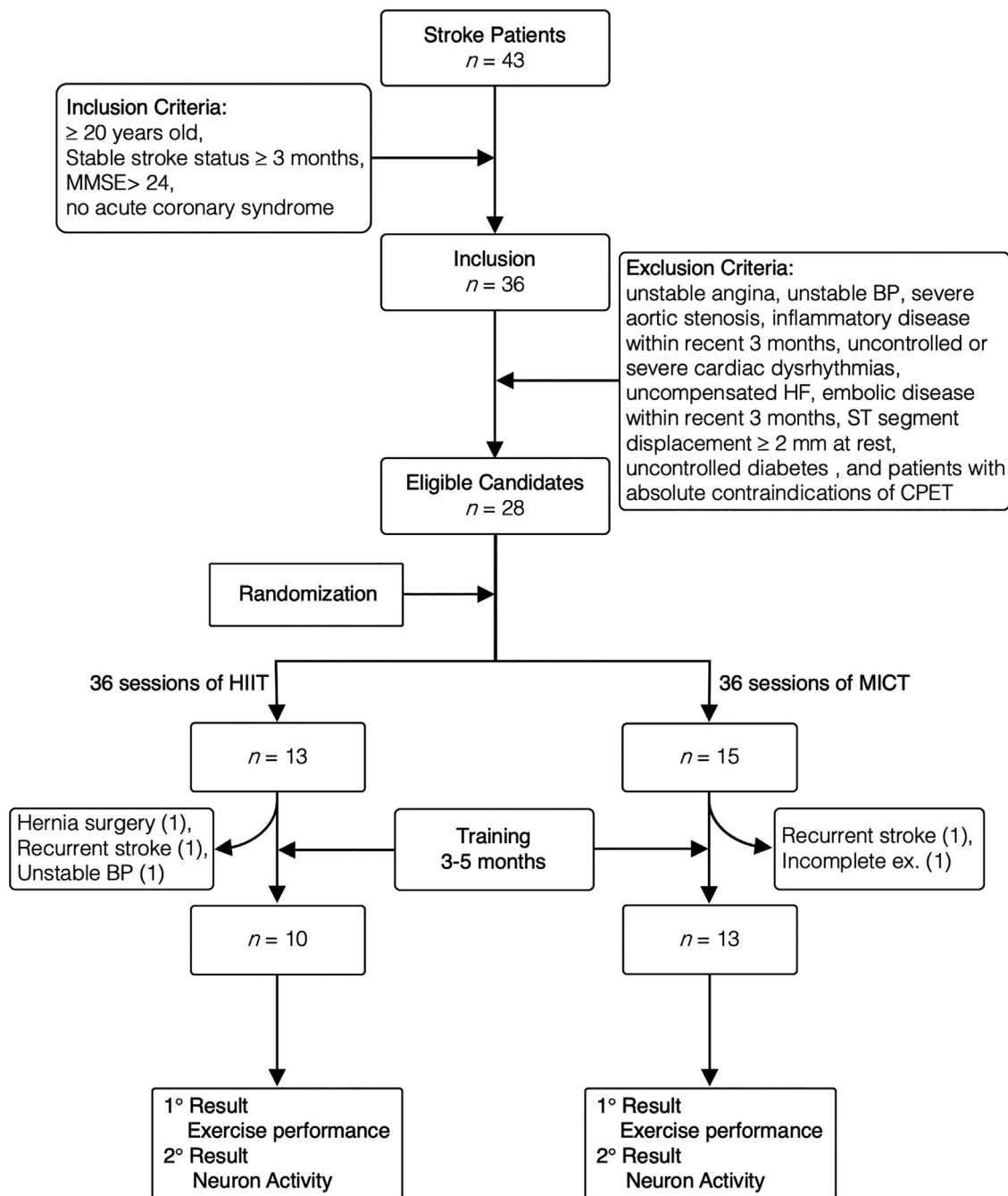


Fig. 1. Flow of participants in the study. BP: blood pressure; CPET: cardiopulmonary exercise test; HF: heart failure; HIIT: high-intensity interval training; MICT: moderate-intensity continuous training; MMSE: mini-mental status examination.

(Fig. 3A). Improvement in health- or cognition-related findings at the late stroke stage were similar between the groups after exercise training (Appendix 2).

3.4. Effect of exercise training on circulating BDNF level and neural reactivities

Circulating BDNF level increased significantly after HIIT (median pre- vs. post-HIIT = 6.06 vs. 7.91 ng/mL, $P = 0.012$), but decreased significantly after MICT (median pre- vs. post-MICT = 7.30 vs. 5.88 ng/mL, $P = 0.009$) (Table 2). Serum BDNF level significantly increased after HIIT vs. after MICT ($P < 0.001$) (Fig. 3B).

Dendritic growth was significantly increased in neuroblastic cells treated with serum from stroke patients after HIIT ($P = 0.017$) as compared with those treated with serum after MICT (Table 2). On low-power-field examination, cells treated with serum obtained after HIIT showed distinct dendritic growth with long dendrites (Fig. 4A–D) as well as redistribution of mitochondria along the newly developed dendrites associated with dendritic spines and synapse (Fig. 4E–H).

3.5. Correlation between exercise effect and clinical presentation

We pooled all participants to analyze the correlation between training regimens and physiological responses. The HIIT regimen was

Table 1

Baseline demographics of stroke patients undergoing high-intensity interval training (HIIT) and moderate-intensity continuous training (MICT).

	HIIT (n = 10)	MICT (n = 13)	P-value
Thrombosis/hemorrhage	6/4	9/4	0.645
Age, years	58.5 (49.8–67.2)	53.1 (46.2–60.0)	0.483
Sex (F/M)	2/8	1/12	0.385
BMI, kg/m ²	25.5 (23.3–27.8)	26.2 (23.7–28.6)	0.927
Stroke duration, m	38.5 (19.1–57.9)	28.8 (3.35–54.2)	0.166
Affected limbs (R/L)	4/6	8/5	0.855
Modified Rankin scale, n (%)			
1	4 (40)	6 (46)	0.937
2	6 (60)	7 (53)	
Brunnstrom recovery stage, n (%)			
III	1 (10)	2 (15)	0.399
IV	1 (10)	4 (30)	
V	8 (80)	7 (55)	
Risk factors, n (%)			
Hypertension	9 (90)	11 (85)	0.704
Diabetes	2 (20)	4 (31)	0.560
Dyslipidemia	7 (70)	12 (92)	0.162
Cardiac disease	4 (40)	5 (38)	0.940
Sleep apnea	5 (50)	3 (23)	0.179
Obesity	1 (10)	3 (23)	0.412
Smoking	2 (20)	6 (46)	0.192
Medication, n (%)			
ACEI/ARB	8 (80)	9 (69)	0.560
β-blocker	4 (40)	5 (38)	0.940
CCB	7 (70)	11 (85)	0.400
Diuretics	3 (30)	2 (15)	0.400
HMG CoAI	7 (70)	12 (92)	0.162
ASA	6 (60)	8 (62)	0.940
NOAC	1 (10)	2 (15)	0.704

Data are mean (95% confidence interval) or number (%). ACEI: angiotensin converting enzyme inhibitor; ARB: angiotensin receptor blocker; ASA: acetylsalicylic acid; BMI: body mass index; CCB: calcium channel blocker; F/M: female/male; HMG CoAI: hydroxymethylglutaryl-CoA reductase inhibitor; L/R: left/right; NOAC: non-vitamin K antagonist oral anticoagulant.

positively correlated with serum BDNF level ($r = 0.658$, $P = 0.001$), % neurites ($r = 0.625$, $P = 0.013$), and $\Delta[\text{HHb}]$ ($r = 0.564$, $P = 0.018$). $\text{VO}_{2\text{peak}}$ was positively correlated with $\Delta[\text{HHb}]$ ($r = 0.634$, $P = 0.006$) and % neurites ($r = 0.551$, $P = 0.041$). Cognitive function was inversely correlated with age ($r = -0.541$, $P = 0.011$).

4. Discussion

To avoid confounding factors of spontaneous neurological recovery, we analyzed the effect of different exercise training regimens on brain oxygenation and neuron activities > 3 months after stroke onset [24]. HIIT induced a greater increase of $\text{VO}_{2\text{peak}}$ and serum BDNF level in chronic stroke patients as compared with MICT. $\Delta[\text{HHb}]$ provides a highly sensitive measure of relative tissue deoxygenation and is closely associated with changes in venous O_2 content due to O_2 utilization [6]. HIIT-improved systemic and cerebral tissue O_2 utilization in this study support this point of view. The high cerebral tissue deoxygenation and redistribution regional blood flow to the involved FC after HIIT implies increased neural reactivities, which may be related to release of neurotrophic factors from the cerebral tissue in chronic stroke patients. These physiological adaptations after HIIT may further stimulate dendritic growth and increase mitochondria activities in neurons.

The rapid deterioration of physical fitness leads to cardiorespiratory complications and prevents acute stroke patients from participating in rehabilitation therapy and limits their independence [5]. Despite aggressive supervised cardiopulmonary training, the aerobic capacity of patients with stroke in the chronic

Table 2

Effect of HIIT and MICT on physical, cognitive and health-related quality of life features in stroke patients.

	Initial	End of training	P-value
HIIT, (n = 10)	3.70 (3.19–4.21)		
Training period, m			
$\text{VO}_{2\text{peak}}$, O_2 mL/min/kg	16.4 (15.0–17.8)	19.8 (18.3–21.3)	0.008 ^a
CO (L/min)	8.35 (6.93–9.77)	9.80 (7.68–11.9)	0.038 ^a
AV $\text{O}_{2\text{diff}}$ (mL/dL)	13.9 (11.7–16.0)	14.6 (12.1–17.1)	0.214
ΔNIRS			
$\Delta[\text{O}_2\text{Hb}]$ (μM)	3.14 (0.67–5.61)	4.58 (1.28–7.88)	0.345
$\Delta[\text{HHb}]$ (μM)	1.24 (0.53–1.94)	2.81 (1.62–4.01)	0.046 ^a
$\Delta[\text{THb}]$ (μM)	3.34 (0.53–6.16)	6.30 (1.85–10.7)	0.046 ^a
BDNF, ng/mL	6.06 (3.80–8.32)	7.91 (5.86–9.96)	0.012 ^a
Cell-bearing neurites, %	38.8 (30.6–47.0)	45.2 (35.2–55.2)	0.017 ^a
MMSE	28.0 (26.7–29.3)	28.2 (26.7–29.7)	0.157
SF-36			
PCS	43.5 (39.0–47.9)	44.6 (41.0–48.1)	0.859
MCS	44.3 (36.2–52.5)	48.4 (41.2–55.6)	0.139
MICT, (n = 13)			
Training period, m	3.62 (3.20–4.03)		
$\text{VO}_{2\text{peak}}$, O_2 mL/min/kg	17.4 (14.9–20.0)	19.1 (16.9–21.2)	0.046 ^a
CO (L/min)	9.78 (8.76–10.8)	10.1 (8.29–11.9)	0.637
AV $\text{O}_{2\text{diff}}$ (mL/dL)	12.2 (10.7–13.7)	14.6 (12.5–16.6)	0.117
ΔNIRS			
$\Delta[\text{O}_2\text{Hb}]$ (μM)	5.09 (3.27–6.92)	5.62 (3.69–7.56)	0.594
$\Delta[\text{HHb}]$ (μM)	1.51 (0.94–2.07)	1.58 (1.13–2.03)	0.859
$\Delta[\text{THb}]$ (μM)	5.80 (3.79–7.80)	6.55 (4.49–8.61)	0.594
BDNF, ng/mL	7.30 (6.06–8.53)	5.88 (4.72–7.04)	0.009 ^a
Cell-bearing neurites, %	45.7 (37.1–54.3)	34.3 (19.5–49.1)	0.115
MMSE			
SF-36			
PCS	28.5 (27.1–29.9)	28.4 (26.5–30.3)	1.000
MCS	44.7 (41.3–48.2)	45.8 (41.2–50.4)	0.917
	40.0 (33.5–46.4)	41.7 (36.0–47.4)	0.753

AV $\text{O}_{2\text{diff}}$: arteriovenous O_2 difference; BDNF: brain-derived neurotrophic factor; CO: cardiac output; ΔNIRS: near-infrared spectroscopy measurement between involved and uninvolved hemispheres (involved-uninvolved); $\Delta[\text{HHb}]$: deoxyhemoglobin; $\Delta[\text{O}_2\text{Hb}]$: oxyhemoglobin; $\Delta[\text{THb}]$: total hemoglobin; HIIT: high-intensity interval training; MICT: moderate-intensity interval training; MMSE: mini-mental status examination; PCS: physical component score; SF-36: Medical Outcomes Study Short Form-36; $\text{VO}_{2\text{peak}}$: peak oxygen consumption.

^a Data are mean (95% CI). Statistical significance was assessed by Wilcoxon matched-pair signed-rank test.

phase is still lower than that of healthy individuals [25,26]. Thus, the American Heart Association advocates aerobic exercise training for stroke patients to help them regain independent daily living activity rather than promote cognitive function [27]. The quality of evidence for aerobic exercise training to promote cognitive function in stroke patients is still insufficient, especially for people with chronic stroke > 12 months, and further investigation is indicated [28]. Exercise intensity due to cardiorespiratory fitness is critical for the redistribution of cerebral blood flow as well as increased cerebral oxygenation and its possible effect on cognitive function in community indwelling women [29]. A previous report showed that after more than 4 months of MICT in stroke patients, their overall cerebral blood perfusion did not increase, but the distribution of blood flow to the temporal lobe increased, which further improves cognitive function [30]. In-depth analysis of our NIR findings revealed cerebral blood flow redistributed to the involved hemisphere after HIIT, as reflected by the increased change to the involved FC cerebral blood flow. Increased cerebral tissue O_2 utilization in the involved hemisphere, supported by the significant increase in $\Delta[\text{HHb}]$, was associated with increased systemic tissue O_2 extraction after HIIT vs. MICT. Therefore, exercise intensity is associated with cerebral blood flow redistribution and cerebral tissue O_2 utilization.

A single bout of high-intensity cycling at workloads of 200 to 315 W in healthy young adults significantly increased peripheral BDNF level even 7 days after the exercise intervention [31]. A randomized clinical study of 61 patients with chronic ischemic

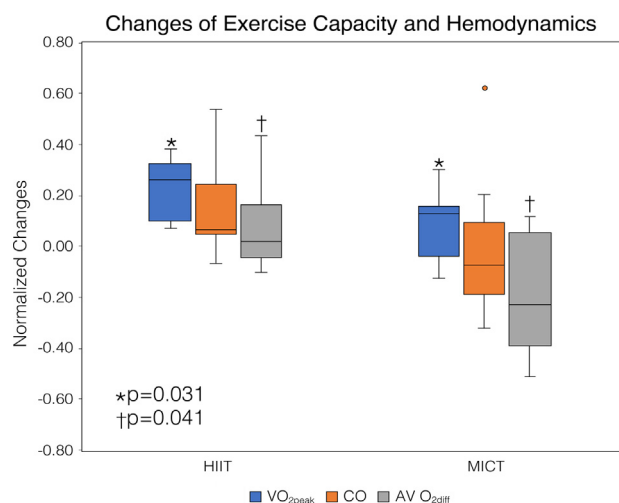


Fig. 2. Effect of exercise training regimens on exercise performance and hemodynamics. Horizontal bar is the median, box edges are 1st and 3rd quartiles and error bars are 95% confidence interval (CI) of tested values. Changes in VO_{2peak} and AV O_{2diff} were normalized as [(PostEx – PreEx)/PreEx]. Outliers are shown with dots. *: Mann-Whitney U test for VO_{2peak}; †: Mann-Whitney U test for AV O_{2diff}; AV O_{2diff}: arteriovenous oxygen difference; CO: cardiac output; HIIT: high-intensity interval training; MICT: moderate-intensity continuous training; PostEx: post-exercise assessment; PreEx: pre-exercise assessment; VO_{2peak}: peak oxygen consumption.

stroke (>6 months) showed improved cardiovascular fitness after treadmill exercise training (3X/week) at 60% to 70% HR reserve for 6 months, but cognition status after interventions was not discussed [11]. An aerobic exercise training at unknown intensity for ischemic stroke patients about 50 years old increased serum BDNF level [12]. Preliminary evidence from 4 randomized controlled trials and 6 single-session cross-over studies reported HIIT-associated improvements in post-stroke neuroplastic outcomes [17]. The exercise-induced increase in serum BDNF level may be intensity-dependent, but the optimal intensity to facilitate BDNF release remains undefined [13]. In humans, serum BDNF originates from the liver, skeletal muscles, vascular endothelium, and central nervous system [32]. However, a striking BDNF release from the brain, evidenced by samples obtained from the right internal jugular vein, was increased 2- to 3-fold and contributed

70% to 80% of circulating BDNF during exercise [33]. In the present work, HIIT at alternating intensity of 80% and 40% of VO_{2peak} instead of MICT at 60% of VO_{2peak} increased serum BDNF level. A significant decrease in serum BDNF level in MICT participants was similar to the 3 weeks of BDNF level follow-up in stroke patients [34], which implies that moderate-intensity is not adequate for brain recovery in stroke patients [35]. Thus, HIIT may be effective for improving brain health in stroke patients.

Reduced serum BDNF level, detected in acute ischemic stroke patients and those with post-stroke depression, was found associated with poor functional outcome at 2 years after stroke onset [36]. Cognitive deficit in aged mice with ischemic prefrontal cortex could be treated by intracerebral hydrogels loaded with a BDNF decoy, which suggests that the recovery of cognitive function is BDNF-dependent [37]. A study of 30 young stroke patients with disease duration of 3 to 18 months reported improved cognitive function positively correlated with increased serum BDNF level [12]. Therefore, serum BDNF level has been used as an indicator reflecting cognitive function and the effectiveness of behavioral or pharmacologic interventions for stroke patients [36]. BDNF is highly expressed in the brain and has potent effects on dendritic spine formation. The synergistic interactions between neuronal activity and synaptic plasticity by BDNF make it an ideal and essential regulator underlying complex cognitive behavior [38].

Mitochondria, dynamically redistributed into dendritic protrusions in response to synaptic excitation, are associated with dendritic spine formation and critical to serve the differential spatial and temporal demands of neurons [39]. Increased dendritic growth as well as spine formation and mitochondria distribution in dendrites were observed in neurons treated with serum from participants after HIIT. The correlation between aerobic capacity and dendritic growth was also identified. Hence, greater improvement of exercise performance with HIIT could enhance neurogenesis and synaptic plasticity in stroke patients.

In contrast to the previous studies, cognitive function was not significantly improved in stroke patients. The change in BDNF level was not correlated with change in cognitive function or mental health. These observations may be caused by enrolling patients with stroke duration > 24 months. Limited benefits of aerobic exercise to improve cognition in stroke patients at such a chronic stage could be expected. With this limitation, age becomes the most dominant factor deteriorating cognitive function, with failure

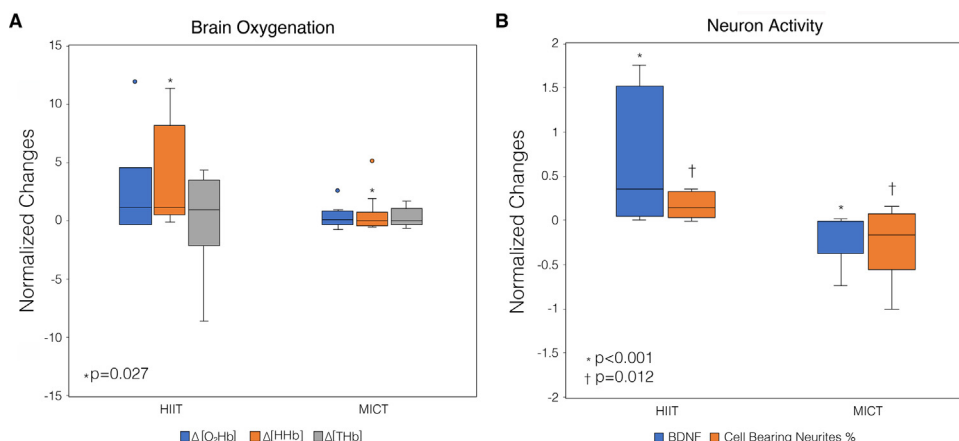


Fig. 3. Effect of exercise regimens on differences in (A) brain oxygenation and between involved and uninvolved (involved-uninvolved) hemispheres and (B) neuron activity. Change in above measurements was normalized according to the following equation, [(PostEx – PreEx)/PreEx]. Horizontal bar is the median, box edges are 1st and 3rd quartiles and error bars are 95% CI of tested values. Outliers are shown as dots. *: Mann-Whitney U test for Δ[HbHb] (A) and serum BDNF level (B) between the 2 groups. †: Mann-Whitney U test for cell-bearing neurites (B). Δ[HbHb]: difference in deoxyhemoglobin concentration between the involved and uninvolved hemispheres; Δ[O₂Hb]: difference in oxyhemoglobin concentration between the involved and uninvolved hemispheres; Δ[THb]: difference in total hemoglobin concentration between the involved and uninvolved hemispheres; HIIT: high-intensity interval training; MICT: moderate-intensity continuous training; PostEx: post-exercise assessment; PreEx: pre-exercise assessment.

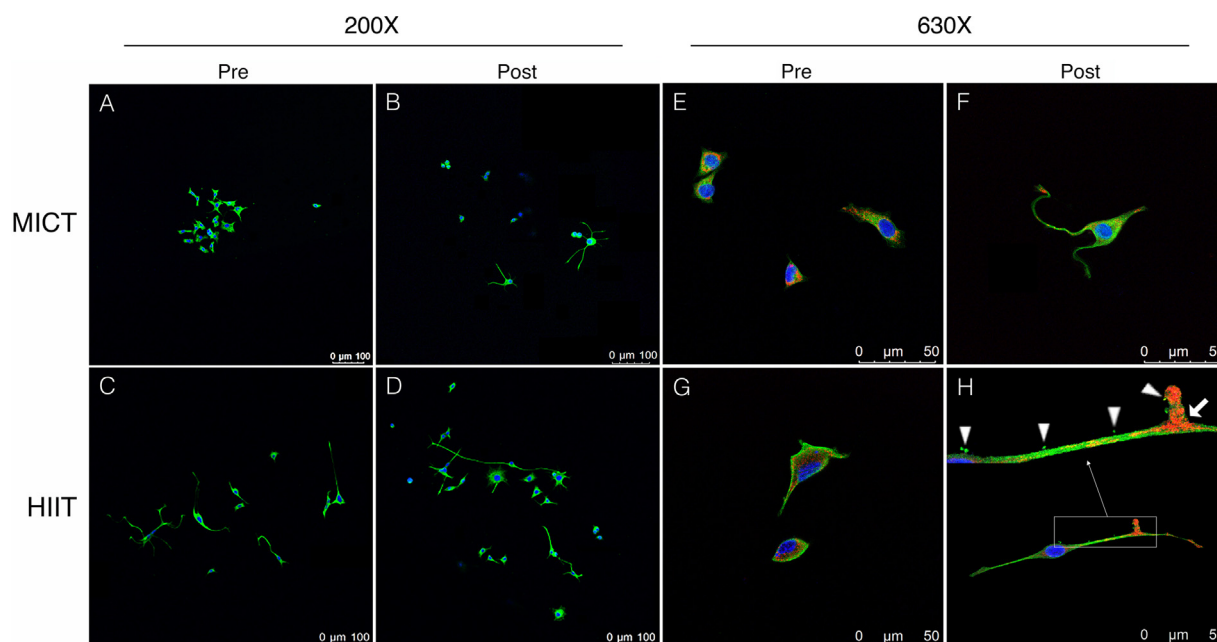


Fig. 4. Effect of different exercise training regimens on dendritic protrusions and mitochondria distribution in neuroblastic cells. A–D. Low-power field (200X) showing long dendrites in cells treated with serum from stroke patients after high-intensity interval training (HIIT) and moderate-intensity continuous training (MICT). Microtubules (green) distributed in the cell body and dendrites. The oval shape nucleus (blue) in the body is the neuron. E–H. With high power field (630X), cells treated with pre-exercise serum showed most mitochondria (red) in the peri-nuclear (blue) region. Mitochondria redistributed along microtubules in new growth dendrites. Magnification of the rectangle area showed dendritic spines (arrowheads) and possible synapse (arrow) in cells treated with serum from patients after HIIT.

to increase serum BDNF level after aerobic exercise training. The other drawback was that only bilateral prefrontal cortex oxygenation was measured, not the whole hemisphere.

5. Conclusions

An exercise strategy involving high-intensity exercise training significantly improved aerobic fitness. This physiological adaptation allowed for better regional cerebral blood flow with increased O_2 utilization in the brain and would translate into improved executive and motor performance [40]. Increased BDNF level released from neurons responding to the above changes may further result in the growth and branching of neuron dendrites, which are crucial for the recovery of central nervous system function in stroke patients.

Funding

This research was funded by the Keelung Chang Gung Medical Research Program (CMRPD310021, CMRPG2G0011, and CMRPG2G0012).

Authors' contributions

Conceived and designed the experiments: CCH and JSW. Performed the experiments: TCF and SCH. Analyzed the data: CCH, TCF, SCH and JSW. Wrote original draft: CCH. Reviewed and edited the draft: JSW. All authors critically revised the manuscript for important intellectual content and approved the final manuscript.

Disclosure of interest

The authors declare that they have no competing interest.

Acknowledgements

We thank Mr. Hsiao-Tung Liu in the Laser Scanning Confocal Microscopy Room, Keelung Chang Gung Memorial Hospital, for

providing excellent fluorescent images; Pei-Shuan Lin in the Department of Physical Medicine and Rehabilitation, Keelung Chang Gung Memorial Hospital, for contributions to the cell biology experiment. This manuscript was edited for English language by Laura Smales (BioMedEditing).

Appendix A. Supplementary data

Supplementary data associated with this article can be found, in the online version at: <https://doi.org/10.1016/j.rehab.2020.03.010>.

References

- [1] Sacco RL, Kasner SE, Broderick JP, Caplan LR, Connors JJ, Culebras A, et al. An updated definition of stroke for the 21st century: a statement for healthcare professionals from the American Heart Association/American Stroke Association. *Stroke* 2013;44:2064–89.
- [2] Kumar S, Selim MH, Caplan LR. Medical complications after stroke. *Lancet Neurol* 2010;9:105–18.
- [3] McDonald MV, Black SE, Copland DA, Corbett D, Dijkhuizen RM, Farr TD, et al. Cognition in stroke rehabilitation and recovery research: consensus-based core recommendations from the second Stroke Recovery and Rehabilitation Roundtable. *Int J Stroke* 2019;14:774–82.
- [4] GBD 2016 Stroke Collaborators. Global, regional, and national burden of stroke, 1990–2016: a systematic analysis for the Global Burden of Disease Study 2016. *Lancet Neurol* 2019;18:439–58.
- [5] Kelly JO, Kilbreath SL, Davis GM, Zeman B, Raymond J. Cardiorespiratory fitness and walking ability in subacute stroke patients. *Arch Phys Med Rehabil* 2003;84:1780–5.
- [6] Wang JS, Wu MH, Mao TY, Fu TC, Hsu CC. Effects of normoxic and hypoxic exercise regimens on cardiac, muscular, and cerebral hemodynamics suppressed by severe hypoxia in humans. *J Appl Physiol* 2010;109:219–29.
- [7] Santos GL, Alcântara CC, Silva-Couto MA, García-Salazar LF, Russo TL. Decreased brain-derived neurotrophic factor serum concentrations in chronic post-stroke subjects. *J Stroke Cerebrovasc Dis* 2016;25:2968–74.
- [8] Bathina S, Das UN. Brain-derived neurotrophic factor and its clinical implications. *Arch Med Sci* 2015;11:1164–78.
- [9] Gagrani M, Faiq MA, Sidhu T, Dada R, Yadav RK, Sihota R, et al. Meditation enhances brain oxygenation, upregulates BDNF and improves quality of life in patients with primary open angle glaucoma: a randomized controlled trial. *Restor Neurol Neurosci* 2018;36:741–53.
- [10] Cotman CW, Berchtold NC, Christie L-A. Exercise builds brain health: key roles of growth factor cascades and inflammation. *Trends Neurosci* 2007;30:464–72.

- [11] Macko RF, Ivey FM, Forrester LW, Hanley D, Sorkin JD, Katzel LI, et al. Treadmill exercise rehabilitation improves ambulatory function and cardiovascular fitness in Patients with chronic stroke: a randomized, controlled trial. *Stroke* 2005;36:2206–11.
- [12] El-Tamawy MS, Abd-Allah F, Ahmed SM, Darwish MH, Khalifa HA. Aerobic exercises enhance cognitive functions and brain derived neurotrophic factor in ischemic stroke patients. *NeuroRehabilitation* 2014;34:209–13.
- [13] Ferris LT, Williams JS, Shen CL. The effect of acute exercise on serum brain-derived neurotrophic factor levels and cognitive function. *Med Sci Sports Exerc* 2007;39:728–34.
- [14] Jeon YK, Ha CH. The effect of exercise intensity on brain derived neurotrophic factor and memory in adolescents. *Environ Health Prev Med* 2017;22:27.
- [15] Fu TC, Wang CH, Lin PS, Hsu CC, Cherng WJ, Huang SC, et al. Aerobic interval training improves oxygen uptake efficiency by enhancing cerebral and muscular hemodynamics in patients with heart failure. *Int J Cardiol* 2013;167:41–50.
- [16] Gossard D, Haskell WL, Taylor CB, Mueller JK, Rogers F, Chandler M, et al. Effects of low- and high-intensity home-based exercise training on functional capacity in healthy middle-aged men. *Am J Cardiol* 1986;57:446–9.
- [17] Crozier J, Roig M, Eng JJ, MacKay-Lyons M, Fung J, Ploughman M, et al. High-intensity interval training after stroke: an opportunity to promote functional recovery, cardiovascular health, and neuroplasticity. *Neurorehabil Neural Repair* 2018;32:543–56.
- [18] Hsu CC, Tsai HH, Fu TC, Wang JS. Exercise training enhances platelet mitochondrial bioenergetics in stroke patients: a randomized controlled trial. *J Clin Med* 2019;8:2186.
- [19] Quaney BM, Boyd LA, McDowd JM, Zahner LH, He J, Mayo MS, et al. Aerobic exercise improves cognition and motor function poststroke. *Neurorehabil Neural Repair* 2009;23:879–85.
- [20] Ainslie PN, Cotter JD, George KP, Lucas S, Murrell C, Shave R, et al. Elevation in cerebral blood flow velocity with aerobic fitness throughout healthy human ageing. *J Physiol* 2008;586:4005–10.
- [21] Pescatello LS, Arena R, Riebe D, Thompson PD. ACSM's guidelines for exercise testing and prescription, 9th ed., Philadelphia, PA: Wolters Kluwer/Lippincott Williams & Wilkins; 2014.
- [22] Delorme M, Vergotte G, Perrey S, Froger J, Laffont I. Time course of sensorimotor cortex reorganization during upper extremity task accompanying motor recovery early after stroke: an fNIRS study. *Restor Neurol Neurosci* 2019;37:207–18.
- [23] Huang CH, Cheng JC, Chen JC, Tseng CP. Evaluation of the role of Disabled-2 in nerve growth factor-mediated neurite outgrowth and cellular signalling. *Cell Signal* 2007;19:1339–47.
- [24] Lee KB, Lim SH, Kim KH, Kim KJ, Kim YR, Chang WN, et al. Six-month functional recovery of stroke patients: a multi-time-point study. *Int J Rehabil Res* 2015;38:173–80.
- [25] Fu TC, Wang CH, Hsu CC, Cherng WJ, Huang SC, Wang JS. Suppression of cerebral hemodynamics is associated with reduced functional capacity in patients with heart failure. *Am J Physiol Heart Circ Physiol* 2011;300:H1545–5.
- [26] Tsai CF, Thomas B, Sudlow CL. Epidemiology of stroke and its subtypes in Chinese vs. white populations: a systematic review. *Neurology* 2013;81:264–72.
- [27] Gordon NF, Gulanick M, Costa F, Fletcher G, Franklin BA, Roth EJ, et al. Physical activity and exercise recommendations for stroke survivors: an American Heart Association scientific statement from the council on clinical cardiology, subcommittee on exercise, cardiac rehabilitation, and prevention; the council on cardiovascular nursing; the council on nutrition, physical activity, and metabolism; and the stroke council. *Circulation* 2004;109:2031–41.
- [28] Liu-Ambrose T, Eng JJ. Exercise training and recreational activities to promote executive functions in chronic stroke: a proof-of-concept study. *J Stroke Cerebrovasc Dis* 2015;24:130–7.
- [29] Albinet CT, Mandrick K, Bernard PL, Perrey S, Blain H. Improved cerebral oxygenation response and executive performance as a function of cardiorespiratory fitness in older women: a fNIRS study. *Front Aging Neurosci* 2014;6:272.
- [30] Moore SA, Hallsworth K, Jakovljevic DG, Blamire AM, He J, Ford GA, et al. Effects of community exercise therapy on metabolic, brain, physical, and cognitive function following stroke: a randomized controlled pilot trial. *Neurorehabil Neural Repair* 2015;29:623–35.
- [31] Skriver K, Roig M, Lundbye-Jensen J, Pingel J, Helge JW, Kiens B, et al. Acute exercise improves motor memory: exploring potential biomarkers. *Neurobiol Learn Mem* 2014;116:46–58.
- [32] Klein AB, Williamson R, Santini MA, Clemmensen C, Ettrup A, Rios M, et al. Blood BDNF concentrations reflect brain-tissue BDNF levels across species. *Int J Neuropsychopharmacol* 2011;14:347–53.
- [33] Rasmussen P, Brassard P, Adser H, Pedersen MV, Leick L, Hart E, et al. Evidence for a release of brain-derived neurotrophic factor from the brain during exercise. *Exp Physiol* 2009;94:1062–9.
- [34] Luo W, Liu T, Li S, Wen H, Zhou F, Zafonte R, et al. The serum BDNF level offers minimum predictive value for motor function recovery after stroke. *Transl Stroke Res* 2019;10:342–51.
- [35] Zembron-Lacny A, Dziubek W, Rynkiewicz M, Morawin B, Woźniowski M. Peripheral brain-derived neurotrophic factor is related to cardiovascular risk factors in active and inactive elderly men. *Braz J Med Biol res* 2016;49:e5253.
- [36] Stanne TM, Åberg ND, Nilsson S, Jood K, Blomstrand C, Andreasson U, et al. Low circulating acute brain-derived neurotrophic factor levels are associated with poor long-term functional outcome after ischemic stroke. *Stroke* 2016;47:1943–5.
- [37] Houlton J, Zhou LYY, Barwick D, Gowing EK, Clarkson AN. Stroke induces a BDNF-dependent improvement in cognitive flexibility in aged mice. *Neural Plast* 2019;2019:1460890.
- [38] Luine V, Frankfurt M. Interactions between estradiol, BDNF and dendritic spines in promoting memory. *Neuroscience* 2013;239:34–45.
- [39] Li Z, Okamoto K, Hayashi Y, Sheng M. The importance of dendritic mitochondria in the morphogenesis and plasticity of spines and synapses. *Cell* 2004;119:873–87.
- [40] Perrey S. Promoting motor function by exercising the brain. *Brain Sci* 2013;3:101–22.



Research paper



Association of *XRCC2* rs2040639 with the survival of patients with oral squamous cell carcinoma undergoing concurrent chemoradiotherapy

Thomas Senghore^{a,b}, Wen-Chang Wang^c, Huei-Tzu Chien^{d,e,f}, You-Xin Chen^a,
Chi-Kuang Young^g, Shiang-Fu Huang^{d,h,*}, Chih-Ching Yeh^{a,i,j,k,*}

^a School of Public Health, College of Public Health, Taipei Medical University, Taipei, Taiwan

^b Department of Nursing and Reproductive Health, School of Medicine and Allied Health Sciences, University of The Gambia, Independence Drive, Banjul, Gambia

^c Ph.D. Program for Translational Medicine, College of Medical Science and Technology, Taipei Medical University, Taipei, Taiwan

^d Department of Public Health, Chang Gung University, Taoyuan, Taiwan

^e Department of Nutrition and Health Sciences, Chang Gung University of Science and Technology, Taoyuan, Taiwan

^f Research Center for Chinese Herbal Medicine, College of Human Ecology, Chang Gung University of Science and Technology, Taoyuan, Taiwan

^g Department of Otolaryngology, Chang Gung Memorial Hospital, Keelung, Taiwan

^h Department of Otolaryngology, Head and Neck Surgery, Chang Gung Memorial Hospital, Linkou, Taoyuan, Taiwan

ⁱ Department of Public Health, College of Public Health, China Medical University, Taichung, Taiwan

^j Cancer Center, Wan Fang Hospital, Taipei Medical University, Taipei, Taiwan

^k Master Program in Applied Molecular Epidemiology, College of Public Health, Taipei Medical University, Taipei, Taiwan

ARTICLE INFO

Keywords:

Genetic polymorphisms
DNA double-strand break
Chemotherapy
Radiotherapy

ABSTRACT

Objective: To investigate the association between the variants of DNA double-strand break repair genes and the clinical outcomes of patients with oral squamous cell carcinoma (OSCC) undergoing concurrent chemoradiotherapy.

Methods: Five variants of DNA double-strand break repair genes in samples from 319 patients with OSCC were genotyped using the Sequenom iPLEX MassARRAY system. Kaplan–Meier curves and Cox proportional hazards analysis were used to identify the factors associated with patient survival.

Results: The *XRCC2* rs2040639 (G3063A) polymorphism in the codominant model was associated with decreased recurrence risk (hazard ratio [HR] = 0.55, 95% confidence interval [CI] = 0.31–0.98; $p = 0.042$). A marginally significant interaction was observed between *XRCC2* rs2040639 and *PRKDC* rs7003908 in patients carrying the AA and AA genotypes; these patients showed reduced recurrence risk (HR = 0.36, 95% CI = 0.17–0.79; $p = 0.010$).

Conclusion: The A-allele of *XRCC2* rs2040639 is a favorable prognostic factor for disease-free survival. Patients with these genotypes may benefit from concurrent chemoradiotherapy. Additional confirmation from studies with larger samples or other ethnic populations is warranted.

1. Introduction

Despite therapeutic and diagnostic advances in recent decades, oral cancer remains a leading cause of cancer mortality, making it a major public health concern, particularly among men in Taiwan (Chiang et al.,

2016). Oral squamous cell carcinoma (OSCC) is the most common subtype, accounting for approximately 90% of all oral cancers (Chiang et al., 2016). In most cases, OSCC is diagnosed at an advanced stage, which renders surgical resection an inappropriate option. Adjuvant concurrent chemoradiotherapy (CCRT) with surgery is considered the

Abbreviations: AJCC, American Joint Committee on Cancer; BMI, Body mass index; CCR, Concurrent chemoradiotherapy; CIs, confidence intervals; DFS, Disease-free survival; DNA-PKcs, DNA-dependent protein kinase; DSB, Double-strand break; HRs, hazard ratios; NHEJ, Non-homologous end-joining; OS, Overall survival; OSCC, Oral squamous cell carcinoma; SNPs, Single-nucleotide polymorphisms; TNM, Tumor, nodes, and metastasis.

* Corresponding authors at: School of Public Health, College of Public Health, Taipei Medical University, 250 Wu-Hsing Street, Taipei 11031, Taiwan (C.-C. Yeh), Department of Otolaryngology, Head and Neck Surgery, Chang Gung Memorial Hospital, Linkou, Taiwan. No. 5, Fuxing St., Guishan Dist., Taoyuan City 33305, Taiwan (S.-F. Huang).

E-mail addresses: shiangfu.huang@gmail.com (S.-F. Huang), ccyeh@tmu.edu.tw (C.-C. Yeh).

<https://doi.org/10.1016/j.gene.2020.145283>

Received 27 March 2020; Received in revised form 15 October 2020; Accepted 26 October 2020

Available online 1 November 2020

0378-1119/© 2020 Elsevier B.V. All rights reserved.

standard treatment for such cases. However, the 5-year overall survival (OS) of these patients is generally poor (Hill and Price, 1994; Zini et al., 2010; Amit et al., 2013). A genetic basis for tumor cell response to ionizing radiation and platinum-based agents in cancer therapy has been hypothesized (Mladenov et al., 2013; Srivastava and Raghavan, 2015) because patients receiving similar treatment respond differently to chemotherapy and radiotherapy. Therefore, the identification of genetic biomarkers for patients with advanced OSCC may help identify patients who may benefit from CCRT.

The DNA double-strand break (DSB) repair mechanism constitutes a crucial part of the DNA damage repair system that constitutes the biological basis for radiotherapy and chemotherapy with platinum-based agents—tumor cells are more sensitive than are normal cells to DSBs (Mladenov et al., 2013). Two primary mechanisms for recognizing and repairing DSBs are homologous recombination and nonhomologous end-joining (NHEJ). Several key proteins such as RAD51 and its paralogs (XRCC2, XRCC3, RAD51B, RAD51C, and RAD51D) have been identified as participating in the homologous recombination repair process (Liu et al., 1998; San Filippo et al., 2008). XRCC5, which participates in multiple processes, together with PRKDC proteins plays a crucial role in the NHEJ repair mechanism (Sishc and Davis, 2017). Studies on genetic variants have shown that the genetic background of an individual plays a key role in their response to cancer treatment and survival (Carrassa and Damia, 2017). In addition, single-nucleotide polymorphisms (SNPs) in DSB repair genes may modulate the repair capacity of proteins coded by these genes through their expression, which ultimately influences patient survival (Li et al., 2006; Costa et al., 2008; Liu et al., 2008; Yin et al., 2011). The genetic variant *RAD51* rs1801320 is associated with OS in patients with non-small-cell lung cancer who received definitive radiochemotherapy (Yin et al., 2011) and survival in patients with acute myelocytic leukemia treated with chemotherapy (Liu et al., 2008). *XRCC3* rs861539 is correlated with clinical outcomes in pancreatic cancer (Li et al., 2006) and acute myelocytic leukemia (Liu et al., 2008). The variant *XRCC2* rs3218536 is associated with OS in patients with pancreatic cancer (Li et al., 2006) and patients with non-small-cell lung cancer who received definitive radiochemotherapy (Yin et al., 2011).

Because the variant of DSB repair genes may affect the response of cancer cells to CCRT (Li et al., 2006; Costa et al., 2008; Liu et al., 2008; Yin et al., 2011), these variants may be key predictive factors for CCRT treatment outcomes. Based on these observations, we conducted a retrospective cohort study to investigate the association between the variants of DSB repair genes and the survival of patients with advanced OSCC who received adjuvant CCRT. Five SNPs (*XRCC2* rs2040639, *XRCC3* rs861539, *RAD51* rs1801320, *XRCC5* rs1051677, and *PRKDC* rs7003908) in key DSB genes were genotyped, and their associations with clinical outcomes were investigated in alternative genetic models, namely codominant, additive, dominant, recessive, and allelic models.

2. Materials and methods

2.1. Ethics statement

The Ethics Review Committees of Taipei Medical University (IRB No. N201802083) and Chang Gung Memorial Hospital (IRB No. 201800213B0) approved the study. All patients provided written informed consent after receiving detailed explanations of the study objectives.

2.2. Study population

Patients were recruited from the Head and Neck Surgery Department, Chang Gung Memorial Hospital, Linkou, Taiwan. The patients were entered in the cancer registry of the department from 1999 to 2016. The procedure for patient recruitment and data collection has been previously described (Senghore et al., 2019). In summary, the registry included 2528 patients; however, after excluding patients with

incomplete information ($n = 63$), those without blood specimens ($n = 105$), those who did not receive CCRT ($n = 1974$), those with tumor stage I or II ($n = 12$), those in whom the genotyping experiment failed ($n = 7$), those of aboriginal ethnicity ($n = 13$), and female patients ($n = 35$), a total of 319 patients were considered eligible, and their data were included in the analysis. The sociodemographic and clinical data of the patients were obtained through an interviewer-administered questionnaire and from their medical history and laboratory test results. The information included age, ethnicity, education, lifestyle habits (past and current history of smoking, alcohol drinking, and betel quid chewing), and family history of cancer. The weight and height of the patients were also measured, and body mass index (BMI) was calculated as weight/height² (kg/m²). Clinical and laboratory information included blood chemistry, abdominal ultrasound, and whole-body bone scan or positron emission tomography scan, magnetic resonance imaging, or computed tomography of the head and neck. The tumors of the patients were assessed for stage; depth; level of tissue differentiation; nodal and extranodal status; and perineural, vascular, and lymphatic invasions. The tumor, nodes, and metastasis (TNM) staging system of the Seventh Edition of the American Joint Committee on Cancer (AJCC; Edge and Compton, 2010) was used for tumor staging. Only the patients who were confirmed to have OSCC with TNM stages III and IV were included in this study.

2.3. SNP selection and genotyping

Five key genetic variants in *XRCC2* (rs2040639), *XRCC3* (rs861539),

Table 1
Demographic and clinical characteristics of male patients with OSCC who were treated with CCRT.

Variable	Number (n = 319)	%
Mean age (SD), years	49.72 (9.8)	
Age, years		
<50	164	51.41
≥50	155	48.59
Mean BMI (SD), kg/m ²	23.81 (3.9)	
BMI, kg/m ²		
<18.5	22	6.90
18.5–23.9	157	49.22
≥24	140	43.89
Ethnicity		
Taiwanese	230	72.10
Hakka	72	22.57
Mainland Chinese	17	5.33
Cigarette smoking	272	85.27
Alcohol drinking	221	69.28
Betel quid chewing	275	86.21
Tea drinking	156	48.90
Coffee drinking	76	23.82
Tumor differentiation		
Well	51	16.14
Moderate	210	66.45
Poor	55	17.41
Primary tumor size		
T1	26	8.15
T2	96	30.09
T3	38	11.91
T4	159	49.84
Nodal involvement		
N0	30	11.91
N+	281	88.09
Perineural invasion	177	55.49
Vascular invasion	19	5.96
Lymphatic invasion	40	12.54
Extranodal extension	205	64.26
Pathological TNM Stage		
III	42	13.17
IV	277	86.83

SD, standard deviation; BMI, body mass index; OSCC, oral squamous cell carcinoma; CCRT, concurrent chemoradiotherapy.

Table 2

Univariate association between demographic and clinical factors and survival from OSCC in male patients treated with adjuvant CCRT.

Variable	No.	Event	OS		Event	DFS	
			HR (95% CI)	p value		HR (95% CI)	p value
Age, years							
<50	164	54	1.00		69	1.00	
≥50	155	40	0.71 (0.47–1.07)	0.104	60	0.82 (0.57–1.16)	0.262
Ethnicity							
Taiwanese	230	69	1.00		98	1.00	
Hakka	72	19	0.93 (0.56–1.56)	0.786	19	0.64 (0.39–1.04)	0.073
Mainland Chinese	17	6	1.25 (0.54–2.88)	0.601	12	1.80 (0.99–3.29)	0.056
BMI, kg/m ²							
18.5–23.9	157	53	1.00		66	1.00	
<18.5	22	7	0.90 (0.41–1.97)	0.787	11	1.44 (0.76–2.72)	0.269
≥24	140	34	0.66 (0.43–1.02)	0.058	52	0.82 (0.57–1.20)	0.306
Smoking cigarettes							
Never	47	16	1.00		20	1.00	
Ever	272	78	0.89 (0.51–1.53)	0.661	109	0.96 (0.59–1.57)	0.874
Drinking alcohol							
Never	98	31	1.00		41	1.00	
Ever	221	63	1.00 (0.65–1.54)	0.994	88	1.00 (0.69–1.46)	1.000
Chewing betel quid							
Never	44	13	1.00		15	1.00	
Ever	275	81	0.96 (0.54–1.73)	0.900	114	1.37 (0.79–2.39)	0.268
Drinking tea							
Never	163	50	1.00		63	1.00	
Ever	156	44	0.82 (0.55–1.24)	0.359	66	1.06 (0.75–1.51)	0.745
Drinking coffee							
Never	243	78	1.00		93	1.00	
Ever	76	16	0.63 (0.37–1.07)	0.088	36	1.26 (0.85–1.86)	0.249
Tumor differentiation							
Well	51	19	1.00		24	1.00	
Moderate	210	61	0.92 (0.55–1.53)	0.735	80	0.89 (0.56–1.42)	0.622
Poor	55	13	0.81 (0.40–1.63)	0.550	24	1.14 (0.64–2.02)	0.662
Primary tumor size							
T1–T2	160	43	1.00		59	1.00	
T3–T4	159	51	1.41 (0.93–2.13)	0.102	70	1.47 (1.03–2.09)	0.034*
Nodal involvement							
N0	102	19	1.00		35	1.00	
N+	217	75	3.76 (1.38–10.26)	0.010*	94	1.36 (0.78–2.38)	0.280
Perineural invasion							
No	142	41	1.00		56	1.00	
Yes	177	53	1.15 (0.77–1.74)	0.493	73	1.19 (0.83–1.70)	0.340
Vascular invasion							
No	300	86	1.00		122	1.00	
Yes	19	8	1.51 (0.73–3.13)	0.266	7	0.94 (0.44–2.02)	0.876
Lymphatic invasion							
No	279	75	1.00		110	1.00	
Yes	40	19	2.22 (1.32–3.72)	0.003*	19	1.37 (0.82–2.30)	0.224
Extranodal extension							
No	114	14	1.00		36	1.00	
Yes	205	80	3.78 (2.14–6.68)	<0.0001*	93	1.87 (1.26–2.78)	0.002*
Pathological TNM Stage							
III	42	10	1.00		14	1.00	
IV	277	84	1.62 (0.83–3.15)	0.154	115	1.66 (0.93–2.94)	0.086

BMI, body mass index; HR, hazard ratio; CI, confidence interval; OSCC, oral squamous cell carcinoma; CCRT, concurrent chemoradiotherapy; OS, overall survival; DFS, disease-free survival *Significance at $p < 0.05$

RAD51 (rs1801320), *XRCC5* (rs1051677), and *PRKDC* (rs7003908) genes involved in DSB repair pathways were selected through a literature review and based on their effects on cancers (Yen et al., 2008; Yin et al., 2011; Cheng-Hong et al., 2015; Hu et al., 2016). We further conducted network analysis of these genes on GeneMANIA (<https://genemania.org/>), a bioinformatic web interface for generating gene interaction networks. The query returned physical interaction, coexpression, prediction, colocation, and pathway values of 67.6%, 13.5%, 6.4%, 6.2%, and 4.4%, respectively. Using the standard phenol–chloroform method, genomic DNA was extracted from the buffy coat and prepared for genotyping. Genotyping was performed using the Sequenom iPLEX MassARRAY System (Sequenom, Inc., San Diego, CA, USA), as previously described (Senghore et al., 2019). For quality control, a 10% random sample that showed 100% concordance for all SNPs was reanalyzed.

2.4. Patient treatment and follow-up

All patients underwent surgery that entailed radical tumor excision with neck dissection following preoperative tumor surgery. The primary tumors were resected 1 cm above the safety margins, whereas neck dissection was performed as per the examination status. Bilateral neck dissection was performed if the lesion was deeply invasive and crossing the midline, as in tongue cancer. CCRT was performed at a radiation dose of 6000–6600 cGy, with 40–60 mg/m² intravenous cisplatin administered biweekly or triweekly and oral 5-fluorouracil administered for 4–8 weeks after surgery. During and after treatment, the patients underwent monthly clinical and radiological examinations for the first 6 months, twice-monthly examinations for the next 6 months, thrice-monthly evaluations within the second year, and, finally, evaluations every 6 months. History of biopsy or imaging was used to confirm any

case of relapse, and death from OSCC was confirmed based on the death certificates of the patients.

2.5. Statistical analysis

The baseline characteristics of the patients are summarized as means and standard deviations for continuous variables and as frequency and proportions for categorical variables. The major clinical endpoint was OS or disease-free survival (DFS). DFS was defined as the time (in months) from the date of treatment commencement to the date of recurrence, metastasis, or death from any cause. OS was defined as the time (in months) from the date of treatment commencement to the date of death. Any patient without an event at the time of the last contact was censored or was considered to be a case of administrative censoring by the last date of follow-up (April 10, 2019). The hazard ratios (HRs) with 95% confidence intervals (CIs) were calculated using Cox proportional hazards regression models to evaluate the influence of various genotypes on OS or DFS. The models were adjusted for clinicopathological variables that were significant at $p < 0.10$ in the univariate model. Several genetic models were constructed to evaluate the effect of various genotypes on survival; specifically, these were codominant, additive, dominant, recessive, and allelic models. Owing to the significant association of *XRCC2* rs2040639 with DFS, its interaction with other SNPs was further assessed using the likelihood ratio test. Kaplan–Meier survival curves and the log-rank test were used to evaluate the effect of various genotypes on the cumulative probability of OS and DFS. We performed linkage disequilibrium (LD) analysis of the selected SNPs using Haploview (version 4.2, Board Institute, Cambridge, MA, USA). For two SNPs found to be in high LD, further haplotype analysis was performed using PHASE software (version 2.1). Two-tailed p values were reported in all cases, and $p < 0.05$ indicated statistical significance. SAS software (version 9.4; SAS Institute, Cary, NC, USA) was used for all statistical analyses.

3. Results

3.1. Population characteristics

Table 1 shows the demographic and clinical characteristics of the 319 men with OSCC who received adjuvant CCRT. Their mean age was

49.72 \pm 9.8 years, and the majority of them (51%) were younger than 50 years. Their mean BMI was 23.81 \pm 3.9 kg/m², and almost half of them (49.22%) had a normal BMI. The patients were predominantly (72.10%) of Taiwanese ethnicity. Over two-thirds of the patients smoked cigarettes (85.27%), consumed alcohol (69.28%), or chewed betel quid (86.21%). Tumors were poorly differentiated in 17.41% of the patients; almost half of the patients (49.84%) had stage T4 primary tumors, and 88.09% of them had nodal involvement. Perineural invasion, extranodal extension, and pathological TNM stage IV were present in 55.49%, 64%, and 86.83% of the patients, respectively.

The entire follow-up duration was 199 months, with mean OS and DFS times of 16 and 13 months, respectively. The clinical factors associated with OS or DFS in the univariate analysis are presented in Table 2. Nodal involvement (HR = 3.76, 95% CI = 1.38–10.26; $p = 0.010$), lymphatic invasion (HR = 2.22, 95% CI = 1.32–3.72; $p = 0.003$), and extranodal extension (HR = 3.78, 95% CI = 2.14–6.68; $p < 0.0001$) were associated with an increased mortality risk, whereas T3 to T4 primary tumor stage (HR = 1.47, 95% CI = 1.03–2.09; $p = 0.034$) and extranodal extension (HR = 1.87, 95% CI = 1.26–2.78; $p = 0.002$) were associated with an increased risk of recurrence.

3.2. Association between DSB repair SNPs and OSCC survival

Fig. 1 shows the Kaplan–Meier survival curves and log-rank test for the association between *XRCC1* rs2040639 and DFS. A marginally significant difference was observed in DFS (log-rank test: $p = 0.0702$). However, no statistically significant difference was observed in OS (log-rank test: $p = 0.9599$; Supplementary Fig. 1). Table 3 shows the genotype distribution of SNPs and the association between genotypes and OS or DFS. In the univariate analysis, no statistically significant association was observed between the selected SNPs and OS or DFS. However, the *XRCC2* rs2040639 polymorphism in the codominant model (AA compared with GG, HR = 0.55, 95% CI = 0.31–0.98; $p = 0.044$), additive model (HR = 0.77, 97% CI = 0.59–0.99; $p = 0.044$), and allelic model (HR = 0.77, 95% CI = 0.59–0.99; $p = 0.045$) was a favorable prognostic factor for DFS. After adjustment in the multivariate analysis, statistical significance remained for *XRCC2* rs2040639 in the codominant (HR = 0.55, 95% CI = 0.31–0.98; $p = 0.042$), additive (HR = 0.77, 95% CI = 0.60–1.00; $p = 0.048$), and allelic models (HR = 0.77, 95% CI = 0.59–1.00; $p = 0.048$). The A-allele carriers exhibited a protective

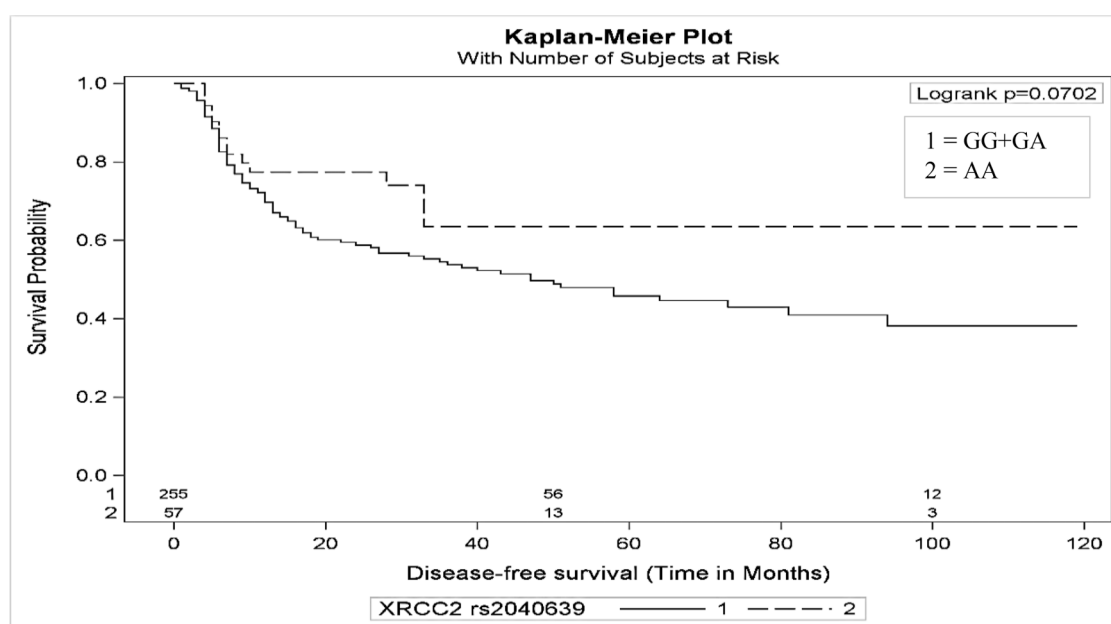


Fig. 1. Kaplan–Meier survival curves and log-rank test of disease-free survival for *XRCC1* rs2040639. The AA genotype showed marginally significantly longer survival time than that of the GG + GA genotype (log-rank test $p = 0.0702$).

effect for DFS. A marginally significant interaction was observed between *XRCC2* rs2040639 and *PRKDC* rs7003908 ($p = 0.050$). The combination of rs2040639 AA and rs7003908 AA genotypes (HR = 0.36, 95% CI = 0.17–0.79; $p = 0.010$) was a favorable prognostic factor for DFS (Table 4). No significant interaction was observed between other SNPs (data not shown). The results of the LD analysis showed that *XRCC2* rs2040639 and *RAD51* rs1801320 ($D' = 91$ and $R^2 = 1$) were in high LD (Supplementary Fig. 2). We constructed a haplotype LD block to explore their effects on survival (Supplementary Table 1). However, these analyses did not yield any statistically significant results.

4. Discussion

The DNA DSB repair system is a critical process for maintaining genomic stability (Aparicio et al., 2014; Srivastava and Raghavan, 2015). Its inactivation may lead to uncontrolled cell growth and an

increased risk of tumor development (Aparicio et al., 2014). However, the DSB repair system may affect the efficacy of CCRT by allowing the repair of damaged DNA in tumor cells (Carrassa and Damia, 2017), thereby affecting patient survival. In this retrospective cohort study, we investigated the contributions of five SNPs in the DNA DSB repair genes to the survival of Taiwanese patients with OSCC. We observed that *XRCC2* rs2040639 was a favorable prognostic factor for DFS. A marginally significant interaction of *XRCC2* rs2040639 and *PRKDC* rs7003908 with DFS was observed, and the AA genotype carriers of both SNPs exhibited a lower risk of recurrence than did the carriers of other genotypes. Thus, to the best of our knowledge, this is the first study to show that the A-allele of *XRCC2* rs2040639 is a crucial factor in the survival of patients with OSCC.

Both radiotherapy and chemotherapy introduce DSBs that are repaired by the DSB repair mechanism. The *XRCC2* protein is a core component of the DSB homologous recombination repair system and a

Table 3

Association between DSB repair candidate SNPs and overall and disease-free survival in patients with OSCC who were treated with adjuvant CCRT.

SNP	No	Event	OS				Event	DFS			
			Univariate		Multivariate ^a			Univariate		Multivariate ^b	
			HR (95% CI)	p-value	HR (95% CI)	p value		HR (95% CI)	p value	HR (95% CI)	p value
XRCC2											
rs2040639											
GG	102	30	1.00		1.00		49	1.00		1.00	
GA	159	48	1.03 (0.65–1.63)	0.907	1.01 (0.63–1.60)	0.981	64	0.83 (0.57–1.21)	0.336	0.86 (0.59–1.26)	0.438
AA	58	16	1.02 (0.55–1.86)	0.961	1.03 (0.56–1.91)	0.927	16	0.55 (0.31–0.98)	0.044*	0.55 (0.31–0.98)	0.042*
Additive model			0.99 (0.73–1.34)	0.961	1.01 (0.75–1.37)	0.932		0.77 (0.59–0.99)	0.044*	0.77 (0.60–1.00)	0.048*
Dominant model	217	64	1.03 (0.66–1.58)	0.913	1.01 (0.65–1.58)	0.959	80	0.76 (0.53–1.08)	0.127	0.77 (0.53–1.11)	0.159
Recessive model	58	16	1.00 (0.58–1.71)	0.997	1.03 (0.59–1.77)	0.927	16	0.61 (0.36–1.05)	0.077	0.60 (0.35–1.03)	0.062
A-allele			1.01 (0.76–1.35)	0.943	1.01 (0.76–1.36)	0.934		0.77 (0.59–0.99)	0.045*	0.77 (0.59–1.00)	0.048*
XRCC3											
rs861539											
CC	281	87	1.00		1.00		116	1.00		1.00	
CT	37	7	0.66 (0.31–1.44)	0.299	0.75 (0.34–1.64)	0.469	13	0.84 (0.46–1.52)	0.565	0.79 (0.43–1.46)	0.458
TT	1	0	–	0.985	–	0.987	0	–	0.981	–	0.981
Additive model			0.63 (0.30–1.34)	0.229	0.73 (0.34–1.57)	0.416		0.78 (0.44–1.38)	0.391	0.74 (0.41–1.35)	0.328
Dominant model	37	7	0.64 (0.30–1.38)	0.254	0.74 (0.34–1.61)	0.440	13	0.80 (0.44–1.45)	0.465	0.76 (0.41–1.40)	0.383
Recessive model	1	0	–	0.985	–	0.987	0	–	0.981	–	0.981
T-allele			0.63 (0.29–1.33)	0.225	0.73 (0.34–1.57)	0.424		0.77 (0.43–1.38)	0.385	0.75 (0.42–1.35)	0.333
RAD51											
rs1801320											
GG	228	69	1.00		1.00		97	1.00		1.00	
GC	84	24	0.97 (0.61–1.55)	0.908	0.98 (0.61–3.23)	0.918	30	0.85 (0.56–1.29)	0.445	0.90 (0.59–1.38)	0.619
CC	7	1	0.48 (0.07–3.47)	0.469	0.45 (0.06–3.23)	0.423	2	0.61 (0.15–2.47)	0.488	0.62 (0.15–2.54)	0.504
Additive model			0.91 (0.60–1.37)	0.638	0.90 (0.59–1.36)	0.607		0.83 (0.58–1.20)	0.322	0.87 (0.60–1.25)	0.443
Dominant model	91	25	0.93 (0.59–1.48)	0.772	0.93 (0.59–1.48)	0.758	32	0.83 (0.55–1.25)	0.366	0.87 (0.57–1.32)	0.513
Recessive model	7	1	0.49 (0.07–3.48)	0.472	0.45 (0.06–3.24)	0.426	2	0.63 (0.16–2.57)	0.523	0.63 (0.15–2.60)	0.525
C-allele			0.91 (0.60–1.37)	0.640	0.90 (0.59–1.36)	0.608		0.83 (0.58–1.20)	0.321	0.87 (0.60–1.25)	0.443
XRCC5											
rs1051677											
TT	243	75	1.00		1.00		101	1.00		1.00	
TC	73	18	0.79 (0.47–1.32)	0.361	0.86 (0.51–1.45)	0.575	28	0.82 (0.53–1.26)	0.367	0.89 (0.57–1.37)	0.591
CC	3	1	0.88 (0.12–6.34)	0.897	0.71 (0.10–5.17)	0.735	0	–	0.980	–	0.980
Additive model			0.81 (0.51–1.30)	0.386	0.86 (0.54–1.37)	0.521		0.75 (0.50–1.13)	0.171	0.78 (0.52–1.18)	0.235
Dominant model	76	19	0.79 (0.48–1.31)	0.362	0.85 (0.51–1.42)	0.537	28	0.78 (0.50–1.20)	0.253	0.82 (0.53–1.27)	0.382
Recessive model	3	1	0.93 (0.13–6.67)	0.939	0.73 (1.00–5.31)	0.096	0	–	0.980	–	0.980
C-allele			0.82 (0.51–1.30)	0.398	0.86 (0.54–1.37)	0.524		0.76 (0.50–1.14)	0.181	0.78 (0.52–1.18)	0.237
PRKDC											
rs7003908											
AA	212	67	1.00		1.00		88	1.00		1.00	
AC	93	25	0.86 (0.54–1.36)	0.520	0.82 (0.52–1.31)	0.410	36	0.98 (0.66–1.45)	0.928	0.91 (0.61–1.35)	0.635
CC	14	2	0.41 (0.10–1.67)	0.213	0.68 (0.16–2.89)	0.601	5	0.88 (0.36–2.17)	0.782	1.22 (0.48–3.10)	0.678
Additive model			0.78 (0.53–1.14)	0.203	0.82 (0.55–1.24)	0.346		0.96 (0.71–1.32)	0.813	0.98 (0.71–1.35)	0.892
Dominant model	107	27	0.80 (0.51–1.25)	0.316	0.81 (0.52–1.27)	0.362	41	0.97 (0.67–1.41)	0.867	0.94 (0.65–1.37)	0.743
Recessive model	14	2	0.43 (0.11–1.74)	0.235	0.72 (0.17–3.04)	0.653	5	0.89 (0.36–2.17)	0.789	1.25 (0.49–3.16)	0.639
C-allele			0.77 (0.52–1.14)	0.188	0.83 (0.56–1.24)	0.357		0.96 (0.70–1.33)	0.811	0.98 (0.71–1.35)	0.893

BMI, body mass index; HR, hazard ratio; CI, confidence interval; DSB, double-strand break; SNP, single-nucleotide polymorphism; OSCC, oral squamous cell carcinoma; CCRT, concurrent chemoradiotherapy; OS, overall survival; DFS, disease-free survival

*Significance at $p < 0.05$

^a Adjusted for age, BMI, drinking coffee, nodal involvement, lymphatic invasion, and extranodal extension

^b Adjusted for age, ethnicity, primary tumor size, extranodal extension and pathological TNM stage

Table 4Interaction between *XRCC2* rs2040639 and *PRKDC* rs7003908 on the prognosis of OSCC in patients treated with CCRT.

<i>XRCC2</i>	<i>PRKDC</i>	No.	Event	OS		Event	DFS	
rs2040639	rs7003908			HR (95% CI) ^a	<i>p</i> value		HR (95% CI) ^b	<i>p</i> value
GG	AA	68	21	1.00		35	1.00	
GG	AC	30	8	0.67 (0.29–2.05)	0.340	14	0.67 (0.35–1.26)	0.211
GG	CC	4	1	1.57 (0.21–12.05)	0.662	0	–	0.982
GA	AA	104	37	0.97 (0.55–1.69)	0.900	44	0.72 (0.45–1.15)	0.175
GA	AC	46	10	0.78 (0.36–1.67)	0.523	15	0.65 (0.35–1.20)	0.165
GA	CC	9	1	0.45 (0.06–3.46)	0.444	5	1.31 (0.49–3.48)	0.590
AA	AA	40	9	0.87 (0.39–1.91)	0.724	9	0.36 (0.17–0.79)	0.010*
AA	AC	17	7	1.02 (0.42–2.49)	0.968	7	0.74 (0.32–1.67)	0.461
AA	CC	1	0	–	0.986	0	–	0.987
<i>p</i> for interaction				0.685			0.050	

BMI, body mass index; HR, hazard ratio; CI, confidence interval; OSCC, oral squamous cell carcinoma; CCRT, concurrent chemoradiotherapy; OS, overall survival; DFS, disease-free survival.

* Significance at $p < 0.05$.

^a Adjusted for age, BMI, coffee drinking, N stage, lymphatic invasion and extracapsular spread.

^b Adjusted for age, ethnicity, T size, extracapsular spread and pathological TNM stage.

member of the RecA/RAD51-related protein family that is essential for chromosome stability and DSB repair (Liu et al., 1998; Heyer et al., 2010). Evidence suggests that *XRCC2* is pivotal in DSB repair and is sensitive to chemotherapeutic agents (Liu et al., 1998; Johnson et al., 1999). For instance, compared with parental cells, *XRCC2*-deficient cells were shown to have reduced homologous recombination repair capacity (Johnson et al., 1999), and the loss of *XRCC2* protein expression was found to sensitize cells to DSB-damaging agents (Liu et al., 1998). In this study, the A-allele carriers of *XRCC2* rs2040639 showed a lower risk of recurrence than did noncarriers. rs2040639 is an upstream variant located in the promoter region of *XRCC2*, and it may affect gene expression through transcription, mRNA decay, or RNA interference (Rana, 2007; Wang et al., 2008; de Vooght et al., 2009). This could lead to reduced DSB homologous recombination repair capacity and sensitivity to CCRT and a subsequent low risk of recurrence. However, direct evidence to collaborate or contradict our findings is lacking; we were unable to find previous studies on *XRCC2* rs2040639 and cancer survival. Most reported studies have focused on other neighboring SNPs or cancer risk (Yen et al., 2008; Garcia-Quispes et al., 2011; Lin et al., 2011).

PRKDC operates in the NHEJ DNA repair pathway and encodes the catalytic subunit of DNA-dependent protein kinase (DNA-PKcs); this kinase functions with the Ku70/Ku80 heterodimer protein in DNA DSB repair (Sishc and Davis, 2017). In PRKDC, rs7003908 is an intron variant that was previously found to be associated with the survival of patients with high-grade glioma (Hu et al., 2016). In our study, we did not observe any significant association between rs7003908 and survival, possibly due to the small number of the patients with the homozygous variant genotype. However, in the gene–gene interaction analysis, PRKDC rs7003908 exhibited a marginally significant interaction with *XRCC2* rs2040639. The patients carrying the AA and AA genotypes of both SNPs had a significantly lower risk of recurrence than did those carrying other genotypes. Previous evidence has shown that PRKDC is highly expressed in several advanced cancer types (Hosoi et al., 2004; Tonotsuka et al., 2006). The suppression of DNA-PKcs was found to inhibit tumor metastasis (Goodwin et al., 2015). Hu et al. found that patients with the AA genotype of rs7003908 had a lower risk of recurrence than did patients with other genotypes (Hu et al., 2016). Thus, in our study, the results revealed that the AA genotype of rs7003908 interacted with the AA genotype of rs2040639 to reduce the repair capacity of tumor cells, leading to chemo- and radio-sensitivity and resulting in a relatively low risk of recurrence.

In this study, we did not observe any significant association between SNPs in *XRCC3*, *RAD51*, and *XRCC5* and survival in OSCC. Research on the association between these SNPs and survival in oral cancer is scant, and the results of studies on other cancer types are inconsistent (Liu

et al., 2008, 2012; Ruzzo et al., 2008). For instance, *XRCC3* rs861539 was associated with survival in patients with various cancers, including myelocytic leukemia (Liu et al., 2008), pancreatic cancer (Li et al., 2006), and advanced colorectal cancer (Ruzzo et al., 2008), whereas no association was observed in patients with colorectal cancer who underwent chemotherapy (Liu et al., 2012; Negandhi et al., 2013). In patients with non-small-cell lung cancer who received definitive radiochemotherapy, *RAD51* rs1801320 was associated with OS (Yin et al., 2011). The aforementioned findings are related to various cancer types; therefore, they are not comparable with our results. In addition, the differences between these results and our results may be attributed to differences in sample sizes, ethnicities, and treatment modalities. Thus, additional studies may be required to clarify our findings.

This study has several limitations. First, not all SNPs in the DSB repair system were included in the study; other SNPs may affect survival. Second, the small number of patients carrying certain genotypes, particularly the homozygous variants, may have led to the nonsignificant associations observed for other SNPs. Finally, the generalizability of our results may be limited because all participants were recruited from a single hospital. The strength of our study lies in its long follow-up period and the use of a homogenous sample. All participants were men with similar tumor stages who received similar treatment, thus eliminating the effects of these factors on survival.

5. Conclusion

In this study, we investigated the effects of DNA DSB repair genetic variants on the survival of Taiwanese men with advanced OSCC and found that the A-allele carriers of *XRCC2* rs2040639 showed a lower risk of recurrence than did the noncarriers. In addition, both the *XRCC2* rs2040639 and PRKDC rs7003908 carriers of the AA genotypes had a lower risk of recurrence than did the noncarriers. These findings support the role of these two genotypes in the survival of patients with OSCC. Patients carrying these alleles may benefit from CCRT. However, additional studies with large samples are warranted.

Funding

This work was supported by the Ministry of Science and Technology, Taiwan [MOST 107-2314-B-038-071, MOST 108-2314-B-038-088, and MOST 106-2314-B-182-025-MY3], the Health and Welfare Surcharge on Tobacco Products, Ministry of Health and Welfare [MOHW109-TDU-B-212-134016]; and Chang Gung Memorial Hospital [CMRPG3H0793, CMRPG3J0591, CMRPG3J0592, and CMRPG3J0593]. The funders had no role in the conduct of the research and/or preparation of the article and in the decision to submit the article for publication.

CRedit authorship contribution statement

Thomas Senghore: Data curation, Formal analysis, Methodology, Validation, Writing - original draft, Writing - review & editing. **Wen-Chang Wang:** Conceptualization, Methodology, Writing - review & editing. **Huei-Tzu Chien:** Data curation, Investigation, Resources, Validation. **You-Xin Chen:** Data curation, Formal analysis, Resources, Validation. **Chi-Kuang Young:** Investigation, Resources. **Shiang-Fu Huang:** Conceptualization, Funding acquisition, Methodology, Supervision, Writing - review & editing. **Chih-Ching Yeh:** Conceptualization, Funding acquisition, Methodology, Project administration, Supervision, Writing - review & editing.

Declaration of Competing Interest

The authors declare that they have no known competing financial interests or personal relationships that could have appeared to influence the work reported in this paper.

Acknowledgements

The authors are thankful to the study participants. This manuscript was edited by Wallace Academic Editing.

Appendix A. Supplementary data

Supplementary data to this article can be found online at <https://doi.org/10.1016/j.gene.2020.145283>.

References

- Amit, M., Yen, T.C., Liao, C.T., Chaturvedi, P., Agarwal, J.P., Kowalski, L.P., Ebrahimi, A., Clark, J.R., Kreppel, M., Zoller, J., Fridman, E., Bolzoni, V.A., Shah, J. P., Binenbaum, Y., Patel, S.G., Gil, Z., 2013. Improvement in survival of patients with oral cavity squamous cell carcinoma: An international collaborative study. *Cancer* 119, 4242–4248.
- Aparicio, T., Baer, R., Gautier, J., 2014. DNA double-strand break repair pathway choice and cancer. *DNA Repair (Amst)* 19, 169–175.
- Carrassa, L., Damia, G., 2017. DNA damage response inhibitors: Mechanisms and potential applications in cancer therapy. *Cancer Treat. Rev.* 60, 139–151.
- Cheng-Hong, Y., Yu-Da, L., Ching-Yui, Y., Li-Yeh, C., Hsueh-Wei, C., 2015. A Systematic Gene-Gene and Gene-Environment Interaction Analysis of DNA Repair Genes XRCC1, XRCC2, XRCC3, XRCC4, and Oral Cancer Risk. *OMICS* 19, 238–247.
- Chiang, C.J., Lo, W.C., Yang, Y.W., You, S.L., Chen, C.J., Lai, M.S., 2016. Incidence and survival of adult cancer patients in Taiwan, 2002–2012. *J. Formos. Med. Assoc.* 115, 1076–1088.
- Costa, S., Pinto, D., Pereira, D., Rodrigues, H., Cameselle-Teijeiro, J., Medeiros, R., Schmitt, F., 2008. XRCC1 Arg399Gln and RAD51 5'UTR G135C polymorphisms and their outcome in tumor aggressiveness and survival of Portuguese breast cancer patients. *Breast Cancer Res. Treat.* 109, 183–185.
- de Vooght, K.M.K., van Wijk, R., van Solinge, W.W., 2009. Management of Gene Promoter Mutations in Molecular Diagnostics. *Clin. Chem.* 55, 698–708.
- Edge, S.B. and Compton, C.C., 2010. The American Joint Committee on Cancer: the 7th edition of the AJCC cancer staging manual and the future of TNM. *Ann Surg Oncol* 17, 1471–1474.
- Garcia-Quispe, W.A., Perez-Machado, G., Akdi, A., Pastor, S., Galofre, P., Biarnes, F., Castell, J., Velazquez, A., Marcos, R., 2011. Association studies of OGG1, XRCC1, XRCC2 and XRCC3 polymorphisms with differentiated thyroid cancer. *Mutat. Res.* 709–710, 67–72.
- Goodwin, J.F., Kothari, V., Drake, J.M., Zhao, S., Dylgjeri, E., Dean, J.L., Schiewer, M.J., McNair, C., Jones, J.K., Aytes, A., Magee, M.S., Snook, A.E., Zhu, Z., Den, R.B., Birbe, R.C., Gomella, L.G., Graham, N.A., Vashisht, A.A., Wohlschlegel, J.A., Graeber, T.G., Karnes, R.J., Takhar, M., Davicioni, E., Tomlins, S.A., Abate-Shen, C., Sharifi, N., Witte, O.N., Feng, F.Y., Knudsen, K.E., 2015. DNA-PKcs-Mediated Transcriptional Regulation Drives Prostate Cancer Progression and Metastasis. *Cancer Cell* 28, 97–113.
- Heyer, W.D., Ehmsen, K.T., Liu, J., 2010. Regulation of homologous recombination in eukaryotes. *Annu. Rev. Genet.* 44, 113–139.
- Hill, B.T., Price, L.A., 1994. Lack of survival advantage in patients with advanced squamous cell carcinomas of the oral cavity receiving neoadjuvant chemotherapy prior to local therapy, despite achieving an initial high clinical complete remission rate. *Am. J. Clin. Oncol.* 17, 1–5.
- Hosoi, Y., Watanabe, T., Nakagawa, K., Matsumoto, Y., Enomoto, A., Morita, A., Nagawa, H., Suzuki, N., 2004. Up-regulation of DNA-dependent protein kinase activity and Sp1 in colorectal cancer. *Int. J. Oncol.* 25, 461–468.
- Hu, M., Du, J., Cui, L., Huang, T., Guo, X., Zhao, Y., Ma, X., Jin, T., Li, G., Song, J., 2016. IL-10 and PRKDC polymorphisms are associated with glioma patient survival. *Oncotarget* 7, 80680–80687.
- Johnson, R.D., Liu, N., Jasin, M., 1999. Mammalian XRCC2 promotes the repair of DNA double-strand breaks by homologous recombination. *Nature* 401, 397–399.
- Li, D., Liu, H., Jiao, L., Chang, D.Z., Beinart, G., Wolff, R.A., Evans, D.B., Hassan, M.M., Abbruzzese, J.L., 2006. Significant effect of homologous recombination DNA repair gene polymorphisms on pancreatic cancer survival. *Cancer Res.* 66, 3323–3330.
- Lin, W.Y., Camp, N.J., Cannon-Albright, L.A., Allen-Brady, K., Balasubramanian, S., Reed, M.W.R., Hopper, J.L., Apicella, C., Giles, G.G., Southey, M.C., Milne, R.L., Arias-Perez, J.I., Menendez-Rodriguez, P., Benitez, J., Grundmann, M., Dubrowskaja, N., Park-Simon, T.W., Dork, T., Garcia-Closas, M., Figueroa, J., Sherman, M., Lissowska, J., Easton, D.F., Dunning, A.M., Rajaraman, P., Sigurdson, A.J., Doody, M.M., Linet, M.S., Pharoah, P.D., Schmidt, M.K., Cox, A., 2011. A role for XRCC2 gene polymorphisms in breast cancer risk and survival. *J. Med. Genet.* 48, 477–484.
- Liu, L., Yang, L., Zhang, Y., Xu, Z.F., Yu, M.H., Wang, J.X., Xiao, Z.J., 2008. Polymorphisms of RAD51(G135C) and XRCC3(C241T) genes and correlations thereof with prognosis and clinical outcomes of acute myeloid leukemia. *Zhonghua Yi Xue Za Zhi* 88, 378–382.
- Liu, N., Lamerdin, J.E., Tebbs, R.S., Schild, D., Tucker, J.D., Shen, M.R., Brookman, K.W., Siciliano, M.J., Walter, C.A., Fan, W., Narayana, L.S., Zhou, Z.Q., Adamson, A.W., Sorensen, K.J., Chen, D.J., Jones, N.J., Thompson, L.H., 1998. XRCC2 and XRCC3, new human Rad51-family members, promote chromosome stability and protect against DNA cross-links and other damages. *Mol. Cell* 1, 783–793.
- Liu, Y., Chen, H., Chen, L., Hu, C., 2012. Prediction of genetic polymorphisms of DNA repair genes XRCC1 and XRCC3 in the survival of colorectal cancer receiving chemotherapy in the Chinese population. *Hepatogastroenterology* 59, 977–980.
- Mladenov, E., Magin, S., Soni, A., Iliakis, G., 2013. DNA double-strand break repair as determinant of cellular radiosensitivity to killing and target in radiation therapy. *Front. Oncol.* 3, 113–113.
- Negandhi, A.A., Hyde, A., Dicks, E., Pollett, W., Younghusband, B.H., Parfrey, P., Green, R.C., Savas, S., 2013. MTHFR Glu429Ala and ERCC5 His46His Polymorphisms Are Associated with Prognosis in Colorectal Cancer Patients: Analysis of Two Independent Cohorts from Newfoundland. *PLoS ONE* 8, e61469.
- Rana, T.M., 2007. Illuminating the silence: understanding the structure and function of small RNAs. *Nat. Rev. Mol. Cell Biol.* 8, 23–36.
- Ruzzo, A., Graziano, F., Loupakis, F., Santini, D., Catalano, V., Bissoni, R., Ficarelli, R., Fontana, A., Andreoni, F., Falcone, A., Canestrari, E., Tonini, G., Mari, D., Lippe, P., Pizzagalli, F., Schiavon, G., Alessandrini, P., Giustini, L., Maltese, P., Testa, E., Menichetti, E.T., Magnani, M., 2008. Pharmacogenetic profiling in patients with advanced colorectal cancer treated with first-line FOLFIRI chemotherapy. *Pharmacogenomics* 9, 278–288.
- San Filippo, J., Sung, P., Klein, H., 2008. Mechanism of eukaryotic homologous recombination. *Annu. Rev. Biochem.* 77, 229–257.
- Senghore, T., Wang, W.C., Chien, H.T., Chen, Y.X., Young, C.K., Huang, S.F., Yeh, C.C., 2019. Polymorphisms of Mismatch Repair Pathway Genes Predict Clinical Outcomes in Oral Squamous Cell Carcinoma Patients Receiving Adjuvant Concurrent Chemoradiotherapy. *Cancers Basel*, 11.
- B.J. Sishc A.J. Davis The Role of the Core Non-Homologous End Joining Factors in Carcinogenesis and Cancer 2017 *Cancers (Basel)* 9.
- Srivastava, M., Raghavan, S.C., 2015. DNA Double-Strand Break Repair Inhibitors as Cancer Therapeutics. *Chem. Biol.* 22, 17–29.
- Tonotsuka, N., Hosoi, Y., Miyazaki, S., Miyata, G., Sugawara, K., Mori, T., Ouchi, N., Satomi, S., Matsumoto, Y., Nakagawa, K., Miyagawa, K., Ono, T., 2006. Heterogeneous expression of DNA-dependent protein kinase in esophageal cancer and normal epithelium. *Int. J. Mol. Med.* 18, 441–447.
- Wang, J.X., Lee, E.R., Morales, D.R., Lim, J., Breaker, R.R., 2008. Riboswitches that sense S-adenosylhomocysteine and activate genes involved in coenzyme recycling. *Mol. Cell* 29, 691–702.
- Yen, C.-Y., Liu, S.-Y., Chen, C.-H., Tseng, H.-F., Chuang, L.-Y., Yang, C.-H., Lin, Y.-C., Wen, C.-H., Chiang, W.-F., Ho, C.-H., Chen, H.-C., Wang, S.-T., Lin, C.-W., Chang, H.-W., 2008. Combinational polymorphisms of four DNA repair genes XRCC1, XRCC2, XRCC3, and XRCC4 and their association with oral cancer in Taiwan. *J. Oral Pathol. Med.* 37, 271–277.
- Yin, M., Liao, Z., Huang, Y.-J., Liu, Z., Yuan, X., Gomez, D., Wang, L.-E., Wei, Q., 2011. Polymorphisms of homologous recombination genes and clinical outcomes of non-small cell lung cancer patients treated with definitive radiotherapy. *PLoS ONE* 6, e20055-e20055.
- Zini, A., Czerninski, R., Sgan-Cohen, H.D., 2010. Oral cancer over four decades: epidemiology, trends, histology, and survival by anatomical sites. *J. Oral Pathol. Med.* 39, 299–305.

Available online at www.sciencedirect.com

ScienceDirect

journal homepage: www.jfda-online.com

Original Article

Polysaccharide-containing fraction from *Artemisia argyi* inhibits tumor cell-induced platelet aggregation by blocking interaction of podoplanin with C-type lectin-like receptor 2



Ching-Ping Tseng^{a,b,c,d,1}, Yu-Ling Huang^{e,1}, Yao-Wen Chang^{b,e},
Hsiang-Ruei Liao^{a,e,f}, Yu-Li Chen^e, Pei-Wen Hsieh^{a,e,f,g,*}

^a Graduate Institute of Biomedical Sciences, College of Medicine, Chang Gung University, Taoyuan 333, Taiwan

^b Department of Medical Biotechnology and Laboratory Science, College of Medicine, Chang Gung University, Taoyuan 333, Taiwan

^c Molecular Medicine Research Center, Chang Gung University, Taoyuan 333, Taiwan

^d Department of Laboratory Medicine, Chang Gung Memorial Hospital, Linkou, Taiwan

^e Graduate Institute of Natural Products, School of Traditional Chinese Medicine, College of Medicine, Chang Gung University, Taoyuan 333, Taiwan

^f Department of Anesthesiology, Chang Gung Memorial Hospital, Linkou, Taiwan

^g Research Center for Chinese Herbal Medicine, Chang Gung University of Science and Technology, Taoyuan, Taiwan

ARTICLE INFO

Article history:

Received 22 March 2019

Received in revised form

11 July 2019

Accepted 13 August 2019

Available online 26 September 2019

Keywords:

Tumor cell-induced platelet aggregation

Podoplanin

C-type lectin-like receptor 2

ABSTRACT

Tumor cell-induced platelet aggregation (TCIPA) is a mechanism that involves the protection of tumor cells in the circulation and the promotion of tumor cell invasion and metastases. The C-type lectin-like receptor 2 (CLEC-2) that binds podoplanin (PDPN) is on the platelet surface and facilitates the TCIPA. Selective blockage of the PDPN-mediated platelet-tumor cell interaction is thereby a plausible strategy for inhibiting metastases. In a search for antagonists of PDPN- and tumor cell-induced platelet aggregation, traditional Chinese medicines were screened and it was found that the water extract of *Artemisia argyi* leaves selectively inhibited the PDPN-induced platelet aggregation. Bioactivity-guided fractionation analysis was performed for defining a polysaccharide-containing fraction (AAWAP) characterized by inhibition of PDPN activity and tumor cell-induced platelet aggregation. The pharmacological effects of AAWAP on PDPN-activated CLEC-2 signaling were determined by using Western blot and alpha screening analyses. AAWAP was non-toxic to the cells and platelets and it suppressed PDPN- and tumor cell-induced

Abbreviations: 2CP, N-(2-benzamidoethyl)-2-hydroxy-5-nitrobenzamide; ALI, acute lung injury; ARDS, acute respiratory distress syndrome; CLEC-2, C-type lectin-like receptor 2; Co-HP, cobalt hematoporphyrin; DVT, deep vein thrombosis; LDH, lactose dehydrogenase; PDPN, podoplanin; PMP, 1-phenyl-3-methyl-5-pyrazolone; TCIPA, tumor cell-induced platelet aggregation; TCM, traditional Chinese medicine.

* Corresponding author. Graduate Institute of Natural Products, School of Traditional Chinese Medicine, Chang Gung University 259 Wen-Hwa 1st Road, Kwei-Shan, Taoyuan 333, Taiwan. Fax: +886 3 2118643.

E-mail addresses: ctseng@mail.cgu.edu.tw (C.-P. Tseng), tps40418@yahoo.com.tw (Y.-L. Huang), d9701408@gmail.com (Y.-W. Chang), liao@mail.cgu.edu.tw (H.-R. Liao), oo66931@gmail.com (Y.-L. Chen), pewehs@mail.cgu.edu.tw (P.-W. Hsieh).

¹ These authors contribute equally to this work and are considered as co-first authors.

<https://doi.org/10.1016/j.jfda.2019.08.002>

1021-9498/Copyright © 2019, Food and Drug Administration, Taiwan. Published by Elsevier Taiwan LLC. This is an open access article under the CC BY-NC-ND license (<http://creativecommons.org/licenses/by-nc-nd/4.0/>).

Polysaccharides
Artemisia argyi

platelet aggregation by irreversibly blocking the interaction between PDPN and CLEC-2 in a dose-dependent manner. These findings indicate that AAWAP is an antagonist of the PDPN-CLEC-2 interaction. This action by AAWAP may result in the prevention of tumor cell metastases, and if so, could become an effective pharmacological agent in treating cancer patients.

Copyright © 2019, Food and Drug Administration, Taiwan. Published by Elsevier Taiwan LLC. This is an open access article under the CC BY-NC-ND license (<http://creativecommons.org/licenses/by-nc-nd/4.0/>).

1. Introduction

Cancer-associated thrombosis commonly occurs in patients with lung, breast, head and neck, and colorectal cancer, and is a marker of a poor prognosis for cancer patients [1]. Tumor cell-induced platelet aggregation (TCIPA) protects tumor cells by forming a platelet “shield” that allows tumor cells to tolerate attacks by immune cells and promotes tumor cell invasion and metastasis [2–5]. Therefore, inhibition of the TCIPA should be considered as a potential therapeutic strategy in the treatment of cancer.

Podoplanin (PDPN) is a type-I transmembrane sialoglycoprotein that is expressed in various cancer cell types and plays a critical role in facilitating tumor invasion and metastasis [4,5]. PDPN expression is highly associated with cancer-related mortality [6]. PDPN affects cellular behavior by interacting with a number of cellular proteins including C-type lectin-like receptor 2 (CLEC-2), galectin 8, and CD44 [6]. Of these PDPN-interacting proteins, CLEC-2 is a platelet surface receptor that binds PDPN and facilitates TCIPA [4,7]. Antibodies or synthetic agents targeting PDPN or CLEC-2 inhibit tumor cell growth, migration, invasion, metastasis, and tumor cell-induced thrombus formation [6–9]. Because the suppression of PDPN/CLEC-2-induced platelet aggregation does not affect normal physiological hemostasis [4], selective blockage of PDPN-CLEC-2 binding or its downstream signaling represents an apparently safe anti-metastasis strategy.

Traditional Chinese medicine (TCM) and botanical products are important sources of healthy foods and therapeutic agents [10]. Thirteen water extracts of TCMs were prepared and their inhibitory effects on PDPN-induced platelet aggregation were evaluated as possible antagonists of TCIPA. Of these, the water extracts (100 µg/mL) of leaves of *Artemisia argyi* (AAW), spikes of *Prunella vulgaris* (PVW), seeds of *Cassia obtusifolia* (COW), rhizomes of *Davallia mariesii* (DMW), and flowers of *Inula japonica* (IJW) showed inhibitory effects on PDPN-induced platelet aggregation. AAW was the only extract that selectively inhibited PDPN- but not other agonists-induced platelet aggregation (Fig. S1) and was chosen as the candidate TCMs to develop and identify new antagonists against TCIPA.

A. argyi and its congeners are widely distributed and their leaves have been used as traditional medicine, food ingredients, and herbal teas in China, Japan, Korea, Taiwan, and Russia [11,12]. The genus *Artemisia* plants have been used for the treatment of menstruation-related symptoms and gastric disease [11]. *A. argyi* elicits anti-cancer, anti-inflammatory,

anti-obesity, anti-Trypanosome, and antioxidant activity [12–15]. The therapeutic effects of *Artemisia* plants are mainly mediated by a variety of flavonoids [16], terpenoids [17,18], and caffeoylquinic acids [19].

In this study, the water extract of *A. argyi* leaves was fractionated via a bioassay-directed fractionation method to identify the fractions that elicited anti-PDPN-induced platelet aggregation activity. The cellular toxicity and the putative mechanisms of action for the active constituents were also addressed.

2. Materials and methods

2.1. Materials and reagents

Recombinant human PDPN and His-tagged CLEC-1B were purchased from Sino Biological Inc. (Beijing, China). The recombinant human PDPN-Fc chimera was purchased from R&D Systems Inc. (Minneapolis, MN). Thrombin, apyrase, prostacyclin I₂ (PGI₂), heparin, bovine serum albumin (BSA), mannose, rhamnose, galaturonic acid, glucose, galactose, xylose, arabinose, glucosamine hydrochloride, fucose, acetic acid, 3-phenylphenol, sodium tetraborate, and phosphate-buffered saline (PBS) were purchased from Sigma–Aldrich (St Louis, MO). Collagen and U46619 were purchased from Chrono-Log Co. (Havertown, PA). Anti-phospho-specific antibodies for PLCγ2 (Y1217), SLP-76 (Y145), Syk (Y525/526), Akt1 (S473), PDK1 (S241), PKD/PKCμ (S744/748), cPLA₂ (S505), p38 (Y180/182), Erk1/2 (Y202/204), and horseradish peroxidase (HRP)-conjugated secondary antibody were purchased from Cell Signaling Technology Inc. (Beverly, MA). The anti-β-actin antibody was purchased from Novus Biological (Mill Valley, CA). The lactate dehydrogenase (LDH) activity assay kit was purchased from Promega Inc. (Madison, WI). The Bio-Rad protein assay dye reagent concentrate (#5000006) was purchased from Bio-Rad (Hercules, CA). Dextran T standards were purchased from Pharmacosmos (Holbaek, Denmark).

2.2. Genomic identification of the leaves of *Artemisia argyi*

Dried leaves of *A. argyi* were purchased from a Chinese medicine store (Huang-De-An, New Taipei City, Taiwan). ITS sequence analysis was performed to confirm that the dried leaves belonged to the species of *A. argyi* (see Supplementary

information). Sequence similarity was determined and analyzed by alignment with the genome sequence in the NCBI genome database (accession #GU724269).

2.3. Preparation of the bioactive polysaccharide-containing fraction (AAWAP)

The bioactive crude polysaccharide fraction (8.0 g) of the dried leaves from *A. argyi* (120 g) was prepared as previously described [20]. The crude polysaccharide fraction (8.0 g) was dissolved into ddH₂O (1:20, w/v), then sequentially fractionated by 100 and 300 kDa MWCO Vivaspin 20 (Little Chalfont, GE Healthcare) to yield three sub-fractions of AAWPU (>100 kDa, 2.2 g), AAWPD (<100 kDa, 4.4 g), and AAWPUU (>300 kDa, 1.4 g). AAWPUU (658.6 mg) was dissolved in ddH₂O (50 mg/mL) and centrifuged at 8000 g for 10 min to remove insoluble material. Acetic acid (99.8%) was added to the supernatant until the pH reached 3.0. The subsequent precipitate (AAWAP, 261.2 mg) was collected by centrifuging at 8000 g for 10 min. The average molecular weight of AAWAP was 4255 kDa. The carbohydrate, uronic acid and protein contents in AAWAP was 15.25%, 8.33%, and 23.61%, respectively [20]. PDPN-induced platelet aggregation assays were then performed to determine the bioactivity of each fraction (Fig. S2).

2.4. Monosaccharide composition of AAWAP

AAWAP (10 mg) was hydrolyzed, and then the hydrolysis product or monosaccharide standards (mannose, rhamnose, galaturonic acid, glucose, galactose, xylose, arabinose, glucosamine hydrochloride, and fucose) were dissolved in ddH₂O, labeled with 1-phenyl-3-methyl-5-pyrazolone (PMP), and analyzed by HPLC as previously described [20,21].

2.5. Human blood collection and preparation of washed human platelets

All experimental protocols and procedures were approved by the Institutional Review Board of Chang Gung Memorial Hospital (Linkou, Taiwan, Republic of China) with the approval ID 201800448A3 and 102–4838C. Healthy volunteers had not taken any drugs that might influence hematological function within the last two weeks of blood collection and had no history of hematological diseases.

The washed platelets were prepared as previously described with some modifications [22]. Briefly, platelet-rich plasma (PRP) was obtained by centrifugation of the whole blood premixed with 3.2% trisodium citrate solution (9:1) at 220 g for 15 min. PRP was centrifuged at 980 g for 8 min to pellet the platelets. After washing the platelets twice using Tyrode's buffer (137 mM NaCl, 12 mM NaHCO₃, 5.5 mM glucose, 5 mM HEPES, 2 mM KCl, 2 mM CaCl₂, 1 mM MgCl₂, 0.3 mM NaH₂PO₄, pH 7.3) containing 0.6 μM PGI₂, 8 units/mL heparin, and 0.02 units/mL apyrase, the platelets were re-suspended in Tyrode's buffer and then diluted to 3 × 10⁵ platelets/mL for the thrombin, collagen, or U46619-induced platelet aggregation assays, or 3 × 10⁸ platelets/mL for the PDPN- and tumor cell-induced platelet aggregation assays.

2.6. Platelet aggregation and TCIPA

Washed platelets were pre-incubated with PBS or sample solutions (2.5 μL) for 3 min (4 min for TCIPA assay) at 37 °C with constant stirring (900 rpm) prior to the addition of the platelet agonists: collagen (2 μg/mL), U46619 (2 μM), thrombin (0.1 U/mL), or tumor cells (1.5 × 10⁶ cells). For the PDPN-induced platelet aggregation assays, washed platelets were pre-incubated with PBS or sample solutions (2 μL) for 3 min at 37 °C with constant stirring (1000 rpm) in the presence of the anti-human CD32 (FcγRII) blocking solution (1 μL). Subsequently, PDPN (5 μg/mL) was added to trigger platelet aggregation [22,23]. These assays were performed by using a platelet aggregometer (Chrono-Log Corp., Havertown, PA). The time to reach 50% maximal aggregation was recorded and defined as the aggregation time.

2.7. Lactose dehydrogenase (LDH) cytotoxicity assays

Cytotoxicity toward platelets and tumor cells was evaluated using a commercial LDH activity assay kit according to the manufacturer's instruction. Briefly, washed platelets (1 × 10⁹/mL) were pre-incubated for 1 min at 37 °C with constant stirring (900 rpm). Then 2 μL of PBS, AAWAP (10–100 μg/mL) or a 1% Triton X-100 solution (positive control) was added to the reaction mixtures and incubated for an additional 15 min. The supernatants were collected after centrifugation at 3000 g for 5 min and 10,000 g for 5 min. Tumor cells (1 × 10⁵ cells/well) were cultured in a 12-well plate and treated with AAWAP (100 μg/mL) for 0–24 h. The supernatants of the cell cultures were collected as described above for the LDH cytotoxicity assay.

The LDH cytotoxicity assay was performed by mixing 50 μL of the cell or platelet suspension with 50 μL of the reagent mix (diaphorase, tetrazolium INT, NAD⁺, and lactate) in an optical 96-well flat microplate. The reaction was incubated at room temperature for 30 min and then quenched by adding 50 μL of the stop solution. The LDH activity of the samples was determined by measuring the absorbance at 492 nm using an ELISA plate reader (Thermo Labsystems, Franklin, MA). The supernatant from platelets that were lysed with 0.1% Triton X-100 was used as a control for total LDH activity [22,24].

2.8. Western blot analysis

Platelets were mixed with 125 μL of 5X lysis buffer (300 mM NaCl, 100 mM Tris–HCl, pH 7.5, 5 mM EGTA, 5 mM PMSF, 5 mM Na₃VO₄, 5% Triton X-100, 20 μg/mL leupeptin, and 20 μg/mL aprotinin) and kept on ice for 2 h. Subsequently, 156 μL of the sample buffer (60 mM Tris–HCl pH 6.8, 2% SDS, 10% glycerol, 0.1% bromophenol blue, and 50 mM DTT) was added to the platelet lysates and the mixture was heated to 95 °C for 10 min. The lysates were kept at –80 °C until use.

The extracted proteins were fractionated using a 10% polyacrylamide gel and transferred to polyvinylidene fluoride membranes (Pall Corp., Ann Arbor, MI). After blocking with 5% non-fat dry milk, membranes were incubated with appropriate primary antibody at 4 °C overnight. The membranes were washed with Tris-buffered saline containing 0.1% Tween 20 (TBS-T), and then incubated with a HRP-conjugated

secondary antibody prepared in 5% BSA for 1 h at room temperature. After washing with TBS-T, the proteins were detected by using an enhanced chemiluminescence detection kit (Millipore Corp., Bedford, MA). The relative protein expression was normalized to β -actin expression [22].

2.9. Alpha screen

AAWAP (2.44–156.25 $\mu\text{g/mL}$) or PBS (10 μL) was incubated with 5 μL of His-tagged human CLEC-2 protein (330 nM) in a 96-well plate for 15 min at 37 °C. Subsequently, 5 μL of PDPN-Fc protein (2.75 nM) was added to the reaction and the solution was mixed by shaking for 1 h at 37 °C. Protein A acceptor beads (20 $\mu\text{g/mL}$, 10 μL) and nickel chelate donor beads (20 $\mu\text{g/mL}$, 10 μL) (Perkin Elmer, Waltham, MA) were then added to the mixture. After incubation for 1 h at room temperature, binding intensity was determined using an EnVision plate reader (Perkin Elmer, Waltham, MA) [25].

2.10. Statistical analysis

All experiments were repeated at least three times and the results were expressed as the mean \pm S.E.M. Data were analyzed by a Student's t-test or a one-way ANOVA as appropriate using GraphPad Prism 4 (San Diego, CA, USA). $P < 0.05$ indicates statistical significance.

3. Results

3.1. AAWAP selectively inhibited PDPN-induced platelet aggregation

Using a bioactivity-guided fractionation protocol, a crude polysaccharide fraction of AAWPU (5 $\mu\text{g/mL}$) elicited inhibitory activity against PDPN-induced platelet aggregation. This crude polysaccharide fraction was subdivided by molecular weight and the sub-fraction AAWPUU (>300 kDa) was found to be more potent than the crude polysaccharide fraction. After acetic acid precipitation, the precipitate fraction (AAWAP) showed the most potent inhibitory effect on PDPN-induced platelet aggregation in a dose-dependent manner (Figs. 1A, D, and S2). This fraction was selected for further analysis in the following studies.

Analysis of AAWAP showed that its contents included carbohydrates (15.25%), uronic acid (8.33%), and proteins (23.61%). AAWAP may belong to a group of sulfated polysaccharides that have a low content of carbohydrates, uronic acid, and protein [26,27]. The monosaccharide molar ratio of AAWAP was glucose (2.42), galactose (1.00), arabinose (0.79), mannose (0.34), and galaturonic acid (0.25, respectively (Fig. S3).

3.2. AAWAP inhibited tumor cell-induced platelet aggregation

Two PDPN-expressing human osteosarcoma cell lines, HOS and MG63, were used to test the effects of AAWAP on TCIPA. AAWAP inhibited TCIPA in both cell lines in a dose-dependent manner (Fig. 1B, C). The time to reach 50% platelet aggregation

for AAWAP-treated (10 $\mu\text{g/mL}$) HOS and MG63 cells (944.6 ± 53.1 and 1626.0 ± 111.0 s) was significantly longer than that for the control (633.7 ± 26.7 and 723.0 ± 41.3 s), respectively (Fig. 1E, F). The LDH assay revealed that AAWAP (100 $\mu\text{g/mL}$) was not cytotoxic to tumor cells. LDH release occurred only in platelets pre-treated with high concentrations of AAWAP (>50 $\mu\text{g/mL}$) (Fig. 2). At concentrations lower than 50 $\mu\text{g/mL}$, cytotoxicity is not a factor related to the inhibitory effects of AAWAP on PDPN- and tumor cell-induced platelet aggregation.

3.3. AAWAP suppressed PDPN-induced CLEC-2 signaling

An analysis of the effect of AAWAP on PDPN-activated signaling proteins downstream of CLEC-2 was compared to the effect of 2CP, an antagonist of PDPN-CLEC-2 binding, on PDPN-induced platelet aggregation (Fig. 3A) [22]. Phosphorylation of Syk (Y525/526), PLC γ 2 (Y1217), Akt1 (S473), p38 (Y180/Y182), cPLA2 (S505), PKC μ (S748), and Erk (Y202/204) was increased in the PDPN-treated group. Both AAWAP and 2CP significantly suppressed PDPN-induced dose-dependent phosphorylation of these proteins (Fig. 3B). The phosphorylation of PDK1 (S241) that was decreased by PDPN was restored by AAWAP and 2CP (Fig. 3B). These results indicate that AAWAP, similar to 2CP, inhibits PDPN-induced platelet aggregation through modulation of CLEC-2-mediated signaling.

3.4. AAWAP irreversibly blocked the interaction between PDPN and CLEC-2

An alpha screen-based competition assay was performed to determine whether or not AAWAP interfered with PDPN binding to CLEC-2. The PDPN-CLEC-2 interaction was attenuated by AAWAP in a concentration-dependent manner with an IC_{50} of 26.53 $\mu\text{g/mL}$ (Fig. 4A). AAWAP (25 $\mu\text{g/mL}$) suppressed the maximum value and changed the slope of the PDPN-CLEC-2 response curve, indicating that AAWAP may irreversibly block the interaction between PDPN and CLEC-2 (Fig. 4B).

4. Discussion

Polysaccharides are major bioactive constituents of natural products with diverse bioactivities, including immunomodulatory, anti-diabetic, anti-inflammatory, and antitumor activities [20,28]. In particular, injection of the polysaccharide of *Astragalus membranaceus* (PG2®) was approved for treatment of cancer-related fatigue in Taiwan [29]. Polysaccharides such as lentinan, schizophyllan, and krestin have been used as immunomodulatory agents in several countries [30]. Polysaccharides thereby represent a source of healthy foods and therapeutic agents.

Several polysaccharides have been isolated from *Artemisia* sp. with potent immunomodulatory effects [21,30]. Among them, ASKP-1, a novel polysaccharide of *Artemisia sphaerocephala* composed of mannose, glucose, and galactose with an average molecular weight of 908 kDa elicits macrophage-activating effects through modulating MAPK, PI3K/Akt and NF- κ B signaling [22]. FAAP-02 is an octomeric polysaccharide

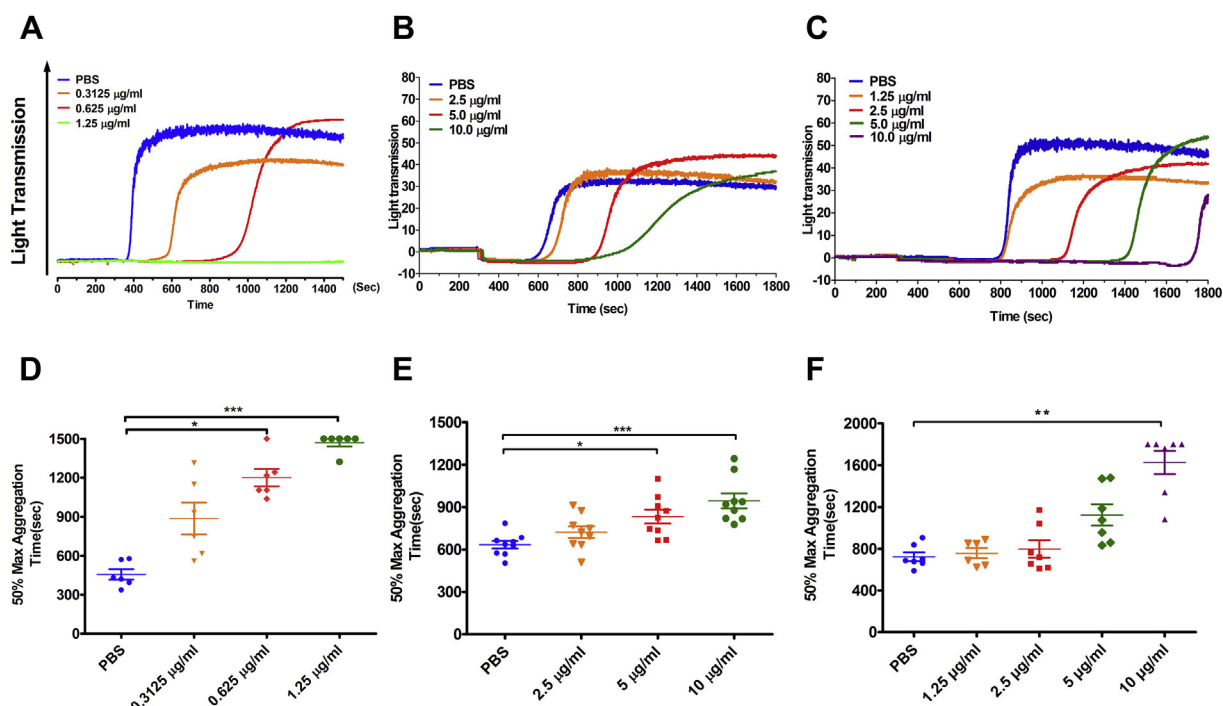


Fig. 1 – AAWAP inhibited PDPN- and tumor cell-induced platelet aggregation. (A and D) Washed platelets were treated with PBS or different concentrations of AAWAP (0.3125 $\mu\text{g/mL}$: orange; 0.625 $\mu\text{g/mL}$: red; 1.25 $\mu\text{g/mL}$: green) followed by stimulation with PDPN. Representative traces of platelet aggregation and the time to reach 50% of the maximal aggregation was defined as the aggregation time. The value is set to 1500 s when no platelet aggregation was observed. (B and E) AAWAP (1.25 $\mu\text{g/mL}$: orange; 2.5 $\mu\text{g/mL}$: red; 5.0 $\mu\text{g/mL}$: green; 10.0 $\mu\text{g/mL}$: purple) attenuated HOS cell-induced platelet aggregation in a dose-dependent manner. (C and F) AAWAP (2.5 $\mu\text{g/mL}$: orange; 5.0 $\mu\text{g/mL}$: red; 10.0 $\mu\text{g/mL}$: green) attenuated MG-63-induced platelet aggregation in a dose-dependent manner. The value is set to 1800 s when no platelet aggregation was observed. Data represent the mean \pm S.E.M of six independent experiments. * $P < 0.05$ and *** $P < 0.001$ when compared to the PBS-group.

from *A. argyi* exhibiting antitumor activity via immunostimulatory effects [30]. In the present study, a polysaccharide-containing fraction (AAWAP) with an average molecular weight of 4255 kDa inhibited PDPN- and tumor cell-induced platelet aggregation through direct and irreversible inhibition of the PDPN and CLEC-2 interaction. To the best of our understanding, this is the first natural product reported to act as an antagonist of PDPN-CLEC-2 binding. TCMs may be excellent sources for screening more novel agents that inhibit the PDPN-CLEC-2 interaction.

2CP, a 5-nitrobenzoate derivative, inhibits PDPN- and tumor cell-induced platelet aggregation through direct binding to CLEC-2 with a dissociation constant of 33.2 μM , thereby inhibits PDPN- and tumor cell-induced platelet aggregation at concentration of 12.1 and 20 μM [22]. This inhibition is also observed with protoporphyrin IX (H2-PP). H2-PP was modified at its hematoporphyrin moiety, and a cobalt-conjugating derivative (cobalt hematoporphyrin, Co-HP) was synthesized. At concentrations between 1.53 μM and 3.05 μM , Co-HP selectively inhibits platelet aggregation induced by PDPN-expressing CHO cells and rhodocytin [4]. AAWAP inhibited PDPN- and tumor cell-induced platelet aggregation at the concentrations of 0.3–2.3 nM (1.25–10.0 $\mu\text{g/mL}$) and was more potent than other known inhibitors of the PDPN-CLEC-2

interaction. In addition, it is a firstly inhibitors of the PDPN-CLEC-2 interaction from natural source.

PDPN and CLEC-2 may be involved in tumor cells metastasis and are recognized as critical regulators of many diseases such as acute lung injury (ALI), acute respiratory distress syndrome (ARDS), and deep vein thrombosis (DVT) [4,31–34]. The interaction between platelets and immune cells regulates the pathogenic mechanisms of ARDS and ALI. CLEC-2 expressed on platelets interacts with PDPN expressed on alveolar macrophages. The interaction inhibits neutrophil recruitment and improves lung function in animal models of ARDS/ALI [31,32]. DVT and its major complication, pulmonary embolism is associated with high mortality. Platelet CLEC-2 and PDPN expressed on the pathological venous wall may be responsible for thrombus formation and DVT [4,33,34]. Treating DVT with Co-HP and platelet-specific deficiency in CLEC-2 significantly decreases thrombus formation and protects against DVT [4,33]. The inhibitory effect of AAWAP on PDPN binding may be effective in preventing metastases and protection against DVT.

In conclusion, AAWAP, a non-cytotoxic polysaccharide-containing fraction, was prepared from water extracts of *A. argyi* leaves using a bioactivity-guided fractionation protocol. AAWAP suppressed PDPN- and tumor cell-induced platelet

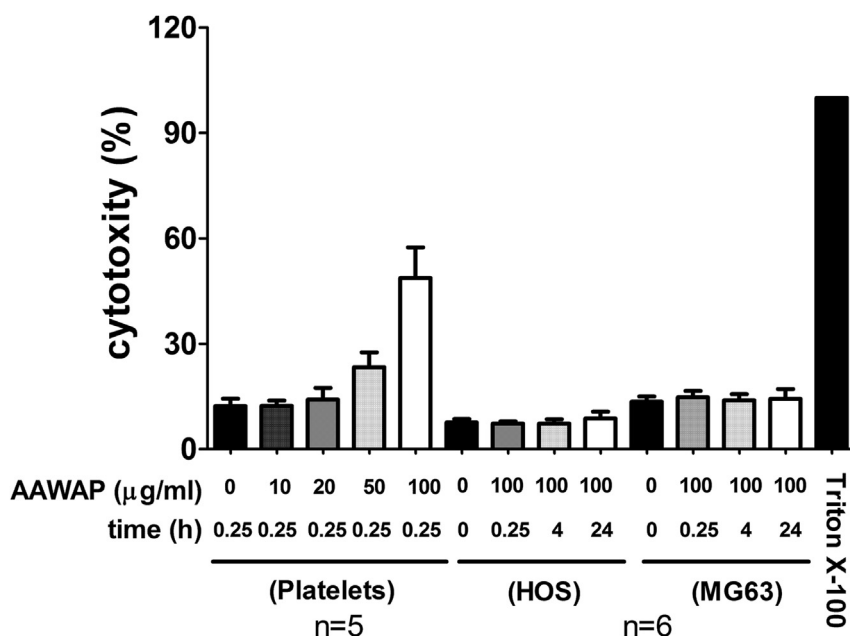


Fig. 2 – The effect of AAWAP on LDH release in human platelets and osteosarcoma cells. Platelets and osteosarcoma cells (HOS and MG63) were incubated with the indicated concentrations of AAWAP at 37 °C. The cell-free supernatants were collected for measurement of LDH activity. The supernatant from platelets lysed by 0.1% Triton X-100 was used as a control for total LDH activity (100%). The released LDH activity was used as an indicator of cytotoxicity. Data represent the mean \pm S.E.M of five to six independent experiments.

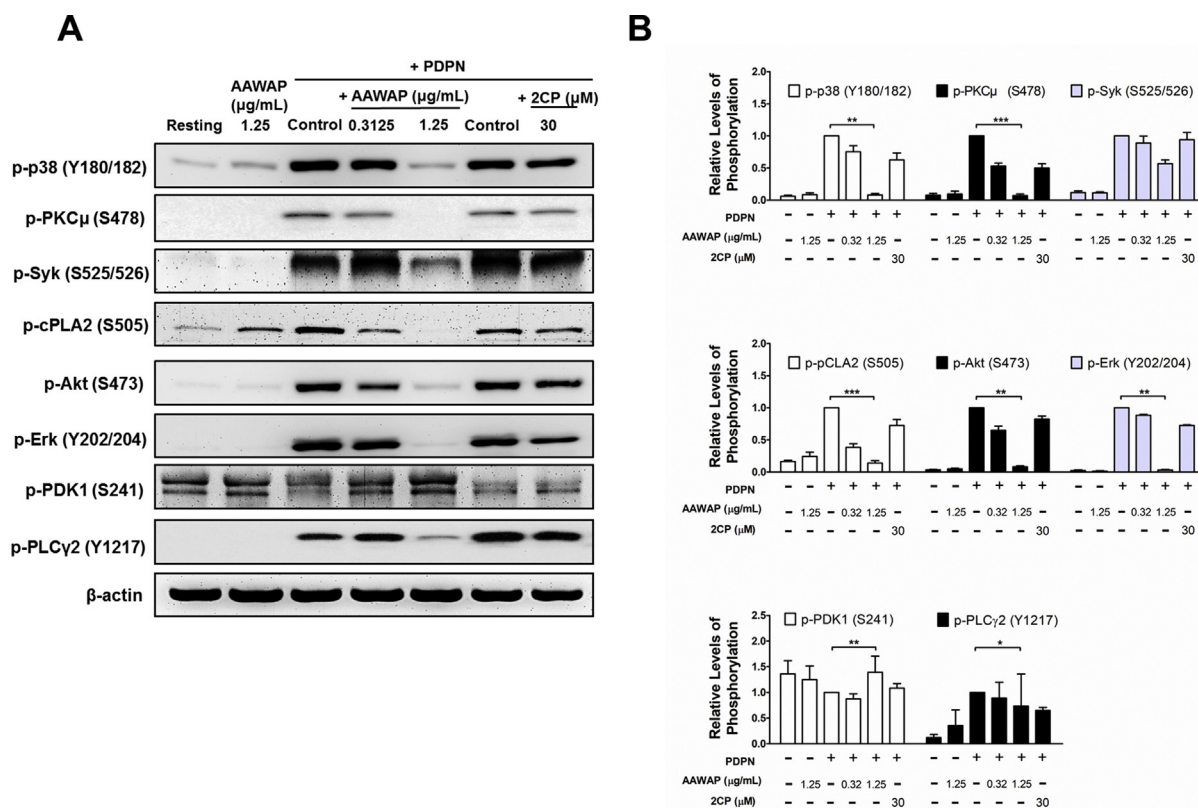


Fig. 3 – AAWAP reversed the signal transduction of PDPN-induced platelet aggregation. (A) AAWAP and 2CP reversed PDPN-modulated phosphorylation of p38, PKC μ , Syk, cPLA2, Akt, Erk, PDK1, and PLC γ 2. (B) The relative phosphorylation level of the indicated proteins were determined and quantified using ImageJ software (NIH). Data represent the mean \pm S.E.M (n \geq 3). ***P < 0.001, **P < 0.01, and *P < 0.05 when compared to the control group.

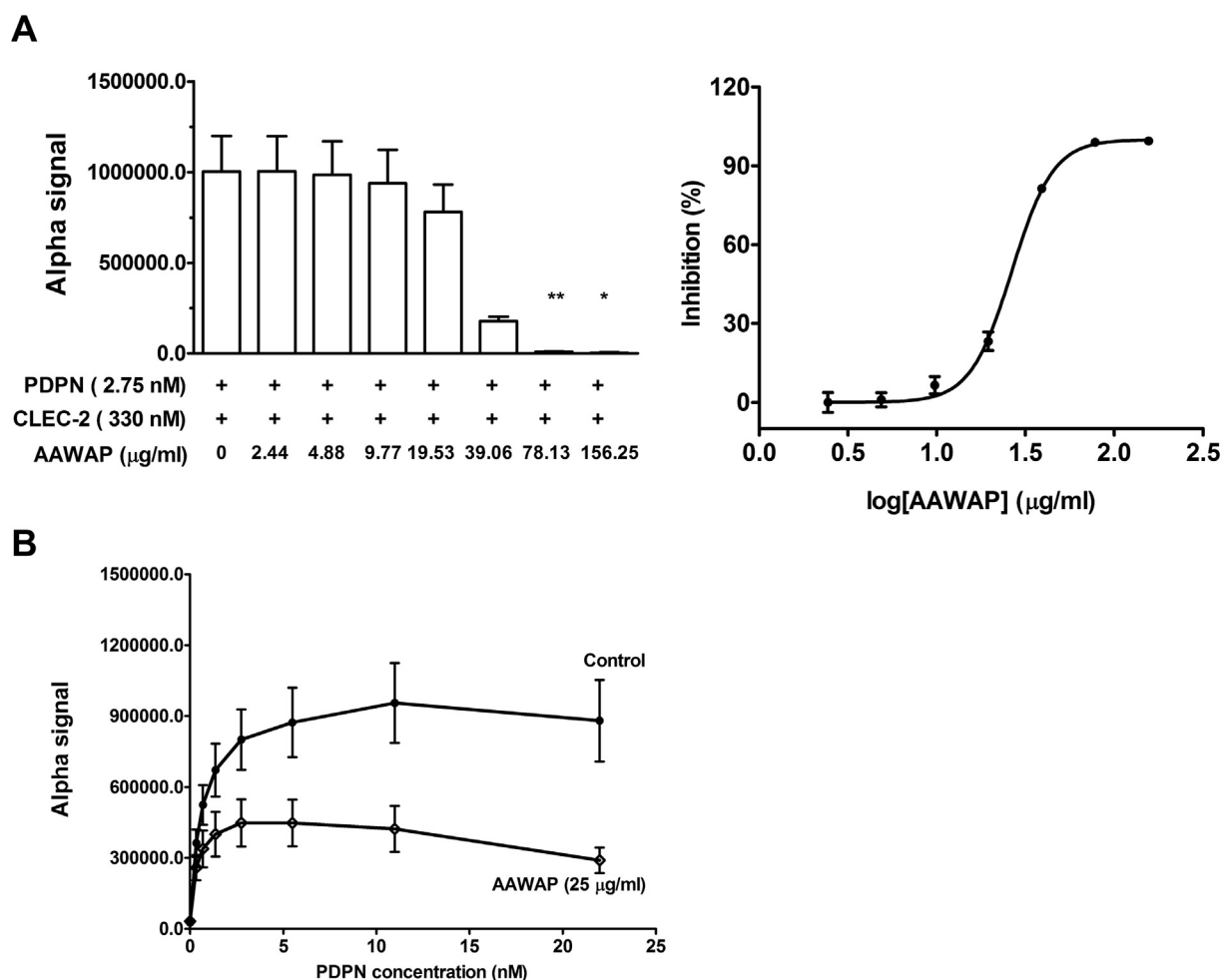


Fig. 4 – AAWAP irreversibly blocked the interaction between PDPN and CLEC-2. (A) His-tagged CLEC-2 protein was incubated with PBS or different concentrations of AAWAP in a 96-well plate. PDPN was then added to each well. After incubating with alpha screen beads, the intensity of alpha screen fluorescence signals representing the binding intensity of PDPN-CLEC-2 was determined (left panel). AAWAP elicited dose-dependent inhibition of PDPN-CLEC-2 binding (right panel). (B) His-tagged CLEC-2 protein was incubated with AAWAP (25 μg/mL) in a 96-well plate. The indicated concentrations of PDPN were then added to each well followed by an alpha screen assay to determine the intensity of alpha screen fluorescence signal. Data represent the mean \pm S.E.M ($n \geq 4$). ** $P < 0.01$ and * $P < 0.05$ when compared to the control group.

aggregation by irreversibly blocking the interaction between PDPN and CLEC-2. These findings indicate that AAWAP is an antagonist of the PDPN-CLEC-2 interaction. This action by AAWAP may result in the prevention of tumor cell metastases, and if so, could become an effective pharmacological agent in treating cancer patients.

Conflicts of interest

The authors declare no conflict of interest.

Author contributions

Conception and design of the research: Y.L.H., C.P.T., and P.W.H.; performed experiments: Y.L.H., C.P.T., and P.W.H.; acquired and analyzed data: C.P.T., Y.L.H. and P.W.H.; drafted

and edited the manuscript: C.P.T., Y.L.H. and P.W.H.; assisted with experiments: Y.W.C, H.R.L. and Y.L.C.; data discussion and review of the manuscript; C.P. T., Y.L.H. and P.W.H.

Acknowledgements

We acknowledge Professor Arnold Stern (New York University School of Medicine) for his editorial help, and the technique supports from Bioproduction Engineering Technology Department, Biomedical Technology and Device Research Laboratories, ITR (Hsinchu, Taiwan) for performing genomic analysis of plant material. This work was supported by the Ministry of Science and Technology grants (MOST102-2320-B-182-008-MY3 and MOST106-2320-B-182-003-MY3 to P.-W. Hsieh and MOST105-2320-B-182-029-MY3 and MOST106-2320-B-182-027-MY3 to C.-P. Tseng), and the Chang Gung

Memorial Hospital grants (CMRPD1F0561-2 and BMRPB23 to P.-W. Hsieh, and CMRPD1E0181-3, CMRPD1F0611-3, CMRPD1H0211-3 and BMRP466 to C.-P. Tseng). The funders had no role in the study design, the data collection and analysis, the decision to publish, or the preparation of the manuscript.

Appendix A. Supplementary data

Supplementary data to this article can be found online at <https://doi.org/10.1016/j.jfda.2019.08.002>.

REFERENCES

- [1] Bambace NM, Holmes CE. The platelet contribution to cancer progression. *J Thromb Haemast* 2011;9:237–49.
- [2] Takemoto A, Miyata K, Fujita N. Platelet-activating factor podoplanin: from discovery to drug development. *Cancer Metastasis Rev* 2017;36:225–34.
- [3] Gresle P, Malvestiti M, Moni S. Anti-platelet treatments in cancer: basic and clinical research. *Thromb Res* 2018;164:S106–11.
- [4] Tsukiji N, Osada M, Sasaki T, Shirai T, Satoh K, Inoue O, et al. Cobalt hematoporphyrin inhibits CLEC-2-podoplanin interaction, tumor metastasis, and arterial/venous thrombosis in mice. *Blood Adv* 2018;2:2214–25.
- [5] Schlesinger M. Role of platelets and platelet receptors in cancer metastasis. *J Hematol Oncol* 2018;11:125.
- [6] Krishnan H, Rayes J, Miyashita T, Ishii G, Retzbach EP, Sheehan SA, et al. Podoplanin: an emerging cancer biomarker and therapeutic target. *Cancer Sci* 2018;109:1292–9.
- [7] Miyata K, Takemoto A, Okumura S, Nishio M, Fujita N. Podoplanin enhances lung cancer cell growth in vivo by inducing platelet aggregation. *Sci Rep* 2017;7:4059.
- [8] Sasaki T, Shirai T, Tsukiji N, Otake S, Tamura S, Ichikawa J, et al. Functional characterization of recombinant snake venom rhodocytin: rhodocytin mutant blocks CLEC-2/podoplanin-dependent platelet aggregation and lung metastasis. *J Thromb Haemast* 2018;16:960–72.
- [9] Zara M, Canobbio I, Visconte C, Canino J, Torti M, Guidetti GF. Molecular mechanisms of platelet activation and aggregation induced by breast cancer cells. *Cell Signal* 2018;48:45–53.
- [10] Chen YL, Hwang TL, Yu HP, Fang JY, Chong KY, Chang YW, et al. *Ilex kaushue* and its bioactive component 3,5-dicaffeoylquinic acid protected mice from lipopolysaccharide-induced acute lung injury. *Sci Rep* 2016;6:34243.
- [11] Li S, Zhou S, Yang W, Meng D. Gastro-protective effect of edible plant *Artemisia argyi* in ethanol-induced rats via normalizing inflammatory responses and oxidative stress. *J Ethnopharmacol* 2018;214:207–17.
- [12] Yu Y, Mendoza TM, Ribnick DM, Poulev A, Noland RC, Mynatt RL, et al. An extract of Russian tarragon prevents obesity-related ectopic lipid accumulation. *Mol Nutr Food Res* 2018;62:e1700856.
- [13] Ahuja A, Yi YS, Kim MY, Cho JY. Ethnopharmacological properties of *Artemisia asiatica*: a comprehensive review. *J Ethnopharmacol* 2018;220:117–28.
- [14] Naß J, Efferth T. The activity of *Artemisia* spp. and their constituents against Trypanosomiasis. *Phytomedicine* 2018;47:184–91.
- [15] Ye CL, Lai YF. Optimization of extraction process and antioxidant activity of polysaccharides from leaves of *Artemisia argyi* Lev. et Vant. *J Food Process Preserv* 2015;39:1309–17.
- [16] Lv JL, Li ZZ, Zhang LB. Two new flavonoids from *Artemisia argyi* with their anticoagulation activities. *Nat Prod Res* 2018;64:1–8.
- [17] Kim JH, Kim HK, Jeon SB, Son KH, Kim EH, Kang SK, et al. New sesquiterpene-monoterpene lactone, artemisolid, isolated from *Artemisia argyi*. *Tetrahedron Lett* 2002;43:6205–8.
- [18] Lee SH, Seo Y, Kim HK, Kang HM, Kim JH, Son KH, et al. New inhibitors of farnesyl protein transferase from *Artemisia argyi*. *J Org Chem* 2002;67:7670–5.
- [19] Kang JY, Lee DS, Park SK, Ha JS, Kim JM, Ha GJ, et al. Cognitive function of *Artemisia argyi* H. fermented by *Monascus purpureus* under TMT-induced learning and memory. *Evid Based Complement Altern Med* 2017;209:108–15.
- [20] Chen YL, Hwang TL, Fang JY, Lan YH, Chong KY, Hsieh PW. Polysaccharides from *Kochia scoparia* fruits protect mice from lipopolysaccharide-mediated acute lung injury by inhibiting neutrophil elastase. *J Funct Foods* 2017;38:582–90.
- [21] Ren D, Lin D, Alim A, Zheng Q, Yang X. Chemical characterization of a novel polysaccharide ASKP-1 from *Artemisia sphaerocephala* Krasch seed and its macrophage activation via MAPK, PI3k/Akt and NF- κ B signaling pathways in RAW246.7 cells. *Food Funct* 2017;8:1299–312.
- [22] Chang YW, Hsieh PW, Chang YT, Lu MH, Huang TF, Chong KY, et al. Identification of a novel platelet antagonist that binds to CLEC-2 and suppresses podoplanin-induced platelet aggregation and cancer metastasis. *Oncotarget* 2015;6:42733–48.
- [23] Kung PH, Hsieh PW, Lin YT, Lee JH, Chen IH, Wu CC. HPW-RX40 prevents human platelet activation by attenuating cell surface protein disulfide isomerases. *Redox Biol* 2017;13:266–77.
- [24] Chang YW, Tseng CP, Lee CH, Hwang TL, Chen YL, Su MT, et al. β -Nitrostyrene derivatives attenuate LPS-mediated acute lung injury via the inhibition of neutrophil-platelet interactions and NET release. *Am J Physiol Lung Cell Mol Physiol* 2018;314:L654–69.
- [25] Sekiguchi T, Takemoto A, Takagi S, Takatori K, Sato S, Takami M, et al. Targeting a novel domain in podoplanin for inhibiting platelet-mediated tumor metastasis. *Oncotarget* 2018;7:3934–46.
- [26] Di T, Chen G, Sun Y, Ou S, Zeng X, Ye H. Antioxidant and immunostimulating activities in vitro of sulfated polysaccharides isolated from *Gracilaria rubra*. *J Funct Foods* 2017;28:64–75.
- [27] Liu QM, Xu SS, Li L, Pan TM, Shi CL, Liu H, et al. In vitro and in vivo immunomodulatory activity of sulfated polysaccharide from *Porphyra haitanensis*. *Carbohydr Polym* 2017;165:189–96.
- [28] Zhang Q, Xu Y, Lv J, Cheng M, Wu Y, Cao K, et al. Structure characterization of two functional polysaccharides from *Polygonum multiflorum* and its immunomodulatory. *Int J Biol Macromol* 2017;113:195–204.
- [29] Chen CC, Chen XX, Li TC, Lin HL, Chu YT, Lee HC, et al. PG2 for patients with acute spontaneous intracerebral hemorrhage: a double-blind, randomized, placebo-controlled study. *Sci Rep* 2017;7:45628.
- [30] Bao X, Yuan H, Wang C, Liu J, Lan M. Antitumor and immunomodulatory activities of a polysaccharide from *Artemisia argyi*. *Carbohydr Polym* 2013;98:1236–43.
- [31] Lax S, Reyes J, Wichaiyo S, Haining EJ, Lowe K, Grygielska B, et al. Platelet CLEC-2 protects against lung injury via effects of its ligand podoplanin on inflammatory alveolar

- macrophages in the mouse. *Am J Physiol Lung Cell Mol Physiol* 2017;313:L1016–29.
- [32] Rayes J, Lax S, Wchaiyo S, Watson SK, Di Y, Lombard S, et al. The podoplanin-CLEC-2 axis inhibits inflammation in sepsis. *Nat Commun* 2017;8:2239.
- [33] Payne H, Pnonmaryov T, Watson SP, Brill A. Mice with a deficiency in CLEC-2 are protected against deep vein thrombosis. *Blood* 2017;129:2013–20.
- [34] Budnik I, Brill A. Immune factors in deep vein thrombosis initiation. *Trends Immunol* 2018;39:610–23.

Article

Sponge-Derived 24-Homoscalaranes as Potent Anti-Inflammatory Agents

Bo-Rong Peng ^{1,2,3}, Kuei-Hung Lai ^{4,5} , Yu-Chia Chang ⁵ , You-Ying Chen ^{3,6}, Jui-Hsin Su ^{3,7}, Yusheng M. Huang ⁸, Po-Jen Chen ⁹, Steve Sheng-Fa Yu ^{2,10,*}, Chang-Yih Duh ^{1,6,*} and Ping-Jyun Sung ^{3,6,7,11,12,*} 

¹ Doctoral Degree Program in Marine Biotechnology, National Sun Yat-Sen University, Kaohsiung 804201, Taiwan; pengpojung@gmail.com

² Doctoral Degree Program in Marine Biotechnology, Academia Sinica, Taipei 115201, Taiwan

³ National Museum of Marine Biology and Aquarium, Pingtung 944401, Taiwan; zoeblack0108@gmail.com (Y.-Y.C.); x2219@nmmba.gov.tw (J.-H.S.)

⁴ Graduate Institute of Pharmacognosy, College of Pharmacy, Taipei Medical University, Taipei 110301, Taiwan; mos19880822@gmail.com

⁵ Research Center for Chinese Herbal Medicine, College of Human Ecology, Chang Gung University of Science and Technology, Taoyuan 333324, Taiwan; jay0404@gmail.com

⁶ Department of Marine Biotechnology and Resources, National Sun Yat-Sen University, Kaohsiung 804201, Taiwan

⁷ Graduate Institute of Marine Biology, National Dong Hwa University, Pingtung 944401, Taiwan

⁸ Department of Marine Recreation, National Penghu University of Science and Technology, Penghu 880011, Taiwan; yusheng@npu.edu.tw

⁹ Department of Cosmetic Science, Providence University, Taichung 433303, Taiwan; litlep@hotmail.com

¹⁰ Institute of Chemistry, Academia Sinica, Taipei 115201, Taiwan

¹¹ Chinese Medicine Research and Development Center, China Medical University Hospital, Taichung 404333, Taiwan

¹² Graduate Institute of Natural Products, Kaohsiung Medical University, Kaohsiung 807377, Taiwan

* Correspondence: sfyu@chem.sinica.edu.tw (S.S.-F.Y.); yihduh@mail.nsysu.edu.tw (C.-Y.D.); pjsung@nmmba.gov.tw (P.-J.S.); Tel.: +886-2-5572-8650 (S.S.-F.Y.); +886-7-525-2000 (ext. 5036) (C.-Y.D.); +886-8-882-5037 (P.-J.S.); Fax: +886-2-2783-1237 (S.S.-F.Y.); +886-7-525-5020 (C.-Y.D.); +886-8-882-5087 (P.-J.S.)

Received: 8 July 2020; Accepted: 14 August 2020; Published: 19 August 2020



Abstract: Scalarane-type sesterterpenoids are known for their therapeutic potential in cancer treatments. However, the anti-inflammatory properties of this class of metabolites remain elusive. Our current work aimed to investigate the anti-inflammatory scalaranes from marine sponge *Lendenfeldia* sp., resulting in the isolation of six new 24-homoscalaranes, lendenfeldaranes E–J (1–6). The structures of the new metabolites were determined by extensive spectroscopic analyses, and the absolute configuration of **1** was established by electronic circular dichroism (ECD) calculations. Compounds **2** and **3** were discovered to individually reduce the generation of superoxide anions, and compound **1** displayed an inhibitor effect on the release of elastase. These three compounds were proven to be the first anti-neutrophilic scalaranes.

Keywords: 24-homoscalarane; sesterterpenoid; lendenfeldarane; *Lendenfeldia*; anti-neutrophilic inflammation; superoxide anion; NADPH oxidase; elastase release

1. Introduction

The marine sponges of genus *Lendenfeldia* have been studied for decades since first being reported in 1982 [1]. Further investigation of this genus revealed more than 50 compounds categorized into scalarane-type sesterterpenoids [1–5], other types of sesterterpenoids [4], amino acids [6],

steroids [7,8], iminosugars [9], naphthalenes [10], lipid [10,11], and diphenyl ethers [12]. Our group has extensively studied scalarane-type sesterterpenoids over the past few years and has found that they demonstrate a wide structural diversity [5,13–16]. This class of compounds possesses a pentamethyl-D-homoandrostane skeleton. Alkylated scalaranes are usually known as homoscalarane, exhibiting methylation at C-20 or C-24. In the current report, we summarize a series of structural classification for scalaranes from the *Lendenfeldia* sp. sponge. In detail, a normal 25-carbon scalarane represents the basic type of scalarane, while the 26-carbon ones can be further sorted into tetra- and pentacyclic homoscalarane groups. Nor-homoscalaranes were characterized with a missing methyl at position 18 and bishomoscalaranes are defined for the scalaranes with a pair of methylations at both C-20 and C-24. Additionally, it is noteworthy that most of them present a different oxidation in positions C-12, C-16, C-22, C-24, and C-25 [17]. The biological properties of scalarane-type sesterterpenoids were extensively studied with special emphasis on cytotoxic and anti-proliferative properties [5]. For instance, the scalaranes isolated from sponges of *Hyrtios*, *Hippospongia*, *Lendenfeldia*, *Phyllospongia*, and *Psammocinia* genus were examined to show potent cytotoxicity against A498, ACHN, MIA-paca, PANC-1, CV-1, molt-4, K562, DLD-1, HCT-116, and T-47D cancer cell lines at low concentrations ($< 4 \mu\text{M}$) [5,15,18]. The previous pharmacological studies on scalaranes have also revealed several possible anti-proliferative mechanisms, including the inhibition of Hsp90 and topoisomerase II [16], and the binding of DNA [19]. In addition, these sesterterpenoids were also reported to exhibit other pharmacological activities, such as anti-microbial, anti-fungal, anti-viral, and so on [16]. However, only few studies have explored the anti-inflammatory activity of this class of metabolites. A sponge-derived scalarane, named deacetylphylloketa, was reported to exhibit anti-inflammatory activity by regulating the expression levels of pro-inflammatory factors (TNF- α , IL-6, and IL-1 β) and anti-inflammatory factors (Nrf-2 and HO-1). It could downregulate the expressions of iNOS and COX-2, as well as attenuate nuclear translocation of NF- κ B [20]. Recently, we focused our ongoing studies on a marine sponge identified as *Lendenfeldia* sp. From the result of our studies on this species, we report herein the isolation, structural determination, and bioactivity of six new 24-homoscalaranes, lendenfeldaranes E–J (1–6) (Figure 1). Moreover, the extensive biological screening suggested the isolates significantly inhibited superoxide anion generation and elastase release in neutrophils responding to *N*-formyl-methionyl-leucyl-phenylalanine (fMLF).

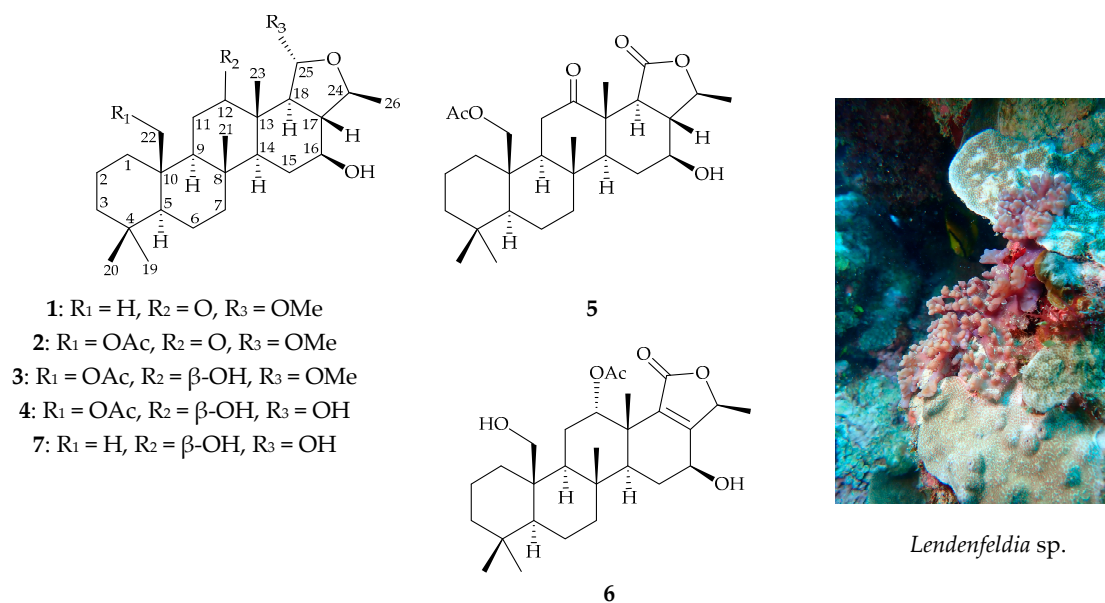


Figure 1. Structures of lendenfeldaranes E–J (1–6) and felixin E (7) and a picture of *Lendenfeldia* sp.

2. Results and Discussion

Specimens of the marine sponge *Lendenfeldia* sp. were collected by hand by self-contained underwater breathing apparatus (scuba) diving off the coast of Southern Taiwan in 2012, and stored frozen at -20°C until extraction. The frozen sponge was minced and extracted with ethyl acetate (EtOAc). The fractionation of the EtOAc-soluble extract led to the production of 11 fractions A–K. Fractions I and J were further purified by normal-phase and reversed-phase HPLC to afford scalaranes **1**–**6**.

Lendenfeldarane E (**1**), isolated as an amorphous powder, has a molecular formula of $\text{C}_{27}\text{H}_{44}\text{O}_4$ as determined from its (+)-HRESIMS at m/z 455.31340 (calcd. for $\text{C}_{27}\text{H}_{44}\text{O}_4 + \text{Na}$, 455.31318) implying 6 degrees of unsaturation. The IR spectrum showed absorptions for OH (3438 cm^{-1}) and C=O (1701 cm^{-1}) functionalities. The ^1H NMR data (Table 1) demonstrated five tertiary methyls at δ_{H} 0.82, 0.85, 0.86, 1.07, and 1.36 (each 3H \times s); one secondary methyl at δ_{H} 1.40 (3H, d, $J = 6.0\text{ Hz}$); one methoxy at δ_{H} 3.30 (3H, s); as well as three oxymethine protons at 3.43 (1H, ddd, $J = 10.4, 10.4, 4.4\text{ Hz}$), 3.84 (1H, qd, $J = 6.0, 2.4\text{ Hz}$), and 5.35 (1H, d, $J = 4.0\text{ Hz}$). The ^{13}C NMR (Table 1), heteronuclear single quantum correlation (HSQC), and distortionless enhancement by polarization transfer (DEPT) spectra revealed in total 27 carbon signals including a few oxygenated ones, such as a ketone (δ_{C} 215.3), a ketal carbon (δ_{C} 104.8), and two oxymethine carbons (δ_{C} 74.8 and 78.7).

Table 1. ^1H (400 MHz, CDCl_3) and ^{13}C (100 MHz, CDCl_3) NMR data for 24-homoscalaranes **1** and **2**.

C/H	1		2	
	δ_{H} (J in Hz)	δ_{C} Mult.	δ_{H} (J in Hz)	δ_{C} Mult.
1	1.59 m; 0.80 m	39.4, CH_2	1.99 m; 0.77 m	34.3, CH_2
2	1.43 m; 1.58 m	18.1, CH_2	1.46 m; 1.58 m	17.9, CH_2
3	1.10 m; 1.36 m	41.8, CH_2	1.14 m; 1.43 m	41.4, CH_2
4		33.3, C		33.0, C
5	0.81 m	56.6, CH	0.97 m	56.9, CH
6	1.43 m	18.4, CH_2	1.46 m	18.1, CH_2
7	0.92 ddd (12.8, 12.8, 4.0) 1.82 ddd (12.8, 2.8, 2.8)	41.9, CH_2	0.98 m; 1.90 m	42.2, CH_2
8		37.8, C		37.7, C
9	1.15 m	61.3, CH	1.26 m	61.1, CH
10		38.1, C		41.2, C
11	2.66 dd (14.4, 13.6) 2.24 dd (13.6, 2.0)	35.1, CH_2	2.99 dd (14.8, 13.6) 2.43 dd (13.6, 2.4)	37.9, CH_2
12		215.3, C		214.8, C
13		51.8, C		51.9, C
14	1.13 m	59.6, CH	1.13 m	59.7, CH
15	1.52 m; 1.90 m	30.8, CH_2	1.56 m; 1.92 m	31.0, CH_2
16	3.43 ddd (10.4, 10.4, 4.4)	74.8, CH	3.43 ddd (10.0, 10.0, 4.4)	74.6, CH
17	1.89 m	49.6, CH	1.91 m	49.5, CH
18	1.62 m	53.0, CH	1.60 m	52.8, CH
19	0.82 s	21.3, CH_3	0.84 s	21.8, CH_3
20	0.85 s	33.2, CH_3	0.87 s	33.7, CH_3
21	1.07 s	17.1, CH_3	1.15 s	16.5, CH_3
22	0.86 s	15.7, CH_3	4.19 dd (12.4, 1.6); 4.65 d (12.4)	64.6, CH_2
23	1.36 s	15.3, CH_3	1.37 s	15.4, CH_3
24	3.84 qd (6.0, 2.4)	78.7, CH	3.83 qd (6.0, 2.0)	78.8, CH
25	5.35 d (4.0)	104.8, CH	5.33 d (4.4)	104.7, CH
26	1.40 d (6.0)	23.5, CH_3	1.40 d (6.0)	23.5, CH_3
22-OAc				170.7, C
			2.04 s	21.1, CH_3
25-OMe	3.30 s	54.4, CH_3	3.28 s	54.4, CH_3

After the detailed analysis of above NMR data, one degree of unsaturation (ketone) was found to form a part of total. Then the rest of the five unsaturated degrees obscured a pentacyclic homoscalarane.

This inference can be further confirmed from the heteronuclear multiple bond correlation (HMBC) (Figure 2) of H₃-19 to C-3, C-4, C-5, and C-20; H₃-21 to C-7, C-8, C-9, and C-14; H₃-22 to C-1, C-5, C-9, and C-10; H₃-23 to C-12, C-13, C-14, and C-18; H-24 to C-16, C-17, C-18, and C-25; H₃-26 to C-17 and C-24; 25-methoxy to C-25, and further confirmed by the ¹H-¹H correlation spectroscopy (COSY) (Figure 2). Thus, it indicated that compound **1** is a 6/6/6/6/5 pentacyclic scalarane sesterterpene, having a 2-methoxy-5-methyltetrahydrofuran. A detailed analysis of these NMR data with those of a known metabolite, felixin E (**7**) [14], suggested that the structure of **1** is closely related to that of **7**, with the only difference being an α -hydroxy group at C-25 in **7** replaced by an α -methoxy group in **1** [14]. All naturally occurring scalarane sesterterpenoids displayed the H-5 *trans* to Me-22, assigned as α - and β -orientation, respectively [17]. Then, the relative stereochemistry of **1** was established by nuclear Overhauser effect spectroscopy (NOESY) spectral analysis. The NOESY experimental data (Figure 3) demonstrated the correlations H₃-22/H₃-20, H₃-22/H₃-21, H₃-21/H₃-23, H₃-23/H-17, H₃-23/H-25, H-5/H-9, H-9/H-14, H-14/16, H-14/H-18, and H-16/H-24, supporting the β -Me-20, β -Me-21, β -Me-23, β -H-17, α -OMe-25, α -H-9, α -H-14, β -OH-16, α -H-18, and β -Me-26 assignments. The aforementioned results enabled the establishment of the relative configuration of **1**. Based on the above findings; the configurations of stereogenic carbons of **1** were determined as 5*S**, 8*R**, 9*S**, 10*R**, 13*S**, 14*S**, 16*S**, 17*S**, 18*S**, 24*S**, and 25*R**. To further determine the absolute configuration of **1**, the electronic circular dichroism (ECD) calculations for the enantiomers of **1**, including **1a** (5*S*, 8*R*, 9*S*, 10*R*, 13*S*, 14*S*, 16*S*, 17*S*, 18*S*, 24*S*, and 25*R*) and **1b** (5*R*, 8*S*, 9*R*, 10*S*, 13*R*, 14*R*, 16*R*, 17*R*, 18*R*, 24*R*, and 25*S*) were performed using the method at the B3LYP/6-31pG* level with Gaussian 9.0 software (Figure 4). By comparison of the experimental and calculated ECD spectra, the result of compound **1** was in good agreement with that of **1a**, inferring the 5*S*, 8*R*, 9*S*, 10*R*, 13*S*, 14*S*, 16*S*, 17*S*, 18*S*, 24*S*, and 25*R* configurations. Hence, the structure, including the absolute configuration of lendenfeldarane E (**1**) was unambiguously assigned as shown in Figures 1 and 3 (Supplementary Materials, Figures S1–S8).

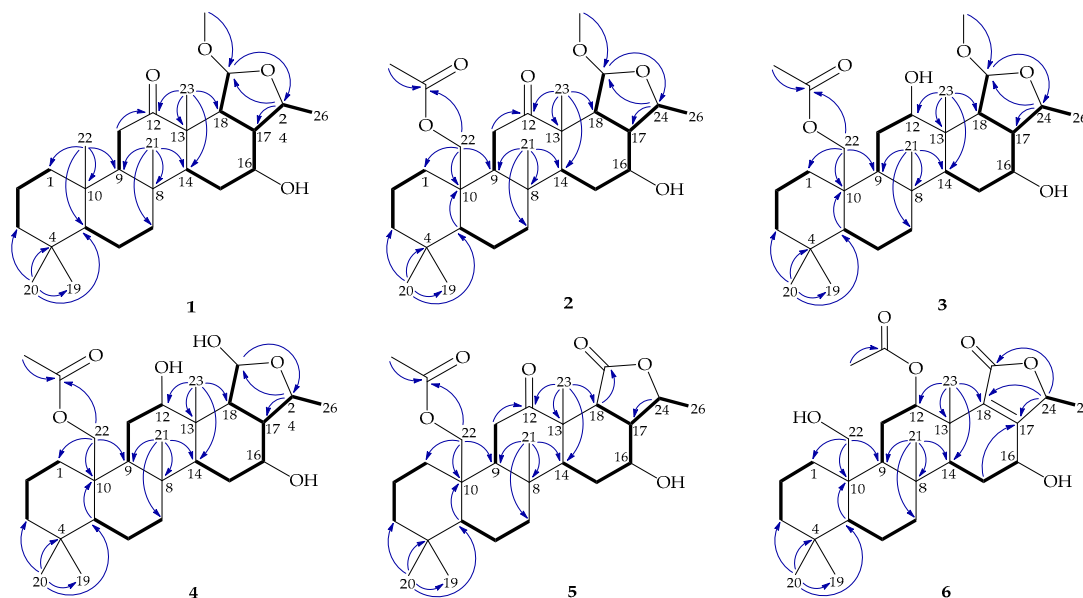


Figure 2. The COSY (—) and HMBC (—) of 1–6.

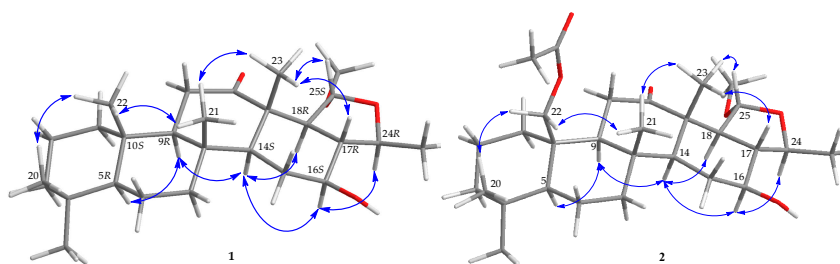


Figure 3. The selected NOESY correlations (↷) of **1** and **2**.

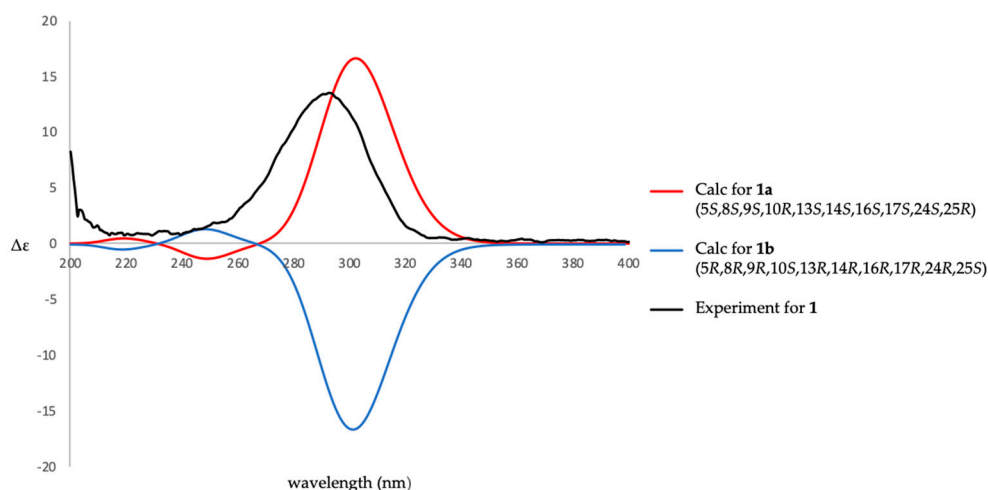


Figure 4. Calculated and experimental electronic circular dichroism (ECD) spectra of **1**.

Lendenfeldarane F (**2**), an amorphous powder, showed the molecular formula $C_{29}H_{46}O_6$ determined by (+)-HRESIMS and ^{13}C NMR data, implying seven unsaturated degrees. The IR spectra indicated the presence of OH (3451 cm^{-1}), ester carbonyl (1731 cm^{-1}), and C=O (1700 cm^{-1}) functional groups. The 1H , ^{13}C , DEPT, and HSQC spectra (Table 1) displayed seven methyls, one oxymethylene, two oxymethines, one ester carbonyl, one ketone, and one ketal carbon, representing two unsaturated calculations. Thus, the above NMR data and the rest of the five unsaturated degrees of **2** implied a pentacyclic homoscalarane. The NMR data of **2** resembled those of **1** with the exception of an additional oxymethylene signal (δ_C 64.6; δ_H 4.19, 1H, dd, $J = 12.4, 1.6\text{ Hz}$; 4.65, 1H, d, $J = 12.4\text{ Hz}$, CH_2 -22), and an acetoxyl group (δ_H 2.04, 3H, s; δ_C 170.7, C; 21.1, CH_3). An ethyl acetate substitution at position 10 can be deduced by HMBC cross-peaks from H_2 -22 to C-1, C-5, C-9, C-10, and acetate carbonyl. The stereochemical configuration was identical to that of other scalarane sesterterpenes based on the NOESY cross-correlations at H_3 -22/ H_3 -20, H_2 -22/ H_3 -21, H_3 -21/ H_3 -23, H_3 -23/ H_3 -25, H-5/H-9, H-9/H-14, H-14/16, H-14/H-18, and H-16/H-24 (Figure 3). Based on the above findings, the configurations of stereogenic carbons of **2** were determined to be 5S*, 8R*, 9S*, 10R*, 13S*, 14S*, 16S*, 17S*, 18S*, 24S*, and 25R*. As 24-homoscalaranes **2–6** were isolated along with **1** from the same target organism, it is reasonable on biogenetic grounds to assume that **2–6** have the same absolute configurations as that of **1**. Therefore, the configurations of stereogenic centers of **2** were determined as 5S, 8R, 9S, 10R, 13S, 14S, 16S, 17S, 18S, 24S, and 25R (Supplementary Materials, Figures S9–S16).

Compound **3** (lendenfeldarane G) was obtained as an amorphous powder. Its molecular formula was determined to be $C_{29}H_{48}O_6$ by (+)-HRESIMS with six degrees of unsaturation. The IR spectra indicated the presence of OH (3462 cm^{-1}) and ester carbonyl (1729 cm^{-1}) functionalities. 1D and 2D NMR data disclosed a 6/6/6/6/5 pentacyclic skeleton, which was closely related to compound **2**. The only difference between these two compounds was a reductive substitution at C-12 in **3**. Comparing the 1H and ^{13}C NMR data (Table 2) of **3** with those of **2** showed an extra oxymethine signal (δ_C 72.0; δ_H 3.57, 1H,

br s, CH-12) and the 12-ketonic group was absent in **3**. Moreover, the substitution with -OH at position 12 can also be confirmed by HMBC (Figure 2) from H₃-23 (δ_{H} 0.93, 3H, s) to C-12 (δ_{C} 72.0), as well the COSY correlation (Figure 2) H₂-11/H-12. The configuration of **3** was confirmed to be unanimous as that of **2**. The NOESY correlations from H₃-23 to H-12 supported an *S* assignment of oxymethine carbon at C-12, then established the structure illumination of lendenfeldarane G (Supplementary Materials, Figures S17–S24).

Table 2. ¹H (400 MHz, CDCl₃) and ¹³C (100 MHz, CDCl₃) NMR data for 24-homoscalaranes **3** and **4**.

C/H	3		4	
	δ_{H} (J in Hz)	δ_{C} Mult.	δ_{H} (J in Hz)	δ_{C} Mult.
1	2.04 m; 0.82 m	34.5, CH ₂	2.03 m; 0.84 m	34.6, CH ₂
2	1.45 m; 1.56 m	18.4, CH ₂	1.45 m; 1.56 m	18.4, CH ₂
3	1.18 m; 1.43 m	41.5, CH ₂	1.17 br d (3.6); 1.42 m	41.5, CH ₂
4		32.9, C		33.0, C
5	1.10 m	56.6, CH	1.09 m	56.6, CH
6	1.56 m	18.1, CH ₂	1.56 m	18.1, CH ₂
7	1.09 m; 1.78 ddd (12.8, 3.2, 3.2)	42.0, CH ₂	1.08 m; 1.79 ddd (12.4, 3.2, 3.2)	42.1, CH ₂
8		37.6, C		37.6, C
9	1.57 m	52.0, CH	1.58 m	52.1, CH
10		40.1, C		40.2, C
11	1.89 m; 1.29 m	31.3, CH ₂	1.90 m; 1.29 m	31.3, CH ₂
12	3.57 br s	72.0, CH	3.67 ddd (3.2, 3.2, 3.2)	72.1, CH
13		39.0, C		39.0, C
14	1.38 m	52.2, CH	1.40 m	52.2, CH
15	1.86–1.98 m	25.9 CH ₂	1.91 m, 2.00 m	26.1 CH ₂
16	3.55 ddd (10.0, 10.0, 4.8)	72.9, CH	3.58 ddd (10.0, 10.0, 4.8)	73.0, CH
17	1.57 m	51.7, CH	1.58 m	52.1, CH
18	1.92 m	55.8, CH	1.94 m	56.7, CH
19	0.82 s	21.8, CH ₃	0.82 s	21.8, CH ₃
20	0.86 s	33.7, CH ₃	0.87 s	33.7, CH ₃
21	0.90 s	16.1, CH ₃	0.91 s	16.1, CH ₃
22	4.17 d (11.6); 4.56 d (11.6)	65.0, CH ₂	4.18 dd (12.0, 0.8); 4.57 d (12.0)	65.0, CH ₂
23	0.93 s	16.3, CH ₃	0.94 s	16.2, CH ₃
24	3.98 qd (6.0, 3.2)	79.5, CH	4.09 qd (6.0, 3.2)	79.7, CH
25	4.85 d (6.4)	103.9, CH	5.35 dd (6.8, 3.2)	96.5, CH
26	1.37 d (6.0)	20.3, CH ₃	1.36 d (6.0)	20.5, CH ₃
22-OAc		171.0, C		171.0, C
	2.05 s	21.2, CH ₃	2.06 s	21.2, CH ₃
25-OMe	3.45 s	56.6, CH ₃		

Lendenfeldarane H (**4**) was also obtained as an amorphous powder. The (+)-HRESIMS (*m/z* 501.31879, calculated for C₂₈H₄₆O₆ + Na, 501.31866) and NMR data of **4** indicated a molecular formula C₂₈H₄₆O₆ with six degrees of unsaturation. The IR spectra revealed the presence of OH (3292 cm^{−1}) and ester carbonyl (1740 cm^{−1}) groups. Based on the analysis of the NMR spectra between **3** and **4** (Table 2), a missing methoxy group signal was found, together with different assignments at position 25 (**4**: δ_{H} 5.35, 1H, dd, *J* = 6.8, 3.2 Hz/ δ_{C} 96.5; **3**: δ_{H} 4.85, 1H, d, *J* = 6.4 Hz/ δ_{C} 103.9). The HMBC cross peak (Figure 2) further revealed the replacement of an α -hydroxy group in **4**. The configuration of **4** was confirmed to be identical to that of **3** by NOESY experiment (Figure 5). Compound **4** was finally assigned, as shown in Figure 1 (Supplementary Materials, Figures S25–S32).

Lendenfeldarane I (**5**) was isolated as a white powder. The (+)-HRESIMS at *m/z* 497.28757 (calculated for C₂₈H₄₂O₆ + Na, 497.28736) indicated a molecular formula of C₂₈H₄₂O₆. The IR spectra showed absorptions for OH (3460 cm^{−1}), C=O (1701 cm^{−1}), and ester carbonyl (1745 cm^{−1}) functionalities. The ¹³C NMR data (Table 3) revealed 28 carbons signals stored by HSQC and DEPT, including a ketone at δ_{C} 211.9 and two ester carbonyls at δ_{C} 170.7 and 172.3. Therefore, three degrees of unsaturation

were built up, then the rest of the five unsaturated degrees were speculated to come from a pentacyclic homoscalarane. The 1D and 2D NMR data disclosed the existence of a compound 5-like 6/6/6/6/5 pentacyclic skeleton. The only found divergence was located at E-ring, the disappearance of the ketal carbon in **2** was replaced by an ester carbonyl in **5**. Then the HMBC (Figure 2) cross-peak from H-24 to C-17, C-18, and C-25 allowed the establishment of a γ -valerolactone. The stereochemical configuration was identical to that of other scalarane sesterterpenes [5] based on the NOESY (Figure 6) correlations at H₃-22/H₃-20, H₂-22/H₃-21, H₃-21/H₃-23, H-5/H-9, H-9/H-14, H-14/16, H-14/H-18, and H-16/H-24. Consequently, compound **5** was assigned as shown in Figure 1 (Supplementary Materials, Figures S33–S40).

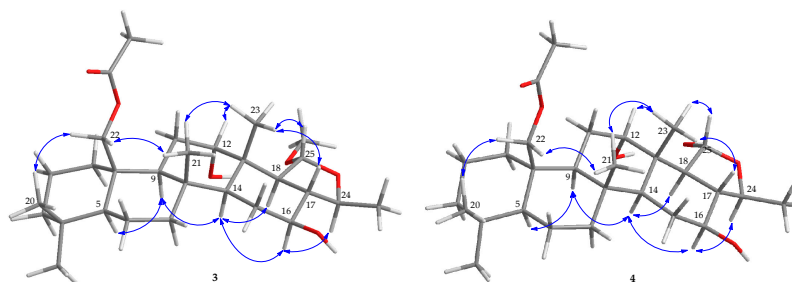


Figure 5. The selected NOESY correlations (↔) of **3** and **4**.

Table 3. ¹H and ¹³C NMR data for 24-homoscalaranes **5** and **6**.

C/H	5		6	
	δ_H (J in Hz) ^a	δ_C Mult. ^b	δ_H (J in Hz) ^c	δ_C Mult. ^d
1	1.99 m; 0.80 m	34.4, CH ₂	2.10 m; 0.51 ddd (12.6, 12.6, 3.6)	34.3, CH ₂
2	1.49 m; 1.64 m	18.0, CH ₂	1.43 m; 1.56 m	18.1, CH ₂
3	1.15 m; 1.45 m	41.4, CH ₂	1.13 m; 1.44 m	41.7, CH ₂
4		33.0, C		33.0, C
5	0.97 m	57.0, CH	0.98 dd (12.6, 2.4)	57.0, CH
6	1.50 m; 1.60 m	18.1, CH ₂	1.42 m; 1.57 m	17.9, CH ₂
7	0.99 m; 1.87 m	41.9, CH ₂	1.12 m, 1.90 m	42.0, CH ₂
8		38.5, C		37.0, C
9	1.28 br d (14.0)	63.3, CH	1.31 dd (7.2, 7.2)	53.5, CH
10		41.6, C		41.8, C
11	3.15 dd (14.0, 12.4); 2.51 dd (12.4, 2.4)	37.6, CH ₂	1.87–1.95 m	27.9, CH ₂
12		211.9, C	5.51 t (3.0)	73.8, CH
13		50.0, C		39.0, C
14	0.95 m	59.3, CH	1.79 dd (12.6, 2.4)	46.2, CH
15	1.50 m; 1.97 m	31.1, CH ₂	2.21 m	23.9 CH ₂
16	3.61 ddd (9.6, 9.6, 4.4)	72.0, CH	4.46 dd (5.4, 5.4)	61.7, CH
17	1.92 m	51.4, CH		161.3, C
18	2.58 d (14.4)	49.7, CH		135.7, C
19	0.84 s	21.8, CH ₃	0.77 s	21.8, CH ₃
20	0.87 s	33.7, CH ₃	0.87 s	33.8, CH ₃
21	1.18 s	16.6, CH ₃	1.10 s	16.3, CH ₃
22	4.17 dd (11.6, 1.6); 4.67 d (11.6)	64.6, CH ₂	3.88 dd (11.4, 4.8); 4.04 d (11.4)	62.8, CH ₂
23	1.38 s	14.7, CH ₃	1.16 s	19.4, CH ₃
24	4.30 qd (6.0, 2.4)	79.5, CH	5.07 q (6.6)	76.5, CH
25		172.3, C		170.5, C
26	1.53 d (6.0)	20.1, CH ₃	1.41 d (6.6)	18.3, CH ₃
12-OAc			1.98 s	169.8, C
22-OAc		170.7, C		21.2, CH ₃
	2.06 s	21.1, CH ₃		

^a 400 MHz, CDCl₃. ^b 100 MHz, CDCl₃. ^c 600 MHz, CDCl₃. ^d 150 MHz, CDCl₃.

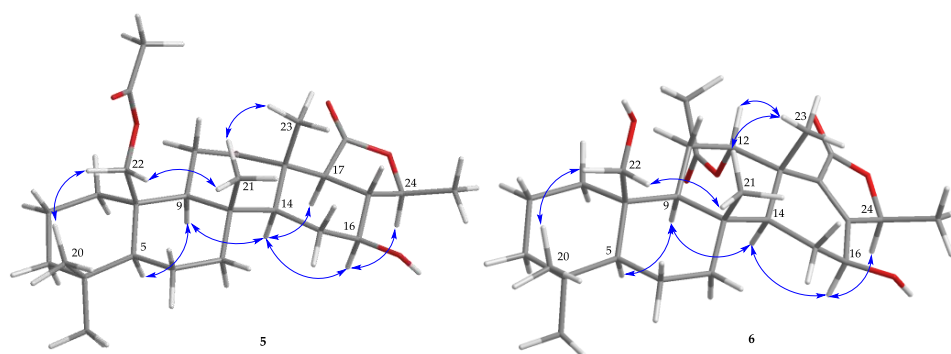


Figure 6. The selected NOESY correlations (↔) of **5** and **6**.

The molecular formula of lendenfeldarane **J** (**6**) was determined as $C_{28}H_{42}O_6$ from an $[M + Na]^+$ sodiated adduct ion at m/z 497.28729 (calcd. for $C_{28}H_{42}O_6 + Na$, 497.28736) and NMR data, revealing eight degrees of unsaturation. The 1H NMR data (Table 3) of **6** showed the five uncoupled (singlet) methyls at δ_H 0.77, 0.87, 1.10, 1.16, and 1.98; one doublet coupled methyl at δ_H 1.41 ($J = 6.6$ Hz); and two oxymethines at δ_H 5.51 (1H, t, $J = 3.0$ Hz) and 4.46 (1H, dd, $J = 5.4, 5.4$ Hz). The diastereotopic geminal proton at δ_H 3.88 (1H, dd, $J = 11.4, 4.8$ Hz) and 4.04 (1H, d, $J = 11.4$ Hz) were assumed to be an oxymethylene group. Based on the ^{13}C spectrum, **6** was found to possess an oxymethylene (δ_C 62.8), two oxymethines (δ_C 61.7 and 75.5), two ester carbonyls (δ_C 170.5 and 169.8), as well as a tetra-substituted olefin (δ_C 135.7 and 161.3) that accounted for an unsaturated degree. Thus, the above NMR data and the remaining five unsaturated degrees of **6** required a pentacyclic analogue. Based on the COSY and HMBC correlations (Figure 2), the planer structure of **6** was determined as shown in Figure 1. Compound **6** held a methylfuran-2(5H)-one moiety determined by HMBC cross-correlations from H-24 to C-17, C-18, and C-25. Furthermore, the relative configuration was confirmed by NOESY (Figure 6) correlations (H-12/H₃-23, H-16/H-14, and H-16/H-24) and the comparison with related compounds [5,21] (Supplementary Materials, Figures S41–S47).

Several lines of scientific and clinical evidences indicated that neutrophil oxidants and elastase secreted by inflammatory cells play critical roles in the pathogenesis of several inflammation-related disorders, such as psoriasis, arthritis, acute respiratory distress syndrome, and systemic lupus erythematos [22]. NADPH oxidase type 2 (NOX2) is an important enzyme that causes superoxide generation during respiratory burst, a predominant neutrophil function against foreign pathogens. An excessive amount of superoxide release can damage host tissues and lead to neutrophilic inflammation. Besides, another critical role, elastase, can contribute to neutrophil migration toward the inflammatory site, and activates neutrophil degranulation that causes the release of more elastolytic proteases to degrade the proteins from invading pathogens. Many recent studies have revealed that the pharmacological inhibition of NOX2 and elastase can restrict inflammatory responses, indicating the promising therapeutic potential of NOX2 and elastase inhibitors for treating neutrophil-dominant inflammatory disorders [23].

In the current study, the inhibition of fMLF-activated superoxide anion generation and elastase release were evaluated on metabolites **1–6** to characterize their property of anti-neutrophilic inflammation (Table 4). From these results, compound **1** showed the most potent inhibitory effect independently against elastase release, as well as a slight enhancing property in superoxide generation. With an additional acetyl functionality at C-22, compounds **2** and **3** both displayed activity of superoxide inhibition, but not elastase inhibition. These results suggest a crucial role of C-22-acetylation of homoscalarane on specifically affecting neutrophilic targets, such as NOX2 and elastase.

Table 4. Inhibitory effects of 24-homoscalaranes 1–6 on superoxide anion generation and elastase release by human neutrophils in response to fMLF.

Compound	Superoxide Anions			Elastase Release		
	IC ₅₀ (μM) ^a	Inh (Enh) ^b %		IC ₅₀ (μM) ^a	Inh %	
1		(11.35 ± 3.65)	*	1.74 ± 0.08	82.80 ± 3.91	***
2	6.17 ± 0.16	70.68 ± 3.86	***		26.15 ± 3.40	**
3	6.81 ± 0.52	62.92 ± 2.58	***		25.19 ± 4.01	**
4		7.13 ± 3.69			2.97 ± 1.63	
5		9.97 ± 4.38			6.81 ± 2.46	
6		4.52 ± 2.91			1.16 ± 0.89	

Percentage of inhibition (Inh %) at 10 μM. Results are presented as mean ± S.E.M. (*n* = 3–5). * *p* < 0.05, ** *p* < 0.01, *** *p* < 0.001 compared with the control (DMSO). ^a Concentration necessary for 50 % inhibition (IC₅₀). ^b Inh = inhibition, Enh = Enhancement.

3. Material and Methods

3.1. General Experimental Procedures

Optical rotations spectra were recorded on a JASCO P-1010 polarimeter (cell length 10 mm) (JASCO, Tokyo, Japan). IR spectra were obtained with a Thermo Scientific Nicolet iS5 FT-IR spectrophotometer (Thermo Fisher Scientific, Waltham, MA, USA). ECD spectra were recorded on JASCO-815 CD spectrometer. The NMR spectra were obtained on a JEOL ECZ 400S or an ECZ 600R NMR (JEOL, Tokyo, Japan), using the residual CHCl₃ signals (δ_H 7.26 ppm) and CDCl₃ (δ_C 77.0 ppm) as the internal standards for ¹H and ¹³C NMR, respectively. The coupling constants (*J*) are presented in Hz. ESIMS and HRESIMS data were collected on a Bruker 7 Tesla solariX FTMS system (Bruker, Bremen, Germany). TLC was performed on Kieselgel 60 F₂₅₄ (0.25 mm, Merck, Darmstadt, Germany) and/or RP-18 F_{254S} (0.25 mm, Merck, Darmstadt, Germany) coated plates and then visualized by spraying with 10% H₂SO₄ and heating on a hot plate. Silica gel 60 (Merck, 40–63 and 63–200 μm) were used for column chromatography. Normal-phase HPLC (NP-HPLC) was performed using a system comprising a pump (L-7110; Hitachi, Tokyo, Japan), an injection port (Rheodyne, 7725; Rohnert Park, CA, USA), and a semi-preparative normal-phase column (YMC-Pack SIL, SIL-06, 250 × 20 mm, D. S-5 μm; Sigma-Aldrich, St. Louis, MO, USA). Reverse-phase HPLC (RP-HPLC) was performed using a system comprising a pump (L-2130; Hitachi), a photodiode array detector (L-2455; Hitachi), an injection port (Rheodyne; 7725), and a reverse-phase column (Luna 5 μm, C18(2) 100Å AXIA Packed, 250 × 21.2 mm; phenomenex, Torrance, CA, USA).

3.2. Animal Material

Specimen of the marine sponges *Lendenfeldia* sp. was collected by hand using self-contained underwater breathing apparatus (scuba) diving off the coast of Southern Taiwan on September 5, 2012, and stored in a freezer until extraction. The specimen was identified by one of the authors (Y.M. Huang). A voucher specimen (NMMBA-TWSP-12006) was deposited in the National Museum of Marine Biology and Aquarium, Pingtung, Taiwan.

3.3. Extraction and Isolation

Sliced bodies of *Lendenfeldia* sp. (wet weight 1.21 kg) were extracted with ethyl acetate (EtOAc). The EtOAc layer (5.09 g) was separated on silica gel and eluted using a mixture of hexanes and EtOAc (stepwise, 100:1—pure EtOAc) to yield 11 fractions A–K. Fraction I was separated by NP-HPLC using a mixture of dichloromethane and acetone (4:1, flow rate: 3.0 mL/min) to afford 22 fractions I1–I22. Fraction I4 was separated by RP-HPLC using a mixture of MeOH and H₂O (85:15, flow rate: 5.0 mL/min) to afford **5** (1.3 mg). Fraction I6 was separated by RP-HPLC using a mixture of MeOH and H₂O (8:2, flow rate: 5.0 mL/min) to afford **6** (0.2 mg). Fraction I17 was separated by RP-HPLC using a mixture of MeOH and H₂O (8:2, flow rate: 5.0 mL/min) to afford **4** (3.2 mg). Fraction J was

separated by NP-HPLC using a mixture of *n*-hexane and acetone (2:1, flow rate: 2.0 mL/min) to afford **1** (0.2 mg), **2** (10.0 mg) and **3** (14.8 mg).

Lendenfeldarane E (**1**): Amorphous powder; $[\alpha]_D^{25}$ -94 (c 0.07, CHCl₃); IR (ATR) ν_{\max} 3438, 1701 cm⁻¹; ¹H and ¹³C NMR spectroscopic data, see Table 1; ESIMS: *m/z* 455 [M + Na]⁺; HRESIMS: *m/z* 455.31340 (calcd. for C₂₇H₄₄O₄ + Na, 455.31318).

Lendenfeldarane F (**2**): Amorphous powder; $[\alpha]_D^{25}$ $+38$ (c 0.50, CHCl₃); IR (ATR) ν_{\max} 3451, 1731, 1700 cm⁻¹; ¹H and ¹³C NMR spectroscopic data, see Table 1; ESIMS: *m/z* 513 [M + Na]⁺; HRESIMS: *m/z* 513.31878 (calcd. for C₂₉H₄₆O₆ + Na, 513.31866).

Lendenfeldarane G (**3**): Amorphous powder; $[\alpha]_D^{25}$ $+59$ (c 0.74, CHCl₃); IR (ATR) ν_{\max} 3462, 1729 cm⁻¹; ¹H and ¹³C NMR spectroscopic data, see Table 2; ESIMS: *m/z* 515 [M + Na]⁺; HRESIMS: *m/z* 515.33437 (calcd. for C₂₉H₄₈O₆ + Na, 515.33431).

Lendenfeldarane H (**4**): Amorphous powder; $[\alpha]_D^{25}$ $+73$ (c 0.16, CHCl₃); IR (ATR) ν_{\max} 3292, 1740 cm⁻¹; ¹H and ¹³C NMR spectroscopic data, see Table 2; ESIMS: *m/z* 501 [M + Na]⁺; HRESIMS: *m/z* 501.31879 (calcd. for C₂₈H₄₆O₆ + Na, 501.31866).

Lendenfeldarane I (**5**): Amorphous powder; $[\alpha]_D^{25}$ $+20$ (c 0.07, CHCl₃); IR (ATR) ν_{\max} 3460, 1745, 1701 cm⁻¹; ¹H and ¹³C NMR spectroscopic data, see Table 3; ESIMS: *m/z* 497 [M + Na]⁺; HRESIMS: *m/z* 497.28757 (calcd. for C₂₈H₄₂O₆ + Na, 497.28736).

Lendenfeldarane J (**6**): Amorphous powder; $[\alpha]_D^{25}$ -25 (c 0.07, CHCl₃); IR (ATR) ν_{\max} 3463, 1738 cm⁻¹; ¹H and ¹³C NMR spectroscopic data, see Table 3; ESIMS: *m/z* 497 [M + Na]⁺; HRESIMS: *m/z* 497.28729 (calcd. for C₂₈H₄₂O₆ + Na, 497.28736).

3.4. ECD Calculations

The lowest energies of **1a** (5*S*,8*R*,9*S*,10*R*,13*S*,14*S*,16*S*,17*S*,18*S*,24*S*, and 25*R*) and **1b** (5*R*,8*S*,9*R*,10*S*, 13*R*,14*R*,16*R*,17*R*,18*R*,24*R*, and 25*S*) were calculated and the data were performed by the Gaussian 09 software (Gaussian Inc., Wallingford, CT, USA). The density functional theory (DFT) at the B3LYP/6-31G(d) level in the gas phase were used to obtain the restricted conformation. The final ECD files were generated by GaussSum 2.2.5 software with a bandwidth σ of 0.5 eV. The calculated ECD and experimental ECD curves were drawn by Excel.

3.5. Superoxide Anion Generation and Elastase Release by Human Neutrophils

Human neutrophils were obtained from healthy human volunteers and were isolated by Ficoll centrifugation and dextran sedimentation. Purified neutrophils were re-suspended in calcium (Ca²⁺)-free Hank's balanced salt solution (HBSS) buffer at pH 7.4 and were maintained at 4 °C before use. For the superoxide anion generation assay, neutrophils (6×10^5 cell/mL) were equilibrated in ferricytochrome *c* (0.6 mg/mL) and Ca²⁺ (1 mM) at 37 °C for 5 min and incubated with DMSO (0.1%) or tested compounds for another 5 min [24]. Cells were activated with formyl-methionyl-leucyl-phenylalanine (fMLF, 0.1 μ M) for 10 min after priming with cytochalasin B (CB, 1 μ g/mL) for 3 min. The change in absorbance was monitored continuously at 550 nm with a spectrophotometer (Hitachi U-3010). For the elastase release assay, neutrophils (6×10^5 cell/mL) were equilibrated in MeO-Suc-Ala-Ala-Pro-Val-*p*-nitroanilide (100 μ M) and Ca²⁺ (1 mM) at 37 °C for 5 min and incubated with dimethyl sulfoxide (DMSO) (0.1%) or test compounds for another 5 min. The cells were activated with fMLF (0.1 μ M) for 10 min after the priming with CB (0.5 μ g/mL) for 3 min. The change in absorbance was monitored continuously at 405 nm with a spectrophotometer [24]. The results are recorded as the mean \pm SEM of three measurements. The inhibition % was measured at 10 μ M concentration of each compound, and IC₅₀ values were estimated from dose-response curves. Statistical analysis was carried out using Student's *t*-tests with SigmaPlot (Systat Software, San Jose, CA, USA).

4. Conclusions

The current work is the first to illustrate the anti-neutrophilic inflammatory properties of scalarane-type sesterterpenoids, and reported a series of metabolites with novel structures, lendenfeldaranes E–J (1–6). These results also suggested a structural dependent specificity of C-22-acetylation in neutrophilic targets, which motivates future research to illustrate structural dependent specificity as well as further clarify the corresponding molecular mechanisms of the active leads.

Supplementary Materials: Supplementary Materials according to this article can be found online at <http://www.mdpi.com/1660-3397/18/9/434/s1>. HRESIMS, 1D and 2D NMR spectra of compounds 1–6.

Author Contributions: B.-R.P., S.S.-F.Y., C.-Y.D., and P.-J.S. conceived and designed the experiments; B.-R.P., Y.-Y.C., J.-H.S., Y.-C.C. and Y.M.H. performed the sample collections, species identification, extraction, isolation, and structures determination; the pharmacological experiments were carried out by P.-J.C.; P.-J.S. contributed reagents and analysis tools; B.-R.P., K.-H.L. and P.-J.S. participated in data interpretation, wrote the manuscript and revised the paper. All authors have read and agreed to the published version of the manuscript.

Funding: The research was founded by the Ministry of Science and Technology of Taiwan (MOST 106-2320-B-291-001-MY3, 107-2320-B-291-001-MY3, and 109-2320-B-291-001-MY3).

Acknowledgments: This work was mainly supported by grants from the National Museum of Marine Biology and Aquarium; and the Ministry of Science and Technology (Grant Nos MOST 106-2320-B-291-001-MY3, 107-2320-B-291-001-MY3, and 109-2320-B-291-001-MY3), Taiwan, awarded to P.-J.S.

Conflicts of Interest: The authors declare no conflict of interest.

References

- Kazlauskas, R.; Murphy, P.T.; Wells, R.J. Five new C₂₆ tetracyclic terpenes from a sponge (*Lendenfeldia* sp.). *Aust. J. Chem.* **1982**, *35*, 51–59. [\[CrossRef\]](#)
- Alvi, K.A.; Crews, P. Homoscalarane sesterterpenes from *Lendenfeldia frondosa*. *J. Nat. Prod.* **1992**, *55*, 859–865. [\[CrossRef\]](#) [\[PubMed\]](#)
- Stessman, C.C.; Ebel, R.; Corvino, A.J.; Crews, P. Employing dereplication and gradient 1D NMR methods to rapidly characterize sponge-derived sesterterpenes. *J. Nat. Prod.* **2002**, *65*, 1183–1186. [\[CrossRef\]](#) [\[PubMed\]](#)
- Chill, L.; Rudi, A.; Akinin, M.; Loya, S.; Hizi, A.; Kashman, Y. New sesterterpenes from Madagascan *Lendenfeldia* sponges. *Tetrahedron* **2004**, *60*, 10619–10626. [\[CrossRef\]](#)
- Peng, B.-R.; Lai, K.-H.; Chen, Y.-Y.; Su, J.-H.; Huang, Y.M.; Chen, Y.-H.; Lu, M.-C.; Yu, S.S.-F.; Duh, C.-Y.; Sung, P.-J. Probing anti-proliferative 24-homoscalaranes from a sponge *Lendenfeldia* sp. *Mar. Drugs* **2020**, *18*, 76. [\[CrossRef\]](#)
- Oda, Y.; Zhang, Q.; Matsunaga, S.; Fujita, M.J.; Sakai, R. Two new mycosporine-like amino acids LC-343 and mycosporine-ethanolamine from the Micronesian marine sponge *Lendenfeldia chondrodes*. *Chem. Lett.* **2017**, *46*, 1272–1274. [\[CrossRef\]](#)
- Sera, Y.; Adachi, K.; Shizuri, Y. A new epidioxy sterol as an antifouling substance from a Palauan marine sponge, *Lendenfeldia chondrodes*. *J. Nat. Prod.* **1999**, *62*, 152–154. [\[CrossRef\]](#)
- Radwan, M.M.; Manly, S.P.; Ross, S.A. Two new sulfated sterols from the marine sponge *Lendenfeldia dendyi*. *Nat. Prod. Commun.* **2019**, *2*, 901–904. [\[CrossRef\]](#)
- Sakai, R.; Kamiya, H. 1-Deoxynojirimycin derivatives from the marine sponge *Lendenfeldia chondrodes*. *J. Antibiot.* **2006**, *59*, 507–511. [\[CrossRef\]](#)
- Dai, J.; Liu, Y.; Zhou, Y.-D.; Nagle, D.G. Cytotoxic metabolites from an Indonesian sponge *Lendenfeldia* sp. *J. Nat. Prod.* **2007**, *70*, 1824–1826. [\[CrossRef\]](#)
- Liu, Y.; Liu, R.; Mao, S.-C.; Morgan, J.B.; Jekabsons, M.B.; Zhou, Y.-D.; Nagle, D.G. Molecular-targeted antitumor agents. 19. Furospingolide from a marine *Lendenfeldia* sp. sponge inhibits hypoxia-inducible factor-1 activation in breast tumor cells. *J. Nat. Prod.* **2008**, *71*, 1854–1860. [\[CrossRef\]](#) [\[PubMed\]](#)
- Radwan, M.M.; Wanas, A.S.; Fronczek, F.R.; Jacob, M.R.; Ross, S.A. Polybrominated diphenyl ethers from the marine organisms *Lendenfeldia dendyi* and *Simularia dura* with anti-MRsa activity. *Med. Chem. Res.* **2015**, *24*, 3398–3404. [\[CrossRef\]](#)

13. Lai, Y.-Y.; Chen, L.-C.; Wu, C.-F.; Lu, M.-C.; Wen, Z.-H.; Wu, T.-Y.; Fang, L.-S.; Wang, L.-H.; Wu, Y.-C.; Sung, P.-J. New cytotoxic 24-homosclalarane sesterterpenoids from the sponge *Ircinia felix*. *Int. J. Mol. Sci.* **2015**, *16*, 21950–21958. [[CrossRef](#)] [[PubMed](#)]
14. Lai, Y.-Y.; Lu, M.-C.; Wang, L.-H.; Chen, J.-J.; Fang, L.-S.; Wu, Y.-C.; Sung, P.-J. New scalarane sesterterpenoids from the Formosan sponge *Ircinia felix*. *Mar. Drugs* **2015**, *13*, 4296–4309. [[CrossRef](#)] [[PubMed](#)]
15. Chang, Y.-C.; Tseng, S.-W.; Liu, L.-L.; Chou, Y.; Ho, Y.-S.; Lu, M.-C.; Su, J.-H. Cytotoxic sesterterpenoids from a sponge *Hippospongia* sp. *Mar. Drugs* **2012**, *10*, 987–997. [[CrossRef](#)]
16. Lai, K.-H.; Liu, Y.-C.; Su, J.-H.; El-Shazly, M.; Wu, C.-F.; Du, Y.-C.; Hsu, Y.-M.; Yang, J.-C.; Weng, M.-K.; Chou, C.-H.; et al. Antileukemic scalarane sesterterpenoids and meroditerpenoid from *Carteriospongia* (*Phyllospongia*) sp., induce apoptosis via dual inhibitory effects on topoisomerase II and Hsp90. *Sci. Rep.* **2016**, *6*, 36170. [[CrossRef](#)]
17. González, M.A. Scalarane sesterterpenoids. *Curr. Bioact. Compd.* **2010**, *6*, 178–206. [[CrossRef](#)]
18. Hahn, D.; Won, D.H.; Mun, B.; Kim, H.; Han, C.; Wang, W.; Chun, T.; Park, S.; Yoon, D.; Choi, H.; et al. Cytotoxic scalarane sesterterpenes from a Korean marine sponge *Psammocinia* sp. *Bioorg. Med. Chem. Lett.* **2003**, *23*, 2336–2339. [[CrossRef](#)]
19. Alarif, W.M.; Al-Lihaibi, S.S.; Ghandourah, M.A.; Orif, M.I.; Basaif, S.A.; Ayyad, S.E.N. Cytotoxic scalarane-type sesterterpenes from the Saudi Red Sea sponge *Hyrtios erectus*. *J. Asian Nat. Prod. Res.* **2016**, *18*, 611–617. [[CrossRef](#)]
20. Lee, S.M.; Kim, N.-H.; Lee, S.; Kim, Y.N.; Heo, J.D.; Jeong, E.J.; Rho, J.-R. Deacetylphylloketal, a new phylloketal derivative from a marine sponge, genus *Phyllospongia*, with potent anti-inflammatory activity in in vitro co-culture model of intestine. *Mar. Drugs* **2019**, *17*, 634. [[CrossRef](#)]
21. Fu, X.; Zeng, L.M.; Su, J.Y.; Pais, M.; Potier, P. Scalarane-type bishomosesterterpenes from the sponge *Phyllospongia foliascens*. *J. Nat. Prod.* **1992**, *55*, 1607–1613. [[CrossRef](#)]
22. Sachs, C.W.; Christensen, R.H.; Pratt, P.C.; Lynn, W.S. Neutrophil elastase activity and superoxide production are diminished in neutrophils of alcoholics. *Am. Rev. Respir. Dis.* **1990**, *141*, 1249–1255. [[CrossRef](#)] [[PubMed](#)]
23. Liu, F.-C.; Yu, H.-P.; Chen, P.-J.; Yang, H.-W.; Chang, S.-H.; Tzeng, C.-C.; Cheng, W.-J.; Chen, Y.-R.; Chen, Y.-L.; Hwang, T.-L. A novel NOX2 inhibitor attenuates human neutrophil oxidative stress and ameliorates inflammatory arthritis in mice. *Redox Biol.* **2019**, *26*, 101273. [[CrossRef](#)] [[PubMed](#)]
24. Chen, P.-J.; Ko, I.-L.; Lee, C.-L.; Hu, H.-C.; Chang, F.-R.; Wu, Y.-C.; Leu, Y.-L.; Wu, C.-C.; Lin, C.-Y.; Pan, C.-Y.; et al. Targeting allosteric site of AKT by 5,7-dimethoxy-1,4-phenanthrenequinone suppresses neutrophilic inflammation. *EBioMedicine* **2019**, *40*, 528–540. [[CrossRef](#)] [[PubMed](#)]



© 2020 by the authors. Licensee MDPI, Basel, Switzerland. This article is an open access article distributed under the terms and conditions of the Creative Commons Attribution (CC BY) license (<http://creativecommons.org/licenses/by/4.0/>).



Article

Preparation and Characterization of Surface Heat Sintered Nanohydroxyapatite and Nanowhitlockite Embedded Poly (Lactic-co-glycolic Acid) Microsphere Bone Graft Scaffolds: In Vitro and in Vivo Studies

Gils Jose ¹, K.T. Shalumon ^{1,*}, Han-Tsung Liao ² , Chang-Yi Kuo ¹ and Jyh-Ping Chen ^{1,2,3,4,*}

¹ Department of Chemical and Materials Engineering, Chang Gung University, Kwei-San, Taoyuan 33302, Taiwan; gilsjose84@gmail.com (G.J.); onesky1997@gmail.com (C.-Y.K.)

² Department of Plastic and Reconstructive Surgery and Craniofacial Research Center, Chang Gung Memorial Hospital, Linkou, Chang Gung University School of Medicine, Kwei-San, Taoyuan 33305, Taiwan; lia01211@gmail.com

³ Research Center for Food and Cosmetic Safety, Research Center for Chinese Herbal Medicine, College of Human Ecology, Chang Gung University of Science and Technology, Taoyuan 33302, Taiwan

⁴ Department of Materials Engineering, Ming Chi University of Technology, Tai-Shan, New Taipei City 24301, Taiwan

* Correspondence: shalumon@gmail.com (K.T.S.); jpchen@mail.cgu.edu.tw (J.-P.C.); Tel.: +886-3211-8800 (ext. 3741) (K.T.S.); +886-3211-8800 (ext. 5298) (J.-P.C.)

Received: 9 December 2019; Accepted: 10 January 2020; Published: 14 January 2020



Abstract: In the context of using bone graft materials to restore and improve the function of damaged bone tissues, macroporous biodegradable composite bone graft scaffolds have osteoinductive properties that allow them to provide a suitable environment for bone regeneration. Hydroxyapatite (HAP) and whitlockite (WLKT) are the two major components of hard tissues such as bone and teeth. Because of their biocompatibility and osteoinductivity, we synthesized HAP (nHAP) and WLKT nanoparticles (nWLKT) by using the chemical precipitation method. The nanoparticles were separately incorporated within poly (lactic-co-glycolic acid) (PLGA) microspheres. Following this, the composite microspheres were converted to macroporous bone grafts with sufficient mechanical strength in pin or screw shape through surface sintering. We characterized physico-chemical and mechanical properties of the nanoparticles and composites. The biocompatibility of the grafts was further tested through in vitro cell adhesion and proliferation studies using rabbit bone marrow stem cells. The ability to promote osteogenic differentiation was tested through alkaline phosphatase activity and immunofluorescence staining of bone marker proteins. For in vivo study, the bone pins were implanted in tibia bone defects in rabbits to compare the bone regeneration ability through H&E, Masson's trichrome and immunohistochemical staining. The results revealed similar physico-chemical characteristics and cellular response of PLGA/nHAP and PLGA/nWLKT scaffolds but the latter is associated with higher osteogenic potential towards BMSCs, pointing out the possibility to use this ceramic nanoparticle to prepare a sintered composite microsphere scaffold for potential bone grafts and tissue engineered implants.

Keywords: whitlockite; hydroxyapatite; poly (lactic-co-glycolic acid); microsphere; bone graft; bone marrow stem cells

1. Introduction

Bone fractures and bone disorders among middle aged people are increasing day by day, which demands the development of suitable bone grafts as an essential prerequisite to fix bone defects.

Recent advancements in bone graft materials including polylactide, titanium, and hydroxyapatite (HA) have led to the introduction of various products including bone plates and biodegradable bone pins that can cure many bone defects [1,2]. Although many bone grafts and similar tissue engineering scaffolds possess biodegradability, biocompatibility, and adequate mechanical strength, their ability to reconstruct defected areas has not been very high in many experiments [3]. Hence, developing a bio-absorbable bone graft with osteogenic properties will be helpful to achieve a better success rate. Osteobiologic materials are engineered biomaterials that can serve as implant materials for bone repair and remodeling. Due to the capacity of these osteobiologic materials to promote the healing of bone fractures, they have been the most discussed biomaterials in the past decade [4]. The osteobiologic materials are expected to provide a biocompatible surface that can promote cell attachment and migration after implantation. Due to the similarities of these materials with the body, the scaffolds made of osteobiologic materials can mimic the bodies' inherent capacity to heal defects and to regenerate bone tissues [5]. Although various organic materials have been used in clinical applications for bone regeneration, using bioceramics to treat damaged hard tissue has also gained significant attention [6]. Among the biomimicking ceramics, calcium phosphate-based bioceramics have been widely used due to their compositional similarity with human hard tissue and excellent biocompatibilities [7]. Hydroxyapatite ($\text{Ca}_{10}(\text{PO}_4)_6(\text{OH})_2$) and whitlockite ($\text{Ca}_{18}\text{Mg}_2(\text{HPO}_4)_2(\text{PO}_4)_{12}$) are the most widely used materials in this family due to their osteoconductivity and their compositional and crystallographic similarities with natural bone materials [8]. Moreover, nanoparticles prepared from these bioceramic materials can further enhance their physical as well as biological properties, due to the greater surface area provided [9,10].

Hydroxyapatite (HAP), the most commonly used form of calcium phosphate ceramics, has been used for a variety of biomedical applications, including matrices for controlled drug release and bone tissue engineering scaffolding materials [11,12]. Due to the chemical similarity of HAP with the inorganic component of a bone matrix, it exhibits osteoconductivity as well as a strong affinity towards hosting hard tissues. It possesses high thermodynamic stability in physiological conditions and is able to form direct chemical bonding to the bone [13]. In addition to this, synthetic HAP offers high biocompatibility, slow biodegradability in situ, as well as good osteoconductive and osteoinductive properties [14,15]. On the other hand, whitlockite (WLKT), consisting of Ca^{2+} , Mg^{2+} , and PO_4^{3-} ions, is another component that constitutes about 20 to 30 wt% of the inorganic phase of human bone [16,17]. The WLKT is the second most abundant ceramic material present in bones and also known to exist with a high ratio in early stage bone tissue formation [18,19]. As bone stores 99% of the Ca^{2+} and more than 50% of the Mg^{2+} in our body, WLKT is used as a storehouse for Mg^{2+} since the other major bone mineral HAP could hardly accommodate Mg^{2+} in its lattice structure [19]. Although biocompatibility and chemical compositions of WLKT and HAP are quite similar, the capacity of WLKT to enhance both cell proliferation and mineralization is comparatively high compared to HAP [20]. In addition to this, different studies suggest the stability of WLKT in acidic condition is higher than HAP [21]. The acidic stability of WLKT plays a major role in its capability to promote bone mineralization. This property is connected with the better resorption of organic bone matrices through proteinase in an acidic pH condition, which is necessary for bone formation. Even though HAP and WLKT hold all the biological properties required for rapid bone formation, the low mechanical strength and fracture toughness act as an obstacle for the load-bearing applications [22]. Hence, the fabrication of composites by incorporating bioceramics in polymeric materials is an obvious solution for the aforementioned problem [14]. Among the various polymeric materials available, poly (lactic-co-glycolic acid) (PLGA) is a biocompatible and biodegradable material that can provide enough mechanical strength for the composite to act as a bone graft [23].

In this work, we prepared a composite PLGA microsphere containing nanosized HAP (nHAP) or WLKT (nWLKT) to combine the advantages of improved mechanical properties of a polymeric material and the osteogenic properties of bioceramic nanoparticles (Figure 1, step 1 and 2). The composite microspheres were heat sintered to fabricate macroporous bone grafts in different shapes such as pins and screws (Figure 1, step 3). The PLGA/nHAP and PLGA/nWLKT microsphere based bone grafts thus fabricated were subsequently used for comparison of the physico-chemical, mechanical properties, and biological properties. In vitro studies were then conducted using rabbit bone marrow stem cells (BMSCs) to study cell attachment, proliferation, and differentiation within the porous grafts. Further, in vivo experiments were performed using the rabbit tibia defect model to examine the efficacy of the grafts for bone regeneration.

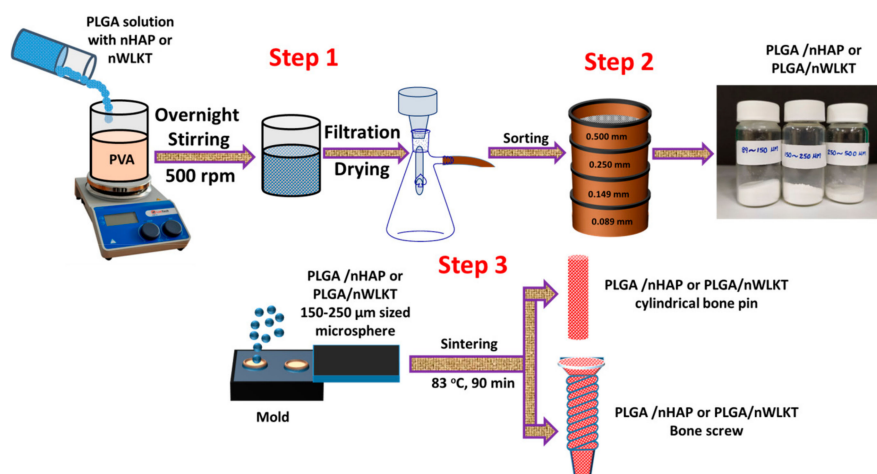


Figure 1. The schematic representation of poly (lactic-co-glycolic acid) (PLGA)/nHAP or PLGA/nWLKT microsphere preparation (step 1, 2) and the subsequent fabrication process of microsphere scaffold by using surface sintering (step 3).

2. Results and Discussion

2.1. Characterization of nHAP and nWLKT

The morphology of prepared nHAP and nWLKT particles was analyzed using scanning electron microscopy (SEM) analysis, from which particles were found to be uniform in size and shape, and with minimum agglomeration (Figure 2A,B). The nHAP particles displayed a round-shaped morphology with an average diameter of ~100 nm (Figure 2A), while nWLKT particles showed its characteristic rhombohedral shape (Figure 2B) [16]. The elemental compositions of both samples were identified through energy dispersive X-ray spectroscopy (EDS) analysis. In nHAP, the measured calcium (Ca) to phosphate (P) stoichiometric ratio was 1.87 (Figure 2C). As this value is slightly higher than the theoretical value of 1.67, we hypothesized that this might be due to the formation of calcium-rich hydroxyapatite. The EDS spectrum of nWLKT revealed the presence of Mg elemental peak with its $\text{Ca}_{18}\text{Mg}_2(\text{HPO}_4)_2(\text{PO}_4)_{12}$ molecular structure in contrast to $\text{Ca}_{10}(\text{PO}_4)_6(\text{OH})_2$ for nHAP (Figure 2D). Moreover, the experimental stoichiometric ratio of Ca/P was 1.26, close to the theoretical value of 1.29.

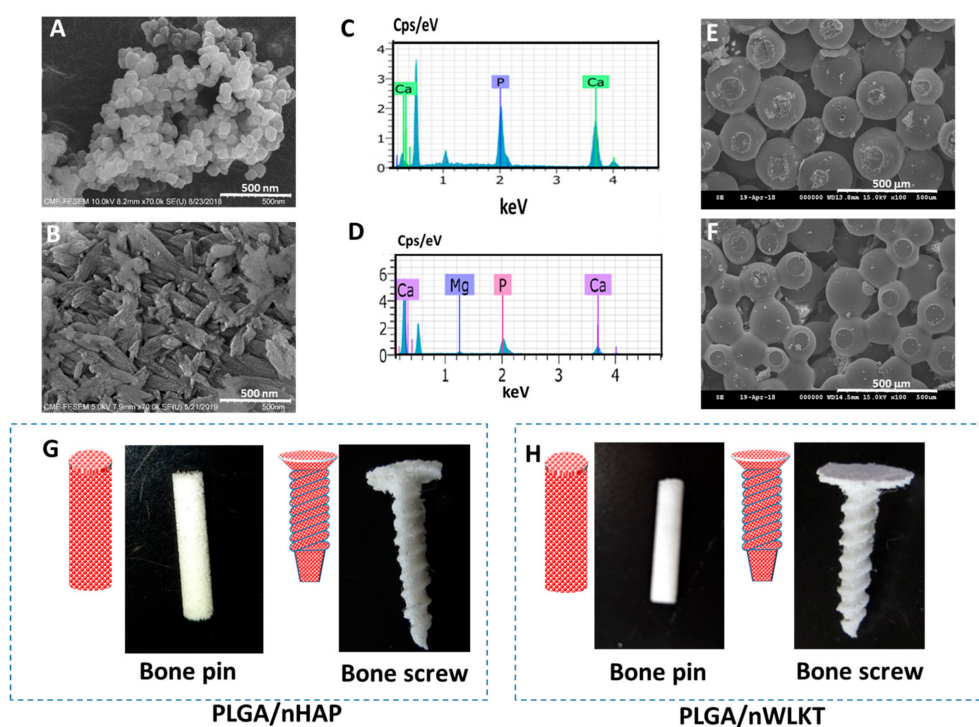


Figure 2. The characterization of nHAP and nWLKT by using scanning electron microscopy (SEM) (A,B) and electron dispersive X-ray spectroscopy (EDS) (C,D). The SEM images of PLGA/nHAP microsphere scaffold (E) and PLGA/nWLKT microsphere scaffold (F) confirm uniform surface sintering. Schematic drawings and photographs of PLGA/nHAP (G) and PLGA/nWLKT (H) bone grafts in a pin and screw shape after the surface sintering process.

2.2. Characterization of PLGA/nHAP and PLGA/nWLKT

PLGA microspheres containing nHAP or nWLKT with sizes ranging from 150 to 250 μm were chosen from the crude samples and further fabricated into scaffolds in pin or screw shapes (Figure 1). The SEM images of the microspheres are shown in Figure S1. In order to obtain the required microsphere size for surface sintering, the PLGA concentration and rotation speed during the mixing process were optimized to be 13.3% and 600 rpm. The PLGA concentration and rotation speed were optimized by using the trial-and-error method. As the concentration varied, the size and size distribution of the microspheres as well as the yield of microspheres changed (Figure S2, Supplementary Materials). All microspheres were washed in double distilled (DD) water to avoid surface attachment of PVA and were dried prior to storage in a desiccator. Since it is desirable to reach similar final concentrations of nHAP and nWLKT in the microsphere, an initial trial-and-error pilot study was conducted to estimate the final loading percentage of nHAP and nWLKT in the microsphere beforehand. It was found that the encapsulation efficacy of nHAP and nWLKT in the composite microspheres was drastically different, as the latter showed a lower value. A series of experiments with a range of nWLKT concentrations in PLGA solution further concluded that encapsulation of 1.2 g nWLKT in 4 g PLGA led to the same encapsulation amount of nanoparticles using 0.8 g nHAP and 4 g PLGA. This was confirmed by the thermogravimetric analysis (TGA) shown in Figure S3 (Supplementary Materials). This condition was thus utilized for preparing PLGA/nHAP and PLGA/nWLKT microspheres. The SEM images of sintered microsphere scaffold of PLGA/nHAP (Figure 2E) and PLGA/nWLKT (Figure 2F) confirmed the uniform surface-to-surface sintering with an average pore size of $234 \pm 64 \mu\text{m}$ and $286 \pm 82 \mu\text{m}$, which could be seen in the lower and higher magnification SEM images in Figure S4 (Supplementary Materials). The gross views of the pin and screw shaped scaffolds of PLGA/nHAP (Figure 2G) and PLGA/nWLKT (Figure 2H) indicate that the intended shape and morphology of the bone graft could be achieved through surface sintering of the composite microspheres, which endorsed the possibility

of applying this manufacturing process to fabricate bone grafts with suitable shapes for bone surgeries. Another relevant issue while considering scaffolds for tissue replacements is the porosity. Although our bone pin was intended as an acellular bone graft implant without cells, its porosity was also crucial for cellular penetration of stem cells from the surrounding tissues into the graft interior. It therefore was helpful to encompass the use of a 3D scaffold to provide a suitable microenvironment for cell ingrowth and differentiation to regenerate damaged tissues [24]. Since macroporous materials can also efficiently handle waste and nutrient exchange more efficiently during the regeneration phase, achieving adequate porosity without tailoring mechanical properties is a tactical factor in bone graft development. The fabricated bone pin developed here attained a porosity of 49.6% (PLGA/nHAP) and 47.3% (PLGA/nWLKT), which is sufficient for cell penetration [25].

The Fourier-transformed infrared spectroscopy (FTIR) analysis was conducted to identify the chemical compositions within the microsphere scaffolds (Figure 3A). The characteristic stretching and bending vibrations of the scaffolds were recorded and compared with the pristine nHAP, nWLKT and PLGA. Considering the nHAP spectrum, phosphate stretching vibrations were observed at 564, 617, and 1030 cm^{-1} . The band at 1412 cm^{-1} belonged to the hydroxyl group. The sharp peak at 1644 cm^{-1} and a broad absorption at 3339–3579 cm^{-1} might be due to the moisture present in the samples. nWLKT also had similar peaks due to its structural resemblance with nHAP where bands at 542 and 617 cm^{-1} could be assigned to the phosphate group, while bands at 3444 cm^{-1} could be due to the hydroxyl stretching. PLGA displayed characteristic peaks for the alkyl group in the broad range of 2942–3010 cm^{-1} , the hydroxyl vibrations were observed at 760 and 3526–3669 cm^{-1} , C=O stretching at 1765 cm^{-1} and C-C stretching bands at 1104 cm^{-1} [26]. Both PLGA/nHAP and PLGA/nWLKT microsphere scaffolds displayed all characteristic peaks associated with PLGA, nHAP, and nWLKT. The bands at 572, 617, 1037, 1435, 1637, and 3514 cm^{-1} as well as at 580, 1089, 1644, and 3022 cm^{-1} denoted the presence of nHAP and nWLKT, respectively. Similarly, the peaks that appeared around 767, 872, 1773, and 3010 cm^{-1} in both scaffolds confirmed the presence of PLGA. Thus, the FTIR study clearly proved the effective incorporation of nHAP and nWLKT in PLGA microsphere scaffolds. In addition to FTIR, the presence of the ceramic counterparts in the composites was further examined through the identification of crystalline peaks by X-ray diffraction (XRD) analysis. As shown in Figure 3B, nHAP had major diffraction peaks at 2θ values 25.9 and 32°, along with other minor peaks at 33.1, 34.2, 39.9, 46.8, and 49.5°. PLGA had only a single diffraction peak at 25.5°. When combined with nHAP, PLGA/nHAP displayed all the characteristic peaks associated with nHAP and PLGA (Figure 3B). When examining the XRD pattern of nWLKT, peaks at 2θ values of 26.5, 31.2, and 34.7° were found to be unique in comparison with the nHAP pattern, which again all appeared in the pattern of PLGA/nWLKT.

The thermal stability of all samples was evaluated using thermogravimetric analysis (TGA). As shown in Figure 3C, PLGA copolymer possesses low thermal stability compared with ceramics and started to decompose at 180 °C, while complete decomposition occurred at around 340 °C [27]. In contrast, nHAP and nWLKT remained almost unchanged in weight up to 700 °C. The TGA curves for both PLGA/nHAP and PLGA/nWLKT showed ~12.4% residual weight when the temperature was increased to 700 °C, indicating the same weight ratio of the ceramic material (12.4%) was loaded into the composite microspheres. As explained before, it was observed that the loading efficiency of nWLKT in the microspheres were lower than that of nHAP during the emulsification step and therefore pilot TGA experiments were performed with different nWLKT loading concentrations to achieve a desirable final concentration of nWLKT in the microspheres. The overlapping TGA curves PLGA/nHAP and PLGA/nWLKT therefore justified the rationale to compare two different composite scaffolds based on the same ceramic content in the bone graft implant. The higher thermal stability of PLGA/nHAP or PLGA/nWLKT could be further confirmed from the increase of peak decomposition temperature from 346 °C to 375 °C after incorporating nHAP or nWLKT in PLGA (Figure 3D).

As a bone pin scaffold was intended to be applied in a load bearing condition, the compressive mechanical properties of the scaffolds were examined first. The respective stress-strain curves of

PLGA/nHAP and PLGA/nWLKT bone pins in a dry state are shown in Figure 3E. The Young's modulus and the yield stress were found to be similar for both pin-shaped scaffolds, which showed good mechanical properties with unbreakable strength, and even reached the maximum loading capacity of the testing machine. The Young's modulus calculated from the stress-strain curve was 80.39 ± 17.5 for PLGA/nHAP and 77.25 ± 13.1 MPa for PLGA/nWLKT, which is of suitable mechanical strength to be used as a bone substitute. The high mechanical strength of both scaffolds could be ascribed to their surface-to-surface interconnectivity, which offers physical surface sintering and blending of surface PLGA in neighboring microspheres after heating. In order to evaluate the mechanical properties that simulate the wet condition in vivo, the samples were immersed in PBS for one hour before the mechanical testing. As shown in Figure 3F, the stress-strain curves which showed a similar trend to before were obtained in the wet state, where scaffolds remained unbroken, even after reaching the maximum loading capacity. Nonetheless, the Young's modulus decreased to 37.37 ± 8.7 (PLGA/nHAP) and 39.86 ± 11.8 MPa (PLGA/nWLKT) and no significant difference was found to in the dry state.

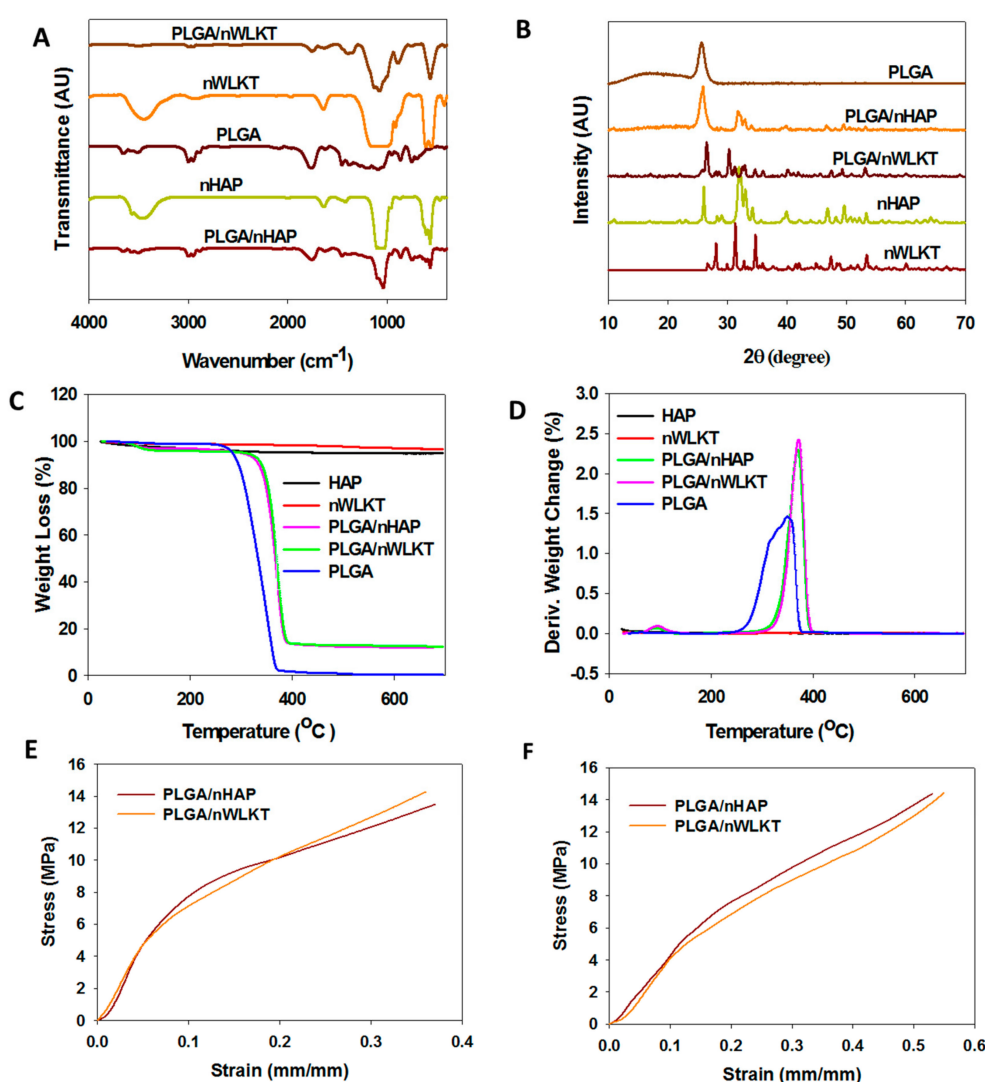


Figure 3. Characterization of nHAP, nWLKT, PLGA, PLGA/nHAP, and PLGA/nWLKT by Fourier-transformed infrared spectroscopy (FTIR) (A), X-ray diffraction (XRD) (B), thermogravimetric analysis (TGA) (C), and differential thermogravimetry (DTG) (D). The stress-strain curves of PLGA/nHAP and PLGA/nWLKT microsphere scaffold obtained through compressive mechanical testing are shown in (E) and (F) for dry and wet samples.

2.3. In Vitro Studies

2.3.1. Cell Morphology

The morphology of BMSCs cultured in PLGA/nHAP and PLGA/nWLKT microsphere scaffolds up to 28 days was observed under SEM and reported in Figure 4. Though the graft is an acellular implant scaffold, possible cell interaction after in vivo grafting should be assessed through cellular response from in vitro BMSCs culture. At day 0, the cells displayed more rounded morphology in both samples by weakly adhering to the microsphere surface. However, a rapid change in adhesion pattern was observed after seven days, where most of the cells spread alongside the curved surface of the microsphere. A higher density of cell population was observed within the pores of the scaffold on day 14, confirming the presence of homogenous cell growth that was ideal for regeneration. Cells started to migrate to the whole microsphere surface and also to the microsphere intersections after 21 days, leading to bridging between microsphere surfaces while filling the pores, which is ideal for tissue regeneration [28]. A thick cell covering layer was found on day 28 for both scaffolds. Apart from covering individual microspheres, the pores inside the scaffolds were also filled with cellular extensions due to continued cell growth with time. The mineralized nodules observed after 14 days further confirmed the initiation of osteogenic differentiation of BMSCs towards the bone lineage. More interestingly, there was no significant difference in cell spreading morphology between scaffolds, which confirmed the identical cellular responses of nHAP and nWLKT towards cell adhesion.

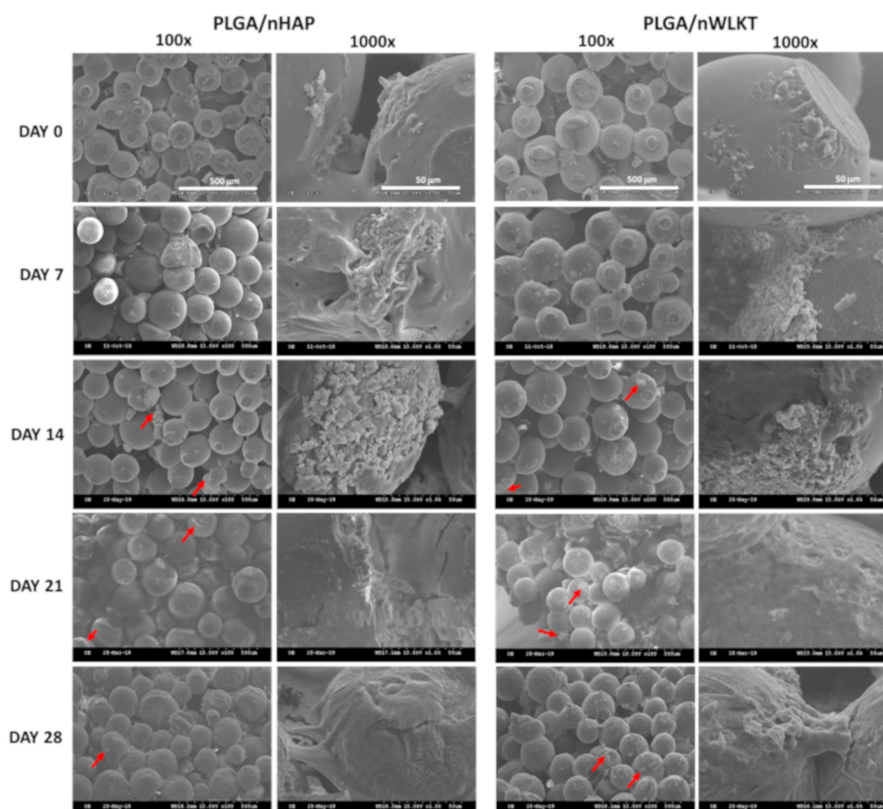


Figure 4. Assessment of cell morphology in PLGA/nHAP and PLGA/nWLKT microsphere scaffolds on day 0, 7, 14, 21, and 28 through scanning electron microscopy (SEM) at 100× (bar = 500 µm) and 1000× (bar = 50 µm) magnification. The red arrows indicate mineralized nodules.

The cell morphology was further validated through staining of the actin cytoskeleton of adhered cells [29]. It is well known that the cytoskeleton has a vital role in determining the morphology of cells, the pattern of adhesion and the subsequent cell growth through signaling [30], and therefore it is crucial in cell migration and division. The major components of cytoskeleton are actin filaments,

intermediate filaments, and microtubules with F-actin as the backbone. Unlike SEM analysis, actin staining helped to visualize the migration and proliferation of the cells within the three-dimensional structure of the scaffold, due to the versatility of the confocal microscope to scan various planes while providing a maximum projection. As observed from SEM analysis, the cells shifted from a more rounded and less intense cell adhesion pattern to a well spread and high intense adhesion scenario from day 0 to day 28 (Figure 5). Consistent with the SEM observation, less F-actin expression was detected due to early cell adhesion on day 0. A monolayer of more spread cell morphology on the microsphere was found after seven days and the pattern of cell spreading in both scaffolds on day 14 was slightly different from early stages due to possible cell differentiation. A preferential cell growth around the gap within the microsphere intersections was found at later stages. The relatively brighter spots in the scaffolds at these stages could be correlated with the multiple layering of cellular extensions, as clearly visible from the higher magnification images of individual microspheres. Thus, the cell morphology analysis confirmed the curved cell-spreading around the microspheres with an enhancement of F-actin stretching with respect to time. Interestingly, both scaffolds exhibited similar cellular cytoskeleton arrangements, with similar F-actin stress fibers within the gaps of microspheres. More detailed studies could reveal the relative efficiency of PLGA/nHAP and PLGA/nWLKT scaffolds towards bone regeneration from a bone graft aspect.

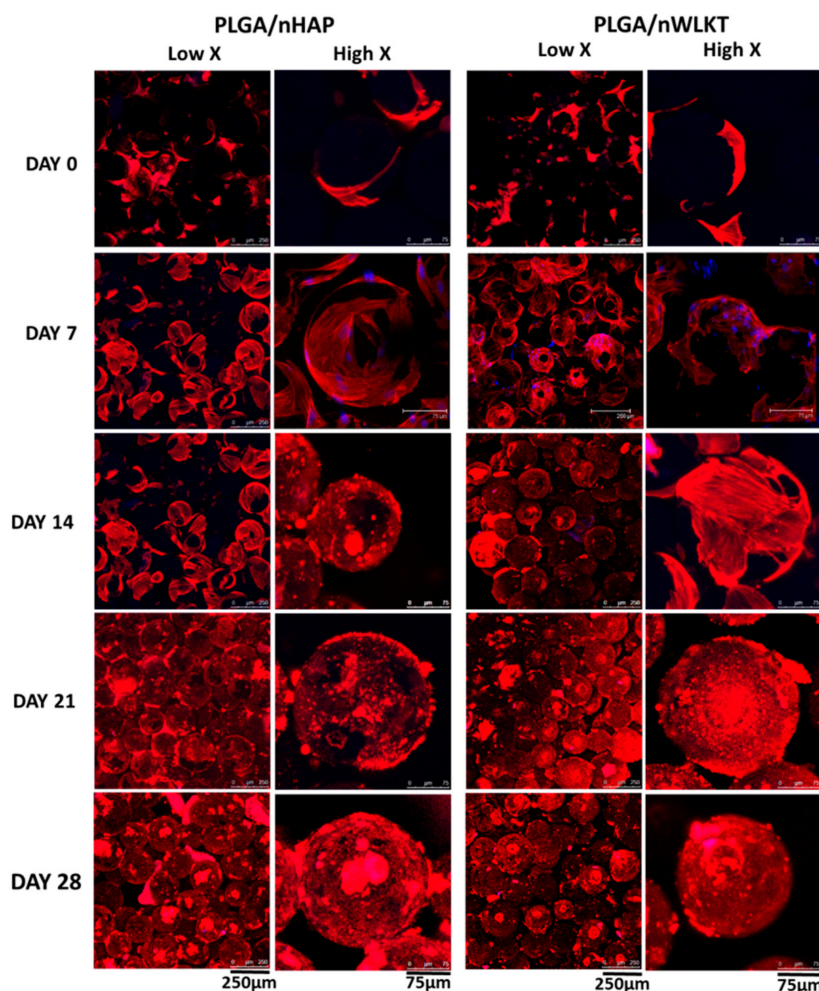


Figure 5. Visualization of the cytoskeletal arrangement in PLGA/nHAP and PLGA/nWLKT scaffolds through F-actin staining at low and high magnifications. Cell cytoskeleton was labeled with red fluorescence-producing phalloidin-tetramethylrhodamine B isothiocyanate and cell nuclei were counterstained with blue fluorescence-producing Hoechst 33,342 (Bar: low X = 250 µm, high X = 75 µm).

2.3.2. Cell Viability and Proliferation

The biocompatibility of both scaffolds was evaluated through the Live/Dead cell viability staining displayed in Figure 6A. The results obtained for the Live/Dead staining show a similar trend as observed in Figures 4 and 5. Furthermore, the percentage of dead cell (red) in both scaffolds throughout the observation period up to 28 days was negligible in comparison with viable cells (green), and thus confirms the excellent biocompatibility of the scaffolds. As seen in the cell morphology pattern earlier, early stage cell adhesion resulted in less cell density and rounded morphology, while later stages revealed more spread cells. Only scattered live cells were visualized as green spots on day 0 during the initiation of cell spreading after attachment, which developed into a more cell-covered microsphere during cell proliferation to result in an ascending order of green fluorescence intensity with time. Similar to previous results, both scaffolds showed similar cellular response results with no distinguishable differences from Live/Dead staining.

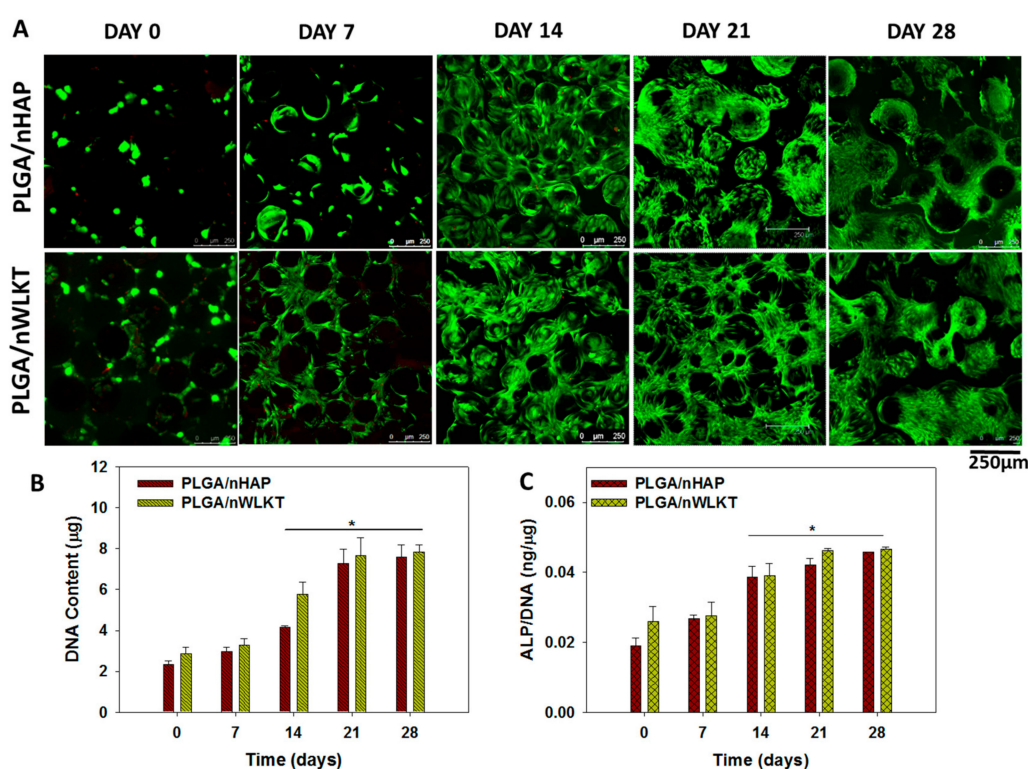


Figure 6. (A) Cell viability assessment of BMSCs in PLGA/nHAP and PLGA/nWLKT microsphere scaffolds through Live/Dead staining (bar = 250 µm). The quantitative estimation of cell proliferation and osteogenic differentiation of BMSCs seeded in the microsphere scaffolds was determined from DNA content (B) and normalized ALP activity (C) (* $p < 0.05$ compared to day 0).

Quantitative estimation of cell proliferation is essential to investigate the trend of increasing cell density around microspheres seen earlier. The rationale behind selecting BMSCs is due to its better proliferation and differentiation capabilities in a 3D micro-environment to mimic the natural architecture in bone [31]. Therefore, BMSCs cultured in both scaffolds were analyzed for cell proliferation through DNA analysis (Figure 6B). The DNA content increased with time due to cell division, which re-confirmed the results from SEM (Figure 4), the cytoskeleton expression from F-actin staining (Figure 5), and the Live/Dead cell viability assay (Figure 6A). The DNA content was lowest on day 0, increased before reaching a maximum at 21 days and plateaued thereafter. There was no significant difference in DNA content between PLGA/nHAP and PLGA/nWLKT throughout the culture period. The appearance of a cell number plateau during cell proliferation should be due to the differentiation of BMSCs induced by

nHAP or nWLKT in both scaffolds, as stem cells will usually become more mature and exhibit growth arrest during osteogenic differentiation [32].

2.3.3. Alkaline Phosphatase (ALP) Activity

Alkaline phosphatase (ALP) is an enzyme found in our body with higher concentrations in bones and the liver. A high level ALP can be observed during the cell maturation and mineralization stage during bone formation. Thus, the elevated ALP levels can be attributed to the production of a mineralized matrix. The ALP activity was shown in Figure S5 (Supplementary Materials), while the normalized ALP activity (to DNA content) is shown in Figure 6C. As can be seen in Figure 6C, the normalized ALP activity on day 0 and 7 was significantly lower compared to those on day 14. Elevation in ALP production thus initiated on day 14, increased further to day 21, and reached a plateau afterwards till day 28. This trend was supported by the early osteogenesis marker nature of ALP [33]. This osteo-induction nature of BMSCs was triggered from nHAP or nWLKT present in the microspheres and thus rationalizes the higher ALP content observed after seven days. Although there was no significant difference in ALP activity between PLGA/nHAP and PLGA/nWLKT at any time points, the latter did show a trend of a higher ALP level compared to the former. More quantitative studies and biochemical tests may be implemented to confirm the difference in relative osteogenic differentiation capability induced by nHAP and nWLKT in PLGA, if there is any.

2.3.4. Immunofluorescent Staining of Type I Collagen (COL I) and Osteocalcin (OCN)

The osteogenic differentiation potential of PLGA/nHAP and PLGA/nWLKT scaffolds was verified through immunofluorescent (IF) staining of type I collagen (COL I) and osteocalcin (OCN) after observing from confocal microscopy in both low and high magnification (Figure 7A). The scaffolds were tested for the presence of COL I and OCN, which are bone-specific protein markers synthesized by osteoblasts during osteogenic maturation of BMSCs [34]. Presence of proteins were represented by the FITC-green fluorescence while blue is the DAPI-stained nucleus. Production of both COL I and OCN by BMSCs in PLGA/nHAP and PLGA/nWLKT was found to increase with time, with a fluorescence signal from the stained protein distributed around the individual microspheres on day 14 while a more intense fluorescence signal was found to fill the pores between microspheres on day 28. This not only confirmed the more protein production at later stages but also supported the claims that PLGA/nHAP and PLGA/nWLKT induced osteogenic differentiation of BMSCs into osteoblasts in vitro. The empty gap between individual microspheres on day 14 for both scaffolds denoted the absence of cell bridging and thereby endorsed the results observed through SEM, cytoskeletal staining and cell proliferation earlier. Furthermore, the relative intensity of blue colored DAPI stains on day 14 and 28 was not drastically different than for supporting cell growth arrest during differentiation in later cell culture periods. However, there was a trend of higher protein production on day 28 and PLGA/nWLKT appeared to display a relatively higher protein production rate irrespective of when COL I or OCN was used. This could be seen in the higher magnification images where bridging of cells in the pores and hence protein production observed in PLGA/nWLKT was visibly superior (red dashed circles) compared to PLGA/nHAP (white dashed circles).

The qualitative output of protein expression was further substantiated through PAX-it!TM image analysis software quantification, which distinguishes objects by their color, size, or shape [35]. When using this method, the varied color intensity level above a chosen level is compared to the total image area for a quantitative comparison between groups. As shown in Figure 7B, the expression of protein was not significantly different between PLGA/nHAP and PLGA/nWLKT on day 14, although the mean value of PLGA/nWLKT was higher than that of PLGA/nHAP for COL I (48.7 vs. 37.4) and OCN (41.7 vs. 34.0). BMSCs in on both scaffolds produced significantly higher COL I and OCN protein on day 28 compared to day 14. PLGA/nWLKT revealed significantly higher protein expression compared to PLGA/nHAP, which accounted for the cell bridging characteristics observed in Figure 7A. The fact that the respective area percentage of COL I and OCN in PLGA/nWLKT was 1.27 and 1.12

times greater than that in PLGA/nHAP on day 28 may support the use of the former as a bone graft implant in vivo in the bone defective region.

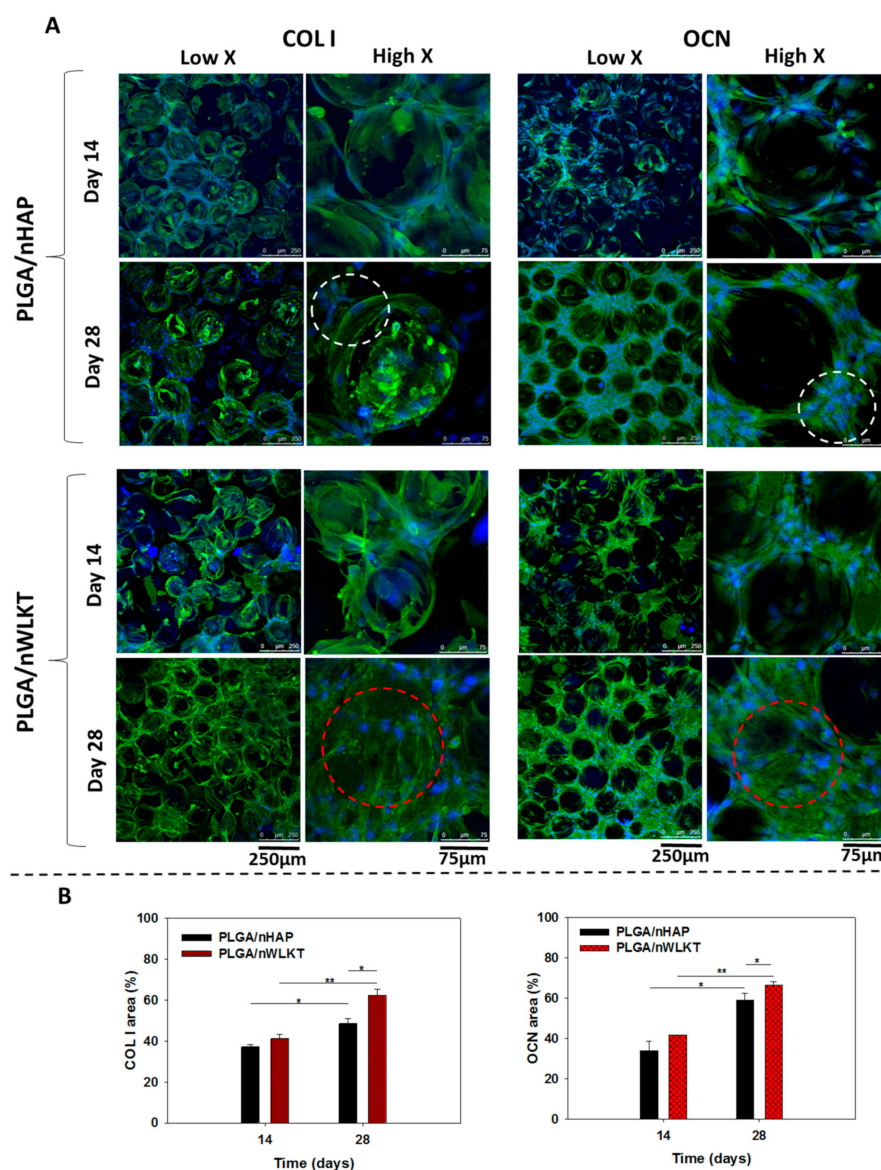


Figure 7. (A) Expression of collagen I (COL I) and osteocalcin (OCN) protein by BMSCs when cultured in PLGA/nHAP and PLGA/nWLKT scaffolds on day 14 and 28 by immunofluorescence (IF) staining. The cell nucleus labeled with Hoechst 33,342 is in blue while proteins labeled with FITC-conjugated antibody are in green (bar: low X = 250 μ m, high X = 75 μ m). (B) The semi-quantitative analysis of protein expression developed by an image analysis software (* $p < 0.05$, ** $p < 0.005$).

2.4. In Vivo Studies

2.4.1. Gross Observation

Being an acellular graft implant intended for use as a bone pin or screw, both scaffolds were selected to be implanted in the tibia of rabbits without seeded cells. Due to the complexity of making screw shaped defects, only sintered microsphere scaffold in cylindrical bone pin shape were selected for the in vivo studies. Since both scaffolds were osteoinductive in nature from in vitro studies, it was necessary to evaluate its comparative in vivo bone formation efficiency. Figure 8 shows the gross view images of sterile acellular bone pins prior to implantation, tibia defects created for bone pin

grafting, and tibia defects implanted with bone pins. An empty control without bone pin grafting was also shown and included in the experiment. It could be confirmed that both implants (white arrows) were well fitted in the defect cavities through mechanical pressure without leading to any physical deformation, due to their high mechanical strength (Figure 3E,F). The oozing blood observed within the bone pin implanted in tibia from the inserts in Figure 8 confirms that the macroporous structure of the graft is suitable for cell infiltration from surrounding bone tissue. After 12 weeks post-operative period, the rabbits were sacrificed, and the samples were explanted from the animal for gross view observation and histological analysis.

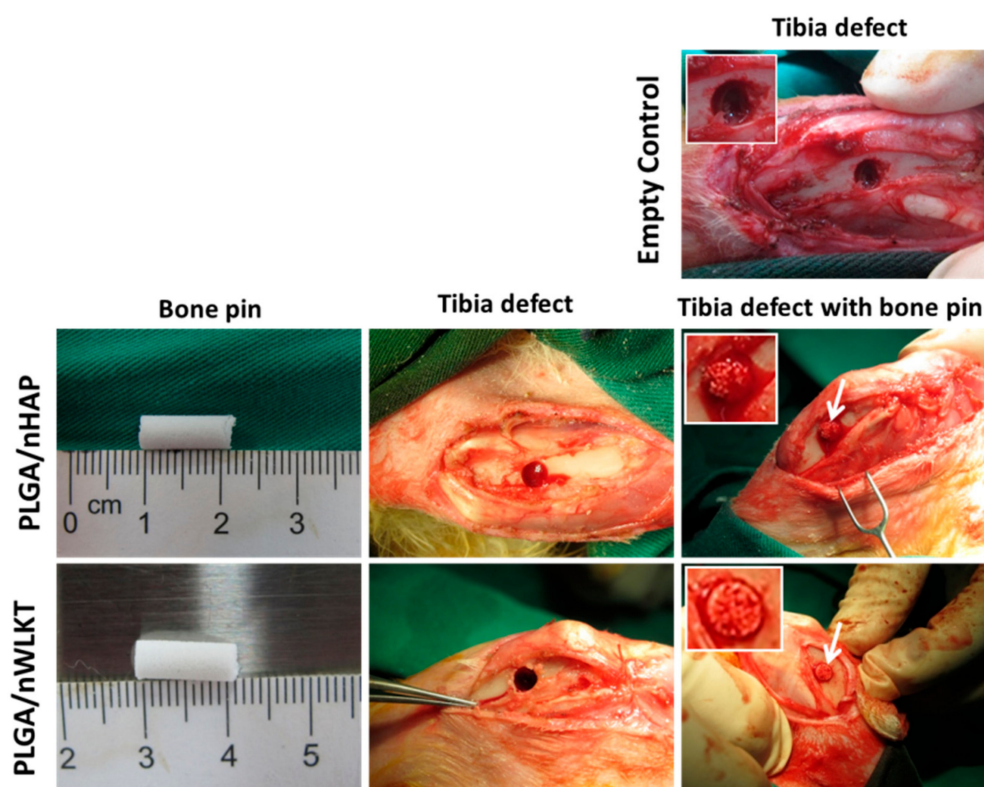


Figure 8. Gross view of the surgical procedure for the implantation of bone pin grafts in rabbit tibia defects. The white arrows denote the implanted bone pine graft. The inserts are enlarged views of the bone defects.

2.4.2. Histological Analysis

The regeneration capability of both PLGA/nHAP and PLGA/nWLKT bone pin implants were assessed through histological and immunohistochemical (IHC) staining (Figure 9A). H&E staining showed that relatively fewer cells were found within the defect compared to native bone (NB) in all groups. The narrow rounded appearance of extracellular matrix within the sample should have been due to the infiltration of cells towards the scaffold interior. The irregular empty voids with purple outline morphology confirmed the attachment of infiltrated cells, probably from native bone tissue. This had to be further confirmed with Masson's trichrome staining, where a deep blue color observed due to the presence of collagen in native bone was evident. Considering the implant area, microsphere circumference was stained light blue for PLGA/nHAP while it was slightly deeper and intense for PLGA/nWLKT. The blue-colored region generally represents the formation of osteoid [36], and thus could be correlated with the initiation of tissue matrix deposition. In comparison with the empty control group, both the PLGA/nHAP and PLGA/nWLKT groups showed higher cellularity from H&E stain and collagen deposition from Masson's trichrome staining to support the ability of both pin shaped bone grafts to regenerate bone tissue.

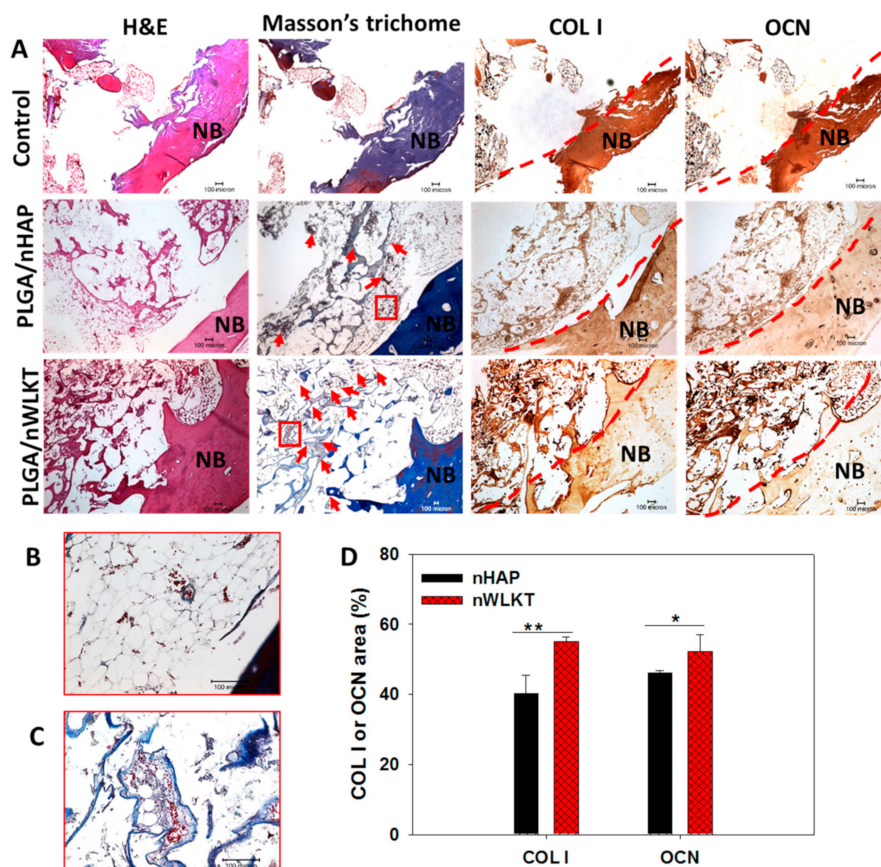


Figure 9. (A) The H&E, Masson's trichrome and immunohistochemical (IHC) staining of COL I and OCN in the rabbit tibia defect repaired with PLGA/nHAP and PLGA/nWLKT microsphere scaffolds (scale bar = 100 μ m). The red arrows indicate newly formed blood vessels and NB indicates native bone. The red squares in Masson's trichrome staining images were further enlarged for PLGA/nHAP (B) and PLGA/nWLKT (C) to show the newly formed blood vessel. (D) The semi-quantitative analysis of protein expression by image analysis from IHC staining (* $p < 0.05$, ** $p < 0.005$).

The trend seen in both H&E and Masson's trichrome staining was further confirmed by using COL I and OCN IHC staining. Similar to HE and Masson's trichrome staining, the empty control group generated very light brown intensities, whereas the microsphere circumference showed brownish staining in the experiment groups. In comparison to the intensities obtained for the PLGA/nHAP scaffold, the PLGA/nWLKT group showed comparatively higher staining density. Previously, WLKT incorporated chitosan scaffolds prepared by freeze drying was shown to have a better rat calvarial bone regeneration ability compared to HAP containing counterparts in vivo [37]. Similarly, PLGA/nWLKT composite scaffolds prepared by salt leaching were found to facilitate bone-specific differentiation in vitro and induce similar or better bone regeneration in a rat calvarial defect model in vivo compared to PLGA/nHAP [17].

The absence of purple colored cell nuclei should be due to the lesser cellular intensity for an acellular scaffold compared to a traditional cellular tissue engineered scaffold. Nonetheless, the results conclude that PLGA/nWLKT and PLGA/nHAP bone pin implants have the ability to allow cellular infiltration into the interiors of the scaffold from surrounding bone. This underlines the potential of surface sintered microsphere scaffolds to be suitable bone grafts in any shapes, without sacrificing the mechanical stability requirement. In addition to this, the Masson's trichrome staining showed the uneven distribution of red dots that reveals the existence of newly formed blood vessels in the implanted area [38]. It is interesting to note that PLGA/nWLKT shows more pronounced effect to promote blood vessel formation (labeled by red arrows) compared with PLGA/nHAP from the enlarged

square areas shown in Figure 9B,C. This property may be correlated with the release of Mg^{2+} ions from WKLT, which can promote angiogenesis [39]. This is consistent with a recent report indicating the angiogenic potential of nWKLT embedded in injectable carrageenan hydrogel in vitro [40], although only minimum angiogenesis effect could be seen here in vivo. To substantiate the preference of PLGA/nWKLT, the IHC staining images were further analyzed semi-quantitatively from image analysis as in IF staining by selecting the area of the scaffold (Figure 9D). The expression of both COL I and OCN in PLGA/nWKLT was found to be significantly higher compared with PLGA/nHAP where the stained area percentage increased by 1.37 fold (COL I) and 1.13 fold (OCN).

In summary, the physico-chemical characterizations and in vitro studies conducted for the PLGA/nHAP and PLGA/nWKLT scaffolds suggest that both scaffolds have comparable properties. However, the in vivo results reveal that PLGA/nWKLT have higher osteogenic potential towards BMSCs compared to PLGA/nHAP bone graft.

3. Materials and Methods

3.1. Materials

Poly (lactic-co-glycolic acid) (PLGA, intrinsic viscosity = 0.96 dL/g, lactide/glycolide ratio = 85/15) was purchased from Green Square Materials Inc., Taiwan. Poly (vinyl alcohol) (PVA), calcium hydrogen phosphate ($Ca_2HPO_4 \cdot 2H_2O$) and cetylpyridinium chloride were obtained from Sigma Aldrich (St Louis, MO, USA). Calcium carbonate ($CaCO_3$) was purchased from Scharlau Chemie S.A., Spain. Dichloromethane was obtained from Alfa Aesar (Haverhill, MA, USA). Fetal bovine serum (FBS) was purchased from Gibco (Waltham, MA, USA). Dulbecco's Modified Eagle's medium (DMEM) was from Invitrogen (Carlsbad, CA, USA) while ortho-phosphoric acid (85%) was from Merck (Darmstadt, Germany). For nuclear staining, we used 6-diamidino-2-phenylindole dihydrochloride (DAPI) from Life Technologies (Carlsbad, CA, USA). All chemicals were used as received without further purification.

3.2. Preparation of Hydroxyapatite Nanoparticles (nHAP)

To prepare HAP nanoparticles from $Ca_2HPO_4 \cdot 2H_2O$ and $CaCO_3$, the chemical precipitation method was used as described before [32]. In this procedure, 25.8 g calcium hydrogen phosphate and 10 g of calcium carbonate were mixed together and added to 1 L of 2.5 M NaOH solution maintained at 75 °C. The mixture was allowed to react for another 1 h, and finally the reaction was terminated by keeping the mixture in an ice bath. Subsequently, the precipitate was washed with double distilled (DD) water, centrifuged, and dried at 70 °C for 24 h to obtain nHAP.

3.3. Preparation of Whitlockite Nanoparticles (nWLKT)

The WLKT nanoparticles were prepared by using precipitation of calcium hydroxide magnesium hydroxide with ortho-phosphoric acid, as described previously [16,19,41]. In brief, a conical flask containing 100 mL de-ionized (DI) water was heated up to 80 °C, followed by mixing of 5.48 g of $Ca(OH)_2$ and 1.516 g of $Mg(OH)_2$ in the solution and was then stirred for 1 h. Subsequently, 100 mL ortho-phosphoric acid (1 M) was added dropwise to the above mixture with continued stirring for another 16 h. The nWLKT particles were separated by centrifugation, washed, and lyophilized for storage.

3.4. Preparation of PLGA/nHAP and PLGA/nWLKT Microspheres

The PLGA/nHAP microspheres were prepared based on the emulsion-solvent evaporation technique as described earlier [29]. Briefly, 4 g PLGA was dissolved in 30 mL dichloromethane (DCM) in a vortex shaker and 800 mg of nHAP was added to obtain a solution containing 20% (*w/w*) nHAP. The PLGA solution containing homogeneously distributed nHAP nanoparticles were then poured into 1800 mL of 0.5% (*w/v*) PVA solution kept on a magnetic stirrer and allowed to stir at 700 rpm for 18 h for microsphere formation. The microspheres were recovered and washed multiple times with DD water,

filtered under vacuum and dried. The PLGA/nWLKT microspheres were prepared using the same method as described before for PLGA/nHAP microsphere. In this case, instead of 800 mg nHAP used for PLGA/nHAP microspheres, 1.2 g of nWLKT was used to prepare 30% (*w/w*) theoretical loading of nWLKT in PLGA/nWLKT. This difference in loading ratio between nHAP and nWLKT was chosen to achieve a similar actual loading percentage of nHAP and nWLKT in the microspheres through pilot experiments. The mixture was then emulsified in 1800 mL of 0.5% (*w/v*) PVA solution kept on a magnetic stirrer and stirred at 700 rpm for 18 h. It was then continued with the same washing and drying steps as before to obtain PLGA/nWLKT microspheres (Figure 1, step 1).

3.5. Preparation of PLGA/nHAP and PLGA/nWLKT Microsphere Scaffolds

The PLGA/nHAP and PLGA/nWLKT microspheres were sieved using an array of steel meshes having gradient pore sizes ranging from 88 to 500 μm and microspheres within a size range of 150 to 250 μm was selected for the scaffold fabrication process (Figure 1, step 2). The selected microspheres were filled into a prefabricated cavity shaped stainless steel mold (4 mm height \times 4 mm diameter). The microspheres were closely filled inside the cavity by applying pressure using a stainless steel rod that can fit inside the mold cavity. Followed by this, the mold was screw tightened with the mold top and sintered at 83 $^{\circ}\text{C}$ for 90 min. Similarly, the conceptual model of bone pin or screw was made from a pre-fabricated clay based negative mold. A metallic screw was kept inside a square shaped clay, heated at 60 $^{\circ}\text{C}$, and then the screw was removed by cutting with a surgical knife. The cut pieces from the negative mold were clipped together and microspheres of a selected size range were filled inside through a narrow orifice until the cavity became tight packed. The clay mold was sintered at 86 $^{\circ}\text{C}$ for 90 min to obtain a microsphere based bone pin or screw scaffolds (Figure 1, step 3).

3.6. Physico-Chemical Characterization of Nanoparticles, Microspheres and Scaffolds

The morphology of prepared microspheres, microspheres, and scaffolds were characterized using a scanning electron microscope (SEM, S3000N) or a field emission scanning electron microscope (FESEM, SU8010), both of which were from Hitachi, Tokyo, Japan. The elemental composition of nHAP and nWLKT nanoparticles was quantified using energy dispersive X-ray spectroscopy (EDS, Bruker AXS-5030, Billerica, MA, USA). The chemical compositions and the crystallinity of nHAP, nWLKT, and composite microspheres were identified through Fourier-transform infrared spectroscopy (FTIR, RX1, Perkin-Elmer, Waltham, MA, USA) and X-ray diffraction spectroscopy (XRD, D5005, Siemens AG, Munich, Germany), respectively. The thermal behavior of the materials was examined through thermogravimetric analysis (TGA) under nitrogen atmosphere from 25 $^{\circ}\text{C}$ to 700 $^{\circ}\text{C}$ with a platinum pan containing 10 mg of sample in a TA Instruments TGA 2050 thermogravimetric analyzer (New Castle, DE, USA).

The percentage of pores in the microsphere scaffolds (porosity) was measured using the liquid displacement method with a non-solvent of the polymer, ethanol [42]. In brief, pre-weighed microsphere scaffold was placed in a syringe with a known volume of ethanol. Followed by this, the liquid was forced to penetrate into the pores of the scaffold by a series of evacuation/re-pressurization cycles. The porosity was calculated by dividing the volume of ethanol in the scaffold (void volume) with the volume of the whole scaffold (void + solid volume).

The compressive mechanical properties of cylindrical shaped microsphere scaffolds in 4 mm \times 4 mm (height \times diameter) dimensions were evaluated to confirm their load bearing capacity. The samples were kept on top of the horizontal stainless steel plate and compression mechanical testing was performed using an ElectroForce[®] 5200 BioDynamic[™] Test Instrument (TA Instruments, New Castle, DE, USA) with a 250 N load cell and 0.01 mm/min cross head speed. The mechanical properties of the scaffold were measured in terms of a stress-strain curve, and the Young's modulus was determined from the initial slope of the stress-strain curve from a 0.01 to 0.05 stain value.

3.7. In Vitro Cell Culture Studies

3.7.1. Isolation and Culture of Bone Marrow-Derived Stem Cells (BMSCs)

Rabbit bone marrow-derived mesenchymal stem cells (BMSCs) were isolated from young New Zealand white rabbits as per the standard procedures reported earlier [43]. Animals were anesthetized and the blood was withdrawn from the bone marrow. The anticoagulant (5 mL heparin) was taken in the aspiration needle prior to blood withdrawal and the whole procedures were done according to the rules and regulations of Institutional Animal Care and Use Committee of Chang Gung University (IACUC Approval No.: CGU106-021, 1 July 2017)). Phosphate buffer saline (PBS) was mixed with the blood and the solution was centrifuged at 4 °C. After removing the supernatant, an equal volume of cell culture medium (80% DMEM, 20% FBS, 1% penicillin-streptomycin and 2 µg/mL fibroblast growth factor-2) was added to the concentrated cell solution. Another centrifugation was done, the supernatant was removed and a dark-red solution containing BMSCs was obtained. The cell suspension was uniformly distributed in T-75 flasks with 10 mL of cell culture medium and was incubated at 37 °C. After the removal of non-adherent cells, the BMSCs were further sub-cultured and stored in liquid nitrogen for future studies.

3.7.2. Evaluation of Cell Adhesion and Distribution

The PLGA/nHAP and PLGA/WLKT microsphere scaffolds were sterilized in 75% ethanol under UV for 24 h, rinsed another three times with PBS, and kept in a 24-well cell culture plate (Thermo Fisher Scientific, Carlsbad, CA, USA) containing 1 mL cell culture medium (90% DMEM, 10% FBS and 1% antibiotic/antimitotic). After 1 h incubation, we removed the culture medium from each well in the cell culture plate, followed by adding 10 µL of cell suspension containing 1×10^5 BMSCs to each pre-wetted scaffold. The cell-seeded scaffold was placed in a CO₂ incubator maintained at 37 °C for 4 h to allow cell attachment. The cell/scaffold sample was transferred to another well in the 24-well culture plate, 1 mL of cell culture medium was added, and cell culture analysis was carried out up for 28 days at 37 °C in a CO₂ incubator.

The morphology of adhered BMSCs in both microsphere scaffolds was examined through SEM (S-3000N from Hitachi, Tokyo, Japan) while the cytoskeletal arrangements were visualized through a confocal laser scanning microscope (Zeiss LSM 510 Meta, Carl Zeiss AG, Oberkochen, Germany). The samples were first fixed in 2.5% glutaraldehyde solution for 30 min followed through washing with PBS. Alcohol gradient was used to remove water content, followed by critical point drying prior to SEM observation. In cytoskeletal observation, the glutaraldehyde fixed samples were permeabilized with 0.1% Triton X-100 for 10 min at room temperature before staining with red fluorescence-producing phalloidin-tetramethylrhodamine B isothiocyanate (1%, Sigma-Aldrich) and blue fluorescence-producing Hoechst 33,342 (1 µg/mL, Thermo Fisher Scientific).

3.7.3. Cell Viability Analysis

The viability of BMSCs within the microsphere scaffolds was determined through the Live/Dead cell viability assay following standard protocols [44]. The cells were stained with calcein AM/ethidium homodimer in the LIVE/DEAD viability/cytotoxicity kit for mammalian cells (Thermo Fisher Scientific, Waltham, MA, USA). After the staining, the scaffolds were washed with PBS and observed under a confocal laser scanning microscopy (Zeiss LSM 510 Meta).

3.7.4. Cell Proliferation and Differentiation

To evaluate cell proliferation, cell-seeded scaffolds were retrieved at predetermined time points and the DNA content was analyzed using the bis-benzimidazole dye (Hoechst 33258). The DNA was extracted by a digestion buffer containing papain and aliquots of digested solution were mixed with the dye solution and the fluorescence emission was measured. The intracellular alkaline phosphatase (ALP) activity of BMSCs was measured using a SensoLyte pNPP ALP assay kit (AnaSpec, Fremont,

CA, USA), using standard protocols. The cell-seeded scaffolds retrieved at specific time points were transferred to the cell lysis solution containing 1 mL of 0.1% Triton X-100 and 5 mM MgCl_2 for cell lysis and the lysate was centrifuged at 10,000 rpm for 15 min at 4 °C. To measure ALP activity, 50 μL of the lysate supernatant was mixed with 100 μL of 5 mM p-nitrophenyl phosphate (PNPP) solution prepared in 2-amino-2-methyl-1-propanol buffer solution (150 mM). The mixture was allowed to react for 30 min at room temperature in the dark. To terminate the reaction, 50 μL of 0.2 N NaOH was added, followed by measuring the optical density of the solution at 405 nm (OD405) in an enzyme-linked immunosorbent assay (ELISA) reader.

3.7.5. Immunofluorescence (IF) Staining of Bone Marker Proteins

The presence of osteogenic bone markers in the *in vitro* cultured sample were detected by the immunofluorescence (IF) staining of type I collagen (COL I) and osteocalcin (OCN). The 14 and 28 days BMSCs-seeded samples were collected, washed with PBS, and fixed in 4% formaldehyde for 30 min. Subsequently, the samples were washed with a PBST solution containing PBS and 0.1% Tween 20, for 15 min. The nonspecific proteins present in the sample were blocked by treating the sample with HyBlock 1-min Blocking Buffer® (Goal Bio, Taipei, Taiwan) and washed with PBST again. For COL I, the samples were incubated with antibody for COL I (monoclonal anti-COL I antibody produced in mouse, Novus Biologicals, Littleton, CO, USA) for 8 h at 4 °C, rinsed with PBST for 20 min and incubated in FITC-conjugated goat anti-mouse IgG secondary antibody (Jacksons Laboratories, Bar Harbor, ME, USA) for 1 h. For OCN, the primary antibody used was polyclonal anti-OCN antibody produced in guinea pigs (Cloud-Clone Co., Houston, TX, USA) and the secondary antibody was FITC-conjugated goat anti-guinea pig IgG (Abcam, Cambridge, UK). After we counterstained the cell nucleus with Hoechst 33342, the samples were visualized under a confocal laser scanning microscope (Zeiss LSM 510 Meta) to observe the blue-stained nuclei embedded within the green-stained proteins. For semi-quantitative determination of production of COL I and OCN, the PAX-it!™ image analysis software from PAX-it Inc. (Villa Park, IL, USA) was used. The area percentage of the green fluorescence signal corresponding to COL I or OCN was calculated from six randomly selected fields from microscopic observation and used for protein content quantification.

3.8. *In Vivo* Studies

Eight male New Zealand white rabbits weighing 3 to 4 kg was selected for the study and they were carefully examined for 10 days prior to the experiments and the surgeries were performed under aseptic conditions in accordance with the standard procedures approved by the Institutional Animal Care and Use Committee of Chang Gung University (IACUC Approval No.: CGU106-021, 1 July 2017). Briefly, all rabbits were anesthetized using a mixture of Zoletil 50 (18 mg/kg) and Rompun 20 (1 mg/kg), followed by intramuscularly injecting Atropin (0.3 mg/kg). The tibias of rabbits were shaved. Afterwards, their skin surfaces were disinfected with iodine solution and the tibia part of the leg was carefully exposed via skin incision. After a PBS wash, a 4.2 mm pilot hole was drilled using a round dental bur under profuse saline irrigation. Subsequently, PLGA/nWLKT and PLGA/nHAP pin-shaped scaffolds were inserted into the holes. A control group established by keeping the created hole empty was used for comparison. After the implantation, muscle and skin were sutured separately and the surgical sites were then closed in layers using 4-0 Ethicon sutures. Further, the wounds were sterilized and dressed with gentamicin ointment. All rabbits received intramuscular injections of gentamicin (3 mg/kg) for three days after the surgery and were returned to their normal cages for free movement.

Twelve weeks post-operation, all rabbits were euthanized by lethal doses of pentobarbital and the tibias were dissected out for gross evaluation. The samples from all groups (grafts and control) were fixed in 10% formaldehyde and fixed samples were dehydrated and embedded in paraffin to make 10 μm slice sections on glass slides. Samples were then subject to hematoxylin and eosin (H&E) and Masson's trichrome staining following standard protocols. Another set of slides were allowed to undergo immunohistochemical (IHC) staining using primary antibodies for COL I (mouse monoclonal

anti-collagen I, Novus Biologicals, Littleton, CO, USA) and OCN (mouse monoclonal anti-osteocalcin, Abcam, Cambridge, UK). New bone formation within the implanted PLGA/nHAP and PLGA/nWLKT bone grafts was assessed by recording the images under an inverted optical microscope (Olympus IX-71, Tokyo, Japan).

3.9. Statistical Analysis

All quantitative data were expressed as mean \pm standard deviation and the statistics used Student *T*-test with a *p* value less than 0.05 considered significant.

4. Conclusions

We successfully fabricated macroporous PLGA microsphere based bone grafts containing nHAP (PLGA/nHAP) or nWLKT (PLGA/nWLKT) and compared the properties of each grafts to assess their physico-chemical and osteogenic properties. Most characteristics of both grafts including morphology, mechanical strength, porosity, thermal stability, biocompatibility, and cell viability were found to be similar, suggesting the identical nature of nHAP and nWLKT as a bone graft implant. Nonetheless, judging from COLI and OCN bone marker protein production in vitro and in vivo, PLGA/nWLKT revealed higher osteogenic potential towards BMSCs compared to PLGA/nHAP bone graft. Overall, this study discloses the potential of a relatively less explored nWLKT ceramic nanoparticle as an alternative to nHAP for preparing composite sintered microsphere scaffolds with PLGA for potential bone grafts and tissue engineered implants in pin or screw shapes.

Supplementary Materials: The following are available online at <http://www.mdpi.com/1422-0067/21/2/528/s1>. Figure S1. The SEM images of PLGA microspheres at different magnifications. Figure S2. The optical microscopic images of PLGA microspheres obtained at different PLGA concentrations for the optimization of PLGA concentration. Figure S3. The TGA results for the assay conducted for microsphere scaffold containing two different concentrations of nWLKT for the optimization of nWLKT loading. Figure S4. The SEM images of low and high magnification of PLGA/nHAP microsphere scaffold (A and B) and PLGA/nWLKT microsphere scaffold (C and D). Figure S5. The ALP activity of BMSCs in PLGA/nHAP and PLGA/nWLKT microsphere scaffolds.

Author Contributions: G.J., K.T.S. and J.-P.C. conceived and designed the experiments; G.J., K.T.S., H.-T.L. and C.-Y.K. performed the experiments; G.J., K.T.S. and J.-P.C. analyzed the data; G.J., K.T.S. and J.-P.C. wrote the paper. All authors have read and agreed to the published version of the manuscript.

Funding: This research was funded by Chang Gung Memorial Hospital, Keelung grant number CMRPD3G0081, CMRPD3G0082 and CMRPD3G0083.

Acknowledgments: We would like to express our appreciation for the financial support provided by Chang Gung Memorial Hospital, Keelung (CMRPD3G0083) and facility use provided by the Microscope Core Laboratory and the Laboratory Animal Center, Chang Gung Memorial Hospital, Linkou.

Conflicts of Interest: The authors declare no conflict of interest.

References

1. Haers, P.E.; Suuronen, R.; Lindqvist, C.; Sailer, H. Biodegradable polylactide plates and screws in orthognathic surgery: Technical note. *J. Cranio Maxillofac. Surg.* **1998**, *26*, 87–91. [CrossRef]
2. Elisseeff, J.; Puleo, C.; Yang, F.; Sharma, B. Advances in skeletal tissue engineering with hydrogels. *Orthod. Craniofacial Res.* **2005**, *8*, 150–161. [CrossRef]
3. Andreas, S.S.; Parag, K.J.; Wasim, S.K. Clinical Applications of Mesenchymal Stem Cells in the Treatment of Fracture Non-Union and Bone Defects. *Curr. Stem Cell Res. Ther.* **2012**, *7*, 127–133.
4. Hasan, A.; Byambaa, B.; Morshed, M.; Cheikh, M.I.; Shakoar, R.A.; Mustafy, T.; Marei, H.E. Advances in osteobiologic materials for bone substitutes. *J. Tissue Eng. Regen. Med.* **2018**, *12*, 1448–1468. [CrossRef]
5. Lienemann, P.S.; Lutolf, M.P.; Ehrbar, M. Biomimetic hydrogels for controlled biomolecule delivery to augment bone regeneration. *Adv. Drug Deliv. Rev.* **2012**, *64*, 1078–1089. [CrossRef]
6. Kalita, S.J.; Bhardwaj, A.; Bhatt, H.A. Nanocrystalline calcium phosphate ceramics in biomedical engineering. *Mater. Sci. Eng. C* **2007**, *27*, 441–449. [CrossRef]

7. Albee, F.H. Studies in bone growth: Triple calcium phosphate as a stimulus to osteogenesis. *Ann. Surg.* **1920**, *71*, 32–39. [[CrossRef](#)] [[PubMed](#)]
8. Al-Sanabani, J.S.; Madfa, A.A.; Al-Sanabani, F.A. Application of calcium phosphate materials in dentistry. *Int. J. Biomater.* **2013**, *2013*, 876132. [[CrossRef](#)]
9. Gatoo, M.A.; Naseem, S.; Arfat, M.Y.; Dar, A.M.; Qasim, K.; Zubair, S. Physicochemical properties of nanomaterials: Implication in associated toxic manifestations. *BioMed Res. Int.* **2014**, *2014*, 498420. [[CrossRef](#)]
10. Shin, S.W.; Song, I.H.; Um, S.H. Role of physicochemical properties in nanoparticle toxicity. *Nanomaterials (Basel)* **2015**, *5*, 1351–1365. [[CrossRef](#)]
11. Ginebra, M.P.; Traykova, T.; Planell, J.A. Calcium phosphate cements as bone drug delivery systems: A review. *J. Control. Release* **2006**, *113*, 102–110. [[CrossRef](#)] [[PubMed](#)]
12. Zhou, H.; Lee, J. Nanoscale hydroxyapatite particles for bone tissue engineering. *Acta Biomater.* **2011**, *7*, 2769–2781. [[CrossRef](#)] [[PubMed](#)]
13. Pan, H.; Liu, X.Y.; Tang, R.; Xu, H.Y. Mystery of the transformation from amorphous calcium phosphate to hydroxyapatite. *Chem. Commun.* **2010**, *46*, 7415–7417. [[CrossRef](#)]
14. Wang, W.; Yeung, K.W.K. Bone grafts and biomaterials substitutes for bone defect repair: A review. *Bioact. Mater.* **2017**, *2*, 224–247. [[CrossRef](#)] [[PubMed](#)]
15. Yu, X.; Tang, X.; Gohil, S.V.; Laurencin, C.T. Biomaterials for bone regenerative engineering. *Adv. Healthc. Mater.* **2015**, *4*, 1268–1285. [[CrossRef](#)] [[PubMed](#)]
16. Muthiah Pillai, N.S.; Eswar, K.; Amirthalingam, S.; Mony, U.; Kerala Varma, P.; Jayakumar, R. Injectable Nano Whitlockite Incorporated Chitosan Hydrogel for Effective Hemostasis. *ACS Appl. Bio Mater.* **2019**, *2*, 865–873. [[CrossRef](#)]
17. Jang, H.L.; Zheng, G.B.; Park, J.; Kim, H.D.; Baek, H.-R.; Lee, H.K.; Lee, K.; Han, H.N.; Lee, C.-K.; Hwang, N.S.; et al. In vitro and in vivo evaluation of whitlockite biocompatibility: Comparative study with hydroxyapatite and β -tricalcium phosphate. *Adv. Healthc. Mater.* **2016**, *5*, 128–136. [[CrossRef](#)]
18. Cheng, H.; Chabok, R.; Guan, X.; Chawla, A.; Li, Y.; Khademhosseini, A.; Jang, H.L. Synergistic interplay between the two major bone minerals, hydroxyapatite and whitlockite nanoparticles, for osteogenic differentiation of mesenchymal stem cells. *Acta Biomater.* **2018**, *69*, 342–351. [[CrossRef](#)]
19. Jang, H.L.; Jin, K.; Lee, J.; Kim, Y.; Nahm, S.H.; Hong, K.S.; Nam, K.T. Revisiting whitlockite, the second most abundant biomineral in bone: Nanocrystal synthesis in physiologically relevant conditions and biocompatibility evaluation. *ACS Nano* **2014**, *8*, 634–641. [[CrossRef](#)]
20. Jeong, J.; Kim, J.H.; Shim, J.H.; Hwang, N.S.; Heo, C.Y. Bioactive calcium phosphate materials and applications in bone regeneration. *Biomater. Res.* **2019**, *23*, 4. [[CrossRef](#)]
21. Kim, H.D.; Jang, H.L.; Ahn, H.-Y.; Lee, H.K.; Park, J.; Lee, E.-S.; Lee, E.A.; Jeong, Y.-H.; Kim, D.-G.; Nam, K.T.; et al. Biomimetic whitlockite inorganic nanoparticles-mediated in situ remodeling and rapid bone regeneration. *Biomaterials* **2017**, *112*, 31–43. [[CrossRef](#)] [[PubMed](#)]
22. Choi, J.W.; Kong, Y.M.; Kim, H.E.; Lee, I.S. Reinforcement of hydroxyapatite bioceramic by addition of Ni₃Al and Al₂O₃. *J. Am. Ceram. Soc.* **1998**, *81*, 1743–1748. [[CrossRef](#)]
23. Gentile, P.; Nandagiri, V.K.; Daly, J.; Chiono, V.; Mattu, C.; Tonda-Turo, C.; Ciardelli, G.; Ramtoola, Z. Localised controlled release of simvastatin from porous chitosan-gelatin scaffolds engrafted with simvastatin loaded PLGA-microparticles for bone tissue engineering application. *Mater. Sci. Eng. C Mater. Biol. Appl.* **2016**, *59*, 249–257. [[CrossRef](#)] [[PubMed](#)]
24. Rider, P.; Kacarevic, Z.P.; Alkildani, S.; Retnasingh, S.; Schnettler, R.; Barbeck, M. Additive manufacturing for guided bone regeneration: A perspective for alveolar ridge augmentation. *Int. J. Mol. Sci.* **2018**, *19*. [[CrossRef](#)] [[PubMed](#)]
25. Guimaraes, P.P.; Oliveira, M.F.; Gomes, A.D.; Gontijo, S.M.; Cortes, M.E.; Campos, P.P.; Viana, C.T.; Andrade, S.P.; Sinisterra, R.D. PLGA nanofibers improves the antitumoral effect of daunorubicin. *Colloids Surf. B Biointerfaces* **2015**, *136*, 248–255. [[CrossRef](#)] [[PubMed](#)]
26. Qi, C.; Chen, F.; Wu, J.; Zhu, Y.-J.; Hao, C.-N.; Duan, J.-L. Magnesium whitlockite hollow microspheres: A comparison of microwave-hydrothermal and conventional hydrothermal syntheses using fructose 1,6-bisphosphate, and application in protein adsorption. *RSC Adv.* **2016**, *6*, 33393–33402. [[CrossRef](#)]
27. Amirthalingam, S.; Ramesh, A.; Lee, S.S.; Hwang, N.S.; Jayakumar, R. Injectable in situ shape-forming osteogenic nanocomposite hydrogel for regenerating irregular bone defects. *ACS Appl. Bio Mater.* **2018**, *1*, 1037–1046. [[CrossRef](#)]

28. Hannink, G.; Arts, J.J.C. Bioresorbability, porosity and mechanical strength of bone substitutes: What is optimal for bone regeneration? *Injury* **2011**, *42*, S22–S25. [\[CrossRef\]](#)
29. Shalumon, K.T.; Sheu, C.; Fong, Y.T.; Liao, H.T.; Chen, J.P. Microsphere-based hierarchically juxtapositioned biphasic scaffolds prepared from poly(lactic-co-glycolic acid) and nanohydroxyapatite for osteochondral tissue engineering. *Polymers* **2016**, *8*, 429. [\[CrossRef\]](#)
30. Vishavkarma, R.; Raghavan, S.; Kuyyamudi, C.; Majumder, A.; Dhawan, J.; Pullarkat, P.A. Role of Actin filaments in correlating nuclear shape and cell spreading. *PLoS ONE* **2014**, *9*, e107895. [\[CrossRef\]](#)
31. Yousefi, A.-M.; James, P.F.; Akbarzadeh, R.; Subramanian, A.; Flavin, C.; Oudadesse, H. Prospect of stem cells in bone tissue engineering: A review. *Stem Cells Int.* **2016**, *2016*, 6180487. [\[CrossRef\]](#) [\[PubMed\]](#)
32. Lai, G.J.; Shalumon, K.T.; Chen, J.P. Response of human mesenchymal stem cells to intrafibrillar nanohydroxyapatite content and extrafibrillar nanohydroxyapatite in biomimetic chitosan/silk fibroin/nanohydroxyapatite nanofibrous membrane scaffolds. *Int. J. Nanomed.* **2015**, *10*, 567–584.
33. Wan, Y.; Chang, P.; Yang, Z.; Xiong, G.; Liu, P.; Luo, H. Constructing a novel three-dimensional scaffold with mesoporous TiO₂ nanotubes for potential bone tissue engineering. *J. Mater. Chem. B* **2015**, *3*, 5595–5602. [\[CrossRef\]](#)
34. Thitiset, T.; Damrongsakkul, S.; Bunaprasert, T.; Leeanansaksiri, W.; Honsawek, S. Development of collagen/demineralized bone powder scaffolds and periosteum-derived cells for bone tissue engineering application. *Int. J. Mol. Sci.* **2013**, *14*, 2056–2071. [\[CrossRef\]](#)
35. Shalumon, K.T.; Kuo, C.-Y.; Wong, C.-B.; Chien, Y.-M.; Chen, H.-A.; Chen, J.-P. Gelatin/nanohydroxyapatite cryogel embedded poly(lactic-co-glycolic acid)/nanohydroxyapatite microsphere hybrid scaffolds for simultaneous bone regeneration and load-bearing. *Polymers* **2018**, *10*, 620. [\[CrossRef\]](#)
36. Shalumon, K.T.; Lai, G.J.; Chen, C.H.; Chen, J.P. Modulation of bone-specific tissue regeneration by incorporating bone morphogenetic protein and controlling the shell thickness of silk fibroin/chitosan/nanohydroxyapatite core-shell nanofibrous membranes. *ACS Appl. Mater. Interfaces* **2015**, *7*, 21170–21181. [\[CrossRef\]](#)
37. Zhou, D.; Qi, C.; Chen, Y.X.; Zhu, Y.J.; Sun, T.W.; Chen, F.; Zhang, C.Q. Comparative study of porous hydroxyapatite/chitosan and whitlockite/chitosan scaffolds for bone regeneration in calvarial defects. *Int. J. Nanomed.* **2017**, *12*, 2673–2687. [\[CrossRef\]](#)
38. Du, B.; Liu, W.; Deng, Y.; Li, S.; Liu, X.; Gao, Y.; Zhou, L. Angiogenesis and bone regeneration of porous nano-hydroxyapatite/coralline blocks coated with rhVEGF165 in critical-size alveolar bone defects in vivo. *Int. J. Nanomed.* **2015**, *10*, 2555–2565.
39. Zhai, W.; Lu, H.; Wu, C.; Chen, L.; Lin, X.; Naoki, K.; Chen, G.; Chang, J. Stimulatory effects of the ionic products from Ca–Mg–Si bioceramics on both osteogenesis and angiogenesis in vitro. *Acta Biomater.* **2013**, *9*, 8004–8014. [\[CrossRef\]](#)
40. Yegappan, R.; Selvaprithiviraj, V.; Amirthalingam, S.; Mohandas, A.; Hwang, N.S.; Jayakumar, R. Injectable angiogenic and osteogenic carrageenan nanocomposite hydrogel for bone tissue engineering. *Int. J. Biol. Macromol.* **2019**, *122*, 320–328. [\[CrossRef\]](#)
41. Chaisri, W.; Hennink, W.E.; Okonogi, S. Preparation and characterization of cephalixin loaded PLGA microspheres. *Curr. Drug Deliv.* **2009**, *6*, 69–75. [\[CrossRef\]](#) [\[PubMed\]](#)
42. Loh, Q.L.; Choong, C. Three-dimensional scaffolds for tissue engineering applications: Role of porosity and pore size. *Tissue Eng. B Rev.* **2013**, *19*, 485–502. [\[CrossRef\]](#) [\[PubMed\]](#)
43. Chen, J.P.; Chang, Y.S. Preparation and characterization of composite nanofibers of polycaprolactone and nanohydroxyapatite for osteogenic differentiation of mesenchymal stem cells. *Colloids Surf. B Biointerfaces* **2011**, *86*, 169–175. [\[CrossRef\]](#) [\[PubMed\]](#)
44. Zhang, X.; Chang, W.; Lee, P.; Wang, Y.; Yang, M.; Li, J.; Kumbar, S.G.; Yu, X. Polymer-ceramic spiral structured scaffolds for bone tissue engineering: Effect of hydroxyapatite composition on human fetal osteoblasts. *PLoS ONE* **2014**, *9*, e85871. [\[CrossRef\]](#) [\[PubMed\]](#)





Kan-Lu-Hsiao-Tu-Tan, a traditional Chinese medicine formula, inhibits human neutrophil activation and ameliorates imiquimod-induced psoriasis-like skin inflammation

Chiang Chih-Chao^{a,b,c}, Wei-Jen Cheng^{a,d,e}, Cheng-Yu Lin^f, Kuei-Hung Lai^g, Seanson-Chance Ju^f, Chuan Lee^f, Sien-Hung Yang^{d,e}, Tsong-Long Hwang^{f,g,h,i,j,*}

^a Graduate Institute of Clinical Medical Sciences, College of Medicine, Chang Gung University, Taoyuan, 333, Taiwan

^b Supervisory Board, Taoyuan Chinese Medicine Association, Taoyuan, 338, Taiwan

^c Puxin Fengze Chinese Medicine Clinic, Taoyuan, 326, Taiwan

^d Center for Traditional Chinese Medicine, Chang Gung Memorial Hospital, Taoyuan, 333, Taiwan

^e School of Traditional Chinese Medicine, Chang Gung University, Taoyuan, 333, Taiwan

^f Graduate Institute of Natural Products, College of Medicine, Chang Gung University, Taoyuan, 333, Taiwan

^g Research Center for Chinese Herbal Medicine, Research Center for Food and Cosmetic Safety, and Graduate Institute of Health Industry Technology, Chang Gung University of Science and Technology, Taoyuan, 333, Taiwan

^h Chinese Herbal Medicine Research Team, Healthy Aging Research Center, Chang Gung University, Taoyuan, 333, Taiwan

ⁱ Department of Anesthesiology, Chang Gung Memorial Hospital, Taoyuan, 333, Taiwan

^j Department of Chemical Engineering, Ming Chi University of Technology, New Taipei City, 243, Taiwan



ARTICLE INFO

Keywords:

Kan-Lu-Hsiao-Tu-Tan

Human neutrophils

Reactive oxygen species

Neutrophil extracellular traps

Psoriasis

ABSTRACT

Ethnopharmacological relevance: Kan-Lu-Hsiao-Tu-Tan (KLHTT) is a popular traditional Chinese medicine for treating various inflammatory diseases.

Aim of the study: The aim of the present study was to investigate the anti-inflammatory effects of KLHTT on human neutrophils and its therapeutic potential in treating imiquimod (IMQ)-induced psoriasis-like skin inflammation.

Materials and methods: Spectrophotometry, flow cytometry, and microscopy with immunohistochemical staining were used to evaluate superoxide anion generation, elastase release, CD11b expression, adhesion, and neutrophil extracellular trap (NET) formation in activated human neutrophils. Reactive oxygen species (ROS) and reactive nitrogen species in cell-free systems were measured using a multi-well fluorometer or a spectrophotometer. A psoriasis-like skin inflammation was induced in mice using the IMQ cream.

Results: KLHTT suppressed superoxide anion generation, ROS production, CD11b expression, and adhesion in activated human neutrophils. In contrast, KLHTT failed to alter elastase release in activated human neutrophils. Additionally, KLHTT had an ROS-scavenging effect in the AAPH assay, but it did not scavenge superoxide anions directly in the xanthine/xanthine oxidase assay. Protein kinase C (PKC)-induced NET formation most commonly occurs through ROS-dependent mechanisms. KLHTT significantly inhibited phorbol 12-myristate 13-acetate, a PKC activator, inducing NET formation. Furthermore, topical KLHTT treatment reduced the area affected by psoriasis area and severity index (PASI) score and ameliorated neutrophil infiltration in IMQ-induced psoriasis-like skin inflammation in mice.

Conclusions: Our data show that KLHTT has anti-neutrophilic inflammatory effects in inhibiting ROS generation

Abbreviations: AAPH, 2,2-azobis(2-amidinopropane) dihydrochloride; CD11b, cluster of differentiation molecule 11b; fMLF, N-formyl-L-methionyl-L-leucyl-L-phenylalanine; IMQ, imiquimod; KLHTT, Kan-Lu-Hsiao-Tu-Tan; m-3M3FBS, 2,4,6-trimethyl-N-(meta-3-trifluoromethyl-phenyl)-benzenesulfonamide; NETs, neutrophil extracellular traps; PASI, psoriasis area and severity index; PKC, protein kinase C; PMA, phorbol 12-myristate 13-acetate; ROS, reactive oxygen species

* Corresponding author. Graduate Institute of Natural Products, College of Medicine, Chang Gung University, 259 Wenhwa 1st Road, Kweishan, Taoyuan, 333, Taiwan.

E-mail addresses: moonlight0604@hotmail.com (C.-C. Chiang), misterarren@gmail.com (W.-J. Cheng), god100240847@gmail.com (C.-Y. Lin), mos19880822@gmail.com (K.-H. Lai), 107sju@gmail.com (S.-C. Ju), max869301@gmail.com (C. Lee), dryang@mail.cgu.edu.tw (S.-H. Yang), htl@mail.cgu.edu.tw (T.-L. Hwang).

<https://doi.org/10.1016/j.jep.2019.112246>

Received 9 April 2019; Received in revised form 5 September 2019; Accepted 16 September 2019

Available online 17 September 2019

0378-8741/ © 2019 Elsevier B.V. All rights reserved.

and cell adhesion. KLHTT also mitigated NET formation, mainly via an ROS-dependent pathway. In addition, KLHTT reduced neutrophil infiltration and improved the severity of IMQ-induced psoriasis-like skin inflammation in mice. Therefore, KLHTT may prove to be a safe and effective psoriasis therapy in the future.

1. Introduction

Neutrophils, the most abundant circulating white blood cells, regulate innate immunity via several mechanisms such as phagocytosis, respiratory bursts with superoxide anion generation, degranulation with elastase release, cytokine production, and neutrophil extracellular trap (NET) formation (Delgado-Rizo et al., 2017). Neutrophils also regulate adaptive immunity (El-Benna et al., 2016). However, excessive amounts of reactive oxygen species (ROS), proteolytic enzymes, and NETs are harmful and can cause various pathological conditions, including infectious diseases like sepsis (Navegantes et al., 2017), chronic inflammatory disorders like atherosclerosis and chronic obstructive pulmonary disease (Amulic et al., 2012), autoimmune conditions like systemic lupus erythematosus and psoriasis (Hoffmann and Enk, 2016), and other diseases like cancer and diabetes mellitus (Papayannopoulos, 2017).

Psoriasis is a chronic immune-mediated skin disease affecting approximately 2% of the global population (> 125 million people) (Ogawa et al., 2017). Men and woman are affected equally at all ages (Michalek et al., 2017). Psoriasis manifests as thickened, erythematous, and scaly plaques that can appear on any part of the body (Parmar et al., 2017). It is characterized by excessive proliferation and abnormal differentiation of keratinocytes and by infiltration of diverse innate and adaptive immune cells, including neutrophils, T cells, and dendritic cells (Greb et al., 2016). The accumulation of neutrophils is a unique feature of psoriasis (Schon et al., 2017). Neutrophils have been found to be involved in amplification feedback during the maintenance stage of psoriasis, and NET formation correlates with psoriasis severity (Hu et al., 2016; Lowes et al., 2014). Patients with intractable psoriasis have been shown to experience a dramatic improvement after human neutrophil depletion (Ikeda et al., 2013). Therefore, neutrophils are a promising target for the treatment of psoriasis.

Kan-Lu-Hsiao-Tu-Tan (KLHTT) is a well-known formula in traditional Chinese medicine (TCM) for the treatment of “warm diseases”. KLHTT was first prescribed by Ye Gui in the “Supplement to the Classified Case Histories of Famous Physicians” in the Qing Dynasty of China (Hsieh et al., 2016). KLHTT is composed of 11 herbs (Table 1). TCM doctors use KLHTT to treat various infections and inflammatory conditions (Wei et al., 2016) such as influenza (Bi et al., 2014), acute sinusitis (Zhang, 2004), hepatitis B (Huang et al., 2000), enterovirus infections (Hsieh et al., 2016), gout (Xin and Fan, 2012), and chronic dermatitis (Xu, 2010). However, the pharmacological effects and its underlying mechanisms of KLHTT in neutrophils still need further investigation. Here, we investigated the anti-inflammatory effects of KLHTT on human neutrophils and its therapeutic potential in treating imiquimod (IMQ)-induced psoriasis-like skin inflammation.

2. Materials and methods

2.1. Reagents

Baicalin, baicalein, wogonoside, and wogonin were supplied by Dr. Leu Yann-Lii from Chang Gung University, Taiwan. Chlorogenic acid

and forsythin were purchased from Tauto (Shanghai, China). Hanks' balanced salt solution (HBSS) was purchased from GIBCO (Grand Island, NY, USA). Leukotriene B₄ (LTB₄) and H-Leu-Glu-Ser-Ile-Phe-Arg-Ser-Leu-Leu-Phe-Arg-Val-Met-CONH₂ (MMK-1) were purchased from Tocris Bioscience (Ellisville, MO, USA). Lactate dehydrogenase (LDH) assay kits were purchased from Promega (Madison, WI). Xanthine was obtained from Santa Cruz Biotechnology (Santa Cruz, CA, USA). Water-soluble tetrazolium-1 (WST-1) was purchased from Dojindo Laboratories (Kumamoto, Japan). FITC-labeled anti-cluster of differentiation molecule 11b (CD11b), anti-lymphocyte antigen 6 complex locus G6D (Ly6G), and anti-myeloperoxidase (MPO) antibodies were purchased from eBioscience (San Diego, CA, USA). Other bioassay reagents were ordered from Sigma-Aldrich (St. Louis, MO, USA).

2.2. Sample preparation

The KLHTT water extract was provided by Sun Ten Pharmaceutical Company (New Taipei City, Taiwan). Briefly, total 11 herbs (27.93 g) was extracted with ddH₂O (335.16 mL) at 100 °C for 1 h (Table 1). The KLHTT water extract was concentrated using a freeze dryer (LABCO-NCO, USA). A voucher specimen (CGU_KLHTT-01) was deposited in the Graduate Institute of Natural Products, Chang Gung University. KLHTT powder was dissolved in ddH₂O, filtered through a 0.45 µm filter, and stored at −20 °C before the bioassay.

2.3. High-performance liquid chromatography (HPLC) of KLHTT

The methods, including the machine equipment used, standard solutions used, and the sample HPLC solution preparation, have been described in detail by Hsieh et al. (2016). Baicalin, baicalein, wogonoside, wogonin, chlorogenic acid, and forsythin were used as the standard references. Subsequently, KLHTT fingerprinting was

Table 1
Kan-Lu-Hsiao-Tu-Tan (KLHTT).

Herb	Binomial nomenclature	Weight (g)
Huashi (滑石)	Soapstone [Mg ₃ (Si ₄ O ₁₀) (OH) ₂]	6.25
Yinchenhao (茵陳蒿)	<i>Artemisia capillaris</i> Thunb.	4.58
Huangqin (黃芩)	<i>Scutellaria baicalensis</i> Georgi	4.17
Shichangpu (石菖蒲)	<i>Acorus gramineus</i> Soland.	2.50
Mutong (木通)	<i>Clematis armandii</i> Franch.	2.08
Chuanbeimu (川貝母)	<i>Fritillaria cirrhosa</i> D. Don	2.08
Huoxiang (藿香)	<i>Pogostemon cablin</i> (Blanco) Benth.	1.67
Lianqiao (連翹)	<i>Forsythia suspensa</i> (Thunb.) Vahl	1.67
Baidoukou (白豆蔻)	<i>Amomum kravanh</i> Pierre ex Gagnep.	1.67
Baohe (薄荷)	<i>Mentha haplocalyx</i> Briq.	1.67
Shegan (射干)	<i>Belamcanda chinensis</i> (L.) DC.	1.67

Total eleven herbs (27.93 g) was extracted with ddH₂O (335.16 mL) at 100 °C for 1 h by Sun Ten Pharmaceutical Corporation. The batch number was 0503-2-403-01.

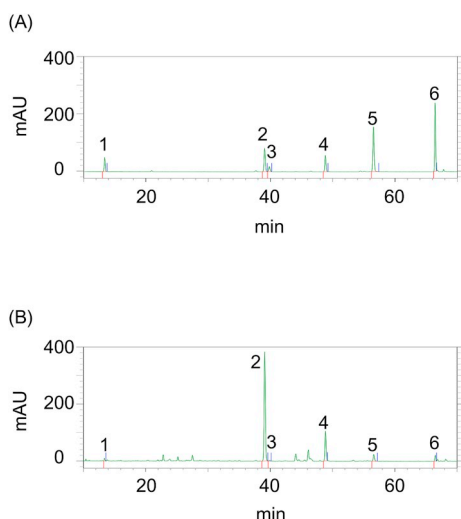


Fig. 1. Chemical fingerprint profile of Kan-Lu-Hsiao-Tu-Tan (KLHTT). Chromatograms obtained from HPLC-UV at 272 nm. (A) Six standard references including 1: Chlorogenic acid; 2: Baicalin; 3: Forsythin; 4: Wogonoside; 5: Baicalein; 6: Wogonin. (B) HPLC-UV fingerprint profile of KLHTT.

performed at 272 nm using a Hitachi chromatograph system (Hitachi, Tokyo, Japan).

2.4. Human neutrophil isolation

The institutional review board of Chang Gung Memorial Hospital approved this study. All volunteers (20–32 years old) were healthy and signed informed consent forms before blood donation. Human neutrophil preparation was performed using a standard protocol that included dextran sedimentation, centrifugation in a Ficoll-Hypaque gradient, and hypotonic lysis of red blood cells. The isolated human neutrophils were suspended in Ca^{2+} -free Hanks' balanced salt solution (HBSS) at 4 °C prior to analysis (Tsai et al., 2015).

2.5. Reactive oxygen species (ROS)

2.5.1. Measurement of extracellular superoxide anion production

Human neutrophils (3×10^5 or 6×10^5 cells/ml) supplemented with 1 mM CaCl_2 and 0.5 mg/ml ferricytochrome *c* at 37 °C were incubated with ddH₂O (0.1%, as control) or KLHTT (1, 3, or 10 $\mu\text{g}/\text{ml}$) for 5 min. Cells were then activated by *N*-formyl-L-methionyl-L-leucyl-L-phenylalanine (fMLF; 0.1 μM for 10 min), MMK-1 (0.1 μM for 10 min), 2,4,6-trimethyl-*N*-(meta-3-trifluoromethyl-phenyl)-benzenesulfonamide (m-3M3FBS; 15 μM for 10 min), or sodium fluoride (NaF; 20 mM for 30 min) in the pretreatment of cytochalasin B (CB; 1 $\mu\text{g}/\text{ml}$ for fMLF, MMK-1, and m-3M3FBS; 2 $\mu\text{g}/\text{ml}$ for NaF) or phorbol 12-myristate 13-acetate (PMA; 10 nM for 5 min). The absorbance change was detected spectrophotometrically at 550 nm (Yu et al., 2011).

Table 2

Retention times (t_R) and content of six standard references detected in KLHTT.

Peak no	Retention time (min)	Name	Content (%)
1	13.393	Chlorogenic acid	0.035%
2	39.120	Baicalin	1.03%
3	39.877	Forsythin	0.025%
4	48.877	Wogonoside	0.39%
5	56.630	Baicalein	0.03%
6	66.530	Wogonin	0.02%

Chlorogenic acid, baicalin, forsythin, wogonoside, baicalein, wogonin were used as standard solutions to detect KLHTT through HPLC-UV at 272 nm. The retention times and content were observed and calculated.

2.5.2. Measurement of intracellular superoxide anion generation

Human neutrophils (1×10^6 cells/ml) were labeled with hydroethidine bromide (HE) for 10 min at 37 °C, and then ddH₂O or KLHTT (3 and 10 $\mu\text{g}/\text{ml}$) were added for 5 min before activating with fMLF (0.1 μM) in the pretreatment of CB (0.5 $\mu\text{g}/\text{ml}$) for another 5 min. The generation of intracellular superoxide anions was analyzed using flow cytometry (Yang et al., 2018).

2.5.3. Total ROS release assays

Intracellular and extracellular ROS were detected using luminol-enhanced chemiluminescence. Human neutrophils (7×10^5 cells/ml) were mixed with 6 U/ml horseradish peroxidase (HRP) and 37.5 μM luminol for 5 min, and then ddH₂O or KLHTT (1, 3, and 10 $\mu\text{g}/\text{ml}$) were added for 5 min before activating with fMLF (0.1 μM). A 96-well chemiluminometer (Tecan, Infinite F200 Pro; Tecan Group, Männedorf, Switzerland) was used to observe the chemiluminescence response (Tsai et al., 2015).

2.6. Measurement of elastase release

The method used to detect elastase release, which represents the degranulation of azurophilic granules, has been previously described by Lee et al. (2013). Meo-Suc-Ala-Ala-Pro-Val-*p*-nitroanilide was the elastase-specific substrate. Human neutrophils (6×10^5 or 1×10^6 cells/ml) mixed with 0.1 mM substrate at 37 °C were incubated with ddH₂O or KLHTT (1, 3, or 10 $\mu\text{g}/\text{ml}$) for 5 min. Human neutrophils were activated using different stimulants, including 0.1 μM fMLF, 0.1 μM MMK-1, 15 μM m-3M3FBS, 100 ng/ml interleukin 8 (IL-8), 0.1 μM LTB₄, or 1 μM platelet activating factor (PAF) in the pretreatment of CB (0.5 or 2 $\mu\text{g}/\text{ml}$) for 3 min. The absorbance changes were detected spectrophotometrically at 405 nm.

2.7. LDH release

The commercially available protocol (Promega, Madison, WI, USA) has previously been described in Chang et al. (2008). Human neutrophils were incubated with ddH₂O or KLHTT for 15 min or 3 h. Cytotoxicity was evaluated using the percentage of total LDH release, which was determined by lysing cells with 0.1% Triton X-100 at 37 °C for 30 min.

2.8. ROS-scavenging activity

2.8.1. Superoxide anion scavenging analysis

The xanthine/xanthine oxidase cell-free system was used to determine the superoxide anion scavenging abilities of KLHTT (Lin et al., 2009). After adding 0.1 mM xanthine to a buffer containing Tris (pH 7.4), 0.3 mM WST-1, and 0.02 U/ml xanthine oxidase at 30 °C for 10 min, the absorbance changes were detected spectrophotometrically at 450 nm.

2.8.2. 2,2'-Azobis(2-amidinopropane) dihydrochloride (AAPH)-scavenging analysis

KLHTT (1, 3, and 10 µg/ml) or Trolox (12.5–100 µM) were incubated with fluorescein (80 nM) dissolved in a 75 mM sodium phosphate buffer (pH 7.4) for 5 min at 37 °C. After adding AAPH (25 mM),

the fluorescence changes were detected every 3 min for 2 h. The excitation wavelength was 485 nm, and the emission wavelength was 535 nm (Betigeri et al., 2005).

2.9. Reactive nitrogen species (RNS)-scavenging activity

2.9.1. 1,1-Diphenyl-2-picrylhydrazyl (DPPH)-scavenging assay

DPPH is a stable nitrogen-centered free radical. After adding KLHTT (1, 3, and 10 µg/ml) or vitamin E (3, 15, and 30 µM) to DPPH (100 µM in methanol), the absorbance was determined at 517 nm after 15 min (Lin et al., 2009).

2.9.2. 2,2'-Azino-bis(3-ethylbenzothiazoline-6-sulfonic acid) diammonium salt (ABTS)-scavenging analysis

ABTS is another nitrogen-centered free radical. After adding KLHTT

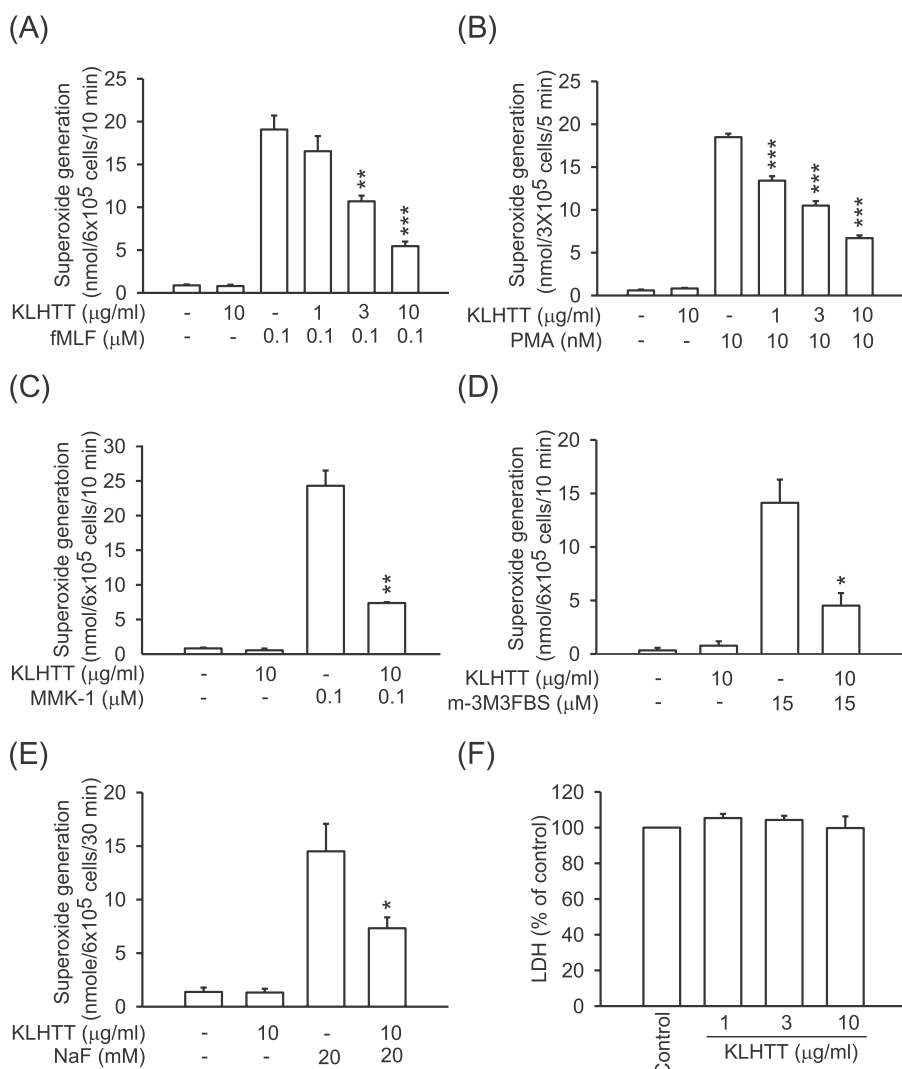


Fig. 2. KLHTT inhibits extracellular superoxide anion generation in activated human neutrophils. Human neutrophils were incubated with ddH₂O (0.1%, as a control) or KLHTT (1, 3, or 10 µg/ml) for 5 min and were activated by (A) fMLF, (C) MMK-1, or (D) m-3M3FBS for 10 min, (B) PMA for 5 min, or (E) NaF for 30 min. Superoxide anion production was monitored using ferricytochrome c reduction at 550 nm. (F) Human neutrophils were incubated with ddH₂O or KLHTT for 15 min. Cytotoxicity was represented by LDH release in the cell-free medium as a percentage of total LDH release. Total LDH release was determined from cells lysed with 0.1% Triton X-100 for 30 min at 37 °C. All data are expressed as mean ± S.E.M. (n = 3 or 4). *p < 0.05, **p < 0.01, ***p < 0.001 compared to different stimulants alone.

(1, 3, and 10 $\mu\text{g/ml}$) or vitamin C (10, 15, and 30 μM) to ABTS (2.45 mM in potassium persulfate), the absorbance at 734 nm was detected after 15 min (Re et al., 1999).

2.10. CD11b expression analysis

Human neutrophils (2.5×10^6 cells/ml) were incubated with ddH₂O or KLHTT (3 and 10 $\mu\text{g/ml}$) for 5 min and then activated by fMLF (0.1 μM)/CB (1 $\mu\text{g/ml}$) for another 5 min. After centrifugation at $200 \times g$ for 8 min, the cells were resuspended in HBSS containing 0.5% bovine serum albumin (BSA). FITC-labeled anti-CD11b (1 μg) was added at 4 °C for 90 min in the dark, and the immunofluorescence was detected immediately using flow cytometry (Tsai et al., 2015).

2.11. Adhesion study

Human neutrophils (4×10^6 cells/ml) were mixed with 1 ng/ml Hoechst 3342 for 10 min at 37 °C. The supernatant was cleared using centrifugation ($200 \times g$, 8 min). The cells were resuspended and activated by adding fMLF (0.1 μM)/CB (1 $\mu\text{g/ml}$) for 10 min and were

transferred to wells containing bEND 3 cells. After co-incubating for 15 min, the cells were washed with HBSS and were fixed with 4% paraformaldehyde. Adherent neutrophils were counted using fluorescent microscopy (Chen et al., 2016).

2.12. Analysis of NET formation

2.12.1. Quantification of NETs

Human neutrophils (1×10^6 cells/ml) were incubated with ddH₂O or KLHTT (10 $\mu\text{g/ml}$) for 10 min and then activated by PMA (10 nM) for 3 h. SYTOX Green nucleic acid stain (2.5 μM) was added for 15 min, and the fluorescence was detected at 485–535 nm (Yang et al., 2018).

2.12.2. Photography of NETs

Human neutrophils (2.5×10^5 cells/ml) containing 0.05% BSA (w/v) were placed on poly-L-lysine coated glasses and incubated at 37 °C for 30 min. KLHTT (10 $\mu\text{g/ml}$) was added for 10 min before stimulating with PMA (10 nM) for 3 h. A solution of 4% paraformaldehyde was added to fix the cells, and 0.05% (v/v) Triton X-100 was used to lyse cells. Afterwards, 0.5% (v/v) anti-human elastase antibody (MABS461),

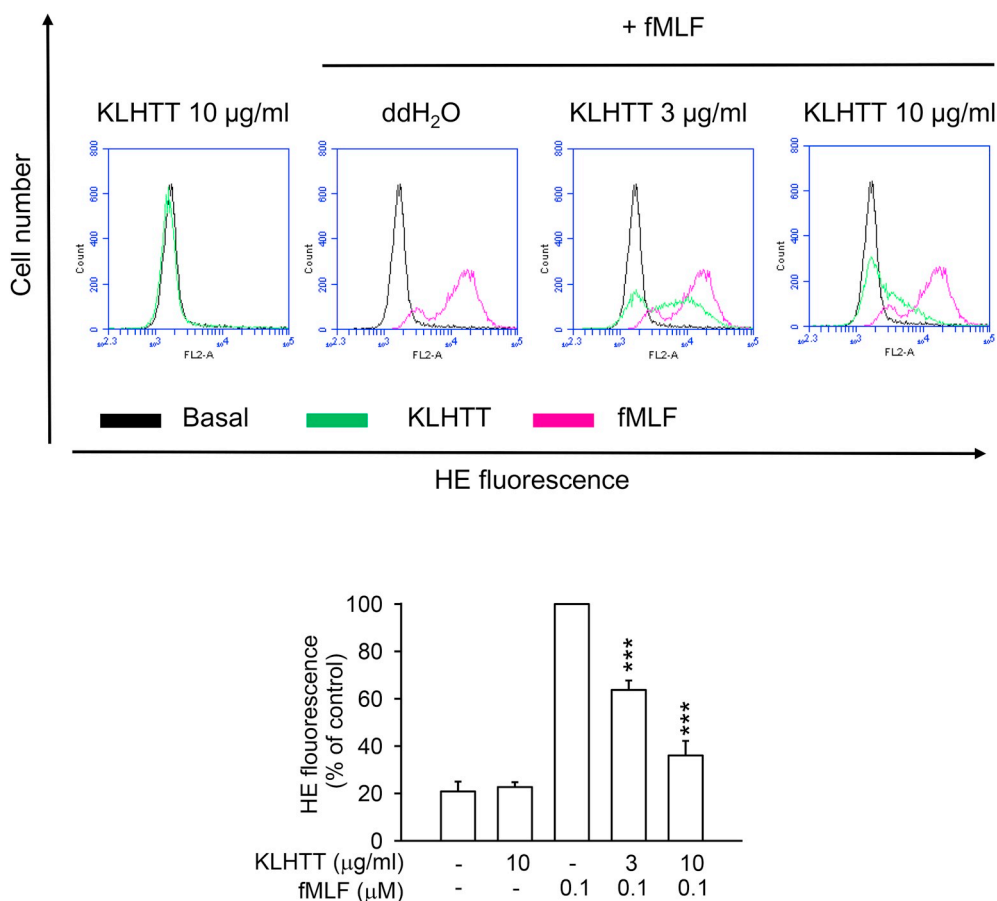


Fig. 3. KLHTT inhibits intracellular superoxide anion generation in activated human neutrophils. Human neutrophils were incubated with ddH₂O or KLHTT (3 and 10 $\mu\text{g/ml}$) for 5 min and were activated by fMLF. Superoxide anion production was measured using the reduction in HE fluorescence. All data are expressed as mean \pm S.E.M. (n = 3). ***p < 0.001 compared with fMLF alone.

0.5% (v/v) anti-MPO antibody (ab9535), and 1 ng/ml Hoechst 33342 were used to stain NETs for photography (Remijsen et al., 2011).

2.13. Anti-psoriasis activity

2.13.1. Imiquimod-induced psoriasis animal model

Eight-week-old male mice weighing about 20 g were used in this experiment. This study was approved by Institutional Animal Care and Use Committee of Chang Gung University, Taiwan. Mice were divided into five groups as follows: Group 1, sham-operated mice treated with the vehicle (40% ethanol and 60% ddH₂O, 100 μ L); Group 2, sham-operated mice treated with KLHTT (10 mg/ml, 100 μ L); Group 3, mice treated with the vehicle and IMQ; Group 4, mice treated with KLHTT

(10 mg/ml, 100 μ L) before IMQ; and Group 5, mice treated with KLHTT (10 mg/ml, 100 μ L) after IMQ. The backs of mice were shaved using depilatory machine and cream. Aldara (3M Health Care Limited, UK) containing 5% imiquimod (IMQ) was used to induce psoriasis-like skin inflammation with a daily dose of 62.5 mg from day 1 to day 5, consecutively. KLHTT (10 mg/ml) was dissolved in a vehicle containing 40% ethanol and 60% ddH₂O. The pretreatment groups were treated topically with KLHTT (10 mg/ml, 100 μ L) daily from day 1 to day 5. The posttreatment groups were treated topically with KLHTT (10 mg/ml, 100 μ L) from day 2 to day 5. Skin samples from the backs of the mice were isolated on day 6, fixed in 10% paraformaldehyde, and stained with hematoxylin-eosin (HE), ki67, Ly6G, and MPO based on a standard protocol (El Malki et al., 2013).

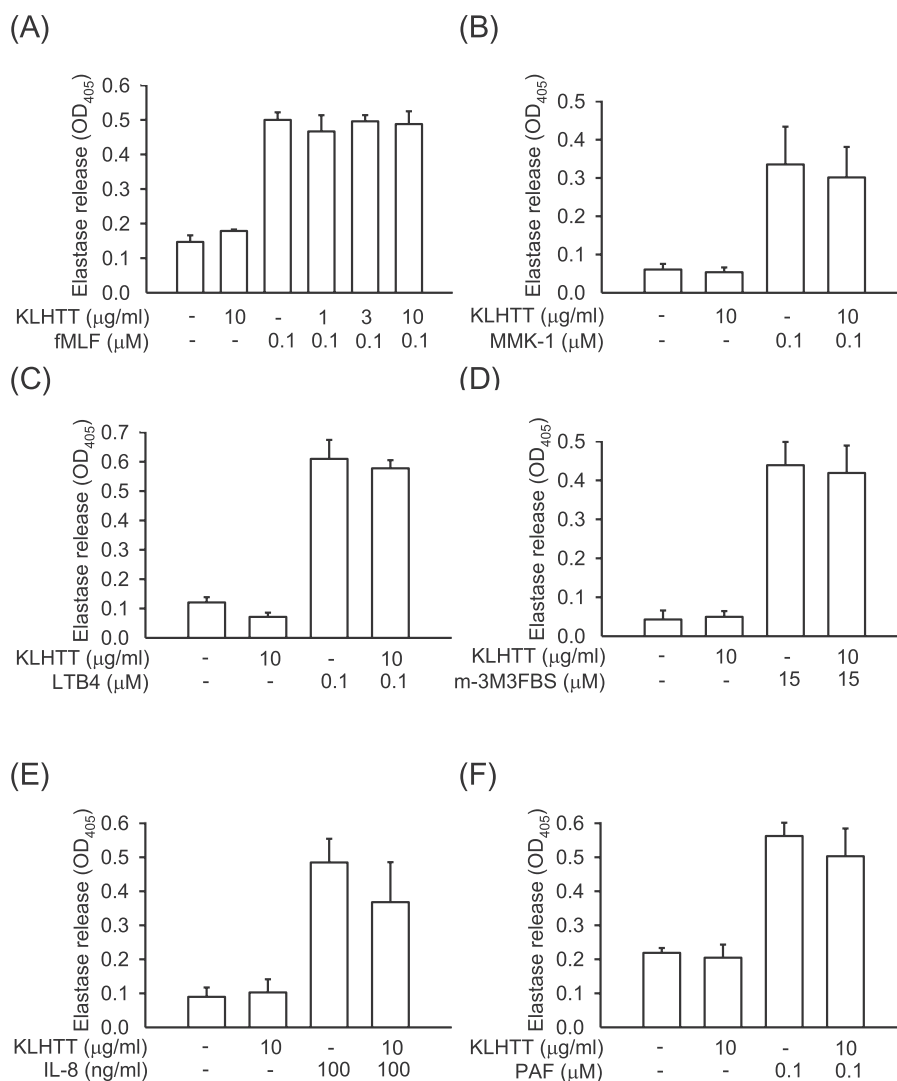


Fig. 4. KLHTT does not inhibit elastase release in activated human neutrophils. Human neutrophils were incubated with ddH₂O or KLHTT (1, 3, or 10 μ g/ml) for 5 min and were activated using (A) fMLF, (B) MMK-1, (C) LTB₄, (D) m-3M3FBS, (E) IL-8, or (F) PAF for 10 min. Elastase release was measured spectrophotometrically at 405 nm. All data are expressed as mean \pm S.E.M. (n = 3).

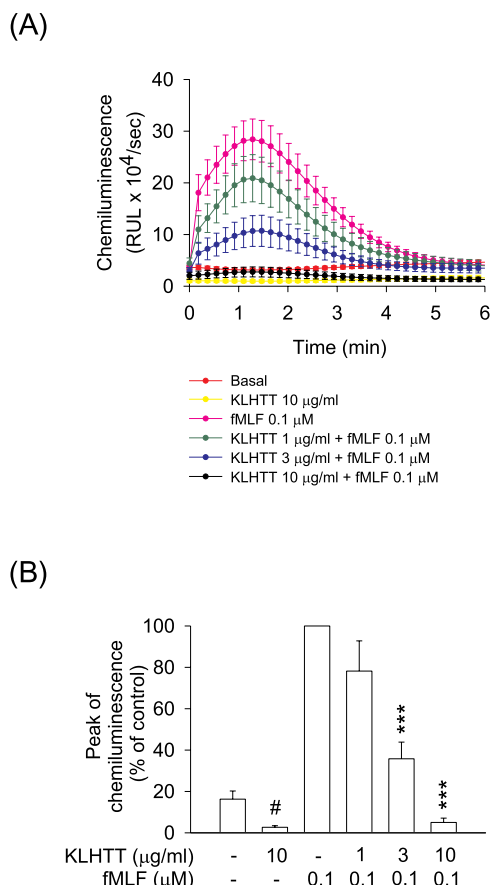


Fig. 5. KLHTT inhibits ROS generation in activated human neutrophils. (A) Human neutrophils (7×10^5 cells/ml) were incubated with ddH₂O or KLHTT (1, 3, and 10 µg/ml) for 5 min and were stimulated with fMLF for 6 min. (B) Peak chemiluminescence is expressed as mean \pm S.E.M. (n = 6). ****p* < 0.001 compared to fMLF alone. #*p* < 0.001 compared to basal level.

2.13.2. Scoring of psoriatic lesions

The severity of psoriatic lesions was evaluated on day 6 using a psoriasis area and severity index (PASI) score based on the human PASI score. Erythema, scaling, and thickness were independently assigned a score between 0 and 4: 0 for no effect; 1 for a mild effect; 2 for an intermediate effect; 3 for a severe effect; and 4 for a very severe effect (El Malki et al., 2013).

2.14. Statistical analysis

Statistical significance was calculated using Student's *t*-tests with SigmaPlot (Systat Software, San Jose, CA, USA). All data were expressed as mean \pm S.E.M. A *P*-value of *P* < 0.05 was considered statistically significant.

3. Results

3.1. High-performance liquid chromatography (HPLC) analysis of KLHTT

Chlorogenic acid, baicalin, forsythin, wogonoside, baicalein, and wogonin were used as the standard references and had retention times of 13.393 min, 39.120 min, 39.877 min, 48.877 min, 56.630 min, and 66.530 min, respectively (Fig. 1). The percentage compositions of the standard references were found to be: baicalin, 1.03%; wogonoside, 0.39%; chlorogenic acid, 0.035%; baicalein, 0.03%; forsythin, 0.025%; and wogonin, 0.02% (Table 2).

3.2. KLHTT attenuates ROS production but not elastase release in activated human neutrophils

Neutrophils produce large amounts of ROS, including the main superoxide anion, by activating NADPH oxidase in a process called respiratory burst (Nagarkoti et al., 2018). KLHTT (10 µg/ml) significantly attenuated extracellular superoxide anion generation in fMLF-, PMA-, MMK-1-, m-3M3FBS-, and NaF-activated human neutrophils. KLHTT did not change superoxide anion generation in resting human neutrophils, and it did not induce LDH release under experimental conditions (Fig. 2).

KLHTT (10 µg/ml) also decreased intracellular superoxide production in HE-labeled human neutrophils (Fig. 3). In addition, different stimulants were used to activate human neutrophils to study degranulation, which releases many granules containing proteolytic enzymes like elastase (Schulz-Fincke et al., 2017). Even at a high concentration (10 µg/ml), KLHTT failed to affect elastase release (Fig. 4). These data suggested that KLHTT selectively inhibited oxidative stress caused by activated human neutrophils. Corroborating this hypothesis, KLHTT (1, 3, and 10 µg/ml) significantly suppressed total ROS generation in fMLF-activated human neutrophils in a concentration-dependent manner (Fig. 5).

3.3. KLHTT reduces neutrophil-dependent oxidative stress via direct and indirect effects

To understand the ROS-scavenging effects of KLHTT, ROS generation assays in cell-free systems were used. KLHTT (1, 3, and 10 µg/ml) did not inhibit superoxide anion production in a cell-free xanthine/xanthine oxidase system (Fig. 6A), suggesting that KLHTT inhibited superoxide anion generation in activated human neutrophils by regulating cell activation. Superoxide dismutase (20 U/ml) was used as a positive control. The antioxidant ability of KLHTT was further assessed using oxygen-radical absorbance capacity assays. Fig. 6B–D shows that KLHTT and Trolox had potent antioxidant effects in preventing fluorescent degeneration. In contrast, KLHTT showed only minor effects in ABTS and DPPH radical assays. Vitamin C and vitamin E were used as positive controls (Fig. 6E and F). These data suggest that KLHTT is more sensitive to scavenging ROS than RNS.

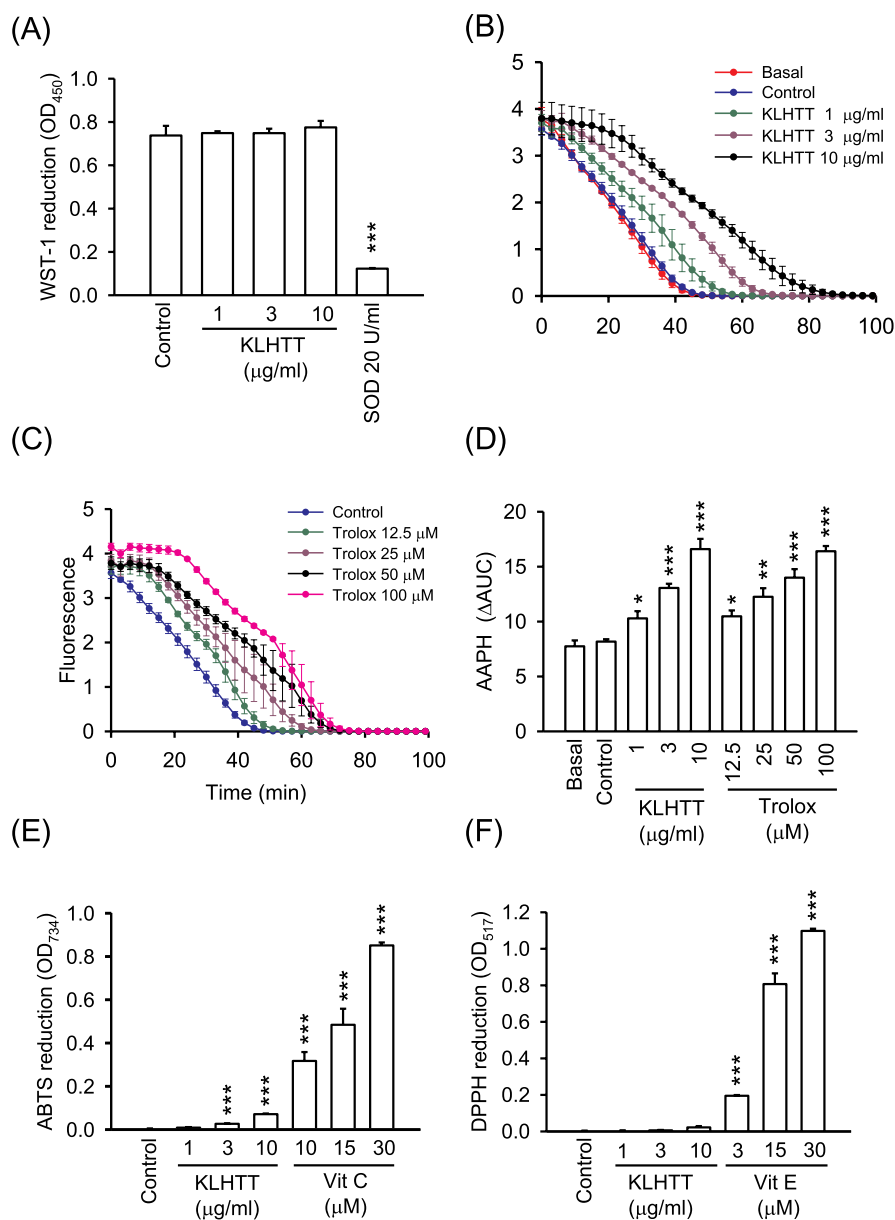


Fig. 6. KLHTT has an ROS scavenging effect. (A) Xanthine oxidase was incubated with ddH₂O, KLHTT (1, 3, and 10 µg/ml), or 20 U/ml superoxide dismutase (SOD, as a positive control) for 3 min, and then xanthine (0.1 mM) was added for 10 min. The reduction of WST-1 by xanthine/xanthine oxidase-induced superoxide anions was measured spectrophotometrically at 450 nm. (B, C) Fluorescence decay curves of AAPH in the presence of KLHTT and Trolox (D) The area under the curve (AUC) (E) ABTS was incubated with ddH₂O, KLHTT (1, 3, and 10 µg/ml), or vitamin C (10, 15, and 30 µM). ABTS reduction was measured spectrophotometrically at 734 nm. (F) DPPH was incubated with ddH₂O, KLHTT (1, 3, and 10 µg/ml), or vitamin E (3, 15, and 30 µM). The reduction of DPPH was measured spectrophotometrically at 517 nm. All data are expressed as mean ± S.E.M. (n = 3). **p* < 0.05, ***p* < 0.01, and ****p* < 0.001 compared to the control.

3.4. KLHTT inhibits NET formation

NETs are web-like structures containing decondensed chromatin with many granules and cytosolic proteins like elastase and MPO. Human neutrophils released NETs in response to PMA for 3 h. KLHTT (10 µg/ml) inhibited NET release in PMA-activated human neutrophils (Fig. 7A and B). Incubation with KLHTT for 3 h, even at the high concentration of 10 µg/ml, did not cause LDH release (Fig. 7C). This indicated that the inhibitory effect of KLHTT on NET formation was not due to cytotoxicity.

3.5. KLHTT inhibits CD11b expression and cell adhesion in activated human neutrophils

Circulating human neutrophils sense inflammatory signals and express various cell-surface receptors, such as CD11b, for adhesion. Later on, human neutrophils migrate and accumulate at inflammation sites (Futosi and Mocsai, 2016). Human neutrophil CD11b expression was increased in response to fMLF (Fig. 8) and enhanced adhesion to bEND 3 cells was also observed (Fig. 9A). Our data showed that KLHTT decreased CD11b expression in activated human neutrophils (Fig. 8) and

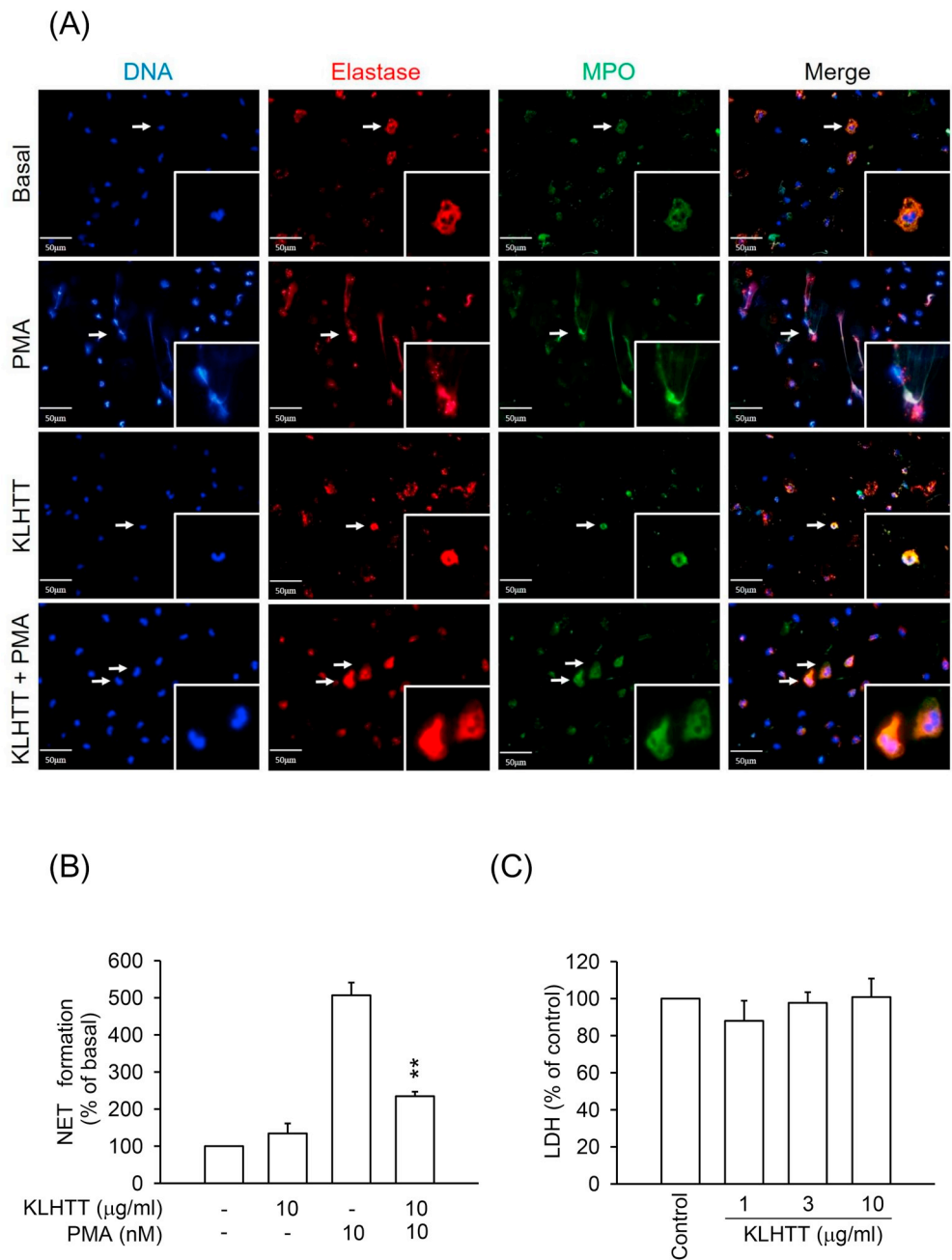


Fig. 7. KLHTT decreases NET formation. (A) Human neutrophils (2.5×10^5 cells/ml) were incubated on poly-L-lysine coated glasses with ddH₂O or KLHTT (10 μ g/ml). Neutrophils were stimulated using 10 nM PMA for 3 min and were hand fixed in paraformaldehyde for 10 min. The antibodies 0.5% (v/v) anti-human elastase (MABS461) and 0.5% (v/v) anti-MPO (ab9535), and 1 ng/ml Hoechst 33342 were used to stain NETs. Scale bar = 50 μ m. (B) Human neutrophils were incubated with ddH₂O or KLHTT (10 μ g/ml) for 10 min and were activated with 10 nM PMA for 3 h. SYTOX Green nucleic acid stain was added to quantify NET formation. (C) Human neutrophils were incubated with ddH₂O or KLHTT (1, 3, and 10 μ g/ml) for 3 h. Cytotoxicity was represented by LDH release in the cell-free medium as a percentage of the total LDH release. Total LDH release was determined from cells lysed with 0.1% Triton X-100 for 30 min at 37 $^{\circ}$ C. All data are expressed as mean \pm S.E.M. (n = 3). **p < 0.01 compared to PMA alone.

attenuated neutrophil adhesion to bEND 3 cells (Fig. 9A and B).

3.6. KLHTT ameliorates IMQ-induced psoriasis-like skin inflammation in mice

The topical application of IMQ, a toll-like receptor (TLR)-7/8 agonist, on mouse skin caused symptoms similar to those of human

psoriasis, including erythema, scaling, skin thickening, hyperkeratosis, formation of micro-abscesses, and neutrophil accumulation (El Malki et al., 2013).

Based on the gross appearance observed using a digital camera and hand-held digital microscope, it was concluded that the application of IMQ cream caused psoriasis-like skin inflammation. KLHTT was used to alleviate this IMQ-induced psoriasis-like skin inflammation. Both the

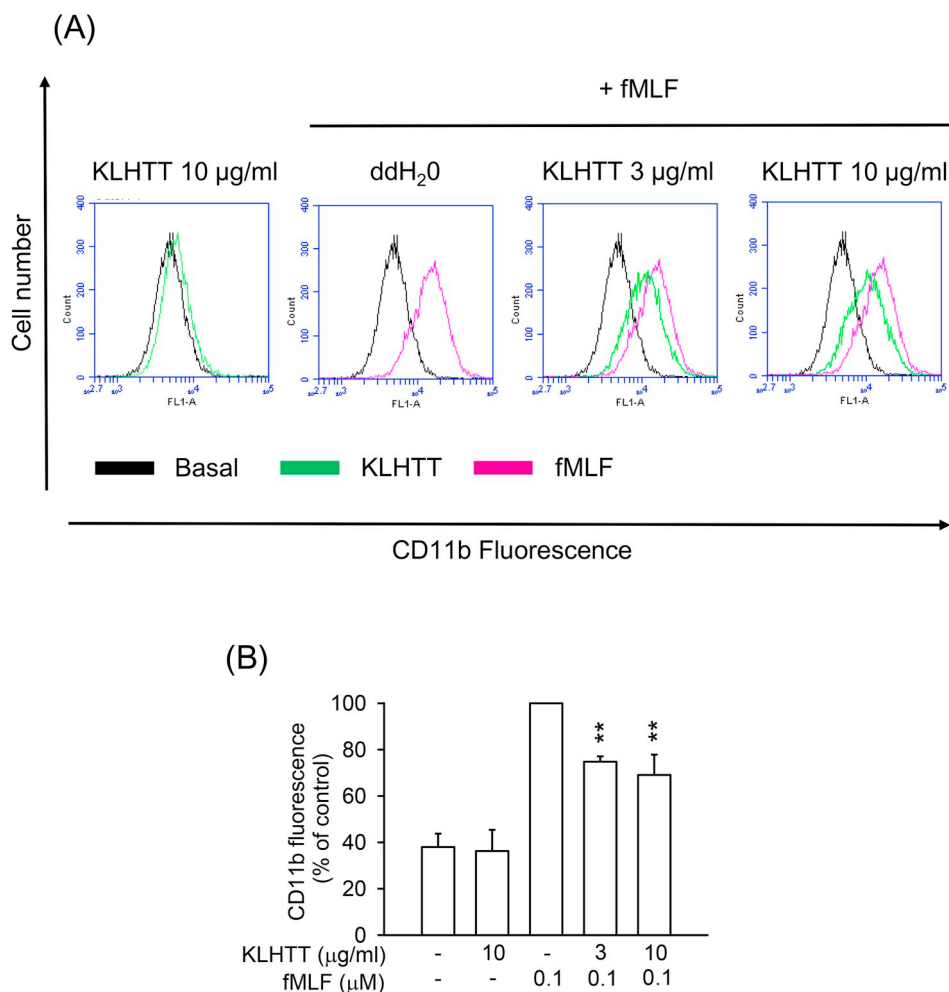


Fig. 8. KLHTT inhibits CD11b expression in activated human neutrophils. Human neutrophils (2.5×10^6 cells/ml) were incubated with ddH₂O or KLHTT (3 and 10 µg/ml) for 5 min and were activated with fMLF for 5 min. The fluorescence intensity of FITC-labeled anti-CD11b was measured using flow cytometry. The mean fluorescence intensity is expressed as mean \pm S.E.M. (n = 3). ** $p < 0.01$ compared to fMLF alone.

sham group and the KLHTT-without-IMQ-induction group had normal skin appearance (Fig. 10A). Furthermore, topical KLHTT (10 mg/ml) significantly improved IMQ-induced psoriasis-like skin inflammation and reduced the PASI score based on scaling, erythema, and thickness. The PASI scores were 0 in both the sham group and in the group treated with KLHTT without IMQ (Fig. 10B).

In the IMQ induced group, HE staining and IHC staining of Ki67 (the epidermal proliferation marker) revealed a thickened epidermis (acanthosis). IHC staining of MPO and Ly6G uncovered increased neutrophil recruitment and severe neutrophil infiltration in the dermis and epidermis (Munro's micro-abscesses). In the KLHTT pretreatment group (application of KLHTT before IMQ induction) and posttreatment group (application of KLHTT after IMQ induction), KLHTT reduced epidermal

thickness and significantly alleviated the infiltration and recruitment of neutrophils. The sham group and the KLHTT-without-IMQ-induction group both had a normal epidermis and did not display neutrophil infiltration (Fig. 11).

4. Discussion

Psoriasis is a chronic immune disease with skin symptoms such as erythema, thickness, and scaling. Neutrophil accumulation in the skin is a histological hallmark of psoriasis (Schon et al., 2017). Neutrophils in psoriasis participate in amplification feedback, leading to the release of many chemokines from keratinocytes (Lowes et al., 2014). Moreover, NETs are correlated with psoriasis severity in patients (Di Domizio and

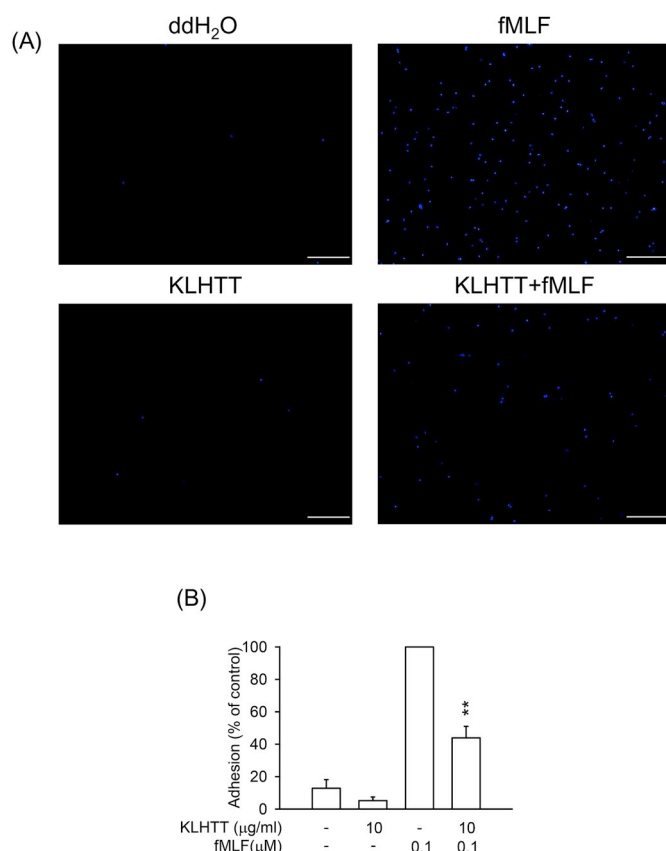


Fig. 9. KLHTT represses the adherence of activated human neutrophils to endothelial cells. (A) Hoechst 3342-labeled human neutrophils (4×10^6 cells/ml) were incubated with ddH₂O or KLHTT (10 μg/ml) for 5 min fMLF (0.1 μM) was used as the stimulant. The stimulated human neutrophils were added to bEND 3 cells for 15 min. Neutrophil adherence on bEND 3 cells was evaluated using fluorescent microscopy. Scale bar = 200 μm. (B) Representative histograms for fluorescent microscopy were made after counting and quantification of the adhered human neutrophils. All data are expressed as mean \pm S.E.M. (n = 3). ** $p < 0.01$ compared to fMLF alone.

Gilliet, 2019; Hu et al., 2016). Neutrophil depletion has been shown to dramatically improve intractable psoriasis in humans (Ikeda et al., 2013). Therefore, neutrophils and their associated ROS and NETs play important roles in psoriasis.

IMQ is a TLR-7/8 agonist drug that can result in psoriasis-like skin inflammation after topical application. The skin symptoms include redness, scaling, and thickening. Microscopically observable features include neutrophil infiltration, micro-abscess formation, acanthosis, and hyperkeratosis (El Malki et al., 2013). Irrespective of whether KLHTT was applied before or after IMQ induction, topical KLHTT significantly improved both individual and cumulative PASI scores.

Topical KLHTT also decreased neutrophil infiltration and thinned the epidermis in IMQ-induced psoriasis-like skin inflammation. Therefore, KLHTT may be an appropriate choice for psoriasis treatment.

This study indicated that KLHTT inhibited superoxide anion generation and the associated ROS release in human neutrophils activated by different stimuli. KLHTT exerted ROS-scavenging effects in the AAPH assay. However, KLHTT did not directly scavenge superoxide anion generated in the cell-free xanthine/xanthine oxidase system. Therefore, our data indicate that KLHTT decreases neutrophil ROS formation via direct scavenging and indirect regulation of cell responses. Moreover, we showed that KLHTT attenuated NET formation in PMA-activated human neutrophils. NETs are web-like structures composed of decondensed chromatin coated with many neutrophilic components like elastase and MPO. NETs result in a highly immunogenic environment (Hoffmann and Enk, 2016). The formation of NETs occurs mostly through ROS-dependent mechanisms. ROS stimulate MPO and elastase to decondense chromatin, which subsequently leads to NET formation (Papayannopoulos, 2017). Our data suggest that KLHTT inhibits NET formation by inhibiting the ROS-dependent pathway. KLHTT also decreased CD11b expression and cell adhesion in activated human neutrophils. In patients with psoriasis, there is an increase in the occurrence of respiratory burst in neutrophils with overproduction of ROS (Bloomfield and Young, 1988). Moreover, NET formation is increased in psoriasis, and the number of NETs is correlated with severity (Hu et al., 2016). In conclusion, KLHTT ameliorates IMQ-induced psoriasis-like skin inflammation in mice by suppressing neutrophil activation, which may occur via ROS attenuation, inhibition of CD11b expression and adhesion, and restriction of NET formation.

TCM doctors use KLHTT to treat various inflammatory conditions that may be related to neutrophils. KLHTT contains 11 herbs: huashi, yinchenhao, huangqin, shichangpu, mutong, chuanbeimu, huoxiang, lianqiao, baidoukou, baohe, and shegan (Hsieh et al., 2016). Huangqin contains baicalin and baicalein, which have been shown to inhibit neutrophil activation and improve psoriasis in mouse models (Huang et al., 2016; Shen et al., 2003; Wu et al., 2015). Yinchenhao, lianqiao, and baohe contain chlorogenic acid, which affects neutrophil adhesion and locomotion (Hebeda et al., 2011). The 19-hydroxyabda-8 (17),13(Z)-dien-15-oic acid, ursolic acid, and alphitolic acid in lianqiao suppress superoxide anion generation in activated neutrophils (Kuo et al., 2017). Isorhapontigenin, found in shegan, represses neutrophil respiratory burst (Fang and Liu, 2002). Huoxiang has anti-inflammatory properties (Li et al., 2013). For thousands of years, TCM doctors have prescribed formulations containing complex mixtures of herbs, finding that formulation expresses synergistic and coordinated effects for higher curative quality and efficacy than a single herb (Ho et al., 2013).

In summary, our results show that KLHTT has potent anti-inflammatory effects on human neutrophils. We also indicate that KLHTT is an effective TCM for treating psoriasis-like skin inflammation. Hence, the topical application of KLHTT may be an effective modality to improve the treatment of patients with psoriasis in the future.

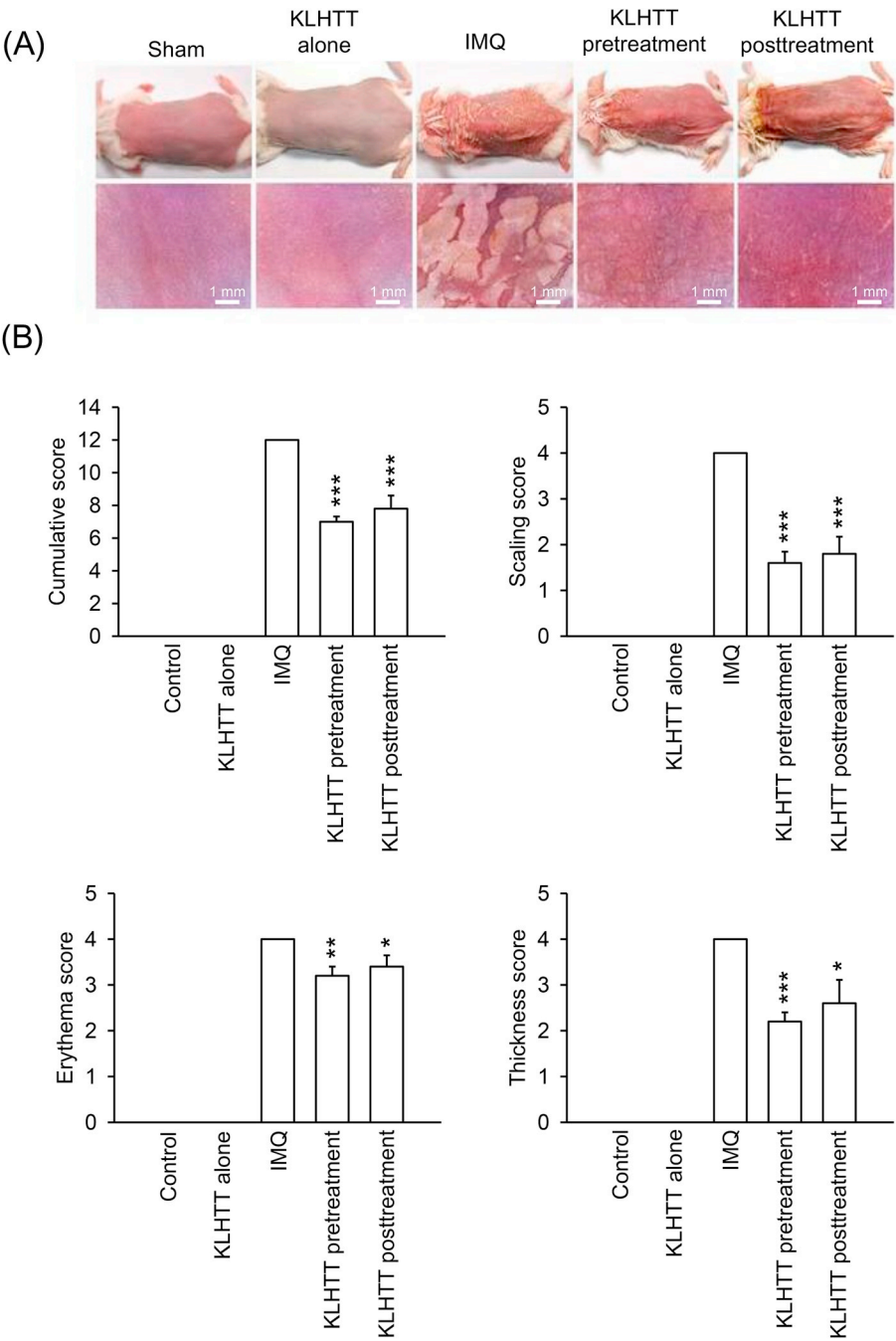


Fig. 10. KLHTT improves the severity of IMQ-induced psoriasis-like skin inflammation. (A) IMQ-induced psoriasis-like skin inflammations were observed using a digital camera and a hand-held digital microscope. Scale bar = 1 mm. Five days after treatment, topical KLHTT (10 mg/ml) improved erythema, thickness, and scaling in the groups treated both before and after IMQ induction. (B) KLHTT (10 mg/ml) significantly improved the erythema score, thickness score, scaling score, and cumulative score in both KLHTT-treated groups. All data are expressed as mean \pm S.E.M. (n = 5). * p < 0.05, ** p < 0.01, and *** p < 0.001 compared to the IMQ alone group.

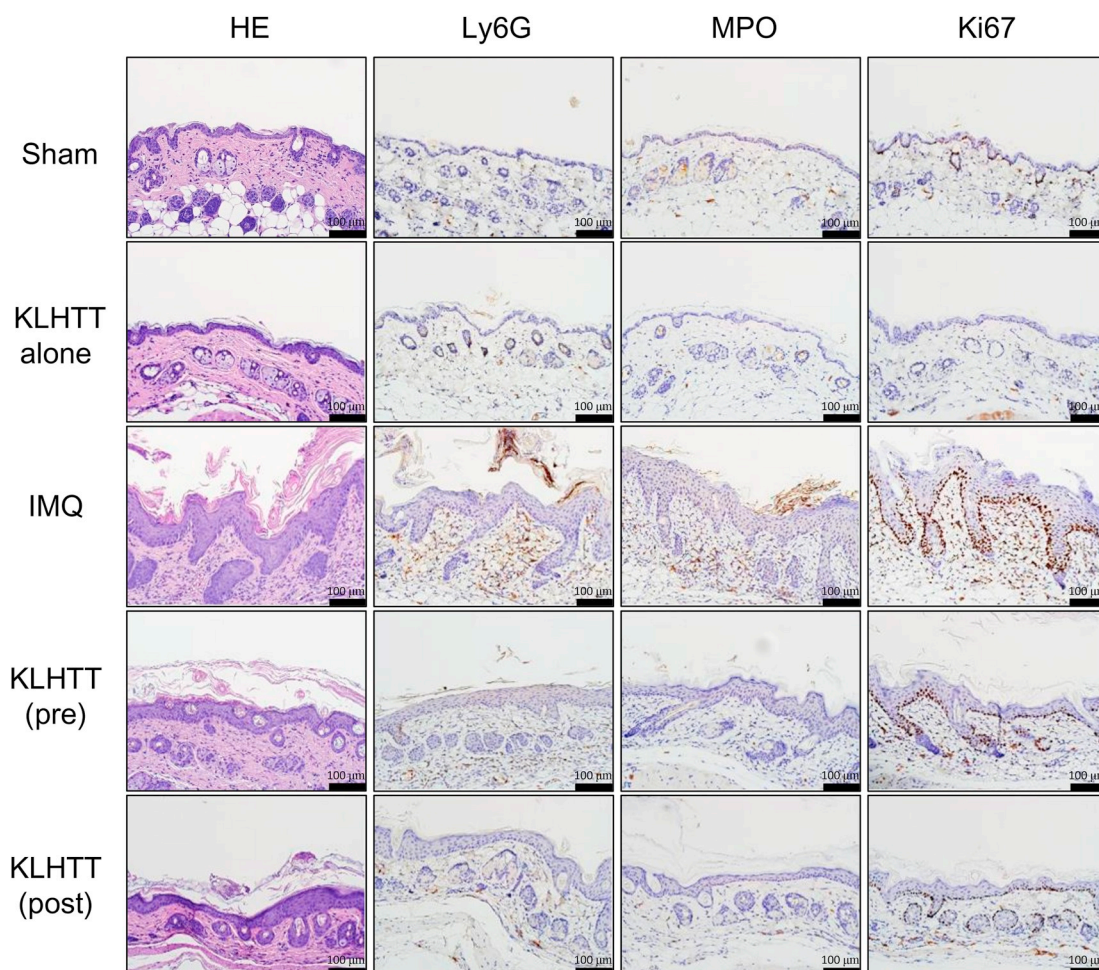


Fig. 11. KLHTT reduces the epidermal thickness and neutrophil infiltration in IMQ-induced psoriasis-like skin inflammation in mice. The mice were euthanized on day 6, and the back skin was collected and subjected to hematoxylin-eosin (HE) staining and immunohistochemical staining for Ly6G, MPO (the neutrophil infiltration markers), and Ki67 (the epidermal proliferation marker), after which the samples were observed under a microscope. In both KLHTT-treated groups, KLHTT (10 mg/ml) significantly improved epidermal thickness and neutrophil infiltration in IMQ-induced psoriasis-like inflammation in mice. Scale bar = 100 μm.

Herbs studied in this article

Kan-Lu-Hsiao-Tu-Tan includes Soapstone [$\text{Mg}_3\text{Si}_4\text{O}_{10}(\text{OH})_2$] (Huashi滑石), *Artemisia capillaris* Thunb. (Yinchenhao 茵陳蒿), *Scutellaria baicalensis* Georgi (Huangqin 黃芩), *Acorus gramineus* Soland. (Shichangpu 石菖蒲), *Clematis armandii* Franch. (Mutong 木通), *Fritillaria cirrhosa* D. Don (Chuanbeimu 川貝母), *Pogostemon cablin* (Blanco) Benth. (Huoxiang 藿香), *Forsythia suspensa* (Thunb.) Vahl (Lianqiao 連翹), *Amomum kravanh* Pierre ex Gagnep. (Baidoukou 白豆蔻), *Mentha haplocalyx* Briq (Baohe 薄荷), *Belamcanda chinensis* (L.) DC. (Shegan 射干).

Author contributions

Conceptualization: Tsong-Long Hwang. Conduct experiments: Chih-Chao Chiang, Wei-Jen Cheng, Cheng-Yu Lin, Kuei-Hung Lai, Seanson-Chance Ju, Chuan Lee. Data curation: Tsong-Long Hwang. Formal analysis: Tsong-Long Hwang. Funding acquisition: Tsong-Long Hwang. Investigation: Chih-Chao Chiang, Wei-Jen Cheng. Methodology: Chih-Chao Chiang, Wei-Jen Cheng, Kuei-Hung Lai, Tsong-Long Hwang. Resources: Chih-Chao Chiang, Cheng-Yu Lin. Software: Chih-Chao Chiang,

Cheng-Yu Lin. Supervision: Tsong-Long Hwang. Validation: Tsong-Long Hwang. Visualization: Tsong-Long Hwang. Writing – original draft: Chih-Chao Chiang, Wei-Jen Cheng, Cheng-Yu Lin. Writing – review & editing: Chih-Chao Chiang, Sien-Hung Yang, Tsong-Long Hwang.

Declaration of interest

The authors declare no conflicts of interest.

Acknowledgements

The study was supported by the grants from the Ministry of Science Technology (MOST 106-2320-B-255-003-MY3 and MOST 108-2320-B-255-003-MY3), Ministry of Education (EMRPD1I0441), Chang Gung University (EMRPD1I0501), Chang Gung University of Science and Technology (ZRRPF3H0101 and ZRRPF3H0111), and Chang Gung Memorial Hospital (CMRPF1F0011~3, CMRPF1F0061~3, CMRPF1G0241~3, CMRPG5F0161, CORPG5G0031, and BMRP450), Taiwan.

References

- Amulic, B., Cazalet, C., Hayes, G.L., Metzler, K.D., Zychlinsky, A., 2012. Neutrophil function: from mechanisms to disease. *Annu. Rev. Immunol.* 30, 459–489.
- Betigeri, S., Thakur, A., Raghavan, K., 2005. Use of 2,2'-azobis(2-amidinopropane) dihydrochloride as a reagent tool for evaluation of oxidative stability of drugs. *Pharm. Res.* 22 (2), 310–317.
- Bi, Y., Yue, D., Li, X., Zhang, H., Zhuo, Y., 2014. Research summary of TCM prevention and treatment of influenza. *Jilin J. Trad. Chin. Med.* 11, 1109–1113.
- Bloomfield, F.J., Young, M.M., 1988. Enhanced chemiluminescence production by phagocytosing neutrophils in psoriasis. *Inflammation* 12 (2), 153–159.
- Chang, H.L., Chang, F.R., Chen, J.S., Wang, H.P., Wu, Y.H., Wang, C.C., Wu, Y.C., Hwang, T.L., 2008. Inhibitory effects of 16-hydroxycyclohexa-3,13(14)E-dien-15-oic acid on superoxide anion and elastase release in human neutrophils through multiple mechanisms. *Eur. J. Pharmacol.* 586, 332–339.
- Chen, P.J., Wang, Y.L., Kuo, L.M., Lin, C.F., Chen, C.Y., Tsai, Y.F., Shen, J.J., Hwang, T.L., 2016. Honokiol suppresses TNF- α -induced neutrophil adhesion on cerebral endothelial cells by disrupting polyubiquitination and degradation of IkappaB α . *Sci. Rep.* 6, 26554.
- Delgado-Rizo, V., Martinez-Guzman, M.A., Iniguez-Gutierrez, L., Garcia-Orozco, A., Alvarado-Navarro, A., Fafutis-Morris, M., 2017. Neutrophil extracellular traps and its implications in inflammation: An overview. *Front. Immunol.* 8, 81.
- Di Domizio, J., Gilliet, M., 2019. Psoriasis caught in the NET. *J. Investig. Dermatol.* 139 (7), 1426–1429.
- El-Benna, J., Hurtado-Nedelec, M., Marzaioli, V., Marie, J.C., Gougerot-Pocidal, M.A., Dang, P.M., 2016. Priming of the neutrophil respiratory burst: role in host defense and inflammation. *Immunol. Rev.* 273, 180–193.
- El Malki, K., Karbach, S.H., Huppert, J., Zayoud, M., Reissig, S., Schuler, R., Nikolaev, A., Karram, K., Munzel, T., Kuhlmann, C.R., Lühmann, H.J., von Stebut, E., Wortge, S., Kurschus, F.C., Waisman, A., 2013. An alternative pathway of imiquimod-induced psoriasis-like skin inflammation in the absence of interleukin-17 receptor signaling. *J. Investig. Dermatol.* 133, 441–451.
- Fang, Y.N., Liu, G.T., 2002. Effect of isorhapontigenin on respiratory burst of rat neutrophils. *Phytomedicine* 9, 734–738.
- Futosi, K., Mocsai, A., 2016. Tyrosine kinase signaling pathways in neutrophils. *Immunol. Rev.* 273 (1), 121–139.
- Greb, J.E., Goldminz, A.M., Elder, J.T., Lebwohl, M.G., Gladman, D.D., Wu, J.J., Mehta, N.N., Finlay, A.Y., Gottlieb, A.B., 2016. Psoriasis. *Nat. Rev.* 2, 16082.
- Hebeda, C.B., Bolonheis, S.M., Nakasato, A., Belinati, K., Souza, P.D., Gouvea, D.R., Lopes, N.P., Farsky, S.H., 2011. Effects of chlorogenic acid on neutrophil locomotion functions in response to inflammatory stimulus. *J. Ethnopharmacol.* 135, 261–269.
- Ho, L.J., Chang, W.L., Chen, A., Chao, P., Lai, J.H., 2013. Differential immunomodulatory effects by *Tripterygium wilfordii* Hook f-derived refined extract PG27 and its purified component PG490 (triptolide) in human peripheral blood T cells: potential therapeutics for arthritis and possible mechanisms explaining in part Chinese herbal theory “Junn-Chenn-Zuou-SS”. *J. Transl. Med.* 11, 294.
- Hoffmann, J.H., Enk, A.H., 2016. Neutrophil extracellular traps in dermatology: Caught in the NET. *J. Dermatol. Sci.* 84, 3–10.
- Hsieh, Y.J., Yen, M.H., Chiang, Y.W., Yeh, C.F., Chiang, L.C., Shieh, D.E., Yeh, I., Chang, J.S., 2016. Gan-Lu-Siao-Du-yin, a prescription of traditional Chinese medicine, inhibited enterovirus 71 replication, translation, and virus-induced cell apoptosis. *J. Ethnopharmacol.* 185, 132–139.
- Hu, S.C., Yu, H.S., Yen, F.L., Lin, C.L., Chen, G.S., Lan, C.C., 2016. Neutrophil extracellular trap formation is increased in psoriasis and induces human beta-defensin-2 production in epidermal keratinocytes. *Sci. Rep.* 6, 31119.
- Huang, K.F., Ma, K.H., Liu, P.S., Chen, B.W., Chueh, S.H., 2016. Baicalin increases keratin 1 and 10 expression in HaCaT keratinocytes via TRPV4 receptor activation. *Exp. Dermatol.* 25, 623–629.
- Huang, R.L., Chen, C.C., Chang, Y.S., Chang, C.G., Chen, C.F., 2000. Anti-human hepatitis B virus activities of Chinese medicinal prescriptions for the treating of liver disease: anti-HBV effects of six traditional Chinese prescriptions. *J. Chin. Med.* 11, 1–8.
- Ikedo, S., Takahashi, H., Suga, Y., Eto, H., Etoh, T., Okuma, K., Takahashi, K., Kanbara, T., Seishima, M., Morita, A., Imai, Y., Kanekura, T., 2013. Therapeutic depletion of myeloid lineage leukocytes in patients with generalized pustular psoriasis indicates a major role for neutrophils in the immunopathogenesis of psoriasis. *J. Am. Acad. Dermatol.* 68, 609–617.
- Kuo, P.C., Hung, H.Y., Nian, C.W., Hwang, T.L., Cheng, J.C., Kuo, D.H., Lee, E.J., Tai, S.H., Wu, T.S., 2017. Chemical constituents and anti-inflammatory principles from the fruits of *Forsythia suspensa*. *J. Nat. Prod.* 80, 1055–1064.
- Lee, C.L., Hwang, T.L., He, W.J., Tsai, Y.H., Yen, C.T., Yen, H.F., Chen, C.J., Chang, W.Y., Wu, Y.C., 2013. Anti-neutrophilic inflammatory steroidal glycosides from *Solanum torvum*. *Phytochemistry* 95, 315–321.
- Li, C.W., Wu, X.L., Zhao, X.N., Su, Z.Q., Chen, H.M., Wang, X.F., Zhang, X.J., Zeng, H.F., Chen, J.N., Li, Y.C., Su, Z.R., 2013. Anti-inflammatory property of the ethanol extract of the root and rhizome of *Pogostemon cablin* (Blanco) Benth. *ScientificWorldJournal* 2013, 434151.
- Lin, Y.K., Leu, Y.L., Huang, T.H., Wu, Y.H., Chung, P.J., Su Pang, J.H., Hwang, T.L., 2009. Anti-inflammatory effects of the extract of indigo naturalis in human neutrophils. *J. Ethnopharmacol.* 125 (1), 51–58.
- Lowes, M.A., Suarez-Farinas, M., Krueger, J.G., 2014. Immunology of psoriasis. *Annu. Rev. Immunol.* 32, 227–255.
- Michalek, I.M., Loring, B., John, S.M., 2017. A systematic review of worldwide epidemiology of psoriasis. *J. Eur. Acad. Dermatol. Venereol.* 31, 205–212.
- Nagarkoti, S., Dubey, M., Awasthi, D., Kumar, V., Chandra, T., Kumar, S., Dikshit, M., 2018. S-Glutathionylation of p47phox sustains superoxide generation in activated neutrophils. *Biochim. Biophys. Acta* 1865, 444–454.
- Navegantes, K.C., de Souza Gomes, R., Pereira, P.A., Czaikoski, P.G., Azevedo, C.H., Monteiro, M.C., 2017. Immune modulation of some autoimmune diseases: the critical role of macrophages and neutrophils in the innate and adaptive immunity. *J. Transl. Med.* 15, 36.
- Ogawa, E., Sato, Y., Minagawa, A., Okuyama, R., 2018. Pathogenesis of psoriasis and development of treatment. *J. Dermatol.* 45 (3), 264–272.
- Papayannopoulos, V., 2018. Neutrophil extracellular traps in immunity and disease. *Nat. Rev. Immunol.* 18 (2), 134–147.
- Parmar, K.M., Itankar, P.R., Joshi, A., Prasad, S.K., 2017. Anti-psoriatic potential of *Solanum xanthocarpum* stem in imiquimod-induced psoriatic mice model. *J. Ethnopharmacol.* 198, 158–166.
- Re, R., Pellegrini, N., Proteggente, A., Pannala, A., Yang, M., Rice-Evans, C., 1999. Antioxidant activity applying an improved ABTS radical cation decolorization assay. *Free Radic. Biol. Med.* 26 (9–10), 1231–1237.
- Remijsen, Q., Vanden Berghe, T., Wirawan, E., Asselbergh, B., Parthoens, E., De Rycke, R., Noppen, S., Delforge, M., Willems, J., Vandenabeele, P., 2011. Neutrophil extracellular trap cell death requires both autophagy and superoxide generation. *Cell Res.* 21 (2), 290–304.
- Schon, M.P., Broekaert, S.M., Erpenbeck, L., 2017. Sexy again: the renaissance of neutrophils in psoriasis. *Exp. Dermatol.* 26, 305–311.
- Schulz-Finke, A.C., Tikhomirov, A.S., Braune, A., Gribel, T., Gilberg, E., Bajorath, J., Blaut, M., Nourshargh, S., Gutschow, M., 2017. Design of an activity-based probe for human neutrophil elastase: implementation of the Lossen rearrangement to induce Förster resonance energy transfers. *Biochemistry* 57 (5), 742–752.
- Shen, Y.C., Chiou, W.F., Chou, Y.C., Chen, C.F., 2003. Mechanisms in mediating the anti-inflammatory effects of baicalin and baicalein in human leukocytes. *Eur. J. Pharmacol.* 465, 171–181.
- Tsai, Y.F., Yu, H.P., Chung, P.J., Leu, Y.L., Kuo, L.M., Chen, C.Y., Hwang, T.L., 2015. Osthol attenuates neutrophilic oxidative stress and hemorrhagic shock-induced lung injury via inhibition of phosphodiesterase 4. *Free Radic. Biol. Med.* 89, 387–400.
- Wei, S., Yue, D., Wei, J., Yu, L., Cui, K., Bi, Y., 2016. Research overview of Ganlu Xiaodu Dan in preventing disease with syndrome of damp-heat. *Clin. J. Trad. Chin. Med.* 28, 266–268.
- Wu, J., Li, H., Li, M., 2015. Effects of baicalin cream in two mouse models: 2,4-dinitrofluorobenzene-induced contact hypersensitivity and mouse tail test for psoriasis. *Int. J. Clin. Exp. Med.* 8, 2128–2137.
- Xin, X., Fan, X., 2012. Traditional Chinese medicine treats gout: 4 case reports (Print in Chinese). *Xinjiang J. Trad. Chin. Med.* 30, 106–107.
- Xu, Y., 2010. Variant ganlu Xiaodu Dan treating chronic dermatitis in 47 cases (Print in Chinese). *Clin. J. Trad. Chin. Med.* 22, 514–515.
- Yang, S.C., Chen, P.J., Chang, S.H., Weng, Y.T., Chang, F.R., Chang, K.Y., Chen, C.Y., Kao, T.I., Hwang, T.L., 2018. Luteolin attenuates neutrophilic oxidative stress and inflammatory arthritis by inhibiting Raf 1 activity. *Biochem. Pharmacol.* 154, 384–396.
- Yu, H.P., Hsieh, P.W., Chang, Y.J., Chung, P.J., Kuo, L.M., Hwang, T.L., 2011. 2-(2-Fluorobenzamido)benzoate ethyl ester (EFB-1) inhibits superoxide production by human neutrophils and attenuates hemorrhagic shock-induced organ dysfunction in rats. *Free Radic. Biol. Med.* 50, 1737–1748.
- Zhang, Q., 2004. Clinical observation of Kan-Lu-Hsiao-Tu-Tan in treating acute sinusitis (Print in Chinese). *Hubei J. Trad. Chin. Med.* 26, 36.

Inhalable Dual-Targeted Hybrid Lipid Nanocore–Protein Shell Composites for Combined Delivery of Genistein and All-Trans Retinoic Acid to Lung Cancer Cells

Nayra M. Kamel,^{†,‡} Maged W. Helmy,^{†,§} Elsayeda-Zeinab Abdelfattah,^{||} Sherine N. Khattab,^{†,⊥} Doaa Ragab,[‡] Magda W. Samaha,[‡] Jia-You Fang,^{*,#,▽,○} and Ahmed O. Elzoghby^{*,†,‡,&,%}

[†]Cancer Nanotechnology Research Laboratory (CNRL), Faculty of Pharmacy, Alexandria University, Alexandria 21521, Egypt

[‡]Department of Industrial Pharmacy, Faculty of Pharmacy, Alexandria University, Alexandria 21521, Egypt

[§]Department of Pharmacology and Toxicology, Faculty of Pharmacy, Damanhour University, Damanhour, Egypt

^{||}Medical Research Institute, Alexandria University, Alexandria, Egypt

[⊥]Department of Chemistry, Faculty of Science, Alexandria University, Alexandria 21321, Egypt

[#]Pharmaceutics Laboratory, Graduate Institute of Natural Products, Chang Gung University, Taoyuan 333, Taiwan

[▽]Research Center for Industry of Human Ecology and Research Center for Chinese Herbal Medicine, Chang Gung University of Science and Technology, Kweishan, Taoyuan 333, Taiwan

[○]Department of Anesthesiology, Chang Gung Memorial Hospital, Kweishan, Taoyuan 333, Taiwan

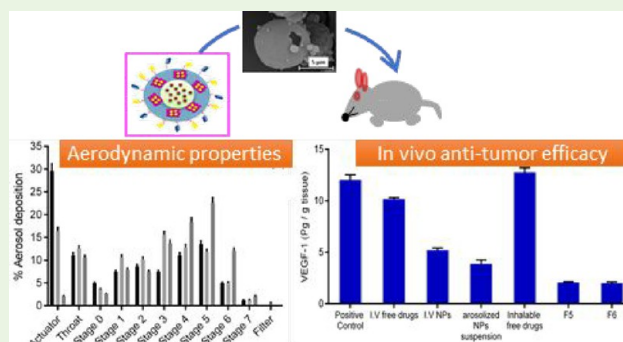
[&]Division of Engineering in Medicine, Department of Medicine, Brigham and Women's Hospital, Harvard Medical School, Boston, Massachusetts 02115, United States

[%]Harvard-MIT Division of Health Sciences and Technology, Cambridge, Massachusetts 02139, United States

Supporting Information

ABSTRACT: Localized pulmonary delivery of anticancer agents to lungs has proven to be pioneering approach for lung cancer therapy. Hybrid lipid nanocore-protein shell nanoparticles (HLPNPs) coloaded with all-trans retinoic acid (ATRA) and genistein (GNS) were prepared via sequential solvent evaporation followed by nanoprecipitation of zein shell onto the lipid core. The outer protein shell of HLPNPs provided additional drug reservoir for encapsulation of ATRA/stearyl amine ion pair and enabled dual tumor-targeting with biotin and ATRA. Enhanced uptake and cytotoxic activity of HLPNPs against A549 lung cancer cells was confirmed. To improve their deep lung deposition, dual-targeted drug-loaded HLPNP nanocomposites were fabricated. The nanocomposites prepared using mannitol/HPβCD/leucine demonstrated favorable aerosolization (MMAD = 2.47 μm and FPF = 70.81%). In vivo, the inhalable nanocomposites were superior to aerosolized or i.v. nanoparticle suspension against lung carcinoma bearing mice. Overall, inhalable dual-targeted HLPNPs nanocomposites provided localized codelivery of GNS and ATRA for lung cancer therapy.

KEYWORDS: hybrid lipid protein nanoparticles, all-trans retinoic acid, genistein, dual targeting, inhalable nanocomposites, lung cancer



1. INTRODUCTION

Recently, the world has witnessed an increased mortality rate due to lung carcinoma, mainly non-small-cell lung cancer (NSCLC).¹ Preliminary treatment strategies of lung cancer were based on surgery, radiotherapy, chemotherapy, and, in some cases, combination of therapies. However, these treatment strategies have been assigned with serious side effects on healthy tissues.² Furthermore, systemic administration of anticancer agents resulted in a reduced therapeutic efficiency. This is partially due to lack of targeting to cancer

cells³ in addition to the hydrophobic nature of most anticancer drugs. On the basis of these interests, drug-loaded nanocarriers have attracted great attention by providing increased

Special Issue: Biomaterials Science and Engineering in the Middle East

Received: November 4, 2018

Accepted: March 6, 2019

Published: March 6, 2019

therapeutic effect, decreased toxicity on normal tissues, and reduced macrophage clearance by the immune system.²

In this context, lipid nanoparticles (LNPs) are good candidates as vehicles for both hydrophilic and hydrophobic anticancer drugs.⁴ LNPs offer the advantages of being biocompatible and biodegradable, in addition to their ability to sustain the release of incorporated drugs as well as a high affinity for uptake by cancer cells.^{1,5} Despite these interests, LNPs have limited physical stability and high possibility to leach out the encapsulated drugs. Therefore, the current research presents different strategies to overcome limitations of LNPs. One strategy is to prepare hybrid core-shell lipid-protein nanoparticles (HLPNPs). The outer shell, composed of a natural hydrophobic protein, zein,⁶ is intended to overcome the stability limitations of LNPs, help more sustained drug release characteristics, provide an additional reservoir/compartment for loading another hydrophobic drug, and enable a more readily functionalizable surface via its abundant functional groups.^{7,8}

Nanocarriers usually extravasate through pores in endothelium cells of tumor capillary via the enhanced permeability and retention (EPR) referred to as passive targeting. On the other hand, in the active targeting approach, tumor-targeted nanocarriers can be designed through conjugation of specific targeting ligands on the nanocarrier surface that can recognize their receptors overexpressed by tumor cells.^{9,10} However, the slow turnover of some of these receptors can produce saturation easily and allow a relatively low capacity of uptake through receptor-mediated endocytosis of the drug-loaded NPs. Therefore, the dual-targeting approach has emerged as a promising strategy that would increase differentiation between normal and cancer cells and enable more selective nanocarrier-based drug delivery to tumor cells compared with the single targeting ligand modification. Biotin (vitamin B7) is a growth promoter needed by tumor cells to sustain their rapid proliferation. Streptavidin, neutravidin, and avidin are receptors of biotin in cell membrane that enhanced the uptake of biotinylated NPs into cancer cells.¹¹ Simultaneously, all-trans retinoic acid (ATRA) is the vitamin A derivative that is an essential component in the regulation of cell proliferation and differentiation. ATRA binds to the type of nuclear receptors known as retinoic acid receptors (RARs) that are expressed at high levels inside tumor cells and at low levels in normal cells.¹²

To overcome the ineffective systemic delivery of nanocarriers to lung cancer cells, pulmonary administration is currently used to deliver drugs directly to the lung. Compared to the conventional intravenous administration, the pulmonary route provides better patient compliance and less patient complications.¹³ To enhance pulmonary deposition, the production of nanocomposites as a dry powder inhaler has been suggested as a possible formulation strategy that consists of drug-loaded nanoparticles and excipients in microsize particles.¹⁴ These nanocomposite microparticles are intended to disintegrate into their original drug-loaded nanoparticles once reaching lung tissue and thus NPs will be easily taken up by cancer cells.¹⁵

In the current study, genistein (GNS), a potent tyrosine kinase inhibitor, was combined with ATRA for combination therapy of lung cancer. All-trans retinoic acid (ATRA), a metabolite of vitamin A, exerts its antiproliferative action by causing cell cycle arrest at the G1 phase and apoptosis through binding to nuclear retinoic acid receptors (RARs) and affecting

DNA synthesis.^{16,17} GNS interferes with the cell cycle at the G2/M phase, induces autophagocytosis, and inhibits angiogenesis in cancer cells. Moreover, GNS blocks the expression of vascular endothelial growth factor (VEGF) and thus inhibits the resistance of lung cancer toward ATRA which is mainly mediated through up-regulation of VEGF. Therefore, coencapsulation of GNS and ATRA would be hypothesized to enhance their anticancer activity and reduce their doses, thus decreasing their toxicity and inhibiting the resistance to ATRA action.¹⁷

In our study, we propose the design of inhalable dry powder nanocomposites of dual-targeted hybrid lipid-zein NPs for codelivery of GNS and ATRA to lung cancer cells. First, hybrid lipid core-protein shell nanoparticles were prepared by sequential emulsification followed by the zein nanoprecipitation technique to facilitate coencapsulation of the hydrophobic drugs, GNS and ATRA. Second, the zein shell assembled onto the lipid core would act as a substrate for decorating the surface of NPs via coupling of both targeting ligands, biotin and ATRA, through carbodiimide coupling. Therefore, biotin can increase internalization of nanoparticles into cancer cells via membrane-receptor-mediated endocytosis and ATRA can then enhance their entry into the nucleus where GNS acts by inhibition of topoisomerase II and PIP kinase.¹⁸ Third, for deep lung deposition, inhalable nanocomposite microparticles were fabricated by spray-drying of the prepared NPs with inert carriers.¹⁹ Finally, the prepared inhalable system was evaluated in vitro and in vivo to compare their antitumor efficacy with that of the free drugs and intravenous nanoparticles.

2. MATERIALS AND METHODS

2.1. Materials. Genistein (GNS) was purchased from Xian Natural Field Biotechnology Co., Ltd. (Shaanxi, China). All-trans retinoic acid (ATRA), zein, biotin (Bio), stearyl amine (SA), *N*-(3-(dimethylamino)propyl)-*N'*-ethyl carbodiimide hydrochloride (EDC-HCl), *N*-hydroxy succinimide (NHS), D-mannitol, maltodextrin, leucine, hydroxypropyl- β -cyclodextrin (HP β CD), and 3-(4,5-dimethylthiazol-2-yl)-2,5-diphenyltetrazolium bromide (MTT) were obtained from Sigma-Aldrich (St. Louis, MO, USA). Glycerol monostearate (GMS) was kindly supplied by Gattefossé (France). Lipoid S 75 (L-S75) soybean phospholipids were kindly supplied by Lipoid GmbH (Ludwigshafen, Germany). Tween 80, poly(ethylene glycol) 400, absolute ethanol, and dimethyl sulfoxide (DMSO) were obtained from El-Nasr Pharmaceutical Chemicals Co. (Cairo, Egypt). Sodium chloride intravenous normal saline 0.9% was obtained from Otsuka Pharmaceutical Co. (Alexandria, Egypt). Methanol and acetonitrile HPLC grade were purchased from JT Baker (Phillipsburg, NJ, USA).

2.2. Preparation of Dual-Targeted ATRA/Bio-zein. Biotin and ATRA were conjugated with zein through amide bond formation via carbodiimide coupling between their carboxylic groups and amino groups of zein.¹² First, biotin (6.7 mg, 0.027 mmol) was dissolved in 2 mL of DMSO and its carboxylic group was activated by EDC-HCl (6.7 mg, 0.035 mmol) and NHS (4 mg, 0.035 mmol) under stirring for 1 h. Zein solution (200 mg in 3 mL of DMSO) was added to the activated biotin solution and stirred overnight. After 24 h, ATRA solution (30 mg, 0.1 mmol) in 2 mL of DMSO was preactivated with EDC-HCl (23 mg, 0.12 mmol) and NHS (13.8 mg, 0.12 mmol) for 1 h and was added to the reaction mixture (Bio-zein conjugate), followed by stirring overnight. The ATRA/Bio-zein conjugate was dialyzed against DMSO for 24 h to remove nonreacted ATRA and biotin. The solution was then dialyzed against water to remove the residual organic solvent. The final solution was lyophilized for 48 h to obtain ATRA/Bio-zein conjugate powder using a LyoQuest laboratory freeze-dryer (Telstar, Spain).

2.3. Chemical Characterization of ATRA/Bio-zein Conjugate. **2.3.1. ATRA Conjugation Efficiency.** The percent conjugation efficiency of ATRA was calculated indirectly through measuring the absorbance of unconjugated ATRA by UV spectrophotometer (UV-1700, Shimadzu, Japan) at 349 nm, after detecting that all other reaction components do not interfere with ATRA analysis.²⁰

2.3.2. Differential Scanning Calorimetry (DSC). DSC thermograms were recorded for zein, biotin, pure ATRA, Bio-zein, and ATRA/Bio-zein using a differential scanning calorimeter (PerkinElmer, USA)²¹ according to the method detailed in the [Supporting Information](#).

2.3.3. Proton NMR Spectra. Proton NMR spectra (¹H NMR) of pure zein, Bio-zein, and ATRA/Bio-zein conjugates were recorded via nuclear magnetic resonance (NMR), JEOL 500 MHz spectrometers (Japan) at ambient temperature. Chemical shifts were reported in parts per million (ppm) and referenced relative to residual solvent (e.g., DMSO at δ 2.50 ppm for DMSO-*d*₆) to obtain the structural configuration of each sample.

2.4. Preparation of GNS/ATRA-Loaded Lipid-Zein Core-Shell NPs. The LNP core was prepared by the solvent evaporation technique.²² Briefly, glyceryl monostearate (GMS) was dissolved in ethanol (200 mg/3 mL) and heated up to 55 °C in a type 3047 Kottermann shaking water bath (Hanigsen, Germany). A predetermined amount of GNS (20 mg) was added to the organic phase and then rapidly injected into 50 mL of aqueous phase, containing 1% w/v Tween 80 and 0.2% w/v lipid S75 preserved at the same temperature. The whole mixture was then homogenized (Ultra-Turrax, T-25, Ika Labortechnik, Germany) at 4000 rpm for 15 min. The NPs were cooled down to room temperature under continuous magnetic stirring (100 rpm for 15 min). The nanoprecipitation technique was then used to encapsulate ATRA into the zein shell coating LNP core. Therefore, ATRA and stearyl amine (SA) as an ion pairing reagent were dissolved in 3 mL of ethanol for 10 min under stirring and then added to 94.5% v/v ethanolic solution containing 200 mg of zein, Bio-zein, or ATRA/Bio-zein. The zein/ATRA/SA ethanolic solution was then added to the aqueous LNPs suspension under homogenization for 5 min at room temperature. The obtained lipid-zein hybrid NP (HLPNP) suspension was stored at 4 °C until further characterization.

2.5. Physicochemical Characterization of Lipid-Zein NPs. Drug content,²³ in vitro drug release,²⁴ particle size,²⁵ zeta potential, morphology,^{26,27} and physical stability of the prepared HLPNPs were measured according to methods demonstrated in the [Supporting Information](#).

2.6. Determination of Cytotoxicity by MTT Assay. The in vitro cytotoxicity of free GNS, free ATRA, free GNS/ATRA combination, ATRA/GNS-HLPNPs, Bio-ATRA/GNS-HLPNPs, and ATRA/Bio-ATRA/GNS-HLPNPs against A549 lung cancer cells was determined using MTT assay. The detailed method was illustrated in the [Supporting Information](#). The CompuSyn software (version 1) was employed to calculate the IC₅₀ for GNS, ATRA, and their different nanocombinations against the A549 cell line according to the method of Chou and Talaly.²⁸ The CompuSyn software was used to calculate the DRI for ATRA and GNS in A549 cells. The combination index (CI) was calculated for determination of synergism or antagonism of the two drugs, where CI < 1, = 1, and > 1 reflect synergistic, additive, or antagonistic effects, respectively.

2.7. Cellular Internalization. Coumarin-6 as a hydrophobic fluorescent dye was incorporated in the place of GNS during preparation of the lipid core to obtain coumarin-loaded NPs. The cellular internalization behavior of free coumarin-6, coumarin-loaded HLPNPs, Bio-HLPNPs, or ATRA/Bio-HLPNPs was determined by CLSM toward A549 cells, as illustrated in the [Supporting Information](#).

2.8. Preparation of Inhalable Spray-Dried Nanocomposites. Dual-targeted ATRA/GNS-HLPNPs were microencapsulated within various carriers using spray-drying. HLPNPs were dispersed in aqueous solution of the carrier at 1:4 NPs/carrier mass ratio under magnetic stirring. The mixed solution was then spray-dried using a B-290 mini spray-dryer (BÜCHI, Flawil, Switzerland), provided with a

high-performance cyclone. The spray-drying process was conducted under the following conditions: inlet air temperature (110 °C), pump flow rate (15%), aspirator (100%), and atomizing air flow rate (320 L/h). The carrier type (carbohydrates or carbohydrate/amino acid mixture) has been investigated and presented in [Table 3](#). The samples were collected with a cyclone, and the spray-dried powders were stored in vacuum desiccators over calcium carbonate for further analysis.

2.9. Characterization of Spray-Dried Nanocomposite. The yield, particle morphology, aqueous redispersibility, solid state properties, and long-term stability of the spray-dried powder nanocomposites were measured depending on the methodology illustrated in the [Supporting Information](#).

2.10. Aerodynamic Properties. Aerodynamic properties of the inhalable nanocomposites were assessed using an Andersen Cascade Impactor (ACI) (Copley Scientific Ltd., Nottingham, U.K.) as previously reported.²⁹ The methodology was illustrated in the [Supporting Information](#).

2.11. In Vivo Study. **2.11.1. Animals.** The antitumor activity of different formulations was evaluated on male Albino mice (15–20 g). All experiments followed the protocol approved by the Animal Care and Use Committee of the Faculty of Pharmacy, Alexandria University, as demonstrated in the [Supporting Information](#).

2.11.2. Induction of Lung Tumor. Mice received a single i.p. injection of 1.5 g/kg urethane that was dissolved in saline (0.9% NaCl) followed by a poster dose in the eighth week of induction. Mice were observed after 12–16 weeks for induction of lung cancer. Monitoring of lung cancer induction was done both by histopathological examination and evaluation of some tumor growth biomarkers.

2.11.3. Treatment Protocol. The animals were divided into eight groups (six mice in each one):

- Group 1: positive control (untreated mice bearing lung carcinoma)
- Group 2: healthy mice (negative control)
- Group 3: mice received inhalable dry ATRA/Bio-ATRA/GNS-HLPNP nanocomposites (F5) prepared using mannitol/leucine using dry powder insufflators (model-DP-4M, Penn-Century, PA, USA)
- Group 4: mice received inhalable dry ATRA/Bio-ATRA/GNS-HLPNP nanocomposites (F6) prepared using HPβCD/mannitol/leucine by insufflation³⁰
- Group 5: mice received inhalable spray-dried mixture of free GNS/ATRA combination with mannitol/HPβCD/leucine by insufflation
- Group 6: mice received ATRA/Bio-ATRA/GNS-HLPNP aqueous suspension by a Microsprayer (model 1A-1B, Penn-Century Inc., USA)
- Group 7: mice were i.v. injected with ATRA/Bio-ATRA/GNS-HLPNP aqueous suspension into the tail vein
- Group 8: mice were i.v. injected with combined free GNS/ATRA cosolvent (50% saline, 47.5% PEG 400, and 2.5% DMSO) in the tail vein

All mice groups were administered the different formulations equivalent to 0.38 mg/kg for ATRA 3 times per week for 2 weeks, and then, they were sacrificed after 15 days of treatment. For pulmonary administration, anesthesia was applied to mice using xylazine (1.5 mg/kg) and ketamine (12.5 mg/kg) through i.p. injection. Mice must be placed in a supine position. The insufflator powder chamber was connected to a syringe that pumped 0.2 mL of air. Finally, this insufflator powder chamber must be weighed before and after each dose to determine the actual quantity of sample to reach the lungs.

2.11.4. Evaluation of Antitumor Efficacy. i. Lung and Body Weight. The body weight of mice was assessed periodically during the course of treatment. At the end of the experiment at the 15th day of treatment, the animals were sacrificed and excised lungs were weighed, morphologically examined, and divided for tumor growth biomarker measurement after freezing at −80 °C and histological and immunological examinations to assess the therapeutic activity after fixation with 4% paraformaldehyde solution

ii. **Quantification of Angiogenesis and Apoptosis by ELISA.** One part of excised lung tumors was used for quantification of tumor growth biomarkers using ELISA, as illustrated in the [Supporting Information](#).

iii. **Histopathological and Immunohistochemical Analysis.** Another part of excised lung tumor was used in determination of histopathological neoplastic changes, average number of microscopic metastatic lung foci, their diameter, and cellular proliferation of tumor through Ki-67 protein staining ([Supporting Information](#)).

2.12. Statistical Analysis. All data were expressed as means (\pm SD). The statistical analysis was done using GraphPad Software, Inc., La Jolla, CA, USA (Prism Version 5). ANOVA; F test (analysis of variance) was used for comparisons between the studied groups for distributed quantitative data. Furthermore, Tukey's multiple comparison test were used. In addition, a P value <0.05 was considered significant.

3. RESULTS AND DISCUSSION

3.1. Synthesis and Characterization of Dual-targeted ATRA/Bio-zein Conjugate. In an attempt to promote better stability and enhanced tumor-targetability of lipid nanocarriers, a protein shell with dual-targeting modality was assembled onto the lipid nanocore. For this purpose, a dual-targeted zein conjugate was first prepared and characterized ([Figure 1](#)). Zein

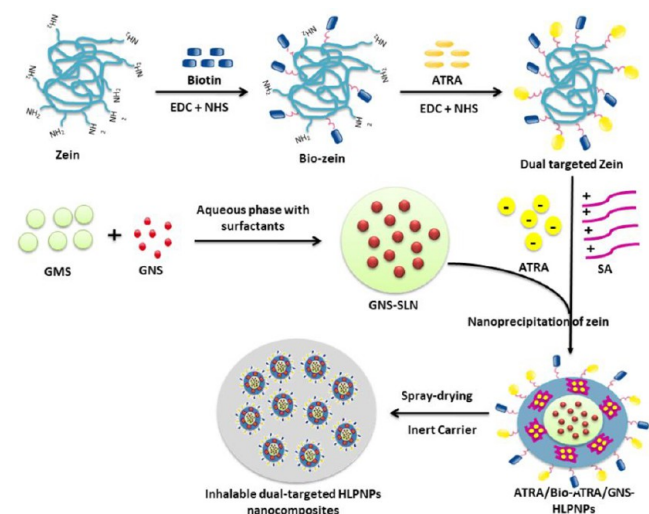


Figure 1. Schematic presentation for the formulation of ATRA/Bio-zein conjugate and HLPNPs.

consists of 22% of glutamine and asparagine in addition to a few arginine residues.⁸ Therefore, both biotin and ATRA were chemically conjugated onto the protein backbone of zein via a simple carbodiimide coupling reaction.³¹ This reaction occurred by subsequent coupling of the carboxylic groups of biotin and ATRA, preactivated using EDC-HCl and NHS reagents, with the free amino groups in zein molecules to form covalent amide bonds¹¹ ([Figure S2 in the Supporting Information](#)).

The conjugation efficiency of ATRA reacted with Bio-zein was determined by an indirect method. The unreacted free ATRA found in reaction dialyzate was measured through its UV absorbance at 349 nm, which enabled the calculation of the ATRA conjugated with Bio-zein that was 8.5 mg/200 mg of Bio-zein. The DSC thermograms of pure biotin and ATRA showed sharp peaks at 231.7 and 184.3 °C corresponding to their melting points of biotin and ATRA, respectively ([Figure 2](#)).^{32,33} These peaks were absent in the thermograms of Bio-

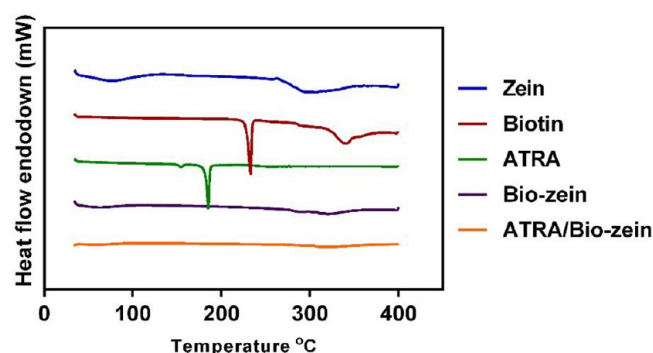


Figure 2. Characterization of dual-targeted ATRA/Bio-zein conjugate; DSC thermograms for zein, biotin, ATRA, Bio-zein, and ATRA/Bio-zein.

zein and ATRA/Bio-zein conjugates, indicating that ATRA and biotin were consumed in the formation of the new conjugate with zein macromolecule.

For further structural investigations, ¹H NMR spectra of zein, Bio-zein, and ATRA/Bio-zein conjugates were performed. The biotin ring structure exhibited ureic protons at 6.37 and 6.45 ppm ([Figure 3](#)).³⁴ The spectra of the functionalized Bio-zein and ATRA/Bio-zein conjugates were characterized by the disappearance of the acidic protons of ATRA and biotin at 12.02 and 11.99 ppm, respectively, referring to the absence of free molecules of biotin or ATRA and their replacement by an increase of proton integration at 9.24 ppm ([Figure 3](#)).¹² The increase of integration is indicative of ATRA/biotin conjugation through amide bond formation and the presence of additional NH—C=O protons, which accordingly indicates the successful conjugation of ATRA and biotin with zein.^{34,35}

Moreover, the appearance of new signals in the spectra of the functionalized conjugates at ca. 6.52 ppm referring to ureic protons of biotin which were absent in the spectrum of pure zein is a further confirmation. In addition, ATRA contains six sp² protons which could also be observed at 6.52 ppm. The increase of proton integration at 6.52 ppm in the ATRA/Bio-zein conjugate compared to the Bio-zein one confirmed the coupling of ATRA to the Bio-zein conjugate. Moreover, referring to FTIR results, the sharp band at 1700 cm⁻¹ corresponding to the OH and C=O groups of the carboxylic group characteristic to ATRA and biotin disappeared, as illustrated in the [Supporting Information \(Figure S5\)](#). On the basis of these results, the chemical bonding of zein with biotin and ATRA molecules in the ATRA/Bio-zein conjugate has been confirmed.

3.2. Fabrication of Hybrid Core–Shell HLPNPs. Dual-targeted core–shell hybrid lipid–protein nanoparticles were prepared by sequential solvent evaporation/nanoprecipitation in two consecutive steps. First, the GNS-loaded lipid nanocore was developed by the solvent evaporation injection method. The GMS lipid phase containing GNS in ethanol at temperatures higher than the melting point of lipid was added rapidly to the aqueous phase containing surfactants as emulsifying agents with continuous mixing. After solvent evaporation, the lipid was precipitated in nanosize cores encapsulating GNS inside while stabilized by the surrounding surfactant molecules.³⁶ This step was followed by the formation of the ATRA-loaded zein shell via the nanoprecipitation technique. The electrostatic interaction between the acidic drug ATRA ($pK_a \sim 4$) at pH 7.0 and the cationic ion

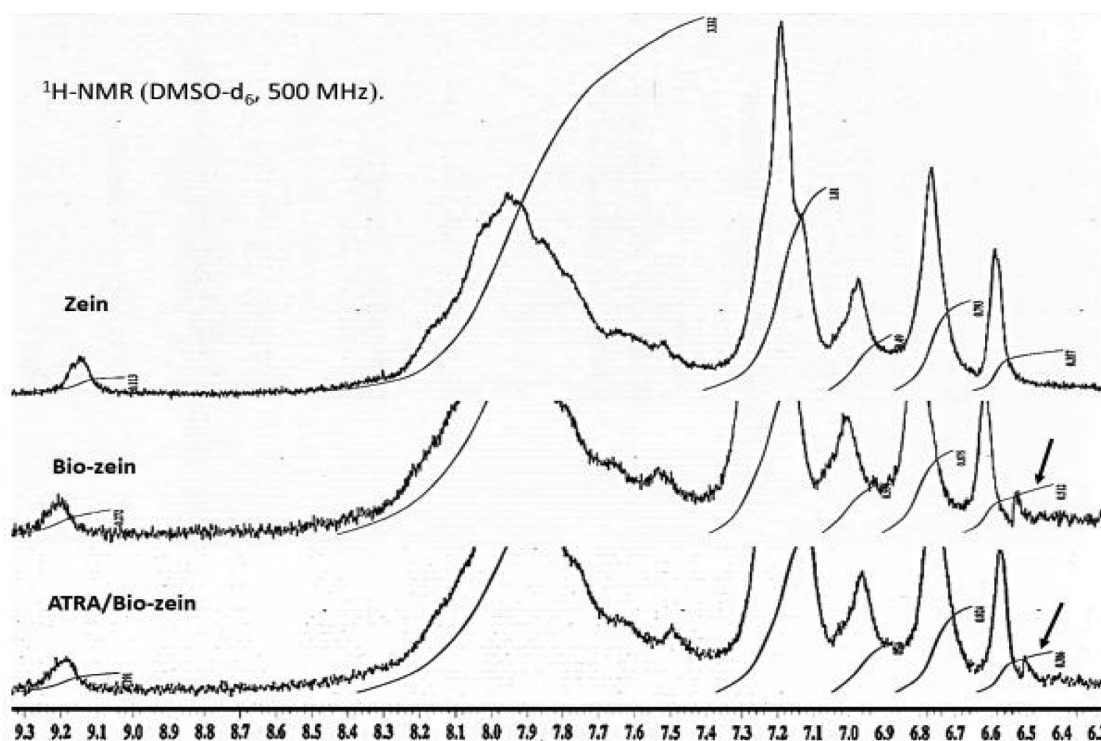


Figure 3. Characterization of dual-targeted ATRA/Bio-zein conjugate; ^1H NMR ($\text{DMSO}-d_6$, 500 MHz) spectra of zein, Bio-zein, and ATRA/Bio-zein.

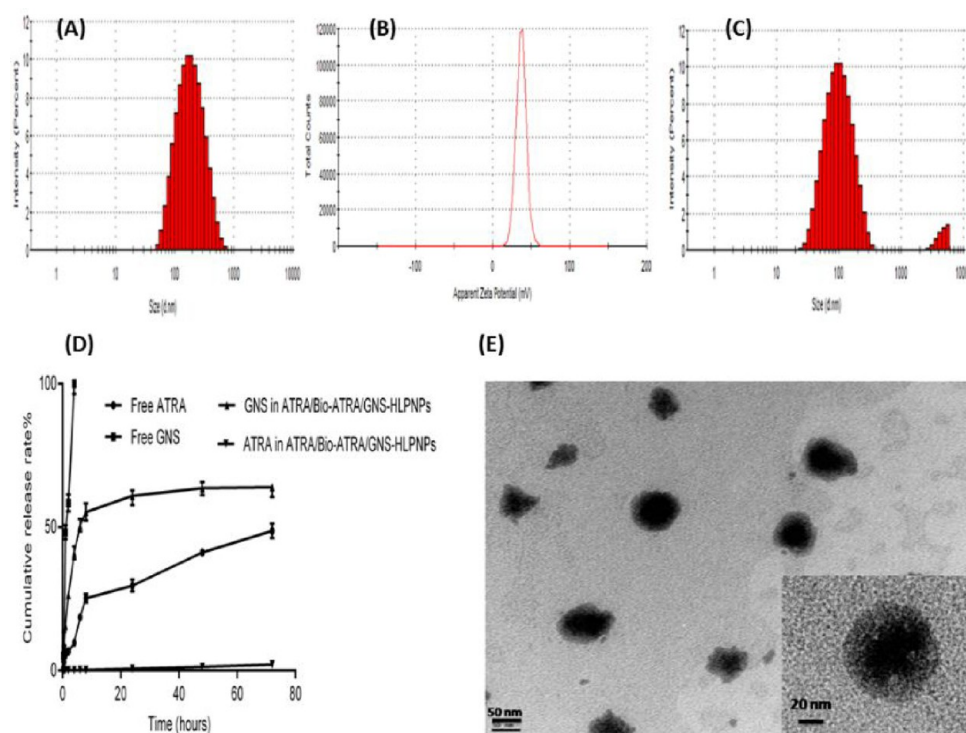


Figure 4. Physicochemical properties of the prepared dual-targeted ATRA/GNS-HLPNPs: (A) particle size distribution histograms and (B) zeta potential chart of dual-targeted ATRA/GNS-HLPNPs; (C) particle size distribution histograms of GNS-SLN; (D) in vitro release profile of GNS and ATRA from ATRA/Bio-ATRA/GNS-HLPNPs compared to free GNS and free ATRA in PBS with 0.5% Tween 80 in pH 7.4 at 37 °C; (E) TEM photograph illustrating the core-shell structure of ATRA/Bio-ATRA/GNS-HLPNPs.

pairing agent (stearylamine, SA) was necessary to enable entrapment of ATRA in the hydrophobic zein shell and increase the stability of the formed nanoparticles. Therefore,

ethanolic solution of the ATRA/SA hydrophobic ion pair was mixed with zein solution and then added to the aqueous lipid nanosuspension, resulting in precipitation of the zein/ATRA

Table 1. Physicochemical Properties of GNS/ATRA Loaded HLPNPs

nanocarriers	entrapment efficiency (% w/w)		particle size (nm)	PDI	zeta potential (mV)
	GNS	ATRA			
nontargeted HLPNPs	90.2 ± 1.2	97.0 ± 3.1	165.9 ± 1.15	0.17	+37.4 ± 3.1
Bio-targeted HLPNPs	90.1 ± 2.1	98.8 ± 3.9	183.2 ± 2.2	0.19	+31.4 ± 3.4
ATRA/Bio-dual-targeted HLPNPs	87.5 ± 1.4	98.7 ± 2.8	206.0 ± 2.5	0.20	+37.0 ± 1.8

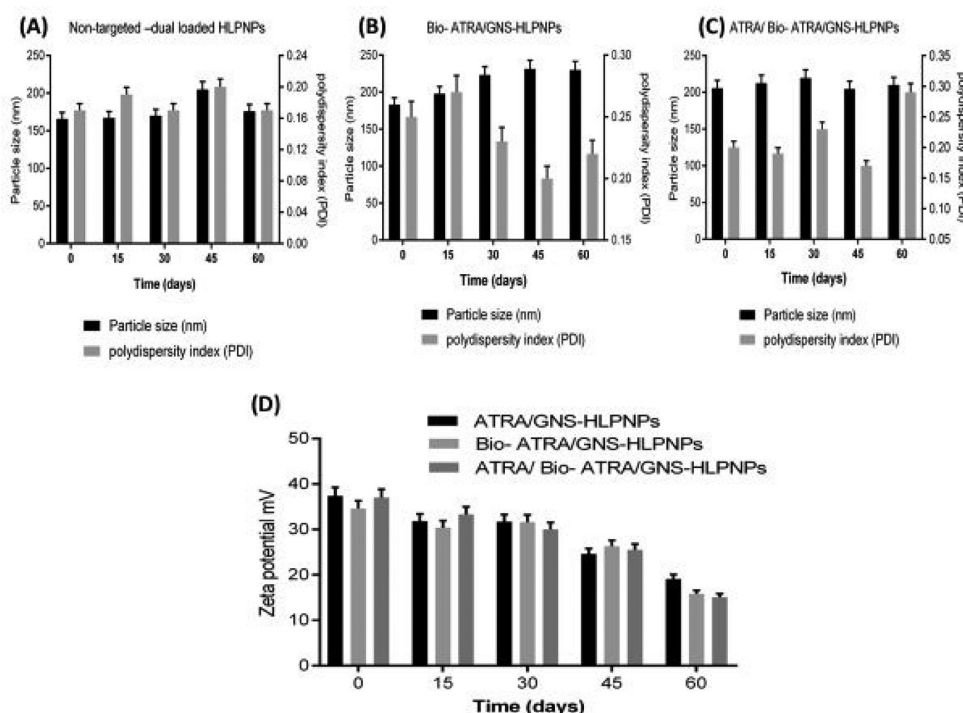


Figure 5. Physical stability of (A) nontargeted ATRA/GNS-HLPNPs, (B) Bio-targeted ATRA/GNS-HLPNPs, and (C) dual-targeted ATRA/GNS-HLPNPs and (D) zeta potential of nontargeted and targeted ATRA/GNS-HLPNPs.

shell onto the GNS-loaded lipid nanocore. Hydrophobic bonding between the zein shell and the lipid core may contribute to stabilization of the hybrid system.

3.3. Physicochemical Characterization of Dual-Targeted NPs. The developed nontargeted ATRA/GNS-HLPNPs showed a small size of 165.9 nm (PDI = 0.17) with a positive zeta potential (+37.4 mV). In comparison, without a zein shell, the particle size of GNS-SLN was significantly smaller (109.8 nm, PDI = 0.29) (Figure 4C). This difference may be explained by the precipitation of a thick zein layer onto the surface of the lipid nanocore. Coupling of targeting ligands to the zein shell of nanocarriers was found to cause a significant increase in their size. Conjugation of the biotin ligand to the zein shell has increased the particle size of the nanohybrids to 183.2 nm (PDI = 0.19) with a positive surface charge (+34.6 mV). Moreover, the conjugation of ATRA and biotin onto the surface of NPs has increased the size of HLPNPs to 206.2 nm with a narrow size distribution (PDI = 0.2) (Figure 4A) with no difference in zeta potential (+37 mV) (Figure 4B). The high positive charge of NPs is related to the cationic ion pairing reagent (SA) that interacts electrostatically with the anionic drug ATRA to increase its entrapment in NPs.³⁷

Both GNS and ATRA were efficiently incorporated into dual-targeted ATRA/GNS-HLPNPs with encapsulation efficiencies of 87.5 and 98.7%, respectively. The high drug entrapment is related to the hydrophobic nature of both drugs

and hence their high affinity toward the hydrophobic carriers, GMS and zein, respectively. On the other hand, no differences were observed in the content of both GNS and ATRA for dual-targeted and nontargeted NPs, as illustrated in Table 1. In vitro, the dual-targeted core-shell HLPNPs depicted a biphasic pattern of GNS release demonstrated as an initial burst, characterized by fast release during the first 0.25–8 h with about 55% of drug being released after 8 h, followed by a slower sustained release up to 65% drug release after 72 h (Figure 4D). In comparison, free GNS was completely released (100%) after 4 h.³⁸ On the other hand, the release of ATRA from dual-targeted HLPNPs was found to be very slow, reaching only 2% after 72 h. However, 48% free ATRA was released from its solution within 72 h. A similar slow release of ATRA was observed by Zuccari et al. where the release rate of ATRA from micellar poly(vinyl alcohol)–nicotinoyl ester complexes after 48 h did not exceed 8%.³⁹ This sequential drug release from HLPNPs with faster GNS release helps delay the emergence of resistance of lung cancer cells to the action of the slowly released ATRA.

The nontargeted, Bio-targeted, and dual-targeted HLPNPs exhibited excellent physical stability. After 60 days of storage at 4 °C, there was a very slight increase in the mean particle size for dual-targeted HLPNPs from 206 to 210 nm (Figure 5C). In addition, the zeta potential of NPs was still high (+15.1 mV) after 60 days, which could contribute to the high stability of NPs (Figure 5D).

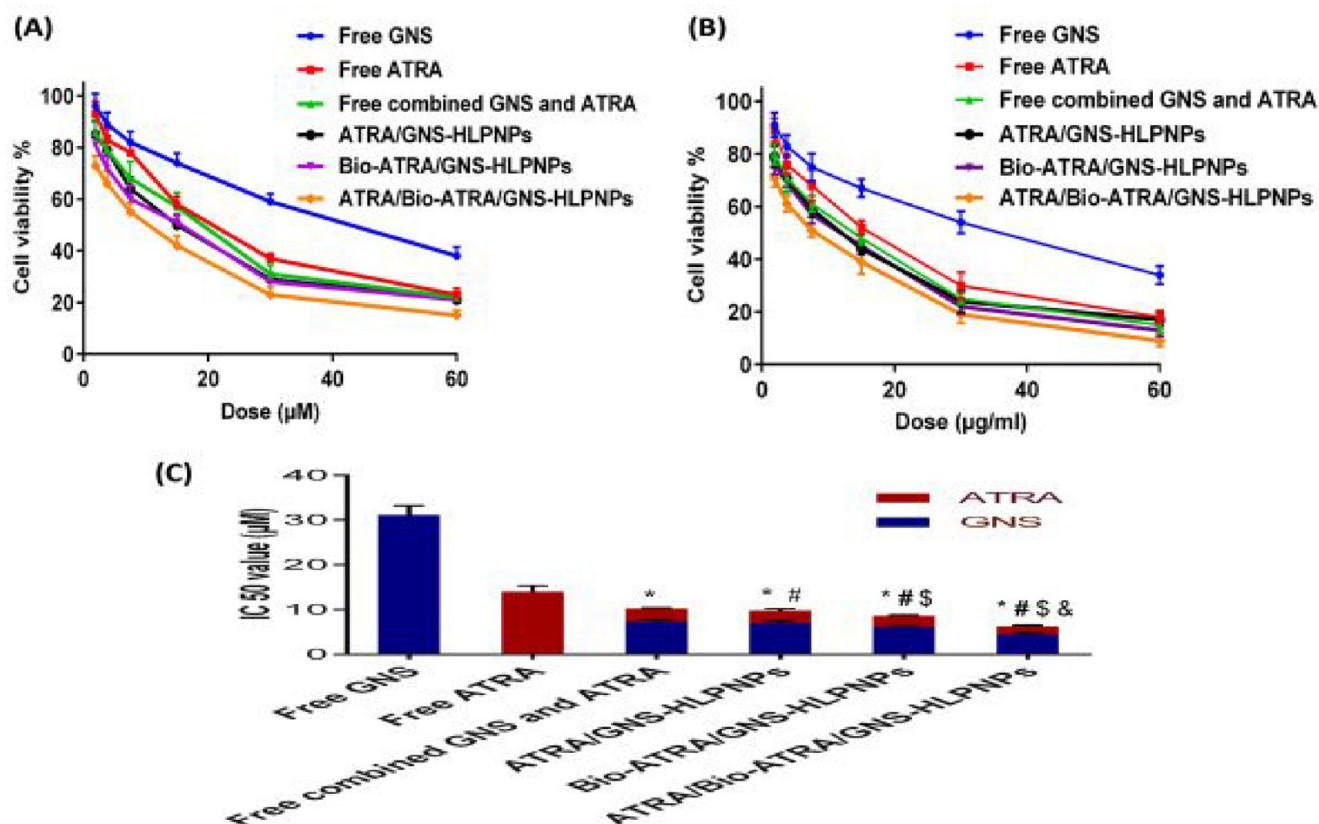


Figure 6. In vitro cytotoxicity analysis for different formulations in comparison with free GNS, free ATRA, and free combined ATRA/GNS on the A549 cell line using MTT assay through (A) 24 and (B) 48 h; (C) IC₅₀ values (μM) for different formulations on the A549 cell line through 48 h. **P* < 0.05 vs free drug, #*P* < 0.05 vs I.V. free combined GNS and ATRA, \$*P* < 0.05 vs nontargeted ATRA/GNS-HLPNPs, and &*P* < 0.05 vs Bio-ATRA/GNS-HLPNPs.

Table 2. IC₅₀ Values of Free Drugs Compared to Drug-Loaded HLPNPs on A549 Cells after 48 h

drug/combo	CI value	total IC ₅₀ of combination	GNS dose	ATRA dose	DRI of GNS	DRI of ATRA
free GNS			31.11 ± 1.53			
free ATRA				14.03 ± 0.64		
blank HLPNPs		1732.35 ± 75.6				
free comb. GNS/ATRA	0.934 ± 0.044	10.25 ± 0.57	7.278 ± 0.49	2.97 ± 0.12	4.27 ± 0.19	4.72 ± 0.22
nontargeted ATRA/GNS-HLPNPs	0.904 ± 0.042	9.84 ± 0.38	6.986 ± 0.39	2.854 ± 0.13	4.45 ± 0.20	4.92 ± 0.25
Bio-targeted ATRA/GNS-HLPNPs	0.891 ± 0.045	8.6 ± 0.61	6.106 ± 0.48	2.494 ± 0.12	5.09 ± 0.25	5.63 ± 0.27
ATRA/Bio-dual-targeted ATRA/GNS-HLPNPs	0.810 ± 0.03	6.3 ± 0.27	4.473 ± 0.22	1.827 ± 0.07	6.96 ± 0.28	7.68 ± 0.32

Morphological TEM micrographs show the spherical shape of dual-targeted HLPNPs demonstrating average diameters of about 85 nm smaller than the results obtained from the DLS technique (Figure 4E). A smaller size of the dried particles is usually detected by TEM after particle shrinkage, while DLS measures the hydrodynamic diameter of the particles in a hydrated state associated with the solvent phase.⁴⁰ Furthermore, the core-shell structure was evident as a gray membrane covering the lipid core, demonstrating the successful hybridization of the lipid surface with a layer of zein shell.⁴¹

3.4. In Vitro Cytotoxicity Analysis. The in vitro cytotoxicity of free GNS, free ATRA, free combined ATRA/GNS, nontargeted, and single- and dual-targeted ATRA/GNS-HLPNPs against A549 lung cancer cells for 24 and 48 h was evaluated through MTT assay. As shown in Figure 6, the dual-targeted ATRA/GNS-HLPNPs produced the maximum cell inhibition effect compared to the other nanocarriers.

Consistently, the IC₅₀ value of dual-targeted ATRA/GNS-HLPNPs was 1.5- and 1.9-fold lower than Bio-targeted HLPNPs and nontargeted HLPNPs for 24 h, respectively. The enhanced cytotoxic effect of dual-targeted ATRA/GNS-HLPNPs was correlated to the increased accumulation of NPs in cancer cells via binding to biotin membrane receptors overexpressed on A549 cells.^{11,12} After their cellular uptake, the NPs will immediately escape the endocytic compartments and drugs will be released to diffuse into the cell.¹⁹ Eventually, the high drug accumulation in A549 cells resulted in a strong proliferation inhibition effect. Moreover, surface modification with ATRA enables nuclear delivery of nanocarriers through binding to nuclear retinoic acid receptors (RARs), resulting in higher antiproliferative activity. In previous literature, functionalization of DOX-PLGA-lecithin-PEG NPs with biotin enhanced their cytotoxicity against HepG2 cells.⁴²

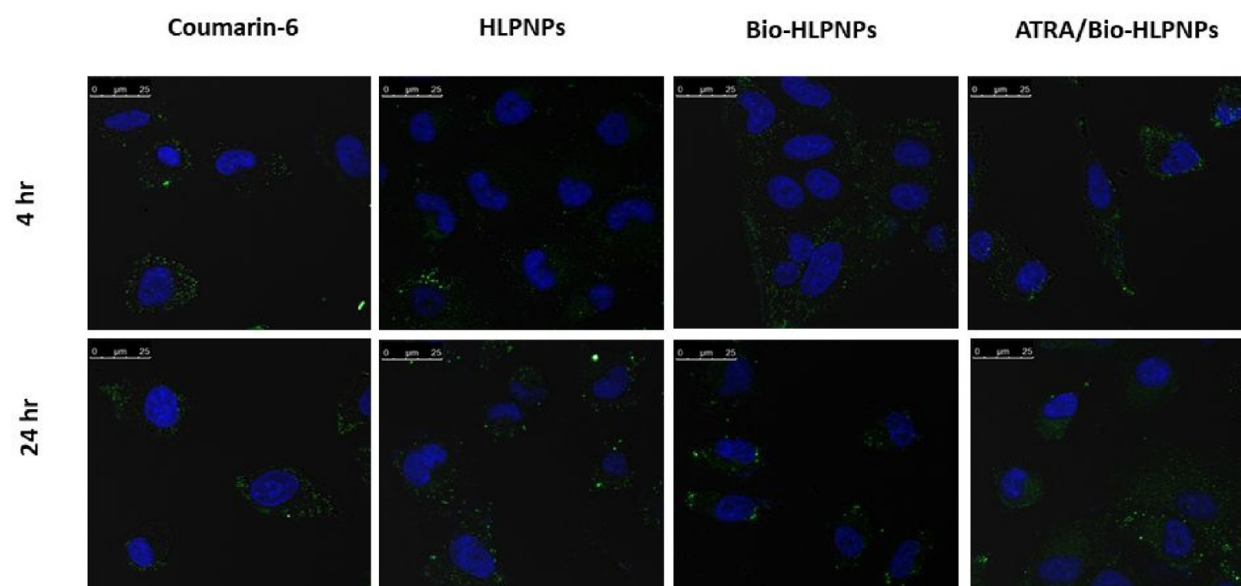


Figure 7. Confocal images showing cellular uptake of free coumarin, nontargeted HLPNPs, Bio-HLPNPs, and ATRA/Bio-HLPNPs with A549 cells after incubation for 4 and 24 h.

Table 3. Composition and Physicochemical Properties of Spray-Dried Nanocomposites Prepared Using Various Carriers

	nanoparticle formulation	composition of spray-dryer feed solution		yield (% w/w)	redispersibility index (RI)
		microparticle composition (w/w)	stearylamine concentration (mg/mL)		
F1	GNS-HLPNPs	mannitol		69.4 ± 5.1	1.13 ± 0.06
F2	GNS-HLPNPs	mannitol:leucine (3:1)		66.86 ± 3.6	0.91 ± 0.038
F3	GNS-HLPNPs	mannitol:maltodextrin:leucine (1.5:1.5:1)		72.59 ± 4.5	1.07 ± 0.05
F4	GNS-HLPNPs	mannitol:HPβCD:leucine (1.5:1.5:1)		70.65 ± 2.9	0.9 ± 0.02
F5	ATRA/GNS-HLPNPs	mannitol:leucine (3:1)	0.73	78.9 ± 3.2	1.00 ± 0.03
F6	ATRA/GNS-HLPNPs	mannitol:HPβCD:leucine (1.5:1.5:1)	0.73	71.8 ± 2.4	0.94 ± 0.02

Further statistical analysis of cytotoxicity studies was conducted using CompuSyn software (version 1) described by Chou and Talaly,²⁸ where the dose reduction index (DRI) and combination index (CI) were used in comparing the free drug combination and the different nanocarriers. The results ensure the synergistic effect of combining ATRA and GNS where their free combination had a CI lower than 1 (0.934) (Table 2 and Figure 6). Zhou et al. found that a combined administration of genistein and ATRA increased the cytotoxic activity and apoptosis of A549 lung cancer cells compared with the single drug use.¹⁷

Moreover, the combination indices (CIs) of Bio-targeted and dual-targeted ATRA/GNS-HLPNPs were 0.891 and 0.81, respectively, confirming that both nanocarriers could provide synergy between ATRA and GNS. Furthermore, the DRIs of GNS were 5.09 and 6.96 in Bio-targeted and dual-targeted ATRA/GNS-HLPNPs, respectively, while the DRIs of ATRA were 5.63 and 7.68 in Bio-targeted and dual-targeted ATRA/GNS-HLPNPs, respectively. Overall, all of the obtained results confirm the superiority of dual-targeted ATRA/GNS-HLPNPs.

3.5. Cellular Uptake Study. Dual-targeted HLPNPs loaded with coumarin-6 as a fluorescent dye showed a higher green fluorescence intensity in A549 cells than Bio-targeted and nontargeted HLPNPs (Figure 7). In contrast, the low fluorescence intensity in cells incubated with free coumarin solution can be correlated to a low degree of internalization. The remarkable uptake of dual-targeted HLPNPs was referred to as receptor-mediated endocytosis. Bio present on the surface

of NPs has a specific affinity toward biotin receptors on the cell membrane, and ATRA can then enhance NP entry into the nucleus. Both receptors are overexpressed by lung cancer cells, while the cellular uptake of Bio-HLPNPs was mediated by interaction with only the biotin receptor.^{11,12}

On the other hand, the internalization of nontargeted HLPNPs followed a nonspecific adsorption within the cells demonstrated as lower uptake compared with ligand-conjugated HLPNPs.³⁵ In agreement with our results, anchoring ATRA onto the surface of chitosan–albumin hybrid NPs loaded with sodium fluorescein led to their rapid accumulation into HepG2 cancer cells.^{11,12} Moreover, the positively charged NPs were reported to be more significantly internalized by cancer cells than neutral or negatively charged ones.⁴³

3.6. Fabrication of Inhalable Nanocomposite Microcarriers for Pulmonary Delivery of Dual-Targeted ATRA/GNS-HLPNPs. Parenteral administration of ATRA or genistein can induce systemic toxicity as well as inefficient delivery to lung cancer tissues. Therefore, inhalable formulations of those drugs were developed. Nebulization of a water-miscible formulation of ATRA resulted in elevation of drug concentration in the lungs of guinea pigs associated with a dose-dependent protein expression, without apparent toxic effects.⁴⁴ In another study, nebulization of niosomal formulations of ATRA has successfully generated aerosol droplets with MMAD of 3.7 μm suitable for pulmonary deposition.⁴⁵ On the other hand, inhalable liposomes coentrapping genistein

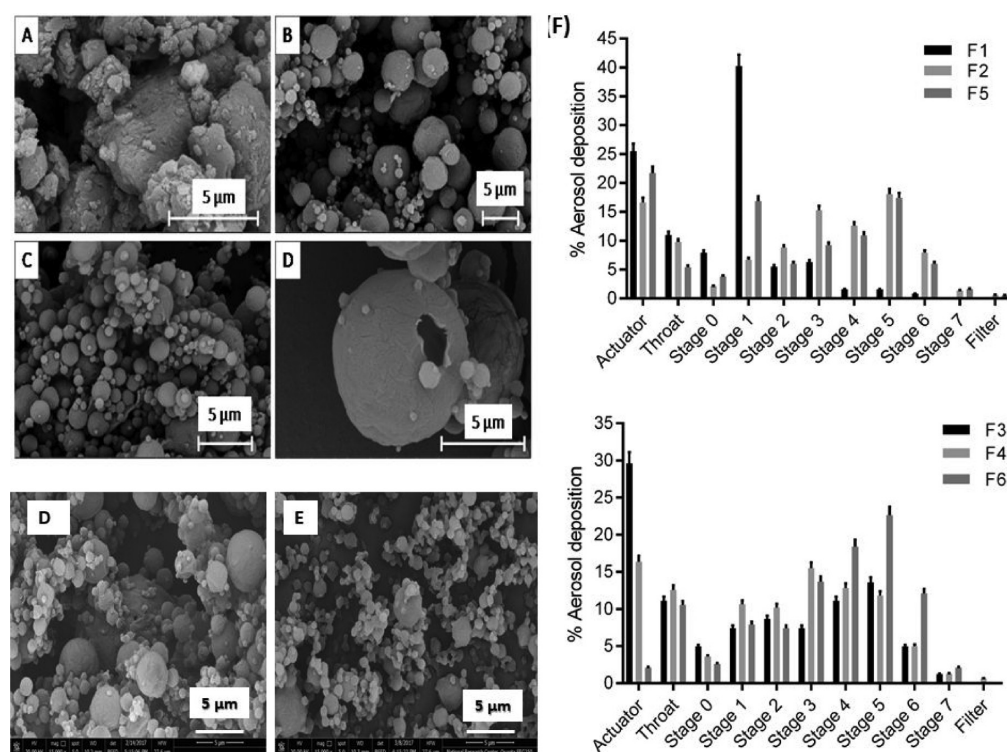


Figure 8. Scanning electron micrographs (SEMs) of spray-dried nanocomposite formulations prepared using different carriers: (A) mannitol (F1), (B) mannitol:leucine (F2), (C) mannitol:maltodextrin:leucine (F3), (D) HPβCD:mannitol:leucine (F4), and (E) SA:HPβCD:mannitol:leucine (F6). (F) In vitro aerosol deposition profiles of spray-dried dual-targeted HLPNP nanocomposites (F1–F6) using Andersen Cascade Impactor (ACI); experiments were performed at air flow rate 28.5 L/min.

and erlotinib were developed by Nimmano et al.⁴⁶ The authors proved that liposomes were more efficiently delivered by an air-jet nebulizer rather than by a vibrating-mesh nebulizer.

Pulmonary delivery of anticancer drugs via nanoparticles has many challenges, such as their physical instability and high chance of exhalation, following their pulmonary administration, due to their nanoscale size.^{15,47} However, development of microcarriers for pulmonary administration of nanoparticles represents an outstanding strategy. With their 1–5 μm size range, formulating microcarriers of nanoparticle drug delivery systems outweighs the disadvantages of nanoparticles and enables deep lung deposition.⁴⁸ Therefore, in our study, the spray-drying technique was applied for developing inhalable nanocomposite microcarrier systems consisting of HLPNPs and excipients. Different types of carriers, such as carbohydrates (mannitol, maltodextrin, and hydroxypropyl β-cyclodextrin) and amino acids (leucine), were investigated (Table 3). After pulmonary administration, these carriers would be easily dissolved releasing the nanoparticles into lung tissue, thus overcoming their clearance by macrophages.⁴⁹ The nanoparticles were then internalized by lung cancer cells rather than normal ones by virtue of the dual-targeting strategy. On another avenue, the presence of these carriers is important to protect the lipid core from melting and the protein shell from denaturation during the spray-drying process.⁵⁰

3.7. Physicochemical Characteristics of Inhalable Nanocomposite Microcarriers. **3.7.1. Spray-Drying Yield, Degree of Reconstitution, and Surface Morphology.** Spray-dried powder nanocomposites showed properties of both NPs and MPs with controllable and uniform size.¹⁵ In this study, the majority of nanocomposites showed a high spray-drying

yield (66.86–78.9%, Table 3). However, spray-dried powder nanocomposites prepared using mannitol (F1) were collected primarily in the cyclone part of the spray-dryer. Meanwhile, addition of leucine (F2) improved the powder flow properties which was readily collected in the collection flask. Compared with the study of Marchiori et al., ATRA nanoemulsion was converted into microparticles using 10% w/v lactose as the auxiliary excipient via spray-drying process where the powder yield was 40% w/w.⁵¹

In our study, all spray-dried powders (F1–F6) have an S_f/S_i ratio <1.2, indicating good redispersibility of NPs and ensuring their complete reconstitution at the target site (Table 3).⁴⁹ Leucine acts as a dispersibility enhancer by reducing attraction between nanoparticles during the spray-drying process. In addition, the nanocomposites prepared using HPβCD as a carrier (F4 and F6) displayed complete water reconstitution (S_f/S_i ratio ≈ 1). HPβCD presents the highest aqueous solubility and its external surface is polar due to the presence of hydroxyl groups, which allows hydrogen bonding with water molecules.^{52,53}

Powders prepared using mannitol (F1, Figure 8A) had an irregular shape, with a significant degree of sintering between particles. However, a smooth surface and spherical shape particles were observed for powders prepared with mannitol:leucine (F2, Figure 8B). Amino acids such as leucine with nonpolar side chains have a higher tendency to the particle surface, thus reducing interaction forces between adjacent surfaces and decreasing particles' aggregation.^{54–56} Similarly, spherical particles with a smooth surface were obtained by addition of maltodextrin (F3, Figure 8C). Interestingly, addition of HPβCD (F4, Figure 8D) improved the particles' porous structure and reduced the density of particles. This

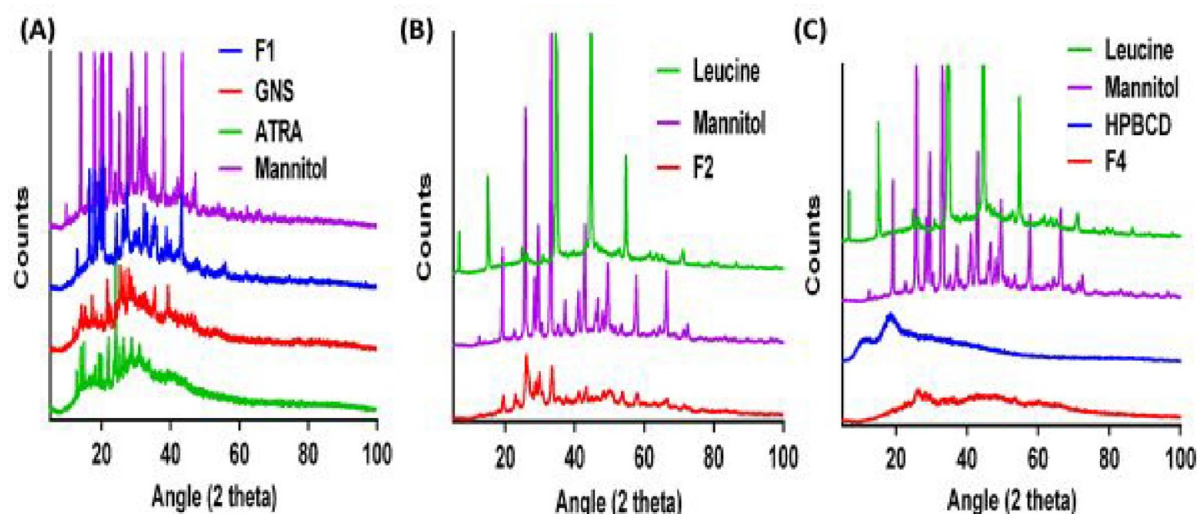


Figure 9. XRD patterns of free drugs, carriers, and the spray-dried dual-targeted HLPNP nanocomposites (F1, F2, and F4).

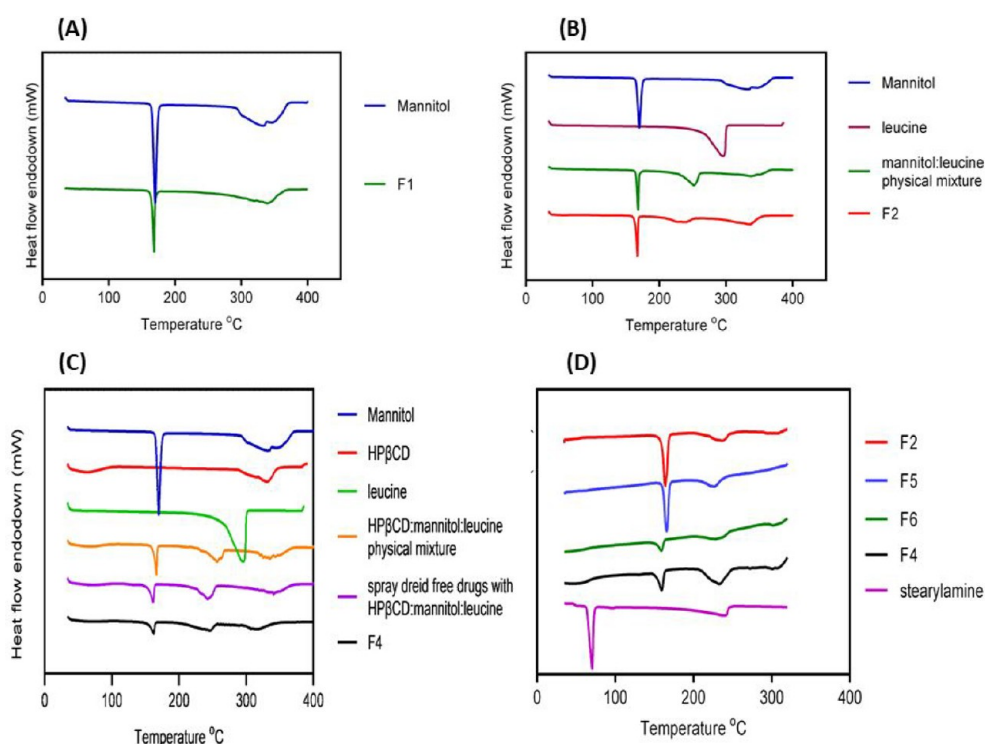


Figure 10. Physical state characterization of different spray-dried dual-targeted HLPNP nanocomposites through their DSC thermograms compared with their carriers.

could be attributed to the β -cyclodextrin cavity, which provided the internal pores in microparticles.²⁹ Moreover, some NPs were clearly detected on the surface of those porous microparticles, thus confirming the nanocomposition of our microparticles (Figure 8D). On the other hand, O'Connor et al. prepared inhalable ATRA encapsulated in spherical poly(D,L-lactide-co-glycolide) microparticles using a closed spray-drying system without excipients.⁵⁷ The ATRA-loaded microparticles exhibited a size of 2.07 μm which is favorable for lung deposition.

3.7.2. Physical State Characterization. Unwanted inflammatory response might be caused upon pulmonary administration due to long-term persistence of poorly water-soluble

particles on the lung epithelial surface. Therefore, using the amorphous form of excipients, that has a higher dissolution rate compared to the crystalline form, in dry powder inhalers (DPIs) is recommended to avoid those problems induced by water insoluble particles. Furthermore, once those amorphous nanocomposites reach the alveolar surface, they rapidly disintegrate into their primary NPs to avoid macrophage clearance.⁵⁵

Wide-angle X-ray powder diffraction (XRD) spectra of GNS, ATRA, and dual-targeted ATRA/GNS-HLPNPs (F1) were illustrated in Figure 9A. The XRD pattern of ATRA showed sharp peaks at $2\theta = 12.72, 13.91, 14.82, 22.03, 24.22,$ and 26.39° . Also, GNS showed crystalline peaks at $2\theta = 15.19,$

Table 4. Aerodynamic Properties of Spray-Dried Nanocomposites with Different Carriers^a

nanocomposite formulation	FPF (%)	ED (%)	MMAD (μm)	GSD
F1	13.68 \pm 0.6	74.8 \pm 4.6	6.8 \pm 0.5	1.27 \pm 0.08
F2	67.04 \pm 2.9	83.3 \pm 4.1	2.8 \pm 0.17	1.86 \pm 0.08
F3	54.39 \pm 1.9	70.37 \pm 2.7	3.14 \pm 0.12	2.13 \pm 0.11
F4	56.09 \pm 2.1	83.8 \pm 3.2	3.6 \pm 0.17	1.7 \pm 0.07
F5	58.74 \pm 2.5	78.14 \pm 3.4	3.28 \pm 0.15	2.13 \pm 0.1
F6	70.81 \pm 3.1	97.9 \pm 4.1	2.47 \pm 0.09	2.13 \pm 0.08

^aThe fine particle fraction (FPF) was calculated as the percentage of the particle size less than 5 μm . The particle size at the 50% cumulative fraction versus the effective cutoff diameter was calculated and defined as the mass median aerodynamic diameter (MMAD). In order to measure the distribution of an aerodynamic particle size, the geometric standard deviation (GSD) was obtained from the ratio diameters at 84 and 16% of the contained aerosol mass.

14.16, 17.26, 21.65, and 25.41°. These peaks are the evidence of the crystalline state for both drugs. In contrast, these peaks were absent in XRD patterns of ATRA/GNS-HLPNPs (F1), indicating that GNS and ATRA were successfully entrapped inside the core-shell NPs in an amorphous state.

According to Figure 9, the raw mannitol has intrinsic peaks referring to its high crystallinity that still appeared in XRD patterns of F1 and F2 nanocomposites at the same position. Thus, mannitol maintained its crystallinity in these formulations. However, the XRD pattern of F4 nanocomposites showed a smooth line without observing specific peaks characteristics for carriers as mannitol and leucine. Therefore, it can be concluded that addition of HP β CD to mannitol and leucine carrier mixture during spray-drying of F4 nanocomposites promoted the amorphous state formation which in turn helped improve the pulmonary characteristics of F4 nanocomposites (Figure 9C).

In our study, the DSC thermogram of spray-dried mannitol nanocomposites (F1) demonstrated a sharp endothermic peak at 169 °C that was attributed to the existence of mannitol in the crystalline state after the spray-drying process similar to pure mannitol (Figure 10A).^{29,56} Moreover, leucine crystals sublime upon heating rather than melting, as revealed by its thermal analysis. When leucine was combined with mannitol in the nanocomposite formulation (F2), the sublimation of leucine occurred at about 60 °C lower than that of pure leucine. This may be related to its possible hydrogen bond formation with mannitol (Figure 10B).^{54–56} This result was confirmed through the reduction in the sublimation temperature that occurred when leucine and mannitol were physically mixed. However, mannitol was still in the crystalline state. Furthermore, by incorporation of HP β CD in the nanocomposite formulation (F4, Figure 10C), a small endothermic peak at 169 °C was observed, reflecting reduction of mannitol crystallinity in the presence of HP β CD during spray-drying compared to the physical mixture.⁵⁸

As illustrated in Figure 10D, a sharp endothermic peak at 57.1 °C representing the melting point of crystalline stearyl amine (SA) was observed. The thermograms of nanocomposite powders (F5 and F6) showed no peaks of SA due to the presence of SA in an amorphous form. Being amorphous, SA, the fatty primary amine, allowed the particles to collapse during solidification in the spray-drying process, thus leading to the observed narrowest particle size distribution (Figure 8E).²⁹ On the contrary, being a crystalline component as stearyl and cetostearyl alcohol provided a rigid structure that pierced through the solvent evaporation bubbles, resulting in particles with sponge-like structure and lower aerodynamic properties than particles prepared with SA.⁵⁹

Therefore, the nanocomposite microparticles (F6) were porous with spherical shape and low density.

3.7.3. Long-Term Stability of Spray-Dried Nanocomposites. Inhalable dry powders had several benefits including long-term stability in the dry form. The encapsulated drugs were preserved in the dry powder as long as it was stored under controlled conditions. In the case of F6 nanocomposites prepared using mannitol/HP β CD/leucine, the powder maintained its physicochemical properties without any aggregation. After reconstitution in distilled water, the particle size analysis showed a very slight increase (219.6 nm with PDI of 0.3) after 7 months of storage compared to the initial size (206.2 nm with PDI of 0.2). On the contrary, F5 nanocomposites fabricated using mannitol/leucine have demonstrated a remarkable increase in particle size and PDI values (372.8 nm with PDI of 0.5). Therefore, F6 nanocomposites were considered as the optimum formulation designed to deliver the dual-targeted GNS/ATRA-HLPNPs to lung tissue. These results confirmed that spray-dried nanocomposites succeeded to maintain the stability of nanoparticles over a long period of time and ensured the powder would be dispersed into primary drug-loaded NPs in a deep lung site.

3.8. Aerosolization Performance of Nanocomposite Microparticles. In our study, the FPF and MMAD values of nanocomposites prepared using mannitol (F1), detected using an Andersen Cascade Impactor (ACI), were 13.6% and 6.8 μm , respectively (Table 4). As shown in Figure 7F, the majority of powder (90%) was deposited from the actuator to stage 2 and relatively very lower fractions reached the lower stages. This could be attributed to the presence of mannitol in the crystalline form with irregular aggregated particles.²⁹ Alternatively, the decrease in aggregation between microparticles in F4 nanocomposites as well as their increased porosity resulted in improvement of the FPF data (56.09%) and enhanced their deposition in lower stages of ACI relating to the presence of HP β CD and leucine combined with mannitol. HP β CD is characterized by the β -cyclodextrin cavity, which improved microparticles' aerodynamic properties through providing internal pores and reducing the particles' density. Furthermore, the presence of leucine reduced the fraction deposited in the throat and the device. The increase in aerosol deposition, by the effect of leucine, was significantly observed by the significant increase in FPF values from F1 (13.7%) to F2 (67%) (Figure 7F and Table 4).^{29,60} Using leucine in a spray-drying mixture was reported to improve the aerosolization behavior of powder by reducing surface tension of microparticles and decreasing nanoagglomeration.⁶¹

During the preparation of dual drug-loaded nanoparticles, SA was used as an ion-pairing agent to form an ionic complex

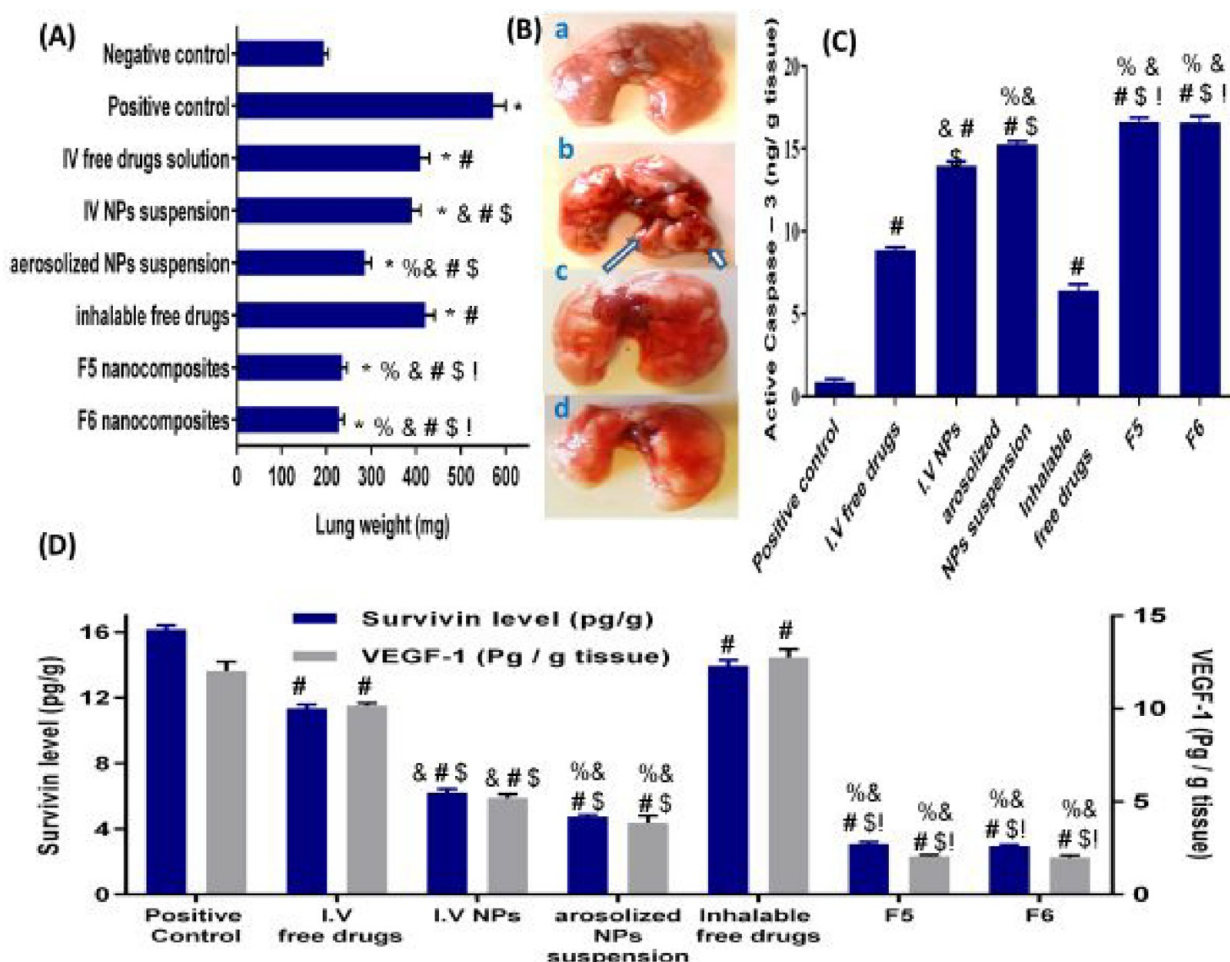


Figure 11. In vivo therapeutic antitumor activity of different formulations on (A) lung tumor weight and (B) morphology of lungs excised from treatment groups; (Ba) negative control, (Bb) positive control, (Bc) inhalable free drugs, and (Bd) F6 nanocomposites. Levels of tumor marker values in lung cancer bearing mice treated with different formulations compared to untreated positive control including (C) survivin, (D) active caspase-3, and (E) VEGF-1. * $P < 0.05$ vs negative control, # $P < 0.05$ vs positive control, & $P < 0.05$ vs inhalable free drugs, % $P < 0.05$ vs I.V. targeted NPs, \$ $P < 0.05$ vs I.V. free drugs, ! $P < 0.05$ vs aerosolized NPs suspension.

with ATRA.¹⁶ The presence of SA in the nanoparticle structure has reversed the charge of nanoparticles from -27 to $+37$ mV. The electrostatic charge in spray-dried powder can significantly influence the deposition of inhalable particles in the lung tissue.⁶² The electrostatic charge of powders has a strong effect on material loss during actuation of the inhaler where the charged particles may adhere to the inhaler material, thus affecting the emitted dose.⁶² For this reason, we investigated the change in the aerodynamic properties of nanocomposites as a result of the presence of SA with different carriers (F5 and F6) compared to F2 and F4 nanocomposites (prepared without SA). The positively charged NPs in F5 nanocomposites were coated with neutral carriers such as mannitol and leucine, resulting in an FPF value of 58.7%. However, the mannitol:leucine carriers used in F2 nanocomposites could coat the low negatively charged NPs, resulting in a higher FPF value (67%). Therefore, the reduction of the ED value from 83.3% in F2 to 78.14% upon using SA in F5 indicated the adherence of particles to the inhaler device and hence their deposition in upper stages of ACL.⁵⁹

HP β CD is a cyclic oligosaccharide with D-(+)-glucopyranose units, one group of hydroxypropyl per unit. The high content of HP β CD in the formulations provides a large number of oxygen atoms that have a larger electron cloud.⁶³ Thus,

HP β CD carriers in F4 nanocomposites increased the net charge of particles, resulting in low FPF (56%) and ED (83.8%) values. However, the positive charge of NPs in F6 nanocomposites could be reduced by HP β CD and decreased the powder entrapped in the inhaler device, as demonstrated by the increase in ED (97.9%) and FPF (70.8%) values.²⁹ Therefore, F6 nanocomposite powder prepared using HP β CD/mannitol/leucine was considered as the optimum inhalable nanocomposites that could deliver the ATRA/GNS drug nanocomposition to target tumor tissue in deep lung and produce their therapeutic effect.

Compared to the relatively small size of microparticles measured by the cascade impaction method, the particles seem to be aggregated in SEM images. During the cascade impaction process, the particles were aerosolized to simulate the real condition during powder inhalation in humans. However, for SEM measurement, the powders were not aerosolized and measured in their static state. Therefore, measurement of the diameter of inhalable particles depends mainly on cascade impaction technology while SEM gives an idea about their surface topography.

3.9. In Vivo Anticancer Efficacy. 3.9.1. Lung and Body Weight. The antitumor efficacy of different formulations with various routes of administration was evaluated in mice bearing

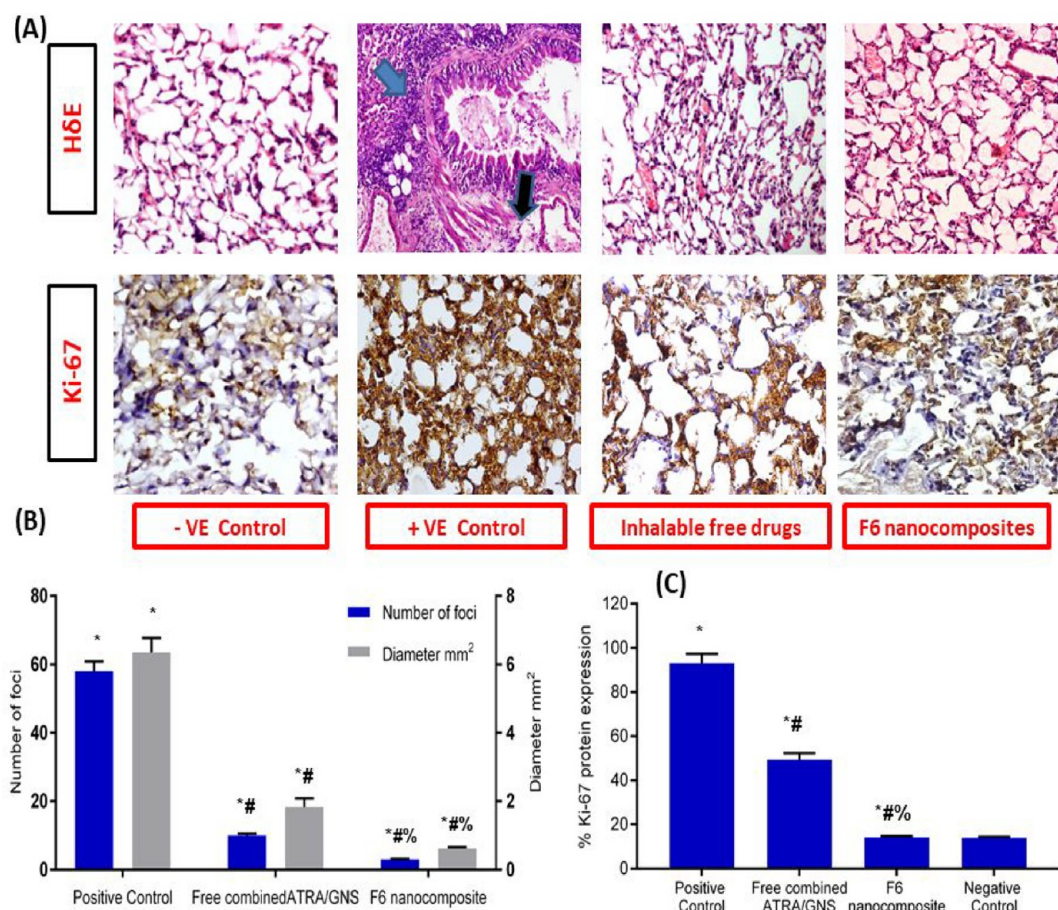


Figure 12. Histopathological and Immunohistochemical analysis: (A) representative histopathological images of lung sections of different treatment groups and immunohistochemical analysis of Ki-67 from lung sections collected from mice treated with different treatments; (B) effect of different treatments on the number and diameter of lung tumor foci in a urethane induced lung cancer mouse model; (C) % Ki-67 proliferation marker in lung cancer tissues of different treatment groups. * $P < 0.05$ vs negative control, # $P < 0.05$ vs positive control, % $P < 0.05$ vs free combination.

lung cancer. As illustrated in Figure 11B, the excised lungs from mice bearing a lung tumor exhibited tumor surface lesions, while lungs harvested from mice of the negative control group demonstrated normal physiological characteristics. The lungs of mice treated with inhalable spray-dried free ATRA/GNS combination exhibited a slightly lower number of lesions than the positive control group. However, the inhalable F6 spray-dried nanocomposite-treated groups displayed the lowest lung lesion numbers like the negative control group, indicating an effective therapeutic effect of those formulations.

The lung tumors in the untreated positive control grew rapidly with an average lung weight of 571.5 mg ($P < 0.05$), while the lung weight in the negative control group at the end of the experiment was much smaller (194 mg) ($P < 0.05$) without lesions in tissue (Figure 11A). For treated mice, specifically, the reduction in lung weight ($P < 0.05$) for the F6 dry powder nanocomposite-treated group was greatly lower with 58.9% than free drugs dry powder- and aerosolized NPs suspension-treated groups (26.4 and 46.6%, respectively) compared to the positive control. On another avenue, there was a slight change in lung weight after i.v. administration for free drugs or NP suspensions from the positive control due to the low concentration of drugs reaching the lung after systemic dilution.⁶⁴ These results indicated the superior efficacy of localized therapy particularly using inhalable dry powder

nanocomposites (F6) that outweighed other formulations in anticancer efficacy. In previous literature, ATRA was successfully combined with chemotherapeutics for synergistic lung cancer therapy. Zhang et al. have developed poly(ethylene glycol)-*b*-polyaspartate (PEG-*b*-PAsp) micelles as nanocarriers for PTX and ATRA to lung. Treatment of A549 tumor-bearing mice with the drug-loaded micelles via the i.v. route resulted in a great tumor growth inhibition compared with free drugs.⁶⁵ However, no inhalable nanocarriers have been developed for ATRA combined lung cancer therapy until now.

The change in body weight of treated mice was used as the indicator of the safety profile of various formulations. The group treated with inhalable NP powder showed an increase in body weight near that of the negative control group, indicating the improved health of the mice and the low toxicity of the formulation (Figure S9).⁶⁶ The slight change in the body weight of the group treated with an aerosolized NP suspension was attributed to the low toxicity of formulations on normal tissue in mice and uptake in cancer cells, but they had a body weight higher than inhalable powder. On the other hand, the inhalable free drugs and parenteral administration of free drugs and NP suspension had a body weight near that of the positive control group referred to the wide distribution of free drugs on the whole body and hence causing a toxic effect on normal tissue.⁶⁴

3.9.2. Tumor Growth Biomarkers. The tumor biomarkers were measured in homogenized lung to evaluate the inhibition effect on tumor growth which differed between various formulations, as illustrated in Figure 11. From these data, there were no remarkable differences in markers between F5 dry powder (survivin, 3.08 pg/g; VEGF, 2.06 pg/g) and F6 dry powder (survivin, 2.95 pg/g; VEGF, 1.99 pg/g) ($P < 0.05$); however, the aerosolized NP suspension had higher values of survivin (4.75 pg/g) and VEGF (3.86 pg/g) ($P < 0.05$) (Figure 11D). As illustrated in previous studies, the formulation administered as dry powder increased the concentration of drugs in the lung compared to the aerosolized formulation suspension. This may be related to the high chance of exhalation of the aerosolized formulation, following their administration, due to their nanoscale size compared to the microsize nanocomposites.^{48,67}

On the contrary, the tumor markers were higher in lungs of mice treated with the NP suspension after i.v. administration (survivin, 6.23 pg/g; VEGF, 5.2 pg/g) ($P < 0.05$) compared with the aerosolized NP suspension. Pulmonary administration leads to a relatively higher accumulation of NPs in lungs with a very low amount absorbed to serum, while the i.v. administered NP suspension distributed to all body tissues with low concentration reaching the lung tissue.⁶⁷

On the other hand, the inhalable F6 dry powder nanocomposites increased caspase-3 expression as an apoptotic indicator to 19.5-fold compared to the positive control group (Figure 11C). Moreover, the groups treated with inhalable free combined ATRA/GNS dry powder and aerosolized NP suspension had 7.5- and 17.5-fold lower caspase-3 expression ($P < 0.05$), respectively, in comparison to tumors of the positive control group. However, treatment with i.v. NP suspension or free ATRA/GNS combination slightly increased caspase-3 expression compared to the positive control group. These results acted as additional evidence for the superior therapeutic effect of inhalable dry powder nanocomposites compared to other routes of administration.

3.9.3. Histopathological and Immunohistochemical Analysis. Mice bearing urethane-induced adenomas were sacrificed after the treatment, and the tumors were dissected and stained with H&E and Ki-67. Normal alveoli epithelial tissues with a single layer were demonstrated in the negative control group, while the positive control group was characterized by unclear cell morphology with various lesions for necrotic cells (Figure 12A). These preneoplastic to neoplastic lesions ranged from epithelial hyperplasia to adenoma (blue arrow).⁶⁸ Furthermore, the black and white arrows in the positive control group referred to the infiltration of inflammatory and hemorrhage cells, respectively. Mice administered with inhalable free drug powder mixture exhibited a decrease in the histopathological neoplastic transformation, while the inhalable F6 nanocomposite-treated group exhibited superior improvement of the carcinogenic histopathological profile.⁶⁹ The inhalable F6 nanocomposites exhibited a 19.3-fold decrease in the average number of microscopic metastatic lung adenomatous foci with significantly lower diameter (0.62 mm) ($P < 0.05$) compared with the positive control group (Figure 12B). On another avenue, immunohistochemical analysis was performed to measure tumor proliferation using Ki-67 analysis. Analysis of a lung section showed that the expression of Ki-67 was greatly decreased by 6.6-fold in the group treated with inhalable F6

nanocomposites ($P < 0.05$) compared with the positive control group (Figure 12C).

4. CONCLUSIONS

In summary, inhalable dual-targeted hybrid lipid–protein core–shell nanocomposites (HLPNPs) coloaded with ATRA and GNS were developed for localized therapy of lung cancer. The sequential solvent evaporation/nanoprecipitation technique was used to elaborate lipid nanocore–zein shell hybrid nanocarriers. The nanocarriers displayed favorable characteristics including small particle size, charged surface, and sustained drug release. Coupling of both biotin and ATRA to the zein shell of nanocarriers resulted in the highest internalization and cytotoxicity against A549 lung cancer cells compared to single biotin-targeted and nontargeted nanocarriers. To enhance their deposition at deep lung tissues, the prepared dual-targeted nanocarriers were formulated into inhalable dry powder nanocomposite microcarriers via spray-drying. Different types of pulmonary carriers were investigated for the preparation of nanocomposite particles with optimal aerodynamic properties. Both in vitro aerosolization and in vivo antitumor efficacy studies proved the superiority of inhalable spray-dried nanocomposites fabricated using mannitol:HP β CD:leucine in 1.5:1.5:1 mass ratio as a carrier mixture for localized codelivery of ATRA and GNS to lung cancer cells rather than normal ones. The nanocomposites exhibited deep lung deposition, as demonstrated by their small MMAD (2.47 μ m) and high FPF (70.81%). The enhanced in vivo anticancer activity of the inhalable nanocomposites was confirmed by the significant decrease of lung weights, numbers, and diameters of metastatic foci and tumor biomarkers. In comparison, administration of free drugs or drug nanoparticle suspensions either by inhalation or intravenous injection resulted in lower therapeutic effects. Overall, the developed inhalable dual-targeted lipid core–zein shell nanocomposites coloaded with ATRA and GNS could offer a potential route for localized lung cancer therapy.

■ ASSOCIATED CONTENT

§ Supporting Information

The Supporting Information is available free of charge on the ACS Publications website at DOI: 10.1021/acsbomaterials.8b01374.

Further information about HPLC method development for dual drugs, the characterization of ATRA/Bio-zein conjugate, physicochemical characterization of ATRA/Bio-ATRA/GNS-HLPNPs, in vitro cytotoxicity, physical characterization of spray-dried nanocomposite, quantification of angiogenesis and apoptosis by ELISA, and histopathological analysis and immunohistochemical analysis methodology (PDF)

■ AUTHOR INFORMATION

Corresponding Authors

*E-mail: fajy@mail.cgu.edu.tw.

*E-mail: aelzoghby@bwh.harvard.edu, ahmed_elzoghby@alexu.edu.eg. Cell: (001) 781-366-8703. Phone: (001) 617-768-8994.

ORCID

Sherine N. Khattab: 0000-0002-3162-6386

Jia-You Fang: 0000-0003-2114-7709

Ahmed O. Elzoghby: 0000-0002-5193-7536

Author Contributions

The rationale of the study and design of the experiments was developed by A.O.E. The practical experiments were performed by N.M.K. The manuscript was written and revised through contributions of all authors. All authors have given approval to the final version of the manuscript.

Notes

The authors declare no competing financial interest.

ACKNOWLEDGMENTS

This work was supported by the research grant (No. 5731) of Science and Technology Development Fund (STDF), Ministry of Scientific Research, Egypt.

REFERENCES

- (1) Soni, N.; Soni, N.; Pandey, H.; Maheshwari, R.; Kesharwani, P.; Tekade, R. K. Augmented delivery of gemcitabine in lung cancer cells exploring mannose anchored solid lipid nanoparticles. *J. Colloid Interface Sci.* **2016**, *481*, 107–16.
- (2) Babu, A.; Templeton, A. K.; Munshi, A.; Ramesh, R. Nanoparticle-based drug delivery for therapy of lung cancer: progress and challenges. *J. Nanomater.* **2013**, *2013*, 863951.
- (3) Varshosaz, J.; Hassanzadeh, F.; Mardani, A.; Rostami, M. Feasibility of haloperidol-anchored albumin nanoparticles loaded with doxorubicin as dry powder inhaler for pulmonary delivery. *Pharm. Dev. Technol.* **2015**, *20* (2), 183–96.
- (4) Kabary, D. M.; Helmy, M. W.; Elkhodairy, K. A.; Fang, J. Y.; Elzoghby, A. O. Hyaluronate/lactoferrin layer-by-layer-coated lipid nanocarriers for targeted co-delivery of rapamycin and berberine to lung carcinoma. *Colloids Surf., B* **2018**, *169*, 183–194.
- (5) Ezzati Nazhad Dolatabadi, J.; Hamishehkar, H.; Valizadeh, H. Development of dry powder inhaler formulation loaded with alendronate solid lipid nanoparticles: solid-state characterization and aerosol dispersion performance. *Drug Dev. Ind. Pharm.* **2015**, *41* (9), 1431–7.
- (6) Sabra, S. A.; Elzoghby, A. O.; Sheweita, S. A.; Haroun, M.; Helmy, M. W.; Eldemellawy, M. A.; Xia, Y.; Goodale, D.; Allan, A. L.; Rohani, S. Self-assembled amphiphilic zein-lactoferrin micelles for tumor targeted co-delivery of rapamycin and wogonin to breast cancer. *Eur. J. Pharm. Biopharm.* **2018**, *128*, 156–169.
- (7) Mandal, B.; Mittal, N. K.; Balabathula, P.; Thoma, L. A.; Wood, G. C. Development and in vitro evaluation of core-shell type lipid-polymer hybrid nanoparticles for the delivery of erlotinib in non-small cell lung cancer. *Eur. J. Pharm. Sci.* **2016**, *81*, 162–71.
- (8) Elzoghby, A.; Freag, M.; Mamdouh, H.; Elkhodairy, K. Zein-based Nanocarriers as Potential Natural Alternatives for Drug and Gene Delivery: Focus on Cancer Therapy. *Curr. Pharm. Des.* **2018**, *23* (35), 5261–5271.
- (9) Danhier, F.; Feron, O.; Préat, V. To exploit the tumor microenvironment: passive and active tumor targeting of nanocarriers for anti-cancer drug delivery. *J. Controlled Release* **2010**, *148* (2), 135–146.
- (10) Sabra, S.; Abdelmoneem, M.; Abdelwakil, M.; Mabrouk, M. T.; Anwar, D.; Mohamed, R.; Khattab, S.; Bekhit, A.; Elkhodairy, K.; Freag, M.; Elzoghby, A. Self-Assembled Nanocarriers Based on Amphiphilic Natural Polymers for Anti-Cancer Drug Delivery Applications. *Curr. Pharm. Des.* **2018**, *23* (35), 5213–5229.
- (11) Russo, A.; Pellosi, D. S.; Pagliara, V.; Milone, M. R.; Pucci, B.; Caetano, W.; Hioka, N.; Budillon, A.; Ungaro, F.; Russo, G. Biotin-targeted Pluronic® P123/F127 mixed micelles delivering niclosamide: A repositioning strategy to treat drug-resistant lung cancer cells. *Int. J. Pharm.* **2016**, *511* (1), 127–139.
- (12) Varshosaz, J.; Hassanzadeh, F.; Sadeghi, H.; Khan, Z. G.; Rostami, M. Retinoic acid decorated albumin-chitosan nanoparticles for targeted delivery of doxorubicin hydrochloride in hepatocellular carcinoma. *J. Nanomater.* **2013**, *2013*, 1.
- (13) Wauthoz, N.; Deleuze, P.; Saumet, A.; Duret, C.; Kiss, R.; Amighi, K. Temozolomide-based dry powder formulations for lung tumor-related inhalation treatment. *Pharm. Res.* **2011**, *28* (4), 762–75.
- (14) Ali, M. E.; Lamprecht, A. Spray freeze drying for dry powder inhalation of nanoparticles. *Eur. J. Pharm. Biopharm.* **2014**, *87* (3), 510–517.
- (15) Abdelaziz, H. M.; Gaber, M.; Abd-Elwakil, M. M.; Mabrouk, M. T.; Elgohary, M. M.; Kamel, N. M.; Kabary, D. M.; Freag, M. S.; Samaha, M. W.; Mortada, S. M.; Elkhodairy, K. A.; Fang, J. Y.; Elzoghby, A. O. Inhalable particulate drug delivery systems for lung cancer therapy: Nanoparticles, microparticles, nanocomposites and nanoaggregates. *J. Controlled Release* **2018**, *269*, 374–392.
- (16) Schultze, E.; Ourique, A.; Yurgel, V. C.; Beghini, K. R.; Thurow, H.; de Leon, P. M.; Campos, V. F.; Dellagostin, O. A.; Guterres, S. R.; Pohlmann, A. R.; Seixas, F. K.; Beck, R. C.; Collares, T. Encapsulation in lipid-core nanocapsules overcomes lung cancer cell resistance to tretinoin. *Eur. J. Pharm. Biopharm.* **2014**, *87* (1), 55–63.
- (17) Zhou, R. J.; Yang, X. Q.; Wang, D.; Zhou, Q.; Xia, L.; Li, M. X.; Zeng, L. L.; Wang, G.; Yang, Z. Z. Anti-tumor effects of all-trans retinoic acid are enhanced by genistein. *Cell Biochem. Biophys.* **2012**, *62* (1), 177–84.
- (18) Adachi, N.; Miyaike, M.; Kato, S.; Kanamaru, R.; Koyama, H.; Kikuchi, A. Cellular distribution of mammalian DNA topoisomerase II is determined by its catalytically dispensable C-terminal domain. *Nucleic acids research* **1997**, *25* (15), 3135–3142.
- (19) Long, J. T.; Cheang, T. Y.; Zhuo, S. Y.; Zeng, R. F.; Dai, Q. S.; Li, H. P.; Fang, S. Anticancer drug-loaded multifunctional nanoparticles to enhance the chemotherapeutic efficacy in lung cancer metastasis. *J. Nanobiotechnol.* **2014**, *12*, 37.
- (20) Sharma, P.; Dube, B.; Sawant, K. Synthesis of cytarabine lipid drug conjugate for treatment of meningeal leukemia: development, characterization and in vitro cell line studies. *J. Biomed. Nanotechnol.* **2012**, *8* (6), 928–937.
- (21) Elzoghby, A. O.; Mostafa, S. K.; Helmy, M. W.; Eldemellawy, M. A.; Sheweita, S. A. Multi-Reservoir Phospholipid Shell Encapsulating Protamine Nanocapsules for Co-Delivery of Letrozole and Celecoxib in Breast Cancer Therapy. *Pharm. Res.* **2017**, *34* (9), 1956–1969.
- (22) Sahu, P. K.; Mishra, D. K.; Jain, N.; Rajoriya, V.; Jain, A. K. Mannosylated solid lipid nanoparticles for lung-targeted delivery of Paclitaxel. *Drug Dev. Ind. Pharm.* **2015**, *41* (4), 640–9.
- (23) Elzoghby, A. O.; El-Lakany, S. A.; Helmy, M. W.; Abu-Serie, M. M.; Elgindy, N. A. Shell-crosslinked zein nanocapsules for oral codelivery of exemestane and resveratrol in breast cancer therapy. *Nanomedicine (London, U. K.)* **2017**, *12* (24), 2785–2805.
- (24) Elzoghby, A. O.; Mostafa, S. K.; Helmy, M. W.; Eldemellawy, M. A.; Sheweita, S. A. Superiority of aromatase inhibitor and cyclooxygenase-2 inhibitor combined delivery: Hyaluronate-targeted versus PEGylated protamine nanocapsules for breast cancer therapy. *Int. J. Pharm.* **2017**, *529* (1–2), 178–192.
- (25) Khattab, S. N.; Naim, S. E. A.; El-Sayed, M.; El Bardan, A. A.; Elzoghby, A. O.; Bekhit, A. A.; El-Faham, A. Design and synthesis of new s-triazine polymers and their application as nanoparticulate drug delivery systems. *New J. Chem.* **2016**, *40* (11), 9565–9578.
- (26) El-Far, S. W.; Helmy, M. W.; Khattab, S. N.; Bekhit, A. A.; Hussein, A. A.; Elzoghby, A. O. Phytosomal bilayer-enveloped casein micelles for codelivery of monascus yellow pigments and resveratrol to breast cancer. *Nanomedicine (London, U. K.)* **2018**, *13* (5), 481–499.
- (27) Elgindy, N.; Elkhodairy, K.; Molokhia, A.; ElZoghby, A. Biopolymeric Nanoparticles for Oral Protein Delivery: Design and In Vitro Evaluation. *J. Nanomed. Nanotechnol.* **2011**, *2* (3), 1000110.
- (28) Chou, T. C.; Talaly, P. A simple generalized equation for the analysis of multiple inhibitions of Michaelis-Menten kinetic systems. *J. Biol. Chem.* **1977**, *252* (18), 6438–42.
- (29) Parsian, A. R.; Vatanara, A.; Rahmati, M. R.; Gilani, K.; Khosravi, K. M.; Najafabadi, A. R. Inhalable budesonide porous

microparticles tailored by spray freeze drying technique. *Powder Technol.* **2014**, *260*, 36–41.

(30) Kim, I.; Byeon, H. J.; Kim, T. H.; Lee, E. S.; Oh, K. T.; Shin, B. S.; Lee, K. C.; Youn, Y. S. Doxorubicin-loaded highly porous large PLGA microparticles as a sustained-release inhalation system for the treatment of metastatic lung cancer. *Biomaterials* **2012**, *33* (22), 5574–5583.

(31) Chuacharoen, T.; Sabliov, C. M. Zein nanoparticles as delivery systems for covalently linked and physically entrapped folic acid. *J. Nanopart. Res.* **2017**, *19* (2), 81.

(32) Taheri, A.; Dinarvand, R.; Atyabi, F.; Nouri, F.; Ahadi, F.; Ghahremani, M. H.; Ostad, S. N.; Boroujeni, A. T.; Mansoori, P. Targeted delivery of methotrexate to tumor cells using biotin functionalized methotrexate-human serum albumin conjugated nanoparticles. *J. Biomed. Nanotechnol.* **2011**, *7* (6), 743–753.

(33) Das, S.; Ng, W. K.; Kanaujia, P.; Kim, S.; Tan, R. B. Formulation design, preparation and physicochemical characterizations of solid lipid nanoparticles containing a hydrophobic drug: effects of process variables. *Colloids Surf., B* **2011**, *88* (1), 483–489.

(34) Balan, V.; Petrache, I. A.; Popa, M. I.; Butnaru, M.; Barbu, E.; Tsiouklis, J.; Verestiuc, L. Biotinylated chitosan-based SPIONs with potential in blood-contacting applications. *J. Nanopart. Res.* **2012**, *14* (2), 730.

(35) Tran, T. H.; Bae, B.-c.; Lee, Y.-k.; Na, K.; Huh, K. M. Heparin-folate-retinoic acid bioconjugates for targeted delivery of hydrophobic photosensitizers. *Carbohydr. Polym.* **2013**, *92* (2), 1615–1624.

(36) Tran, T. H.; Ramasamy, T.; Truong, D. H.; Shin, B. S.; Choi, H.-G.; Yong, C. S.; Kim, J. O. Development of vorinostat-loaded solid lipid nanoparticles to enhance pharmacokinetics and efficacy against multidrug-resistant cancer cells. *Pharm. Res.* **2014**, *31* (8), 1978–1988.

(37) Castro, G. A.; Coelho, A. L. L.; Oliveira, C. A.; Mahecha, G. A.; Oréfice, R. L.; Ferreira, L. A. Formation of ion pairing as an alternative to improve encapsulation and stability and to reduce skin irritation of retinoic acid loaded in solid lipid nanoparticles. *Int. J. Pharm.* **2009**, *381* (1), 77–83.

(38) Andrade, L. M.; de Fátima Reis, C.; Maione-Silva, L.; Anjos, J. L. V.; Alonso, A.; Serpa, R. C.; Marreto, R. N.; Lima, E. M.; Taveira, S. F. Impact of lipid dynamic behavior on physical stability, in vitro release and skin permeation of genistein-loaded lipid nanoparticles. *Eur. J. Pharm. Biopharm.* **2014**, *88* (1), 40–47.

(39) Zuccari, G.; Bergamante, V.; Carosio, R.; Gotti, R.; Montaldo, P.; Orienti, I. Micellar complexes of all-trans retinoic acid with polyvinylalcohol-nicotinoyl esters as new parenteral formulations in neuroblastoma. *Drug Delivery* **2009**, *16* (4), 189–195.

(40) Kaasalainen, M.; Aseyev, V.; von Haartman, E.; Karaman, D. S.; Makila, E.; Tenhu, H.; Rosenholm, J.; Salonen, J. Size, Stability, and Porosity of Mesoporous Nanoparticles Characterized with Light Scattering. *Nanoscale Res. Lett.* **2017**, *12* (1), 74.

(41) Hu, Y.; Ehrich, M.; Fuhrman, K.; Zhang, C. In vitro performance of lipid-PLGA hybrid nanoparticles as an antigen delivery system: lipid composition matters. *Nanoscale Res. Lett.* **2014**, *9* (1), 434.

(42) Dai, Y.; Xing, H.; Song, F.; Yang, Y.; Qiu, Z.; Lu, X.; Liu, Q.; Ren, S.; Chen, X.; Li, N. Biotin-conjugated multilayer poly [D, L-lactide-co-glycolide]-lecithin-polyethylene glycol nanoparticles for targeted delivery of doxorubicin. *J. Pharm. Sci.* **2016**, *105* (9), 2949–2958.

(43) Hu, Y.; Hoerle, R.; Ehrich, M.; Zhang, C. Engineering the lipid layer of lipid-PLGA hybrid nanoparticles for enhanced in vitro cellular uptake and improved stability. *Acta Biomater.* **2015**, *28*, 149–159.

(44) Schäffer, M. W.; Roy, S. S.; Mukherjee, S.; Ong, D. E.; Das, S. K. Uptake of all-trans retinoic acid-containing aerosol by inhalation to lungs in a guinea pig model system—A pilot study. *Exp. Lung Res.* **2010**, *36* (10), 593–601.

(45) Desai, T. R.; Finlay, W. H. Nebulization of niosomal all-trans-retinoic acid: an inexpensive alternative to conventional liposomes. *Int. J. Pharm.* **2002**, *241* (2), 311–317.

(46) Nimmano, N.; Somavarapu, S.; Taylor, K. M. Aerosol characterisation of nebulised liposomes co-loaded with erlotinib and genistein using an abbreviated cascade impactor method. *Int. J. Pharm.* **2018**, *542* (1–2), 8–17.

(47) Elzoghby, A. Editorial (Thematic Issue: Nanocarriers Based on Natural Polymers as Platforms for Drug and Gene Delivery Applications). *Curr. Pharm. Des.* **2016**, *22* (22), 3303–3304.

(48) Meenach, S. A.; Anderson, K. W.; Zach Hilt, J.; McGarry, R. C.; Mansour, H. M. Characterization and aerosol dispersion performance of advanced spray-dried chemotherapeutic PEGylated phospholipid particles for dry powder inhalation delivery in lung cancer. *Eur. J. Pharm. Sci.* **2013**, *49* (4), 699–711.

(49) Lebbardt, T.; Roesler, S.; Uusitalo, H. P.; Kissel, T. Surfactant-free redispersible nanoparticles in fast-dissolving composite microcarriers for dry-powder inhalation. *Eur. J. Pharm. Biopharm.* **2011**, *78* (1), 90–6.

(50) Li, Y. Z.; Sun, X.; Gong, T.; Liu, J.; Zuo, J.; Zhang, Z. R. Inhalable microparticles as carriers for pulmonary delivery of thymopentin-loaded solid lipid nanoparticles. *Pharm. Res.* **2010**, *27* (9), 1977–86.

(51) Marchiori, M.; Ourique, A.; Silva, C. d. B.; Raffin, R.; Pohlmann, A.; Guterres, S.; Beck, R. Spray-dried powders containing tretinoin-loaded engineered lipid-core nanocapsules: development and photostability study. *J. Nanosci. Nanotechnol.* **2012**, *12* (3), 2059–2067.

(52) Yergey, A. L.; Blank, P. S.; Cologna, S. M.; Backlund, P. S.; Porter, F. D.; Darling, A. J. Characterization of hydroxypropyl-beta-cyclodextrins used in the treatment of Niemann-Pick Disease type C1. *PLoS One* **2017**, *12* (4), No. e0175478.

(53) Morais, W. A.; Barros Neto, B. c. d.; Cavalcanti, I. M. F.; Xavier Junior, F. H.; Santos-Magalhães, N. S.; Maciel, M. A. M. Coencapsulation of trans-Dehydrocrotonin and trans-Dehydrocrotonin:hydroxypropyl-β-cyclodextrin into Microparticles. *J. Braz. Chem. Soc.* **2017**, *28*, 1494–1505.

(54) LeClair, D. A.; Cranston, E. D.; Xing, Z.; Thompson, M. R. Evaluation of excipients for enhanced thermal stabilization of a human type 5 adenoviral vector through spray drying. *Int. J. Pharm.* **2016**, *506* (1–2), 289–301.

(55) Chen, L.; Okuda, T.; Lu, X.-Y.; Chan, H.-K. Amorphous powders for inhalation drug delivery. *Adv. Drug Delivery Rev.* **2016**, *100*, 102–115.

(56) Laaksonen, T.; Liu, P.; Rahikkala, A.; Peltonen, L.; Kauppinen, E. I.; Hirvonen, J.; Jarvinen, K.; Raula, J. Intact nanoparticulate indomethacin in fast-dissolving carrier particles by combined wet milling and aerosol flow reactor methods. *Pharm. Res.* **2011**, *28* (10), 2403–11.

(57) O'Connor, G.; Krishnan, N.; Fagan-Murphy, A.; Cassidy, J.; O'Leary, S.; Robertson, B. D.; Keane, J.; O'Sullivan, M. P.; Cryan, S.-A. Inhalable poly (lactic-co-glycolic acid) (PLGA) microparticles encapsulating all-trans-Retinoic acid (ATRA) as a host-directed, adjunctive treatment for Mycobacterium tuberculosis (Mtb) infection. *Eur. J. Pharm. Biopharm.* **2019**, *134*, 153.

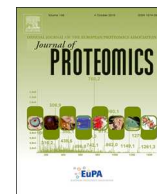
(58) Peters, B. H.; Staels, L.; Rantanen, J.; Molnar, F.; De Beer, T.; Lehto, V. P.; Ketolainen, J. Effects of cooling rate in microscale and pilot scale freeze-drying - Variations in excipient polymorphs and protein secondary structure. *Eur. J. Pharm. Sci.* **2016**, *95*, 72–81.

(59) Martinelli, F.; Balducci, A. G.; Kumar, A.; Sonvico, F.; Forbes, B.; Bettini, R.; Buttini, F. Engineered sodium hyaluronate respirable dry powders for pulmonary drug delivery. *Int. J. Pharm.* **2017**, *517* (1), 286–295.

(60) Amaro, M. I.; Tewes, F.; Gobbo, O.; Tajber, L.; Corrigan, O. I.; Ehrhardt, C.; Healy, A. M. Formulation, stability and pharmacokinetics of sugar-based salmon calcitonin-loaded nanoporous/nanoparticulate microparticles (NMPs) for inhalation. *Int. J. Pharm.* **2015**, *483* (1–2), 6–18.

(61) Wang, Y.; Kho, K.; Cheow, W. S.; Hadinoto, K. A comparison between spray drying and spray freeze drying for dry powder inhaler formulation of drug-loaded lipid-polymer hybrid nanoparticles. *Int. J. Pharm.* **2012**, *424* (1–2), 98–106.

- (62) Wong, J.; Lin, Y. W.; Kwok, P. C.; Niemela, V.; Crapper, J.; Chan, H. K. Measuring Bipolar Charge and Mass Distributions of Powder Aerosols by a Novel Tool (BOLAR). *Mol. Pharmaceutics* **2015**, *12* (9), 3433–40.
- (63) Zia, V.; Rajewski, R. A.; Stella, V. J. Effect of cyclodextrin charge on complexation of neutral and charged substrates: comparison of (SBE)7M-beta-CD to HP-beta-CD. *Pharm. Res.* **2001**, *18* (5), 667–73.
- (64) Chen, L.; Sha, X.; Jiang, X.; Chen, Y.; Ren, Q.; Fang, X. Pluronic P105/F127 mixed micelles for the delivery of docetaxel against Taxol-resistant non-small cell lung cancer: optimization and in vitro, in vivo evaluation. *Int. J. Nanomed.* **2013**, *8*, 73.
- (65) Zhang, Y.; Peng, L.; Chu, J.; Zhang, M.; Sun, L.; Zhong, B.; Wu, Q. pH and redox dual-responsive copolymer micelles with surface charge reversal for co-delivery of all-trans-retinoic acid and paclitaxel for cancer combination chemotherapy. *Int. J. Nanomed.* **2018**, *13*, 6499.
- (66) Patel, A. R.; Chougule, M.; Singh, M. EphA2 targeting pegylated nanocarrier drug delivery system for treatment of lung cancer. *Pharm. Res.* **2014**, *31* (10), 2796–2809.
- (67) Costabile, G.; d'Angelo, I.; di Villa Bianca, R. d. E.; Mitidieri, E.; Pompili, B.; Del Porto, P.; Leoni, L.; Visca, P.; Miro, A.; Quaglia, F. Development of inhalable hyaluronan/mannitol composite dry powders for flucytosine repositioning in local therapy of lung infections. *J. Controlled Release* **2016**, *238*, 80–91.
- (68) Choi, S. H.; Byeon, H. J.; Choi, J. S.; Thao, L.; Kim, I.; Lee, E. S.; Shin, B. S.; Lee, K. C.; Youn, Y. S. Inhalable self-assembled albumin nanoparticles for treating drug-resistant lung cancer. *J. Controlled Release* **2015**, *197*, 199–207.
- (69) Lv, S.; Tang, Z.; Li, M.; Lin, J.; Song, W.; Liu, H.; Huang, Y.; Zhang, Y.; Chen, X. Co-delivery of doxorubicin and paclitaxel by PEG-polypeptide nanovehicle for the treatment of non-small cell lung cancer. *Biomaterials* **2014**, *35* (23), 6118–6129.



Assessment of candidate biomarkers in paired saliva and plasma samples from oral cancer patients by targeted mass spectrometry

Lang-Ming Chi^{a,1}, Yung-Chin Hsiao^{b,c,1}, Kun-Yi Chien^{b,d,1}, Szu-Fan Chen^b, Yao-Ning Chuang^b, Shih-Yu Lin^b, Wei-Shun Wang^b, Ian Yi-Feng Chang^b, Chi Yang^b, Lichieh Julie Chu^{b,c}, Wei-Fan Chiang^{e,f}, Chih-Yen Chien^{g,h}, Yu-Sun Chang^{b,i}, Kai-Ping Chang^{b,i,**}, Jau-Song Yu^{b,c,d,j,*}

^a Clinical Proteomics Core Laboratory, Chang Gung Memorial Hospital, Taoyuan, Taiwan

^b Molecular Medicine Research Center, Chang Gung University, Taoyuan, Taiwan

^c Liver Research Center, Chang Gung Memorial Hospital, Linkou, Taiwan

^d Department of Biochemistry and Molecular Biology, College of Medicine, Chang Gung University, Taoyuan, Taiwan

^e Department of Oral and Maxillofacial Surgery, Chi-Mei Medical Center, Liouying, Tainan, Taiwan

^f School of Dentistry, National Yang Ming University, Taipei, Taiwan

^g Department of Otolaryngology, Kaohsiung Chang Gung Memorial Hospital, Kaohsiung, Taiwan

^h College of Medicine, Chang Gung University, Taoyuan, Taiwan

ⁱ Department of Otolaryngology-Head, Department of Neck Surgery, Chang Gung Memorial Hospital, Linkou, Taiwan

^j Research Center for Food and Cosmetic Safety, Research Center for Chinese Herbal Medicine, College of Human Ecology, Chang Gung University of Science and Technology, Taoyuan, Taiwan

ARTICLE INFO

Keywords:

Oral cancer
Saliva
Plasma
Biomarker
Quantification
MRM-MS
SISCAPA-MRM

ABSTRACT

For oral cancer, numerous saliva- and plasma-derived protein biomarker candidates have been discovered and/or verified; however, it is unclear about the behavior of these candidates as saliva or plasma biomarkers. In this study, we developed two targeted assays, MRM and SISCAPA-MRM, to quantify 30 potential biomarkers in both plasma and saliva samples collected from 30 healthy controls and 30 oral cancer patients. Single point measurements were used for target quantification while response curves for assay metric determination. In comparison with MRM assay, SISCAPA-MRM effectively improved (> 1.5 fold) the detection sensitivity of 11 and 21 targets in measurement of saliva and plasma samples, respectively. The integrated results revealed that the salivary levels of these 30 selected biomarkers weakly correlated ($r < 0.2$) to their plasma levels. Five candidate biomarkers (MMP1, PADI1, TNC, CSTA and MMP3) exhibited significant alterations and disease-discriminating powers (AUC = 0.914, 0.827, 0.813, 0.77, and 0.753) in saliva sample; nevertheless, no such targets could be found in plasma samples. Our data support the notion that saliva may be more suitable for the protein biomarker-based detection of oral cancer, and the newly developed SISCAPA-MRM assay could be applied to verify multiple oral cancer biomarker candidates in saliva samples.

Significance: In this work we systematically determined the abundance of 30 selected targets in the paired saliva and plasma samples to evaluate the utility of saliva and plasma samples for protein biomarker-based detection of oral cancer. Our study provides significant evidence to support the use of saliva, but not blood samples, offer more opportunity to achieve the success of protein biomarker discovery for oral cancer detection.

1. Introduction

Oral cavity cancer is a major worldwide health problem with high prevalence and mortality. Oral squamous cell carcinoma (OSCC) accounts for $> 90\%$ of oral cavity cancer cases. Although conventional

survey policy and therapy regimens of surgery and anticancer drug treatment have improved, the survival outcome of OSCC patients has not significantly improved in recent decades. The main reasons for poor outcome are delay diagnosis of lesions in advanced stages, secondary cancer occurrence, local recurrence, and metastasis [1–3].

* Correspondence to: J. Yu, Department of Cell and Molecular Biology, College of Medicine, Chang Gung University, Taoyuan, Taiwan.

** Correspondence to: K. Chang, Department of Otolaryngology-Head, Department of Neck Surgery, Chang Gung Memorial Hospital, Linkou, Taiwan.

E-mail addresses: dr.kpchang@gmail.com (K.-P. Chang), yusong@mail.cgu.edu.tw (J.-S. Yu).

¹ These authors contribute equally to this work.

<https://doi.org/10.1016/j.jprot.2019.103571>

Received 3 June 2019; Received in revised form 26 October 2019; Accepted 30 October 2019

Available online 02 November 2019

1874-3919/© 2019 Elsevier B.V. All rights reserved.

Epidemiological studies have shown that the 5-year survival rates of OSCC patients in stages I, II, III and IV are 72–90%, 39–85%, 27–70% and 12–50%, respectively [1,3,4]. Therefore, better strategies for detecting early-stage OSCC and/or predicting the aggressiveness of tumor lesions are urgently needed to improve the diagnosis and treatment of OSCC.

Body fluid-accessible biomarkers hold potential for detecting early-stage cancers, which are often manageable and curable. Serum and plasma are the major sample types in routine clinical practice for disease screening, diagnosis, and monitoring. They are different blood matrices imposing different considerations (regarding pre-analytical and analytical methods) and detection tendencies [5]. For instance, a team effort made by the HUPO Plasma Proteome Project (HUPO PPP) had found the dramatic differences in peptide contents between serum and plasma samples, presumably due to various ex vivo processes occur during processing of venous blood into serum, leading to neogeneration of many peptides [6]. Based on this finding, the Specimens Committee of HUPO PPP concluded that plasma is preferable to serum, due to less degradation ex vivo, for certain peptidomic studies [7]. For oral cavity disease, saliva is the biofluid most proximal to oral lesions, and can be obtained easily and non-invasively [8,9]. By a meta-analysis, the usefulness of the salivary biomarkers for the OSCC detection has been suggested [10]. During the past two decades, numerous candidate biomarkers for OSCC have been discovered by different laboratories using serum, plasma and/or saliva specimens, including proteins, RNAs, DNAs, metabolites and exosomes [11–16]. However, their clinical utilities for OSCC detection and prognostic prediction remain to be further validated. For example, Wang et al. explored and showed the potential of tumor-specific DNA (somatic mutations or human papillomavirus genes) in the saliva and plasma as a valuable biomarker for detection of head and neck squamous cell carcinomas (93 cases in this study) [17]. In addition, Gleber-Netto et al. evaluated the discriminatory power of salivary transcriptomic (7 mRNAs) and proteomic (2 proteins) biomarkers in differentiating OSCC cases from controls and potentially malignant oral disorders (180 cases in this study) and concluded the combination of mRNA and protein markers is of great value for OSCC detection [18].

Recently, we have reported the verification of 49 candidate OSCC biomarkers in 460 saliva samples using multiple reaction monitoring-mass spectrometry (MRM-MS) assays [19], as well as the development of a 24-plex SISCAPA-MRM (stable isotope standards and capture by anti-peptide antibodies coupled with MRM-MS) assay for verifying OSCC candidate biomarkers in saliva samples [20]. For those 49 candidate biomarkers selected for our previous verification study, which were prioritized from 302 proteins examined in 277 papers with small-size clinical specimens, our literature mining revealed that 23 targets had been quantified in plasma/serum specimens but only 6 targets were measured in saliva samples (see Table S2 in Ref. [20]). This observation indicates the previous preference of using blood samples for measuring OSCC biomarkers. Although studies from our and other groups have shown the high potential of specific salivary proteins for OSCC detection, to our knowledge, only a few studies explored the behavior of biomarker candidates as saliva or plasma biomarkers in the same cohort. A recent study verified the serum and salivary levels of chemerin and MMP-9 in OSCC and showed that the elevated levels of MMP-9 (in saliva) and chemerin (in both saliva and serum) might be considered as diagnostic biomarkers [21]. In contrast to consistent changes of chemerin in serum and saliva samples, the inverse changes of serum and salivary EGFR were observed in OSCC patients compared with health subjects [22]. Moreover, Lee et al. measured 14 cytokines in both plasma and saliva samples from the same individuals using Luminex Bead-based multiplex assay and found that the correlation between saliva and plasma biomarkers in OSCC was weak [23].

Targeted mass spectrometry has recently been demonstrated as a robust technology platform for identifying and quantifying multiple proteins in complex biological samples for disease biomarker discovery

and verification. The MRM-MS assay is a targeted acquisition technique capable of verifying the presence and abundance of > 100 candidates of interest in a single analysis [24–27]. Employing spiked-in, stable heavy isotope-labeled peptides with known amounts as a standard, liquid chromatography (LC)-MRM-MS measurements enable sensitive, reproducible and specific quantification of 100 or more peptide features in complex biological matrices [28,29]. Further coupling peptide immunoaffinity enrichment with LC-MRM-MS analyses, known as SISCAPA-MRM [30] or immuno-MRM [31,32], can improve the sensitivity and specificity of MRM-MS assays in quantitatively measuring disease biomarkers and cellular signaling proteins.

Although a few studies have explored the behavior of biomarker candidates as saliva or plasma biomarkers in the same cohort, most of them are cytokines [23], and only three proteins (MMP-9, chemerin and EGFR) other than cytokines were investigated [21,22]. Since many cytokines are known to be also activated in non-cancer, inflammatory conditions, a more comprehensive blood/saliva comparative study of biomarker candidates other than cytokines should benefit future development of clinically useful OSCC biomarkers. In the present study, we established two types of targeted MS assays for 30 potential OSCC protein biomarkers selected from the literature and our in-house studies [19,20], and then applied these assays to determine the abundance of selected targets in paired saliva and plasma samples from 30 controls and 30 OSCC cases. Because various ex vivo degradation processes are highly enhanced in serum compared to plasma samples, which might have a strong effect on the peptide-based targeted MS assays [7], we thus chose the paired plasma/saliva, but not serum/saliva samples for this comparative study. Our data demonstrated the superiority of SISCAPA-MRM versus MRM assay for quantifying larger numbers of selected targets in both saliva and plasma samples, and showed that both methods could reliably quantify more targets in saliva than plasma samples. More importantly, we found that many candidate biomarkers were significantly elevated in saliva, but not paired plasma samples, from OSCC patients.

2. Materials and methods

2.1. Study subjects and sample collection

Thirty individuals with no signs of cancer (healthy controls) and 30 OSCC patients were enrolled at Chang Gung Memorial Hospital (Linkou, Taiwan) with Institutional Review Board approval (IRB No. 102-5685A3). All subjects signed an informed consent form to participate and permit the use of plasma/saliva samples collected before treatment. The demographic characteristics of these subjects are summarized in Supplemental Table S1. All experiments were performed in accordance with the approved guidelines. The plasma and saliva samples from the donors were collected simultaneously in the morning or afternoon. One hour before collection at least, the donors avoided eating, drinking, smoking, and using oral hygiene products for collecting saliva samples. Before saliva collection, donors were asked to rinse the mouth with clean water. The passive drooled saliva samples from the donors were collected using 15-ml sterile centrifuge tubes, and the obtained saliva samples were centrifuged at 3000 × g for 15 min at 4 °C. The resulting supernatant was collected, treated with a protease inhibitor cocktail (v/v 1:50, Sigma, St. Louis, MO, US), and stored in aliquots at –80 °C. Whole blood sample were collected into commercially available EDTA-containing tube, and then centrifuged at 2000 × g for 15 min at 4 °C. The resulting supernatant was collected, treated with a protease inhibitor cocktail (v/v 1:50, Sigma, St. Louis, MO, US), and stored in aliquots at –80 °C. The time from collection to centrifugation for all samples were within 90 min. Protein concentrations in saliva and plasma samples were determined using a BCA assay kit (Pierce Chemical, Rockford, IL, US) according to the manufacturer's protocol.

2.2. Selection of protein targets and surrogate peptides

Protein targets were selected from literature survey and prioritized according to their clinical and scientific relevance as OSCC-related biomarker candidates, including 1) the number of articles; 2) the consistency in the differential expression under two different conditions (cancer versus healthy control) among multiple studies; and 3) detection in multiple sample types (tissue and body fluids) of OSCC. Detailed descriptions of the 30 selected targets are summarized in Supplemental Table S2. Thirty surrogate tryptic peptides representing these 30 proteins (one peptide for each target protein) were selected as previously described [19]. Briefly, the list of tryptic peptides was generated in silico by the MRMPilot software (version 2.1; AB-Sciex, Foster, CA, US) and further selected according to the following criteria: (a) peptides without terminal RP and KP sequences that could potentially lead to missed cleavages; (b) unique peptides containing 8 to 23 residues without any known post-translational modification sites; (c) peptides without chemically reactive amino acids (such as Cys, Met) and unstable sequences (such as NG, DG, QG, and N-ter Q). (d) peptides containing more hydrophilic, charged, or branched amino acids and/or proline residue in consideration of antigenicity for anti-peptide antibody production. However, for which no suitable peptide fully fitted in the above criteria, we reluctantly allowed the presence of unstable sequences (NG, DG, QG or N-ter Q). The uniqueness of these selected peptides was further checked via a BLAST search with human protein database of UniProt. The sequence and mass values of the surrogate peptides and their heavy version are summarized in Supplemental Table S3.

2.3. Peptide synthesis

Synthetic (light) peptides were purchased from Kelowna International Scientific (Taipei, Taiwan). The heavy version of [$^{13}\text{C}_6$ $^{15}\text{N}_2$]Lys- and [$^{13}\text{C}_6$ $^{15}\text{N}_4$]Arg-coded proteotypic peptides, used as stable isotope standard (SIS) peptides, were synthesized and purified at the UVic-Genome BC Proteomics Centre (Victoria, BC, Canada). The purity of synthetic stable isotope-labeled peptides was at least 90%, and in most cases was > 95%. The powder of each synthetic peptide was resolved in 0.1% FA and divided into aliquots of 1 nmol. The aliquots were then dried by Speed-Vac and stored at -80°C .

2.4. Production and characterization of mouse monoclonal anti-peptide antibodies

The synthetic peptides with a C-terminal cysteine or GSGC linker (purchased from Kelowna International Scientific) were chemically conjugated to a carrier protein and used as the antigens. Mouse monoclonal anti-peptide antibodies against 30 target proteins were produced and characterized according to previously described procedures [20], including selection of the signature peptide for each target protein, preparation of peptide-carrier protein conjugates, mouse immunization, enzyme-linked immunosorbent assay (ELISA)-based monoclonal antibody screening, measurement of antibody-peptide antigen binding kinetics using surface plasmon resonance, and screening of the peptide-capture ability of produced antibodies by immuno-affinity enrichment-conjugated qTOF MS analysis. The characteristics of these 30 mouse monoclonal anti-peptide antibodies are described in Supplemental Table S4.

2.5. Sample preparation

Based on the BCA assay, the total protein concentration of each sample was defined (Supplemental Table S5). Triplicate aliquots of each sample containing 30 μg (saliva) or 120 μg (plasma) proteins was diluted with an appropriate amount (as indicated in Supplemental Table

S5) of 100 mM Tris-HCl buffer at pH 8.5 (Sigma) to achieve the final volume of 60 μL and then mixed with 20 μL of 20% sodium deoxycholate (DOC; Sigma). The samples were heated at 100°C for 5 mins, and the denatured proteins were then reduced with 5 mM Tris(2-carboxyethyl)phosphine hydrochloride (TCEP; Sigma) at 60°C for 30 min and alkylated with 10 mM iodoacetamide (Sigma) at 37°C for 30 min in the dark. The samples were further diluted with 100 mM Tris-HCl buffer to achieve 1% DOC before adding trypsin (Agilent, Santa Clara, CA, US) to the substrate protein solution. At an enzyme to substrate ratio (w/w) of 1:25, the digestion was performed at 37°C overnight, and then stopped by boiling for 15 min. To remove DOC, the samples were adjusted to 0.1% trifluoroacetic acid (TFA; Alfa Aesar, Haverhill, MA, US) and 0.4% formic acid (FA; J.T. Baker, Phillipsburg, NJ, US) and then centrifuged at $15,000 \times g$ for 10 min at room temperature. Afterwards, the supernatants were mixed with a set of SIS peptides containing 90 fmol (for saliva) or 360 fmol (for plasma) of each target peptide and then desalted by solid-phase extraction (SPE) equipment using Waters Oasis HLB 96-well plates (10 mg) (Waters, Milford, MA, US), as described previously [20]. Finally, the aliquots of saliva (25 μg) and plasma (100 μg) were taken for target peptide enrichment using anti-peptide antibodies coupled with LC-MRM-MS measurement (SISCAPA-MRM). The residual samples were lyophilized and stored at -20°C until the analysis of LC-MRM-MS (MRM).

2.6. Automated and multiplexed SISCAPA assay

A KingFisher magnetic particle processor was used for automated handling of the multiplexed SISCAPA assay against 30 target peptides, as described previously [20]. Briefly, the slurry of 200 μL protein G magnetic beads (GE Healthcare, Little Chalfont, UK) was washed and suspended in phosphate buffered saline (PBS) with 0.03% 3-[(3-cholamidopropyl)dimethylammonio]-1-propanesulfonate (CHAPS) (USB Corp., Cleveland, OH, US). The pre-washed beads were incubated with 1 μg of specific anti-peptide antibodies for each of 30 analytes (Supplemental Table S4) for 1 h under a medium mixing condition, and then transferred to next plate which contained trypsin-digested saliva or plasma samples for a 2-h incubation. The beads were washed twice with 200 μL of PBS (plates 4 and 5) and once with $1/10 \times$ PBS. The captured peptides were then eluted in plate 7 which contained 50 μL of 5% acetic acid (J.T. Baker) and 70% ACN (the elution buffer). The eluted samples were lyophilized and stored at -20°C until further analysis by LC-MRM-MS.

2.7. LC-MRM-MS analysis

A nanoACQUITY HPLC system equipped with a nanoACQUITY UPLC C18 column (100 $\mu\text{m} \times 100 \text{ mm}$, 1.7- μm particle size; Waters) was coupled with a triple quadrupole mass spectrometer (QTRAP 5500; AB Sciex, Redwood, CA, US). The lyophilized samples were rehydrated with appropriate amount of 0.1% formic acid to achieve the concentration of 0.25 $\mu\text{g}/\mu\text{L}$, and 4 μL of each eluate was injected onto the LC-MRM-MS system. After 20-min injection of sample with 3% buffer B, samples were separated at a flow rate of 0.4 $\mu\text{L}/\text{min}$ with a 38-minute linear gradient from 3% to 22% of buffer B, a 5-minute linear gradient from 22% to 30% of buffer B, a 5-minute flat of 30% buffer B, and a final 2-minute linear gradient from 30% to 95% of buffer B, followed by a re-generation with a 2-minute linear gradient from 95% to 5% of buffer B and a 5-minute flat of 5% buffer B. The resolved fractions were applied to an AB/MDS Sciex 5500 QTRAP with a nano-electrospray ionization source controlled by Analyst 1.5.1 software (all from AB Sciex). The acquisition parameters (collision energy, CE; declustering potential, DP; entrance potential, EP; collision entrance potential, CEP; and collision exit potential, CXP) for each target peptides were experimentally determined as described in our previous studies [19,20]. The instrument setting of acquisition methods: ion spray voltage,

2300 V; curtain gas setting, 20 psi (UHP nitrogen); interface heater temperature, 150 °C; auto-sampler temperature, 4 °C; MS operating pressure, 1.1×10^{-5} Torr; Q1 and Q3 were set to unit resolution (0.6–0.8 Da full width at half height). A scheduled MRM option using three MRM ion pairs per peptide (Supplemental Table S3) was used for all data acquisition with a target cycle time of 1.5 s and a 6-min scheduled MRM detection window. As the overlapping number of transitions ≤ 72 transitions, the 1.5-seconds cycle time would offer a dwell time ≥ 20 msec per transition in our experiments. The triplicate samples prepared from each clinical specimen were continuously subjected to LC-MRM analysis, and each sample run was separated by two wash runs with a short gradient (from 3% to 95% ACN within 30 mins).

2.8. Generation of response curves

Bulk saliva or plasma protein digests were prepared as background matrices. As shown in Supplemental Table S6, the digests were mixed with a constant amount of a set of light peptides and a variable amount of heavy peptides for the generation of reverse response curves. The samples with > 2000 -fold range of levels from 0.024 to 50 fmol/ μ g (MRM in plasma), from 0.01 to 40 fmol/ μ g (MRM in saliva), from 0.0061 to 12.5 fmol/ μ g (SISCAPA-MRM in plasma), and from 0.00976 to 20 fmol/ μ g (SISCAPA-MRM in saliva) along with a zero sample were subjected to MRM and SISCAPA-MRM analyses, respectively. The quintuplet samples of each level were prepared, and the data acquisition was sequentially performed from zero sample to the highest concentration sample followed by a blank sample (0.4% FA) for one replicate. Each sample run was separated by two wash runs with a short gradient (from 3% to 95% ACN within 30 mins). According to the linear regression of log-to-log scales, the data point nearest to the turning point of the slope (i.e. the point at which the slope begins to flatten out) was determined as the low end of curve. The quantifier ion (a single transition per peptide) was selected according to the following criteria: (1) lower value of LOD and/or CV% obtained in the response curve, and (2) lower interference status in clinical samples.

2.9. Bead-based suspension immunoassay for the detection of MMP1, MMP3, LGALS3BP and TNC

Protein concentration of MMP-1, MMP-3, LGALS3BP, and tenascin (TNC) in saliva and plasma specimens were determined by Luminex multiplex assay kit (R&D Systems, Minneapolis, MN, US) according to the manufacturer's protocol. By using filter-bottom 96-well microplates (Millipore, Burlington, MA, US) and vacuum manifold, the recommend protocols were performed automatically. At the end of all reactions, the beads were suspended in assay buffer and analyzed using the Bio-Plex 200 system (Bio-Rad Laboratories, Hercules, CA, US). The detection range was 36.95–26,939 pg/mL for MMP-1, 27.6–60,364 pg/mL for MMP-3, 249.64–545,970 pg/mL for LGALS3BP, and 33.67–24,545 pg/mL for TNC. Saliva and plasma specimens were respectively analyzed in 5-fold and 20-fold dilution, and the detected protein concentration lower than the detection limit was considered as zero.

2.10. Data analysis and statistical methods

All MRM data were processed using Skyline software based on the defined precursor (Q1) and fragment (Q3) mass list of the target peptides [33]. All spectra were manually double-checked for confident quantitative results, and the unqualified signals were recorded as zero concentration for the quantification of clinical samples. The single point measurements were used for the quantification of targets in clinical samples. The levels (fmol/ μ g) of the target peptides in each sample were determined as the ratio of the peak area to that of the heavy-labeled peptides, and multiplied by the known input of each heavy peptide. The concentrations (ng/mL) of target proteins were

determined as the observed levels (i.e. fmol/ μ g) multiplied by the molecular weight of each target protein and multiplied by the total protein concentration of each sample. The reverse response curves were generated for assay metric determination. The limit of detection (LOD) and lower limit of quantification (LLOQ) of each target were determined based on response curves generated using the MRM statistical software, QuaSAR, as previously reported [34]. The LLOQ was calculated as the LOD value multiplied by 3. The differences in biomarker levels between two groups were analyzed using the Mann Whitney test. The area under the receiver operating characteristic (ROC) curve (AUC) was analyzed using SPSS statistical software. Consistency between quantifications by MRM and SISCAPA-MRM assay were analyzed using linear regression. Correlations between plasma levels and saliva levels of candidate proteins were analyzed by Pearson's correlation. The statistical significance of each target in multiple comparison assay was further adjusted by Benjamini–Hochberg procedure with the false discovery rate defined as 5%.

3. Results

3.1. Establishment of 30-plex MRM and SISCAPA-MRM assays for target protein quantification in saliva and plasma samples

Based on our previous study of OSCC-related biomarker in saliva samples [19], we attempted to verify the potential of applying these biomarkers in plasma samples and compare the levels of biomarkers in both plasma and saliva samples collected from the same individuals. In this study, we adapted two approaches, MRM and SISCAPA-MRM, to quantify the protein biomarkers in both plasma and saliva samples. The MRM and SISCAPA-MRM assay methods used in this study were primarily established in our previous studies [19,20] against 24 targets, and the additional 6 targets (ENO1, MYO5A, OASL, PADI1, S100A2, and SERPINE1) with newly in-house produced anti-peptide antibodies were included for establishing the 30-plex MRM and SISCAPA-MRM assays. The sequence and mass values of the surrogate peptides and their heavy version are summarized in Supplemental Table S3. A representative run shows the intensity and liquid chromatography distribution of the 30 peptides analyzed by scheduled MRM-MS (Supplemental Fig. S1). The single chromatograms of light and heavy XICs for the 30 target peptides are shown in Supplemental Fig. S2. The characteristics of these 30 mouse monoclonal anti-peptide antibodies are described in Supplemental Table S4. After optimization of instrument parameters for peptide detection and protocols for sample preparation and immuno-enrichment, we constructed reverse response curves for the 30 target peptides using a serial dilution of heavy peptides (13 designed data points) plus a constant amount of light peptides of each target, which was mixed with saliva or plasma digest as background matrix. Limit of detection (LOD) and lower limit of quantification (LLOQ) values for 30-plex MRM and SISCAPA-MRM assays in saliva and plasma samples were determined by reference to reverse response curves. The different set points of the dynamic range and input amount of saliva or plasma digest in MRM and SISCAPA-MRM assays are detailed in Supplemental Table S6.

In consideration of the application in clinical use, we intended to use 1 μ g saliva or plasma digest for direct MRM assay. For SISCAPA-MRM measurements, 25-fold or 100-fold more digests (25 μ g saliva or 100 μ g plasma protein digests, finally) than the one used in MRM assay were tested to enhance the signals of selected targets. Therefore, we used the determined amount of digest as background matrices for MRM and SISCAPA-MRM assay response curves, respectively. The detection sensitivity (LOD and LLOQ) and linearity (slope and r^2) of assays as applied to saliva and plasma matrices are shown in Supplemental Table S7 (for MRM assay) and Supplemental Table S8 (for SISCAPA-MRM assay). The performance of the MRM and SISCAPA-MRM assays using

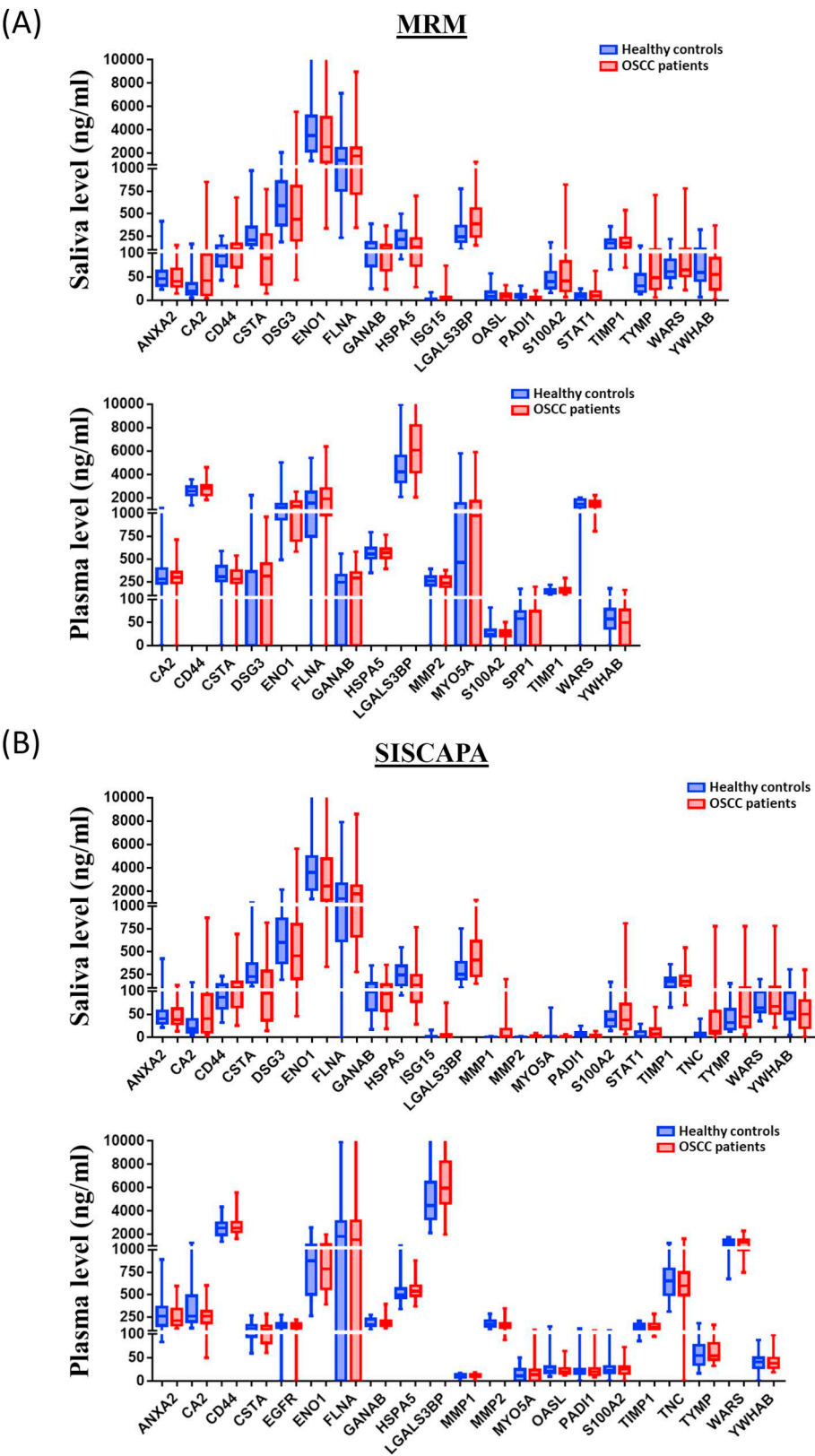


Fig. 1. Abundance of target proteins in saliva and plasma samples, determined by MRM and SISCAPA-MRM assays. (A) For MRM assay, shown here are the quantification results of 19 and 16 targets which could be measured in > 30 saliva and plasma samples among total 60 samples, respectively. (B) For SISCAPA-MRM assay, shown here are the quantification results of 22 and 21 targets which could be measured in > 30 saliva and plasma samples among total 60 samples, respectively. Box-whisker plot showing the levels of the proteins quantified in Hc (blue) and Oc group (red), presented as the upper and lower quartiles and range (box), the median value (horizontal line), and the middle 90% distribution (whisker line). (For interpretation of the references to colour in this figure legend, the reader is referred to the web version of this article.)

saliva were much better than that using plasma. As expected, SISCAPA-MRM assay showed improvement of LLOQ to its corresponding MRM assay. Applying an additional immuno-enrichment step using the anti-peptide antibodies effectively improved (> 1.5 fold) the detection sensitivity of 11 targets in saliva samples and 21 targets in plasma samples (Supplemental Table S8).

3.2. Abundance of the 30 biomarker candidates in paired saliva and plasma samples from healthy subjects and OSCC patients, determined by MRM and SISCAPA-MRM analyses

We applied the developed 30-plex MRM and SISCAPA-MRM assays to determine the levels of 30 selected candidates using single point

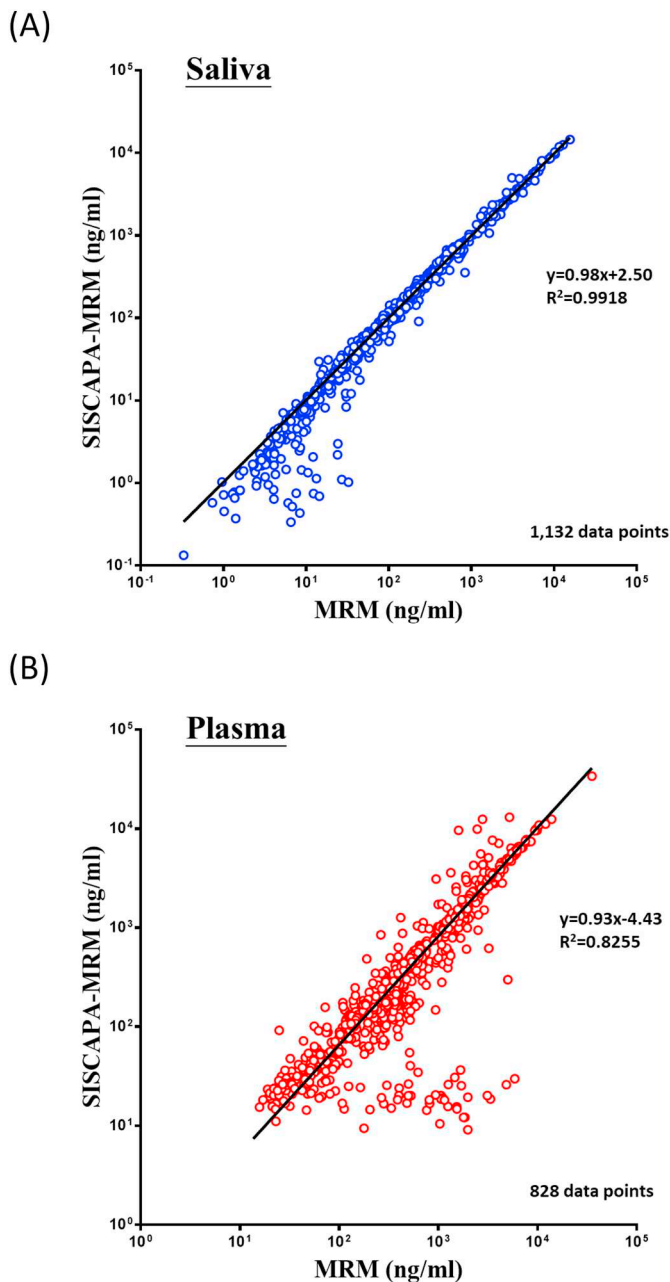


Fig. 2. Consistency analysis of target protein abundance determined by MRM versus SISCAPA-MRM assay in saliva and plasma samples. A total of 1800 data points (30 targets \times 60 samples) were obtained using MRM (or SISCAPA-MRM) assay in saliva (or plasma) samples. (A) In saliva samples, 1132 data points for target proteins that could be quantified (i.e., target protein concentration > 0) by both MRM and SISCAPA-MRM assays were used in a linear regression analysis to evaluate the consistency between measurements obtained by MRM and SISCAPA-MRM assays. The results are shown in a log-scale plot. (B) Similar analysis is shown for plasma samples, in which 828 data points were used for the analysis.

measurements in both saliva and plasma samples from each of the 30 healthy subjects and 30 OSCC patients. Of the 30 candidate biomarkers measured directly by MRM, 19 and 16 targets could be measured in > 30 saliva and plasma samples among total 60 samples, respectively (Fig. 1A). We further applied anti-peptide antibodies to capture 30 targets from larger amounts of samples (saliva samples, 25 μ g; plasma samples, 100 μ g) to improve the detection power of the established MRM assay. Consequently, 22 and 21 detectable targets could be measured in ≥ 30 saliva and plasma samples, respectively, using this

newly developed 30-plex SISCAPA-MRM assay (Fig. 1B). Quantification data for these 30 targets in paired saliva and plasma samples from the 60 individuals are detailed in Supplemental Tables S9. The measured abundance of these proteins ranged from 0.16 ng/mL (IL6) to 4175.59 ng/mL (ENO1) in saliva and from 0.57 ng/mL (ISG15) to 7475.53 ng/mL (LGALS3BP) in plasma. The dynamic range of detection of MRM and SISCAPA-MRM assays covered five orders of magnitude. In addition, an analysis of the consistency between the two MS-based quantification assays revealed a good linear correlation ($R^2 = 0.9918$) and good accuracy (slope = 0.98) in saliva samples (Fig. 2A) as well as in plasma samples ($R^2 = 0.8255$; slope = 0.93; Fig. 2B). Collectively, these results indicate that inclusion of an immuno-enrichment process prior to LC-MRM-MS analysis improves detection sensitivity while retaining detection accuracy in both saliva and plasma samples.

3.3. Relative abundance of each target in saliva and plasma samples from 60 individuals

To evaluate the relative abundance of each target in saliva and plasma samples from the 60 individuals, the log₂ ratio of the determined concentration in each sample to the mean concentration of the healthy group was calculated and displayed in Fig. 3. Among total 1800 quantitative data events (30 targets \times 60 samples) in saliva or plasma samples, the SISCAPA-MRM results showed that the levels of many candidate biomarkers, including CA2, EGFR, ISG15, MMP1, MMP2, MMP3, OASL, SERPINE1, TNC and TYMP, were elevated in saliva, but not plasma samples, from OSCC patients (Fig. 3). Similar results could be obtained from the MRM analysis, which are shown in Supplemental Fig. S3. We further analyzed the correlation between saliva levels and plasma levels of these 10 biomarkers except two targets (MMP3 and SERPINE1) which didn't have pairwise data in both saliva and plasma samples. All the eight targets, except ISG15, showed poor correlation between their saliva and plasma levels ($r < 0.2$); for ISG15, its levels in saliva and plasma exhibited positive correlation (Pearson's $r = 0.688$, $p = .0192$) although there are only 11 pairwise data points (Supplemental Fig. S4). Moreover, for all target proteins simultaneously measurable by MRM or SISCAPA-MRM in paired saliva and plasma samples, we obtained correlation r values of 0.0736 (for MRM) and 0.1358 (for SISCAPA-MRM) between saliva and plasma (Supplemental Fig. S5A and B), indicating that the determined concentrations of multiple candidate biomarkers in these paired saliva and plasma samples were very poorly correlated ($r < 0.2$). These results reveal that the plasma concentration of proteins was not reflective of saliva concentrations, and suggest that the concentration of these candidate protein biomarkers in saliva is more meaningful for oral cancer detection.

3.4. Evaluation of the discrimination power of candidate biomarkers quantified using SISCAPA-MRM

Since the SISCAPA-MRM assay was capable of greater detection sensitivity and measured more data points, we further investigated the quantitative results of SISCAPA-MRM analysis to address clinical utility of each target in use of the two biofluid sample types (saliva and plasma). Ten targets—CSTA, EGFR, HSPA5, ISG15, LGALS3BP, MMP1, MMP3, PADI1, SERPINE1, TNC—showed significant ($p < .05$) changes in saliva levels in the OSCC group compared with the healthy group (Fig. 4A & Supplemental Table S10); however, only one target (LGALS3BP) displayed a significant relative increase in levels (Oc/Hc = 1.5) in plasma (Fig. 4B & Supplemental Table S11). Concerning the multiple comparisons could affect the statistical finding, we further adjusted the statistical significance by Benjamini-Hochberg procedure and found that seven targets (CSTA, ISG15, MMP1, MMP3, PADI1, SERPINE1, and TNC) still remained significant change in saliva samples but no such targets could be found in plasma samples (Supplemental Table S12). Consequently, seven candidates elevated in saliva samples

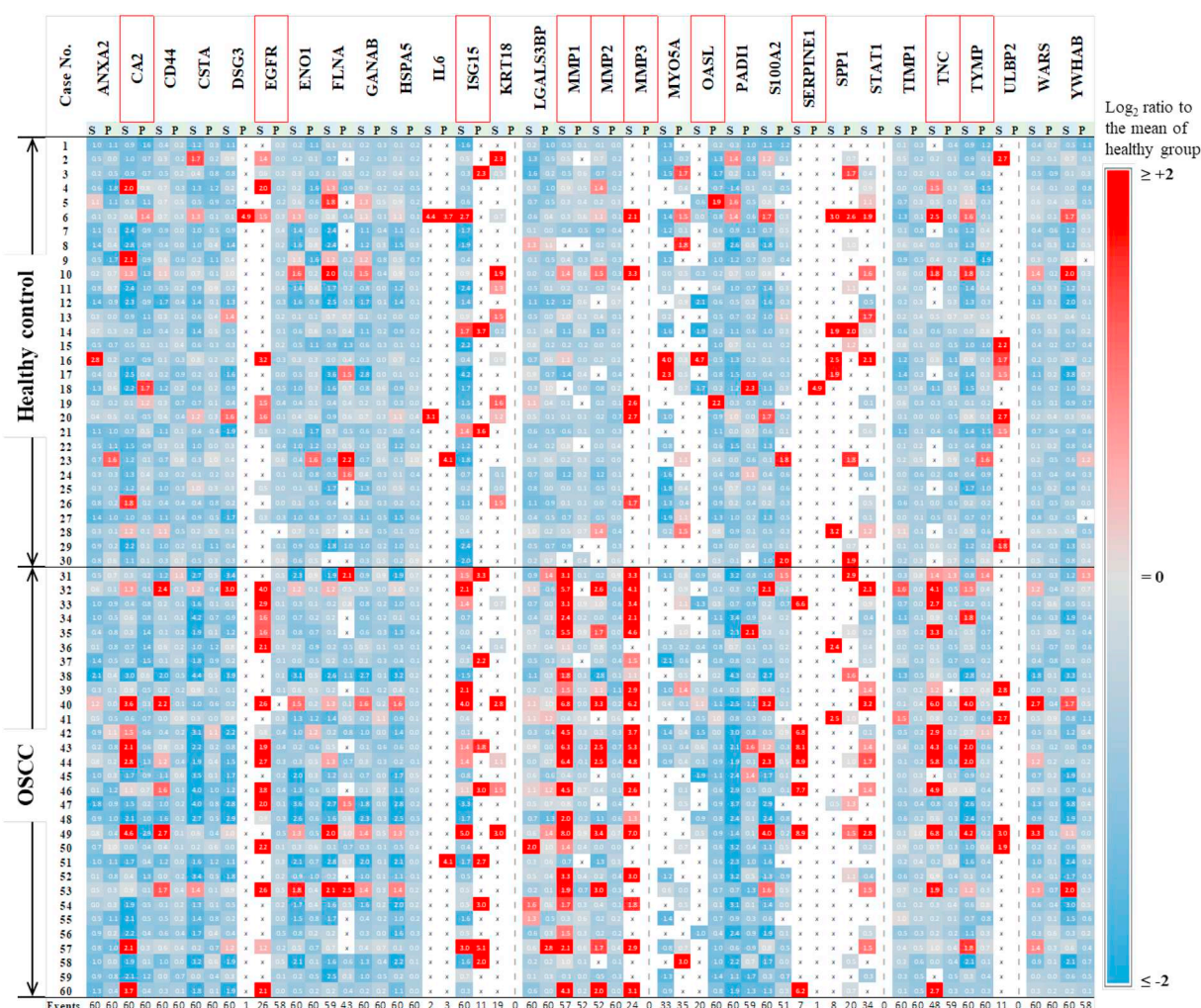


Fig. 3. Heat maps of the relative abundance of each target in saliva and plasma samples from 60 individuals. The levels of each target protein in paired saliva (S) and plasma (P) samples from each of the 30 healthy subjects and 30 OSCC patients were quantified by SISCAPA-MRM assay. For each target protein, the log₂ ratio of the determined concentration to the mean concentration of the healthy group (case numbers 1–30) was first calculated in the 60 saliva or plasma samples, and data from the 30 target proteins were then combined to generate the heat map, which illustrates significant changes in candidate proteins in OSCC patients. “X” indicates that the protein in question was not detectable in the corresponding sample, and “|” denotes the protein in question was not detectable in any sample.

of OSCC groups were selected, and their assay results are detailed in Table 1. In addition to fold-change and *p*-value, the ROC curve analysis further showed that five of the seven targets (MMP1, PADI1, TNC, CSTA and MMP3) showed AUC values being 0.914, 0.827, 0.813, 0.77 and 0.753, suggesting their good potential for further clinical validation. To further confirm the results observed by using MS-based quantification, we performed multiplexed bead-based immunoassays to quantify the protein levels of four selected targets (MMP1, MMP3, TNC and LGALS3BP) in both saliva and plasma samples. As shown in Fig. 5, the results are, in principle, consistent with those obtained using the MS-based assay, which also indicated the elevated saliva levels of three targets (MMP1, MMP3 and TNC) in OSCC cases versus healthy controls while only one target (LGALS3BP) elevated in plasma samples from OSCC cases.

4. Discussion

Detection of disease biomarkers in body fluids has great impact for disease diagnostics and treatment. Both saliva and blood samples have been widely used for oral cancer biomarker discovery, but there is limited information about the systematic comparison of disease-discriminating power of candidate protein biomarkers measured in these two biofluids. The study by Lee et al. [23] represents one such effort to

address this issue, which measured 14 cytokines and found that the levels of several cytokines, such as IL1 β , IL-6, IL-8 and TNF- α , were significantly increased in saliva from OSCC patients but showed no obvious difference in plasma samples between patient (*n* = 41) and control (*n* = 24) groups. Our current study addressed the same issue but focusing on quantification of candidate biomarkers other than cytokines (which were prioritized from a review of literatures) using in-house developed, MS-based multiplex assays. Our data showed that five candidates (MMP1, PADI1, TNC, CSTA and MMP3) with significantly altered levels and displaying high disease-discriminating power (AUC = 0.914, 0.827, 0.813, 0.77 and 0.753) were only observed in saliva, but not plasma, samples from OSCC patients (Table 1). Taken together with the findings by Lee et al. [23], these results indicate that, for OSCC, disease-caused alterations in protein biomarkers in the local microenvironment of the oral cavity may poorly be reflected in the systemic circulation. Our study highlights the importance to validate the oral cancer biomarkers in saliva, which is less invasive and close to tumor nest than blood samples.

While serum/plasma is generally regarded as one of standard specimens for evaluation of systemic alternations including malignant disease, saliva is a local infiltrate of oral cavity, respiratory tract and digestive tract. Approximate one third of the whole-saliva proteins are found in plasma, and nearly 40% of biomarker candidates discovered in

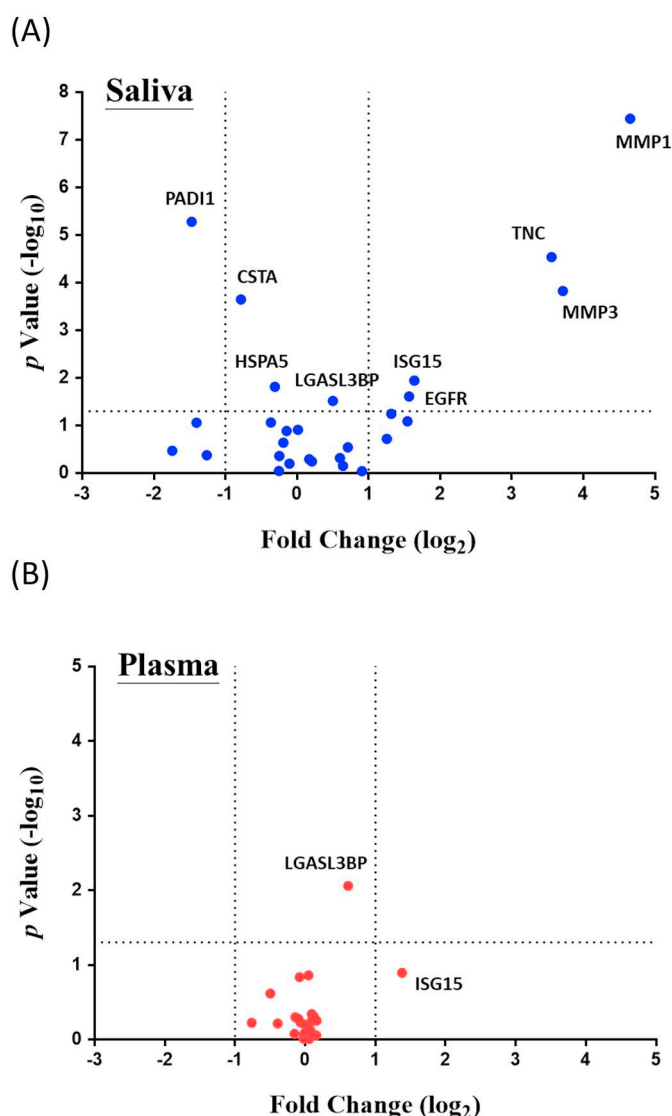


Fig. 4. Evaluation of the performance of SISCAPA-MRM-quantified candidate biomarkers in distinguishing oral cancer patients from healthy controls using saliva and plasma samples. A volcano plot (fold change vs. *p*-value) of 29 targets quantified in saliva (A) and 26 targets quantified in plasma (B) showing significant ($p < .05$) changes in nine targets in saliva and one target in plasma. The horizontal dotted line indicates $p = .05$, and the vertical dotted line denotes fold-change = 2. It is noted that the saliva level of SERPINE1 was significantly elevated in OSCC group ($p = .006$), but its fold change between healthy and OSCC group couldn't be estimated (the average concentration of SERPINE1 in healthy group was zero). Therefore, SERPINE1 is not shown in this figure.

plasma also existed in saliva [26,35,36]. However, the correlation of protein abundances between saliva and plasma was not largely explored. A previous study compared the expression levels of multiple biomarkers (27 cytokines) in plasma and saliva samples from 50 healthy adults, and only two cytokines (IL-6 and MIP-1 β) showed weak correlation ($r = 0.31$ and 0.34) between saliva and plasma [37]. We performed correlation analysis between saliva and plasma samples in the abundance levels (Supplemental Fig. S5) and relative abundance levels (Supplemental Fig. S4) and obtained similar results to support the weak correlation of protein level between saliva and plasma. However, some factors such as the variation of concentration of salivary substances affected by the collection time and dietary habits of donors have to be considered and further evaluated. In the concern of this issue, we have reported that the average variation of 90 proteins in the intraday-

and interday-collected saliva samples from the same subjects was 38% and 43%, respectively [38], suggesting that the variation of concentration of proteins in saliva samples collected via a well-controlled protocol might be small.

For biomarker discovery, the reproducibility and sensitivity of the applied assays would profoundly affect the reliability and validity of the results. The extreme dynamic range of protein concentration in plasma appears to be the major factor affecting the sensitivity of MRM assays. As expected, the detection sensitivity of many targets in both plasma and saliva was enhanced using the SISCAPA-MRM assay (Supplemental Table S8); specifically, up to 21 targets in plasma showed improvement (2.4- to 22.9-fold) in LLOQ values compared with those determined using the MRM assay. In our experimental design, 100 μ g of plasma protein (equivalent to 1–2 μ L of plasma) was used for the SISCAPA-MRM assay. Improving the LLOQ value to near sub-nanogram per milliliter levels could require \sim 1-mL plasma samples [32]. On the other hand, LLOQ values determined by SISCAPA-MRM assay were unsatisfactory in 12 targets in saliva and 2 targets in plasma (SISCAPA-MRM/MRM < 0.66; Supplemental Table S8). Lower-affinity of antigen-antibody interactions might account for this observation. Therefore, antibodies with higher capture efficiencies are recommended to achieve higher quality and sensitivity of SISCAPA-MRM assays.

In the present study, single point measurements based on the internal standards were used for the quantification of targets in clinical samples while the reverse response curves were generated for the determination of signal linearity and LOD/LLOQ corresponding to the selected peptides. The concentration ranges of 8 proteins (EGFR, IL6, KRT18, MMP2, MYO5A, SERPINE1, SPP1 and ULBP2) below the respective assay LLOQs will challenge the accuracy of the quantification results (Supplemental Tables S7, S8, S10 and S11). However, if both stable-isotope-labeled internal standards and endogenous peptides could be detected with confident peak sharp and co-elution feature, the determined values were included for quantification analysis. Among the 30 targets, 12 have been detected in saliva and/or plasma samples by immuno-based assays in previous studies (Supplemental Table S2). In comparison of our quantitative results (Supplemental Tables S10 and S11) with the concentration ranges reported (Supplemental Table S2), the levels measured by MS-based assay were similar to those by immuno-based assays for IL6 and CD44 (saliva sample), and TNC, LGALS3BP, MMP2, and SPP1 (plasma sample). However, it is quite different between MS-based and immuno-based quantifications for some proteins, such as LGALS3BP, MMP1, MMP3 (saliva sample) and CD44 (plasma sample). Percy et al. reported the concentration ranges of 158 proteins in healthy donor's saliva samples by LC-MRM assay [26]. Among the 6 target proteins measured in both our and Percy's studies, four targets (CD44, HSPA5, LGALS3BP, and TIMP1) showed similar concentrations but two targets (CSTA and ENO1) displayed different levels. The differences in method and target peptide selected for quantification, as well as the race of study subjects might contribute to the observed discrepancies between studies.

By statistical analysis and AUC value evaluation of the SISCAPA-MRM assay results, our study revealed significant increase of three proteins (MMP1, MMP3 and TNC) and decrease of two proteins (CSTA and PADI1) in saliva samples from OSCC patients (Table 1). Although sample cohort of this study is small, the salivary levels of MMP1, MMP3, and CSTA have been verified in a large cohort consisting of 460 individuals enrolled in an oral cancer screening program in our previous study, showing that MMP1 is the most highly increased protein in the OSCC group with a disease-discriminating power value (AUC) being 0.871 [19]. It has been shown that metalloproteinases, a family of multifunctional proteins, are up-regulated in various types of cancer, including oral cavity cancers [39–41]. Transcriptional assays and multiplex sandwich-ELISAs have shown that the RNA and protein levels of both MMP1 and MMP3 are highly elevated in tumor tissues and saliva from OSCC patients and display an increasing trend with higher disease stage [39]. Increases in tenascin-C (TNC) in oral cancer are

Table 1

Concentrations of seven candidate biomarkers in saliva and plasma samples, determined by SISCAPA-MRM assay.

Protein	Hc (n = 30)		Oc (n = 30)		Oc vs. Hc				
	Concentration ^a (ng/mL)	Detectable	Concentration (ng/mL)	Detectable	Fold-change ^b	p	Rank	(i/m)Q ^c	AUC
Saliva sample									
MMP1	0.784 ± 0.501	27	19.728 ± 39.983	30	25.18	< 0.0001	1	0.002	0.914
PADI1	8.591 ± 6.440	30	3.099 ± 2.902	30	0.36	< 0.0001	2	0.003	0.827
TNC	7.145 ± 8.797	20	83.967 ± 170.794	28	11.75	< 0.0001	3	0.005	0.813
MMP3	0.829 ± 2.029	5	10.865 ± 21.537	19	13.11	< 0.0001	4	0.007	0.753
CSTA	314.332 ± 223.102	30	182.679 ± 212.763	30	0.58	< 0.0001	5	0.008	0.770
SERPINE1	0.000 ± 0.000	0	5.685 ± 13.035	7	–	0.006	6	0.010	0.617
ISG15	2.368 ± 3.083	30	7.381 ± 14.804	30	3.12	0.011	7	0.012	0.689
Plasma sample									
MMP1	9.838 ± 5.023	25	11.008 ± 4.902	27	1.12	0.564	12	0.020	0.544
PADI1	24.761 ± 20.545	29	26.095 ± 21.305	30	1.05	0.764	18	0.030	0.523
TNC	669.708 ± 216.236	30	668.396 ± 310.371	29	1.00	0.633	17	0.028	0.537
MMP3	0.000 ± 0.000	0	0.000 ± 0.000	0	–	–	–	–	–
CSTA	132.910 ± 52.051	30	124.247 ± 52.917	30	0.93	0.532	11	0.018	0.548
SERPINE1	12.325 ± 67.505	1	0.000 ± 0.000	0	–	0.334	7	0.012	0.483
ISG15	0.572 ± 1.866	3	1.489 ± 3.741	8	2.60	0.128	2	0.003	0.578

^a Mean ± SD.

^b Fold change of protein levels in OSCC group over healthy control group.

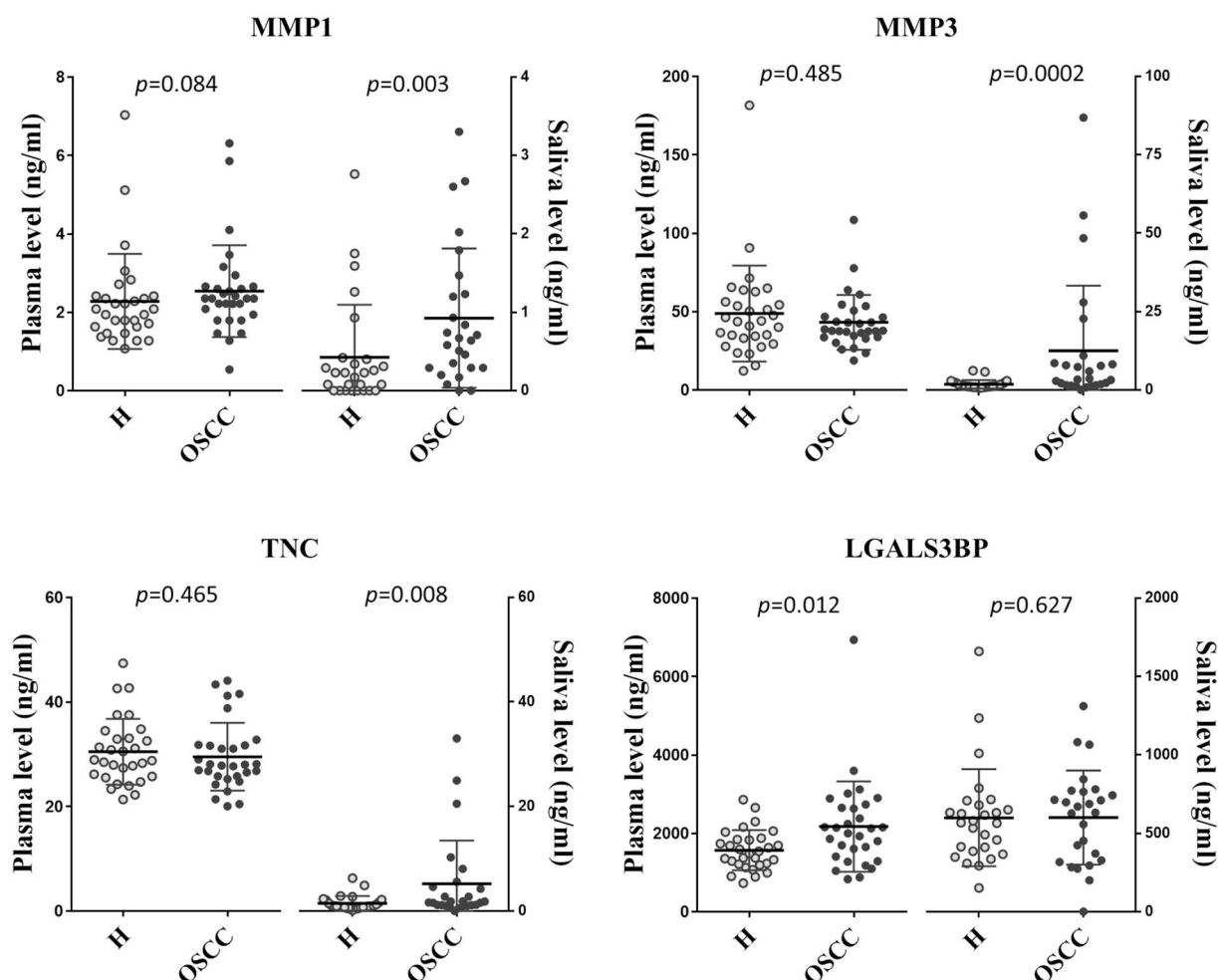
^c (i/m)Q, where i is the rank, m is the total number of tests, and Q is the false discovery rate defined as 5%; significance adjusted according to p < (i/m)Q.


Fig. 5. Quantification of four targets in plasma and saliva samples using the multiplexed bead-based immunoassay. For plasma sample, 60 samples (30 H and 30 OSCC) were diluted 20-fold with sample diluent and then subjected to the multiplexed bead-based immunoassay (R&D luminax) according to the manufacture's protocol. For saliva samples, 53 samples (27 H and 26 OSCC among 30 cases each group) remained enough amount for this analysis. The saliva samples were diluted 5-fold with sample diluent and then analyzed.

positively associated with tumor metastasis, implicating TNC in modulation of the extracellular matrix at the invasive tumor front [42]. However, no previous studies have investigated its salivary levels in OSCC patients. Cysteine protease inhibitor cystatin A (CSTA), belonging to type 1 cystatin super-family, acts as a tumor suppressor in many cancers, including esophageal, skin and Lung cancers. In head and neck cancer, overexpression of CSTA was found in tumor tissues as compared with the non-tumor part, but the risk of tumor recurrence was high in patients with low CSTA level [43,44]. PADI1, encoding peptidyl arginine deiminase type-1, was found to be down-regulated in oral cancer tissue specimens using Affymetrix cDNA arrays. PADI1 can catalyze the post-translational deamination of proteins such as filaggrin and keratins by converting arginine residues into citrulines in the last steps of epidermal differentiation, a process that may support the growth and movement of tumor cells [45,46]. Due to the small sample size tested in this study, the saliva biomarkers found in this study have to be further verified in a large cohort to clarify their clinical relevance and significance.

5. Conclusions

We have developed 30-plex MRM and SISCAPA-MRM assays for candidate OSCC biomarkers and applied these assays to compare the disease-discriminating power of selected biomarkers in paired saliva and plasma samples from 60 subjects. SISCAPA-MRM assay has higher detection sensitivity than MRM assay and can quantify more targets in both saliva and plasma samples. For most quantified targets, a very poor correlation was observed between their saliva and plasma levels. Five targets (MMP1, PADI1, TNC, CSTA and MMP3) displayed significantly altered salivary levels in OSCC patients as compared to healthy subjects with AUC = 0.914, 0.827, 0.813, 0.77 and 0.753, but none of these alterations could be observed in the plasma samples from the same subjects. Our data support the notion that saliva may be more suitable for protein biomarker-based detection of oral cancer. Moreover, the newly developed 30-plex SISCAPA-MRM assay could be used to verify the clinical utility of multiple oral cancer biomarker candidates in a large cohort of saliva samples in future studies.

Funding

This study was supported by the “Molecular Medicine Research Center, Chang Gung University” from The Featured Areas Research Center Program within the framework of the Higher Education Sprout Project by the Ministry of Education (MOE) in Taiwan. This work was also supported by grants from the Ministry of Science and Technology, Taiwan (MOST 103-2320-B-182A-014 and MOST 107-2314-B-182A-113 to LMC, MOST 107-2320-B-182-027-MY3 to YCH, MOST 106-2632-B-182-002 and MOST 106-2320-B-182-029-MY3 to JSY) and the Chang Gung Memorial Hospital, Linkou, Taiwan (CLRPD1J0011, CLRPD190019, CMRPD1H0251 to JSY, CIRPG3B0014 to KPC and CMRPG3G0501~CMRPG3G0503, CMRPG3E1132, CMRPG3C1613 to LMC).

Availability of data and material

All data generated or analyzed during this study are included in this article and its additional files. The raw files of mass spectrometry-based quantitative data have been deposited to the Peptide Atlas with the link of https://db.systemsbiology.net/sbeams/cgi/PeptideAtlas/PASS_View. Dataset title: Assessment of candidate biomarkers in paired saliva and plasma samples from oral cancer patients by targeted mass spectrometry; Dataset identifier: PASS01299; Password: HN9894s. The raw files include the four sets of response curve (MRM and SISCAPA-MRM assay in each of saliva or plasma), applications of two assays on individual samples.

Authors' contributions

LMC, YCH, and JSY contributed to analysis and interpretation of data and drafting of the manuscript. KYC contributed to acquisition of data and technical support. SFC, YNC, SYL, and WSW contributed to acquisition of data and processing of raw data. IYC, CY, and LJC contributed to statistical analysis of data. WFC, CYC, and KPC contributed to collection of clinical sample and providing clinical information. YSC, KPC and JSY contributed to study concept and design.

Ethics approval and consent to participate

This study was approved by the Institutional Review Board of Chang Gung Memorial Hospital, and all subjects signed an informed consent form to participate and permit the use of plasma/saliva samples collected before treatment.

Consent for publication

Not applicable.

Declaration of Competing Interest

The authors declare that they have no competing interests and no potential conflict of interest.

Appendix A. Supplementary data

Supplementary data to this article can be found online at <https://doi.org/10.1016/j.jprote.2019.103571>.

References

- [1] C.T. Liao, J.T. Chang, H.M. Wang, S.H. Ng, C. Hsueh, L.Y. Lee, C.H. Lin, I.H. Chen, S.F. Huang, A.J. Cheng, T.C. Yen, Analysis of risk factors of predictive local tumor control in oral cavity cancer, *Ann. Surg. Oncol.* 15 (3) (2008) 915–922.
- [2] C.T. Liao, C.Y. Lin, K.H. Fan, C. Hsueh, L.Y. Lee, H.M. Wang, S.F. Huang, I.H. Chen, C.J. Kang, S.H. Ng, C.H. Lin, Y.C. Huang, T.C. Yen, Outcome analyses of unusual site neck recurrence in oral cavity cancer, *Ann. Surg. Oncol.* 20 (1) (2013) 257–266.
- [3] W.L. Lo, S.Y. Kao, L.Y. Chi, Y.K. Wong, R.C. Chang, Outcomes of oral squamous cell carcinoma in Taiwan after surgical therapy: factors affecting survival, *J. Oral Maxillofac. Surg.* 61 (7) (2003) 751–758.
- [4] Y.J. Chen, J.T. Chang, C.T. Liao, H.M. Wang, T.C. Yen, C.C. Chiu, Y.C. Lu, H.F. Li, A.J. Cheng, Head and neck cancer in the betel quid chewing area: recent advances in molecular carcinogenesis, *Cancer Sci.* 99 (8) (2008) 1507–1514.
- [5] M. Plebani, G. Banfi, S. Bernardini, F. Bondanini, L. Conti, R. Dorizzi, F.E. Ferrara, R. Mancini, T. Trenti, Serum or plasma? An old question looking for new answers, *Clin. Chem. Lab. Med.* (2019), <https://doi.org/10.1515/cclm-2019-0719> Sep 17. pii: /j/cclm.ahead-of-print/cclm-2019-0719/cclm-2019-0719.xml. (Epub ahead of print).
- [6] G.S. Omenn, D.J. States, M. Adamski, T.W. Blackwell, R. Menon, H. Hermjakob, R. Apweiler, B.B. Haab, R.J. Simpson, J.S. Eddes, E.A. Kapp, R.L. Moritz, D.W. Chan, A.J. Rai, A. Admon, R. Aebersold, J. Eng, W.S. Hancock, S.A. Hefta, H. Meyer, Y.K. Paik, J.S. Yoo, P. Ping, J. Pounds, J. Adkins, X. Qian, R. Wang, V. Wasinger, C.Y. Wu, X. Zhao, R. Zeng, A. Archakov, A. Tsugita, I. Beer, A. Pandey, M. Pisano, P. Andrews, H. Tammen, D.W. Speicher, S.M. Hanash, Overview of the HUPO Plasma Proteome Project: results from the pilot phase with 35 collaborating laboratories and multiple analytical groups, generating a core dataset of 3020 proteins and a publicly-available database, *Proteomics* 5 (13) (2005) 3226–3245.
- [7] A.J. Rai, C.A. Gelfand, B.C. Haywood, D.J. Warunek, J. Yi, M.D. Schuchard, R.J. Mehlig, S.L. Cockrill, G.B. Scott, H. Tammen, P. Schulz-Knappe, D.W. Speicher, F. Vitzthum, B.B. Haab, G. Siest, D.W. Chan, HUPO Plasma Proteome Project specimen collection and handling: towards the standardization of parameters for plasma proteome samples, *Proteomics* 5 (13) (2005) 3262–3277.
- [8] T. Pfaffe, J. Cooper-White, P. Beyerlein, K. Kostner, C. Punyadeera, Diagnostic potential of saliva: current state and future applications, *Clin. Chem.* 57 (5) (2011) 675–687.
- [9] J.M. Yoshizawa, C.A. Schafer, J.J. Schafer, J.J. Farrell, B.J. Paster, D.T. Wong, Salivary biomarkers: toward future clinical and diagnostic utilities, *Clin. Microbiol. Rev.* 26 (4) (2013) 781–791.
- [10] E.N. Guerra, A.C. Acevedo, A.F. Leite, D. Gozal, H. Chardin, G. De Luca Canto, Diagnostic capability of salivary biomarkers in the assessment of head and neck cancer: a systematic review and meta-analysis, *Oral Oncol.* 51 (9) (2015) 805–818.
- [11] L. Arantes, A.C. De Carvalho, M.E. Melendez, A. Lopes Carvalho, Serum, plasma and saliva biomarkers for head and neck cancer, *Expert. Rev. Mol. Diagn.* 18 (1) (2018)

- 85–112.
- [12] S. Hu, M. Arellano, P. Boontheung, J. Wang, H. Zhou, J. Jiang, D. Elashoff, R. Wei, J.A. Loo, D.T. Wong, Salivary proteomics for oral cancer biomarker discovery, *Clin. Cancer Res.* 14 (19) (2008) 6246–6252.
 - [13] G. Troiano, L. Boldrup, F. Ardito, X. Gu, L. Lo Muzio, K. Nylander, Circulating miRNAs from blood, plasma or serum as promising clinical biomarkers in oral squamous cell carcinoma: a systematic review of current findings, *Oral Oncol.* 63 (2016) 30–37.
 - [14] D. Babji, R. Nayak, K. Bhat, V. Kotrashetti, Cell-free tumor DNA: emerging reality in oral squamous cell carcinoma, *J. Oral Maxillofac. Pathol.* 23 (2) (2019) 273–279.
 - [15] X. Chen, D. Yu, Metabolomics study of oral cancers, *Metabolomics* 15 (2) (2019) 22.
 - [16] D. Zlotogorski-Hurvitz, G. Dayan, T. Chaushu, M.V. Salo, Morphological and molecular features of oral fluid-derived exosomes: oral cancer patients versus healthy individuals, *J. Cancer Res. Clin. Oncol.* 142 (1) (2016) 101–110.
 - [17] Y. Wang, S. Springer, C.L. Mulvey, N. Silliman, J. Schaefer, M. Sausen, N. James, E.M. Rettig, T. Guo, C.R. Pickering, J.A. Bishop, C.H. Chung, J.A. Califano, D.W. Eisele, C. Fakhry, C.G. Gourin, P.K. Ha, H. Kang, A. Kiess, W.M. Koch, J.N. Myers, H. Quon, J.D. Richmon, D. Sidransky, R.P. Tufano, W.H. Westra, C. Bettgowda, L.A. Diaz Jr., N. Papadopoulos, K.W. Kinzler, B. Vogelstein, N. Agrawal, Detection of somatic mutations and HPV in the saliva and plasma of patients with head and neck squamous cell carcinomas, *Sci. Transl. Med.* 7 (293) (2015) 293ra104.
 - [18] F.O. Gleber-Netto, M. Yakob, F. Li, Z. Feng, J. Dai, H.K. Kao, Y.L. Chang, K.P. Chang, D.T. Wong, Salivary biomarkers for detection of oral squamous cell carcinoma in a Taiwanese population, *Clin. Cancer Res.* 22 (13) (2016) 3340–3347.
 - [19] J.S. Yu, T.T. Chen, W.F. Chiang, Y.C. Hsiao, L.J. Chu, L.C. See, C.S. Wu, H.T. Tu, H.W. Chen, C.C. Chen, W.C. Liao, Y.T. Chang, C.C. Wu, C.Y. Lin, S.Y. Liu, S.T. Chiou, S.L. Chia, K.P. Chang, C.Y. Chien, S.W. Chang, C.J. Chang, J.D. Young, C.C. Pao, Y.S. Chang, L.H. Hartwell, Saliva protein biomarkers to detect oral squamous cell carcinoma in a high-risk population in Taiwan, *Proc. Natl. Acad. Sci. U. S. A.* 113 (41) (2016) 11549–11554.
 - [20] Y.C. Hsiao, L.M. Chi, K.Y. Chien, W.F. Chiang, S.F. Chen, Y.N. Chuang, S.Y. Lin, C.C. Wu, Y.T. Chang, L.J. Chu, Y.T. Chen, S.L. Chia, C.Y. Chien, K.P. Chang, Y.S. Chang, J.S. Yu, Development of a multiplexed assay for oral cancer candidate biomarkers using peptide immunoaffinity enrichment and targeted mass spectrometry, *Mol. Cell. Proteomics* 16 (10) (2017) 1829–1849.
 - [21] N.A. Ghallab, O.G. Shaker, Serum and salivary levels of chemerin and MMP-9 in oral squamous cell carcinoma and oral premalignant lesions, *Clin. Oral Investig.* 21 (3) (2017) 937–947.
 - [22] L. Zanotti, A. Paderno, C. Piazza, E. Pagan, E. Bignotti, C. Romani, E. Bandiera, S. Calza, F. Del Bon, P. Nicolai, Epidermal growth factor receptor detection in serum and saliva as a diagnostic and prognostic tool in oral cancer, *Laryngoscope* 127 (11) (2017) E408–E414.
 - [23] L.T. Lee, Y.K. Wong, H.Y. Hsiao, Y.W. Wang, M.Y. Chan, K.W. Chang, Evaluation of saliva and plasma cytokine biomarkers in patients with oral squamous cell carcinoma, *Int. J. Oral Maxillofac. Surg.* 47 (6) (2018) 699–707.
 - [24] A.G. Paulovich, J.R. Whiteaker, Quantifying the human proteome, *Nat. Biotechnol.* 34 (10) (2016) 1033–1034.
 - [25] A.J. Percy, J. Yang, D.B. Hardie, A.G. Chambers, J. Tamura-Wells, C.H. Borchers, Precise quantitation of 136 urinary proteins by LC/MS-MS using stable isotope labeled peptides as internal standards for biomarker discovery and/or verification studies, *Methods* 81 (2015) 24–33.
 - [26] A.J. Percy, D.B. Hardie, A. Jardim, J. Yang, M.H. Elliott, S. Zhang, Y. Mohammed, C.H. Borchers, Multiplexed panel of precisely quantified salivary proteins for biomarker assessment, *Proteomics* 17 (6) (2017).
 - [27] A.J. Percy, A.G. Chambers, J. Yang, D.B. Hardie, C.H. Borchers, Advances in multiplexed MRM-based protein biomarker quantitation toward clinical utility, *Biochim. Biophys. Acta* 1844 (5) (2014) 917–926.
 - [28] T.A. Addona, S.E. Abbatiello, B. Schilling, S.J. Skates, D.R. Mani, D.M. Bunk, C.H. Spiegelman, L.J. Zimmerman, A.J. Ham, H. Keshishian, S.C. Hall, S. Allen, R.K. Blackman, C.H. Borchers, C. Buck, H.L. Cardasis, M.P. Cusack, N.G. Dodder, B.W. Gibson, J.M. Held, T. Hiltke, A. Jackson, E.B. Johansen, C.R. Kinsinger, J. Li, M. Mesri, T.A. Neubert, R.K. Niles, T.C. Pulsipher, D. Ransohoff, H. Rodriguez, P.A. Rudnick, D. Smith, D.L. Tabb, T.J. Tegeler, A.M. Variyath, L.J. Vega-Montoto, A. Wahlander, S. Waldemarson, M. Wang, J.R. Whiteaker, L. Zhao, N.L. Anderson, S.J. Fisher, D.C. Liebler, A.G. Paulovich, F.E. Regnier, P. Tempst, S.A. Carr, Multi-site assessment of the precision and reproducibility of multiple reaction monitoring-based measurements of proteins in plasma, *Nat. Biotechnol.* 27 (7) (2009) 633–641.
 - [29] J.R. Whiteaker, C. Lin, J. Kennedy, L. Hou, M. Trute, I. Sokal, P. Yan, R.M. Schoenherr, L. Zhao, U.J. Voytovich, K.S. Kelly-Spratt, A. Krasnoselsky, P.R. Gafken, J.M. Hogan, L.A. Jones, P. Wang, L. Amon, L.A. Chodosh, P.S. Nelson, M.W. McIntosh, C.J. Kemp, A.G. Paulovich, A targeted proteomics-based pipeline for verification of biomarkers in plasma, *Nat. Biotechnol.* 29 (7) (2011) 625–634.
 - [30] N.L. Anderson, N.G. Anderson, L.R. Haines, D.B. Hardie, R.W. Olafson, T.W. Pearson, Mass spectrometric quantitation of peptides and proteins using Stable Isotope Standards and Capture by Anti-Peptide Antibodies (SISCAPA), *J. Proteome Res.* 3 (2) (2004) 235–244.
 - [31] J.R. Whiteaker, L. Zhao, P. Yan, R.G. Ivey, U.J. Voytovich, H.D. Moore, C. Lin, A.G. Paulovich, Peptide immunoaffinity enrichment and targeted mass spectrometry enables multiplex, quantitative pharmacodynamic studies of phospho-signaling, *Mol. Cell. Proteomics* 14 (8) (2015) 2261–2273.
 - [32] J.R. Whiteaker, L. Zhao, H.Y. Zhang, L.C. Feng, B.D. Piening, L. Anderson, A.G. Paulovich, Antibody-based enrichment of peptides on magnetic beads for mass-spectrometry-based quantification of serum biomarkers, *Anal. Biochem.* 362 (1) (2007) 44–54.
 - [33] B. MacLean, D.M. Tomazela, N. Shulman, M. Chambers, G.L. Finney, B. Frewen, R. Kern, D.L. Tabb, D.C. Liebler, M.J. MacCoss, Skyline: an open source document editor for creating and analyzing targeted proteomics experiments, *Bioinformatics* 26 (7) (2010) 966–968.
 - [34] H. Chen, Y.C. Hsiao, S.F. Chiang, C.C. Wu, Y.T. Lin, H. Liu, H. Zhao, J.S. Chen, Y.S. Chang, J.S. Yu, Quantitative analysis of wild-type and V600E mutant BRAF proteins in colorectal carcinoma using immunoenrichment and targeted mass spectrometry, *Anal. Chim. Acta* 933 (2016) 144–155.
 - [35] J.A. Loo, W. Yan, P. Ramachandran, D.T. Wong, Comparative human salivary and plasma proteomes, *J. Dent. Res.* 89 (10) (2010) 1016–1023.
 - [36] W. Yan, R. Apweiler, B.M. Balgley, P. Boontheung, J.L. Bundy, B.J. Cargile, S. Cole, X. Fang, M. Gonzalez-Begne, T.J. Griffin, F. Hagen, S. Hu, L.E. Wolinsky, C.S. Lee, D. Malamud, J.E. Melvin, R. Menon, M. Mueller, R. Qiao, N.L. Rhodus, J.R. Sevinsky, D. States, J.L. Stephenson, S. Than, J.R. Yates, W. Yu, H. Xie, Y. Xie, G.S. Omenn, J.A. Loo, D.T. Wong, Systematic comparison of the human saliva and plasma proteomes, *Proteomics Clin. Appl.* 3 (1) (2009) 116–134.
 - [37] S. Williamson, C. Munro, R. Pickler, M.J. Grap, R.K. Elswick Jr., Comparison of biomarkers in blood and saliva in healthy adults, *Nurs. Res. Pract.* 2012 (2012) 246178.
 - [38] Y.C. Hsiao, L.J. Chu, Y.T. Chen, L.M. Chi, K.Y. Chien, W.F. Chiang, Y.T. Chang, S.F. Chen, W.S. Wang, Y.N. Chuang, S.Y. Lin, C.Y. Chien, K.P. Chang, Y.S. Chang, J.S. Yu, Variability assessment of 90 salivary proteins in intraday and interday samples from healthy donors by multiple reaction monitoring-mass spectrometry, *Proteomics Clin. Appl.* 12 (2) (2018), <https://doi.org/10.1002/prca.201700039>.
 - [39] M. Stott-Miller, J.R. Houck, P. Lohavanichbutr, E. Mendez, M.P. Upton, N.D. Futran, S.M. Schwartz, C. Chen, Tumor and salivary matrix metalloproteinase levels are strong diagnostic markers of oral squamous cell carcinoma, *Cancer Epidemiol. Biomark. Prev.* 20 (12) (2011) 2628–2636.
 - [40] M. Yakob, L. Fuentes, M.B. Wang, E. Abemayor, D.T. Wong, Salivary biomarkers for detection of oral squamous cell carcinoma - current state and recent advances, *Curr. Oral Health Rep.* 1 (2) (2014) 133–141.
 - [41] H. Kadeh, S. Saravani, F. Heydari, M. Keikha, V. Rigi, Expression of matrix metalloproteinase-10 at invasive front of squamous cell carcinoma and verrucous carcinoma in the oral cavity, *Asian Pac. J. Cancer Prev.* 16 (15) (2015) 6609–6613.
 - [42] P. Berndt, H. Richter, M.F. Kosmehl, Tenascin-C and carcinoma cell invasion in oral and urinary bladder cancer, *Cell Adhes. Migr.* 9 (1–2) (2015) 105–111.
 - [43] P. Stojan, M. Budihna, L. Smid, B. Svetic, I. Vrhovec, J. Kos, J. Skrk, Prognostic significance of cysteine proteinases cathepsins B and L and their endogenous inhibitors stefins A and B in patients with squamous cell carcinoma of the head and neck, *Clin. Cancer Res.* 6 (3) (2000) 1052–1062.
 - [44] Y. Ma, Y. Chen, Y. Li, K. Grun, A. Berndt, Z. Zhou, I. Petersen, Cystatin A suppresses tumor cell growth through inhibiting epithelial to mesenchymal transition in human lung cancer, *Oncotarget* 9 (18) (2018) 14084–14098.
 - [45] C. Chen, E. Mendez, J. Houck, W. Fan, P. Lohavanichbutr, D. Doody, B. Yueh, N.D. Futran, M. Upton, D.G. Farwell, S.M. Schwartz, L.P. Zhao, Gene expression profiling identifies genes predictive of oral squamous cell carcinoma, *Cancer Epidemiol. Biomark. Prev.* 17 (8) (2008) 2152–2162.
 - [46] M.C. Mechlin, M. Enji, R. Nachat, S. Chavanas, M. Charveron, A. Ishida-Yamamoto, G. Serre, H. Takahara, M. Simon, The peptidylarginine deiminases expressed in human epidermis differ in their substrate specificities and subcellular locations, *Cell. Mol. Life Sci.* 62 (17) (2005) 1984–1995.

Article

Probing Anti-Proliferative 24-Homoscalaranes from a Sponge *Lendenfeldia* sp.

Bo-Rong Peng ^{1,2,3}, Kuei-Hung Lai ⁴ , You-Ying Chen ^{3,5}, Jui-Hsin Su ^{3,6}, Yusheng M. Huang ⁷, Yu-Hsin Chen ³, Mei-Chin Lu ^{3,6}, Steve Sheng-Fa Yu ^{2,8,*}, Chang-Yih Duh ^{1,5,*} and Ping-Jyun Sung ^{3,5,6,9,10,*} 

¹ Doctoral Degree Program in Marine Biotechnology, National Sun Yat-sen University, Kaohsiung 80424, Taiwan; pengpojung@gmail.com

² Doctoral Degree Program in Marine Biotechnology, Academia Sinica, Taipei 11529, Taiwan

³ National Museum of Marine Biology and Aquarium, Pingtung 94450, Taiwan; zoeblack0108@gmail.com (Y.-Y.C.); x2219@nmmba.gov.tw (J.-H.S.); kb5634@yahoo.com.tw (Y.-H.C.); jinx6609@nmmba.gov.tw (M.-C.L.)

⁴ Research Center for Chinese Herbal Medicine, College of Human Ecology, Chang Gung University of Science and Technology, Taoyuan 33303, Taiwan; mos19880822@gmail.com

⁵ Department of Marine Biotechnology and Resources, National Sun Yat-sen University, Kaohsiung 80424, Taiwan

⁶ Graduate Institute of Marine Biology, National Dong Hwa University, Pingtung 94450, Taiwan

⁷ Department of Marine Recreation, National Penghu University of Science and Technology, Penghu 88046, Taiwan; yusheng@npu.edu.tw

⁸ Institute of Chemistry, Academia Sinica, Taipei 11529, Taiwan

⁹ Chinese Medicine Research and Development Center, China Medical University Hospital, Taichung 40447, Taiwan

¹⁰ Graduate Institute of Natural Products, Kaohsiung Medical University, Kaohsiung 80708, Taiwan

* Correspondence: sfyu@chem.sinica.edu.tw (S.S.-F.Y.); yihduh@mail.nsysu.edu.tw (C.-Y.D.); pjsung@nmmba.gov.tw (P.-J.S.); Tel.: +886-2-5572-8650 (S.S.-F.Y.); +886-7-525-2000 (ext. 5036) (C.-Y.D.); +886-8-882-5037 (P.-J.S.); Fax: +886-2-2783-1237 (S.S.-F.Y.); +886-7-525-5020 (C.-Y.D.); +886-8-882-5087 (P.-J.S.)

Received: 30 December 2019; Accepted: 22 January 2020; Published: 24 January 2020



Abstract: In the current study, an NMR spectroscopic pattern-based procedure for probing scalarane derivatives was performed and four new 24-homoscalaranes, lendenfeldaranes A–D (**1–4**), along with three known compounds, 12 α -acetoxy-22-hydroxy-24-methyl-24-oxoscalar-16-en-25-al (**5**), felixin F (**6**), and 24-methyl-12,24,25-trioxoscalar-16-en-22-oic acid (**7**) were isolated from the sponge *Lendenfeldia* sp. The structures of scalaranes **1–7** were elucidated on the basis of spectroscopic analysis. Scalaranes **1–7** were further evaluated for their cytotoxicity toward a series of human cancer cell lines and the results suggested that **5** and **7** dominated in the anti-proliferative activity of the extract. The 18-aldehyde functionality was found to play a key role in their activity.

Keywords: scalarane; sesterterpenoid; anti-proliferation; *Lendenfeldia*

1. Introduction

Since the first scalarane-type derivative, scalarin, was originally isolated from *Cocaspongia scalaris* [1], more than three hundred scalarane sesterterpenoids have been obtained from cyanobacteria and marine organisms [2,3]. Compounds of this type demonstrate a wide spectrum of interesting biological properties, such as anti-inflammation [4], cytotoxicity [5–7], anti-feedant [8–10], anti-microbial activity [11,12], ichthyotoxicity [13], anti-tubercular activity [14], anti-HIV [15], and inhibition of the nuclear hormone receptor [16]. In order to seek novel anti-proliferative substances from marine

organisms, a chemical and bioactive investigation was carried out on the organic extracts of a marine sponge identified as *Lendenfeldia* sp. (family—Thorectidae). The ethyl acetate (EtOAc) extract of *Lendenfeldia* sp. was found to exhibit anti-proliferative activity against human cancer cell lines, including human acute lymphoblastic leukemia (MOLT-4), human chronic myelogenous leukemia (K-562), human histiocytic lymphoma (U-937), and human T-cell lymphoblastic lymphoma (SUP-T1) with IC_{50} values $< 0.625 \mu\text{g/mL}$. The bioassay-guided isolation, combined with an NMR spectroscopic pattern-based procedure, was used to explore the anti-proliferative scalarane substances, and led to the isolation four new 24-homoscalaranes, lendenfeldaranes A–D (1–4), along with three known metabolites, 12 α -acetoxy-22-hydroxy-24-methyl-24-oxoscalar-16-en-25-al (5) [17], felixin F (6) [18], and 24-methyl-12,24,25-trioxoscalar-16-en-22-oic acid (7) [17]. In the current study, the comprehensive workflow of isolation, structure elucidation and an anti-proliferative evaluation were implemented on scalaranes 1–7 (Figure 1).

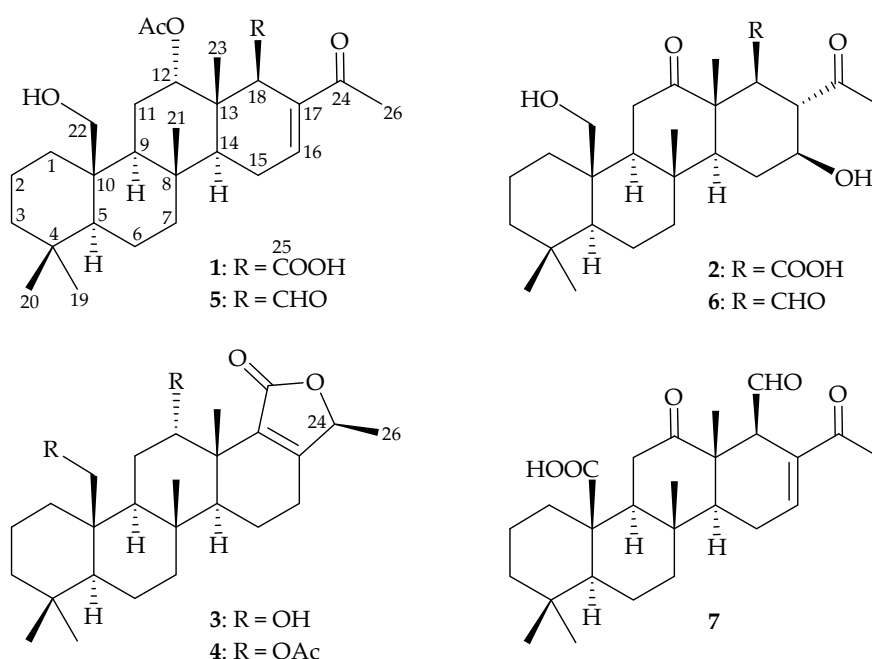


Figure 1. The structures of lendenfeldaranes A–D (1–4), 12 α -acetoxy-22-hydroxy-24-methyl-24-oxoscalar-16-en-25-al (5), felixin F (6), and 24-methyl-12,24,25-trioxoscalar-16-en-22-oic acid (7).

2. Results and Discussion

Lendenfeldarane A (1) was obtained as an amorphous powder and assigned the molecular formula $C_{28}H_{42}O_6$ (eight degrees of unsaturation) from its (+)-HRESIMS at m/z 497.28736 $[M + Na]^+$ (calcd. for $C_{28}H_{42}O_6 + Na$, 497.28712). The ^1H NMR data of 1 (Table 1), showed six singlet methyls at δ_H 0.75, 0.86, 0.96, 1.16, 2.14, and 2.29, one olefinic proton at δ_H 6.90 (1H, br s), and one oxymethine proton at δ_H 4.77 (1H, br s). The diastereotopic geminal protons at δ_H 3.85 (1H, d, $J = 11.6$ Hz) and 4.02 (1H, d, $J = 11.6$ Hz) were assumed to be an oxymethylene group. Analyses of the ^{13}C and distortionless enhancement by polarization transfer (DEPT) spectra of 1 (Table 1) revealed the existence of 28 carbon resonances, including six methyls, eight sp^3 methylenes (including one oxymethylene), five sp^3 methines (including one oxymethine), four sp^3 quaternary carbons, one sp^2 methine, and four sp^2 quaternary carbons (including three carbonyls). Based on the ^1H and ^{13}C NMR spectra, 1 was found to possess an acetoxy group (δ_H 2.14, 3H, s; δ_C 170.4, C; 21.5, CH_3). An additional unsaturated functionality was indicated by ^{13}C resonances at δ_C 139.7 (CH-16) and 137.9 (C-17), suggesting the presence of a trisubstituted olefin. Thus, four degrees of unsaturation were accounted for, and the above NMR data—as well as the unassigned degrees of unsaturation of 1—implied a tetracyclic analogue.

Table 1. The ^1H and ^{13}C NMR data for 24-homoscalaranes **1** and **2** (CDCl_3).

C/H	1		2	
	δ_{H} (J in Hz) ^a	δ_{C} Multiple ^b	δ_{H} (J in Hz) ^c	δ_{C} Multiple ^d
1	2.12 m; 0.48 ddd (12.8, 12.8, 3.2)	34.4, CH_2	2.13 m; 0.80 m	33.8, CH_2
2	1.50 m	17.8, CH_2	1.44 m; 1.65 m	17.9, CH_2
3	1.19 m; 1.43 m	41.6, CH_2	1.18 m; 1.43 m	41.4, CH_2
4		33.0, C		33.0, C
5	0.94 m	56.8, CH	0.95 br d (12.6)	56.8, CH
6	1.43 m	18.3, CH_2	1.53 m	18.2, CH_2
7	1.03 m; 1.82 ddd (12.8, 3.2, 3.2)	42.2, CH_2	0.96 m; 1.91 ddd (13.2, 3.6, 3.6)	42.1, CH_2
8		37.8, C		38.7, C
9	1.50 m	49.3, CH	1.26 m	62.8, CH
10		41.7, C		42.8, C
11	2.07 m	24.9, CH_2	2.62 dd (12.6, 1.8); 3.34 dd (14.4, 12.6)	39.0, CH_2
12	4.77 br s	75.7, CH		221.9, C
13		38.9, C		52.8, C
14	1.31 m	52.2, CH	1.21 m	58.0, CH
15	2.27 m	23.3, CH_2	1.65 m; 1.94 ddd (12.6, 4.2, 1.8)	30.1, CH_2
16	6.90 br s	139.7, CH	3.53 ddd (10.8, 10.8, 4.8)	72.7, CH
17		137.9, C	3.22 dd (12.0, 10.8)	54.8, CH
18	3.79 br s	48.0, CH	3.18 d (12.0)	51.3, CH
19	0.75 s	21.9, CH_3	0.76 s	21.7, CH_3
20	0.86 s	33.8, CH_3	0.87 s	33.7, CH_3
21	1.16 s	16.1, CH_3	1.30 s	16.4, CH_3
22	3.85 d (11.6); 4.02 d (11.6)	62.9, CH_2	3.93 dd (11.4, 1.2); 4.08 d (11.4)	62.7, CH_2
23	0.96 s	15.5, CH_3	1.34 s	15.3, CH_3
24		199.3, C		212.6, C
25		175.1, C		172.4, C
26	2.29 s	25.3, CH_3	2.40 s	33.4, CH
OAc-12		170.4, C		
	2.14 s	21.5, CH_3		

^a 400 MHz. ^b 100 MHz. ^c 600 MHz. ^d 150 MHz.

The gross structure of **1** was further established from its 2D NMR spectra. From the coupling information in the COSY spectrum of **1** (Figure 2), it was possible to establish four partial structure units between $\text{H}_2\text{-1}/\text{H}_2\text{-2}/\text{H}_2\text{-3}$, $\text{H-5}/\text{H}_2\text{-6}/\text{H}_2\text{-7}$, $\text{H-9}/\text{H}_2\text{-11}/\text{H-12}$, and $\text{H-14}/\text{H}_2\text{-15}/\text{H}_2\text{-16}$. The heteronuclear multiple bond correlation (HMBC) spectrum connected these substructures by the connectivity between $\text{H-5}/\text{C-10}$; $\text{H-16}/\text{C-17}$; $\text{H}_3\text{-20}/\text{C-3}$, C-4, C-5, C-19; $\text{H}_3\text{-21}/\text{C-7}$, C-8, C-9, C-14; $\text{H}_2\text{-22}/\text{C-1}$, C-9, C-10; $\text{H}_3\text{-23}/\text{C-12}$, C-13, C-14, C-18; and $\text{H}_3\text{-26}/\text{C-17}$, C-24, indicating a scalarane-type sesterterpenoid structure (Figure 2). Furthermore, the acetoxy and carboxylic acid groups positioned at C-12 and C-18 were determined by the HMBC, from H-12 to the acetate carbonyl at δ_{C} 170.4 and from H-18 to C-25 (δ_{C} 175.1), respectively.

The relative stereochemistry of **1** was elucidated by correlations in the NOESY experiment. Using the conventional method for analyzing the stereochemistry, the α - and β -configurations were assigned at H-5 and C-10-hydroxymethyl, respectively, to anchor the stereochemical analysis. In the NOESY spectrum of **1** (Figure 3), H-9 correlated with H-5, but not with $\text{H}_3\text{-21}$ and $\text{H}_2\text{-22}$, suggesting that these two protons (H-5 and H-9) were situated on the same face and were α -oriented, and that the Me-21 and C-10-hydroxymethyl groups were β -oriented at C-8 and C-10, respectively. H-14 exhibited correlations with H-9 and H-18, but not with $\text{H}_3\text{-21}$ and $\text{H}_3\text{-23}$, demonstrating that H-14 and H-18 were α -oriented. Additionally, the proton signal of a methyl group at δ_{H} 0.96 ($\text{H}_3\text{-23}$) displayed a correlation

with H-12 (δ_{H} 4.77), which indicated the β -orientations of Me-23 and H-12. The NOESY spectrum showed a correlation between H₃-26 and H-16, revealing the *E* geometry of the C-16/17 carbon–carbon double bond. It was found that the NMR data of **1** were similar to those of a known scalarane analogue, 12 α -acetoxy-22-hydroxy-24-methyl-24-oxoscalar-16-en-25-al (**5**), from an Australian sponge, *Lendenfeldia* sp. [17], except that the aldehyde group in **5** was replaced by a carboxylic acid group in **1**. Based on the above findings, the structure of **1** was accordingly assigned, as shown in Figure 1, and named lendenfeldarane A (Supplementary Materials, Figures S1–S8).

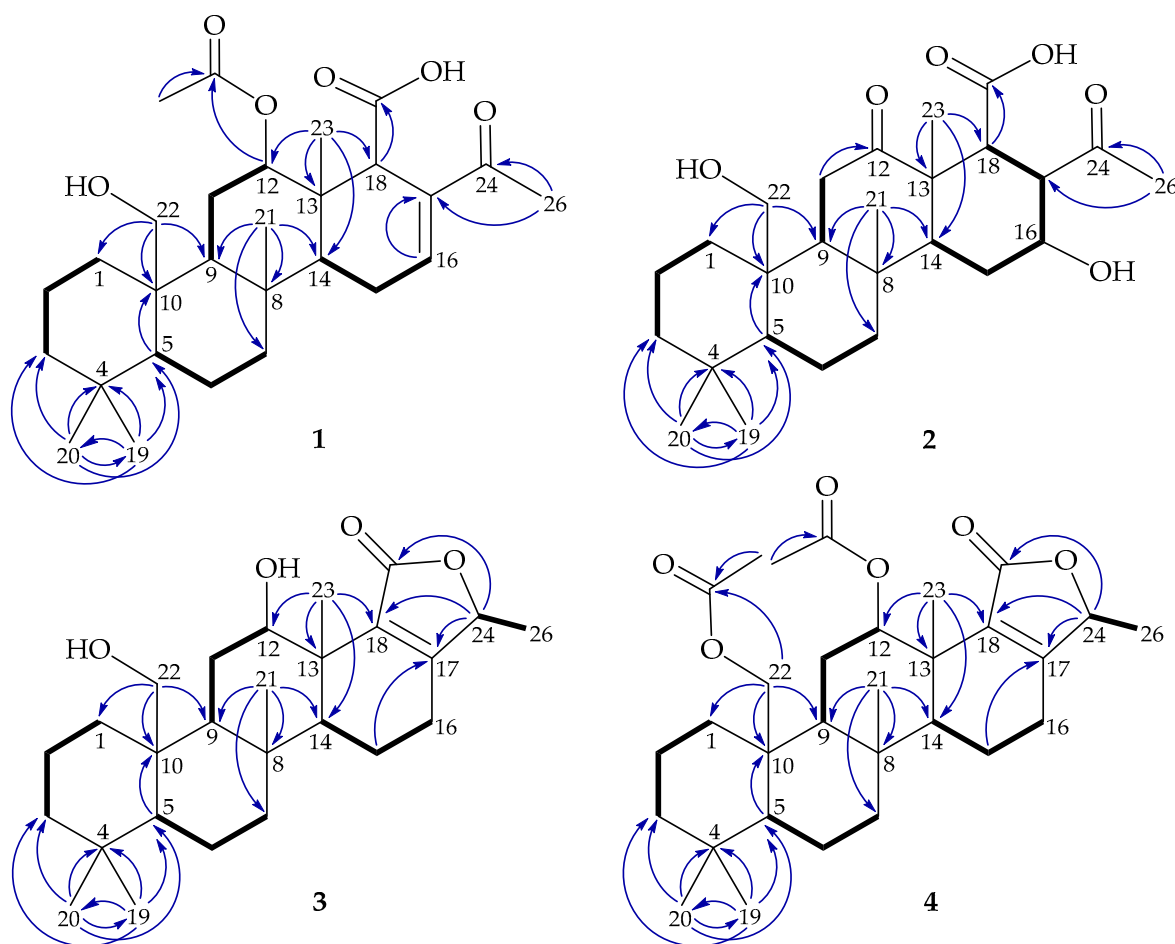


Figure 2. The key COSY correlations (—) and heteronuclear multiple bond correlation (HMBC) (---) of **1**–**4**.

Compound **2** (lendenfeldarane B) was obtained as an amorphous powder and its molecular formula was determined as $\text{C}_{26}\text{H}_{40}\text{O}_6$, based on a sodiated adduct ion peak $[\text{M} + \text{Na}]^+$ at m/z 471.27171 in (+)-HRESIMS (calcd. for $\text{C}_{26}\text{H}_{40}\text{O}_6 + \text{Na}$, 471.27142). The ^1H NMR data of **2** (Table 1) showed five singlet methyls at δ_{H} 0.76, 0.87, 1.30, 1.34, and 2.40 and one oxymethine proton at δ_{H} 3.53 (1H, ddd, $J = 10.8, 10.8, 4.8$ Hz). The diastereotopic geminal protons at δ_{H} 3.93 (1H, dd, $J = 11.4, 1.2$ Hz) and 4.08 (1H, d, $J = 11.4$ Hz) were assumed to be an oxygenated methylene group. The ^{13}C and DEPT data of **2** suggested the presence of 26 carbons that were similar to those of a known scalarane, felixin F (**6**) [18], including a carboxylic carbon at δ_{C} 172.4, two ketone carbons at δ_{C} 212.6 and 221.9, an oxymethine carbon at δ_{C} 72.7, and an oxymethylene carbon at δ_{C} 62.7. Analysis of these NMR data suggested that compounds **2** and **6** are closely related, with the only difference being that the β -aldehyde group at C-18 in **6** was replaced by a β -carboxylic acid group in **2**. Based on the analyses of the COSY, HMBC, and NOESY spectra, as well as the specific rotation data (**2**: $[\alpha]_{\text{D}}^{20} +49$ (c 0.99, CHCl_3), **6**: $[\alpha]_{\text{D}}^{20} +55$

(c 0.04, CHCl_3); ref [18] **6**: $[\alpha]_D^{25} +54$ (c 0.4, CHCl_3)), Compound **2** was finally assigned, as shown in Figure 1, and named as lendenfeldarane B (Supplementary Materials, Figures S9–S16).

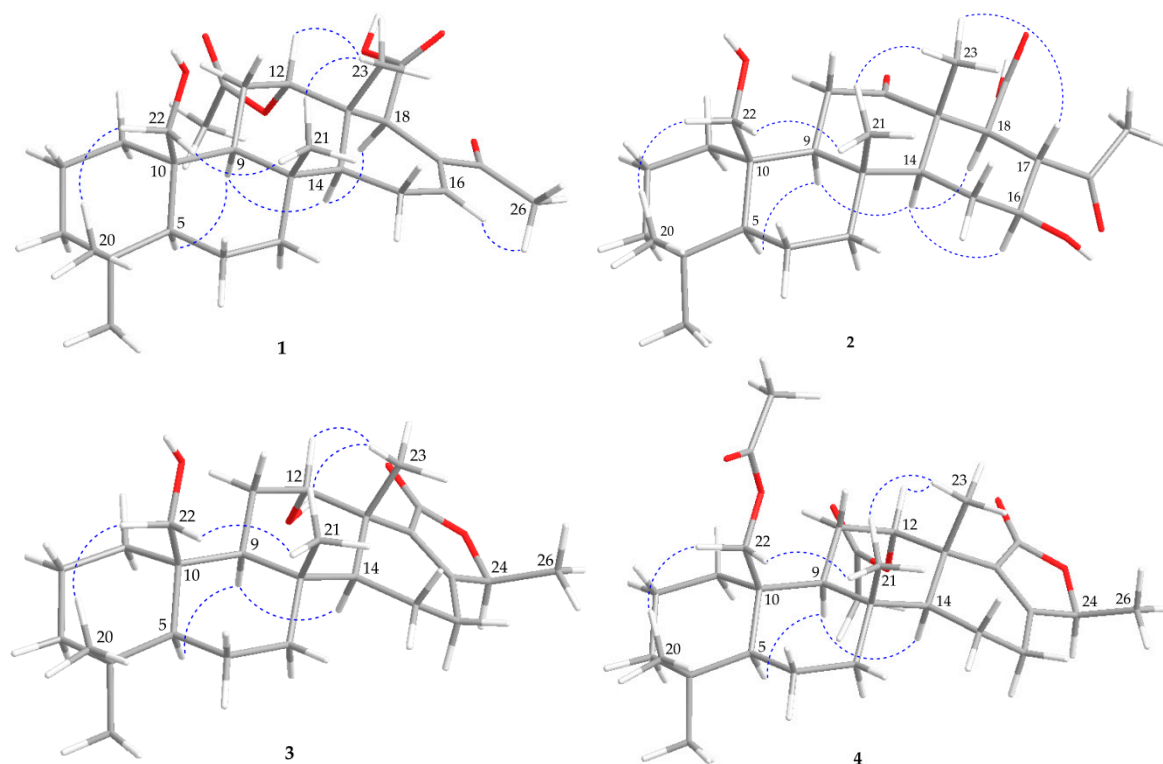


Figure 3. The selected NOESY correlations (---) of 1–4.

The molecular formula of lendenfeldarane C (**3**) was determined as $\text{C}_{26}\text{H}_{40}\text{O}_4$ from an $[\text{M} + \text{Na}]^+$ ion at m/z 439.28188 (calcd. for $\text{C}_{26}\text{H}_{40}\text{O}_4 + \text{Na}$, 439.28174) and NMR data (Table 2), indicating seven degrees of unsaturation. The ^1H NMR data of **3** showed four singlet methyls at δ_{H} 0.78, 0.86, 1.08, 1.13, one doublet methyl at δ_{H} 1.37 ($J = 6.5$ Hz), and two oxymethine protons at δ_{H} 4.60 (1H, br s) and 4.79 (1H, q, $J = 6.5$ Hz). The diastereotopic geminal protons at δ_{H} 3.92 (1H, d, $J = 11.5$ Hz) and 4.05 (1H, d, $J = 11.5$ Hz) were assumed to be an oxymethylene group. Analyses of the ^{13}C NMR and DEPT spectrum of **3** revealed the existence of 26 carbon resonances, including five methyls, nine sp^3 methylenes (including one oxymethylene), five sp^3 methines (including two oxymethines), four sp^3 quaternary carbons, and three sp^2 quaternary carbons (including one ester carbonyl). Based on the ^{13}C spectrum, **3** was found to possess an ester carbonyl (δ_{C} 172.6) and an unsaturated degree was indicated by the ^{13}C chemical shifts at δ_{C} 133.5 (C-18) and 165.2 (C-17), suggesting the presence of a tetrasubstituted olefin. Thus, the above NMR data and the remaining five unsaturated degrees of **3** required a pentacyclic analogue.

The gross structure of **3** was constructed from its 2D NMR spectra. From the COSY spectrum (Figure 2), five partial structure units between $\text{H}_2\text{-1}/\text{H}_2\text{-2}/\text{H}_2\text{-3}$, $\text{H}_5\text{-1}/\text{H}_2\text{-6}/\text{H}_2\text{-7}$, $\text{H}_9\text{-1}/\text{H}_2\text{-11}/\text{H}_2\text{-12}$, $\text{H}_4\text{-1}/\text{H}_2\text{-15}/\text{H}_2\text{-16}$, and $\text{H}_4\text{-24}/\text{H}_3\text{-26}$ were established. The HMBC spectrum connected these fractional structures by the key correlations between $\text{H}_5\text{-1}/\text{C}-10$; $\text{H}_2\text{-15}/\text{C}-17$; $\text{H}_3\text{-20}/\text{C}-3$, C-4, C-5, C-19; $\text{H}_3\text{-21}/\text{C}-7$, C-8, C-9, C-14; $\text{H}_2\text{-22}/\text{C}-1$, C-9, C-10; and $\text{H}_3\text{-23}/\text{C}-12$, C-13, C-14, C-18, indicating a scalarane skeleton. The COSY correlation between $\text{H}_3\text{-26}/\text{H}_4\text{-24}$ and the HMBC from $\text{H}_4\text{-24}$ to C-17, C-18, and C-25 allowed the establishment of a 5-methyl-2(5H)-furanone. In the NOESY experiment of **3** (Figure 3), $\text{H}_3\text{-23}$ correlated with $\text{H}_3\text{-21}$ and $\text{H}_2\text{-12}$, indicating the β -orientation of Me-23 and $\text{H}_2\text{-12}$, respectively. The orientation of Me-26 was determined to be β -oriented, based on the comparison of the NMR chemical shifts of Me-26 (δ_{H} 1.37, 3H, d, $J = 6.5$ Hz; δ_{C} 18.5) in **3** with those of previous reported scalarane analogues, phyllactones A (δ_{H} 1.51, 3H, d, $J = 6.5$ Hz; δ_{C} 19.6) and B (δ_{H} 1.38, 3H, d, $J = 6.5$ Hz; δ_{C} 18.5) (Figure 4) [5].

Hence, the structure of **3** was determined to be a new sesterterpenoid and this metabolite was found to be the 12-epi-compound of a known 24-homoscalarane, 23-hydroxy-20-methylscalarolide [19,20], and should be named lendenfeldarane C (Supplementary Materials, Figures S17–S24).

Table 2. The ^1H and ^{13}C NMR data for 24-homoscalaranes **3** and **4** (CDCl_3).

C/H	3		4	
	δ_{H} (J in Hz) ^a	δ_{C} Multiple ^b	δ_{H} (J in Hz) ^c	δ_{C} Multiple ^d
1	2.16 m; 0.80 m	34.0, CH_2	2.01 m; 0.52 ddd (13.8, 13.8, 3.0)	34.7, CH_2
2	1.63 m	18.4, CH_2	1.63 m	18.2, CH_2
3	1.18 m; 1.43 m	41.7, CH_2	1.15 ddd (9.0, 9.0, 4.2); 1.43 m	41.5, CH_2
4		33.0, C		33.0, C
5	1.05 m	56.8, CH	1.01 dd (13.8, 3.6)	57.1, CH
6	1.56 m; 1.91 m	16.9, CH_2	1.56 m; 1.93 m	17.0, CH_2
7	1.10 m; 1.89 m	42.0, CH_2	1.11 ddd (12.0, 12.0, 4.2); 1.92 m	41.9, CH_2
8		37.6, C		37.5, C
9	1.56 m	52.3, CH	1.26 m	53.2, CH
10		41.8, C		40.2, C
11	1.89 m; 2.18 m	27.1, CH_2	1.99 m; 2.20 m	23.3, CH_2
12	4.60 br s	69.9, CH	5.54 t (3.0)	73.8, CH
13		40.2, C		38.4, C
14	1.60 m	50.0, CH	1.55 m	51.2, CH
15	2.18 m; 2.35 m	24.1, CH_2	2.23 m; 2.39 m	24.0, CH_2
16	1.46 m; 1.56 m	18.0, CH_2	1.60 m	18.0, CH_2
17		165.2, C		163.6, C
18		133.5, C		132.6, C
19	0.78 s	21.8, CH_3	0.83 s	21.9, CH_3
20	0.86 s	33.9, CH_3	0.89 s	33.7, CH_3
21	1.08 s	16.3, CH_3	0.98 s	16.4, CH_3
22	3.92 d (11.5); 4.05 d (11.5)	63.0, CH_2	4.15 dd (12.0, 1.2); 4.58 d (12.0)	64.7, CH_2
23	1.13 s	21.7, CH_3	1.19 s	21.3, CH_3
24	4.79 q (6.5)	78.2, CH	4.78 q (6.0)	77.7, CH
25		172.6, C		171.1, C
26	1.37 d (6.5)	18.5, CH_3	1.36 d (6.0)	18.6, CH_3
OAc-12				169.9, C
			1.97 s	21.2, CH_3
OAc-22				170.9, C
			2.07 s	21.2, CH_3

^a 500 MHz. ^b 125 MHz. ^c 600 MHz. ^d 150 MHz.

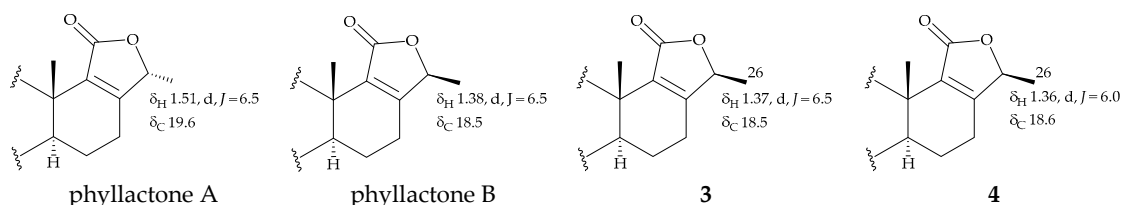


Figure 4. The ^1H and ^{13}C NMR chemical shifts in the methyl group in the α,β -unsaturated- γ -lactone moiety in phyllactones A and B and lendenfeldaranes C (**3**) and D (**4**).

Compound **4** (lendenfeldarane D) has a molecular formula of $\text{C}_{30}\text{H}_{44}\text{O}_6$, as established by (+)-HRESIMS at m/z 523.30301 (calcd. for $\text{C}_{30}\text{H}_{44}\text{O}_6 + \text{Na}$, 523.30307). The ^1H and ^{13}C NMR data indicated that **4** possessed a structural skeleton similar to that of **3** (Table 2). Comparison of the ^1H and ^{13}C NMR spectra of **4** with those of **3** revealed that the C-12 oxymethine resonance at δ_{C} 69.9 observed in **3** was moved to δ_{C} 73.8 in **4**, and the C-22 oxymethene resonance at δ_{C} 63.0 observed in **3** was moved to δ_{C}

64.7 in **4**. Similarly, the ^1H NMR spectrum of **4** displayed two additional acetate methyl signals at δ_{H} 1.97 and 2.07 (both $3\text{H} \times \text{s}$), relative to **3**. Therefore, the differences between compounds **3** and **4** are that the hydroxy groups at C-12 and C-22 in **3** were replaced by acetoxy groups in **4**. The gross structure of **4** is supported by the HMBC and COSY correlations (Figure 2). The stereochemical configuration was identical to that of other scalarane sesterterpenes based on the NOESY cross-peaks at H-5/H-9, H-9/H-14, H₃-20/H-22, H-22/H₃-21, H₃-21/H₃-23, and H₃-23/H-12 (Figure 3). Thus, the structure of **4** was determined and named as lendenfeldarane D (Supplementary Materials, Figures S25–S32).

Based on the cytotoxicity that was demonstrated by the EtOAc extract of *Lendenfeldia* sp., all of the isolates **1–7** were assessed for their cytotoxicity toward the cancer cell lines MOLT-4, K-562, U-937, and SUP-T1 (Table 3). Compound **5** showed the most potent cytotoxicity toward MOLT-4 cells ($\text{IC}_{50} = 0.31 \mu\text{M}$). Since both compounds **5** and **7** were the major components, it was suggested that the cytotoxicity of the extract from *Lendenfeldia* sp. was attributed to these two scalaranes and the aldehyde groups in **5** and **7** played a significant role in their cytotoxicity.

Table 3. The anti-proliferative effects of scalaranes **1–7**.

Compound	Cell lines IC_{50} (μM)			
	MOLT-4	K-562	U-937	SUP-T1
1	39.54	NA	NA	33.02
2	34.93	NA	NA	NA
3	6.31	11.69	5.74	9.00
4	29.83	NA	NA	NA
5	0.31	3.04	2.35	5.90
6	5.67	9.71	6.97	12.33
7	1.49	1.04	5.88	7.49
Doxorubicin ^a	0.02	0.13	0.04	0.09

^a Doxorubicin was used as a positive control; NA: not active at $20 \mu\text{g/mL}$ for 72 h.

3. Material and Methods

3.1. General Experimental Procedures

The optical rotation values were measured using a Jasco P-1010 digital polarimeter (Jasco, Tokyo, Japan). The IR spectra were obtained with a Thermo Scientific Nicolet iS5 FT-IR spectrophotometer (Thermo Fisher Scientific, Waltham, MA, USA). The NMR spectra were recorded on a 600 or a 400 MHz Jeol ECZ NMR (Jeol, Tokyo, Japan) and a 500 MHz Varian Unity INOVA NMR spectrometer (Varian, Palo Alto, CA, USA), using the residual CHCl_3 signals (δ_{H} 7.26 ppm) and CDCl_3 (δ_{C} 77.0 ppm) as the internal standards for ^1H and ^{13}C NMR, respectively. The coupling constants (J) are presented in Hz. ESIMS and HRESIMS were recorded using a Bruker 7 Tesla solarix FTMS system (Bruker, Bremen, Germany). The column chromatography was carried out with silica gel (230–400 mesh; Merck, Darmstadt, Germany). The TLC was performed on plates that were precoated with Kieselgel 60 F₂₅₄ (0.25 mm thick, Merck, Darmstadt, Germany), then sprayed with 10% H_2SO_4 solution, followed by heating to visualize the spots. The normal-phase HPLC (NP-HPLC) was performed using a system comprising a pump (L-7110; Hitachi, Tokyo, Japan), an injection port (Rheodyne, 7725; Rohnert Park, CA, USA), and a semi-preparative normal-phase column (YMC-Pack SIL, $250 \times 20 \text{ mm}$, $5 \mu\text{m}$; Sigma-Aldrich, St. Louis, MO, USA). The reverse-phase HPLC (RP-HPLC) was performed using a system comprising a pump (L-2130; Hitachi), a photodiode array detector (L-2455; Hitachi), an injection port (Rheodyne; 7725), and a reverse-phase column (Luna $5 \mu\text{m}$, C18(2) 100Å AXIA Packed, $250 \times 21.2 \text{ mm}$; Phenomenex, Torrance, CA, USA).

3.2. Animal Material

The specimens of the marine sponge *Lendenfeldia* sp. were collected by hand, using self-contained underwater breathing apparatus (SCUBA), while diving off the coast of Southern Taiwan on 5 September 2012, and stored in a freezer until extraction. The sponge material was identified by Dr. Yusheng M. Huang, Department of Marine Recreation, National Penghu University of Science and Technology, Taiwan, by comparison—as described in a previous publication [21]. A voucher specimen (NMMBA-TWSP-12006) was deposited in the National Museum of Marine Biology and Aquarium, Pingtung, Taiwan.

3.3. Extraction and Isolation

The sliced bodies of *Lendenfeldia* sp. (wet weight 1.21 kg) were extracted with EtOAc. The EtOAc layer (5.09 g) was separated on silica gel and eluted using a mixture of *n*-hexane and EtOAc (stepwise, 100:1–pure EtOAc) to yield 11 fractions A–K. Fraction F was separated by NP-HPLC, using a mixture of *n*-hexane and EtOAc (3:1, flow rate: 3.0 mL/min) to afford seven fractions F1–F7. Fraction F3 was separated by RP-HPLC using a mixture of MeOH and H₂O (7:3, flow rate: 5 mL/min) to afford **4** (1.2 mg). Fraction G was chromatographed on silica gel and eluted using *n*-hexane/acetone (8:1—pure acetone) to afford eight fractions G1–G8. Fraction G3 was separated by NP-HPLC using a mixture of *n*-hexane and acetone (2.5:1, flow rate: 3.0 mL/min) to afford 10 fractions G3A–G3J, including Compound **7** (fraction G3C, 57.5 mg). Fraction G3D was separated by RP-HPLC using a mixture of MeOH and H₂O (8:2, flow rate: 5 mL/min) to afford **3** (0.8 mg). Fraction H was separated on silica gel and eluted using a mixture of *n*-hexane and acetone (6:1–2:1) to obtain 14 fractions H1–H14. Fraction H5 was re-purified by NP-HPLC, using a mixture of *n*-hexane and acetone (5:1, flow rate: 3.0 mL/min) to afford **5** (49.2 mg) and **6** (2.0 mg), respectively. Fraction K was separated by NP-HPLC using a mixture of *n*-hexane and acetone (2:1, flow rate: 3.0 mL/min) to afford **1** (11.4 mg) and **2** (7.6 mg).

Lendenfeldarane A (**1**): amorphous powder; $[\alpha]_D^{20} +17$ (c 0.99, CHCl₃); IR (ATR) ν_{\max} 3552–2420 (broad), 3467, 1716, 1667 cm^{−1}; ¹H (CDCl₃, 400 MHz) and ¹³C (CDCl₃, 100 MHz) NMR data, see Table 1; ESIMS: *m/z* 497 [M + Na]⁺; HRESIMS: *m/z* 497.28736 (calcd. for C₂₈H₄₂O₆ + Na, 497.28712).

Lendenfeldarane B (**2**): amorphous powder; $[\alpha]_D^{20} +49$ (c 0.99, CHCl₃); IR (ATR) ν_{\max} 3444–2309 (broad), 3399, 1740, 1730 cm^{−1}; ¹H (CDCl₃, 600 MHz) and ¹³C (CDCl₃, 150 MHz) NMR data, see Table 1; ESIMS: *m/z* 471 [M + Na]⁺; HRESIMS: *m/z* 471.27171 (calcd. for C₂₆H₄₀O₆ + Na, 471.27142).

Lendenfeldarane C (**3**): amorphous powder; $[\alpha]_D^{20} +56$ (c 0.04, CHCl₃); IR (ATR) ν_{\max} 3436, 1731 cm^{−1}; ¹H (CDCl₃, 500 MHz) and ¹³C (CDCl₃, 125 MHz) NMR data, see Table 2; ESIMS: *m/z* 439 [M + Na]⁺; HRESIMS: *m/z* 439.28188 (calcd. for C₂₆H₄₀O₄ + Na, 439.28174).

Lendenfeldarane D (**4**): amorphous powder; $[\alpha]_D^{20} +38$ (c 0.05, CHCl₃); IR (ATR) ν_{\max} 1738, 1672 cm^{−1}; ¹H (CDCl₃, 600 MHz) and ¹³C (CDCl₃, 150 MHz) NMR data, see Table 2; ESIMS: *m/z* 523 [M + Na]⁺; HRESIMS: *m/z* 523.30301 (calcd. for C₃₀H₄₄O₆ + Na, 523.30307).

12 α -Acetoxy-22-hydroxy-24-methyl-24-oxoscalar-16-en-25-al (**5**): amorphous powder; $[\alpha]_D^{20} +24$ (c 2.46, CHCl₃); IR (ATR) ν_{\max} 1732, 1702, 1662 cm^{−1}; ¹H (CDCl₃, 400 MHz) and ¹³C (CDCl₃, 100 MHz) NMR data were found to be in complete agreement with previous report [17]; ESIMS: *m/z* 481 [M + Na]⁺.

Felixin F (**6**): amorphous powder; $[\alpha]_D^{20} +55$ (c 0.04, CHCl₃) (ref. [18] $[\alpha]_D^{25} +54$ (c 0.4, CHCl₃)); IR (ATR) ν_{\max} 3430, 1701 cm^{−1}; ¹H (CDCl₃, 400 MHz) and ¹³C (CDCl₃, 100 MHz) NMR data were found to be in complete agreement with previous report [18]; ESIMS: *m/z* 455 [M + Na]⁺.

24-Methyl-12,24,25-trioxoscalar-16-en-22-oic acid (**7**): amorphous powder; $[\alpha]_D^{20} +68$ (c 0.04, CHCl₃) (ref. [17] $[\alpha]_D^{21} +33.5$ (c 1, CHCl₃)); IR (ATR) ν_{\max} 3468–2388 (broad), 1732, 1702, 1662 cm^{−1}; ¹H (CDCl₃, 400 MHz) and ¹³C (CDCl₃, 100 MHz) NMR data were found to be in complete agreement with previous report [17]; ESIMS: *m/z* 451 [M + Na]⁺.

3.4. MTT Cell Proliferative Assay

The anti-proliferative properties of the metabolites against a limited panel of human tumor cell lines, including MOLT-4, K-562, U-937, and SUP-T1, were assayed. The cell lines were purchased from the American Type Culture Collection (ATCC). The cells were seeding at 2×10^4 and were cultured in 96-well plates. The cytotoxic effect of the tested compounds was determined by the (3-(4,5-dimethylthiazol-2-yl)-2,5-diphenyltetrazolium bromide (MTT)-cell proliferation assay (Sigma-M2128; Sigma-Aldrich, St. Louis, MO, USA) after 72 h. A total of 50 μ L of MTT solution was added to each well for 1 h and an ELISA reader (Anthoslabtec Instrument, Salzburg, Austria) was used ($OD = OD_{570} - OD_{620}$) for the IC_{50} value, calculated with CalcuSyn software.

4. Conclusions

The marine sponge belonging to the genus *Lendenfeldia* has proven to be a prolific producer of bioactive metabolites, especially sesterterpenoids with a scalarane skeleton. In the present study, seven 24-homoscalaranes were obtained from the *Lendenfeldia* sp. that was collected from the waters of Southern Taiwan, including four new 24-homoscalaranes, lendenfeldaranes A–D (1–4), along with three known analogues, 12 α -acetoxy-22-hydroxy-24-methyl-24-oxo-scalar-16-en-25-al (5), felixin F (6), and 24-methyl-12,24,25-trioxoscalar-16-en-22-oic acid (7). The anti-cancer assessments indicated that 5–7 showed the most promising anti-proliferative activities against tumor cells. The structure-activity relationship (SAR) discussions also suggested the pivotal role of 18-aldehyde functionality in the activity against leukemia and lymphoma. Overall, these results can support the potential use of the marine sponge, genus *Lendenfeldia*, as a therapeutic agent in the treatment of cancer. We have therefore begun to culture this potentially useful sponge in tanks, using our highly developed aquaculture technology, for the extraction of natural products in order to establish a stable supply of bioactive materials, which will also protect the natural population and habitats from over-exploitation.

Supplementary Materials: The following are available online at <http://www.mdpi.com/1660-3397/18/2/76/s1>. HRESIMS, 1D, and 2D NMR spectra of compounds 1–4.

Author Contributions: B.-R.P., S.S.-F.Y., C.-Y.D., and P.-J.S. conceived and designed the experiments; B.-R.P., Y.-Y.C., J.-H.S., Y.M.H., and Y.-H.C. performed the sample collections, species identification, extraction, isolation, and structures determination; the pharmacological experiments were carried out by Y.-Y.C. and M.-C.L.; J.-H.S. and P.-J.S. contributed reagents and analysis tools; B.-R.P., K.-H.L. and P.-J.S. participated in data interpretation, wrote the manuscript and revised the paper. All authors have read and agreed to the published version of the manuscript.

Acknowledgments: This research was supported by grants from the National Museum of Marine Biology and Aquarium; the National Dong Hwa University; and the Ministry of Science and Technology (Grant Nos: MOST 106-2320-B-291-001-MY3 and 107-2320-B-291-001-MY3), Taiwan, awarded to P.-J.S.

Conflicts of Interest: The authors declare no conflict of interest.

References

1. Fattorusso, E.; Magno, S.; Santacroce, C.; Sica, D. Scalarin, a new pentacyclic C-25 terpenoid from the sponge *Cacospongia scalaris*. *Tetrahedron* **1972**, *28*, 5993–5997. [\[CrossRef\]](#)
2. Mo, S.; Kronic, A.; Pegan, S.D.; Franzblau, S.G.; Orjala, J. An antimicrobial guanidine-bearing sesterterpene from the cultured cyanobacterium *Scytonema* sp. *J. Nat. Prod.* **2009**, *72*, 2043–2045. [\[CrossRef\]](#) [\[PubMed\]](#)
3. González, M.A. Scalarane sesterterpenoids. *Curr. Bioact. Compd.* **2010**, *6*, 178–206. [\[CrossRef\]](#)
4. Marshall, L.A.; Winkler, J.D.; Griswold, D.E.; Bolognese, B.; Roshak, A.; Sung, C.-M.; Webb, E.F.; Jacobs, R. Effects of scalaradial, a type II phospholipase A₂ inhibitor, on human neutrophil arachidonic acid mobilization and lipid mediator formation. *J. Pharmacol. Exp. Ther.* **1994**, *268*, 709–717.
5. Fu, X.; Zeng, L.M.; Su, J.Y.; Pais, M.; Potier, P. Scalarane-type bishomosesterterpenes from the sponge *Phyllospongia foliascens*. *J. Nat. Prod.* **1992**, *55*, 1607–1613. [\[CrossRef\]](#)
6. Jiménez, J.I.; Yoshida, W.Y.; Scheuer, P.J.; Lobkovsky, E.; Clardy, J.; Kelly, M. Honulactones: new bishomoscalarane sesterterpenes from the Indonesian sponge *Strepsichordaia aliena*. *J. Org. Chem.* **2000**, *65*, 6837–6840. [\[CrossRef\]](#)

7. Chill, L.; Rudi, A.; Akinin, M.; Loya, S.; Hizi, A.; Kashman, Y. New sesterterpenes from Madagascan *Lendenfeldia* sponges. *Tetrahedron* **2004**, *60*, 10619–10626. [[CrossRef](#)]
8. Cimino, G.; De Rosa, S.; De Stefano, S.; Sodano, G. The chemical defense of four Mediterranean nudibranchs. *Comp. Biochem. Physiol.* **1982**, *73*, 471–474. [[CrossRef](#)]
9. Rogers, S.D.; Paul, V.J. Chemical defenses of three *Glossodoris* nudibranchs and their dietary *Hyrtios* sponges. *Mar. Ecol. Prog. Ser.* **1991**, *77*, 221–232. [[CrossRef](#)]
10. Avila, C.; Paul, V.J. Chemical ecology of the nudibranch *Glossodoris pallida*: Is the location of diet-derived metabolites important for defense? *Mar. Ecol. Prog. Ser.* **1997**, *150*, 171–180. [[CrossRef](#)]
11. Kamel, H.N.; Kim, Y.B.; Rimoldi, J.M.; Fronczek, F.R.; Ferreira, D.; Slattery, M. Scalarane sesterterpenoids: Semisynthesis and biological activity. *J. Nat. Prod.* **2009**, *72*, 1492–1496. [[CrossRef](#)]
12. Bergquist, P.R.; Cambie, R.C.; Kernan, M.R. Scalarane sesterterpenes from *Collospongia auris*, a new thorectid sponge. *Biochem. Syst. Ecol.* **1990**, *18*, 349–357. [[CrossRef](#)]
13. Gavagnin, M.; Mollo, E.; Docimo, T.; Guo, Y.-W.; Cimino, G. Scalarane metabolites of the nudibranch *Glossodoris rufomarginata* and its dietary sponge from the South China Sea. *J. Nat. Prod.* **2004**, *67*, 2104–2107. [[CrossRef](#)]
14. Youssef, D.T.A.; Shaala, L.A.; Emara, S. Antimycobacterial scalarane-based sesterterpenes from the Red Sea sponge *Hyrtios erecta*. *J. Nat. Prod.* **2005**, *68*, 1782–1784. [[CrossRef](#)]
15. Chang, L.C.; Otero-Quintero, S.; Nicholas, G.M.; Bewley, C.A. Phyllolactones A–E: New bishomoscalarane sesterterpenes from the marine sponge *Phyllospongia lamellosa*. *Tetrahedron* **2001**, *57*, 5731–5738. [[CrossRef](#)]
16. Nam, S.-J.; Ko, H.; Shin, M.; Ham, J.; Chin, J.; Kim, Y.; Kim, H.; Shin, K.; Choi, H.; Kang, H. Farnesoid X-activated receptor antagonists from a marine sponge *Spongia* sp. *Bioorg. Med. Chem. Lett.* **2006**, *16*, 5398–5402. [[CrossRef](#)]
17. Kazlauskas, R.; Murphy, P.T.; Wells, R.J. Five new C₂₆ tetracyclic terpenes from a sponge (*Lendenfeldia* sp.). *Aust. J. Chem.* **1982**, *35*, 51–59. [[CrossRef](#)]
18. Lai, Y.-Y.; Chen, L.-C.; Wu, C.-F.; Lu, M.-C.; Wen, Z.-H.; Wu, T.-Y.; Fang, L.-S.; Wang, L.-H.; Wu, Y.-C.; Sung, P.-J. New cytotoxic 24-homoscalarane sesterterpenoids from the sponge *Ircinia felix*. *Int. J. Mol. Sci.* **2015**, *16*, 21950–21958. [[CrossRef](#)]
19. Hochlowski, J.E.; Faulkner, D.J.; Bass, L.S.; Clardy, J. Metabolites of the dorid nudibranch *Chromodoris sedan*. *J. Org. Chem.* **1983**, *48*, 1738–1740. [[CrossRef](#)]
20. Harinantenaina, L.; Brodie, P.J.; Maharavo, J.; Bakary, G.; TenDyke, K.; Shen, Y.; Kingston, D.G.I. Antiproliferative homoscalarane sesterterpenes from two Madagascan sponges. *Bioorg. Med. Chem.* **2013**, *21*, 2912–2917. [[CrossRef](#)]
21. Bergquist, P.R. A revision of the supraspecific classification of the orders Dictyoceratida, Dendroceratida, and Verongida (class Demospongiae). *N. Z. J. Zool.* **1980**, *7*, 443–503. [[CrossRef](#)]



© 2020 by the authors. Licensee MDPI, Basel, Switzerland. This article is an open access article distributed under the terms and conditions of the Creative Commons Attribution (CC BY) license (<http://creativecommons.org/licenses/by/4.0/>).

RESEARCH

Open Access



Oleic acid-based nanosystems for mitigating acute respiratory distress syndrome in mice through neutrophil suppression: how the particulate size affects therapeutic efficiency

Huang-Ping Yu^{1,2†}, Fu-Chao Liu^{1,2†}, Ani Umoro³, Zih-Chan Lin⁴, Ahmed O. Elzoghby^{5,6,7},
Tsong-Long Hwang^{1,3,8,9,10*} and Jia-You Fang^{1,3,8,9*} 

Abstract

Background: Oleic acid (OA) is reported to show anti-inflammatory activity toward activated neutrophils. It is also an important material in nanoparticles for increased stability and cellular internalization. We aimed to evaluate the anti-inflammatory activity of injectable OA-based nanoparticles for treating lung injury. Different sizes of nanocarriers were prepared to explore the effect of nanoparticulate size on inflammation inhibition.

Results: The nanoparticles were fabricated with the mean diameters of 105, 153, and 225 nm. The nanocarriers were ingested by isolated human neutrophils during a 5-min period, with the smaller sizes exhibiting greater uptake. The size reduction led to the decrease of cell viability and the intracellular calcium level. The OA-loaded nanosystems dose-dependently suppressed the superoxide anion and elastase produced by the stimulated neutrophils. The inhibition level was comparable for the nanoparticles of different sizes. In the ex vivo biodistribution study, the pulmonary accumulation of nanoparticles increased following the increase of particle size. The nanocarriers were mainly excreted by the liver and bile clearance. Mice were exposed to intratracheal lipopolysaccharide (LPS) to induce acute respiratory distress syndrome (ARDS), like lung damage. The lipid-based nanocarriers mitigated myeloperoxidase (MPO) and cytokines more effectively as compared to OA solution. The larger nanoparticles displayed greater reduction on MPO, TNF- α , and IL-6 than the smaller ones. The histology confirmed the decreased pulmonary neutrophil recruitment and lung-architecture damage after intravenous administration of larger nanoparticles.

Conclusions: Nanoparticulate size, an essential property governing the anti-inflammatory effect and lung-injury therapy, had different effects on activated neutrophil inhibition and in vivo therapeutic efficacy.

Keywords: Oleic acid, Lipid-based nanoparticles, Size, Anti-inflammation, Neutrophil, Acute respiratory distress syndrome

Background

Oleic acid (OA) is a monounsaturated omega-9 fatty acid that is abundant in plant and animal fats. This fatty acid can have both favorable and unfavorable effects in the immune system. OA can suppress, enhance, or synergize

*Correspondence: htl@mail.cgu.edu.tw; fajy@mail.cgu.edu.tw

[†]Huang-Ping Yu and Fu-Chao Liu contributed equally to this work

³ Graduate Institute of Natural Products, Chang Gung University, 259

Wen-Hwa 1st Road, Kweishan 333, Taoyuan, Taiwan

Full list of author information is available at the end of the article



© The Author(s) 2020. This article is licensed under a Creative Commons Attribution 4.0 International License, which permits use, sharing, adaptation, distribution and reproduction in any medium or format, as long as you give appropriate credit to the original author(s) and the source, provide a link to the Creative Commons licence, and indicate if changes were made. The images or other third party material in this article are included in the article's Creative Commons licence, unless indicated otherwise in a credit line to the material. If material is not included in the article's Creative Commons licence and your intended use is not permitted by statutory regulation or exceeds the permitted use, you will need to obtain permission directly from the copyright holder. To view a copy of this licence, visit <http://creativecommons.org/licenses/by/4.0/>. The Creative Commons Public Domain Dedication waiver (<http://creativecommons.org/publicdomain/zero/1.0/>) applies to the data made available in this article, unless otherwise stated in a credit line to the data.

the hyperactivity of human neutrophils depending on the experimental condition and applied dose [1]. Our previous study [2] demonstrated the effectiveness of OA for inhibiting upregulated superoxide anion and elastase in activated neutrophils. Gonçalves-de-Albuquerque et al. [3] also affirmed the usefulness of OA for decreasing sepsis mortality via reactive oxygen species (ROS) reduction. OA is a compound with an extremely high lipophilicity (*n*-octanol–water partition coefficient = 6.8). It is infeasible to formulate OA into a conventional drug vehicle, especially the injectable aqueous formulation [4]. Nanoparticulate encapsulation is an efficient approach to improving the solubility of highly lipophilic molecules while retaining injectability [5]. The other benefits of injectable nanocarriers for drug delivery include sustained release, prolonged half-life in circulation, increased drug stability, and targeting capability to a nidus [6]. Among the nanocarriers, lipid-based nanosystems show an ideal biodegradability and biocompatibility to entrap lipophilic chemicals. Our previous investigation [7] showed that OA loading in cilomilast-containing lipid nanocarriers could synergize the inhibition of psoriatic inflammation. In addition to the role as an active ingredient, OA can be a stabilizing and emulsifying agent in nanoparticles to produce highly uniform nanosystems [8–10].

The composition and size of nanocarriers is critical to governing the cellular uptake, targeting facility, and therapeutic outcome [11]. In order to maximize the therapeutic and delivery efficiency, we aimed to modulate the particulate size of OA-loaded nanocarriers for evaluating activated neutrophil inhibition, biodistribution, and anti-inflammatory therapy. The present work developed the injectable nanosystems using generally regarded as safe (GRAS-approved) materials such as OA, mineral oil, soy phosphatidylcholine (SPC), and Poloxamer 188. We successfully fabricated lipid-based nanocarriers between 105 and 225 nm by simply changing the amount of mineral oil. The primary human neutrophils were used as a cellular model to explore the anti-inflammatory activity of the lipid-based nanoparticles in this study. We utilized a lipopolysaccharide (LPS)-stimulated mouse model of acute respiratory distress syndrome (ARDS) as an *in vivo* disease model. ARDS is a severe form of acute lung injury (ALI) caused by infection, sepsis, collagen vascular disease, and pulmonary hemorrhage [12]. ARDS is characterized by a massive neutrophil infiltration into the lung [13]. This had led to the potential targeting of neutrophils for ARDS attenuation.

Due to the acute property of ARDS, a quickly effective medication by injection is needed to reduce the associated mortality. Lipid-based nanocarriers are suitable for pulmonary delivery because of the possibility of

deep lung deposition, prolonged release, and low toxicity [14]. We assessed the biodistribution and inflammation suppression of the nanoparticles of different sizes in the ARDS mouse model. The possible influence of the particulate size on anti-inflammation was discussed in this work. The present study's evidence leads to the rational design of anti-inflammatory lipid-based nanoformulations.

Results

Physicochemical properties of OA-loaded nanocarriers

The expected chemical configurations of three nanocarriers are illustrated in Fig. 1a. The nanoparticles were formed consisting of core lipids and emulsifier membrane. Table 1 summarizes the particulate size, polydispersity index (PDI), and zeta potential of the three nanoformulations. The average hydrodynamic diameter of the small (AS), medium (AM), and large (AL) nanoparticles determined by laser-scattering method was 105, 153, and 225 nm, respectively. This indicates that the size could be adjusted by varying the amount of mineral oil, the major material in the lipid core. The prepared nanocarriers exhibited a monodispersity. A narrow PDI (< 0.3) was achieved for AS and AM. All nanocarriers revealed a highly negative zeta potential, with the larger-sized formulations showing a greater negative surface charge. Figure 1b displays the emission spectrum of Nile red in lipid-based nanosystems. The fluorescence would be quenched in the molecular environment with lower lipophilicity. The larger-sized nanoformulations showed a weaker fluorescence, demonstrating the lesser lipophilicity as compared to the smaller size.

The neutrophil uptake of nanocarriers

The OA-loaded nanocarriers should interact with neutrophils for the following endocytosis and bioactivity. We investigated the effect of different sizes on nanoparticle uptake by primary human neutrophils. Flow cytometry was the tool used to offer a quantitative assessment of cellular uptake. As shown in Fig. 1c, a clear increase in the fluorescence signal was detected with decreasing particulate size. We next employed confocal microscopy to observe the uptake of nanoparticles by neutrophils as illustrated in Fig. 1d. The cells were imaged 5 min after nanoparticle exposure. The nanoparticles were quickly internalized into the neutrophils within 5 min. The fluorescence was mainly distributed in the cytoplasm without deterioration of the intact nuclei morphology. As with the use of flow cytometry, the smaller sizes showed greater uptake into the cells than the larger ones.

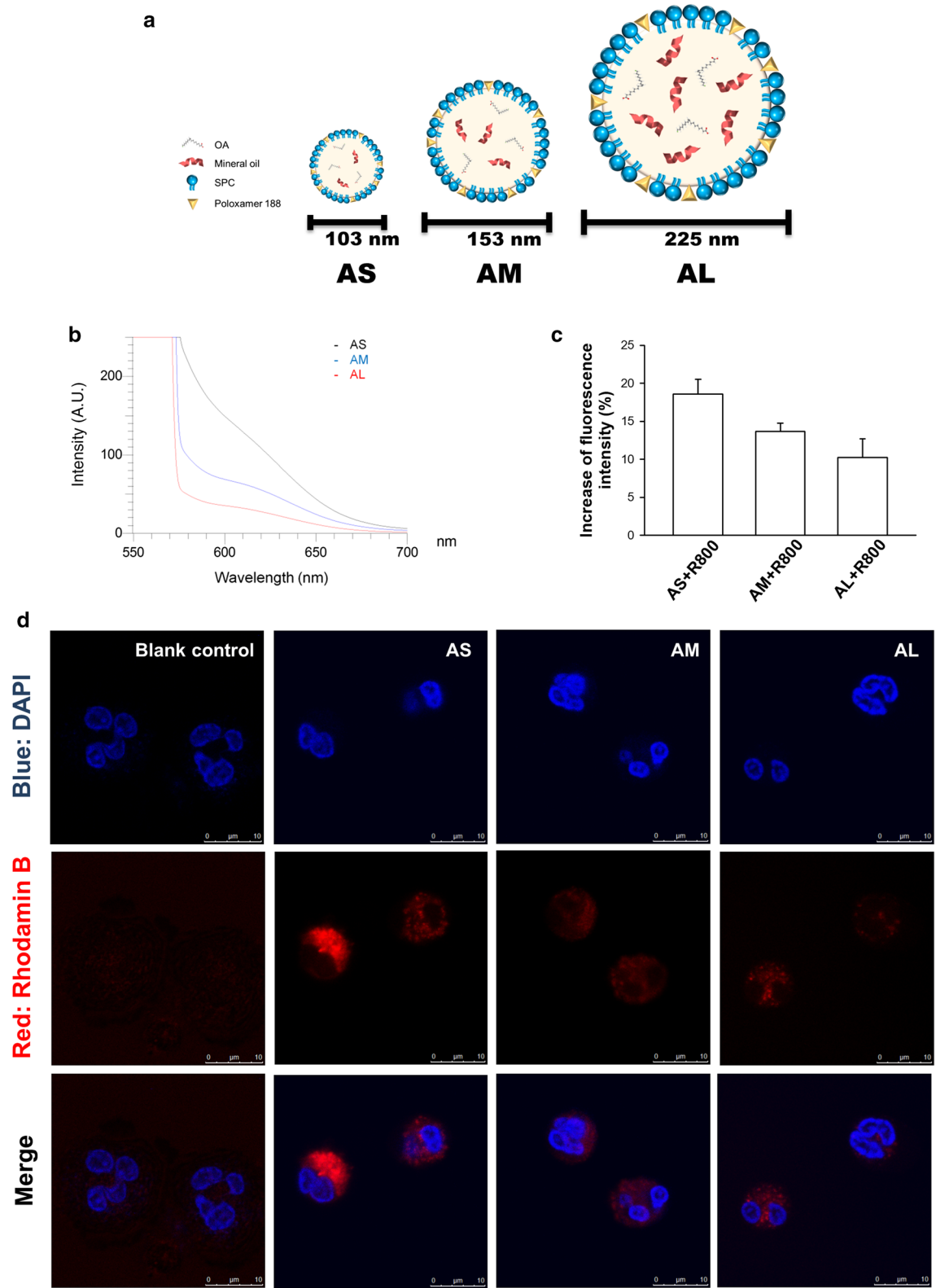


Fig. 1 The uptake of rhodamine 800-loaded OA nanocarriers by human neutrophils. **a** The schematic exhibition of the structures of AS, AM, and AL. **b** Molecular environment (polarity) of the nanocarriers examined by Nile red fluorescence intensity. **c** The fluorescence intensity of rhodamine 800 in the neutrophils analyzed by flow cytometry. **d** Confocal microscopy of neutrophils demonstrated that rhodamine 800-loaded OA nanocarriers (red color) were internalized. Neutrophils nucleus stained (blue) were visualized by DAPI. All data represent mean \pm SEM ($n = 6$)

Table 1 Physiochemical properties of the lipid nanocarriers on nanoparticulate size, polydispersity index (PDI) and zeta potential

Formulation	Size (nm)	PDI	Zeta potential (mV)
AS	102.8 ± 2.8	0.25 ± 0.05	−41.0 ± 0.7
AM	152.6 ± 1.1	0.23 ± 0.01	−46.6 ± 0.7
AL	224.5 ± 4.4	0.33 ± 0.01	−52.6 ± 0.1

Each value represents the mean ± SEM ($n = 3$)

Neutrophil viability

The cytotoxicity assay was conducted by lactate dehydrogenase (LDH) release. As depicted in Fig. 2a, free OA induced no toxicity toward the neutrophils even at a high concentration of 10 µg/ml. Nanocarrier exposure showed no cytotoxicity at OA doses of 1 and 3 µg/ml (Fig. 2b–d). The viability following treatment of nanocarriers was significantly reduced at an OA concentration of 10 µg/ml. The smaller sizes showed higher cytotoxicity against neutrophils than the larger ones at 10 µg/ml.

Superoxide anion production and elastase release

Superoxide anion and elastase leakage are essential indicators of oxidative stress and degranulation in stimulated neutrophils, respectively. We tested the superoxide production and elastase release of neutrophils after the exposure of free or nanoparticulate OA. The OA concentrations of 0.3–10 µg/ml were chosen in this experiment due to the previous experience of effective neutrophil activation inhibition by free fatty acids within this concentration range [2], although the dose of 10 µg/ml caused some cytotoxicity. As shown in Fig. 3a, free OA inhibited superoxide generation in a concentration-dependent manner. Free OA at 3 µg/ml induced a nearly fivefold decrease of superoxide. The same tendency was observed in the case of AS. No superoxide suppression was found by incubation of AS in the absence of OA (blank AS). This suggests that the confinement of neutrophil activation was derived from OA but not from the other ingredients in the nanoparticles. The nanocarriers of different sizes revealed a comparable inhibition on superoxide anion. Free OA has the capacity to dose-dependently impede elastase release as shown in Fig. 3b. This effect was still detectable after encapsulation into nanoparticles. There was no difference in the elastase

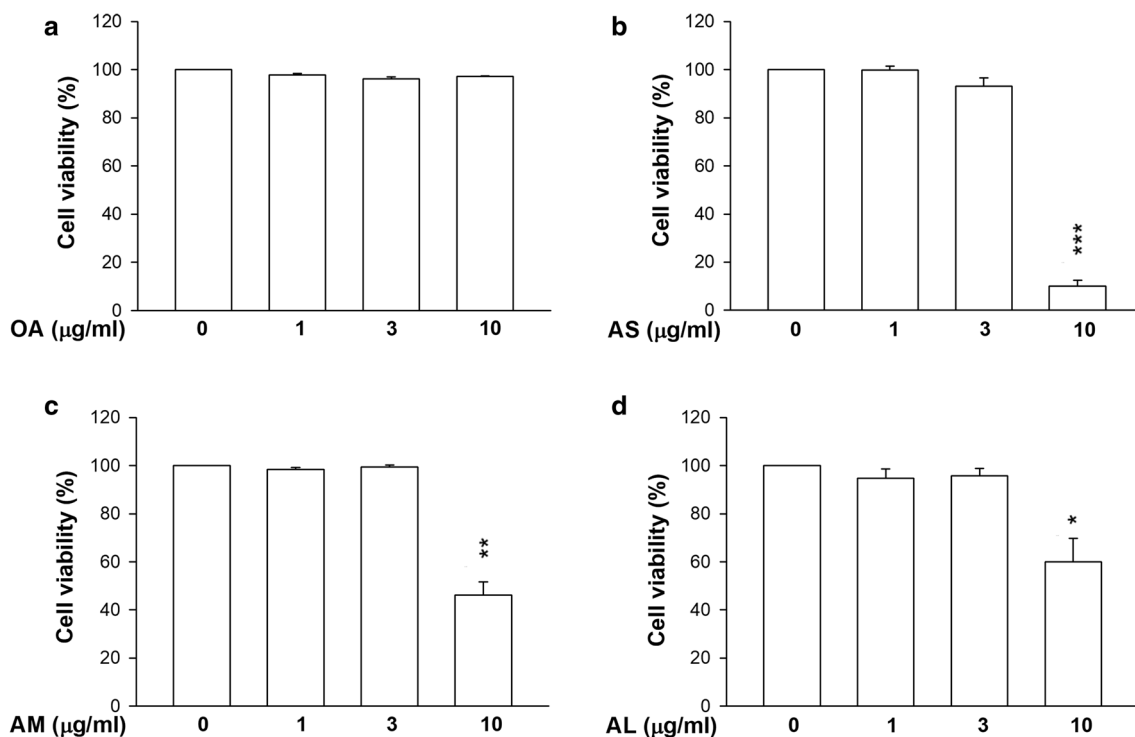
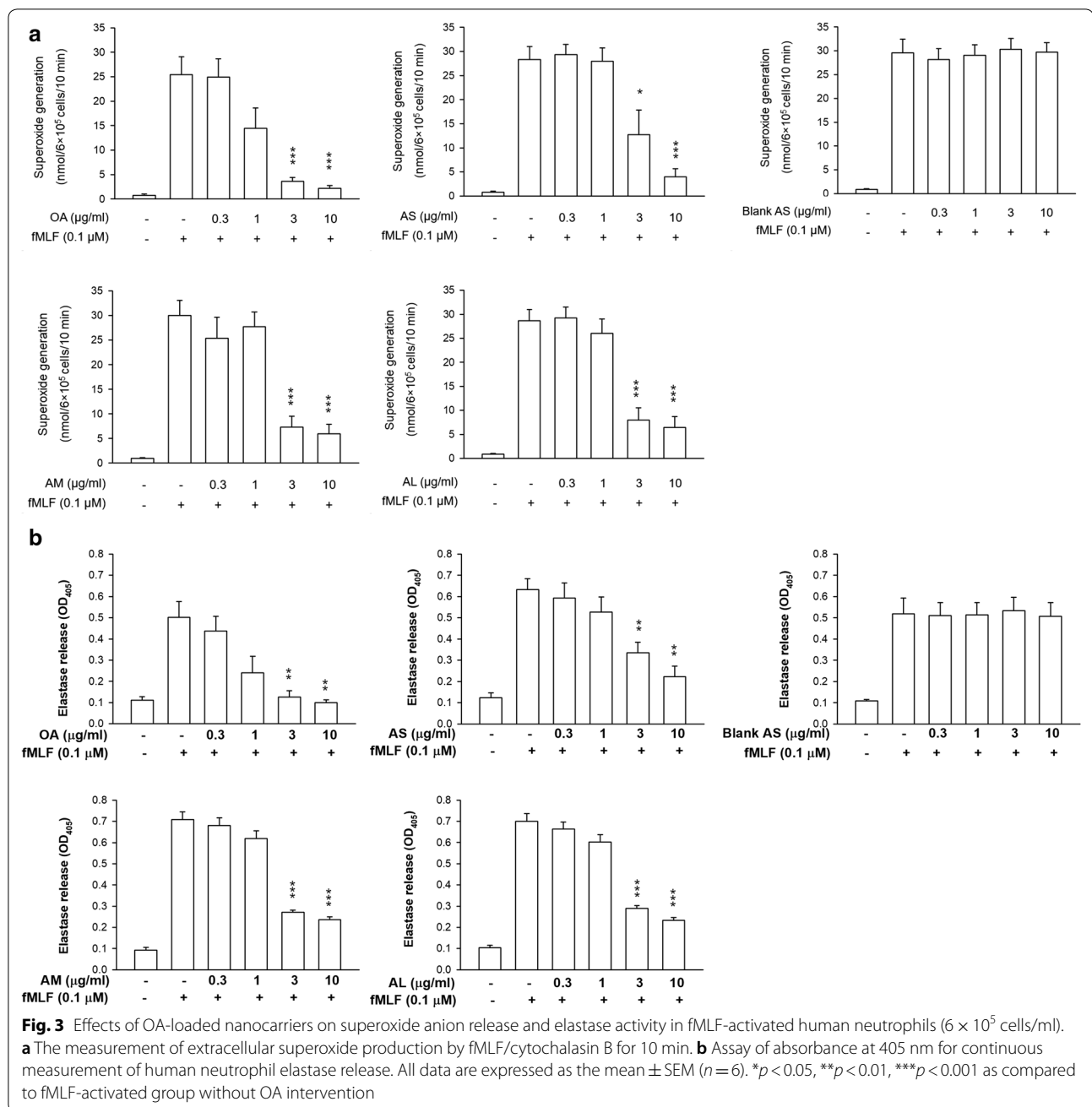


Fig. 2 Neutrophil cytotoxicity assay by treatment of OA-loaded nanocarriers with different droplet sizes. **a** The neutrophils (6×10^5 cells/ml) were treated with free OA. **b** The neutrophils (6×10^5 cells/ml) were treated with AS. **c** The neutrophils (6×10^5 cells/ml) were treated with AM. **d** The neutrophils (6×10^5 cells/ml) were treated with AL. The cytotoxicity was measured by LDH assay. All data are expressed as the mean ± SEM ($n = 6$). * $p < 0.05$, ** $p < 0.01$, *** $p < 0.001$ as compared to control

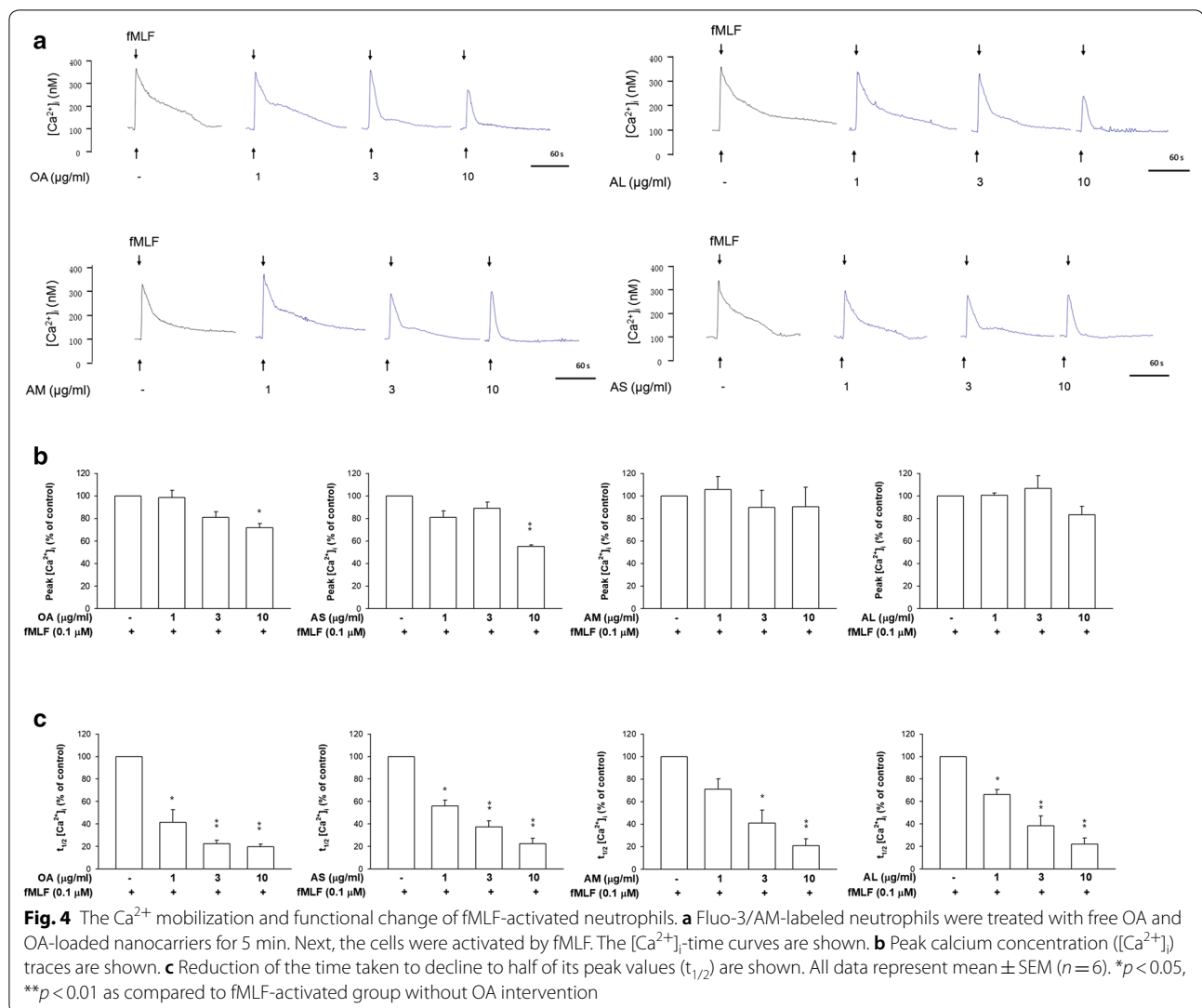


inhibition by nanocarriers with different diameters. Nanoparticle treatment showed less potency on elastase inhibition than the free control.

Intracellular Ca²⁺ ([Ca²⁺]_i) assay

[Ca²⁺]_i presents an important role in the function of activated neutrophils. Formyl-l-methionyl-l-leucyl-l-phenylalanine (fMLF) stimulation results in a fast [Ca²⁺]_i increase as shown in Fig. 4a. This elevation evoked neutrophil activation. The fMLF-stimulated

neutrophils were treated by free and nanoparticulate OA for observing the change of [Ca²⁺]_i. The peak value of [Ca²⁺]_i in spectrofluometry shown in Fig. 4a was computed. As illustrated in Fig. 4b, peak [Ca²⁺]_i could be diminished in the treatments of free OA and AS at a high concentration (10 μg/ml). AM and AL failed to restrain [Ca²⁺]_i. The time needed for [Ca²⁺]_i to return to half of the peak (t_{1/2}) was calculated as presented in Fig. 4c. The t_{1/2} showed a reduction trend in response to free and nanoparticulate OA at all concentrations



tested. The difference of $t_{1/2}$ among all groups tested was limited.

The formation of neutrophil extracellular traps (NETs)

Activated neutrophils undergo degranulation to release NETs. We used phorbol myristate acetate (PMA) to induce the generation of NETs. As shown in Fig. 5, PMA increased NETs by about fivefold as compared to the nontreatment control. Surprisingly, free OA at 10 $\mu\text{g/ml}$ raised the amount of NETs in the absence or presence of PMA (Fig. 5a). The same tendency was detected for all nanocarriers tested (Fig. 5b–d). Since the OA dose of 10 $\mu\text{g/ml}$ could cause cytotoxicity, we selected another dose (3 $\mu\text{g/ml}$) for examining the production of NETs. This low OA dose still increased NETs in the PMA-induced neutrophils.

Biodistribution of nanocarriers

The biodistribution of an active agent entrapped in nanoparticles is controlled by the size and is different from the free form. It is vital to monitor the biodistribution to understand the therapeutic efficacy. The OA-loaded nanoparticles were prepared with the addition of near infrared (NIR) dye to enable visualization using a bioimaging system. Nanoparticle encapsulation minimally changes the NIR intensity of the free dye (Fig. 6a). The three dye-containing nanocarrier samples showed a comparable NIR intensity. The nanoparticles were intravenously injected into the mice. Organs were resected at 2 h post-injection to observe NIR intensity. This time point was adequate to observe the distribution of injectable lipid-based nanoparticles in organs. Since the NIR intensity of the different nanocarrier samples might be somewhat different, we had calibrated the ex vivo organ images by

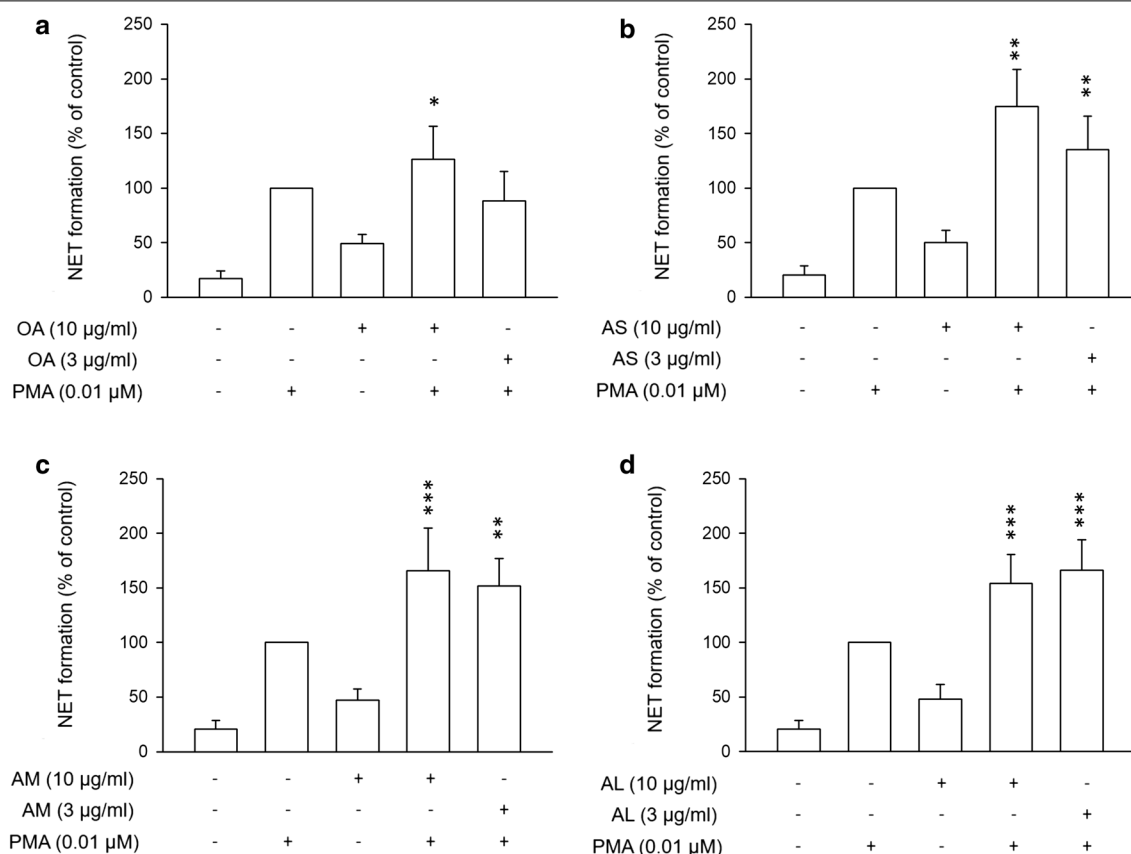


Fig. 5 Effects of OA-loaded nanocarriers on the NET formation. **a** The PMA-activated neutrophils were treated with free OA. **b** The PMA-activated neutrophils were treated with AS. **c** The PMA-activated neutrophils were treated with AM. **d** The PMA-activated neutrophils were treated with AL. * $p < 0.05$, ** $p < 0.01$, *** $p < 0.001$ as compared to PMA-activated group without OA intervention

the intensity of different formulations. Thus the organ images from different nanocarriers could be reasonably compared according to the same criterion. As manifested in Fig. 6b, nanoparticle accumulation is apparently high in the gastrointestinal (GI) tract, the liver, and the lung. A negligible signal was observed in the brain, indicating the minimal penetration of the nanocarriers across the blood–brain barrier. The signal in the heart and spleen was also insignificant. The larger-sized nanocarriers had a higher uptake level in the organs than the smaller ones. Figure 6c summarizes the NIR intensity percentage in the different organs. The OA nanoparticles were primarily distributed to the GI, followed by the liver and the lung. The accumulation percentages of nanosystems in the lung were 10–20%. The lung distribution was increased as size increased. Particulate size exerted an unappreciable effect on the deposition of the other organs.

The effect of nanocarriers on ARDS treatment in mice

An LPS-induced mouse ARDS model was used for pharmacodynamic evaluation of nanoformulations to

corroborate the biodistribution findings and therapeutic efficacy. Intravenous free OA or OA-loaded nanoparticles were administered into the ARDS-like mice. The animals were sacrificed 6 h after LPS instillation to excise the lung for the subsequent histological and biochemical assays. A 6-h period for LPS stimulation is sufficient to induce the ARDS-like syndromes. The hematoxylin and eosin (H&E) staining revealed the cause of inflammation in the LPS group (Fig. 7a), including immune cell infiltration, alveolar hemorrhage, and edema. Free OA marginally ameliorated the inflammatory signs. At the study endpoint, the inflammatory symptoms were further improved by the injectable nanocarriers. Both MPO and Ly6G are the biomarkers of neutrophil recruitment for characterizing the ARDS feature. As shown in Fig. 7b, c, a significant increase of MPO and Ly6G production in pulmonary tissue was found after LPS instillation. The neutrophil accumulation could be decreased by free and nanoparticulate OA, with the nanoparticles displaying better mitigation. The larger nanoparticles showed higher neutrophil inhibition than the smaller ones. To

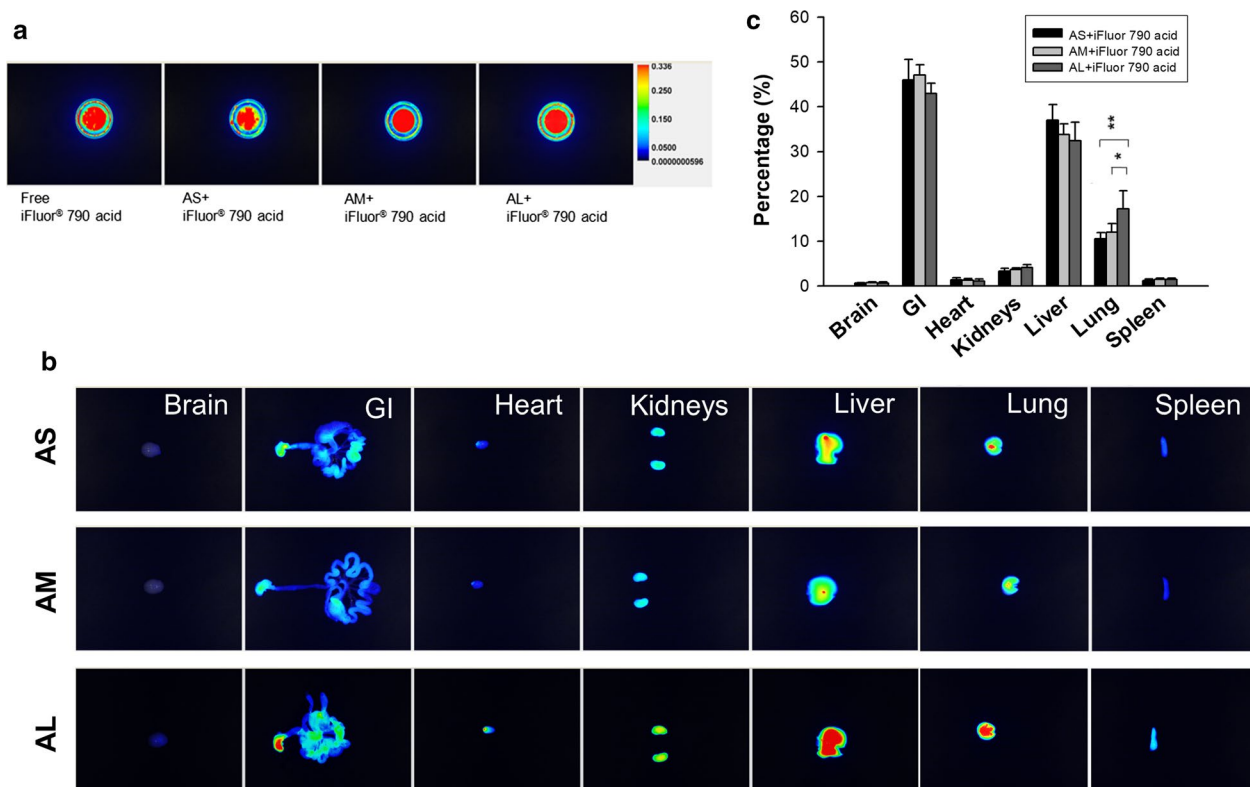


Fig. 6 Ex vivo bioimaging of organs of the mice receiving intravenous iFluor 790 acid-loaded OA nanocarriers. **a** The NIR signal of the prepared samples of free iFluor 790 acid and iFluor 790 acid-loaded OA nanocarriers. **b** The ex vivo bioimaging of organs of representative animals. **c** The percentage (%) of NIR intensity of iFluor 790 acid in different organs analyzed by Pearl Impulse. The scale of bioimaging was calibrated by the intensity of the formulations for impartial comparison. All data represent mean \pm SEM ($n=6$). * $p < 0.05$, ** $p < 0.01$ as compared to AL

further confirm the histology result, we quantified the MPO amount by ELISA analysis. As shown in Fig. 7d, MPO decreased in response to the administration of free and nanoparticulate OA. The highest MPO inhibition was observed in the AL group.

We also quantified the cytokine levels in the lung to explore nanoparticle activity on proinflammatory mediators. In the case of TNF- α (Fig. 7e), the prophylactic administration of AM and AL resulted in a significantly lower expression as compared to the LPS group. This effect was not found in the groups of free OA and AS. IL-1 β expression exhibited no marked inhibition by free OA (Fig. 7f). Treatment of nanocarriers significantly reduced IL-1 β , with similar inhibition for the three nanoformulations. In the case of IL-6 (Fig. 7g), only AL significantly reduced its expression in the LPS-treated lung. The chemokine CXCL-2 was determined as depicted in Fig. 7h. Although the OA-loaded nanosystems clearly inhibited cytokine production in the animal model, an increase of CXCL-2 expression was achieved when administering free or nanoparticulate OA to LPS-treated mice.

Discussion

In this study, we reported the effect of OA-loaded lipid-based nanoparticles on anti-inflammatory potency against neutrophils and the ability to mitigate ARDS in a mouse model. Our ability to control the nanoparticulate size made it possible to elucidate how the specific sizes affected anti-inflammatory efficacy. Our major findings were that the smaller sizes showed greater internalization and cytotoxicity in neutrophils. Nanoparticulate OA inhibited the superoxide and elastase of activated neutrophils with less potency compared to the free control. However, injectable OA-loaded nanoparticles demonstrated greater mitigation on lung injury in vivo than free OA. The larger-sized nanocarriers were beneficial to ameliorate ARDS with greater efficiency. There are limited drugs for treating ARDS-induced inflammation. Current data on the use of steroids in ARDS indicate no definitive evidence of reducing mortality [15]. OA-loaded nanosystems may provide an opportunity to treat ARDS in the future.

Previous study [11] demonstrated that the particulate diameters ranging between 10 and 200 nm are most

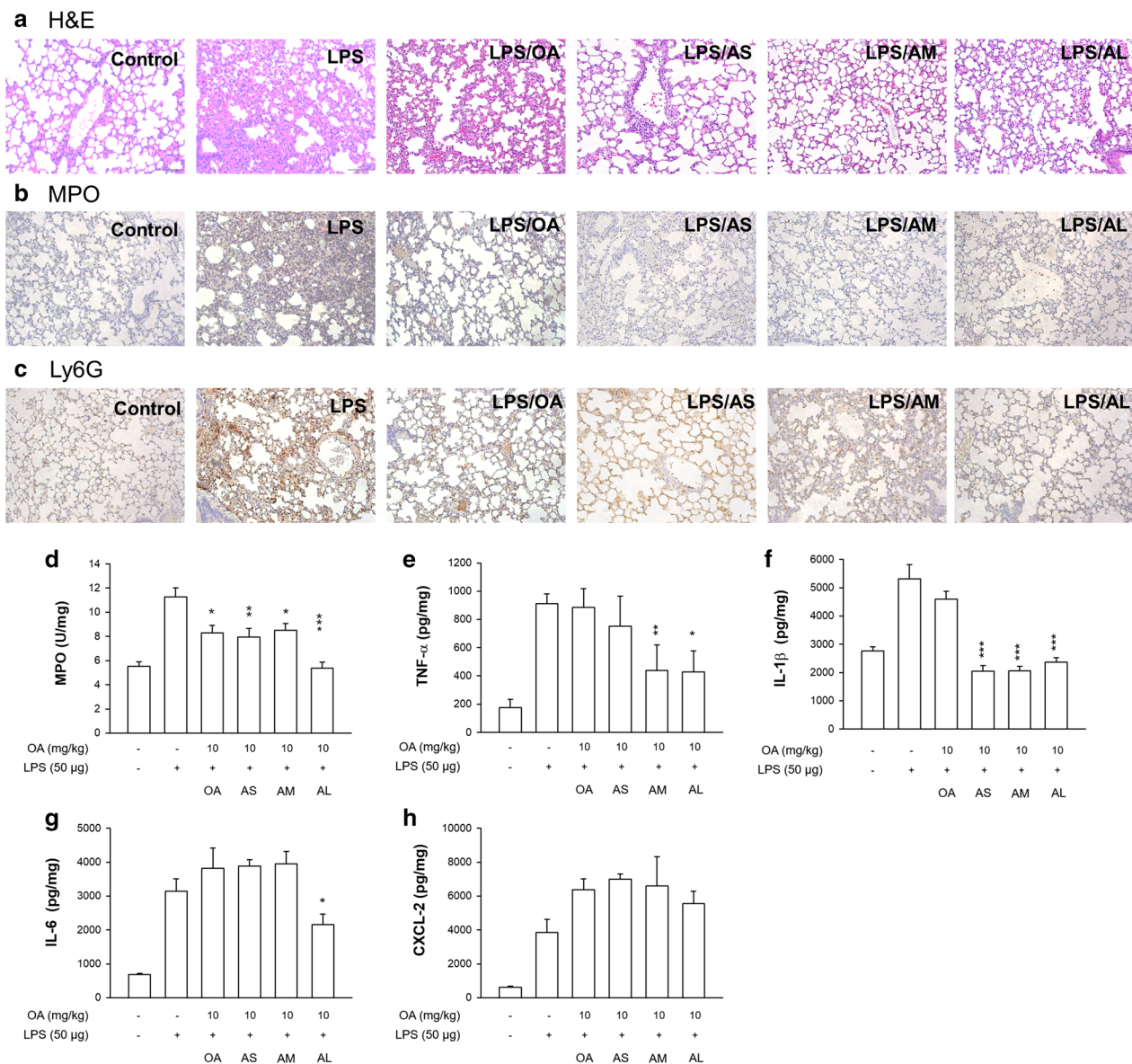


Fig. 7 The effect of intravenous free OA and OA-loaded nanocarriers on LPS-induced lung injury in mice. **a** The lung histology (H&E staining) of LPS-challenged mice treated by free OA and OA-loaded nanocarriers. **b** The immunohistochemistry (MPO antibody staining) of LPS-challenged mice treated by free OA and OA-loaded nanocarriers. **c** The immunohistochemistry (Ly6G antibody staining) of LPS-challenged mice treated by free OA and OA-loaded nanocarriers. **d** MPO expression. **e** TNF- α expression. **f** IL-1 β expression. **g** IL-6 expression. **h** CXCL-2 expression. All data represent mean \pm SEM ($n = 6$). * $p < 0.05$, ** $p < 0.01$, *** $p < 0.001$ as compared to LPS-treated group without OA intervention

relevant for physical and biochemical targeting to specific tissues. Our nanoparticles fell within this range. OA was expected to remain in the lipid core of the nanoparticles because of its high lipophilicity capable of mixing with mineral oil, the main ingredient of the lipid matrix. Nevertheless, the emulsifier nature of OA might lead to the possible intercalation of some OA molecules in the emulsifier layer of the particulate surface. The carboxyl moiety of OA is responsible for negative zeta potential since this

moiety is deprotonated in the physiological environment [4]. We found that the blank AS without OA displayed a negative surface charge of -35.2 mV, which was less than that of OA-loaded AS (-41.0 mV). This confirmed the coating of some OA on the nanoparticulate shell. Zeta potential serves as a predominant factor to offer electrostatic repulsion among the charged nanoparticles for storage stability [16]. The high zeta potential of our nanosystems signified a great repulsion for increased

stability. We developed the nanocarriers with negative surface charges with the aim of injectable anionic nanoparticles being favorable for longer circulation, leading to the possibility of enhanced distribution to the target site [17]. The anionic nanoparticles are also well tolerated in the lung whereas the cationic nanoparticles are detrimental to pulmonary function [18]. Mucin in the mucus layer of the lung is negatively charged. Mucin can capture cationic nanoparticles to retard the penetration into the alveolar space [19]. The negatively charged nanoparticles facilitate transport across the mucus barrier into the alveolar space. The various sizes of OA-loaded nanoparticles are expected to penetrate through the mucus layer with a pore size range of 60–300 nm [20].

The OA nanoparticles were quickly internalized into the neutrophil cytoplasm. The surface functionalization of the nanocarriers is key to their reaction to cellular uptake. OA as the nanoparticulate stabilizer increases the probability of insertion into the cells [21]. OA interaction with membrane phospholipid bilayers can increase and disturb cellular membrane fluidity to increase invagination [1, 22]. This may be one of the reasons for the cytotoxicity induced by OA nanoparticles at a high concentration. The higher surface-to-mass ratio of AS than AM and AL for higher frequency of neutrophil interaction may contribute to the greater cytotoxicity at 10 µg/ml. Previous study [23] also suggests the enhancement of the phagocytic capacity of neutrophils by OA. Lipid-based nanocarriers could be recognized as the soft but not rigid nanoparticles. The soft nanoparticles are easily deformed by the cells for phagocytosis although the negative charge of nanoparticulate surface might retard the interaction between cell membrane and nanoparticles. This internalization process is less energetically favorable [24]. Nanoparticulate size is a physicochemical factor to influence immune cell uptake [25]. It is generally acknowledged that the increased nanoparticulate size correlates with increased uptake by phagocytic cells [26]. This was not the case in the present study. We showed an increased neutrophil ingestion with decreased size of OA-loaded nanoparticles. The size range of our nanocarriers was 105–225 nm. The previous studies that concluded that increased size resulted in increased uptake usually used the particulate size of ≥ 300 nm as the representative of larger particles, e.g. the microscale versus nanoscale [25] and 500 nm versus 150 nm [27]. Wang et al. [28] also demonstrated the inefficient phagocytosis of nanoparticles of < 100 nm by phagocytic macrophages. Of course, the different experimental conditions and nanoparticle types might be responsible for the different results. The size range of OA-loaded lipid-based nanoparticles might display a unique property for neutrophil uptake.

Some investigations support the inverse correlation between particle size and neutrophil uptake. Kelley et al. [29] demonstrated the increased human neutrophil uptake following the size reduction of polystyrene nanoparticles. Gifford et al. [30] suggested a facile uptake of iron oxide nanoparticles with a mean diameter of 110 nm by leukocytes. The increased total surface area-to-mass ratio of the smaller sizes has promoted the opportunity to interact with cells. The smaller-sized nanoparticles often need less driving energy in the internalization procedure. The role of the surface charge and the molecular environment on neutrophil uptake cannot be ignored. The greater zeta potential causes more hydrophilicity of the nanoparticles, decreasing the cellular uptake through a stealth effect [31]. The negative surface charge and hydrophilicity of OA nanocarriers increased following the size increase, leading to less internalization. Basically, the nanoparticles would fuse with the lysosomes after invagination into the cells. The lysosomes degraded the nanoparticles to release active ingredients for revealing the bioactivity.

$[Ca^{2+}]_i$ is a second messenger contributing to neutrophil activation. It is a potential target for anti-inflammation. Our results showed that AS but not AM and AL significantly impeded fMLF-induced Ca^{2+} influx amplification. This could be due to neutrophils' facile uptake of AS. All nanoformulations hastened the speed of $[Ca^{2+}]_i$ decline. The ability of OA to inhibit Ca^{2+} influx has been proved in neutrophils and T lymphocytes [2, 7, 32]. The augmentation of $[Ca^{2+}]_i$ results in neutrophil activation, producing oxidative stress and degranulation. Excess superoxide production by activated neutrophils contributes to lung tissue damage in ARDS via the release of cytokines and chemokines [13]. Elastase also holds an apparent capacity for the pathogenesis of ARDS [33]. Increased superoxide anion production and elastase release by activated neutrophils were abrogated in neutrophils internalizing OA nanoparticles. It should be noted that the inhibitory effect of the lipid-based nanocarriers at a high OA dose (10 µg/ml) was partly mediated via the cytotoxic result. No significant difference in this inhibition was detected for the nanosystems of different sizes. This suggests that although different particulate sizes showed different levels of neutrophil uptake, this effect did not influence the following alleviation of oxidative stress and degranulation. However, the cellular uptake level did affect the cytotoxicity and peak $[Ca^{2+}]_i$.

NETosis is a process of neutrophil degranulation in response to microbial invasion to release elastase, MPO, histones, and extracellular DNA fibers [34]. The creation of NETs is associated with ARDS severity [35]. Although OA nanoparticles could inhibit the release of elastase, NETs were augmented by this treatment. Some

nanoparticles act directly on the neutrophil membrane to activate the generation of NETs. These include lipid-based, silver, polystyrene, and graphene oxide nanoparticles [36–39]. A similar effect might be found in our case. As already mentioned, OA shows controversial data involving inflammation through different mechanisms. Further investigation is necessary to elucidate the detailed mechanisms related to nanoparticle-induced NETosis. It is generally recognized that NETosis is a unique type of neutrophil death via the NADPH-oxidase (Nox)-dependent pathway [40]. Previous evidence [41] expressed that OA only induces Nox-dependent NETosis in human neutrophils. This explains the enhanced NET formation and cell death by the nanosystems with an OA dose at 10 µg/ml.

We aimed to deliver OA-loaded nanocarriers to the lung to treat ARDS. A rationale for nanoformulation design to achieve this intention was the incorporation of SPC and Poloxamer 188 as the emulsifiers. The activated neutrophils migrate to the alveolar space in ARDS development [33], promoting a large number of proinflammatory mediators. The nanoparticles should penetrate across the alveolar epithelium to reach the neutrophils. The epithelium is covered with the lining layer containing pulmonary surfactants. The main components of pulmonary surfactants are phospholipids, neutral lipids, and proteins. These surfactants can be used as efficient carriers associated with nanoparticles for delivery into the airspace [42, 43]. Our previous study [44] showed that the nanovesicles with abundant SPC were beneficial for interacting with pulmonary surfactants for lung targeting. The nanoparticles with a negative surface charge generally have a higher biodistribution than those with a positive charge [45]. The bioimaging assay displayed a broad organ distribution by intravenous OA nanocarriers. A differential response in biodistribution was detected with the different nanocarriers, with larger nanoparticles representing a more-extensive biodistribution in the peripheral organs. This can account for the longer half-life of the smaller nanoparticles in circulation after intravenous injection [26, 45]. Because of the soft and deformable characters of lipid-based nanoparticles, the larger nanoparticles such as AL facily transported across the biological barriers such as the capillary wall.

The lung accumulation of the OA nanoparticles was size-dependent, with the larger sizes exhibiting greater uptake. The nanoparticles even with a large diameter can enter the lung tissue since the pulmonary epithelium in ARDS reveals an elevated microvascular permeability [46]. Dysfunction of the epithelial barrier facilitates the diffusion of macromolecules and nanoparticles into the alveolar space. It is well known that the lung can act as the first mechanical filter in the circulation. The lung

vasculature has an extensive vascular network with 30% of the total endothelial surface. This unique characteristic enables larger nanoparticles to deposit in the lung [45, 47]. Another possibility for greater lung accumulation of larger OA-loaded nanocarriers could be that hydrophilic nanoparticles such as AL tend to rapidly penetrate across pulmonary surfactant film [48]. The plasma proteins easily adsorbed onto the intravenous nanoparticle surface to form a protein corona. This opsonization facilitated the recognition of nanoparticles by a mononuclear phagocyte system and was then engulfed by a reticuloendothelial system such as the liver, spleen, and lung. Previous investigations [47, 49] inferred that the nanoparticles between 100 and 200 nm were largely stored in the liver, whereas the nanoparticles of <50 nm were mainly delivered to the spleen. Our data fitted this criterion, demonstrating that the OA nanocarriers showed a notable liver accumulation but a low spleen uptake. The high level of OA nanoparticles in the GI may suggest the large excretion through the biliary system from the liver to the GI tract. It is possible that nanoparticles deliver epithelial cells and hepatocytes into the bile via the bile duct [50].

MPO and cytokines in ARDS-like pulmonary tissue were analyzed to examine the anti-inflammatory effect of OA nanoparticles. MPO expressed in neutrophil granules is a major mediator of lung injury. Neutrophils also secrete some cytokines such as TNF- α , IL-1 β , and IL-6 to deteriorate ARDS [51]. An attenuation of ARDS by nanoparticulate OA was found, based on the reduction of MPO and cytokines. Histological observation also confirmed a suppression of neutrophil infiltration in mice receiving OA nanoparticles. Neutrophils could be the predominant cells affected. The larger nanoparticles demonstrated greater improvement according to the data of MPO, TNF- α , and IL-6. This result correlated well with the biodistribution in the lung. Though the larger nanoparticles exhibited less capability for neutrophil uptake, the superoxide and elastase inhibition was comparable to that of the smaller sizes. The ARDS mitigation was far superior with nanocarriers than with free OA. By using nanoparticles, a robust increase of OA in the pulmonary tissue could be accomplished. Because of the extremely lipophilic feature, OA was tightly loaded in the lipid matrix with minimal leakage over an extended period, increasing the stability to prevent enzymatic attack. OA encapsulated in lipid-based nanoparticles safely delivered into the lung for neutrophil internalization, resulting in anti-inflammatory action. Free OA possibly even damaged the alveolar endothelium to evoke pulmonary capillary permeability, causing lung injury [52].

ARDS is highly associated with the activation of neutrophils. Our data verified that the inhibition of neutrophil stimulation lessened the signs of pulmonary

inflammation. Although this study focused on the role of neutrophils in lung injury, the other cells related to ARDS cannot be overlooked. Lung injury involves a mixture of cells with origins of neutrophils, alveolar macrophages, dendritic cells, and T lymphocytes [53]. Cytokines can be produced by different immune cells. For instance, IL-6 is a key proinflammatory mediator secreted by neutrophils, macrophages, and T cells to induce an inflammatory cascade in ARDS [51]. Alveolar macrophages are important phagocytic cells in the lung for nanoparticle internalization. Though the larger OA nanoparticles showed less uptake by neutrophils, the larger sizes present a great opportunity to be endocytosed by macrophages [26]. Fromen et al. [18] also indicated that the nanoparticles with a high negative charge are beneficial for internalization by alveolar macrophages. Our results demonstrated the higher negative zeta potential of AL compared to that of AS and AM. NETs appear in the pulmonary microvasculature of ALI patients [54]. However, NETs can be phagocytosed and cleared by macrophages [55]. Although OA nanoparticles elicited the NET creation, this negative effect might be absent in the *in vivo* ARDS model due to the participation of the macrophages.

Another concern is the CXCL-2 upregulation by OA. This suggests the mechanisms other than cytokine inhibition mediated neutrophil chemoattraction. OA is proved to increase chemokines CXCL-8 and MIP-1 α in lung tissue [56]. Oral OA induces CXCL-3 release and neutrophil-endothelium interaction in the air pouch [57]. The increase of CXCL-2 did not affect the overall improvement of the ARDS-like lesion by OA-loaded nanoparticles. There are some limitations in the present study. The mouse neutrophils behave differently from human neutrophils. This can cause difficulty in directly linking or correlating the *in vitro* results with the *in vivo* profiles. According to previous and present investigations, OA treatment demonstrated both advantageous and detrimental impacts on pulmonary tissue. The independent studies are hard to compare due to the variation in experimental setups such as nanoparticle types, cell models, animal models, and the administered doses. Although our nanoformulations were validated as being useful for inhibiting pulmonary inflammation, whether this effect is still maintained with different doses and clinical status remains uncertain. Further study is needed to clarify these questions.

Conclusions

OA-based nanoparticles have attracted interest as the anti-inflammatory nanosystems against neutrophil stimulation. In the present study, we examined how the particulate size of OA nanocarriers influences inflammation suppression and the therapeutic efficiency on lung

injury. The results indicated that neutrophil uptake was strongly size-dependent. Increased nanoparticle ingestion by neutrophils was observed following the decrease in size, leading to the lower cell viability and $[Ca^{2+}]_i$ peak. However, the constrained superoxide anion production and elastase release by nanoparticles were not affected by the size. The nanocarriers could specifically deliver to the pulmonary tissue to treat ARDS-like inflammation in mice. The greater particle diameter demonstrated superior accumulation in the lung. Compared to the smaller-sized nanoparticles, the larger sizes significantly improved the therapeutic effect against ARDS and reduced neutrophilic infiltration in the lung. The nanosystems with larger size (AL) are a better choice for ARDS treatment than the other nanoformulations because of the greater deposition in lung tissue for mitigating lung injury signs, whereas the inhibition of superoxide and elastase in stimulated neutrophils was comparable for all nanosystems. Herein, we suggest how the anti-inflammatory activity, biodistribution, and lung-injury treatment can be modulated using nanoparticle-size modification. The injectable OA-loaded nanoformulations used in this investigation can serve as an effective delivery system for ARDS therapy.

Methods

Fabrication of lipid-based nanocarriers

Three lipid-based nanosystems with different diameters were produced by the emulsification method. The lipid phase consisted of OA (1% of the final product, w/v), SPC (1.5%), and mineral oil. The percentage of mineral oil was 1.5%, 5%, and 10% for development of the final products with small (AS), medium (AM), and large (AL) size, respectively. The aqueous phase consisted of Poloxamer 188 (1.5%) and water. Both phases were heated separately at 85 °C for 20 min. The water phase was then added in drop form into the lipid phase via high-shear homogenization at 12,000 rpm for 20 min, followed by agitation through a probe-type sonicator (35 W) for 20 min. The nanocarriers were used in the experiments after cooling to room temperature.

The size and zeta potential of the nanocarriers

The average diameter, PDI, and zeta potential of the OA-loaded nanoparticles were measured by a laser-scattering procedure (Nano ZS90, Malvern). The nanoparticles were diluted 100-fold with water before measurement.

Molecular environment of the nanocarriers

The degree of lipophilicity of the nanoparticles was determined by fluorescence spectrophotometry based on the solvatochromism of Nile red [58]. Nile red (1×10^{-3} mg/ml) was incorporated in the lipid phase of

the nanosystems. The emission spectra of dye-containing nanosystems were scanned from 550 to 700 nm. The excitation wavelength was set at 546 nm.

Human neutrophil purification

The protocol for this purification was approved by the Institutional Review Board of Chang Gung Memorial Hospital. All subjects (20–30 years old) had signed an informed consent. The blood was collected by venipuncture. The neutrophils were isolated using dextran sedimentation before centrifugation in a Ficoll-Hypaque gradient as previously described [59].

The neutrophil uptake of nanocarriers

The lipid-based nanoparticles were labeled with rhodamine 800 (0.1 mg/ml) as a dye to visualize neutrophil uptake (1.8×10^7 cells/ml). The nanoparticles were treated with the cells for 5 min. The degree of uptake was quantified by measuring the dye fluorescence in flow cytometry. The nuclei were stained by 4',6-diamidino-2-phenylindole (DAPI). The nanoparticle ingestion was observed under confocal microscopy (TCS SP2, Leica).

Neutrophil viability

The neutrophil survival after nanoparticle treatment was measured by LDH release. LDH was analyzed using a commercial kit (CytoTox 96, Promega). The cells (6×10^5 cells/ml) were equilibrated at 37 °C for 2 min. Subsequently, the nanocarriers with OA (1–10 µg/ml) were added into neutrophil suspension for 15 min. The OA doses used in this study were 1, 3, and 10 µg/ml. The total LDH leakage was detected after the treatment by Triton X-100.

Superoxide anion production

We used the superoxide dismutase-inhibitable decrease of ferricytochrome *c* to detect superoxide production [59]. At first, neutrophils (6×10^5 cells/ml) were equilibrated for 2 min after supplementation with ferricytochrome *c* (0.5 mg/ml) and CaCl_2 (1 mM). Then, the nanoformulations were added to the cell suspension for 5 min. The OA doses tested were 0.3, 1, 3, and 10 µg/ml. The cells were activated by fMLF at 100 nM for 10 min. The absorbance with the reduction of ferricytochrome *c* at 550 nm was quantified by a UV/visible spectrophotometer.

Elastase release

Meo-Suc-Ala-Ala-Pro-Val-*p*-nitroanide was employed as the substrate of elastase for detecting elastase release [60]. After the incorporation with the substrate (100 µM), the cells were equilibrated for 2 min and then treated with the nanoformulations for 5 min. We used the OA

dose of 0.3, 1, 3, or 10 µg/ml for testing elastase inhibition. The neutrophils were activated by 100-nM fMLP. Absorbance at 405 nm was obtained by a UV/visible spectrophotometer.

Intracellular Ca^{2+} ($[\text{Ca}^{2+}]_i$) assay

Furo-3/AM (2 µM) was used to treat the neutrophils (3×10^6 cells/ml) at 35 °C for 45 min, followed by centrifugation and resuspension in Hank's balanced salt solution with CaCl_2 (1 mM). The cells were exposed with nanosystems for 5 min at OA dose of 1, 3, or 10 µg/ml. The $[\text{Ca}^{2+}]_i$ in response to fMLF was detected using a fluorescence spectrophotometer with the excitation and emission wavelength at 488 nm and 520 nm, respectively.

The formation of neutrophil extracellular traps (NETs)

The isolated neutrophils (1×10^6 cells/ml) were incubated with nanocarriers at OA concentration of 3 or 10 µg/ml for 10 min and then stimulated with PMA at 10 nM for 3 h. SYTO Green nucleic acid stain (2.5 µM) was added to the cell suspension for 15 min. The fluorescence intensity was quantified at 485 (excitation) and 535 (emission) nm, respectively [61].

Animals

Male C57BL/6 mice (20–25 g) acquired from the National Laboratory Animal Center (Taipei, Taiwan) were used. All study procedures were conducted in accordance with the protocols approved by the Institutional Animal Care and Use Committee of Chang Gung University.

Biodistribution of nanocarriers

We employed an NIR bioimaging system (Pearl Impulse, Li-Cor) to monitor the nanoparticle biodistribution. iFluor 790 acid (0.08%) as the NIR dye was incorporated into the nanocarriers. The nanosystems (2 ml/kg) were intravenously injected into the tail vein of the anesthetized mice. The mice were sacrificed after 2 h. The organs were excised to monitor the NIR signal using the Pearl Impulse bioimaging system.

LPS-induced ARDS

The mice with ARDS-like signs were divided into five groups: ARDS without therapy and ARDS treated with intravenous free OA, AS, AM, or AL. An intratracheal challenge of LPS was carried out as described before [62]. In brief, we injected free OA or OA-loaded nanocarriers into the mice. LPS at 8 mg/kg was administered to the animals after a 30-min injection. The mice were sacrificed 6 h after LPS stimulation. The pulmonary tissue was excised for histological observation and ELISA analysis.

Histological observation

The lung specimen was added into formaldehyde (10%) and embedded in paraffin. The samples were cut to a 3- μ m thickness for H&E staining. For the immunohistochemistry, the slices were incubated with anti-MPO or anti-Ly6G antibody for 1 h. Subsequently, the biotinylated donkey anti-goat IgG was used to treat the samples for 20 min. A light microscope was used to visualize the slices.

ELISA analysis

MPO activity in the lung tissue was measured by the colorimetric assay of combined *o*-dianisidine HCl and H₂O₂ as described previously [63]. Cytokines and chemokines in the pulmonary tissue were quantified by ELISA. The tissue was extracted with buffer containing complete protease inhibitors under homogenization (MagNA Lyser, Roche). The homogenate was centrifuged at 11,500 \times g for 10 min. The supernatant was taken to measure TNF- α , IL-1 β , IL-6, and CXCL-2 employing commercial kits (BioLegend).

Statistical assay

The statistical difference in the data of the various treatments was analyzed by the Kruskal–Wallis test. The post hoc test for checking individual differences was Dunn's test. The 0.05, 0.01, and 0.001 levels of probability were taken as statistically significant.

Authors' contributions

T-LH and J-YF designed the study. H-PY, F-CL, and AU performed the experiments. F-CL, Z-CL, and AOE collected, analyzed, and interpreted the data. H-PY and J-YF prepared the manuscript. T-LH revised the manuscript. All authors read and approved the final manuscript.

Funding

The authors are grateful for the financial support from Ministry of Science and Technology of Taiwan (MOST-108-2314-B-182A-058-MY2 and MOST-108-2314-B-182A-059-MY2) and Chang Gung Memorial Hospital (CMRPG3G1601-2 and CMRPG3H0811-3).

Availability of data and materials

All data and materials in this study are available in this published article.

Ethics approval and consent to participate

All procedures related to animal experiments were carried out in a bioassay laboratory and approved by the Institutional Animal Care and Use Committee of Chang Gung University. All procedures related to the use of human neutrophils were approved by the Institutional Review Board at Chang Gung Memorial Hospital, and written informed consent was obtained from each volunteer.

Consent for publication

Not applicable.

Competing interests

The authors declare that they have no competing interests.

Author details

¹ Department of Anesthesiology, Chang Gung Memorial Hospital, Kweishan, Taoyuan, Taiwan. ² School of Medicine, College of Medicine, Chang Gung University, Kweishan, Taoyuan, Taiwan. ³ Graduate Institute of Natural Products, Chang Gung University, 259 Wen-Hwa 1st Road, Kweishan 333, Taoyuan, Taiwan. ⁴ Graduate Institute of Biomedical Sciences, Chang Gung University, Kweishan, Taoyuan, Taiwan. ⁵ Division of Engineering in Medicine, Department of Medicine, Brigham and Women's Hospital, Harvard Medical School, Boston, MA, USA. ⁶ Harvard-MIT Division of Health Sciences and Technology, Cambridge, MA, USA. ⁷ Cancer Nanotechnology Research Laboratory (CNRL) and Department of Industrial Pharmacy, Faculty of Pharmacy, Alexandria University, Alexandria, Egypt. ⁸ Chinese Herbal Medicine Research Team, Healthy Aging Research Center, Chang Gung University, Kweishan, Taoyuan, Taiwan. ⁹ Research Center for Food and Cosmetic Safety and Research Center for Chinese Herbal Medicine, Chang Gung University of Science and Technology, Kweishan, Taoyuan, Taiwan. ¹⁰ Department of Chemical Engineering, Ming Chi University of Technology, New Taipei City, Taiwan.

Received: 27 November 2019 Accepted: 21 January 2020

Published online: 31 January 2020

References

- Carrillo C, Cavia DM, Alonso-Torre S. Role of oleic acid in immune system; mechanism of action; a review. *Nutr Hosp*. 2012;27(4):978–90.
- Hwang TL, Su YC, Chang HL, Leu YL, Chung PJ, Kuo LM, Chang YJ. Suppression of superoxide anion and elastase release by C₁₈ unsaturated fatty acids in human neutrophils. *J Lipid Res*. 2009;50(7):1395–408.
- Gonçalves-de-Albuquerque CF, Medeiros-de-Moraes IM, de Jesus Oliveira FM, Burth P, Bozza PT, Faria MVC, Silva AR, de Castro-Faria-Neto HC. Omega-9 oleic acid induces fatty acid oxidation and decreases organ dysfunction and mortality in experimental sepsis. *PLoS ONE*. 2016;11(4):e0153607.
- Choi KO, Choe J, Suh S, Ko S. Positively charged nanostructured lipid carriers and their effect on the dissolution of poorly soluble drugs. *Molecules*. 2016;21(5):672.
- Natarajan JV, Nugraha C, Ng XW, Venkatraman S. Sustained-release from nanocarriers: a review. *J Control Release*. 2014;193:122–38.
- Lin MH, Lin CF, Yang SC, Hung CF, Fang JY. The interplay between nanoparticles and neutrophils. *J Biomed Nanotechnol*. 2018;14(1):66–85.
- Lin CY, Hsu CY, Elzoghby AO, Alalawi A, Hwang TL, Fang JY. Oleic acid as the active agent and lipid matrix in cilomilast-loaded nanocarriers to assist PDE4 inhibition of activated neutrophils for mitigating psoriasis-like lesions. *Acta Biomater*. 2019;90:350–61.
- Bloemen M, Brullot W, Luong TT, Geukens N, Gils A, Verbiest T. Improved functionalization of oleic acid-coated iron oxide nanoparticles for biomedical applications. *J Nanopart Res*. 2012;14(9):1100.
- Tran PHL, Tran TTD, Lee BJ. Enhanced solubility and modified release of poorly water-soluble drugs via self-assembled gelatin-oleic acid nanoparticles. *Int J Pharm*. 2013;455(1–2):235–40.
- Shah K, Chan LW, Wong TW. Critical physicochemical and biological attributes of nanoemulsions for pulmonary delivery of rifampicin by nebulization technique in tuberculosis treatment. *Drug Deliv*. 2017;24(1):1631–47.
- Hickey JW, Santos JL, Williford JM, Mao HQ. Control of polymeric nanoparticle size to improve therapeutic delivery. *J Control Release*. 2015;219:536–47.
- Butt Y, Kurdowska A, Allen TC. Acute lung injury: a clinical and molecular review. *Arch Pathol Lab Med*. 2016;140(4):345–50.
- Potey PMD, Rossi AG, Lucas CD, Dordard DA. Neutrophils in the initiation and resolution of acute pulmonary inflammation: understanding biological function and therapeutic potential. *J Pathol*. 2019;247(5):672–85.
- Weber S, Zimmer A, Pardeike J. Solid lipid nanoparticles (SLN) and nanostructured lipid carriers (NLC) for pulmonary application: a review of the state of the art. *Eur J Pharm Biopharm*. 2014;86(1):7–22.
- Hough CL. Should we ever give steroids to ARDS patients? *Clin Chest Med*. 2014;35(4):781–95.
- Fang JY, Lin YK, Wang PW, Alalawi A, Yang YC, Yang SC. The droplet-size effect of squalene@cetylpyridinium chloride nanoemulsions on

- antimicrobial potency against planktonic and biofilm MRSA. *Int J Nanomed*. 2019;14:8133–47.
17. Zhao Z, Ukidve A, Krishnan V, Mitragotri S. Effect of physicochemical and surface properties on in vivo fate of drug nanocarriers. *Adv Drug Deliv Rev*. 2019;143:3–21.
 18. Fromen CA, Rahhal TB, Robbins GR, Kai MP, Shen TW, Luft JC, DeSimone JM. Nanoparticle surface charge impacts distribution, uptake and lymph node trafficking by pulmonary antigen-presenting cells. *Nanomed Nanotechnol Biol Med*. 2016;12(3):677–87.
 19. Suk JS, Kim AJ, Trehan K, Schneider CS, Cebotaru L, Woodward OM, Boylan NJ, Boyle MP, Lai SK, Guggino WB, Hanes J. Lung gene therapy with highly compacted DNA nanoparticles that overcome the mucus barrier. *J Control Release*. 2014;178:8–17.
 20. Song JH, Kim JY, Piao C, Lee S, Kim B, Song SJ, Choi JS, Lee M. Delivery of the high mobility group box 1 box A peptide using heparin in the acute lung injury animal models. *J Control Release*. 2016;234:33–40.
 21. Schütz C, Staedler D, Crosbie-Staunton K, Movia D, Bernasconi CC, Kenzaoui BH, Prina-Mello A, Juillerat-Jeanneret L. Differential stress reaction of human colon cells to oleic-acid-stabilized and unstabilized ultrasmall iron oxide nanoparticles. *Int J Nanomed*. 2014;9:3481–98.
 22. Fang B, Zhang M, Wu H, Fan X, Ren F. Internalization properties of the anti-tumor α -lactalbumin-oleic acid complex. *Int J Biol Macromol*. 2017;96:44–51.
 23. Padovese R, Curi R. Modulation of rat neutrophil function in vitro by cis- and trans-MUFA. *Br J Nutr*. 2009;101(9):1351–9.
 24. Anselmo AC, Mitragotri S. Impact of particle elasticity on particle-based drug delivery systems. *Adv Drug Deliv Rev*. 2017;108:51–67.
 25. Boraschi D, Italiani P, Palomba R, Decuzzi P, Duschl A, Fadeel B, Moghimi SM. Nanoparticles and innate immunity: new perspectives on host defense. *Semin Immunol*. 2017;34:33–51.
 26. Hoshyar N, Gray S, Han H, Bao G. The effect of nanoparticle size on in vivo pharmacokinetics and cellular interaction. *Nanomedicine*. 2016;11(6):673–92.
 27. He C, Hu Y, Yin L, Tang C, Yin C. Effects of particle size and surface charge on cellular uptake and biodistribution of polymeric nanoparticles. *Biomaterials*. 2010;31(13):3657–66.
 28. Wang B, He X, Zhang Z, Zhao Y, Feng W. Metabolism of nanomaterials in vivo: blood circulation and organ clearance. *Acc Chem Res*. 2013;46(3):761–9.
 29. Kelley WJ, Fromen CA, Lopez-Cazares G, Eniola-Adefeso O. PEGylation of model drug carriers enhances phagocytosis by primary human neutrophils. *Acta Biomater*. 2018;79:283–93.
 30. Gifford G, Vu VP, Banda NK, Holers VM, Wang G, Groman EV, Backos D, Scheinman R, Moghimi SM, Simberg D. Complement therapeutics meets nanomedicine: overcoming human complement activation and leukocyte uptake of nanomedicines with soluble domains of CD55. *J Control Release*. 2019;302:181–9.
 31. Alexis F, Pridgen E, Molnar LK, Farokhzad OC. Factors affecting the clearance and biodistribution of polymeric nanoparticles. *Mol Pharm*. 2008;5(4):505–15.
 32. Gamberucci A, Fulcieri R, Benedetti A. Inhibition of store-dependent capacitative Ca^{2+} influx by unsaturated fatty acids. *Cell Calcium*. 1997;21(5):375–85.
 33. Grommes J, Soehnlein O. Contribution of neutrophils to acute lung injury. *Mol Med*. 2011;17(3–4):293–307.
 34. Twaddell SH, Baines KJ, Grainge C, Gibson PG. The emerging role of neutrophil extracellular traps in respiratory disease. *Chest*. 2019;156(4):774–82.
 35. Lefrançois E, Mallavia B, Zhuo H, Calfee CS, Looney MR. Maladaptive role of neutrophil extracellular traps in pathogen-induced lung injury. *JCI Insight*. 2018;3(3):98178.
 36. Hwang TL, Aljuffali IA, Hung CF, Chen CH, Fang JY. The impact of cationic solid lipid nanoparticles on human neutrophil activation and formation of neutrophil extracellular traps (NETs). *Chem-Biol Interact*. 2015;235:106–14.
 37. Liz R, Simard JC, Leonardi LB, Girard D. Silver nanoparticles rapidly induce atypical human neutrophil cell death by a process involving inflammatory caspases and reactive oxygen species and induce neutrophil extracellular traps release upon cell adhesion. *Int Immunopharmacol*. 2015;28(1):616–25.
 38. Muñoz LE, Bilyy R, Biermann MH, Kienhöfer D, Maueröder C, Hahn J, Brauner JM, Weidner D, Chen J, Scharin-Mehlmann M, Janko C, Friedrich RP, Mielenz D, Dumych T, Lootsik MD, Schauer C, Schett G, Hoffmann M, Zhao Y, Herrmann M. Nanoparticles size-dependently initiate self-limiting NETosis-driven inflammation. *Proc Natl Acad Sci U S A*. 2016;113(40):5856–65.
 39. Mukherjee SP, Lazzaretto B, Hultenby K, Newman L, Rodrigues AF, Lozano N, Kostarelos K, Malmberg P, Fadeel B. Graphene oxide elicits membrane lipid change and neutrophil extracellular trap formation. *Chem*. 2018;4(2):334–58.
 40. Ravindran M, Khan MA, Pananiyar N. Neutrophil extracellular trap formation: physiology, pathology and pharmacology. *Biomolecules*. 2019;9(8):365.
 41. Khan MA, Pace-Asciak C, Al-Hassan JM, Afzal M, Liu YF, Oommen S, Paul BM, Nair D, Palaniyar N. Furanoid F-acid F6 uniquely induces NETosis compared to C16 and C18 fatty acids in human neutrophils. *Biomolecules*. 2018;8(4):144.
 42. De Backer L, Cerrada A, Pérez-Gil J, De Smedt SC, Raemdonck K. Bio-inspired materials in drug delivery: exploring the role of pulmonary surfactant in siRNA inhalation therapy. *J Control Release*. 2015;220:642–50.
 43. Hidalgo A, Cruz A, Pérez-Gil J. Barrier or carrier? Pulmonary surfactant and drug delivery. *Eur J Pharm Biopharm*. 2015;95:117–27.
 44. Hsu CY, Sung CT, Aljuffali IA, Chen CH, Hu KY, Fang JY. Intravenous anti-MRSA phosphatidylserine mediate enhanced affinity to pulmonary surfactants for effective treatment of infectious pneumonia. *Nanomed Nanotechnol Biol Med*. 2018;14(2):215–25.
 45. Javidi J, Haeri A, Nowroozi F, Dadashzadeh S. Pharmacokinetics, tissue distribution and excretion of Ag_2S quantum dots in mice and rats: the effects of injection dose, particle size and surface charge. *Pharm Res*. 2019;36(3):46.
 46. D'Almeida APL, de Oliveira MTP, de Souza ÉT, de Sá Coutinho D, Ciambarella BT, Gomes CR, Terroso T, Guterres SS, Pohlmann AR, Silva PMR, Martins MA, Bernardi A. α -bisabolol-loaded lipid-core nanocapsules reduce lipopolysaccharide-induced pulmonary inflammation in mice. *Int J Nanomed*. 2017;12:4479–91.
 47. Xue W, Liu Y, Zhang N, Yao Y, Ma P, Wen H, Huang S, Luo Y, Fan H. Effects of core size and PEG coating layer of iron oxide nanoparticles on the distribution and metabolism in mice. *Int J Nanomed*. 2018;13:5719–31.
 48. Hu G, Jiao B, Shi X, Valle RP, Fan Q, Zuo YY. Physicochemical properties of nanoparticles regulate translocation across pulmonary surfactant monolayer and formation of lipoprotein corona. *ACS Nano*. 2013;7(12):10525–33.
 49. Longmire M, Choyke PL, Kobayashi H. Clearance properties of nanosized particles and molecules as imaging agents: considerations and caveats. *Nanomedicine*. 2018;3(5):703–17.
 50. Poon W, Zhang YN, Ouyang B, Kingston BR, Wu JLY, Wilhelm S, Chan WCW. Elimination pathways of nanoparticles. *ACS Nano*. 2019;13(5):5785–98.
 51. Qin M, Qiu Z. Changes in TNF- α , IL-6, IL-10 and VEGF in rats with ARDS and the effects of dexamethasone. *Exp Ther Med*. 2019;17(1):383–7.
 52. Xu X, Zhu Q, Zhang R, Wang Y, Niu F, Wang W, Sun D, Wang A. ITRAQ-based proteomics analysis of acute lung injury induced by oleic acid in mice. *Cell Physiol Biochem*. 2017;44(5):1949–64.
 53. Shaver CM, Bastarache JA. Clinical and biological heterogeneity in ARDS: direct versus indirect lung injury. *Clin Chest Med*. 2014;35(4):639–53.
 54. Caudrillier A, Kessenbrock K, Gilliss BM, Nguyen JX, Marques MMB, Monestier M, Toy P, Werb Z, Looney MR. Platelets induce neutrophil extracellular traps in transfusion-related acute lung injury. *J Clin Invest*. 2012;122(7):2661–71.
 55. Farrera C, Fadeel B. Macrophage clearance of neutrophil extracellular traps is a silent process. *J Immunol*. 2013;191(5):2647–56.
 56. Gonçalves-de-Albuquerque CF, Silva AR, Burth P, Castro-Faria MV, Castro-Faria-Neto HC. Acute respiratory distress syndrome: role of oleic acid-triggered lung injury and inflammation. *Mediators Inflamm*. 2015;2015:260465.
 57. Rodrigues HG, Vinolo MA, Magdalon MA, Fujiwara J, Cavalcanti H, Farsky DM, Calder SH, Hatanaka PC, Curi E. Dietary free oleic and linoleic acid enhances neutrophil function and modulates the inflammatory response in rats. *Lipids*. 2010;45(9):809–19.
 58. Pan TL, Wang PW, Hung CF, Aljuffali IA, Dai YS, Fang JY. The impact of retinol loading and surface charge on the hepatic delivery of lipid nanoparticles. *Colloids Surf B*. 2016;141:584–94.

59. Yu HP, Hsieh PW, Chang YJ, Chung PJ, Kuo LM, Hwang TL. 2-(2-Fluoroben-zamido)benzoate ethyl ester (EFB-1) inhibits superoxide production by human neutrophils and attenuates hemorrhagic shock-induced organ dysfunction in rats. *Free Radic Biol Med*. 2011;50(12):1737–48.
60. Hsieh PW, Yu HP, Chang YJ, Hwang TL. Synthesis and evaluation of benzoxazinone derivatives on activity of human neutrophil elastase and on hemorrhagic shock-induced lung injury in rats. *Eur J Med Chem*. 2010;45(7):3111–5.
61. Yang SC, Chen PJ, Chang SH, Weng YT, Chang FR, Chang KY, Chen CY, Kao TZ, Hwang TL. Luteolin attenuates neutrophilic oxidative stress and inflammatory arthritis by inhibiting Raf1 activity. *Biochem Pharmacol*. 2018;154:384–96.
62. Asti C, Ruggieri V, Porzio S. Lipopolysaccharide-induced lung injury in mice. I. Concomitant evaluation of inflammatory cells and haemorrhagic lung damage. *Pulm Pharmacol Ther*. 2000;13(2):61–9.
63. Tsai YF, Yu HP, Chung PJ, Leu YL, Kuo LM, Chen CY, Hwang TL. Osthol attenuates neutrophilic oxidative stress and hemorrhagic shock-induced lung injury in rats. *Biochem Pharmacol*. 2015;89:387–400.

Publisher's Note

Springer Nature remains neutral with regard to jurisdictional claims in published maps and institutional affiliations.

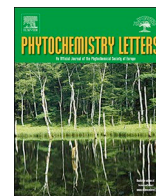
Ready to submit your research? Choose BMC and benefit from:

- fast, convenient online submission
- thorough peer review by experienced researchers in your field
- rapid publication on acceptance
- support for research data, including large and complex data types
- gold Open Access which fosters wider collaboration and increased citations
- maximum visibility for your research: over 100M website views per year

At BMC, research is always in progress.

Learn more biomedcentral.com/submissions





New trihydroxybriarane diterpenoids from an octocoral *Briareum* sp

Chiung-Chin Hu^a, Nai-Cheng Lin^a, Bo-Rong Peng^a, You-Ying Chen^a, Zhi-Hong Wen^b,
Yu-Chia Chang^c, Gene-Hsiang Lee^d, Yang-Chang Wu^{e,f,*}, Ping-Jyun Sung^{a,b,f,g,h,*}

^a National Museum of Marine Biology and Aquarium, Pingtung, 94450, Taiwan

^b Department of Marine Biotechnology and Resources, National Sun Yat-sen University, Kaohsiung, 80424, Taiwan

^c Research Center for Chinese Herbal Medicine, Research Center for Food and Cosmetic Safety, Graduate Institute of Healthy Industry Technology, College of Human Ecology, Chang Gung University of Science and Technology, Taoyuan, 33303, Taiwan

^d Instrumentation Center, National Taiwan University, Taipei, 10617, Taiwan

^e Graduate Institute of Integrated Medicine, College of Chinese Medicine, China Medical University, Taichung, 40402, Taiwan

^f Chinese Medicine Research and Development Center, China Medical University Hospital, Taichung, 40447, Taiwan

^g Graduate Institute of Marine Biology, National Dong Hwa University, Pingtung, 94450, Taiwan

^h Graduate Institute of Natural Products, Kaohsiung Medical University, Kaohsiung, 80708, Taiwan

ARTICLE INFO

Keywords:

Briareum
Excavatulide
Briaviolide
Briarane
iNOS
COX-2

ABSTRACT

Chemical investigation of the extract from the supercritical CO₂ extraction of an octocoral identified as *Briareum* sp., afforded a known briarane-type diterpenoid, excavatulide B (1), and a pair of new briaranes, briaviolides Y (2) and Z (3). The absolute configuration of 1 was determined by a single-crystal diffraction analysis and the structures of briaranes 2 and 3 were elucidated by using spectroscopic methods. Additionally, anti-inflammatory analysis showed that briarane 3 suppressed the iNOS and COX-2 levels, in LPS-stimulated RAW264.7 cells.

1. Introduction

Since 1977, the first briarane-type diterpenoid, briarein A, was reported from the Caribbean octocoral *Briareum asbestinum* (Burks et al., 1977), over 700 marine-origin briarane analogues containing a γ -lactone in a bicyclo[8.4.0] system have been isolated from various octocorals (Su et al., 2017). In order to fit the tendency of green chemistry, an encrusting octocoral identified as *Briareum* sp. (kingdom Animalia, phylum Cnidaria, class Anthozoa, order Alcyonacea, family Briareidae) (Fig. 1), distributed in the tropical waters of Taiwan, was extracted by supercritical CO₂ and a known briarane, excavatulide B (1) (Sheu et al., 1998; Yao et al., 2019) and a pair of new briaranes, briaviolides Y (2) and Z (3), featuring with an 11 β ,12 α -dihydroxy-13(Z)-en moiety, were isolated (Fig. 1). We reported herein the isolation and structural elucidation of briaranes 1–3 as well as anti-inflammatory activity of briaranes 2 and 3 to inhibit the accumulation of pro-inflammatory iNOS and COX-2 protein.

2. Results and discussion

Excavatulide B (1) was first isolated from the octocoral *Briareum excavatum*; and the structure of this compound was elucidated by

spectroscopic methods and X-ray analysis (Sheu et al., 1998; Yao et al., 2019). The structure, including the absolute configuration of 1 was established in this study by a single-crystal X-ray diffraction analysis (Flack parameter $x = 0.01(3)$) and the ORTEP diagram (Fig. 1) showed the configurations of stereogenic carbons are 1R,2R,3S,7S,8R,9S,10S,11R, 12S,14S and 17R.

Briaviolide Y (2) was found to have the molecular formula C₂₄H₃₂O₁₀ and nine degrees of unsaturation, as indicated from the HRESIMS at m/z 503.18868 (calcd for C₂₄H₃₂O₁₀ + Na, 503.18877). The IR absorptions at 3363, 1777 and 1717 cm⁻¹, indicated that the presence of hydroxy, γ -lactone and ester groups. The structure of 2 was directly inferred from its ¹³C NMR spectra (Table 1), where it indicated that there were 20 carbon signals in total after subtraction of 4 carbons ascribed to two acetate groups. Comparison of the ¹³C and DEPT data with the molecular formula indicated that there must be three exchangeable protons, requiring the presence of three hydroxy groups. The ¹³C NMR data confirmed the presence of 24 signals, characterized by DEPT spectra as 6 methyls, 1 sp³-CH₂, 6 sp³-CH (including 5 oxymethines), 4 sp³ quaternary carbons (including 3 oxygenated quaternary carbons), 3 sp²-CH, 1 sp² quaternary carbon and 3 sp² carbonyls. Based on the ¹H and ¹³C NMR data (Table 1), 2 was determined to possess a disubstituted olefin (δ_H 5.94, 1H, dd, $J = 10.0, 5.2$ Hz, H-13;

* Corresponding authors at: National Museum of Marine Biology and Aquarium, Pingtung, 94450, Taiwan.

E-mail addresses: yachwu@gmail.com (Y.-C. Wu), pjsung@nmmba.gov.tw (P.-J. Sung).

<https://doi.org/10.1016/j.phytol.2019.10.003>

Received 26 June 2019; Received in revised form 6 October 2019; Accepted 21 October 2019

Available online 10 November 2019

1874-3900/ © 2019 Phytochemical Society of Europe. Published by Elsevier Ltd. All rights reserved.

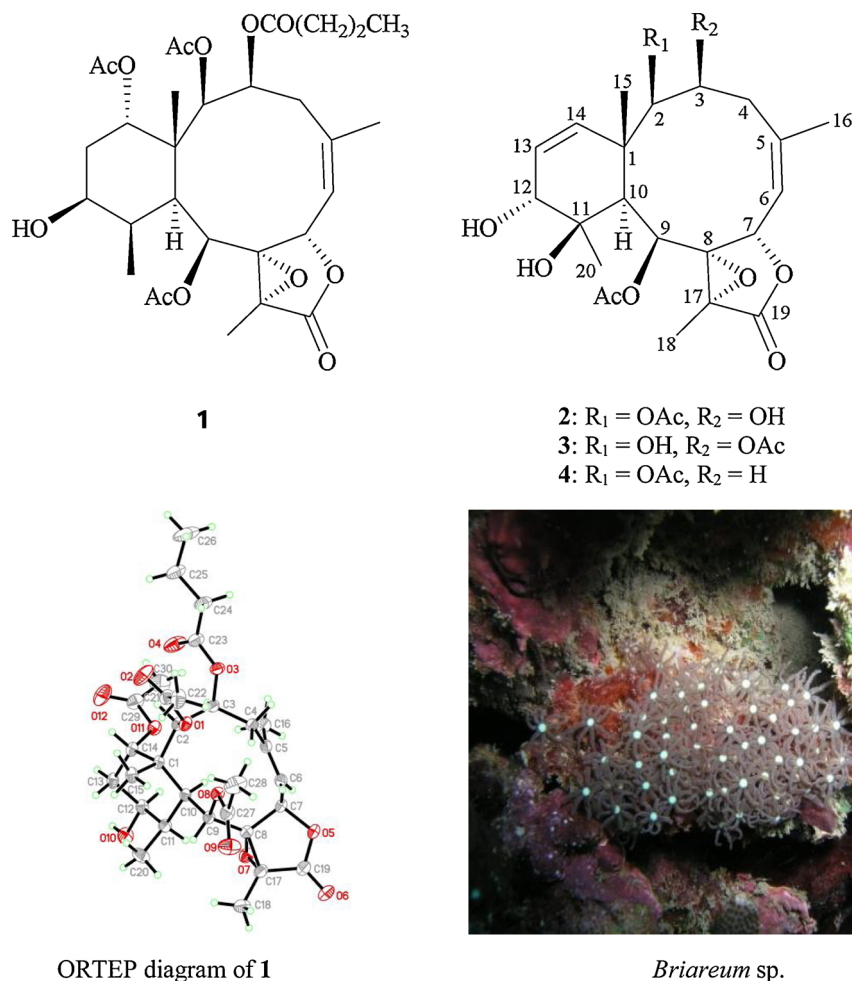


Fig. 1. Structures of excavatolide B (1), briaviolides Y (2) and Z (3), the computer-generated ORTEP diagram of 1 and a picture of *Briareum* sp.

5.52, 1H, d, $J = 10.0$ Hz, H-14; δ_C 125.1, CH-13; 138.7, CH-14), a tri-substituted olefin (δ_H 5.41, 1H, dd, $J = 10.0, 1.2$ Hz, H-6; δ_C 141.4, C-5; 121.2, CH-6), two acetoxyl groups (δ_H 2.36, 2.16, each 3H s; δ_C 21.3, 21.9, 2 \times acetate methyls; 172.4, 170.1, 2 \times acetate carbonyls) and a γ -lactone moiety (δ_C 171.7, C-19). A tetrasubstituted epoxide containing a methyl substituent was confirmed from the signals of two quaternary oxygenated carbons at δ_C 71.0 (C-8) and 62.2 (C-17) and from the proton signal of a methyl at δ_H 1.50 (3H, s, H-18). Based on the ^{13}C NMR data and numbers of unsaturation, 2 was established as a tetracyclic briarane diterpenoid.

The ^1H NMR coupling information in the COSY spectrum analysis of 2 enabled the determination of proton sequences between H-3/H-4 β , H-6/H-7, H-9/H-10 and H-12/H-13/H-14 units (Fig. 2), which were assembled with the assistance of an HMBC experiment (Fig. 2). The HMBC between protons and quaternary carbons, such as H-2, H-10, H-13, H-14, H₃-15/C-1; H₂-4, H-7, H₃-16/C-5; H-9, H-10, H₃-18/C-8; H-9, H-10, H-12, H-13, H₃-20/C-11; H₃-18/C-17; and H₃-18/C-19, permitted elucidation of the carbon skeleton. The presence of a vinyl methyl group on C-5 was supported by HMBC between H₂-4, H-6/C-16; H₃-16/C-4, C-5, C-6, and further supported by an allylic coupling between H-6/H₃-16 ($J = 1.2$ Hz). The methyl group (Me-15) on C-1 was substantiated by the HMBC from H₃-15/C-1, C-2, C-10, C-14; and H-2, H-10, H-14/C-15. Furthermore, HMBC from the oxymethine protons at δ_H 4.59 (H-2) and 5.63 (H-9) to the ester carbonyls at δ_C 172.4 and 170.1, respectively, placed the acetoxyl groups on C-2 and C-9, respectively. Furthermore, a COSY correlation from H-3 (δ_H 3.87) to a hydroxy proton at δ_H 3.41 suggested the existence of a hydroxy group at C-3. Eight of the ten oxygen atoms in the molecular formula of 2 could be

accounted for the presence of a γ -lactone, two esters, an epoxide and a hydroxy group. Thus, the remaining two oxygen atoms had to be positioned at C-11 and C-12 as hydroxy group respectively, as indicated by characteristic ^{13}C and ^1H NMR signal analysis (δ_C 73.7, C-11; δ_H 3.76, 1H, d, $J = 5.2$ Hz; δ_C 71.6, CH-12). The aforementioned data defined the molecular framework of 2.

Based on previous studies, all naturally occurring briarane diterpenoids have the H-10 *trans* to Me-15, and are assigned as α - and β -oriented, respectively, as shown in most briarane derivatives (Su et al., 2017). The relative stereochemistry of 2 was established by NOESY spectral analysis. In the NOESY experiment for 2 (Fig. 3), H-10 was found to show correlations with H-3, H-9 and H₃-20, suggested that H-3, H-9, H-10 and Me-20 were on the α -face and Me-15 was β -oriented at C-1. A lack of constant coupling was detected between H-2 and H-3, indicating that the dihedral angle between H-2 and H-3 is approximately 90° , and correlations were found between H-2 with H-3, H-14 and H₃-15, indicating that H-2 should be α -oriented by modeling study. NOESY spectrum showed correlations of H₃-16 with H-3 and H-6 revealing the *Z* geometry of the C-5/6 double bond. Furthermore, one of the methylene protons at C-4 (δ_H 2.02) exhibited a correlation with H₃-16 was assigned as H-4 α while the other (δ_H 2.82) was denoted as H-4 β . A correlation between H-4 β and H-7, reflected the β -orientation of proton at C-7. Since H-12 showed correlations to H-13 and H₃-20, as well as a 5.2 Hz coupling constant was found between H-12 and H-13, demonstrating that H-12 should be β -oriented by modeling analysis. Furthermore, by comparison the chemical shifts of C-11 (δ_C 73.7), CH-12 (δ_H 3.76, 1H, d, $J = 5.2$ Hz; δ_C 71.6) and Me-20 (δ_H 1.40, 3H, s; δ_C 27.2) of 2 with those a known briarane, briaexcavatin

Table 1
¹H and ¹³C NMR data for briaranes **2** and **3**.

Position	2		3	
	δ_H (J in Hz) ^a	δ_C , Mult. ^b	δ_H (J in Hz) ^a	δ_C , Mult. ^b
1		44.5, C		45.6, C
2	4.59 s	91.6, CH	3.62 d (3.6)	84.7, CH
3	3.87 dd (9.6, 9.6)	69.6, CH	4.90 d (9.6)	73.8, CH
4 α	2.02 br d (14.4) 2.82	38.6, CH ₂	1.80 d (13.8) 3.69 dd	34.4, CH ₂
β	dd (14.4, 9.6)		(13.8, 9.6)	
5		141.4, C		141.5, C
6	5.41 dd (10.0, 1.2)	121.2, CH	5.46 dd (9.6, 1.2)	122.2, CH
7	5.58 d (10.0)	74.1, CH	5.97 d (9.6)	74.2, CH
8		71.0, C		70.7, C
9	5.63 d (4.8)	68.8, CH	5.63 d (5.4)	69.3, CH
10	3.05 d (4.8)	38.4, CH	3.13 d (5.4)	38.8, CH
11		73.7, C		73.9, C
12	3.76 d (5.2)	71.6, CH	3.74 dd (5.4, 3.6)	71.9, CH
13	5.94 dd (10.0, 5.2)	125.1, CH	5.87 dd (10.2, 5.4)	124.4, CH
14	5.52 d (10.0)	138.7, CH	5.37 d (10.2)	139.0, CH
15	1.20 s	21.6, CH ₃	1.28 s	21.5, CH ₃
16	1.88 d (1.2)	24.7, CH ₃	1.92 d (1.2)	24.6, CH ₃
17		62.2, C		62.2, C
18	1.50 s	10.2, CH ₃	1.50 s	10.3, CH ₃
19		171.7, C		171.6, C
20	1.40 s	27.2, CH ₃	1.41 s	27.1, CH ₃
2-OAc		172.4, C		
	2.36 s	21.3, CH ₃		
3-OAc				169.8, C
			2.23 s	21.8, CH ₃
9-OAc		170.1, C		170.1, C
	2.16 s	21.9, CH ₃	2.08 s	21.3, CH ₃
2-OH			1.78 d (3.6)	
3-OH	3.41 d (9.6)			
11-OH	–		3.67 s	
12-OH	–		3.67 d (3.6)	

^aSpectra recorded at 400 MHz in CDCl₃ at 25°C.

^bSpectra recorded at 100 MHz in CDCl₃ at 25°C.

^cSpectra recorded at 600 MHz in CDCl₃ at 25°C.

^dSpectra recorded at 150 MHz in CDCl₃ at 25°C.

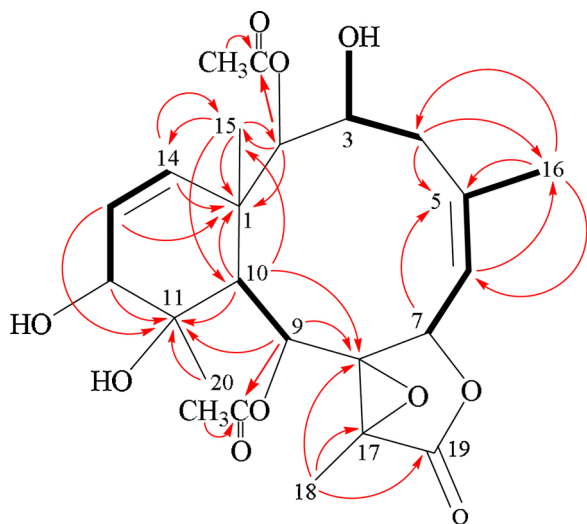


Fig. 2. The COSY (–) correlations and selective HMBC (→) of **2**.

W (**4**) (δ_C 74.5, C-11; δ_H 3.74, 1H, d, J = 5.6 Hz; δ_C 71.8, CH-12; δ_H 1.41, 3H, s; δ_C 27.5, Me-20), (Fig. 1) (Sung et al., 2009a), further supporting that the hydroxy groups at C-11 and C-12 are β - and α -oriented, respectively. Additionally, the proton signal of a methyl group at δ_H 1.50 displayed a correlation with H-9 (δ_H 5.63), which indicated that the Me-18 at C-17 was α -oriented. The *cis* geometry of C-13/14 double bond was indicated by a correlation between H-13 (δ_H 5.94) and H-14 (δ_H 5.52) and confirmed by a 10.0 Hz coupling

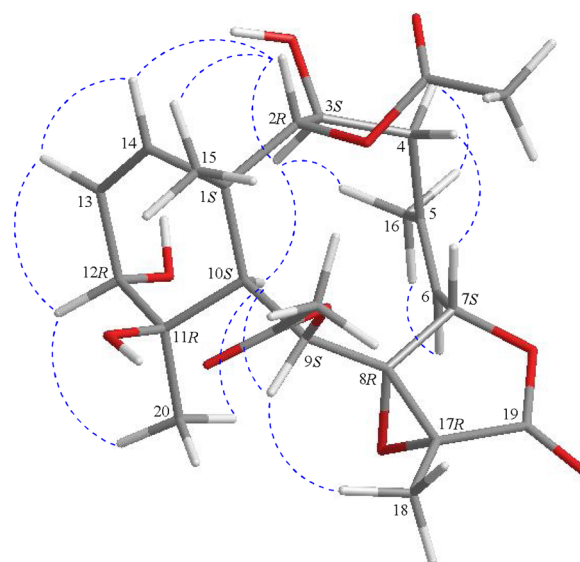


Fig. 3. Selective NOESY correlations of briarane **2** (→).

constant between these two olefin protons. The aforementioned results enabled establishment of the relative configuration of **2**. Based on above findings, the configurations of the stereogenic carbons of **2** were determined as 1*S**, 2*R**, 3*S**, 7*S**, 8*R**, 9*S**, 10*S**, 11*R**, 12*R** and 17*R**. As briaranes **2** and **3** were isolated along with **1** from the same target organism, it is reasonable on biogenetic grounds to assume that **2** and **3** have the same absolute configurations as **1**. Therefore, the configurations of stereogenic carbons of **2** were determined as 1*S*, 2*R*, 3*S*, 7*S*, 8*R*, 9*S*, 10*S*, 11*R*, 12*R* and 17*R*.

Briarane **3** has the same molecular formula as that of **2**, C₂₄H₃₂O₁₀, as determined by HRESIMS at m/z 503.18860 (calcd for C₂₄H₃₂O₁₀ + Na, 503.18877). The NMR data of **3** (Table 1) were similar to those of **2**. However, the polarity of **3**, which was checked by TLC, was substantially different from that of **2**, indicating that these two compounds are isomers. In the ¹H NMR spectrum, two acetate methyls were observed at δ_H 2.23 and 2.08 (each 3H × s). A correlation observed in the HMBC experiment further revealed the connectivity between H-9 (δ_H 5.63) and the carbonyl carbon (δ_C 170.1) of acetate group at C-9. Thus, the remaining acetoxy group was on C-3, for its characteristic NMR signals (δ_H 4.90, 1H, d, J = 9.6 Hz; δ_C 73.8, CH-3), although no HMBC was observed from H-3 to any ester carbonyl. In addition, by comparison of the NOESY correlations of **3** with those of **2**, the stereogenic centers of **3** were confirmed to be the same as those of **2** and assigned as 1*S*, 2*R*, 3*S*, 7*S*, 8*R*, 9*S*, 10*S*, 11*R*, 12*R* and 17*R*. It is interesting to note that all briarane analogues possessing an 11*β*, 12*α*-dihydroxy-13(*Z*)-ene moiety, including briaexcavatins K and W (Sung et al., 2008, 2009a), excavatoids B and I (Sung et al., 2009b, 2010) and briaranes **2** (briarane Y) and **3** (briarane Z) in this study, are isolated from the octocorals belonging to the genus *Briareum*, collected from the waters of Taiwan.

Anti-inflammatory activity assays using an *in vitro* cell culture model were performed in this study, and western blot analysis was employed to evaluate the changes in pro-inflammatory iNOS and COX-2 proteins in lipopolysaccharides (LPS)-stimulated pro-inflammatory response in a murine macrophage RAW264.7 cell line. As compared with cells stimulated with LPS alone, macrophages treated with a concentration of 10 μ M, briarane **3** exhibited reduced the levels of iNOS and COX-2 to 82.47 and 73.45%, respectively (Fig. 4 and Table 2). Using trypan blue staining to measure the cytotoxic effects of the compounds, it was observed that **2** and **3** did not induce significant cytotoxicity in RAW264.7 macrophage cells. Briarane **3** showed anti-inflammatory activities against the expressions of iNOS and COX-2 and **2** was found to be inactive in terms of reducing the expressions of iNOS and COX-2,

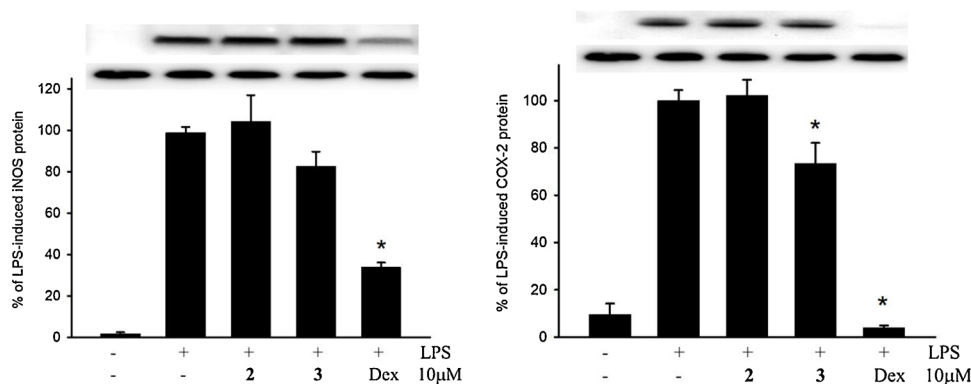


Fig. 4. Effects of compounds **2** and **3** on the expression of pro-inflammatory iNOS and COX-2 proteins in murine RAW264.7 macrophage cell. Using immunoblot analysis, briarane **3** was demonstrated to reduce lipopolysaccharides (LPS)-induced expressions of COX-2. Data were normalized to those of cells treated with LPS alone, and cells treated with dexamethasone (Dex, 10 μ M) were used as a positive control (which has been shown to reduce the levels of iNOS and COX-2 to 33.73 and 3.91%, respectively). Data are expressed as the mean \pm SEM ($n = 3$). * Significantly different from cells treated with LPS ($p < 0.05$).

Table 2

Effects of briaranes **2** and **3** on LPS-induced iNOS and COX-2 protein expressions in macrophages.

Compound	iNOS Expression (% of LPS)	COX-2	β -Actin
Negative Control	1.72 \pm 0.85	9.55 \pm 4.65	101.10 \pm 7.78
LPS	98.81 \pm 2.79	100.03 \pm 4.41	101.61 \pm 3.20
2	104.09 \pm 12.89	102.20 \pm 6.63	104.34 \pm 1.96
3	82.47 \pm 7.22	73.45 \pm 8.69	91.29 \pm 1.91
DEX ^a	33.73 \pm 2.37	3.91 \pm 1.10	115.99 \pm 10.52

^a Dexamethasone (DEX, 10 μ M) was used as a positive control.

indicating that the anti-inflammatory activity of these compounds is largely dependent on the functional groups at C-2 and C-3.

3. Experimental

3.1. General

NMR spectra were recorded on 400 or 600 MHz Jeol ECZ NMR spectrometers using the residual CHCl_3 signal (δ_{H} 7.26 ppm) and CDCl_3 (δ_{C} 77.1 ppm) as internal references for ^1H NMR and ^{13}C NMR, respectively. ESIMS and HRESIMS were obtained from the Bruker mass spectrometer with 7 T magnets (model: Solarix FTMS system). Column chromatography, IR spectra and optical rotation were performed according to our earlier research (Xu et al., 2018).

3.2. Animal material

Specimens of *Briareum* sp. were collected in June 2017 by hand by self-contained underwater breathing apparatus (SCUBA) divers off the coast of Lanyu Island (Orchid Island), Taiwan. The samples were then stored in a -20°C freezer until extraction. A voucher specimen was deposited in the National Museum of Marine Biology and Aquarium (NMMBA), Taiwan (NMMBA-TW-SC- 2017-418). Identification of the species of this organism was performed by comparison as described in previous publications (Samimi-Namin and van Ofwegen, 2016).

3.3. Extraction and isolation

The freeze-dried and sliced bodies (wet/dry weight = 1344/568 g) of the coral specimen were prepared and extracted with supercritical CO_2 to give 58.9 g of extract. Partial extract (22.5 g) was then applied on silica gel column and eluted with gradients of n-hexane/EtOAc (100% n-hexane – 100% EtOAc, stepwise), to furnish **2** (593.7 mg) and 11 fractions (fractions: A – K). Fraction E was chromatographed on silical gel with a mixture of dichloromethane and EtOAc (4:1) to obtain **1** (1.85 g). Fraction I was then separated by normal-phase HPLC using a mixture of n-hexane and Me_2CO (with volume: volume = 3:2; at a flow rate = 3.0 mL/min) to afford **3** (0.3 mg).

3.4. Excavatolide B (**1**)

Colorless prisms; all the physical (melting point and rotation value) and spectroscopic (IR, MS, ^1H and ^{13}C NMR) data were found to be in absolute agreement with previous studies (Sheu et al., 1998; Yao et al., 2019).

3.5. Briaviolide Y (**2**)

Amorphous powder; $[\alpha]_{\text{D}} -85$ (c 0.1, MeOH), IR (ATR) ν_{max} 3363, 1777, 1717 cm^{-1} ; ^1H and ^{13}C NMR data, see Table 1. ESIMS: m/z 503 $[\text{M} + \text{Na}]^+$, HRESIMS: m/z 503.18868 (calcd for $\text{C}_{24}\text{H}_{32}\text{O}_{10} + \text{Na}$, 503.18877).

3.6. Briaviolide z (**3**)

Amorphous powder; $[\alpha]_{\text{D}} -95$ (c 0.3, CHCl_3), IR (ATR) ν_{max} 3487, 1778, 1724 cm^{-1} ; ^1H and ^{13}C NMR data, see Table 1. ESIMS: m/z 503 $[\text{M} + \text{Na}]^+$, HRESIMS: m/z 503.18860 (calcd for $\text{C}_{24}\text{H}_{32}\text{O}_{10} + \text{Na}$, 503.18877).

3.7. Single-crystal X-ray crystallography of excavatolide B (**1**)

Suitable colorless prisms of **1** were obtained from a solution of MeOH. The crystal ($0.321 \times 0.157 \times 0.091 \text{ mm}^3$) belongs to the monoclinic system, space group $\text{P}2_1$ (#4), with $a = 10.2194(4) \text{ \AA}$, $b = 9.6577(3) \text{ \AA}$, $c = 15.1066(5) \text{ \AA}$, $V = 1490.23(9) \text{ \AA}^3$, $Z = 2$, $D_{\text{calcd}} = 1.325 \text{ Mg/m}^3$, λ (Cu K α) = 1.54178 \AA . Intensity data were measured on a Bruker D8 Venture diffractometer up to θ_{max} of 75.0° . All 10362 reflections were collected. The structure was solved by direct methods and refined by a full-matrix least-squares procedure. The refined structural model converged to a final $R1 = 0.0317$; $wR2 = 0.0861$ for 6105 observed reflections [$I > 2\sigma(I)$] and 388 variable parameters. The absolute configuration was determined by Flack parameter $x = 0.01(3)$ (Flack, 1983; Flack and Bernardinelli, 1999). Crystallographic data for the structure of excavatolide B (**1**) have been deposited with the Cambridge Crystallographic Data Center as supplementary publication number CCDC 1876574. These data can be obtained free of charge via <http://www.ccdc.cam.ac.uk/conts/retrieving.html> (or from the CCDC, 12 Union Road, Cambridge CB2 1EZ, UK; fax: +44 1223 336033; e-mail: deposit@ccdc.cam.ac.uk).

3.8. In vitro anti-inflammatory assay anti-inflammatory assay

Murine macrophage-like RAW264.7 cell line was purchased from the American Type Culture Collection (ATCC, No TIB-71). The *in vitro* model of the assay, which was used to evaluate the anti-inflammatory activities of compounds **2** and **3**, was performed using RAW264.7 cells pre-treated with compounds **2** and **3** then incubated with LPS to induce pro-inflammatory protein expressions. The inhibition effects of the

compounds on the expressions of LPS-induced pro-inflammatory iNOS and COX-2 proteins in the cells were assessed using western blot analysis (Huang et al., 2012; Jean et al., 2008, 2009). Briefly, RAW264.7 cells were untreated or pre-treated with 10 μ M compounds **2** and **3** and 10 μ M dexamethasone as a positive control for 10 min, followed by adding 10 ng/mL LPS (2 nM) and incubating for 16 h. The cell lysates were then collected for western blotting analysis. Protein expression levels were calculated based on the intensities of the bands on the blots representing the immunoreactivity to the iNOS and COX-2 antibodies. The cytotoxic effects of compounds **2** and **3** were also evaluated using a trypan blue exclusion assay (Jean et al., 2008, 2009). Statistical analyses were performed using one-way analysis of variance (ANOVA), and data were further processed by the Student–Newman–Keuls *post hoc* test for multiple comparisons. A *p*-value of < 0.05 was considered to indicate a significant difference between two treatments.

Acknowledgments

This research was supported by grants from the National Museum of Marine Biology and Aquarium; and the Ministry of Science and Technology, Taiwan (Grant Nos: MOST 104-2320-B-291-001-MY3 and 107-2320-B-291-001-MY3) awarded to Ping-Jyun Sung.

Appendix A. Supplementary data

Supplementary data associated with this article can be found, in the online version, at <https://doi.org/10.1016/j.phytol.2019.10.003>.

References

- Burks, J.E., van der Helm, D., Chang, C.Y., Ciereszko, L.S., 1977. The crystal and molecular structure of briarein A, a diterpenoid from the gorgonian *Briareum asbestinum*. *Acta Cryst. B* 33, 704–709.
- Flack, H.D., 1983. On enantiomorph-polarity estimation. *Acta Cryst. A* 39, 876–881.
- Flack, H.D., Bernardinelli, G., 1999. Absolute structure and absolute configuration. *Acta Cryst. A* 55, 908–915.
- Huang, S.-Y., Chen, N.-F., Chen, W.-F., Hung, H.-C., Lee, H.-P., Lin, Y.-Y., Wang, H.-M., Sung, P.-J., Sheu, J.-H., Wen, Z.-H., 2012. Sinularin from indigenous soft coral attenuates nociceptive responses and spinal neuroinflammation in carrageenan-induced inflammatory rat model. *Mar. Drugs* 10, 1899–1919.
- Jean, Y.-H., Chen, W.-F., Duh, C.-Y., Huang, S.-Y., Hsu, C.-H., Lin, C.-S., Sung, C.-S., Chen, I.-M., Wen, Z.-H., 2008. Inducible nitric oxide synthase and cyclooxygenase-2 participate in anti-inflammatory and analgesic effects of the natural marine compound lemnalol from Formosan soft coral *Lemnalia cervicorni*. *Eur. J. Pharmacol.* 578, 323–331.
- Jean, Y.-H., Chen, W.-F., Sung, C.-S., Duh, C.-Y., Huang, S.-Y., Lin, C.-S., Tai, M.-H., Tzeng, S.-F., Wen, Z.-H., 2009. Capnellene, a natural marine compound derived from soft coral, attenuates chronic constriction injury-induced neuropathic pain in rats. *Br. J. Pharmacol.* 158, 713–725.
- Samimi-Namin, K., van Ofwegen, L.P., 2016. Overview of the genus *Briareum* (Cnidaria, Octocorallia, Briareidae) in the Indo-Pacific, with the description of a new species. *ZooKeys* 557, 1–44.
- Su, Y.-D., Su, J.-H., Hwang, T.-L., Wen, Z.-H., Sheu, J.-H., Wu, Y.-C., Sung, P.-J., 2017. Briarane diterpenoids isolated from octocorals between 2014 and 2016. *Mar. Drugs* 15, 44 and previous review articles in this series.
- Sheu, J.-H., Sung, P.-J., Cheng, M.-C., Liu, H.-Y., Fang, L.-S., Duh, C.-Y., Chiang, M.Y., 1998. Novel cytotoxic diterpenes, excavatolides A–E, isolated from the Formosan gorgonian *Briareum excavatum*. *J. Nat. Prod.* 61, 602–608.
- Sung, P.-J., Lin, M.-R., Su, Y.-D., Chiang, M.Y., Hu, W.-P., Su, J.-H., Cheng, M.-C., Hwang, T.-L., Sheu, J.-H., 2008. New briaranes from the octocoral *Briareum excavatum* (Briareidae) and *Junceella fragilis* (Ellisellidae). *Tetrahedron* 64, 2596–2604.
- Sung, P.-J., Lin, M.-R., Chiang, M.Y., Hwang, T.-L., 2009a. Briarexcatins V–Z, discovery of new briaranes from a cultured octocoral *Briareum excavatum*. *Bull. Chem. Soc. Jpn.* 82, 987–996.
- Sung, P.-J., Su, Y.-D., Li, G.-Y., Chiang, M.Y., Lin, M.-R., Huang, I.-C., Li, J.-J., Fang, L.-S., Wang, W.-H., 2009b. Excavatoids A–D, new polyoxygenated briaranes from the octocoral *Briareum excavatum*. *Tetrahedron* 65, 6918–6924.
- Sung, P.-J., Chen, B.-Y., Chiang, M.Y., Hou, C.-H., Su, Y.-D., Hwang, T.-L., Chen, Y.-H., Chen, J.-J., 2010. Excavatoids G–K, new 8,17-epoxybriaranes from the cultured octocoral *Briareum excavatum* (Briareidae). *Bull. Chem. Soc. Jpn.* 83, 549–545.
- Xu, J.-H., Lai, K.-H., Su, Y.-D., Chang, Y.-C., Peng, B.-R., Backlund, A., Wen, Z.-H., Sung, P.-J., 2018. Briaviolides K–N, new briarane-type diterpenoids from cultured octocoral *Briareum violaceum*. *Mar. Drugs* 16, 75.
- Yao, J.-W., Chi, W.-C., Lee, G.-H., Su, J.-H., Hwang, T.-L., Wu, Y.-J., Su, T.-R., Sheu, J.-H., 2019. 2-Acetoxybriaranes from *Briareum violaceum*. *Tetrahedron* 75, 3751–3757.



Encapsulating curcumin in ethylene diamine- β -cyclodextrin nanoparticle improves topical cornea delivery

Chi-Hsien Liu^{a,b,c,d,*}, Guan-Wei Lee^e, Wei-Chi Wu^{d,f}, Chun-Chao Wang^g

^a Department of Chemical and Materials Engineering, Chang Gung University, 259, Wen-Hwa First Road, Kwei-Shan, Tao-Yuan, 333, Taiwan

^b Research Center for Chinese Herbal Medicine and Research Center for Food and Cosmetic Safety, College of Human Ecology, Chang Gung University of Science and Technology, 261, Wen-Hwa First Road, Taoyuan, Taiwan

^c Department of Chemical Engineering, Ming Chi University of Technology, 84, Gung-Juan Road, New Taipei City, Taiwan

^d Department of Ophthalmology, Chang Gung Memorial Hospital, 5, Fu-Hsing Street, Taoyuan, Taiwan

^e Graduate Institute of Biomedical Engineering, Chang Gung University, 259, Wen-Hwa First Road, Kwei-Shan, Tao-Yuan 333, Taiwan

^f College of Medicine, Chang Gung University, 259, Wen-Hwa First Road, Taoyuan, Taiwan

^g Institute of Molecular Medicine & Department of Medical Science, National Tsing Hua University, 101, Kuang-Fu Road, Hsinchu, Taiwan

ARTICLE INFO

Keywords:

Ethylene diamine
 β -cyclodextrin
Curcumin
Ocular delivery
Nanoparticles

ABSTRACT

Curcumin is a powerful scavenger of reactive oxygen species and could prevent the corneal cells from oxidative damage. However, the clinical efficacy of curcumin is limited by its low aqueous solubility and stability, leading to poor bioavailability. β -cyclodextrin, with a hydrophilic surface and a hydrophobic cavity and self-assembling properties, can form inclusion complexes with lipophilic drugs such as curcumin for ocular delivery. We synthesized ethylene diamine (EDA)-modified β -cyclodextrin and prepared the curcumin complexation using the solvent evaporation method. The EDA- β -cyclodextrin provided a better thermodynamic stability and higher complex yield for curcumin complexes, compared to β -cyclodextrin, which were demonstrated on the analysis of their van't Hoff plots and phase solubility diagrams. We characterized EDA- β -cyclodextrin curcumin nanoparticles and determined that the EDA modified β -cyclodextrin is a more suitable carrier than parental β -cyclodextrin, using FT-IR, XRD, TEM, and analyses of solubility and storage stability. In addition, the curcumin-EDA- β -cyclodextrin nanoparticles had better *in vitro* corneal penetration and 3-h cumulative flux in a porcine cornea experiment, and displayed an improved biocompatibility, confirmed by the histological examination of porcine corneas and cell viability of bovine corneal epithelial cells. These results together revealed a role of EDA modification in the β -cyclodextrin carrier, including the improvement of curcumin complex formation, thermodynamic properties, cytotoxicity, and the *in vitro* corneal penetration. The EDA- β -cyclodextrin inclusion can provide curcumin a higher degree of aqueous solubility and corneal permeability.

1. Introduction

Curcumin (diferuloylmethane, PubMed CID: 969,516), a polyphenol extracted from turmeric, has shown several pharmacological functions, as it is a strong antioxidant, anti-inflammatory, and anti-infectious agent [1]. Curcumin can suppress key regulators of the inflammatory response, such as 5-lipoxygenase, cyclooxygenase-2, and nitric oxide synthase [2]. This makes curcumin practically effective in many ocular diseases, including chronic anterior uveitis, diabetic retinopathy, glaucoma, age-related macular degeneration, and dry eye syndrome [3]. However, the bioavailability study has indicated the low absorption and quick clearance of curcumin in humans [4]. Due to its

hydrophobic nature, curcumin suffers from low water solubility. As a consequence, curcumin is classified as a class IV compound in the biopharmaceutical classification system on the basis of its poor aqueous solubility and permeability through epithelial cells [5]. It is necessary to develop new strategies to improve the effectiveness and safety of ocular curcumin delivery.

To achieve this goal, suitable carrier materials that can enhance the solubility, stability and bioavailability of drug molecules are used. The supramolecular complexation of carbohydrates can improve the solubility and bioavailability of hydrophobic drugs [6]. Among the supramolecular materials, β -cyclodextrins are popular, especially for their biological application. β -cyclodextrins are cyclic oligosaccharides

* Corresponding author at: Department of Chemical and Materials Engineering, Chang Gung University, 259, Wen-Hwa First Road, Kwei-Shan, Tao-Yuan 333, Taiwan.

E-mail address: CHL@mail.cgu.edu.tw (C.-H. Liu).

<https://doi.org/10.1016/j.colsurfb.2019.110726>

Received 27 August 2019; Received in revised form 5 November 2019; Accepted 12 December 2019

Available online 13 December 2019

0927-7765/© 2019 Elsevier B.V. All rights reserved.

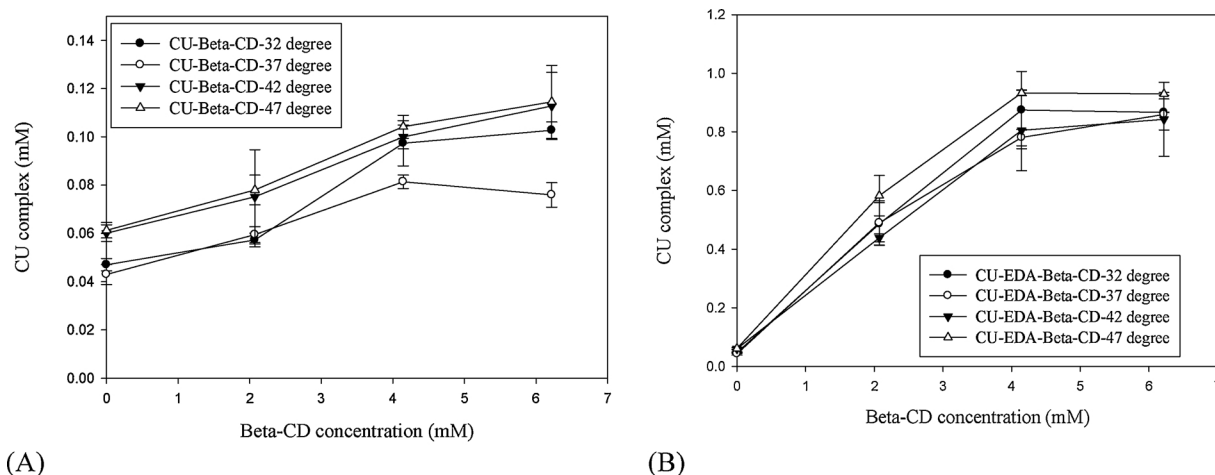


Fig. 1. Effect of temperature on curcumin (CU) complex with (A) β -cyclodextrin, (B) EDA- β -cyclodextrin ($n = 3$).

consisting of seven α -(1,4)-linked glucopyranose subunits. Some works have been dedicated to the encapsulation of curcumin into β -cyclodextrin derivatives, including hydroxypropyl-, sulfobutylether-, and surfactant-modified cyclodextrins [7–10], and provided evidence that curcumin- β -cyclodextrin inclusion complex enhances the curcumin delivery to prostate cancer cells and melanoma cells *in vitro* [8,10]. Cyclodextrins also decrease drug irritation by limiting the free drug concentration to a nonirritating level. Therefore, cyclodextrins can stabilize drugs, reduce irritation, and enhance drug solubility and permeability [11,12].

Drug delivery to various parts of the eye *in vivo* is one of the most challenging fields because of the complex anatomical structure of the eye, such as corneal epithelium and blood-retinal barriers. These physiological barriers cause poor bioavailability of drugs. As a result, insoluble drugs delivered through conventional administration forms are limited [13]. Most topical drug delivery systems are in the form of aqueous eye drop solutions. In eye drop solutions, lipophilic drugs can be encapsulated in the hydrophobic cave of cyclodextrin and delivered through the aqueous tear fluid to the eye. There, cyclodextrins function as permeation enhancers by adhering around the eye surface and sustaining the drug release [14]. For example, randomly methylated β -cyclodextrin provides good complex efficiencies with the antibiotic chloramphenicol [15]. The hydroxypropylated and sulphobutylether β -cyclodextrins have already been approved as the excipient of ophthalmic formulations of diclofenac and voriconazole [16]. Cyclodextrin derivatives, such as 2-hydroxypropyl-, sulfobutylether-, methyl- β -cyclodextrins, and 2-hydroxypropyl- γ -cyclodextrins, have been used in pharmaceutical excipients [17]. A good example is the γ -cyclodextrin nanoparticle eye drops with dorzolamide, which is used to decrease intraocular pressure and reduce local irritation [18]. In addition, the cyclodextrin derivatives effectively enhance the topical bioavailability of dexamethasone for macular edema disease [19].

Ethylene diamine (EDA), the simplest 1,2-diamine, is low-toxicity, low-cost and without any immunogenicity. Our hypothesis was the creation of diamine group on the parental β -cyclodextrin could improve the corneal curcumin delivery. We developed an easy and efficient strategy to synthesize EDA-modified β -cyclodextrin and evaluated the effects of EDA- β -cyclodextrin on the curcumin complexation and corneal delivery. We also characterized the inclusion complex (the complex stability, thermodynamic information, morphology, size distribution, and molecular weight), examined the partition coefficient and accumulation of curcumin in porcine corneas, analyzed the antioxidant activity, and evaluated their biocompatibility in corneal cells.

2. Materials and method

2.1. Materials

β -cyclodextrin was obtained from Fengyuan Biotech (Jiangsu, China). Acetone, methanol, and ethanol were provided by Echo Chemicals (Taiwan). Curcumin was obtained from Masterasia (Taiwan). EDA, p-tolylsulfonyl chloride, 1,1-diphenyl-2-picrylhydrazyl (DPPH), and sodium chloride were bought from Sigma-Aldrich. Fresh porcine eyes were kindly donated from Ya-Shin Pork Industry (Taoyuan, Taiwan). The other chemicals were bought from Sigma-Aldrich.

2.2. Synthesis of EDA- β -cyclodextrin

Mono-6-deoxy-6-(p-tolylsulfonyl)- β -Cyclodextrin was first synthesized according to a previous method [20]. Briefly, 6-gram β -cyclodextrin was suspended in 50 ml of double distilled water, and 2 ml of 16.4 N NaOH was added slowly to the suspension within six minutes. The suspension became slightly yellow and homogenous, after which 1.08 g of p-tolylsulfonyl chloride in 3 ml of acetonitrile was added to modify on the 6-hydroxyl group of β -cyclodextrin. The recovered mono-6-deoxy-6-(p-tolylsulfonyl)- β -cyclodextrin was reacted with EDA to form EDA-modified β -cyclodextrin. Cold acetone was added to the mixture to precipitate the white EDA- β -cyclodextrin.

2.3. Estimation of the stability constant and thermodynamic parameters

Usually, one drug molecule forms a complex with one cyclodextrin molecule [21]. The stability constant (K_c) is then obtained from the slope of the equilibrium diagram of phase solubility using the following equation:

$$K_c = \frac{\text{Slope}}{(S_0)(1 - \text{Slope})} \quad (1)$$

where S_0 is the saturation concentration of curcumin in the solution free of cyclodextrin and the slope is the tangent line in the phase diagram.

The value of the slope ($\Delta \text{drug complex} / \Delta \text{cyclodextrin}$) was obtained from the linear regression of phase solubility data after measuring the concentrations of curcumin complexes at different amounts of cyclodextrin (Fig. 1). For most substances, the tangent line in the solubility plot has a positive slope indicating the drug complex increases with the cyclodextrin concentration. The experiment for the phase solubility diagram is performed according to a previous report [7]. Briefly, different amounts of cyclodextrin (0, 20, 40, 60, 80, 100, and 120 mg) were added to 4.5 ml of de-ionized water separately. The solutions were preheated at 32°C to dissolve the cyclodextrin

completely. Curcumin in the acetone solution (2 mL) was added to each of the freshly prepared cyclodextrin solutions. The solution was continuously stirred for 4 h at a fixed temperature using the solvent evaporation procedure. The bottle cap was removed for the evaporation of acetone. After being centrifuged at 10,000 rpm for 10 min, the complex in the supernatant was then filtrated using a 0.22 μm pore-size filter and lyophilized for further HPLC assay. The HPLC system (Jasco, Tokyo, Japan) included an analytical column (Lichrospher, RP-18, 250 \times 5 mm), a mobile phase (the methanol *versus* 0.5% phosphoric acid solution ratio was 86:14, with a 1 mL/min flow rate), and a fluorescence detector (excitation wavelength of 430 nm; emission wavelength of 540 nm). The stoichiometry of the cyclodextrin/curcumin complex is 1:1 according to Tønnesen's conclusion [7]. For poorly soluble molecule, it can be difficult to obtain accurate S_0 values. Under such condition, complexation efficiency (CE) is defined as follows:

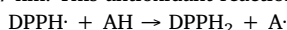
$$\text{CE} = \frac{[\text{curcumin-cyclodextrin complex}]}{[\text{equilibrium cyclodextrin}]} = \frac{\text{Slope}}{(1-\text{Slope})} = K_c \cdot (S_0) \quad (2)$$

The corresponding thermodynamic parameters, ΔH , ΔS , and ΔG , were estimated according to the van't Hoff equation [22]:

$$\ln K_c = -\frac{\Delta H}{RT} + \frac{\Delta S}{R} = -\frac{\Delta G}{RT} \quad (3)$$

2.4. Scavenging activity analysis

To analyze the scavenging activity, a relatively stable free radical (DPPH) was used. DPPH had a specific absorbance at a wavelength of 517 nm. This antioxidant reaction is as follows:



After the centrifugation of EDA- β -cyclodextrin and curcumin, the nanoparticles in the supernatant were dried in the oven. The complex powder was dissolved in water to obtain various concentrations of EDA- β -cyclodextrin. Fifty μL of different concentrations (3.125, 6.25, 12.5, 25, 50, and 100 ppm) of the complexes was placed into a 96-well dish, and 100 μL of freshly prepared 0.1 mM DPPH / methanol solution was added and mixed well. After allowing it to react for 30 min at room temperature in the dark, a microplate spectrophotometer was used to measure the absorbance at 517 nm. In the control group, the complex was replaced with de-ionized water in the reaction. The absorbance value of the blank was the background absorbance but without DPPH. The scavenging activity was calculated by the following equation:

$$\text{Scavenging activity (\%)} = \left[1 - \frac{(S_{517\text{nm}})}{(C_{517\text{nm}})} \right] \times 100\%$$

$S_{517\text{nm}}$: absorbance at 517 nm after the sample reaction

$C_{517\text{nm}}$: absorbance at 517 nm after the reaction in the control group

2.5. Characterization of the inclusion nanoparticles

The size distribution and zeta potential of the inclusion complexes were characterized using a Zetasizer Nano ZS 90 (Malvern, Worcestershire, UK) at a fixed angle of 90° and temperature of 32 °C. The size distribution was also measured by the Zetasizer after 100-fold dilution with water. Cyclodextrin inclusion complexes were diluted 1:25 with Milli-Q water and dried on carbon film (CF200-Cu, Electron Microscopy Science, Washington, PA, USA) for 12 h. Then samples were analyzed by transmission electron microscopy (TEM, JEOL JEM 2000 EXII, Tokyo, Japan). The size distribution of nanoparticles in TEM images was analyzed by Image J software. The crystalline structures of EDA-cyclodextrin and its inclusion complex were investigated using an x-ray diffractometer (XRD, D2 Phaser, Bruker CO., Germany). The powder samples were used for the XRD measurement. Diffractograms were scanned from the initial angle of 20° to the final angle of 40°. The obtained data were collected with a step width of 0.02 and a count time of one second. The functional group analyses for the inclusion complex

and its physical mixture were performed using Fourier transform infrared spectroscopy (FT-IR, Alpha, Bruker Co., Germany). The IR spectra were recorded in the range of 500–4000 cm^{-1} with a resolution of 2 cm^{-1} at room temperature using a KBr pellet. The background signals were corrected with a pure KBr pellet. An average of 25-scan data was collected for each sample. The FT-IR data were analyzed with Bruker Opus software.

2.6. Biocompatibility evaluation

Bovine corneal epithelium (BCE) and retinal ganglion cells (RGCs) were respectively maintained in Eagle's minimum essential medium (MEM) and Dulbecco's modified Eagle's medium (DMEM) with a 10% fetal bovine serum supplement at a condition of 37°C, 5% CO₂, and 95% relative humidity. After 48 h, the culture medium was removed from the 96-well plate and replaced by 0.1 mL/well sample for 24 h. The cell viability was evaluated using the cell counting kit (Dojindo Co. Japan).

$$\text{Cell viability (\%)} = \frac{\text{Sample OD}}{\text{Control OD}} \times 100\%$$

2.7. Accumulation, penetration, and partition of the curcumin complex in corneal tissues

To investigate the penetration and retention in the ocular tissues, the following experiments were performed to measure the partition coefficient and accumulation rate of curcumin in porcine corneas. The accumulation of curcumin into the ocular tissue was estimated by measuring its partition coefficient between the porcine corneas and the formulation at 32°C. *in vitro* permeation and release studies of curcumin were performed in static Franz diffusion cells. The devices consisted of donor and receptor chambers between which a corneal tissue was positioned. A total volume of 0.5 mL curcumin containing sample was applied to the donor compartment. The receptor fluid (5.5 mL) consisted of PBS: ethanol (1:1). The addition of ethanol in the receptor medium was chosen because of the insufficient solubility of curcumin in aqueous buffer. Each receptor chamber contained a stirring magnetic bar to maintain the solution's homogeneity. The temperature of the receptor chamber was controlled at 32°C by a water circulator. The whole buffer in the receptor chamber was taken and fresh buffer was replenished at fixed intervals. Curcumin in the buffer was analyzed by HPLC. The curcumin partition coefficient in the cornea was calculated based on our previous report [23]. The calculation of the curcumin permeability coefficient through the cornea (flux/curcumin concentration in cyclodextrin) was done according to a previous paper [24]. The average thickness of the porcine corneas used in this study was 1243.33 \pm 60.46 μm , respectively ($n = 10$). Statistical analysis of the comparison between the measurements was performed using an unpaired Student's *t*-test. A 0.05 level of probability was taken as the level of significance.

3. Results and discussion

3.1. EDA-modification enhanced the encapsulation of curcumin into β -cyclodextrin

Drug molecules and cyclodextrins have tendency to not only form complexes, but also self-assemble in aqueous solutions. At high cyclodextrins concentrations, these aggregates may precipitate [25]. To clearly understand the complexation process of EDA- β -cyclodextrin and curcumin, we performed the experiments for phase solubility. The stability constants (K_c) of curcumin- β -cyclodextrin and curcumin-EDA- β -cyclodextrin were obtained from the slope and the saturated curcumin concentration in the phase solubility diagrams (Eq 1) using the solvent evaporation method. At the same temperature, when the

concentrations of β -cyclodextrins or EDA- β -cyclodextrins increased, more curcumins were encapsulated into their host cavities, and more curcumin/cyclodextrin nanoparticles were formed (Fig. 1(A) (B)). The curcumin nanoparticles with β -cyclodextrin have limited solubility in the media and the inclusion complex saturated at 0.1 mM when the β -cyclodextrin concentration reached 4 mM (Fig. 1(A)). This is usually associated with the limited solubility of natural β -cyclodextrin in the aqueous solution [26]. The poor solubility of β -cyclodextrin can be explained in terms of the effect of the intermolecular hydrogen bonding [27]. In contrast, the EDA modified β -cyclodextrin could significantly enhance the curcumin complex concentration to 0.9 mM at 47 °C compared with the 0.1 mM of β -cyclodextrin complex. This suggested that reaction of the EDA modified β -cyclodextrin enhanced the solubilizing potential of the parental β -cyclodextrin. This effect could be observed in a wide temperature range of 32–47 °C for curcumin β -cyclodextrin complex (Fig. 1(A) (B)).

According to the phase-solubility diagram (Fig. 1), linear diagrams showed that curcumin solubility increases as a function of cyclodextrin concentration. The stability constants (K_c) and complexation efficiency (CE) of curcumin-cyclodextrin complex in the tested temperatures (32–47 °C) are listed in Table 1. The K_c and CE of the curcumin-EDA- β -cyclodextrin were much higher than those of curcumin- β -cyclodextrin, where the increases were 16–21-fold and 22–26-fold, respectively. The higher CE of the cyclodextrin complex indicated that there were more guest molecules loaded into cyclodextrin cavities [28]. This result suggested EDA modification enhanced K_c by affecting the strength of host-guest binding and the hydrophobic surface area of β -cyclodextrin [29]. Particularly, the higher K_c values of EDA- β -cyclodextrin (4790 M^{-1}) than β -cyclodextrin (291 M^{-1}) was likely due to the following factors: (a) curcumin-EDA- β -cyclodextrin complexes were more stable than curcumin- β -cyclodextrin complexes in the aqueous solution; (b) the binding force between curcumin and EDA- β -cyclodextrin was stronger than that between curcumin and β -cyclodextrin; and (c) the substituent diamine group disturbed the intermolecular hydrogen bonds in the parental β -cyclodextrin cavity, preventing the inclusion of curcumin. Interestingly, the K_c constants decreased as the temperature increased in both cyclodextrins. This can be explained by the motion of molecules at higher temperature, curcumin and solvent molecules in the cavity of β -cyclodextrin have more freedom of movement than those at low temperature, resulting in unstable inclusion complexes and decreased K_c . Together, we concluded that the introduction of the EDA moiety on the hydroxyl group of β -cyclodextrin may help the accommodation of curcumin into cyclodextrin cavity.

3.2. Estimation of thermodynamic parameters

We performed the thermodynamic analysis to estimate the changes of enthalpy (ΔH), entropy (ΔS), and free energy (ΔG) during the complex formation using K_c values obtained from different conditions, the Gibbs (Eq (4)) and van't Hoff equations (Eq (3)).

$$\Delta G = \Delta H - T\Delta S \quad (4)$$

Table 1

Stability constants and complexation efficiency of curcumin-cyclodextrin complex under different temperatures.

K_c (M^{-1}) ^a	32 °C	37 °C	42 °C	47 °C
CU- β -cyclodextrin	290.93	222.97	165.69	181.50
CU-EDA- β -cyclodextrin	4789.60	4027.97	3527.63	2967.03
Increase ratio	16.5	18.1	21.3	16.3
CE ^b	32 °C	37 °C	42 °C	47 °C
CU- β -cyclodextrin	0.012	0.009	0.010	0.010
CU-EDA- β -cyclodextrin	0.27	0.22	0.22	0.26
Increase ratio	22.2	24.7	22.0	26.6

^a Stability constants (K_c , Eq (2)).

^b Complexation efficiency (CE, Eq (2)).

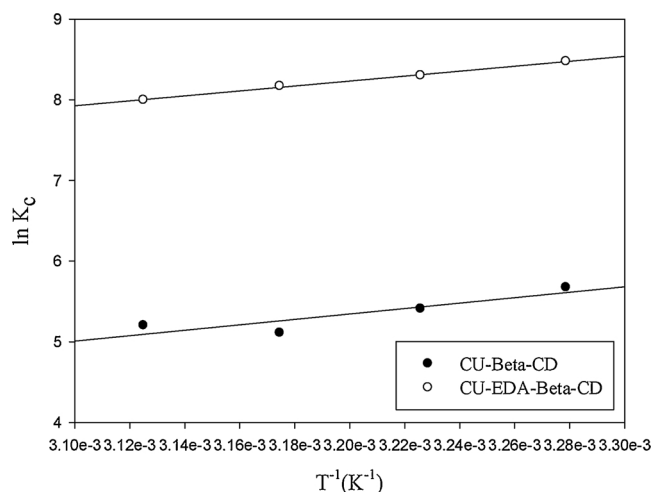


Fig. 2. The van't Hoff plot for two kinds of curcumin- β -cyclodextrin complexes.

We constructed the van't Hoff plot of $\ln K_c$ versus $1/T$, which yields a slope of $-\Delta H/R$ and an intercept of $\Delta S/R$, as shown in Fig. 2. The ΔG at a specific temperature can be obtained using Eq (4). The contribution of three thermodynamic factors, ΔG , ΔH , and ΔS , to the complex formation was examined and summarized in Table 2. The negative values of free energy change ΔG confirmed the feasibility of the formation of two complexes. The values of ΔG of curcumin- β -cyclodextrin formation were slightly increased from -13.8 to -14.4 $kJ\ mol^{-1}$ when the temperature shifted from 47 to 42 °C, suggesting the process was becoming more infeasible at elevated temperatures. This drawback could be overcome with our EDA modification since the values of ΔG for the curcumin-EDA- β -cyclodextrin formation were almost temperature-independent (-21.5 $kJ\ mol^{-1}$ (32 °C), -21.4 $kJ\ mol^{-1}$ (37 °C), -21.4 $kJ\ mol^{-1}$ (42 °C), and -21.3 $kJ\ mol^{-1}$ (47 °C)). The larger negative value of ΔG curcumin-EDA- β -cyclodextrin (compared to the ones of the curcumin- β -cyclodextrin) indicated the higher K_c . That means in equilibrium, EDA modification enhanced the curcumin encapsulation and made β -cyclodextrins better drug carriers.

The enthalpy changes (ΔH) for the formations of the curcumin- β -cyclodextrin and the curcumin-EDA- β -cyclodextrin were listed in Table 2. The negative values of ΔH showed that the curcumin encapsulation processes for both EDA- β -cyclodextrin and β -cyclodextrin were exothermic, which was similar to the results of previous reports studying the cyclodextrin complex with quercetin [30,31]. The large negative ΔH has been attributed to strong van der Waals interactions due to strong size and shape complementarities as well as the formation of hydrogen bonds between myricetin and β -cyclodextrin [32]. The values of entropy change ΔS of both complex formations appears to be negative, suggesting they are entropy restricted processes (Table 2). The decreases in entropy during inclusion complexation is resulted from the size-fit matching between the host and curcumin molecules [33–35]. It shall be noted that the impedance of ΔS in β -cyclodextrin (-45 $J\ mol^{-1}\ K^{-1}$) was much higher than that of EDA- β -cyclodextrin (-13 $J\ mol^{-1}\ K^{-1}$). In conclusion, the phase solubility results and the thermodynamic analysis indicated that EDA modification provided

Table 2

Thermodynamic parameters of curcumin- β -cyclodextrin complexes at 32 °C.

	curcumin- β -cyclodextrin	curcumin -EDA- β -cyclodextrin
ΔH ($kJ\ mol^{-1}$)	-27.97	-25.46
ΔS ($J\ mol^{-1}\ K^{-1}$)	-45.07	-13.05
$\Delta S \times T$ ($kJ\ mol^{-1}$) ^a	-13.58	-3.97
ΔG ($kJ\ mol^{-1}$)	-14.39	-21.49

^a At 32 °C condition.

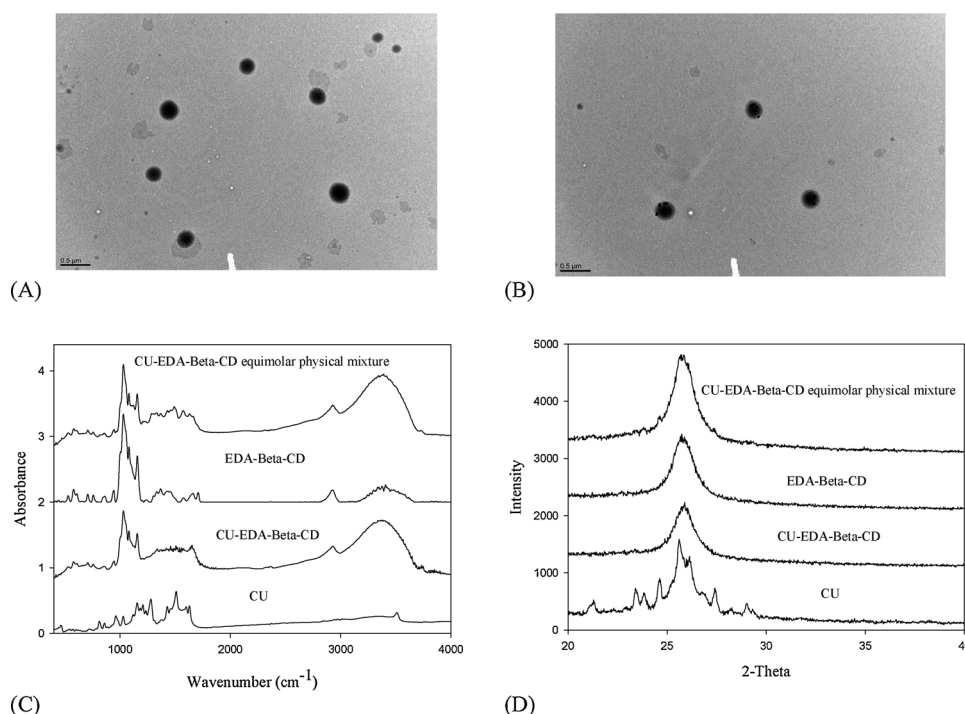


Fig. 3. TEM images of the aggregates of (A) EDA-β-cyclodextrin, (B) curcumin-EDA-β-cyclodextrin. FT-IR (C) and XRD (D) spectra of curcumin, EDA-β-cyclodextrin, their physical mixture, and inclusion complexes

natural β-cyclodextrin favorable conformational changes for curcumin encapsulation. EDA-β-cyclodextrins were better carriers for curcumin when using the solvent evaporation method.

3.3. Morphology and characterization

Transmission electron microscopy (TEM) was used to characterize the structural features (the morphology and size distribution) of dehydrated EDA-cyclodextrin and its curcumin complex. EDA-β-cyclodextrin and curcumin-EDA-β-cyclodextrin displayed spherical morphologies and the particle sizes were 189 and 300 nm analyzed by Image J software (Fig. 3(A) (B)). Encapsulated curcumins appeared as dots and could be clearly observed around the shells of complexes (Fig. 3(B)). In addition, we used the dynamic light scattering technique to analyze β-cyclodextrin particles in liquid, and found the distributions of EDA-β-cyclodextrin and curcumin-EDA-β-cyclodextrin were 238 ± 107 and 287 ± 57 nm respectively in pure water. Our EDA-β-cyclodextrin can form nanoparticles in aqueous solution, which is consistent with many self-assembled cyclodextrin nanoparticle, reported before [36,37].

Fourier-transform infrared spectroscopy (FT-IR) analysis can be used to reveal the interactions between the guest and host molecules in the solid state. Changes in the characteristic bands of the guest molecule, such as disappearance or broadening in peak intensity or shifts in their wave number, can be indicative of complex formation. Further supporting evidence for the curcumin encapsulation could be provided by FT-IR analysis. Curcumin and EDA-β-cyclodextrin displayed the respective absorption bands in the spectra (Fig. 3(C)). For example, EDA-β-cyclodextrin had a broad OH peak present at 3360 cm^{-1} . In the curcumin containing samples, there were no bands in the most significant carbonyl region ($1800\text{--}1650 \text{ cm}^{-1}$), indicating that curcumin was existed in the keto-enol form [38]. The physical mixture showed bands related to curcumin and EDA-β-cyclodextrin. For the inclusion complex, the curcumin included into the cavity of β-cyclodextrin would restrict the stretching vibrations carbonyl C=O or aromatic C=C groups around $1510\text{--}1650 \text{ cm}^{-1}$. The vibration of C=O of curcumin

reduced as it was encapsulated (Fig. 3(C)). In addition, the EDA-β-cyclodextrin masked the molecular vibrations of the guest curcumin around $1350\text{--}1500 \text{ cm}^{-1}$. Thus, the IR spectra of curcumin-EDA-β-cyclodextrin complex prepared by the solvent evaporation method and that of the physical mixture were different.

X-ray diffraction (XRD) is a non-destructive technique to determine the crystallinity or amorphization of the finely ground powder samples. The sample does not suffer physical change during the spectrum recording and it can be reused for other analyses. XRD analysis has been used in the characterization of different cyclodextrins and their inclusion complexes [39]. The comparison of the XRD patterns of the single components, their physical mixture and the inclusion complex is shown in Fig. 3(D). The 2-Theta range in XRD was around 27° . Curcumin and EDA-β-cyclodextrin were characterized by the XRD peaks, indicating both of them were in crystalline form. Curcumin had strong sharp peaks at 21° , $23\text{--}27^\circ$, and 29° in the XRD spectra. The curcumin peaks were observed in the physical mixture diffraction pattern. By contrast, the complex of curcumin-EDA-β-cyclodextrin did not have those characteristic peaks of curcumin indicating that the inclusion complex was successfully prepared without free curcumin left, consistent with the observation reported by Anirudhan et al. [40]. Thus, the data from XRD analysis, together with the results from FT-IR study, provided the evidence of the existence of inclusion complex that was prepared by the solvent evaporation method.

To investigate the average molecular weight of CD complex, the static light scattering (SLS) technique was followed for determining the weight of the suspended particles. In Rayleigh theory, the intensity of scattered light produced by macromolecules is proportional to the molecular weight of these molecules. The Debye plot can obtain the molecular weight of a protein by generating a linear equation of KC/R_oP as a function of the different concentrations of protein. Molecular weight is the inverse of the intercept value in the Debye plot. K is an optical constant, C is the concentration of the particle, and R_o is the Rayleigh ratio. From the inverse of the intercept of Y-axis (KC/R_oP), the calculated molecular weight for the complex was 1546 Da, and for the EDA-cyclodextrin was 1178 Da, respectively (Fig. S1). The increased

molecular weight of CD complex indicated an inclusion of curcumin into the CD.

Eye drops with a lower viscosity are preferred for administrations [41]. We measured the viscosity, solubility, and curcumin loading efficiency of β -cyclodextrin and EDA- β -cyclodextrins (Table S1). The EDA modification enhanced the curcumin loading efficiency from 32.17 % (β -cyclodextrin) to 37.78% (EDA- β -cyclodextrin). In addition, EDA modification increased the solubility of both β -cyclodextrin alone and curcumin encapsulated β -cyclodextrin. The solubility of pure β -cyclodextrin, EDA- β -cyclodextrin, and their curcumin-encapsulated complexes are 1.85 , 21.34 ± 0.77 , 13.95 ± 0.17 , and $28.57 \pm 0.25\%$ (w/v), respectively (Table S1). Importantly, in all conditions the viscosities of these β -cyclodextrins carriers were less than 3 mPa·s, which are good flowing abilities for drug carriers on the eye surface. Thus, we established the potential of EDA- β -cyclodextrins for drug delivery in topical eye delivery.

3.4. Curcumin-EDA- β -cyclodextrin nanoparticles in *in vitro* corneal delivery

It was reported that β -cyclodextrin can enhance the corneal delivery of some small compounds, such as riboflavin, anandamide, and cholesterol, in the bovine cornea and corneas of rabbits [42,43]. To investigate possible drug penetration or retention of our system, we measured the accumulation, penetration flux and partition coefficient of both β -cyclodextrin alone and curcumin encapsulated β -cyclodextrin in the porcine cornea *in vitro* for 3-h diffusion. These *in vitro* diffusion parameters were measured by using the Franz diffusion device and porcine cornea as the passive diffusion model between the curcumin vehicles and the corneal tissue. As shown in Fig. 4(A), (B) and Table S2, curcumin-EDA- β -cyclodextrin had more curcumin penetration and accumulation in the porcine cornea compared with the curcumin aqueous solution. EDA modification caused 3.74-fold and 6.61-fold increases in the corneal partition coefficient and the permeability constant of curcumin (Table S2). It is clear that EDA- β -cyclodextrin encapsulation could hugely promote the corneal curcumin delivery.

3.5. Histological examination of porcine corneal tissue

Although there is no irritation observed in patients using the cyclodextrin eye drop solutions, a previous study reported that a small fraction of the applied cyclodextrin could penetrate into the cornea and extract lipid components from the cornea [44]. To evaluate the safety of our systems, we performed the histological examination of the porcine corneas, using hematoxylin and eosin (H&E) staining, to understand the

impact of vehicles on the corneal tissue. The porcine corneas were treated with curcumin aqueous solution and curcumin-EDA- β -cyclodextrin for 3 h before the HE staining (Fig. S2 (A) & (B)). Three layers of the epithelium, Bowman membrane, and stroma were clearly visualized in both images. The corneal epithelium, the upmost layer of cells, directly contacted the curcumin vehicles. Some fibrous areas were observed in the stroma layers treated by both curcumin solutions. In general, no structural damage was observed in the corneal epithelium in both vehicles. The curcumin-EDA- β -cyclodextrin complex did not affect the corneal morphology in the *in vitro* porcine cornea model.

3.6. Radical scavenging and antioxidant activity of the curcumin-EDA- β -cyclodextrin

Free radicals cause many ocular diseases, including dry eye syndrome, anterior uveitis, and conjunctivitis [3]. Protection against free radicals can be achieved using ocular antioxidant delivery [45]. One of the protection mechanisms for antioxidants, the radical scavenging, can quench peroxide radicals directly [46]. Assays based on the use of free radical-containing 1,1-diphenyl-2-picryl-hydrazyl (DPPH) can be used to evaluate the antioxidant capacity of compounds, since the purple color of DPPH fades rapidly when it encounters radical scavengers [47]. We performed *in vitro* DPPH assay to determine the antioxidant capacity of curcumin aqueous solution, curcumin in methanol, curcumin inclusion complex (CU- β -CD), and the positive control vitamin C (Fig. 5). The antioxidant activities were in the order of vitamin C > curcumin in methanol solution > CU- β -CD > curcumin in water. The sample, curcumin in methanol, had good solubility and an effective scavenging power since methanol was used as the solvent in the DPPH assay. The low scavenging activity of the curcumin aqueous solution was because water used as solvent alone was weak and not able to completely keep curcumin soluble. However, the CU- β -CD complex successfully rescued the radical scavenging ability of the curcumin. Our results indicated that the curcumin inclusion with EDA- β -cyclodextrin preserved the DPPH radical scavenging activity.

3.7. The biocompatibility of EDA- β -cyclodextrin in BCE and RGC-5 cell

Human studies and animal models have proved that curcumin is safe even at high doses [48]. Here, we evaluated if EDA- β -cyclodextrin carriers can maintain the safety profile of curcumin in *in vitro* cell models. BCE cell line has been used to test biocompatibility of biodegradable polymers in ophthalmology [49] and RGC-5 cell line has been used to study the protective mechanism of lutein [50]. We observed

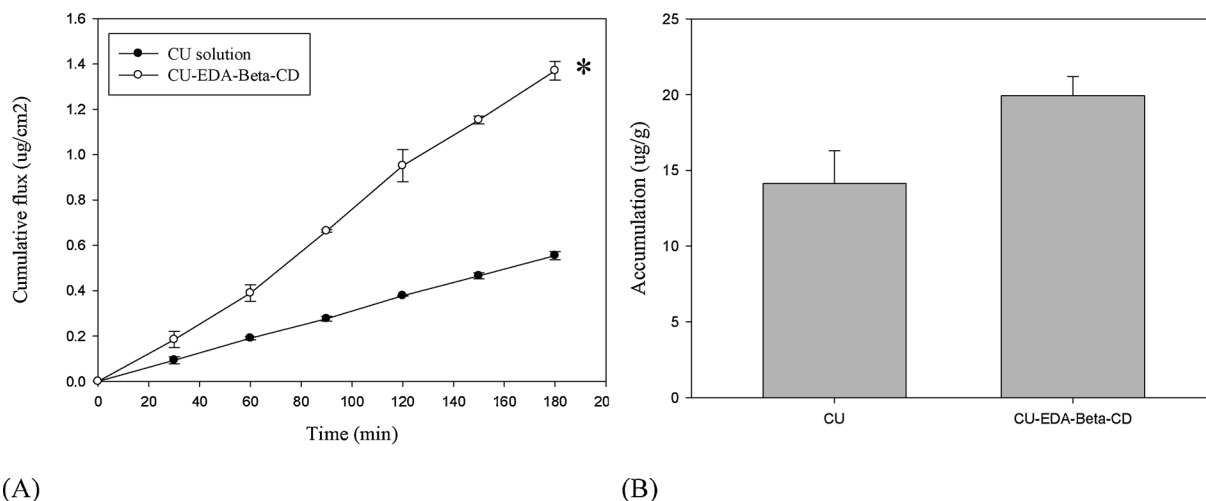


Fig. 4. Cumulative flux (A) and accumulation (B) of curcumin in porcine cornea using curcumin solution and CU-EDA- β -cyclodextrin in Franz diffusion cells for 3 h (n = 2, * indicates P < 0.05).

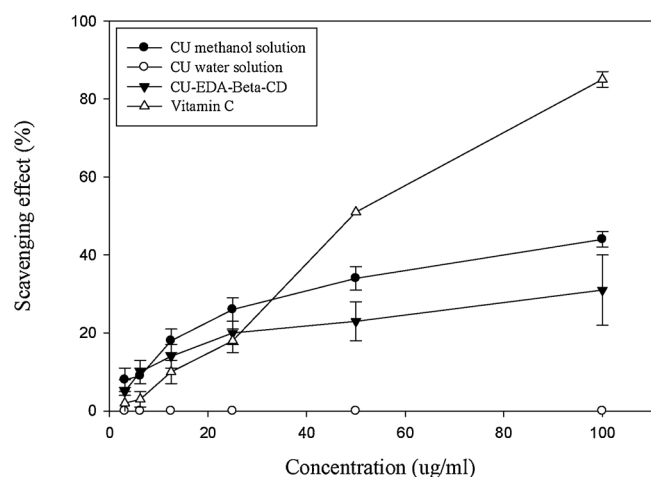


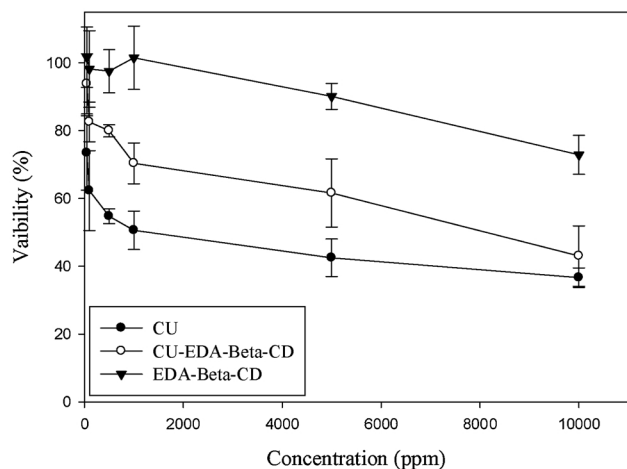
Fig. 5. The scavenging activity of curcumin and CU-EDA- β -cyclodextrin.

that in both cell lines, the toxicity ranking was in the order of curcumin > curcumin-EDA- β -cyclodextrin complex > EDA- β -cyclodextrin (Fig. 6(A) & (B)). The low toxicity of curcumin could be even more

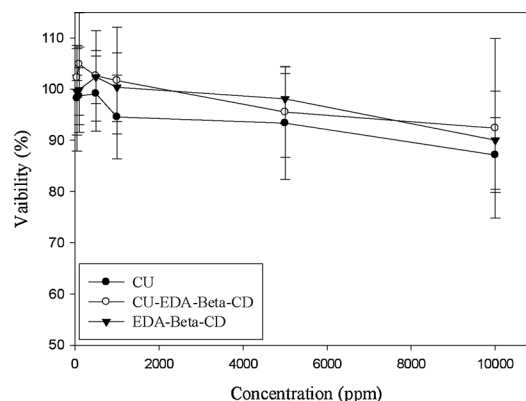
reduced when encapsulated in EDA- β -cyclodextrin. These biocompatibility results indicated that EDA- β -cyclodextrin was an excellent carrier for curcumin.

3.8. Storage stability of the curcumin inclusion nanoparticles

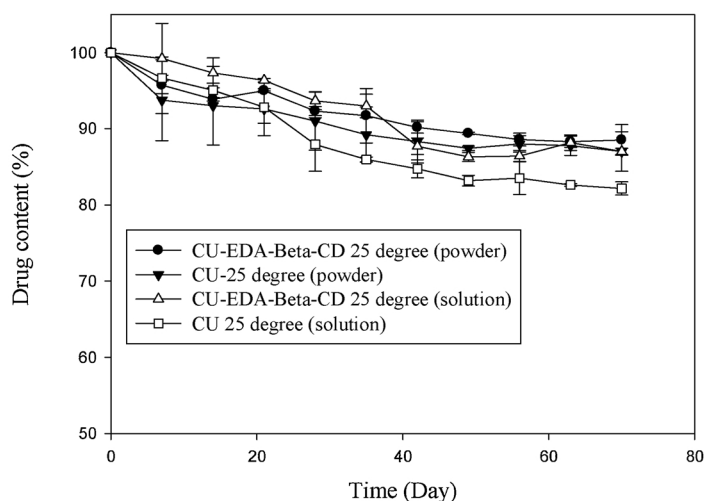
One of the major challenges that limit curcumin bioavailability is its instability [1]. At physiological conditions, curcumin rapidly degrades chemically or undergoes biotransformation in the presence of metabolizing enzymes [51]. Cyclodextrins were reported to be able to enhance the stability of wide variety of drugs in aqueous solutions [13]. Fig. 6(C) shows the stability of the curcumin and curcumin-EDA- β -cyclodextrin complexes stored at 25 °C, in aqueous solution or in their dried, powdered form for 10 weeks. Curcumin degraded at the rate of 2% per week in aqueous solution, but was stable in the dried form. Importantly, curcumin-EDA- β -cyclodextrin complexes in both forms were more stable; they decomposed only 10% after 10-week storage. The results confirmed that the EDA- β -cyclodextrin could protect the encapsulated curcumin from degradation in the aqueous environment. The enhanced stability may be attributed to the lipophilic moiety of curcumin being protected inside the cavity of doughnut-shaped molecules.



(A)



(B)



(C)

Fig. 6. Dose effects of EDA- β -cyclodextrin, curcumin, and their inclusion complex on the viability of retinal ganglion cells (A) and bovine corneal epithelial cells (B). The stability of curcumin-EDA- β -cyclodextrin complex stored at 25 °C (C). n = 2.

4. Conclusion

Using the solvent evaporation method, we prepared the novel EDA- β -cyclodextrin and its curcumin complex. We characterized the EDA- β -cyclodextrin and its complex, using the van't Hoff plot, phase solubility diagram, FT-IR, XRD, TEM, and evaluation of solubility and storage stability. The EDA- β -cyclodextrin complex had better thermodynamic stability and higher complex yield than the parental β -cyclodextrin. The EDA- β -cyclodextrin complex displayed high corneal penetration and cumulative flux in the cornea diffusion experiment *in vitro*. The histological examination of the porcine corneas and cell viability test of two ocular cell lines confirmed the biocompatibility of the inclusion complex. Together, our results supported that curcumin-EDA- β -cyclodextrin nanoparticles were potent for ocular curcumin delivery.

Declaration of Competing Interest

The authors declare that they have no conflict of interest.

Acknowledgements

We express gratitude to Ministry of Science and Technology, Taiwan (MOST 108-2221-E-182-039), Chang Gung University (BMRP 758) and Chang Gung Memorial Hospital (CMRPD 2H0071, 2H0072) for funding and supporting this research. We appreciate the technical assistance of Gaurav Tripathi from Indian Institute Technology (BHU), India.

Appendix A. Supplementary data

Supplementary material related to this article can be found, in the online version, at doi:<https://doi.org/10.1016/j.colsurf.2019.110726>.


References

- [1] K.M. Nelson, J.L. Dahlin, J. Bisson, J. Graham, G.F. Pauli, M.A. Walters, The essential medicinal chemistry of curcumin, *J. Med. Chem.* 60 (2017) 1620–1637.
- [2] H. Mirzaei, A. Shakeri, B. Rashidi, A. Jalili, Z. Banikazemi, A. Sahebkar, Phytosomal curcumin: a review of pharmacokinetic, experimental and clinical studies, *Biomed. Pharmacother.* 85 (2017) 102–112.
- [3] N. Pescosolido, R. Giannotti, A.M. Plateroti, A. Pascarella, M. Nebbioso, Curcumin: Therapeutic potential in ophthalmology, *Planta Med.* 80 (2014) 249–254.
- [4] C. Mohanty, S.K. Sahoo, Curcumin and its topical formulations for wound healing applications, *Drug Discov. Today* 22 (2017) 1582–1592.
- [5] B. Wahlang, Y.B. Pawar, A.K. Bansal, Identification of permeability-related hurdles in oral delivery of curcumin using the Caco-2 cell model, *Eur. J. Pharm. Biopharm.* 77 (2011) 275–282.
- [6] X. Ma, Y. Zhao, Biomedical applications of supramolecular systems based on host-guest interactions, *Chem. Rev.* 115 (2015) 7794–7839.
- [7] H.H. Tønnesen, M. Masson, T. Loftsson, Studies of curcumin and curcuminoids. XXVII. Cyclodextrin complexation: solubility, chemical and photochemical stability, *Int. J. Pharm.* 244 (2002) 127–135.
- [8] M.M. Yallapu, M. Jaggi, S.C. Chauhan, Beta-Cyclodextrin-curcumin self-assembly enhances curcumin delivery in prostate cancer cells, *Colloids Surf. B Biointerfaces* 79 (2010) 113–125.
- [9] A.B. Hegge, T.T. Nielsen, K.L. Larsen, E. Bruzell, H.H. Tønnesen, Impact of curcumin supersaturation in antibacterial photodynamic therapy-effect of cyclodextrin type and amount: studies on curcumin and curcuminoids XLV, *J. Pharm. Sci.* 101 (2012) 1524–1537.
- [10] M. Poorghorban, U. Das, O. Alaidi, J.M. Chitanda, D. Michel, J. Dimmock, R. Verrall, P. Grochulski, I. Badea, Characterization of the host-guest complex of a curcumin analog with β -cyclodextrin and β -cyclodextrin-gemini surfactant and evaluation of its anticancer activity, *Int. J. Nanomedicine* 10 (2015) 503–515.
- [11] Thorsteinn Loftsson, Marcus E. Brewster, Cyclodextrins as functional excipients: methods to enhance complexation efficiency, *J. Pharm. Sci.* 101 (2012) 3019–3032.
- [12] T. Loftsson, M.E. Brewster, Pharmaceutical applications of cyclodextrins: effects on drug permeation through biological membranes, *J. Pharm. Pharmacol.* 63 (2011) 1119–1135.
- [13] C. Muankaew, T. Loftsson, Cyclodextrin-Based Formulations: A Non-Invasive Platform for Targeted Drug Delivery, *Basic Clin. Pharmacol. Toxicol.* 122 (2018) 46–55.
- [14] R. Iacovino, J.V. Caso, C. Di Donato, G. Maligneri, M. Palmieri, L. Russo, C. Isernia, Cyclodextrins as complexing agents: preparation and applications, *Curr. Org. Chem.* 21 (2017).
- [15] T. Loftsson, T. Jarvinen, Cyclodextrins in ophthalmic drug delivery, *Adv. Drug Deliv. Rev.* 36 (1999) 59–79.
- [16] M.E. Brewster, T. Loftsson, Cyclodextrins as pharmaceutical solubilizers, *Adv. Drug Delivery Rev.* 59 (2007) 645–666.
- [17] P. Jansook, S.V. Kurkov, T. Loftsson, Cyclodextrins as solubilizers: formation of complex aggregates, *J. Pharm. Sci.* 99 (2010) 719–729.
- [18] H.H. Sigurdsson, E. Stefansson, E. Gudmundsdottir, T. Eysteinnsson, M. Thorsteinsdottir, T. Loftsson, Cyclodextrin formulation of dorzolamide and its distribution in the eye after topical administration, *J. Control. Release* 102 (2005) 255–262.
- [19] M. Tanito, K. Hara, Y. Takai, Y. Matsuoka, N. Nishimura, P. Jansook, T. Loftsson, E. Stefansson, A. Ohira, Topical dexamethasone-cyclodextrin microparticle eye drops for diabetic macular edema, *Invest. Ophthalmol. Vis. Sci.* 52 (2011) 7944–7948.
- [20] Y.Y. Liu, X.D. Fan, L. Gao, Synthesis and characterization of β -Cyclodextrin based functional monomers and its copolymers with N-isopropylacrylamide, *Macromol. Biosci.* 3 (2003) 715–719.
- [21] M.E. Brewster, T. Loftsson, Cyclodextrins as pharmaceutical solubilizers, *Adv. Drug Deliv. Rev.* 59 (2007) 645–666.
- [22] D.J. Wales, P. Salamon, Observation time scale, free-energy landscapes, and molecular symmetry, *Proc. Natl. Acad. Sci.* 111 (2014) 617–622.
- [23] C.H. Liu, Y.C. Huang, J.W. Jhang, Y.H. Liu, W.C. Wu, Quercetin delivery to porcine cornea and sclera by solid lipid nanoparticles and nanoemulsion, *RSC Adv.* 5 (2015) 100923–100933.
- [24] C.H. Liu, F.Y. Chang, D.K. Hung, Terpene microemulsions for transdermal curcumin delivery: effects of terpenes and cosurfactants, *Colloids Surf. B Biointerfaces* 82 (2011) 63–70.
- [25] P. Jansook, N. Ogawa, T. Loftsson, Cyclodextrins: structure, physicochemical properties and pharmaceutical applications, *Int. J. Pharm.* 535 (2018) 272–284.
- [26] P. Saokham, C. Muankaew, P. Jansook, T. Loftsson, Solubility of cyclodextrins and Drug/Cyclodextrin complexes, *Molecules* 23 (2018).
- [27] E. Sabadini, T. Cosgrove, C. Egidio Fdo, Solubility of cyclomaltooligosaccharides (cyclodextrins) in H₂O and D₂O: a comparative study, *Carbohydr. Res.* 341 (2006) 270–274.
- [28] T. Loftsson, M.E. Brewster, Cyclodextrins as functional excipients: methods to enhance complexation efficiency, *J. Pharm. Sci.* 101 (2012) 3019–3032.
- [29] M.M. Al Omari, M.B. Zughul, J.E.D. Davies, A.A. Badwan, Sildenafil/cyclodextrin complexation: stability constants, thermodynamics, and guest-host interactions probed by ¹H NMR and molecular modeling studies, *J. Pharm. Biomed. Anal.* 41 (2006) 857–865.
- [30] Lina Dong, Min Liu, Aiju Chen, Yong Wang, Dezhi Sun, Solubilities of quercetin in three β -cyclodextrin derivative solutions at different temperatures, *J. Mol. Liq.* 177 (2013) 204–208.
- [31] Y. Zheng, I.S. Haworth, Z. Zuo, M.S. Chow, A.H. Chow, Physicochemical and structural characterization of quercetin-beta-cyclodextrin complexes, *J. Pharm. Sci.* 94 (2005) 1079–1089.
- [32] S. Chakraborty, S. Basu, S. Basak, Effect of β -cyclodextrin on the molecular properties of myricetin upon nano-encapsulation: insight from optical spectroscopy and quantum chemical studies, *Carbohydr. Polym.* 99 (2014) 116–125.
- [33] M.V. Rekharsky, Y. Inoue, Complexation thermodynamics of cyclodextrins, *Chem. Rev.* 98 (1998) 1875–1917.
- [34] K. Taguchi, Transient binding mode of Phenolphthalein- β -Cyclodextrin complex: an example of induced geometrical distortion, *J. Am. Chem. Soc.* 108 (1986) 2705–2709.
- [35] M.H. Mohamed, L.D. Wilson, J.V. Headley, K.M. Peru, Thermodynamic properties of inclusion complexes between β -cyclodextrin and naphthenic acid fraction components, *Energy Fuels* 29 (2015) 3591–3600.
- [36] X. Li, H. Liu, J. Li, Z. Deng, L. Li, J. Liu, J. Yuan, P. Gao, Y. Yang, S. Zhong, Micelles via self-assembly of amphiphilic beta-cyclodextrin block copolymers as drug carrier for cancer therapy, *Colloids Surf. B Biointerfaces* 183 (2019).
- [37] H. Liu, J. Chen, X. Li, Z. Deng, P. Gao, J. Li, T. Ren, L. Huang, Y. Yang, S. Zhong, Amphipathic β -cyclodextrin nanocarriers serve as intelligent delivery platform for anticancer drug, *Colloids Surf. B Biointerfaces* 180 (2019) 429–440.
- [38] C.S. Mangolim, C. Moriwaki, A.C. Nogueira, F. Sato, M.L. Baesso, A.M. Neto, G. Mاتيoli, Curcumin- β -cyclodextrin inclusion complex: stability, solubility, characterisation by FT-IR, FT-Raman, X-ray diffraction and photoacoustic spectroscopy, and food application, *Food Chem.* 153 (2014) 361–370.
- [39] J. Li, Q. Jiang, P. Deng, Q. Chen, M. Yu, J. Shang, W. Li, The formation of a host-guest inclusion complex system between beta-cyclodextrin and baicalin and its dissolution characteristics, *J. Pharm. Pharmacol.* 69 (2017) 663–674.
- [40] T.S. Anirudhan, P.L. Divya, J. Nima, Synthesis and characterization of novel drug delivery system using modified chitosan based hydrogel grafted with cyclodextrin, *Chem. Eng. J.* 284 (2016) 1259–1269.
- [41] L.J. Hill, R.J.A. Moakes, C. Vareechon, G. Butt, A. Ng, K. Brock, G. Chouhan, R.C. Vincent, S. Abbondante, R.L. Williams, N.M. Barnes, E. Pearlman, G.R. Wallace, S. Rauz, A. Logan, L.M. Grover, Sustained release of decorin to the surface of the eye enables scarless corneal regeneration, *NPJ Regen. Med.* 3 (2018) 23.
- [42] P.W.J. Morrison, C.J. Connon, V.V. Khutoryanskiy, Cyclodextrin-mediated enhancement of riboflavin solubility and corneal permeability, *Mol. Pharm.* 10 (2013) 756–762.
- [43] P. Jarho, A. Urtti, D.W. Pate, P. Suhonen, T. Jarvinen, Increase in aqueous solubility, stability and *in vitro* corneal permeability of anandamide by hydroxypropyl-beta-cyclodextrin, *Int. J. Pharm.* 137 (1996) 209–216.
- [44] T. Loftsson, E. Stefansson, Cyclodextrins in ocular drug delivery: theoretical basis with dexamethasone as a sample drug, *J. Drug Deliv. Sci. Technol.* 17 (2007) 3–9.
- [45] M.N. Alam, N.J. Bristi, M. Rafiqzaman, Review on *in vivo* and *in vitro* methods

- evaluation of antioxidant activity, *J. Saudi Pharm. Soc.* 21 (2013) 143–152.
- [46] J.R. Soares, T.C. Dinis, A.P. Cunha, L.M. Almeida, Antioxidant activities of some extracts of *Thymus zygis*, *Free Radic. Res.* 26 (1997) 469–478.
- [47] O.P. Sharma, T.K. Bhat, DPPH antioxidant assay revisited, *Food Chem.* 113 (2009) 1202–1205.
- [48] M. Kanai, Y. Otsuka, K. Otsuka, M. Sato, T. Nishimura, Y. Mori, M. Kawaguchi, E. Hatano, Y. Kodama, S. Matsumoto, Y. Murakami, A. Imaizumi, T. Chiba, J. Nishihira, H. Shibata, A phase I study investigating the safety and pharmacokinetics of highly bioavailable curcumin (Theracurmin) in cancer patients, *Cancer Chemother. Pharmacol.* 71 (2013) 1521–1530.
- [49] A. Huhtala, T. Pohjonen, L. Salminen, A. Salminen, K. Kaarniranta, H. Uusitalo, In vitro biocompatibility of degradable biopolymers in cell line cultures from various ocular tissues: direct contact studies, *J. Biomed. Mater. Res. - Part A* 83 (2007) 407–413.
- [50] S.Y. Li, A.C.Y. Lo, Lutein protects RGC-5 cells against hypoxia and oxidative stress, *Int. J. Mol. Sci.* 11 (2010) 2109–2117.
- [51] G. Garcea, D.J. Jones, R. Singh, A.R. Dennison, P.B. Farmer, R.A. Sharma, W.P. Steward, A.J. Gescher, D.P. Berry, Detection of curcumin and its metabolites in hepatic tissue and portal blood of patients following oral administration, *Br. J. Cancer* 90 (2004) 1011–1015.

Article

CXCL1/CXCR2 Paracrine Axis Contributes to Lung Metastasis in Osteosarcoma

Chia-Chia Chao ^{1,†}, Chiang-Wen Lee ^{2,3,4,†}, Tsung-Ming Chang ⁵, Po-Chun Chen ^{6,7,8} and Ju-Fang Liu ^{6,8,9,*} 

¹ Department of Respiratory Therapy, Fu Jen Catholic University, New Taipei City 24205, Taiwan; 095457@mail.fju.edu.tw

² Department of Orthopaedic Surgery, Chang Gung Memorial Hospital, Puzi City, Chiayi County 61363, Taiwan; cwlee@mail.cgu.edu.tw

³ Department of Nursing, Division of Basic Medical Sciences, and Chronic Diseases and Health Promotion Research Center, Chang Gung University of Science and Technology, Puzi City, Chiayi County 61363, Taiwan

⁴ Research Center for Industry of Human Ecology and Research Center for Chinese Herbal Medicine, Chang Gung University of Science and Technology, Guishan Dist., Taoyuan City 33303, Taiwan

⁵ School of Medicine, Institute of Physiology, National Yang-Ming University, Taipei City 11221, Taiwan; briancoinage@ym.edu.tw

⁶ Translational medicine Center, Shin-Kong Wu Ho-Su Memorial Hospital, Taipei City 11101, Taiwan; blibra1002@hotmail.com

⁷ Department of Biotechnology, College of Medical and Health Science, Asia University, Taichung 41354, Taiwan

⁸ Department of Medical Research, China Medical University Hospital, China Medical University, Taichung 40402, Taiwan

⁹ School of Oral Hygiene, College of Oral Medicine, Taipei Medical University, Taipei 11031, Taiwan

* Correspondence: T010615@ms.skh.org.tw or jufangliu@tmu.edu.tw; Tel.: +(886)-2-2833-2211 (ext. 9420)

† These authors contributed equally to this work.

Received: 14 January 2020; Accepted: 13 February 2020; Published: 17 February 2020



Abstract: Osteosarcoma, the most common of all bone malignancies, has a high likelihood of lung metastasis. Up until now, the molecular mechanisms involved in osteosarcomas with lung metastases are not clearly understood. Recent observations have shown that the chemokine CXCL1 and its receptor CXCR2 assist with the homing of neutrophils into the tumor microenvironment. Here, we show that the CXCL1/CXCR2 paracrine axis is crucial for lung metastasis in osteosarcoma. In an in vivo lung metastasis model of osteosarcoma, lung blood vessels expressed CXCL1 and osteosarcoma cells expressed the CXCR2 receptor. CXCR2 expression was higher in osteosarcoma cell lines than in normal osteoblast cells. Immunohistochemistry staining of clinical osteosarcoma specimens revealed positive correlations between CXCR2 expression and pathology stage and also vascular cell adhesion molecule 1 (VCAM-1) expression. High levels of CXCL1 secreted by human pulmonary artery endothelial cells (HPAECs) promoted osteosarcoma cell mobility, which was mediated by the upregulation of VCAM-1 expression. When HPAECs-conditioned media was incubated in osteosarcoma cells, we observed that the CXCR2 receptor and FAK/PI₃K/Akt/NF- κ B signaling cascade were required for VCAM-1 expression. Our findings illustrate a molecular mechanism of lung metastasis in osteosarcoma and indicate that CXCL1/CXCR2 is worth targeting in treatment schemas.

Keywords: Osteosarcoma; CXCL1; CXCR2; migration; VCAM-1

1. Introduction

Of all bone malignancy diagnoses in children and young adults, osteosarcoma is the most common and frequently presents with metastasis at diagnosis, which contributes to mortality [1].

Approximately one-third of patients presenting with localized disease will relapse, as will about three-quarters of patients with metastases at diagnosis. As many as 90% of these relapses are due to lung metastases [2]. Therapy that effectively prevents osteosarcoma lung metastasis is urgently required.

Each type of carcinoma has its preferred sites of metastasis. Organs involved in metastasis secrete attractant molecules that guide cancer cells to specific sites [3]. It is also known that chemokines, low molecular chemotactic cytokines that mediate connection between different cell types, help to regulate leukocyte homing besides promoting cancer growth [4]. Indeed, chemokines play important roles in various biological functions including cell migration, angiogenesis, and hematopoietic cell homing [5]. They also play crucial roles in the progression and metastasis of different cancers. In breast cancer, the CXCL12/CXCR4 axis is implicated in the homing of cancer cells to metastatic sites [6,7]. Metastatic breast cancer cells express high levels of CXCR4 and stromal cells in distant organs express high levels of CXCL12, the CXCR4 ligand. The CXCL12/CXCR4 axis compromises adjuvant therapy in breast cancer [8].

Since it was first identified in culture supernatants of melanoma cell lines, CXCL1 has been implicated in inflammation, angiogenesis, tumorigenesis, and wound healing [9]. CXCL1 binds to CXCR2, which is highly expressed on neutrophil surfaces [10]. Tumor-derived CXCL1 modulates the tumor microenvironment by regulating various cells, such as macrophages, fibroblasts [11], neutrophils [12], and osteoclasts [13]. Increased levels of CXCL1 are associated with tumor size, advancing stage, depth of invasion, and patient survival [14–16]. Silencing of CXCL1 can inhibit tumor growth in hepatocellular carcinoma [17], while knockdown of CXCL1 expression can inhibit tumor growth in colorectal cancer liver metastasis [18]. CXCL1 autocrine and paracrine networks can also promote tumor invasion and metastasis [19–22]. However, although the pro-metastatic functions of CXCL1 are recognized in tumor progression, its role remains unclear in osteosarcoma.

This report is the first to demonstrate that human pulmonary artery endothelial cells secrete CXCL1 and contribute to lung metastasis by increasing VCAM-1 expression. It also shows that CXCL1-promoted VCAM-1 expression is regulated by the CXCR2/FAK/PI₃K/Akt/NF- κ B pathway. Our results show that CXCL1 plays a pivotal role in metastatic osteosarcoma.

2. Materials and Methods

2.1. Materials

Anti-mouse and anti-rabbit IgG-conjugated horseradish peroxidase, rabbit polyclonal antibodies specific for CXCL1, CXCR2, VCAM-1, p-FAK, FAK, p85 α , p-p85 α , Akt, p-Akt, p-IKK α / β , IKK α / β , p-I κ B α , I κ B α , p-p65, p65, and β -Actin were purchased from GeneTex International Corporation (Hsinchu City, Taiwan). Recombinant human CXCL1 was purchased from PeproTech (Rocky Hill, NJ, USA). Short hairpin RNA (shRNA) plasmid for knocking down gene expression was purchased from the National RNAi Core Facility Platform (Taipei, Taiwan). All siRNAs were ON-TARGETplus siRNAs, purchased from Dharmacon Research (Lafayette, CO, USA). All other chemicals were obtained from Sigma-Aldrich (St. Louis, MO, USA).

2.2. Cell Culture

Human osteosarcoma cell lines (MG63, U2OS, and HOS) and normal osteoblast cell lines (hFOB1.19) were obtained from the American Type Cell Culture Collection (Manassas, VA, USA). Human pulmonary artery endothelial cells (HPAECs) were purchased from Lonza Clonetics (Walkersville, MD, USA). hFOB1.19 cells were cultured in DMEM/F12 medium, U2OS cells were cultured in McCoy's 5A medium and MG63 and HOS cells were cultured in Eagle's minimum essential medium. All cells were supplemented with contained with 20 mM HEPES, 10% heat-inactivated fetal bovine serum, 2 mM-glutamine, penicillin (100 U/mL), and streptomycin (100 μ g/mL) at 37 °C with 5% CO₂. The HPAECs were maintained in EGMTM-2 endothelial cell growth medium-2 BulletKit (Lonza), which contains basic growth medium (EBM-2), fetal bovine serum (FBS) and antibiotics, ascorbic acid, vascular

endothelial growth factor (VEGF), human fibroblast growth factor (hFGF-B), hydrocortisone, human epidermal growth factor (hEGF), R3-IGF (insulin-like growth factor)-1, and heparin. Unless otherwise stated, cells were maintained in a 37 °C incubator with 5% CO₂. Migration-prone MG63 cells were selected according to their differential migration ability; the cell culture insert system was used as described earlier [23]. After 24 h of migration, cells that penetrated through pores and migrated to the underside of the filters were trypsinized and harvested for a second selection process. Any of the original cells that did not pass through membrane pores were designated as M0. After 10 selection rounds, the migration-prone subline was designated as M10. After 20 selection rounds, the migration-prone subline was designated as M20.

2.3. Preparation of Conditioned Media

The HPAECs were seeded and grown overnight in 10-cm culture dishes. The cells were washed with PBS and cultured in EGM-2 medium for 48 h. The culture supernatants (conditioned media (CM)) were collected. To normalize for differences in cell density due to proliferation, the cells from each plate were collected, and the total DNA content per dish was determined (spectrophotometric absorbance, 260 nm).

2.4. Western Blot

The cells were lysed in RIPA lysis buffer and total cell lysates were collected. Resolved proteins were determined with SDS-PAGE and transferred to Immobilon™ polyvinylidene difluoride (PVDF) membranes. Blots were blocked with 5% nonfat milk for 1 h at room temperature then incubated with primary antibodies for another 1 h at room temperature. After three washes, blots were incubated with peroxidase-conjugated secondary antibody (1:5000) for 1 h at room temperature. The blots were visualized using a charge-coupled device camera-based detection system (UVP Inc., Upland, CA, USA). Quantitative data were obtained using ImageJ software (National Institutes of Health, USA). All original western blot figures can be found in the supplementary file.

2.5. RNA Extraction and Quantitative Real-Time Polymerase Chain Reaction

Total RNA was extracted from cells using Total RNA preparation kits (easy-Blue Total RNA Extraction kit) purchased from iNtRON Biotechnology (Seongnam, Korea), following the manufacturer's protocol. In brief, cells were added to 0.5 mL easy-Blue reagent, homogenized and incubated at room temperature for 3 min. After extraction with chloroform (0.1 mL) and precipitation with isopropanol (0.4 mL), RNA was washed with 75% ethanol, and then the RNA pellet was dissolved in 10 µL of RNase-free water. RNA yield and purity were determined by measuring absorbance at 260 and 280 nm using a Nanodrop spectrophotometer (Thermo Fisher Scientific, Inc., Waltham, MA, USA). Complementary DNA (cDNA) was generated by reverse transcription of total RNA, according to the manufacturer's instructions (Invitrogen, Carlsbad, CA, USA).

Real-time quantitative polymerase chain reaction (qPCR) was performed using SYBR Green (KAPA Biosystems, Woburn, MA, USA), according to the manufacturer's protocol, and reactions were performed using a StepOnePlus machine (Applied Biosystems, Foster City, CA, USA). Human VCAM-1 and glyceraldehyde 3-phosphate dehydrogenase (GAPDH) purchased from Sigma-Aldrich were used as primers to amplify the target genes. The expression levels of the target genes were determined by normalization to GAPDH levels. We calculated the results using this equation: $\text{Ratio} = 2^{-\Delta\Delta C_t}$, where $\Delta\Delta C_t = (C_{t \text{ target}} - C_{t \text{ GAPDH}})_{\text{Sample}} - (C_{t \text{ target}} - C_{t \text{ GAPDH}})_{\text{Control}}$. Each sample was assayed in triplicate, and the data represent three independent experiments.

2.6. Transwell Cell Migration Assay

Cell migration assays were performed with Transwell inserts (8-µm pore size; Costar, NY, USA) in 24-well dishes. Cells (2×10^4 cell/well) were pretreated for 90 min with the designated inhibitor then incubated with the culture supernatants for 24 h. The cells were seeded in the upper Transwell

chamber, and 300 µL of medium was placed in the lower chamber. After 24 h, the cells were fixed in 3.7% formaldehyde for 30 min and stained with 0.05% crystal violet for 60 min. Cells on the upper side of the chamber were removed with cotton-tipped swabs, and the chamber were washed with PBS. Cells on the underside of the filters were examined and counted under a microscope. Each experiment was repeated at least three times.

2.7. Immunofluorescence Microscopy

MG63 cells (5×10^3 cell/well) were seeded on glass coverslips and treated under the indicated conditions, rinsed once with PBS, and fixed in 3.7% paraformaldehyde for 15 min at room temperature. Cells were washed three times with PBS and blocked with 4% BSA for 15 min. After blocking, the cells were incubated with anti-human p65 (1:100) for 1 h at room temperature. After undergoing three washes with PBS, the cells were incubated with FITC-conjugated goat anti-rabbit IgG for 1 h. Finally, the cells were washed, mounted, and photographed using the Leica TCS SP2 Spectral Confocal System.

2.8. Chromatin Immunoprecipitation Assay

Chromatin immunoprecipitation (ChIP) analysis was performed as described previously [24]. DNA were extracted from treated samples and immunoprecipitated by anti-p65 antibody. The immunoprecipitated DNA were further subjected to purification by using phenol–chloroform. The purified DNA pellet was subjected to PCR then resolved using 1.5% agarose gel electrophoresis and visualized by ultraviolet illumination. Primers 5'-ACAGAGAGAGGAGCTTCAGCAGTGAGAGCA-3' and 5'-GTCTGTGCTTTATAAAGGGTCTTGTTCAG-3' were used to amplify across the human promoter region of the NF-κB region (-2167 and -1967) in the promoter region of VCAM-1.

2.9. Reporter Assay

The NF-κB report plasmid, pSV-β-galactosidase vector and luciferase assay kit were purchased from Promega (Madison, WI, USA). Cells (2×10^5 cell/well) were co-transfected with NF-κB report plasmid and pSV-β-galactosidase vector for 24 h using Lipofectamine 3000™ (Invitrogen). Transactivation was determined by monitoring firefly luciferase levels in the pGL2 vector. The luciferase assay was performed by adding lysis buffer (100 µL), and cells were harvested by centrifugation (13,200 rpm for 5 min). The supernatant was transferred to fresh tubes, and 20 µL of cell lysate was added to 80 µL of fresh luciferase assay buffer in an assay tube. Luciferase activity was measured using a microplate luminometer and normalized to transfection efficiency based on the cotransfected β-galactosidase expression vector.

2.10. In Vivo Tumor Xenograft Study

All mice were obtained from the Lasco (Taipei, Taiwan). Ethical approval was obtained for the use of the animals, and all experiments were performed in accordance with the Guidelines for Animal Care of the Institutional Animal Care and Use Committee of College of Medicine, National Taiwan University (Approval No: 20150357). All experiments were performed in National Taiwan University. Four-week-old male CB17/SCID mice were purchased from Lasco and maintained under pathogen-free conditions. Seven animals per group were used, and the experiment was repeated twice. For assessing lung metastasis in osteosarcoma cells in the in vivo xenograft model. Two times 1×10^6 cells were resuspended in 0.1 mL of PBS and injected into the lateral tail vein. After 4 weeks, mice were sacrificed using CO₂. The lungs were removed and fixed in 10% formalin. The number of lung tumor nodules was counted using a dissecting microscope.

2.11. Immunohistochemistry (IHC) Staining

For investigating CXCR2 and VCAM-1 expression in clinical specimens, human osteosarcoma tissue arrays (BO244, T261, T262, T262A, T263, and OS804b) containing 11 cases of normal bone,

7 cases of stage I osteosarcoma, 49 cases of stage II osteosarcoma, and 7 cases of stage III osteosarcoma were purchased from Biomax (Rockville, MD, USA). The tissues were rehydrated, and incubated in 3% hydrogen peroxide to block endogenous peroxidase activity. After antigen retrieval, the sections were in 3% bovine serum albumin then incubated with the primary mouse polyclonal anti-CXCR2 and VCAM-1 antibody at 1:100 dilutions, at 4 °C overnight. After undergoing three PBS washes, samples were incubated with a 1:100 dilution of biotin-labeled goat anti-mouse IgG secondary antibody. Bound antibodies were detected using the ABC Kit (Vector Laboratories, Burlingame, CA, USA). Slides were stained with the chromogen diaminobenzidine, washed, counterstained with Delafield's hematoxylin, dehydrated, treated with xylene, and then mounted.

Stained specimens were photographed by microscope. Tumor cell staining intensities were scored from 0–5, where 0 = no staining or unspecific staining, 1 = very weak (intensity), 2 = weak staining, 3 = moderate staining, 4 = strong staining, and 5 = very strong staining. A pathologist scored staining intensity in all samples.

2.12. Statistical Analysis

Data are presented as the mean \pm standard deviation (S.D). Statistical comparisons between two samples were performed using the Student's *t*-test. Statistical comparisons of more than two groups were performed using one-way analysis of variance (ANOVA) with Fisher LSD post hoc tests. A *p*-value of less than 0.05 was considered to be statistically significant.

3. Results

3.1. Metastatic Colonies in Osteosarcoma Arise in Pulmonary Vasculature In Vivo

Previous findings suggest that metastatic colonies originate from pulmonary vasculature cells and, in the early stages of disease, micrometastases are contained entirely within the vasculature [25]. To clarify the mechanism involved in osteosarcoma lung metastasis, we created a metastatic lung cancer model using intravenous injections of MG63 cells. Intact organ microscopy revealed the formation of metastatic colonies in pulmonary vascular walls (Figure 1A). The establishment of metastatic colonies at distant sites is only superficially understood. One of the most important mechanisms underlying this process involves homeostatic chemokines and their receptors, which play a key role in cancer homing [26]. As the CXCL1/CXCR2 axis is required for lung metastasis in breast cancer [19], we therefore analyzed levels of CXCL1/CXCR2 expression in lung specimens. Interestingly, CXCL1 was highly expressed in pulmonary vasculature, whereas CXCR2 was only weakly stained in lung tissue. In contrast, lung metastatic foci showed strong CXCR2 expression (Figure 1A). CXCR2 expression was also determined in osteosarcoma cell lines and normal osteoblast cells. As expected, osteosarcoma cell lines expressed CXCR2 and expression levels were positively correlated with anchorage-independent growth ability, as described in a previous report [27] (Figure 1B,C). To clarify the role of CXCR2 in osteosarcoma metastasis, Transwell migration assays established MG63 sublines with high migration ability; CXCR2 expression levels were elevated in the high migration-prone sublines (MG63, M10, and M20) (Figure 1D). This evidence suggests that the CXCL1/CXCR2 axis plays a pivotal role in osteosarcoma lung metastasis.

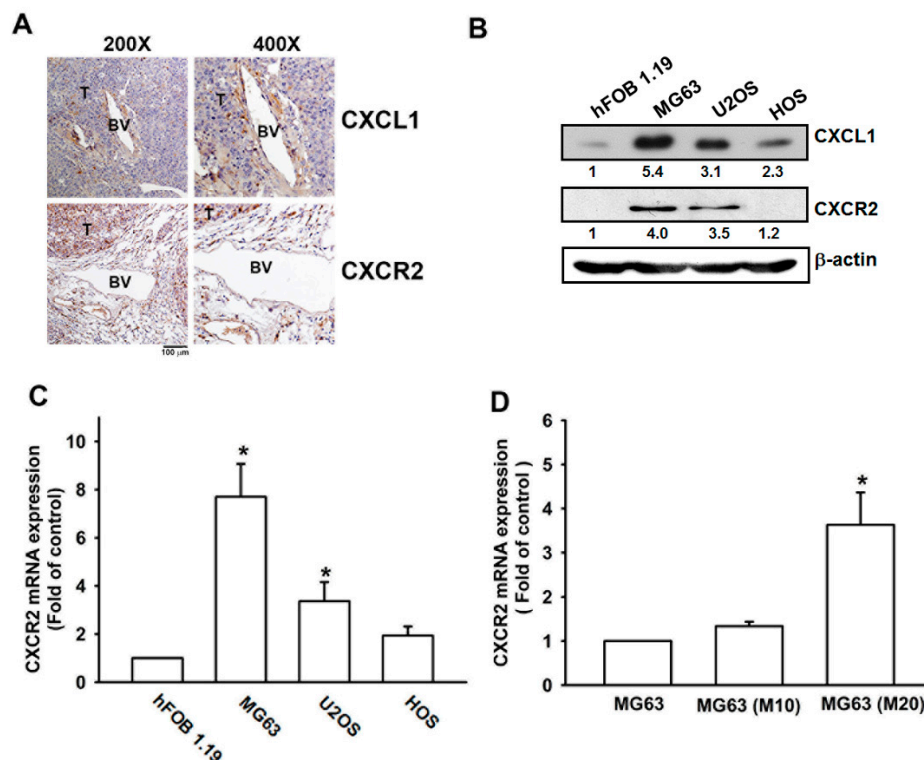


Figure 1. Expression of CXCL1 and CXCR2 in osteosarcoma lung metastasis. (A) The lung metastasis model was established by intravenous injection of MG63 osteosarcoma cells into CB17-SCID mice. Four weeks later, the lung specimens from sacrificed mice were stained with CXCL1 and CXCR2 antibodies, then photographed by optical microscope. T: tumor; BV: blood vessel. (B,C) Total cell lysate and RNA were extracted from hFOB1.19, MG63, U2OS and HOS cells, and CXCR2 expression was examined by Western blot and qPCR analysis. (D) The migration-prone MG63 cells were subjected to qPCR analysis to detect CXCR2 expression. Results are expressed as the mean \pm SD. * $p < 0.05$ compared with the hFOB1.19 group.

3.2. VCAM-1 Expression Is Positively Correlated with CXCR2 in Osteosarcoma Specimens

We next examined levels of CXCR2 expression in osteosarcoma specimens, to determine the prognostic relevance of CXCR2 in osteosarcoma progression. IHC results revealed that CXCR2 expression increased with disease progression (Figure 2A). Extravasation is a critical step in metastasis, by which cancer cells are arrested in small capillaries, are extravasated, adhere to the vasculature endothelium and migrate through the vasculature wall, to establish metastatic foci. Cell adhesion molecules (CAMs) have been implicated in tumor metastasis during the extravasation process [28]. However, very little is known about CAM regulation in human osteosarcoma cells. We, therefore, examined the expression levels of VCAM-1, which has a pivotal role in tumor metastasis [29]. We found that VCAM-1 expression increased with tumor stage (Figure 2B) and was positively correlated with CXCR2 expression in osteosarcoma specimens (Figure 2C). Thus, CXCR2 expression correlates with VCAM-1 expression and tumor progression in osteosarcoma.

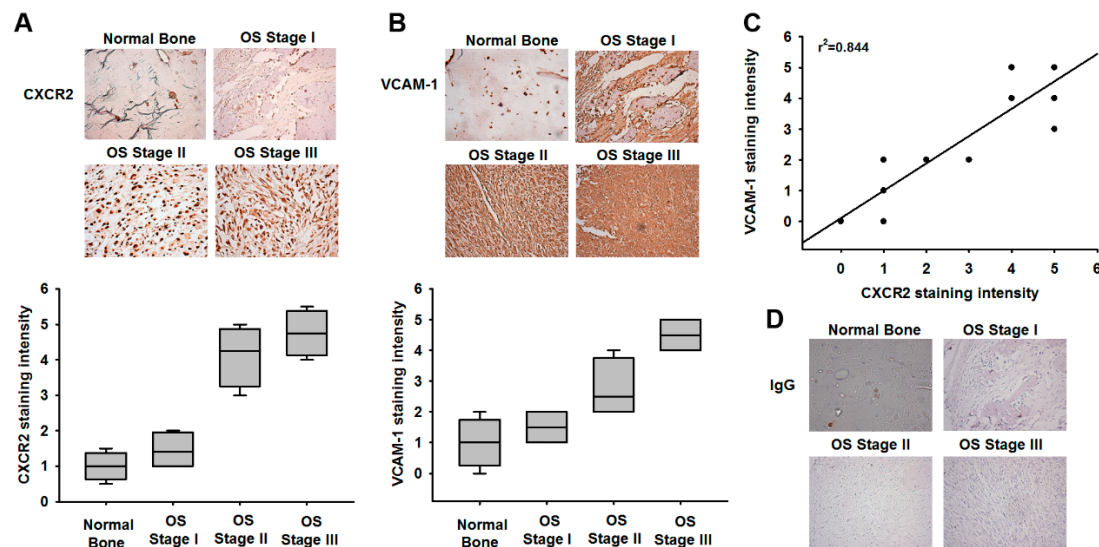


Figure 2. Osteosarcoma specimens exhibit significant correlations between CXCR2 and VCAM-1 expression, and tumor progression. **(A,B)** Tumor specimens were stained with CXCR2 and VCAM-1 antibodies, then photographed by optical microscope. The lower panels quantify the expression levels of CXCR2 and vascular cell adhesion molecule 1 (VCAM-1) in different disease stages. **(C)** Immunohistochemistry (IHC) staining scores of CXCR2 and VCAM-1 were paired from the same specimens and the correlation between CXCR2 and VCAM-1 expression levels was shown by linear regression in prostate cancer specimens. **(D)** Control IgG antibody was used as a negative control in IHC staining.

3.3. Human Pulmonary Artery Endothelial Cell Secretion of CXCL1 Contributes to Osteosarcoma Cell Migration

To determine whether the CXCL1/CXCR2 axis is involved in osteosarcoma lung metastasis, we examined the expression of CXCL1 in human pulmonary artery endothelial cells (HPAECs), which reside in pulmonary vasculature, where metastatic foci are found. HPAECs CM was collected and subjected to enzyme-linked immunosorbent assay (ELISA) to examine CXCL1 secretion by the HPAECs. Compared with control media, high levels of CXCL1 were found in the HPAECs CM (Figure 3A). Further testing revealed that HPAECs CM promoted migration of osteosarcoma cells, suggesting that HPAECs-secreted factor recruits osteosarcoma cells, thus contributing to homing of cancer cells (Figure 3B). This migratory ability was also seen when osteosarcoma cells were incubated with HPAECs CM in the wound healing assay (Figure 3C). To validate whether HPAECs-secreted CXCL1 plays a major role in osteosarcoma homing and migration, we used CXCL1 neutralizing antibody to block the CXCL1/CXCR2 interaction between HPAECs and osteosarcoma cells. HPAECs CM pretreated with CXCL1 antibody significantly inhibited recruitment and the migratory ability of osteosarcoma cells (Figure 3D,E). Our data show that HPAECs-secreted CXCL1 directs the homing of osteosarcoma cells to the lung, thus promoting lung metastasis in osteosarcoma.

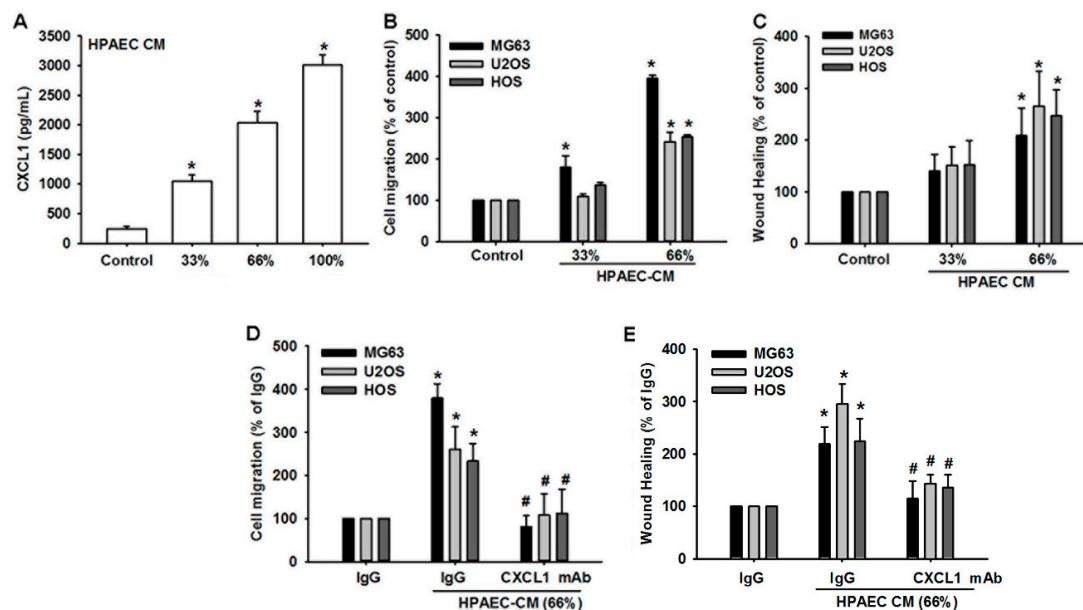


Figure 3. Human pulmonary artery endothelial cell (HPAECs)-secreted CXCL1 promotes migration of osteosarcoma cells. **(A)** HPAECs conditioned media (CM) was collected and levels of CXCL1 secretion were determined by ELISA. **(B)** HPAECs CM was placed in the lower chamber of the Transwell plate. MG63, U2OS, and HOS osteosarcoma cells were seeded in the upper chamber of the Transwell plate and cell mobility was determined after 20 h. **(C)** Osteosarcoma cells were incubated with the indicated concentrations of HPAECs CM for 24 h. Cell mobility was assessed by a wound healing assay. **(D)** HPAECs CM was placed in the lower chamber of the Transwell apparatus in the presence of CXCL1 neutralizing antibody or control IgG (1 μ g/mL). MG63, U2OS, and HOS osteosarcoma cells were seeded in the upper chamber of the Transwell apparatus and cell mobility was determined after 20 h. **(E)** Osteosarcoma cells were incubated with the indicated concentrations of HPAECs CM in the presence of CXCL1 neutralizing antibody or control IgG for 24 h. The cells were subjected to wound healing assays to assess cell mobility. Results are expressed as the mean \pm SD. * $p < 0.05$ compared with control or the control IgG group. # $p < 0.05$ compared with the HPAECs CM-treated group.

3.4. HPAECs-Secreted CXCL1 Stimulates VCAM-1 Expression in Osteosarcoma Cells

In consideration of the fact that HPAECs-secreted CXCL1 recruits osteosarcoma cells and contributes to lung metastasis, and our findings showing that VCAM-1 expression is positively correlated with CXCR2 in osteosarcoma tissue, we analyzed VCAM-1 expression after HPAECs CM treatment. VCAM-1 expression levels in osteosarcoma cells were dramatically increased after treatment with HPAECs CM (Figure 4A,B). Furthermore, the recruitment of osteosarcoma cells by HPAECs CM was inhibited by transfection with VCAM-1 shRNA (Figure 4C). Preincubation of HPAECs CM with CXCL1 neutralized antibody reversed VCAM-1 expression, demonstrating that HPAECs-secreted CXCL1 can directly stimulate VCAM-1 expression in osteosarcoma cells (Figure 4D). Next, to examine whether CXCR2, the specific receptor of the ligand CXCL1, is involved in CXCL1-induced cell migration, comparison of CXCR2 among MG63, HOS, and U2OS is important. We examined the levels of CXCR2 in osteosarcoma cells by immunofluorescence, Western blotting and flow cytometry. The level of CXCR2 was significantly elevated in MG63, HOS, and U2OS cell lines (Figure 4E–G). Finally, the CXCR2 chemical inhibitor SB225002 and CXCR2 shRNA confirmed that the CXCL1/CXCR2 axis is required for VCAM-1 expression and mobility of osteosarcoma cells (Figure 4H–K).

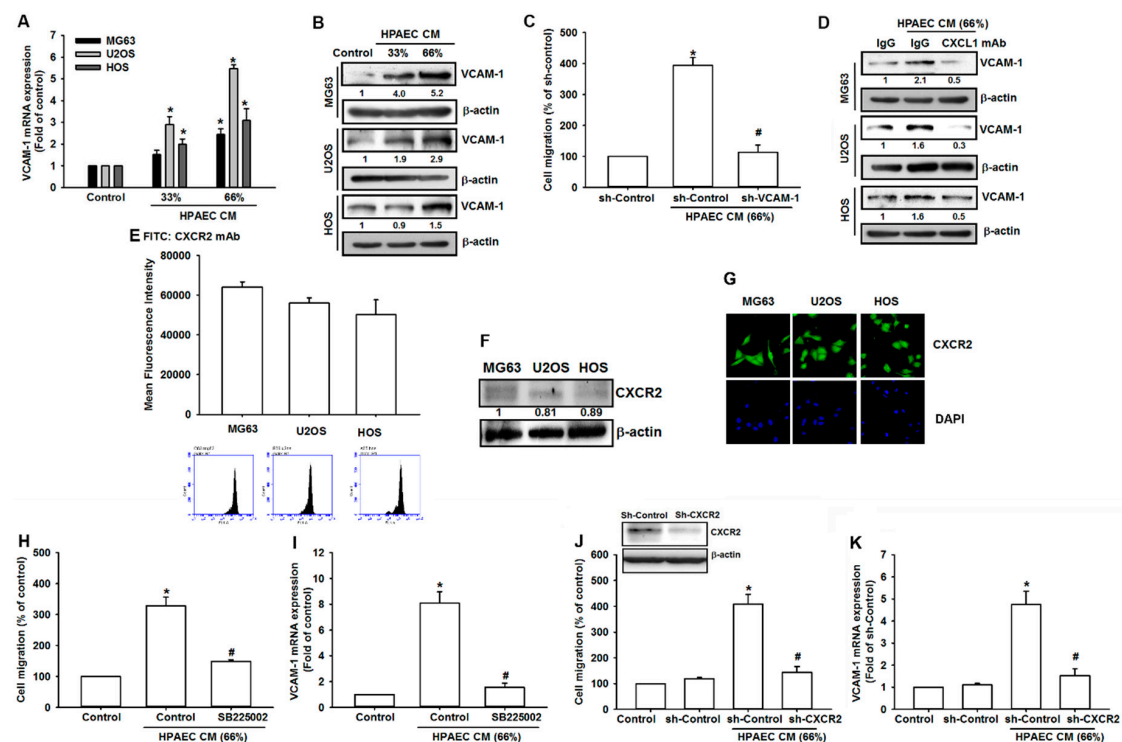


Figure 4. HPAECs CM promotes osteosarcoma cell mobility by upregulating VCAM-1 expression. (A,B) MG63, U2OS and HOS osteosarcoma cells were incubated with increasing concentrations of HPAECs CM. Total mRNA and protein were extracted from the osteosarcoma cells and levels of VCAM-1 expression were detected by qPCR and Western blot. (C) MG63 cells were transfected with VCAM-1 shRNA and incubated with the indicated concentrations of HPAECs CM, and cell mobility was assessed by the Transwell migration assay. (D) MG63, U2OS, and HOS osteosarcoma cells were incubated with the indicated concentrations of HPAECs CM in the presence of CXCL1 neutralizing antibody or control IgG (1 μ g/mL). Total protein was collected and VCAM-1 expression was evaluated by Western blot. (E–G) Total protein were collected from the indicated cell lines, and CXCR2 expression was detected using flow cytometry, Western blotting, and immunofluorescence. (H) MG63 cells were pretreated with the CXCR2 inhibitor SB225002 for 90 min and seeded in the upper chamber of the Transwell apparatus; then the HPAECs CM was placed in the lower chamber, and cell migration was evaluated after 20 h. (I) MG63 cells were pretreated with the CXCR2 inhibitor SB225002, and then incubated with HPAECs CM for 24 h. Levels of VCAM-1 mRNA expression were determined by qPCR. (J) MG63 cells were transfected with CXCR2 shRNA and incubated with the indicated concentrations of HPAECs CM, and cell mobility was assessed by the Transwell migration assay. (K) MG63 cells were transfected with CXCR2 shRNA and incubated with the indicated concentrations of HPAECs CM for 24 h, and VCAM-1 mRNA expression levels were determined by qPCR. Results are expressed as the mean \pm SD. * p < 0.05 compared with control or the control shRNA group. # p < 0.05 compared with the HPAECs CM-treated group.

3.5. The FAK/PI3K/AKT/NF- κ B Signaling Cascade Is Required for HPAECs CM-Induced Increases in VCAM-1 Expression and Cell Migration

CXCR1/CXCR2 chemokine receptors elicit the PI₃K/Akt, mitogen-activated protein kinase (MAPK) signaling cascade, in which several serine/threonine kinases are co-localized via their interaction with scaffolding proteins, in close proximity to cell-surface receptors [30]. Moreover, CXCL8/IL-8 activates protein tyrosine kinases, such as FAK and c-Src, through the CXCR2 receptor [31]. To explore which signal pathways are activated after stimulation of CXCR2 receptors with CXCL1, we screened for candidate signal pathways downstream of CXCR2. Pretreatment with pathway inhibitors (FAKi, LY294002, Wortmannin, Akti, TPCK, and PDTC) clearly inhibited cell migration and VCAM-1 expression

in osteosarcoma cells (Figure 5A,B). Moreover, FAK, PI₃K, Akt, and NF- κ B were activated in response to HPAECs CM (Figure 5C,D). The dominant negative mutants of these pathway components abolished HPAECs CM-induced promotion of cell migration and VCAM-1 expression (Figure 5E,F). These findings suggest that HPAECs CM promotes cell migration and VCAM-1 through the FAK/PI₃K/Akt/NF- κ B pathway in osteosarcoma cells.

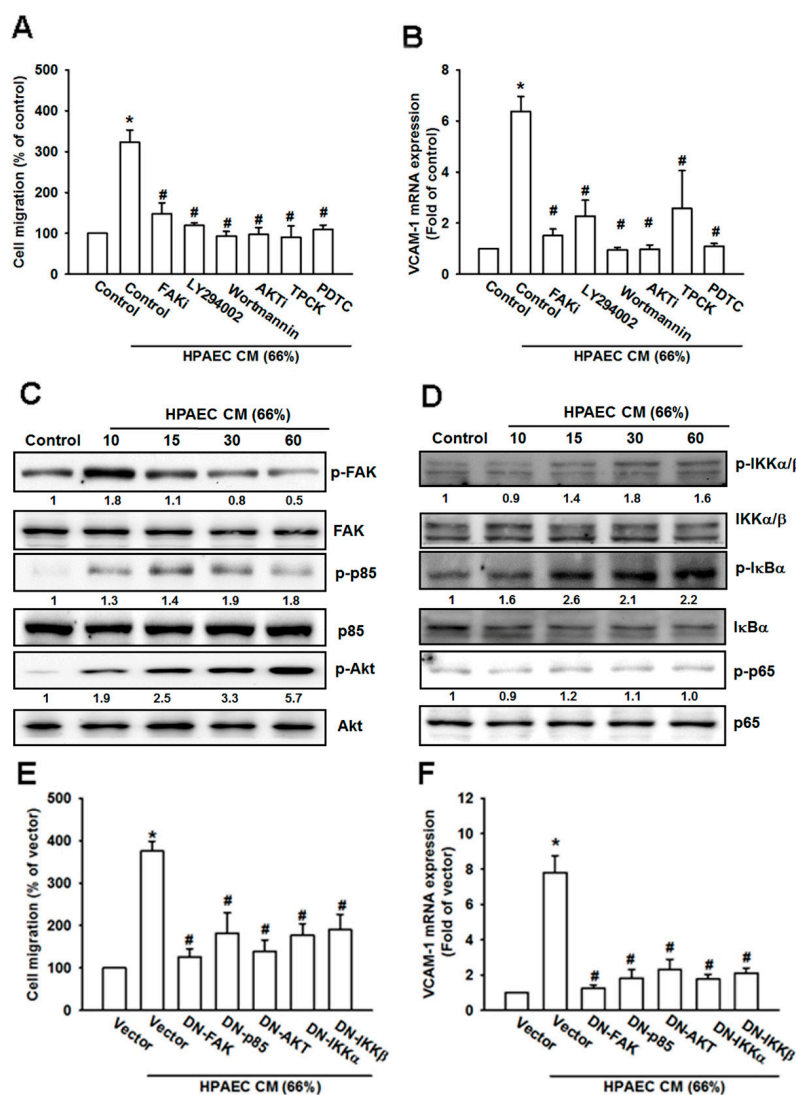


Figure 5. HPAECs CM increases VCAM-1 expression and cell mobility via the FAK/PI₃K/Akt/NF- κ B signaling cascade. (A) MG63 cells were pretreated with FAK, PI₃K, Akt, and NF- κ B inhibitors (FAKi, LY294002, Wortmanin, Akti, TPCK, and PDTC) for 90 min and seeded in the upper chamber of the Transwell plate; then the HPAECs CM was placed in the lower chamber, and cell migration was evaluated after 20 h. (B) MG63 cells were pretreated with FAK, PI₃K, Akt, and NF- κ B inhibitors (FAKi, LY294002, Wortmanin, Akti, TPCK and PDTC) for 90 min and then incubated with HPAECs CM for 24 h. VCAM-1 expression was investigated by qPCR. (C,D) MG63 cells were incubated with HPAECs CM for different time intervals (0, 10, 15, 30, or 60 min). Total protein was collected and phosphorylation of FAK, p85, Akt, IKK α / β , I κ B α , and p65 was determined by Western blot. (E) MG63 cells were transfected with FAK, p85, Akt, IKK α , and IKK β DN mutants for 24 h and then subjected to the Transwell migration assay. (F) MG63 cells were treated as described in (E) and mRNA was extracted, then VCAM-1 expression was determined by qPCR. Results are expressed as the mean \pm SD. * $p < 0.05$ compared with control or the control vector group. # $p < 0.05$ compared with the HPAECs CM-treated group.

3.6. The NF- κ B Signaling Pathway Is Involved in HPAECs CM-Induced Increases in VCAM-1 Expression and Cell Migration

Previous research has indicated that NF- κ B is an crucial transcription factor that is correlated with cancer cell migration and invasion [32]. To confirm our finding of a signaling transduction cascade, the cells were pretreated with FAK, PI₃K, and Akt inhibitors and then incubated with HPAECs CM. The cells were subjected to Western blot to evaluate p65 phosphorylation and nuclear translocation. The inhibitors reversed HPAECs CM-induced p65 phosphorylation and nuclear translocation, confirming the involvement of the FAK/PI₃K/Akt/NF- κ B signaling cascade (Figure 6A,B). We also examined whether NF- κ B transcriptional activation participates in HPAECs CM-induced increases in VCAM-1 expression. Incubation of osteosarcoma cells with HPAECs CM dramatically increased NF- κ B reporter activity, in a dose-dependent manner (Figure 6C). Pretreatment with pathway inhibitors, including CXCR2, FAK, PI₃K, and Akt, strongly inhibited NF- κ B reporter activity in osteosarcoma cells incubated with HPAECs CM (Figure 6D). Knockdown of these pathway inhibitors also reduced HPAECs CM-induced promotion of NF- κ B transcriptional activation (Figure 6E). Finally, the ChIP assay confirmed recruitment of p65 to the NF- κ B binding element and its abolishment by pathway inhibitors (Figure 6F). These results indicate that transcriptional activation of NF- κ B is required in order for HPAECs CM to induce increases in VCAM-1 expression.

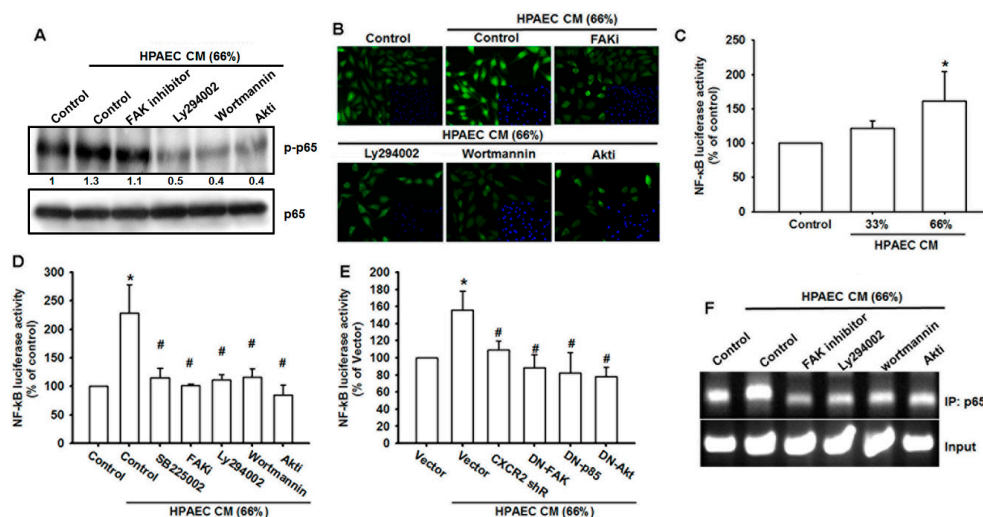


Figure 6. NF- κ B transcriptional activation is required for cell mobility and VCAM-1 expression in osteosarcoma cells incubated with HPAECs CM. (A) MG63 cells were pretreated with pathway inhibitors (FAKi, LY294002, Wortmanin, Akti, TPCK, and PDTC) for 90 min and then incubated with HPAECs CM for 1 h. p65 activation was evaluated by Western blot. (B) MG63 cells were treated as described in (A) and then subjected to immunofluorescence by anti-p65 antibody staining. Nuclei were counterstained with DAPI (4',6-diamidino-2-phenylindole). Representative microscopy images are shown. (C) MG63 cells were transfected with NF- κ B reporter vector for 24 h and then incubated with different concentrations of HPAECs CM for 24 h. NF- κ B transcriptional activity was examined by reporter assay. (D) MG63 cells were transfected with the NF- κ B reporter vector for 24 h and then incubated with HPAECs CM in the presence of the indicated inhibitors for 24 h. NF- κ B transcriptional activity was examined by reporter assay. (E) MG63 cells were co-transfected with the indicated vectors (CXCR2 shRNA, DN-FAK, DN-p85 or DN-Akt) and the NF- κ B reporter vector for 24 h and then incubated with HPAECs CM for 24 h. NF- κ B transcriptional activity was examined by reporter assay. (F) MG63 cells were treated as described in (A). Chromatin immunoprecipitation was performed with anti-p65. One percent of immunoprecipitated chromatin was assayed to verify equal loading (input). Results are expressed as the mean \pm SD of triplicate samples. * $p < 0.05$ compared with control or the control vector group. # $p < 0.05$ compared with the HPAECs CM-treated group.

4. Discussion

This study is the first to investigate the mechanism of lung metastasis in osteosarcoma. Human pulmonary artery endothelial cells secrete CXCL1, thus promoting the migration and homing of osteosarcoma cells to the lung. As osteosarcoma cells contain high levels of CXCR2, a chemokine receptor of CXCL1, their response to HPAECs secretion of CXCL1 promotes lung metastasis. Our investigation supports the development of CXCL1/CXCR2 as a therapeutic target to inhibit or prevent metastatic spread of disease (Figure 7).

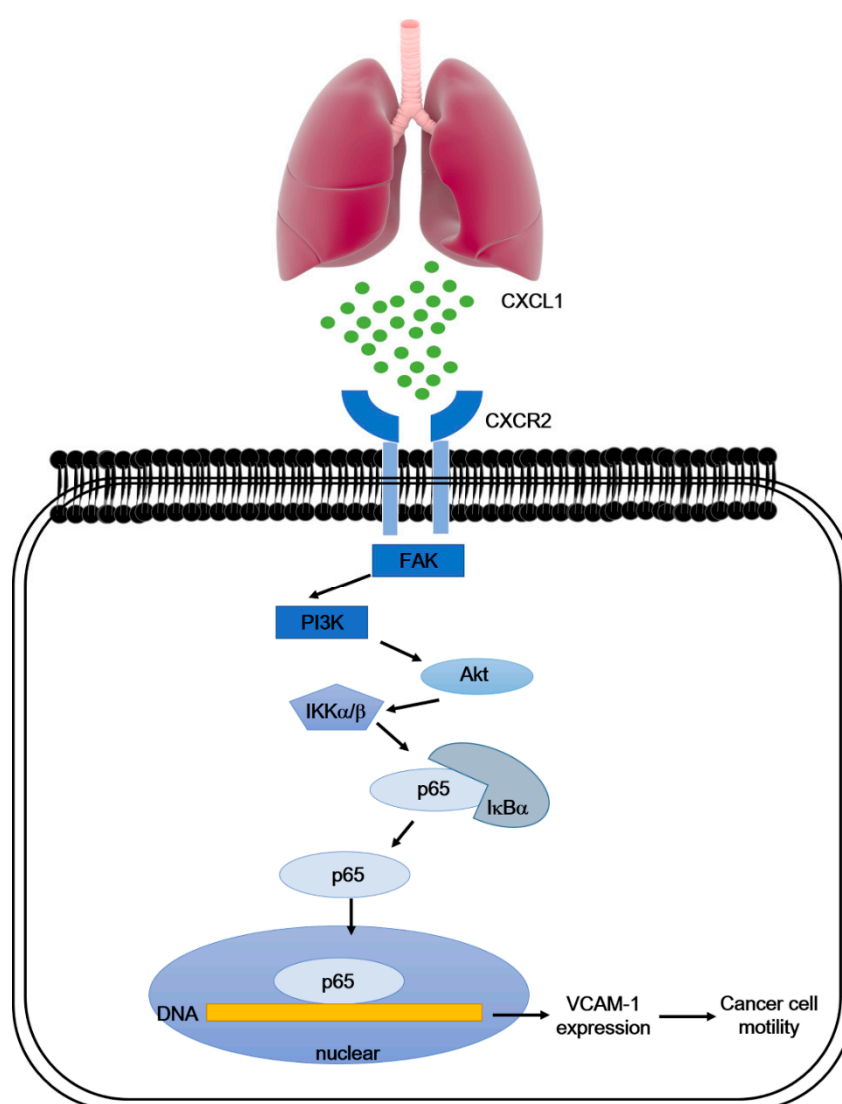


Figure 7. Schematic diagram summarizes the mechanism whereby CXCL 1 promotes VCAM-1 expression and cell migration in osteosarcoma. High levels of CXCL1 secreted by human pulmonary artery endothelial cells (HPAECs) promoted osteosarcoma cell mobility. When HPAECs conditioned media was incubated in osteosarcoma cells, we observed that the CXCR2 receptor and FAK/PI₃K/Akt/NF-κB signaling cascade were required for VCAM-1 expression.

Chemokines are small pro-inflammatory chemoattractant cytokines involved in cell activation, differentiation, adhesion and trafficking [33]. It is well known that organ-specific metastasis occurs when cancer cells are influenced by chemokine gradients at distant sites [34]. Increasing evidence indicates a pivotal role for the CXCL12/CXCR4 axis in organ-specific metastasis of various cancers [3,35–37]. The role of the CXCL12/CXCR4 axis in determining metastatic sites was first proposed in breast

cancer [3]. Not only does the future metastatic organ express high levels of CXCL1, but its chemokine receptors CXCR4 and CCR7 are also highly expressed in human breast cancer cells. On the other hand, CXCR4/SDF-1 pathway might have a role in osteosarcoma tumor progression, supporting some of the sequential events that are involved in metastasis formation [38]. The CXCL12-CXCR4 interaction is therefore considered crucial for attracting cancer cells to a distal organ.

Recent evidence has demonstrated that tumor-secreted CXCL1 enhances tumor growth via the recruitment of various inflammatory cells [16,39] or stroma cells [40,41] into the tumor microenvironment via paracrine or autocrine mechanisms. We are the first to provide evidence showing that HPAECs-induced secretion of CXCL1 recruits CXCR2-expressing osteosarcoma cells to pre-metastatic pulmonary sites. This finding agrees with the proposed CXCL12/CXCR4 interaction in breast cancer metastasis. Clearly, chemokines and their receptors are involved in tumor metastasis, and a better understanding of chemokine signaling in this process could lead to new therapeutic strategies for cancer.

Primary tumors release cancer cells into the circulation long before diagnosis. To establish disseminated cancer cells that may eventually progress to metastases, circulating cancer cells must first transmigrate across endothelial capillary walls and then adapt to new environmental stress [42]. Transendothelial migration of monocytes is the process by which monocytes or leukocytes leave the circulatory system and extravasate through the endothelial lining of the blood vessel wall, before entering the underlying tissue [43]. Similarly to leukocyte extravasation, lung metastasis requires that cancer cells cross the lung endothelium [44]. VCAM-1 has been implicated in early leukocyte transmigration [43] and its relevance for tumorigenesis and metastasis has recently been reviewed [29]. We found that HPAECs-induced secretion of CXCL1 promoted VCAM-1 expression in osteosarcoma cells, which suggests that VCAM-1 may assist with the transendothelial migration of cancer cells. Future research should verify the role of VCAM-1 in the transendothelial migration of HPAECs.

Previous investigations have described the activation of signaling pathways stimulated by the CXCR2 receptor [30], and research has reviewed the involvement of the serine/threonine kinases, including the PI₃K/Akt and MAPK signaling cascades [31]. HPAECs-secreted CXCL1 activates PI₃K/Akt signaling in osteosarcoma cells. The PI₃K/Akt oncogenic pathway is critical in almost all human cancers [45], and active Akt signaling has been found by Kinome profiling in most osteosarcoma cell lines [46]. Dysregulation of this pathway is implicated in many of the pathological processes in osteosarcoma, such as tumorigenesis, proliferation, invasion, cell cycle progression, apoptosis, angiogenesis, metastasis, and chemoresistance. The evidence indicates that targeting PI3K/Akt signaling would be worthwhile in osteosarcoma metastasis.

5. Conclusions

Our results provide a novel insight into osteosarcomas with lung metastases. The paracrine CXCL1/CXCR2 network links HPAECs and osteosarcoma cells, provides a metastatic trace for the cells, and directs their destination.

Supplementary Materials: The following are available online at <http://www.mdpi.com/2072-6694/12/2/459/s1>, all original western blot figures can be found in the supplementary file.

Author Contributions: C.-C.C., P.-C.C. and J.-F.L. conceived and designed the experiments, which were performed by C.-W.L., T.-M.C. and P.-C.C. P.-C.C. analyzed the data. C.-W.L. contributed reagents/materials/analysis tools. J.-F.L. wrote the paper. All authors read and approved the final manuscript.

Funding: This work was supported by grants from the Ministry of science and technology (MOST-106-2314-B-341-001-MY3; MOST-106-2320-B-030-005) and Shin-Kong Wu Ho-Su Memorial Hospital (106-SKH-FJU-07). Chang Gung Medical Research Program Foundation from the Chang-Gung Memorial Hospital Taiwan (CMRPF6J0051; CMRPF6K0041), Chang Gung University of science foundation grant ZRRPF6J0011 and the Ministry of Science and Technology (NMRPG6G0031, 32 and 33).

Conflicts of Interest: The authors state no conflict of interest.

References

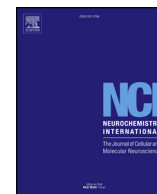
- Munajat, I.; Zulmi, W.; Norazman, M.Z.; Wan Faisham, W.I. Tumour volume and lung metastasis in patients with osteosarcoma. *J. Orthop. Surg. (Hong Kong)* **2008**, *16*, 182–185. [\[CrossRef\]](#) [\[PubMed\]](#)
- Briccoli, A.; Rocca, M.; Salone, M.; Guzzardella, G.A.; Ballardelli, A.; Bacci, G. High grade osteosarcoma of the extremities metastatic to the lung: Long-term results in 323 patients treated combining surgery and chemotherapy, 1985–2005. *Surg. Oncol.* **2010**, *19*, 193–199. [\[CrossRef\]](#)
- Muller, A.; Homey, B.; Soto, H.; Ge, N.; Catron, D.; Buchanan, M.E.; McClanahan, T.; Murphy, E.; Yuan, W.; Wagner, S.N.; et al. Involvement of chemokine receptors in breast cancer metastasis. *Nature* **2001**, *410*, 50–56. [\[CrossRef\]](#) [\[PubMed\]](#)
- Strieter, R.M. Chemokines: Not just leukocyte chemoattractants in the promotion of cancer. *Nat. Immunol.* **2001**, *2*, 285–286. [\[CrossRef\]](#) [\[PubMed\]](#)
- Vandercappellen, J.; Van Damme, J.; Struyf, S. The role of CXC chemokines and their receptors in cancer. *Cancer Lett.* **2008**, *267*, 226–244. [\[CrossRef\]](#) [\[PubMed\]](#)
- Burger, J.A.; Kipps, T.J. CXCR4: A key receptor in the crosstalk between tumor cells and their microenvironment. *Blood* **2006**, *107*, 1761–1767. [\[CrossRef\]](#) [\[PubMed\]](#)
- Sun, X.; Cheng, G.; Hao, M.; Zheng, J.; Zhou, X.; Zhang, J.; Taichman, R.S.; Pienta, K.J.; Wang, J. CXCL12/CXCR4/CXCR7 chemokine axis and cancer progression. *Cancer Metastasis Rev.* **2010**, *29*, 709–722. [\[CrossRef\]](#)
- Epstein, R.J. The CXCL12-CXCR4 chemotactic pathway as a target of adjuvant breast cancer therapies. *Nat. Rev. Cancer* **2004**, *4*, 901–909. [\[CrossRef\]](#)
- Dhawan, P.; Richmond, A. Role of CXCL1 in tumorigenesis of melanoma. *J. Leukoc. Biol.* **2002**, *72*, 9–18.
- Eash, K.J.; Greenbaum, A.M.; Gopalan, P.K.; Link, D.C. CXCR2 and CXCR4 antagonistically regulate neutrophil trafficking from murine bone marrow. *J. Clin. Invest.* **2010**, *120*, 2423–2431. [\[CrossRef\]](#)
- Miyake, M.; Hori, S.; Morizawa, Y.; Tatsumi, Y.; Nakai, Y.; Anai, S.; Torimoto, K.; Aoki, K.; Tanaka, N.; Shimada, K.; et al. CXCL1-Mediated Interaction of Cancer Cells with Tumor-Associated Macrophages and Cancer-Associated Fibroblasts Promotes Tumor Progression in Human Bladder Cancer. *Neoplasia* **2016**, *18*, 636–646. [\[CrossRef\]](#) [\[PubMed\]](#)
- Yuan, M.; Zhu, H.; Xu, J.; Zheng, Y.; Cao, X.; Liu, Q. Tumor-Derived CXCL1 Promotes Lung Cancer Growth via Recruitment of Tumor-Associated Neutrophils. *J. Immunol. Res.* **2016**, *2016*. [\[CrossRef\]](#) [\[PubMed\]](#)
- Hardaway, A.L.; Herroon, M.K.; Rajagurubandara, E.; Podgorski, I. Marrow adipocyte-derived CXCL1 and CXCL2 contribute to osteolysis in metastatic prostate cancer. *Clin. Exp. Metastasis* **2015**, *32*, 353–368. [\[CrossRef\]](#) [\[PubMed\]](#)
- Ogata, H.; Sekikawa, A.; Yamagishi, H.; Ichikawa, K.; Tomita, S.; Imura, J.; Ito, Y.; Fujita, M.; Tsubaki, M.; Kato, H.; et al. GROalpha promotes invasion of colorectal cancer cells. *Oncol. Rep.* **2010**, *24*, 1479–1486. [\[PubMed\]](#)
- Xiang, Z.; Jiang, D.P.; Xia, G.G.; Wei, Z.W.; Chen, W.; He, Y.; Zhang, C.H. CXCL1 expression is correlated with Snail expression and affects the prognosis of patients with gastric cancer. *Oncol. Lett.* **2015**, *10*, 2458–2464. [\[CrossRef\]](#) [\[PubMed\]](#)
- Li, L.; Xu, L.; Yan, J.; Zhen, Z.J.; Ji, Y.; Liu, C.Q.; Lau, W.Y.; Zheng, L.; Xu, J. CXCR2-CXCL1 axis is correlated with neutrophil infiltration and predicts a poor prognosis in hepatocellular carcinoma. *J. Exp. Clin. Cancer Res.* **2015**, *34*, 129. [\[CrossRef\]](#) [\[PubMed\]](#)
- Han, K.Q.; He, X.Q.; Ma, M.Y.; Guo, X.D.; Zhang, X.M.; Chen, J.; Han, H.; Zhang, W.W.; Zhu, Q.G.; Zhao, W.Z. Targeted silencing of CXCL1 by siRNA inhibits tumor growth and apoptosis in hepatocellular carcinoma. *Int. J. Oncol.* **2015**, *47*, 2131–2140. [\[CrossRef\]](#)
- Bandapalli, O.R.; Ehrmann, F.; Ehemann, V.; Gaida, M.; Macher-Goeppinger, S.; Wente, M.; Schirmacher, P.; Brand, K. Down-regulation of CXCL1 inhibits tumor growth in colorectal liver metastasis. *Cytokine* **2012**, *57*, 46–53. [\[CrossRef\]](#)
- Acharyya, S.; Oskarsson, T.; Vanharanta, S.; Malladi, S.; Kim, J.; Morris, P.G.; Manova-Todorova, K.; Leversha, M.; Hogg, N.; Seshan, V.E.; et al. A CXCL1 paracrine network links cancer chemoresistance and metastasis. *Cell* **2012**, *150*, 165–178. [\[CrossRef\]](#)

20. Xu, J.; Zhang, C.; He, Y.; Wu, H.; Wang, Z.; Song, W.; Li, W.; He, W.; Cai, S.; Zhan, W. Lymphatic endothelial cell-secreted CXCL1 stimulates lymphangiogenesis and metastasis of gastric cancer. *Int. J. Cancer* **2012**, *130*, 787–797. [\[CrossRef\]](#)
21. Cheng, W.L.; Wang, C.S.; Huang, Y.H.; Tsai, M.M.; Liang, Y.; Lin, K.H. Overexpression of CXCL1 and its receptor CXCR2 promote tumor invasion in gastric cancer. *Ann. Oncol.* **2011**, *22*, 2267–2276. [\[CrossRef\]](#) [\[PubMed\]](#)
22. Kawanishi, H.; Matsui, Y.; Ito, M.; Watanabe, J.; Takahashi, T.; Nishizawa, K.; Nishiyama, H.; Kamoto, T.; Mikami, Y.; Tanaka, Y.; et al. Secreted CXCL1 is a potential mediator and marker of the tumor invasion of bladder cancer. *Clin. Cancer Res.* **2008**, *14*, 2579–2587. [\[CrossRef\]](#)
23. Hou, C.H.; Lin, F.L.; Hou, S.M.; Liu, J.F. Cyr61 promotes epithelial-mesenchymal transition and tumor metastasis of osteosarcoma by Raf-1/MEK/ERK/Elk-1/TWIST-1 signaling pathway. *Mol. Cancer* **2014**, *13*, 236. [\[CrossRef\]](#)
24. Astarci, E.; Sade, A.; Cimen, I.; Savas, B.; Banerjee, S. The NF-kappaB target genes ICAM-1 and VCAM-1 are differentially regulated during spontaneous differentiation of Caco-2 cells. *FEBS J.* **2012**, *279*, 2966–2986. [\[CrossRef\]](#) [\[PubMed\]](#)
25. Al-Mehdi, A.B.; Tozawa, K.; Fisher, A.B.; Shientag, L.; Lee, A.; Muschel, R.J. Intravascular origin of metastasis from the proliferation of endothelium-attached tumor cells: A new model for metastasis. *Nat. Med.* **2000**, *6*, 100–102. [\[CrossRef\]](#) [\[PubMed\]](#)
26. Zlotnik, A.; Burkhardt, A.M.; Homey, B. Homeostatic chemokine receptors and organ-specific metastasis. *Nat. Rev. Immunol.* **2011**, *11*, 597–606. [\[CrossRef\]](#)
27. Lauvrak, S.U.; Munthe, E.; Kresse, S.H.; Stratford, E.W.; Namlos, H.M.; Meza-Zepeda, L.A.; Myklebost, O. Functional characterisation of osteosarcoma cell lines and identification of mRNAs and miRNAs associated with aggressive cancer phenotypes. *Br. J. Cancer* **2013**, *109*, 2228–2236. [\[CrossRef\]](#)
28. Miles, F.L.; Pruitt, F.L.; van Golen, K.L.; Cooper, C.R. Stepping out of the flow: Capillary extravasation in cancer metastasis. *Clin. Exp. Metastasis* **2008**, *25*, 305–324. [\[CrossRef\]](#)
29. Schlesinger, M.; Bendas, G. Vascular cell adhesion molecule-1 (VCAM-1)—an increasing insight into its role in tumorigenicity and metastasis. *Int. J. Cancer* **2015**, *136*, 2504–2514. [\[CrossRef\]](#)
30. Waugh, D.J.; Wilson, C. The interleukin-8 pathway in cancer. *Clin. Cancer Res.* **2008**, *14*, 6735–6741. [\[CrossRef\]](#)
31. Cohen-Hillel, E.; Yron, I.; Meshel, T.; Soria, G.; Attal, H.; Ben-Baruch, A. CXCL8-induced FAK phosphorylation via CXCR1 and CXCR2: Cytoskeleton- and integrin-related mechanisms converge with FAK regulatory pathways in a receptor-specific manner. *Cytokine* **2006**, *33*, 1–16. [\[CrossRef\]](#) [\[PubMed\]](#)
32. Tang, C.H.; Tan, T.W.; Fu, W.M.; Yang, R.S. Involvement of matrix metalloproteinase-9 in stromal cell-derived factor-1/CXCR4 pathway of lung cancer metastasis. *Carcinogenesis* **2008**, *29*, 35–43. [\[CrossRef\]](#) [\[PubMed\]](#)
33. Balkwill, F. Cancer and the chemokine network. *Nat. Rev. Cancer* **2004**, *4*, 540–550. [\[CrossRef\]](#) [\[PubMed\]](#)
34. Zlotnik, A. Involvement of chemokine receptors in organ-specific metastasis. *Contrib. Microbiol.* **2006**, *13*, 191–199. [\[CrossRef\]](#)
35. Sun, Y.X.; Schneider, A.; Jung, Y.; Wang, J.; Dai, J.; Wang, J.; Cook, K.; Osman, N.I.; Koh-Paige, A.J.; Shim, H.; et al. Skeletal localization and neutralization of the SDF-1(CXCL12)/CXCR4 axis blocks prostate cancer metastasis and growth in osseous sites in vivo. *J. Bone Miner. Res.* **2005**, *20*, 318–329. [\[CrossRef\]](#)
36. Phillips, R.J.; Burdick, M.D.; Lutz, M.; Belperio, J.A.; Keane, M.P.; Strieter, R.M. The stromal derived factor-1/CXCL12-CXC chemokine receptor 4 biological axis in non-small cell lung cancer metastases. *Am. J. Respir. Crit. Care Med.* **2003**, *167*, 1676–1686. [\[CrossRef\]](#)
37. Yasumoto, K.; Koizumi, K.; Kawashima, A.; Saitoh, Y.; Arita, Y.; Shinohara, K.; Minami, T.; Nakayama, T.; Sakurai, H.; Takahashi, Y.; et al. Role of the CXCL12/CXCR4 axis in peritoneal carcinomatosis of gastric cancer. *Cancer Res.* **2006**, *66*, 2181–2187. [\[CrossRef\]](#)
38. Perissinotto, E.; Cavalloni, G.; Leone, F.; Fonsato, V.; Mitola, S.; Grignani, G.; Surrenti, N.; Sangiolo, D.; Bussolino, F.; Piacibello, W.; et al. Involvement of chemokine receptor 4/stromal cell-derived factor 1 system during osteosarcoma tumor progression. *Clin. Cancer Res.* **2005**, *11*, 490–497.
39. Shih, C.H.; Chang, Y.J.; Huang, W.C.; Jang, T.H.; Kung, H.J.; Wang, W.C.; Yang, M.H.; Lin, M.C.; Huang, S.F.; Chou, S.W.; et al. EZH2-mediated upregulation of ROS1 oncogene promotes oral cancer metastasis. *Oncogene* **2017**, *36*, 6542–6554. [\[CrossRef\]](#)

40. Zhang, T.; Tseng, C.; Zhang, Y.; Sirin, O.; Corn, P.G.; Li-Ning-Tapia, E.M.; Troncoso, P.; Davis, J.; Pettaway, C.; Ward, J.; et al. CXCL1 mediates obesity-associated adipose stromal cell trafficking and function in the tumour microenvironment. *Nat. Commun.* **2016**, *7*. [[CrossRef](#)]
41. Kasashima, H.; Yashiro, M.; Nakamae, H.; Masuda, G.; Kinoshita, H.; Morisaki, T.; Fukuoka, T.; Hasegawa, T.; Nakane, T.; Hino, M.; et al. Clinicopathologic significance of the CXCL1-CXCR2 axis in the tumor microenvironment of gastric carcinoma. *PLoS ONE* **2017**, *12*. [[CrossRef](#)] [[PubMed](#)]
42. Husemann, Y.; Geigl, J.B.; Schubert, F.; Musiani, P.; Meyer, M.; Burghart, E.; Forni, G.; Eils, R.; Fehm, T.; Riethmuller, G.; et al. Systemic spread is an early step in breast cancer. *Cancer Cell* **2008**, *13*, 58–68. [[CrossRef](#)] [[PubMed](#)]
43. Muller, W.A. Mechanisms of leukocyte transendothelial migration. *Annu. Rev. Pathol.* **2011**, *6*, 323–344. [[CrossRef](#)] [[PubMed](#)]
44. el-Sabban, M.E.; Pauli, B.U. Adhesion-mediated gap junctional communication between lung-metastatic cancer cells and endothelium. *Invasion Metastasis* **1994**, *14*, 164–176.
45. Porta, C.; Paglino, C.; Mosca, A. Targeting PI3K/Akt/mTOR Signaling in Cancer. *Front. Oncol.* **2014**, *4*, 64. [[CrossRef](#)]
46. Kuijjer, M.L.; van den Akker, B.E.; Hilhorst, R.; Mommersteeg, M.; Buddingh, E.P.; Serra, M.; Burger, H.; Hogendoorn, P.C.; Cleton-Jansen, A.M. Kinome and mRNA expression profiling of high-grade osteosarcoma cell lines implies Akt signaling as possible target for therapy. *BMC Med. Genom.* **2014**, *7*, 4. [[CrossRef](#)]



© 2020 by the authors. Licensee MDPI, Basel, Switzerland. This article is an open access article distributed under the terms and conditions of the Creative Commons Attribution (CC BY) license (<http://creativecommons.org/licenses/by/4.0/>).



Xanthohumol, an active constituent from hops, affords protection against kainic acid-induced excitotoxicity in rats

Che Chuan Wang^{c,d}, Yu Hsuan Ho^b, Chi Feng Hung^a, Jinn Rung Kuo^{c,d}, Su Jane Wang^{a,b,e,*}

^a School of Medicine, Fu Jen Catholic University, No.510, Zhongzheng Rd., Xinzhuang Dist., New Taipei City, 24205, Taiwan

^b Graduate Institute of Biomedical and Pharmaceutical Science, Fu Jen Catholic University, No.510, Zhongzheng Rd., Xinzhuang Dist., New Taipei City, 24205, Taiwan

^c Department of Neurology, Chi Mei Medical Center, Tainan, Taiwan

^d Biotechnology, Southern Taiwan University of Science and Technology, Tainan, Taiwan

^e Research Center for Chinese Herbal Medicine, College of Human Ecology, Chang Gung University of Science and Technology, Taoyuan City, Taiwan

ARTICLE INFO

Keywords:

Xanthohumol
Kainic acid
Glutamate excitotoxicity
Neuroprotection
Hippocampus

ABSTRACT

Excitotoxicity induced by excessive glutamate has been implicated in many brain disorders. Xanthohumol is a natural product derived from hops (*Humulus lupulus* L.), which is reported to have glutamate release-inhibiting activity. However, it is unknown whether xanthohumol has protective effects against glutamate-induced excitotoxicity. This study investigated the potential action of xanthohumol in a rat model of excitotoxicity induced by intraperitoneal injection of kainic acid (KA). Xanthohumol (10 or 50 mg/kg) administered intraperitoneally 30 min prior to KA (15 mg/kg) considerably ameliorated KA-induced seizures, glutamate concentration elevation, and CA3 neuron death. The decrease of mitochondrial fusion protein Mfn-2 and antiapoptotic protein Bcl-2 expression in hippocampal tissues following KA injection were reversed by xanthohumol. Moreover, apoptotic protease activating factor 1 (Apaf-1) expression and caspase-3 activation in the hippocampus were inhibited by xanthohumol. These results suggest that xanthohumol up-regulates Mfn-2 and Bcl-2 to preserve mitochondrial function and suppress Apaf-1 and caspase-3 activation, thereby increasing neuron survival in rats after KA treatment. Therefore, xanthohumol has great potential for development into a therapeutic agent for improving glutamate-related nervous system diseases.

1. Introduction

Excitotoxicity is a common pathological process in many acute and chronic brain disorders, including stroke, traumatic brain injury, epilepsy, Alzheimer's disease (AD), and Parkinson's disease (PD) (Lewerenz and Maher, 2015; Dong et al., 2009; Mehta et al., 2013). It is caused by excessive concentrations of the excitatory neurotransmitter glutamate, which overactivates glutamate receptors such as α -amino-3-hydroxy-5-methyl-4-isoxazolepropionic acid (AMPA), N-methyl-D-aspartate (NMDA), and kainate receptors (Choi, 1988). The overstimulation of glutamate receptors causes excessive Ca^{2+} influx into neurons and induces a variety of death pathways, which include protease activation, reactive oxygen species accumulation, and mitochondrial dysfunction (Bano and Ankarcrona, 2018). Therefore, attenuating glutamate excitotoxicity represents a possible therapeutic target for excitotoxic processes (Gardoni and Di Luca, 2006). In addition, compounds that reduce the amount of glutamate release may counteract excitotoxic

injuries and could be regarded as potential drug candidates (Dohare et al., 2014; Wong et al., 2015; Lin et al., 2016).

Natural products have gained increasing attention due to their benefits for the brain and fewer side effects compared with conventional pharmaceuticals. Xanthohumol is one of the major prenyl-flavonoids present in hops (*Humulus lupulus* L.), an ingredient of beer (Stevens and Page, 2004). It has multiple bioactivities, including antiviral, anti-bacterial, anti-cancer, anti-inflammatory, anti-oxidant, and immunomodulatory effects (Magalhães et al., 2009; Yamaguchi et al., 2009; Lee et al., 2011; Venturelli et al., 2016). Regarding its neuroprotective effects, xanthohumol has been reported to protect PC12 cells from H_2O_2 - and 6-OHDA-induced cell damage (Yao et al., 2015), to alleviate neuroinflammation and brain damage in both stroke-induced rats and in male senescence-accelerated prone mice (Yen et al., 2012; Rancán et al., 2017), to promote neurite growth in mouse neuronal cells (Oberbauer et al., 2013), and to improve cognitive function in young mice (Zamzow et al., 2014). Notably, xanthohumol was shown to

Abbreviations: KA, kainic acid; AMPA, α -amino-3-hydroxy-5-methyl-4-isoxazolepropionic acid; NMDA, N-methyl-D-aspartate; AD, Alzheimer's disease; PD, Parkinson's disease; i.p., intraperitoneal; DMSO, dimethylsulfoxide; PBS, phosphate-buffered saline; Mfn-2, mitofusin; Apaf-1, apoptotic protease activating factor 1

* Corresponding author. School of Medicine, Fu Jen Catholic University, No.510, Zhongzheng Rd., Xinzhuang Dist., New Taipei City, 24205, Taiwan.

E-mail address: med0003@mail.fju.edu.tw (S.J. Wang).

<https://doi.org/10.1016/j.neuint.2019.104629>

Received 30 August 2019; Received in revised form 29 November 2019; Accepted 5 December 2019

Available online 06 December 2019

0197-0186/ © 2019 Elsevier Ltd. All rights reserved.

display glutamate release-inhibiting effect in our previous work (Chang et al., 2016). However, the protective effect of xanthohumol on glutamate-induced neurotoxicity has not been reported to the best of our knowledge.

One well-accepted and commonplace glutamate excitotoxicity animal model is generated by intraperitoneal (i.p.) injection of kainic acid (KA), a glutamate analog (Nadler, 1981; Lévesque et al., 2016). KA causes seizures and neuronal death that resemble effects induced by the pathological release of glutamate, mitochondrial dysfunction, and endoplasmic reticulum stress (Kim et al., 2016; Xue et al., 2017). These KA-induced pathological changes share similarities with those found in patients with epilepsy and neurodegenerative diseases (Ferkany and Coyle, 1983; Ben-Ari, 1985; Wang et al., 2005). In the present study, we utilized the KA-induced excitotoxicity rat model to examine the effects of xanthohumol on seizure activity, elevated glutamate levels, mitochondrial dysfunction pathways, and neuronal death in the hippocampus.

2. Materials and methods

2.1. Animals

Male Sprague-Dawley rats weighing 150–200 g were purchased from BioLASCO, Taiwan. The animals were housed on a 12 h light/dark cycle under regulated temperature and humidity and fed with standard diet and water ad libitum. All the experiments were approved by the Fu Jen Institutional Animal Care and Utilization Committee. The rats were randomly divided into six groups: dimethylsulfoxide (DMSO, Sigma-Aldrich Co, MO, USA)-treated group (control), xanthohumol 10 mg/kg-treated group, xanthohumol 50 mg/kg-treated group, KA only-treated group, xanthohumol 10 mg/kg + KA group, and xanthohumol 50 mg/kg + KA group. KA (Sigma-Aldrich Co, MO, USA) dissolved in 0.9% NaCl (pH 7.0), at a dose of 15 mg/kg, was injected intraperitoneally (i.p.). Xanthohumol (ChemFaces, Hubei, PRC) dissolved in 1% DMSO (Sigma, St. Louis, MO, USA) was administered i.p. for 30 min prior to KA injection. The rats in the xanthohumol-only group were injected i.p. with xanthohumol alone. The dose of KA and schedule of administration were selected on the basis of our previous experiments (Lin et al., 2016; Chang et al., 2018) and literature data (Friedman et al., 1994; Spigolon et al., 2010). Seizure activity of rats ($n = 30$) was rated during a 4 h period after KA injection using the Racine scale (Racine, 1972). Eighty-four percent of the KA-injected rats survived, of which ninety-five percent developed a epileptic seizures corresponding to stages 4 or 5 on the Racine scale and were used for subsequent experiments. The rats were killed at 4 h or 72 h after KA treatment.

2.2. Determination of glutamate by high-performance liquid chromatography

Glutamate concentration was measured from dissected tissues as described previously (Lin et al., 2016). Briefly, animals ($n = 30$) were sacrificed through decapitation and the brains were removed immediately. The hippocampi were dissected and homogenized in 300 μ l of 200 mM ice-cold perchloric acid. After centrifugation (4000 rpm for 10 min at 4 °C), the supernatant (20 μ l) was filtered and injected directly into a high-performance liquid chromatography system with an electrochemical detection (HTEC-500, Eicom, Kyoto, Japan).

2.3. Evaluation of neuronal injury using neutral red and Fluoro Jade B staining

Animals ($n = 30$) were anesthetized (chloral hydrate 650 mg/kg, i.p., Sigma-Aldrich Co, MO, USA) and perfused transcardially with heparinized saline, followed by 4% paraformaldehyde (Sigma-Aldrich Co, MO, USA) in 0.1 M phosphate-buffered saline (PBS). The brains were removed and post-fixed overnight in 4% paraformaldehyde

containing 30% sucrose. Fixed brain were cut into 40- μ m-thick coronal sections and these sections were mounted onto glass slides. For neutral red staining, slides were air-dried, dehydrated in ethanol, and stained with neutral red solution. Stained samples were rehydrated in ethanol, cleared in xylene (Sigma-Aldrich Co, MO, USA), air dried, coverslipped using dibutylphthalate polystyrene xylene (DPX), and visualized with a DM 2000 LED light microscope (LEICA, Valladolid, ES). For Fluoro-Jade B staining, slides were air-dried, dehydrated in ethanol, and immersed in 0.06% KMnO_4 for 15 min, rinsed for 1 min in distilled water, and then incubated in 0.001% Fluoro-Jade B (Roche, Basel, CH) in 0.1% acetic acid (Sigma-Aldrich Co, MO, USA) for 30 min in the dark. Slides were washed three times in distilled water, air-dried, cleared in xylene, coverslipped, and examined with a fluorescence microscope (Zeiss Axioskop 40, Goettingen, Germany). The hippocampal CA3 region was visualized under 100 \times magnification through upright fluorescence microscopy (Zeiss Axioskop 40, Goettingen, Germany); the digitized photomicrographs used for analysis were captured using a digital camera (Nikon D80, Tokyo, Japan). The number of Fluoro-Jade B-positive cells was counted in a 255 \times 255 μ m area of the hippocampal CA3 in 5 randomly selected sections in each rat, and the count was averaged for each rat by using a computer-assisted image analysis system (Image J; NIH Image, National Institutes of Health, Bethesda, MD, USA) by an examiner blinded to the experimental conditions. The results of labelled cells per 0.1 mm^2 are expressed as mean \pm SEM.

2.4. Transmission electron microscopy

As described in our previous studies (Chang et al., 2018), fixed brain from rats ($n = 4$) were cut into 200- μ m-thick coronal slices by using a vibratome (VT1000S, Leica, Germany). The CA3 areas of hippocampus were cut out from the coronal slices and fixed in 4% paraformaldehyde and 2.5% glutaraldehyde for 1 day. The specimens were then washed in PBS, postfixed in 1% osmium tetroxide for 2h, dehydrated, and embedded in epoxy resin. 70-nm-thick sections were prepared with the ultramicrotome (EM UC7, Leica Microsystems, Wetzlar, Germany). The ultrastructure of hippocampal CA3 area was imaged using transmission electron microscopy (Model JEM-1400, JEOL Ltd, Tokyo, Japan) at 80 KV.

2.5. Western blot

Animals ($n = 30$) were decapitated and the hippocampi were rapidly dissected. Hippocampi were homogenized and protein extracts were prepared as described previously (Lin et al., 2016). Protein extracts (20 μ g) were loaded onto 10% sodium dodecylsulfate polyacrylamide gel, separated by gel electrophoresis, and transferred onto nitrocellulose membranes (Millipore, Billerica, MA, USA). Membranes were blocked with 5% non-fat milk for 1 h at room temperature, then incubated overnight at 4 °C with primary antibodies: anti-Mfn-2 (1: 100, Santa Cruz Biotechnology, Texas, USA), anti-Bcl-2 (1: 1000, Cell Signaling Technology, Danvers, USA), anti-Apaf-1 (1: 8000, Novus Biologicals, Colorado, USA), anti-cleaved caspase-3 (1: 1000, Cell Signaling Technology, Danvers, USA), and anti- β actin (1: 5000, GeneTex, Antonio, USA). After being washed in PBS, membranes were probed with secondary antibodies (anti-Mouse IgG, 1:5000; anti-Rabbit IgG, 1: 5000, GeneTex, Antonio, USA). The blots were visualized using enhanced chemiluminescence (Amersham, Buckinghamshire, UK) and quantified using the Syngene software (SynGene, Cambridge, UK).

2.6. Statistics

Statistical analysis was performed using one-way analysis of variance (ANOVA) followed by a post hoc Bonferroni test. Difference with a P value less than 0.05 was considered as statistically significant. All data are expressed as the mean \pm SEM.

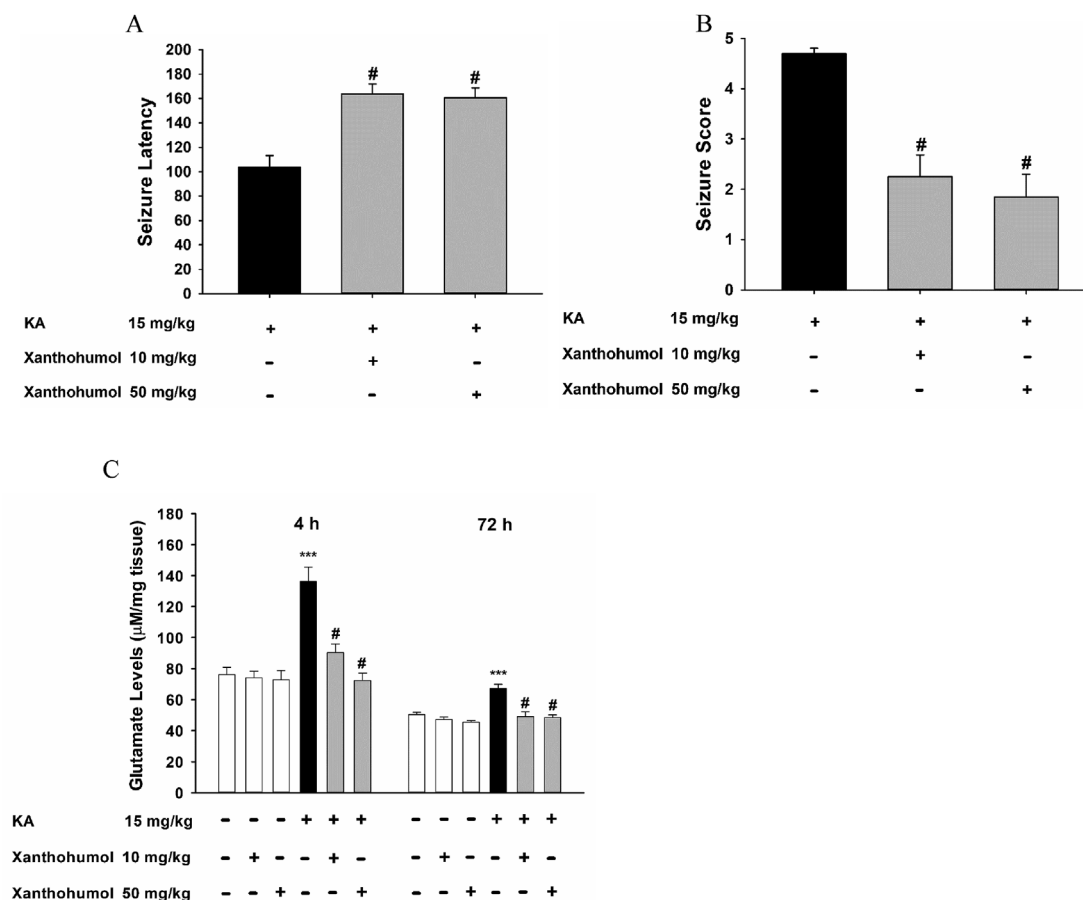


Fig. 1. Effect of xanthohumol on KA-induced seizures and glutamate elevation in the hippocampus. Xanthohumol (10 or 50 mg/kg) was administered i.p. 30 min prior to KA (15 mg/kg, i.p.). The seizure latency (A) and seizure score (B) were evaluated during 1–4 h after KA administration ($n = 19$ –20). (C) The glutamate levels in the hippocampus was examined at 4 h and 72 h after KA injection by HPLC ($n = 5$). Each bar represents mean \pm S.E.M. Symbols: ***significant difference ($P < 0.001$) from control; #significant difference ($P < 0.05$) from KA.

3. Results

3.1. KA-induced seizure behavior and glutamate concentration elevation is attenuated by xanthohumol pretreatment

Administration of KA (15 mg/kg, i.p.) to animals caused seizures with latency and score of 113.6 ± 10.1 min and 4.2 ± 0.3 , respectively (Fig. 1A and B). Xanthohumol, at the doses of 10 and 50 mg/kg, administered (i.p.) 30 min prior to KA, increased the seizure latency [$F(2, 56) = 15.3$, $P < 0.001$; Fig. 1A] and decreased the seizure score [$F(2, 56) = 17.8$, $P < 0.001$; Fig. 1B]. In addition, in agreement with previously published data (Lin et al., 2016; Chang et al., 2018), a significant elevation of glutamate levels in the hippocampus was observed at 4 h after KA administration (i.p.) ($P < 0.001$; Fig. 1C). The xanthohumol pretreated group (10 or 50 mg/kg, i.p.) offered significant restoration of glutamate levels in comparison to KA-only group [$F(3,17) = 21.5$, $P < 0.001$; Fig. 1C]. In the group of xanthohumol alone, there was no significant difference in glutamate levels, when compared to the DMSO-treated group (control) [$F(2,14) = 0.11$, $P = 0.89$; Fig. 1C]. A similar effect of xanthohumol on hippocampal glutamate levels was observed at 72 h after KA administration [$F(3,18) = 14.2$, $P < 0.001$; Fig. 1C].

3.2. Xanthohumol protects CA3 neurons against KA-induced excitotoxicity

At 72 h after KA administration (15 mg/kg, i.p.), neutral red or Fluoro-Jade B staining was used to assess surviving neurons and degenerating neurons, respectively. Neutral red staining showed that KA

caused extensive loss of hippocampal neurons in CA3 region as compared to DMSO-treated group (control) (Fig. 2A). Xanthohumol (10 or 50 mg/kg, i.p.) administration before KA injection was found to significantly reduce KA-induced neuronal death in CA3 region compared with KA-only (Fig. 2A). The xanthohumol-only group showed no obvious neuronal loss in CA3 compared with the control group (Fig. 2A). On the other hand, no Fluoro-Jade B-labelled neurons were found in the control and xanthohumol-only groups (Fig. 2B). In KA-injected rats, the number of Fluoro-Jade B-positive neurons in CA3 region was increased, as compared to DMSO-treated group (control) ($P < 0.001$; Fig. 2B and C). However, in KA-treated groups that received pretreatment of xanthohumol (10 or 50 mg/kg, i.p.), the number of Fluoro-Jade B-positive neurons in CA3 was significantly lower than that in KA-only [$F(2,11) = 68.4$, $P < 0.001$; Fig. 2B and C].

We also used transmission electron microscopy to elucidate the ultrastructure of hippocampal CA3 neurons. In 72 h DMSO-i.p. treated (control) rats, the hippocampal CA3 nerve cells had normal morphological appearance (Fig. 3). However, morphological alterations were observed in the hippocampal CA3 nerve cells of KA-i.p. treated rats. Nerve cells displayed deformed nuclei with condensed, vacuoles, swollen mitochondria, and dilated endoplasmic reticula (ER) (Fig. 3). In KA-treated groups that received pretreatment of xanthohumol (10 or 50 mg/kg, i.p.), the morphological appearance of hippocampal CA3 nerve cells was relatively normal when compared to KA-only (Fig. 3). In the mitochondrial ultrastructure, in addition to the mitochondrial swelling and disruption, decreased size (indicating the occurrence of mitochondrial fragmentation) was also observed in the hippocampal CA3 of KA-injected rats. These KA-caused alterations in the

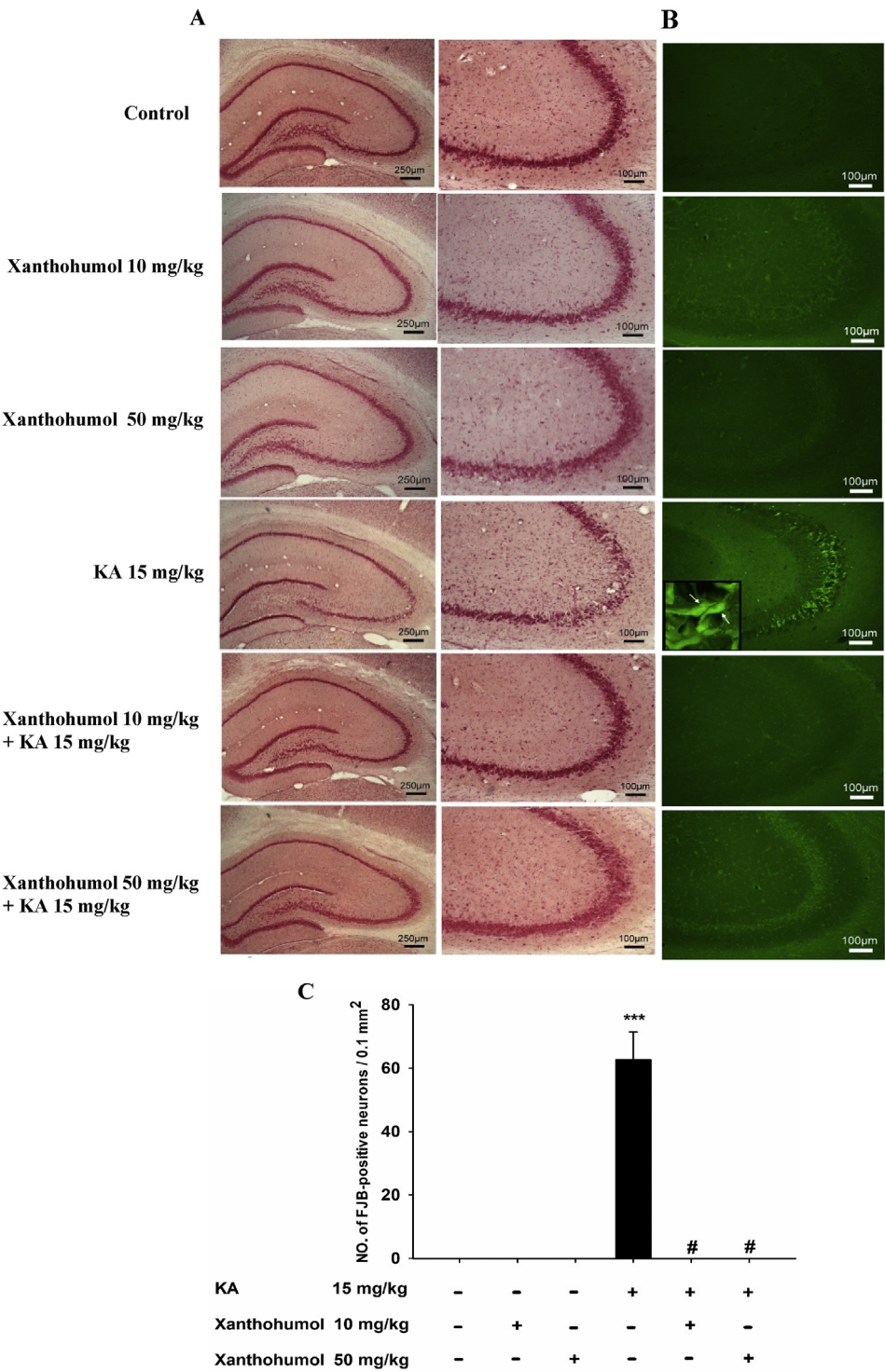


Fig. 2. Effect of xanthohumol on KA-induced neuronal damage in the hippocampal CA3 region. Xanthohumol was administrated (10 or 50 mg/kg, i.p.) 30 min prior to KA injection (15 mg/kg, i.p.). Neutral red (A) and Fluoro-Jade B (B) staining were used to examine neuronal loss and degeneration in the hippocampus of KA and/or xanthohumol treated animals. The inset is high magnification micrograph of CA3 neurons. Numbers of Fluoro-Jade B-positive neuron in CA3 region were quantified in (C). Each bar represents as mean \pm S.E.M. (n = 5). Symbols: ***significant difference ($P < 0.001$) from control; #significant difference ($P < 0.05$) from KA.

mitochondrion were ameliorated by xanthohumol pretreatment (Fig. 3).

3.3. Xanthohumol inhibits KA-induced decrease in Mfn-2 expression in the hippocampus

Mitofusin 2 (Mfn-2), a mitochondrial fusion protein, is known to be downregulated in KA-induced mitochondrial dysfunction and neuronal death (Wang et al., 2015; Xue et al., 2017). It was therefore of interest to determine whether xanthohumol affects the Mfn-2 expression in KA-treated rats. As shown in Fig. 4, at 72 h after KA administration (15 mg/

kg, i.p.), the expression of Mfn-2 in the hippocampus was decreased, as compared to DMSO-treated group (control) ($P < 0.001$). In KA-treated groups that received pretreatment of xanthohumol (10 or 50 mg/kg, i.p.), the expression levels of Mfn-2 was significantly increased compared with KA-only [$F(3,16) = 10.5$, $P < 0.001$; Fig. 4A and B]. There was no significant difference in Mfn-2 levels between xanthohumol-only group and DMSO-treated group (control) [$F(2,15) = 0.48$, $P = 0.63$; Fig. 4B]. In addition, the expression of dynamin-related protein 1 (Drp-1), a mitochondrial fission protein, was examined. However, the protein level of Drp-1 remained unchanged (Fig. 4A). The one-way ANOVA showed no significant differences in the hippocampal

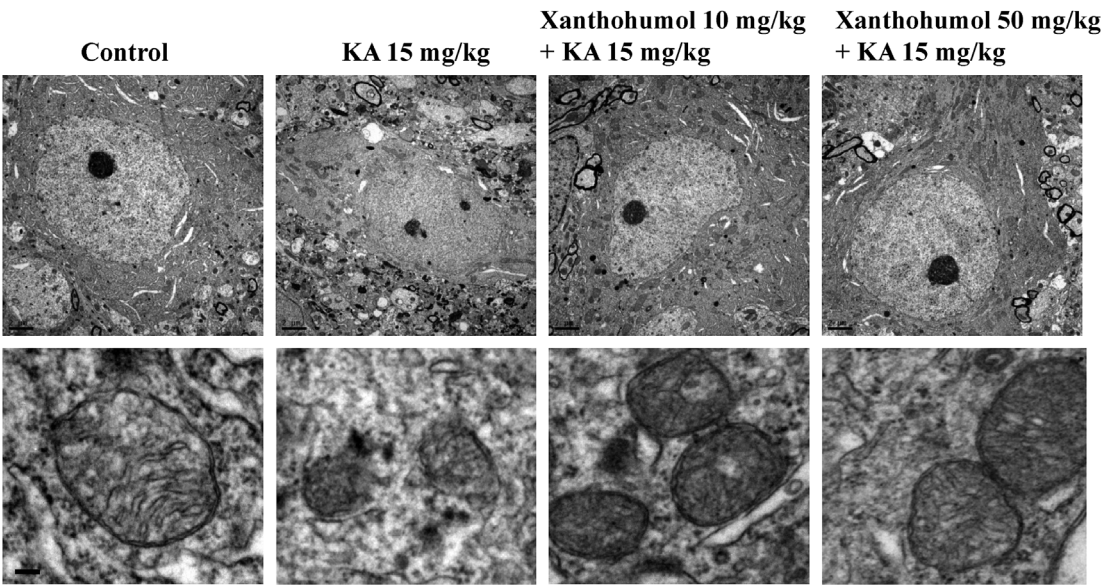


Fig. 3. Representative transmission electron micrographs of the hippocampal CA3 nerve cell. Ultrastructure of the hippocampal CA3 nerve cell in KA and/or xanthohumol treated animals. Scale bar, 2 μ m. Higher magnification of mitochondrial ultrastructure in the hippocampal CA3 regions from differently treated groups. Scale bar, 0.5 μ m.

Drp-1 expression levels among the groups [$F(5, 24) = 0.31, P = 0.9$; Fig. 4C].

3.4. Xanthohumol inhibits KA-induced Apaf-1 and caspase-3 expression in the hippocampus

In excitotoxic conditions, the downregulation of Mfn-2 can increase apoptotic protease activating factor 1 (Apaf-1) and caspase-3 activation, thereby leading apoptosis (Zhao et al., 2015). We next determined

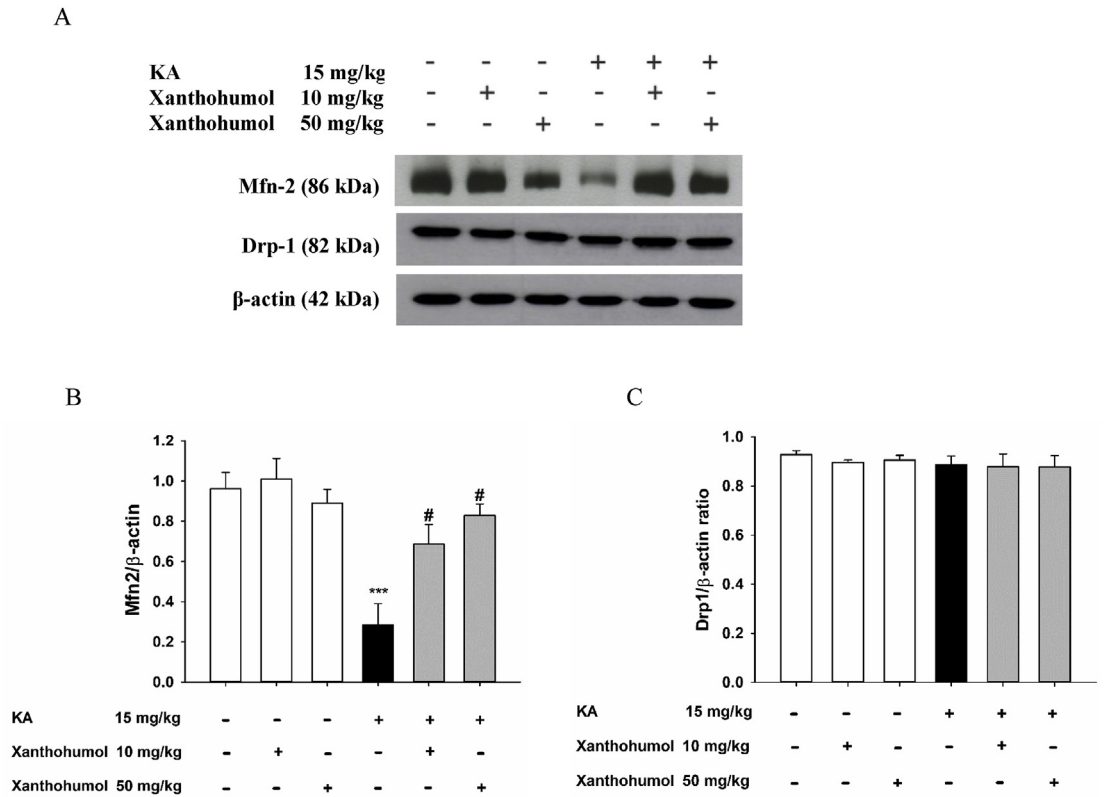


Fig. 4. Effect of xanthohumol on KA-induced decrease in Mfn-2 expression in the hippocampus. Xanthohumol was administrated (10 or 50 mg/kg, i.p.) 30 min prior to KA injection (15 mg/kg, i.p.) and Mfn-2 or Drp-1 expression was assessed by Western blot. Protein extracts were prepared at 72 h after KA administration from the hippocampus and results are presented as mean \pm S.E.M (n = 5–6). Symbols: ***significant difference ($P < 0.001$) from control; #significant difference ($P < 0.05$) from KA.

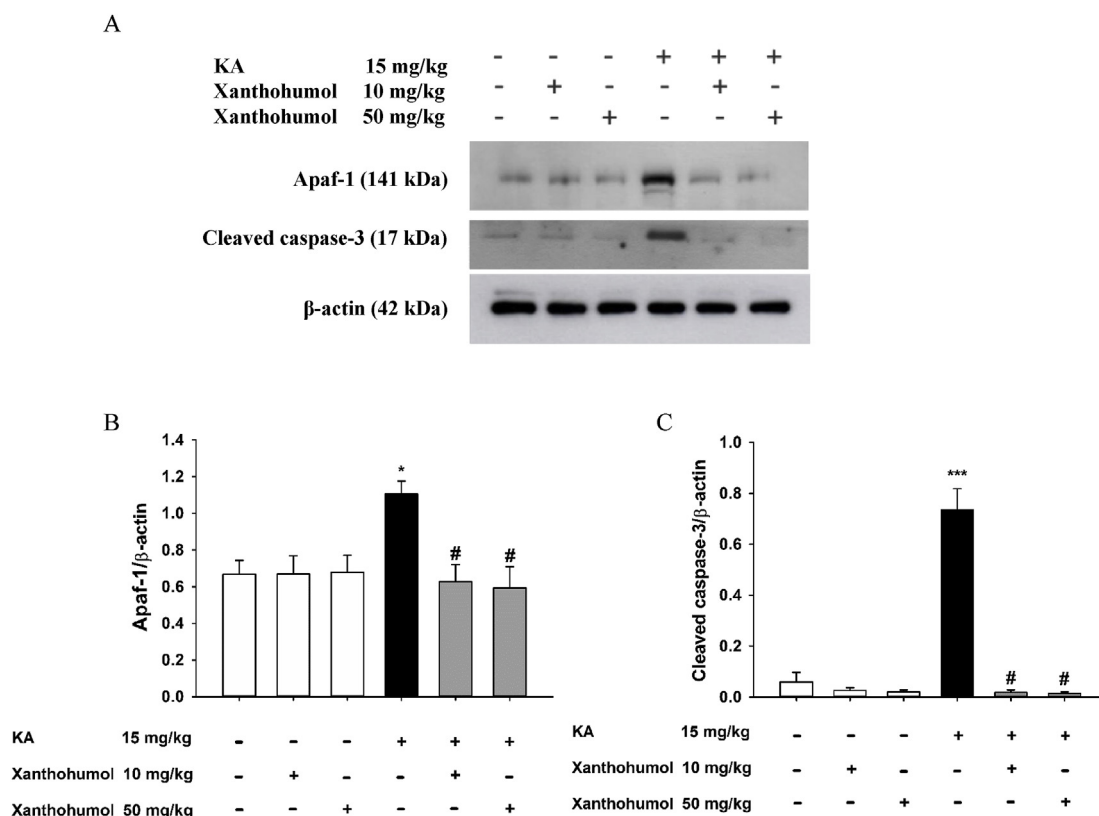


Fig. 5. Effect of xanthohumol on KA-induced Apaf-1 and caspase-3 expression in the hippocampus. Xanthohumol was administrated (10 or 50 mg/kg, i.p.) 30 min prior to KA injection (15 mg/kg, i.p.), and Apaf-1 and activated caspase-3 expression were assessed by Western blot. Protein extracts were prepared at 72 h after KA administration from the hippocampus and results are presented as mean \pm S.E.M (n = 5–6). Symbols: ***significant difference ($P < 0.001$) from control; #significant difference ($P < 0.05$) from KA.

whether the xanthohumol-increased Mfn-2 expression is accompanied by the inhibition of Apaf-1 and cleaved caspase-3 expression in the hippocampus (Fig. 5A). The results showed that the expression of Apaf-1 and cleaved caspase-3 in hippocampus was increased significantly at 72 h after KA administration as compared to the DMSO-treated group (control) ($P < 0.001$). Such increases were suppressed by xanthohumol pretreatment as compared to KA-only [Apaf-1, $F(3,16) = 6.9$, $P < 0.01$; cleaved caspase-3, $F(3,16) = 65.2$, $P < 0.001$; Fig. 5B and C]. In addition, there was no significant difference in Apaf-1 and cleaved caspase-3 expression between xanthohumol-only group and DMSO-treated group (control) [apaf-1, $F(2,12) = 0.01$, $P = 0.99$; caspase-3, $F(2,15) = 0.79$, $P = 0.47$, Fig. 5B and C].

3.5. Xanthohumol inhibits the KA-induced inhibition of Bcl-2 expression in the hippocampus

Since Bcl-2 is an anti-apoptotic protein that plays a key role in suppressing mitochondrial-mediated apoptotic cell death (D'Orsi et al., 2017; Suhaili et al., 2017), it was therefore of interest to determine whether xanthohumol affects Bcl-2 expression levels in KA-treated rats. Consistent with previous studies (Chang et al., 2018; Lu et al., 2018), Bcl-2 expression in the hippocampus was decreased at 72 h after KA administration as compared to the DMSO-treated group (control) ($P < 0.01$). In KA-treated groups that received pretreatment of xanthohumol (10 or 50 mg/kg, i.p.), the expression levels of Bcl-2 was significantly increased, as compared to KA-only [$F(3,19) = 8.4$, $P < 0.01$; Fig. 6]. In addition, there was no significant difference in Bcl-2 levels between xanthohumol-only group and DMSO-treated group (control) [$F(2,18) = 0.15$, $P = 0.86$; Fig. 6].

4. Discussion

Excitotoxicity induced by excessive glutamate is a common pathogenic process in numerous neurological conditions and therapeutic strategies inhibiting or providing protection against glutamate excitotoxicity are of interest to researchers (Traynelis et al., 2010; Mayor and Tymianski, 2018). Xanthohumol, a hop-derived prenylated flavonoid present in beer, has multiple biological activities, including neuroprotective effects (Yen et al., 2012; Rancán et al., 2017). In our previous work, we demonstrated that xanthohumol inhibits glutamate release from rat hippocampal nerve terminals by suppressing N- and P/Q-type Ca^{2+} channels and Ca^{2+} -calmodulin/adenylate cyclase/cAMP/protein kinase A cascade (Chang et al., 2016). Therefore, we hypothesized that xanthohumol is capable of protecting against glutamate-induced brain injury. This hypothesis was confirmed in this study by using a rat model of excitotoxicity induced by systemic administration of a glutamate analog KA.

In the present study, it was observed that KA (15 mg/kg, i.p.) administration induced seizure activity, elevated glutamate levels in the hippocampus, and caused neurodegeneration and neuronal death in the CA3 region of the hippocampus, which is consistent with the results obtained from previous studies (Friedman et al., 1994; Sperk, 1994; Śmiałowska et al., 2012). However, pretreatment with xanthohumol (10 or 50 mg/kg, i.p.) 30 min before KA could reverse these KA-induced trends. For example, xanthohumol reduced the seizure score and increased seizure latency, suggesting that xanthohumol has antiepileptic activity. Xanthohumol also reduced KA-provoked glutamate level increase and CA3 neuron damage. As excessive glutamate is involved in KA-induced seizures and neuronal death (Śmiałowska et al., 2012), we suggest that the protective effect of xanthohumol in KA-induced excitotoxicity is associated with a reduction of glutamate levels, which

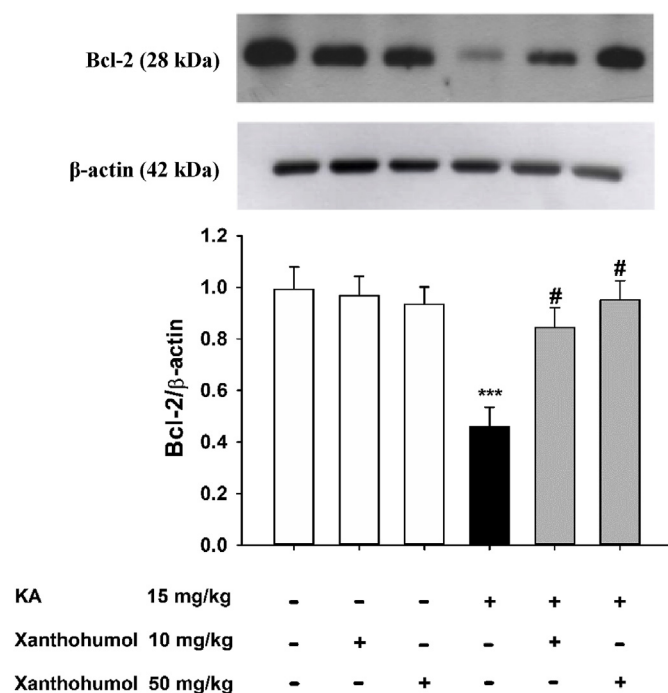


Fig. 6. Effect of xanthohumol on KA-induced inhibition of Bcl-2 expression in the hippocampus. Xanthohumol was administrated (10 or 50 mg/kg, i.p.) 30 min prior to KA injection (15 mg/kg, i.p.) and Bcl-2 expression were assessed by Western blot. Protein extracts were prepared at 72 h after KA administration from the hippocampus and results are presented as mean \pm S.E.M (n = 5–7). Symbols: ***significant difference ($P < 0.001$) from control; #significant difference ($P < 0.05$) from KA.

subsequently suppresses glutamate receptor activation and death signaling pathways. In fact, KA is an agonist for a subtype ionotropic glutamate receptors, KA and AMPA (α-amino-3-hydroxy-5-methylisoxazole-4-propionyl acid) receptors. Overstimulation of these receptors is believed to contribute to KA-induced neurodegeneration (Ferkany et al., 1982; Chittajallu et al., 1996). Thus, the current study does not exclude the possibility that the suppression of KA-induced neuronal cell death by xanthohumol is linked to antagonism at the KA/AMPA receptors. In addition, it was unclear how xanthohumol affects glutamate levels in the hippocampus. Further studies are warranted to clarify precise molecular mechanisms involved in the xanthohumol-induced inhibition of glutamate levels in KA-injected animal models.

One of the events associated with excitotoxic injury-caused brain damage is mitochondrial dysfunction, which disrupts the integrity of the mitochondrial membrane, increases the release of mitochondrial cytochrome c, activates Apaf-1 and caspase-3 and thus, leads to apoptosis (Schinder et al., 1996; Shin et al., 2009; Prentice et al., 2015). Therefore, maintaining mitochondrial function represents a promising approach to alleviate glutamate neurotoxicity. In our present study, KA administration (15 mg/kg, i.p.) led to mitochondrial ultrastructure alteration in the CA3 region of the hippocampus including mitochondrial disruption and fragmentation, which is consistent with the results obtained by other investigators (Chuang et al., 2004; Xue et al., 2017). These KA-induced mitochondrial defects were relieved by xanthohumol pretreatment, indicating that a decrease in KA-induced mitochondrial fragmentation and dysfunction is involved in the mechanism through which xanthohumol exerts neuroprotective effects. Mfn-2, a mitochondrial fusion protein, is shown to play an important role in maintaining mitochondrial morphology and function (Detmer and Chan, 2007; de Brito and Scorrano, 2009). Decreased Mfn-2 expression has been reported to participate in the cascade of events leading to mitochondrial fragmentation/dysfunction and neuronal death induced by glutamate or KA administration (Wang et al., 2015; Xue et al., 2017).

Furthermore, Mfn-2 overexpression can alleviate glutamate-induced mitochondrial damage and neuronal death in spinal cord motor neurons (Wang et al., 2015). In this work, we found that Mfn-2 expression was considerably decreased in the KA-treated hippocampus, which is consistent with previous research (Xue et al., 2017). Xanthohumol pretreatment restored Mfn-2 expression reduced by KA administration. However, the level of mitochondrial fission protein Drp-1 in our study remained unchanged, which is consistent with previous study (Xue et al., 2017). Therefore, we suggest that xanthohumol exerts its protective effects by increasing Mfn-2 expression, thus preventing mitochondrial dysfunction and neuronal death induced by KA. Additionally, the downregulation of Mfn-2 has been shown to increase Apaf-1 and caspase-3 activation, thereby leading to apoptosis (Zhao et al., 2015); this mitochondrial apoptotic process is involved in glutamate excitotoxicity (Ma et al., 2017). Also in this study, we found that KA administration increased apaf-1 and active caspase-3 expression, and this phenomenon was suppressed by xanthohumol pretreatment. This is similar to previous research, which showed that xanthohumol alleviates brain damage in rats with cerebral ischemia through the inhibition of caspase-3 activation (Yen et al., 2012). Therefore, we suggest that the mechanism by which xanthohumol prevents neuronal death caused by KA involves reducing Apaf-1 and caspase-3 activation.

In addition to Mfn-2, the antiapoptotic protein Bcl-2 plays a key role in maintaining mitochondrial function and suppressing the mitochondrial apoptotic pathway (D'Orsi et al., 2017; Suhaili et al., 2017). For example, Bcl-2 can stabilize mitochondrial integrity, inhibit cytochrome c release from the mitochondria, and suppress caspase-3 activation, leading to cell survival and apoptosis inhibition (Czabotar et al., 2014). Furthermore, experimental studies have indicated that Bcl-2 overexpression protects against excitotoxic insults (Howard et al., 2002; Okazaki et al., 2008). Congruent with previous studies (Chang et al., 2018; Lu et al., 2018), we observed decreased Bcl-2 expression in the hippocampus of rats following KA exposure. Xanthohumol pretreatment rescued KA-induced decrease in Bcl-2 expression, suggesting that the neuroprotective effect of xanthohumol may also be mediated by an increase of the anti-apoptotic protein Bcl-2. The current results suggest that xanthohumol up-regulates mitochondrial fusion protein Mfn-2 and anti-apoptotic protein Bcl-2 to preserve mitochondrial function and suppress Apaf-1 and caspase-3 activation, thereby increasing neuron survival in rats after KA treatment (Fig. 7).

Xanthohumol has received increasing attention due to its distribution in the brain (Zamzow et al., 2014) and has an excellent safety profile (Dorn et al., 2010). For example, oral administration of xanthohumol (700–1000 mg/kg/day) to mice for 3–4 weeks had no adverse effects on major organ functions (Vanhoelcke et al., 2005). Many studies have shown neuroprotective effects of xanthohumol on animal disease models, which is consistent with our findings. For example, xanthohumol was found to alleviate ischemia and aging-induced neuroinflammation and brain damage (Yen et al., 2012; Rancán et al., 2017), to improve cognitive dysfunction (Zamzow et al., 2014), and to promote neurogenesis (Oberbauer et al., 2013). Regarding the mechanism underlying the neuroprotective effects of xanthohumol, the suppression of inflammatory responses and free radical production have been reported (Yen et al., 2012; Rancán et al., 2017). In addition to these possible mechanisms, our previous (Chang et al., 2016) and present study results presume that inhibiting glutamate release and antiexcitotoxic properties may partly contribute to the neuroprotective effects of xanthohumol in the brain. In addition, oral administration of xanthohumol to rats at a dose of 16.9 mg/kg results in the maximum concentration of 31 μ g/L and the bioavailability of 11% (Legette et al., 2012). Human studies also revealed that the maximum xanthohumol concentration is 67 μ g/L after oral administration of a single xanthohumol dose (60 mg/kg) (Legette et al., 2014). The dose of xanthohumol (10–50 mg/kg) used in our study is similar to these studies and this makes our data more relevant to clinical practice.

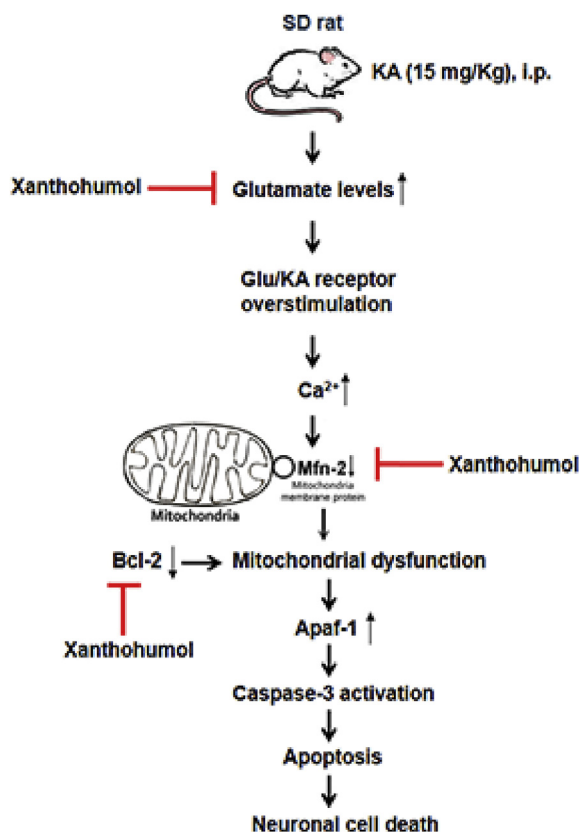


Fig. 7. Proposed mechanisms involved in the xanthohumol-mediated neuroprotective effect against KA-induced excitotoxicity in the rat hippocampus, which includes reduction of glutamate levels, upregulation of Mfn-2 and Bcl-2, and suppression of Apaf-1 and caspase-3 activation.

5. Conclusion

The present study revealed that xanthohumol confers substantial neuroprotection against KA-induced excitotoxicity by suppressing the mitochondria-dependent apoptotic process through the upregulation of Mfn-2 and Bcl-2 activity. To the best of our knowledge, this is the first study demonstrating that xanthohumol protects against excitotoxic injury, a feature that may expand its therapeutic potential for the treatment of brain diseases in which excessive glutamate is involved, such as ischemic brain injury and neurodegenerative disorders.

Declaration of competing interest

The authors declare there are no conflicts of interest.

Acknowledgments

This work was supported by the research grants from the Chi Mei Medical Center (105-CM-FJU-04).

References

- Bano, D., Ankarcrona, M., 2018. Beyond the critical point: an overview of excitotoxicity, calcium overload and the downstream consequences. *Neurosci. Lett.* 663, 79–85.
- Ben-Ari, Y., 1985. Limbic seizure and brain damage produced by kainic acid: mechanisms and relevance to human temporal lobe epilepsy. *Neuroscience* 14, 375–403.
- Chang, Y., Lin, T.Y., Lu, C.W., Huang, S.K., Wang, Y.C., Wang, S.J., 2016. Xanthohumol-induced presynaptic reduction of glutamate release in the rat hippocampus. *Food Funct.* 7, 212–226.
- Chang, Y., Lu, C.W., Chen, Y.J., Lin, T.Y., Huang, S.K., Wang, S.J., 2018. Astaxanthin protects against kainic acid-induced seizures and pathological consequences. *Neurochem. Int.* 116, 85–94.
- Chittajallu, R., Vignes MDev, K.K., Barnes, J.M., Collingridge, G.L., Henley, J.M., 1996.

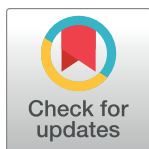
- Regulation of glutamate release by presynaptic kainate receptors in the hippocampus. *Nature* 379, 78–91.
- Choi, D.W., 1988. Glutamate neurotoxicity and diseases of the nervous system. *Neuron* 1, 623–634.
- Chuang, Y.C., Chang, A.Y.W., Lin, J.W., Hsu, S.P., Chan, S.H.H., 2004. Mitochondrial dysfunction and ultrastructural damage in the hippocampus during kainic acid-induced status epilepticus in the rat. *Epilepsy* 45, 1201–1209.
- Czabotar, P.E., Lessene, G., Strasser, A., Adams, J.M., 2014. Control of apoptosis by the BCL-2 protein family: implications for physiology and therapy. *Nat. Rev. Mol. Cell Biol.* 15, 49–63.
- de Brito, O.M., Scorrano, L., 2009. Mitofusin-2 regulates mitochondrial and endoplasmic reticulum morphology and tethering: the role of Ras. *Mitochondrion* 9, 222–226.
- Detmer, S.A., Chan, D.C., 2007. Functions and dysfunctions of mitochondrial dynamics. *Nat. Rev. Mol. Cell Biol.* 8, 870–879.
- Dohare, P., Hyzinski-García, M.C., Vipani, A., Bowens, N.H., Nalwalk, J.W., Feustel, P.J., Keller Jr., R.W., Jourdeuil, D., Mongin, A.A., 2014. The neuroprotective properties of the superoxide dismutase mimetic tempol correlate with its ability to reduce pathological glutamate release in a rodent model of stroke. *Free Radic. Biol. Med.* 77, 168–182.
- Dong, X.X., Wang, Y., Qin, Z.H., 2009. Molecular mechanisms of excitotoxicity and their relevance to pathogenesis of neurodegenerative diseases. *Acta Pharmacol. Sin.* 30, 379.
- Dorn, C., Bataille, F., Gaebele, E., Heilmann, J., Hellerbrand, C., 2010. Xanthohumol feeding does not impair organ function and homeostasis in mice. *Food Chem. Toxicol.* 48, 1890–1897.
- D'Orsi, B., Mateyka, J., Prehn, J.H., 2017. Control of mitochondrial physiology and cell death by the Bcl-2 family proteins Bax and Bok. *Neurochem. Int.* 109, 162–170.
- Ferkany, J.W., Zaczek, R., Coyle, J.T., 1982. Kainic acid stimulates excitatory amino acid neurotransmitter release at presynaptic receptors. *Nature* 298, 757–759.
- Ferkany, J.W., Coyle, J.T., 1983. Kainic acid selectively stimulates the release of endogenous excitatory amino acid. *J. Pharmacol. Exp. Ther.* 225, 399–406.
- Friedman, L.K., Pellegrini-Giamperio, D.E., Sperber, E.F., Bennett, M., Moshe, S.L., Zukin, R.S., 1994. Kainate-induced status epilepticus alters glutamate and GABA_A receptor gene expression in adult rat hippocampus: an in situ hybridization study. *J. Neurosci.* 14, 2697–2707.
- Gardoni, F., Di Luca, M., 2006. New targets for pharmacological intervention in the glutamatergic synapse. *Eur. J. Pharmacol.* 545, 2–10.
- Howard, S., Bottino, C., Brooke, S., Cheng, E., Giffard, R.G., Sapolsky, R., 2002. Neuroprotective effects of bcl-2 overexpression in hippocampal cultures: interactions with pathways of oxidative damage. *J. Neurochem.* 83, 914–923.
- Kim, H., Lee, J.Y., Park, K.J., Kim, W.H., Roh, G.S., 2016. A mitochondrial division inhibitor, Mdivi-1, inhibits mitochondrial fragmentation and attenuates kainic acid-induced hippocampal cell death. *BMC Neurosci.* 17, 33.
- Lee, I.S., Lim, J., Gal, J., Kang, J.C., Kim, H.J., Kang, B.Y., Choi, H.J., 2011. Anti-inflammatory activity of xanthohumol involves heme oxygenase-1 induction via NRF2-ARE signaling in microglial BV2 cells. *Neurochem. Int.* 58, 153–160.
- Legette, L., Ma, L., Reed, R.L., Miranda, C.L., Christensen, J.M., Rodriguez-Proteau, R., Stevens, J.F., 2012. Pharmacokinetics of xanthohumol and metabolites in rats after oral and intravenous administration. *Mol. Nutr. Food Res.* 56, 466–474.
- Legette, L., Karnpracha, C., Reed, R.L., Choi, J., Bobe, G., Christensen, J.M., Rodriguez-Proteau, R., Purnell, J.Q., Stevens, J.F., 2014. Human pharmacokinetics of xanthohumol, an antihyperglycemic flavonoid from hops. *Mol. Nutr. Food Res.* 58, 248–255.
- Lévesque, M., Avoli, M., Bernard, C., 2016. Animal models of temporal lobe epilepsy following systemic chemoconvulsant administration. *J. Neurosci. Methods* 260, 45–52.
- Lewerenz, J., Maher, P., 2015. Chronic glutamate toxicity in neurodegenerative diseases—what is the evidence? *Front. Neurosci.* 9, 469.
- Lin, T.Y., Lu, C.W., Wang, S.J., 2016. Luteolin protects the hippocampus against neuron impairments induced by kainic acid in rats. *Neurotoxicology* 55, 48–57.
- Lu, C.W., Hsieh, H.L., Lin, T.Y., Hsieh, T.Y., Huang, S.K., Wang, S.J., 2018. Echinacoside, an active constituent of *cistanche herba*, exerts a neuroprotective effect in a kainic acid rat model by inhibiting inflammatory processes and activating the Akt/GSK3 β pathway. *Biol. Pharm. Bull.* 41, 1685–1693.
- Ma, Y.M., Ibeanu, G., Wang, L.Y., Zhang, J.Z., Chang, Y., Dong, J.D., Li, P.A., Jing, L., 2017. Selenium suppresses glutamate-induced cell death and prevents mitochondrial morphological dynamic alterations in hippocampal HT22 neuronal cells. *BMC Neurosci.* 18, 15.
- Magalhães, P.J., Carvalho, D.O., Cruz, J.M., Guido, L.F., Barros, A.A., 2009. Fundamentals and health benefits of xanthohumol, a natural product derived from hops and beer. *Nat. Prod. Commun.* 4, 591–610.
- Mayor, D., Tymianski, M., 2018. Neurotransmitters in the mediation of cerebral ischemic injury. *Neuropharmacology* 134, 178–188.
- Mehta, A., Prabhakar, M., Kumar, P., Deshmukh, R., Sharma, P., 2013. Excitotoxicity: bridge to various triggers in neurodegenerative disorders. *Eur. J. Pharmacol.* 698, 6–18.
- Nadler, J.V., 1981. Kainic acid as a tool for the study of temporal lobe epilepsy. *Life Sci.* 29, 2031–2042.
- Oberbauer, E., Urmann, C., Steffenhagen, C., Bieler, L., Brunner, D., Furtner, T., Humpel, C., Bäumer, B., Bandtlow, C., Couillard-Despres, S., 2013. Chroman-like cyclic prenylflavonoids promote neuronal differentiation and neurite outgrowth and are neuroprotective. *J. Nutr. Biochem.* 24, 1953–1962.
- Okazaki, T., Magaki, T., Takeda, M., Kajiwar, Y., Hanaya, R., Sugiyama, Arita, K., Nishimura, M., Kato, Y., Kurisu, K., 2008. Intravenous administration of bone marrow stromal cells increases survivin and Bcl-2 protein expression and improves sensorimotor function following ischemia in rats. *Neurosci. Lett.* 430, 109–114.
- Prentice, H., Modi, J.P., Wu, J.Y., 2015. Mechanisms of neuronal protection against

- excitotoxicity, endoplasmic reticulum stress, and mitochondrial dysfunction in stroke and neurodegenerative diseases. *Oxid. Med. Cell. Longev.* 1–7 2015.
- Racine, R.J., 1972. Modification of seizure activity by electrical stimulation: II. Motor seizure. *Electroencephalogr. Clin. Neurophysiol.* 32, 281–294.
- Rancán, L., Paredes, S.D., García, I., Muñoz, P., García, C., de Hontanar, G.L., de la Fuente, M., Vara, E., Tresguerres, J.A., 2017. Protective effect of xanthohumol against age-related brain damage. *J. Nutr. Biochem.* 49, 133–140.
- Schinder, A.F., Olson, E.C., Spitzer, N.C., Montal, M., 1996. Mitochondrial dysfunction is a primary event in glutamate neurotoxicity. *J. Neurosci.* 16, 6125–6133.
- Shin, E.J., Jeong, J.H., Kim, A.Y., Koh, Y.H., Nah, S.Y., Kim, W.K., Ko, K.H., Kim, H.J., Wie, M.B., Kwon, Y.S., 2009. Protection against kainate neurotoxicity by ginsenosides: attenuation of convulsive behavior, mitochondrial dysfunction, and oxidative stress. *J. Neurosci. Res.* 87, 710–722.
- Śmiałowska, M., Golembiowska, K., Kajta, M., Zięba, B., Dziubina, A., Domin, H., 2012. Selective mGluR1 antagonist EMQMCM inhibits the kainate-induced excitotoxicity in primary neuronal cultures and in the rat hippocampus. *Neurotox. Res.* 21, 379–392.
- Sperk, G., 1994. Kainic acid seizures in the rat. *Prog. Neurobiol.* 42, 1–32.
- Stevens, J.F., Page, J.E., 2004. Xanthohumol and related prenylflavonoids from hops and beer: to your good health. *Phytochemistry* 65, 1317–1330.
- Suhaili, S.H., Karimian, H., Stellato, M., Lee, T.H., Aguilar, M.I., 2017. Mitochondrial outer membrane permeabilization: a focus on the role of mitochondrial membrane structural organization. *Biophys. Rev.* 9, 443–457.
- Traynelis, S.F., Wollmuth, L.P., McBain, C.J., Menniti, F.S., Vance, K.M., Ogden, K.K., Hansen, K.B., Yuan, H., Myers, S.J., Dingledine, R., 2010. Glutamate receptor ion channels: structure, regulation, and function. *Pharmacol. Rev.* 62, 405–496.
- Vanhoecke, B.W., Delporte, F., Van Braeckel, E., Heyerick, A., Depypere, H.T., Nuytinck, M., De Keukeleire, D., Bracke, M.E., 2005. A safety study of oral tangeretin and xanthohumol administration to laboratory mice. *In Vivo* 19, 103–107.
- Venturelli, S., Burkard, M., Biendl, M., Lauer, U.M., Frank, J., Busch, C., 2016. Prenylated chalcones and flavonoids for the prevention and treatment of cancer. *Nutrition* 32, 1171–1178.
- Wang, W., Zhang, F., Li, L., Tang, F., Siedlak, S.L., Fujioka, H., Liu, Y., Su, B., Pi, Y., Wang, X., 2015. MFN2 couples glutamate excitotoxicity and mitochondrial dysfunction in motor neurons. *J. Biol. Chem.* 290, 168–182.
- Wang, Q., Yu, S., Simonyi, A., Sun, G.Y., Sun, A.Y., 2005. Kainic acid-mediated excitotoxicity as a model for neurodegeneration. *Mol. Neurobiol.* 31, 3–16.
- Wong, S.B., Cheng, S.J., Hung, W.C., Lee, W.T., Min, M.Y., 2015. Rosiglitazone suppresses in vitro seizures in hippocampal slice by inhibiting presynaptic glutamate release in a model of temporal lobe epilepsy. *PLoS One* 10, e0144806.
- Xue, F., Shi, C., Chen, Q., Hang, W., Xia, L., Wu, Y., Tao, S.Z., Zhou, J., Shi, A., Chen, J., 2017. Melatonin mediates protective effects against kainic acid-induced neuronal death through safeguarding ER stress and mitochondrial disturbance. *Front. Mol. Neurosci.* 10, 49.
- Yamaguchi, N., Satoh-Yamaguchi, K., Ono, M., 2009. In vitro evaluation of antibacterial, anticollagenase, and antioxidant activities of hop components (*Humulus lupulus*) addressing acne vulgaris. *Phytomedicine* 16, 369–376.
- Yao, J., Zhang, B., Ge, C., Peng, S., Fang, J., 2015. Xanthohumol, a polyphenol chalcone present in hops, activating Nrf2 enzymes to confer protection against oxidative damage in PC12 cells. *J. Agric. Food Chem.* 63, 1521–1531.
- Yen, T.L., Hsu, C.K., Lu, W.J., Hsieh, C.Y., Hsiao, G., Chou, D.S., Wu, G.J., Sheu, J.R., 2012. Neuroprotective effects of xanthohumol, a prenylated flavonoid from hops (*humulus lupulus*), in ischemic stroke of rats. *J. Agric. Food Chem.* 60, 1937–1944.
- Zamzow, D.R., Elias, V., Legette, L.L., Choi, J., Stevens, J.F., Magnusson, K.R., 2014. Xanthohumol improved cognitive flexibility in young mice. *Behav. Brain Res.* 275, 1–10.
- Zhao, N., Zhang, Y., Liu, Q., Xiang, W., 2015. Mfn2 affects embryo development via mitochondrial dysfunction and apoptosis. *PLoS One* 10, e0125680.

RESEARCH ARTICLE

Pathogenesis of local necrosis induced by *Naja atra* venom: Assessment of the neutralization ability of Taiwanese freeze-dried neurotoxic antivenom in animal models

Chien-Chun Liu¹✉, Yu-Shao Chou²✉, Chun-Yu Chen², Kuei-Lin Liu³, Guo-Jen Huang⁴, Jau-Song Yu^{1,5,6,7}✉, Cho-Ju Wu⁸, Geng-Wang Liaw⁹, Cheng-Hsien Hsieh^{2,10*}, Chun-Kuei Chen^{10*}



1 Molecular Medicine Research Center, Chang Gung University, Taoyuan, Taiwan, **2** Department of Emergency Medicine, En Chu Kong Hospital, New Taipei City, Taiwan, **3** Faculty of Biotechnology and Laboratory Science in Medicine, School of Medical Technology and Engineering, National Yang-Ming University, Taipei, Taiwan, **4** Department and Graduate Institute of Biomedical Sciences, College of Medicine, Chang Gung University, Taoyuan, Taiwan, **5** Department of Cell and Molecular Biology, College of Medicine, Chang Gung University, Taoyuan, Taiwan, **6** Liver Research Center, Chang Gung Memorial Hospital, Linkou, Taoyuan, Taiwan, **7** Research Center for Food and Cosmetic Safety, Research Center for Chinese Herbal Medicine, College of Human Ecology, Chang Gung University of Science and Technology, Taoyuan, Taiwan, **8** Department of Emergency Medicine, Chang Gung Memorial Hospital and Chang Gung University College of Medicine, Taoyuan, Taiwan, **9** Department of Emergency Medicine, Yeezen General Hospital, Taoyuan, Taiwan, **10** Graduate Institute of Clinical Medicine, College of Medicine, Taipei Medical University, Taipei, Taiwan

✉ These authors contributed equally to this work.

* sogahsieh@gmail.com (CHH); master198012@gmail.com (CKC)

OPEN ACCESS

Citation: Liu C-C, Chou Y-S, Chen C-Y, Liu K-L, Huang G-J, Yu J-S, et al. (2020) Pathogenesis of local necrosis induced by *Naja atra* venom: Assessment of the neutralization ability of Taiwanese freeze-dried neurotoxic antivenom in animal models. PLoS Negl Trop Dis 14(2): e0008054. <https://doi.org/10.1371/journal.pntd.0008054>

Editor: Elda Eliza Sanchez, Texas A&M University Kingsville, UNITED STATES

Received: September 1, 2019

Accepted: January 14, 2020

Published: February 7, 2020

Copyright: © 2020 Liu et al. This is an open access article distributed under the terms of the [Creative Commons Attribution License](https://creativecommons.org/licenses/by/4.0/), which permits unrestricted use, distribution, and reproduction in any medium, provided the original author and source are credited.

Data Availability Statement: All relevant data are within the manuscript and its Supporting Information files.

Funding: This work was supported by Chang Gung Memorial Hospital, Taiwan (grants CMRPG3H1091 to CKChen and CMRPG3J1231 to CJWu), by En Chu Kong Hospital, Taiwan (ECKH_W10711 and ECKH_W10802 to CHHsieh), and by the "Molecular Medicine Research Center, Chang Gung

Abstract

Naja atra envenomation is one of the most significant clinical snakebite concerns in Taiwan. Taiwanese freeze-dried neurotoxic antivenom (FNAV) is currently used clinically for the treatment of cobra snakebite, and has been shown to limit the mortality of cobra envenomation to less than 1%. However, more than half of victims (60%) require surgery because of local tissue necrosis, a major problem in patients with cobra envenomation. Although the importance of evaluating the neutralizing effect of FNAV on this pathology is recognized, whether FNAV is able to prevent the local necrosis extension induced by *N. atra* venom has not been investigated in detail. Cytotoxins (CTXs) are considered as the major components of *N. atra* venom that cause necrosis. In the current study, we isolated CTXs from whole cobra venom and used both whole venom and purified CTXs to develop animal models for assessing the neutralization potential of FNAV against venom necrotizing activity. Local necrotic lesions were successfully produced in mice using CTXs in place of whole *N. atra* venom. FNAV was able to rescue mice from a subcutaneously injected lethal dose of cobra venom; however, it was unable to prevent CTX-induced dermo-necrosis. Furthermore, using the minimal necrosis dose (MND) of CTXs and venom proteome data, we found a dose of whole *N. atra* venom suitable for FNAV and developed a workable protocol for inducing local necrosis in rodent models that successfully imitated the clinical circumstance of cobra envenoming. This information provides a more comprehensive understanding of

University” from The Featured Areas Research Center Program within the framework of the Higher Education Sprout Project by the Ministry of Education (MOE) in Taiwan. The funders had no role in study design, data collection and analysis, decision to publish, or preparation of the manuscript.

Competing interests: The authors have declared that no competing interests exist.

the pathophysiology of *N. atra* envenomation, and serves as a guide for improving current antivenom strategies and advancing clinical snakebite management in Taiwan.

Author summary

Naja atra envenomation is an important public health issue in Taiwan. Although the mortality rate of cobra snakebite is controlled using antivenom, more than half of victims develop symptoms of local necrosis and require surgical intervention. Whether the Taiwanese freeze-dried neurotoxic antivenom (FNAV) currently in clinical use is able to prevent the local necrosis extension induced by *N. atra* venom is still unclear. In this study, we developed a dermo-necrosis animal model using purified cytotoxins (CTXs), the major necrosis-related proteins from *N. atra* venom. We found that FNAV was able to neutralize the lethality of whole cobra venom, but was unable to neutralize the necrosis induced by CTXs *in vivo*. This finding introduced an example that supplementary quality control assays may be necessary to determine the effectiveness of antivenoms in neutralizing specific pathology induced by the venom; only evaluating the rodent lethality prevention is insufficient. Our results provide insights that should help improve current antivenoms and advance cobra snakebite management in Taiwan.

Introduction

Envenomation by snakebite is a significant global public health issue, but is a particularly important issue in tropical (subtropical) countries and some poor rural communities [1]. Epidemiological studies have estimated that at least 1,800,000 envenoming events and 82,000 associated deaths occur each year due to snakebite [2]. Because snakes are ectothermic animals, snakebite cases are particularly burdensome in regions with a warmer climate, such as South Asia, Southeast Asia, and Africa [2–4].

Taiwan (formerly known as Formosa) is a subtropical island located in East Asia that is home to more than 40 snake species [5], six of which are of highly venomous [6]. According to the World Health Organization (WHO) categorizations in the guideline for antivenom production, four of these venomous snakes—*Bungarus multicinctus*, *Naja atra*, *Trimeresurus stejnegeri*, and *Protobothrops mucrosquamatus*—belong to the category 1, whereas the other two—*Deinagkistrodon acutus* and *Daboia russelii siamensis*—belong to the category 2 [7]. There are approximately 1,000 envenoming incidents in Taiwan each year, about 23.5–36% of which are *N. atra* envenoming [6, 8].

The government of Taiwan has produced snake antivenom for more than nine decades. After a series of improvements and refinements in the production process, there are now four types of antivenoms against the six most clinically significant snakebites available for clinical use. All are in the form of lyophilized F(ab)₂ from equine serum—two as bivalent antivenoms, and two as monovalent antivenoms [5, 9]. The first two are freeze-dried hemorrhagic antivenom (FHAV) against *T. stejnegeri* and *P. mucrosquamatus* and freeze-dried neurotoxic antivenom (FNAV) against *B. multicinctus* and *N. atra*, whereas the latter two are freeze-dried *D. acutus* antivenom against *D. acutus* and freeze-dried *D. russelii siamensis* antivenom against *D. russelii siamensis*. A complete antivenom system against all clinically significant snakebites would greatly aid in the control of snakebite-related mortality, which currently stands at less than 1% in Taiwan [8].

The cobra (genus *Naja*) is one of the most important venomous snakes that contribute to snakebite injury in Southeast Asia, including Taiwan [2, 10]. Cobra (*N. atra*) envenoming in Taiwan causes significant local tissue necrosis with swelling, in addition to inducing weak systemic neurotoxic effects [11, 12]. Although the bivalent FNAV, produced by the Centers for Disease Control, ROC (Taiwan), is clinically available for treatment of cobra envenoming, the surgical intervention rate still remains high (60–65%) [11, 13, 14]. Despite early antivenom administration (<6 h), more than half of cobra envenoming patients develop local tissue necrosis requiring debridement or other surgical intervention [11]; thus, limits to the ability of FNAV to neutralize the cytotoxicity of *N. atra* have been widely discussed.

Snake venom is a mixture of components. The major toxic proteins in *N. atra* venom are neurotoxins, phospholipase A₂ (PLA₂) proteins and cytotoxins (CTXs) [15], the latter of which have been reported to induce necrosis symptoms [16–18]. The potential of FNAV to neutralize *N. atra* venom is currently determined based on its ability to prevent lethality of *N. atra* venom in mice. However, whether FNAV is effective in neutralizing the local necrosis induced by *N. atra* venom has not been systematically investigated. In the present study, we purified and characterized the major components of *N. atra* venom and assessed the lethality and necrosis-promoting ability of whole venom and purified CTXs in animal models. The effectiveness of FNAV against the mortality and morbidity (necrosis) induced by *N. atra* venom was evaluated by pre-administration of venom proteins and antivenom.

Materials and methods

The snake venom and antivenom

The crude venom of *N. atra* was obtained from the world snake king education farm, Tainan, Taiwan. It was immediately lyophilized and stored at -20 °C until used. The FNAV (batch number: FN10201, FN10302 and FN10303) was purchased from Center of Disease and Control, R.O.C (Taiwan). The lyophilized antivenom powder was dissolved at 80 mg/ml in antivenom diluted buffer, providing with antivenom, for use in this investigation.

C₁₈ reverse-phase high-performance liquid chromatography (RP-HPLC) fractionation of *N. atra* venom

The venom of *N. atra* was separated by RP-HPLC, as previously described [19]. Briefly, crude venom (100 µg protein) was dissolved in solvent A (water containing 0.1% trifluoroacetic acid (TFA)), and separated by RP-HPLC using a Supelco Discovery 300 Å C₁₈ (4.6 × 150 mm, 3 µm particle size) column (Sigma-Aldrich, St. Louis, Missouri, USA). The flow rate was set to 0.7 mL/min, and the column was developed with a linear gradient of solvent A and solvent B (acetonitrile containing 0.1% TFA) as follows: isocratic 5% solution B for 3 minutes, followed by linear gradients of 5–10% solvent B for 2 minutes, 10–16% solvent B for 6 minutes, 16–28% solvent B for 4 minutes, 28–41% solvent B for 32 minutes, 41–52% solvent B for 5 minutes, 52–80% solvent B for 3 minutes, 80–100% solvent B for 1 minutes, 100% solvent B for 1 minutes, 100–5% solvent B for 2 minutes, and re-equilibration with 5% solvent B for 1 minutes. Peaks were detected by monitoring absorbance at 280 nm. Chromatographic fractions were collected manually. This process was performed to separate 15 mg of *N. atra* venom proteins. Then, fractions were lyophilized and stored at -20 °C for further analysis.

Sodium dodecyl sulfate-polyacrylamide gel electrophoresis (SDS-PAGE)

The lyophilized fractions from RP-HPLC were dissolved by PBS. The protein concentration of each fraction was measured using the Pierce BCA Protein Assay Kit (Thermo Fisher Scientific,

Waltham, Massachusetts, USA). Two microgram of each fraction proteins was analyzed by SDS-PAGE under reducing condition. Briefly, samples were dissolved in sample buffer (125 mM Tris, 25% glycerol, 10% 2-mercaptoethanol, 4% SDS, 0.05% bromophenol blue) and heated at 95 °C for 5 minutes. Samples were then loaded onto a 15% gel and further separated by SDS-PAGE. The location of proteins in SDS-PAGE gels was visualized by Coomassie Brilliant Blue staining.

In-direct enzyme-linked immunosorbent assay (Indirect ELISA)

Each fraction of *N. atra* venom (50 ng) was diluted in 100 µl phosphate-buffered saline (PBS) and coated onto 96-well polystyrene microplates (Corning Inc., Corning, New York, USA) by incubating at 4 °C overnight. The plates were washed six times with 200 µl of PBST (contain 0.1% Tween-20) and blocked with 200 µl of 1% ovalbumin in PBS at room temperature for 2 hours. After repeating the washing step for six times, FNAV (8 mg/ml) was diluted (1:5000) in PBS, and added to each well. After incubation at room temperature for 2 hours, the excess antibodies were removed by washing 6 times with PBST. Then, the alkaline phosphatase-conjugated secondary antibody (Santa Cruz Biotechnology, Dallas, Texas, USA) was diluted (1:5000) in PBS and added to each well and incubated at room temperature for 1 hour. After finally washing each well 6 times with PBST, the substrate 4-methyl umbelliferyl phosphate (100 µM, 100 µl/well) was added to each well and incubated for 10 minutes. The fluorescence was measured with a SpectraMax M5 microplate reader (Molecular Devices, Silicon Valley, CA, USA) at excitation and emission wavelengths of 355 and 460 nm, respectively.

In-solution tryptic digestion of protein

For protein identification, the proteins in each fraction were subjected to tryptic digestion before liquid chromatography-tandem mass spectrometry (LC-MS/MS) analysis, as described previously [20]. Briefly, 1 µg of protein was reduced by incubation with 10 mM dithiothreitol (DTT) at 60 °C for one hour and alkylated by incubation with 30 mM iodoacetamide (IAM) at room temperature in the dark for 30 minutes. Samples were then equilibrated by incubation again with 10 mM DTT at room temperature for 10 minutes. Proteins were digested with freshly prepared trypsin solution containing 20 µg/mL of trypsin (Promega, Madison, WI, USA) in 50 mM ammonium bicarbonate at 37 °C for 16 hours, following heated sample at 100 °C for 10 minutes to denature the trypsin enzyme. A 96-well Oasis HLB µElution plate (Waters, Milford, Massachusetts, USA) was used to desalt each sample according to the manufacturer's protocol. After the sample was desalted, the tryptic peptides were lyophilized by SpeedVac and stored at -20 °C before LC-MS/MS analysis.

LC-MS/MS analysis

Each peptide sample was reconstituted with 0.1% formic acid (FA), and then analyzed on a nano-LC-LTQ-Orbitrap Hybrid Mass Spectrometer (Thermo Fisher, San Jose, CA, USA), as described previously [21]. Briefly, the sample was loaded across a trap column (Zorbax 300SB-C18, 0.3 × 5 mm; Agilent Technologies, Wilmington, DE, USA) at a flow rate of 0.2 µl/min in HPLC buffer (0.1% FA), and separated on a resolving 10-cm analytical C18 column (inner diameter, 75 µm) using a 15-µm tip (New Objective, Woburn, MA, USA). The peptides were eluted using a linear gradient of 0–10% HPLC buffer B (100% ACN containing 0.1% FA) for 3 minutes, 10–30% buffer B for 35 minutes, 30–35% buffer B for 4 minutes, 35–50% buffer B for 1 minute, 50–95% buffer B for 1 minute and 95% buffer B for 8 minute, with a flow rate of 0.25 µl/min across the analytical column. The resolution of the Orbitrap is 30,000, and the ion signal of $(\text{Si}(\text{CH}_3)_2\text{O})_6\text{H}^+$ at 445.120025 (m/z) was used as a

lock mass for internal calibration. A procedure that alternated between one MS scan followed by 10 MS/MS scans for the 10 most abundant precursor ions in the MS scan was applied. The m/z values selected for MS/MS were dynamically excluded for 180 seconds. For MS scans, the m/z value of the scan range was 400 to 2000 Da. For MS/MS scans, more than 1×10^4 ions were accumulated in the ion trap to generate MS/MS spectra. Both MS and MS/MS spectra were acquired using one scan with maximum fill-times of 1000 and 100 ms for MS and MS/MS analysis, respectively. For database searching, MS raw data files were analyzed by Proteome Discoverer Software (version 1.4.1.14; Thermo Fisher, San Jose, CA, USA), and searched against other lobe-finned fish and tetrapod clade taxonomy in the Swiss-Prot database using MASCOT. The enzyme specificity parameter was set to “trypsin” and one missed cleavage was allowed. Carbamidomethylation of cysteine was set as a static modification and oxidation of methionine, acetyl (protein N-term) and Gln- > pyro-Glu (N-term Q) was set as dynamic modification. The tolerance of MS is 10 ppm and MS/MS is 0.5 Da. The criteria of minimal number of peptide per identified protein is 2.

Animal

Experiments were performed on seven-week-old littermate ICR (CD1) mice with a defined weight range (30–35 g). Mice were maintained in specific pathogen-free conditions. They were housed in a 12:12 hour light dark cycle at a temperature of 22°C and a humidity level of 60–70%. Animals had ad libitum access to food and water.

Animal ethics statement

Experiments involving the care and injection of mice with various venoms were reviewed and approved by the Institutional Animal Care and Use Committee of Chang Gung University (Permit Number: CGU106-194). The protocol of animal study on mice was based on the guidelines given by the law of animal protection act in Taiwan and the Council for International Organizations of Medical Sciences (CIOMS) [22].

The median lethal dose (LD₅₀) assay

Groups of 5 mice are subcutaneously injected, in the dorsal skin, with 0.1 ml of sterile saline solution containing different doses of venom (0.2–0.45 mg/kg). LD₅₀ was determined by recording deaths 24 hours after injection, and the value of LD₅₀ is estimated with Probit analysis [23]. One venom LD₅₀ is defined as the minimal amount of venom causing death in 50% of the mice.

The minimal necrosis dose (MND) assay

Groups of 3 mice were intradermally injected, in the dorsal region, with varying amount (0–60 µg) of *N. atra* venom (or cytotoxins), dissolved in 0.05 ml sterile saline solution. Animals were sacrificed by CO₂ inhalation three-day post-injection. The dorsal skin was then removed and the necrotic lesion in the inner side of the skin was measured, and the MND is estimated with linear regression analysis. The MND was defined as the dose which induced an area of necrosis with 5 mm diameter three days after injection [24].

The median effective dose (ED₅₀) assay

This test involves incubation of a challenge dose, 5 LD₅₀, of venom with different volumes (0.25–5 µl) of the antivenom, adjusted to a constant volume (0.1 ml) with saline solution. The mixtures were incubated for 30 minutes at 37°C, then 0.1-ml aliquots of each mixture were

injected subcutaneously into groups of mice ($n = 5/\text{group}$). Mice in the control group were injected with a saline solution containing the challenge dose of venom alone, which induces 100% lethality. ED_{50} was determined by recording deaths 24 hours after injection, and the value of ED_{50} was calculated using probit analysis. One ED_{50} is defined as the ratio of amount of venom to the volume dose of antivenom that keep 50% alive of mice. Another term called “potency”, expressed as the amount of venom that is completely neutralized per milliliter of antivenom, was calculated as previously described [25, 26].

The MND-median effective dose (MND_{50}) assay

The test is carried out as above, using 3 mice per group. 1.5 MND of venom (or cytotoxins) is selected as the challenge dose. The challenge dose was mixed with different doses of FNAV in 0.05 ml saline solution and incubated at 37 °C for 30 minutes, and the control group including venom solutions incubated with physiological saline solution alone. The mixture was then intradermally injected in the dorsal skin of lightly anaesthetized mice. The diameter of necrotic lesions is quantified 3 days after injection. The neutralizing ability of antivenom, expressed as MND-median effective dose (MND_{50}), is estimated as the volume of antivenom which reduces the diameter of necrotic lesions by 50% when compared with the diameter of the lesion in mice injected with the control venom/saline mixture. The antivenom was considered ineffective when none of mice, administered with the maximum amount of antivenom, survived.

Histological analysis

Mice were intradermally injected, as described above, with saline solution and 1.5 MND of CTXs, respectively. Animals were sacrificed by CO_2 inhalation three-day post-injection. The dorsal skin was then removed and immediately placed in 10% formaldehyde for 24 h. After routine processing and embedding in paraffin, 3 μm sections were obtained and stained with hematoxylin and eosin (HE) for histological observation. All samples were analyzed with a light microscope.

Envenoming and rescue rodent models

Groups of 3 mice were intradermally injected, in the dorsal region, with a mixture of anti-venom (40 μl) and varying amount (80–160 μg) of *N. atra* venom. The time-course of survival rate was recorded each half hour in the 12-hour period. The surviving mice were additionally fed for 60 hr and sacrificed by CO_2 inhalation. The dorsal skin was then removed and the necrotic lesion in the inner side of the skin was measured.

Statistical analysis

Statistical analysis was performed using one-way ANOVA followed by Tukey’s Multiple comparison test, and t-tests. All statistical analyses were performed using Graphpad Prism 5 software (La Jolla, California, USA). Differences were considered statistically significant when $p\text{-value} \leq 0.05$.

Results

Description and preparation of major protein components from *N. atra* venom

The crude venom of *N. atra* was separated by RP-HPLC (Fig 1). Consistent with previous studies using similar methods [15, 19], we purified and collected five major protein components. To confirm the identity of protein components in each fraction, we performed in-solution

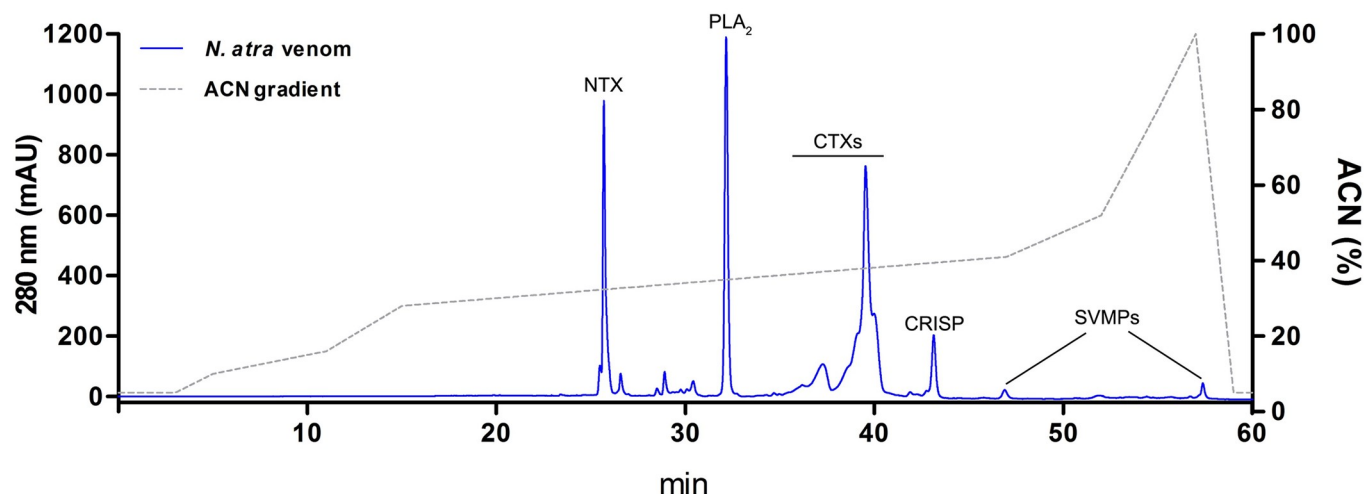


Fig 1. RP-HPLC fractionation of venom components from *N. atra*. Venom powder (100 µg protein) was dissolved in 0.1% formic acid and subjected to RP-HPLC analysis. Major proteins in resolved fractions were identified by LC-MS/MS. The identity of major protein components is indicated above each HPLC-separated fraction.

<https://doi.org/10.1371/journal.pntd.0008054.g001>

digestion together with LC-MS/MS. These results are summarized in [S1 Table](#). The five major peaks in the RP-HPLC spectrum were identified as neurotoxin (NTX), phospholipase A₂ (PLA₂), cytotoxins (CTXs), cysteine-rich secretory protein (CRISP), and snake venom metalloproteinase (SVMP) ([Fig 1](#)).

The relative abundance of these toxic components was calculated based on the absorbance intensity of their peaks in the RP-HPLC spectrum ([Fig 2](#)). More than half (54.2%) of *N. atra* venom consisted of CTXs. PLA₂, NTX, CRISP, and SVMP constituted 20.3%, 15.7%, 4.0%, and 1.1%, respectively, of the total; the remaining 4.7% of venom proteins were other components. Collectively, CTX, PLA₂, and NTX accounted more than 90% of protein components of *N. atra* venom. It has been claimed that CTXs are the major components that contribute to local necrosis [27]. To obtain a large amount of CTXs for further studies, we used HPLC methodology to purify 7 mg of CTXs from 15 mg of crude *N. atra* venom.

Immuno-recognition of *N. atra* venom by FNAV

To characterize fractionated venom components, we resolved proteins by sodium dodecyl sulfate-polyacrylamide gel electrophoresis (SDS-PAGE) and performed Coomassie Blue staining ([Fig 3A](#)). NTX, PLA₂, CTXs and CRISP fractions each yielded a single major band on gels. The SVMP fraction appeared as two protein bands corresponding to molecular weights (MW) of 55 and 70 kDa. Results of MW and LC-MS/MS analyses ([S1 Table](#)) suggested that the upper and lower bands were zinc metalloproteinase disintegrin-like atragin (D3TTC2) and metalloproteinase disintegrin-like kaouthiagin-like (D3TTC1), respectively. The MWs of all protein bands coincided with the theoretical MWs based on protein identification results ([S1 Table](#)).

To evaluate and compare the titer of FNAV against each venom protein, we performed indirect enzyme-linked immunosorbent assays (ELISAs) using FNAV as the detection antibody ([Fig 3B](#)). FNAV showed the ability to recognize all five major venom components from *N. atra*. Surprisingly, the titer of FNAV toward SVMP was highest, even though the relative abundance of SVMP was the lowest of these five toxins. FNAV-interaction signals were almost equal for NTX, CTXs and CRISP, which did not significantly differ among each other, and the titer against PLA₂ was the lowest.

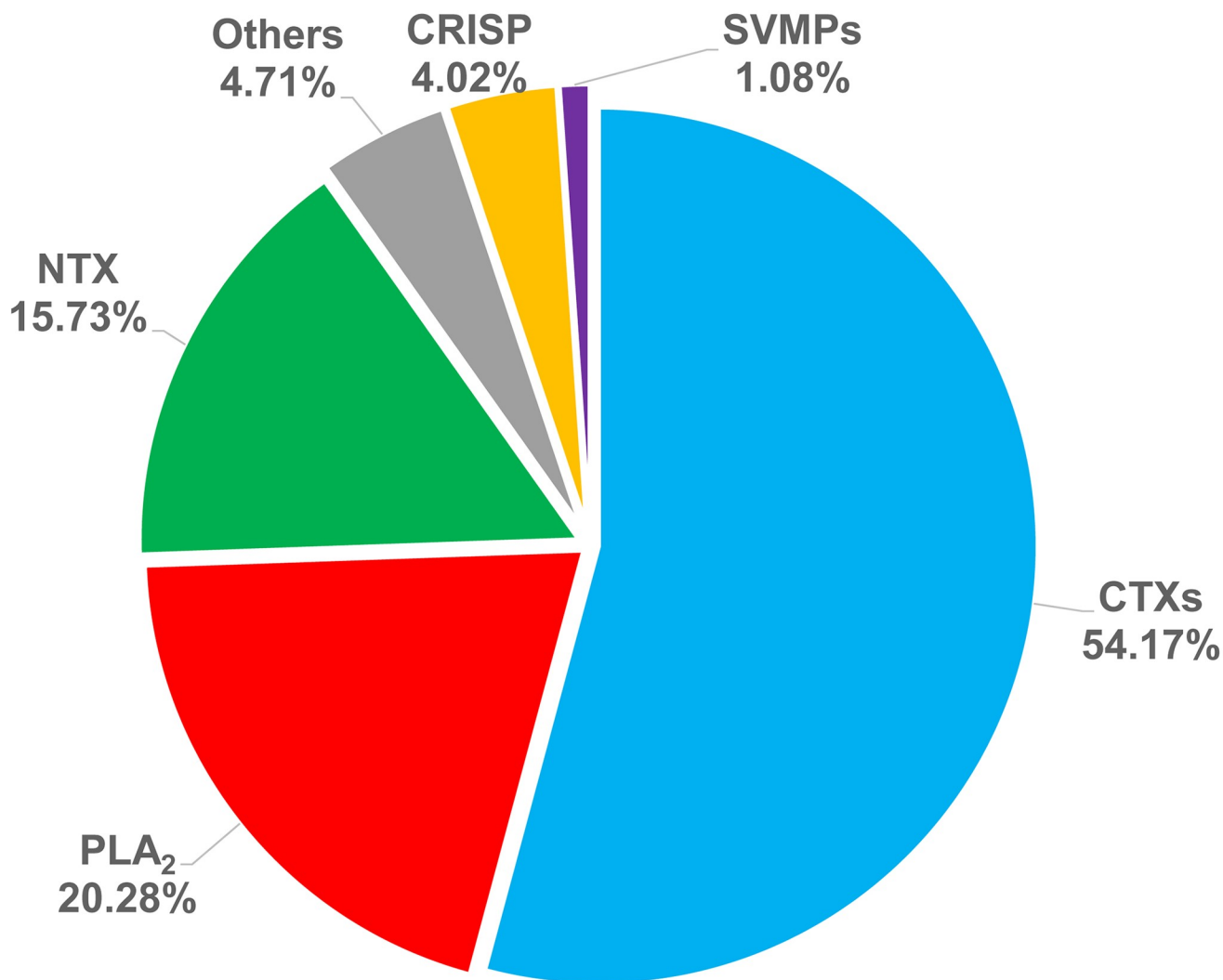


Fig 2. The relative abundance of venom components in *N. atra* venom. The relative abundance of each protein was calculated based on the peak area (280 nm) in RP-HPLC.

<https://doi.org/10.1371/journal.pntd.0008054.g002>

Development of an animal model of CTX-induced necrosis

To evaluate the necrosis-inducing activity of venom *in vivo*, we sought to develop a dermo-necrosis mouse model, followed WHO criteria for biological standardization [7]. First, we administered whole *N. atra* venom to mice to induce necrosis in the dorsal skin. Intradermal injection of mice with a total amount of venom greater than 30 µg resulted in the death of all mice within 12 hours. However, no necrotic lesions were observed in the dorsal skin following injection of whole venom. We next tested administration of purified CTXs. Necrotic lesions were observed in the dorsal skin following injection of more than 30 µg CTXs (Fig 4A), and the size of necrotic lesions increased with increasing CTX dose (Fig 4B). Calculations showed that the minimum necrotizing dose (MND) of CTX was 47 µg (Table 1). We also evaluated the 50% lethal dose (LD₅₀) of whole cobra venom and purified CTX for subsequent assessment of neutralization ability. The LD₅₀ of whole cobra venom was 0.29 µg/g; in contrast, mice survived injection of 100 µg (~3.3 µg/g) of CTXs (Table 1). Twitch, muscle weakness and

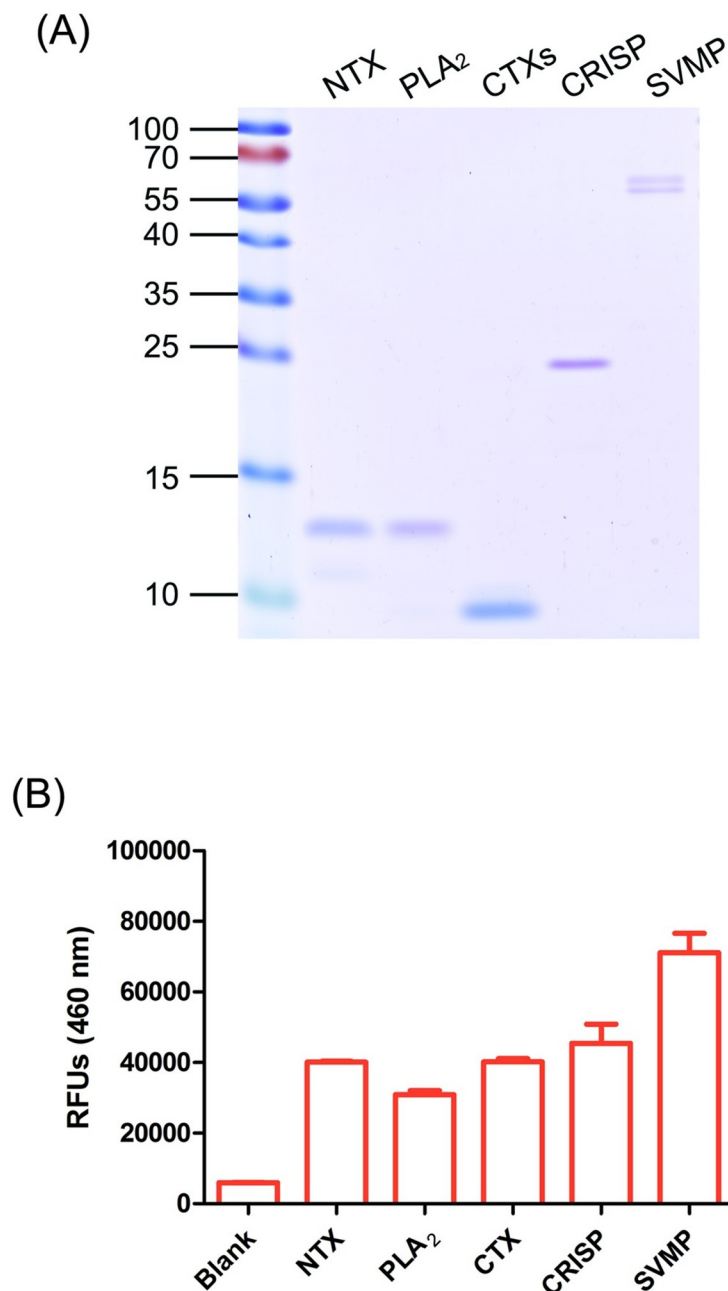


Fig 3. Immuno-profiling of FNAV against major components in *N. atra* venom. (A) Each component was analyzed by resolving 1 μ g protein by SDS-PAGE. Gel bands were visualized by Coomassie Blue staining. (B) An equal amount of each protein was coated on 96-well plates and subjected to indirect ELISA using FNAV as the detecting antibody. The bar chart shows signals (means \pm SD) from triplicate determinations.

<https://doi.org/10.1371/journal.pntd.0008054.g003>

respiratory paralysis occurred in venom-administrated mice, whereas these symptoms were not observed in CTX-administrated mice.

To analyze histopathologic changes associated with CTX-induced necrosis, we evaluated sections of skin samples under a light microscope (Fig 4C and 4D & S1 Fig). Dorsal skin of mice injected with saline solution displayed normal epidermis and dermis histological structures (Fig 4C). In contrast, the epidermis was loosened and formed a hyaline fibrinoid material

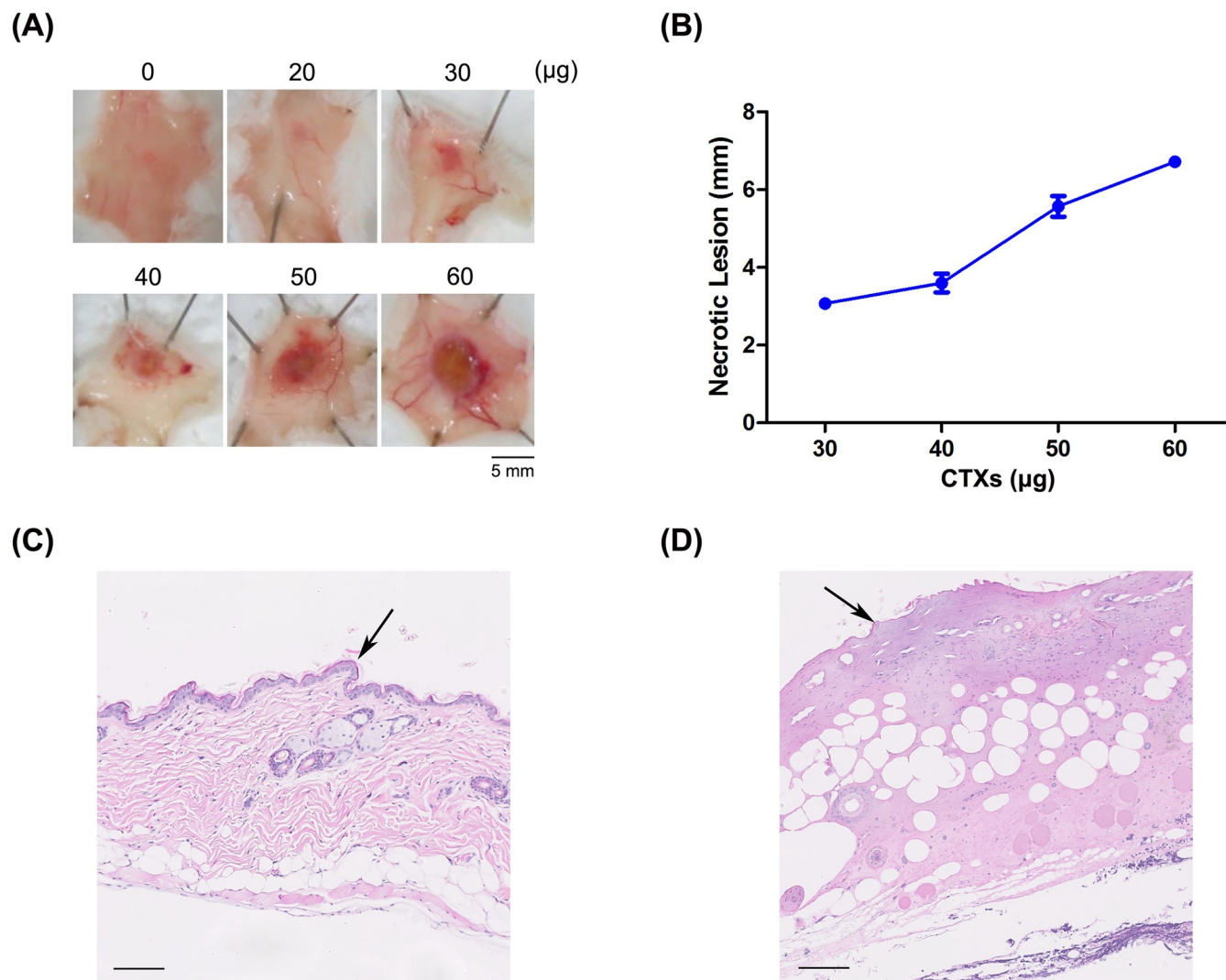


Fig 4. CTX-induced necrosis in mouse models. (A) Different amounts (0–60 µg) of CTXs were intradermally injected into mice, and the sizes of necrotic lesions in the dorsal skin of injected mice were measured. (B) MNDs for CTXs, calculated from measured sizes of necrotic lesions. H&E-stained sections of dorsal skins injected with (C) saline solution or (D) CTXs were analyzed histologically under a light microscope. Arrows highlight alterations in the epidermis. Scale bar: 100 µm.

<https://doi.org/10.1371/journal.pntd.0008054.g004>

Table 1. Neutralization of toxic activities of *N. atra* venom by FNAV.

<i>N. atra</i>	Lethality	Necrosis	Neutralization ability of FNAV			
			Lethal ability		Necrotic ability	
	LD ₅₀ (µg/g)	MND (µg)	ED ₅₀ (mg/ml)	Potency (mg/ml)	MND ₅₀ (mg/ml)	Potency (mg/ml)
whole venom	0.29 (0.14–0.37)	NA	47.86 (30.17–110.56)	38.3	ND	
cytotoxins	NA ^a	47 (43.9–50.3)	ND ^b		NE ^c	

Results were presented as means and 95% confidence limits.

^aNA: no activity was detected.

^bND: neutralization ability not determined because proteins lacked activity.

^cNE: neutralization activity was not affected by administration of the maximum dosage of FNAV.

<https://doi.org/10.1371/journal.pntd.0008054.t001>

in skin samples from CTX-injected mice, and there was obvious evidence of inflammatory infiltrate in the dermis (Fig 4D).

Evaluation of the ability of FNAV to neutralize CTX-induced necrosis

Next, we used the CTX-induced necrotic mouse model to assess the potential of FNAV to prevent necrosis. In these experiments, antivenom was pre-incubated with CTXs before injection. Surprisingly, dermo-necrosis was still observed following administration of the highest volume of FNAV (40 μ l) (Fig 5A). Moreover, the size of necrotic lesions did not decrease with

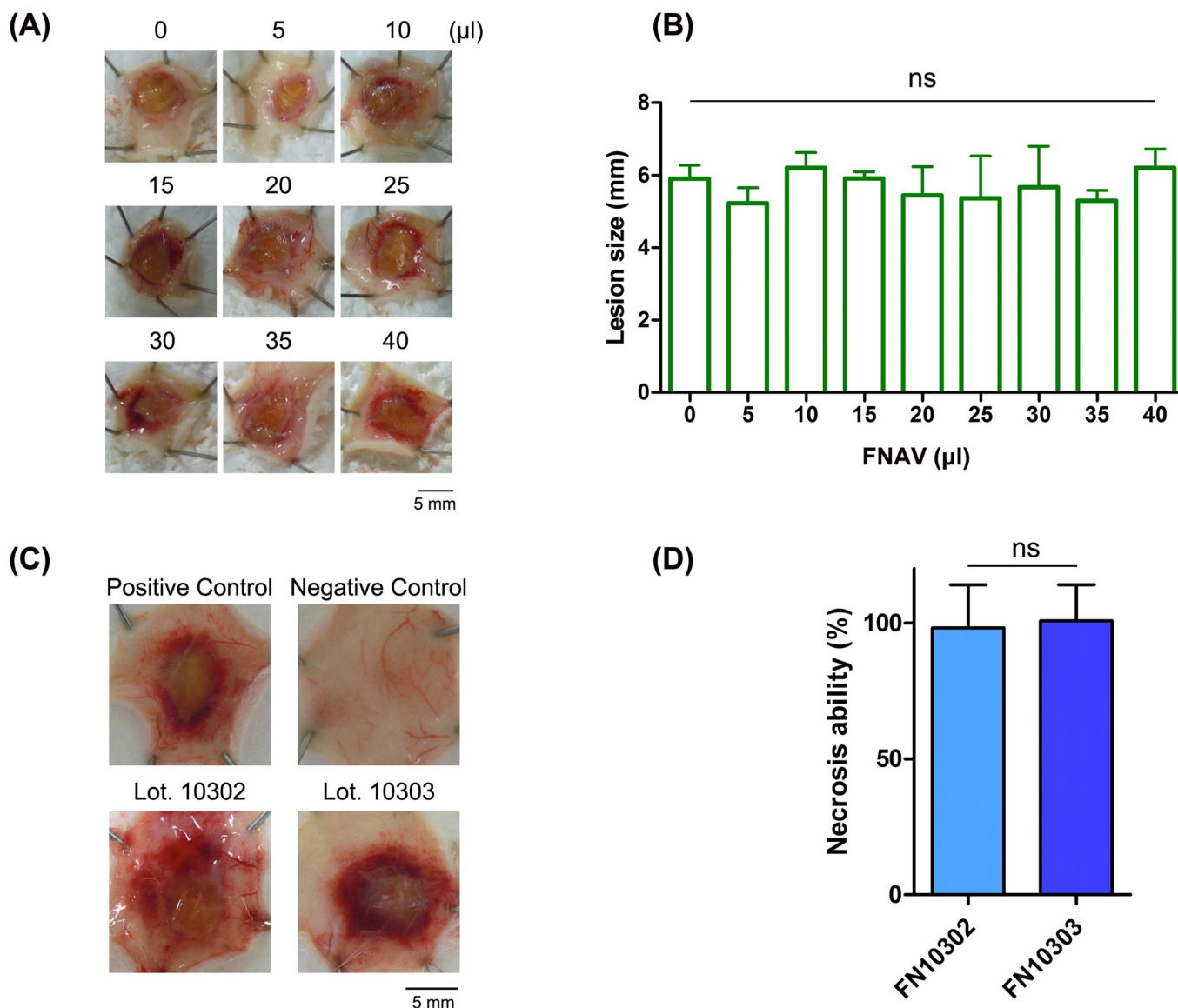


Fig 5. Evaluation of the ability of FNAV to neutralize CTX-induced necrosis. (A) Different volumes of FNAV (0–40 μ l) were pre-incubated with a fixed amount of CTXs (1.5 MND), and then intradermally injected into mice. The sizes of necrotic lesions in the dorsal skin of injected mice were measured. (B) Average size of necrotic lesions ($n = 3$) after neutralization by different volumes of FNAV. One-way ANOVA followed by Tukey's multiple comparison test was performed to analyze differences. (C) The sizes of necrotic lesions were recorded after mice had been administered two additional batches of FNAV (40 μ l). Positive controls were injected with 1.5 MND of CTXs, and negative controls received the same volume of PBS. (D) Necrosis-inducing ability presented as the size of necrotic lesions compared with that of positive controls. Each bar represents means \pm SD of triplicates (ns: not significant; two sample t-test).

<https://doi.org/10.1371/journal.pntd.0008054.g005>

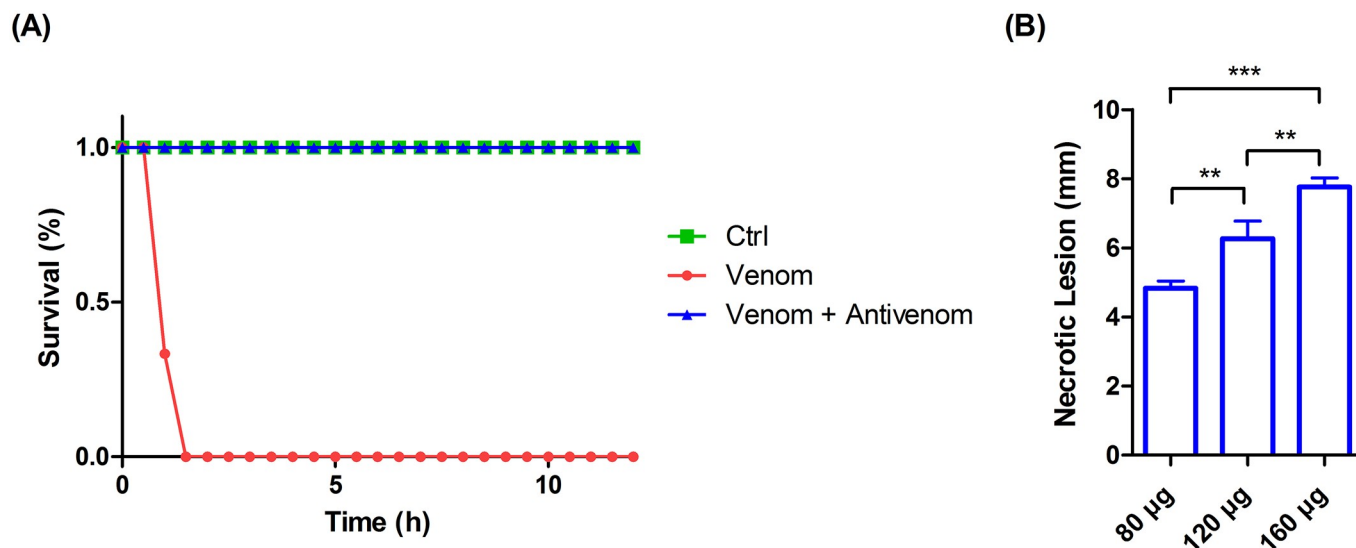


Fig 6. Development of local necrosis in mice administrated whole *N. atra* venom and FNAV. (A) The protective effect of FNAV was evaluated in mice. Mice ($n = 3$ per group) were administrated PBS (Ctrl), 80 µg of *N. atra* venom (Venom), or 80 µg of *N. atra* venom plus 40 µl of FNAV (Venom + Antivenom). The survival rate of mice was recorded every half-hour for 12 hours. (B) The sizes of necrotic lesions in mice that survived for 72 hours were measured and recorded. Each bar represents means \pm SD of triplicates (*, $p \leq 0.05$; **, $p \leq 0.01$; ***, $p \leq 0.001$; one-way ANOVA followed by Tukey's multiple comparison test).

<https://doi.org/10.1371/journal.pntd.0008054.g006>

increasing volumes of added FNAV and remained larger than 5 mm in diameter (Fig 5B). By contract, FNAV successfully neutralized the lethality of whole cobra venom, with an ED₅₀ of ~47.9 mg/ml (Table 1).

These data seem to indicate that FNAV has limited potential for preventing the occurrence of local necrosis. However, antivenoms exhibit batch-to-batch variation, and individual horses in which FNAV was raised may have different immune responses toward CTXs, resulting in differences in antibody titer against CTXs. Thus, two additional batches of FNAV, FN1302 and FN1303, were selected and their ability to prevent the CTX-induced necrosis was accessed. Western blotting was performed to confirm that these batches of FNAV were active and able to recognize *N. atra* venom (S2 Fig). Again, FNAV (40 µl) from each batch was preincubated with 1.5 MND of CTX for 30 minutes, and then intradermally injected into the dorsal skin of mice. As shown in Fig 5C, necrotic lesions were observed in mice 3 days after injection. The sizes of necrotic lesions did not differ significantly compared with that in positive controls injected with 1.5 MND of CTX alone (Fig 5D).

Development of an animal model of whole venom-induced necrosis

As described above, our original attempt to induce necrosis in the dorsal skin of mice by intradermally injecting the whole *N. atra* venom failed because all mice died within 12 hours after injection. Our finding that FNAV could neutralize the lethality of CTX, but could not prevent the CTX-induced necrosis in mice (Fig 5), raises the intriguing possibility of creating a whole venom-induced necrosis mouse model by simultaneously injecting whole *N. atra* venom and FNAV into mice at appropriate amounts and ratios. In developing snakebite animal models and assessing the ED₅₀ of FNAV, researchers generally use 2.5–5 LD₅₀ of *N. atra* venom as a challenge dose. However, our venom proteome (Fig 2) and lethality test results (Table 1) indicate that 5 LD₅₀ of *N. atra* venom corresponds to about 20 µg of CTXs, which is incapable of inducing overt necrotic lesions. Thus, we used 80 µg, or approximately 9 LD₅₀, of cobra venom as a challenge dose in the absence or presence of 40 µl FNAV. In the time-course experiments

(Fig 6A), all mice in the control group (PBS injected) and the group administrated both cobra venom and FNAV survived the initial 12-hour period, whereas mice administered only cobra venom did not survive more than 1.5 hr. An examination of surviving mice in the cobra venom plus FNAV group, maintained on a normal diet for an additional 60 hours, revealed obvious dorsal skin necrosis. (S3 Fig). We also tested two groups of mice that were challenged with increased doses of cobra venom (120 and 160 µg) in the presence of FNAV. All mice in both groups survived and developed dorsal skin necrosis 3 days after injection (S3 Fig), and the average size of necrotic lesions increased in a challenge dose-dependent manner (Fig 6B).

Discussion

Snakebite accidents involving *N. atra* are important in an emergency medicine setting in Taiwan. In this study, we characterized the venom proteome of *N. atra*, isolated necrosis-related CTX components, and evaluated the neutralization ability of FNAV—the clinically therapeutic antivenom for *N. atra* envenoming—against CTX-induced necrosis. Our results showed that more than half of *N. atra* venom proteins are CTXs. These components are the key cause of necrosis, which contributes to pathogenic complications in *N. atra* envenomation victims. Despite this contribution, our data showed that CTXs alone are not lethal (Table 1), suggesting that death observed in mice is predominantly caused by other toxic components. Furthermore, although CTXs were found to be immunogenic, such that FNAV was able to recognize CTXs in native form (Fig 3), antibodies in FNAV were unable to prevent the progression of CTX-induced necrosis. These results raise critical issues regarding the need for further discussion and improvement in antivenom production and evaluation of therapeutic efficacy.

CTXs, PLA₂ and NTX account for ~90% of venom protein constituents [15, 19]. The structure of CTXs, the most dominant proteins in *N. atra* venom, is characterized by a three-fingered fold comprising loops I–III [28]. The tips of loop I–III form a hydrophobic core flanked by polar residues, which represent a membrane-binding motif [29–31]. This motif allows CTXs to bind cell membranes, an interaction that has been reported to cause a conformational change in the membrane and structural deformation of lipid bilayers [32, 33]. Several *in vitro* studies using model membranes or cell lines have suggested that CTXs are the major toxins that contribute to necrosis—a major pathological consequence of cobra envenomation [29, 30, 34–36]. In the current study, we used mouse models to further confirm that, although the pathological activity of CTXs is related to the symptom of local necrosis, CTX toxicity is not a determining factor in the fatality of cobra envenomation.

Although *N. atra* belongs to the *Elapidae* family, neurotoxic symptoms are not a clinically significant consequence of *N. atra* envenomation, unlike the case for other members of this family [11]. This is somewhat surprising, given that our investigation found that NTX constitutes about 15% of venom components of Taiwanese cobra. Importantly, LD₅₀ assays reported here found that mice developed muscle weakness and respiratory paralysis after subcutaneous injection of *N. atra* venom, neurological effects that were also previously documented in mice [37, 38]. The reason for the discrepancy between neurotoxic effects of *N. atra* envenomation in mice and those in humans is still unclear. The NTX in *N. atra* venom is a short-chain α-neurotoxin. α-Neurotoxins are competitive antagonists that bind to nicotinic acetylcholine receptors (nAChR) in post-synaptic membranes, causing a neuromuscular-blocking effect [39–41]. The α-subunit of nAChR plays a critical role in α-neurotoxin binding, and the protein sequence of loop C in the α-subunit shows few amino acid differences between human and mouse [42, 43]. Furthermore, the inhibition of human nAChR induced by α-elapitoxin, a short chain α-neurotoxin from *Pseudechis porphyriacus*, was shown to be completely reversible within 6 minutes, a rate that is significantly faster than that for mouse nAChR [43]. This suggests that species-

specific differences in nAChR underlie differences in neurotoxic effects between rodents and humans, and may be the reason for discrepancies in the pathogenesis of *N. atra* envenoming.

PLA₂ constitutes about 20% of *N. atra* venom proteins (Fig 2), indicating that it may be an important factor in the pathogenesis of cobra envenoming. PLA₂ from *N. atra* has been shown to exhibit strong binding activity toward zwitterionic membranes [44]. Additionally, PLA₂ from *Naja kaouthia* venom was reported to promote CTX-induced cytotoxicity in cell models [45], indicating that cobra PLA₂ may play a role in the pathogenesis of necrosis. Although the relative abundances of SVMP and CRISP are lower than those of the three major components in *N. atra* venom, they may contribute to the pathogenesis of cobra envenoming. SVMPs have the ability to inhibit classical and alternative pathways of the complement system by cleaving complement factors [46], and activating mast cells [47], indicating that the effect of SVMPs in cobra venom may act to disturb the immune system in local tissues. CRISP targets various ion channels, and weakly blocks muscle contraction evoked by potassium ions, similar to the weak toxicity exhibited by other snake venom cysteine-rich proteins [48, 49]. Despite considerable previous research effort, the detailed roles of *N. atra* PLA₂, SVMP, and CRISP in clinical sequelae among snakebite victims remains unclear and should be further elucidated.

Antivenom for snakebite treatment, produced using horses, has been available in Taiwan since the 1920s [37]. Our ELISA results showed that the horse bivalent antivenom, FNAV, has the ability to recognize all five major components of *N. atra* venom (Fig 3B). Cobra venom exhibits high immunogenicity in a horse model, despite co-immunization with *B. multicinctus* venom. Here, we found that FNAV was able to neutralize cobra venom lethality in a mouse model with high potency, but lacked the ability to prevent CTX-induced necrosis. It is unclear why CTX-recognizing antivenom is unable to neutralize CTX toxicity. One possible explanation is that FNAV-recognized epitopes are not the toxicity-related domains on CTXs, resulting in a lack of neutralization ability toward CTXs. Another possibility is that CTX is a low molecular weight protein (<10 kDa) exhibiting lower immunogenicity than other high molecular weight venom components [15, 50]. Immunization of crude cobra venom to prepare FNAV may cause the CTX-neutralizing antibodies are less than expected.

Currently, the suggested dosage of FNAV for treating envenomation by *N. atra* or *B. multicinctus* is based on the ability to reduce lethality in a mouse model. Our investigation suggests that the symptoms in venom-injected mice—primarily muscle weakness and respiratory paralysis—are attributable to NTX, whereas the major venom component, CTX, does not cause death when subcutaneously injected into mice. This indicates that NTX may be the major toxin in *N. atra* venom that contributes to rodent death. However, unlike observations in mice, cobra envenomation does not lead to life-threatening neurotoxicity in the clinic; instead, local necrosis—a hallmark of cobra snakebite—is usually the main symptom. Whether FNAV can neutralize CTXs and prevent the development of local necrosis was previously unclear. The results of the present study show that FNAV is not able to prevent the extension of local necrosis induced by CTX from *N. atra* venom (Fig 5). This raises critical issues about the efficacy tests used during antivenom production prior to submitting the antivenom for clinical use. Indeed, the rodent lethality-prevention assay is the WHO-recommended standard for testing the efficacy of snake antivenom before a production run is released [7]. However, snake venoms induce a variety of systemic pathological effects, including hemorrhage, pro-coagulopathy, anti-coagulopathy, neurotoxicity, myotoxicity and necrosis, among others. Moreover, not all pathologies are related to lethality. Sometimes, the antivenom has the ability to neutralize the lethal effects of a snake venom, but is unable to prevent or eliminate its most clinically relevant pathophysiological effects. Our study provides a good case in point, showing that FNAV did not prevent necrosis, a specific pathogenic feature induced by *N. atra* venom, despite being able to neutralize venom-induced lethality in a mouse model. Thus, supplementary assays to determine

antivenom neutralization of specific venom-induced pathologies may be necessary for quality control of antivenom production.

Most cases of cobra envenoming will develop local necrosis [24, 51, 52]. Although this pathological effect is not life threatening, it usually leads to an irreversible outcome for snakebite victims. Once the local necrosis occurs, patients will require debridement, fasciotomy, or even amputation. These surgeries permanently impact a patient's life, and may further detrimentally affect a family if the victim is the primary source of income. Thus, although necrosis may not cause lethality, its consequences are far from trivial. Therefore, whether an antivenom is effective in protecting against the occurrence of local necrosis is a critical issue for countries where cobra snakebite is a constant threat. In the manufacture of antivenom for cobra envenoming, not only for *N. atra*, but also for other *Naja* species, we strongly recommend that manufacturers perform MND₅₀ assays to determine whether a particular batch of antivenom is able to eliminate local necrosis or prevent expansion of the local necrosis—the most clinically relevant pathological effect induced by cobra venoms—before antivenoms are submitted to clinical use.

Given our finding that FNAV is, at best, only partially effective in controlling the local necrotic damage induced by *N. atra* venom, it is important to develop novel therapeutic interventions for treating *N. atra* envenomation in Taiwan. Several advanced biotechnological tools have recently been adopted for developing alternative strategies for antivenom production [53, 54]. Applying expertise in synthetic biology, antibody research and immunology, a number of researchers have attempted to develop recombinant antivenoms and investigate their ability to neutralize toxins from snake venom [55–59]. Recombinant antivenoms containing several monoclonal antibodies or single-chain variable fragments (scFv) that target CTXs may be a promising source material for solving the problem of *N. atra*-induced local tissue damage. A previous study reported a situation similar to our case [56], showing that the currently used equine polyvalent antivenom exhibited a limited ability to neutralize dendrotoxin-mediated neurotoxicity. In this case, the researchers developed a cocktail of a few humanized monoclonal antibodies against this neurotoxin. We could follow these authors' strategy to screen for anti-CTX monoclonal antibodies that are capable of preventing venom-induced local necrosis extension. These anti-CTXs monoclonal antibodies could then be combined with current FNAV to serve as a novel recombinant antivenom for treatment of cobra envenomation in Taiwan. This recombinant antivenom would not only conserve the original potential of FNAV to neutralize cobra-induced lethality, it would also have the additional ability to prevent the occurrence of local tissue necrosis. In addition, a novel hydrogel nanoparticle that inhibits *Naja nigricollis* venom-induced dermo-necrosis *in vivo* has been reported [60]. These engineered nanoparticles bind to PLA₂ and three-finger toxins from *Elapidae* snakes and sequester them, preventing them from interacting with their membrane targets and thereby inhibiting their biological activities. This specific therapeutic application demonstrates the potential for inhibiting the cytotoxicity and dermo-necrosis ability of African spitting cobra venom in cells and animal models. It may be an alternative to solve the problem of local necrosis induced by cobra envenomation in Taiwan.

Whether FNAV has the potential to prevent local necrosis extension induced by *N. atra* venom has been debated for more than a decade in Taiwan [9, 11–14]. Following the standard protocol described previously [61, 62] has failed to yield a mouse model of *N. atra* venom-induced necrosis for investigating the neutralization potential of FNAV *in vivo*. Venom-injected mice would die due to neurotoxicity before necrotic lesions developed. In the present study, we used RP-HPLC to purify CTXs—the necrosis-related toxins—to successfully develop a local necrosis mouse model. This resulting model is a good tool for evaluating the necrosis-neutralizing ability of antivenom, or other potential drugs, toward *N. atra* venom *in vivo*.

Despite having developed a necrotic animal model and used it to assess the ability of FNAV to neutralize cobra venom-induced necrosis, there are three limitations to our work. First, our

strategy ignored direct or synergistic contributions of other cobra venom proteins to the pathogenesis of necrosis. As noted above, PLA₂ proteins in *N. atra* venom may have synergistic effects that promote local necrotic damage [44, 45, 63]. Furthermore, clinical effects of other proteins in *N. atra* venom, such as CRISP and SVMP, are unclear, and may be involved in the pathogenesis of necrosis. Whether these proteins contribute to necrosis or other specific physiological processes associated with clinical symptoms should be further evaluated. Second, our results demonstrated that FNAV has limited potential for preventing the occurrence of local necrosis. Although three batches of FNAV were evaluated in our study, we should further evaluate additional batches or antiserum from different horses, to verify our findings. Finally, although pre-incubation of venom and antivenom before delivery to animal models is the WHO-recommended procedure for evaluating neutralization efficacy, these necrosis neutralization assays do not completely recapitulate the real circumstance of cobra snakebite. Accordingly, these experiments neglected to take into account the influence of the toxicokinetics of venoms and the pharmacokinetics of antivenom. Efficacy tests should be further investigated under conditions in which antivenom is administered in mice after injection of venom so as to more accurately mimic the actual circumstances of snakebite.

Taken together, the data provided here show that isolated CTXs, the major necrosis-related proteins in *N. atra* venom, were able to produce dermo-necrosis in rodent models, but did not induce lethality, even at high doses. FNAV, the conventional antivenom for *N. atra* treatment in Taiwan, was highly potent in neutralizing the lethality of whole cobra venom; however, it was unable to prevent CTX-induced necrosis *in vivo*. Moreover, dermo-necrosis was still observed in mice following subcutaneous injection of a high dose of cobra venom mixed with FNAV, which imitated the clinical circumstance of cobra envenoming in Taiwan. This finding provides insights that should help improve current antivenoms and advance cobra envenoming management in Taiwan. In addition, our case provides an example in which supplementary quality control assays may be necessary to determine the effectiveness of antivenoms in neutralizing specific pathologies induced by the venom; evaluating only the ability to prevent rodent lethality is insufficient. Thus, characterizing and including supplementary quality control assays is encouraged in antivenom production worldwide, focusing on specific pathologies of snake envenoming.

Supporting information

S1 Table. Identification of major protein fractions in *N. atra* venom.
(XLSX)

S1 Fig. Microscopic images of hemorrhagic spots in the dorsal skin. H&E-stained sections of dorsal skin of mice injected with (A) saline solution or (B) CTXs were observed under a light microscope. Images correspond to an area near hemorrhagic spots. Scale bar: 100 μm.
(TIF)

S2 Fig. Immunorecognition of *N. atra* venom by two different batches of FNAV. SDS-PAGE was performed to separate *N. atra* venom. After transferring *N. atra* venom proteins onto PVDF membranes, each lane was probed with FNAV batches FN1302 and FN1303.
(TIF)

S3 Fig. Necrotic lesions in mice induced by whole *N. atra* venom in the presence of FNAV. Different amounts of *N. atra* venom were mixed with a fixed volume (40 μl) of FNAV. Each mixture was administered into mice, and necrotic lesions in mouse dorsal skin were measured and recorded 72 hours after injection.
(TIF)

Acknowledgments

We would like to thank Dr. Kun-Yi Chien from the Chang Gung University Proteomics Core Laboratory for the excellent assistance with the LC-MS analysis of snake venom proteome presented in this investigation.

Author Contributions

Conceptualization: Chien-Chun Liu, Yu-Shao Chou, Guo-Jen Huang, Jau-Song Yu, Cheng-Hsien Hsieh, Chun-Kuei Chen.

Data curation: Chien-Chun Liu, Jau-Song Yu.

Formal analysis: Chien-Chun Liu, Chun-Yu Chen, Geng-Wang Liaw.

Funding acquisition: Jau-Song Yu, Cho-Ju Wu, Cheng-Hsien Hsieh, Chun-Kuei Chen.

Investigation: Chien-Chun Liu, Chun-Yu Chen, Kuei-Lin Liu, Guo-Jen Huang.

Methodology: Chien-Chun Liu, Guo-Jen Huang.

Project administration: Chien-Chun Liu, Yu-Shao Chou, Jau-Song Yu, Cheng-Hsien Hsieh, Chun-Kuei Chen.

Software: Geng-Wang Liaw.

Supervision: Yu-Shao Chou, Jau-Song Yu.

Validation: Yu-Shao Chou, Jau-Song Yu, Cheng-Hsien Hsieh, Chun-Kuei Chen.

Visualization: Chien-Chun Liu.

Writing – original draft: Chien-Chun Liu, Cheng-Hsien Hsieh.

Writing – review & editing: Jau-Song Yu, Chun-Kuei Chen.

References

1. Harrison RA, Hargreaves A, Wagstaff SC, Faragher B, Laloo DG. Snake envenoming: a disease of poverty. *PLoS Negl Trop Dis*. 2009; 3(12):e569. Epub 2009/12/23. <https://doi.org/10.1371/journal.pntd.0000569> PMID: 20027216
2. Gutierrez JM, Calvete JJ, Habib AG, Harrison RA, Williams DJ, Warrell DA. Snakebite envenoming. *Nat Rev Dis Primers*. 2017; 3:17063. Epub 2017/09/15. <https://doi.org/10.1038/nrdp.2017.63> PMID: 28905944
3. Kasturiratne A, Wickremasinghe AR, de Silva N, Gunawardena NK, Pathmeswaran A, Premaratna R, et al. The global burden of snakebite: a literature analysis and modelling based on regional estimates of envenoming and deaths. *PLoS Med*. 2008; 5(11):e218. Epub 2008/11/07. <https://doi.org/10.1371/journal.pmed.0050218> PMID: 18986210
4. Longbottom J, Shearer FM, Devine M, Alcoba G, Chappuis F, Weiss DJ, et al. Vulnerability to snakebite envenoming: a global mapping of hotspots. *Lancet*. 2018; 392(10148):673–84. Epub 2018/07/19. [https://doi.org/10.1016/S0140-6736\(18\)31224-8](https://doi.org/10.1016/S0140-6736(18)31224-8) PMID: 30017551
5. Liao MY, Huang RJ. Toxoids and antivenoms of venomous snakes in Taiwan. *J Toxicol-Toxin Rev*. 1997; 16(3):163–75.
6. Hung DZ. Taiwan's venomous snakebite: epidemiological, evolution and geographic differences. *Trans R Soc Trop Med Hyg*. 2004; 98(2):96–101. Epub 2004/02/18. [https://doi.org/10.1016/s0035-9203\(03\)00013-0](https://doi.org/10.1016/s0035-9203(03)00013-0) PMID: 14964809
7. Cichutek K, Epstein J, Griffiths E, Hindawi S, Jivapaisarnpong T, Klein H, et al. WHO Expert Committee on Biological Standardization Sixty-seventh report. *Who Tech Rep Ser*. 2017; 1004:1–591.
8. Chang KP, Lai CS, Lin SD. Management of poisonous snake bites in southern Taiwan. *Kaohsiung J Med Sci*. 2007; 23(10):511–8. Epub 2007/12/07. [https://doi.org/10.1016/S1607-551X\(08\)70009-3](https://doi.org/10.1016/S1607-551X(08)70009-3) PMID: 18055297

9. Chieh-Fan C, Tzeng-Jih L, Wen-Chi H, Hua-Wei Y. Appropriate Antivenom Doses for Six Types of Envenomations Caused by Snakes in Taiwan. *J Venom Anim Toxins*. 2009; 15(3):479–90.
10. Alirol E, Sharma SK, Bawaskar HS, Kuch U, Chappuis F. Snake bite in South Asia: a review. *PLoS Negl Trop Dis*. 2010; 4(1):e603. Epub 2010/02/04. <https://doi.org/10.1371/journal.pntd.0000603> PMID: 20126271
11. Mao YC, Liu PY, Chiang LC, Lai CS, Lai KL, Ho CH, et al. *Naja atra* snakebite in Taiwan. *Clin Toxicol (Phila)*. 2018; 56(4):273–80. Epub 2017/08/24.
12. Hung DZ, Liao MY, Lin-Shiau SY. The clinical significance of venom detection in patients of cobra snakebite. *Toxicon*. 2003; 41(4):409–15. Epub 2003/03/27. [https://doi.org/10.1016/s0041-0101\(02\)00336-7](https://doi.org/10.1016/s0041-0101(02)00336-7) PMID: 12657310
13. Lin CC, Chaou CH, Tseng CY. An investigation of snakebite antivenom usage in Taiwan. *J Formos Med Assoc*. 2016; 115(8):672–7. Epub 2015/08/08. <https://doi.org/10.1016/j.jfma.2015.07.006> PMID: 26250942
14. Su HY, Wang MJ, Li YH, Tang CN, Tsai MJ. Can surgical need in patients with *Naja atra* (Taiwan or Chinese cobra) envenomation be predicted in the emergency department? *Hong Kong Med J*. 2016; 22(5):435–44. <https://doi.org/10.12809/hkmj154739> PMID: 27516567
15. Huang HW, Liu BS, Chien KY, Chiang LC, Huang SY, Sung WC, et al. Cobra venom proteome and glycome determined from individual snakes of *Naja atra* reveal medically important dynamic range and systematic geographic variation. *J Proteomics*. 2015; 128:92–104. Epub 2015/07/22. <https://doi.org/10.1016/j.jprot.2015.07.015> PMID: 26196238
16. Standker L, Harvey AL, Furst S, Mathes I, Forssmann WG, Escalona de Motta G, et al. Improved method for the isolation, characterization and examination of neuromuscular and toxic properties of selected polypeptide fractions from the crude venom of the Taiwan cobra *Naja naja atra*. *Toxicon*. 2012; 60(4):623–31. Epub 2012/06/09. <https://doi.org/10.1016/j.toxicon.2012.05.013> PMID: 22677803
17. Braganca BM, Patel NT, Badrinath PG. Isolation and properties of a cobra venom factor selectively cytotoxic to Yoshida sarcoma cells. *Biochim Biophys Acta*. 1967; 136(3):508–20. Epub 1967/04/25. [https://doi.org/10.1016/0304-4165\(67\)90009-8](https://doi.org/10.1016/0304-4165(67)90009-8) PMID: 6066619
18. Lai MK, Wen CY, Lee CY. Local lesions caused by cardiotoxin isolated from Formosan cobra venom. *Taiwan Yi Xue Hui Za Zhi*. 1972; 71(6):328–32. Epub 1972/06/28. PMID: 4512908
19. Liu CC, You CH, Wang PJ, Yu JS, Huang GJ, Liu CH, et al. Analysis of the efficacy of Taiwanese freeze-dried neurotoxic antivenom against *Naja kaouthia*, *Naja siamensis* and *Ophiophagus hannah* through proteomics and animal model approaches. *PLoS Negl Trop Dis*. 2017; 11(12):e0006138. Epub 2017/12/16. <https://doi.org/10.1371/journal.pntd.0006138> PMID: 29244815
20. Chen PC, Huang MN, Chang JF, Liu CC, Chen CK, Hsieh CH. Snake venom proteome and immunoprofiling of the hundred-pace viper, *Deinagkistrodon acutus*, in Taiwan. *Acta Trop*. 2018. Epub 2018/10/01.
21. Wu CC, Hsu CW, Chen CD, Yu CJ, Chang KP, Tai DI, et al. Candidate serological biomarkers for cancer identified from the secretomes of 23 cancer cell lines and the human protein atlas. *Mol Cell Proteomics*. 2010; 9(6):1100–17. Epub 2010/02/04. <https://doi.org/10.1074/mcp.M900398-MCP200> PMID: 20124221
22. Howard-Jones N. A CIOMS ethical code for animal experimentation. *WHO Chron*. 1985; 39(2):51–6. PMID: 4090462
23. Finney DJ. Probit analysis: a statistical treatment of the sigmoid response curve. 2d ed. Cambridge Eng.: University Press; 1952. xiv, 318 p. p.
24. Petras D, Sanz L, Segura A, Herrera M, Villalta M, Solano D, et al. Snake venomomics of African spitting cobras: toxin composition and assessment of congeneric cross-reactivity of the pan-African EchiTAb-Plus-ICP antivenom by antivenomics and neutralization approaches. *J Proteome Res*. 2011; 10(3):1266–80. Epub 2010/12/22. <https://doi.org/10.1021/pr101040f> PMID: 21171584
25. Morais V, Ifran S, Berasain P, Massaldi H. Antivenoms: potency or median effective dose, which to use? *J Venom Anim Toxins*. 2010; 16(2):191–3.
26. Araujo HP, Bourguignon SC, Boller MA, Dias AA, Lucas EP, Santos IC, et al. Potency evaluation of antivenoms in Brazil: the national control laboratory experience between 2000 and 2006. *Toxicon*. 2008; 51(4):502–14. Epub 2007/12/25. <https://doi.org/10.1016/j.toxicon.2007.11.002> PMID: 18155119
27. Gasanov SE, Dagda RK, Rael ED. Snake Venom Cytotoxins, Phospholipase A2s, and Zn(2+)-dependent Metalloproteinases: Mechanisms of Action and Pharmacological Relevance. *J Clin Toxicol*. 2014; 4(1):1000181. Epub 2014/06/21. <https://doi.org/10.4172/2161-0495.1000181> PMID: 24949227
28. Bhaskaran R, Huang CC, Chang DK, Yu C. Cardiotoxin III from the Taiwan cobra (*Naja naja atra*). Determination of structure in solution and comparison with short neurotoxins. *J Mol Biol*. 1994; 235(4):1291–301. Epub 1994/01/28. <https://doi.org/10.1006/jmbi.1994.1082> PMID: 8308891

29. Gasanov SE, Kamaev FG, Salakhutdinov BA, Aripov TF. [The fusogenic properties of the cytotoxins of cobra venom in a model membrane system]. Nauchnye Doki Vyssh Shkoly Biol Nauki. 1990;(2):42–50. Epub 1990/01/01. PMID: [2162221](#)
30. Dubovskii PV, Konshina AG, Efremov RG. Cobra cardiotoxins: membrane interactions and pharmacological potential. Curr Med Chem. 2014; 21(3):270–87. Epub 2013/11/05. <https://doi.org/10.2174/09298673113206660315> PMID: [24180277](#)
31. Konshina AG, Boldyrev IA, Utkin YN, Omel'kov AV, Efremov RG. Snake cytotoxins bind to membranes via interactions with phosphatidylserine head groups of lipids. PLoS One. 2011; 6(4):e19064. Epub 2011/05/12. <https://doi.org/10.1371/journal.pone.0019064> PMID: [21559494](#)
32. Tjong SC, Wu PL, Wang CM, Huang WN, Ho NL, Wu WG. Role of glycosphingolipid conformational change in membrane pore forming activity of cobra cardiotoxin. Biochemistry. 2007; 46(43):12111–23. Epub 2007/10/09. <https://doi.org/10.1021/bi700871x> PMID: [17918958](#)
33. Forouhar F, Huang WN, Liu JH, Chien KY, Wu WG, Hsiao CD. Structural basis of membrane-induced cardiotoxin A3 oligomerization. J Biol Chem. 2003; 278(24):21980–8. Epub 2003/03/28. <https://doi.org/10.1074/jbc.M208650200> PMID: [12660250](#)
34. Feofanov AV, Sharonov GV, Astapova MV, Rodionov DI, Utkin YN, Arseniev AS. Cancer cell injury by cytotoxins from cobra venom is mediated through lysosomal damage. Biochem J. 2005; 390:11–8. <https://doi.org/10.1042/BJ20041892> PMID: [15847607](#)
35. Gasanov SE, Aripov TF, Salakhutdinov BA. [Intermembrane exchange of lipids induced by cobra venom cytotoxins]. Biofizika. 1990; 35(6):958–62. Epub 1990/11/01. PMID: [1965687](#)
36. Ebrahim K, Shirazi FH, Mirakabadi AZ, Vatanpour H. Cobra venom cytotoxins; apoptotic or necrotic agents? Toxicon. 2015; 108:134–40. Epub 2015/10/21. <https://doi.org/10.1016/j.toxicon.2015.09.017> PMID: [26482932](#)
37. YC M, DZ H. Management of Snake Envenomation in Taiwan. In: Gopalakrishnakone P., Faiz A., Fernando R., Gnanathasan C., Habib A., Yang CC. (eds) Clinical Toxinology in Asia Pacific and Africa. Toxinology. 2015; vol 2. Springer.
38. Tseng LF, Chiu TH, Lee CY. Absorption and distribution of 131I-labeled cobra venom and its purified toxins. Toxicol Appl Pharmacol. 1968; 12(3):526–35.
39. Chang CC, Chuang ST, Lee CY, Wei JW. Role of cardiotoxin and phospholipase A in the blockade of nerve conduction and depolarization of skeletal muscle induced by cobra venom. Br J Pharmacol. 1972; 44(4):752–64. Epub 1972/04/01. <https://doi.org/10.1111/j.1476-5381.1972.tb07313.x> PMID: [5041453](#)
40. Chang CC, Lee CY. Electrophysiological study of neuromuscular blocking action of cobra neurotoxin. Br J Pharmacol Chemother. 1966; 28(2):172–81. Epub 1966/11/01. <https://doi.org/10.1111/j.1476-5381.1966.tb01883.x> PMID: [5972624](#)
41. Ranawaka UK, Laloo DG, de Silva HJ. Neurotoxicity in snakebite—the limits of our knowledge. PLoS Negl Trop Dis. 2013; 7(10):e2302. Epub 2013/10/17. <https://doi.org/10.1371/journal.pntd.0002302> PMID: [24130909](#)
42. Yu J, Zhu X, Zhang L, Kudryavtsev D, Kasheverov I, Lei Y, et al. Species specificity of rat and human alpha7 nicotinic acetylcholine receptors towards different classes of peptide and protein antagonists. Neuropharmacology. 2018; 139:226–37. Epub 2018/07/22. <https://doi.org/10.1016/j.neuropharm.2018.07.019> PMID: [30025921](#)
43. Silva A, Cristofori-Armstrong B, Rash LD, Hodgson WC, Isbister GK. Defining the role of post-synaptic alpha-neurotoxins in paralysis due to snake envenoming in humans. Cell Mol Life Sci. 2018; 75(23):4465–78. Epub 2018/08/03. <https://doi.org/10.1007/s00018-018-2893-x> PMID: [30069700](#)
44. Sumandea M, Das S, Sumandea C, Cho W. Roles of aromatic residues in high interfacial activity of *Naja naja atra* phospholipase A2. Biochemistry. 1999; 38(49):16290–7. Epub 1999/12/10. <https://doi.org/10.1021/bi9921384> PMID: [10587453](#)
45. Gasanov SE, Alsarraj MA, Gasanov NE, Rael ED. Cobra venom cytotoxin free of phospholipase A2 and its effect on model membranes and T leukemia cells. J Membr Biol. 1997; 155(2):133–42. Epub 1997/01/15. <https://doi.org/10.1007/s002329900165> PMID: [9049107](#)
46. Sun QY, Bao J. Purification, cloning and characterization of a metalloproteinase from *Naja atra* venom. Toxicon. 2010; 56(8):1459–69. Epub 2010/09/15. <https://doi.org/10.1016/j.toxicon.2010.08.013> PMID: [20837040](#)
47. Wei JF, Mo YZ, Qiao LY, Wei XL, Chen HQ, Xie H, et al. Potent histamine-releasing activity of atraha-gin, a novel snake venom metalloproteinase. Int J Biochem Cell Biol. 2006; 38(4):510–20. Epub 2005/11/29. <https://doi.org/10.1016/j.biocel.2005.10.011> PMID: [16310401](#)
48. Chang LS, Liou JC, Lin SR, Cheng YC. Purification and characterization of Taiwan cobra venom proteins with weak toxicity. Toxicon. 2005; 45(1):21–5. Epub 2004/12/08. <https://doi.org/10.1016/j.toxicon.2004.09.002> PMID: [15581679](#)

49. Wang F, Li H, Liu MN, Song H, Han HM, Wang QL, et al. Structural and functional analysis of natrin, a venom protein that targets various ion channels. *Biochem Biophys Res Commun*. 2006; 351(2):443–8. Epub 2006/10/31. <https://doi.org/10.1016/j.bbrc.2006.10.067> PMID: 17070778
50. Calvete JJ, Sanz L, Angulo Y, Lomonte B, Gutierrez JM. Venoms, venomics, antivenomics. *FEBS Lett*. 2009; 583(11):1736–43. Epub 2009/03/24. <https://doi.org/10.1016/j.febslet.2009.03.029> PMID: 19303875
51. Faiz MA, Ahsan MF, Ghose A, Rahman MR, Amin R, Hossain M, et al. Bites by the Monocled Cobra, *Naja kaouthia*, in Chittagong Division, Bangladesh: Epidemiology, Clinical Features of Envenoming and Management of 70 Identified Cases. *Am J Trop Med Hyg*. 2017; 96(4):876–84. Epub 2017/02/01. <https://doi.org/10.4269/ajtmh.16-0842> PMID: 28138054
52. Kularatne SA, Budagoda BD, Gawarammana IB, Kularatne WK. Epidemiology, clinical profile and management issues of cobra (*Naja naja*) bites in Sri Lanka: first authenticated case series. *Trans R Soc Trop Med Hyg*. 2009; 103(9):924–30. Epub 2009/05/15. <https://doi.org/10.1016/j.trstmh.2009.04.002> PMID: 19439335
53. Laustsen AH, Maria Gutierrez J, Knudsen C, Johansen KH, Bermudez-Mendez E, Cerni FA, et al. Pros and cons of different therapeutic antibody formats for recombinant antivenom development. *Toxicon*. 2018; 146:151–75. Epub 2018/03/15. <https://doi.org/10.1016/j.toxicon.2018.03.004> PMID: 29534892
54. Bermudez-Mendez E, Fuglsang-Madsen A, Fons S, Lomonte B, Gutierrez JM, Laustsen AH. Innovative Immunization Strategies for Antivenom Development. *Toxins (Basel)*. 2018; 10(11). Epub 2018/11/08.
55. Lee CH, Leu SJ, Lee YC, Liu CI, Lin LT, Mwale PF, et al. Characterization of Chicken-Derived Single Chain Antibody Fragments against Venom of *Naja Naja Atra*. *Toxins (Basel)*. 2018; 10(10). Epub 2018/09/27.
56. Laustsen AH, Karatt-Vellatt A, Masters EW, Arias AS, Pus U, Knudsen C, et al. In vivo neutralization of dendrotoxin-mediated neurotoxicity of black mamba venom by oligoclonal human IgG antibodies. *Nat Commun*. 2018; 9(1):3928. Epub 2018/10/04. <https://doi.org/10.1038/s41467-018-06086-4> PMID: 30279409
57. Julve Parreno JM, Huet E, Fernandez-Del-Carmen A, Segura A, Venturi M, Gandia A, et al. A synthetic biology approach for consistent production of plant-made recombinant polyclonal antibodies against snake venom toxins. *Plant Biotechnol J*. 2018; 16(3):727–36. Epub 2017/08/30. <https://doi.org/10.1111/pbi.12823> PMID: 28850773
58. Schneider FS, Nguyen DL, Castro KL, Cobo S, Machado de Avila RA, Ferreira Nde A, et al. Use of a synthetic biosensor for neutralizing activity-biased selection of monoclonal antibodies against atroxlysin-I, an hemorrhagic metalloproteinase from *Bothrops atrox* snake venom. *PLoS Negl Trop Dis*. 2014; 8(4):e2826. Epub 2014/04/26. <https://doi.org/10.1371/journal.pntd.0002826> PMID: 24762927
59. Riano-Umbarila L, Ledezma-Candanoza LM, Serrano-Posada H, Fernandez-Taboada G, Olamendi-Portugal T, Rojas-Trejo S, et al. Optimal Neutralization of *Centruroides noxius* Venom Is Understood through a Structural Complex between Two Antibody Fragments and the Cn2 Toxin. *J Biol Chem*. 2016; 291(4):1619–30. Epub 2015/11/22. <https://doi.org/10.1074/jbc.M115.685297> PMID: 26589800
60. O'Brien J, Lee SH, Gutierrez JM, Shea KJ. Engineered nanoparticles bind elapid snake venom toxins and inhibit venom-induced dermonecrosis. *PLoS Negl Trop Dis*. 2018; 12(10):e0006736. Epub 2018/10/05. <https://doi.org/10.1371/journal.pntd.0006736> PMID: 30286075
61. Gutierrez JM, Solano G, Pla D, Herrera M, Segura A, Vargas M, et al. Preclinical Evaluation of the Efficacy of Antivenoms for Snakebite Envenoming: State-of-the-Art and Challenges Ahead. *Toxins (Basel)*. 2017; 9(5). Epub 2017/05/16.
62. Gutierrez JM, Rojas E, Quesada L, Leon G, Nunez J, Laing GD, et al. Pan-African polyspecific anti-venom produced by caprylic acid purification of horse IgG: an alternative to the antivenom crisis in Africa. *Trans R Soc Trop Med Hyg*. 2005; 99(6):468–75. Epub 2005/04/20. <https://doi.org/10.1016/j.trstmh.2004.09.014> PMID: 15837359
63. Kang TS, Georgieva D, Genov N, Murakami MT, Sinha M, Kumar RP, et al. Enzymatic toxins from snake venom: structural characterization and mechanism of catalysis. *FEBS J*. 2011; 278(23):4544–76. Epub 2011/04/08. <https://doi.org/10.1111/j.1742-4658.2011.08115.x> PMID: 21470368

Inhalable Lactoferrin/Chondroitin-Functionalized Monoolein Nanocomposites for Localized Lung Cancer Targeting

Hadeer M. Abdelaziz, Ahmed O. Elzoghby,* Maged W. Helmy, Elsayeda-Zeinab A. Abdelfattah, Jia-You Fang, Magda W. Samaha, and May S. Freag*



Cite This: *ACS Biomater. Sci. Eng.* 2020, 6, 1030–1042



Read Online

ACCESS |



Metrics & More



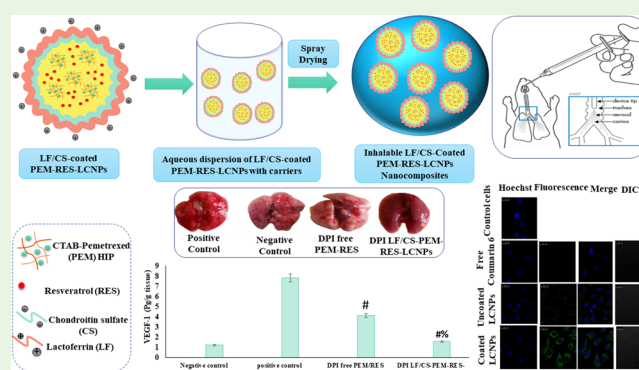
Article Recommendations



Supporting Information

ABSTRACT: Localized drug delivery to lung cancer can overcome the limitations of systemic nanocarriers including low drug amounts reaching lung tissues and severe off-target toxicity. The current work presented novel inhalable nanocomposites as noninvasive platforms for lung cancer therapy. Nanoparticulate liquid crystals (LCNPs) based on monoolein were developed for synergistic co-encapsulation of the cytotoxic chemotherapeutic drug, pemetrexed, and the phytoherbal drug, resveratrol (PEM-RES-LCNPs). For active tumor targeting, lactoferrin (LF) and chondroitin sulfate (CS), natural polymers with intrinsic tumor-targeting capabilities, were exploited to functionalize the surface of LCNPs using a layer-by-layer (LbL) self-assembly approach. To maximize their deep lung deposition, LF/CS-coated PEM-RES-LCNPs were then microencapsulated within various carriers to obtain inhalable nanocomposites via spray-drying techniques. The inhalable dry powder nanocomposites prepared using a mannitol–inulin–leucine (1:1:1 wt) mixture displayed superior in vitro aerosolization performance ($2.72\ \mu\text{m}$ of MMAD and 61.6% FPF), which ensured deep lung deposition. In lung cancer-bearing mice using urethane as a chemical carcinogen, the inhalable LF/CS-coated PEM-RES-LCNP nanocomposites showed superior antitumor activity as revealed by a considerable decrease of the average lung weight, reduced number and diameter of cancerous lung foci, decreased expression of VEGF-1, and increased expression of active caspase-3 as well as reduced Ki-67 expression compared to the spray-dried free PEM/RES powder mixture and positive control. Moreover, the in vivo fluorescence imaging confirmed successful lung deposition of the inhalable nanocomposites. Conclusively, the inhalable liquid crystalline nanocomposites elaborated in the current work could open new avenues for noninvasive lung cancer treatment.

KEYWORDS: inhalable nanocomposites, chondroitin, lactoferrin, layer-by-layer (LbL) coating, nanoparticulate liquid crystals, lung cancer



1. INTRODUCTION

Lung cancer is considered one of the major mortality etiologic factors all over the world.¹ In advanced stages of lung cancer, the conventional chemotherapeutic cytotoxic drugs are given as first line therapy. However, the nonspecific systemic delivery of chemotherapeutics limits their satisfactory results due to extensive dilution by the large blood volume resulting in low amounts of drug reaching the lung tissues as well as off-target toxicity.² Anticancer drug nanoparticles passively accumulate in tumor tissues after intravenous injection via extravasation through the leaky tumor vasculature. However, human tumors much differ from murine ones in the rate of growth, heterogeneity of tumor endothelial fenestrations, and extent of blood flow through tissues.^{3,4} Therefore, while the enhanced permeability and retention phenomenon was proven to be effective in animals, its success in humans is still doubtful.

On another avenue, localized administration of tumor therapeutics to lung tumor tissues does not need EPR effects.

Thus, localized delivery of drug-loaded nanocarriers to lung cancer via inhalation can bypass the hurdles of EPR-based nanomedicine in systemic lung cancer therapy.^{4,5} Moreover, localized delivery of conventional anticancer agents via inhalation could be a potential noninvasive substitute overcoming the drawbacks associated with systemic delivery.⁵ Compared to liquid aerosol nebulizers, the inhaled dry powders represent a more suitable method for administration of poorly soluble chemotherapeutics and provide long-term stability.⁶ Inhalable nanocarriers represent a promising approach as they can avoid natural barriers of the lungs such

Received: October 28, 2019

Accepted: January 21, 2020

Published: January 21, 2020



ACS Publications

© 2020 American Chemical Society

1030

<https://dx.doi.org/10.1021/acsbiomaterials.9b01639>
ACS Biomater. Sci. Eng. 2020, 6, 1030–1042

970

as alveolar macrophages, mucociliary clearance, and enzymatic degradation in addition to their efficient accumulation in the lung tissues utilizing both passive and active targeting mechanisms.⁷ However, the major obstacle that hinders the clinical application of inhaled nanocarriers is their nanometric diameter, which facilitates their easy exhalation before reaching the tumor site. In contrast, the use of inhalable 1–5 μm particles could enable efficient deposition in deep lung tissues although their clearance by macrophages of the alveoli still hinders their wide application. Therefore, many efforts have been directed to improve the delivery efficiency of drugs to lung tissues by combining the privileges of both micro- and nanoparticles. Among those strategies, the nanocomposites where nanocarriers are embedded in the carrier matrix of microparticles represent a promising approach.^{6,7}

In recent years, combined drug cancer therapy has become a cornerstone in oncology to avoid drug resistance and reduce the optimal drug dose and hence minimize the side effects. Pemetrexed (PEM) (Alimta) is a hydrophilic, FDA-approved anti-folate chemotherapeutic agent that is used alone or combined with other chemotherapeutic drugs as first-line therapy of lung cancer.⁸ PEM successfully damages the *de novo* biosynthesis of purine and thymidine nucleotides and inhibits three folate-dependent enzymes. However, PEM is associated with multiple adverse effects including thrombocytopenia and hepato- and nephrotoxicity that hinder its systemic administration.⁹

Recently, herbal drugs show great promise in sensitizing resistant cancerous cells and enable synergistic anticancer efficacy with cytotoxic chemotherapy.^{10,11} Resveratrol (RES) is a naturally occurring herbal drug with multiple pharmacological activities such as antioxidant, anti-inflammatory, and unique chemopreventive activity.¹² Additionally, RES inhibits the activity of the efflux P-glycoprotein pump thus increasing the concentration of co-administered chemotherapy in cancer cells.¹³ The synergistic activity between PEM and RES for lung cancer therapy was previously reported where PEM could potentiate the cytotoxic activity of RES due to its tendency to knock down the expression levels of both ERCC1 and phospho-p38 MAPK.¹⁴ However, RES's lipophilicity, instability, short half-life, and extensive metabolism hinder its wide application even at high doses.¹⁵ Therefore, it is crucial to tailor a suitable drug delivery system co-encapsulating hydrophilic PEM and lipophilic RES to combine the merits of both drugs in lung cancer treatment.

Liquid crystalline nanoparticles (LCNPs) are promising lipid-based nanocarriers, which could efficiently incorporate and deliver hydrophilic, lipophilic, and/or amphiphilic molecules. Lyotropic LCNPs are crystalline structures that can be self-assembled into nanoparticles when a polar lipid such as monoolein is dispersed in a suitable solvent, most commonly water, stabilized by a surfactant (e.g., poloxamer).¹⁶ LCNPs possess many characteristics that make them potential carriers for cancer therapy including biocompatibility, biodegradability, elevated drug loading, and controlled drug release in addition to ease of surface functionalization.¹⁷

To confer tumor-targeting capability, LbL assembly was utilized as a simple approach for surface functionalization of LCNPs.¹⁸ The LbL assembly technique involves deposition of alternate layers of oppositely charged ionizable polymers on the nanocarrier's surface.¹⁹ In the current study, chondroitin sulfate (CS) and lactoferrin (LF) were selected as oppositely charged natural biodegradable polymers.^{20,21} CS is a

polyanionic linear sulfated glycosaminoglycan that is attached to proteoglycans at the cell surface.^{22,23} Additionally, CS is considered a potential targeting ligand to cancer cells overexpressing CD44 receptors like NSCLC cells.²⁴ LF is a non-heme iron-binding cationic protein that belongs to the transferrin (Tf) family that plays an important role in anti-inflammatory, antioxidant, and anti-carcinogenic activities.²⁵ Surface decoration of NPs by LF via either carbodiimide coupling or electrostatic interactions represents a potential approach for targeting cancer cells overexpressing LF and Tf receptors (LF and Tf-Rs).^{26,27}

Based on the abovementioned information, the current research aimed to fabricate novel inhalable dry powder nanocomposites of LF/CS-coated nanoparticulate liquid crystals for combined administration of PEM and RES to lung tumor. First, to enable its encapsulation into the LCNPs, the water-soluble chemotherapeutic drug, PEM, was in situ complexed with the cationic surfactant CTAB thus increasing its hydrophobicity and hence maximizing its entrapment. Second, the phytochemical drug RES was co-entrapped together with the PEM ion pair into the lipid nanoparticles via a hydrotrope technique to increase its anticancer effect and delay the onset of drug resistance. Third, for maximal tumor targeting efficacy, CS and LF were electrostatically deposited via LbL assembly onto the surface of LCNPs. Finally, to maximize their deposition in deep lung tissues, the developed PEM/RES-loaded LCNPs were converted into stable inhalable nanocomposite powder by co-spray drying with various pulmonary carriers. The fabricated nanocomposites were thoroughly characterized *in vitro* and *in vivo*. Moreover, *in vivo* imaging was done on a chemical carcinogen-induced model of lung cancer to visualize the lung accumulation of the inhaled nanocomposites.

2. MATERIALS AND METHODS

2.1. Materials. The details of materials including drugs, chemicals, kits, and solvents are illustrated in the [Supporting Information](#).

2.2. Preparation of CTAB-Modified LCNPs for Codelivery of RES and PEM. In situ CTAB-modified PEM-RES-LCNPs were prepared via the hydrotrope method.²⁸ Briefly, 0.18 mL of ethanol was added to 200 mg of glyceryl monooleate (GMO) to obtain an isotropic mixture in which 10 mg of RES was dissolved. The isotropic mixture was added drop wise under magnetic stirring to 2 mL of 0.5% w/v aqueous solution of poloxamer 407 containing 10 mg of PEM and 34 mg of CTAB. The resultant mixture was left to equilibrate at RT for 24 h and then homogenized with another 6 mL of poloxamer 407 solution at 13,000 rpm for 3 min. The effect of various formulation parameters on the physicochemical properties of the fabricated PEM-RES-LCNPs was assessed.

2.3. Preparation of LF/CS-Coated PEM-RES-LCNPs. Layer-by-layer-coated LCNPs were prepared via an electrostatic assembly process. First, 2 mL of positively charged PEM-RES-LCNPs was titrated against anionic chondroitin sulfate (CS) solution (2.5 mg/mL) at different volumes (0.5–3 mL). The nanoparticle suspension was then incubated for 30 min under mild magnetic stirring (100 rpm). To finally obtain LF/CS-coated PEM-RES-LCNPs, a second positively charged layer was implemented by titrating varied volumes (0.5–2 mL) of lactoferrin (LF) solution (30 mg/mL) against CS-coated PEM-RES-LCNPs under magnetic stirring at 100 rpm for additional 30 min.

2.4. Physicochemical Characterization of LCNPs. The methods of assessment of the entrapment efficiency, particle hydrodynamic diameter, zeta potential, microscopical examination, and rate of drug release^{29–32} are illustrated in detail in the [Supporting Information](#).

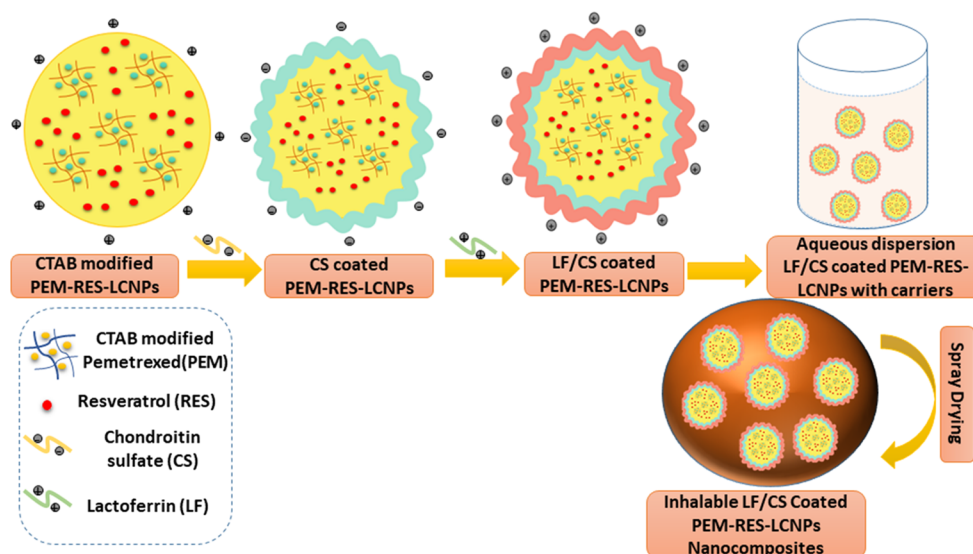


Figure 1. Schematic illustration showing the preparation steps of inhalable LF/CS-coated PEM-RES-LCNP nanocomposites.

2.5. In Vitro Anticancer Study. A methylthiazoltetrazolium (MTT) test was carried out to examine the viability of A549 lung cancer cells treated with free PEM, free RES, a mixture of free PEM/RES, blank LCNPs, PEM-RES-LCNPs (F2), and LF/CS-coated PEM-RES-LCNPs (F3). Details of the cell culture protocol and cytotoxicity evaluation method are illustrated in the [Supporting Information](#).

2.6. Cellular Internalization. An in vitro cellular internalization test was performed to investigate the influence of surface functionalization on the cellular internalization of the optimized LCNPs into A549 lung cancer cells. Details of the method are illustrated in the [Supporting Information](#).

2.7. Development of LF/CS-Coated PEM-RES-LCNP-Enriched Inhalable Dry Powder Nanocomposites. A spray-drying technique was applied to prepare inhalable nanocomposites enriched with LF/CS-coated PEM-RES-LCNPs as described previously.^{33,34} Simply, 4 mL of optimized LF/CS-coated PEM-RES-LCNPs (F3) was added to 20 mL of water containing a mannitol, inulin, and leucine mixture at a ratio of 1:3 w/w under magnetic stirring at 50 rpm to ensure proper mixing. The resultant feed suspension was subsequently spray-dried using a B-290 Mini spray-dryer (BÜCHI Labortechnik AG, Switzerland) according to a previously published protocol in additional reference illustrated in the [Supporting Information](#).

2.8. Physicochemical Characterization of Nanocomposites. The methodology of characterization of LF/CS-coated PEM-RES-LCNP nanocomposites including production yield, morphology, and solid-state characteristics and their re-dispersibility index are illustrated in the [Supporting Information](#).

2.9. In Vitro Pulmonary Drug Deposition. The in vitro aerosolization performance of inhalable LCNP nanocomposites was carried out using eight stages of the nonviable Copley Andersen cascade impactor (U.K.) according to previous protocols^{34–36} as illustrated in the [Supporting Information](#).

2.10. In Vivo Studies. **2.10.1. Animals and Induction of Tumor.** For induction of lung cancer in male BALB/c mice (3–4 weeks old, 15–20 g), a single dose of urethane (ethyl carbamate, 1 g/kg) in 0.9% saline was intraperitoneally injected. Fifteen days later, a booster dose of urethane (0.5 g/kg) was injected into the mice. The mice were housed in cages and given the balanced nutrients of chow as food and water. After 12–16 weeks, mice were euthanized using overdose of thiopental, and the excised lungs were examined histopathologically using H&E staining to assess the precancerous lesions and index of tumor incidence. The protocol of animal use is mentioned in the [Supporting Information](#).

2.10.2. In Vivo Antitumor Efficacy. The in vivo anticancer effect of the dry inhalable powder of LF/CS-coated PEM-RES-LCNPs (S4) was assessed on lung cancer mice models. The animals were grouped into four (seven mice per group). The first group of mice received spray-dried powder of a free combined PEM/RES mixture. The second group received the inhalable LF/CS-coated PEM-RES-LCNP nanocomposites (S4) using a DP-4 M dry powder insufflator (Penn Century, U.S.A.). In the current study, untreated lung cancer-bearing mice served as the positive control, while healthy mice served as the negative control group. The animals were first anesthetized via intraperitoneally injecting with ketamine (12.5 mg/kg) and xylazine (1.5 mg/kg), positioned against an angled restraining stand in a supine position to expose trachea and then given their inhalation twice weekly for three consecutive weeks.³⁷ The doses of PEM and RES in each formula were fixed at 0.342 mg/kg. All surviving mice were sacrificed on the 25th day of treatment. The excised lungs were weighed and then divided into two parts. The first part was frozen at -80°C until biological evaluation of tumor biomarkers, and the other part was fixed using 4% paraformaldehyde solution for histopathological and immunohistochemical examination.

2.10.3. Tumor Markers. ELISA was used for quantification of the expression levels of tumor markers ([Supporting Information](#)).

2.10.4. Histopathological and Immunohistochemical Analysis. Histopathological changes, number and diameters of lung cancerous foci, and the expression level of the Ki-67 protein as an index of proliferation were assessed for the excised lungs ([Supporting Information](#)).

2.10.5. In Vivo Imaging. Herein, mice with lung cancer were divided into two groups (five mice per group) and isolated in the dark for 6 h prior to imaging. The first group received spray-dried powder of free coumarin-6, and the other one was given coumarin-6-labeled inhalable LCNP nanocomposites. After anaesthetizing mice using isoflurane, the spray-dried powder of free coumarin-6 and coumarin-6-labeled inhalable LCNP nanocomposites were traced after their administration to mice via PhotonIMAGER Optima (Biospace Lab, France). The mice were imaged 4 and 24 h after dry-powder administration displaying the whole-lung regions of interest, which are located approximately 8 mm above the liver and diaphragm. The fluorescent intensities of obtained images were quantitatively analyzed via M3 vision software provided by the device.

2.11. Statistical Analysis. Details of statistical analysis of the results are included in the [Supporting Information](#).

Table 1. Composition and Physicochemical Characterization of PEM-RES-Loaded LCNPs (F2) and LF/CS-Coated PEM-RES-LCNPs (F3)^a

LCNPs	ethanol (% w/v)	P 407 (% w/v)	PEM (mg)	RES (mg)	CTAB (mg)	particle size (nm)	PDI	ζ potential (mV)	RES (% EE)	PEM (% EE)
F1	1.75	0.5	10	10		161 ± 4.36	0.22 ± 0.01	−34.34 ± 4.15	91.3 ± 1.13	69.4 ± 1.25
F2	1.75	0.5	10	10	34.7	165 ± 2.16	0.19 ± 0.01	+40.0 ± 4.42	97.5 ± 2.01	96.8 ± 2.11
F3	1.75	0.5	10	10	34.7	220 ± 2.16	0.21 ± 0.02	+11.0 ± 3.21	96.1 ± 3.49	95.6 ± 4.64

^aAll nanocarriers were fabricated using 2.5% w/v monoolein relative to the total dispersion volume.

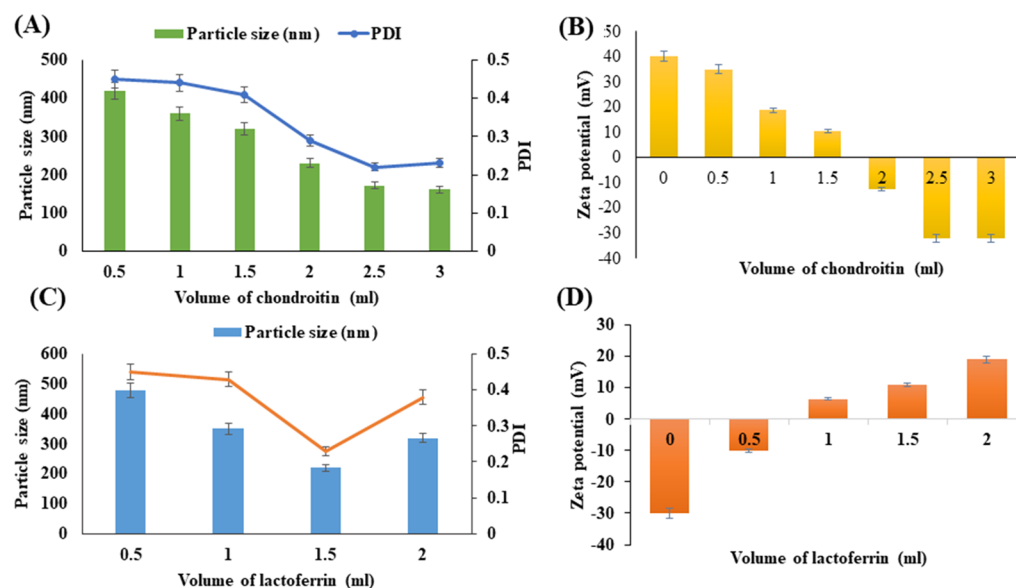


Figure 2. Layer-by-Layer (LbL) self-assembly of chondroitin sulfate (CS) and lactoferrin (LF) onto PEM-RES-LCNPs. Impact of the gradual titration of CS on optimized PEM-RES-LCNPs (F2): (A) the particle size and PDI and (B) the corresponding ζ potential. Impact of the additional deposition of LF on CS-coated PEM-RES-LCNPs: (C) the particle size and PDI and (D) the corresponding ζ potential.

3. RESULTS

3.1. Preparation and Characterization of LF/CS-Coated PEM-RES-LCNPs. The current study aimed to fabricate novel inhalable nanocomposites enriched with LF/CS-coated PEM-RES-LCNPs to target lung cancer cells that overexpress LF- and Tf-Rs. The developed LF/CS-PEM-RES-LCNPs were then co-sprayed with various carriers to finally obtain nanocomposites for effective lung deposition as illustrated in Figure 1. First, PEM-RES-loaded LCNPs were prepared using the hydrotrope method. The optimized CTAB-modified PEM-RES-LCNPs (F2; Table 1) showed a promising PS of 165 ± 2.16 nm, PDI of 0.19 ± 0.01 , ζ potential of $+40 \pm 4.42$ mV, and high EE of RES ($97\% \pm 2.01$) as well as PEM ($96\% \pm 2.11$). Upon polarizing microscopical analysis, both unloaded and PEM-RES-loaded LCNPs exhibited a dark diffraction pattern revealing the isotropic nature of the nanocarriers.³⁸ The details of optimization are plotted in the Supporting Information. The positive surface charge of LCNPs was exploited to electrostatically functionalize the surface of our formulated PEM-RES-LCNPs (F2) using a layer-by-layer self-assembly approach. Addition of the first CS layer was optimized via gradual addition of variable volumes (0.5–3 mL) of CS solution onto a fixed volume of a positively charged-LCNP formulation (2 mL). Obvious aggregations were noticed at initial additions of the CS solution (0.5–1.5 mL) confirmed via significant increases ($p < 0.05$) in both PDI and PS. However, upon a further increase in the volume of CS solution added, a homogenous dispersion was obtained, which was confirmed by reduction of the PDI value. Gradual addition

of CS was continued until a certain inflection point at which the ζ potential was shifted to a negative charge. The final two additions of CS solution (2.5 and 3 mL) showed insignificant change in the ζ-potential value, which indicated complete coverage of the LCNP surface with CS.

According to the results displayed in Figure 2A,B, 2.5 mL of CS solution (2.5 mg/mL) was selected for optimum coating of the LCNPs (2 mL), which displayed a uniform particle size of 172 nm and acceptable inflection point of surface charge from +40 to −32 mV. Assembly of the second outer layer of LF over the surface of negatively charged CS-coated LCNPs was achieved via addition of variable volumes (0.5–2 mL) of LF solution (30 mg/mL) onto a fixed volume of CS-coated LCNPs. The results indicated that the initial added volume of LF solution (0.5–1 mL) was associated with aggregations evidenced by increased PS and PDI (Figure 2C). A further increase in the volume of LF solution added resulted in adequate inflection in the ζ potential and subsequent reduction in PS. Increasing the volume of LF solution added beyond 1.5 mL led to a further increase in the ζ potential (Figure 2D); however, an unacceptable increase in both PS and PDI as well as aggregates was observed. Therefore, 1.5 mL of LF aqueous solution (30 mg/mL) was chosen as the most suitable volume required for coating of CS-coated LCNP dispersion. The optimized LF/CS-coated PEM-RES-LCNPs (F3; Table 1) displayed a hydrodynamic diameter of 220 nm and ζ potential of +11 mV with good physical stability up to six months (Table S1).

As depicted in Figure 3A,B, both uncoated and coated LCNPs displayed nonuniform spherical particles with an

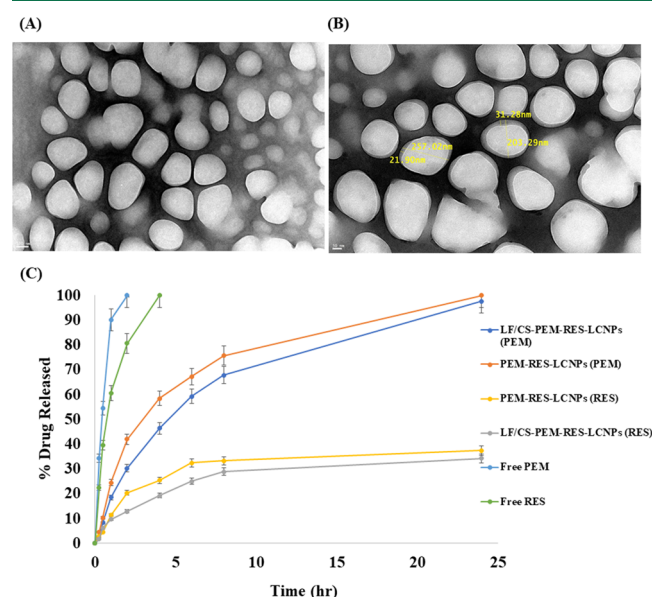


Figure 3. Transmission electron micrograph (TEM) displaying the morphology of (A) PEM-RES-LCNPs (F2) and (B) LF/CS-coated PEM-RES-LCNPs (F3). (C) In vitro release of PEM and RES from CTAB-modified PEM-RES-LCNPs (F2) and LF/CS-coated PEM-RES-LCNPs (F3) compared with free PEM and RES solution in PBS (pH 7.4) at 100 rpm and 37 °C using a dialysis-bag diffusion method.

average particle size like that obtained by DLS. LF/CS-coated PEM-RES-LCNPs (Figure 3B) revealed an outer layer surrounding the particles, which indicated successful deposition of the polymeric layers over LCNPs. In vitro release performance was investigated for free RES, free PEM, PEM-RES-LCNPs (F2), and LF/CS-coated PEM-RES-LCNPs (F3) in phosphate buffer saline (PBS, pH = 7.4). As depicted in Figure 3C, LF/CS-coated PEM-RES-LCNPs (F3) exhibited a biphasic drug release pattern with a relatively initial fast release within the first 3–4 h followed by a prolonged release behavior of both PEM and RES for up to 24 h. Meanwhile, free PEM

and RES displayed an initial burst release profile characterized by prompt and entire release after 2 and 4 h, respectively.

3.2. In Vitro Cytotoxicity and Uptake Studies. As depicted in Figure 4A,B, blank LCNPs showed excellent cell compatibility with insignificant cytotoxicity to A549 lung cancer cells (cell viability was more than 87%) after 24 and 48 h. However, free PEM and RES showed dose-dependent cytotoxicity on lung cancer cells. The combined IC_{50} of the PEM/RES mixture (4.12 $\mu\text{g/mL}$) confirmed the synergistic activity between both drugs with higher inhibitory effects than those of either free PEM or free RES (Table S2; IC_{50} = 6.92 and 7.52 $\mu\text{g/mL}$, respectively). It is worth mentioning that LF/CS-coated PEM-RES-LCNPs (F3) displayed the highest cytotoxic profile (IC_{50} = 2.56 $\mu\text{g/mL}$) compared with PEM-RES-LCNPs (F2) (Table S2; IC_{50} 3.85 $\mu\text{g/mL}$). The cytotoxicity results were further confirmed by cellular uptake study. As shown in Figure 5A,B, LCNPs exhibited enhanced cellular internalization compared with free dye after incubation with A549 cells for 4 and 24 h. Additionally, it was obviously demonstrated that polyelectrolyte coating of LCNPs with CS and LF resulted in significant enhancement in cellular uptake compared with uncoated formulation.

3.3. Characterization of Inhalable Nanocomposites Enriched with LF/CS-Coated PEM-RES-LCNPs. As shown in Table 2, different spray-dried formulations (S1–S4) displayed yields ranging from 45 to 78%. The percent yield of the nanocomposites prepared by spray-drying of LF/CS-coated PEM-RES-LCNPs with mannitol alone (S1) was calculated as 52%. We found that addition of leucine to mannitol (S2) at a ratio of 1:2 during spray drying led to a partial yield increase up to 60%. However, it was noted that addition of trehalose to the nanocomposites prepared using a mannitol:leucine mixture (S3) decreased the yield to 45%. Interestingly, co-spray drying of LF/CS-coated PEM-RES-LCNPs with a carrier mixture composed of mannitol:inulin:leucine (1:1:1) at a weight ratio of 1:3 (S4) resulted in the highest yield of 78% and best redispersibility profile with an S_f/S_i ratio \approx 1. These results were further confirmed by investigation of the in vitro aerosolization performance of different nanocomposites prepared using various carrier mixtures in terms of FPF, MMAD, and GSD using the Andersen cascade impactor (ACI) (Table 2). The percent deposition of nanocomposite powder on each stage of the

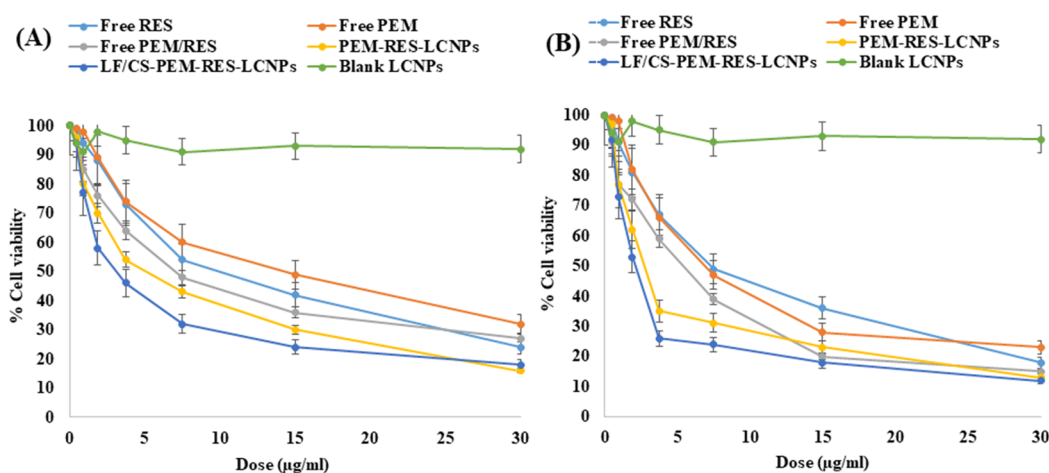


Figure 4. In vitro cytotoxicity analysis of LF/CS-coated PEM-RES-LCNPs (F3) compared with free PEM, free RES, and free PEM/RES cosolvent, blank LCNPs, and PEM-RES-LCNPs (F2) on A549 lung cancer cells at a concentration of 0.468 to 30 $\mu\text{g/mL}$ after (A) 24 h and (B) 48 h.

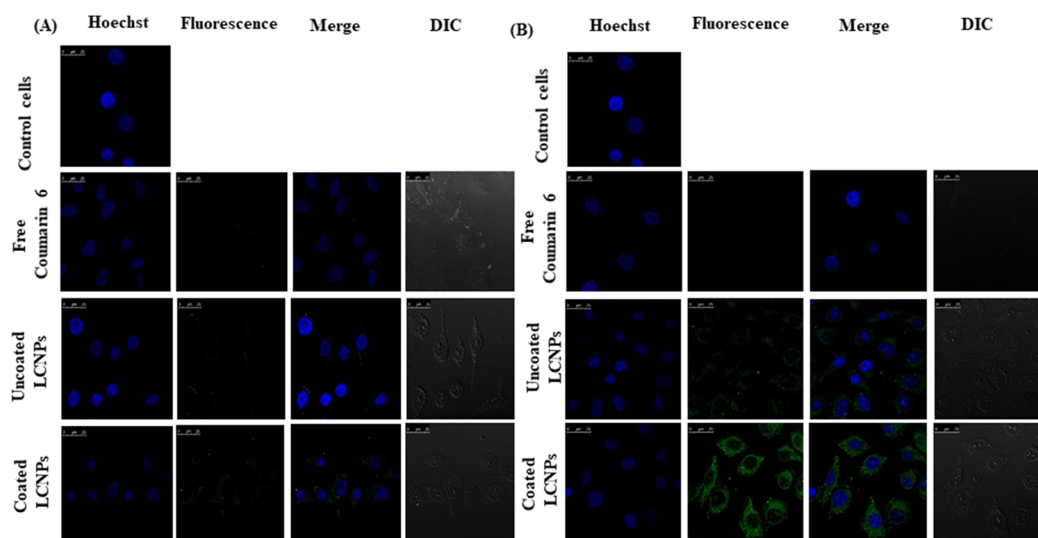


Figure 5. Confocal microscopical images displaying the internalization of LF/CS-coated coumarin-6 LCNPs into A549 lung cancer cells relative to free coumarin-6, coumarin-6 LCNPs, and control cells after incubation for (A) 4 h and (B) 24 h.

Table 2. Composition and Characterization of Inhalable Spray-Dried Nanocomposites^a

nanocomposites	carrier composition (weight ratio)	% yield	RI	MMAD (μm)	% FPF	GSD
S1	mannitol	52.21 \pm 4.21	1.21 \pm 0.02	4.25 \pm 0.31	40.2 \pm 5.42	2.13 \pm 0.04
S2	mannitol:leucine (2:1)	60.45 \pm 3.46	1.14 \pm 0.02	3.14 \pm 0.42	55.64 \pm 3.62	2.25 \pm 0.02
S3	mannitol:trehalose:leucine (1:1:1)	45.34 \pm 5.13	1.43 \pm 0.01	6.61 \pm 0.34	15.87 \pm 4.31	1.85 \pm 0.02
S4	mannitol:inulin:leucine (1:1:1)	78.42 \pm 3.89	1.01 \pm 0.01	2.72 \pm 0.21	61.62 \pm 4.74	2.41 \pm 0.03

^aAll nanocomposites were prepared at a nanoparticles:carrier 1:3 weight ratio.

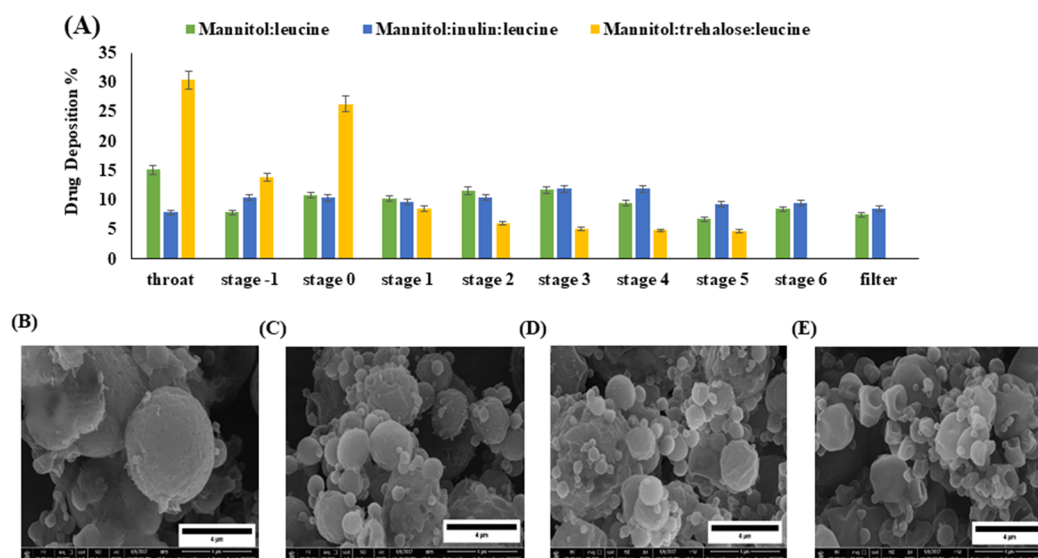


Figure 6. (A) In vitro aerosol deposition profile of spray-dried LF/C-coated PEM-RES-LCNPs displaying the percentage of drug content in each stage of the cascade impactor using different carriers at a 1:3 weight ratio. Scanning electron micrograph (SEM) of spray-dried powder of LF/CS-coated PEM-RES-LCNPs using different carriers at 1:3 w/w: (B) mannitol, (C) mannitol:leucine, (D) mannitol:trehalose:leucine, and (E) mannitol:inulin:leucine at 30,000 \times magnification.

impactor using different carrier mixtures is displayed in Figure 6A, whereas the aerosolization parameters are depicted in Figure S1. It was obvious that spray drying of LF/CS-coated PEM-RES-LCNPs with mannitol alone (S1) resulted in poor aerosolization behavior with an FPF of 40% and MMAD of 4.25 μm . The addition of hydrophobic leucine to mannitol (S2) significantly improved the aerodynamic profile and minimized the residual deposition in the inhaler device and

oropharynx (55% FPF, 3 μm MMAD). However, using mannitol in combination with trehalose and leucine (S3) as a carrier mixture resulted in nanocomposites showing the worst aerosolization profile with an FPF of 15% and MMAD of 6.628 μm . Strikingly, addition of inulin to mannitol and leucine resulted in nanocomposites showing the best aerosolization performance with an FPF of 61.6% and MMAD of 2.41 μm . According to the literature, our optimized nanocomposites

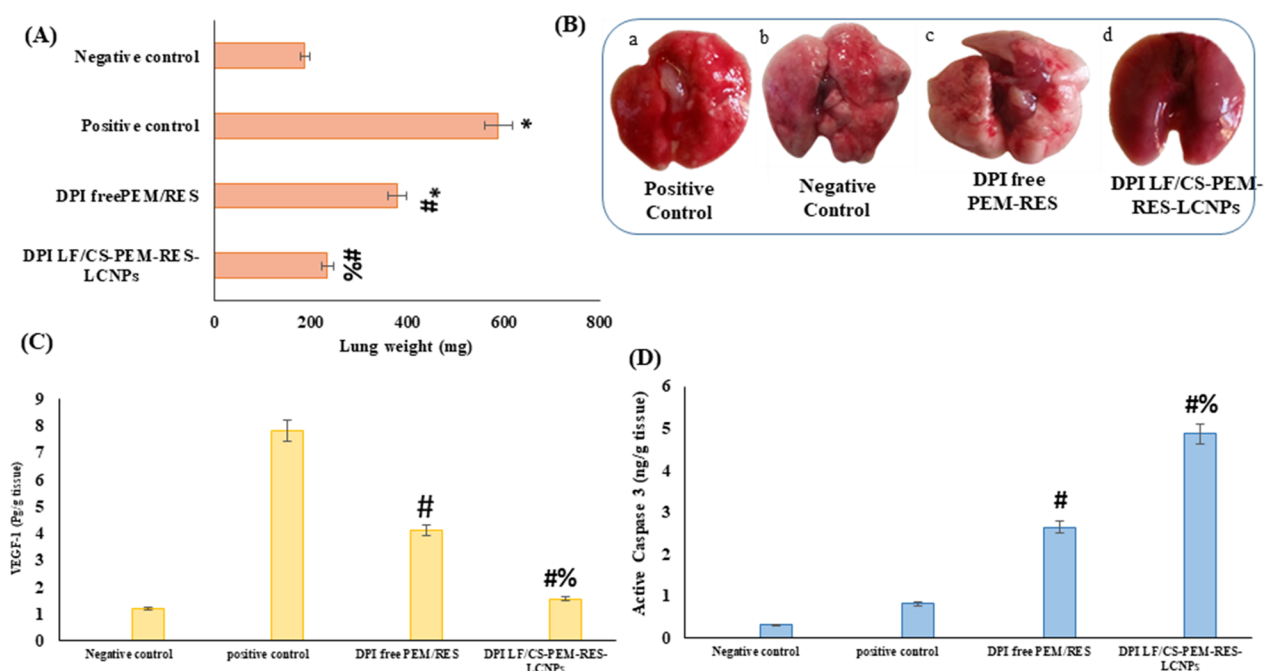


Figure 7. In vivo antitumor activity. (A) Average lung weight and (B) representative images of excised lungs after 3 weeks of treatment: (a) positive control, (b) negative control, (c) DPI free PEM-RES mixture, and (d) DPI LF/CS-PEM-RES-LCNPs. Level of the tumor biomarkers: (C) VEGF and (D) caspase-3 in lung cancer-bearing mice. * $P < 0.05$ vs negative control, # $P < 0.05$ vs positive control, and % $P < 0.05$ vs dry powder inhaler (DPI) of the free PEM/RES mixture.

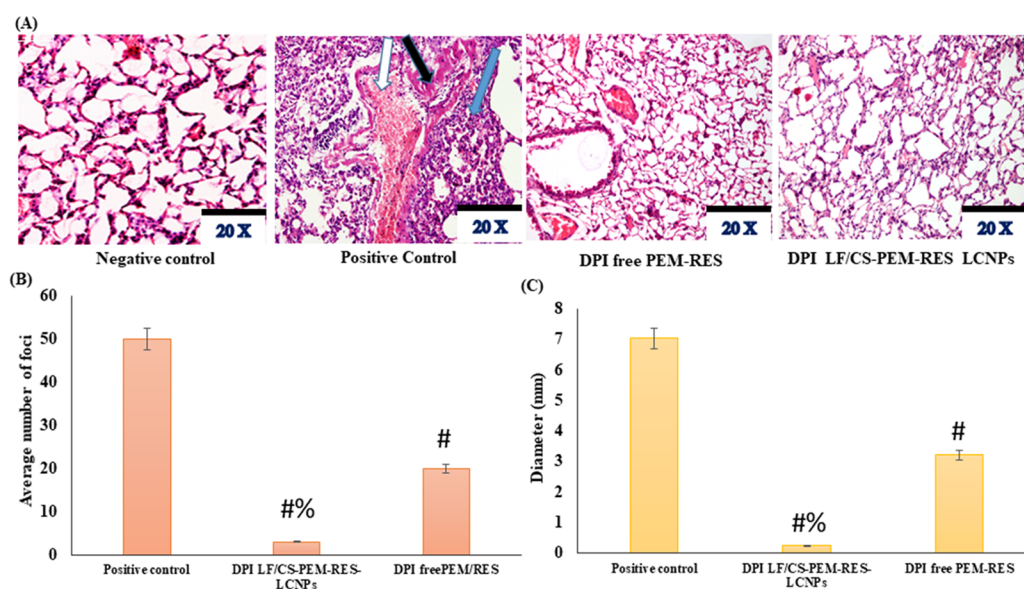


Figure 8. (A) Histopathological analysis of H&E-stained lung sections harvested from different mice groups; (B) number of adenomatous lung foci of excised lungs and (C) their corresponding diameters (mm).

possess an FPF percentage higher than that of the currently available DPIs in the market (10–20%).^{33,39} SEM images indicated that most particles possessed a diameter of less than 5 μm where the nanocomposites prepared using mannitol:trehalose:leucine (S3) displayed a spherical shape with a broad smooth surface due to the negative impact of trehalose in reducing the corrugation of particles (Figure 6D). In contrast, those nanocomposites prepared using mannitol:inulin:leucine (S4) showed dimpled particles with prominent surface corrugations (Figure 6E). From the abovementioned results, the spray-dried nanocomposites (S4) were highly respirable with good flowability, high FPF, and good uniformity across

different fields where each 1 mg of powder contains 3 μg of each drug, so it was chosen as the optimized nanocomposites for further analysis.

3.4. In Vivo Anticancer Efficacy and Toxicity Studies.

The anticancer effect of inhalable dry powder of the free PEM/RES mixture and inhalable LF/CS-coated PEM-RES-LCNPs nanocomposites (S4) was assessed using urethane as a chemical carcinogen to induce lung cancer in mice via both macroscopic and microscopic examinations. As presented in Figure 7A, the average lung weight of mice received with inhalable LF/CS-coated PEM-RES-LCNPs (S4; 235 ± 5 mg) was significantly lower than that received with inhalable free

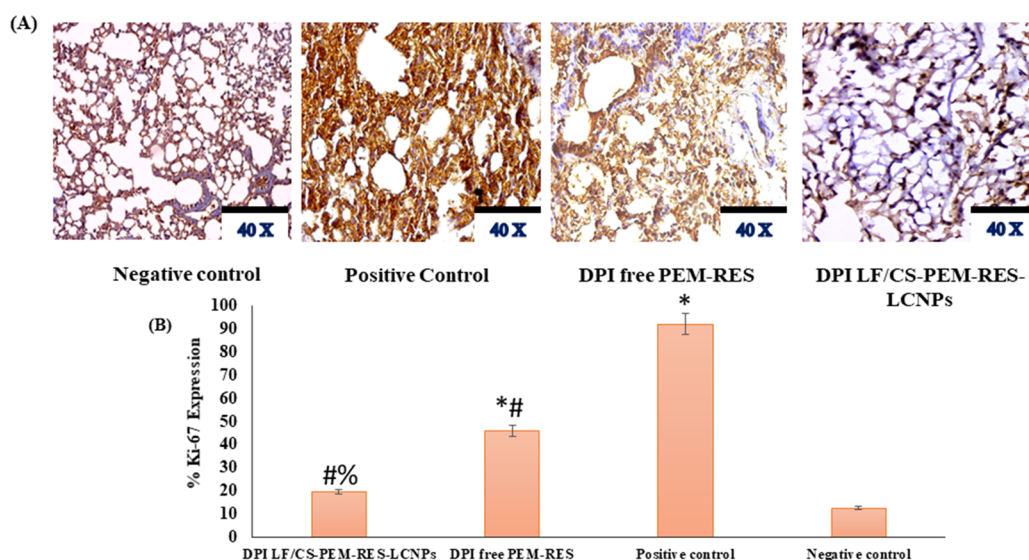


Figure 9. Immunohistochemical analysis. (A) Ki-67 staining; (B) % expression of Ki-67 of excised lungs from different mice groups. * $P < 0.05$ vs negative control, # $P < 0.05$ vs positive control, and % $P < 0.05$ vs dry powder inhaler (DPI) of free PEM/RES.

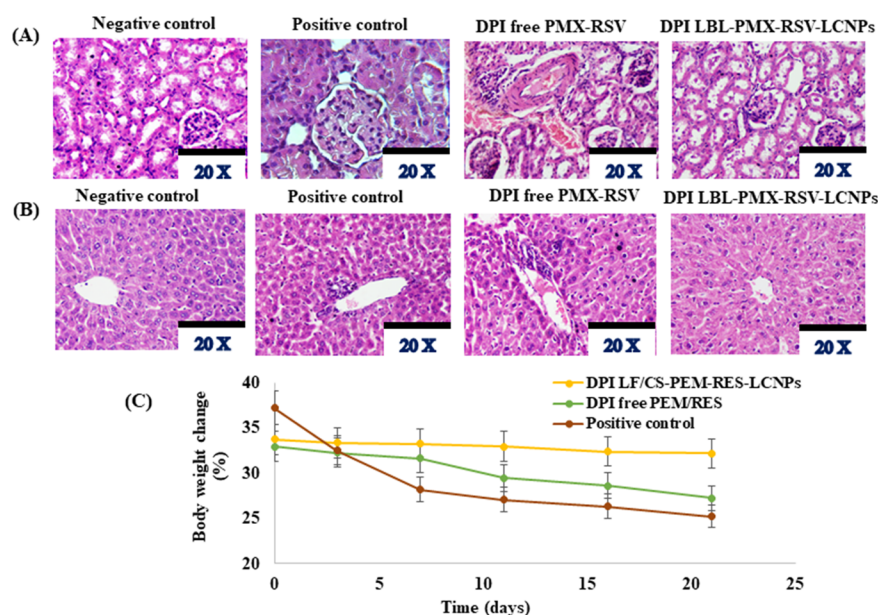


Figure 10. Safety profile of inhalable dry powder of LF/CS-coated PEM-RES-LCNPs including histopathological H&E-stained (A) kidney and (B) liver tissues of different treatment groups and (C) average body weights of different mice groups during the study period.

PEM/RES powder (380 ± 10 mg). Figure 7B shows the morphological appearance of lungs harvested from different mice groups where the surface of untreated, positive-control lungs exhibited malignant lesions with many lung cancerous foci; however, the lungs harvested from mice treated with inhalable LF/CS-coated PEM-RES-LCNPs (S4) showed normal physiological characteristics with remarkably diminished malignant surface lesions. Furthermore, the optimized dry powder nanocomposites (S4) exhibited the best tumor inhibitory effect characterized by the lowest level of VEGF-1 (1.56 pg/g) and highest active caspase-3 level (4.87 ng/g) compared to the spray-dried powder of the free PEM/RES mixture with VEGF-1 (4.11 pg/g) and active caspase-3 (2.65 ng/g) (Figure 7C,D) and the positive control.

The histopathological study displayed that the excised lungs of the positive-control group had pre-neoplastic to neoplastic

lesions showing a range of epithelial hyperplasia to adenoma as pointed by the blue arrow (Figure 8A). Furthermore, they were associated with hemorrhage and infiltration of inflammatory cells revealed as white and black, respectively. On the contrary, the lungs of the negative-control group maintained their normal physiological attributes with normal alveoli lined with single epithelial tissues. Meanwhile, mice treated with the inhalable free PEM/RES mixture demonstrated a marked decrease of neoplastic transformation as revealed by the histopathological profile. The best improvement in the carcinogenic histopathological profile was displayed by mice treated with inhalable dry powder of LF/CS-coated PEM-RES-LCNPs (S4). Additionally, the lungs isolated from tumor-bearing mice treated with inhalable dry powder of free PEM/RES displayed considerable reduction in the number of lung adenomatous foci (Figure 8B,C). However, mice treated with

inhalable dry powder of LF/CS-coated PEM-RES-LCNPs (S4) displayed a great reduction in lesion numbers as well as lung adenomatous foci.

Immunohistochemical analysis illustrating the expression of nuclear proliferating proteins (Ki67) confirmed the superiority of the inhalable dry powder of LF/CS-coated PEM-RES-LCNPs in attenuating urethane-induced adenoma proliferation (Figure 9A,B). It is worth mentioning that the inhalable dry powder of LF/CS-coated PEM-RES-LCNPs has improved the therapeutic outcomes and the safety profile of the nanoformulations. This could be attributed to the hepato- and nephroprotective effect of RES, which managed to alleviate the well-known hepato- and nephrotoxicity of PEM.

The histopathological analysis of the excised kidney and liver (Figure 10A,B, respectively) confirmed the great tendency of the inhalable dry powder of LF/CS-coated PEM-RES-LCNPs in maintaining the functions of the kidney and liver of treated mice without inducing damage unlike the positive control or mice treated with the DPI free PEM/RES mixture. This reflected the ability of mice treated with the optimized inhalable dry powder of LF/CS-coated PEM-RES-LCNPs to continue growth without significant body weight loss, while a remarkable loss in body weight was observed in mice of other groups during the study period (Figure 10C). Notably, the inhalable dry powder of PEM-RES-LCNPs administered to mice via the insufflator significantly enhanced the survival rates of tumor-bearing mice with an 80% survival rate during the study period of 25 days, whereas mice treated with inhalable dry powder of the free PEM/RES mixture showed survival rates of 50%. For further confirmation, *in vivo* imaging of lung cancer-bearing mice treated with inhalable dry powder of free coumarin-6 and coumarin-6-loaded LF/CS-LCNPs was performed after 4 and 24 h.

Figure 11 reveals that mice treated with dry powder of free coumarin-6 exhibited weak fluorescence represented by a lower

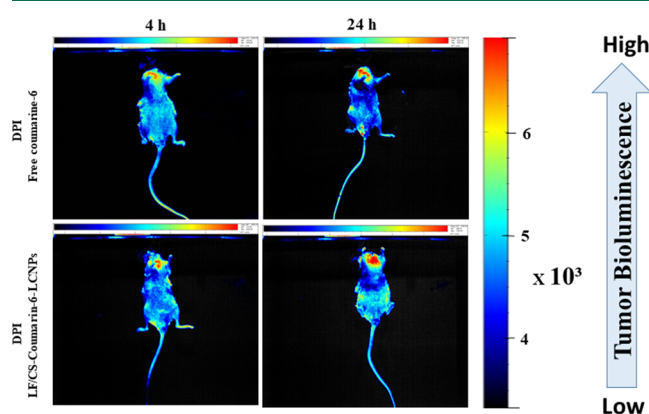


Figure 11. *In vivo* fluorescence imaging of tumor-bearing mice subjected to DPI of free coumarin-6 and coumarin-6-labeled LF/CS-LCNPs.

intensity of the RGB scale, whereas mice treated with inhalable dry powder of LF/CS-coated coumarin-6-LCNPs showed significantly higher fluorescence. After 24 h, an obvious increase in intensity of the RGB scale in the center and throughout lungs without any luminescence in other regions of the body was observed, which confirmed higher localization and uptake of inhalable dry powder of LF/CS-coated coumarin-6-LCNPs.

4. DISCUSSION

The current study shed light on the fabrication of inhalable nanocomposites of lyotropic LCNPs co-loaded with hydrophilic (PEM) and lipophilic (RES) drugs for lung cancer treatment. The novelty of our inhalable nanocomposites entails the following: (1) the first inhalable dry powder formulation of PEM for lung cancer patients, (2) synergistic combination of PEM and RES as chemotherapy/herbal combination for lung cancer therapy, (3) our nanocomposites combining the merits of both nano- and microparticles, which guarantee deep lung deposition as well as active targeting and efficient internalization of the NPs into lung cancer cells, and (4) a layer-by-layer tumor targeting approach via electrostatic assembly of chondroitin (CS) and lactoferrin (LF) to ensure targeting of lung cancer cells rather than affecting healthy normal cells.⁴⁰ This can markedly enhance the therapeutic outcomes and minimize the undesirable side effects of the conventional systemic drug delivery in addition to improving the patient's compliance.²³ Thus, our proposed system opens the frontiers for management of lung cancer. LCNPs were simply prepared via a hydrotrope method previously reported by Spicer et al.²⁸ Gradual addition of a GMO/ethanol isotropic mixture to water stabilized with poloxamer 407 resulted in a prompt formation of stable nanometric LCNPs.¹⁷ The hydrotrope method was adopted in the current study to avoid the harsh preparation conditions associated with the other common methods such as elevated temperature and pressure, thereby ensuring the integrity of the thermosensitive RES during preparation.¹⁶ An *in situ* hydrophobic ion pairing (HIP) strategy was applied to decrease the aqueous solubility of the anionic drug (PEM) and increase its entrapment efficiency within the lipid-based delivery system (LCNPs).⁴¹ An HIP technique had great potential in imparting a hydrophobic nature to PEM, thus decreasing its partitioning into the external aqueous phase.⁴² CTAB was chosen as the model cationic ion pair that successfully interacted with negatively charged PEM and increased its EE up to 96% without affecting LCNP properties. The positive ζ potential owned by PEM-RES-LCNPs, attributed to cationic CTAB, was exploited to electrostatically functionalize the surface of our formulated PEM-RES-LCNPs via an LbL self-assembly technique to enable active targeting to lung cancer cells.¹⁸ A combination of chondroitin sulfate (CS) and lactoferrin (LF) as the respective anionic and cationic polymers was selected for the LbL assembly process. Since the LbL technique depends mainly on the electrostatic interaction between oppositely charged electrolytes, the charge density of both polymers was maximized by adjusting the pH of CS ($pK_a = 3.3$) and LF ($pK_a = 8.7$) solutions to pH 7 to ensure maximum ionization of the carboxylate group of CS and maximum protonation of amino groups of LF.²⁹ Optimization of the amount of polyelectrolytes used during the LbL process was critical for uniform coating onto the surface of LCNPs and has a remarkable influence on LCNP properties.¹⁷ Therefore, excess and unnecessary polyelectrolytes were avoided via careful detection of the polyelectrolyte concentration desired for reversal of the charge on PEM-RES-LCNPs by titration methods.⁴³ It is worth mentioning that a nonwashing LbL assembly approach was utilized in this study to avoid the tedious repetitive centrifugation and washing steps accompanied by traditional LbL assembly techniques. First, the amount of CS was gradually increased till complete neutralization of the positively charged LCNPs. After that,

the LF layer was assembled over CS-coated LCNPs where the strong electrostatic interactions between the two polyelectrolytes CS and LF resulted in stiffer NPs with smaller particle size.¹⁷

The *in vitro* release study revealed that incorporating both drugs in LCNPs resulted in a remarkable biphasic release profile. The initial fast release behavior could be attributed to the nanometric size of LCNPs, which provides a relatively large surface area-to-volume ratio, whereas the additional controlled release of both drugs from PEM-RES-LCNPs could be correlated to the diffusion of both drugs from the lipidic bicontinuous bilayer of the liquid crystalline structure.^{30,44,45} Moreover, the *in situ* HIP formation between PEM and CTAB played a crucial role in providing additional sustained release of the hydrophilic PEM.⁴⁶ Interestingly, LF/CS-coated PEM-RES-LCNPs manifested a comparable release profile to that of uncoated PEM-RES-LCNPs in spite of the additional diffusional barrier resulting from the thickness of polyelectrolytes covering the surface of LCNPs. This could be explained by the additional time required for the coating step that resulted into partitioning of the drugs from the lipid matrix toward the aqueous phase.⁴⁷ Such sustained drug-release behavior is generally favored to decrease the toxic undesirable effects of the drug and ensure that the tumor site receives a constant and controlled amount of the drug.

A combination of PEM and RES was reported to exhibit a synergistic cytotoxic effect to lung cancer cells, which was further evidenced in our study. The enhanced cytotoxicity elucidated by our proposed liquid crystalline nanoparticles could be explained by their enhanced cellular uptake achieved via both bioadhesive characteristics of GMO and energy-independent internalization of LCNPs, thus leading to increased accumulation of both RES and PEM within cancer cells over a prolonged time.⁴⁷ Meanwhile, the superior cytotoxicity of LF/CS-coated PEM-RES-LCNPs was ascribed to their enhanced cellular internalization mediated by the interaction of the LF corona with LF- or Tf-receptor-mediated endocytosis.^{48,49} These results were confirmed by the cellular uptake studies where polyelectrolyte coating of LCNPs with CS and LF resulted in significant enhancement in cellular uptake compared with uncoated LCNPs facilitated by receptor-mediated endocytosis owing to the outer LF layer.

The current study reported for the first time, to our knowledge, a localized inhalable dry powder of PEM in combination with a promising herbal drug, RES. Novel inhalable nanocomposites were successfully fabricated in which the LF/CS-coated PEM-RES-LCNPs (F3) were embedded into a microparticulate system via a spray-drying technique. Mannitol was selected as a model nonreducing sugar during spray drying of the nanoformulation (F3) to avoid the possible Millard reaction with amino acids of the LF protein.³³ The improvement in the percentage yield observed after addition of leucine was attributed to the relative hydrophobicity of leucine adsorbed at the surface of droplets during the spray-drying process, which inhibits the cohesion of particles by virtue of its lubricating effect.⁵⁰ Moreover, leucine played a crucial role in minimizing the hygroscopicity associated with spray drying of mannitol-polymer mixtures.³³ Numerous studies reported that addition of leucine to spray-dried powder increased the yield of low-density powders composed of small, low-cohesive particles with rough wrinkled surfaces.^{51–53} The decreased yield after addition of trehalose to the mannitol:leucine mixture (S3) was attributed to the

reported tendency of trehalose to produce cohesive particles that tended to form aggregates and lead to poor redispersibility of the spray-dried powder.⁵² The redispersibility index is an essential parameter that evaluates the quality of reconstitution of nanoparticles (S_f/S_i) from the spray-dried nanocomposites and ensures their complete dispersion at the target site.⁶ The superior redispersibility behavior of the nanocomposites (S4) confirmed the ability of this carrier system to protect LCNPs from high temperature and maintain their properties during the spray-drying process. The best aerosolization performance owned by the nanocomposites constituted with a mixture of mannitol:leucine:inulin 1:1:1 w/w (S4) was attributed to the remarkable role of inulin in stabilizing the amorphous structure of mannitol and preventing its recrystallization.^{33,54} The aerosol particle size (aerodynamic diameter, d_{ae}) is considered an important parameter for evaluating aerosolization performance and predicting the mechanism of aerosol deposition within lungs. Careful tailoring of the d_{ae} of particles in the range of 1–5 μm is essential for deep lung deposition of inhaled particles. Particles with $d_{ae} < 1 \mu\text{m}$ are easily exhaled, while microparticles with $d_{ae} > 5 \mu\text{m}$ are deposited in the oropharynx region via inertial impaction.⁶ The large aerodynamic diameter and irregular aggregations manifested by spray-dried powder with mannitol in combination with trehalose and leucine (S3) hindered particle deposition in lower stages 4 and 5 resulting in the least efficient aerosolization performance.⁵² In contrast, the dimpled morphology and optimum aerodynamic diameter of S4 nanocomposites could guarantee deep lung deposition and make them good candidates for pulmonary drug delivery.

The *in vivo* antitumor efficacy study showed the superiority of dry-powder, inhalable LCNP nanocomposites. The superior therapeutic outcomes of mice treated with inhalable LF/CS-coated PEM-RES-LCNPs could be attributed to direct localization of dry powder within tumor cells of lungs via inhalation, thus concentrating therapeutic payloads within lungs and avoiding their dilution along the systemic circulation.⁵⁵ Once they have reached the target site, the alveolar fluids dissolve the multicarrier leaving behind the surface-functionalized LCNPs.⁶ Surface functionalization of LCNPs with LF and CS could enhance the binding of LCNPs with their corresponding receptors over-expressed by lung cancer cells leading to improved cellular internalization.^{47,56} The obtained bioimages were in accordance with *in vivo* study results, which further confirmed the superiority of inhalable dry-powder LF/C-coated PEM-RES-LCNPs for lung cancer treatment.⁵⁷

5. CONCLUSIONS

The current research proposed novel inhalable dry nanocomposite powder of LCNPs co-loaded with a synergistic combination of chemoherbals drugs (PEM and RES) for localized lung cancer treatment. The concept of using lactoferrin and chondroitin as coating materials proved their efficacy in tumor targeting and enhanced cancer cell internalization. Moreover, it was revealed that spray drying is a promising technique for development of inhalable dry-powder nanocomposites. Using a pulmonary carrier mixture composed of 1:1:1 mannitol/inulin/leucine at a 1:3 w/w ratio was efficient in enabling deep lung deposition, which guarantees maximal therapeutic efficacy. This was demonstrated as improved aerosolization behavior of the developed powder nanocomposites (MMAD of 2.41 μm and PPF of 61.6%), and

in turn, this improvement was reflected as superior in vivo anti-tumor efficacy. Conclusively, the current work could open a new avenue in lung cancer treatment via a pulmonary route.

■ ASSOCIATED CONTENT

Supporting Information

The Supporting Information is available free of charge at <https://pubs.acs.org/doi/10.1021/acsbiomaterials.9b01639>.

Information about the preparation and characterization of nanocarriers, physicochemical characterization of dual drug-loaded nanocarriers and nanocomposites, methodology for assessment of in vitro cytotoxicity, cellular uptake, quantification of angiogenesis and apoptosis, and histopathological and immunohistochemical analysis (PDF)

■ AUTHOR INFORMATION

Corresponding Authors

Ahmed O. Elzoghby – Cancer Nanotechnology Research Laboratory (CNRL), Faculty of Pharmacy and Department of Industrial Pharmacy, Faculty of Pharmacy, Alexandria University, Alexandria 21521, Egypt; Division of Engineering in Medicine, Department of Medicine, Brigham and Women's Hospital, Harvard Medical School, Boston, Massachusetts 02115, United States; Harvard-MIT Division of Health Sciences & Technology, Cambridge, Massachusetts 02139, United States; orcid.org/0000-0002-5193-7536; Phone: (001) 781-366-8703; Email: aelzoghby@bwh.harvard.edu, ahmed_elzoghby@alexu.edu.eg

May S. Freag – Cancer Nanotechnology Research Laboratory (CNRL), Faculty of Pharmacy and Department of Pharmaceutics, Faculty of Pharmacy, Alexandria University, Alexandria 21521, Egypt; Division of Engineering in Medicine, Department of Medicine, Brigham and Women's Hospital, Harvard Medical School, Boston, Massachusetts 02115, United States; Harvard-MIT Division of Health Sciences & Technology, Cambridge, Massachusetts 02139, United States; Phone: (001) 781-600-6892; Email: mfreag@bwh.harvard.edu, may.s.freag@alexu.edu.eg

Authors

Hadeer M. Abdelaziz – Cancer Nanotechnology Research Laboratory (CNRL), Faculty of Pharmacy, Alexandria University, Alexandria 21521, Egypt; Department of Pharmaceutics, Faculty of Pharmacy, Damanhour University, Damanhour 22511, Egypt

Maged W. Helmy – Cancer Nanotechnology Research Laboratory (CNRL), Faculty of Pharmacy, Alexandria University, Alexandria 21521, Egypt; Department of Pharmacology & Toxicology, Faculty of Pharmacy, Damanhour University, Damanhour 22511, Egypt

Elsayed-Zeinab A. Abdelfattah – Medical Research Institute, Alexandria University, Alexandria 21521, Egypt

Jia-You Fang – Pharmaceutics Laboratory, Graduate Institute of Natural Products, Chang Gung University, Taoyuan 333, Taiwan; Research Center for Industry of Human Ecology and Research Center for Chinese Herbal Medicine, Chang Gung University of Science and Technology, Taoyuan 333, Taiwan; Department of Anesthesiology, Chang Gung Memorial Hospital, Taoyuan 333, Taiwan; orcid.org/0000-0003-2114-7709

Magda W. Samaha – Cancer Nanotechnology Research Laboratory (CNRL), Faculty of Pharmacy and Department of

Industrial Pharmacy, Faculty of Pharmacy, Alexandria University, Alexandria 21521, Egypt

Complete contact information is available at: <https://pubs.acs.org/doi/10.1021/acsbiomaterials.9b01639>

Author Contributions

M.S.F. and A.O.E. conceived the idea and designed the experiments. H.M.A. performed the experiments. J.-Y.F. and M.W.S. analyzed the data. M.W.H. designed and supervised the in vivo studies. H.M.A. wrote the manuscript. M.S.F. and A.O.E. are responsible for the overall design and supervision of the study and editing the manuscript. All authors reviewed and approved the manuscript.

Notes

The authors declare no competing financial interest.

■ ACKNOWLEDGMENTS

This work was supported by the research grant (no. 5731) of Science and Technology Development Fund (STDF), Ministry of Scientific Research, Egypt. The authors also acknowledge Westland Milk Products (Hokitika, New Zealand) for their kind donation of lactoferrin.

■ REFERENCES

- (1) Zappa, C.; Mousa, S. A. Non-small cell lung cancer: current treatment and future advances. *Transl. Lung Cancer Res.* **2016**, *5*, 288–300.
- (2) Chidambaram, M.; Manavalan, R.; Kathiresan, K. Nano-therapeutics to overcome conventional cancer chemotherapy limitations. *J. Pharm. Pharm. Sci.* **2011**, *14*, 67–77.
- (3) Cryer, A. M.; Chan, C.; Eftychidou, A.; Maksoudian, C.; Mahesh, M.; Tetley, T. D.; Spivey, A. C.; Thorley, A. J. Tyrosine Kinase Inhibitor Gold Nanoconjugates for the Treatment of Non-Small Cell Lung Cancer. *ACS Appl. Mater. Interfaces* **2019**, 16336.
- (4) Nel, A.; Ruoslahti, E.; Meng, H. New insights into “permeability” as in the enhanced permeability and retention effect of cancer nanotherapeutics. *ACS Nano* **2017**, 9567.
- (5) Danhier, F. To exploit the tumor microenvironment: since the EPR effect fails in the clinic, what is the future of nanomedicine? *J. Controlled Release* **2016**, *244*, 108–121.
- (6) Abdelaziz, H. M.; Gaber, M.; Abd-Elwakil, M. M.; Mabrouk, M. T.; Elgohary, M. M.; Kamel, N. M.; Kabary, D. M.; Freag, M. S.; Samaha, M. W.; Mortada, S. M.; Elkhodairy, K. A.; Fang, J.-Y.; Elzoghby, A. O. Inhalable particulate drug delivery systems for lung cancer therapy: Nanoparticles, microparticles, nanocomposites and nanoaggregates. *J. Controlled Release* **2018**, *269*, 374–392.
- (7) El-Sherbiny, I. M.; El-Baz, N. M.; Yacoub, M. H. Inhaled nano- and microparticles for drug delivery. *Global Cardiol. Sci. Pract.* **2015**, *2015*, 2.
- (8) Cohen, M. H.; Johnson, J. R.; Wang, Y. C.; Sridhara, R.; Pazdur, R. FDA drug approval summary: pemetrexed for injection (Alimta) for the treatment of non-small cell lung cancer. *Oncologist* **2005**, *10*, 363–368.
- (9) Wei, R.; Gaohua, L.; Xiao, L.; Ling, G. Side effects of pemetrexed in the maintenance therapy of nonsmall-cell lung cancer at advanced stage and the nursing measures. *Mod. Clin. Nurs.* **2015**, *5*, 48–50.
- (10) El-Far, S. W.; Helmy, M. W.; Khatib, S. N.; Bekhit, A. A.; Hussein, A. A.; Elzoghby, A. O. Phytosomal bilayer-enveloped casein micelles for codelivery of monascus yellow pigments and resveratrol to breast cancer. *Nanomedicine* **2018**, *13*, 481–499.
- (11) Freag, M. S.; Saleh, W. M.; Abdallah, O. Y. Self-assembled phospholipid-based phytosomal nanocarriers as promising platforms for improving oral bioavailability of the anticancer celastrol. *Int. J. Pharm.* **2017**, 18.

- (12) Varoni, E. M.; Lo Faro, A. F.; Sharifi-Rad, J.; Iriti, M. Anticancer Molecular Mechanisms of Resveratrol. *Front. Nutr.* **2016**, *3*, 8.
- (13) Junco, J. J.; Mancha, A.; Malik, G.; Wei, S.-J.; Kim, D. J.; Liang, H.; Slaga, T. J. Resveratrol and P-glycoprotein Inhibitors Enhance the Anti-skin Cancer Effects of Ursolic Acid. *Mol. Cancer Res.* **2013**, *11*, 1521.
- (14) Chen, R. S.; Ko, J. C.; Chiu, H. C.; Wo, T. Y.; Huang, Y. J.; Tseng, S. C.; Chen, H. J.; Huang, Y. C.; Jian, Y. J.; Lee, W. T.; Lin, Y. W. Pemetrexed downregulates ERCC1 expression and enhances cytotoxicity effected by resveratrol in human nonsmall cell lung cancer cells. *Naunyn-Schmiedeberg's Arch. Pharmacol.* **2013**, *386*, 1047–1059.
- (15) Elzoghby, A. O.; El-Lakany, S. A.; Helmy, M. W.; Abu-Serie, M. M.; Elgindy, N. A. Shell-crosslinked zein nanocapsules for oral codelivery of exemestane and resveratrol in breast cancer therapy. *Nanomedicine* **2017**, *12*, 2785–2805.
- (16) Freag, M. S.; Elnaggar, Y. S.; Abdelmonsif, D. A.; Abdallah, O. Y. Stealth, biocompatible monoolein-based lyotropic liquid crystalline nanoparticles for enhanced aloe-emodin delivery to breast cancer cells: in vitro and in vivo studies. *Int. J. Nanomed.* **2016**, *11*, 4799–4818.
- (17) Freag, M. S.; Elnaggar, Y. S.; Abdelmonsif, D. A.; Abdallah, O. Y. Layer-by-layer-coated lyotropic liquid crystalline nanoparticles for active tumor targeting of rapamycin. *Nanomedicine* **2016**, *11*, 2975–2996.
- (18) Oh, K. S.; Lee, H.; Kim, J. Y.; Koo, E. J.; Lee, E. H.; Park, J. H.; Kim, S. Y.; Kim, K.; Kwon, I. C.; Yuk, S. H. The multilayer nanoparticles formed by layer by layer approach for cancer-targeting therapy. *J. Controlled Release* **2013**, *165*, 9–15.
- (19) Kabary, D. M.; Helmy, M. W.; Elkhodairy, K. A.; Fang, J.-Y.; Elzoghby, A. O. Hyaluronate/lactoferrin layer-by-layer-coated lipid nanocarriers for targeted co-delivery of rapamycin and berberine to lung carcinoma. *Colloids Surf., B* **2018**, *169*, 183–194.
- (20) Sabra, S.; Abdelmoneem, M.; Abdelwakil, M.; Mabrouk, M. T.; Anwar, D.; Mohamed, R.; Khattab, S.; Bekhit, A.; Elkhodairy, K.; Freag, M.; Elzoghby, A. Self-assembled nanocarriers based on amphiphilic natural polymers for anti-cancer drug delivery applications. *Curr. Pharm. Des.* **2017**, DOI: 10.2174/1381612823666170526111029.
- (21) AbdElhamid, A. S.; Helmy, M. W.; Ebrahim, S. M.; Bahey-El-Din, M.; Zayed, D. G.; Zein El Dein, E. A.; El-Gizawy, S. A.; Elzoghby, A. O. Layer-by-layer gelatin/chondroitin quantum dots-based nanotheranostics: combined rapamycin/celecoxib delivery and cancer imaging. *Nanomedicine* **2018**, *13* (), DOI: 10.2217/nmm-2018-0028.
- (22) Wegrowski, Y.; Maquart, F. X. Chondroitin Sulfate Proteoglycans in Tumor Progression. In *Advances in Pharmacology*; Academic Press: 2006; Vol. 53, pp 297–321. DOI: [https://doi.org/10.1016/S1054-3589\(05\)53014-X](https://doi.org/10.1016/S1054-3589(05)53014-X).
- (23) Elzoghby, A. O. Editorial: Polymeric Nanocarriers as Robust Platforms for Cancer Therapy. *Curr. Pharm. Des.* **2018**, *23*, 5211–5212.
- (24) Jiang, H.; Zhao, W.; Shao, W. Prognostic value of CD44 and CD44v6 expression in patients with non-small cell lung cancer: meta-analysis. *Tumour Biol.* **2014**, *35*, 7383–7389.
- (25) Gibbons, J. A.; Kanwar, R. K.; Kanwar, J. R. Lactoferrin and cancer in different cancer models. *Front. Biosci.* **2011**, *3*, 1080–1088.
- (26) Chaharband, F.; Kamalinia, G.; Atyabi, F.; Mortazavi, S. A.; Mirzaie, Z. H.; Dinarvand, R. Formulation and in vitro evaluation of curcumin-lactoferrin conjugated nanostructures for cancerous cells. *Artif. Cells, Nanomed., Biotechnol.* **2017**, 626–636.
- (27) Gaber, M.; Medhat, W.; Hany, M.; Saher, N.; Fang, J. Y.; Elzoghby, A. Protein-lipid nanohybrids as emerging platforms for drug and gene delivery: Challenges and outcomes. *J. Controlled Release* **2017**, *254*, 75–91.
- (28) Spicer, P. T.; Hayden, K. L.; Lynch, M. L.; Ofori-Boateng, A.; Burns, J. L. Novel Process for Producing Cubic Liquid Crystalline Nanoparticles (Cubosomes). *Langmuir* **2001**, *17*, 5748–5756.
- (29) Ramasamy, T.; Tran, T. H.; Choi, J. Y.; Cho, H. J.; Kim, J. H.; Yong, C. S.; Choi, H.-G.; Kim, J. O. Layer-by-layer coated lipid-polymer hybrid nanoparticles designed for use in anticancer drug delivery. *Carbohydr. Polym.* **2014**, *102*, 653–661.
- (30) Khattab, S. N.; Naim, S. E. A.; El-Sayed, M.; El Bardan, A. A.; Elzoghby, A. O.; Bekhit, A. A.; El-Faham, A. Design and synthesis of new s-triazine polymers and their application as nanoparticulate drug delivery systems. *New J. Chem.* **2016**, *40*, 9565–9578.
- (31) Abdelmoneem, M. A.; Mahmoud, M.; Zaky, A.; Helmy, M. W.; Sallam, M.; Fang, J.-Y.; Elkhodairy, K. A.; Elzoghby, A. O. Dual-targeted casein micelles as green nanomedicine for synergistic phytotherapy of hepatocellular carcinoma. *J. Controlled Release* **2018**, *287*, 78–93.
- (32) Anwar, D. M.; Khattab, S. N.; Helmy, M. W.; Kamal, M. K.; Bekhit, A. A.; Elkhodairy, K. A.; Elzoghby, A. O. Lactobionic/folate dual-targeted amphiphilic maltodextrin-based micelles for targeted co-delivery of sulfasalazine and resveratrol to hepatocellular carcinoma. *Bioconjugate Chem.* **2018**, 3026.
- (33) Sou, T.; McIntosh, M. P.; Kaminskas, L. M.; Prankerd, R. J.; Morton, D. A. V. Designing a Multicomponent Spray-Dried Formulation Platform for Pulmonary Delivery of Biomacromolecules: The Effect of Polymers on the Formation of an Amorphous Matrix for Glassy State Stabilization of Biomacromolecules. *Drying Technol.* **2013**, *31*, 1451–1458.
- (34) Elgohary, M. M.; Helmy, M. W.; Abdelfattah, E.-Z. A.; Ragab, D. M.; Mortada, S. M.; Fang, J.-Y.; Elzoghby, A. O. Targeting sialic acid residues on lung cancer cells by inhalable boronic acid-decorated albumin nanocomposites for combined chemo/herbal therapy. *J. Controlled Release* **2018**, *285*, 230–243.
- (35) Ohashi, K.; Kabasawa, T.; Ozeki, T.; Okada, H. One-step preparation of rifampicin/poly(lactic-co-glycolic acid) nanoparticle-containing mannitol microspheres using a four-fluid nozzle spray drier for inhalation therapy of tuberculosis. *J. Controlled Release* **2009**, *135*, 19–24.
- (36) Kabary, D. M.; Helmy, M. W.; Abdelfattah, E.-Z. A.; Fang, J.-Y.; Elkhodairy, K. A.; Elzoghby, A. O. Inhalable multi-compartmental phospholipid enveloped lipid core nanocomposites for localized mTOR inhibitor/herbal combined therapy of lung carcinoma. *Eur. J. Pharm. Biopharm.* **2018**, *130*, 152–164.
- (37) Abd Elwakil, M. M.; Mabrouk, M. T.; Helmy, M. W.; Abdelfattah, E.-Z. A.; Khiste, S. K.; Elkhodairy, K. A.; Elzoghby, A. O. Inhalable lactoferrin–chondroitin nanocomposites for combined delivery of doxorubicin and ellagic acid to lung carcinoma. *Nanomedicine* **2018**, *13*, 2015.
- (38) Swarnakar, N. K.; Thanki, K.; Jain, S. Bicontinuous cubic liquid crystalline nanoparticles for oral delivery of doxorubicin: implications on bioavailability, therapeutic efficacy, and cardiotoxicity. *Pharm. Res.* **2014**, *31*, 1219–1238.
- (39) Hindle, M. Aerosol Drug Delivery. In *Pharmaceutical Sciences Encyclopedia*; John Wiley & Sons, Inc., 2010. DOI: DOI: 10.1002/9780470571224.pse357.
- (40) Elzoghby, A. Editorial (Thematic Issue: Nanocarriers Based on Natural Polymers as Platforms for Drug and Gene Delivery Applications). *Curr. Pharm. Des.* **2016**, *22*, 3303–3304.
- (41) Devrim, B.; Bozkir, A. Design and Evaluation of Hydrophobic Ion-Pairing Complexation of Lysozyme with Sodium Dodecyl Sulfate for Improved Encapsulation of Hydrophilic Peptides/Proteins by Lipid-Polymer Hybrid Nanoparticles. *J. Nanomed. Nanotechnol.* **2015**, *6*, 1.
- (42) Meyer, J. D.; Manning, M. C. Hydrophobic Ion Pairing: Altering the Solubility Properties of Biomolecules. *Pharm. Res.* **1998**, *15*, 188–193.
- (43) Freag, M. S.; Saleh, W. M.; Abdallah, O. Y. Laminated chitosan-based composite sponges for transmucosal delivery of novel protamine-decorated tripterine phytosomes: Ex-vivo mucopenetration and in-vivo pharmacokinetic assessments. *Carbohydr. Polym.* **2018**, *188*, 108–120.
- (44) Elzoghby, A. O.; Mostafa, S. K.; Helmy, M. W.; ElDemellawy, M. A.; Sheweita, S. A. Superiority of aromatase inhibitor and

cyclooxygenase-2 inhibitor combined delivery: Hyaluronate-targeted versus PEGylated protamine nanocapsules for breast cancer therapy. *Int. J. Pharm.* **2017**, *529*, 178–192.

(45) Elzoghby, A. O.; Mostafa, S. K.; Helmy, M. W.; ElDemellawy, M. A.; Sheweita, S. A. Multi-Reservoir Phospholipid Shell Encapsulating Protamine Nanocapsules for Co-Delivery of Letrozole and Celecoxib in Breast Cancer Therapy. *Pharm. Res.* **2017**, *34*, 1956–1969.

(46) Jain, V.; Swarnakar, N. K.; Mishra, P. R.; Verma, A.; Kaul, A.; Mishra, A. K.; Jain, N. K. Paclitaxel loaded PEGylated glyceryl monooleate based nanoparticulate carriers in chemotherapy. *Biomaterials* **2012**, *33*, 7206–7220.

(47) Thapa, R. K.; Choi, J. Y.; Poudel, B. K.; Hiep, T. T.; Pathak, S.; Gupta, B.; Choi, H. G.; Yong, C. S.; Kim, J. O. Multilayer-Coated Liquid Crystalline Nanoparticles for Effective Sorafenib Delivery to Hepatocellular Carcinoma. *ACS Appl. Mater. Interfaces* **2015**, *7*, 20360–20368.

(48) Tsuda, H.; Sekine, K.; Fujita, K.-I.; Iigo, M. Cancer prevention by bovine lactoferrin and underlying mechanisms — a review of experimental and clinical studies. *Biochem. Cell Biol.* **2002**, *80*, 131–136.

(49) Abdelmoneem, M. A.; Elnaggar, M. A.; Hammady, R. S.; Kamel, S. M.; Helmy, M. W.; Abdulkader, M. A.; Zaky, A.; Fang, J.-Y.; Elkhodairy, K. A.; Elzoghby, A. O. Dual-Targeted Lactoferrin Shell-Oily Core Nanocapsules for Synergistic Targeted/Herbal Therapy of Hepatocellular Carcinoma. *ACS Appl. Mater. Interfaces* **2019**, 26731.

(50) Arora, S.; Kappl, M.; Haghi, M.; Young, P. M.; Traini, D.; Jain, S. An investigation of surface properties, local elastic modulus and interaction with simulated pulmonary surfactant of surface modified inhalable voriconazole dry powders using atomic force microscopy. *RSC Adv.* **2016**, *6*, 25789–25798.

(51) Sou, T.; Orlando, L.; McIntosh, M. P.; Kaminskas, L. M.; Morton, D. A. V. Investigating the interactions of amino acid components on a mannitol-based spray-dried powder formulation for pulmonary delivery: A design of experiment approach. *Int. J. Pharm.* **2011**, *421*, 220–229.

(52) Yang, F.; Liu, X.; Wang, W.; Liu, C.; Quan, L.; Liao, Y. The effects of surface morphology on the aerosol performance of spray-dried particles within HFA 134a based metered dose formulations. *Asian J. Pharm. Sci.* **2015**, *10*, 513–519.

(53) Sou, T.; Kaminskas, L. M.; Nguyen, T.-H.; Carlberg, R.; McIntosh, M. P.; Morton, D. A. V. The effect of amino acid excipients on morphology and solid-state properties of multi-component spray-dried formulations for pulmonary delivery of biomacromolecules. *Eur. J. Pharm. Biopharm.* **2013**, *83*, 234–243.

(54) Kamel, N. M.; Helmy, M. W.; Abdelfattah, E.-Z.; Khatib, S. N.; Ragab, D.; Samaha, M. W.; Fang, J.-Y.; Elzoghby, A. O. Inhalable dual-targeted hybrid lipid nanocore-protein shell composites for combined delivery of genistein and all-trans retinoic acid to lung cancer cells. *ACS Biomater. Sci. Eng.* **2019**, 71.





(55) Roa, W. H.; Azarmi, S.; Al-Hallak, M. H. D. K.; Finlay, W. H.; Magliocco, A. M.; Löbenberg, R. Inhalable nanoparticles, a non-invasive approach to treat lung cancer in a mouse model. *J. Controlled Release* **2011**, *150*, 49–55.

(56) Sabra, S. A.; Elzoghby, A. O.; Sheweita, S. A.; Haroun, M.; Helmy, M. W.; ElDemellawy, M. A.; Xia, Y.; Goodale, D.; Allan, A. L.; Rohani, S. Self-assembled amphiphilic zein-lactoferrin micelles for tumor targeted co-delivery of rapamycin and wogonin to breast cancer. *Eur. J. Pharm. Biopharm.* **2018**, *128*, 156–169.

(57) Elzoghby, A. O.; Hemasa, A. L.; Freag, M. S. Hybrid protein-inorganic nanoparticles: From tumor-targeted drug delivery to cancer imaging. *J. Controlled Release* **2016**, *243*, 303–322.

Article

Hydroxygenkwanin Suppresses Non-Small Cell Lung Cancer Progression by Enhancing EGFR Degradation

Yann-Lii Leu ^{1,2,†} , Tong-Hong Wang ^{3,4,†} , Chih-Ching Wu ^{5,6} , Kuo-Yen Huang ⁷,
Yu-Wen Jiang ³, Yi-Chiung Hsu ^{8,*}  and Chi-Yuan Chen ^{3,4,*}

¹ Graduate Institute of Natural Products, Chang Gung University, Taoyuan 333, Taiwan; ylleu@mail.cgu.edu.tw

² Center for Traditional Chinese Medicine, Chang Gung Memorial Hospital at Linkou, Taoyuan 333, Taiwan

³ Graduate Institute of Health Industry Technology and Research Center for Food and Cosmetic Safety, Research Center for Chinese Herbal Medicine, College of Human Ecology, Chang Gung University of Science and Technology, Taoyuan 333, Taiwan; cellww@gmail.com (T.-H.W.); sjiang0715@gmail.com (Y.-W.J.)

⁴ Tissue Bank, Chang Gung Memorial Hospital at Linkou, Taoyuan 333, Taiwan

⁵ Department of Medical Biotechnology and Laboratory Science, College of Medicine, Chang Gung University, Taoyuan 333, Taiwan; luckywu@mail.cgu.edu.tw

⁶ Department of Otolaryngology-Head&Neck Surgery, Chang Gung Memorial Hospital at Linkou, Taoyuan 333, Taiwan

⁷ Institute of Biomedical Sciences, Academia Sinica, Taipei 115, Taiwan; kyhuang0222@gmail.com

⁸ Department of Biomedical Sciences and Engineering, National Central University, Taoyuan 320, Taiwan

* Correspondence: syicncu@g.ncu.edu.tw (Y.-C.H.); d49417002@gmail.com (C.-Y.C.); Tel.: +886-3-4227151 (Y.-C.H.); +886-3-2118999 (C.-Y.C.); Fax: +886-3-4226062 (Y.-C.H.); +886-3-2118866 (C.-Y.C.)

† These authors have contributed equally to this work.

Received: 23 January 2020; Accepted: 18 February 2020; Published: 19 February 2020



Abstract: Epidermal growth factor receptor (EGFR) is frequently overexpressed and mutated in non-small cell lung cancer (NSCLC), which is the major type of lung cancer. The EGFR tyrosine kinase inhibitors (TKIs) are the approved treatment for patients harboring activating mutations in the EGFR kinase. However, most of the patients treated with EGFR-TKIs developed resistance. Therefore, the development of compounds exhibiting unique antitumor activities might help to improve the management of NSCLC patients. The total flavonoids from *Daphne genkwa* Sieb. et Zucc. have been shown to contain antitumor activity. Here, we have isolated a novel flavonoid hydroxygenkwanin (HGK) that displays selective cytotoxic effects on all of the NSCLC cells tested. In this study, we employed NSCLC cells harboring EGFR mutations and xenograft mouse model to examine the antitumor activity of HGK on TKI-resistant NSCLC cells. The results showed that HGK suppressed cancer cell viability both in vitro and in vivo. Whole-transcriptome analysis suggests that EGFR is a potential upstream regulator that is involved in the gene expression changes affected by HGK. In support of this analysis, we presented evidence that HGK reduced the level of EGFR and inhibited several EGFR-downstream signalings. These results suggest that the antitumor activity of HGK against TKI-resistant NSCLC cells acts by enhancing the degradation of EGFR.

Keywords: *Daphne genkwa*; hydroxygenkwanin; NSCLC; EGFR; apoptosis

1. Introduction

The epidermal growth factor receptor (EGFR) pathway is one of the most dysregulated molecular pathways in human cancers. The activating mutations of EGFR occur in approximately ~10% of non-small cell lung cancer (NSCLC) cases in North America and Western Europe patients and approximately

30–50% in East Asian patients [1]. These tumors are oncogene-addicted to EGFR-mediated survival pathway and they are highly sensitive to apoptosis induction by tyrosine kinase inhibitors (TKIs) [2]. The TKIs are approved treatments for patients harboring activating mutations in the EGFR kinase. Several generations of TKIs have been developed and these drugs are superior to conventional chemotherapy in prolonging progression-free survival (PFS) of NSCLC patients harboring common EGFR mutations, including exon 19 deletions (Del19) and L858R [3]. However, most of the patients treated with TKIs developed resistance within 9–14 months [4,5]. Therefore, the development of compounds exhibiting unique pharmacologic properties and antitumor activities for NSCLC patients at high risk of recurrence is urgently needed to help in the management of NSCLC patients.

Daphne genkwa Sieb. et Zucc. has been used in traditional Chinese medicine for thousands of years. The flower buds of this plant (“Genkwa Flos”) are mainly used for the treatment of cancer, asthma, and edema [6–9]. It contains several types of compounds, including flavonoids, biscoumarin, lignans, volatile oils, diterpene esters, chlorogenic acids, and phenolic glycosides. The flavonoids and diterpene esters are thought to be the major efficacy components [10,11]. Yuanhuadine, a Daphnane diterpene from Genkwa Flos, has been reported to inhibit the growth of human lung cancer cells, which was accompanied with cell cycle arrest, up-regulation of p21, and down-regulation of c-Myc, CDK2, CDK4, and cyclins [12]. Yuanhuadine also inhibits ligand-induced EGFR and c-Met signaling [12]. Yuanhuacine, a Daphnane diterpenoid from Genkwa Flos, has been shown to modulate the AMPK/mTORC2 signaling pathway and actin cytoskeleton organization in NSCLC cells [13]. The total flavonoids from Genkwa Flos have been shown to inhibit the growth of Lewis lung carcinoma in C57BL6 mice and colorectal cancer cells [14,15]. However, the active components in the flavonoids of Genkwa Flos have not been characterized. In this study, we have identified hydroxygenkwanin (HGK) as one of the active flavonoids that display anti-tumor activity against TKI-resistant NSCLC cells in vitro and in vivo.

2. Results

2.1. Isolation and Identification of Flavonoids from Genkwa Flos

Genkwa Flos were extracted with methanol and then concentrated to give brown syrup. The syrup was partitioned first in CHCl₃/water (1:1) and then in *n*-butanol/water (1:1) [16]. The cytotoxic effects of the fractionated extracts on lung cancer cells A549 were investigated by treating the cells with extracted compounds at 30 µg/mL for 48 h and the cell viability was determined by MTT assay. The chloroform fraction had the highest cytotoxic effects in A549 cells (viability 38.50%) as compared with the water (viability 99.84%) or *n*-butanol fractions (viability 75.38%), which suggested that the anti-NSCLC agents are mainly contained in the chloroform fraction. To identify and isolate the active compounds that display anti-tumor activity, the chloroform fraction was subjected to silica gel column chromatography (see Materials and Methods) in order to obtain three known flavonoid compounds (Figure 1A), including genkwanin, 3-methoxy genkwanin, and hydroxygenkwanin (HGK). The identity of these three compounds has been confirmed by comparing their UV, IR, NMR, and MS data with those of authentic compounds and/or with those that were reported in the literature [10,17,18].

The three flavonoid compounds that were isolated from the chloroform fraction of Genkwa Flos extract were first tested for their selective cytotoxicity against lung cancer cells. The lung cancer cells A549 and normal fibroblasts HFF3 were treated with each compound for 24 h and then assayed for viability by MTT assay. The HGK exhibited the strongest selective cytotoxicity against lung cancer cells, as shown in Table 1. The half maximal inhibitory concentration (IC₅₀) of HGK for A549 cells was about 22 µM (Figure 1B), while the IC₅₀s of genkwanin and 3-methoxy genkwanin against A549 cells were >100 µM. A search of the literature has revealed that HGK that was isolated from the leaves of *Blumea balsamifera* DC displayed strong cytotoxicity against human lung cancer cells (NCI-H187) and a moderate toxicity against oral cavity cancer cells lines (KB) [19]. HGK induced DNA damage, cell cycle arrest, and cell apoptosis in glioma [20]. HGK inhibited cell migration, invasion, and proliferation in

oral squamous cell carcinoma and hepatocellular carcinoma [21,22]. These data suggest that HGK is one of the active antitumor flavonoids in the Genkwa Flos extract.

Table 1. Cytotoxic effects of the compounds Genkwanin, 3'-Methoxy genkwanin, and hydroxygenkwanin (HGK).

Name of Compounds (100 μ M)	Cell Viability (%)	
	HFF3	A549
Genkwanin	86.46 \pm 2.4	91.64 \pm 11.0
3'-Methoxy genkwanin	55.15 \pm 6.9	67.31 \pm 5.0
Hydroxygenkwanin (HGK)	74.87 \pm 3.4	22.03 \pm 2.9

Cells were treated with the indicated compound at 100 μ M for 24 h, and cell viability was analyzed by MTT assay. Data are expressed as mean \pm SD of three independent experiments.

2.2. The Cytotoxic Effect of HGK

The cytotoxic effects of HGK on PC9 (EGFR Del19, TKI-sensitive), and H1975 (EGFR L858R/T790M, TKI-resistant) were compared to that of a NSCLC cell line A549 and normal fibroblasts HFF3 cells to evaluate whether HGK displays antitumor effects against NSCLC cells harboring constitutive activating EGFR mutations. As shown in Figure 1B, HGK displayed greater cytotoxic effects on all three lung cancer cells than the normal fibroblasts HFF3. The half maximal inhibitory concentration (IC₅₀) of HGK for A549, PC9, and H1975 cells were 22.0 \pm 0.9 μ M, 18.3 \pm 3.1 μ M, and 18.3 \pm 0.3 μ M, respectively. Since the A549 cells that were treated with HGK at 100 μ M (Table 1) had a similar survival as that treated at 50 μ M (Figure 1B), this suggests that the cytotoxic effects of this drug peaked at around 50 μ M. Therefore, the highest dose of HGK used in all of the subsequent experiments was set at 50 μ M. Next, we examined the effects of HGK on the foci formation of NSCLC cells. As shown in Figure 1C, HGK inhibited foci formation in a concentration-dependent manner in all three NSCLC cells. Together, these results indicate that the TKI-sensitive and TKI-resistant NSCLC cells are all sensitive to the treatment of HGK.

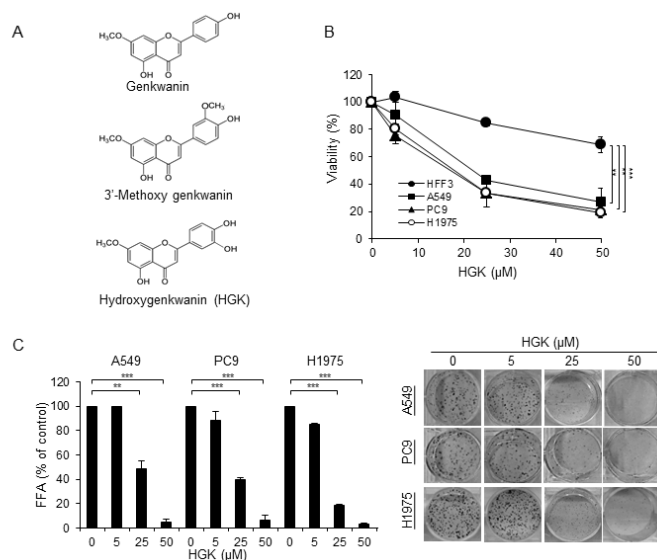


Figure 1. Effects of hydroxygenkwanin (HGK) on the viability of non-small cell lung cancer (NSCLC) cells. (A) Structures of genkwanin, 3'-methoxy genkwanin, and HGK. (B) Cells were treated with various concentrations of HGK for 24 h and the viability of treated cells was evaluated by staining with trypan blue. (C) Cells were treated with various concentrations of HGK for 24 h and then cultured in the absence of HGK for an additional five days. The number of foci was scored, and the data are presented as relative focus-forming ability (FFA). Data are expressed as mean \pm SD of three independent experiments. ** p < 0.01; and *** p < 0.001, as analyzed with the unpaired t -test.

2.3. Effects of HGK on the Cell Cycle Progression and Apoptosis

The effects of HGK on cell cycle progression and apoptosis were examined to investigate the cytotoxic mechanism of HGK. For cell cycle analysis, the NSCLC cells were treated with HGK for 24 h and examined by flow cytometry using propidium iodide (PI) staining. As shown in Figure 2A, the percentage of treated-cells in the sub-G1 region was only significantly increased in the H1975 cells that were treated with HGK. An accumulation of cells in G2/M phase, and reduced distribution in the G0/G1 and S phase, were also only observed in HGK-treated H1975 cells, but not the HGK-treated A549 or PC9 cells. Therefore, HGK appears to affect cell cycle progression only in H1975 cells, despite HGK having similar cytotoxic effects on the three NSCLC cells (Figure 1B,C). To determine whether HGK induces apoptosis, the phosphatidylserine exposure in the cell surface and the cleavage of PARP and caspase 9 were examined. As shown in the upper and lower right quadrants of Figure 2B, cells that were positively stained with Annexin V-FITC were readily detected in all of the NSCLC cells treated with HGK at 50 μ M for 24 h. Similarly, the cleavage of PARP and caspase 9 were readily detected in the HGK-treated NSCLC cells (Figure 3B,C). These data suggest that the cytotoxic effect of HGK is mediated through its induction of apoptosis.

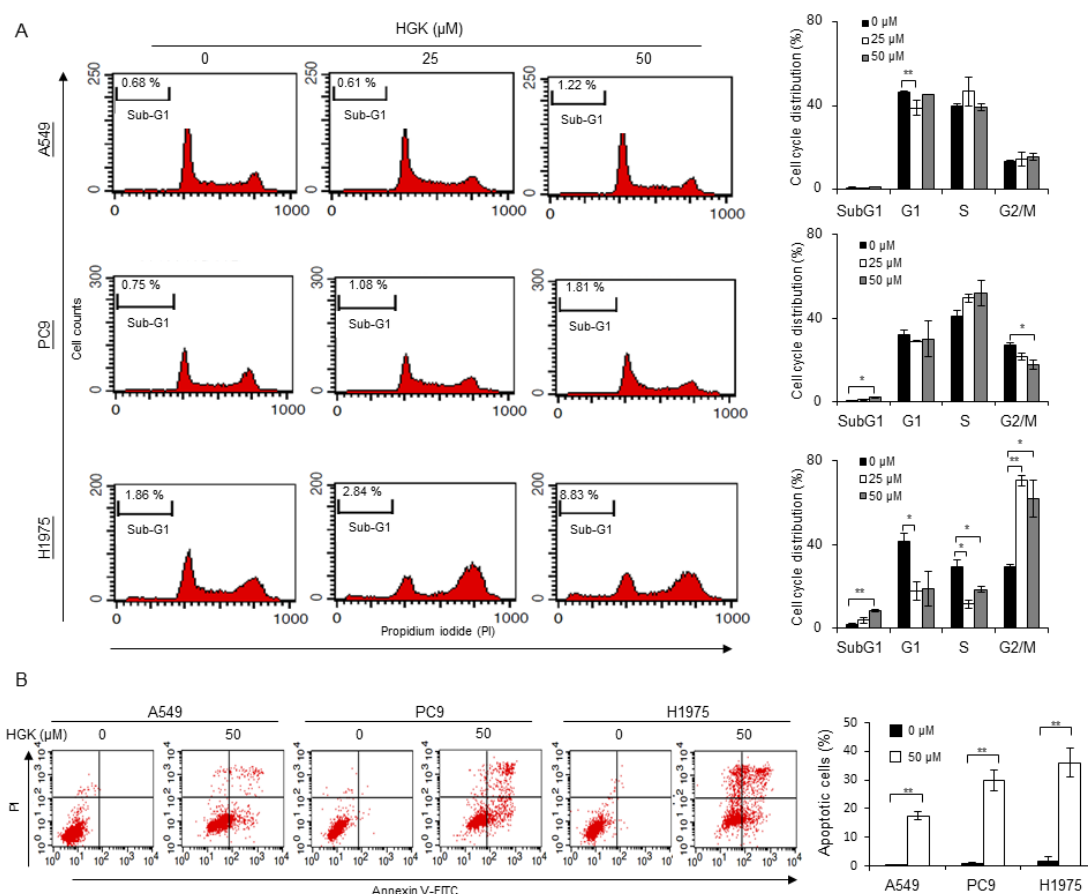


Figure 2. Effects of HGK on cell cycle and apoptosis in NSCLC cells. Cells were treated with HGK at the indicated concentrations for 24 h. (A) The distribution of cells in different phases of cell cycle was analyzed by flow cytometry of cells stained with propidium iodide. (B) Apoptosis was detected by flow cytometry of cells stained with Annexin V-FITC. The data shown are expressed as the mean \pm SD of three independent experiments. Symbols: * $p < 0.05$ and ** $p < 0.01$, as analyzed by unpaired t -tests.

2.4. The Molecular Mechanism of Antitumor Activity by HGK in H1975 Cells

We employed whole-transcriptome sequencing to analyze the effects of HGK on gene expression to further explore the mechanism of the action affected by HGK on H1975 cells. A total of 2345

putative genes showed a statistically significant two-fold difference in the expression level of H1975 cells that were treated with HGK at 50 μ M when compared to the untreated cells. Next, we used the Ingenuity Pathway Analysis (IPA) for Canonical pathway analysis to conduct functional enrichment analysis of these differentially expressed (DE) genes [23]. The results showed that these DE genes were enriched in mitochondrial dysfunction ($p = 5.5 \times 10^{-22}$), oxidative phosphorylation ($p = 4.41 \times 10^{-18}$), and protein ubiquitination pathway ($p = 5.23 \times 10^{-16}$) (Table 2). Table 3 shows the top molecular and cellular functions of DE genes identified by IPA. The top five cellular functions that were affected by HGK suggest that the major activity of HGK is to affect the cell death and survival. Upstream regulator analysis in IPA was used to predict the upstream transcriptional regulators from the dataset. The overlap value was used to predict the potential transcriptional regulator through the gene expression database. EGFR (overlap p -value = 1.22×10^{-11}) was a potential upstream regulator that is involved the gene expression changes in H1975 cells treated with HGK at 50 μ M. Figure 3A shows the putative function of EGFR regulator in the network. These analyses reveal that HGK might modulate EGFR regulator and, thus, affect cell proliferation and death pathways in H1975 cells.

Table 2. Functional enrichment analysis of the differentially expressed genes in H1975 cells treated with HGK at 50 μ M.

Ingenuity Canonical Pathways	p -Value
Mitochondrial Dysfunction	5.55×10^{-22}
Sirtuin Signaling Pathway	1.29×10^{-20}
Oxidative Phosphorylation	4.41×10^{-18}
Protein Ubiquitination Pathway	5.23×10^{-16}
Estrogen Receptor Signaling	4.34×10^{-12}

Table 3. Top molecular and cellular functions of the differentially expressed genes in H1975 cells treated with HGK at 50 μ M.

Molecular and Cellular Functions	p -Value
Cell Death and Survival	2.32×10^{-6} to 2.37×10^{-42}
Cellular Development	2.05×10^{-6} to 2.40×10^{-39}
Cellular Growth and Proliferation	2.05×10^{-6} to 2.40×10^{-39}
RNA Post-Transcriptional Modification	8.49×10^{-7} to 2.98×10^{-38}
Cell Cycle	2.26×10^{-6} to 1.61×10^{-33}

2.5. The Effects of HGK on EGFR Expression and Downstream Pathways

A549, PC9, and H1975 cells were treated with HGK at 0, 25, and 50 μ M, and examined for the expression of EGFR and EGFR-related signaling pathways to address whether HGK might modulate EGFR and its downstream signaling. As shown in Figure 3B,C, the levels of total EGFR were decreased in a dose-dependent manner in HGK-treated A549, PC9, and H1975 cells. The levels of phospho-EGFR (pEGFR) were similarly reduced in the HGK-treated PC9 and H1975 cells. Accompanied with reduced EGFR levels in HGK-treated cells, several EGFR-downstream signaling pathways, including phospho-STAT3 (pSTAT3), phospho-AKT (pAKT), and phospho-ERK (pERK), were also inhibited in HGK-treated PC9 and H1975 cells. These results indicate that HGK modulates EGFR and its downstream pathways in NSCLC cells.

We examined the effects of HGK on the mRNA expression of EGFR to address whether the reduced expression of EGFR in the HGK-treated cells might be mediated by transcriptional downregulation of EGFR. The levels of EGFR mRNA stayed unchanged in all of HGK-treated NSCLC cells, as shown in Figure 3D. These results suggest that HGK might modulate EGFR by affecting the stability of EGFR

protein. We postulate that HGK might modulate EGFR signaling by accelerating EGFR degradation, as HGK is predicted to affect protein ubiquitination pathway ($p = 5.23 \times 10^{-16}$) (Table 2) based on transcriptome analysis. H1975 cells were treated cycloheximide in the presence or absence of HGK, and the levels of EGFR were determined by Western blot, to determine the effects of HGK on the protein stability of EGFR. As shown in Figure 3E, the level of total EGFR gradually reduced in the absence of HGK treatment. However, the level of EGFR was rapidly decreased in HGK-treated H1975 cells. We examined the effect of proteasome inhibitor (MG132) on the EGFR stability in H1975 to address whether the instability of EGFR protein by HGK treatment might be due to proteasome-mediated degradation [24,25]. The treatment of H1975 cells with MG132 at 10 μM or lower concentrations had no effect on cell proliferation (Supplementary Figure S1A). In the presence of MG132 at 10 μM , the level of EGFR was no longer reduced following treatment of HGK at 50 μM in H1975 cells (Figure 3F). Under this experimental condition, the combination of MG132 and HGK treatment for 12 h had no effect on cell cytotoxicity (Supplementary Figure S1B) or apoptosis induction, as evidenced by the lack of procaspase 9 cleavage (Figure 3F). Collectively, these results suggest that HGK can promote proteasome-mediated degradation of EGFR in NSCLC cells, which leads to the inhibition of cell proliferation and cell death.

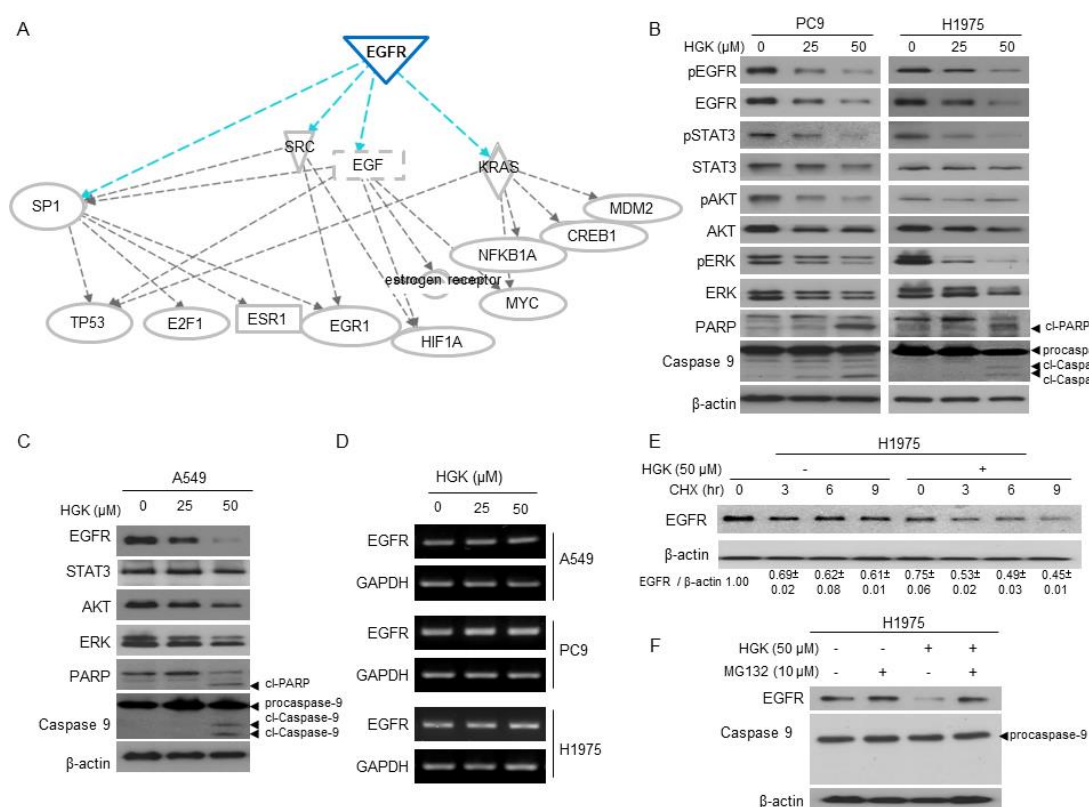


Figure 3. Effects of HGK on epidermal growth factor receptor (EGFR) signaling pathway in NSCLC cells. (A) The prediction of EGFR as the upstream transcriptional regulators by using the Ingenuity Pathway Analysis (IPA). (B and C) Cells were treated with indicated concentrations of HGK for 24 h. The expression levels of phosphor-EGFR (pEGFR), EGFR, phospho-STAT3 (pSTAT3), phospho-AKT (pAKT), AKT, phospho-ERK (pERK), ERK, as well as the level of cleaved poly (ADP-ribose) polymerase (cl-PARP) and cleaved caspase 9 (cl-caspase 9) were determined by Western blot. β -actin served as a loading control. (D) The expression level of EGFR mRNA in HGK-treated cells was determined by RT-PCR. GAPDH served as the loading control. (E) H1975 cells were incubated with cycloheximide (CHX) 100 mg/mL for the indicated times in absence or presence of HGK 50 μM . The relative expression levels of EGFR were quantified and shown at the bottom. (F) H1975 cells were incubated with HGK in the presence or absence of MG132 for 12 h. The expression levels of EGFR and caspase 9 were analyzed by Western blot. β -actin used as a loading control. The data shown in (A) to (F) are from one of three similar results.

2.6. Antitumor Activity of HGK in a Xenograft Mouse Model

A xenograft mouse model was used in this work to evaluate the antitumor activity of HGK *in vivo*. The H1975 cells were subcutaneously inoculated in the right flank of nude mice. When the H1975 xenograft tumors reached around 50 mm³, we administered HGK (1.0 mg/kg body weight) in 100 µL of PBS by i.p. injection every two days. As shown in Figure 4A,B, the administration of HGK significantly inhibited tumor progression. There was no recognizable alteration in body weight or overt sign of toxicity in all of the treated mice (Figure 4C). IHC staining of the tumor xenografts showed the heavy staining of phospho-EGFR (pEGFR) and EGFR in untreated H1975 tumor xenografts (Figure 4D; upper panel), whereas weak staining of pEGFR and EGFR was detected in HGK-treated tumor (Figure 4D; lower panel). These results indicate that HGK displays antitumor activity against TKI-resistant NSCLC cells *in vivo*.

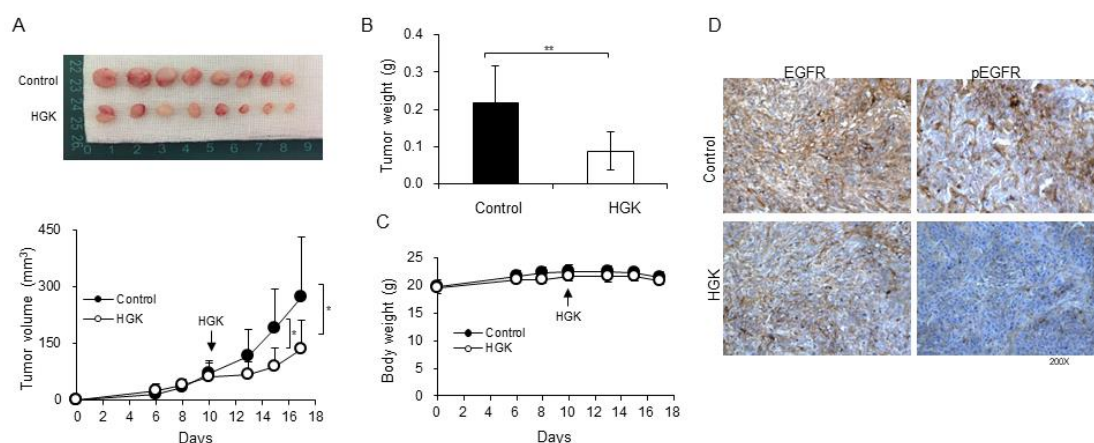


Figure 4. The antitumor effects of HGK *in vivo*. (A) The H1975 cells were inoculated subcutaneously in the right flank of nude mice. When the H1975 xenograft tumors reached around 50 mm³ at day 10 (as indicated by arrow), HGK was intraperitoneal injected every two days. The tumor volume was detected as described in Materials and Methods and is shown in the bottom panel. The excised xenograft tumors are shown in the upper panel. The effects of HGK treatment on the tumor net weights and body weights of mice are shown in (B) and (C), respectively. (D) Immunohistochemical staining of xenograft tumor sections for EGFR and phosphor-EGFR (pEGFR). The data that are shown in A B, C are presented as mean \pm SD and they were analyzed by Student's *t*-test. Asterisks denote statistically significant.

3. Discussion

In the study, we have isolated three flavonoid compounds from Genkwa Flos (Figure 1A), and have identified HGK as one of the active flavonoids that display anti-tumor activity against NSCLC cells. HGK displayed cytotoxic effects against NSCLC cells harboring constitutive activating EGFR mutations, including TKI-resistant H1975 and TKI-sensitive PC9 cells (Figure 1). Similar to the report by Wang et al., [20], HGK induced apoptosis in all of NSCLC cells that were used in this study (Figures 2B and 3B,C). However, flow cytometric analysis of cell cycle progression revealed that HGK only induces cell cycle arrest in H1975 cells, but not in A549 and PC9 cells (Figure 2A). Therefore, the effects of HGK on cell cycle progression do not appear to be universal for all cancer cells. The discrepancy between the results of apoptosis shown in Figure 2A,B may reflect the different methods used for detecting apoptosis, i.e., an increase in the sub G1 phase (Figure 2A) versus phosphatidylserine exposure in the cell surface (Figure 2B), which detects an early event of apoptosis.

While the antitumor activity of HGK is likely related to its ability to induce apoptosis in cancer cells, the molecular basis for such an activity is not known. In this study, whole-transcriptome sequencing and Ingenuity Pathway Analysis (IPA) of the differentially expressed genes was used to analyze the molecular and cellular functions of DE genes and predict the upstream transcriptional

regulators involved. These analyses suggest that HGK might affect certain factors that are involved in EGFR signaling and proteasome-mediated proteolysis (Figure 3A). Indeed, we have shown that HGK reduced the protein level of EGFR via proteasomal-dependent degradation (Figure 3B–F). As one of the most important post-translational modifications that facilitate EGFR degradation is ubiquitination [26] and that our analysis showed that the differentially expressed genes were enriched, including protein ubiquitination pathway (Table 2), it is likely that HGK might act to enhance the ubiquitination of EGFR and, thus, accelerates the proteasome-mediated process. The attachment of casitas B-lineage lymphoma (CBL), an E3 ubiquitin ligase, to activated EGFR is known to mediate the receptor degradation through the ubiquitin- proteasome system [27]. This raises the possibility that HGK may regulate CBL to enhance EGFR ubiquitination [24]. Future investigations are needed to test such a postulate.

Lastly, we have shown that HGK displays antitumor activity against xenografted H1975 cells in nude mice (Figure 4). HGK down-regulated EGFR and slowed down the growth of tumors, but not the total inhibition of tumor growth. Therefore, this compound might not be effective by itself in eradicating tumors, but it can be added as an adjuvant drug. For example, a combination of HGK and apigenin, a flavonoid compound that is commonly present in vegetables and fruits, has been shown to significantly increase the antitumor effects of apigenin in C6 glioma cells [20]. Therefore, HGK might hold capacity as an adjuvant drug in the treatment of NSCLC. As HGK is able to inhibit the tumor growth of TKI-resistant NSCLC cells (Figures 1 and 4), the potential inclusion of HGK as an adjuvant drug in the treatment of NSCLC patients harboring activating EGFR mutations might be explored.

In conclusion, this study has identified HGK as one of the active flavonoids from Genkwa Flos that displays antitumor activity against NSCLC cells harboring activated EGFR mutations. Our molecular studies suggest a model that HGK functions by inducing the proteasome-mediated degradation of EGFR, thus inhibiting EGFR-downstream signaling and inducing apoptosis. The findings from this study may have potential applications in the future development of HGK as an anticancer agent that displays unique pharmacologic properties and anti-tumorigenesis activities against specific lung cancer patients.

4. Materials and Methods

4.1. Plant Material and Extraction

The Department of Pharmacy, Chang Gung Memorial Hospital at Chiayi, Taiwan, provided and authenticated dry flower buds of *Daphne genkwa*. A voucher specimen (No. CGU-DG-1) was deposited in the herbarium of Chang Gung University, Taoyuan, Taiwan [16]. The extraction of dried buds of *Daphne genkwa* Sieb. et Zucc. was as described in earlier work [16]. Briefly, dry flower buds of *Daphne genkwa* (5.0 Kg) were extracted with MeOH (30 L \times 4) and then concentrated to give brown syrup (745.75 g). The syrup was suspended in H₂O and partitioned first in CHCl₃/water (1:1) and then in *n*-butanol/water (1:1), successively. The CHCl₃ extract (511.19 g) was used in this study to isolate and identify the flavonoids that exhibit antitumor activity.

4.2. Isolation and Identification of Flavonoids

The CHCl₃ extract was subjected to silica gel column chromatography by eluting with stepwise gradients of CHCl₃: MeOH to obtain fourteen fractions. The fourth fraction was further chromatographed in the silica gel column by eluting with a mixture of *n*-hexane and acetone (3:1) to isolate 3'-methoxy genkwanin [18] (151.9 mg). The fifth fraction was further chromatographed in the silica gel column by eluting with a step gradients of CHCl₃ and acetone to isolate genkwanin [10] (373.9 mg). The seventh fraction was further chromatographed in silica gel column by eluting with a step gradients of *n*-hexane and acetone to isolate HGK [17] (206.4 mg). The structures of these compounds were confirmed by comparison of their spectral data with the corresponding literature values. These compounds were dissolved in dimethyl sulfoxide (DMSO) to make a stock concentration at 100 mM and then stored at -20°C before use.

4.3. Cell Lines and Culture

A549 and H1975 were obtained from the American Type Culture Collection (Manassas, VA, USA). Dr. Tzu-Chien V. Wang (Chang Gung University, Taoyuan, Taiwan) kindly provided the primary normal human foreskin fibroblasts (HFF3) and Dr. Pan-Chyr Yang kindly provided PC9 (National Taiwan University, Taiwan). A549 cells express wild-type EGFR; PC9 cells contain a deletion in exon 19 of EGFR; and, H1975 cells harbor two mutations (L858R and T790M) in EGFR. All of the cells were cultivated in RPMI-1640 medium containing 10% fetal bovine serum (FBS), 2 mM sodium pyruvate, 100 U/mL penicillin, and 100 U/mL streptomycin. The cells were grown at 37 °C in a humidified incubator containing 5% CO₂.

4.4. Antibodies, Oligonucleotides, and Reagents

The culture media, FBS, and chemical compounds were purchased from Life Technologies (Grand Island, NY, USA). Antibodies against phospho-EGFR (Tyr1068), phospho-STAT3 (Tyr705), phospho-AKT (Ser473), phospho-ERK (Thr202/Tyr204), caspase 9, and poly (ADP-ribose) polymerase (PARP) (Asp214) were purchased from Cell Signaling (Temecula, CA, USA). Anti-EGFR, anti-STAT3, anti-AKT, anti-ERK, and β -actin were purchased from Santa Cruz Biotechnology (Santa Cruz, CA, USA). Cycloheximide and MG132 were purchased from Sigma (St. Louis, MO, USA).

4.5. Assays for Viability, Cell Proliferation Capacity, Clonogenic Ability, and Apoptosis

Cell viability assay was carried out by plating 3000 cells/well into 96-well plates. In the following day, the cells were treated with various concentrations of HGK and then incubated for 24 h. Cell viability was measured while using MTT assay and staining with trypan blue. For MTT assay, 10 μ L of MTT (5 mg/mL) solution was added to the cells in each well containing 100 μ L of medium. After incubating at 37 °C for 3 h, the supernatant was removed and 200 μ L of DMSO was added to the cells. The MTT color reaction was examined while using a microplate reader set at A560 nm. For trypan blue assay, the cells were trypsinized and stained with 0.4% trypan blue. The number of unstained viable cells was counted in a hemocytometer under microscope. The data were presented as means \pm standard deviations from three independent experiments. The Student's *t*-test was used for statistical analyses with the SPSS 16.0 software (IBM, New York, NY, USA). The unstained viable cells were determined by counting with a hemocytometer under microscope. The cell proliferation capacity was examined with an xCELLigence real-time cell analyzer (Roche Life Science, Indiana, USA) according to the manufacturer's instructions [28]. For clonogenic ability, the cells were plated in six-well plates (500 cells/well). In the following day, the cells were treated with various concentrations of HGK for 24 h. The treated cells were then incubated in the absence of HGK for five days, stained with crystal violet, and the number of foci formation was determined. For apoptosis assay, the cells were seeded in six-well plates (1×10^5 cells/well) with growth media. In the following day, the cells were placed in the media containing various concentrations of HGK for 24 h. Apoptosis was examined by the detection of phosphatidylserine exposure with Annexin V-FITC Apoptosis Detection Kit I (BD Biosciences, New Jersey, USA) [29], and by the cleaved PARP and caspase 9, as described previously [30].

4.6. Cell-Cycle Analysis

The cells were seeded in six-well plates (1×10^5 cells/well) with growth media. In the following day, the cells were treated with various concentrations of HGK for 24 h. Cells was fixed in -20 °C absolute ethanol for 4 h and resuspended in 1 mL of PBS containing ribonuclease A at 20 μ g/mL. After incubating at 37 °C for 30 min. and propidium iodide was added to each sample at 100 μ g/mL. Cell cycle distribution was analyzed by flow cytometry (BD FACSCalibur TM system, Becton–Dickinson).

4.7. RT-PCR, Western Blotting, and Immunohistochemistry (IHC)

The cells were seeded in six-well plates (1×10^5 cells/well) with growth media. In the following day, the cells were treated with various concentrations of HGK for 24 h. The cell lysate were then collected for analysis by RT-PCR and Western blotting, as described previously [31]. IHC was performed, as described previously [29]. The primary antibodies used for staining were targeted against EGFR and pEGFR [32].

4.8. Whole-Transcriptome Sequencing

The total RNA from H1975 cells treated with and without HGK at 50 μ M for 24 h was isolated while using Trizol® Reagent (Invitrogen, Massachusetts, USA), according to the manufacturer's instruction. RNA was quantified at OD_{260nm} by using a ND-1000 spectrophotometer (Nanodrop Technology, Wilmington, USA). The RNA 6000 LabChip® kit (Agilent Technologies, USA) was used with the Bioanalyzer 2100 (Agilent Technologies, Santa Clara, California, USA) to check the integrity and concentration of total RNA samples. RNA sample preparation for sequencing analysis was carried out according to the protocol that was provided by Illumina. Agilent's SureSelect Strand Specific RNA Library Preparation Kit was used for library construction and 150–200 bp cDNAs were purified by AMPure XP Beads size selection (Beckman Coulter, High Wycombe, Bucks, UK). The DNA sequence was determined while using an Illumina HiSeq 2000 platform.

4.9. Functional Enrichment Analysis

The Ingenuity Pathway Analysis (IPA) (QIAGEN company, Redwood City, CA, USA), a web-based computational platform, was used to conduct functional enrichment analysis of genes [23]. A total of 2345 differential expression (DE) genes (>two fold change) were analyzed by the Core analysis enrichment tool that was based on gene expression database. Canonical pathways and Upstream Regulator Analysis found by core analysis in IPA are given with a *p*-value.

4.10. In Vivo Tumor Xenograft Study

The in vivo antitumor activity of HGK against human NSCLC was studied while using six-week-old nude BALB/c nu/nu male mice (*n* = eight per group). The animals were inoculated subcutaneously in the right flank with H1975 tumor cells (3×10^6) in 100 μ L on day 0. Drug treatment was started when the tumor volume reached around 50 mm³ on day 10. The mice were randomized into control and drug treatment groups with eight animals in each group. The powder of HGK dissolved in 100 μ L of PBS was administered by intra-peritoneal (i.p.) injection (1.0 mg/kg body weight) every two days. The control group was treated with an equal volume of PBS. The tumor volume was monitored every two days while using calipers, and tumor volume was estimated according to the following formula: tumor volume = length \times width² / 2. On day 17, the tumor-bearing mice was weighed and then sacrificed for the assay of tumor biology. The animals were also evaluated for body weights and consumption of food to access apparent signs of toxicity. All of the animal experiments were performed after obtaining the approval of the Institutional Animal Care and Use Committee (IACUC) of Chang Gung Memorial Hospital (IACUC approval no.: 2018031301, approval date: 6/19/2018).

4.11. Statistical Analysis

The presented results were representative of three independent experiments with similar results. Statistical differences was evaluated while using the Student's *t*-test, and it was considered to be significant at *p* < 0.05.

Supplementary Materials: The following are available online at <http://www.mdpi.com/1420-3049/25/4/941/s1>, Figure S1: The cell proliferation capacity of H1975 cells treated with MG132 or/ and HGK.

Author Contributions: Conceptualization, Y.-L.L., T.-H.W., Y.-C.H. and C.-Y.C.; formal analysis, C.-C.W., K.-Y.H. and Y.-W.J.; software, Y.-C.H.; investigation, C.-C.W., K.-Y.H. and Y.-W.J.; methodology, Y.-L.L., T.-H.W., Y.-C.H.

and C.-Y.C.; project administration, Y.-L.L., T.-H.W. and C.-Y.C.; data curation, C.-C.W., K.-Y.H. and Y.-W.J.; resources, Y.-L.L., T.-H.W. and C.-Y.C.; supervision, T.-H.W.; validation, Y.-C.H.; visualization, Y.-L.L., T.-H.W. and C.-Y.C.; writing, original draft, Y.-C.H. and C.-Y.C.; writing, review and editing, Y.-L.L., T.-H.W., Y.-C.H. and C.-Y.C. All authors have read and agreed to the published version of the manuscript.

Funding: This work was supported by grants from Chang Gung Memorial Hospital (CMRPF1I0011), Ministry of Science and Technology of Taiwan (107-2320-B-255-004-), Chang Gung University of Science and Technology (ZRRPF3H0091). The funders had no role in study design, data collection, data analysis, publication decisions or manuscript preparation.

Conflicts of Interest: The authors declare no conflict of interest.

References

- Sharma, S.V.; Bell, D.W.; Settleman, J.; Haber, D.A. Epidermal growth factor receptor mutations in lung cancer. *Nat. Rev. Cancer* **2007**, *7*, 169–181. [\[CrossRef\]](#) [\[PubMed\]](#)
- Linardou, H.; Dahabreh, I.J.; Bafaloukos, D.; Kosmidis, P.; Murray, S. Somatic EGFR mutations and efficacy of tyrosine kinase inhibitors in NSCLC. *Nat. Rev. Clin. Oncol.* **2009**, *6*, 352–366. [\[CrossRef\]](#) [\[PubMed\]](#)
- Pao, W.; Chmielecki, J. Rational, biologically based treatment of EGFR-mutant non-small-cell lung cancer. *Nat. Rev. Cancer* **2010**, *10*, 760–774. [\[CrossRef\]](#) [\[PubMed\]](#)
- Chong, C.R.; Jänne, P.A. The quest to overcome resistance to EGFR-targeted therapies in cancer. *Nat. Med.* **2013**, *19*, 1389–1400. [\[CrossRef\]](#)
- Thress, K.S.; Pawelczak, C.P.; Felip, E.; Cho, B.C.; Stetson, D.; Dougherty, B.; Lai, Z.; Markovets, A.; Vivancos, A.; Kuang, Y.; et al. Acquired EGFR C797S mutation mediates resistance to AZD9291 in non-small cell lung cancer harboring EGFR T790M. *Nat. Med.* **2015**, *21*, 560–562. [\[CrossRef\]](#)
- Kai, H.; Koine, T.; Baba, M.; Okuyama, T. Pharmacological Effects of Daphne genkwa and Chinese Medical Prescription, “Jyu-So-To”. *Yakugaku Zasshi* **2004**, *124*, 349–354. [\[CrossRef\]](#)
- Zhan, Z.J.; Fan, C.Q.; Ding, J.; Yue, J.M. Novel diterpenoids with potent inhibitory activity against endothelium cell HMEC and cytotoxic activities from a well-known TCM plant Daphne genkwa. *Bioorg. Med. Chem.* **2005**, *13*, 645–655. [\[CrossRef\]](#)
- Lee, M.-Y.; Park, B.-Y.; Kwon, O.-K.; Yuk, J.-E.; Oh, S.-R.; Kim, H.-S.; Lee, H.-K.; Ahn, K.-S. Anti-inflammatory activity of (–)-aptosimon isolated from Daphne genkwa in RAW264.7 cells. *Int. Immunopharmacol.* **2009**, *9*, 878–885. [\[CrossRef\]](#)
- Park, B.-Y.; Min, B.S.; Ahn, K.-S.; Kwon, O.-K.; Joung, H.; Bae, K.-H.; Lee, H.-K.; Oh, S.-R. Daphnane diterpene esters isolated from flower buds of Daphne genkwa induce apoptosis in human myelocytic HL-60 cells and suppress tumor growth in Lewis lung carcinoma (LLC)-inoculated mouse model. *J. Ethnopharmacol.* **2007**, *111*, 496–503. [\[CrossRef\]](#)
- Park, B.-Y.; Min, B.-S.; Oh, S.-R.; Kim, J.-H.; Bae, K.-H.; Lee, H.-K. Isolation of flavonoids, a biscoumarin and an amide from the flower buds of Daphne genkwa and the evaluation of their anti-complement activity. *Phytotherapy Res.* **2006**, *20*, 610–613. [\[CrossRef\]](#)
- Wang, C.-F.; Li, R.-R.; Huang, L.-L.; Zhong, L.-Q.; Yuan, S.-T. [Studies on chemical constituents of Daphne genkwa]. *J. Chin. Med. Mater.* **2009**, *32*, 508–511.
- Hong, J.-Y.; Chung, H.-J.; Lee, H.-J.; Park, H.J.; Lee, S.K. Growth Inhibition of Human Lung Cancer Cells via Down-regulation of Epidermal Growth Factor Receptor Signaling by Yuanhuadine, a Daphnane Diterpene from Daphne genkwa. *J. Nat. Prod.* **2011**, *74*, 2102–2108. [\[CrossRef\]](#) [\[PubMed\]](#)
- Kang, J.I.; Hong, J.Y.; Lee, H.J.; Bae, S.Y.; Jung, C.; Park, H.J.; Lee, S.K. Anti-Tumor Activity of Yuanhuacine by Regulating AMPK/mTOR Signaling Pathway and Actin Cytoskeleton Organization in Non-Small Cell Lung Cancer Cells. *PLoS ONE* **2015**, *10*, e0144368. [\[CrossRef\]](#) [\[PubMed\]](#)
- Zheng, W.; Gao, X.; Chen, C.; Tan, R. Total flavonoids of Daphne genkwa root significantly inhibit the growth and metastasis of Lewis lung carcinoma in C57BL6 mice. *Int. Immunopharmacol.* **2007**, *7*, 117–127. [\[CrossRef\]](#) [\[PubMed\]](#)
- Du, W.-J.; Yang, X.-L.; Song, Z.-J.; Wang, J.-Y.; Zhang, W.-J.; He, X.; Zhang, R.-Q.; Zhang, C.-F.; Li, F.; Yu, C.; et al. Antitumor Activity of Total Flavonoids from Daphne genkwa in Colorectal Cancer. *Phytotherapy Res.* **2015**, *30*, 323–330. [\[CrossRef\]](#) [\[PubMed\]](#)
- Chang, C.-W.; Leu, Y.-L.; Horng, J.-T. Daphne Genkwa Sieb. et Zucc. Water-Soluble Extracts Act on Enterovirus 71 by Inhibiting Viral Entry. *Viruses* **2012**, *4*, 539–556. [\[CrossRef\]](#)

17. Ulubelen, A.; Bücken, R.; Mabry, T.J. Flavone 5-O-glucosides from *Daphne sericea*. *Phytochemistry* **1982**, *21*, 801–803. [[CrossRef](#)]
18. Das, K.C.; Farmer, W.J.; Weinstein, B. Phytochemical studies. IX. A new flavone, velutin. *J. Org. Chem.* **1970**, *35*, 3989–3990. [[CrossRef](#)]
19. Pang, Y.-X.; Wang, D.; Fan, Z.; Chen, X.L.; Yu, F.-L.; Hu, X.; Wang, K.; Yuan, L. *Blumea balsamifera*—A Phytochemical and Pharmacological Review. *Molecules* **2014**, *19*, 9453–9477. [[CrossRef](#)]
20. Wang, Y.; Xu, Y.S.; Yin, L.H.; Na Xu, L.; Jinyong, P.; Zhou, H.; Kang, W. Synergistic anti-glioma effect of Hydroxygenkwanin and Apigenin in vitro. *Chem. Interact.* **2013**, *206*, 346–355. [[CrossRef](#)]
21. Huang, Y.-C.; Lee, P.-C.; Wang, J.J.; Hsu, Y.-C. Anticancer Effect and Mechanism of Hydroxygenkwanin in Oral Squamous Cell Carcinoma. *Front. Oncol.* **2019**, *9*, 911. [[CrossRef](#)] [[PubMed](#)]
22. Chou, L.-F.; Chen, C.-Y.; Yang, W.-H.; Chen, C.-C.; Chang, J.-L.; Leu, Y.-L.; Liou, M.-J.; Wang, T.H. Suppression of Hepatocellular Carcinoma Progression through FOXM1 and EMT Inhibition via Hydroxygenkwanin-Induced miR-320a Expression. *Biomolology* **2019**, *10*, 20. [[CrossRef](#)] [[PubMed](#)]
23. Krämer, A.; Green, J.; Pollard, J.; Tugendreich, S. Causal analysis approaches in Ingenuity Pathway Analysis. *Bioinformatics* **2013**, *30*, 523–530. [[CrossRef](#)]
24. Huang, K.-Y.; Kao, S.-H.; Wang, W.-L.; Hong, T.-M.; Chen, C.-Y.; Hsiao, T.-H.; Salunke, S.B.; Chen, J.J.W.; Su, K.-Y.; Yang, S.-C.; et al. Small Molecule T315 Promotes Casitas B-Lineage Lymphoma-Dependent Degradation of Epidermal Growth Factor Receptor via Y1045 Autophosphorylation. *Am. J. Respir. Crit. Care Med.* **2016**, *193*, 753–766. [[CrossRef](#)]
25. Chen, C.-Y.; Yu, Z.-Y.; Chuang, Y.-S.; Huang, R.-M.; Wang, T.-C. Sulforaphane attenuates EGFR signaling in NSCLC cells. *J. Biomed. Sci.* **2015**, *22*, 38. [[CrossRef](#)]
26. Sigismund, S.; Algisi, V.; Nappo, G.; Conte, A.; Pascolutti, R.; Cuomo, A.; Bonaldi, T.; Argenzio, E.; Verhoef, L.G.G.C.; Maspero, E.; et al. Threshold-controlled ubiquitination of the EGFR directs receptor fate. *EMBO J.* **2013**, *32*, 2140–2157. [[CrossRef](#)]
27. Vucic, D.; Dixit, V.M.; Wertz, I.E. Ubiquitylation in apoptosis: A post-translational modification at the edge of life and death. *Nat. Rev. Mol. Cell Biol.* **2011**, *12*, 439–452. [[CrossRef](#)]
28. Chen, C.-C.; Chen, C.-Y.; Ueng, S.-H.; Hsueh, C.; Yeh, C.-T.; Ho, J.-Y.; Chou, L.-F.; Wang, T.H. Corylin increases the sensitivity of hepatocellular carcinoma cells to chemotherapy through long noncoding RNA RAD51-AS1-mediated inhibition of DNA repair. *Cell Death Dis.* **2018**, *9*, 543. [[CrossRef](#)]
29. Yeh, Y.-M.; Chen, C.-Y.; Huang, P.-R.; Hsu, C.-W.; Wu, C.-C.; Wang, T.-C. Proteomic analyses of genes regulated by heterogeneous nuclear ribonucleoproteins A/B in Jurkat cells. *Proteomics* **2014**, *14*, 1357–1366. [[CrossRef](#)]
30. Wang, T.-H.; Chan, C.-W.; Fang, J.-Y.; Shih, Y.-M.; Liu, Y.-W.; Wang, T.-C.; Chen, C.-Y. 2-O-Methylmagnolol upregulates the long non-coding RNA, GAS5, and enhances apoptosis in skin cancer cells. *Cell Death Dis.* **2017**, *8*, e2638. [[CrossRef](#)]
31. Chen, C.-Y.; Jan, C.-I.; Lo, J.-F.; Yang, S.-C.; Chang, Y.-L.; Pan, S.-H.; Wang, W.-L.; Hong, T.-M.; Yang, P.-C. Tid1-L Inhibits EGFR Signaling in Lung Adenocarcinoma by Enhancing EGFR Ubiquitinylation and Degradation. *Cancer Res.* **2013**, *73*, 4009–4019. [[CrossRef](#)] [[PubMed](#)]
32. Wang, T.-H.; Lin, Y.-H.; Yang, S.-C.; Chang, P.-C.; Wang, T.-C.; Chen, C.-Y. Tid1-S regulates the mitochondrial localization of EGFR in non-small cell lung carcinoma. *Oncogenesis* **2017**, *6*, e361. [[CrossRef](#)] [[PubMed](#)]



© 2020 by the authors. Licensee MDPI, Basel, Switzerland. This article is an open access article distributed under the terms and conditions of the Creative Commons Attribution (CC BY) license (<http://creativecommons.org/licenses/by/4.0/>).



Enterovirus and Encephalitis

Bo-Shiun Chen^{1,2}, Hou-Chen Lee¹, Kuo-Ming Lee¹, Yu-Nong Gong^{1,3} and Shin-Ru Shih^{1,3,4,5,6,7*}

¹ Research Center for Emerging Viral Infections, College of Medicine, Chang Gung University, Taoyuan, Taiwan, ² Department of Neuroscience and Regenerative Medicine, Medical College of Georgia, Augusta University, Augusta, GA, United States, ³ Department of Laboratory Medicine, Linkou Chang Gung Memorial Hospital, Taoyuan, Taiwan, ⁴ Department of Medical Biotechnology and Laboratory Science, College of Medicine, Chang Gung University, Taoyuan, Taiwan, ⁵ Research Center for Chinese Herbal Medicine, College of Human Ecology, Chang Gung University of Science and Technology, Taoyuan, Taiwan, ⁶ Research Center for Food and Cosmetic Safety, College of Human Ecology, Chang Gung University of Science and Technology, Taoyuan, Taiwan, ⁷ Graduate Institute of Health Industry Technology, College of Human Ecology, Chang Gung University of Science and Technology, Taoyuan, Taiwan

Enterovirus-induced infection of the central nervous system (CNS) results in acute inflammation of the brain (encephalitis) and constitutes a significant global burden to human health. These viruses are thought to be highly cytolytic, therefore normal brain function could be greatly compromised following enteroviral infection of the CNS. A further layer of complexity is added by evidence showing that some enteroviruses may establish a persistent infection within the CNS and eventually lead to pathogenesis of certain neurodegenerative disorders. Interestingly, enterovirus encephalitis is particularly common among young children, suggesting a potential causal link between the development of the neuroimmune system and enteroviral neuroinvasion. Although the CNS involvement in enterovirus infections is a relatively rare complication, it represents a serious underlying cause of mortality. Here we review a selection of enteroviruses that infect the CNS and discuss recent advances in the characterization of these enteroviruses with regard to their routes of CNS infection, tropism, virulence, and immune responses.

Keywords: enterovirus, encephalitis, CNS, Picornaviridae, RNA virus

INTRODUCTION

Enteroviruses belong to the family Picornaviridae, a highly diverse group of small, non-enveloped, icosahedral-shaped viruses with single positive-strand RNA genomes. Based on the sequence diversity, they have been divided into 15 species: enterovirus A to L and rhinovirus A to C. Human enteroviruses containing four enterovirus species (A to D) and three rhinovirus species (A to C) infect millions of people worldwide every year. Although infections are frequently asymptomatic, human enteroviruses can cause a variety of symptoms comprising fever, headache, respiratory illness, sore throat, and, occasionally, vomiting and diarrhea. Importantly, several members of human enteroviruses are neurotropic pathogens with a wide range of clinical disorders ranging from aseptic meningitis to more severe encephalitis. In the United States, enterovirus has been shown to be the most common etiology of meningitis/encephalitis (Hasbun et al., 2017; Balada-Llasat et al., 2019). About 58% of the infected infants and children and 52% of the infected adults diagnosed with meningitis/encephalitis is due to enterovirus. In addition, age is highly associated with the clinical presentation with severe infections including CNS disease, myocarditis and

OPEN ACCESS

Edited by:

Erna Geessien Kroon,
Federal University of Minas Gerais,
Brazil

Reviewed by:

Sara Louise Cosby,
Agri-Food and Biosciences Institute
(AFBI), United Kingdom
Varpu Seija Marjomäki,
University of Jyväskylä, Finland

*Correspondence:

Shin-Ru Shih
srshih@mail.cgu.edu.tw

Specialty section:

This article was submitted to
Virology,
a section of the journal
Frontiers in Microbiology

Received: 06 November 2019

Accepted: 04 February 2020

Published: 20 February 2020

Citation:

Chen B-S, Lee H-C, Lee K-M,
Gong Y-N and Shih S-R (2020)
Enterovirus and Encephalitis.
Front. Microbiol. 11:261.
doi: 10.3389/fmicb.2020.00261

sepsis-like illness occurring most frequently in neonates and infants. The best-known neurotropic enterovirus is the poliovirus (PV), which belongs to the species Enterovirus C and is believed to have almost been eradicated by vaccinations from circulation in human populations. Non-polio enteroviruses are also known to infect the CNS and account for the majority of recent enteroviral infections with neurological disorders. Among the non-polio enteroviruses, the species Enterovirus A like enterovirus 71 (EV-A71), coxsackievirus A6 (CV-A6), and CV-A16 (Goto et al., 2009; Xu et al., 2012; Huang Y. et al., 2015; Holmes et al., 2016; B'Krong et al., 2018; Suresh et al., 2018), the species Enterovirus B like CV-B1 (Sun et al., 2019), CV-B3 (Fan and Liu, 2019), CV-B5 (Mao et al., 2018), CV-A9, Echovirus 6 (E-6), E-7, E-11, and E-13 (Holmes et al., 2016; Chen et al., 2017; B'Krong et al., 2018; Suresh et al., 2018; Chen et al., 2019; Ramalho et al., 2019; Sun et al., 2019), the species Enterovirus C like CV-A24 (Tapparel et al., 2013; B'Krong et al., 2018; Suresh et al., 2018), and the species Enterovirus D like EV-D68 (Tapparel et al., 2013; Messacar et al., 2018) have been shown to involve the CNS and cause diverse neurological complications such as encephalitis, meningitis and acute flaccid paralysis (AFP) (Tapparel et al., 2013) (see **Table 1** for details).

ENTEROVIRUS LIFE CYCLE

The enterovirus genome contains approximately 7.5 kb with a single open reading frame flanked by 5'- and 3'-untranslated regions (UTR) and is enclosed in a capsid. While the 5' end is covalently attached to a viral protein genome-linked (VPg) required for replication, the polyadenylated 3' terminus is important not only for the negative-stranded RNA synthesis but also for translation and RNA stability (Zoll et al., 2009; Kempf and Barton, 2015). The life cycle of enteroviruses begins with binding to one or more specific receptors on the cell surface. The cell receptors for enteroviruses are quite divergent. For example, the cell surface receptor for PV is cluster of differentiation 155 (CD155), whereas EV-A71 has nine cell surface receptors including human scavenger receptor class B member 2 (hSCARB2), human P-selectin glycoprotein ligand 1 (hPSGL1), annexin II (Anx2), heparan sulfate, sialylated glycan, dendritic cell-specific ICAM3-grabbing non-integrin, vimentin, nucleolin and human tryptophanyl-tRNA synthetase (hWARS) (Baggen et al., 2018; Yeung et al., 2018). Receptor binding allows viruses to enter host cells via receptor-mediated endocytosis. There are several endocytic pathways that can mediate the entry of receptor-bound enterovirus particles at the plasma membrane, including macropinocytosis, clathrin-dependent endocytosis and clathrin-independent uptake such as caveolae-dependent and non-caveolae-dependent endocytosis (Marjomaki et al., 2015). The specific endocytic pathways that virus exploits to enter the cells depend on the viral species and serotype, host cell type and local microenvironment (such as pH and temperature). For instance, EV-A71 enters rhabdomyosarcoma (RD) cells through the clathrin-dependent pathway, whereas the caveolae-mediated pathway is used to enter Jurkat cells. EV-A71 exhibits distinct endocytic pathways in different host cells, partly because of the

diversity of the EV-A71 surface receptors (Yamayoshi et al., 2014). Upon entry into host cells, virus uncoating releases its viral RNA genome into the cytoplasm and translation is initiated from an internal ribosome sequence in the 5' UTR, which is called internal ribosome entry site (IRES). An IRES is a *cis*-acting RNA element that forms secondary and tertiary structures to allow cap-independent initiation of translation (Shih et al., 2011; Lee et al., 2017). Translation of viral RNA yields a single polyprotein, which is proteolytically processed by viral proteases to produce four capsid proteins (VP4, VP2, VP3, and VP1) required for virion packaging, and seven non-structural proteins (2A-2B-2C and 3A-3B-3C-3D^{Pol}) as well as some stable precursors, which function in virus replication and disrupting the host cellular immune system. Viral RNA replication is catalyzed by the virally encoded RNA-dependent RNA polymerases, 3D^{Pol}, which utilizes VPg as a protein primer to initiate the replication process. The synthesis of viral RNA takes place on the virus-induced remodeling of intracellular membranes that form replication organelles and leads to double-stranded RNA formation, which in turn will be transcribed into positive single-stranded RNA (Hsu et al., 2010; van der Schaar et al., 2016). Newly synthesized RNA may either serve as a template for translation and replication or be packaged into new infectious virions.

CNS INVASION

Enteroviruses infect humans primarily through the fecal-oral route and replicate in the gastrointestinal tract with the exception of some enteroviruses, e.g., rhinovirus and EV-D68, which can cause respiratory infection and spread via respiratory secretion. After initial infection in the first exposed area, the enteroviruses can gain access to the CNS through multiple pathways, which are not mutually exclusive (**Figure 1**; Rhoades et al., 2011; Huang and Shih, 2015). First, most neurotropic viruses including enteroviruses spread through the bloodstream to reach the CNS. The spread of virus particles from the blood to the CNS is normally restricted by the blood brain barrier (BBB), which is a highly selective semipermeable barrier between the brain's blood vessels and the cells in the brain. However, BBB integrity can be compromised by direct infection of the brain microvascular endothelial cells (BMECs) that make up the BBB or by the cytokines that are produced locally in the CNS during viral infections. For example, PV has been shown to invade the CNS via BBB transmission (Yang et al., 1997). Recent evidence has further demonstrated that mouse transferrin receptor 1 is responsible for PV attachment to the cell surface of BMECs, allowing invasion into the CNS via the BBB (Mizutani et al., 2016). Secondly, enteroviruses can invade the CNS through the peripheral circulating immune cells, which carry intracellular viruses (Tabor-Godwin et al., 2010). This is known as the Trojan horse route. Although the brain has been considered a site of immune-privilege, it has an active immune surveillance system that involves the recruitment of non-specific leukocytes such as phagocytes and lymphocytes into the meninges and cerebrospinal fluid (CSF) (Forrester et al., 2018). Indeed, it has been shown that the CSF contains a trafficking population of mononuclear

TABLE 1 | Neurological symptoms of non-polio enteroviruses that involve the CNS.

Species	Serotype	CNS symptoms	References
A	EV-A71	E/M/AFP	Huang Y. et al., 2015; Mao et al., 2016; B'Krong et al., 2018; Suresh et al., 2018; Ramalho et al., 2019
	EV-A76	AFP	Suresh et al., 2018
	EV-A90	AFP	Suresh et al., 2018
	CV-A2	M/AFP	Holmes et al., 2016; Suresh et al., 2018
	CV-A3	AFP	Suresh et al., 2018
	CV-A4	AFP	Suresh et al., 2018
	CV-A5	AFP	Suresh et al., 2018
	CV-A6	E/M/AFP	Huang Y. et al., 2015; Holmes et al., 2016; Suresh et al., 2018
	CV-A7	AFP	Suresh et al., 2018
	CV-A10	E/M/AFP	Huang Y. et al., 2015; Mao et al., 2016; B'Krong et al., 2018; Suresh et al., 2018
	CV-A12	AFP	B'Krong et al., 2018; Suresh et al., 2018
	CV-A14	AFP	Suresh et al., 2018
B	CV-A16	E/M/AFP	Goto et al., 2009; Xu et al., 2012; Huang Y. et al., 2015; Holmes et al., 2016; Suresh et al., 2018
	CV-A9	E/M/AFP	Holmes et al., 2016; Chen et al., 2017; B'Krong et al., 2018; Suresh et al., 2018; Ramalho et al., 2019; Sun et al., 2019
	CV-B1	E/M/AFP	Holmes et al., 2016; B'Krong et al., 2018; Suresh et al., 2018; Fan and Liu, 2019; Ramalho et al., 2019; Sun et al., 2019
	CV-B2	E/M/AFP	Holmes et al., 2016; B'Krong et al., 2018; Suresh et al., 2018; Fan and Liu, 2019; Ramalho et al., 2019
	CV-B3	E/M/AFP	Holmes et al., 2016; Mao et al., 2016; Mao et al., 2018; Suresh et al., 2018; Fan and Liu, 2019; Ramalho et al., 2019; Sun et al., 2019
	CV-B4	E/M/AFP	Holmes et al., 2016; Mao et al., 2016; B'Krong et al., 2018; Mao et al., 2018; Suresh et al., 2018; Sun et al., 2019
	CV-B5	E/M/AFP	Holmes et al., 2016; Mao et al., 2016; Chen et al., 2017; B'Krong et al., 2018; Mao et al., 2018; Suresh et al., 2018; Ramalho et al., 2019; Sun et al., 2019
	CV-B6	M/AFP	Tapparel et al., 2013; Suresh et al., 2018
	E-1	M/AFP	Tapparel et al., 2013; Suresh et al., 2018
	E-2	M/AFP	Tapparel et al., 2013; Suresh et al., 2018
	E-3	E/M/AFP	Tapparel et al., 2013; Suresh et al., 2018; Ramalho et al., 2019
	E-4	E/M/AFP	Tapparel et al., 2013; B'Krong et al., 2018; Suresh et al., 2018
	E-5	E/M/AFP	Tapparel et al., 2013; Holmes et al., 2016; Suresh et al., 2018
	E-6	E/M/AFP	Holmes et al., 2016; Chen et al., 2017; B'Krong et al., 2018; Suresh et al., 2018; Ramalho et al., 2019; Sun et al., 2019
	E-7	E/M/AFP	Tapparel et al., 2013; Holmes et al., 2016; Suresh et al., 2018; Ramalho et al., 2019
	E-9	E/M/AFP	Holmes et al., 2016; B'Krong et al., 2018; Suresh et al., 2018; Ramalho et al., 2019; Sun et al., 2019
	E-11	E/M/AFP	Holmes et al., 2016; Suresh et al., 2018; Ramalho et al., 2019; Sun et al., 2019
	E-12	M/AFP	Tapparel et al., 2013; B'Krong et al., 2018; Suresh et al., 2018
	E-13	E/M/AFP	Tapparel et al., 2013; Holmes et al., 2016; Suresh et al., 2018; Ramalho et al., 2019
	E-14	E/M/AFP	Chen et al., 2017; Suresh et al., 2018; Ramalho et al., 2019; Sun et al., 2019
	E-15	M/AFP	Suresh et al., 2018; Ramalho et al., 2019
	E-16	E/M/AFP	Holmes et al., 2016; B'Krong et al., 2018; Suresh et al., 2018; Sun et al., 2019
	E-17	E/M/AFP	Tapparel et al., 2013; Holmes et al., 2016; Suresh et al., 2018
	E-18	E/M/AFP	Holmes et al., 2016; Chen et al., 2017; B'Krong et al., 2018; Suresh et al., 2018; Chen et al., 2019; Ramalho et al., 2019; Sun et al., 2019
	E-19	E/M/AFP	Tapparel et al., 2013; B'Krong et al., 2018; Suresh et al., 2018
	E-20	M/AFP	Tapparel et al., 2013; Suresh et al., 2018
	E-21	E/M/AFP	Holmes et al., 2016; Suresh et al., 2018; Ramalho et al., 2019; Sun et al., 2019
	E-22	AFP	Suresh et al., 2018
	E-24	E/M/AFP	Tapparel et al., 2013; B'Krong et al., 2018; Suresh et al., 2018
	E-25	E/M/AFP	Holmes et al., 2016; B'Krong et al., 2018; Suresh et al., 2018; Ramalho et al., 2019; Sun et al., 2019
	E-26	AFP	Suresh et al., 2018
	E-27	E/M/AFP	Tapparel et al., 2013; B'Krong et al., 2018; Suresh et al., 2018
	E-29	M/AFP	Tapparel et al., 2013; Suresh et al., 2018
	E-30	E/M/AFP	Holmes et al., 2016; Mao et al., 2016; Chen et al., 2017; B'Krong et al., 2018; Suresh et al., 2018; Ramalho et al., 2019; Sun et al., 2019
	E-31	M/AFP	Tapparel et al., 2013; Suresh et al., 2018
	E-32	M/AFP	Tapparel et al., 2013; Suresh et al., 2018
	E-33	E/M/AFP	Tapparel et al., 2013; Suresh et al., 2018; Sun et al., 2019
	EV-B73	AFP	Suresh et al., 2018

(Continued)

TABLE 1 | Continued

Species	Serotype	CNS symptoms	References
C	EV-B74	AFP	Suresh et al., 2018
	EV-B75	AFP	Tapparel et al., 2013; Suresh et al., 2018
	EV-B77	AFP	Tapparel et al., 2013; Suresh et al., 2018
	EV-B79	AFP	Suresh et al., 2018
	EV-B80	AFP	Suresh et al., 2018
	EV-B81	AFP	Tapparel et al., 2013; Suresh et al., 2018
	EV-B85	AFP	Tapparel et al., 2013; Suresh et al., 2018
	EV-B86	AFP	Tapparel et al., 2013; Suresh et al., 2018
	EV-B87	AFP	Tapparel et al., 2013; Suresh et al., 2018
	EV-B88	AFP	Tapparel et al., 2013; Suresh et al., 2018
	EV-B93	AFP	Tapparel et al., 2013; Suresh et al., 2018
	EV-B97	AFP	Tapparel et al., 2013; Suresh et al., 2018
	EV-B100	AFP	Tapparel et al., 2013; Suresh et al., 2018
	EV-B106	AFP	Suresh et al., 2018
	EV-B107	AFP	Suresh et al., 2018
	CV-A1	AFP	Tapparel et al., 2013
	CV-A11	E/M/AFP	Tapparel et al., 2013; Suresh et al., 2018
	CV-A13	E/M/AFP	Tapparel et al., 2013; Suresh et al., 2018
	CV-A17	M/AFP	Tapparel et al., 2013; Suresh et al., 2018
	CV-A20	AFP	Tapparel et al., 2013; Suresh et al., 2018
D	CV-A21	AFP	Tapparel et al., 2013
	CV-A22	M/AFP	Suresh et al., 2018
	CV-A24	M/AFP	Tapparel et al., 2013; Suresh et al., 2018
	EV-C96	AFP	Tapparel et al., 2013; B'Krong et al., 2018; Suresh et al., 2018
	EV-C99	AFP	Suresh et al., 2018
	EV-C109	AFP	Tapparel et al., 2013
	EV-D68	E/M/AFP	Tapparel et al., 2013; Messacar et al., 2018; Suresh et al., 2018
	EV-D70	E/M/AFP	Tapparel et al., 2013; Suresh et al., 2018
	EV-D94	AFP	Tapparel et al., 2013; Suresh et al., 2018

E, encephalitis; M, meningitis; AFP, acute flaccid paralysis.

cells, consisting of T cells (~90%), B cells (~5%), monocytes (~5%), and dendritic cells (<1%) (Ransohoff and Engelhardt, 2012). Once these leukocytes are infected, they can act as carriers to bring viruses into the CNS. For instance, CV-B3-infected myeloid cells have been shown to cross the blood-CSF barrier in the choroid plexus (Tabor-Godwin et al., 2010). Upon entry into the CNS, the virus is likely released from myeloid cells and subsequently infect neurons and/or glia in the brain. There is also evidence that EV-A71 can infect leukocytes through binding to hPSGL1, a sialomucin membrane protein primarily expressed on leukocytes (Nishimura et al., 2009). Whether EV-A71-infected leukocytes can bring viruses into the CNS is not clear. Thirdly, certain enteroviruses can enter the CNS through peripheral nerves via retrograde axonal transport and *trans-synaptic* propagation (Gromeier and Wimmer, 1998; Chen et al., 2007; Ong et al., 2008). Axonal transport is an essential cellular process in neurons required for the movement of synaptic vesicles, lipids, proteins, and organelles including mitochondria, lysosomes, autophagosomes, and endosomes, to and from the cell body. It is well known that some neurotropic viruses can hijack the retrograde axonal transport to invade the CNS. For example, studies have shown that intramuscularly inoculated

PV is taken up by endocytosis at the neuromuscular junctions (Ohka et al., 2004). The endocytosed viral particles in the axon terminal are moved in the retrograde direction toward the cell body via dynein-mediated vesicular transport without initiating uncoating (Ohka et al., 2009). The uncoating event takes place upon arrival at the cell body of the motor neuron. EV-A71 and EV-D68 can also enter and infect the CNS by retrograde axonal transport via peripheral spinal motor nerves (Chen et al., 2007; Ong et al., 2008; Hixon et al., 2019). Interestingly, a recent report has demonstrated that EV-A71 can directly infect the brainstem via cranial nerves, suggesting that the virus can use not only the motor components of spinal nerves but also cranial nerves to enter the CNS (Tan et al., 2014).

TROPISM

Each enterovirus has a distinct tropism that is determined by a combination of host and virus factors (Figure 2; Lin and Shih, 2014). Although neurotropic enteroviruses can invade the CNS and are associated with neurological disorders, dissemination of the virus to the CNS seems to occur sporadically and it is not clear

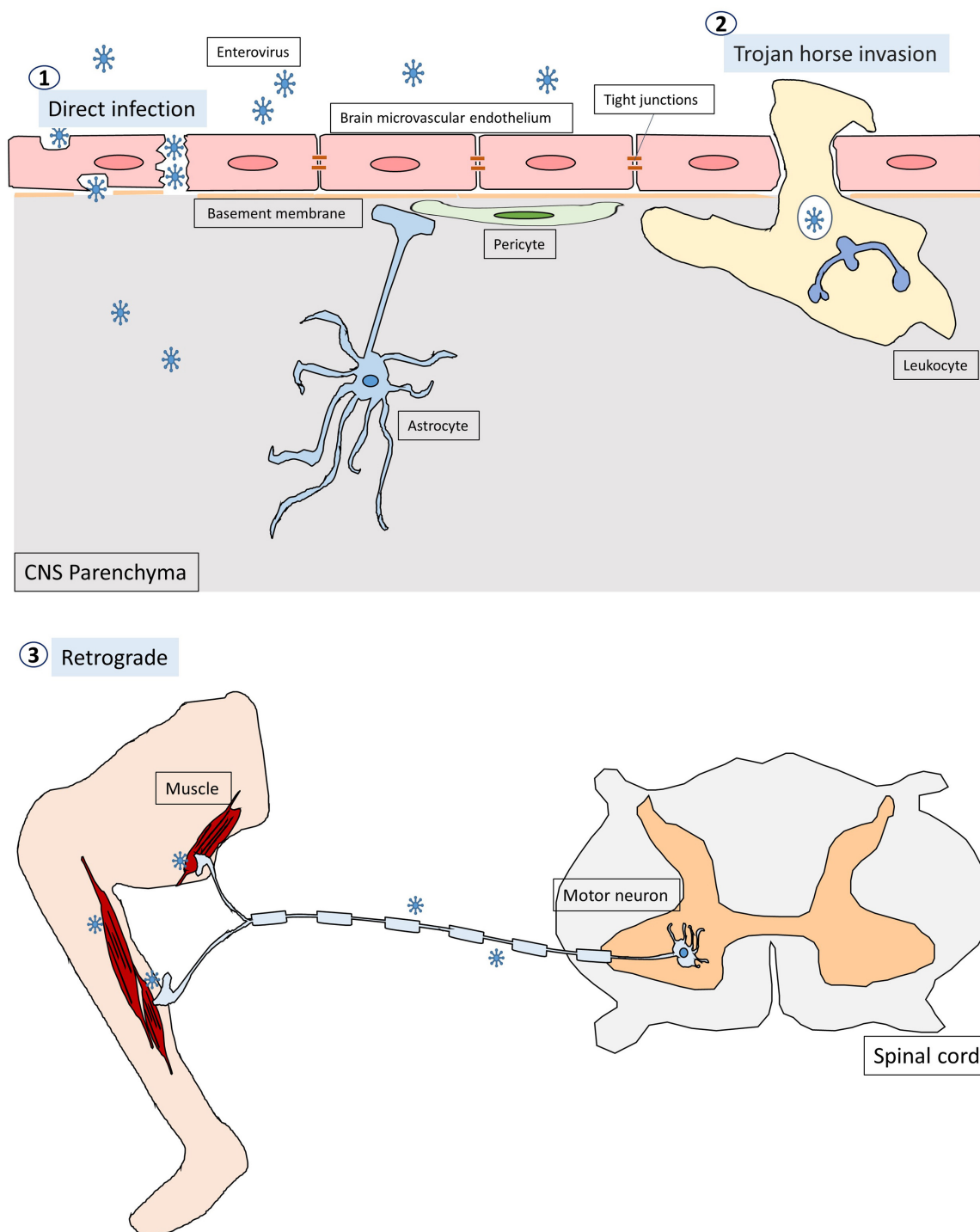
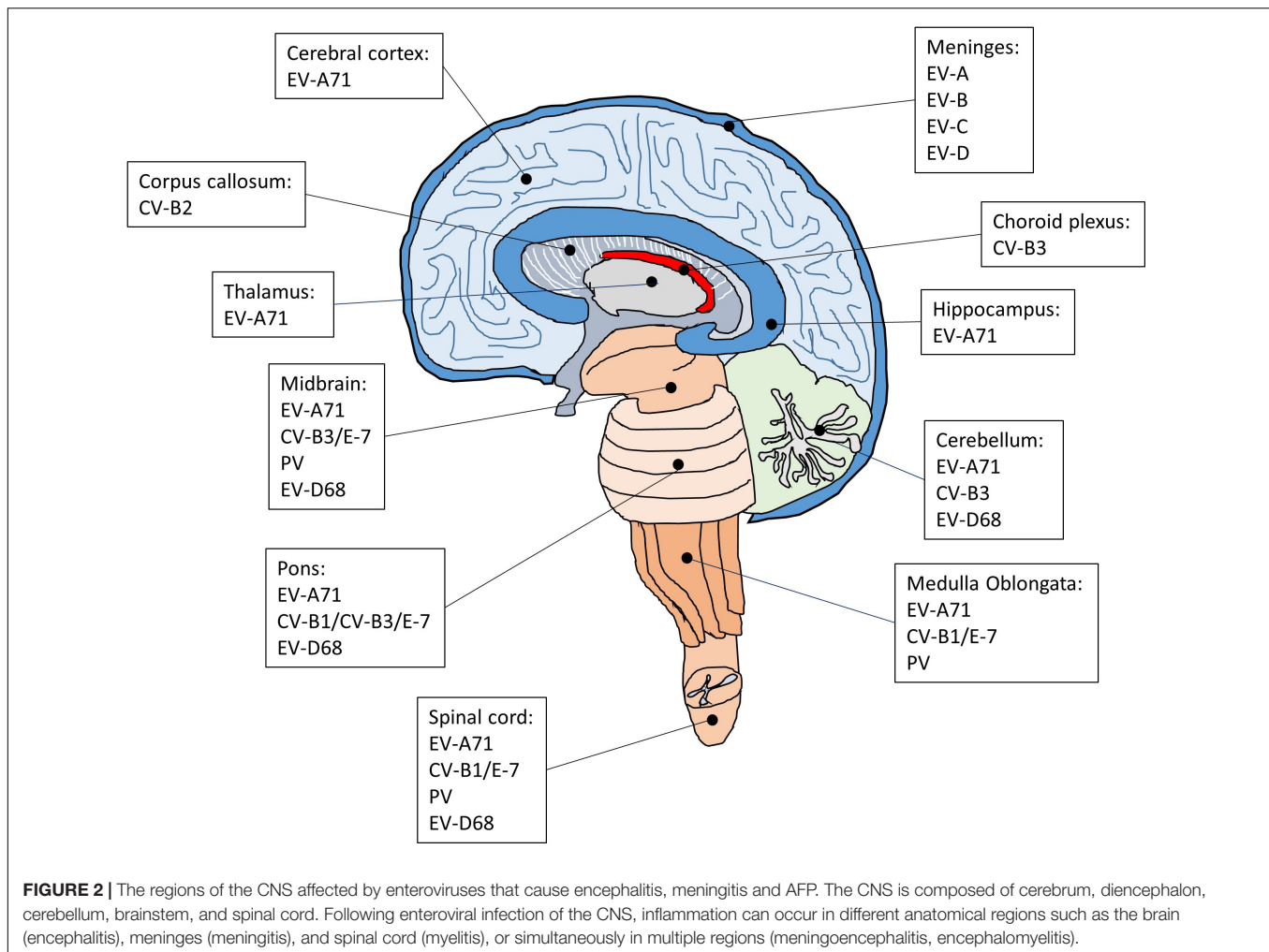


FIGURE 1 | The pathways through which enteroviruses can gain access to the CNS. Enteroviruses can invade the CNS through three pathways. First, they infect BMECs, compromising and crossing the BBB to reach the CNS directly. The second pathway is known as Trojan horse route, in which enterovirus-infected leukocytes act as carriers and transverse the brain barriers bringing virus into the CNS. Thirdly, enteroviruses are able to hijack the retrograde axonal transport to enter the CNS from muscles into the motor neurons in the spinal cord.

how enterovirus targets specific regions and cell types in the brain and spinal cord. Earlier studies on poliovirus have suggested that virus tropism is determined by the cellular receptor for virus

entry (Holland, 1961). However, the PV receptor CD155 is found in tissues that are not sites of PV infection (Mendelsohn et al., 1989; Freistadt et al., 1990; Koike et al., 1990), indicating that the



cellular receptor is required for susceptibility to PV infection but not the sole determinant for virus tropism. Subsequent studies have suggested that the tissue-specific activity of IRES on viral RNAs also plays an important role in determining virus tropism (Gromeier et al., 1996; Yanagiya et al., 2003). For example, a chimeric PV carrying the IRES of hepatitis C virus replicates well in the liver but not in the brain of a mouse model for poliomyelitis, whereas the control poliovirus replicates well both in the liver and brain (Yanagiya et al., 2003). There is also evidence that innate immune antiviral activities such as the interferon (IFN) response is critical for virus tropism (Wessely et al., 2001; Ida-Hosonuma et al., 2005). In transgenic mice containing human CD155, PV replicates and produces severe lesions in the brain and spinal cord, whereas other tissues did not show severe pathological changes. However, in the CD155 transgenic mice lacking alpha/beta IFN, severe lesions are detected in the liver, spleen, and pancreas in addition to the CNS, suggesting that the alpha/beta IFN system is an important determinant for the differential susceptibility of tissue to PV. Poliovirus invades the CNS, which leads to the development of a paralytic disease in about 1% of virus-infected people (Melnick, 1996). Therefore, it has been suggested that, in 99% of the infected cases, the

IFN response limits PV replication in extraneural tissues to prevent the invasion of the CNS (Racaniello, 2006). In the CNS, PV infects and replicates mainly in motor neurons in the anterior horn of the spinal cord, resulting in poliomyelitis (Nagata et al., 2004; Arita et al., 2006). In the most severe cases, PV attacks the neurons of the brainstem, causing bulbar poliomyelitis. In addition to neurons, the CNS contains three major types of non-neuronal cells called glial cells, including astrocytes, oligodendrocytes, and microglia. These glial cells play critical roles in maintaining homeostasis, myelin formation and providing support and protection for neurons. Interestingly, astrocytes and oligodendrocytes are also susceptible to PV infection in primary mouse culture prepared from the cerebral cortex of neonatal CD155 transgenic mice (Couderc et al., 2002). Whether these glial cells are targets for PV infection in the human brain is not known.

Although EV-A71 also invade the CNS, the infected areas are quite distinct compared with poliovirus. Brainstem encephalitis is the most common neurological presentation of EV-A71 infection. Consistently, viral lesions are mainly observed in the brainstem and predominantly located in the ventral, medial and caudal areas of the medulla oblongata (Kao et al., 2004). A few

lesions are also found in the cortex, cerebellum, and spinal cord. In severe cases of EV-A71 infection, the major histopathological changes in the CNS are characterized by inflammatory damage, which selectively leads to neurogenic pulmonary edema and cardiac failure. In agreement with the main CNS lesion locations of EV-A71 infection, the neurons in the medulla oblongata have been implicated in the onset of neurogenic pulmonary edema (Davison et al., 2012). In addition, several autopsy results have suggested that EV-A71 may infect neurons and cause neuronal degeneration, which would activate inflammatory responses in the lesion area and cause encephalitis (Yan et al., 2000; Khong et al., 2012; Yao et al., 2012). Indeed, studies have shown that neurons are susceptible to EV-A71 infection (Huang et al., 2014; Feng et al., 2016). Intriguingly, although neurons can be infected by EV-A71, neural progenitor cells and astrocytes appear to be the main targets for EV-A71 infection in the CNS (Huang et al., 2014; Feng et al., 2016). Both of these cell types are similar in that they are capable of mitosis, which may be critical for virus replication (Yu et al., 2015). Neural progenitor cells are the progenitor cells of the CNS that give rise to many, if not all, of the neuronal and glial cell types and are important for many brain functions including learning and memory and cognition. Thus, the loss of neural progenitor cells due to EV-A71 infection may cause long-term abnormalities of the CNS. This is supported by a long-term follow-up study showing that a large proportion of children after EV-A71 infection with severe CNS involvement and cardiopulmonary failure exhibited delayed neurodevelopment and reduced cognitive function (Chang et al., 2007). Astrocytes also perform many functions in the brain, such as contribution to the formation of the blood-brain barrier, maintenance of extracellular ionic and chemical homeostasis and involvement in the injury response. Since astrocytes are mitotic and localized in a much broader area in the brain than neural progenitor cells, the preferential infection of astrocytes over neurons may create a reservoir for viral proliferation and enable the viral progeny to quickly spread in the CNS and induce massive inflammatory responses. It would be of interest to understand how EV-A71 show a preference for neural progenitor cells and astrocytes.

Similar to EV-A71, coxsackievirus has also been shown to infect neural progenitor cells in addition to neurons (Feuer et al., 2005). Studies have revealed that CV-B3 can infect proliferating neural progenitor cells located in the neonatal subventricular zone and hippocampus. Interestingly, CV-B3 preferentially replicates and induces cytopathic effects in undifferentiated neural progenitor cells (Tsueng et al., 2011). CV-B3 mediated loss of neural progenitor cells leads to a rapid decline in neurogenesis and may eventually cause developmental defects and CNS dysfunction (Ruller et al., 2012). However, the determinants of CV-B3 tropism in the CNS remain unclear. CV-B3 binds to target cells through two main receptors: decay-accelerating factor (DAF) (Bergelson et al., 1995) and coxsackievirus and adenovirus receptor (CAR) (Bergelson, 2009), which has been found to be highly expressed in the developing brain (Xu and Crowell, 1996). There is evidence that immature neurons express relatively high levels of CAR compare to their fully differentiated counterparts (Ahn et al., 2008), suggesting that the level of virus

receptor is one of the critical determinants in preferential virus replication in undifferentiated neural progenitor cells. Besides, CAR exists as multiple isoforms and a specific isoform of CAR that is expressed at high levels in human pancreatic beta cells has been suggested to be prone to coxsackievirus infection (Ifie et al., 2018). Whether this specific isoform of CAR plays a role in coxsackievirus infection in the CNS is not known.

PERSISTENT INFECTION

Though enteroviruses have been considered as cytolytic viruses and diseases caused by infection with enteroviruses are typically short-lived, several studies have indicated that some enteroviruses may be associated with lifelong disorders including post-polio syndrome (Muir et al., 1995; Julien et al., 1999), schizophrenia (Rantakallio et al., 1997; Suvisaari et al., 2003; Khandaker et al., 2012), amyotrophic lateral sclerosis (Woodall et al., 1994; Berger et al., 2000; Giraud et al., 2001), type 1 diabetes (Richardson and Morgan, 2018), and chronic viral cardiomyopathy (Chapman and Kim, 2008). The cause of these enterovirus-associated lifelong disorders is still not clear, but it has been hypothesized that persistent infection of enterovirus may occur based on the presence of enterovirus RNA and protein in the affected tissues at stages of disease after acute infection (Chapman and Kim, 2008). Consistently, the spread of enteroviruses within tissues is not always accompanied by cell death (Bird et al., 2014). Two major groups of persistent infection have been observed *in vitro* (Pinkert et al., 2011). One group, called steady-state infection, is characterized by infection of all cells, while the other group, named carrier-state infection, is characterized by a cytolitic infection of a small proportion of cells, which spares the majority of cells in culture from cytolysis. There is evidence that enteroviruses establish carrier-state infection *in vitro* (Heim et al., 1992; Heim et al., 1995; Pinkert et al., 2011). The carrier-state infection is thought to be induced by the selection of virus mutants that are less cytopathic and may involve the coevolution of both cells and viruses. For example, following CV-B3 infection, expression of the CV-B3 receptor CAR has evolved to be downregulated or eliminated in a subpopulation of cells (Pinkert et al., 2011), which is known to be associated with a decrease of CV-B3 infection and cell lysis (Werk et al., 2005; Fechner et al., 2007). As a result, these evolved cells are protected from virus infection and cell lysis and become dominant in the culture within several passages. In the meantime, the virus also adapts to persist by gaining a CAR-independent entry mechanism (Pinkert et al., 2011). Thus, during the development of persistent infection, viruses and cells have co-evolved such that cellular resistance to viral replication is balanced. In addition to the coevolution model, other viral genomic alterations that cause persistent infection have been reported in the highly conserved 5' UTR, which is critical for viral replication. For instance, CV-B mutants with deletions in the 5' end of the viral genome persist in host tissues, and RNA of the variants can be stably detected from heart tissue of mice experimentally inoculated with wild type CV-B3 and from human cases of

myocarditis (Kim et al., 2005; Chapman et al., 2008; Kim et al., 2008), suggesting that viral replication is important for persistent infection *in vivo*. Nonetheless, it has also been suggested that persistence of CV-B1 RNA in skeletal muscle or CV-B3 RNA in the CNS is not facilitated by genetic alterations that give rise to replication-defective forms, but occurs primarily through formation of stable and atypical double-stranded RNA complex (Tam and Messner, 1999; Feuer et al., 2009). Interestingly, besides the reduction of CAR, other cellular factors have also been shown to play an important role in persistent infection of CV-B3. In particular, CV-B3 replication is affected by the cell cycle status, suggesting that the persistence of CV-B3 may dependent on infection of quiescent cells in which viral replication is lowered or suppressed (Feuer et al., 2002; Feuer et al., 2004). Therefore, the differences between these mechanisms are likely due to distinct patterns of virus-host interactions and there may be tissue- or cell-specific mechanisms for establishing a persistent infection.

Early viral infection of the CNS can cause severe physical and intellectual disability and, in some cases, results in unexpected neurological disorders years after acute infection. For example, approximately 30 percent of polio victims experience new symptoms (post-polio syndrome) about 50 years after the primary infection. Some studies have shown that post-polio syndrome is correlated with the presence of viral RNA in the CNS, suggesting that PV can persist and cause long-term damage in the CNS (Muir et al., 1995). In consistent with these findings, it has been shown that poliovirus strains are not fully lytic in neuroblastoma cell lines (Colbere-Garapin et al., 1989). Following PV infection, massive cytopathic effects are observed in cultured cells, but some cells survive infection without further observable cytopathic effects in spite of continuous viral production. During persistent infection, PV mutants are constantly selected, and many of the identified mutations occur at positions known to be involved in the binding of PV receptors, suggesting that the interactions of the virus with its receptor is critical for the establishment of persistent infections (Colbere-Garapin et al., 1998). Although there is not a single mechanism for establishing a persistent infection, it is believed that the virus must evade host's antiviral immune response. Because enteroviruses have high mutation rates due to the lack of proofreading ability in RNA polymerases, they can generate a variety of mutants not only to affect receptor binding and virus replication but also to evade the immune system. The CNS is relatively inaccessible to immune surveillance compared with other tissues, which makes it particularly vulnerable to persistent infection. Using *in vivo* imaging, a recent study has demonstrated that EV-A71 infection of AG129 mice, in which alpha/beta and gamma interferon receptors are deficient, shows rapid spread and long-term persistence of the virus in the brain of surviving animals (Caine and Osorio, 2017). Interestingly, high viral loads are maintained in the brain even at 6 weeks following infection, whereas viral loads in other tissues including heart, lung, liver, spleen and intestine are gradually reduced to a lower level. In agreement with these findings, *in vitro* studies have shown that in contrast to RD cells or neuroblastoma cell lines, motor neuron-like hybrid cell line (NSC-34) infected by EV-A71 does not display cytopathic effect and the viral particles adopt a non-lytic

exit pathway through autophagy (Too et al., 2016). Furthermore, there is evidence that EV-A71 RNA is present in stool weeks after initial infection (Han et al., 2010). Taken together, all these findings suggest that similar to PV and CV-B3, EV-A71 can also establish a persistent infection in the CNS, but the long-term impact of EV-A71 infection in the CNS remains elusive.

NEUROVIRULENCE

Some enteroviruses can cause diseases within the nervous system. The most thoroughly studied neurovirulent enterovirus is PV. To eradicate global poliomyelitis, much effort has been made to develop polio vaccines including an inactivated PV given by injection and an attenuated PV given by mouth. Although both types of polio vaccines are effective, oral polio vaccines are superior not only in administration but also in providing longer-lasting immunity. The attenuated PV was developed based on the observation that the virus no longer caused disease after many passages in different animals and cell cultures, but replicated sufficiently to induce protective immunity. Genetic analysis of the attenuated PV has shown that a point mutation within the IRES of the vaccine strains is a critical determinant of the attenuation phenotype (Evans et al., 1985; Kawamura et al., 1989; Ren et al., 1991). For instance, the C472U mutation in the IRES of poliovirus type 3 causes a translation defect, which leads to reduced replication in the CNS and attenuation of neurovirulence (La Monica and Racaniello, 1989; Gutierrez et al., 1997; Ohka and Nomoto, 2001). Subsequent studies have shown that the C472U mutation reduces the efficiency of binding of the polypyrimidine-tract binding protein (PTB) to the IRES, which is required for initiation of translation (Guest et al., 2004). Sequence analysis has also identified additional mutations in the capsid region of the vaccine strains. These capsid mutations are likely to disrupt viral particle binding to host cells and reduce the capsid stability, which may contribute to and stabilize the attenuation phenotype. However, PV is notably adaptable and attenuated viruses can increase its virulence through mutation and/or recombination (Jorba et al., 2008; Minor, 2009). Thus, although unusual, immunization with the attenuated vaccine strains may cause vaccine-associated paralytic poliomyelitis, which could be due to the reversion of the mutations in the viral genome that confer the attenuation phenotype and/or acquisition of new mutations with enhanced virulence (Kew et al., 2005; Famulare et al., 2016). Moreover, these vaccine-derived polioviruses (VDPV) have caused outbreaks of poliomyelitis in areas with low routine immunization rates (Burki, 2019). Using approach combining phylogenetic analysis of sequence data from outbreaks of VDPV and an experimental evolution approach in cell culture, a recent study has provided a model describing the evolutionary steps sufficient for the vaccine strain to lose its attenuation and become virulent (Stern et al., 2017). In the first step, the critical mutations for the attenuation phenotype are reverted to increase the viral replication. This is followed by recombination events with co-circulating enterovirus strains, most often a coxsackievirus strain, but in some cases a circulating PV strain to optimize viral replication in the

human gut. In the final step, the virus continues to slowly revert to sequences that are conserved across wild-type PV to enhance the fitness of the virus. The information provides a powerful framework for developing safer vaccine strains and for forecasting virulence of viruses.

EV-A71 has emerged as a serious threat to public health across the Asia-Pacific region. EV-A71 causes hand, foot and mouth disease (HFMD) and herpangina, and occasionally severe neurological disorders. Unlike PV in which a point mutation within the IRES can attenuate neurovirulence, the association between EV-A71 neurovirulence and viral genome sequences remains largely unknown. So far, there are only a few reports showing that the neurovirulence can be weakened by mutations in the viral genome of EV-A71. For example, studies have shown that defined genetic manipulation of the EV-A71 genome based on the temperature-sensitive determinants of a poliovirus vaccine strain results in attenuated neurovirulence in monkeys (Arita et al., 2005). The generated EV-A71 mutant strain contains four mutations in the conserved regions of the enterovirus genome including one in the 5' UTR, two in the 3D polymerase gene and one in the 3' UTR, and all of them are required for substantial attenuation (Arita et al., 2008). Like PV, the capsid proteins also play an important role in EV-A71 virulence. For instance, the amino acid residue 145 of EV-A71 VP1, which affects receptor usage for cell surface attachment of the viral particles (Nishimura et al., 2013; Tan et al., 2017), has been shown to confer mouse adaptation with a G145E replacement (Arita et al., 2008; Chua et al., 2008) and influence the virulence in mice (Chua et al., 2008; Zaini and McMinn, 2012). Consistent with earlier results, a recent study has further demonstrated that the VP1-145 is a key determinant for EV-A71 neurovirulence in monkeys (Fujii et al., 2018). In addition, changes of nucleotides in the 5' UTR and an amino acid replacement in the 2A or 3C protein have been identified to play an important role for virulence determination of EV-A71 (Li et al., 2011; Yeh et al., 2011; Li et al., 2017). Whether they attenuate EV-A71 neurovirulence is unknown. Nonetheless, it is expected that all these findings would contribute to not only our understanding of EV-A71 but also the development of live attenuated EV-A71 vaccine in the future.

EV-D68 is another non-polio enterovirus that has an association with a polio-like neurological disorder known as acute flaccid myelitis (AFM) with symptoms such as dysneuria and muscle weakness although the most common clinical symptom of EV-D68 infection is respiratory illness (Holm-Hansen et al., 2016; Messacar et al., 2018). EV-D68 is quite unique among enteroviruses because it carries some characteristic features of respiratory enteroviruses (Rhinovirus A-C) including optimal growth temperature of 33°C allowing better replication in the nasal cavity and inability to survive in the stomach due to acid sensitivity, but is genetically more closely related to enteric enteroviruses based on phylogenetic analysis. EV-D68 has become an emerging pathogen since an outbreak occurred in 2014 in the United States. Studies have shown that six mutations including M291T, V341A, T860N, D297N, S1108G, and R2005K are associated with neurovirulence of the outbreak EV-D68 strains causing AFM in 2014 (Greninger et al., 2015). Interestingly, another study has identified 3 nucleotide variables,

C1817T, C3277A, and A4020G, in the 2014 outbreak strains, which differ significantly from previously identified EV-D68 strains (Huang W. et al., 2015). Among these three variables, C3277A causes amino acid substitution T860N in the protease 2A cleavage site between VP1 and 2A, whereas A4020G results in amino acid substitution S1108G in a protease 3C cleavage site between 2B and 2C, suggesting that mutation of these two sites may alter the cleavage efficiency and increase replication and transmission rates. However, using a mouse model of paralytic myelitis caused by EV-D68, a recent study has shown that the 2014 outbreak EV-D68 strains isolated from patients without AFM can also produce paralysis in neonatal mice (Hixon et al., 2017). Thus, further comparative analyses using infectious clones containing different combinations of previously identified mutations will be needed to establish the determinants of EV-D68 neurovirulence.

IMMUNE RESPONSES IN THE CNS

About 3% of enterovirus infected people will develop encephalitis while most people never show evidence of CNS infection (Koskiniemi et al., 1991). Since encephalitis only occurs in a small percentage of infected people, it is thought that host-pathogen interactions and immune responses in peripheral sites prevent viruses from gaining access to and causing infection within the CNS. Patients with enterovirus encephalitis may present symptoms that range in severity from mild cognitive impairment and memory loss to permanent CNS damage and death. The symptoms are mainly caused by virus-induced inflammatory responses in the brain. Inflammation is the body's protective immune response against infection, but the brain was thought to be immune-privileged based on two predominant beliefs. First, the BBB prevents the entry of circulating immune cells and antibodies into the brain. Secondly, there is no lymphatic drainage to alert the immune system to the presence of CNS antigens. However, these two beliefs have been questioned by the detection of small numbers of leukocytes in the CSF and the newly identified lymphatics that allow leukocyte egress (Engelhardt et al., 2017). In addition to the BBB, two other brain barrier structures have been described: (1) blood – CSF barrier to the choroid plexus, which is located at the ventricles of the brain, and (2) blood – CSF barrier to the pia arachnoid, which is located at the surface of the brain. It is important to note that CSF spaces in these two brain barriers do not exhibit the same immune privilege as the CNS parenchyma and contain diverse immune cells to monitor the CSF for the presence of immune signals in response to viral pathogens. Therefore, the immune privilege of the brain is not absolute but instead is relative to other organs.

Enterovirus encephalitis is reported to occur more frequently in younger children. Although the exact cause remains unknown, it has been suggested that a compromised or immature immune system may be involved in the observed effect. Studies have shown that expression of CD40-ligand on activated T cells and interleukin 4 (IL-4) production are significantly lower in EV-A71 infected children with meningoencephalitis than those without it (Yang et al., 2001). CD40-ligand plays a pivotal role

in co-stimulation and regulation of the immune responses. It binds to the CD40 receptor on antigen-presenting cells including B cells and macrophages to facilitate cell-cell communication and modulate adaptive immunity. Interleukin-4 (IL-4) is also a key regulator in adaptive immunity. It is a cytokine that has many functions including the stimulation of activated B cell and T cell proliferation and the differentiation of naïve helper T cells and B cells into Th2 cells and plasma cells, respectively. Thus, a reduction in CD40-ligand and IL-4 may indicate that adaptive immunity is compromised. In addition, differences in the polymorphism of the cytotoxic T lymphocyte antigen-4 (CTLA-4) have been noted between children with and without meningoencephalitis in the same study (Yang et al., 2001). CTLA-4 is a surface receptor on T cells, which functions to downregulate T cell activity and polymorphism of CTLA-4 has been shown to be associated with certain autoimmune diseases (Marron et al., 1997). Interestingly, a recent study has reported a correlation between human leukocyte antigen (HLA) genotype and enterovirus infectivity in young children (Sioofy-Khojine et al., 2018). Consistently, there is evidence that genetic differences between individuals may affect the immune response to infection (Kim-Hellmuth et al., 2017). Taken together, these results suggest that genetic factors may confer susceptibility to neurological complications following enterovirus infection.

Although genetic susceptibility may provide clues to why enterovirus encephalitis only occurs in some children but not in others, it cannot explain why younger children infected with enteroviruses are at higher risk for developing encephalitis. It has been suggested that the immaturity of the BBB in early development may account, at least in part, for the age-related difference in viral neuroinvasion (Saunders et al., 2014). The development of the BBB is a multistep process that starts with the growth of new vessels into the embryonic neuroectoderm from pre-existing vessels (Blanchette and Daneman, 2015). This is followed by the expression of tight junction proteins and nutrient transporter in BMECs that lines blood vessels in the brain. The BBB becomes mature as nascent vessels come into close contact with pericytes and astrocytes, which provide structural and functional support to the BBB. In addition, the other cell types present at the BBB, including neurons, microglia, and perivascular macrophages also contribute to the properties of the BBB (Banerjee and Bhat, 2007). Interestingly, it has been shown that the BBB is capable of restricting entry of proteins and small molecules during embryogenesis prior to postnatal astrocyte generation and ensheathment of the vessels (Daneman et al., 2010; Saunders et al., 2014), suggesting that the BBB is functionally mature even without astrocytes in early development. Although astrocytes are not required for initial BBB formation, there is strong evidence that astrocytes play an important role in regulating the function of the BBB during postnatal development (Haseloff et al., 2005). For example, astrocytes secrete trophic factors that lead to tighter tight junctions between BMECs (Dehouck et al., 1990; Rubin et al., 1991). In addition to its role in regulating the BBB, astrocytes receive signals from neighboring neurons and responding to them with the release of neuroactive substances to modulate synaptic strength in the CNS (Santello et al., 2019). Moreover,

there is also evidence that astrocytes convey signals from neurons to the vasculature, leading to arteriolar dilation and an increase in local blood flow (Anderson and Nedergaard, 2003; Zonta et al., 2003). Thus, astrocytes link neuronal activity to functional properties of the BBB. Given that astrocytes are critical for structural support and the maintenance of the BBB, the developing brain containing immature astrocytes may have higher BBB permeability compared to that in the adult brain and is likely to be more vulnerable to viral neuroinvasion.

The CNS immune system may also be involved in the age-related difference in developing enterovirus encephalitis. Microglia, the primary resident immune cells of the brain, play a key role in regulating signaling pathways during CNS inflammation (Rivest, 2009). Although microglia are phenotypically and developmentally different from peripheral macrophages, they use phagocytic and cytotoxic mechanisms to destroy foreign pathogens and act as antigen-presenting cells to initiate T cell-mediated adaptive immune responses similar to macrophages. In addition, microglia have been shown to induce the recruitment of monocytes into the brain during viral infection (Fekete et al., 2018). However, whether microglia are fully functional during early development is not clear. Microglia in the early postnatal brain exhibit different morphologies compared to the adult brain (Cuadros and Navascues, 1998). They are largely non-ramified and take on an ameboid shape during early development, and gradually differentiate into mature/ramified microglia as the brain matures. Consistently, distinct sets of genes are expressed in microglia during different phases of development (Bennett et al., 2016; Matcovitch-Natan et al., 2016). The ameboid morphology observed in developing microglia is similar to activated phagocytic microglia from the adult brain, suggesting that microglia are in a constitutively “activated” state in the developing brain (Lenz and Nelson, 2018). Interestingly, it has been shown that activated microglia produce inflammatory cytokines such as TNF α and IL-1 β (Nishioku et al., 2010; Yang et al., 2015), that increase BBB permeability and downregulate tight-junction proteins between BMECs (Gu et al., 2015; Almutairi et al., 2016). Taken together, these results suggest that developing microglia may increase BBB permeability by releasing inflammatory cytokines. Intriguingly, another study has shown that gene expression profiles are distinct between activated microglia from the adult brain and microglia from a control neonatal brain (Włodarczyk et al., 2017). Therefore, developing microglia are not the same as adult “activated” microglia even both of them exhibit a remarkable similarity in morphology. Nonetheless, this may provide a logical explanation of why younger children infected with enteroviruses are at higher risk for developing encephalitis.

CONCLUSION

Enterovirus infection is a major public health concern considering the increase in outbreaks of serious neurological complications. Although there has been considerable progress in studying the complex interplay between enteroviruses and the infected cell in a culture dish, more complicated interaction

between virus and host *in vivo* is largely unknown and how enteroviruses gain access to and spread in the well-protected CNS remains to be explored. For example, a common feature of enteroviral encephalitis is the involvement of brainstem (Wasserstrom et al., 1992; Huang et al., 1999; Shen et al., 1999; Lum et al., 2002; Brecht et al., 2010; Fan and Liu, 2019), but some studies have revealed cerebral white matter lesions without brainstem involvement in neonatal enteroviral encephalitis (Verboon-Macielek et al., 2006; Hirata et al., 2011; Wu et al., 2014; Correia et al., 2016), suggesting that age and brain maturation may play an important role in the pathogenesis of enteroviral encephalitis. In the current review, we propose that there is a causal link between the development of the neuroimmune system and enteroviral neuroinvasion and have suggested that the age-related difference in developing enterovirus encephalitis may be associated with the development of neuroimmune system such as maturation of astrocytes and/or microglia. Future work will need to include the further characterization of the complex interactions between host and enteroviruses using appropriate animal models and the developmental roles of astrocytes and microglia in

regulating BBB permeability. We also need to better understand the regulation of immune responses in the CNS caused by enteroviruses.

AUTHOR CONTRIBUTIONS

All authors contributed to the writing and discussion of this review article and approved the final version of the manuscript. H-CL made the figure and table.

FUNDING

This work was financially supported by the Research Center for Emerging Viral Infections from the Featured Areas Research Center Program within the framework of the Higher Education Sprout Project by the Ministry of Education (MOE) in Taiwan, the Ministry of Science and Technology (MOST), Taiwan (MOST 108-3017-F-182-001) and the Chang Gung Memorial Hospital (CORPD1J0061).

REFERENCES

- Ahn, J., Jee, Y., Seo, I., Yoon, S. Y., Kim, D., Kim, Y. K., et al. (2008). Primary neurons become less susceptible to coxsackievirus B5 following maturation: the correlation with the decreased level of CAR expression on cell surface. *J. Med. Virol.* 80, 434–440. doi: 10.1002/jmv.21100
- Almutairi, M. M., Gong, C., Xu, Y. G., Chang, Y., and Shi, H. (2016). Factors controlling permeability of the blood-brain barrier. *Cell. Mol. Life Sci.* 73, 57–77. doi: 10.1007/s00018-015-2050-8
- Anderson, C. M., and Nedergaard, M. (2003). Astrocyte-mediated control of cerebral microcirculation. *Trends Neurosci.* 26, 340–344; author reply 344–345.
- Arita, M., Ami, Y., Wakita, T., and Shimizu, H. (2008). Cooperative effect of the attenuation determinants derived from poliovirus sabin 1 strain is essential for attenuation of Enterovirus 71 in the NOD/SCID mouse infection model. *J. Virol.* 82, 1787–1797. doi: 10.1128/jvi.01798-07
- Arita, M., Nagata, N., Sata, T., Miyamura, T., and Shimizu, H. (2006). Quantitative analysis of poliomyelitis-like paralysis in mice induced by a poliovirus replicon. *J. Gen. Virol.* 87, 3317–3327. doi: 10.1099/vir.0.82172-0
- Arita, M., Shimizu, H., Nagata, N., Ami, Y., Suzuki, Y., Sata, T., et al. (2005). Temperature-sensitive mutants of Enterovirus 71 show attenuation in cynomolgus monkeys. *J. Gen. Virol.* 86, 1391–1401. doi: 10.1099/vir.0.80784-0
- Baggen, J., Thibaut, H. J., Strating, J., and Van Kuppeveld, F. J. M. (2018). The life cycle of non-polio Enteroviruses and how to target it. *Nat. Rev. Microbiol.* 16, 368–381. doi: 10.1038/s41579-018-0005-4
- Balada-Llasat, J. M., Rosenthal, N., Hasbun, R., Zimmer, L., Bozzette, S., Duff, S., et al. (2019). Cost of managing meningitis and encephalitis among infants and children in the United States. *Diagn. Microbiol. Infect. Dis.* 93, 349–354. doi: 10.1016/j.diagmicrobio.2018.10.012
- Banerjee, S., and Bhat, M. A. (2007). Neuron-glia interactions in blood-brain barrier formation. *Annu. Rev. Neurosci.* 30, 235–258. doi: 10.1146/annurev.neuro.30.051606.094345
- Bennett, M. L., Bennett, F. C., Liddelow, S. A., Ajami, B., Zamanian, J. L., Fernhoff, N. B., et al. (2016). New tools for studying microglia in the mouse and human CNS. *Proc. Natl. Acad. Sci. U.S.A.* 113, E1738–E1746. doi: 10.1073/pnas.1525528113
- Bergelson, J. M. (2009). Intercellular junctional proteins as receptors and barriers to virus infection and spread. *Cell Host Microbe* 5, 517–521. doi: 10.1016/j.chom.2009.05.009
- Bergelson, J. M., Mohanty, J. G., Crowell, R. L., St John, N. F., Lublin, D. M., and Finberg, R. W. (1995). Coxsackievirus B3 adapted to growth in RD cells binds to decay-accelerating factor (CD55). *J. Virol.* 69, 1903–1906. doi: 10.1128/jvi.69.3.1903-1906.1995
- Berger, M. M., Kopp, N., Vital, C., Redl, B., Aymard, M., and Lina, B. (2000). Detection and cellular localization of Enterovirus RNA sequences in spinal cord of patients with ALS. *Neurology* 54, 20–25.
- Bird, S. W., Maynard, N. D., Covert, M. W., and Kirkegaard, K. (2014). Nonlytic viral spread enhanced by autophagy components. *Proc. Natl. Acad. Sci. U.S.A.* 111, 13081–13086. doi: 10.1073/pnas.1401437111
- B'Krong, N., Minh, N. N. Q., Qui, P. T., Chau, T. T. H., Nghia, H. D. T., Do, L. A. H., et al. (2018). Enterovirus serotypes in patients with central nervous system and respiratory infections in Viet Nam 1997–2010. *Virol. J.* 15:69. doi: 10.1186/s12985-018-0980-0
- Blanchette, M., and Daneman, R. (2015). Formation and maintenance of the BBB. *Mech. Dev.* 138(Pt 1), 8–16. doi: 10.1016/j.mod.2015.07.007
- Brecht, M., Jyoti, R., Mcguire, W., and Chauhan, M. (2010). A case of neonatal coxsackie B virus brainstem encephalitis. *J. Paediatr. Child Health* 46, 699–701.
- Burki, T. (2019). Vaccine derived poliovirus cases exceed wild types. *Lancet Infect. Dis.* 19:140. doi: 10.1016/s1473-3099(19)30012-x
- Caine, E. A., and Osorio, J. E. (2017). In vivo imaging with bioluminescent Enterovirus 71 allows for real-time visualization of tissue tropism and viral spread. *J. Virol.* 91:e01759-16. doi: 10.1128/JVI.01759-16
- Chang, L. Y., Huang, L. M., Gau, S. S., Wu, Y. Y., Hsia, S. H., Fan, T. Y., et al. (2007). Neurodevelopment and cognition in children after Enterovirus 71 infection. *N. Engl. J. Med.* 356, 1226–1234. doi: 10.1056/nejmoa065954
- Chapman, N. M., and Kim, K. S. (2008). Persistent coxsackievirus infection: Enterovirus persistence in chronic myocarditis and dilated cardiomyopathy. *Curr. Top. Microbiol. Immunol.* 323, 275–292. doi: 10.1007/978-3-540-75546-3_13
- Chapman, N. M., Kim, K. S., Drescher, K. M., Oka, K., and Tracy, S. (2008). 5' terminal deletions in the genome of a coxsackievirus B2 strain occurred naturally in human heart. *Virology* 375, 480–491. doi: 10.1016/j.virol.2008.02.030
- Chen, C. S., Yao, Y. C., Lin, S. C., Lee, Y. P., Wang, Y. F., Wang, J. R., et al. (2007). Retrograde axonal transport: a major transmission route of Enterovirus 71 in mice. *J. Virol.* 81, 8996–9003. doi: 10.1128/jvi.00236-07
- Chen, X., Ji, T., Guo, J., Wang, W., Xu, W., and Xie, Z. (2019). Molecular epidemiology of echovirus 18 circulating in mainland China from 2015 to 2016. *Virol. Sin.* 34, 50–58. doi: 10.1007/s12250-018-0080-8
- Chen, X., Li, J., Guo, J., Xu, W., Sun, S., and Xie, Z. (2017). An outbreak of echovirus 18 encephalitis/meningitis in children in Hebei Province, China, 2015. *Emerg. Microbes Infect.* 6:e54.

- Chua, B. H., Phuektes, P., Sanders, S. A., Nicholls, P. K., and Mcminn, P. C. (2008). The molecular basis of mouse adaptation by human Enterovirus 71. *J. Gen. Virol.* 89, 1622–1632. doi: 10.1099/vir.0.83676-0
- Colbere-Garapin, F., Christodoulou, C., Crainic, R., and Pelletier, I. (1989). Persistent poliovirus infection of human neuroblastoma cells. *Proc. Natl. Acad. Sci. U.S.A.* 86, 7590–7594. doi: 10.1073/pnas.86.19.7590
- Colbere-Garapin, F., Duncan, G., Pavio, N., Pelletier, I., and Petit, I. (1998). An approach to understanding the mechanisms of poliovirus persistence in infected cells of neural or non-neural origin. *Clin. Diagn. Virol.* 9, 107–113. doi: 10.1016/s0928-0197(98)00009-9
- Correia, J., Alves, J. E., Ferreira, P., Ferreira, M., Pires, P., and Garrido, C. (2016). Enterovirus 71 meningoencephalitis with extensive white matter damage. *Pediatr. Infect. Dis. J.* 35, 1277–1278. doi: 10.1097/inf.0000000000001292
- Couderc, T., Guivel-Benhassine, F., Calaora, V., Gosselin, A. S., and Blondel, B. (2002). An ex vivo murine model to study poliovirus-induced apoptosis in nerve cells. *J. Gen. Virol.* 83, 1925–1930. doi: 10.1099/0022-1317-83-8-1925
- Cuadros, M. A., and Navascues, J. (1998). The origin and differentiation of microglial cells during development. *Prog. Neurobiol.* 56, 173–189. doi: 10.1016/s0301-0082(98)00035-5
- Daneman, R., Zhou, L., Kebede, A. A., and Barres, B. A. (2010). Pericytes are required for blood-brain barrier integrity during embryogenesis. *Nature* 468, 562–566. doi: 10.1038/nature09513
- Davison, D. L., Terek, M., and Chawla, L. S. (2012). Neurogenic pulmonary edema. *Crit. Care* 16:212.
- Dehouck, M. P., Meresse, S., Delorme, P., Fruchart, J. C., and Cecchelli, R. (1990). An easier, reproducible, and mass-production method to study the blood-brain barrier in vitro. *J. Neurochem.* 54, 1798–1801. doi: 10.1111/j.1471-4159.1990.tb01236.x
- Engelhardt, B., Vajkoczy, P., and Weller, R. O. (2017). The movers and shapers in immune privilege of the CNS. *Nat. Immunol.* 18, 123–131. doi: 10.1038/ni.3666
- Evans, D. M., Dunn, G., Minor, P. D., Schild, G. C., Cann, A. J., Stanway, G., et al. (1985). Increased neurovirulence associated with a single nucleotide change in a noncoding region of the sabin type 3 poliovaccine genome. *Nature* 314, 548–550. doi: 10.1038/314548a0
- Famulare, M., Chang, S., Iber, J., Zhao, K., Adeniji, J. A., Bukbuk, D., et al. (2016). Sabin vaccine reversion in the field: a comprehensive analysis of sabin-like poliovirus isolates in Nigeria. *J. Virol.* 90, 317–331. doi: 10.1128/JVI.01532-15
- Fan, Y. K., and Liu, Y. P. (2019). Magnetic resonance imaging features of pediatric coxsackievirus encephalitis. *J. Belg. Soc. Radiol.* 103:6. doi: 10.5334/jbsr.1685
- Fechner, H., Pinkert, S., Wang, X., Sipo, I., Suckau, L., Kurreck, J., et al. (2007). Coxsackievirus B3 and adenovirus infections of cardiac cells are efficiently inhibited by vector-mediated RNA interference targeting their common receptor. *Gene Ther.* 14, 960–971. doi: 10.1038/sj.gt.3302948
- Fekete, R., Cserep, C., Lenart, N., Toth, K., Orsolits, B., Martinecz, B., et al. (2018). Microglia control the spread of neurotropic virus infection via P2Y12 signalling and recruit monocytes through P2Y12-independent mechanisms. *Acta Neuropathol.* 136, 461–482. doi: 10.1007/s00401-018-1885-0
- Feng, M., Guo, S., Fan, S., Zeng, X., Zhang, Y., Liao, Y., et al. (2016). The preferential infection of astrocytes by Enterovirus 71 plays a key role in the viral neurogenic pathogenesis. *Front. Cell. Infect. Microbiol.* 6:192. doi: 10.3389/fcimb.2016.00192
- Feuer, R., Mena, I., Pagarigan, R., Slifka, M. K., and Whitton, J. L. (2002). Cell cycle status affects coxsackievirus replication, persistence, and reactivation in vitro. *J. Virol.* 76, 4430–4440. doi: 10.1128/jvi.76.9.4430-4440.2002
- Feuer, R., Mena, I., Pagarigan, R. R., Hassett, D. E., and Whitton, J. L. (2004). Coxsackievirus replication and the cell cycle: a potential regulatory mechanism for viral persistence/latency. *Med. Microbiol. Immunol.* 193, 83–90. doi: 10.1007/s00430-003-0192-z
- Feuer, R., Pagarigan, R. R., Harkins, S., Liu, F., Hunziker, I. P., and Whitton, J. L. (2005). Coxsackievirus targets proliferating neuronal progenitor cells in the neonatal CNS. *J. Neurosci.* 25, 2434–2444. doi: 10.1523/jneurosci.4517-04.2005
- Feuer, R., Ruller, C. M., An, N., Tabor-Godwin, J. M., Rhoades, R. E., Maciejewski, S., et al. (2009). Viral persistence and chronic immunopathology in the adult central nervous system following Coxsackievirus infection during the neonatal period. *J. Virol.* 83, 9356–9369. doi: 10.1128/JVI.02382-07
- Forrester, J. V., Mcmenamin, P. G., and Dando, S. J. (2018). CNS infection and immune privilege. *Nat. Rev. Neurosci.* 19, 655–671. doi: 10.1038/s41583-018-0070-8
- Freistadt, M. S., Kaplan, G., and Racaniello, V. R. (1990). Heterogeneous expression of poliovirus receptor-related proteins in human cells and tissues. *Mol. Cell Biol.* 10, 5700–5706. doi: 10.1128/mcb.10.11.5700
- Fujii, K., Sudaka, Y., Takashino, A., Kobayashi, K., Kataoka, C., Suzuki, T., et al. (2018). VP1 amino acid residue 145 of Enterovirus 71 is a key residue for its receptor attachment and resistance to neutralizing antibody during cynomolgus monkey infection. *J. Virol.* 92:e00682-18. doi: 10.1128/JVI.00682-18
- Giraud, P., Beaulieux, F., Ono, S., Shimizu, N., Chazot, G., and Lina, B. (2001). Detection of enteroviral sequences from frozen spinal cord samples of Japanese ALS patients. *Neurology* 56, 1777–1778. doi: 10.1212/wnl.56.12.1777
- Goto, K., Sanefuji, M., Kusuha, K., Nishimura, Y., Shimizu, H., Kira, R., et al. (2009). Rhombencephalitis and coxsackievirus A16. *Emerg. Infect. Dis.* 15, 1689–1691. doi: 10.3201/eid1510.090594
- Greninger, A. L., Naccache, S. N., Messacar, K., Clayton, A., Yu, G., Somasekar, S., et al. (2015). A novel outbreak Enterovirus D68 strain associated with acute flaccid myelitis cases in the USA (2012–14): a retrospective cohort study. *Lancet Infect. Dis.* 15, 671–682. doi: 10.1016/S1473-3099(15)70093-9
- Gromeier, M., Alexander, L., and Wimmer, E. (1996). Internal ribosomal entry site substitution eliminates neurovirulence in intergeneric poliovirus recombinants. *Proc. Natl. Acad. Sci. U.S.A.* 93, 2370–2375. doi: 10.1073/pnas.93.6.2370
- Gromeier, M., and Wimmer, E. (1998). Mechanism of injury-provoked poliomyelitis. *J. Virol.* 72, 5056–5060. doi: 10.1128/jvi.72.6.5056-5060.1998
- Gu, X., Wei, Z. Z., Espinera, A., Lee, J. H., Ji, X., Wei, L., et al. (2015). Pharmacologically induced hypothermia attenuates traumatic brain injury in neonatal rats. *Exp. Neurol.* 267, 135–142. doi: 10.1016/j.expneurol.2015.02.029
- Guest, S., Pilipenko, E., Sharma, K., Chumakov, K., and Roos, R. P. (2004). Molecular mechanisms of attenuation of the Sabin strain of poliovirus type 3. *J. Virol.* 78, 11097–11107. doi: 10.1128/jvi.78.20.11097-11107.2004
- Gutierrez, A. L., Denova-Ocampo, M., Racaniello, V. R., and Del Angel, R. M. (1997). Attenuating mutations in the poliovirus 5' untranslated region alter its interaction with polypyrimidine tract-binding protein. *J. Virol.* 71, 3826–3833. doi: 10.1128/jvi.71.5.3826-3833.1997
- Han, J., Ma, X. J., Wan, J. F., Liu, Y. H., Han, Y. L., Chen, C., et al. (2010). Long persistence of EV71 specific nucleotides in respiratory and feces samples of the patients with Hand-Foot-Mouth Disease after recovery. *BMC Infect. Dis.* 10:178. doi: 10.1186/1471-2334-10-178
- Hasbun, R., Rosenthal, N., Balada-Llasat, J. M., Chung, J., Duff, S., Bozzette, S., et al. (2017). Epidemiology of meningitis and encephalitis in the United States, 2011–2014. *Clin. Infect. Dis.* 65, 359–363. doi: 10.1093/cid/cix319
- Haseloff, R. F., Blasig, I. E., Bauer, H. C., and Bauer, H. (2005). In search of the astrocytic factor(s) modulating blood-brain barrier functions in brain capillary endothelial cells in vitro. *Cell. Mol. Neurobiol.* 25, 25–39. doi: 10.1007/s10571-004-1375-x
- Heim, A., Brehm, C., Stille-Siegener, M., Muller, G., Hake, S., Kandolf, R., et al. (1995). Cultured human myocardial fibroblasts of pediatric origin: natural human interferon-alpha is more effective than recombinant interferon-alpha 2a in carrier-state coxsackievirus B3 replication. *J. Mol. Cell. Cardiol.* 27, 2199–2208. doi: 10.1016/s0022-2828(95)91515-x
- Heim, A., Canu, A., Kirschner, P., Simon, T., Mall, G., Hofschneider, P. H., et al. (1992). Synergistic interaction of interferon-beta and interferon-gamma in coxsackievirus B3-infected carrier cultures of human myocardial fibroblasts. *J. Infect. Dis.* 166, 958–965. doi: 10.1093/infdis/166.5.985
- Hirata, O., Ishikawa, N., Mizoguchi, Y., Nakamura, K., and Kobayashi, M. (2011). A case of neonatal coxsackie B2 meningo-encephalitis in which serial magnetic resonance imaging findings reveal the development of lesions. *Neuropediatrics* 42, 156–158. doi: 10.1055/s-0031-1285876
- Hixon, A. M., Clarke, P., and Tyler, K. L. (2019). Contemporary circulating Enterovirus D68 strains infect and undergo retrograde axonal transport in spinal motor neurons independent of sialic acid. *J. Virol.* 93:e00578-19. doi: 10.1128/JVI.00578-19
- Hixon, A. M., Yu, G., Leser, J. S., Yagi, S., Clarke, P., Chiu, C. Y., et al. (2017). A mouse model of paralytic myelitis caused by Enterovirus D68. *PLoS Pathog.* 13:e1006199. doi: 10.1371/journal.ppat.1006199
- Holland, J. J. (1961). Receptor affinities as major determinants of Enterovirus tissue tropisms in humans. *Virology* 15, 312–326. doi: 10.1016/0042-6822(61)90363-4
- Holmes, C. W., Koo, S. S., Osman, H., Wilson, S., Xerry, J., Gallimore, C. I., et al. (2016). Predominance of Enterovirus B and echovirus 30 as cause of viral

- meningitis in a UK population. *J. Clin. Virol.* 81, 90–93. doi: 10.1016/j.jcv.2016.06.007
- Holm-Hansen, C. C., Midgley, S. E., and Fischer, T. K. (2016). Global emergence of Enterovirus D68: a systematic review. *Lancet Infect. Dis.* 16, e64–e75. doi: 10.1016/S1473-3099(15)00543-5
- Hsu, N. Y., Illytska, O., Belov, G., Santiana, M., Chen, Y. H., Takvorian, P. M., et al. (2010). Viral reorganization of the secretory pathway generates distinct organelles for RNA replication. *Cell* 141, 799–811. doi: 10.1016/j.cell.2010.03.050
- Huang, C. C., Liu, C. C., Chang, Y. C., Chen, C. Y., Wang, S. T., and Yeh, T. F. (1999). Neurologic complications in children with Enterovirus 71 infection. *N. Engl. J. Med.* 341, 936–942. doi: 10.1056/nejm199909233411302
- Huang, H. I., Lin, J. Y., Chen, H. H., Yeh, S. B., Kuo, R. L., Weng, K. F., et al. (2014). Enterovirus 71 infects brain-derived neural progenitor cells. *Virology* 468–470, 592–600. doi: 10.1016/j.virol.2014.09.017
- Huang, H. I., and Shih, S. R. (2015). Neurotropic Enterovirus infections in the central nervous system. *Viruses* 7, 6051–6066. doi: 10.3390/v7112920
- Huang, W., Wang, G., Zhuge, J., Nolan, S. M., Dimitrova, N., and Fallon, J. T. (2015). Whole-genome sequence analysis reveals the Enterovirus D68 isolates during the United States 2014 outbreak mainly belong to a novel clade. *Sci. Rep.* 5:15223. doi: 10.1038/srep15223
- Huang, Y., Zhou, Y., Lu, H., Yang, H., Feng, Q., Dai, Y., et al. (2015). Characterization of severe hand, foot, and mouth disease in Shenzhen, China, 2009–2013. *J. Med. Virol.* 87, 1471–1479. doi: 10.1002/jmv.24200
- Ida-Hosonuma, M., Iwasaki, T., Yoshikawa, T., Nagata, N., Sato, Y., Sata, T., et al. (2005). The alpha/beta interferon response controls tissue tropism and pathogenicity of poliovirus. *J. Virol.* 79, 4460–4469. doi: 10.1128/jvi.79.7.4460-4469.2005
- Ifie, E., Russell, M. A., Dhayal, S., Leete, P., Sebastiani, G., Nigi, L., et al. (2018). Unexpected subcellular distribution of a specific isoform of the Coxsackie and adenovirus receptor, CAR-SIV, in human pancreatic beta cells. *Diabetologia* 61, 2344–2355. doi: 10.1007/s00125-018-4704-1
- Jorba, J., Campagnoli, R., De, L., and Kew, O. (2008). Calibration of multiple poliovirus molecular clocks covering an extended evolutionary range. *J. Virol.* 82, 4429–4440. doi: 10.1128/JVI.02354-07
- Julien, J., Leparac-Goffart, I., Lina, B., Fuchs, F., Foray, S., Janatova, I., et al. (1999). Postpolio syndrome: poliovirus persistence is involved in the pathogenesis. *J. Neurol.* 246, 472–476. doi: 10.1007/s004150050386
- Kao, S. J., Yang, F. L., Hsu, Y. H., and Chen, H. I. (2004). Mechanism of fulminant pulmonary edema caused by Enterovirus 71. *Clin. Infect. Dis.* 38, 1784–1788. doi: 10.1086/421021
- Kawamura, N., Kohara, M., Abe, S., Komatsu, T., Tago, K., Arita, M., et al. (1989). Determinants in the 5' noncoding region of poliovirus Sabin 1 RNA that influence the attenuation phenotype. *J. Virol.* 63, 1302–1309. doi: 10.1128/jvi.63.3.1302-1309.1989
- Kempf, B. J., and Barton, D. J. (2015). Picornavirus RNA polyadenylation by 3D(pol), the viral RNA-dependent RNA polymerase. *Virus Res.* 206, 3–11. doi: 10.1016/j.virusres.2014.12.030
- Kew, O. M., Sutter, R. W., De Gourville, E. M., Dowdle, W. R., and Pallansch, M. A. (2005). Vaccine-derived polioviruses and the endgame strategy for global polio eradication. *Annu. Rev. Microbiol.* 59, 587–635. doi: 10.1146/annurev.micro.58.030603.123625
- Khandaker, G. M., Zimbron, J., Dalman, C., Lewis, G., and Jones, P. B. (2012). Childhood infection and adult schizophrenia: a meta-analysis of population-based studies. *Schizophr. Res.* 139, 161–168. doi: 10.1016/j.schres.2012.05.023
- Khong, W. X., Yan, B., Yeo, H., Tan, E. L., Lee, J. J., Ng, J. K., et al. (2012). A non-mouse-adapted Enterovirus 71 (EV71) strain exhibits neurotropism, causing neurological manifestations in a novel mouse model of EV71 infection. *J. Virol.* 86, 2121–2131. doi: 10.1128/JVI.06103-11
- Kim, K. S., Chapman, N. M., and Tracy, S. (2008). Replication of coxsackievirus B3 in primary cell cultures generates novel viral genome deletions. *J. Virol.* 82, 2033–2037. doi: 10.1128/jvi.01774-07
- Kim, K. S., Tracy, S., Tappich, W., Bailey, J., Lee, C. K., Kim, K., et al. (2005). 5'-Terminal deletions occur in coxsackievirus B3 during replication in murine hearts and cardiac myocyte cultures and correlate with encapsidation of negative-strand viral RNA. *J. Virol.* 79, 7024–7041. doi: 10.1128/jvi.79.11.7024-7041.2005
- Kim-Hellmuth, S., Bechheim, M., Putz, B., Mohammadi, P., Nedelec, Y., Giangreco, N., et al. (2017). Genetic regulatory effects modified by immune activation contribute to autoimmune disease associations. *Nat. Commun.* 8:266. doi: 10.1038/s41467-017-00366-1
- Koike, S., Horie, H., Ise, I., Okitsu, A., Yoshida, M., Iizuka, N., et al. (1990). The poliovirus receptor protein is produced both as membrane-bound and secreted forms. *EMBO J.* 9, 3217–3224. doi: 10.1002/j.1460-2075.1990.tb07520.x
- Koskiniemi, M., Rautonen, J., Lehtokoski-Lehtiniemi, E., and Vaheri, A. (1991). Epidemiology of encephalitis in children: a 20-year survey. *Ann. Neurol.* 29, 492–497. doi: 10.1002/ana.410290508
- La Monica, N., and Racaniello, V. R. (1989). Differences in replication of attenuated and neurovirulent polioviruses in human neuroblastoma cell line SH-SY5Y. *J. Virol.* 63, 2357–2360. doi: 10.1128/jvi.63.5.2357-2360.1989
- Lee, K. M., Chen, C. J., and Shih, S. R. (2017). Regulation mechanisms of viral IRES-driven translation. *Trends Microbiol.* 25, 546–561. doi: 10.1016/j.tim.2017.01.010
- Lenz, K. M., and Nelson, L. H. (2018). Microglia and beyond: innate immune cells as regulators of brain development and behavioral function. *Front. Immunol.* 9:698. doi: 10.3389/fimmu.2018.00698
- Li, B., Yue, Y., Zhang, Y., Yuan, Z., Li, P., Song, N., et al. (2017). A novel Enterovirus 71 (EV71) virulence determinant: the 69th residue of 3C protease modulates pathogenicity. *Front. Cell. Infect. Microbiol.* 7:26. doi: 10.3389/fcimb.2017.00026
- Li, R., Zou, Q., Chen, L., Zhang, H., and Wang, Y. (2011). Molecular analysis of virulent determinants of Enterovirus 71. *PLoS One* 6:e26237. doi: 10.1371/journal.pone.0026237
- Lin, J. Y., and Shih, S. R. (2014). Cell and tissue tropism of Enterovirus 71 and other Enteroviruses infections. *J. Biomed. Sci.* 21:18. doi: 10.1186/1423-0127-21-18
- Lum, L. C., Chua, K. B., Mcminn, P. C., Goh, A. Y., Muridan, R., Sarji, S. A., et al. (2002). Echovirus 7 associated encephalomyelitis. *J. Clin. Virol.* 23, 153–160. doi: 10.1016/s1386-6532(01)00214-1
- Mao, Q., Hao, X., Hu, Y., Du, R., Lang, S., Bian, L., et al. (2018). A neonatal mouse model of central nervous system infections caused by Coxsackievirus B5. *Emerg. Microbes Infect.* 7:185. doi: 10.1038/s41426-018-0186-y
- Mao, Q., Wang, Y., Bian, L., Xu, M., and Liang, Z. (2016). EV-A71 vaccine licensure: a first step for multivalent Enterovirus vaccine to control HFMD and other severe diseases. *Emerg. Microbes Infect.* 5:e75. doi: 10.1038/emi.2016.73
- Marjomaki, V., Turkki, P., and Huttunen, M. (2015). Infectious entry pathway of Enterovirus B species. *Viruses* 7, 6387–6399. doi: 10.3390/v7122945
- Marron, M. P., Raffel, L. J., Garchon, H. J., Jacob, C. O., Serrano-Rios, M., Martinez Larrad, M. T., et al. (1997). Insulin-dependent diabetes mellitus (IDDM) is associated with CTLA4 polymorphisms in multiple ethnic groups. *Hum. Mol. Genet.* 6, 1275–1282. doi: 10.1093/hmg/6.8.1275
- Matcovitch-Natan, O., Winter, D. R., Giladi, A., Vargas Aguilar, S., Spinrad, A., Sarrazin, S., et al. (2016). Microglia development follows a stepwise program to regulate brain homeostasis. *Science* 353:aad8670. doi: 10.1126/science.aad8670
- Melnick, J. L. (1996). Current status of poliovirus infections. *Clin. Microbiol. Rev.* 9, 293–300. doi: 10.1128/cmr.9.3.293-300.1996
- Mendelsohn, C. L., Wimmer, E., and Racaniello, V. R. (1989). Cellular receptor for poliovirus: molecular cloning, nucleotide sequence, and expression of a new member of the immunoglobulin superfamily. *Cell* 56, 855–865. doi: 10.1016/0092-8674(89)90690-9
- Messacar, K., Asturias, E. J., Hixon, A. M., Van Leer-Buter, C., Niesters, H. G. M., Tyler, K. L., et al. (2018). Enterovirus D68 and acute flaccid myelitis-evaluating the evidence for causality. *Lancet Infect. Dis.* 18, e239–e247. doi: 10.1016/S1473-3099(18)30094-X
- Minor, P. (2009). Vaccine-derived poliovirus (VDPV): impact on poliomyelitis eradication. *Vaccine* 27, 2649–2652. doi: 10.1016/j.vaccine.2009.02.071
- Mizutani, T., Ishizaka, A., and Nihei, C. (2016). Transferrin receptor 1 facilitates poliovirus permeation of mouse brain capillary endothelial cells. *J. Biol. Chem.* 291, 2829–2836. doi: 10.1074/jbc.M115.690941
- Muir, P., Nicholson, F., Sharief, M. K., Thompson, E. J., Cairns, N. J., Lantos, P., et al. (1995). Evidence for persistent Enterovirus infection of the central nervous system in patients with previous paralytic poliomyelitis. *Ann. N. Y. Acad. Sci.* 753, 219–232. doi: 10.1111/j.1749-6632.1995.tb27548.x
- Nagata, N., Iwasaki, T., Ami, Y., Sato, Y., Hatano, I., Harashima, A., et al. (2004). A poliomyelitis model through mucosal infection in transgenic mice bearing

- human poliovirus receptor, TgPVR21. *Virology* 321, 87–100. doi: 10.1016/j.virol.2003.12.008
- Nishimura, Y., Lee, H., Hafenstein, S., Kataoka, C., Wakita, T., Bergelson, J. M., et al. (2013). Enterovirus 71 binding to PSGL-1 on leukocytes: VP1-145 acts as a molecular switch to control receptor interaction. *PLoS Pathog.* 9:e1003511. doi: 10.1371/journal.ppat.1003511
- Nishimura, Y., Shimojima, M., Tano, Y., Miyamura, T., Wakita, T., and Shimizu, H. (2009). Human P-selectin glycoprotein ligand-1 is a functional receptor for Enterovirus 71. *Nat. Med.* 15, 794–797. doi: 10.1038/nm.1961
- Nishioku, T., Matsumoto, J., Dohgu, S., Sumi, N., Miyao, K., Takata, F., et al. (2010). Tumor necrosis factor- α mediates the blood-brain barrier dysfunction induced by activated microglia in mouse brain microvascular endothelial cells. *J. Pharmacol. Sci.* 112, 251–254. doi: 10.1254/jphs.09292sc
- Ohka, S., Matsuda, N., Tohyama, K., Oda, T., Morikawa, M., Kuge, S., et al. (2004). Receptor (CD155)-dependent endocytosis of poliovirus and retrograde axonal transport of the endosome. *J. Virol.* 78, 7186–7198. doi: 10.1128/jvi.78.13.7186-7198.2004
- Ohka, S., and Nomoto, A. (2001). The molecular basis of poliovirus neurovirulence. *Dev. Biol.* 105, 51–58.
- Ohka, S., Sakai, M., Bohnert, S., Igarashi, H., Deinhardt, K., Schiavo, G., et al. (2009). Receptor-dependent and -independent axonal retrograde transport of poliovirus in motor neurons. *J. Virol.* 83, 4995–5004. doi: 10.1128/JVI.02225-08
- Ong, K. C., Badmanathan, M., Devi, S., Leong, K. L., Cardosa, M. J., and Wong, K. T. (2008). Pathologic characterization of a murine model of human Enterovirus 71 encephalomyelitis. *J. Neuropathol. Exp. Neurol.* 67, 532–542. doi: 10.1097/NEN.0b013e31817713e7
- Pinkert, S., Klingel, K., Lindig, V., Dorner, A., Zeichhardt, H., Spiller, O. B., et al. (2011). Virus-host coevolution in a persistently coxsackievirus B3-infected cardiomyocyte cell line. *J. Virol.* 85, 13409–13419. doi: 10.1128/JVI.00621-11
- Racaniello, V. R. (2006). One hundred years of poliovirus pathogenesis. *Virology* 344, 9–16. doi: 10.1016/j.virol.2005.09.015
- Ramalho, E., Sousa, I. Jr., Burlandy, F., Costa, E., Dias, A., Serrano, R., et al. (2019). Identification and phylogenetic characterization of human Enteroviruses isolated from cases of aseptic meningitis in Brazil, 2013–2017. *Viruses* 11:E690. doi: 10.3390/v11080690
- Ransohoff, R. M., and Engelhardt, B. (2012). The anatomical and cellular basis of immune surveillance in the central nervous system. *Nat. Rev. Immunol.* 12, 623–635. doi: 10.1038/nri3265
- Rantakallio, P., Jones, P., Moring, J., and Von Wendt, L. (1997). Association between central nervous system infections during childhood and adult onset schizophrenia and other psychoses: a 28-year follow-up. *Int. J. Epidemiol.* 26, 837–843. doi: 10.1093/ije/26.4.837
- Ren, R. B., Moss, E. G., and Racaniello, V. R. (1991). Identification of two determinants that attenuate vaccine-related type 2 poliovirus. *J. Virol.* 65, 1377–1382. doi: 10.1128/jvi.65.3.1377-1382.1991
- Rhoades, R. E., Tabor-Godwin, J. M., Tsueng, G., and Feuer, R. (2011). Enterovirus infections of the central nervous system. *Virology* 411, 288–305. doi: 10.1016/j.virol.2010.12.014
- Richardson, S. J., and Morgan, N. G. (2018). Enteroviral infections in the pathogenesis of type 1 diabetes: new insights for therapeutic intervention. *Curr. Opin. Pharmacol.* 43, 11–19. doi: 10.1016/j.coph.2018.07.006
- Rivest, S. (2009). Regulation of innate immune responses in the brain. *Nat. Rev. Immunol.* 9, 429–439. doi: 10.1038/nri2565
- Rubin, L. L., Hall, D. E., Porter, S., Barbu, K., Cannon, C., Horner, H. C., et al. (1991). A cell culture model of the blood-brain barrier. *J. Cell Biol.* 115, 1725–1735.
- Ruller, C. M., Tabor-Godwin, J. M., Van Deren, D. A. Jr., Robinson, S. M., Maciejewski, S., Gluhm, S., et al. (2012). Neural stem cell depletion and CNS developmental defects after enteroviral infection. *Am. J. Pathol.* 180, 1107–1120. doi: 10.1016/j.ajpath.2011.11.016
- Santello, M., Toni, N., and Volterra, A. (2019). Astrocyte function from information processing to cognition and cognitive impairment. *Nat. Neurosci.* 22, 154–166. doi: 10.1038/s41593-018-0325-8
- Saunders, N. R., Dreifuss, J. J., Dziegielewska, K. M., Johansson, P. A., Habgood, M. D., Mollgard, K., et al. (2014). The rights and wrongs of blood-brain barrier permeability studies: a walk through 100 years of history. *Front. Neurosci.* 8:404. doi: 10.3389/fnins.2014.00404
- Shen, W. C., Chiu, H. H., Chow, K. C., and Tsai, C. H. (1999). MR imaging findings of enteroviral encephalomyelitis: an outbreak in Taiwan. *AJNR Am. J. Neuroradiol.* 20, 1889–1895.
- Shih, S. R., Stollar, V., and Li, M. L. (2011). Host factors in Enterovirus 71 replication. *J. Virol.* 85, 9658–9666. doi: 10.1128/JVI.05063-11
- Sioofy-Khojine, A. B., Oikarinen, S., Honkanen, H., Huhtala, H., Lehtonen, J. P., Briesse, T., et al. (2018). Molecular epidemiology of Enteroviruses in young children at increased risk of type 1 diabetes. *PLoS One* 13:e0201959. doi: 10.1371/journal.pone.0201959
- Stern, A., Yeh, M. T., Zinger, T., Smith, M., Wright, C., Ling, G., et al. (2017). The evolutionary pathway to virulence of an RNA virus. *Cell* 169, 35–46.e19. doi: 10.1016/j.cell.2017.03.013
- Sun, Y., Miao, Z., Yan, J., Gong, L., Chen, Y., Chen, Y., et al. (2019). Sero-molecular epidemiology of Enterovirus-associated encephalitis in Zhejiang Province, China, from 2014 to 2017. *Int. J. Infect. Dis.* 79, 58–64. doi: 10.1016/j.ijid.2018.11.002
- Suresh, S., Forgie, S., and Robinson, J. (2018). Non-polio Enterovirus detection with acute flaccid paralysis: a systematic review. *J. Med. Virol.* 90, 3–7. doi: 10.1002/jmv.24933
- Suvisaari, J., Mautemps, N., Haukka, J., Hovi, T., and Lonnqvist, J. (2003). Childhood central nervous system viral infections and adult schizophrenia. *Am. J. Psychiatry* 160, 1183–1185. doi: 10.1176/appi.ajp.160.6.1183
- Tabor-Godwin, J. M., Ruller, C. M., Bagalzo, N., An, N., Pagarigan, R. R., Harkins, S., et al. (2010). A novel population of myeloid cells responding to coxsackievirus infection assists in the dissemination of virus within the neonatal CNS. *J. Neurosci.* 30, 8676–8691. doi: 10.1523/JNEUROSCI.1860-10.2010
- Tam, P. E., and Messner, R. P. (1999). Molecular mechanisms of coxsackievirus persistence in chronic inflammatory myopathy: viral RNA persists through formation of a double-stranded complex without associated genomic mutations or evolution. *J. Virol.* 73, 10113–10121. doi: 10.1128/jvi.73.12.10113-10121.1999
- Tan, C. W., Sam, I. C., Lee, V. S., Wong, H. V., and Chan, Y. F. (2017). VP1 residues around the five-fold axis of Enterovirus A71 mediate heparan sulfate interaction. *Virology* 501, 79–87. doi: 10.1016/j.virol.2016.11.009
- Tan, S. H., Ong, K. C., and Wong, K. T. (2014). Enterovirus 71 can directly infect the brainstem via cranial nerves and infection can be ameliorated by passive immunization. *J. Neuropathol. Exp. Neurol.* 73, 999–1008. doi: 10.1097/NEN.000000000000122
- Tapparel, C., Siegrist, F., Petty, T. J., and Kaiser, L. (2013). Picornavirus and Enterovirus diversity with associated human diseases. *Infect. Genet. Evol.* 14, 282–293. doi: 10.1016/j.meegid.2012.10.016
- Too, I. H., Yeo, H., Sessions, O. M., Yan, B., Libau, E. A., Howe, J. L., et al. (2016). Enterovirus 71 infection of motor neuron-like NSC-34 cells undergoes a non-lytic exit pathway. *Sci. Rep.* 6:36983. doi: 10.1038/srep36983
- Tsueng, G., Tabor-Godwin, J. M., Gopal, A., Ruller, C. M., Deline, S., An, N., et al. (2011). Coxsackievirus preferentially replicates and induces cytopathic effects in undifferentiated neural progenitor cells. *J. Virol.* 85, 5718–5732. doi: 10.1128/JVI.02261-10
- van der Schaar, H. M., Dorobantu, C. M., Albulescu, L., Strating, J., and Van Kuppeveld, F. J. M. (2016). Fat(al) attraction: picornaviruses usurp lipid transfer at membrane contact sites to create replication organelles. *Trends Microbiol.* 24, 535–546. doi: 10.1016/j.tim.2016.02.017
- Verboon-Macielek, M. A., Groenendaal, F., Cowan, F., Govaert, P., Van Loon, A. M., and De Vries, L. S. (2006). White matter damage in neonatal Enterovirus meningoencephalitis. *Neurology* 66, 1267–1269. doi: 10.1212/01.wnl.0000208429.69676.23
- Wasserstrom, R., Mamourian, A. C., McGary, C. T., and Miller, G. (1992). Bulbar poliomyelitis: MR findings with pathologic correlation. *AJNR Am. J. Neuroradiol.* 13, 371–373.
- Werk, D., Schubert, S., Lindig, V., Grunert, H. P., Zeichhardt, H., Erdmann, V. A., et al. (2005). Developing an effective RNA interference strategy against a plus-strand RNA virus: silencing of coxsackievirus B3 and its cognate coxsackievirus-adenovirus receptor. *Biol. Chem.* 386, 857–863.
- Wessely, R., Klingel, K., Knowlton, K. U., and Kandolf, R. (2001). Cardiospecific infection with coxsackievirus B3 requires intact type I interferon signaling: implications for mortality and early viral replication. *Circulation* 103, 756–761. doi: 10.1161/01.cir.103.5.756

- Wlodarczyk, A., Holtman, I. R., Krueger, M., Yogev, N., Bruttger, J., Khorooshi, R., et al. (2017). A novel microglial subset plays a key role in myelinogenesis in developing brain. *EMBO J.* 36, 3292–3308. doi: 10.15252/embj.201696056
- Woodall, C. J., Riding, M. H., Graham, D. I., and Clements, G. B. (1994). Sequences specific for Enterovirus detected in spinal cord from patients with motor neurone disease. *BMJ* 308, 1541–1543. doi: 10.1136/bmj.308.6943.1541
- Wu, T., Fan, X. P., Wang, W. Y., and Yuan, T. M. (2014). Enterovirus infections are associated with white matter damage in neonates. *J. Paediatr. Child Health* 50, 817–822. doi: 10.1111/jpc.12656
- Xu, R., and Crowell, R. L. (1996). Expression and distribution of the receptors for coxsackievirus B3 during fetal development of the Balb/c mouse and of their brain cells in culture. *Virus Res.* 46, 157–170. doi: 10.1016/s0168-1702(96)01398-6
- Xu, W., Liu, C. F., Yan, L., Li, J. J., Wang, L. J., Qi, Y., et al. (2012). Distribution of Enteroviruses in hospitalized children with hand, foot and mouth disease and relationship between pathogens and nervous system complications. *Viol. J.* 9:8. doi: 10.1186/1743-422X-9-8
- Yamayoshi, S., Fujii, K., and Koike, S. (2014). Receptors for Enterovirus 71. *Emerg. Microbes Infect.* 3:e53. doi: 10.1038/emi.2014.49
- Yan, J. J., Wang, J. R., Liu, C. C., Yang, H. B., and Su, I. J. (2000). An outbreak of Enterovirus 71 infection in Taiwan 1998: a comprehensive pathological, virological, and molecular study on a case of fulminant encephalitis. *J. Clin. Virol.* 17, 13–22. doi: 10.1016/s1386-6532(00)00067-6
- Yanagiya, A., Ohka, S., Hashida, N., Okamura, M., Taya, C., Kamoshita, N., et al. (2003). Tissue-specific replicating capacity of a chimeric poliovirus that carries the internal ribosome entry site of hepatitis C virus in a new mouse model transgenic for the human poliovirus receptor. *J. Virol.* 77, 10479–10487. doi: 10.1128/jvi.77.19.10479-10487.2003
- Yang, K. D., Yang, M. Y., Li, C. C., Lin, S. F., Chong, M. C., Wang, C. L., et al. (2001). Altered cellular but not humoral reactions in children with complicated Enterovirus 71 infections in Taiwan. *J. Infect. Dis.* 183, 850–856. doi: 10.1086/319255
- Yang, W. X., Terasaki, T., Shiroki, K., Ohka, S., Aoki, J., Tanabe, S., et al. (1997). Efficient delivery of circulating poliovirus to the central nervous system independently of poliovirus receptor. *Virology* 229, 421–428. doi: 10.1006/viro.1997.8450
- Yang, Y., Salayandia, V. M., Thompson, J. F., Yang, L. Y., Estrada, E. Y., and Yang, Y. (2015). Attenuation of acute stroke injury in rat brain by minocycline promotes blood-brain barrier remodeling and alternative microglia/macrophage activation during recovery. *J. Neuroinflammation* 12:26. doi: 10.1186/s12974-015-0245-4
- Yao, P. P., Qian, L., Xia, Y., Xu, F., Yang, Z. N., Xie, R. H., et al. (2012). Enterovirus 71-induced neurological disorders in young gerbils, *Meriones unguiculatus*: development and application of a neurological disease model. *PLoS One* 7:e51996. doi: 10.1371/journal.pone.0051996
- Yeh, M. T., Wang, S. W., Yu, C. K., Lin, K. H., Lei, H. Y., Su, I. J., et al. (2011). A single nucleotide in stem loop II of 5'-untranslated region contributes to virulence of Enterovirus 71 in mice. *PLoS One* 6:e27082. doi: 10.1371/journal.pone.0027082
- Yeung, M. L., Jia, L., Yip, C. C. Y., Chan, J. F. W., Teng, J. L. L., Chan, K. H., et al. (2018). Human tryptophanyl-tRNA synthetase is an IFN-gamma-inducible entry factor for Enterovirus. *J. Clin. Invest.* 128, 5163–5177. doi: 10.1172/JCI99411
- Yu, J., Zhang, L., Ren, P., Zhong, T., Li, Z., Wang, Z., et al. (2015). Enterovirus 71 mediates cell cycle arrest in S phase through non-structural protein 3D. *Cell Cycle* 14, 425–436. doi: 10.4161/15384101.2014.980631
- Zaini, Z., and McMinin, P. (2012). A single mutation in capsid protein VP1 (Q145E) of a genogroup C4 strain of human Enterovirus 71 generates a mouse-virulent phenotype. *J. Gen. Virol.* 93, 1935–1940. doi: 10.1099/vir.0.043893-0
- Zoll, J., Heus, H. A., Van Kuppeveld, F. J., and Melchers, W. J. (2009). The structure-function relationship of the Enterovirus 3'-UTR. *Virus Res.* 139, 209–216. doi: 10.1016/j.virusres.2008.07.014
- Zonta, M., Angulo, M. C., Gobbo, S., Rosengarten, B., Hossmann, K. A., Pozzan, T., et al. (2003). Neuron-to-astrocyte signaling is central to the dynamic control of brain microcirculation. *Nat. Neurosci.* 6, 43–50. doi: 10.1038/nn980

Conflict of Interest: The authors declare that the research was conducted in the absence of any commercial or financial relationships that could be construed as a potential conflict of interest.

Copyright © 2020 Chen, Lee, Lee, Gong and Shih. This is an open-access article distributed under the terms of the Creative Commons Attribution License (CC BY). The use, distribution or reproduction in other forums is permitted, provided the original author(s) and the copyright owner(s) are credited and that the original publication in this journal is cited, in accordance with accepted academic practice. No use, distribution or reproduction is permitted which does not comply with these terms.

CCL5 of glioma-associated microglia/macrophages regulates glioma migration and invasion via calcium-dependent matrix metalloproteinase 2

Caren Yu-Ju Wu, Chia-Hua Chen, Chun-Yen Lin, Li-Ying Feng, Yung-Chang Lin, Kuo-Chen Wei, Chung-Yin Huang, Jia-You Fang, and Pin-Yuan Chen

Graduate Institute of Biomedical Sciences, Pharmaceuticals Laboratory, Graduate Institute of Natural Products, Chang Gung University, Taoyuan, Taiwan (C.-Y.J.W., J.-Y.F.); Department of Neurosurgery (C.-H.C., L.-Y.F., K.-C.W., C.-Y.H., P.-Y.C.), Department of Gastroenterology and Hepatology (C.-Y.L., Y.-C.L.), and Department of Anesthesiology (J.-Y.F), Linkou Chang Gung Memorial Hospital, Taoyuan, Taiwan; Department of Neurosurgery, Keelung Chang Gung Memorial Hospital, Keelung, Taiwan (C.-Y.J.W., P.-Y.C.); School of Medicine, Chang Gung University, Taoyuan, Taiwan (C.-Y.L., K.-C.W., P.-Y.C.); Research Center for Food and Cosmetic Safety and Research Center for Chinese Herbal Medicine, Chang Gung University of Science and Technology, Taoyuan, Taiwan (J.-Y.F)

Corresponding Authors: Pin-Yuan Chen, MD, PhD, Department of Neurosurgery, Chang Gung Memorial Hospital, No. 222, Mai-jin Rd., Anle Dist., Keelung 20401, Taiwan (pinyuanc@gmail.com); Jia-You Fang, PhD, Graduate Institute of Natural Products, Chang Gung University, No. 259, Wenhwa 1st Road, Guishan Dist., Taoyuan 33302, Taiwan (fajy@mail.cgu.edu.tw).

Abstract

Background. Glioma-associated microglia/macrophages (GAMs) comprise macrophages of peripheral origin and brain-intrinsic microglia, which support tumor progression. Chemokine C-C ligand 5 (CCL5) is an inflammatory mediator produced by immune cells and is involved in tumor growth and migration in several cancers, including glioma. However, the mechanisms detailing how CCL5 facilitates glioma invasion remain largely unresolved.

Methods. Glioma migration and invasion were determined by wound healing, transwell assay, and 3D μ -slide chemotaxis assay. The expression levels of CCL5, CD68, matrix metalloproteinase 2 (MMP2), phosphorylated Ca^{2+} /calmodulin-dependent protein kinase II (p-CaMKII), p-Akt, and phosphorylated proline-rich tyrosine kinase 2 were determined by cytokine array, quantitative PCR, western blot, or immunohistochemistry. Zymography and intracellular calcium assays were used to analyze MMP2 activity and intracellular calcium levels, respectively.

Results. CCL5 modulated the migratory and invasive activities of human glioma cells in association with MMP2 expression. In response to CCL5, glioma cells underwent a synchronized increase in intracellular calcium levels and p-CaMKII and p-Akt expression levels. CCL5-directed glioma invasion and increases in MMP2 were suppressed after inhibition of p-CaMKII. Glioma cells tended to migrate toward GAM-conditioned media activated by granulocyte-macrophage colony-stimulating factor (GM-CSF) in which CCL5 was abundant. This homing effect was associated with MMP2 upregulation, and could be ameliorated either by controlling intracellular and extracellular calcium levels or by CCL5 antagonism. Clinical results also revealed the associations between CCL5 and GAM activation.

Conclusion. Our results suggest that modulation of glioma CaMKII may restrict the effect of CCL5 on glioma invasion and could be a potential therapeutic target for alleviating glioma growth.

Key Points

1. Glioma migration and invasion increased by CCL5 were associated with CaMKII-dependent MMP2 expression.
2. CCL5 of GM-CSF-activated GAMs may increase glioma invasion as the disease progresses.

Importance of the Study

GAMs are the largest portion of infiltrating immune cells and act to reciprocate the various factors in the tumor mass supporting glioma growth. We identified the GM-CSF-activated GAMs (which may enrich the level of CCL5 in the glioma microenvironment) that human glioma tended to home toward, in which CCL5 was abundantly expressed, and the cellular and molecular events that underlie CCL5-directed glioma

invasion. In addition, we showed that intracellular calcium level and p-CaMKII expression were mediators of MMP2 expression. Moreover, we demonstrated that chelation of extracellular calcium and inhibition of p-CaMKII could eliminate CCL5-directed glioma invasion. Collectively, our findings suggest that the CCL5/CC receptor 5 axis may be an important antitumor drug target.

Glioblastoma (GBM) is the most lethal type of primary malignant brain tumor and is characterized by diffusely infiltrative growth.¹ Despite current optimal therapies, including surgery, radiation, and chemotherapy, the prognosis of patients with GBM remains poor, with a median survival of about 1.5 years due to therapeutic resistance and tumor recurrence.² Recurrent glioma arising from residual invasive cells may undergo a multistep reactivation process that facilitates adhesion to the extracellular matrix, secretion of enzymes that degrade the surrounding matrix, and migration through the glioma microenvironment prior to tumorigenesis.^{3,4} This process involves cross-talk between neoplastic and nonneoplastic cells residing in the tumor microenvironment and reciprocation of the autocrine and paracrine chemotactic factors that give rise to tumor recurrence.^{5,6} Recently, tumor-associated immune cells including lymphocytes and macrophages/microglia identified in the tumor mass have been shown to induce intrinsic inflammation, thereby contributing to a pro-tumorigenic microenvironment.^{7,8} As critical immune cells of the central nervous system, microglia/macrophages demonstrably represent the major regulators of pro-angiogenic factors and facilitate glioma development.⁹ In glioma, chronic inflammation always accompanies tumor development as part of the organism's self-defense, but this ultimately involves feedback mechanisms that tend to benefit tumor growth.¹⁰ Various chemotactic factors, including CC chemokines and colony-stimulating factors, have been identified in the human glioma microenvironment and are associated with immune cell development and migration along with glioma progression.¹¹

Chemokine C-C ligand 5 (CCL5), also known as RANTES (regulated on activation, normal T cell expressed and secreted), is identified as a pro-inflammatory mediator secreted by multiple cell types, including cancer cells and immune cells.¹² CCL5 elicits a strong chemotactic activity toward T lymphocytes and monocytes, which are the primary origin of CCL5 associated with chronic inflammatory diseases, including cancers.¹³ The expression of CCL5 has been shown to positively regulate tumor growth and angiogenesis via the mammalian target of rapamycin/Akt pathway in breast cancer,¹⁴ and phosphorylated (p-)Akt activation in glioma.¹⁵ Recently, CCL5 from tumor-associated microglia/macrophages was demonstrated to promote tumor progression via CC receptor 5 (CCR5) in gastric cancer and glioma.^{13,16} Glioma patients with high CCR5 levels have poor survival. Glioma-associated microglia/

macrophages (GAMs) have been postulated to play a role in glioma development.^{15,17}

The CCL5/CCR5 axis has been demonstrated to enhance tumor local invasiveness via the induction of intracellular calcium cascades and matrix metalloproteinases (MMPs).^{18–20} Cell migration depends on adhesion to the extracellular matrix mediated by calcium-induced integrin activation^{21,22} and proline-rich tyrosine kinase 2 (PYK2).^{23,24} As a family of zinc-dependent extracellular endopeptidases, MMPs facilitate tissue remodeling, tissue repair, and tumorigenesis via the degradation of extracellular matrix components.^{25,26} Most MMPs are secreted as inactive pro-MMPs and become activated when cleaved by extracellular proteinases such as membrane type 1 (MT1)-MMP.^{27,28} Several studies have indicated that MMP2 is highly expressed in human GBM tissues^{29,30} and that this can regulate tumor invasion.^{28,31} The expression of MMPs has been associated with the phosphorylation of Akt and Ca²⁺/calmodulin-dependent protein kinase II (CaMKII) and to be synchronized with calcium influx in neurons and glioma.^{28,32} Downregulation of phosphatidylinositol-3 kinase/Akt signaling has been previously reported to diminish MMP2 gelatinolytic activity,²⁸ and silencing of MT1-MMP has been shown to hinder both MMP2 expression and intracellular calcium mobility during glioma invasion, indicating the involvement of calcium signaling in MMP-regulated cell invasiveness.^{21,27,33} In addition, intracellular calcium influx has been demonstrated to produce a synergistic effect during the tumor invasive process as tumor microtubules emerge to consolidate intercellular connections.³

Recently, GAMs have been identified as a critical source of CCL5, which serves to establish a potent paracrine regulatory circuit for glioma growth.^{16,34,35} As CD8+ tumor-infiltrating lymphocytes (TILs) are also associated with glioma prognosis,³⁶ the involvement of GAMs and CD8+ TILs and the underlying mechanism of CCL5-regulated glioma invasion await validation. In the present study, we sought to determine the regulatory effect of CCL5 produced by GAMs and TILs on glioma migration and invasion. We found that CCL5 enhances the invasiveness of glioma cells through a novel calcium-dependent MMP2 signaling pathway, which could be suppressed via CaMKII small interfering (si)RNA-mediated knockdown. GAMs appeared to provide a more critical source of CCL5 relative to CD8+ TILs, and glioma displayed an increased homing effect along with MMP2 expression toward activated GAM-conditioned media (GAM-CM) in which CCL5 was

enriched by granulocyte-macrophage colony-stimulating factor (GM-CSF) stimulation. This MMP2 upregulation was downregulated after depletion of intracellular calcium or blockage of CCL5. Collectively, these findings broaden the concept that the production of CCL5 by GAMs is reinforced by growth factors such as GM-CSF residing in the glioma microenvironment, and that this regulates glioma migration and invasion and facilitates intracellular calcium mobilization.

Materials and Methods

Glioma Patient Sample Collection and Usage

This study was approved by the Chang Gung Medical Foundation institutional review board (no. 104-9839B). Records of all patients with a diagnosis of GBM over a 10-year period were retrospectively reviewed. Whole blood samples were collected from glioma patients recruited from the Department of Neurosurgery at Chang Gung Memorial Hospital, Taiwan, between 2015 and 2017. All eligible patients were informed about the details of the study, and written consents regarding utilization of patient samples were obtained prior to sample collection. Patient criteria and characteristics are outlined in [Supplementary Tables 1 and 2](#).

Cell Culture

Human A172 and U87 GBM cells were obtained from the American Type Culture Collection and were maintained in Dulbecco's modified Eagle's medium or Minimum Essential Medium. The patient-derived GBM cell line, W802, was obtained from Dr Kuo-Chen Wei at Chang Gung Memorial Hospital. The identity of W802 was validated via short tandem repeat analysis.

Preparation of GAMs from Patient Samples

Tumor biosamples and blood were collected from patients with primary glioma diagnosed histopathologically according to current World Health Organization criteria ([Supplementary Figure 1](#)). Tumor tissues were freshly collected during surgery into Roswell Park Memorial Institute (RPMI) medium and separated under sterile conditions as described previously.^{37,38} Briefly, tissues were washed, digested, and filtered extensively to obtain a single-cell suspension. Cells were labeled with CD11b MicroBeads and isolated using magnetic activated cell sorting separation (Miltenyi Biotec). Isolated GAMs were confirmed to have approximately 90% purity, and day 3 post-culture viability was confirmed with an average of 67% of the cells characterized with Ki-67+ CD11b+ (detailed in [Supplementary Figure 2C–F](#)).

Immunohistochemistry

Paraffin sections of glioma tissues were deparaffinized and dehydrated in a graded ethanol series. Antigens were

retrieved in boiling citric acid buffer following blockage of nonspecific binding and permeabilization by incubating sections in 5% bovine serum albumin and 0.01% Triton X-100. The sections were stained overnight in polyclonal and monoclonal primary antibodies against human p-CaMKII, CCL5 (Santa Cruz), or cluster of differentiation (CD)68 (Abcam) with 1:500 dilution at 4°C overnight. The samples were then washed and stained with Alexa Fluor-tagged secondary antibody (Thermo Fisher) for 2 h at room temperature. The samples were then counterstained with 4',6'-diamidino-2-phenylindole (DAPI) and mounted in fluorescent mounting medium (Dako), and images were captured on an upright microscope (DM2500, Leica).

GAM-Conditioned Medium

GAMs collected from tumors of glioma patients were cultured in RPMI-1640 and seeded after reaching confluence. They were then treated with the indicated stimulators, and the medium was collected after 72 h and immediately applied to cultured A172 and U87 cells for analysis (see the [Supplementary Material](#)).

Flow Cytometry Analysis

GAMs and lymphocytes were stained with multiple cell surface markers to determine the cell types and percentages of GAM and CD8+T cells in the tumor tissues and peripheral blood mononuclear cells (see the [Supplementary Material](#)).

Cytokine Protein Array

Human glioma tissue lysates were analyzed using a Proteome Profiler human XL cytokine array kit (R&D Systems) according to the manufacturer's instructions.

Quantitative Real-Time PCR

Quantitative RT-PCR was performed as described in the [Supplementary Materials and Methods](#). The oligonucleotide primers used for RT-PCR are shown in [Supplementary Table 3](#).

Migration and Invasion Assays

Cell invasion was assessed using Matrigel-coated transwell inserts (8.0- μ m pore size; Falcon). Cells were seeded to Matrigel-coated inserts (Corning), and the invading cells on the underside of the inserts were fixed and stained with crystal violet. The number of invading cells was counted. A 3D μ -slide chemotaxis assay (Ibidi) was performed to determine the chemotactic responses of glioma cells. Cells were mixed with Matrigel and suspended in a polymerizable 3D gel and treated with GAM-CM to induce chemotactic invasion. Images of cell-free areas covered by invasive cells were measured at 24 h and quantified using ImageJ software v1.47 (NIH; see the [Supplementary Material](#)).

Western Blotting

Cells were treated with CCL5, the CaMKII inhibitor KN-93 (KN), the calcium chelator BAPTA-AM (1,2-bis-(2-aminophenoxy)ethane-N,N',N'-tetraacetic acid-tetra(acetoxymethyl) ester) (BAP) (Sigma-Aldrich), Met-CCL5 (MET), or anti-GM-CSF (R&D Systems) for the indicated time periods. Protein samples were prepared and transferred to polyvinylidene difluoride membranes, blocked, and probed with primary antibodies against human species. After extensive washing and incubation with secondary antibodies, the blots were visualized using Amersham Hyperfilm electrochemiluminescence (GE Healthcare; see the Supplementary Material).

Zymography Analysis

The culture media of A172 and U87 cells were collected after the indicated treatment to evaluate MMP activity. The culture medium was mixed with non-reducing sample buffer and separated by sodium dodecyl sulfate-polyacrylamide gel electrophoresis containing 1% bovine type B gelatin (Sigma-Aldrich) followed by washing with 2.5% Triton X-100 to remove sodium dodecyl sulfate and rinsing with 50 mM Tris-HCl (pH 7.5). The gel was incubated in developing buffer for at least 24 h at 37°C for gelatin digestion by MMPs. The enzyme activities of MMPs were determined by staining the gels with 2% Coomassie blue.

Intracellular Calcium Assay

Intracellular calcium was detected using a calcium detection kit according to the manufacturer's instructions (Abcam).

Small Interfering RNA Transfection

Cells were grown to confluence and transfected with Dharmacon On-Target siRNA (GE Healthcare) against CaMKII or a scramble siRNA according to the manufacturer's protocol. The siRNA target sequences are outlined in [Supplementary Table 4](#).

Enzyme-Linked Immunosorbent Assay

The CM of GAMs was used to determine CCL5 and GM-CSF levels using a CCL5 and GM-CSF enzyme-linked immunosorbent assay kit (R&D Systems) according to the manufacturer's instructions.

Statistical Analysis

All results are presented as means \pm SE from at least 3 independent experiments unless otherwise stated. Statistical analyses were performed using 2-tailed unpaired Student's *t*-tests to determine statistical significance between the groups using SPSS v19, and *P*-values of <0.05 were considered significant.

Results

CCL5 Level, Tumor Volume, and Survival in Glioma Patients

We analyzed the CCR5 ligands in tumor biopsies of 4 newly diagnosed GBMs using protein cytokine arrays. As shown in [Figure 1A](#), the level of CCL5 in comparison to CCL3 and CCL4 was higher in the tumor biopsies than in tumor margin ([Supplementary Figure 3A](#)). We confirmed this elevated CCL5 expression using a larger sample size including patients with 15 newly diagnosed GBMs ([Figure 1B](#)), and the results showed that this elevation of the CCL5 mRNA was even higher in the paired-recurrent gliomas ([Figure 1C](#); [Supplementary Figure 3B](#)). The clinical data verified a significant negative correlation between CCL5 and overall survival (OS) of the newly diagnosed cases ([Supplementary Figure 3C](#)). Kaplan-Meier survival plots validated that the patients with a low CCL5 level had a substantially longer OS than those with a high CCL5 level (median OS = 1637 vs 909 days; [Figure 1D](#)). The database of the National Cancer Institute's Repository of Molecular Brain Neoplasia Data (REMBRANDT) confirmed a significant survival advantage for patients with a low CCL5 level (median OS = 406 vs 598 days; [Figure 1D](#)). Progression-free survival was weakly associated with CCL5 ([Supplementary Figure 3D and E](#)). To further investigate the influence of CCL5, we stratified glioma patients based on grading, and isocitrate dehydrogenase (IDH) status. Low-grade glioma patients with low CCL5 levels had longer OS than high-grade glioma patients with high CCL5 levels (hazard ratio [HR] = 0.02, *P* = 0.001; [Figure 1E](#)). While including IDH status, IDH wildtype (WT) was associated with shorter OS (HR = 4.3, *P* = 0.001; [Supplementary Figure 3F](#)). Patients with mutant IDH/low CCL5 were associated with better outcome than those with WT IDH/high CCL5 (HR = 49.46, *P* = 0.001; [Figure 1E](#)). When adjusting for tumor size, age, sex, grade, IDH, and CCL5 status in the multivariate analysis, CCL5 showed minor prognostic value (HR = 1.08, *P* = 0.90), whereas the prognostic values of grade (HR = 8.30, *P* < 0.01) and tumor size (HR = 4.06, *P* = 0.02; [Supplementary Table 5](#)) were statistically significant. Further analysis of linear regression revealed that tumor volume was a significant predictor of CCL5 expression level, indicating associations between increased tumor volume and increased CCL5 expression (beta = 0.42, *P* < 0.01; [Supplementary Table 6](#)).

CCL5 Promotes Heterogeneous Glioma Migration and Invasion

To clarify the direct effect of CCL5 on glioma infiltration, wound-healing and transwell invasion assays were performed on A172 and U87 cells in the presence of CCL5 at different concentrations (0–10 ng/mL). There was no significant reduction in cell-free gaps without the addition of CCL5 after 12 h. However, in the presence of CCL5, the gaps were significantly covered by migrating cells in both the A172 and U87 groups, and this was associated with an increase in gap reduction rate in a CCL5

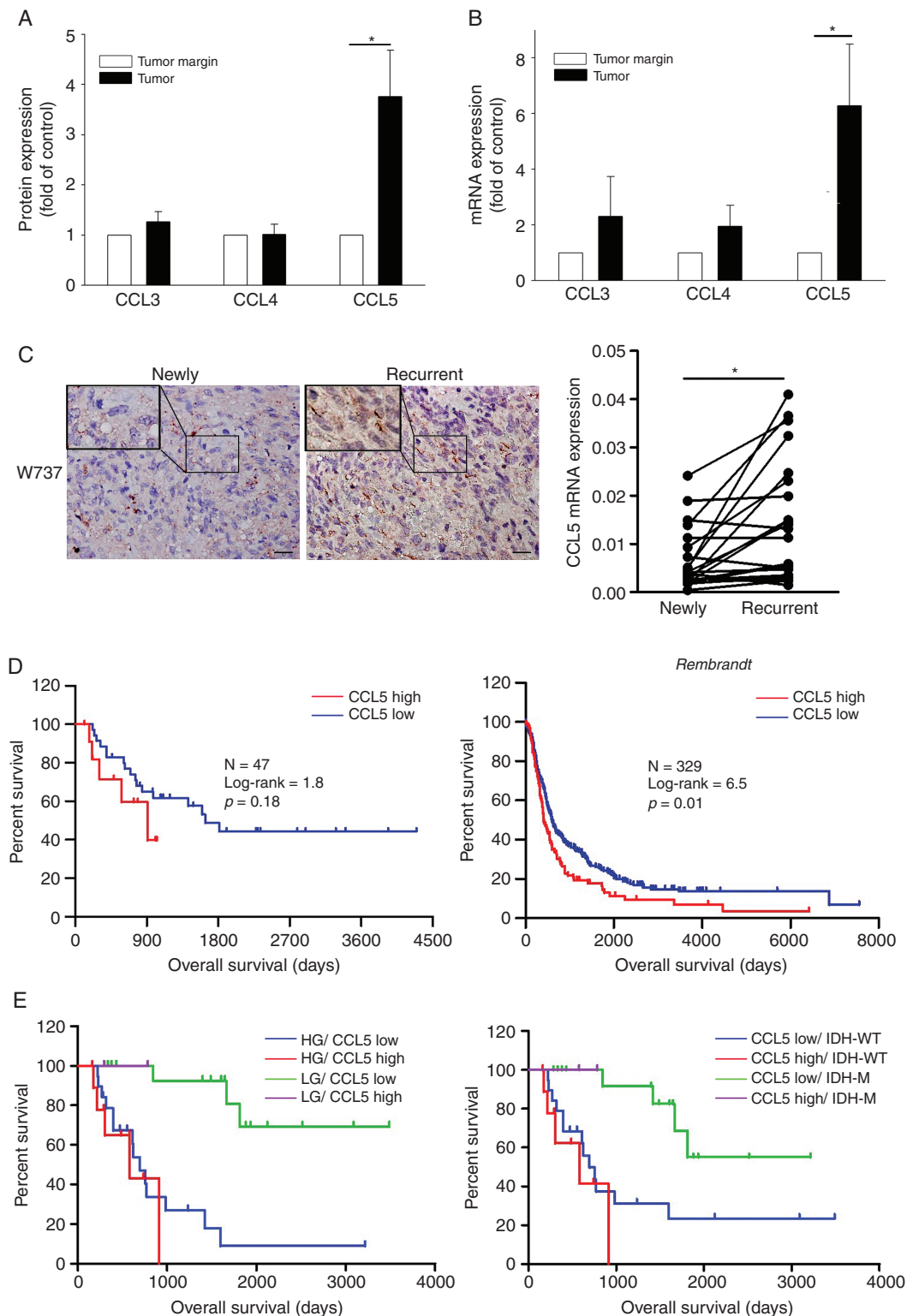


Fig. 1 Survival analysis results for CCL5 in newly diagnosed glioma. (A) CCL5 expression quantified from 4 newly diagnosed GBM tissues. (B) The CCL5 mRNA expression of newly diagnosed gliomas ($n = 15$) relative to the tumor margin was determined. (C) IHC staining of CCL5 (brown) in paired newly diagnosed and recurrent GBM tumor sections. CCL5 mRNA identified in paired newly diagnosed ($n = 20$) and recurrent GBM ($n = 20$) tumors. (D) Kaplan–Meier survival plots for glioma patients with a low CCL5 level (low = 12, high = 35) showed a longer OS. Using the REMBRANDT database, Kaplan–Meier survival plots confirmed a survival advantage in the patients with a low CCL5 level (low = 83, high = 246). (E) Glioma patients ($n = 47$) were stratified based on CCL5, grading, and IDH status. LG: low-grade; HG: high-grade; IDH-M: mutant IDH. Bar: 100 μ m. All data are presented as means \pm SE. * $P < 0.05$, # $P < 0.01$.

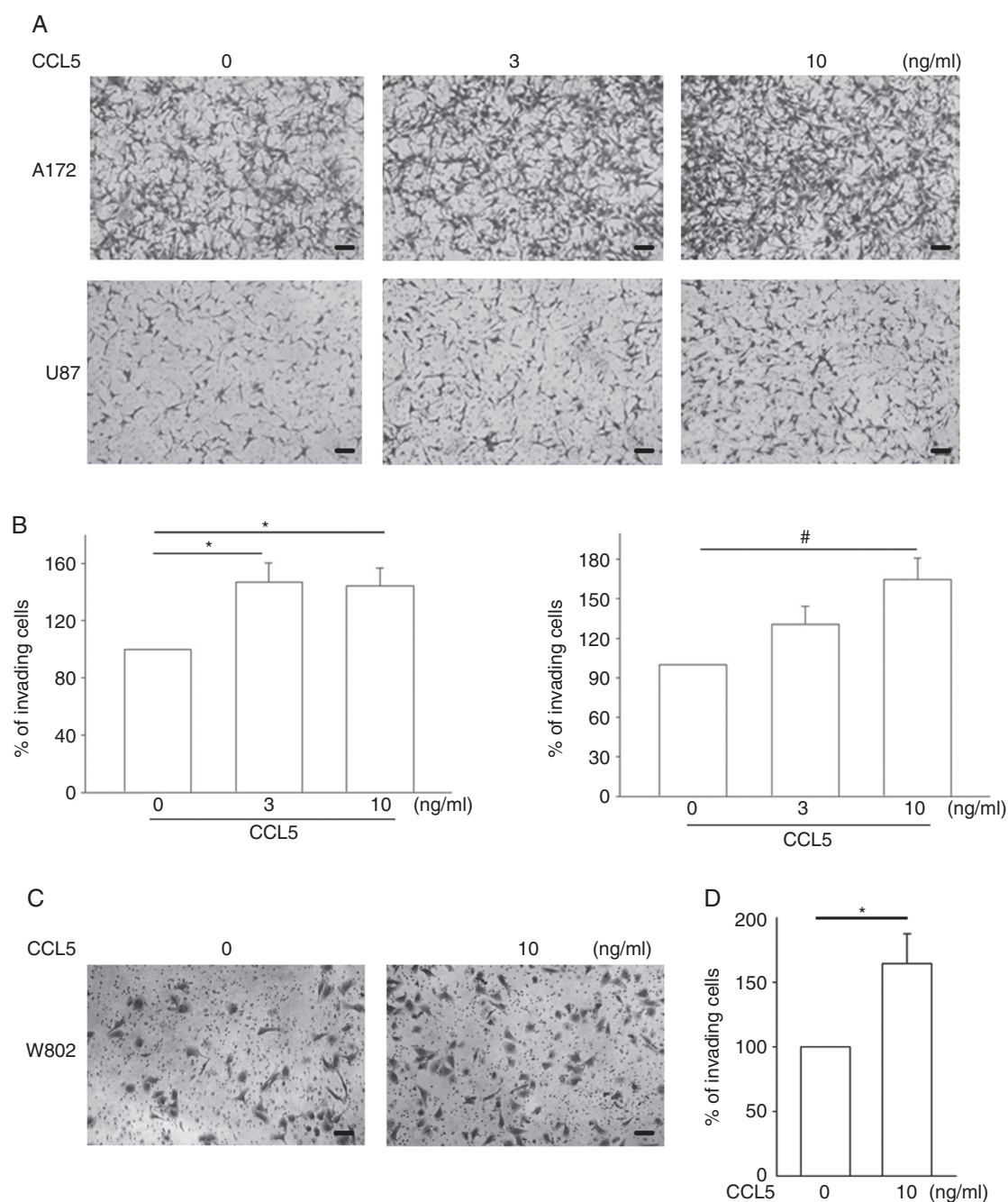


Fig. 2 CCL5 promotes heterogeneous glioma invasive activity. (A, C) The effect of CCL5 on glioma invasion was analyzed. The numbers of invading cells were increased in CCL5-treated A172, U87, and W802 cells after 24 h. (B, D) The number of invading cells are presented as percent of invading cells. Bar: 100 μ m. All data are presented as means \pm SE. * $P < 0.05$, # $P < 0.01$.

dose-dependent manner (Supplementary Figure 4A–D). In addition, the transwell invasion assays showed that CCL5 enhanced cell invasiveness, with an approximate 1.5-fold increase in 10 ng/mL CCL5-treated A172 and U87 cells (Figure 2A) and W802 (Figure 2C) cells. Cell invasion ability was quantified as percent of invading cells compared with the groups without CCL5 stimulation (Figure 2B and D).

CCL5 Induces PYK2 Phosphorylation and MMP2 Activation

As CCL5 could significantly enhance cell migration and invasion initiated by MMP2 upregulation, we examined the involvement of PYK2 and MMP2 in the CCL5 signaling pathway. As shown in Figure 3A and B, CCL5 induced time- and concentration-dependent phosphorylation of

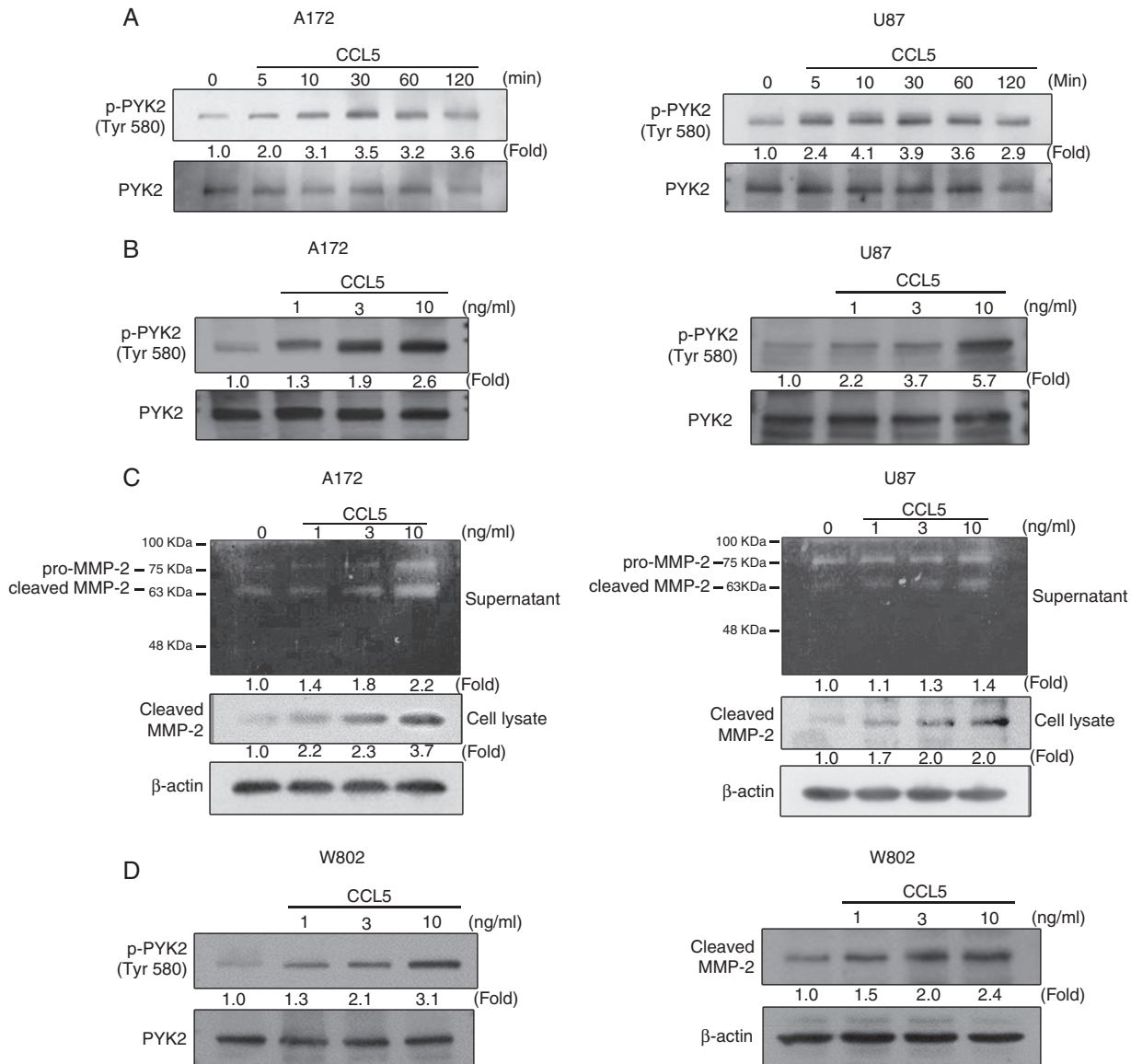
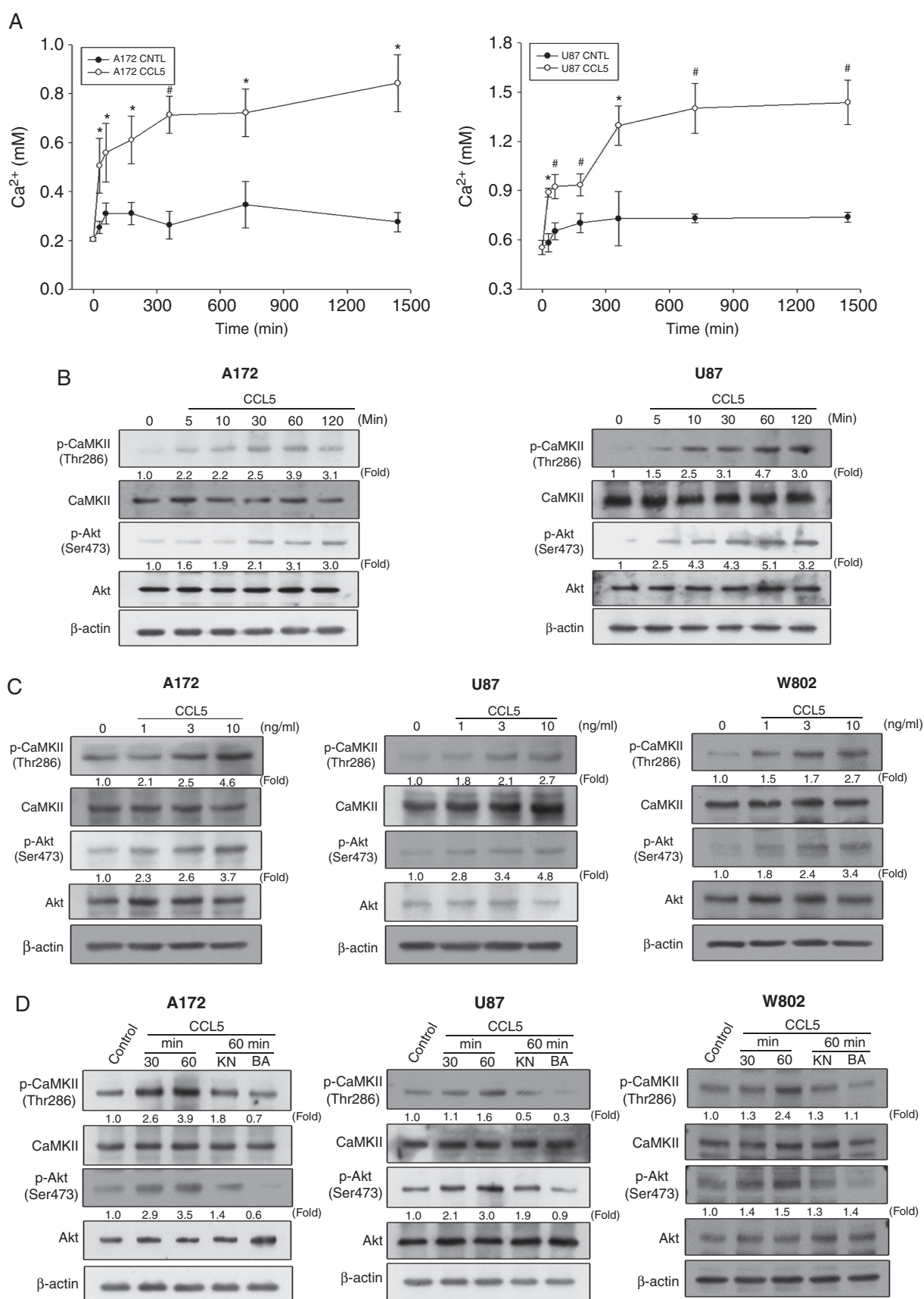


Fig. 3 CCL5 induces PYK2 phosphorylation and MMP2 activation in glioma cells. (A) PYK2 phosphorylation in A172 and U87 cells was induced by CCL5 (10 ng/mL) in a time-dependent manner. (B) CCL5 (0–10 ng/mL) induced a concentration-dependent increase in PYK2 phosphorylation in A172 and U87 cells. (C) MMP2 protease activity and protein expression were induced by 24 h of CCL5 treatment (10 ng/mL) in both A172 and U87 cells. (D) CCL5 (0–10 ng/mL) induced an increase in PYK2 phosphorylation and cleaved MMP2 expression in W802 cells. Blots are quantified as fold of control.

PYK2 in both A172 and U87 cells. The amounts of cleaved MMP2 in gelatin zymography and western blot using CM from CCL5-treated glioma cells were increased in a CCL5 dose-dependent manner in A172 and U87 cells (Figure 3C). W802 cells also showed CCL5-directed upregulation of p-PYK2 and cleaved MMP2 protein expression levels (Figure 3D).

Controlling Calcium Levels Eliminates CCL5-Regulated Calcium-Dependent Protein Kinases in Glioma

We next investigated whether CCL5 stimulation was correlated with intracellular calcium elevation and the phosphorylation of Akt and CaMKII. The intracellular calcium



concentration significantly increased after the addition of CCL5 in both A172 and U87 cells compared with the control groups (Figure 4A). The phosphorylation of CaMKII and Akt was induced after the addition of CCL5 for 5 min, and gradually increased within 60 min of treatment (Figure 4B). Treatment of glioma cells with different concentrations of CCL5 induced concentration-dependent phosphorylation of Akt and CaMKII (Figure 4C). Immunocytochemistry results validated the CCL5-induced phosphorylation of CaMKII in A172, U87, and W802 cells (Supplementary Figure 5A–C), which was consistent with the p-CaMKII expression identified in newly diagnosed and recurrent GBM (Supplementary Figure 5D). Inhibition of CaMKII phosphorylation by KN or blocking of calcium influx via BAP significantly reduced Akt and CaMKII phosphorylation in response to CCL5 stimulation (Figure 4D).

Inhibition of CaMKII Phosphorylation Suppresses CCL5-Induced MMP2 Expression

To elucidate the relationship between CaMKII phosphorylation and MMP2 expression levels, KN was applied to glioma cells at different concentrations (10–50 μ M) for 1 h prior to CCL5 stimulation. The protein expression and activity of cleaved MMP2 were downregulated with increasing concentrations of KN (Figure 5A and B, Supplementary Figure 6A). Furthermore, knockdown of CaMKII via siRNA (si-CaMKII) in the glioma cells suppressed the expression levels of CaMKII protein and CCL5-induced cleaved MMP2 (Figure 5C). The transwell invasion assays revealed that si-CaMKII suppressed CCL5-stimulated cell invasion. The number of invading cells was increased in the presence of CCL5 and was significantly reduced following si-CaMKII treatment (Figure 5D), which was quantified as percent of invading cells compared with control siRNA (Figure 5E).

Inhibition of Calcium-Dependent Signaling Reduces GAM-CM with GM-CSF–Induced MMP2 Expression in Glioma Cells

As GAMs represent a crucial source of CCL5 regulating gliomagenesis, we speculated that the GAMs of newly diagnosed cases would be pivotal for CCL5 production. Immunohistochemistry (IHC) results of newly diagnosed gliomas revealed the co-localization of microglia/macrophages (CD68) with CCL5 (Figure 6A) in approximately 30% of the glioma microenvironment (Supplementary Figure 6B, Supplementary Figure 2A), with a higher GAM percentage in high-grade glioma (40% vs 13%; Supplementary Figure 2B). We then investigated whether activated GAMs contributed to CCL5 production and glioma invasion. A 3D chemotaxis assay was performed to validate the chemotactic invasion of glioma toward

GAM-CM with GM-CSF (GM-CM) or without GM-CSF (CM) stimulation, since GM-CSF is a critical growth factor for GAM activation and is known to be involved in glioma progression.³⁹ We observed that glioma cells tended to preferentially invade toward GM-CM relative to CM after 24 h of incubation (Supplementary Figure 6C). This homing effect of glioma was unlikely to be mediated by activated-CD8+ TILs after anti-CD3/CD28 stimulation, as they resulted in the downregulation of CCL5 production (Supplementary Figure 7). Furthermore, GM-CSF was neutralized in GM-CM (anti-GM-CM; Supplementary Figure 6D), and this appeared to elicit similar invasive activity in W802 cells (Figure 6B). CCL5 mRNA expression in GAMs and protein secretion in GAM-CM were both increased after GM-CSF stimulation compared with those without stimulation (Figure 6C and D). To elucidate the invasive ability of GM-CM–treated glioma cells, MMP2 mRNA expression was also assessed and was found to be elevated in glioma cells treated with anti-GM-CM compared with cells treated with GM-CSF only (Figure 6E and Supplementary Figure 6E and F). Blockade of calcium influx by BAP, inhibition of CaMKII phosphorylation by KN, or antagonism of CCL5 by MET significantly reduced PYK2 phosphorylation and cleaved MMP2 expression levels induced by GM-CM treatment (Figure 6F).

Discussion

Glioma is relatively rare compared with other human cancers, and the aggressiveness of glioma is due to its high migratory potential and recurrence rate.^{40,41} The secretion of matrix metalloproteinases is an important step for cancer metastasis and facilitates cancer invasion. Emerging evidence has demonstrated that autoregulation of CCL5 in GAMs can influence glioma growth and that it is associated with a poor prognosis in patients with glioma.^{5,16,34,35} The influence of GAMs and TILs on glioma progression is not fully understood as there are fundamental differences between GAMs and TILs, and their effects on glioma development remain to be elucidated. Our results highlight the clinical value of CCL5 production and its association with GAM activation. We analyzed the involvement of the CCL5/CCR5 axis on glioma invasion with regard to the different CCR5 ligands, including CCL3, CCL4, and CCL5, of which CCL5 is critical in newly diagnosed GBM (Figure 1A and B). We demonstrated that the newly diagnosed cases with a high CCL5 level were associated with increased tumor volume (Supplementary Table 6). GAMs of GBM were involved in the production of CCL5, whereas the impact on CCL5 production by CD8+ TILs was negligible. CCL5 is known to mediate its biological activities via activation of G-protein coupled receptors or binding to glycosaminoglycans.^{42,43} Previous clinical

Fig. 4 Continued. CCL5 induces a calcium-dependent signaling pathway in a concentration- and time-dependent manner in glioma cells. (A) CCL5 (10 ng/mL) induced an increase in intracellular calcium from 60 to 1440 min in A172 and U87 cells. (B) CCL5 (10 ng/mL) induced CaMKII and Akt phosphorylation over the indicated time periods. (C) CaMKII and Akt phosphorylation was increased in a concentration-dependent manner by CCL5 (0–10 ng/mL). (D) CaMKII and Akt phosphorylation was determined after cells pretreated with KN (20 μ M) or BAP (20 μ M) followed by CCL5 (10 ng/mL) treatment. The data are presented as means \pm SE. * P < 0.05, # P < 0.01 compared with control. Blots are quantified as fold of control.

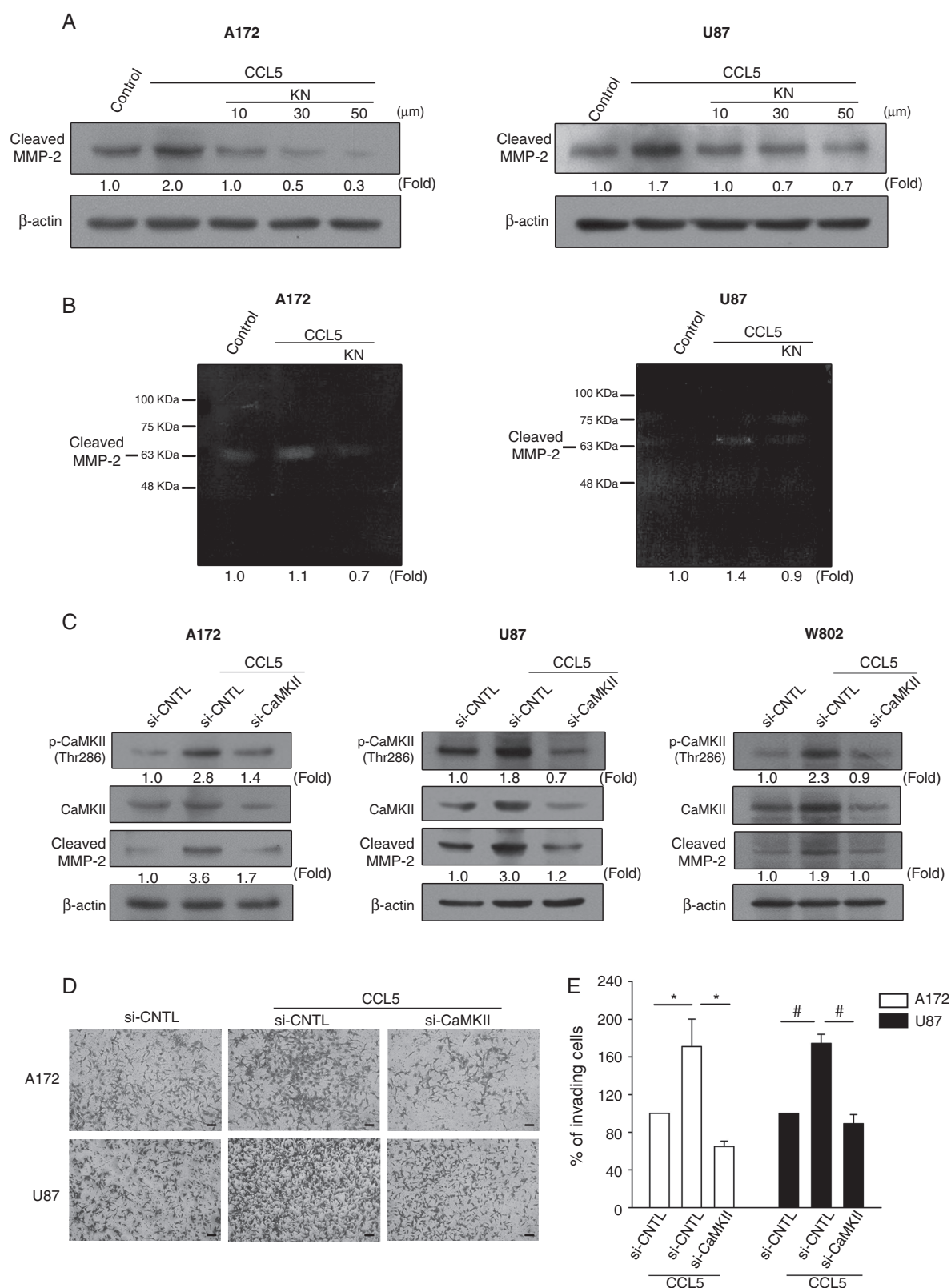


Fig. 5 Inhibition of CaMKII phosphorylation downregulates CCL5-induced MMP2 expression. (A, B) Cells pretreated with KN (10–50 μM) followed by CCL5 treatment showed inhibition of cleaved MMP2 expression. (C) Glioma cells transfected with CaMKII siRNA followed by CCL5 (10 ng/mL) treatment showed inhibited CaMKII phosphorylation and cleaved MMP2 protein expression. (D) Invasive activity was inhibited in the glioma cells with si-CaMKII followed by CCL5 (10 ng/mL) treatment. (E) The invading cells in (D) were quantified and presented as percent of invading cells. Bar: 100 μm. The data are presented as means ± SE. * $P < 0.05$, # $P < 0.01$. Blots are quantified as fold of control.

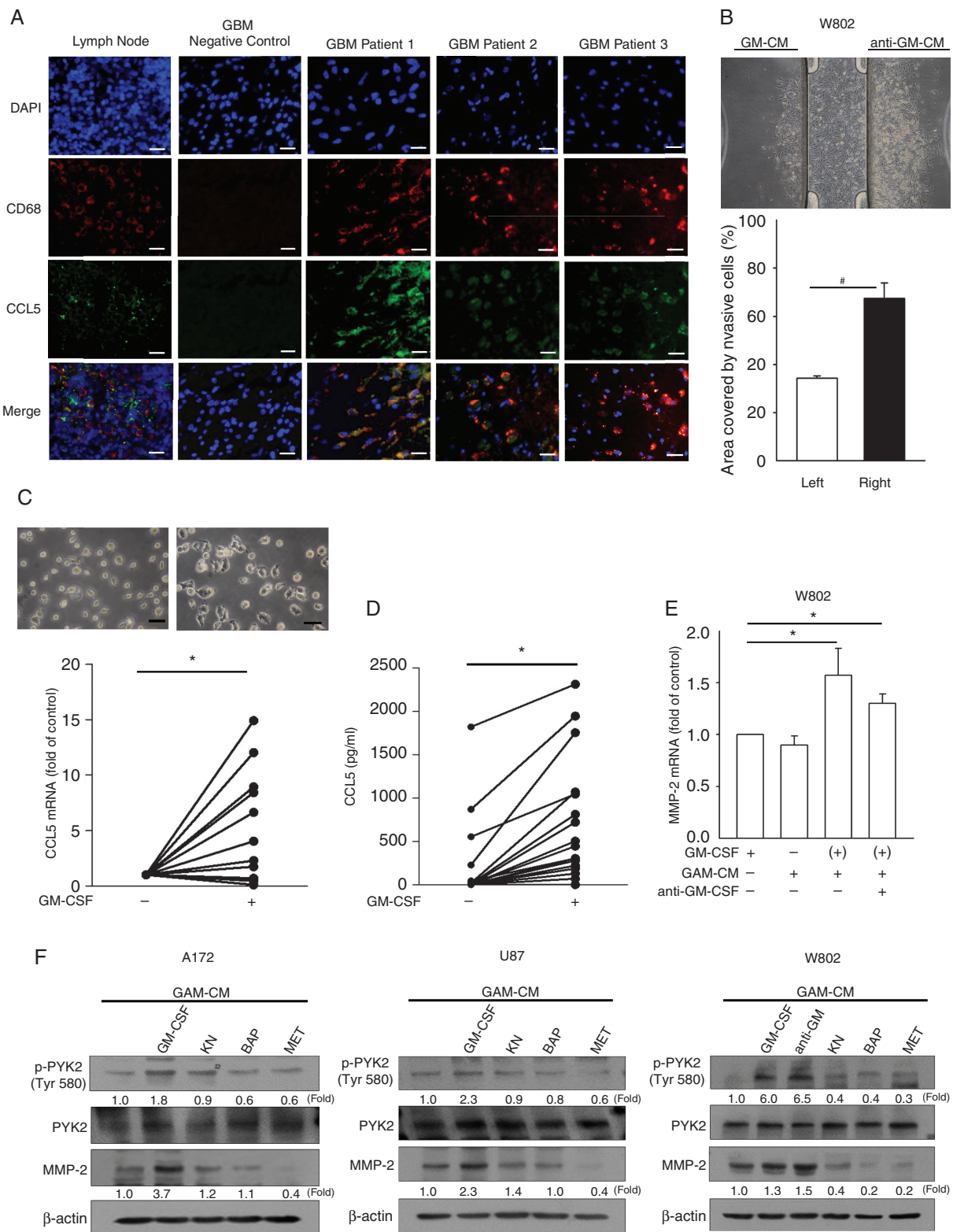


Fig. 6 The increased MMP2 expression by GM-CM is suppressed by inhibition of calcium-related signaling pathways. (A) IHC staining of CD68 (red), CCL5 (green), and DAPI (blue) in newly diagnosed GBM tumor sections ($n = 3$). (B) W802 cells invaded toward the reservoir containing anti-GM-CM. Percentages of areas covered by invading W802 cells are shown. (C) Representative images of GAMs stimulated with or without GM-CSF, which showed that the CCL5 mRNA level was increased in GM-CSF-stimulated GAMs ($n = 21$). (D) The amounts of CCL5 in CM and GM-CM were

results have suggested that CCR5 appears to be involved in tumorigenesis, with a stronger expression in high-grade glioma.⁴⁴ This upregulation of CCR5 in the glioma microenvironment is presumably due to the production of CCL5 from GAMs leading to direct glioma growth and metastasis,^{34,35} and it has also been associated with intracellular calcium mobilization.⁴⁵ Our results are partially consistent with previous reports, since we observed that high-grade glioma contained a higher level of GAM infiltration, as characterized by CD11b+CD45-/CD11b+CD45+, of which CD11b+CD45- cells were predominant (Supplementary Figure 2A and B).

GM-CSF has been demonstrated to act as an autocrine growth factor in astrocytic cell lines isolated from human glioma, and its expression has been significantly correlated with higher-grade tumors.³⁹ Animal models have shown that GM-CSF-secreting glioma/glioma stem cells can promote the differentiation of monocytes into macrophages characterized by CD11c^{high}, and this has been shown to promote tumorigenesis.⁷ Similarly, mice with GL261-induced glioma have been shown to display higher GM-CSF expression along with microglia/macrophage infiltration.⁴⁶ In addition, GM-CSF is known to promote the production of GAMs.⁷ This prompted us to investigate whether exposing GAMs to GM-CSF would promote stronger glioma invasion. We determined that GM-CSF-activated GAMs from human glioma secreted higher levels of CCL5. The invasive ability of glioma toward GAM-CM was verified, and glioma cells elicited a more robust homing response toward GM-CSF-activated GAM-CM (Figure 6B). Importantly, the elevation of CCL5 in the glioma microenvironment did not appear to be critically mediated by activated-CD8+TILs, since CCL5 downregulation was observed after anti-CD3/CD38 stimulation (Supplementary Figure 7A and B). In addition, GAMs accounted for the largest portion (~30–50%) of infiltrating immune cells, of which the propagation of pro-inflammatory cytokines such as interleukin-1 β and tumor necrosis factor alpha are crucial in modulating glioma GM-CSF production and relative functional proteins that aid tumorigenesis, including MMPs.^{39,47} The burst of CCL5 production by GAMs after contact with GM-CSF from glioma may have a considerable impact on glioma progression. As such, the connection between glioma and GAMs in relation to GM-CSF stimulation and CCL5 production might be a potential starting point for new therapeutic approaches.

The expression of MMPs, including MMP2, has been shown to coordinate calcium mobilization and regulate glioma invasion.^{21,33} In this study, we demonstrated that CCL5-regulated glioma migration and invasion were associated with the expression levels of p-PYK2 and MMP2. Consistently, the addition of CCL5 increased the level of intracellular calcium in glioma, which was dependent on the time of exposure to CCL5. Importantly, the intracellular calcium levels did not rise above physiological concentrations (1.2–2.5 mM) following 24 h of CCL5 stimulation (Figure 4A), suggesting that the time of exposure to CCL5 with

respect to alterations in calcium level may be critical for glioma invasion.⁴⁸ Increased levels of calcium-dependent p-CaMKII and p-Akt were observed in response to CCL5 stimulation in both time- and concentration-dependent manners. Moreover, alterations in calcium levels following treatment with KN-93 or BAPTA-AM resulted in downregulation of p-PYK2 and MMP2 (Figure 6F). These results indicated that CCL5-induced glioma invasion requires the calcium-dependent regulation of p-PYK2 and MMP2. Moreover, restriction of intracellular and extracellular calcium flux or CCL5 level eliminated the effect of GAMs in relation to glioma invasion (Supplementary Figure 8). Taken together, our results indicate that the chemokine axis in the glioma microenvironment is subject to CCL5-mediated invasion, and such regulation is facilitated by GAM activation. Moreover, restriction of calcium-dependent pathways may be pivotal for eliminating CCL5/GAM-regulated glioma invasion.

Supplementary Material

Supplementary data are available at Neuro-Oncology online.

Keywords

CCL5 | glioma | invasion | microglia | MMP2

Funding

This work was supported by grants from the Ministry of Science and Technology, Taiwan (107-2314-B-182A-168, 105-2314-B-182-007 and 106-2119-M-182-001), the National Health Research Institutes, Taiwan (NHRI-EX108-10502NI) and Chang Gung Memorial Hospital (CMRPG3F1732).

Conflict of interest statement. The authors have no conflicts to disclose.

Authorship statement. C.Y.-J.W., C.-Y.L., C.-Y.F., and P.-Y.C. were involved in the conception and design of the study; C.Y.-J.W., and L.-Y.F. performed the experiments; C.-Y.L., L.-Y.F., and C.-H.C. provided technical support; C.Y.-J.W., L.-Y.F., C.-H.C., C.-Y.L., Y.-C.L., C.-Y.H., and P.-Y.C. analyzed the data; K.-C.W. and P.-Y.C. provided important materials and critical revision of the manuscript; C.Y.-J.W., P.-Y.C., and C.-Y.F. wrote the manuscript.

Fig. 6 Continued. determined ($n = 21$). (E) MMP2 mRNA expression in glioma cells was determined after 24 h of treatment with CM or GM-CM. (F) Glioma cells pretreated with KN, BAP, or MET prior to GM-CM or CM treatment showed downregulation of PYK2 phosphorylation and cleaved MMP2 protein expression. "(+)" represents CM collected from GM-CSF-activated GAMs. Bar: 100 μ m. All data are presented as means \pm SE. * $P < 0.05$, # $P < 0.01$. Blots are quantified as fold of control.

References

- Hsieh WT, Yeh WL, Cheng RY, et al. Exogenous endothelin-1 induces cell migration and matrix metalloproteinase expression in U251 human glioblastoma multiforme. *J Neurooncol*. 2014;118(2):257–269.
- Chen J, Li Y, Yu TS, et al. A restricted cell population propagates glioblastoma growth after chemotherapy. *Nature*. 2012;488(7412):522–526.
- Osswald M, Jung E, Sahm F, et al. Brain tumour cells interconnect to a functional and resistant network. *Nature*. 2015;528(7580):93–98.
- Galvao RP, Kasina A, McNeill RS, et al. Transformation of quiescent adult oligodendrocyte precursor cells into malignant glioma through a multistep reactivation process. *Proc Natl Acad Sci U S A*. 2014;111(40):E4214–E4223.
- Hambardzumyan D, Gutmann DH, Kettenmann H. The role of microglia and macrophages in glioma maintenance and progression. *Nat Neurosci*. 2016;19(1):20–27.
- Eder K, Kalman B. The dynamics of interactions among immune and glioblastoma cells. *Neuromolecular Med*. 2015;17(4):335–352.
- Kokubu Y, Tabu K, Muramatsu N, et al. Induction of protumoral CD11c(high) macrophages by glioma cancer stem cells through GM-CSF. *Genes Cells*. 2016;21(3):241–251.
- Liang H, Yi L, Wang X, Zhou C, Xu L. Interleukin-17 facilitates the immune suppressor capacity of high-grade glioma-derived CD4 (+) CD25 (+) Foxp3 (+) T cells via releasing transforming growth factor beta. *Scand J Immunol*. 2014;80(2):144–150.
- Brandenburg S, Müller A, Turkowski K, et al. Resident microglia rather than peripheral macrophages promote vascularization in brain tumors and are source of alternative pro-angiogenic factors. *Acta Neuropathol*. 2016;131(3):365–378.
- Hao C, Parney IF, Roa WH, Turner J, Petruk KC, Ramsay DA. Cytokine and cytokine receptor mRNA expression in human glioblastomas: evidence of Th1, Th2 and Th3 cytokine dysregulation. *Acta Neuropathol*. 2002;103(2):171–178.
- Mostofa AG, Punganuru SR, Madala HR, Al-Obaide M, Srivenugopal KS. The process and regulatory components of inflammation in brain oncogenesis. *Biomolecules*. 2017;7(2):1–33.
- Lapteva N, Huang XF. CCL5 as an adjuvant for cancer immunotherapy. *Expert Opin Biol Ther*. 2010;10(5):725–733.
- Ding H, Zhao L, Dai S, Li L, Wang F, Shan B. CCL5 secreted by tumor associated macrophages may be a new target in treatment of gastric cancer. *Biomed Pharmacother*. 2016;77:142–149.
- Sax MJ, Gasch C, Athota VR, et al. Cancer cell CCL5 mediates bone marrow independent angiogenesis in breast cancer. *Oncotarget*. 2016;7(51):85437–85449.
- Zhao L, Wang Y, Xue Y, Lv W, Zhang Y, He S. Critical roles of chemokine receptor CCR5 in regulating glioblastoma proliferation and invasion. *Acta Biochim Biophys Sin (Shanghai)*. 2015;47(11):890–898.
- Pan Y, Smithson LJ, Ma Y, Hambardzumyan D, Gutmann DH. Ccl5 establishes an autocrine high-grade glioma growth regulatory circuit critical for mesenchymal glioblastoma survival. *Oncotarget*. 2017;8(20):32977–32989.
- Pham K, Luo D, Liu C, Harrison JK. CCL5, CCR1 and CCR5 in murine glioblastoma: immune cell infiltration and survival rates are not dependent on individual expression of either CCR1 or CCR5. *J Neuroimmunol*. 2012;246(1–2):10–17.
- Aldinucci D, Colombatti A. The inflammatory chemokine CCL5 and cancer progression. *Mediators Inflamm*. 2014;2014:292376.
- Tang CH, Yamamoto A, Lin YT, Fong YC, Tan TW. Involvement of matrix metalloproteinase-3 in CCL5/CCR5 pathway of chondrosarcomas metastasis. *Biochem Pharmacol*. 2010;79(2):209–217.
- Shen Z, Li T, Chen D, et al. The CCL5/CCR5 axis contributes to the perineural invasion of human salivary adenoid cystic carcinoma. *Oncol Rep*. 2014;31(2):800–806.
- Fortier S, Labelle D, Sina A, Moreau R, Annabi B. Silencing of the MT1-MMP/ G6PT axis suppresses calcium mobilization by sphingosine-1-phosphate in glioblastoma cells. *FEBS Lett*. 2008;582(5):799–804.
- Brzdak P, Włodarczyk J, Mozyrmas JW, Wojtowicz T. Matrix metalloproteinase 3 activity supports hippocampal EPSP-to-spike plasticity following patterned neuronal activity via the regulation of NMDAR function and calcium flux. *Mol Neurobiol*. 2017;54(1):804–816.
- Sulzmaier FJ, Jean C, Schlaepfer DD. FAK in cancer: mechanistic findings and clinical applications. *Nat Rev Cancer*. 2014;14(9):598–610.
- Hsin H, Kim MJ, Wang CF, Sheng M. Proline-rich tyrosine kinase 2 regulates hippocampal long-term depression. *J Neurosci*. 2010;30(36):11983–11993.
- Freitas-Rodriguez S, Folgueras AR, Lopez-Otin C. The role of matrix metalloproteinases in aging: Tissue remodeling and beyond. *Biochim Biophys Acta*. 2017;1864(11):2015–2025.
- Poincloux R, Lizarraga F, Chavrier P. Matrix invasion by tumour cells: a focus on MT1-MMP trafficking to invadopodia. *J Cell Sci*. 2009;122(Pt 17):3015–3024.
- Kheradmand F, Rishi K, Werb Z. Signaling through the EGF receptor controls lung morphogenesis in part by regulating MT1-MMP-mediated activation of gelatinase A/MMP2. *J Cell Sci*. 2002;115(Pt 4):839–848.
- Kwiatkowska A, Kijewska M, Lipko M, Hibner U, Kaminska B. Downregulation of Akt and FAK phosphorylation reduces invasion of glioblastoma cells by impairment of MT1-MMP shuttling to lamellipodia and downregulates MMPs expression. *Biochim Biophys Acta*. 2011;1813(5):655–667.
- Tabouret E, Boudouresque F, Farina P, et al. MMP2 and MMP9 as candidate biomarkers to monitor bevacizumab therapy in high-grade glioma. *Neuro-Oncol*. 2015;17(8):1174–1176.
- Du R, Petritsch C, Lu K, et al. Matrix metalloproteinase-2 regulates vascular patterning and growth affecting tumor cell survival and invasion in GBM. *Neuro Oncol*. 2008;10(3):254–264.
- Chang L, Zhao D, Liu HB, et al. Activation of sonic hedgehog signaling enhances cell migration and invasion by induction of matrix metalloproteinase-2 and -9 via the phosphoinositide-3 kinase/AKT signaling pathway in glioblastoma. *Mol Med Rep*. 2015;12(5):6702–6710.
- Xu J, Kurup P, Bartos JA, Patriarchi T, Hell JW, Lombroso PJ. Striatal-enriched protein-tyrosine phosphatase (STEP) regulates Pyk2 kinase activity. *J Biol Chem*. 2012;287(25):20942–20956.
- Han KY, Dugas-Ford J, Seiki M, Chang JH, Azar DT. Evidence for the involvement of MMP14 in MMP2 processing and recruitment in exosomes of corneal fibroblasts. *Invest Ophthalmol Vis Sci*. 2015;56(9):5323–5329.
- Solga AC, Pong WW, Kim KY, et al. RNA sequencing of tumor-associated microglia reveals Ccl5 as a stromal chemokine critical for neurofibromatosis-1 glioma growth. *Neoplasia*. 2015;17(10):776–788.
- Toonen JA, Anastasaki C, Smithson LJ, et al. NF1 germline mutation differentially dictates optic glioma formation and growth in neurofibromatosis-1. *Hum Mol Genet*. 2016;25(9):1703–1713.
- Han S, Zhang C, Li Q, et al. Tumour-infiltrating CD4(+) and CD8(+) lymphocytes as predictors of clinical outcome in glioma. *Br J Cancer*. 2014;110(10):2560–2568.
- Olah M, Raj D, Brouwer N, et al. An optimized protocol for the acute isolation of human microglia from autopsy brain samples. *Glia*. 2012;60(1):96–111.
- Menck K, Behme D, Pantke M, et al. Isolation of human monocytes by double gradient centrifugation and their differentiation to macrophages in teflon-coated cell culture bags. *J Vis Exp*. 2014(91):e51554.
- Revoltella RP, Menicagli M, Campani D. Granulocyte-macrophage colony-stimulating factor as an autocrine survival-growth factor in human gliomas. *Cytokine*. 2012;57(3):347–359.

40. Ostrom QT, Gittleman H, Xu J, et al. CBTRUS statistical report: primary brain and other central nervous system tumors diagnosed in the United States in 2009–2013. *Neuro Oncol.* 2016;18(suppl_5):v1–v75.
41. Lin YJ, Chiu HY, Chiou MJ, et al. Trends in the incidence of primary malignant brain tumors in Taiwan and correlation with comorbidities: a population-based study. *Clin Neurol Neurosurg.* 2017;159:72–82.
42. Wu L, LaRosa G, Kassam N, et al. Interaction of chemokine receptor CCR5 with its ligands: multiple domains for HIV-1 gp120 binding and a single domain for chemokine binding. *J Exp Med.* 1997;186(8):1373–1381.
43. Martin L, Blanpain C, Garnier P, Wittamer V, Parmentier M, Vita C. Structural and functional analysis of the RANTES-glycosaminoglycans interactions. *Biochemistry.* 2001;40(21):6303–6318.
44. Kouno J, Nagai H, Nagahata T, et al. Up-regulation of CC chemokine, CCL3L1, and receptors, CCR3, CCR5 in human glioblastoma that promotes cell growth. *J Neuro Oncol.* 2004;70(3):301–307.
45. Chernova I, Lai JP, Li H, et al. Substance P (SP) enhances CCL5-induced chemotaxis and intracellular signaling in human monocytes, which express the truncated neurokinin-1 receptor (NK1R). *J Leukoc Biol.* 2009;85(1):154–164.
46. Gabrusiewicz K, Ellert-Miklaszewska A, Lipko M, Sielska M, Frankowska M, Kaminska B. Characteristics of the alternative phenotype of microglia/macrophages and its modulation in experimental gliomas. *PLoS One.* 2011;6(8):e23902.
47. Sielska M, Przanowski P, Wylot B, et al. Distinct roles of CSF family cytokines in macrophage infiltration and activation in glioma progression and injury response. *J Pathol.* 2013;230(3):310–321.
48. Bronner F. Extracellular and intracellular regulation of calcium homeostasis. *Sci World J.* 2001;1:919–925.



Hydroxygenkwanin Inhibits Class I HDAC Expression and Synergistically Enhances the Antitumor Activity of Sorafenib in Liver Cancer Cells

Chi-Yuan Chen^{1,2†}, Chin-Chuan Chen^{1,3†}, Wen-Yu Chuang⁴, Yann-Lii Leu^{3,5,6}, Shir-Hwa Ueng⁴, Chuen Hsueh^{1,4}, Chau-Ting Yeh^{7*} and Tong-Hong Wang^{1,2,7*}

¹ Tissue Bank, Chang Gung Memorial Hospital, Taoyuan, Taiwan, ² Research Center for Chinese Herbal Medicine, Graduate Institute of Health Industry Technology and Research Center for Food and Cosmetic Safety, College of Human Ecology, Chang Gung University of Science and Technology, Taoyuan, Taiwan, ³ Graduate Institute of Natural Products, Chang Gung University, Taoyuan, Taiwan, ⁴ Department of Anatomic Pathology, Chang Gung Memorial Hospital, Chang Gung University School of Medicine, Taoyuan, Taiwan, ⁵ Chinese Herbal Medicine Research Team, Healthy Aging Research Center, Chang Gung University, Taoyuan, Taiwan, ⁶ Center for Traditional Chinese Medicine, Chang Gung Memorial Hospital, Taoyuan, Taiwan, ⁷ Department of Hepato-Gastroenterology, Liver Research Center, Chang Gung Memorial Hospital, Taoyuan, Taiwan

OPEN ACCESS

Edited by:

Sanjay K. Srivastava,
Texas Tech University Health Sciences
Center, Abilene, United States

Reviewed by:

Nor Eddine Sounni,
University of Liège, Belgium
Guoyin Kai,
Zhejiang Chinese Medical
University, China

*Correspondence:

Tong-Hong Wang
cellww@adm.cgmh.org.tw
Chau-Ting Yeh
chautingy@gmail.com

[†]These authors have contributed
equally to this work

Specialty section:

This article was submitted to
Pharmacology of Anti-Cancer Drugs,
a section of the journal
Frontiers in Oncology

Received: 15 October 2019

Accepted: 07 February 2020

Published: 25 February 2020

Citation:

Chen C-Y, Chen C-C, Chuang W-Y,
Leu Y-L, Ueng S-H, Hsueh C, Yeh C-T
and Wang T-H (2020)
Hydroxygenkwanin Inhibits Class I
HDAC Expression and Synergistically
Enhances the Antitumor Activity of
Sorafenib in Liver Cancer Cells.
Front. Oncol. 10:216.
doi: 10.3389/fonc.2020.00216

Abnormal histone deacetylase (HDAC) expression is closely related to cancer development and progression. Many HDAC inhibitors have been widely used in cancer treatment; however, severe side effects often limit their clinical application. In this study, we attempted to identify natural compounds with HDAC inhibitory activity and low physiological toxicity and explored their feasibility and mechanisms of action in liver cancer treatment. A yeast screening system was used to identify natural compounds with HDAC inhibitory activity. Further, western blotting was used to verify inhibitory effects on HDAC in human liver cancer cell lines. Cell functional analysis was used to explore the effects and mechanisms and the *in vitro* results were verified in BALB/c nude mice. We found that hydroxygenkwanin (HGK), an extract from *Daphne genkwa*, inhibited class I HDAC expression, and thereby induced expression of tumor suppressor p21 and promoted acetylation and activation of p53 and p65. This resulted in the inhibition of growth, migration, and invasion of liver cancer cells and promoted cell apoptosis. Animal models revealed that HGK inhibited tumor growth in a synergistic manner with sorafenib. HGK inhibited class I HDAC expression and had low physiological toxicity. It has great potential as an adjuvant for liver cancer treatment and may be used in combination with anticancer drugs like sorafenib to improve therapeutic efficacy.

Keywords: hydroxygenkwanin (HGK), liver cancer, histone deacetylase (HDAC), p21, sorafenib

INTRODUCTION

Liver cancer is the second most common cause of cancer-related deaths worldwide (1). Due to primary drug resistance and the propensity for metastasis, liver cancer is one of the most refractory cancers (2). Currently, surgery is the main treatment option, but for patients with advanced liver cancer that has metastasized, chemotherapy or radiotherapy is the main treatment approach (3, 4). However, most chemotherapeutic agents have strong side effects, which negatively impact patient quality of life. Therefore, the development of effective liver cancer treatments with low side effects is urgently needed.

Targeted therapy is a new approach in cancer treatment. Since it targets and deactivates specific proteins that cause carcinogenesis, targeted therapy has the advantages of high specificity and low adverse effects and is widely used in the treatment of various cancers (5, 6). Currently, the most commonly used drugs for liver cancer treatment are sorafenib and bevacizumab (7). Sorafenib inhibits the activation of multiple kinases related to tumor growth and angiogenesis and is currently the most effective drug for targeted therapy of liver cancer. In contrast, bevacizumab is a monoclonal antibody that targets vascular endothelial growth factor and inhibits tumor growth by inhibiting angiogenesis inside the tumor (8, 9). The causes of liver cancer are complex, often involving mutations in more than two carcinogenic pathways. This complexity, coupled with the heterogeneous nature of liver cancer tumors, results in the efficacy of treatments usually being limited (10, 11). Even sorafenib can only prolong survival by ~3 months (4, 12). Therefore, the development of drugs with multiple targets to improve the efficacy against liver cancer and low side effects is crucial for liver cancer research.

Histone deacetylase (HDAC) regulates the de-acetylation of histone and non-histone proteins, thereby regulating gene expression or protein stability and activity (13, 14). De-acetylation of histone proteins results in increased binding of the coiled chromonema, thereby inhibiting gene expression. Non-histone protein de-acetylation is closely related to their activity and affects the binding ability of these proteins to DNA and other proteins, indirectly regulating the activation or expression of other proteins (15, 16). Currently, 18 human HDACs have been identified, which are divided into four types, including class I (HDAC1, HDAC2, HDAC3, HDAC8), class IIa (HDAC4, HDAC5, HDAC7, HDAC9), class IIb (HDAC6, HDAC10), class III Sir2-like enzymes (consisting of seven sirtuins), and class IV (HDAC11). Among these, class I HDACs are over-expressed in most cancers, including liver cancer, making these a treatment target for many cancers (17–19). Currently, HDAC inhibitors such as trichostatin A, vorinostat (suberoylanilide hydroxamic acid, SAHA), trapoxin A, and valproic acid (VPA) have been widely used with good results in the treatment of lung cancer, breast cancer, and esophageal cancer (20–22). However, application of these HDAC inhibitors alone fails to achieve satisfactory results in the treatment of liver cancer, likely due to tumor heterogeneity. Recent studies have found that HDAC inhibitors have considerably improved efficacy against liver cancer if combined with sorafenib (23, 24). However, since most HDAC inhibitors cause strong physiological side effects, it remains necessary to carefully assess the physiological conditions of patients prior to administration.

Numerous studies have confirmed that some natural compounds have specific anticancer effects. Compared with drugs of Western medicine, these natural compounds have low physiological side effects and are thus suitable for use as therapeutic adjuvants in combination with other drugs to improve efficacy (25, 26). Currently, drugs such as artemisinin and curcumin have been used in the treatment of liver cancer and have been confirmed to considerably inhibit tumor growth and metastasis and to prolong patient survival (27–29). Certain

Chinese herbal extracts such as sulforaphane have inhibitory activity against HDAC, giving them the potential for use in the treatment of a variety of diseases, including cancer (30–32). In the current study, we used a yeast analysis platform and identified hydroxygenkwanin (HGK) as an herbal extract with class I HDAC inhibitory activity. We found that HGK, a bioactive substance extracted from *Daphne genkwa* Sieb. et Zucc., inhibited expression of class I HDAC, induced expression of tumor suppressor p21, and promoted acetylation of p53 and p65, thereby inhibiting the proliferation, migration, and invasion of liver cancer cells. In addition, HGK had a synergistic effect with sorafenib, suggesting that its combination with sorafenib may enhance the inhibitory effects on liver cancer cells in clinical practice.

MATERIALS AND METHODS

Cell Lines and Yeast

The hepatocellular carcinoma cell lines Huh7 and HepG2 were purchased from the American Type Culture Collection (Manassas, VA, USA). Human skin fibroblasts (HFB) were kindly provided by Dr. P. C. Yang of Taiwan University. The cells were routinely maintained in Dulbecco's Modified Eagle Medium (DMEM; GIBCO, Gaithersburg, MD, USA) supplemented with 10% fetal bovine serum at 37°C with 5% CO₂ in a humidified incubator. Yeast cultures were grown for 12 to 14 h in yeast extract-peptone (YEP) media containing lactic acid.

Antibodies and Drugs

Antibodies against HDAC1, HDAC2, HDAC3, HDAC8, p21, p53, p65, acetyl-p53, acetyl-p65, and β -actin, and antibodies for histone H3 and acetyl-histone H3 were purchased from Cell Signaling Technology (Beverly, MA, USA) and Genetex (Irvine, CA, USA). Antibody for cyclin D1 was purchased from ABclonal Technology (Woburn, MA, USA) and antibody for CDK4 was purchased from Proteintech (Rosemont, IL, USA). Secondary antibodies were purchased from Santa Cruz Biotechnology (Santa Cruz, CA, USA). Prestained protein marker and TOOLS[®] RNA extractor were purchased from BIOTOOLS (New Taipei City, Taiwan). HGK powder (purity >98% as measured by HPLC) was purchased from Shanghai BS Bio-Tech Co., Ltd (Shanghai, China). SAHA (purity >98% as measured by HPLC) and Sorafenib was purchased from Sigma-Aldrich (St. Louis, MO, USA).

Real-Time RT-PCR Analysis

Total RNA from Huh7 and HepG2 cells under different treatment conditions was extracted using an RNeasy Mini Kit (QIAGEN, Gaithersburg, MD, USA) according to the manufacturer's instructions. Complementary DNA (cDNA) was synthesized from the total RNA using a Reverse Transcription Kit (QIAGEN) and ToolScript MMLV RT Kit (BIOTOOLS CO., LTD., Taiwan), and used as template in quantitative real-time PCR assays using the TaqMan Gene Expression Kit (Applied Biosystems, Foster City, CA, USA) and an ABI StepOnePlus[™] System (Applied Biosystems) to detect p21, p53, and p65 expression. GAPDH was used as an internal control.

Western Blotting Analysis

Huh7 and HepG2 cells were treated with various concentrations HGK, sorafenib, or DMSO for 48 h followed by being washed twice with phosphate-buffered saline (PBS) and lysed in RIPA lysis buffer (BIOTOOLS CO., LTD., Taiwan) containing protease inhibitors. Protein samples (30 µg) were separated using SDS-polyacrylamide gel electrophoresis (PAGE), transferred to nitrocellulose membranes, and analyzed by western blot. β -actin served as a loading control. Immuno-reactive bands were detected using an ECL Chemiluminescence Kit (NEN Life Science Products, Boston, MA, USA) and developed using X-ray film. The relative intensities of the protein bands were quantified using ImageQuant 5.2 software (GE Healthcare, Piscataway, NJ, USA).

Cell Proliferation Assay

Cell proliferation capacity was monitored using an xCELLigence Real-Time Cell Analyzer (Roche Life Science, Indiana, USA) according to the manufacturer's instructions.

Cell Migration and Invasion Assay

Cell migration and invasion activity was analyzed using a Transwell assay as previously described (33, 34). For the migration assay, cells at a concentration of 5×10^4 were resuspended in 100 µl serum-free culture medium (DMEM) with/without HGK and placed in the upper chambers. The lower chambers were filled with 500 µl DMEM medium containing 10% FBS. Twenty-four hours after treatment, the cells were fixed with methanol, and the cells on the upper surface of the membrane were removed using cotton swabs. The membrane was washed twice with PBS and stained with 0.1% crystal violet. The stained cells were imaged using the ImagePro 6.2 software. Cell counts were obtained from five random fields at 100 \times magnification. For the invasion assay, the membrane was coated with 30 mg/cm² Matrigel (ECM gel, Sigma-Aldrich, St. Louis, MO, USA) to form a matrix barrier. The procedure followed for the invasion assay was the same as that for the migration assay except that the permeating time for the cells was 48 h.

Terminal Deoxynucleotidyl Transferase dUTP Nick End Labeling (TUNEL) Assay

Apoptosis status of Huh7 cells was determined using a DeadEndTM Fluorometric TUNEL Assay Kit (Promega, Madison, WI) according to the manufacturers' protocol. In brief, Huh7 cells were treated with HGK (40 µM), sorafenib (5 µM), or both, for 48 h. The cells were then subjected to a TUNEL assay. The cells were then counted using a microscope (magnification, $\times 100$). Cells in five different microscopic fields/dish were analyzed for each experiment.

Cell-Cycle Analysis

Cells were trypsinized, washed twice, and incubated in PBS containing 0.12% Triton X-100, 0.12 mmol/L EDTA, and 100 mg/mL ribonuclease A. Propidium iodide (50 µg/mL) was then added to each sample for 20 min at 4°C. Cell cycle distribution was analyzed by flow cytometry (Beckman Coulter Epics Elite, Beckman, Inc.).

In vivo Study

Six-week-old male BALB/c nude mice were purchased from the National Laboratory Animal Center (Taipei, Taiwan), maintained under specific pathogen-free conditions, and manipulated according to protocols approved by the Institutional Animal Care and Use Committee (IACUC) of Chang Gung Memorial Hospital (IACUC approval no.: 2018031301, approval date: 6/19/2018). A total of 5×10^6 Huh7 cells were resuspended in 100 µl of saline with 50% Matrigel (BD Biosciences) and the suspensions were subcutaneously implanted into the left and right flank regions of the mice. All tumors were allowed to grow for 1 wk prior to the initiation of drug treatments. At the start of the second week, the mice with tumors were intraperitoneally injected 3 d/wk with 100 µl of HGK (1 mg/kg of body weight), sorafenib (15 mg/kg), or an equal volume of DMSO, which served as a control. Subcutaneous growth of the tumors was measured every 3 d and tumor volumes were calculated using the following equation: length \times width² \times 0.5. Twenty-one days after drug administration, the mice were sacrificed and the tumors were subjected to immunohistochemical staining and analysis.

Immunohistochemistry

The tumors of the mice were fixed in formalin and embedded in paraffin. Consecutive 2-µm-thick sections were cut from the paraffin-embedded tissue blocks and floated onto glass slides. The slide-mounted tissue sections were subjected to immunohistochemical staining as described previously (35).

Chromatin Immunoprecipitation (ChIP)-qPCR Analysis

Chromatin immunoprecipitation assays were carried out using an Acetyl-Histone H3 Immunoprecipitation Assay Kit (Merck Millipore, Temecula, CA) according to manufacturer's instruction. Each of the purified DNAs (5 µl) were used as template for 60 cycles of PCR amplification using p21 promoter-specific primers (36) and TOOLS 2x SYBR qPCR Mix (BIOTOOLS CO., LTD., Taiwan).

Statistical Analysis

All data were recorded as continuous variants and analyzed using Student's *t*-test. All statistical analyses were performed using SPSS 16.0 and Excel 2007 software. All statistical tests were two-sided and the *p*-values of significance were established at < 0.05 (*), < 0.01 (**), or < 0.001 (***), as indicated.

RESULTS

HGK Inhibited the Expression of Class I HDAC in Yeast

Previous studies have shown that over-expression of class I HDAC is closely related to the development and progression of liver cancer. To identify natural compounds with inhibitory activity against class I HDAC, we used a yeast analysis platform previously established for drug screening (37). After treating the yeasts with different natural compounds, western blotting was performed to analyze the expression of reduced potassium dependency 3 (Rpd3) corresponding to human class I HDAC.

We found that the amount of Rpd3 expressed in yeast treated with HGK was significantly lower compared to that in the vehicle control group (**Figures 1A,B**). The results showed that HGK may have inhibitory activity against class I HDAC in human cell lines.

HGK Inhibited Class I HDAC Expression and Suppressed Proliferation, Migration, and Invasion Capacities of Liver Cancer Cells

To determine whether HGK inhibits the expression of class I HDAC in liver cancer cell lines, western blotting was used to

analyze class I HDAC expression in HepG2 and Huh7 cells following treatment with different concentrations of HGK. The results demonstrated that expression levels of HDAC 1, 2, 3, and 8 were significantly decreased by HGK treatment in a dose-dependent manner (**Figures 1C–G**), suggesting that HGK was able to inhibit class I HDAC expression in liver cancer cells. In order to further understand the effect of HGK on the acetylation of histone proteins, we performed western blot analysis on the acetylation status of histone H4 in liver cancer cell lines treated with HGK. We found that, after treatment, the proportion of acetylated histone H4 was significantly increased compared with that of the vehicle group (**Figure 1H**), indicating that HGK promotes the acetylation of histone by inhibiting HDAC.

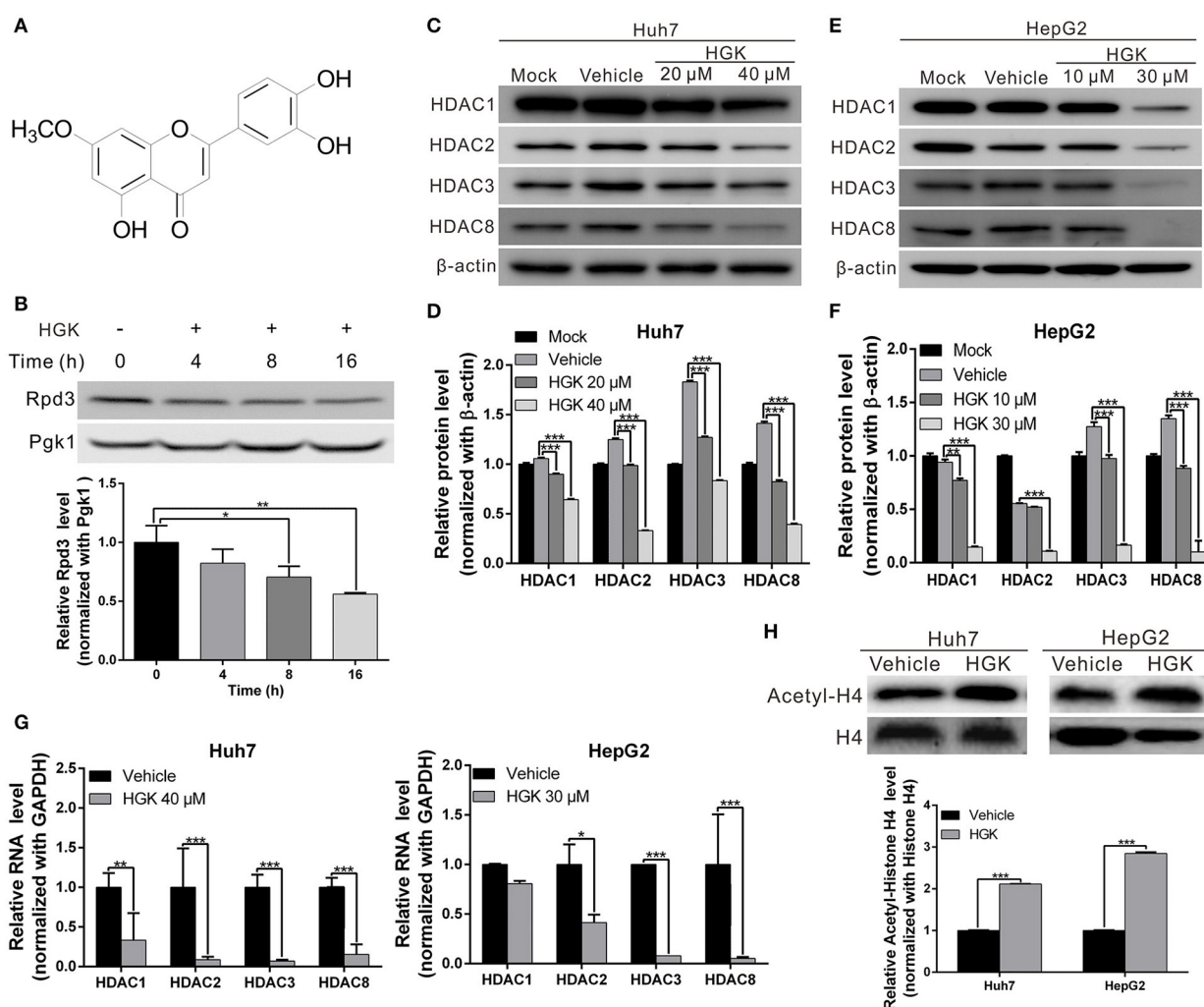


FIGURE 1 | Hydroxyginkwanin (HGK) inhibited the expression of class I histone deacetylase (HDAC) in yeast and human liver cancer cell lines. **(A)** Chemical structure of HGK. **(B)** Western blot analysis revealed the effect on Rpd3 expression in yeast after the 48 h of 1 mM HGK treatment. Quantitative results are shown in lower panel. $p < 0.05$ (*), $p < 0.01$ (**), as assessed using the Student's *t*-test. **(C,E)** Huh7 and HepG2 cells were treated with HGK or vehicle for 48 h. The expression levels of HDAC 1, 2, 3, and 8 were determined using western blotting. Quantitative results are shown **(D,F)**. **(G)** RNA expression levels of HDAC 1, 2, 3, and 8 in Huh7 and HepG2 cells following treatment with vehicle (DMSO) or HGK analyzed by quantitative real-time RT-PCR. **(H)** The levels of acetylated histone H4 were determined by western blotting after 48 h of HGK treatment. Quantitative results are shown in the lower panel. $p < 0.001$ (***). All data are expressed as the mean \pm standard deviation (SD) of three independent experiments.

To elucidate the effect of HGK on the physiology of liver cancer cells, we performed cell functional analysis to detect changes in proliferation, migration, and invasion of liver cancer cell lines Huh7 and HepG2. The results revealed that proliferation, migration, and invasion abilities of the two cell lines were significantly lower in HGK-treated cells compared to those of control cells. Additionally, increased HGK concentrations resulted in greater inhibition (**Figures 2A–F**), showing that HGK may exert its anticancer activity by inhibiting class I HDAC. The half-maximal inhibitory concentration (IC_{50}) of HGK toward Huh7 and HepG2 cells was calculated using GraphPad Prism software and was about 40 and 30 μ M, respectively. However, no inhibitory effect was observed on the growth of human skin fibroblast cell line HFB at the above concentrations (**Figure 2B**).

This indicated that HGK selectively inhibits the growth of liver cancer cells without significant toxicity to normal cells.

Moreover, we compared the efficacy of HGK against liver cancer with the clinically used HDAC inhibitor SAHA and its toxicity to normal cells. The half-maximal inhibitory concentration (IC_{50}) of SAHA toward Huh7 and HepG2 cells was about 3 μ M. We found that the physiological toxicity of HGK to human skin fibroblast (HFB) cell line was significantly lower than that of SAHA at the half maximal inhibitory concentration (**Figure S1D**). In addition, after 30 h of treatment, both HGK and SAHA significantly inhibited the growth of the liver cancer cell lines. However, the inhibitory effect of SAHA was better than that of HGK, as SAHA obviously triggered apoptosis (data not shown). Flow cytometry results also confirmed that the tumor

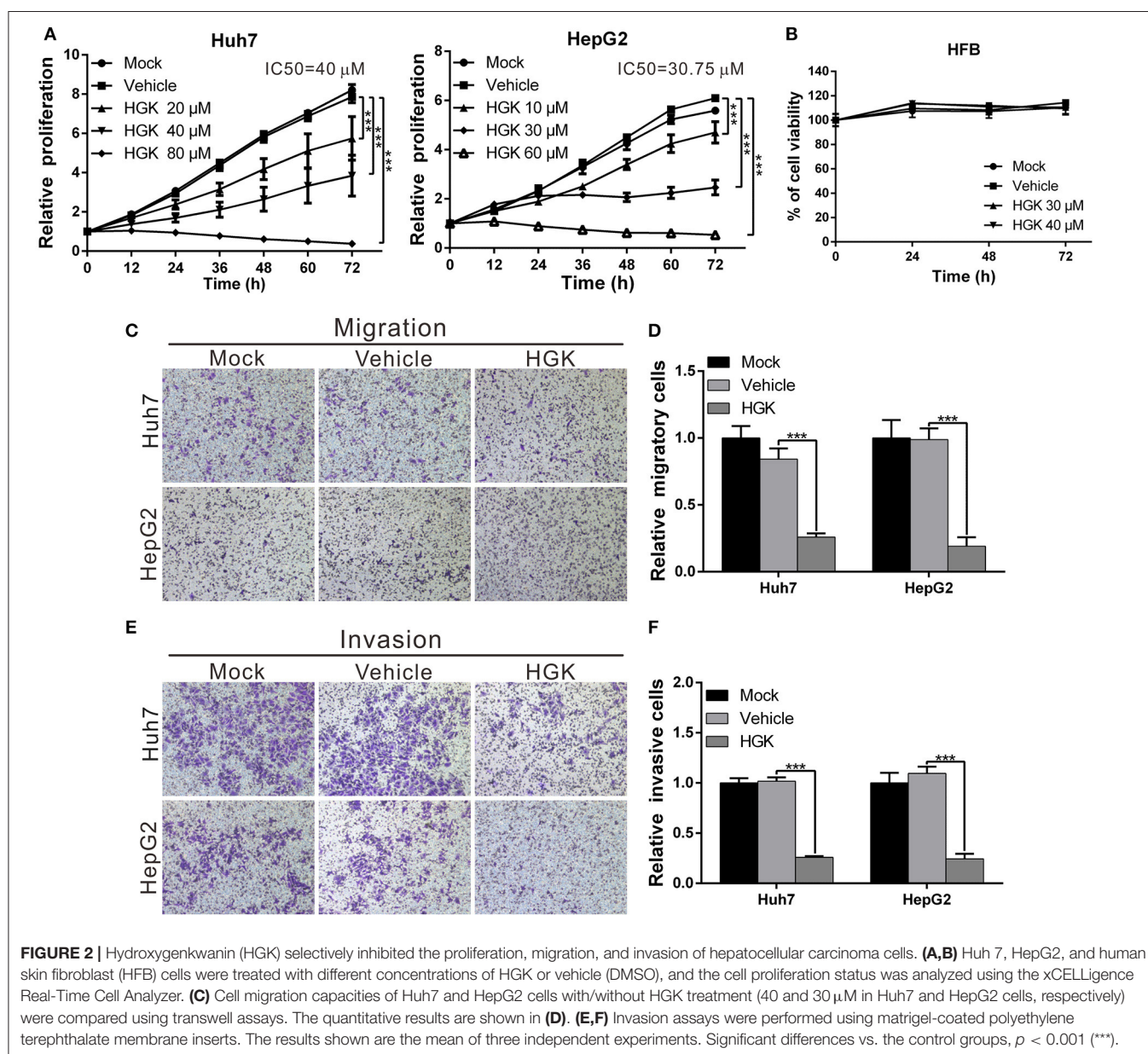


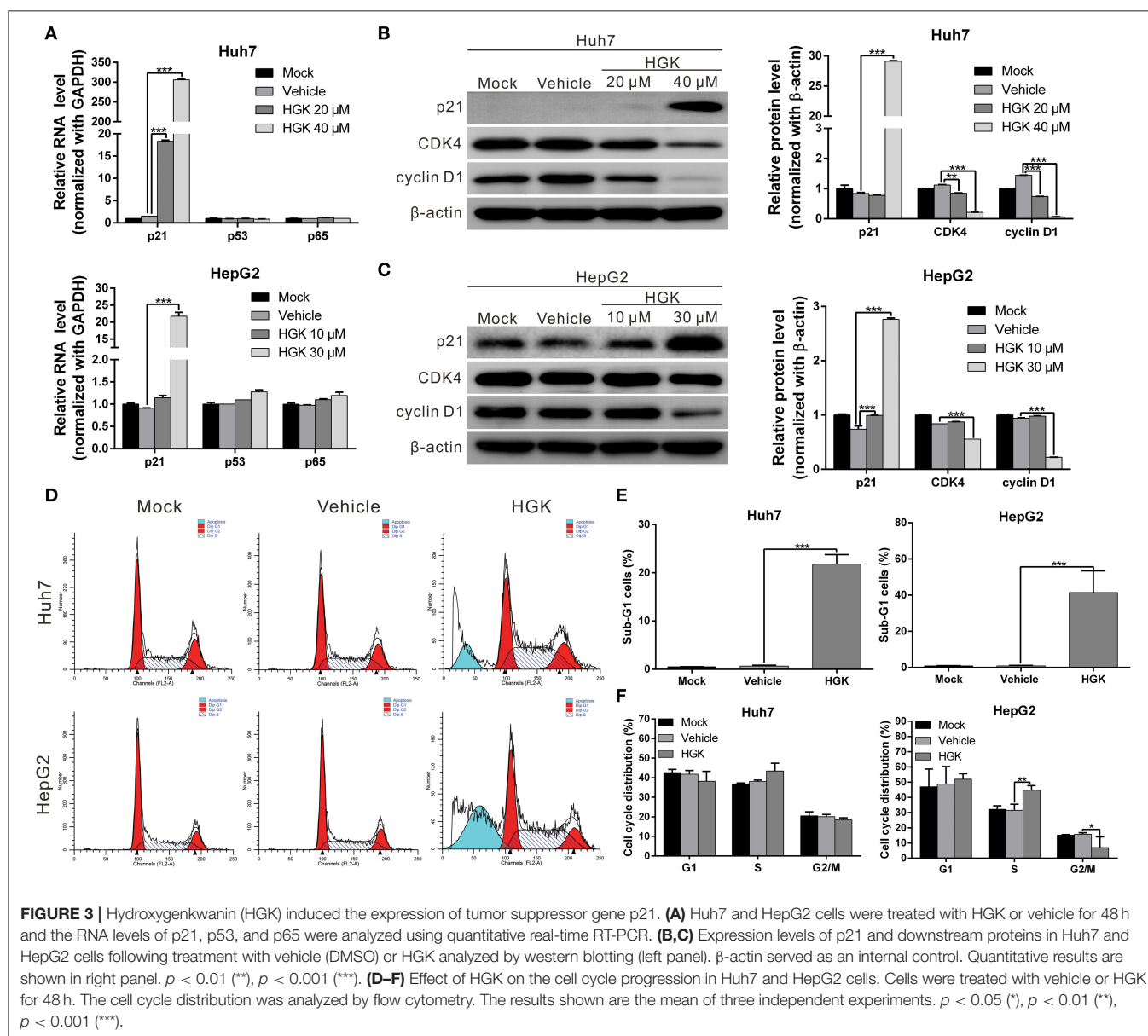
FIGURE 2 | Hydroxygenkwanin (HGK) selectively inhibited the proliferation, migration, and invasion of hepatocellular carcinoma cells. **(A,B)** Huh 7, HepG2, and human skin fibroblast (HFB) cells were treated with different concentrations of HGK or vehicle (DMSO), and the cell proliferation status was analyzed using the xCELLigence Real-Time Cell Analyzer. **(C)** Cell migration capacities of Huh7 and HepG2 cells with/without HGK treatment (40 and 30 μ M in Huh7 and HepG2 cells, respectively) were compared using transwell assays. The quantitative results are shown in **(D)**. **(E,F)** Invasion assays were performed using matrigel-coated polyethylene terephthalate membrane inserts. The results shown are the mean of three independent experiments. Significant differences vs. the control groups, $p < 0.001$ (***).

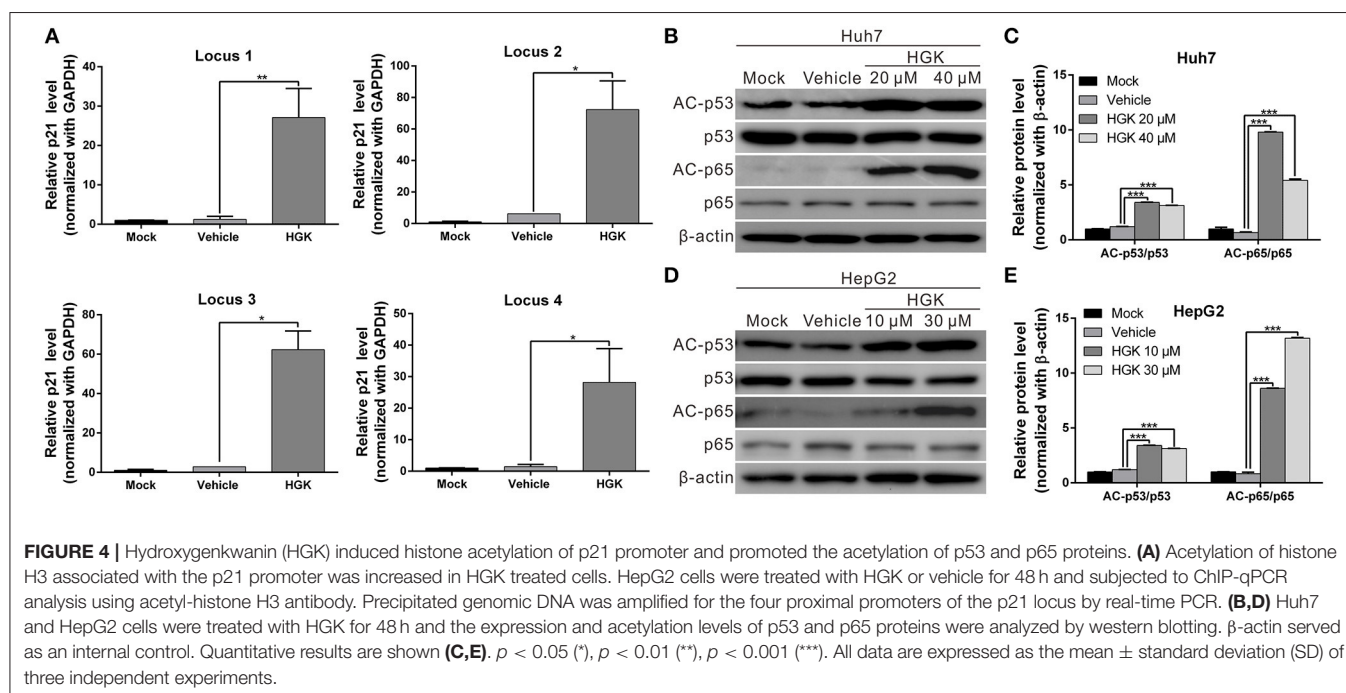
suppressor mechanism of HGK mainly caused cell cycle arrest, while SAHA caused apoptosis (Figures S1A–C).

HGK Effects on p21, p53, and p65 Gene

HDAC regulates the de-acetylation of histone and non-histone proteins, affecting gene expression or protein activation. Previous studies have shown that class I HDAC inhibits the expression of the tumor suppressor gene p21 and alters the acetylation and activation of p53 and p65 proteins, which in turn promote carcinogenesis (38–41). To determine the effect of HGK on tumor suppressor molecules, real-time RT-PCR and western blotting were used to analyze the expression of p21 and acetylation of p53 and p65 in liver cancer cell lines treated with HGK (Figures 3A–C). The results showed that compared with that in the vehicle control group, expression

levels of p21 mRNA and protein significantly increased in Huh7 and HepG2 cells treated with HGK, which inhibited the expression of cell cycle regulatory proteins CDK4 and cyclin D1, thereby inducing S-phase cell cycle arrest and promoting apoptosis (Figures 3D–F). To further confirm that HGK increased expression from the p21 gene region by modulating acetylation of histones, we performed a chromatin immunoprecipitation (ChIP) assay. The assay demonstrated that the degree of histone H3 acetylation in four distinct p21 promoter regions were significantly increased following treatment with HGK (Figure 4A). This suggested that HGK enhanced p21 expression by promoting the acetylation of histone H3 in the p21 promoter region. Moreover, the degree of p53 and p65 protein acetylation in the two cell lines was significantly increased following HGK treatment (Figures 4B–E), showing that HGK





altered the activation of tumor suppressor proteins, such as p53 and p65.

Synergistic Effect of HGK and Sorafenib

Previous studies have shown that HDAC inhibitors have synergistic effects with sorafenib that enhance cancer suppression efficacy. To determine whether HGK and sorafenib had synergistic effects, liver cancer cell lines were treated with HGK and sorafenib, separately and combined, and the cells were analyzed for apoptosis. The results demonstrated that treatment with HGK or sorafenib alone slightly induced cell apoptosis. However, when both compounds were administered simultaneously, the cytotoxic effects on the cell lines were significantly greater compared with that observed in cells that received single-drug treatments (Figure 5A). Moreover, the combination of the two drugs inhibited cancer cell proliferation, migration, and invasion by more than 1-fold compared to the inhibition by either HGK or sorafenib alone (Figures 5B–F). These results confirmed that the combined use of HGK and sorafenib had synergistic effects against liver cancer cells.

Combination of HGK and Sorafenib Enhanced Efficacy Against Liver Cancer *in vivo*

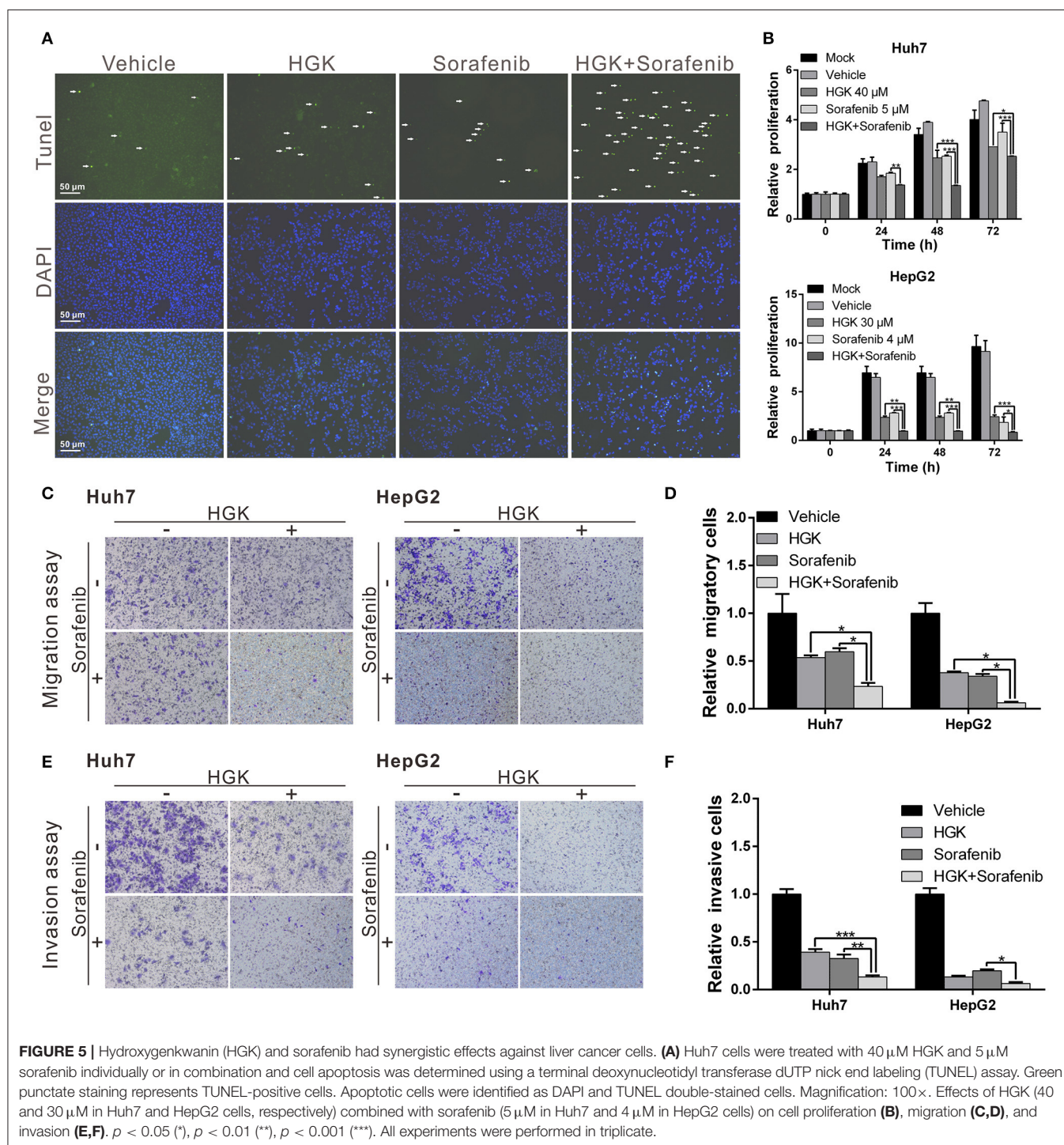
To verify that HGK had anticancer effects *in vivo* and to confirm the regulatory mechanisms involved, a mouse xenograft model was used. Huh7 cells were injected into the back of mice and HGK and sorafenib were periodically administered by intraperitoneal injection, either separately or in combination. The results showed that tumor growth in mice treated with HGK, sorafenib, or both was significantly inhibited compared with that in the vehicle dimethyl sulfoxide (DMSO)-treated group.

Moreover, the inhibitory effects of the combination treatment on the tumors were significantly greater compared to that of single-drug treatment (Figures 6A–D), showing a synergistic efficacy for HGK and sorafenib. Additionally, there was no significant difference in body weight between the mice given HGK alone and the vehicle group (Figure 6E), nor were there any significant abnormalities in the serological test results for the two groups of mice (Figure 6F). This indicated that HGK failed to demonstrate any noteworthy physiological toxicity.

In addition, expression of class I HDAC genes was analyzed using immunohistochemical staining of mouse tumor tissues. Interestingly, the results were consistent with those from the *in vitro* experiments. Expression levels of class I HDAC were significantly decreased in mouse tumors treated with HGK (Figure 7A). These results confirmed that HGK induced expression of a tumor suppressor genes by inhibiting class I HDAC, thereby promoting apoptosis in liver cancer cells and inhibiting tumor growth (Figure 7B).

DISCUSSION

Abnormal regulation of epigenetics is closely related to tumorigenesis, which is partly regulated by HDAC. Previous studies have demonstrated that class I HDACs are highly expressed in liver cancer tissues and closely associated with tumor development and progression, which makes them important targets for liver cancer treatment (42–44). In the current study, we determined that the natural compound HGK possessed class I HDAC inhibitory activity and low physiological toxicity. We also confirmed that HGK induced expression or activation of p21, p53, p65, and other tumor suppressor genes to inhibit the growth of liver cancer tumors. Importantly, we determined that HGK



exhibited a synergistic effect with sorafenib in enhancing tumor-suppressing effects. To our knowledge, this is the first study to identify HGK as a class I HDAC inhibitor and to demonstrate its therapeutic potential for liver cancer treatment.

HDAC regulates gene expression and protein activation by regulating the acetylation of histone and non-histone proteins; however, the regulatory mechanism of cancer physiology is

extremely diverse and complex and the carcinogenic and tumor-suppressing pathways regulated in various cancers are different. In the current study, we limited our analyses to tumor suppressor genes such as p21, p53, and p65, which explains only part of the anticancer mechanism of HGK. We believe that there are multiple key factors involved; however, this needs to be clarified with further experiments.

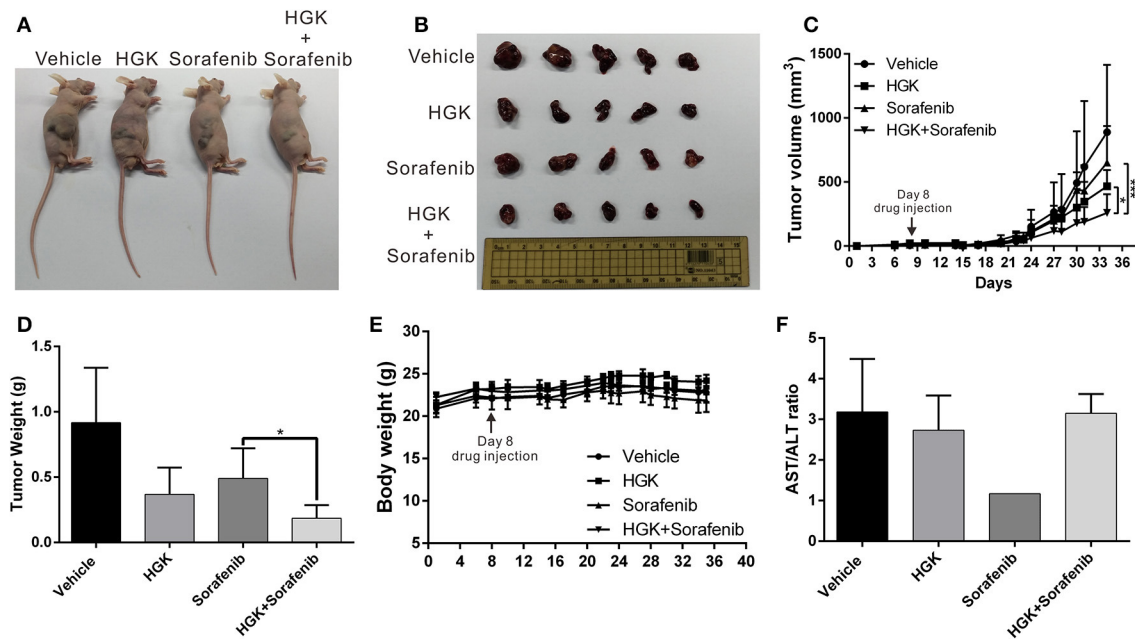


FIGURE 6 | Combination of hydroxygenkwamin (HGK) and sorafenib enhanced *in vivo* anticancer efficacy. **(A,B)** A total of 5×10^6 Huh7 cells were inoculated into nude mice ($n = 5$ per group). The mice with tumors were intraperitoneally injected three times per wk with 100 μ l of HGK (1 mg/kg of body weight), sorafenib (15 mg/kg), or an equal volume of dimethyl sulfoxide (DMSO), which served as a control. Representative images show the tumor xenografts at 4 wk post-implantation. **(C)** Tumor volumes were recorded every 3 d after injection as follows: length \times width² \times 0.5. The error bars indicate the S.D. $p < 0.05$ (*), $p < 0.001$ (***). Tumor weights **(D)** and body weights **(E)** were calculated every 3 d after injection. **(F)** Serological test results of the four groups of mice.

In the present study, we found that HGK promoted histone acetylation in the p21 promoter region, which in turn upregulated p21 expression. p21 is a cyclin-dependent kinase inhibitor (CKI) that acts on cyclin-dependent kinases (CDKs), consequently inhibiting cell cycle progression (45). The p21 gene is also one of the genes regulated by p53. Previous studies have shown that acetylation of the p53 protein enhances its stability allowing it to bind to the target gene promoter, thereby upregulating the expression of tumor suppressor genes, such as p21 and BAX (46, 47). The results of the present study indicate that HGK can promote the acetylation of p53 at lysine 382 (K382), suggesting that HGK can also indirectly promote p21 expression through the regulation of p53 acetylation (48). Furthermore, previous research has determined that acetylation at different sites on the p65 protein produces different effects on p65 activity (49). For example, acetylation of p65 at K310 enhances the ability of p65 to bind to the target gene promoter, which in turn regulates the expression of tumor suppressor genes, such as miR21 and DR5, and activates the downstream pathways. Therefore, the acetylation of p65 at K310 is also regarded as an indicator of the anticancer activity of p65. In the present study, we found that p65 acetylation at K310 was significantly increased in HGK-treated cells, showing that HGK can achieve anticancer effects by activating p65 and upregulating the expression of its downstream tumor suppressor genes.

Currently, histone deacetylase inhibitors (HDACi) are widely used in cancer treatment and have achieved good therapeutic effects in treating various cancers. Suberoylanilide hydroxamic

acid (SAHA) and romidepsin, two widely studied HDACi, have been approved by the US FDA for treatment of T-cell lymphomas (50). Many studies have shown that these HDACi can also inhibit the progression of cancers such as breast cancer, lung cancer, and prostate cancer (51–54). Furthermore, many clinical trials have demonstrated that the concomitant use of HDACi and other anticancer drugs provides synergistic therapeutic effects (55–57). For instance, the concomitant use of SAHA and bortezomib can synergistically induce ROS-driven caspase-dependent apoptosis of nasopharyngeal carcinoma (58); the concomitant use of romidepsin with cisplatin and nivolumab can enhance the therapeutic effects of the individual medications on triple-negative breast cancer; and a combination therapy using pralatrexate and romidepsin enhances the therapeutic effects on relapsed and refractory T-cell lymphoma [56]. Studies on liver cancer have also indicated a similar synergistic killing effect on liver cancer cell lines when using the HDACi valproic acid (VPA) along with aspirin (59). In the present study, we found that the concomitant use of HGK and sorafenib significantly enhanced their inhibitory effects on the growth and metastasis of malignant liver tumors. Thus, the different mechanisms by which HGK and sorafenib achieve their anticancer effects result in synergism during concomitant use. This result also suggests that HGK can potentially be used as an adjuvant agent in clinical treatment.

SAHA is an HDAC inhibitor that is currently approved by the FDA for the treatment of T-cell lymphoma. It can specifically bind to the zinc-containing catalytic domains of class I, II, and VI histone deacetylases (HDACs), thereby suppressing

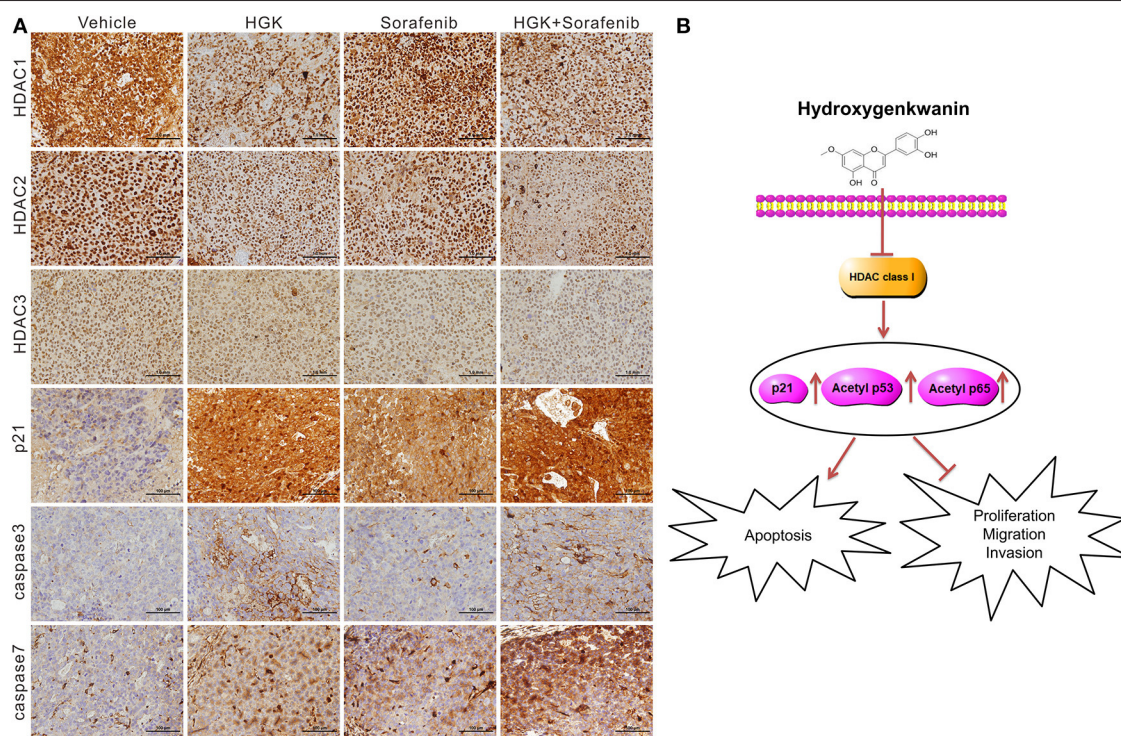


FIGURE 7 | Hydroxygenkwanin (HGK) repressed tumor growth by inhibiting class I histone deacetylase (HDAC). **(A)** Immunohistochemical staining representing the effect of HGK on class I HDACs, p21, caspase 3, and caspase 7 expression in mice xenograft tumors. Magnification: 400 \times . **(B)** Schematic representation summarizing the anti-hepatocellular carcinoma mechanism of HGK.

their enzymatic activities. However, HGK inhibits the growth of liver cancer cells by inhibiting the expression of class I HDAC, which is different from the mechanism of action of SAHA. In addition, in our recent study, we found that HGK can also inhibit the expression of FOXM1, thereby inhibiting EMT progression by regulating miR320a expression (60). The anti-HCC effect of HGK is known to involve two or more regulatory mechanisms. In this study, we aimed to show that HGK can inhibit the progression of liver cancer by inhibiting the expression of class I HDAC. Although its efficacy and specificity are not as good as SAHA, the results of our study indicate that HGK has lower physiological toxicity to normal cells and can be potentially used as a therapeutic adjuvant in the treatment of liver cancer.

Class I HDAC is highly expressed in most tumor tissues, including liver cancer, breast cancer, lung cancer, and colorectal cancer, and is one of the main targets for cancer treatment (61–64). Therefore, we focused on the regulation of class I HDAC by HGK. However, in yeast, HGK also inhibited the expression of Sir2, suggesting that it may also have class III HDAC inhibitory activity in human cells (data not shown). Previous studies have shown that class III HDAC is closely related to tumorigenesis and prognosis in leukemia, glioblastoma, prostate cancer, colorectal cancer, and skin cancer (65–69). Therefore, we plan to continue exploring whether HGK inhibits human class III HDAC and to test its inhibitory effect on

multiple cancer cell types in effort to assess whether HGK might be used to treat other types of cancer. In addition, further studies are needed to understand how HGK upregulates HDACs expression.

Although high HDAC expression levels are closely related to tumor progression and patient outcome in most cancers, HDAC deactivation due to gene mutations has been observed in some cancers. For example, HDAC1 somatic mutations have been found in 8.3% of dedifferentiated liposarcoma and HDAC4 homozygous deletions are found in 4% of melanoma (70, 71). These mutations result in deactivation of HDAC and slows tumor growth. However, since mutations increase resistance to HDAC inhibitors, it is speculated that this is one reason why many cancers, including liver cancer, are not sensitive to HDAC inhibitors. Therefore, the combination of different drugs in cancer treatment is crucial for improving efficacy.

CONCLUSIONS

While HDAC inhibitors have been widely used in treating various cancers, their side effects cause bottlenecks in treatment. In the current study, we identified HGK, a natural compound with class I HDAC inhibitory activity, as an anticancer compound that acted synergistically with sorafenib. Importantly, since HGK is not physiologically toxic, it is suitable as a therapeutic adjuvant

in combination with other anticancer drugs to enhance their therapeutic effects.

DATA AVAILABILITY STATEMENT

All datasets generated for this study are included in the article/**Supplementary Material**.

ETHICS STATEMENT

The animal study was reviewed and approved by Institutional Animal Care and Use Committee (IACUC) of Chang Gung Memorial Hospital, Taiwan (IACUC approval no.: 2018031301, approval date: 6/19/2018).

AUTHOR CONTRIBUTIONS

Conceptualization: T-HW and C-CC. Data curation: C-YC and T-HW. Formal analysis: C-TY, W-YC, and Y-LL. Investigation and project administration: T-HW, C-CC, and C-YC. Methodology: CH and C-TY. Resources: Y-LL and CH. Supervision: T-HW. Validation: S-HU. Visualization: S-HU, W-YC, and CH. Writing of the original manuscript draft and manuscript review and editing: T-HW and C-YC. All authors contributed to manuscript revision and have read and approved the submitted version.

REFERENCES

- Liao SH, Su TH, Jeng YM, Liang PC, Chen DS, Chen CH, et al. Clinical manifestations and outcomes of patients with sarcomatoid hepatocellular carcinoma. *Hepatology*. (2019) 69:209–21. doi: 10.1002/hep.30162
- Niu L, Liu L, Yang S, Ren J, Lai PBS, Chen GG. New insights into sorafenib resistance in hepatocellular carcinoma: Responsible mechanisms and promising strategies. *Biochim Biophys Acta Rev Cancer*. (2017) 1868:564–70. doi: 10.1016/j.bbcan.2017.10.002
- Llovet JM. Liver cancer: time to evolve trial design after everolimus failure. *Nat Rev Clin Oncol*. (2014) 11:506–7. doi: 10.1038/nrclinonc.2014.136
- Worns MA, Galle PR. HCC therapies—lessons learned. *Nat Rev Gastroenterol Hepatol*. (2014) 11:447–52. doi: 10.1038/nrgastro.2014.10
- Muntane J, De la Rosa AJ, Docobo F, Garcia-Carbonero R, Padillo FJ. Targeting tyrosine kinase receptors in hepatocellular carcinoma. *Curr Cancer Drug Targets*. (2013) 13:300–12. doi: 10.2174/15680096113139990075
- Cidon EU. Systemic treatment of hepatocellular carcinoma: past, present and future. *World J Hepatol*. (2017) 9:797–807. doi: 10.4254/wjh.v9.i18.797
- Kudo M. Systemic therapy for hepatocellular carcinoma: latest advances. *Cancers*. (2018) 10:E412. doi: 10.3390/cancers10110412
- Frenette C, Gish R. Targeted systemic therapies for hepatocellular carcinoma: clinical perspectives, challenges and implications. *World J Gastroenterol*. (2012) 18:498–506. doi: 10.3748/wjg.v18.i6.498
- Bhayani NH, Jiang Y, Hamed O, Kimchi ET, Staveley O'Carroll KE, Gusani NJ. Advances in the pharmacologic treatment of hepatocellular carcinoma. *Curr Clin Pharmacol*. (2015) 10:299–304. doi: 10.2174/1574884710666151020100059
- Finn RS. Emerging targeted strategies in advanced hepatocellular carcinoma. *Semin Liver Dis*. (2013) 33:S11–19. doi: 10.1055/s-0033-1333632
- Llovet JM, Hernandez-Gea V. Hepatocellular carcinoma: reasons for phase III failure and novel perspectives on trial design. *Clin Cancer Res*. (2014) 20:2072–9. doi: 10.1158/1078-0432.CCR-13-0547

FUNDING

This research was partially supported by the Ministry of Science and Technology, Taiwan (grant MOST 107-2314-B-182A-140-MY3) and Chang Gung Medical Research Program, Taiwan (grant CMRPG3H1001).

ACKNOWLEDGMENTS

We would like to thank the Tissue Bank at the Chang Gung Memorial Hospital, Lin-Kou, Taiwan for their excellent tissue processing. We thank Ying Chen and Shu-Fang Cheng for excellent technical assistance in this project.

SUPPLEMENTARY MATERIAL

The Supplementary Material for this article can be found online at: <https://www.frontiersin.org/articles/10.3389/fonc.2020.00216/full#supplementary-material>

Figure S1 | Comparison of antiproliferative effect and physiological toxicity of HGK and SAHA. **(A,B)** Effect of HGK and SAHA on the cell cycle progression in Huh7 and HepG2 cells. Cells were treated with or without stated concentrations of HGK or SAHA for 30 h. The cell cycle distribution was analyzed by flow cytometry. The quantitative results were shown in **(C)**. **(D)** Human skin fibroblast (HFB) cells were treated with stated concentrations of HGK, SAHA, or vehicle (DMSO), and the cell viability was analyzed using the xCELLigence Real-Time Cell Analyzer. The results shown are the mean of three independent experiments. Significant differences versus the control group (vehicle), *** $p < 0.001$.

- Raza A, Sood GK. Hepatocellular carcinoma review: current treatment, and evidence-based medicine. *World J Gastroenterol*. (2014) 20:4115–27. doi: 10.3748/wjg.v20.i15.4115
- Petta V, Gkiozos I, Strimpakos A, Syrigos K. Histones and lung cancer: Are the histone deacetylases a promising therapeutic target? *Cancer Chemother Pharmacol*. (2013) 72:935–52. doi: 10.1007/s00280-013-2223-9
- Tang J, Yan H, Zhuang S. Histone deacetylases as targets for treatment of multiple diseases. *Clin Sci*. (2013) 124:651–62. doi: 10.1042/CS20120504
- Frew AJ, Johnstone RW, Bolden JE. Enhancing the apoptotic and therapeutic effects of HDAC inhibitors. *Cancer Lett*. (2009) 280:125–33. doi: 10.1016/j.canlet.2009.02.042
- Bassett SA, Barnett MP. The role of dietary histone deacetylases (HDACs) inhibitors in health and disease. *Nutrients*. (2014) 6:4273–301. doi: 10.3390/nu6104273
- Newbold A, Falkenberg KJ, Prince HM, Johnstone RW. How do tumor cells respond to HDAC inhibition? *FEBS J*. (2016) 283:4032–46. doi: 10.1111/febs.13746
- Miller SM, Goulet DR, Johnson GL. Targeting the breast cancer kinome. *J Cell Physiol*. (2017) 232:53–60. doi: 10.1002/jcp.25427
- Zhang H, Shang YP, Chen HY, Li J. Histone deacetylases function as novel potential therapeutic targets for cancer. *Hepatol Res*. (2017) 47:149–59. doi: 10.1111/hepr.12757
- Konsoula Z, Velen A, Lee R, Dritschilo A, Jung M. Histone deacetylase inhibitor: antineoplastic agent and radiation modulator. *Adv Exp Med Biol*. (2011) 720:171–9. doi: 10.1007/978-1-4614-0254-1_14
- McConkey DJ, White M, Yan W. HDAC inhibitor modulation of proteotoxicity as a therapeutic approach in cancer. *Adv Cancer Res*. (2012) 116:131–63. doi: 10.1016/B978-0-12-394387-3.00004-5
- Mottamal M, Zheng S, Huang TL, Wang G. Histone deacetylase inhibitors in clinical studies as templates for new anticancer agents. *Molecules*. (2015) 20:3898–941. doi: 10.3390/molecules20033898

23. Hamed HA, Yamaguchi Y, Fisher PB, Grant S, Dent P. Sorafenib and HDAC inhibitors synergize with TRAIL to kill tumor cells. *J Cell Physiol.* (2013) 228:1996–2005. doi: 10.1002/jcp.24362
24. Chen CH, Chen MC, Wang JC, Tsai AC, Chen CS, Liou JP, et al. Synergistic interaction between the HDAC inhibitor, MPT0E028, and sorafenib in liver cancer cells in vitro and in vivo. *Clin Cancer Res.* (2014) 20:1274–87. doi: 10.1158/1078-0432.CCR-12-3909
25. Li-Weber M. Targeting apoptosis pathways in cancer by Chinese medicine. *Cancer Lett.* (2013) 332:304–12. doi: 10.1016/j.canlet.2010.07.015
26. Wang Z, Li J, Ji Y, An P, Zhang S, Li Z. Traditional herbal medicine: a review of potential of inhibitory hepatocellular carcinoma in basic research and clinical trial. *Evid Based Complement Alternat Med.* (2013) 2013:268963. doi: 10.1155/2013/268963
27. Terlikowska KM, Witkowska AM, Zujko ME, Dobrzycka B, Terlikowski SJ. Potential application of curcumin and its analogues in the treatment strategy of patients with primary epithelial ovarian cancer. *Int J Mol Sci.* (2014) 15:21703–22. doi: 10.3390/ijms151221703
28. Hong M, Tan HY, Li S, Cheung F, Wang N, Nagamatsu T, et al. Cancer stem cells: the potential targets of chinese medicines and their active compounds. *Int J Mol Sci.* (2016) 17:E893. doi: 10.3390/ijms17060893
29. Slezakova S, Ruda-Kucerova J. Anticancer activity of artemisinin and its derivatives. *Anticancer Res.* (2017) 37:5995–6003. doi: 10.21873/anticancer.12046
30. Myzak MC, Tong P, Dashwood WM, Dashwood RH, Ho E. Sulforaphane retards the growth of human PC-3 xenografts and inhibits HDAC activity in human subjects. *Exp Biol Med.* (2007) 232:227–34. doi: 10.3181/00379727-207-2320227
31. Liu Y, Tong Y, Yang X, Li F, Zheng L, Liu W, et al. Novel histone deacetylase inhibitors derived from *Magnolia officinalis* significantly enhance TRAIL-induced apoptosis in non-small cell lung cancer. *Pharmacol Res.* (2016) 111:113–25. doi: 10.1016/j.phrs.2016.05.028
32. Yang F, Wang F, Liu Y, Wang S, Li X, Huang Y, et al. Sulforaphane induces autophagy by inhibition of HDAC6-mediated PTEN activation in triple negative breast cancer cells. *Life Sci.* (2018) 213:149–57. doi: 10.1016/j.lfs.2018.10.034
33. Wang TH, Lin YS, Chen Y, Yeh CT, Huang YL, Hsieh TH, et al. Long non-coding RNA AOC4P suppresses hepatocellular carcinoma metastasis by enhancing vimentin degradation and inhibiting epithelial-mesenchymal transition. *Oncotarget.* (2015) 6:23342–57. doi: 10.18632/oncotarget.4344
34. Chen CY, Chen CC, Shieh TM, Hsueh C, Wang SH, Leu YL, et al. Corylin Suppresses hepatocellular carcinoma progression via the inhibition of epithelial-mesenchymal transition, mediated by long noncoding RNA GAS5. *Int J Mol Sci.* (2018) 19:E380. doi: 10.3390/ijms19020380
35. Chen CC, Chen CY, Ueng SH, Hsueh C, Yeh CT, Ho JY, et al. Corylin increases the sensitivity of hepatocellular carcinoma cells to chemotherapy through long noncoding RNA RAD51-AS1-mediated inhibition of DNA repair. *Cell Death Dis.* (2018) 9:543. doi: 10.1038/s41419-018-0575-0
36. Noh JH, Jung KH, Kim JK, Eun JW, Bae HJ, Xie HJ, et al. Aberrant regulation of HDAC2 mediates proliferation of hepatocellular carcinoma cells by deregulating expression of G1/S cell cycle proteins. *PLoS ONE.* (2011) 6:e28103. doi: 10.1371/journal.pone.0028103
37. Chen CC, Huang JS, Wang TH, Kuo CH, Wang CJ, Wang SH, et al. Dihydrocoumarin, an HDAC inhibitor, increases DNA damage sensitivity by inhibiting Rad52. *Int J Mol Sci.* (2017) 18:E2655. doi: 10.3390/ijms18122655
38. Lehmann A, Denkert C, Budczies J, Buckendahl AC, Darb-Esfahani S, Noske A, et al. High class I HDAC activity and expression are associated with RelA/p65 activation in pancreatic cancer *in vitro* and *in vivo*. *BMC Cancer.* (2009) 9:395. doi: 10.1186/1471-2407-9-395
39. Wagner T, Brand P, Heinzel T, Kramer OH. Histone deacetylase 2 controls p53 and is a critical factor in tumorigenesis. *Biochim Biophys Acta.* (2014) 1846:524–38. doi: 10.1016/j.bbcan.2014.07.010
40. Ruscetti M, Dadashian EL, Guo W, Quach B, Mulholland DJ, Park JW, et al. HDAC inhibition impedes epithelial-mesenchymal plasticity and suppresses metastatic, castration-resistant prostate cancer. *Oncogene.* (2016) 35:3781–95. doi: 10.1038/ncr.2015.444
41. Wang L, Li H, Ren Y, Zou S, Fang W, Jiang X, et al. Targeting HDAC with a novel inhibitor effectively reverses paclitaxel resistance in non-small cell lung cancer via multiple mechanisms. *Cell Death Dis.* (2016) 7:e2063. doi: 10.1038/cddis.2015.328
42. Wu LM, Yang Z, Zhou L, Zhang F, Xie HY, Feng XW, et al. Identification of histone deacetylase 3 as a biomarker for tumor recurrence following liver transplantation in HBV-associated hepatocellular carcinoma. *PLoS ONE.* (2010) 5:e14460. doi: 10.1371/journal.pone.0014460
43. Wu J, Du C, Lv Z, Ding C, Cheng J, Xie H, et al. The up-regulation of histone deacetylase 8 promotes proliferation and inhibits apoptosis in hepatocellular carcinoma. *Dig Dis Sci.* (2013) 58:3545–53. doi: 10.1007/s10620-013-2867-7
44. Zhao J, Gray SG, Wabitsch M, Greene CM, Lawless MW. The therapeutic properties of resminostat for hepatocellular carcinoma. *Oncoscience.* (2018) 5:196–208. doi: 10.18632/oncoscience.420
45. Dutto I, Tillhon M, Cazzalini O, Stivala LA, Prosperi E. Biology of the cell cycle inhibitor p21(CDKN1A): molecular mechanisms and relevance in chemical toxicology. *Arch Toxicol.* (2015) 89:155–78. doi: 10.1007/s00204-014-1430-4
46. Batta K, Kundu TK. Activation of p53 function by human transcriptional coactivator PCA: role of protein-protein interaction, DNA bending, and posttranslational modifications. *Mol Cell Biol.* (2007) 27:7603–14. doi: 10.1128/MCB.01064-07
47. Reed SM, Quelle DE. p53 Acetylation: regulation and consequences. *Cancers.* (2014) 7:30–69. doi: 10.3390/cancers7010030
48. Zhao Y, Lu S, Wu L, Chai G, Wang H, Chen Y, et al. Acetylation of p53 at lysine 373/382 by the histone deacetylase inhibitor depeptide induces expression of p21(Waf1/Cip1). *Mol Cell Biol.* (2006) 26:2782–90. doi: 10.1128/MCB.26.7.2782-2790.2006
49. Singh BN, Zhang G, Hwa YL, Li J, Dowdy SC, Jiang SW. Nonhistone protein acetylation as cancer therapy targets. *Expert Rev Anticancer Ther.* (2010) 10:935–54. doi: 10.1586/era.10.62
50. Licciardi PV, Ververis K, Tang ML, El-Osta A, Karagiannis TC. Immunomodulatory effects of histone deacetylase inhibitors. *Curr Mol Med.* (2013) 13:640–7. doi: 10.2174/1566524011313040013
51. Molife LR, Attard G, Fong PC, Karavasilis V, Reid AH, Patterson S, et al. Phase II, two-stage, single-arm trial of the histone deacetylase inhibitor (HDACi) romidepsin in metastatic castration-resistant prostate cancer (CRPC). *Ann Oncol.* (2010) 21:109–13. doi: 10.1093/annonc/mdp270
52. Lee YJ, Won AJ, Lee J, Jung JH, Yoon S, Lee BM, et al. Molecular mechanism of SAHA on regulation of autophagic cell death in tamoxifen-resistant MCF-7 breast cancer cells. *Int J Med Sci.* (2012) 9:881–93. doi: 10.7150/ijms.5011
53. Hui KF, Cheung AK, Choi CK, Yeung PL, Middeldorp JM, Lung ML, et al. Inhibition of class I histone deacetylases by romidepsin potently induces Epstein-Barr virus lytic cycle and mediates enhanced cell death with ganciclovir. *Int J Cancer.* (2016) 138:125–36. doi: 10.1002/ijc.29698
54. Gerelchuluun A, Maeda J, Manabe E, Brents CA, Sakae T, Fujimori A, et al. Histone deacetylase inhibitor induced radiation sensitization effects on human cancer cells after photon and hadron radiation exposure. *Int J Mol Sci.* (2018) 19:E496. doi: 10.3390/ijms19020496
55. Hui KF, Chiang AK. Combination of proteasome and class I HDAC inhibitors induces apoptosis of NPC cells through an HDAC6-independent ER stress-induced mechanism. *Int J Cancer.* (2014) 135:2950–61. doi: 10.1002/ijc.28924
56. Berghauer Pont LM, Kleijn A, Kloezezan JJ, van den Bossche W, Kaufmann JK, de Vrij J, et al. The HDAC inhibitors scriptaid and LBH589 combined with the oncolytic virus delta24-RGD exert enhanced anti-tumor efficacy in patient-derived glioblastoma cells. *PLoS ONE.* (2015) 10:e0127058. doi: 10.1371/journal.pone.0127058
57. Caponigro F, Di Gennaro E, Ionna F, Longo F, Aversa C, Pavone E, et al. Phase II clinical study of valproic acid plus cisplatin and cetuximab in recurrent and/or metastatic squamous cell carcinoma of Head and Neck-V-CHANCE trial. *BMC Cancer.* (2016) 16:918. doi: 10.1186/s12885-016-2957-y
58. Hui KF, Lam BH, Ho DN, Tsao SW, Chiang AK. Bortezomib and SAHA synergistically induce ROS-driven caspase-dependent apoptosis of nasopharyngeal carcinoma and block replication of Epstein-Barr virus. *Mol Cancer Ther.* (2013) 12:747–58. doi: 10.1158/1535-7163.MCT-12-0811
59. Li X, Zhu Y, He H, Lou L, Ye W, Chen Y, et al. Synergistically killing activity of aspirin and histone deacetylase inhibitor valproic acid (VPA) on hepatocellular cancer cells. *Biochem Biophys Res Commun.* (2013) 436:259–64. doi: 10.1016/j.bbrc.2013.05.088
60. Chou LF, Chen CY, Yang WH, Chen CC, Chang JL, Leu YL, et al. Suppression of hepatocellular carcinoma progression through FOXM1

- and EMT inhibition via hydroxygenkwanin-induced miR-320a expression. *Biomolecules*. (2019) 10:E20. doi: 10.3390/biom10010020
61. Mariadason JM. HDACs and HDAC inhibitors in colon cancer. *Epigenetics*. (2008) 3:28–37. doi: 10.4161/epi.3.1.5736
 62. Zhu L, Wu K, Ma S, Zhang S. HDAC inhibitors: a new radiosensitizer for non-small-cell lung cancer. *Tumori*. (2015) 101:257–62. doi: 10.5301/tj.5000347
 63. Damaskos C, Garmis N, Valsami S, Kontos M, Spartalis E, Kalampokas T, et al. Histone Deacetylase Inhibitors: An Attractive Therapeutic Strategy Against Breast Cancer. *Anticancer Res*. (2017) 37:35–46. doi: 10.21873/anticancer.11286
 64. Heers H, Stanislaw J, Harrelson J, Lee MW. Valproic acid as an adjunctive therapeutic agent for the treatment of breast cancer. *Eur J Pharmacol*. (2018) 835:61–74. doi: 10.1016/j.ejphar.2018.07.057
 65. Hida Y, Kubo Y, Murao K, Arase S. Strong expression of a longevity-related protein, SIRT1, in Bowen's disease. *Arch Dermatol Res*. (2007) 299:103–6. doi: 10.1007/s00403-006-0725-6
 66. Nosh K, Shima K, Irahara N, Kure S, Firestein R, Baba Y, et al. SIRT1 histone deacetylase expression is associated with microsatellite instability and CpG island methylator phenotype in colorectal cancer. *Mod Pathol*. (2009) 22:922–32. doi: 10.1038/modpathol.2009.49
 67. Wang JC, Kafeel MI, Avezbakiyev B, Chen C, Sun Y, Rathnasabapathy C, et al. Histone deacetylase in chronic lymphocytic leukemia. *Oncology*. (2011) 81:325–9. doi: 10.1159/000334577
 68. Lovaas JD, Zhu L, Chiao CY, Byles V, Faller DV, Dai Y. SIRT1 enhances matrix metalloproteinase-2 expression and tumor cell invasion in prostate cancer cells. *Prostate*. (2013) 73:522–30. doi: 10.1002/pros.22592
 69. Schneckeburger M, Goffin E, Lee JY, Jang JY, Mazumder A, Ji S, et al. Discovery and characterization of R/S-N-3-cyanophenyl-N'-(6-tert-butoxycarbonylamino-3,4-dihydro-2,2-dimethyl-2H-1-benzopyran-4-yl)urea, a new histone deacetylase class III inhibitor exerting antiproliferative activity against cancer cell lines. *J Med Chem*. (2017) 60:4714–33. doi: 10.1021/acs.jmedchem.7b00533
 70. Stark M, Hayward N. Genome-wide loss of heterozygosity and copy number analysis in melanoma using high-density single-nucleotide polymorphism arrays. *Cancer Res*. (2007) 67:2632–42. doi: 10.1158/0008-5472.CAN-06-4152
 71. Taylor BS, DeCarolis PL, Angeles CV, Brenet F, Schultz N, Antonescu CR, et al. Frequent alterations and epigenetic silencing of differentiation pathway genes in structurally rearranged liposarcomas. *Cancer Discov*. (2011) 1:587–97. doi: 10.1158/2159-8290.CD-11-0181


Conflict of Interest: The authors declare that the research was conducted in the absence of any commercial or financial relationships that could be construed as a potential conflict of interest.

Copyright © 2020 Chen, Chen, Chuang, Leu, Ueng, Hsueh, Yeh and Wang. This is an open-access article distributed under the terms of the Creative Commons Attribution License (CC BY). The use, distribution or reproduction in other forums is permitted, provided the original author(s) and the copyright owner(s) are credited and that the original publication in this journal is cited, in accordance with accepted academic practice. No use, distribution or reproduction is permitted which does not comply with these terms.



Review

Radiosensitization of Hepatocellular Carcinoma through Targeting Radio-Associated MicroRNA

Cheng-Heng Wu ¹, Cheng-Yi Chen ², Chau-Ting Yeh ³ and Kwang-Huei Lin ^{1,3,4,*} 

¹ Department of Biochemistry, College of Medicine, Chang Gung University, Taoyuan 333, Taiwan; rubio9615151@gmail.com

² Department of Cell Biology and Anatomy, College of Medicine, National Cheng Kung University, Tainan 70101, Taiwan; csmc8972@hotmail.com

³ Liver Research Center, Chang Gung Memorial Hospital, Taoyuan 333, Taiwan; chauting@adm.cgmh.org.tw

⁴ Research Center for Chinese Herbal Medicine, College of Human Ecology, Chang Gung University of Science and Technology, Taoyuan 333, Taiwan

* Correspondence: khlin@mail.cgu.edu.tw; Tel./Fax: +886-3-2118263

Received: 21 February 2020; Accepted: 6 March 2020; Published: 9 March 2020



Abstract: Hepatocellular carcinoma (HCC) is the fourth leading cause of cancer-related deaths worldwide. For patients who are resistant to monotherapy, multimodal therapy is a basic oncologic principle that incorporates surgery, radiotherapy (RT), and chemotherapy providing survival benefits for patients with most types of cancer. Although liver has low tolerance for radiation, high-precision RT for local HCC minimizes the likelihood of radiation-induced liver disease (RILD) in noncancerous liver tissue. RT have several therapeutic benefits, including the down-staging of tumors to make them resectable and repression of metastasis. The DNA damage response (DDR) is a cellular response to irradiation (IR), including DNA repair of injured cells and induction of programmed cell death, thereby resulting in maintenance of cell homeostasis. Molecules that block the activity of proteins in DDR pathways have been found to enhance radiotherapeutic effects. These molecules include antibodies, kinase inhibitors, siRNAs and miRNAs. MicroRNAs (miRNAs) are short non-coding regulatory RNAs binding to the 3'-untranslated regions (3'-UTR) of the messenger RNAs (mRNAs) of target genes, regulating their translation and expression of proteins. Thus, miRNAs and their target genes constitute complicated interactive networks, which interact with other molecules during carcinogenesis. Due to their promising roles in carcinogenesis, miRNAs were shown to be the potential factors that mediated radiosensitivity and optimized outcomes of the combination of systemic therapy and radiotherapy.

Keywords: radiation; microRNA; DNA damage; apoptosis; cell cycle; liver cancer

1. Introduction

HCC is the fourth leading cause of cancer-related deaths worldwide. Most patients with HCC have underlying chronic liver disease caused by viral hepatitis and/or nonalcoholic/alcoholic fatty liver disease. These chronic liver diseases are competing comorbidity risks for mortality in many patients [1].

Surgery, such as partial hepatectomy or liver transplantation, remains the gold standard for curative treatment of HCC. Although transplantation is associated with an 84% rate of the two-year overall survival (OS), only 15% to 30% of patients are candidates for transplantation at diagnosis due to tumor extent and underlying liver dysfunction. Other liver-directed therapies (LDTs) evaluated in multidisciplinary settings can include bridge-to-transplant, definitive/curative treatment, and/or palliation, depending on treatment intent. LDTs administered to most patients

with non-metastatic HCC over their course of treatment can include radiofrequency ablation (RFA), transarterial chemoembolization (TACE), transarterial radioembolization (TARE), and external beam RT.

In addition to LDTs, the modern strategy of systemic therapy in progressive HCC is a kinase inhibitor Nexavar, which is also known as sorafenib. Sorafenib is a small-molecule multikinase inhibitor against PDGFR, VEGFR and Raf kinases including B-Raf and c-Raf. The Sorafenib HCC Assessment Randomized Protocol (SHARP) Trial randomized controlled trials of sorafenib vs. placebo and have demonstrated modest but significant improvements in OS with sorafenib [2]. In another randomized trial, the Asia-Pacific Trial [3], sorafenib was also associated with an improvement of overall survival. However, the effect of sorafenib-induced overall survival was reduced in the Asia-Pacific Trial as compared with the SHARP trial, due to the increased enrollment of patients with advanced HCC (such as a higher number of intrahepatic tumors or increased extrahepatic disease burden).

For patients who could not tolerate sorafenib or with progression during treatment, there are already early clinical data supporting that multimodal therapy is the next stage of HCC trial studies besides the improvements of the first-line setting. Multimodal therapy is a basic oncologic principle that incorporates surgery, RT, and chemotherapy. These treatments provide survival benefits for patients with most types of cancer. Although guidelines suggest that patients should be treated with single modality therapy during each stage of HCC, the multimodal approach may benefit individual patients, depending on the characteristics of their disease.

As the liver has a low tolerance for radiation, RT was previously not indicated for HCC. However, technological improvements in RT, including three-dimensional conformal RT (3D-CRT), intensity-modulated RT (IMRT), image-guided RT, and stereotactic body RT (SBRT), have enabled the delivery of high-precision RT for local HCC while minimizing the likelihood of RILD in noncancerous liver tissue. These improvements in RT have therapeutic benefits, including the down-staging of tumors to make them resectable and repression of metastasis. Synergic treatment of radiotherapy and target agents is the ongoing field of research. The potential of target drugs as radiosensitizers, especially sorafenib, was supported by retrospective data [4]. In a phase II study, 40 patients who were not candidates for hepatectomy received sorafenib 400 mg twice a day and radiotherapy. 83% of patients completed the course of treatment, a 55% rate of completed or partial response, a 32% rate of the two-year OS, and in-field PFS of 39% in a phase II single-arm study demonstrated that concurrent and sequential sorafenib with radiotherapy was associated with impressive response rates [5]. Recently, Phase I-dose escalation study of combination treatment of sorafenib and SBRT reported the dose-limiting toxicities, aiming to determine dose-limiting toxicities of sorafenib combining with SBRT. The patients with irradiated liver volume (V_{eff}) < 30% were treated by SBRT (39Gy–54Gy) and 400 mg sorafenib daily without any dose-limiting toxicities. In a clinical study, 15 patients were pre-treated with sorafenib for 1 week and followed by RT with sorafenib concurrently. There was a reduction in the liver volume of patients who were treated with sorafenib and RT. This evidence supported the importance of careful assessment before a period of treatment [6].

Although the cooperative interaction of combination therapy enlarged the curative effect, it is also accompanied by increase toxicities or unexpected RILD. The major challenge of combination therapy is the relief or prevention of unexpected side effects and toxicities; this is still the ongoing area of research.

2. miRNAs-Mediated Radiosensitivity

2.1. miRNAs Involved in the DNA Damage Response

miRNAs are short non-coding regulatory RNAs consisting of about 22 nucleotides. Binding of miRNAs to the 3'-UTR of their target genes controls the expression of these target genes at the post-transcriptional level in a complete/incomplete complementary manner. The gene encoding each miRNA is first transcribed into a pri-miRNA, which is converted to pre-miRNA by the enzyme Drosha. The Exportin-5/Ran-guanosine triphosphate complex promotes the translocation of pre-miRNA from

the nucleus to the cytoplasm. Subsequently, the maturation of miRNA is completed by the enzyme Dicer, which catalyzes the removal of the stem-loop structure.

Mature miRNAs target the mRNAs of target genes, regulating their translation and expression of proteins. Individual genes can be regulated by several miRNAs, whereas individual miRNAs can target multiple genes. Thus, miRNAs and their target genes constitute complicated interactive networks, which interact with other molecules during carcinogenesis. These miRNAs can affect various biological processes during tumorigenesis and play an important role in cancer development by influencing tumor cell growth, cycling, differentiation, and apoptosis. Due to their promising roles in carcinogenesis, miRNAs were shown to be the potential factors that mediated radiosensitivity and optimized outcomes of the combination of systemic therapy and radiotherapy.

The DDR is a cellular response to IR, reversing DNA damage and maintaining genome integrity, thereby resulting in cell survival. Although cells have various DDR pathways, their DDRs consisted of three major components: sensors, signal transducers, and effectors.

When DNA damage is induced by IR, poly [ADP-ribose] polymerase-1 (PARP-1) is responsible for DNA single strand breaks (SSBs). The most common form of IR-induced damage, the sensing of DNA double strand breaks (DSBs), is completed by the MRN complex, MRE11/RAD50/NBS1. After they sense damage, ataxia-telangiectasia mutated (ATM) and ATM and Rad3-related (ATR), the pivotal kinases of the DDR that trigger downstream DDR cascades, can be used to detect DNA damage. Generally, ATR regulates SSBs, whereas ATM activates the DDR involving DSBs.

As DSB is a major type of IR-induced damage, we focused on the miRNAs that regulate ATM. miR-203a-3p targeting ATM was found to repress the proliferation, migration, and invasion of ovarian cancer cells and to facilitate their apoptosis through the Akt/GSK-3 β /Snail signaling pathway [7]. Moreover, up-regulation of miR-18a-5p inhibited the levels of expression of ATM and pATM (phospho S1981) and enhanced the radiosensitivity of A549 and CD133⁺ stem-like cells [8]. Enhanced miR-203 also inhibited ATM activity and suppressed the ATM-Snail pathway, increasing E-cadherin, and thereby preventing the migration and invasion of gastric cancer cells [9].

ATM was found to be the direct target of miR-203 in colorectal cancer (CRC) cells. Mutation of the putative miR-203 binding site in the 3'-UTR of ATM mRNA abrogated the inhibitory effect of miR-203 on ATM, with miR-203 inducing oxaliplatin resistance in CRC cells [10]. Overexpression of miR-18a was found to down-regulate ATM expression by directly targeting the ATM-3'-UTR, reducing DNA damage repair activity and increasing cellular radiosensitivity to IR treatment [11]. miR-421 was found to suppress ATM expression in LA-N-1 and LA-N-5 neuroblastoma cells in vitro by targeting the 3'-UTR of ATM transcripts, with ATM 3'-UTR rescuing the radioresistance phenotype caused by miR-421 [12].

ATM is responsible for the phosphorylation of histone H2AX, which mediates DSBs' repair and recruits DNA repair proteins to the site of damage. Knockdown of miR-328 was reported to up-regulate histone H2AX expression and increase the number of TUNEL-positive cells in vitro. Down-regulation of miR-328 decreased the incidence of lung cancer induced by *Chlamydia pneumoniae*, reduced tumor volume, increased caspase-3 activity, and facilitated tumor cell apoptosis in vivo. These findings revealed that histone H2AX is the target of miR-328 and participates in lung cancer regulation, and that reductions in miR-328 levels promote apoptosis of lung cancer tissue [13]. miR-138 was shown to directly target the 3'-UTR of histone H2AX, with overexpression of miR-138 inhibiting homologous recombination and enhancing cellular sensitivity to multiple DNA damaging agents. Expression of histone H2AX in miR-138 overexpressing cells attenuated miR-138-mediated sensitization to radiotherapy and to chemotherapy with DNA damaging agents [14].

Activation of ATM and histone H2AX also involves RAD51, DNA-dependent protein kinase (DNA-PK), breast cancer susceptibility gene 1 (BRCA1) and breast cancer susceptibility gene 2 (BRCA2), all of which play essential roles in completion of DNA damage repair. Cells possess two major DNA repair pathways: homologous recombination repair (HRR) and non-homologous end-joining (NHEJ). DNA-PK is a pivotal factor for NHEJ in the DDR. miR-101 was reported to reduce the expression of ATM

or DNA-dependent protein kinase, catalytic subunit (DNA-PKcs), the catalytic subunit of DNA-PK by binding to their own 3'-UTR sequences, sensitizing the GBM cell line U87MGD to radiation [15]. miR-101 had similar effects in pancreatic cancer cells [16]. RAD51 was found to participate in HRR to avoid illegitimate recombination events leading to genetic instability. miR-34a was shown to regulate RAD51 by directly binding to its 3'-UTR, controlling HR and promoting radiosensitivity in NSCLC cells [17]. In addition, miR-155 was reported to regulate DNA repair activity and sensitivity to IR by repressing RAD51 in breast cancer cells [18], and miR-34a/b/c-5p was shown to directly target the RAD51 mRNA 3'-UTR or indirectly inhibit RAD51 expression via the p53 signaling pathway, indicating that miR-34s overexpression reduces the efficiency of HR repair and induces DSBs by down-regulating RAD51 expression [19].

BRCA1 was shown to be involved in several important cellular pathways, including DNA damage repair, chromatin remodeling, and checkpoint activation, thereby affecting the outcomes of cancer therapy. Overexpression of miR-212 down-regulated BRCA1 expression, and knockdown of BRCA1 attenuated IR-induced apoptosis [20]. Increased expression of miR-7-5p was found to further repress PARP-1 and BRCA1 expression in lymphoblastoid cells, increasing apoptosis and inhibiting cell proliferation [21]. miR-9 was also reported to directly regulate BRCA1 expression in ovarian cancer, having more therapeutic potential than treatment with PARP-1 inhibitors [22].

BRCA2 is a major component of the homologous recombination DNA repair pathway. Testing of interactions between BRCA2 and miR-19a/miR-19b in 15 cell lines derived from pancreatic, breast, colon, and kidney cancers showed that overexpression of these two miRNAs reduced BRCA2 expression by directly binding to its 3'-UTR [23]. In addition, miR-1245 was found to directly bind to the 3'-UTR of BRCA2 and suppress its translation, impairing HR-mediated repair, reducing the number of DNA damage-induced RAD51 nuclear foci, and rendering cells hypersensitive to γ -irradiation (IR). Furthermore, the c-myc protein was observed to up-regulate miR-1245 expression via direct binding to the miR-1245 promoter, down-regulating BRCA2 and reducing the efficiency of HR [24].

2.2. miRNAs Involving the Cell Cycle

The cell cycle in humans consists of four phases, in which transitions were regulated by cell cycle checkpoints through cyclins and cyclin-dependent kinases (CDKs). Deregulation of the cell cycle was frequently observed in carcinomas and affected by treatments such as radiotherapy. IR-induced DNA damage can trigger cell cycle checkpoints, arresting the cell cycle and allowing time for DNA damage repair. Thus, inhibiting the transition of other working checkpoints prevents cell cycle progression, allowing more tumor cells to be killed by radiotherapy.

Repair of DNA damage allows cells to re-enter the cell cycle. If damage is not repaired, however, these cells will progress to apoptosis or senescence, preventing tumorigenesis resulting from genomic instability. Chk1 and Chk2 are the major cell cycle checkpoint inhibitors. Chk1 is a direct target of miR-195, with down-regulation of miR-195 sensitizing HCT-116 cells to treatment with 5-FU [25]. In addition, miR-200c was reported to repress Chk1 through targeting of LINC02582 [26].

Cdc25a contains highly conserved domains for dual-specificity phosphatases, which dephosphorylate and activate cyclin-dependent kinase complexes. Irradiation and other DNA-damaging agents activate the signal cascade from ATM and ATR to Chk1 and Chk2, whereas activation of Cdc25a by Chk-1 initiates the procedure leading to cell-cycle arrest. This Cdc25a axis is thought to be the main pathway of cell cycle arrest independent of p53 and a critical regulator of the cell-cycle checkpoint in response to DNA damage caused by IR, oxidative stress, and other DNA-damaging agents. miR-21 knockdown was found to enhance RT-induced GBM cell growth arrest and apoptosis by directly or indirectly modulating Cdc25a levels, thereby reducing G2/M cell cycle accumulation [27].

Irradiation of LNCaP cells has been shown to induce miR-449a, which targets Cdc25a both directly and indirectly. Suppression of Cdc25a reduced Rb phosphorylation, E2F1 expression and the Cdc2/cyclin B1 complex, leading to G2/M phase arrest and sensitizing cancer cells to ionizing radiation [28].

2.3. miRNAs Involved in Apoptosis

p53 is a multifunctional tumor suppressor capable of activating transient cell cycle checkpoints and accelerating DNA repair (e.g., rejoining of DNA double strand breaks; DSBs) to promote survival, and inducing growth arrest through stress-induced premature senescence (SIPS) or activating programmed cell death (e.g., apoptosis) to eliminate highly injured cells from the proliferating population [29]. SIPS is a sustained growth-arrested state resembling replicative senescence, triggered by DNA-damaging agents. It is a prominent reaction of cells that express wild-type p53 to genotoxic stress (ionizing radiation) [29–31]. Failure of cells to properly engage p53-mediated responses (checkpoints, SIPS, apoptosis) under stressful conditions can result in the creation of polyploid/multinucleated giant cells (MNGCs). Such giant cells exhibit resistance to genotoxic agents and can give rise to tumor repopulating progeny that has been reported for several carcinomas [32–35]. For targeting these dormant cancer cells, a recent literature reported that down-regulating the Bcl-XL/Bcl-2 pathway in multinucleated colon carcinoma cells (HCT116) results in the rapid death of multinucleated giant cells through the treatment of ABT-263 (a small-molecule inhibitor of Bcl-X, Bcl-2 and Bcl-w) [36].

p53 can activate apoptotic signaling through its proline-rich region or inducing the expression of pro-apoptotic proteins such as PUMA (interaction with Bcl-2 and Bcl-XL), Bax and NOXA (resulting cytochrome c releasing from mitochondria) [37]. Concurrently, p53 transcriptionally activates DNAJB9 and inhibits apoptosis through direct interaction with it. p21 can also be activated by p53, preventing p14^{ARF}-modulated MDM2 degradation and induction of WIP1 (a phosphatase targeting p53 and its upstream kinase) [38].

The final outcome of p53 signaling in response to genotoxic stress in terms of sustained growth arrest or apoptotic cell death depends on the genetic background of the cells' several factors and genotoxic stress. In most human cells, exposure to moderate doses of ionizing radiation, UV, or chemotherapeutic drugs promotes a high degree of SIPS rather than apoptosis [39]. Stress-induced growth arrest in cancer cells results in the emergence of cancer repopulating progeny. Selective targeting of those growth-arrested cancer cells from arrest to apoptosis through lowering the apoptotic threshold was a potential strategy for the effectiveness of genotoxic cancer therapy [40].

Two basic apoptotic signaling pathways have been described to date, the intrinsic and extrinsic apoptotic pathways. The intrinsic apoptotic pathway is triggered by numerous stimuli, including DNA damage and oxidative stress, leading to the formation of apoptosomes, which are composed of apoptotic protease activating factor 1 (Apaf-1), cytochrome c and procaspase-9. p53 modulates the expression of several members of the Bcl-2 family, including anti-apoptotic Bcl-2, Bcl-xL, Mcl-1, and pro-apoptotic Bax, Bak, Bim, Bid. Bcl-2 family mediates apoptotic response through the interplay of each other, thus facilitating mitochondrial membrane permeabilization and the release of cytochrome c. miR-365 was found to directly target pro-apoptotic protein Bax and adaptor protein Src Homology 2 Domain Containing 1 (SHC1), inducing resistance of gemcitabine in pancreatic cancer cells [41]. Bak1 was targeted by miR-125b, leading to suppression of Taxol-induced apoptosis and increased resistance to Taxol [42]. miR-133a was found to be down-regulated in osteosarcomas, with its expression correlating with tumor progression and patient prognosis. Expression of miR-133a could reduce cell proliferation, promote cell apoptosis, and suppress tumorigenicity by targeting Bcl-xL and Mcl-1 and reducing their expression [42]. Bcl-xL was also directly targeted by miR-491, contributing to miR-491-induced apoptosis. Treatment with miR-491 also suppressed tumor growth in vivo, suggesting that miRNAs may have therapeutic potential through regulation of Bcl-xL in CRC cells [43]. Bcl-xL was found to be a direct target of miR-608, with expression of miR-608 inducing apoptosis in chordoma cells [44]. miR-148a can induce apoptosis in CRC cells through posttranscriptional repression of Bcl-2 [45]. Moreover, miR-24-2 was shown to target the antiapoptotic gene Bcl-2, with overexpression of miR-24-2 inducing apoptosis by down-regulating Bcl-2 expression [46]. Down-regulation of miR-204 was found to correlate with increased expression of Bcl-2 protein in gastric cancers (GCs). Moreover, miR-204 increased the sensitivity of GC cells to treatment with 5-fluorouracil and oxaliplatin by targeting Bcl-2, whereas restoration of Bcl-2 protein counteracted this response to 5-fluorouracil [47]. Expression levels

of miR-15a and miR-16-1 correlated negatively to Bcl-2 expression in chronic lymphocytic leukemia (CLL), which was characterized by malignant B cells with overexpression of Bcl-2. Both microRNAs repressed Bcl-2 at a posttranscriptional level. Bcl-2 down-regulation by these microRNAs was found to induce apoptosis and could be used for therapy of Bcl-2-overexpressing tumors [48].

Apoptotic protease activating factor-1 (Apaf-1) was repressed by miR-23a/b and miR-27a/b, which regulate neuronal apoptosis [49], and by miR-24a in the developing neural retina [50].

The extrinsic pathway of apoptosis is initiated by the binding of death ligands (Fas ligand (FasL), TNF-related apoptosis-inducing ligand (TRAIL), TNF- α , and TNF-like weak inducer of apoptosis (TWEAK) etc.) to death receptors belonging to the TNF receptor (TNFR) superfamily. These death ligand/death receptor complexes activate pro-caspase-8, with the resultant caspase-8 triggering the activation of pro-caspase-3, inducing apoptosis. FasL expression induced cancer cell apoptosis after gemcitabine treatment, an apoptotic process partially counteracted by the ectopic expression of miR-21 [51]. miR-20a suppressed Fas expression in osteosarcoma, contributing to the ability of osteosarcoma cells to metastasize to the lungs [52].

miR-146a, which targets Fas, was shown to be involved in the pathogenesis of autoimmune lymphoproliferative syndrome (ALPS) [53], whereas the miR-196b-induced reduction in FAS expression significantly promoted leukemogenesis [54]. miR-25 was shown to target TRAIL/death receptor-4 (DR4) complexes, suppressing TRAIL-induced apoptosis, whereas antagonism of miR-25 was found to sensitize cells to apoptotic death [55]. TNF- α overexpression was found to induce apoptosis, whereas ectopic expression of miR-181c partially protected neurons from cell death [56]. Ectopic expression of miR-187 [57], miR-34a-5p and miR-34a-3p [58] consistently and selectively reduced TNF α -induced apoptosis in monocytes. Fas-associated death domain-containing protein (FADD) and caspase-3 were found to be the key factors in FasL–Fas signaling. Ectopic expression of miR-155 in human NP cells repressed FADD and caspase-3 expression; whereas knockdown of miR-155 restored their expression. Ectopic expression of miR-128a conferred Fas-resistance on Jurkat cells by directly targeting FADD. Thus, antagonizing miR-155 [59] and miR-128a [60] can target Fas-mediated apoptosis. Although caspase-3 was well-characterized as an apoptotic factor in both intrinsic and extrinsic pathways, many literatures also report that caspase-3-mediated secretion of PGE2 and tumor repopulation is associated with these stress-induced cells [61]. However, this repopulation could be abrogated by treatment with a PGE2-neutralizing antibody or PGE-2 inhibitor (such as celecoxib, a pharmacological inhibitor which repressed the production of PGE-2 through targeting cyclooxygenase-2) [62].

2.4. miRNAs Involved in Radio-Related Signal Transduction Pathways

Four well-recognized pathways have been confirmed as playing roles in radiotherapy and to be closely associated with radiosensitivity. Three of these pathways, the PI3K/Akt pathway, the mitogen-activated protein kinase (MAPK) pathway, and the pathway involving nuclear factor-kappa B (NF- κ B) and transforming growth factor- β (TGF β), are regarded as being associated with radiation. Radiation-induced activation of the PI3K/Akt and MAPK/ERKs pathways was shown to suppress intrinsic apoptosis through repression of downstream target genes, including *Bad* and *Bim*. In contrast, the NF- κ B/ TGF β pathway enhances intrinsic apoptosis by increasing the expression of the antiapoptotic protein, Mcl-1. By affecting apoptosis, these pathways contribute to tumor radioresistance.

In addition to participating in cell death, the PI3K/Akt and MAPK/ERK pathways are activated by radiation and affect DNA damage repair pathways by influencing DNA-PKcs, the major components of the NHEJ pathway, thereby modulating tumor radioresistance. Moreover, epidermal growth factor receptor and insulin-like growth factor receptor were found to be directly involved in the process of NHEJ after their translocation to the nucleus. These growth factors also affect DNA-PKcs activities, contributing to tumor radioresistance. In addition to these three pathways in DDR, the TGF β pathway contributes to two major repair pathways in DDR, the NHEJ and HR pathways, by activating the *ATM* gene.

The importance of radio-related signal transduction pathways has led to therapeutic approaches that enhance tumor radiosensitivity and reduce tumor radioresistance. Molecules that block the activity of proteins in signal transduction pathways have been found to enhance apoptosis and reduce DNA damage repair, increasing tumor radiosensitivity and radiotherapeutic effects. These molecules, including antibodies, kinase inhibitors, siRNAs and miRNAs, have been used to suppress the function of crucial signaling pathways, such as those involving PI3K, Akt, MAPK, NF- κ B and TGF β . PTEN is a tumor suppressor gene that acts upstream of Akt. The miRNAs miR-21, miR-26, miR-486, miR-221/222, and miR-216a/217 control the activation of Akt by regulating the expression of PTEN. In addition, miR-155, miR-205 and miR-375 control Akt activation by regulating the expression of the SH2-containing inositol 5'-polyphosphatase (SHIP) and PDK1 genes. Moreover, miR-126 and miR-320 control PI3K expression, affecting the downstream activities of PIP3, and altering the levels of expression of total and phosphorylated Akt protein [63]. miR-486 can directly target PTEN and Foxo1a, contributing to Akt phosphorylation, with phosphorylated Akt shown to phosphorylate GSK3 β , a negative regulator of Foxo1a, ensuring constant activation of the PI3K/Akt pathway [64].

The miRNAs, miR-221 and miR-222, have been found to regulate the viability, apoptosis, cell cycle progression and invasive ability of gastric cancer cells by down-regulating PTEN expression and enhancing Akt phosphorylation. Suppression of miR-221 and miR-222 may represent a novel therapeutic strategy for gastric cancer through the PI3K/Akt pathway [65]. The miR-17-92 cluster, composed of miR-17-5p, miR-17-3p, miR-18a, miR-19a, miR-20a, miR-19b, and miR-92-1, has been linked to cancer pathogenesis. miR-17-5p was shown to be overexpressed in HCC, resulting in the suppression of the p38 MAPK pathway through the miR-17-5p/E2F1/Wip1 axis [66].

Transcriptional active heterodimer of NF- κ B is repressed by I κ B, and I κ B degradation is regulated by I κ B kinase complex (IKK) through phosphorylation. NF- κ B signaling is mediated by various miRNAs through targeting I κ B or IKK. I κ B α is repressed by miR-668 in breast cancer; I κ B β is suppressed by miR20a in gastric cancer; IKK α is negatively modulated by miR-156-5p in colorectal cancer; IKK β is down-regulated by miR-218 in glioma cancer, miR-199a in ovarian cancer, miR-451 in HCC and miR-429 in cervical cancer. miR-223 targeted both IKK α and IKK β in lung cancer. Moreover, NF- κ B repressing factor NKRF is targeted by miR-301a, repressing the activity of the p50 subunit of NF- κ B [67].

2.5. Radiation-Associated miRNAs in HCC

HCC is usually diagnosed at a late stage; most of the patients will not be the candidates for hepatectomy and liver transplantation. In addition, the impairment of liver function also restricts the efficacy of systemic therapy such as chemotherapy or targeted therapy due to intolerable side effects. Sorafenib exerts its anti-tumor functions mainly through repressing tumor cell proliferation and angiogenesis. However, HCC patients could acquire resistance, happening within 6 months. The high incidence of sorafenib resistance has become a limiting factor in its clinical application; combining with radiotherapy is an ideal option for current treatment. However, the combination treatment of sorafenib and radiotherapy increases toxicity; minimizing toxicity through sensitizing tumors to radiotherapy is an ongoing area of research.

Replication protein A3 (RPA3) can affect DNA recombination, repair, and replication, as well as cell cycle checkpoints. Up-regulation of RPA3 expression has been reported to promote HCC progression. miR-146a-5p can suppress the proliferation of HCC cells and their radiosensitivity and apoptosis by activating DNA repair pathways and inhibiting RPA3 [68].

WEE1 is a tyrosine kinase that acts to regulate the cell cycle. Down-regulation of WEE1 was found to enhance the radiosensitivity of HCC cells, as evidenced by reduced survival and enhanced apoptosis of Huh7 and PLC5 cells. WEE1 was shown to be a direct target of miR-101-3p. NEAT1_2 was shown to up-regulate WEE1 through sponging by lncRNA miR-101-3p and down-regulation of lncRNA NEAT1_2, resulting in the radiosensitization of HCC cells [69]. PTEN deficiency was thought to be the leading cause of hyperactivation of the PI3K/Akt signaling pathway. Forced expression of miR-20a

activated the PI3K/Akt signaling pathway, an effect reversed by the PI3K tyrosine kinase inhibitor LY294002, indicating the importance of the miR-20a mediated PI3K/Akt pathway in radioresistance [70].

It has been reported B-cell-specific Moloney leukemia virus insertion site 1 (Bmi-1) was correlated with poor overall survival in various cancer and involved in tumor initiation, progression and radiosensitivity through mediated transcription of p16^{Ink4a} and p14^{ARF} [71,72]. The bioinformatics prediction and the result of luciferase assay identified that Bmi-1 was directly targeted by miR-203, which radiosensitized cancer cells through repression of Bmi-1, ectopic expression of Bmi-1 without 3'-UTR could reverse the improvement of radiosensitivity by miR-203 [73].

F-box and WD repeat domain containing 7 (FBXW7), a member of the F-box protein family, which has been reported to function as a tumor suppressor in various human cancers. Notably, the former findings indicate that FBXW7 is implicated in prognosis and induction of apoptosis through repression of YAP expression in HCC [74]. FBXW7 was a direct target of miR-106a and its interference reversed the regulatory effect of miR-106a abrogation on migration, invasion, and radiosensitivity in HCC cells [75].

The SET domain bifurcated 1 (SETDB1) is a methyltransferase that mediates the transcriptional inhibition of euchromatin through catalyzing the methylation of histones, mainly H3K9me3. SETDB1 is one of the highly expressed genes of various malignant tumors in the TCGA database and related to the progression of carcinoma. In previous literature, SETDB1 forms a complex with p53 and catalyzes the dimethylation of p53K370me2, leading to degradation of p53 via MDM2 in HCC cells [76]. SETDB1 was a direct target gene of miR-621, enhancing the radiosensitivity of HCC cells and activating the p53-signaling pathway via inhibiting the expression of SETDB1 as a radiosensitizer in HCC [77].

It has been reported that the down-regulation of miR-26b in HCC is correlated with cancer progression and poor prognosis. Erythropoietin-producing hepatocellular carcinoma A2 (EphA2) mediates tissue renewal and embryonic morphogenesis, but its dysregulation has been associated with tumorigenesis and metastasis in many cancers [78]. The expression profiles and the result of dual reporter assay revealed the interrelationship of miR-26b and EphA2. Transfection of miR-26b mimics or EphA2-shRNA leading to radiosensitization of 97H HCC cells and overexpression of EphA2 can protect 97H HCC cells from irradiation [79].

As aforementioned, activation of anti-apoptotic proteins and/or suppression of pro-apoptotic proteins could lead to apoptosis resistance in cancer cells. Several pieces of literature have been reported that miRNAs targeting the anti-apoptotic genes (such as Mcl-1, Bcl-xL) can enhance the sorafenib-induced apoptosis. miR-193b can sensitize the HBV-positive HCC cells to sorafenib through targeting Mcl-1 directly [80]. Let-7 miRNA is negatively correlated with Bcl-xL in HCC tissues and sensitizes hepatoma cells to sorafenib-induce apoptosis through targeting 3'-UTR of Bcl-xL [81].

Besides, there are miRNAs promoting sorafenib resistance of HCC through the repression of pro-apoptotic genes. The aberrant expression of miR-221 has been reported in HCC; overexpression of miR-221 in chemical-induced HCC rat model and xenograft mouse model were leading to sorafenib resistance through caspase-3 modulation [82]. Moreover, liver-specific miR-122 is repressed in HBV-related HCC, UDP-N-acetyl- α -d-galactosamine: polypeptide N-acetylgalactosaminyltransferase-10 (GALNT10) is the target by miR-122. Repression of GALNT10 decreases the expression of Mcl-1 and Bcl-2, increasing sorafenib and doxorubicin resistance of hepatoma cells [83].

3. Discussion

As the incidence of HCC increases, the need for study and effective treatment options have become even more pivotal. Sorafenib remains the recommended first-line effective systemic targeted agent for patients with metastatic or locally advanced HCC who are not candidates for local therapies, but outcomes remain poor. In addition to systemic therapy, aggressive local therapy, like radiotherapy, has emerged as a safe and effective treatment option in patients with advanced disease; a randomized trial of sequential radiotherapy with sorafenib is ongoing. The potential for synergy of radiotherapy and target agents remains an area of research. As aforementioned, miRNAs play roles in the radiosensitivity

of cancer cells (Figure 1). These miRNAs affect cell survival through the signal cascades of DNA damage response from upstream to downstream. These findings suggest that miRNAs may be an ideal clinical target to modulate cellular radiosensitivity, and that the regulatory roles of miRNAs in tumor radiosensitivity may be useful clinically in the near future. The potential role of miRNAs as radiosensitizers in the combination of radiotherapy and sorafenib raises the possibility of minimizing RILD in HCC patients and improves treatment efficacy, improving the killing rate of radiation and enhancing the OS of advanced HCC patients. Although these miRNAs have shown activity in vitro, future studies are needed to evaluate the effects of miRNAs on radiosensitivity in vivo. Improvements in miRNA delivery techniques have raised the possibility of the successful development of a new class of radiosensitizers for cancer patients.

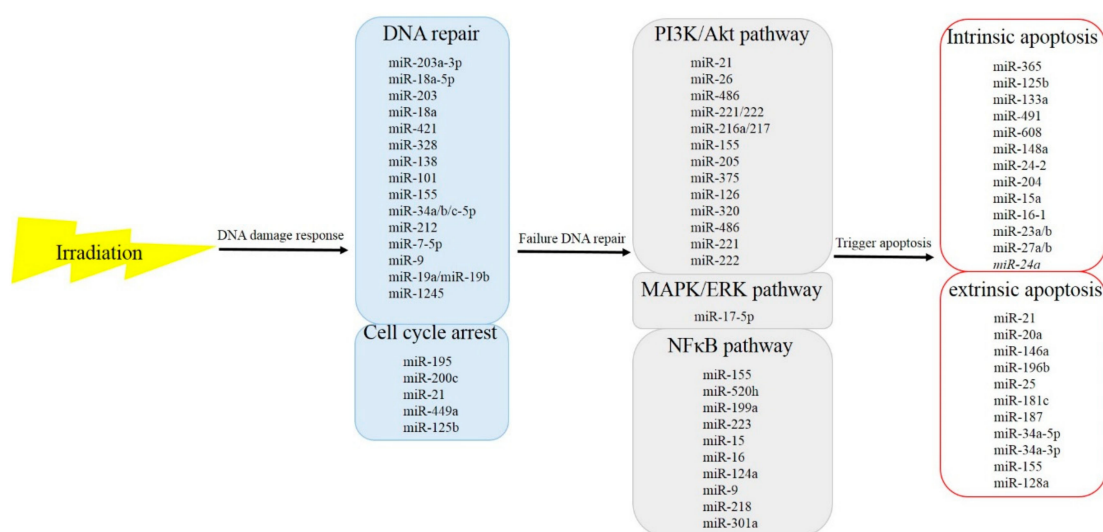


Figure 1. microRNAs that respond to irradiation and the functional pathways in which they participate.

Author Contributions: Conceptualization, C.-H.W. and K.-H.L.; investigation, C.-H.W. and C.-Y.C.; writing—original draft preparation, C.-H.W.; writing—review and editing, K.-H.L.; visualization, supervision, C.-T.Y. and K.-H.L.; funding acquisition, K.-H.L. All authors have read and agreed to the published version of the manuscript.

Funding: This research was funded by grants from Chang Gung Memorial Hospital, Taoyuan, Taiwan. (CMRPD1J0051, CMRPD1H0631, CMRPD1H0632 to K.H. Lin) and from the Ministry of Science and Technology of the Republic of China (MOST 106-2320-B-182-031-MY3 and 106-2320-B-182-032-MY3 to K.H. Lin). The APC was funded by Chang Gung Memorial Hospital, Taoyuan, Taiwan.

Conflicts of Interest: The authors declare no conflict of interest. The funders had no role in the design of the study; in the collection, analyses, or interpretation of data; in the writing of the manuscript, or in the decision to publish the results.

References

1. Akinyemiju, T.; Abera, S.; Ahmed, M.; Alam, N.; Alemayohu, M.A.; Allen, C.; Al-Raddadi, R.; Alvis-Guzman, N.; Amoako, Y.; Artaman, A.; et al. The Burden of Primary Liver Cancer and Underlying Etiologies From 1990 to 2015 at the Global, Regional, and National Level: Results From the Global Burden of Disease Study 2015. *JAMA Oncol.* **2017**, *3*, 1683–1691. [\[PubMed\]](#)
2. Llovet, J.M.; Ricci, S.; Mazzaferro, V.; Hilgard, P.; Gane, E.; Blanc, J.F.; de Oliveira, A.C.; Santoro, A.; Raoul, J.L.; Forner, A.; et al. Sorafenib in advanced hepatocellular carcinoma. *N. Engl. J. Med.* **2008**, *359*, 378–390. [\[CrossRef\]](#)
3. Cheng, A.L.; Kang, Y.K.; Chen, Z.; Tsao, C.J.; Qin, S.; Kim, J.S.; Luo, R.; Feng, J.; Ye, S.; Yang, T.S.; et al. Efficacy and safety of sorafenib in patients in the Asia-Pacific region with advanced hepatocellular carcinoma: A phase III randomised, double-blind, placebo-controlled trial. *Lancet Oncol.* **2009**, *10*, 25–34. [\[CrossRef\]](#)

4. Huang, C.Y.; Lin, C.S.; Tai, W.T.; Hsieh, C.Y.; Shiau, C.W.; Cheng, A.L.; Chen, K.F. Sorafenib enhances radiation-induced apoptosis in hepatocellular carcinoma by inhibiting STAT3. *Int. J. Radiat. Oncol. Biol. Phys.* **2013**, *86*, 456–462. [[CrossRef](#)] [[PubMed](#)]
5. Chen, S.W.; Lin, L.C.; Kuo, Y.C.; Liang, J.A.; Kuo, C.C.; Chiou, J.F. Phase 2 study of combined sorafenib and radiation therapy in patients with advanced hepatocellular carcinoma. *Int. J. Radiat. Oncol. Biol. Phys.* **2014**, *88*, 1041–1047. [[CrossRef](#)]
6. Swaminath, A.; Knox, J.J.; Brierley, J.D.; Dinniwel, R.; Wong, R.; Kassam, Z.; Kim, J.; Coolens, C.; Brock, K.K.; Dawson, L.A. Changes in Liver Volume Observed Following Sorafenib and Liver Radiation Therapy. *Int. J. Radiat. Oncol. Biol. Phys.* **2016**, *94*, 729–737. [[CrossRef](#)]
7. Liu, H.Y.; Zhang, Y.Y.; Zhu, B.L.; Feng, F.Z.; Zhang, H.T.; Yan, H.; Zhou, B. MiR-203a-3p regulates the biological behaviors of ovarian cancer cells through mediating the Akt/GSK-3 β /Snail signaling pathway by targeting ATM. *J. Ovarian Res.* **2019**, *12*, 60. [[CrossRef](#)]
8. Chen, X.; Wu, L.; Li, D.; Xu, Y.; Zhang, L.; Niu, K.; Kong, R.; Gu, J.; Xu, Z.; Chen, Z.; et al. Radiosensitizing effects of miR-18a-5p on lung cancer stem-like cells via downregulating both ATM and HIF-1 α . *Cancer Med.* **2018**, *7*, 3834–3847. [[CrossRef](#)]
9. Zhou, P.; Jiang, N.; Zhang, G.X.; Sun, Q. MiR-203 inhibits tumor invasion and metastasis in gastric cancer by ATM. *Acta Biochim. Biophys. Sin. (Shanghai)* **2016**, *48*, 696–703. [[CrossRef](#)]
10. Zhou, Y.; Wan, G.; Spizzo, R.; Ivan, C.; Mathur, R.; Hu, X.; Ye, X.; Lu, J.; Fan, F.; Xia, L.; et al. miR-203 induces oxaliplatin resistance in colorectal cancer cells by negatively regulating ATM kinase. *Mol. Oncol.* **2014**, *8*, 83–92. [[CrossRef](#)]
11. Song, L.; Lin, C.; Wu, Z.; Gong, H.; Zeng, Y.; Wu, J.; Li, M.; Li, J. miR-18a impairs DNA damage response through downregulation of ataxia telangiectasia mutated (ATM) kinase. *PLoS ONE* **2011**, *6*, e25454. [[CrossRef](#)] [[PubMed](#)]
12. Hu, H.; Du, L.; Nagabayashi, G.; Seeger, R.C.; Gatti, R.A. ATM is down-regulated by N-Myc-regulated microRNA-421. *Proc. Natl. Acad. Sci. USA* **2010**, *107*, 1506–1511. [[CrossRef](#)] [[PubMed](#)]
13. Shen, M.; Cai, L.; Jiang, K.; Xu, W.; Chen, Y.; Xu, Z. The therapeutic role of inhibition of miR-328 on pulmonary carcinoma induced by chlamydia pneumoniae through targeting histone H2AX. *Cancer Biomark.* **2018**. [[CrossRef](#)] [[PubMed](#)]
14. Wang, Y.; Huang, J.W.; Li, M.; Cavenee, W.K.; Mitchell, P.S.; Zhou, X.; Tewari, M.; Furnari, F.B.; Taniguchi, T. MicroRNA-138 modulates DNA damage response by repressing histone H2AX expression. *Mol. Cancer Res.* **2011**, *9*, 1100–1111. [[CrossRef](#)]
15. Yan, D.; Ng, W.L.; Zhang, X.; Wang, P.; Zhang, Z.; Mo, Y.Y.; Mao, H.; Hao, C.; Olson, J.J.; Curran, W.J.; et al. Targeting DNA-PKcs and ATM with miR-101 sensitizes tumors to radiation. *PLoS ONE* **2010**, *5*, e11397. [[CrossRef](#)]
16. Hu, H.; He, Y.; Wang, Y.; Chen, W.; Hu, B.; Gu, Y. micorRNA-101 silences DNA-PKcs and sensitizes pancreatic cancer cells to gemcitabine. *Biochem. Biophys. Res. Commun.* **2017**, *483*, 725–731. [[CrossRef](#)]
17. Cortez, M.A.; Valdecanas, D.; Niknam, S.; Peltier, H.J.; Diaio, L.; Giri, U.; Komaki, R.; Calin, G.A.; Gomez, D.R.; Chang, J.Y.; et al. In Vivo Delivery of miR-34a Sensitizes Lung Tumors to Radiation Through RAD51 Regulation. *Mol. Ther. Nucleic Acids* **2015**, *4*, e270. [[CrossRef](#)]
18. Gasparini, P.; Lovat, F.; Fassan, M.; Casadei, L.; Cascione, L.; Jacob, N.K.; Carasi, S.; Palmieri, D.; Costinean, S.; Shapiro, C.L.; et al. Protective role of miR-155 in breast cancer through RAD51 targeting impairs homologous recombination after irradiation. *Proc. Natl. Acad. Sci. USA* **2014**, *111*, 4536–4541. [[CrossRef](#)]
19. Chen, S.; Liu, R.; Wang, Q.; Qi, Z.; Hu, Y.; Zhou, P.; Wang, Z. MiR-34s negatively regulate homologous recombination through targeting RAD51. *Arch. Biochem. Biophys.* **2019**, *666*, 73–82. [[CrossRef](#)]
20. He, X.; Fan, S. hsa-miR-212 modulates the radiosensitivity of glioma cells by targeting BRCA1. *Oncol. Rep.* **2018**, *39*, 977–984. [[CrossRef](#)]
21. Luo, H.; Liang, H.; Chen, Y.; Chen, S.; Xu, Y.; Xu, L.; Liu, J.; Zhou, K.; Peng, J.; Guo, G.; et al. miR-7-5p overexpression suppresses cell proliferation and promotes apoptosis through inhibiting the ability of DNA damage repair of PARP-1 and BRCA1 in TK6 cells exposed to hydroquinone. *Chem. Biol. Interact.* **2018**, *283*, 84–90. [[CrossRef](#)] [[PubMed](#)]
22. Sun, C.; Li, N.; Yang, Z.; Zhou, B.; He, Y.; Weng, D.; Fang, Y.; Wu, P.; Chen, P.; Yang, X.; et al. miR-9 regulation of BRCA1 and ovarian cancer sensitivity to cisplatin and PARP inhibition. *J. Natl. Cancer Inst.* **2013**, *105*, 1750–1758. [[CrossRef](#)] [[PubMed](#)]

23. Mogilyansky, E.; Clark, P.; Quann, K.; Zhou, H.; Londin, E.; Jing, Y.; Rigoutsos, I. Post-transcriptional Regulation of BRCA2 through Interactions with miR-19a and miR-19b. *Front. Genet.* **2016**, *7*, 143. [[CrossRef](#)] [[PubMed](#)]
24. Song, L.; Dai, T.; Xie, Y.; Wang, C.; Lin, C.; Wu, Z.; Ying, Z.; Wu, J.; Li, M.; Li, J. Up-regulation of miR-1245 by c-myc targets BRCA2 and impairs DNA repair. *J. Mol. Cell Biol.* **2012**, *4*, 108–117. [[CrossRef](#)]
25. Kim, C.; Hong, Y.; Lee, H.; Kang, H.; Lee, E.K. MicroRNA-195 desensitizes HCT116 human colon cancer cells to 5-fluorouracil. *Cancer Lett.* **2018**, *412*, 264–271. [[CrossRef](#)] [[PubMed](#)]
26. Wang, B.; Zheng, J.; Li, R.; Tian, Y.; Lin, J.; Liang, Y.; Sun, Q.; Xu, A.; Zheng, R.; Liu, M.; et al. Long noncoding RNA LINC02582 acts downstream of miR-200c to promote radioresistance through CHK1 in breast cancer cells. *Cell Death Dis.* **2019**, *10*, 764. [[CrossRef](#)]
27. Li, Y.; Zhao, S.; Zhen, Y.; Li, Q.; Teng, L.; Asai, A.; Kawamoto, K. A miR-21 inhibitor enhances apoptosis and reduces G(2)-M accumulation induced by ionizing radiation in human glioblastoma U251 cells. *Brain Tumor Pathol.* **2011**, *28*, 209–214. [[CrossRef](#)]
28. Mao, A.; Zhao, Q.; Zhou, X.; Sun, C.; Si, J.; Zhou, R.; Gan, L.; Zhang, H. MicroRNA-449a enhances radiosensitivity by downregulation of c-Myc in prostate cancer cells. *Sci. Rep.* **2016**, *6*, 27346. [[CrossRef](#)]
29. Mirzayans, R.; Andrais, B.; Scott, A.; Wang, Y.W.; Murray, D. Ionizing radiation-induced responses in human cells with differing TP53 status. *Int. J. Mol. Sci.* **2013**, *14*, 22409–22435. [[CrossRef](#)]
30. Mirzayans, R.; Andrais, B.; Scott, A.; Paterson, M.C.; Murray, D. Single-cell analysis of p16(INK4a) and p21(WAF1) expression suggests distinct mechanisms of senescence in normal human and Li-Fraumeni Syndrome fibroblasts. *J. Cell. Physiol.* **2010**, *223*, 57–67.
31. Wang, M.; Morsbach, F.; Sander, D.; Gheorghiu, L.; Nanda, A.; Benes, C.; Kriegs, M.; Krause, M.; Dikomey, E.; Baumann, M.; et al. EGF receptor inhibition radiosensitizes NSCLC cells by inducing senescence in cells sustaining DNA double-strand breaks. *Cancer Res.* **2011**, *71*, 6261–6269. [[CrossRef](#)] [[PubMed](#)]
32. Zhang, S.; Zhang, D.; Yang, Z.; Zhang, X. Tumor Budding, Micropapillary Pattern, and Polyploidy Giant Cancer Cells in Colorectal Cancer: Current Status and Future Prospects. *Stem Cells Int.* **2016**, *2016*, 4810734. [[CrossRef](#)] [[PubMed](#)]
33. Fei, F.; Zhang, D.; Yang, Z.; Wang, S.; Wang, X.; Wu, Z.; Wu, Q.; Zhang, S. The number of polyploid giant cancer cells and epithelial-mesenchymal transition-related proteins are associated with invasion and metastasis in human breast cancer. *J. Exp. Clin. Cancer Res.* **2015**, *34*, 158. [[CrossRef](#)]
34. Lv, H.; Shi, Y.; Zhang, L.; Zhang, D.; Liu, G.; Yang, Z.; Li, Y.; Fei, F.; Zhang, S. Polyploid giant cancer cells with budding and the expression of cyclin E, S-phase kinase-associated protein 2, stathmin associated with the grading and metastasis in serous ovarian tumor. *BMC Cancer* **2014**, *14*, 576. [[CrossRef](#)] [[PubMed](#)]
35. Zhang, S.; Mercado-Urbe, I.; Xing, Z.; Sun, B.; Kuang, J.; Liu, J. Generation of cancer stem-like cells through the formation of polyploid giant cancer cells. *Oncogene* **2014**, *33*, 116–128. [[CrossRef](#)]
36. Shah, O.J.; Lin, X.; Li, L.; Huang, X.; Li, J.; Anderson, M.G.; Tang, H.; Rodriguez, L.E.; Warder, S.E.; McLoughlin, S.; et al. Bcl-XL represents a druggable molecular vulnerability during aurora B inhibitor-mediated polyploidization. *Proc. Natl. Acad. Sci. USA* **2010**, *107*, 12634–12639. [[CrossRef](#)]
37. Janicke, R.U.; Sohn, D.; Schulze-Osthoff, K. The dark side of a tumor suppressor: Anti-apoptotic p53. *Cell Death Differ.* **2008**, *15*, 959–976. [[CrossRef](#)]
38. Lee, H.J.; Kim, J.M.; Kim, K.H.; Heo, J.I.; Kwak, S.J.; Han, J.A. Genotoxic stress/p53-induced DNAJB9 inhibits the pro-apoptotic function of p53. *Cell Death Differ.* **2015**, *22*, 86–95. [[CrossRef](#)]
39. Mirzayans, R.; Andrais, B.; Kumar, P.; Murray, D. Significance of Wild-Type p53 Signaling in Suppressing Apoptosis in Response to Chemical Genotoxic Agents: Impact on Chemotherapy Outcome. *Int. J. Mol. Sci.* **2017**, *18*, 928. [[CrossRef](#)]
40. Kracikova, M.; Akiri, G.; George, A.; Sachidanandam, R.; Aaronson, S.A. A threshold mechanism mediates p53 cell fate decision between growth arrest and apoptosis. *Cell Death Differ.* **2013**, *20*, 576–588. [[CrossRef](#)]
41. Hamada, S.; Masamune, A.; Miura, S.; Satoh, K.; Shimosegawa, T. MiR-365 induces gemcitabine resistance in pancreatic cancer cells by targeting the adaptor protein SHC1 and pro-apoptotic regulator BAX. *Cell Signal.* **2014**, *26*, 179–185. [[CrossRef](#)]
42. Zhou, M.; Liu, Z.; Zhao, Y.; Ding, Y.; Liu, H.; Xi, Y.; Xiong, W.; Li, G.; Lu, J.; Fodstad, O.; et al. MicroRNA-125b confers the resistance of breast cancer cells to paclitaxel through suppression of pro-apoptotic Bcl-2 antagonist killer 1 (Bak1) expression. *J. Biol. Chem.* **2010**, *285*, 21496–21507. [[CrossRef](#)] [[PubMed](#)]

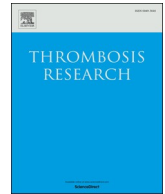
43. Nakano, H.; Miyazawa, T.; Kinoshita, K.; Yamada, Y.; Yoshida, T. Functional screening identifies a microRNA, miR-491 that induces apoptosis by targeting Bcl-X(L) in colorectal cancer cells. *Int. J. Cancer* **2010**, *127*, 1072–1080. [\[CrossRef\]](#) [\[PubMed\]](#)
44. Zhang, Y.; Schiff, D.; Park, D.; Abounader, R. MicroRNA-608 and microRNA-34a regulate chordoma malignancy by targeting EGFR, Bcl-xL and MET. *PLoS ONE* **2014**, *9*, e91546. [\[CrossRef\]](#) [\[PubMed\]](#)
45. Zhang, H.; Li, Y.; Huang, Q.; Ren, X.; Hu, H.; Sheng, H.; Lai, M. MiR-148a promotes apoptosis by targeting Bcl-2 in colorectal cancer. *Cell Death Differ.* **2011**, *18*, 1702–1710. [\[CrossRef\]](#)
46. Srivastava, N.; Manvati, S.; Srivastava, A.; Pal, R.; Kalaiarasan, P.; Chattopadhyay, S.; Gochhait, S.; Dua, R.; Bamezai, R.N. miR-24-2 controls H2AFX expression regardless of gene copy number alteration and induces apoptosis by targeting antiapoptotic gene BCL-2: A potential for therapeutic intervention. *Breast Cancer Res.* **2011**, *13*, R39. [\[CrossRef\]](#)
47. Sacconi, A.; Biagioni, F.; Canu, V.; Mori, F.; Di Benedetto, A.; Lorenzon, L.; Ercolani, C.; Di Agostino, S.; Cambria, A.M.; Germoni, S.; et al. miR-204 targets Bcl-2 expression and enhances responsiveness of gastric cancer. *Cell Death Dis.* **2012**, *3*, e423. [\[CrossRef\]](#) [\[PubMed\]](#)
48. Cimmino, A.; Calin, G.A.; Fabbri, M.; Iorio, M.V.; Ferracin, M.; Shimizu, M.; Wojcik, S.E.; Aqeilan, R.I.; Zupo, S.; Dono, M.; et al. miR-15 and miR-16 induce apoptosis by targeting BCL2. *Proc. Natl. Acad. Sci. USA* **2005**, *102*, 13944–13949. [\[CrossRef\]](#)
49. Chen, Q.; Xu, J.; Li, L.; Li, H.; Mao, S.; Zhang, F.; Zen, K.; Zhang, C.Y.; Zhang, Q. MicroRNA-23a/b and microRNA-27a/b suppress Apaf-1 protein and alleviate hypoxia-induced neuronal apoptosis. *Cell Death Dis.* **2014**, *5*, e1132. [\[CrossRef\]](#)
50. Walker, J.C.; Harland, R.M. microRNA-24a is required to repress apoptosis in the developing neural retina. *Genes Dev.* **2009**, *23*, 1046–1051. [\[CrossRef\]](#)
51. Wang, P.; Zhuang, L.; Zhang, J.; Fan, J.; Luo, J.; Chen, H.; Wang, K.; Liu, L.; Chen, Z.; Meng, Z. The serum miR-21 level serves as a predictor for the chemosensitivity of advanced pancreatic cancer, and miR-21 expression confers chemoresistance by targeting FasL. *Mol. Oncol.* **2013**, *7*, 334–345. [\[CrossRef\]](#) [\[PubMed\]](#)
52. Huang, G.; Nishimoto, K.; Zhou, Z.; Hughes, D.; Kleinerman, E.S. miR-20a encoded by the miR-17-92 cluster increases the metastatic potential of osteosarcoma cells by regulating Fas expression. *Cancer Res.* **2012**, *72*, 908–916. [\[CrossRef\]](#) [\[PubMed\]](#)
53. Guo, Q.; Zhang, J.; Li, J.; Zou, L.; Zhang, J.; Xie, Z.; Fu, X.; Jiang, S.; Chen, G.; Jia, Q.; et al. Forced miR-146a expression causes autoimmune lymphoproliferative syndrome in mice via downregulation of Fas in germinal center B cells. *Blood* **2013**, *121*, 4875–4883. [\[CrossRef\]](#) [\[PubMed\]](#)
54. Li, Z.; Huang, H.; Chen, P.; He, M.; Li, Y.; Arnovitz, S.; Jiang, X.; He, C.; Hyjek, E.; Zhang, J.; et al. miR-196b directly targets both HOXA9/MEIS1 oncogenes and FAS tumour suppressor in MLL-rearranged leukaemia. *Nat. Commun.* **2012**, *3*, 688. [\[CrossRef\]](#) [\[PubMed\]](#)
55. Razumilava, N.; Bronk, S.F.; Smoot, R.L.; Fingas, C.D.; Werneburg, N.W.; Roberts, L.R.; Mott, J.L. miR-25 targets TNF-related apoptosis inducing ligand (TRAIL) death receptor-4 and promotes apoptosis resistance in cholangiocarcinoma. *Hepatology* **2012**, *55*, 465–475. [\[CrossRef\]](#) [\[PubMed\]](#)
56. Zhang, L.; Dong, L.Y.; Li, Y.J.; Hong, Z.; Wei, W.S. The microRNA miR-181c controls microglia-mediated neuronal apoptosis by suppressing tumor necrosis factor. *J. Neuroinflamm.* **2012**, *9*, 211. [\[CrossRef\]](#) [\[PubMed\]](#)
57. Rossato, M.; Curtale, G.; Tamassia, N.; Castellucci, M.; Mori, L.; Gasperini, S.; Mariotti, B.; De Luca, M.; Mirolo, M.; Cassatella, M.A.; et al. IL-10-induced microRNA-187 negatively regulates TNF-alpha, IL-6, and IL-12p40 production in TLR4-stimulated monocytes. *Proc. Natl. Acad. Sci. USA* **2012**, *109*, E3101–E3110. [\[CrossRef\]](#)
58. Guennewig, B.; Roos, M.; Dogar, A.M.; Gebert, L.F.; Zagalak, J.A.; Vongrad, V.; Metzner, K.J.; Hall, J. Synthetic pre-microRNAs reveal dual-strand activity of miR-34a on TNF-alpha. *RNA* **2014**, *20*, 61–75. [\[CrossRef\]](#)
59. Wang, H.Q.; Yu, X.D.; Liu, Z.H.; Cheng, X.; Samartzis, D.; Jia, L.T.; Wu, S.X.; Huang, J.; Chen, J.; Luo, Z.J. Deregulated miR-155 promotes Fas-mediated apoptosis in human intervertebral disc degeneration by targeting FADD and caspase-3. *J. Pathol.* **2011**, *225*, 232–242. [\[CrossRef\]](#)
60. Yamada, N.; Noguchi, S.; Kumazaki, M.; Shinohara, H.; Miki, K.; Naoe, T.; Akao, Y. Epigenetic regulation of microRNA-128a expression contributes to the apoptosis-resistance of human T-cell leukaemia jurkat cells by modulating expression of fas-associated protein with death domain (FADD). *Biochim. Biophys. Acta* **2014**, *1843*, 590–602. [\[CrossRef\]](#)

61. Mirzayans, R.; Andrais, B.; Kumar, P.; Murray, D. The Growing Complexity of Cancer Cell Response to DNA-Damaging Agents: Caspase 3 Mediates Cell Death or Survival? *Int. J. Mol. Sci.* **2016**, *17*, 708. [[CrossRef](#)]
62. Kurtova, A.V.; Xiao, J.; Mo, Q.; Pazhanisamy, S.; Krasnow, R.; Lerner, S.P.; Chen, F.; Roh, T.T.; Lay, E.; Ho, P.L.; et al. Blocking PGE2-induced tumour repopulation abrogates bladder cancer chemoresistance. *Nature* **2015**, *517*, 209–213. [[CrossRef](#)] [[PubMed](#)]
63. Sayed, D.; Abdellatif, M. AKT-ing via microRNA. *Cell Cycle* **2010**, *9*, 3213–3217. [[CrossRef](#)] [[PubMed](#)]
64. Small, E.M.; O'Rourke, J.R.; Moresi, V.; Sutherland, L.B.; McAnally, J.; Gerard, R.D.; Richardson, J.A.; Olson, E.N. Regulation of PI3-kinase/Akt signaling by muscle-enriched microRNA-486. *Proc. Natl. Acad. Sci. USA* **2010**, *107*, 4218–4223. [[CrossRef](#)]
65. Zhang, C.-Z.; Han, L.; Zhang, A.-L.; Fu, Y.-C.; Yue, X.; Wang, G.-X.; Jia, Z.-F.; Pu, P.-Y.; Zhang, Q.-Y.; Kang, C.-S. MicroRNA-221 and microRNA-222 regulate gastric carcinoma cell proliferation and radioresistance by targeting PTEN. *BMC Cancer* **2010**, *10*, 367.
66. Yang, F.; Yin, Y.; Wang, F.; Wang, Y.; Zhang, L.; Tang, Y.; Sun, S. miR-17-5p Promotes migration of human hepatocellular carcinoma cells through the p38 mitogen-activated protein kinase-heat shock protein 27 pathway. *Hepatology* **2010**, *51*, 1614–1623. [[CrossRef](#)]
67. Wu, J.; Ding, J.; Yang, J.; Guo, X.; Zheng, Y. MicroRNA Roles in the Nuclear Factor Kappa B Signaling Pathway in Cancer. *Front. Immunol.* **2018**, *9*, 546. [[CrossRef](#)] [[PubMed](#)]
68. Luo, J.; Si, Z.Z.; Li, T.; Li, J.Q.; Zhang, Z.Q.; Chen, G.S.; Qi, H.Z.; Yao, H.L. MicroRNA-146a-5p enhances radiosensitivity in hepatocellular carcinoma through replication protein A3-induced activation of the DNA repair pathway. *Am. J. Physiol. Cell Physiol.* **2019**, *316*, C299–C311. [[CrossRef](#)]
69. Chen, X.; Zhang, N. Downregulation of lncRNA NEAT1_2 radiosensitizes hepatocellular carcinoma cells through regulation of miR-101-3p/WEE1 axis. *Cell Biol. Int.* **2019**, *43*, 44–55. [[CrossRef](#)]
70. Zhang, Y.; Zheng, L.; Ding, Y.; Li, Q.; Wang, R.; Liu, T.; Sun, Q.; Yang, H.; Peng, S.; Wang, W.; et al. MiR-20a Induces Cell Radioresistance by Activating the PTEN/PI3K/Akt Signaling Pathway in Hepatocellular Carcinoma. *Int. J. Radiat. Oncol. Biol. Phys.* **2015**, *92*, 1132–1140. [[CrossRef](#)] [[PubMed](#)]
71. Silva, J.; Garcia, J.M.; Pena, C.; Garcia, V.; Dominguez, G.; Suarez, D.; Camacho, F.I.; Espinosa, R.; Provencio, M.; Espana, P.; et al. Implication of polycomb members Bmi-1, Mel-18, and Hpc-2 in the regulation of p16INK4a, p14ARF, h-TERT, and c-Myc expression in primary breast carcinomas. *Clin. Cancer Res.* **2006**, *12*, 6929–6936. [[CrossRef](#)] [[PubMed](#)]
72. Guney, I.; Wu, S.; Sedivy, J.M. Reduced c-Myc signaling triggers telomere-independent senescence by regulating Bmi-1 and p16(INK4a). *Proc. Natl. Acad. Sci. USA* **2006**, *103*, 3645–3650. [[CrossRef](#)] [[PubMed](#)]
73. Shao, Y.; Zhang, D.; Li, X.; Yang, J.; Chen, L.; Ning, Z.; Xu, Y.; Deng, G.; Tao, M.; Zhu, Y.; et al. MicroRNA-203 Increases Cell Radiosensitivity via Directly Targeting Bmi-1 in Hepatocellular Carcinoma. *Mol. Pharm.* **2018**, *15*, 3205–3215. [[CrossRef](#)] [[PubMed](#)]
74. Tu, K.; Yang, W.; Li, C.; Zheng, X.; Lu, Z.; Guo, C.; Yao, Y.; Liu, Q. Fbxw7 is an independent prognostic marker and induces apoptosis and growth arrest by regulating YAP abundance in hepatocellular carcinoma. *Mol. Cancer* **2014**, *13*, 110. [[CrossRef](#)]
75. Deng, P.; Wu, Y. Knockdown of miR-106a suppresses migration and invasion and enhances radiosensitivity of hepatocellular carcinoma cells by upregulating FBXW7. *Int. J. Clin. Exp. Pathol.* **2019**, *12*, 1184–1193.
76. Fei, Q.; Shang, K.; Zhang, J.; Chuai, S.; Kong, D.; Zhou, T.; Fu, S.; Liang, Y.; Li, C.; Chen, Z.; et al. Histone methyltransferase SETDB1 regulates liver cancer cell growth through methylation of p53. *Nat. Commun.* **2015**, *6*, 8651. [[CrossRef](#)]
77. Shao, Y.; Song, X.; Jiang, W.; Chen, Y.; Ning, Z.; Gu, W.; Jiang, J. MicroRNA-621 Acts as a Tumor Radiosensitizer by Directly Targeting SETDB1 in Hepatocellular Carcinoma. *Mol. Ther.* **2019**, *27*, 355–364. [[CrossRef](#)]
78. Fokas, E.; Kamlah, F.; Hanze, J.; Engenhart-Cabillic, R.; Rose, F.; An, H.X. EphA2 blockade enhances the anti-endothelial effect of radiation and inhibits irradiated tumor cell-induced migration of endothelial cells. *Thorac. Cancer* **2010**, *1*, 153–162. [[CrossRef](#)]
79. Jin, Q.; Li, X.J.; Cao, P.G. MicroRNA-26b Enhances the Radiosensitivity of Hepatocellular Carcinoma Cells by Targeting EphA2. *Tohoku J. Exp. Med.* **2016**, *238*, 143–151. [[CrossRef](#)]
80. Mao, K.; Zhang, J.; He, C.; Xu, K.; Liu, J.; Sun, J.; Wu, G.; Tan, C.; Zeng, Y.; Wang, J.; et al. Restoration of miR-193b sensitizes Hepatitis B virus-associated hepatocellular carcinoma to sorafenib. *Cancer Lett.* **2014**, *352*, 245–252. [[CrossRef](#)]

81. Shimizu, S.; Takehara, T.; Hikita, H.; Kodama, T.; Miyagi, T.; Hosui, A.; Tatsumi, T.; Ishida, H.; Noda, T.; Nagano, H.; et al. The let-7 family of microRNAs inhibits Bcl-xL expression and potentiates sorafenib-induced apoptosis in human hepatocellular carcinoma. *J. Hepatol.* **2010**, *52*, 698–704. [[CrossRef](#)] [[PubMed](#)]
82. Fornari, F.; Pollutri, D.; Patrizi, C.; La Bella, T.; Marinelli, S.; Casadei Gardini, A.; Marisi, G.; Baron Toaldo, M.; Baglioni, M.; Salvatore, V.; et al. In Hepatocellular Carcinoma miR-221 Modulates Sorafenib Resistance through Inhibition of Caspase-3-Mediated Apoptosis. *Clin. Cancer Res.* **2017**, *23*, 3953–3965. [[CrossRef](#)] [[PubMed](#)]
83. Wu, Q.; Liu, H.O.; Liu, Y.D.; Liu, W.S.; Pan, D.; Zhang, W.J.; Yang, L.; Fu, Q.; Xu, J.J.; Gu, J.X. Decreased expression of hepatocyte nuclear factor 4alpha (Hnf4alpha)/microRNA-122 (miR-122) axis in hepatitis B virus-associated hepatocellular carcinoma enhances potential oncogenic GALNT10 protein activity. *J. Biol. Chem.* **2015**, *290*, 1170–1185. [[CrossRef](#)] [[PubMed](#)]



© 2020 by the authors. Licensee MDPI, Basel, Switzerland. This article is an open access article distributed under the terms and conditions of the Creative Commons Attribution (CC BY) license (<http://creativecommons.org/licenses/by/4.0/>).



Full Length Article

High-intensity interval training recuperates capacity of endogenous thrombin generation in heart failure patients with reduced ejection fraction[☆]

Chih-Chin Hsu^a, Tieh-Cheng Fu^a, Shu-Chun Huang^b, Jong-Shyan Wang^{a,c,d,*}^a Heart Failure Center, Department of Physical Medicine and Rehabilitation, Chang Gung Memorial Hospital, Keelung, Taiwan^b Department of Physical Medicine and Rehabilitation, Chang Gung Memorial Hospital, Tao-Yuan, Taiwan^c Healthy Aging Research Center, Graduate Institute of Rehabilitation Science, Medical College, Chang Gung University, Tao-Yuan, Taiwan^d Research Center for Chinese Herbal Medicine, College of Human Ecology, Chang Gung University of Science and Technology, Tao-Yuan, Taiwan

ARTICLE INFO

Keywords:

Heart failure

Exercise

Microparticles

Thrombin

ABSTRACT

Objective: Consumptive coagulopathy is associated with increased mortality in patients with heart failure (HF). Physical activity influences the risk of major vascular thrombotic events. This study investigates how high-intensity interval training (HIIT) affects the capacity of endogenous thrombin generation (TG) by modulating circulatory procoagulant microparticles (MPs) in HF patients.

Methods: Thirty-eight HF patients with reduced ejection fraction (HFrEF) and 38 age- and gender-matched normal counterparts (NC) were recruited into this study. The HFrEF group performed HIIT (3-min intervals at 40% and 80%VO_{2peak}) on a bicycle ergometer for 30 min/day, 3 days/week for 12 weeks, whereas the NC group did not receive any form of intervention. Plasma TG kinetics, procoagulant MPs, coagulation-related factors, and oxidative stress/proinflammatory status were analyzed.

Results: The HFrEF group exhibited (i) less endogenous thrombin potential (ETP) and TG rate, (ii) lower concentration/activity of tissue factor (TF) and counts of TF-rich MPs derived from blood cells, and (iii) higher vascular endothelial shedding and plasma myeloperoxidase and interleukin-6 concentrations, compared to the NC group did. However, HIIT elevated TG rate and TF concentration/activity in plasma, as well as, TF-rich MP counts derived from blood cells in patients with HFrEF. Moreover, the exercise regimen also decreased vascular endothelial shedding and plasma myeloperoxidase and interleukin-6 concentrations in HFrEF patients.

Conclusion: HFrEF reduces the capacity of endogenous TG in plasma, which is associated with decreased (or consumed) circulatory procoagulant MP levels. However, HIIT alleviates HFrEF-declined endogenous TG capacity and vascular endothelial damage through recuperating TF-related coagulation activity and suppressing oxidative stress/proinflammatory status.

1. Introduction

Ischemic etiology of the cardiomyopathy and lower ejection fraction (EF) were found to be independent predictors of systemic embolization [1]. A clinical investigation has reported that heart failure patients with reduced ejection fraction (HFrEF) have higher crude rates of thromboembolism, compared with those of HF patients with preserved ejection fraction (HFpEF) [2]. Moreover, HFrEF patients with an embolic event suffered a significantly higher mortality (38.9%) during the follow-up period when compared to those without an embolic event (10.3%) [3].

Advanced HF predisposes to the development of consumptive coagulopathy [4–6], whereas low plasma concentrations of coagulant factors are associated with increased risk of mortality in patients with HF [7]. Thrombin activity is critical to determining the severity of hemostatic reactions [8]. The procoagulant microparticles (MPs) derived from blood cells can effectively trigger thrombin generation (TG) [9]. Our recent investigation showed that elevated oxidative stress and further consequence of vascular endothelial damage led to the development of consumptive coagulopathy, which contributed to attenuated capacity of endogenous TG in patients with HF [10]. Accordingly, regional tissue

Abbreviations: HFrEF, heart failure patients with reduced ejection fraction; TG, thrombin generation; MP, procoagulant microparticle

[☆] Financial support: This study was supported by grants NSC106-2314-B-182-048-MY3, CMRPD3I0021 and EMRPD1A0841.

* Corresponding author at: Graduate Institute of Rehabilitation Science, Chang Gung University, 259 Wen-Hwa 1st Road, Kwei-Shan, Tao-Yuan 333, Taiwan.

E-mail address: s5492@mail.cgu.edu.tw (J.-S. Wang).

<https://doi.org/10.1016/j.thromres.2020.01.013>

Received 26 October 2019; Received in revised form 7 January 2020; Accepted 13 January 2020

Available online 15 January 2020

0049-3848/© 2020 Elsevier Ltd. All rights reserved.

ischemia, stagnant blood flow, elevated oxidative stress, and/or imbalanced neurohormonal factors may confer to the development of consumptive coagulopathy in patients with HF [4–6].

Regular exercise improves cardiopulmonary fitness and reduces the risk of major vascular thrombotic events [11,12]. However, physical activity imposes, paradoxically, both enhancing and suppressing effects on thrombogenesis, depending on the type and intensity of exercise [11]. An early study demonstrated that warmup exercise (40%VO_{2max}) reduce high-intensity exercise (80%VO_{2max})-induced risks of inflammatory thrombosis associated with leukocytes and platelets, which is a form of preconditioning [13]. Recently, our investigation further revealed that high-intensity interval exercise training (HIIT) that consists of alternating mild-(40%VO_{2max}) and high-(80%VO_{2max}) intensity exercise significantly suppressed hypoxia-induced inflammatory thrombosis in healthy sedentary men [14]. However, no clear and comprehensive pictures of HIIT effects on endogenous TG capacity and blood coagulation in HFrEF patients have become available.

To answer the above questions, this investigation evaluated the effects of HIIT on (i) the concentrations or activities of coagulation-related factors in plasma, (ii) the levels of vascular endothelial shedding and circulatory procoagulant MPs, (iii) the kinetic properties of endogenous TG in plasma, and (iv) the levels of plasma peroxide and proinflammatory cytokine in HFrEF patients. The aim of the present study is to establish an effective exercise strategy for improving aerobic capacity and simultaneously retarding the development of consumptive coagulopathy in patients with HFrEF.

2. Materials and methods

2.1. Subjects

This study enrolled 38 patients diagnosed with HFrEF from August 2015 to July 2017 in the Heart Failure Center, Department of Internal Medicine, Chang Gung Memorial Hospital, Keelung, Taiwan. HFrEF was diagnosed if the patients had a left ventricular ejection fraction (LVEF) < 40%. All HFrEF patients were New York Heart Association (NYHA) functional class II or III and had received optimal treatment for at least 12 months according to American Heart Association/American College of Cardiology guidelines. Patients with the presence of atrial fibrillation/flutter, second/third degree heart block, history of life-threatening ventricular arrhythmias, recent unstable angina, myocardial infarction or coronary revascularization (< 4 weeks), uncontrolled diabetes mellitus, severe chronic obstructive pulmonary disease, or symptomatic cerebral vascular disease within 12 months, collagen vascular disease, alcohol or drug abuse during the previous 12 months or significant renal or hepatic disease were excluded. Additionally, normal control (NC) group was carefully selected to recruit 38 age- and gender-matched subjects who had no cardiopulmonary and hematological disorders. The investigation was performed according to the Helsinki declaration, and was approved by the Institutional Review Board of Chang Gung Memorial Hospital, Taiwan (IRB no. 102-5561B) and the clinical trial registration number was [NCT01229670](#). All subjects provided informed consent after the experimental procedures were explained.

2.2. Graded exercise test

The participants performed the graded exercise test on a bicycle ergometer (Ergoselect 150P, Germany) by one rehabilitation physician who was blinded to the HFrEF or NC subjects to assess their cardiopulmonary parameters. Moreover, the data collector was isolated from the data analytic specialist. Each participant was instructed to fast for at least 8 h and to refrain from exercise for at least 24 h before the test. All participants arrived at the testing center at 9:00 a.m. to eliminate diurnal effects. The test comprised 2 min of unloaded pedaling, followed by a progressive increase in work-rate of 10 W/min until

exhaustion (progressive exercise to peak oxygen consumption, VO_{2peak}). Minute ventilation (V_E), oxygen consumption (VO₂), and carbon dioxide production (VCO₂) were measured in a breath-by-breath basis, using a computer-based system (Master Screen CPX, Cardinal-health Germany). Heart rate (HR) was determined from the R-R interval on a 12-lead electrocardiogram, mean arterial pressure (MAP) was measured using an automatic blood pressure system (Tango, SunTech Medical, UK), and arterial O₂ saturation was monitored through finger pulse-oximetry (model 9500, Nonin Onyx, Plymouth, MN, USA) [15,16]. VO_{2peak} was defined by the following criteria: VO₂ increased by < 2 mL/kg/min over at least 2 min, HR > 85% of its predicted upper threshold, respiratory exchange ratio > 1.15, or some other symptom/sign limitations in accordance with the guidelines of the American College of Sports Medicine for exercise testing [17].

Ventilation and VCO₂ responses, acquired from the initiation of exercise to the peak values, were used to calculate the V_E-VCO₂ slope, using least-squares linear regression ($y = m \cdot x + b$, $m = \text{slope}$) [18]. O₂ uptake efficiency slope (OUES) is an estimation of the efficiency of ventilation with respect to VO₂ [19]. OUES was derived from the slope of a natural logarithm plot of V_E vs. VO₂, with greater slopes indicating higher ventilatory efficiency [20].

2.3. Training protocols

The HFrEF patients performed supervised hospital-based training on a bicycle ergometer (Ergoselect 150P, Germany), completing three weekly sessions for 12 weeks [15,16]. The HIIT group warmed up for 3 min at 30% of VO_{2peak} [$\approx 30\%$ heart rate reserve (HRR); $\approx 30\% \cdot (\text{HR}_{\text{peak}} - \text{HR}_{\text{rest}}) + \text{HR}_{\text{rest}}$] before exercise five 3-minute intervals at 80% of VO_{2peak} ($\approx 80\%$ HRR). Each interval was followed by 3-minute exercise at 40% of VO_{2peak} ($\approx 40\%$ HRR). The exercise session was terminated by a 3-minute cool-down at 30% of VO_{2peak}. An HR monitor (Tango, SunTech Medical, UK) was used for all patients to calibrate the assigned intensity of exercise. The Borg 6-to-20 scale was used to assess the rate of perceived exertion during and after each exercise session. The work-rate of the bicycle ergometer was adjusted continuously to ensure that exercise intensity matched the target HR throughout the training period. Patients were instructed to immediately stop exercise training if they experienced chest pain or other cardiac symptoms/signs. The compliance rate with HFrEF patients were 100%.

2.4. Microparticles derived from blood cells and shedding endothelial cells

An amount of 20 mL of blood was sampled just prior to each exercise test performed. The first 2 mL was discarded, then the remaining blood sample was used for the measurements of hematological parameters. Each blood sampling was performed after holding medication (anti-platelet or anticoagulant) for 48 h, medication in thrombotic prevention was restarted after the procedure. Blood cells were enumerated using a Sysmax SF-3000 cell counter (GMI Inc., Ramsey, MN, USA). Platelet-poor plasma (PPP) was separated from whole blood by centrifugation at 1600g for 10 min at room temperature. The quantification of MPs in PPP was determined by a three-color FACSscan flow cytometer (Becton Dickinson), as described in previous studies [21–23]. Briefly, PPP was incubated with a saturating concentration of Cy5-conjugated annexin V (BioVision), phycoerythrin-conjugated (American Diagnostica Industry) TF, and a cell-specific monoclonal antibody [fluorescein isothiocyanate (FITC)-conjugated CD45 (clone 2D1, eBioscience) for leukocytes, FITC-conjugated CD41a (clone HIP8, eBioscience) for platelets, FITC-conjugated CD235a (clone HIR2, eBioscience) for erythrocytes, or FITC-conjugated CD144 (clone 55-7H1, BD Pharmingen) for endothelial cells] in darkness for 30 min at 4 °C. Standard size beads of 0.5, 0.9 and 3 µm were used to set the gating scale for MPs in forward light scatter. The particles (size < 1.0 µm) labelled with annexin V and CD41a, CD45, CD235a, or CD144 in PPP were expressed as definition of MPs derived from platelets (PMPs),

leukocytes (LMPs), erythrocytes (RMPs), or endothelial cells (unit = MPs/mL), respectively. Afterward, the TF-stained events observed in the MP gate were represented as the TF-rich MPs (unit = MPs/mL). For the MP calculation, the acquisition period was counted and stopped after 50,000 events under “low run condition” (0.012 mL/min), and MP number per mL was calculated using the following formula: $N = 50,000 \times C \times 10^3 / [(12/60) \times T]$, where C is the percentage of PMPs, LMPs, RMPs, or EMPs in total MP count and T is total acquisition time in seconds [21–23].

2.5. Thrombin generation assay

The calibrated automated thrombogram (CAT) assay (Synapse/Thromboscope BV) was performed as described in the authors' earlier work [14,22,23]. Twenty microliters of reagents containing TF with or without phospholipids (PS) were mixed with the plasma samples to obtain a final concentration of 20 pM TF plus 4 μM phosphatidylserine (PS) (high TF + PS) or 0.5 pM TF only (low TF), respectively. Coagulation was started by adding 0.1 M CaCl₂ (20 μL) in a fresh mixture of fluobuffer (containing 20 mM HEPES and 60 mg/mL bovine serum albumin in pH 7.35) containing 2.5 mM Z-Gly-Gly-Arg-AMC (the fluorogenic substrate) (Sigma). Upon cleaving by thrombin, the fluorescent AMC (7-amino-4-methylcoumarin) is released and measured with a 390-nm-excitation and a 460-nm-emission filter set in an Ascent Fluoroskan (ThermoLabsystems). All reagents were warmed to 37 °C before the experiment began. Fluorescence was recorded for 90 min. The fluorescence signal was corrected for substrate consumption, plasma color variability and inner filter fluorescence effect by running in parallel calibrating wells where 80 microliter plasma samples were mixed with 20 microliter Thrombin Calibrator from Thromboscope BV.

Fluorescence data were then analyzed with the Thromboscope software (Thromboscope BV). The following parameters were recorded: (i) endogenous thrombin potential (ETP): area under the curve, which stands for the total amount of thrombin generated over the time; (ii) TG_{lag time}: time to burst of thrombin generation, which roughly represents the clotting time; (iii) TG_{peak height}: the highest thrombin concentration reached during the time course of thrombin formation and inhibition; and (iv) TG rate: peak height divided by the difference between time to peak and lag time, which recommends the initial slope of thrombin generation [14,22,23].

2.6. Coagulation-related factors, pro-inflammatory cytokine and lipid peroxide in plasma

An additional 5-mL blood sample was obtained from all subjects, placed in a cold centrifuge tube containing EDTA (final concentration, 4 mM), and immediately centrifuged at 3000g for 10 min at 4 °C. The plasma samples were then stored at −80 °C until assay. Plasma myeloperoxidase (MPO, Immunology Consultants Laboratory) and interleukin-6 (IL-6, eBioscience) concentrations, as well as, TF level (Assaypro) and activity (Assaypro) were measured by commercially available ELISA kits.

2.7. Statistical analysis

Data were presented as median with the interquartile range (IQR) or as numbers with the percentage. The statistical software package StatView was employed to analyze the data. Kolmogorov–Smirnov's goodness-of-fit test was used and normal distribution was observed in the present study. The effect size was calculated from the most used variable, VO_{2peak}, from the author's previous study to compute the required sample size [15]. With the average improvement of VO_{2peak} up to 30% after HIIT, the statistical power by G*power 3.1 for the matched pairs analysis revealed that at least 26 patients were required to detect a large effect size (0.9) in VO_{2peak} with a power of 90% and a two-sided

Table 1

Demographic and clinical characteristics in heart failure patients with reduced ejection fraction and normal counterparts.

		NC	HFrEF	
			Pre-training	Post-training
Anthropometrics/clinical characteristics				
Gender	N (M/F)	38 (22/16)	38 (22/16)	38 (22/16)
Age	years	59.3 (54.2–64.5)	59.7.5 (54.2–65.2)	–
Height	cm	162.6 (156.2–169.4)	165.1 (160.3–170.1)	165.1 (160.3–170.1)
Weight	kg	66.9 (62.4–71.3)	68.4 (63.7–73.1)	67.8 (62.5–73.0)
Heart rate	bpm	79 (74–83)	81 (77–86)	79 (75–84)
Systolic BP	mmHg	133 (123–141)	134 (122–145)	132 (120–143)
Diastolic BP	mmHg	78 (71–85)	80 (73–89)	78 (72–87)
Etiology (primary cause)				
Ischemic heart disease	N (%)	0 (0%)	24 (64%)	–
Hypertension	N (%)	0 (0%)	7 (18%)	–
Cardiomyopathy	N (%)	0 (0%)	6 (16%)	–
Heart failure duration	Years	–	5.1 ± 1.7	–
Echocardiography				
LVEF	(%)	–	35.7 (29.5–38.2)	43.0 (37.3–48.8)*
Clinical outcome				
Thrombotic events	N (%)	0 (0%)	0 (0%)	0 (0%)
Rehospitalization	N (%)	0 (0%)	0 (0%)	0 (0%)
Death	N (%)	0 (0%)	0 (0%)	0 (0%)
Hematology				
Red blood cells	× 10 ⁶ /μL	4.36 (4.02–4.70)	4.04 (3.72–4.36)	4.18 (3.83–4.51)
Hemoglobin	g/dL	13.5 (12.3–14.5)	12.4 (11.2–13.8)	13.0 (11.7–14.2)
Hematocrit	%	40.1 (37.8–42.2)	37.7 (35.6–39.8)	38.2 (36.0–40.5)
Leukocytes	× 10 ³ /μL	6.72 (5.88–7.54)	6.00 (5.27–6.72)	6.35 (5.58–7.11)
Platelets	× 10 ³ /μL	216 (176–254)	196 (157–234)	207 (172–241)
Medications				
ASA	N (%)	0 (0%)	15 (39%)	15 (39%)
NOAC	N (%)	0 (0%)	6 (16%)	6 (16%)
β-Blockers	N (%)	0 (0%)	28 (74%)	28 (74%)
Ca ²⁺ channel blockers	N (%)	0 (0%)	2 (5%)	2 (5%)
Digoxin	N (%)	0 (0%)	3 (8%)	3 (8%)
ACEI/ARB	N (%)	0 (0%)	29 (76%)	29 (76%)
Diuretics	N (%)	0 (0%)	17 (45%)	17 (45%)

Values are expressed as the median and interquartile range (IQR) or as numbers with the percentage. NC, normal control; HFrEF, heart failure with reduced ejection fraction; LVEF, left ventricular ejection fraction; WBC, white blood cells; RBC, red blood cells; Hb, hemoglobin; Hct, hematocrit; ASA, acetylsalicylic acid; NOAC, non-vitamin K antagonist oral anticoagulant; ACEI/ARB, angiotensin converting enzyme inhibitor/angiotensin II receptor blocker; M, male; F, female; N, numbers. Pre-training vs. Post-training.

* $P < 0.05$, Pre-training vs. Post-training.

5% significance level. Since this investigation was a longitudinal study in which one group of patients (HIIT), the experimental results were analyzed by pair *t*-test to compare cardiopulmonary fitness, plasma TG kinetics, procoagulant MPs, vascular endothelial shedding, coagulation-related factors, and peroxide/proinflammatory cytokine at the beginning of this study and after 12 weeks of HIIT in HF patients. The differences in cardiopulmonary fitness, plasma TG kinetics, procoagulant MPs, vascular endothelial shedding, coagulation-related factors, and peroxide/proinflammatory cytokine between HFrEF and NC groups were analyzed by unpaired *t*-test. The criterion for significance was $P < 0.05$.

Table 2

The effect of high-intensity interval training on cardiopulmonary responses to exercise in heart failure patients with reduced ejection fraction.

NC			HFrEF	
			Pre-training	Post-training
Exercise performance				
Work-rate	Watt	115 (100–130)	80 (70–90) ⁺	105 (90–120) ⁺
Circulatory responses at peak performance				
HR	bpm	153 (145–161)	132 (122–138) ⁺	137 (129–144)
Systolic BP	mmHg	176 (169–184)	158 (148 ± 166) ⁺	162 (152–172)
Diastolic BP	mmHg	87 (81–92)	91 (82–100)	88 (81–94)
MAP	mmHg	123 (117–129)	116 (109–121) ⁺	117 (113–125)
Respiratory responses at peak performance				
V _E	L/min	66.8 (61.2–72.3)	47.1 (41.5–52.6) ⁺	60.5 (55.6–65.3) ⁺
VO ₂	mL/ min/kg	25.3 (22.3–28.2)	16.8 (14.7–18.7) ⁺	21.7 (19.2–24.2) ⁺
VCO ₂	mL/ min/kg	29.4 (26.1–32.6)	20.6 (17.6–23.5) ⁺	26.0 (22.5–29.5) ⁺
OUES	Unit	1729 (1612–18,450)	1184 (1023–1345) ⁺	1527 (1445–1602) ⁺
VE-VCO ₂ slope	Unit	26.3 (24.3–28.7)	35.5 (32.5–38.3) ⁺	31.3 (29.3–33.7) ⁺

Values are expressed as the median and interquartile range (IQR). NC, normal control; HFrEF, heart failure with reduced ejection fraction; HR, heart rate; BP, blood pressure; MAP, mean arterial pressure; VE, minute ventilation; VO₂, O₂ consumption; VCO₂, CO₂ production; OUES, oxygen uptake efficiency slope. NC vs. HFrEF; Pre-training vs. Post-training.

⁺ $P < 0.05$, NC vs. HFrEF.

^{*} $P < 0.05$, Pre-training vs. Post-training.

3. Results

3.1. Cardiopulmonary fitness and hematologic parameters

All NC and HF subjects have no occurred thrombotic events, re-hospitalization, and death throughout experimental periods (Table 1). Regarding myocardial contractility, the HIIT regimen resulted in significantly elevated left-ventricular ejection fraction (LVEF) from 35% to 42% (Table 1, $P < 0.05$) in patients with HF. However, hematological parameters (i.e., erythrocyte, hemoglobin, hematocrit, leukocyte, and platelet) did not change significantly after 12-week HIIT in the HFrEF group (Table 1).

Before the intervention, the HFrEF group had lower work-rate, V_E, VO₂, and VCO₂ at peak exercise, as well as, less OUES and steeper V_E-VCO₂ slope during exercise than the NC group (Table 2, $P < 0.05$). However, 12-week HIIT significantly increased peak work-rate, V_E, VO₂, and VCO₂, elevated OUES, and lowered V_E-VCO₂ slope during the graded exercise test in patients with HFrEF (Table 2, $P < 0.05$).

3.2. TF-rich MPs derived from blood cells, coagulant-related factors, and dynamic TG in plasma

The HFrEF group before HIIT revealed lower levels of PS⁺- and PS⁺TF⁺-rich total MPs (TMPs) ($P < 0.05$) and PMPs, LMPs, and RMPs ($P < 0.05$) in plasma than the NC group (Table 3). Moreover, the HFrEF group also displayed lower dynamic TG in plasma, which were reflected to smaller ETP ($P < 0.05$), longer TG lag time ($P < 0.05$), lower TG peak height ($P < 0.05$) and less TG rate ($P < 0.05$), compared to those of the NC group (Table 4). While in vitro addition of high TF and PS to plasma, the differences of ETP, TG lag time, TG peak height, and TG rate between the HFrEF and NC groups became negligible (Table 4).

Table 3

The effect of high-intensity interval training on procoagulant microparticles, endothelial shedding, lipid peroxide, and pro-inflammatory cytokine in heart failure patients with reduced ejection fraction.

	NC	HFrEF	
		Pre-training	Post-training
Plasma microparticles ($\times 10^3$ particles/mL)			
PS ⁺ TMPs	603 (541–662)	305 (272–342) ⁺	417 (361–472) ⁺
TF ⁺ PS ⁺ TMPs	242 (212–271)	82 (51–112) ⁺	164 (121–204) ⁺
Blood cell-derived PS ⁺ microparticles ($\times 10^3$ particles/mL)			
PS ⁺ PMPs	72 (48–94)	30 (17–42) ⁺	62 (48–76) ⁺
PS ⁺ LMPs	73 (52–93)	41 (24–53) ⁺	70 (59–82) ⁺
PS ⁺ RMPs	192 (152–228)	115 (87–139) ⁺	159 (136–191) ⁺
Blood cell-derived TF ⁺ PS ⁺ microparticles ($\times 10^3$ particles/mL)			
TF ⁺ PS ⁺ PMPs	29 (21–36)	14 (8–20) ⁺	24 (18–31) ⁺
TF ⁺ PS ⁺ LMPs	32 (22–42)	11 (6–14) ⁺	22 (17–28) ⁺
TF ⁺ PS ⁺ RMPs	74 (53–94)	34 (21–45) ⁺	54 (42–68) ⁺
Plasma EMPs ($\times 10^3$ particles/mL)	115 (81–149)	243 (201–291) ⁺	155 (123–189) ⁺
Plasma myeloperoxidase (ng/mL)	50.7 (41.4–60.1)	70.2 (62.3–84.5) ⁺	55.2 (44.3–61.2) ⁺
Plasma interleukin-6 (pg/mL)	2.44 (1.87–3.01)	4.28 (3.21–5.34) ⁺	2.81 (2.01–3.57) ⁺

Values are expressed as the median and interquartile range (IQR). TF, tissue factor; PS, phosphatidylserine; NC, normal counterpart; HFrEF, heart failure with reduced ejection fraction; TMPs, PMPs, LMPs, RMPs: microparticles derived from total blood cells, platelets, leukocytes, and erythrocytes; EMPs, endothelial microparticles in plasma, respectively.

⁺ $P < 0.05$, NC vs. HFrEF.

^{*} $P < 0.05$, Pre-training vs. Post-training.

3.3. Vascular endothelial shedding and peroxide/proinflammatory cytokine

The HFrEF patients revealed higher count of EMP ($P < 0.05$) and concentrations of MPO ($P < 0.05$) and IL-6 ($P < 0.05$) in plasma than those of NC subjects (Table 3). However, plasma levels of EMP ($P < 0.05$), MPO ($P < 0.05$), and IL-6 ($P < 0.05$) were lowered following 12-week HIIT in patients with HFrEF (Table 3).

The HIIT for 12 weeks increased PS⁺- and PS⁺TF⁺-rich total TMP (Table 3, $P < 0.05$) and PMP, LMP, and RMP counts (Table 3, $P < 0.05$) and were accompanied by enlarged ETP ($P < 0.05$), shortened TG lag time ($P < 0.05$), elevated TG peak height ($P < 0.05$), and increased TG rate ($P < 0.05$) in the HFrEF group (Table 4). Fig. 1(A) and (B) shows the samples of dynamic TG in plasma with in vitro addition of low TF (A) or high TF and PS (B) in an NC subject and an HFrEF patient at pre- and post-HIIT status.

On the other hand, the HFrEF group had lower plasma TF concentration and activity than the NC group ($P < 0.05$, Table 4). However, 12 weeks of HIIT increased plasma TF concentration and activity in the HFrEF group ($P < 0.05$, Table 4).

4. Discussion

This investigation clearly demonstrates that HFrEF reduces the amount and rate of TG in plasma by diminishing the levels of blood cell-derived procoagulant MPs and coagulation-related factors. However, HIIT for 12 weeks alleviates HFrEF-induced endogenous TG reduction and vascular endothelial damage through recuperating blood coagulation activity and suppressing oxidative stress/proinflammatory status.

Previous studies have demonstrated that circulating MPs released from blood cells act as potent pro-coagulants at a distance from the site of the cell activation [24,25]. The negatively charged PS on MPs can bind intrinsic coagulation factors, providing a strongly catalytic surface

Table 4

The effect of high-intensity interval training on dynamic thrombin generation and coagulation-related factor in heart failure patients with reduced ejection fraction.

		NC	HFrEF	
			Pre-training	Post-training
Dynamic thrombin generation				
Plasma with low TF				
Lag time	min	7.8 (5.8–9.7)	10.6 (8.8–12.9) ⁺	7.7 (6.1–9.2) [*]
Peak height	nM	100.8 (80.3–121.2)	62.9 (52.5–73.2) ⁺	90.7 (78.3–103.2) [*]
ETP	nM	1465 (1312–1622)	851 (791–910) ⁺	1122 (972–1276) [*]
Rate	nM/min	14.12 (12.01–16.13)	5.42 (4.61–6.23) ⁺	7.99 (6.87–9.10) [*]
Plasma with high TF + PS				
Lag time	min	1.56 (1.32–1.77)	1.71 (1.49–1.92)	1.65 (1.41–1.85)
Peak height	nM	293.6 (252.4–332.2)	264.2 (231.6–296.4)	279.3 (253.5–305.2)
ETP	nM	2059 (1806–2310)	1763 (1512–2010)	1812 (1613–2101)
Rate	nM/min	102.4 (87.2–117.5)	92.3 (78.2–106.3)	93.8 (80.2–107.3)
Plasma coagulation-related factor				
TF concentration	pg/mL	26.8 (22.2–31.3)	12.9 (10.3–15.1) ⁺	19.4 (14.8–24.2) [*]
TF Activity	pM	100.6 (87.2–114.2)	73.4 (63.5–83.2) ⁺	94.3 (81.3–106.5) [*]

Values are expressed as the median and interquartile range (IQR). NC, normal control; HFrEF, heart failure with reduced ejection fraction; TF, tissue factor; PS, phosphatidylserine; low TF, 0.5 pM TF; high TF + PS, 20 pM TF plus 4 μ M PS; ETP, endogenous thrombin potential.

⁺ $P < 0.05$, NC vs. HFrEF.

^{*} $P < 0.05$, Pre-training vs. Post-training.

for the assembly of prothrombinase and tenase [24]. The TF on MP membranes also catalyzes TG from prothrombin via activating extrinsic coagulation pathway, resulting in the formation of a fibrin clot [25].

Congestive HF caused by ischemic cardiomyopathy has been frequently diagnosed with disseminated intravascular coagulation (DIC) [26]. In this investigation, HFrEF patients revealed lesser counts of total and TF-

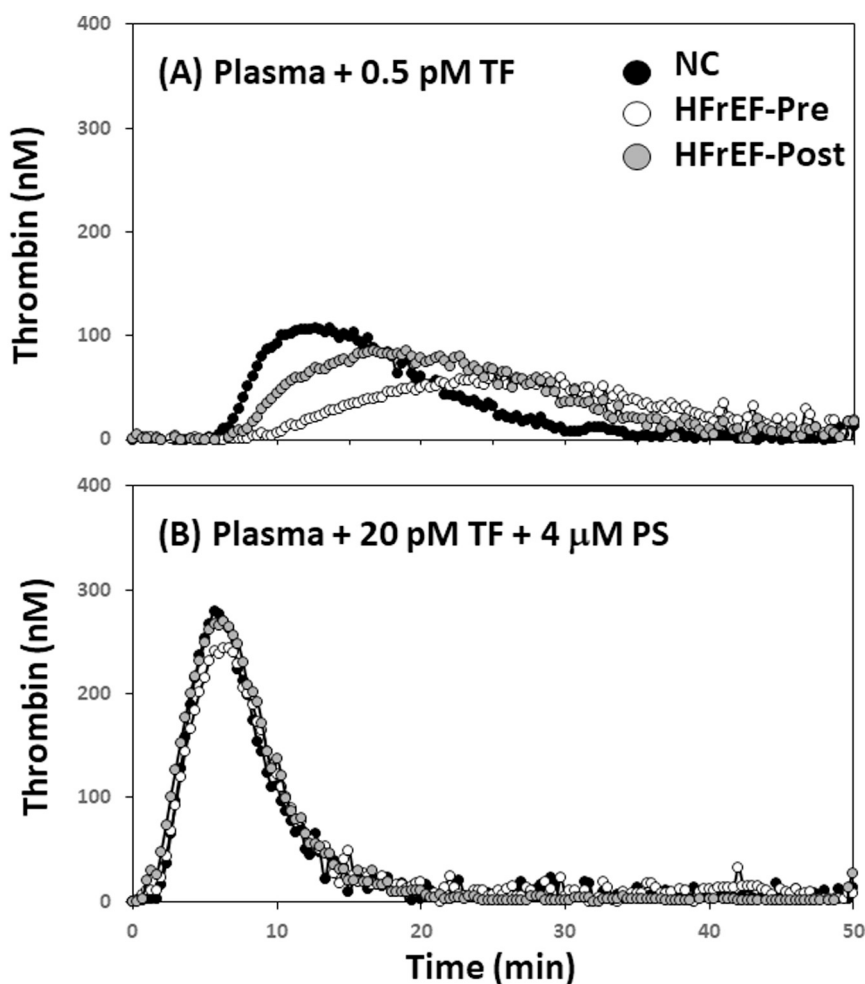


Fig. 1. Graph showing the samples of dynamic thrombin generation in plasma with in vitro addition of low tissue factor (TF, 0.5 pM) (2A) or high TF (20 pM) and phosphatidylserine (PS, 4- μ M) (2B) in a heart failure patient with reduced ejection fraction (HFrEF) before (Pre) and after (Post) high-intensity interval training and a normal counterpart (NC).

rich MPs derived from leukocytes, platelets, and erythrocytes and lower TF concentration/activity in plasma, compared to those of normal counterparts. Moreover, the reductions of procoagulant MPs and TF in HFrEF were accompanied by diminished ETP, as well as, lengthened lag time, lowered peak height, and decreased rate of TG in plasma. While in vitro addition of high TF and PS to plasma, the kinetic properties of plasma TG in HFrEF patients were similar to those in normal counterparts. These findings suggest that the HFrEF-declined dynamic TG may be associated with lowered procoagulant MPs derived from blood cells and TF concentration/activity in plasma.

In this study, HFrEF patients exhibited higher levels of plasma MPO and IL-6 and circulating EMPs than normal counterparts did. Elevated oxidative stress and further consequence of vascular endothelial damage may contribute to the development of consumptive coagulopathy in patients with HF [10]. The HF-related consumptive coagulopathy presenting as DIC may prolong clotting time, elevate fibrin degradation products, decrease plasma fibrinogen concentration, further impairing blood coagulation [6,26]. Furthermore, low plasma concentrations of coagulant factors have been observed to increased risk of mortality in the elderly with HF symptoms [7]. Therefore, we speculate that HFrEF may result in vascular endothelial damage by elevating oxidative stress and pro-inflammatory status, subsequently consuming to reduce coagulation-related factors in blood, eventually lowering endogenous TG in blood.

A previous investigation has shown that patients with ischemic heart disease developed a warm-up phenomenon during repeated exercise testing, characterized by delayed on set of angina pain and reduced electrocardiographic evidence of myocardial ischemia, an effect that comprised a form of preconditioning [28]. Previous studies have revealed that exercise preconditioning improved myocardial tolerance to ischemia by activating mitochondrial ATP-sensitive K^+ channel [29,30]. Moreover, the protective effects of exercise training on cardiovascular systems are associated with up-regulating expression of antioxidant enzymes and stress-related proteins [29,30]. Our previous study using sedentary males showed that prior exercise intensity lowered to 40% VO_{2max} (warm-up exercise) attenuated the enhancements of platelets binding to neutrophils and production of neutrophil reactive oxygen species promoted by heavy-intensity exercise (80% VO_{2max}) [13]. Additionally, the HIIT-induced alternating changes of aerobic and anaerobic metabolisms may serve as preconditioning to oxidative stress induced by hypoxia, which may increase the resistance to hypoxia-induced endothelial dysfunction [31] and inflammatory thrombosis [14]. This present investigation also indicated that HIIT significantly decreased plasma levels of MPO and IL-6 and was accompanied by depressed endothelial shedding and recuperating TG capacity in HF patients. Accordingly, we posit that these HIIT-induced physiological adaptations protect against oxidative stress and inflammation associated with consumptive coagulopathy in patients with HFrEF.

5. Study limitations

Major limitations of this study are the lacks of D-dimer measurement that directly reflects the phenomenon of consumptive coagulopathy and the design of control HFrEF group that these patients only receive general healthcare without exercise training. However, a previous study indicated that the analysis of endogenous TG kinetics is superior to traditional D-dimer measurement [32]. Despite the lack of control HFrEF design, this study compared the differences in blood coagulation between HFrEF patients and normal counterparts, that indirectly explains why HFrEF results in consumptive coagulopathy. However, a longitudinal investigation in HFrEF-related consumptive coagulopathy needs to further explore.

6. Conclusions

The progression of HFrEF may impair the kinetic properties of

endogenous TG, which is associated with decreased levels of blood cell-derived procoagulant MPs and depressed activation of coagulation pathway. However, HIIT for 12 weeks alleviates HFrEF-induced endogenous TG reduction and vascular endothelial damage through recuperating blood coagulation activity and suppressing oxidative stress/proinflammatory status. These findings provide a new insight into how HIIT alleviates dysfunction of blood coagulation, further developing a suitable exercise strategy for improving regulation of hemostasis in the HF progression.

Author contribution

Jong-Shyan Wang was involved in conception and design of research; Chih-Chin Hsu, Tieh-Cheng Fu, and Shu-Chun Huang performed experiments; Jong-Shyan Wang and Chih-Chin Hsu analyzed data, interpreted results of experiments, prepared the figures and drafted the paper; Jong-Shyan Wang and Chih-Chin Hsu edited and revised the paper; Jong-Shyan Wang, Chih-Chin Hsu, Tieh-Cheng Fu, and Shu-Chun Huang approved the final version of paper.

Funding sources

This work was supported by the National Science Council of Taiwan (grant number NSC 106-2314-B-182-048-MY3), Chang Gung Medical Research Program (grant number CMRPD3I0021), and Healthy Aging Research Center, Chang Gung University (grant number EMRPD1A0841).

Acknowledgments

The authors would like to thank the volunteers for their enthusiastic participation.

Declaration of competing interest

No conflicts of interest, financial or otherwise, are declared by the authors.

References

- [1] R.L. Wilensky, S.C. Jung, Thromboembolism in patients with decreased left ventricular function: incidence, risk, and treatment, *J. Cardiovasc. Risk* 2 (1995) 91–96.
- [2] G.Y. Lip, C. Laroche, M.I. Popescu, L.H. Rasmussen, L. Vitali-Serdoz, G.A. Dan, Z. Kalarus, H.J. Crijns, M.M. Oliveira, L. Tavazzi, A.P. Maggioni, G. Boriani, Heart failure in patients with atrial fibrillation in Europe: a report from the EURObservational Research Programme Pilot survey on Atrial Fibrillation, *Eur. J. Heart Fail.* 17 (2015) 570–582.
- [3] N.D. Sharma, P.A. McCullough, E.F. Philbin, W.D. Weaver, Left ventricular thrombus and subsequent thromboembolism in patients with severe systolic dysfunction, *Chest* 117 (2000) 314–320.
- [4] R. Itani, Y. Minami, S. Haruki, E. Watanabe, N. Hagiwara, Prognostic impact of disseminated intravascular coagulation score in acute heart failure patients referred to a cardiac intensive care unit: a retrospective cohort study, *Heart Vessels* 32 (2017) 872–879.
- [5] A. Sarcon, X. Liu, D. Ton, J. Haywood, T. Hitchcock, Advanced congestive heart failure associated with disseminated intravascular coagulopathy, *J. Investig. Med. High Impact Case Rep.* 3 (2015) 2324709615623298.
- [6] D. Belov, R. Lyubarova, S. Fein, M. Torosoff, Disseminated intravascular coagulation with congestive heart failure and left ventricular thrombus: a case report with literature review of 7 cases, *Am. J. Case Rep.* 16 (2015) 53–56.
- [7] U. Alehagen, U. Dahlstrom, T.L. Lindahl, Low plasma concentrations of coagulation factors II, VII and XI indicate increased risk among elderly with symptoms of heart failure, *Blood Coagul. Fibrinolysis* 21 (2010) 62–69.
- [8] R. Al Dieri, B. de Laat, H.C. Hemker, Thrombin generation: what have we learned? *Blood Rev.* 26 (2012) 197–203.
- [9] O. Morel, F. Toti, B. Hugel, B. Bakouboula, L. Camoin-Jau, F. Dignat-George, J.M. Freyssinet, Procoagulant microparticles: disrupting the vascular homeostasis equation? *Arterioscler. Thromb. Vasc. Biol.* 26 (2006) 2594–2604.
- [10] Y.W. Chen, Y.C. Chen, T.C. Fu, C.H. Wang, S.C. Huang, J.S. Wang, Anemic comorbidity reduces capacity of endogenous thrombin generation and is associated with consumptive coagulopathy in patients with heart failure, *Int. J. Cardiol.* 168 (2013) 4965–4967.

- [11] J.S. Wang, Exercise prescription and thrombogenesis, *J. Biomed. Sci.* 13 (2006) 753–761.
- [12] K.W. Lee, G.Y. Lip, Acute versus habitual exercise, thrombogenesis and exercise intensity, *Thromb. Haemost.* 91 (2004) 416–419.
- [13] J.S. Wang, H.L. Yen, C.M. Yang, Warm-up exercise suppresses platelet-eosinophil aggregation and platelet-promoted release of eosinophil oxidant products enhanced by severe exercise under shear flow and inflammation in men, *Thromb. Haemost.* 207 (2006) 174–186.
- [14] Y.C. Chen, C.W. Ho, H.H. Tsai, J.S. Wang, Interval and continuous exercise regimens suppress neutrophil-derived microparticle formation and neutrophil-promoted thrombin generation under hypoxic stress, *Clin. Sci.* 128 (2015) 425–436.
- [15] T.C. Fu, C.H. Wang, P.S. Lin, C.C. Hsu, W.J. Cherng, S.C. Huang, M.H. Liu, C.L. Chiang, J.S. Wang, Aerobic interval training improves oxygen uptake efficiency by enhancing cerebral and muscular hemodynamics in patients with heart failure, *Int. J. Cardiol.* 167 (2013) 41–50.
- [16] C.H. Chou, T.C. Fu, H.H. Tsai, C.C. Hsu, C.H. Wang, J.S. Wang, High-intensity interval training enhances mitochondrial bioenergetics of platelets in patients with heart failure, *Int. J. Cardiol.* 274 (2019) 214–220.
- [17] American College of Sports Medicine, General principle of exercise prescription, in: W.R. Thompson, N.F. Gordon, L.S. Pescatello (Eds.), *ACSM's Guidelines for Exercise Testing and Prescription*, Lippincott Williams & Wilkins, Philadelphia, 2010, pp. 152–182.
- [18] R. Arena, M. Guazzi, J. Myers, Ventilatory abnormalities during exercise in heart failure: a mini review, *Curr. Respir. Med. Rev.* 3 (2007) 179–187.
- [19] M. Hollenberg, I.B. Tager, Oxygen uptake efficiency slope: an index of exercise performance and cardiopulmonary reserve requiring only submaximal exercise, *J. Am. Coll. Cardiol.* 36 (2000) 194–201.
- [20] C. Van Laethem, N. Van De Veire, G. De Backer, S. Bihija, T. Seghers, D. Cambier, M. Vanderheyden, J. De Sutter, Response of the oxygen uptake efficiency slope to exercise training in patients with chronic heart failure, *Eur. J. Heart. Fail.* 9 (2007) 625–629.
- [21] L. Burnier, P. Fontana, B.R. Kwak, A. Angelillo-Scherrer, Cell-derived microparticles in haemostasis and vascular medicine, *Thromb. Haemost.* 101 (2009) 439–451.
- [22] Y.W. Chen, J.K. Chen, J.S. Wang, Strenuous exercise promotes shear-induced thrombin generation by increasing the shedding of procoagulant microparticles from platelets, *Thromb. Haemost.* 104 (2010) 293–301.
- [23] J.S. Wang, Y.L. Chang, Y.C. Chen, H.H. Tsai, T.C. Fu, Effects of normoxic and hypoxic exercise regimens on monocyte-mediated thrombin generation in sedentary men, *Clin. Sci.* 129 (2015) 363–374.
- [24] E.I. Sinauridze, D.A. Kireev, N.Y. Popenko, A.V. Pichugin, M.A. Panteleev, O.V. Krymskaya, F.I. Ataullakhanov, Platelet microparticle membranes have 50- to 100-fold higher specific procoagulant activity than activated platelets, *Thromb. Haemost.* 97 (2007) 425–434.
- [25] I. Müller, A. Klocke, M. Alex, et al., Intravascular tissue factor initiates coagulation via circulating microvesicles and platelets, *FASEB J.* 17 (2003) 476–478.
- [26] T.A. Heckman, M.H. Rosove, Massive left ventricular mural thrombosis with consumption coagulopathy in congestive heart failure, *West. J. Med.* 133 (1980) 442–444.
- [27] I.A. Paraskevaidis, E.K. Iliodromitis, S. Mavrogeni, G.K. Karavolias, G.N. Theodorakis, M. Georgiadis, D.T. Kremastinos, Repeated exercise stress testing identifies early and late preconditioning, *Int. J. Cardiol.* 98 (2005) 221–226.
- [28] S. Gielen, G. Schuler, V. Adams, Cardiovascular effects of exercise training: molecular mechanisms, *Circulation* 122 (2010) 1221–1238.
- [29] E. Crimi, L.J. Ignarro, F. Cacciatore, C. Napoli, Mechanisms by which exercise training benefits patients with heart failure, *Nat. Rev. Cardiol.* 6 (2009) 292–300.
- [30] H.H. Tsai, C.P. Lin, Y.H. Lin, C.C. Hsu, J.S. Wang, High-intensity Interval training enhances mobilization/functionality of endothelial progenitor cells and depressed shedding of vascular endothelial cells undergoing hypoxia, *Eur. J. Appl. Physiol.* 116 (2016) 2375–2388.
- [31] H.C. Hemker, P. Giesen, R. Al Dieri, V. Regnault, E. de Smed, R. Wagenvoort, T. Lecompte, S. Béguin, The calibrated automated thrombogram (CAT): a universal routine test for hyper- and hypocoagulability, *Pathophysiol. Haemost. Thromb.* 32 (2002) 249–253.



An immuno-MALDI mass spectrometry assay for the oral cancer biomarker, matrix metalloproteinase-1, in dried saliva spot samples

Yung-Chin Hsiao ^{a, b}, Shih-Yu Lin ^a, Kun-Yi Chien ^{c, d}, Szu-Fan Chen ^a, Chia-Chun Wu ^a, Ya-Ting Chang ^a, Lang-Ming Chi ^d, Lichieh Julie Chu ^{a, b}, Wei-Fan Chiang ^{e, f}, Chih-Yen Chien ^{g, h}, Kai-Ping Chang ^{a, i}, Yu-Sun Chang ^{a, i}, Jau-Song Yu ^{a, b, c, j, *}

^a Molecular Medicine Research Center, Chang Gung University, Taoyuan, Taiwan

^b Liver Research Center, Chang Gung Memorial Hospital, Linkou, Taiwan

^c Department of Biochemistry and Molecular Biology, College of Medicine, Chang Gung University, Taoyuan, Taiwan

^d Clinical Proteomics Core Laboratory, Chang Gung Memorial Hospital, Taoyuan, Taiwan

^e Department of Oral and Maxillofacial Surgery, Chi-Mei Medical Center, Liouying, Tainan, Taiwan

^f School of Dentistry, National Yang Ming University, Taipei, Taiwan

^g Department of Otolaryngology, Kaohsiung Chang Gung Memorial Hospital, Kaohsiung, Taiwan

^h College of Medicine, Chang Gung University, Taoyuan, Taiwan

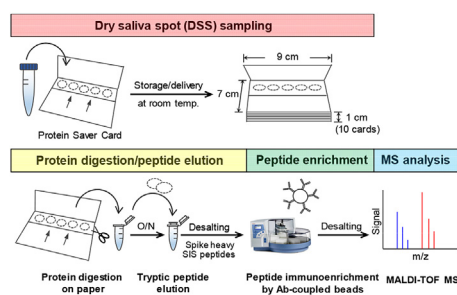
ⁱ Departments of Otolaryngology-Head & Neck Surgery, Chang Gung Memorial Hospital, Linkou, Taiwan

^j Research Center for Food and Cosmetic Safety, Research Center for Chinese Herbal Medicine, College of Human Ecology, Chang Gung University of Science and Technology, Taoyuan, Taiwan

HIGHLIGHTS

- Quantification of the oral cancer biomarker, MMP1, in DSS samples with a novel immuno-MALDI assay is presented.
- DSS sampling, on-paper protein digestion and elution are optimized for recovery of MMP1-derived peptides.
- Magnetic beads coupled with an anti-peptide antibody against MMP1 are used to enrich MMP1-derived peptides.
- KingFisher magnetic particle processor is used for automation of immunoenrichment.
- The developed assay is successfully used for MMP1 measurement in DSS samples from oral cancer patients.

GRAPHICAL ABSTRACT



Abbreviations: ACN, acetonitrile; CHAPS, 3-[(3-cholamidopropyl)dimethylammonio]-1-propanesulfonate; CV, coefficient of variation; DOC, sodium deoxycholate; DSS, dried saliva spot; ELISA, enzyme-linked immunosorbent assay; FA, formic acid; IAM, iodoacetamide; immuno-MALDI, immuno-enrichment coupled MALDI-TOF MS; LOQ, limit of quantification; MALDI-TOF MS, matrix assisted laser desorption ionization-time of flight mass spectrometry; MMP1, matrix metalloproteinase-1; MRM, multiple reaction monitoring; OSCC, oral squamous cell carcinoma; PBS, phosphate buffered saline; SIS, stable isotope-coded internal standard; TCEP, Tris(2-carboxyethyl)phosphinehydrochloride; TFA, trifluoroacetic acid.

* Corresponding author. Molecular Medicine Research Center, Chang Gung University, Taoyuan, Taiwan.

E-mail address: yusong@mail.cgu.edu.tw (J.-S. Yu).

<https://doi.org/10.1016/j.aca.2019.12.006>

0003-2670/© 2019 Elsevier B.V. All rights reserved.

ARTICLE INFO

Article history:

Received 10 August 2019

Received in revised form

19 November 2019

Accepted 1 December 2019

Available online 3 December 2019

Keywords:

Oral cancer

Biomarker

Metalloproteinase-1

Dried saliva spot

Immuno-MALDI

ABSTRACT

Oral cavity cancer is a common cancer type that presents an increasingly serious global problem. Oral squamous cell carcinoma (OSCC) accounts for >90% oral cancer cases. No biomarker tests are currently available for management of this cancer type in clinical practice. Previously, we validated matrix metalloproteinase-1 (MMP1) as one of the most promising salivary biomarkers for OSCC detection. Development of a convenient, rapid and high-throughput assay should further facilitate application of salivary MMP1 measurement for early detection of OSCC. The present study aimed to develop a workflow comprising dry saliva spot (DSS) sampling and immunoenrichment-coupled MALDI-TOF MS (immuno-MALDI) analysis to quantify salivary MMP1. We generated recombinant MMP1 protein and anti-peptide antibodies against MMP1, which were used to optimize the procedures of the entire workflow, including DSS sampling, on-paper protein digestion and elution, KingFisher magnetic particle processor-assisted immuno-enrichment and MALDI-TOF MS analysis. The established workflow was applied to measure salivary MMP1 levels in DSS samples from 5 healthy donors and 9 OSCC cases. The newly developed workflow showed good precision (intra-day and inter-day variations <10%) and accuracy (80–100%) in quantification of MMP1 in DSS samples, with the limit of quantification at 3.07 ng/ml. Using this assay, we successfully detected elevated salivary MMP1 levels (ranging from 5.95 to 242.52 ng/ml) in 7 of 9 OSCC cases while MMP1 was not detectable in samples from the 5 healthy donors. In comparison, the traditional immunoassay was not effective in measuring MMP1 in DSS samples, highlighting the significant advantage of our immuno-MALDI assay. The DSS sampling format confers high flexibility and convenience of collection, storage and delivery of saliva specimens and the KingFisher-assisted immuno-MALDI analysis renders the assay as suitable for high-throughput screening. By combining the two features, the workflow developed in this study should facilitate improvement of molecular diagnostic tests for OSCC using salivary MMP1 as a biomarker.

© 2019 Elsevier B.V. All rights reserved.

1. Introduction

Oral cavity cancer is a common cancer type representing a serious global problem [1,2]. While more than one-third of the new cases and half of the associated deaths are reported in developing countries, the incidence in West has also increased steadily over the past two decades [3–5]. Oral squamous cell carcinoma (OSCC) accounts for more than 90% oral cancer cases. The majority of OSCC cases develop from oral epithelial dysplasia termed oral potentially malignant disorders (OPMD), including erythroplakia, submucous fibrosis, heterogeneous leukoplakia and verrucous hyperplasia, thin homogeneous leukoplakia and lichen planus [6–8]. Although visual inspection of oral mucosa and pathological examination of dysplasia tissue biopsies aid in detection of OSCC, over 60% patients present with stage III and IV disease [9]. Many OPMD lesions comprise a mixture of potentially malignant cells reflecting the field cancerization phenomenon [10,11], leading to considerable discrepancies in interpretation of the same lesion by different clinicians and significant complications of biopsy-based diagnostic procedures [12–14]. These factors make early clinical detection of OSCC a challenge and highlight the urgent medical need for effective novel approaches, such as biomarker tests, that could facilitate early identification of cancer in high-risk OPMD lesions and/or monitoring of malignant transformation. Stage at diagnosis is the key determinant of 5-year survival, with survival rates approaching 80% for OSCC patients with stage I disease and decreasing significantly for those with late-stage disease [15,16].

Over the past two decades, numerous non-invasive biomarker candidates identified in body fluid samples, such as serum/plasma and saliva, have shown potential in early detection and diagnosis of OSCC [17–19]. However, only a few have been carefully evaluated in a large cohort of samples for further validation of their utility. The lack of a rapid, convenient and reliable format of testing for a promising biomarker in an appropriate specimen type presents an obvious bottleneck for successful translation of biomarker candidates in the clinic. Saliva is the most proximal fluid of oral lesions

and can be collected in a relatively non-invasive manner, compared to blood. Thus, accumulating studies have focused on using saliva samples for biomarker discovery and verification of oral cancer [20–22]. For the purpose of convenient storage and delivery, arid saliva may present an attractive format for sample collection on the basis that dry spot sampling of whole blood sample (DBS) has been widely applied in official newborn screening tests for many years [23]. However, limited studies have demonstrated the utility of dry saliva spot (DSS) for detection of drug compounds and metabolites using mass spectrometry (MS)-based approaches [24,25]. To our knowledge, the applicability of DSS in detection of protein biomarkers of disease has not been evaluated to date.

The generation of appropriate reagents/technology platforms for rapid and reliable quantification should provide a further step towards successful application of biomarkers in the clinic. Traditionally, clinical laboratories primarily use enzymatic colorimetric methods for target protein quantification, such as substrate-based activity assays for proteins with enzymatic activity and enzyme-linked immunosorbent assay (ELISA) for non-enzymatic proteins. Recently, MS techniques have been increasingly used as routine procedures in clinical laboratories, such as tandem MS for drug compounds or metabolites and MALDI-TOF for microbiota [26,27]. Over the past decade, the liquid chromatography-coupled multiple-reaction-monitoring MS (LC-MRM-MS) approach has been widely applied for multiplexed and targeted quantification of several proteins in different biofluids, such as plasma, urine and saliva [28–30]. In addition to the LC-based MS approach, combination of immunoenrichment with MALDI-based MS (immuno-MALDI) has recently been developed as a highly sensitive and specific method for high-throughput analysis of samples over a short time-period [31–33].

Matrix metalloproteinase 1 (MMP1, also known as interstitial collagenase), an enzyme that can break down interstitial collagens, is involved in normal physiological and disease processes. Overexpression of MMP1 in OSCC tissues is associated with malignant behavior, such as cervical lymph node metastasis [34], poor survival

[35], poorly differentiated grade [36], recurrence [37], and tumor progression [38]. Elevated salivary MMP1 levels in OSCC patients, compared with healthy donors, have been detected via immunoassay [39,40]. We recently compared the disease-discriminating power of 28 candidate OSCC biomarkers by measuring their concentrations in saliva samples from 460 subjects using the LC-MRM-MS assay, which disclosed MMP1 as one of the most promising salivary biomarkers for OSCC detection [30]. More recently, we produced and characterized anti-peptide mouse monoclonal antibodies (mAb) and developed a peptide immunoaffinity enrichment-coupled LC-MRM-MS assay for quantifying 24 OSCC candidate biomarkers, including MMP1, in saliva samples [41]. To validate the utility of salivary MMP1 as a biomarker in a large cohort of patients from multiple hospitals, we developed a workflow incorporating both DSS sampling and immuno-MALDI for effective measurement of salivary MMP1 in the present study.

2. Materials and methods

2.1. Peptide synthesis and monoclonal antibody production

One proteotypic peptide (DIYSSFGFPR, $m/z = 1188.5684$) for MMP1 (MMP1_HUMAN, P03956) was selected from tryptic peptides as described previously [30,41]. The synthetic (light) peptide was purchased from Kelowna International Scientific (Taipei, Taiwan). Two versions of stable isotope-coded internal standard (SIS) peptides (DIYSSFGFPR, [$^{13}\text{C}_6^{15}\text{N}_4$]Arg-coded, $m/z = 1198.648$; DIYSSFGFPR, [$^{13}\text{C}_6^{15}\text{N}_4$]Tyr- and [$^{13}\text{C}_6^{15}\text{N}_4$]Arg-coded, $m/z = 1208.609$) were purchased from UVic-Genome BC Proteomics Centre (BC, CA) and New England peptide, Inc. (Gardner, MA, US), respectively. Initial MALDI-TOF MS analysis of the [$^{13}\text{C}_6^{15}\text{N}_4$]Arg-coded SIS peptide in a saliva background revealed the existence of a strong interference signal with $m/z = 1197.68$ (Fig. S1). Accordingly, we used the [$^{13}\text{C}_6^{15}\text{N}_4$]Tyr- and [$^{13}\text{C}_6^{15}\text{N}_4$]Arg-coded SIS peptide for developing the quantitative assay. An anti-peptide monoclonal antibody (mAb) against MMP1 proteotypic peptide (DIYSSFGFPR) produced and characterized in a previous study by our group [41] was employed, which possesses high affinity ($K_D = 1.48 \times 10^{-10}$) and peptide-capturing capability (40–50% recovery rate) for its peptide antigen.

2.2. Production of recombinant MMP1 protein

Recombinant human MMP1 protein was produced using the baculovirus-insect cell expression system according to a previously described protocol [42,43]. Human MMP1 cDNA was obtained from transOMIC technologies Inc. (AL, USA). To generate recombinant baculovirus vAc-MMP1-Rhir-EGFP, full-length MMP1 cDNA containing $6 \times \text{His}$ at the C-terminus was generated using the bicistronic vector, pBacMCS-Rhir-EGFP, to obtain pBacMCS-Rhir-EGFP-MMP1-His. The pBacMCS-Rhir-EGFP-MMP1-His transfer vector was co-transfected with BaculoGold™ baculovirus DNA into *Spodoptera frugiperda* IPBL-Sf21 (Sf21) cells and the presence of recombinant virus confirmed via green fluorescent protein expression. Recombinant MMP1 in Sf21 culture medium was purified using Ni-NTA-FPLC according to the manufacturer's protocol (GE Healthcare, IL, US). Eluted fractions containing recombinant MMP1 were collected, dialyzed against storage buffer and stored at -40°C . The purity of intact recombinant MMP1 was determined to be 92%, evaluated via the densitometry analysis of the Coomassie blue-stained SDS-PAGE, and its identity was confirmed by MALDI-TOF MS analysis (Fig. S5).

2.3. Saliva sample collection and dried spot sampling

Saliva samples from five healthy controls and nine OSCC patients were collected in the Chi-Mei Medical Center (Liouying, Taiwan) with the approval of the Institutional Review Board (IRB No. 10408-L06). The study population consist only male subjects because 90% of OSCC patients in Taiwan were males according to a population-based study over a 28-year period [44]. Prior to collection of saliva samples, each subject signed an informed consent form to permit their use for study. Basic information on the 14 subjects is presented in Table S1. The donors were requested to avoid eating, drinking, smoking or using oral hygiene products for at least 1 h prior to collection, and unstimulated whole saliva was collected as described previously [30,45]. All samples were centrifuged at $3000 \times g$ for 15 min at 4°C to remove cells and debris. The supernatant fractions were treated with a protease inhibitor cocktail (Cat. No. 11836145001; Sigma, MO, US) and stored at -80°C . For dried spot sampling, an aliquot of 25 μl saliva was spotted on one circle (half-inch in diameter) of filter paper (903 Protein Saver Card, Whatman, UK) once, followed by drying for 30 min at room temperature. The collection cards were bent to facilitate drying of saliva-soaked filter paper and prevent loss caused by contact with the wrapper before drying. For immuno-MALDI analysis, 100 μl saliva sample from each subject was spotted sequentially on two circles of filter paper card. After spotting 25 μl saliva on each circle, the arid circle was re-spotted with another 25 μl saliva sample and dried for a further 30 min. Dried cards were folded within their wrappers and stored at room temperature.

2.4. Immobilization of antibodies on protein G magnetic beads

To immobilize antibodies on protein G magnetic beads, a cross-linker reagent, disuccinimidyl suberate (Thermo Scientific, MA, US), was applied to promote an amine coupling reaction between antibody and protein G beads according to the manufacturer's protocol. The anti-peptide monoclonal antibody against MMP1 used in this study had been produced and characterized earlier by our group [41]. Briefly, a 1 ml slurry of protein G magnetic beads (Protein G Mag Sepharose Xtra, GE Healthcare) was washed twice with phosphate buffered saline (PBS) and incubated with 100 μg antibody in a microtube placed on a rotator (Intelli-Mixer RM-2L, ELMI, LV) for 30 min at room temperature. Antibody-bound beads were collected using a magnet and the supernatant removed. Collected beads were conditioned in 100 mM sodium phosphate and 150 mM sodium chloride (pH 7.0) and incubated with the cross-linker reagent (final concentration of 200 μM) for 30 min at room temperature. The reaction was quenched by replacing the supernatant with an equal volume of 1 M Tris-HCl (pH 7.5) buffer. Beads were washed once with quenching buffer and twice with PBS. Antibody-coupled beads were stored in PBS at 4°C until use. For each immunoenrichment experiment, 10 μl slurry of protein G magnetic beads bound with $\sim 1 \mu\text{g}$ antibody was used to capture the target peptide in each sample.

2.5. Tryptic digestion and desalting of saliva samples

Digestion and desalting of saliva samples were performed according to previous protocols [41,46]. Briefly, 25 μl saliva sample was diluted with an appropriate amount of 100 mM Tris-HCl (Sigma) containing 5% (w/v) sodium deoxycholate (DOC; Sigma) and boiled for 5 min. Denatured proteins were reduced by 30 min incubation with 5 mM Tris(2-carboxyethyl)phosphinehydrochloride (TCEP; Sigma) at 60°C and alkylated via 30 min incubation with 10 mM iodoacetamide (IAM; Sigma) at 37°C in the dark. The

resulting mixture was diluted 3-fold with 100 mM Tris-HCl and digested with 1 μ g trypsin (Proteomics Grade Trypsin; Agilent, CA, US) at 37 °C overnight. The reaction was terminated by boiling the sample for 15 min. An appropriate amount of SIS peptide was added to the digested samples, followed by further acidification with trifluoroacetic acid (TFA; Alfa Aesar, MA, US) (final concentration of 0.2%) and formic acid (FA; J.T. Baker, NJ, US) (final concentration, 0.4%) to precipitate DOC. Precipitated DOC was removed via centrifugation at 15,000 \times g for 30 min. The supernatant was desalted via solid-phase extraction (Oasis HLB plate 2 mg/96-well, Waters MA, US) using the procedure described below. The plate was equilibrated using a decreasing concentration gradient (100%, 75%, 30%, and 3%) of acetonitrile (ACN; J.T. Baker, NJ, US) with 0.1% TFA. The sample was loaded onto the column and passed through twice, followed by washing the column twice with a solution of 3% ACN/0.1% TFA. Bound peptides were eluted twice with 100 μ l 75% ACN/0.1% TFA. Eluted fractions containing digested and SIS peptides were lyophilized using a spin vacuum and stored at –20 °C until use.

2.6. On-paper digestion and peptide elution of DSS

For on-paper digestion of salivary proteins, the tryptic digestion protocol was modified as specified below. Entire circles containing dried saliva were punched from the protein saver card. Two circular punches containing the dried contents of 100 μ l saliva were placed in a microtube, immersed in 400 μ l solution comprising 260 μ l of 100 mM Tris-HCl pH8.5, 100 μ l of 20% (w/v) DOC, and 40 μ l of 50 mM TCEP, and further incubated for 30 min at 60 °C followed by a 5-min sonication period. Denatured proteins were further alkylated by adding 44.5 μ l 100 mM IAM for an additional 30 min incubation period at 37 °C. The DOC concentration was adjusted to <1% with the addition of 1360 μ l of 100 mM Tris-HCl. The sample was digested with 4 μ g trypsin dissolved in 0.1% formic acid (1 μ g/ μ l) at 37 °C overnight. Next, the reaction was terminated by boiling the sample for 15 min and the solution harvested. Filter papers containing peptide residues were further centrifuged at 860 \times g for 1 min using a home-made cartridge as shown in Fig. S2. An additional centrifugation step was performed after rehydrating the filter paper with 30 μ l of 100 mM Tris-HCl or 40%ACN/1% TFA solution in the indicated experiments and pooled with the reaction solution. Digested peptides were further spiked with SIS peptides and desalted as described above.

2.7. Peptide quantification

The Pierce Quantitative Colorimetric Peptide Assay kit (Thermo Scientific) was used to evaluate peptide concentrations. Serially diluted standards (125, 62.5, 31.3, 15.6, 7.8 and 0 μ g/ml) and working reagent (Reagent A, B and C mixed at a 50:48:2 ratio) were prepared as described by the manufacturer. Lyophilized saliva sample digests were dissolved in 20 μ l of 50% ACN, and 0.5 μ l dissolved sample was acquired and diluted to a volume of 20 μ l for quantification of the peptide concentration. Serially diluted standards and individual samples (20 μ l each) were added into wells of 96-well microplate and mixed with 180 μ l working reagent using an 8-channel pipette. The plate was mixed thoroughly on a plate shaker for 1 min and incubated at 37 °C for 15 min. Absorbance at 480 nm for each well was measured using a spectrophotometer (SpectraMax M5, Molecular Devices, USA) and used to calculate the peptide concentration of each sample based on the standard curve.

2.8. Automatic enrichment of target peptides using antibody-coupled magnetic beads

A KingFisher magnetic particle processor system (KingFisher™ Flex Purification System, Thermo Fisher Scientific) was used for automated handling of magnetic beads [47]. The automatic process involving peptide binding, washing and elution steps was operated as described previously [41]. Briefly, antibody-coupled magnetic beads (containing ~1 μ g mAb) were suspended in 200 μ l PBS containing 0.03% 3-[(3-cholamidopropyl)dimethylammonio]-1-propanesulfonate (CHAPS; USB Corp., OH, US). Beads were washed on plate 1 and automatically transferred to plate 2 containing the digested samples in 100 μ l PBS/0.03% CHAPS. Lyophilized samples were rehydrated with 20 μ l of 50% ACN, vortexed for 15 min, and diluted with 80 μ l PBS/0.03% CHAPS. The mixture of antibody-coupled beads and digested sample on plate 2 was agitated using tip comb for 2 h. After the immunocapture step, peptide-bound beads were washed three times on plates 3, 4 and 5 containing 200 μ l PBS (plates 3 and 4) or 0.1x PBS (plate 5). Bound peptides were eluted with 50 μ l of 5% acetic acid (J.T. Baker, NJ, US) and 70% ACN on plate 6 and collected for lyophilization. For further clean-up of undesired antibody, a home-made tip column packed with 2–3 μ l Alkyl-DIOL-Silica (ADS) beads (LiChrospher ADS; Millipore, MA, US) was applied for separation of peptides from antibody molecules. Columns were equilibrated using a decreasing concentration gradient (100%, 75%, 30%, and 3%) of ACN with 0.1% TFA. Immuno-enriched products were loaded onto the column and passed through twice via centrifugation at 500 rpm, followed by washing of the column twice with a solution of 3% ACN/0.1% TFA. Bound peptides were eluted twice with 30 μ l of 75% ACN/0.1% TFA. Eluted peptides were lyophilized and stored at –20 °C for further MALDI-TOF analysis. To examine the immunoaffinity efficiency, a model sample containing 500 fmol synthetic light peptide in digested saliva matrix from healthy donor was subjected to automatic enrichment of the target peptide using antibody-coupled magnetic beads. After immunoaffinity enrichment step, the eluted sample was spiked with 100 fmol heavy peptide and subjected to MALDI-TOF analysis for measuring the amount of the recovered light peptide. The recovery rate of the light peptide was calculated and used to evaluate the immunoaffinity efficiency.

2.9. Combinational curve of pure peptide for MALDI-TOF analysis

The combination curve was prepared according to the protocol of Anderson et al. [48]. Light (L) and heavy (H) peptides were initially prepared at a concentration of 500 fmol/ μ l, and different ratios of L and H generated by intermediate dilutions in which equal volumes of two prior solutions were mixed that created a concentration precisely halfway between the two concentrations of input solution while maintaining a constant total amount of peptide (L + H). The stepwise combinations generated the first 11-point curve including L/H ratios of 10, 4.18, 2.38, 1.51, 1.23, 1, 0.81, 0.66, 0.42, 0.24 and 0.1 while the total L + H amount was 110 fmol/ μ l, serving as Curve one (Table S2). The other descending curves were yielded by 5-fold serial dilution of each concentration point, with the total L + H amounts being 22, 4.4, and 0.88 fmol/ μ l for Curves 2, 3, and 4, respectively. For MALDI analysis, 2 μ l individual concentration points were dotted on the AnchorChip plate. All quantifications were performed in triplicate.

2.10. Reverse response curves of synthetic peptide spiked in saliva for immuno-MALDI analysis

A wider dynamic range was explored in the reverse response curve as described previously [41,47,48]. The curve was generated

by directly spiking various amounts of heavy peptide (200, 100, 50, 25, 12.5, 6.25, 3.13, 1.56 and 0 fmol) along with a constant amount of light peptide (100 fmol) into a matrix sample (digest generated from 100 μ l saliva). Triplicate aliquots of each point of the curve were independently processed for immuno-MALDI analysis. Samples eluted from immuno-enrichment were desalted via solid-phase extraction (Oasis HLB plate, 2 mg/96-well) as described previously, followed by MALDI-TOF quantification. The lowest point of the response curve quantified with CV% of triplicate less than 20% and accuracy in the range of 80–120% was defined as the limit of quantification (LOQ). The concentrations (ng/mL) of LOQ were determined as the observed levels (i.e. fmol) multiplied by the molecular weight (54,007 Da) over the volume of 100 μ l saliva.

2.11. MALDI-based mass spectrometry analysis

MALDI spectra were acquired in the positive ion mode using an Ultraflex TOF/TOF mass spectrometer (Bruker Daltonics, Bremen, Germany). Briefly, lyophilized samples were rehydrated with 10 μ l of 50% ACN by vortexing on a rotator for 15 min, followed by dotting 1–2 μ l on an MTP AnchorChip TM 600/384 TF target plate (Bruker Daltonics). After samples had dried on the plate, 0.2 μ l α -cyano-4-hydroxycinnamic acid (CHCA) matrix (2 mg/ml CHCA in 70% ACN/0.5% TFA)-containing internal mass standard peptides were dotted onto each sample. All spectra were automatically acquired over a mass range of 600–4000 Da in the positive-ion reflector mode with 25% laser power and a total of 1000 shots of laser desorption were accumulated. Mass accuracy was calibrated before sample data acquisition using the four internal mass standard peptides [Sar1, Thr8]-angiotensin II (956.53 Da), angiotensin I (1296.69 Da), renin substrate tetradecapeptide (1758.93 Da) and adrenocorticotrophic hormone (fragment 18–39, human; 2465.20 Da). Data were analyzed using FlexAnalysis v2.4 (Bruker Daltonics) and DataAnalysis v4.3 (Bruker Daltonics) software for automatic baseline subtraction, peak detection, re-calibration and peak area calculation. The criteria for peak detection were as follows: signal-to-noise ratio > 5, peak width > 0.1 m/z , and maximum picking number of peak as 100. According to accurate mass measurement with 100 ppm tolerance, the target peptide was automatically retrieved from the peak list with a VBA script executed in Excel software.

2.12. Quantification of MMP1 in DSS and liquid saliva samples via bead-based suspension immunoassay

The concentrations of MMP1 in saliva samples were determined with a Luminex multiplex assay kit (R&D Systems, MN, US) in keeping with the manufacturer's protocol. Procedures were performed automatically with filter-bottom 96-well microplates (Millipore, MA, US) operated using vacuum manifold. At the end of the reactions, beads were suspended in assay buffer and analyzed using the Bio-Plex 200 system (Bio-Rad Laboratories, CA, US). The detection range was 23.87–17400 pg/ml, and DSS and liquid saliva were analyzed based on 8-fold and 80-fold dilution, respectively. For eluting proteins from DSS samples, the circular punches of protein saver cards containing dried proteins were placed in a microtube, immersed in 400 μ l solution containing PBS and 1% Tween 20, and further incubated for 1 h at 4 °C with constant agitation. The solution was harvested from the tube, transferred to a new tube, and centrifuged at 860 \times g for 1 min. The resulting supernatant was collected and subjected to immunoassay.

2.13. LC-MRM mass spectrometry

A nanoACQUITY HPLC system equipped with a nanoACQUITY UPLC C18 column (100 μ m \times 100 mm, 1.7 μ m particle size; Waters,

MA, US) was employed for liquid chromatography (LC) separation. Resolved fractions were applied to an AB/MDS Sciex 5500 QTRAP (AB Sciex, Singapore) with a nano-electrospray ionization (ESI) source controlled by Analyst 1.5.1 software (AB Sciex). Lyophilized samples were rehydrated in 4 μ l of 0.1% FA by vortexing on a rotator for 15 min and injected into the C18 resolving analytical column at a flow rate of 0.6 μ l/min in 99% buffer A (0.1% FA in H₂O) and 1% buffer B (0.1% FA in ACN) for 15 min. Samples were separated at a flow rate of 0.4 μ l/min with a 38 min linear gradient (3–22% buffer B), a 5-min linear gradient (22–30% buffer B), and a final 2 min linear gradient (30–95% buffer B). Multiple reaction monitoring (MRM) acquisition methods developed in our previous studies were applied [30,41]. The instrument setting of acquisition methods: ion spray voltage, 2300 V; curtain gas setting, 20 psi (UHP nitrogen); interface heater temperature, 150 °C; auto-sampler temperature, 4 °C; MS operating pressure, 1.1×10^{-5} Torr; Q1 and Q3 were set to unit resolution (0.6–0.8 Da full width at half height). All MRM data were processed using Skyline software.

2.14. Statistical analysis

Correspondence of peak area ratio to concentration ratio was calculated via linear regression with a standard $1/x$ (x = concentration ratio) weighting option, a commonly used method for establishment of the calibration curve [29]. Correlation of quantitative results between two methods (such as MALDI-TOF vs. LC-MRM and protein concentration vs. peptide concentration) was evaluated with linear regression based on R^2 and p values. Regression of the experimental to theoretical concentration was performed using the second-order polynomial (quadratic) fitting method, which was generated from the reverse response curve of immuno-MALDI analysis and further applied for quantitative calculations. Technical variations of measurements in triplicate were calculated as the coefficient of variation (CV) percentage defined as standard deviation (SD)/mean of triplicate experiments.

3. Results

3.1. Study design

To develop an accurate, high-throughput quantitative assay for salivary MMP1 appropriate for room temperature saliva storage and shipping, we developed a workflow combining DSS sampling and immuno-MALDI analysis. A schematic presentation of the strategy used is shown in Fig. 1. We initially assessed the precision and accuracy of MMP1 peptide quantification using MALDI-TOF MS and subsequently evaluated the performance of automatic immuno-enrichment of MMP1 peptide from a saliva background matrix using magnetic bead-coupled anti-peptide mAb and the KingFisher magnetic particle processor. Subsequently, we examined the optimal conditions for DSS sampling, on-paper protein digestion and elution, and quantification of MMP1 peptide eluted from DSS using KingFisher-assisted immuno-MALDI. The optimized protocol was finally applied to assess MMP1 levels in DSS samples prepared from several healthy donors and OSCC patients. Moreover, the performance of our newly developed immuno-MALDI was compared to that of traditional immunoassay for quantifying MMP1 in DSS samples.

3.2. Precision and accuracy of MMP1 peptide quantification via MALDI-TOF MS

To assess the precision and dynamic range of MALDI-TOF analysis, a series of 11 mixtures in which the ratio of unlabeled light (L) and stable isotope-labeled heavy (H) versions of proteotypic

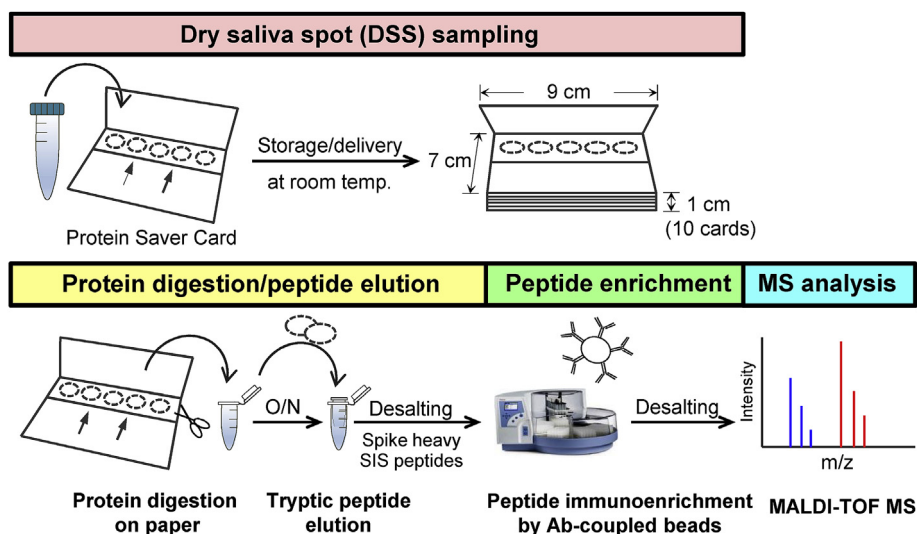


Fig. 1. Workflow of DSS sampling combined with immuno-MALDI for measuring salivary MMP1 in clinical specimens. Please refer to the text for details.

peptide (DIYSSFGFPR) of MMP1 varied from 1:10 to 10:1 were measured using MALDI-TOF MS. While the total amount of light and heavy peptides remained constant for each point, determined as 110, 22, 0.44, and 0.088 fmol for the four curves, the L/H peptide ratios in the 11 curve points were 10, 4.18, 2.38, 1.51, 1.23, 1, 0.81, 0.66, 0.42, 0.24 and 0.1. Spectra of light and heavy peptides at an adjusted equimolar ratio (1:1) are shown in Fig. 2a. The preparation

of different combinations of L and H peptides for curve 1 (110 fmol total peptide) is described in supplementary Table S2. The other three curves were serially 5-fold diluted from curve 1. The L/H peak area ratios of individual points of the four curves measured using the reflector mode are shown based on the light peptide content (Fig. 2b). Samples of each data point were applied to 3 spots on the target plate for triplicate quantification and the coefficient of

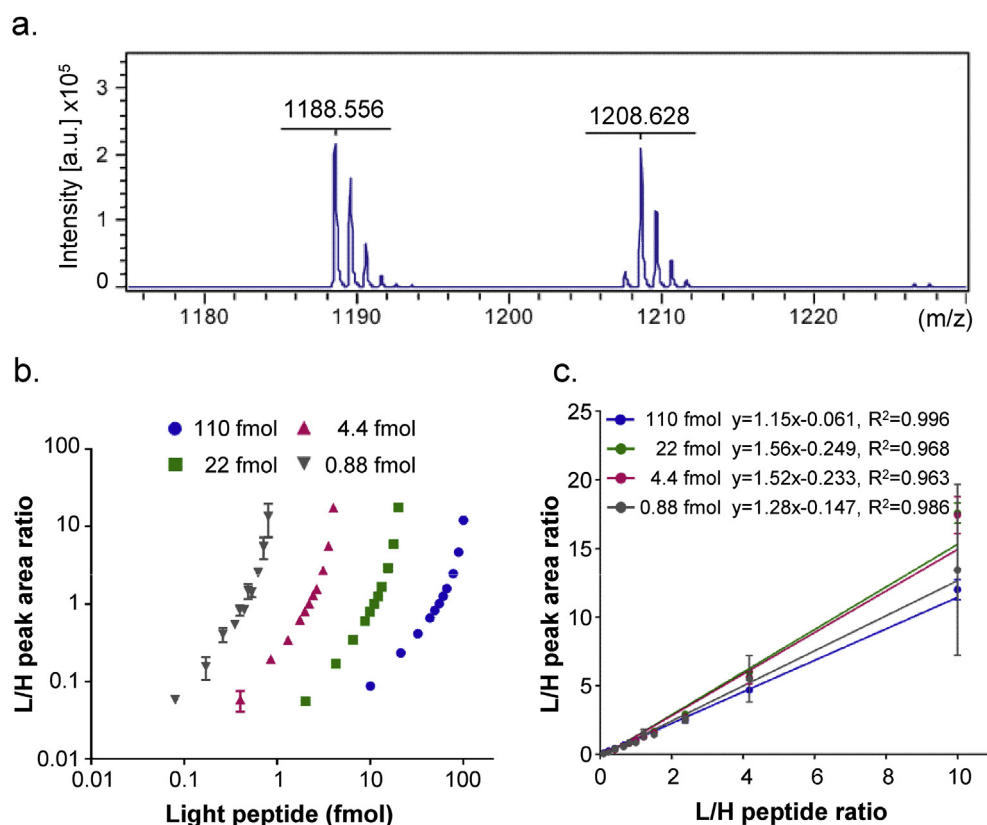


Fig. 2. Detection of target peptides with the reflector mode of MALDI-TOF MS. (a) Spectra of light peptide (left peak, $m/z = 1188.556$) and stable isotope-labeled heavy peptide (right peak, $m/z = 1208.628$) at adjusted equimolar amounts are presented. (b) Each of the four combination curves contained 11 samples in which the L/H ratios were 10, 4.18, 2.38, 1.51, 1.23, 1, 0.81, 0.66, 0.42, 0.24 and 0, respectively, while the combined amount of light and heavy peptide remained constant in each curve (110, 22, 0.44, and 0.088 fmol). Error bars are not shown for some data points because they were shorter than the height of the symbol. (c) Regression curves were generated via linear regression with a standard $1/x$ (x = concentration ratio) weighting option, which assists with better fitting at the lower concentration of target peptide.

variation (CV%) calculated to establish the precision of quantification (Fig. S3a). CV% values of most data-points on the three curves (110, 22, and 0.44 fmol) were <10%, and for the fourth curve (0.088 fmol), CV% values of the central 7 data-points were near or less than 20%. Our results collectively indicate that MALDI-TOF MS analysis can be successfully applied to precisely measure the peptide signal from the lowest concentration of 0.26 fmol (L amount at L/H = 0.42, H amount at L/H = 2.38 on the fourth curve) to the highest concentration of 100 fmol (L amount at L/H = 10, H amount at L/H = 0.1 on the first curve).

To determine the performance of MALDI-TOF MS in quantification, regression curves were generated via linear regression with a standard $1/x$ (x = concentration ratio) weighting option (Fig. 2c), and the accuracy of the experimental L/H peak area ratio to theoretical L/H peptide ratio calculated (Fig. S3b). The slope and coefficient of determination (R^2) generated from the four curves ranged from 1.15 (110 fmol) to 1.56 (22 fmol) and 0.963 (4.4 fmol) to 0.996 (110 fmol), respectively (Fig. 2c). The accuracy of the entire range of the first curve (110 fmol) and central 7 points of the other three curves remained within 80–120% of the expected L/H ratio (Fig. S3b). Overvalued and undervalued peak area ratios were obtained from the terminal regions (top and bottom ends) of the curves (Fig. S3c). Representative spectra of the terminals of the four curves are presented in Fig. S4. These results suggest that extreme light to heavy ratio causes inaccurate quantification, especially in samples containing target peptide at concentrations lower than 10 fmol.

3.3. Immunoaffinity enrichment-coupled MALDI-TOF MS assay

To generate a high-throughput quantification assay for MMP1, we attempted to establish an immunoaffinity enrichment-coupled MALDI-TOF MS (immuno-MALDI) assay. The target peptide derived from trypsin-digested MMP1 protein was enriched and purified from a complex background of biological samples using an anti-peptide antibody for MALDI-TOF MS. We initially produced a His-tagged recombinant MMP1 protein using the baculovirus-insect cell expression system, which was purified to near-homogeneity using the Ni-NTA-FPLC column (Fig. S5). A model sample (60 ng recombinant MMP1 protein spiked in 100 μ l saliva sample from healthy donors) was digested with trypsin and the target peptide enriched using antibody-conjugated protein G-magnetic beads. As expected, the target peptide signal was clearly observed in the enriched sample (Fig. 3b) but not the unenriched sample (Fig. 3a). To optimize the immunoaffinity enrichment protocol, we evaluated the peptide-capturing recovery rates of three different magnetic beads (M280, anti-mouse IgG dynabeads; Dyna, protein G dynabeads; GE, protein G beads purchased from GE Comp.) in the two following formats: non-covalent and covalent conjugation with the same amount of anti-peptide antibody. For the covalent coupling reaction, minimal loss of antibody through a series of steps (antibody binding, disuccinimidyl suberate reaction, and quenching reaction) was demonstrated via SDS-PAGE (Fig. S6a). To examine the peptide capturing capability of antibody-bound/conjugated beads, 500 fmol synthetic light peptide spiked into 1 μ g saliva digest was affinity-captured using the antibody-bead complex (10 or 20 μ l) and measured via MALDI-TOF MS with 100 fmol heavy peptide as a reference standard (Fig. 3c). For non-covalent antibody-bound beads, higher volumes of beads were used to obtain a higher recovery rate of the spiked peptide. The covalent coupling reaction led to a reduction in the target peptide recovery rate in all three bead types, potentially resulting from partial disruption of antibody caused by chemical reaction of covalent conjugation (Fig. 3c). Notably, target peptide captured by antibody-coupled GE beads displayed a higher peak area signal (Fig. S6b) and signal-to-

noise ratio (Fig. S6c), compared to that among the three types of beads and between non-covalently conjugated and covalently coupled beads. To standardize the sample preparation process for future clinical applications, covalently coupled beads could be prepared once and divided into aliquots prior to long-term experiments. Therefore, we proposed a format of 10 μ l GE beads conjugated with 1 μ g anti-peptide antibody as the affinity reagent for target enrichment, which yielded a $32.2 \pm 4.3\%$ recovery rate against MMP1 peptide (Fig. 3c).

To characterize the performance of this immuno-MALDI assay for verification of MMP1 in saliva samples, a reverse response curve was constructed that included a series of heavy-to-light peptide ratios (2, 1, 0.5, 0.25, 0.125, 0.0625, 0.03125, 0.015625, 0) in a background of 100 μ l saliva digest, followed by analyses as described in Materials and methods. The heavy peptide signals were detected on points of the curve ranging from 6.25 to 200 fmol. Representative spectra of each data-point are shown in Fig. S7. Due to limitations of non-linear dynamic range detection using MALDI-TOF, we employed the second-order polynomial (quadratic) fitting method to calculate regression of the peak area to peptide ratio, which presented an excellent coefficient of determination ($R^2 = 0.999$) (Fig. 3d). Based on the fitting formula, the adjusted peak area ratio precisely (CV% <15%) reflected the theoretical heavy to light peptide ratio with accuracy of 90.89–112.90% (Table S3). Based on the limit of quantification (LOQ) defined as the lowest concentration point with CV% <20% and accuracy in the range of 80–120%, a value of 5.68 fmol was obtained, representing 3.07 ng/ml MMP1 protein, for the newly developed immuno-MALDI-TOF assay.

3.4. Sample preparation of dried saliva spots for MS-based analysis

In addition to high-throughput MALDI-TOF MS analysis, a convenient format of saliva sample collection for storage and transport, such as the dried saliva spot (DSS) sampling method, should facilitate effective application of biomarker tests in clinical practice. To this end, we examined three procedures for elution of blotted proteins from filter paper and protein digestion. First, proteins were eluted with Tris-HCl buffer and digested in tube. Second, proteins were eluted with 40% ACN/1% TFA and digested in tube. Third, proteins were digested on filter paper and subsequently eluted with 40% ACN/1% TFA. Afterwards, samples were directly subjected to LC-MRM-MS to evaluate the protein recovery rate. Compared to the amount of spike-in recombinant MMP1 protein (60 ng), the digestion efficiencies of the three procedures and in-solution digestion were calculated as $62.1 \pm 3.8\%$, $63.1 \pm 1.4\%$, $70.5 \pm 3.6\%$, and $90 \pm 0.2\%$, respectively (Fig. 4a, **bottom panel**). When the amount of MMP1 detected from in-solution digestion was taken as 100% (control), the recovery rates of the three procedures were determined as 69%, 70%, and 78%, respectively (Fig. 4a, **upper panel**).

Since the protein concentration in saliva samples (~ 0.3 – 3μ g/ml) is markedly lower than that in serum/plasma samples (~ 70 – 150μ g/ml), the protein amount in 25 μ l saliva absorbed on one circle of the protein saver card may be insufficient for usage in the biomarker test. Accordingly, we assessed the possibility of repeated blotting on one arid spot. A model sample containing 60 ng recombinant MMP1 protein in 100 μ l saliva collected from a healthy donor was blotted on four spots (25 μ l per circle), two spots (50 μ l per circle, blotted twice) and one spot (100 μ l per circle, blotted four times). The dried saliva samples were digested on filter paper and eluted with 40% ACN/1% TFA for LC-MRM-MS analysis. Under the three experimental conditions, we observed $74.5 \pm 1.6\%$, $76.5 \pm 2.2\%$, and $74 \pm 5.2\%$ digestion efficiency, respectively, relative to $91.5 \pm 1.0\%$ efficiency of in-solution digestion (control) (Fig. 4b, **bottom panel**). Different spot numbers of the same sample had no

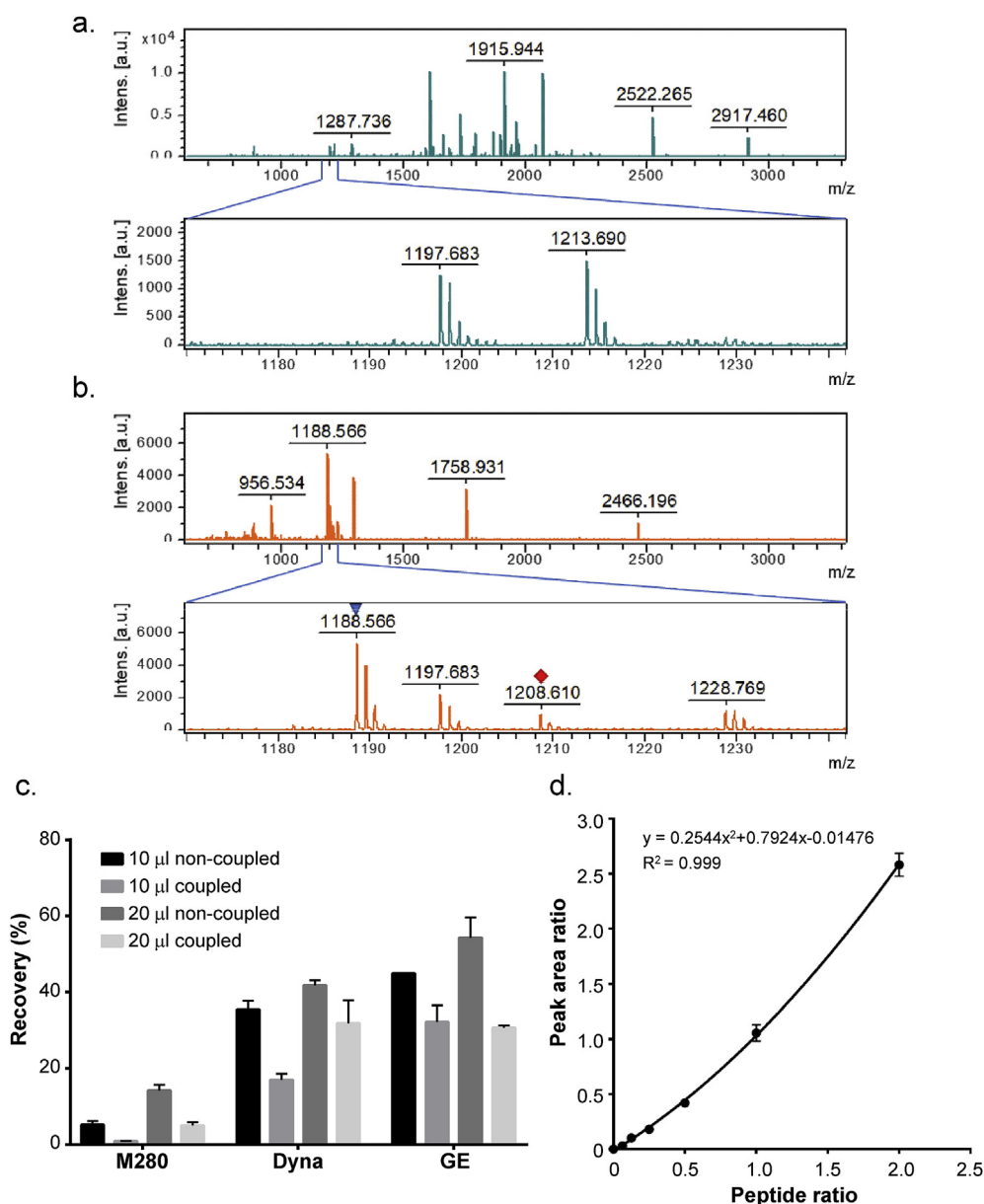


Fig. 3. Immunoaffinity enrichment of target peptide for detection via MALDI-TOF MS. (a, b) A model sample (60 ng recombinant MMP1 protein spiked in a 100 µl saliva sample from healthy donors) was digested with trypsin and subsequently analyzed either directly (a) or after immunoaffinity enrichment using an anti-peptide antibody (b). The blue inverted triangle indicates the monoisotopic peak of the light peptide and the red rhombus indicates the peak of the heavy peptide. Three different magnetic beads (M280, anti-mouse IgG dynabeads; Dyna, protein G dynabeads; GE, protein G beads purchased from GE Comp.) were used for non-covalent conjugation (non-coupling) and covalent coupling while 1 µg antibody was mixed with 10 µl or 20 µl bead slurry. (c) Based on the initial input amount of 500 fmol synthetic light peptide, enriched peptide was quantified and the recovery rate (%) further calculated. (d) Reverse response curve showing regression between peak area ratio and peptide ratio using the second-order polynomial (quadratic) fitting method. The R^2 value represents the coefficient of determination. (For interpretation of the references to color in this figure legend, the reader is referred to the Web version of this article.)

significant effects on digestion efficiency (Fig. 4b, upper panel). Based on the collective data, we conclude that the protocol incorporating 100 µl saliva samples blotted on two spots (50 µl per circle, blotted twice), digested on paper and eluted from paper with 40% ACN/1% TFA is optimal for MS-based quantification of MMP1 protein in the DSS format.

3.5. Applicability of the immuno-MALDI assay for quantification of MMP1 in DSS samples

According to the optimized procedure described above, serially diluted MMP1 protein (120, 60, 30, 15, and 7.5 ng) spiked in 100 µl

saliva samples was blotted on the protein saver card and processed for immuno-MALDI analysis. As shown in Fig. 5a, levels of MMP1 were measured as 5.6 ± 0.6 , 9.5 ± 1.2 , 23.0 ± 0.7 , 44.7 ± 1.1 , and 82.3 ± 1.1 ng, which increased in a dose-dependent manner with good recovery of quantification (63.5–76.5%), and coefficients of variation (CV) of quantification conducted in triplicate were 1.3%, 2.5%, 3.3%, 2.0%, and 10.0%, respectively. To evaluate pre-analytic variations (target stability during storage), a model sample (50 ng MMP1 protein in 100 µl saliva) was spotted on the saver card, stored at ambient temperature for 1, 2, 4, and 8 days, and processed for immuno-MALDI analysis (Fig. 5b). MMP1 levels were quantified as 33.7 ± 1.1 , 36.0 ± 1.7 , 32.3 ± 2.1 , and 33.2 ± 2.5 ng, indicating good

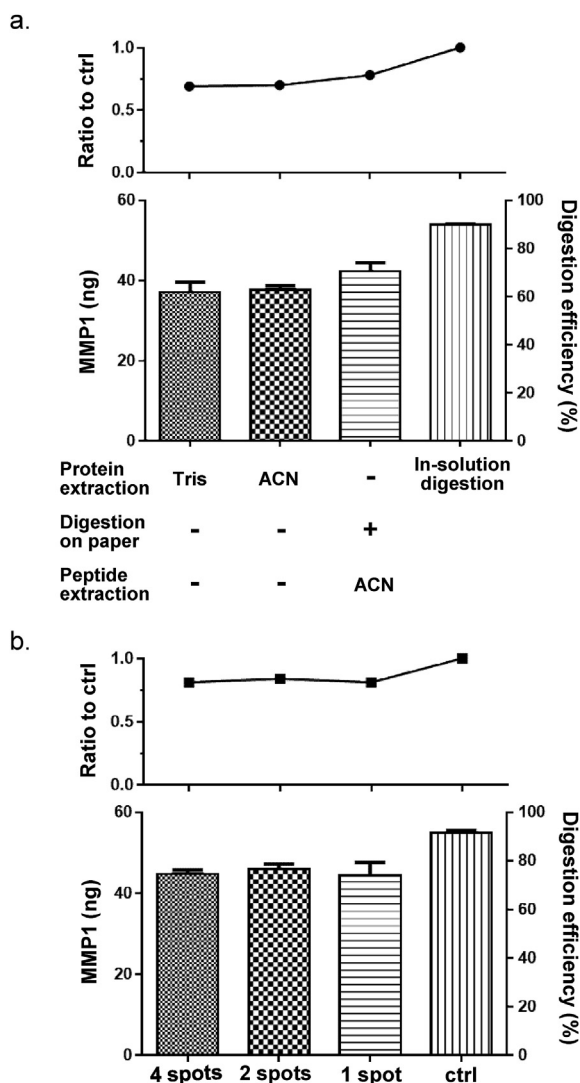


Fig. 4. Assessment of protein elution and blot conditions for DSS samples. A model sample containing 60 ng recombinant MMP1 protein in 100 μ l saliva from healthy donors was prepared for further investigation. **(a)** Aliquots of saliva (25 μ l) were blotted on circles of filter paper (protein saver card) and the dried saliva spots processed using different procedures. (i) Dried salivary proteins were eluted from filter paper with Tris-HCl buffer and digested in tube. (ii) Dried salivary proteins were eluted from filter paper with 40% ACN/1%TFA and digested in tube. (iii) Dried salivary proteins were digested on filter paper and subsequently eluted with 40% ACN/1%TFA. In-solution digestion of liquid saliva sample served as the control (ctrl). **(b)** Aliquots of saliva (100 μ l) were blotted on 4 spots (25 μ l per circle), 2 spots (50 μ l per circle, blotted twice) or one spot (100 μ l per circle, blotted 4 times). Digests of the indicated samples were mixed with 200 fmol heavy peptide before DOC elimination and desalting. All tests were performed in triplicate and subjected to MRM analysis.

stability in the dried spot sample after storage for different time intervals. The recovery of quantified protein ranged from 61.7 to 75.4%, and intra-day and inter-day CV values were 4.4 ± 2.3 and 4.6% , respectively. Our findings clearly indicate that DSS sampling coupled with immuno-MALDI assay is stable and feasible for MMP1 quantification, with $>60\%$ recovery of protein.

Since SIS peptides were spiked prior to immuno-enrichment and subsequently co-precipitated with endogenous digested peptide, loss of target peptide (recovery $\sim 60\text{--}75\%$) may be significantly attributable to digestion and elution efficiency. To address this issue, three saliva samples (in liquid or DSS format) with spiked MMP1 (20, 40 or 80 ng/ml) were subjected to MMP1 immuno-MALDI assay (Fig. 5c). The MMP1 quantity was estimated as

15.21 ± 0.64 , 24.20 ± 0.39 , and 54.73 ± 2.43 ng/ml in DSS samples and 14.04 ± 2.13 , 29.40 ± 5.45 , and 60.24 ± 1.80 ng/ml in liquid samples, respectively (Fig. 5c). The results suggest that the digestion efficiency may contribute to underestimation of MMP1 quantification in liquid saliva samples and efficiency of elution could further reduce the MMP1 content measured in DSS samples.

Additionally, we examined the capability of the immunoassay to measure MMP1 protein eluted from the three DSS samples. MMP1 levels measured via immunoassay in the three liquid saliva samples were used as positive controls. As shown in Fig. 5d, the bead-based suspension immunoassay could be effectively applied to measure MMP1 in the three liquid saliva samples in a dose-dependent manner (6.83 ± 0.39 , 21.25 ± 1.48 , and 45.04 ± 1.15 ng/ml). However, the immunoassay could detect significantly lower levels of MMP1 eluted from the three DSS samples (0.64 ± 0.01 , 1.57 ± 0.13 , and 2.94 ± 0.29 ng/ml). Clearly, the immuno-MALDI assay developed in this study outperforms the immunoassay in terms of MMP1 quantification in DSS samples.

3.6. Quantification of MMP1 in clinical samples using DSS and immuno-MALDI assay

Next, we applied the optimized DSS-coupled immuno-MALDI protocol to measure MMP1 levels in clinical samples. Saliva samples from 5 healthy donors (cases 1–5) and 9 OSCC patients (cases 6–14) were collected, and 100 μ l of each sample blotted on protein saver cards (50 μ l per circle, blotted twice) in triplicate. The MMP1 protein was efficiently detected in 7 of the 9 OSCC samples ($5.95\text{--}242.52$ ng/ml) in triplicate but not in all 5 samples from healthy donors (Table 1), consistent with our previous findings [30,41]. We further measured the protein concentration (before blotting) and peptide concentration (after digestion and elution) of each saliva sample, and observed a significant correlation between protein and digested peptide ($R^2 = 0.914$, Fig. S8a), suggesting that this technique provides a feasible way to evaluate the sample quality of DSS in clinical practice without the requirement for any additional processes before blotting saliva on saver cards. In addition to MALDI-TOF, all immuno-enriched samples were simultaneously analyzed using the LC-MRM platform. As expected, the concentrations of MMP1 quantified with MALDI-TOF and LC-MRM were highly correlated ($R^2 = 0.989$, Fig. S8b). Representative spectra of quantifications in triplicate are shown for both MALDI-TOF (Fig. S9) and LC-MRM (Fig. S10) analyses. The results clearly validate the applicability of the DSS-coupled immuno-MALDI assay for MMP1 quantitation in clinical samples.

4. Discussion

Saliva is a useful body fluid for biomarker-based detection of OSCC [20–22]. To our knowledge, most OSCC-related investigations to date have used frozen saliva as the study material. Here, we demonstrated for the first time that in combination with immuno-MALDI technology, the DSS format can be employed to precisely measure the level of MMP1, a promising recently validated salivary biomarker for OSCC [30,40]. The advantages of using DSS in OSCC salivary biomarker research, such as significantly reducing the requirement for storage and shipping of saliva specimens, provide considerable flexibility for application in the biomarker test.

In recent years, the immuno-MALDI technology has been applied to develop quantitative assays for targets with important clinical implications. For example, Mason et al. successfully developed a duplex immuno-MALDI assay to detect angiotensin I and angiotensin II in plasma [31], and applied such assay to measure plasma renin activity in clinical samples [49]. Similarly, Razavi et al. applied this technology to the measurement of a surrogate

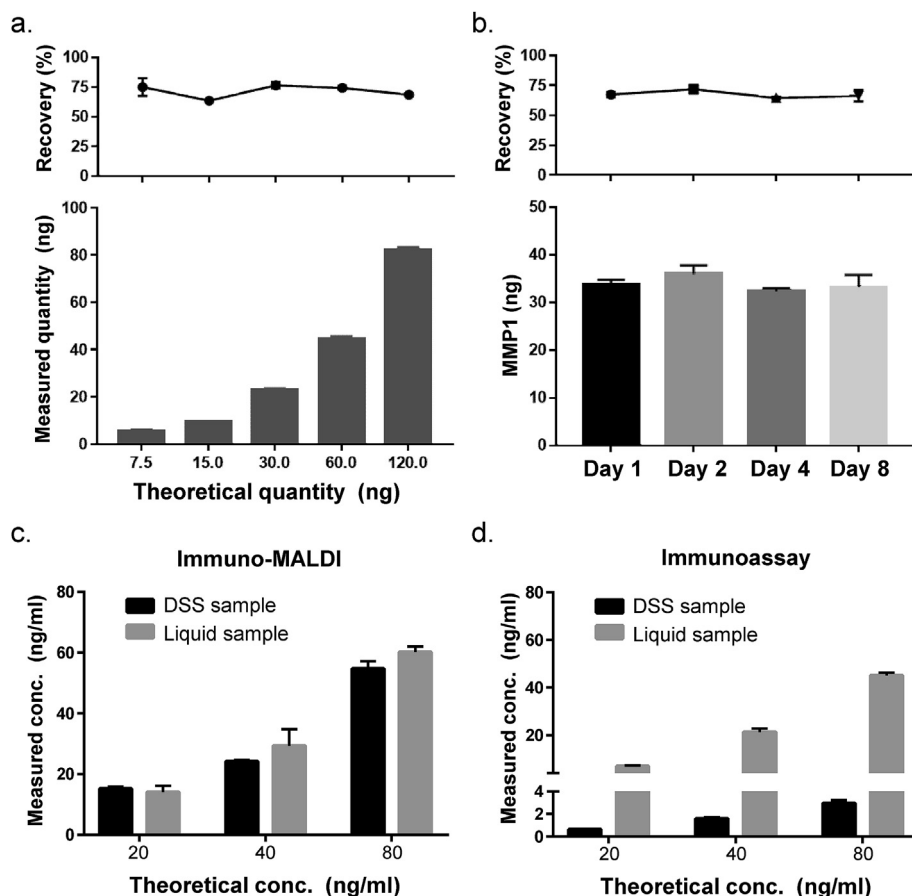


Fig. 5. Applicability of the immuno-MALDI assay for quantification of MMP1 in DSS samples. (a) Saliva samples (100 µl) containing various amounts of recombinant MMP1 protein (120, 60, 30, 15, and 7.5 ng) were blotted on a protein saver card. DSS samples were processed for the immuno-MALDI assay for quantification of MMP1. The amounts of MMP1 were measured (bottom panel) and the protein recovery levels calculated (upper panel). (b) Aliquots (100 µl) of a model saliva sample containing 50 ng MMP1 were blotted on the protein saver card. After storage at room temperature for 1, 2, 4 and 8 days, DSS samples were processed for the MMP1 immuno-MALDI assay. The amounts of MMP1 spiked in the saliva sample were measured (bottom panel) and recovery of quantified protein calculated (upper panel). (c, d) Three saliva samples with spiked recombinant MMP1 (20, 40 and 80 ng/ml) protein were prepared in the liquid or dry spot format and subjected to immuno-MALDI (c) and ELISA (d) for MMP1 quantification. Aliquots of each sample were quantified in triplicate and presented as means \pm SD, as shown in the bar chart.

Table 1

Quantification of MMP1 in DSS samples prepared from healthy donors and OSCC patients using immuno-MALDI.

Case No.		Total protein concentration (µg/µl) ^a	Total peptide concentration (µg/µl) ^b	MMP1 concentration (ng/ml) ^c	
				MALDI-TOF	LC-MRM
Healthy donors	1	0.42	0.26	0	0.30 \pm 0.04
	2	0.47	0.28	0	0.33 \pm 0.04
	3	1.49	0.90	0	1.28 \pm 0.11
	4	0.36	0.22	0	0.22 \pm 0.06
	5	1.28	0.79	0	1.22 \pm 0.34
OSCC patients	6	0.62	0.32	36.59 \pm 0.01	45.52 \pm 0.48
	7	1.45	0.80	32.83 \pm 0.03	41.52 \pm 0.96
	8	0.45	0.25	0	0.56 \pm 0.14
	9	3.35	2.02	12.79 \pm 0.04	8.74 \pm 0.15
	10	4.79	1.87	242.52 \pm 0.16	205.64 \pm 2.06
	11	0.74	0.49	0	3.69 \pm 0.19
	12	2.07	1.17	5.95 ^d	4.69 \pm 0.09
	13	0.76	0.44	16.90 \pm 0.01	18.60 \pm 0.92
	14	3.14	1.54	20.82 \pm 0.04	20.50 \pm 0.29

^a Liquid saliva sample measured using BCA.

^b Digested sample from DSS measured using the peptide assay.

^c Samples digested and eluted from DSS were subjected to immunoenrichment, followed by quantification using MALDI-TOF MS and LC-MRM-MS. Concentrations are presented as means \pm SD of triplicate measurements.

^d MMP1 was only quantified in one of the triplicate measurements.

proteotypic peptide from protein C inhibitor (PCI) in sera from patients with prostate cancer, and found the association between decreased serum concentrations of the PCI peptide and the recurrence of prostate cancer in patients treated with radiation with or without hormone therapy [50]. Moreover, Gao et al. established a novel four-plex immuno-MALDI assay to quantify the inflammatory markers C-reactive protein (CRP), serum amyloid A (SAA), and calprotectin (S100A8/9) and the kidney function marker cystatin C (CysC), with low limits of detection (0.01–0.06 µg/mL), low coefficients of variation (3.8–9.4%) and good between-assay agreement with immuno-turbidimetry (for CRP), ELISA (for SAA and S100A8/9), and nephelometry for CysC [51]. Another study by Ahn et al. combined lectin-enrichment and immuno-MALDI assay to measure the lectin-captured glycoforms of tissue inhibitor of metalloproteinase 1 (TIMP1) in serum samples and demonstrated the aberrantly glycosylated TIMP1 as a potent biomarker candidate for colorectal cancer [52]. In addition to the measurement of body-fluid accessible targets, the immuno-MALDI assay has also been applied to quantify targets that play critical roles in cancer development and progression. Popp et al. developed a duplex immuno-MALDI assay to measure AKT1 and AKT2, isoforms of protein kinase B that promotes survival and growth in response to extracellular signals linked to a range of diseases such as cancer and type II diabetes, in breast and colorectal cancer cell lines and tumor samples [33]. All these studies have demonstrated the advantages of using immuno-MALDI assay to measure targets in biological samples and clinical specimens, including low sample consumption, low limit-of-detection and high sample throughput.

Generally, quantification of specific targets in complex samples (such as clinical specimens) using MALDI-based MS analysis is difficult owing to the lack of pre-fractionation step(s) to reduce sample complexity. By incorporating an immuno-enrichment step using an anti-peptide Ab, we optimized the utility of MALDI-TOF MS to quantify MMP1 peptide eluted from trypsin-digested DSS samples. Although the LC-MRM assay could also be applied to quantify MMP1 peptide from DSS samples in a more sensitive manner (Table 1), this process is considerably more time-consuming than MALDI-TOF MS due to the lengthy process of liquid chromatography. A comparison of time costs between the two methods (immune-MALDI and LC-MRM) to quantify a specific target in one and 32 samples is presented in Fig. S11. In our previous study, we demonstrated that the LLOQ value of MMP1 in saliva measured using LC-MRM is 18.98 ng/ml, which indicates 0.12 fmol of peptides quantifiable in the injection of 1 µg sample [53]. In the present study, we showed that the lowest level of MMP1 peptide that can be precisely measured by MALDI-TOF analysis is 0.26 fmol (Fig. 2 and Fig. S3), indicating the lower detection sensitivity of MALDI-TOF as compared to LC-MRM. However, introducing an immuno-enrichment step prior to MALDI-TOF analysis provides an opportunity to increase the amount of input sample and thus improve the detection sensitivity. By increasing the amount of saliva sample to 100 µl, the immuno-MALDI assay showed a significant improvement of the LOQ value at 3.07 ng/ml (Fig. 3d and Table S3).

LC-MRM analysis has been widely applied in biomarker validation for multiple targets. Using well designed, scheduled MRM coupled with stable isotope-coded standard peptides, CV values for triplicate quantification of multiple proteins were <15% within and across laboratories [54,55]. In this study, we addressed the precision, dynamics of detection, and stability of the newly developed immuno-MALDI assay. The MALDI-TOF assay could precisely and accurately detect pure peptide within a limit of 0.26 fmol (the third point of combination curve 4) based on CV% <20% (Fig. S3a) and accuracy within 80–100% (Fig. S3b). However, the peak area ratios of the top and bottom points of the combination curves were

overvalued and undervalued, respectively (Fig. S3c). The same phenomenon has been consistently reported by other researchers. One potential reason is that the MALDI ionization mode restricts the analysis of widely disparate peptide abundance due to its obvious ion suppression effects [48]. Moreover, automatic subtraction of baseline noise would equally reduce the baseline intensity of all spectra, leading to a significant decrease in the signals of low-abundance peaks with no obvious effects on high-abundance peaks. This would aggravate the peak area ratio of light to heavy peptide when one peptide is 10-fold more abundant than the other. Evidently, the concentration response of peptide in MALDI-TOF analysis is nonlinear, particularly in the case of analyte peptide, which is 10-fold higher/lower than the SIS peptide. Therefore, we used the second-order polynomial (quadratic) fitting method to establish the response curve of signal to concentration (Fig. 3d) and adjusted the peak area ratio for accurate quantification (Table S3). Accordingly, the precision (CV% <15%) and accuracy (90.89–112.90%) of immuno-MALDI assay against MMP1 were qualified for clinical application (Table S3). In addition to response curve generated by synthetic peptides, a model sample containing recombinant MMP1 protein was also precisely and accurately quantified by immuno-MALDI assay (Fig. 4a, c). Moreover, the workflow from DSS sampling to immuno-MALDI quantification exhibited intra-day variations (CV% of triplicate quantification) and inter-day variations (CV% of multiple-day quantification, up to 8 days) less than 15%, which indicated a good reproducibility of the assay and a good stability of DSS storage (Fig. 5b).

5. Conclusions

Currently, no high-throughput protein biomarker assay workflows are available for DSS samples. Here, we have developed a workflow incorporating DSS sampling and immuno-MALDI analysis for precise (intra-day and inter-day variation <10%), accurate (80–100%) and sensitive (LOQ at 3.07 ng/ml) quantification of salivary MMP1 for OSCC detection. We optimized all the procedures including DSS sampling, on-paper protein digestion and elution, KingFisher magnetic particle processor-assisted immuno-enrichment and MALDI-TOF MS analysis, and successfully applied the established workflow to measure salivary MMP1 levels from DSS samples of OSCC patients. The DSS sampling format confers high flexibility and convenience of collection, storage and delivery of saliva specimens while KingFisher-assisted immuno-MALDI analysis renders the assay high-throughput. Our novel workflow combining the two features should improve the efficiency of molecular diagnostic testing in OSCC using salivary MMP1 as a biomarker. Additionally, since our data validate the compatibility between DSS sampling and peptide-based quantitative MS assay, this strategy could be applied to develop targeted assays for other medically important proteins in saliva.

Author contributions

Yung-Chin Hsiao and Jau-Song Yu: Conceptualization.
Yung-Chin Hsiao and Shih-Yu Lin: Methodology.
Yung-Chin Hsiao, Shih-Yu Lin and Szu-Fan Chen: Investigation.
Yung-Chin Hsiao and Shih-Yu Lin: Formal analysis.
Kun-Yi Chien, Chia-Chun Wu, Lang-Ming Chi, Ya-Ting Chang, Yu-Sun Chang, Lichieh Julie Chu, Wei-Fan Chiang, Chih-Yen Chien and Kai-Ping Chang: Resources.
Yung-Chin Hsiao and Jau-Song Yu: Writing - original draft; Writing - review & editing.
Yung-Chin Hsiao, Shih-Yu Lin and Jau-Song Yu: Visualization.
Jau-Song Yu: Supervision.
Yung-Chin Hsiao and Jau-Song Yu: Project administration.

Yung-Chin Hsiao and Jau-Song Yu: Funding acquisition.

Declaration of competing interest

The authors declare that they have no known competing financial interests or personal relationships that could have appeared to influence the work reported in this paper.

Acknowledgements

This study was supported by the “Molecular Medicine Research Center, Chang Gung University” from The Featured Areas Research Center Program within the framework of the Higher Education Sprout Project by the Ministry of Education (MOE) in Taiwan. This work was also supported by grants from the Ministry of Science and Technology, Taiwan (MOST 107-2320-B-182-027-MY3 to YCH, MOST 107-2320-B-182-028-MY3 to LJC and MOST 106-2320-B-182-029-MY3 to JSY); and the Chang Gung Memorial Hospital, Linkou, Taiwan (CLRPD1J0011, CLRPD190019, CMRPD1H0251 to JSY, CIRPG3B0014 to KPC).

Appendix A. Supplementary data

Supplementary data to this article can be found online at <https://doi.org/10.1016/j.aca.2019.12.006>.

References

- [1] S. Warnakulasuriya, Global epidemiology of oral and oropharyngeal cancer, *Oral Oncol.* 45 (2009) 309–316.
- [2] A.C. Chi, T.A. Day, B.W. Neville, Oral cavity and oropharyngeal squamous cell carcinoma—an update, *Ca - Cancer J. Clin.* 65 (2015) 401–421.
- [3] L.A. Torre, F. Bray, R.L. Siegel, J. Ferlay, J. Lortet-Tieulent, A. Jemal, Global cancer statistics, 2012, *Ca - Cancer J. Clin.* 65 (2015) 87–108.
- [4] J. Ferlay, D.M. Parkin, E. Steliarova-Foucher, Estimates of cancer incidence and mortality in Europe in 2008, *Eur. J. Cancer* 46 (2010) 765–781.
- [5] J. Ferlay, E. Steliarova-Foucher, J. Lortet-Tieulent, S. Rosso, J.W. Coebergh, H. Comber, et al., Cancer incidence and mortality patterns in Europe: estimates for 40 countries in 2012, *Eur. J. Cancer* 49 (2013) 1374–1403.
- [6] H. Mortazavi, M. Baharvand, M. MehdiPour, Oral potentially malignant disorders: an overview of more than 20 entities, *J. Dent. Res. Dent. Clin. Dent. Prospects* 8 (2014) 6–14.
- [7] I. van der Waal, Potentially malignant disorders of the oral and oropharyngeal mucosa; terminology, classification and present concepts of management, *Oral Oncol.* 45 (2009) 317–323.
- [8] T. Amagasa, M. Yamashiro, N. Uzawa, Oral premalignant lesions: from a clinical perspective, *Int. J. Clin. Oncol.* 16 (2011) 5–14.
- [9] M.W. Lingen, J.R. Kalmar, T. Karrison, P.M. Speight, Critical evaluation of diagnostic aids for the detection of oral cancer, *Oral Oncol.* 44 (2008) 10–22.
- [10] B.J. Braakhuis, M.P. Tabor, J.A. Kummer, C.R. Leemans, R.H. Brakenhoff, A genetic explanation of Slaughter's concept of field cancerization: evidence and clinical implications, *Cancer Res.* 63 (2003) 1727–1730.
- [11] B.J. Braakhuis, M.P. Tabor, C.R. Leemans, I. van der Waal, G.B. Snow, R.H. Brakenhoff, Second primary tumors and field cancerization in oral and oropharyngeal cancer: molecular techniques provide new insights and definitions, *Head Neck* 24 (2002) 198–206.
- [12] J.J. Lee, H.C. Hung, S.J. Cheng, C.P. Chiang, B.Y. Liu, C.H. Yu, et al., Factors associated with underdiagnosis from incisional biopsy of oral leukoplakic lesions, *Oral Surg. Oral Med. Oral Pathol. Oral Radiol. Endod.* 104 (2007) 217–225.
- [13] D.J. Fischer, J.B. Epstein, T.H. Morton, S.M. Schwartz, Interobserver reliability in the histopathologic diagnosis of oral pre-malignant and malignant lesions, *J. Oral Pathol. Med.* 33 (2004) 65–70.
- [14] D.J. Fischer, J.B. Epstein, T.H. Morton Jr., S.M. Schwartz, Reliability of histologic diagnosis of clinically normal intraoral tissue adjacent to clinically suspicious lesions in former upper aerodigestive tract cancer patients, *Oral Oncol.* 41 (2005) 489–496.
- [15] K.E. Rusthoven, D. Raben, J.I. Song, M. Kane, T.A. Altoos, C. Chen, Survival and patterns of relapse in patients with oral tongue cancer, *J. Oral Maxillofac. Surg.* 68 (2010) 584–589.
- [16] W.L. Lo, S.Y. Kao, L.Y. Chi, Y.K. Wong, R.C. Chang, Outcomes of oral squamous cell carcinoma in Taiwan after surgical therapy: factors affecting survival, *J. Oral Maxillofac. Surg.* 61 (2003) 751–758.
- [17] S. Blatt, M. Kruger, T. Ziebart, K. Sagheb, E. Schiegnitz, E. Goetze, et al., Biomarkers in diagnosis and therapy of oral squamous cell carcinoma: a review of the literature, *J. Cranio-Maxillo-Fac. Surg.* 45 (2017) 722–730.
- [18] A. Fernandez-Olavarria, R. Mosquera-Perez, R.M. Diaz-Sanchez, M.A. Serrera-Figallo, J.L. Gutierrez-Perez, D. Torres-Lagares, The role of serum biomarkers in the diagnosis and prognosis of oral cancer: a systematic review, *J. Clin. Exp. Dent.* 8 (2016) 184–193.
- [19] Y.H. Ni, L. Ding, Q.G. Hu, Z.C. Hua, Potential biomarkers for oral squamous cell carcinoma: proteomics discovery and clinical validation, *Proteom. Clin. Appl.* 9 (2015) 86–97.
- [20] M. Yakob, L. Fuentes, M.B. Wang, E. Abemayor, D.T. Wong, Salivary biomarkers for detection of oral squamous cell carcinoma - current state and recent advances, *Curr. Oral Health Rep.* 1 (2014) 133–141.
- [21] T. Radhika, N. Jeddy, S. Nithya, R.M. Muthumeenakshi, Salivary biomarkers in oral squamous cell carcinoma - an insight, *J. Oral Biol. Craniofac. Res.* 6 (1) (2016) S51–S54.
- [22] V.T. Stuan, C.M. Rubira, A.C. Sant'Ana, P.S. Santos, Salivary biomarkers as tools for oral squamous cell carcinoma diagnosis: a systematic review, *Head Neck* 39 (2017) 797–811.
- [23] R.S. George, S.J. Moat, Effect of dried blood spot quality on newborn screening analyte concentrations and recommendations for minimum acceptance criteria for sample analysis, *Clin. Chem.* 62 (2016) 466–475.
- [24] N. Zheng, J. Zeng, Q.C. Ji, A. Angeles, A.F. Aubry, S. Basdeo, et al., Bioanalysis of dried saliva spot (DSS) samples using detergent-assisted sample extraction with UHPLC-MS/MS detection, *Anal. Chim. Acta* 934 (2016) 170–179.
- [25] M. Numako, T. Takayama, I. Noge, Y. Kitagawa, K. Todoroki, H. Mizuno, et al., Dried saliva spot (DSS) as a convenient and reliable sampling for bioanalysis: an application for the diagnosis of diabetes mellitus, *Anal. Chem.* 88 (2016) 635–639.
- [26] P.J. Jannetto, R.L. Fitzgerald, Effective use of mass spectrometry in the clinical laboratory, *Clin. Chem.* 62 (2016) 92–98.
- [27] A. Sloan, G. Wang, K. Cheng, Traditional approaches versus mass spectrometry in bacterial identification and typing, *Clin. Chim. Acta* 473 (2017) 180–185.
- [28] M.A. Kuzlyk, D. Smith, J. Yang, T.J. Cross, A.M. Jackson, D.B. Hardie, et al., Multiple reaction monitoring-based, multiplexed, absolute quantitation of 45 proteins in human plasma, *Mol. Cell. Proteom.* 8 (2009) 1860–1877.
- [29] Y.T. Chen, H.W. Chen, D. Domanski, D.S. Smith, K.H. Liang, C.C. Wu, et al., Multiplexed quantification of 63 proteins in human urine by multiple reaction monitoring-based mass spectrometry for discovery of potential bladder cancer biomarkers, *J. Proteomics* 75 (2012) 3529–3545.
- [30] J.S. Yu, Y.T. Chen, W.F. Chiang, Y.C. Hsiao, L.J. Chu, L.C. See, et al., Saliva protein biomarkers to detect oral squamous cell carcinoma in a high-risk population in Taiwan, *Proc. Natl. Acad. Sci. U S A* 113 (2016) 11549–11554.
- [31] D.R. Mason, J.D. Reid, A.G. Camenzind, D.T. Holmes, C.H. Borchers, Duplexed iMALDI for the detection of angiotensin I and angiotensin II, *Methods* 56 (2012) 213–222.
- [32] Y.H. Ahn, K.H. Kim, P.M. Shin, E.S. Ji, H. Kim, J.S. Yoo, Identification of low-abundance cancer biomarker candidate TIMP1 from serum with lectin fractionation and peptide affinity enrichment by ultrahigh-resolution mass spectrometry, *Anal. Chem.* 84 (2012) 1425–1431.
- [33] R. Popp, H. Li, A. LeBlanc, Y. Mohammed, A. Aguilar-Mahecha, A.G. Chambers, et al., Immuno-matrix-assisted laser desorption/ionization assays for quantifying AKT1 and AKT2 in breast and colorectal cancer cell lines and tumors, *Anal. Chem.* 89 (2017) 10592–10600.
- [34] M. Nagata, H. Fujita, H. Ida, H. Hoshina, T. Inoue, Y. Seki, et al., Identification of potential biomarkers of lymph node metastasis in oral squamous cell carcinoma by cDNA microarray analysis, *Int. J. Cancer* 106 (2003) 683–689.
- [35] Y.Y. Chiang, M.H. Tsai, T.Y. Lin, I.P. Chiang, Expression profile of metastasis-related genes in invasive oral cancers, *Histol. Histopathol.* 23 (2008) 1213–1222.
- [36] A. George, K. Ranganathan, U.K. Rao, Expression of MMP-1 in histopathological different grades of oral squamous cell carcinoma and in normal buccal mucosa - an immunohistochemical study, *Cancer Biomark.* 7 (2010) 275–283.
- [37] P.P. Reis, L. Waldron, B. Perez-Ordóñez, M. Pintilie, N.N. Galloni, Y. Xuan, et al., A gene signature in histologically normal surgical margins is predictive of oral carcinoma recurrence, *BMC Canc.* 11 (2011) 437.
- [38] Z. Zhang, J. Pan, L. Li, Z. Wang, W. Xiao, N. Li, Survey of risk factors contributed to lymphatic metastasis in patients with oral tongue cancer by immunohistochemistry, *J. Oral Pathol. Med.* 40 (2011) 127–134.
- [39] M. Stott-Miller, J.R. Houck, P. Lohavanichbutr, E. Mendez, M.P. Upton, N.D. Futran, et al., Tumor and salivary matrix metalloproteinase levels are strong diagnostic markers of oral squamous cell carcinoma, *Cancer Epidemiol. Biomark. Prev.* 20 (2011) 2628–2636.
- [40] T. Nosrati, E. Alijani, M. Moodi, Salivary MMP-1, MMP-2, MMP-3 and MMP-13 levels in patients with oral lichen planus and squamous cell carcinoma, *Asian Pac. J. Cancer Prev. APJCP* 18 (2017) 1947–1951.
- [41] Y.C. Hsiao, L.M. Chi, K.Y. Chien, W.F. Chiang, S.F. Chen, Y.N. Chuang, et al., Development of a multiplexed assay for oral cancer candidate biomarkers using peptide immunoaffinity enrichment and targeted mass spectrometry, *Mol. Cell. Proteom.* 16 (2017) 1829–1849.
- [42] W.S. Chen, O.B. Villaflores, T.R. Jinn, M.T. Chan, Y.C. Chang, T.Y. Wu, Expression of recombinant human interferon-gamma with antiviral activity in the bi-cistronic baculovirus-insect/larval system, *Biosci. Biotechnol. Biochem.* 75 (2011) 1342–1348.
- [43] T.Y. Wu, Y.J. Chen, C.Y. Teng, W.S. Chen, O. Villaflores, A bi-cistronic baculovirus expression vector for improved recombinant protein production, *Bioeng. Bugs* 3 (2012) 129–132.
- [44] K.D. Lee, T.Y. Wang, C.H. Lu, C.E. Huang, M.C. Chen, The bidirectional

- association between oral cancer and esophageal cancer: a population-based study in Taiwan over a 28-year period, *Oncotarget* 8 (2017) 44567–44578.
- [45] S. Hu, Y. Xie, P. Ramachandran, R.R. Ogorzalek Loo, Y. Li, J.A. Loo, et al., Large-scale identification of proteins in human salivary proteome by liquid chromatography/mass spectrometry and two-dimensional gel electrophoresis-mass spectrometry, *Proteomics* 5 (2005) 1714–1728.
- [46] J.L. Proc, M.A. Kuzyk, D.B. Hardie, J. Yang, D.S. Smith, A.M. Jackson, et al., A quantitative study of the effects of chaotropic agents, surfactants, and solvents on the digestion efficiency of human plasma proteins by trypsin, *J. Proteome Res.* 9 (2010) 5422–5437.
- [47] J.R. Whiteaker, L. Zhao, L. Anderson, A.G. Paulovich, An automated and multiplexed method for high throughput peptide immunoaffinity enrichment and multiple reaction monitoring mass spectrometry-based quantification of protein biomarkers, *Mol. Cell. Proteom.* 9 (2010) 184–196.
- [48] N.L. Anderson, M. Razavi, T.W. Pearson, G. Kruppa, R. Paape, D. Suckau, Precision of heavy-light peptide ratios measured by maldi-tof mass spectrometry, *J. Proteome Res.* 11 (2012) 1868–1878.
- [49] A.G. Camenzind, J.G. van der Gugten, R. Popp, D.T. Holmes, C.H. Borchers, Development and evaluation of an immuno-MALDI (iMALDI) assay for angiotensin I and the diagnosis of secondary hypertension, *Clin. Proteonomics* 10 (2013) 20.
- [50] M. Razavi, L.D. Johnson, J.J. Lum, G. Kruppa, N.L. Anderson, T.W. Pearson, Quantification of a proteotypic peptide from protein C inhibitor by liquid chromatography-free SISCAPA-MALDI mass spectrometry: application to identification of recurrence of prostate cancer, *Clin. Chem.* 59 (2013) 1514–1522.
- [51] J. Gao, K. Meyer, K. Borucki, P.M. Ueland, Multiplex Immuno-MALDI-TOF MS for Targeted Quantification of protein biomarkers and their proteoforms related to inflammation and renal dysfunction, *Anal. Chem.* 90 (2018) 3366–3373.
- [52] Y.H. Ahn, K.H. Kim, P.M. Shin, E.S. Ji, H. Kim, J.S. Yoo, Identification of low-abundance cancer biomarker candidate TIMP1 from serum with lectin fractionation and peptide affinity enrichment by ultrahigh-resolution mass spectrometry, *Anal. Chem.* 84 (2012) 1425–1431.
- [53] L.M. Chi, Y.C. Hsiao, K.Y. Chien, S.F. Chen, Y.N. Chuang, S.Y. Lin, et al., Assessment of candidate biomarkers in paired saliva and plasma samples from oral cancer patients by targeted mass spectrometry, *J. Proteomics* 211 (2019 Nov 2) 103571, <https://doi.org/10.1016/j.jpro.2019.103571> [Epub ahead of print].
- [54] E. Kuhn, J.R. Whiteaker, D.R. Mani, A.M. Jackson, L. Zhao, M.E. Pope, et al., Interlaboratory evaluation of automated, multiplexed peptide immunoaffinity enrichment coupled to multiple reaction monitoring mass spectrometry for quantifying proteins in plasma, *Mol. Cell. Proteom.* 11 (2012). M111 013854.
- [55] T.A. Addona, S.E. Abbatiello, B. Schilling, S.J. Skates, D.R. Mani, D.M. Bunk, et al., Multi-site assessment of the precision and reproducibility of multiple reaction monitoring-based measurements of proteins in plasma, *Nat. Biotechnol.* 27 (2009) 633–641.

Fractional Laser-Mediated siRNA Delivery for Mitigating Psoriasis-like Lesions via IL-6 Silencing

Woan-Ruoh Lee,^{1,2,10} Yin-Ku Lin,^{3,4,10} Ahmed Alalaiwe,⁵ Pei-Wen Wang,⁶ Pei-Yin Liu,⁷ and Jia-You Fang^{7,8,9}

¹Graduate Institute of Medical Sciences, Taipei Medical University, Taipei, Taiwan; ²Department of Dermatology, Taipei Medical University Shuang Ho Hospital, New Taipei City, Taiwan; ³School of Traditional Chinese Medicine, Chang Gung University, Kweishan, Taoyuan, Taiwan; ⁴Department of Traditional Chinese Medicine, Chang Gung Memorial Hospital at Keelung, Keelung, Taiwan; ⁵Department of Pharmaceutics, College of Pharmacy, Prince Sattam Bin Abdulaziz University, Al Kharj, Saudi Arabia; ⁶Department of Medical Research, China Medical University Hospital, China Medical University, Taichung, Taiwan; ⁷Pharmaceutics Laboratory, Graduate Institute of Natural Products, Chang Gung University, Kweishan, Taoyuan, Taiwan; ⁸Research Center for Food and Cosmetic Safety and Research Center for Chinese Herbal Medicine, Chang Gung University of Science and Technology, Kweishan, Taoyuan, Taiwan; ⁹Department of Anesthesiology, Chang Gung Memorial Hospital at Linkou, Kweishan, Taoyuan, Taiwan

The poor permeability of topically applied macromolecules such as small interfering RNA (siRNA) has inhibited the translation to clinical application. In this study, the fractional CO₂ laser-assisted approach was developed to describe siRNA permeation enhancement mediated by the created microchannels for silencing the gene to treat psoriasiform lesions. *In vitro* permeation using Franz cell and *in vivo* interleukin (IL)-6 silencing using psoriasis-like plaque in mice were evaluated to verify the impact of the laser irradiation. Low-fluence laser exposure enabled a significant increase in skin transport of siRNA, peptide, and 5-fluorouracil (5-FU). The laser treatment resulted in the enhancement of siRNA flux by 33- and 14-fold as compared to the control in nude mouse and pig skin, respectively. The laser exposure also promoted siRNA penetration across psoriatic and photoaging skins with the deficient barrier, although the enhancement level was minor compared to that of intact skin. The 3D images of confocal microscopy revealed a diffusion of macromolecules into the laser-created microchannels; the radial and vertical distribution to the surrounding and deep tissues followed this. A single laser treatment and the following topical siRNA administration were able to reduce IL-6 expression by 64% in the psoriatic skin model. Laser assistance led to the marked improvement in the plaque and the reduction of specific cytokine expression, keratinocyte proliferation, and neutrophil infiltration. Our data support the use of the fractional laser for delivery of functional nucleic acid into the skin and the target cells.

INTRODUCTION

Small interfering RNA (siRNA) is a class of small double-stranded RNA silencing genes that interfere with the expression of specific genes by interrupting DNA translation into proteins. RNA interference (RNAi) provides the potential to treat an extensive variety of diseases. The targeting of a given gene mutation by siRNA design leads to a promising future for precision medicine. The US Food and Drug

Administration (USFDA) approved the first RNAi therapy in August 2018. Patisiran, developed by Alnylam Pharmaceuticals, can silence the gene that underlies hereditary transthyretin amyloidosis.¹ Cutaneous disorders are the most common diseases, affecting >70% of the population worldwide.² siRNA therapeutics are effective in treating a number of skin conditions such as psoriasis, atopic dermatitis, epidermolysis bullosa, epidermolytic palmoplantar keratoderma, pachyonychia congenita, and skin cancers.³ Topical administration is a suitable route for delivering siRNA into the skin due to the easy administration, accessibility of the target site, and the resulting avoidance of systemic adverse effects. Despite the possibility of using siRNA for skin-disorder treatment, the difficulty in siRNA delivery through the cutaneous barrier and insufficient cellular uptake limit the translation to clinical use.⁴ Delivery of siRNA across the *stratum corneum* (SC) is a challenge because of the large molecular size, negative charge, and hydrophilic characteristic.⁵ The rapid enzymatic degradation in the skin also hampers topical siRNA administration.⁶ Currently, intradermal injection is used as an efficient delivery approach for siRNA to treat skin diseases. This method shows poor patient compliance because it causes severe pain, is invasive, and requires the assistance of medical professionals.

RNAi for cutaneous therapy can be achieved if its delivery hurdles can be conquered. In recent years, fractional laser ablation has been proven to magnify topical absorption of macromolecules by controlled and safe removal of the SC.^{7,8} Fractional modality creates microscopic vertical channels on the cutaneous surface with unaffected viable tissue surrounding the microchannels. The ablated area can be recovered within 1 day.⁹ Fractional laser treatment may be feasible for siRNA

Received 23 January 2019; accepted 8 November 2019;
<https://doi.org/10.1016/j.omtn.2019.11.013>.

¹⁰These authors contributed equally to this work.

Correspondence: Jia-You Fang, Pharmaceutics Laboratory, Graduate Institute of Natural Products, Chang Gung University, 259 Wen-Hwa 1st Road, Kweishan, Taoyuan 333, Taiwan.

E-mail: fajy@mail.cgu.edu.tw



absorption, as it offers a strategy for delivering the polar macromolecules through the lipid-rich SC to a specific region and cellular population. Psoriasis is an inflammatory autoimmune skin disease affecting 125 million individuals each year.¹⁰ It has a complex etiology involving genetic and environmental factors. siRNA has been proven to be useful for psoriasis treatment.^{11–13} It is reported that the majority of psoriasis patients are not satisfied with the current topical therapy.¹⁴ Fractional laser treatment may be useful for skin delivery of siRNA to manage psoriasis. Purposed with investigating this possibility, we used a low-fluence CO₂ ablative laser to assist skin permeation of siRNA for psoriasis mitigation in a mouse model.

Using interleukin (IL)-6 siRNA as the test permeant, three lines of experiments were performed. First, the appearance and histology of intact and psoriasis skins after laser irradiation were visualized. Second, we evaluated laser-mediated siRNA permeation by using various barrier-damaged skins. Topical therapy was proposed for use in diseased skin. The transport nature of siRNA in diseased skin is quite different from that in healthy skin.¹⁵ Besides the psoriasis-like mouse skin, the photoaging mouse skin developed by UVB exposure was used as another diseased-skin model for siRNA absorption. The cutaneous transport is largely related to the molecular characteristics of the permeants. In addition to the DNA-based macromolecule, the peptide-based macromolecule and hydrophilic 5-fluorouracil (5-FU) with low skin permeability were employed to examine skin absorption for comparison. Finally, the therapeutic efficacy of laser-assisted siRNA treatment on psoriasis was assessed in the imiquimod (IMQ)-activated psoriasis-like mouse model. For the first time, we provided a basis for laser-enhanced siRNA delivery for psoriasis treatment.

RESULTS

The Appearance of Skin Surface

Figure 1A illustrates en face images of the mouse skin with and without photoaging or psoriasis-like inflammation. The laser-irradiated healthy nude and hairy mouse skins demonstrated an array of dark-colored micropores on the cutaneous surface. The created microchannels had a diameter of 200–300 μm , approximating the microscopic thermal zone (MTZ) of the fractional laser (300 μm). There were flaky scales and erythema on the UVB-treated nude mouse skin surface. The en face image of the psoriasiform skin exhibited silvery scales. The size of the scaly lesion created by IMQ was larger than that created by UVB. As with normal skin, CO₂ laser treatment produced discrete channels with a circular appearance on diseased skins. The light micrographs with higher magnification were taken as depicted in Figure 1B. The micropores caused by CO₂ laser were found in all skin types (arrows). The opening showed a round or ovary shape on the skin surface with a mean diameter of 150–200 μm . The dark region surrounding the pores could be the coagulation induced by the CO₂ laser.

The skin histology demonstrated more details about the microchannel structure as shown in Figure 1C. The healthy skin had all layers of the intact skin with no impairment. The laser exposure removed the SC and some epidermal layers (arrows). The holes were surrounded

by the residual thermal coagulation extended down to the upper dermis. Examination of the photoaging skin section revealed the superficial scaling and epidermal hyperplasia. The immune cell infiltration was observed in the dermis, indicating an inflammatory condition. The laser irradiation on the UVB-treated skin penetrated the SC and extended into the epidermis. The H&E staining showed hyperkeratosis, epidermal thickening, and immune-cell infiltration in the psoriasis-like skin. The laser was effective for removing the SC and the upper epidermis of IMQ-treated skin. Some carbonization layers (coagulation) were visible around the ablated zone.

Permeation via Barrier-Defective Skins

We examined the flux of permeants across nude mouse and pig skins with pretreatment of SC stripping and removal of lipid, sebum, or protein. Because the nude mouse and baby pig skins were not as thick as human skin, the flux could be regarded as the permeant delivery to the deeper skin strata. Figure 2A summarizes the fluorescent-labeled siRNA flux across nude mouse and pig skins. Passive siRNA flux across the intact control skin indicated relatively low diffusion for both animal skins. The SC-stripped skin resulted in increased siRNA flux. This was the greatest permeation among the barrier-defective skins, followed by de-protein, de-lipid, and de-sebum skins. The laser was evaluated for the capability to promote fluorescently tagged siRNA penetration. The flux was 33- and 14-fold higher than across the untreated skin when the fractional ablation was employed in the case of intact mouse and pig skin, respectively. The laser did not greatly increase the flux in the case of SC stripping, suggesting that the laser had already diminished the barrier function of the SC. Contrary to this result, the laser greatly enhanced the flux in the case of sebum removal (>25-fold). The laser-assisted flux across de-protein skin was 5- to 7-fold higher than with the untreated control. The trend with nude mouse skin was similar to that of pig skin, except that the laser increased the siRNA flux across de-lipid pig skin by 7-fold but had no effect on de-lipid mouse skin.

Peptide represents a convenient and typical model macromolecule for a skin permeation test. As shown in Figure 2B, the flux of peptide across intact skin indicated low passive permeation in both animal skins. SC stripping led to a significant increase of flux, which was 22-fold higher than that with intact mouse skin. The peptide flux tendency of the barrier-defective skins was similar to that of siRNA flux. The laser exposure did not promote the peptide flux across SC-stripped skin. The laser-induced enhancement on de-lipid skin was also limited. Compared to de-sebum skin without laser irradiation, the peptide flux rose about 7-fold after fractional ablation. Laser application resulted in a 3-fold greater flux across de-protein skin compared to passive application for both animals. The permeation of the small-molecule drug 5-FU was also examined, as shown in Figure 2C. Both SC stripping and lipid removal increased the 5-FU flux across the mouse and pig skins at the same level. This indicates that the SC lipid bilayers were the predominant barrier for 5-FU transport. The laser did not facilitate 5-FU flux across the SC-stripped and de-lipid skins. Alternatively, in the case of intact skin, laser-mediated permeation was significantly 3-fold greater than in the untreated control. Laser

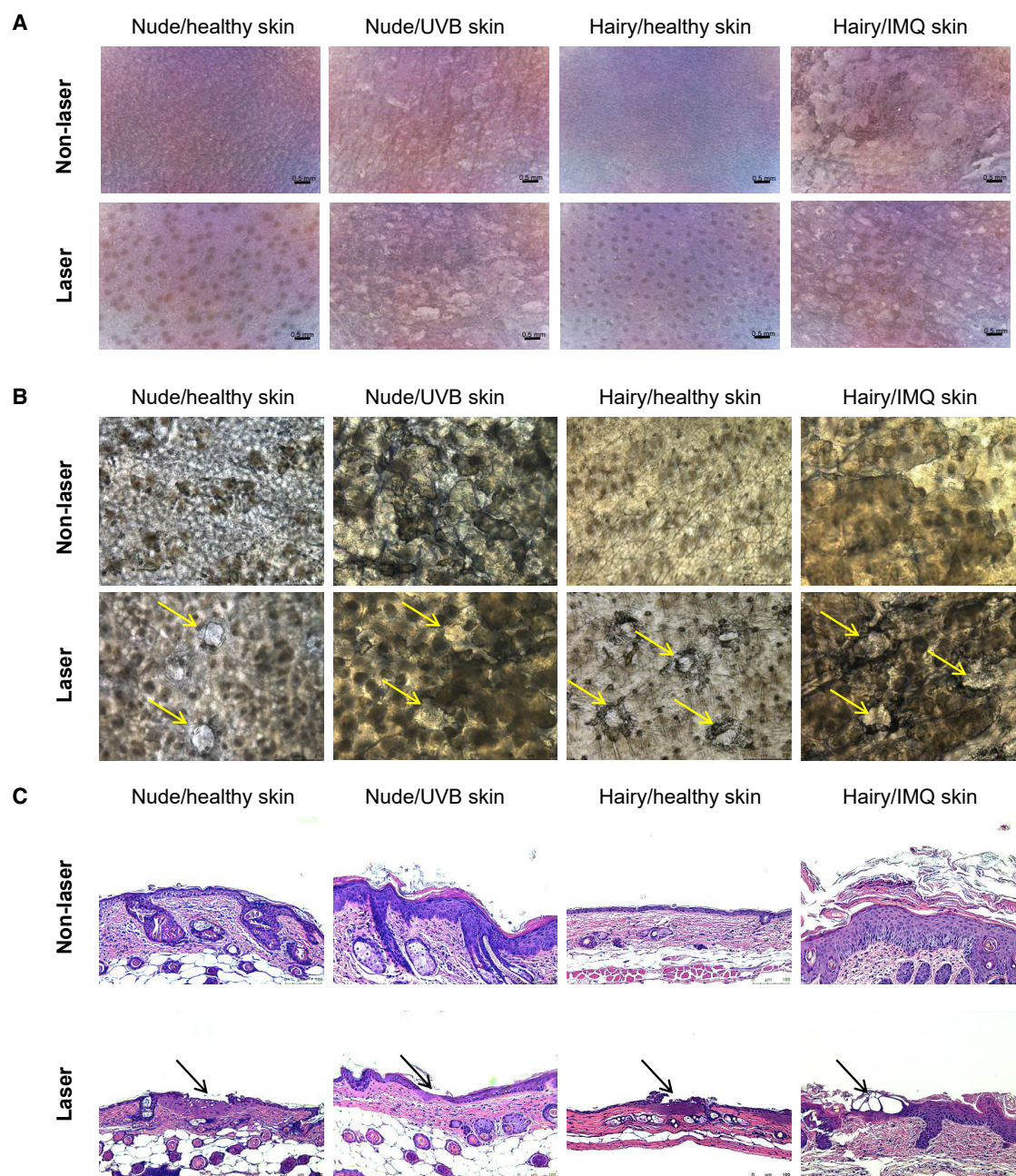


Figure 1. Macroscopic and Microscopic Observations of the Skin Treated by Fractional CO₂ Laser-Treated Skin as a Function of Different Recovery Times
(A) Skin surface imaging captured by handheld digital magnifier. (B) Skin surface imaging captured by optical microscopy. (C) H&E staining of the skin observed by optical microscopy. Arrows in the images indicate the micropores.

treatment on de-protein mouse skin increased 5-FU flux from 14 to 71 nmol/cm², which was a 13-fold enhancement. A 3-fold increase was observed in the case of de-protein pig skin.

Permeation via Diseased Skins

Photoaging and psoriasis-like skins were induced by treating UVB and IMQ in nude and hairy mice, respectively. The permeation of siRNA

and 5-FU into (skin deposition) and across (flux) the diseased skin was evaluated as shown in Figure 3. The deposition in animal skin can be a predictor of permeant accumulation in a superior skin layer. As shown in Figures 3A and 3B, the laser was unable to enhance the flux and skin deposition of siRNA via photoaging skin. Fractional laser treatment led to increased siRNA flux across healthy BALB/c mouse skin, with a 35-fold enhancement versus the untreated control. The

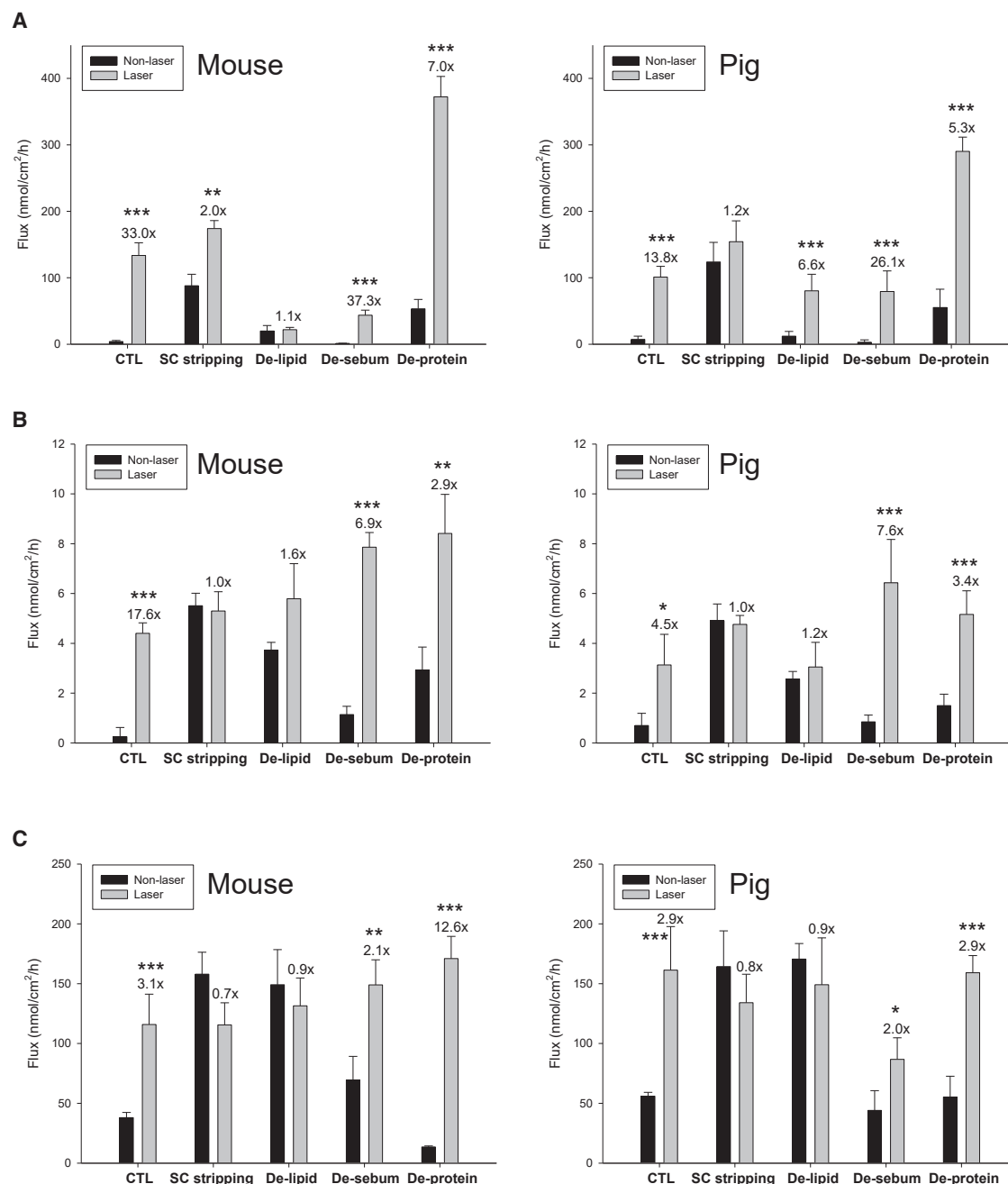


Figure 2. Flux (nmol/cm²/h) of the Permeants via Intact and Barrier-Defective Skins with or without Fractional CO₂ Laser Treatment

(A) Flux of fluorescently labeled siRNA via nude mouse and pig skins. (B) Flux of fluorescently labeled peptide via nude mouse and pig skins. (C) Flux of 5-FU via nude mouse and pig skins. Data are presented as the mean of four experiments \pm SD. * $p < 0.05$, ** $p < 0.01$, *** $p < 0.001$.

BALB/c mouse skin permeability for siRNA significantly increased after IMQ treatment, indicating the loss of barrier function in the psoriasisform type. A similar trend was observed in the skin deposition of IMQ-treated skin versus normal skin, although the enhancement level was much lower than that of the flux. The laser intervention permitted a 3- and 2-fold increase in psoriasis-like skin flux and deposition,

respectively. Figures 3C and 3D show the flux and skin deposition of 5-FU in the diseased skin. An 8-fold increase in 5-FU flux was found using the laser as compared to the passive permeation in the UVB-treated skin. However, the 5-FU deposition lessened after laser intervention on photoaging skin. A significant enhancement in hairy mouse flux and deposition with laser irradiation was achieved, with the

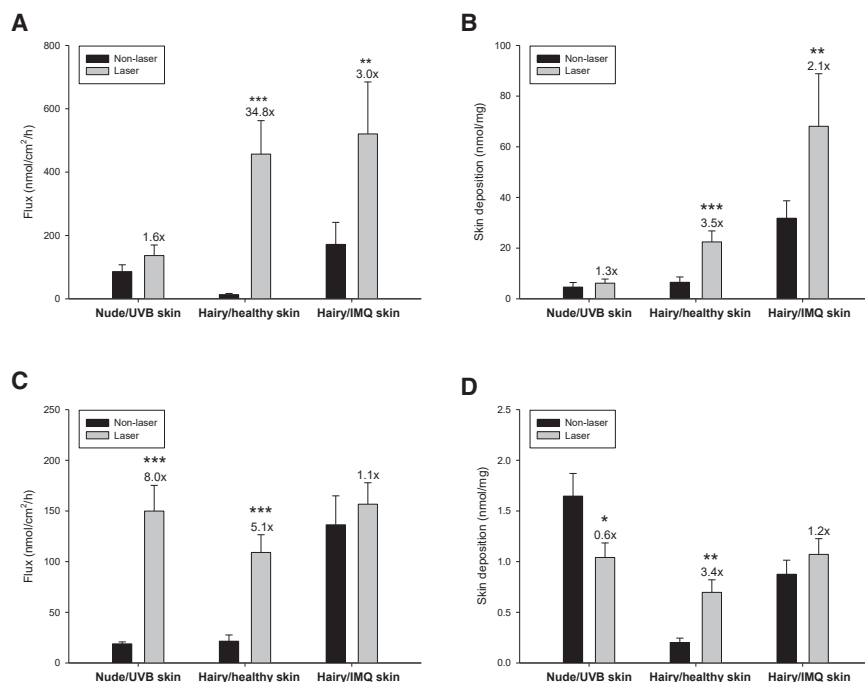


Figure 3. Flux (nmol/cm²/h) and Skin Deposition (nmol/mg) of the Permeants via Intact and Diseased Skins with or without Fractional CO₂ Laser Treatment

(A) Flux of fluorescently labeled siRNA via nude and hairy skins. (B) Skin deposition of fluorescently labeled siRNA in nude and hairy skins. (C) Flux of 5-FU via nude and hairy skins. (D) Skin deposition of 5-FU in nude and hairy skins. The data are presented as the mean of four experiments \pm SD. * $p < 0.05$, ** $p < 0.01$, *** $p < 0.001$.

enhancement being 5- and 3-fold greater than in the control group, respectively. 5-FU flux through laser-treated psoriatic skin was found to be 136 nmol/cm²/h, which was comparable to the untreated control (157 nmol/cm²/h). The laser also did not promote 5-FU deposition in psoriatic skin. This demonstrates the usefulness of CO₂ laser to assist 5-FU absorption in the IMQ-treated skin.

Distribution of siRNA and Peptide in the Skin

Cutaneous distribution of fluorescently labeled siRNA and peptide was acquired by confocal microscopy in a horizontal scanning fashion. Following the application of macromolecules using the laser approach, the skin sample was imaged as shown in Figure 4. The untreated skin served as a negative control, and no fluorescence was visualized in the skin tissue (data not shown). Figure 4A illustrates siRNA distribution in healthy and photoaging nude mouse skins with and without laser irradiation. The left panel of each group in the planar image is the summing of 15 separate sections. The right panel is the 3D skin structure seen in the photographs. A faint fluorescence distribution was observed in the healthy skin without laser treatment. UVB irradiation on the skin could increase siRNA distribution. After laser exposure, the distribution of siRNA fluorescence increased. The confocal images demonstrate a homogeneous siRNA distribution in the laser-treated photoaging skin. It was shown that laser-mediated siRNA could be delivered into the deeper layers of photoaging skin. In the case of psoriatic skin as shown in Figure 4B, the passive transport of siRNA into healthy BALB/c mouse skin has resulted in superficial distribution. Because of the barrier disruption by IMQ-induced inflammation, the fluorescence was increased. Following fractional ablation, there was pronounced siRNA distributed within the healthy and psoriatic skins with deeper penetration

compared to the control. The green fluorescence was evident around the microchannels (arrows). An intense fluorescence was visualized at sites lateral to the channels, indicating a radial siRNA diffusion.

As seen in Figure 4C, the passive peptide application resulted in the distribution within the superficial layer of normal nude mouse skin. UVB exposure was able to increase peptide absorption. The laser further facilitated peptide delivery into the healthy and photoaging skins. We could not find the obvious microchannels in the laser-treated healthy skin. In the case of laser-treated photoaging skin, the peptide appeared to migrate along the microchannels and into the deeper skin strata (arrows). The openings of the micropores could be clearly visualized. The diameter of the peptide-stained area was larger than that of siRNA, suggesting a significant peptide spread from the channels via lateral diffusion. The same result was detected in the peptide application on psoriasisiform skin, as shown in Figure 4D. Laser treatment created the microchannels to form the depots for peptide residence, followed by the perpendicular and lateral diffusion to increase the penetration depth and distribution.

Laser-Assisted siRNA Delivery for Silencing IL-6 in Psoriasisiform Skin

A psoriatic skin model in mice was employed to examine the *in vivo* activity of IL-6 siRNA delivered by laser assistance. The capability of siRNA to induce a therapeutic response was first proved *in vitro* as revealed in Figure 5A. Incubation with siRNA resulted in 55% IL-6 knockdown relative to the control in 3T3-L1 cells. These data confirmed the IL-6 gene-silencing effect using siRNA. No significant cytotoxicity was detected following incubation with siRNA. To determine whether silencing IL-6 expression in psoriasisiform skin by laser-assisted siRNA leads to therapeutic efficacy, we first assessed H&E-stained histology as shown in Figure 5B. The representative images exhibited the severity of hyperplasia and scaling in the order of IMQ \geq IMQ+siRNA > IMQ+siRNA+laser > untreated healthy control. The laser group proved to be more effective than the group without laser intervention. No microchannel was revealed in the laser-treated skin. This was because the micrographs were taken 3 days post-irradiation. The wounds were closed and

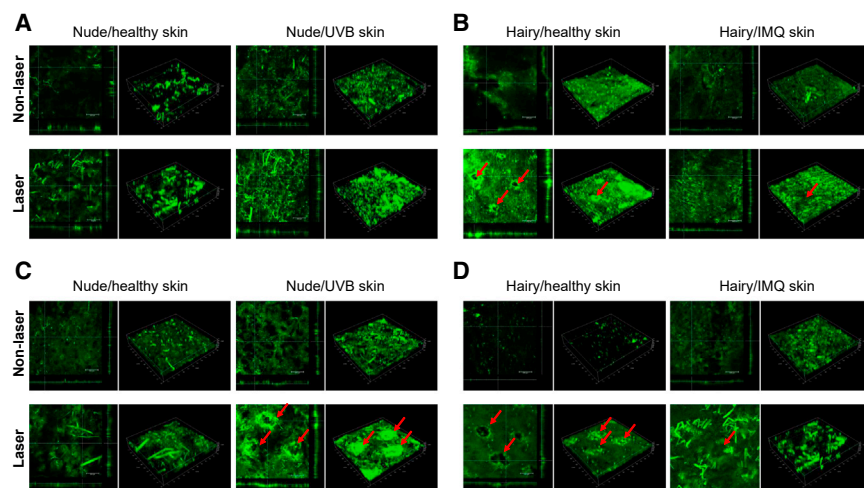


Figure 4. Biodistribution of the Permeants in the Fractional CO₂ Laser-Treated Skin Monitored by Confocal Microscopy

(A) Topical application of fluorescently labeled siRNA on nude mouse skin with or without UVB treatment. (B) Topical application of fluorescently labeled siRNA on hairy mouse skin with or without IMQ treatment. (C) Topical application of fluorescently labeled peptide on nude mouse skin with or without UVB treatment. (D) Topical application of fluorescently labeled peptide on hairy mouse skin with or without IMQ treatment. The left panel is the 2D (x-y axis) imaging of the skin structure. The right panel is the 3D (x-y-z axis) imaging of the skin structure.

recovered on the intact skin. In addition to H&E staining, specific psoriatic biomarkers were analyzed using immunohistochemistry. The increased IL-6 and IL-17A expression was observed for IMQ-treated skin compared to healthy skin as shown in Figures 5C and 5D, respectively. The immunohistochemical staining displayed a markedly decreased brown color for IL-6 and IL-17A by laser-assisted siRNA, signifying reduced inflammation and epidermal thickening.

The impact on keratinocyte proliferation was analyzed by Ki67, a proliferation marker highly expressed in psoriatic skin. Figure 5E represents a broad distribution of Ki67 throughout the basal layer of the epidermis following IMQ stimulation. Topically applied siRNA produced a decrease in Ki67 staining, with greater reduction by the laser group. Increased neutrophil infiltration in the dermis is profound in psoriatic lesions. The presence of brown staining by Ly6G in Figure 5F is considered a positive identification for neutrophils. A marked neutrophil migration was apparent in the dermis of the IMQ group. Laser treatment caused a significant decrease in neutrophils. Figure 5G shows the epidermal thickness calculated by histology. The thickness was increased from 12 to 164 μ m by IMQ stimulation, while the thickness for siRNA treatment with and without laser was reduced to 75 and 146 μ m, respectively. Figure 5H shows the microabscesses estimated by histopathology. The microabscesses were reduced by siRNA application with laser by 2-fold less than those in the IMQ group. Transdermal water loss (TEWL) as an indicator of skin-barrier function was determined as shown in Figure 5I. A 4-fold increase of TEWL was achieved in the psoriatic lesions as compared to normal skin. The application of siRNA did not improve the barrier function disrupted by IMQ. We used the ELISA method to quantify the psoriasis-related cytokines in the skin. These included IL-6, IL-17A, IL-23, and tumor necrosis factor alpha (TNF- α) (Figures 6A to 6D). IMQ activation resulted in the increase of all cytokines compared with the control. Topical siRNA administration without laser treatment was unable to reduce the protein expression. In contrast, laser-assisted siRNA

reduced cytokine expression significantly compared to the IMQ group. The laser-mediated siRNA application could lower the interleukin family to the normal control baseline. The laser intervention induced a knockdown of siRNA with a 64% inhibition.

DISCUSSION

RNAi strategy is valid for treating inflamed skin diseases such as psoriasis, atopic dermatitis, and contact allergy. The conventional route of siRNA delivery for dermatological treatment is injection. However, the associated intense pain and difficult self-administration have limited the use of injection. The less invasive topical delivery is a focus for improving the siRNA delivery approach. The intrinsic barrier nature of the skin combined with the large molecule and negative charge leads to restricted siRNA skin permeation. Our previous work demonstrated the effective enhancement of siRNA absorption by low-fluence laser irradiation on the skin.^{16,17} Nevertheless, whether this enhanced delivery can silence the gene to show the promising therapeutic benefit has not yet been established. In the present study, we used laser-assisted siRNA delivery for treating psoriasiform lesions via IL-6 silencing. The micropores formed by the laser ablation enabled the facile entry of siRNA and other low-absorption permeants into the skin. This effect still remained in the barrier-defective skins. The *in vivo* result demonstrated a significant improvement of the psoriatic lesions by laser-mediated siRNA administration. This is the first report of successful *in vivo* application of topical siRNA delivery using laser microporation.

Fractional laser illuminates the skin with a distinct microchannel array. The intact tissue around the microchannels accelerates the healing of the treated tissue, shortening the recovery time.¹⁸ Our previous study suggested the closure of the CO₂ laser-treated micropore opening within 16 h.¹⁹ The lining of coagulation surrounding the micropores was found after laser treatment. According to the microscopic observation, the micropores were smaller than the irradiated area of the fractional laser dot (300 μ m). The effective treatment zone on the laser-treated skin may contain the micropores and thermal coagulation. The skin was artificially prepared to develop barrier-defective models for mimicking diseased skin in a controllable

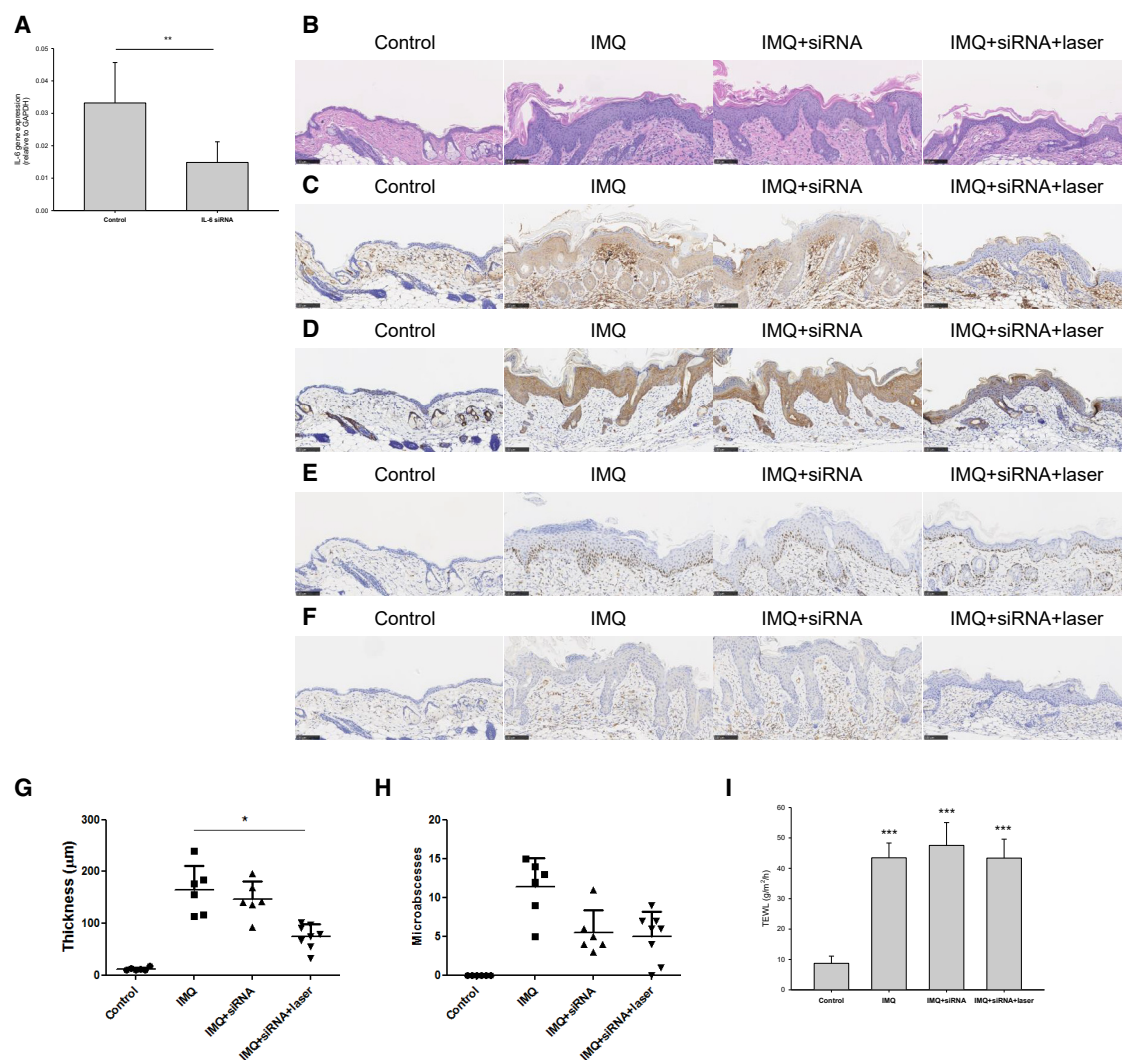


Figure 5. *In Vivo* Topical Application of IL-6 siRNA in IMQ-Induced Psoriasiform Lesion with or without Fractional CO₂ Laser Treatment

(A) IL-6 gene expression in 3T3-L1 cells with treatment by siRNA. (B) H&E staining of the skin observed by optical microscopy. (C) Immunohistochemical IL-6 staining of the skin observed by optical microscopy. (D) Immunohistochemical IL-17A staining of the skin observed by optical microscopy. (E) Immunohistochemical Ki67 staining of the skin observed by optical microscopy. (F) Immunohistochemical Ly6G staining of the skin observed by optical microscopy. (G) Epidermal thickness quantified by H&E staining. (H) Total counts of abscesses by H&E staining. (I) TEWL measurement. Data are presented as the mean of six to eight experiments \pm SD. * $p < 0.05$, ** $p < 0.01$, *** $p < 0.001$.

condition. These included SC stripping, lipid removal, sebum removal, and protein denaturalization.

The drugs should be lipophilic and small to achieve a meaningful passive permeation across intact skin. Healthy skin is almost impermeable for the charged, hydrophilic, and large molecules.²⁰ The permeants selected in this study are the molecules with poor skin penetration. Topical delivery of siRNA, peptide, and 5-FU remains a challenge. 5-FU was proved to be efficient for treating psoriasis, vitiligo, actinic keratosis, and skin tumors.²¹ The CO₂ laser-assisted 5-FU delivery is evaluated in clinical trials for skin-cancer management.^{22–24} Since the topical drug therapy is always applied on the barrier-defective diseased skin, we first pre-

pared the impaired skin according to the standardized methods for examining permeation. The greater enhancement of siRNA flux by tape stripping indicated an important barrier of SC. It was possible that siRNA interacted with the SC and hence SC stripping dramatically elevated its delivery. The diffusion routes of the SC are mainly the lipid bilayers and intercellular proteins. The de-protein skin showed a greater siRNA permeability than did the de-lipid skin, demonstrating the stronger barrier of protein compared to lipid for siRNA transport. A contrary tendency was detected for peptide delivery across de-lipid and de-protein skins. The sebaceous glands produce sebum to cover the outermost skin surface. The permeant should partition into the sebum layer and then penetrate the SC.²⁵ Sebum removal significantly decreased siRNA

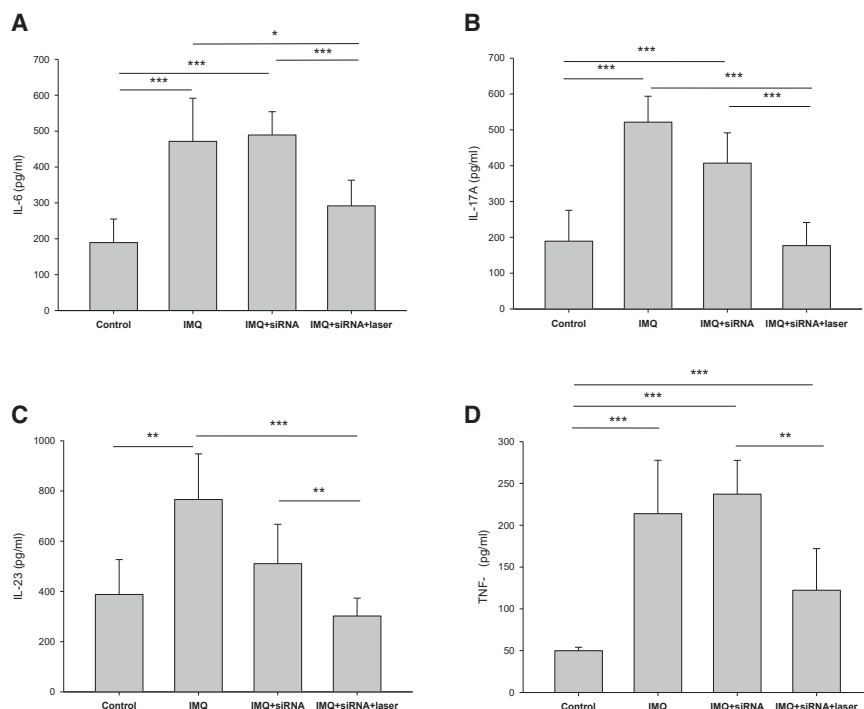


Figure 6. Cytokine Expression in the Skin after In Vivo Topical Application of IL-6 siRNA in IMQ-Induced Psoriasiform Lesion with or without Fractional CO₂ Laser Treatment

(A) IL-6. (B) IL-17A. (C) IL-23. (D) TNF-α. Data are presented as the mean of six to eight experiments ± SD. *p < 0.05, **p < 0.01, ***p < 0.001.

flux compared to intact skin, suggesting the importance of sebum partitioning for siRNA permeation.

A previous study²⁶ manifested the difficulty of peptide partitioning to a lipophilic skin surface. This difficulty has led to the higher peptide permeation via de-sebum skin than via intact skin. The sebum was not as significant for 5-FU partitioning due to the comparable flux between intact and de-sebum skins. The permeation enhancement of 5-FU by SC stripping was notably lower as compared to that for macromolecules. This indicates that the small molecules are still better able than macromolecules to pass across the SC. The cutaneous transport of hydrophilic small molecules is predominantly attributed to the polar pathway. This is why 5-FU flux was increased by protein removal but not lipid extraction.

Our results demonstrated that fractional laser treatment overcame the barrier of the SC to enhance the permeation of all permeants tested. This denoted the usefulness of laser-mediated delivery for the permeants with a molecular weight (MW) range from at least 130 to 8,490 g/mol. The SC is usually the main barrier for the delivery of macromolecules and hydrophilic molecules. The creation of microchannels by fractional laser treatment exposed the permeants to the underlying epidermis with a hydrophilic matrix.²⁷ The fractional pathway filled with aqueous permeant vehicle to produce hydrophilic channels in the viable tissue. The permeants facily traversed into the channels to partition into the viable skin for broad biodistribution. The effortless delivery into the microchannels was evidenced by confocal imaging. The formation of microchannels increased the total contact surface area of the skin for drug delivery. In addition to ver-

tical penetration into the deeper skin layer, the permeants in the microchannels diffused to the lateral region via radial permeation.²⁸ The confocal micrographs illustrated the possibility of horizontal diffusion from the channels. The smaller molecular size of the peptide compared to siRNA contributed to the larger diffusion radius of the horizontal penetration area. The irradiated area of the dot of the fractional laser was 300 μm, which was an overestimation of the created micropores (150–200 μm) according to microscopic imaging. This was probably due to the formation of thermal coagulation around the micropores by the fractional CO₂ laser dot.²⁹ The constituents of coagulation are mainly the platelets and fibrin fibers. The matrix serves as a protective shield against pathogenic microbes.³⁰ Hence, it is also the obstruction for drug delivery.³¹ This layer prevented a fast release of macromolecules from the channels to the surrounding tissue, establishing a permeant reservoir inside the micropores for prolonged and sustained delivery. The filling of fluorescently labeled microchannels inside some pores could confirm this inference. The thermal denaturation hinders drug passage across the microchannels, especially for hydrophilic small molecules.^{31–33} This could be the reason for the low enhancement level of 5-FU flux after fractional laser exposure.

The fractional laser was still effective in inducing the enhancement of permeant delivery in barrier-defective and diseased skin, although the enhancement level was lower than that in the intact skin. Tape stripping can be a robust model for dermatitis.³⁴ The laser did not promote the flux of all permeants across SC-stripped skin, except siRNA penetration via SC-stripped mouse skin. This indicates that the laser almost eliminated the barrier function of the SC. De-lipid skin mimics the diseased condition of psoriasis, xerosis, and ichthyosis.³⁵ The denaturation of protein in the SC resembles the model of atopic dermatitis and photoaging.³⁶ Our results demonstrated a lesser enhancement of laser-mediated delivery in de-lipid skin than in de-protein skin, suggesting a stronger laser impact on lipid bilayers than on proteins and corneocytes. The CO₂ laser can elicit a photo-mechanical wave for the enlargement of lacunar space in lipid bilayers, facilitating drug passage.⁷ Both photoaging and psoriatic skins are characterized by an impaired barrier property. The fractional laser assisted the delivery of permeants into the diseased skins. The enhancement was lower compared to that of healthy skin because

of the already compromised barrier in the inflamed skin. The comparison of different permeants generally showed the greatest absorption enhancement for laser-assisted siRNA in all skin types. This suggests greater selectivity of siRNA to diffuse through the microchannels than for the other permeants.

An ideal delivery approach for topical siRNA therapy is to enhance nucleic acid transport across the SC and facilitate efficient uptake by target cells.³⁷ We further delivered IL-6 siRNA into the skin in a targeted fashion by using the fractional laser *in vivo*. IL-6 plays a critical role in the psoriasis triggering. We observed that IL-6 was significantly inhibited by laser-assisted siRNA. The result also demonstrated that the laser reduced cytokines, keratinocyte proliferation, and inflammation, which was less than with the passive siRNA delivery and IMQ-only stimulation. The silencing effect and anti-inflammatory ability in psoriasis-like plaque could be the result of laser ablation for enhancing siRNA permeation. In addition to IL-6, IMQ is reported to elevate cytokines IL-17 and IL-23.³⁸ IL-17 can synergize with TNF- α to activate psoriatic inflammation.³⁹ The neutralizing of TNF- α is an important indicator for therapeutic efficiency against psoriasis. All of these cytokines were downregulated by laser-mediated siRNA in our *in vivo* psoriasis-like model. The reduction of proinflammatory cytokines led to the repair of IMQ-induced skin inflammation and damage. No microchannel or coagulation was observed in the skin histology taken 3 days after laser irradiation, indicating a safe use of the fractional laser for psoriasis mitigation. The 3-(4,5-dimethylthiazol-2-yl)-2,5-dimethyltetrazolium bromide (MTT)-based assay in 3T3-L1 cells also revealed that IL-6 siRNA was nontoxic.

Once siRNA delivers into the skin, additional effort is necessary to reach the target cells and promote the cellular uptake. Transporting the nucleic acid family into the cells is problematic because of the large size and negative charge.¹² A previous study⁴⁰ has suggested a negligible knockdown of IL-6 by siRNA due to the insufficient cell uptake. In order to improve the nucleic acid uptake into the cells, an active approach is especially beneficial. Our data showed an efficient IL-6 silencing by laser treatment. A laser-enhanced cell uptake was possible. IL-17A is mainly released by neutrophils, T cells, and innate lymphoid cells. IL-6 is known as an upstream cytokine of IL-17A.⁴¹ In psoriatic lesions, keratinocytes and dendritic cells produce a high level of IL-23.³⁹ The laser irradiation might increase the uptake in a variety of cells. Previous studies^{26,42} have revealed that the fractional laser can act at a cellular level to increase the uptake of macromolecular vaccines and nanoparticles. Further study is needed to explore the detailed mechanisms of laser-assisted cell uptake. Cutaneous diseases related to inflammation are suitable for siRNA therapy because of the presence of determined molecular targets for silencing. Our results suggested that laser-assisted IL-6 siRNA could inhibit psoriatic plaque in a mouse model in the absence of transfection reagents. The enhanced knockdown was achieved with only one application of laser pulse and could be sustained over time. Some approaches, including ultrasound, iontophoresis, electroporation, and microneedles, are employed to facilitate nucleic acid permeation across the SC. Most

of them need a prolonged period of application to obtain enhanced efficiency. Fractional laser is an ideal permeation-enhanced strategy with the advantages of a very short application time and avoidance of cross-contamination risk.

The present study had some limitations. We chiefly evaluated the skin delivery of the permeants by the *in vitro* Franz cell. The use of excised skin *in vitro* may exhibit some differences from the *in vivo* and clinical status. Although mouse and pig skins are extensively accepted as an alternative model for human skin, it is difficult to compare the cutaneous delivery in the different skin types. Further study is needed to clarify the laser-mediated siRNA absorption in humans. Another concern is that the laser-enhanced IL-6 siRNA transport could not completely reverse the psoriatic lesion to the normal baseline according to histology and TEWL. A complete silencing of the gene target is not required to accomplish the therapeutic benefit.⁴³ A previous study³ suggests that a 50% expression reduction in the target gene via topical RNAi is adequate to treat keratinizing skin diseases. The experimental data showed a 64% decline of IL-6 expression by fractional CO₂ laser in the psoriasis mouse model, verifying the usefulness of the laser approach.

Conclusions

To date, several RNAi clinical trials have been conducted, but only one product (Patisiran) has obtained USFDA approval. RNAi has the potential for skin-disease treatment if the delivery approaches can be improved. Here, we develop fractional laser-mediated delivery for topical siRNA application. In this study, the macromolecules and hydrophilic small molecules were transported through the breached SC along the microchannels to reach the deeper skin strata. In the *in vivo* psoriasis-like lesion model, laser-assisted siRNA delivery was able to silence IL-6 in the epidermis. The psoriatic plaque was thus ameliorated. Laser-assisted siRNA permeation proved to be a potential therapeutic management for psoriasis. Further clinical study is warranted to verify the possible application of RNAi therapy by laser aid.

MATERIALS AND METHODS

Permeants

The siRNA containing fluorescein isothiocyanate (FITC) for the skin permeation test exhibited the sequences of 5'-FITC-UGCUGACUC-CAAAG-3' and 3'-ACGACUGAGGUUC-5' (MW = 8,490 g/mol). The IL-6 siRNA sequences were 5'-UUCUCCGAACGUGUCA CGUTT-3' and 3'-ACGUGACACGUUCGAGAATT-5' (MW = 12,856 g/mol). Both siRNAs were synthesized by GenZyme (Miaoli, Taiwan). The FITC-conjugated peptide with the sequence of FITC-NH₂-Pro-Arg-Leu-Leu-Tyr-Ser-Trp-His-Arg-Ser-His-Arg-Ser-His-COOH was purchased from Biotools (New Taipei City, Taiwan). 5-FU was provided by Sigma-Aldrich (St. Louis, MO, USA).

Animals

The 8-week-old female nude and BALB/c mice were supplied by the National Laboratory Animal Center (Taipei, Taiwan). The pathogen-free 1-week-old pig was purchased from the Animal Technology

Institute of Taiwan (Miaoli, Taiwan). All experiments were conducted in strict accordance with the recommendations in the *Guidelines for the Care and Use of Laboratory Animals* of Chang Gung University.

Preparation of Barrier-Defective and Diseased Skins

Adhesive tape (Scotch, 3M) was applied to the surface of the excised nude mouse or pig skin and then removed, with the application/removal being done a total of 20 times to achieve SC-stripped skin. De-lipid skin was prepared by incubating the skin surface with chloroform/methanol (2:1) for 2 h. The de-sebum skin was obtained by a cold hexane (4°C) wash repeated five times.⁴⁴ We prepared the de-protein skin using ethanol/water (2:3) incubation on the skin surface for 2 h.⁴⁵ In the induction of photoaging skin, the back of the nude mice was exposed under UVB at 312 nm (Vilber Lourmat, Marne-la-Vallée, France).⁴⁶ The spectral irradiance was 175 mJ/cm². The dorsal area was exposed to UVB once a day for 5 days. The induction of a psoriasis-like lesion was performed according to the previous protocol.⁴⁷ In brief, the skin on the shaved back of the hairy mice was topically applied with IMQ cream (Aldara, 3M) at a dose of 62.5 mg each day for 6 consecutive days. The applied region was covered with Tegaderm and nonwoven cloth after the IMQ application.

Laser System

The fractional CO₂ laser (Mosaic eCO₂, Lutronic, San Jose, CA, USA) emitted a 10,600-nm irradiation with a scanning area of 14 × 14 mm. There were 400 spots in 1 cm² to produce a microscopic thermal zone (MTZ). The MTZ diameter was 300 μm with a fluence of 4 mJ and pulse duration of 80 μs.

The Appearance of the Skin Surface

The intact nude and BALB/c mice skins as well as UVB- and IMQ-treated skins were irradiated *in vivo* by CO₂ laser. The gross observation of the skin surface was accomplished using a handheld digital magnifier (Mini Scope-V, M&T Optics, Taipei, Taiwan). The microscopic observation of the skin surface was achieved by optical microscopy (DMi8, Leica, Wetzlar, Germany) with ×200 magnification.

H&E Staining

The excised skin with or without laser treatment was immersed in a 10% buffered formalin using ethanol embedded in paraffin wax; it was sliced at a thickness of 3 μm for H&E staining. The longitudinal section of the skin was visualized by optical microscopy.

Skin Permeation Assessment

Franz cell was used to assess the skin delivery of the permeants. The intact or barrier-defective skin with or without laser exposure was mounted between the donor and receptor with the SC facing toward the donor. The donor compartment was filled with 0.5 mL of FITC-conjugated siRNA (0.4 μM) in nuclease-free water, peptide (150 μM) in pH 7.4 buffer, or 5-FU (15 mM) in pH 7.4 buffer. The receptor medium was nuclease-free water for siRNA. The pH 7.4 buffer was the receptor solution for peptide and 5-FU. The effective permeation area was 0.789 cm². The stirring rate and receptor temperature were kept at 600 rpm and 37°C, respectively. The 300-μL aliquot in

the receptor was withdrawn at the determined intervals. At the end of the experiment (24 h), the skin was removed to determine the skin deposition of the permeants. The skin was extracted by 0.1 N HCl in a homogenizer (MagNA Lyser, Roche). The homogenate was centrifuged at 10,000 × g for 10 min. The receptor amount and skin deposition of siRNA and peptide were quantified by fluorescence spectrophotometry. 5-FU was analyzed by high-performance liquid chromatography (HPLC) according to the previous condition.⁴⁸

Distribution of siRNA and Peptide in the Skin

siRNA or peptide in the medium the same as the skin permeation assessment was applied in the Franz cell donor. The application duration was 6 h. Then, the skin was washed with water. The skin was positioned onto the stage plate of a confocal laser scanning microscope (TCS SP2, Leica). The skin thickness was scanned at 5-μm increments via z axis from the surface. The images were summed by 15 fragments. The 3D image of the skin was processed by confocal microscopy software.

IL-6 Silencing by siRNA in Cells

The mouse 3T3-L1 cell line was cultured in DMEM and was then supplemented with 10% fetal bovine serum (FBS) and 1% penicillin-streptomycin in 5% CO₂ at 37°C. The cells were transfected by IL-6 siRNA with Lipofectamine 2000 for 4 h. After an incubation of 24 h, the cells were collected to detect the mRNA level of IL-6. Total RNA was extracted by TRIzol (Thermo Fisher Scientific). cDNA was synthesized by reverse transcription with an iScript cDNA synthesis kit (Bio-Rad). Quantitative real-time PCR was carried out by iQ SYBR Green Supermix (Bio-Rad). The GAPDH gene expression was employed as a housekeeping gene to normalize IL-6 gene expression. The 3T3-L1 cell viability was analyzed by an MTT assay.

In Vivo Topical siRNA Administration on Psoriasiform Lesions

The BALB/c mice with IMQ treatment were enrolled in this experiment. IMQ cream was topically applied on the mouse back for 6 days. On day 3, a fractional laser was irradiated on the dorsal area. IL-6 siRNA at 20 μM (60 μL) was then applied on the mouse back. We applied siRNA each day for 3 days. TEWL was monitored by Tewameter TM300 (Courage and Khazaka, Köln, Germany). The animals were sacrificed on day 6 for the further examination of skin histology and cytokines.

Immunohistochemical Staining

The skin samples were fixed in 10% formalin buffered in phosphate saline for immunohistochemical staining. The detailed procedure was described in the previous study.⁴⁹ The skin sections were incubated with anti-IL-6 antibody, anti-IL-17A antibody, anti-Ki67 antibody, and anti-Ly6G antibody for 1 h, and subsequently incubated with biotinylated donkey anti-goat IgG for 20 min. Photomicrographs were taken using Leica DMi8 microscopy.

Cytokine Measurement

The number of cytokines in the skin was assessed by ELISA. The detailed process was shown in our previous work.⁴⁹ The level of

IL-6, IL-17A, IL-23, and TNF- α was measured using commercial kits (BioLegend, San Diego, CA, USA) according to the manufacturer's instructions.

Statistical Analysis

The statistical difference in the data of the different treatment groups was analyzed using a Kruskal-Wallis test. The *post hoc* test for checking individual differences was the Dunn's test. The 0.05, 0.01, and 0.001 levels of probability were taken as statistically significant.

AUTHOR CONTRIBUTIONS

J.-Y.F. initiated the study and drafted the manuscript. J.-Y.F. and W.-R.L. involved in the design of all experiments. W.-R.L., Y.-K.L., and P.-Y.L. carried out the experiments. Y.-K.L. and A.A. analyzed data and wrote the manuscript. J.-Y.F. supervised the entire project. W.-R.L. and P.-W.W. reviewed critically and approved the final manuscript. All authors read and approved the final manuscript.

CONFLICTS OF INTEREST

The authors declare no competing interests.

ACKNOWLEDGMENTS

The authors are grateful for the financial support by the Ministry of Science and Technology of Taiwan (MOST-105-2320-B-182-010-MY3) and the Chang Gung Memorial Hospital (CMRPD1F0231-3 and CMRPG2F0491-3).

REFERENCES

- Adams, D., Gonzalez-Duarte, A., O'Riordan, W.D., Yang, C.C., Ueda, M., Kristen, A.V., Tourné, I., Schmidt, H.H., Coelho, T., Berk, J.L., et al. (2018). Patisiran, an RNAi therapeutic, for hereditary transthyretin amyloidosis. *N. Engl. J. Med.* 379, 11–21.
- Hay, R.J., Johns, N.E., Williams, H.C., Bolliger, I.W., Dellavalle, R.P., Margolis, D.J., Marks, R., Naldi, L., Weinstock, M.A., Wulf, S.K., et al. (2014). The global burden of skin disease in 2010: an analysis of the prevalence and impact of skin conditions. *J. Invest. Dermatol.* 134, 1527–1534.
- Hegde, V., Hickerson, R.P., Nainamalai, S., Campbell, P.A., Smith, F.J., McLean, W.H., and Pedrioli, D.M. (2014). In vivo gene silencing following non-invasive siRNA delivery into the skin using a novel topical formulation. *J. Control. Release* 196, 355–362.
- Rosa, J., Suzuki, I., Kravicz, M., Caron, A., Pupo, A.V., Praça, F.G., and Bentley, M.V.L.B. (2018). Current non-viral siRNA delivery systems as a promising treatment of skin diseases. *Curr. Pharm. Des.* 24, 2644–2663.
- Ita, K. (2017). Dermal/transdermal delivery of small interfering RNA and antisense oligonucleotides—advances and hurdles. *Biomed. Pharmacother.* 87, 311–320.
- Aljuffali, I.A., Lin, C.F., Chen, C.H., and Fang, J.Y. (2016). The codrug approach for facilitating drug delivery and bioactivity. *Expert Opin. Drug Deliv.* 13, 1311–1325.
- Lin, C.H., Aljuffali, I.A., and Fang, J.Y. (2014). Lasers as an approach for promoting drug delivery via skin. *Expert Opin. Drug Deliv.* 11, 599–614.
- Zorec, B., Škrabelj, D., Marinček, M., Miklavčič, D., and Pavšelj, N. (2017). The effect of pulse duration, power and energy of fractional Er:YAG laser for transdermal delivery of differently sized FITC dextrans. *Int. J. Pharm.* 516, 204–213.
- Lee, W.R., Shen, S.C., Sung, C.T., Liu, P.Y., and Fang, J.Y. (2018). Is the fractional laser still effective in assisting cutaneous macromolecule delivery in barrier-deficient skin? Psoriasis and atopic dermatitis as the disease models. *Pharm. Res.* 35, 128.
- Greb, J.E., Goldminz, A.M., Elder, J.T., Lebwohl, M.G., Gladman, D.D., Wu, J.J., Mehta, N.N., Finlay, A.Y., and Gottlieb, A.B. (2016). Psoriasis. *Nat. Rev. Dis. Primers* 2, 16082.
- Desmet, E., Bracke, S., Forier, K., Taevernier, L., Stuart, M.C., De Spiegeleer, B., Raemdonck, K., Van Gele, M., and Lambert, J. (2016). An elastic liposomal formulation for RNAi-based topical treatment of skin disorders: Proof-of-concept in the treatment of psoriasis. *Int. J. Pharm.* 500, 268–274.
- Boakye, C.H.A., Patel, K., Doddapaneni, R., Bagde, A., Marepally, S., and Singh, M. (2017). Novel amphiphilic lipid augments the co-delivery of erlotinib and IL36 siRNA into the skin for psoriasis treatment. *J. Control. Release* 246, 120–132.
- Desmet, E., Van Gele, M., Grine, L., Remaut, K., and Lambert, J. (2018). Towards the development of a RNAi-based topical treatment for psoriasis: proof-of-concept in a 3D psoriasis skin model. *Exp. Dermatol.* 27, 463–469.
- Vaidya, T.S., and Alikhan, A. (2017). Treatment satisfaction among patients with psoriasis at a large academic center: an observational study. *J. Dermatolog. Treat.* 28, 288–289.
- Zakrewsky, M., and Mitragotri, S. (2016). Therapeutic RNAi robed with ionic liquid moieties as a simple, scalable prodrug platform for treating skin disease. *J. Control. Release* 242, 80–88.
- Lee, W.R., Shen, S.C., Zhuo, R.Z., Wang, K.C., and Fang, J.Y. (2009). Enhancement of topical small interfering RNA delivery and expression by low-fluence erbium:YAG laser pretreatment of skin. *Hum. Gene Ther.* 20, 580–588.
- Lee, W.R., Shen, S.C., Chen, W.Y., Aljuffali, I.A., Suen, S.Y., and Fang, J.Y. (2014). Noninvasive delivery of siRNA and plasmid DNA into skin by fractional ablation: erbium:YAG laser versus CO₂ laser. *Eur. J. Pharm. Biopharm.* 86, 315–323.
- Borges, J., Manela-Azulay, M., and Cuzzi, T. (2016). Photoaging and the clinical utility of fractional laser. *Clin. Cosmet. Investig. Dermatol.* 9, 107–114.
- Lee, W.R., Hsiao, C.Y., Huang, T.H., Wang, C.L., Alalawi, A., Chen, E.L., and Fang, J.Y. (2019). Post-irradiation recovery time strongly influences fractional laser-facilitated skin absorption. *Int. J. Pharm.* 564, 48–58.
- Prausnitz, M.R., and Langer, R. (2008). Transdermal drug delivery. *Nat. Biotechnol.* 26, 1261–1268.
- Moore, A.Y. (2009). Clinical applications for topical 5-fluorouracil in the treatment of dermatological disorders. *J. Dermatolog. Treat.* 20, 328–335.
- Glenn, C.J., Parlette, E.C., and Mitchell, C. (2015). Fractionated CO₂ laser-assisted delivery of topical 5-fluorouracil as a useful modality for treating field cutaneous squamous cell carcinomas. *Dermatol. Surg.* 41, 1339–1342.
- Nguyen, B.T., Gan, S.D., Konnikov, N., and Liang, C.A. (2015). Treatment of superficial basal cell carcinoma and squamous cell carcinoma in situ on the trunk and extremities with ablative fractional laser-assisted delivery of topical fluorouracil. *J. Am. Acad. Dermatol.* 72, 558–560.
- Hsu, S.H., Gan, S.D., Nguyen, B.T., Konnikov, N., and Liang, C.A. (2016). Ablative fractional laser-assisted topical fluorouracil for the treatment of superficial basal cell carcinoma and squamous cell carcinoma in situ: a follow-up study. *Dermatol. Surg.* 42, 1050–1053.
- Schneider, D., Dennerlein, K., Göen, T., Schaller, K.H., Drexler, H., and Korinth, G. (2016). Influence of artificial sebum on the dermal absorption of chemicals in excised human skin: a proof-of-concept study. *Toxicol. In Vitro* 33, 23–28.
- Fujimoto, T., Wang, J., Baba, K., Oki, Y., Hiruta, Y., Ito, M., Ito, S., and Kanazawa, H. (2017). Transcutaneous drug delivery by liposomes using fractional laser technology. *Lasers Surg. Med.* 49, 525–532.
- Taudorf, E.H., Lerche, C.M., Erlendsson, A.M., Philipsen, P.A., Hansen, S.H., Janfelt, C., Paasch, U., Anderson, R.R., and Haedersdal, M. (2016). Fractional laser-assisted drug delivery: laser channel depth influences biodistribution and skin deposition of methotrexate. *Lasers Surg. Med.* 48, 519–529.
- Kumar, M.N.K., Zhou, C., and Wu, M.X. (2016). Laser-facilitated epicutaneous immunotherapy to IgE-mediated allergy. *J. Control. Release* 235, 82–90.
- Banzhaf, C.A., Lin, L.L., Dang, N., Freeman, M., Haedersdal, M., and Prow, T.W. (2018). The fractional laser-induced coagulation zone characterized over time by laser scanning confocal microscopy—a proof of concept study. *Lasers Surg. Med.* 50, 70–77.
- Minutti, C.M., Knipper, J.A., Allen, J.E., and Zaiss, D.M. (2017). Tissue-specific contribution of macrophages to wound healing. *Semin. Cell Dev. Biol.* 61, 3–11.

31. Nguyen, H.X., and Banga, A.K. (2018). Delivery of methotrexate and characterization of skin treated by fabricated PLGA microneedles and fractional ablative laser. *Pharm. Res.* 35, 68.
32. Choi, J.H., Shin, E.J., Jeong, K.H., and Shin, M.K. (2017). Comparative analysis of the effects of CO₂ fractional laser and sonophoresis on human skin penetration with 5-aminolevulinic acid. *Lasers Med. Sci.* 32, 1895–1900.
33. Meesters, A.A., Nieboer, M.J., Kezic, S., de Rie, M.A., and Wolkerstorfer, A. (2018). Parameters in fractional laser assisted delivery of topical anesthetics: role of laser type and laser settings. *Lasers Surg. Med.* 50, 813–818.
34. Abdel-Mottaleb, M.M.A., and Lamprecht, A. (2016). In vivo skin penetration of macromolecules in irritant contact dermatitis. *Int. J. Pharm.* 515, 384–389.
35. Sahle, F.F., Gebre-Mariam, T., Dobner, B., Wohlrab, J., and Neubert, R.H. (2015). Skin diseases associated with the depletion of stratum corneum lipids and stratum corneum lipid substitution therapy. *Skin Pharmacol. Physiol.* 28, 42–55.
36. Biniek, K., Levi, K., and Dauskardt, R.H. (2012). Solar UV radiation reduces the barrier function of human skin. *Proc. Natl. Acad. Sci. USA* 109, 17111–17116.
37. González-González, E., Speaker, T.J., Hickerson, R.P., Spitler, R., Flores, M.A., Leake, D., Contag, C.H., and Kaspar, R.L. (2010). Silencing of reporter gene expression in skin using siRNAs and expression of plasmid DNA delivered by a soluble protrusion array device (PAD). *Mol. Ther.* 18, 1667–1674.
38. Desai, P.R., Marepally, S., Patel, A.R., Voshavar, C., Chaudhuri, A., and Singh, M. (2013). Topical delivery of anti-TNF α siRNA and capsaicin via novel lipid-polymer hybrid nanoparticles efficiently inhibits skin inflammation in vivo. *J. Control. Release* 170, 51–63.
39. Grine, L., Dejager, L., Libert, C., and Vandenbroucke, R.E. (2015). An inflammatory triangle in psoriasis: TNF, type I IFNs and IL-17. *Cytokine Growth Factor Rev.* 26, 25–33.
40. Depieri, L.V., Borgheti-Cardoso, L.N., Campos, P.M., Otaguiri, K.K., Vicentini, F.T., Lopes, L.B., Fonseca, M.J., and Bentley, M.V.L.B. (2016). RNAi mediated IL-6 in vitro knockdown in psoriasis skin model with topical siRNA delivery system based on liquid crystalline phase. *Eur. J. Pharm. Biopharm.* 105, 50–58.
41. Croxford, A.L., Karbach, S., Kurschus, F.C., Wörtge, S., Nikolaev, A., Yogeve, N., Klebow, S., Schüler, R., Reissig, S., Piotrowski, C., et al. (2014). IL-6 regulates neutrophil microabscess formation in IL-17A-driven psoriasiform lesions. *J. Invest. Dermatol.* 134, 728–735.
42. Chen, X., Shah, D., Kosiratna, G., Manstein, D., Anderson, R.R., and Wu, M.X. (2012). Facilitation of transcutaneous drug delivery and vaccine immunization by a safe laser technology. *J. Control. Release* 159, 43–51.
43. Lara, M.F., González-González, E., Speaker, T.J., Hickerson, R.P., Leake, D., Milstone, L.M., Contag, C.H., and Kaspar, R.L. (2012). Inhibition of CD44 gene expression in human skin models, using self-delivery short interfering RNA administered by dissolvable microneedle arrays. *Hum. Gene Ther.* 23, 816–823.
44. Campbell, C.S., Contreras-Rojas, L.R., Delgado-Charro, M.B., and Guy, R.H. (2012). Objective assessment of nanoparticle disposition in mammalian skin after topical exposure. *J. Control. Release* 162, 201–207.
45. Chuang, S.Y., Lin, Y.K., Lin, C.F., Wang, P.W., Chen, E.L., and Fang, J.Y. (2017). Elucidating the skin delivery of aglycone and glycoside flavonoids: how the structures affect cutaneous absorption. *Nutrients* 9, 1304.
46. Hung, C.F., Chen, W.Y., Aljuffali, I.A., Lin, Y.K., Shih, H.C., and Fang, J.Y. (2015). Skin aging modulates percutaneous drug absorption: the impact of ultraviolet irradiation and ovariectomy. *Age (Dordr.)* 37, 21.
47. van der Fits, L., Mourits, S., Voerman, J.S., Kant, M., Boon, L., Laman, J.D., Cornelissen, F., Mus, A.M., Floencia, E., Prens, E.P., and Lubberts, E. (2009). Imiquimod-induced psoriasis-like skin inflammation in mice is mediated via the IL-23/IL-17 axis. *J. Immunol.* 182, 5836–5845.
48. Fang, J.Y., Hung, C.F., Fang, Y.P., and Chan, T.F. (2004). Transdermal iontophoresis of 5-fluorouracil combined with electroporation and laser treatment. *Int. J. Pharm.* 270, 241–249.
49. Lin, Z.C., Hsieh, P.W., Hwang, T.L., Chen, C.Y., Sung, C.T., and Fang, J.Y. (2018). Topical application of anthranilate derivatives ameliorates psoriatic inflammation in a mouse model by inhibiting keratinocyte-derived chemokine expression and neutrophil infiltration. *FASEB J.* 32, fj201800354.



Comorbidity of Narcolepsy and Psychotic Disorders: A Nationwide Population-Based Study in Taiwan

Jia-Yin Yeh¹, Yu-Chiau Shyu^{2,3,4}, Sheng-Yu Lee^{5,6}, Shin-Sheng Yuan⁷, Chun-Ju Yang^{2,8}, Kang-Chung Yang^{2,8}, Tung-Liang Lee⁹, Chi-Chin Sun¹⁰ and Liang-Jen Wang^{1*}

¹ Department of Child and Adolescent Psychiatry, Kaohsiung Chang Gung Memorial Hospital and Chang Gung University College of Medicine, Kaohsiung, Taiwan, ² Community Medicine Research Center, Keelung Chang Gung Memorial Hospital, Keelung, Taiwan, ³ Institute of Molecular Biology, Academia Sinica, Taipei, Taiwan, ⁴ Department of Nursing, Department of Nutrition and Health Sciences, Research Center for Food and Cosmetic Safety, and Research Center for Chinese Herbal Medicine, College of Human Ecology, Chang Gung University of Science and Technology, Taoyuan, Taiwan, ⁵ Department of Psychiatry, Kaohsiung Veterans General Hospital, Kaohsiung, Taiwan, ⁶ Department of Psychiatry, College of Medicine and Hospital, National Cheng Kung University, Tainan, Taiwan, ⁷ Institute of Statistical Science, Academia Sinica, Taipei, Taiwan, ⁸ Institute of Biopharmaceutical Sciences, National Yang-Ming University, Taipei, Taiwan, ⁹ Department of Radiation Oncology, University of Texas MD Anderson Cancer Center, Houston, TX, United States, ¹⁰ Department of Ophthalmology, Keelung, Chang Gung Memorial Hospital, Keelung, Taiwan

OPEN ACCESS

Edited by:

Fernando Rodriguez de Fonseca,
University of Málaga, Spain

Reviewed by:

Jan Dirk Blom,
Parnassia Psychiatric Institute,
Netherlands
Francisco Alen,
Complutense University of Madrid,
Spain

*Correspondence:

Liang-Jen Wang
wangliangjen@gmail.com

Specialty section:

This article was submitted to
Psychopharmacology,
a section of the journal
Frontiers in Psychiatry

Received: 12 March 2019

Accepted: 02 March 2020

Published: 25 March 2020

Citation:

Yeh J-Y, Shyu Y-C, Lee S-Y,
Yuan S-S, Yang C-J, Yang K-C,
Lee T-L, Sun C-C and Wang L-J
(2020) Comorbidity of Narcolepsy and
Psychotic Disorders: A Nationwide
Population-Based Study in Taiwan.
Front. Psychiatry 11:205.
doi: 10.3389/fpsy.2020.00205

Background: Narcolepsy is a chronic sleep disorder that is likely to have neuropsychiatric comorbidities. Psychotic disorders are characterized by delusion, hallucination, and reality impairments. This study investigates the relationship between narcolepsy and psychotic disorders.

Design and Methods: This study involves patients who were diagnosed with narcolepsy between January 2002 and December 2011 ($n = 258$) and age- and gender-matched controls ($n = 2580$) from Taiwan's National Health Insurance database. Both the patients and the controls were monitored from January 1, 2002 to December 31, 2011 to identify any occurrence of a psychotic disorder. Drugs that have been approved for treating narcolepsy: immediate-release methylphenidate (IR-MPH), osmotic controlled-release formulations of methylphenidate (OROS-MPH), and modafinil, were analyzed. A multivariate logistic regression model was used to evaluate the potential comorbidity of narcolepsy with psychotic disorders.

Results: During the study period, 8.1% of the narcoleptic patients exhibited comorbidity with a psychotic disorder, whereas only 1.5% of the control subjects (1.5%) had psychotic disorders (aOR, 4.07; 95% CI, 2.21–7.47). Of the narcolepsy patients, 41.5, 5.4, and 13.2% were treated with MPH-IR, MPH-OROS, and modafinil, accordingly. Pharmacotherapy for narcolepsy did not significantly affect the risk of exhibiting a psychotic disorder.

Conclusions: This nationwide study revealed that narcolepsy and psychotic disorders commonly co-occur. Pharmacotherapy for narcolepsy was not associated with the risk of psychotic disorders. Our findings serve as a reminder that clinicians must consider the comorbidity of narcolepsy and psychosis.

Keywords: narcolepsy, comorbidity, epidemiology, psychosis, stimulants

INTRODUCTION

Narcolepsy is a chronic disabling sleep disorder with an estimated lifetime prevalence of approximately 1 in 2,000 in the general population and it can severely influence daily activities (1, 2). Clinically, it is characterized by excessive daytime sleepiness (EDS) with sudden sleep attacks, rapid eye movement sleep abnormalities such as cataplexy, sleep paralysis, and hypnagogic or hypnopompic hallucinations, nocturnal dyssomnia with fragmented sleep and awakenings (3). The symptoms usually begin in adolescence (4). It has been hypothesized to be caused by a combination of genetic and environmental factors, trigger an autoimmune process that results in hypothalamic destruction, with a loss of hypocretin-1-containing cells, causing the hypocretin deficiency (4, 5). Psychiatric comorbidities with narcolepsy are frequent, and include mood, anxiety, attention deficit hyperactivity, eating disorders, and psychosis (6–9).

Psychotic disorders, consisting of a group of severe mental disorders, are a leading cause of disability globally (10). People with psychotic disorders manifest symptoms of delusion, hallucination, and reality impairment. They suffer from significant functional impairment and have elevated risks of suicide, physical morbidity and premature mortality, loss of productivity, and being difficult to care for caregivers (11, 12). Among narcoleptic symptoms, the hallucinatory episodes, which involve hypnagogic and hypnopompic hallucinations, can be mistaken for an active psychotic state of schizophrenia (13–15). Sleep disturbances, and particularly poor-quality sleep, are also common in schizophrenia (16). Furthermore, the development of narcolepsy in patients with schizophrenia may not be identified because their sleepiness may be attributed to their antipsychotic treatment, and cataplexy may be alleviated or masked by antidopaminergic treatment (17). The overlapping symptoms and similar ages of onset lead to a possibility of misdiagnosis between the two conditions (18–20). These difficulties that are faced by clinicians in correctly diagnosing narcolepsy and psychosis may delay well-targeted treatment.

Modafinil and methylphenidate (MPH) are two effective treatments for narcolepsy. In 1998, the U.S. Food and Drug Administration approved modafinil, an oral agent, for the treatment of EDS that is associated with narcolepsy (21). Modafinil is a wakefulness-promoting drug that probably functions by increasing the extracellular concentration of dopamine and enhancing glutaminergic activity with the result of improved alertness (22). It reacts with histamine and blocks the reuptake of noradrenaline by the noradrenergic terminals on the sleep-promoting neurons from the ventrolateral preoptic nucleus (23). If modafinil cannot be prescribed, then methylphenidate (MPH) is the second-best option. Methylphenidate is a dopamine and catecholamine reuptake inhibitor that also promotes serotonin transmission. MPH reduces EDS, promotes the onset of sleep; increases REM sleep latency, and reduces the percentage of REM sleep (23). However, patients with narcolepsy may develop or experience aggravated psychosis as a consequence of stimulant therapy (such as with methylphenidate or modafinil) (6), although this side-effect

seems to be rare even in patients who are treated with high doses of stimulants over a long period (14, 24, 25).

This nationwide population-based analysis was performed to elucidate the co-occurrence rate of narcolepsy and psychotic disorders. The potential effect of pharmacotherapy for narcolepsy on the risk of developing psychotic disorder is also examined.

MATERIALS AND METHODS

Data Source

This retrospective cohort study used data from the ambulatory claims database of the National Health Insurance Research Database of Taiwan (NHIRD-TW), which includes outpatient, ambulatory, hospital inpatient care and dental service data. National Health Insurance (NHI), a compulsory universal health insurance program, was implemented in Taiwan on March 1, 1995. At the end of the year 2000, it covered the delivery of all health care for 22.3 million people in Taiwan (more than 96% of the national population). The Institutional Review Board of Chang Gung Memorial Hospital reviewed and approved this investigation.

In this study, two subjects of the NHIRD-TW, the Longitudinal Health Insurance Database 2000 (LHID2000) and the Longitudinal Health Insurance Database 2005 (LHID2005), were used. They respectively comprise the original claims data for one million beneficiaries that were randomly sampled from the 2000 and 2005 Registries of Beneficiaries of the NHIRD-TW. LHID2000 and LHID2005 include data on all of the medical procedures and prescriptions of two million people (approximately 9% of the population) in Taiwan. A previous study has already demonstrated the reliability of the diagnostic codes in the NHIRD (26–29).

Study Subjects

The 347.XX codes of the International Classification of Disease, Ninth Revision (ICD-9), were used to identify cases of narcolepsy. A case of narcolepsy was identified by at least one NHI claim record per visit with a diagnosis of narcolepsy (ICD-9 codes: 347). The LHID2000 and LHID2005 database included 258 such cases of narcolepsy (N = 258) between January 1, 2002 and December 31, 2011. The day when narcolepsy was first diagnosed was set as the index date, and the patients' medical records were traced until a psychotic disorder was diagnosed or until December 31, 2011.

A matching control for each patient in the patient group was selected at random from LHID2000 or LHID2005 using the propensity score matching technique (and a ratio of narcolepsy cases to controls was 1:10). The propensity score was obtained using a multivariable logistic regression model with age and sex as covariates. January 1, 2002 was set as the initial observation date, and the 2,580 control subjects were monitored from the entry date until December 31, 2011 or the diagnosis of a psychotic disorder.

Variables and Outcomes

The following relevant disorders that were known to be commonly comorbid with narcolepsy were identified in this

study (23, 30); attention-deficit hyperactivity disorder (ADHD) (ICD-9-CM code 314.X), autism spectrum disorder (ASD) (ICD-9-CM code 299.X), intellectual disability (ICD-9-CM codes 317 to 319), epilepsy (ICD-9-CM code 345), and alcohol use disorders (ICD-9-CM code 303.X). The results of this study were determined using a diagnosis of any psychotic disorder (ICD-9-CM code 295.X, 297.X, or 298.X).

Medications were identified using the Anatomical Therapeutic Chemical (ATC) classification system. According to the Food and Drug Administration of Taiwan, only three drugs were licensed for treating narcolepsy before 2011; they were immediate-release methylphenidate (IR-MPH) (ATC code N06BA04), osmotic controlled-release formulations of methylphenidate (OROS-MPH) (ATC code N06BA04), and modafinil (ATC code N06BA07). These drugs are restricted by the Bureau of NHI in Taiwan, and ideally any prescription for narcolepsy is recorded in an ambulatory care, pharmacy, or hospital care claim.

Statistical Analysis

To study the distribution of the study population, the characteristics of the narcolepsy group were compared with those of the control group using a chi-square (χ^2) test or *t*-test. To compare the ages at the diagnosis of a psychotic disorder between the two groups, a Mann-Whitney U test was conducted. A multivariate logistic regression model was used to evaluate the potential comorbidity of a psychotic disorder with narcolepsy across all study subjects. Multivariate logistic regression was also used to investigate the potential effect of a pharmacotherapy prescription for narcolepsy on the risk of a psychotic disorder among narcoleptic patients. The results are presented as an adjusted odds ratio (aOR) and 95% confidence intervals (CIs). All data management and statistical analyses were carried out using the Statistical Package for the Social Sciences (SPSS) Version 16.0 (SPSS Inc., Chicago, IL, USA). A two-tailed value of $p < 0.05$ indicated statistical significance.

RESULTS

Table 1 presents the characteristics of the narcolepsy group and the control group. No significant difference in age and sex between the two groups. The narcolepsy group was more likely than the control group to exhibit comorbidities among ADHD (8.9%), ASD (2.3%), intellectual disability (2.3%), and epilepsy (8.9%). Of patients with narcolepsy, 41.5, 5.4, and 13.2% were prescribed MPH-IR, MPH-OROS, and modafinil, respectively. In the monitoring period, 8.1% of the cases of narcolepsy were comorbid with a psychotic disorder. In contrast, 1.5% of the control subjects had a psychotic disorder. The age at diagnosis of a psychotic disorder was lower for narcoleptic patients (29.4 years) than for the controls (36.3 years).

The multivariate logistic regression models (**Table 2**) indicate that patients with narcolepsy were more likely than the control subjects to be diagnosed with a psychotic disorder (aOR, 4.07; 95% CI, 2.21–7.47). Moreover, subjects who were diagnosed with ASD (aOR, 8.13; 95% CI, 1.74–38.05), intellectual disability (aOR, 4.33; 95% CI, 1.05–17.90), and epilepsy (aOR, 5.15; 95% CI, 2.23–11.93) had a higher risk of being diagnosed with a psychotic disorder.

Table 3 provides the effects of pharmacotherapy for narcolepsy on a comorbid psychotic disorder. Prescription of methylphenidate or modafinil for the narcoleptic patients was not significantly associated with a psychotic disorder. However, patients with ASD had a higher risk of having a psychotic disorder (aOR, 10.42; 95% CI, 1.40–77.52).

We further analyzed the individual effect of IR-MPH, OROS-MPH, and modafinil on psychotic disorders (**Supplementary Table 1**). We also examined that association between the risk of psychotic disorders, antipsychotic drugs, antidepressant drugs, and alcohol use disorders. We found that prescription of IR-MPH, OROS-MPH, or modafinil for the narcoleptic patients was not significantly associated with a psychotic disorder. However, prescription of antipsychotic drugs was associated with a higher risk of having a psychotic disorder (aOR, 12.65; 95% CI, 2.90–55.13).

TABLE 1 | Characteristics of patients with narcolepsy and control subjects in Taiwan from 2002 to 2011.

Characteristics	Narcolepsy (N = 258)	Controls (N = 2,580)	Statistics	P-value
Age (years)	29.3 ± 20.4	30.2 ± 20.9	0.60 ^a	0.552
Gender			0.47 ^b	0.495
Female	118 (45.7)	1,123 (43.5)		
Male	140 (54.3)	1,457 (56.5)		
Comorbidity				
ADHD	23 (8.9)	24 (0.9)	91.81 ^b	< 0.001*
ASD	6 (2.3)	6 (0.2)	24.40 ^b	< 0.001*
Intellectual disability	6 (2.3)	19 (0.7)	6.78 ^b	0.009*
Epilepsy	23 (8.9)	38 (1.5)	61.76 ^b	< 0.001*
Medication treatment				
Methylphenidate-IR	107 (41.5)	23 (0.9)	883.72 ^b	< 0.001*
ethylphenidate-OROS	14 (5.4)	7 (0.3)	84.86 ^b	< 0.001*
Modafinil	34 (13.2)	0 (0)	344.12 ^b	< 0.001*
Diagnosed a psychotic disorder	21 (8.1)	39 (1.5)	49.79 ^b	< 0.001*
Age at diagnosis (years)	29.4 ± 21.2	36.3 ± 17.5	2.08 ^c	0.038*

Data is expressed by n (%) or mean ± SD; Statistic values: ^a *t* using an independent *t*-test; ^b Pearson's χ^2 ; ^c *Z* using Mann-Whitney U test; ADHD, attention-deficit hyperactivity disorder; ASD, Autism Spectrum Disorder; Age, age at diagnosis or at recruitment; * $P < 0.05$.

TABLE 2 | Logistic regression models for the risk of diagnosis with a psychotic disorder among all participants, controlling for gender, age, and comorbidities.

Variables	Psychotic disorder		
	n (%)	aOR (95% CI)	P-value
Diagnostic group			
Controls (N = 2,580)	39 (1.5)	1	
Narcolepsy (N = 258)	21 (8.1)	4.07 (2.21–7.47)	<0.001*
Age at recruitment	–	1.01 (1.00–1.02)	0.156
Gender			
Male (N = 1,241)	33 (2.1)	1	
Female (N = 1,597)	27 (2.2)	0.99 (0.58–1.70)	0.965
ADHD			
Without (N = 2,791)	53 (1.9)	1	
With (N = 47)	7 (14.9)	1.74 (0.51–5.87)	0.373
ASD			
Without (N = 2,826)	55 (1.9)	1	
With (N = 12)	5 (41.7)	8.13 (1.74–38.05)	0.008*
Intellectual disability			
Without (N = 2,813)	55 (2.0)	1	
With (N = 25)	5 (20.0)	4.33 (1.05–17.90)	0.043*
Epilepsy			
Without (N = 2,777)	50 (1.8)	1	
With (N = 61)	10 (16.4)	5.15 (2.23–11.93)	<0.001*

ADHD, attention-deficit hyperactivity disorder; ASD, Autism Spectrum Disorder; aOR, adjusted odds ratios; 95% CI, 95% confidence interval; n, number of diagnosed psychotic disorders.

*P < 0.05.

TABLE 3 | Risk factors of diagnosis with a psychotic disorder in narcoleptic patients.

Variables	Psychotic disorder		
	n (%)	aOR (95% CI)	P-value
Age at recruitment	–	1.00 (0.98–1.03)	0.755
Gender			
Male (N = 140)	12 (8.6)	1	
Female (N = 118)	9 (7.6)	1.00 (0.38–2.66)	1.000
ADHD			
Without (N = 235)	16 (6.8)	1	
With (N = 23)	5 (21.7)	1.21 (0.26–5.59)	0.812
ASD			
Without (N = 252)	18 (7.1)	1	
With (N = 6)	3 (50.0)	10.42 (1.40–77.52)	0.022*
Intellectual disability			
Without (N = 252)	19 (7.5)	1	
With (N = 6)	2 (33.2)	3.25 (0.38–27.68)	0.280
Epilepsy			
Without (N = 235)	17 (7.2)	1	
With (N = 23)	4 (17.4)	2.02 (0.53–7.67)	0.302
Methylphenidate			
Without (N = 151)	9 (6.0)	1	
With (N = 107)	12 (11.2)	2.39 (0.83–6.86)	0.106
Modafinil			
Without (N = 224)	19 (8.5)	1	
With (N = 34)	2 (5.9)	0.59 (0.11–3.04)	0.528

ADHD, attention-deficit hyperactivity disorder; ASD, Autism Spectrum Disorder; aOR, adjusted odds ratios; 95% CI, 95% confidence interval; n, number of diagnosed psychotic disorders.

*P < 0.05.

DISCUSSION

The Prevalence of Narcolepsy

According to our study, the prevalence of narcolepsy in Taiwan is about 12.9 per 100,000, slightly lower than the global mean prevalence of approximately 30 per 100,000 (31). To our

knowledge, reliable evidence about the prevalence of narcolepsy in Taiwan is still lacking currently. In Asia, the prevalence in Korea and China is 15 and 30 per 100,000, respectively (31). For incidence rates, Dodd et al. (32) reported that narcolepsy incidence in Taiwan was 0.29 per 100,000 person-years, relatively lower than those in European Union

and North America. The lower incidence/prevalence of narcolepsy in Taiwan may be related to under diagnosis or under treatment. Moreover, polymorphism of HLA-DQB1*0602, H1N1 influenza vaccination, and H1N1 infection itself have been associated with narcolepsy susceptibility (31) (33). Various genetic or environment factors may also contribute to the discrepancies in prevalence of narcolepsy across countries.

Narcolepsy and the Increased Risk of a Psychotic Disorder

This nationwide, population-based cohort study revealed that narcolepsy was associated with a four-fold greater risk of a psychotic disorder. Most relevant studies have discussed the risk of psychosis rather than the psychotic illness among narcoleptic patients.

An association between psychosis and narcolepsy has been reported in both adults and children with frequencies in the range 1 to 10% (18, 19, 25, 34, 35). A cross-sectional observational study of 28 narcolepsy and 21 schizophrenia patients found that narcoleptic and schizophrenic patients did not differ with respect to frequency or sensory modality of hallucinations. It also found that the lifetime prevalence of hallucinations did not differ between individuals with schizophrenia and those with narcolepsy (36). Some reports have found narcolepsy patients with challenging differential diagnoses of psychotic disorders (37, 38). Diagnostic and therapeutic challenges exist for patients with comorbid narcolepsy and psychotic disorder owing to their similar onset times (usually in early life and often in childhood) and their overlapping symptoms (13, 14, 19, 37–41). However, our cohort revealed that the age at diagnosis of a psychotic disorder was lower for narcoleptic patients (29.4 years) than for the controls (36.3 years). There were some possible explanations for this. First, patients have dual diagnoses of narcolepsy and schizophrenia have strong biological tendency and tend to onset earlier than patients who had schizophrenia only. The second explanation is that the psychotic disorders among patients who had narcolepsy were diagnosed earlier due to their hypnagogic or hypnopompic hallucination.

A cohort study found that narcolepsy is not an under-recognized disease in adult patients with schizophrenia or schizoaffective disorder (42). It also indicated a possible age-dependent relationship between schizophrenia and narcolepsy, with patients who initially experienced narcolepsy in childhood or early adolescence at a higher risk of developing schizophrenia (6, 42). However, the study did not consider the effects of psychotic disorders on risk of narcolepsy. Additionally, its exclusion of patients who were considered to be unable to answer a questionnaire might have generated bias, such as by the failure to include patients with possibly highly severe functional impairment.

Numerous pathophysiological mechanisms potentially explain the high comorbidity of narcolepsy and psychotic disorder. Dopaminergic neurons in ventral tegmental area (VTA) contribute to the regulation of sleep-awake cycle and are involved in the mechanism of cataplexy (43). Hypocretinergic neurotransmission regulates dopamine firing in ascending

midbrain neurons in the ventral tegmental area and prefrontal cortex, and possibly at the level of the nucleus accumbens, which are critical areas in schizophrenia pathophysiology. Therefore, hypocretin, which is known to be an important cause of narcolepsy (4), may also influence dopamine signaling, causing dysfunction of the mesocorticolimbic and mesocorticostriatal circuits, which are the two main pathways that are implicated in the pathophysiology of psychotic symptoms (44).

Some reports have suggested an overlapping autoimmune pathogenesis between narcolepsy and schizophrenia-like psychosis, associated with both HLA and autoantibodies (34, 35, 45–47). An autoimmune basis of schizophrenia has been suggested (48), and several studies have examined investigated its association with the HLA region and DQ6 alleles, particularly of the DQB1*0602 subtype (45–47). Narcolepsy is also strongly associated with the HLA DQB1 * 0602 subtype, which is found in up to 98% of patients (36).

Previous studies have studied a potential autoimmune basis of the relationship between schizophrenia and narcolepsy by assessing NMDAR autoantibodies in either the serum or CSF of patients with anti-NMDA encephalitis, but discordant results have been obtained with respect to narcolepsy (6, 34, 35). Some environmental clues about autoimmunity also suggest the overlapping pathogenesis of narcolepsy and psychosis. Several upper airway infections (streptococcal and H1N1 influenza) and Pandemrix vaccinations have been reported as triggering narcolepsy (49). Prenatal maternal infection with herpes simplex virus type 2, influenza, or cytomegalovirus has been associated with the risk of adult schizophrenia (50). Early-life infections that are caused by viruses or bacteria have also been associated with the risk of adult psychotic illness (51, 52).

A recent review study indicates that severe sleep deprivation itself may cause psychosis (53). Within 24–48 h of sleep deprivation, perceptual distortions and depersonalization occur. After 48–90 h without sleep, complex hallucinations and delusion develop, yielding psychotic states indistinguishable from acute psychosis or toxic delirium. The underlying biological mechanism may be neuronal instability or a related defect in neural transmission, especially cholinergic, and central chromatolysis (53).

Pharmacotherapy and Psychotic Disorder in Narcoleptic Patients

Our data do not support an association between the use of MPH or modafinil and the development of incident psychotic disorder. Among adolescents and young adults with ADHD who were receiving prescription stimulants, new-onset psychosis occurred in approximately 1 in 660 patients. Amphetamine use was associated with a greater risk of psychosis than MPH (54). A study revealed that initiation of MPH treatment did not increase the risk of psychotic events in adolescents and young adults, including in those individuals with a history of psychosis (55). Few investigations have found that a high dose of modafinil may cause mania and psychosis in patients with medical or psychiatric diseases and those who are shift-workers (56, 57).

However, in a recent study, modafinil-induced psychosis was identified in only a few case reports (58, 59).

In the present study, MPH users among patients with narcolepsy were more likely than others to have a psychotic disorder but not significantly so ($OR = 2.39$, $P\text{-value} = 0.106$). We further analyzed the individual effect of IR-MPH, OROS-MPH, and modafinil on development of psychosis, and there was still no significant association between drug treatment and psychotic disorders. A self-controlled case series revealed no increased risk of incident psychotic events during MPH-exposure relative to periods of non-exposure (incidence rate ratio: 1.02, 95%: 0.53–1.97) (60). Nonetheless, the prevalence of MPH-induced psychosis has been reported as 18.2% among MPH-treated patients, and this effect should not be considered rare (6, 24, 25). Notably, previous studies demonstrated a significantly higher occurrence of psychosis, substance misuse, and psychiatric hospitalizations in patients using high-dose stimulants compared to those using standard doses (24, 25). However, the doses of medication were not available in this study. Further investigations with a larger sample size and comprehensive information about stimulants prescription are warranted to clarify the relationship between stimulants doses and psychotic disorders.

One study reviewed data from 49 randomized controlled clinical trials, analyzed the association between psychotic symptoms and the use of ADHD drugs, and found a rate of psychosis/mania events of 1.48 per 100 person-years in the ADHD treatment group. However, only two events were identified in trials of modafinil and four in trials of MPH (61). We found that prescription of antipsychotic drugs, but not antidepressant drugs or alcohol use disorders, was associated with a higher risk of having a psychotic disorder. This is not surprising because patients who suffered from psychotic symptoms may be prescribed antipsychotic drugs for treating psychotic symptoms.

A recent nation-wide study comprised 789 patients with schizophrenia suggested that the use of CNS stimulant (including modafinil and methylphenidate) may reduce in the overall number of psychiatric bed-days (62). Although CNS stimulant use is not recommended in any treatment guidelines for psychosis, it may be beneficial for cognition, negative symptoms, and the overall function of the patient with schizophrenia. Positive symptoms of schizophrenia are known to be caused by excess dopamine in the midbrain and substantia nigra. CNS stimulants, such as modafinil, may only increase dopamine in the prefrontal cortex. The brain target site influenced by CNS stimulant is different from that for pathophysiology of schizophrenia may count for the possible mechanism that CNS stimulants not seem to enhance psychosis (63, 64).

Comorbidities and an Increased Risk of Psychotic Disorder

In this investigation, intellectual disability and epilepsy were risk factors for psychotic disorder. Various studies have demonstrated that intellectual disability and epilepsy are risk factors for comorbidity of a psychotic disorder. A cohort study of

people with intellectual disability and the general population found an increased diagnosis of psychotic disorders among patients with intellectual disability ($OR:10.4$) (65).

A systemic review found that individuals with epilepsy have approximately an eight-fold greater risk of psychosis than those without and 6% of them have a comorbid psychotic illness with an even higher prevalence of psychosis in cases of temporal lobe epilepsy (7%) (66). The neurotoxic effect of epilepsy, a “kindling” process by which acute seizure discharges, a “forced normalization” process, on-going subictal activity in the limbic system, antiepileptic medication, similar structural brain abnormalities and genetic abnormalities in patients with schizophrenia and patients with epilepsy, all may explain the high comorbidity (66).

According to recent studies, ASD seems not to be a common comorbidity of narcolepsy. Our research identified only five cases of concomitant narcolepsy and ASD (67, 68). However, around 2.33% of the patients with narcolepsy had also been diagnosed with ASD in our study. Patients with narcolepsy and ASD were found to have a higher risk of psychotic disorder than those with only narcolepsy. Owing to the few data on the association between narcolepsy and ASD, the pathophysiological pathway of the co-occurrence remains unclear. In narcoleptic patients, ASD may be an additional neurodevelopmental disorder (67).

Although ASD is now believed to be distinct from psychotic disorders, they share multiple phenotypic similarities and risk factors, and reportedly co-occur. Psychotic disorder rates of patients with ASD range from 5 to 16% (69). Several models have been used explain the association and comorbidity between psychotic disorders and ASD. They include a potential autoimmune basis for a relationship among narcolepsy, ASD and psychotic disorder.

Maternal mild acute inflammation that is caused by infection, including influenza, triggers abnormal activation of microglia and overexpression of inflammatory cytokines. This reaction has been observed in animal models. This maternal immune activation generates imbalanced cytokine profiles and characteristics of the offspring that are similar to ASD and schizophrenia (70). The overlapping pathophysiological mechanisms (49) potentially explain the association among narcolepsy, ASD, and psychotic disorder.

Strengths and Limitations

To the best of our knowledge, this study is the first to investigate the association between narcolepsy and psychotic disorders, and the first to elucidate the relationship between psychotic disorders and pharmacotherapy in narcoleptic patients. The strengths of the investigation include its use of a nationwide population-based database to provide a nationally representative sample, an appropriate observation period, physician-based diagnoses to identify cases of narcolepsy and psychotic disorder, and clear information about the prescription of medications. The use of registration of medical claim data from the NHIRD prevents recall bias and selection bias.

However, this investigation has certain limitations. First, misclassifications may arise from the fact that the diagnoses of narcolepsy and psychotic disorders were taken from the registration database rather than made using validated structural diagnostic

instruments. Patients with idiopathic hypersomnia or other hypersomnolence disorders may have been coded as narcoleptics. Besides, the ICD-9-CM does not differentiate between type 1 and type 2 narcolepsy. Moreover, the diagnostic codes for narcolepsy and psychotic disorders in the NHIRD have not been validated, although the accuracy of disease diagnoses in the National Health Insurance system in 1990 to 1991 was reportedly between 54 and 85% (71), and the validity of diagnosis codes in the NHIRD has been confirmed in previous studies (26–29). Second, previous studies have examined many comorbidities of narcolepsy, but this study considered only ADHD, ASD, intellectual disability, and epilepsy. Other confounding factors, such as other organic diseases and psychiatric disorders, may have had an unrecognized effect. Third, the NHIRD is an administrative database that does not contain comprehensive clinical information, such as medication compliance and laboratory examination data. Therefore, our results merely reveal increased associations between psychotic disorders and narcolepsy and no increased associations between psychotic disorders and MPH or modafinil use in narcoleptic patients. This investigation did not analyze whether a psychiatric condition persisted following the diagnosis of narcolepsy or discontinuation of relevant medication. Hence, it could not establish a causal relationship and further longitudinal research is warranted. Finally, this study was carried out among Taiwan's population, and therefore its generalizability to other countries requires further investigation. Besides, the prevalence of narcolepsy varies in different countries and ethnic groups (31). However, we were unable to control for ethnicity because such information was not registered in the NHIRD. With increasing immigrants in Taiwan, such bias influenced by the different susceptibility to narcolepsy across ethnicity might require other form of study.

CONCLUSION

This population-based longitudinal study provides evidence that patients with narcolepsy had higher rates of psychotic disorders than a control group. Among narcoleptic patients, the prescription of MPH or modafinil was not associated with a psychotic disorder. However, narcoleptic patients with ASD were found to have a higher risk of a psychotic disorder than those without. Further comprehensive research is warranted to enhance the public awareness of narcolepsy and the possible co-occurrence of psychotic disorders, especially those comorbid with ASD. Continuous efforts must also be made to identify exactly the associated pathophysiological mechanisms and the causal relationship between narcolepsy and psychotic disorders.

DATA AVAILABILITY STATEMENT

The datasets for this manuscript are not publicly available because: The data are provided by the National Health

Insurance Administration, Ministry of Health and Welfare and managed by the National Health Research Institutes. Requests to access the datasets should be directed to nhird@nhri.org.tw.

ETHICS STATEMENT

This study has been approved by the institutional review board at Chang Gung Memorial Hospital.

AUTHOR CONTRIBUTIONS

J-YY and Y-CS are joint first authors and contribute equally to this manuscript. J-YY participated in reviewing references and drafting the manuscript. Y-CS executed the statistical analysis. S-YL, S-SY, C-JY, K-CY, T-LL, and C-CS participated in the design of the study. L-JW interpreted the data and revised the manuscript. All authors read and approved the final manuscript and contributed to the drafting and revising of the paper.

FUNDING

This study was sponsored by the Chang Gung Memorial Hospital Research Projects (CMRPG8D0581, CMRPG2G0071, CLRPG2C0023, and CGRPG2F0021).

ACKNOWLEDGMENTS

This study is based in part on data from the NHIRD-TW provided by the National Health Insurance Administration, Ministry of Health and Welfare and managed by the National Health Research Institutes (registration number: NHIRD-102-088). The interpretations and conclusions contained herein do not represent those of the National Health Insurance Administration, Ministry of Health and Welfare, or National Health Research Institutes.

SUPPLEMENTARY MATERIAL

The Supplementary Material for this article can be found online at: <https://www.frontiersin.org/articles/10.3389/fpsy.2020.00205/full#supplementary-material>

REFERENCES

- Overeem S, Mignot E, van Dijk JG, Lammers GJ. Narcolepsy: clinical features, new pathophysiological insights, and future perspectives. *J Clin Neurophysiol* (2001) 18(2):78–105. doi: 10.1097/00004691-200103000-00002
- Goswami M. The influence of clinical symptoms on quality of life in patients with narcolepsy. *Neurology* (1998) 50(2 Suppl 1):S31–6. doi: 10.1212/WNL.50.2_Suppl_1.S31
- Dauvilliers Y, Arnulf I, Mignot E. Narcolepsy with cataplexy. *Lancet* (2007) 369(9560):499–511. doi: 10.1016/S0140-6736(07)60237-2
- Mignot E, Lammers GJ, Ripley B, Okun M, Nevssimalova S, Overeem S, et al. The role of cerebrospinal fluid hypocretin measurement in the diagnosis of narcolepsy and other hypersomnias. *Arch Neurol* (2002) 59(10):1553–62. doi: 10.1001/archneur.59.10.1553
- De la Herran-Arita AK, Kornum BR, Mahlios J, Jiang W, Lin L, Hou T, et al. CD4+ T cell autoimmunity to hypocretin/orexin and cross-reactivity to a 2009 H1N1 influenza A epitope in narcolepsy. *Sci Transl Med* (2013) 5(216):216ra176. doi: 10.1126/scitranslmed.3007762
- Dauvilliers Y, Gaig C, Barateau L, Graus F, Iranzo A, Lopez R, et al. Absence of NMDA receptor antibodies in the rare association between Type 1 Narcolepsy and Psychosis. *Sci Rep* (2016) 6:25230. doi: 10.1038/srep25230
- Lee MJ, Lee SY, Yuan SS, Yang CJ, Yang KC, Lee TL, et al. Comorbidity of narcolepsy and depressive disorders: a nationwide population-based study in Taiwan. *Sleep Med* (2017) 39:95–100. doi: 10.1016/j.sleep.2017.07.022
- Scammell TE. Narcolepsy. *N Engl J Med* (2015) 373(27):2654–62. doi: 10.1056/NEJMra1500587
- Nallu S, Guerrero GY, Lewis-Croswell J, Wittine LM. Review of Narcolepsy and Other Common Sleep Disorders in Children. *Adv Pediatr* (2019) 66:147–59. doi: 10.1016/j.yapd.2019.03.008
- Global Burden of Disease Study C. Global, regional, and national incidence, prevalence, and years lived with disability for 301 acute and chronic diseases and injuries in 188 countries, 1990–2013: a systematic analysis for the Global Burden of Disease Study 2013. *Lancet* (2015) 386(9995):743–800. doi: 10.1016/S0140-6736(15)60692-4
- Chang WC, Wong CSM, Chen EYH, Lam LCW, Chan WC, Ng RMK, et al. Lifetime Prevalence and Correlates of Schizophrenia-Spectrum, Affective, and Other Non-affective Psychotic Disorders in the Chinese Adult Population. *Schizophr Bull* (2017) 43(6):1280–90. doi: 10.1093/schbul/sbx056
- Jablensky A. Epidemiology of schizophrenia: the global burden of disease and disability. *Eur Arch Psychiatry Clin Neurosci* (2000) 250(6):274–85. doi: 10.1007/s004060070002
- Douglass AB, Shipley JE, Haines RF, Scholten RC, Dudley E, Tapp A. Schizophrenia, narcolepsy, and HLA-DR15, DQ6. *Biol Psychiatry* (1993) 34(11):773–80. doi: 10.1016/0006-3223(93)90066-M
- Kishi Y, Konishi S, Koizumi S, Kudo Y, Kurosawa H, Kathol RG. Schizophrenia and narcolepsy: a review with a case report. *Psychiatry Clin Neurosci* (2004) 58(2):117–24. doi: 10.1111/j.1440-1819.2003.01204.x
- Ullman KC. Narcolepsy and schizophrenia. *Am J Psychiatry* (1977) 134(7):822. doi: 10.1176/ajp.134.7.822b
- Benson KL. Sleep in schizophrenia: impairments, correlates, and treatment. *Psychiatr Clin North Am* (2006) 29(4):1033–45. abstract ix-x. doi: 10.1016/j.psc.2006.08.002
- Okura M, Riehl J, Mignot E, Nishino S. Sulpiride, a D2/D3 blocker, reduces cataplexy but not REM sleep in canine narcolepsy. *Neuropsychopharmacology* (2000) 23(5):528–38. doi: 10.1016/S0893-133X(00)00140-8
- Fortuyn HA, Lappenschaar GA, Nienhuis FJ, Furer JW, Hodiament PP, Rijnders CA, et al. Psychotic symptoms in narcolepsy: phenomenology and a comparison with schizophrenia. *Gen Hosp Psychiatry* (2009) 31(2):146–54. doi: 10.1016/j.genhosppsych.2008.12.002
- Canellas F, Lin L, Julia MR, Clemente A, Vivas-Bauza C, Ollila HM, et al. Dual cases of type 1 narcolepsy with schizophrenia and other psychotic disorders. *J Clin Sleep Med* (2014) 10(9):1011–8. doi: 10.5664/jcsm.4040
- Jardri R, Bartels-Velthuis AA, Debbané M, Jenner JA, Kelleher I, Dauvilliers Y, et al. From phenomenology to neurophysiological understanding of hallucinations in children and adolescents. *Schizophr Bull* (2014) 40 Suppl 4:S221–32. doi: 10.1093/schbul/sbu029
- Kallweit U, Bassetti CL. Pharmacological management of narcolepsy with and without cataplexy. *Expert Opin Pharmacother* (2017) 18(8):809–17. doi: 10.1080/14656566.2017.1323877
- Golicki D, Bala MM, Niewada M, Wierzbicka A. Modafinil for narcolepsy: systematic review and meta-analysis. *Med Sci Monit* (2010) 16(8):RA177–86.
- Rocca FL, Pizza F, Ricci E, Plazzi G. Narcolepsy during Childhood: An Update. *Neuropediatrics* (2015) 46(3):181–98. doi: 10.1055/s-0035-1550152
- Pawluk LK, Hurwitz TD, Schluter JL, Ullevig C, Mahowald MW. Psychiatric morbidity in narcoleptics on chronic high dose methylphenidate therapy. *J Nerv Ment Dis* (1995) 183(1):45–8. doi: 10.1097/00005053-199501000-00009
- Auger RR, Goodman SH, Silber MH, Krahn LE, Pankratz VS, Slocumb NL. Risks of high-dose stimulants in the treatment of disorders of excessive somnolence: a case-control study. *Sleep* (2005) 28(6):667–72. doi: 10.1093/sleep/28.6.667
- Su VY, Liu CJ, Wang HK, Wu LA, Chang SC, Perng DW, et al. Sleep apnea and risk of pneumonia: a nationwide population-based study. *CMAJ* (2014) 186(6):415–21. doi: 10.1503/cmaj.131547
- Lin YS, Chen TH, Chi CC, Lin MS, Tung TH, Liu CH, et al. Different Implications of Heart Failure, Ischemic Stroke, and Mortality between Nonvalvular Atrial Fibrillation and Atrial Flutter—a View From a National Cohort Study. *J Am Heart Assoc* (2017) 6(7):pii:e006406. doi: 10.1161/JAHA.117.006406
- Chang SL, Huang YL, Lee MC, Hu S, Hsiao YC, Chang SW, et al. Association of Varicose Veins With Incident Venous Thromboembolism and Peripheral Artery Disease. *JAMA* (2018) 319(8):807–17. doi: 10.1001/jama.2018.0246
- Su VY, Su WJ, Yen YF, Pan SW, Chuang PH, Feng JY, et al. Statin Use Is Associated With a Lower Risk of TB. *Chest* (2017) 152(3):598–606. doi: 10.1016/j.chest.2017.04.170
- Nevssimalova S. Narcolepsy in childhood. *Sleep Med Rev* (2009) 13(2):169–80. doi: 10.1016/j.smrv.2008.04.007
- Dye TJ, Gurbani N, Simakajornboon N. Epidemiology and Pathophysiology of Childhood Narcolepsy. *Paediatr Respir Rev* (2018) 25:14–8. doi: 10.1016/j.prrv.2016.12.005
- Dodd CN, de Ridder M, Huang WT, Weibel D, Giner-Soriano M, Perez-Vilar S, et al. Incidence rates of narcolepsy diagnoses in Taiwan, Canada, and Europe: The use of statistical simulation to evaluate methods for the rapid assessment of potential safety issues on a population level in the SOMNIA study. *PLoS One* (2018) 13(10):e0204799. doi: 10.1371/journal.pone.0204799
- Sarkonen TO, Alakujala APE, Dauvilliers YA, Partinen MM. Incidence of narcolepsy after H1N1 influenza and vaccinations: Systematic review and meta-analysis. *Sleep Med Rev* (2018) 38:177–86. doi: 10.1016/j.smrv.2017.06.006
- Huang YS, Guilleminault C, Chen CH, Lai PC, Hwang FM. Narcolepsy-cataplexy and schizophrenia in adolescents. *Sleep Med* (2014) 15(1):15–22. doi: 10.1016/j.sleep.2013.09.018
- Tsutsui K, Kanbayashi T, Tanaka K, Boku S, Ito W, Tokunaga J, et al. Anti-NMDA-receptor antibody detected in encephalitis, schizophrenia, and narcolepsy with psychotic features. *BMC Psychiatry* (2012) 12:37. doi: 10.1186/1471-244X-12-37
- Plazzi G, Fabbri C, Pizza F, Serretti A. Schizophrenia-like symptoms in narcolepsy type 1: shared and distinctive clinical characteristics. *Neuropsychobiology* (2015) 71(4):218–24. doi: 10.1159/000432400
- Szucs A, Janszky J, Hollo A, Miglecz G, Halasz P. Misleading hallucinations in unrecognized narcolepsy. *Acta Psychiatrica Scand* (2003) 108(4):314–6; discussion 6–7. doi: 10.1034/j.1600-0447.2003.00114.x
- Takeuchi N, Mukai M, Uchimura N, Satomura T, Sakamoto T, Maeda H. A narcoleptic patient exhibiting hallucinations and delusion. *Psychiatry Clin Neurosci* (2000) 54(3):321–2. doi: 10.1046/j.1440-1819.2000.00696.x
- Undurraga J, Garrido J, Santamaria J, Parellada E. Treatment of narcolepsy complicated by psychotic symptoms. *Psychosomatics* (2009) 50(4):427–8. doi: 10.1176/appi.psy.50.4.427
- Walterfang M, Upjohn E, Velakoulis D. Is schizophrenia associated with narcolepsy? *Cognit Behav Neurol* (2005) 18(2):113–8. doi: 10.1097/01.wnn.0000160822.53577.2c
- Bhat SK, Galang R. Narcolepsy presenting as schizophrenia. *Am J Psychiatry* (2002) 159(7):1245. doi: 10.1176/appi.ajp.159.7.1245
- Sansa G, Gavalda A, Gaig C, Monreal J, Ercilla G, Casamitjana R, et al. Exploring the presence of narcolepsy in patients with schizophrenia. *BMC Psychiatry* (2016) 16:177. doi: 10.1186/s12888-016-0859-9
- Szabo ST, Thorpy MJ, Mayer G, Peever JH, Kilduff TS. Neurobiological and immunogenetic aspects of narcolepsy: Implications for pharmacotherapy. *Sleep Med Rev* (2019) 43:23–36. doi: 10.1016/j.smrv.2018.09.006

44. Pizza F, Magnani M, Indrio C, Plazzi G. The hypocretin system and psychiatric disorders. *Curr Psychiatry Rep* (2014) 16(2):433. doi: 10.1007/s11920-013-0433-9
45. Grosskopf A, Muller N, Malo A, Wank R. Potential role for the narcolepsy- and multiple sclerosis-associated HLA allele DQB1*0602 in schizophrenia subtypes. *Schizophr Res* (1998) 30(2):187–9. doi: 10.1016/S0920-9964(97)00148-5
46. Debnath M, Cannon DM, Venkatasubramanian G. Variation in the major histocompatibility complex [MHC] gene family in schizophrenia: associations and functional implications. *Prog Neuropsychopharmacol Biol Psychiatry* (2013) 42:49–62. doi: 10.1016/j.pnpbp.2012.07.009
47. Stefansson H, Ophoff RA, Steinberg S, Andreassen OA, Cichon S, Rujescu D, et al. Common variants conferring risk of schizophrenia. *Nature* (2009) 460(7256):744–7. doi: 10.1038/nature08186
48. Fessel WJ. Autoimmunity and mental illness. A preliminary report. *Arch Gen Psychiatry* (1962) 6:320–3. doi: 10.1001/archpsyc.1962.01710220062008
49. Partinen M, BR K, Plazzi G, Jennum P, Julkunen I, Vaarala O. Narcolepsy as an autoimmune disease: the role of H1N1 infection and vaccination. *Lancet Neurol* (2014) 13(6):600–13. doi: 10.1016/S1474-4422(14)70075-4
50. Khandaker GM, Zimbron J, Lewis G, Jones PB. Prenatal maternal infection, neurodevelopment and adult schizophrenia: a systematic review of population-based studies. *Psychol Med* (2013) 43(2):239–57. doi: 10.1017/S0033291712000736
51. Nielsen PR, Benros ME, Mortensen PB. Hospital contacts with infection and risk of schizophrenia: a population-based cohort study with linkage of Danish national registers. *Schizophr Bull* (2014) 40(6):1526–32. doi: 10.1093/schbul/sbt200
52. Khandaker GM, Stochl J, Zammit S, Lewis G, Jones PB. Childhood Epstein-Barr Virus infection and subsequent risk of psychotic experiences in adolescence: a population-based prospective serological study. *Schizophr Res* (2014) 158(1–3):19–24. doi: 10.1016/j.schres.2014.05.019
53. Waters F, Chiu V, Atkinson A, Blom JD. Severe Sleep Deprivation Causes Hallucinations and a Gradual Progression Toward Psychosis With Increasing Time Awake. *Front Psychiatry* (2018) 9:303. doi: 10.3389/fpsy.2018.00303
54. Moran LV, Ongur D, Hsu J, Castro VM, Perlis RH, Schneeweiss S. Psychosis with Methylphenidate or Amphetamine in Patients with ADHD. *N Engl J Med* (2019) 380(12):1128–38. doi: 10.1056/NEJMoa1813751
55. Hollis C, Chen Q, Chang Z, Quinn PD, Viktorin A, Lichtenstein P, et al. Methylphenidate and the risk of psychosis in adolescents and young adults: a population-based cohort study. *Lancet Psychiatry* (2019) 6(8):651–8. doi: 10.1016/S2215-0366(19)30189-0
56. Mariani JJ, Hart CL. Psychosis associated with modafinil and shift work. *Am J Psychiatry* (2005) 162(10):1983. doi: 10.1176/appi.ajp.162.10.1983
57. Wu P, Jones S, Ryan CJ, Michail D, Robinson TD. Modafinil-induced psychosis. *Intern Med J* (2008) 38(8):677–8. doi: 10.1111/j.1445-5994.2008.01710.x
58. Aytas O, Dilek Yalvac H. Modafinil-Induced Psychosis: A Case Report. *Noro Psikiyatr Ars* (2015) 52(1):99–101. doi: 10.5152/npa.2015.7160
59. DiSciullo AA, English CD, Horn WT. Modafinil Induced Psychosis in a Patient with Bipolar I Depression. *Case Rep Psychiatry* (2018) 2018:3732958. doi: 10.1155/2018/3732958
60. Man KK, Coghill D, Chan EW, Lau WC, Hollis C, Liddle E, et al. Methylphenidate and the risk of psychotic disorders and hallucinations in children and adolescents in a large health system. *Transl Psychiatry* (2016) 6(11):e956. doi: 10.1038/tp.2016.216
61. Mosholder AD, Gelperin K, Hammad TA, Phelan K, Johann-Liang R. Hallucinations and other psychotic symptoms associated with the use of attention-deficit/hyperactivity disorder drugs in children. *Pediatrics* (2009) 123(2):611–6. doi: 10.1542/peds.2008-0185
62. Rohde C, Polcwiartek C, Asztalos M, Nielsen J. Effectiveness of Prescription-Based CNS Stimulants on Hospitalization in Patients With Schizophrenia: A Nation-Wide Register Study. *Schizophr Bull* (2018) 44(1):93–100. doi: 10.1093/schbul/sbx043
63. Saavedra-Velez C, Yusim A, Anbarasan D, Lindenmayer JP. Modafinil as an adjunctive treatment of sedation, negative symptoms, and cognition in schizophrenia: a critical review. *J Clin Psychiatry* (2009) 70(1):104–12. doi: 10.4088/JCP.07r03982
64. Yamamuro K, Makinodan M, Kimoto S, Kishimoto N, Morimoto T, Toritsuka M, et al. Differential patterns of blood oxygenation in the prefrontal cortex between patients with methamphetamine-induced psychosis and schizophrenia. *Sci Rep* (2015) 5:12107. doi: 10.1038/srep12107
65. Axmon A, Bjorne P, Nylander L, Ahlstrom G. Psychiatric diagnoses in older people with intellectual disability in comparison with the general population: a register study. *Epidemiol Psychiatr Sci* (2018) 27(5):479–91. doi: 10.1017/S2045796017000051
66. Clancy MJ, Clarke MC, Connor DJ, Cannon M, Cotter DR. The prevalence of psychosis in epilepsy: a systematic review and meta-analysis. *BMC Psychiatry* (2014) 14:75. doi: 10.1186/1471-244X-14-75
67. Prihodova I, Dudova I, Mohaplova M, Hrdlicka M, Nevsimalova S. Childhood narcolepsy and autism spectrum disorders: four case reports. *Sleep Med* (2018) 51:167–70. doi: 10.1016/j.sleep.2018.07.017
68. Szakacs A, Hallbook T, Tideman P, Darin N, Wentz E. Psychiatric comorbidity and cognitive profile in children with narcolepsy with or without association to the H1N1 influenza vaccination. *Sleep* (2015) 38(4):615–21. doi: 10.5665/sleep.4582
69. Buck TR, Viskochil J, Farley M, Coon H, McMahon WM, Morgan J, et al. Psychiatric comorbidity and medication use in adults with autism spectrum disorder. *J Autism Dev Disord* (2014) 44(12):3063–71. doi: 10.1007/s10803-014-2170-2
70. Prata J, Santos SG, Almeida MI, Coelho R, Barbosa MA. Bridging Autism Spectrum Disorders and Schizophrenia through inflammation and biomarkers - pre-clinical and clinical investigations. *J Neuroinflammation* (2017) 14(1):179. doi: 10.1186/s12974-017-0938-y
71. Yeoh C, Davies H. Clinical coding: completeness and accuracy when doctors take it on. *BMJ* (1993) 306(6883):972. doi: 10.1136/bmj.306.6883.972

Conflict of Interest: The authors declare that the research was conducted in the absence of any commercial or financial relationships that could be construed as a potential conflict of interest.

Copyright © 2020 Yeh, Shyu, Lee, Yuan, Yang, Yang, Lee, Sun and Wang. This is an open-access article distributed under the terms of the Creative Commons Attribution License (CC BY). The use, distribution or reproduction in other forums is permitted, provided the original author(s) and the copyright owner(s) are credited and that the original publication in this journal is cited, in accordance with accepted academic practice. No use, distribution or reproduction is permitted which does not comply with these terms.



Article

Sesamol Alleviates Airway Hyperresponsiveness and Oxidative Stress in Asthmatic Mice

Chian-Jiun Liou ^{1,2,†} , Ya-Ling Chen ^{3,†}, Ming-Chin Yu ⁴ , Kuo-Wei Yeh ², Szu-Chuan Shen ^{5,*} and Wen-Chung Huang ^{2,6,*}

¹ Division of Basic Medical Sciences, Department of Nursing, Research Center for Chinese Herbal Medicine, and Graduate Institute of Health Industry Technology, Chang Gung University of Science and Technology, No.261, Wenhua 1st Rd., Guishan Dist., Taoyuan City 33303, Taiwan; ccliu@mail.cgu.edu.tw

² Division of Allergy, Asthma, and Rheumatology, Department of Pediatrics, Chang Gung Memorial Hospital, Linkou, Guishan Dist., Taoyuan City 33305, Taiwan; kwyeh@cgmh.org.tw

³ School of Nutrition and Health Sciences, Taipei Medical University, 250 Wu-Hsing Street, Taipei City 11031, Taiwan; ylchen01@tmu.edu.tw

⁴ Department of Surgery, Chang Gung Memorial Hospital, Linkou, Guishan Dist., Taoyuan City 33305, Taiwan; mingchin2000@gmail.com

⁵ Graduate Program of Nutrition Science, National Taiwan Normal University, 88 Ting-Chow Rd., Sec 4, Taipei 11676, Taiwan

⁶ Graduate Institute of Health Industry Technology, Research Center for Food and Cosmetic Safety, Research Center for Chinese Herbal Medicine, College of Human Ecology, Chang Gung University of Science and Technology, No.261, Wenhua 1st Rd., Guishan Dist., Taoyuan City 33303, Taiwan

* Correspondence: sjwu@mail.cgu.edu.tw (S.-C.S.); wchuang@mail.cgu.edu.tw (W.-C.H.); Tel.: +886-3-77491437 (S.-C.S.); +886-3-2118999 (ext. 5112) (W.-C.H.)

† These authors contributed equally to this paper.

Received: 27 February 2020; Accepted: 30 March 2020; Published: 1 April 2020



Abstract: Sesamol, isolated from sesame seeds (*Sesamum indicum*), was previously shown to have antioxidative, anti-inflammatory, and anti-tumor effects. Sesamol also inhibited lipopolysaccharide (LPS)-induced pulmonary inflammatory response in rats. However, it remains unclear how sesamol regulates airway inflammation and oxidative stress in asthmatic mice. This study aimed to investigate the efficacy of sesamol on oxidative stress and airway inflammation in asthmatic mice and tracheal epithelial cells. BALB/c mice were sensitized with ovalbumin, and received oral sesamol on days 14 to 27. Furthermore, BEAS-2B human bronchial epithelial cells were treated with sesamol to investigate inflammatory cytokine levels and oxidative responses in vitro. Our results demonstrated that oral sesamol administration significantly suppressed eosinophil infiltration in the lung, airway hyperresponsiveness, and T helper 2 cell-associated (Th2) cytokine expressions in bronchoalveolar lavage fluid and the lungs. Sesamol also significantly increased glutathione expression and reduced malondialdehyde levels in the lungs of asthmatic mice. We also found that sesamol significantly reduced proinflammatory cytokine levels and eotaxin in inflammatory BEAS-2B cells. Moreover, sesamol alleviated reactive oxygen species formation, and suppressed intercellular cell adhesion molecule-1 (ICAM-1) expression, which reduced monocyte cell adherence. We demonstrated that sesamol showed potential as a therapeutic agent for improving asthma.

Keywords: airway hyperresponsiveness; asthma; eosinophil infiltration; oxidative stress; sesamol

1. Introduction

Asthma is an allergic respiratory disease that is important globally. The pathological characteristics of allergic asthma include inflammation and allergic reactions in the airways and increased eosinophil

infiltration in the lungs. These conditions lead to airway hyperresponsiveness (AHR), airway remodeling due to smooth muscle hyperplasia, and narrow airways [1]. Sudden asthma attacks are characterized by paroxysmal wheezing, dry cough, shortness of breath, and chest tightness [2]. In patients with asthma, airway smooth muscle contraction and goblet cell hyperplasia stimulate mucus secretion, which obstructs the airway and causes difficulty breathing [3]. Hence, severe asthma attacks require urgent medication to avoid suffocation.

The pathological development of asthma is mainly related to excessive activation of T helper 2 (Th2) lymphocytes. Activated Th2 cells can secrete excessive cytokines, including interleukin (IL)-4, IL-5, and IL-13, which affect AHR, airway remodeling, eosinophil infiltration, and excessive mucus secretion in the trachea [4]. In recent years, clinical drugs have been developed to improve the symptoms of asthma with potential therapeutic effects on IL-4, IL-5, and IL-13 expression levels [5]. However, some patients with asthma have not responded well to these new treatments. Therefore, it is necessary to develop and design other treatment methods or drugs to regulate the effects of Th2 activation in patients with asthma.

Tracheal epithelial cells can defend against microorganism and allergen invasions to reduce the entry of harmful substances into the lungs. Allergens and inflammatory mediators stimulate tracheal epithelial cell activation [6]. Activated tracheal epithelial cells release cytokines, which induce an inflammatory response, and chemokines, which attract more immune cells to the lungs. These immune cells release more inflammatory and oxidative molecules to increase lung inflammation, which damages lung cells and tissues [7]. In addition, inflammatory epithelial cells can stimulate the expression of oxidases, such as nicotinamide adenine dinucleotide phosphate (NADPH) oxidase and inducible nitric oxide synthase, which produce reactive oxygen species (ROS) and nitric oxide. These conditions cause oxidative stress, which leads to airway remodeling, smooth muscle thickening, and pulmonary cell damage [8]. Therefore, in the airways, ROS and inflammatory response cytokines are dangerous signaling molecules that cause persistent respiratory cell damage and respiratory dysfunction.

Sesamun indicum, Linn. (Sesame) is a common source of sesame seeds, which can be refined to produce sesame oil. This edible vegetable oil contains high levels unsaturated fatty acids, including linolenic acid and linoleic acid [9]. Sesamol is a polyphenol lignan isolated from sesame seeds. Sesamol has shown multiple biologically active functions in animal and cellular disease models [10,11]. Sesamol alleviated the expression of inflammatory mediators by suppressing the nuclear factor- κ B (NF- κ B) and mitogen-activated protein kinase (MAPK) signaling pathways. Sesamol also displayed antioxidant effects by promoting nuclear factor erythroid 2-related factor 2/ heme oxygenase-1 (Nrf2/HO-1) expression in LPS-stimulated macrophages [12]. Moreover, sesamol reduced oxidative stress by regulating the sirtuin 1/ forkhead box class O 3a (SIRT1/FOXO3a) signaling pathway in human neuronal cells [13]. Recently, sesamol was shown to improve neutrophil infiltration and the inflammatory response in mouse lungs after an LPS-induced acute lung injury [14]. However, it remains unclear whether sesamol might improve airway inflammation, eosinophil infiltration, and oxidative stress in asthmatic lungs. In the present study, we investigated whether sesamol could regulate the molecular mechanisms involved in oxidative stress and the inflammatory response in an ovalbumin (OVA)-induced asthmatic mouse model and in inflamed human tracheal epithelial cells.

2. Materials and Methods

2.1. Animals

Six-week-old female BALB/c mice were purchased from the National Laboratory Animal Center, Taiwan. All mice were raised in air-conditioned animal housing under a 12-h light/dark cycle with food and water ad libitum. All animal experiment protocols in this study were approved by the Laboratory Animal Care Committee of Chang Gung University of Science and Technology (IACUC approval number: 2018-003).

Sesamol ($\geq 98\%$ purity; Sigma-Aldrich, St. Louis, MO, USA) was dissolved in normal saline before administration. Mice were divided into the following five treatment groups (each group, $n = 8$): (1) Mice were sensitized with normal saline and received normal saline, administered orally (N group); (2) mice were sensitized with OVA and received normal saline orally (OVA group); (3) mice were sensitized with OVA and were fed 10 or 30 mg/kg sesamol (S10 and S30 groups, respectively); and (4) mice were sensitized with OVA and were fed 10 mg/kg prednisolone (P group; the positive control).

2.2. Establishment of an Asthma Model and Sesamol Administration

Asthma was induced in mice as shown in Figure 1A. Briefly, mice were sensitized with intraperitoneal injections of a sensitization solution (0.8 mg aluminum hydroxide; Thermo, Rockford, IL) and 50 μ g ovalbumin (OVA; Sigma) in 200 μ L of normal saline) on days 1–3 and 14. Next, mice inhaled 2% OVA administered with an ultrasonic nebulizer for 30 min to induce asthma symptoms (DeVilbiss Pulmo-Aide 5650D, United States) on days 14, 17, 20, 23, and 27. Then, for 2 weeks (days 14–27), in addition to their regular diet, each mouse group received a daily dose of saline (N and OVA groups), sesamol (S10 and S30 groups), or prednisolone (P group). On day 28, we calculated the AHR in all mice; then, on day 29, we sacrificed mice to investigate the asthma pathology, immune regulation, inflammation, and oxidative stress.

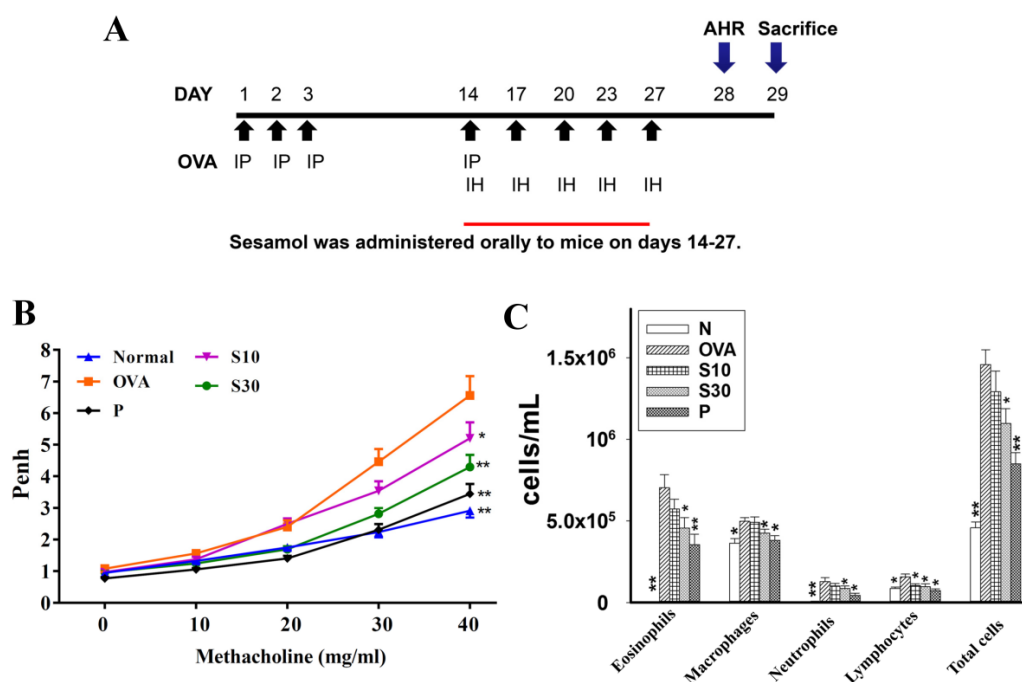


Figure 1. The effect of sesamol on AHR and immune cell counts in the BALF of mice. (A) Experimental procedures for asthmatic mouse studies. For sensitization, mice received an intraperitoneal injection (I.P.) of OVA on days 1–3 and 14. Next, mice were challenged with 2% OVA inhalation (I.H.) on days 14, 17, 20, 23, and 27. Different mouse groups were fed saline (normal and OVA groups), sesamol (S10 and S30 groups), or prednisolone (P groups), daily for 2 weeks (days 14–27; $n = 8$ mice/group). (B) Mouse AHRs measured on day 28 with increasing metacholine challenges; results are expressed as Penh values. (C) Inflammatory cells measured in BALF. All data are the means \pm SEM. * $p < 0.05$, ** $p < 0.01$ compared to the OVA control group. AHR: airway hyperresponsiveness; BALF: bronchoalveolar lavage fluid; OVA: ovalbumin; Penh: enhanced pause.

2.3. Airway Hyperresponsiveness Assay

Airway function was examined after administering aerosolized methacholine, as described previously [15]. Briefly, methacholine doses were prepared (0, 10, 20, 30, and 40 mg/mL) in normal saline solution, and mice inhaled various doses of aerosolized methacholine for 3 min. Then, mice were

placed in a closed system to record the enhanced pause (Penh) with a whole-body plethysmograph; the Penh was used to calculate the AHR (Buxco Electronics, Troy, NY, USA) on day 28.

2.4. Histological Analysis of Lung Tissue

Mice were anesthetized and sacrificed. Lung tissues were removed and fixed in 10% neutral buffered formalin (Sigma). Lung tissues were embedded into paraffin and cut into 6- μ m-thick sections. Then, the lung tissue sections were stained with a hematoxylin and eosin (HE) solution to calculate eosinophil infiltration (pathological scores), based on a five-point grading system described previously [16]. Briefly, the pathological degree of eosinophil infiltration was scored as follows: 0, no cell; 1, a few cells; 2, a ring of inflammatory cells one cell layer; 3, a ring of inflammatory cells two to four cells layer; and 4, a ring of inflammatory cells > four cells layer [17]. Lung sections were also stained with a periodic acid-Schiff (PAS) solution (Sigma) to evaluate goblet cell hyperplasia in the trachea and bronchial epithelium, as described previously [17].

2.5. Bronchoalveolar Lavage Fluid and Cell Counting

Mice were anesthetized and sacrificed to collect bronchoalveolar lavage fluid (BALF), as previously described [18]. Briefly, an indwelling needle was inserted into the trachea, and the end was connected to a 1-mL syringe. The lungs and airways were washed by loading lavage fluid into the syringe, then moving the plunger back and forth three times. Next, the BALF was centrifuged at 1500 rpm for 5 min, and the supernatant was collected and stored at -80°C . These samples were later assayed to detect cytokine and chemokine levels. Furthermore, BALF cells were treated with red blood cell lysis buffer and stained with Giemsa stain (Sigma). Then, cells were counted to determine the total cell number and the numbers of different types of immune cells.

2.6. Serum Collection

Mice were anesthetized and blood was collected from a submandibular vein. Blood was centrifuged to obtain the serum. Serum was analyzed with an ELISA to detect OVA-specific antibodies, as previously described [19].

2.7. ELISA Assay

We analyzed the supernatants of cell cultures and BALF from mice with commercial ELISA kits (R&D Systems, Minneapolis, MN), according to the manufacturer's instructions. We determined the levels of IL-6, tumor necrosis factor- α (TNF- α), IL-4, IL-5, IL-8, IL-13, intercellular adhesion molecule 1 (ICAM-1), monocyte chemoattractant protein-1 (MCP-1), chemokine (C-C motif) ligand 24 (CCL24), CCL11, and CCL5, as previously described [17]. Furthermore, we used a specific ELISA kit (BD Biosciences, San Diego, CA) to determine serum OVA-specific immunoglobulin (Ig) E, IgG1, and IgG2a levels. For OVA-IgE levels, serum samples were diluted 5-fold and the optical density (OD) was measured at 450 nm. OVA-IgG1 and OVA-IgG2a standard curves were created with mixed serum samples from OVA-sensitized mice. Cytokine and antibody levels were detected at an OD of 450 nm with a microplate reader (Multiskan FC, Thermo, Waltham, MA, USA).

2.8. Malondialdehyde Activity

Malondialdehyde (MDA) activity in the lung was examined with a lipid peroxidation assay kit (Sigma), as described previously [17]. Briefly, lung tissues were homogenized and centrifuged, and the supernatants were isolated. Then, we added perchloric acid to the supernatants to precipitate the proteins. These samples were centrifuged, and the supernatant was collected. We detected MDA activity with a multi-mode microplate reader (SpectraMax i3X, Molecular Devices, San Jose, CA, USA).

2.9. Glutathione Assay

The glutathione (GSH) levels in lung tissues were examined with a glutathione assay kit (Sigma), as described previously [17]. Briefly, lung tissues were homogenized in 5% 5-sulfosalicylic acid in a homogenizer (FastPrep-24, MP Biomedicals, Santa Ana, CA, USA). We centrifuged the samples and

collected the supernatant. GSH levels were detected with a microplate reader (Thermo) at an OD of 412 nm.

2.10. Real-Time PCR Analysis

Total RNA was extracted with TRI reagent (Sigma). cDNA was reverse transcribed from 100 ng RNA with a cDNA synthesis kit (Bio-Rad, San Francisco, CA, USA), according to the manufacturer's instructions. Next, specific genes were PCR-amplified and quantified with the SYBR Green Master Mix kit (Bio-Rad) and a spectrofluorometric thermal cycler (iCycler; Bio-Rad), as described previously [15]. The PCR conditions were: 95 °C for 10 min, and 40 cycles of 95 °C for 15 s and 60 °C for 60 s.

2.11. BEAS-2B Cell Culture and Sesamol Treatment

Sesamol was dissolved in phosphate buffered saline (PBS), and a 100 mM stock solution was prepared. Human bronchial epithelial cells (BEAS-2B, American Type Culture Collection, Manassas, VA) were cultured in dulbecco's modified eagle medium (DMEM)/F12 medium, and seeded into 24-well plates. Cell viability was determined using the 3-(4,5-Dimethylthiazol-2-yl)-2,5-diphenyltetrazolium bromide (MTT) solution (Sigma), as described previously [20]. BEAS-2B cells were treated with sesamol (0–100 μ M) for 1 h, then cells were stimulated with or without 10 ng/mL TNF- α and 10 ng/mL IL-4 for 24 h. Harvested cells were centrifuged, and the supernatants were collected. We determined chemokine and cytokine production with specific commercial ELISA kits.

2.12. Cell-Cell Adhesion Assay

BEAS-2B cells were treated with various concentrations of sesamol and stimulated with or without TNF- α /IL-4 for 24 h. Human monocytic cells (THP-1, Bioresource Collection and Research Center, Taiwan) were cultured in RPMI 1640 medium. THP-1 cells were stained with calcein-AM solution (Sigma). Next, THP-1 cells were co-cultured with BEAS-2B cells, and adherent THP-1 cells were evaluated with fluorescence microscopy (Olympus, Tokyo, Japan), as previously described [21].

2.13. Reactive Oxygen Species Assay

BEAS-2B cells were treated with sesamol for 1 h, and stimulated with or without 10 ng/mL TNF- α /IL-4 for 24 h. Then, BEAS-2B cells were incubated with 20 μ M dichloro-dihydro-fluorescein diacetate for 30 min, as previously described [17]. Briefly, three images were calculated for each result, and three areas were selected for each image to quantify the fluorescence intensity with a fluorescence microscope (Olympus). Cells were then lysed, and ROS levels were measured by exciting at 485 nm and recording emissions at 528 nm with a Multi-Mode microplate reader (SpectraMax i3X, Molecular Devices).

2.14. Statistical Analysis

Statistical analyses were performed with a one-way analysis of variance (ANOVA), followed by Dunnett's post hoc test for normally distributed data. Non-normally distributed data used non-parametric Kruskal–Wallis analysis. All data are expressed as the means \pm standard error of the mean (SEM), based on at least three independent experiments. *p*-values <0.05 were considered significant.

3. Results

3.1. Sesamol Effects on AHR in Asthmatic Mice

Asthmatic mice received oral sesamol administrations once daily from days 14 to 27. On day 28, all mice inhaled increasing doses (0–40 mg/mL) of methacholine to examine AHR. We found that the Penh values were significantly higher in the OVA group of asthmatic mice compared to normal mice (Figure 1B). At 40 mg/mL of inhaled methacholine, we observed significant attenuations in the

Penh values of the sesamol and prednisolone groups, compared to the OVA group. Thus, oral sesamol administration inhibited AHR in asthmatic mice.

3.2. Effect of Sesamol on Inflammatory Cells in BALF

In BALF, inflammatory cells were stained with Giemsa. We found significantly higher numbers of eosinophils in the OVA group of asthmatic mice ($7.1 \times 10^5 \pm 7.8 \times 10^4$) compared to normal mice. Moreover, the numbers of eosinophils in OVA-treated asthmatic mice were significantly reduced with a high sesamol concentration (S10: $5.7 \times 10^5 \pm 5.8 \times 10^4$, $p = 0.21$; S30: $4.6 \times 10^5 \pm 6.3 \times 10^4$, $p < 0.05$) and prednisolone ($3.5 \times 10^5 \pm 4.4 \times 10^4$, $p < 0.01$). The total cell numbers in asthmatic mice were significantly reduced after treatment with sesamol (S10: $1.29 \times 10^6 \pm 1.27 \times 10^5$, $p = 0.06$; S30: $1.09 \times 10^6 \pm 9.11 \times 10^4$, $p < 0.05$) or prednisolone ($8.5 \times 10^5 \pm 6.91 \times 10^4$, $p < 0.01$), compared to the OVA group ($1.46 \times 10^6 \pm 9.15 \times 10^4$; Figure 1C).

3.3. Sesamol Effects on Eosinophil Infiltration and Goblet Cell Hyperplasia in Lungs

HE staining demonstrated that more eosinophils infiltrated the lungs of asthmatic mice, compared to normal mice. In OVA-sensitized mice, sesamol or prednisolone suppressed lung eosinophil infiltration compared to the OVA group of asthmatic mice (Figure 2A). Sesamol also significantly improved the inflammatory pathology score in asthmatic mice (Figure 2B). PAS staining showed goblet cell hyperplasia in the tracheas of OVA-sensitized mice. Both sesamol and prednisolone significantly reduced goblet cell hyperplasia compared to the OVA group (Figure 2C,D).

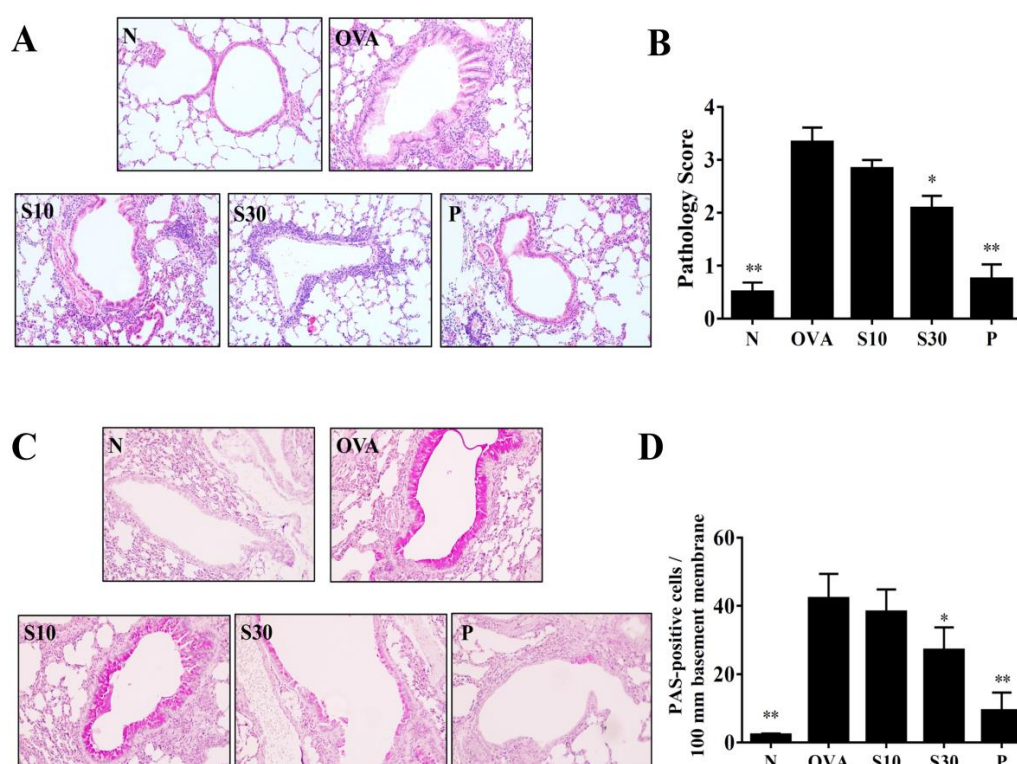


Figure 2. Sesamol effects on asthmatic lung tissues. Histological sections of lung tissues are shown from normal (N) and OVA-stimulated (OVA) mice treated with or without prednisolone (P) or sesamol (S10 and S30). (A) HE staining shows eosinophil infiltration (200× magnification); (B) pathological scores reflect the degree of eosinophil infiltration in lung sections. (C) PAS staining shows goblet cell hyperplasia (200× magnification); (D) the number of PAS-positive cells per 100 μm of basement membrane. All data are the means \pm SEM. * $p < 0.05$, ** $p < 0.01$ compared to the OVA control group; HE: hematoxylin and eosin; OVA: ovalbumin; PAS: periodic acid-Schiff.

3.4. Sesamol Effects on Cytokine and Chemokine Levels in BALF and Lung Tissue

In BALF, sesamol significantly reduced the levels of IL-4, IL-5, IL-13, IL-6, TNF- α , CCL11, and CCL24, compared to OVA-sensitized asthmatic mice (Figure 3). Moreover, an analysis of the gene expression in lung tissues showed that sesamol inhibited IL-4, IL-5, IL-13, IL-6, TNF- α , cyclooxygenase (COX)-2, CCL11, and CCL24 expression compared to asthmatic mice (Figure 4). Conversely, sesamol significantly promoted interferon (IFN)- γ levels in BALF and lung tissues, compared to asthmatic mice (Figures 3 and 4).

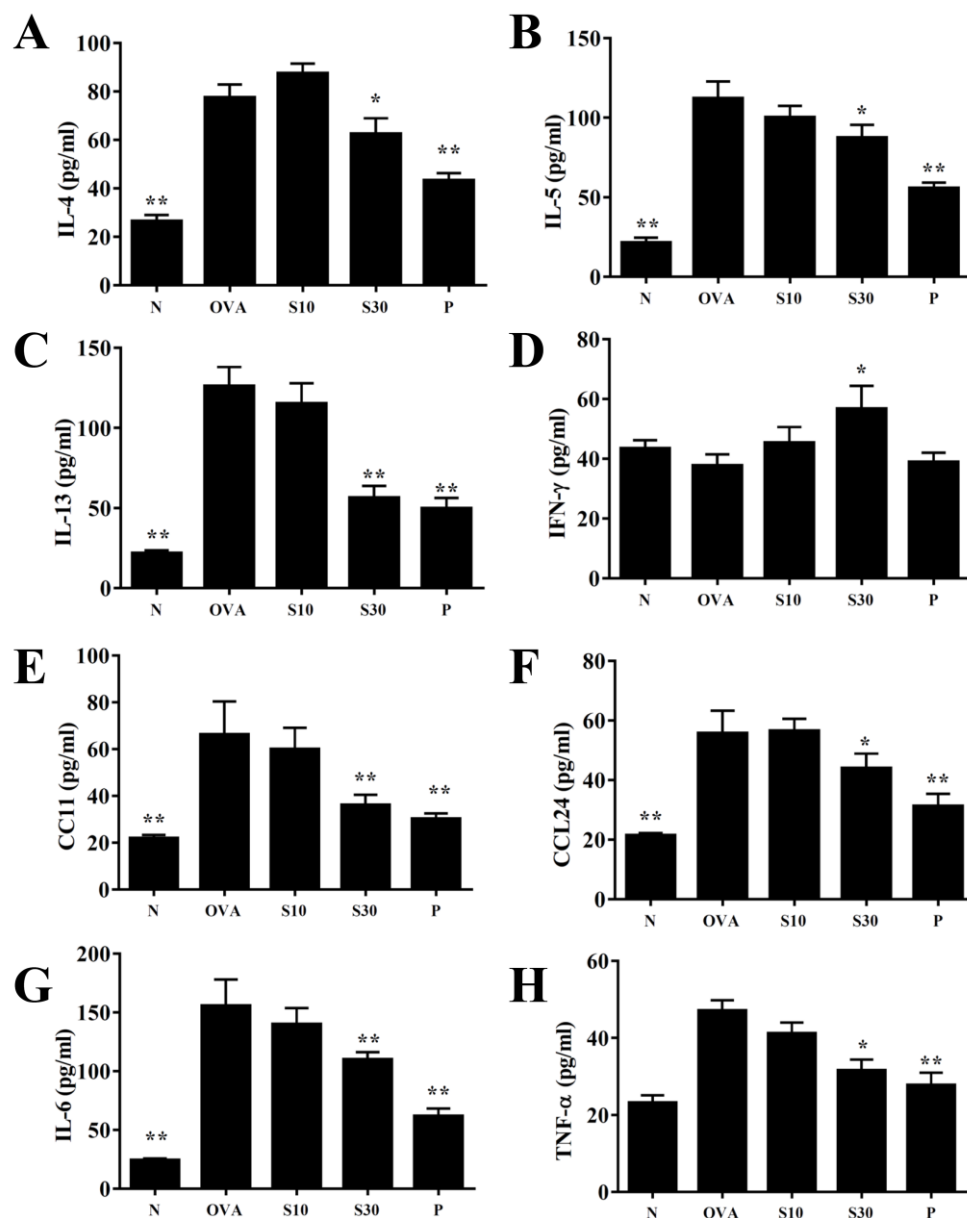


Figure 3. Effects of sesamol on cytokine and chemokine levels in BALF. ELISA results show the concentrations of (A) IL-4, (B) IL-5, (C) IL-13, (D) IFN- γ , (E) CCL11, (F) CCL24, (G) IL-6, and (H) TNF- α in BALF from normal (N) and OVA-stimulated (OVA) mice treated without or with prednisolone (P) or sesamol (S10 and S30). All data are the means \pm SEM. * $p < 0.05$, ** $p < 0.01$ compared to the OVA control group. BALF: bronchoalveolar lavage fluid; OVA: ovalbumin.

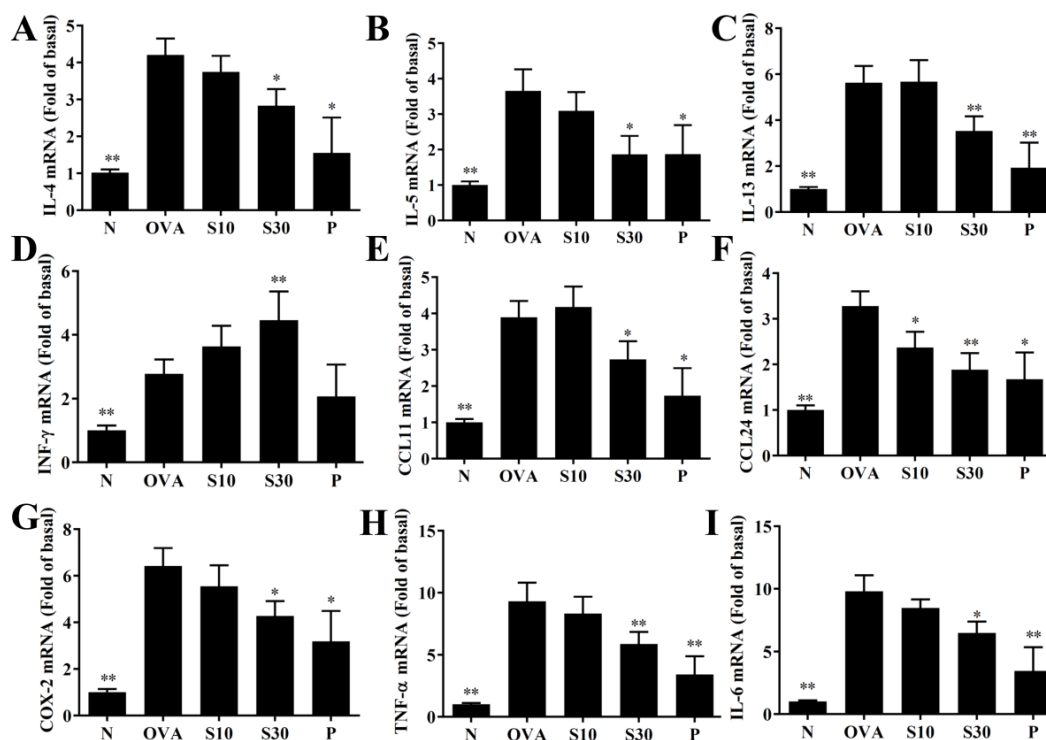


Figure 4. Sesamol effects on gene expression in the lungs. mRNAs extracted from lung tissues were amplified with real-time RT-PCR. Results show gene expression levels in normal (N) and OVA-stimulated (OVA) mice treated without or with prednisolone (P) or sesamol (S10 and S30). The results show the expression levels of (A) IL-4, (B) IL-5, (C) IL-13, (D) IFN- γ , (E) CCL11, (F) CCL24, (G) COX-2, (H) TNF- α , and (I) IL-6. Fold-changes in expression were measured relative to β -actin expression levels (internal control). All data are the means \pm SEM. * $p < 0.05$, ** $p < 0.01$ compared to the OVA control group. OVA: ovalbumin.

3.5. Sesamol Modulated GSH and MDA Activities in Lung issues

Asthma attacks can induce oxidative stress in the lung and attenuate lung function [22]. We homogenized mouse lung tissues to assay GSH and MDA levels. We found that sesamol significantly enhanced GSH levels and reduced MDA activity compared to OVA-treated asthmatic mice (Figure 5A,B).

3.6. Sesamol Modulated ICAM-1 and Mucin 5AC (Muc5Ac) Expression in Lung Tissues

We performed PCR to detect ICAM-1 and Muc5Ac gene expression in lung tissues. We found that sesamol significantly reduced ICAM-1 expression (Figure 5C) and suppressed Muc5AC expression in asthmatic mice (Figure 5D).

3.7. Sesamol Effect on Serum OVA-Specific Antibodies

Sesamol significantly reduced the serum levels of OVA-IgE and OVA-IgG1, compared to OVA-treated mice (Figure 6A,B). Interestingly, sesamol significantly increased the OVA-IgG2a levels, compared to OVA-treated mice (Figure 6C). In contrast, oral prednisolone administration significantly suppressed the levels of all OVA-specific antibodies, compared to OVA-treated mice (Figure 6).

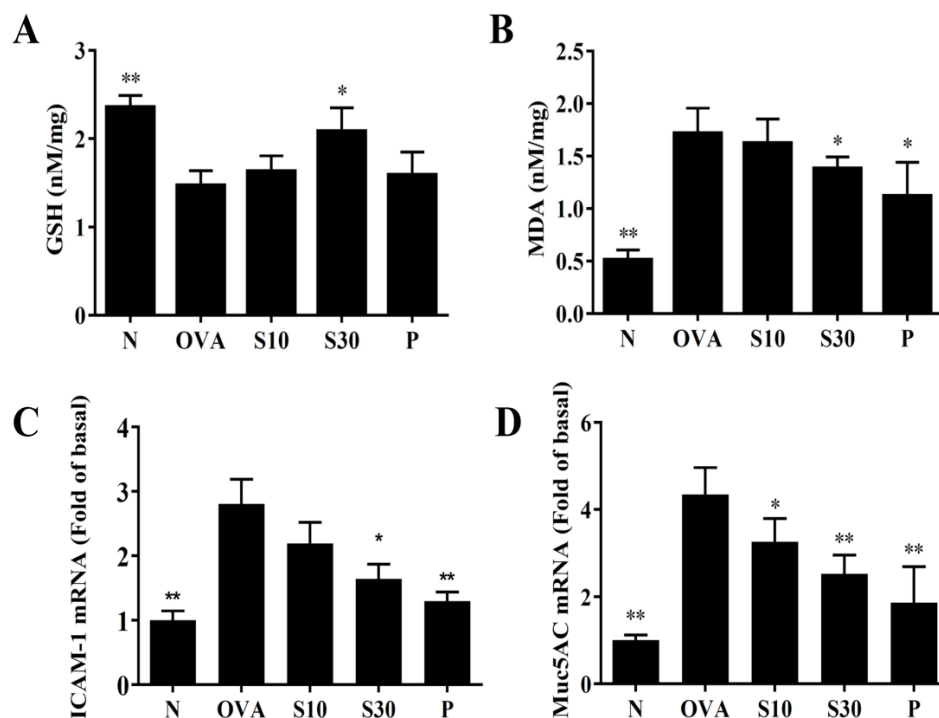


Figure 5. Sesamol regulation of oxidative activities in the lung. (A) GSH activity and (B) MDA activity were measured in the lung tissues of normal (N) and OVA-stimulated (OVA) mice treated without or with prednisolone (P) or sesamol (S10 and S30). Sesamol suppressed the expression of (C) ICAM-1 and (D) Muc5Ac genes in the lungs. All data are the means ± SEM. * $p < 0.05$, ** $p < 0.01$ compared to the OVA control group. ICAM-1: intercellular adhesion molecule 1; GSH: glutathione; MDA: malondialdehyde; muc5Ac: mucin 5Ac protein; OVA: ovalbumin.

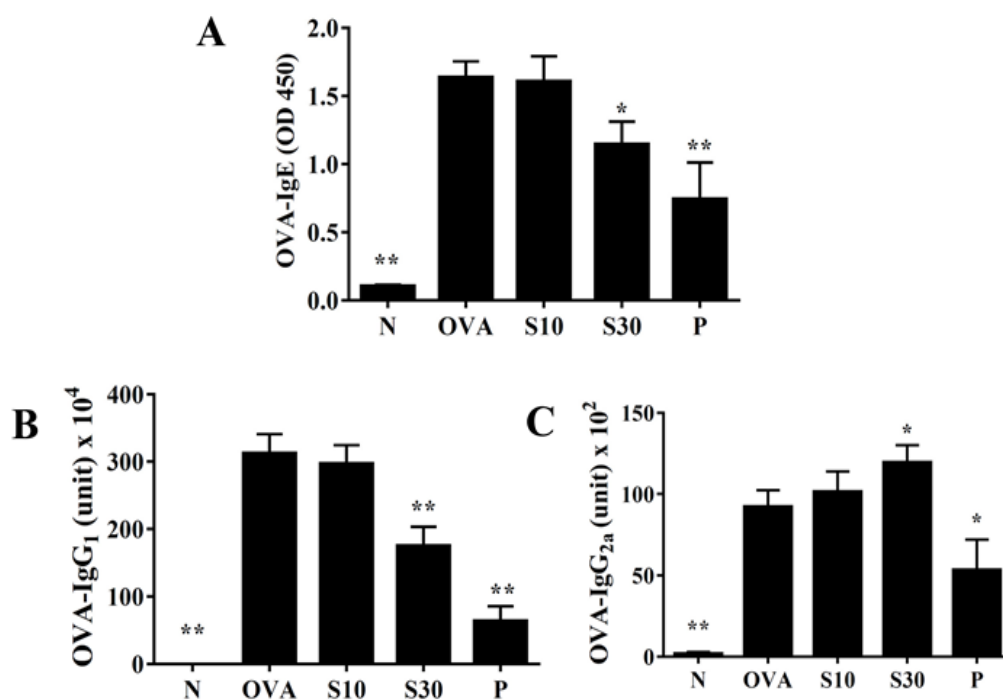


Figure 6. Sesamol effects on OVA-specific antibodies in serum. Serum levels of (A) OVA-IgE, (B) OVA-IgG₁, and (C) OVA-IgG_{2a} are shown for normal (N) and OVA-stimulated (OVA) mice treated without or with prednisolone (P) or sesamol (S10 and S30). All data are the means ± SEM. * $p < 0.05$, ** $p < 0.01$ compared to the OVA control group. OVA: ovalbumin.

3.8. Sesamol Suppressed Proinflammatory Cytokine and Chemokine Production in BEAS-2B Cells

In this study, the cytotoxicity of sesamol in BEAS-2B cells was determined using the MTT assay. Sesamol did not show significant cytotoxic effects at doses ≤ 100 μM , and subsequent experiments used sesamol at 10–100 μM concentrations (data not shown). BEAS-2B cells treated with various sesamol concentrations were stimulated with 10 ng/mL TNF- α /IL-4. We found that sesamol significantly dose-dependently reduced the levels of CCL11, CCL24, CCL5, MCP-1, IL-6, and IL-8, compared to BEAS-2B cells stimulated with TNF- α /IL-4 alone (Figure 7).

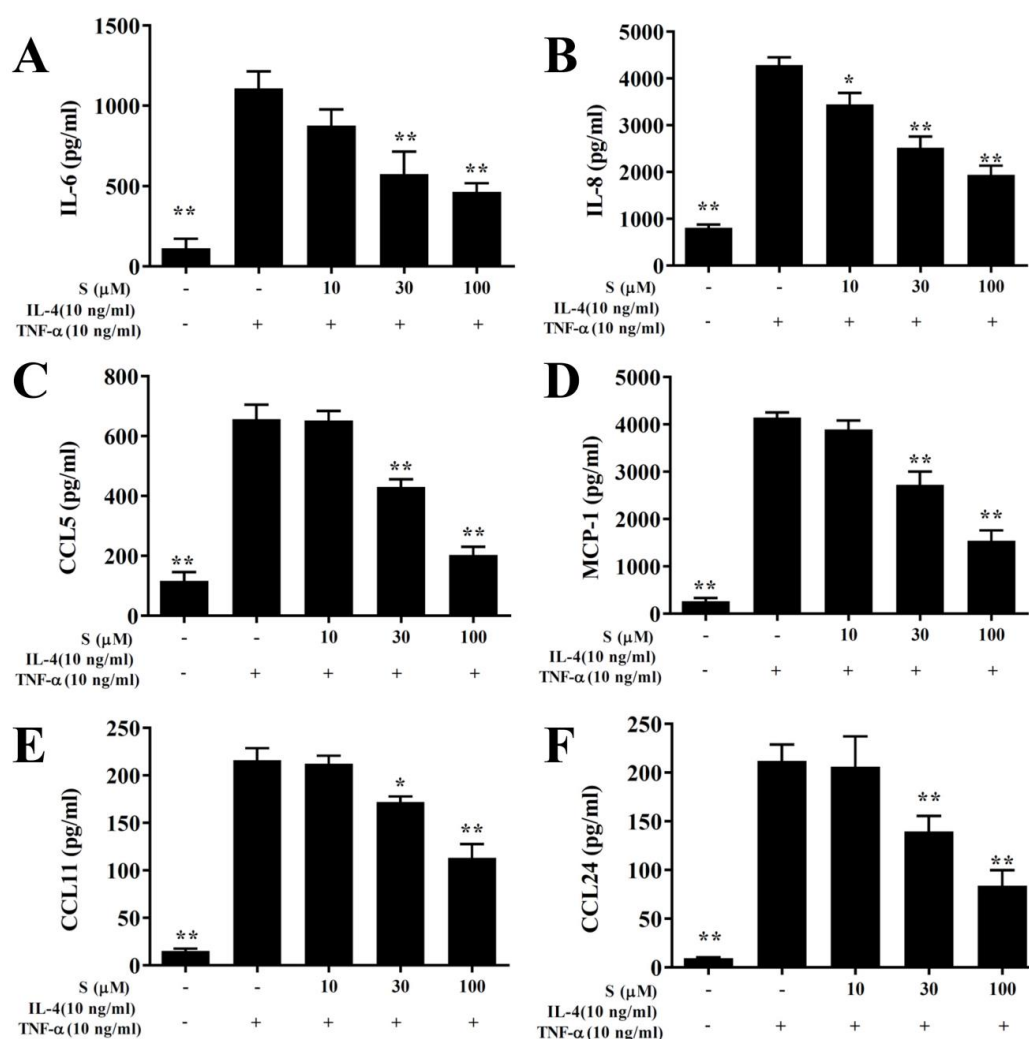


Figure 7. Sesamol effects on cytokine and chemokine production in BEAS-2B cells. ELISA results show sesamol (S) effects on the concentrations of (A) IL-6, (B) IL-8, (C) CCL5, (D) MCP-1, (E) CCL11, (F), and CCL24 in TNF- α /IL-4-activated BEAS-2B cells. The data represent the mean \pm SEM; * $p < 0.05$, ** $p < 0.01$, compared to BEAS-2B cells stimulated with 10 ng/mL TNF- α /IL-4.

3.9. Sesamol Suppressed THP-1 Cell Adhesion to BEAS-2B Cells

We found that TNF- α /IL-4 stimulated ICAM-1 expression in BEAS-2B cells, and sesamol significantly reduced ICAM-1 levels after TNF- α /IL-4 treatment (Figure 8A). Next, we stained THP-1 cells with calcein-AM and co-cultured them with BEAS-2B cells. We found that sesamol significantly reduced THP-1 cell adherence to TNF- α /IL-4-treated BEAS-2B cells (Figure 8B,C).

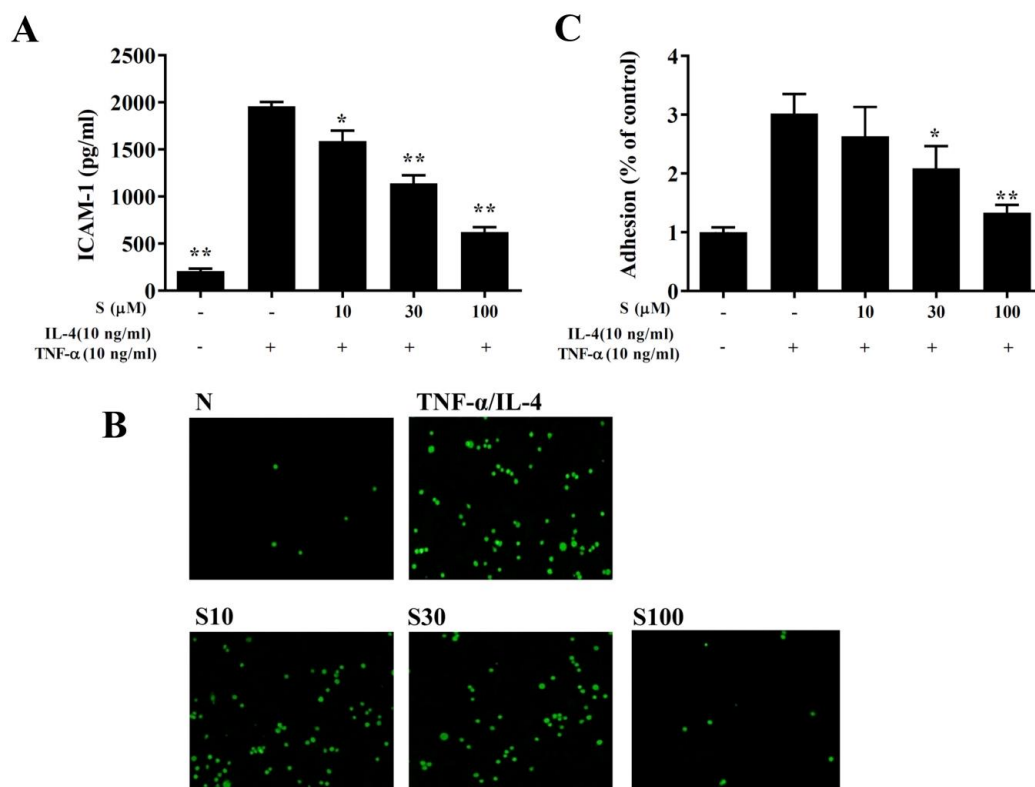


Figure 8. Sesamol inhibited THP-1 cell adherence to BEAS-2B cells. (A) Sesamol (S) reduced the levels of ICAM-1 in TNF- α /IL-4-activated BEAS-2B cells. (B) Fluorescence images show the adhesion of THP-1 cells to TNF- α /IL-4-stimulated BEAS-2B cells. (C) Fluorescence intensities were evaluated to determine the percent of THP-1 adhesion to BEAS-2B cells. The data represent the mean \pm SEM of three independent experiments; * $p < 0.05$, ** $p < 0.01$, compared to BEAS-2B cells stimulated with TNF- α and IL-4.

3.10. Sesamol Effects on ROS Production

BEAS-2B cells were incubated with dichloro-dihydro-fluorescein diacetate to label intracellular ROS. Fluorescence microscopy showed that sesamol reduced the intracellular ROS levels in BEAS-2B cells treated with TNF- α /IL-4 (Figure 9A,B). Furthermore, when ROS levels were measured with a Multi-Mode microplate reader, we found that sesamol significantly attenuated ROS levels, compared to BEAS-2B cells treated with TNF- α /IL-4 (Figure 9C).

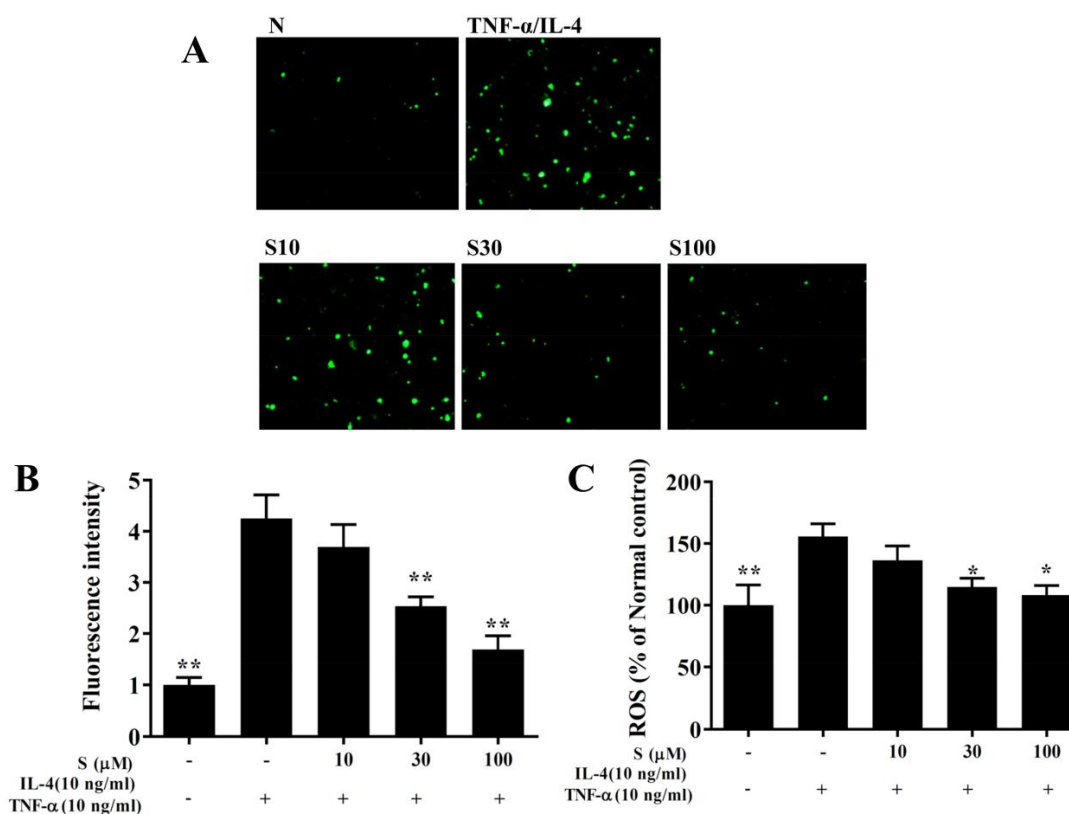


Figure 9. Sesamol effects on ROS production in activated BEAS-2B cells. (A) Fluorescence images show intracellular ROS in normal inactivated (N) and in TNF- α /IL-4-activated BEAS-2B cells treated without or with sesamol (S). (B) Fluorescence intensities indicate the levels of intracellular ROS in BEAS-2B cells. (C) The percentage of ROS detected in TNF- α /IL-4-activated BEAS-2B cells compared to that detected in normal control cells. All data represent the mean \pm SEM; * $p < 0.05$, ** $p < 0.01$, compared to BEAS-2B cells stimulated with TNF- α and IL-4.

4. Discussion

Sesamol is a lignin isolated from sesame seeds [7]. Sesamol has many biological functions, which produce anti-inflammatory, antioxidant, and anti-tumor effects [10]. Studies have shown that sesamol could induce apoptosis in cancer cells and inhibit the effects of proliferation and autophagy in lung cancer and colon cancer [11]. We and other research groups also discovered that sesamol could inhibit the secretion of inflammatory cytokines and reduce oxidative damage caused by inflammatory macrophages [12,23]. Other studies found that sesamol could ameliorate the effects of oxidative stress and inflammation in focal cerebral ischemia/reperfusion injury in the rat brain [24]. Sesamol also reduced inflammatory cell secretions of TNF- α and IL-6, promoted superoxide dismutase expression to increase antioxidation effects, and reduced neutrophil infiltration in a rat model of LPS-induced acute lung injury [14]. Taken together, these findings have shown that sesamol is a natural lignin with excellent antioxidant and anti-inflammatory properties. Therefore, we hypothesized that sesamol might improve inflammation and show antioxidant effects in asthmatic lungs.

Excessive Th2 cell activation is considered the main factor involved in pathological symptoms in the lung during asthma development [25]. In the lungs of patients with asthma, Th2 cells secrete excess IL-4, IL-5, and IL-13 to inhibit the expression of Th1 cells, which reduces IFN- γ secretion [4]. Th2 cells secrete excess IL-4 to induce B cell activation and the secretion of more IgE antibodies [26]. When allergens combine with IgE and mast cells, the complex induces mast cells to release an excess of histamine and leukotriene, which causes a severe allergic reaction [27]. We found that sesamol could inhibit IL-4 expression in BALF and lungs, and it reduced serum OVA-specific IgE levels in asthmatic mice. Many previous studies have shown that Th1 cell-associated cytokines could stimulate

B cells to secrete IgG2a, and that Th2 cytokines could induce B cells to produce IgG1 in mice [28]. Prednisone has anti-inflammatory and immunosuppressive properties. Prednisone could suppress Th1 and Th2 cell activity to decrease inflammation and allergic reactions in patients with asthma [5]. Hence, asthmatic mice treated with prednisone could reduce inflammation of the lungs and improve asthma symptoms in mice by blocking the expression of Th1- and Th2-associated cytokines. Interestingly, our results showed that sesamol inhibited OVA-IgG1 expression, promoted OVA-IgG2 levels in serum, and increased INF- γ production in the BALF and lungs of asthmatic mice. Therefore, we demonstrated that oral sesamol administration could increase Th1 cell activity and inhibit Th2 cell activity, which improved the pathological features of asthma.

Asthma is an allergic inflammatory respiratory disease. Patients with chronic asthma continuously display chronic inflammation and oxidative stress [8]. Furthermore, pulmonary epithelial cells and immune cells are continuously activated, and they release various inflammatory cytokines, inflammatory mediators, and oxidative molecules that damage cells and tissues, which reduces lung function [6,29]. Previous studies have shown that some natural products could reduce airway inflammation in asthmatic mice [30,31]. For example, asthmatic mice treated with an intraperitoneal injection of curcumin showed reduced IL-6 and TNF- α secretion in BALF [32]. Intraperitoneal injections of casticin and licochalcone A also improved airway inflammation in asthmatic mice, by suppressing inflammatory cytokines and chemokines in inflammatory tracheal epithelial cells [9,19]. In the present study, sesamol was dissolved in PBS or normal saline, and it was administered orally to asthmatic mice with a gastric tube. We found that sesamol reduced inflammation in the BALF and lungs of asthmatic mice. Many previous studies showed that lung tissues accumulate excessive amounts of the inflammatory cytokines, TNF- α and IL-6, which cause damage to lung cells, and might also induce the development of lung fibrosis [33,34]. In addition, allergens and inflammatory cytokines were shown to stimulate an inflammatory response in tracheal epithelial cells and increase lung tissue damage caused by inflammation [25,35,36]. The present study demonstrated that sesamol could attenuate the inflammatory response in TNF- α /IL-4-stimulated tracheal epithelial cells. Therefore, we concluded that sesamol improved lung inflammation in asthmatic mice, which inhibited asthma development.

Airway remodeling is a structural change of the airways in patients with asthma. Airway remodeling includes airway narrowing and enhanced airway resistance [37]. In patients with chronic asthma, airway smooth muscle thickening and reduced connective tissue elasticity reduces the alveolar surface tension and elasticity, which worsens lung compliance [38,39]. Clinically, AHR is used to detect the airflow and respiratory rate in airways to evaluate pathological characteristics and pulmonary function in patients with asthma [1]. Many previous studies have pointed out that oxidative stress and inflammation exacerbated AHR values, which reflected the exacerbation the deterioration of lung function [15,17,19]. We employed whole-body plethysmography to detect AHRs in asthmatic mice. Our results demonstrated that sesamol could reduce AHR, which reflected improved physiological respiratory function. In patients with asthma, excessive Th2 cell activation increases AHR; indeed, IL-13 is a pleiotropic Th2 cytokine that induces AHR [40]. Moreover, IL-13-deficient asthmatic mice showed significantly less AHR than wild-type asthmatic mice [41]. Our results demonstrated that sesamol could attenuate IL-13 gene expression in the lungs and BALF of asthmatic mice. Hence, we concluded that sesamol improved AHR mainly by reducing IL-13 expression in asthmatic mice.

Patients with acute asthma often show large amounts of eosinophil infiltration in the lungs [42]. Many previous studies found that activated eosinophils released increased amounts eosinophil cationic proteins into cellular vesicles. Eosinophil cationic proteins caused respiratory inflammation and induced damage or apoptosis in lung cells, which decreased lung function [43]. In addition, eosinophils released eosinophil peroxidase, which caused oxidative damage to alveolar cells [2]. Th2 cells also released excessive IL-5, which induced bone marrow cells to differentiate to mature eosinophils [42,44]. In patients with asthma, tracheal epithelial cells release high amounts of eotaxin, which induces eosinophil migration and infiltration into the lungs [45]. Therefore, reducing Th2 cell activation and the inflammatory response of tracheal epithelial cells might regulate eosinophilic infiltration in the lung.

We found that sesamol reduced the number of total cells and eosinophils in the BALF of asthmatic mice, compared to asthmatic mice. In addition, sesamol inhibited eosinophil infiltration into the lungs of asthmatic mice. Sesamol also reduced IL-5 expression in the BALF and lung, and it reduced eotaxin expression in the lung and tracheal epithelium. Moreover, sesamol reduced ICAM-1 expression in inflamed airway epithelial cells, which inhibited the adherence of THP-1 immune cells. Therefore, we concluded that sesamol improved the allergic and inflammatory responses in asthmatic mice by reducing IL-5 expression in the lung and by inhibiting eosinophil infiltration into the lung.

Respiratory mucus glycoproteins can protect the lungs from microorganisms or allergens that can invade the lower respiratory tract. Additionally, mucus is an important secretory substance for maintaining respiratory functions [3]. However, during asthma onset, the patient's airway narrows, and excessive mucus secretion increases airway obstruction, which leads to dyspnea or even suffocation [37]. Mucus is mainly secreted by tracheal epithelial cells. Allergens stimulate tracheal epithelial cells to differentiate into goblet cells and proliferate. This leads to excess mucus secretion in patients with asthma [46]. We used the PAS stain to detect goblet cells in asthmatic mice. We found that sesamol reduced goblet cell hyperplasia in the trachea and attenuated Muc5Ac gene expression in the lungs, which reduced mucus production. Previous studies demonstrated that IL-4 and IL-13 were released by overactivated Th2 cells and they induced goblet cell proliferation in the tracheas of asthmatic mice [47]. Here, we demonstrated that sesamol reduced IL-4 and IL-13 levels in the BALF and lungs. These results suggested that the sesamol inhibition of IL-4 and IL-13 expression caused a reduction in goblet cell proliferation in the trachea.

Previous studies pointed out that, in patients with asthma, the airways are stimulated to induce excessive oxidative stress, which aggravates mucus and sputum production and also damages lung cells [48,49]. Asthmatic mouse models and in vitro cellular experiments showed that allergens or inflammatory cytokines could stimulate airway epithelial cell activation, which increased chemokine release, attracted inflammatory immune cell infiltration into the lungs, and induced ROS production in tracheal epithelial cells [8,50]. Animal experiments also showed that these inflamed immune cells released high levels of inflammatory mediators in the lungs and induced oxidative stress, which damaged lung cells and attenuated lung function [51,52]. In the present study, we found that sesamol inhibited ROS production in inflammatory BEAS-2B cells and reduced CCL11 and CCL24 expression, which inhibited eosinophil infiltration. Moreover, reducing the amounts of eosinophil peroxidase released by eosinophils reduced the oxidative damage to lung cells. Sesamol also reduced the levels of MCP-1 and IL-8, which suppressed macrophage (monocyte) and neutrophil migration into the lungs of asthmatic mice. Moreover, high doses of sesamol reduced the numbers of macrophages and neutrophils in BALF. Hence, sesamol suppressed ROS release, and thus maintained lung function in asthmatic mice. We employed a lipid peroxidation assay to detect MDA activity, an identifying marker of oxidative stress in cells or tissues [8]. Additionally, glutathione is an important antioxidant enzyme that regulates oxidative stress in the lungs of patients with asthma [53]. We found that sesamol significantly attenuated the MDA levels and promoted GSH expression in the lungs of asthmatic mice. These activities regulated peroxidation effects in the lungs of asthmatic mice. These findings were consistent with previous studies, which showed that sesamol increased GSH and decreased MDA levels in rat ischemic cortex tissues [24]. Sesamol regulation of GSH and MDA levels also reduced oxidative stress and improved cognitive impairments in mouse brains [54]. Hence, sesamol had a protective effect against oxidative stress, and thus maintained lung function in asthmatic mice.

5. Conclusions

In conclusion, our findings confirmed that sesamol ameliorates airway inflammation, inhibits eosinophil infiltration into the lung, and attenuates tracheal mucus secretion by suppressing Th2-associated cytokine and eotaxin release in asthmatic mice. More specifically, sesamol showed potential for improving inflammation and oxidative stress in asthma.

Author Contributions: Experimental design and performance: C.-J.L., Y.-L.C., M.-C.Y., S.-C.S. and W.-C.H.; Data analysis and interpretation: C.-J.L., Y.-L.C., M.-C.Y., and K.-W.Y.; Drafting the manuscript: C.-J.L., S.-C.S. and W.-C.H. All authors have read and agreed to the published version of the manuscript.

Funding: This study was supported, in part, by grants from Chang Gung Memorial Hospital (CMRPF1H0022, CMRPF1H0041, CMRPF1H0042, and CMRPF1J0021) and the Ministry of Science and Technology in Taiwan (105-2320-B-255-003).

Conflicts of Interest: The authors have no conflicts of interest to declare.

References

1. Fergusson, J.E.; Patel, S.; Lockey, R.F. Acute asthma, prognosis and treatment. *J. Allergy Clin. Immunol.* **2017**, *139*, 438–447. [\[CrossRef\]](#)
2. Yancey, S.W.; Keene, O.N.; Albers, F.C.; Ortega, H.; Bates, S.; Bleecker, E.R.; Pavord, I. Biomarkers for severe eosinophilic asthma. *J. Allergy Clin. Immunol.* **2017**, *140*, 1509–1518. [\[CrossRef\]](#) [\[PubMed\]](#)
3. Santus, P.; Radovanovic, D.; Chiumello, D.A. Mucins and asthma: Are we headed to the revolutionary road? *J. Clin. Med.* **2019**, *8*, 1955. [\[CrossRef\]](#) [\[PubMed\]](#)
4. Caminati, M.; Pham, D.L.; Bagnasco, D.; Canonica, G.W. Type 2 immunity in asthma. *World Allergy Organ.* **2018**, *11*, 13. [\[CrossRef\]](#) [\[PubMed\]](#)
5. Sehmi, R.; Lim, H.F.; Mukherjee, M.; Huang, C.; Radford, K.; Newbold, P.; Boulet, L.P.; Dorscheid, D.; Martin, J.G.; Nair, P. Benralizumab attenuates airway eosinophilia in prednisone-dependent asthma. *J. Allergy Clin. Immunol.* **2018**, *141*, 1529–1532.e8. [\[CrossRef\]](#)
6. Roan, F.; Obata-Ninomiya, K.; Ziegler, S.F. Epithelial cell-derived cytokines: More than just signaling the alarm. *J. Clin. Investig.* **2019**, *129*, 1441–1451. [\[CrossRef\]](#)
7. Lloyd, C.M.; Saglani, S. Epithelial cytokines and pulmonary allergic inflammation. *Curr. Opin. Immunol.* **2015**, *34*, 52–58. [\[CrossRef\]](#)
8. De Groot, L.E.S.; van der Veen, T.A.; Martinez, F.O.; Hamann, J.; Lutter, R.; Melgert, B.N. Oxidative stress and macrophages: Driving forces behind exacerbations of asthma and chronic obstructive pulmonary disease? *Am. J. Physiol. Lung Cell Mol. Physiol.* **2019**, *316*, L369–L384. [\[CrossRef\]](#)
9. Michailidis, D.; Angelis, A.; Aligiannis, N.; Mitakou, S.; Skaltsounis, L. Recovery of sesamin, sesamol, and minor lignans from sesame oil using solid support-free liquid-liquid extraction and chromatography techniques and evaluation of their enzymatic inhibition properties. *Front. Pharmacol.* **2019**, *10*, 723. [\[CrossRef\]](#)
10. Wu, M.S.; Aquino, L.B.B.; Barbaza, M.Y.U.; Hsieh, C.L.; Castro-Cruz, K.A.; Yang, L.L.; Tsai, P.W. Anti-inflammatory and anticancer properties of bioactive compounds from *Sesamum indicum* L.—A review. *Molecules* **2019**, *24*, 4426. [\[CrossRef\]](#)
11. Majdalawieh, A.F.; Mansour, Z.R. Sesamol, a major lignan in sesame seeds (*Sesamum indicum*): Anti-cancer properties and mechanisms of action. *Eur. J. Pharmacol.* **2019**, *855*, 75–89. [\[CrossRef\]](#) [\[PubMed\]](#)
12. Wu, X.L.; Liou, C.J.; Li, Z.Y.; Lai, X.Y.; Fang, L.W.; Huang, W.C. Sesamol suppresses the inflammatory response by inhibiting NF-kappaB/MAPK activation and upregulating AMP kinase signaling in RAW 264.7 macrophages. *Inflamm. Res.* **2015**, *64*, 577–588. [\[CrossRef\]](#) [\[PubMed\]](#)
13. Ruankham, W.; Suwanjang, W.; Wongchitrat, P.; Prachayasittikul, V.; Prachayasittikul, S.; Phopin, K. Sesamin and sesamol attenuate H₂O₂-induced oxidative stress on human neuronal cells via the SIRT1-SIRT3-FOXO3a signaling pathway. *Nutr. Neurosci.* **2019**, 1–12. [\[CrossRef\]](#) [\[PubMed\]](#)
14. Chu, P.Y.; Chien, S.P.; Hsu, D.Z.; Liu, M.Y. Protective effect of sesamol on the pulmonary inflammatory response and lung injury in endotoxemic rats. *Food Chem. Toxicol.* **2010**, *48*, 1821–1826. [\[CrossRef\]](#) [\[PubMed\]](#)
15. Huang, W.C.; Fang, L.W.; Liou, C.J. Phloretin attenuates allergic airway inflammation and oxidative stress in asthmatic mice. *Front. Immunol.* **2017**, *8*, 134. [\[CrossRef\]](#) [\[PubMed\]](#)
16. Myou, S.; Leff, A.R.; Myo, S.; Boetticher, E.; Tong, J.; Meliton, A.Y.; Liu, J.; Munoz, N.M.; Zhu, X. Blockade of inflammation and airway hyperresponsiveness in immune-sensitized mice by dominant-negative phosphoinositide 3-kinase-TAT. *J. Exp. Med.* **2003**, *198*, 1573–1582. [\[CrossRef\]](#) [\[PubMed\]](#)
17. Huang, W.C.; Liu, C.Y.; Shen, S.C.; Chen, L.C.; Yeh, K.W.; Liu, S.H.; Liou, C.J. Protective effects of licochalcone A improve airway hyper-responsiveness and oxidative stress in a mouse model of asthma. *Cells* **2019**, *8*, 617. [\[CrossRef\]](#)

18. Liou, C.J.; Huang, W.C.; Kuo, M.L.; Yang, R.C.; Shen, J.J. Long-term oral administration of *Gynostemma pentaphyllum* extract attenuates airway inflammation and Th2 cell activities in ovalbumin-sensitized mice. *Food Chem. Toxicol.* **2010**, *48*, 2592–2598. [\[CrossRef\]](#)
19. Liou, C.J.; Cheng, C.Y.; Yeh, K.W.; Wu, Y.H.; Huang, W.C. Protective effects of casticin from *Vitex trifolia* alleviate eosinophilic airway inflammation and oxidative stress in a murine asthma model. *Front. Pharmacol.* **2018**, *9*, 635. [\[CrossRef\]](#)
20. Huang, W.C.; Dai, Y.W.; Peng, H.L.; Kang, C.W.; Kuo, C.Y.; Liou, C.J. Phloretin ameliorates chemokines and ICAM-1 expression via blocking of the NF-kappaB pathway in the TNF-alpha-induced HaCaT human keratinocytes. *Int. Immunopharmacol.* **2015**, *27*, 32–37. [\[CrossRef\]](#)
21. Peng, H.L.; Huang, W.C.; Cheng, S.C.; Liou, C.J. Fisetin inhibits the generation of inflammatory mediators in interleukin-1beta-induced human lung epithelial cells by suppressing the NF-kappaB and ERK1/2 pathways. *Int. Immunopharmacol.* **2018**, *60*, 202–210. [\[CrossRef\]](#) [\[PubMed\]](#)
22. Sordillo, J.E.; Rifas-Shiman, S.L.; Switkowski, K.; Coull, B.; Gibson, H.; Rice, M.; Platts-Mills, T.A.E.; Kloog, I.; Litonjua, A.A.; Gold, D.R.; et al. Prenatal oxidative balance and risk of asthma and allergic disease in adolescence. *J. Allergy Clin. Immunol.* **2019**, *144*, 1534–1541.e5. [\[CrossRef\]](#)
23. Duarte, A.R.; Chenet, A.L.; Souza de Almeida, F.J.; Balbinotti Andrade, C.M.; Roberto de Oliveira, M. The inhibition of heme oxygenase-1 (HO-1) abolishes the mitochondrial protection induced by sesamol in LPS-treated RAW 264.7 cells. *Chem. Biol. Interact.* **2018**, *296*, 171–178. [\[CrossRef\]](#) [\[PubMed\]](#)
24. Gao, X.J.; Xie, G.N.; Liu, L.; Fu, Z.J.; Zhang, Z.W.; Teng, L.Z. Sesamol attenuates oxidative stress, apoptosis and inflammation in focal cerebral ischemia/reperfusion injury. *Exp. Ther. Med.* **2017**, *14*, 841–847. [\[CrossRef\]](#) [\[PubMed\]](#)
25. Lambrecht, B.N.; Hammad, H.; Fahy, J.V. The cytokines of asthma. *Immunity* **2019**, *50*, 975–991. [\[CrossRef\]](#)
26. Bush, A. Cytokines and chemokines as biomarkers of future asthma. *Front. Pediatr.* **2019**, *7*, 72. [\[CrossRef\]](#)
27. Krohn, I.K.; Lund, G.; Frandsen, P.M.; Schiotz, P.O.; Dahl, R.; Hoffmann, H.J. Mast cell FcRI density and function dissociate from dependence on soluble IgE concentration at very low and very high IgE concentrations. *J. Asthma* **2013**, *50*, 117–121. [\[CrossRef\]](#)
28. Wu, L.C.; Scheerens, H. Targeting IgE production in mice and humans. *Curr. Opin. Immunol.* **2014**, *31*, 8–15. [\[CrossRef\]](#)
29. Goleva, E.; Berdyshev, E.; Leung, D.Y. Epithelial barrier repair and prevention of allergy. *J. Clin. Investig.* **2019**, *129*, 1463–1474. [\[CrossRef\]](#)
30. Huang, W.C.; Chan, C.C.; Wu, S.J.; Chen, L.C.; Shen, J.J.; Kuo, M.L.; Chen, M.C.; Liou, C.J. Matrine attenuates allergic airway inflammation and eosinophil infiltration by suppressing eotaxin and Th2 cytokine production in asthmatic mice. *J. Ethnopharmacol.* **2014**, *151*, 470–477. [\[CrossRef\]](#)
31. Liou, C.J.; Huang, W.C. Dehydroepiandrosterone suppresses eosinophil infiltration and airway hyperresponsiveness via modulation of chemokines and Th2 cytokines in ovalbumin-sensitized mice. *J. Clin. Immunol.* **2011**, *31*, 656–665. [\[CrossRef\]](#) [\[PubMed\]](#)
32. Shakeri, F.; Boskabady, M.H. Anti-inflammatory, antioxidant, and immunomodulatory effects of curcumin in ovalbumin-sensitized rat. *Biofactors* **2017**, *43*, 567–576. [\[CrossRef\]](#) [\[PubMed\]](#)
33. Malaviya, R.; Laskin, J.D.; Laskin, D.L. Anti-TNFalpha therapy in inflammatory lung diseases. *Pharmacol. Ther.* **2017**, *180*, 90–98. [\[CrossRef\]](#) [\[PubMed\]](#)
34. Shen, Q.Y.; Wu, L.; Wei, C.S.; Zhou, Y.N.; Wu, H.M. Sevoflurane prevents airway remodeling via downregulation of VEGF and TGF-beta1 in mice with OVA-induced chronic airway inflammation. *Inflammation* **2019**, *42*, 1015–1022. [\[CrossRef\]](#)
35. Rossi, A.; Caiazzo, E.; Bilancia, R.; Riemma, M.A.; Pagano, E.; Cicala, C.; Ialenti, A.; Zjawiony, J.K.; Izzo, A.A.; Capasso, R.; et al. Salvinorin A inhibits airway hyperreactivity induced by ovalbumin sensitization. *Front. Pharmacol.* **2016**, *7*, 525. [\[CrossRef\]](#)
36. Kleinjan, A. Airway inflammation in asthma: Key players beyond the Th2 pathway. *Curr. Opin. Pulm. Med.* **2016**, *22*, 46–52. [\[CrossRef\]](#)
37. Kudo, M.; Ishigatsubo, Y.; Aoki, I. Pathology of asthma. *Front. Microbiol.* **2013**, *4*, 263. [\[CrossRef\]](#)
38. Song, W.J.; Lee, J.H.; Kang, Y.; Joung, W.J.; Chung, K.F. Future risks in patients with severe asthma. *Allergy Asthma Immunol. Res.* **2019**, *11*, 763–778. [\[CrossRef\]](#)
39. Pelaia, C.; Paoletti, G.; Puggioni, F.; Racca, F.; Pelaia, G.; Canonica, G.W.; Heffler, E. Interleukin-5 in the pathophysiology of severe asthma. *Front. Physiol.* **2019**, *10*, 1514. [\[CrossRef\]](#)

40. Parulekar, A.D.; Kao, C.C.; Diamant, Z.; Hanania, N.A. Targeting the interleukin-4 and interleukin-13 pathways in severe asthma: Current knowledge and future needs. *Curr. Opin. Pulm. Med.* **2018**, *24*, 50–55. [[CrossRef](#)]
41. Chen, W.; Sivaprasad, U.; Gibson, A.M.; Ericksen, M.B.; Cunningham, C.M.; Bass, S.A.; Kinker, K.G.; Finkelman, F.D.; Wills-Karp, M.; Khurana Hershey, G.K. IL-13 receptor alpha2 contributes to development of experimental allergic asthma. *J. Allergy Clin. Immunol.* **2013**, *132*, 951–958.e6. [[CrossRef](#)] [[PubMed](#)]
42. Coverstone, A.M.; Seibold, M.A.; Peters, M.C. Diagnosis and management of T2-high asthma. *J. Allergy Clin. Immunol. Pract.* **2020**, *8*, 442–450. [[CrossRef](#)] [[PubMed](#)]
43. McBrien, C.N.; Menzies-Gow, A. The Biology of Eosinophils and Their Role in Asthma. *Front. Med.* **2017**, *4*, 93. [[CrossRef](#)] [[PubMed](#)]
44. Johansson, K.; Malmhall, C.; Ramos-Ramirez, P.; Radinger, M. Bone marrow type 2 innate lymphoid cells: A local source of interleukin-5 in interleukin-33-driven eosinophilia. *Immunology* **2018**, *153*, 268–278. [[CrossRef](#)]
45. Ghaffar, O.; Hamid, Q.; Renzi, P.M.; Allakhverdi, Z.; Molet, S.; Hogg, J.C.; Shore, S.A.; Luster, A.D.; Lamkhioed, B. Constitutive and cytokine-stimulated expression of eotaxin by human airway smooth muscle cells. *Am. J. Respir. Crit Care Med.* **1999**, *159*, 1933–1942. [[CrossRef](#)]
46. Bonser, L.R.; Erle, D.J. Airway mucus and asthma: The role of MUC5AC and MUC5B. *J. Clin. Med.* **2017**, *6*, 112. [[CrossRef](#)]
47. Moran, A.; Pavord, I.D. Anti-IL-4/IL-13 for the treatment of asthma: The story so far. *Expert. Opin. Biol. Ther.* **2020**. [[CrossRef](#)]
48. Sussan, T.E.; Gajghate, S.; Chatterjee, S.; Mandke, P.; McCormick, S.; Sudini, K.; Kumar, S.; Breyse, P.N.; Diette, G.B.; Sidhaye, V.K.; et al. Nrf2 reduces allergic asthma in mice through enhanced airway epithelial cytoprotective function. *Am. J. Physiol. Lung Cell Mol. Physiol.* **2015**, *309*, L27–L36. [[CrossRef](#)]
49. Sol, I.S.; Kim, Y.H.; Park, Y.A.; Lee, K.E.; Hong, J.Y.; Kim, M.N.; Kim, Y.S.; Oh, M.S.; Yoon, S.H.; Kim, M.J.; et al. Relationship between sputum clusterin levels and childhood asthma. *Clin. Exp. Allergy* **2016**, *46*, 688–695. [[CrossRef](#)]
50. Rogers, L.K.; Cismowski, M.J. Oxidative stress in the lung—The essential paradox. *Curr. Opin. Toxicol.* **2018**, *7*, 37–43. [[CrossRef](#)]
51. Zahiruddin, A.S.; Grant, J.A.; Sur, S. Role of epigenetics and DNA-damage in asthma. *Curr. Opin. Allergy Clin. Immunol.* **2018**, *18*, 32–37. [[CrossRef](#)] [[PubMed](#)]
52. Menzel, M.; Ramu, S.; Calven, J.; Olejnicka, B.; Sverrild, A.; Porsbjerg, C.; Tufvesson, E.; Bjermer, L.; Akbarshahi, H.; Uller, L. Oxidative stress attenuates TLR3 responsiveness and impairs anti-viral mechanisms in bronchial epithelial cells from COPD and asthma patients. *Front. Immunol.* **2019**, *10*, 2765. [[CrossRef](#)] [[PubMed](#)]
53. Fatani, S.H. Biomarkers of oxidative stress in acute and chronic bronchial asthma. *J. Asthma* **2014**, *51*, 578–584. [[CrossRef](#)] [[PubMed](#)]
54. Ren, B.; Yuan, T.; Diao, Z.; Zhang, C.; Liu, Z.; Liu, X. Protective effects of sesamol on systemic oxidative stress-induced cognitive impairments via regulation of Nrf2/Keap1 pathway. *Food Funct.* **2018**, *9*, 5912–5924. [[CrossRef](#)]



© 2020 by the authors. Licensee MDPI, Basel, Switzerland. This article is an open access article distributed under the terms and conditions of the Creative Commons Attribution (CC BY) license (<http://creativecommons.org/licenses/by/4.0/>).

PAPER

[View Article Online](#)
[View Journal](#)


Cite this: DOI: 10.1039/c9fo02487e

Supplementation of nano-bubble curcumin extract improves gut microbiota composition and exercise performance in mice

 Yi-Ming Chen,^{†a} Wan-Chun Chiu,^{†b,c} Yen-Shuo Chiu,^{b,d} Tong Li,^a
 Hsin-Ching Sung^{e,f} and Chien-Yu Hsiao^{*f,g,h}

Background: In a previous study, we evaluated the potential beneficial effect of nano-bubble curcumin extract (NCE) in reducing exercise-related injuries and improving performance. **Methods:** In this study, we seek to investigate changes in the gut microbiota composition upon NCE supplementation in relation to health and exercise performance. Male ICR mice were divided into 3 groups ($n = 8$ per group) and orally administered NCE once daily for six weeks at 0 (vehicle), 3.075 (NCE-1X) and 15.375 g kg⁻¹ day⁻¹ (NCE-5X). The gut microbiota from the mice was analyzed using 16S rRNA gene sequencing. **Results:** NCE-5X did not appear to obviously cluster with the vehicle group, although NCE-5X groups showed an increased Firmicutes/Bacteroidetes ratio compared with the vehicle group. In addition, anti-fatigue activity and exercise performance were evaluated by investigating the exhaustive swimming time, forelimb grip strength and serum levels of lactate, ammonia, glucose, blood urea nitrogen (BUN), creatine kinase (CK) and lactate dehydrogenase (LDH) after swimming. The NCE-1X and NCE-5X groups showed a significantly longer exhaustive swimming time and higher relative forelimb grip strength than the vehicle group. Tissue glycogen content, an important energy source for exercise, increased significantly with NCE supplementation. **Conclusion:** Taken together, our results indicate that NCE supplementation alters the gut microbiota composition and aids in overcoming physical fatigue. Curcumin may be acting on the gut microbiome to modulate the gut system towards improving exercise performance.

Received 24th October 2019,

Accepted 8th March 2020

DOI: 10.1039/c9fo02487e

rsc.li/food-function

Introduction

The stability of nanobubbles (NBs), together with their high surface area per volume and the possibility of high gas transfer, oxidant production and enhanced pollutant bio-

degradation, endows them with important and useful properties.¹ NBs are able to enhance pollutant biodegradation and extraction due to their ability to preferentially bind small hydrophobic particles. This causes them to merge as larger agglomerates due to the large capillary forces that develop, allowing them to dissolve substances without the use of a solvent or detergent². In recent years, NBs have been applied in wastewater treatment technologies to degrade organic pollutants³. In addition, NBs could have additional biological effects through the production of submicromolar hydroxyl radicals ([•]OH) and superoxide ions (O₂^{•-}).⁴ Recent research indicated that nanobubble water significantly increased the dissolved oxygen concentration of water and effectively promoted the growth of plants, fishes, and mice⁵. Nano-bubble water could cause hyperoxia and induce a hypermetabolic state to maintain a higher rate of food digestion and absorption.^{5,6} In our previous studies, curcumin NB supplementation reduces the risk of lower body injury in women.⁷ In addition, due to its high bioavailability and oxidation properties, curcumin is able to reduce exercise-induced muscle damage.^{8,9} According to Vamanu *et al.*, 2019, the curcumin supplementation on hypertensive patients changed their microbiota activity decrease in

^aHealth Technology College, Jilin Sport University, Changchun 130022, Jilin, China.
 E-mail: 1021302@ntsui.edu.tw

^bSchool of Nutrition and Health Sciences, College of Nutrition, Taipei Medical University, Taipei 11031, Taiwan

^cResearch Center of Geriatric Nutrition, College of Nutrition, Taipei Medical University, Taipei City 11031, Taiwan

^dDepartment of Orthopedics, Shuang Ho Hospital, Taipei Medical University, Taipei 23561, Taiwan

^eDepartment of Anatomy, College of Medicine, Chang Gung University, Taoyuan 33302, Taiwan

^fAesthetic Medical Center, Department of Dermatology, Chang Gung Memorial Hospital, Taoyuan 33305, Taiwan. E-mail: mozart@gw.cgust.edu.tw

^gDepartment of Nutrition and Health Sciences, Chang Gung University of Science and Technology, Taoyuan 33303, Taiwan

^hResearch Center for Industry of Human Ecology and Research Center for Chinese Herbal Medicine, College of Human Ecology, Chang Gung University of Science and Technology, Taoyuan 33303, Taiwan

[†]These authors contributed equally to this work.

the unfavorable strain by a high degree of curcumin biotransformation in the other phenolic compounds.¹⁰ Thus, a high level of curcumin could have potential microbiota modulation.

Fatigue, as defined by the inability to maintain a desired power output or exercise intensity during short-term, high-intensity anaerobic exercise, is in part due to the accumulation of lactic acid, ammonia and blood urea nitrogen (BUN) in the serum and muscles.¹¹ Sustained high intensity contractions during exercise can rapidly deplete muscle glycogen and precipitate muscle fatigue.^{12,13} Fatigue is a matter of concern for aerobic endurance athletes and is commonly referred to as “hitting the wall”. Symptoms of significantly reduced blood glucose include weakness, dizziness and decreased motivation. Supplement intake by athletes has been shown to improve performance and reduce fatigue.¹⁴

Chen *et al.*¹⁵ showed that the consumption of pre- and probiotics has positive health benefits in improving performance and recovery after exercise. Prebiotics as non-digestible food ingredients selectively stimulate the growth and the activity of probiotics (bifidobacteria or lactobacilli) in the host.¹⁶ The polysaccharides are metabolized by probiotics, generating short-chain fatty acids (SCFAs).¹⁷ Curcumin has previously been described as a prebiotic with beneficial health benefits in humans.¹⁸ There is evidence pointing to curcumin's ability in restoring the intestinal barrier function by modulating the paracellular permeability in the intestinal barrier system.¹⁹ Serum lactate that accumulates during exercise is able to cross the epithelial barrier into the lumen of the gut to affect exercise performance.²⁰ Thus, NCE could be acting as a prebiotic to potentially affect exercise performance through its modulation of the gut system.

Some studies have shown that exercise is associated with changes in microbiome composition and diversity,^{21,22} although the effect of these microbial genera on phenotype remains unknown. This raises the question of whether there is a causal link between NCE supplementation with gut microbiota changes and exercise performance improvement. Few studies have directly investigated the anti-fatigue activity of NCE and its effect on the gut microbiota composition. This study seeks to investigate the effectiveness and safety of NCE supplementation in modulating the gut microbiome and reducing fatigue.

Methods

Nano-bubble curcumin extract (NCE) preparation

Nanobubbles (also called ultrafine bubbles) are sub-micron gas-containing cavities in aqueous solution. Nanobubble water (NB) was generated by using a controllable platform of instant high pressure based on high speed grinding and cutting of water molecules. Crude curcumin was soaked in NBs for 3–5 min until the NBs impacted all curcumin particles. After NB processing, the crude curcumin was ground to powder. The NB technology was kindly provided by Mr Yung-hsiang Tseng from the Leading Auto. Bio Co. Ltd. One gram of NCE

contains 2.87 kcal and constitutes 76.67 mg protein, 14 mg fat, 4 mg saturated fat, 0 g transfat, 0.72 g carbohydrate, 14.67 mg sugar, 0.23 g fiber, and 0.18 mg sodium.

Determination of curcumin, demethoxycurcumin, and bisdemethoxycurcumin

The contents of curcuminoids in the NCE sample were determined by means of a high-performance liquid chromatography (HPLC) method. The HPLC system comprised a gradient delivery system (600, Waters, Milford, MA, USA), an auto-sampler (717 Plus, Waters), a column heater (U-620, Sugai, Wakayama, Japan), and a photodiode array (PDA) detector (2996, Waters). A Cosmosil 5C18-MS-II column (250 × 4.6 mm, i.d. 5 µm; Nacalai Tesque, Kyoto, Japan) with a Lichrospher RP-18 end-capped guard column (10 × 4.0 mm, i.d. 5 µm; Merck, Darmstadt, Germany) was used in the HPLC separation. The NCE sample was pulverized and accurately weighed to be 0.2 g. Then the sample underwent ultrasonic-assisted extraction for 15 min using 40 mL of methanol under room temperature. After centrifugation at 8000g for 5 min, the supernatant portion was taken and methanol was added to the volume of 50 mL. The final extract was filtered by using a 0.45 µm syringe filter and subjected to the HPLC system. The mobile phase, 2% acetic acid : acetonitrile (6 : 4, v/v), was delivered isocratically at 2 mL min⁻¹. The injection volume was 10 µL and the runtime was 20 min. The column temperature was maintained at 35 °C and the UV detection wavelength was 420 nm.

Animals

Male ICR mice (six weeks old; average 25 g) were purchased from Liaoning Changsheng Biotechnology (Liaoning, China). The mice were given rodent chow 5001 and distilled water *ad libitum*. They were housed at room temperature (24 ± 2 °C) under humidity-controlled (50 ± 5%) conditions on a regular 12 h light/dark cycle. The animal protocol (IACUC-19002) was reviewed and approved by the Institutional Animal Care and Use Committee (IACUC) of Jilin Sport University, Changchun City, China. The mice were subjected to daily oral gavage of vehicle, 3.075 g kg⁻¹ day⁻¹ (1X) or 15.375 g kg⁻¹ day⁻¹ (5X) NCE doses for 6 weeks⁷. Vehicle group was of the same volume and same calorific value (2.87 kcal g⁻¹) as that of glucose water equivalent to individual BWs by oral gavage.

Exhaustive swimming test and forelimb grip strength

On Day 41 of the supplementation period, 30 min after the NCE supplementation, the exhaustive swimming test was carried out according to the method previously described by Chen *et al.*²³ The swimming time from beginning to exhaustion was used to evaluate endurance performance. A low-force testing system (PicoScope 2000, Pico Technology Limited, Cambridgeshire, UK) was used to measure the forelimb absolute grip strength as previously described.²³ The forelimb grip strength test was performed on Day 40, one hour after the vehicle/NCE dose was administered. Maximal force (in grams)

recorded by this low-force system was used as an indicator of the grip strength.

Fatigue-associated biochemical indices

On Day 43, blood samples were collected 15 min after the swimming exercise. Blood was centrifuged for 10 min (1500g) at 4 °C and sera were collected for analysis. Lactate, ammonia, creatine kinase (CK), glucose, blood urea nitrogen (BUN), and lactate dehydrogenase (LDH) levels were determined using an autoanalyzer (SYSMEX XT-2000iv, Sysmex Corp., Kobe, Japan).

Tissue glycogen determination

At the end of the study on Day 45, the glycogen contents of liver and muscles were analyzed. Glycogen analysis was carried out according to a previously described method.²⁰

Histological staining of tissues

Different tissues were collected and fixed in 10% formalin after the mice were sacrificed. Hematoxylin and eosin staining was carried out as previously described.²¹

Blood biochemical assessments

At the end of the study on Day 45, all mice were fasted for 8 h, sacrificed using 95% CO₂ asphyxiation and had blood withdrawn through cardiac puncture. Serum was collected through centrifugation and the levels of aspartate aminotransferase (AST), alanine aminotransferase (ALT), lactate dehydrogenase (LDH), CK, BUN, albumin, uric acid (UA), total cholesterol (TC), triacylglycerol (TG) creatinine, total protein (TP) and glucose were assessed using an autoanalyzer (SYSMEX XT-2000iv, Sysmex Corp., Kobe, Japan).

Bacterial DNA extraction and 16S rRNA sequencing

Cecum samples were collected from the sacrificed mice on Day 45 and immediately stored at −80 °C for DNA extraction. Total genomic DNA was extracted from the cecum using a Power Soil DNA isolation kit (MO Bio, USA) according to the manufacturer's instructions. The integrity of the DNA was confirmed with 1% agarose gel electrophoresis and the DNA concentration was determined with a Picodrop microliter spectrophotometer (Picodrop, Saffron Walden, Essex, UK). The hyper-variable V3–V4 region of the bacterial 16S rRNA gene was

amplified using PCR with bar-coded universal primers 341F (F, forward primer; 5'-CCTAYGGGRBGCASCAG-3') and 806R (R, reverse primer; 5'-GGACTACNNGGTATCTAAT-3'). A pair-end library (insert size of 450–470 bp for each sample) was constructed using a TruSeq DNA PCR-Free Sample Preparation kit (Illumina, San Diego, CA, USA). Sequencing was performed according to the manufacturer's protocol at Personal Biotechnology Co., Ltd, Shanghai, China (454 Life Sciences, Roche, the Netherlands). The sequence data derived from the sequencing process were demultiplexed and clustered into operational taxonomic units (OTU) using closed-reference OTU picking against the Greengenes 13.8 reference OTU database (<http://greengenes.secondgenome.com/>) with a 97% similarity threshold.^{24,25} Singletons (OTUs that were observed to be fewer than 2 times) and OTUs that had less than 0.01% of the total observation were discarded. The dataset was rarified to 65 004 OTU for the analysis of diversity and species richness. Principal coordinates analysis (PCoA) was performed on the 97% OTU composition and abundance matrix using both weighted and unweighted unique fraction metric (UniFrac) distances that measure the phylogenetic distance between sets of taxa in a phylogenetic tree as the fraction of the branch length of the tree.²⁶ The results of bacterial groups were analyzed based on LDA effect size (LEfSe) to show the graphical cladogram.²⁷

Statistical analysis

Data are expressed as mean ± SD ($n = 8$). Significant differences between multiple groups were calculated using one-way analysis of variance (ANOVA) and *post-hoc* Duncan's test. Values <0.05 were considered significant. The Cochran–Armitage trend test was used to examine the dose-dependent effect.

Results

Phytochemical properties of NCE

The bioactive constituents of NCE, curcuminoids, were qualitatively and quantitatively confirmed. The contents of curcumin, demethoxycurcumin, and bisdemethoxycurcumin in NCE were 8.53, 2.56, and 2.45 mg g^{−1}, respectively. The HPLC chromatogram of NCE is depicted in Fig. 1.

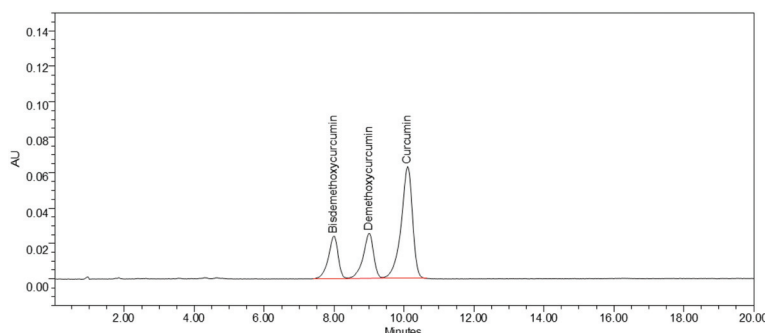


Fig. 1 The chromatogram of nano-bubble curcumin extract (NCE) analyzed using HPLC-PDA.

Table 1 General characteristics of mice with nano-bubble curcumin extract (NCE) supplementation

Characteristic	Vehicle	NCE-1X	NCE-5X	Trend analysis
Initial BW (g)	30.5 ± 1.7	30.5 ± 0.7	30.6 ± 1.5	0.9073
Final BW (g)	39.7 ± 1.7	39.5 ± 1.0	38.5 ± 1.8	0.1700
Food intake (g day ⁻¹)	4.58 ± 0.48 ^{ab}	4.73 ± 0.42 ^b	4.35 ± 0.78 ^a	0.0997
Water intake (g day ⁻¹)	5.51 ± 0.42	5.64 ± 1.10	5.58 ± 0.87	0.9332
Liver (g)	1.82 ± 0.22	1.85 ± 0.22	1.89 ± 0.30	0.5399
Kidneys (g)	0.54 ± 0.06	0.53 ± 0.04	0.55 ± 0.05	0.7553
EFP(g)	1.13 ± 0.19 ^b	0.63 ± 0.10 ^a	0.56 ± 0.16 ^a	<0.0001
Heart (g)	0.23 ± 0.03	0.22 ± 0.03	0.22 ± 0.03	0.3163
Lung (g)	0.24 ± 0.02	0.24 ± 0.03	0.24 ± 0.06	0.7708
Muscle (g)	0.37 ± 0.03 ^a	0.43 ± 0.03 ^b	0.41 ± 0.03 ^b	0.076
BAT (g)	0.044 ± 0.010 ^a	0.048 ± 0.013 ^b	0.038 ± 0.005 ^a	0.2383
Cecum (g)	0.45 ± 0.06	0.45 ± 0.05	0.44 ± 0.06	0.6358
Relative liver weight (%)	4.61 ± 0.48	5.01 ± 0.62	5.25 ± 0.80	0.0399
Relative kidney weight (%)	1.42 ± 0.17	1.43 ± 0.10	1.47 ± 0.12	0.3267
Relative EFP weight (%)	2.85 ± 0.35 ^b	1.71 ± 0.27 ^a	1.51 ± 0.41 ^a	<0.0001
Relative heart weight (%)	0.57 ± 0.08	0.60 ± 0.08	0.59 ± 0.08	0.6813
Relative lung weight (%)	0.61 ± 0.06	0.64 ± 0.09	0.64 ± 0.18	0.7445
Relative muscle weight (%)	0.95 ± 0.09 ^a	1.16 ± 0.08 ^b	1.13 ± 0.11 ^b	0.0093
Relative BAT weight (%)	0.11 ± 0.02 ^a	0.13 ± 0.03 ^b	0.10 ± 0.01 ^a	0.3153
Relative cecum weight (%)	1.13 ± 0.14	1.20 ± 0.12	1.22 ± 0.14	0.2122

Data are presented as mean ± SD, $n = 8$ mice/group. Different letters (^a, ^b) in the same row indicate a significant difference at $p < 0.05$. Muscle mass includes both gastrocnemius and soleus muscles at the back part of the lower legs. BW, body weight; BAT, brown adipose tissue; EFP, epididymal fat pad. The mice were supplemented for 6 weeks with vehicle (glucose water), NCE-1X (3.075 g kg⁻¹ day⁻¹ NCE) or NCE-5X (15.375 g kg⁻¹ day⁻¹ NCE).

Effect of 6-week NCE supplementation on tissue weight, body weight, food and water intake

Table 1 shows the tissue weight, body weight, and food and water intake of the mouse groups over the study period. The initial body weight (BW), final BW, food intake and water intake were not significantly different between the groups, suggesting that NCE supplementation had no effect on the mouse BW. Tissues and organs were obtained from the sacrificed mice after the study period and weighed. The epididymal fat pad (EFP) weight from the vehicle, NCE-1X and NCE-5X groups were 1.13 ± 0.19, 0.63 ± 0.10 and 0.56 ± 0.16 g, respectively. The EFP weights were significantly lower in the NCE-1X (44.20%, $p < 0.0001$) and NCE-5X groups (50.72%, $p < 0.0001$), compared with the vehicle group. The muscle weights of the NCE-1X and NCE-5X groups were significantly higher than the vehicle group by 1.15-fold

($p = 0.0001$) and 1.11-fold ($p = 0.0116$), respectively. There was no significant difference in the liver, kidneys, heart, lungs, brown adipose tissue (BAT) and cecum weights between the mouse groups. The relative weights of the EFP and muscle in the NCE-1X and NCE-5X groups were higher than the vehicle group.

Effect of six-week NCE supplementation on the exhaustive swimming test and forelimb grip strength

As shown in Fig. 2A, the exhaustive swimming time of the NCE-1X group was 12.0 ± 5.6 min, 1.90-fold longer than that of the vehicle group ($p = 0.0205$). The exhaustive swimming time of the NCE-5X group was 11.6 ± 5.7 min, significantly longer (1.84-fold, $p = 0.0397$) than the vehicle group ($p = 0.0397$). The relative strengths normalized to individual body weights in the vehicle, NCE-1X and NCE-5X groups were 534 ± 55, 670 ± 85

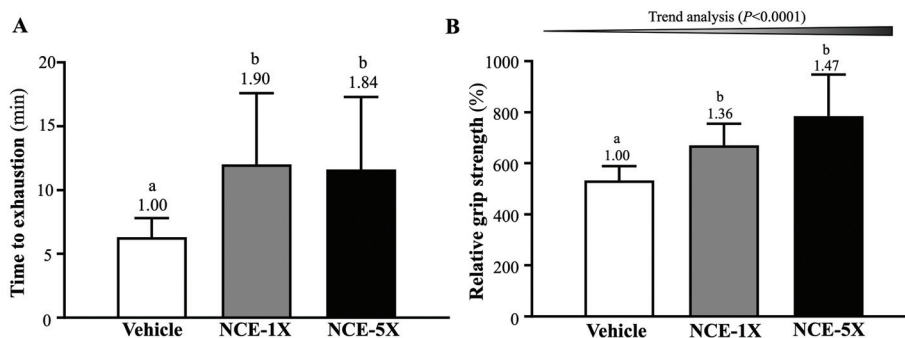


Fig. 2 Effect of nano-bubble curcumin extract (NCE) supplementation on the (A) exhaustive swimming test and (B) relative forelimb grip strength (calculated as grip strength (g) as % of body weight (g)). Data are presented as mean ± SD, $n = 8$. Bars with different letters (^a, ^b) indicate significant difference at $p < 0.05$, determined using one-way ANOVA.

and $785 \pm 164\%$, respectively (Fig. 2B). The NCE-1X and NCE-5X supplementation groups showed significantly higher relative strengths (1.25-fold, $p = 0.0239$ and 1.47-fold, $p = 0.0002$, respectively) to the vehicle group. Furthermore, a significant dose-dependent effect on relative forelimb grip strength was observed ($p < 0.0001$).

Effect of six-week NCE supplementation on fatigue-related profile after the 15-min swimming test

On Day 43 of the supplementation period, the mice were subjected to a 15 min swimming test to evaluate the levels of several fatigue-related indicators (Fig. 3A). Serum lactate levels in the NCE-1X ($4.7 \pm 0.4 \text{ mmol L}^{-1}$) and NCE-5X ($4.2 \pm 0.5 \text{ mmol L}^{-1}$) groups were seen to be significantly lower at 21.70% ($p < 0.0001$) and 29.66% ($p < 0.0001$) compared to the vehicle group ($6.0 \pm 0.4 \text{ mmol L}^{-1}$). In addition, a significant dose-dependent effect on the blood lactate level was observed ($p < 0.0001$) after the 15 min swimming test. The serum ammonia levels in the NCE-1X ($139 \pm 13 \text{ } \mu\text{mol L}^{-1}$) and NCE-5X ($139 \pm 14 \text{ } \mu\text{mol L}^{-1}$) groups were 23.88% ($p < 0.0001$) and 24.15% ($p < 0.0001$), respectively, lower than that in the

vehicle group ($183 \pm 23 \text{ } \mu\text{mol L}^{-1}$) (Fig. 3B). The glucose levels in the NCE-5X ($202.9 \pm 94.4 \text{ mg dL}^{-1}$) group were significantly higher (2.36-fold, $p = 0.0005$) than the vehicle group ($86.0 \pm 11.4 \text{ mg dL}^{-1}$) (Fig. 3C). Moreover, a significant dose-dependent effect on the glucose level was observed ($p < 0.0001$). The BUN levels in the NCE-1X ($7.67 \pm 0.86 \text{ mmol L}^{-1}$) and NCE-5X ($6.49 \pm 1.09 \text{ mmol L}^{-1}$) groups were significantly lower (12.24%, $p = 0.0184$ and 25.75%, $p < 0.0001$, respectively) than the vehicle group ($8.74 \pm 0.44 \text{ mmol L}^{-1}$) (Fig. 3D). A significant dose-dependent effect on the BUN levels was observed ($p < 0.0001$). The serum CK levels in the NCE-1X ($557 \pm 241 \text{ U L}^{-1}$) and NCE-5X ($667 \pm 176 \text{ U L}^{-1}$) groups were significantly lower (50.75%, $p = 0.0009$ and 41.09%, $p = 0.0049$) than the vehicle group ($1132 \pm 417 \text{ U L}^{-1}$) (Fig. 3E). Similarly, a significant dose-dependent effect on the CK level was observed ($p = 0.0198$). In Fig. 3F, the LDH levels in the NCE-1X ($363 \pm 80 \text{ U L}^{-1}$) and NCE-5X ($300 \pm 70 \text{ U L}^{-1}$) groups were significantly lower (40.90%, $p = 0.0002$ and 51.10%, $p < 0.0001$) compared with that in the vehicle group ($614 \pm 165 \text{ U L}^{-1}$). A significant dose-dependent effect on LDH levels was also observed ($p < 0.0001$).

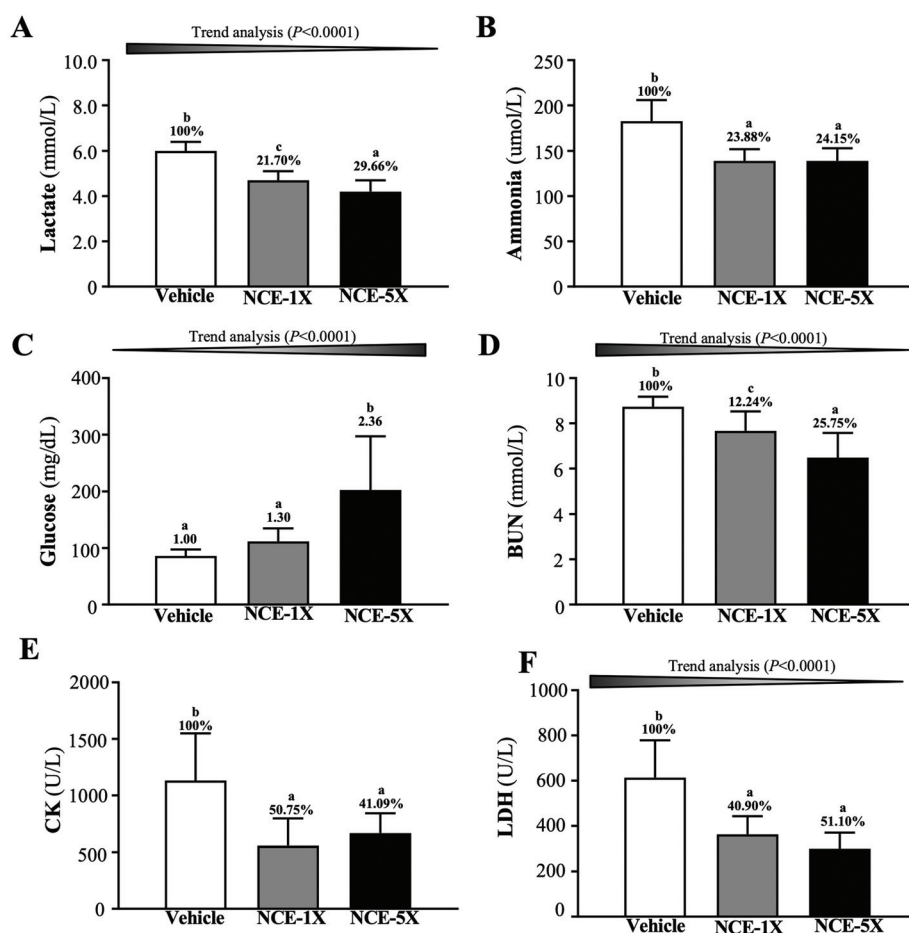


Fig. 3 Effect of nano-bubble curcumin extract (NCE) supplementation on the serum levels of (A) lactate, (B) ammonia, (C) glucose, (D) blood urea nitrogen (BUN), (E) creatine kinase (CK), and (F) lactate dehydrogenase (LDH) after a 15 min swimming test. Data are presented as mean \pm SD, $n = 8$. Bars with different letters (^a, ^b, ^c) indicate significant differences at $p < 0.05$ by one-way ANOVA.

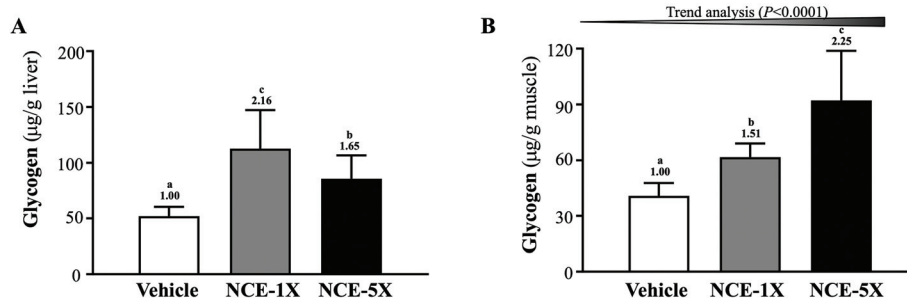


Fig. 4 Effect of NCE supplementation on (a) liver glycogen and (b) muscle glycogen. Data are presented as mean \pm SD, $n = 8$. Bars with different letters (a, b, c) indicate significant differences at $p < 0.05$ by one-way ANOVA.

Effect of six-week NCE supplementation on liver and muscular glycogen

As shown in Fig. 4A, liver glycogen contents in the NCE-1X ($112.6 \pm 34.7 \mu\text{g g}^{-1}$ liver) and NCE-5X ($85.7 \pm 21.0 \mu\text{g g}^{-1}$ liver) groups were significantly higher (2.16-fold, $p < 0.0001$; 1.56-fold and 1.65-fold, $p = 0.0104$) than the vehicle group ($52.0 \pm 8.4 \mu\text{g g}^{-1}$ liver). Muscle glycogen levels in the NCE-1X ($61.7 \pm 7.2 \mu\text{g g}^{-1}$) and NCE-5X ($92.3 \pm 26.5 \mu\text{g g}^{-1}$) groups were higher (1.51-fold, $p = 0.0260$; and 2.25-fold, $p < 0.0001$) than those in the vehicle group ($40.9 \pm 6.9 \mu\text{g g}^{-1}$) (Fig. 4B). A significant dose-dependent effect on muscle glycogen content was observed ($p < 0.0001$).

Effect of 6-week NCE supplementation on tissue histopathology and biochemical variables

At the end of the study period, the mice were sacrificed and major organs and tissues were removed for histopathological analyses. Representative histopathological sections of the liver, lungs, muscle, heart, kidneys and EFP tissues are shown in Fig. 5. We observed no histopathology differences between the NCE-1X and NCE-5X groups with the vehicle group. Likewise, we did not detect any clinical signs of organ-specific toxicity in the NCE-treated mice. The levels of aspartate aminotransferase (AST), lactate dehydrogenase (LDH), creatine kinase (CK), uric acid (UA), total cholesterol (TC) and triacylglycerol (TG) in the mice from the NCE-5X group were significantly lower than those from the vehicle group. In addition, NCE supplementation showed a dose-dependent effect on the AST, LDH, CK, BUN, UA, TC and TG levels. Creatine levels were higher in the NCE-1X and NCE-5X groups than in the vehicle group. Other biochemical indices, including ALT, ALP, albumin, TP and glucose, did not differ among the 3 groups (Table 2).

Effect of six-week NCE supplementation on the gut microbiota

We analyzed the gut microbiota composition in the vehicle, NCE-1X and NCE-5X supplemented mice using 16S rRNA gene sequencing. However, weighted principal coordinates analysis (PCoA) showed differences in the beta diversity of the gut microbial communities in the vehicle, NCE-1X and NCE-5X groups (Fig. 6A and B). The weighted PCoA plot (Fig. 6A) does not appear to have obvious clustering, with NCE-5X showing a distance from both vehicle and NCE-1X. The PCoA of

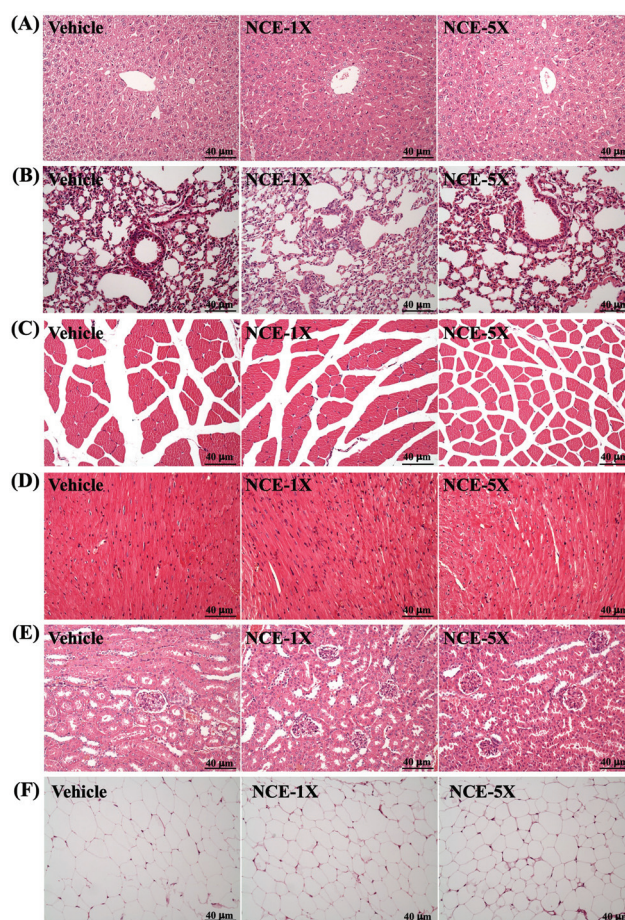


Fig. 5 Representative histological sections showing the effect of NCE supplementation on the (A) liver, (B) lungs, (C) muscle, (D) heart, (E) kidneys and (F) epididymal fat pad (EFP). Specimens were observed using light microscopy. Hematoxylin and eosin stain, magnification: $\times 200$.

unweighted UniFrac distances between samples (Fig. 6B) showed that the NCE-5X group had a different microbial population from the vehicle and NCE-1X groups, suggesting that 5X NCE supplementation significantly altered the gut microbial population. Fig. 6C shows the overall composition of the gut microbiome at the phylum level. The gut microbiome was dominated by the phyla Bacteroidetes (32.98% for the vehicle

Table 2 Effect of 6-week NCE supplementation on biochemical variables

Parameter	Vehicle	NCE-1X	NCE-5X	Trend analysis
AST (U L ⁻¹)	152 ± 42 ^b	133 ± 27 ^b	94 ± 22 ^a	<0.0001
ALT (U L ⁻¹)	160 ± 86	142 ± 40	100 ± 45	0.1374
ALP (U L ⁻¹)	85.8 ± 19.8	79.7 ± 11.4	95.9 ± 23.0	0.3172
LDH (U L ⁻¹)	738 ± 171 ^b	581 ± 137 ^{ab}	483 ± 185 ^a	0.0095
CK (U L ⁻¹)	1260 ± 392 ^b	1340 ± 451 ^b	543 ± 261 ^a	<0.0001
BUN (mg dL ⁻¹)	9.6 ± 1.0 ^b	7.3 ± 0.5 ^c	5.1 ± 0.7 ^a	<0.0001
Albumin (g dL ⁻¹)	35.6 ± 1.9	34.0 ± 0.7	34.2 ± 1.4	0.3370
UA (mg dL ⁻¹)	111 ± 26 ^b	58 ± 14 ^a	61 ± 23 ^a	0.0001
TC (mg dL ⁻¹)	150 ± 26 ^b	113 ± 13 ^a	104 ± 14 ^a	<0.0001
TG (mg dL ⁻¹)	276 ± 63 ^b	236 ± 35 ^c	97 ± 19 ^a	<0.0001
Creatinine (mg dL ⁻¹)	55.3 ± 2.9 ^a	60.4 ± 4.6 ^b	59.6 ± 2.3 ^b	0.0003
TP (g dL ⁻¹)	57.5 ± 2.8	58.7 ± 2.0	59.0 ± 2.2	0.3497
Glucose (mg dL ⁻¹)	153 ± 27	157 ± 14	167 ± 35	0.4256

Data are expressed as mean ± SD, $n = 8$ mice/group. Different letters (^a, ^b) in the same row indicate significant differences at $p < 0.05$ by one-way ANOVA. AST, aspartate aminotransferase; ALT, alanine aminotransferase; ALP, alkaline phosphatase; LDH, lactate dehydrogenase; CK, creatine kinase; BUN, blood urea nitrogen; UA, uric acid; TC, total cholesterol; TG, triacylglycerol; TP, total protein.

group, 30.98% for the NCE-1X group, 16.18% for the NCE-5X group) and Firmicutes (50.85% for the vehicle group, 51.35% for the NCE-1X group and 67.60% for the NCE-5X group). The NCE-5X group showed a significantly reduced proportion of the Bacteroidetes phylum compared with the vehicle group ($p = 0.0127$). The phyla detected in all 3 mouse groups include Proteobacteria, TM7, Actinobacteria, Verrucomicrobia, Deferribacteres and Tenericutes.

The gut microbiota of all the mice were dominated by Bacteroidetes, Firmicutes and Proteobacteria (together accounting for approximately 95%). However, NCE-5X supplemented mice had a reduced proportion of Bacteroidetes and an increased proportion of Firmicutes. The Firmicutes/Bacteroidetes (F/B) ratio in the NCE-5X group was 4.18, higher than the F/B ratios in the NCE-1X (1.66) and vehicle (1.54) groups. The graphical cladogram analysis showing the most differentially abundant taxa enriched in the gut microbiota is shown in Fig. 6D. The graphical cladogram indicates that the number of bacteria from the family Lactobacillaceae and

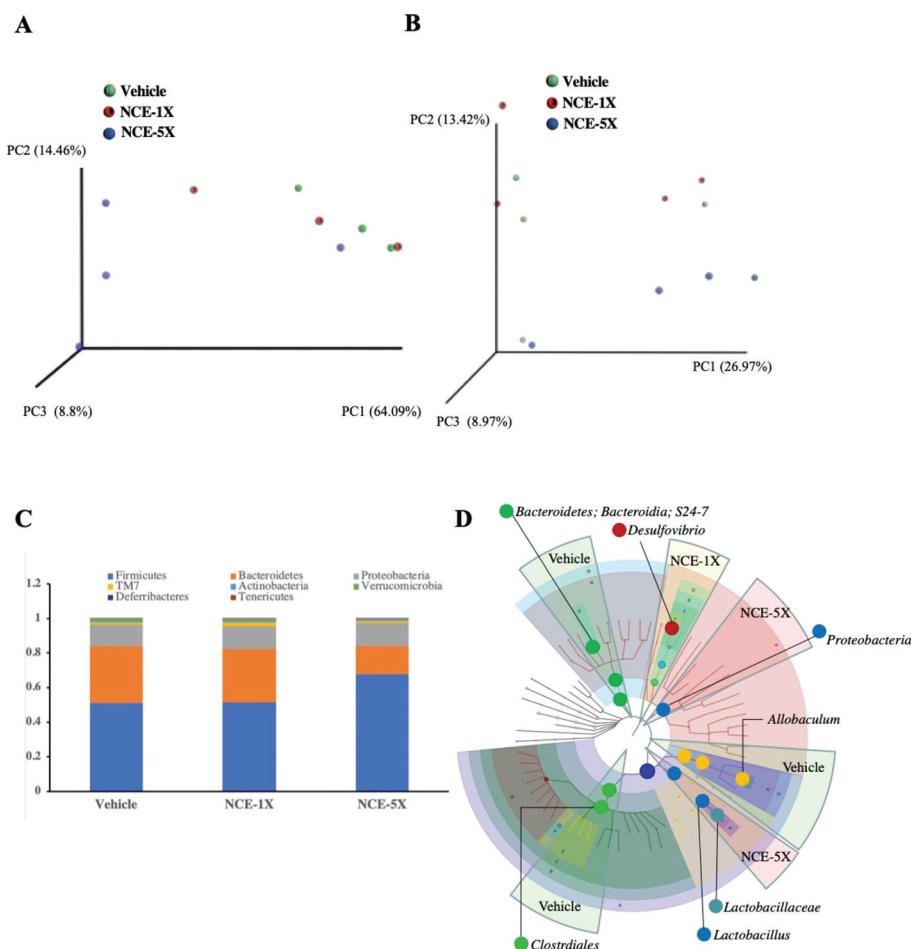


Fig. 6 Effect of NCE supplementation on PCoA plots of weighted and unweighted UniFrac distances based on the UniFrac distance matrix generated from cecal 16S rRNA gene sequencing (A) Weighted PCoA and (B) unweighted PCoA. Each dot represents a sample from the vehicle (green dots), NCE-1X (red dots) and NCE-5X (blue dots) groups. (C) Effect of NCE supplementation on the phylum-level gut microbiota composition of mice. Only the top 8 most abundant phyla are included. (D) The cladogram was generated from the cladogram analysis, showing the most differentially abundant taxa enriched in the microbiota of vehicle, NCE-1X and NCE-5X supplemented mice.

Lactobacillus genus was higher in the NCE-5X group than in the vehicle or NCE-1X group. The NCE-5X-treated mice had higher proportions of Proteobacteria than the mice from the vehicle group. However, the proportions of Clostridiales, *Allobaculum* and Bacteroidetes were higher in the vehicle group than in the NCE groups.

Discussion

Recent studies have investigated the use of high dose curcumin as an ergogenic aid to reduce the risk of muscle damage in downhill running exercises,²⁸ eccentric exercises²⁹ and plyometric exercises (drop jump), as well as reducing muscle soreness.³⁰ Ray Hamidie *et al.* showed that curcumin could enhance skeletal muscle performance through the regulation of mitochondrial biogenesis *via* an increase in the level of cAMP.³¹ The use of curcumin has been limited by its poor solubility, poor absorption in the gut, rapid metabolism and systemic elimination.³² One possible mechanism by which curcumin exerts its bioactivity is through functioning as a prebiotic to modulate the gut microbiome.

During high-intensity exercise when the anaerobic threshold is reached, lactate production outpaces the intracellular buffering capacity, causing excess lactate to be transported out of the cell. As the exercise intensity increases, the blood lactate level increases in an exponential fashion. Lactate clearance capacity thereby affects muscle performance.³³ Another important index for exercise fatigue is ammonia. During exercise, the amino group (NH₂) is converted into ammonia (NH₃) in the liver. Ammonia is then converted into urea, which passes into the blood and is eventually eliminated by the kidneys into the urine. NCE supplementation is able to improve both lactate and ammonia clearance after exercise, thereby reducing physical fatigue (Fig. 3A and B). Increased BUN levels reflect protein decomposition, which has an adverse effect on muscle contraction and strength, leading to fatigue. Decreased BUN levels with NCE supplementation suggest that NCE is able to reduce the fatigue induced by acute exercise (Fig. 3D). CK is another important clinical biomarker for muscle damage, muscular dystrophy and severe muscle breakdown.²³ The reduction of CK levels by NCE suggests a reduced accumulation of damage-induced metabolites during exercise, resulting in improved exercise performance (Fig. 3E).

In a previous study,²⁰ Scheiman *et al.* showed that systemic lactate produced during exercise crosses the gut lumen and is metabolized by gut microorganisms in the colon to propionate (one of the short chain fatty acids), which serves to promote exercise performance. Lactate dehydrogenase (LDH) is the enzyme responsible for the first step of lactate metabolism. LDHs are commonly thought to be responsible for lactate utilization during the stationary phase of aerobic growth in *Lactobacillus plantarum*.³⁴ In a previous study, *Veillonella atypica*, isolated from the stool samples of marathon runners and inoculated into the mice, led to a significantly increased exhaustive treadmill run time. *Veillonella atypica* was able to

enhance athletic performance *via* its metabolic conversion of exercise-induced lactate into propionate.²⁰ In our study, we also found that NCE supplementation decreased the lactate and LDH levels after exercise (Fig. 3B and F). The gut microbiome may play a role in fermenting lactate into butyrate *via* specific pathways. Lactate generated during sustained bouts of exercise becomes accessible to the microbiome and is converted to short chain fatty acids (SCFAs), which are known to improve athletic performance.^{35,36}

The main carbohydrate sources during exercise are muscle and liver glycogen, liver gluconeogenesis (the production of carbohydrate from noncarbohydrate sources) and ingested carbohydrate. The glycogen stores and glucose intake by skeletal muscles are the primary substrates being oxidized to provide energy during prolonged exercise.³⁶ Thereby, glycogen content is a determining factor for fatigue. We also found that NCE supplementation increases glycogen accumulation to improve aerobic and anaerobic exercise capacity. Muscle glycogen may directly increase exercise performance and reduce physical fatigue.

Studies have shown a relationship between the Proteobacteria found in the human gut with obesity and metabolic disorder.³⁷ Compared to healthy subjects, patients with inflammatory bowel disease (IBD) are characterized by low microbial diversity and an increased proportion of the Proteobacteria phylum accompanied by a concomitant depletion of Firmicutes.^{38,39} Interestingly, we observed that the cecum microbial diversity was not decreased by NCE supplementation, but that the Proteobacteria and *Lactobacillus* phyla became more abundant. In a previous study, there is similar evidence that high levels of curcumin could decrease the microbiota dysbiosis.¹⁰ Thus, the high content of curcumin was the key that correlated to a decrease in the unfavorable strain or increase in the probiotic strain. The Firmicutes and Bacteroidetes are the two predominant phyla in the human colon and together comprise >90% of the microbiome population.⁴⁰ The short-chain fatty acid (SCFA) production and F/B ratio vary together, suggesting that they be interrelated.⁴¹ Short chain fatty acids (SCFAs) such as acetate, propionate and butyrate are important energy sources for colonocytes and are assumed to play key roles in gut health. Indigestible carbohydrate and gut microbiota from individuals with different F/B ratios influence SCFA production patterns.^{42,43} A previous study suggested that a higher F/B ratio may be associated with increased energy harvest from colonic fermentation and increased production of SCFA in an obese animal model.⁴⁴ In our study, the final BWs were not significantly different between the groups, but the F/B ratio and Proteobacteria population were seen to increase with 5X NCE supplementation. Further studies will be required to determine how Proteobacteria influences SCFA production and leads to benefits for athletes. In our previous study, we demonstrated how a probiotic supplementation (*Lactobacillus plantarum* TWK10) triggered an anti-fatigue effect by lowering serum lactate, ammonia and CK levels while increasing muscle glycogen storage, together enhancing the exercise performance in

mice.¹⁵ Our current study suggests that NCE may be a probiotic trigger to shift the gut microbial composition and increase the abundance of the Lactobacillaceae family to enhance exercise performance.

The timing of carbohydrate consumption is an area of great interest in sports nutrition, having a significant impact on many athletes. Prebiotics, or indigestible carbohydrates, may be more effective than digestible carbohydrates in improving exercise performance. Taken together, our results suggest that NCE is able to modify the gut microbiota and affect the metabolic network to reduce physical fatigue. Further studies are warranted to better understand the energy homeostasis behind nutrition supplementation.

Conclusions

In the present study, we found that six weeks of NCE supplementation was able to modulate the gut microbiota and yield anti-fatigue effects by lowering fatigue-related serum markers. As a result, forelimb grip strength, exhaustive swimming time and exercise performance improved in the mice. NCE might be useful in reducing physical fatigue, with the gut microbiome playing a critical role in physical performance, possibly by fermenting lactate into butyrate or other SCFAs. These SCFAs are then able to improve athletic performance. Taken together, our results shed new light on the prebiotic role of NCE in shifting the gut microbiome and enhancing exercise performance *via* decreasing the fatigue indicators of lactate and LDH levels.

Abbreviations

NCE	Nano-bubble curcumin extract
EFP	Epididymal fat pad
BAT	Brown adipose tissue
AST	Aspartate aminotransferase
ALT	Alanine aminotransferase
ALP	Alkaline phosphatase
LDH	Lactate dehydrogenase;
BUN	Blood urea nitrogen
UA	Uric acid
TC	Total cholesterol
TG	Triacylglycerol
TP	Total protein
CK	Creatine kinase
SCFAs	Short chain fatty acids

Ethics approval and consent to participate

The animal protocol (IACUC-19002) was reviewed and approved by the Institutional Animal Care and Use Committee (IACUC) of Jilin Sport University, Changchun City, China. This

research adheres to the ARRIVE guidelines (<https://www.nc3rs.org.uk/arrive-guidelines>).

Author contributions

YMC and YSC designed the experiments. YMC, TL, HCS and CYH performed the laboratory experiments. YMC and WCC analyzed the data, interpreted the results, prepared the figures and wrote the manuscript. YMC, YSC and CYH contributed reagents, materials, and analysis platforms. All authors have read and approved the manuscript.

Funding

This work is partially financially supported by Ministry of Science and Technology of Taiwan (grant no. MOST 106-2320-B-038-033 to Dr. Wan-Chun Chiu) and Chang Gung Memorial Hospital Grants (CMRPF1G0172).

Conflicts of interest

All authors declare that they have no conflicts of interest with regard to the contents of this article.

Acknowledgements

We thank Mr. Yung-hsiang Tseng of Leading Auto. Bio Co. Ltd. for kindly providing the NBs technology. The authors are grateful to Dr. Chien-Chao Chiu for his technical assistance in the histopathological examination. We also thank Shanghai Personal Biotechnology Co., Ltd. for kindly providing the gut microbiota technology.

References



- 1 Y. Xing, X. Gui and Y. Cao, The hydrophobic force for bubble-particle attachment in flotation - a brief review, *Phys. Chem. Chem. Phys.*, 2017, **19**, 24421–24435.
- 2 P. Knüpfer, L. Ditscherlein and U. A. Peuker, Nanobubble enhanced agglomeration of hydrophobic powders, *Colloids Surf., A*, 2017, **530**, 117–123.
- 3 T. Temesgen, T. T. Bui, M. Han, T. I. Kim and H. Park, Micro and nanobubble technologies as a new horizon for water-treatment techniques: A review, *Adv. Colloid Interface Sci.*, 2017, **246**, 40–51.
- 4 S. Liu, S. Oshita, S. Kawabata, Y. Makino and T. Yoshimoto, Identification of ros produced by nanobubbles and their positive and negative effects on vegetable seed germination, *Langmuir*, 2016, **32**, 11295–11302.
- 5 K. Ebina, K. Shi, M. Hirao, J. Hashimoto, Y. Kawato, S. Kaneshiro, T. Morimoto, K. Koizumi and H. Yoshikawa, Oxygen and air nanobubble water solution promote the

- growth of plants, fishes, and mice, *PLoS One*, 2013, **8**, e65339.
- 6 T. Owerkowicz, R. M. Elsey and J. W. Hicks, Atmospheric oxygen level affects growth trajectory, cardiopulmonary allometry and metabolic rate in the American alligator (*Alligator mississippiensis*), *J. Exp. Biol.*, 2009, **212**, 1237–1247.
 - 7 I. L. Wang, C. Y. Hsiao, Y. H. Li, F. B. Meng, C. C. Huang and Y. M. Chen, Nanobubbles water curcumin extract reduces injury risks on drop jumps in women: a pilot study, *J. Evidence-Based Complementary Altern. Med.*, 2019, **2019**, 8647587.
 - 8 J. M. Davis, E. A. Murphy, M. D. Carmichael, M. R. Zielinski, C. M. Groschwitz, A. S. Brown, J. D. Gangemi, A. Ghaffar and E. P. Mayer, Curcumin effects on inflammation and performance recovery following eccentric exercise-induced muscle damage, *Am. J. Physiol.: Regul., Integr. Comp. Physiol.*, 2007, **292**, R2168–R2173.
 - 9 M. Takahashi, K. Suzuki, H. K. Kim, Y. Otsuka, A. Imaizumi, M. Miyashita and S. Sakamoto, Effects of curcumin supplementation on exercise-induced oxidative stress in humans, *Int. J. Sports Med.*, 2014, **35**, 469–475.
 - 10 E. Vamanu, F. Gatea, I. Sarbu and D. Pelinescu, An in vitro study of the influence of curcuma longa extracts on the microbiota modulation process, in patients with hypertension, *Pharmaceutics*, 2019, **11**, 191.
 - 11 S. Nikolaidis, I. Kosmidis, M. Sougioultzis, A. Kabasakalis and V. Mougios, Diurnal variation and reliability of the urine lactate concentration after maximal exercise, *Chronobiol. Int.*, 2018, **35**, 24–34.
 - 12 J. T. Gonzalez, C. J. Fuchs, J. A. Betts and L. J. van Loon, Liver glycogen metabolism during and after prolonged endurance-type exercise, *Am. J. Physiol.: Endocrinol. Metab.*, 2016, **311**, 543–553.
 - 13 R. G. Shulman, F. Hyder and D. L. Rothman, Cerebral energetics and the glycogen shunt: neurochemical basis of functional imaging, *Proc. Natl. Acad. Sci. U. S. A.*, 2001, **98**, 6417–6422.
 - 14 P. S. Harty, M. L. Cottet, J. K. Malloy and C. M. Kerksick, Nutritional and supplementation strategies to prevent and attenuate exercise-induced muscle damage: a brief review, *Sports Med. Open*, 2019, **5**, 1.
 - 15 Y. M. Chen, L. Wei, Y. S. Chiu, Y. J. Hsu, T. Y. Tsai, M. F. Wang and C. C. Huang, *Lactobacillus plantarum* TWK10 supplementation improves exercise performance and increases muscle mass in mice, *Nutrients*, 2016, **8**, 205.
 - 16 A. Terpou, A. Papadaki, I. K. Lappa, V. Kachrimanidou, L. A. Bosnea and N. Kopsahelis, Probiotics in food systems: significance and emerging strategies towards improved viability and delivery of enhanced beneficial value, *Nutrients*, 2019, **11**, 1591.
 - 17 H. D. Holscher, Dietary fiber and prebiotics and the gastrointestinal microbiota, *Gut Microbes*, 2017, **8**, 172–184.
 - 18 P. S. Panesar, S. Kumari and R. Panesar, Biotechnological approaches for the production of prebiotics and their potential applications, *Crit. Rev. Biotechnol.*, 2013, **33**, 345–364.
 - 19 K. Tajiri, Y. Futsukaichi, S. Kobayashi, S. Yasumura, T. Takahara, M. Minemura and T. Sugiyama, L-carnitine for the treatment of overt hepatic encephalopathy in patients with advanced liver cirrhosis, *J. Nutr. Sci. Vitaminol.*, 2018, **64**, 321–328.
 - 20 J. Scheiman, J. M. Lubner, T. A. Chavkin, T. MacDonald, A. Tung, L. D. Pham, M. C. Wibowo, R. C. Wurth, S. Punthambaker, B. T. Tierney, Z. Yang, M. W. Hattab, J. Avila-Pacheco, C. B. Clish, S. Lessard, G. M. Church and A. D. Kostic, Meta-omics analysis of elite athletes identifies a performance-enhancing microbe that functions via lactate metabolism, *Nat. Med.*, 2019, **25**, 1104–1109.
 - 21 S. F. Clarke, E. F. Murphy, O. O'Sullivan, A. J. Lucey, M. Humphreys, A. Hogan, P. Hayes, M. O'Reilly, I. B. Jeffery, R. Wood-Martin, D. M. Kerins, E. Quigley, R. P. Ross, P. W. O'Toole, M. G. Molloy, E. Falvey, F. Shanahan and P. D. Cotter, Exercise and associated dietary extremes impact on gut microbial diversity, *Gut*, 2014, **63**, 1913–1920.
 - 22 W. Marlicz and I. Loniewski, The effect of exercise and diet on gut microbial diversity, *Gut*, 2015, **64**, 519–520.
 - 23 Y. M. Chen, C. L. Lin, L. Wei, Y. J. Hsu, K. N. Chen, C. C. Huang and C. H. Kao, Sake protein supplementation affects exercise performance and biochemical profiles in power-exercise-trained mice, *Nutrients*, 2016, **8**, 106.
 - 24 M. Blaxter, J. Mann, T. Chapman, F. Thomas, C. Whitton, R. Floyd and E. Abebe, Defining operational taxonomic units using DNA barcode data, *Philos. Trans. R. Soc. London, Ser. B*, 2005, **360**, 1935–1943.
 - 25 T. Z. DeSantis, P. Hugenholtz, N. Larsen, M. Rojas, E. L. Brodie, K. Keller, T. Huber, D. Dalevi, P. Hu and G. L. Andersen, Greengenes, a chimera-checked 16S rRNA gene database and workbench compatible with ARB, *Appl. Environ. Microbiol.*, 2006, **72**, 5069–5072.
 - 26 A. Ramette, Multivariate analyses in microbial ecology, *FEMS Microbiol. Ecol.*, 2007, **62**, 142–160.
 - 27 N. Segata, J. Izard, L. Waldron, D. Gevers, L. Miropolsky, W. S. Garrett and C. Huttenhower, Metagenomic biomarker discovery and explanation, *Genome Biol.*, 2011, **12**, R60.
 - 28 R. Jager, M. Purpura and C. M. Kerksick, Eight weeks of a high dose of curcumin supplementation may attenuate performance decrements following muscle-damaging exercise, *Nutrients*, 2019, **11**, 1692.
 - 29 Y. Choi, Y. Tanabe, N. Akazawa, A. Zempo-Miyaki and S. Maeda, Curcumin supplementation attenuates the decrease in endothelial function following eccentric exercise, *J. Exerc. Nutr. Biochem.*, 2019, **23**, 7–12.
 - 30 S. A. Basham, H. S. Waldman, B. M. Krings, J. Lamberth, J. W. Smith and M. J. McAllister, Effect of curcumin supplementation on exercise-induced oxidative stress, inflammation, muscle damage, and muscle soreness, *J. Diet. Suppl.*, 2019, **2019**, 1–14.

- 31 R. D. Ray Hamidie, T. Yamada, R. Ishizawa, Y. Saito and K. Masuda, Curcumin treatment enhances the effect of exercise on mitochondrial biogenesis in skeletal muscle by increasing cAMP levels, *Metabolism*, 2015, **64**, 1334–1347.
- 32 P. Anand, A. B. Kunnumakkara, R. A. Newman and B. B. Aggarwal, Bioavailability of curcumin: problems and promises, *Mol. Pharm.*, 2007, **4**, 807–818.
- 33 J. Hoff, O. Storen, A. Finstad, E. Wang and J. Helgerud, Increased blood lactate level deteriorates running economy in world class endurance athletes, *J. Strength Cond. Res.*, 2016, **30**, 1373–1378.
- 34 P. Goffin, F. Lorquet, M. Kleerebezem and P. Hols, Major role of NAD-dependent lactate dehydrogenases in aerobic lactate utilization in *Lactobacillus plantarum* during early stationary phase, *J. Bacteriol.*, 2004, **186**, 6661–6666.
- 35 J. Pluznick, A novel SCFA receptor, the microbiota, and blood pressure regulation, *Gut Microbes*, 2014, **5**, 202–207.
- 36 I. Kimura, D. Inoue, T. Maeda, T. Hara, A. Ichimura, S. Miyauchi, M. Kobayashi, A. Hirasawa and G. Tsujimoto, Short-chain fatty acids and ketones directly regulate sympathetic nervous system via G protein-coupled receptor 41 (GPR41), *Proc. Natl. Acad. Sci. U. S. A.*, 2011, **108**, 8030–8035.
- 37 N. Fei and L. Zhao, An opportunistic pathogen isolated from the gut of an obese human causes obesity in germfree mice, *ISME J.*, 2013, **7**, 880–884.
- 38 I. Mukhopadhyay, R. Hansen, E. M. El-Omar and G. L. Hold, IBD-what role do Proteobacteria play?, *Nat. Rev. Gastroenterol. Hepatol.*, 2012, **9**, 219–230.
- 39 N. R. Shin, T. W. Whon and J. W. Bae, Proteobacteria: microbial signature of dysbiosis in gut microbiota, *Trends Biotechnol.*, 2015, **33**, 496–503.
- 40 P. B. Eckburg, E. M. Bik, C. N. Bernstein, E. Purdom, L. Dethlefsen, M. Sargent, S. R. Gill, K. E. Nelson and D. A. Relman, Diversity of the human intestinal microbial flora, *Science*, 2005, **308**, 1635–1638.
- 41 J. Fernandes, W. Su, S. Rahat-Rozenbloom, T. M. Wolever and E. M. Comelli, Adiposity, gut microbiota and faecal short chain fatty acids are linked in adult humans, *Nutr. Diabetes*, 2014, **4**, e121.
- 42 S. Rahat-Rozenbloom, J. Fernandes, G. B. Gloor and T. M. Wolever, Evidence for greater production of colonic short-chain fatty acids in overweight than lean humans, *Int. J. Obes.*, 2014, **38**, 1525–1531.
- 43 S. G. Peters, E. W. Pomare and C. A. Fisher, Portal and peripheral blood short chain fatty acid concentrations after caecal lactulose instillation at surgery, *Gut*, 1992, **33**, 1249–1252.
- 44 P. J. Turnbaugh, R. E. Ley, M. A. Mahowald, V. Magrini, E. R. Mardis and J. I. Gordon, An obesity-associated gut microbiome with increased capacity for energy harvest, *Nature*, 2006, **444**, 1027–1031.

Article

Isolation of Lobane and Prenyleudesmane Diterpenoids from the Soft Coral *Lobophytum varium*

Chuan-Hsiang Chang ^{1,†}, Atallah F. Ahmed ^{2,3,†} , Tian-Sheng Yang ^{1,†}, You-Cheng Lin ⁴,
Chiung-Yao Huang ¹, Tsong-Long Hwang ^{5,6,7}  and Jyh-Horng Sheu ^{1,4,8,9,10,*}

¹ Department of Marine Biotechnology and Resources, National Sun Yat-sen University, Kaohsiung 804, Taiwan; hunter02141991@gmail.com (C.-H.C.); b025020004@student.nsysu.edu.tw (T.-S.Y.); betty8575@yahoo.com.tw (C.-Y.H.)

² Department of Pharmacognosy, College of Pharmacy, King Saud University, Riyadh 11451, Saudi Arabia; afahmed@ksu.edu.sa

³ Department of Pharmacognosy, Faculty of Pharmacy, Mansoura University, Mansoura 35516, Egypt

⁴ Doctoral Degree Program in Marine Biotechnology, National Sun Yat-sen University, Kaohsiung 804, Taiwan; cand93@yahoo.com.tw

⁵ Graduate Institute of Natural Products, College of Medicine, Chang Gung University, Taoyuan 333, Taiwan; htl@mail.cgu.edu.tw

⁶ Research Center for Chinese Herbal Medicine, Research Center for Food and Cosmetic Safety, and Graduate Institute of Health Industry Technology, College of Human Ecology, Chang Gung University of Science and Technology, Taoyuan 333, Taiwan

⁷ Department of Anesthesiology, Chang Gung Memorial Hospital, Taoyuan 333, Taiwan

⁸ Department of Medical Research, China Medical University Hospital, China Medical University, Taichung 404, Taiwan

⁹ Graduate Institute of Natural Products, Kaohsiung Medical University, Kaohsiung 807, Taiwan

¹⁰ Frontier Center for Ocean Science and Technology, National Sun Yat-sen University, Kaohsiung 804, Taiwan

* Correspondence: sheu@mail.nsysu.edu.tw; Tel.: +886-7-5252000 (ext. 5030); Fax: +886-7-5255020

† These authors contributed equally to this work.

Received: 25 March 2020; Accepted: 16 April 2020; Published: 22 April 2020



Abstract: Further chemical investigation of the EtOAc extract of the soft coral *Lobophytum varium* resulted in the discovery of eleven new diterpenoids lobovarols F–P (**1–11**) of lobane- and prenyleudesmane-types, along with two known metabolites (**12** and **13**). The structures of the new metabolites were established by spectroscopic analyses, including 2D NMR experiments. The absolute configuration of **1** was determined using Mosher's method. The complete assignment of ¹H and ¹³C NMR spectroscopic data of **12** and **13** and the identification of pyran-derived moieties in the prenyleudesmanes were reported for the first time. Anti-inflammatory activities of the isolated compounds in suppressing elastase release and superoxide anion generation in human neutrophils were disclosed for **1**, **2**, **4**, **12**, and **13**. A stereospecific biosynthesis for lobanes and prenyleudesmanes from the related prenylgermacranes could explain the coexistence of lobanes and prenylgermacranes in *L. varium*.

Keywords: lobane; prenyleudesmane; anti-inflammatory activity; *Lobophytum varium*

1. Introduction

Soft corals belonging to genus *Lobophytum* (Alcyoniidae) were shown to be the main biological sources of lobane [1–7], prenyleudesmane [1,8–11], and spatane-type diterpenoids [8]. Some lobane and prenyleudesmane diterpenoids have displayed antimicrobial [2], cytotoxic [2,6,8], and anti-inflammatory activities [1]. Cembranoids have also been isolated from this genus, and have been

shown to exhibit significant cytotoxic [12–14], antiviral [15], and anti-inflammatory activities [14,16–18]. Our previous chemical study on the EtOAc extract of a Formosan soft coral, *Lobophytum varium* has led to the discovery of five new metabolites of lobane- and prenyleudesmane-types, of which some were found to possess anti-inflammatory activity through the suppression of elastase release and/or superoxide anion generation in challenged neutrophils [1]. The present study was aimed to further discover new bioactive diterpenoids from continuing investigation of the organic fractions of *L. varium*. This study not only led to the isolation of new metabolites but also gave strong evidence for the biosynthetic mechanism of lobane and prenyleudesmane from the corresponding prenylgermacrane biosynthetic intermediate was proposed, which could explain the common coexistence of lobane and prenylgermacranes in *L. varium*.

2. Results and Discussion

The terpenoids containing fractions of the EtOAc extract of *L. varium* were repeatedly purified using a series of chromatographic techniques, including HPLC, to afford compounds 1–13 (Figure 1). The structures of the new compounds (1–11) were established on the basis of NMR data (Tables 1–3) and spectroscopic analyses (Supplementary Materials, Figures S1 to S79).

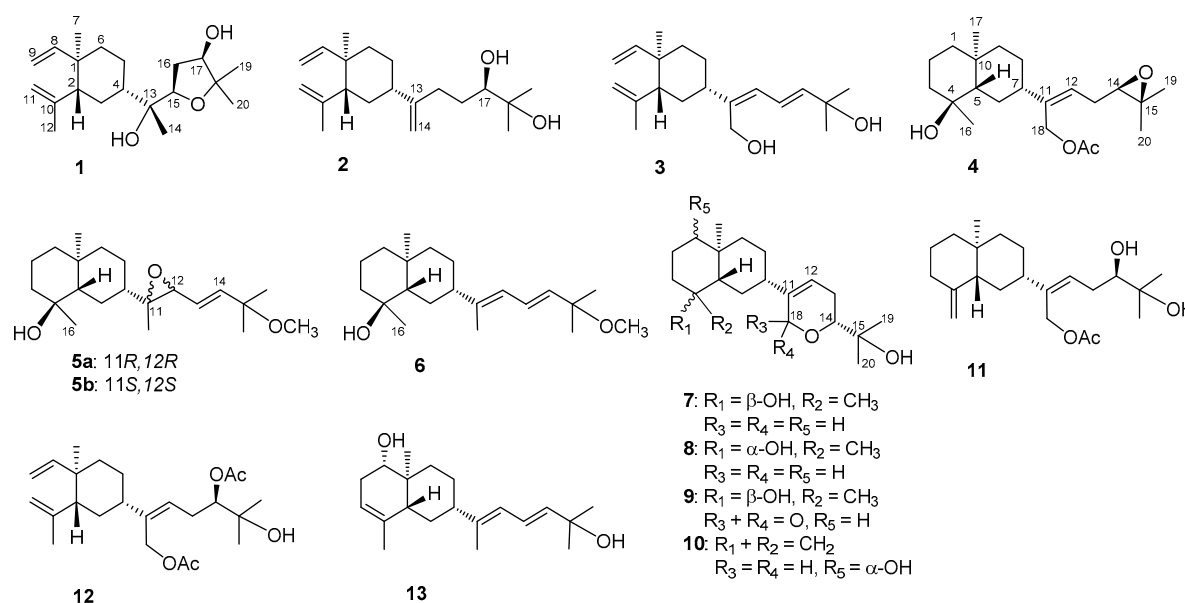


Figure 1. Structures of compounds 1–13.

Lobovarol F (1) was found to possess a molecular formula $\text{C}_{20}\text{H}_{34}\text{O}_3$ as established by high-resolution electrospray ionization mass spectrometry (HRESIMS, m/z 345.2403, $[\text{M} + \text{Na}]^+$), indicating four degrees of unsaturation. The IR absorption at 3393 cm^{-1} designated the presence of the hydroxy group. The NMR signals (Table 1) showed the presence of a vinyl (δ_{C} 150.0, CH and 110.0, CH_2 ; δ_{H} 5.80, dd, $J = 18.0, 10.4\text{ Hz}$, 4.90 d, $J = 10.4\text{ Hz}$, and 4.89, br d, $J = 18.0\text{ Hz}$), an isopropenyl (δ_{C} 147.6, C; 112.1, CH_2 and 24.9, CH_3 ; δ_{H} 4.83 and 4.59, each 1H, s; and 1.71, 3H, s), a ring-juncture methyl (δ_{C} 16.6, CH_3 ; δ_{H} 0.99, 3H, s) and methine (δ_{C} 52.4, CH; δ_{H} 1.98, m) of a β -elemene segment of lobane-type diterpenoids [1–3]. Thus, the proton signals at δ_{H} 1.30, 1.26, and 1.15 (each 3H, s) should be the methyls attached to the oxygen-bearing carbons of the side chain. The analysis of correlations spectroscopy (COSY) and heteronuclear multiple bond correlation (HMBC) led to the establishment of a 2,2-dimethyl-3-hydroxytetrahydrofuran attached to a methyl-bearing oxygenated carbon (δ_{C} 75.0, C-13) to form the side chain of 1 (Figure 2). Accordingly, the HMBC correlations from H_3 -14 (δ_{H} 1.26) and from both H_3 -19 and H_3 -20 (δ_{H} 1.15 and 1.30) to the downfield shifted oxycarbons (δ_{C} 80.4, CH and 84.0, C), respectively, assigned the 15,18-ether linkage of the tetrahydrofuran ring. Moreover, the

HMBC correlations observed from H₃-14 and from both of H₃-19 and H₃-20 to oxycarbons (δ_C 75.0, C and 76.6, CH) positioned the two hydroxy groups at C-13 and C-17, respectively.

The relative configurations of **1** at C-1, C-2, C-4, C-13, C-15, and C-17 were assigned by the nuclear Overhauser effect spectroscopy (NOESY) correlation analysis (Figure 3a) and supported by MM2 force-field modeling and NMR data. From the NOE correlations displayed for H₃-7/H₃-12 and H-2/H-4 and by comparison of the chemical shifts of C-1 to C-12 with those of the previously reported lobane-type diterpenoids [1,2,5,6,19], the 1*R**,2*R**,4*S** configurations of **1** was determined. Moreover, H₃-14 and H-15 showed the NOE interactions with the β -oriented H-4 and H₂-5, leading to the assignment of the corresponding β - and α -orientations of H₃-14 and H-15, respectively. The α -orientation for the hydroxy group at C-13 was thus suggested and also supported by the down-field shifted H-3 (δ_H 1.70, m) relative to those of lobane-type diterpenoids having a β -orientated hydroxy group [1]. A conformation analysis for **1** and its 13-epimer, using MM2 calculations and measuring distances between protons showing key NOEs, also revealed the α -orientation of 13-OH, as the distances between both H-15/H₂-5 and H-4/H₃-14 were found to be shorter than 2.8 Å in **1**. Furthermore, the NOE correlations between H₃-19 (δ_H 1.15, 3H, s) and both H-15 and H-17 disclosed the β -orientations of the hydroxy at C-17. The *R**-configurations for C-13, C-15, and C-17 were thus assigned. By using Mosher's method [20,21], the absolute *R* configuration for C-17 was proven by the analysis of the calculated $\Delta\delta$ ($\delta_S - \delta_R$) values of the neighboring protons to C-17 from the ¹H NMR data of 17-(*S*)- and 17-(*R*)- α -methoxy- α -(trifluoromethyl)phenylacetyl (MTPA) esters of **1** (**1a** and **1b**), respectively (Figure 3b). Based on the above findings, lobovarol F (**1**) was determined to be (1*R*,2*R*,4*S*,13*R*,15*R*,17*R*)-15,18-epoxyloba-8,10-dien-13,17-diol. To the best of own knowledge, **1** is the first lobane diterpene with a tetrahydrofuran-containing side chain.

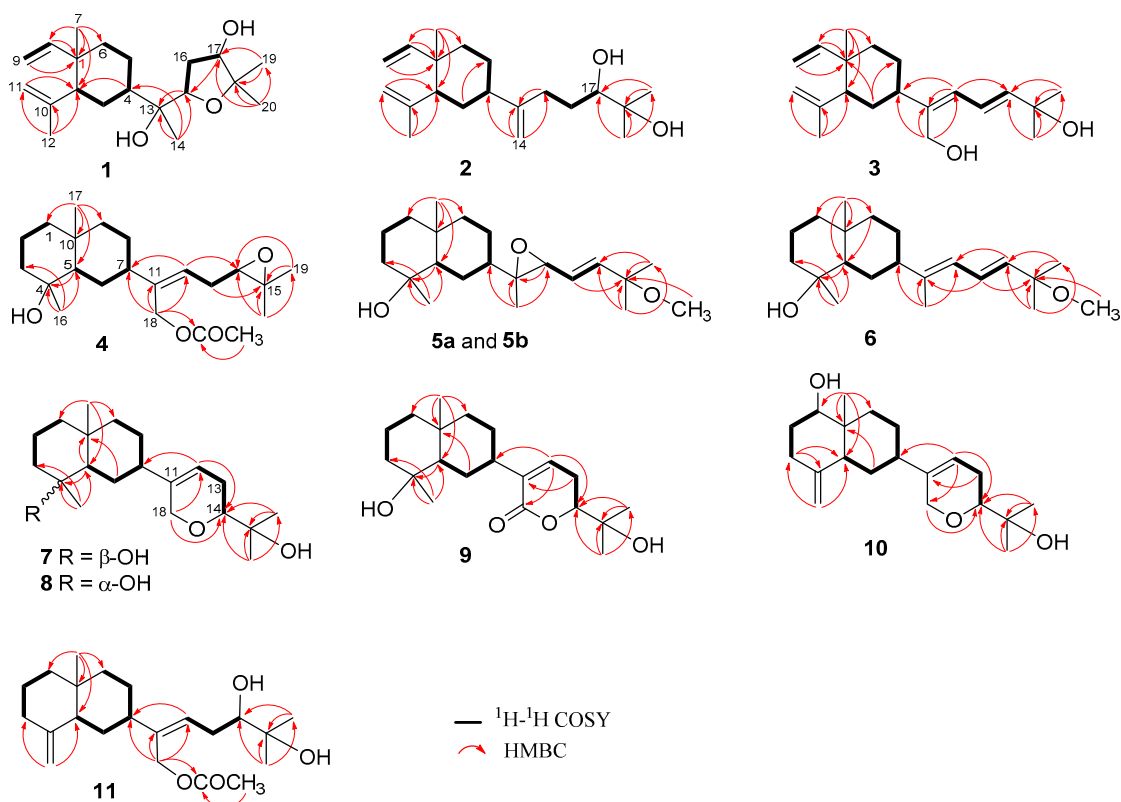


Figure 2. ¹H-¹H COSY and HMBC correlations of **1**–**11**.

Table 1. ^{13}C and ^1H NMR spectroscopic data of compounds 1–4.

Position	1		2		3		4	
	δ_{C}^a (Mult.) ^b	δ_{H}^c (J in Hz)	δ_{C}^a (Mult.)	δ_{H}^c (J in Hz)	δ_{C}^d (Mult.)	δ_{H}^e (J in Hz)	δ_{C}^a (Mult.)	δ_{H}^c (J in Hz)
1	39.9, C		39.8, C		39.7, C		41.0, CH ₂	1.38 m; 1.08 m
2	52.4, CH	1.98 m	52.8, CH	2.01 m	52.8, CH	2.04 dd (7.5, 7.5)	20.1, CH ₂	1.55–1.15 m
3	27.4, CH ₂	1.70 m; 1.50 m	33.3, CH ₂	1.58 m	33.4, CH ₂	1.60 m	43.4, CH ₂	1.80 d (13.2); 1.40 m
4	45.1, CH	1.52 m	44.4, CH	1.93 m	43.6, CH	2.20 m	72.2, C	
5	23.1, CH ₂	1.35 m; 1.24 m	27.4, CH ₂	1.66 m; 1.47 m	27.2, CH ₂	1.64 m; 1.52 m	54.9, CH	1.27 m
6	39.7, CH ₂	1.42 m	39.7, CH ₂	1.52 m; 1.47 m	39.9, CH ₂	1.50 m	27.2, CH ₂	1.52 m
7	16.6, CH ₃	0.99 s	16.6, CH ₃	1.01 s	16.6, CH ₃	1.02 s	44.7, CH	2.06 m
8	150.0, CH	5.80 dd (18.0, 10.4)	150.2, CH	5.82 dd (17.2, 10.8)	150.1, CH	5.82 dd (17.5, 11.5)	26.4, CH ₂	1.85 d (12.0); 1.22 m
9	110.0, CH ₂	4.90 d (10.4)	110.0, CH ₂	4.90 d (17.2)	110.0, CH ₂	4.92 d (11.5)	44.6, CH ₂	1.45 m
		4.89 br d (18.0)		4.90 d (10.8)		4.89 d (17.5)		1.21 m
10	147.6, C		147.6, C		147.5, C		34.6, C	
11	112.1, CH ₂	4.83 s; 4.59 s	112.1, CH ₂	4.59 s; 4.82 br s	112.2, CH ₂	4.82 s; 4.59 s	141.0, C	
12	24.9, CH ₃	1.71 s	24.8, CH ₃	1.71 s	24.8, CH ₃	1.71 s	124.7, CH	5.58 dd (8.0, 6.8)
13	75.0, C		154.5, C		145.3, C		27.9, CH ₂	2.39–2.30 m
14	20.4, CH ₃	1.26 s	107.4, CH ₂	4.82 s	60.0 CH ₂	4.31 d (12.5)	63.7 CH	2.76 dd (6.4, 6.4)
				4.77 s		4.29 d (12.5)		
15	80.4, CH	4.01 dd (9.2, 4.0)	32.0, CH ₂	2.35 m; 2.12 m	126.1, CH	6.02 d (11.0)	58.6, C	
16	34.3, CH ₂	2.39 ddd (14.4, 9.2, 6.0)	30.0, CH ₂	1.64 m	121.9, CH	6.61 dd (15.0, 11.0)	22.7, CH ₃	1.12 s
		1.95 dd (14.4, 4.0)		1.47 m				
17	76.6, CH	3.78 br d (6.0)	78.4, CH	3.78 d (10.8)	142.0, CH	5.88 d (15.0)	18.7, CH ₃	0.90 s
18	84.0, C		73.1, C		70.9, C		61.2, CH ₂	4.62 d (12.0); 4.61 d (12.0)
19	25.5, CH ₃	1.15 s	23.3, CH ₃	1.18 s	29.8, CH ₃	1.36 s	24.8, CH ₃	1.33 s
20	22.2, CH ₃	1.30 s	26.5, CH ₃	1.23 s	29.8, CH ₃	1.36 s	18.7, CH ₃	1.31 s
Ac							171.0, C	
							21.1, CH ₃	2.06 s

^a Spectrum recorded at 100 MHz in CDCl₃. ^b Attached protons were deduced by the distortionless enhancement by polarization transfer (DEPT) experiment. ^c Spectrum recorded at 400 MHz in CDCl₃. ^d Spectrum recorded at 125 MHz in CDCl₃. ^e Spectrum recorded at 500 MHz in CDCl₃.

Table 2. ^{13}C and ^1H NMR spectroscopic data of compounds 5–8.

Position	5a + 5b		6		7		8	
	δ_{C}^a (Mult.) ^b	δ_{H}^c (J in Hz)	δ_{C}^d (Mult.)	δ_{H}^e (J in Hz)	δ_{C}^d (Mult.)	δ_{H}^e (J in Hz)	δ_{C}^d (Mult.)	δ_{H}^e (J in Hz)
1	42.1, CH ₂	1.37 m; 1.06 m	41.0, CH ₂	1.42 m; 1.11 m	41.0, CH ₂	1.40 m; 1.07 m	41.5, CH ₂	1.44 m; 1.08 m
2	20.9, CH ₂	1.53 m; 1.49 m	20.1, CH ₂	1.58 m; 1.55 m	20.1, CH ₂	1.58–1.53 m	18.0, CH ₂	1.85 m; 1.65 m
3	44.3, CH ₂	1.71 m	43.3, CH ₂	1.82 m; 1.38 m	43.4, CH ₂	1.78 br d (12.0); 1.38 m	41.3, CH ₂	1.69 m; 1.44 m
4	71.4, C		72.2, C		72.2, C		71.9, C	
5	55.2/55.3, CH	1.21 m	54.9, CH	1.25 m	54.9, CH	1.25 m	51.8, CH	1.07 m
6	23.8/23.9, CH ₂	1.54 m	26.5, CH ₂	1.53 m; 1.51 m	26.0, CH ₂	1.86 br d (9.2); 1.14 m	25.7, CH ₂	1.70 m; 1.34 m
7	48.2/48.3, CH	1.20 m	48.3, CH	2.01 m	42.5, CH	1.86 br d (9.2)	42.9, CH	1.85 m
8	23.0, CH ₂	2.00 m	25.8, CH ₂	1.81 m; 1.26 m	27.0, CH ₂	1.48 m; 1.42 m	27.3, CH ₂	1.48 m
9	45.2, CH ₂	1.41 m; 1.16 m	44.6, CH ₂	1.47 m; 1.22 m	44.6, CH ₂	1.42 m; 1.19 m	43.8, CH ₂	1.36 m; 1.14 m
10	35.4, C		34.6, C		34.6, C		33.7, C	
11	65.7, C		143.4, C		141.4, C		141.5, C	
12	62.6/62.8, CH	3.24/3.26 d (7.0)	122.5, CH	5.90 d (10.8)	116.3, CH	5.57 br d (5.6)	116.4, CH	5.59 br d (4.0)
13	126.3/126.4, CH	5.557/5.563 dd (16.0, 7.0)	126.0, CH	6.39 dd (15.6, 10.8)	25.3, CH ₂	2.14 br d (13.6, 12.8)	25.3, CH ₂	2.16 m
						1.97 m		1.98 m
14	141.7/141.8, CH	5.84 d (16.0)	136.6 CH	5.57 d (15.6)	80.3 CH	3.26 dd (11.2, 3.6)	80.3 CH	3.27 dd (10.8, 3.2)
15	75.1, C		75.1, C		71.1, C		71.7, C	
16	23.1, CH ₃	1.07 s	22.7, CH ₃	1.12 s	22.7, CH ₃	1.11 s	30.3, CH ₃	1.15 s
17	19.1, CH ₃	0.90 s	18.7, CH ₃	0.90 s	18.6 CH ₃	0.88 s	18.6, CH ₃	1.04 s
18	14.3/14.4, CH ₃	1.23 s	15.3, CH ₃	1.80 s	68.2, CH ₂	4.18 d (16.4)	68.2, CH ₂	4.19 d (16.4)
						4.23 d (16.4)		4.21 d (16.4)
19	26.0/26.1, CH ₃	1.24 s	26.0, CH ₃	1.30 s	26.1, CH ₃	1.21 s	26.1, CH ₃	1.21 s
20	26.3/26.4, CH ₃	1.24 s	26.0, CH ₃	1.30 s	23.6, CH ₃	1.17 s	23.6, CH ₃	1.17 s
OCH ₃	50.4, CH ₃	3.10 s	50.4, CH ₃	3.18 s				

^a Spectrum recorded at 125 MHz in acetone-d₆. ^b Attached protons were deduced by the DEPT experiment. ^c Spectrum recorded at 500 MHz in acetone-d₆. ^d Spectrum recorded at 100 MHz in CDCl₃. ^e Spectrum recorded at 400 MHz in C.

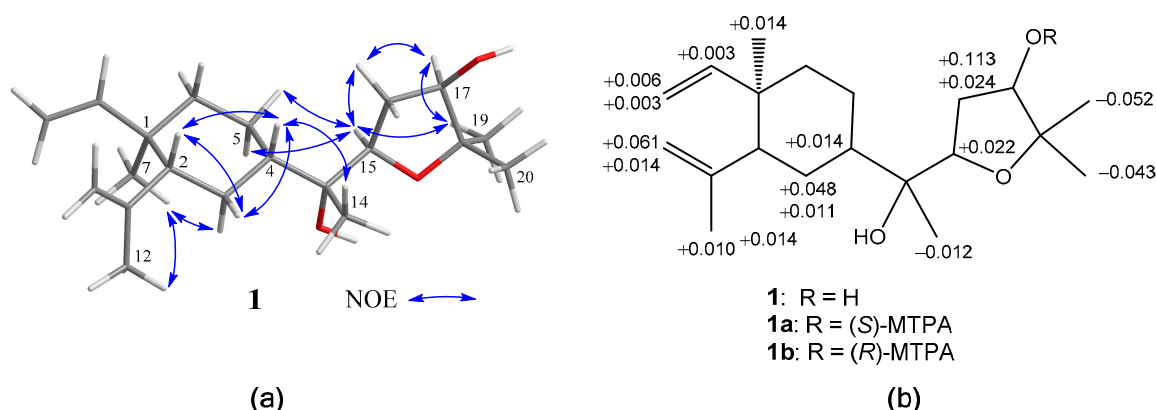


Figure 3. (a) Key nuclear Overhauser effect (NOE) correlations of **1**; (b) ^1H NMR chemical shift differences $\Delta(\delta_S - \delta_R)$ in ppm for the MTPA esters of **1**.

Lobovarol G (**2**) displayed a sodiated ion peak at m/z 329.2453 in the HRESIMS spectrum, appropriate for a molecular formula $\text{C}_{20}\text{H}_{34}\text{O}_2$. The IR absorption at 3392 cm^{-1} also indicated the presence of hydroxy group. The NMR data of **2** (Table 1) showed resonances and coupling patterns identical to those of the β -elemene ring system in **1** as well as other lobane-type diterpenoids [1–7]. The fourth degree of unsaturation has arisen from an 1,1-disubstituted double bond (δ_{C} 154.5, C and 107.4, CH_2 ; and δ_{H} 4.82 and 4.77, each 1H, s). NMR data showed that **2** differs with (1*R*,2*R*,4*S*,17*R*)-loba-8,10,13(15)-trien-17,18-diol, isolated from the same organism (*L. varium*) [1] and *L. pauciflorum* [2], only in the position of the double bond of the side chain. The analysis of HMBC correlations further confirmed the C-17 and C-18 positions of the hydroxy groups in the side chain (Figure 2). Compound **2** should possess the same 1*R*,2*R*,4*S*-configuration of the β -elemene ring system as that of **1** by the biogenetic relationship with **1** and the previously reported lobane diterpenoids isolated from genus *Lobophytum* [1,5,19]. Comparison of NMR data of the side chain of **2** (Table 1) with the corresponding data of chokol E (**14**) [22] and 10-*epi*-chokol E (**15**) [23] of known absolute configurations (Figure 4), allowed the elucidation of 17*R** configuration in **2**. As **1** and **2** should share the same biosynthetic pathway, therefore, the structure of **2** was suggested to be (1*R*,2*R*,4*S*,17*R*)-loba-8,10,13-trien-17,18-diol.

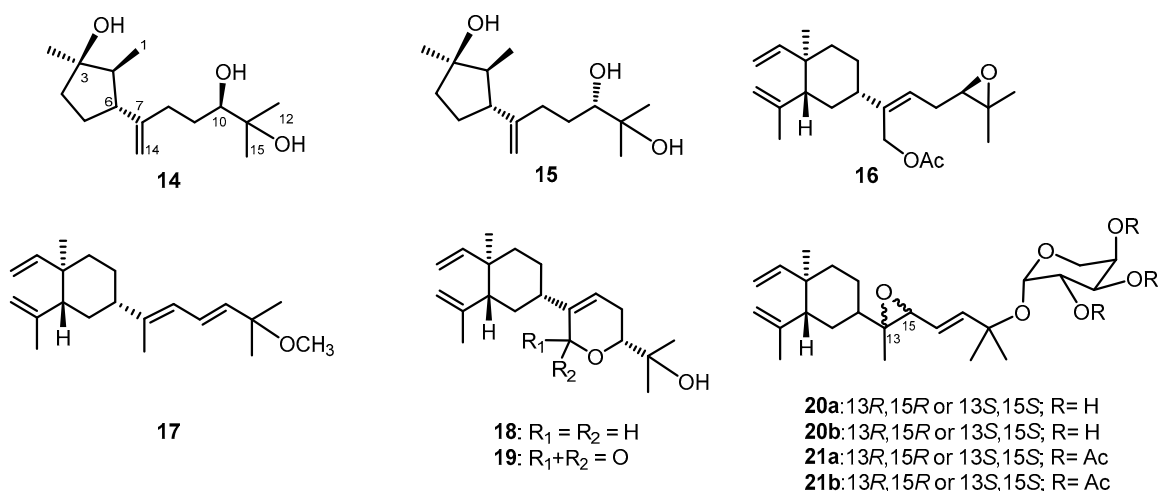


Figure 4. Known sesquiterpenoids chokol E (**14**) and 10-*epi*-chokol E (**15**); lobane diterpenoids (**16**–**19**); fucosides C and D (**20a** and **20b**), and fucosides C and D acetates (**21a** and **21b**).

Lobovarol H (**3**) possessed a molecular formula $C_{20}H_{32}O_2$ (HRESIMS: m/z 327.2294 $[M + Na]^+$) and showed the presence of hydroxy and olefinic functionalities from the IR absorptions at 3352 and 1645 cm^{-1} . The NMR data (Table 1) revealed that **3** is a lobane diterpenoid, with the presence of a trisubstituted (δ_C 145.3, C and 126.1, CH; δ_H 6.02, d, $J = 11.0$ Hz) and an 1,2-disubstituted double bond (δ_C 142.0, CH and 121.9, CH; δ_H 6.61, dd, $J = 15.0, 11.0$ Hz and 5.88, d, $J = 15.0$ Hz); and hydroxymethylene group (δ_C 60.0 CH_2 ; δ_H 4.31 and 4.29, each 1H, d, $J = 12.5$ Hz) in the side chain.

The NMR data of the side chain of **3** was found to be the same as the corresponding data of known compound **13** except the olefinic methyl of **13** was replaced by a hydroxymethylene group (δ_H 4.31 and 4.29, each 1H, d, $J = 12.5$ Hz) in **3**. The HMBC correlations of **3** further confirmed the C-13, C-13/C-15, C-16/C-17, and C-18 positions of the hydroxymethylene, two conjugated double bonds, and a hydroxy group, respectively (Figure 2). Finally, the strong NOE correlation of H₂-14/H-16 and the large J value of H-16 and H-17 (15.0 Hz) determined the *Z* and *E* configurations of C-13/C-15 and C-16/C-17 double bonds, respectively. Compound **3** was thus established as (1*R*,2*R*,4*S*,13*Z*,16*E*)-loba-8,10,13(15),16-tetraen-14,18-diol.

Lobovarol I (**4**) displayed a sodiated ion peak $[M + Na]^+$ at m/z 387.2504 in the HRESIMS, appropriate for a molecular formula $C_{22}H_{36}O_4$, and five degrees of unsaturation. The IR absorptions at 3278 and 1740 cm^{-1} revealed the presence of the hydroxy and ester carbonyl groups. The NMR data (Table 1) showed the presence of a trisubstituted double bond (δ_C 141.0, C and 124.7, CH; δ_H 5.58, dd, $J = 8.0, 6.8$ Hz), a trisubstituted epoxide (δ_C 58.6, C; 63.7, CH; δ_H 2.76, 1H, dd, $J = 6.4, 6.4$ Hz), and an acetoxy group (δ_C 171.0, C; 21.1 CH_3 ; δ_H 2.06, 3H, s). The remaining two degrees of unsaturation have arisen from the presence of two rings. A decalin bicarbocyclic structure with an angular methyl (δ_H 0.90, 3H, s) and a methine (δ_C 54.9, CH; δ_H 1.27, m) was elucidated from the COSY and HMBC correlations (Figure 2) which showed **4** to be a prenyleudesmane type diterpene [9,10]. The C-4 position of the hydroxy group was confirmed from the HMBC correlation of H₃-16 (δ_H 1.12, s,) to C-5 (δ_C 54.9, CH) and C-4 (δ_C 72.2, C). Moreover, the NMR data of the side chain of **4** were found to be identical in all aspects to those of the side chain of acetoxylobaoxide (**16**) (Figure 4) [5], the gross structure of **4** was thus established unambiguously.

The relative configuration of **4** was determined based on biogenetic consideration, NOESY correlations (Figure 5a) and NMR data comparison of related metabolites. Accordingly, the steric orientations of H₃-17, H-5, and H-7 in the bicarbocyclic ring system of prenyleudesmanes **4** and **5–11** (*vide infra*) should be α , β , and β , respectively, as the same with the corresponding H₃-17, H-2, and H-4 of the ring system of the lobanes (**1–3**), as the showed by the NOESY analysis of lobovarol I (**4**) (Figure 5a). Consequently, the NOE interaction displayed between H₃-17 and H₃-16 indicated the β -orientation of the hydroxy group at C-4. Furthermore, the NMR data of the side chain in **4** were identical to those of the side chain in acetoxylobaoxide (**16**), of which the *R* absolute configuration at C-14 has been determined after reduction of the C-14/C-15 epoxide [5]. From the above results, the structure of **4** was determined as (4*S*,5*S*,7*S*,10*S*,11*Z*,14*R*)-14,15-epoxy-18-acetoxyprenyleudesma-11-en-4-ol.

Lobovarol J (**5a** and **5b**) were obtained as an inseparable mixture ($\approx 1:1$) of two isomers as revealed from the NMR spectra which displayed two sets of signals with an only slight difference in the chemical shifts for certain carbon and proton atoms. The HRESIMS (m/z 359.2555 $[M + Na]^+$) was determining a molecular formula ($C_{21}H_{36}O_3$) for the mixture of two isomers. Comparison of the NMR data of **5a** and **5b** (Table 2) with those of **4** (Table 1) revealed that lobovarol J possessed the same bicarbocyclic system as that of **4** (Table 2) and the similar side chain of fuscoides C & D triacetates (**21a** and **21b**) [24], except that the sugar moiety in **21a** or **21b** (Figure 4) was replaced by a methoxy group (δ_C 50.4, CH_3 ; δ_H 3.10, 3H, s) in **5**. The planar structure of **5a** and **5b** was then established, as illustrated in Figure 2. The *E* configuration of the 13,14-double bond and the *trans* 11,12-epoxide were deduced from the J values of H-13 and H-14 (16.0 Hz) and the NOE correlations (Figure 5b), respectively. However, by using MM2 calculation for either stable conformation of **5a** or **5b**, it was found that either isomer showed a distance of near 2.4 Å between the NOE-interacting protons H-12 and H-7 (Figure 5b). Therefore, the two new compounds were defined as 11*R*,12*R*- (**5a**) and 11*S*,12*S*-

(5b) isomers of (4*S*,5*S*,7*S*,10*S*,13*E*)-11,12-epoxy-15-methoxyprenyleudesma-13-en-4-ol with the exact NMR spectroscopic data for each isomer remained for further elucidation.

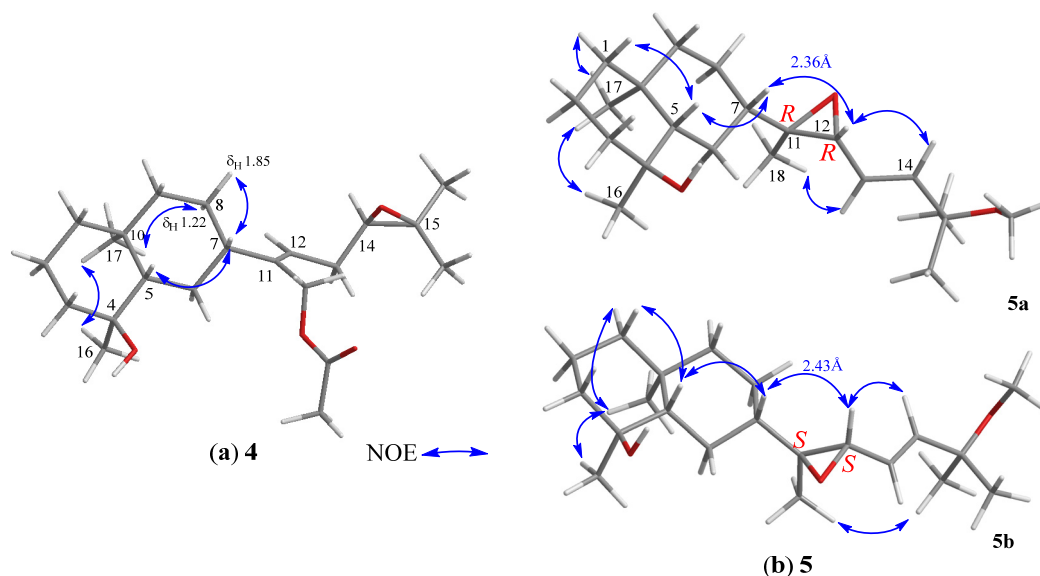


Figure 5. (a) Selected NOE correlations of **4**; (b) Selected NOE correlations of 11,12-bisepimers.

Lobovarol K (**6**) has a molecular formula $C_{21}H_{36}O_2$, as displayed from the sodiated ion peak in the HRESIMS (m/z 343.2606 $[M + Na]^+$), and showed the presence of a hydroxy group (IR 3431 cm^{-1}). The NMR spectroscopic data of **6** (Table 2) are similar to a methoxylated (δ_C 50.4, CH_3 and δ_H 3.18, 3H, s) prenyleudesmane, including signals of five methyls. The 1H and ^{13}C NMR data of **6** further revealed that it is a diterpene possessing the same side chain as that of lobane **17** [2]. The chemical shifts of C-18 (δ_C 15.3, CH_3) and J value of H-13 and H-14 (15.6 Hz) indicated the *E*-geometry for the 11,12- and 13,14-double bonds, respectively. The NOE correlations (Figure 6a) and the above-mentioned biogenetic consideration established **6** as (4*S*,5*S*,7*S*,10*S*,11*E*,13*E*)-15-methoxyprenyleudesma-11,13-dien-4-ol.

Lobovarol L (**7**) possessed a molecular formula $C_{20}H_{34}O_3$ (HRESIMS m/z 345.2401 $[M + Na]^+$). Compound **7** displayed the combined NMR data of the eudesmane ring system in **4**–**6** (Table 2), and the side chain of lobatriene (**18**) [19]. The planar structure was further established by the analysis of COSY and NMR correlations (Figure 2). The configuration of **7** was established after the structure determination of **8**. NOE correlations between the known α -oriented H_3 -17 and H_3 -16, and β -oriented H-7 with H-5, but not between H-5 and both H_3 -16 and H_3 -17 led to the structure of **7** to be determined as shown in formula **7**.

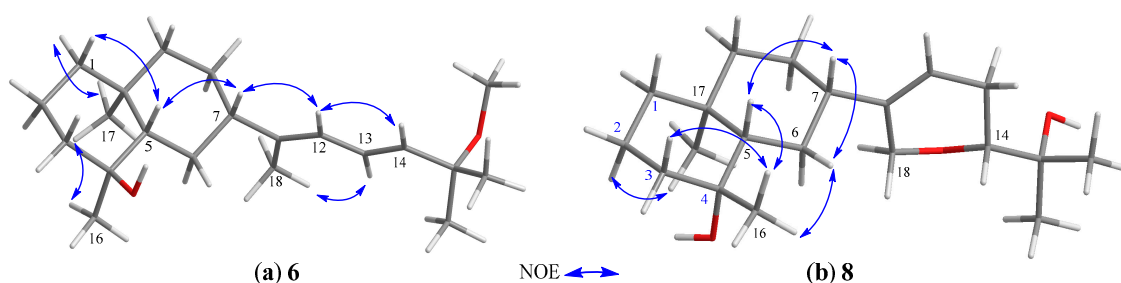


Figure 6. (a) Selected NOE correlations of **6**; (b) selected NOE correlations of **8**.

The HRESIMS of lobovarol M (**8**) showed the same molecular formula $C_{20}H_{34}O_3$ as that of **7**, suggesting **8** to be an isomer for **7**. The NMR data of **8** were found to be very similar to those of **7** (Table 2); however, **8** exhibited more upfield chemical shifts for carbons around C-4, in particular

C-2, C-3, and C-5 ($\Delta\delta_C$ −2.1, −2.1, and −3.1, respectively) relative to the correspondent carbons in **7**, supporting that **8** is the 4-epimer of **7**. Unlike the NOE correlations of **7**, **8** exhibited correlations (Figure 6b) between H₃-17 and H-2 α , but not between H₃-17 and H₃-16. Also, H₃-16 showed NOE interactions with both H-3 β and H-5, and H-5 displayed correlation with the β -oriented H-7, thus **8** was determined as 4-epimer of **7**.

Table 3. ¹³C and ¹H NMR spectroscopic data of compounds **9–11**.

Position	9		10		11	
	δ_C^a (Mult.) ^b	δ_H^c (J in Hz)	δ_C^d (Mult.)	δ_H^e (J in Hz)	δ_C^d (Mult.)	δ_H^e (J in Hz)
1	40.9, CH ₂	1.40 m; 1.10 m	79.2, CH	3.42 dd (11.5, 4.0)	41.8, CH ₂	1.44 m; 1.28 m
2	20.1, CH ₂	1.56 m	31.4, CH ₂	1.82 m; 1.56 m	23.4, CH ₂	1.63 m
3	43.6, CH ₂	1.83 m; 1.80 m	34.1, CH ₂	2.32 m; 2.11 m	36.8, CH ₂	2.31 m; 2.01 m
4	72.1, C		148.5, C		150.7, C	
5	54.9, CH	1.32 m	47.5, CH	1.77 m	49.9, CH	1.83 d (11.5)
6	25.4, CH ₂	1.90 m	28.8, CH ₂	1.64 m; 1.31 m	29.7, CH ₂	1.56 m; 1.26 m
7	39.5, CH	2.57 m	41.2, CH	1.83 m	44.0, CH	2.01 m
8	27.9, CH ₂	1.67 m; 1.30 m	26.7, CH ₂	1.59 m; 1.42 m	27.5, CH ₂	1.60 m; 1.42 m
9	44.6, CH ₂	1.43 m; 1.34 m	36.9, CH ₂	1.94 m; 1.20 m	41.2, CH ₂	1.51 m; 1.42 m
10	34.6, C		40.2, C		35.9, C	
11	137.2, C		141.2, C		141.6, C	
12	136.7, CH	6.63 d (5.6)	116.4, CH	5.58 d (5.5)	126.6, CH	5.61 t (7.5)
13	24.5, CH ₂	2.49 m; 2.36 m	25.3, CH ₂	2.17 m; 1.96 m	30.4, CH ₂	2.32 m
14	83.3 CH	4.13 dd (12.8, 3.6)	80.3 CH	3.28 dd (11.0, 3.5)	77.6 CH	3.42 m
15	71.0, C		71.7, C		72.7, C	
16	22.5, CH ₃	1.12 s	107.0, CH ₂	4.76 s; 4.50 s	105.5, CH ₂	4.71 s; 4.42 s
17	18.7, CH ₃	0.91 s	10.2 CH ₃	0.70 s	16.4, CH ₃	0.73 s
18	164.7, C		68.2, CH ₂	4.20 br s	61.6, CH ₂	4.54 d (12.0)
						4.76 d (12.0)
19	24.4, CH ₃	1.25 s	23.7, CH ₃	1.17 s	23.8, CH ₃	1.20 s
20	25.9, CH ₃	1.33 s	26.1, CH ₃	1.22 s	26.3, CH ₃	1.24 s
Ac					171.3, C	
					21.1, CH ₃	2.06 s

^a Spectrum recorded at 100 MHz in CDCl₃. ^b Attached protons were deduced by the DEPT experiment. ^c Spectrum recorded at 400 MHz in CDCl₃. ^d Spectrum recorded at 125 MHz in CDCl₃. ^e Spectrum recorded at 500 MHz in CDCl₃.

Lobovarol N (**9**) displayed a sodiated ion peak at m/z 359.2191 [M + Na]⁺ in the HRESIMS spectrum of a molecular formula C₂₀H₃₂O₄ and IR absorptions at 3430 and 1700 cm^{−1} of the hydroxy and ester carbonyl functionalities. The ¹³C and ¹H NMR data (Table 3) were similar to those of **7** except the replacement of the 18-hydroxymethylene signals (δ_C 68.2, CH₂; δ_H 4.23 and 4.18, each br d, J = 16.4 Hz) in **7** by a signal at δ_C 164.7 (C) in **9**. Thus, **9** is the 16-oxo derivative of **7**. The NMR data of the side chain of **9** are also nearly identical with those of lobatrienolide (**19**) [5] coexisting in the same organism [1]. A combination of 2D NMR analyses (Figure 2) and biogenetic relationship with the coexisting biogenetically related lobanes **1,19** [5], and 17,18-epoxyloba-8,10,13(15)-trien-16-ol [1] with confirmed absolute configurations established the structure of **9** as (4*S*,5*S*,7*S*,10*S*,11*Z*,14*R*)-14,18-epoxyprenyleudesma-11-en-4,15-diol-18-one.

The sodium adduct ion peak [M + Na]⁺ of lobovarol O (**10**) at m/z 343.2242 in the HRESIMS showed a molecular formula C₂₀H₃₂O₃ of **10**. NMR data (Table 3) of **10** showed that it has the same cyclic ether ring as **7**, **8**, and lobatriene (**18**) [19] in the side chain. In comparison of the NMR spectroscopic data of **10** (Table 3) with those of **7** and **8** (Table 2) and analysis of COSY spectrum which showed the proton sequence of H-1 (δ_H 3.42, dd, J = 11.5, 4.0 Hz) to H-3 and the HMBC correlations of H₃-17 (δ_H 0.70, 3H, s) to C-1 (δ_C 79.2), C-5 (δ_C 47.5), C-9 (δ_C 36.9), and C-10 (δ_C 40.2), confirmed the presence of a hydroxy group at C-1 and the prenyleudesmane molecular skeleton of **10**. Furthermore, NOE correlations of H-1 with the β -oriented H-5 and one proton of H₂-9 (δ_H 1.20, m) showed the β -orientation of H-1 and this H-9. The other proton at C-9 (δ_H 1.94, m) was thus assigned as H-9 α which exhibited NOE correlation with H₃-17, but not with both H-1 and H-5, thus H₃-17 was assigned as α -oriented.

Lobovarol P (**11**) has the molecular formula C₂₂H₃₆O₄ (HRESIMS: m/z 387.2504 [M + Na]⁺). The NMR data (Table 3) revealed that it possesses the same decalin bicyclic structures [10] and the same

side-chain [3] of known compounds. The gross structure of **11** was thus determined and the relative configuration of **11** was further established by analysis of the NOESY spectrum which exhibited NOE interactions of the β -oriented H-5 (δ_{H} 1.83, d, $J = 11.5$ Hz) with both H-1 β (δ_{H} 1.28, m) and H-7 (δ_{H} 2.10, m), and H-1 α (δ_{H} 1.28, m) with H₃-17 (δ_{H} 0.73, 3H, s). Thus, H-7 was determined to be positioned on the β face. By the biogenetic consideration, lobovarol P was found to possess (5*R*,7*S*,10*S*)-configuration, the same as that of lobovarol E [1].

Although 5,6-dihydro-2H-pyran and 5,6-dihydro-2H-pyran-2-one moieties have been known to be present in the side chain of lobane diterpenoid isolated from genus *Lobophytum* [1–3,5], this is the first report about discovering both pyran and pyranone systems in the structures of prenyleudesmanes. The structures of two known compounds loba-8,10,13(15)-trien-14,17,18-triol-14,17-diacetate (**12**) [3] and the eudesmane derivative (**13**) [9] were established mainly based on the MS and partial ¹H NMR data. The detailed 1D and 2D NMR spectroscopic analysis enabled us to fully assign the ¹H and ¹³C NMR data of these two diterpenoids for the first time.

Cytotoxicity for compounds **1**, **2**, **4**, **7**, **8**, **12**, and **13** against the growth of human colon adenocarcinoma (DLD-1), human colon carcinoma (HT-29), and human liver bile duct carcinoma (HuCCT-1); and for **3**, **5**, **6**, and **9–11** against DLD-1 and mouse lymphocytic leukemia (P388) cancer cell lines using the Alamar Blue assay has been screened [25,26]. The results showed that all of the tested metabolites did not exhibit cytotoxicity towards the above cell lines ($\text{IC}_{50} > 40 \mu\text{g/mL}$) compared to doxorubicin HCl (IC_{50} 0.9–7.4 $\mu\text{g/mL}$).

The anti-inflammatory activities of diterpenoids **2–13** against the fMLF/CB-induced pro-inflammatory responses on human neutrophils were evaluated [27,28], too. The results (Table 4) showed that **12** and **13** have potent inhibitory effect against the elastase release (IC_{50} 6.9 ± 2.7 and $4.4 \pm 0.7 \mu\text{M}$, respectively). Compounds **2** and **4** could suppress elastase release (IC_{50} 18.8 ± 1.8 and $20.0 \pm 3.0 \mu\text{M}$), too, while **13** is the only compound also could significantly suppress the superoxide anion generation (IC_{50} $13.7 \pm 4.4 \mu\text{M}$). Thus **2**, **4**, **12**, and **13**, in particular **12** and **13**, have the potential to become anti-inflammatory agents. Compound **1** was found to strongly suppress elastase release in the absence of fMLF/CB, and is worthy for further biological study.

Table 4. Inhibitory effects of compounds **1–13** on the generation of superoxide anion and release of elastase in fMLF/CB-stimulated human neutrophils.

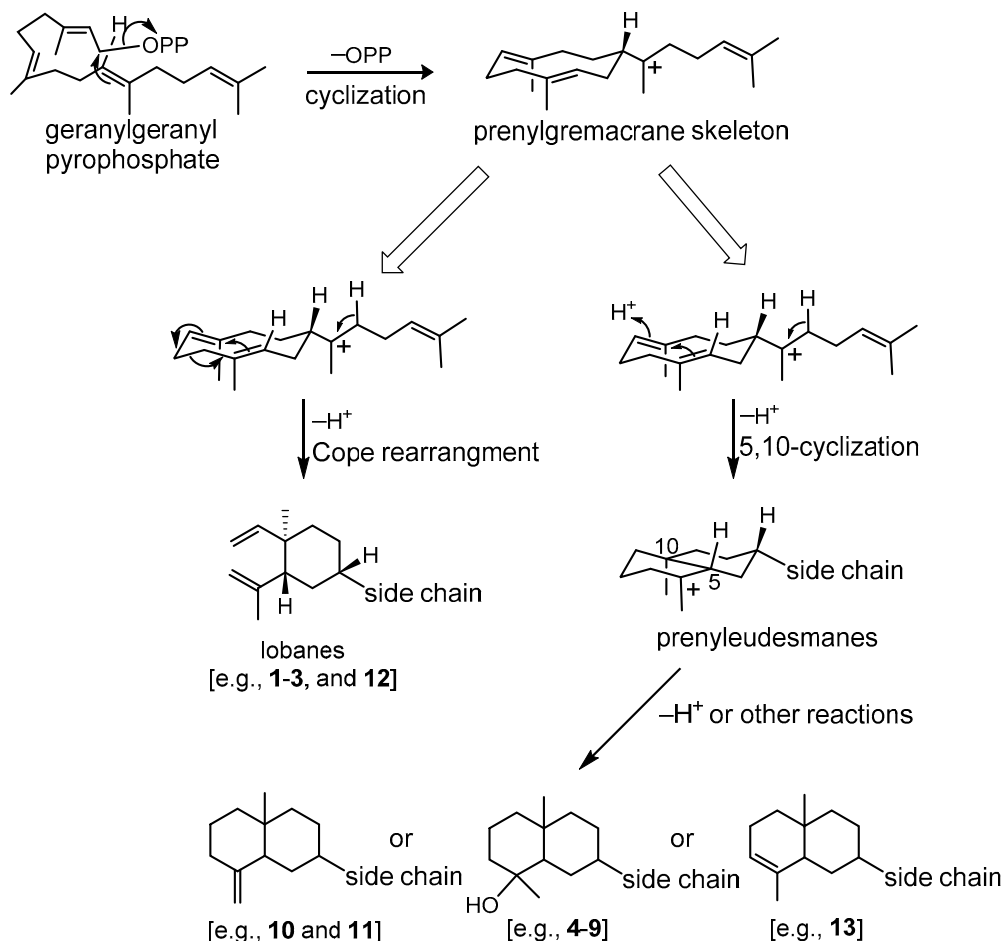
Compound	Superoxide Anion			Elastase Release		
	IC_{50} (μM)	Inh % ^a		IC_{50} (μM)	Inh %	
1	>20	4.6 ± 3.8 ^b		>20	64.3 ± 3.7 ^b	
2	>20	18.1 ± 4.0	*	18.8 ± 1.8	87.3 ± 7.9	***
3	>20	4.3 ± 4.2		>20	3.8 ± 2.6	
4	>20	40.2 ± 7.3	**	20.0 ± 3.0	53.2 ± 0.2	***
5	>20	8.4 ± 7.4		>20	3.5 ± 1.4	
6	>20	4.2 ± 4.4		>20	-10.9 ± 5.1	
7	>20	22.9 ± 7.6	*	NT ^c	NT	
8	>20	19.1 ± 6.9	*	>20	37.8 ± 6.2	***
9	>20	5.3 ± 3.2		>20	5.5 ± 0.6	***
10	>20	2.7 ± 5.0		>20	5.3 ± 1.6	*
11	>20	8.9 ± 7.0		>20	12.0 ± 4.4	
12	>20	46.5 ± 5.8	***	6.9 ± 2.7	73.7 ± 2.4	***
13	13.7 ± 4.4	72.4 ± 5.9	***	4.4 ± 0.7	117.3 ± 3.2	***
Idelalisib ^d	0.07 ± 0.01		***	0.30 ± 0.10		***

^a Inh% at 10 $\mu\text{g/mL}$. ^b **1** induced superoxide generation and elastase release in the absence of fMLF/CB. ^c NOT tested.

^d Positive control. Results are presented as mean \pm S.E.M. ($n = 3-4$). * $p < 0.05$, ** $p < 0.01$, *** $p < 0.001$ compared with the control (DMSO).

Although the structures of lobanes **1–3**, and **12** and eudesmanes **4–11**, and **13**, along with the previously reported related metabolites from the same organism [1] possess different ring structures, they are coexisted in *L. varium* and are biogenetically related to each other

A prenylgermacrene has been regarded as the same biosynthetic precursor [8,9] and we further propose a stereospecific biosynthesis for lobane and prenyleudesmane diterpenoids through Cope rearrangement and acid-catalyzed cyclization, respectively [9,29], as illustrated in Scheme 1. Thus, the co-occurrence of lobanes and prenyleudesmanes could be found in the same soft coral as in the cases of *L. varium* [1], *Lobophytum* sp. [9], *Eunicea fusca* [24], *Simularia gyrosa* [30], and *Simularia polydactyla* [31], is scientifically reasonable.



Scheme 1. Plausible biosynthetic pathway of lobanes and prenyleudesmane-type diterpenoids.

3. Experimental Section

3.1. General Experimental Procedures

Optical rotations and IR spectra were measured on a JASCO P-1020 polarimeter and FT/IR-4100 infrared spectrophotometer (Jasco Corporation, Tokyo, Japan), respectively. ESIMS and HRESIMS experiments were performed on VG Quattro GC/MS and Bruker APEX II mass spectrometers, respectively. The NMR spectra were recorded on a Varian Unity Inova 500 FT-NMR (Varian Inc., Palo Alto, CA, USA) at 500 and 125 MHz for ¹H and ¹³C, respectively; or on a Varian 400 FT-NMR at 400 and 100 MHz for ¹H and ¹³C, respectively. Silica gel 60 or reversed-phase silica gel (RP-18; 230–400 mesh) and precoated silica gel plates (Kieselgel 60 F254, 0.2 mm) (Merck, Darmstadt, Germany) were used for open column chromatography (CC) and analytical TLC analysis, respectively. Isolation and purification of isolates by HPLC were performed by Hitachi L-2455 instrument equipped with an RP-18 column (ODS-3, 5 μm, 250 × 20 mm; Sciences Inc., Tokyo, Japan).

3.2. Amino Material

The soft coral *L. varium* (Tixier-Durivault, 1970) was collected in March 2013 at a depth of 10 to 15 m at Jihui Fish Port, Taitung, Taiwan (23°7'2" N, 121°23'49.2" E) and identified by Professor Chang-Feng Dai, Institute of Oceanography, National Taiwan University, Taipei, Taiwan [1].

3.3. Extraction and Isolation

The sliced frozen soft coral *L. varium* (1.3 kg, wet weight) was exhaustively extracted with EtOAc, and the resulting solvent-free extract (55.40 g) was fractionated by silica gel column chromatography into 24 fractions (F1 to F24) as described before¹. F19 (1.39 g), eluting with 50% EtOAc in *n*-hexane, was permeated through a column of Sephadex LH-20 using acetone to afford two diterpenoid-rich fractions F19-1 (105.0 mg) and F19-2 (94.0 mg). F19-1 was chromatographed over silica gel and eluted with EtOAc–*n*-hexane (1:3) to give two subfractions F19-1a (70.5 mg) and F19-1b (15.0 mg). F19-1a was further divided by reverse phase (RP-18) column chromatography, using MeOH–H₂O, into two subfractions F19-1a1 and F19-1a2 which were purified separately by RP-18 HPLC, using CH₃CN–H₂O (2:1), to yield **1** (2.4 mg) and **2** (3.1 mg) from F19-1a1, and **12** (10.0 mg) from F19-1a2, respectively. F19-1b (15.0 mg) was purified by RP-18 HPLC using CH₃CN–H₂O (1.5:1) to afford **4** (1.1 mg). F19-2 was also primarily chromatographed over silica gel column using EtOAc–*n*-hexane (1:3) where the eluted diterpenoid-rich fraction (50.1 mg) was further isolated by RP-18 column chromatography, using MeOH–H₂O (9:1 then 2:1), to yield **13** (1.4 mg), **7** (1.5 mg), and **8** (4.8 mg), respectively. F20 (1.20 g), eluted with 66.7% EtOAc in *n*-hexane, was fractionated over silica gel column, using EtOAc–*n*-hexane (5:95 to 0:100, gradient), to yield four fractions (F20-1 to F20-4). Isolation of F20-1 over RP-18 silica gel column, using MeOH–H₂O (9:1), gave **5** (2.2 mg) and **6** (3.8 mg), respectively. F20-2 was further separated by RP-HPLC, using MeOH–H₂O (6:1), to afford **10** (2.0 mg) and **11** (3.2 mg), respectively. F21 (0.50 g), eluted with 100% EtOAc, was similarly further fractionated, as for fractionation of F20, to give F21-1 and F21-2. RP-18 silica gel column chromatography was then applied to purify F21-1, using MeOH–H₂O (5:1), to afford **3** (5.0 mg) and to further purify F21-2, using MeOH–H₂O (6:1), to yield **9** (4.0 mg).

Lobovarol F (**1**): Colorless oil; $[\alpha]_D^{24} + 2.8$ (c 2.4, CHCl₃); IR (neat) ν_{\max} 3393, 2926, 1643, 1532, 1462, 1147, 1024, and 897 cm^{−1}; ¹³C and ¹H NMR data (see Table 1); ESIMS m/z 345 [M + Na]⁺; HRESIMS m/z 345.2403 [M + Na]⁺ (calcd for C₂₀H₃₄O₃Na, 345.2400).

Lobovarol G (**2**): Colorless oil; $[\alpha]_D^{24} + 44.5$ (c 3.1, CHCl₃); IR (neat) ν_{\max} 3392, 2926, 2860, 1642, 1523, and 891 cm^{−1}; ¹³C and ¹H NMR data (see Table 1); ESIMS m/z 329 [M + Na]⁺; HRESIMS m/z 329.2453 [M + Na]⁺ (calcd for C₂₀H₃₄O₂Na, 329.2451).

Lobovarol H (**3**): Colorless oil; $[\alpha]_D^{24} - 46.7$ (c 0.57, CHCl₃); IR (neat) ν_{\max} 3352, 2926, 1645, 1456, 1374, and 898 cm^{−1}; ¹³C and ¹H NMR data (see Table 1); ESIMS m/z 327 [M + Na]⁺; HRESIMS m/z 327.2294 [M + Na]⁺ (calcd for C₂₀H₃₂O₂Na, 327.2295).

Lobovarol I (**4**): Colorless oil; $[\alpha]_D^{24} + 66.0$ (c 1.1, CHCl₃); IR (neat) ν_{\max} 3278, 2919, 2852, 1740, and 1531 cm^{−1}; ¹³C and ¹H NMR data (see Table 1); ESIMS m/z 387 [M + Na]⁺; HRESIMS m/z 387.2504 [M + Na]⁺ (calcd for C₂₂H₃₆O₄Na, 387.2506).

Lobovarol J (mixture of **5a** and **5b**): Colorless oil; $[\alpha]_D^{24} + 14.2$ (c 0.63, CHCl₃); IR (neat) ν_{\max} 3443, 2929, 1531, 1456, 1378, and 1068 cm^{−1}; ¹³C and ¹H NMR data (see Table 2); ESIMS m/z 359 [M + Na]⁺; HRESIMS m/z 359.2555 [M + Na]⁺ (calcd for C₂₁H₃₆O₃Na, 359.2557).

Lobovarol K (**6**): Colorless oil; $[\alpha]_D^{24} - 10.9$ (c 0.46, CHCl₃); IR (neat) ν_{\max} 3431, 2922, 1670, 1535, 1458, 1377, and 1071 cm^{−1}; ¹³C and ¹H NMR data (see Table 2); ESIMS m/z 343 [M + Na]⁺; HRESIMS m/z 343.2606 [M + Na]⁺ (calcd for C₂₁H₃₆O₂Na, 343.2608).

Lobovarol L (7): Colorless oil; $[\alpha]_D^{24} + 99.2$ (c 1.5, CHCl_3); IR (neat) ν_{max} 3378, 2922, 2852, 1540, 1458, 1089, 906, and 670 cm^{-1} ; ^{13}C and ^1H NMR data (see Table 2); ESIMS m/z 345 $[\text{M} + \text{Na}]^+$; HRESIMS m/z 345.2401 $[\text{M} + \text{Na}]^+$ (calcd for $\text{C}_{20}\text{H}_{34}\text{O}_3\text{Na}$, 345.2400).

Lobovarol M (8): Colorless oil; $[\alpha]_D^{24} + 87.7$ (c 4.8, CHCl_3); IR (neat) ν_{max} 3459, 2927, 2852, 1451, 1378, 1161, 1088, and 756 cm^{-1} ; ^{13}C and ^1H NMR data (see Table 2); ESIMS m/z 345 $[\text{M} + \text{Na}]^+$; HRESIMS m/z 345.2401 $[\text{M} + \text{Na}]^+$ (calcd for $\text{C}_{20}\text{H}_{34}\text{O}_3\text{Na}$, 345.2400).

Lobovarol N (9): Colorless oil; $[\alpha]_D^{24} + 59.7$ (c 0.54, CHCl_3); IR (neat) ν_{max} 3430, 2924, 1700, 1429, 1376, and 1096 cm^{-1} ; ^{13}C and ^1H NMR data (see Table 3); ESIMS m/z 359 $[\text{M} + \text{Na}]^+$; HRESIMS m/z 359.2191 $[\text{M} + \text{Na}]^+$ (calcd for $\text{C}_{20}\text{H}_{32}\text{O}_4\text{Na}$, 359.2193).

Lobovarol O (10): Colorless oil; $[\alpha]_D^{24} + 48.1$ (c 0.57, CHCl_3); IR (neat) ν_{max} 3433, 2926, 1696, 1532, 1024, and 670 cm^{-1} ; ^{13}C and ^1H NMR data (see Table 3); ESIMS m/z 343 $[\text{M} + \text{Na}]^+$; HRESIMS m/z 343.2242 $[\text{M} + \text{Na}]^+$ (calcd for $\text{C}_{20}\text{H}_{32}\text{O}_3\text{Na}$, 343.2244).

Lobovarol P (11): Colorless oil; $[\alpha]_D^{24} - 54.0$ (c 0.71, CHCl_3); IR (neat) ν_{max} 3503, 2925, 1731, 1373, and 1237 cm^{-1} ; ^{13}C and ^1H NMR data (see Table 3); ESIMS m/z 387 $[\text{M} + \text{Na}]^+$; HRESIMS m/z 387.2504 $[\text{M} + \text{Na}]^+$ (calcd for $\text{C}_{22}\text{H}_{36}\text{O}_4\text{Na}$, 387.2506).

Compound 12: Colorless oil; $[\alpha]_D^{24} + 57.0$ (c 14.3, CHCl_3); IR (neat) ν_{max} 3496, 2927, 2937, 1736, 1640, 1442, 1373, and 1027 cm^{-1} ; ^1H NMR (CDCl_3 , 400 MHz): δ_{H} 5.80 (1H, dd, $J = 17.6, 10.4\text{ Hz}$, H-8), 5.48 (1H, dd, $J = 7.2, 7.2\text{ Hz}$, H-15), 4.89 (1H, d, $J = 17.6\text{ Hz}$, H-9a), 4.89 (1H, d, $J = 10.4\text{ Hz}$, H-9b), 4.85 (1H, dd, $J = 9.2, 4.0\text{ Hz}$, H-17), 4.81 (1H, s, H-11a), 4.66 (1H, d, $J = 12.0\text{ Hz}$, H-14a), 4.58 (1H, d, $J = 12.0\text{ Hz}$, H-14b), 4.56 (1H, s, H-11b), 2.46, (2H, m, H-6, H₂-16), 2.06 (3H, s, 17-OCOCH₃), 2.05 (3H, s, 14-OCOCH₃) 2.03, (1H, m, H-4), 1.99 (1H, dd, $J = 11.6, 3.6\text{ Hz}$, H-2), 1.69 (3H, s, H₃-12), 1.53, (2H, m, H₂-5), 1.49 (2H, m, H₂-3), 1.41 (2H, m, H₂-6), 1.22 (6H, s, H₃-19 and H₃-20), 0.98 (3H, s, H₃-7); ^{13}C NMR (CDCl_3 , 100 MHz): δ_{C} 171.0 (C, 14-OCOCH₃), 170.6 (C, 17-OCOCH₃), 150.0 (CH, C-8), 147.4 (C, C-10), 140.7 (C, C-13), 125.6 (CH, C-15), 112.2 (CH₂, C-11), 110.0 (CH₂, C-9), 78.9 (CH, C-17), 72.1 (C, C-18), 61.1 (CH₂, C-14), 52.6 (CH, C-2), 43.7 (CH, C-4), 39.8 (CH₂, C-6), 39.7 (C, C-1), 33.1 (CH₂, C-3), 28.2 (CH₂, C-16), 27.1 (CH₂, C-5), 26.5 (CH₃, C-19), 25.3 (CH₃, C-20), 24.8 (CH₃, C-12), 21.1 (CH₃, 14-OCOCH₃), 20.9 (CH₃, 17-OCOCH₃), 16.5 (CH₃, C-7); ESIMS m/z 429 $[\text{M} + \text{Na}]^+$; HRESIMS m/z 429.2609 $[\text{M} + \text{Na}]^+$ (calcd for $\text{C}_{24}\text{H}_{38}\text{O}_5\text{Na}$, 429.2612).

Compound 13: Colorless oil; $[\alpha]_D^{24} - 81.0$ (c 1.4, CHCl_3); IR (neat) ν_{max} 3254, 2925, 2857, 1640, 1450, and 1023 cm^{-1} ; ^1H NMR (CDCl_3 , 500 MHz): δ_{H} 6.50 (1H, dd, $J = 15.5, 11.0\text{ Hz}$, H-13), 5.90 (1H, d, $J = 11.0\text{ Hz}$, H-12), 5.78 (1H, d, $J = 15.5\text{ Hz}$, H-14), 5.29 (1H, s, H-3), 4.58 (1H, dd, $J = 7.0, 7.0\text{ Hz}$, H-1), 3.55 (1H, dd, $J = 7.0, 7.0\text{ Hz}$, H-1), 2.31 (1H, m, H-2a), 1.98 (2H, m, H-2b and H-7), 1.95 (1H, m, H-5), 1.92 (1H, m, H-9a), 1.71 (1H, m, H-6a), 1.80 (3H, s, H₃-18), 1.60 (2H, m, H₂-8), 1.58 (3H, s, H₃-16), 1.36 (6H, s, H₃-19 and H₃-20), 1.29 (1H, m, H-6b), 1.14 (1H, m, H-9b), 0.79 (3H, s, H₃-17); ^{13}C NMR (CDCl_3 , 125 MHz): δ_{C} 143.6 (C, C-11), 139.3 (CH, C-14), 135.2 (C, C-4), 123.0 (CH₂, C-13), 122.7 (CH, C-12), 119.5 (CH, C-3), 76.4 (CH, C-1), 71.0 (C, C-15), 52.8 (CH₂, C-2), 48.0 (CH, C-7), 46.6 (CH, C-5), 37.4 (C, C-10), 35.0 (CH₂, C-9), 29.9 (2 x CH₃, C-19 and C-20), 28.2 (CH₂, C-6), 26.0 (CH₂, C-8), 20.8 (CH₃, C-16), 15.0 (CH₃, C-18), 9.5 (CH₃, C-17); ESIMS m/z 327 $[\text{M} + \text{Na}]^+$; HRESIMS m/z 327.2296 $[\text{M} + \text{Na}]^+$ (calcd for $\text{C}_{20}\text{H}_{32}\text{O}_2\text{Na}$, 327.2295).

Preparation of (S)- and (R)-MTPA Esters of 1

To a solution of **1** (1.0 mg, 3.1 μmol) in anhydrous pyridine (200 μL) was added S-(+)- α -methoxy- α -(trifluoromethyl)phenylacetyl (MTPA) chloride (20 μL), and the mixture was further reacted for 20 h at room temperature. The reaction mixture was then processed as previously described [20,21] to yield the (R)-MTPA ester **1a** (0.5 mg, 0.93 μmol , 30%). The correspondent (S)-MTPA ester **1b** was similarly yielded from the reaction of R-(−)-MTPA chloride with **1**. ^1H NMR (CDCl_3 , 400 MHz) of **1a**: δ_{H} 5.8005 (1H, dd, $J = 17.6, 10.4\text{ Hz}$, H-8), 4.892 (1H, d, $J = 12\text{ Hz}$, H-9b), 5.114 (1H, dd,

$J = 5.6, 5.6$ Hz, H-17), 4.8895 (1H, d, $J = 16.4$ Hz, H-9a), 4.822 (1H, s, H-11b), 4.591 (1H, s, H-11a), 3.949 (1H, dd, $J = 8.4, 6.8$ Hz, H-15), 2.395 (1H, ddd, $J = 10.0, 6.8, 6.8$ Hz, H-16b), 1.994 (1H, m, H-16a), 1.9475 (1H, m, H-2), 1.708 (3H, s, H₃-12), 1.689 (1H, d, $J = 15.2$, H-3b), 1.522 (1H, m, H-3a), 1.367 (1H, m, H-4), 1.394–1.229 (4H, m, H₂-5 and H₂-6), 1.279 (3H, s, H₃-20), 1.210 (3H, s, H₃-14), 1.158 (3H, s, H₃-19), 0.981 (3H, s, H₃-7); ^1H NMR (CDCl_3 , 400 MHz) of **1b**: δ_{H} 5.803 (1H, dd, $J = 17.6, 10.4$ Hz, H-8), 4.895 (1H, d, $J = 12$ Hz, H-9b), 5.136 (1H, dd, $J = 6.0, 6.0$ Hz, H-17), 4.8945 (1H, d, $J = 16.4$ Hz, H-9a), 4.883 (1H, s, H-11b), 4.605 (1H, s, H-11a), 3.971 (1H, dd, $J = 8.0, 7.6$ Hz, H-15), 2.419 (1H, ddd, $J = 9.6, 6.8, 6.8$ Hz, H-16b), 2.107 (1H, m, H-16a), 1.989 (1H, m, H-2), 1.718 (3H, s, H₃-12), 1.7665 (1H, br d, $J = 14.0$, H-3b), 1.5325 (1H, m, H-3a), 1.415 (1H, m, H-4), 1.394–1.256 (4H, m, H₂-5 and H₂-6), 1.236 (3H, s, H₃-20), 1.198 (3H, s, H₃-14), 1.106 (3H, s, H₃-19), 0.995 (3H, s, H₃-7).

3.4. Cytotoxic Testing

Cytotoxicities of **1–11** were assayed using Almar Blue assay [25,26]. Doxorubicin HCl, employed as positive control, displayed cytotoxic activity toward DLD-1, HT-29, HuCCT-1, and P388 cell lines with IC_{50} 0.9, 4.4, 2.6, and 7.4 $\mu\text{g/mL}$, respectively.

3.5. In Vitro Anti-Inflammatory Testing

The experiment for measuring superoxide anion generation and elastase release were manipulated according to previously reported method [28,32,33].

4. Conclusions

In conclusion, our further chemical investigation and biological evaluation on the EtOAc extract of the soft coral *L. varium* disclosed three new lobane and eight prenyleudesmane diterpenoids along with two known derivatives. Compound **1** is the first labane possessing a tetrahydrofuran ring at the end of the side chain, and displayed ability to inhibit elastase release in the absence of fMLF/CB. Compounds **2**, **4**, **12**, and **13**, in particular **12** and **13**, displayed the potential to be the leads for anti-inflammatory medicines. Our proposed stereospecific biosynthetic pathway can explain the common coexistence of both lobanes and prenyleudesmanes in the soft coral *L. varium*.

Supplementary Materials: HRESIMS, ^1H , ^{13}C , COSY, heteronuclear single quantum coherence spectroscopy (HSQC), HMBC, and NOESY spectra of new compounds **1–11** and ^1H NMR spectrum of MTPA ester of **1** are available online at <http://www.mdpi.com/1660-3397/18/4/223/s1>, Figure S1: HRESIMS spectrum of **1**, Figure S2: ^1H NMR spectrum of **1** in CDCl_3 at 400 MHz, Figure S3: ^{13}C NMR spectrum of **1** in CDCl_3 at 100 MHz, Figure S4: ^1H - ^1H COSY spectrum of **1** in CDCl_3 , Figure S5: HSQC spectrum of **1** in CDCl_3 , Figure S6: HMBC spectrum of **1** in CDCl_3 , Figure S7: NOESY spectrum of **1** in CDCl_3 , Figure S8: ^1H NMR spectrum of (*S*)-MTPA ester of **1** (**1a**) in CDCl_3 at 400 MHz, Figure S9: ^1H NMR spectrum of (*R*)-MTPA ester of **1** (**1b**) in CDCl_3 at 400 MHz, Figure S10: HRESIMS spectrum of **2**, Figure S11: ^1H NMR spectrum of **2** in CDCl_3 at 400 MHz, Figure S12: ^{13}C NMR spectrum of **2** in CDCl_3 at 100 MHz, Figure S13: ^1H - ^1H COSY spectrum of **2** in CDCl_3 , Figure S14: HSQC spectrum of **2** in CDCl_3 , Figure S15: HMBC spectrum of **2** in CDCl_3 , Figure S16: NOESY spectrum of **2** in CDCl_3 , Figure S17: HRESIMS spectrum of **3**, Figure S18: ^1H NMR spectrum of **3** in CDCl_3 at 500 MHz, Figure S19: ^{13}C NMR spectrum of **3** in CDCl_3 at 125 MHz, Figure S20: ^1H - ^1H COSY spectrum of **3** in CDCl_3 , Figure S21: HSQC spectrum of **3** in CDCl_3 , Figure S22: HMBC spectrum of **3** in CDCl_3 , Figure S23: NOESY spectrum of **3** in CDCl_3 , Figure S24: HRESIMS spectrum of **4**, Figure S25: ^1H NMR spectrum of **4** in CDCl_3 at 400 MHz, Figure S26: ^{13}C NMR spectrum of **4** in CDCl_3 at 100 MHz, Figure S27: ^1H - ^1H COSY spectrum of **4** in CDCl_3 , Figure S28: HSQC spectrum of **4** in CDCl_3 , Figure S29: HMBC spectrum of **4** in CDCl_3 , Figure S30: NOESY spectrum of **4** in CDCl_3 , Figure S31: HRESIMS spectrum of **5a** and **5b**, Figure S32: ^1H NMR spectrum of **5a** and **5b** acetone-*d*₆ at 500 MHz, Figure S33: ^{13}C NMR spectrum of **5a** and **5b** in acetone-*d*₆ at 125 MHz, Figure S34: ^1H - ^1H COSY spectrum of **5a** and **5b** in acetone-*d*₆, Figure S35: HSQC spectrum of **5a** and **5b** in acetone-*d*₆, Figure S36: HMBC spectrum of **5a** and **5b** in acetone-*d*₆, Figure S37: NOESY spectrum of **5a** and **5b** in acetone-*d*₆, Figure S38: HRESIMS spectrum of **6**, Figure S39: ^1H NMR spectrum of **6** in CDCl_3 at 400 MHz, Figure S40: ^{13}C NMR spectrum of **6** in CDCl_3 at 100 MHz, Figure S41: ^1H - ^1H COSY spectrum of **6** in CDCl_3 , Figure S42: HSQC spectrum of **6** in CDCl_3 , Figure S43: HMBC spectrum of **6** in CDCl_3 , Figure S44: NOESY spectrum of **6** in CDCl_3 , Figure S45: HRESIMS spectrum of **7**, Figure S46: ^1H NMR spectrum of **7** in CDCl_3 at 400 MHz, Figure S47: ^{13}C NMR spectrum of **7** in CDCl_3 at 100 MHz, Figure S48: ^1H - ^1H COSY spectrum of **7** in CDCl_3 , Figure S49: HSQC spectrum of **7** in CDCl_3 , Figure

S50: HMBC spectrum of **7** in CDCl₃, Figure S51: NOESY spectrum of **7** in CDCl₃, Figure S52: HRESIMS spectrum of **8**, Figure S53: ¹H NMR spectrum of **8** in CDCl₃ at 400 MHz, Figure S54: ¹³C NMR spectrum of **8** in CDCl₃ at 100 MHz, Figure S55: ¹H-¹H COSY spectrum of **8** in CDCl₃, Figure S56: HSQC spectrum of **8** in CDCl₃, Figure S57: HMBC spectrum of **8** in CDCl₃, Figure S58: NOESY spectrum of **8** in CDCl₃, Figure S59: HRESIMS spectrum of **9**, Figure S60: ¹H NMR spectrum of **9** in CDCl₃ at 400 MHz, Figure S61: ¹³C NMR spectrum of **9** in CDCl₃ at 100 MHz, Figure S62: ¹H-¹H COSY spectrum of **9** in CDCl₃, Figure S63: HSQC spectrum of **9** in CDCl₃, Figure S64: HMBC spectrum of **9** in CDCl₃, Figure S65: NOESY spectrum of **9** in CDCl₃, Figure S66: HRESIMS spectrum of **10**, Figure S67: ¹H NMR spectrum of **10** in CDCl₃ at 500 MHz, Figure S68: ¹³C NMR spectrum of **10** in CDCl₃ at 125 MHz, Figure S69: ¹H-¹H COSY spectrum of **10** in CDCl₃, Figure S70: HSQC spectrum of **10** in CDCl₃, Figure S71: HMBC spectrum of **10** in CDCl₃, Figure S72: NOESY spectrum of **10** in CDCl₃, Figure S73: HRESIMS spectrum of **11**, Figure S74: ¹H NMR spectrum of **11** in CDCl₃ at 500 MHz, Figure S75: ¹³C NMR spectrum of **11** in CDCl₃ at 125 MHz, Figure S76: ¹H-¹H COSY spectrum of **11** in CDCl₃, Figure S77: HSQC spectrum of **11** in CDCl₃, Figure S78: HMBC spectrum of **11** in CDCl₃, Figure S79: NOESY spectrum of **11** in CDCl₃.

Author Contributions: J.-H.S. designed and guided the whole experiment; C.-H.C. and T.-S.Y. isolated the compounds and performed structure elucidation; A.F.A. and Y.-C.L. performed structure elucidation and manuscript preparation; C.-Y.H. performed cytotoxicity assay; T.-L.H. performed the anti-inflammatory activity assay. All authors have read and agreed to the published version of the manuscript.

Funding: The research was funded by the Ministry of Science and Technology of Taiwan (MOST 102-2628-B-110-002-MY2, 104-2320-B-110-001-MY2, 105-2113-M-110-002- and 105-2811-M-110-013-) and the Deanship of Scientific Research at King Saud University, Saudi Arabia (RG-1440-127).

Acknowledgments: This work was mainly supported by grants from Ministry of Science and Technology (MOST 102-2628-B-110-002-MY2, 104-2320-B-110-001-MY2, 105-2113-M-110-002- and 105-2811-M-110-013-) awarded to J.-H.S., A.F.A. would like to extend appreciation to the Deanship of Scientific Research at King Saud University for further funding this work through research group RG-1440-127.

Conflicts of Interest: The authors declare no conflicts of interest.

References

1. Ahmed, A.F.; Teng, W.T.; Hung, C.Y.; Dai, C.F.; Hwang, T.L.; Sheu, J.H. Anti-inflammatory lobane and prenyleudesmane diterpenoids from the soft coral *Lobophytum varium*. *Mar. Drugs* **2017**, *15*, 300. [\[CrossRef\]](#) [\[PubMed\]](#)
2. Edrada, R.A.; Proksch, P.; Wray, V.; Witte, L.; van Ofwegen, L. Four new bioactive lobane diterpenes of the soft coral *Lobophytum pauciflorum* from Mindoro, Philippines. *J. Nat. Prod.* **1998**, *61*, 358–361. [\[CrossRef\]](#) [\[PubMed\]](#)
3. Dunlop, R.W.; Wells, R.J. Isolation of some novel diterpenes from a soft coral of the genus *Lobophytum*. *Aust. J. Chem.* **1979**, *32*, 1345–1351. [\[CrossRef\]](#)
4. Lakshmana Raju, B.; Subbaraju, G.V.; Bheemasankara Rao, C.; Trimurtulu, G. Two new oxygenated lobanes from a soft coral of *Lobophytum* species of the Andaman and Nicobar coasts. *J. Nat. Prod.* **1993**, *56*, 961–966. [\[CrossRef\]](#)
5. Hamada, T.; Kusumi, T.; Ishitsuka, M.O.; Kakisawa, H. Structures and absolute configurations of new lobane diterpenoids from the Okinawan soft coral *Sinularia flexibilis*. *Chem. Lett.* **1992**, *21*, 33–36. [\[CrossRef\]](#)
6. Govindam, S.V.; Yoshioka, Y.; Kanamoto, A.; Fujiwara, T.; Okamoto, T.; Ojika, M. Cyclolobatriene, a novel prenylated germacrene diterpene, from the soft coral *Lobophytum pauciflorum*. *Bioorg. Med. Chem.* **2012**, *20*, 687–692. [\[CrossRef\]](#)
7. Minh, C.V.; Kiem, P.V.; Nhiem, N.X.; Cuong, N.X.; Thao, N.P.; Nam, N.H.; Anh, H.L.T.; Thung, D.C.; Thuy, D.T.T.; Kang, H.K.; et al. Cytotoxic and antioxidant activities of diterpenes and sterols from the Vietnamese soft coral *Lobophytum compactum*. *Bioorg. Med. Chem. Lett.* **2011**, *21*, 2155–2159. [\[CrossRef\]](#)
8. Li, L.; Sheng, L.; Wang, C.Y.; Zhou, Y.B.; Huang, H.; Li, X.B.; Li, J.; Mollo, E.; Gavagnin, M.; Guo, Y.W. Diterpenes from the Hainan soft coral *Lobophytum cristatum* Tixier-Durivault. *J. Nat. Prod.* **2011**, *74*, 2089–2094. [\[CrossRef\]](#)
9. Coll, J.C.; Bowden, B.F.; König, G.M.; Braslau, R.; Price, I.R. Studies of Australian soft corals. XXXX.1 The natural products chemistry of Alcyonacean soft corals with special reference to the genus *Lobophytum*. *Bull. Soc. Chim. Belg.* **1986**, *95*, 815–834. [\[CrossRef\]](#)
10. Matthee, G.F.; König, G.M.; Wright, A.D. Three new diterpenes from the marine soft coral *Lobophytum crassum*. *J. Nat. Prod.* **1998**, *61*, 237–240. [\[CrossRef\]](#)

11. Bowden, B.F.; Coll, J.C.; Liyanage, N.; Mitchell, S.J.; Stokie, G.J.; van Altena, I. A novel bicyclic diterpene was obtained from a soft coral *Lobophytum hedleyi*. *Aust. J. Chem.* **1978**, *31*, 163–170. [\[CrossRef\]](#)
12. Chao, C.H.; Wen, Z.H.; Wu, Y.C.; Yeh, Y.C.; Sheu, J.H. Cytotoxic and anti-inflammatory cembranoids from the soft coral *Lobophytum crassum*. *J. Nat. Prod.* **2008**, *71*, 1819–1824. [\[CrossRef\]](#) [\[PubMed\]](#)
13. Lee, N.L.; Su, J.H. Tetrahydrofuran cembranoids from the cultured soft coral *Lobophytum crassum*. *Mar. Drugs* **2011**, *9*, 2526–2536. [\[CrossRef\]](#)
14. Roy, P.K.; Roy, S.; Ueda, K. New cytotoxic cembranolides from an Okinawan soft coral, *Lobophytum* sp. *Fitoterapia* **2019**, *136*, 104162. [\[CrossRef\]](#) [\[PubMed\]](#)
15. Rashid, M.A.; Gustafson, K.R.; Boyd, M.R. HIV-inhibitory cembrane derivatives from a Philippines collection of the soft coral *Lobophytum* species. *J. Nat. Prod.* **2000**, *63*, 531–533. [\[CrossRef\]](#) [\[PubMed\]](#)
16. Kao, C.Y.; Su, J.H.; Lu, M.C.; Hwang, T.L.; Wang, W.H.; Chen, J.J.; Sheu, J.H.; Kuo, Y.H.; Weng, C.F.; Fang, L.S.; et al. New cembrane-type diterpenoids from the soft coral *Lobophytum crassum*. *Mar. Drugs* **2011**, *9*, 1319–1331. [\[CrossRef\]](#) [\[PubMed\]](#)
17. Lai, K.H.; You, Y.J.; Lin, C.C.; El-Shazly, M.; Liao, Z.J.; Su, J.H. Anti-Inflammatory cembranoids from the soft coral *Lobophytum crassum*. *Mar. Drugs* **2017**, *15*, 327. [\[CrossRef\]](#)
18. Thao, N.P.; Luyen, B.T.T.; Ngan, N.T.T.; Song, S.B.; Cuong, N.X.; Nam, N.H.; Kiem, P.V.; Kim, Y.H.; Minh, C.V. New anti-inflammatory cembranoid diterpenoids from the Vietnamese soft coral *Lobophytum crassum*. *Bioorg. Med. Chem. Lett.* **2014**, *24*, 228–232. [\[CrossRef\]](#)
19. Kusumi, T.; Hamada, T.; Ishitsuka, M.O.; Ohtani, I.; Kakisawa, H. Elucidation of the relative and absolute stereochemistry of lobatriene, a marine diterpene, by a modified Mosher method. *J. Org. Chem.* **1992**, *57*, 1033–1035. [\[CrossRef\]](#)
20. Peng, C.-C.; Huang, C.-Y.; Ahmed, A.F.; Hwang, T.-L.; Dai, C.-F.; Sheu, J.-H. New cembranoids and a biscembranoid peroxide from the soft coral *Sarcophyton cheronnieri*. *Mar. Drugs* **2018**, *16*, 276. [\[CrossRef\]](#)
21. Ohtani, I.; Kusumi, T.; Kashman, Y.; Kakisawa, H. High-Field FT NMR application of Mosher's Method. The absolute configurations of marine terpenoids. *J. Am. Chem. Soc.* **1991**, *113*, 4092–4096. [\[CrossRef\]](#)
22. Hiroyuki, K.; Satoshi, T.; Shun-ichi, T.; Yoshihara, T.; Sakamura, S.; Shimanuki, T.; Sato, T.; Tajimi, A. New fungitoxic sesquiterpenoids, chokols A-G, from stromata of *Epichloe typhina* and the absolute configuration of chokol E. *Agric. Biol. Chem.* **1989**, *53*, 789–796. [\[CrossRef\]](#)
23. Pérez Morales, C.; Catalán, J.; Domingo, V.; González Delgado, J.A.; Dobado, J.A.; Herrador, M.M.; Quilez del Moral, J.F.; Barrero, A.F. Protecting-group-free synthesis of chokols. *J. Org. Chem.* **2011**, *76*, 2494–2501. [\[CrossRef\]](#) [\[PubMed\]](#)
24. Shin, J.; Fenical, W. Fuscoides A-D: Anti-inflammatory diterpenoid glycosides of new structural classes from the caribbean gorgonian *Eunicea fusca*. *J. Org. Chem.* **1991**, *56*, 3153–3158. [\[CrossRef\]](#)
25. O'Brien, J.; Wilson, I.; Orton, T.; Pognan, F. Investigation of the Alamar Blue (resazurin) fluorescent dye for the assessment of mammalian cell cytotoxicity. *Eur. J. Biochem.* **2000**, *267*, 5421–5426. [\[CrossRef\]](#)
26. Nakayama, G.R.; Caton, M.C.; Nova, M.P.; Parandoosh, Z. Assessment of the Alamar Blue assay for cellular growth and viability in vitro. *J. Immunol. Methods* **1997**, *204*, 205–208. [\[CrossRef\]](#)
27. Hwang, T.L.; Yeh, S.H.; Leu, Y.L.; Chern, C.Y.; Hsu, H.C. Inhibition of superoxide anion and elastase release in human neutrophils by 3'-isopropoxychalcone via a cAMP-dependent pathway *Br. J. Pharmacol.* **2006**, *148*, 78–87.
28. Hwang, T.L.; Su, Y.C.; Chang, H.L.; Leu, Y.L.; Chung, P.J.; Kuo, L.M.; Chang, Y.J. Suppression of superoxide anion and elastase release by C18 unsaturated fatty acids in human neutrophils. *J. Lipid Res.* **2009**, *50*, 1395–1408. [\[CrossRef\]](#)
29. De Kraker, J.W.; Franssen, M.C.R.; de Groot, A.; König, W.A.; Bouwmeester, H.J. (+)-Germacrene a biosynthesis: The committed step in the biosynthesis of bitter sesquiterpene lactones in chicory. *Plant Physiol.* **1998**, *117*, 1381–1392. [\[CrossRef\]](#)
30. Cheng, S.Y.; Chuang, C.T.; Wang, S.K.; Wen, Z.H.; Chiou, S.F.; Hsu, C.H.; Dai, C.F.; Duh, C.Y. Antiviral and anti-inflammatory diterpenoids from the soft coral *Simularia gyrosa*. *J. Nat. Prod.* **2010**, *73*, 1184–1187. [\[CrossRef\]](#)
31. Ye, F.; Zhu, Z.D.; Gu, Y.C.; Li, J.; Zhu, W.L.; Guo, Y.W. Further New Diterpenoids as PTP1B Inhibitors from the Xisha Soft Coral *Simularia polydactyla*. *Mar. Drugs* **2018**, *16*, 103. [\[CrossRef\]](#) [\[PubMed\]](#)

32. Yang, S.C.; Chung, P.J.; Ho, C.M.; Kuo, C.Y.; Hung, M.F.; Huang, Y.T.; Chang, W.Y.; Chang, Y.W.; Chan, K.H.; Hwang, T.L. Propofol inhibits superoxide production, elastase release, and chemotaxis in formyl peptide-activated human neutrophils by blocking formyl peptide receptor 1. *J. Immunol.* **2013**, *190*, 6511–6519. [[CrossRef](#)] [[PubMed](#)]
33. Yu, H.P.; Hsieh, P.W.; Chang, Y.J.; Chung, P.J.; Kuo, L.M.; Hwang, T.L. 2-(2-Fluorobenzamido)benzoate ethyl ester (EFB-1) inhibits superoxide production by human neutrophils and attenuates hemorrhagic shock-induced organ dysfunction in rats. *Free Radic. Biol. Med.* **2011**, *50*, 1737–1748. [[CrossRef](#)] [[PubMed](#)]



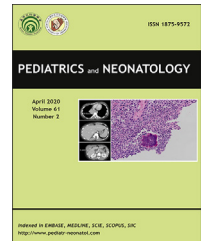
© 2020 by the authors. Licensee MDPI, Basel, Switzerland. This article is an open access article distributed under the terms and conditions of the Creative Commons Attribution (CC BY) license (<http://creativecommons.org/licenses/by/4.0/>).



Available online at www.sciencedirect.com

ScienceDirect

journal homepage: <http://www.pediatr-neonatal.com>



Original Article

Investigation and successful control of an echovirus 11 outbreak in neonatal intensive care units



Sheng-Yuan Ho^{a,b}, Cheng-Hsun Chiu^{c,d}, Yhu-Chering Huang^{c,d},
Chih-Jung Chen^{c,d}, Reyin Lien^{b,c}, Shih-Ming Chu^{b,c},
Chung-Guei Huang^{e,f,g}, Kuo-Chien Tsao^{e,g},
Shin-Ru Shih^{e,f,g,h,i,j}, Jen-Fu Hsu^{b,c,*}

^a Department of Pediatrics, Tri-Service General Hospital, National Defense Medical Center, Taipei, Taiwan

^b Division of Neonatology, Department of Pediatrics, Chang Gung Memorial Hospital, Taoyuan, Taiwan

^c College of Medicine, Chang Gung University, Taoyuan, Taiwan

^d Division of Pediatric Infectious Disease, Department of Pediatrics, Chang Gung Memorial Hospital, Taoyuan, Taiwan

^e Research Center for Emerging Viral Infections, Chang Gung University, Taoyuan, Taiwan

^f Graduate Institute of Biomedical Sciences, Department of Medical Biotechnology and Laboratory Science, College of Medicine, Chang Gung University, Taoyuan, Taiwan

^g Department of Laboratory Medicine, Linkou Chang Gung Memorial Hospital, Taoyuan, Taiwan

^h Research Center for Chinese Herbal Medicine, College of Human Ecology, Chang Gung University of Science and Technology, Taoyuan, Taiwan

ⁱ Research Center for Food and Cosmetic Safety, College of Human Ecology, Chang Gung University of Science and Technology, Taoyuan, Taiwan

^j Graduate Institute of Health Industry Technology, College of Human Ecology, Chang Gung University of Science and Technology, Taoyuan, Taiwan

Received Aug 5, 2019; received in revised form Sep 18, 2019; accepted Sep 24, 2019

Available online 4 October 2019

Key Words

echovirus 11;
outbreak;
neonatal intensive
care unit

Background: Echovirus 11 emerged as a predominant enterovirus strain and was associated with neonatal mortalities in Taiwan in 2018. We investigated an echovirus 11 outbreak in the neonatal intensive care units (NICUs) in a tertiary hospital in northern Taiwan and analyzed infection control efforts.

Methods: Between May and June 2018, an outbreak of 10 infants with echovirus 11 infections occurred in the NICUs. Comprehensive surveillance, including virus isolation, real-time reverse

* Corresponding author. Division of Pediatric Neonatology, Department of Pediatrics, Chang Gung Memorial Hospital, College of Medicine, Chang Gung University No. 5, Fushing St, Guishan Dist, Taoyuan City 333, Taiwan. Fax: +886 3 3288957.

E-mail address: jeff0724@gmail.com (J.-F. Hsu).

transcription-polymerase chain reaction (RT-PCR), and consequential degenerate hybrid oligonucleotide primer (CODEHOP) methods, were arranged for specimens (rectal or throat swabs), which were obtained from all contacts, newly admitted cases, and suspected cases during the outbreak since June 2.

Results: Ten cases were identified with echovirus 11 infection in this outbreak. Eight of these 10 confirmed cases were identified by viral isolation, and the remaining two cases were identified by RT-PCR surveillance. In addition to confirmed cases, the surveillance of 19 contacts, 47 newly admitted cases, and nine suspected cases showed negative results. All confirmed cases eventually recovered.

Conclusion: RT-PCR and CODEHOP methods significantly shorten the time of laboratory diagnosis of enterovirus infection compared with conventional methods. The outbreak of echovirus 11 in the NICUs was caused by three imported cases and was successfully controlled by the implementation of isolation, rapid surveillance, reinforced disinfection, and infection control measures.

Copyright © 2019, Taiwan Pediatric Association. Published by Elsevier Taiwan LLC. This is an open access article under the CC BY-NC-ND license (<http://creativecommons.org/licenses/by-nc-nd/4.0/>).

1. Introduction

Enterovirus (EV) infection is one of the most frequent viral outbreaks in neonatal intensive care units (NICUs)¹ and nurseries.² However, the majority of infants who acquired nonpolio EVs were asymptomatic or had a mild infection; infants who acquired severe EV infection still had high mortality rates.^{3–5} Severe neonatal EV infection is difficult to differentiate from severe bacterial infection, which leads to unnecessary interventions and antibiotics exposure. The predominant types of severe neonatal EV infection included echovirus 11, coxsackieviruses B2-5, and parechovirus 3 in previous research.⁵

Echovirus 11, which is categorized into nonpolio enteroviruses, is one of the predominant causative agents of epidemics of EV infection in nurseries.^{2,4,6–11} However, the outbreaks of echovirus 11 infections have rarely been reported in the NICU.¹² This article reports an outbreak of echovirus 11, which led to EV control efforts that occurred in the NICUs and intermediate care units (IMCUs) of a tertiary hospital in northern Taiwan. The identification of the outbreak on May 31 led to the quick implementation of infection control measures in the hospital. We also highlight the impact of infection control measures on healthcare-associated EV infection and the results of molecular epidemiologic surveillance.

2. Patients and methods

2.1. Study populations

This was a retrospective study, including three NICUs (referred to as A, B, and C) and two IMCUs (referred to below as D and E), which could accommodate up to 47 and 54 patients, respectively, at Chang Gung Memorial Hospital in northern Taiwan between the months of May and June, 2018 (Fig. 1). Each area has six to 10 facilities that allow healthcare workers to practice hand hygiene and alcohol-

based hand rub is accessible at the point of care at each bedside. Admissions to NICUs A, B, and C were more critical cases than those in other areas, and we adjusted the patient's admission area according to the clinical condition. This study was approved by the Chang Gung Memorial Hospital Institutional Review Board (IRB#201801167A3).

A confirmed case was defined as an infant within 3 months of age in our IMCUs or NICUs who presented with symptoms with laboratory-confirmed echovirus 11. A case of healthcare-associated EV infection was defined as disease onset 3 days after admission. The definition of severe complicated EV infection, which was modified from the definition provided by the committee of the Taiwan Society of Neonatology and Taiwan Centers for Disease Control (CDC) in 2016, included confirmed cases meeting one of the following criteria: (1) myocarditis or pericarditis; (2) hepatitis with coagulopathy; (3) encephalitis; (4) pneumonia complicated with respiratory failure; and (5) sepsis and excluded other common pathogens. Hepatitis with coagulopathy was defined as a serum aspartate aminotransferase (AST) level higher than three times the upper limit of normal, thrombocytopenia (platelet count $<10^5/\text{mm}^3$), and prolonged prothrombin time/activated partial thromboplastin time.¹³ Myocarditis was defined as ejection fraction $<50\%$ on echocardiography, arrhythmia, or an elevation in the serum level of the cardiac fraction of creatine kinase or troponin-I, which couldn't be explained by other reasons.

2.2. The outbreak

On May 31, a clinician reported a probable echovirus 11 outbreak in both the NICUs and IMCUs to the infection control department and national public health authorities, with ten patients affected. A Hospital Emergency Response Team was then organized to manage the situation, initiate the epidemiological investigation, and implement infection control measures on May 31. The epidemiological investigation led to the retrospective identification of three potential cases, which might be responsible for this outbreak

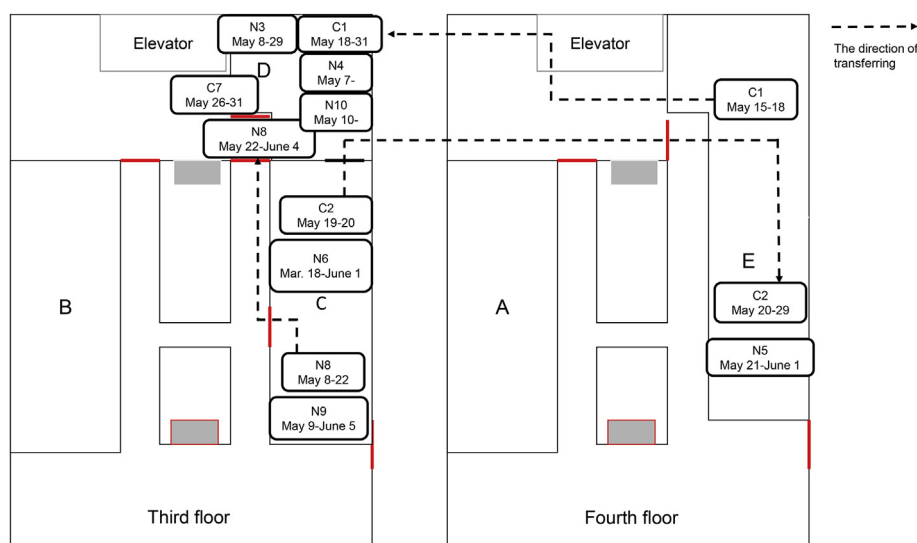


Figure 1 There are three NICUs (referred to as follows as A, B and C) and two IMCUs (referred to below as D and E) in Chang Gung Memorial Hospital. The way of transferring, hospitalization locations and hospitalized time of the 10 confirmed cases, of which three were community transmission (C1, 2, 7) and seven were healthcare-associated transmission (N3-6, 8–10), with echovirus 11 infection are shown. (NICU, neonatal intensive care unit; IMCU, intermediate care unit).

in our NICU. Case 1 (index case 1) was an outborn neonate and presented with fever on May 15. Echovirus 11 infection of Case 1 was identified on May 21. The secondary imported index case was Case 2, a 1-day-old outborn neonate, who was admitted to the NICU in area C because of petechiae on May 19. Fever and oral ulcer were found in Case 2 on May 23, and echovirus 11 infection was identified on May 29. These two index cases were investigated for viral infection on the day of admission but were not placed in isolated rooms. The index cases were transferred extensively in our NICUs and IMCUs while transmissible. The third imported index case, Case 7, was a 1-month-old infant who presented with fever and emesis two days before admission. All index cases were born in different clinics and had no relationship in the community before admission. Cases 3–6 were cared for in close proximity to the index cases during this epidemic. Inpatient Case 9 was only exposed to Case 6 during the incubation period. We could not identify the epidemiological links of Case 6 and Case 10 because of multiple infectious cases in the later periods. Case 10 was identified by rapid screening on June 4 and presented with symptoms on June 7. Patient transfers and the dates of hospitalization are shown in Fig. 1. The epidemic curve indicating the dates of onset of echovirus 11 infections, and the dates of interventions are shown in Fig. 2. Therefore, no further cases have been identified or linked to this hospital setting after interventions (described below) were conducted in June.

2.3. Clinical investigation and intervention

An isolation area was created in part of area D to evaluate possible and confirmed cases in the IMCUs after the on-site inspection on May 31. Bundle implementation, including hand washing (with povidone-iodine and water, and bedside disinfectant with 75% ethanol then 95% ethanol for 20–30 s), glove and isolation gown use, was reinforced to

healthcare workers and visitors. Only one visitor was allowed, and the entrance of people with EV-associated symptoms was prohibited during this epidemic. In addition, patient transfers were restricted to the same floor. The infection control practitioners conducted strict monitoring of hand hygiene and provided feedback to improve compliance with outbreak control measures. The environment was disinfected with a 1:100 dilution of sodium hypochlorite with a concentration of 500 ppm for 10 min every day. Pacifiers and baby bottles that had been used by confirmed cases were concentrated for pasteurization and were not shared with others. Quarantine measures and rapid screening tools with real-time RT-PCR surveillance (described below) were applied to 19 contacts, 47 quarantined, and nine possible cases between June 2 and June 15, 2018.

2.4. Laboratory investigations

Specimens (cerebrospinal fluid [CSF], rectal or throat swabs, and similar items) were collected from cases admitted to our neonatal units and sent to our laboratory. In the laboratory confirmation process, samples are isolated and identified by viral isolation and immunofluorescence assay (IFA), real-time reverse transcription-polymerase chain reaction (RT-PCR), or consensus degenerate hybrid oligonucleotide primer (CODEHOP) detection of EV. Virus isolation and identification with an indirect IFA was performed by the methods provided in detail previously.^{14,15} Pan-Enterovirus RT-PCR was used for specimens from the throat and rectal swabs since June 2. Viral RNA was extracted from the clinical specimens using a Viral RNA Extraction Mini Kit (QIAgen, Germany). An RT-PCR procedure was applied, and PCR amplification was performed using Pan-Enterovirus primers as previously described.^{16,17} Pan-Enterovirus RT-PCR was replaced by CODEHOP methods since June 6. The EV VP1 gene was amplified by

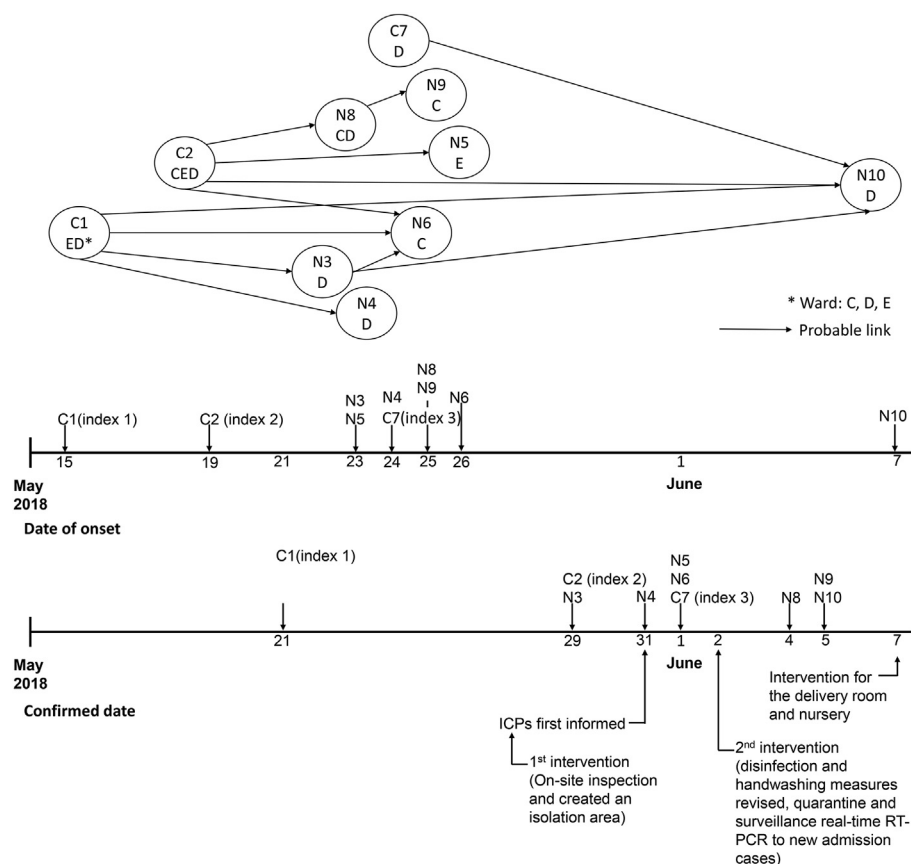


Figure 2 Epidemiologic curve indicating the date of interventions, the date of onset, and the date of confirmed echovirus 11 infection from 10 patients, of which three were community transmission (C1, 2, 7) and seven were healthcare-associated transmission (N3–6, 8–10) in neonatal units in one tertiary hospital, northern Taiwan, May–June, 2018. (ICP, infection control practitioner; RT-PCR, reverse transcription-polymerase chain reaction).

VP1 RT-snPCR from each of these extracted RNA templates. The amplified DNA was sequenced using an ABI 3730 XL DNA Analyzer (Applied Biosystem Inc., Foster City, CA). Nucleotide sequences of the partial VP1 gene were analyzed and aligned, as described in detail previously.^{15,17,18}

3. Results

3.1. Descriptive epidemiology

The 10 confirmed patients had a mean age of onset of 21.5 days (interquartile range [IQR]: 13.8–59.3 days), mean gestational age of 35 weeks (IQR: 32–39 weeks), and mean birth weight of 2007.5 g (IQR: 1552.5–3165.0 g). Detailed demographic data are summarized in Table 1. The common manifestations included fever (80%), and tachycardia or bradycardia (70%). Elevated serum C-reactive protein concentrations (>15.8 mg/l) were noted in eight cases (80%), whereas thrombocytopenia was found in three infants (30%). Only Case 1 met the definition of neonatal EV infection with severe complications (hepatitis with coagulopathy), and immunoglobulin (1 g/kg/dose) was administered intravenously. One case developed acute myocarditis, and five cases developed meningitis. Among the ten confirmed cases, the infection source of the three

index cases was almost certainly from the community, and the remaining seven were healthcare-associated infections. All patients survived.

3.2. Laboratory investigations

Eight cases with echovirus 11 infections (Cases 1–8) were subjected to viral isolation. Among Cases 1–8, four were detected from throat swabs, five were detected from rectal swabs, and five were detected from CSF samples. Another nine suspected cases received Pan-Enterovirus RT-PCR or the CODEHOP method. Only Case 9 was identified from a rectal swab using Pan-Enterovirus RT-PCR, and Case 10 was identified from a rectal swab by the CODEHOP method. The viral studies of the 10 confirmed neonates in this outbreak are shown in Table 1. Besides confirmed cases, 19 hospitalized contacts and 47 quarantined cases in NICUs and IMCUs were screened by real-time RT-PCR between May 31 and June 15, which showed negative findings.

3.3. Further interventions

3.3.1. Rapid screening and quarantine measures

New patient admissions were suspended until the quarantine areas in IMCUs of areas D and E were established on

Table 1 Demographic data and laboratory results of the ten echovirus 11 infected infants.

Case	Sex	GA (wk)	Birth wt (g)	Date of Admission	Date of Onset	Age at Onset (days)	Date of Laboratory Confirmation	Laboratory Investigation			Clinical Manifestations
								Viral isolation	Pan-EV PCR	CODEHOP	
C1	M	38	3120	May 15	May 15	7	May 21	U(+), T(-), CSF(+)	NM	NM	Fever, hepatitis, coagulopathy, thrombocytopenia, tachycardia
C2	M	40	3300	May 19	May 19	1	May 29	T(+), R(+), CSF(+)	NM	NM	Fever, oral ulcer, petechiae, thrombocytopenia
N3	F	36	1876	May 3	May 23	57	May 29	T(+), R(+)	NM	NM	Fever, apnea, cyanosis
N4	M	33	2200	May 7	May 24	17	May 31	CSF(+)	NM	NM	Fever, tachycardia
N5	F	27	618	Mar. 18	May 23	66	June 1	T(+), R(+), CSF(+)	NM	NM	Fever, poor activity, tachycardia
N6	M	27	1140	Feb. 25	May 26	90	June 1	T(+), R(+)	NM	NM	Fever, tachycardia
C7	M	40	3505	May 26	May 24	38	June 1	R(+)	NM	NM	Fever, cough
N8	M	35	2075	May 8	May 25	17	June 4	CSF(+)	T(-)	NM	Fever
N9	M	34	1940	May 9	May 25	16	June 5	R(+)	T(-), R(+)	NM	Feeding intolerance, apnea, cyanosis, tachycardia, thrombocytopenia
N10	F	33	1690	May 10	June 7	26	June 5	NM	T(-)	T(+)	Feeding intolerance, apnea, bradycardia, cyanosis, emesis

CODEHOP, consequential degenerate hybrid oligonucleotide primer; CSF, cerebrospinal fluid; EV, enterovirus; GA, gestational age; NM, not measured; RT-PCR, reverse transcription-polymerase chain reaction; T, throat; U, urine; R, rectum.

June 2. To reduce the source of community infection, extra beds were set up in general wards to receive the non-critical outborn neonates. New critical patients of admission to the NICUs of area A, B, and C were quarantined in situ. Throat and rectal swabs from all new cases were investigated with real-time RT-PCR surveillance. If the result of real-time RT-PCR was negative, the case could come out of quarantine. However, if a case had EV-associated presentations, additional virus isolation had to be tested and kept quarantined until the negative result of viral isolation was confirmed. Our team reviewed the results of rapid screening tests daily. We have known that EV can be detected from feces for up to two months,¹⁹ so two months isolation is recommended for confirmed cases who require long-term hospitalization. The comprehensive screening of new admission cases was terminated on June 15, which was the date of diagnosis of the last confirmed case plus a maximum incubation period of 10 days. The neonatal division provided up-to-date EV epidemic information from national and hospital sources weekly and established standard quarantine measures (Supplementary Figures S1 and S2) based on the experience learned from this outbreak.

3.3.2. Hospital information system settings

Confirmed cases or patients who were exposed from May 15 to June 1 were all noted as EV contacts in the information system for tracking by the emergency department or outpatient department. These patients were followed up by clinicians one week later after being discharged. The

hospital sent out text messages about the newly confirmed results of cases with EV infection to healthcare workers via cellphone and the information system immediately.

3.3.3. Infection control measures for the delivery room and nursery

Infection control measures were conducted at the nursery and delivery room to prevent the risk of EV vertical transmission from mothers. Care from the same visitor during the hospitalization was advised. We designed a questionnaire, including three questions, to be filled out by each mother (Table 2). If the mother answered "Yes" to one of these three questions, her neonate was quarantined in an isolation area in the nursery. Control measures and device disinfection were as same as the isolation areas in NICUs. Breastfeeding and rooming-in were prohibited. Posters were created to raise public awareness of EV infection in the delivery room and the nursery. Neonates, who became symptomatic, were transferred to the quarantined areas of the NICUs or IMCUs. During this epidemic, 52 cases were quarantined in the nursery, and there were no confirmed cases of EV infection.

4. Discussion

This investigation is the first study of an echovirus 11 outbreak in NICUs in Taiwan in 2018, and the source of this outbreak could be traced back to three community cases. There are two possible causes for the outbreak in this

Table 2 Survey questionnaire for a parturient woman during the prevalent season of enterovirus infection.

	Item	Yes	No
1.	Have you or the family members you live with had any of the following symptoms: fever, abdominal pain, cough, runny nose, chest pain, in the last two weeks?	<input type="checkbox"/>	<input type="checkbox"/>
2.	Have your other children been infected with the enterovirus in the last two weeks?	<input type="checkbox"/>	<input type="checkbox"/>
3.	Have you been exposed to patients with the enterovirus infection in the last two weeks?	<input type="checkbox"/>	<input type="checkbox"/>

Table is modified from the "Recommendations for the Prevention of Enterovirus Infection" of the Infectious Diseases Society of Taiwan and Child Health Research Center of National Health Research Institute of Taiwan.

study. First, it is challenging to differentiate presentations of neonatal EV infection from other common diseases (e.g., sepsis, respiratory distress syndrome, and transient tachypnea of newborns). Without tools for rapid surveillance, healthcare workers may ignore the possibility of EV infection. Second, some healthcare workers seemed to underestimate the attack rate of this outbreak and delayed the implementation of stricter isolation and control measures. The neonate's ability to respond to infections is limited, so they may be susceptible to contracting EV infection and have a higher risk of EV outbreak in NICUs.^{20–22} In this outbreak, index cases from the community were not adequately isolated. The echovirus 11 might have subsequently spread to another seven cases because contacts were cared for by the same healthcare workers during the same shift as index cases. Therefore, reinforcing stricter isolation and setting up a quarantine area in general wards to receive non-critical outborn neonates would be an effective control measure to reduce the possible infection sources from the community during this epidemic. During the prevalent seasons of EV from April to October, healthcare workers should inquire about perinatal events, contact history, and EV-related manifestations by continuous medical education on infection control issues.

EV infection is common in pregnant women, and up to 42% of pregnant women were found to be infected with EVs in a serology study.²³ Neonates can acquire EV transmission in uterine, intrapartum, or postpartum through contact with feces and mucosal secretions,²⁴ with an average incubation period of 3–10 days.²⁵ EV is most infectious within one week after the onset of disease,^{26,27} and can be shed in feces for as long as 8–12 weeks.¹⁹ Neonates with disease onset between one and seven days of life may have acquired EV infection from vertical transmission with majority of intrapartum exposure.^{5,28,29} Therefore, the two cases of community infections, Case 1 and Case 2, with disease onset on days 1 and 7 of life were classified as vertical transmissions in this outbreak. Case 7 (index 3) developed symptoms before admission. The other seven cases were eligible for secondary infection. Contagious viral shedding was detected before the onset of symptoms as previously mentioned,^{26,27} so rapid surveillance was performed in all quarantined cases during this epidemic. The neonatal EV infection also could be transmitted via infected parents during rooming-in³⁰ or via breastfeeding in some studies.^{31,32} Therefore, rooming-in and breastfeeding were prohibited from the quarantined neonates in the nursery during this outbreak in our hospital. Using sodium

hypochlorite as an environmental disinfectant is known to be effective.³³ In addition to handwashing with soap and water, past research has confirmed that the use of gloves and 90%–95% alcohol-based hand rub offer benefits in compliance and effectiveness.^{34,35} The same strategy for hand and environmental disinfection was conducted in this outbreak and seemed successful. As of September 14, 2018, 35 cases with neonatal echovirus 11 infection were notified at the national level on the surveillance system provided by the Taiwan CDC, with eight severely complicated cases. Echovirus 11 infection was prevalent in the community and was the predominant enterovirus type in northern Taiwan from the seventeenth to the thirty-first week (April 22 to August 4) of 2018, and we also found a similar trend from the laboratory database in our hospital (Fig. 3). We successfully stopped this outbreak in our NICUs by following infection control measures in the twenty-third week of 2018.

Echovirus 11 was the predominant serotype of severely complicated EV infection in Taiwan in 2018 through laboratory surveillance by the Taiwan CDC. As previously mentioned, echovirus 11 accounted for 14% of neonatal EV infections, of which 19% were fatal in the United States.⁹ Echovirus 11 outbreaks and the first case of a patient dying of echovirus 11 sepsis in Taiwan was reported in 2003.^{28,29} Among the last epidemics in 2003, an echovirus 11 outbreak was reported in an obstetric clinic in Taiwan, during which 13 infants were admitted to the NICU; one infant died, and one patient presented with fulminant hepatitis. The Taiwan CDC investigated the outbreak in the above obstetric clinic and found that echovirus 11 was also detected in two asymptomatic neonates.²⁹ Therefore, comprehensive surveillance for asymptomatic cases was also conducted in this study.

Previous studies confirmed that using the CODEHOP method as a tool for EV surveillance is more sensitive and saves time compared with virus isolation.^{17,18} Using the CODEHOP method, we can facilitate timely intervention as early as 48 h in cases with severe complications, and reduce unnecessary use of antibiotics and hospitalization. However, the cost of the CODEHOP method is higher than that of traditional methods. The use of the CODEHOP method as a comprehensive screening tool is not cost effective for asymptomatic cases because of all the negative results in this outbreak. Compared with comprehensive CODEHOP surveillance, early awareness of possible EV infection, strict quarantine and isolation, and implementation of hand hygiene may be more cost effective. Many studies have

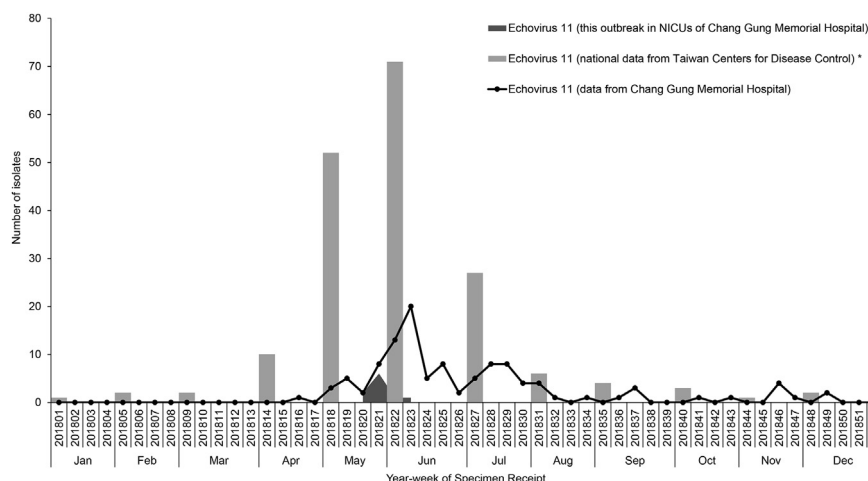


Figure 3 Chronological trend of weekly isolated echovirus 11 infection cases in Chang Gung Memorial Hospital and monthly isolated echovirus infection cases at the national level in Taiwan Centers for Disease Control in 2018. Data were from the laboratories of Chang Gung Memorial Hospital and Taiwan CDC. * National data from Taiwan CDC were presented as month of specimen receipt. (CDC, Centers for Disease Control).

documented that the 5' nontranslated region of the Pan-Enterovirus RT-PCR is more timesaving but less sensitive than the CODEHOP method for the detection of EV infection.^{17,36} In our study, only Case 10 received both the Pan-Enterovirus RT-PCR and CODEHOP methods. Echovirus 11 was detected by the CODEHOP method but revealed a negative result by Pan-Enterovirus RT-PCR in Case 10.

There are several limitations to this study. First, this was a retrospective study. No further phylogenetic analysis was performed to confirm the propagation path of this outbreak. Further molecular typing of isolated strains in this outbreak should be applied to confirm the propagation path subsequently. Second, the costs associated with outbreak control have not been estimated, but may be considerable.

In conclusion, RT-PCR and CODEHOP methods significantly shorten the time of laboratory diagnosis of EV infection compared with conventional methods but have higher medical expenses. Through a series of outbreak control measures, including epidemic investigation, stricter isolation, and the bundle implementation of disinfection and hand washing, we successfully stopped the spread of EV infection in this outbreak.

Declaration of Competing Interest

The authors declare no conflicts of interest.

References

- Civardi E, Tzialla C, Baldanti F, Strocchio L, Manzoni P, Stronati M. Viral outbreaks in neonatal intensive care units: what we do not know. *Am J Infect Control* 2013;41:854–6.
- Modlin JF. Perinatal echovirus infection: insights from a literature review of 61 cases of serious infection and 16 outbreaks in nurseries. *Rev Infect Dis* 1986;8:918–26.
- Morens DM. Enteroviral disease in early infancy. *J Pediatr* 1978; 92:374–7.
- Jenista JA, Powell KR, Menegus MA. Epidemiology of neonatal enterovirus infection. *J Pediatr* 1984;104:685–90.
- Abzug MJ. Presentation, diagnosis, and management of enterovirus infections in neonates. *Paediatr Drugs* 2004;6: 1–10.
- Piraino FF, Sedmak G, Raab K. Echovirus 11 infections of newborns with mortality during the 1979 enterovirus season in Milwaukee, Wis. *Public Health Rep* 1982;97:346–53.
- Bowen GS, Fisher MC, DeForest A, Thompson Jr CM, Kleger B, Friedman H. Epidemic of meningitis and febrile illness in neonates caused by ECHO type 11 virus in Philadelphia. *Pediatr Infect Dis* 1983;2:359–63.
- Chow CB, Chan KY, Tam A, Ho LC, Ho WY, Chang WK. Outbreak of echo virus type 11 infection in newborn infants in a maternity ward: clinical presentation. *J Trop Pediatr* 1987;33: 305–8.
- Khetsuriani N, Lamonte A, Oberste MS, Pallansch M. Neonatal enterovirus infections reported to the national enterovirus surveillance system in the United States, 1983–2003. *Pediatr Infect Dis J* 2006;25:889–93.
- Abedi GR, Watson JT, Pham H, Nix WA, Oberste MS, Gerber SI. Enterovirus and human parechovirus surveillance - United States, 2009–2013. *MMWR Morb Mortal Wkly Rep* 2015;64: 940–3.
- Cabrerizo M, Diaz-Cerio M, Muñoz-Almagro C, Rabella N, Tarragó D, Romero MP, et al. Molecular epidemiology of enterovirus and parechovirus infections according to patient age over a 4-year period in Spain. *J Med Virol* 2017;89: 435–42.
- Isaacs D, Dobson SR, Wilkinson AR, Hope PL, Eglin R, Moxon ER. Conservative management of an echovirus 11 outbreak in a neonatal unit. *Lancet* 1989;1:543–5.
- Lin TY, Kao HT, Hsieh SH, Huang YC, Chiu CH, Chou YH, et al. Neonatal enterovirus infections: emphasis on risk factors of severe and fatal infections. *Pediatr Infect Dis J* 2003;22: 889–94.
- Lin TL, Li YS, Huang CW, Hsu CC, Wu HS, Tseng TC, et al. Rapid and highly sensitive coxsackievirus a indirect immunofluorescence assay typing kit for enterovirus serotyping. *J Clin Microbiol* 2008;46:785–8.
- Chen YJ, Chang SC, Tsao KC, Shih SR, Yang SL, Lin TY, et al. Comparative genomic analysis of coxsackievirus A6 strains of different clinical disease entities. *PLoS One* 2012;7:e52432.

16. Tsao LY, Lin CY, Yu YY, Wang BT. Microchip, reverse transcription-polymerase chain reaction and culture methods to detect enterovirus infection in pediatric patients. *Pediatr Int* 2006;**48**:5–10.
17. Chiang PS, Huang ML, Luo ST, Lin TY, Tsao KC, Lee MS. Comparing molecular methods for early detection and serotyping of enteroviruses in throat swabs of pediatric patients. *PLoS One* 2012;**7**:e48269.
18. Chung WY, Chiang PS, Luo ST, Lin TY, Tsao KC, Lee MS. A molecular approach applied to enteroviruses surveillance in northern Taiwan, 2008-2012. *PLoS One* 2016;**11**:e0167532.
19. Chung PW, Huang YC, Chang LY, Lin TY, Ning HC. Duration of enterovirus shedding in stool. *J Microbiol Immunol Infect* 2001;**34**:167–70.
20. Risdon G, Gaddy J, Horie M, Broxmeyer HE. Alloantigen priming induces a state of unresponsiveness in human umbilical cord blood T cells. *Proc Natl Acad Sci U S A* 1995;**92**:2413–7.
21. Sautois B, Fillet G, Beguin Y. Comparative cytokine production by in vitro stimulated mononucleated cells from cord blood and adult blood. *Exp Hematol* 1997;**25**:103–8.
22. Tolar J, Hippen KL, Blazar BR. Immune regulatory cells in umbilical cord blood: T regulatory cells and mesenchymal stromal cells. *Br J Haematol* 2009;**147**:200–6.
23. Brown GC, Karunas RS. Relationship of congenital anomalies and maternal infection with selected enteroviruses. *Am J Epidemiol* 1972;**95**:207–17.
24. Tebruegge M, Curtis N. Enterovirus infections in neonates. *Semin Fetal Neonatal Med* 2009;**14**:222–7.
25. Zaoutis T, Klein JD. Enterovirus infections. *Pediatr Rev* 1998;**19**:183–91.
26. Haston JC, Dixon TC. Nonpolio enterovirus infections in neonates. *Pediatr Ann* 2015;**44**:e103–7.
27. Noor A, Krilov LR. Enterovirus infections. *Pediatr Rev* 2016;**37**: 505–15.
28. Hsiao CC, Tsao LY, Chen HN. Echovirus 11 sepsis in a neonate: report of one case. *Acta Paediatr Taiwan* 2003;**44**:104–5.
29. Chen JH, Chiu NC, Chang JH, Huang FY, Wu KB, Lin TL. A neonatal echovirus 11 outbreak in an obstetric clinic. *J Microbiol Immunol Infect* 2005;**38**:332–7.
30. Groneck P, Jahn P, Schuler-Lüttmann S, Beyrer K. Neonatal enterovirus meningitis: transmission via parents during rooming-in and current epidemiology in Germany. *Z Geburtshilfe Neonatol* 2011;**215**:1–5 [Article in German].
31. Chang ML, Tsao KC, Huang CC, Yen MH, Huang CG, Lin TY. Coxsackievirus B3 in human milk. *Pediatr Infect Dis J* 2006;**25**: 955–7.
32. Maus MV, Posencheg MA, Geddes K, Elkan M, Peñaranda S, Oberste MS, et al. Detection of echovirus 18 in human breast milk. *J Clin Microbiol* 2008;**46**:1137–40.
33. Narang HK, Codd AA. Action of commonly used disinfectants against enteroviruses. *J Hosp Infect* 1983;**4**:209–12.
34. Davies JG, Babb JR, Bradley CR, Ayliffe GA. Preliminary study of test methods to assess the virucidal activity of skin disinfectants using poliovirus and bacteriophages. *J Hosp Infect* 1993;**25**:125–31.
35. Chang SC, Li WC, Huang KY, Huang YC, Chiu CH, Chen CJ, et al. Efficacy of alcohols and alcohol-based hand disinfectants against human enterovirus 71. *J Hosp Infect* 2013;**83**:288–93.
36. Nix WA, Oberste MS, Pallansch MA. Sensitive, seminested PCR amplification of VP1 sequences for direct identification of all enterovirus serotypes from original clinical specimens. *J Clin Microbiol* 2006;**44**:2698–704.

Appendix A. Supplementary data

Supplementary data to this article can be found online at <https://doi.org/10.1016/j.pedneo.2019.09.012>.



Article

Glycofullerenes Inhibit Particulate Matter Induced Inflammation and Loss of Barrier Proteins in HaCaT Human Keratinocytes

Chiang-Wen Lee ^{1,2,3,4}, Yu-Han Su ⁵, Yao-Chang Chiang ^{1,2} , I-Ta Lee ⁶, Sin-Yu Li ^{1,2}, Hui-Chun Lee ^{2,7}, Lee-Fen Hsu ^{2,7,8}, Yi-Ling Yan ^{2,4}, Hsing-Yen Li ^{5,9}, Ming-Chun Chen ⁵, Kuo-Ti Peng ^{1,4,*} and Chian-Hui Lai ^{5,9,*}

¹ Department of Orthopaedic Surgery, Chang Gung Memorial Hospital, Puzi City, Chiayi County 61363, Taiwan; cwlee@gw.cgust.edu.tw (C.-W.L.); yaochang.chiang@gmail.com (Y.-C.C.); 0426cyndi@gmail.com (S.-Y.L.)

² Department of Nursing, Division of Basic Medical Sciences, and Chronic Diseases and Health Promotion Research Center, and Research Center for Chinese Herbal Medicine, Chang Gung University of Science and Technology, Puzi City, Chiayi County 61363, Taiwan; hcli@cgust.edu.tw (H.-C.L.); lfhsu@mail.cgust.edu.tw (L.-F.H.); iling410@hotmail.com (Y.-L.Y.)

³ Department of Safety Health and Environmental Engineering, Ming Chi University of Technology, New Taipei City 24301, Taiwan

⁴ College of Medicine, Chang Gung University, Guishan Dist., Taoyuan City 33303, Taiwan

⁵ Graduate Institute of Biomedical Engineering, National Chung Hsing University, Taichung 40227, Taiwan; goat2658@gmail.com (Y.-H.S.); black910255@gmail.com (H.-Y.L.); daniel0044789@gmail.com (M.-C.C.)

⁶ School of Dentistry, College of Oral Medicine, Taipei Medical University, Taipei 11031, Taiwan; itlee0128@tmu.edu.tw

⁷ Department of Respiratory Care, Chang Gung University of Science and Technology, Puzi City, Chiayi County 61363, Taiwan

⁸ Division of Neurosurgery, Department of Surgery, Chang Gung Memorial Hospital, Puzi City, Chiayi County 61363, Taiwan

⁹ Department of Medicinal and Applied Chemistry, Kaohsiung Medical University, Kaohsiung 80708, Taiwan

* Correspondence: mr3497@cgmh.org.tw (K.-T.P.); chianhuilai@dragon.nchu.edu.tw (C.-H.L.); Tel.: +886-5-53621000(ext. 2004) (K.-T.P.); +886-4-22840733 (ext. 634) (C.-H.L.)

Received: 18 February 2020; Accepted: 26 March 2020; Published: 28 March 2020



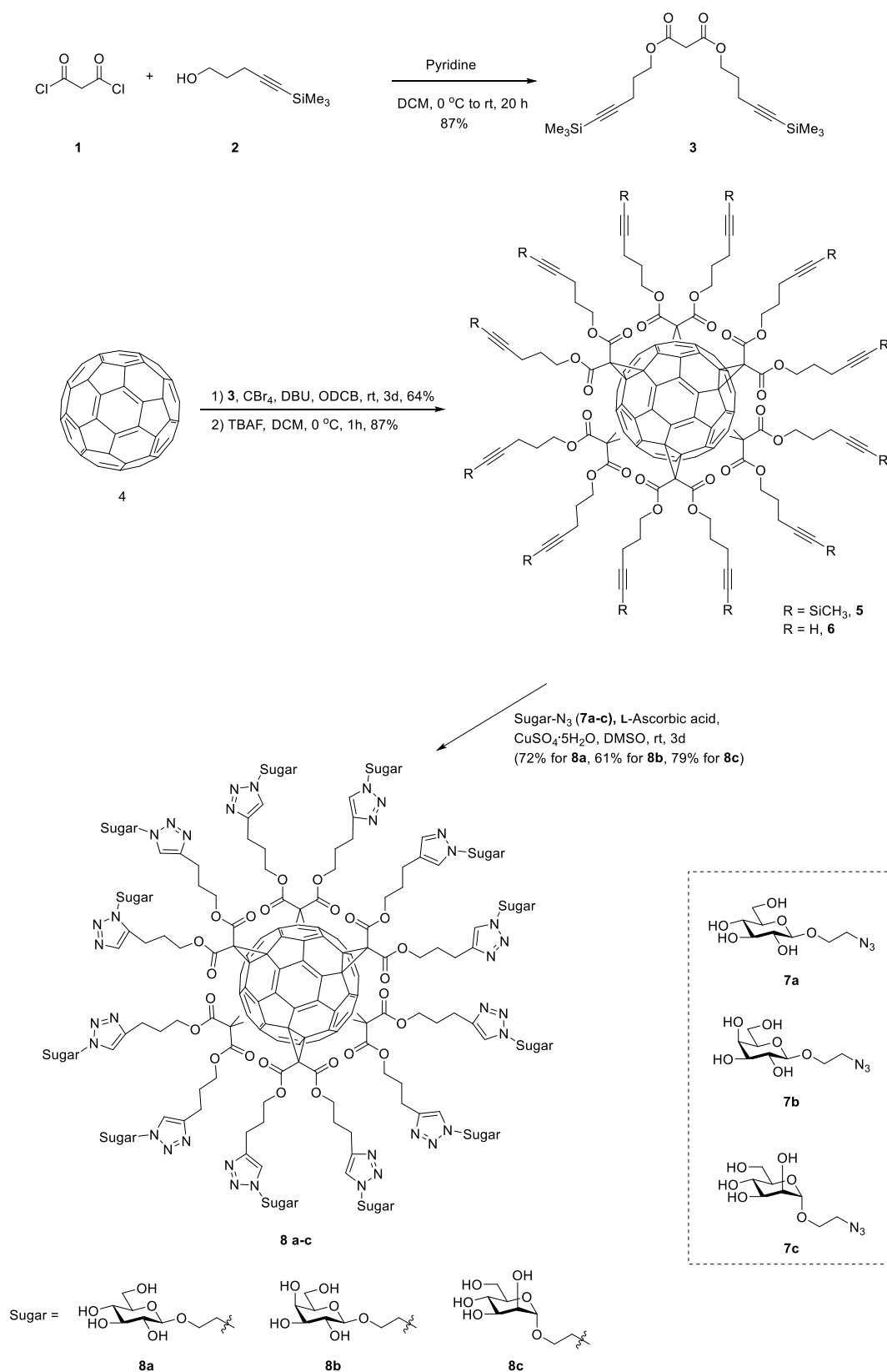
Abstract: Exposure to particulate matter (PM) has been linked to pulmonary and cardiovascular dysfunctions, as well as skin diseases, etc. PM impairs the skin barrier functions and is also involved in the initiation or exacerbation of skin inflammation, which is linked to the activation of reactive oxygen species (ROS) pathways. Fullerene is a single C₆₀ molecule which has been reported to act as a good radical scavenger. However, its poor water solubility limits its biological applications. The glyco-modification of fullerenes increases their water solubility and anti-bacterial and anti-virus functions. However, it is still unclear whether it affects their anti-inflammatory function against PM-induced skin diseases. Hence, glycofullerenes were synthesized to investigate their effects on PM-exposed HaCaT human keratinocytes. Our results showed that glycofullerenes could reduce the rate of PM-induced apoptosis and ROS production, as well as decrease the expression of downstream mitogen-activated protein kinase and Akt pathways. Moreover, PM-induced increases in inflammatory-related signals, such as cyclooxygenase-2, heme oxygenase-1, and prostaglandin E2, were also suppressed by glycofullerenes. Notably, our results suggested that PM-induced impairment of skin barrier proteins, such as filaggrin, involucrin, repetin, and loricrin, could be reduced by pre-treatment with glycofullerenes. The results of this study indicate that glycofullerenes could be potential candidates for treatments against PM-induced skin diseases and that they exert their protective effects via ROS scavenging, anti-inflammation, and maintenance of the expression of barrier proteins.

Keywords: glycofullerenes; particulate matter; reactive oxygen species; human keratinocytes; antioxidant; anti-inflammation

1. Introduction

Ambient air pollution (AAP), particularly with fine particulate matter (PM), has been reported to be harmful to human health by the World Health Organization (WHO) [1] and was responsible for 4.2 million deaths in 2016 [1]. AAP is greatly associated with various diseases, such as chronic obstructive pulmonary disease, cancer, cardiovascular diseases, and stroke [1]. Air pollutants can be produced by a variety of sources, including industries, households, fuel combustion by vehicles, or the burning of biomass. PM can be divided into categories based on the particle size, namely ultrafine particles (particle size of $< 0.1 \mu\text{m}$, UFP), fine particles (particle size of $< 2.5 \mu\text{m}$, $\text{PM}_{2.5}$), and coarse particles (particle size of $< 10 \mu\text{m}$, PM_{10}) [2]. The level of $\text{PM}_{2.5}$ in the air on the weather forecast is an important daily environmental indication. The polyaromatic hydrocarbon coating on PM particles can cause inflammation by increasing oxidative stress levels and activating downstream mitogen-activated protein kinase (MAPK) signaling pathways. The skin constitutes the first line of defense of the human body against air pollutants, as the skin is the largest and outermost organ of the body. Notably, PM exposure has also been associated with skin aging, cancer, and inflammatory or allergic skin conditions, such as atopic dermatitis, eczema, psoriasis, or acne [3]. The increased levels of reactive oxygen species (ROS) and inflammatory factors, as well as a decreased expression of barrier proteins, are hypothesized to play a role in the pathological mechanisms of PM-induced skin diseases [4,5].

Fullerene (C_{60}) is a good radical scavenger, with a single C_{60} molecule able to interact and add up to 34 methyl radicals [6]. However, its poor water solubility limits its biological applications. Fullerene was discovered by Smalley and co-workers in 1985 [7], with the first macroscopic synthesis taking place in 1990 [8]. Moreover, there has been a rapid increase in attention regarding chemically functionalized fullerenes, due to their different applications [9,10]. Fullerenes entrapped in polyvinylpyrrolidone (PVP), resulting in a water-soluble compound which was termed a ‘radical sponge’ and was expected to act as an anti-ultraviolet A (UVA)-preventive agent in human skin keratinocytes [11]. Fullerene nanoparticles (NPs) have been used for dermatological and cosmetic applications (skin whitening, sunscreen, etc.) due to their high reactivity with ROS [12]. Notably, water-soluble fullerenes with direct functional derivatives have had a significant impact in the biological field [13,14] by exhibiting superior membranotropic functions, greater biological affinity to certain nucleic acids and proteins, as well as an increase in their ROS scavenging activity in target cells or tissues [14]. Water-soluble fullerenes were also shown to protect cell growth from various toxins, as well as promote recovery after ischemic stroke [10,15–17]. Of particular interest are fullerene derivatives substituted with sugar residues, known as glycofullerenes [17,18]. ROS damage is potentially prevented in the case of hexa-substituted glycol-fullerene derivatives, which have a globular structure and a T_h -symmetrical octahedral addition pattern [18]. The synthesis of these hexa-substituted glycofullerenes could be achieved via a chemical reaction method, namely Cu(I) alkyne–azide cycloaddition (CuAAC), which is a very powerful synthetic tool for the functionalization of alkyne–fullerene building blocks **6** (as shown in Scheme 1) [18]. Dodecavalent galactoside fullerene-based glyoclusters has been synthesized and showed to have promising multivalent interactions with bacterial lectin PA-IL and a 12,000-fold binding ability [19]. Similarly, the dodecavalent heptoside fullerene sugar ball showed good inhibition of heptosyltransferase WaaC, a glycosyltransferase which catalyzes the incorporation of the first L-heptose into lipopolysaccharides [20]. Moreover, mannosylated fullerene sugar balls have been shown to have antiviral activity in an Ebola pseudotyped infection model [18,21,22]. A classical 3-(4,5-Dimethylthiazol-2-yl)-2,5-diphenyltetrazolium bromide (MTT) assay has also been recently performed using various fullerene sugar balls and the results indicated that they did not exert cytotoxicity [18].



Scheme 1. The synthesis procedure of the glycofullerenes **8a** C₆₀(Glc)₁₂, **8b** C₆₀(Gal)₁₂, and **8c** C₆₀(Man)₁₂.

The HaCaT cell line was first generated by Boukamp et. al. [23] and it can be a reliable differentiation model to estimate the inflammatory and repair response, as well as a cell platform for the development of novel treatments and the investigation of disease mechanisms [5,24–28]. In our previous study [27,29], we prepared water-soluble 7, 3', 4'-trihydroxyisoflavone NPs by using the planetary ball mill method [27] and eupafolin NP delivery system [25,29] to investigate their individual antioxidant and anti-inflammatory activities in PM-induced skin inflammation [5,24,25,29]. The results of our previous study suggested that PM-induced skin cell inflammation regulated the AhR/p47 phox/NADPH oxidase pathway, and subsequently increased ERK1/2, p38/nuclear factor kappa-light-chain-enhancer of activated B cells (NF- κ B), and c-Jun N-terminal kinase (JNK)/Activator protein 1 (AP-1) levels [5]. Moreover, it also upregulated the expression of cyclooxygenase-(COX-2) and prostaglandin E2 (PGE2) and downregulated filaggrin, thereby resulting in the impaired ability of barrier proteins, as well as skin function. ROS scavengers (*N*-acetylcysteine) and the apocynin (a Nox2 inhibitor) could suppress PM-induced ROS production. Fullerene has been shown to have radical scavenger activity. However, the biofunctions of glycofullerenes, especially their protective effects against PM-induced skin cell inflammation and expression of barrier protein have not yet been studied.

In order to further investigate this manner, we tried to develop and synthesize three different glycofullerenes, based on the CuAAC reaction, which differed based on their sugar substituent and had glucosides, galactosides, and mannosides substitutions, resulting in **8a** C₆₀(Glc)₁₂, **8b** C₆₀(Gal)₁₂, and **8c** C₆₀(Man)₁₂ (Scheme 1). Moreover, we investigated their ability to attenuate PM-induced oxidative stress and inflammation in HaCaT keratinocytes. These glycofullerenes were characterized by nuclear magnetic resonance spectroscopy (NMR), Fourier-transform infrared spectroscopy (FTIR), ultraviolet–visible spectroscopy (UV–Vis), dynamic light scattering (DLS), and zeta-potential at each step of the synthesis process. In all of the biological experiments, the fullerenes which were not soluble in water (represented as C₆₀-H₂O) were used as a comparison. Annexin V-Fluorescein isothiocyanate (FITC)/propidium iodide staining was used to detect the stage of HaCaT cell apoptosis by flow cytometry. The typical molecular biological mechanism study models for antioxidant and anti-inflammation pathways were applied. Regarding the ability of the skin to repair, the expression of proteins which have been reported to be disrupted by PM [5], including loricrin, filaggrin, involucrin, and repetin, was also investigated.

2. Materials and Methods

2.1. Materials

PM (Standard Reference Material 1649b, SRM-1649b) was purchased from the National Institute of Standards and Technology (Gaithersburg, MD, USA). Fullerene, tetrabutylammonium hydroxide (TBAH), sodium hydroxide (NaOH), malonyl dichloride, tetrabromomethane (CBr₄), tetra-*n*-butylammonium fluoride (TBAF), 1,8-diazabicyclo [5.4.0]undec-7-ene (DBU), L-Ascorbic acid, CuSO₄·5H₂O, magnesium sulfate (MgSO₄), and Sephadex LH-20 resin were purchased from Sigma-Aldrich (St. Louis, MO, USA). All solvents including toluene (Tol), dimethyl sulfoxide (DMSO), methanol (MeOH), pyridine (Py), 1,2-dichlorobenzene (ODCB), dichloromethane (DCM), tetrahydrofuran (THF), and methanol (MeOH) were dried and distilled by standard techniques. Analytical thin-layer chromatography (TLC) was performed on precoated plates (Silica Gel 60). Silica gel 60 (E. Merck, Darmstadt, Germany) was employed for all flash chromatography. All reactions were carried out in oven-dried glassware (100 °C) under an atmosphere of nitrogen unless indicated otherwise. Low-resolution and high-resolution mass spectra were recorded under Electrospray Ionization Time-of-Flight (ESI-TOF) mass spectra conditions. ¹H and ¹³C NMR spectra were recorded on Varian Mercury-400 MHz. Chemical shifts are expressed in ppm using residual CDCl₃ (7.24 ppm) or CD₃OD (3.31 ppm) or D₂O (4.67 ppm at 298 k) as internal standard. Fourier-transform infrared spectroscopy (FTIR) spectra were recorded on a Thermo Nicolet iS5 FTIR spectrometer (Thermo Fisher Scientific Inc., Waltham, MA, USA). The absorption spectra of the fullerene derivatives were

measured by Thermo Genesys 6 UV-Visible (Thermo Fisher Scientific Inc., Waltham, MA, USA) spectrophotometer. HaCaT cells were purchased from AddexBio (San Diego, CA, USA). All buffers and solutions were prepared by using Millipore water. Dulbecco's modified Eagle medium (DMEM) was obtained from GIBCO (Grand Island, NY, USA). Fetal bovine serum (FBS) was purchased from Hazelton Product (Denver, PA, USA). The bicinchoninic acid (BCA) protein assay kit was obtained from Pierce (Rockford, IL, USA). Western blotting enhanced chemiluminescence (ECL) detection kit and Hyperfilms were purchased from GE Healthcare Biosciences (Buckinghamshire, UK). Antibodies for Western blotting (total and phospho-p38, ERK, JNK, and phospho-Akt) were purchased from Cell Signaling Technology (Danvers, MA, USA). Total-Akt and cytosolic phospholipase A2 (cPLA2) antibodies were purchased from Santa Cruz Biotechnology (Dallas, TX, USA). Metalloproteinase-9 (MMP-9), involucrin, and repetin antibodies were purchased from Proteintech Group Inc. (Rosemont, IL, USA). Heme oxygenase-1 (HO-1) and COX-2 antibodies were obtained from Abcam (Cambridge, UK). Anti-loricrin antibody was purchased from Boster (Pleasanton, CA, USA). Filaggrin antibody was purchased from Genetex (Hsinchu, Taiwan). Anti-GAPDH antibody was purchased from Biogenesis (Bournemouth, UK). All of other chemicals were ACS reagent grade and purchased from Sigma-Aldrich (St. Louis, MO, USA).

2.2. Synthesis of Bis(5-(Trimethylsilyl)pent-4-yn-1-yl) Malonate (3)

Malonyl dichloride **1** (0.50 mL, 5.14 mmol) was dropwisely added to a solution of 5-(trimethylsilyl)-4-pentyn-1-ol **2** (1.87 mL, 10.28 mmol), pyridine (0.84 mL, 10.33 mmol), and dry DCM (73 mL) at 0 °C for stirring 1 h. The reaction mixture was then warmed to room temperature and stirred for 19 h. The solution was evaporated and co-evaporated with DCM three times. The crude was purified by column chromatography to afford **3** (1.70 g, 87%). ¹H NMR (400 MHz, CDCl₃) δ 4.22 (t, *J* = 6.3 Hz, 4H), 3.36 (s, 2H), 2.30 (t, *J* = 7.0 Hz, 4H), 1.85 (p, *J* = 6.7 Hz, 4H), 0.12 (s, 18H). NMR spectrum of **3** is also provided in Figure S1 in Supplementary Data.

2.3. Synthesis of Dodecatrimethylsilylalkyne-Fullerene (5)

To a solution of fullerene **4** (201.8 mg, 0.28 mmol) in *O*-dichlorobenzene (ODCB) (6.0 mL) was added **3** (1.07 g, 2.80 mmol), CBr₄ (9.29 g, 28.0 mmol), and 1,8-diazabicyclo[5.4.0]undec-7-ene (DBU) (0.84 mL, 5.60 mmol). The reaction mixture was stirred at room temperature for 3 days. The solvent was evaporated in vacuo, then the crude was purified by column chromatography to afford **5** (527.9 mg, 64%). IR (neat): 2177 (C≡C), 1747 (C=O); ¹H NMR (400 MHz, CDCl₃) δ 4.62–4.17 (m, 24H), 2.53–2.15 (m, 24H), 2.09–1.74 (m, 24H), 0.12 (s, 108H). NMR, IR, and UV absorption spectrum of **5** were also provided in Figures S2–S4 in Supplementary Data.

2.4. Synthesis of Dodecaalkyne-Fullerene (6)

A 1M solution of TBAF in THF (2.1 mL, 7.50 μmol) was dropwisely added to a solution of **5** (448.8 mg, 0.15 mmol) in dry DCM (15 mL) at 0 °C for stirring 1 h. The solution was diluted with DCM, washed with water, dried over MgSO₄, and concentrated under reduced pressure. The crude was purified by column chromatography to afford **6** (276.4 mg, 87%). IR (neat): 3288 (≡C-H), 2116 (C≡C), 1742 (C=O); ¹H NMR (400 MHz, CDCl₃) δ 4.61–4.21 (m, 24H), 2.43–2.19 (m, 24H), 2.07–1.76 (m, 36H). NMR, IR, and UV absorption spectrum of **6** were also provided in Figures S5–S7 in Supplementary Data.

2.5. Synthesis of Glycofullerenes: 8a C₆₀(Glc)₁₂, 8b C₆₀(Gal)₁₂, 8c C₆₀(Man)₁₂

Compound **8a** C₆₀(Glc)₁₂: To a reaction mixture of **6** (38.0 mg, 17.87 μmol) and **7a** (97.2 mg, 0.39 mmol) in DMSO (7 mL) was added L-ascorbic acid (7.9 mg, 44.68 μmol) and CuSO₄·5H₂O (3.6 mg, 14.30 μmol) and stirred at room temperature for 3 d. The reaction mixture was concentrated in vacuo. The crude was purified by Sephadex LH-20 to afford **8a** (65.8 mg, 72%). IR (neat): 3375 (O-H), 1736 (C=O); ¹H NMR (400 MHz, DMSO) δ 7.92 (s, 12H), 5.06 (s, 10H), 4.98–4.88 (m, 17H), 4.59–4.15 (m, 77H), 4.05 (s, 14H), 3.86 (s, 12H), 3.65 (s, 11H), 3.49–3.38 (m, 14H), 3.20–2.90 (m, 41H), 2.71 (d, *J* = 37.5 Hz,

31H), 2.21 (s, 29H), 2.06–1.65 (m, 48H); HRMS (ESI): calcd for $C_{234}H_{245}N_{36}O_{96}Na$ $[M + Na]^+$: 5117.5293; found: 5140.4565. Synthetic route of 7a were showed in Figure S8. NMR, IR, UV absorption and mass spectrum of 8a were also provided in Figures S9–S12 in Supplementary Data.

Compound **8b** $C_{60}(Gal)_{12}$: Similar experiment procedure as described for 8a. The reaction contained with 6 (40.0 mg, 18.81 μ mol), 7b (102.2 mg, 0.41 mmol), L-ascorbic acid (8.3 mg, 47.03 μ mol) and $CuSO_4 \cdot 5H_2O$ (3.8 mg, 15.05 μ mol) in DMSO (8 mL) at room temperature for 3 d. The reaction mixture was concentrated in vacuo. The crude was purified by Sephadex LH-20 to afford 8b (58.7 mg, 61%). IR (neat): 3383 (O-H), 1738 (C=O); 1H NMR (400 MHz, DMSO) δ 7.90 (s, 12H), 4.93 (s, 12H), 4.72 (s, 12H), 4.66–4.42 (m, 36H), 4.37 (s, 24H), 4.20–4.11 (m, 12H), 4.04 (s, 12H), 3.83 (s, 12H), 3.61 (s, 12H), 3.57–3.40 (m, 24H), 3.28 (s, 24H), 2.66 (s, 24H), 1.96 (s, 24H); HRMS (ESI): calcd for $C_{234}H_{245}N_{36}O_{96}Na$ $[M + Na]^+$: 5117.5294; found: 5117.5535. Synthetic route of 7b were showed in Figure S8R, IR, UV absorption and mass spectrum of 8b were also provided in Figures S13–S16 in Supplementary Data.

Compound **8c** $C_{60}(Man)_{12}$: Similar experiment procedure as described for 8a. The reaction contained with 6 (37.4 mg, 18.81 μ mol), 7c (97.2 mg, 0.39 mmol), L-Ascorbic acid (7.7 mg, 43.98 μ mol) and $CuSO_4 \cdot 5H_2O$ (3.5 mg, 14.07 μ mol) in DMSO (7 mL) at room temperature for 3 d. The reaction mixture was concentrated in vacuo. The crude was purified by Sephadex LH-20 to afford 8c (71.1 mg, 79%). IR (neat): 3397 (O-H), 1735 (C=O); 1H NMR (400 MHz, DMSO) δ 7.90 (s, 12H), 4.71 (m, 24H), 4.55 (m, 29H), 4.44 (m, 40H), 4.28 (m, 15H), 3.87 (s, 12H), 3.72 (s, 12H), 3.51 (m, 48H), 3.05 (m, 12H), 2.51 (m, 24H), 1.91 (m, 24H); HRMS (ESI): calcd for $C_{234}H_{246}N_{36}O_{96}Na$ $[M + Na]^+$: 5118.5372; found: 5118.6387. Synthetic route of 7c were showed in Figure S8. NMR, IR, UV absorption and mass spectrum of 8c were also provided in Figures S17–S20 in Supplementary Data.

2.6. Transmission Electron Microscopy Analysis of Glycofullerene Particle Size

Transmission electron microscopy (TEM) was performed by using a JEOL microscope (Model JEM-2100) (JEOL Ltd., Tokyo, Japan) operated at 200 keV to analyze the sizes and dispersion of the synthetic glycofullerenes. A drop of the glycofullerenes solution ($\sim 1 \mu$ L) was dropped on a carbon-coated 200-mesh copper grid. The grid was left to dry at room temperature for hours. Before the TEM analysis, the grid was then further dried under vacuum overnight.

2.7. Particle Size of Glycofullerene Analysis by Dynamic Light Scattering and Zeta-Potential Measurement

The hydro-diameter size and zeta potential of the glycofullerene particles were analyzed using a particle analyzer with dynamic light scattering (DLS) technique (Horiba, SZ-100V2, Kyoto, Japan) at 25 °C with a laser angle of 90°. The samples were diluted with pure water. Each value was measured in triplicate.

2.8. Cell Culture Condition

Human epidermal keratinocyte (HaCaT) cells were purchased from AddexBio (San Diego, CA, USA). The HaCaT cell line was seeded in a 12 well plate (2×10^5 per well) with 1 mL Dulbecco's Modified Eagle Medium (DMEM, Gibco, Grand Island, NY, USA) supplemented with 10% FBS (Hazelton Research Products, Denver, PA, USA) and 1% penicillin–streptomycin (Gibco, USA), and incubated at 37 °C in a humidified atmosphere containing 5% CO_2 /95% air. After cells were seeded for 24 h to ensure that they were stable, the medium was renewed and followed experiments were performed. Cells were treated with 0.05% (*w/v*) trypsin/0.53 mM EDTA for 5 min at 37 °C, when cultures reached confluence. The cell viability was also simultaneously tested using the 3-(4,5-Dimethylthiazol-2-yl)-2,5-diphenyltetrazolium bromide (MTT) assay, to ensure a survival rate of at least 90% with each passage. The HaCaT cells passages within 5 to 12 were used for preforming experiments.

2.9. Measurement of Cell Apoptosis

The flow cytometry with the Annexin V-fluorescein isothiocyanate (FITC)/propidium iodide (Thermo Fisher Scientific, Waltham, MA, USA) staining were used for measuring the cell apoptosis. Different types of glycofullerenes (1 μ M) were dissolved with pure water and pre-treated to HaCaT cells for 1 h, then treated with PM (SRM-1649b) with 50 μ g/cm² for another 24 h. After 24 h of PM administration, these of cells were followed to stain with the dye—Annexin V-FITC and propidium iodide (for 30 min), according to the manual, and subjected to detect by flow cytometry (Accuri C6, BD Biosciences, San Jose, CA, USA). Data were repeated and collected from at least three independent experiments.

2.10. Determination of ROS Productions from Cellular and Mitochondrial Areas

The ROS production from cellular area was measured using the 2',7'-dichlorodihydrofluorescein diacetate (H2DCFDA) and CellROX assay. HaCaT cells were seeded onto 12-well plates (2×10^5 per well) and incubated 24 h for stable. Cells were treated with different types of glycofullerene (1 μ M) for 1 h and then administered PM (50 μ g/cm²) for another 2 h. Cells were stained with H2DCFDA and CellROX reagents (Thermo Fisher Scientific, USA). The fluorescence intensity of the cells was measured using flow cytometry (excitation/emission wavelength, 488/530 nm). Furthermore, MitoSOX™ (Molecular Probes, Eugene, OR, USA) was used for assaying the levels of the mitochondrial ROSs with the same treatment schedule as mentioned above. The excitation wavelength and emission wavelength for flow cytometry were set as 488 and 585 nm, respectively. The data were collected from at least three times of independent experiments.

2.11. Immunoblotting for MAPKs and Epidermal-Related Proteins Measurement

HaCaT after being seeded and incubated onto 12-well plates (2×10^5 per well) for 24 h, were pre-treated with 1 μ M of different types of glycofullerenes (1 μ M) for 1 h and then exposed to PM (50 μ g/cm²) for another 6 h (kinases) or 24 h (inflammatory- and protection-related proteins). After treatment, the cells were lysed with lysis buffer for protein extraction. Equal amounts of the protein were loaded and separated by electrophoresis in the SDS-polyacrylamide gel (10–12.5% polyacrylamide) and then transferred onto nitrocellulose membranes. The primary antibodies, phospho-p38, ERK, JNK and phospho-Akt, cPLA2, MMP-9, involucrin and repetin, HO-1 and COX-2, loricrin, and filaggrin were utilized to measure the expression levels of these of targets. Next, the horseradish peroxidase conjugated secondary antibodies with were added, and the enhanced chemiluminescence (ECL) detection system was used to assess the immunoreactivities. The signals were detected on a ChemiDoc™ XRS+ image system (Bio-Rad Laboratories, Hercules, CA, USA) and GAPDH signal was used as a loading control. At least three independent replicates with a similar pattern of blotting data were collected. The values were calculated from those of figures, then a figure with closer pattern of statistical values was selected for presentation.

2.12. Measurement of Prostaglandin E2 Production

HaCaT cells were cultured in 12-well culture plates (2×10^5 per well) and incubated for 24 h to ensure stable for followed experiments. After reaching confluence, cells were pre-treated with 1 μ M of different types of glycofullerene for 1 h and then exposed to PM (50 μ g/cm²) for another 24 h. After treatment, medium was collected and stored at -80°C until assays were performed. PGE2 levels were measured by PGE2 enzyme immunoassay kit (Cayman Chemical, Ann Arbor, MI, USA), according to the manufacturer's instructions. Experiments were repeated at least three times and the data were collected.

2.13. Statistical Analysis

Data were expressed as mean \pm standard error of the mean (SEM). One-way ANOVA followed by post-hoc Tukey's multiple comparison (multiple groups) were used to analyze the data with version 5 of GraphPad Prism software (GraphPad, San Diego, CA, USA). A p -value < 0.05 was considered significant.

3. Results

3.1. Synthesis and Characterization of Glycofullerenes

The steps required for the synthesis of the glycofullerenes **8a** $C_{60}(\text{Glc})_{12}$, **8b** $C_{60}(\text{Gal})_{12}$, and **8c** $C_{60}(\text{Man})_{12}$ are shown in Scheme 1 (synthetic route, UV, NMR, and Mass spectra are shown in the Supplementary Data, Figures S1–S20). The reaction of malonyl dichloride **1** with 5-(trimethylsilyl)-4-pentyn-1-ol **2** in the presence of pyridine led to the production of malonate **3** with a yield of 87%. The hexakis-adduct (dodecatrimethylsilylalkyne-fullerene) **5** was then synthesized via the reaction between fullerene C_{60} **4** (1 equiv.) and malonate **3** (10 equiv.), CBr_4 (100 equiv.), and DBU (20 equiv.) in *o*-dichlorobenzene (ODCB) at room temperature for 3 days. The resulting product was then purified on a fresh silica-gel column to obtain **5**, with a 64% yield. Subsequently, treatment of **5** with tetra-*n*-butylammonium fluoride (TBAF) in CH_2Cl_2 led to the synthesis of dodecaalkyne-fullerene **6** with an 87% yield. The ^1H NMR spectrum of **6** indicates the disappearance of the trimethylsilyl (TMS)-protecting groups at ~ 0.12 ppm (Figure S5). Moreover, the chemical structure of the fullerenes derivatives was easily confirmed by FTIR analysis. As shown in Figure 1a, the fullerene C_{60} **4** powder in KBr shows a typical IR signal at ~ 1482 , ~ 1180 , ~ 575 , and ~ 526 cm^{-1} . The dodecatrimethylsilylalkyne-fullerene **5** has a signal at 2177 and 1747 cm^{-1} for the alkyne ($\text{C}\equiv\text{C}$) and carbonyl ($\text{C}=\text{O}$) groups, respectively. After removal of the TMS protecting group, compound **6** exhibits a terminal alkyne ($\equiv\text{C-H}$) C-H bond stretching signal at 3288 cm^{-1} .

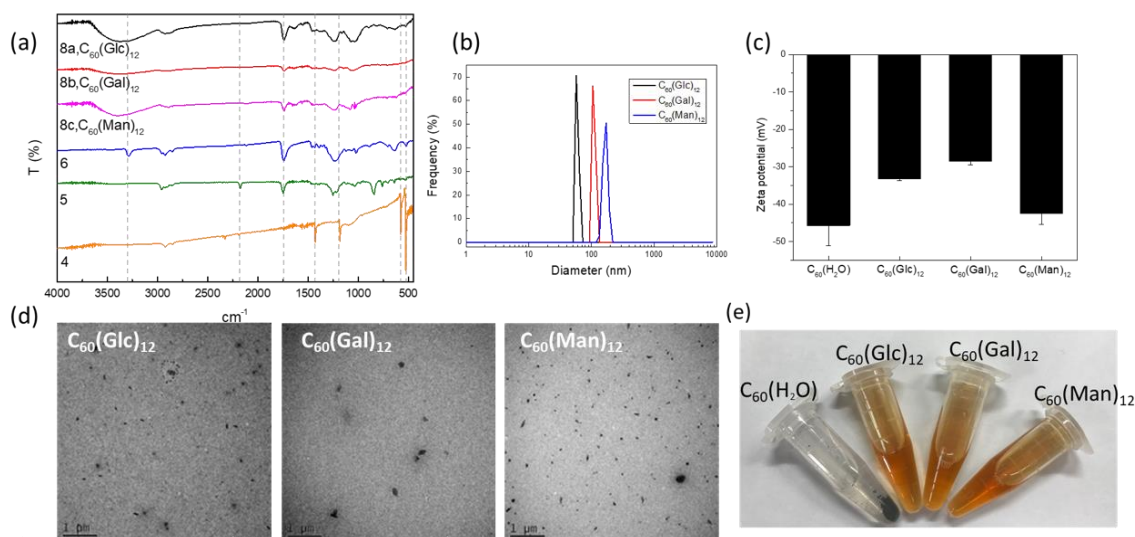


Figure 1. (a) FTIR, (b) dynamic light scattering (DLS), (c) zeta-potential, and (d) TEM data for $C_{60}(\text{Glc})_{12}$, $C_{60}(\text{Gal})_{12}$, and $C_{60}(\text{Man})_{12}$, respectively. (e) Images of the newly synthesized glycofullerenes dissolved in water. $C_{60}\text{-H}_2\text{O}$ formed a precipitate in the Eppendorf tube.

To synthesize the glycofullerenes **8a** $C_{60}(\text{Glc})_{12}$, **8b** $C_{60}(\text{Gal})_{12}$, and **8c** $C_{60}(\text{Man})_{12}$ (Scheme 1), we used an optimized CuAAC method, known as the click chemistry strategy. Different glycofullerenes can be prepared relatively easy using this methodology, by reacting the twelve terminal alkynes on **6** with azido-sugar such as **7a** (Glc-N_3), **7b** (Gal-N_3), and **7c** (Man-N_3) [18]. As such, the mixture of

6 (1 equiv.), **7** (**7a**, **7b**, or **7c**, 22 equiv.), $\text{CuSO}_4 \cdot 5\text{H}_2\text{O}$ (0.8 equiv.), and sodium ascorbate (2.5 equiv.) in DMSO was stirred at room temperature for 3 days. The crude products were purified by using a size exclusion Sephadex LH-20 column to obtain **8a** $\text{C}_{60}(\text{Glc})_{12}$, **8b** $\text{C}_{60}(\text{Gal})_{12}$, or **8c** $\text{C}_{60}(\text{Man})_{12}$, in a yield of 72%, 61% or 79%, respectively. These glycofullerenes display 12 carbohydrate epitopes on their periphery, in a globular topology. The molecular weight of **8a** $\text{C}_{60}(\text{Glc})_{12}$, **8b** $\text{C}_{60}(\text{Gal})_{12}$, and **8c** $\text{C}_{60}(\text{Man})_{12}$ was recorded by using electrospray ionization (ESI) high-resolution mass spectrometry (Figures S12, S16, and S20). The FTIR spectrum (Figure 1a) indicated a broad single signal at around 3350 cm^{-1} , a typical O-H stretching for the sugar moieties of **8a** $\text{C}_{60}(\text{Glc})_{12}$, **8b** $\text{C}_{60}(\text{Gal})_{12}$, and **8c** $\text{C}_{60}(\text{Man})_{12}$, respectively.

The **8a** $\text{C}_{60}(\text{Glc})_{12}$, **8b** $\text{C}_{60}(\text{Gal})_{12}$, and **8c** $\text{C}_{60}(\text{Man})_{12}$ glycofullerenes were characterized regarding their hydrodynamic diameter (Figure 1b), zeta potential (Figure 1c) for their surface charge by DLS, and particle morphology by TEM (Figure 1d). The UV absorption spectra show almost identical bands between 190 and 290 nm for the fullerene derivatives **5**, **6**, **8a** $\text{C}_{60}(\text{Glc})_{12}$, **8b** $\text{C}_{60}(\text{Gal})_{12}$, and **8c** $\text{C}_{60}(\text{Man})_{12}$ (Figure S4–S19 in the Supplementary Data). The hydrodynamic diameters of **8a** $\text{C}_{60}(\text{Glc})_{12}$, **8b** $\text{C}_{60}(\text{Gal})_{12}$, and **8c** $\text{C}_{60}(\text{Man})_{12}$ were 69.3 ± 5.2 , 103.2 ± 6.1 , and 172.0 ± 17.7 nm, respectively. The zeta potential of **8a** $\text{C}_{60}(\text{Glc})_{12}$, **8b** $\text{C}_{60}(\text{Gal})_{12}$, and **8c** $\text{C}_{60}(\text{Man})_{12}$ in water were -33.23 ± 0.5 , -28.57 ± 0.9 , and -42.43 ± 3.0 , respectively. As shown in Figure 1e, **8a** $\text{C}_{60}(\text{Glc})_{12}$, **8b** $\text{C}_{60}(\text{Gal})_{12}$, and **8c** $\text{C}_{60}(\text{Man})_{12}$ can be dissolved in an aqueous solution. In contrast, $\text{C}_{60}\text{-H}_2\text{O}$ was not soluble in water and formed a precipitate in the Eppendorf tube.

3.2. Glycofullerenes Reduced the Ratio of PM-Induced Cell Apoptosis

Flow cytometry with Annexin V-FITC and propidium iodide staining at 24 h was used to determine cell apoptosis. The times for the apoptosis, ROS, and Western blot assays were based on our previous study on HaCaT cells [5]. Based on the properties of Annexin V-FITC and propidium iodide, this staining could be used to identify the early or late stages of apoptosis and necrosis by analyzing the combination of positive/negative signals of Annexin V-FITC and propidium iodide, a method which has been used to detect the different stages of apoptosis in HaCaT cells via flow cytometry [30–32]. As shown in Figure 2A, incubation with glycofullerenes and $\text{C}_{60}\text{-H}_2\text{O}$ did not significantly induce HaCaT apoptosis, while PM did. Moreover, as observed in Figure 2B, pre-treatment for 1 h with 1 μM of **8a** $\text{C}_{60}(\text{Glc})_{12}$, **8b** $\text{C}_{60}(\text{Gal})_{12}$, or **8c** $\text{C}_{60}(\text{Man})_{12}$ could reduce the ratio of early-stage of PM (SRM 1649b, $50\text{ }\mu\text{g}/\text{cm}^2$)-induced cell apoptosis, while the non-soluble fullerene $\text{C}_{60}\text{-H}_2\text{O}$ did not show a notable inhibition effect on PM-induced apoptosis in HaCaT cells.

3.3. Glycofullerenes Suppressed PM-Induced Production of Cellular and Mitochondrial Reactive Oxygen Species

It is well known that PM could cause ROS accumulation and subsequently initiate the development of diseases [5,33]. Previously, fullerenes have been shown to have ROS scavenging activity, which could be enhanced by their water-soluble properties [14]. Hence, the effects of glycofullerenes on ROS generation in the cell and mitochondria were investigated. H2DCFDA and the CellROX Red dye were mainly used to measure the ROS production in the cytoplasm area by detecting the activity of hydroxyl and peroxy groups (H_2O_2) (by H2DCFDA) and the oxidation of various ROS (by CellROX). MitoSox was used to detect the ROS in the mitochondria due to its specific sensitivity to the superoxide produced by the mitochondria. As shown in Figure 3A, H2DCFDA, an agent used to determine cellular ROS, was used to stain the cells for flow cytometry, which were treated with 1 μM of **8a** $\text{C}_{60}(\text{Glc})_{12}$, **8b** $\text{C}_{60}(\text{Gal})_{12}$, or **8c** $\text{C}_{60}(\text{Man})_{12}$, and the non-soluble fullerene, $\text{C}_{60}\text{-H}_2\text{O}$. Our results showed that the cells treated with the indicated fullerenes had lower ROS production when compared with the vehicle (water) treated control group, while PM exposure significantly increased ROS levels. As expected, glycofullerenes were found to reduce PM-induced ROS production but the non-soluble fullerene, $\text{C}_{60}\text{-H}_2\text{O}$ did not (Figure 3B). The bar graphs in Figure 3C illustrate the cumulative counts of the H2DCFDA flow cytometry results. A similar pattern was obtained by using another cellular ROS staining reagent—CellROX (Figure 3D–F). In addition, mitochondrial ROS levels

after treatment with glycofullerenes and PM were detected by using flow cytometry with MitoSOX staining (Figure 4). As shown in Figure 4C, ROS levels were increased by PM treatment, while treatment with glycofullerenes alone did not induce mitochondrial ROS production. Moreover, pre-treatment with 1 μ M of **8a** C₆₀(Glc)₁₂, **8b** C₆₀(Gal)₁₂, or **8c** C₆₀(Man)₁₂ was shown to suppress PM-triggered mitochondrial ROS production in HaCaT cells. The results indicate that the PM-induced increase in cellular and mitochondrial ROS (H₂O₂ and superoxide) could be suppressed by pre-treatment with the **8a** C₆₀(Glc)₁₂, **8b** C₆₀(Gal)₁₂, or **8c** C₆₀(Man)₁₂ glycofullerenes, but not by the non-soluble fullerene, C₆₀-H₂O.

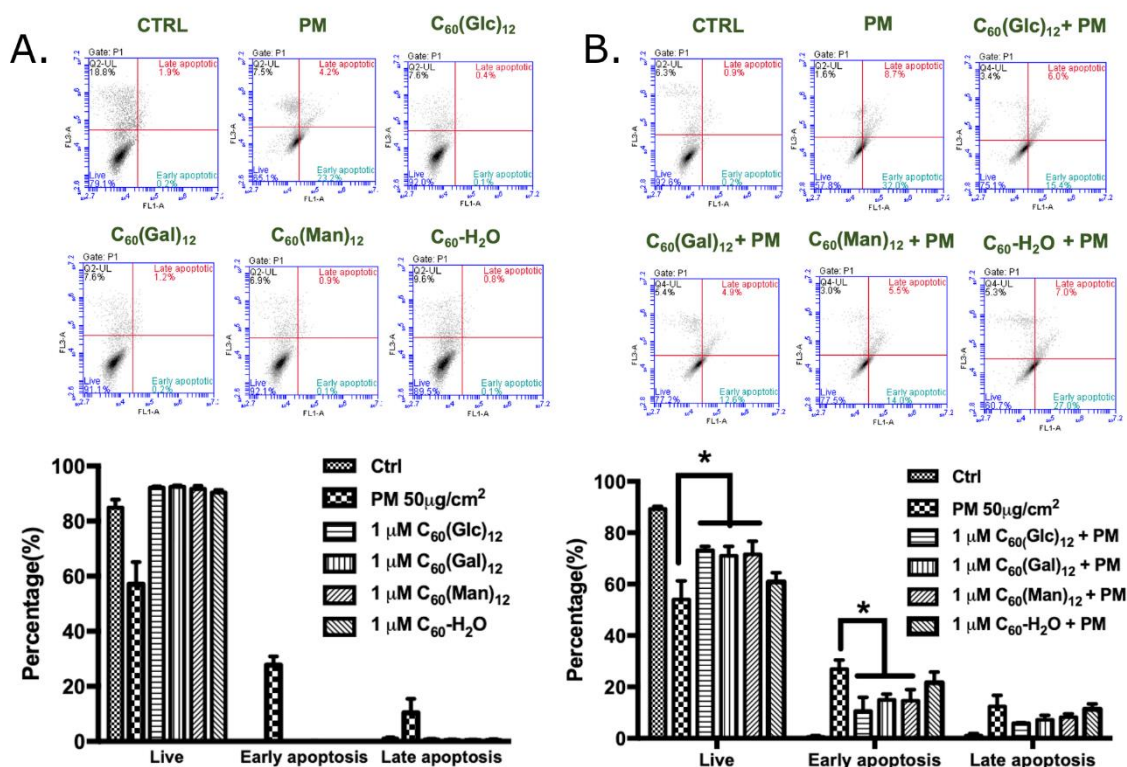


Figure 2. The effects of glycofullerenes and particulate matter (PM) on cell apoptosis in human skin keratinocyte (HaCaT) cells. (A) Glycofullerenes (1 μ M) or PM (SRM 1649b, 50 μ g/cm²) treatment of HaCaT cells for 24 h, (B) pre-treatment with glycofullerenes for 1 h and then incubation with PM for another 24 h. The images were obtained by flow cytometry using the Annexin V-FITC and propidium iodide staining. The upper panel of (A,B) show the raw data obtained by flow cytometry and the right lower quadrant of each raw figure indicates the level of early apoptosis in the cells. The bar graphs illustrate the cumulative counts obtained by flow cytometry. Data are expressed as mean \pm standard error of mean (SEM) from at least three individual experiments. * $p < 0.05$ as compared to the PM exposure group.

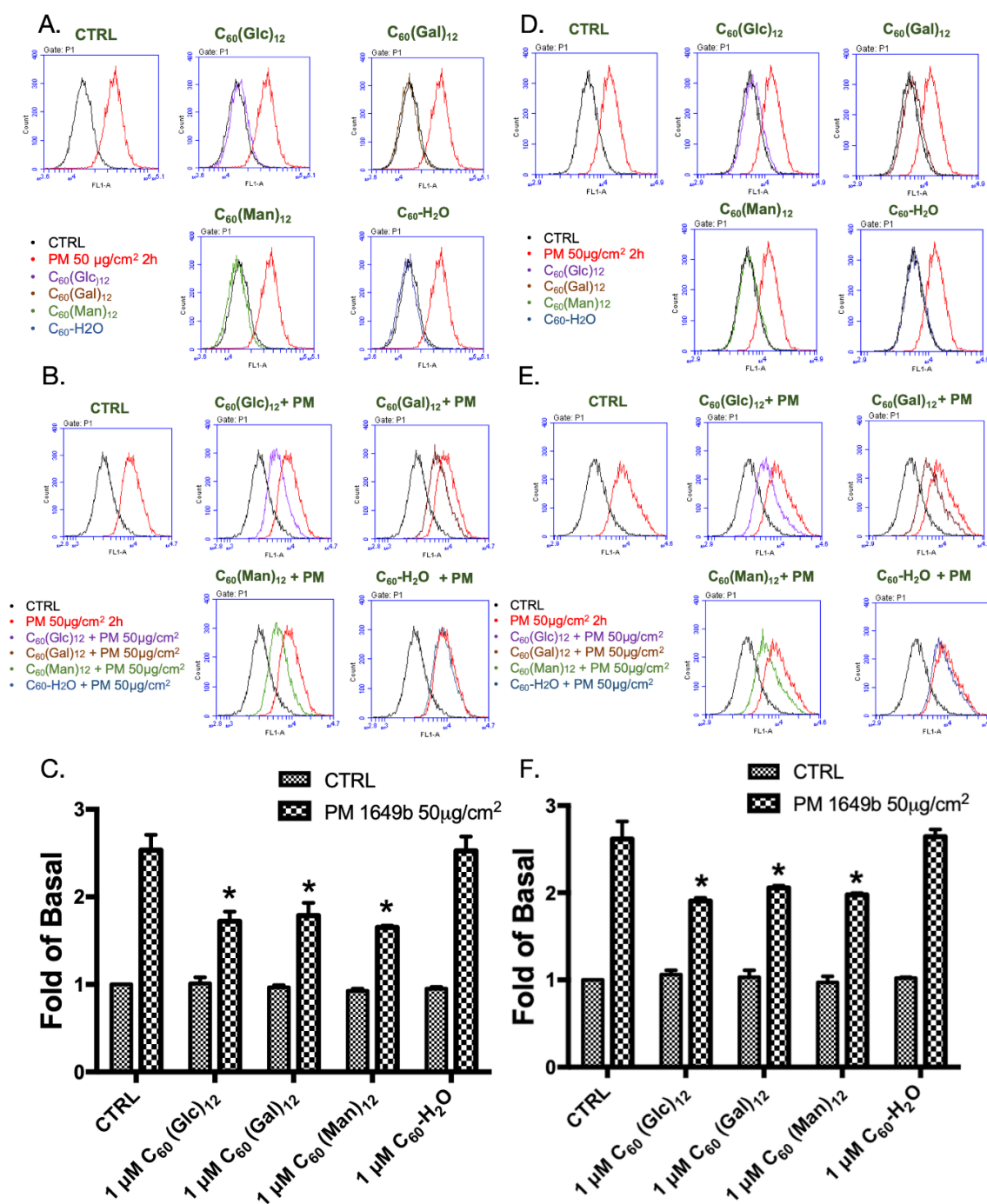


Figure 3. The cellular production of reactive oxygen species (ROS) following treatment with glycofullerenes and particulate matter (PM) in HaCaT cells. (A) graphs of flow cytometry raw data following treatment with glycofullerenes (1 μM) or PM (SRM 1649b, 50 μg/cm²) alone and (B) pre-treatment with glycofullerenes for 1 h followed by incubation with PM for another 2 h. The signals were detected by H2DCFDA staining. (C) The bar graphs illustrate the cumulative counts of H2DCFDA results obtained by flow cytometry. (D) Flow cytometry data from cells treated with only glycofullerenes or PM and (E) pre-treated with glycofullerenes for 1 h followed by incubation with PM for another 2 h. The signals were detected by using CellROX staining. (F) The bar graphs illustrate the cumulative counts of CellROX results obtained by flow cytometry. All bar graphs data were collected from at least three individual experiments and expressed as mean ± SEM. * $p < 0.05$ when compared to the PM exposure group.

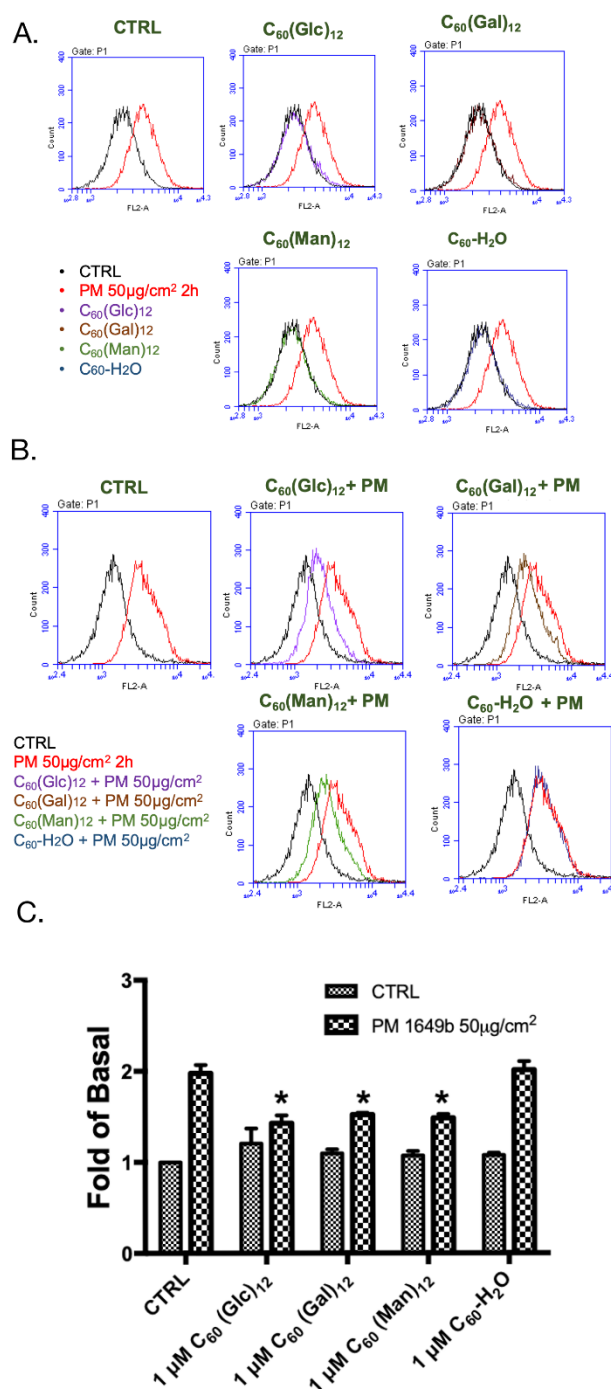


Figure 4. Effect of glycofullerenes and particulate matter (PM) on mitochondrial reactive oxygen species (ROS) production (determined by flow cytometry after staining with MitoSOX) in HaCaT cells. (A) Graphs of the raw flow cytometry data from cells treated with glycofullerenes (1 µM) or PM (SRM 1649b, 50 µg/cm²) alone and (B) pre-treated with glycofullerenes for 1 h followed by incubation with PM for another 2 h. (C) The bar graph illustrates the cumulative counts of MitoSOX results obtained by flow cytometry. All bar graphs data were collected from at least three individual experiments and expressed as mean ± SEM. * $p < 0.05$ when compared to the PM exposure group.

3.4. Glycofullerenes Suppressed the PM-Induced Phosphorylation of Mitogen-Activated Protein Kinases and Akt Proteins

The mitogen-activated protein kinase (MAPK) and Akt (also known as protein kinase B) pathways play roles in various cellular processes and have been demonstrated to be possibly regulated by

ROS [5,34]. As such, the effects of the glycofullerenes on the change in the protein levels of the MAPK and Akt pathways following PM exposure in a HaCaT cell model were further evaluated by immunoblotting methods. As shown in Figure 5, treatment with **8a** C₆₀(Glc)₁₂, **8b** C₆₀(Gal)₁₂, or **8c** C₆₀(Man)₁₂ and the non-soluble fullerene, C₆₀-H₂O alone did not significantly alter the total and phosphorylated protein levels of extracellular signal-regulated kinase (ERK1/2, pp42, and pp44), P38, c-Jun N-terminal kinase 1/2 (JNK 1/2), and Akt. Moreover, the increased expression of phosphorylated ERK, P38, JNK, and Akt induced by PM exposure in HaCaT cells was significantly suppressed by pre-treatment with 1 µM of glycofullerenes, while pre-treatment with the non-soluble fullerene, C₆₀-H₂O alone did not influence those of phosphorylated protein levels.

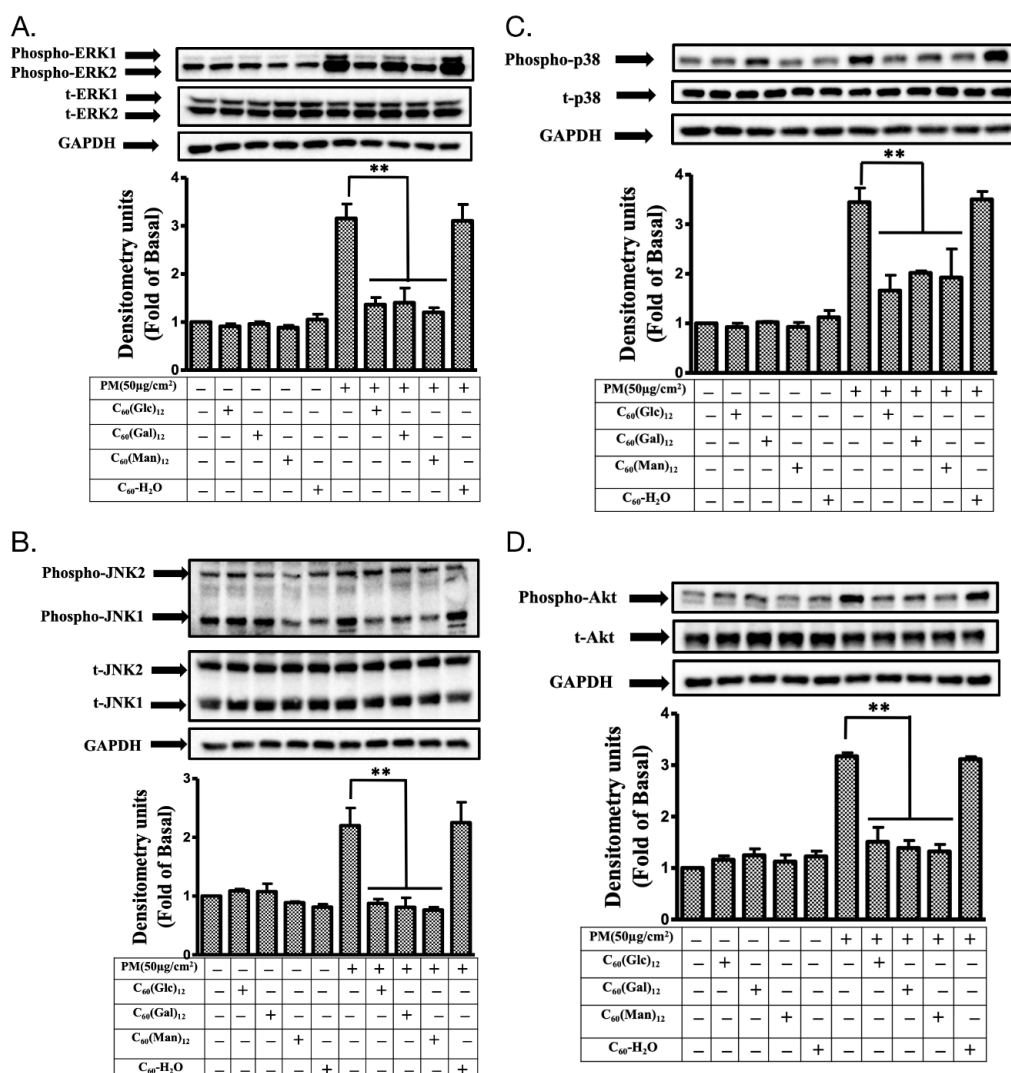


Figure 5. The phosphorylation of mitogen-activated protein kinase (MAPK) and Akt proteins in HaCaT cells treated with glycofullerenes and particulate matter (PM). The effects of the treatment on different kinases (A) extracellular signal-regulated kinase (ERK, pp42/pp44), (B) c-Jun N-terminal kinase (JNK), (C) p38, and (D) Akt were measured by immunoblotting in HaCaT cells with or without pre-treatment with 1 µM of **8a** C₆₀(Glc)₁₂, **8b** C₆₀(Gal)₁₂, **8c** C₆₀(Man)₁₂, or non-soluble fullerene, C₆₀-H₂O, respectively, for 1 h and then incubation with PM (SRM 1649b, 50 µg/cm²) for 6 h. Glyceraldehyde 3-phosphate dehydrogenase (GAPDH) was used as a loading control. The bar graphs were calculated from the phospho-ERK, JNK, p38, and Akt blot signals, respectively. The blots were representative of three independent experiments. The data were collected from at least three individual experiments and expressed as mean ± SEM. ** $p < 0.01$ when compared to the PM exposure group.

3.5. Glycofullerenes Suppressed PM-Induced Changes in the Expression of Inflammatory Proteins

ROS also trigger the expression of several inflammatory proteins and cause cell and tissue injury by regulating the cellular kinase pathways [5,35]. Therefore, the level of COX-2, intercellular adhesion molecular-1 (ICAM-1), HO-1, cPLA2, MMP-9, and PGE2 were measured after PM or glycofullerenes treatment. As shown in Figure 6, treatment with 1 μ M of **8a** C₆₀(Glc)₁₂, **8b** C₆₀(Gal)₁₂, **8c** C₆₀(Man)₁₂ or non-soluble fullerene, C₆₀-H₂O did not change the base level of COX-2, ICAM-1, HO-1, cPLA2, MMP-9, and PGE2 when compared with the vehicle-treated control. Notably, all the glycofullerenes were shown to significantly reduce PM-induced increases in COX-2, ICAM-1, HO-1, cPLA2, and MMP-9 expression, as well as PGE2 production. However, pre-treatment with non-soluble fullerene, C₆₀-H₂O could not decrease the PM-induced increase in the expression of inflammatory proteins.

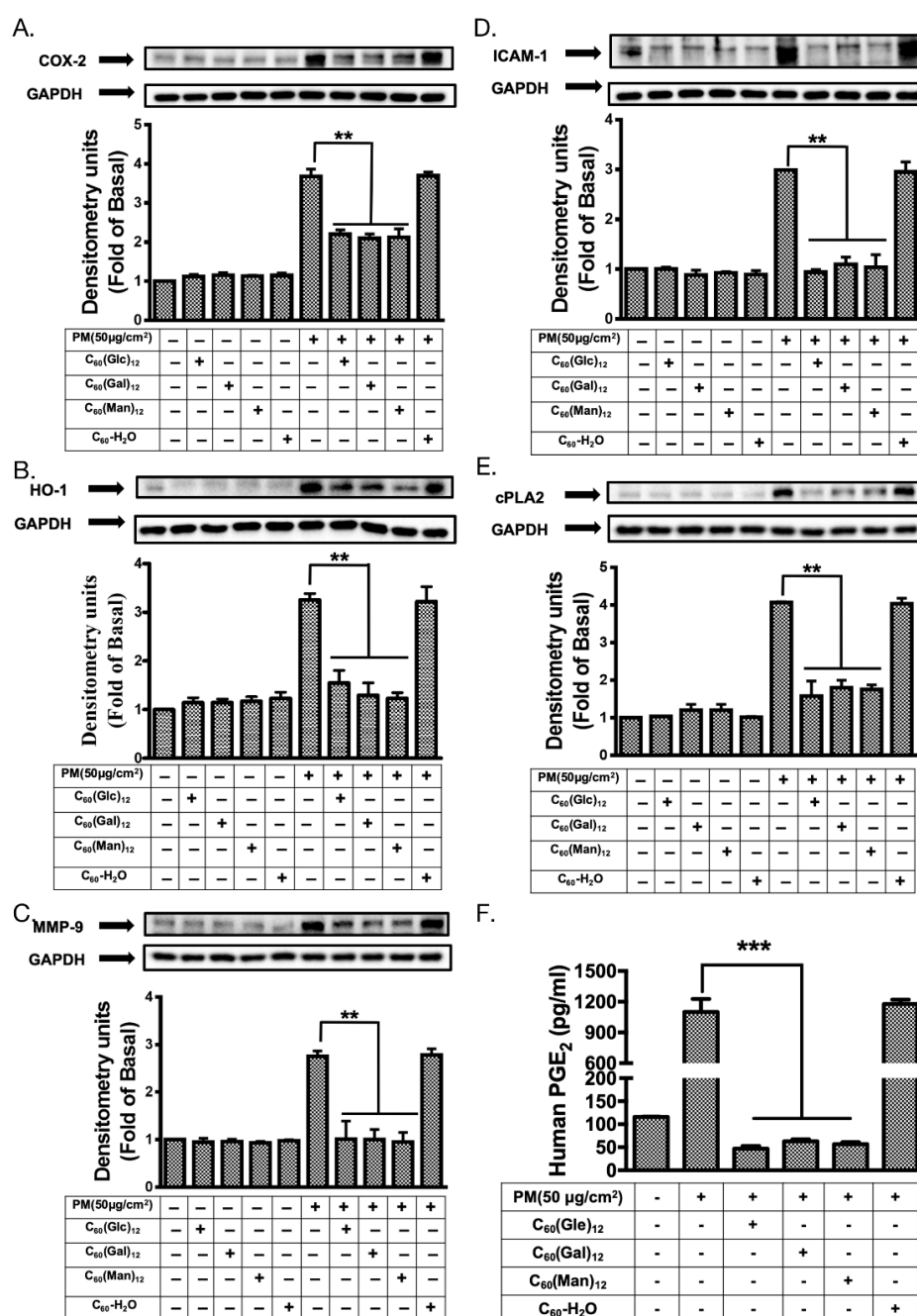


Figure 6. The effects of glycofullerenes and particulate matter (PM) treatment on inflammatory pathways-related proteins in HaCaT cells. Effects of the treatment on inflammatory pathways-related

proteins (A) cyclooxygenase-2 (COX-2), (B) intercellular adhesion molecular-1 (ICAM-1), (C) heme oxygenase-1 (HO-1), (D) cytosolic phospholipase A2 (cPLA2), and (E) metalloproteinase-9 (MMP-9) were measured by immunoblotting and (F) prostaglandin E2 (PGE2) levels were measured by using an ELISA kit in HaCaT cells with or without pre-treatment with 1 μ M of **8a** C₆₀(Glc)₁₂, **8b** C₆₀(Gal)₁₂, **8c** C₆₀(Man)₁₂, or non-soluble fullerene, C₆₀-H₂O for 1 h and then incubation with PM (SRM 1649b, 50 μ g/cm²) for 24 h. Glyceraldehyde 3-phosphate dehydrogenase (GAPDH) was used as a loading control. The blots were representative of three independent experiments. The data were collected from at least three individual experiments and expressed as mean \pm SEM. ** $p < 0.01$, *** $p < 0.001$ when compared to the PM exposure group.

3.6. Pre-Treatment with Glycofullerenes Maintained the Level of Protection Proteins in Keratinocytes under PM-Exposure

Several proteins, such as filaggrin, involucrin, and loricrin, act as a barrier against the damage caused by PM in keratinocytes [5,36]. Therefore, we investigated whether glycofullerenes have a protective effect in PM exposed HaCaT cells. As shown in Figure 7, we observed a notable suppression effect on PM-induced filaggrin, involucrin, loricrin, and repetin loss (at 24 h) in cells pre-treated with 1 μ M of **8a** C₆₀(Glc)₁₂, **8b** C₆₀(Gal)₁₂, and **8c** C₆₀(Man)₁₂, while pre-treatment with the non-soluble fullerene, C₆₀-H₂O did not induce any change. This indicates that the glycofullerenes could preserve the levels of protection-related proteins in keratinocytes under PM exposure.

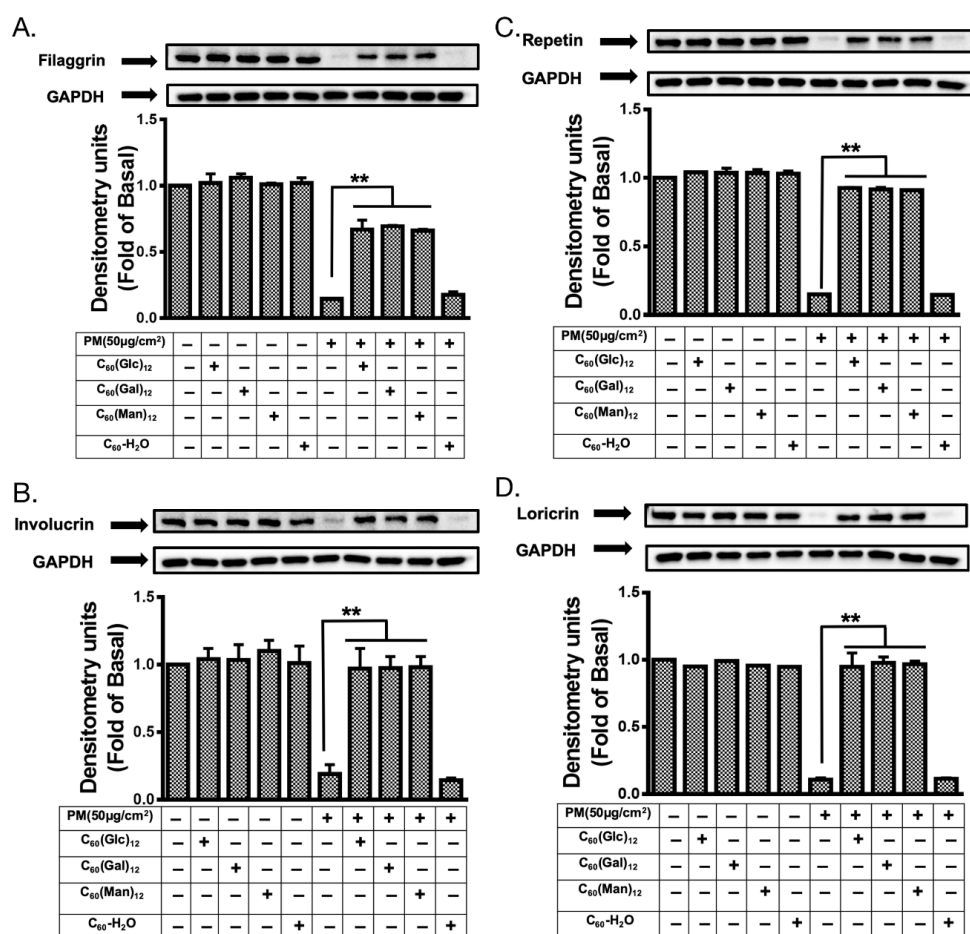


Figure 7. The expression levels of skin protection proteins in HaCaT cells treated with glycofullerenes and particulate matter (PM). The changes in the level of protection-related proteins (A) filaggrin, (B) involucrin, (C) repetin, and (D) loricrin were measured by immunoblotting in HaCaT cells with or

without pre-treatment with 1 μ M of **8a** C₆₀(Glc)₁₂, **8b** C₆₀(Gal)₁₂, **8c** C₆₀(Man)₁₂, or non-soluble fullerene, C₆₀-H₂O for 1 h and then incubation with PM (50 μ g/cm²) for 24 h. Glyceraldehyde 3-phosphate dehydrogenase (GAPDH) was used as a loading control. The blots were representative of three independent experiments. The data were collected from at least three individual experiments and expressed as mean \pm SEM. ** $p < 0.01$ when compared to the PM exposure group.

4. Discussion

The present study was focused on the synthesis of water-soluble fullerenes, particularly that of glycofullerenes, and aimed to investigate their protective effects against PM-induced inflammation and oxidative stress. In the current study, the Standard Reference Material® 1649b (SRM 1649b), which has been certified by the National Institute of Standards and Technology with organic constituents (such as polycyclic aromatic hydrocarbons and polychlorinated biphenyl), was selected to mimic the real effects of PM-induced damage which is attributable to urban dust on skin cells. According to the certificate of SRM 1649b, the PM was collected from the Washington, DC area in 1976 and 1977 and passed through a 63 μ m filter (230 mesh). This indicates that SRM 1649b includes PM with various particle sizes (coarse, fine particles, and ultrafine particles). The use of SRM 1649b could prevent the recording of effects due to unknown compounds in the composition of PM and enable easy comparison between the results of other studies. Firstly, we discussed the synthetic procedure used, as well as the characterization of the newly synthesized glycofullerenes. As non-modified fullerenes **4** are non-soluble in water, we first synthesized glycofullerenes **8a** C₆₀(Glc)₁₂, **8b** C₆₀(Gal)₁₂, and **8c** C₆₀(Man)₁₂ using an effective click chemistry strategy to obtain water-soluble glycofullerene derivatives (Scheme 1). FTIR measurements (Figure 1a) indicate the typical signals of fullerene derivative functional groups for the synthesis steps. Moreover, the DLS data (Figure 1b) provided direct and fast information of the hydrodynamic diameter ranges of the glycofullerenes, while TEM images were used to estimate the sizes and further provide information regarding the surface morphology (Figure 1d). The negative charge obtained by the zeta potential measurement (Figure 1c) of **8a** C₆₀(Glc)₁₂, **8b** C₆₀(Gal)₁₂, and **8c** C₆₀(Man)₁₂ was attributed to the hydroxyl group (-OH) of the sugar moieties on the glycofullerenes.

Previous studies have suggested that fullerenes may act as a potential antioxidant in biological systems [10]. Due to their intrinsic structure, fullerenes exhibit a unique chemical property, namely having many conjugated double bonds in the lowest unoccupied molecular orbital (LUMO). This enables easy acceptance of an electron, therefore increasing the likelihood of it attacking and neutralizing radical species [10]. The non-water-soluble fullerene (also known as an aqueous dispersion of fullerene), which was termed as C₆₀-H₂O in the present study, has been reported to be a powerful antioxidant with no lethal, acute or subacute effects on liver cells or animals [37,38]. Its anti-oxidant effects may occur via inactivation of hydroxyl radicals which attach to the double bonds or acquire a positive charge, as well as absorption of protons in the mitochondria [39]. However, studies have also shown that it exerts toxic effects in living systems by inducing oxidative stress, such as anti-bacterial or anti-viral effects [10]. The ROS generation induced by fullerene may be associated with light exposure and oxygen concentration [40]. Generally, fullerenes dispersed in water with no organic solvent are safe in mammals [10,38]. In the current study, we selected a dose of C₆₀-H₂O (with no organic solvent) which would not cause significant effects in our test platform in order to identify the potential effects of glycofullerenes and non-water-soluble fullerene. All cellular biomacromolecules, including lipids, sugars, proteins, and DNA, can react with ROS. However, the generated secondary ROS products can be even more dangerous to the cell than the initially formed ROS. In normal condition, cells can defend themselves against ROS damage by using either enzymes or small antioxidant molecules. These enzymes can be catalase, superoxide dismutase, lactoperoxidase, peroxiredoxin, and glutathione peroxidase, while small antioxidant molecules can be α -tocopherol (vitamin E), vitamin C, and glutathione. ROS play a role as a double-edged sword, as they maintain redox homeostasis in physiological conditions, while also being involved in various pathological processes in the cell [41–43].

Under physiological conditions, ROS are involved in phagocytosis, activation of downstream cell signaling, and maintaining homeostasis. In this case, ROS levels are regulated by endogenous cells scavenging systems which neutralize and eliminate excess ROS [44,45]. However, under unbalanced, oxidative stress conditions, cellular lipids, proteins, and DNA can be oxidized by higher concentrations of ROS. Subsequently, several diseases and phenomena can be promoted or induced by excess ROS, such as tissues inflammation, organ aging, neurodegeneration, and cancer [45–49]. PM can cause aberrant ROS accumulation [5,33]. Here, we used 1 μ M of glycofullerenes **8a** C₆₀(Glc)₁₂, **8b** C₆₀(Gal)₁₂, and **8c** C₆₀(Man)₁₂, respectively, and non-water-soluble C₆₀-H₂O as a comparison to study their protective effects against PM-induced inflammation and oxidative stress. The results of the cell apoptosis assays were first to reveal that **8a** C₆₀(Glc)₁₂, **8b** C₆₀(Gal)₁₂, **8c** C₆₀(Man)₁₂, and non-water-soluble C₆₀-H₂O did not significantly induce apoptosis of HaCaT cells at the concentration used in this study, while PM (50 μ g/cm²) treatment did. Notably, our results showed that pre-treatment with all of the glycofullerenes could suppress PM-triggered early-apoptosis, while C₆₀-H₂O pre-treatment had no effect.

The major advantage of water-soluble fullerenes for use as an antioxidant in the medical field is their potential ability to localize within the cell to the mitochondria [50] and other cellular compartments, where the production of free radicals is increased. Here, cellular ROS production was measured via H2DCFDA and CellROX staining (Figure 3). All cellular ROS assays performed indicated that PM exposure significantly raised ROS levels in the cell, while glycofullerenes pre-treatment could reduce PM-induced ROS production. However, this suppression effect could not be observed in the group treated with non-soluble fullerene C₆₀-H₂O. Furthermore, we used MitoSOX staining (Figure 4) to detect the levels of ROS generated by the mitochondria. As expected, glycofullerenes were found to effectively decrease PM-induced ROS production in the mitochondria, while C₆₀-H₂O did not.

The MAPK superfamily consists of three main protein kinase families: ERKs, c-JNKs, and p38. Each was shown to play major roles in the regulation of the intracellular metabolism and gene expression. Moreover, they play a critical role in regulating various cellular processes, such as gene expression, mitosis, differentiation, apoptosis, cellular responses to external stresses, and disease [51]. These three main kinases of the MAPK family may be regulated by different signaling cascades and play different roles. For example, phospho-ERK1/2 plays an essential role in the downstream phosphorylation of p38 in HaCaT cells. In most mammalian tissues, ERK2 was shown to have a higher expression level than ERK1, which may be due to the strength of its proximal promoter [52]. Studies have also suggested that ERK1 and 2 may play different roles in various cells and experimental conditions [52]. Furthermore, our previous study suggested that PM-stimulated phosphorylation of ERK1/2, JNK1/2, and p38 was mediated by ROS in HaCaT cells [5,29]. This indicates that the activation of the MAPK pathways is associated with PM-induced increase in ROS, as well as inflammatory processes in skin cells. In this study, the PM-activated MAPK pathways could be suppressed by pre-treatment with glycofullerenes (Figure 5). However, in the current stage, our results could not distinguish between the effects of glycofullerene treatment on the individual regulatory roles of ERK1 and 2 in PM-exposed HaCaT cells, due to the similarity between the regulation patterns of ERK1 and 2 after PM and glycofullerenes treatment. Additionally, JNK-1 and -2 were also shown to play different roles in various conditions [53]. Under normal conditions, in several cells and animal models (such as the proliferation of keratinocytes in the mouse skin), JNK1 acts as a positive regulator, while JNK2 exhibits a negative or downregulatory function [54]. JNK-2 has been also reported to be more important than JNK-1 in some skin diseases, such as human squamous cell carcinoma [55]. However, JNK-1 was found to be more affected than JNK-2 in our PM-exposure cell model. We hypothesized that the increase in JNK-1 levels following PM exposure may lead to resistance to PM-induced damage. However, PM is a mixture of components and may induce complicated effects on signal transduction. Hence, our findings could not identify the individual roles of JNK-1 and 2 in PM-induced inflammation in skin cells and, therefore, require further investigation. The Akt pathway is important for skin aging [56] and has been suggested to promote tissue regeneration and wound healing [57,58]. Loss of Akt leads to a thinner epidermal layer and delayed development of the hair follicle [59]. These findings

indicate that the MAPK and Akt pathways are involved in the mechanisms which protect skin cells from damage induced by environmental toxins. As such, maintenance of the MAPK and Akt pathways within physiological conditions could help maintain the health of skin cells. In the current study, our results suggested that glycofullerenes could dramatically suppress PM-induced phosphorylation of MAPKs and Akt proteins, while $C_{60}\text{-H}_2\text{O}$ had no effect. These results imply that the water-solubility of glycofullerenes may play a critical role in their bioactivity and signal transduction for skin cells.

Previously, we found that the MAPK signaling pathways were involved in the PM-induced ROS-mediated COX-2/PGE2 and MMP-9 inflammation pathway [5,29]. Previous studies have reported that HO-1 may be induced by oxidative or nitrosative stress [60] and play antioxidant and anti-inflammatory roles in various pathological conditions [61–63]. In addition, it is well known that ICAM-1 is highly expressed during lymphoid infiltration of epidermal keratinocytes and plays an important role in inflammatory-related mechanisms, such as lymphocyte transendothelial migration [64–66]. cPLA2 is an enzyme which hydrolyzes phospholipids to produce arachidonic acid or lysophospholipids and is also a type of inflammatory factor. Notably, cPLA2 inhibitors may be potential therapeutic agents for inflammatory skin diseases [67,68]. Our results revealed that glycofullerenes could inhibit the expression of COX-2, HO-1, MMP-9, ICAM-1, and cPLA2, as well as the production of PGE2, induced by PM treatment, while $C_{60}\text{-H}_2\text{O}$ did not (Figure 6). Furthermore, PM exposure can induce an increase in COX-2 expression and decrease in filaggrin expression [5]. Filaggrin, repetin, involucrin, and loricrin act as barrier/protective proteins in keratinocytes to help the skin defend against the external environment (pathogens and allergens entry or chemical damage) and reduce water loss [69]. Moreover, filaggrin levels have been shown to be linked with the activation of inflammatory pathways [70]. Therefore, maintaining the expression level of filaggrin, repetin, involucrin, and loricrin protects the keratinocytes against the damage caused by PM [5,36]. Here, we further revealed that our glycofullerenes could maintain the level of protection-related proteins in keratinocytes under PM exposure (Figure 7). This result proves that glycofullerenes are promising potential protective agents against PM-induced skin damage.

5. Conclusions

The three glycofullerenes designed in this study, **8a** $C_{60}(\text{Glc})_{12}$, **8b** $C_{60}(\text{Gal})_{12}$, and **8c** $C_{60}(\text{Man})_{12}$, were shown for the first time to have good protective effects against PM-induced oxidative stress, inflammation, and impairment of barrier proteins in HaCaT keratinocytes (Figure 8). In contrast, the poor water-solubility of $C_{60}\text{-H}_2\text{O}$ may be the cause of its lack of antioxidant and anti-inflammation activity, and barrier proteins preservation effects. The glycofullerenes may have great potential applications as cosmeceutical products to protect the skin from PM-induced inflammation and oxidative stress damage or as medicine to treat ROS-caused skin diseases in the future.

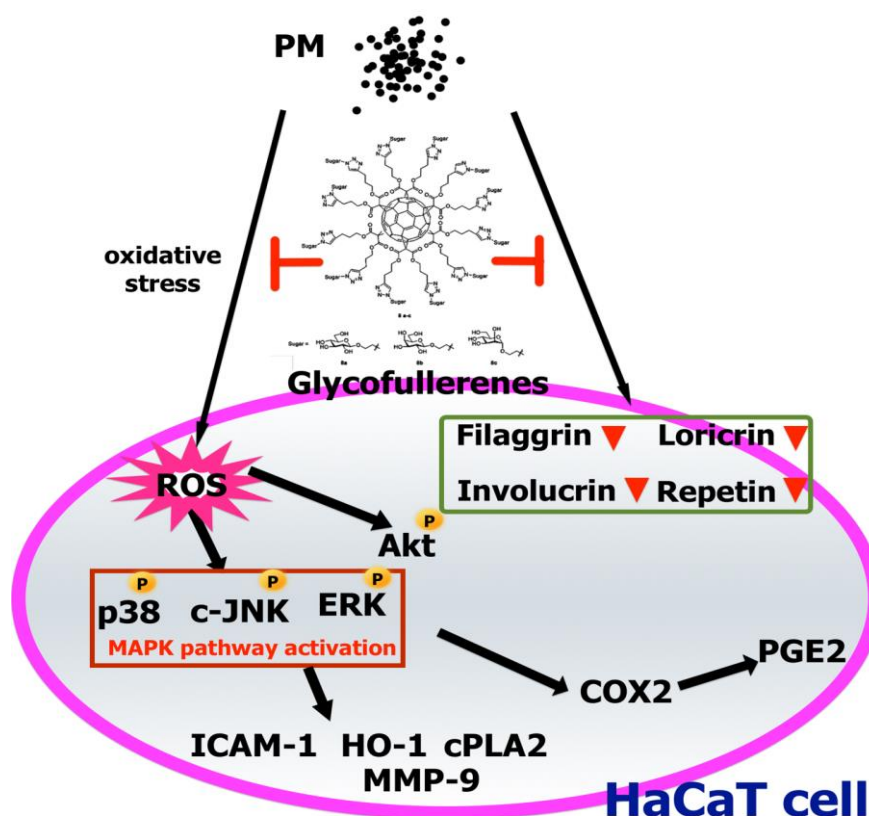


Figure 8. A model for the molecular mechanisms underlying the suppressive effects of glycofullerenes on particulate matter (PM)-triggered oxidation, inflammation, and loss of barrier proteins in HaCaT cells. PM increased ROS generation and activated the MAPK and Akt pathways, followed by upregulation of the expressions of inflammatory proteins (ICAM-1, COX-2, HO-1, and PGE2, etc.). Additionally, the levels of barrier proteins were decreased by PM exposure. Finally, cell apoptosis occurred. Pre-treatment with glycofullerenes could inhibit the PM-induced adverse effects via mechanisms such as ROS scavenging, anti-inflammation, and maintenance of the expressions of barrier proteins in HaCaT cells.

Supplementary Materials: The following are available online at <http://www.mdpi.com/2218-273X/10/4/514/s1>, Figure S1: NMR spectrum of compound 3, Figure S2: NMR spectrum of compound 5, Figure S3: IR spectra of compound 5, Figure S4: UV spectra of compound 5 in DMSO, Figure S5: NMR spectrum of compound 6, Figure S6: IR spectra of compound 6, Figure S7: UV spectra of compound 6 in DMSO, Figure S8: Synthetic route of glucoside 7a, galactoside 7b, and mannoside 7c, Figure S9: NMR spectrum of compound 8a, Figure S10: IR spectra of compound 8a, Figure S11: UV spectra of compound 8a in DMSO, Figure S12: Mass spectra of compound 8a, Figure S13: NMR spectrum of compound 8b, Figure S14: IR spectra of compound 8b, Figure S15: UV spectra of compound 8b in DMSO, Figure S16: Mass spectra of compound 8b, Figure S17: NMR spectrum of compound 8c, Figure S18: IR spectra of compound 8c, Figure S19: UV spectra of compound 8c in DMSO, Figure S20: Mass spectra of compound 8c.

Author Contributions: Conceptualization, C.-W.L., K.-T.P., and C.-H.L.; investigation, methodology, and compound synthesis, Y.-H.S., Y.-L.Y., H.-Y.L., M.-C.C., and C.-H.L.; western blotting, flow, and oversight analysis of the results, S.-Y.L., H.-C.L., I.-T.L., L.-F.H., Y.-C.C., Y.-H.S., Y.-L.Y., and C.-W.L.; writing—original draft preparation, C.-W.L., K.-T.P., Y.-C.C., and C.-H.L.; writing—review and editing, C.-W.L., I.-T.L., Y.-C.C., and C.-H.L.; supervision, C.-W.L., K.-T.P., and C.-H.L.; project administration, C.-W.L. and C.-H.L.; All authors have read and approved the final manuscript.

Funding: We thank National Chung Hsing University and Ministry of Science and Technology of Taiwan for the financial support under contracts MOST 106-2320-B-255-001-, 106-2314-B-255-007-, 107-2113-M-005-014-, 108-2113-M-005-004-, Chang Gung University of Science Foundation (grants ZRRPF3J0081, ZRRPF6J0011) and Chang Gung Medical Research Program Foundation (grants CMRPF6G0081, CMRPF6H0041, CMRPF6H0042, CMRPF6J0051, CMRPF6K0041).

Conflicts of Interest: The authors declare no conflict of interest and the funders had no role in the design of the study; in the collection, analyses, or interpretation of data; in the writing of the manuscript, or in the decision to publish the results.

Abbreviations

AP-1	Activator protein 1
COX-2	Cyclooxygenase
cPLA2	Cytosolic phospholipases A2
DLS	Dynamic light scattering
ERK	Extracellular regulated protein kinase
FITC	Fluorescein isothiocyanate
GAPDH	Glyceraldehyde 3-phosphate dehydrogenase
H2DCFDA	2',7'-dichlorodihydrofluorescein diacetate
HO-1	Heme oxygenase-1
ICAM-1	Intercellular adhesion molecular-1
IR	Infrared spectroscopy
JNK	c-Jun N-terminal kinase
LUMO	Lowest unoccupied molecular orbital
MAPK	Mitogen-activated protein kinase
MMP-9	Metalloproteinase-9
NF-κB	nuclear factor kappa-light-chain-enhancer of activated B cells
NMR	Nuclear magnetic resonance spectroscopy
PM	Particulate matter
PGE2	Prostaglandin E2
ROS	Reactive oxygen species
TEM	Transmission electron microscopy
TLC	Thin-layer chromatography
UV-Vis	Ultraviolet-visible spectroscopy

References

1. Prüss-Ustün, A.J.W.; Corvalán, C.; Bos, R.; Neira, M. Preventing Disease Through Healthy Environments: A Global Assessment of the Burden of Disease from Environmental Risks. Available online: https://www.who.int/quantifying_ehimpacts/publications/preventing-disease/en/ (accessed on 2 May 2019).
2. Bernstein, J.A.; Alexis, N.; Barnes, C.; Bernstein, I.L.; Nel, A.; Peden, D.; Diaz-Sanchez, D.; Tarlo, S.M.; Williams, P.B.; Bernstein, J.A. Health effects of air pollution. *J. Allergy Clin. Immunol.* **2004**, *114*, 1116–1123. [CrossRef] [PubMed]
3. Drakaki, E.; Dessinioti, C.; Antoniou, C.V. Air pollution and the skin. *Front. Environ. Sci.* **2014**, *2*. [CrossRef]
4. Parrado, C.; Mercado-Saenz, S.; Perez-Davo, A.; Gilaberte, Y.; Gonzalez, S.; Juarranz, A. Environmental stressors on skin aging. Mechanistic insights. *Front. Pharmacol.* **2019**, *10*. [CrossRef] [PubMed]
5. Lee, C.W.; Lin, Z.C.; Hu, S.C.; Chiang, Y.C.; Hsu, L.F.; Lin, Y.C.; Lee, I.T.; Tsai, M.H.; Fang, J.Y. Urban particulate matter down-regulates filaggrin via COX2 expression/PGE2 production leading to skin barrier dysfunction. *Sci. Rep.* **2016**, *6*, 27995. [CrossRef] [PubMed]
6. Krusic, P.J.; Wasserman, E.; Keizer, P.N.; Morton, J.R.; Preston, K.F. Radical reactions of C₆₀. *Science* **1991**, *254*, 1183–1185. [CrossRef] [PubMed]
7. Kroto, H.W.; Heath, J.R.; O'Brien, S.C.; Curl, R.F.; Smalley, R.E. C₆₀: Buckminsterfullerene. *Nature* **1985**, *318*, 162. [CrossRef]
8. Krätschmer, W.; Lamb, L.D.; Fostiropoulos, K.; Huffman, D.R. Solid C₆₀: A new form of carbon. *Nature* **1990**, *347*, 354. [CrossRef]
9. Yan, W.; Seifermann, S.M.; Pierrat, P.; Bräse, S. Synthesis of highly functionalized C₆₀ fullerene derivatives and their applications in material and life sciences. *Org. Biomol. Chem.* **2015**, *13*, 25–54. [CrossRef] [PubMed]
10. Bakry, R.; Vallant, R.M.; Najam-Ul-Haq, M.; Rainer, M.; Szabo, Z.; Huck, C.W.; Bonn, G.K. Medicinal applications of fullerenes. *Int. J. Nanomed.* **2007**, *2*, 639–649.

11. Xiao, L.; Takada, H.; Gan, X.H.; Miwa, N. The water-soluble fullerene derivative ‘Radical Sponge®’ exerts cytoprotective action against UVA irradiation but not visible-light-catalyzed cytotoxicity in human skin keratinocytes. *Bioorganic Med. Chem. Lett.* **2006**, *16*, 1590–1595. [\[CrossRef\]](#)
12. Mousavi, S.Z.; Nafisi, S.; Maibach, H.I. Fullerene nanoparticle in dermatological and cosmetic applications. *Nanomed. Nanotechnol. Biol. Med.* **2017**, *13*, 1071–1087. [\[CrossRef\]](#) [\[PubMed\]](#)
13. Castro, E.; Hernandez Garcia, A.; Zavala, G.; Echegoyen, L. Fullerenes in biology and medicine. *J. Mater. Chem. B* **2017**, *5*, 6523–6535. [\[CrossRef\]](#) [\[PubMed\]](#)
14. Tzirakis, M.D.; Orfanopoulos, M. Radical reactions of fullerenes: From synthetic organic chemistry to materials science and biology. *Chem. Rev.* **2013**, *113*, 5262–5321. [\[CrossRef\]](#) [\[PubMed\]](#)
15. Hsieh, F.-Y.; Zhilenkov, A.V.; Voronov, I.I.; Khakina, E.A.; Mischenko, D.V.; Troshin, P.A.; Hsu, S.-H. Water-soluble fullerene derivatives as brain medicine: Surface chemistry determines if they are neuroprotective and antitumor. *ACS Appl. Mater. Interfaces* **2017**, *9*, 11482–11492. [\[CrossRef\]](#)
16. Monti, D.; Moretti, L.; Salvioli, S.; Straface, E.; Malorni, W.; Pellicciari, R.; Schettini, G.; Bisaglia, M.; Pincelli, C.; Fumelli, C.; et al. C₆₀ carboxyfullerene exerts a protective activity against Oxidative stress-induced apoptosis in human peripheral blood mononuclear cells. *Biochem. Biophys. Res. Commun.* **2000**, *277*, 711–717. [\[CrossRef\]](#)
17. Fluri, F.; Grünstein, D.; Cam, E.; Ungethüm, U.; Hatz, F.; Schäfer, J.; Samnick, S.; Israel, I.; Kleinschnitz, C.; Orts-Gil, G.; et al. Fullerenols and glucosamine fullerenes reduce infarct volume and cerebral inflammation after ischemic stroke in normotensive and hypertensive rats. *Exp. Neurol.* **2015**, *265*, 142–151. [\[CrossRef\]](#)
18. Nierengarten, I.; Nierengarten, J.F. Fullerene sugar balls: A new class of biologically active fullerene derivatives. *Chem. Asian J.* **2014**, *9*, 1436–1444. [\[CrossRef\]](#)
19. Cecioni, S.; Oerthel, V.; Iehl, J.; Holler, M.; Goyard, D.; Praly, J.P.; Imbert, A.; Nierengarten, J.F.; Vidal, S. Synthesis of dodecavalent fullerene-based glycoclusters and evaluation of their binding properties towards a bacterial lectin. *Chemistry* **2011**, *17*, 3252–3261. [\[CrossRef\]](#)
20. Durka, M.; Buffet, K.; Iehl, J.; Holler, M.; Nierengarten, J.F.; Vincent, S.P. The inhibition of liposaccharide heptosyltransferase WaaC with multivalent glycosylated fullerenes: A new mode of glycosyltransferase inhibition. *Chemistry* **2012**, *18*, 641–651. [\[CrossRef\]](#)
21. Luczkowiak, J.; Munoz, A.; Sanchez-Navarro, M.; Ribeiro-Viana, R.; Ginieis, A.; Illescas, B.M.; Martin, N.; Delgado, R.; Rojo, J. Glycofullerenes inhibit viral infection. *Biomacromolecules* **2013**, *14*, 431–437. [\[CrossRef\]](#)
22. Muñoz, A.; Illescas, B.M.; Luczkowiak, J.; Lasala, F.; Ribeiro-Viana, R.; Rojo, J.; Delgado, R.; Martín, N. Antiviral activity of self-assembled glycodendro[60]fullerene monoadducts. *J. Mater. Chem. B* **2017**, *5*, 6566–6571. [\[CrossRef\]](#)
23. Boukamp, P.; Petrussevska, R.T.; Breitkreutz, D.; Hornung, J.; Markham, A.; Fusenig, N.E. Normal keratinization in a spontaneously immortalized aneuploid human keratinocyte cell line. *J. Cell Biol.* **1988**, *106*, 761–771. [\[CrossRef\]](#) [\[PubMed\]](#)
24. Schoop, V.M.; Mirancea, N.; Fusenig, N.E. Epidermal organization and differentiation of HaCaT keratinocytes in organotypic coculture with human dermal fibroblasts. *J. Invest. Dermatol.* **1999**, *112*, 343–353. [\[CrossRef\]](#) [\[PubMed\]](#)
25. Lin, Z.C.; Lee, C.W.; Tsai, M.H.; Ko, H.H.; Fang, J.Y.; Chiang, Y.C.; Liang, C.J.; Hsu, L.F.; Hu, S.C.; Yen, F.L. Eupafolin nanoparticles protect HaCaT keratinocytes from particulate matter-induced inflammation and oxidative stress. *Int. J. Nanomed.* **2016**, *11*, 3907–3926. [\[CrossRef\]](#)
26. Colombo, I.; Sangiovanni, E.; Maggio, R.; Mattozzi, C.; Zava, S.; Corbett, Y.; Fumagalli, M.; Carlino, C.; Corsetto, P.A.; Scaccabarozzi, D.; et al. HaCaT cells as a reliable in vitro differentiation model to dissect the inflammatory/repair response of human keratinocytes. *Mediat. Inflamm.* **2017**, *2017*, 12. [\[CrossRef\]](#)
27. Huang, P.H.; Tseng, C.H.; Lin, C.Y.; Lee, C.W.; Yen, F.L. Preparation, characterizations and anti-pollutant activity of 7,3',4'-trihydroxyisoflavone nanoparticles in particulate matter-induced HaCaT keratinocytes. *Int. J. Nanomed.* **2018**, *13*, 3279–3293. [\[CrossRef\]](#)
28. Peng, K.T.; Hsieh, M.Y.; Lin, C.T.; Chen, C.F.; Lee, M.S.; Huang, Y.Y.; Chang, P.J. Treatment of critically sized femoral defects with recombinant BMP-2 delivered by a modified mPEG-PLGA biodegradable thermosensitive hydrogel. *BMC Musculoskelet. Disord.* **2016**, *17*, 286. [\[CrossRef\]](#)
29. Lee, C.W.; Lin, Z.C.; Hsu, L.F.; Fang, J.Y.; Chiang, Y.C.; Tsai, M.H.; Lee, M.H.; Li, S.Y.; Hu, S.C.; Lee, I.T.; et al. Eupafolin ameliorates COX-2 expression and PGE2 production in particulate pollutants-exposed human keratinocytes through ROS/MAPKs pathways. *J. Ethnopharmacol.* **2016**, *189*, 300–309. [\[CrossRef\]](#)

30. Narayanapillai, S.; Agarwal, C.; Tilley, C.; Agarwal, R. Silibinin is a potent sensitizer of UVA radiation-induced oxidative stress and apoptosis in human keratinocyte HaCaT cells. *Photochem. Photobiol.* **2012**, *88*, 1135–1140. [\[CrossRef\]](#)
31. Fujisaki, H.; Futaki, S.; Yamada, M.; Sekiguchi, K.; Hayashi, T.; Ikejima, T.; Hattori, S. Respective optimal calcium concentrations for proliferation on type I collagen fibrils in two keratinocyte line cells, HaCaT and FEPE1L-8. *Regen. Ther.* **2018**, *8*, 73–79. [\[CrossRef\]](#)
32. Lee, C.W.; Chi, M.C.; Peng, K.T.; Chiang, Y.C.; Hsu, L.F.; Yan, Y.L.; Li, H.Y.; Chen, M.C.; Lee, I.T.; Lai, C.H. Water-soluble fullereneol C₆₀(OH)₃₆ toward effective anti-air pollution induced by urban particulate matter in HaCaT cell. *Int. J. Mol. Sci.* **2019**, *20*, 4259. [\[CrossRef\]](#) [\[PubMed\]](#)
33. Rao, X.; Zhong, J.; Brook, R.D.; Rajagopalan, S. Effect of particulate matter air pollution on cardiovascular oxidative stress pathways. *Antioxid. Redox. Signal* **2018**, *28*, 797–818. [\[CrossRef\]](#) [\[PubMed\]](#)
34. Son, Y.; Cheong, Y.K.; Kim, N.H.; Chung, H.T.; Kang, D.G.; Pae, H.O. Mitogen-activated protein kinases and reactive oxygen species: How can ROS activate MAPK pathways? *J. Signal Transduct.* **2011**, *2011*, 792639. [\[CrossRef\]](#) [\[PubMed\]](#)
35. Mittal, M.; Siddiqui, M.R.; Tran, K.; Reddy, S.P.; Malik, A.B. Reactive oxygen species in inflammation and tissue injury. *Antioxid. Redox. Signal* **2014**, *20*, 1126–1167. [\[CrossRef\]](#)
36. Li, Q.; Kang, Z.; Jiang, S.; Zhao, J.; Yan, S.; Xu, F.; Xu, J. Effects of ambient fine particles PM 2.5 on human HaCaT cells. *Int. J. Environ. Res. Public Health* **2017**, *14*, 72. [\[CrossRef\]](#)
37. Gharbi, N.; Pressac, M.; Hadchouel, M.; Szwarc, H.; Wilson, S.R.; Moussa, F. [60]Fullerene is a powerful antioxidant in vivo with no acute or subacute toxicity. *Nano Lett.* **2005**, *5*, 2578–2585. [\[CrossRef\]](#)
38. Andrievsky, G.; Klochov, V.; Derevyanchenko, L. Is the C₆₀ fullerene molecule toxic?! *Fuller. Nanotub. Carbon Nanostruct.* **2005**, *13*, 363–376. [\[CrossRef\]](#)
39. Chistyakov, V.A.; Smirnova, Y.O.; Prazdnova, E.V.; Soldatov, A.V. Possible mechanisms of fullerene C(6)(0) antioxidant action. *Biomed. Res. Int.* **2013**, *2013*, 821498. [\[CrossRef\]](#)
40. Kong, L.; Zepp, R.G. Production and consumption of reactive oxygen species by fullerenes. *Environ. Toxicol. Chem.* **2012**, *31*, 136–143. [\[CrossRef\]](#)
41. Brandes, R.P.; Weissmann, N.; Schroder, K. Nox family NADPH oxidases: Molecular mechanisms of activation. *Free Radic. Biol. Med.* **2014**, *76*, 208–226. [\[CrossRef\]](#)
42. Day, B.J. Antioxidant therapeutics: Pandora's box. *Free Radic. Biol. Med.* **2014**, *66*, 58–64. [\[CrossRef\]](#) [\[PubMed\]](#)
43. Singh, S.; Bocker, C.; Koppaka, V.; Chen, Y.; Jackson, B.C.; Matsumoto, A.; Thompson, D.C.; Vasiliou, V. Aldehyde dehydrogenases in cellular responses to oxidative/electrophilic stress. *Free Radic. Biol. Med.* **2013**, *56*, 89–101. [\[CrossRef\]](#) [\[PubMed\]](#)
44. Devasagayam, T.P.; Tilak, J.C.; Bloor, K.K.; Sane, K.S.; Ghaskadbi, S.S.; Lele, R.D. Free radicals and antioxidants in human health: Current status and future prospects. *J. Assoc. Physicians India* **2004**, *52*, 794–804. [\[PubMed\]](#)
45. Trachootham, D.; Alexandre, J.; Huang, P. Targeting cancer cells by ROS-mediated mechanisms: A radical therapeutic approach? *Nat. Rev. Drug. Discov.* **2009**, *8*, 579–591. [\[CrossRef\]](#)
46. Farmer, E.E.; Mueller, M.J. ROS-mediated lipid peroxidation and RES-activated signaling. *Annu. Rev. Plant Biol.* **2013**, *64*, 429–450. [\[CrossRef\]](#)
47. Radak, Z.; Zhao, Z.; Goto, S.; Koltai, E. Age-associated neurodegeneration and oxidative damage to lipids, proteins and DNA. *Mol. Asp. Med.* **2011**, *32*, 305–315. [\[CrossRef\]](#)
48. Zhang, W.; Xiao, S.; Ahn, D.U. Protein oxidation: Basic principles and implications for meat quality. *Crit. Rev. Food Sci. Nutr.* **2013**, *53*, 1191–1201. [\[CrossRef\]](#)
49. Schieber, M.; Chandel, N.S. ROS function in redox signaling and oxidative stress. *Curr. Biol.* **2014**, *24*, R453–R462. [\[CrossRef\]](#)
50. Foley, S.; Crowley, C.; Smaih, M.; Bonfils, C.; Erlanger, B.F.; Seta, P.; Larroque, C. Cellular localisation of a water-soluble fullerene derivative. *Biochem. Biophys. Res. Commun.* **2002**, *294*, 116–119. [\[CrossRef\]](#)
51. Cargnello, M.; Roux, P.P. Activation and function of the MAPKs and their substrates, the MAPK-activated protein kinases. *Microbiol. Mol. Biol. Rev.* **2011**, *75*, 50–83. [\[CrossRef\]](#)
52. Busca, R.; Pouyssegur, J.; Lenormand, P. ERK1 and ERK2 map kinases: Specific roles or functional redundancy? *Front. Cell Dev. Biol.* **2016**, *4*, 53. [\[CrossRef\]](#) [\[PubMed\]](#)

53. Sabapathy, K.; Wagner, E.F. JNK2: A negative regulator of cellular proliferation. *Cell Cycle* **2004**, *3*, 1520–1523. [[CrossRef](#)] [[PubMed](#)]
54. Bode, A.M.; Dong, Z. The functional contrariety of JNK. *Mol. Carcinog.* **2007**, *46*, 591–598. [[CrossRef](#)] [[PubMed](#)]
55. Ke, H.; Harris, R.; Coloff, J.L.; Jin, J.Y.; Leshin, B.; Miliani de Marval, P.; Tao, S.; Rathmell, J.C.; Hall, R.P.; Zhang, J.Y. The c-Jun NH2-terminal kinase 2 plays a dominant role in human epidermal neoplasia. *Cancer Res.* **2010**, *70*, 3080–3088. [[CrossRef](#)]
56. Chen, H.; Wang, X.; Han, J.; Fan, Z.; Sadia, S.; Zhang, R.; Guo, Y.; Jiang, Y.; Wu, Y. AKT and its related molecular feature in aged mice skin. *PLoS ONE* **2017**, *12*, e0178969. [[CrossRef](#)]
57. Castilho, R.M.; Squarize, C.H.; Gutkind, J.S. Exploiting PI3K/mTOR signaling to accelerate epithelial wound healing. *Oral. Dis.* **2013**, *19*, 551–558. [[CrossRef](#)]
58. Gao, Y.L.; Liu, C.S.; Zhao, R.; Wang, L.L.; Li, S.S.; Liu, M.; Zhang, M.; Jiang, S.K.; Tian, Z.L.; Wang, M.; et al. Effects of PI3K/Akt pathway in wound healing process of mice skin. *Fa Yi Xue Za Zhi* **2016**, *32*, 7–12.
59. Di-Poi, N.; Ng, C.Y.; Tan, N.S.; Yang, Z.; Hemmings, B.A.; Desvergne, B.; Michalik, L.; Wahli, W. Epithelium-mesenchyme interactions control the activity of peroxisome proliferator-activated receptor beta/delta during hair follicle development. *Mol. Cell. Biol.* **2005**, *25*, 1696–1712. [[CrossRef](#)]
60. Paine, A.; Eiz-Vesper, B.; Blasczyk, R.; Immenschuh, S. Signaling to heme oxygenase-1 and its anti-inflammatory therapeutic potential. *Biochem. Pharm.* **2010**, *80*, 1895–1903. [[CrossRef](#)]
61. Vile, G.F.; Basu-Modak, S.; Waltner, C.; Tyrrell, R.M. Heme oxygenase 1 mediates an adaptive response to oxidative stress in human skin fibroblasts. *Proc. Natl. Acad. Sci. USA* **1994**, *91*, 2607–2610. [[CrossRef](#)]
62. Wu, M.L.; Ho, Y.C.; Lin, C.Y.; Yet, S.F. Heme oxygenase-1 in inflammation and cardiovascular disease. *Am. J. Cardiovasc. Dis.* **2011**, *1*, 150–158. [[PubMed](#)]
63. Turkseven, S.; Kruger, A.; Mingone, C.J.; Kaminski, P.; Inaba, M.; Rodella, L.F.; Ikehara, S.; Wolin, M.S.; Abraham, N.G. Antioxidant mechanism of heme oxygenase-1 involves an increase in superoxide dismutase and catalase in experimental diabetes. *Am. J. Physiol. Heart Circ. Physiol.* **2005**, *289*, H701–H707. [[CrossRef](#)] [[PubMed](#)]
64. Muller, W.A. Mechanisms of leukocyte transendothelial migration. *Annu. Rev. Pathol.* **2011**, *6*, 323–344. [[CrossRef](#)] [[PubMed](#)]
65. Viac, J.; Schmitt, D.; Claudy, A. Adhesion molecules and inflammatory dermatoses. *Allerg. Immunol.* **1994**, *26*, 274–277.
66. Singer, K.H.; Tuck, D.T.; Sampson, H.A.; Hall, R.P. Epidermal keratinocytes express the adhesion molecule intercellular adhesion molecule-1 in inflammatory dermatoses. *J. Investig. Dermatol.* **1989**, *92*, 746–750. [[CrossRef](#)]
67. Mruwat, R.; Cohen, Y.; Yedgar, S. Phospholipase A(2) inhibition as potential therapy for inflammatory skin diseases. *Immunotherapy* **2013**, *5*, 315–317. [[CrossRef](#)]
68. Soubhye, J.; van Antwerpen, P.; Dufasne, F. Targeting cytosolic phospholipase A2 α for novel anti-inflammatory agents. *Curr. Med. Chem.* **2018**, *25*, 2418–2447. [[CrossRef](#)]
69. Sandilands, A.; Sutherland, C.; Irvine, A.D.; McLean, W.H. Filaggrin in the frontline: Role in skin barrier function and disease. *J. Cell Sci.* **2009**, *122*, 1285–1294. [[CrossRef](#)]
70. Jin, S.H.; Choi, D.; Chun, Y.J.; Noh, M. Keratinocyte-derived IL-24 plays a role in the positive feedback regulation of epidermal inflammation in response to environmental and endogenous toxic stressors. *Toxicol. Appl. Pharmacol.* **2014**, *280*, 199–206. [[CrossRef](#)]



© 2020 by the authors. Licensee MDPI, Basel, Switzerland. This article is an open access article distributed under the terms and conditions of the Creative Commons Attribution (CC BY) license (<http://creativecommons.org/licenses/by/4.0/>).

11-Keto- β -Boswellic Acid Attenuates Glutamate Release and Kainic Acid-Induced Excitotoxicity in the Rat Hippocampus

Authors

Cheng Wei Lu^{1,3}, Tzu Yu Lin^{1,3}, Su Jane Wang^{2,4}

Affiliations

- 1 Department of Anesthesiology, Far-Eastern Memorial Hospital, New Taipei City, Taiwan
- 2 School of Medicine, Fu Jen Catholic University, New Taipei City, Taiwan
- 3 Department of Mechanical Engineering, Yuan Ze University, Taoyuan City, Taiwan
- 4 Research Center for Chinese Herbal Medicine, College of Human Ecology, Chang Gung University of Science and Technology, Taoyuan City, Taiwan

Key words

Burseraceae, *Boswellia serrata*, KBA, presynaptic glutamate release, kainic acid, neuroprotection, hippocampus

received October 29, 2019

revised January 20, 2020

accepted January 28, 2020

Bibliography

DOI <https://doi.org/10.1055/a-1107-9337>

published online | Planta Med © Georg Thieme Verlag KG
Stuttgart · New York | ISSN 0032-0943

Correspondence

Su Jane Wang

School of Medicine, Fu Jen Catholic University
No. 510, Chung-Cheng Rd., New Taipei City 24205,
Hsin-Chuang, Taiwan

Phone: + 88 62 29 05 34 65, Fax: + 88 62 29 05 20 96
med0003@mail.fju.edu.tw

ABSTRACT

Excessive glutamate concentration induces neuronal death in acute brain injuries and chronic neurodegenerative diseases. Natural compounds from medicinal plants have attracted considerable attention for their use in the prevention and treatment of neurological disorders. 11-Keto- β -boswellic acid, a triterpenoid found in the medicinal plant *Boswellia serrata*, has neuroprotective potential. The present study investigated the effect of 11-keto- β -boswellic acid on glutamate release *in vitro* and kainic acid-induced glutamate excitotoxicity *in vivo* in the rat hippocampus. In rat hippocampal nerve terminals (synaptosomes), 11-keto- β -boswellic acid dose-dependently inhibited 4-aminopyridine-stimulated glutamate release. This effect was dependent on extracellular calcium, persisted in the presence of the glutamate transporter inhibitor DL-threo- β -benzyloxyaspartate, and was blocked by the vesicular transporter inhibitor bafilomycin A1. In addition, 11-keto- β -boswellic acid reduced the 4-aminopyridine-induced increase in intrasynaptosomal Ca^{2+} levels. The N- and P/Q-type channel blocker ω -conotoxin MVIIC and the protein kinase A inhibitor H89 significantly suppressed the 11-keto- β -boswellic acid-mediated inhibition of glutamate release, whereas the intracellular Ca^{2+} -releasing inhibitors dantrolene, CGP37157, and xestospongine C, mitogen-activated protein kinase inhibitor PD98059, as well as protein kinase C inhibitor calphostin C had no effect. In a rat model of excitotoxicity induced by intraperitoneal kainic acid injection (15 mg/kg), intraperitoneal 11-keto- β -boswellic acid administration (10 or 50 mg/kg) 30 min before kainic acid injection considerably ameliorated kainic acid-induced glutamate concentration elevation and CA3 neuronal death. These data suggested that 11-keto- β -boswellic acid inhibits glutamate release from the rat hippocampal synaptosomes by suppressing N- and P/Q-type Ca^{2+} channels and protein kinase A activity, as well as exerts protective effects against kainic acid-induced excitotoxicity *in vivo*.

Introduction

Glutamate is the most prominent excitatory neurotransmitter in the CNS and plays a critical role in neurological processes, including cognition, learning, and memory [1]. However, under pathophysiological conditions, excessive glutamate release causes overactivation

of glutamate receptors, consequently resulting in neuronal damage and death [2]. This glutamate excitotoxicity has also been observed in numerous brain diseases, such as ischemia, stroke, epilepsy, and neurodegenerative diseases [3,4]. Various neuroprotective compounds have been developed to treat these brain disorders; however, satisfactory drug treatments in clinical practice are

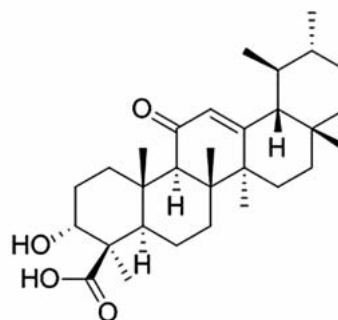
ABBREVIATIONS

4-AP	4-aminopyridine
CGP37157	7-chloro-5-(2-chlorophenyl)-1,5-dihydro-4,1-benzothiazepin-2(3H)-one
CNS	central nervous system
DL-TBOA	DL-threo- β -benzyloxyaspartate
GF109203X	bisindolylmaleimide I
H89	N-[2-(p-bromocinnamylamino)ethyl]-5-isoquinolinesulfonamide
i. p.	intraperitoneal
KA	kainic acid
KBA	11-keto- β -boswellic acid
MAPK	mitogen-activated protein kinase
PKA	protein kinase A
PKC	protein kinase C
PD98059	2-(2-amino-3-methoxyphenyl)-4H-1-benzopyran-4-one
VDCCS	voltage-dependent Ca^{2+} channels

limited [5,6]. Therefore, developing new neuroprotective drugs against glutamate excitotoxicity is a crucial research goal.

Medicinal plants are attractive sources of new drugs and have demonstrated promising results for preventing and treating brain disorders [7–9]. *Boswellia serrata*, a medicinal plant of family Burseraceae, has been widely used in traditional medicine to treat various chronic inflammatory diseases such as osteoarthritis, chronic bowel diseases, arthritis, and asthma [10,11]. *B. serrata* extracts have multiple pharmacological properties, including anticancer, antidiabetic, immunomodulatory, antioxidant, and anti-inflammatory activities [12–14]. In addition to the aforementioned pharmacological properties, the neuroprotective effects of *B. serrata* extracts under different conditions have been documented. For example, the extract attenuates oxygen-glucose-serum deprivation-induced or glutamate-induced neuronal cell death in PC12 cells [15,16], reduces brain damage and alleviates neurological deficits in animal models of cerebral ischemia and Parkinson's disease [17–19], as well as enhances learning capability in type 2 diabetic and aged rats [20,21]. *B. serrata* extract contains multiple compounds, such as terpenoids and triterpenoids, which contribute to its pharmacological activities [11]. In the present study, KBA (► Fig. 1) was selected because it is one of the major constituents in the triterpenoid fraction of the extract [14]. Furthermore, the efficacy of KBA in the CNS has been evaluated, including its distribution in the brain [22] and neuroprotective effects [23].

Considering that the increase in glutamate is one of the major culprits for neuronal degeneration in various brain disorders, reduction in presynaptic glutamate release is considered a potential mechanism for neuroprotective actions [24,25]. KBA has shown neuroprotective effects; however, studies on the effect of KBA on glutamate release are lacking. Therefore, the present study evaluated the effect of KBA on glutamate release from synaptosomal preparations and the possible protective role in a rat model of KA-induced glutamate excitotoxicity.



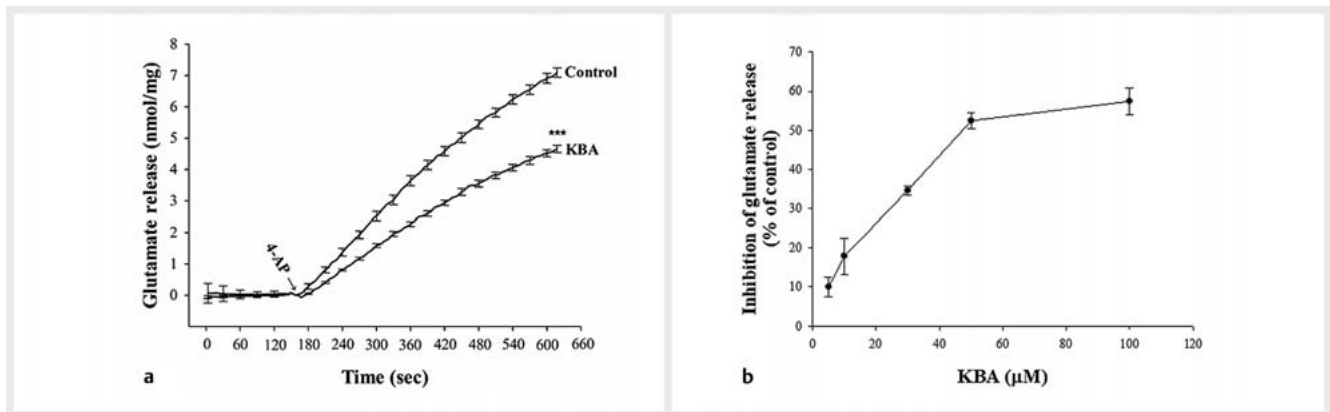
► Fig. 1 Chemical structures of KBA (11-keto- β -boswellic acid).

Results

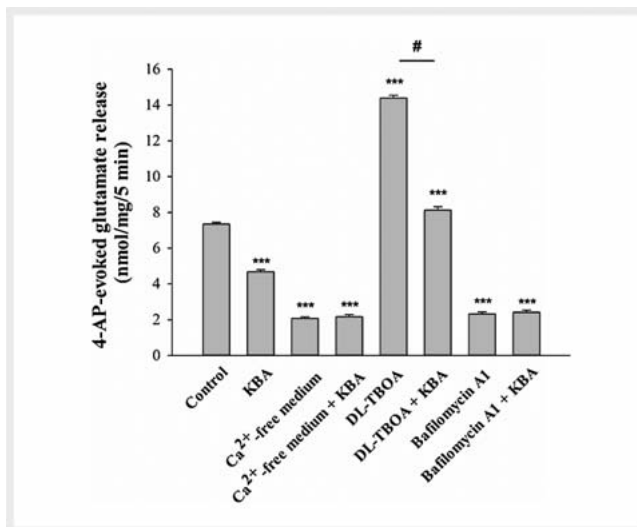
To examine the presynaptic action of KBA specifically, nerve terminals (synaptosomes) were depolarized with the K^+ channel blocker 4-AP, which opens VDCCs and induces the release of glutamate [26]. In ► Fig. 2a, 1 mM 4-AP evoked a glutamate release of 7.1 ± 0.1 nmol/mg/5 min from synaptosomes incubated in the presence of 1.2 mM CaCl_2 . Preincubation of synaptosomes with 50 μM KBA for 10 min caused an inhibition of 4-AP-stimulated release of about 50% to 3.4 ± 0.1 nmol/mg/5 min [$t(8) = 19.8$, $p < 0.001$] (► Fig. 2b). KBA did not alter the basal release of glutamate. The KBA-mediated inhibition of glutamate release was concentration dependent, with 5, 10, 30, 50, and 100 μM KBA reducing glutamate release by 10 ± 2.5 , 17.9 ± 4.6 , 34.6 ± 1.2 , 52.4 ± 2.1 , and $57.4 \pm 3.4\%$, respectively (► Fig. 2b). A maximum inhibition occurred with 50–100 μM KBA. The IC_{50} value for KBA inhibition of 4-AP-stimulated glutamate release, derived from a log dose-response curve, was 31 μM .

We next examined whether the effect of KBA on 4-AP-stimulated glutamate release reflected an effect on exocytotic vesicular release, or on Ca^{2+} -independent release attributable to cytosolic efflux via reversal of the glutamate transporter [27]. ► Fig. 3 shows that glutamate release stimulated by 4-AP in extracellular Ca^{2+} -free solution containing 0.3 mM EGTA was significantly reduced [$F(2,17) = 862.1$, $p < 0.001$]. In the absence of extracellular Ca^{2+} , 4-AP-stimulated glutamate release was unaffected by 50 μM KBA ($p > 0.05$). In addition, in the presence of 10 μM DL-TBOA, a potent inhibitor of the plasma membrane glutamate transporter, although 4-AP-stimulated glutamate release increased (because of inhibition of reuptake of released glutamate) ($p < 0.001$), 50 μM KBA continued to significantly reduce the 4-AP-stimulated release of glutamate [$F(2,17) = 1047.5$, $P < 0.001$] (► Fig. 3). In contrast, the vesicular transporter inhibitor bafilomycin A1 (0.1 μM) reduced 4-AP-stimulated glutamate release [$F(2,17) = 901.2$, $p < 0.001$] (► Fig. 3). However, in the presence of bafilomycin A1, KBA induced a statistically insignificant inhibition ($p = 0.7$).

To further investigate the mechanism of KBA-mediated inhibition of glutamate release, we determined the $[\text{Ca}^{2+}]_i$ with the Ca^{2+} indicator Fura-2. ► Table 1 shows that 4-AP (1 mM) caused an increase in $[\text{Ca}^{2+}]_i$ to a plateau level of 191.9 ± 5.3 nM. The presence of 50 μM KBA reduced the 4-AP-evoked $[\text{Ca}^{2+}]_i$ increase by 25 nM



► **Fig. 2** Effect of 11-keto- β -boswellic acid (KBA) on 4-aminopyridine (4-AP)-stimulated glutamate release from rat synaptosomes. **a** Glutamate release was triggered by the addition of 1 mM 4-AP in the absence (control) and presence of 50 μ M KBA added 10 min before the addition of 4-AP. **b** Dose-response curve showing the effect of KBA (5–100 μ M) on 4-AP-stimulated glutamate release. Data are the mean \pm SEM values of independent experiments using synaptosomal preparations from four to five animals. *** P < 0.001 compared with the control (Student's unpaired t -test).



► **Fig. 3** Effect of 11-keto- β -boswellic acid (KBA) on 4-aminopyridine (4-AP)-stimulated glutamate release in extracellular Ca^{2+} -free solution, or in the presence of the glutamate transporter blocker DL-TBOA and the vesicular transporter inhibitor bafilomycin A1. KBA, DL-TBOA, or bafilomycin A1 was added 10 min before the addition of 4-AP. Each column is the mean \pm SEM values of independent experiments using synaptosomal preparations from five animals. *** P < 0.001 compared with the control (Student's unpaired t -test). # P < 0.05 compare with the DL-TBOA-treated group (one-way ANOVA).

(165.7 ± 4.8 nM) [$t(8) = 8.5$, $p < 0.001$]. In ► **Table 1**, the inhibitory effect of KBA was also evident with the KCl-evoked (15 mM) increase in $[\text{Ca}^{2+}]_i$, which reduced 46% [$t(8) = 4.3$, $p < 0.001$]. The basal $[\text{Ca}^{2+}]_i$ was not altered by KBA ($p > 0.05$).

In synaptic terminals, a depolarization-induced increase in $[\text{Ca}^{2+}]_C$, coupled to glutamate release, is mediated by the extracellular Ca^{2+} influx through VDCCs and intracellular store Ca^{2+} release [28, 29]. To understand the effect of KBA on $[\text{Ca}^{2+}]_i$, a comparative

study using a VDCC inhibitor or intracellular Ca^{2+} -release inhibitors and KBA was performed on the release of glutamate stimulated by 4-AP. In ► **Fig. 4**, the N- and P/Q-type Ca^{2+} channel inhibitor ω -conotoxin MVIIC, at a concentration of 4 μ M, significantly reduced glutamate release evoked by 1 mM 4-AP [$F(2,17) = 279.1$, $p < 0.001$]. Application of 50 μ M KBA was not able to further reduce 4-AP-stimulated glutamate release in the presence of ω -conotoxin MVIIC ($p = 0.9$), indicating the involvement of a reduction of Ca^{2+} entry through N- and P/Q-type Ca^{2+} channels. On the other hand, the Ca^{2+} -induced Ca^{2+} -release inhibitor dantrolene (10 μ M) reduced 4-AP-stimulated glutamate release [$F(2,17) = 133.5$, $p < 0.001$] (► **Fig. 4**). However, the inhibitory action of KBA on 4-AP-stimulated glutamate release persisted in the presence of dantrolene ($p < 0.05$). Similar results were observed with 10 μ M CGP37157 a specific inhibitor of Na^+ -dependent Ca^{2+} release from mitochondria [$F(2,17) = 185.4$, $p < 0.001$], and 1 μ M xestospongion C, a selective IP₃ receptor antagonist [$F(2,17) = 134.8$, $p < 0.001$], as shown in ► **Fig. 4**. KBA (50 μ M) still produced a statistically significant inhibition in the presence of CGP37157 or xestospongion C ($p < 0.05$).

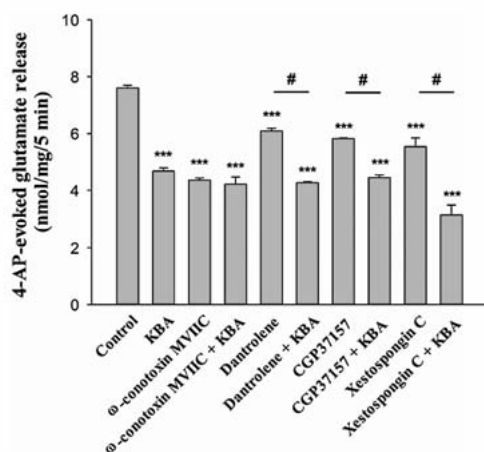
Several protein kinases have been shown to regulate glutamate release [30, 31]. In order to investigate which type of protein kinase signaling pathway participated in the KBA-mediated inhibition of glutamate release, various protein kinase inhibitors were used to examine the effect of KBA on 4-AP-stimulated glutamate release. In ► **Fig. 5**, 1 mM 4-AP-stimulated glutamate release was reduced by the PKA inhibitor H89 (100 μ M) [$F(2,17) = 170.6$, $p < 0.001$], MAPK inhibitor PD98059 (50 μ M) [$F(2,17) = 381.5$, $p < 0.001$], and the PKC inhibitor GF109203X (10 μ M) [$F(2,17) = 123.8$, $p < 0.001$]. In the presence of PD98059 or GF109203X, the inhibitory action of KBA on 4-AP-stimulated glutamate release persisted ($p < 0.05$). However, KBA was not able to further reduce 4-AP-stimulated glutamate release in the presence of H89 ($p > 0.05$).

On the basis of the KBA-mediated inhibition of glutamate release *in vitro*, we further examined whether KBA executed a protective action in a rat model of excitotoxicity induced by KA. As

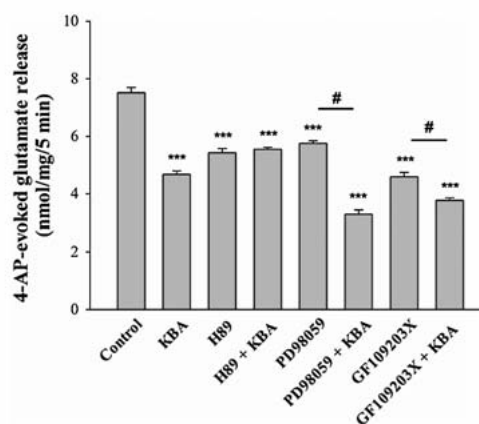
► **Table 1** Effect of KBA on the 4-AP- and KCl-induced increase in $[Ca^{2+}]_i$ in synaptosomes.

	$[Ca^{2+}]_i$ (nM)					
	Basal	4-AP (1 mM)	n	Basal	KCl (15 mM)	n
Control	152.4 ± 3.8	191.9 ± 5.4	5	145.6 ± 4.9	177.6 ± 3.1	5
KBA	149.5 ± 4.2	165.7 ± 4.8***	5	141.6 ± 2.1	155.3 ± 2.3**	5

***P < 0.001, **p < 0.01 compare with the control. KBA, 11-keto- β -boswellic acid; 4-AP, 4-aminopyridine



► **Fig. 4** Effects of 11-keto- β -boswellic acid (KBA) on 4-aminopyridine (4-AP)-stimulated glutamate release in the presence of N- and P/Q-type calcium channel blocker ω -conotoxin MVIIC or intracellular Ca^{2+} release inhibitors dantrolene, CGP37157, and xestospongin C. KBA, ω -conotoxin MVIIC, dantrolene, CGP37157, or xestospongin C was added 10 min before the addition of 4-AP. Each column is the mean \pm SEM values of independent experiments using synaptosomal preparations from five animals. ***P < 0.001 compared with the control; #p < 0.05 compared with the dantrolene-, CGP37157-, or xestospongin C-treated group (one-way ANOVA).



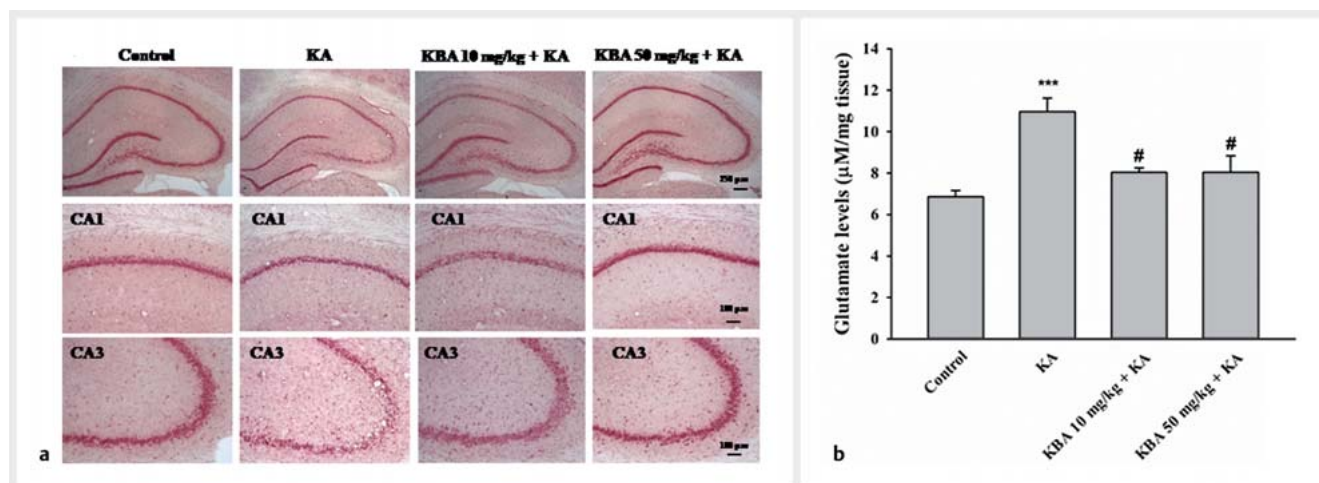
► **Fig. 5** Effects of 11-keto- β -boswellic acid (KBA) on 4-aminopyridine (4-AP)-stimulated glutamate release in the presence of the PKA inhibitor H89, MAPK inhibitor PD98059, and PKC inhibitor GF109203X. KBA was added 10 min before the addition of 4-AP and other drugs 30 min before this. Each column is the mean \pm SEM values of independent experiments using synaptosomal preparations from five animals. ***P < 0.001 compared with the control (Student's unpaired t-test). #P < 0.05 compared with the PD98059- or GF109203X-treated group (one-way ANOVA).

shown in ► **Fig. 6a**, i.p. administration of KA (15 mg/kg) to animals caused extensive loss of hippocampal neurons in the CA3 region compared to the DMSO-treated group (control). No significant neuronal death was observed in the CA1 and dentate gyrus regions in the KA-injected rats. KBA, at the doses of 10 and 50 mg/kg, administered (i.p.) 30 min prior to KA reduced KA-induced neuronal death in the CA3 region compared with KA only. On the other hand, in agreement with previously published data [32,33], a significant elevation of glutamate levels in the hippocampus was observed at 4 h after KA administration (i.p.) (p < 0.001) (► **Fig. 6b**). The KBA-pretreated group (10 or 50 mg/kg, i.p.) offered significant restoration of glutamate levels in comparison to the KA-only group [$F(3,17) = 10.1$, p < 0.01] (► **Fig. 6b**).

Discussion

One of the crucial findings of the current study is that KBA reduced 4-AP-stimulated glutamate release from the rat hippocampal synaptosomes (► **Fig. 2**). The released glutamate produced by

synaptosomes depolarization consists of two components: a physiologically relevant Ca^{2+} -dependent component produced by the exocytosis of synaptic vesicles containing glutamate, and a Ca^{2+} -independent component attributed to the reversal efflux of glutamate by the glutamate transporter due to prolonged depolarization [27]. The present data indicated that KBA does not have an effect on Na^{+} -dependent glutamate transporters but reduces the amount of glutamate released by the vesicular-mediated effects. First, the inhibitory effect of KBA on 4-AP-stimulated glutamate release was dependent on extracellular calcium, persisting in the presence of the glutamate transporter inhibitor DL-TBOA, and blocked by the vesicular transporter inhibitor bafilomycin A1 (► **Fig. 3**). Second, the 4-AP- and KCl-evoked increase in $[Ca^{2+}]_i$ was reduced in the presence of KBA (► **Table 1**). This suggested that a direct reduction in Ca^{2+} channel activity was involved in the KBA-mediated inhibition of glutamate release, because 4-AP-mediated depolarization/VDCC activation involves the action of Na^{+} and Ca^{2+} channels and 15 mM external KCl-mediated depolarization/VDCC activation involves only Ca^{2+} channels [34,35].

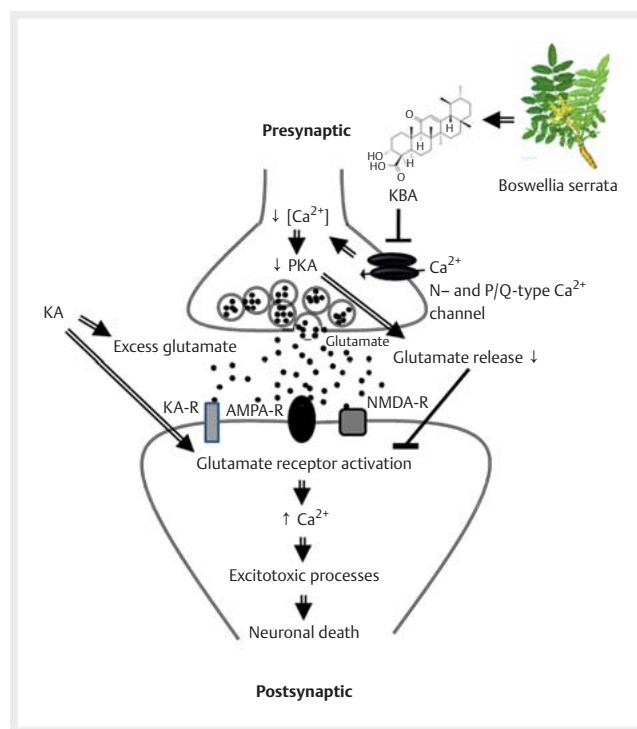


► **Fig. 6** Effect of 11-keto-β-boswellic acid (KBA) on kainic acid (KA)-induced neuronal damage and glutamate elevation in the hippocampus. KBA (10 or 50 mg/kg) was administered i. p. 30 min prior to KA (15 mg/kg, i. p.). **a** Neutral red staining was used to examine neuronal loss in the hippocampus of KA- and/or KBA-treated animals. **b** The glutamate levels in the hippocampus were examined at 4 h after KA injection by HPLC. Each bar represents the mean ± SEM; n = 5 animals for each group. ***Significant difference ($p < 0.001$) from control; #significant difference ($p < 0.05$) from KA (one-way ANOVA).

Finally, the inhibitory effect of KBA on 4-AP-stimulated glutamate release was significantly abolished by the N- and P/Q-type Ca^{2+} channel blocker ω -conotoxin MVIIC, whereas the intracellular Ca^{2+} release inhibitors dantrolene, CGP37157, and xestospongine C did not have any effect (► **Fig. 4**), indicating the involvement of N- and P/Q-type Ca^{2+} channel suppression. However, the KBA effect was not completely abolished by blocking the N- and P/Q-type calcium channels. The possibility that KBA inhibits glutamate release through a mechanism other than suppressing N- and P/Q-type calcium channels cannot be ruled out.

In addition, some signal transduction pathways during the glutamate exocytotic process are activated, especially the PKA cascade [30]. For example, increased cytosolic Ca^{2+} levels activate PKA and facilitate glutamate release [36, 37]. In the present study, the inhibitory effect of KBA on 4-AP-stimulated glutamate release was efficiently blocked by a PKA inhibitor and not by an MAPK inhibitor and PKC inhibitor (► **Fig. 5**), thus indicating the involvement of PKA. On the basis of the rat hippocampal synaptosome data, we conclude that KBA reduces Ca^{2+} influx through N- and P/Q-type calcium channels, subsequently suppressing PKA activity and decreasing the evoked glutamate release (► **Fig. 7**). However, the mechanism of KBA-induced suppression of VDCC activity remains to be addressed.

A significant increase in the glutamate level has been observed in many brain disorders [3, 4]. Because KBA inhibited glutamate release in the current study, KBA can also attenuate glutamate excitotoxicity. As presented in ► **Fig. 6**, KBA exerts a neuroprotective effect in a rat model of excitotoxicity induced by KA administration (15 mg/kg, i. p.). KA is a nonselective agonist of KA and ionotropic glutamate receptors, and its administration to animals results in selective neuronal death in specific brain regions, especially in the hippocampal CA3 region [33, 38], which has the highest density of KA receptors [39]. KA-induced neuronal death is associated with the pathological release of glutamate [40, 41]. Sim-



► **Fig. 7** Potential mechanisms by which 11-keto-β-boswellic acid (KBA) inhibits glutamate release and protects against kainic acid (KA)-induced excitotoxicity in the rat hippocampus. KBA decreases the Ca^{2+} influx through N- and P/Q-type Ca^{2+} channels, which subsequently reduces PKA activity to cause a decrease in glutamate release and glutamate excitotoxicity. KBA, 11-keto-β-boswellic acid; KA, kainic acid; PKA, protein kinase A; KA-R, kainate receptor; NMDA-R, N-methyl-D-aspartate receptor; AMPA-R, α-amino-3-hydroxy-5-methyl-4-isoxazolepropionic acid receptor.

ilarly, in the current study, KA administration (15 mg/kg, i.p.) led to neuronal death in the CA3 region of the hippocampus and increased glutamate levels in the hippocampus. However, pretreatment with KBA (10 or 50 mg/kg, i.p.) 30 min before KA could reverse these KA-induced trends. Consistent with our finding, Ding et al. reported that KBA (25 mg/kg, i.p.) alleviated brain damage and neurologic deficits in ischemic rats [23]. This neuroprotection was a result of enhanced antioxidant capacity. As we found that KBA has a glutamate release-inhibiting effect *in vitro* and excessive glutamate is involved in KA-induced neuronal death [40,41], the protective effect of KBA on KA-induced excitotoxicity is associated with the inhibition of glutamate release (► Fig. 7), which subsequently suppresses glutamate receptor activation and death signaling pathways. Supporting this finding, several drugs inhibiting glutamate release, such as rosiglitazone, bupropion, and lidocaine, display neuroprotective effects based on their ability to prevent glutamate excitotoxicity and inhibit neuronal cell death [25, 42, 43]. Further studies are warranted to clarify the precise molecular mechanisms involved in the KBA-induced protective effects in KA-injected animal models.

In summary, KBA, an active constituent of *B. serrata*, inhibits 4-AP-evoked glutamate release from hippocampal synaptosomes by attenuating the voltage-dependent calcium channel and PKA activity as well as effectively prevents KA-induced glutamate elevation and excitotoxicity *in vivo*. Thus, KBA has potential to be used for the clinical management of glutamate-induced neurological disorders.

Materials and Methods

Chemicals

KBA (purity >98%) was purchased from ChemFaces. DL-TBOA, bafilomycin A1, dantrolene, GP37157, GF109203X, PD98059, and H89 were purchased from Tocris Cookson. ω -Conotoxin MVIIIC was purchased from Alomone Laboratories. Xestospongine C was purchased from Cayman Chemical. Fura-2-acetoxymethyl ester (Fura-2-AM) was obtained from Life Technologies. 4-AP, KA, and all other reagents were obtained from Sigma-Aldrich. The purity of all compounds was >90%.

Animals

All experiments described in this report were performed with male Sprague-Dawley rats (200–250 g) purchased from BioLASCO Inc. Animal orders were placed by Animal Care Services of Fu Jen Catholic University, Taiwan. Upon receipt, rats were housed under standardized environmental conditions (22°C, 55% relative humidity, 12-h light/dark cycle) and allowed unlimited access to food and water. Animal experiments were approved by the ethical committee [January 10, 2018; IACUC-2018(2)-MOST-01].

In vitro studies

Synaptosome preparation

Synaptosomes were prepared as previously described [44]. Rats were briefly anesthetized with isoflurane (5% in O₂) and decapitated. The hippocampus from each rat was homogenized in 0.32 M sucrose with a Teflon glass homogenizer and centrifuged

at 3000 × *g* for 2 min. The supernatant was subjected to a discontinuous 3, 10, and 23% Percoll density gradient solution centrifugation at 32 500 × *g* for 7 min. The synaptosomal fraction was isolated from the band at 10 and 23% Percoll interface, diluted with HEPES buffer medium, and centrifuged at 27 000 × *g* for 10 min. The pellet was used for protein measurements and the glutamate release assay.

Release of glutamate from synaptosomes

Glutamate release was assayed by online fluorometry [45]. Pelleted synaptosomes were resuspended in HEPES buffer medium containing bovine serum albumin, and the suspension was then transferred to stirred quartz cuvette thermostated at 37°C in an LS-55 spectrofluorimeter (PerkinElmer Life Sciences). After 5 min incubation, NADP⁺ (1 mM) and glutamate dehydrogenase (50 units/mL) were added in the presence of 1.2 mM CaCl₂. Following a 2-min incubation, 4-AP (1 mM) was added to stimulate glutamate release. The amount of glutamate released was monitored as an increase in fluorescence due to NADPH forming from NADP⁺ as a result of the oxidative deamination of released glutamate by glutamate dehydrogenase. The fluorescence of NADPH was measured at 2 s intervals for 5 min and calibrated by a glutamate standard (5 nmol). Released glutamate was expressed as nanomoles of glutamate per milligram of synaptosomal protein (nmol/mg).

Intrasyntosomal Ca²⁺ concentration

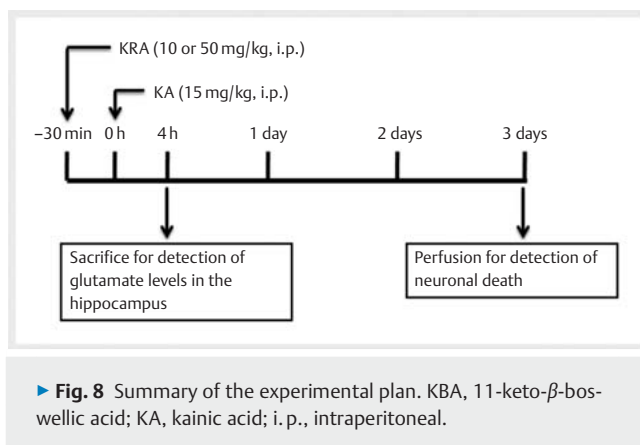
Intraterminal Ca²⁺ concentration ([Ca²⁺]_i) was measured with Fura-2 as previously described [44]. Synaptosomes were preincubated in HEPES buffer medium containing 5 μM Fura-2-AM, 0.1 mM CaCl₂, and 16 μM BSA for 35 min at 37°C. The suspension was then centrifuged for 1 min at 10 000 × *g*. Pelleted synaptosomes were resuspended and treated as described for glutamate release experiments. Fura-2-Ca fluorescence was assayed at the excitation wavelengths of 340 and 380 nm (emission wavelength, 505 nm) and data accumulated at 5 s intervals. The [Ca²⁺]_i was calculated by using calibration procedures and equations described previously [46].

In vivo studies

The rats were randomly divided into four groups: DMSO-treated group (control), KA only-treated group, KBA 10 mg/kg + KA group, and KBA 50 mg/kg + KA group. KA was dissolved in 0.9% NaCl (pH 7.0), at a dose of 15 mg/kg, and was injected (i.p.). The dose of administration was chosen based on previous experiments of our group and others [32,33,38]. KBA dissolved in 1% DMSO was administered i.p. for 30 min prior to KA injection. The experimental design is shown in ► Fig. 8. Rats were either sacrificed 4 h or 3 days after KA injection with an overdose of anesthetic (chloral hydrate, 650 mg/kg, i.p.). The rats sacrificed at 4 h were used for detecting glutamate levels, whereas those used for neuronal death were euthanized 3 days after KA administration.

Evaluation of neuronal injury using neutral red staining

Neutral red staining was conducted as described previously [32]. Animals were anesthetized (chloral hydrate 650 mg/kg, i.p.) and perfused transcardially with heparinized saline, followed by 4%



paraformaldehyde in 0.1 M PBS. The brains were removed and post-fixed overnight in 4% paraformaldehyde containing 30% sucrose. Fixed brains were cut into 40 μ m thick coronal sections and these sections were mounted onto glass slides. For neutral red staining, slides were air dried, dehydrated in ethanol, and stained with neutral red solution. Stained samples were rehydrated in ethanol, cleared in xylene (Sigma-Aldrich), air dried, coverslipped using dibutylphthalate polystyrene xylene (DPX), and visualized with a DM 2000 LED light microscope (LEICA).

Determination of glutamate by high-performance liquid chromatography

Glutamate concentration was measured from dissected hippocampus tissues as described previously [32,33]. Briefly, animals were sacrificed through decapitation and the brains were removed immediately. The hippocampi were dissected and homogenized in 500 μ L of 200 mM ice-cold perchloric acid. After centrifugation (1500 \times g for 10 min at 4°C), the supernatant (10 μ L) was filtered and injected directly into a high-performance liquid chromatography system with an electrochemical detection (HTEC-500). Peak heights were recorded with an integrator, and the concentration of glutamate was calculated on the basis of known standards.

Data analysis

The data are expressed as the mean \pm standard error of the mean (SEM). Statistical analyses were performed using Student's unpaired t-test or one-way ANOVA with Scheffe's post hoc test (SPSS 17.0), as detailed in the legend section. A p value < 0.05 was considered statistically significant.

Acknowledgements

This research was financially supported by the Ministry of Science and Technology (MOST 107-2314-B-418-005; MOST 106-2320-B-030-002 MY3), Taiwan.

Conflict of Interest

The authors declare that they have no conflict of interest.

References

- [1] Zhou Y, Danbolt NC. Glutamate as a neurotransmitter in the healthy brain. *J Neural Transm* 2014; 121: 799–817
- [2] Bano D, Ankarcrona M. Beyond the critical point: an overview of excitotoxicity, calcium overload and the downstream consequences. *Neurosci Lett* 2018; 663: 79–85
- [3] Choi DW. Glutamate neurotoxicity and diseases of the nervous system. *Neuron* 1988; 1: 623–634
- [4] Lewerenz J, Maher P. Chronic glutamate toxicity in neurodegenerative diseases – What is the evidence? *Front Neurosci* 2015; 9: 469
- [5] Danysz W, Parsons CG. Glycine and N-methyl-D-aspartate receptors: physiological significance and possible therapeutic applications. *Pharmacol Rev* 1998; 50: 597–664
- [6] Ikonomidou C, Turski L. Why did NMDA receptor antagonists fail clinical trials for stroke and traumatic brain injury? *Lancet Neurol* 2002; 1: 383–386
- [7] Wu PF, Zhang Z, Wang F, Chen JG. Natural compounds from traditional medicinal herbs in the treatment of cerebral ischemia/reperfusion injury. *Acta Pharmacol Sin* 2010; 31: 1523–1531
- [8] Kim MH, Kim SH, Yang WM. Mechanisms of action of phytochemicals from medicinal herbs in the treatment of Alzheimer's disease. *Planta Med* 2014; 80: 1249–1258
- [9] Russo P, Frustaci A, Del Bufalo A, Fini M, Cesario A. From traditional European medicine to discovery of new drug candidates for the treatment of dementia and Alzheimer's disease: acetylcholinesterase inhibitors. *Curr Med Chem* 2013; 20: 976–983
- [10] Siddiqui M. *Boswellia serrata*, a potential antiinflammatory agent: an overview. *Indian J Pharm Sci* 2011; 73: 255
- [11] Abdel-Tawab M, Werz O, Schubert-Zsilavecz M. *Boswellia serrata*: an overall assessment of *in vitro*, preclinical, pharmacokinetic and clinical data. *Clin Pharmacokinet* 2011; 50: 349–369
- [12] Ammon HP. Boswellic acids in chronic inflammatory diseases. *Planta Med* 2006; 72: 1100–1116
- [13] Beghelli D, Isani G, Roncada P, Andreani G, Bistoni O, Bertocchi M, Lupidi G, Alunno A. Antioxidant and *Ex vivo* immune system regulatory properties of *Boswellia serrata* extracts. *Oxid Med Cell Longev* 2017; 2017: 7468064
- [14] Roy NK, Parama D, Banik K, Bordoloi D, Devi AK, Thakur KK, Padmavathi G, Shakibaei M, Fan L, Sethi G, Kunnumakara AB. An update on pharmacological potential of boswellic acids against chronic diseases. *Int J Mol Sci* 2019; 20: 4101
- [15] Rajabian A, Boroushaki MT, Hayatdavoudi P, Sadeghnia HR. *Boswellia serrata* protects against glutamate-induced oxidative stress and apoptosis in PC12 and N2a cells. *DNA Cell Biol* 2016; 35: 666–679
- [16] Sadeghnia HR, Arjmand F, Ghorbani A. Neuroprotective effect of *Boswellia serrata* and its active constituent acetyl 11-keto- β -boswellic acid against oxygen-glucose-serum deprivation-induced cell injury. *Acta Pol Pharm* 2017; 74: 911–920
- [17] Ding Y, Chen M, Wang M, Wang M, Zhang T, Park J, Zhu Y, Guo C, Jia Y, Li Y, Wen A. Neuroprotection by acetyl-11-keto- β -Boswellic acid, in ischemic brain injury involves the Nrf2/HO-1 defense pathway. *Sci Rep* 2014; 4: 7002
- [18] Forouzanfar F, Hosseinzadeh H, Ebrahimzadeh Bideskan A, Sadeghnia HR. Aqueous and ethanolic extracts of *Boswellia serrata* protect against focal cerebral ischemia and reperfusion injury in rats. *Phytother Res* 2016; 30: 1954–1967
- [19] Doaaee P, Rajaei Z, Roghani M, Alaei H, Kamalinejad M. Effects of *Boswellia serrata* resin extract on motor dysfunction and brain oxidative stress in an experimental model of Parkinson's disease. *Avicenna J Phytomed* 2019; 9: 281–290

- [20] Gomaa AA, Makboul RM, Al-Mokhtar MA, Nicola MA. Polyphenol-rich *Boswellia serrata* gum prevents cognitive impairment and insulin resistance of diabetic rats through inhibition of GSK3 β activity, oxidative stress and pro-inflammatory cytokines. *Biomed Pharmacother* 2019; 109: 281–292
- [21] Hosseini-Sharifabad M, Kamali-Ardakani R, Hosseini-Sharifabad A. Beneficial effect of *Boswellia serrata* gum resin on spatial learning and the dendritic tree of dentate gyrus granule cells in aged rats. *Avicenna J Phytomed* 2016; 6: 189–197
- [22] Reising K, Meins J, Bastian B, Eckert G, Mueller WE, Schubert-Zsilavecz M, Abdel-Tawab M. Determination of boswellic acids in brain and plasma by high-performance liquid chromatography/tandem mass spectrometry. *Anal Chem* 2005; 77: 6640–6645
- [23] Ding Y, Chen M, Wang M, Li Y, Wen A. Posttreatment with 11-keto- β -boswellic acid ameliorates cerebral ischemia-reperfusion injury: Nrf2/HO-1 pathway as a potential mechanism. *Mol Neurobiol* 2015; 52: 1430–1439
- [24] Dohare P, Hyzinski-García MC, Vipani A, Bowens NH, Nalwalk JW, Feustel PJ, Keller RW jr., Jourdain D, Mongin AA. The neuroprotective properties of the superoxide dismutase mimetic tempol correlate with its ability to reduce pathological glutamate release in a rodent model of stroke. *Free Radic Biol Med* 2014; 77: 168–182
- [25] Wong SB, Cheng SJ, Hung WC, Lee WT, Min MY. Rosiglitazone suppresses *in vitro* seizures in hippocampal slice by inhibiting presynaptic glutamate release in a model of temporal lobe epilepsy. *PLoS One* 2015; 10: e0144806
- [26] McMahon HT, Nicholls DG. Transmitter glutamate release from isolated nerve terminals: evidence for biphasic release and triggering by localized Ca²⁺. *J Neurochem* 1991; 56: 86–94
- [27] Nicholls DG, Sihra TS, Sanchez-Prieto J. Calcium dependent and -independent release of glutamate from synaptosomes monitored by continuous fluorometry. *J Neurochem* 1987; 49: 50–57
- [28] Millán C, Sánchez-Prieto J. Differential coupling of N- and P/Q-type calcium channels to glutamate exocytosis in the rat cerebral cortex. *Neurosci Lett* 2002; 330: 29–32
- [29] Berridge MJ. Neuronal calcium signaling. *Neuron* 1998; 21: 13–26
- [30] Millán C, Torres M, Sánchez-Prieto J. Co-activation of PKA and PKC in cerebrocortical nerve terminals synergistically facilitates glutamate release. *J Neurochem* 2003; 87: 1101–1111
- [31] Pereira DB, Carvalho AP, Duarte CB. Non-specific effects of the MEK inhibitors PD98059 and U0126 on glutamate release from hippocampal synaptosomes. *Neuropharmacology* 2002; 42: 9–19
- [32] Lin TY, Lu CW, Wang SJ. Luteolin protects the hippocampus against neuron impairments induced by kainic acid in rats. *Neurotoxicology* 2016; 55: 48–57
- [33] Chang Y, Lu CW, Chen YJ, Lin TY, Huang SK, Wang SJ. Astaxanthin protects against kainic acid-induced seizures and pathological consequences. *Neurochem Int* 2018; 116: 85–94
- [34] Barrie AP, Nicholls DG, Sanchez-Prieto J, Sihra TS. An ion channel locus for the protein kinase C potentiation of transmitter glutamate release from guinea pig cerebrocortical synaptosomes. *J Neurochem* 1991; 57: 1398–1404
- [35] Nicholls DG. Presynaptic modulation of glutamate release. *Prog Brain Res* 1998; 116: 15–22
- [36] Andrade-Talavera Y, Duque-Feria P, Negrete-Díaz JV, Sihra TS, Flores G, Rodríguez-Moreno A. Presynaptic kainate receptor-mediated facilitation of glutamate release involves Ca²⁺-calmodulin at mossy fiber-CA3 synapses. *J Neurochem* 2012; 122: 891–899
- [37] Rodríguez-Moreno A, Sihra TS. Presynaptic kainate receptor-mediated facilitation of glutamate release involves Ca²⁺-calmodulin and PKA in cerebrocortical synaptosomes. *FEBS Lett* 2013; 587: 788–792
- [38] Friedman LK, Pellegrini-Giampietro DE, Sperber EF, Bennett M, Moshe SL, Zukin RS. Kainate-induced status epilepticus alters glutamate and GABA_A receptor gene expression in adult rat hippocampus: an *in situ* hybridization study. *J Neurosci* 1994; 14: 2697–2707
- [39] Bahn S, Volk B, Widsen W. Kainate receptor gene expression in the developing rat brain. *J Neurosci* 1994; 14: 5525–5547
- [40] Śmiałowska M, Golembiowska K, Kajta M, Zięba B, Dziubina A, Domin H. Selective mGluR1 antagonist EMQMCM inhibits the kainate-induced excitotoxicity in primary neuronal cultures and in the rat hippocampus. *Neurotox Res* 2012; 21: 379–392
- [41] Domin H, Zięba B, Golembiowska K, Kowalska M, Dziubina A, Śmiałowska M. Neuroprotective potential of mGluR5 antagonist MTEP: effects on kainate-induced excitotoxicity in the rat hippocampus. *Pharmacol Rep* 2010; 62: 1051–1061
- [42] Lin KC, Wang CC, Wang SJ. Bupropion attenuates kainic acid-induced seizures and neuronal cell death in rat hippocampus. *Prog Neuropsychopharmacol Biol Psychiatry* 2013; 45: 207–214
- [43] Chiu KM, Lu CW, Lee MY, Wang MJ, Lin TY, Wang SJ. Neuroprotective and anti-inflammatory effects of lidocaine in kainic acid-injected rats. *Neuroreport* 2016; 27: 501–507
- [44] Lu CW, Lin TY, Chang CY, Huang SK, Wang SJ. Ciproxifan, a histamine H₃ receptor antagonist and inverse agonist, presynaptically inhibits glutamate release in rat hippocampus. *Toxicol Appl Pharmacol* 2017; 319: 12–27
- [45] Nicholls DG, Sihra TS. Synaptosomes possess an exocytotic pool of glutamate. *Nature* 1986; 321: 772–773
- [46] Grynkiewicz G, Poenie M, Tsien RY. A new generation of Ca²⁺ indicators with greatly improved fluorescence properties. *J Biol Chem* 1985; 260: 3440–3450

ARTICLE

Open Access

Profiling of subcellular EGFR interactome reveals hnRNP A3 modulates nuclear EGFR localization

Tong-Hong Wang^{1,2}, Chih-Ching Wu^{3,4,5,6}, Kuo-Yen Huang⁷, Wen-Yu Chuang⁸, Chuen Hsueh¹, Hsin-Jung Li⁹ and Chi-Yuan Chen^{1,2}

Abstract

The aberrant subcellular translocation and distribution of epidermal growth factor receptor (EGFR) represent a major yet currently underappreciated cancer development mechanism in non-small cell lung cancer (NSCLC). In this study, we investigated the subcellular interactome of EGFR by using a spectral counting-based approach combined with liquid chromatography–tandem mass spectrometry to understand the associated protein networks involved in the tumorigenesis of NSCLC. A total of 54, 77, and 63 EGFR-interacting proteins were identified specifically in the cytosolic, mitochondrial, and nuclear fractions from a NSCLC cell line, respectively. Pathway analyses of these proteins using the KEGG database shown that the EGFR-interacting proteins of the cytosol and nucleus are involved in the ribosome and spliceosome pathways, respectively, while those of the mitochondria are involved in metabolizing propanoate, fatty acid, valine, leucine, and isoleucine. A selected nuclear EGFR-interacting protein, hnRNP A3, was found to modulate the accumulation of nuclear EGFR. Downregulation of hnRNP A3 reduced the nuclear accumulation of EGFR, and this was accompanied by reduced tumor growth ability in vitro and in vivo. These results indicate that variations in the subcellular translocation and distribution of EGFR within NSCLC cells could affect tumor progression.

Introduction

The epidermal growth factor receptor (EGFR) signaling is one of the most commonly deregulated pathways in human tumor. Despite the firmly-established significance of this pathway in tumor growth, however, targeted treatment aimed to disrupt EGFR has yielded only modest medical success in the past 2 decades. An exception is non-small cell lung cancer (NSCLC) patients carrying EGFR activation mutations: such patients initially showed very promising responses to treatment with an EGFR kinase inhibitor, but almost all of the treated patients eventually developed resistance to the EGFR kinase

inhibitor¹. These unsatisfactory effects are, in part, due to the highly complex of the EGFR network pathway.

Significant research efforts have sought to gain deeper information of the EGFR signaling and EGFR-mediated fatal oncology in human cancer. Recent studies have shown that activated EGFR may escape lysosome-mediated degradation and recycle to the plasma membrane or undergo intracellular trafficking to subcellular organelles, such as nuclei^{2,3} and mitochondria^{4,5}. Within these organelles, EGFR may exert novel functions that differ from its typical function as a transmembrane receptor tyrosine kinase. In support of this view, the functionality of EGFR has been shown to depend on its subcellular location⁶, and EGFR was shown to undergo shuttling into the cell nucleus and mitochondrion upon ligand binding, EGFR-targeted therapy, and other stimuli (e.g., radiation)⁷. As the EGFR localized in these organelles can display novel functions and may regulate the response of a tumor to therapy, it is important to characterize the novel functions of EGFR in these organelles.

Correspondence: Chi-Yuan Chen (d49417002@gmail.com)

¹Graduate Institute of Health Industry Technology and Research Center for Food and Cosmetic Safety, Research Center for Chinese Herbal Medicine, College of Human Ecology, Chang Gung University of Science and Technology, Taoyuan 333, Taiwan

²Tissue Bank, Chang Gung Memorial Hospital at Linkou, Taoyuan 333, Taiwan

Full list of author information is available at the end of the article

These authors contributed equally: Tong-Hong Wang, Chih-Ching Wu

© The Author(s) 2020



Open Access This article is licensed under a Creative Commons Attribution 4.0 International License, which permits use, sharing, adaptation, distribution and reproduction in any medium or format, as long as you give appropriate credit to the original author(s) and the source, provide a link to the Creative Commons license, and indicate if changes were made. The images or other third party material in this article are included in the article's Creative Commons license, unless indicated otherwise in a credit line to the material. If material is not included in the article's Creative Commons license and your intended use is not permitted by statutory regulation or exceeds the permitted use, you will need to obtain permission directly from the copyright holder. To view a copy of this license, visit <http://creativecommons.org/licenses/by/4.0/>.

The presence of full-length EGFR in the nucleus has been recognized for over 20 years⁸. Nuclear EGFR performs as a tyrosine kinase, transcriptional mediator, and regulator of other biological functions. Within the cell nucleus, EGFR roles as a transcriptional mediator through its specific transactivation domain⁹ and through its connections with RNA helicase A¹⁰ and/or DNA-binding transcription factors that are highly presented in tumors, including STAT3², E2F1¹¹, and STAT5¹². The nuclear increase of EGFR has been associated with cancer malignancy, poor patient survival, and drug resistance^{3,13,14}. In line with these links, studies have shown that nuclear EGFR activates the expression of cyclin D1⁹, inducible nitric oxide synthase², B-Myb¹¹, COX-2¹⁵, aurora A¹², c-Myc¹⁶, and breast cancer resistance protein¹⁷. Nuclear EGFR also keeps its tyrosine kinase activity and phosphorylates proliferating cell nuclear antigen to stimulate cell growth and DNA repair¹⁸. Heterogeneous nuclear ribonucleoprotein A3 (hnRNP A3) has been reported to interact with nuclear EGFR and stabilize mRNAs involved in aerobic glycolysis in response to irradiation¹⁹. Overall, the current evidence suggests that blocking the nuclear functions of EGFR may maximize the efficacy of EGFR-targeting agents and other anti-cancer therapies. However, the natural and pathological significances of nuclear EGFR in cancers remain mostly unidentified. Efforts to map the relationships at work within the subcellular interactome of EGFR could help us fundamentally understand the mechanisms that govern tumor development and therapeutic resistance, leading to alternative treatment strategies. To address this issue, we employed a label-free spectral counting-based proteomics approach to investigate the EGFR subcellular interactome in a NSCLC cell line. We further examined a selected nuclear EGFR-interacting protein, hnRNP A3, and found that it contributes to the nuclear accumulation of EGFR in NSCLC.

Results

Profiling of the subcellular EGFR interactome in CL1-5 cells

The translocation of EGFR to non-canonical subcellular locations, including the nucleus and mitochondria, represents a major yet underappreciated mechanism of NSCLC development. To further understand the putative functions of subcellularly distributed EGFR and EGFR signaling at different subcellular locations, we investigated the EGFR interactome at three subcellular locations (cytosol, mitochondria, and nucleus) to characterize the proteins that interact with the EGFR at these subcellular locations. As previous studies have shown that EGFR are internalized to nucleus and mitochondria without EGF treatment^{20–22}, we investigated the subcellular interactome of EGFR in the physiological condition without any stimulation in this study. Figure 1a shows an overview

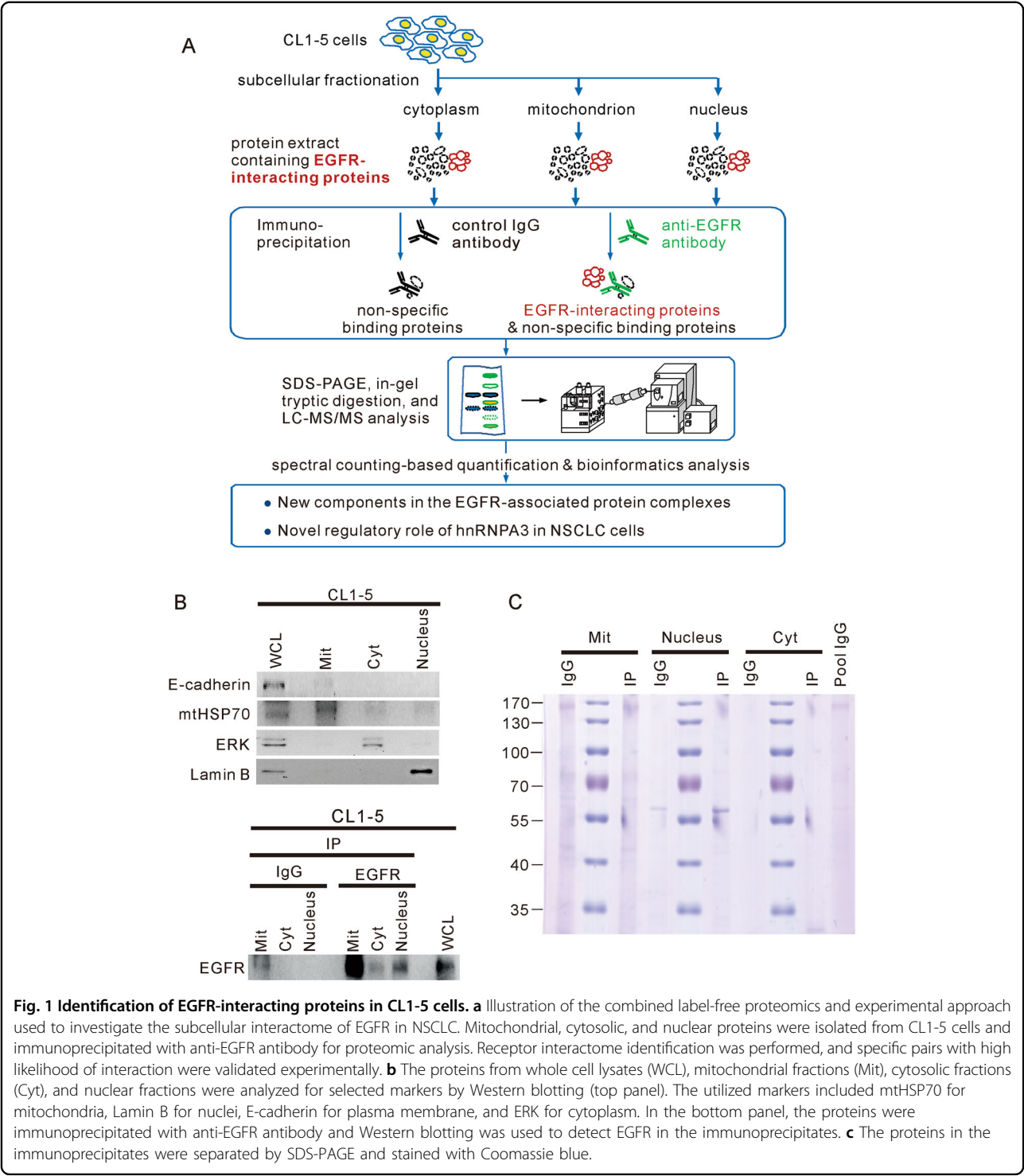
of the strategy used to analyze the EGFR interactome at each subcellular location and functionally explore each identified interacting protein. We used the NSCLC cell line, CL1-5, which is a highly invasive cell line that was derived from CL1-0 cells²³ and displays higher EGFR expression compared to the less-invasive CL1-0 cell line²⁴. Proteins were isolated from the mitochondria, nucleus, and cytoplasm, and immunoprecipitated with an antibody against EGFR (Fig. 1b). The subcellular proteins in the EGFR-immunoprecipitates were separated by sodium dodecyl sulfate-polyacrylamide gel electrophoresis (SDS-PAGE, Fig. 1c), extracted from the gel, and identified by free-labeling approaches combined with liquid chromatography–tandem mass spectrometry (LC–MS/MS).

Spectral counting-based quantification of identified EGFR-interacting proteins

To further assess the proteins that appeared to interact with EGFR, the relative amounts of proteins identified in the immunoprecipitates were determined by spectral counting-based protein quantification. The fold change for each protein was determined from the ratio of the average spectral count (SC) of the protein in the anti-EGFR fraction versus that in the control IgG fraction. Proteins with fold changes more than two standard deviations (SD) above the mean ratio (i.e., above 6.92, 7.92, and 17.84 for the cytosolic, mitochondrial, and nuclear fractions, respectively) were considered to be EGFR-interacting proteins. Based on the cutoff, 58, 79, and 67 EGFR-interacting proteins were observed in the cytosolic, mitochondrial, and nuclear fractions, respectively (Supplementary Table 1). Among them, 54, 77, and 63 proteins were specific to the cytosolic, mitochondrial, and nuclear groups, respectively (Supplementary Table 1). In contrast, glucose-6-phosphate isomerase was found in the cytosolic and mitochondrial groups; 60S ribosomal protein L6 was detected in the mitochondrial and nuclear groups; and filaggrin, desmocollin-1, and suprabasin were identified in the cytosolic and nuclear groups.

Bioinformatics analysis of the EGFR interactome

To determine the biological processes that are most likely to be affected by the presence of the EGFR-associated complexes, we used DAVID to annotate the functions of the EGFR-interacting proteins in each subcellular fraction (Supplementary Table 1). The enriched biological processes were as follows: for the cytosolic fraction, translation, rRNA processing, protein complex biogenesis, regulation of apoptosis, and epidermis development; for the mitochondrial fraction, energy generation, oxidation/reduction, mitochondrion organization, membrane organization, and transmembrane transport; and for the nuclear fraction, RNA processing and



ribonucleoprotein complex biogenesis (Table 1). Pathway analyses performed using the KEGG database revealed that the EGFR-interacting proteins of the cytosolic fraction were involved in ribosome-related pathways, those of the nuclear fraction were involved in spliceosome-related pathways, and those of the mitochondrial group were

related to pathways involved in the metabolism of propanoate, fatty acid, valine, leucine, and isoleucine (Table 2).

We further used the STRING online database to establish a network of protein–protein interactions (PPIs) between the identified EGFR-interacting proteins

Table 1 Biological processes enriched among EGFR-interacting proteins.

Biological process ^a	Identified proteins involved in the process	p Value
Cytoplasm		
Translation	EGFR, RPL17, RPL27A, RPS15A, RPS9, RPL23A, RPS2, RPS4X, RPS5, RPS3, RPS7, RPS25, EIF3B, RPS19, RPS16, RPS3A, RPS17, RPS14, RPL9, FAU, RPS10, RPS20, RPS23	1.60×10^{-29}
rRNA processing	RPS19, RPS16, RPS17, RPS14, RPS7	7.90×10^{-8}
Peptide cross-linking	TGM1, TGM2, DSP, TGM3, FN1	3.42×10^{-6}
Protein complex biogenesis	JUP, TCP1, RPS14, TUBB2C, TGM2, TGM3, HSPA4, CAT, KPNB1, FLNA	9.26×10^{-4}
Regulation of apoptosis	EGFR, HMGB1, RPS3A, TUBB2C, CFL1, TGM2, CAT, PRDX1, YWHAE, RPS3	4.78×10^{-3}
Epidermis development	C1ORF68, FLG, TGM1, DSP, TGM3	6.58×10^{-3}
Mitochondria		
Generation of precursor metabolites and energy	SLC25A12, GPI, NDUFB5, OXA1L, ND4, NDUFV1, SUCLG1, IDH3B, SUCLA2, ATP6V0A2, ETFB, IDH3A	3.83×10^{-8}
Oxidation reduction	NDUFB5, OXA1L, ALDH18A1, ACADM, ND4, IDH3B, IDH3A, VAT1, COQ6, SLC25A12, ALDH7A1, ALDH1B1, HMOX1, NDUFV1, ACAD9, ETFB	8.59×10^{-7}
Cofactor metabolic process	DBT, HMOX1, SUCLG1, IDH3B, ACOT1, SUCLA2, IDH3A, COQ6	1.97×10^{-5}
Mitochondrion organization	OXA1L, OPA1, GFM1, MTX1, BCS1L, DNAJA3	7.80×10^{-4}
Membrane organization	EGFR, NRCAM, STX4, OXA1L, OPA1, LDLR, MTCH1, SUN2	3.76×10^{-3}
Transmembrane transport	SLC25A12, CPT2, SLC35B2, SLC25A10, MTCH1, ABCB10, ABCC1, ABCB7, ATP6V0A2	9.66×10^{-3}
Nucleus		
RNA processing/splicing	RALY, TRA2A, SYNRIP, PNN, PRPF19, SFRS6, NONO, HNRNPA3, HNRNPM, SFRS7, DDX17, DKC1, PRPF8, PCBP1, SFRS9, DHX15, PABPN1, RPL35A, DHX9, EFTUD2, RNPS1, SNW1, CDC5L, SFRS1, HNRNPA0, FBL, PRPF6, RSL1D1, HNRPDL, NOP2, HNRNPUL1, SNRNP200, KHSRP, NOP58, NOP56, PES1, RBM14	2.13×10^{-36}
Ribonucleoprotein complex biogenesis	RPL35A, GTPBP4, SFRS1, FBL, PRPF6, SFRS6, NOP2, DKC1, SNRNP200, SFRS9, NOP58, NOP56, PES1	8.95×10^{-12}
Cellular macromolecular complex assembly	SFRS6, H1FO, HP1BP3, SNRNP200, SFRS9, TRIM27, SFRS1, NEFL, PRPF6	3.58×10^{-4}

^aThe Database for Annotation, Visualization, and Integrated Discovery (DAVID, version 6.7) was applied to functionally annotate enriched proteins, using the annotation category GOTERM_BP_FAT. Processes with at least five protein members and *p* values less than 0.01 were considered significant.

(Supplementary Table 1). The analyses yielded 268, 24, and 204 strong interaction links between the EGFR-interacting proteins identified in the cytosolic, mitochondrial, and nuclear fractions, respectively (Fig. 2). In line with the results from our DAVID and KEGG analyses (Tables 1, 2), the STRING analysis generated a module that depicted interactions between EGFR and proteins grouped into the RNA processing/splicing and ribonucleoprotein complex biogenesis interaction networks (Fig. 2). The RNA processing/splicing group primarily included hnRNP family proteins, such as hnRNP A0, hnRNP A3, hnRNP DL, hnRNP M, and hnRNP UL1. The highest score was found for hnRNP A3, which is involved in RNA processing/splicing and the spliceosome (Tables 1, 2). Since hnRNP A3 is reportedly overexpressed in lung cancer²⁵ and has been shown to interact with nuclear EGFR in A549 cells¹⁹, we selected hnRNP A3 for further

study, and set out to examine the functional role of its interaction with nuclear EGFR.

Expression levels of hnRNP A3 and EGFR in paired NSCLC tumor and adjacent normal tissues

To address the functional role of the putative EGFR–hnRNP A3 interaction in the nucleus, we used immunohistochemistry (IHC) to detect the expression levels of hnRNP A3 and EGFR in 15 NSCLC tumor tissues and paired adjacent normal sections. The clinical characteristics of the patients are summarized in Supplementary Table 2. Representative IHC results for hnRNP A3 and EGFR (brown staining) from an overall stage 1 patient are shown in Fig. 3a. The percentage of positive staining ranged from 0 to 100% in all samples. The clinical relevance of hnRNP A3 and EGFR expression in paired NSCLC tumor and adjacent normal tissue samples is

Table 2 Pathway analysis of the EGFR-interacting proteins.

Term in the KEGG pathway ^a	Identified proteins involved in the pathway	p Value
Cytoplasm		
Ribosome	RPL17, RPL27A, RPS15A, RPS9, RPL23A, RPS2, RPS4X, RPS5, RPS3, RPS7, RPS25, RPS19, RPS16, RPS3A, RPS17, RPL9, FAU, RPS10, RPS20, RPS23	4.63×10^{-25}
Mitochondria		
Propanoate metabolism	MUT, ALDH7A1, ACADM, ALDH1B1, SUCLG1, SUCLA2	4.55×10^{-6}
Fatty acid metabolism	ALDH7A1, CPT2, ACADM, ALDH1B1, CPT1A	2.70×10^{-4}
Valine, leucine and isoleucine degradation	DBT, MUT, ALDH7A1, ACADM, ALDH1B1	3.91×10^{-4}
Nucleus		
Spliceosome	EFTUD2, TRA2A, SNW1, CDC5L, SFRS1, PRPF6, HNRNPA3, SFRS6, PRPF19, SFRS7, HNRNPM, PCBP1, PRPF8, SNRNP200, SFRS9, DHX15, ACIN1	5.01×10^{-22}

^aDAVID was applied to functionally annotate the enriched proteins. The knowledge base used was the KEGG pathway database. Processes with at least five protein members and *p* values less than 0.01 were considered significant.

summarized in Supplementary Table 3. Elevated expression of hnRNP A3 and EGFR was detected in the tumor section compared with the adjacent normal section. To determine if hnRNP A3 showed nuclear colocalization with EGFR in NSCLC, we used immunofluorescence (IF) staining to examine the expression patterns of these proteins in the paired tumor and adjacent normal tissues of an overall stage 3 patient. As shown in Fig. 3b, c, hnRNP A3 and EGFR showed elevated colocalization in tumor sections compared with adjacent normal sections. The elevated colocalization of hnRNP A3 and EGFR in tumor sections was also examined by IHC double staining in a NSCLC patient. As shown in Fig. 3d, the colocalization of EGFR and hnRNP A3 was clearly much higher in the tumor sections than the hyperplasia sections. In addition, the tissue extract was prepared from a frozen NSCLC tissue and immunoprecipitated with anti-hnRNP A3 or anti-IgG. As shown in Fig. 3e, EGFR was readily detected in the immunoprecipitates pulled down by anti-hnRNP A3. These results suggest that nuclear hnRNP A3 and EGFR interact in NSCLC.

hnRNP A3 and EGFR interact in the nuclei of NSCLC cells

To confirm that hnRNP A3 interacts with EGFR in the nucleus, we immunoprecipitated the nuclear proteins of CL1-5 and A549 cells using an antibody against EGFR. As shown in Fig. 4a, hnRNP A3 was detected in EGFR immunoprecipitates from both CL1-5 and A549 cells. To further evaluate the nuclear colocalization of EGFR with hnRNP A3, we used *in situ* IF staining to analyze the subcellular distributions of EGFR, hnRNP A3 and DAPI (a nuclear marker). As shown in Fig. 4b, hnRNP A3 and EGFR were highly colocalized in the nuclei of both cell lines. As shown in Fig. 4c, about 35 and 55% of EGFR

were localized in the nucleus of CL1-5 and A549 cells, respectively. Three-channel colocalization analysis indicated that about 20 and 30% of colocalization of EGFR, hnRNP A3, and DAPI in CL1-5 and A549 cells, respectively. Taken together, these results, together with those from our analyses of the interactome and clinical tissues, strongly indicate that hnRNP A3 and EGFR interact *in vitro* and *in vivo*.

hnRNP A3 is essential for the nuclear translocation of EGFR

As hnRNP A3 has been shown to shuttle cargo between the cytosol and nucleus^{26–28}, we postulated that it might perform this function for EGFR. To test this hypothesis, we used IF staining to examine the effects of hnRNP A3 knockdown on the cellular distribution of EGFR. As shown in Fig. 5a, b, the colocalization of EGFR with DAPI was decreased in CL1-5 and A549 cells depleted of hnRNP A3. To confirm these IF staining results, we employed nuclear fractionation and Western blot analysis to examine the expression levels of EGFR and hnRNP A3 in nuclear and whole-cell lysates (WCL). As shown in Fig. 5c, while the level of hnRNP A3 was greatly reduced in the hnRNP A3-depleted cells, the level of EGFR in the whole-cell lysates remained unchanged. In contrast, the levels of nuclear EGFR were greatly reduced in hnRNP A3-depleted CL1-5 cells compared to the siN control (Fig. 5d). As the total level of EGFR was not affected by the depletion of hnRNP A3, it is likely that the reduced localization of EGFR in the nucleus of hnRNP A3-depleted cells was accompanied by the redistribution of EGFR to membrane, cytoplasm, or cytoplasmic organelles. In addition, we also examined how stable depletion of hnRNP A3 affected the nuclear localization of EGFR. CL1-5 cells stably depleted of hnRNP A3 by

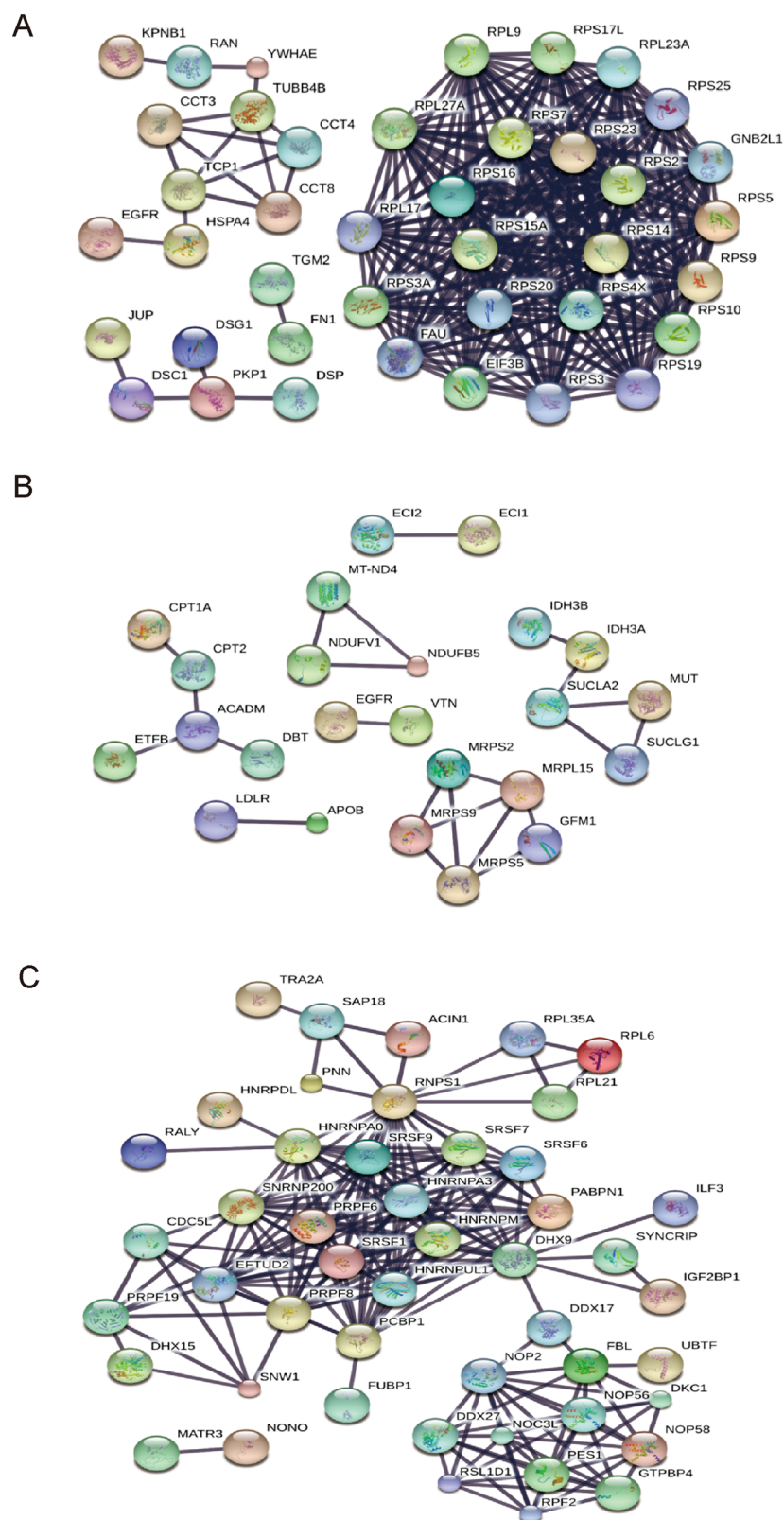
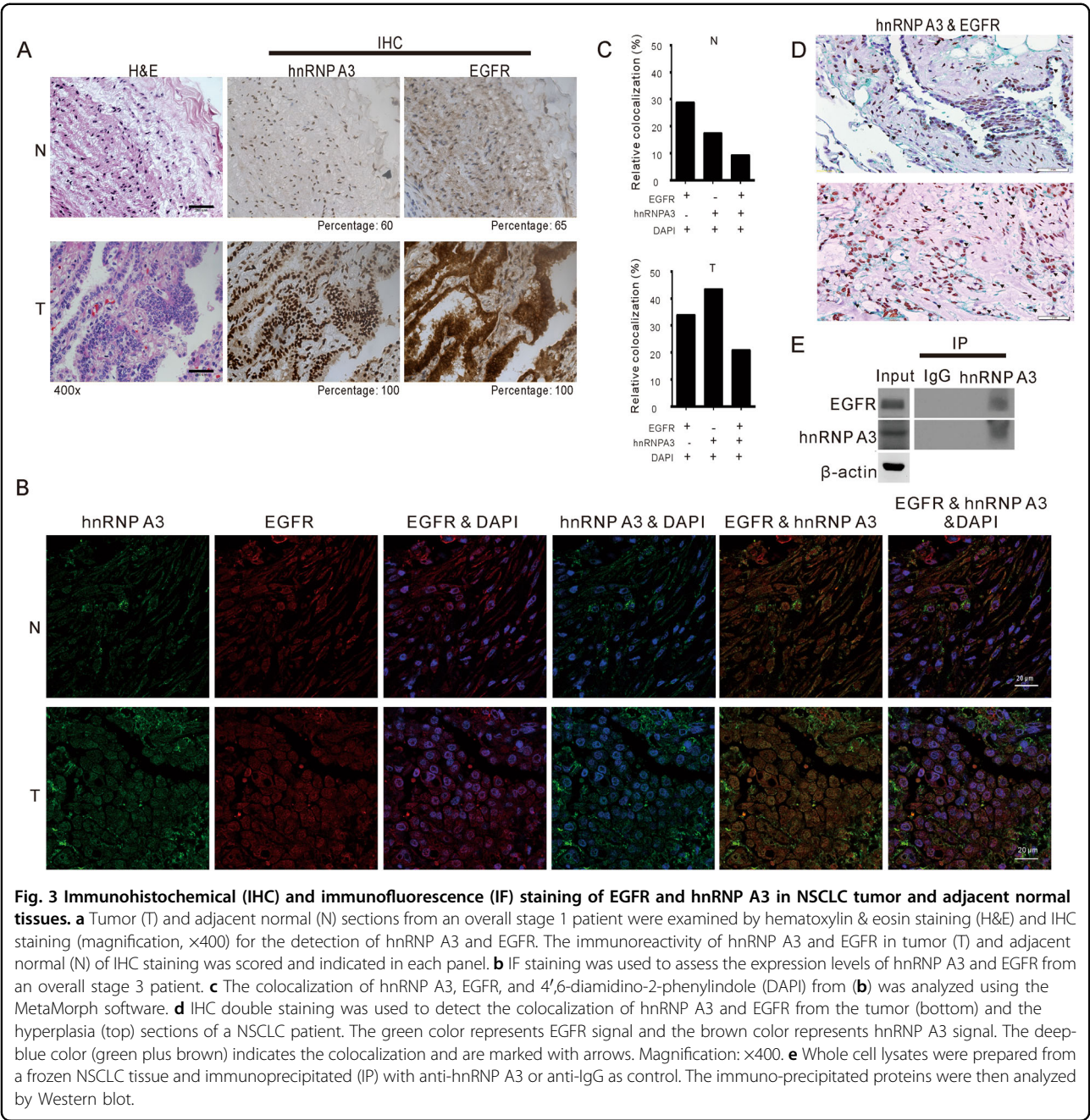


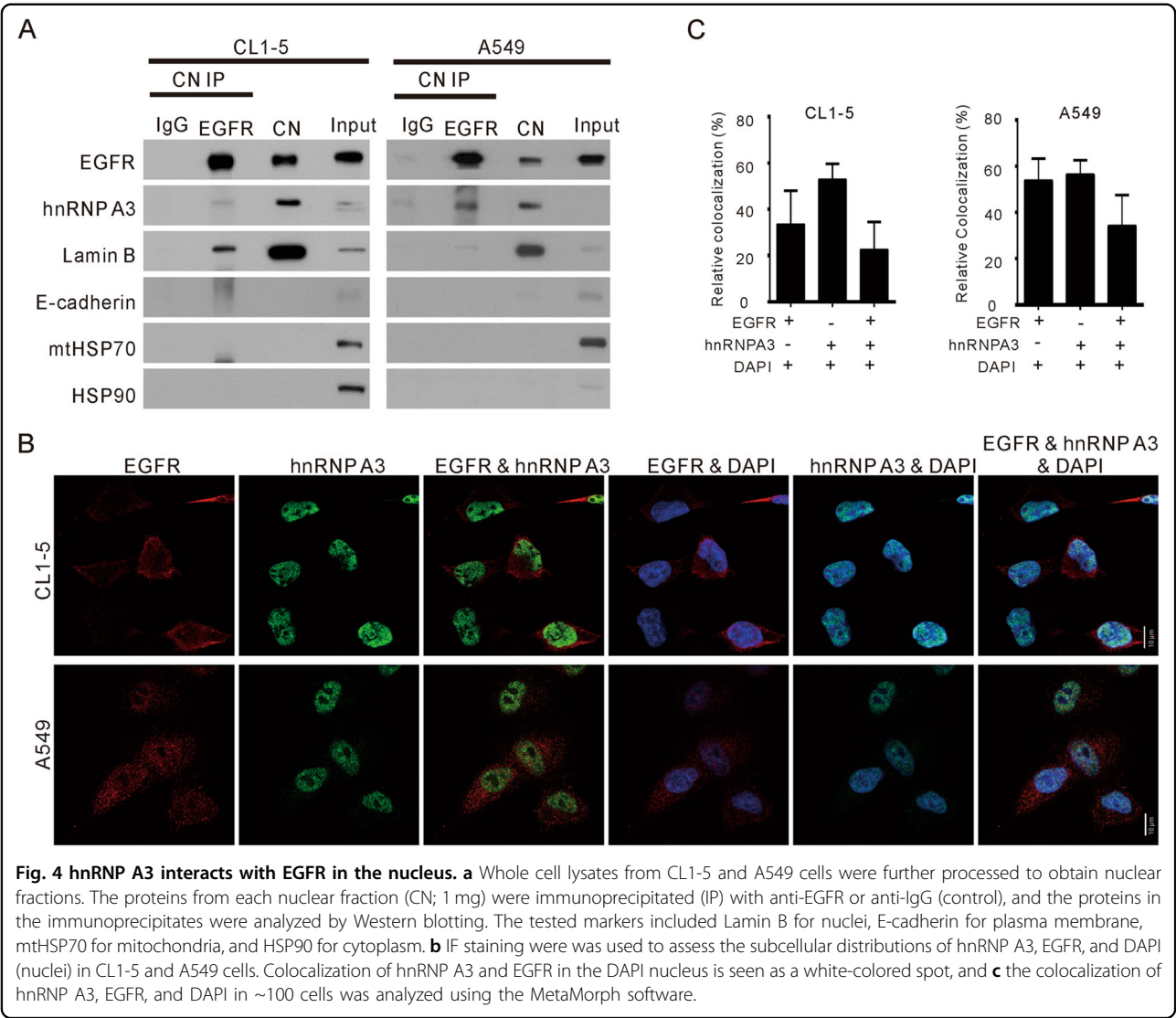
Fig. 2 Protein–protein interaction (PPI) network analysis of EGFR-interacting proteins. PPI networks of the EGFR-interacting proteins identified in the cytoplasm (a), mitochondria (b), and nucleus (c) were constructed using the STRING v10.5 database. A combined score >0.9 (indicating the highest confidence) was used as the cutoff criterion. The interaction links between individual nodes/proteins are shown as solid lines.



sh-hnRNP A3 (shA3-1 and shA3-2) were subjected to nuclear fractionation, and the levels of EGFR in nuclear and whole-cell lysates were assayed by Western blot analysis. As shown in Fig. 5e, the levels of total EGFR in WCL of shA3-1- and shA3-2-depleted CL1-5 cells were similar to that of the sh-V control, whereas the levels of nuclear EGFR were greatly reduced in shA3-1- and shA3-2-depleted CL1-5 cells compared to the sh-V control. Collectively, these results show that hnRNP A3 modulates the nuclear localization of EGFR in NSCLC.

Effects of hnRNP A3 depletion on the cell proliferation, anchorage-independent growth, and in vivo tumor growth of NSCLC

As hnRNP A3 is reportedly overexpressed in lung cancer²⁵, we next examined its effects on cell proliferation and anchorage-independent growth in CL1-5 and A549 cells. As shown in Fig. 6a, transient depletion of hnRNP A3 inhibited cell proliferation in CL1-5 cells (Fig. 6a, left panel) and A549 cells (Fig. 6a, right panel). Similarly, stable depletion of hnRNP A3 by shRNA suppressed the



anchorage-independent growth ability of CL1-5 cells (Fig. 6b). These results suggest that hnRNP A3 may be involved in the tumorigenesis of NSCLC. To determine if hnRNP A3 affects NSCLC tumorigenesis in vivo, we examined how stable depletion of hnRNP A3 affected tumor growth in a xenograft mouse model. As shown in Fig. 6c, the growth of shA3-1 cell-derived tumors was slower than that of sh-V control cell-derived tumors. Similarly, the excised shA3-1 tumors were considerably smaller than the sh-V control tumors. To evaluate if the depletion of hnRNP A3 also reduced the nuclear localization of EGFR, we subjected the excised tumors to IF staining of hnRNP A3 and EGFR. As shown in Fig. 6d, e, the levels of hnRNP A3, nuclear EGFR, cMyc, cyclin D1, aurora A, and COX-2 were greatly decreased in shA3-1 tumors compared to sh-V tumors. These results indicate that the downregulation of hnRNP A3 reduced tumor growth in vivo, possibly by decreasing the levels of nuclear

EGFR and its target regulation, including cMyc, cyclin D1, aurora A, and COX-2.

Discussion

In this study, we examined the EGFR interactome at three subcellular locations (cytosol, mitochondria, and nucleus) in order to deduce the functionality of EGFR at these subcellular locations. Using free-labeling approaches combined with LC-MS/MS, we identified 58, 79, and 67 EGFR-interacting proteins in the cytosol, mitochondria, and nucleus, respectively (Supplementary Table 1). Our enrichment analysis of categories belonging to biological processes revealed that the cytosolic EGFR-interacting proteins were associated with translation, rRNA processing, peptide cross-linking, protein complex biogenesis, regulation of apoptosis, and epidermis development (Table 1). Pathway analyses using the KEGG database revealed that the cytosolic EGFR-interacting

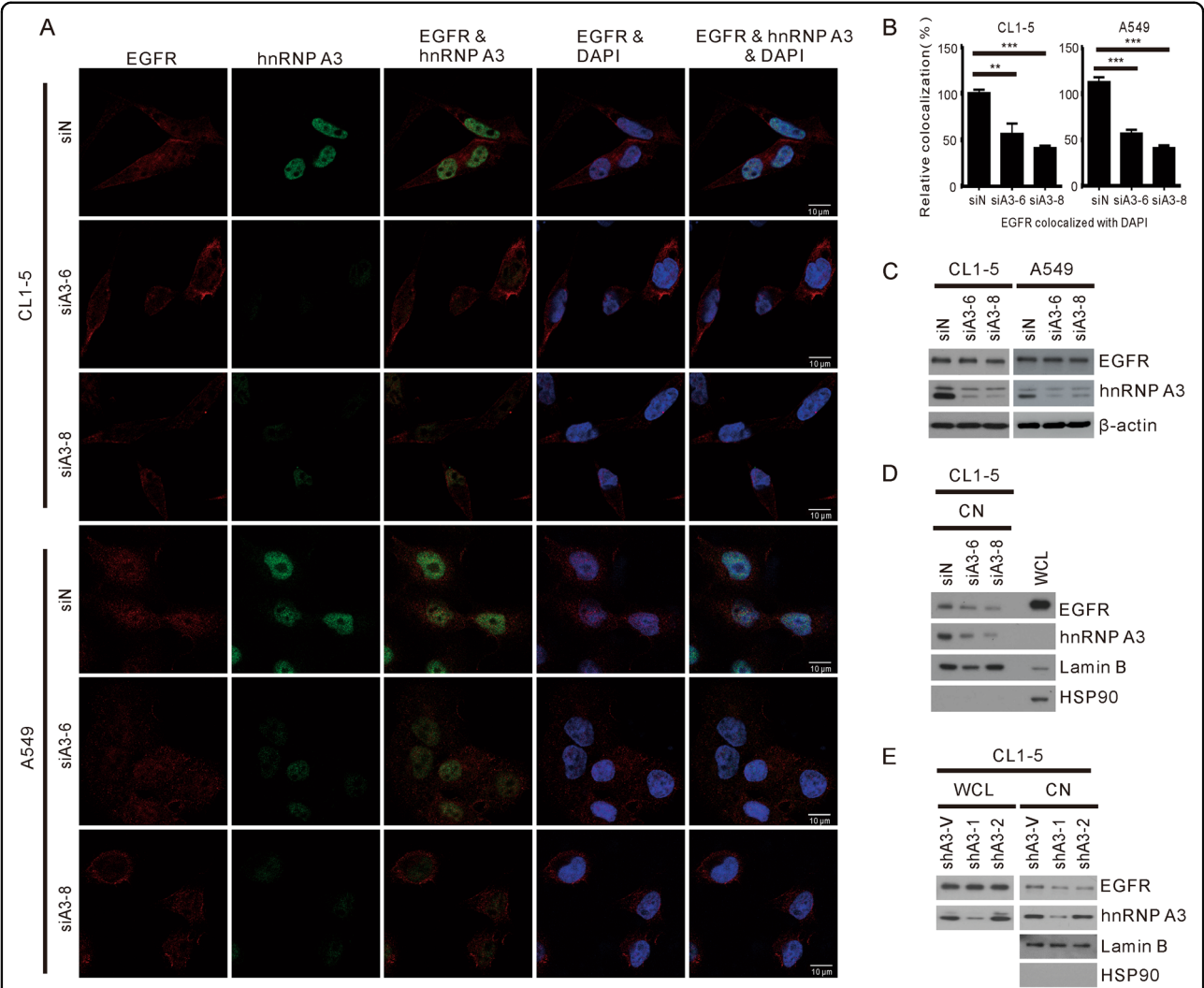
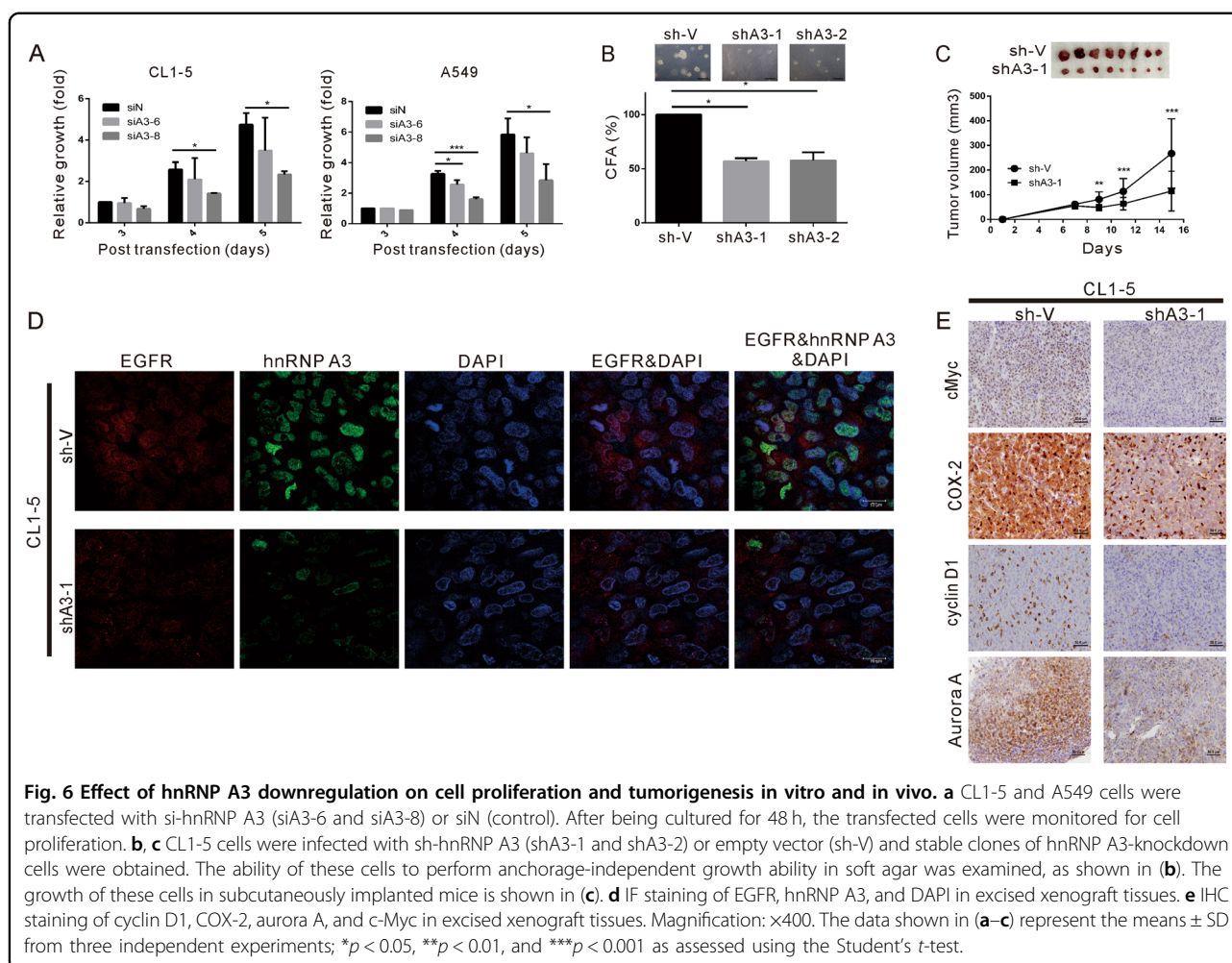


Fig. 5 Effects of hnRNP A3 downregulation on translocation of EGFR into the nucleus. CL1-5 and A549 cells were transfected with si-hnRNP A3 (siA3-6 and siA3-8) or siN (control). At 72 h post-transfection, the cells were IF stained with anti-EGFR and -hnRNP A3 antibodies. Representative IF staining results are shown in (a). The scores for the localization of EGFR in nucleus from ~100 cells were calculated using the MetaMorph software. The summary data shown in (b) indicate the means \pm SD from three independent experiments; $**p < 0.01$ and $***p < 0.001$, as assessed with the Student's *t*-test. c Western blot analysis for the expression level of hnRNP A3 and EGFR. β -Actin was used as a loading control. d The lysates of CL1-5 cells transfected with si-hnRNP A3 were fractionated to isolate nuclear fraction for Western blot analysis. e CL1-5 cells were infected with sh-hnRNP A3 (sh-A3-1 and sh-A3-2) or sh-V (control) and stable clones of hnRNP A3-knockdown cells were obtained. The levels of relevant proteins in nuclear fractions (CN, 10 μ g) and WCL (20 μ g) were analyzed by Western blot analysis. The cytoplasmic marker, HSP90, and nuclear marker, Lamin B, were included to validate the purity of the nuclear fraction.

proteins were involved in ribosome-related pathways (Table 2). Our findings suggested a previously unknown function of EGFR, namely that cytosolic EGFR may interact with ribosomal proteins to promote the translational program in NSCLC. In tumor cells, the activation of survival signaling pathways increases overall protein synthesis and enhances cellular metabolism, tumor growth, and metastasis^{29–31}, and the deregulation of translation can enable tumors to resist clinical treatment³². In this regard, it is interesting to speculate that the deregulation of translation and ribosomes may

contribute to drug resistance, especially in the NSCLC cells harboring constitutively activating mutations of EGFR. The EGFR-interacting proteins in mitochondria were found to correlate with precursor metabolite generation, energy production, and mitochondrion organization (Table 1). The mitochondrial EGFR-interactome included Dnaja3 (Table 1, also known as Tid-1); this protein has been shown to govern the mitochondrial localization of EGFR, and the mitochondrial accumulation of EGFR has been shown to promote metastasis in NSCLC³³. While



the functions of mitochondrial EGFR remain poorly understood, our pathway analyses revealed that many of the mitochondrial EGFR-interacting proteins are involved in the metabolism of propanoate, fatty acids, and degradation of valine, leucine, and isoleucine (Table 2). The palmitoylation of mitochondrial EGFR has been shown to induce mitochondrial fusion and promote cell survival in prostate and breast cancer³⁴. The products of valine, leucine, and isoleucine catabolism may enter the citric acid cycle and link to the metabolism of propanoate and fatty acids³⁵. In the future, it could be interesting to investigate exactly how mitochondrial EGFR modulates these metabolic pathways to promote metastasis.

The EGFR-interacting proteins in the nucleus were found to be involved in RNA processing/splicing, ribonucleoprotein complex biogenesis, and cellular macromolecular complex assembly (Table 1). Pathway analyses revealed that the nuclear EGFR-interacting proteins were involved in spliceosome-related pathways (Table 2). Consistent with this finding, our STRING-based EGFR interactome profiling generated an EGFR interaction

module that grouped into the RNA processing/splicing and ribonucleoprotein complex biogenesis interaction networks (Fig. 2). The RNA processing/splicing group primarily included hnRNP family proteins, including hnRNP A0, hnRNP A3, hnRNP DL, hnRNP M, and hnRNP UL1. Several members of hnRNP A/Bs, which are comprised of A1, A2, A3, and A0³⁶ have been identified in the nuclear EGFR interactome (Supplementary Table 1). HnRNP A1, A2, and A3 have been shown to copurify with the splicing complexes^{37,38}. The functions of hnRNP A1 and A2 in the splicing of oncogenes and tumor-related genes may explain the frequent dysregulation of hnRNP A/Bs in different types of cancers^{39,40}. HnRNP A3 has been reported to interact with nuclear EGFR and stabilize the mRNA involved in the aerobic glycolysis in response to irradiation¹⁹. However, compared to the well-studied members of hnRNP A1 and A2, the role of hnRNP A0 and A3 in RNA processing/splicing are poorly understood. In this study, hnRNP A3 was detected as a spliceosome component that interacted with nuclear EGFR and is predicted to function in a related manner similar to that

of hnRNP A1 and A2. Nuclear EGFR has also been shown to regulate the stability of mRNAs related to the VEGF pathway in stress-exposed NSCLC and head and neck cancer cell lines⁴¹. It is also quite possible that the ability of nuclear EGFR to activate the expression of cyclin D1⁹, inducible nitric oxide synthase², B-Myb¹¹, COX-2¹⁵, aurora A¹², c-Myc¹⁶, and breast cancer resistance protein¹⁷ may be related to this RNA processing function.

From among the nuclear EGFR-interacting proteins, we selected hnRNP A3 for further study. Our results suggest that hnRNP A3 is involved in the nuclear accumulation of EGFR in NSCLC. For example, IF staining of EGFR and hnRNP A3 in tumor and adjacent normal tissues obtained from NSCLC patients revealed that hnRNP A3 and EGFR exhibited elevated colocalization in tumor sections compared with adjacent normal sections (Fig. 3). Consistent with a previous study, hnRNP A3 was detected predominantly in nucleus with a minor expression in the cytosol⁴². Depletion of hnRNP A3 did not affect the total level of EGFR, but reduced the nuclear accumulation of EGFR (Fig. 5). These data suggest that the reduced nuclear EGFR accumulation is accompanied with increased relocation of EGFR to membrane, cytoplasm, or cytoplasmic organelles. Depletion of hnRNP A3 also reduced anchorage-independent growth ability and tumor cell growth both in vitro and in vivo (Fig. 6). These results suggest that nuclear EGFR plays an important role in the tumorigenesis of NSCLC. Since hnRNP A/Bs have been reported to be overexpressed in lung cancer⁴³, our identification of hnRNP A/Bs as nuclear EGFR interacting proteins suggests that such an interaction may involve yet-to-be identified mechanism to facilitate the functions of hnRNP A/Bs in mRNA processing/trafficking. Nuclear EGFR may employ its kinase activity to phosphorylate hnRNP A/Bs or it may function as transcriptional regulator to regulate the expression of hnRNP A/Bs. Thus, the phosphorylation status and the expression levels of hnRNP A/Bs may be affected by the nuclear EGFR.

In summary, we herein examined subcellular EGFR interactomes, analyzed the putative functions of EGFR at these subcellular locations, and report that a nuclear EGFR-interacting protein selected for further study, hnRNP A3, modulates nuclear EGFR accumulation and tumor growth in NSCLC.

Materials and methods

Cell lines and culture media

The human NSCLC cell line, CL1-5, was established from CL1-0 cells via selecting for increased invasive capability using a Transwell chamber assay²³. These cells were kindly provided by Dr. Pan-Chyr Yang (Department of Internal Medicine, College of Medicine, National Taiwan University, Taipei, Taiwan). A549 cells were obtained from the American Type Culture Collection (Manassas,

VA, USA). CL1-5 and A549 cells express wild-type EGFR⁴⁴. In the absence of ligand stimulation, EGFR was not phosphorylated in these cells. CL1-5 cells were cultivated in RPMI-1640 supplemented with 10% fetal bovine serum (FBS) and 100 U/ml penicillin and streptomycin together. A549 cells were cultured in Dulbecco's modified Eagle's medium containing 10% FBS, 2.5 mM L-glutamine, 0.5 mM sodium pyruvate, and 100 U/ml penicillin and streptomycin. All cell lines were confirmed by short tandem repeat analysis and mycoplasma PCR. All culture media and FBS were purchased from Life Technologies (Grand Island, NY, USA).

Antibodies

Antibodies against EGFR (1005), lamin B (C-20), hnRNP A3 (A15), ERK (K-23), E-cadherin, c-Myc (N-262), cyclin D1 (HD11), and HSP90 were purchased from Santa Cruz Biotechnology, Inc. (Santa Cruz, CA, USA). The antibody against mitochondrial HSP70 (MA3-02) was purchased from Thermo Fisher Scientific, Inc. (Waltham, MA, USA). The antibody against COX-2 (ab15191) and aurora A (35C1) were purchased from Abcam (Cambridge, UK). The antibody against β -actin was purchased from Sigma (St. Louis, MO, USA). Alexa Fluor® 594 donkey anti-rabbit IgG (A21207), Alexa Fluor® 647 donkey anti-goat IgG (A21447), and Alexa Fluor® 488 goat anti-mouse IgG (A11001) were purchased from Life Technologies-Molecular Probes.

Tumor specimens

The 15 paired tumor and adjacent normal tissues were obtained from NSCLC patients who underwent surgical resection at Chang Gung Memorial Hospital. This study was approved by the Ethics Committee of Chang Gung Memorial Hospital. Written informed consent was obtained from all patients.

Subcellular fractionation

Nuclear, cytoplasmic, and mitochondrial fractions were obtained from lung cancer cells using a Qproteome mitochondria isolation kit (Qiagen, Venlo, Netherlands) according to the manufacturer's protocol³³. Cells were suspended in a lysis buffer, which selectively disrupts the cell membrane without solubilizing it, resulting in the isolation of cytosolic proteins.

Western blotting, immunoprecipitation, and immunofluorescence staining

Western blotting, immunoprecipitation, and immunofluorescence (IF) were performed as described previously^{24,33}. The distributions of hnRNP A3 and EGFR in NSCLC tissues and cells were determined by IF staining as described previously³³. Cells or tissues were visualized under confocal microscopy (LSM 700; Carl Zeiss, Jena,

Germany) and the MetaMorph software was used to examine colocalization (MetaMorph Inc., Nashville, TN, USA). The analysis colocalization of EGFR (red) and hnRNP A3 (green) in nucleus (DAPI/blue) using MetaMorph software are illustrated in Supplementary Fig. S1.

Immunohistochemical assay

Immunohistochemical staining for EGFR and hnRNP A3 was performed as described previously²⁴. These tissues were examined for the extent of EGFR and hnRNP A3 staining by a pathologist (W. Y. Chuang) in a blinded manner⁴⁵. The immunoreactivity for the hnRNP A3 and EGFR was semiquantitatively scored by the percentage of positive-staining tumor cells in a representative large section of each tissue specimen. The immunoreactivity was grouped into four groups according to the percentage of the positive tumor cells: negative (0%), low (1–50%), medium (51–95%), and high (96–100%). IHC double staining was performed with MultiView (mouse-HRP/rabbit-DAB) IHC kit (Enzo Life Sciences, Inc., NY, USA), by following the protocols provided by the manufacturer.

In-gel digestion and mass spectrometric analysis

The immunoprecipitates were separated by 10% SDS-PAGE and stained with a Colloidal Blue Staining Kit (Thermo Fisher Scientific). Destaining was performed with 10% methanol and 5% acetic acid, each gel lane was cut into 10 pieces, and each piece was further separated into two replicates. The pieces were then dehydrated in acetonitrile (Mallinckrodt Baker) and dried in a SpeedVac. Proteins were reduced with 25 mM NH_4HCO_3 containing 10 mM dithiothreitol at 60 °C for 30 min, alkylated with 55 mM iodoacetamide at room temperature for 30 min, and then digested by trypsin (20 $\mu\text{g}/\text{ml}$; Promega, Madison, WI, USA) overnight at 37 °C. The digested peptides were extracted by acetonitrile and dried in a SpeedVac.

The extracted peptides were identified by LTQ-Orbitrap Discovery (Thermo Fisher, Waltham, MA) coupled with high-performance liquid chromatography. Briefly, peptide extracts were reconstituted in solution A (0.1% formic acid), loaded across a trap column (Zorbax 300SB- C_{18} , $0.3 \times 5 \text{ mm}^2$; Agilent Technologies, Taiwan) at a flow rate of 0.2 $\mu\text{L}/\text{min}$ in solution A, and separated on a resolving 100-mm analytical C_{18} column (inner diameter, 75 μm) using a 15- μm tip (New Objective, Woburn, MA, USA). The peptides were eluted with a 60-min gradient at a flow rate of 0.25 $\mu\text{L}/\text{min}$. The LTQ Orbitrap was operated using the Xcalibur 2.0 software (Thermo Fisher). The data were acquired in a data-dependent mode containing one MS scan, using the Orbitrap at a resolution of 30,000 and 10 MS/MS scans (in the linear ion trap) for the 10 most abundant precursor ions. The m/z scan range for the MS scans was set as 350–2000 Da, and the ion signal of $(\text{Si}(\text{CH}_3)_2\text{O})_6\text{H}^+$ at m/z 445.120025 was used as a lock mass

for internal calibration. To increase identification coverage, the precursor ions selected for MS/MS analysis were dynamically excluded for 180 s^{46–48}.

Database searching and protein identification

The obtained spectra were searched with the Mascot algorithm (Version 2.1; Matrix Science, Boston, MA, USA) against the Swiss-Prot human sequence database (released March 2018, selected for *Homo sapiens*, 20,198 entries) of the European Bioinformatics Institute. The peak list was generated using the Thermo ExtractMSn software (Version 1.0.0.8, May 2012 release). The mass tolerances for parent and fragment ions were set as 10 ppm and 0.5 Da, respectively. Oxidation on methionine (+15.99 Da) and carbamidomethylation on cysteine (+57 Da) were set as variable and fixed modifications, respectively. The enzyme was set as trypsin and up to one missed cleavage was allowed. The random sequence database was used to estimate false positive rates for protein matches. The resulting files were further integrated using the Scaffold software (Version 4.2.1; Proteome Software, Portland, OR, USA), which included the PeptideProphet algorithm⁴⁹ for assignment of peptide MS spectra and the ProteinProphet algorithm⁵⁰ for grouping peptides to a unique protein or protein family (if the peptides are shared among several isoforms). The thresholds for PeptideProphet and ProteinProphet probability were set as 0.95 to ensure an overall false discovery rate below 0.5%. Only proteins with two unique matching peptides were retained.

Spectral counting-based protein quantification and bioinformatics analysis

To identify the binding partners of EGFR, we compared the protein levels between immunoprecipitation products of the control vector and EGFR vector groups using a previously described label-free spectral counting-based quantification method⁵¹. Briefly, the exclusive spectrum count for each identified protein was exported from the Scaffold software in Excel format (Microsoft, Redmond, WA, USA). To reduce differences between analyses, the normalized spectral count (NSC) of each protein was calculated by the spectral count (SC) for that protein divided by the total SC of the analysis. The fold change was estimated as the ratio of the average of normalized SCs in the EGFR group to that in the control group. Because not all proteins were identified in all replicates, the SCs of unidentified proteins or missing values in a certain sample were assigned a value of one; this enabled us to avoid overestimating the fold changes and dividing by zero.

The biological pathways and processes involved with the EGFR-interacting proteins were revealed using the Kyoto Encyclopedia of Genes and Genomes (KEGG)

database (<http://www.genome.jp/kegg/pathway.html>) and the Database for Annotation, Visualization, and Integrated Discovery (DAVID, version 6.8, <https://david.ncicrf.gov/>), respectively⁵². The known and predicted associations between the EGFR-interacting partners were analyzed with the STRING online software (version 10.5, <https://string-db.org/cgi/input.pl>). A combined confidence score of ≥ 0.9 was used as the cutoff criterion⁵³.

RNA interference (RNAi)

hnRNP A3 was downregulated using RNAi from Dharmacon (Lafayette, CO, USA), with a nontargeting siRNA (D-001810-01, Dharmacon) used as a control. The two siRNAs targeting the human hnRNP A3 mRNA covered nucleotides 785–803 from the start codon (A3-6: GGAGGGAACUUUGGAGGUG) and nucleotides 1041–1059 (A3-8: ACAUGAAGGAGGAAAUUU). Transfection was performed by using the Dharmafect 1 transfection reagent (Dharmacon) according to the manufacturer's instructions, as described previously⁵⁴.

Plasmids and establishment of stable knockdown subclones

Stable knockdown of hnRNP A3 was achieved using a short hairpin RNA approach (shRNAs). Packed lentiviruses expressing shRNAs designed to knock down hnRNP A3 (TRCN0000245295 and TRCN0000074511) were obtained from the RNA interference consortium (National RNAi Core Facility, Academia Sinica, Taipei, Taiwan). Cells were infected with lentivirus and cultured in the presence of puromycin for 2 weeks. The stable knockdown CL1-5 cells were designated shA3-1 and shA3-2, while the control was called sh-V (control).

Assays for cell viability and anchorage-independent growth

Trypan blue exclusion assay for viable cell counts and soft agar colony formation assays for anchorage-independent growth were performed as described previously^{55,56}.

Subcutaneous xenografts

Each xenograft was established by subcutaneously injecting 2×10^6 cells into the right flank of 6-week-old male Balb/c nude mice ($n=8$ per group, National Laboratory Animal Center, Taipei, Taiwan). Tumor volumes were measured twice a week using calipers, and tumor volumes were calculated according to the formula $V = 0.5 \times W^2 L$, where W was taken as the smaller diameter and L was taken as the larger diameter. Mice were sacrificed by CO₂ asphyxiation on day 15 after inoculation. All animal experiments were performed according to the guidelines for the Animal Care Ethics Commission of Chang Gung Memorial Hospital.

Statistical analysis

The presented results represent three independent experiments with similar results. Statistical differences were evaluated using the Student's *t*-test and considered significant at $p < 0.05$.

Acknowledgements

This work was supported by grants from Chang Gung Memorial Hospital (CMRPF110012) and the Ministry of Science and Technology of Taiwan (108-2314-B-255-002- and 108-2320-B-182-030-MY3). The proteomics experiments were performed by the Proteomics Core Laboratory, Molecular Medicine Research Center, Chang Gung University, Taiwan (Grants CLRPD1J0011 and CLRPD190019). The funders had no role in the study design, data collection, data analysis, publication decisions, or manuscript preparation.

Author details

¹Graduate Institute of Health Industry Technology and Research Center for Food and Cosmetic Safety, Research Center for Chinese Herbal Medicine, College of Human Ecology, Chang Gung University of Science and Technology, Taoyuan 333, Taiwan. ²Tissue Bank, Chang Gung Memorial Hospital at Linkou, Taoyuan 333, Taiwan. ³Department of Otolaryngology-Head & Neck Surgery, Chang Gung Memorial Hospital at Linkou, Taoyuan 333, Taiwan. ⁴Department of Medical Biotechnology and Laboratory Science, College of Medicine, Chang Gung University, Taoyuan 333, Taiwan. ⁵Molecular Medicine Research Center, Chang Gung University, Taoyuan 333, Taiwan. ⁶Research Center for Emerging Viral Infections, College of Medicine, Chang Gung University, Taoyuan 333, Taiwan. ⁷Institute of Biomedical Sciences, Academia Sinica, Taipei 115, Taiwan. ⁸Department of Pathology, Chang Gung Memorial Hospital at Linkou and Chang Gung University, Taoyuan 333, Taiwan. ⁹Institute of Cellular and Organismic Biology, Academia Sinica, Taipei 115, Taiwan

Conflict of interest

The authors declare that they have no conflict of interest.

Publisher's note

Springer Nature remains neutral with regard to jurisdictional claims in published maps and institutional affiliations.

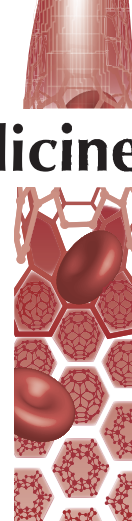
Supplementary Information accompanies this paper at (<https://doi.org/10.1038/s41389-020-0225-0>).

Received: 25 October 2019 Revised: 4 April 2020 Accepted: 7 April 2020
Published online: 22 April 2020


References

1. Maemondo, M. et al. Gefitinib or chemotherapy for non-small-cell lung cancer with mutated EGFR. *N. Engl. J. Med.* **362**, 2380–2388 (2010).
2. Lo, H. W. et al. Nuclear interaction of EGFR and STAT3 in the activation of the iNOS/NO pathway. *Cancer Cell* **7**, 575–589 (2005).
3. Lo, H. W. Nuclear mode of the EGFR signaling network: biology, prognostic value, and therapeutic implications. *Discov. Med.* **10**, 44–51 (2010).
4. Boerner, J. L., Demory, M. L., Silva, C. & Parsons, S. J. Phosphorylation of Y845 on the epidermal growth factor receptor mediates binding to the mitochondrial protein cytochrome c oxidase subunit II. *Mol. Cell. Biol.* **24**, 7059–7071 (2004).
5. Demory, M. L. et al. Epidermal growth factor receptor translocation to the mitochondria: regulation and effect. *J. Biol. Chem.* **284**, 36592–36604 (2009).
6. Han, W. & Lo, H. W. Landscape of EGFR signaling network in human cancers: biology and therapeutic response in relation to receptor subcellular locations. *Cancer Lett.* **318**, 124–134 (2012).
7. Liccardi, G., Hartley, J. A. & Hochhauser, D. EGFR nuclear translocation modulates DNA repair following cisplatin and ionizing radiation treatment. *Cancer Res.* **71**, 1103–1114 (2011).
8. Marti, U. et al. Localization of epidermal growth factor receptor in hepatocyte nuclei. *Hepatology* **13**, 15–20 (1991).

9. Lin, S. Y. et al. Nuclear localization of EGF receptor and its potential new role as a transcription factor. *Nat. Cell Biol.* **3**, 802–808 (2001).
10. Huo, L. et al. RNA helicase A is a DNA-binding partner for EGFR-mediated transcriptional activation in the nucleus. *Proc. Natl Acad. Sci. U.S.A.* **107**, 16125–16130 (2010).
11. Hanada, N. et al. Co-regulation of B-Myb expression by E2F1 and EGF receptor. *Mol. Carcinog.* **45**, 10–17 (2006).
12. Hung, L. Y. et al. Nuclear epidermal growth factor receptor (EGFR) interacts with signal transducer and activator of transcription 5 (STAT5) in activating Aurora-A gene expression. *Nucleic Acids Res.* **36**, 4337–4351 (2008).
13. Li, C., Iida, M., Dunn, E. F., Ghia, A. J. & Wheeler, D. L. Nuclear EGFR contributes to acquired resistance to cetuximab. *Oncogene* **28**, 3801–3813 (2009).
14. Lo, H. W. et al. Novel prognostic value of nuclear epidermal growth factor receptor in breast cancer. *Cancer Res.* **65**, 338–348 (2005).
15. Lo, H. W., Cao, X., Zhu, H. & Ali-Osman, F. Cyclooxygenase-2 is a novel transcriptional target of the nuclear EGFR-STAT3 and EGFR/STAT3 signaling axes. *Mol. Cancer Res.* **8**, 232–245 (2010).
16. Jaganathan, S. et al. A functional nuclear epidermal growth factor receptor, SRC and Stat3 heteromeric complex in pancreatic cancer cells. *PLoS ONE* **6**, e19605 (2011).
17. Huang, W. C. et al. Nuclear translocation of epidermal growth factor receptor by Akt-dependent phosphorylation enhances breast cancer-resistant protein expression in gefitinib-resistant cells. *J. Biol. Chem.* **286**, 20558–20568 (2011).
18. Wang, S. C. et al. Tyrosine phosphorylation controls PCNA function through protein stability. *Nat. Cell Biol.* **8**, 1359–1368 (2006).
19. Dittmann, K. et al. Nuclear EGFR renders cells radio-resistant by binding mRNA species and triggering a metabolic switch to increase lactate production. *Radiother. Oncol.* **116**, 431–437 (2015).
20. Bitler, B. G., Goverdhan, A. & Schroeder, J. A. MUC1 regulates nuclear localization and function of the epidermal growth factor receptor. *J. Cell Sci.* **123**, 1716–1723 (2010).
21. Che, T. F. et al. Mitochondrial translocation of EGFR regulates mitochondria dynamics and promotes metastasis in NSCLC. *Oncotarget* **6**, 37349–37366 (2015).
22. Tan, X., Thapa, N., Sun, Y. & Anderson, R. A. A kinase-independent role for EGF receptor in autophagy initiation. *Cell* **160**, 145–160 (2015).
23. Chu, Y. W. et al. Selection of invasive and metastatic subpopulations from a human lung adenocarcinoma cell line. *Am. J. Respir. Cell Mol. Biol.* **17**, 353–360 (1997).
24. Chen, C. Y. et al. Tid1-L inhibits EGFR signaling in lung adenocarcinoma by enhancing EGFR Ubiquitinylation and degradation. *Cancer Res.* **73**, 4009–4019 (2013).
25. Boukakis, G., Patrino-Georgoula, M., Lekaraku, M., Valavanis, C. & Guialis, A. Deregulated expression of hnRNP A/B proteins in human non-small cell lung cancer: parallel assessment of protein and mRNA levels in paired tumour/non-tumour tissues. *BMC Cancer* **10**, 434 (2010).
26. Katahira, J. T. et al. Nuclear RNA export factor 7 is localized in processing bodies and neuronal RNA granules through interactions with shuttling hnRNPs. *Nucleic Acids Res.* **36**, 616–628 (2008).
27. Mishra, N., Reddy, K. S., Timilsina, U., Gaur, D. & Gaur, R. Human APOBEC3B interacts with the heterogeneous nuclear ribonucleoprotein A3 in cancer cells. *J. Cell. Biochem.* **119**, 6695–6703 (2018).
28. Pelisch, F. et al. Involvement of hnRNP A1 in the matrix metalloproteinase-3-dependent regulation of Rac1 pre-mRNA splicing. *J. Cell. Biochem.* **113**, 2319–2329 (2012).
29. Cunningham, J. T., Moreno, M. V., Lodi, A., Ronen, S. M. & Ruggero, D. Protein and nucleotide biosynthesis are coupled by a single rate-limiting enzyme, PRPS2, to drive cancer. *Cell* **157**, 1088–1103 (2014).
30. Hsieh, A. C. et al. The translational landscape of mTOR signalling steers cancer initiation and metastasis. *Nature* **485**, 55–61 (2012).
31. Silvera, D., Formenti, S. C. & Schneider, R. J. Translational control in cancer. *Nat. Rev. Cancer* **10**, 254–266 (2010).
32. Truitt, M. L. & Ruggero, D. New frontiers in translational control of the cancer genome. *Nat. Rev. Cancer* **16**, 288–304 (2016).
33. Wang, T. H. et al. Tid1-S regulates the mitochondrial localization of EGFR in non-small cell lung carcinoma. *Oncogenesis* **6**, e361 (2017).
34. Bollu, L. R. et al. Involvement of de novo synthesized palmitate and mitochondrial EGFR in EGF induced mitochondrial fusion of cancer cells. *Cell Cycle* **13**, 2415–2430 (2014).
35. Halama, A. et al. Metabolic switch during adipogenesis: from branched chain amino acid catabolism to lipid synthesis. *Arch. Biochem. Biophys.* **589**, 93–107 (2016).
36. He, Y. & Smith, R. Nuclear functions of heterogeneous nuclear ribonucleoproteins A/B. *Cell. Mol. Life Sci.* **66**, 1239–1256 (2009).
37. Jurica, M. S., Licklider, L. J., Gygi, S. R., Grigorieff, N. & Moore, M. J. Purification and characterization of native spliceosomes suitable for three-dimensional structural analysis. *RNA* **8**, 426–439 (2002).
38. Rappsilber, J., Ryder, U., Lamond, A. I. & Mann, M. Large-scale proteomic analysis of the human spliceosome. *Genome Res.* **12**, 1231–1245 (2002).
39. He, Y., Brown, M. A., Rothnagel, J. A., Saunders, N. A. & Smith, R. Roles of heterogeneous nuclear ribonucleoproteins A and B in cell proliferation. *J. Cell Sci.* **118**, 3173–3183 (2005).
40. Patry, C. et al. Small interfering RNA-mediated reduction in heterogeneous nuclear ribonucleoprotein A1/A2 proteins induces apoptosis in human cancer cells but not in normal mortal cell lines. *Cancer Res.* **63**, 7679–7688 (2003).
41. Dittmann, K., Mayer, C., Czernmel, S., Huber, S. M. & Rodemann, H. P. New roles for nuclear EGFR in regulating the stability and translation of mRNAs associated with VEGF signaling. *PLoS ONE* **12**, e0189087 (2017).
42. Papadopoulou, C., Boukakis, G., Ganou, V., Patrino-Georgoula, M. & Guialis, A. Expression profile and interactions of hnRNP A3 within hnRNP/mRNP complexes in mammals. *Arch. Biochem. Biophys.* **523**, 151–160 (2012).
43. Tauler, J., Zudaire, E., Liu, H., Shih, J. & Mulshine, J. L. hnRNP A2/B1 modulates epithelial-mesenchymal transition in lung cancer cell lines. *Cancer Res.* **70**, 7137–7147 (2010).
44. Chen, C. Y., Yu, Z. Y., Chuang, Y. S., Huang, R. M. & Wang, T. C. Sulforaphane attenuates EGFR signaling in NSCLC cells. *J. Biomed. Sci.* **22**, 38 (2015).
45. Wang, C. L. et al. Discovery of retinoblastoma-associated binding protein 46 as a novel prognostic marker for distant metastasis in non-small cell lung cancer by combined analysis of cancer cell secretome and pleural effusion proteome. *J. Proteome Res.* **8**, 4428–4440 (2009).
46. Kuo, R. L. et al. Interactome analysis of the NS1 protein encoded by influenza A H1N1 virus reveals a positive regulatory role of host protein PRP19 in viral replication. *J. Proteome Res.* **15**, 1639–1648 (2016).
47. Kuo, R. L. et al. Interactome analysis of NS1 protein encoded by influenza A H7N9 virus reveals an inhibitory role of NS1 in host mRNA maturation. *J. Proteome Res.* **17**, 1474–1484 (2018).
48. Wu, C. C., Chu, H. W., Hsu, C. W., Chang, K. P. & Liu, H. P. Saliva proteome profiling reveals potential salivary biomarkers for detection of oral cavity squamous cell carcinoma. *Proteomics* **15**, 3394–3404 (2015).
49. Keller, A., Nesvizhskii, A. I., Kolker, E. & Aebersold, R. Empirical statistical model to estimate the accuracy of peptide identifications made by MS/MS and database search. *Anal. Chem.* **74**, 5383–5392 (2002).
50. Nesvizhskii, A. I., Keller, A., Kolker, E. & Aebersold, R. A statistical model for identifying proteins by tandem mass spectrometry. *Anal. Chem.* **75**, 4646–4658 (2003).
51. Hsu, C. W. et al. Proteomic profiling of paired interstitial fluids reveals dysregulated pathways and salivary NID1 as a biomarker of oral cavity squamous cell carcinoma. *Mol. Cell. Proteomics* **18**, 1939–1949 (2019).
52. Huang, da, W., Sherman, B. T. & Lempicki, R. A. Systematic and integrative analysis of large gene lists using DAVID bioinformatics resources. *Nat. Protoc.* **4**, 44–57 (2009).
53. Szklarczyk, D. et al. STRING v10: protein-protein interaction networks, integrated over the tree of life. *Nucleic Acids Res.* **43**, D447–D452 (2015).
54. Wang, T. H. et al. Heterogeneous nuclear ribonucleoproteins A1 and A2 function in telomerase-dependent maintenance of telomeres. *Cancers* **11**, E334 (2019).
55. Chen, C. Y. et al. Tid1 functions as a tumour suppressor in head and neck squamous cell carcinoma. *J. Pathol.* **219**, 347–355 (2009).
56. Chen, C. Y. et al. Heterogeneous nuclear ribonucleoproteins A1 and A2 modulate expression of Tid1 isoforms and EGFR signaling in non-small cell lung cancer. *Oncotarget* **7**, 16760–16772 (2016).



Suppression of neutrophilic inflammation can be modulated by the droplet size of anti-inflammatory nanoemulsions

Huang-Ping Yu^{‡,1,2} , Fu-Chao Liu^{‡,1,2}, Cheng-Yu Lin³, Ani Umoro⁴, Jiří Trousil⁵, Tsong-Long Hwang^{**}, ^{1,4,6,7,8} & Jia-You Fang^{*}, ^{1,4,6,7}

¹Department of Anesthesiology, Chang Gung Memorial Hospital, Kweishan, Taoyuan, 333, Taiwan

²School of Medicine, College of Medicine, Chang Gung University, Kweishan, Taoyuan, 333, Taiwan

³Graduate Institute of Biomedical Sciences, Chang Gung University, Kweishan, Taoyuan, 333, Taiwan

⁴Graduate Institute of Natural Products, Chang Gung University, Kweishan, Taoyuan, 333, Taiwan

⁵Institute of Macromolecular Chemistry, Czech Academy of Sciences, Prague, 11720, Czech Republic

⁶Chinese Herbal Medicine Research Team, Healthy Aging Research Center, Chang Gung University, Kweishan, Taoyuan, 333, Taiwan

⁷Research Center for Food & Cosmetic Safety & Research Center for Chinese Herbal Medicine, Chang Gung University of Science & Technology, Kweishan, Taoyuan, 333, Taiwan

⁸Department of Chemical Engineering, Ming Chi University of Technology, New Taipei City, 243, Taiwan

*Author for correspondence: Tel.: +886 3 211 8800; Fax: +886 3 211 8236; fajy@mail.cgu.edu.tw

**Author for correspondence: Tel.: +886 3 211 8800; Fax: +886 3 211 8506; htl@mail.cgu.edu.tw

‡ Authors contributed equally

Aim: We aimed to develop nanoemulsions containing phosphodiesterase 4 inhibitor rolipram with different droplet sizes, to evaluate the anti-inflammatory effect against activated neutrophils and a related lung injury. **Materials & methods:** We prepared nanoemulsions of three different sizes, 68, 133 and 188 nm. **Results:** The nanoemulsion inhibited the superoxide anion but not elastase release in primary human neutrophils. The large-sized nanoemulsions were mostly internalized by neutrophils, resulting in the reduction of intracellular Ca^{2+} half-life. The peripheral organ distribution of near-infrared dye-tagged nanoemulsions increased, following the decrease in droplet diameter. Rolipram entrapment into intravenous nanoemulsions ameliorated pulmonary inflammation. The smallest droplet size showed improvement, compared with the largest size. **Conclusion:** We established a foundation for the development of nanoemulsions against inflamed lung disease.

First draft submitted: 29 October 2019; Accepted for publication: 30 January 2020; Published online: 20 March 2020

Keywords: anti-inflammation • lung injury • nanoemulsion • neutrophil • rolipram • size effect

Inflammatory lung disorders pose a great health threat in modern society. Chronic lung inflammation such as chronic obstructive pulmonary disease (COPD) and asthma are the leading causes of death in the USA [1]. Acute lung inflammation occurs in pneumonia, acute lung injury (ALI) and acute respiratory distress syndrome (ARDS). ARDS is a complex and cascading condition resulting from ALI. The mortality associated with ARDS has been higher than 40% over the last decade [2]. Both COPD and ARDS are difficult to treat using the drug therapy currently available. The overwhelming stimulation of neutrophils majorly contributes to the pathogenesis of COPD and ARDS [3]. Neutrophils, which are phagocytic leukocytes, play the greatest role in the immune response. The regulation of the activated neutrophils is essential to control pulmonary damage [4]. PDE4 inhibitors are currently developed as anti-inflammatory drugs via the suppression of neutrophil activation. PDE4 inhibition upregulates cAMP expression to prevent the production of pro-inflammatory mediators and reactive oxygen species from neutrophils [5]. Recently, the US FDA approved the first PDE4 inhibitor; roflumilast, for treating chronic respiratory inflammatory diseases. However, it is evident that the application of PDE4 inhibitors is hampered due to safety concerns. PDE4 inhibitors facily penetrate across the blood–brain barrier (BBB) to enter the brain, causing the side effects of headache, nausea and insomnia [6]. The novel strategy to overcome the side effects and improve the therapeutic index is a major focus of PDE4 inhibitor development.

Nanocarriers for efficient drug delivery are gaining attention in the field of therapeutic application. The unique properties of nanoparticles, including large surface area–mass proportion, strong reactivity and the capability to functionalize on particulate surfaces contribute to the amelioration of pharmacokinetics and achievement of the desired bioactivity at the target nidus [7,8]. This targeting capability can reduce the possible side effects of the drugs. Among different nanoparticles, nanoemulsions are attractive drug carriers because of their ability to enhance drug delivery across biomembranes and prolong half-life ($t_{1/2}$) in the body and their high encapsulation of lipophilic drugs [9–11]. Nanoemulsions are heterogeneous liquid dispersions with the oil droplet size generally ranging from 100 to 250 nm. The nanoparticulate size demonstrates a critical role in influencing the cellular uptake, targeting efficiency, pharmacokinetics and the final outcome of the drugs [12]. The impact of nanoparticulate size on the cellular interaction, pharmacokinetics and pharmacodynamics for metallic nanoparticles, polymeric nanoparticles and liposomes has been extensively studied [13,14]. However, there is no report on the effect of the nanoemulsions' droplet size on these aspects. Herein, we investigated the possibility of modulating activated neutrophil suppression, biodistribution and drug therapy by controlling the size of anti-inflammatory nanoemulsions.

The PDE4 selective inhibitor; rolipram, was chosen as the model drug encapsulated in nanoemulsions in this study because it shows the potential for suppressing asthma and ALI [15,16]. Clinical trial results have demonstrated the failure of rolipram, which has had undesired adverse effects [17]. Methods to create nanoparticles with well-controlled size and narrow particle distribution are limited [18]. We successfully fabricated nanoemulsions with droplet size controlled between 60 and 190 nm. The primary human neutrophils were utilized in this study as the model cells for exploring the interaction with nanosystems. The biodistribution of the nanoemulsions was examined by determining *ex vivo* bioimaging and the rolipram concentration in different organs. The *in vivo* disease model was the lung instillation of lipopolysaccharide (LPS) for generating ARDS-like inflammation.

Materials & methods

Fabrication of nanoemulsions

The oil and water phases of nanoemulsions were separately prepared. The oil phase consisted of rolipram (0.27% of the final product, w/w), soy phosphatidylcholine (SPC, 1.5%) and squalene. The squalene percentage was 2, 5 and 7% for formation of small (RS), medium (RM) and large (RL) size, respectively. The water phase containing Poloxamer 188 (2%) and water for all nanoemulsions. The lipid and aqueous phases were heated at 85°C for 20 min. The aqueous phase was then incorporated with the oil phase through the homogenization at 12,000 rpm (85°C for 20 min). Then an agitation through a probe-type sonicator for 20 min was carried out. The final step was the cooling of the nanoemulsions at room temperature.

Dynamic laser-scattering of the nanoemulsions

The average size, polydispersity index (PDI) and ζ -potential were detected by a dynamic laser-scattering method (Nano ZS90, Worcestershire, UK). The formulations were diluted 100-fold with water before the measurement.

Rolipram encapsulation percentage in nanoemulsions

The rolipram entrapment in oil droplets was examined using an ultracentrifugation technique (Optima MAX, Beckman Coulter, CA, USA). The prepared nanoformulations were centrifuged at $48,000 \times g$ and 4°C for 30 min to divide them into encapsulated and unencapsulated rolipram. The supernatant and precipitate were withdrawn to measure the encapsulation percentage by high-performance liquid chromatography (HPLC). The HPLC setup was described previously [19].

Molecular environment of nanoemulsions

The molecular environment of the nanoemulsions was estimated by fluorescence spectrophotometry based on Nile red solvatochromism [20]. The nanoemulsions were loaded with Nile red (1 ppm in the final product). The emission spectra of nanoemulsions were scanned from 550 to 700 nm. The excitation wavelength was set at 546 nm.

Rolipram release from nanoemulsions

Rolipram release was evaluated by Franz diffusion cell. A cellulose membrane with pores of a 6000–8000 g/ml cutoff was mounted between the donor and receptor compartments. Free rolipram or rolipram-loaded nanoemulsions (0.5 ml) were positioned in the donor. A 30% ethanol in pH 7.4 buffer was used as the receptor medium. The

other procedures were the same as in the previous study [21]. The released rolipram amount in the receptor was quantified by HPLC.

Isolation of primary human neutrophils

The protocol of this isolation was approved by the Institutional Review Board of Chang Gung Memorial Hospital. Each of the volunteers, between 20–30 years of age, signed and gave informed consent. The blood was obtained by venipuncture. The neutrophils were separated with a dextran sedimentation method before centrifugation in a Ficoll-Hypaque gradient. The processes were described in detail previously [22].

Lactate dehydrogenase of neutrophils

The lactate dehydrogenase (LDH) level of neutrophils treated with or without nanoemulsions was analyzed by a commercial method (CytoTox 96, Promega, WI, USA). Neutrophils (6×10^5 cells/ml) were equilibrated at 37°C for 2 min. Then, the nanoemulsions with rolipram at different concentrations were added to the neutrophil suspension for 15 min. The total LDH release was determined by 0.1% Triton X-100 treatment.

Superoxide generation of neutrophils

The assay of superoxide was based on the previous work [22]. In brief, neutrophils (6×10^5 cells/ml) were equilibrated for 2 min after mixing with a 0.5-mg/ml ferricytochrome *c* and 1-mM CaCl_2 . The suspension was incubated with nanoemulsions for 5 min. The neutrophils were stimulated by a 100-nM formyl-L-methionyl-L-leucyl-L-phenylalanine (fMLP) for 10 min. The absorbance change at 550 nm was quantified under a UV/visible spectrophotometer (U3010, Tokyo, Japan).

Elastase release of neutrophils

MeO-Suc-Ala-Ala-Pro-Val-p-nitroanilide was used as the elastase substrate to determine the elastase release [23]. After supplementation with the substrate (100 μM), neutrophils were equilibrated for 2 min and then treated with the nanoemulsions for 5 min. The cells were stimulated by fMLP at a concentration of 100 nM. The changes in absorbance at 405 nm were detected by a UV/visible spectrophotometer.

Intracellular Ca^{2+} concentration of neutrophils

The primary human neutrophils (3×10^6 cells/ml) were incubated with Furo-3/AM agent at 2 μM in a condition of 35°C for 45 min. The cells were resuspended with Ca^{2+} -free Hank's balanced salt solution (HBSS) after washing. The neutrophil suspension was treated with nanoemulsions for 5 min. fMLP was employed to increase intracellular Ca^{2+} concentration ($[\text{Ca}^{2+}]_i$) in the presence of CaCl_2 (1 mM). The changes in fluorescence intensity at the excitation and emission wavelength of 488 and 520 nm, respectively, were monitored by a fluorescence spectrophotometer (F4500, Hitachi). $[\text{Ca}^{2+}]_i$ was calibrated by fluorescence intensity.

The uptake of nanoemulsions by neutrophils

Rhodamine 800 at 0.1 mg/ml was the dye incorporating into the nanoemulsion to visualize neutrophil uptake. The nanoemulsions were incubated with the neutrophils (1.8×10^7 cells/ml) for 5 min. The uptake was visualized by confocal laser-scanning microscopy (TCS SP2, Leica, Wetzlar, Germany). The uptake was also analyzed by measuring the rhodamine 800 fluorescence in flow cytometry.

Animals

Male C57BL/6 mice (20–25 g) acquired from the National Laboratory Animal Center (Taipei, Taiwan) were used in the *ex vivo* and *in vivo* experiments. All animal study procedures were conducted in accordance with the protocols approved by the Institutional Animal Care and Use Committee of Chang Gung University.

Ex vivo bioimaging of nanoemulsions

iFlour 790 acid (0.08%) was used as the near-infrared (NIR) dye to monitor the biodistribution of nanoemulsions in different organs. After the mice were anesthetized, the nanoemulsions (2 ml/kg) were intravenously applied into the tail vein. The mice were then sacrificed at 2 h. The organs were taken for visualizing nanoemulsion biodistribution in mice by a bioimaging system (Pearl Impulse, Li-Cor, NE, USA).

Table 1. Physicochemical properties of the nanoemulsions on droplet size, polydispersity index and ζ -potential.

Formulation	Size (nm)	PDI	ζ -potential
Nanoemulsions with small diameter	67.8 \pm 0.7	0.31 \pm 0.02	-42.6 \pm 2.2
Nanoemulsions with medium diameter	133.0 \pm 1.0	0.21 \pm 0.01	-47.7 \pm 0.2
Nanoemulsions with large diameter	188.2 \pm 2.2	0.23 \pm 0.01	-49.2 \pm 0.1

Each value represents the mean \pm standard error of the mean (n = 3).
PDI: Polydispersity index.

Biodistribution of rolipram

The blood samples were taken 2 h after the intravenous bolus of free rolipram or rolipram-loaded nanoemulsions (60 mg/kg). Then, the mice were immediately sacrificed to remove the organs to determine the rolipram concentration. The detailed procedures of organ homogenization and rolipram extraction from plasma and organs were described previously [19]. The rolipram concentration in the organs was calibrated from ng/ μ l to ng/mg, given the homogenate volume and organ weight.

Establishment of lung injury

The mice with lung injury were divided into five groups: lung injury without therapy and lung injury treated with intravenous free rolipram, RS, RM or RL. Intratracheal instillation of LPS was performed as previously described [24]. Briefly, intravenous-free rolipram or nanoemulsions were administered to the mice. After 30 min, the anesthetized mice received instilled LPS (8 mg/kg) by a tracheostomy. The animals were sacrificed 6 h after LPS treatment. The lung was excised for the following histology and ELISA assay.

Histological observation

The pulmonary sample was positioned into 10% formalin and embedded in paraffin. The specimens were cut to a thickness of 3 μ m for hematoxylin and eosin staining. For immunohistochemistry staining, the sections were incubated with anti-Ly6G antibody (the clone of antibody: RB6-8C5) for 1 h and were then treated with biotinylated donkey anti-goat IgG.

ELISA assay

Myeloperoxidase (MPO), cytokines and chemokines in the lung were detected by ELISA. The lung was extracted by phosphate-buffered saline containing protease inhibitors under homogenization (MagNA Lyser, Roche, Penzberg, Germany). The supernatant was taken after centrifugation (11,500 $\times g$ for 10 min) for quantifying MPO, IL-1 β , IL-6, TNF- α and CXCL-1 using the commercially available kits (BioLegend, CA, USA) according to the manufacturer's instructions.

Statistical analysis

The statistical analysis was performed by Kruskal–Wallis test. The *post hoc* test used in the present study was Dunn's test. The 0.05, 0.01 and 0.001 probability levels were selected as statistically significant.

Results

Physicochemical properties of nanoemulsions

The droplet size, PDI and ζ -potential of the nanoemulsions are summarized as depicted in Table 1. The hydrodynamic diameter was 68, 133 and 188 nm for small (RS), medium (RM) and large (RL) nanoemulsions, respectively, depending on the squalene amount from 2–7%. All nanoformulations revealed a unimodal size distribution with PDI \leq 0.31, demonstrating a narrow size distribution. The ζ -potential exhibited negative values ranging from -43 to -49 mV, with the bigger droplet size showing a slightly higher negative charge. Entrapment of rolipram resulted in a higher encapsulation percentage (>95%) for all nanosystems. The lipophilic property of rolipram would be retained in the oil core of nanoemulsions, resulting in great loading efficiency. Figure 1A illustrates the emission spectrum of Nile red-loaded nanoemulsions. The fluorescence would be quenched in the nanocarriers with less lipophilicity. The larger-sized nanosystems demonstrated a lower lipophilicity compared with the smaller ones. Rolipram release from nanoemulsions was conducted in Franz cell. The rolipram control solution was investigated in parallel. All curves of release amount-time profiles fitted zero-order fashion. Figure 1B shows the release rate calculated from the slopes. Significantly different release rates were detected for different formulations. Rolipram

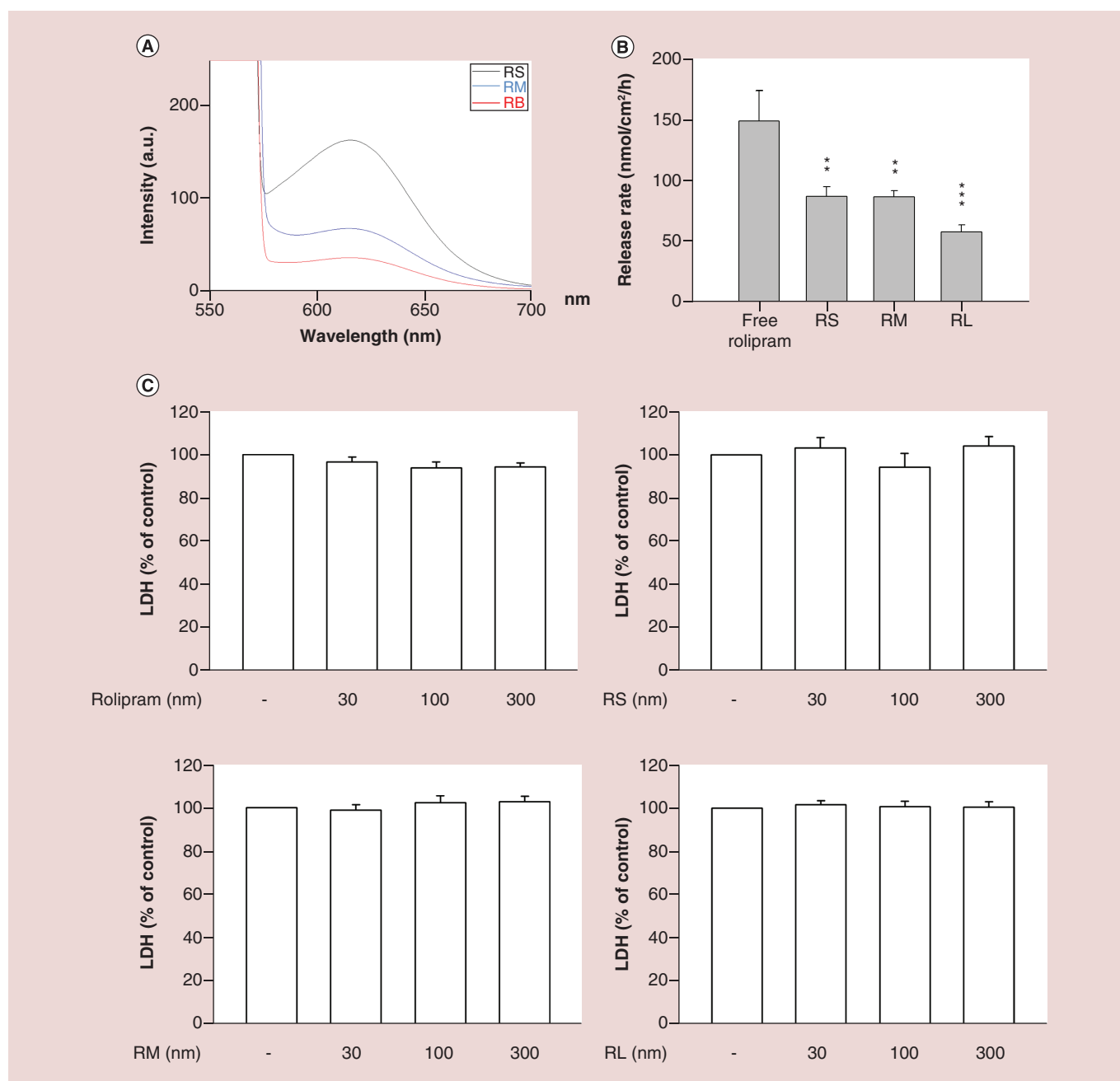


Figure 1. Design of rolipram-loaded nanoemulsions with different droplet sizes and neutrophil cytotoxicity assay. (A) Molecular environment (polarity) of the nanoemulsions examined by Nile red fluorescence intensity. **(B)** Rolipram release rate from free control and rolipram-loaded nanoemulsions. **(C)** The neutrophils (6×10^5 cells/ml) were treated with free rolipram, RS, RM and RL for 15 min. The cytotoxicity was measured by LDH assay. All data are expressed as the mean \pm standard error of mean (n = 6).

* $p < 0.05$; ** $p < 0.01$; *** $p < 0.001$ as compared with free rolipram.

LDH: Lactate dehydrogenase; RL: Nanoemulsion with large diameter; RM: Nanoemulsion with medium diameter; RS: Nanoemulsion with small diameter.

was released more slowly from the nanoemulsions than the control solution. RS and RM had a similar release rate and rolipram was released more slowly from RL than the smaller-sized nanoemulsions.

Anti-inflammatory nanoemulsions inhibit neutrophil stimulation

A cell model of isolated human neutrophils was employed to investigate the anti-inflammatory activity of nanoemulsions. A cytotoxicity study was first conducted by LDH release. As shown in Figure 1C, neither free rolipram nor rolipram-loaded nanoemulsions induced cytotoxicity toward neutrophils at the concentrations between 30 and 300 nM. The nanoemulsions were also tested in activated neutrophils to assess the ability to inhibit superoxide generation and elastase release. All rolipram formulations did not alter the basal superoxide and elastase level under resting conditions (data not shown). As depicted in Figure 2A, we found that nontoxic concentrations of free rolipram reduced superoxide in fMLP-stimulated neutrophils in a dose-dependent manner. Free rolipram at 300 nM induced a nearly fourfold decrease of superoxide. As with free rolipram, superoxide production decreased in response to nanoemulsion treatment. There was no difference among the superoxide inhibition of nanoemulsions of different sizes. Treatment with nanoemulsions decreased the superoxide level by about 85%, showing more potency than the control solution. However, the IC₅₀ of rolipram on superoxide inhibition showed no significant difference for all formulations (Figure 2B). RS without rolipram was also examined for comparison. The nanoemulsions without the drug (blank RS) show no ability to inhibit superoxide (Figure 2A), demonstrating that rolipram played a main role to confine neutrophil activation. Neutrophil degranulation was determined based on the release of elastase as shown in Figure 2C. Free rolipram could not suppress elastase release. Elastase revealed a trend of slight reduction in response to nanoemulsions, however, this trend did not achieve statistical significance.

The oxidative stress of neutrophil activation is regulated via a process involving the magnitude and duration of $[Ca^{2+}]_i$. We next surveyed whether nanoemulsions could reverse increase $[Ca^{2+}]_i$ and thus alleviate inflammation. As shown in the profiles of spectrofluorometry (Figure 3A), fMLP induces a fast and transient increase of $[Ca^{2+}]_i$. The peak value of $[Ca^{2+}]_i$ in spectrofluorometry was calculated as shown in Figure 3B. All rolipram formulations failed to diminish the $[Ca^{2+}]_i$ peak. Nevertheless, rolipram decreases the time needed for $[Ca^{2+}]_i$ to return to half of the peak (Figure 3C). The larger-sized nanoemulsions (RM and RL) showed a significantly greater decrease of $t_{1/2}$ than smaller-sized nanoemulsions (RS) at the low rolipram concentration (30 nM). The statistical assay demonstrated no significant reduction of $t_{1/2}$ by free rolipram and RS at this low dose.

Facile uptake of nanoemulsions by neutrophils

We investigated the effect of nanoemulsion size on droplet uptake by human neutrophils as shown in Figure 4. As early as 5 min after dye-loaded nanoemulsion application, an intense fluorescence was observed within the cells (Figure 4A). RM and RL accumulated in neutrophils to a greater degree as compared with RS. This suggests the maximum uptake by the nanosystems with larger sizes. The nanoemulsions were mainly located within the cytosol. The uptake efficiency was also analyzed by flow cytometry. As found with visualization under microscopy, the larger sizes had better internalization than the smaller sizes (Figure 4B).

Ex vivo bioimaging of nanoemulsions

To evaluate the retention of injected nanoemulsions in the organs, the nanocarriers were fabricated with the entrapment of NIR dye to enable visualization through the bioimaging system. The organs were harvested for observing nanoemulsion distribution after a 2 h bolus. As depicted in Figure 5A, we showed that the nanoemulsion accumulation in all peripheral organs increased as the size decreased. This result could account for the rapid and extensive delivery of small-sized nanoemulsions from the circulation to the peripheral tissues. The signal in the brain was negligible for all nanosystems tested. Quantitative analysis of NIR intensity was performed as shown in Figure 5B. As observed from the bioimaging, a significantly higher intensity was measured in RS than RM and RL. Figure 5C summarizes the percentage of NIR intensity in different organs. No significant difference in the NIR accumulation percentage was found as a function of droplet sizes for all organs. The nanoemulsions were more accumulated in the gastrointestinal tract and liver by about 45 and 40%, respectively, than in the other organs.

Biodistribution of rolipram

The rolipram concentration in the peripheral organs was examined 2 h postinjection as shown in Figure 6. The brain had the greatest rolipram accumulation by control solution injection (Figure 6A). Rolipram encapsulation into nanoemulsions allowed a decrease in brain accumulation by sevenfold. The nanoemulsion uptake by the brain exhibited no correlation to droplet size. RS and RL had a similar drug concentration in the heart and kidney as compared with free rolipram, whereas there was a decreased distribution for RM (Figure 6B & C). RS exhibited a twofold greater accumulation of rolipram in the liver than in the free control (Figure 6D). The hepatic uptake of

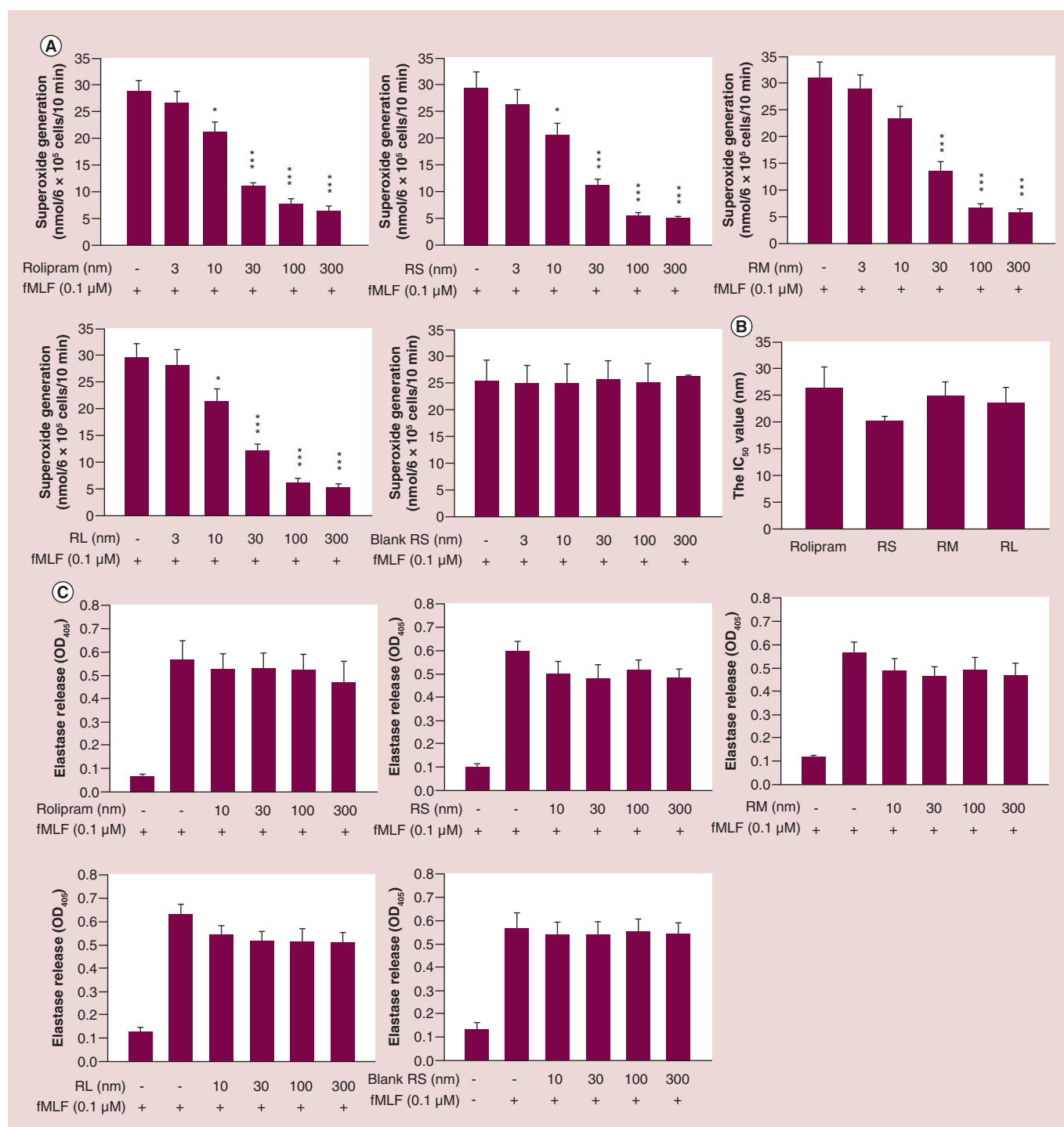


Figure 2. Effects of rolipram-loaded nanoemulsions on superoxide anion release and elastase activity in formyl-L-methionyl-L-leucyl-L-phenylalanine-activated human neutrophils (6 × 10⁵ cells/ml). (A) Measurement of extracellular superoxide production by fMLP/cytochalasin B for 10 min. (B) Rolipram concentration with a 50% inhibition (IC₅₀) value of rolipram in different formulations for inhibiting superoxide generation. (C) Assay of absorbance at 405 nm for continuous measurement of human neutrophil elastase release. All data are expressed as the mean ± standard error of the mean (n = 6).

*p < 0.05; ***p < 0.001 as compared with fMLP-activated group without rolipram intervention.

fMLP: Formyl-L-methionyl-L-leucyl-L-phenylalanine; OD: Optical density; RL: Nanoemulsion with large diameter; RM: Nanoemulsion with medium diameter; RS: Nanoemulsion with small diameter.

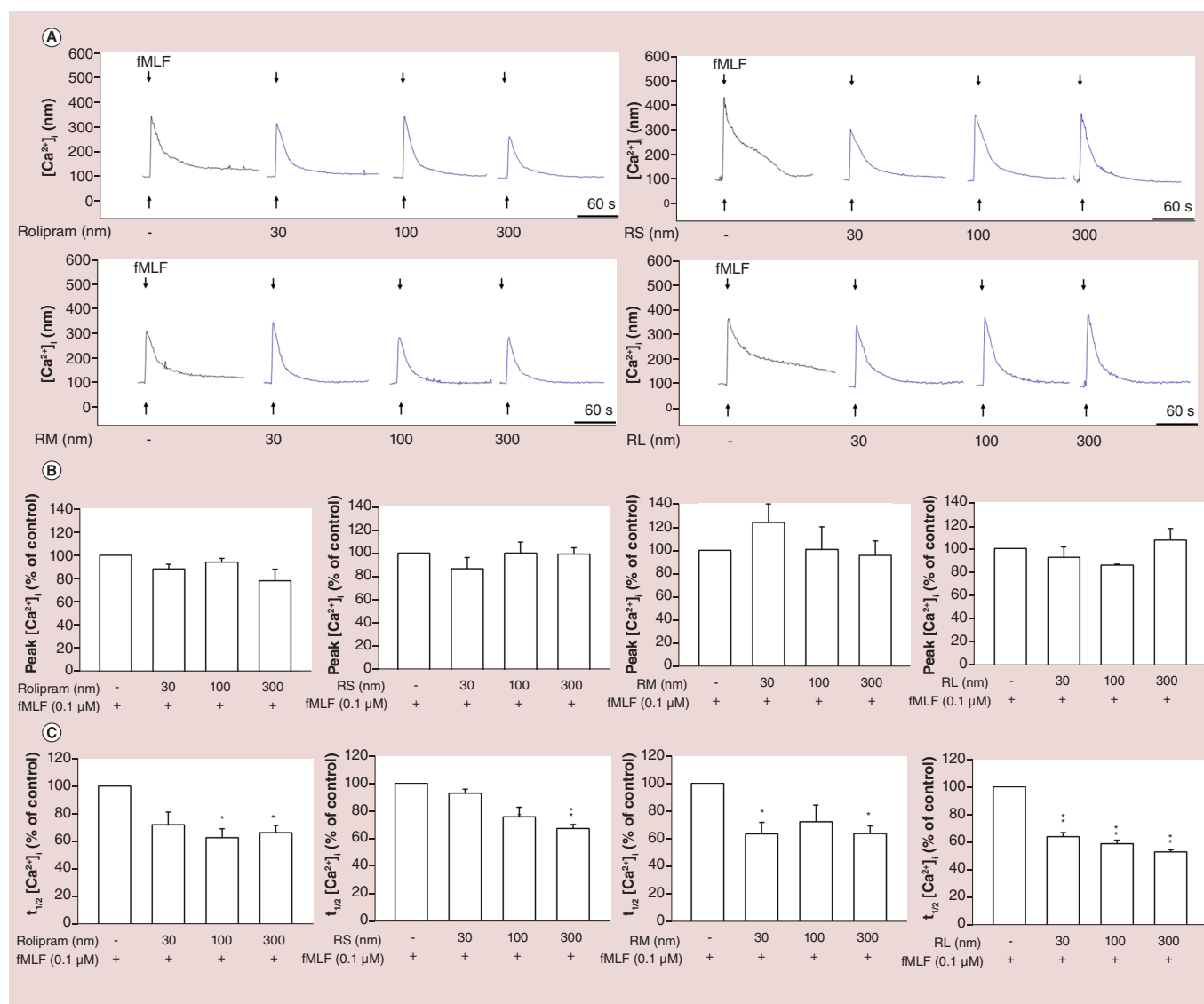


Figure 3. The Ca^{2+} mobilization and functional change of formyl-L-methionyl-L-leucyl-L-phenylalanine-activated neutrophils. (A) Fluo-3/AM-labeled neutrophils were treated with free rolipram and rolipram-loaded nanoemulsions for 5 min. Next, the cells were activated by fMLP. The $[Ca^{2+}]_i$ -time curves are shown. **(B)** Peak calcium concentration ($[Ca^{2+}]_i$) traces are shown. **(C)** Reduction of the time taken to decline to half of its peak values ($t_{1/2}$) are shown. All data represent mean \pm standard error of the mean ($n = 6$).

* $p < 0.05$; ** $p < 0.01$ as compared with fMLP-activated group without rolipram intervention.

$[Ca^{2+}]_i$: Intracellular Ca^{2+} concentration; fMLP: Formyl-L-methionyl-L-leucyl-L-phenylalanine; RL: Nanoemulsion with large diameter; RM: Nanoemulsion with medium diameter; RS: Nanoemulsion with small diameter.

RM and RL was comparable to that in the control. Rolipram showed the highest distribution in the lung by the administration of RS (11.82 ng/mg), followed by RL, the free control and RM (Figure 6E). The nanoemulsions with larger size (RL) but not those with smaller size (RS and RM) increased the spleen accumulation as compared with the free control (Figure 6F). The control and nanoemulsions displayed quite different rolipram concentrations in the circulation (Figure 6G). The control solution resulted in the highest concentration in the plasma. The plasma concentration was decreased by 85, 48 and 47% after injection of RS, RM and RL, respectively. Since our aim was to increase lung targeting and minimize the side effects of PDE4 inhibitor originated from the brain and plasma, the lung/brain and lung/plasma ratios of rolipram accumulation were calculated as shown in Figure 6H & I, respectively. RS showed the highest ratio for both lung/brain and lung/plasma, followed by RL. This indicates a possibility of improved therapy with minimal side effects for RS or RL treatment of lung inflammation. The ratios for the free control and RM were relatively low compared with RS and RL.

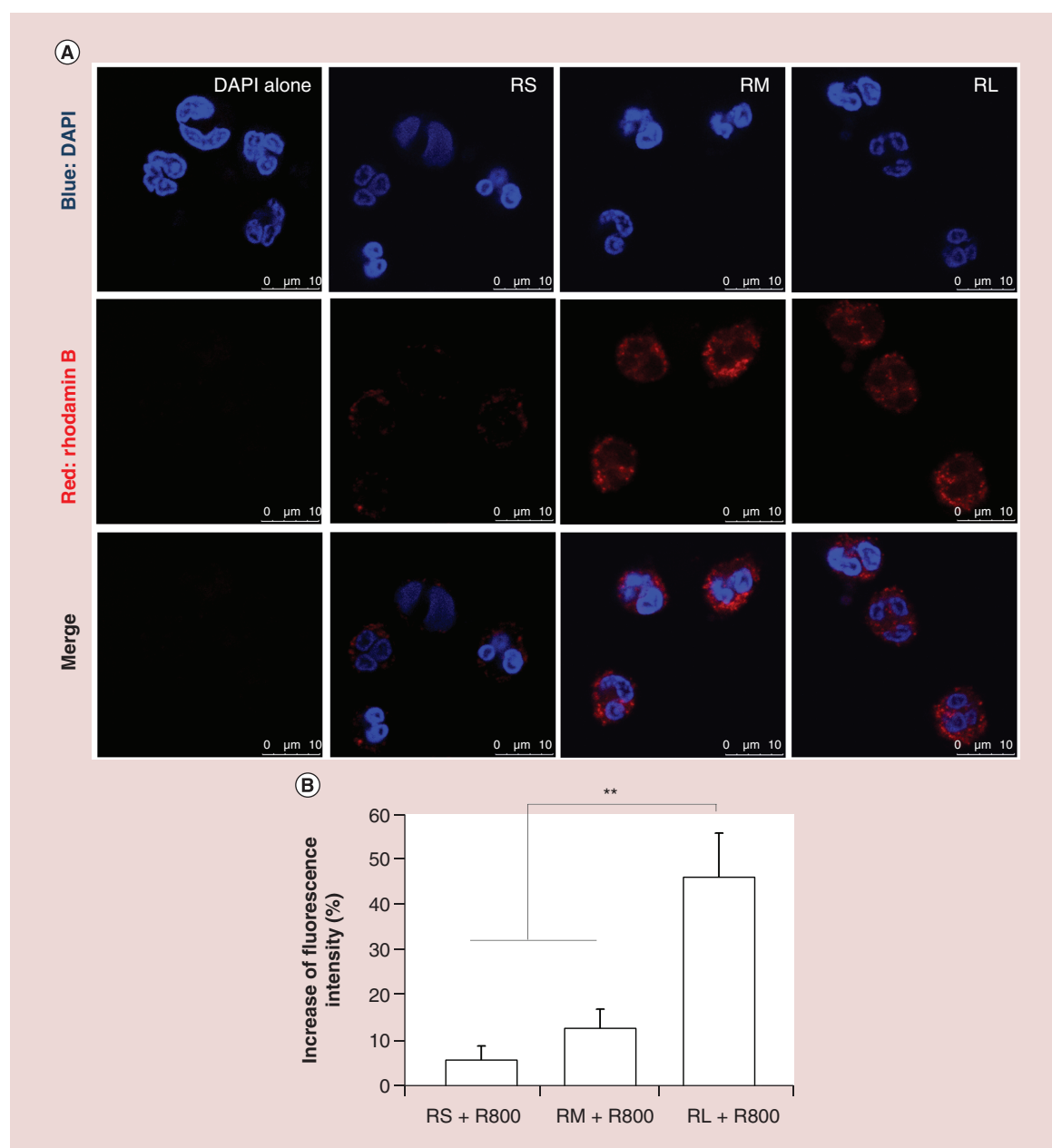


Figure 4. The uptake of rhodamine 800-loaded nanoemulsions by human neutrophils. (A) Confocal microscopy of neutrophils demonstrated that rhodamine 800-loaded nanoemulsions (red color) were internalized. Neutrophils nucleus stained (blue) were visualized by DAPI. **(B)** The fluorescence intensity of rhodamine 800 in the neutrophils analyzed by flow cytometry. All data represent mean \pm standard error of the mean ($n = 6$). ** $p < 0.01$.

DAPI: 4',6-diamidino-2-phenylindole; RL: Nanoemulsion with large diameter; RM: Nanoemulsion with medium diameter; RS: Nanoemulsion with small diameter.

The mitigation of lung injury by nanoemulsions

Given the inhibitory effect of anti-inflammatory nanoemulsions on neutrophil activation, we tested whether systemic application of nanoemulsions protected against LPS-induced lung injury. The lung section of hematoxylin and eosin staining displayed hemorrhage, interstitial edema and the disruption and thickening of the alveolar wall after LPS instillation (Figure 7A). The immune cell infiltration in the alveoli and interstitium was also observed. The decreased inflammation and edema as well as the enlarged airspace were visualized in the LPS-treated lung architecture after rolipram formulation administration. The inflammatory cell infiltration was further ameliorated

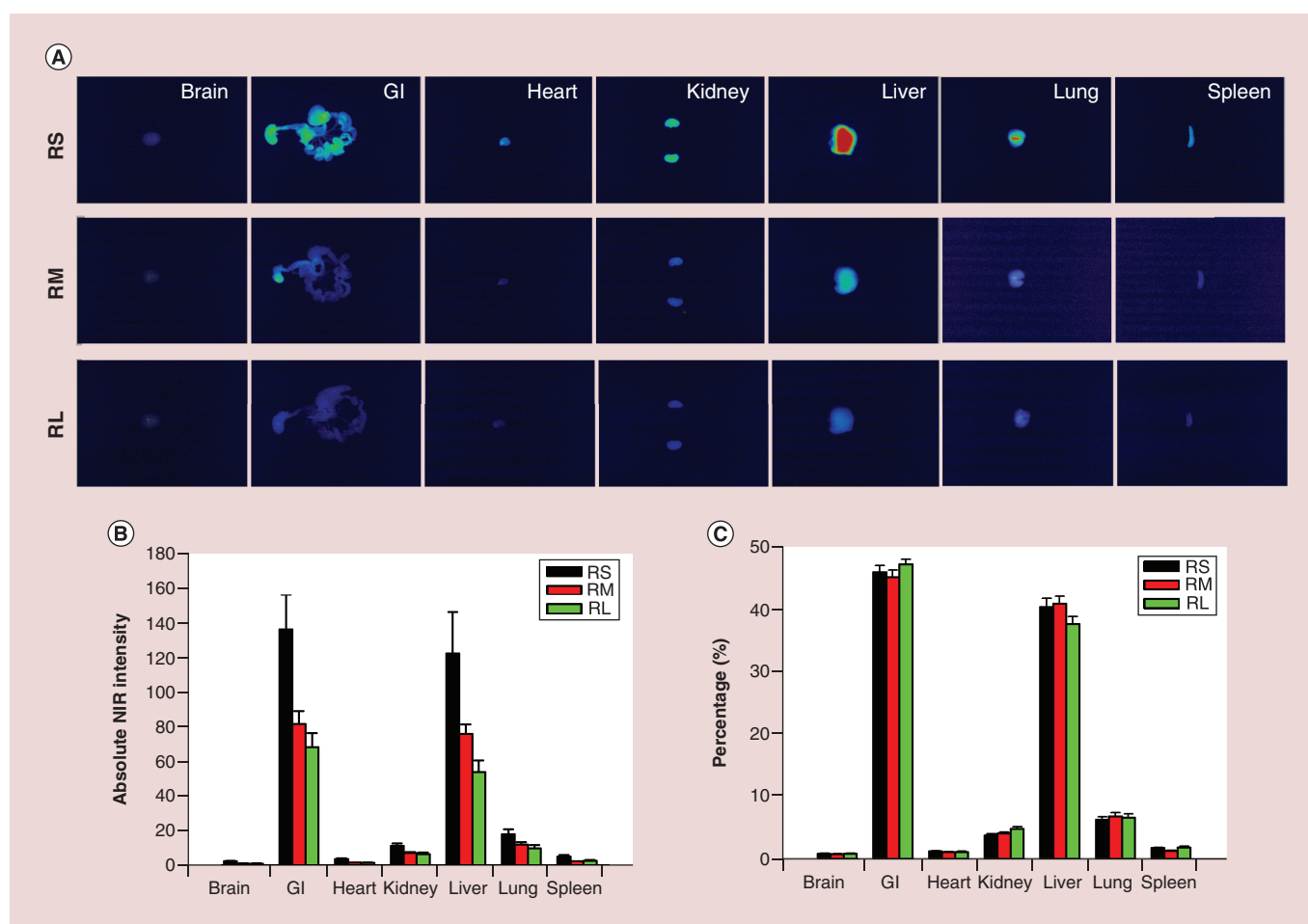


Figure 5. Ex vivo bioimaging of organs of the mice receiving intravenous iFlour 790 acid-loaded nanoemulsions. (A) Ex vivo bioimaging of organs of representative animals. **(B)** NIR intensity of iFlour 790 acid in the organs analyzed by Pearl Impulse. **(C)** The percentage (%) of NIR intensity of iFlour 790 acid in different organs analyzed by Pearl Impulse. The scale of bioimaging was calibrated by the intensity of the formulations for impartial comparison. All data represent mean \pm standard error of the mean ($n = 6$).

NIR: Near-infrared; RL: Nanoemulsion with large diameter; RM: Nanoemulsion with medium diameter; RS: Nanoemulsion with small diameter.

by nanoemulsions as compared with the control solution. The three nanoformulations did not significantly differ with respect to the signs of injury. The immunohistochemistry of Ly6G for labeling neutrophils showed a greater number of neutrophils in the LPS-treated lung tissue (Figure 7B). Rolipram formulation treatment revealed a trend toward diminishing the total neutrophil number, with RS and RL demonstrating a notable improvement. The lung exposed to RS or RL displayed focal areas of neutrophils while the neighboring regions were less affected.

We determined the expression of MPO and proinflammatory mediators in the lung by ELISA. The neutrophil-specific marker MPO was increased in the LPS-treated lung, and the application of rolipram formulations significantly reduced the level (Figure 7C). Free rolipram decreased MPO from 11.2 to 8.4 U/mg. The MPO of the LPS/RS and LPS/RM groups was lower than that of the LPS group, but comparable with that of the free control group. RL demonstrated further MPO reduction as compared with the other nanocarriers. The MPO level of LPS/RL could be suppressed to the baseline control. A contrary result was found in IL-1 β expression (Figure 7D). The IL-1 β reduction in the LPS-treated lung was less significant for the administration of RL than RS and RM. Free rolipram lacked the capability for inhibiting IL-1 β and IL-6 (Figure 7D & E). A significant IL-6 reduction of the LPS-treated lung was detected for RS and RL. TNF- α was elevated by LPS, and a significant inhibition was observed for all rolipram formulations (Figure 7F). The TNF- α of the nanoemulsion groups was lower than that of free rolipram. LPS induced the elevation of chemokine CXCL-1 as shown in Figure 7G. Surprisingly,

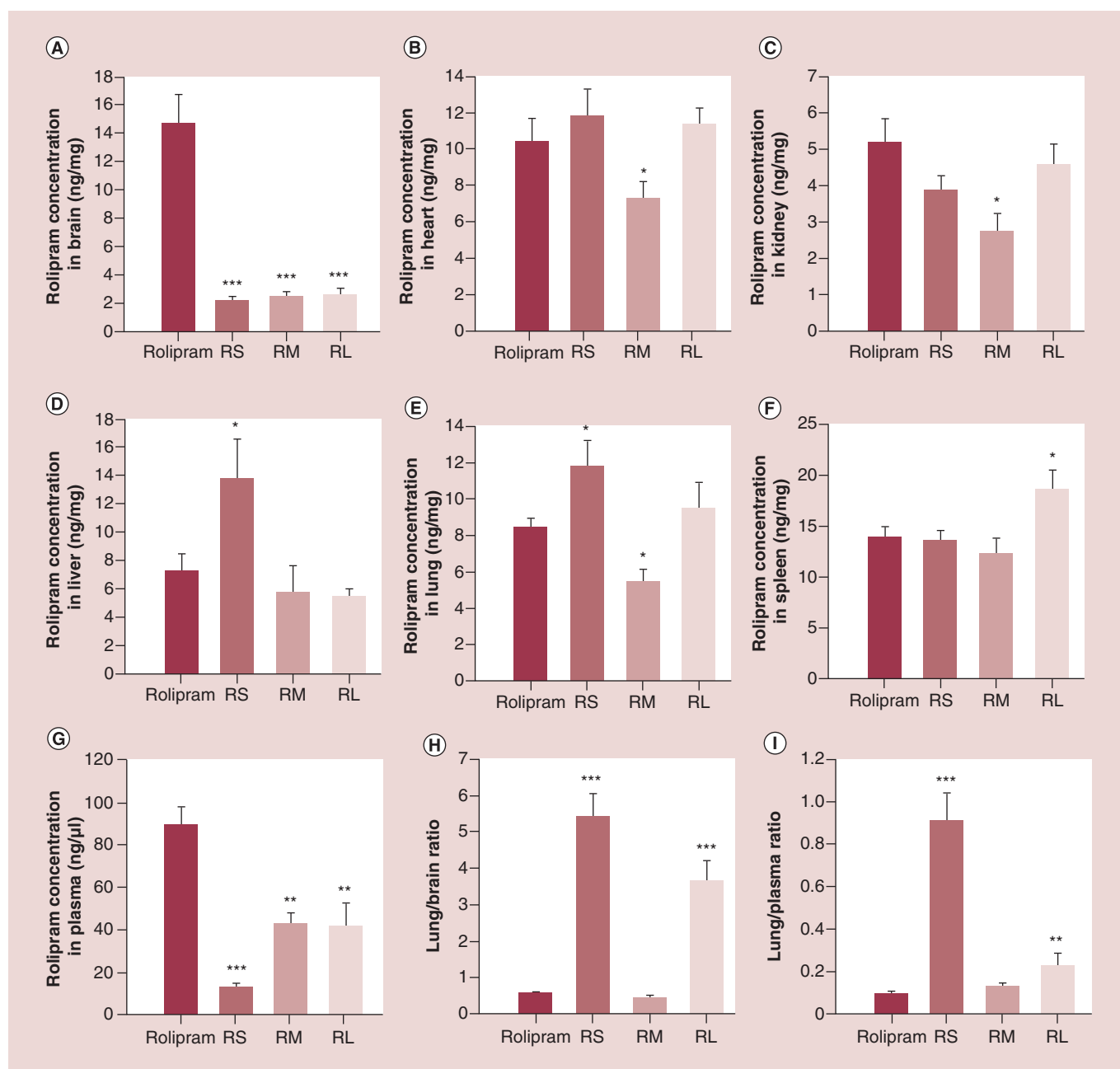


Figure 6. *In vivo* biodistribution of rolipram in different organs after intravenous injection of control solution and nanoemulsions. (A) Brain; (B) heart; (C) kidney; (D) liver; (E) lung; (F) spleen and (G) plasma. (H) Ratio of rolipram concentration between lung and brain. (I) Ratio of rolipram concentration between lung and plasma. All data represent mean \pm standard error of the mean ($n = 6$). * $p < 0.05$; ** $p < 0.01$; *** $p < 0.001$ as compared with free rolipram. RL: Nanoemulsion with large diameter; RM: Nanoemulsion with medium diameter; RS: Nanoemulsion with small diameter.

a further increase of CXCL-1 was found when administering free rolipram to LPS-treated mice. Nanoemulsion encapsulation could decrease this elevation caused by the free drug to the level approximating LPS treatment alone.

Discussion

Rolipram is a PDE4 inhibitor demonstrating potential to treat pulmonary neutrophilia [25]. PDE4 inhibitors are known to manage neutrophil-induced inflammation for suppressing COPD and ARDS [26,27]. In order to test the feasibility of nanoemulsions as rolipram vehicles for enhancing therapeutic efficiency, primary human neutrophils

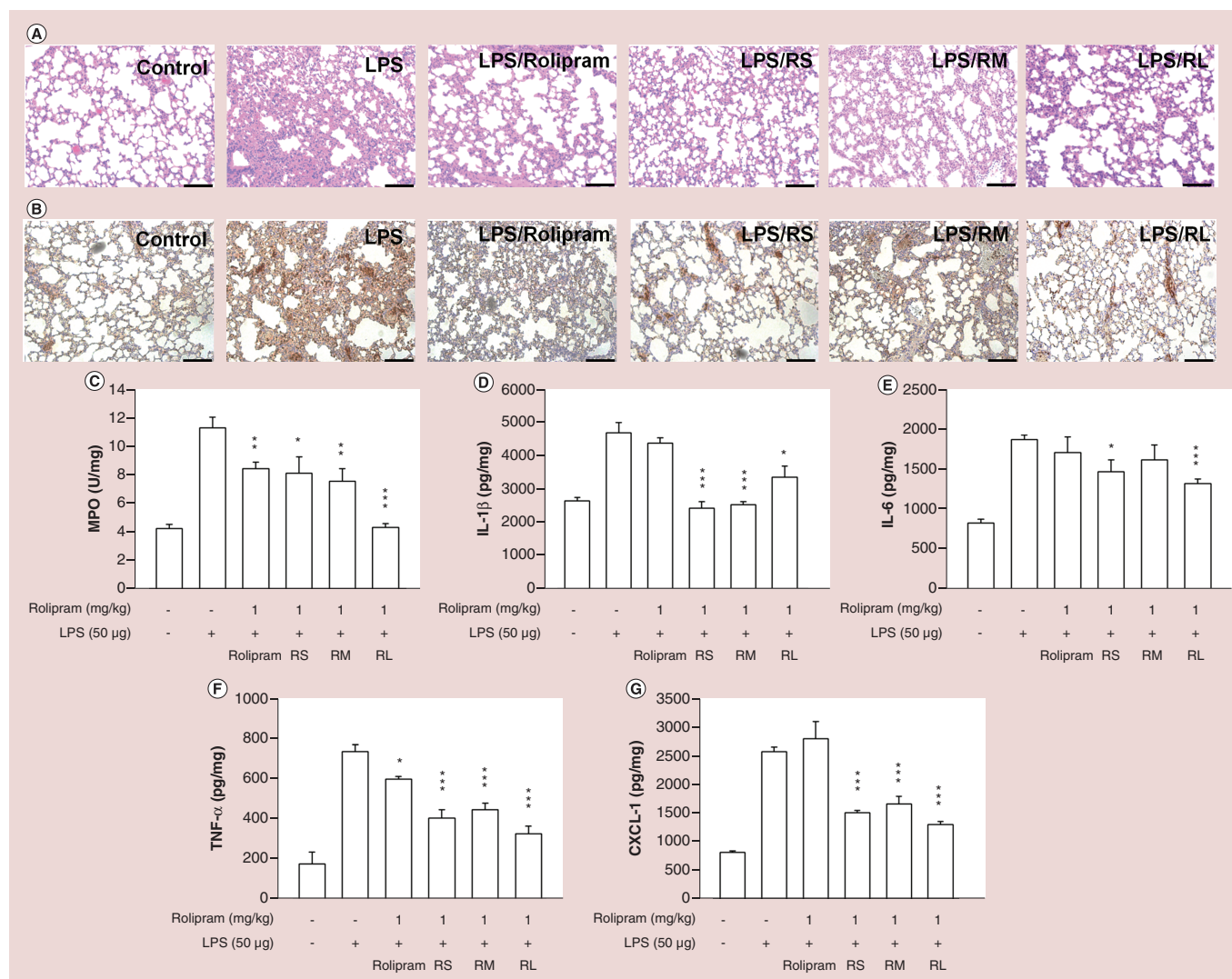


Figure 7. The effect of intravenous-free rolipram and rolipram-loaded nanoemulsions on lipopolysaccharide-induced lung injury in mice. (A) Lung H&E staining of LPS-challenged mice treated by free rolipram and rolipram-loaded nanoemulsions. **(B)** Lymphocyte antigen 6 complex locus G6D (Ly6G) antibody staining of LPS-challenged mice treated by free rolipram and rolipram-loaded nanoemulsions. **(C)** MPO expression; **(D)** IL-1 β expression; **(E)** IL-6 expression; **(F)** TNF- α expression and **(G)** CXCL-1 expression. * $p < 0.05$; ** $p < 0.01$; *** $p < 0.001$ as compared with LPS-treated group without rolipram intervention. The scale bar is 100 μm . H&E: Hematoxylin and eosin; LPS: Lipopolysaccharide; MPO: Myeloperoxidase; RL: Nanoemulsion with large diameter; RM: Nanoemulsion with medium diameter; RS: Nanoemulsion with small diameter.

and LPS-activated ARDS in mice were used as the *in vitro* and *in vivo* models. The association of neutrophils with ARDS is proven previously [28,29]. The droplet size had some effects on activated neutrophils, with the larger size showing greater capability to decrease $[\text{Ca}^{2+}]_i$; half-life and enhance cellular uptake. We provided evidence that the entrapment by nanoemulsions significantly reduced the brain accumulation of rolipram. This is an expectation to lessen the side effects involving the CNS. In our work, the nanoemulsions could mitigate the severity of the lung injury induced by LPS. RS and RL generally exhibited better therapeutic outcomes than RM although the difference was not large.

Physicochemical properties of nanoemulsions

We simply prepared the nanoemulsions of different droplet sizes by changing the amount of squalene, an inert hydrocarbon. The size ratio of about 1:2:3 for RS, RM and RL was ideal to distinctly compare their effect on inflammation attenuation. Previous study [18] suggested that the sizes ranged between 10 and 200 nm are most

suitable for physical and biochemical distribution to specific organs or tissues. The nanoemulsions tested in the present work fell within this scope. The nanoemulsions with negative surface charge were designed since the negatively charged nanoparticles are basically well tolerated by pulmonary tissue [30]. The negative surface charge of the nanoemulsions attributed to the incorporation of SPC with anionic character. The negative charge was slightly increased following the increase of particulate size. This could be due to the larger surface area for the bigger droplet than smaller one, contributing to the more SPC molecules decorating on the surface. Positively charged nanoparticles are known to be detrimental to the lung because of the formation of aggregates with serum proteins to create embolisms in pulmonary microvessels [31]. The anionic nanoparticles can penetrate across the pulmonary mucus layer more easily than those with a positive charge due to the capture of cationic molecules by anionic mucin [32]. Another drawback of positively charged nanoparticles is the association with antigen-presenting cells such as dendritic cells and macrophages in the lung [33]. This may reduce the targeting of nanocarriers to neutrophils. The high negative charge of nanoemulsions led to the satisfied storage stability because of the repulsion between the droplets. The use of Poloxamer surfactant as the emulsifier also provided a long-term stability via the steric stabilization. The lower rolipram release of nanoemulsions compared with the free control indicates a constant and sustained delivery of the drug through dissolution and diffusion. RL showed the slowest release since there is usually a burst drug release for the smaller-sized nanocarriers [34].

Anti-inflammatory nanoemulsions inhibit neutrophil stimulation

The neutrophils maintained the viability after a 15-min treatment with nanoemulsions. Most of the experiments involved in neutrophils were treated in a short time due to the rapid response of the neutrophils for the external stimuli. These cells appear to be refractory to necrosis after a short period of treatment [35]. The neutrophils undergo spontaneous apoptosis after 24 h. The short treatment duration for the nanoemulsions on neutrophils might not induce a significant apoptosis. The necrosis and apoptosis of neutrophils by nanoemulsion treatment can be excluded since we focused on the management of acute inflammation. Oxidative stress and degranulation of activated neutrophils correlate with the severity of lung injury [36]. PDE4 inhibition can attenuate superoxide production and elastase release of neutrophils, which is an efficient strategy to decrease the inflammatory response of respiratory diseases such as COPD and asthma [37]. $[Ca^{2+}]_i$ is in line with neutrophil migration in COPD and other pulmonary inflammation diseases [38]. The suppression of oxidative stress of neutrophils by anti-inflammatory nanoemulsions could be mediated through an enhancement of $[Ca^{2+}]_i$ clearance. Free and nanoemulsion-encapsulated rolipram did not reduce the peak $[Ca^{2+}]_i$ but hastened the rate of $[Ca^{2+}]_i$ decline. The decline rate was predominated by the clearance efficiency of $[Ca^{2+}]_i$. Our results demonstrated a significant $t_{1/2}$ reduction by the nanoemulsions of larger sizes (RM and RL) but not RS and free rolipram at a concentration of 30 nM, implying the superior inflammation alleviation by the larger-sized nanocarriers.

Facile uptake of nanoemulsions by neutrophils

The interaction between nanoparticles and neutrophils facilitated nanoparticle phagocytosis into the cells [39]. The high surface charge, positive or negative, of nanoparticles is a driver for phagocytosis by neutrophils [40]. Soft nanoparticles such as nanoemulsions are easily deformed in the phagocytic step with less energy as compared with rigid nanoparticles [18]. These characteristics verified the facile nanoemulsion internalization by neutrophils. Basically, the phagocytic cells displayed increased uptake following the increase in nanoparticulate size, while nonphagocytic cells showed a contrary tendency [13]. The previous studies [41,42] proved that the larger nanoparticles were ingested by neutrophils better than the smaller ones. The small nanoparticles should aggregate at the cellular surface for triggering uptake [43]. Our results demonstrated a facile internalization of large-sized nanoemulsions by neutrophils. The effective uptake of nanocarriers can induce anti-inflammatory activity to a higher degree according to the data of $[Ca^{2+}]_i$. Although the low lipophilicity of large-sized nanoemulsions may restrict the interaction with the cells, the major factor governing invagination can be the droplet diameter but not lipophilicity. In phagocytosis, the nanoparticles fuse with endosomes and then route to lysosomes for further degradation. The larger-sized nanocarriers are more difficult to load into lysosomes, resulting in the decreased degradation and prolonged retention of nanoparticles for sustained drug release and bioactivity. Although the droplet sizes did influence the neutrophil uptake, this impact did not affect the subsequent alleviation of superoxide generation. This suggests that lesser RS uptake by neutrophils was sufficient to inhibit oxidative stress. However, it should be noticed that the neutrophil internalization level did affect $[Ca^{2+}]_i$. We did not detect the downstream cytokines of neutrophils *in vitro* since cytokine production needs a prolonged time due to the role of downstream proinflammatory mediators

in the later stage of activation. The treatment period of nanoemulsions in the *in vitro* experiments was very short (<30 min). It was difficult to observe a significant change of cytokine level during the short time.

Biodistribution of nanoemulsions

The biodistribution of drug-loaded nanocarriers largely influences therapeutic activity and adverse effects. The size of the particles is an important factor for the alteration of biodistribution. For instance, the increase of the quantum dot diameter can commonly shorten the circulation time and promote peripheral organ accumulation [44]. This was not the case in our nanoemulsions since the larger-sized nanoemulsions showed lower organ uptake than the smaller ones according to *ex vivo* bioimaging. In our case, it was reasonable that the smaller droplets facily passed through the capillaries and were broadly distributed in various organs. The NIR intensity of brain treated by nanoemulsions was minimal. This result was in line with the data pertaining to rolipram biodistribution. However, the trend in different sizes differed between *ex vivo* bioimaging and rolipram biodistribution. For example, rolipram showed greater spleen accumulation by RL than the other nanoemulsions, whereas the NIR signal was extremely low for dye loaded RL. One explanation is that the incorporation of NIR dye into the nanoemulsions might change the pharmacokinetics and biodistribution. Another cause could be the release of rolipram from nanoemulsions in the body. The rolipram molecules detected in the organs included both free and nanoemulsion-encapsulated forms. Further study is needed to elucidate the possibility.

Control solution injection led to a high rolipram uptake in the brain. This considerable accumulation in the brain has been proved in previous research [45,46]. Rolipram binds to the high affinity rolipram binding site conformation of PDE4 in CNS, which accounts for PDE4 inhibition in area postrema to generate the adverse effects of nausea, vomiting and gastric acid release [47]. Compared with free rolipram, nanoemulsions largely reduced drug exposure in the brain, which is of great importance for limiting the side effects. *Ex vivo* bioimaging also showed a negligible uptake of nanoemulsions by the brain. Since the area postrema is not totally behind the BBB, the high rolipram concentration in the plasma by the control solution was accessible to the area postrema to induce marked side effects. The high rolipram amount in the circulation is another concern since one of the adverse reactions of rolipram is low blood pressure [5]. Nanoemulsion loading significantly decreased the plasma concentration. The negatively charged nanoparticles revealed a vital clearance from the circulation because of the favorable uptake by the phagocytic cells [48]. Previous studies [31,49] demonstrated that anionic or neutral nanoparticles 100–200 nm in size and an extended hydrophilic nature have prolonged circulation retention. RM and RL fitted these criteria to produce a higher rolipram concentration in the plasma than RS.

The nanoparticles internalized by phagocytic cells are easily transferred to the reticuloendothelial system (RES), which includes the liver, lung and spleen. Increasing the lipophilicity of the nanosystems is an approach to increasing the RES uptake [50]. RS with a strong lipophilic nature showed a greater rolipram concentration in the liver and lung than RM and RL. The incorporation of SPC and Poloxamer 188 on the nanoparticulate surface was also beneficial for pulmonary delivery [21,51]. RS exhibited the highest lung accumulation, followed by RL. Because of the lung tissue's leaky endothelium, the smaller droplets might easily penetrate across the endothelial wall. The larger droplets showed good retention but poor permeability via the endothelium. The high lung/brain and lung/plasma ratios of RS and RL indicated the possible achievement of passive targeting to the lung with the decrease in side effects. The pore size of the hepatic fenestrated capillary is about 100 nm, which allows the penetration of nanoparticles of <100 nm [52]. This is the reason for the high rolipram uptake in the liver by RS injection. This effect also elucidates the low plasma concentration of RS because the uptake of nanoparticles by the liver would elevate biliary clearance to reduce the circulation amount [44]. Contrary to the result of liver accumulation, RL showed the highest retention in the spleen. The structure of the blood–spleen barrier is relatively looser than that of the BBB because of the absence of a tight junction [53]. The nanoparticles of <100 nm are difficult to keep in the spleen [31]. On the other hand, the spleen captures the nanoparticles of >150–200 nm due to the complementary activation [41,54]. This is also observed in the case of nanoemulsions [55].

The mitigation of lung injury by nanoemulsions

Chronic inflammatory conditions such as COPD and asthma as well as acute conditions such as ALI and ARDS are typically associated with neutrophil recruitment in the lung. Various pathological stresses such as pneumonia, trauma and sepsis contribute to the occurrence of ARDS. The hyperactivation of neutrophils in the lung can be elicited by LPS. The lung injury induced by LPS can serve as a general model for a wide range of pulmonary inflammation diseases. Nanoemulsions demonstrated stronger amelioration of LPS-induced lung injury than the

control solution. The pharmacokinetics and biodistribution of the drug markedly affect the therapeutic outcome. The rolipram concentration in the lung by control-solution administration was not low. The sustained release and efficient neutrophil internalization of nanoemulsions may account for the stronger injury mitigation of nanosystems compared with free rolipram. Another possibility is that the surfactants in nanoemulsions could supply the depletion of pulmonary surfactants caused by neutrophil recruitment in the lung [56]. Neutrophil-derived cytokines can be of foremost importance as the biomarkers in the *in vivo* inflammation condition because that the neutrophils are usually the majority of infiltrating cells in the inflamed tissue [57]. In general, the ability of injury amelioration for RS and RL was greater than RM according to the histology and a number of cytokine profiles. A high level of drug accumulation in the target organ usually results in an enhanced therapy. Although RS represented the highest pulmonary rolipram accumulation, the *in vivo* pharmacodynamic potency of RS was comparable to that of RL. RS and RL somewhat varied in their ability to reduce the inflammatory markers. For instance, the MPO inhibition in the inflamed lung under RL treatment was greater than that of RS. An opposite response was found in the case of IL-1 β .

The attenuation of neutrophil recruitment and inhibition of neutrophil activation by PDE4 inhibitors is an important factor to reduce pulmonary injury [58]. MPO is a specific marker for neutrophils. The strong MPO inhibition by RL could be due to the greater RL uptake by neutrophils and the reduction of $[Ca^{2+}]_i$ $t_{1/2}$ compared with the smaller-sized nanoemulsions. The lung's surfactant film showed greater interaction with the smaller nanoparticles than with the larger ones [59]. RS might chiefly locate in the surfactant film after penetration into the lung. Most of the neutrophils infiltrated into the airspace but not the surfactant film [60]. RL was expected to deliver into the airspace, the right place, for neutrophil uptake. However, this does not explain the lower ability of IL-1 β suppression by RL. It should be noted that numerous cells besides neutrophils, including monocytes, mast cells, lymphocytes and macrophages, play a role in lung inflammation [61]. The cytokines are not only released by activated neutrophils but also by other immune cells in the lung [36,62]. The therapeutic level of nanoemulsions could be reached by the effect on different inflammatory cell types. The LPS instillation causes pulmonary inflammation by increased cell numbers of neutrophils and macrophages [63]. Alveolar macrophages easily internalize anionic nanocarriers including nanoemulsions [33,64]. The macrophage uptake of nanoparticles in the liver results in the high accumulation in the hepatic tissue [44]. The greater accumulation of RS in the liver than seen with the other nanoemulsions may indicate the facile uptake of RS by alveolar macrophages for restraining pulmonary cytokines such as IL-1 β .

IL-1 β , IL-6 and TNF- α are cytokines showing important mediators in the development of pulmonary injury. The capability of rolipram to inhibit TNF- α in pulmonary inflammation was confirmed previously [65]. The LPS-induced IL-1 β and IL-6 were inhibited by nanoemulsions but not by free rolipram. The previous research [66] demonstrated that rolipram failed to treat pulmonary inflammation due to the inability to downregulate pulmonary cytokines such as IL-6 and IL-13. Rolipram even promoted CXCL-1 expression in an LPS-treated lung in our study. CXCL-1 is a key chemotactic factor for neutrophil migration to the lung in COPD patients [58]. It is possible that free rolipram increased CXCL-1 because rolipram or other PDE4 inhibitors have immunomodulatory actions to upregulate cytokine and chemokine expression in some cells [17,67,68]. Nanoemulsions could shield CXCL-1 upregulation by rolipram to the baseline of LPS treatment alone. The advantages of RS are the favorable rolipram accumulation in the lung and possible intake by alveolar macrophages for inhibiting inflammation. The advantages of RL are the sustained rolipram release and the vital uptake by neutrophils that play a principal role in pulmonary injury. The bipolar droplet sizes, but not medium size, were preferred in the treated neutrophil-related inflamed lung. It should be emphasized that the size effect on anti-inflammatory activity cannot be regarded as very significant according to *in vitro* and *in vivo* results. The size effect on bioactivity is nanocarrier-dependent and does not universally apply to all drug-loaded nanocarriers. A recent study by Bisso *et al.* [14] suggests a size-dependent neutrophil interaction for metallic and polymeric nanoparticles, whereas the size dependence for the lipid-based nanovesicles is limited. We can infer that the size-dependent inflammation inhibition by nanoemulsions is only moderate.

Conclusion

The main goal of the current study was to investigate the effectiveness of PDE4 inhibitor-entrapped nanoemulsions on anti-inflammatory activity against stimulated neutrophils and a related lung injury. We also aimed to design the optimized nanoformulations based on the difference in droplet sizes to achieve greater improvement in therapeutic efficacy. The therapeutic effect on pulmonary injury was ameliorated by nanoemulsions compared

with free rolipram. Some size effects were found to influence the rolipram biodistribution. The significant effect of nanoemulsion size was also observed in the biodistribution of dye-loaded nanocarriers in the bioimaging study. Although, the larger-sized nanoemulsions (RL) showed more efficient internalization into activated neutrophils for inducing higher anti-inflammatory activity based on the shortened $[Ca^{2+}]_i$ $t_{1/2}$, the bipolar-sized nanoemulsions (RS and RL) generally showed a comparable therapeutic potency in the animal study. This could be due to the large accumulation of small-sized nanoemulsions in the pulmonary tissue and the possible uptake by immune cells other than neutrophils. The molecular environment of the nanoemulsions affected by the size difference was also another factor to influence the anti-inflammatory effect. The evidence in this study could lead to the rational design of anti-inflammatory nanoemulsions.

Future perspective

We proved that the size of nanoemulsions largely affected neutrophil activation and ARDS-like lesion amelioration. The experimental results are beneficial to provide the strategy for the formulation design of anti-inflammatory nanocarriers. We completed *in vitro* and *in vivo* studies to explore the usefulness of nanoemulsions for treating lung inflammation. Further improvement of formulations is needed to achieve better therapy and minimal adverse effect, promoting the possibility of applicability in humans. The size range of our nanoemulsions ranged between 68 and 188 nm. An extensive size range of the prepared nanoemulsions can clearly observe the effect of size on the level of inflammation suppression. It is our next aim for the following investigation.

Summary points

- This study endeavored to develop anti-inflammatory nanocarriers with different droplet sizes to evaluate the anti-inflammatory effect against activated neutrophils and the related lung injury.
- The characteristics of biodistribution and inflamed lung suppression *in vivo* were examined.
- Rolipram-loaded nanoemulsions exerted an anti-inflammatory effect against activated neutrophils by restraining superoxide anion production and shortening the time taken for intracellular Ca^{2+} concentration to reach half of its peak.
- The droplet size had some effects on activated neutrophils, with the larger size showing greater capability to decrease intracellular Ca^{2+} concentration half-life and enhance cellular uptake.
- The entrapment by nanoemulsions significantly reduced the brain accumulation of rolipram to lessen the side effects involving the CNS.
- The nanoemulsions could mitigate the severity of the lung injury induced by lipopolysaccharide.
- Either neutrophils or other immune cells such as macrophages involve in the lung inflammation mitigation by the nanoemulsions, especially the smaller one.
- The smaller and larger particles of the nanoemulsions demonstrated comparable lung injury attenuation but different mechanisms.

Financial & competing interests disclosure

The authors are grateful for the financial support from Ministry of Science and Technology of Taiwan (MOST-105-2314-B-182A-012-MY3 and MOST-107-2320-B-182-016-MY3). The Czech-Taiwan collaboration was supported by the Czech Academy of Sciences (VAJVA-19-55). The authors have no other relevant affiliations or financial involvement with any organization or entity with a financial interest in or financial conflict with the subject matter or materials discussed in the manuscript apart from those disclosed.

Writing assistance was utilized from Choice Language Service Company in the production of this manuscript.

Ethical conduct of research

All animal study procedures were conducted in accordance with the protocols approved by the Institutional Animal Care and Use Committee of Chang Gung University. The authors state that they have obtained appropriate institutional review board approval or have followed the principles outlined in the Declaration of Helsinki for all human or animal experimental investigations. In addition, for investigations involving human subjects, informed consent has been obtained from the participants involved.

References

Papers of special note have been highlighted as: • of interest; •• of considerable interest

1. Scherer PM, Chen DL. Imaging pulmonary inflammation. *J. Nucl. Med.* 57(11), 1764–1770 (2016).
2. Butt Y, Kurdowska A, Allen TC. Acute lung injury: a clinical and molecular review. *Arch. Pathol. Lab. Med.* 140, 345–350 (2016).

- **Review introducing lung inflammation.**

3. Hidalgo A, Chilvers ER, Summers C, Koenderman L. The neutrophil life cycle. *Trend Immunol.* 40(7), 584–597 (2019).
4. Mortaz E, Alipoor SD, Adcock IM, Mumby S, Koenderman L. Uptake on neutrophil function in severe inflammation. *Front. Immunol.* 9, 2171 (2018).
5. Lin CH, Chang SH, Fang JY. Recent advances using phosphodiesterase 4 (PDE4) inhibitors to treat inflammatory disorders: animal and clinical studies. *Curr. Drug Ther.* 11(1), 21–40 (2016).

- **Review introducing PDE4 inhibitors for managing inflammatory diseases.**

6. Rogliani P, Calzetta L, Cazzola M, Matera MG. Drug safety evaluation of roflumilast for the treatment of COPD: a meta-analysis. *Expert Opin. Drug Saf.* 15(8), 1133–1146 (2016).
7. Ikoba U, Peng H, Li H, Miller C, Yu C, Wang Q. Nanocarriers in therapy of infectious and inflammatory diseases. *Nanoscale* 7(10), 4291–4305 (2015).

- **Review describing the application of drug-loaded nanocarriers for treating inflammatory diseases.**

8. Ahmed N, Ahmad I, Umar S, Iqbal Z, Samim M, Ahmed FJ. PNIPAM nanoparticles for targeted and enhanced nose-to-brain delivery of curcuminoids: UPLC/ESI-Q-ToF-MS/MS-based pharmacokinetics and pharmacodynamic evaluation in cerebral ischemia model. *Drug Deliv.* 23(7), 2095–2114 (2016).
9. Ahmad N, Ahmad R, Naqvi AA *et al.* The effect of safranal loaded mucoadhesive nanoemulsion on oxidative stress markers in cerebral ischemia. *Artif. Cells Nanomed. Biotechnol.* 45(4), 775–787 (2017).
10. Ahmad N, Ahmad R, Naqvi AA *et al.* Intranasal delivery of quercetin-loaded mucoadhesive nanoemulsion for treatment of cerebral ischaemia. *Artif. Cells Nanomed. Biotechnol.* 46(4), 717–729 (2018).
11. Tayeb HH, Sainsbury F. Nanoemulsions in drug delivery: formulation to medical application. *Nanomedicine* 13(19), 2507–2525 (2018).
12. Wang J, Bai R, Yang R *et al.* Size- and surface chemistry-dependent pharmacokinetics and tumor accumulation of engineered gold nanoparticles after intravenous administration. *Metallomics* 7(3), 516–524 (2015).
13. Hoshyar N, Gray S, Han H, Bao G. The effect of nanoparticle size on *in vivo* pharmacokinetics and cellular interaction. *Nanomedicine* 11(6), 673–692 (2016).
14. Bisso PW, Gaglione S, Guimarães PPG, Mitchell MJ, Langer R. Nanomaterial interactions with human neutrophils. *ACS Biomater. Sci. Eng.* 4(12), 4255–4265 (2018).
15. Kanehiro A, Ikemura T, Makela MJ *et al.* Inhibition of phosphodiesterase 4 attenuates airway hyperresponsiveness and airway inflammation in a model of secondary allergen challenge. *Am. J. Respir. Crit. Care Med.* 163(1), 173–184 (2001).
16. de Visser YP, Walther FJ, Laghmani EH, van Wijngaarden S, Nieuwland K, Wagenaar GTM. Phosphodiesterase-4 inhibition attenuates pulmonary inflammation in neonatal lung injury. *Eur. Respir. J.* 31(3), 633–644 (2008).
17. Bielekova B, Richert N, Howard T *et al.* Treatment with the phosphodiesterase type-4 inhibitor rolipram fails to inhibit blood–brain barrier disruption in multiple sclerosis. *Mult. Scler.* 15(10), 1206–1214 (2009).

- **The side effects of rolipram.**

18. Hickey JW, Santos JL, Williford JM, Mao HQ. Control of polymeric nanoparticle size to improve therapeutic delivery. *J. Control. Rel.* 219, 536–547 (2015).
19. Fang CL, Wen CJ, Aljuffali IA, Sung CT, Huang CL, Fang JY. Passive targeting of phosphatidosomes increases rolipram delivery to the lungs for treatment of acute lung injury: an animal study. *J. Control. Rel.* 213, 69–78 (2015).
20. Pan TL, Wang PW, Hung CF, Aljuffali IA, Dai YS, Fang JY. The impact of retinol loading and surface charge on the hepatic delivery of lipid nanoparticles. *Colloids Surf. B.* 141, 584–594 (2016).
21. Hsieh PW, Wen CJ, Yu HP, Aljuffali IA, Huang YH, Fang JY. Nanostructured lipid carriers containing a high percentage of a pluronic copolymer increase the biodistribution of novel PDE4 inhibitors for the treatment of traumatic hemorrhage. *J. Biomed. Nanotechnol.* 10(8), 1520–1535 (2014).
22. Yu HP, Hsieh PW, Chang YJ, Chung PJ, Kuo LM, Hwang TL. 2-(2-Fluorobenzamido)benzoate ethyl ester (EFB-1) inhibits superoxide production by human neutrophils and attenuates hemorrhagic shock-induced organ dysfunction in rats. *Free Radic. Biol. Med.* 50(12), 1737–1748 (2011).
23. Hsieh PW, Yu HP, Chang YJ, Hwang TL. Synthesis and evaluation of benzoxazinone derivatives on activity of human neutrophil elastase and on hemorrhagic shock-induced lung injury in rats. *Eur. J. Med. Chem.* 45(7), 3111–3115 (2010).
24. Asti C, Ruggieri V, Porzio S. Lipopolysaccharide-induced lung injury in mice. I. Concomitant evaluation of inflammatory cells and haemorrhagic lung damage. *Pulm. Pharmacol. Ther.* 13(2), 61–69 (2000).
25. Spond J, Chapman R, Fine J *et al.* Comparison of PDE4 inhibitors, rolipram and SB 207499 (arifo), in a rat model of pulmonary neutrophilia. *Pulm. Pharmacol. Ther.* 14(2), 157–164 (2001).
26. Matera MG, Rogliani P, Calzetta L, Cazzola M. Phosphodiesterase inhibitors for chronic obstructive pulmonary disease: what does the future hold? *Drugs* 74(17), 1983–1992 (2014).

27. Tang HF, Lu JJ, Tang JF *et al.* Action of a novel PDE4 inhibitor ZL-n-91 on lipopolysaccharide-induced acute lung injury. *Int. Immunopharmacol.* 10(4), 406–411 (2010).
28. Kangelaris KN, Prakash A, Liu KD *et al.* Increased expression of neutrophil-related genes in patients with early sepsis-induced ARDS. *Am. J. Physiol. Lung Cell Mol. Physiol.* 308(11), 1102–1113 (2015).
29. Bendib I, de Chaisemartin L, Mekontso Dessap A, Chollet-Martin S, de Prost N. Understanding the role of neutrophil extracellular traps in patients with severe pneumonia and ARDS. *Chest* 156(6), 1278–1280 (2019).
30. Roberts RA, Shen T, Allen IC, Hasan W, DeSimone JM, Ting JP. Analysis of the murine immune response to pulmonary delivery of precisely fabricated nano- and microscale particles. *PLoS ONE* 8, e62115 (2013).
31. Li SD, Huang L. Pharmacokinetics and biodistribution of nanoparticles. *Mol. Pharm.* 5(4), 496–504 (2008).
- **The overview of the pharmacokinetics and biodistribution of intravenous nanoparticles.**
32. Song JH, Kim JY, Piao C *et al.* Delivery of the high mobility group box 1 box A peptide using heparin in the acute lung injury animal models. *J. Control. Rel.* 234, 33–40 (2016).
33. Fromen CA, Rahhal TB, Robbins GR *et al.* Nanoparticle surface charge impacts distribution, uptake and lymph node trafficking by pulmonary antigen-presenting cells. *Nanomed. Nanotechnol. Biol. Med.* 12(3), 677–687 (2016).
34. Natarajan JV, Nugraha C, Ng XW, Venkatraman S. Sustained-release from nanocarriers: a review. *J. Control. Rel.* 193, 122–138 (2014).
35. Geering B, Simon HU. Peculiarities of cell death mechanisms in neutrophils. *Cell Death Differ.* 18(9), 1457–1469 (2011).
36. Potey PMD, Rossi AG, Lucas CD, Dorward DA. Neutrophils in the initiation and resolution of acute pulmonary inflammation: understanding biological function and therapeutic potential. *J. Pathol.* 247(5), 672–685 (2019).
37. Spina D. PDE4 inhibitors: current status. *Br. J. Pharmacol.* 155(3), 308–315 (2008).
38. Ruljancic N, Popovic-Grle S, Rumenjak V *et al.* COPD: magnesium in the plasma and polymorphonuclear cells of patients during a stable phase. *COPD* 4(1), 41–47 (2007).
39. Lin MH, Lin CF, Yang SC, Hung CF, Fang JY. The interplay between nanoparticles and neutrophils. *J. Biomed. Nanotechnol.* 14(1), 66–85 (2018).
- **The elucidation of nanoparticle interaction with neutrophils.**
40. Kelley WJ, Fromen CA, Lopez-Cazares G, Eniola-Adefeso O. PEGylation of model drug carriers enhances phagocytosis by primary human neutrophils. *Acta Biomater.* 79, 283–293 (2018).
41. Faraji AH, Wipf P. Nanoparticles in cellular drug delivery. *Bioorg. Med. Chem.* 17(8), 2950–2962 (2009).
42. Boraschi D, Italiani P, Palomba R *et al.* Nanoparticles and innate immunity: new perspectives on host defense. *Semin. Immunol.* 34, 33–51 (2017).
- **The effect of nanoparticles on the innate immunity.**
43. Jiang X, Rocker C, Hafner M, Brandholt S, Dorlich RM, Nienhaus GU. Endo- and exocytosis of zwitterionic quantum dot nanoparticles by live HeLa cells. *ACS Nano.* 4(11), 6787–6797 (2010).
44. Javidi J, Haeri A, Nowroozi F, Dadashzadeh S. Pharmacokinetics, tissue distribution and excretion of Ag₂S quantum dots in mice and rats: the effects of injection dose, particle size and surface charge. *Pharm. Res.* 36(3), 46 (2019).
45. Sprague DR, Fujita M, Ryu YH, Liow JS, Pike VW, Innis RB. Whole-body biodistribution and radiation dosimetry in monkeys and humans of the phosphodiesterase 4 radioligand [¹¹C](R)-rolipram: comparison of two-dimensional planar, bisected and quadrisectioned image analyses. *Nucl. Med. Biol.* 35(4), 493–500 (2008).
46. Kraft P, Schwarz T, Göb E *et al.* The phosphodiesterase-4 inhibitor rolipram protects from ischemic stroke in mice by reducing blood–brain-barrier damage, inflammation and thrombosis. *Exp. Neurol.* 247, 80–90 (2013).
47. Zhao Y, Zhang HT, O'Donnell JM. Inhibitor binding to type 4 phosphodiesterase (PDE4) assessed using [³H]piclamilast and [³H]rolipram. *J. Pharmacol. Exp. Ther.* 305(2), 565–572 (2003).
48. Su Z, Niu J, Xiao Y *et al.* Effect of octreotide-polyethylene glycol(100) monostearate modification on the pharmacokinetics and cellular uptake of nanostructured lipid carrier loaded with hydroxycamptothecin. *Mol. Pharm.* 8(5), 1641–1651 (2011).
49. Perry JL, Reuter KG, Kai MP *et al.* PEGylated PRINT nanoparticles: the impact of PEG density on protein binding, macrophage association, biodistribution, and pharmacokinetics. *Nano Lett.* 12(10), 5304–5310 (2012).
50. Zhao Z, Ukidve A, Krishnan V, Mitragotri S. Effect of physicochemical and surface properties on in vivo fate of drug nanocarriers. *Adv. Drug Deliv. Rev.* 143, 3–21 (2019).
51. Hsu CY, Sung CT, Aljuffali IA, Chen CH, Hu KY, Fang JY. Intravenous anti-MRSA phosphatiosomes mediate enhanced affinity to pulmonary surfactants for effective treatment of infectious pneumonia. *Nanomed. Nanotechnol. Biol. Med.* 14(2), 215–225 (2018).
52. Wang B, He X, Zhang Z, Zhao Y, Feng W. Metabolism of nanomaterials *in vivo*: blood circulation and organ clearance. *Acc. Chem. Res.* 46(3), 761–769 (2013).
53. Tarantino G, Savastano S, Capone D, Colao A. Spleen: a new role for an old player? *World J. Gastroenterol.* 7(33), 3776–3784 (2011).

54. Moghimi SM, Hunter AC, Andresen TL. Factors controlling nanoparticle pharmacokinetics: an integrated analysis and perspective. *Ann. Rev. Pharmacol. Toxicol.* 52, 481–503 (2012).
55. Ahmad G, Gattacecca F, El Sadda R *et al.* Biodistribution and pharmacokinetic evaluations of a novel taxoid DHA-SBT-1214 in an oil-in-water nanoemulsion formulation in naïve and tumor-bearing mice. *Pharm. Res.* 35(4), 91 (2018).
56. Kosutova P, Mikolka P, Kolomaznik M *et al.* Reduction of lung inflammation, oxidative stress and apoptosis by the PDE4 inhibitor roflumilast in experimental model of acute lung injury. *Physiol. Res.* 67(Suppl. 4), S645–S654 (2018).
57. Tecchio C, Micheletti A, Cassatella MA. Neutrophil-derived cytokines: facts beyond expression. *Front. Immunol.* 5, 508 (2014).
58. Dunne AE, Kawamatawong T, Fenwick PS *et al.* Direct inhibitory effect of PDE4 inhibitor roflumilast on neutrophil migration in chronic obstructive pulmonary disease. *Am. J. Respir. Cell Mol. Biol.* 60(4), 445–453 (2019).
59. Hidalgo A, Cruz A, Pérez-Gil J. Barrier or carrier? Pulmonary surfactant and drug delivery. *Eur. J. Pharm. Biopharm.* 95, 117–127 (2015).
60. Zhu Q, Wang H, Wang H *et al.* Protective effects of ethyl pyruvate on lipopolysaccharide-induced acute lung injury through inhibition of autophagy in neutrophils. *Mol. Med. Rep.* 15, 1272–1278 (2017).
61. Guiedem E, Ikomey GM, Nkenfou C *et al.* Chronic obstructive pulmonary disease (COPD): neutrophils, macrophages and lymphocytes in patients with anterior tuberculosis compared to tobacco related COPD. *BMC Res. Notes* 11(1), 192 (2018).
- **The relationship between chronic obstructive pulmonary disease and neutrophils.**
62. Smith KR, Leonard D, McDonald JD, Tesfaigzi Y. Inflammation, mucous cell metaplasia, and Bcl-2 expression in response to inhaled lipopolysaccharide aerosol and effect of rolipram. *Toxicol. Appl. Pharmacol.* 253(3), 253–260 (2011).
63. Baudiß K, Vieira RDP, Cicko S *et al.* C1P attenuates lipopolysaccharide-induced acute lung injury by preventing NF-κB activation in neutrophils. *J. Immunol.* 196, 2319–2326 (2016).
64. Davalapally H, Zhou F, McDade J *et al.* Optimization of PEGylated nanoemulsions for improved pharmacokinetics of BCS class II compounds. *Drug Deliv.* 22(4), 467–474 (2015).
65. Wollin L, Bundschuh DS, Wohlsen A, Marx D, Beume MR. Inhibition of airway hyperresponsiveness and pulmonary inflammation by roflumilast and other PDE4 inhibitors. *Pulm. Pharmacol. Ther.* 19(5), 343–352 (2006).
66. Singh SP, Mishra NC, Rir-sima-ah J *et al.* Maternal exposure to secondhand cigarette smoke primes the lung for induction of phosphodiesterase-4D5 isozyme and exacerbated Th2 responses: rolipram attenuates the airway hyperreactivity and muscarinic receptor expression but not lung inflammation and atopy. *J. Immunol.* 183(3), 21978–21983 (2009).
67. Hertz AL, Bender AT, Smith KC *et al.* Elevated cyclic AMP and PDE4 inhibition induce chemokine expression in human monocyte-derived macrophages. *Proc. Natl Acad. Sci. USA* 106(51), 21978–21983 (2009).
68. Chang W, Chen J, Schlueter CF, Rando RJ, Pathak YV, Hoyle GW. Inhibition of chlorine-induced lung injury by the type 4 phosphodiesterase inhibitor rolipram. *Toxicol. Appl. Pharmacol.* 263(2), 251–258 (2012).



Article

Preparation of Peptide and Recombinant Tissue Plasminogen Activator Conjugated Poly(Lactic-Co-Glycolic Acid) (PLGA) Magnetic Nanoparticles for Dual Targeted Thrombolytic Therapy

Huai-An Chen ¹, Yunn-Hwa Ma ² , Tzu-Yuan Hsu ² and Jyh-Ping Chen ^{1,3,4,5,*}

¹ Department of Chemical and Materials and Materials Engineering, Chang Gung University, Kwei-San, Taoyuan 33302, Taiwan; eam012331@gmail.com

² Department of Physiology and Pharmacology and Healthy Aging Research Center, Chang Gung University, Kwei-San, Taoyuan 33302, Taiwan; yhma@mail.cgu.edu.tw (Y.-H.M.); w1314lin@gmail.com (T.-Y.H.)

³ Department of Plastic and Reconstructive Surgery and Craniofacial Research Center, Chang Gung Memorial Hospital, Linkou, Kwei-San, Taoyuan 33305, Taiwan

⁴ Research Center for Food and Cosmetic Safety, Research Center for Chinese Herbal Medicine, College of Human Ecology, Chang Gung University of Science and Technology, Taoyuan 33302, Taiwan

⁵ Department of Materials Engineering, Ming Chi University of Technology, Tai-Shan, New Taipei City 24301, Taiwan

* Correspondence: jpchen@mail.cgu.edu.tw; Tel.: +886-3211-8800 (ext. 5298)

Received: 10 March 2020; Accepted: 10 April 2020; Published: 13 April 2020



Abstract: Recombinant tissue plasminogen activator (rtPA) is the only thrombolytic agent that has been approved by the FDA for treatment of ischemic stroke. However, a high dose intravenous infusion is required to maintain effective drug concentration, owing to the short half-life of the thrombolytic drug, whereas a momentous limitation is the risk of bleeding. We envision a dual targeted strategy for rtPA delivery will be feasible to minimize the required dose of rtPA for treatment. For this purpose, rtPA and fibrin-avid peptide were co-immobilized to poly(lactic-co-glycolic acid) (PLGA) magnetic nanoparticles (PMNP) to prepare peptide/rtPA conjugated PMNPs (pPMNP-rtPA). During preparation, PMNP was first surface modified with avidin, which could interact with biotin. This is followed by binding PMNP-avidin with biotin-PEG-rtPA (or biotin-PEG-peptide), which was prepared beforehand by binding rtPA (or peptide) to biotin-PEG-maleimide while using click chemistry between maleimide and the single –SH group in rtPA (or peptide). The physicochemical property characterization indicated the successful preparation of the magnetic nanoparticles with full retention of rtPA fibrinolysis activity, while biological response studies underlined the high biocompatibility of all magnetic nanoparticles from cytotoxicity and hemolysis assays in vitro. The magnetic guidance and fibrin binding effects were also confirmed, which led to a higher thrombolysis rate in vitro using PMNP-rtPA or pPMNP-rtPA when compared to free rtPA after static or dynamic incubation with blood clots. Using pressure-dependent clot lysis model in a flow system, dual targeted pPMNP-rtPA could reduce the clot lysis time for reperfusion by 40% when compared to free rtPA at the same drug dosage. From in vivo targeted thrombolysis in a rat embolic model, pPMNP-rtPA was used at 20% of free rtPA dosage to restore the iliac blood flow in vascular thrombus that was created by injecting a blood clot to the hind limb area.

Keywords: magnetic nanoparticles; tissue plasminogen activator; poly(lactic-co-glycolic acid); targeted drug delivery; clot lysis; nanomedicine

1. Introduction

Within the two ischemic and hemorrhagic categories of stroke, the ischemic stroke accounts for ~87% of all cases, according to the American Stroke Association [1]. A multitude of molecular pathways may be involved in the onset and progression of ischemic stroke, thus an equally diverse arsenal of intervention strategies is needed. To date, the gold standard for intravenous (IV) intervention of ischemic stroke is by administering recombinant tissue plasminogen activator (rtPA), a thrombolytic drug that dissolves clots to restore blood flow. As a serine protease, rtPA is the major enzyme that is responsible for clot dissolution by catalyzing the conversion of plasminogen to plasmin. It is currently the only thrombolytic agent approved by the U.S. Food and Drug Administration (FDA) for the treatment of ischemic stroke [2]. A major issue in rtPA therapeutic use is the short half-life (4–8 min) in the circulation due to autolysis and the influences of inhibitors, enzymes, and antibodies in blood [3]. The poor affinity of rtPA toward thrombus also reduces its thrombolysis efficacy and might cause ischemia reperfusion injury to the neuron beyond the thrombolysis window [4]. Other limitations of rtPA for clinical use include the short window time for treatment (usually within 3 h) and the risk of hemorrhagic side effects [5]. Consequently, several strategies have emerged to improve the thrombolytic efficacy of rtPA, such as ultrasound-based thrombolysis, targeting thrombolysis, and immobilized thrombolytic drug to improve the safety and effectiveness of thrombolytic therapy [6].

Nanomedicine using nanoparticles for drug delivery is a novel field for the diagnosis and treatment of diseases. Although with similar biologic molecular scale when compared with traditional medicine, the unique properties of nanoparticles provide more strategic advantages and application flexibility over pure molecular therapeutics [7]. Using nanoparticles as rtPA carrier for thrombolytic therapy has also been widely explored. For example, biodegradable polymers conjugated with rtPA can provide the protection from the inhibitor in the circulation to prolong its circulation time, which might also confer the possibility for controlled release in encapsulated drug formulation [8]. In recent years, magnetic nanoparticles (MNP), especially iron oxide (Fe_3O_4) MNP, are frequently employed as a nano-carrier for drug delivery. Not only to be useful as a magnetic resonance imaging contrast agent, the MNP can also be endowed with other advantages, such as magnetic targeting (physical targeting) and localized heating by magnetic field induction or near-infrared laser irradiation [9]. In addition to pristine nanoparticles, MNP could be also surface modified to enhance their functionality as a drug delivery vehicle. The most common example is surface modification with polyethylene glycol (PEG) to prevent uptake by the mononuclear phagocyte system during circulation, thus prolonging the life time of injected drug [10]. Conjugation with ligand is another commonly used strategy for nanoparticle-based targeted drug delivery. Indeed, ligand-mediated drug delivery could offer a highly specific binding between the ligand molecule immobilized to the nano-carrier and the receptor molecule highly expressed in the diseased area, which could enhance the treatment efficacy by inducing drug accumulation and increasing local drug concentration in the targeted area [11].

Many groups have proposed nanomedicine using targeted rtPA delivery strategy for thrombolysis [12]. We have extensively studied different MNP-based polymeric nano-carrier for magnetically targeted delivery of rtPA, being prepared either by immobilization of rtPA on the particle surface or by encapsulation within the polymeric matrix, and demonstrated the improved thrombolytic efficacy both in vitro and in vivo [13–15]. Recently, we also pioneered the use of thermosensitive magnetic liposomes for targeted delivery and temperature-sensitive release of rtPA [16,17]. Other groups used different ligands for targeting fibrin in a blood clot or different moieties that are associated with the blood clot. For example, the ligands used for rtPA delivery targeting thrombus include peptide targeting FXIII [18], fibrin antibody targeting fibrin [19], Arg-Gly-Asp (RGD) [20], cyclicRGD [21], or other peptides [22] targeting GP IIb/IIIa, and fucoidan targeting p-selectin [23]. Those targeted thrombolysis strategies have demonstrated promising results in improving thrombolytic efficiency with shorter clot lysis time, which makes possible the use of reduced drug dosage to circumvent associated side effects, such as the bleeding risk [24].

Consider a ligand targeting fibrin, which is a trimeric molecule consisting of α -, β -, and γ -chains and a major constituent of fresh or old blood clots. Although the actual quantity of fibrin content in a clot varies from clot to clot, fibrin is the major component in a clot and it exists on the surface of a clot that is slowly dissolving either spontaneously or during therapeutic thrombolytic intervention. It is conceivable that a peptide specific for fibrin could be labelled with radioisotopes and used as an imaging agent to detect vascular thrombosis. This was demonstrated from a previous study using ^{99m}Tc labelled pentapeptide Gly-Pro-Arg-Pro-Pro (GPRPP), which has high affinity for the fibrin α -chain, for the imaging of vascular thrombosis in animals [25]. The peptide GGSKGC was later added to the C-terminus of GPRPP in order to impart functionality on the peptide. This peptide (GPRPPGGSKGC) was later shown to have high fibrin-avid affinity and high resistance to proteolysis [26].

Although using a magnetic field to magnetically guide the movement of MNP for rtPA delivery is promising, the optimization of a magnetic field might be the limiting factor, especially for clinical application. On the other hand, ligand targeting for rtPA delivery might pose challenges, such as specificity and possible immunogenicity of the targeting moiety. Therefore, a dual targeting mechanism for rtPA and for other thrombolytic drugs delivery in general is warranted. This dual targeted strategy for rtPA delivery has rarely been investigated [21]. A recent paper using two peptides as ligands to construct dual targeted liposomes for delivery of a neuroprotective agent proved to be a safe and effective treatment for ischemic stroke [27]. By integrating different targeting functionalities, dual and even multi-targeted nanoparticles could be designed to provide a paradigm for precise drug delivery to the targeted site. Through sequential or synchronized navigation of the drug-loaded nano-sized carrier, highly controllable drug delivery by synergistic function of the targeting moieties could be accomplished when compared to conventional targeting strategies [28].

Therefore, with the aim of enhancing thrombolysis efficacy, we postulated that a dual targeted rtPA nano-drug would be feasible to achieve better thrombolytic outcomes for translation into a clinical setting. When compared with the single targeting strategy, nanoparticles engineered with dual targeting mechanism, either augment the single targeting ligand with a second ligand or with magnetic targeting, has successfully been used for cancer therapy, but it has never have been demonstrated for targeted thrombolysis in vivo. Because dual-targeting nanoparticles were shown to increase differentiation between cancer and normal cells and lead to enhanced accumulation of the drug in tumors [29], the same principle is deemed to be feasible for more selectively targeted delivery of thrombolytic agents to thrombus. Specifically, magnetic PLGA nanoparticles have been explored in a dual targeted delivery of paclitaxel and curcumin in brain tumor therapy [30] and protein antigen delivery for immune stimulation [31].

In the present study, PLGA MNP (PMNP) was prepared to encapsulate Fe_3O_4 nanoparticles in a single oil-in-water emulsion step. Thrombolytic agent (rtPA) and fibrin-affinity peptide (GPRPPGGSKGC) were conjugated to PMNP surface that was modified with avidin to prepare pPMNP-rtPA, through avidin-biotin interaction and thiol-maleimide “click” reactions using biotin-PEG-maleimide (Figure 1). The physico-chemical properties of nanoparticles during preparation were analyzed, followed by biocompatibility and thrombolysis analysis in vitro. Finally, the clot thrombolysis efficiency of pPMNP-rtPA was tested in vivo in a rat embolic model.

2. Results and Discussion

2.1. Preparation of Peptide and rtPA Conjugated PLGA Magnetic Nanoparticles

Iron oxide MNP are prone to agglomeration in biological fluids due to high surface energy and the tendency to adsorb proteins, which might limit their in vivo application. After entrapping in a polymer matrix, the MNP improve stability in biological fluids and increase the half-life during circulation in vivo [32]. Therefore, in this study, PLGA was used as a polymer matrix to encapsulate hydrophobic oleic acid-coated iron oxide MNP (OMNP) and form PLGA magnetic nanoparticles (PMNP) in a single oil-in-water (O/W) emulsion step in order to prevent aggregation of iron oxide MNP. After modifying

PLGA surface with avidin through carbodiimide-mediated covalent bond formation between the carboxyl groups of PLGA and the amine groups of avidin, avidin-biotin interaction was explored for facile synthesis of rtPA and/or peptide conjugated nanoparticles (Figure 1). Avidin is a protein showing considerable affinity for biotin, which is an important co-factor in many biological processes. Avidin has the ability to bind up to four biotin molecules with the strongest non-covalent interaction being known to exist between a protein and its ligand ($K_d = 10^{-15}$ M) [33]. In addition, the bond formation between biotin and avidin is very rapid and the formed bond is unaffected by pH, organic solvents, or temperature, which facilitates the conjugation of rtPA (or peptide) to PMNP-avidin. The one-to-four binding ratio of avidin toward biotin also allows high loading of rtPA on nanoparticle surface in a controllable manner to exert high thrombolytic activity.

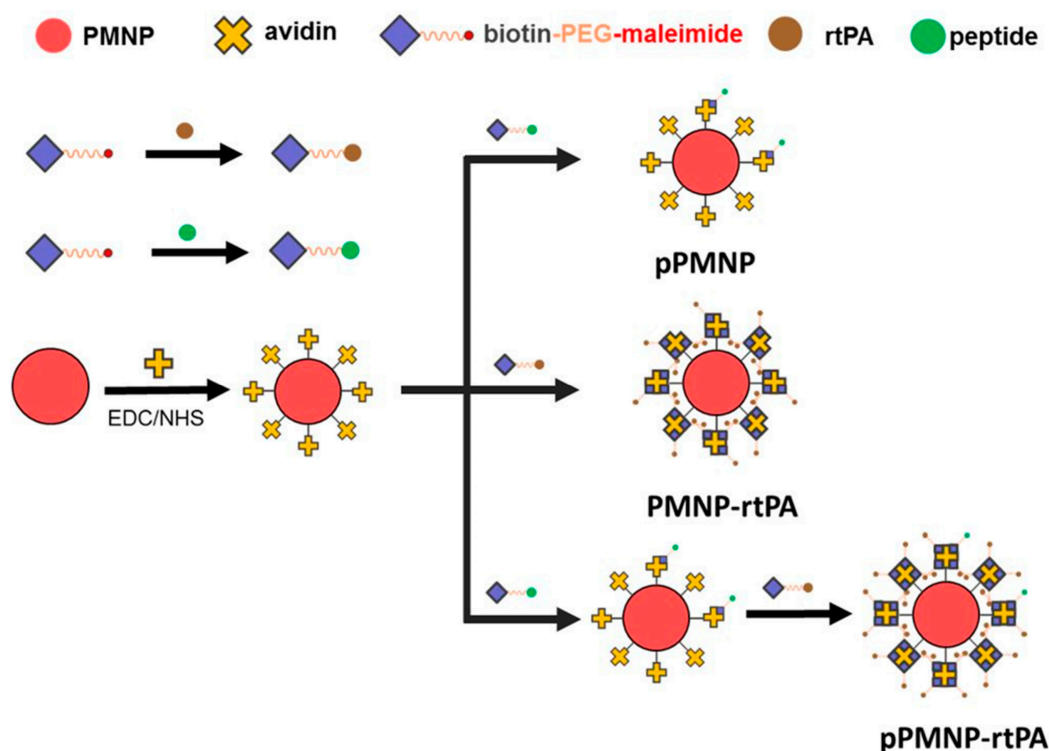


Figure 1. The schematic diagram showing the preparation of peptide conjugated poly(lactic-co-glycolic acid) (PLGA) magnetic nanoparticles (pPMNP), recombinant tissue plasminogen activator (rtPA) conjugated PLGA magnetic nanoparticles (PMNP-rtPA), and peptide/rtPA conjugated PLGA magnetic nanoparticles (pPMNP-rtPA).

Therefore, we used biotin as a mediator in this study to introduce rtPA and peptide to PMNP-avidin. This was accomplished using biotin-PEG-maleimide, which could interact with the nanoparticle through avidin/biotin interaction in one end and conjugate rtPA (or peptide) at the other using thiol–maleimide “click” chemistry [34]. It is well known that maleimide specifically reacts with the sulfhydryl group between pH 6.5 to 7.5 and forms a stable irreversible thioether linkage. It should be noted, however, a more alkaline conditions (pH > 8.5) favors reaction with primary amines and the rate of maleimide hydrolysis increases [35]. The facile conjugation rtPA and peptide to PMNP-avidin is through binding of rtPA (or peptide) to biotin-PEG-maleimide with a 1:1 molar ratio of maleimide: rtPA (or peptide). This could be accomplished, as either GPRPPGGSKGC or rtPA has only one thio (–SH) group from the cysteine (C) residue at one end of the peptide or an unpaired cysteine residue in rtPA (contains 35 cysteine residues and 17 disulfide linkages) [36].

It is imperative to first modify PMNP surface with vast amount of avidin for conjugating with abundant biotin-PEG-rtPA in order to optimize the preparation of pPMNP-rtPA. This high specific fibrinolytic activity of immobilized rtPA per unit weight of nanoparticle will render the use of minimum

amount of nanoparticles for effective thrombolysis *in vivo*. For this purpose, the influence of the amount of avidin used for immobilization on the amount of immobilized avidin protein per mg of nanoparticle was studied. The immobilized avidin content increased with the amount of avidin used during the modification step and reached a plateau at around 0.2 mg avidin, as shown in Figure 2a. Therefore, the optimum avidin modification condition is reached when 0.2 mg avidin is reacted with 1 mg PMNP for preparation of PMNP-avidin where $63.5 \pm 1.5 \mu\text{g}$ avidin/mg PMNP loading content could be achieved. Using this PMNP-avidin preparation, we proceeded to study effect of the amount of rtPA used for immobilization on the amidolytic activity of immobilized rtPA activity per mg of nanoparticle. The loading activity increases with rtPA used for conjugation until reaching 0.5 mg rtPA and decreases thereafter, as shown in Figure 2b. Therefore, the optimum drug loading is reached when 0.5 mg rtPA is reacted with 1 mg PMNP-avidin to fabricate PMNP-rtPA with $0.35 \pm 0.02 \text{ U}$ rtPA/mg PMNP-avidin loading activity. For the proper preparation of pPMNP-rtPA without overloading PMNP-avidin, PMNP-avidin was first reacted with biotin-PEG-peptide corresponding to 5 mol% of rtPA in the first step, followed by reacting with biotin-PEG-rtPA to fabricate pPMNP-rtPA (Figure 1). The final loading of peptide on pPMNP-rtPA was $0.46 \pm 0.03 \text{ mg/mg}$ nanoparticle, while the rtPA activity slightly reduced to $0.32 \pm 0.01 \text{ U}$ rtPA/mg nanoparticle.

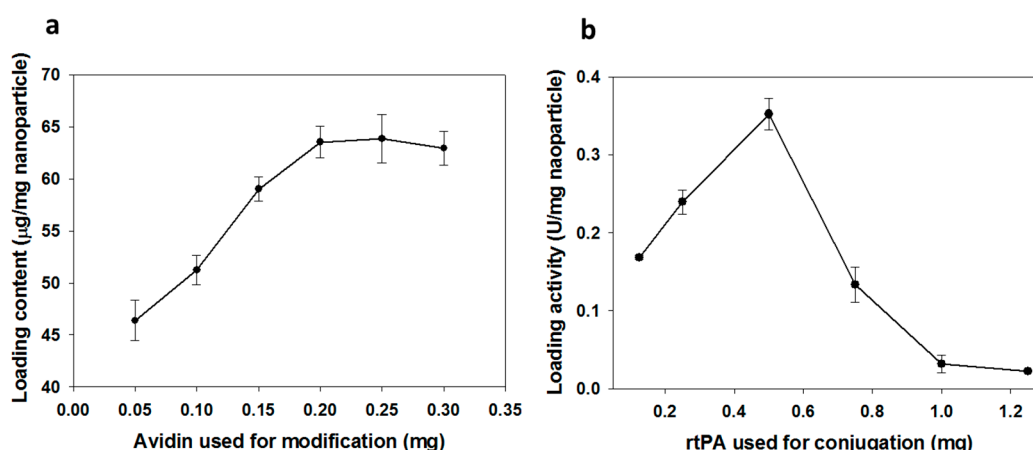


Figure 2. The effect of avidin and rtPA used during for immobilization on the loading of avidin protein (a) and rtPA activity (b).

The activity of rtPA determined above is the amidolytic activity (U) to hydrolyze a low molecular weight substrate (S-2288), but not associated with the clot lysis thrombolytic activity. The fibrinolytic property of free and immobilized rtPA was compared from the agar plate assay to show the thrombin-mediated fibrinolytic activity of rtPA for application in thrombolysis in order to ascertain the retention of biological activity of rtPA, which is likely to change and diminish the clot lysis activity due to protein denaturation [37]. To validate this assay method, the dosage dependent sensitivity was first confirmed by determining the thickness of clear zones around sample holes, containing different amount of rtPA, due to the enzymatic action of the drug. The thickness of a clear zone around the sample hole of the solidified agar, due to lysis of fibrin gel with rtPA enzymatic function, increased with the amount of rtPA used for the assay, as shown in Figure 3a,b. When PMNP-rtPA or pPMNP-rtPA was placed in the sample hole on the agar plate, the size of the clear zone created by the action of immobilized rtPA was equal to that created by free rtPA at the same drug dosage (Figure 3a,c), endorsing that rtPA conjugated to PMNP and pPMNP could fully retain its lytic action against fibrin clot. Most importantly, nano-carrier conjugated with the peptide ligand (pPMNP-rtPA) showed the same clot lysis activity when compared to the non-conjugated one (PMNP-rtPA), implying that modifying PMNP with the targeting peptide ligand would not influence the thrombolysis activity of rtPA. The absence of any clear zone around the phosphate buffered saline (PBS), PMNP and pPMNP-containing sample

hole shows that they have no fibrinolytic activity to hydrolyze the fibrin and the lysis of agar plate is solely due to the fibrinolytic activity of rtPA (Figure 3a).

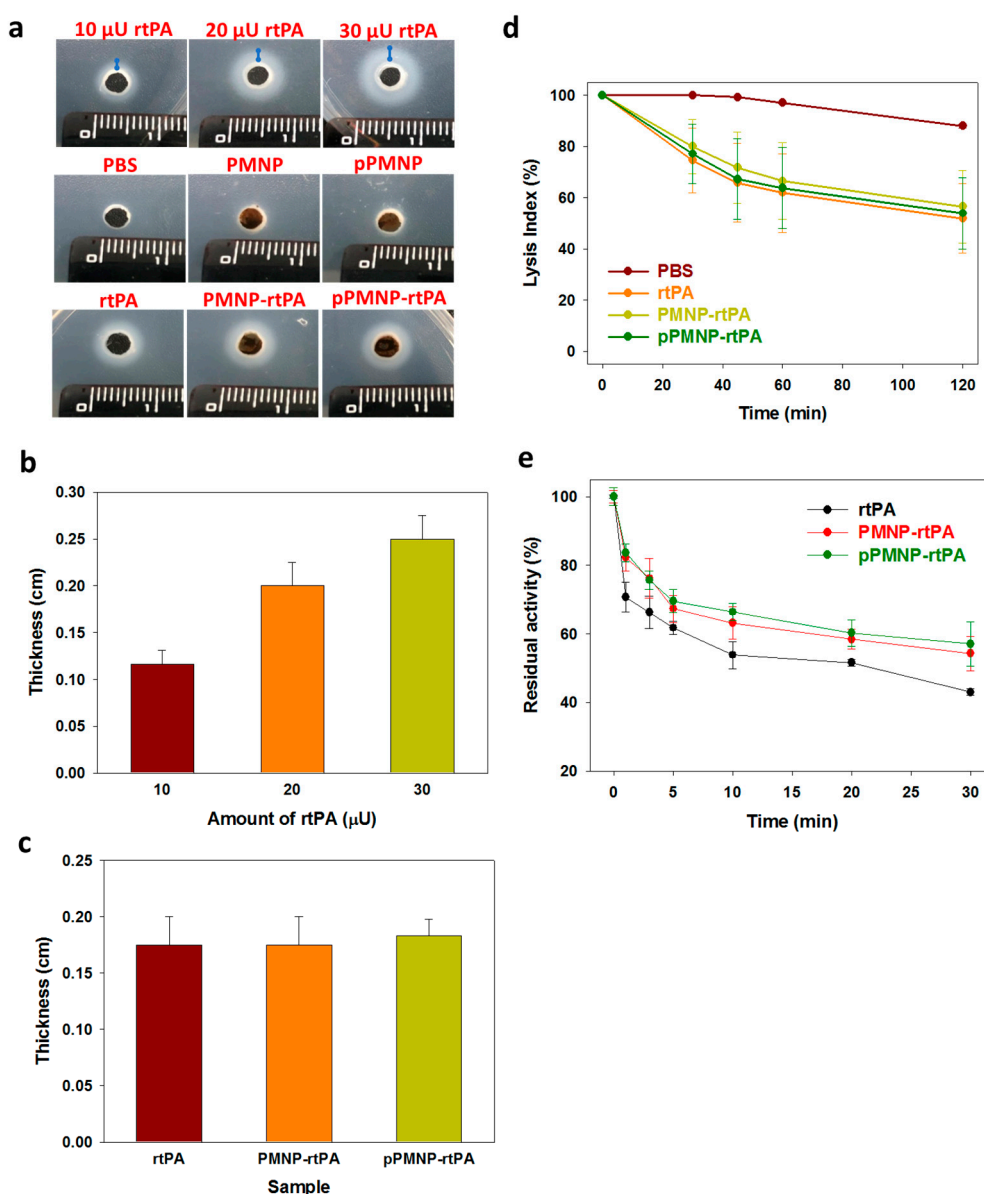


Figure 3. The clot lysis ability of free and immobilized rtPA from the fibrinolytic activity assay using the agar plate. Fibrinolysis activity was observed from a clear zone around the sample hole after incubation at 37 °C for 24 h using free rtPA at 10, 20, and 30 μ U and PMNP-rtPA and pPMNP-rtPA at 20 μ U (a). The thickness of the clear zone (blue lines) in (a) was measured and compared between free rtPA at different dosage (b), and between free rtPA, PMNP-rtPA, and pPMNP-rtPA (c). (d) Comparison of the fibrinolytic activity of phosphate buffered saline (PBS) (control), rtPA, PMNP-rtPA and pPMNP-rtPA from the lysis index using thromboelastometry at 1.7 μ U/mL rtPA dosage. (e) The inhibition of free rtPA, PMNP-rtPA, and pPMNP-rtPA by plasminogen activator inhibitor-1 (PAI-1) in vitro by measuring the residual amidolytic activity of rtPA after incubating with PAI-I at 37 °C for different times.

We further used thromboelastometry to determine blood clots lysis induced by rtPA by measuring the lysis index, which was shown to be dosage-dependent on free rtPA concentration used for the assay, to evaluate the thrombolytic effects [38]. As shown in Figure 3d, there is no significant difference in lysis index among free rtPA, PMN-rtPA and pPMNP rtPA irrespective of assay time (30, 45, 60 and 120 min) at the same rtPA drug dosage, which is in accordance with those from agar plate assays

(Figure 3c). Taken together, both assays confirm the full retention of rtPA fibrinolytic activity after conjugation to PMNP, irrespective of peptide conjugation by using the pre-designed conjugation step as shown in Figure 1, which facilitate the use of pPMNP-rtPA for dual targeted rtPA delivery.

The plasminogen activator inhibitor-1 (PAI-1) is the main inhibitor of circulating rtPA and inactivation of rtPA by PAI-1 is the main cause for the short half-life of rtPA [39]. Therefore, it will be highly desirable that the PMNP-rtPA and pPMNP-rtPA developed in this study will not only retain its fibrinolytic activity (Figure 3c), but also prolong the circulation time of rtPA. Therefore, we used the chromogenic substrate S-2288 to determine the amidolytic activity of PMNP-rtPA and pPMNP-rtPA when pre-incubated with PAI-1 for different times and compared with that of free rtPA. The immobilized rtPA was inactivated by PAI-1 more slowly than free rtPA, indicating that the rtPA in PMNP-rtPA and pPMNP-rtPA was protected from PAI-1 to some extent, as shown in Figure 3e. This might be due to the effects of steric hindrance of the nano-carrier for accessibility of PAI-1 to bind rtPA or due to the inaccessibility of the PAI-1-binding site in the bound rtPA [40].

2.2. Characterization of Physico-Chemical Properties

From the transmission electron microscope (TEM) images that are shown in Figure 4a–d, iron oxide MNP and OMNP agglomerated in water at low magnification due to Van der Waals force or weak magnetic attractions from magnetic dipole–dipole interactions [41]. Nonetheless, the average particle size of discrete nanoparticles could still be estimated to be around 10 nm from high magnification micrographs and consistent with similar researches that also used co-precipitation method to prepare iron oxide MNP [42]. After the encapsulation of OMNP in PLGA, PMNP shows smooth and spherical surface morphology of ~300 nm diameter and an agglomerate core of iron oxide MNPs (Figure 4e,f). This indicates that all OMNP were well encapsulated within the PLGA matrix after a single oil-in-water (o/w) emulsion/solvent evaporation step. Modification with avidin (PMNP-avidin), conjugation with rtPA (PMNP-rtPA), and conjugation with peptide (pPMNP-rtPA) do not lead to much change of particle size and surface morphology (Figure 4g–l). Nonetheless, a gray layer around the round contours from 1% phosphotungstic acid staining, which binds to the basic groups (lysine and arginine residues) of proteins, suggests that both avidin and rtPA were successfully immobilized on the nanoparticle surface.

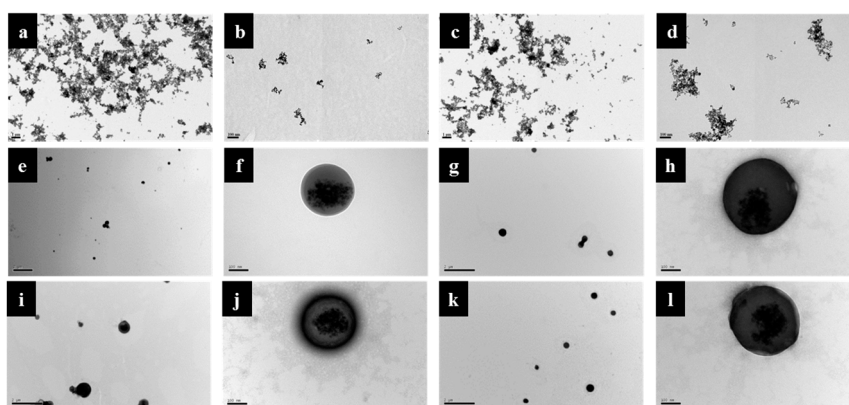


Figure 4. The transmission electron microscope (TEM) images of Fe_3O_4 magnetic nanoparticles (MNP) (a,b), oleic acid coated magnetic nanoparticles (OMNP) (c,d), PLGA magnetic nanoparticles (PMNP) (e,f), avidin-modified PLGA magnetic nanoparticles (PMNP-avidin) (g,h), rtPA-conjugated PLGA magnetic nanoparticles (PMNP-rtPA) (i,j), and peptide/rtPA-conjugated PLGA magnetic nanoparticles (pPMNP-rtPA) (k,l). Bar = 2 μm (e,g,i,k), 1 μm (a,c) and 100 nm (b,d,f,h,j,l).

From the dynamic light scattering (DLS) results that are shown in Figure 5a, the average hydrodynamic diameters for MNP, OMNP, PMNP, PMNP-avidin, PMNP-rtPA, and pPMNP-rtPA are 230.7, 229.4, 252.7, 278.8, 291.2, and 321.1 nm, respectively (Table 1) and consistent with the trend observed from TEM (Figure 4). The particle size constantly increased during the sequential

modification/conjugation steps from PMNP to pPMNP-rtPA due to increasing amount of molecules coated on nanoparticle surface. The polydispersity index (PDI) were all below 0.22 (Table 1), indicating that the particle size distribution is uniform for all samples, and every sample has good suspension stability [43].

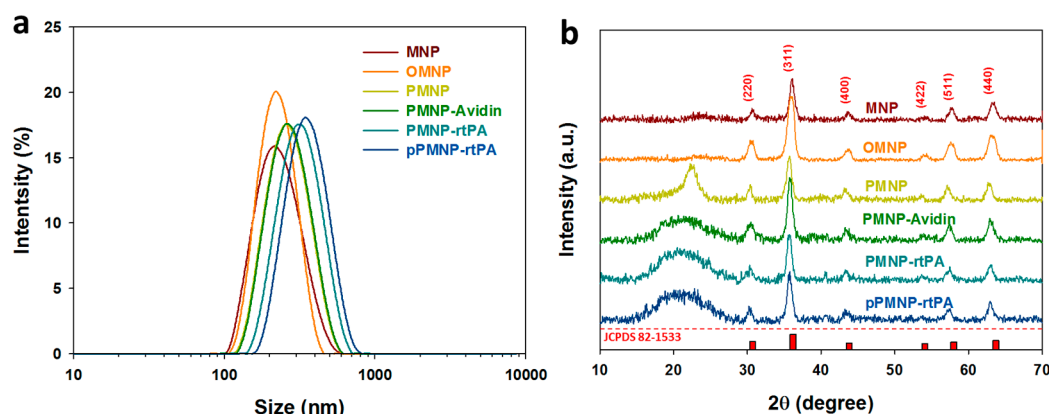


Figure 5. Characterization of Fe_3O_4 magnetic nanoparticles (MNP), oleic acid coated magnetic nanoparticles (OMNP), PLGA magnetic nanoparticles (PMNP), avidin-conjugated PLGA magnetic nanoparticles (PMNP-avidin), rtPA-conjugated PLGA magnetic nanoparticles (PMNP-rtPA), and peptide/rtPA-conjugated PLGA magnetic nanoparticles (pPMNP-rtPA) by dynamic light scattering (DLS) (a) and X-ray diffraction (XRD) (b).

Table 1. The average particle size, polydispersity index (PDI), zeta potential, and crystal size of different nanoparticles.

Sample ¹	Average Diameter ² (nm)	PDI	Zeta Potential (mV)	Crystal Size ³ (nm)
MNP	230.7 ± 17.1	0.19 ± 0.05	12.1 ± 2.9	10.2
OMNP	229.3 ± 18.5	0.20 ± 0.01	−17.6 ± 0.9	10.5
PMNP	252.7 ± 13.4	0.19 ± 0.04	−30.0 ± 1.3	10.3
PMNP-avidin	278.8 ± 19.1	0.21 ± 0.02	−25.8 ± 0.4	11.7
PMNP-rtPA	291.2 ± 27.3	0.21 ± 0.04	−24.4 ± 1.1	10.7
pPMNP-rtPA	321.1 ± 26.9	0.22 ± 0.05	−22.1 ± 2.0	10.9

¹ MNP: iron oxide magnetic nanoparticles, OMNP: oleic acid coated magnetic nanoparticles, PMNP: PLGA magnetic nanoparticles, PMNP-avidin: avidin-conjugated PLGA magnetic nanoparticles, PMNP-rtPA: rtPA-conjugated PLGA magnetic nanoparticles, pPMNP-rtPA: peptide/rtPA-conjugated PLGA magnetic nanoparticles. ² Determined from dynamic light scattering (DLS). ³ Determined from x-ray diffraction (XRD).

From electrophoretic mobility measurements, the average zeta potential of MNP is positive at 12.1 mV, due to residual ammonium ions associated with the particles as ammonia was used for the co-precipitation of ferric and ferrous ions during the synthesis (Table 1). This value changed to negative values for OMNP (−17.6 mV) and PMNP (−30 mV) due to the carboxylic group of oleic acid and PLGA. The zeta potential shifted to −25.8 mV after avidin modification as the isoelectric point (pI) of this protein is approximately 10 [44]. A similar effect due to the positive change of rtPA (pI = 7.6) and peptide (pI = 10) slightly changed the zeta potential to −24.4 mV (PMNP-rtPA) and −22.1 mV (pPMNP-rtPA).

The x-ray diffraction (XRD) patterns that are shown in Figure 5b reveal six characteristic peaks at $2\theta = 30.3^\circ, 35.7^\circ, 43.4^\circ, 53.87^\circ, 57.4^\circ$, and 63.1° for all samples, which represent the (220), (311), (400), (422), (511), and (440) planes of a cubic cells and corresponds to the magnetite structure (JCPDS file no. 82-1533). This confirms that all of the nanoparticles were pure Fe_3O_4 with a spinel structure and PLGA encapsulation or surface conjugation steps did not lead to phase change of Fe_3O_4 . The average crystal size calculated from the Scherrer equation, using the highest diffraction peak at $2\theta = 35.7^\circ$, with the

XRD line broadening and assuming spherical crystals, ranged from 10 to 12 nm (Table 1), supporting the results from TEM.

The Fourier transform infrared (FTIR) spectra are shown in Figure 6a for all samples. The characteristic peak of Fe_3O_4 MNP at 640 and 570 cm^{-1} represented the Fe–O bond while the peak in the 3200 to 3600 cm^{-1} range and at 1650 cm^{-1} might represent the N–H bond contributed from residual ammonia, as observed from its positive zeta potential (Table 1). For OMNP, the characteristic peak at 2950, 2900, and 2850 cm^{-1} represented the C–H bond of –CH, –CH₂, and –CH₃, respectively. The characteristic peak that ranged 1750–1680 cm^{-1} represented the C=O (carboxylic acid) bond, while the characteristic peak ranged 1450–1400 cm^{-1} represented the O–H (carboxylic acid) bond and the C–H bond, supporting oleic acid coating. For PMNP, the characteristic peak at 1180 cm^{-1} and 1080 cm^{-1} represented the C–O bond of ester and alcohol, indicating the successful entrapment of OMNP in PLGA. A new characteristic peak at 1350 cm^{-1} that was assigned to the C–N (acryl) bond was observed for PMNP-avidin, supporting surface modification of PMNP with avidin. No new peaks could be identified after peptide and rtPA conjugation, as expected.

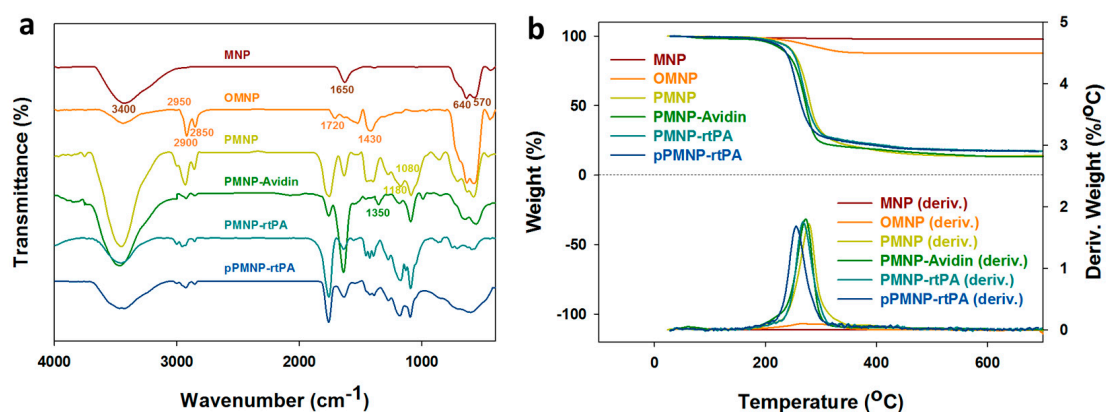


Figure 6. Characterization of Fe_3O_4 magnetic nanoparticles (MNP), oleic acid coated magnetic nanoparticles (OMNP), PLGA coated magnetic nanoparticles (PMNP), avidin-conjugated PLGA coated magnetic nanoparticles (PMNP-Avidin), rtPA-conjugated PLGA coated magnetic nanoparticles (PMNP-rtPA) and peptide/rtPA-conjugated PLGA magnetic nanoparticles (pPMNP-rtPA) by Fourier transform infrared (FTIR) spectroscopy (a) and thermogravimetric analysis (TGA) (b).

The thermogravimetric analysis (TGA) results that are shown in Figure 6b reveal weight loss starting from 270 °C for OMNP compared with MNP due to the decomposition of the organic oleic acid molecules on Fe_3O_4 MNP and the final residual weight at 700 °C indicates 10% (*w/w*) oleic acid in OMNP (Table 2). For PLGA-encapsulated nanoparticles, substantial weight loss near 275 °C was evident due to PLGA decomposition and the residual weights of PMNP, PMNP-avidin, PMNP-rtPA, and pPMNP-rtPA at 700 °C were approximately 14.0%, 13.4%, 17.1%, and 16.9%, respectively (Table 2). For comparison, the Fe_3O_4 content that was determined from inductively coupled plasma-optical emission spectrometry (ICP-OES) for MNP, OMNP, PMNP, PMNP-avidin, PMNP-rtPA, and pPMNP-rtPA are 97.8%, 87.1%, 13.5%, 12.3%, 10.5%, and 10.1%, respectively (Table 2). Separate experiment indicates the residual weight of PLGA, avidin, and rtPA after burning to 700 °C in nitrogen were 0%, 20.1%, and 33.7%, respectively, due to their respective synthetic and natural material characteristics (data not shown). When considering the residual weight of avidin and rtPA, the Fe_3O_4 content from TGA and ICP-OES experiments could be deemed to be consistent.

Table 2. The residual weight at 700 °C from thermogravimetric analysis (TGA) and the Fe₃O₄ content determined from inductively coupled plasma-optical emission spectrometry (ICP-OES) and superconducting quantum interference device (SQUID).

Sample ¹	Residual Weight from TGA (%)	Fe ₃ O ₄ from ICP-OES (%)	Fe ₃ O ₄ from SQUID (%)
MNP	97.9	97.8 ± 1.6	100.0 ± 0.05
OMNP	87.7	87.1 ± 2.1	90.9 ± 0.11
PMNP	14.0	13.5 ± 0.3	15.5 ± 0.06
PMNP-avidin	13.4	12.3 ± 0.8	14.4 ± 0.11
PMNP-rtPA	17.1	10.5 ± 0.3	13.3 ± 0.07
pPMNP-rtPA	16.9	10.1 ± 0.4	13.5 ± 0.07

¹ MNP: iron oxide magnetic nanoparticles, OMNP: oleic acid coated magnetic nanoparticles, PMNP: PLGA magnetic nanoparticles, PMNP-avidin: avidin-conjugated PLGA magnetic nanoparticles, PMNP-rtPA: rtPA-conjugated PLGA magnetic nanoparticles, pPMNP-rtPA: peptide/rtPA-conjugated PLGA magnetic nanoparticles.

Figure 7a shows the magnetization curves of all samples from superconducting quantum interference device (SQUID) analysis at room temperature. The remnant (residue) magnetization (without magnetic field) was determined from Figure 7b to determine the superparamagnetic property. The remnant magnetization of MNP is close to zero (0.21 emu/g), endorsing its superparamagnetic property and consistent with its ~10 nm size from TEM and XRD experiments and in accordance with reported extremely low or non-existent remanence of Fe₃O₄ NMP [45]. The remnant magnetization values of OMNP, PMNP, PMNP-avidin, PMNP-rtPA, and pPMNP-rtPA are also close to zero (< 0.3 emu/g) (Table 2), indicating MNP retained the characteristic superparamagnetism behavior during the synthesis of PLGA-based nanoparticles. The superparamagnetism behavior refers that all magnetic nano-carriers can be magnetized when an external magnetic field is applied and there is no residual magnetic interaction after removing the magnetic field. This behavior depends on the size of iron oxide MNP and it generally occurs below ~20 nm particle size, which supports the characterizing results from TEM and XRD. Undoubtedly, the use of superparamagnetic pPMNP-rtPA confers an important property for in vivo application as the drug-conjugated magnetic nano-carrier could be easily dispersed after guidance to the target site by removing the applied magnetic field, which can prevent undesirable particle agglomeration and possible vessel blockage [46]. The saturation magnetization value of OMNP reduced to 90% of that of MNP, consistent with the trend of MNP content from TGA or ICP-OES. This value reduced drastically to ~15% of that of MNP for all PLGA-encapsulated nanoparticles (i.e., PMNP, PMNP-avidin, PMNP-rtPA, and pPMNP-rtPA), which is due to the reduced MNP weight in the nanoparticles. Although the magnetization value is deemed to be sufficient for magnetic guidance in magnetically targeted thrombolytic drug delivery [47], dual targeting through synergistic ligand targeting will undoubtedly improve the drug targeting and clot lysis efficacy.

2.3. In Vitro Biocompatibility

The biocompatibility was first determined from the cytocompatibility of PMNP at different concentrations after being incubated with NIH 3T3 fibroblasts for 24 and 48 h. The relative cell viability after contacting with PMNP shows no significance difference from that of control (without PMNP) up to 0.2 mg/mL, indicating PMNP is not toxic, even at concentrations suitable for in vivo injection, as shown from Figure 8a. Using this concentration, we further tested the cytotoxicity of all nanoparticles during pPMNP-rtPA synthesis. The relative cell viability of all samples not only remained above 70% at both time points, to conform with the cytocompatibility standards of ISO 10993-5, no significance difference was found for all groups when compared to the control (PBS), as shown in Figure 8b.

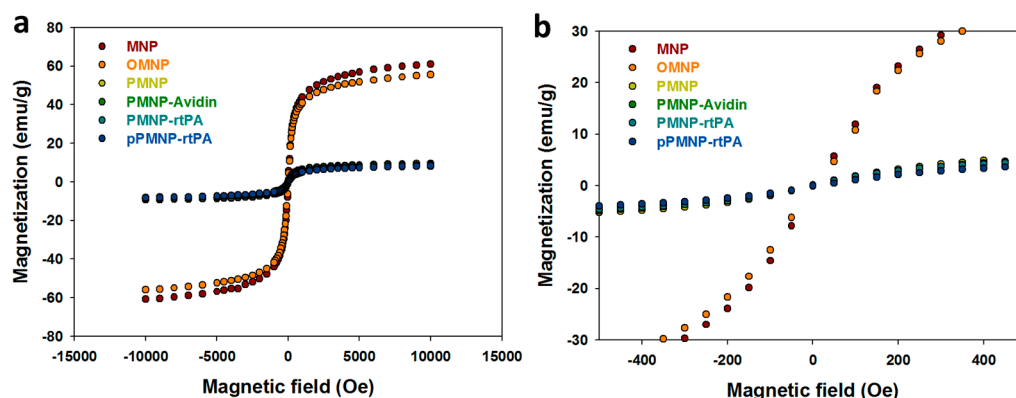


Figure 7. Characterization of Fe_3O_4 magnetic nanoparticles (MNP), oleic acid coated magnetic nanoparticles (OMNP), PLGA coated magnetic nanoparticles (PMNP), avidin-conjugated PLGA coated magnetic nanoparticles (PMNP-avidin), rtPA-conjugated PLGA coated magnetic nanoparticles (PMNP-rtPA), and peptide/rtPA-conjugated PLGA magnetic nanoparticles (pPMNP-rtPA) by superconducting quantum interference device (SQUID) hysteresis magnetization curves (a). The remnant (residue) magnetization of all samples is close to zero, as shown in (b).

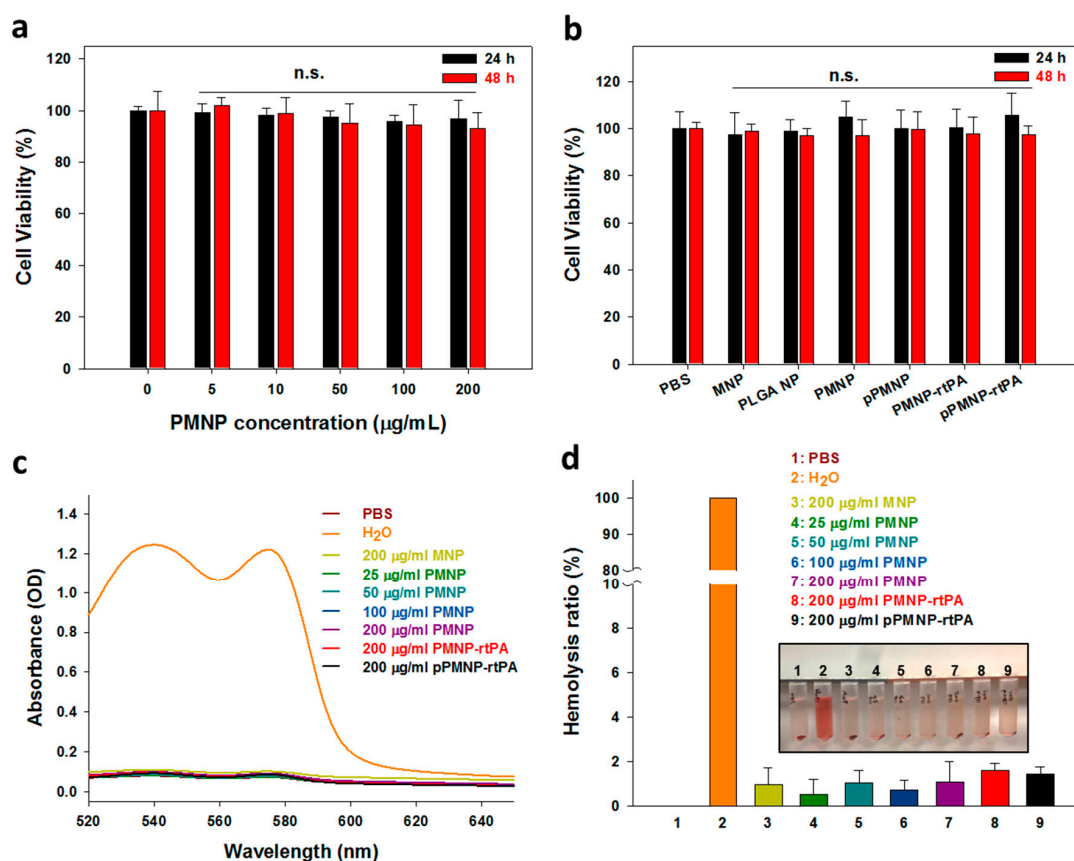


Figure 8. Cytocompatibility of PMNP at different concentrations (n.s.: not significant compared to 0 μg/mL at 24 or 48 h, all samples) (a) and of different nanoparticles at 200 μg/mL (n.s.: not significant compared to PBS at 24 or 48 h, all samples) (b) by MTT assay after contacting with NIH 3T3 cells. Hemocompatibility of different nanoparticles was determined from the hemolysis assay by incubation with diluted red blood cells in PBS at 37 °C for 2 h to obtain the full-wavelength absorption spectra of the supernatant (c) and the hemolysis ratio from OD₅₄₀ (d). Water and PBS were used as the positive and the negative controls, respectively.

Other than cytocompatibility, further biocompatibility consideration is through hemocompatibility to determine whether nanoparticles may induce hemolysis when administrated through intravenous injection. After incubation with purified rat red blood cells diluted in PBS at 37 °C for 2 h, the absorption spectra of the supernatant of MNP, pPMNP, PMNP-rtPA, and pPMNP-rtPA was the same as PBS (negative control), but not water (positive control), due to busting of red blood cells and release of oxyhemoglobin to show absorbance maxima at 540 and 577 nm (Figure 8c). The hemolysis effect was further examined through a quantitative comparison of the hemolysis ratio by using the difference in OD₅₄₀ between the sample and the negative control (PBS) divided by the difference between the positive control (water) and the negative control. No visible hemolysis was observed between all samples and PBS, but not water, and the hemolysis ratio was lower than 2% for every nanoparticle (Figure 8d), indicating the good hemocompatibility of the nanoparticles synthesized according to the hemocompatibility standards of ASTM F756–08. Taken together, the good cytocompatibility and negligible hemolytic activity of pPMNP-rtPA underlines its excellent biocompatibility for in vivo application [48].

2.4. Targeting Effects

The magnetic targeting effect was examined by magnetic guiding experiments by visually observing the solution turbidity after placing a magnet at the side of a tube containing 1 mg/mL nanoparticle for 5 min. From Figure 9a, the time-lapsed change of supernatant turbidity indicated a magnetic field that was created by using a 1700 gauss magnet was effective to guide magnetic nanoparticles synthesized in this study to tube side against the gravity force, which reveals the possibility of using pPMNP-rtPA for magnetically guided thrombolysis. We used pre-synthesized Cy 5.5-encapsulated magnetic nanoparticles to demonstrate the fibrin binding ability of pPMNP and the ligand targeting effect. The fluorescently labelled nanoparticles were placed in a fibrin plate, shaken for 10 min, washed, and examined under an inverted fluorescence microscope to reveal the difference in binding ability between PMNP and pPMNP toward fibrin. In contrast to control with PBS showing no background fluorescence, Cy 5.5-labelled PMNP showed minimum fluorescence signal due to non-specific binding, in contrast to abundant scattered fluorescence associated with pPMNP due to specific peptide-fibrin binding, as shown in Figure 9b. The peptide GPRPPGGSKGC used here has been conjugated to fluorescently labeled MNP and showed high affinities for thrombi for multimodal fluorescence and magnetic resonance imaging of intravascular thrombus [49]. Therefore, the peptide-conjugated magnetic nanoparticles (pPMNP) offer the possibility for ligand-mediated fibrin-targeted thrombolytic drug delivery to induce thrombolysis. When compared with using monoclonal antibody against fibrin as a targeting ligand, the peptides are smaller in size, easier to produce than monoclonal antibodies, less likely to induce any immunologic reaction, but still in most cases, show high specificity and binding constants as monoclonal antibodies [50].

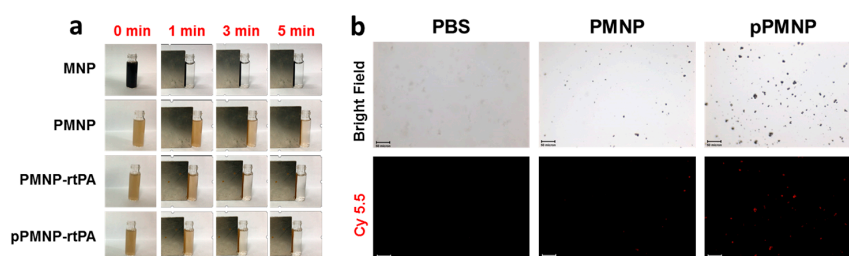


Figure 9. (a) Magnetic field guiding efficiency of different magnetic nanoparticles by attaching a magnet (1700 gauss) to the side of a tube containing 1 mg/mL nanoparticle in PBS for 5 min. (b) Fibrin-binding efficiency of PLGA magnetic nanoparticles (PMNP) and peptide-conjugated PLGA magnetic nanoparticles (pPMNP) was determined by contacting Cy 5.5-labelled magnetic nanoparticles (0.1 mg/mL) with a fibrin plate for 10 min. The fluorescence signal from the remnant nanoparticles bound to fibrin was observed under an inverted fluorescence microscope after washing (bar = 50 μ m).

2.5. In Vitro Thrombolysis

Static in vitro thrombolysis in vertical position, using a blood clot made from rat whole blood, was performed with or without a magnet, to determine the effectiveness of magnetic targeting in blood clot lysis (Figure 10a) [51]. For this purpose, the extent of clot lysis when pre-formed blood clot was treated by rtPA and PMNP-rtPA in a sample tube was compared under the influence of downward magnetic pulling force generated from a magnet placed at the bottom of the tube. The clots treated in PBS and PMNP were taken as controls. Blood clot lysis was monitored spectrophotometrically by measuring the absorbance of the supernatant at 415 nm (OD_{415}) after 10 min. In PBS or PMNP without rtPA, the blood clot remains intact with the solution transparency similar to 0 min, as observed from Figure 10b. Nonetheless, the contact with rtPA or PMNP-rtPA resulted in red-colored supernatant solution due to release of red blood cell residues from the tight fibrin network in the blood clot. By comparing the OD_{415} values presented in Figure 10c, there is no significant difference in OD_{415} for rtPA and PMNP-rtPA without magnet, as observed before from the agar plate clot lysis assays (Figure 3c). Most importantly, only PMNP-rtPA, but not rtPA, shows magnet-sensitive lysis activity. The OD_{415} increased significantly (1.83 folds) due to a downward magnetic force being generated by the magnet to attract PMNP-rtPA toward the blood clot for enhanced fibrinolysis.

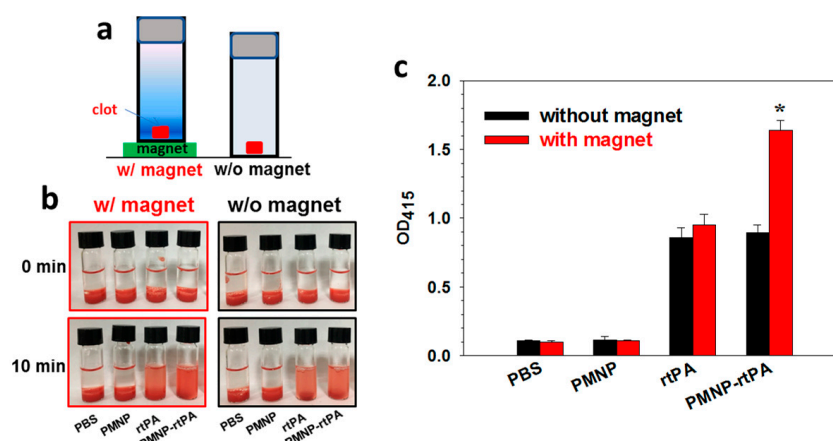


Figure 10. The in vitro static clot lysis with or without magnetic guidance in vertical position was carried out as illustrated in (a). The solution appearance after blood clot lysis (b) and the solution absorbance measured at 415 nm (OD_{415}) (c) after incubating the blood clot with PBS, PMNP, rtPA or PMNP-rtPA solution (25 μ U rtPA). * $p < 0.05$ compared with pPMNP-rtPA without magnet.

Dynamic in vitro thrombolysis was employed to verify enhanced clot lysis due to the conjugated peptide ligand at 37 °C and 43 °C by slowly rotating the clot-containing vial (Figure 11a). The mixing of a blood clot with the nanocarrier was deemed to be necessary for showing the ligand targeting effect of pPMNP-rtPA originated from fibrin binding. As in static test, the color intensity of the red-colored supernatant solution increased only for rtPA, PMNP-rtPA, and pPMNP-rtPA with the thrombolytic action of rtPA releasing red blood cell residues from the clot (Figure 11b). Most importantly, a significant difference in OD_{415} was found between pPMNP-rtPA and pPMNP-rtPA, regardless of temperature (Figure 11c). This underscores the importance of using fibrin-avid peptide moiety to upregulate the clot lysis activity of immobilized rtPA, due to the preferential binding to fibrin (Figure 9b). That temperature-dependent lysis was only being shown in rtPA-containing samples further supports rtPA-induced clot lysis, with higher rtPA enzymatic activity at 43 °C.

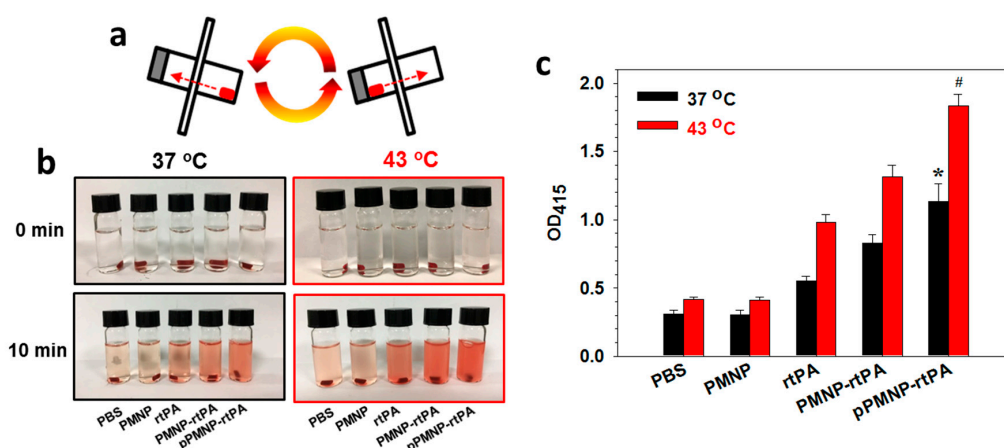


Figure 11. The in vitro dynamic clot lysis was carried out as illustrated in (a). The solution appearance after blood clot lysis (b) and the solution absorbance measured at 415 nm (OD₄₁₅) (c) after incubating the blood clot with PBS, PMNP, rtPA, PMNP-rtPA, or pPMNP-rtPA solution (50 μ U rtPA activity). * $p < 0.05$ compared with PMNP-rtPA at 37 °C, # $p < 0.05$ compared with PMNP-rtPA at 43 °C.

After thrombolysis testing in a closed system, we studied simulated vascular embolization induced by a blood clot and pressure-driven clot lysis in a flow system (Figure 12a). The best pPMNP-rtPA sample was tested in the flow thrombolysis model at 37 °C while using a water jacketed glass tube. A blood clot was placed at the bottom of a tube with reduced diameter and lodged tightly within the tube inner circumference, in order to restrict lysis from the clot surface, and the sample was injected from a side opening. A magnet was placed below the clot, outside of the tube to introduce magnetic guidance. A fluid pressure gradient was generated with PBS flow from the top at 0.5 mL/min using a syringe pump. At time zero, a different sample was introduced into the flow system and the reperfusion time for clot dissolution (clot lysis time) was compared among different treatment groups to determine the lysis efficiency. The blood clot lysis efficiency of pPMNP-rtPA treatment was enhanced with significantly reduced clot lysis time (51 min), when reperfusion and disengaging of clot from the tube occurs. This could be compared with free rtPA (86 min) as shown in Figure 12b. The combination of magnetic and ligand targeting resulted in the shortest reperfusion time with 2.3-fold increase in lysis efficiency when compared to the pPMNP group.

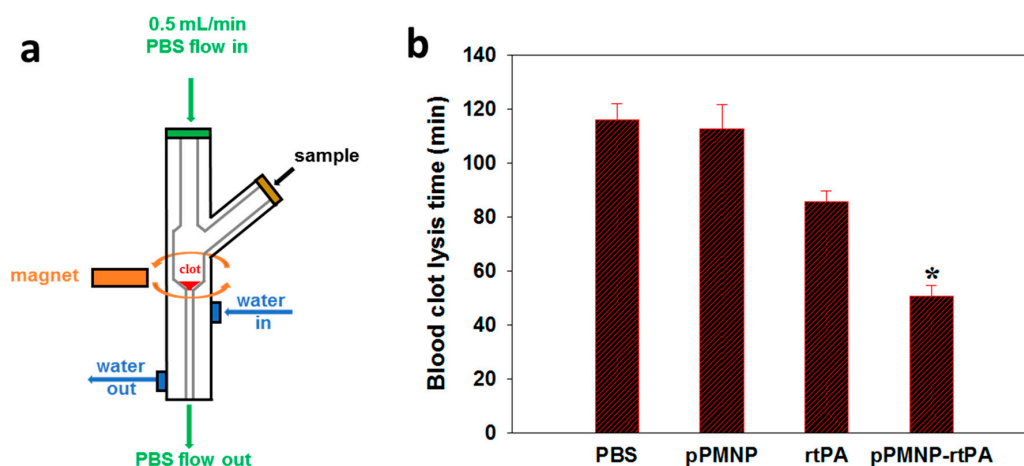


Figure 12. The schematic diagram of a flow model to evaluate pressure-driven thrombolysis at 0.5 mL/min (a). At time zero, different sample (PBS, pPMNP, rtPA, or pPMNP-rtPA) was introduced into the flow system and the blood clot lysis time was recorded when reperfusion occurs to determine the lysis efficiency (b). * $p < 0.05$ compared with rtPA.

2.6. In Vivo Thrombolysis

The clinical application potential of dual targeted delivery of rtPA was evaluated by determining the in vivo fibrinolytic efficacy of pPMNP-rtPA where induce targeted thrombolysis under magnetic guidance was assessed in a rat embolic model [48]. Five minutes after lodging the left iliac artery upstream of the pubic epigastric artery with a blood clot, pPMNP (vehicle), free rtPA, or pPMNP-rtPA was administered intra-arterially via the right iliac artery. Magnetic guidance with a 0.5 T magnet started immediately after drug administration. This was repeated in five successive cycles (5 min each) from the branch of abdominal aorta and iliac artery to the branch of iliac artery and the femoral artery (1 min) and to the lower extremities (4 min) (Figure 13a). The blood flow pattern changes around the surrounding areas of the hind limb was acquired using a laser speckle contrast imager, while the rates of iliac blood flow (IBF) and aortic blood flow (ABF) were determined using ultrasonic flow probes.

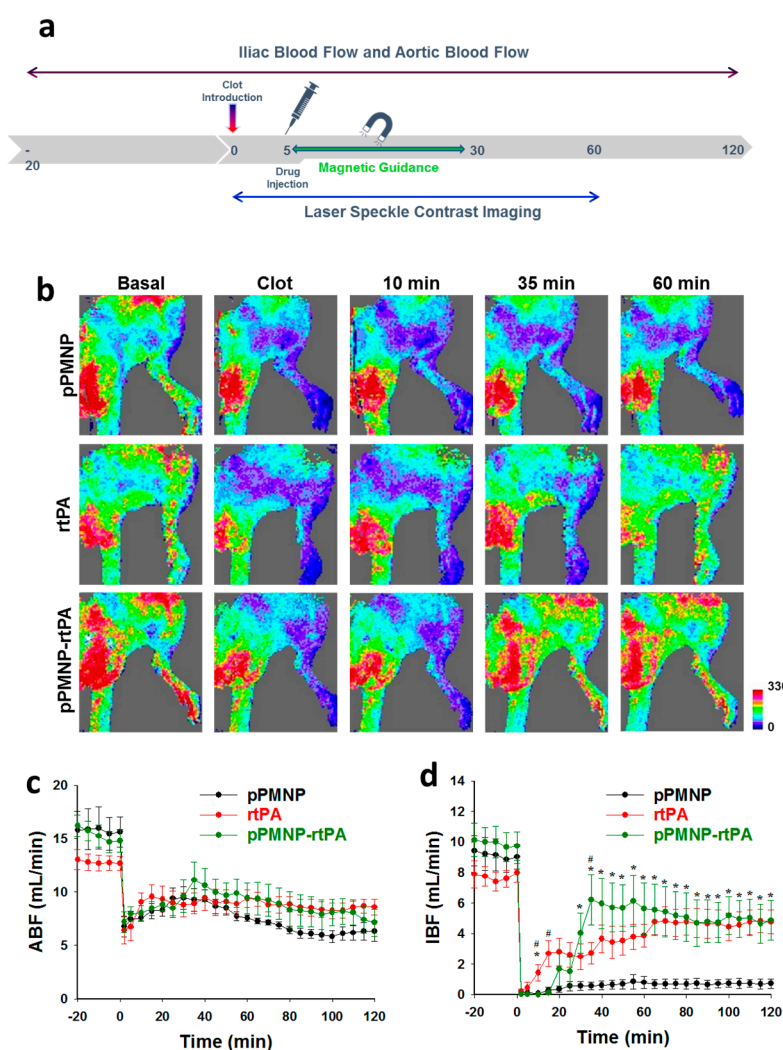


Figure 13. The in vivo thrombolytic effects of pPMNP-rtPA by evaluating targeted thrombolysis in a rat embolic model. (a) A blood clot was lodged into the left iliac artery and after 5 min pPMNP ($n = 5$), rtPA (1.5 U/kg; $n = 5$) or pPMNP-rtPA (0.3 U/kg; $n = 5$) was delivered from the right iliac artery and subject to magnetic guidance for 25 min. (b) Representative images of blood perfusion rate in the hind limb area at different time points after clot introduction using a laser speckle contrast imager. The abdominal aortic blood flow (ABF) (c) and iliac blood flow (IBF) (d) before and after blood clot introduction (0 min) was determined from ultrasonic flow probes. * $p < 0.05$ rtPA or pPMNP-rtPA vs. PMNP, # $p < 0.05$ rtPA vs. pPMNP-rtPA.

The hind limb perfusion reduced dramatically from the basal after introducing the clot, which created vascular thrombosis for evaluation of the fibrinolytic activity of rtPA *in vivo*, as shown in Figure 13b. It is evident that pPMNP-rtPA injection improved the blood perfusion in the hind limb 35 min post-treatment due to restoring the blood flow downstream of the blood clot site, which was not achievable in both pPMNP and rtPA groups. The rtPA group showed increased blood perfusion only after 60 min treatment to be similar to the pPMNP-rtPA, while the pPMNP group showed a similar thrombosis condition without any improvement of the perfusion rate (Figure 13b). The time-lapsed hemodynamics results, including ABF (Figure 13c) and IBF (Figure 13d), were shown after different treatments. Before clot lodging, the IBF values were 9.4 ± 1.0 , 7.9 ± 0.9 and 10.1 ± 1.1 mL/min for pPMNP, rtPA, and pPMNP-rtPA, respectively. Nonetheless, the IBF values reduced to nearly 0% for all groups after thromboembolism, due to the complete occlusion of the left iliac artery. Simultaneously, the ABF also reduced to 6 mL/min in all groups. After the treatment, the IBF restored to 0.7 ± 0.3 , 4.8 ± 0.8 , and 4.9 ± 1.3 mL/min for pPMNP, rtPA, and pPMNP-rtPA, which was $8.1 \pm 3.5\%$, $60.7 \pm 8.8\%$, and $46.9 \pm 10.8\%$ of the respective initial value. From 10 to 35 min, there was a significant difference in IBF between rtPA and pPMNP-rtPA, as revealed from the perfusion image (Figure 13b). However, there was no significant difference in IBF between rtPA and pPMNP-rtPA from 40 min to 120 min, but both showed significant difference from pPMNP. In comparison, the ABF did not show dramatic recovery as IBF, although some recovery of ABF was also observed for the rtPA and pPMNP-rtPA groups after 100 min due to downstream restoration of IBF. Most importantly, as the dosage of pPMNP-rtPA was 0.3 U/kg compared to 1.5 U/kg for rtPA, we demonstrated comparable efficacy in restoring blood flow and *in vivo* thrombolysis using only 20% dosage of free rtPA. By allowing the use of a lower rtPA dosage with shortened clot lysis time, this dual targeted nanomedicine approach will be a feasible strategy for improving the efficacy and safety of rtPA in reducing bleeding risk [52]. Overall, the *in vivo* study suggested the clinical feasibility using dual targeted delivery strategy for rtPA and that dual targeted pPMNP is an efficient functional nano-carrier for comparable *in vivo* thrombolysis outcomes at reduced rtPA dosage, which might reduce the hemorrhagic side effects in clinical thrombolytic therapy.

3. Materials and Methods

3.1. Materials

1-(3-Dimethylaminopropyl)-3-ethylcarbodiimide hydrochloride (EDC), *N*-hydroxysuccinimide (NHS), iron (II) chloride tetrahydrate, and iron(III) chloride hexahydrate were purchased from Organics, Thermo Fisher Scientific (Geel, Belgium). Acetone, dichloromethane (DCM), oleic acid, polyvinyl alcohol (PVA) (hydrolyzed, M.W. 30,000–70,000), and plasminogen activator inhibitor-1 (PAI-1) were purchased from Sigma-Aldrich (St Louis, MO, USA). Poly(lactic-co-glycolic acid) (PLGA) (lactide/glycolide = 50/50, molecular weight = 15,000~30,000, intrinsic viscosity = 0.35 ± 0.05 dL/g) was purchased from Green Square Co. (Taoyuan, Taiwan). Recombinant tissue plasminogen activator (rtPA, Actilyse®) was provided from Boehringer Ingelheim (Ingelheim am Rhein, Germany). Avidin and biotin-PEG-maleimide (M.W. 3500) were purchased from Merck (Darmstadt, Germany) and JenKem Technology USA Inc. (Plano, TX, USA), respectively.

3.2. Preparation of Magnetic Nanoparticles

The oleic acid coated iron oxide magnetic nanoparticles (OMNP) were prepared by the co-precipitation method. $\text{FeCl}_3 \cdot 6\text{H}_2\text{O}$ (2.15 g) and $\text{FeCl}_2 \cdot 4\text{H}_2\text{O}$ (0.79 g) were dissolved in 50 mL ddH₂O in a three necks glass reactor. Nitrogen was purged for 10 min to remove oxygen, followed by heating the solution to 60 °C. Five milliliter of NH_4OH was added dropwise with a needle into the reactor and then reacted for 30 min under nitrogen by stirring at 500 rpm. The solution was cooled to room temperature while under continuous nitrogen purging. The magnetic nanoparticles was washed three times with distilled deionized water (ddH₂O) after recovering with a magnet and the final solution pH was adjusted to 5 using 0.1 N HCl. The solution was sonicated for 10 min,

followed by nitrogen purging for 10 min before heating to 60 °C. Ten milliliters of 2.77% (*v/v*) oleic acid solution prepared in acetone was then added dropwise with a needle into the reactor and reacted for 30 min under 500 rpm stirring. Nitrogen purge continued while cooling down the solution to room temperature. After removing acetone by evaporation, OMNPs was dispersed in chloroform to 1% (*w/w*) for storage.

The OMNPs prepared above were entrapped in PLGA polymer matrix by the single emulsion-solvent evaporation method to prepare PLGA MNP (PMNP). Fifty milligram of PLGA was dissolved in 2.5 mL organic solvent mixture (2.25 mL acetone and 0.25 mL DCM), followed by sonicating for 10 min. Five hundred microliters of OMNPs prepared above (10 mg OMNPs in 1 mL chloroform) was added, vortexed for 1 min and sonicated for 1 min in a sonication bath. The mixture was quickly poured into 25 mL phosphate buffered saline (PBS), vortexed for 1 min and sonicated for 5 min (Q700, Qsonica, Newtown, CT, USA). The resulting solution containing PMNPs was added dropwise into 50 mL 0.3% (*w/v*) PVA solution prepared in PBS and stirred at 1000 rpm. After incubating at 30 °C for 12 h, the solution was placed in a rotary evaporator and then dried for 1 h at 30 °C for removing residual solvents and washed twice with ddH₂O using magnetic decantation. To modify the surface of PMNPs with avidin, 1 mg/mL PMNPs in PBS (pH 7.4) was mixed with 0.5 mL EDC (0.5 mg/mL) and 0.5 mL NHS (0.5 mg/mL) prepared in 0.5 M pH 5 MES buffer and rotated at 6 rpm for 1 h at room temperature for the activation of the carboxyl groups in PLGA. After washing twice with PBS, activated PMNP was recovered by magnetic decantation and re-dispersed in 1 mL PBS, followed by adding 1 mL avidin (0.2 mg/mL) in PBS and mixed by rotation at 6 rpm for 3 h at room temperature. After washing twice with PBS, PMNP that was conjugated with avidin (PMNP-avidin) was recovered by magnetic decantation and re-dispersed in 1 mL PBS for immobilization of peptide/rtPA using biotin-PEG-peptide/biotin-PEG-rtPA through avidin-biotin interaction (Figure 1). To prepare biotin-PEG-peptide, 0.65 µg biotin-PEG-maleimide was mixed with 0.21 µg fibrin-avid peptide (GPRPPGSKGC) in 1 mL PBS and then mixed at 4 °C for 24 h. Similarly, 27 µg biotin-PEG-maleimide was mixed with 0.5 mg rtPA in 1 mL PBS at 4 °C for 24 h to obtain biotin-PEG-rtPA. The solutions prepared above were mixed successively with PMNP-avidin, first by adding biotin-PEG-peptide to PMNP-avidin and mixed for 24 h at 4 °C, followed by adding biotin-PEG-rtPA and mixed for another 24 h at 4 °C. Finally, the particles were washed twice with PBS to obtain peptide/rtPA conjugated PLGA magnetic nanoparticles (pPMNP-rtPA). As a control, the peptide conjugated PLGA magnetic nanoparticles (pPMNP) or rtPA conjugated PLGA magnetic nanoparticles (PMNP-rtPA) were also prepared without adding biotin-PEG-peptide or biotin-PEG-rtPA during synthesis (Figure 1).

3.3. Determination of rtPA and Peptide Conjugation

The amount of avidin loading on nanoparticles was measured by the Pierce™ BCA protein assay kit from Thermo Fisher Scientific (Geel, Belgium). All of the samples were collected after modification and dilute with PBS to appropriate concentration. Fifty microliter sample (1 mg/mL) and 1 mL BCA reagent were added into a 2 mL brown centrifuge tube and reacted for 30 min at 37 °C. After cooling to room temperature, the chromogenic product was measured by an UV-Vis spectrophotometer at 562 nm. The loading content of rtPA was determined as mg of protein per mg of nanoparticles. For rtPA loading, the activity of immobilized rtPA was spectrophotometrically determined from its amidolytic activity using S-2288 as a specific protease chromogenic substrate (Chromogenix, Mölndal, Sweden) following that manufacturer's protocols. Two hundred microliter of samples (rtPA, PMNP-rtPA and pPMNP-rtPA) was diluted with 0.2 mL 0.1 M pH 7.4 Tris buffer and incubated at 37 °C for 5 min. Two hundred microliter of S-2288 substrate (1 mM) was added and vortexed immediately before incubating at 37 °C. To stop the enzymatic reaction, 0.1 mL acetic acid (20% (*v/v*)) was added after 30 s and solution absorbance was determined for the chromogenic product using an UV-Vis spectrophotometer at 405 nm (OD₄₀₅) after magnetic separation. The amidolytic activity (U) was calculated as $OD_{405} \times 0.313 \times 0.2/0.5$ using respective nanoparticles as the blank.

3.4. Characterization of Physico-Chemical Properties

The particle morphology of the prepared sample was analyzed using a transmission electron microscope (TEM, JEOL JEM2000 EXII, Tokyo, Japan) at an accelerating voltage of 100 kV. For OMNP, a diluted sample that was prepared in ethanol was used while other samples were prepared in ddH₂O. After dropping a sample solution on the surface of copper grids, it was dried in a 37 °C oven for 24 h and blotted with a filter paper. The sample was stained with 1% (*w/v*) phosphotungstic acid aqueous solution for 1 min before analysis. The particles size distribution was analyzed using a Zetasizer (Nano ZS 90, Malvern Instruments, Malvern UK) at 25 °C. The measurement was carried out by setting equilibration time at 30 s, measurement duration at automatic, number of measurement at 3, and delay between measurements at 5 s. The OMNP sample was prepared by dispersing in ethanol at 0.1 mg/mL, while other samples were prepared by dispersing in ddH₂O. The thermal property of the prepared sample was analyzed using a Q50 thermogravimetric analyzer (TGA) from TA Instruments (New Castle, DE, USA) while using a platinum pan and then purged with nitrogen at 60 mL/min. The temperature was raised from room temperature to 700 °C at a heating rate of 10 °C/min. All of the samples were dried in a 37 °C oven for 24 h before analysis.

The element content of the prepared sample was analyzed using an inductively coupled plasma optical emission spectrometer (ICP-OES, 710-ES, Varian Inc., Palo Alto, CA, USA). All of the samples were digested in 37% HCl for 2 h at 60 °C and diluted with ddH₂O into 15 mL before filtration through a 0.22 µm PVDF filter. The chemical structure of prepared sample was analyzed using X-ray diffraction (XRD, D2 PHASER, Bruker, MA, USA) using Cu-Kα radiation ($\lambda = 1.54060 \text{ \AA}$). The 2θ range was from 10 to 70° with 0.02° increment. All of the samples were dried in a 37 °C oven for 24 h before measurements. The crystalline size was calculated by the Debye–Scherrer equation.

$$d = \frac{k \times \lambda}{\beta \times \cos \theta} \quad (1)$$

In Equation (1), d is the mean size of the crystalline domains, k is a dimensionless shape factor (0.9), λ is the X-ray wavelength, β is the line broadening at half the maximum intensity, and θ is the Bragg angle. The magnetic moment of prepared sample was analyzed using a superconducting quantum interference device (SQUID) magnetometer (MPMS XL-7, Quantum Design, San Diego, CA, USA). The magnetic field-dependent magnetization was measured from −10,000 to 10,000 Oe at 298 °K. All of the samples were dried in a 37 °C oven for 24 h and 40–50 mg of samples was analyzed. The magnetic field guidance of prepared samples was tested in PBS by attaching a magnet (1700 gauss) at side of a tube containing 1 mg/mL nanoparticle for 5 min.

3.5. Fibrin Binding Efficiency and Fibrinolysis Assay

An agar solution was prepared by dissolving 0.2 g low-melting agar in 10 mL pH 7.4 Tris buffer and heated in a microwave. To induce clotting, 5 mg fibrinogen in 1 mL pH 7.4 Tris buffer, 10 mL clotting factor solution (1.8% NaCl and 0.3% CaCl₂), and 5 mL thrombin solution (25 U) were added to the agar solution under stirring. For fibrin binding efficiency, 100 µL solution prepared above was added into a 96-well cell culture plate and incubated at 4 °C for 30 min to form solidified fibrin gel. To prepare fluorescently labelled nanoparticles, 5 µL Cy 5.5 (1 mg/mL) in dimethyl sulfoxide was added to the organic solvent mixture during PMNP and pPMNP preparation. For fibrin binding ability, 0.2 mL of test sample (PBS, 0.1 mg/mL PMNP or 0.1 mg/mL pPMNP) was added to each well and shaken for 10 min. After washing twice with PBS, microscopic images were taken using an inverted fluorescence microscope (Olympus IX71, Tokyo, Japan).

For the agar plate fibrinolysis assay, the solution prepared above was poured into a 15 cm cell culture dish and spread evenly to obtain a homogeneous gel, which was then placed in a 4 °C refrigerator and incubated for 30 min to form solidified fibrin gel. After making nine 4-mm diameter holes on the agar plate as sample reservoirs, 10 µL of sample (20 µU rtPA) and 15 µL plasminogen

prepared in PBS (1 mg/mL) were added into each hole and then incubated for 24 h at 37 °C to induce fibrinolysis. The fibrinolytic activity was determined by measuring the thickness of the clear zone around the sample hole well induced by the fibrinolytic activity of rtPA. The dose-dependent sensitivity of the test was confirmed from the same agar plate assay with 10 to 30 µU free rtPA following the same procedure.

To study the inhibition of rtPA by PAI-1, 50 µM rtPA (free rtPA, PMNP-rtPA, or pPMNP-rtPA) and 50 µM PAI-1 were mixed in 40 µL 0.1 M Tris buffer (pH 7.4). After incubation at 37 °C for different times, 20 µL Tris buffer and 20 µL S-2288 substrate (1 mM) were added and incubated for another 30 min at 37 °C, followed by adding 20 µL acetic acid (20% (v/v)) to stop the reaction. The amidolytic activity was calculated from the solution absorbance at 405 nm after magnetic separation using an ELISA reader, as described above.

3.6. Determination of Thrombolysis Using Rotational Thromboelastometry

Thromboelastography is a method to test blood coagulation efficiency by measuring the viscoelastic properties of developing whole blood clot and used in this study for in vitro thrombolysis assays from the percentage of clot that has lysed at different time points after rtPA treatment [53]. The whole blood that was obtained from Sprague-Dawley (SD) rats using cardiac puncture was citrated and incubated at 37 °C for 30 min before use. Thrombus formation was initiated by adding 300 µL whole blood, 20 µL PBS or rtPA sample (28.9 µU/mL), and 20 µL 12 mM CaCl₂ in the sample cup, after which a thromboelastogram could be recorded with time using rotational thromboelastometry (ROTEM, Delta2000, Tem Innovations GmbH, Munich, Germany). The clot lysis index at different time points was calculated by dividing the amplitude at a given time with the maximum amplitude corresponding to the maximum clot firmness from the thromboelastogram to evaluate the thrombolysis effect that is induced by rtPA in vitro.

3.7. In Vitro Biocompatibility and Hemocompatibility

To test biocompatibility, the in vitro cytotoxicity of nanoparticles was determined using NIH 3T3 cells and MTT assays. Briefly, 1×10^4 NIH 3T3 cells were seeded in a 96-well cell culture plate and then cultured in DMEM medium supplemented with 10% fetal bovine serum at 37 °C in 5% CO₂ atmosphere. After 24 h, the medium was removed and replenished with samples solution containing nanoparticles prepared in fresh medium and cultured for 24 and 48 h before measuring the mitochondria activity by the MTT assay. For MTT assay, the medium was removed and 100 µL MTT solution (10 µL 5mg/mL MTT reagent diluted with 90 µL medium) was added to each well and then incubated at 37 °C in 5% CO₂ for 2 h. After dissolving the formazan crystals with dimethyl sulfoxide, the solution absorbance in each well was determined while using a microplate reader (Synergy HT, BioTek, Winooski, VT, USA) at 570 nm (OD₅₇₀).

To test blood compatibility, the possible hemolysis effect that was induced by nanoparticles was analyzed. Briefly, rat whole blood was collected, washed, and then diluted ten times with in volume with PBS first. 0.3 mL diluted red blood cell solution was mixed with 1.2 mL test sample solution and gently shaken before incubation at 37 °C for 2 h. Deionized water and PBS were used as the positive and negative controls, respectively. After centrifugation, the absorbance of the supernatant solution was recorded using a UV-Vis spectrophotometer from 500 to 650 nm. The difference in solution absorbance at 540 nm (OD₅₄₀) between the sample and the negative control was divided by the difference in OD₅₄₀ between the positive control and the negative control to calculate the hemolysis ratio.

3.8. In Vitro Blood Clot Lysis

For static clot lysis, a blood clot was prepared from rat whole blood after diluting with equal volume PBS. The diluted blood (0.5 mL) was mixed with 100 µL thrombin solution (5 U/mL) in 1.8% NaCl and 0.3% CaCl₂ solution in a 4 mL vial and pipetting for 20 times to form the clot. After 30 min, the vial was washed twice with PBS and 50 µL of sample (25 µU rtPA activity) was added to the vial

containing 2 mL PBS. The vial was placed in a 37 °C oven for 10 min before measuring absorbance of the supernatant solution at 415 nm using a UV-Vis spectrophotometer. For the sample under magnetic guidance, a magnet (80 mm × 50 mm × 10 mm, 1700 gauss) was placed at the bottom of the vial during the incubation period.

For dynamic clot lysis, 1 mL diluted blood was mixed with 0.2 mL thrombin solution and pipetting for 20 times. The blood solution was placed in a silicone tube (4 mm diameter) and then incubated at room temperature for 1 h. After clot formation, the tube was cut into 5-mm long pieces and the blood clot was flushed out from the tube with PBS. The blood clot was placed in a 4 mL vial and 50 µL of sample (50 µU rtPA activity) was added to the vial containing 4 mL PBS. The vial was incubated in a 37 °C or 43 °C oven in a Multi Bio RS-24 programmable rotator at 10 rpm for 10 min and the absorbance of the supernatant solution at 415 nm was measured using a UV-Vis spectrophotometer.

The experiment was performed at 37 °C using a water bath for clot lysis in a flow model in a flow system employing flow occlusion induced by a blood clot (Figure 12a). A 4 mm diameter × 5 mm length blood clot prepared above was lodged tightly within a reduction point at the bottom of a tube where the inner diameter decreased from 4 mm to 3 mm. A fluid pressure gradient was generated to start flow of PBS using a syringe pump at 0.5 mL/min from the top while a magnet 80 mm × 50 mm × 10 mm, 1700 gauss) was placed below the clot for magnetic guidance. At time zero, different samples were introduced into the flow system by injecting 200 µL PBS, pPMNP, rtPA, or pPMNP-rtPA solution (100 µU rtPA) from a side opening and the reperfusion time for dissolution of the clot was measured to determine the lysis efficiency.

3.9. *In Vivo* Thrombolysis Using Rat Embolic Model

A rat embolic model was used with the protocols that the Institutional Animal Care and Use Committee of Chang Gung University approved to determine the thrombolysis efficacy *in vivo*. Male SD rats were anesthetized by intraperitoneal injection with Inactin® (100 mg/kg). Mean arterial pressure was measured by carotid artery cannulation and a pressure transducer. The right iliac artery was cannulated with the tip of the catheter and reached to the bifurcation of abdominal aorta. A 3 mm × 3 mm blood clot was introduced from the right iliac artery, and lodged in the left iliac artery upstream of the pubic epigastric artery. The sample (pPMNP, rtPA, and pPMNP-rtPA) was administered via the right iliac artery and guided by a 0.5 T magnet from the abdominal aorta and iliac artery branch to the iliac artery and the femoral artery for 1 min, followed by magnetic guiding to the lower extremities for 4 min. The guiding cycle was repeated four times. The rate of iliac blood flow (IBF) and aortic blood flow (ABF) were determined by placing ultrasonic flow probes (T206, Transonic System Inc., Ithaca, NY, USA) on the left iliac artery and the aorta upstream of left renal artery, respectively. Real-time, high-resolution blood flow images at different time points after treatment were carried out by laser speckle contrast analysis while using a MoorFLPI laser speckle contrast imager from Moor Instruments (Devon, UK).

3.10. Statistical Analysis

All of the results were presented as mean ± standard deviation (SD), except for *in vivo* experiments, which were presented as mean ± standard error of mean (SEM). For statistical analysis, the data are subject to one-way analysis of variance (ANOVA) and Tukey's test with statistical significance declared with a *p* value of less than 0.05.

4. Conclusions

In the study, we demonstrated the preparation of functional PLGA MNP modified through avidin-biotin interaction for the immobilization of fibrin-avid peptide (GPRPPGGSKGC) and thrombolytic drug (rtPA) in dual targeted thrombolytic therapy *in vitro* and *in vivo*. Iron oxide magnetic nanoparticles were well encapsulated in PLGA MNP, as confirmed by physico-chemical characterization, which allowed for drug delivery through magnetic guidance. Under the optimized

preparation conditions, rtPA retains the same clot-lysis efficiency after conjugation to the dual targeted nanoparticle (pPMNP-rtPA) to facilitate its use in thrombolytic therapy. The magnetic guiding and fibrin binding ability associated with the dual targeted nanoparticle further reveal the preference of pPMNP-rtPA over free rtPA for in vitro and in vivo thrombolysis. The dual targeting thrombolytic nano-drug will have the potential to improve the efficacy of a thrombolytic drug and facilitate in vivo thrombolysis for future clinical application.

Author Contributions: H.-A.C., Y.-H.M., T.-Y.H. and J.-P.C. conceived and designed the experiments; H.-A.C. and T.-Y.H. performed the experiments; H.-A.C., Y.-H.M., T.-Y.H. and J.-P.C. analyzed the data; H.-A.C. and J.-P.C. wrote the paper. All authors have read and agreed to the published version of the manuscript.

Funding: This research was funded by Ministry of Science and Technology, Taiwan grant number NERPD2C0461.

Acknowledgments: We would like to express our appreciation for the financial support provided by Chang Gung Memorial Hospital (CMRPD250023, CMRPD1E0011 and BMRP249). The Microscopy Center in Chang Gung University is acknowledged for the transmission electron microscopy analysis.

Conflicts of Interest: The authors declare no conflict of interest.

References

- Shiber, J.R.; Fontane, E.; Adewale, A. Stroke registry: Hemorrhagic vs ischemic strokes. *Am. J. Emerg. Med.* **2010**, *28*, 331–333. [\[CrossRef\]](#) [\[PubMed\]](#)
- Zivin, J.A. Acute stroke therapy with tissue plasminogen activator (tPA) since it was approved by the U.S. Food and Drug Administration (FDA). *Ann. Neurol.* **2009**, *66*, 6–10. [\[CrossRef\]](#) [\[PubMed\]](#)
- Gurman, P.; Miranda, O.R.; Nathan, A.; Washington, C.; Rosen, Y.; Elman, N.M. Recombinant tissue plasminogen activators (rtPA): A review. *Clin. Pharmacol. Ther.* **2015**, *97*, 274–285. [\[CrossRef\]](#)
- Burrows, F.E.; Bray, N.; Denes, A.; Allan, S.M.; Schiessl, I. Delayed reperfusion deficits after experimental stroke account for increased pathophysiology. *J. Cereb. Blood Flow Metabol.* **2015**, *35*, 277–284. [\[CrossRef\]](#) [\[PubMed\]](#)
- Gravanis, I.; Tsirka, S.E. Tissue-type plasminogen activator as a therapeutic target in stroke. *Expert Opin. Ther. Targets* **2008**, *12*, 159–170. [\[CrossRef\]](#) [\[PubMed\]](#)
- Zamanlu, M.; Farhoudi, M.; Eskandani, M.; Mahmoudi, J.; Barar, J.; Rafi, M.; Omid, Y. Recent advances in targeted delivery of tissue plasminogen activator for enhanced thrombolysis in ischaemic stroke. *J. Drug Target* **2018**, *26*, 95–109. [\[CrossRef\]](#)
- Doane, T.L.; Burda, C. The unique role of nanoparticles in nanomedicine: Imaging, drug delivery and therapy. *Chem. Soc. Rev.* **2012**, *41*, 2885–2911. [\[CrossRef\]](#)
- Bonnard, T.; Gauberti, M.; Martinez de Lizarondo, S.; Campos, F.; Vivien, D. Recent advances in nanomedicine for ischemic and hemorrhagic stroke. *Stroke* **2019**, *50*, 1318–1324. [\[CrossRef\]](#)
- Chu, M.; Shao, Y.; Peng, J.; Dai, X.; Li, H.; Wu, Q.; Shi, D. Near-infrared laser light mediated cancer therapy by photothermal effect of Fe₃O₄ magnetic nanoparticles. *Biomaterials* **2013**, *34*, 4078–4088. [\[CrossRef\]](#)
- Kim, J.Y.; Kim, J.K.; Park, J.S.; Byun, Y.; Kim, C.K. The use of PEGylated liposomes to prolong circulation lifetimes of tissue plasminogen activator. *Biomaterials* **2009**, *30*, 5751–5756. [\[CrossRef\]](#)
- Yu, M.K.; Park, J.; Jon, S. Targeting strategies for multifunctional nanoparticles in cancer imaging and therapy. *Theranostics* **2012**, *2*, 3–44. [\[CrossRef\]](#) [\[PubMed\]](#)
- Ma, Y.-H.; Liu, C.-H.; Liang, Y.; Chen, J.-P.; Wu, T. Targeted delivery of plasminogen activators for thrombolytic therapy: An integrative evaluation. *Molecules* **2019**, *24*, 3407. [\[CrossRef\]](#) [\[PubMed\]](#)
- Ma, Y.-H.; Wu, S.-Y.; Wu, T.; Chang, Y.-J.; Hua, M.-Y.; Chen, J.-P. Magnetically targeted thrombolysis with recombinant tissue plasminogen activator bound to polyacrylic acid-coated nanoparticles. *Biomaterials* **2009**, *30*, 3343–3351. [\[CrossRef\]](#) [\[PubMed\]](#)
- Chen, J.-P.; Yang, P.-C.; Ma, Y.-H.; Wu, T. Characterization of chitosan magnetic nanoparticles for in situ delivery of tissue plasminogen activator. *Carbohydr. Polym.* **2011**, *84*, 364–372. [\[CrossRef\]](#)
- Chen, J.-P.; Yang, P.-C.; Ma, Y.-H.; Tu, S.-J.; Lu, Y.-J. Targeted delivery of tissue plasminogen activator by binding to silica-coated magnetic nanoparticle. *Int. J. Nanomed.* **2012**, *7*, 5137–5149. [\[CrossRef\]](#)
- Hsu, H.-L.; Chen, J.-P. Preparation of thermosensitive magnetic liposome encapsulated recombinant tissue plasminogen activator for targeted thrombolysis. *J. Magn. Magn. Mater.* **2017**, *427*, 188–194. [\[CrossRef\]](#)

17. Liu, C.-H.; Hsu, H.-L.; Chen, J.-P.; Wu, T.; Ma, Y.-H. Thrombolysis induced by intravenous administration of plasminogen activator in magnetoliposomes: Dual targeting by magnetic and thermal manipulation. *Nanomed. Nanotechnol. Biol. Med.* **2019**, *20*, 101992. [[CrossRef](#)]
18. McCarthy, J.R.; Sazonova, I.Y.; Erdem, S.S.; Hara, T.; Thompson, B.D.; Patel, P.; Botnaru, I.; Lin, C.P.; Reed, G.L.; Weissleder, R.; et al. Multifunctional nanoagent for thrombus-targeted fibrinolytic therapy. *Nanomed. Nanotechnol. Biol. Med.* **2012**, *7*, 1017–1028. [[CrossRef](#)]
19. Yurko, Y.; Maximov, V.; Andreozzi, E.; Thompson, G.L.; Vertegel, A.A. Design of biomedical nanodevices for dissolution of blood clots. *Mater. Sci. Eng. C* **2009**, *29*, 737–741. [[CrossRef](#)]
20. Hua, X.; Zhou, L.; Liu, P.; He, Y.; Tan, K.; Chen, Q.; Gao, Y.; Gao, Y. In vivo thrombolysis with targeted microbubbles loading tissue plasminogen activator in a rabbit femoral artery thrombus model. *J. Thromb. Thrombol.* **2014**, *38*, 57–64. [[CrossRef](#)]
21. Zhou, J.; Guo, D.; Zhang, Y.; Wu, W.; Ran, H.; Wang, Z. Construction and evaluation of Fe₃O₄-based plga nanoparticles carrying rtpa used in the detection of thrombosis and in targeted thrombolysis. *ACS Appl. Mater. Interfaces* **2014**, *6*, 5566–5576. [[CrossRef](#)] [[PubMed](#)]
22. Absar, S.; Kwon, Y.M.; Ahsan, F. Bio-responsive delivery of tissue plasminogen activator for localized thrombolysis. *J. Control. Release* **2014**, *177*, 42–50. [[CrossRef](#)] [[PubMed](#)]
23. Juenet, M.; Aid-Launais, R.; Li, B.; Berger, A.; Aerts, J.; Ollivier, V.; Nicoletti, A.; Letourneur, D.; Chauvierre, C. Thrombolytic therapy based on fucoidan-functionalized polymer nanoparticles targeting P-selectin. *Biomaterials* **2018**, *156*, 204–216. [[CrossRef](#)] [[PubMed](#)]
24. Huang, T.; Li, N.; Gao, J. Recent strategies on targeted delivery of thrombolytics. *Asian J. Pharm. Sci.* **2019**, *14*, 233–247. [[CrossRef](#)] [[PubMed](#)]
25. Aruva, M.R.; Daviau, J.; Sharma, S.S.; Thakur, M.L. Imaging thromboembolism with fibrin-avid 99mTc-peptide: Evaluation in swine. *J. Nuclear Med.* **2006**, *47*, 155–162.
26. Thakur, M.L.; Pallela, V.R.; Consigny, P.M.; Rao, P.S.; Vessileva-Belnikolovska, D.; Shi, R. Imaging vascular thrombosis with 99mTc-labeled fibrin alpha-chain peptide. *J. Nuclear Med.* **2000**, *41*, 161–168.
27. Zhao, Y.; Jiang, Y.; Lv, W.; Wang, Z.; Lv, L.; Wang, B.; Liu, X.; Liu, Y.; Hu, Q.; Sun, W.; et al. Dual targeted nanocarrier for brain ischemic stroke treatment. *J. Control. Release* **2016**, *233*, 64–71. [[CrossRef](#)]
28. Luo, Y.; Yang, H.; Zhou, Y.-F.; Hu, B. Dual and multi-targeted nanoparticles for site-specific brain drug delivery. *J. Control. Release* **2020**, *317*, 195–215. [[CrossRef](#)]
29. Zhang, W.; Yu, Z.-L.; Wu, M.; Ren, J.-G.; Xia, H.-F.; Sa, G.-L.; Zhu, J.-Y.; Pang, D.-W.; Zhao, Y.-F.; Chen, G. Magnetic and folate functionalization enables rapid isolation and enhanced tumor-targeting of cell-derived microvesicles. *ACS Nano* **2017**, *11*, 277–290. [[CrossRef](#)]
30. Cui, Y.; Zhang, M.; Zeng, F.; Jin, H.; Xu, Q.; Huang, Y. Dual-targeting magnetic plga nanoparticles for codelivery of paclitaxel and curcumin for brain tumor therapy. *ACS Appl. Mater. Interfaces* **2016**, *8*, 32159–32169. [[CrossRef](#)]
31. Saengruengrit, C.; Ritprajak, P.; Wanichwecharungruang, S.; Sharma, A.; Salvan, G.; Zahn, D.R.T.; Insin, N. The combined magnetic field and iron oxide-PLGA composite particles: Effective protein antigen delivery and immune stimulation in dendritic cells. *J. Colloid Interface Sci.* **2018**, *520*, 101–111. [[CrossRef](#)] [[PubMed](#)]
32. Boyer, C.; Priyanto, P.; Davis, T.P.; Pissuwan, D.; Bulmus, V.; Kavallaris, M.; Teoh, W.Y.; Amal, R.; Carroll, M.; Woodward, R.; et al. Anti-fouling magnetic nanoparticles for siRNA delivery. *J. Mater. Chem.* **2010**, *20*, 255–265. [[CrossRef](#)]
33. Livnah, O.; Bayer, E.A.; Wilchek, M.; Sussman, J.L. Three-dimensional structures of avidin and the avidin-biotin complex. *Proc. Natl. Acad. Sci. USA* **1993**, *90*, 5076–5080. [[CrossRef](#)] [[PubMed](#)]
34. Northrop, B.H.; Frayne, S.H.; Choudhary, U. Thiol-maleimide “click” chemistry: Evaluating the influence of solvent, initiator, and thiol on the reaction mechanism, kinetics, and selectivity. *Polym. Chem.* **2015**, *6*, 3415–3430. [[CrossRef](#)]
35. Ravasco, J.M.J.M.; Faustino, H.; Trindade, A.; Gois, P.M.P. Bioconjugation with Maleimides: A Useful Tool for Chemical Biology. *Chem. Eur. J.* **2019**, *25*, 43–59. [[CrossRef](#)]
36. Wu, S.-L.; Jiang, H.; Hancock, W.S.; Karger, B.L. Identification of the unpaired cysteine status and complete mapping of the 17 disulfides of recombinant tissue plasminogen activator using LC-MS with electron transfer dissociation/collision induced dissociation. *Anal. Chem.* **2010**, *82*, 5296–5303. [[CrossRef](#)]
37. Absar, S.; Nahar, K.; Kwon, Y.M.; Ahsan, F. Thrombus-targeted nanocarrier attenuates bleeding complications associated with conventional thrombolytic therapy. *Pharm. Res.* **2013**, *30*, 1663–1676. [[CrossRef](#)]

38. Chen, J.-P.; Liu, C.-H.; Hsu, H.-L.; Wu, T.; Lu, Y.-J.; Ma, Y.-H. Magnetically controlled release of recombinant tissue plasminogen activator from chitosan nanocomposites for targeted thrombolysis. *J. Mater. Chem. B* **2016**, *4*, 2578–2590. [[CrossRef](#)]
39. Lin, H.; Xu, L.; Yu, S.; Hong, W.; Huang, M.; Xu, P. Therapeutics targeting the fibrinolytic system. *Exp. Mol. Med.* **2020**, 1–13. [[CrossRef](#)]
40. Tang, Z.; Li, D.; Wang, X.; Gong, H.; Luan, Y.; Liu, Z.; Brash, J.L.; Chen, H. A t-PA/nanoparticle conjugate with fully retained enzymatic activity and prolonged circulation time. *J. Mater. Chem. B* **2015**, *3*, 977–982. [[CrossRef](#)]
41. Lalatonne, Y.; Richardi, J.; Pileni, M.P. Van der Waals versus dipolar forces controlling mesoscopic organizations of magnetic nanocrystals. *Nat. Mater.* **2004**, *3*, 121–125. [[CrossRef](#)]
42. Singh, M.; Ulbrich, P.; Prokopec, V.; Svoboda, P.; Šantavá, E.; Štěpánek, F. Effect of hydrophobic coating on the magnetic anisotropy and radiofrequency heating of γ -Fe₂O₃ nanoparticles. *J. Magn. Magn. Mater.* **2013**, *339*, 106–113. [[CrossRef](#)]
43. Danaei, M.; Dehghankhold, M.; Ataei, S.; Hasanzadeh Davarani, F.; Javanmard, R.; Dokhani, A.; Khorasani, S.; Mozafari, M.R. Impact of particle size and polydispersity index on the clinical applications of lipidic nanocarrier systems. *Pharmaceutics* **2018**, *10*, 57. [[CrossRef](#)] [[PubMed](#)]
44. Hermanson, G.T. Chapter 11—(Strept)avidin-Biotin Systems. In *Bioconjugate Techniques*, 3rd ed.; Hermanson, G.T., Ed.; Academic Press: Boston, MA, USA, 2013; pp. 465–505. [[CrossRef](#)]
45. Caruntu, D.; Caruntu, G.; O'Connor, C.J. Magnetic properties of variable-sized Fe₃O₄ nanoparticles synthesized from non-aqueous homogeneous solutions of polyols. *J. Phys. D Appl. Phys.* **2007**, *40*, 5801–5809. [[CrossRef](#)]
46. Wahajuddin Arora, S. Superparamagnetic iron oxide nanoparticles: Magnetic nanoplatforms as drug carriers. *Int. J. Nanomed.* **2012**, *7*, 3445–3471. [[CrossRef](#)] [[PubMed](#)]
47. Torno, M.D.; Kaminski, M.D.; Xie, Y.; Meyers, R.E.; Mertz, C.J.; Liu, X.; O'Brien, W.D., Jr.; Rosengart, A.J. Improvement of in vitro thrombolysis employing magnetically-guided microspheres. *Thromb. Res.* **2008**, *121*, 799–811. [[CrossRef](#)] [[PubMed](#)]
48. Gentile, P.; Chiono, V.; Carmagnola, I.; Hatton, P.V. An overview of poly(lactic-co-glycolic) acid (PLGA)-based biomaterials for bone tissue engineering. *Int. J. Mol. Sci.* **2014**, *15*, 3640–3659. [[CrossRef](#)]
49. McCarthy, J.R.; Patel, P.; Botnaru, I.; Haghayeghi, P.; Weissleder, R.; Jaffer, F.A. Multimodal nanoagents for the detection of intravascular thrombi. *Bioconjug Chem.* **2009**, *20*, 1251–1255. [[CrossRef](#)]
50. Runge, M.S.; Quertermous, T.; Zavodny, P.J.; Love, T.W.; Bode, C.; Freitag, M.; Shaw, S.Y.; Huang, P.L.; Chou, C.C.; Mullins, D.; et al. A recombinant chimeric plasminogen activator with high affinity for fibrin has increased thrombolytic potency in vitro and in vivo. *Proc. Natl. Acad. Sci. USA* **1991**, *88*, 10337–10341. [[CrossRef](#)]
51. Chapurina, Y.E.; Drozdov, A.S.; Popov, I.; Vinogradov, V.V.; Dudanov, I.P.; Vinogradov, V.V. Streptokinase@alumina nanoparticles as a promising thrombolytic colloid with prolonged action. *J. Mater. Chem. B* **2016**, *4*, 5921–5928. [[CrossRef](#)]
52. Liu, S.; Feng, X.; Jin, R.; Li, G. Tissue plasminogen activator-based nanothrombolysis for ischemic stroke. *Expert Opin. Drug Deliv.* **2018**, *15*, 173–184. [[CrossRef](#)] [[PubMed](#)]
53. Whiting, D.; Dinardo, J. TEG and ROTEM: Technology and clinical applications. *Am. J. Hematol.* **2014**, *89*. [[CrossRef](#)] [[PubMed](#)]



Article

Dysregulated FAM215A Stimulates LAMP2 Expression to Confer Drug-Resistant and Malignant in Human Liver Cancer

Po-Shuan Huang ¹, Yang-Hsiang Lin ², Hsiang-Cheng Chi ¹, Yi-Hsin Tseng ³, Cheng Yi Chen ⁴, Tzu-Kang Lin ⁵, Chau-Ting Yeh ² and Kwang-Huei Lin ^{1,2,6,7,*} 

¹ Department of Biochemistry, College of Medicine, Chang Gung University, Taoyuan 333, Taiwan; leo_6813@msn.com (P.-S.H.), nonbalance@gmail.com (H.-C.C.)

² Liver Research Center, Chang Gung Memorial Hospital, Linkou, Taoyuan 333, Taiwan; sam4915@yahoo.com.tw (Y.-H.L.), chauting@adm.cgmh.org.tw (C.-T.Y.)

³ Institute of Stem Cell and Translational Cancer Research, Chang Gung Memorial Hospital at Linkou, and Chang Gung University, Taoyuan 333, Taiwan; akiraest@yahoo.com.tw

⁴ Department of Cell Biology and Anatomy, College of Medicine, National Cheng Kung University, Tainan 70101, Taiwan; cychen@gs.ncku.edu.tw

⁵ Neurosurgery, Fu Jen Catholic University Hospital and School of Medicine, Fu Jen Catholic University, New Taipei City 24205, Taiwan; tklin100@cgmh.org.tw

⁶ Research Center for Chinese Herbal Medicine, College of Human Ecology, Chang Gung University of Science and Technology, Taoyuan 333, Taiwan

⁷ Graduate Institute of Biomedical Sciences, College of Medicine, Chang Gung University, Taoyuan 333, Taiwan

* Correspondence: khlin@mail.cgu.edu.tw; Tel./Fax: +886-3-2118263

Received: 1 April 2020; Accepted: 13 April 2020; Published: 14 April 2020



Abstract: Hepatocellular carcinoma (HCC) is one of the most common and aggressive human malignancies worldwide. Long non-coding (lnc) RNAs regulate complex cellular functions, such as cell growth, differentiation, metabolism, and metastasis. Although deregulation of lncRNA expression has been detected in HCC, many of the hepato-carcinogenesis-associated lncRNAs remain yet unidentified. Here, we aimed to investigate the involvement of a specific HCC-dysregulated lncRNA, FAM215A, and characterize its molecular regulation mechanism. We show for the first time that FAM215A is overexpressed in HCC, and its expression level correlates with tumor size, vascular invasion, and pathology stage. Overexpression of FAM215A accelerates cell proliferation and metastasis in HCC cells. According to Gene Expression Omnibus Dataset analysis, FAM215A is induced in doxorubicin (DOX)-resistant HCC cells. Overexpression of FAM215A increases DOX resistance in two HCC cell lines, and this is associated with enhanced expression of lysosome-associated membrane protein 2 (LAMP2). FAM215A interacts with LAMP2 to protect it from ubiquitination. Together, our results show that the lncRNA, FAM215A, is highly expressed in HCC, where it interacts with and stabilizes LAMP2 to increase tumor progression while decreasing doxorubicin sensitivity.

Keywords: HCC; Long non-coding RNA; FAM215A; Lysosome; LAMP2

1. Introduction

Hepatocellular carcinoma (HCC) ranks among the most common cancers in many countries and is the second most common cause of cancer death worldwide. Most HCC is associated with liver cirrhosis that represents major risk factors (HBV- or HCV-related chronic liver disease, toxins and drugs) for HCC development, being implicated in more than 70% of HCC cases worldwide [1,2]. The lifestyle of a high-calorie, low-fiber diet and lack of exercise are highly correlated with obesity

to cause non-alcoholic fatty liver disease (NAFLD). NAFLD covers a range of clinical diseases from hepatic steatosis to severe inflammatory steatohepatitis (NASH) [3]. A variety of genomic alterations have been identified in fully developed HCC. In the clinic, alpha-fetoprotein (AFP) is the main tumor biomarker available to guide the management of HCC; however, its low accuracy limits its usefulness as a screening test [4]. The survival rate of HCC is usually poor due to the high probability of tumor recurrence and metastasis after treatment. We therefore urgently need to identify novel therapeutic targets and biomarkers, with the goal of developing effective strategies to improve the prognosis of HCC [5].

Traditionally, studies of gene regulation have tended to focus on protein-coding genes. However, multiple lines of evidence from numerous high-throughput genomic platforms suggest that it more strongly reflects the regulatory potential of non-coding RNAs (ncRNAs) than the number of protein-coding genes, even when protein diversification by alternative splicing and post-translational regulation are taken into account [6,7].

Various small ncRNAs, such as siRNAs, miRNAs, and piRNAs, have been studied, and the research has shown that they are highly conserved and involved in transcriptional and posttranscriptional regulation of gene expression through specific base pairing with their targets. Another class of ncRNAs are the long non-coding RNAs (lncRNAs), which are operationally defined as RNAs larger than 200 base-pairs that do not “appear” to have coding potential, are poorly conserved, and regulate gene expression by diverse mechanisms that are complex and not yet fully understood [6].

Some lines of evidences indicate that most nuclear lncRNAs function by guiding chromatin modifiers to specific genomic locations. These lncRNAs recruit DNA methyltransferase 3 (DNMT3) and histone modifiers, such as the polycomb repressive complex (PRC2) and histone H3 lysine 9 (H3K9) methyltransferases. The resultant DNA and histone modifications predominantly correlate with repressive heterochromatin formation and transcriptional repression [7,8]. Many other lncRNA-mediated gene regulation mechanisms have been identified in the cytoplasm. The involved lncRNAs often show sequence complementarity with other transcripts; they may recognize the target by complementary base pairing, leading to modulation of translational processes. The target sites of lncRNAs differ between the so-called cis- and trans-acting lncRNAs; the former control the expression of genes that are positioned near the transcription site of that lncRNA, with their effects sometimes spreading across great distances on the same chromosome; in contrast, trans-acting lncRNAs can affect the expression of independently located genes [7,9].

Although few lncRNAs have been fully characterized, many have been shown to exhibit cell-specific expression and to be associated with cancer. Numerous studies have indicated that lncRNAs modulate cancer initiation and progression by affecting various biological pathways [10]. For example, lncRNAs have been reported to be aberrantly expressed in HCC and to play roles in modulating malignant phenotypes. Maternally expressed gene 3 (MEG3), which is an imprinted lncRNA located on chromosome 14q32.3 within the DLK-1 locus, is downregulated in 60% of HCC cases; this is correlated with increased DNA methylation, reduced tumor cell growth, and increased apoptosis [11]. HOX transcript antisense RNA (HOTAIR) is expressed from the developmental HOX-C locus located on chromosome 12q13.13, and was found to be up-regulated in patients with large primary HCC and those with nodal involvement. HOTAIR acts as an oncogene; it may positively regulate the expression levels of multiple genes involved in promoting metastatic processes, such as vascular endothelial growth factor (VEGF) and matrix metalloproteinase 9 (MMP9). HOTAIR acts as a scaffolding molecule that binds polycomb repressive complex 2 (PRC2) and lysine-specific demethylase 1 (LSD1) and increases the recruitment of enzymes involved in epigenetic modification to repress tumor suppressor genes [12–14].

Lysosomes are acidic (pH 4.5–5) catabolic organelles that are found in all mammalian cells. They are responsible for the disposal and recycling of worn-out and damaged cellular macromolecules and organelles, and the digestion of extracellular and foreign materials that are delivered to them by endocytosis, autophagy, and phagocytosis [15]. It has been well documented that during the process

of cellular transformation and cancer progression, lysosomes exhibit changes in their localization, composition, and volume; moreover, lysozymes can, through the release of their enzymes, promote invasive growth, angiogenesis, and drug resistance [15,16]. Lysosomal-associated membrane protein (LAMP) 1 and 2 comprise nearly 50% of the lysosomal transmembrane, and they are essential for maintaining the structural integrity of the lysosomal compartment [15]. In addition to its expression on the lysosomal membrane, LAMP2 is reportedly relocalized to the cell surface of some highly metastatic tumor cells, such as melanoma and colon cancer cells [17,18]. In HCC, LAMP2 is required for tumor growth and promotes tumor recurrence [19]. Currently, we aimed to determine the function of a specific HCC-dysregulated lncRNA, FAM215A, and characterize its molecular action involvement of LAMP2 function.

2. Materials and Methods

2.1. Human HCC Specimens and Cancer Cell Lines

All clinical studies were performed in accordance with the approved guidelines of the Chang Gung Memorial Hospital Institutions Review Board (IRB: 201601542B0). Informed consent was obtained from all patients involved in this study. The human hepatoma cell lines, Hep3B, Mahlavu, and J7, were routinely grown in DMEM supplemented with 10% fetal bovine serum. Cells were cultured at 37 °C in a humidified atmosphere of 95% air and 5% CO₂.

2.2. Quantitative Reverse Transcription-Polymerase Chain Reaction (qRT-PCR)

Total RNA was purified using the TRIzol reagent (Life Technologies, Carlsbad, CA, USA) according to the supplier's protocol (MAN0016385), and cDNA was synthesized using a Superscript II kit (Life Technologies, Karlsruhe, Germany). The sequences of the primer pairs for FAM215A amplification were: forward primer, 5'-GCGGTAGCTCACCAATCCAA-3', and reverse primer, 5'-CTCCTTATTAAACGCACTGTTGTATCA-3'. All reactions were conducted in an ABI PRISM 7500 sequencer (Applied Biosystems, Foster City, CA, USA). The other primers information for qRT-PCR were listed in the Supplementary Table S1.

2.3. Rapid Amplification of cDNA Ends (RACE)

A partial sequence of lncRNA-FAM215A was obtained from NCBI, and RACE PCR was performed to obtain the full-length sequence. Total RNA from Hep3B cells was used as the template for nested-PCR reactions using a 5'/3'-RACE Kit, 2nd Generation (Catalog No. 03353621001; Roche Applied Science, CA, USA, according to the manufacturer's instructions. The products obtained from RACE PCR were cloned into a TA vector and sequenced.

2.4. Fractionation of Nuclear and Cytoplasmic RNA

To obtain nuclear and cytoplasmic RNA fractions, cells were washed twice with ice-cold PBS and centrifuged for 5 min at 290 g at 4 °C. Each cell pellet was resuspended in 1 mL RSB buffer (10 mM Tris-Cl [pH 7.4], 10 mM NaCl, and 3 mM MgCl₂) and incubated for 3 min on ice. Cells were pelleted at 1500 g for 3 min at 4 °C, the supernatant was discarded, and the cells were lysed by gentle resuspension in 150 µL RSBG40 buffer (10 mM Tris-Cl [pH 7.4], 10 mM NaCl, 3 mM MgCl₂, 10% glycerol, and 0.5% Nonidet P-40). Samples were centrifuged at 4500 g for 3 min at 4 °C. The supernatant (cytoplasmic fraction) was collected in a new Eppendorf tube, and 1 mL TRIzol reagent was added to each sample (nuclear pellet and cytoplasmic supernatant) to extract the relevant RNA fractions.

2.5. Establishment of FAM215A-Overexpressing Cells

The FAM215A plasmid was cloned into expression vector pLAS5w.PeGFP-I2-Bsd and prepared using an EasyPrep EndoFree Maxi Plasmid Extraction Kit (DPT-BA17; Biotools Co., Ltd., Taipei, Taiwan). The generated plasmid was transfected to Mahlavu and J7 cells using a lentivirus-based method and a

FAM215A-encoding lentivirus (System Biosciences). The plasmid and lentiviral packaging plasmids were co-transfected to Hek-293T cells using a Turbofect Reagent Kit (Thermo Fisher Scientific, Waltham, MA, USA), and produced a virus in Hek-293T cell. The Mahlavu and J7 cells were infected with viruses collected from 24 h cultures of virus-producing Hek-293T cells. After 48 h of incubation, cells were transferred to medium containing blasticidin (3 µg/mL) for selection of infected cells, and FAM215A expression was confirmed by qRT-PCR.

2.6. Establishment of FAM215A-Knockdown Cells

The FAM215A shRNA plasmid was constructed by following the guidelines of the TRC shRNA Design Process from the National RNAi Core Facility (Institute of Molecular Biology, Academia Sinica, Taipei, Taiwan), and cloning the obtained shRNA sequence into the pLKO-TRC001 vector. The primers used to construct the sh-FAM215A#1 plasmid were: forward primer, 5'-CCGG GGTAGCTACCAATCCAATGCCTCGAGGCATTGGATTGGTGAGCTACCTTTT-3'; and reverse primer, 5'-AATTAAAAAGGTAGCTACCAATCCAATGCCTCGAGGCATTGGA TTGGTGAGCT ACC-3'. Those used to construct the sh-FAM215A#2 plasmid were: forward primer, 5'-CCGGTTTGGGATGGTTGATTAGGACCTCGAGGTCCTAATCAACCATCCCAAATTTT-3'; and reverse primer, 5'-AATTAAAAATTTG GGATGGTTGATTAGGACCTCGAGGTCCTAATCAA CCATCCCAA-3'. Each plasmid was transfected to Hep3B and J7 cells by a lentivirus-based method. The lentivirus of shRNA FAM215A was purchased from System Biosciences. The plasmid and lentiviral packaging plasmids were co-transfected to Hek-293T cells using the Turbofect Reagent, and produced virus in Hek-293T cell. After 24 h, viral soup was collected and used to infect Hep3B and J7 cells. After 48 h of incubation, the cells were transferred to a medium containing puromycin (0.3 µg/mL) for the selection of lentivirus-infected cells, and FAM215A expression was confirmed by qRT-PCR.

2.7. Establishment of LAMP2-Overexpressing and -Knockdown Cells

The LAMP2 plasmid was cloned into the pcDNA3 expression vector, which was transfected to FAM215A-knockdown Hep3B and J7 cells using the Turbofect Reagent. LAMP2 expression was confirmed by Western blot analysis. LAMP2 shRNAs were purchased from the National RNAi Core Facility (Institute of Molecular Biology, Academia Sinica, Taiwan). Stable LAMP2-knockdown Mahlavu and J7 cell lines infected with lentivirus-expressing shRNA against LAMP2 were established by culturing cells in selection medium consisting of DMEM with 10% fetal bovine serum and puromycin (0.3 µg/mL).

2.8. Wound-Healing Assay

To assess the cell migration capacity, 1.5×10^6 cells/well were seeded to 6-well plates in 10% FBS DMEM and incubated for 24 h. A pipette tip was used to scratch (wound) the monolayer, and the medium was changed to 1% DMEM. The same positions were recorded under a microscope at 0 to 12 h post-wounding.

2.9. Invasion and Migration Assay

To assess cell invasive capacity, we used transwell chambers coated with (to assess invasion) or without (to assess migration) Matrigel (Collaborative Biomedical Products, Bedford, MA, USA). Briefly, 4×10^4 cells in serum-free DMEM were seeded to the upper chambers of transwell filter devices; DMEM containing 20% FBS was added to the lower chambers, and the devices were incubated overnight. The next day, the migrated or invaded cells on the underside of the filter were stained with crystal violet and visualized with a microscope.

2.10. Cell Proliferation Assay

Cells were seeded at 3×10^4 cells in a 6-well plate and incubated for 1 to 5 days. Staining with 0.4% Trypan Blue Solution was used to assess cell viability (viable cells excluded the dye), and a hemocytometer was used to count cell numbers.

2.11. Western Blot Analysis

Protein expression levels were determined by immunoblot analysis, which was performed according to a previous description [20]. Primary antibodies were obtained to detect LAMP2 (Abcam, Cambridge, MA, USA, ab-125068), TWIST (GeneTex, Irvine, CA, USA; GTX127310), SLUG, SNAIL, ERK, and phospho-ERK (Cell Signaling, Hitchin, UK; #9585, #3895, #4695 and #4370, respectively).

2.12. Ubiquitination Assay

Cells were treated for 4 h with the proteasome inhibitor, MG132 (10 μ M), and whole-cell lysates were extracted. The cell lysates were incubated with protein A (Santa Cruz Biotechnology, Santa Cruz, CA, USA) for 1 h to eliminate non-specific binding, and then with anti-LAMP2 (Abcam, Cambridge, MA, country, ab-125068) overnight at 4 °C. Total lysates were then incubated with protein A for 1 h at 4 °C and centrifuged, and the pelleted proteins were eluted from the beads by being heated in 50 μ L of SDS loading buffer for 5 min. Ubiquitinated LAMP2 was detected by Western blot analysis using an anti-ubiquitin antibody (Santa Cruz Biotechnology; sc-8017).

2.13. Drug Resistance Assay

The MTT assay was used to assess the viability of cells treated with doxorubicin (5 μ M), cisplatin (10 μ M), or sorafenib (2 μ M). The cells were seeded at 3×10^4 cells in 96 well plate, grown for 1–5 days, and subjected to the MTT assay (Thiazolyl Blue Tetrazolium Bromide, 298-93-1, Sigma-Aldrich, St. Louis, MO, USA).

2.14. Lysosomal Content Assay

Cells were incubated with LysoTracker Red dye (LysoTracker™ Red DND-99, L7528, Carlsbad, CA, USA) for 1 h at 37 °C in the dark, washed three times with PBS, and fixed in 3.7% formaldehyde for 10 min. Fluorescent images were captured and recorded using a fluorescent microscope and a CCD camera. The images were analyzed and quantified using the Image J software.

2.15. RNA Immunoprecipitation (RIP)

Cells were washed twice with ice-cold PBS, removed from the culture plate using a cell scraper, and placed in a 10-cm dish containing 1 mL of ice-cold polysomal lysis buffer (100 mM KCl, 5 mM MgCl₂, 10 mM HEPES [pH 7.0], 0.5% NP40, 1 mM DTT, 50 U RNase inhibitor, and protease inhibitor). The resulting suspension was passed through a 27.5-G needle eight times to promote cell lysis. Whole-cell extracts were collected by centrifugation (12,000 rpm, 15 min) and pre-cleared with magnetic protein-A beads (Invitrogen) at 4 °C for 1 h. For immunoprecipitation, anti-LAMP2 was added to the pre-cleared extracts and the mixtures were incubated at 4 °C overnight. Magnetic protein-A beads were added to the IP samples and the mixtures were rotated for 1 h at 4 °C. The beads were pelleted and washed with polysomal lysis buffer. After several washes, 20 U of DNase I (Roche) and 10X reaction buffer was added and the mixtures were incubated at 37 °C for 15 min to remove contaminating DNA. Finally, 1 mL of TRIzol reagent was added to the beads and the RNA was extracted.

2.16. Mouse Xenograft Model

The metastatic ability of FAM215A-knockdown J7 cells was determined. Briefly, FAM215A-knockdown and shControl J7 cells (5×10^5 /100 μ L PBS) were intravenously injected to the tail veins of severe combined immunodeficiency (SCID) mice (n = 5/group). All animals were sacrificed at 4 weeks

after tumor inoculation, and lungs were removed. For establishment of solid tumors in nude mice ($n = 5/\text{group}$), 1×10^6 stable FAM215A-knockdown J7 cells/100 μL PBS were subcutaneously injected and tumor growth was measured. When J7 shControl tumors reached $>50 \text{ mm}^3$ in volume, mice were injected intraperitoneally with doxorubicin (4 mg/kg body weight) twice per week. Animal experiments were performed in accordance with the United States National Institutes of Health guidelines and the Chang-Gung Institutional Animal Care (Taoyuan, Taiwan) and Use Committee Guide for Care and Use of Laboratory Animals.

2.17. Statistical Analysis

Statistical analyses were carried out using means and standard deviations, one-way analysis of variance (ANOVA), and Tukey's honest significant difference post-hoc test.

3. Results

3.1. lncRNA FAM215A Is Up-Regulated in Hepatocellular Carcinoma and Is Associated with Tumor Progression and Metastasis

Our previous microarray analysis identified the lncRNA, FAM215A, as being highly expressed and dysregulated in human hepatoma samples [21]. To verify the alteration of FAM215A expression in HCC, 156 paired HCC tissues and corresponding adjacent normal tissues were collected and qRT-PCR was used to assess the levels of FAM215A. Indeed, FAM215A expression was found to be significantly upregulated in 78% (123 of 156, ≥ 1.5 fold) of the cancerous tissue samples compared with their normal counterparts (Figure 1A). The sequence of FAM215A is presented in Figure 1B. The encoding gene is located on chromosome 17 in humans; it consists of a single 773-nt exon, as determined by RACE (rapid amplification of cDNA ends) assay in Hep3B cells (Supplemental Figure S1A). To examine the physiological significance of FAM215A overexpression in HCC, we assessed whether it was associated with various clinicopathological features of HCC patients. Indeed, high FAM215A expression was significantly correlated with tumor size, vascular invasion, and pathology stage in HCC, and FAM215A upregulation was also closely correlated with the recurrence-free survival of HCC patients (Figure 1B,C). The genes encoding lncRNAs constitute a large fraction of the mammalian transcriptome, yet relatively few lncRNAs have been subjected to a comprehensive, high-quality annotation of their gene structure and boundaries [22]. Similar to proteins, the functions of lncRNAs can depend on their subcellular localization [23]. Here, we found that FAM215A is expressed in both nuclear and cytoplasmic fractions of Mahlavu and J7 cells. In these experiments (Supplemental Figure S1B), GAPDH was used as a cytoplasmic marker and U1 was used as a nuclear marker.

3.2. FAM215A Promotes HCC Cell Metastasis and Proliferation

To investigate the potential role of FAM215A in HCC cells, we established stable expression lines using Mahlavu and J7 cells. qRT-PCR assays verified that FAM215A expression was significantly increased in the stable expression lines (Figure 1D). A wound-healing assay showed that overexpression of FAM215A significantly increased cell migration in Mahlavu and J7 cells compared with the corresponding control cells (Figure 2A). Similarly, a transwell assay revealed that migration and invasion were significantly increased in Mahlavu and J7 cells overexpressing FAM215A (Figure 2B), as were cell metastasis and cell proliferation (Figure 2D). We generated Hep3B and J7 cells with stable knockdown of FAM215A, as verified by qRT-PCR assays (Figure 1E), and found that the significant depletion of FAM215A decreased cell metastasis and proliferation (Figure 2C, E). We also assessed the epithelial-mesenchymal transition (EMT), which is classically associated with the relocation of cells from a basement membrane microenvironment into a fibrillar ECM [24,25]. Upon knockdown of FAM215A, many EMT-related transcription factors, such as SNAIL, SLUG, and TWIST, were repressed, as assessed by Western blot analysis (Supplemental Figure S1C). Extracellular signal-related kinase 1/2 (ERK1/2) is a member of the mitogen-activated protein kinase (MAPK) family and is reportedly associated with

cell proliferation [26]. Interestingly, knockdown of FAM215A repressed the phosphorylation of ERK (Supplemental Figure S1E). Our findings clearly indicate that FAM215A plays an oncogenic role in HCC cell lines.

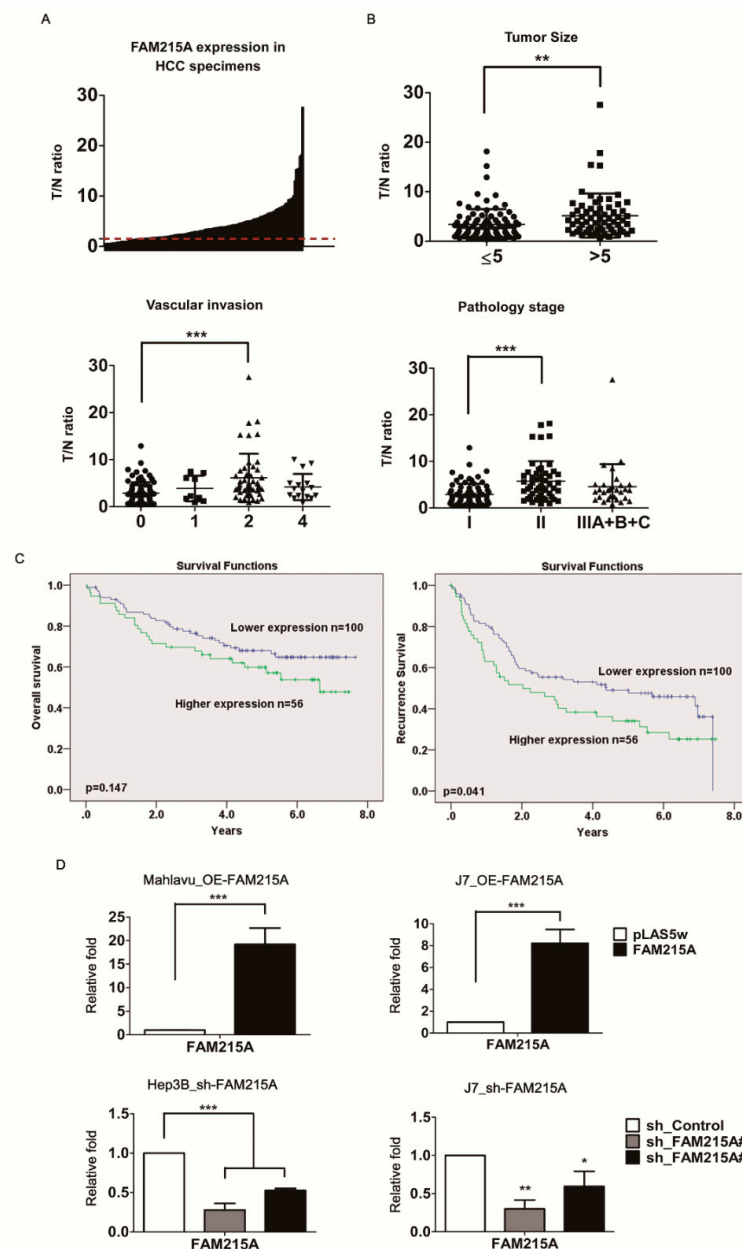


Figure 1. FAM215A dysregulated in HCC and correlated with HCC tumorigenesis. To verify the role and expression of FAM215A in 156 pairs of HCC clinical specimens by qRT-PCR. (A) FAM215A is highly expressed in 156 pairs of HCC specimens. (B) Clinical significance of FAM215A. (C) Overall survival or recurrence free survival. The average value of expression is the cutoff (high or low). (D) Overexpression or depletion of FAM215A cells by using lentivirus. Expression of FAM215A was determined by qRT-PCR. 18s rRNA was used as the loading controls. Data are presented as means \pm s.d. (* $p < 0.05$; ** $p < 0.01$; *** $p < 0.001$) of three independent experiments. Data show as tumor/adjacent normal (T/N ratio). Vascular invasion: 0. Absent, 1. Capsular vein invasion, 2. Portal vein tumor thrombosis (micro), 3. Portal vein tumor thrombosis (grossly) and 4. Portal vein tumor thrombosis (gross and micro). Pathology stage is according to TNM stage: Stage I. T1, Stage II. T2 and Stage III. T3-4. The square, triangle and circle are used to indicate the labels of different pathological groups.

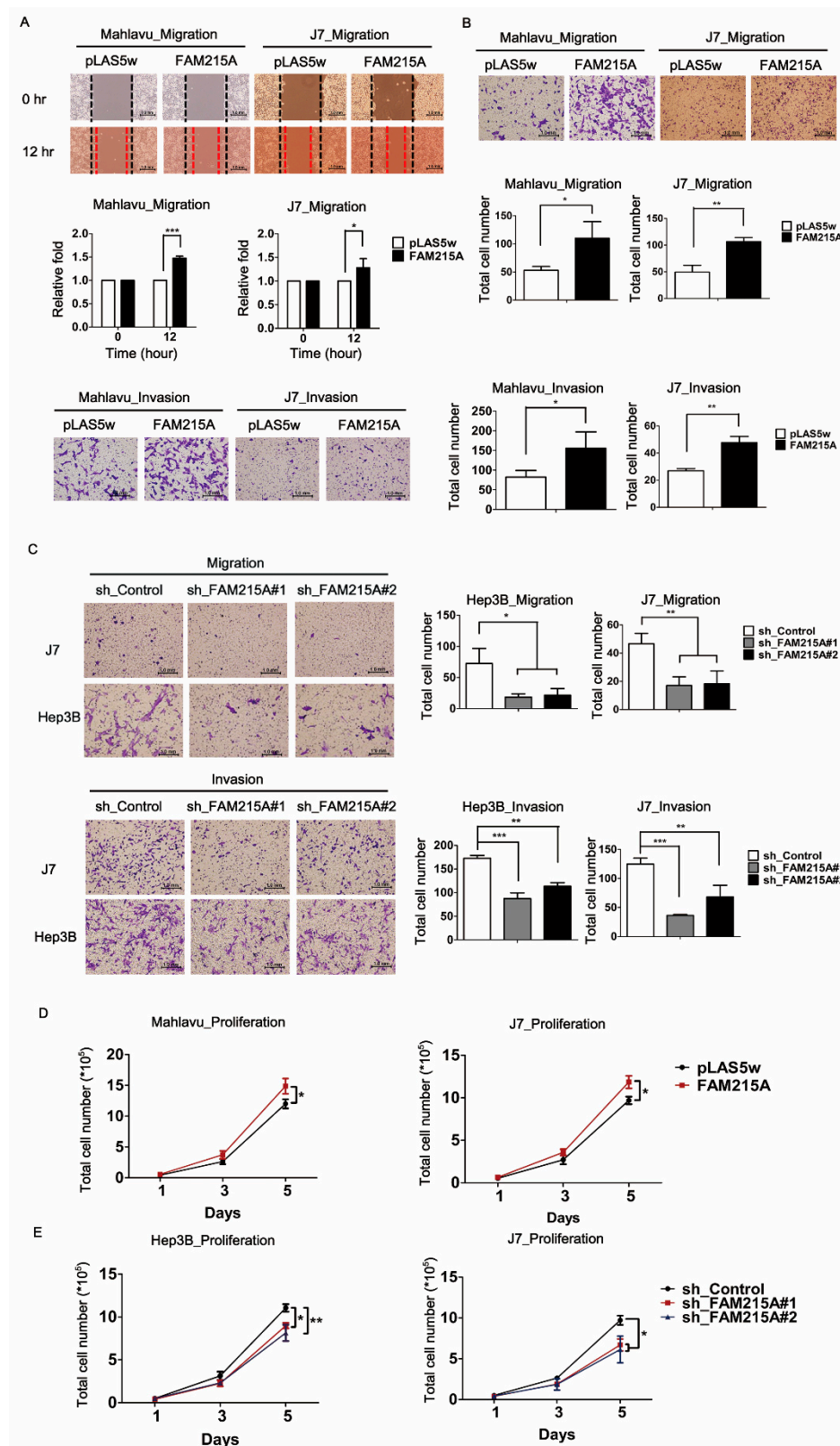


Figure 2. FAM215A promotes cell metastasis and proliferation in HCC. Migration and invasion capacity in FAM215A-expressing or depletion cells were determined by (A) Wound healing assay, (B) Transwell assay in Mahlavu and J7 cell lines. (C) Migration and invasion ability assayed by transwell in Hep3B and J7 cell lines. (D,E) Proliferation rate measured by the total cell numbers (1-5 days). Data are presented as means \pm SD of three independent experiments (*, $p < 0.05$; **, $p < 0.01$; ***, $p < 0.001$).

3.3. FAM215A Promotes Doxorubicin Resistance and Is Highly Expressed in Doxorubicin-Resistant HCC Cells

Chemoresistance is a major obstacle limiting the success of systemic chemotherapy and targeted therapy for patients with advanced HCC. Doxorubicin (DOX) is one of the most widely used anti-HCC drugs for chemotherapy [27]. Analysis of the Gene Expression Omnibus (GEO) datasets [28] revealed that FAM215A is specifically induced in DOX-resistant HCC cells (7.24-fold) but not in cisplatin (CP)-resistant HCC cells. To verify this result, we used qRT-PCR to examine the expression of FAM215A in Hep3B and J7 cells treated with various doses of DOX. Our results revealed that doxorubicin treatment induced FAM215A by ~1.8–2.2-fold and 2.3–5.5-fold in Hep3B and J7 cells, respectively (Figure 3A). To ascertain the importance of FAM215A to drug resistance in HCC cells, we performed MTT assays on FAM215A-overexpressing and -knockdown HCC cells treated with Doxorubicin. Indeed, our results revealed that FAM215A increases the Doxorubicin resistance of HCC cells (Figure 3B). As Doxorubicin induces apoptosis by activating caspase-3 [29], we assessed the level of activated caspase-3 in Doxorubicin-treated FAM215A-overexpressing and -knockdown HCC cells. Our results indicated that FAM215A represses the Doxorubicin-induced activation of caspase-3 in the tested HCC cell lines (Figure 3C). Our findings indicate that FAM215A promotes Doxorubicin resistance in HCC cells.

3.4. FAM215A Increases HCC Progression and Drug Resistance through LAMP2

Similarly, cells treated with Cisplatin or Sorafenib in FAM215A-overexpression or -knockdown conditions, the same results that are consistent with the treated doxorubicin can be obtained by MTT assay (Supplemental Figure S1D,E). However, cisplatin did not affect FAM215A expression (Supplemental Figure S1F). Based on the FAM215A influence on different drugs' sensitivity, we examined the lysosome expression of strong correlation with the multidrug resistance (MDR) of cancer cells [30]. We found that overexpression and knockdown of FAM215A will positively affect the lysosomal content, as assessed by LysoTracker (Figure 4A). Lysosomes are membrane-bound intracellular organelles that receive macromolecules delivered by endocytosis, phagocytosis, and autophagy for degradation and recycling [31]. The lysosomal membranes contain several highly N-glycosylated proteins, including LAMP1 and LAMP2 [32]. LAMP2A expression in HCC contributes to tumor cell viability and promotes tumor growth and recurrence. Thus, it has been speculated that LAMP2A could be targeted as a novel treatment strategy for HCC [19]. Indeed, inhibition or genetic knockdown of LAMP2A resulted in the sensitization of tumor cells to Doxorubicin and radiation therapy [16]. Here, we found that FAM215A was affected by different doses of Doxorubicin (Figure 3A). We also observed that LAMP2 and FAM215A exhibited a positive correlation in Hep3B and J7 cells treated with different doses of Doxorubicin (Figure 4B). The protein expression level of LAMP2 was increased in FAM215A-overexpressing HCC cells and decreased in FAM215A-knockdown HCC cells (Figure 4C). To further verify the role of LAMP2 in HCC cells, we established LAMP2-depleted Mahlavu and J7 cells. The proliferation and viability of LAMP2-knockdown cells were reduced by Doxorubicin treatment (Figure 4D). To address the possible involvement of LAMP2 in the FAM215A-mediated promotion of doxorubicin resistance, LAMP2 was re-expressed in FAM215A-knockdown J7 and Hep3B cells. Whereas the knockdown of FAM215A in J7 and Hep3B cells inhibited their Doxorubicin resistance, this parameter was restored following the re-expression of LAMP2 (Figure 5A). Our findings indicate that FAM215A increases LAMP2 expression to induce Doxorubicin resistance in HCC cells.

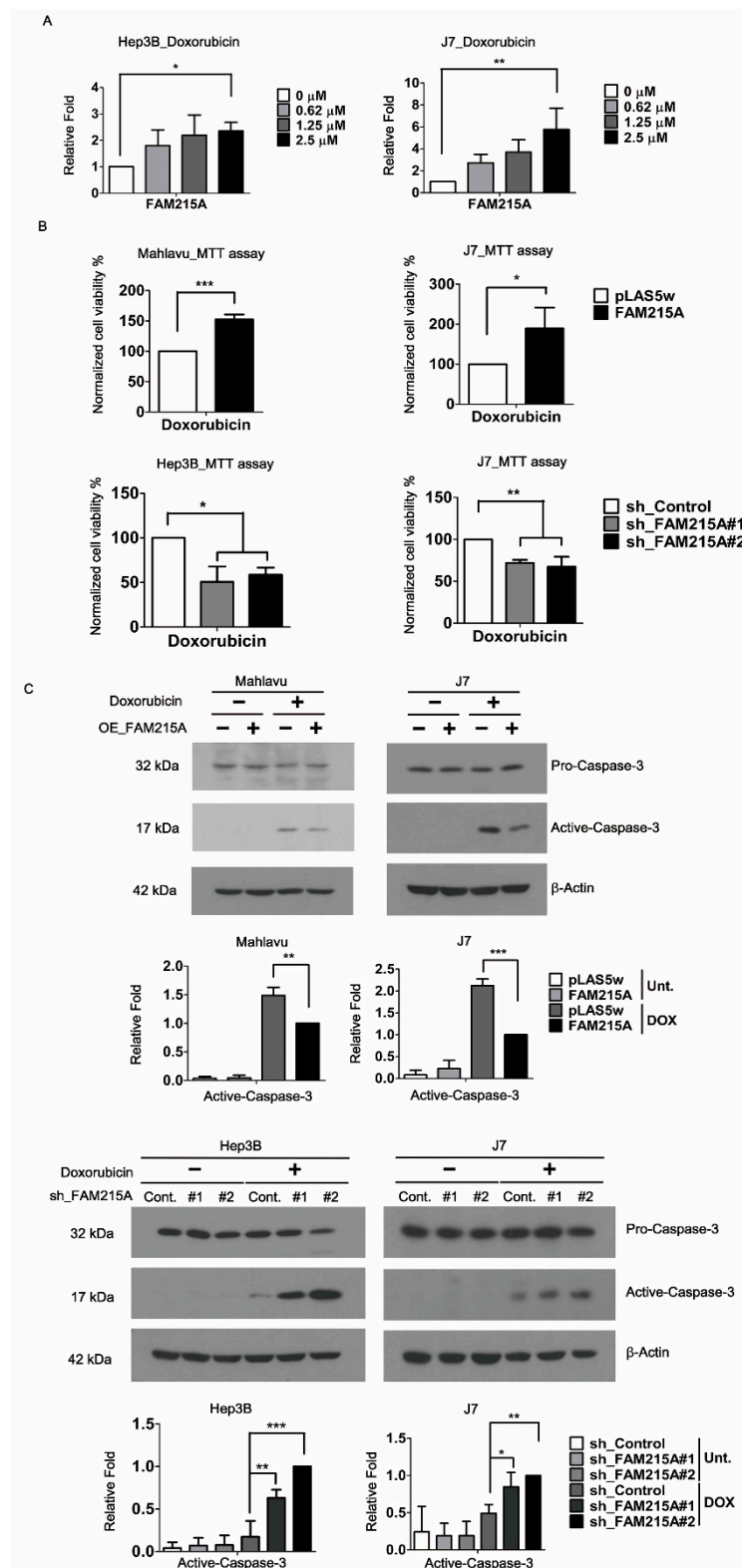


Figure 3. FAM215A is regulated by Doxorubicin and inhibits apoptosis. (A) Doxorubicin (0–2.5 μ M) regulates FAM215A expression in Hep3B and J7 cells determined by qRT-PCR. (B) Cell viability treated with Doxorubicin with/without FAM215A expression. The data are normalized to the untreated groups. (C) Expression of apoptosis marker active caspase-3 and the pro-caspase-3 detected in FAM215A-expressing or knockdown HCC cells treated with Doxorubicin 5 μ M for 24 h by western blot. 18s rRNA and β -Actin was used as the loading controls. Data are presented as means \pm SD of three independent experiments (*, $p < 0.05$; **, $p < 0.01$; ***, $p < 0.001$).

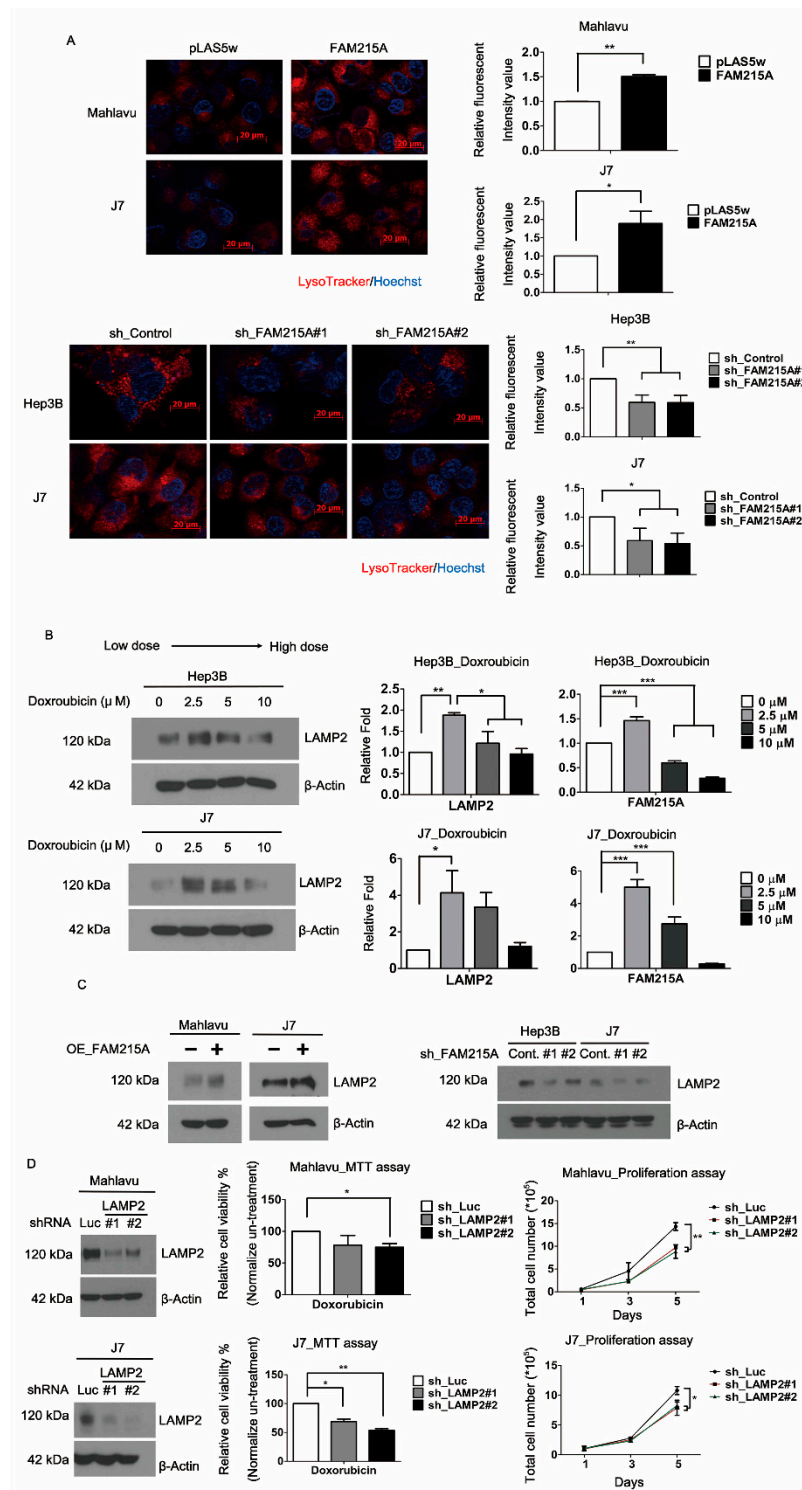


Figure 4. FAM215A affects lysosomes and the oncogene LAMP2 expression in HCC. **(A)** Lysosome expression (red fluorescent) in FAM215A-expressing or knockdown J7 cells determined by LysoTracker. Blue fluorescent is Hoechst that indicates nucleus. The signal was detected by fluorescence microscopy images and analysis with ImageJ. **(B)** The effects of Doxorubicin (0–10 μM, 24 hours) on the expression of FAM215A and LAMP2 detected by Western blot and qRT-PCR. **(C)** Expression of LAMP2 in FAM215A-expressing or knockdown cells assayed by Western blot. **(D)** Proliferation rate measured by MTT in LAMP2-depleted Mahlavu and J7 cells with/without 5 μM Doxorubicin for 24 h. All the data are normalized with un-treatment groups. Data are presented as means ± SD of three independent experiments (*, $p < 0.05$; **, $p < 0.01$; ***, $p < 0.001$).

3.5. FAM215A Interacts with and Stabilizes LAMP2

To further investigate the mechanism by which FAM215A affects LAMP2 expression, we used cycloheximide (CHX) treatment to examine the protein stability of LAMP2 in FAM215A-knockdown and -overexpressing cells. We found that the protein stability of LAMP2 was repressed by FAM215A knockdown and increased by FAM215A overexpression in J7 or Mahlavu cells (Figure 5B). To test whether this stability change involved proteasome-mediated degradation, we assessed the ubiquitination of LAMP2 in MG132-treated FAM215A-overexpressing or -knockdown HCC cells. We found that LAMP2 ubiquitination was decreased in FAM215A-overexpressing J7 or Mahlavu cells, whereas it was increased in FAM215A-repressing Hep3B and J7 cells (Figure 5C). We further used an RNA immunoprecipitation (RIP) assay to determine whether FAM215A and LAMP2 interacted in HepG2 or J7 cells, and found that FAM215A interacts with LAMP2 (Figure 5D) to increase its protein stability in HCC cells.

3.6. FAM215A Increases HCC Progression and Drug Resistance In Vivo

To determine whether the in vitro effects of FAM215A could be replicated in vivo, we used xenograft mouse models. Indeed, tumors derived from FAM215A-knockdown J7 cells administered by tail vein injection exhibited less tumor metastasis compared to those of mice injected with control cells (Figure 6A). In metastatic tumors found in the lungs of such mice, LAMP2 expression was decreased in mice with FAM215A-knockdown cell-derived tumors compared to mice injected with control cells (Figure 6B). To validate the role of FAM215A in tumor formation and DOX resistance, FAM215A-depleted J7 cells were subcutaneously injected into nude mice. Our results revealed that mice injected with FAM215A-knockdown cells displayed decreased tumor growth compared to mice injected with control cells (Figure 6C). We also examined whether stable knockdown of FAM215A increased the DOX sensitivity of J7 cell-derived tumors in mice. DOX was administered twice a week via intraperitoneal injection, beginning when the tumor volume of the J7 control group reached $\sim 50 \text{ mm}^3$. Indeed, our data showed that FAM215A knockdown was associated with decreased tumor growth and further repression of the tumor size in DOX-treated mice. The slope of the growth curve was decreased nearly 51% (slope, Control-DOX 11.84/30.28 versus sh-FAM215A-DOX 0.88/4.41) (Figure 6C,D). The expression levels of FAM215A and LAMP2 were decreased in the tumor tissues with FAM215A-knockdown cell-derived tumors compared to mice injected with control cells (Figure 6E,F). Together, our findings clearly indicate that FAM215A increases tumor progression and DOX resistance in HCC by interacting with and increasing the stability of LAMP2 (Figure 6G).

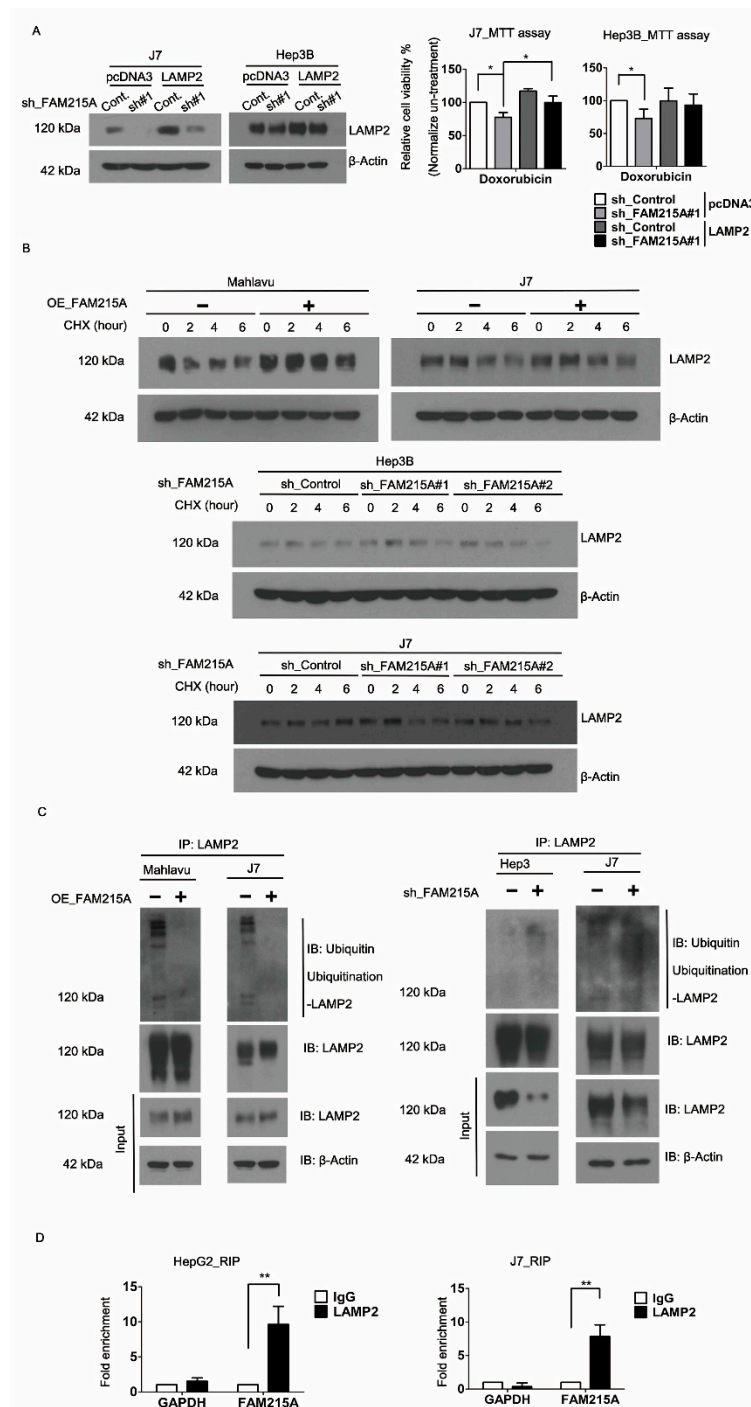


Figure 5. FAM215A confers Doxorubicin resistance in HCC by affecting the LAMP2 stability. **(A)** To restore LAMP2 expression in FAM215A knockdown of Hep3B and J7 cell lines detected by Western blot. The cell viability assay was performed on MTT assay with Doxorubicin 5 μ M 24 h. **(B)** The protein stability of LAMP2 was assessed by treatment CHX 10 μ g for 1–6 h in FAM215A-expressing or knockdown cells detected by Western blot. **(C)** The ubiquitination of LAMP2 was assessed by immunoprecipitation (IP) that was treated with MG132 for 4 h in FAM215A-expressing or knockdown cells. **(D)** Interaction of FAM215A and LAMP2 assessed by RNA immunoprecipitation (RIP) in HepG2 and J7 cells, IgG as the control antibody and GAPDH as the negative control. β -Actin and 18s rRNA were used as the loading controls. Data are presented as means \pm SD of three independent experiments (*, $p < 0.05$; **, $p < 0.01$).

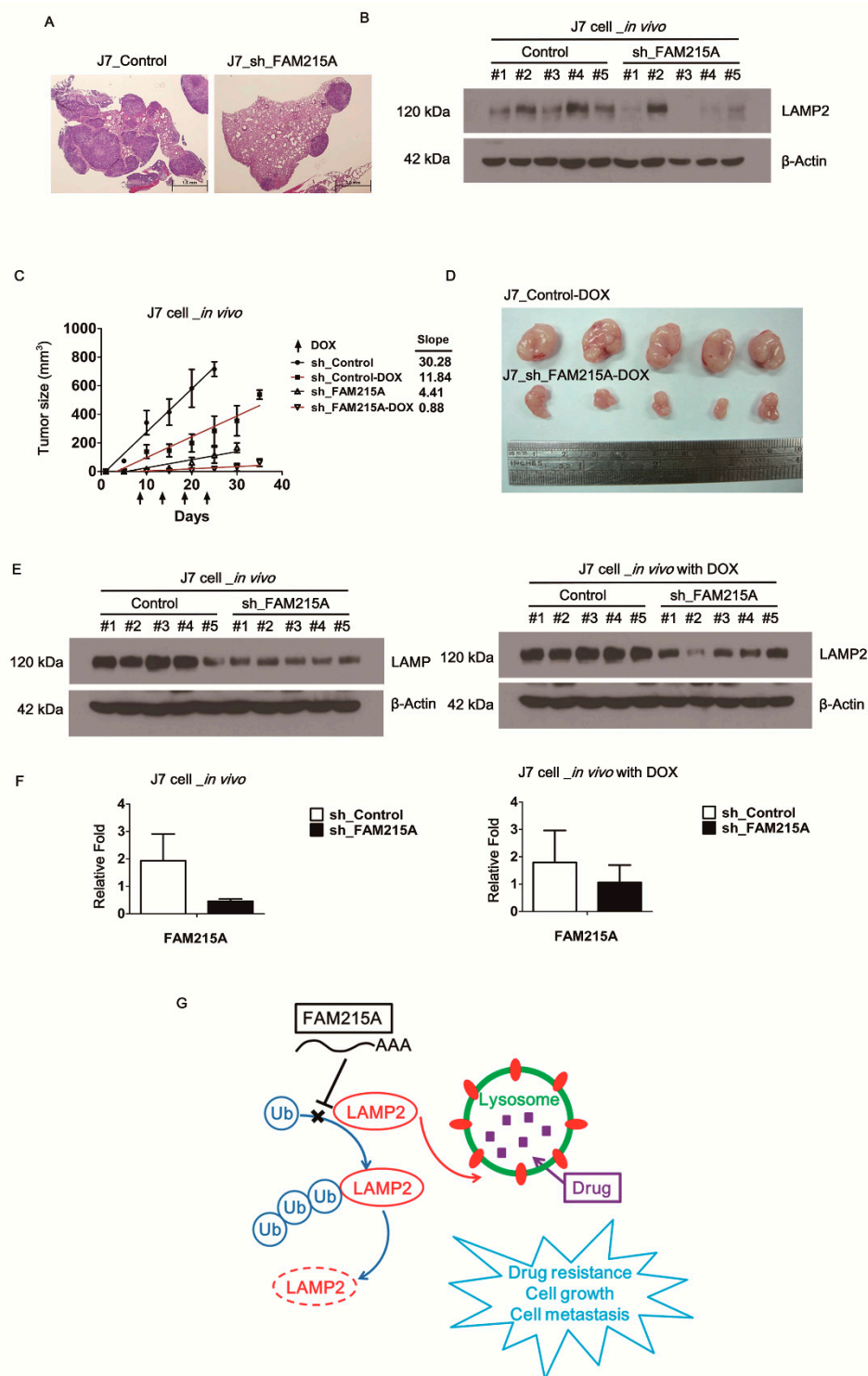


Figure 6. FAM215A promotes tumor progression and drug resistance in vivo by xenograft mouse. (A) Injection of the FAM215A knockdown in J7 cells by tail vein in severe combined immunodeficiency (SCID) mice (n = 5). The hematoxylin and eosin (H&E) staining of the tumor in lung tissues was used to determine the metastasis capacity. (B) LAMP2 expression from the tumor in the lung by Western blot. (C,D) Affect FAM215A on the tumor growth curve (slope) and drug resistance capacity treated with Doxorubicin (4 mg/kg). FAM215A depleted in J7 cells were subcutaneously injected into nude mice (n = 5). (E,F) Expression of the LAMP2 and FAM215A determined by Western blot or qRT-PCR. β-Actin and 18s rRNA were used as the loading controls. Arrow indicates the time of Doxorubicin treatment. Data are presented as means ± SD of five independent experiments. (G) Diagram of FAM215A inhibits LAMP2-ubiquitination to confer drug-resistant in HCC.

4. Discussion

Recent studies have shown that lncRNAs have important functions in modulating various tumor progression in HCC, such as growth arrest-specific 5 (GAS5), nuclear-enriched autosomal transcript 1 (NEAT1), and taurine upregulated gene 1 (TUG1) [21,33,34]. FAM215A is a novel dysregulated lncRNA that our previous microarray analysis identified as being highly expressed in human hepatoma tissues [21]. Conversely, in ovarian cancer, FAM215A is associated with favorable overall survival [35]. In the current study, we show that FAM215A is highly expressed in human hepatoma samples and associated with clinical markers of tumor progression, including tumor size, vascular invasion, and pathologic stage. Moreover, high-level expression of FAM215A in HCC is associated with a poor recurrence-survival ratio. We obtained consistent results when we analyzed data from the Cancer Genome Atlas (TCGA) using the cBio Cancer Genomics Portal [36]. Further, FAM215A leads to HCC cell metastasis, and up-regulation of EMT-related transcription factors, including TWIST, SNAIL, and SLUG, is seen in FAM215A-overexpressing J7 and Hep3B cells. The latter finding is relevant because EMT-related phenotypes have been found to exhibit significant associations with clinicopathological factors indicating aggressive biologic behavior and poor outcome in patients with liver cancer and other types of cancer [37–39]. In addition to cell metastasis, FAM215A increases cell growth and induces the phosphorylation of ERK1/2, in which it has been shown that growth factor could enhance cell proliferation and survival through the activation of the ERK1/2 pathway [40]. ERK1/2 also plays an important role in the metabolism of the liver. ERK1/2 can affect liver metabolism by positively affecting the activation of Peroxisome proliferator-activated receptors (PPARs)-alpha, a gene related to liver fat metabolism [41,42]. PPAR is a ligand-activated transcription factor that regulates mitochondrial function, ATP generation, antioxidant, immune responses, and fatty acid oxidation [43].

Doxorubicin is one of the most widely used drugs for chemotherapy in HCC [44]. Doxorubicin mainly plays a role in chemotherapy cancer through two different mechanisms of action. (I) Doxorubicin intercalates into DNA and interference of topoisomerase II-mediated DNA repair. (II) Doxorubicin generation of reactive oxygen species (ROS) leads to lipid peroxidation and membrane damage, DNA damage, oxidative stress, and severe inflammatory responses to triggers apoptotic pathways of cell death [45,46]. In the analyzed Gene Expression Omnibus (GEO) datasets, FAM215A is a highly expressing gene in doxorubicin-resistant HCC cells [28]. Here, we show that FAM215A is specifically regulated by doxorubicin, but not cisplatin. This suggests that FAM215A may act as a survival factor under Doxorubicin therapy in HCC. Several other genes have been found to be upregulated in drug-adapted cells. For example, NGFR is highly expressed in cells exposed to vemurafenib (a RAF inhibitor), allowing these cells to transiently exit the cell cycle and induce an adaptive response, thereby making them drug-resistant. Interestingly, pathway enrichment analysis showed that various pathways found to be altered by upregulation of NGFR (e.g., the cell adhesion, ECM remodeling, and EMT pathways) are also altered by the upregulation of other factors, including the ECM component, thrombospondin-1 (TSP-1), adhesive glycoprotein, laminin subunits LAMA1 and LAMC1, and several integrin family receptors. Additionally, integrin β 1 is regulated in a manner similar to FAM215A when cells are treated with different dose drugs [47]. The lncRNA promoter of CDKN1A antisense DNA-damage-activated RNA (PANDAR) has been reported to serve as a negative regulator of cisplatin sensitivity, and cisplatin has been shown to induce higher levels of PANDAR than doxorubicin or paclitaxel in human ovarian cancer cells [41]. Moreover, PANDAR exhibited higher expression in cisplatin-resistant ovarian cancer tissues and cells, compared with cisplatin-sensitive tissues and cells, and mechanistic studies showed that it negatively regulates cisplatin sensitivity in human ovarian cancer via PANDAR-SRFS2-p53 feedback regulation in the nucleus [48]. By analogy, these studies strengthen our concept regarding the relationship between FAM215A and doxorubicin in liver cancer cells. Here, we clearly show that FAM215A increases the resistance of HCC cells to doxorubicin by mechanisms that go beyond simply increasing cell proliferation and the capacity for metastasis.

In addition to its regulation of doxorubicin sensitivity, FAM215A also affects the sensitivity of cancer cells to other anticancer drugs, such as cisplatin and sorafenib. We thus analyzed a mechanism

of action that is known to be related to multiple drug resistance (MDR). Lysosomal sequestration (or lysosomal drug entrapment) of anti-cancer compounds reduces drug availability at intracellular target sites, thereby limiting drug sensitivity and inducing chemoresistance [30,49]. Lysosomes mediate MDR in many cancers, such as those showing resistance to cisplatin, sorafenib, doxorubicin, and oxaliplatin [30]. Lysosomes recycle organelles and proteins in cells [50] and they play extensive roles in various diseases, including cancers, making them an attractive and targetable node for therapeutic intervention. In liver cancer, lysosomes are known to be involved in the chemoresistance of HCC cells [51,52]. Here, we used LysoTracker probes to assess the lysosomal contents of cells and found that FAM215A had a positive effect on the lysosomal content of HCC cells. Mechanistically, the lysosomal membrane proteins, LAMP1 and LAMP2, are estimated to contribute to about 50% of all lysosome membrane proteins [53]. LAMP2 has been shown to play roles in many diseases, but few such studies have been performed in liver cancer [16,54,55]. Here, we report that doxorubicin had similar effects on the expression levels of FAM215A and LAMP2. Indeed, we generally observed a positive correlation between FAM215A and LAMP2 in HCC cells. In previous studies, LAMP2 was shown to act as an oncogene, to be required for tumor growth, and to promote tumor recurrence [19]. Consistent with our data, LAMP2 knockdown in HCC cells repressed doxorubicin resistance. Our results therefore collectively suggest that FAM215A induces tumor progression, metastasis, and doxorubicin resistance, potentially through LAMP2. Consistent with this proposal, re-expression of LAMP2 in FAM215A-depleted HCC cells rescued their doxorubicin resistance.

To explore a mechanism through which FAM215A could affect LAMP2 protein expression, we used the eukaryotic translation inhibitor, cycloheximide (CHX), to assess changes in the protein stability of LAMP2 in our various cell lines. Our data showed that FAM215A increased LAMP2 protein stability. This result was further confirmed by assessing the ubiquitination of LAMP2 in MG132-treated cells. Our findings indicated that FAM215A prevents the ubiquitination of LAMP2 to decrease its degradation. Moreover, RNA immunoprecipitation (RIP) showed that FAM215A and LAMP2 interact. Similarly, previous work showed that the lncRNA, metastasis-associated lung adenocarcinoma transcript 1 (MALAT1), interacts with SREBP-1c to stabilize nuclear SREBP-1c protein and thereby promote hepatic steatosis and insulin resistance [56]. We propose that FAM215A acts analogously to stabilize LAMP2 and alter downstream functions. The glycoprotein-specific F-box protein, FBXO27, is part of the SCF (SKP1/CUL1/F-box protein) ubiquitin ligase complex, and is also important for the ubiquitination of LAMP2. The N-myristoylation of FBXO27 localizes it to membranes, allowing it to accumulate rapidly around damaged lysosomes. Meanwhile, LAMP2 is ubiquitinated and degraded to enhance recruitment of the autophagic machinery to damaged lysosomes [57]. Finally, we used animal models to confirm that the *in vitro* effects of FAM215A can be replicated *in vivo*. Our results collectively indicate that FAM215A induces tumor metastasis, enhances tumor growth, and increases the doxorubicin resistance capacity in HCC.

Currently, we report that FAM215A increases the ability of liver cancer cells to resist different anti-cancer drugs. At the same time, FAM215A improves the ability of LAMP2, which plays an important role in the process of autophagy, and also seems to imply a new treatment strategy to overcome the failure of anti-cancer drug treatment caused by autophagy [30,58,59]. In conclusion, we herein show for the first time that the lncRNA, FAM215A, is highly expressed in HCC, where it interacts with and prevents the ubiquitination of LAMP2 to increase tumor progression and decrease doxorubicin sensitivity.

Supplementary Materials: The following are available online at <http://www.mdpi.com/2073-4409/9/4/961/s1>, Figure S1: FAM215A information and its role with cisplatin and sorafenib in HCC., Table S1: Primer sets used for qRT-PCR analysis.

Author Contributions: P.-S.H., Y.-H.L., H.-C.C. and C.Y.C. performed the experiments, Y.-H.T., T.-K.L. and C.-T.Y. provided experimental materials, K.-H.L. supervised and wrote the manuscript with input from all authors. All authors have read and agreed to the published version of the manuscript.

Funding: This research received no external funding.

Acknowledgments: This work was supported by grants from Chang Gung Memorial Hospital, Taoyuan, Taiwan (CMRPD1G0421, CMRPD1G0422, CMRPD1G0423, CMRPD1J0051, NMRPD1G0943, and NMRPD1G0953 to K. H. Lin) and from the Ministry of Science and Technology of the Republic of China (MOST 106-2320-B-182-031-MY3 and 106-2320-B-182-032-MY3 to K. H. Lin). We would like to thank the Taiwan Liver Cancer Network (TLCN) for providing the hepatoma tissue samples and related clinical data (all anonymous).

Conflicts of Interest: The authors declare no conflict of interests.

References

- Levrero, M. Viral hepatitis and liver cancer: The case of hepatitis C. *Oncogene* **2006**, *25*, 3834–3847. [[CrossRef](#)] [[PubMed](#)]
- Ferlay, J.; Soerjomataram, I.; Dikshit, R.; Eser, S.; Mathers, C.; Rebelo, M.; Parkin, D.M.; Forman, D.; Bray, F. Cancer incidence and mortality worldwide: Sources, methods and major patterns in GLOBOCAN 2012. *Cancer* **2015**, *136*, E359–E386. [[CrossRef](#)] [[PubMed](#)]
- Strathearn, L.S.; Stepanov, A.I.; Font-Burgada, J. Inflammation in Primary and Metastatic Liver Tumorigenesis-Under the Influence of Alcohol and High-Fat Diets. *Nutrients* **2020**, *12*, 933. [[CrossRef](#)] [[PubMed](#)]
- Charriere, B.; Maulat, C.; Suc, B.; Muscari, F. Contribution of alpha-fetoprotein in liver transplantation for hepatocellular carcinoma. *Hepatology* **2016**, *8*, 881–890. [[CrossRef](#)]
- Wu, S.M.; Lin, S.L.; Lee, K.Y.; Chuang, H.C.; Feng, P.H.; Cheng, W.L.; Liao, C.J.; Chi, H.C.; Lin, Y.H.; Tsai, C.Y.; et al. Hepatoma cell functions modulated by NEK2 are associated with liver cancer progression. *Cancer* **2017**, *140*, 1581–1596. [[CrossRef](#)]
- Wang, K.C.; Chang, H.Y. Molecular mechanisms of long noncoding RNAs. *Mol. Cell* **2011**, *43*, 904–914. [[CrossRef](#)]
- Fatica, A.; Bozzoni, I. Long non-coding RNAs: New players in cell differentiation and development. *Nature Rev. Genet.* **2014**, *15*, 7–21. [[CrossRef](#)]
- Rinn, J.L.; Chang, H.Y. Genome regulation by long noncoding RNAs. *Annu. Rev. Biochem.* **2012**, *81*, 145–166. [[CrossRef](#)]
- Wilusz, J.E.; Sunwoo, H.; Spector, D.L. Long noncoding RNAs: Functional surprises from the RNA world. *Genes Dev.* **2009**, *23*, 1494–1504. [[CrossRef](#)]
- He, Y.; Meng, X.M.; Huang, C.; Wu, B.M.; Zhang, L.; Lv, X.W.; Li, J. Long noncoding RNAs: Novel insights into hepatocellular carcinoma. *Cancer Lett.* **2014**, *344*, 20–27. [[CrossRef](#)]
- Braconi, C.; Kogure, T.; Valeri, N.; Huang, N.; Nuovo, G.; Costinean, S.; Negrini, M.; Miotto, E.; Croce, C.M.; Patel, T. microRNA-29 can regulate expression of the long non-coding RNA gene MEG3 in hepatocellular cancer. *Oncogene* **2011**, *30*, 4750–4756. [[CrossRef](#)] [[PubMed](#)]
- Yang, Z.; Zhou, L.; Wu, L.M.; Lai, M.C.; Xie, H.Y.; Zhang, F.; Zheng, S.S. Overexpression of long non-coding RNA HOTAIR predicts tumor recurrence in hepatocellular carcinoma patients following liver transplantation. *Ann. Surg. Oncol.* **2011**, *18*, 1243–1250. [[CrossRef](#)] [[PubMed](#)]
- Kogo, R.; Shimamura, T.; Mimori, K.; Kawahara, K.; Imoto, S.; Sudo, T.; Tanaka, F.; Shibata, K.; Suzuki, A.; Komune, S.; et al. Long noncoding RNA HOTAIR regulates polycomb-dependent chromatin modification and is associated with poor prognosis in colorectal cancers. *Cancer Res.* **2011**, *71*, 6320–6326. [[CrossRef](#)] [[PubMed](#)]
- Ghidini, M.; Braconi, C. Non-Coding RNAs in Primary Liver Cancer. *Front. Med.* **2015**, *2*, 36. [[CrossRef](#)] [[PubMed](#)]
- Kallunki, T.; Olsen, O.D.; Jaattela, M. Cancer-associated lysosomal changes: Friends or foes? *Oncogene* **2013**, *32*, 1995–2004. [[CrossRef](#)] [[PubMed](#)]
- Alessandrini, F.; Pezze, L.; Ciribilli, Y. LAMPs: Shedding light on cancer biology. *Semin. Oncol.* **2017**, *44*, 239–253. [[CrossRef](#)]
- Krishnan, V.; Bane, S.M.; Kawle, P.D.; Naresh, K.N.; Kalraiya, R.D. Altered melanoma cell surface glycosylation mediates organ specific adhesion and metastasis via lectin receptors on the lung vascular endothelium. *Clin. Exp. Meta.* **2005**, *22*, 11–24. [[CrossRef](#)]

18. Saitoh, O.; Wang, W.C.; Lotan, R.; Fukuda, M. Differential glycosylation and cell surface expression of lysosomal membrane glycoproteins in sublines of a human colon cancer exhibiting distinct metastatic potentials. *Biolo. Chem.* **1992**, *267*, 5700–5711.
19. Ding, Z.B.; Fu, X.T.; Shi, Y.H.; Zhou, J.; Peng, Y.F.; Liu, W.R.; Shi, G.M.; Gao, Q.; Wang, X.Y.; Song, K.; et al. Lamp2a is required for tumor growth and promotes tumor recurrence of hepatocellular carcinoma. *Oncology* **2016**, *49*, 2367–2376. [[CrossRef](#)]
20. Huang, P.S.; Chung, I.H.; Lin, Y.H.; Lin, T.K.; Chen, W.J.; Lin, K.H. The Long Non-Coding RNA MIR503HG Enhances Proliferation of Human ALK-Negative Anaplastic Large-Cell Lymphoma. *Mol. Sci.* **2018**, *19*, 1463. [[CrossRef](#)]
21. Lin, Y.H.; Wu, M.H.; Huang, Y.H.; Yeh, C.T.; Cheng, M.L.; Chi, H.C.; Tsai, C.Y.; Chung, I.H.; Chen, C.Y.; Lin, K.H. Taurine up-regulated gene 1 functions as a master regulator to coordinate glycolysis and metastasis in hepatocellular carcinoma. *Hepatology* **2018**, *67*, 188–203. [[CrossRef](#)]
22. Lagarde, J.; Uszczynska-Ratajczak, B.; Santoyo-Lopez, J.; Gonzalez, J.M.; Tapanari, E.; Mudge, J.M.; Steward, C.A.; Wilming, L.; Tanzer, A.; Howald, C.; et al. Extension of human lncRNA transcripts by RACE coupled with long-read high-throughput sequencing (RACE-Seq). *Nat. Commun.* **2016**, *7*, 12339. [[CrossRef](#)]
23. Chen, L.L. Linking Long Noncoding RNA Localization and Function. *Trends Biochem. Sci.* **2016**, *41*, 761–772. [[CrossRef](#)]
24. Zeisberg, M.; Neilson, E.G. Biomarkers for epithelial-mesenchymal transitions. *Clin. Invest.* **2009**, *119*, 1429–1437. [[CrossRef](#)]
25. Garg, M. Epithelial-mesenchymal transition activating transcription factors multifunctional regulators in cancer. *Stem Cells* **2013**, *5*, 188–195. [[CrossRef](#)] [[PubMed](#)]
26. Sun, Y.; Liu, W.Z.; Liu, T.; Feng, X.; Yang, N.; Zhou, H.F. Signaling pathway of MAPK/ERK in cell proliferation, differentiation, migration, senescence and apoptosis. *Recep. Signal Trans. Res.* **2015**, *35*, 600–604. [[CrossRef](#)] [[PubMed](#)]
27. Yang, Y.; Zhang, J.; Wu, T.; Xu, X.; Cao, G.; Li, H.; Chen, X. Histone deacetylase 2 regulates the doxorubicin (Dox) resistance of hepatocarcinoma cells and transcription of ABCB1. *Life Sci.* **2019**, *216*, 200–206. [[CrossRef](#)] [[PubMed](#)]
28. Ng, K.T.; Lo, C.M.; Guo, D.Y.; Qi, X.; Li, C.X.; Geng, W.; Liu, X.B.; Ling, C.C.; Ma, Y.Y.; Yeung, W.H.; et al. Identification of transmembrane protein 98 as a novel chemoresistance-conferring gene in hepatocellular carcinoma. *Mol. Cancer Thera.* **2014**, *13*, 1285–1297. [[CrossRef](#)]
29. Ueno, M.; Kakinuma, Y.; Yuhki, K.; Murakoshi, N.; Iemitsu, M.; Miyauchi, T.; Yamaguchi, I. Doxorubicin induces apoptosis by activation of caspase-3 in cultured cardiomyocytes in vitro and rat cardiac ventricles in vivo. *Pharmacol. Sci.* **2006**, *101*, 151–158. [[CrossRef](#)]
30. Sheng, J.; Qin, H.; Zhang, K.; Li, B.; Zhang, X. Targeting autophagy in chemotherapy-resistant of hepatocellular carcinoma. *Cancer Res.* **2018**, *8*, 354–365.
31. Piao, S.; Amaravadi, R.K. Targeting the lysosome in cancer. *Sciences* **2016**, *1371*, 45–54. [[CrossRef](#)]
32. Eskelinen, E.L.; Illert, A.L.; Tanaka, Y.; Schwarzmann, G.; Blanz, J.; Von Figura, K.; Saftig, P. Role of LAMP-2 in lysosome biogenesis and autophagy. *Mol. Biol. Cell* **2002**, *13*, 3355–3368. [[CrossRef](#)]
33. Yan, K.; Fu, Y.; Zhu, N.; Wang, Z.; Hong, J.L.; Li, Y.; Li, W.J.; Zhang, H.B.; Song, J.H. Repression of lncRNA NEAT1 enhances the antitumor activity of CD8(+)T cells against hepatocellular carcinoma via regulating miR-155/Tim-3. *Biochem. Cell Biol.* **2019**, *110*, 1–8. [[CrossRef](#)]
34. Chen, F.; Li, Y.; Li, M.; Wang, L. Long noncoding RNA GAS5 inhibits metastasis by targeting miR-182/ANGPTL1 in hepatocellular carcinoma. *Cancer Res.* **2019**, *9*, 108–121.
35. Fu, Y.; Biglia, N.; Wang, Z.; Shen, Y.; Risch, H.A.; Lu, L.; Canuto, E.M.; Jia, W.; Katsaros, D.; Yu, H. Long non-coding RNAs, ASAP1-IT1, FAM215A, and LINC00472, in epithelial ovarian cancer. *Gynecol. Oncol.* **2016**, *143*, 642–649. [[CrossRef](#)] [[PubMed](#)]
36. Cerami, E.; Gao, J.; Dogrusoz, U.; Gross, B.E.; Sumer, S.O.; Aksoy, B.A.; Jacobsen, A.; Byrne, C.J.; Heuer, M.L.; Larsson, E.; et al. The cBio cancer genomics portal: An open platform for exploring multidimensional cancer genomics data. *Cancer Dis.* **2012**, *2*, 401–404. [[CrossRef](#)] [[PubMed](#)]

37. Van Zijl, F.; Zulehner, G.; Petz, M.; Schneller, D.; Kornauth, C.; Hau, M.; Machat, G.; Grubinger, M.; Huber, H.; Mikulits, W. Epithelial-mesenchymal transition in hepatocellular carcinoma. *Future Oncol.* **2009**, *5*, 1169–1179. [[CrossRef](#)] [[PubMed](#)]
38. Han, L.L.; Yin, X.R.; Zhang, S.Q. miR-103 promotes the metastasis and EMT of hepatocellular carcinoma by directly inhibiting LATS2. *Oncology* **2018**, *53*, 2433–2444. [[CrossRef](#)]
39. Bae, Y.K.; Choi, J.E.; Kang, S.H.; Lee, S.J. Epithelial-Mesenchymal Transition Phenotype Is Associated with Clinicopathological Factors That Indicate Aggressive Biological Behavior and Poor Clinical Outcomes in Invasive Breast Cancer. *Breast Cancer* **2015**, *18*, 256–263. [[CrossRef](#)]
40. Guegan, J.P.; Fremin, C.; Baffet, G. The MAPK MEK1/2-ERK1/2 Pathway and Its Implication in Hepatocyte Cell Cycle Control. *Int. J. Hepatol.* **2012**, *2012*, 328372. [[CrossRef](#)]
41. Moreno, M.; Lombardi, A.; Silvestri, E.; Senese, R.; Cioffi, F.; Goglia, F.; Lanni, A.; de Lange, P. PPARs: Nuclear Receptors Controlled by, and Controlling, Nutrient Handling through Nuclear and Cytosolic Signaling. *PPAR Res.* **2010**, *2010*. [[CrossRef](#)] [[PubMed](#)]
42. Valenzuela, R.; Videla, L.A. Impact of the Co-Administration of N-3 Fatty Acids and Olive Oil Components in Preclinical Nonalcoholic Fatty Liver Disease Models: A Mechanistic View. *Nutrients* **2020**, *12*, 499. [[CrossRef](#)] [[PubMed](#)]
43. Corona, J.C.; Duchon, M.R. PPARgamma as a therapeutic target to rescue mitochondrial function in neurological disease. *Free Radic. Biol. Med.* **2016**, *100*, 153–163. [[CrossRef](#)]
44. Ye, P.; Xing, H.; Lou, F.; Wang, K.; Pan, Q.; Zhou, X.; Gong, L.; Li, D. Histone deacetylase 2 regulates doxorubicin (Dox) sensitivity of colorectal cancer cells by targeting ABCB1 transcription. *Cancer Chemother. Pharmacol.* **2016**, *77*, 613–621. [[CrossRef](#)]
45. Thorn, C.F.; Oshiro, C.; Marsh, S.; Hernandez-Boussard, T.; McLeod, H.; Klein, T.E.; Altman, R.B. Doxorubicin pathways: Pharmacodynamics and adverse effects. *Pharmacogen. Genom.* **2011**, *21*, 440–446. [[CrossRef](#)] [[PubMed](#)]
46. Wang, L.; Chen, Q.; Qi, H.; Wang, C.; Wang, C.; Zhang, J.; Dong, L. Doxorubicin-Induced Systemic Inflammation Is Driven by Upregulation of Toll-Like Receptor TLR4 and Endotoxin Leakage. *Cancer Res.* **2016**, *76*, 6631–6642. [[CrossRef](#)] [[PubMed](#)]
47. Fallahi-Sichani, M.; Becker, V.; Izar, B.; Baker, G.J.; Lin, J.R.; Boswell, S.A.; Shah, P.; Rotem, A.; Garraway, L.A.; Sorger, P.K. Adaptive resistance of melanoma cells to RAF inhibition via reversible induction of a slowly dividing de-differentiated state. *Mol. Syst. Biol.* **2017**, *13*, 905. [[CrossRef](#)]
48. Wang, H.; Fang, L.; Jiang, J.; Kuang, Y.; Wang, B.; Shang, X.; Han, P.; Li, Y.; Liu, M.; Zhang, Z.; et al. The cisplatin-induced lncRNA PANDAR dictates the chemoresistance of ovarian cancer via regulating SFRS2-mediated p53 phosphorylation. *Cell Death Dis.* **2018**, *9*, 1103. [[CrossRef](#)]
49. Gavini, J.; Dommann, N.; Jakob, M.O.; Keogh, A.; Bouchez, L.C.; Karkampouna, S.; Julio, M.K.; Medova, M.; Zimmer, Y.; Schlafli, A.M.; et al. Verteporfin-induced lysosomal compartment dysregulation potentiates the effect of sorafenib in hepatocellular carcinoma. *Cell Death Dis.* **2019**, *10*, 749. [[CrossRef](#)]
50. Towers, C.G.; Thorburn, A. Targeting the Lysosome for Cancer Therapy. *Cancer Dis.* **2017**, *7*, 1218–1220. [[CrossRef](#)]
51. Colombo, F.; Trombetta, E.; Cetrangolo, P.; Maggioni, M.; Razini, P.; De Santis, F.; Torrente, Y.; Prati, D.; Torresani, E.; Porretti, L. Giant Lysosomes as a Chemotherapy Resistance Mechanism in Hepatocellular Carcinoma Cells. *PLoS ONE* **2014**, *9*, e114787. [[CrossRef](#)]
52. Fennelly, C.; Amaravadi, R.K. Lysosomal Biology in Cancer. *Methods Mol. Biol.* **2017**, *1594*, 293–308.
53. Eskelinen, E.L. Roles of LAMP-1 and LAMP-2 in lysosome biogenesis and autophagy. *Molecular Aspects Med.* **2006**, *27*, 495–502. [[CrossRef](#)] [[PubMed](#)]
54. Dubois, A.; Furstoss, N.; Calleja, A.; Zerhouni, M.; Cluzeau, T.; Savy, C.; Marchetti, S.; Hamouda, M.A.; Boulakirba, S.; Orange, F.; et al. LAMP2 expression dictates azacytidine response and prognosis in MDS/AML. *Leukemia* **2019**, *33*, 1501–1513. [[CrossRef](#)] [[PubMed](#)]
55. Ma, S.; Zhang, M.; Zhang, S.; Wang, J.; Zhou, X.; Guo, G.; Wang, L.; Wang, M.; Peng, Z.; Guo, C.; et al. Characterisation of Lamp2-deficient rats for potential new animal model of Danon disease. *Sci. Rep.* **2018**, *8*, 6932. [[CrossRef](#)] [[PubMed](#)]

56. Yan, C.; Chen, J.; Chen, N. Long noncoding RNA MALAT1 promotes hepatic steatosis and insulin resistance by increasing nuclear SREBP-1c protein stability. *Sci. Rep.* **2016**, *6*, 22640. [[CrossRef](#)] [[PubMed](#)]
57. Yoshida, Y.; Yasuda, S.; Fujita, T.; Hamasaki, M.; Murakami, A.; Kawawaki, J.; Iwai, K.; Saeki, Y.; Yoshimori, T.; Matsuda, N.; et al. Ubiquitination of exposed glycoproteins by SCF(FBXO27) directs damaged lysosomes for autophagy. *Proc. Acad. Sci. USA* **2017**, *114*, 8574–8579. [[CrossRef](#)] [[PubMed](#)]
58. Yang, S.; Yang, L.; Li, X.; Li, B.; Li, Y.; Zhang, X.; Ma, Y.; Peng, X.; Jin, H.; Li, H. New insights into autophagy in hepatocellular carcinoma: Mechanisms and therapeutic strategies. *Cancer Res.* **2019**, *9*, 1329–1353.
59. Sun, T.; Liu, H.; Ming, L. Multiple Roles of Autophagy in the Sorafenib Resistance of Hepatocellular Carcinoma. *Cell. Physiol. Biochem.: Exp. Cell. Physiol. Biochem. Pharmacol.* **2017**, *44*, 716–727. [[CrossRef](#)]



© 2020 by the authors. Licensee MDPI, Basel, Switzerland. This article is an open access article distributed under the terms and conditions of the Creative Commons Attribution (CC BY) license (<http://creativecommons.org/licenses/by/4.0/>).



Nano-Based Drug Delivery or Targeting to Eradicate Bacteria for Infection Mitigation: A Review of Recent Advances

Yuan-Chieh Yeh^{1,2}, Tse-Hung Huang^{1,3,4,5}, Shih-Chun Yang⁶, Chin-Chang Chen^{1,7} and Jia-You Fang^{7,8,9,10*}

¹ Department of Traditional Chinese Medicine, Chang Gung Memorial Hospital, Keelung City, Taiwan, ² Program in Molecular Medicine, School of Life Sciences, National Yang Ming University, Taipei, Taiwan, ³ School of Traditional Chinese Medicine, Chang Gung University, Taoyuan City, Taiwan, ⁴ Graduate Institute of Health Industry Technology, Chang Gung University of Science and Technology, Taoyuan City, Taiwan, ⁵ School of Nursing, National Taipei University of Nursing and Health Sciences, Taipei, Taiwan, ⁶ Department of Cosmetic Science, Providence University, Taichung City, Taiwan, ⁷ Chinese Herbal Medicine Research Team, Healthy Aging Research Center, Chang Gung University, Taoyuan City, Taiwan, ⁸ Pharmaceuticals Laboratory, Graduate Institute of Natural Products, Chang Gung University, Taoyuan City, Taiwan, ⁹ Research Center for Food and Cosmetic Safety and Research Center for Chinese Herbal Medicine, Chang Gung University of Science and Technology, Taoyuan City, Taiwan, ¹⁰ Department of Anesthesiology, Chang Gung Memorial Hospital, Taoyuan City, Taiwan

OPEN ACCESS

Edited by:

Tivadar Feczko,
Hungarian Academy of
Sciences, Hungary

Reviewed by:

Manoranjana Arakha,
Siksha 'O' Anusandhan
University, India
Konstantinos Simeonidis,
Aristotle University of
Thessaloniki, Greece

*Correspondence:

Jia-You Fang
fajy@mail.cgu.edu.tw

Specialty section:

This article was submitted to
Nanoscience,
a section of the journal
Frontiers in Chemistry

Received: 09 January 2020

Accepted: 23 March 2020

Published: 24 April 2020

Citation:

Yeh Y-C, Huang T-H, Yang S-C,
Chen C-C and Fang J-Y (2020)
Nano-Based Drug Delivery or
Targeting to Eradicate Bacteria for
Infection Mitigation: A Review of
Recent Advances.
Front. Chem. 8:286.
doi: 10.3389/fchem.2020.00286

Pathogenic bacteria infection is a major public health problem due to the high morbidity and mortality rates, as well as the increased expenditure on patient management. Although there are several options for antimicrobial therapy, their efficacy is limited because of the occurrence of drug-resistant bacteria. Many conventional antibiotics have failed to show significant amelioration in overall survival of infectious patients. Nanomedicine for delivering antibiotics provides an opportunity to improve the efficiency of the antibacterial regimen. Nanosystems used for antibiotic delivery and targeting to infection sites render some benefits over conventional formulations, including increased solubility, enhanced stability, improved epithelium permeability and bioavailability, prolonged antibiotic half-life, tissue targeting, and minimal adverse effects. The nanocarriers' sophisticated material engineering tailors the controllable physicochemical properties of the nanoparticles for bacterial targeting through passive or active targeting. In this review, we highlight the recent progress on the development of antibacterial nanoparticles loaded with antibiotics. We systematically introduce the concepts and amelioration mechanisms of the nanomedical techniques for bacterial eradication. Passive targeting by modulating the nanoparticle structure and the physicochemical properties is an option for efficient drug delivery to the bacteria. In addition, active targeting, such as magnetic hyperthermia induced by iron oxide nanoparticles, is another efficient way to deliver the drugs to the targeted site. The nanoparticles are also designed to respond to the change in environment pH or enzymes to trigger the release of the antibiotics. This article offers an overview of the benefits of antibacterial nanosystems for treating infectious diseases.

Keywords: nanomedicine, antibiotic, bacteria, drug delivery, drug targeting

INTRODUCTION

Microorganisms including viruses, bacteria, fungi, and parasites can cause infectious diseases. Infection-related illness is a leading cause of death globally. According to the report from World Health Organization, three infectious diseases were ranked in the top 10 death causes in 2016: lower respiratory infection (fourth place), diarrhea disease (ninth place), and tuberculosis (tenth place). Among the infectious microorganisms, bacteria remain the leading cause of death in children, the elderly and immunodeficient patients (Zhang L. et al., 2019). Pathogenic bacteria represent a main public health problem because of the high morbidity and mortality, as well as the increased expenditure on patient management (Woodford and Livermore, 2009). The development of antibiotics since the 1940s proved important in eradicating bacteria, thereby saving millions of patients' lives. However, the conventional antibiotics used for anti-bacterial therapy exhibit some limitations in modern medicine, including the low bioavailability, minimal permeation to the infection nidus, and the rise of drug-resistant bacteria (superbugs) (Pizzolato-Cezar et al., 2019). The abuse and misuse of antibiotics has led to the emergence of antibiotic-resistant bacteria threatening human health. Antimicrobial resistance has become one of the leading causes of death worldwide in recent years. Novel approaches for either the enhancement of the therapeutic efficiency of existing antibiotics or the development of new antibiotics are necessary to resolve antibiotic resistance. Currently, several strategies, such as chemical modification of antibiotics, combinatorial therapy, photothermal agents, antimicrobial peptides, cationic polymers, and nanoparticles have been reported to be useful for conquering antibiotic resistance (Gebreyohannes et al., 2019).

In the past decade, a great advance in nanomedicine holds promise for bacterial infection treatment. The nanoparticles can act as antibacterial agents or the carriers for loading antibacterial drugs to promote the bioavailability and effectiveness of antibiotics (Baptista et al., 2018). Antibacterial nanoparticles

without the need of drugs are developed using diverse materials, including metals, chitosan, and surfactants (Taylor and Webster, 2011). The net-positive charge of cationic compounds can bind to the negatively charged membrane surface of bacteria, while the amphiphilic structure of some nanoparticles prompts membrane damage (Chen et al., 2012). The encapsulation of antibiotic drugs into nanocarriers is another strategy to enhance bacteria eradication and bioavailability. The delivery of the drugs from nanosystems improves the efficacy, while reducing the possible toxicity in comparison to conventional therapy. Due to the high surface-to-volume ratio, the possibility of surface functionalization, and the capacity to load drug molecules, nanoparticles contribute to the efficient antibacterial activity with their high affinity to bacteria (Zazo et al., 2016). The nanoparticles can protect the drugs from enzymatic attack and sustain the drug release to increase the half-life and bioavailability. The nano-sized nature is beneficial to extravagate through the endothelium in the inflammatory site for efficient accumulation in infectious nidus (Walvekar et al., 2019). The nanomedical strategy to improve antibiotic delivery for bacterial killing indicates the reduction of side effects and drug resistance.

The active targeting of the nanoparticles to bacteria is an efficient management to increase the therapeutic index. The nanocarriers can be functionalized with ligands to the bacterial surface to enhance the targeting to specific pathogens. The design of stimuli-responsive nanosystems, as illustrated in **Figure 1**, is another concept for bacteria targeting through the recognition of bacterial microenvironment and the response in a dynamic process (Canaparo et al., 2019). The nanoparticles, after a suitable design, can respond to the internal stimuli such as varying pH, concentrations of specific enzymes, or chemicals, which are associated with pathological conditions of infection and inflammation (Lee et al., 2018). The antibiotic targeting to bacteria can be also achieved by nanoparticulate response to external physical stimuli, such as magnetic, thermal, light, and ultrasound effects. The application of stimuli to nanoparticulate drug delivery systems leads controlled drug delivery and fast

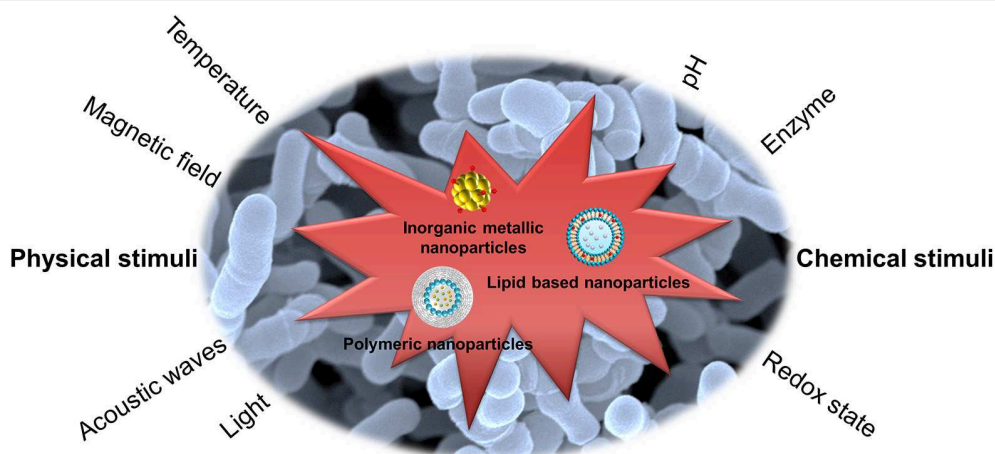


FIGURE 1 | Stimuli-responsive nanoparticles for bacteria targeting via the recognition of bacterial microenvironment and the response in a dynamic process.

response, addressing the pathological events. In addition, the reversibility to the initial state of the nanoparticles is possible to govern the antibacterial effect.

Besides the occurrence of drug-resistant bacteria, the infections associated with biofilm and intracellular residence are difficult to treat due to the inherent resistance to antimicrobial agents and immune cells (Yang et al., 2017). Biofilm is a sessile community of bacteria enclosed by the matrix of extracellular polymer substances (EPS) released by the microbes themselves. Biofilm reveals a rigid structure and high resistance that prevents the entrance of antimicrobial drugs (Mohammed et al., 2018). It is difficult to treat intracellular bacteria because these pathogens become recalcitrant via intracellular persistence in host cells (Cornejo et al., 2017). Some nanoparticles possess the ability to damage the biofilm for facile penetration into biofilm and subsequent bacteria eradication. The large uptake of nanoparticles into the host cells is possible through the functionalization of particulate surface for successful bacteria clearance. There are already 51 nanomedicines approved by the USFDA, including the nanoformulations for antibacterial aims (Bobo et al., 2016). In this review, we highlight recent advances in the application of nanomedicine for treating infection caused by bacteria. We mainly focus on the reports of nanoparticle development of antibacterial nanosystems during the past 5 years using different evaluation platforms, including *in vitro*, *ex vivo*, and *in vivo* examinations. The promising perspective in this emerging application is also discussed.

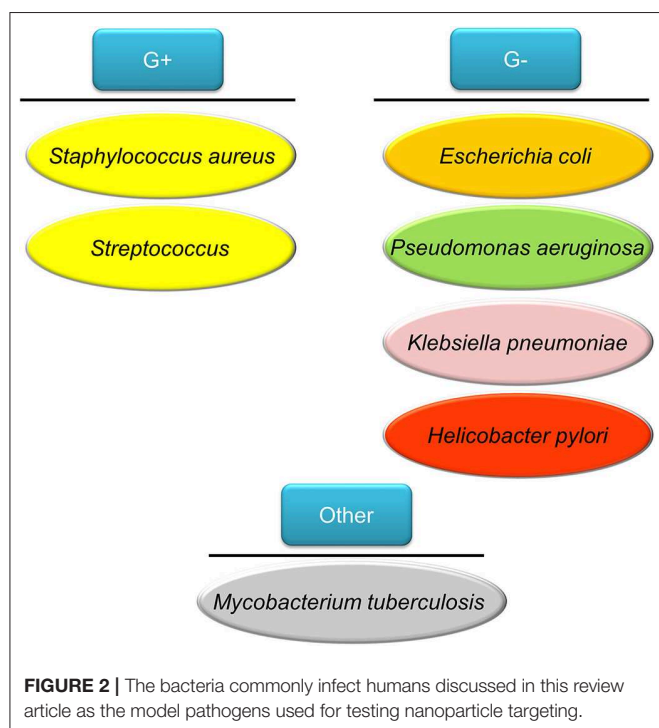
THE BACTERIA FREQUENTLY INFECTING HUMANS

Some bacteria strongly infect the human hosts to generate infectious diseases. The appearance of drug-resistant bacteria can worsen the condition of infection. Prior to the 1950s, antibiotics were extensively used in human medicine and animal agriculture due to their inexpensive cost and low side effects. However, the wide use of antibiotics over a period of several decades has resulted in the serious problem of drug resistance. Gram staining is a technique to differentiate two large groups of bacteria based on the different cell wall constituents (Thomson, 2016). The Gram stain procedure distinguishes between Gram-positive and Gram-negative groups by coloring these microbes violet or red. Gram-positive bacteria stain violet because of the presence of a thick layer of peptidoglycan in the cell walls retaining the crystal violet these cells are stained with. On the other hand, Gram-negative bacteria stain red attributing to a thinner peptidoglycan wall, which does not retain the crystal violet.

We introduce some bacteria frequently used as the cell models for testing the efficiency of nanoparticles on antibacterial assay. *Staphylococcus aureus* belongs to Gram-positive bacteria; it is the major consequence of bacterial infection in community settings and hospitals, eliciting significant morbidity and mortality (Tong et al., 2015). *S. aureus* has the capability to generate a diverse array of infection in different organs or tissues, including skin wound infection, folliculitis, pneumonia, endocarditis, and bacteremia (Price et al., 2017). Some of these diseases can

threaten life. As an intracellular microbe, *S. aureus* is capable of invading macrophages, osteoblasts, and epithelial cells to evade immune surveillance (Fraunholz and Sinha, 2012). Multidrug-resistant *S. aureus*, especially methicillin-resistant *S. aureus* (MRSA), are a rising global health threat and economic burden. MRSA colonization is a predominant risk factor for adverse health outcome with 10–30% of carriers subsequently developing infectious disorders (Poovelikunnel et al., 2015). The resistance of MRSA to several antibiotics makes it necessary to use stronger antibiotics such as vancomycin. Unfortunately, many MRSA-infected patients do not respond favorably to vancomycin due to the recent development of vancomycin-resistant *S. aureus* (VRSA) and vancomycin-intermediate *S. aureus* (VISA) strains in clinics (Zhang et al., 2015). *Streptococcus pneumoniae* is a Gram-positive pathogen colonizing the upper respiratory tract. This strain infects the nasopharynx and spreads, especially in the form within the biofilm (Loughran et al., 2019). *S. pneumoniae* can be a leading cause of bacteremia, meningitis, otitis media, and community-acquired pneumonia. *S. pneumoniae* produces >25,000 deaths of pneumonia patients >50 years each year in the US (Zivich et al., 2018). *Klebsiella pneumoniae* also causes pneumonia although it belongs to the Gram-negative strain. Besides pneumonia, this strain induces multiple infections, including bacteremia, meningitis, liver abscess, and urinary tract infection (Paczosa and Mecsas, 2016). Tigecycline is regarded as the effective and last-line antibiotic to treat *K. pneumoniae*. Nevertheless, the overuse of this antibiotic on *K. pneumoniae*-infected patients has led to the increased drug resistance and reduced sensitivity to tigecycline.

People impaired with pulmonary mucociliary clearance are easily vulnerable to nosocomial infection, especially the Gram-negative *Pseudomonas aeruginosa*. The establishment of *P. aeruginosa* infection relates to the development of biofilm. The biofilm brings about the multidrug resistant *P. aeruginosa* strains (Amin and Ratjen, 2014). This pathogen is associated with cystic fibrosis and chronic obstructive pulmonary disease (COPD) (Hadinoto and Cheow, 2014). *Helicobacter pylori* is a Gram-negative pathogen affecting >50% of the global population (Bocian and Jagusztyn-Krynicka, 2012). *H. pylori* releases urease to hydrolyze urea to ammonia and bicarbonate for neutralizing acidity of stomach pH from 1–3 to 4.5–7, which is a favorable environment for *H. pylori* colonization (Ansari and Yamaoka, 2017). This pathogen plays an important role to elicit chronic gastritis, peptic ulcer, and gastric cancer. The emerging mutation of *H. pylori* has led to resistance to some antibiotics such as clarithromycin, resulting in the failure of therapy (Alba et al., 2017). The tuberculosis induced by *Mycobacterium tuberculosis* infection is one of the top ten causes of death worldwide, with more than 10 million people infected with tuberculosis each year. *M. tuberculosis* possesses a waxy coating on the cell surface because of the presence of mycolic acid. This coating makes the cells impervious to Gram staining. Thus, this pathogen can appear either Gram-positive or Gram-negative staining. Intracellular *M. tuberculosis* in host cells is able to bypass immune defense and modify its metabolic state. The emergence of drug-resistant *M. tuberculosis* has led to the failure of first line therapy and prolonged treatment duration (Seung et al., 2015). The above



bacteria commonly infect individuals and the associated diseases are summarized in **Figure 2**.

THE DIFFERENT PHASES OF BACTERIA

Bacteria in the state of planktonic, biofilm, or intracellular form can infect humans. Planktonic bacteria are free-living bacteria. They live as floating microorganisms in their respective environments. The opposite mode of planktonic bacteria growth is the adherent or sessile type of growth. The bacteria can form biofilm or reside in the host cells. Biofilm and host cells can serve as shelters for bacteria, preventing the attack of antibiotics. Biofilm consists of microbes with altered phenotypes living in a self-organized community adhered to the surface or biomembrane. Bacteria in biofilm show different physiologies compared to the planktonic state, such as a diminished metabolic rate and increased communication between cells (Stewart and Franklin, 2008). The matrix of biofilm is mainly composed of polysaccharides, nucleic acids, lipids, and proteins, as shown in **Figure 3**. This matrix constitutes the protective microenvironment for bacterial colonization and fosters the formidable barrier to antimicrobial agents and the immune system (Di Martino, 2018). Biofilm offers a beneficial environment for gene transfer between the individual bacteria, spreading antibiotic resistance and making the bacteria more virulent (Lebeaux et al., 2014). The biofilm bacteria display a 10- to 1,000-fold higher resistance to antibiotic treatment than the planktonic form (Gebreyohannes et al., 2019). Infection associated with surgical devices and medical implants are always caused by the biofilm adherence. This virulent infection by

biofilm evokes a high morbidity in hospitals. Surgical area infection accounts for about 22% of hospital setting-acquired infection (Magill et al., 2014). The biofilm bacteria release toxins to cause complications like sepsis and hemorrhage shock. For instance, catheter-related sepsis costs an additional USD 57,090 per case (Nakamura et al., 2015). Antibiotic delivery by nanoparticles can be a promising approach to overcome the barrier function of biofilm. The use of fusogenic nanoparticles, nanoparticle targeting, and triggered drug release from nanocarriers are the strategies to maximize the exposure of the biofilm to drugs (Forier et al., 2014). Enzymes such as deoxyribonuclease (DNase) and protease are loaded into nanoparticles to hydrolyze the biofilm structure for enhanced penetration of antibacterial drugs or nanoparticles.

The transportation of bacteria into host cells is a process for inducing intracellular infection. The immune cells are the predominant cells for the intracellular invasion of the bacteria. For instance, macrophages are recruited to the infection site to play a key role in the defense against pathogens. The bacteria facilitate bound to macrophage membrane and subsequently are internalized into phagosomes. Some microbes escape the macrophage-mediated disruption via a tumor necrosis factor (TNF) receptor-dependent pathway (Loeuillet et al., 2006), leading to the bacterial survival and enrichment. Another case is the bacteria infection into neutrophils. The bacteria possibly survive in neutrophils for a prolonged duration. The intracellular residence in the neutrophils protects the bacteria from lethal action by host immune system (Medina et al., 2003). Most of the antibacterial agents demonstrate limited activity against intracellular bacteria. The antibiotic concentrations of less than minimum inhibitory concentration (MIC) are usually found within the intracellular compartment, resulting in the development of drug resistance (Armstead and Li, 2011). Achieving efficient pathogen elimination requires maintaining a high antibiotic concentration in the host cells infected by bacteria. A number of nanoparticles, such as liposomes, polymeric nanoparticles, lipid-based nanoparticles, and silica nanocarriers, are produced for facile internalization into the host cells to eradicate intracellular microbes (Zhang L. et al., 2010). The intracellular nanoparticles can be designed through the increased affinity to host cells or the ligand conjugation on nanoparticulate surface for active targeting to cells.

NANOPARTICLE TYPES USED FOR ANTIBACTERIAL APPLICATION

The nanoparticles can be made by a variety of materials to serve different purposes. There are different types of nanoformulations employed for antibacterial application. For drug delivery, the nanoparticulate core or shell can load several payload drugs. The shape, size, and surface charge of the nanoparticles can be finely tuned by modulation of material types, contents and preparation processes for optimizing drug release and organ/cell targeting (Palange et al., 2014). Inorganic metal, polymeric, lipid-based, micellar, silica, and cell membrane-coated nanoparticles are the commonly studied nanosystems for antibiotic drugs

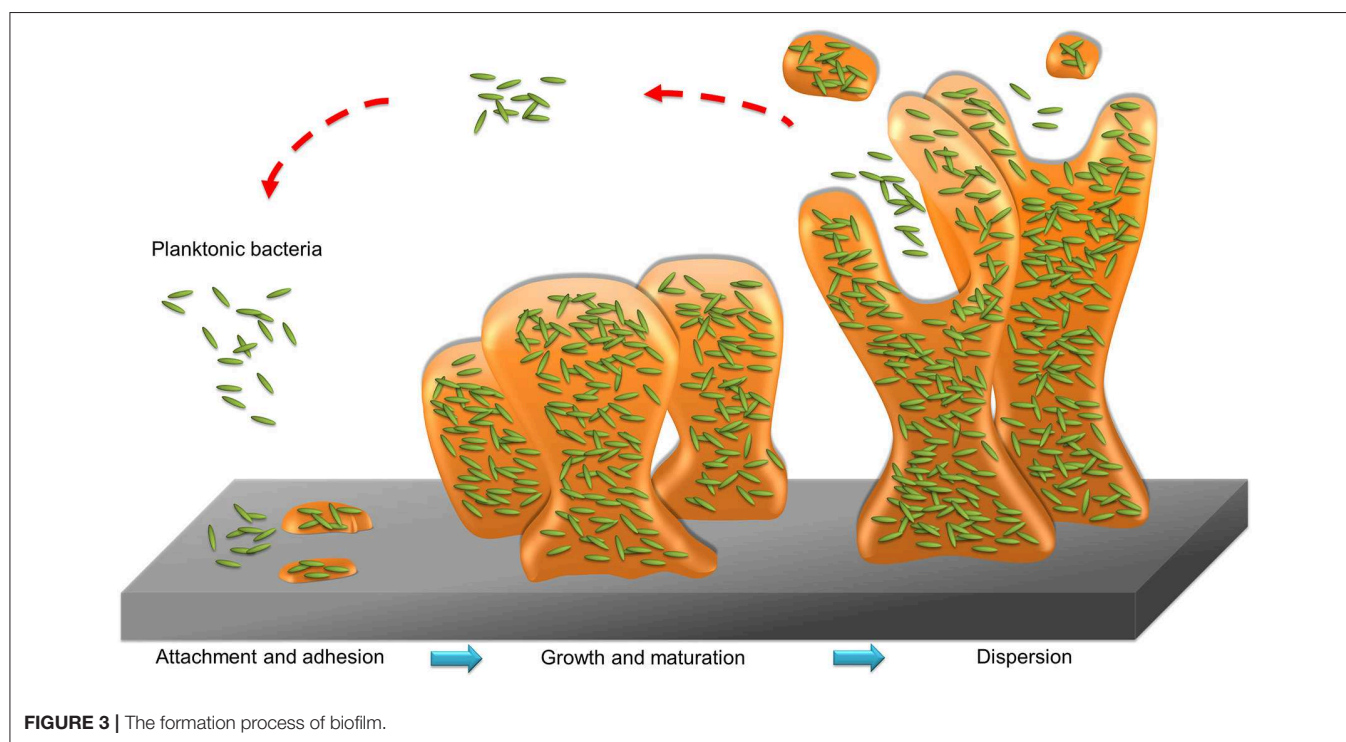


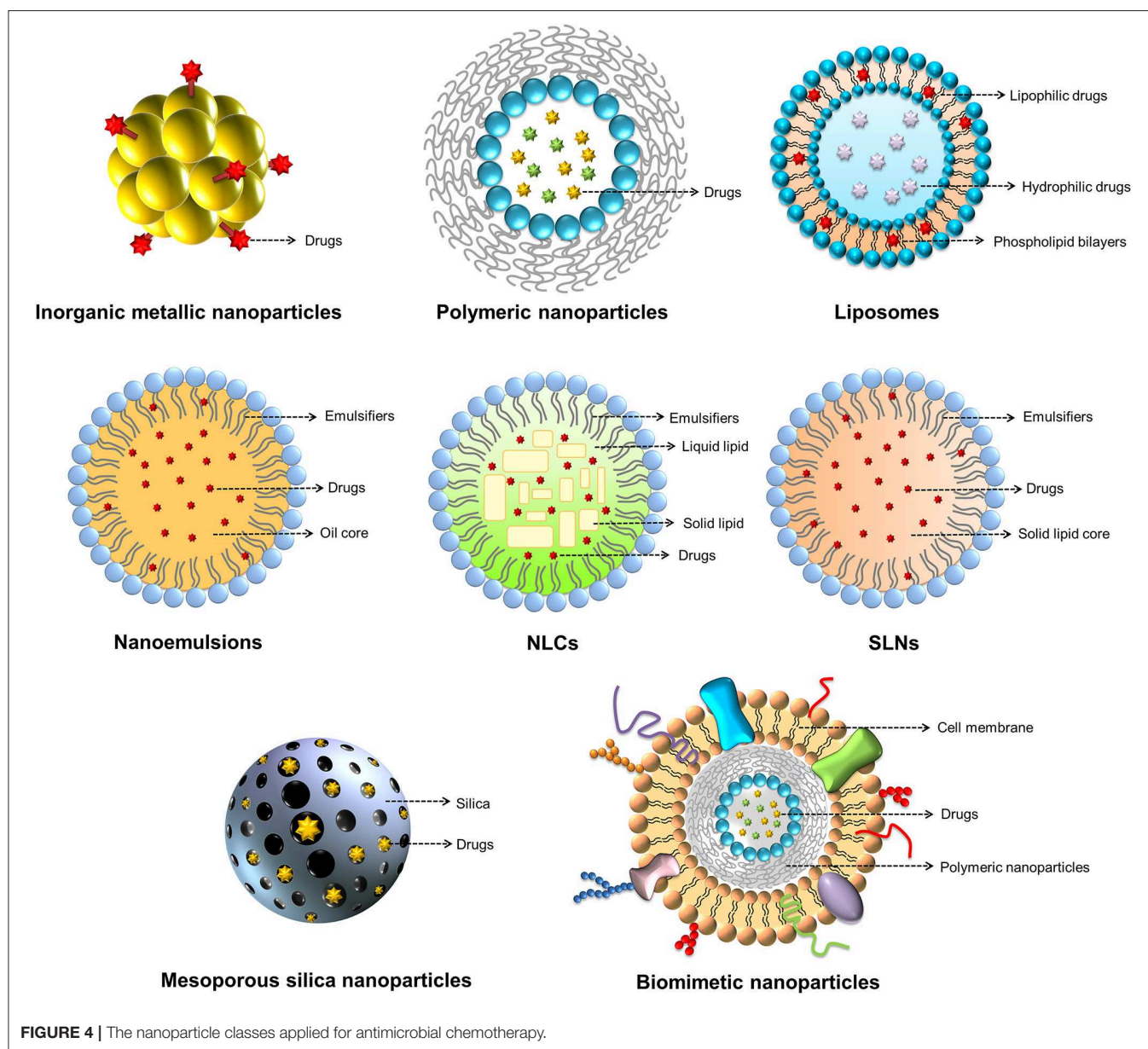
FIGURE 3 | The formation process of biofilm.

(Makowski et al., 2019). **Figure 4** summarizes the nanoparticle classes applied to antimicrobial chemotherapy.

Metallic nanoparticles mainly made by Au, Ag, or Cu are found to present strong antimicrobial activity (Miller et al., 2015). However, the application may be hindered because of their potential toxicity to mammalian cells. Reforming of the metallic nanoparticles is needed to improve the biocompatibility. Compared to the other inorganic metal nanoparticles, Au nanoparticles are attracting great attention due to their acceptable biocompatibility, stable storage, and easy surface functionalization (Cabuzu et al., 2015). Due to the unique physical and chemical characteristics, Au nanoparticles have been extensively applied in drug delivery carrier, bioimaging, and anticarcinogenic therapy (Ramalingam, 2019). The adsorption of drug molecules on the Au particle surface allows the delivery of active ingredients to target sites. Some antimicrobial agents such as antibiotics, antibacterial peptides, and surfactants can be conjugated onto the nanoparticulate shell to initiate potential bactericidal activity (Youghare et al., 2019). Ag nanoparticles themselves reveal a broad spectrum to eradicate bacteria, including some drug-resistant strains (Kasithevar et al., 2017). Nano-sized Ag shows greater biocidal effect than the bulk material (Choi and Hu, 2008). The mechanisms of killing bacteria by Ag nanoparticles are the disintegration of bacterial wall and the subsequent leakage of cytoplasmic contents and inactivation of proteins responsible for DNA and RNA replication. The superparamagnetic iron oxide nanoparticles (SPIONs) are widely investigated as powerful bactericidal agents due to their magnetic hyperthermia property (Javanbakht et al., 2016). Moreover, SPIONs are applicable as bacteria separation agents and bioimaging contrast agents for bacteria diagnosis

(Sabale et al., 2017). SPIONs adsorb electromagnetic radiation and then convert the magnetic energy into heat under a magnetic field with high frequency and amplitude. The hyperthermia causes the increased bacterial membrane permeability to kill the targeted bacteria since most bacteria become vulnerable at the temperature of $>45^{\circ}\text{C}$ (Ibelli et al., 2018). In order to potentiate the antibacterial activity, SPIONs can be functionalized with antibodies, antimicrobial peptides, and aptamers for targeting specific bacteria (Chen et al., 2017). The magnetic nanoparticles made with iron oxide are also effective in deep penetration into biofilm by the triggering of a magnetic field (Park et al., 2011).

Natural or synthetic polymers can be utilized to fabricate nanoparticles for biomedical use. The antibiotics can either be covalently bound to a polymer backbone or physically incorporated into a polymer matrix. The biopolymers can form nanoparticles with high biocompatibility and biodegradability. They are classified into polysaccharides, nucleic acids, and peptides/proteins. Chitosan is one of the biopolymers with linear polysaccharide composed of randomly distributed β -(1 \rightarrow 4)-linked D-glucosamine and N-acetyl-D-glucosamine. Chitosan itself can act as antibacterial and antibiofilm agents due to its polycationic nature's ability to disrupt bacterial membrane (Khan et al., 2020). Chitosan-based nanoparticles have been broadly used as drug delivery systems. The mucoadhesive character of chitosan nanoparticles contributes to the prolonged residence time in biomembranes, such as cornea, gastrointestinal epithelium, and buccal mucosa for sustained drug release (Quiñones et al., 2018). Alginate is another biopolymer commonly used to fabricate drug delivery nanocarriers. Contrary to chitosan, alginate is the anionic polysaccharide derived from the cell wall of algae. Alginate-based nanoparticles are reported



to load antimicrobial agents for treating tuberculosis and fungal infection (Jana et al., 2016). Proteins are interesting ingredients for the preparation of nanoparticles because of the variety of molecular weights and easy chemical modification. Several proteins have been employed to develop nanodelivery systems, such as heat shock albumin, proteins, and ferritin (Tarhini et al., 2017).

Although the synthetic polymers meet the challenges in regard to their biocompatibility and biodegradability, recent studies prove that some synthetic polymers can be generally regarded as safe (GRAS) as recognized by the USFDA. An example is poly(lactide-co-glycolide) (PLGA). This polymer can be hydrolyzed to non-toxic oligomers or monomers of lactic acid and glycolic acid. PLGA nanoparticles are designed for drug delivery to aid therapeutic efficacy by

drug protection, prolonged residence time, and nidus-targeting ability (Swider et al., 2018). According to the industrial consideration, there are many procedures for fabricating PLGA nanoparticles. Most of these techniques are easy to scale-up (Kim et al., 2019). The drug release and degradation rate can be tuned and controlled by changing the ratio of lactic acid and glycolic acid. Another case of synthetic polymers with acceptable biocompatibility is poly(malic acid) (PMLA), a biocompatible amphiphilic polymer based on polyesters. The features of PLMA are water soluble, biodegradable, and less toxic (Loyer and Cammas-Marion, 2014). The pendent carboxyl moieties in PLMA enable the introduction of various chemical modifications for nanoparticle development; these include antibodies, proteins, and specific drugs, including antibiotics (Chi et al., 2016).

Lipid-based nanoformulations, such as liposomes, nanoemulsions, and solid lipid nanoparticles (SLNs), are frequently applied for transporting antibacterial drugs. Lipid nanoparticles can facily fuse with bacterial membrane, delivering antibiotics directly to bacteria (Furneri et al., 2017). Liposomes, as the carriers for drug delivery, can prolong circulation time and accelerate cellular uptake, thus countering therapeutic resistance; these nano-sized vesicles consist of membrane-like phospholipid bilayers in an aqueous solution (Fenske and Cullis, 2008). Liposomes have gained much attention because of their non-toxicity and structural similarity to cells. Liposomes can fuse with mammalian cells, tumor cells, and microbes, facilitating the transport of drugs across biomembranes (Fang et al., 2014). Lipid nanocarriers, such as solid lipid nanoparticles (SLNs), nanostructured lipid carriers (NLCs) and nanoemulsions, appear suitable as drug-carrier systems due to their very low cytotoxicity relative to polymeric nanoparticles (Wen et al., 2011). The predominant difference among SLNs, NLCs and nanoemulsions is the composition of the inner core. SLNs are particles made from crystalline solid lipids, whereas NLCs are composed of a solid lipid matrix with a certain content of a liquid lipid; they are a more advanced generation of SLNs. Nanoemulsions are nanocarriers with neat liquid oil in the inner phase. These lipid nanocarriers were introduced as antibacterial drug carriers for targeting bacteria and diminishing biofilm (Forier et al., 2014).

Because of their physicochemical stability, uniform porosity, great surface area, and biocompatibility, mesoporous silica nanoparticles (MSNs) are widely employed as drug delivery carriers, biosensors, catalysts, and adsorbents (Hao et al., 2017). MSNs with tunable particle size, pore volume, and morphology are promising carriers for drug delivery. The antibacterial agents inside the porous matrix are effectively shielded against enzymatic degradation (Bernardos et al., 2019). The surface chemistry of MSNs can be modified to facilitate the passage through biomembranes. The coating of natural cell membrane on nanoparticles has gained much attention recently. This strategy leverages native cell function for improving therapeutic effect. The biomimetic nanoparticles show therapeutic benefits, including prolonged nanoparticle circulation, cell-specific targeting, and immune system targeting (Gao and Zhang, 2015). The nanoparticles can be coated with the membranes of cancer cells, erythrocytes, neutrophils, macrophages, or platelets to show their capability to bind with the source cells (Vijayan et al., 2018). The platelet membrane-coated nanoparticles are able to mimic the platelet binding with bacteria for targeted antibiotic therapy (Kroll et al., 2017).

THE INTERACTION BETWEEN NANOPARTICLES AND BACTERIAL MEMBRANE

The first step of nanoparticles for killing bacteria is the interaction with bacterial surface. There are some reports describing the interaction between nanoparticles and bacterial wall/membrane, especially the metal-based nanoparticles. The

bacterial surface is basically characterized by cell wall and cell membrane. The bacterial wall lies outside the membrane with a function to maintain the osmotic pressure of the cytoplasm and cellular morphology. Bacterial wall is composed of a homogeneous peptidoglycan layer consisting of sugars and amino acids. Gram-positive strain has one cytoplasmic membrane with multilayer of peptidoglycan polymer and a thicker wall (Fu et al., 2005). On the other hand, the Gram-negative strain wall is composed of two membranes, an outer membrane and a plasma membrane with a thin peptidoglycan layer. Nanoparticles and bacteria can interact intimately. The direct physical interaction of nanoparticles with bacteria is possible. This association is the nanoparticle anchoring onto bacterial wall or incorporation into the bacterial surface (Shrivastava et al., 2007). It is also possible that inorganic metal nanoparticles have the capability to induce irregular pit formation on the bacterial wall to facilitate ions penetrating into the cytoplasm (Pal et al., 2007). The nanoparticle interaction with cell wall can alter the membrane potential to enhance microbial membrane permeability (Vazquez-Muñoz et al., 2019). The dissipation of plasma membrane potential by the metallic nanoparticles leads to ATP depletion and outer membrane destabilization (Lok et al., 2006). Another case is that carbonaceous C₆₀ fullerene nanoparticles can directly interact with bacteria to show cell membrane damage without the influence of energy metabolism (Tang et al., 2007).

The physicochemical features of the nanoparticles such as size, shape, and surface charge are vital to govern the bacterial interaction and antibacterial activity. The size has been shown to largely affect nanoparticle interaction with bacteria. In general, smaller-sized nanoparticles have the higher possibility to interact with bacteria and the following antibacterial potency. The smaller nanocomposites reveal higher surface area-to-mass ratio for increasing the adaption and binding to bacterial surface (Aruguete and Hochella, 2010). Also, the smaller size can facily permeate into the bacterial membrane to manifest greater antibacterial activity (Zhang et al., 2007). The smaller nanoparticles have been shown to create or release more radicals, which are the important factors to eradicate pathogens (Appelrot et al., 2012). In the case of metallic nanoparticles, the smaller-sized nanomaterials increase the dissolution rate of the ions from the particles for association with bacterial surface (Pareek et al., 2018). The increased ion dissolution results in the potentiation of bacterial killing. Nanoparticles may aggregate into larger clusters before and after attaching onto bacterial surface (Tamayo et al., 2014). The nanoparticle aggregates with larger size still can contact the bacterial surface but different manners as compared to the dispersed nanoparticles (Liu et al., 2009). Recent study (Kerisit and Liu, 2009) demonstrated that the aggregates reduced the reactivity with bacteria, resulting in the lower impact upon bacteria. Although it is generally recognized that the smaller-sized nanoparticles have higher ability to eradicate bacteria, however, it cannot be ignored that some studies (El Badawy et al., 2011; Sohm et al., 2015) claimed that the larger nanoparticles are more effective to kill bacteria. In addition to the size, other physicochemical properties, the bacteria model used,

and experimental environment are factors influencing bacterial interaction and the following killing.

The most common shape observed for nanoparticles is spherical type. The other shapes including tube, rod, cube, sheet, plate, triangle, and pyramid are also reported (Slavin et al., 2017). The shape is expected to play a role on the interaction with bacteria. The rod or cube shape seems to be more effective to interact with bacteria than the other types. It can be due to the effect of crystal facet (Wang et al., 2014). The rod-shaped metal nanoparticles possess (111) and (100) facets, whereas the spherical nanoparticles have the (100) facets (Pal et al., 2007). The higher facets with greater atom density exhibit less energy to form oxygen vacancies, linking the greater antibacterial activity. Moreover, the rod or wire morphology of nanoparticles facilitates penetration into bacterial wall as compared to spherical type (Yang et al., 2009). The previous study (Talebian et al., 2013) also indicated a greater biocidal activity of flower-shaped nanoparticles against *S. aureus* than the spherical nanoparticles. Electrostatic adsorption is an important interaction between nanoparticles and bacterial membrane. Positively charged nanoparticles display the strong affinity to negatively charged bacterial surface (Tang et al., 2007). Positively charged nanoparticles tightly adhere to the bacterial surface, followed by the fusion with cell wall, while no attachment was detected for the negatively charged nanoparticles in the case of Ag nanoparticles (Ivask et al., 2014). The cationic nanoparticles also alter the function of electron transport chain in microbes (Slavin et al., 2017). The positive charge in the nanoparticles has led to the damage on cell membrane, which is a mode of antibacterial action. The functionalization of nanoparticulate surface also causes a better interaction and bactericidal activity. For instance, the carboxylic acid-functionalized Au nanoparticles show a preferential attachment to the sub-polar region of bacterial membrane (Jahnke et al., 2016). However, some functionalizations of nanoparticles such as PEGylation and antibody conjugation may retard the attachment to bacteria because of the steric hindrance.

THE POSSIBLE MECHANISMS OF ANTIBACTERIAL NANOPARTICLES

Some nanosystems represent antimicrobial activity without the inclusion of antibiotics. These include metal-based, surfactant-decorated, and chitosan nanoparticles. The bacterial killing mechanisms of these antibacterial nanoparticles include membrane disruption, reactive oxygen species (ROS) production, ATP depletion, and DNA synthesis inhibition (Slavin et al., 2017; Tamara et al., 2018). Nanoparticle adsorption to cell surface causes the depolarization, which changes the typically negative charge of the wall to become more permeable. The bacterial wall would be blurry and degraded to produce the cytoplasm material leakage (Shmarakov et al., 2014). This phenomenon can be found for both Gram-positive and Gram-negative species. The metal ions or cationic surfactants

released from the nanoparticles can directly interact with the bacterial membrane to generate membrane destabilization.

ROS production is recognized to represent an essential role of bacteria killing by antibacterial nanoparticles, particularly the metallic nanocomposites. The toxicity of ROS to the microbes is attributed to the high reactivity and oxidizing property (Zhang H. et al., 2010). Such ROS includes superoxide anion, hydrogen peroxide, and hydroxide. The toxicity of these species involves the destruction of DNA, lipids, and proteins after nanoparticle entrance into bacterial cytoplasm (Abo-Zeid and Williams, 2020). ROS is formed to suppress ATP generation and DNA replication (Ramalingam et al., 2016). For example, bacterial cells treated with Ag nanoparticles inactivate ribosomal subunit protein expression and enzymes essential to ATP production (Yamanaka et al., 2005). The nanocomposites made by ZnO or TiO₂ can generate oxidative stress on bacteria in the presence of UV radiation. ZnO nanoparticles can highly absorb UV light to induce phototoxic effect that produces superoxide anion and hydrogen peroxide (Sirelkhatim et al., 2015). These active species easily diffuse into the bacteria to kill microorganisms. TiO₂ nanoparticles show antibacterial ability through the photocatalyzed generation of radicals under UV irradiation (Brunet et al., 2009).

CELL-BASED EVALUATION OF ANTIBACTERIAL NANOPARTICLES

Antibacterial Nanoparticles Against Planktonic Bacteria

Planktonic bacteria are an original form of bacteria infecting humans; they also contaminate food and medical devices. There are different types of nanoparticles used to eradicate planktonic bacteria, including the multidrug-resistant strains. The methodology frequently used for evaluating the antimicrobial activity of the nanoparticles or compounds includes MIC, minimum bactericidal concentration (MBC), agar diffusion assay, live/dead assay, and colony-forming unit (CFU) quantification. Clinical and Laboratory Standard Institute (CLSI) provides the standard protocol to estimate MIC and agar diffusion analysis, which are the commonly used approaches for examining bacterial growth inhibition. However, the protocol is usually modified to change the treatment periods, bacterial counts, culture media, and temperature in different investigations for the optimization of different bacterial strains and antimicrobial nanoparticles/compounds. Pradeepa et al. (2016) prepared Au nanoparticles by using bacterial exopolysaccharide as the stabilizing agent for treating multidrug-resistant bacteria. The fluoroquinolone antibiotics were loaded into the Au nanoparticles. The nanosystems revealed reduced MIC and MBC against drug-resistant *S. aureus*, *K. pneumoniae*, and *E. coli* compared to the free drugs. In the inhibition zone determination, levofloxacin-, ceftriaxone-, and cefotaxime-loaded nanocarriers at 5 µg/ml exhibited the largest inhibition zones of 7.7, 10.7, and 11.6 mm against *S. aureus*, *K. pneumoniae*, and *E. coli*, respectively. The inhibition of complete bacterial growth could last up to 10 h for the nanoparticles. Antimicrobial

peptides are found in nature. More than 2,000 antimicrobial peptides are demonstrated as effective antimicrobials against a broad spectrum of strains (Mikut et al., 2016). The conjugation of antimicrobial peptides in Au nanoparticles can ameliorate the low stability of these peptides. Casciaro et al. (2017) established the covalent conjugation of antimicrobial peptide esculentin-1a to Au nanoparticles via polyethylene glycol (PEG) linker. This nanoformulation increased the anti-*P. aeruginosa* activity of free esculentin-1a by 15-fold without being toxic to human keratinocytes. The nanoparticles could bear the proteolytic digestion for protecting the peptide.

Bajaj et al. (2017) reported the development of antimicrobial dipeptide-stabilized Au or Ag nanohybrids. The Ag nanoparticles containing dipeptides showed MIC of 0.37–0.93 μM against *S. aureus*, whereas the Ag nanoparticles or dipeptides alone only exhibited the MIC of 2.47 or 24.16–50.83 μM . A synergistic effect could be observed by combining dipeptides and Ag nanoparticles. The dipeptide-capped Au nanoparticles showed no bacterial inhibition. Ag nanoparticles with the size of <30 nm tend to aggregate, resulting in decreased bactericidal activity. Kooti et al. (2018) found that graphene oxide coating on Ag nanoparticles was effective in inhibiting aggregation. The further incorporation of CoFe_2O_4 led to the possibility of magnetic targeting of bacteria. By using ciprofloxacin as the incorporated antibiotic, this nanosystem can release this drug in a controlled manner. The inhibition zone for the ciprofloxacin-loaded nanocomposite increased more than 2-fold compared to that of nanocomposite without drug, and much greater than that of ciprofloxacin alone. The nanocomposite was more effective in eradicating Gram-negative bacteria with an inhibition zone of 34–39 mm than Gram-positive bacteria (30–32 mm). Zomorodian et al. (2018) attempted to encapsulate magnetic Fe_3O_4 by PEG for improving hydrophilicity and biocompatibility. Ag as the antimicrobial agent was coated onto the nanoparticulate shell. The inhibition zone of *S. aureus* for this nanocomposite was 30 mm, which was comparable to the positive control of tetracycline (33 mm). The viability of adipose-derived mesenchymal stem cells was nearly 100% after the intervention of nanocomposite at 8 $\mu\text{g}/\text{ml}$, indicating its safe use. The biodegradable polycarbonates were grafted onto superparamagnetic MnFe_2O_4 nanoparticles for bacterial targeting (Pu et al., 2016). Cationic polycarbonates provide a strong interaction with bacterial surface. Upon increasing the concentration from 15 to 120 $\mu\text{g}/\text{ml}$, the killing percentage of the magnetic nanoparticles against *E. coli* rose from 3 to 97%. The antibacterial potency of the polycarbonate- MnFe_2O_4 nanoparticles was increased 3-fold compared to the polymer alone. The magnetic field was applied to the nanoparticles to produce hyperthermia. This thermal effect, by heating to 52°C, resulted in a killing efficiency of 97% at 8 $\mu\text{g}/\text{ml}$.

Chitosan is commonly used to prepare antibacterial nanoparticles. It has dual roles as bactericidal agent and mucoadhesive material in nanoparticles. Chitosan nanoparticles were used to entrap daptomycin for *Staphylococcus* bacteria, including MRSA (Silva et al., 2015). The encapsulation percentage of daptomycin in nanocarriers was >80%. The complete daptomycin release from the nanocarriers was

4 h. Daptomycin-loaded nanocarriers showed anti-MRSA activity with MIC of 1–2 $\mu\text{g}/\text{ml}$. Ciprofloxacin was loaded into chitosan/heparin nanoparticles to target enteropathogenic bacteria (Kumar et al., 2016). The MIC against *E. coli* of free drug and ciprofloxacin-loaded nanocarriers was 0.25 and 0.125 $\mu\text{g}/\text{ml}$, respectively. The drug-loaded nanocarriers killed nearly 60% of bacteria within 30 min. The proposed bactericidal mechanism was the synergistic effect of the biopolymer and the drug on bacterial membrane disturbance. The combination of biopolymers and synthetic polymers can produce the ideal drug delivery system with suitable biocompatibility and mechanical property. Arif et al. (2018) developed pH-sensitive chitosan/PMLA nanoparticles loaded with amoxicillin for *H. pylori* eradication. This nanosystem was conjugated with cysteine for achieving mucoadhesive and anticoagulant properties. This thiolated nanoformulation could delay amoxicillin release in gastric acid and allow effective delivery to the *H. pylori* infection region. The bacterial growth inhibition after the treatment of amoxicillin-loaded pH-sensitive nanocarriers for 6 h was 49%, which was much higher than that of the nanocarriers without pH response (27%). Proteins represent a versatile biopolymer material for nanoparticle preparation. Steiert et al. (2018) prepared antibacterial protein-based nanoparticles consisting of PEGylated lysozyme. The native lysozyme was selected as the antibacterial agent due to its innate activity as natural antibiotic (Ibrahim et al., 2002). At a concentration of 0.32 $\mu\text{g}/\text{ml}$, the lysozyme-based nanoparticles revealed lower *M. luteus* growth compared to free lysozyme. An adhesive interaction of the nanoparticles with *M. luteus* surface contributed to a sustained release and prolonged attack against peptidoglycan layer.

PLGA is the synthetic GRAS polymer used alone or in combination with the other polymers to produce nanoparticles. The antibiotic rifampicin was loaded into PLGA-N-2-hydroxypropylmethacrylamide (HPMA) nanoparticles to evaluate the bactericidal activity against *M. tuberculosis* (Rani et al., 2018). The rifampicin release from nanocarriers could be maintained in a sustained fashion up to 70 h, while the free drug was completely released within 6 h. The bacterial inhibition by the nanoparticles was 4 times greater than the free control according to the MIC determination. Radovic-Moreno et al. (2012) developed vancomycin-loaded PLGA-poly(L-histidine)-PEG nanoparticles for treating *S. aureus* and *E. coli*. This nanosystem was designed to strongly bind to bacteria in acidity. This mechanism involved the pH response of nanoparticulate surface charge switching by selective protonation of imidazole moieties of poly(L-histidine) in acidic environment. The binding study demonstrated an increased binding of nanoparticles to bacteria by 4 to 6-fold through the pH change from pH 7.4–6.0. The nanosystem reduced the loss of antibacterial efficacy at low pH, with an elevation of MIC of 1.3-fold as compared to 2.0-fold for free vancomycin. The depletion of phosphate in the intestine is a major cue triggering bacterial virulence. It is important to maintain phosphate concentration to prevent virulence expression. Yin et al. (2017) synthesized phosphate- and polyphosphate-crosslinked PEG nanoparticles for sustained delivery of phosphate. The release of phosphate from PEG-based nanocarriers was sustained for 100 h. The nanoformulation was

effective in suppressing pyoverdine and pyocyanin, the virulence biomarkers of *P. aeruginosa*.

The nanoparticulate surface functionalized by carbohydrate/glycan is reported to display antibacterial function via carbohydrate-mediated targeting by bacterial proteins (Xue et al., 2011). Eissa et al. (2016) constructed polymeric glycosylated nanoparticles to encapsulate ampicillin. Poly(N-butyl acrylate) was used as the nanoparticulate core. The ampicillin-loaded glycol-nanoparticles were found to elicit aggregation of *S. aureus* and *E. coli*, resulting in vital bacteria eradication by the antibiotic release in the proximity of the bacterial envelope. Curcumin as a natural compound is well-known for its antibacterial activity (Praditya et al., 2019). Shlar et al. (2017) developed polyquaternium-10-based nanoparticles for curcumin to display anti-*E. coli* activity. Polyquaternium-10 is a cellulose ether with cationic nature. The exposure of *E. coli* to the polyelectrolyte-coated nanoparticles inhibited bacterial proliferation with only minor viability reduction, suggesting bacteriostatic action. Both the bacterial membrane and ATP depolarization were the nanoparticle-related antibacterial mechanisms. Another polyelectrolyte nanosystem for bacteria eradication was the use of polyethyleneimine (PEI) and anionic enzyme-sensitive peptide for targeting *P. aeruginosa* (Insua et al., 2016). This enzyme-responsive nanosystem was selectively degraded in the presence of *P. aeruginosa* elastase, the virulence factor, while no degradation was detected in the presence of human neutrophil elastase. The nanoparticles exerted significant anti-*P. aeruginosa* activity without affecting other non-pathogenic strains.

Lipid-based nanoparticles offer high entrapment to lipophilic antibiotics. The polymers can be incorporated in lipid nanoparticles for developing lipid-polymer hybrid nanosystems. Dave et al. (2017) prepared norfloxacin-loaded hybrid nanoparticles by using soya lecithin and poly (lactic acid) (PLA) as the lipid and polymer components, respectively. The encapsulation efficiency of the antibiotic in the hybrid nanosystem was 72%. The drug release percentage reached 90% within 24 h. The norfloxacin-loaded nanocarriers retained antibacterial activity toward *S. aureus* and *P. aeruginosa* similar to free drug. The skin irritation of topically applied norfloxacin in rats was reduced after nanoparticulate incorporation. SLNs were fabricated to deliver antimicrobial oligonucleotide transcription factor decoys (TFD) (González-Paredes et al., 2019). The nanoparticles are helpful in protecting TDF from nuclease degradation and delivering TDF to target sites. SLNs were coated with either cationic bolaamphiphile 12-bis-tetrahydroacridinium or protamine to form the complexation with TFD. The cationic SLNs displayed extensive *E. coli* membrane binding and aggregation. A >2 log reduction in viable *E. coli* was found after nanoparticle treatment. The MIC was much less than the IC_{50} from cytotoxicity against Caco-2 cells, indicating the selectivity for bactericidal effect over mammalian toxicity. An acid-cleavable lipid was synthesized and used to develop pH-responsive SLNs for delivering vancomycin to acidic infection sites (Kalhapure et al., 2017). Vancomycin release from SLNs was faster at pH 6.5 than pH 7.4. *In vitro* antibacterial activity against MRSA showed that SLNs had enhanced activity at pH 6.5 than pH 7.4. The antimicrobial effect of NLCs loaded with nisin Z was evaluated

by Lewies et al. (2017). Nisin Z is a cationic antimicrobial peptide produced by *Lactococcus lactis*. The incorporation of ethylenediaminetetraacetic acid (EDTA) in NLCs improved anti-*E. coli* activity due to EDTA's ability to destabilize the outer membrane to increase permeability. The antibacterial activity toward Gram-positive strains, such as *S. aureus* and *S. epidermidis*, also increased in the presence of EDTA. Another case of using lipid-based nanocarriers for protecting antimicrobial peptides is the lyotropic liquid crystalline nanostructure (Boge et al., 2016). The liquid crystallines consisting of cubic glycerol monooleate/water and hexagonal glycerol monooleate/oleic acid/water were examined as carriers for three antimicrobial peptides: AP114, DPK-060, and LL-37. The experimental data on MIC against MRSA demonstrated the superior activity of cubosomes over hexosomes, perhaps because the peptides tended to stay in the hexagonal structure with minimal release from the nanostructures.

Dendritic MSNs with center-radial pore architecture, large pore channel, and highly accessible pore volume have emerged as drug delivery system for large molecules such as proteins and DNA (Du and Qiao, 2015). Lysozyme, used as the antimicrobial enzyme to damage bacterial wall, was loaded into dendritic MSNs (Wang et al., 2016). The lysozyme-loaded nanocarriers had lower MIC against *E. coli* compared to free lysozyme (500 vs. 2,500 $\mu\text{g/ml}$). The MSNs released 67% lysozyme within 48 h. The total inhibition of *E. coli* growth by MSNs could be maintained throughout 5 d. The biomembrane-coated nanoparticles are applicable for on-demand antibiotic delivery. Li et al. (2014) prepared gelatin nanoparticles coated with red blood cell (RBC) membrane for delivering vancomycin. RBC membrane can reduce the clearance by the immune system and absorb bacterial exotoxin to relieve bacterial toxicity. The gelatin core was degraded by gelatinase, which is overexpressed in the infection microenvironment; the entrapped antibiotic was then released to kill the bacteria. Upon incubation with gelatinase-positive bacteria (*S. aureus* and *P. aeruginosa*), 62–92% vancomycin was released from the enzyme-responsive nanocarriers, whereas only 20% vancomycin was released in gelatinase-negative strains (*S. epidermidis* and *E. coli*). The MIC against *S. aureus* and *S. epidermidis* was 3 and 12 $\mu\text{g/ml}$, respectively. The antibacterial nanoparticles for eradication of planktonic bacteria evaluated via cell-based study are summarized in Table 1.

Antibacterial Nanoparticles Against Biofilm Bacteria

Nanoparticles provide a unique approach to targeting bacterial biofilm. The nanoparticulate distribution through the biofilm layer is consistent with diffusive permeation. The small size of nanoparticles enables them to transport into the porous matrix (Botequim et al., 2012). It is generalized that nanoparticles diffuse via water-filled pores in the biofilm (Aljuffali et al., 2015). The biofilm is extremely non-wetting, limiting the penetration of some antimicrobial liquids (Sun et al., 2012). The low surface tension of nanoparticles assists the entrance into the non-wetting biofilm. Lambadi et al. (2015) conjugated polymyxin B, a cationic antimicrobial peptide, on Ag nanoparticle surface

TABLE 1 | The summary of antibacterial nanoparticles for eradication of planktonic bacteria evaluated via cell-based study.

Nanoparticle type	Antibacterial agent	Average size	Bacteria strain	The feature of nanoparticles	References
Au	Fluoroquinolones	20–30 nm	Drug-resistant <i>S. aureus</i> , <i>K. pneumoniae</i> , and <i>E. coli</i>	Exopolysaccharide as the stabilizing agent	Pradeepa et al., 2016
Au	Esculentin-1a	14 nm	<i>P. aeruginosa</i>	Increased esculentin-1a stability	Casciaro et al., 2017
Au or Ag	Dipeptides	12–15 nm	<i>S. aureus</i> , <i>E. coli</i> , and <i>S. typhimurium</i>	Both dipeptides and Ag as the antibacterial agents	Bajaj et al., 2017
Ag	Ciprofloxacin	15–16 nm	<i>S. aureus</i> , <i>B. subtilis</i> , <i>E. coli</i> , and <i>P. aeruginosa</i>	Combined with graphene oxide and CoFe ₂ O ₄	Kooti et al., 2018
Fe ₃ O ₄ -Ag	Ag	20–25 nm	<i>S. aureus</i> and <i>E. coli</i>	Increased hydrophilicity and biocompatibility by PEG	Zomorodian et al., 2018
MnFe ₂ O ₄	Polycarbonates	17 nm	<i>S. aureus</i> and <i>E. coli</i>	Increased interaction with bacterial surface	Pu et al., 2016
Chitosan	Daptomycin	About 200 nm	<i>Staphylococcus</i> strains	Mucoadhesive property for ocular treatment	Silva et al., 2015
Chitosan/heparin	Ciprofloxacin	About 250 nm	<i>E. coli</i>	Synergistic effect of chitosan and antibiotic	Kumar et al., 2016
Chitosan/PMLA	Amoxicillin	186 nm	<i>H. pylori</i>	pH-sensitive nanoparticles	Arif et al., 2018
PEGylated lysozyme	Native lysozyme	About 200 nm	<i>M. luteus</i>	Bioadhesive ability to bacteria	Steiert et al., 2018
PLGA-HPMA	Rifampicin	260 nm	<i>M. tuberculosis</i>	Sustained drug release	Rani et al., 2018
PLGA-poly(L-histidine)-PEG	Vancomycin	196 nm	<i>S. aureus</i> and <i>E. coli</i>	pH-sensitive nanoparticles	Radovic-Moreno et al., 2012
PEG	Phosphate and polyphosphate	About 180 nm	<i>P. aeruginosa</i>	Sustained phosphate release	Yin et al., 2017
Poly(N-butyl acrylate)	Ampicillin	302 nm	<i>S. aureus</i> and <i>E. coli</i>	Glycosylated nanoparticles for bacterial aggregation	Eissa et al., 2016
Polyquaternium-10	Curcumin	146 nm	<i>E. coli</i>	A bacteriostatic action for the nanoparticles	Shlar et al., 2017
Poly(ethylene imine)	Poly(ethylene imine)	111 nm	<i>P. aeruginosa</i>	Targeting to <i>P. aeruginosa</i> elastase	Insua et al., 2016
Lipid-polymer hybrid	Norfloxacin	179–221 nm	<i>S. aureus</i> and <i>P. aeruginosa</i>	Less skin irritation	Dave et al., 2017
SLNs	Antimicrobial oligonucleotides	90–124 nm	<i>E. coli</i>	Protection oligonucleotides from enzymatic degradation	González-Paredes et al., 2019
SLNs	Vancomycin	133 nm	MRSA	pH-sensitive nanoparticles	Kalhapure et al., 2017
NLCs	Nisin Z	175–330 nm	<i>S. aureus</i> , <i>S. epidermidis</i> , and <i>E. coli</i>	Increased antibacterial activity by EDTA incorporation	Lewies et al., 2017
Lipid-based liquid crystals	Antimicrobial peptides	127–159 nm	<i>S. aureus</i> , MRSA, <i>P. aeruginosa</i> , and <i>E. coli</i>	Cubosomes showed superior antibacterial activity than hexosomes	Boge et al., 2016
Dendritic MSNs	Lysozyme	79–160 nm	<i>E. coli</i>	Prolonged bacteria growth inhibition	Wang et al., 2016
RBC membrane-coated nanoparticles	Vancomycin	97 nm	<i>S. aureus</i> , <i>S. epidermidis</i> , <i>P. aeruginosa</i> , and <i>E. coli</i>	Enzyme-sensitive nanoparticles	Li et al., 2014

EDTA, ethylenediaminetetraacetic acid; HPMA, N-2-hydroxypropylmethacrylamide; MRSA, methicillin-resistant *S. aureus*; MSNs, mesoporous silica nanoparticles; NLCs, nanostructured lipid carriers; PEG, poly(ethylene glycol); PLGA, poly(lactide-co-glycolide); PMLA, poly(malic acid); RBC, red blood cell; SLNs, solid lipid nanoparticles.

to assess the anti-biofilm activity against multidrug-resistant *P. aeruginosa*. The polymyxin B-capped Ag nanoparticles showed a 3-fold higher biofilm reduction than the neat Ag nanoparticles. In addition, the polymyxin B-capped nanoparticles removed 97% of the endotoxin of *P. aeruginosa*. Another inorganic metal nanosystem employed for biofilm disruption is Au (Giri et al., 2015). The Au nanoparticles were coated with thioalkyl tetra(ethyleneglycol)ated trimethylammonium and tetraethylene

glycol to produce cationic and neutral particles, respectively. The positively charged nanoparticles displayed a significant reduction of *S. aureus* biofilm stained by crystal violet, whereas the neutral nanoparticles showed a lesser degree of diminishing biofilm. The cationic nanosystems are easily bound to biofilm polymers and negatively charged DNA. SPIONs can be targeted to the infection site under an external magnetic force to deeply penetrate into the biofilm (Subbiahdoss et al., 2012). Geilich et al. (2017)

demonstrated biofilm growth inhibition by SPIONs decorated by PEG-*b*-PLA copolymer used to encapsulate methicillin. The application of SPIONs and magnetic field resulted in the deep penetration into *S. epidermidis* biofilm and selective bactericidal effect in the region of the applied magnetic field. The free antibiotic inhibited planktonic bacteria growth without the capability of entering the biofilm.

Chitosan with positive charge is applicable to produce anti-biofilm nanoparticles because of its affinity to polymers and DNA in biofilm. The *S. aureus* biofilm could be diminished by chitosan nanoparticles loaded with oxacillin and DNase I (Tan et al., 2018). DNase I is able to degrade extracellular DNA in biofilm matrix. The nanosystem with oxacillin and DNase I revealed greater biofilm eradication than did the nanoparticles without oxacillin or DNase I. The nanosystem could damage the biofilm via DNA degradation to kill *S. aureus* and reduce biofilm thickness. Repeated nanosystem treatment for 48 h induced a 98% biofilm reduction. Chitosan, PEG, and Fe₃O₄ were used to fabricate the biocompatible magnetic nanoparticles for biofilm eradication (Wang et al., 2018). Gentamicin was the selected antibiotic loaded in the magnetic nanocarriers. Under acidic condition, chitosan and PEG were protonated to facilitate the interaction with bacterial membrane. The magnetic field allowed deep penetration of the nanoparticles into mature *S. aureus* biofilm. The survival of bacteria in biofilm was about 80% and 5% after nanoparticle treatment without and with magnetic force, respectively.

With respect to PLGA nanoparticles, d'Angelo et al. (2015) designed PLGA/chitosan nanoparticles loaded with antimicrobial peptide colistin to eradicate *P. aeruginosa* biofilm. The nanocarriers were freeze-dried to produce the powder form for the future application in pulmonary inhalation. Free colistin at 7.5 and 15 µg/ml had a potent biofilm inhibition with 90% biomass reduction after 24-h treatment. This effect was diminished after 48 h and completely lost after 72 h. The nanocarriers could preserve anti-biofilm effect for 72 h. Baelo et al. (2015) developed ciprofloxacin-loaded PLGA nanoparticles functionalized by DNase I for eradicating *P. aeruginosa* biofilm. The nanoparticles showed a steady release of the antibiotic within 12 h. More than 80% of biofilm reduction was detected by nanoparticle treatment at the ciprofloxacin dose of 0.0156 µg/ml. The repeated application of the nanoparticles for 3 d resulted in biofilm reduction by 95%. Nguyen et al. (2016) determined anti-biofilm activity of poly(oligo(ethylene glycol) methyl ether methacrylate) (POEGMA) nanoparticles capable of storing nitric oxide and gentamicin. Nitric oxide is an agent used to provoke biofilm dispersal into antibiotic-susceptible planktonic form (Barraud et al., 2006). This nanosystem could simultaneously release nitric oxide and antibiotic to demonstrate a synergistic effect, eliminating biofilm and planktonic *P. aeruginosa* by 90 and 95%, respectively. The treatment of free nitric oxide or gentamicin only induced biofilm viability by <20%.

Liposomes are the lipid-based nanovesicles capable of loading antibiotics for biofilm eradication. Nisin was loaded into liposomes to clear the biofilm formed by *Streptococcus mutans* (Yamakami et al., 2013). The liposomes played a role in prolonging nisin release. There was 76% nisin released from

liposomes within 6 h. The nisin concentration for efficacious glucan-biofilm inhibition was reduced 4-fold after liposomal encapsulation. This inhibition could be maintained during 6 h, while no inhibition was observed in the case of free nisin at this time. In another work, Ma and Wu (2016) prepared gentamicin-loaded liposomes to penetrate into alginate-based *Ralstonia insidiosa* biofilm in the presence of acoustic streaming created by pulsed ultrasound. The ultrasound pushed the liposomes into alginate-based biofilm. Afterward, the drug was released from liposomes disintegrated under pulsed ultrasound. This procedure reduced viable bacteria number in biofilm by 72%. Fang et al. (2019) evaluated the effect of cationic nanoemulsion droplet size on anti-biofilm activity against MRSA. The authors prepared three cetylpyridium chloride-coated nanoemulsions with average diameters of 55, 165, and 245 nm. The smaller droplets demonstrated potent anti-biofilm efficacy with a 10-fold reduction of bacteria survival compared with the non-treatment control. The loss of total DNA in bacteria was also increased following the decrease of droplet size. The smaller nanoparticles may be facilely delivered into the pores of the biomass to kill bacteria. Soyaethyl morpholinium ethosulfate (SME) is a cationic surfactant showing antibacterial activity through bacterial membrane lysis. Lin et al. (2017) compared the anti-biofilm activity of SME coated on nanoemulsions and liposomes. The data on MIC/MBC demonstrated superior antimicrobial effect of nanoemulsions compared to liposomes against MRSA and *S. epidermidis*. Nanoemulsions decreased MRSA biofilm thickness 2.4-fold, a result which was higher than liposomes (1.6-fold). The high surface charge, low lipophilicity, and wetting character of nanoemulsions contributed to the greater biofilm suppression as compared to liposomes. The antibacterial nanoparticles for eradication of biofilm bacteria are summarized in Table 2.

Antibacterial Nanoparticles Against Intracellular Bacteria

Two biopolymer nanoparticles were used for treating intracellular bacteria in recent years. Smitha et al. (2015) developed chitin nanoparticles for delivering rifampicin into neutrophils for killing intracellular pathogens. Rifampicin showed a sustained release from the nanoparticles till 72 h. The intracellular rifampicin concentration in neutrophils was enhanced 6- to 7-fold after loading in nanoformulation. The MIC of the nanoparticles to inhibit *E. coli* and *K. pneumoniae* was 20 and 35 µg/ml, respectively. This level was lower than that of free drug (35 and 40 µg/ml), perhaps due to the strong binding of the nanoparticles with bacterial surface. Macrophages are the immune cells serving as a host for *M. tuberculosis*. Rifampicin and levofloxacin were complexed with cyclodextrin and conjugated to curdlan-based nanoparticles for intra-macrophage *M. tuberculosis* eradication (Yunus Basha et al., 2019). Curdlan is a linear glucan derived from *Agrobacterium* and *Rhizobium*. It is recognized by dectin-1 receptor expression in macrophages (Ganbold and Baigude, 2018). The nanoparticle internalization by macrophages was 1.8-fold higher than that by fibroblast cells, indicating the usefulness of curdlan in nanoparticles

TABLE 2 | The summary of antibacterial nanoparticles for eradication of biofilm and intracellular bacteria evaluated via cell-based study.

Nanoparticle type	Antibacterial agent	Average size	Bacteria strain	The state of bacteria	References
Ag	Polymyxin B	About 130 nm	<i>P. aeruginosa</i>	Biofilm	Lambadi et al., 2015
Au	Au	10–12 nm	<i>S. aureus</i>	Biofilm	Giri et al., 2015
SPIONs	Methicillin	About 50 nm	<i>S. epidermidis</i>	Biofilm	Geilich et al., 2017
Chitosan	Oxacillin	167 nm	<i>S. aureus</i>	Biofilm	Tan et al., 2018
Chitosan/PEG/ Fe ₃ O ₄	Gentamicin	About 200 nm	<i>S. aureus</i>	Biofilm	Wang et al., 2018
PLGA/chitosan	Colistin	267 nm	<i>P. aeruginosa</i>	Biofilm	d'Angelo et al., 2015
PLGA	Ciprofloxacin	252 nm	<i>P. aeruginosa</i>	Biofilm	Baelo et al., 2015
POEGMA	Gentamicin	15 nm	<i>P. aeruginosa</i>	Biofilm	Nguyen et al., 2016
Liposomes	Nisin	Unknown	<i>Streptococcus mutans</i>	Biofilm	Yamakami et al., 2013
Liposomes	Gentamicin	182 nm	<i>Ralstonia insidiosa</i>	Biofilm	Ma and Wu, 2016
Nanoemulsions	Cetylpyridinium chloride	55, 165, and 245 nm	MRSA	Biofilm	Fang et al., 2019
Nanoemulsions and liposomes	Soyaethyl morpholinium ethosulfate	214 and 75 nm	MRSA	Biofilm	Lin et al., 2017
Chitin	Rifampicin	350 nm	<i>S. aureus</i> , <i>E. coli</i> , and <i>K. pneumoniae</i>	Intra-neutrophil infection	Smitha et al., 2015
Curdlan	Rifampicin and levofloxacin	619 nm	<i>Mycobacterium smegmatis</i>	Intra-macrophage infection	Yunus Basha et al., 2019

MRSA, methicillin-resistant *S. aureus*; PEG, poly(ethylene glycol); PLGA, poly(lactide-co-glycolide); POEGMA, poly(oligo(ethylene glycol) methyl ether methacrylate); SPIONs, superparamagnetic iron oxide nanoparticles.

for macrophage uptake. The nanocarriers could kill >95% of intra-macrophage bacteria within 4 h, whereas only 53% killing was detected in the group of free rifampicin. The antibacterial nanoparticles for treating intracellular bacteria are summarized in Table 2.

ANIMAL-BASED EVALUATION OF ANTIBACTERIAL NANOPARTICLES

Skin and Subcutaneous Region Infection

The bacteria facily locate in the skin, such as lesions of atopic dermatitis and chronic wounds, playing a critical role in infection-induced inflammation and cutaneous disease progression (Shi et al., 2018). The ideal infection model for assessing the antimicrobial activity of nanomedicine in animal-based studies is the skin and subcutaneous region infection, as one can observe the performance of bacterial infection due to the visible skin appearance. This infection model is also easy and simple to establish by topical bacteria administration or subcutaneous bacteria injection. Various administration routes of nanoparticle delivery can be used to treat cutaneous and subcutaneous infection, including topical, subcutaneous, and intravenous applications. Chitosan and 2-mercapto-1-methylimidazole (MMT) were coated on the surface of Au nanoparticles allowing multivalent interaction with bacterial membrane (Lu et al., 2018). The nanoparticles were crosslinked with gelatin to form wound dressing for treating skin infection. The MRSA-infected wound in rabbit back was topically administered by the nanoparticles. The regenerated skin after treatment of nanocomposite showed an appearance like normal skin, with 92% wound closure, whereas the wound

treated by gauze only revealed 67% closure after 16 d. Liu et al. (2018) developed chemo-photothermal therapy against subcutaneous infection based on polydopamine-coated Au nanorods. Polydopamine coating achieved efficient antibacterial Ag loading in the nanorods. This platform became positively charged in the acidic environment of the bacteria-formed abscess, allowing their accumulation in the infection site as revealed by florescence imaging. The loaded Ag was released in a pH-sensitive manner. This nanosystem was intravenously injected into the mice to treat subcutaneous abscess under near infrared (NIR) irradiation. The hyperthermal effect of NIR led to more Ag release and MRSA killing for abscess ablation and wound healing acceleration.

Allicin is a natural antibacterial compound abundant in garlic (Wallock-Richards et al., 2014). Sharifi-Rad et al. (2014) combined allicin and antibacterial Ag nanoparticles for the management of skin infection in mice produced by MRSA. Topical ointment with allicin and Ag nanoparticles showed a synergistic effect in inhibiting MRSA infection in skin. The bacterial count for control, allicin, Ag, and the combination was 3.8×10^{10} , 4.3×10^6 , 8.0×10^7 , and 0 CFU/ml, respectively. A photothermal nanocomposite of hyaluronic acid (HA)-templated Ag nanoparticles integrated with graphene oxide was prepared to treat *S. aureus* infection in skin (Ran et al., 2017). HA was degraded by hyaluronidase secreted from bacteria to trigger Ag release. NIR illumination on the nanoparticles containing graphene oxide locally raised the hyperthermia to eradicate the bacteria. In the *in vivo* skin wound infection study, the bacterial count of the combined nanoparticles and NIR was 2 orders less as compared to the control and NIR alone. Bacterial contamination in the central venous catheter (CVC) can result

in bacterial consortium and inflammation. Ribeiro et al. (2018) immobilized SPIONs functionalized with antimicrobial peptide clavanin A on CVC for use as an antibacterial prophylactic. The skin infection in mice was induced by introducing CVC (40 mm in length) containing 20 μ l of 1×10^9 CFU/ml *K. pneumoniae*. After irradiation of diode laser (808 nm) on CVC for 5 min, the viability of the attached bacteria was reduced by 88%. The antimicrobial action could be maintained for 7 d. The inflammation was also reduced based on the determination of cytokines. The photothermal therapy was also established by using acetylcysteine-coated Prussian blue nanoparticles (Cai et al., 2019). Acetylcysteine is an antimicrobial agent with mucolytic activity. Prussian blue nanoparticles have been proven as a photothermal agent triggered by NIR (Szaciłowski et al., 2006). The acetylcysteine-coated nanoparticles were prepared based on the co-precipitation of $K_4Fe(CN)_6$ and $FeCl_3$. The irradiation of NIR (980 nm) on nanoparticles at 50 μ g/ml eliminated *S. aureus* and *E. coli* by 74 and 75%, respectively. The NIR exposure after subcutaneous injection of the nanocomposite generated local heat to eradicate *S. aureus* in subcutaneous abscess.

With respect to polymeric nanocarriers, poly(ϵ -caprolactone) (PCL) was used to incorporate carvacrol and then mixed with hydrogel for topical delivery (Mir et al., 2019). Carvacrol is a monoterpene showing bactericidal effect on a broad range of microbes (Nostro and Papalia, 2012). The nanoparticles were enzyme-sensitive to produce carvacrol release in the presence of bacterial lipase. The dermatokinetic study demonstrated an enhanced carvacrol deposition in epidermis from 0.04 to 0.96% of the applied dose after nanoparticle inclusion. The carvacrol-loaded nanoparticles in hydrogel showed MRSA burden reduction by 99.97% in the burn wound of pig skin. About 25% of bacteria residing in skin accumulated in hair follicles (Lange-Asschenfeldt et al., 2011). The bacteria deposited in hair follicles are usually difficult to eliminate. Hsu et al. (2017) developed chloramphenicol-loaded lipid-based nanocarriers for follicular delivery to eradicate MRSA. Dimyristoylphosphatidylcholine (DMPC) or deoxycholic acid (DA) was incorporated into liposomes for producing the malleable vesicles with the aim of easy extrusion into follicles. The flexible liposomes with DMPC and DA elevated intrafollicular uptake of the drug by 1.5- and 2-fold, respectively. *In vivo* topical application demonstrated found no skin irritation after the administration of liposomes for 7 consecutive d. Another case of lipid-based nanoparticles is the simultaneous incorporation of SME and oxacillin in NLCs for synergistic bactericidal effect against MRSA (Alalaiwe et al., 2018). The cationic NLCs could disorganize MRSA membrane to leak the proteins. This disintegration of membrane also promoted oxacillin entrance into the cytoplasm. Topical delivery of NLCs to MRSA abscess in mouse skin reduced MRSA load by 4 logs. The skin architecture and barrier function were also recovered by NLCs.

Yang et al. (2018) developed gentamicin-loaded MSNs coated with lipid bilayer surface. The bilayer shell of MSNs was decorated with *S. aureus*-targeting peptide ubiquicidin. The lipid bilayer could be degraded by bacterial toxins to rapidly release gentamicin. The fast antibiotic release was confirmed in the

presence of planktonic and intra-macrophage *S. aureus*. The intracellular *S. aureus* was subcutaneously injected into mice. The mice were treated with nanocomposite via intravenous administration after 2 d. The bacterial load in the infected area was 2.3×10^7 and 8.4×10^6 CFU/ml upon the injection of PBS and free drug, respectively. The nanoparticles reduced bacterial burden to 1.5×10^4 CFU/ml. Micelles are the supramolecular assembly of surfactants. The antibacterial SME was the cationic surfactant which could form micelles in a nanoscale size (Yang et al., 2016). In the mouse model of subcutaneous MRSA abscess, topically applied SME micelles demonstrated a reduced bacterial burden, compared to vehicle control, by 1.6×10^4 -fold. A negligible cutaneous irritation was found after micelle intervention on healthy mouse skin, suggesting safe application for anti-MRSA therapy. The antibacterial nanoparticles for treating topical infection in skin tissue are listed in Table 3.

Pulmonary Infection

Bacteria can largely invade the human body via the respiratory tract to induce lung-related diseases such as pneumonia, tuberculosis, and cystic fibrosis. Some efforts are conducted to treat lung infection in animals by intravenous or intratracheal administration of nanoformulations. Kang et al. (2019) used tigecycline as the model antibiotic to be encapsulated in intercellular adhesion molecule (ICAM)1-conjugated β - $Ga_2O_3:Cr^{3+}$ nanoparticles. ICAM1 is highly expressed in endothelial cells of inflammation sites. β - $Ga_2O_3:Cr^{3+}$ is a semiconductor material with luminescent property for bioimaging (Wang et al., 2015). Tigecycline-resistant *K. pneumoniae* (TRKP) was administered into the lung via intratracheal route to establish the TRKP-infected pneumonia mice. Only the intravenous nanoparticle-treated mice demonstrated 100% survival against pulmonary infection after 12 d. The survival rate of the mice treated by free drug at 45 mg/kg was 83%, which was still lower than those treated by nanocarriers at 15 mg/kg. The *in vivo* biodistribution showed an increased fluorescence intensity of the nanoparticle-treated lung from 5 to 24 h post-injection, suggesting increased nanoparticle accumulation in the infected area through targeted delivery.

Some polymer-based nanocarriers are fabricated with the aim of treating *P. aeruginosa*-induced pulmonary infection. The inhaled tobramycin represents limited capability to penetrate DNA-rich lung mucus (Kłodzinska et al., 2016). Deacon et al. (2015) synthesized tobramycin-loaded chitosan/alginate nanoparticles functionalized with DNase for inhibiting mucus viscoelasticity by DNA cleavage. The treatment of the biopolymer nanoparticles prior to lung infection with *P. aeruginosa* offered longer protection, doubling the survival rate from 40% with free antibiotic to 80%. The nanoparticles containing DNase improved nanoparticle penetration in the sputum of cystic fibrosis patients. Casciaro et al. (2019) investigated lung infection treated by intratracheal PLGA nanoparticles containing antimicrobial peptide esculentin-1a. The nanoparticles were coated with poly(vinyl alcohol) (PVA) as the stabilizing agent. The neutral hydrophilic nanoparticle surface was favorable to permeate through pulmonary mucus. In the mouse model of lung infection induced by *P. aeruginosa*, the esculentin-1a-loaded

TABLE 3 | The summary of antibacterial nanoparticles for treating bacterial infection of skin and subcutaneous region evaluated via animal-based study.

Nanoparticle type	Antibacterial agent	Average size	Bacteria strain	Animal model	References
Au	Chitosan	8–13 nm	MRSA	Open wound infection in rabbits	Lu et al., 2018
Au nanorods	Ag	Length 68 nm; diameter 21 nm	MRSA	Subcutaneous abscess in mice	Liu et al., 2018
Ag	Allicin and Ag	10–30 nm	MRSA	Open wound infection in mice	Sharifi-Rad et al., 2014
Ag	Ag	20 nm	<i>S. aureus</i>	Open wound infection in mice	Ran et al., 2017
SPIONs	Clavanin A	10 nm	<i>K. pneumoniae</i>	Bacteria-containing CVC introduction in mice	Ribeiro et al., 2018
SPIONs	Acetylcysteine	95 nm	<i>S. aureus</i>	Subcutaneous abscess in mice	Cai et al., 2019
PCL	Carvacrol	164–233 nm	MRSA	Burn wound infection in pig skin	Mir et al., 2019
Liposomes	Chloramphenicol	132–239 nm	MRSA	Skin irritation test in nude mice	Hsu et al., 2017
NLCs	SME and oxacillin	177 nm	MRSA	Subcutaneous abscess in mice	Alalawi et al., 2018
MSNs	Gentamicin	95 nm	<i>S. aureus</i>	Subcutaneous abscess in mice	Yang et al., 2018
Micelles	SME	178 nm	MRSA	Subcutaneous abscess in mice	Yang et al., 2016

CVC, central venous catheter; MRSA, methicillin-resistant *S. aureus*; MSNs, mesoporous silica nanoparticles; NLCs, nanostructured lipid carriers; PCL, poly(ϵ -caprolactone); SME, soyaethyl morpholinium ethosulfate; SPIONs, superparamagnetic iron oxide nanoparticles.

nanocarriers reduced CFU by 3 logs as compared to PBS-treated group. This anti-*P. aeruginosa* activity was 17-fold stronger than that of free esculentin-1a. Amphiphilic PEG-co-PCL copolymer was conjugated with vancomycin as the targeting ligand via pH-cleavable hydrazone bonds to obtain micelle nanocarriers (Chen et al., 2018). Ciprofloxacin was loaded in the nanocomposite for on-demand release. The opening of the vancomycin shell of the nanocomposite under acidic environment could interfere with the hydrophilic/lipophilic balance, leading to micelle size enlargement, facilitating the degradation of PCL by lipase overexpressed in the infection site and ciprofloxacin release for *P. aeruginosa* destruction. The micelle treatment in *P. aeruginosa*-infected mice reduced the bacterial load and alveolar injury in the lung compared to free ciprofloxacin.

To deliver moxifloxacin to the infected lung tissue and enable sustained drug release, a ROS-responsive 4-(hydroxymethyl) phenylboronic acid pinacol ester-modified α -cyclodextrin was coated with phospholipids to form a lipid-coated nanoparticles for lung infection management (Wang et al., 2019). The coating with 1,2-distearoyl-sn-glycero-3-phosphoethanolamine (DSPE)-PEG-folic acid on nanocarriers helped to promote sputum penetration and targeting to the macrophages with overexpressed ROS in the inflammatory region. The nanosystem was intravenously injected into the mice with *P. aeruginosa* infection in lung. The administration of moxifloxacin could increase the survival rate from 20 to 40% after nanoparticulate encapsulation. Almost no pathogen colony was detectable in the lung after nanocomposite treatment. Another lipid-based nanoformulation investigated for ameliorating infectious pneumonia was PEGylated phosphatidylcholine-rich nanovesicles (Hsu et al., 2018). The nanovesicles were loaded with ciprofloxacin for lung targeting to pulmonary surfactants. This could lead to the eradication of intracellular MRSA. The *in vivo* biodistribution result showed a 3.2-fold increase of pulmonary ciprofloxacin accumulation after intravenous

injection of the lipid nanovesicles. The pulmonary MRSA burden was restrained from 4.9×10^8 to 1.2×10^8 and 6.3×10^7 CFU by treatment by control drug and the nanovesicles, respectively.

NZX is an antimicrobial peptide capable of suppressing the growth of drug-resistant *M. tuberculosis*. Tenland et al. (2019) aimed to entrap NZX into MSNs for treating tuberculosis because of the large uptake of MSNs by macrophages. The nanoparticles presented increased intra-macrophage bacteria killing compared to free NZX. In the murine tuberculosis model, the CFU of *M. tuberculosis* in the lung was decreased by 84% and 88% after intratracheal application of free peptide and NZX-containing MSNs, respectively. MSNs were also used for active targeting to treat pulmonary infection (Hussain et al., 2018). The vancomycin-loaded nanoparticles were conjugated with cyclic 9-amino-acid peptide CARGGLKSC (CARG), which could recognize *S. aureus*. CARG specifically bound to *S. aureus* but not *P. aeruginosa in vitro*. The intravenous CARG-conjugated nanoparticles exhibited 8-fold greater deposition in the lung compared to non-targeted nanoparticles. Intratracheal *S. aureus* instillation into the mouse lung led to 67% mortality after 24 h. This survival rate was increased to 100% by CARG-conjugated MSNs. All the mice treated with MSNs survived after 20 d. The antibacterial nanoparticles for treating pulmonary infection *in vivo* are listed in Table 4.

Gastrointestinal (GI) Infection

Antimicrobial nanoparticles can be administered by oral route to treat GI tract infection. The nanocarriers protect the antibiotics from degradation in GI fluids. Some nanoparticles have the bioadhesive feature to prolong the retention in GI tract for enhanced oral bioavailability. Oral MSNs are ideal candidates to protect the drugs from enzymolysis in GI. Zhao et al. (2019) prepared antimicrobial peptide defensin-loaded MSNs for targeting the intestine. Defensin is easily degraded in the stomach. In order to achieve the intention of intestinal

TABLE 4 | The summary of antibacterial nanoparticles for treating bacterial infection of lung evaluated via animal-based study.

Nanoparticle type	Antibacterial agent	Average size	Bacteria strain	Animal model	References
β -Ga ₂ O ₃ :Cr ³⁺	Tigecycline	10–20 nm	TRKP	TRKP-induced pneumonia	Kang et al., 2019
Chitosan/alginate	Tobramycin	505–538 nm	<i>P. aeruginosa</i>	<i>P. aeruginosa</i> -induced infection	Deacon et al., 2015
PLGA	Esculentin-1a	About 250 nm	<i>P. aeruginosa</i>	<i>P. aeruginosa</i> -induced infection	Casciaro et al., 2019
PEG-co-PCL	Ciprofloxacin	77 nm	<i>P. aeruginosa</i>	<i>P. aeruginosa</i> -induced infection	Chen et al., 2018
PSPE-PEG	Moxifloxacin	254 nm	<i>P. aeruginosa</i>	<i>P. aeruginosa</i> -induced infection	Wang et al., 2019
Liposomes	Ciprofloxacin	114 nm	MRSA	MRSA-induced pneumonia	Hsu et al., 2018
MSNs	NZX	About 200 nm	<i>M. tuberculosis</i>	<i>M. tuberculosis</i> -induced tuberculosis	Tenland et al., 2019
MSNs	Vancomycin	About 180 nm	<i>S. aureus</i>	<i>S. aureus</i> -induced infection	Hussain et al., 2018

DSPE, 1,2-distearoyl-sn-glycero-3-phosphoethanolamine; MSNs, mesoporous silica nanoparticles; PCL, poly(ϵ -caprolactone); PEG, poly(ethylene glycol); PLGA, poly(lactide-co-glycolide); TRKP, tigecycline-resistant *K. pneumonia*.

targeting, succinylated casein, that can be degraded by intestinal protease, was coated onto the surface of MSNs. Casein decoration decreased defensin release in acidic environment, whereas a controlled release fashion was found in the presence of trypsin. Multidrug-resistant *E. coli* was administered by oral gavage to evoke intestinal infection. The nanoparticles were orally administered every day for 5 d. The casein-coated nanomedicine significantly lowered bacteria colonization compared with free ciprofloxacin as the positive control. The proinflammatory mediator TNF- α in intestine was decreased by 1.5- and 2.2-fold after casein-coated nanoparticle application, compared to non-coated MSNs and free peptide, respectively.

Montmorillonite is a smectic clay material possessing the ability to attach bacterial EPS and mucoadhesive property (Calabrese et al., 2013). A metronidazole-loaded nanocomposite made with montmorillonite and cationic PEI was designed to treat *H. pylori* infection in GI (Ping et al., 2016). Montmorillonite functions as a bioinspired building block to target bacteria, while PEI can cause bacterial membrane lysis, allowing increased antibiotic entrance into cytoplasm. The orally applied nanoparticles were observed to largely distribute in gastric tissue, confirming their mucoadhesive capability. The nanocarriers were able to eradicate *H. pylori* in GI for improving gastric ulcer and the inflammation response. This antimicrobial efficiency was greater than that of the conventional triple therapy (omeprazole/amoxicillin/metronidazole). For targeting to the infection site of *H. pylori*, gastric epithelial cell membrane was coated onto PLGA nanoparticles for preparing biomimetic nanocarriers containing clarithromycin as the model antibiotic (Angsantikul et al., 2018). The affinity of *H. pylori* with the biomimetic nanocarriers was 10-fold higher than that with non-coated nanoparticles. The bacterial burden in stomach of the infected mice (1.6×10^5 CFU/g) was reduced to 6.5×10^3 and 5.0×10^4 CFU/g by oral delivery of the biomimetic nanoparticles and free drug, respectively.

The Other Infection Sites

The antibacterial nanoparticles were also active to treat systemic, bone, and vaginal infections. The systemic bacterial infection can prompt bacteremia, followed by the occurrence

of sepsis (Huttunen and Aittoniemi, 2011). Rai et al. (2016) conjugated antimicrobial peptide on the Ag nanoparticle surface with high density to eradicate MRSA strain in circulation. The model peptide employed in this study was cecropin-melittin. The nanoparticle size could be controlled to 14 nm. The Au nanoparticles were intraperitoneally injected into the sepsis-like mice to treat bacteremia. The peptide-conjugated nanoparticles decreased MRSA concentration by 2 logs in the circulation compared to the non-conjugated group. Most of the nanoparticles would be distributed to the spleen. Metallic nanoparticles were also utilized to treat bone infection.

Qadri et al. (2017) developed Ag-Cu nanoparticles to eradicate *S. aureus* bone invasion in mice. Boron was added in the nanoparticles to prolong antimicrobial activity since the anticorrosive feature of boron was valuable in delaying Cu oxidation (Prasai et al., 2012). The nanoparticle diameter was about 27 nm. *S. aureus* was incorporated in silk suture and then implanted into the bone of mice to induce osteomyelitis. The intravenous nanoparticle administration at 1 mg/kg reduced bacterial CFU by 10-fold compared to the control. The intramuscular route showed a similar tendency to suppress *S. aureus* accumulation in bone. Osteomyelitis was also treated by magnetic Fe₃O₄ nanoparticles with the induction of hyperthermia to disrupt biofilm (Fang et al., 2017). The SPIONs were implanted in bone infected by *S. aureus*. The inserted implant could be heated to 75°C by magnetic field targeting in the infected bone. The local administration of vancomycin into the femoral canal in the presence of hyperthermia promoted the bacterial eradication in the biofilm. The bone volume of the combined vancomycin and hyperthermia (24%) was greater than that of the infection control (18%). ZnO nanoparticles were proved to display antimicrobial activity at very low concentration (Król et al., 2017). ZnO nanoparticles with the size of 10 nm were incorporated in PVA hydrogel for treating vaginitis via vaginal administration (Bai et al., 2015). The vaginitis mice were established by inoculating *E. coli* in vagina of mice for 5 d. The CFU in vaginal washes was significantly cleared after treatment of the nanoparticles. *E. coli* counting and epithelial exfoliation score determined by histology showed a consistent tendency.

CONCLUSION

When considering the formulation design for antibacterial therapy, it is important to develop the carriers that can stabilize the active ingredients and improve delivery into the infection sites. Increasing attention has been paid to nanomedicine as an approach for applying bacterial targeting or delivery. The use of antibiotic-loaded nanoparticles is considered a valid strategy for bacteria targeting because of its numerous advantages over conventional formulations, including improved stability, controlled antibiotic release, targeted capability, and increased bioavailability. Some issues, such as solubility, drug resistance, and epithelium permeation, can also be resolved by nanocarriers' targeting pathogens. Though many nanocarriers have been developed for testing in cell-based and animal studies, clinical trials for bacteria-delivery application are still limited. This may be due to the high cost of clinical trials and the unknown side effects that should be first identified and explored. Nanosystems are thought to cause more serious adverse effects on organisms compared to the bulk materials, as their very small size causes a correspondingly higher surface area. The researchers should pay attention only not to nanoparticles' therapeutic benefits but also to their toxic responses on human health. Caution should be used in optimizing the feasible conditions of nanomedicine for balancing the effectiveness of antimicrobial therapy and tissue damage. For use in future human applications, the materials utilized for preparing antibacterial nanoparticles should be non-toxic, biodegradable and biocompatible. The materials approved by the FDA may be the first choices for the development of these nanocarriers. There are already some experiences of antibiotic-loaded nanoparticles approved by FDA for clinical application. It is expected that more antibacterial nanoparticles

will be released for clinical use. Because of the improvement of industrial preparation and scale-up in the recent years, the visibility of commercially antibacterial nanoparticles can be raised in the near future. The introduction and description of the nanocarriers for bacterial and infection site targeting outlined in this review may provide relevant information to investigators involved in designing feasible and efficient delivery systems for the treatment of bacteria and its related diseases. It is preferable if some suggestions can be made for selecting the nanoparticles with best antibacterial efficiency. However, this intention is difficult to achieve since different investigations involved in the development of antibacterial nanoparticles employ different evaluation platforms. Although the MIC is the assay most-frequently used, the protocols of MIC determination are always different among different studies. Thus it should be cautious to compare the antimicrobial activity of the various types of nanosystem. Nevertheless, the comparison of antibacterial effect of the nanoparticles with a positive control antibiotic approved for clinical application is suggested.

AUTHOR CONTRIBUTIONS

J-YF conceived the topic of the review article and wrote most of the draft. Y-CY and T-HH took part in the writing and the discussion. S-CY and C-CC wrote sections of the review and prepared the figures. All the authors made comments and suggestions for the writing of the review.

FUNDING

The authors are grateful to the financial support by Chang Gung Memorial Hospital (CMRPG2H0361-2).

REFERENCES

- Abo-Zeid, Y., and Williams, G. R. (2020). The potential anti-infective applications of metal oxide nanoparticles: a systematic review. *Wiley Interdiscip. Rev. Nanomed. Nanobiotechnol.* 12:e1592. doi: 10.1002/wnan.1592
- Alalawi, A., Wang, P. W., Lu, P. L., Chen, Y. P., Fang, J. Y., and Yang, S. C. (2018). Synergistic anti-MRSA activity of cationic nanostructured lipid carriers in combination with oxacillin for cutaneous application. *Front. Microbiol.* 9:1493. doi: 10.3389/fmicb.2018.01493
- Alba, C., Blanco, A., and Alarcón, T. (2017). Antibiotic resistance in *Helicobacter pylori*. *Curr. Opin. Infect. Dis.* 30, 489–497. doi: 10.1097/QCO.0000000000000396
- Aljuffali, I. A., Huang, C. H., and Fang, J. Y. (2015). Nanomedical strategies for targeting skin microbiomes. *Curr. Drug Metab.* 16, 255–271. doi: 10.2174/1389200216666150812124923
- Amin, R., and Ratjen, F. (2014). Emerging drugs for cystic fibrosis. *Expert Opin. Emerg. Drugs* 19, 143–155. doi: 10.1517/14728214.2014.882316
- Angsantikul, P., Thamphiwatana, S., Zhang, Q., Spiekermann, K., Zhuang, J., Fang, R. H., et al. (2018). Coating nanoparticles with gastric epithelial cell membrane for targeted antibiotic delivery against *Helicobacter pylori* infection. *Adv. Ther.* 1:1800016. doi: 10.1002/adtp.201800016
- Ansari, S., and Yamaoka, Y. (2017). Survival of *Helicobacter pylori* in gastric acidic territory. *Helicobacter* 22:e12386. doi: 10.1111/hel.12386
- Applerot, G., Lellouche, J., Lipovsky, A., Nitzan, Y., Lubart, R., Gedanken, A., et al. (2012). Understanding the antibacterial mechanism of CuO nanoparticles: revealing the route of induced oxidative stress. *Small* 8, 3326–3337. doi: 10.1002/sml.201200772
- Arif, M., Dong, Q. J., Raja, M. A., Zeenat, S., Chi, Z., and Liu, C. G. (2018). Development of novel pH-sensitive thiolated chitosan/PMLA nanoparticles for amoxicillin delivery to treat *Helicobacter pylori*. *Mater. Sci. Eng. C Mater. Biol. Appl.* 83, 17–24. doi: 10.1016/j.msec.2017.08.038
- Armstead, A. L., and Li, B. (2011). Nanomedicine as an emerging approach against intracellular pathogens. *Int. J. Nanomed.* 6, 3281–3293. doi: 10.2147/IJN.S27285
- Aruguete, D. M., and Hochella, M. F. (2010). Bacteria-nanoparticle interactions and their environmental implications. *Environ. Chem.* 7, 3–9. doi: 10.1071/EN09115
- Baelo, A., Levato, R., Julián, E., Crespo, A., Astola, J., Gavalda, J., et al. (2015). Disassembling bacterial extracellular matrix with DNase-coated nanoparticles to enhance antibiotic delivery in biofilm infections. *J. Control. Release* 209, 150–158. doi: 10.1016/j.jconrel.2015.04.028
- Bai, X., Li, L., Liu, H., Tan, L., Liu, T., and Meng, X. (2015). Solvothermal synthesis of ZnO nanoparticles and anti-infection application in vivo. *ACS Appl. Mater. Interfaces* 7, 1308–1317. doi: 10.1021/am507532p
- Bajaj, M., Pandey, S. K., Nain, T., Brar, S. K., Singh, P., Singh, S., et al. (2017). Stabilized cationic dipeptide capped gold/silver nanohybrids: Towards enhanced antibacterial and antifungal efficacy. *Colloids Surf. B Biointerfaces* 158, 397–407. doi: 10.1016/j.colsurfb.2017.07.009
- Baptista, P. V., McCusker, M. P., Carvalho, A., Ferreira, D. A., Mohan, N. M., Martins, M., et al. (2018). Nano-strategies to fight multidrug resistant bacteria—“A battle of the Titans”. *Front. Microbiol.* 9:1441. doi: 10.3389/fmicb.2018.01441

- Barraud, N., Hassett, D. J., Hwang, S. H., Rice, S. A., Kjelleberg, S., and Webb, J. S. (2006). Involvement of nitric oxide in biofilm dispersal of *Pseudomonas aeruginosa*. *J. Bacteriol.* 188, 7344–7353. doi: 10.1128/JB.00779-06
- Bernardos, A., Piacenza, E., Sancenón, F., Hamidi, M., Maleki, A., and Turner, R. J., et al. (2019). Mesoporous silica-based materials with bactericidal properties. *Small* 15:e1900669. doi: 10.1002/smll.201900669
- Bobo, D., Robinson, K. J., Islam, J., Thurecht, K. J., and Corrie, S. R. (2016). Nanoparticle-based medicines: a review of FDA-approved materials and clinical trials to date. *Pharm. Res.* 33, 2373–2387. doi: 10.1007/s11095-016-1958-5
- Bocian, K. M., and Jagusztyn-Krynicka, E. K. (2012). The controversy over anti-*Helicobacter pylori* therapy. *Pol. J. Microbiol.* 61, 239–246.
- Boge, L., Byssell, H., Ringstad, L., Wennman, D., Umerska, A., Cassisa, V., et al. (2016). Lipid-based liquid crystals as carriers for antimicrobial peptides: phase behavior and antimicrobial effect. *Langmuir* 32, 4217–4228. doi: 10.1021/acs.langmuir.6b00338
- Botequim, D., Maia, J., Lino, M. M., Lopes, L. M., Simões, P. N., Ilharco, L. M., et al. (2012). Nanoparticles and surfaces presenting antifungal, antibacterial and antiviral properties. *Langmuir* 28, 7646–7656. doi: 10.1021/la300948n
- Brunet, L., Lyon, D. Y., Hotze, E. M., Alvarez, P. J., and Wiesner, M. R. (2009). Comparative photoactivity and antibacterial properties of C60 fullerenes and titanium dioxide nanoparticles. *Environ. Sci. Technol.* 43, 4355–4360. doi: 10.1021/es803093t
- Cabuzu, D., Cirja, A., Puiu, R., and Grumezescu, A. M. (2015). Biomedical applications of gold nanoparticles. *Curr. Top. Med. Chem.* 15, 1605–1613. doi: 10.2174/1568026615666150414144750
- Cai, S., Qian, J., Yang, S., Kuang, L., and Hua, D. (2019). Acetylcysteine-decorated Prussian blue nanoparticles for strong photothermal sterilization and focal infection treatment. *Colloids Surf. B Biointerfaces* 181, 31–38. doi: 10.1016/j.colsurfb.2019.05.007
- Calabrese, I., Cavallaro, G., Scialabba, C., Licciardi, M., Merli, M., and Sciascia, L. (2013). Montmorillonite nanodevices for the colon metronidazole delivery. *Int. J. Pharm.* 457, 224–236. doi: 10.1016/j.ijpharm.2013.09.017
- Canaparo, R., Foglietta, F., Giuntini, F., Della Pepa, C., Dosio, F., and Serpe, L. (2019). Recent developments in antibacterial therapy: focus on stimuli-responsive drug-delivery systems and therapeutic nanoparticles. *Molecules* 24:E1991. doi: 10.3390/molecules24101991
- Casciaro, B., d'Angelo, I., Zhang, X., Loffredo, M. R., Conte, G., Cappiello, F., et al. (2019). Poly(lactide-co-glycolide) nanoparticles for prolonged therapeutic efficacy of esculentin-1a-derived antimicrobial peptides against *Pseudomonas aeruginosa* lung infection: In vitro and in vivo studies. *Biomacromolecules* 20, 1876–1888. doi: 10.1021/acs.biomac.8b01829
- Casciaro, B., Moros, M., Rivera-Fernández, S., Bellelli, A., de la Fuente, J. M., and Mangoni, M. L. (2017). Gold-nanoparticles coated with the antimicrobial peptide esculentin-1a(1-21)NH₂ as a reliable strategy for antipseudomonal drugs. *Acta Biomater.* 47, 170–181. doi: 10.1016/j.actbio.2016.09.041
- Chen, C., Hu, J., Zhang, S., Zhou, P., Zhao, X., Xu, H., et al. (2012). Molecular mechanisms of antibacterial and antitumor actions of designed surfactant-like peptides. *Biomaterials* 33, 592–603. doi: 10.1016/j.biomaterials.2011.09.059
- Chen, J., Andler, S. M., Goddard, J. M., Nugen, S. R., and Rotello, V. M. (2017). Integrating recognition elements with nanomaterials for bacteria sensing. *Chem. Soc. Rev.* 46, 1272–1283. doi: 10.1039/c6cs00313c
- Chen, M., Xie, S., Wei, J., Song, X., Ding, Z., and Li, X. (2018). Antibacterial micelles with vancomycin-mediated targeting and pH/lipase-triggered release of antibiotics. *ACS Appl. Mater. Interfaces* 10, 36814–36823. doi: 10.1021/acsami.8b16092
- Chi, Z., Liu, G. L., Liu, C. G., and Chi, Z. M. (2016). Poly(β -L-malic acid) (PMLA) from *Aureobasidium* spp. and its current proceedings. *Appl. Microbiol. Biotechnol.* 100, 3841–3851. doi: 10.1007/s00253-016-7404-0
- Choi, O., and Hu, Z. (2008). Size dependent and reactive oxygen species related nanosilver toxicity to nitrifying bacteria. *Environ. Sci. Technol.* 42, 4583–4588. doi: 10.1021/es703238h
- Cornejo, E., Schlaermann, P., and Mukherjee, S. (2017). How to rewire the host cell: a home improvement guide for intracellular bacteria. *J. Cell Biol.* 216, 3931–3948. doi: 10.1083/jcb.201701095
- d'Angelo, I., Casciaro, B., Miro, A., Quaglia, F., Mangoni, M. L., and Ungaro, F. (2015). Overcoming barriers in *Pseudomonas aeruginosa* lung infections: engineered nanoparticles for local delivery of a cationic antimicrobial peptide. *Colloids Surf. B Biointerfaces* 135, 717–725. doi: 10.1016/j.colsurfb.2015.08.027
- Dave, V., Yadav, R. B., Kushwaha, K., Yadav, S., Sharma, S., and Agrawal, U. (2017). Lipid-polymer hybrid nanoparticles: Development and statistical optimization of norfloxacin for topical drug delivery system. *Bioact. Mater.* 2, 269–280. doi: 10.1016/j.bioactmat.2017.07.002
- Deacon, J., Abdelghany, S. M., Quinn, D. J., Schmid, D., Megaw, J., Donnelly, R. F., et al. (2015). Antimicrobial efficacy of tobramycin polymeric nanoparticles for *Pseudomonas aeruginosa* infections in cystic fibrosis: formulation, characterisation and functionalisation with dornase alfa (DNase). *J. Control. Release* 198, 55–61. doi: 10.1016/j.jconrel.2014.11.022
- Di Martino, P. (2018). Extracellular polymeric substances, a key element in understanding biofilm phenotype. *AIMS Microbiol.* 4, 274–288. doi: 10.3934/microbiol.2018.2.274
- Du, X., and Qiao, S. Z. (2015). Dendritic silica particles with center-radial pore channels: promising platforms for catalysis and biomedical applications. *Small* 11, 392–413. doi: 10.1002/smll.201401201
- Eissa, A. M., Abdulkarim, A., Sharples, G. J., and Cameron, N. R. (2016). Glycosylated nanoparticles as efficient antimicrobial delivery agents. *Biomacromolecules* 17, 2672–2679. doi: 10.1021/acs.biomac.6b00711
- El Badawy, A. M., Silva, R. G., Morris, B., Scheckel, K. G., Suidan, M. T., and Tolaymat, T. M. (2011). Surface charge-dependent toxicity of silver nanoparticles. *Environ. Sci. Technol.* 45, 283–287. doi: 10.1021/es1034188
- Fang, C. H., Tsai, P. I., Huang, S. W., Sun, J. S., Chang, J. Z., Shen, H. H., et al. (2017). Magnetic hyperthermia enhance the treatment efficacy of peri-implant osteomyelitis. *BMC Infect. Dis.* 17:516. doi: 10.1186/s12879-017-2621-4
- Fang, C. L., Aljuffali, I. A., Li, Y. C., and Fang, J. Y. (2014). Delivery and targeting of nanoparticles into hair follicles. *Ther. Deliv.* 5, 991–1006. doi: 10.4155/tde.14.61
- Fang, J. Y., Lin, Y. K., Wang, P. W., Alalaiwe, A., Yang, Y. C., and Yang, S. C. (2019). The droplet-size effect of squalene@cetylpyridinium chloride nanoemulsions on antimicrobial potency against planktonic and biofilm MRSA. *Int. J. Nanomed.* 14, 8133–8147. doi: 10.2147/IJN.S221663
- Fenske, D. B., and Cullis, P. R. (2008). Liposomal nanomedicines. *Expert Opin. Drug Deliv.* 5, 25–44. doi: 10.1517/17425247.5.1.25
- Forier, K., Raemdonck, K., De Smedt, S. C., Demeester, J., Coenye, T., and Braeckmans, K. (2014). Lipid and polymer nanoparticles for drug delivery to bacterial biofilms. *J. Control. Release* 190, 607–623. doi: 10.1016/j.jconrel.2014.03.055
- Fraunholz, M., and Sinha, B. (2012). Intracellular *Staphylococcus aureus*: live-in and let die. *Front. Cell Infect. Microbiol.* 2:43. doi: 10.3389/fcimb.2012.00043
- Fu, G., Vary, P. S., and Lin, C. T. (2005). Anatase TiO₂ nanocomposites for antimicrobial coatings. *J. Phys. Chem. B* 109, 8889–8898. doi: 10.1021/jp0502196
- Furneri, P. M., Fuochi, V., and Pignatello, R. (2017). Lipid-based nanosized delivery systems for fluoroquinolones: a review. *Curr. Pharm. Des.* 23, 6696–6704. doi: 10.2174/1381612823666171122110103
- Ganbold, T., and Baigude, H. (2018). Design of mannose-functionalized curdlan nanoparticles for macrophage-targeted siRNA delivery. *ACS Appl. Mater. Interfaces* 10, 14463–14474. doi: 10.1021/acsami.8b02073
- Gao, W., and Zhang, L. (2015). Coating nanoparticles with cell membranes for targeted drug delivery. *J. Drug Target.* 23, 619–626. doi: 10.3109/1061186X.2015.1052074
- Gebreyohannes, G., Nyerere, A., Bii, C., and Sbhatu, D. B. (2019). Challenges of intervention, treatment, and antibiotic resistance of biofilm-forming microorganisms. *Heliyon* 5:e02192. doi: 10.1016/j.heliyon.2019.e02192
- Geilich, B. M., Gelfat, I., Sridhar, S., van de Ven, A. L., and Webster, T. J. (2017). Superparamagnetic iron oxide-encapsulating polymersome nanocarriers for biofilm eradication. *Biomaterials* 119, 78–85. doi: 10.1016/j.biomaterials.2016.12.011
- Giri, K., Yepes, L. R., Duncan, B., Parameswaran, P. K., Yan, B., Jiang, Y., et al. (2015). Targeting bacterial biofilms via surface engineering of gold nanoparticles. *RSC Adv.* 5, 105551–105559. doi: 10.1039/C5RA16305F
- González-Paredes, A., Sitia, L., Ruyra, A., Morris, C. J., Wheeler, G. N., McArthur, M., et al. (2019). Solid lipid nanoparticles for the delivery of anti-microbial oligonucleotides. *Eur. J. Pharm. Biopharm.* 134, 166–177. doi: 10.1016/j.ejpb.2018.11.017

- Hadinoto, K., and Cheow, W. S. (2014). Nano-antibiotics in chronic lung infection therapy against *Pseudomonas aeruginosa*. *Colloids Surf. B Biointerfaces* 116, 772–785. doi: 10.1016/j.colsurfb.2014.02.032
- Hao, N., Li, L., and Tang, F. (2017). Roles of particle size, shape and surface chemistry of mesoporous silica nanomaterials on biological systems. *Int. Mater. Rev.* 62, 57–77. doi: 10.1016/j.biomaterials.2009.09.060
- Hsu, C. Y., Sung, C. T., Aljuffali, I. A., Chen, C. H., Hu, K. Y., and Fang, J. Y. (2018). Intravenous anti-MRSA phosphatidylserine mediate enhanced affinity to pulmonary surfactants for effective treatment of infectious pneumonia. *Nanomed. Nanotechnol. Biol. Med.* 14, 215–225. doi: 10.1016/j.nano.2017.10.006
- Hsu, C. Y., Yang, S. C., Sung, C. T., Weng, Y. H., and Fang, J. Y. (2017). Anti-MRSA malleable liposomes carrying chloramphenicol for ameliorating hair follicle targeting. *Int. J. Nanomed.* 12, 827–838. doi: 10.2147/IJN.S147226
- Hussain, S., Joo, J., Kang, J., Kim, B., Braun, G. B., She, Z. G., et al. (2018). Antibiotic-loaded nanoparticles targeted to the site of infection enhance antibacterial efficacy. *Nat. Biomed. Eng.* 2, 95–103. doi: 10.1038/s41551-017-0187-5
- Huttunen, R., and Aittoniemi, J. (2011). New concepts in the pathogenesis, diagnosis and treatment of bacteremia and sepsis. *J. Infect.* 63, 407–419. doi: 10.1016/j.jinf.2011.08.004
- Ibelli, T., Templeton, S., and Levi-Polyachenko, N. (2018). Progress on utilizing hyperthermia for mitigating bacterial infections. *Int. J. Hyperthermia* 34, 144–156. doi: 10.1080/02656736.2017.1369173
- Ibrahim, H. R., Aoki, T., and Pellegrini, A. (2002). Strategies for new antimicrobial proteins and peptides: lysozyme and aprotinin as model molecules. *Curr. Pharm. Des.* 8, 671–693. doi: 10.2174/1381612023395349
- Insua, I., Llamas, E., Zhang, Z., Peacock, A. F., Krachler, A. M., and Fernandez-Trillo, F. (2016). Enzyme-responsive polyion complex (PIC) nanoparticles for the targeted delivery of antimicrobial polymers. *Polym. Chem.* 7, 2684–2690. doi: 10.1039/c6py00146g
- Ivask, A., Elbadawy, A., Kaweeteerawat, C., Boren, D., Fischer, H., Ji, Z., et al. (2014). Toxicity mechanisms in *Escherichia coli* vary for silver nanoparticles and differ from ionic silver. *ACS Nano* 8, 374–386. doi: 10.1021/nn4044047
- Jahnke, J. P., Cornejo, J. A., Sumner, J. J., Schuler, A. J., Atanassov, P., and Ista, L. K. (2016). Conjugated gold nanoparticles as a tool for probing the bacterial cell envelope: the case of *Shewanella oneidensis* MR-1. *Biointerphases* 11:011003. doi: 10.1116/1.4939244
- Jana, S., Sen, K. K., and Gandhi, A. (2016). Alginate based nanocarriers for drug delivery applications. *Curr. Pharm. Des.* 22, 3399–3410. doi: 10.2174/1381612822666160510125718
- Javanbakht, T., Laurent, S., Stanicki, D., and Wilkinson, K. J. (2016). Relating the surface properties of superparamagnetic iron oxide nanoparticles (SPIONs) to their bactericidal effect towards a biofilm of *Streptococcus mutans*. *PLoS ONE* 11:e0154445. doi: 10.1371/journal.pone.0154445
- Kalhapure, R. S., Sikwal, D. R., Rambharose, S., Mocktar, C., Singh, S., Bester, L., et al. (2017). Enhancing targeted antibiotic therapy via pH responsive solid lipid nanoparticles from an acid cleavable lipid. *Nanomed. Nanotechnol. Biol. Med.* 13, 2067–2077. doi: 10.1016/j.nano.2017.04.010
- Kang, X. Q., Shu, G. F., Jiang, S. P., Xu, X. L., Qi, J., Jin, F. Y., et al. (2019). Effective targeted therapy for drug-resistant infection by ICAM-1 antibody-conjugated TPGS modified β -Ga₂O₃:Cr³⁺ nanoparticles. *Theranostics* 9, 2739–2753. doi: 10.7150/thno.33452
- Kasithevar, M., Periakaruppan, P., Muthupandian, S., and Mohan, M. (2017). Antibacterial efficacy of silver nanoparticles against multi-drug resistant clinical isolates from post-surgical wound infections. *Microb. Pathog.* 107, 327–334. doi: 10.1016/j.micpath.2017.04.013
- Kerisit, S., and Liu, C. (2009). Molecular simulations of water and ion diffusion in nanosized mineral fractures. *Environ. Sci. Technol.* 43, 777–782. doi: 10.1021/es8016045
- Khan, F., Pham, D. T. N., Oloketuyi, S. F., Manivasagan, P., Oh, J., and Kim, Y. M. (2020). Chitosan and their derivatives: antibiofilm drugs against pathogenic bacteria. *Colloids Surf. B Biointerfaces* 185:110627. doi: 10.1016/j.colsurfb.2019.110627
- Kim, K. T., Lee, J. Y., Kim, D. D., Yoon, I. S., and Cho, H. J. (2019). Recent progress in the development of poly(lactic-co-glycolic acid)-based nanostructures for cancer imaging and therapy. *Pharmaceutics* 11:280. doi: 10.3390/pharmaceutics11060280
- Kłodzinska, S. N., Priemel, P. A., Rades, T., and Mørck Nielsen, H. (2016). Inhalable antimicrobials for treatment of bacterial biofilm-associated sinusitis in cystic fibrosis patients: challenges and drug delivery approaches. *Int. J. Mol. Sci.* 17:1688. doi: 10.3390/ijms17101688
- Kooti, M., Sedeh, A. N., Motamedi, H., and Rezaatofghi, S. E. (2018). Magnetic graphene oxide inlaid with silver nanoparticles as antibacterial and drug delivery composite. *Appl. Microbiol. Biotechnol.* 102, 3607–3621. doi: 10.1007/s00253-018-8880-1
- Król, A., Pomastowski, P., Rafinska, K., Railean-Plugaru, V., and Buszewski, B. (2017). Zinc oxide nanoparticles: synthesis, antiseptic activity and toxicity mechanism. *Adv. Colloid Interface Sci.* 249, 37–52. doi: 10.1016/j.cis.2017.07.033
- Kroll, A. V., Fang, R. H., and Zhang, L. (2017). Biointerfacing and applications of cell membrane-coated nanoparticles. *Bioconjug. Chem.* 28, 23–32. doi: 10.1021/acs.bioconjchem.6b00569
- Kumar, G. V., Su, C. H., and Velusamy, P. (2016). Ciprofloxacin loaded genipin cross-linked chitosan/heparin nanoparticles for drug delivery application. *Mater. Lett.* 180, 119–122. doi: 10.1016/j.matlet.2016.05.108
- Lambadi, P. R., Sharma, T. K., Kumar, P., Vasnani, P., Thalluri, S. M., Bisht, N., et al. (2015). Facile biofunctionalization of silver nanoparticles for enhanced antibacterial properties, endotoxin removal, and biofilm control. *Int. J. Nanomed.* 10, 2155–2171. doi: 10.2147/IJN.S72923
- Lange-Asschenfeldt, B., Marenbach, D., Lang, C., Patzelt, A., Ulrich, M., Maltusch, A., et al. (2011). Distribution of bacteria in the epidermal layers and hair follicles of the human skin. *Skin Pharmacol. Physiol.* 24, 305–311. doi: 10.1159/000328728
- Lebeaux, D., Ghigo, J. M., and Beloin, C. (2014). Biofilm-related infections: bridging the gap between clinical management and fundamental aspects of recalcitrance toward antibiotics. *Microbiol. Mol. Biol. Rev.* 78, 510–543. doi: 10.1128/MMBR.00013-14
- Lee, S., Stubelius, A., Hamelmann, N., Tran, V., and Almutairi, A. (2018). Inflammation-responsive drug-conjugated dextran nanoparticles enhance anti-inflammatory drug efficacy. *ACS Appl. Mater. Interfaces* 10, 40378–40387. doi: 10.1021/acsami.8b08254
- Lewies, A., Wentzel, J. F., Jordaan, A., Bezuidenhout, C., and Du Plessis, L. H. (2017). Interactions of the antimicrobial peptide nisin Z with conventional antibiotics and the use of nanostructured lipid carriers to enhance antimicrobial activity. *Int. J. Pharm.* 526, 244–253. doi: 10.1016/j.ijpharm.2017.04.071
- Li, L. L., Xu, J. H., Qi, G. B., Zhao, X., Yu, F., and Wang, H. (2014). Core-shell supramolecular gelatin nanoparticles for adaptive and “on-demand” antibiotic delivery. *ACS Nano* 8, 4975–4983. doi: 10.1021/nn501040h
- Lin, M. H., Hung, C. F., Aljuffali, I. A., Sung, C. T., Huang, C. T., and Fang, J. Y. (2017). Cationic amphiphile in phospholipid bilayer or oil-water interface of nanocarriers affects planktonic and biofilm bacteria killing. *Nanomed. Nanotechnol. Biol. Med.* 13, 353–361. doi: 10.1016/j.nano.2016.08.011
- Liu, J., Aruguete, D. M., Murayama, M., and Hochella, M. F. (2009). Influence of size and aggregation on the reactivity of an environmentally and industrially relevant nanomaterial (PbS). *Environ. Sci. Technol.* 43, 8178–8183. doi: 10.1021/es902121r
- Liu, M., He, D., Yang, T., Liu, W., Mao, L., Zhu, Y., et al. (2018). An efficient antimicrobial depot for infectious site-targeted chemo-photothermal therapy. *J. Nanobiotechnol.* 16:23. doi: 10.1186/s12951-018-0348-z
- Loeuillet, C., Martinon, F., Perez, C., Munoz, M., Thome, M., and Meylan, P. R. (2006). *Mycobacterium tuberculosis* subverts innate immunity to evade specific effectors. *J. Immunol.* 177, 6245–6255. doi: 10.4049/jimmunol.177.9.6245
- Lok, C. N., Ho, C. M., Chen, R., He, Q. Y., Yu, W. Y., Sun, H., et al. (2006). Proteomic analysis of the mode of antibacterial action of silver nanoparticles. *J. Proteome Res.* 5, 916–924. doi: 10.1021/pr0504079
- Loughran, A. J., Orihuela, C. J., and Tuomanen, E. I. (2019). *Streptococcus pneumoniae*: invasion and inflammation. *Microbiol. Spectr.* 7:2. doi: 10.1128/microbiolspec.GPP3-0004-2018
- Loyer, P., and Cammas-Marion, S. (2014). Natural and synthetic poly(malic acid)-based derivatives: a family of versatile biopolymers for the design of drug nanocarriers. *J. Drug Target.* 22, 556–575. doi: 10.3109/1061186X.2014.936871
- Lu, B., Ye, H., Shang, S., Xiong, Q., Yu, K., Li, Q., et al. (2018). Novel wound dressing with chitosan gold nanoparticles capped with a small molecule for effective treatment of multiantibiotic-resistant bacterial infections. *Nanotechnology* 29:425603. doi: 10.1088/1361-6528/aad7a7

- Ma, D., and Wu, J. (2016). Biofilm mitigation by drug (gentamicin)-loaded liposomes promoted by pulsed ultrasound. *J. Acoust. Soc. Am.* 140:EL534. doi: 10.1121/1.4972336
- Magill, S. S., Edwards, J. R., Bamberg, W., Beldavs, Z. G., Dumyati, G., Kainer, M. A., et al. (2014). Multistate point-prevalence survey of health care-associated infections. *N. Engl. J. Med.* 370, 1198–1208. doi: 10.1056/NEJMoa1306801
- Makowski, M., Silva, I. C., Pais do Amaral, C., Gonçalves, S., and Santos, N. C. (2019). Advances in lipid and metal nanoparticles for antimicrobial peptide delivery. *Pharmaceutics* 11:588. doi: 10.3390/pharmaceutics11110588
- Medina, E., Rohde, M., and Chhatwal, G. S. (2003). Intracellular survival of *Streptococcus pyogenes* in polymorphonuclear cells results in increased bacterial virulence. *Infect. Immun.* 71, 5376–5380. doi: 10.1128/iai.71.9.5376-5380.2003
- Mikut, R., Ruden, S., Reischl, M., Breitling, F., Volkmer, R., and Hilpert, K. (2016). Improving short antimicrobial peptides despite elusive rules for activity. *Biochim. Biophys. Acta* 1858, 1024–1033. doi: 10.1016/j.bbame.2015.12.013
- Miller, K. P., Wang, L., Benicewicz, B. C., and Decho, A. W. (2015). Inorganic nanoparticles engineered to attack bacteria. *Chem. Soc. Rev.* 44, 7787–7807. doi: 10.1039/c5cs00041f
- Mir, M., Ahmed, N., Permana, A. D., Rodgers, A. M., Donnelly, R. F., and Rehman, A. U. (2019). Enhancement in site-specific delivery of carvacrol against methicillin resistant *Staphylococcus aureus* induced skin infections using enzyme responsive nanoparticles: a proof of concept study. *Pharmaceutics* 11:606. doi: 10.3390/pharmaceutics11110606
- Mohammed, Y. H. E., Manukumar, H. M., Rakesh, K. P., Karthik, C. S., Mallu, P., and Qin, H. L. (2018). Vision for medicine: *Staphylococcus aureus* biofilm war and unlocking key's for anti-biofilm drug development. *Microb. Pathog.* 123, 339–347. doi: 10.1016/j.micpath.2018.07.002
- Nakamura, I., Fukushima, S., Hayakawa, T., Sekiya, K., and Matsumoto, T. (2015). The additional costs of catheter-related bloodstream infections in intensive care units. *Am. J. Infect. Control.* 43, 1046–1049. doi: 10.1016/j.ajic.2015.05.022
- Nguyen, T. K., Selvanayagam, R., Ho, K. K. K., Chen, R., Kutty, S. K., Rice, S. A., et al. (2016). Co-delivery of nitric oxide and antibiotic using polymeric nanoparticles. *Chem. Sci.* 7, 1016–1027. doi: 10.1039/c5sc02769a
- Nostro, A., and Papalia, T. (2012). Antimicrobial activity of carvacrol: current progress and future perspectives. *Recent Pat. Antiinfect. Drug Discov.* 7, 28–35. doi: 10.2174/157489112799829684
- Paczosa, M. K., and Mecsas, J. (2016). *Klebsiella pneumoniae*: going on the offense with a strong defense. *Microbiol. Mol. Biol. Rev.* 80, 629–661. doi: 10.1128/MMBR.00078-15
- Pal, S., Tak, Y. K., and Song, J. M. (2007). Does the antibacterial activity of silver nanoparticles depend on the shape of the nanoparticles? A study of the Gram-negative bacterium *Escherichia coli*. *Appl. Environ. Microbiol.* 73, 1712–1720. doi: 10.1128/AEM.02218-06
- Palange, A. L., Di Mascolo, D., Carallo, C., Gnasso, A., and Decuzzi, P. (2014). Lipid-polymer nanoparticles encapsulating curcumin for modulating the vascular deposition of breast cancer cells. *Nanomed. Nanotechnol. Biol. Med.* 10, 99–1002. doi: 10.1016/j.nano.2014.02.004
- Pareek, V., Gupta, R., and Panwar, J. (2018). Do physico-chemical properties of silver nanoparticles decide their interaction with biological media and bactericidal action? A review. *Mater. Sci. Eng. C Mater. Biol. Appl.* 90, 739–749. doi: 10.1016/j.msec.2018.04.093
- Park, H., Park, H. J., Kim, J. A., Lee, S. H., Kim, J. H., Yoon, J., et al. (2011). Inactivation of *Pseudomonas aeruginosa* PA01 biofilms by hyperthermia using superparamagnetic nanoparticles. *J. Microbiol. Methods* 84, 41–45. doi: 10.1016/j.mimet.2010.10.010
- Ping, Y., Hu, X., Yao, Q., Hu, Q., Amini, S., Miserez, A., et al. (2016). Engineering bioinspired bacteria-adhesive clay nanoparticles with a membrane-disruptive property for the treatment of *Helicobacter pylori* infection. *Nanoscale* 8, 16486–16498. doi: 10.1039/c6nr05551f
- Pizzolato-Cezar, L. R., Okuda-Shinagawa, N. M., and Machini, M. T. (2019). Combinatory therapy antimicrobial peptide-antibiotic to minimize the ongoing rise of resistance. *Front. Microbiol.* 10:1703. doi: 10.3389/fmicb.2019.01703
- Poovelikunnel, T., Gethin, G., and Humphreys, H. (2015). Mupirocin resistance: clinical implications and potential alternatives for the eradication of MRSA. *J. Antimicrob. Chemother.* 70, 2681–2692. doi: 10.1093/jac/dkv169
- Pradeepa, Vidya, S. M., Mutalik, S., Udaya Bhat, K., Huilgol, P., and Avadhani, K. (2016). Preparation of gold nanoparticles by novel bacterial exopolysaccharide for antibiotic delivery. *Life Sci.* 153, 171–179. doi: 10.1016/j.lfs.2016.04.022
- Praditya, D., Kirchhoff, L., Brüning, J., Rachmawati, H., Steinmann, J., and Steinmann, E. (2019). Anti-infective properties of the golden spice curcumin. *Front. Microbiol.* 10:912. doi: 10.3389/fmicb.2019.00912
- Prasai, D., Tuberquia, J. C., Harl, R. R., Jennings, G. K., Rogers, B. R., and Bolotin, K. I. (2012). Graphene: corrosion-inhibiting coating. *ACS Nano* 6, 1102–1108. doi: 10.1021/nn203507y
- Price, J. R., Cole, K., Bexley, A., Kostiou, V., Eyre, D. W., Golubchik, T., et al. (2017). Transmission of *Staphylococcus aureus* between health-care workers, the environment, and patients in an intensive care unit: a longitudinal cohort study based on whole-genome sequencing. *Lancet Infect. Dis.* 17, 207–214. doi: 10.1016/S1473-3099(16)30413-3
- Pu, L., Xu, J., Sun, Y., Fang, Z., Chan-Park, M. B., and Duan, H. (2016). Cationic polycarbonate-grafted superparamagnetic nanoparticles with synergistic dual-modality antimicrobial activity. *Biomater. Sci.* 4, 871–879. doi: 10.1039/c5bm00545k
- Qadri, S., Haik, Y., Mensah-Brown, E., Bashir, G., Fernandez-Cabezudo, M. J., and Al-Ramadi, B. K. (2017). Metallic nanoparticles to eradicate bacterial bone infection. *Nanomed. Nanotechnol. Biol. Med.* 13, 2241–2250. doi: 10.1016/j.nano.2017.05.013
- Quiñones, J. P., Peniche, H., and Peniche, C. (2018). Chitosan based self-assembled nanoparticles in drug delivery. *Polymers* 10:235. doi: 10.3390/polym10030235
- Radovic-Moreno, A. F., Lu, T. K., Puscasu, V. A., Yoon, C. J., Langer, R., and Farokhzad, O. C. (2012). Surface charge-switching polymeric nanoparticles for bacterial cell wall-targeted delivery of antibiotics. *ACS Nano* 6, 4279–4287. doi: 10.1021/nn3008383
- Rai, A., Pinto, S., Velho, T. R., Ferreira, A. F., Moita, C., Trivedi, U., et al. (2016). One-step synthesis of high-density peptide-conjugated gold nanoparticles with antimicrobial efficacy in a systemic infection model. *Biomaterials* 85, 99–110. doi: 10.1016/j.biomaterials.2016.01.051
- Ramalingam, B., Parandhaman, T., and Das, S. K. (2016). Antibacterial effects of biosynthesized silver nanoparticles on surface ultrastructure and nanomechanical properties of Gram-negative bacteria viz. *Escherichia coli* and *Pseudomonas aeruginosa*. *ACS Appl. Mater. Interfaces* 8, 4963–4976. doi: 10.1021/acsami.6b00161
- Ramalingam, V. (2019). Multifunctionality of gold nanoparticles: plausible and convincing properties. *Adv. Colloid Interface Sci.* 271:101989. doi: 10.1016/j.cis.2019.101989
- Ran, X., Du, Y., Wang, Z., Wang, H., Pu, F., Ren, J., et al. (2017). Hyaluronic acid-templated Ag nanoparticles/graphene oxide composites for synergistic therapy of bacteria infection. *ACS Appl. Mater. Interfaces* 9, 19717–19724. doi: 10.1021/acsami.7b05584
- Rani, S., Gothwal, A., Pandey, P. K., Chauhan, D. S., Pachouri, P. K., Gupta, U. D., et al. (2018). HPMA-PLGA based nanoparticles for effective in vitro delivery of rifampicin. *Pharm. Res.* 36:19. doi: 10.1007/s11095-018-2543-x
- Ribeiro, K. L., Frias, I. A. M., Franco, O. L., Dias, S. C., Sousa-Junior, A. A., Silva, O. N., et al. (2018). Clavanin A-bioconjugated Fe₃O₄/Silane core-shell nanoparticles for thermal ablation of bacterial biofilms. *Colloids Surf. B Biointerfaces* 169, 72–81. doi: 10.1016/j.colsurfb.2018.04.055
- Sabale, S., Kandesar, P., Jadhav, V., Komorek, R., Motkuri, R. K., and Yu, X. Y. (2017). Recent developments in the synthesis, properties, and biomedical applications of core/shell superparamagnetic iron oxide nanoparticles with gold. *Biomater. Sci.* 5, 2212–2225. doi: 10.1039/c7bm00723j
- Seung, K. J., Keshavjee, S., and Rich, M. L. (2015). Multidrug-resistant tuberculosis and extensively drug-resistant tuberculosis. *Cold Spring Harb. Perspect. Med.* 5:a017863. doi: 10.1101/cshperspect.a017863
- Sharifi-Rad, J., Hoseini Alfatemi, S., Sharifi Rad, M., and Iriti, M. (2014). Antimicrobial synergic effect of allicin and silver nanoparticles on skin infection caused by methicillin-resistant *Staphylococcus aureus* spp. *Ann. Med. Health. Sci. Res.* 4, 863–868. doi: 10.4103/2141-9248
- Shi, B., Leung, D. Y. M., Taylor, P. A., and Li, H. (2018). MRSA colonization is associated with decreased skin commensal bacteria in atopic dermatitis. *J. Invest. Dermatol.* 138, 1668–1671. doi: 10.1016/j.jid.2018.01.022
- Shlar, I., Droby, S., Choudhary, R., and Rodov, V. (2017). The mode of antimicrobial action of curcumin depends on the delivery system: monolithic

- nanoparticles vs. supramolecular inclusion complex. *RCS Adv.* 7:42559. doi: 10.1039/c7ra07303h
- Shmarakov, I. O., Mukha, I. P., Karavan, V. V., Chunikhin, O. Y., Marchenko, M. M., Smirnova, N. P., et al. (2014). Tryptophan-assisted synthesis reduces bimetallic gold/silver nanoparticle cytotoxicity and improves biological activity. *Nanobiomedicine* 1:6. doi: 10.5772/59684
- Shrivastava, S., Bera, T., Roy, A., Singh, G., Ramachandrarao, P., and Dash, D. (2007). Characterization of enhanced antibacterial effects of novel silver nanoparticles. *Nanotechnology* 18:225103. doi: 10.1088/0957-4484/18/22/225103
- Silva, N. C., Silva, S., Sarmiento, B., and Pintado, M. (2015). Chitosan nanoparticles for daptomycin delivery in ocular treatment of bacterial endophthalmitis. *Drug Deliv.* 22, 885–893. doi: 10.3109/10717544.2013.858195
- Sirelkhatim, A., Mahmud, S., Seeni, A., Kaus, N. H. M., Ann, L. C., Bakhor, S. K. M., et al. (2015). Review on zinc oxide nanoparticles: antibacterial activity and toxicity mechanism. *Nanomicro. Lett.* 7, 219–242. doi: 10.1007/s40820-015-0040-x
- Slavin, Y. N., Asnis, J., Häfeli, U. O., and Bach, H. (2017). Metal nanoparticles: understanding the mechanisms behind antibacterial activity. *J. Nanobiotechnol.* 15:65. doi: 10.1186/s12951-017-0308-z
- Smitha, K. T., Nisha, N., Maya, S., Biswas, R., and Jayakumar, R. (2015). Delivery of rifampicin-chitin nanoparticles into the intracellular compartment of polymorphonuclear leukocytes. *Int. J. Biol. Macromol.* 74, 36–43. doi: 10.1016/j.ijbiomac.2014.11.006
- Sohm, B., Immel, F., Bauda, P., and Pagnout, C. (2015). Insight into the primary mode of action of TiO₂ nanoparticles on *Escherichia coli* in the dark. *Proteomics* 15, 98–113. doi: 10.1002/pmic.201400101
- Steiert, E., Radi, L., Fach, M., and Wich, P. R. (2018). Protein-based nanoparticles for the delivery of enzymes with antibacterial activity. *Macromol. Rapid Commun.* 39:e1800186. doi: 10.1002/marc.201800186
- Stewart, P. S., and Franklin, M. J. (2008). Physiological heterogeneity in biofilms. *Nat. Rev. Microbiol.* 6, 199–210. doi: 10.1038/nrmicro1838
- Subbiahdoss, G., Sharifi, S., Grijsma, D. W., Laurent, S., van der Mei, H. C., Mahmoudi, M., et al. (2012). Magnetic targeting of surface-modified superparamagnetic iron oxide nanoparticles yields antibacterial efficacy against biofilms of gentamicin-resistant staphylococci. *Acta Biomater.* 8, 2047–2055. doi: 10.1016/j.actbio.2012.03.002
- Sun, L. M., Zhang, C. L., and Li, P. (2012). Characterization, antibiofilm, and mechanism of action of novel PEG-stabilized lipid nanoparticles loaded with terpinen-4-ol. *J. Agric. Food Chem.* 60, 6150–6156. doi: 10.1021/jf3010405
- Swider, E., Koshkina, O., Tel, J., Cruz, L. J., de Vries, I. J. M., and Srinivas, M. (2018). Customizing poly(lactic-co-glycolic acid) particles for biomedical applications. *Acta Biomater.* 73, 38–51. doi: 10.1016/j.actbio.2018.04.006
- Szaciłowski, K., Macyk, W., and Stochel, G. (2006). Synthesis, structure and photoelectrochemical properties of the TiO₂ Prussian blue nanocomposite. *J. Mater. Chem.* 16, 4603–4611. doi: 10.1039/b606402g
- Talebian, N., Amininezhad, S. M., and Doudi, M. (2013). Controllable synthesis of ZnO nanoparticles and their morphology-dependent antibacterial and optical properties. *J. Photochem. Photobiol. B* 120, 66–73. doi: 10.1016/j.jphotobiol.2013.01.004
- Tamara, F. R., Lin, C., Mi, F. L., and Ho, Y. C. (2018). Antibacterial effects of chitosan/cationic peptide nanoparticles. *Nanomaterials* 8:E88. doi: 10.3390/nano8020088
- Tamayo, L. A., Zapata, P. A., Vejar, N. D., Azócar, M. I., Gulppi, M. A., Zhou, X., et al. (2014). Release of silver and copper nanoparticles from polyethylene nanocomposites and their penetration into *Listeria monocytogenes*. *Mater. Sci. Eng. C Mater. Biol. Appl.* 40, 24–31. doi: 10.1016/j.msec.2014.03.037
- Tan, Y., Ma, S., Leonhard, M., Moser, D., Haselmann, G. M., Wang, J., et al. (2018). Enhancing antibiofilm activity with functional chitosan nanoparticles targeting biofilm cells and biofilm matrix. *Carbohydr. Polym.* 200, 35–42. doi: 10.1016/j.carbpol.2018.07.072
- Tang, Y. J., Ashcroft, J. M., Chen, D., Min, G., Kim, C. H., Murkhejee, B., et al. (2007). Charge-associated effects of fullerene derivatives on microbial structural integrity and central metabolism. *Nano Lett.* 7, 754–760. doi: 10.1021/nl063020t
- Tarhini, M., Greige-Gerges, H., and Elaissari, A. (2017). Protein-based nanoparticles: from preparation to encapsulation of active molecules. *Int. J. Pharm.* 522, 172–197. doi: 10.1016/j.ijpharm.2017.01.067
- Taylor, E., and Webster, T. J. (2011). Reducing infections through nanotechnology and nanoparticles. *Int. J. Nanomed.* 6, 1463–1473. doi: 10.2147/IJN.S22021
- Tenland, E., Pochert, A., Krishnan, N., Umashankar Rao, K., Kalsum, S., Braun, K., et al. (2019). Effective delivery of the anti-mycobacterial peptide NZX in mesoporous silica nanoparticles. *PLoS ONE* 14:e0212858. doi: 10.1371/journal.pone.0212858
- Thomson, R. B. Jr. (2016). One small step for the Gram stain, one giant leap for clinical microbiology. *J. Clin. Microbiol.* 54, 1416–1417. doi: 10.1128/JCM.00303-16
- Tong, S. Y., Davis, J. S., Eichenberger, E., Holland, T. L., and Fowler, V. G. Jr. (2015). *Staphylococcus aureus* infections: epidemiology, pathophysiology, clinical manifestations, and management. *Clin. Microbiol. Rev.* 28, 603–661. doi: 10.1128/CMR.00134-14
- Vazquez-Muñoz, R., Meza-Villecas, A., Fournier, P. G. J., Soria-Castro, E., Juárez-Moreno, K., Gallego-Hernández, A. L., et al. (2019). Enhancement of antibiotics antimicrobial activity due to the silver nanoparticles impact on the cell membrane. *PLoS ONE* 14:e0224904. doi: 10.1371/journal.pone.0224904
- Vijayan, V., Uthaman, S., and Park, I. K. (2018). Cell membrane coated nanoparticles: an emerging biomimetic nanopatform for targeted bioimaging and therapy. *Adv. Exp. Med. Biol.* 1064, 45–59. doi: 10.1007/978-981-13-0445-3_3
- Wallock-Richards, D., Doherty, C. J., Doherty, L., Clarke, D. J., Place, M., Govan, J. R., et al. (2014). Garlic revisited: antimicrobial activity of allicin-containing garlic extracts against *Burkholderia cepacia* complex. *PLoS ONE* 9:e112726. doi: 10.1371/journal.pone.0112726
- Walvekar, P., Gannamani, R., and Govender, T. (2019). Combination drug therapy via nanocarriers against infectious diseases. *Eur. J. Pharm. Sci.* 127, 121–141. doi: 10.1016/j.ejps.2018.10.017
- Wang, L., He, H., Yu, Y., Sun, L., Liu, S., Zhang, C., et al. (2014). Morphology-dependent bactericidal activities of Ag/CeO₂ catalysts against *Escherichia coli*. *J. Inorg. Biochem.* 135, 45–53. doi: 10.1016/j.jinorgbio.2014.02.016
- Wang, X., Deng, A., Cao, W., Li, Q., Wang, L., Zhou, J., et al. (2018). Synthesis of chitosan/poly (ethylene glycol)-modified magnetic nanoparticles for antibiotic delivery and their enhanced anti-biofilm activity in the presence of magnetic field. *J. Mater. Sci.* 53, 6433–6449. doi: 10.1007/s10853-018-1998-9
- Wang, X. S., Situ, J. Q., Ying, X. Y., Chen, H., Pan, H. F., Jin, Y., et al. (2015). β -Ga₂O₃:Cr³⁺ nanoparticle: a new platform with near infrared photoluminescence for drug targeting delivery and bio-imaging simultaneously. *Acta Biomater.* 22, 164–172. doi: 10.1016/j.actbio.2015.04.010
- Wang, Y., Nor, Y. A., Song, H., Yang, Y., Xu, C., Yu, M., et al. (2016). Small-sized and large-pore dendritic mesoporous silica nanoparticles enhance antimicrobial enzyme delivery. *J. Mater. Chem. B* 4, 2646–2653. doi: 10.1039/c6tb00053c
- Wang, Y., Yuan, Q., Feng, W., Pu, W., Ding, J., Zhang, H., et al. (2019). Targeted delivery of antibiotics to the infected pulmonary tissues using ROS-responsive nanoparticles. *J. Nanobiotechnol.* 17:103. doi: 10.1186/s12951-019-0537-4
- Wen, C. J., Yen, T. C., Al-Suwayeh, S. A., Chang, H. W., and Fang, J. Y. (2011). *In vivo* real-time fluorescence visualization and brain-targeting mechanisms of lipid nanocarriers with different fatty ester:oil ratios. *Nanomedicine* 6, 1545–1559. doi: 10.2217/nnm.11.46
- Woodford, N., and Livermore, D. M. (2009). Infections caused by Gram-positive bacteria: a review of the global challenge. *J. Infect.* 59(Suppl. 1), S4–S16. doi: 10.1016/S0163-4453(09)60003-7
- Xue, X., Pasparakis, G., Halliday, N., Winzer, K., Howdle, S. M., Cramphorn, C. J., et al. (2011). Synthetic polymers for simultaneous bacterial sequestration and quorum sense interference. *Angew. Chem. Int. Ed. Engl.* 50, 9852–9856. doi: 10.1002/anie.201103130
- Yamakami, K., Tsumori, H., Sakurai, Y., Shimizu, Y., Nagatoshi, K., and Sonomoto, K. (2013). Sustainable inhibition efficacy of liposome-encapsulated nisin on insoluble glucan-biofilm synthesis by *Streptococcus mutans*. *Pharm. Biol.* 51, 267–270. doi: 10.3109/13880209.2012.717227
- Yamanaka, M., Hara, K., and Kudo, J. (2005). Bactericidal actions of a silver ion solution on *Escherichia coli*, studied by energy-filtering transmission electron microscopy and proteomic analysis. *Appl. Environ. Microbiol.* 71, 7589–7593. doi: 10.1128/AEM.71.11.7589-7593.2005
- Yang, H., Liu, C., Yang, D., Zhang, H., and Xi, Z. (2009). Comparative study of cytotoxicity, oxidative stress and genotoxicity induced by four typical

- nanomaterials: the role of particle size, shape and composition. *J. Appl. Toxicol.* 29, 69–78. doi: 10.1002/jat.1385
- Yang, S., Han, X., Yang, Y., Qiao, H., Yu, Z., Liu, Y., et al. (2018). Bacteria-targeting nanoparticles with microenvironment-responsive antibiotic release To eliminate intracellular *Staphylococcus aureus* and associated infection. *ACS Appl. Mater. Interfaces* 10, 14299–14311. doi: 10.1021/acsami.7b15678
- Yang, S. C., Aljuffali, I. A., Sung, C. T., Lin, C. F., and Fang, J. Y. (2016). Antimicrobial activity of topically-applied soyaethyl morpholinium ethosulfate micelles against *Staphylococcus* species. *Nanomedicine* 11, 657–671. doi: 10.2217/nmm.15.217
- Yang, S. C., Yen, F. L., Wang, P. W., Aljuffali, I. A., Weng, Y. H., Tseng, C. H., et al. (2017). Naphtho[1,2-*b*]furan-4,5-dione is a potent anti-MRSA agent against planktonic, biofilm, and intracellular bacteria. *Future Microbiol.* 12, 1059–1073. doi: 10.2217/fmb-2017-0044
- Yin, Y., Papavasiliou, G., Zaborina, O. Y., Alverdy, J. C., and Teymour, F. (2017). *De novo* synthesis and functional analysis of polyphosphate-loaded polyethylene glycol hydrogel nanoparticles targeting pyocyanin and pyoverdine production in *Pseudomonas aeruginosa* as a model intestinal pathogen. *Ann. Biomed. Eng.* 45, 1058–1068. doi: 10.1007/s10439-016-1740-1
- Youbare, S., Chang, T. K., Tan, S. H., Kuo, J. C., Hsu, P. H., Su, C. Y., et al. (2019). Antimicrobial gold nanoclusters: recent developments and future perspectives. *Int. J. Mol. Sci.* 20:2924. doi: 10.3390/ijms20122924
- Yunus Basha, R., Sampath Kumar, T. S., and Doble, M. (2019). Dual delivery of tuberculosis drugs via cyclodextrin conjugated curdlan nanoparticles to infected macrophages. *Carbohydr. Polym.* 218, 53–62. doi: 10.1016/j.carbpol.2019.04.056
- Zazo, H., Colino, C. I., and Lanao, J. M. (2016). Current applications of nanoparticles in infectious diseases. *J. Control. Release* 224, 86–102. doi: 10.1016/j.jconrel.2016.01.008
- Zhang, H., Lv, X., Li, Y., Wang, Y., and Li, J. (2010). P25-graphene composite as a high performance photocatalyst. *ACS Nano* 4, 380–386. doi: 10.1021/nn901221k
- Zhang, L., Bao, M., Liu, B., Zhao, H., Zhang, Y., Ji, X., et al. (2019). Effect of andrographolide and its analogs on bacterial infection: a review. *Pharmacology* 105:123–134. doi: 10.1159/000503410
- Zhang, L., Jiang, Y., Ding, Y., Povey, M., and York, D. (2007). Investigation into the antibacterial behavior of suspensions of ZnO nanoparticles (ZnO nanofluids). *J. Nanopart. Res.* 9, 479–489. doi: 10.1007/s11051-006-9150-1
- Zhang, L., Pornpattananangku, D., Hu, C. M., and Huang, C. M. (2010). Development of nanoparticles for antimicrobial drug delivery. *Curr. Med. Chem.* 17, 585–594. doi: 10.2174/092986710790416290
- Zhang, S., Sun, X., Cheng, W., Dai, Y., and Ma, X. (2015). Systematic review and meta-analysis of the epidemiology of vancomycin-intermediate and heterogeneous vancomycin-intermediate *Staphylococcus aureus* isolates. *PLoS ONE* 10:e0136082. doi: 10.1371/journal.pone.0136082
- Zhao, G., Chen, Y., He, Y., Chen, F., Gong, Y., Chen, S., et al. (2019). Succinylated casein-coated peptide-mesoporous silica nanoparticles as an antibiotic against intestinal bacterial infection. *Biomater. Sci.* 7, 2440–2451. doi: 10.1039/c9bm00003h
- Zivich, P. N., Grabenstein, J. D., Becker-Dreps, S. I., and Weber, D. J. (2018). *Streptococcus pneumoniae* outbreaks and implications for transmission and control: a systematic review. *Pneumonia* 10:11. doi: 10.1186/s41479-018-0055-4
- Zomorodian, K., Veisi, H., Mousavi, S. M., Ataabadi, M. S., Yazdanpanah, S., and Bagheri, J., et al. (2018). Modified magnetic nanoparticles by PEG-400-immobilized Ag nanoparticles (Fe₃O₄@PEG-Ag) as a core/shell nanocomposite and evaluation of its antimicrobial activity. *Int. J. Nanomed.* 13, 3965–3973. doi: 10.2147/IJN.S161002

Conflict of Interest: The authors declare that the research was conducted in the absence of any commercial or financial relationships that could be construed as a potential conflict of interest.

Copyright © 2020 Yeh, Huang, Yang, Chen and Fang. This is an open-access article distributed under the terms of the Creative Commons Attribution License (CC BY). The use, distribution or reproduction in other forums is permitted, provided the original author(s) and the copyright owner(s) are credited and that the original publication in this journal is cited, in accordance with accepted academic practice. No use, distribution or reproduction is permitted which does not comply with these terms.



Like Cures Like: Pharmacological Activity of Anti-Inflammatory Lipopolysaccharides From Gut Microbiome

OPEN ACCESS

Edited by:

Ganna Tolstanova,
Taras Shevchenko National University
of Kyiv, Ukraine

Reviewed by:

Shikai Yan,
Shanghai Jiao Tong University, China
Jing Yuan,
Children's Hospital of Capital Institute
of Pediatrics, China

*Correspondence:

Hsin-Chih Lai
hclai@mail.cgu.edu.tw
Chia-Chen Lu
082385@mail.fju.edu.tw

[†]These authors have contributed
equally to this work

Specialty section:

This article was submitted to
Gastrointestinal and
Hepatic Pharmacology,
a section of the journal
Frontiers in Pharmacology

Received: 09 January 2020

Accepted: 14 April 2020

Published: 30 April 2020

Citation:

Lin T-L, Shu C-C, Chen Y-M, Lu J-J,
Wu T-S, Lai W-F, Tzeng C-M, Lai H-C
and Lu C-C (2020) Like Cures Like:
Pharmacological Activity of Anti-
Inflammatory Lipopolysaccharides
From Gut Microbiome.
Front. Pharmacol. 11:554.
doi: 10.3389/fphar.2020.00554

Tzu-Lung Lin^{1,2}, Chin-Chung Shu³, Young-Mao Chen⁴, Jang-Jih Lu⁵, Ting-Shu Wu⁶,
Wei-Fan Lai⁷, Chi-Meng Tzeng⁸, Hsin-Chih Lai^{1,2,9,10*†} and Chia-Chen Lu^{11,12*†}

¹ Department of Medical Biotechnology and Laboratory Science, College of Medicine, Chang Gung University, Taoyuan, Taiwan, ² Microbiota Research Center and Emerging Viral Infections Research Center, Chang Gung University, Taoyuan, Taiwan, ³ Department of Internal Medicine, National Taiwan University Hospital, Taipei, Taiwan, ⁴ Bachelor Degree Program in Marine Biotechnology, College of Life Sciences, National Taiwan Ocean University, Keelung, Taiwan, ⁵ Department of Laboratory Medicine, Linkou Chang Gung Memorial Hospital, Taoyuan, Taiwan, ⁶ Division of Infectious Diseases, Department of Internal Medicine, Linkou Chang Gung Memorial Hospital, Taoyuan, Taiwan, ⁷ Department of Medicine, College of Medicine, Chang Gung University, Taoyuan, Taiwan, ⁸ School of Pharmaceutical Sciences, Xiamen University, Xiamen, China, ⁹ Central Research Laboratory, Xiamen Chang Gung Allergology Consortium, Xiamen Chang Gung Hospital, Xiamen, China, ¹⁰ Research Center for Chinese Herbal Medicine and Research Center for Food and Cosmetic Safety, College of Human Ecology, Chang Gung University of Science and Technology, Taoyuan, Taiwan, ¹¹ Department of Chest Medicine, Internal Medicine, Fu Jen Catholic University Hospital, Fu Jen Catholic University, New Taipei City, Taiwan, ¹² Department of Respiratory Therapy, Fu Jen Catholic University, New Taipei City, Taiwan

Gut microbiome maintains local gut integrity and systemic host homeostasis, where optimal control of intestinal lipopolysaccharides (LPS) activity may play an important role. LPS mainly produced from gut microbiota are a group of lipid-polysaccharide chemical complexes existing in the outer membrane of Gram-negative bacteria. Traditionally, LPS mostly produced from Proteobacteria are well known for their ability in inducing strong inflammatory responses (proinflammatory LPS, abbreviated as P-LPS), leading to septic shock or even death in animals and humans. Although the basic structures and chemical properties of P-LPS derived from different bacterial species generally show similarity, subtle and differential immune activation activities are observed. On the other hand, frequently ignored, a group of LPS molecules mainly produced by certain microbiota bacteria such as Bacteroidetes show blunt or even antagonistic activity in initiating pro-inflammatory responses (anti-inflammatory LPS, abbreviated as A-LPS). In this review, besides the immune activation properties of P-LPS, we also focus on the description of anti-inflammatory effects of A-LPS, and their potential antagonistic mechanism. We address the possibility of using native or engineered A-LPS for immune modulation in prevention or even treatment of P-LPS induced chronic inflammation related diseases. Understanding the exquisite interactive relationship between structure-activity correlation

of P- and A-LPS not only contributes to molecular understanding of immunomodulation and homeostasis, but also re-animates the development of novel LPS-based pharmacological strategy for prevention and therapy of chronic inflammation related diseases.

Keywords: lipopolysaccharides, microbiota, proteobacteria, bacteroidetes, TLR4, immune modulation

INTRODUCTION

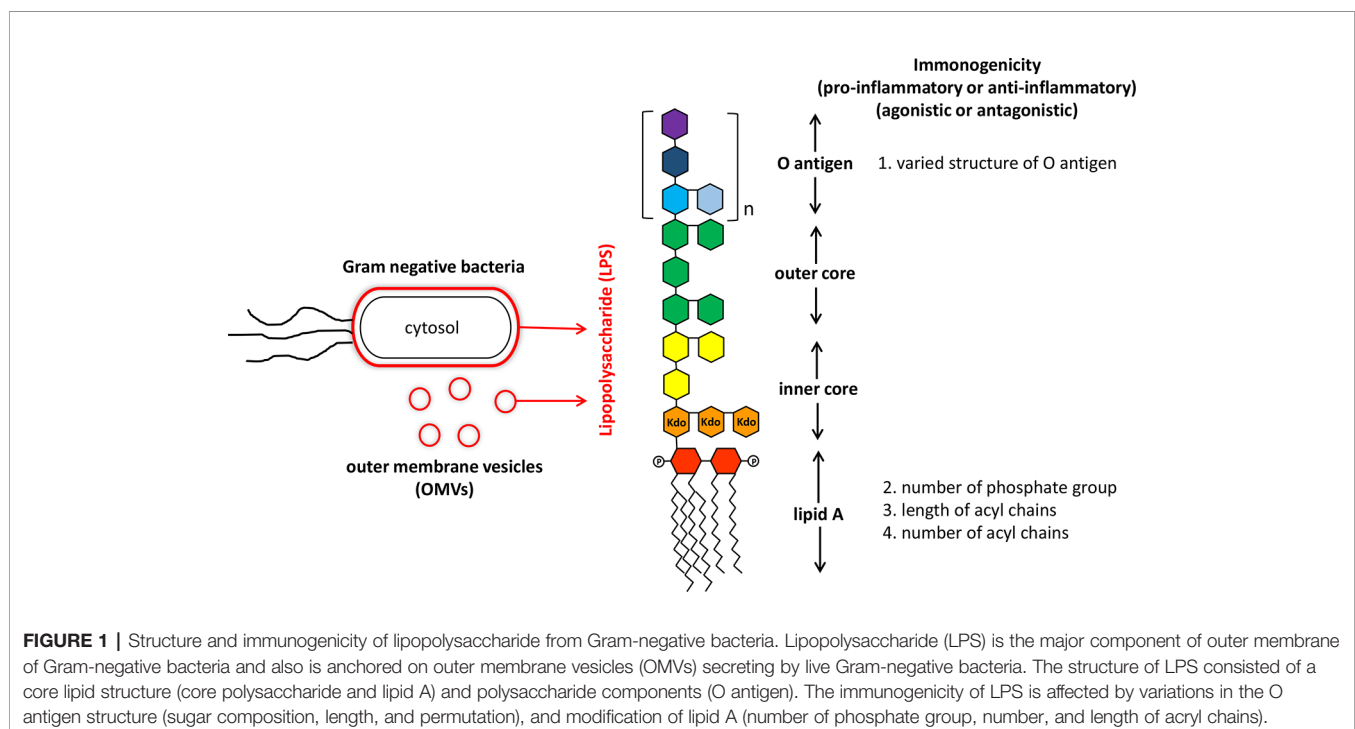
Lipopolysaccharides in General

Lipopolysaccharides (LPS) mainly derived from gut microbiome are chemical molecules located in the outer membrane of Gram-negative bacteria (Sperandeo et al., 2017). It is a pathogen associated molecular pattern (PAMP) molecule consisted of a core lipid structure and polysaccharide components (Nativel et al., 2017). Traditionally, LPS are best known for their eliciting strong immune responses in a variety of eukaryotic species ranging from insects to animals and humans (Alexander and Rietschel, 2001). Increased concentration of LPS in the sera is also closely related to development of sepsis and even mortality (Fink, 2014). Detailed structural analysis indicated that LPS consist of three parts: lipid A, a core oligosaccharide and an O antigen of oligo- or polysaccharide chain (Alexander and Rietschel, 2001). The conserved lipid A entity buried within the Gram-negative bacterial outer membrane is basically composed of a $\beta(1 \rightarrow 6)$ -linked glucosamine disaccharide backbone that is phosphorylated at positions 1 and 4 of the disaccharide, and acylated at positions 2 and 3 of each monosaccharide (Steimle et al., 2016). Covalently attached to lipid A is the core oligosaccharides that link to lipid A through 3-deoxy-D-manno-oct-ulosonic acid (Kdo), and show

variance among LPS purified from different bacterial species (Amor et al., 2000). Located on the outermost part of LPS, the highly versatile O-antigen sugar chain is characterized by significant variation of sugar length, composition, arrangement and the linkages between monosaccharides in different bacterial species, different bacterial strains of the same species, or even different bacterial clones of the same bacterial strain (intrastrain LPS heterogeneity) (Lerouge and Vanderleyden, 2002) (**Figure 1**).

Proinflammatory Lipopolysaccharides

Traditional proinflammatory LPS (P-LPS) are mostly derived from the phylum Proteobacteria such as those from *Escherichia coli*. They have been established to play important roles in increasing the oxidative stress and over-production of inflammatory cytokines/chemokines. Functional activities of P-LPS are widely identified in not only mammals (Wiese et al., 1999), but also other animals including chicken and fish (Komori et al., 2015). While the three parts of P-LPS may all participate in modulation of immune activities, the lipid A is the primary immunostimulatory moiety of P-LPS. After lysis of bacterial cells, exposed lipid A binds to cell surface receptors of target cells such as macrophages and dendritic cells (DCs), initiating downstream inflammatory signaling components. Subsequently,



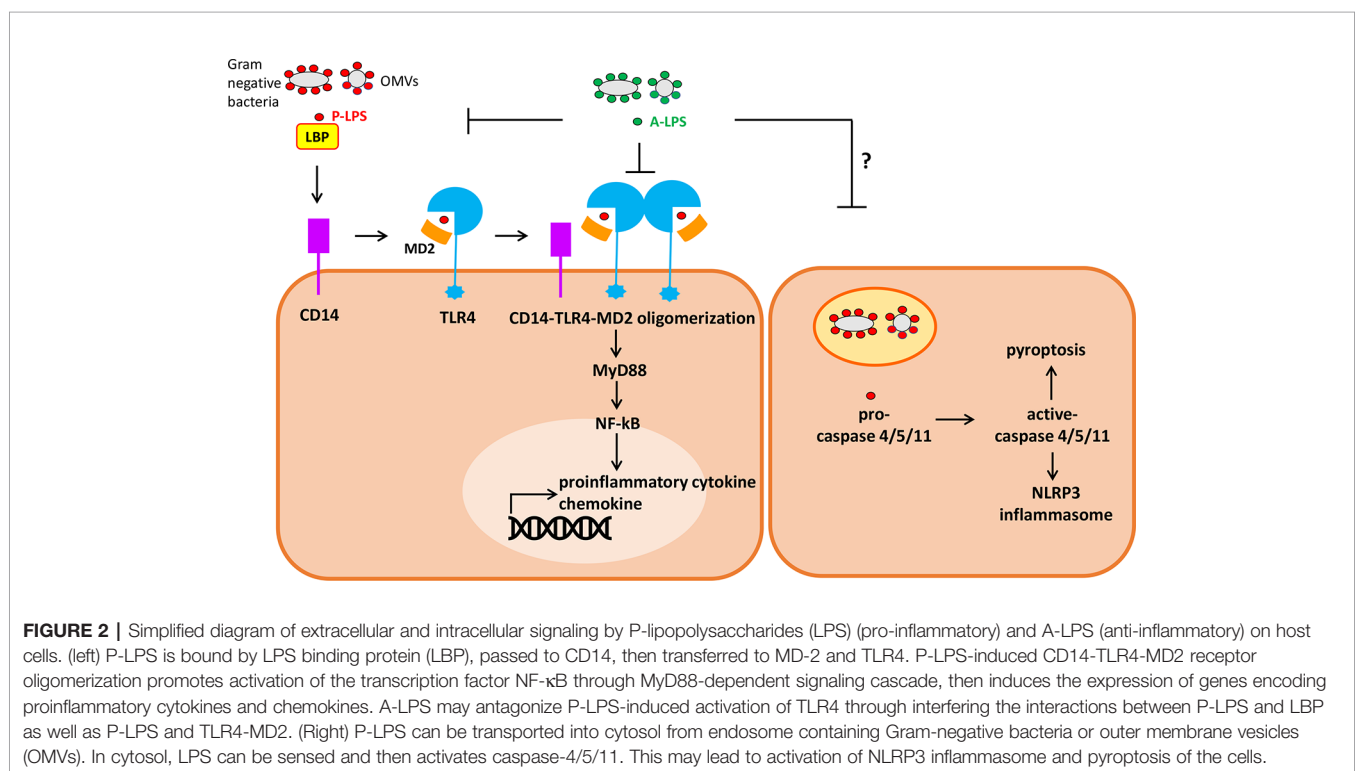
fever, inflammation, and even septic shock are induced. Release of bacterial LPS can not only be achieved after bacterial lysis, but also through secreting outer membrane vesicles (OMVs) by live Gram-negative bacteria (Vanaja et al., 2016) (**Figure 1**). Though proinflammatory, the biological activity of P-LPS molecules show a range of differential activities on target cells. Such effects depend on various factors, including bacterial origin and P-LPS structure, composition, and concentrations (Chantratita et al., 2013). Although lipid A moiety may be the most active component of LPS, the O-antigen part also participates in immune regulation activity (Kadowaki et al., 2013) (**Figure 1**).

Cascades of Proinflammatory Lipopolysaccharides Activated Inflammations

P-LPS act as important molecules initiating local and even systemic inflammations in the host. While there are multiple TLR4-independent P-LPS sensing pathways, TLR4 is currently regarded as a major cell surface pattern recognition molecule receptor (PRR) responsible for initiation and sustaining the inflammatory responses in the host (Nativel et al., 2017; Mazgaen and Gurung, 2020). Upstream interaction between P-LPS and cell surface TLR4 ignites the whole cascade of downstream signaling (**Figure 2**). P-LPS does not directly bind to TLR4. In body fluids, P-LPS micelles first interact with LPS-binding protein (LBP), an acute-phase protein, forming P-LPS/LBP micelles. Sequentially, P-LPS/LBP micelles then interact with CD14. Afterwards, the resulting complex interacts with TLR4/MD-2, leading to oligomerization of TLR4/MD-2/CD14 complex

(Kim and Kim, 2017). Subsequently, aggregated LPS-TLR4 complex (P-LPS/TLR4/MD-2/CD14) activates cells through eliciting the NF- κ B signaling pathway, leading to increased production and secretion of abundant pro-inflammatory cytokines such as IFN- γ , TNF- α , interleukin (IL)-1 β and interleukin (IL)-8 (but little or no IL-4, IL-13 or IL-5), and chemokines, such as monocyte chemoattractant protein 1 (MCP-1) (Chow et al., 1999; Alexander and Rietschel, 2001). Alternatively, P-LPS may also activate immune cells by TLR4 independent pathway. Recent studies indicated that LPS can be transported into cytosol by OMVs and guanylate-binding proteins. In cytosol, LPS can be sensed by the noncanonical inflammasome and directly binds to its intracellular receptor caspase-4/5/11. This may lead to activation of NLRP3 inflammasome and pyroptosis of the cells. The LPS-triggered cytosolic activation of noncanonical inflammasome may play important roles in development of sepsis (Pfalzgraf and Weindl, 2019; Mazgaen and Gurung, 2020).

The P-LPS induced lung inflammations are described here, where sequential multiple biochemical steps occur, leading to final lung pathogenesis development. Following P-LPS-TLR4 interaction, TLR4/MyD88 signaling pathways (Lu et al., 2008) in alveolar macrophages are induced, leading to increased release of proinflammatory cytokines/chemokines such as IL-1 β , IL-6, IL-8, and MCP-1 (Atamas et al., 2013). These subsequently provoke infiltration of various over-activated immune cells including macrophages, neutrophils, and CD8+ T and B lymphocytes (Asti et al., 2000). Proteolytic enzymes activities such as those from elastase, matrix metalloproteinase (MMP-2,



MMP-9, MMP-12) and cathepsins are also increased in lung (Davey et al., 2011). This leads to enhanced degradation of collagen and matrix proteins which further enhance inflammation. Together with other exogenous and endogenous oxidative stresses, the lung parenchyma starts to be damaged. Cell injuries further activate proteases and generate danger-associated molecular patterns (DAMPs) such as hsp70 (Hulina-Tomaskovic et al., 2019) or high mobility group box 1 (HMGB-1) protein (Gangemi et al., 2015). DAMPs continue to activate inflammasome in macrophage, leading to reduced mitochondrial function, cell senescence, apoptosis, and necrosis (Faner et al., 2012).

Proinflammatory Lipopolysaccharides–TLR4 Interaction in Modulation of Immunity and Inflammation

P-LPS derived from the gut microbiota of animals and humans have been shown to cause or contribute to development of chronic inflammation related diseases. The P-LPS levels in blood plasma are normally low, but are found to be elevated in many chronic inflammation related diseases. These include infections and sepsis (Opal, 2010), obesity and type 2 diabetes (Hersoug et al., 2016), gum disease (Brown, 2019), chronic obstructive pulmonary disease (COPD) (Aul et al., 2012; Kobayashi et al., 2013; Gupta et al., 2015), non-alcoholic fatty liver disease (NAFLD) (Fuke et al., 2019), colitis associated cancers (Waldner and Neurath, 2015), and even neurodegenerative diseases such as Alzheimer's disease, Parkinson's disease, and amyotrophic lateral sclerosis (Brown, 2019). Concordantly, dysbiosis in the gut microbiome may increase the production and release of microbial P-LPS which activate gut inflammatory response. Pro-inflammatory cytokines produced in gut can systematically affect host physiology, such as stimulating the afferent vagal nerve which in turn impacts the hypothalamic-pituitary-adrenal (HPA) axis and induces symptoms associated with depression (Simkin, 2019). Gathering evidences strongly indicate the causative relationship between increased P-LPS concentration in body fluids and development of chronic inflammations related diseases. Therefore, it is possible that these diseases may be ameliorated by either decreasing P-LPS levels or antagonizing P-LPS-induced inflammations (Brown, 2019).

P-LPS do not just provoke unfavorable inflammations. These molecules may also contribute to restoring immunity-compromised diseases due to gut microbiota dysbiosis. Using an animal model of antibiotics-induced dysbiosis and bacterial lung infection, previous work has shown that oral supplementation with commensal flora derived P-LPS improves lung defense against *E. coli*-induced pneumonia. Thus, P-LPS derived from the gut microbiota may increase host lung immunity in this context (Chen, Chen et al., 2011). The mechanism underlying the effects of LPS modulatory effects remains to be further examined.

Efficacy of P-LPS activation activity can be significantly affected by variations in the sugar composition, length and permutation, and modification of lipid A, core, and/or O-antigen structure

(Fedele et al., 2008). On the other hand, expression levels or structural variations in the target LBP, CD14, and TLR4 protein complex of host cells may also affect the immune-stimulation activities (Hajjar et al., 2017). In brief, TLR4-MD-2 receptor complex recognizes variations in P-LPS molecule of a particular Gram-negative bacterium and uses multiple sites in interaction. In this situation, subtle tuning of the earliest interaction between the host cell surface and pathogen P-LPS occurs, which affects P-LPS affinity and the subsequent activation activity (Maeshima et al., 2015). For example, LPS derived from Chlamydiaceae shows reduced binding affinity for LBP and CD14, and exhibits weak biological activity against host immune cells such as monocytes (Tsutsumi-Ishii et al., 2008). Besides, studies of LPS derived from *Bordetella pertussis* indicate that distinct charged and uncharged amino acids in TLR4 and MD-2 proteins determine the binding affinity between lipid A and TLR4/MD-2, affecting subsequent macrophage activation (Maeshima et al., 2015). Another example is the involvement of LBP and soluble CD14 (sCD14) in modulation of LPS response in a concentration dependent manner. While low concentration of LBP enhances P-LPS responses, high LBP concentration during acute inflammation and infection inhibits P-LPS bioactivity in contrast. On the other hand, in body fluid, systematic sCD14 may distract P-LPS from membrane-bound CD14 (mCD14) and inhibit TLR4 signaling. Dual stimulatory and inhibitory mechanisms of LBP and sCD14 may therefore exist to modulate the inflammations in infected host (Kitchens and Thompson, 2005). Subtle interactive variations at the host-pathogen interface thus fine-tune the host immune responses to specific P-LPS.

Microbiota Anti-Inflammatory Lipopolysaccharides Counteract Proinflammatory Lipopolysaccharides to Achieve Homeostasis

LPS are mostly produced from gut microbiota, besides those from external infections, the respiratory tract and gum (Brown, 2019). Gut microbiota are mostly strict anaerobes (97%), and play multiple important roles in maintaining host intestinal homeostasis and promoting health (Alexandre et al., 2018). Basic composition of the human gut microbiota is composed of bacteria from the phyla Firmicutes (64%, mainly Gram-positive *Clostridium*, *Bacillus*, *Lactobacillus*, and *Enterococcus* species), and *Bacteroidetes* (23%, mostly Gram-negative *Bacteroides* and *Prevotella* species). Other phyla include Proteobacteria (1–8%), Actinobacteria (3%), and low numbers of the phyla *Fusobacteria*, *Verrucomicrobia*, and TM7 (2%). By contrast, fungi and archaea comprise less than 1% of the total gut microbiota (Cardinelli et al., 2015). Under normobiosis situation, hosts do not develop gut inflammatory phenotypes. This may be due to a harmonic habituating relationship of microbiota bacteria and optimal control of P-LPS activity in the intestine, leading to host intestinal homeostasis and beyond. Within the gut microbiota, intestinal Proteobacteria work as major contributors of P-LPS synthesized. Among these, an average of 14% of total P-LPS produced is of *E. coli* origin in healthy people,

and 5.2% in human microbiome project 1(HMP1) donors (Alexandre et al., 2018).

Recent studies indicated that total LPS prepared from the consortium of gut-resident microbes potentially antagonize the *E. coli* LPS-host TLR4 signaling pathway (Alexander and Rietschel, 2001; d'Hennezel et al., 2017). Further metagenomic sequencing delineated the strain level contributions to the gut LPS pool and found that bacteria across the members of the order Bacteroidales produce antagonistic forms of LPS (A-LPS), thus driving immune silencing for the entire microbial community. Especially, Bacteroidetes species may contribute up to 79% of the A-LPS produced in healthy people and 92.4% of that in HMP1 samples. The estimated average ratio of Bacteroidetes-to-*E. coli* LPS in the gut would be between 6:1 in healthy people and 18:1 in the HMP1 cohort (Alexandre et al., 2018). The abundances of the *Bacteroides* species, and therefore their likely contribution to the whole LPS pool are started to be unraveled to play an important role in intestinal immune homeostasis.

Anti-Inflammatory Lipopolysaccharides Is Characterized by Structure Variations of Lipid A

It is established that natural heterogeneity observed in the lipid A structure portion of LPS may produce differential modulatory effects on immune responses (Chilton et al., 2013). The underlying silencing mechanism of A-LPS is subsequently deciphered to be closely related to their status of lipid A acylation in contrast to P-LPS, where hypoacylation is frequently observed (Coats et al., 2007; d'Hennezel et al., 2017). For example, tetra- or penta-acylation of A-LPS in contrast to the well-established hexaacyl-lipid A of *E. coli* (Reife et al., 2006) is identified. Such hypoacylation characteristic of lipid A structure is expected to be found in many Bacteroidetes bacteria including *Bacteroides dorei*, *Bacteroides fragilis*, *Bacteroides ovatus*, *Bacteroides thetaiotaomicron*, and *Bacteroides uniformis* ... etc. (Poxton and Edmond, 1995; d'Hennezel et al., 2017; Jacobson et al., 2018). Another example is the hypoacylated LPS from a foodborne pathogen *Campylobacter jejuni* that only moderately induces TLR4 dependent immune response (Korneev et al., 2018). Furthermore, *Shigella flexneri* 2a that contains a mixture of hexaacylated, pentaacylated, and predominantly tetraacylated lipid A in its LPS also significantly decreases its stimulatory effects on NF-kappaB signaling pathway in contrast to the hexaacylated *E. coli* LPS (Rallabhandi et al., 2008). On the other hand, structurally similar, pentaacylated LPS of *Porphyromonas gingivalis* and *B. thetaiotaomicron* initiate significantly different innate immune responses (Berezow et al., 2009), highlighting the importance of exquisite structural variations of lipid A of LPS in immune regulation.

Besides hypoacylation, hypophosphorylation of the diglucosamine backbone also decreases LPS toxicity. The A-LPS derived from the intestinal mucosa-associated bacteria *B. thetaiotaomicron* and *Prevotella intermedia* contain monophosphorylated lipid A (MPLA). These A-LPS showed moderate immune-stimulating functions and could work as

immunological adjuvants for antigen-specific immune responses (Chilton et al., 2013). As the immune silencing effect *via* A-LPS seems to be an intrinsic characteristic in healthy hosts, the current belief that robust activation of TLR4 signaling by gut microbiome derived LPS is therefore to be carefully reconsidered (d'Hennezel et al., 2017).

Anti-Inflammatory Lipopolysaccharides Combats Inflammation Induced by Proinflammatory Lipopolysaccharides

A-LPS may show antagonistic effects on P-LPS activity. Taking modulation of colitis by use of A-LPS as an example, mice harboring low levels of Enterobacteriaceae (main P-LPS producer) and high Bacteroidetes (main A-LPS producer) showed intestinal low endotoxicity and maintained mucosal immune homeostasis. By contrast, mice harboring a highly endotoxic gut microbiota (with high Enterobacteriaceae and low Bacteroidetes levels) were prone to develop colitis. In concordance, administration of *E. coli* JM83 (wild-type P-LPS) to mice exacerbated colitis, whereas a mixture of *E. coli* JM83 and *E. coli* htrBPG (mutated LPS, with a lower endotoxicity similar to that of Bacteroidetes) prevented colitis development in mice. These results indicated that the A-LPS produced by the intestinal microbiota may counteract P-LPS dominantly induced colitis development in mice (Gronbach et al., 2014). Another example was *B. dorei* that produces an antagonistic A-LPS affecting the susceptibility of children to allergies and autoimmunity (Vatanen et al., 2016). Besides, *B. fragilis* and *B. ovatus* also alleviated the P-LPS-induced inflammation in mice (Tan et al., 2019), and *Bacteroides vulgatus* and *B. dorei* ameliorated endotoxemia, decreased gut microbial LPS production, and suppressed proinflammatory immune responses (Yoshida et al., 2018). Recently, the intestinal inflammation-reducing properties of weak agonistic A-LPS derived from *B. vulgatus* were reported to be due to inducing a special type of endotoxin tolerance, mainly through the MD-2/TLR4 receptor complex axis in CD11c⁺ cells of intestinal lamina propria (Steimle et al., 2019).

On top of these Bacteroidale bacteria, some Proteobacteria bacteria such as *Rhodobacter capsulatus* and *Rhodobacter sphaeroides* also owned A-LPS that lack potent agonist activity (Alexander and Rietschel, 2001). What's more, A-LPS derived from Rhodobacter, such as E5531 (Rc-LPS derived) and E5564 (eritoran tetrasodium, developed from E5531) further showed potent antagonism of P-LPS-mediated cellular activation (Christ et al., 1995). E5564 was subsequently shown to prevent chronic airway hyperreactivity and inflammation to inhaled P-LPS (Savov et al., 2005). Besides, not only *in vitro* effects, A-LPS also showed protective effect on mice suffered from P-LPS-induced lethality (Barochia et al., 2011). Another example is that, in contrast to P-LPS prepared from *E. coli*, A-LPS prepared from two bacterial strains, the commensal *Endozoicomonas* sp. and the opportunistic bacteria *Pseudoalteromonas* spp., that are associated with the sponge *Suberites domuncula* are non-toxic for mammals. The relatively low acylation of the lipid A of *Pseudoalteromonas* sp. 1A1 and *Endozoicomonas* sp. HEX311

may be a possible reason to explain their A-LPS characteristics (Garderes et al., 2015).

Results from our study also indicated that lipid A of A-LPS derived from the bacterium *Parabacteroides goldsteinii* MTS01 is expected to be pentaacylated, based on genome comparison and structural determination results (unpublished). *P. goldsteinii* MTS01 derived A-LPS (Pg-LPS) antagonizes *E. coli* O111:B4 LPS induced TNF- α production in macrophages RAW264.7, IL-1 β in human PBMC, and over-activation of BCR signaling in B cells (Xu et al., 2008) and reverses the expression of CS-induced inflammations-related genes, leading to alleviating the pathogenesis of COPD in lung and colon tissues (unpublished). Pg-LPS seems to be consistent in their immune inhibiting effect against many different kinds of cells. On the other hand, the antagonistic potential of hypoacylated LPS from *R. sphaeroides* (Rs-LPS) is not consistently seen against many immune cells, and is dependent on the cell sources of mammalian species (Doring et al., 2017). Therefore, complicated and minute interactions occur between LPS and immune cells, which has to be taken into consideration for subsequent development of clinical applications.

Anti-Inflammatory Lipopolysaccharides Competes With Proinflammatory Lipopolysaccharides in TLR4 Signaling Pathway

“Competition” may be the underlying mechanism that hypoacylated A-LPS antagonizes P-LPS activity (Figure 2). Previous study has shown that tetra-acylated LPS derived from *P. gingivalis*, and penta-acylated msbB LPS derived from an *Escherichia coli* mutant strain antagonized the capability of hexa-acylated *E. coli* LPS to activate the TLR4 signaling complex in human endothelial cells (Coats et al., 2005). While expression levels of TLR4 do matter in modulating the efficacy of LPS-dependent antagonism, MD-2 seemed to act as the principal molecular component responsible for the antagonistic effects, due to fact that msbB and *P. gingivalis* LPS could directly bind to hMD-2 (Coats et al., 2005). Subsequent studies showed that these antagonistic A-LPS might utilize at least two distinct mechanisms to block *E. coli* P-LPS-dependent activation of hTLR4: i) directly compete with the *E. coli* P-LPS for the same binding site on hMD-2, and ii) to inhibit complexes interaction between *E. coli* P-LPS-hMD-2 and hTLR4. Besides hMD-2, hTLR4 also participated in species-specific recognition of msbB and *P. gingivalis* A-LPS at the hTLR4 complex (Coats et al., 2007). Results obtained from crystal protein structures studies, as well as targeted mutagenesis analyses of the receptor complex might give some more hints. Combination of intricate electrostatic and hydrophobic interactions primarily occurring within the MD-2 co-receptor, with a contribution from TLR4, may contribute to the species-specific recognition of lipid A by host cells (Oblak and Jerala, 2015). As underacylated LPS has emerged as a novel mechanism utilized by microbiota bacteria to optimally modulate host innate immune responses, these LPS may be developed as prime therapeutic candidates for neutralizing Gram-negative bacteria initiated bacterial sepsis.

Lipopolysaccharides and TLR4 as Targets of Immune Modulation

Varying LPS structures may be used as a means by which Gram-negative bacteria control host immune status. Therefore, engineering LPS structure and chemical properties can be used as a strategy for development of novel immune-regulation agents. For example, controlling the acylation and phosphorylation status of lipid A may be considered. The position of phosphate group on lipid A may change the potency of LPS (Coats et al., 2009; Coats et al., 2011). On the other hand, lipid A without phosphate group due to alkaline phosphatase activity produced from host can even lead to formation of the non-immunostimulatory LPS, as illustrated by the *Eurytmna scolopes-Vibrio fischeri* symbiotic association (Rader et al., 2012). Another example is the lipid A of P-LPS of *V. fischeri* in which heterogeneous mixtures of mono- and diphosphorylated disaccharides, with variable acylation situations from tetra- to octaacylated were identified. These uncommon phosphoglycerol entity and carbohydrate compositions of lipid A may modulate the close interaction between *V. fischeri* and *E. scolopes* during symbiotic development (Phillips et al., 2011; Post et al., 2012), where imbalanced bacteria-host immune response is prevented.

Another example of application by lipid A modification is the mono-phosphorylated lipid A species (MPL) which is less toxic compared to conventional lipid A, and is the first vaccine adjuvant approved by the Food and Drug Administration (FDA) in more than 70 years (Needham et al., 2013). In contrast to the wild-type *E. coli* LPS which mainly acts on TLR4-MyD88 signaling, MPL preferentially effects through TRIF which is less inflammatory (Needham et al., 2013). On top of these, addition of aminoarabinose residues onto lipid A of *Burkholderia cenocepacia* P-LPS enhanced binding efficacy of lipid A to TLR4-MD-2 complex. This might initiate strong activation, despite the lipid A moiety having only five acyl chains (Di Lorenzo et al., 2015). The engineering of lipid A of P-LPS in a human pathogen *B. pertussis* for better control of P-LPS-TLR4 activity is also described. Glucosamine is added into lipid A moiety, leading to promote TLR4 activation in human macrophages. In parallel, site-directed mutagenesis together with a NF- κ B reporter assay are also used to screen TLR4 and MD-2 mutants with changed amino acid residues that change species-specific responses. Results indicate that some uncharged amino acids in both TLR4 and MD-2 are involved in recognition of penta-acylated *B. pertussis* lipid A (Maeshima et al., 2015). These amino acids may be considered as research targets for optimizing P-LPS-TLR4 interaction and activation activity.

Besides lipid A, engineering of O-antigen may also be taken into consideration. Oral or intradermal administration of LPS derived from the bacterium *Pantoea agglomerans*, a bacterium that grows symbiotically in wheat, produce prophylactic and anti-tumor effects, even though no serious side-effects are identified. The main LPS structural difference that involves such biological effects lies in the structure of the O-antigen polysaccharides (Nishizawa et al., 1992). On the other hand, O-antigen defective LPS derived from certain *E. coli* strains may

be anti-inflammatory. For example, the probiotic *E. coli* strain Nissle 1917 given orally to mice exert local and systemic anti-inflammatory effects in a model of LPS-induced sepsis (Arribas et al., 2009). Further analysis show that this strain has a defective LPS biosynthesis pathway that results in production of truncated variable oligosaccharide-antigen chains and gives the bacteria a semi-rough phenotype. Such characteristic may contribute to the probiotic properties of the *E. coli* strain (Guttsches et al., 2012). Another example is the *E. coli* K-12 strain, which shows a defective O-antigen structure, can be converted into a pathogen of *Caenorhabditis elegans* upon restoration of its O antigen structure (Browning et al., 2013). Further studies are ongoing to study how engineered LPS with different structures and components can be exploited to generate a spectrum of immuno-stimulatory molecules for the development of new adjuvants of vaccines and therapeutics (Needham et al., 2013).

FUTURE PERSPECTIVES

Microbiome derived-LPS play important roles in immune modulation and development of inflammatory diseases (Lin et al., 2016). LPS comprise of chemical molecules of very complicated components, though their basic constructions are similar. In concordance, LPS prepared from different bacterial species and strains produce gradient immune-modulation effects on host cells. Intriguingly, dualism that represents two abstract and complementary regulatory effect in LPS seems to exist, after identification and characterization of A-LPS. As counteracting activity exists between A- and P-LPS, engineering LPS structure and composition, or deploying relative LPS ratios may be used to either enhance or inhibit their activities on immunity and inflammation. Therefore, bacterial original or synthesized LPS may be used to modulate the immune response as a preventive or

therapeutic measure for the management of chronic inflammation related diseases. Some difficulties and challenges are expected, especially on how to obtain optimal LPS species or determine relative compositions of A- and P-LPS for potential clinical applications. To circumvent the difficulties, use of modern techniques is proposed. A high-throughput experimentation workflow platform for rapidly and efficiently measuring cytokines, together with high efficacy chemical synthesis pipelines should be established to accelerate the optimization from laboratory-scale discovery to large-scale screening. In parallel, complementary artificial intelligence approaches are just coming into focus.

AUTHOR CONTRIBUTIONS

H-CL, T-LL: Conceptualization, original draft preparation. C-CL: Supervision and contents curation. C-CS: Messages provision and investigation. W-FL, Y-MC, J-JL, T-SW, C-MT: Validation, writing, and reviewing.

FUNDING

We would like to express our thankfulness for funding provided from CORPD1F0013 and CORPD1J0051 from Chang Gung Memorial Hospital, 106-2320-B-182-028-MY3, 108-2321-B-182-002, 108-2320-B-030-005 from Ministry of Science and Technology (MOST), Microbiota Research Center from Chang Gung University, and the Research Center for Emerging Viral Infections from The Featured Areas Research Center Program within the framework of the Higher Education Sprout Project by the Ministry of Education (MOE) in Taiwan and MOST, Taiwan (MOST 108-3017-F-182 -001).

REFERENCES

- Alexander, C., and Rietschel, E. T. (2001). Bacterial lipopolysaccharides and innate immunity. *J. Endotoxin. Res.* 7 (3), 167–202. doi: 10.1179/096805101101532675
- Alexandre, A., Maria, K. D., Alexandre, P. D., Mauro, P., Maddalena, Q., Patrick, R., et al. (2018). Knowledge for Health and Consumer Safety. *The Human Gut Microbiota: Overview and analysis of the current scientific knowledge and possible impact on healthcare and well-being*. Luxembourg: Publications Office of the European Union. doi: 10.2760/17381
- Amor, K., Heinrichs, D. E., Frirdich, E., Ziebell, K., Johnson, R. P., and Whitfield, C. (2000). Distribution of core oligosaccharide types in lipopolysaccharides from *Escherichia coli*. *Infect. Immun.* 68 (3), 1116–1124. doi: 10.1128/IAI.68.3.1116-1124.2000
- Arribas, B., Rodriguez-Cabezas, M. E., Camuesco, D., Comalada, M., Bailon, E., Utrilla, P., et al. (2009). A probiotic strain of *Escherichia coli*, Nissle 1917, given orally exerts local and systemic anti-inflammatory effects in lipopolysaccharide-induced sepsis in mice. *Br. J. Pharmacol.* 157 (6), 1024–1033. doi: 10.1111/j.1476-5381.2009.00270.x
- Asti, C., Ruggieri, V., Porzio, S., Chiusaroli, R., Melillo, G., and Caselli, G. F. (2000). Lipopolysaccharide-induced lung injury in mice. I. Concomitant evaluation of inflammatory cells and haemorrhagic lung damage. *Pulm. Pharmacol. Ther.* 13 (2), 61–69. doi: 10.1006/pupt.2000.0231
- Atamas, S. P., Chapoval, S. P., and Keegan, A. D. (2013). Cytokines in chronic respiratory diseases. *F1000 Biol. Rep.* 5, 3. doi: 10.3410/B5-3
- Aul, R., Armstrong, J., Duvoix, A., Lomas, D., Hayes, B., Miller, B. E., et al. (2012). Inhaled LPS challenges in smokers: a study of pulmonary and systemic effects. *Br. J. Clin. Pharmacol.* 74 (6), 1023–1032. doi: 10.1111/j.1365-2125.2012.04287.x
- Barochia, A., Solomon, S., Cui, X., Natanson, C., and Eichacker, P. Q. (2011). Eritoran tetrasodium (E5564) treatment for sepsis: review of preclinical and clinical studies. *Expert Opin. Drug Metab. Toxicol.* 7 (4), 479–494. doi: 10.1517/17425255.2011.558190
- Berezow, A. B., Ernst, R. K., Coats, S. R., Braham, P. H., Karimi-Naser, L. M., and Darveau, R. P. (2009). The structurally similar, penta-acylated lipopolysaccharides of *Porphyromonas gingivalis* and *Bacteroides* elicit strikingly different innate immune responses. *Microb. Pathog.* 47 (2), 68–77. doi: 10.1016/j.micpath.2009.04.015
- Brown, G. C. (2019). The endotoxin hypothesis of neurodegeneration. *J. Neuroinflammation* 16 (1), 180. doi: 10.1186/s12974-019-1564-7
- Browning, D. F., Wells, T. J., Franca, F. L., Morris, F. C., Sevastyanovich, Y. R., Bryant, J. A., et al. (2013). Laboratory adapted *Escherichia coli* K-12 becomes a pathogen of *Caenorhabditis elegans* upon restoration of O antigen biosynthesis. *Mol. Microbiol.* 87 (5), 939–950. doi: 10.1111/mmi.12144
- Cardinelli, C. S., Sala, P. C., Alves, C. C., Torrinhas, R. S., and Waitzberg, D. L. (2015). Influence of intestinal microbiota on body weight gain: a narrative review of the literature. *Obes. Surg.* 25 (2), 346–353. doi: 10.1007/s11695-014-1525-2
- Chantratita, N., Tandhavanant, S., Myers, N. D., Seal, S., Arayawichanont, A., Kliangsana-Ad, A., et al. (2013). Survey of innate immune responses to

- Burkholderia pseudomallei in human blood identifies a central role for lipopolysaccharide. *PLoS One* 8 (11), e81617. doi: 10.1371/journal.pone.0081617
- Chen, L. W., Chen, P. H., and Hsu, C. M. (2011). Commensal microflora contribute to host defense against *Escherichia coli* pneumonia through Toll-like receptors. *Shock* 36 (1), 67–75. doi: 10.1097/SHK.0b013e3182184ee7
- Chilton, P. M., Hadel, D. M., To, T. T., Mitchell, T. C., and Darveau, R. P. (2013). Adjuvant activity of naturally occurring monophosphoryl lipopolysaccharide preparations from mucosa-associated bacteria. *Infect. Immun.* 81 (9), 3317–3325. doi: 10.1128/IAI.01150-12
- Chow, J. C., Young, D. W., Golenbock, D. T., Christ, W. J., and Gusovsky, F. (1999). Toll-like receptor-4 mediates lipopolysaccharide-induced signal transduction. *J. Biol. Chem.* 274 (16), 10689–10692. doi: 10.1074/jbc.274.16.10689
- Christ, W. J., Asano, O., Robidoux, A. L., Perez, M., Wang, Y., Dubuc, G. R., et al. (1995). E5531, a pure endotoxin antagonist of high potency. *Science* 268 (5207), 80–83. doi: 10.1126/science.7701344
- Coats, S. R., Pham, T. T., Bainbridge, B. W., Reife, R. A., and Darveau, R. P. (2005). MD-2 mediates the ability of tetra-acylated and penta-acylated lipopolysaccharides to antagonize *Escherichia coli* lipopolysaccharide at the TLR4 signaling complex. *J. Immunol.* 175 (7), 4490–4498. doi: 10.4049/jimmunol.175.7.4490
- Coats, S. R., Do, C. T., Karimi-Naser, L. M., Braham, P. H., and Darveau, R. P. (2007). Antagonistic lipopolysaccharides block *E. coli* lipopolysaccharide function at human TLR4 via interaction with the human MD-2 lipopolysaccharide binding site. *Cell Microbiol.* 9 (5), 1191–1202. doi: 10.1111/j.1462-5822.2006.00859.x
- Coats, S. R., Jones, J. W., Do, C. T., Braham, P. H., Bainbridge, B. W., To, T. T., et al. (2009). Human Toll-like receptor 4 responses to *P. gingivalis* are regulated by lipid A 1- and 4'-phosphatase activities. *Cell Microbiol.* 11 (11), 1587–1599. doi: 10.1111/j.1462-5822.2009.01349.x
- Coats, S. R., Berezow, A. B., To, T. T., Jain, S., Bainbridge, B. W., Banani, K. P., et al. (2011). The lipid A phosphate position determines differential host Toll-like receptor 4 responses to phylogenetically related symbiotic and pathogenic bacteria. *Infect. Immun.* 79 (1), 203–210. doi: 10.1128/IAI.00937-10
- d'Hennezel, E., Abubucker, S., Murphy, L. O., and Cullen, T. W. (2017). Total Lipopolysaccharide from the Human Gut Microbiome Silences Toll-Like Receptor Signaling. *mSystems* 2 (6), e00046–17. doi: 10.1128/mSystems.00046-17
- Davey, A., McAuley, D. F., and O'Kane, C. M. (2011). Matrix metalloproteinases in acute lung injury: mediators of injury and drivers of repair. *Eur. Respir. J.* 38 (4), 959–970. doi: 10.1183/09031936.00032111
- Di Lorenzo, F., Kubik, L., Oblak, A., Lore, N. I., Cigana, C., Lanzetta, R., et al. (2015). Activation of Human Toll-like Receptor 4 (TLR4) by Myeloid Differentiation Factor 2 (MD-2) by Hypoacylated Lipopolysaccharide from a Clinical Isolate of *Burkholderia cenocepacia*. *J. Biol. Chem.* 290 (35), 21305–21319. doi: 10.1074/jbc.M115.649087
- Doring, C., Regen, T., Gertig, U., van Rossum, D., Winkler, A., Saiepour, N., et al. (2017). A presumed antagonistic LPS identifies distinct functional organization of TLR4 in mouse microglia. *Glia* 65 (7), 1176–1185. doi: 10.1002/glia.23151
- Faner, R., Rojas, M., Macnee, W., and Agusti, A. (2012). Abnormal lung aging in chronic obstructive pulmonary disease and idiopathic pulmonary fibrosis. *Am. J. Respir. Crit. Care Med.* 186 (4), 306–313. doi: 10.1164/rccm.201202-0282PP
- Fedele, G., Nasso, M., Spensieri, F., Palazzo, R., Frasca, L., Watanabe, M., et al. (2008). Lipopolysaccharides from *Bordetella pertussis* and *Bordetella parapertussis* differently modulate human dendritic cell functions resulting in divergent prevalence of Th17-polarized responses. *J. Immunol.* 181 (1), 208–216. doi: 10.4049/jimmunol.181.1.208
- Fink, M. P. (2014). Animal models of sepsis. *Virulence* 5 (1), 143–153. doi: 10.4161/viru.26083
- Fuke, N., Nagata, N., Suganuma, H., and Ota, T. (2019). Regulation of Gut Microbiota and Metabolic Endotoxemia with Dietary Factors. *Nutrients* 11 (10), 2277. doi: 10.3390/nu11102277
- Gangemi, S., Casciaro, M., Trapani, G., Quartuccio, S., Navarra, M., Pioggia, G., et al. (2015). Association between HMGB1 and COPD: A Systematic Review. *Mediators Inflammation* 2015, 164913. doi: 10.1155/2015/164913
- Garderes, J., Bedoux, G., Koutsouveli, V., Crequer, S., Desriac, F., and Pennec, G. L. (2015). Lipopolysaccharides from Commensal and Opportunistic Bacteria: Characterization and Response of the Immune System of the Host Sponge *Suberites domuncula*. *Mar. Drugs* 13 (8), 4985–5006. doi: 10.3390/md13084985
- Gronbach, K., Flade, I., Holst, O., Lindner, B., Ruscheweyh, H. J., Wittmann, A., et al. (2014). Endotoxicity of lipopolysaccharide as a determinant of T-cell-mediated colitis induction in mice. *Gastroenterology* 146 (3), 765–775. doi: 10.1053/j.gastro.2013.11.033
- Gupta, V., Banyard, A., Mullan, A., Sriskantharajah, S., Southworth, T., and Singh, D. (2015). Characterization of the inflammatory response to inhaled lipopolysaccharide in mild to moderate chronic obstructive pulmonary disease. *Br. J. Clin. Pharmacol.* 79 (5), 767–776. doi: 10.1111/bcp.12546
- Guttsches, A. K., Loseke, S., Zahringer, U., Sonnenborn, U., Enders, C., Gatermann, S., et al. (2012). Anti-inflammatory modulation of immune response by probiotic *Escherichia coli* Nissle 1917 in human blood mononuclear cells. *Innate Immun.* 18 (2), 204–216. doi: 10.1177/1753425910396251
- Hajjar, A. M., Ernst, R. K., Yi, J., Yam, C. S., and Miller, S. I. (2017). Expression level of human TLR4 rather than sequence is the key determinant of LPS responsiveness. *PLoS One* 12 (10), e0186308. doi: 10.1371/journal.pone.0186308
- Hersoug, L. G., Moller, P., and Loft, S. (2016). Gut microbiota-derived lipopolysaccharide uptake and trafficking to adipose tissue: implications for inflammation and obesity. *Obes. Rev.* 17 (4), 297–312. doi: 10.1111/obr.12370
- Hulina-Tomaskovic, A., Heijink, I. H., Jonker, M. R., Somborac-Bacura, A., Grdic Rajkovic, M., and Rumora, L. (2019). Pro-inflammatory effects of extracellular Hsp70 and cigarette smoke in primary airway epithelial cells from COPD patients. *Biochimie* 156, 47–58. doi: 10.1016/j.biochi.2018.09.010
- Jacobson, A. N., Choudhury, B. P., and Fischbach, M. A. (2018). The Biosynthesis of Lipooligosaccharide from *Bacteroides thetaiotaomicron*. *mBio* 9 (2), e02289–17. doi: 10.1128/mBio.02289-17
- Kadowaki, T., Ohno, S., Taniguchi, Y., Inagawa, H., Kohchi, C., and Soma, G. (2013). Induction of nitric oxide production in RAW264.7 cells under serum-free conditions by O-antigen polysaccharide of lipopolysaccharide. *Anticancer Res.* 33 (7), 2875–2879.
- Kim, S. J., and Kim, H. M. (2017). Dynamic lipopolysaccharide transfer cascade to TLR4/MD2 complex via LBP and CD14. *BMB Rep.* 50 (2), 55–57. doi: 10.5483/BMBRep.2017.50.2.011
- Kitchens, R. L., and Thompson, P. A. (2005). Modulatory effects of sCD14 and LBP on LPS-host cell interactions. *J. Endotoxin. Res.* 11 (4), 225–229. doi: 10.1177/09680519050110040701
- Kobayashi, S., Fujinawa, R., Ota, F., Kobayashi, S., Angata, T., Ueno, M., et al. (2013). A single dose of lipopolysaccharide into mice with emphysema mimics human chronic obstructive pulmonary disease exacerbation as assessed by micro-computed tomography. *Am. J. Respir. Cell Mol. Biol.* 49 (6), 971–977. doi: 10.1165/rcmb.2013-0074OC
- Komori, T., Saito, K., Sawa, N., Shibasaki, Y., Kohchi, C., Soma, G., et al. (2015). Innate Immunity Activated by Oral Administration of LPS Is Phylogenetically Preserved and Developed in Broiler Chickens. *Anticancer Res.* 35 (8), 4461–4466.
- Korneev, K. V., Kondakova, A. N., Sviriaeva, E. N., Mitkin, N. A., Palmigiano, A., Kruglov, A. A., et al. (2018). Hypoacylated LPS from Foodborne Pathogen *Campylobacter jejuni* Induces Moderate TLR4-Mediated Inflammatory Response in Murine Macrophages. *Front. Cell Infect. Microbiol.* 8, 58. doi: 10.3389/fcimb.2018.00058
- Lerouge, I., and Vanderleyden, J. (2002). O-antigen structural variation: mechanisms and possible roles in animal/plant-microbe interactions. *FEMS Microbiol. Rev.* 26 (1), 17–47. doi: 10.1111/j.1574-6976.2002.tb00597.x
- Lin, C.-S., Chang, C.-J., Martel, J., Ojcius, D. M., Lai, W.-F., Lu, C.-C., et al. (2016). Lipopolysaccharide: friend or foe? *J. Biomed. Lab. Sci.* 29, 121–126.
- Lu, Y. C., Yeh, W. C., and Ohashi, P. S. (2008). LPS/TLR4 signal transduction pathway. *Cytokine* 42 (2), 145–151. doi: 10.1016/j.cyt.2008.01.006
- Maeshima, N., Evans-Atkinson, T., Hajjar, A. M., and Fernandez, R. C. (2015). *Bordetella pertussis* Lipid A Recognition by Toll-like Receptor 4 and MD-2 Is Dependent on Distinct Charged and Uncharged Interfaces. *J. Biol. Chem.* 290 (21), 13440–13453. doi: 10.1074/jbc.M115.653881
- Mazgaen, L., and Gurung, P. (2020). Recent Advances in Lipopolysaccharide Recognition Systems. *Int. J. Mol. Sci.* 21 (2), 379. doi: 10.3390/ijms21020379

- Nativel, B., Couret, D., Giraud, P., Meilhac, O., d'Hellencourt, C. L., Viranaicken, W., et al. (2017). Porphyromonas gingivalis lipopolysaccharides act exclusively through TLR4 with a resilience between mouse and human. *Sci. Rep.* 7 (1), 15789. doi: 10.1038/s41598-017-16190-y
- Needham, B. D., Carroll, S. M., Giles, D. K., Georgiou, G., Whiteley, M., and Trent, M. S. (2013). Modulating the innate immune response by combinatorial engineering of endotoxin. *Proc. Natl. Acad. Sci. U. S. A.* 110 (4), 1464–1469. doi: 10.1073/pnas.1218080110
- Nishizawa, T., Inagawa, H., Oshima, H., Okutomi, T., Tsukioka, D., Iguchi, M., et al. (1992). Homeostasis as regulated by activated macrophage. I. Lipopolysaccharide (LPS) from wheat flour: isolation, purification and some biological activities. *Chem. Pharm. Bull. (Tokyo)* 40 (2), 479–483. doi: 10.1248/cpb.40.479
- Oblak, A., and Jerala, R. (2015). The molecular mechanism of species-specific recognition of lipopolysaccharides by the MD-2/TLR4 receptor complex. *Mol. Immunol.* 63 (2), 134–142. doi: 10.1016/j.molimm.2014.06.034
- Opal, S. M. (2010). Endotoxins and other sepsis triggers. *Contrib. Nephrol.* 167, 14–24. doi: 10.1159/000315915
- Pfalzgraff, A., and Weindl, G. (2019). Intracellular Lipopolysaccharide Sensing as a Potential Therapeutic Target for Sepsis. *Trends Pharmacol. Sci.* 40 (3), 187–197. doi: 10.1016/j.tips.2019.01.001
- Phillips, N. J., Adin, D. M., Stabb, E. V., McFall-Ngai, M. J., Apicella, M. A., and Gibson, B. W. (2011). The lipid A from *Vibrio fischeri* lipopolysaccharide: a unique structure bearing a phosphoglycerol moiety. *J. Biol. Chem.* 286 (24), 21203–21219. doi: 10.1074/jbc.M111.239475
- Post, D. M., Yu, L., Krasity, B. C., Choudhury, B., Mandel, M. J., Brennan, C. A., et al. (2012). O-antigen and core carbohydrate of *Vibrio fischeri* lipopolysaccharide: composition and analysis of their role in *Euprymna scolopes* light organ colonization. *J. Biol. Chem.* 287 (11), 8515–8530. doi: 10.1074/jbc.M111.324012
- Poxton, I. R., and Edmond, D. M. (1995). Biological activity of *Bacteroides* lipopolysaccharide—reappraisal. *Clin. Infect. Dis.* 20 Suppl 2, S149–S153. doi: 10.1093/clinids/20.Supplement_2.S149
- Rader, B. A., Kremer, N., Apicella, M. A., Goldman, W. E., and McFall-Ngai, M. J. (2012). Modulation of symbiont lipid A signaling by host alkaline phosphatases in the squid-vibrio symbiosis. *mBio* 3 (3), e00093–12. doi: 10.1128/mBio.00093-12
- Rallabhandi, P., Awomoyi, A., Thomas, K. E., Phalipon, A., Fujimoto, Y., Fukase, K., et al. (2008). Differential activation of human TLR4 by *Escherichia coli* and *Shigella flexneri* 2a lipopolysaccharide: combined effects of lipid A acylation state and TLR4 polymorphisms on signaling. *J. Immunol.* 180 (2), 1139–1147. doi: 10.4049/jimmunol.180.2.1139
- Reife, R. A., Coats, S. R., Al-Qutub, M., Dixon, D. M., Braham, P. A., Billharz, R. J., et al. (2006). Porphyromonas gingivalis lipopolysaccharide lipid A heterogeneity: differential activities of tetra- and penta-acylated lipid A structures on E-selectin expression and TLR4 recognition. *Cell Microbiol.* 8 (5), 857–868. doi: 10.1111/j.1462-5822.2005.00672.x
- Savov, J. D., Brass, D. M., Lawson, B. L., McElvania-Tekippe, E., Walker, J. K., and Schwartz, D. A. (2005). Toll-like receptor 4 antagonist (E5564) prevents the chronic airway response to inhaled lipopolysaccharide. *Am. J. Physiol. Lung Cell Mol. Physiol.* 289 (2), L329–L337. doi: 10.1152/ajplung.00014.2005
- Simkin, D. R. (2019). Microbiome and Mental Health, Specifically as It Relates to Adolescents. *Curr. Psychiatry Rep.* 21 (9), 93. doi: 10.1007/s11920-019-1075-3
- Sperandeo, P., Martorana, A. M., and Polissi, A. (2017). Lipopolysaccharide biogenesis and transport at the outer membrane of Gram-negative bacteria. *Biochim. Biophys. Acta Mol. Cell Biol. Lipids* 1862 (11), 1451–1460. doi: 10.1016/j.bbalip.2016.10.006
- Steimle, A., Autenrieth, I. B., and Frick, J. S. (2016). Structure and function: Lipid A modifications in commensals and pathogens. *Int. J. Med. Microbiol.* 306 (5), 290–301. doi: 10.1016/j.ijmm.2016.03.001
- Steimle, A., Michaelis, L., Di Lorenzo, F., Kliem, T., Munzner, T., Maerz, J. K., et al. (2019). Weak Agonistic LPS Restores Intestinal Immune Homeostasis. *Mol. Ther.* 27 (11), 1974–1991. doi: 10.1016/j.ymthe.2019.07.007
- Tan, H., Zhao, J., Zhang, H., Zhai, Q., and Chen, W. (2019). Novel strains of *Bacteroides fragilis* and *Bacteroides ovatus* alleviate the LPS-induced inflammation in mice. *Appl. Microbiol. Biotechnol.* 103 (5), 2353–2365. doi: 10.1007/s00253-019-09617-1
- Tsutsumi-Ishii, Y., Shimada, K., Daida, H., Toman, R., and Nagaoka, I. (2008). Low potency of *Chlamydia* LPS to activate human mononuclear cells due to its reduced affinities for CD14 and LPS-binding protein. *Int. Immunol.* 20 (2), 199–208. doi: 10.1093/intimm/dxm129
- Vanaja, S. K., Russo, A. J., Behl, B., Banerjee, I., Yankova, M., Deshmukh, S. D., et al. (2016). Bacterial Outer Membrane Vesicles Mediate Cytosolic Localization of LPS and Caspase-11 Activation. *Cell* 165 (5), 1106–1119. doi: 10.1016/j.cell.2016.04.015
- Vatanen, T., Kostic, A. D., d'Hennezel, E., Siljander, H., Franzosa, E. A., Yassour, M., et al. (2016). Variation in Microbiome LPS Immunogenicity Contributes to Autoimmunity in Humans. *Cell* 165 (4), 842–853. doi: 10.1016/j.cell.2016.04.007
- Waldner, M. J., and Neurath, M. F. (2015). Mechanisms of Immune Signaling in Colitis-Associated Cancer. *Cell Mol. Gastroenterol. Hepatol.* 1 (1), 6–16. doi: 10.1016/j.jcmgh.2014.11.006
- Wiese, A., Brandenburg, K., Ulmer, A. J., Seydel, U., and Muller-Loennies, S. (1999). The dual role of lipopolysaccharide as effector and target molecule. *Biol. Chem.* 380 (7–8), 767–784. doi: 10.1515/BC.1999.097
- Xu, H., Liew, L. N., Kuo, I. C., Huang, C. H., Goh, D. L., and Chua, K. Y. (2008). The modulatory effects of lipopolysaccharide-stimulated B cells on differential T-cell polarization. *Immunology* 125 (2), 218–228. doi: 10.1111/j.1365-2567.2008.02832.x
- Yoshida, N., Emoto, T., Yamashita, T., Watanabe, H., Hayashi, T., Tabata, T., et al. (2018). *Bacteroides vulgatus* and *Bacteroides dorei* Reduce Gut Microbial Lipopolysaccharide Production and Inhibit Atherosclerosis. *Circulation* 138 (22), 2486–2498. doi: 10.1161/CIRCULATIONAHA.118.033714

Conflict of Interest: The authors declare that the research was conducted in the absence of any commercial or financial relationships that could be construed as a potential conflict of interest.

Copyright © 2020 Lin, Shu, Chen, Lu, Wu, Lai, Tzeng, Lai and Lu. This is an open-access article distributed under the terms of the Creative Commons Attribution License (CC BY). The use, distribution or reproduction in other forums is permitted, provided the original author(s) and the copyright owner(s) are credited and that the original publication in this journal is cited, in accordance with accepted academic practice. No use, distribution or reproduction is permitted which does not comply with these terms.

RESEARCH ARTICLE

A synthesized heterocyclic chalcone inhibits neutrophilic inflammation through K^+ -dependent pH regulation

Shun-Chin Yang^{1,2} | Yi-Hsuan Wang^{2,3} | Yung-Fong Tsai^{4,5} | Ya-Wen Chang² | Tian-Shung Wu^{6,7} | Chiu-Ming Ho¹ | Tsong-Long Hwang^{2,3,4,8,9,10}

¹Department of Anesthesiology, Taipei Veterans General Hospital and National Yang-Ming University, Taipei, Taiwan

²Graduate Institute of Natural Products, College of Medicine, Chang Gung University, Taoyuan, Taiwan

³Division of Natural Products, Graduate Institute of Biomedical Sciences, College of Medicine, Chang Gung University, Taoyuan, Taiwan

⁴Department of Anesthesiology, Chang Gung Memorial Hospital, Taoyuan, Taiwan

⁵Graduate Institute of Clinical Medical Sciences, College of Medicine, Chang Gung University, Taoyuan, Taiwan

⁶Department of Pharmacy, College of Pharmacy and Health Care, Tajen University, Pingtung, Taiwan

⁷School of Pharmacy, College of Medicine, National Cheng Kung University, Tainan, Taiwan

⁸Research Center for Chinese Herbal Medicine, Research Center for Food and Cosmetic Safety, and Graduate Institute of Health Industry Technology, College of Human Ecology, Chang Gung University of Science and Technology, Taoyuan, Taiwan

⁹Chinese Herbal Medicine Research Team, Healthy Aging Research Center, Chang Gung University, Taoyuan, Taiwan

¹⁰Department of Chemical Engineering, Ming Chi University of Technology, New Taipei City, Taiwan

Correspondence

Tsong-Long Hwang, Graduate Institute of Natural Products, College of Medicine, Chang Gung University, 259 Wen-Hwa 1st Road, Kweishan 333, Taoyuan, Taiwan.
Email: htl@mail.cgu.edu.tw

Funding information

Ministry of Science and Technology, Taiwan, Grant/Award Number: 107-2320-B-075-001-MY3, 106-2320-B-255-003-MY3 and 108-2320-B-255-003-MY3; Ministry of Education, Taiwan, Grant/Award Number: EMRPDI10441; Chang Gung University, Grant/Award Number: EMRPDI10501, ZRRPF3H0101 and ZRRPF3H0111; Chang Gung Memorial Hospital, Grant/Award Number: CMRPF1G0241 ~ 3, CMRPF1J0051 ~ 3, CMRPG5F0161, CMRPG6J0141 ~ 3, CMRPG3J1001 ~ 3 and BMRP450; Taipei Veterans

Abstract

Human neutrophils have a vital role in host defense and inflammatory responses in innate immune systems. Growing evidence shows that the overproduction of reactive oxygen species and granular proteolytic enzymes from activated neutrophils is linked to the pathogenesis of acute inflammatory diseases. However, adequate therapeutic targets are still lacking to regulate neutrophil functions. Herein, we report that MVBR-28, synthesized from the Mannich bases of heterocyclic chalcone, has anti-neutrophilic inflammatory effects through regulation of intracellular pH. MVBR-28 modulates neutrophil functions by attenuating respiratory burst, degranulation, and migration. Conversely, MVBR-28 has no antioxidant effects and fails to alter elastase activity in cell-free systems. The anti-inflammatory effects of MVBR-28 are not seen through cAMP pathways. Significantly, MVBR-28 potently inhibits extracellular Ca^{2+} influx in *N*-formyl-methionyl-leucyl-phenylalanine (fMLF)- and thapsigargin-activated human neutrophils. Notably, MVBR-28 attenuates fMLF-induced intracellular alkalization in a K^+ -dependent manner, which is upstream of Ca^{2+} pathways.

Abbreviations: BCECF/AM, 2',7'-bis-(2-carboxyethyl)-5-(and-6)-carboxyfluorescein acetoxymethyl ester; BAPTA-AM, O,O'-bis(2-aminophenyl) ethyleneglycol-N,N,N',N'-tetraacetic acid tetraacetoxymethyl ester; CB, cytochalasin B; DHR123, dihydrorhodamine 123; DMSO, dimethyl sulfoxide; ER, endoplasmic reticulum; fMLF, *N*-formyl-methionyl-leucyl-phenylalanine; Fluo-3/AM, fluo-3 acetoxymethylester; FNLFNKYK, *N*-formyl-Nle-Leu-Phe-Nle-Tyr-Lys; $[Ca^{2+}]_i$, intracellular calcium level; pH_i, intracellular pH value; LDH, lactate dehydrogenase; H89, N-[2-bromo cinnamyl amino]ethyl]-5-isoquinoline sulfonamide; PKA, protein kinase A; ROS, reactive oxygen species; NaF, sodium fluoride; SOD, superoxide dismutase; WKYMVM, Trp-Lys-Tyr-Met-Val-L-Met; WST-1, 2-(4-Iodophenyl)-3-(4-nitrophenyl)-5-(2,4-disulfophenyl)-2H-tetrazolium.

General Hospital, Grant/Award Number: V108B-013 and V109B-001

Collectively, these findings provide new insight into Mannich bases of heterocyclic chalcone regarding the regulation of neutrophil functions and the potential for the development of MVBR-28 as a lead compound for treating neutrophilic inflammatory diseases.

KEYWORDS

alkalization, degranulation, Mannich bases of heterocyclic chalcone, neutrophil, respiratory burst

1 | INTRODUCTION

Circulating neutrophils, identified as critical inducers of inflammation, prevent pathogen invasion, and clear damaged tissues during innate immune responses. Immune responses, including neutrophil adhesion, respiratory burst, and degranulation, are mediated by pathogen- and damage-associated molecular pattern release in infective and sterile inflammation.^{1,2} Hence, overwhelming neutrophil immune responses serve a central role in the development of inflammatory injury. Recent research showed that inflammatory injuries mediated by overwhelming neutrophilic immune reactions are essential in the progression of several diseases such as sepsis, ischemia/reperfusion injury, myocardial injury, and acute lung injury.³⁻⁵ Excessive production of toxic reactive oxygen species (ROS) from activated neutrophils directly destroys lung tissue and indirectly induces interstitial edema due to poorer oxygenation in acute lung injury.^{6,7} Therefore, properly modulating neutrophil immune responses is a way to target controlling these inflammatory injuries and diseases.

Chalcones and their heterocyclic analogues are the important precursors of flavonoids and isoflavonoids existing in many plants. Growing evidence suggesting their pharmacologic potential has shown that they have antioxidant,⁸ anti-bacterial,⁹ and anti-inflammatory effects.⁹⁻¹¹ Notably, heterocyclic chalcones have been demonstrated to exert more potent biological activities among these chalcone derivatives.^{12,13} Numerous methods have been described for the synthesis of chalcones. Among these, Mannich base derivatives showed potent biological activities.^{14,15} Our group previously reported that a series of synthetic Mannich bases of heterocyclic chalcones showed cytotoxicity against tumor cells.¹⁶ We further demonstrated that these compounds displayed anti-inflammatory effects through diminishing respiratory burst as well as degranulation in *N*-formyl-methionyl-leucyl-phenylalanine (fMLF)-stimulated neutrophils. Remarkably, (E)-1-[2-hydroxy-4-methoxy-3-(morpholinomethyl)phenyl]-3-(pyridin-2-yl)-2-propen-1-one (MVBR-28) exhibited more potent anti-inflammatory effects in activated neutrophils among these compounds.¹⁷ However, the action

mechanisms of MVBR-28 in human neutrophils remain unclear and need to be further explored.

The current research investigated the effects of MVBR-28, a synthesized Mannich bases of heterocyclic chalcone, on respiratory burst, degranulation, and the expression of adhesion molecules in human neutrophils. We also demonstrated that the mechanisms of MVBR-28 operated through inhibiting alkalization and calcium mobilization in activated human neutrophils. Herein, our results suggested that the regulation of neutrophil intracellular pH is a potential therapeutic strategy for treating neutrophilic inflammation. We also show that MVBR-28, a synthesized Mannich bases of heterocyclic chalcone, can act as a potential lead for the development of therapeutic drug to control neutrophilic inflammatory diseases.

2 | MATERIALS AND METHODS

2.1 | Reagents

MVBR-28 was synthesized by our group.^{16,17} 2-(4-Iodophenyl)-3-(4-nitrophenyl)-5-(2,4-disulfophenyl)-2H-tetrazolium (WST-1) and O,O'-bis(2-aminophenyl)ethyleneglycol-N,N,N',N'-tetraacetic acid tetraacetoxymethyl ester (BAPTA-AM) was obtained from Dojindo (Kurnamoto, Japan). Methoxysuccinyl-Ala-Ala-Pro-Val-p-nitroanilide, PGE₁, phenylmethylsulfonyl fluoride, and rolipram were obtained from Calbiochem (La Jolla, CA, USA). cAMP enzyme immunoassay kits and Ficoll-Paque were obtained from GE Healthcare (Little Chalfont, Buckinghamshire, UK). Calcium-free Hank's balanced salt solution (HBSS) was obtained from Life Technologies (Paisley, UK). Dihydrorhodamine 123 (DHR123), Fluo-3 acetoxymethylester (Fluo-3/AM), and *N*-formyl-Nle-Leu-Phe-Nle-Tyr-Lys (FNLFNKYK) were obtained from Invitrogen (Eugene, OR, USA). FITC-labeled anti-human CD11b (activation epitope) was obtained from eBioscience (San Diego, CA, USA). APC-labeled anti-human CD63 and FITC-labeled anti-human CD66b were obtained from BioLegend (San Diego, CA, USA). *N*-[2-bromo cinnamyl amino)ethyl]-5-isoquinoline sulfonamide (H89),

2',7'-bis-(2-carboxyethyl)-5-(and-6)-carboxyfluorescein acetoxymethyl ester (BCECF/AM), and other reagents were obtained from Sigma-Aldrich (St. Louis, MO, USA).

2.2 | Isolation of human neutrophils

According to the study protocols approved by the local institutional review board, each healthy volunteer enrolled in this study signed an informed consent form. Venous blood was drawn from these healthy volunteers and collected, using the dextran sedimentation method to isolate the neutrophils. Then, the samples were centrifuged in a Ficoll-Hypaque gradient. The residual erythrocytes were lysed by the hypotonic solution. The final cells, determined by Trypan blue exclusion to confirm viable cells >98%, were suspended in a Ca^{2+} -free HBSS at 4°C for further experiments. HBSS contained 1 mM of Ca^{2+} was used to perform cell assay, excepting fMLF-induced calcium mobilization in a Ca^{2+} -free HBSS.

2.3 | Extracellular superoxide measurement

The method association with the reduction of ferricytochrome *c* was used to measure the superoxide generation in activated human neutrophils.¹⁸ Briefly, neutrophils (6×10^5 cells/mL) were pretreated with ferricytochrome *c* (0.5 mg/mL) in HBSS, and were then treated with 0.1% of dimethyl sulfoxide (DMSO as the control) or MVBR-28 for 5 minutes, followed by triggering with fMLF (0.1 μM), Trp-Lys-Tyr-Met-Val-L-Met (WKYMVM, 100 nM), or sodium fluoride (NaF, 20 mM) in the presence of cytochalasin B (CB, 1 or 2 $\mu\text{g/mL}$). A spectrophotometer (U-3010, Hitachi, Tokyo, Japan) was used to quantify the absorbance change at 550 nm.

2.4 | Intracellular ROS measurement

DHR 123 is a nonfluorescent cell permeability probe that can be converted to cationic green fluorescent rhodamine 123 upon oxidation. Neutrophils (6×10^5 cells/mL) were preloaded with DHR 123 (1 μM) for 15 minutes, and neutrophil ROS were quantified after DMSO (control) or MVBR-28 for 5 minutes followed by triggering with fMLF for 15 minutes at 37°C. The change in fluorescence intensity was quantified by flow cytometry (FACSCalibur; BD Bioscience, San Jose, CA, USA).

2.5 | Lactate dehydrogenase (LDH) release measurement

LDH release was measured by using a commercially available method (Promega, Madison, WI, USA). The result was

based on LDH activity from lysing neutrophils with 0.1% of Triton X-100 at 37°C normalized as the percentage of total LDH activity.

2.6 | Superoxide and 2,2-diphenyl-1-picrylhydrazyl (DPPH) scavenging activity

Superoxide scavenging activity of MVBR-28 was evaluated in a cell-free xanthine/xanthine oxidase system. 0.1 mM of xanthine was added to the assay buffer, which contained 50 mM of Tris (pH 7.4), 0.3 mM of WST-1, and 0.02 U/mL of xanthine oxidase, for 10 minutes at 30°C. Superoxide anion, which induced the reduction of WST-1, was measured at 450 nm by spectrophotometry. Additionally, DPPH scavenging activity of MVBR-28 was determined by the mixture of ethanol solution of DPPH (100 μM) with DMSO or MVBR-28 at 30°C. The absorbance was quantified at 517 nm by spectrophotometry.

2.7 | Elastase release measurement

Elastase release was regarded as the evidence of degranulation, and we used methoxysuccinyl-Ala-Ala-Pro-Val-p-nitroanilide as the elastase substrate. Neutrophils (6×10^5 cells/mL) in HBSS were incubated with elastase substrate and treated with DMSO or MVBR-28 for 5 minutes followed by stimulation with fMLF, WKYMVM, or NaF in the presence of CB (0.5 or 2 $\mu\text{g/mL}$). Change in absorbance was measured at 405 nm by spectrophotometry. The results show the percentage of the control group.

2.8 | Myeloperoxidase (MPO) release assay

Human neutrophils (5×10^6 cells/well) were treated with DMSO or MVBR-28 for 5 minutes, and then, activated by fMLF for 10 minutes in the presence of CB (0.5 $\mu\text{g/mL}$). After centrifugation, supernatants were collected for MPO assay. The supernatant was incubated with MPO substrate buffer (0.001% H_2O_2 and 0.2 mg/mL *o*-Dianisidine dihydrochloride in PBS, pH 6.0) for 45 minutes at 37°C in the dark. MPO (0 to 10 U/mL; USBiological, Salem, MA, USA) were used to obtain standard curve. The absorbance was quantified at 405 nm by ELISA reader (Infinite F200 PRO, Tecan, Crailsheim, Germany).

2.9 | CD63 and CD66b expression assay

Human neutrophils (5×10^5 cells/mL) were incubated with DMSO or MVBR-28 for 5 minutes, and then, activated by fMLF for 10 minutes in the presence of CB (1 $\mu\text{g/mL}$). After

centrifugation at 4°C, the neutrophils were suspended in HBSS containing 0.5% of bovine serum albumin. The mixture was stained with APC-labeled anti-CD63 and FITC-labeled anti-CD66b for 15 minutes at 4°C. The stained samples were measured by flow cytometry.¹⁹

2.10 | CD11b expression assay

Human neutrophils (2.5×10^6 cells/mL) were treated with DMSO or MVBR-28 for 5 minutes and triggered by fMLF in the presence of CB. After centrifugation at 4°C, the neutrophils were suspended in HBSS containing 0.5% of bovine serum albumin. The mixture was stained with FITC-labeled anti-CD11b for 1 hour at 4°C in the dark. Then, the sample was immediately studied by flow cytometry.

2.11 | Migration assay

Cell migration was measured using a 24-well microchemotaxis chamber (pore size 3 μ m; Millipore, Darmstadt, Germany). Neutrophils (2.5×10^5 cells/well) were pretreated with DMSO or MVBR-28 for 5 minutes at 37°C in the top chamber. fMLF were placed in the bottom chamber. After incubation for 60 minutes, migrated cells were collected, and the numbers were analyzed by flow cytometry.²⁰

2.12 | Formyl peptide receptor 1 (FPR1) binding assay

FPR1 binding was detected by the fluorescence-activated cell sorting scan (FACS). A fluorescent analogue of fMLF, FNLFNYK, was used for the assay of receptor binding. Neutrophils (2×10^6 cells/mL) were treated with DMSO or MVBR-28 for 5 minutes at 4°C and loaded with FNLFNYK (4 nM) for 30 minutes. The loaded-cells were suspended in ice-cold HBSS, and immediately studied with FACS. fMLF was used as a positive control.²¹

2.13 | cAMP concentration measurement

Human neutrophils (2.5×10^6 cells/mL) were treated with DMSO or MVBR-28 for 5 minutes and triggered with fMLF. Then, the reaction was stopped by the addition 0.5% of dodecyltrimethylammonium bromide. The supernatant was analyzed with an enzyme immunoassay kit (Amersham Biosciences, Buckinghamshire, UK) after centrifugation at 3000 g for 5 minutes at 4°C. Rolipram was used as a positive control.

2.14 | Intracellular calcium level ($[Ca^{2+}]_i$) measurement

Human neutrophils (3×10^6 cells/mL) were loaded with fluo-3/AM for 35 minutes at 37°C and were then treated with DMSO or MVBR-28 for 5 minutes. fMLF and thapsigargin was then used to activate cells. In addition, fluo-3/AM-labeled neutrophils were incubated in a Ca^{2+} -free HBSS buffer, and then, activated by fMLF followed by the addition of 1 mM of Ca^{2+} . DMSO or MVBR-28 was added before fMLF for 5 minutes or Ca^{2+} for 1 minutes. The $[Ca^{2+}]_i$ were measured with continuous stirring in a quartz cuvette by a Hitachi F-4500 spectrofluorometer. The excitation wavelength was 488 nm and the emission wavelength was 520 nm. $[Ca^{2+}]_i$ was calculated from the fluorescence intensity as follows: $[Ca^{2+}]_i = Kd \times [(F - F_{min}) / (F_{max} - F)]$; where F was the experimental fluorescence intensity, F_{max} and F_{min} were obtained by the addition to the neutrophils of 0.05% Triton X-100 and 20 mM of EGTA, respectively, and Kd was 400 nM.

2.15 | Intracellular pH value (pH_i) measurement

Neutrophils (3×10^6 cells/mL) were resuspended in HBSS with HEPES (10 mM) buffer (136.89 mM NaCl, 5.37 mM KCl, 0.44 mM KH_2PO_4 , 4.17 mM $NaHCO_3$, 0.34 mM Na_2HPO_4 , 5.55 mM D-glucose, 1 mM $CaCl_2$, 1 mM $MgCl_2$, 10 mM HEPES, pH 7.4). HCO_3^- -free solution was prepared by reducing $NaHCO_3$. K^+ -free solutions were prepared by replacing KCl with *N*-methyl-D-glucamine (NMDG) as well as replacing KH_2PO_4 with NaH_2PO_4 . Na^+/K^+ -free solutions contained 10 mM of D-glucose, 136.89 mM of NMDG, 140 mM of HCl, 1 mM of $MgCl_2$, and 10 mM of HEPES.^{22,23} Neutrophils were labeled with BCECF/AM for 30 minutes, and then, treated with DMSO or MVBR-28 for 5 minutes followed by activation by fMLF. The excitation wavelength was 490/440 nm, and the emission wavelength was 535 nm. Fluorescence was measured by spectrofluorometry. pH_i was calculated from the fluorescence intensity as follows: $pH_i = pK + \log [(R_{max} - R) / (R - R_{min})] + \log (F_{440min} / F_{440max})$, where R was the 535 nm emission at 490 nm excitation/535 nm emission at 440 nm excitation ratio; R_{max} were the maximum values at pH values of 9.5; R_{min} were the minimum values at pH values of 4.5; pK was the dissociation constant for the dye, taken as 7.2. $\log (F_{440min} / F_{440max})$ was the ratio of the fluorescence measured at 440 nm of R_{min} and R_{max} .²⁴

2.16 | Measurement of Na^+/H^+ Exchange

BCECF/AM-labeled neutrophils (3×10^6 cells/mL) were suspended in a Na^+/K^+ -free buffer that contained 10 mM of

D-glucose, 136.89 mM of NMDG, 140 mM of HCl, 1 mM of MgCl_2 , and 10 mM of HEPES. The mixture received the addition of nigericin for 2 minutes and was then treated with DMSO or MVBR-28 for 3 minutes followed by adding NaCl (50 mM). Fluorescence was recorded at the 490/440 nm excitation wavelength and the 535 nm emission wavelength.

2.17 | Statistical analysis

All results are presented as mean \pm standard errors of the means (SEM). Statistical analysis was performed using SigmaPlot (Systat Software, San Jose, CA). The half maximal inhibitory concentration (IC_{50}) value was calculated by interpolation. One-way ANOVA analysis followed by Student-Newman-Keuls multiple comparisons tests were used for multiple comparisons. Student's *t* tests were used for simple comparisons between two groups. A value of $P < .05$ was considered statistically significant. All experiments were performed at least four independent experiments.

3 | RESULTS

3.1 | MVBR-28 significantly inhibits fMLF-activated neutrophil immune functions

Respiratory burst, degranulation, and migration are neutrophil immune reactions involved in inflammatory responses.²⁵ To examine the immunomodulatory effects of MVBR-28 in acute inflammation, a FPR1 agonist, fMLF, was used to trigger human neutrophil activation. As shown in Figure 1B, neutrophils were activated by fMLF to produce extracellular superoxide. The dose-dependent inhibition of MVBR-28 on extracellular superoxide generation was achieved under activation conditions in human neutrophils, with the IC_{50} value of $0.59 \pm 0.06 \mu\text{M}$. In light of these observations, we further examined the effects of MVBR-28 on intracellular ROS production by using DHR123. DHR123 was converted to fluorescent rhodamine 123 in the presence of ROS. Under fMLF activation conditions, the fluorescence of rhodamine 123 was obviously increased. In contrast, intracellular ROS production induced by fMLF was dose-dependently attenuated in the presence of MVBR-28, with the IC_{50} value of $1.19 \pm 0.08 \mu\text{M}$ (Figure 1C). The inhibition of superoxide generation and ROS production may have contributed to the antioxidant effects. Therefore, we next used the reduction of WST-1 in the xanthine/xanthine oxidase system and the DPPH assay to explore this hypothesis. Our results showed that MVBR-28 did not affect WST-1 reduction with and without the supplement of superoxide dismutase (SOD) (Figure 1D). In the assay of DPPH, MVBR-28 did not affect the reduction of DPPH (Figure 1E). SOD and α -tocopherol

were used as positive controls, respectively. Collectively, MVBR-28 inhibited extracellular superoxide generation and intracellular ROS production in activated neutrophils. The inhibitory effects of MVBR-28 were not associated with the antioxidant effects. LDH release is an indicator of cytotoxicity. The incubation of MVBR-28 with neutrophils did not have any effects on LDH release even at $30 \mu\text{M}$ (data not shown).

We further studied the effects of MVBR-28 on neutrophil degranulation. Figure 2A showed that elastase release in fMLF-induced human neutrophils was dose-dependently decreased by MVBR-28, with an IC_{50} value of $1.12 \pm 0.11 \mu\text{M}$. To exclude the direct effect on elastase, we determined the effects of MVBR-28 on elastase activity. Our results demonstrated that MVBR-28 did not directly inhibit elastase activity (Figure 2B). MPO was also released from primary granules in activated neutrophils. MPO release in fMLF-activated neutrophils were inhibited by MVBR-28 (Figure 2C). Granule markers CD63 (primary granules) and CD66b (secondary granules) were upregulated after stimulation.²⁶ In Figure 2D,E, the expression of CD63 and CD66b were upregulated in response to fMLF. The treatment of MVBR-28 significantly attenuated the surface expression of CD63 and CD66b in activated neutrophils.

CD11b, a member of the integrin family, is a major cell adhesion molecule of neutrophils. Its immune function is related to the adhesion and migration of neutrophils to endothelium.²⁷ The activation-specific epitopes of CD11b was used to assay the effects of MVBR-28 on surface expression of activated type of CD11b. MVBR-28 alone did not alter the surface expression of CD11b in resting neutrophils; however, it significantly attenuated the upregulated surface expression of CD11b in fMLF-activated neutrophils (Figure 3A,B). Consistently, fMLF-induced neutrophil migration was also inhibited by MVBR-28 (Figure 3C).

Taken together, the results showed that MVBR-28 significantly inhibits respiratory burst, degranulation, and migration of fMLF-stimulated human neutrophils. Of note, the inhibitory effects are not related to antioxidant and cytotoxicity effects, indicating that the anti-inflammatory effects of MVBR-28 occur through modulating the intracellular signaling pathways.

3.2 | MVBR-28 dampens inflammation not through blocking FPR1

Our current results demonstrated that MVBR-28 inhibited neutrophil functions activated by an FPR1 agonist, fMLF. We used a pharmacological method to investigate the anti-inflammatory effects of MVBR-28 in non-FPR1 agonist-activated neutrophils. WKYMVM is a dual FPR1/FPR2 agonist. Our results demonstrated inhibition of superoxide generation and

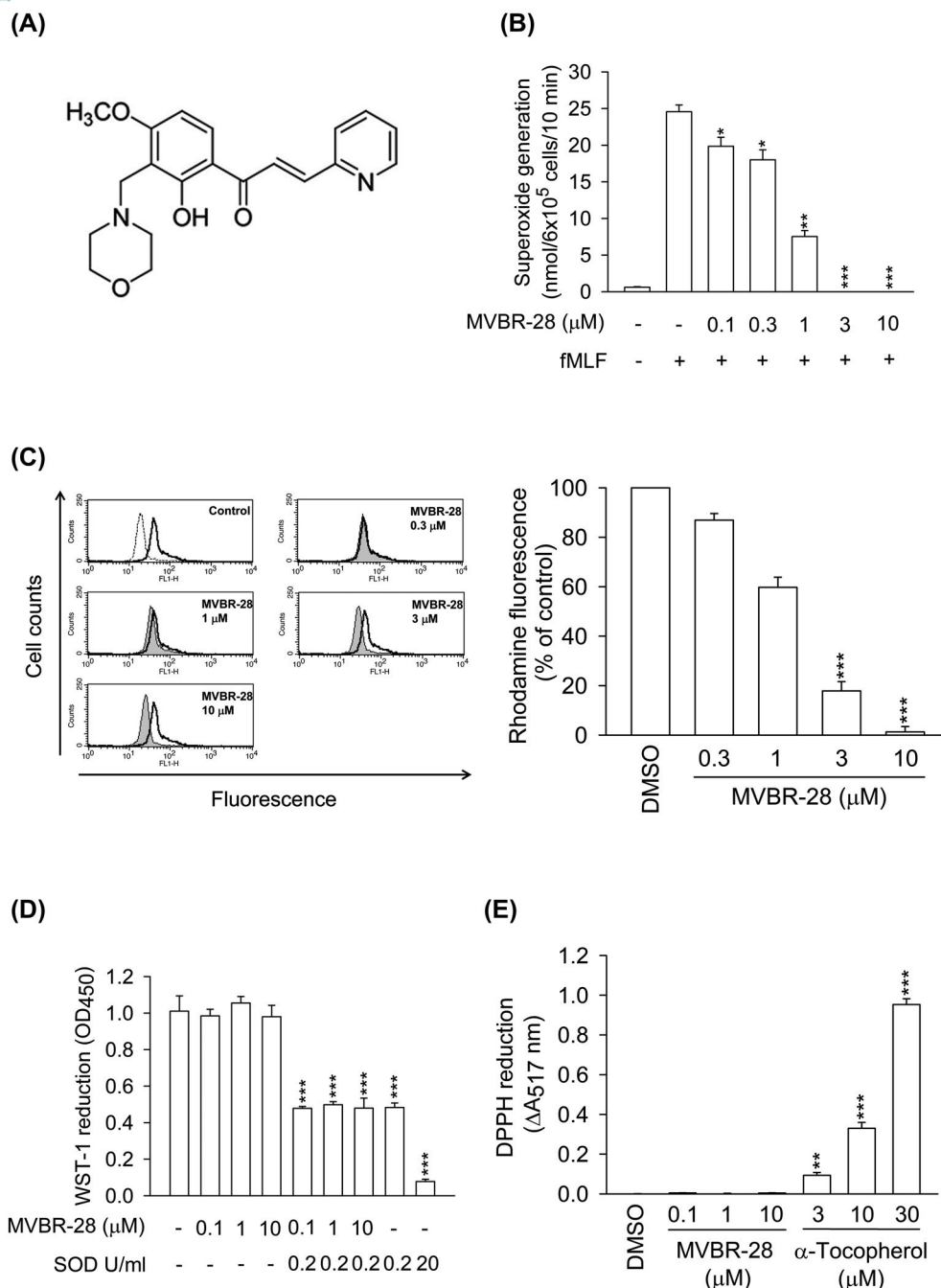


FIGURE 1 MVBR-28 inhibits superoxide generation and ROS production in activated human neutrophils. A, The chemical structure of MVBR-28. B, Human neutrophils (6×10^5 cells/mL) were treated with DMSO (0.1%, as the control), or MVBR-28 (0.1–10 μ M) for 5 minutes, followed by triggering by fMLF for another 10 minutes. Superoxide generation of human neutrophils was measured by using cytochrome *c* reduction. C, Before activation by fMLF, cells (5×10^6 cells/mL) were treated with DMSO (as the control) or MVBR-28 (0.3–10 μ M). Flow cytometry analysis of MVBR-28-treated neutrophils was recorded. Representative histograms demonstrating typical FACS profiles for DHR123 in rest cells (dashed line) and in fMLF-activated cells in the absence (solid lines, white zone) or presence of MVBR-28 at the concentrations indicated (solid lines, gray zone). Measurement of (D) WST-1 and (E) DPPH reduction was performed by spectrophotometry. All data are expressed as the mean \pm SEM ($n = 6$ for B, $n = 5$ for C, D, and E). * $P < .05$, ** $P < .01$, *** $P < .001$ compared with the control

elastase release by MVBR-28 in such activated neutrophils, with the IC_{50} values of 0.77 ± 0.15 μ M and 1.34 ± 0.12 μ M, respectively (Figure 4A,B). NaF is a direct G protein activator. We observed that MVBR-28 also diminished superoxide generation and elastase release in NaF-activated neutrophils,

with the IC_{50} values of 7.06 ± 1.09 μ M and 2.77 ± 0.59 μ M, respectively (Figure 4C,D). To more precisely investigate the potential involvement of FPR1, we next measured the receptor binding capacity of MVBR-28 on FPR1 by using FNLFNK, a fluorescent FPR1 analog. MVBR-28 demonstrated no

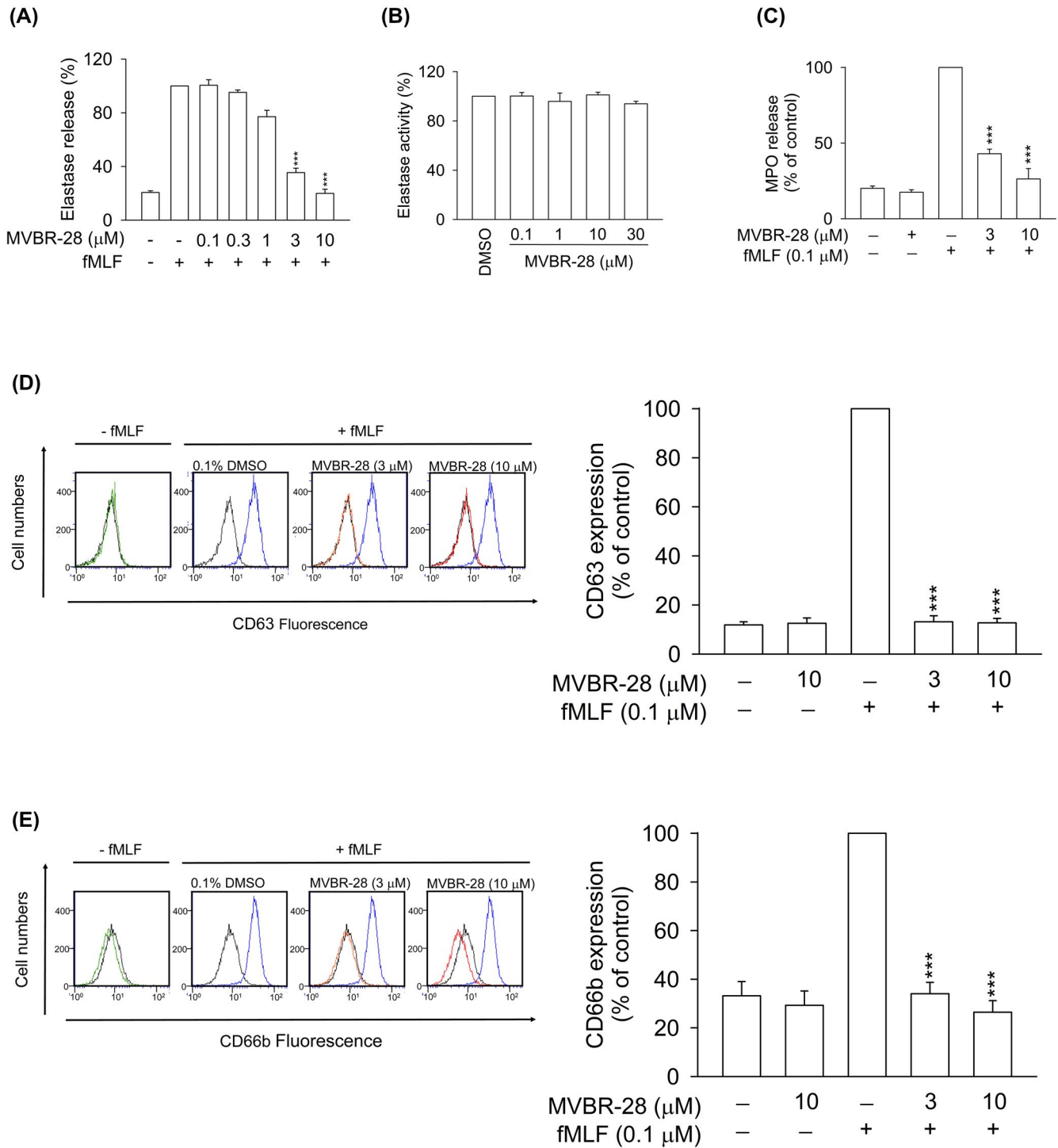


FIGURE 2 MVBR-28 inhibits neutrophil degranulation in activated human neutrophils. A, Human neutrophils (6×10^5 cells/mL) were treated with DMSO (as the control), or MVBR-28 (0.1–10 μ M) for 5 minutes followed by triggering by fMLF for another 10 minutes. Neutrophil degranulation was measured with the breakdown of elastase substrate ($n = 7$). B, The condition medium of activated neutrophils was pretreated with MVBR-28 (0.1–30 μ M) for 5 minutes before the addition of elastase substrate for another 10 minutes. Measurement of elastase activity was recorded by spectrophotometry ($n = 5$ –6). C, Neutrophils (5×10^6 cells/mL) were reacted with DMSO (as the control) or MVBR-28 (3 and 10 μ M) for 5 minutes followed by triggering by fMLF for another 10 minutes. MPO release was measured by the incubation with MPO substrate buffer (0.001% H_2O_2 and 0.2 mg/mL *o*-Dianisidine dihydrochloride in PBS, pH 6.0) ($n = 4$). Human neutrophils (5×10^5 cells/mL) were treated with DMSO (as the control) or MVBR-28 (3 and 10 μ M) for 5 minutes followed by triggering by fMLF. The surface expression of (D) CD63 and (E) CD66b was assessed by flow cytometry. Representative histograms demonstrate basal group (0.1% DMSO, black line) or MVBR-28 (10 μ M, green line) in the absence of fMLF and control group (0.1% DMSO, blue line) or MVBR-28 (3 and 10 μ M, red line) in the presence of fMLF. Mean fluorescence intensity is shown ($n = 4$). All data are expressed as the mean \pm SEM *** $P < .001$ compared with the control

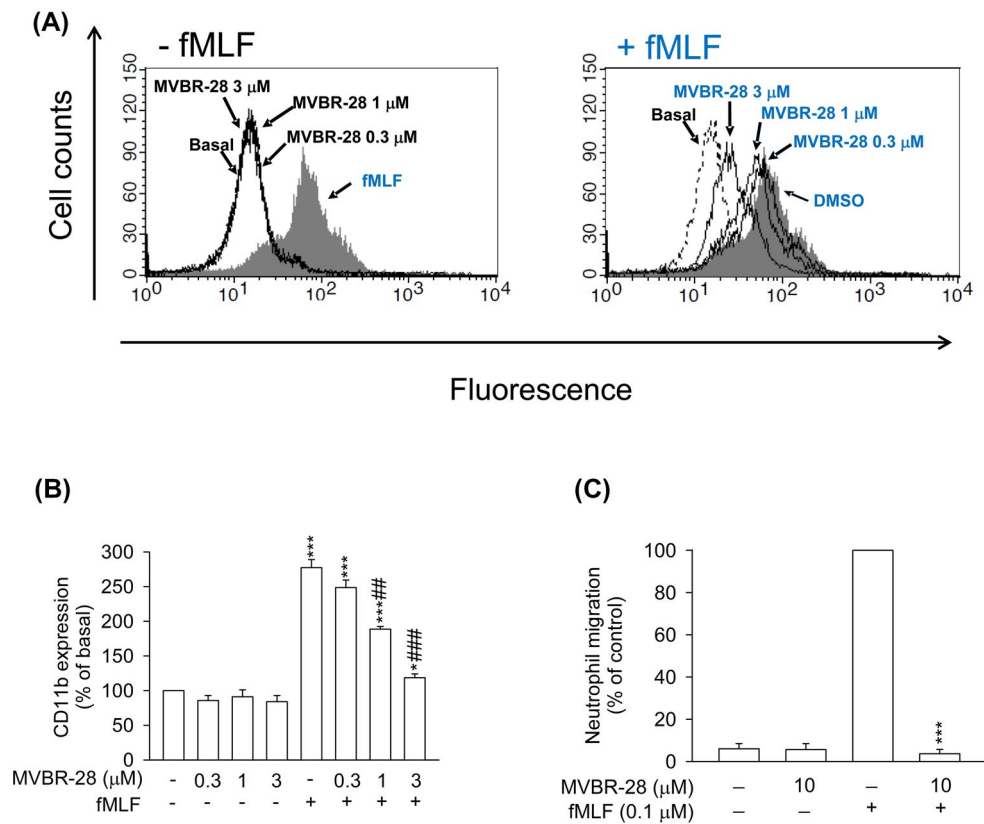


FIGURE 3 MVBR-28 inhibits CD11b expression and migration in activated human neutrophils. A, Cells (2.5×10^6 cells/mL) were treated with DMSO and MVBR-28 (0.3, 1, and 3 μ M) for 5 minutes followed by triggering by fMLF. B, The quantification of fluorescence intensity of FITC-labeled anti-CD11b was measured by flow cytometry. Mean fluorescence intensities are shown as the mean \pm SEM (n = 5-6). * P < .05, *** P < .001 compared to DMSO alone. ## P < .01, ### P < .001 compared to fMLF alone. C, Neutrophils (2.5×10^5 cells/well) were treated with MVBR-28 for 5 minutes in the top chamber. Migrated neutrophils in response to fMLF (0.1 μ M) into the bottom chamber were determined by flow cytometry. Data are expressed as the mean \pm SEM (n = 4). *** P < .001 compared with the control

effects of receptor binding capacity on FPR1 even at 30 μ M. fMLF served as a positive control (Figure 4E). Collectively, the anti-inflammatory effects of MVBR-28 in activated neutrophils did not occur through blocking FPR1.

3.3 | The inhibitory effects of MVBR-28 are not mediated by cAMP signaling pathway

cAMP/PKA pathway has a negative regulatory effect on neutrophil immune responses.²⁸ PGE1 has been found to attenuate activated neutrophil functions through increasing intracellular cAMP.²⁹ Indeed, H89, an inhibitor of protein kinase A (PKA), reversed the inhibitory effects of PGE1, but not MVBR-28, on superoxide generation and elastase release in activated neutrophils (Figure 5A,B). Furthermore, the addition of rolipram (phosphodiesterase 4 inhibitor) increased cAMP levels either in the absence or presence of fMLF, but not MVBR-28 (Figure 5C). Our results suggested that cAMP/PKA pathway is not involved in the inhibitory effects of MVBR-28.

3.4 | MVBR-28 attenuates intracellular alkalization in activated neutrophils

Intracellular pH homeostasis plays a significant role in the regulation of neutrophil immune functions, including respiratory burst and degranulation.³⁰ Figure 6A showed that activated neutrophils exhibited pH_i -increasing effect. Interestingly, a significant reduction of intracellular alkalization in fMLF-activated neutrophils was detected, with a 27% and 33% drop in intracellular alkalization in the presence of 3 μ M and 10 μ M MVBR-28, respectively.

It has been demonstrated that the modification of pH_i is dependent on transmembrane regulation. The inhibition of HCO_3^-/Cl^- exchange contributed to intracellular alkalization.³¹ To determine whether the effects of MVBR-28 on the regulation of pH_i occurred through HCO_3^- influx, we performed the following experiments in a HCO_3^- -free buffer. Our results showed that the reduction of alkalization by MVBR-28 was not altered in fMLF-activated neutrophils in a HCO_3^- -free buffer, indicating that HCO_3^- influx had no effects on the reduction of intracellular alkalization by MVBR-28 in activated neutrophils (Figure 6B).

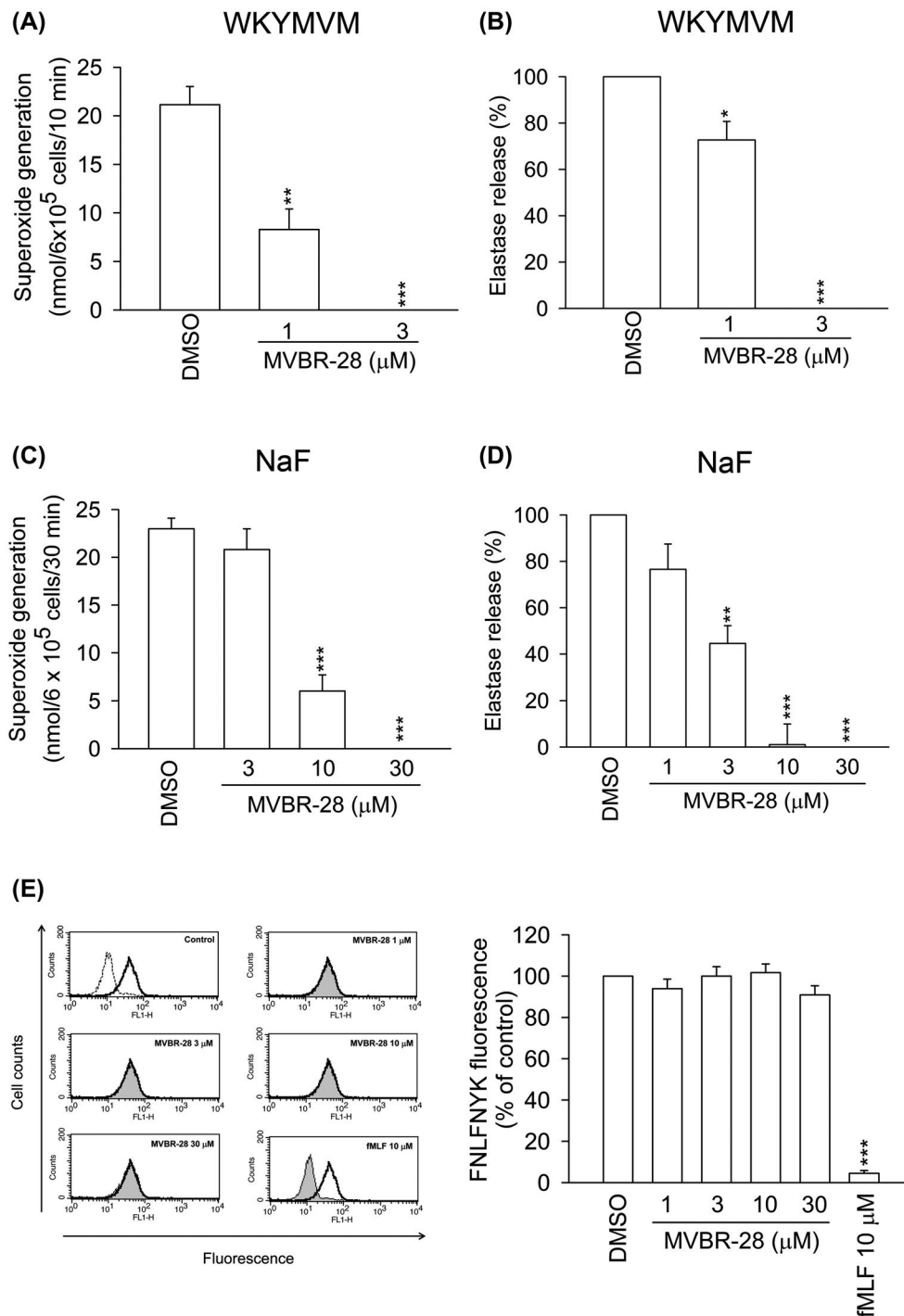


FIGURE 4 The inhibition of MVBR-28 on neutrophil respiratory burst and degranulation is not receptor-specific. Human neutrophils (6×10^5 cells/mL) were treated with DMSO (as the control) or MVBR-28 for 5 minutes, and then, activated by (A) (B) WKYMVM for another 10 minutes and (C) (D) NaF for another 30 minutes. Superoxide generation and elastase release were measured by spectrophotometry. All data were expressed as the mean \pm SEM ($n = 6-7$). E, Human neutrophils (2×10^6 cells/mL) were pretreated with DMSO (as the control), MVBR-28 (1-30 μM), or fMLF (10 μM) for 5 minutes before labeling with FNLNFK (4 nM) for 30 minutes. The intensity of the fluorescence was measured by flow cytometry. Representative histograms demonstrate typical fluorescence in the absence (dashed lines) or presence of the FNLNFK control (solid lines, white zone) or FNLNFK with inhibitors (solid lines, gray zone). Mean fluorescence intensity is shown as the mean \pm SEM ($n = 6$). * $P < .05$, ** $P < .01$, *** $P < .001$ compared with the control

Nigericin, a $\text{K}^+\text{-H}^+$ exchanger, induced intracellular K^+ efflux and H^+ influx leading to intracellular acidosis. A Na^+ supplement increased Na^+/H^+ exchange activities and

restored intracellular alkalization.³² As shown in Figure 6C, the application of nigericin induced a decrease in pH_i , and the NaCl supplement restored pH_i in a Na^+ - and K^+ -free buffer,

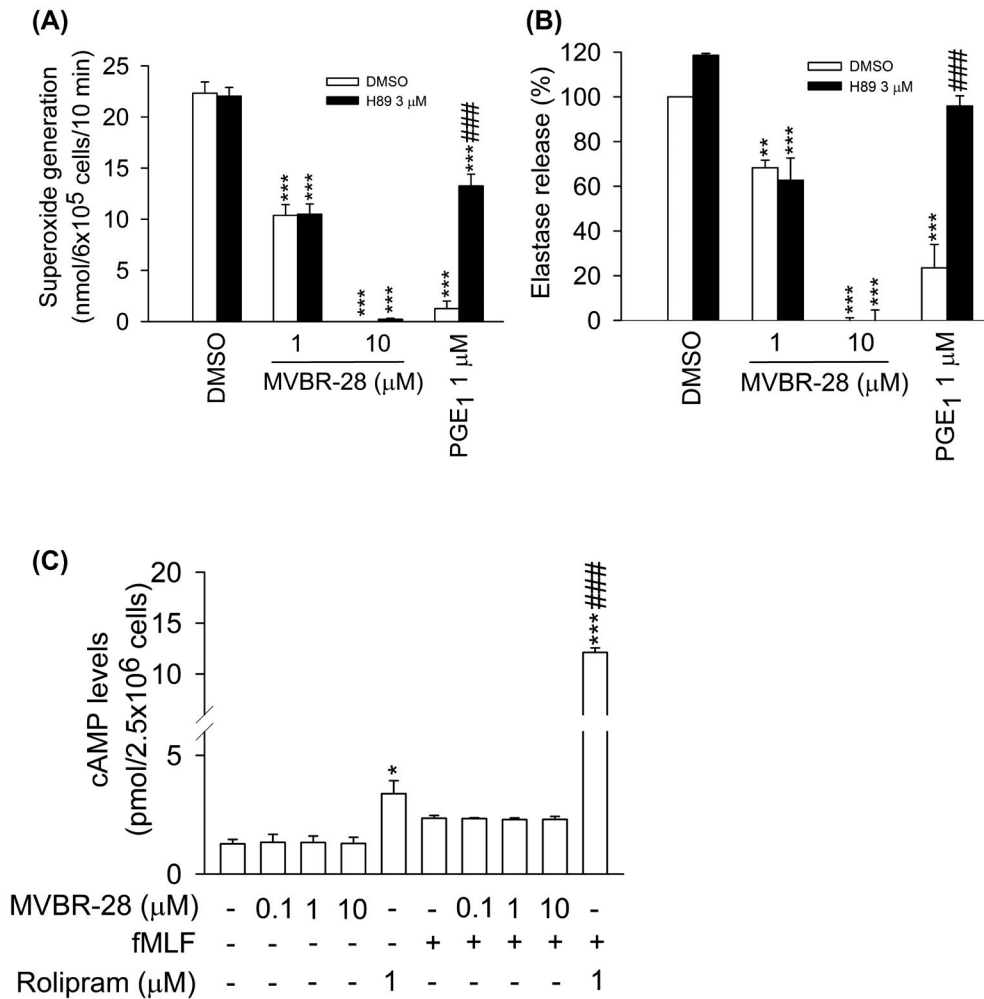


FIGURE 5 The inhibitory effects of MVBR-28 are not dependent on the cAMP/PKA pathway. Human neutrophils (6×10^5 cells/ml) were pretreated with H89 (3 μ M), a PKA inhibitor, for 5 minutes before the addition of MVBR-28 (1 and 10 μ M) or PGE₁ (1 μ M). A, Superoxide generation and (B) elastase release were induced by fMLF for another 10 minutes. The change in absorbance was measured by spectrophotometry. C, Human neutrophils (2.5×10^6 cells/mL) were treated with DMSO (as the control), MVBR-28 (0.1, 1, and 10 μ M), or rolipram (1 μ M) at 37°C for 5 minutes, and then, stimulated with fMLF (0.1 μ M) for another 1 minutes. EIA kits were used to measure the cAMP levels. All data are expressed as the mean \pm SEM ($n = 6$). * $P < .05$, ** $P < .01$, *** $P < .001$ compared with the control. ### $P < .001$ compared with fMLF alone

indicating the supplement of Na⁺ induced intracellular alkalization via the Na⁺-H⁺ exchange. The administration of MVBR-28 had no effects on Na⁺ induced intracellular alkalization, indicating that the regulation of MVBR-28 on pH_i is not accomplished by Na⁺-H⁺ exchange. In the following experiments, we determined the effects of K⁺ on the regulation of pH_i in the presence of MVBR-28. Notably, in a K⁺-free buffer, MVBR-28 did not reduce the alkalization induced by fMLF (Figure 6D). Collectively, the effects of MVBR-28 on the inhibition of intracellular alkalization in activated neutrophils occurred due to K⁺-dependent pH regulation.

3.5 | MVBR-28 attenuates calcium influx in activated neutrophils

Calcium is known to be related to chemoattractant signaling pathways in human neutrophils. Calcium stored in the

endoplasmic reticulum (ER) is released into the cytoplasm under activated conditions. The resulting emptying of calcium stored in the ER further triggered an extracellular calcium influx into the cells.³³ As shown in Table 1 and Figure 7A, a significant high peak of [Ca²⁺]_i was induced by fMLF in human neutrophils. MVBR-28 showed a dose-dependent inhibition of [Ca²⁺]_i triggered by fMLF. The application of MVBR-28 affected the calcium kinetic properties in such cells. Markedly, the results of the time taken for the concentration to drop to half of its peak concentration ($t_{1/2}$) were accelerated by MVBR-28.

It is well known that the elevation of [Ca²⁺]_i contributes to either an ER calcium store release or an extracellular calcium influx into the cells. To further assess the effects of MVBR-28 on the ER store Ca²⁺ release, we measured [Ca²⁺]_i in a Ca²⁺-free buffer. In a Ca²⁺-free and Ca²⁺-reloaded buffer, fMLF induced a biphasic Ca²⁺ signal containing the initial release of ER Ca²⁺ stores followed by Ca²⁺ entry across the

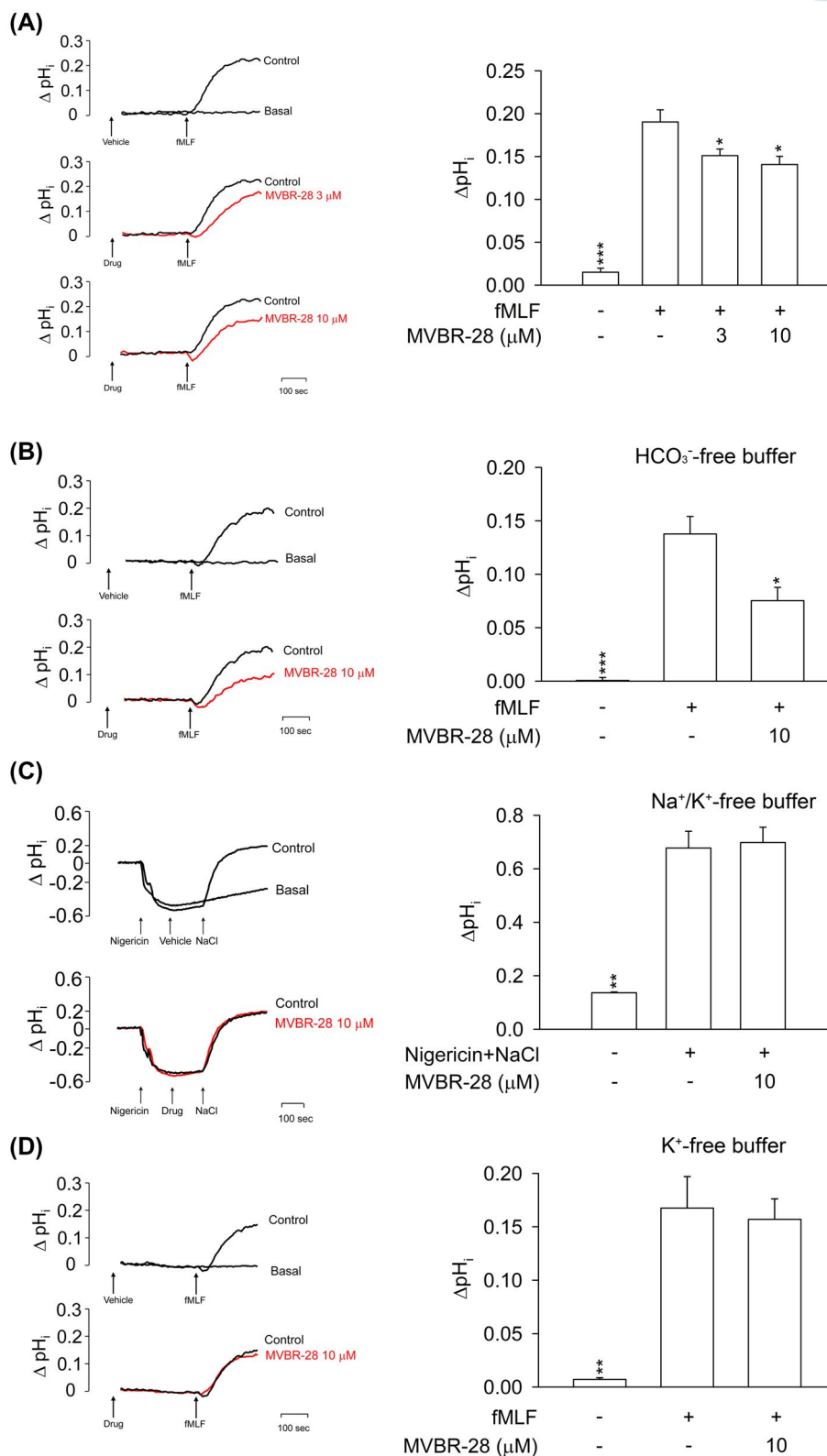


FIGURE 6 MVBR-28 reduces intracellular alkalization in activated human neutrophils. BCECF/AM-loaded human neutrophils (3×10^6 cells/mL) were treated with DMSO (as the control) or MVBR-28 (3 or 10 μM) for 5 minutes before triggering by fMLF (0.1 μM) for another 5 minutes in (A) HEPES buffer, (B) HCO_3^- -free buffer, or (D) K^+ -free buffer. C, Cells (3×10^6 cells/mL) were treated with nigericin (10 μM) for 5 minutes before the addition of NaCl (50 mM) in Na^+/K^+ -free buffer. MVBR-28 (10 μM) was treated for 3 minutes before the addition of NaCl. Representative traces are shown. All data were expressed as the mean \pm SEM ($n = 7$ for A, $n = 4$ for B, C, and D). * $P < .05$, ** $P < .01$, *** $P < .001$ compared with the control

TABLE 1 Effects of MVBR-28 on the peak $[Ca^{2+}]_i$ and time taken for the concentration to drop to half of its peak concentration ($t_{1/2}$) in fMLF-activated neutrophils

Drug	Peak $[Ca^{2+}]_i$ (nM)	$t_{1/2}$ (seconds)
Control	352.36 \pm 11.84	27.42 \pm 1.33
MVBR-28 3 μ M	302.05 \pm 11.49*	24.05 \pm 1.88
MVBR-28 10 μ M	222.96 \pm 12.37***	5.76 \pm 0.54***

Note: Fluo-3/AM-labeled human neutrophils were stimulated with 0.1 μ M of fMLF, and fluorescence was quantified at 37°C with stirring. All data are presented as the mean \pm SEM (n = 5).

* $P < .05$; *** $P < .001$ compared with the fMLF.

cell membrane. MVBR-28 showed only minor effects on the initial ER calcium store release in a Ca^{2+} -free buffer (Table 2 and Figure 7B). Interestingly, both the pretreatment and post-treatment of MVBR-28 significantly inhibited extracellular calcium influx in fMLF-activated neutrophils (Tables 2 and 3, Figure 7B,C). To determine the effects of MVBR-28 on the function of store-operated calcium entry (SOCE), we used thapsigargin to perform further experiments. Thapsigargin, an inhibitor of ER Ca^{2+} ATPase, inhibits calcium restoring into the ER and induces SOCE.³⁴ Our results demonstrated that MVBR-28 dose-dependently inhibited SOCE induced

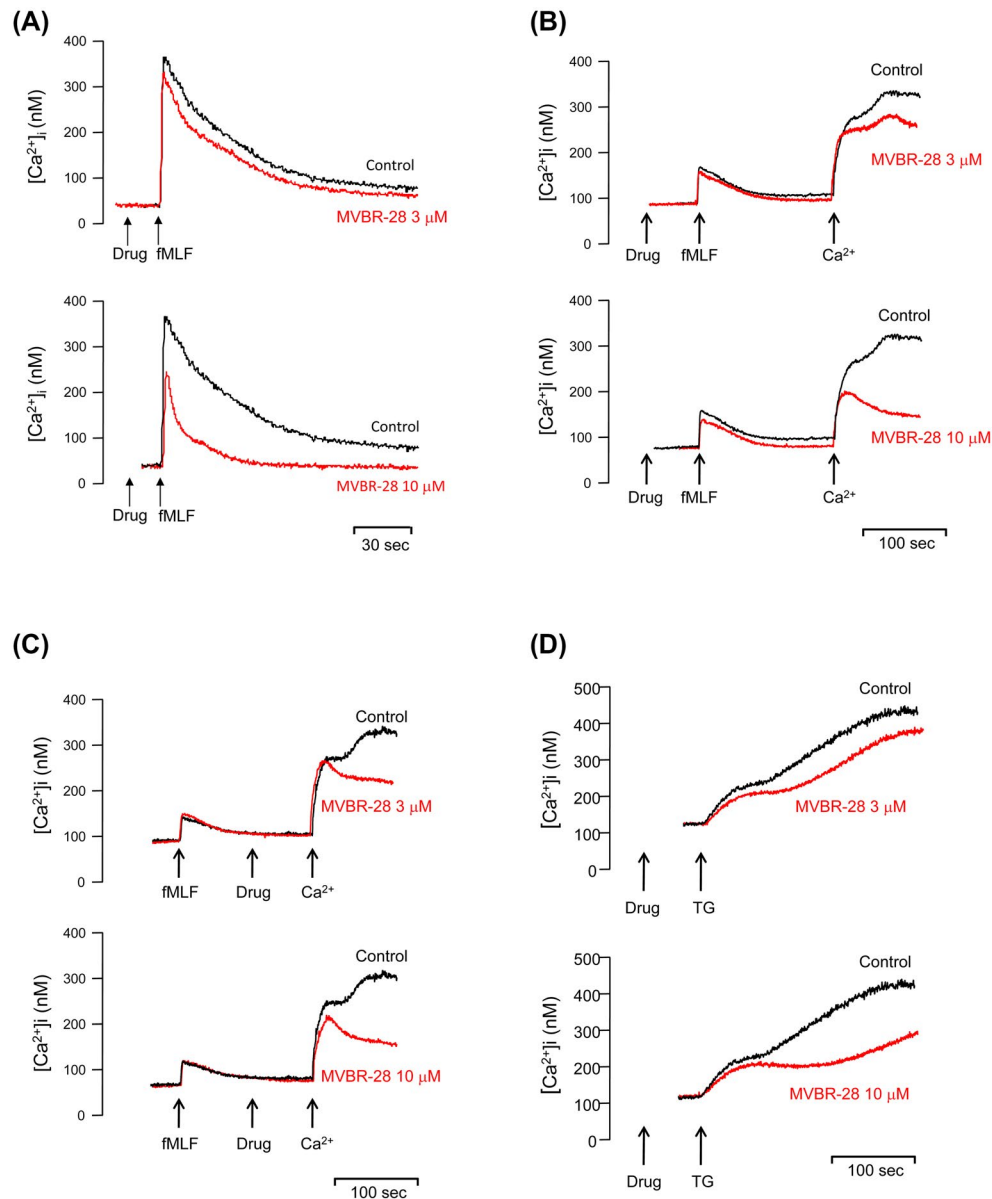


FIGURE 7 MVBR-28 inhibits Ca^{2+} influx through attenuating SOCE in activated human neutrophils. A, Fluo-3/AM-labeled human neutrophils (3×10^6 cells/mL) were treated with DMSO (as the control) or MVBR-28 (3 and 10 μ M) for 5 minutes followed by triggering by fMLF (0.1 μ M). The detection of Ca^{2+} mobilization was determined by spectrofluorometry. B,C, Human neutrophils were activated with fMLF (0.1 μ M) followed by the addition of Ca^{2+} (1 mM). MVBR-28 (3 and 10 μ M) was treated (B) for 5 minutes before or (C) for 2 minutes after the addition of fMLF (0.1 μ M). Representative traces are shown (n = 5 for A, B, and C). D, Human neutrophils (3×10^6 cells/mL) were pretreated with MVBR-28 (3 and 10 μ M) for 5 minutes, and then, stimulated by thapsigargin (TG, 0.5 μ M). Representative traces are shown (n = 6)

TABLE 2 Effects of MVBR-28 pretreatment on the $[Ca^{2+}]_i$ change in fMLF-activated human neutrophils in a Ca^{2+} -free HBSS buffer

Drug	Peak $[Ca^{2+}]_i$ (nM) of fMLF	Sustained $[Ca^{2+}]_i$ (nM) of the addition of Ca^{2+}
Control	66.51 \pm 5.92	178.61 \pm 15.65
MVBR-28 3 μ M	55.71 \pm 7.73	154.47 \pm 13.58
MVBR-28 10 μ M	52.13 \pm 7.57	55.87 \pm 5.38***

Note: Fluo-3/AM-labeled human neutrophils were stimulated with fMLF (0.1 μ M) in a Ca^{2+} -free HBSS buffer followed by the addition of Ca^{2+} (1 mM). MVBR-28 (3 and 10 μ M) was administered for 5 minutes prior to the addition of fMLF, and the fluorescence was quantified at 37°C with stirring. All data are expressed as the mean \pm SEM (n = 5-6).

*** P < .001 compared with the control.

TABLE 3 Effects of MVBR-28 posttreatment on the $[Ca^{2+}]_i$ change in fMLF-activated human neutrophils in a Ca^{2+} -free HBSS buffer

Drug	Peak $[Ca^{2+}]_i$ (nM) of fMLF	Sustained $[Ca^{2+}]_i$ (nM) of the addition of Ca^{2+}
Control	52.52 \pm 5.49	157.54 \pm 18.77
MVBR-28 3 μ M	52.02 \pm 6.51	114.35 \pm 4.53
MVBR-28 10 μ M	50.77 \pm 3.42	85.65 \pm 3.05**

Note: Fluo-3/AM-labeled human neutrophils were activated with fMLF (0.1 μ M) in a Ca^{2+} -free HBSS buffer followed by the addition of Ca^{2+} (1 mM). MVBR-28 (3 and 10 μ M) was administered for 1 minutes before the addition of Ca^{2+} , and fluorescence was quantified at 37°C with stirring. All data are expressed as the mean \pm SEM (n = 5).

** P < .01 compared with the control.

TABLE 4 Effects of MVBR 28 on the $[Ca^{2+}]_i$ in thapsigargin-activated human neutrophils

Drugs	Peak $[Ca^{2+}]_i$ (nM)	Steady curve $[Ca^{2+}]_i$ (nM)
Control	99.28 \pm 3.16	252.02 \pm 13.04
MVBR-28 3 μ M	83.92 \pm 3.26**	182.44 \pm 19.53*
MVBR-28 10 μ M	74.43 \pm 3.79**	131.55 \pm 14.67***

Note: Fluo-3/AM-labeled human neutrophils were incubated with MVBR-28 (3 and 10 μ M) for 5 minutes, and then, activated with thapsigargin (0.5 μ M). The fluorescence was quantified at 37°C with stirring. All data are expressed as the mean \pm SEM (n = 6).

* P < .05; ** P < .01; *** P < .001 compared with the control.

by thapsigargin in a Ca^{2+} buffer (Figure 7D and Table 4). Collectively, MVBR-28's inhibitory effect on $[Ca^{2+}]_i$ may result in attenuating the extracellular calcium influx.

3.6 | MVBR-28 inhibits SOCE in a K^+ -dependent manner

The calcium mobilization induced by fMLF was reduced by MVBR-28 in a K^+ -containing buffer. The decline in

calcium kinetics by MVBR-28 was restored in a K^+ -free buffer (Figure 8A,B), indicating that K^+ is involved in the regulation of MVBR-28 on extracellular Ca^{2+} influx in activated neutrophils. We further studied whether the inhibition of SOCE by MVBR-28 is K^+ -dependent. Noticeably, SOCE induced by thapsigargin was reduced by MVBR-28 in a K^+ -containing buffer. Hence, MVBR-28 failed to further inhibit $[Ca^{2+}]_i$ of SOCE induced by thapsigargin in a K^+ -free buffer (Figure 8C,D), indicating that K^+ is involved in the inhibitory effects of MVBR-28 on SOCE in activated neutrophils. The inhibitory effects of MVBR-28 on superoxide generation and elastase release were assayed in a K^+ -free buffer. The results showed that the inhibitory effects of MVBR-28 at 1 or 3 μ M, but not 10 μ M, were decreased in a K^+ -free buffer (Figure 8E,F), indicating that K^+ -independent pathway is involved in the anti-inflammatory effects of MVBR-28 at high concentration. Taken together, our results suggest that the anti-inflammatory effects of MVBR-28 were mediated, at least in part, by K^+ -dependent calcium influx in human neutrophils.

Next, to determine the roles of Ca^{2+} on pH_i in MVBR-28-treated neutrophils, we performed experiments to determine the effects of MVBR-28 on pH_i in BAPTA/AM, a Ca^{2+} chelator, treated conditions. Our results showed that 10 μ M of MVBR-28 still reduced intracellular alkalization induced by fMLF about 26% in Ca^{2+} -deprived conditions, indicating that the reduction of intracellular alkalization by MVBR-28 was upstream of the Ca^{2+} mobilization (Figure 8G). Collectively, our results indicated that MVBR-28 inhibited intracellular alkalization and Ca^{2+} mobilization in a K^+ -dependent manner.

4 | DISCUSSION

Excess and uncontrolled human neutrophil immune responses contribute to acute and chronic inflammatory diseases. Therefore, regulating neutrophil immune responses is thought to be a potential therapeutic intervention in treating neutrophilic inflammatory diseases.³⁵ Our results showed that MVBR-28 displayed anti-inflammatory abilities by significantly inhibiting respiratory burst, degranulation, adhesion, and migration in activated human neutrophils. The inhibitory effects of MVBR-28 were not due to cytotoxicity or antioxidant effects, and they were independent of FPR1 receptor or cAMP/PKA pathway. We also observed that MVBR-28 attenuated intracellular alkalization with K^+ -dependency in activated cells. Moreover, MVBR-28 modulated calcium mobilization by altering SOCE. Taken together, the immunomodulatory effects of MVBR-28 appear to be mediated by the modulation of pH_i and calcium mobilization through K^+ -dependent regulation (Figure 9).

The hemostasis of pH_i plays an important role on neutrophil respiratory burst and degranulation.^{36,37} Evidence

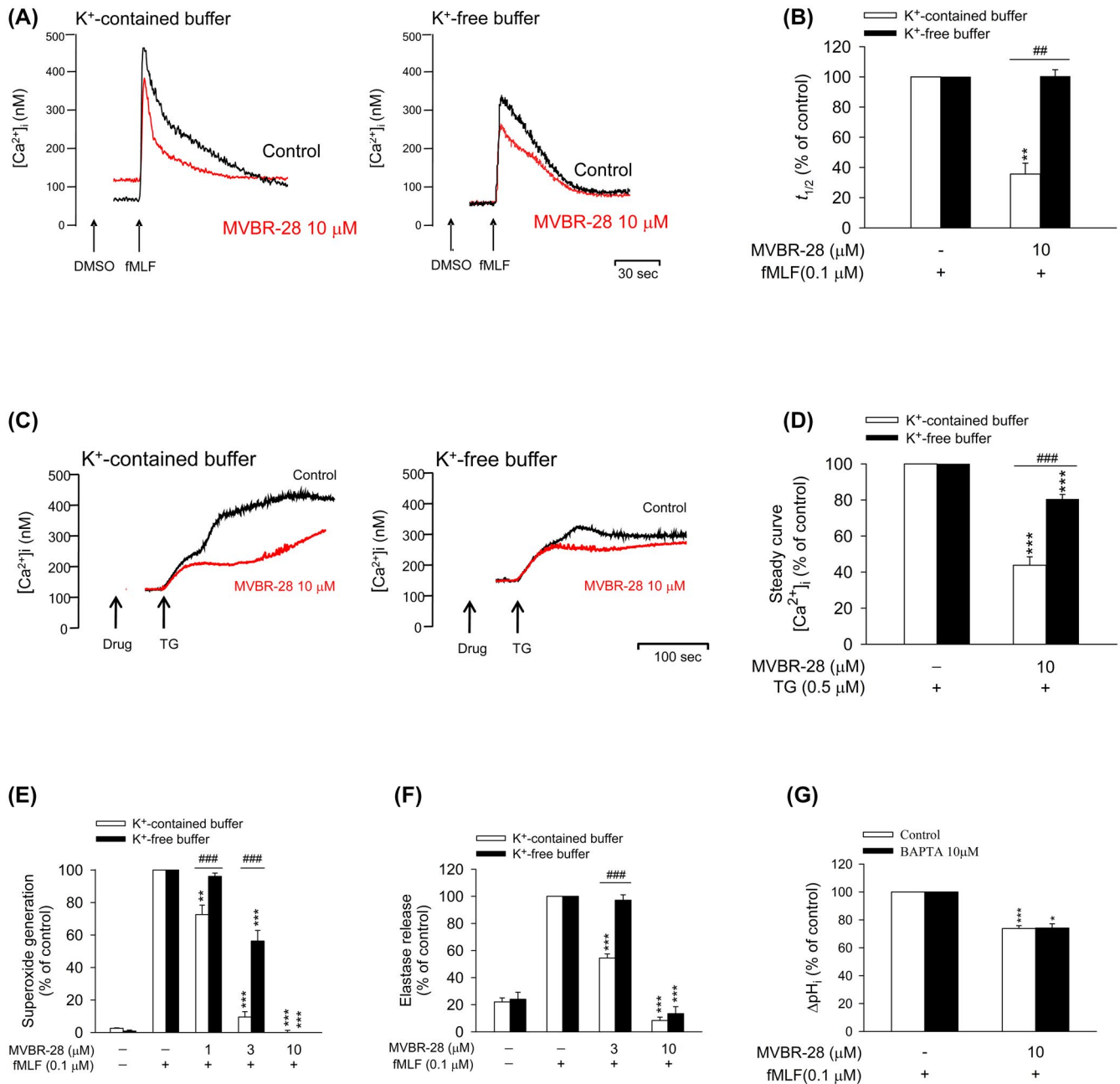


FIGURE 8 MVBR-28 inhibits calcium mobilization in a K⁺-dependent manner. Fluo-3/AM-labeled human neutrophils (3×10^6 cells/mL) were treated with DMSO (as the control) or MVBR-28 (10 μM) for 5 minutes followed by triggering by (A) fMLF (0.1 μM) or (C) TG (0.5 μM) in a K⁺-contained or K⁺-free buffer. Ca²⁺ mobilization was detected by spectrofluorometry. Representative traces are shown. (B) $t_{1/2}$ from A and (D) steady curve [Ca²⁺]_i from C were shown. E, F, Neutrophils (6×10^5 cells/mL) were incubated with DMSO or MVBR-28 for 5 minutes followed by triggering by fMLF for another 10 minutes in a K⁺-contained or K⁺-free buffer. E, Superoxide generation and (F) elastase release were measured by spectrophotography. G, Neutrophils (3×10^6 cells/mL) were pretreated with BAPTA/AM (10 μM) for 5 minutes before the addition of DMSO (as the control) or MVBR-28 (10 μM) in HEBES buffer. The pH_i changes were induced by fMLF (0.1 μM) for another 5 minutes in BCECF/AM-loaded human neutrophils. All data are expressed as the mean \pm SEM ($n = 4$). * $P < .05$, ** $P < .01$, *** $P < .001$ compared with the control. ## $P < .01$, ### $P < .001$ compared to the K⁺-contained group

showed that pH_i changes in activated neutrophils are controlled by many transmembrane regulators, including the HCO₃⁻-dependent transporter, the Na⁺/H⁺ exchanger, and the K⁺-dependent exchanger.³⁸ Notably, H⁺ efflux causes continuous superoxide generation in activated neutrophils

during the respiratory burst.³⁹ Furthermore, K⁺ influx is also related to the release of cationic granule proteins in a pH-dependent manner in response to inflammatory stimulus.⁴⁰ Thus, K⁺-dependent pH_i regulation closely contributes to neutrophil immune responses. Interestingly, our

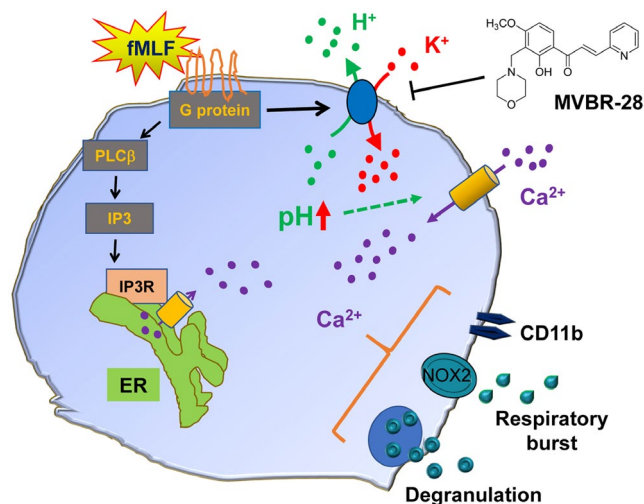


FIGURE 9 Schematic diagram illustrating the anti-inflammatory effects of MVBR-28 in activated human neutrophils. MVBR-28, a Mannich bases of heterocyclic chalcone, inhibits respiratory burst, degranulation, and CD11b expression as well as migration in fMLF-activated human neutrophils. MVBR-28 prevents intracellular alkalization and calcium mobilization in a K^+ -dependent manner. MVBR-28 inhibits neutrophilic inflammation through K^+ -dependent pH regulation

results demonstrated that MVBR-28 failed to inhibit alkalization induced by fMLF in a K^+ -free buffer, implying that the inhibition of MVBR-28 on alkalization is required for extracellular K^+ influx. Except for the K^+ -dependent exchanger, it is well known that the HCO_3^- -dependent transporter plays roles in regulating pH_i in human neutrophils.⁴¹ Hence, our results demonstrated that MVBR-28 still attenuated alkalization in a HCO_3^- -free buffer, suggesting that MVBR-28 did not inhibit alkalization through the HCO_3^- -dependent transporter. The previous research showed that superoxide generation and chemotaxis were regulated by pH_i through activation of the Na^+/H^+ exchanger in neutrophils.^{32,42} Our results also ruled out that Na^+/H^+ exchanger involves in MVBR-28-prevented cellular alkalization.

Calcium signaling plays a major role in the regulation of respiratory burst, degranulation, and adhesion.^{20,43} Calcium mobilization in activated neutrophils has two phases. Initially, the activation of phospholipase $C\beta$ and IP3 induces a rapid release of calcium from intracellular ER stores. Then, there is a prolonged calcium influx mediated by the activation of calcium release-activated cell surface channels, such as SOCE.⁴⁴ Apparently, MVBR-28 significantly inhibited superoxide generation, elastase release, and the expression of adhesion molecule in activated human neutrophils by inhibiting $[Ca^{2+}]_i$ through inhibition of extracellular calcium influx. It has been proven that thapsigargin-induced ER-stored calcium depletion to activate SOCE for the entry of calcium.⁴⁵ Consistently, MVBR-28 suppressed

the secondary elevation of $[Ca^{2+}]_i$ in thapsigargin-activated human neutrophils. Collectively, the regulation of MVBR-28 on calcium influx in activated neutrophils may occur through inhibiting SOCE. In addition, MVBR-28 failed to inhibit extracellular Ca^{2+} entry in a K^+ -free buffer. Taken together, our results demonstrated that MVBR-28 inhibits $[Ca^{2+}]_i$ through K^+ -dependent pH regulation. The roles of Ca^{2+} and K^+ in the regulation of neutrophil inflammatory functions are still controversial. Previous research demonstrated that the killing mechanisms of neutrophils relied on oxidase-dependent protease production through the activation of the Ca^{2+} -activated K^+ channel to generate a K^+ -rich and alkaline intracellular environment.⁴⁶ However, other research demonstrated that the Ca^{2+} -activated K^+ channel was not identified in human neutrophils and did not modulate innate immune functions.⁴⁷

The anti-inflammatory effects of chalcones are controversy.^{11,48,49} Our previous studies have suggested that the anti-neutrophilic inflammatory effects of chalcones are dependent on the chemical structure.^{11,17} Herencia et al demonstrated that the chalcone analogues inhibited superoxide generation through scavenging effects in stimulated human neutrophils.⁵⁰ In contrast, our results showed that the inhibition of extracellular superoxide generation and intracellular ROS production in activated neutrophils by MVBR-28 were not associated with scavenging effects.

In conclusion, our results clearly demonstrated that MVBR-28, a Mannich bases of heterocyclic chalcone, inhibited respiratory burst, degranulation, and migration in activated human neutrophils. The regulation of neutrophil functions by MVBR-28 was through attenuating intracellular alkalization and inhibiting extracellular calcium influx in activated human neutrophils. Interestingly, the regulation of pH_i and calcium mobilization by MVBR-28 in activated neutrophils was K^+ -dependent. Given the importance of neutrophil functions in inflammatory diseases, these results also suggest that MVBR-28 may have potential benefits in protecting against neutrophilic inflammatory diseases.

ACKNOWLEDGMENTS

This research was supported by the grants from the Ministry of Science and Technology (MOST 107-2320-B-075-001-MY3, MOST 106-2320-B-255-003-MY3, and MOST 108-2320-B-255-003-MY3), Ministry of Education (EMRPD1I0441), Chang Gung University (EMRPD1I0501), Chang Gung University of Science and Technology (ZRRPF3H0101 and ZRRPF3H0111), and Chang Gung Memorial Hospital (CMRPF1G0241 ~ 3, CMRPF1J0051 ~ 3, CMRPG5F0161, CMRPG6J0141 ~ 3, CMRPG3J1001 ~ 3, and BMRP450), and projects from Taipei Veterans General Hospital (V108B-013 and V109B-001), Taiwan. The funders had no role in the study design, data collection and analysis, decision to publish, or preparation of the manuscript.

CONFLICT OF INTEREST

The authors declare no competing financial interests.

AUTHOR CONTRIBUTIONS

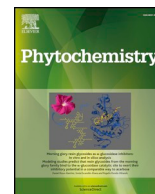
Y.-W. Chang, S.-C. Yang, and Y.-H. Wang performed the study; S.-C. Yang, C.-M. Ho, and Y.-F. Tsai analyzed the data and wrote the manuscript; T.-S. Wu synthesized the MVBR-28; T.-L. Hwang designed the study and reviewed the manuscript; all authors read and approved the final manuscript.

REFERENCES

- Yang SC, Hwang TL. The potential impacts of formyl peptide receptor 1 in inflammatory diseases. *Front Biosci (Elite Ed)*. 2016;8:436-449.
- Dicker AJ, Crichton ML, Pumphrey EG, et al. Neutrophil extracellular traps are associated with disease severity and microbiota diversity in patients with chronic obstructive pulmonary disease. *J Allergy Clin Immunol*. 2018;141:117-127.
- Jorch SK, Kubes P. An emerging role for neutrophil extracellular traps in noninfectious disease. *Nat Med*. 2017;23:279-287.
- Kruger P, Saffarzadeh M, Weber AN, et al. Neutrophils: between host defence, immune modulation, and tissue injury. *PLoS Pathog*. 2015;11:e1004651.
- Ackland GL, Abbott TEF, Cain D, et al. Preoperative systemic inflammation and perioperative myocardial injury: prospective observational multicentre cohort study of patients undergoing non-cardiac surgery. *Br J Anaesth*. 2019;122:180-187.
- Grommes J, Soehnlein O. Contribution of neutrophils to acute lung injury. *Mol Med*. 2011;17:293-307.
- Tsai YF, Yang SC, Chang WY, et al. Garcinia multiflora inhibits FPR1-mediated neutrophil activation and protects against acute lung injury. *Cell Physiol Biochem*. 2018;51:2776-2793.
- Go ML, Wu X, Liu XL. Chalcones: an update on cytotoxic and chemoprotective properties. *Curr Med Chem*. 2005;12:481-499.
- Nowakowska Z. A review of anti-infective and anti-inflammatory chalcones. *Eur J Med Chem*. 2007;42:125-137.
- Hsieh HK, Tsao LT, Wang JP, Lin CN. Synthesis and anti-inflammatory effect of chalcones. *J Pharm Pharmacol*. 2000;52:163-171.
- Hwang TL, Yeh SH, Leu YL, Chern CY, Hsu HC. Inhibition of superoxide anion and elastase release in human neutrophils by 3'-isopropoxychalcone via a cAMP-dependent pathway. *Br J Pharmacol*. 2006;148:78-87.
- Sharma V, Kumar V, Kumar P. Heterocyclic chalcone analogues as potential anticancer agents. *Anticancer Agents Med Chem*. 2013;13:422-432.
- Minders C, Petzer JP, Petzer A, Lourens AC. Monoamine oxidase inhibitory activities of heterocyclic chalcones. *Bioorg Med Chem Lett*. 2015;25:5270-5276.
- Ivanova Y, Momekov G, Petrov O, Karaivanova M, Kalcheva V. Cytotoxic Mannich bases of 6-(3-aryl-2-propenoyl)-2(3H)-benzoxazolones. *Eur J Med Chem*. 2007;42:1382-1387.
- Chiaradia LD, dos Santos R, Vitor CE, et al. Synthesis and pharmacological activity of chalcones derived from 2,4,6-trimethoxyacetophenone in RAW 264.7 cells stimulated by LPS: quantitative structure-activity relationships. *Bioorg Chem*. 2008;16:658-667.
- Reddy MV, Su CR, Chiou WF, et al. Design, synthesis, and biological evaluation of Mannich bases of heterocyclic chalcone analogs as cytotoxic agents. *Bioorg Chem*. 2008;16:7358-7370.
- Reddy MV, Hwang TL, Leu YL, Chiou WF, Wu TS. Inhibitory effects of Mannich bases of heterocyclic chalcones on NO production by activated RAW 264.7 macrophages and superoxide anion generation and elastase release by activated human neutrophils. *Bioorg Chem*. 2011;19:2751-2756.
- Yang SC, Chen PJ, Chang SH, et al. Luteolin attenuates neutrophilic oxidative stress and inflammatory arthritis by inhibiting Raf1 activity. *Biochem Pharmacol*. 2018;154:384-396.
- Brazil JC, Sumagin R, Cummings RD, Louis NA, Parkos CA. Targeting of neutrophil lewis x blocks transepithelial migration and increases phagocytosis and degranulation. *Am J Pathol*. 2016;186:297-311.
- Yang SC, Chung PJ, Ho CM, et al. Propofol inhibits superoxide production, elastase release, and chemotaxis in formyl peptide-activated human neutrophils by blocking formyl peptide receptor 1. *J Immunol*. 2013;190:6511-6519.
- Yang SC, Chang SH, Hsieh PW, et al. Dipeptide HCH6-1 inhibits neutrophil activation and protects against acute lung injury by blocking FPR1. *Free Radic Biol Med*. 2017;106:254-269.
- Ortiz-Acevedo A, Rigor RR, Maldonado HM, Cala PM. Activation of Na⁺/H⁺ and K⁺/H⁺ exchange by calyculin A in *Amphiuma tridactylum* red blood cells: implications for the control of volume-induced ion flux activity. *Am J Physiol Cell Physiol*. 2008;295:C1316-C1325.
- Failli P, Cecchi E, Ruocco C, Fazzini A, Giotti A. Effects of L- and D-arginine and some related esters on the cytosolic mechanisms of alpha-thrombin-induced human platelet activation. *Br J Pharmacol*. 1993;110:213-218.
- Wu ML, Tsai ML, Tseng YZ. DIDS-sensitive pHi regulation in single rat cardiac myocytes in nominally HCO₃-free conditions. *Circ Res*. 1994;75:123-132.
- Chen CY, Tsai YF, Huang WJ, Chang SH, Hwang TL. Propofol inhibits endogenous formyl peptide-induced neutrophil activation and alleviates lung injury. *Free Radic Biol Med*. 2018;129:372-382.
- Lacy P. Mechanisms of degranulation in neutrophils. *Allergy Asthma Clin Immunol*. 2006;2:98-108.
- Bedi P, Davidson DJ, McHugh BJ, Rossi AG, Hill AT. Blood neutrophils are reprogrammed in bronchiectasis. *Am J Respir Crit Care Med*. 2018;198:880-890.
- Yu HP, Hsieh PW, Chang YJ, Chung PJ, Kuo LM, Hwang TL. 2-(2-Fluorobenzamido)benzoate ethyl ester (EFB-1) inhibits superoxide production by human neutrophils and attenuates hemorrhagic shock-induced organ dysfunction in rats. *Free Radic Biol Med*. 2011;50:1737-1748.
- Tsai YF, Yu HP, Chung PJ, et al. Osthon attenuates neutrophilic oxidative stress and hemorrhagic shock-induced lung injury via inhibition of phosphodiesterase 4. *Free Radic Biol Med*. 2015;89:387-400.
- Hidalgo MA, Ojeda F, Eyre P, et al. Platelet-activating factor increases pHi in bovine neutrophils through the PI3K-ERK1/2 pathway. *Br J Pharmacol*. 2004;141:311-321.
- Coakley RJ, Taggart C, Greene C, McElvaney NG, O'Neill SJ. Ambient pCO₂ modulates intracellular pH, intracellular oxidant generation, and interleukin-8 secretion in human neutrophils. *J Leukoc Biol*. 2002;71:603-610.
- De Vito P. The sodium/hydrogen exchanger: a possible mediator of immunity. *Cell Immunol*. 2006;240:69-85.
- Immler R, Simon SI, Sperandio M. Calcium signalling and related ion channels in neutrophil recruitment and function. *Eur J Clin Invest*. 2018;48(Suppl 2):e12964.

34. Schaff UY, Dixit N, Procyk E, Yamayoshi I, Tse T, Simon SI. Orail regulates intracellular calcium, arrest, and shape polarization during neutrophil recruitment in shear flow. *Blood*. 2010;115:657-666.
35. Hellebrekers P, Vrisekoop N, Koenderman L. Neutrophil phenotypes in health and disease. *Eur J Clin Invest*. 2018;48(Suppl 2):e12943.
36. Rotstein OD, Nasmith PE, Grinstein S. The bacteroides by-product succinic acid inhibits neutrophil respiratory burst by reducing intracellular pH. *Infect Immun*. 1987;55:864-870.
37. Denk S, Neher MD, Messerer DAC, et al. Complement C5a functions as a master switch for the pH balance in neutrophils exerting fundamental immunometabolic effects. *J Immunol*. 2017;198:4846-4854.
38. Casey JR, Grinstein S, Orlowski J. Sensors and regulators of intracellular pH. *Nat Rev Mol Cell Biol*. 2010;11:50-61.
39. DeCoursey TE. During the respiratory burst, do phagocytes need proton channels or potassium channels, or both? *Sci STKE*. 2004;pe21.
40. Reeves EP, Lu H, Jacobs HL, et al. Killing activity of neutrophils is mediated through activation of proteases by K^+ flux. *Nature*. 2002;416:291-297.
41. Giambelluca MS, Ciancio MC, Orlowski A, Gende OA, Pouliot M, Aiello EA. Characterization of the Na^+/HCO_3^- cotransport in human neutrophils. *Cell Physiol Biochem*. 2014;33:982-990.
42. Hayashi H, Aharonovitz O, Alexander RT, et al. Na^+/H^+ exchange and pH regulation in the control of neutrophil chemokinesis and chemotaxis. *Am J Physiol Cell Physiol*. 2008;294:C526-C534.
43. Pozzan T, Lew DP, Wollheim CB, Tsien RY. Is cytosolic ionized calcium regulating neutrophil activation? *Science*. 1983;221:1413-1415.
44. Clemens RA, Lowell CA. Store-operated calcium signaling in neutrophils. *J Leukoc Biol*. 2015;98:497-502.
45. Kappala SS, Espino J, Pariente JA, et al. FMLP-, thapsigargin-, and H_2O_2 -evoked changes in intracellular free calcium concentration in lymphocytes and neutrophils of type 2 diabetic patients. *Mol Cell Biochem*. 2014;387:251-260.
46. Ahluwalia J, Tinker A, Clapp LH, et al. The large-conductance Ca^{2+} -activated K^+ channel is essential for innate immunity. *Nature*. 2004;427:853-858.
47. Essin K, Salanova B, Kettritz R, et al. Large-conductance calcium-activated potassium channel activity is absent in human and mouse neutrophils and is not required for innate immunity. *Am J Physiol Cell Physiol*. 2007;293:C45-C54.
48. Sahu NK, Balbhadra SS, Choudhary J, Kohli DV. Exploring pharmacological significance of chalcone scaffold: a review. *Curr Med Chem*. 2012;19:209-225.
49. Mahapatra DK, Bharti SK, Asati V. Chalcone derivatives: anti-inflammatory potential and molecular targets perspectives. *Curr Top Med Chem*. 2017;17:3146-3169.
50. Herencia F, Ferrandiz ML, Ubeda A, et al. Synthesis and anti-inflammatory activity of chalcone derivatives. *Bioorg Med Chem Lett*. 1998;8:1169-1174.

How to cite this article: Yang S-C, Wang Y-H, Tsai Y-F, et al. A synthesized heterocyclic chalcone inhibits neutrophilic inflammation through K^+ -dependent pH regulation. *The FASEB Journal*. 2020;00:1–17. <https://doi.org/10.1096/fj.201903123R>

Anti-inflammatory alkaloids from the root bark of *Hernandia nymphaeifolia*Yu-Wei Lai^{a,b,1}, Shih-Wei Wang^{c,d,1}, Ya-Yun Hu^e, Tsong-Long Hwang^{f,g}, Ming-Jen Cheng^h, Ih-Sheng Chenⁱ, Ping-Jyun Sung^{j,d}, Jih-Jung Chen^{k,l,*}^a Division of Urology, Taipei City Hospital Renai Branch, Taipei, Taiwan^b Department of Urology, School of Medicine, National Yang-Ming University, Taipei, Taiwan^c Graduate Institute of Natural Products, Kaohsiung Medical University, Kaohsiung, Taiwan^d Department of Medicine, Mackay Medical College, New Taipei City, Taiwan^e Graduate Institute of Pharmaceutical Technology, Tajen University, Pingtung, Taiwan^f Graduate Institute of Natural Products, School of Traditional Chinese Medicine, College of Medicine, Chang Gung University, Taoyuan, Taiwan^g Research Center for Chinese Herbal Medicine, Research Center for Food and Cosmetic Safety, Graduate Institute of Health Industry Technology, College of Human Ecology, Chang Gung University of Science and Technology, Taoyuan, Taiwan^h Bioresource Collection and Research Center (BCRC), Food Industry Research and Development Institute (FIRDI), Hsinchu, Taiwanⁱ School of Pharmacy, College of Pharmacy, Kaohsiung Medical University, Kaohsiung, Taiwan^j National Museum of Marine Biology and Aquarium, Pingtung, Taiwan^k Faculty of Pharmacy, School of Pharmaceutical Sciences, National Yang-Ming University, Taipei, Taiwan^l Department of Medical Research, China Medical University Hospital, China Medical University, Taichung, Taiwan

ARTICLE INFO

Keywords:

Hernandia nymphaeifolia

Hernandiaceae

Root bark

Structure elucidation

Alkaloid

Anti-inflammatory activity

ABSTRACT

Four undescribed alkaloids, 7-ethoxy-6-methoxy-2-methylisoquinolin-1(2H)-one, 7,8-dihydroxy-6-methoxy-2-methylisoquinolin-1(2H)-one, *N*-formylhernagine, and 5,6-dihydroxy-*N*-methylphthalimide, were obtained from the root bark of *Hernandia nymphaeifolia*, along with fourteen known compounds. The structures of these compounds were determined through spectroscopic and MS analyses. 7,8-Dihydroxy-6-methoxy-2-methylisoquinolin-1(2H)-one, *N*-formylhernagine, 5,6-dihydroxy-*N*-methylphthalimide, oxohernagine, hernandonine, and *N*-trans-feruloylmethoxytyramine inhibited the superoxide anion ($O_2^{\cdot-}$) production (IC_{50} values $\leq 6.23 \mu\text{g/mL}$) by neutrophils stimulated with formyl-L-methionyl-L-leucyl-L-phenyl-alanine/cytochalasin B (fMLP/CB). Furthermore, 7,8-dihydroxy-6-methoxy-2-methylisoquinolin-1(2H)-one, *N*-formylhernagine, 5,6-dihydroxy-*N*-methylphthalimide, oxohernagine, and *N*-trans-feruloylmethoxytyramine inhibited fMLP/CB-induced elastase release with IC_{50} values $\leq 7.41 \mu\text{g/mL}$. In addition, 7,8-dihydroxy-6-methoxy-2-methylisoquinolin-1(2H)-one, *N*-formylhernagine, oxohernagine, and *N*-trans-feruloylmethoxytyramine showed potent inhibition with IC_{50} values $\leq 28.55 \mu\text{M}$, against lipopolysaccharide (LPS)-induced nitric oxide (NO) generation.

1. Introduction

Hernandia nymphaeifolia (Presl) Kubitzki (Hernandiaceae) is an evergreen tree, distributed in the tropical islands of the western Pacific and Indian Oceans (Yang and Lu, 1996). This plant has been used as a cathartic, depilatory, and hemostatic agent in folk medicine (Kan, 1970). Diverse aporphines (Chen et al., 1997a, 2000, 2001; Wei et al., 2018), lignans (Chen et al., 1997a, 2000; Pettit et al., 2004; Wei et al., 2018), benzylisoquinolines (Chen et al., 1997a), isoquinolones (Chen et al., 1997a), steroids (Chen et al., 2000; Wei et al., 2018), amides (Wei et al., 2018), and their derivatives were isolated from this species in the

past studies. Many of these isolated compounds show cytotoxic (Chen et al., 1997a), anti-platelet aggregation (Chen et al., 2000), vasorelaxing (Chen et al., 2001), antioxidant (Chen et al., 2001), anti-neoplastic (Pettit et al., 2004), and anti-inflammatory (Wei et al., 2018) activities. The inappropriate or extensive activation of neutrophils and/or macrophages results in numerous inflammatory diseases such as asthma, rheumatoid arthritis, chronic obstructive pulmonary disease (COPD), ischemia-reperfusion injury, and metabolic diseases (Borregaard, 1998; Ennis, 2003). In response to different stimuli, activated neutrophils and/or macrophages excrete a series of cytotoxins, such as superoxide anion ($O_2^{\cdot-}$), elastase, bioactive lipids, and nitric

* Corresponding author. Faculty of Pharmacy, School of Pharmaceutical Sciences, National Yang-Ming University, No.155, Sec.2, Linong Street, Taipei, 11221, Taiwan.

E-mail addresses: chenjj@ym.edu.tw, chenjj@gm.ym.edu.tw (J.-J. Chen).

¹ Authors have contributed equally in this manuscript.

<https://doi.org/10.1016/j.phytochem.2020.112326>

Received 7 November 2019; Received in revised form 12 February 2020; Accepted 18 February 2020

Available online 28 February 2020

0031-9422/ © 2020 Elsevier Ltd. All rights reserved.

oxide (NO) (Borregaard, 1998; Roos et al., 2003; Witko-Sarsat et al., 2000). Suppression of the extensive or inappropriate activation of neutrophils and/or macrophages by drugs has been proposed as a way to ameliorate inflammatory diseases. In our studies on the anti-inflammatory constituents of plants in Taiwan, many species have been screened for anti-inflammatory effect, and *H. nymphaeifolia* has been found to be an active species. Four undescribed alkaloids, 7-ethoxy-6-methoxy-2-methylisoquinolin-1(2H)-one (1), 7,8-dihydroxy-6-methoxy-2-methylisoquinolin-1(2H)-one (2), *N*-formylhernagine (3), and 5,6-dihydroxy-*N*-methylphthalimide (4), and fourteen known compounds (5–18) have been isolated and confirmed from the root bark of *H. nymphaeifolia*. This report depicts the structural elucidation of four undescribed compounds 1–4 and the inhibitory activities of all isolated compounds against fMLP/CB-induced $O_2^{\cdot-}$ and elastase release and against LPS-induced NO generation.

2. Results and discussion

2.1. General

Chromatographic isolation of the CH_2Cl_2 -soluble fraction of MeOH extract of root bark of *H. nymphaeifolia* on column chromatography, medium pressure liquid chromatography, and preparative thin-layer chromatography afforded four undescribed (1–4) (Fig. 1) and fourteen known compounds (5–18).

2.2. Structure elucidation of the previously undescribed compounds

Compound 1 was obtained as yellowish needles. Its molecular formula $C_{13}H_{15}NO_3$ was deduced from a sodium adduct ion at m/z 256.0950 $[M + Na]^+$ (calcd 256.0948) in the HR-ESI mass spectrum. The presence of carbonyl group (1680 cm^{-1}) was evident from the IR spectrum. Comparison of the 1H and ^{13}C -NMR data of 1 with those of *N*-methyl-6,7-dimethoxyisoquinoline (Krane and Shamma, 1982) suggested that their structures were closely related, except that the 7-ethoxy group [δ_H 1.52 (3H, t, $J = 7.0\text{ Hz}$, OCH_2CH_3), 4.33 (2H, q, $J = 7.0\text{ Hz}$, OCH_2CH_3)] of 1 replaced the 7-methoxy group of *N*-methyl-6,7-dimethoxyisoquinoline (Krane and Shamma, 1982). This was supported by both HMBC correlations between OCH_2CH_3 (δ_H 4.33) and C-7 (δ_C 148.6), and NOESY correlations between OCH_2CH_3 (δ_H 4.33) and H-8 (δ_H 7.80). This was supported by 1H - 1H COSY, NOESY (Fig. 2),

DEPT, HSQC, and HMBC (Fig. 2) experiments. Therefore, the structure of compound 1 was defined as 7-ethoxy-6-methoxy-2-methylisoquinolin-1(2H)-one.

Compound 2 was isolated as colorless needles. Its molecular formula, $C_{11}H_{11}NO_4$, was determined on the basis of the positive HR-ESI-MS at m/z 244.0586 $[M + Na]^+$ (calcd 244.0589) and supported by the 1H -, ^{13}C -, and DEPT NMR data. IR absorptions for OH (3224 cm^{-1}) and carbonyl (1684 cm^{-1}) functions were observed. The 1H and ^{13}C -NMR data of 2 were similar to those of *N*-methyl-6,7-dimethoxyisoquinoline (Krane and Shamma, 1982), except that the 7,8-dihydroxy groups [δ_H 6.07 (1H, br s, D_2O exchangeable, OH-7), 12.63 (1H, s, D_2O exchangeable, OH-8)] of 2 replaced OMe-7 and H-8 of *N*-methyl-6,7-dimethoxyisoquinoline (Krane and Shamma, 1982). This was supported by the HMBC correlations between OH-7 (δ_H 6.07) and C-6 (δ_C 153.2), C-7 (δ_C 133.9), and C-8 (δ_C 143.0); and between OH-8 (δ_H 12.63) and C-7 (δ_C 133.9), C-8 (δ_C 143.0), and C-8a (δ_C 132.5). The full assignment of 1H and ^{13}C -NMR resonances was supported by 1H - 1H COSY, DEPT, HSQC, NOESY (Fig. 2), and HMBC (Fig. 2) spectral analyses. According to the above data, the structure of 2 was elucidated as 7,8-dihydroxy-6-methoxy-2-methylisoquinolin-1(2H)-one.

Compound 3 was obtained as amorphous powder. The ESI-MS demonstrated the quasi-molecular ion $[M + Na]^+$ at m/z 378, implying a molecular formula of $C_{20}H_{21}NO_5$, which was confirmed by the HR-ESI-MS (m/z 378.1318 $[M + Na]^+$, calcd 378.1317) and by the 1H -, ^{13}C -, and DEPT NMR data. IR absorptions for OH (3422 cm^{-1}) and conjugated carbonyl (1660 cm^{-1}) functions were observed. The 1H -NMR spectrum of *N*-formylhernagine, such as (+)-*N*-formyllovigerine (Chen et al., 1996a) and *N*-acetylnornuciferine (Pachaly et al., 1992), showed two rotational isomers. Compound 3 also displayed two rotational isomers (3a and 3b) in a ratio of 2:1 in the 1H -NMR spectrum, due to the existence of an *N*-formyl group as in the cases of *N*-acylated nor-aporphines (Chen et al., 1996a; Pachaly et al., 1992). The 1H -NMR spectra for two isomers could be clearly differentiated, even though they couldn't be separated. The *Z*-form isomer (3a) exhibited a NOESY correlation between *N*-CNO (δ 8.26) and H_{β} -5 (δ 3.84), while the same experiment for *N*-CNO (δ 8.38) in the *E*-form isomer (3b) correlated with H-6a (δ 4.46). The major isomer 3a showed a C-3 proton at δ 6.71 (1H, s), an *N*-formyl group at δ 8.26 (1H, s), three methoxy groups at δ 3.53 (3H, s, OMe-1), 3.54 (3H, s, OMe-11), and 3.90 (3H, s, OMe-2), and two mutually coupling aromatic protons in ring D at δ 6.90 (1H, d, $J = 8.0\text{ Hz}$, H-9) and 6.94 (1H, d, $J = 8.0\text{ Hz}$, H-8). By contrast, the

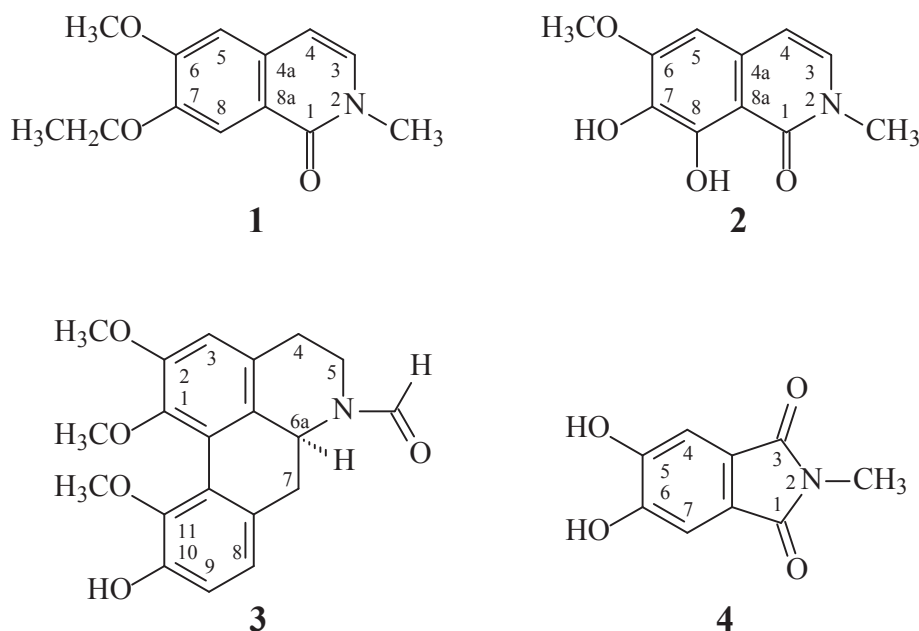


Fig. 1. The chemical structures of previously undescribed compounds 1–4 isolated from *H. nymphaeifolia*.

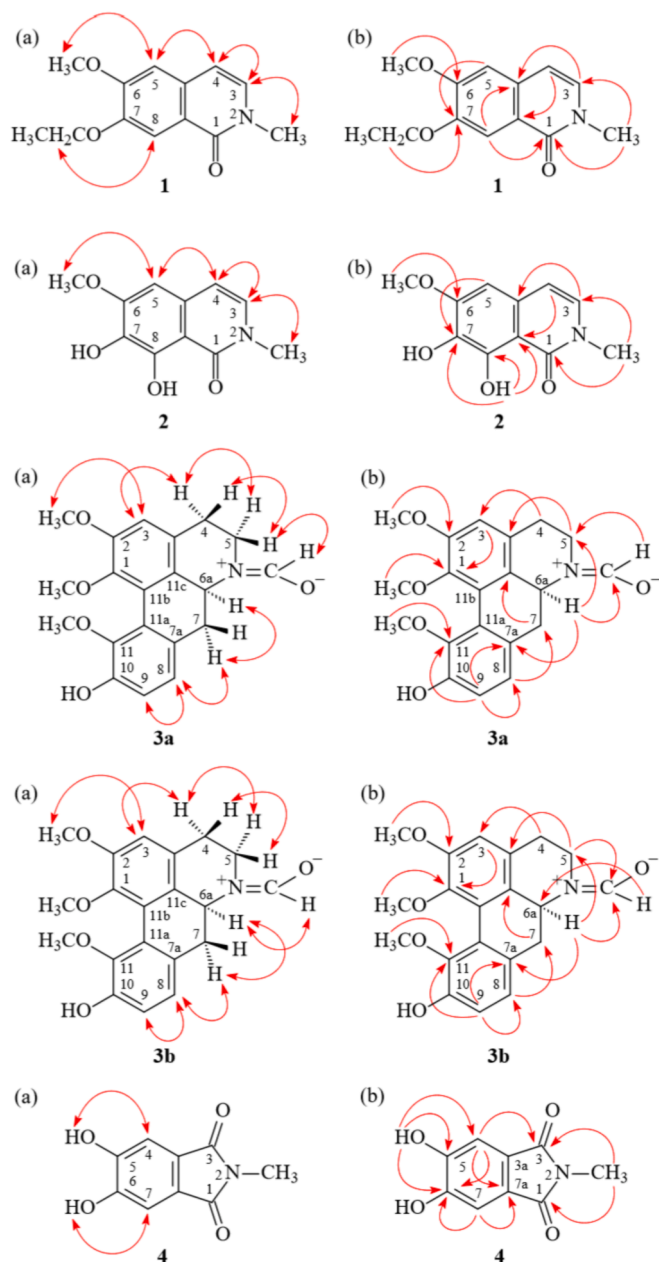


Fig. 2. Key NOESY (a) and HMBC (b) correlations of 1–4.

minor isomer **3b** displayed a corresponding C-3 proton at δ 6.73 (1H, s), an *N*-formyl group at δ 8.38 (1H, s), three methoxy groups at δ 3.53 (3H, s, OMe-1), 3.56 (3H, s, OMe-11), and 3.90 (3H, s, OMe-2), and two mutually coupling aromatic protons in ring D at δ 6.90 (1H, d, J = 8.0 Hz, H-9) and 6.94 (1H, d, J = 8.0 Hz, H-8). The other aliphatic protons of two isomers (**3a** and **3b**) including H-4, H-5, H-6a, and H-7 protons could be well-assigned comparative to those of (+)-*N*-formylhernangerine (Chen et al., 1996a). Comparison of the ^1H and ^{13}C -NMR spectroscopic data of **3** with those of (+)-*N*-formylhernangerine (Chen et al., 1996a) suggested that their structures are closely related, except that the 1,2-dimethoxy groups of **3** replaced the 1,2-methylenedioxy group of (+)-*N*-formylhernangerine (Chen et al., 1996a). This was supported by HMBC correlations between OMe-1 (δ 3.53) and C-1 (δ 148.3), and between OMe-2 (δ 3.90) and C-2 (δ 152.4); and by NOESY correlations between OMe-2 (δ 3.90) and H-3 (δ 6.71). Aporphines isolated from the Hernandiaceae plants usually show the dextrorotatory optical activity and the *S*-configuration at C-6a (Chen et al., 1996a, 2001; Wang and Cheng, 1968). The specific rotation data ($[\alpha]_D^{25}$ = +

298.7) of **3** was similar to those of (+)-*S*-aporphines and opposite to those of (–)-*R*-aporphines, thus **3** possessed a 6a*S*-configuration (Guinaudeau et al., 1988, 1994). The full assignment of ^{13}C and ^1H NMR resonances was affirmed by ^1H – ^1H COSY, NOESY (Fig. 2), DEPT, HMBC (Fig. 2), and HSQC analytical techniques and analyses. On the basis of the above data, structure **3** was elucidated as (*S*)-10-hydroxy-1,2,11-trimethoxy-6a,7-dihydro-4*H*-dibenzo[*de,g*]quinoline-6(5*H*)-carbaldehyde, named *N*-formylhernagine.

Compound **4** was isolated as a colorless needles. The ESI-MS afforded the sodium adduct ion $[\text{M} + \text{Na}]^+$ at m/z 216, suggesting a molecular formula of $\text{C}_9\text{H}_7\text{NO}_4$, which was confirmed by the HR-ESI-MS (m/z 216.0272 $[\text{M} + \text{Na}]^+$, calcd 216.0273). The IR spectrum displayed the presence of OH (3314 cm^{-1}) and carbonyl (1706 cm^{-1}) groups. The ^1H -NMR spectrum of **4** revealed the presence of two hydroxy groups at δ_{H} 5.87 (2H, br s, OH-5 and OH-6), an *N*-Me group at δ_{H} 3.14 (3H, s), and two aromatic protons at δ_{H} 7.25 (2H, s, H-4 and H-7). The ^1H and ^{13}C -NMR data of **4** were similar to those of 6-hydroxy-5-methoxy-*N*-methylphthalimide (Zhang et al., 2004), except that the 5-hydroxy group [δ_{H} 5.87 (1H, br s)] of **4** replaced the 5-methoxy group of 6-hydroxy-5-methoxy-*N*-methylphthalimide (Zhang et al., 2004). This was supported by NOESY correlations between OH-5 (δ_{H} 5.87) and H-4 (δ_{H} 7.25) and by HMBC correlation between OH-5 (δ_{H} 5.87) and C-4 (δ_{C} 109.9), C-5 (δ_{C} 151.1), and C-6 (δ_{C} 151.1). Based on the above evidence, the structure of **4** was elucidated as 5,6-dihydroxy-*N*-methylphthalimide. This was further confirmed by the DEPT, ^1H – ^1H -COSY, NOESY (Fig. 2), HMBC (Fig. 2), and HSQC experiments.

2.3. Structure identification of the known isolates

The known isolates were readily identified by a comparison of physical and spectroscopic data (UV, IR, ^1H -NMR, $[\alpha]_D$, and MS) with corresponding authentic samples or literature values, and this included two aporphines, oxohernagine (**5**) (Chen et al., 1996b) and hernandonine (**6**) (Furukawa et al., 1972), three lignans, dehydrodeoxypodophyllotoxin (**7**) (Yamaguchi et al., 1982), dehydrodeoxypodophyllotoxin (**8**) (Tanoguchi et al., 1987), and podophyllotoxin (**9**) (Ito et al., 1992), an amide, *N*-*trans*-feruloylmethoxytyramine (**10**) (Chen et al., 2010), and eight steroids, mixture of β -sitosterol (**11**) (Chang et al., 2000) and stigmasterol (**12**) (Kojima et al., 1990), mixture of β -sitostenone (**13**) (Chen et al., 1997b) and stigmasterol-4,22-dien-3-one (**14**) (Chen et al., 1997b), mixture of stigmasterol-4-en-3,6-dione (**15**) (Cui et al., 2009) and stigmasterol-4-en-3,6-dione (**16**) (Cui et al., 2009), and mixture of 6 β -hydroxystigmasterol-4-en-3-one (**17**) (Sun et al., 2007; Ayyad, 2002) and 6 β -hydroxystigmasterol-4,22-dien-3-one (**18**) (Sun et al., 2007; Ayyad, 2002).

2.4. Biological studies

Reactive oxygen species (ROS) [e.g., superoxide anion ($\text{O}_2^{\cdot-}$)] and granule proteases (e.g., elastase and proteinase-3) produced by human neutrophils are involved in the pathogenesis of a variety of inflammatory diseases (Borregaard, 1998; Roos et al., 2003; Witko-Sarsat et al., 2000). The effects on neutrophil pro-inflammatory responses of isolated compounds from the root bark of *H. nymphaeifolia* were evaluated by suppressing fMLP/CB-induced superoxide radical anion ($\text{O}_2^{\cdot-}$) generation and elastase release by human neutrophils. The inhibitory activity data on human neutrophil pro-inflammatory responses are shown in Table 1. Diphenyleneiodonium and phenylmethylsulfonyl fluoride were used as positive controls for $\text{O}_2^{\cdot-}$ generation and elastase release, respectively. From the results of our biological tests, the following conclusions can be drawn: (a) 7,8-Dihydroxy-6-methoxy-2-methylisoquinolin-1(2*H*)-one (**2**), *N*-formylhernagine (**3**), 5,6-dihydroxy-*N*-methylphthalimide (**4**), oxohernagine (**5**), hernandonine (**6**), and *N*-*trans*-feruloylmethoxytyramine (**10**) showed potent inhibition ($\text{IC}_{50} \leq 6.23\text{ }\mu\text{g/mL}$) of $\text{O}_2^{\cdot-}$ generation by neutrophils in response to fMLP/CB. (b) 7,8-Dihydroxy-6-methoxy-2-methylisoquinolin-1(2*H*)-

Table 1

Inhibitory effects of compounds **1–18** from the root bark of *H. nymphaeifolia* on superoxide radical anion generation and elastase release by human neutrophils in response to fMet-Leu-Phe/cytochalasin B^a.

Compounds	Superoxide anion	Elastase
	IC ₅₀ [μg/mL] ^b or (Inh %) ^c	
7-Ethoxy-6-methoxy-2-methylisoquinolin-1(2H)-one (1)	8.24 ± 1.04 *	(45.34 ± 5.18) *
7,8-Dihydroxy-6-methoxy-2-methylisoquinolin-1(2H)-one (2)	5.57 ± 0.81 *	6.17 ± 0.75 *
<i>N</i> -Formylhernagine (3)	6.12 ± 0.97 **	7.41 ± 1.36 *
5,6-Dihydroxy- <i>N</i> -methylphthalimide (4)	5.65 ± 0.82 *	6.42 ± 1.03 *
Oxohernagine (5)	2.84 ± 0.78 ***	4.88 ± 0.29 ***
Hernandonine (6)	4.43 ± 0.75 ***	(46.11 ± 6.76) ***
Dehydrodeoxypodophyllotoxin (7)	(37.62 ± 4.03) **	(44.56 ± 3.48)
Dehydropodophyllotoxin (8)	(44.05 ± 3.84) ***	9.33 ± 0.81 ***
Podophyllotoxin (9)	(36.34 ± 4.67) *	(31.85 ± 3.64) *
<i>N-trans</i> -Feruloylmethoxytyramine (10)	6.23 ± 0.63 ***	7.01 ± 0.23 ***
Mixture of β-Sitosterol (11) and Stigmasterol (12)	(11.12 ± 3.36)	(5.73 ± 2.42)
Mixture of β-Sitosterone (13) and Stigmasta-4,22-dien-3-one (14)	(24.58 ± 2.76)	(29.86 ± 2.92)
Mixture of Stigmast-4-en-3,6-dione (15) and Stigmasta-4,22-dien-3,6-dione (16)	(29.87 ± 2.74)	(35.12 ± 3.17)
Mixture of 6β-Hydroxystigmast-4-en-3-one (17) and 6β-Hydroxystigmasta-4,22-dien-3-one (18)	(17.21 ± 2.69) **	7.85 ± 1.23 *
Diphenyleneiodonium ^d	0.54 ± 0.21 ***	–
Phenylmethylsulfonyl fluoride ^d	–	34.3 ± 5.2 ***

**p* < 0.05 compared with the control.

***p* < 0.01 compared with the control.

****p* < 0.001 compared with the control.

^a Results are presented as averages ± SEM (*n* = 4).

^b Concentration necessary for 50% inhibition (IC₅₀). If IC₅₀ value of compound was < 10 μg/mL, it was displayed as IC₅₀ [μg/mL].

^c Percentage of inhibition (Inh %) at 10 μg/mL. If IC₅₀ value of compound was ≥ 10 μg/mL, it was shown as (Inh %) at 10 μg/mL.

^d Diphenyleneiodonium (a NADPH oxidase inhibitor) and phenylmethylsulfonyl fluoride (a serine protease inhibitor) were used as the positive controls in the generation of superoxide anion and release of elastase, respectively.

one (**2**), *N*-formylhernagine (**3**), 5,6-dihydroxy-*N*-methylphthalimide (**4**), oxohernagine (**5**), and *N-trans*-feruloylmethoxytyramine (**10**) displayed potent inhibition (IC₅₀ ≤ 7.41 μg/mL) against fMLP-induced elastase release. (c) Oxoporphine alkaloid, oxohernagine (**5**) (with 1,2,11-trimethoxy and 10-hydroxy groups) displayed more effective inhibition than its analogue, hernandonine (**6**) (with 1,2- and 10,11-dimethylenedioxy groups) against fMLP-induced elastase release and superoxide anion generation. (d) Lignan compound, dehydropodophyllotoxin (**8**) (with 7-hydroxy group) exhibited more effective inhibition than its analogue, dehydrodeoxypodophyllotoxin (**7**) (without 7-hydroxy group) against fMLP-induced elastase release and O₂^{•−} generation. (e) Oxohernagine (**5**) was the most effective among the isolated compounds, with IC₅₀ values of 2.84 ± 0.78 and 4.88 ± 0.29 μg/mL, respectively, against fMLP-induced O₂^{•−} generation and elastase release.

Nitric oxide (NO) is a mediator in the inflammatory response involved in host defense. The anti-inflammatory effects of the compounds isolated from the root bark of *H. nymphaeifolia* were also evaluated by suppressing lipopolysaccharide (LPS)-induced NO generation in macrophage cell line RAW264.7. The inhibitory activity data of the isolates **1–18** on NO generation by macrophages are shown in Table 2. Quercetin was used as the positive control. From the results of our anti-inflammatory assays, the following conclusions can be drawn: (a) 7,8-dihydroxy-6-methoxy-2-methylisoquinolin-1(2H)-one (**2**), *N*-formylhernagine (**3**), oxohernagine (**5**), and *N-trans*-feruloylmethoxytyramine (**10**) showed potent inhibition with IC₅₀ values ≤ 28.55 μM, against lipopolysaccharide (LPS)-induced nitric oxide (NO) generation. (b) Oxohernagine (**5**) (with 1,2,11-trimethoxy and 10-hydroxy groups) displayed more effective inhibition than its analogue, hernandonine (**6**) (with 1,2- and 10,11-dimethylenedioxy groups) against LPS-induced NO generation. (c) Dehydropodophyllotoxin (**8**) (with 7-hydroxy group) exhibited more effective inhibition than its analogue, dehydrodeoxypodophyllotoxin (**7**) (without 7-hydroxy group) against LPS-induced NO generation. (d) *N*-Formylhernagine (**3**) is the most effective among the isolated compounds, with IC₅₀ = 18.60 ± 2.44 μM, against LPS-induced NO production. (e) Cytotoxic effects were tested using MTT experiment. The high cell viability (97, 95, 98, and 93%, respectively) of compounds **2**, **3**, **5**, and **10** at 50 μM showed that their

Table 2

Inhibitory effects of compounds **1–18** from the root bark of *H. nymphaeifolia* on nitric oxide (NO) generation by RAW264.7 murine macrophages in response to lipopolysaccharide (LPS).

Compounds	IC ₅₀ (μM) ^a
7-Ethoxy-6-methoxy-2-methylisoquinolin-1(2H)-one (1)	51.48 ± 4.26*
7,8-Dihydroxy-6-methoxy-2-methylisoquinolin-1(2H)-one (2)	20.57 ± 1.74**
<i>N</i> -Formylhernagine (3)	18.60 ± 2.44*
5,6-Dihydroxy- <i>N</i> -methylphthalimide (4)	56.82 ± 3.70*
Oxohernagine (5)	21.75 ± 1.08*
Hernandonine (6)	44.79 ± 2.86*
Dehydrodeoxypodophyllotoxin (7)	82.35 ± 7.51
Dehydropodophyllotoxin (8)	55.17 ± 4.73
Podophyllotoxin (9)	69.25 ± 4.13
<i>N-trans</i> -Feruloylmethoxytyramine (10)	28.55 ± 3.15**
Mixture of β-Sitosterol (11) and Stigmasterol (12)	> 100
Mixture of β-Sitosterone (13) and Stigmasta-4,22-dien-3-one (14)	> 100
Mixture of Stigmast-4-en-3,6-dione (15) and Stigmasta-4,22-dien-3,6-dione (16)	88.13 ± 6.93
Mixture of 6β-Hydroxystigmast-4-en-3-one (17) and 6β-Hydroxystigmasta-4,22-dien-3-one (18)	> 100
Quercetin ^b	34.12 ± 2.34*

^a The IC₅₀ values were calculated from the slope of the dose-response curves (SigmaPlot). Values are expressed as average ± SEM (*n* = 4). **P* < 0.05, ***P* < 0.01 compared with the control.

^b Quercetin was used as a positive control.

inhibitory activities against LPS-induced NO generation didn't arise from their cytotoxicities.

The above findings indicated that the promising inhibitory activity against fMLP-induced O₂^{•−} and elastase generation and LPS-induced NO release of *H. nymphaeifolia* and its isolates could stimulate future development of new anti-inflammatory agents.

3. Concluding remarks

Eighteen compounds, including four undescribed alkaloids, 7-ethoxy-6-methoxy-2-methylisoquinolin-1(2H)-one (**1**), 7,8-dihydroxy-

6-methoxy-2-methylisoquinolin-1(2*H*)-one (2), *N*-formylhernagine (3), and 5,6-dihydroxy-*N*-methylphthalimide (4), were isolated from root bark of *H. nymphaeifolia*. The structures of these isolates were elucidated according to spectroscopic data. The effects on neutrophil pro-inflammatory responses of isolates were evaluated by suppressing fMLP/CB-induced $O_2^{\cdot-}$ generation and elastase release by human neutrophils. The results of anti-inflammatory assays show that compounds 2–6 and 10 can obviously inhibit fMLP-induced $O_2^{\cdot-}$ generation and/or elastase release. Oxohernagine (5) was the most effective among the isolated compounds, with IC_{50} values of 2.84 ± 0.78 and 4.88 ± 0.29 $\mu\text{g/mL}$, respectively, against fMLP-induced $O_2^{\cdot-}$ generation and elastase release. Furthermore, compounds 2, 3, 5, and 10 showed potent inhibition with IC_{50} values of 20.57 ± 1.74 , 18.60 ± 2.44 , 21.75 ± 1.08 , and 28.55 ± 3.15 μM , respectively, against LPS-induced NO generation. Our research indicates *H. nymphaeifolia* and its isolates (especially 2–6 and 10) are worth further research and may be expectantly developed as candidates for the treatment or prevention of various inflammatory diseases.

4. Experimental

4.1. General experimental procedures

Melting points were determined on a Yanaco micro-melting point apparatus and were uncorrected. The ^1H , ^{13}C , and 2D NMR spectroscopic data were recorded using a Varian Unity 400 or a Varian Inova 500 spectrometer (Varian Inc., Palo Alto, CA, USA) using TMS as an internal standard. ESI-MS and HR-ESI-MS were obtained from the Bruker APEX II (Bruker, Bremen, Germany). Column chromatography, thin-layer chromatography (TLC), preparative thin-layer chromatography (PTLC), IR spectra, UV spectra, and optical rotation were performed according to our earlier research (Chen et al., 2001).

4.2. Plant material

The root barks of *Hernandia nymphaeifolia* (Presl) Kubitzki (Hernandiaceae) were collected from Mudan Township, Pingtung County, Taiwan ($22^\circ14'01.8''\text{N}$ $120^\circ53'48.7''\text{E}$), in August 2008 and identified by Prof. I.-S. Chen. A voucher specimen (Chen 5521) was deposited in School of Pharmacy, Kaohsiung Medical University, Kaohsiung, Taiwan.

4.3. Extraction and isolation

The dried root bark (2.3 kg) of *H. nymphaeifolia* was cut and extracted with MeOH (20 L each) for 3 days. The extract was concentrated under reduced pressure at 35°C , and the residue (225 g) was partitioned between H_2O and CH_2Cl_2 (1:1) to afford the CH_2Cl_2 -soluble fraction (fraction A; 72 g). Fraction A (72 g) was separated by CC (3.5 kg of silica gel, 70–230 mesh; $\text{CH}_2\text{Cl}_2/\text{MeOH}$ gradient) to afford 11 fractions: A1–A11. Fraction A3 (6.5 g) was submitted to CC (300 g of silica gel, 230–400 mesh; *n*-hexane/acetone 20:1–0:1, 850 mL-fractions) to afford 10 subfractions: A3-1–A3-10. Fraction A3-5 (625 mg) was subjected to MPLC (silica column, *n*-hexane/acetone 10:1–0:1) to afford 9 subfractions (each 300 mL, A3-5-1–A3-5-9). Fraction A3-5-6 (70 mg) was purified by preparative TLC (silica gel, *n*-hexane/EtOAc, 8:1) to give mixture of β -sitosterone (13) and stigmasta-4,22-dien-3-one (14) (13.7 mg). Fraction A4 (6.0 g) was subjected to CC (270 g of silica gel, 230–400 mesh; *n*-hexane/EtOAc 10:1–0:1, 850 mL-fractions) to afford 9 subfractions: A4-1–A4-9. Fraction A4-4 (442 mg) was purified by MPLC (silica column, *n*-hexane/acetone 8:1–0:1) to provide 8 subfractions (each 300 mL, A4-4-1–A4-4-8). Fraction A4-4-5 (60 mg) was further purified by preparative TLC (silica gel; *n*-hexane/EtOAc 6:1) to yield mixture of β -sitosterol (11) and stigmasterol (12) (30.5 mg). Fraction A5 (5.9 g) was subjected to CC (270 g of silica gel, 230–400 mesh; $\text{CH}_2\text{Cl}_2/\text{MeOH}$ 12:1–0:1, 900 mL-fractions) to obtain 12 subfractions: A5-1–A5-12.

Fraction A5-3 (455 mg) was subjected to MPLC (silica column, $\text{CHCl}_3/\text{acetone}$ 7:1–0:1) to give 9 subfractions (each 200 mL, A5-3-1–A5-3-9). Fraction A5-3-4 (57 mg) was purified by preparative TLC (silica gel; *n*-hexane/acetone 5:1) to yield mixture of 6 β -hydroxystigmasta-4-en-3-one (17) and 6 β -hydroxystigmasta-4,22-dien-3-one (18) (10.5 mg). Fraction A5-4 (530 mg) was isolated by CC (24 g of silica gel, 230–400 mesh; $\text{CH}_2\text{Cl}_2/\text{EtOAc}$ 8:1–0:1) to provide 7 subfractions (each 300 mL, A5-4-1–A5-4-7). Fraction A5-4-4 (74 mg) was purified by preparative TLC (silica gel; $\text{CH}_2\text{Cl}_2/\text{MeOH}$ 10:1) to yield mixture of stigmasta-4-en-3,6-dione (15) and stigmasta-4,22-dien-3,6-dione (16) (5.6 mg). Part (110 mg) of fraction A5-5 was purified by preparative TLC (silica gel; $\text{CH}_2\text{Cl}_2/\text{acetone}$ 3:1) to obtain 7-ethoxy-6-methoxy-2-methylisoquinolin-1(2*H*)-one (1) (4.5 mg) and dehydrodeoxypodophyllotoxin (7) (5.6 mg). Fraction A6 (6.3 g) was isolated by CC (295 g of silica gel, 230–400 mesh; $\text{CH}_2\text{Cl}_2/\text{MeOH}$ 10:1–0:1, 750 mL-fractions) to provide 11 subfractions: A6-1–A6-11. Part (105 mg) of fraction A6-5 was purified by preparative TLC (silica gel; $\text{CHCl}_3/\text{acetone}$ 5:1) to yield *N*-formylhernagine (3) (4.9 mg). Fraction A6-6 (545 mg) was subjected to MPLC (silica column, $\text{CHCl}_3/\text{MeOH}$ 8:1–0:1) to provide 8 subfractions (each 200 mL, A6-6-1–A6-6-8). Fraction A6-6-4 (80 mg) was purified by preparative TLC (silica gel; $\text{CH}_2\text{Cl}_2/\text{acetone}$ 6:1) to yield podophyllotoxin (9) (4.6 mg). Fraction A6-6-5 (85 mg) was further purified by preparative TLC (silica gel; $\text{CH}_2\text{Cl}_2/\text{acetone}$ 5:1) to yield dehydropodophyllotoxin (8) (5.7 mg). Fraction A7 (6.1 g) was isolated by CC (280 g of silica gel, 230–400 mesh; $\text{CH}_2\text{Cl}_2/\text{MeOH}$ 7:1–0:1, 800 mL-fractions) to provide 9 subfractions: A7-1–A7-9. Part (115 mg) of fraction A7-2 was purified by preparative TLC (silica gel; $\text{CH}_2\text{Cl}_2/\text{EtOAc}$ 3:1) to obtain *N*-trans-feruloylmethoxytyramine (10) (5.1 mg). Fraction A7-3 (480 mg) was subjected to MPLC (silica column, $\text{CH}_2\text{Cl}_2/\text{MeOH}$ 6:1–0:1) to afford 7 subfractions (each 175 mL, A7-3-1–A7-3-7). Fraction A7-3-5 (65 mg) was further purified by preparative TLC (silica gel; $\text{CH}_2\text{Cl}_2/\text{EtOAc}$ 5:1) to obtain hernandonine (6) (6.7 mg). Fraction A7-6 (128 mg) was purified by preparative TLC (silica gel; $\text{CHCl}_3/\text{MeOH}$ 5:1) to afford 7,8-dihydroxy-6-methoxy-2-methylisoquinolin-1(2*H*)-one (2) (3.9 mg) and oxohernagine (5) (5.4 mg). Fraction A9 (5.8 g) was isolated by CC (280 g of silica gel, 230–400 mesh; $\text{CHCl}_3/\text{MeOH}$ 5:1–0:1, 1 L-fractions) to provide 9 subfractions: A9-1–A9-9. Fraction A9-2 (580 mg) was isolated by CC (silica column, $\text{CH}_2\text{Cl}_2/\text{MeOH}$ 5:1–0:1) to afford 8 subfractions (each 300 mL, A9-2-1–A9-2-8). Fraction A9-2-3 (55 mg) was purified by preparative TLC (silica gel; $\text{CH}_2\text{Cl}_2/\text{MeOH}$ 6:1) to obtain 5,6-dihydroxy-*N*-methylphthalimide (4) (5.1 mg).

7-Ethoxy-6-methoxy-2-methylisoquinolin-1(2*H*)-one (1): Yellowish needles; mp $109\text{--}111^\circ\text{C}$ (*n*-hexane); UV (MeOH): λ_{max} ($\log \epsilon$) = 220 (4.48), 260 (4.38), 270 (3.33), 300 (3.36) nm; IR (KBr): ν_{max} = 1680 ($\text{C}=\text{O}$), 1613, 1514, 1475, 1254, 1109, 950, 853 cm^{-1} ; ^1H -NMR spectroscopic data, see Table 3; ^{13}C -NMR spectroscopic data, see Table 4; ESI-MS: m/z = 256 [$\text{M} + \text{Na}$] $^+$; HR-ESI-MS: m/z = 256.0950 [$\text{M} + \text{Na}$] $^+$ (calcd for $\text{C}_{13}\text{H}_{15}\text{NO}_3\text{Na}$, 256.0948).

7,8-Dihydroxy-6-methoxy-2-methylisoquinolin-1(2*H*)-one (2): Colorless needles; mp $125\text{--}127^\circ\text{C}$ ($\text{CH}_2\text{Cl}_2\text{--MeOH}$); UV (MeOH): λ_{max} ($\log \epsilon$) = 221 (4.45), 261 (4.35), 270 (3.30), 331 (3.34) nm; IR (KBr): ν_{max} = 3224 (OH), 1684 ($\text{C}=\text{O}$), 1615, 1516, 1473, 1250, 952 cm^{-1} ; ^1H -NMR spectroscopic data, see Table 3; ^{13}C -NMR spectroscopic data, see Table 4; ESI-MS: m/z = 244 [$\text{M} + \text{Na}$] $^+$; HR-ESI-MS: m/z = 244.0586 [$\text{M} + \text{Na}$] $^+$ (calcd for $\text{C}_{11}\text{H}_{11}\text{NO}_4\text{Na}$, 244.0589).

N-Formylhernagine (3): amorphous powder; $[\alpha]_D^{25} = +298.7^\circ$ (*c* 0.18, CHCl_3); UV (MeOH): λ_{max} ($\log \epsilon$) = 222 (4.37), 271 (3.84), 308 (3.45) nm; IR (KBr): ν_{max} = 3422 (OH), 2924, 1660 ($\text{C}=\text{O}$), 1470, 1290, 1231, 1071, 1044 cm^{-1} ; ^1H -NMR spectroscopic data, see Table 3; ^{13}C -NMR spectroscopic data, see Table 4; ESI-MS: m/z = 378 [$\text{M} + \text{Na}$] $^+$; HR-ESI-MS: m/z = 378.1318 [$\text{M} + \text{Na}$] $^+$ (calcd for $\text{C}_{20}\text{H}_{21}\text{NO}_5\text{Na}$, 378.1317).

5,6-Dihydroxy-*N*-methylphthalimide (4): colorless needles; mp $217\text{--}219^\circ\text{C}$ ($\text{CH}_2\text{Cl}_2\text{--MeOH}$); UV (MeOH): λ_{max} ($\log \epsilon$) = 246 (4.48), 296 (3.12) nm; IR (KBr): ν_{max} = 3314 (OH), 2926, 1706 ($\text{C}=\text{O}$), 1603, 1503, 1433, 1379, 1205, 1020, 746 cm^{-1} ; ^1H -NMR spectroscopic data,

Table 3
¹H NMR data of compounds 1–4.

Position	1 ^a	2 ^b	3a ^a	3b ^a	4 ^b
3	7.00 d (7.2)	6.99 d (7.0)	6.71 s	6.73 s	
4	6.41 d (7.2)	6.39 d (7.0)	2.74 m	2.75 m	7.25 s
			2.89 m	2.79 m	
5	6.86 s	6.84 s	3.38 ddd (12.8, 12.4, 2.8)	3.06 m	
			3.84 ddd (12.8, 4.5, 2.0)	4.45 m	
6a			4.85 dd (13.6, 3.6)	4.46 dd (14.0, 3.6)	
7			2.66 dd (13.6, 13.6)	2.99 dd (14.0, 14.0)	7.25 s
			3.04 dd (13.6, 3.6)	2.76 dd (14.0, 3.6)	
8	7.80 s		6.94 d (8.0)	6.94 d (8.0)	
9			6.90 d (8.0)	6.94 d (8.0)	
1-OCH ₃			3.53 s	3.53 s	
2-OCH ₃			3.90 s	3.90 s	
5-OH					5.87 br s
6-OH					5.87 br s
6-OCH ₃	4.00 s	4.04 s			
7-OH		6.07 br s			
7-OCH ₂ CH ₃	4.33 q (7.0)				
7-OCH ₂ CH ₃	1.52 t (7.0)				
8-OH		12.63 s			
11-OCH ₃			3.54 s	3.56 s	
N-CH ₃	3.60 s	3.58 s			3.14 s
N-CHO			8.26 s	8.38 s	

^a Recorded in CDCl₃ at 400 MHz. Values in ppm (δ). *J* (in Hz) in parentheses.^b Recorded in CDCl₃ at 500 MHz.**Table 4**
¹³C NMR data of compounds 1–4.

Position	1 ^a	2 ^b	3a ^a	3b ^a	4 ^b
1	162.0	161.4	148.3	148.2	169.1
2			152.4	152.6	
3	132.6	131.1	111.5	111.8	169.1
3a			128.3	129.3	126.0
4	105.9	105.4	31.0	29.5	109.9
4a	130.3	130.3			
5	107.1	107.1	42.0	36.1	151.1
6	153.2	153.2			151.1
6a			49.4	53.5	
7	148.6	133.9	34.1	37.8	109.9
7a			129.7	129.1	126.0
8	105.6	143.0	122.6	122.2	
8a	120.0	132.5			
9			113.7	113.8	
10			145.3	145.5	
11			148.2	148.5	
11a			123.3	123.4	
11b			124.8	124.4	
11c			124.9	125.1	
1-OCH ₃			60.7	60.8	
2-OCH ₃			56.0	56.0	
6-OCH ₃	56.2	56.1			
7-OCH ₂ CH ₃	65.0				
7-OCH ₂ CH ₃	14.8				
11-OCH ₃			60.4	60.4	
N-CH ₃	37.2	37.3			24.0
N-CHO			162.1	161.9	

^a Recorded in CDCl₃ at 100 MHz. Values in ppm (δ).^b Recorded in CDCl₃ at 125 MHz.

see Table 3; ¹³C-NMR spectroscopic data, see Table 4; ESI-MS: *m/z* = 216 [M + Na]⁺; HR-ESI-MS: *m/z* = 216.0272 [M + Na]⁺ (calcd for C₉H₇NO₄Na, 216.0273).

4.4. Biological assay

The activity of the isolated compounds on neutrophil pro-inflammatory response was evaluated by monitoring the inhibition of O₂·[−] generation and elastase release in fMLP/CB-activated neutrophils by a concentration-dependent manner.

4.4.1. Preparation of human neutrophils

Preparation of human neutrophils was carried out in accord with methods discussed in the literatures (Boyum, 1968; Jauregui et al., 1981).

4.4.2. Measurement of superoxide anion generation

The assay for measurement of O₂·[−] generation was based on the SOD-inhibitable reduction of ferricytochrome c (Babior et al., 1973; Hwang et al., 2006).

4.4.3. Measurement of elastase release

Degranulation of azurophilic granules was determined by measuring elastase release as reported previously (Hwang et al., 2006).

4.4.4. Determination of NO production

Nitrite concentration was determined by measuring the absorbance at 540 nm using an ELISA plate reader (μ Quant) (Johansson et al., 2002).

4.4.5. Cell viability assay

A MTT colorimetric assay was used to determine cell viability. The assay was modified from that of Mosmann (1983).

4.4.6. Statistical analysis

Results are expressed as the mean ± SEM, and comparisons were made using Tukey's HSD test. A probability of 0.05 or less was considered significant. The software SigmaPlot was used for the statistical analysis.

Declaration of competing interest

The authors declare no conflict of interest.

Acknowledgments

This research was supported by grants from the Ministry of Science and Technology (MOST), Taiwan (No. MOST 106-2320-B-010-033-MY3 and MOST 105-2320-B-010-040), awarded to Prof. J.-J. Chen.

References

- Ayyad, S.N., 2002. A new cytotoxic stigmastane steroid from *Pistia stratiotes*. *Pharmazie* 57, 212–214.
- Babior, B.M., Kipnes, R.S., Curnutte, J.T., 1973. Biological defense mechanisms. The production by leukocytes of superoxide, a potential bactericidal agent. *J. Clin. Invest.* 52, 741–744.
- Borregaard, N., 1998. The human neutrophil. Function and dysfunction. *Eur. J. Haematol.* 41, 401–413.
- Boyum, A., 1968. Isolation of mononuclear cells and granulocytes from human blood. Isolation of mononuclear cells by one centrifugation, and of granulocytes by combining centrifugation and sedimentation at 1 g. *Scand. J. Clin. Lab. Invest.* 97, 77–89.
- Chang, M.H., Wang, G.J., Kuoc, Y.H., Lee, C.K., 2000. The low polar constituents from *Bidens pilosa* L. var. *minor* (Biome) Sherff. *J. Chin. Chem. Soc.* 47, 1131–1136.
- Chen, C.Y., Chang, F.R., Wu, Y.C., 1997b. The constituents from the stems of *Annona cherimola*. *J. Chin. Chem. Soc.* 44, 313–319.
- Chen, C.Y., Wang, Y.D., Wang, H.M., 2010. Chemical constituents from the roots of *Synsepalum dulcificum*. *Chem. Nat. Compd.* 46, 448–449.
- Chen, I.S., Chen, J.J., Duh, C.Y., Tsai, I.L., Chang, C.T., 1997a. New aporphine alkaloids and cytotoxic constituents of *Hernandia nymphaeifolia*. *Planta Med.* 63, 154–157.
- Chen, I.S., Chen, J.J., Tsai, I.L., 1996a. *N*-Formyl- and *N*-hydroxyaporphine alkaloids from Formosan *Hernandia nymphaeifolia*. *Heterocycles* 43, 799–807.
- Chen, J.J., Chang, Y.L., Teng, C.M., Chen, I.S., 2000. Anti-platelet aggregation alkaloids and lignans from *Hernandia nymphaeifolia*. *Planta Med.* 66, 251–256.
- Chen, J.J., Chang, Y.L., Teng, C.M., Chen, I.S., 2001. Vasorelaxing and antioxidant constituents from *Hernandia nymphaeifolia*. *Planta Med.* 67, 593–598.
- Chen, J.J., Tsai, I.L., Chen, I.S., 1996b. New oxoaporphine alkaloids from *Hernandia nymphaeifolia*. *J. Nat. Prod.* 59, 156–158.
- Cui, J.G., Fan, L., Huang, L.L., Liu, H.L., Zhou, A.M., 2009. Synthesis and evaluation of some steroidal oximes as cytotoxic agents: structure/activity studies (I). *Steroids* 74, 62–72.
- Ennis, M., 2003. Neutrophils in asthma pathophysiology. *Curr. Allergy Asthma Rep.* 3, 159–165.
- Furukawa, H., Ueda, F., Ito, M., Ishii, H., Hagiwara, J., 1972. Alkaloids of *Hernandia ovigera*. IV. Constituents of *Hernandia ovigera* collected in the bonin islands. *Yakugaku Zasshi* 92, 150–154.
- Guinaudeau, H., Leboeuf, M., Cavé, A., 1988. Aporphinoid alkaloids, IV. *J. Nat. Prod.* 51, 389–474.
- Guinaudeau, H., Leboeuf, M., Cavé, A., 1994. Aporphinoid alkaloids, V. *J. Nat. Prod.* 57, 1033–1135.
- Hwang, T.L., Leu, Y.L., Kao, S.H., Tang, M.C., Chang, H.L., 2006. Viscolin, a new chalcone from *Viscum coloratum*, inhibits human neutrophil superoxide anion and elastase release via a cAMP-dependent pathway. *Free Radic. Biol. Med.* 41, 1433–1441.
- Ito, C., Matsui, T., Wu, T.S., Furukawa, H., 1992. Isolation of 6,7-demethylenedesoxypodophyllotoxin from *Hernandia ovigera*. *Chem. Pharm. Bull.* 40, 1318–1321.
- Jauregui, H.O., Hayner, N.T., Driscoll, J.L., Williams-Holland, R., Lipsky, M.H., Galletti, P.M., 1981. Trypan blue dye uptake and lactate dehydrogenase in adult rat hepatocytes-freshly isolated cells, cell suspensions, and primary monolayer cultures. *In Vitro* 17, 1100–1110.
- Johansson, M., Köpcke, B., Anke, H., Sterner, O., 2002. Biologically active secondary metabolites from the ascomycete A111-95. 2. Structure elucidation. *J. Antibiot.* 55, 104–106.
- Kan, W.S., 1970. Manual of Medicinal Plants in Taiwan, vol. 1. National Research Institute of Chinese Medicine, Taiwan, pp. 178–179.
- Kojima, H., Sato, N., Hatan, A., Ogura, H., 1990. Sterol glucosides from *Prunella vulgaris*. *Phytochemistry* 29, 2351–2355.
- Krane, B.D., Shamma, M., 1982. The isoquinoline alkaloids. *J. Nat. Prod.* 45, 377–384.
- Mosmann, T., 1983. Rapid colorimetric assay for cellular growth and survival: application to proliferation and cytotoxicity assays. *J. Immunol. Methods* 65, 55–63.
- Pachaly, P., Adnan, A.Z., Will, G., 1992. NMR-Assignments of *N*-acylaporphine alkaloids from *Tinospora crispa*. *Planta Med.* 58, 184–187.
- Pettit, G.R., Meng, Y., Gearing, R.P., Herald, D.L., Pettit, R.K., Dennis, L., Doubek, D.L., Jean-Charles Chapuis, J.-C., Tackett, L.P., 2004. Antineoplastic agents. 522. *Hernandia peltata* (Malaysia) and *Hernandia nymphaeifolia* (Republic of Maldives). *J. Nat. Prod.* 67, 214–220.
- Roos, D., van Bruggen, R., Meischl, C., 2003. Oxidative killing of microbes by neutrophils. *Microb. Infect.* 5, 1307–1315.
- Sun, X.B., Zhao, P.H., Xu, Y.J., Sun, L.M., Cao, M.A., Yuan, C.S., 2007. Chemical constituents from the roots of *Polygonum bistorta*. *Chem. Nat. Compd.* 43, 563–566.
- Tanoguchi, M., Arimoto, M., Saika, H., Yamaguchi, H., 1987. Studies on the constituents of the seeds of *Hernandia ovigera* L. VI. Isolation and structural determination of three lignans. *Chem. Pharm. Bull.* 35, 4162–4168.
- Wang, S.J., Cheng, S.H., 1968. Alkaloids of *Illigeria luzonensis* (Presl) Merr. *Yakugaku Zasshi* 88, 1148–1150.
- Wei, C.Y., Wang, S.W., Ye, J.W., Hwang, T.L., Cheng, M.J., Sung, P.J., Chang, T.H., Chen, J.J., 2018. New anti-inflammatory aporphine and lignan derivatives from the root wood of *Hernandia nymphaeifolia*. *Molecules* 23, 2286.
- Witko-Sarsat, V., Rieu, P., Descamps-Latscha, B., Lesavre, P., Halbwachs-Mecarelli, L., 2000. Neutrophils: molecules, functions and pathophysiological aspects. *Lab. Invest.* 80, 617–653.
- Yang, Y.P., Lu, S.Y., 1996. Hernandiaceae. In: second ed. Flora of Taiwan, vol. 2. Editorial Committee of the Flora of Taiwan, Taipei, Taiwan, pp. 500–503.
- Yamaguchi, H., Arimoto, M., Tanoguchi, M., Ishida, T., Inoue, M., 1982. Studies on the constituents of the seeds of *Hernandia ovigera* L. III. Structures of two new lignans. *Chem. Pharm. Bull.* 30, 3212–3218.
- Zhang, X., Yea, W., Zhao, S., Che, C.T., 2004. Isoquinoline and isoindole alkaloids from *Menispermum dauricum*. *Phytochemistry* 65, 929–932.

Article

¹H NMR-Based Isolation of Anti-Inflammatory 9,11-Secosteroids from the Octocoral *Sinularia leptoclados*

Yu-Chia Chang ¹, Kuei-Hung Lai ¹, Sunil Kumar ², Po-Jen Chen ³, Yi-Hsuan Wu ¹, Ching-Long Lai ^{1,4}, Hsi-Lung Hsieh ^{1,4,5,*}, Ping-Jyun Sung ^{6,7,8,*} and Tsong-Long Hwang ^{1,2,9,10,11,*}

¹ Research Center for Chinese Herbal Medicine, Graduate Institute of Healthy Industry Technology, College of Human Ecology, Chang Gung University of Science and Technology, Taoyuan 333324, Taiwan; jay0404@gmail.com (Y.-C.C.); mos19880822@gmail.com (K.-H.L.); yhwu03@mail.cgust.edu.tw (Y.-H.W.); dinolai@mail.cgust.edu.tw (C.-L.L.)

² Chinese Herbal Medicine Research Team, Healthy Aging Research Center, Chang Gung University, Taoyuan 333323, Taiwan; suniliftm1982@gmail.com

³ Department of Cosmetic Science, Providence University, Taichung 433303, Taiwan; litlep@hotmail.com

⁴ Department of Nursing, Division of Basic Medical Sciences, Chang Gung University of Science and Technology, Taoyuan 333324, Taiwan

⁵ Department of Neurology, Chang Gung Memorial Hospital, Taoyuan 333423, Taiwan

⁶ National Museum of Marine Biology and Aquarium, Pingtung 944401, Taiwan

⁷ Graduate Institute of Marine Biology, National Dong Hwa University, Pingtung 944401, Taiwan

⁸ Chinese Medicine Research and Development Center, China Medical University Hospital, Taichung 404394, Taiwan

⁹ Graduate Institute of Natural Products, College of Medicine, Chang Gung University, Taoyuan 333323, Taiwan

¹⁰ Department of Anaesthesiology, Chang Gung Memorial Hospital, Taoyuan 333423, Taiwan

¹¹ Department of Chemical Engineering, Ming Chi University of Technology, New Taipei City 243303, Taiwan

* Correspondence: hlhsieh@mail.cgust.edu.tw (H.-L.H.); pjsung@nmmba.gov.tw (P.-J.S.); htl@mail.cgu.edu.tw (T.-L.H.); Tel.: +886-3-211-8999 (ext. 5421) (H.-L.H.); +886-8-882-5037 (P.-J.S.); +886-3-211-8800 (T.-L.H.); Fax: +886-8-882-5087 (P.-J.S.); +886-3-211-8506 (T.-L.H.)

Received: 2 May 2020; Accepted: 19 May 2020; Published: 21 May 2020



Abstract: Octocoral *Sinularia leptoclados* has been identified as a source of bioactive 9,11-secosteroids. This study adopted a targeted isolation approach to the discovery and analysis of five 9,11-secosteroids, including two novel compounds named sinleptosterols A (**1**) and B (**2**) as well as five known analogues (8 α H-3 β ,11-dihydroxy-24-methylene-9,11-secocholest-5-en-9-one (**3**), 8 β H-3 β ,11-dihydroxy-24-methylene-9,11-secocholest-5-en-9-one (**4**), leptosterol A (**5**), (24S)-3 β ,11-dihydroxy-24-methyl-9,11-secocholest-5-en-9-one (**6**), and 3 β ,11-dihydroxy-9,11-secogorgost-5-en-9-one (**7**)) in terms of ¹H-NMR patterns and potency against neutrophilic inflammation. The structure of secosteroids **1** and **2** was deduced from general spectroscopic analysis and an examination of NMR spectra. Among the above-mentioned isolates, compound **4** had the most pronounced effect in inhibiting elastase release and superoxide anion generation, with the IC₅₀ values of 2.96 and 1.63 μ M, respectively.

Keywords: *Sinularia leptoclados*; secosteroids; antineutrophilic inflammation; elastase; superoxide anion

1. Introduction

Inflammation is one aspect of the regular host reaction to injury or infection caused by toxic chemicals, dead cells, pathogens, irritants, or allergens. The important role of neutrophils in a variety of infectious and inflammatory diseases makes them an attractive target for therapeutic interventions [1]. Numerous herbs and plant-derived compounds have been found to alleviate inflammation [2]; however, very few sources have been identified in marine environments.

Soft corals are reported to produce a variety of secondary metabolites with diverse pharmacological activities. Most of the metabolites from soft corals are sesquiterpenes, diterpenes, and steroids [3]. The octocoral *Sinularia leptoclados* belongs to the order Alcyonacea, which has been shown to produce a remarkable diversity of steroids in large quantities [4–6]. The 9,11-secosteroids found in marine invertebrates such as sponges, corals, ascidian, and mollusk can be structurally characterized by the C-9/11 oxidative cleavage of the C-ring [7,8]. The potent inhibitory effects of 9,11-secosteroids toward neutrophilic inflammation [9–11] motivated the current study of chemical compositions with this structural feature.

In this study, an ethyl acetate (EtOAc) extract of *S. leptoclados* displayed notable anti-inflammatory activity (superoxide anion generation: IC₅₀ 3.97 µg/mL) following the isolated targeting of 9,11-secosteroids based on ¹H-NMR and bioassay information. Column chromatography revealed two novel 9,11-secosteroids (sinleptosterols A (1) and B (2)) in addition to five known metabolites 3–7 (Figure 1). Most of the 9,11-secosteroids isolated in this study displayed notable inhibitory effects on *N*-formyl-methionyl-leucyl-phenylalanine/cytochalasin B (fMLP/CB)-induced superoxide anion generation and elastase release.

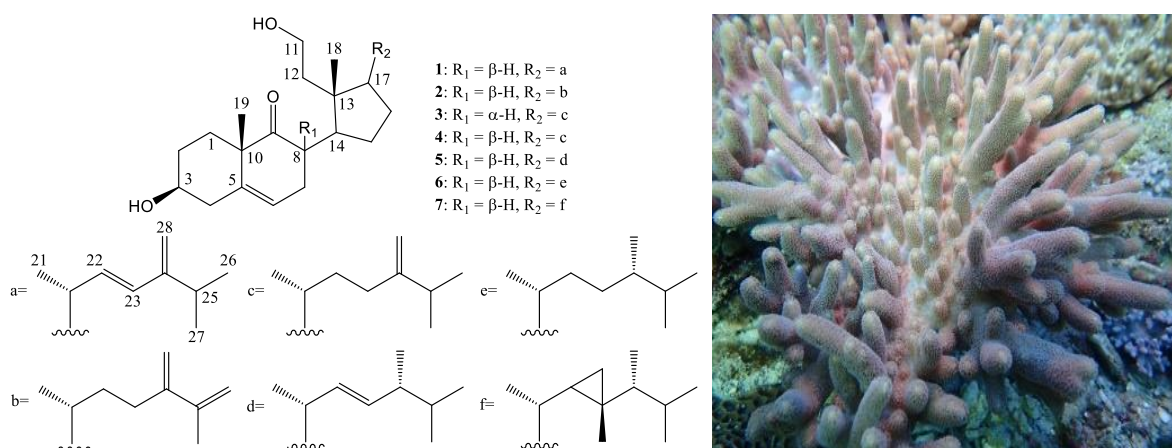


Figure 1. The structures of 9,11-secosteroids sinleptosterols A (1) and B (2), 8αH-3β,11-dihydroxy-24-methylene-9,11-secocholest-5-en-9-one (3), 8βH-3β,11-dihydroxy-24-methylene-9,11-secocholest-5-en-9-one (4), leptosterol A (5), (24S)-3β,11-dihydroxy-24-methyl-9,11-secocholest-5-en-9-one (6), and 3β,11-dihydroxy-9,11-secogorgost-5-en-9-one (7), and a picture of *S. leptoclados*.

2. Results and Discussion

2.1. ¹H NMR-Based Isolation of Anti-Inflammatory 9,11-Secosteroids

Primary silica gel chromatographic fractionation was used to probe anti-inflammatory 9,11-secosteroids within the organic extract from *S. leptoclados*. Comprehensive chemical and biological profiles of all fractions (fractions A–V) were then constructed through ¹H-NMR analysis and an examination of anti-inflammatory activity (Figure 2). Fraction P was selected for subsequent analysis due to its characteristic 9,11-secosteroidal ¹H-NMR patterns (δ_H 3.51, 1H, m, H-3; 3.03, 1H, ddd, *J* = 12.4, 12.8, 6.8, H-8; 3.86, 1H, m; 3.74, 1H, m, H₂-11) and potent anti-inflammatory activities (superoxide anion generation: IC₅₀ 3.57 µg/mL; elastase release: IC₅₀ 6.80 µg/mL). Consecutive column chromatographic

processes (reverse phase) resulted in the isolation of two novel 9,11-secosteroids, (sinleptosterols A (1) and B (2)) as well as 8 α H-3 β ,11-dihydroxy-24-methylene-9,11-secocholest-5-en-9-one (3) [12], 8 β H-3 β ,11-dihydroxy-24-methylene-9,11-secocholest-5-en-9-one (4) [12], leptosterol A (5) [5], (24S)-3 β ,11-dihydroxy-24-methyl-9,11-secocholest-5-en-9-one (6) [5], and 3 β ,11-dihydroxy-9,11-secogorgost-5-en-9-one (7) [12] (Figure 1).

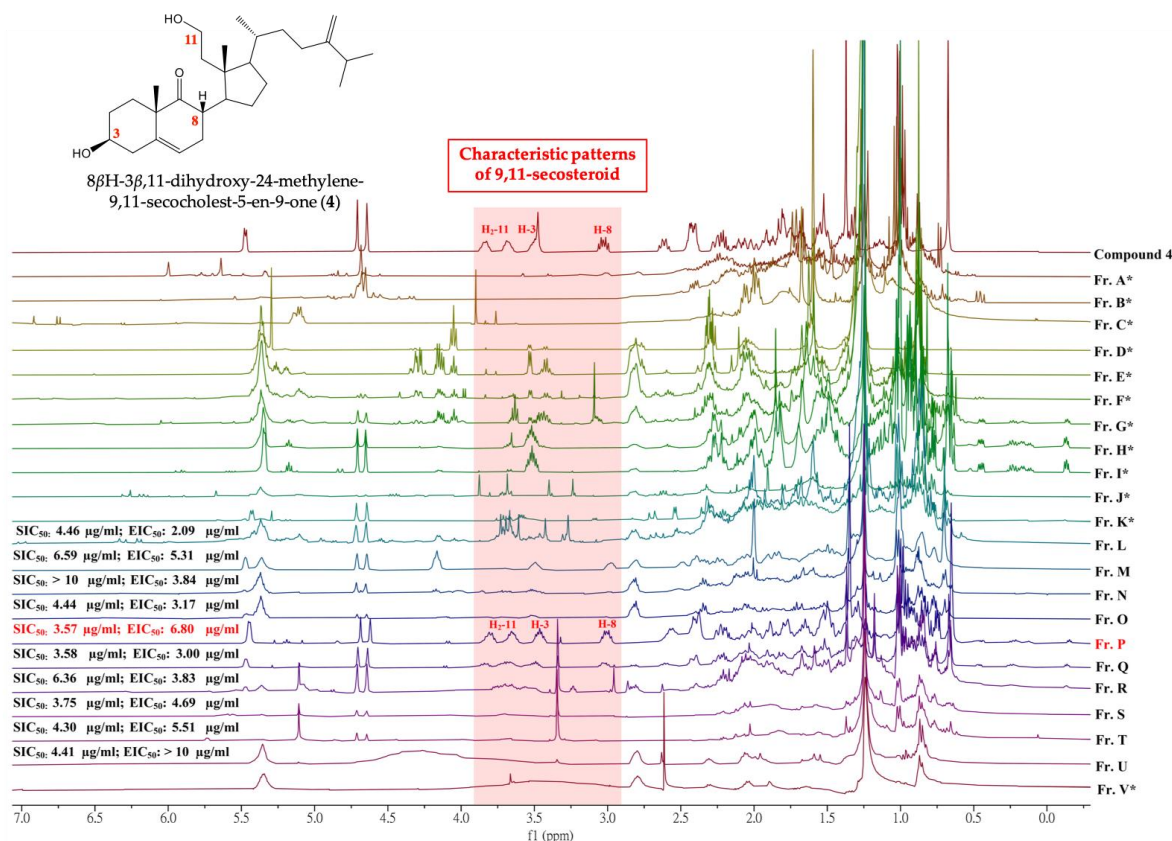


Figure 2. ^1H -NMR spectra of fractions derived from the EtOAc extract of octocoral *S. leptoclados* extract as well as their corresponding inhibitory effects on superoxide anion generation (SIC_{50}) and elastase release (EIC_{50}) in *N*-Formylmethionyl-leucyl-phenylalanine (fMLF)/cytochalasin B (CB)-induced human neutrophils. * Both SIC_{50} and EIC_{50} are over 10 $\mu\text{g/mL}$.

2.2. Chemical Identification of 9,11-Secosterols

Compound 1 was obtained as a colorless oil. Positive mode high resolution electrospray ionization mass spectrum ((+)-HRESIMS) of 1 revealed a sodiated adduct ion peak at m/z 451.31811, which established the molecular formula $\text{C}_{28}\text{H}_{44}\text{O}_3$ (calcd. for $\text{C}_{28}\text{H}_{44}\text{O}_3 + \text{Na}$, 451.31827), indicating seven degrees of unsaturation. IR absorption observed at 3369, 2958, and 1708 cm^{-1} suggested the presence of hydroxy, alkene, and ketonic groups (see Supplementary Materials Figure S2). The ^{13}C and distortionless enhancement by polarization transfer (DEPT) spectroscopic data revealed 28 carbon signals in this compound, (Table 1), including five methyls, eight sp^3 methylenes (including an oxymethylene), one sp^2 methylene, six sp^3 methines (including one oxymethine), two sp^3 quaternary carbons, three sp^2 methines, and three sp^2 quaternary carbons (including two olefin carbons and one ketonic carbonyl) (see Supplementary Materials Figure S5). It was found that the quaternary carbon signal at δ_{C} 217.5 (C-9) and the proton shifts at δ_{H} 1.40 (s, H₃-19), 3.03 (ddd, $J = 12.4, 12.4, 6.8$ Hz, H-8), 3.51 (m, H-3), and 5.47 (d, $J = 5.6$ Hz, H-6) were similar to those of 3-hydroxy-9,11-seco-9-oxosterols (with a 5,6-double bond). A disubstituted alkene was recognized within the carbon signals at δ_{C} 134.6 (CH-22) and 130.2 (CH-23), and was further confirmed by two olefin proton signals at δ_{H} 5.65 (1H, dd, $J = 16.0, 7.2$ Hz, H-22) and 5.93 (1H, d, $J = 16.0$ Hz, H-23) (Table 1). Three methyl doublets at δ_{H} 1.08

(3H, $J = 6.4$ Hz), 1.06 (3H, $J = 6.8$ Hz), and 1.07 (3H, $J = 6.8$ Hz) can respectively be attributed to the Me-21, Me-26, and Me-27 methyl groups. Two sharp methyl singlets for H₃-18 and H₃-19 respectively appeared at δ_{H} 0.69 (3H, s) and 1.40 (3H, s). Taken together, these findings identify compound **1** as a tricyclic compound.

¹H NMR coupling information within the correlation spectroscopy (COSY) data of **1** enabled identification of separate spin systems for H₂-1/H₂-2/H-3/H₂-4, H₂-11/H₂-12, H-6/H₂-7/H-8/H-14/H₂-15/H₂-16/H-17/H-20/H-22/H-23, H-20/H₃-21, and H-25/H₃-26/H₃-27 (Table 1), which were experimentally assembled with the assistance of a heteronuclear multiple bond correlation (HMBC). Key HMBC between protons and quaternary carbons of **1**, such as H-4, H₂-7, H₃-19/C-5; H-8, H-14, H₃-19/C-9; H-6, H₃-19/C-10; H₂-12, H₃-18/C-13 and H-22, H-23, H-25, H₃-26, H₃-27, H₂-28/C-24, permitted elucidation of the carbon skeleton of **1** (Table 1).

Table 1. ¹H (400 MHz, CDCl₃) and ¹³C (100 MHz, CDCl₃) NMR data and COSY and HMBC for **1**.

Position	δ_{H} (J in Hz)	δ_{C} , Type	COSY	HMBC
1a/b	1.50 m; 1.81 m	31.0, CH ₂	H ₂ -2	C-3
2a/b	1.40 m; 1.93 m	30.8, CH ₂	H ₂ -1, H-3	n. o. ^a
3	3.51 m	71.4, CH	H ₂ -2, H ₂ -4	n. o.
4a/b	2.23 m; 2.44 m	40.6, CH ₂	H-3	C-3, C-5, C-6
5	-	140.4, C	-	-
6	5.47 brd (5.6)	121.5, CH	H ₂ -7	C-4, C-7, C-8, C-10
7a/b	1.98 m; 2.40 m	33.1, CH ₂	H-6, H-8	C-5, C-6
8	3.03 ddd (12.4, 12.4, 6.8)	43.8, CH	H ₂ -7, H-14	C-7, C-9, C-14
9	-	217.5, C	-	-
10	-	48.4, C	-	-
11a/b	3.86 m; 3.74m	59.4, CH ₂	H ₂ -12	n. o.
12	1.33 m; 1.67 m	40.2, CH ₂	H ₂ -11	C-11, C-13
13	-	45.5, C	-	-
14	2.61 m	42.1, CH	H-8, H ₂ -15	C-9
15	1.31 m; 1.58 m	24.6, CH ₂	H-14, H ₂ -16	C-14
16	1.31 m; 1.71 m	24.8, CH ₂	H ₂ -15, H-17	n. o.
17	1.78 m	49.6, CH	H ₂ -16, H-20	n. o.
18	0.69 s	17.7, CH ₃	-	C-12, C-13, C-14, C-17
19	1.40 s	22.8, CH ₃	-	C-1, C-5, C-9, C-10
20	2.25 m	38.5, CH	H-17, H ₃ -21, H-22	C-16
21	1.08 d (6.4)	22.1, CH ₃	H-20	C-17, C-20
22	5.65 dd (16.0, 7.2)	134.6, CH	H-20, H-23	C-20, C-21, C-24
23	5.93 d (16.0)	130.2, CH	H-22	C-20, C-24, C-25, C-28
24	-	153.0, C	-	-
25	2.54 m	29.4, CH	H ₃ -26, H ₃ -27	C-24, C-28
26	1.06 d (6.8)	22.4, CH ₃	H-25	C-24, C-25
27	1.07 d (6.8)	21.5, CH ₃	H-25	C-24, C-25
28	4.83 d (6.8)	109.8, CH ₂	-	C-24, C-25

^a n. o. = not observed.

The relative stereochemistry of **1** was explained in terms of correlations observed in a nuclear Overhauser effect spectroscopy (NOESY) experiment, and through a comparison of NMR data between **1** and known secosterol **5**. The results suggest that these two compounds possess the same 9,11-secosterol skeleton as well as the same core A-, B-, and D-rings [5]. The configurations at C-3, C-8, C-10, C-13, C-14, and C-17 in **1** were found to be identical to those of **5**. Key NOESY correlations for **1** displayed interactions between H-8/H₃-18 and H-8/H₃-19. Thus, H-8 should be located on the β -face (Figure 3). A large coupling constant ($J = 16.0$ Hz) indicated a *trans* relationship between H-22 and H-23. All these data allowed to identify compound (**1**) as depicted in Figure 1 and it was named sinleptosterol A.

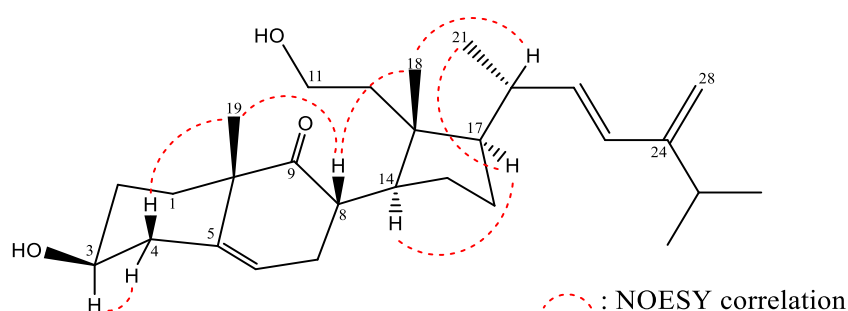


Figure 3. Selected NOESY correlations observed for **1**.

The molecular formula of compound (**2**) was the same as that of **1** ($C_{28}H_{44}O_3$), as determined by (+)-HRESIMS at m/z 451.3239 (calcd. for $C_{28}H_{44}O_3 + Na$, 451.3188), with seven degrees of unsaturation. Its IR bands revealed the presence of hydroxy (3406 cm^{-1}) and ketone (1708 cm^{-1}) groups (see Supplementary Materials Figure S11). On the basis of the above analysis and a comparison of one-dimensional and two-dimensional NMR experiments on **2** (Table 2), the core structural systems of secosterol **2** were established. It was found that the 1H and ^{13}C NMR chemical shifts of **2** (including coupling patterns and coupling constants) resembled those of **1**; however, the signals corresponding to the disubstituted alkene between C-22/23 in **1** were replaced by aliphatic methylenes in **2**, and one of the methyl groups at C-25 in **1** (Me-26) was replaced by an exocyclic carbon-carbon bond in **2**.

Table 2. 1H (400 MHz, $CDCl_3$) and ^{13}C (100 MHz, $CDCl_3$) NMR data and COSY and HMBC for **2**.

Position	δ_H (J in Hz)	δ_C , Type	COSY	HMBC
1a/b	1.53 m; 1.90 m	30.8, CH_2	H_2 -2	n. o. ^a
2a/b	1.31 m; 1.93 m	31.3, CH_2	H_2 -1, H-3	n. o.
3	3.51 m	71.4, CH	H_2 -2, H_2 -4	n. o.
4a/b	2.23 m; 2.44 m	40.6, CH_2	H-3	n. o.
5	-	140.4, C	-	-
6	5.48 brd (5.6)	121.5, CH	H_2 -7	C-4, C-7, C-8
7a/b	2.02 m; 2.39 m	33.0, CH_2	H-6, H-8	n. o.
8	3.03 td (12.4, 6.8)	43.6, CH	H_2 -7, H-14	C-7, C-9, C-14
9	-	217.5, C	-	-
10	-	48.5, C	-	-
11a/b	3.69 m; 3.83m	59.4, CH_2	H_2 -12	n. o.
12	1.32 m; 1.68 m	40.3, CH_2	H_2 -11	n. o.
13	-	45.6, C	-	-
14	2.61 m	41.8, CH	H-8, H_2 -15	n. o.
15	1.30 m; 1.56 m	24.4, CH_2	H-14, H_2 -16	n. o.
16	1.30 m; 1.74 m	25.0, CH_2	H_2 -15, H-17	-
17	1.65 m	49.2, CH	H_2 -16	-
18	0.67 s	17.3, CH_3	-	C-11, C-12, C-13, C-14, C-17
19	1.38 s	22.9, CH_3	-	C-1, C-5, C-9, C-10
20	1.41 m	34.0, CH	H_3 -21	n. o.
21	1.01 d (6.8)	19.4, CH_3	H-20	C-17, C-20, C-22
22	1.17 m; 1.51 m	34.7, CH_2	H-23	n. o.
23	1.81 m; 2.39 m	31.0, CH_2	H-22	n. o.
24	-	148.5, C	-	-
25	-	142.7, C	-	-
26	4.59 d (1.2)	112.5, CH_2	-	C-25
27	1.90 s	21.2, CH_3	-	C-24, C-25, C-26
28	5.06 s	112.0, CH_2	-	C-23, C-24, C-25

^a n. o. = not observed.

The observed HMBC correlations fully supported the locations of the functional groups. An olefinic bond was located at C-25/26 from H_2 -26, H_3 -27, H_3 -28 to C-25, respectively; therefore, sinleptosterol B (**2**) was designated as structure **2**. The relative configurations at C-3, C-8, C-10, C-13, C-14, and C-17 of **2** were found to be the same as those of **1** in the core rings A–C. Note that the stereogenic carbons were

identical to those of **1**, which were in agreement with the observed ^1H and ^{13}C NMR chemical shifts and proton coupling constants. Therefore, compound (**2**) was unambiguously identified as presented in Figure 1 and it was named sinleptosterol B.

Through a comparison of NMR spectroscopic data with those reported in the literature [5,12], the known compounds were identified as $8\alpha\text{H}-3\beta,11\text{-dihydroxy-24-methylene-9,11-secocholest-5-en-9-one}$ (**3**), $8\beta\text{H}-3\beta,11\text{-dihydroxy-24-methylene-9,11-secocholest-5-en-9-one}$ (**4**), leptosterol A (**5**), $(24S)\text{-}3\beta,11\text{-dihydroxy-24-methyl-9,11-secocholest-5-en-9-one}$ (**6**), and $3\beta,11\text{-dihydroxy-9,11-secogorgost-5-en-9-one}$ (**7**).

It is worth noting that the configurations of H-8 for compounds **3** and **4** were elucidated by comparing their ^1H NMR data [12]. A large downfielding of the H-8 as well an upfielding of C-8 were identified to resonate from $\delta_{\text{H}} 2.69/\delta_{\text{C}} 48.6$ (compound **3**) to $\delta_{\text{H}} 3.02/\delta_{\text{C}} 43.8$ (compound **4**). Moreover, the ^1H - and ^{13}C -NMR spectroscopic features for positions 7 and 11 were also found to be different between these two compounds (**3**: $\delta_{\text{H}} 2.20$ (H-7a, m) and $\delta_{\text{H}} 2.60$ (H-7b, m)/ $\delta_{\text{C}} 30.4$ (C-7), 3.72 (H-11, 2H, t, $J = 8.0$ Hz)/ $\delta_{\text{C}} 59.2$ (C-11); **4**: $\delta_{\text{H}} 1.98$ (H-7a, m) and $\delta_{\text{H}} 2.40$ (H-7b, m)/ $\delta_{\text{C}} 33.0$ (C-7), $\delta_{\text{H}} 3.83$ (H-11a, 1H, m) and $\delta_{\text{H}} 3.68$ (H-11b, 1H, m)/ $\delta_{\text{C}} 59.3$ (C-11)) (Supplementary Materials Figures S19–S22).

2.3. Anti-Inflammatory Assessment of Isolated 9,11-Secosterols

The anti-inflammatory properties of metabolites **1–7** were characterized by assessing the inhibition of superoxide anion generation and elastase release by human neutrophils in response to fMLP/CB (Table 3). Compounds **1–5** were shown to inhibit superoxide anion generation and elastase release, at concentrations ranging from 1.63 to 8.07 μM . The IC_{50} values of compounds **3** and **4** were lower than the other isolates. Secosteroid **7** presented activity at a concentration of 10 μM , indicating that the unique gorgosterol side chain nullified the anti-inflammatory activities.

Table 3. Effects of compounds **1–7** on superoxide anion generation and elastase release in fMLP/CB-induced human neutrophils.

Compound	Superoxide Anions		Elastase Release	
	IC_{50} (μM) ^a	Inh %	IC_{50} (μM)	Inh %
1	7.07 ± 0.52	64.76 ± 3.42 ***	7.57 ± 0.40	65.04 ± 2.76 ***
2	4.68 ± 0.57	76.30 ± 5.09 ***	4.29 ± 0.25	105.09 ± 5.25 ***
3	1.97 ± 0.12	90.47 ± 2.44 ***	3.12 ± 0.07	112.23 ± 5.01 ***
4	2.96 ± 0.91	91.11 ± 4.51 ***	1.63 ± 0.15	93.74 ± 1.23 ***
5	8.07 ± 0.53	57.93 ± 2.30 ***	4.73 ± 0.57	86.32 ± 2.91 ***
6	4.09 ± 0.50	60.51 ± 4.06 ***	>10	25.38 ± 6.68 **
7	>10	10.29 ± 5.42 ***	>10	18.87 ± 3.86 ***

Percentage of inhibition (Inh %) at 10 μM concentration. Results are presented as mean \pm S.E.M. ($n = 3$ or 4).

** $p < 0.01$, *** $p < 0.001$ compared with the control (DMSO). ^a Concentration necessary for 50% inhibition (IC_{50}).

N-Formyl peptide receptors (FPRs) are a family of G-protein coupled receptors involved in the switching on of leucocyte responses during inflammation. Human FPR1 is expressed primarily in neutrophils, monocytes, and macrophages. It also initiates immune reactions in response to several formyl peptide ligands derived from bacteria or mitochondria [13]. Researchers have previously proven that compounds acting as FPR1 antagonists exhibit anti-inflammatory activity in vitro and in vivo [14–16].

Flow cytometry was used to determine whether compounds **1–7** possess binding affinity to FPR1, the receptor-binding assay of N-formyl-Nle-Leu-Phe-Nle-Tyr-Lys-fluorescein (fNLFNYK), an FPR1-specific fluorescent analog, on the surface of neutrophils. The results revealed that fMLF (10 μM) entirely inhibited the binding of fNLFNYK (2 nM), whereas only compound **2** presented a low affinity toward the FPR1 receptor at a concentration of 10 μM (Figure 4).

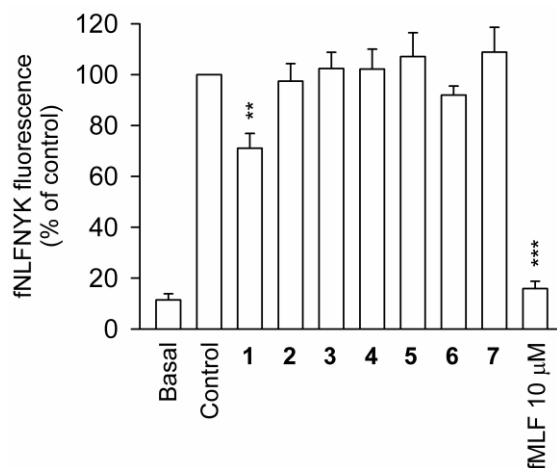


Figure 4. FPR1 receptor binding assay of compounds 1–7 in human neutrophils. Data are representative of three experiments. ** $p < 0.01$, *** $p < 0.001$ versus the control group.

3. Experimental

3.1. General Procedures

The specific rotation of compounds was measured using a Jasco P-1010 digital polarimeter (Japan Spectroscopic Corporation, Tokyo, Japan). IR spectra were acquired using a Jasco FT/IR-4100 spectrometer (Japan Spectroscopic Corporation, Tokyo, Japan). NMR spectra were recorded on a Jeol Resonance ECZ400S NMR spectrometer (at 400 and 100 MHz for ^1H and ^{13}C NMR, respectively) using the residual CHCl_3 signal (δ_{H} 7.26 ppm) as an international standard for ^1H NMR and CDCl_3 (δ_{C} 77.1 ppm) for ^{13}C NMR, respectively. ESIMS and HRESIMS were recorded using a mass spectrometer (7 Tesla Solarix FTMS system; Bruker, Bremen, Germany and Xevo G2-XS QToF; Waters Corporation, Wilmslow, UK). Silica gel (230–400 mesh, Merck, Darmstadt, Germany) was used for open-column chromatography. Reverse-phase MPLC (RP-MPLC) was performed using a system comprising a gradient controller Model 601 (FLOM, Tokyo, Japan) and two Dual Pumps Model 204 (FLOM, Tokyo, Japan). Reversed-phase HPLC (RP-HPLC) was performed using a system comprising of Nexera-i LC-2040C 3D (Shimadzu, Kyoto, Japan) with photodiode-array (PDA) detector and a Rheodyne 7725i injection port (Rheodyne LLC., Rohnert Park, CA, USA). Post-run analysis was performed using Labsolutions 5.90. A Biotage® SNAP Ultra C18 (12 g) flash cartridge (Biotage AB, Uppsala, Sweden) was used for RP-MPLC and a reverse phase column (COSMOSIL C18-AR-II, 10 × 250 mm, Nacal Tesque, Inc., Kyoto, Japan) was used for RP-HPLC.

3.2. Coral Material

In November 2018, samples of the soft coral *Sinularia leptoclados* were obtained by hand using self-contained underwater breathing apparatus (SCUBA) off the coast of Pingtung, Taiwan. The samples were stored in a freezer at $-20\text{ }^{\circ}\text{C}$ until extraction. A specimen voucher was deposited with the Research Center for Chinese Herbal Medicine, Chang Gung University of Science and Technology, Taiwan (specimen No.: CGUST-C004-2018-NOV).

3.3. Extraction and Isolation

Soft coral material (wet weight 1742 g, dry weight 488 g) was cut into small pieces prior to ethyl acetate (EtOAc) extraction at room temperature. The EtOAc layer (9.6 g; superoxide anion generation: IC_{50} 3.97 $\mu\text{g/mL}$; elastase release: $\text{IC}_{50} > 10\text{ }\mu\text{g/mL}$) was separated on silica gel and eluted using *n*-hexane/EtOAc (stepwise, pure *n*-hexane–pure EtOAc–pure MeOH) to yield 22 fractions A–V. Fraction P (superoxide anion generation: IC_{50} 3.57 $\mu\text{g/mL}$; elastase release: IC_{50} 6.80 $\mu\text{g/mL}$) was further separated by RP-MPLC using a mixture of MeOH/ddH₂O ($v:v = 90:10$ of volume ratio) at a

flow rate of 8.0 mL/min) to obtain compound 7 (82.5 mg) and nine subfractions, P1–P9. Subfraction P3 (superoxide anion generation: IC_{50} 2.06 μ g/mL; elastase release: IC_{50} 1.45 μ g/mL) was repurified by RP-HPLC using a mixture of acetonitrile/ddH₂O (volume ratio of $v:v = 90:10$ at a flow rate of 2.0 mL/min) to derive 1 (2.6 mg), 2 (2.0 mg), 3 (3.5 mg), 4 (100.4 mg) and 5 (13.3 mg). Subfraction P4 was purified by RP-HPLC using a mixture of MeOH/ddH₂O (volume ratio of $v:v = 90:10$ at a flow rate of 2.0 mL/min) to yield compound 6 (6.8 mg).

Sinleposterol A (1): colorless oil; $[\alpha]_D^{22} -16.31$ (c 0.095, CHCl₃); IR (neat) ν_{max} 3369, 2958, 1708 cm⁻¹; ¹H (400 MHz, CDCl₃) and ¹³C (100 MHz, CDCl₃) NMR data (see Table 1); ESIMS: m/z 451 [M + Na]⁺; HRESIMS: m/z 451.31811 (calcd. for C₂₈H₄₄O₃ + Na, 451.31827).

Sinleposterol B (2): colorless oil; $[\alpha]_D^{24} -36$ (c 0.1, CHCl₃); IR (neat) ν_{max} 3406, 2954, 1708 cm⁻¹; ¹H (400 MHz, CDCl₃) and ¹³C (100 MHz, CDCl₃) NMR data (see Table 2); ESIMS: m/z 451 [M + Na]⁺; HRESIMS: m/z 451.3239 (calcd. for C₂₈H₄₄O₃ + Na, 451.3188).

3.4. In Vitro Anti-Inflammatory Bioassay

3.4.1. Human Neutrophil Superoxide Anion Generation and Elastase Release

Blood samples were collected from healthy adult donors (20–32 years) via venipuncture in accordance with the standard protocol approved by the local institutional review board. Human neutrophils were isolated from peripheral blood through dextran sedimentation, centrifugation in a Ficoll–Hypaque gradient, and hypotonic lysis of red blood cells. In accordance with the above mentioned protocol, assays were performed to measure superoxide anion generation based on the superoxide dismutase-inhibitable reduction of ferricytochrome C. Note that methoxy-succinyl-alanyl-alanyl-prolyl-valine-*p*-nitroanilide (MeO-Suc-Ala-Ala-Pro-Val-*p*-nitroanilide) was used as the enzyme substrate for the detection of elastase release [17,18].

3.4.2. Receptor Binding Assay

Receptor binding assays were performed via FACScan analysis of fNLFNYK binding, a fluorescent analog of fMLF, as described in [16]. Neutrophils, differentiated THP-1, or FPR1-expressed HEK-293 were preincubated with test compounds at 4 °C for 5 min and then labelled with fNLFNYK for 30 min. Cells were immediately analyzed via flow cytometry.

3.4.3. Statistical Analysis

All experiments were conducted at least three times and the results are presented as the mean \pm SEM. Statistical analysis was performed using the Student's *t*-test, and a *p* value < 0.05 was considered statistically significant. Sigma Plot software (version 8.0, Systat Software, San Jose, CA, USA) was used for all statistical analysis [17].

4. Conclusions

Marine 9,11-secosteroid was first isolated from the gorgonian *Pseudopterogorgia americana* in 1972 [19]. Research since that time has revealed a variety of compounds in this group from a variety of invertebrates, including sponges, gorgonians, octocorals, ascidian, mollusk, and sea hare [7,20,21]. In recent years, 9,11-secosteroids have attracted considerable attention for their anti-inflammatory and antihepafibrosis properties [9,11,22–25]. This study strategically isolated two novel metabolites, sinleptosterols A and B, and five known compounds from the soft coral *Sinularia leptoclados*. The effectiveness of compounds 1–7 in inhibiting fMLP/CB-induced neutrophilic inflammation was also assessed. Compound 3 and 4 presented the most potent anti-inflammatory activities in terms of superoxide anion production and elastase emancipation. Cell free binding assays also demonstrated that the anti-inflammatory properties of these 9,11-secosteroids did not follow the pathway of conventional FPR1 antagonists.

Supplementary Materials: The following are available online at <http://www.mdpi.com/1660-3397/18/5/271/s1>. HRESIMS, IR, 1D (^1H NMR, ^{13}C NMR, and DEPT spectra), and 2D (COSY, HSQC, HMBC, and NOESY) NMR spectra of new compounds **1** and **2**. ^1H NMR and ^{13}C NMR spectra of compounds **3** and **4**.

Author Contributions: Conceptualization, Y.-C.C., P.-J.S. and T.-L.H.; Formal analysis, Y.-C.C., P.-J.C. and Y.-H.W.; Funding acquisition, C.-L.L., H.-L.H. and T.-L.H.; Investigation, Y.-C.C.; Project administration, T.-L.H.; Resources, C.-L.L. and H.-L.H.; Supervision, H.-L.H. and T.-L.H.; Validation, P.-J.C. and Y.-H.W.; Writing—original draft, Y.-C.C.; Writing—review & editing, K.-H.L., S.K. and P.-J.S. All authors have read and agreed to the published version of the manuscript.

Funding: This work was supported by grants from the Chang Gung Medical Research Foundation (BMRP450, CMRPG6J0141~3, CMRPF1G0241~3, CMRPF1H0051~53; CMRPF1I0041~2 and CMRPF1J0051~3), the Chang Gung University of Science and Technology (ZRRPF3H0101, ZRRPF3H0111, ZRRPF3H0131, and ZRRPF3J0081), Ministry of Education (EMRPD1K0421, EMRPD1K0481, EMRPD1I0441 and EMRPD1I0501), and the Ministry of Science and Technology (MOST 106-2320-B-255-003-MY3, 108-2320-B-255-003-MY3, 107-2320-B-182A-004-MY2, MOST107-2320-B-255-003; MOST108-2320-B-255-002-MY3 and 106-2320-B-291-001-MY3), Taiwan.

Conflicts of Interest: The authors declare no conflict of interest.

References

- Németh, T.; Sperandio, M.; Mócsai, A. Neutrophils as emerging therapeutic targets. *Nat. Rev. Drug Discov.* **2020**, *19*, 253–275. [[CrossRef](#)] [[PubMed](#)]
- Lin, S.C.; Shi, L.S.; Ye, Y.L. Advanced molecular knowledge of therapeutic drugs and natural products focusing on inflammatory cytokines in asthma. *Cells* **2019**, *8*, 685. [[CrossRef](#)] [[PubMed](#)]
- Sarma, N.S.; Krishna, M.S.; Pasha, S.G.; Rao, T.S.P.; Venkateswarlu, Y.; Parameswaran, P.S. Marine metabolites: The sterols of soft coral. *Chem. Rev.* **2009**, *109*, 2803–2828. [[CrossRef](#)] [[PubMed](#)]
- Su, J.H.; Tseng, Y.J.; Huang, H.H.; Ahmed, A.F.; Lu, C.K.; Wu, Y.C.; Sheu, J.H. 9,11-Secosterols from the soft corals *Sinularia lochmodes* and *Sinularia leptoclados*. *J. Nat. Prod.* **2006**, *69*, 850–852. [[CrossRef](#)]
- Cheng, S.Y.; Chen, H.P.; Wang, S.K.; Duh, C.Y. Three new 9,11-secosterols from the Formosan soft coral *Sinularia leptoclados*. *Bull. Chem. Soc. Jpn.* **2011**, *84*, 648–652. [[CrossRef](#)]
- Ngoc, N.T.; Hanh, T.T.H.; Thanh, N.V.; Thao, D.T.; Cuong, N.X.; Nam, N.H.; Thung, D.C.; Kiem, P.V.; Minh, C.V. Cytotoxic steroids from the Vietnamese soft coral *Sinularia leptoclados*. *Chem. Pharm. Bull.* **2017**, *65*, 593–597. [[CrossRef](#)]
- Sica, D.; Musumeci, D. Secosteroids of marine origin. *Steroids* **2004**, *69*, 743–756. [[CrossRef](#)]
- Tsai, C.R.; Huang, C.Y.; Chen, B.W.; Tsai, Y.Y.; Shih, S.P.; Hwang, T.L.; Dai, C.F.; Wang, S.Y.; Sheu, J.H. New bioactive steroids from the soft coral *Klyxum flaccidum*. *RSC Adv.* **2015**, *5*, 12546–12554. [[CrossRef](#)]
- Chang, Y.C.; Hwang, T.L.; Sheu, J.H.; Wu, Y.C.; Sung, P.J. New Anti-Inflammatory 9,11-Secosterols with a rare tricyclo[5,2,1,1]decane ring from a formosan gorgonian *Pinnigorgia* sp. *Mar. Drugs* **2016**, *14*, 218. [[CrossRef](#)]
- Chen, W.T.; Liu, H.L.; Yao, L.G.; Guo, Y.W. 9,11-Secosteroids and polyhydroxylated steroids from two South China Sea soft corals *Sarcophyton trocheliophorum* and *Sinularia flexibilis*. *Steroids* **2014**, *92*, 56–61. [[CrossRef](#)]
- Chang, Y.C.; Hwang, T.L.; Kuo, L.M.; Sung, P.J. Pinnisterols D–J, New 11-acetoxy-9,11-secosterols with a 1,4-quinone moiety from Formosan gorgonian coral *Pinnigorgia* sp. (Gorgoniidae). *Mar. Drugs* **2017**, *15*, 11. [[CrossRef](#)] [[PubMed](#)]
- Bonini, C.; Cooper, C.B.; Kazlauskas, R.; Wells, R.J.; Djerassi, C. Minor and trace sterols in marine invertebrates. 41. Structure and stereochemistry of naturally occurring 9,11-seco sterols. *J. Org. Chem.* **1983**, *48*, 2108–2111. [[CrossRef](#)]
- Tsai, Y.F.; Yang, S.C.; Hwang, T.L. Formyl peptide receptor modulators: A patent review and potential applications for inflammatory diseases (2012–2015). *Expert Opin. Ther. Pat.* **2016**, *26*, 1139–1156. [[CrossRef](#)] [[PubMed](#)]
- Schepetkin, I.A.; Kirpotina, L.N.; Khlebnikov, A.I.; Cheng, N.; Ye, R.D.; Quinn, M.T. Antagonism of human formyl peptide receptor 1 (FPR1) by chromones and related isoflavones. *Biochem. Pharmacol.* **2014**, *92*, 627–641. [[CrossRef](#)]
- Kirpotina, L.N.; Schepetkin, I.A.; Khlebnikov, A.I.; Ruban, O.I.; Ge, Y.; Ye, R.D.; Kominsky, D.J.; Quinn, M.T. 4-Aroyl-3-hydroxy-5-phenyl-1H-pyrrol-2(5H)-ones as N-formyl peptide receptor 1 (FPR1) antagonists. *Biochem. Pharmacol.* **2017**, *142*, 120–132. [[CrossRef](#)]






16. Yang, S.C.; Chang, S.H.; Hsieh, P.W.; Huang, Y.T.; Ho, C.M.; Tsai, Y.F.; Hwang, T.L. Dipeptide HCH6-1 inhibits neutrophil activation and protects against acute lung injury by blocking FPR1. *Free Radic. Biol. Med.* **2017**, *106*, 254–269. [[CrossRef](#)]
17. Yang, S.C.; Chung, P.J.; Ho, C.M.; Kuo, C.Y.; Hung, M.F.; Huang, Y.T.; Chang, W.Y.; Chang, Y.W.; Chan, K.H.; Hwang, T.L. Propofol inhibits superoxide production, elastase release, and chemotaxis in formyl peptide-activated human neutrophils by blocking formyl peptide receptor 1. *J. Immunol.* **2013**, *190*, 6511. [[CrossRef](#)]
18. Yu, H.P.; Hsieh, P.W.; Chang, Y.J.; Chung, P.J.; Kuo, L.M.; Hwang, T.L. 2-(2-Fluorobenzamido)-benzoate ethyl ester (EFB-1) inhibits superoxide production by human neutrophils and attenuates hemorrhagic shock-induced organ dysfunction in rats. *Free Radic. Biol. Med.* **2011**, *50*, 1737–1748. [[CrossRef](#)]
19. Enwall, E.L.; van der Helm, D.; Hsu, I.N.; Pattabhiraman, T.; Schmitz, F.J.; Spraggins, R.L.; Weinheimer, A.J. Crystal structure and absolute configuration of two cyclopropane containing marine steroids. *J. Chem. Soc. Chem. Commun.* **1972**, 215–216. [[CrossRef](#)]
20. Van Wyk, A.W.W.; Gray, C.A.; Whibley, C.E.; Osoniyi, O.; Hendricks, D.T.; Caira, M.R.; Davies-Coleman, M.T. Bioactive metabolites from the South African marine mollusk *Trimusculus costatus*. *J. Nat. Prod.* **2008**, *71*, 420–425. [[CrossRef](#)]
21. Kawamura, A.; Kita, M.; Kigoshi, H. Aplysiasecosterol A: A 9,11-Secosteroid with an unprecedented tricyclic γ -diketone structure from the sea hare *Aplysia kurodai*. *Angew. Chem. Int. Ed.* **2015**, *54*, 7073–7076. [[CrossRef](#)] [[PubMed](#)]
22. Chang, Y.C.; Kuo, L.M.; Su, J.H.; Hwang, T.L.; Kuo, Y.H.; Lin, C.S.; Wu, Y.C.; Sheu, J.H.; Sung, P.J. Pinnigorgiols A–C, 9,11-secosterols with a rare ring arrangement from a gorgonian coral *Pinnigorgia* sp. *Tetrahedron* **2016**, *72*, 999–1004. [[CrossRef](#)]
23. Chang, Y.C.; Kuo, L.M.; Hwang, T.L.; Yeh, J.; Wen, Z.H.; Fang, L.S.; Wu, Y.C.; Lin, C.S.; Sheu, J.H.; Sung, P.J. Pinnisterols A–C, New 9,11-secosterols from a gorgonian *Pinnigorgia* sp. *Mar. Drugs* **2016**, *14*, 12. [[CrossRef](#)] [[PubMed](#)]
24. Chang, Y.C.; Hwang, T.L.; Chao, C.H.; Sung, P.J. New marine sterols from a gorgonian *Pinnigorgia* sp. *Molecules* **2017**, *22*, 393. [[CrossRef](#)] [[PubMed](#)]
25. Kuo, L.M.; Chen, P.J.; Sung, P.J.; Chang, Y.C.; Ho, C.T.; Wu, Y.H.; Hwang, T.L. The bioactive extract of *Pinnigorgia* sp. induces apoptosis of hepatic stellate cells via ROS-ERK/JNK-caspase-3 signaling. *Mar. Drugs* **2018**, *16*, 19. [[CrossRef](#)]



© 2020 by the authors. Licensee MDPI, Basel, Switzerland. This article is an open access article distributed under the terms and conditions of the Creative Commons Attribution (CC BY) license (<http://creativecommons.org/licenses/by/4.0/>).

Article

Clerodane Diterpenoids from *Callicarpa hypoleucophylla* and Their Anti-Inflammatory Activity

Yu-Chi Lin ¹ , Jue-Jun Lin ¹, Shu-Rong Chen ¹ , Tsong-Long Hwang ^{2,3,4} , Shu-Yen Fang ², Michal Korinek ^{2,3} , Ching-Yeu Chen ⁵, Yun-Sheng Lin ⁶, Tung-Ying Wu ^{6,7}, Ming-Hong Yen ⁸, Chih-Hsin Wang ^{9,*} and Yuan-Bin Cheng ^{1,10,11,*} 

¹ Graduate Institute of Natural Products, Center for Natural Product Research and Development, College of Pharmacy, Kaohsiung Medical University, Kaohsiung 80708, Taiwan; m8952612@hotmail.com (Y.-C.L.); conk4wu0g3@gmail.com (J.-J.L.); highshorter@hotmail.com (S.-R.C.)

² Graduate Institute of Natural Products, Graduate Institute of Biomedical Sciences, College of Medicine, Chang Gung University, Taoyuan 33302, Taiwan; htl@mail.cgu.edu.tw (T.-L.H.); susan850903@gmail.com (S.-Y.F.); mickorinek@hotmail.com (M.K.)

³ Research Center for Industry of Human Ecology, Research Center for Chinese Herbal Medicine, and Graduate Institute of Health Industry Technology, College of Human Ecology, Chang Gung University of Science and Technology, Taoyuan 33302, Taiwan

⁴ Department of Anesthesiology, Chang Gung Memorial Hospital, Taoyuan 33302, Taiwan

⁵ Department of Physical Therapy, Tzu-Hui Institute of Technology, Pingtung 92641, Taiwan; chingyeu1971@yahoo.com.tw

⁶ Department of Biological Science and Technology, Meiho University, Pingtung 912009, Taiwan; x00010106@meiho.edu.tw (Y.-S.L.); kuma0401@gmail.com (T.-Y.W.)

⁷ Department of Food Science and Nutrition, Meiho University, Pingtung 912009, Taiwan

⁸ School of Pharmacy, College of Pharmacy, Kaohsiung Medical University, Kaohsiung 80708, Taiwan; yen@kmu.edu.tw

⁹ Division of Pharmacy, Zuoying Branch of Kaohsiung Armed Forces General Hospital, Kaohsiung 81342, Taiwan

¹⁰ Department of Marine Biotechnology and Resources, National Sun Yat-sen University, Kaohsiung 80424, Taiwan

¹¹ Department of Medical Research, Kaohsiung Medical University Hospital, Kaohsiung 80708, Taiwan

* Correspondence: hsin610255@gmail.com (C.-H.W.); jmb@kmu.edu.tw (Y.-B.C.); Tel.: +886-0906-7288-62 (C.-H.W.); +886-7312-1101 (ext. 2197) (Y.-B.C.)

Academic Editor: Ping-Chung Kuo

Received: 23 April 2020; Accepted: 12 May 2020; Published: 13 May 2020



Abstract: Plants of the genus *Callicarpa* are known to possess several medicinal effects. The constituents of the Taiwan endemic plant *Callicarpa hypoleucophylla* have never been studied. Therefore, *C. hypoleucophylla* was selected for our phytochemical investigation. Two new clerodane-type diterpenoids, named callihypolins A (**1**) and B (**2**), along with seven known compounds were isolated from the leaves and twigs of the Lamiaceae plant *C. hypoleucophylla* and then characterized. The structures of compounds **1** and **2** were elucidated by spectroscopic data analysis, specifically, two-dimension nuclear magnetic resonance (NMR). The anti-inflammatory activity of compounds **1–9** based on the suppression of superoxide anion generation and elastase release was evaluated. Among the isolates, compounds **2–4** showed anti-inflammatory activity (9.52–32.48% inhibition at the concentration 10 μ m) by suppressing superoxide anion generation and elastase release. Our findings not only expand the description of the structural diversity of the compounds present in plants of the genus *Callicarpa* but also highlight the possibility of developing anti-inflammatory agents from *Callicarpa* endemic species.

Keywords: *Callicarpa hypoleucophylla*; clerodane diterpenoid; anti-inflammatory activity

1. Introduction

Callicarpa (family Lamiaceae) is a genus of about 190 species of herbaceous plants. The plant is geographically found throughout east and southeast Asia, Australia, Madagascar, southeast North America, and South America [1]. Folkloric usage of various parts of *Callicarpa* includes preparations used as fish poisons [2,3], insect repellents [1], and for some medical indications [3]. The phytochemical investigation of this genus has resulted in the identification of diterpenoids, phenylethanoids, phenylpropanoids, and flavonoids. These components display various biological effects, such as anti-inflammatory [4–6], anti-platelet aggregation [7], hemostatic [8], antioxidative [9,10], cytotoxic [6,11,12], and neuroprotective [13], antitubercular [14], hepatoprotective [15,16], antimicrobial [17], anti-arthritic [18], as well as analgesic properties [19]. From the above-mentioned phytochemical and biological studies, we know this genus may offer a rich supply of bioactive phytochemicals. Because the phytochemical profile of the Taiwanese endemic plant *Callicarpa hypoleucophylla* has never been analyzed, we carried out an investigation of the constituents and bioactivity of *C. hypoleucophylla*. A meticulous separation of an ethanolic extract of *C. hypoleucophylla* led to the isolation of two new clerodane-type diterpenoids that we named callihypolins A and B (1 and 2), together with seven known analogues (3–9). The anti-inflammatory evaluation of these isolates is also presented in this paper.

2. Results and Discussion

The leaves and twigs of *C. hypoleucophylla* were extracted with 95% ethanol; the yielded extracts were suspended in H₂O and extracted with ethyl acetate (EtOAc). The EtOAc-soluble part was further partitioned with hexanes/methanol (MeOH)/H₂O (4:3:1) to obtain a MeOH layer. The MeOH layer was subjected to extensive chromatography by normal- and reversed-phase HPLC, using a normal-phase silica gel open column and a Sephadex LH-20 resin column, supplying callihypolins A and B (1 and 2) as well as seven known compounds (4aR,5S,6R,8aR)-5-[2-(2,5-dihydro-5-methoxy-2-oxofuran-3-yl)ethyl]-3,4,4a,5,6,7,8,8a-octahydro-5,6,8a-trimethylnaphthalene-1-carboxylic acid (3) [20], patagonic acid (4) [21], limbatolide F (5) [22], limbatolide A (6) [23], methyl (4aR,5S,6R,8S,8aR)-3,4,4a,5,6,7,8,8a-octahydro-8-hydroxy-5,6,8a-trimethyl-5-[2-(2-oxo-2,5-dihydrofuran-3-yl)ethyl]naphthalene-1-carboxylate (7) [24], clerodermic acid (8) [25], and visclerodol acid (9) [26] (Figure 1).

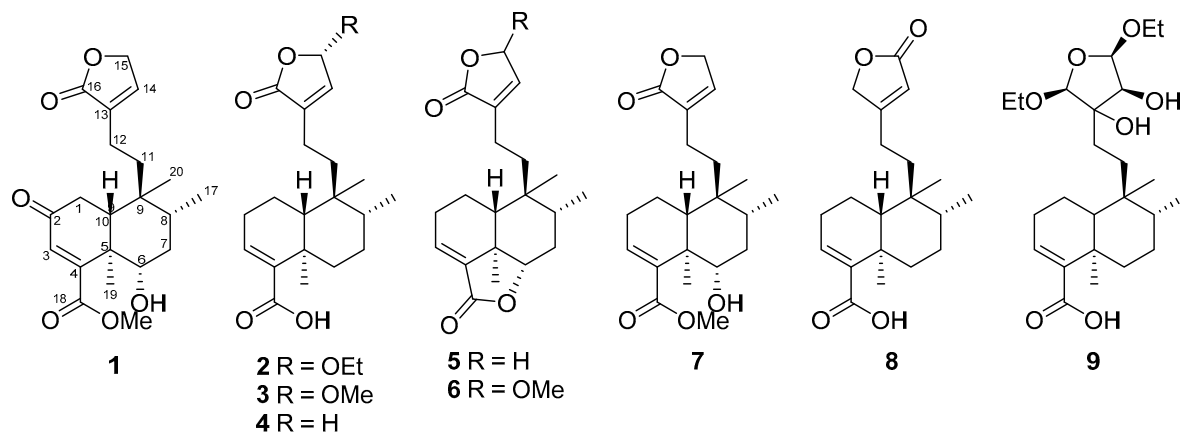


Figure 1. Structures of compounds 1–9 isolated from *Callicarpa hypoleucophylla*.

The molecular formula of compound **1** was established to be $C_{21}H_{28}O_6$ on the basis of the $[M + Na]^+$ peak at m/z 399.17785 (calcd. 399.17781 for $C_{21}H_{28}O_6Na$) obtained from high-resolution electrospray ionization mass spectrometry (HRESIMS) (Figure S13). The IR absorption bands of compound **1** indicated the presence of hydroxy (3451 cm^{-1}), α,β -unsaturated- γ -lactone (1739 cm^{-1}), and carboxyl (1678 cm^{-1}) functionalities. The ^{13}C and distortionless enhancement by polarization transfer (DEPT)-135 NMR data (Figure S2) showed the presence of 21 carbons divided into 7 quaternary carbons (including 3 carbonyls), 5 methines, 5 methylenes, and 4 methyls. The 1H (Figure S1) and ^{13}C NMR signals of compound **1** showed some characteristic peaks such as an olefinic methine singlet (δ_H 5.96, δ_C 126.6, C-3), two tertiary methyls (δ_H 1.33, δ_C 14.0, Me-19; δ_H 0.84, δ_C 17.3, Me-20), a secondary methyl (δ_H 0.90, $J = 6.8\text{ Hz}$, δ_C 15.3, Me-17), as well as a butenolide unit (δ_C 134.0, C-13; δ_H 7.09, 1 H, quin, $J = 1.7\text{ Hz}$, δ_C 143.9, C-14; δ_H 4.77, 1H, dd, $J = 3.8, 1.7\text{ Hz}$, δ_C 70.2, C-15; δ_C 174.0, C-16). The above NMR data indicated that the structure of compound **1** was similar to that of dichrocephnoid E [27], a clerodane diterpenoid, except for a methylene corresponding to C-6 that was replaced by an oxymethine (δ_H 3.84, δ_C 72.5) and an additional methoxy (δ_H 3.81, δ_C 52.8) present in compound **1**. The whole structure of compound **1** was then determined, starting from characteristic signals, by means of correlation spectroscopy (COSY), heteronuclear single quantum correlation (HSQC), and heteronuclear multiple bond correlation (HMBC) NMR correlations (Figures S3–S5). The COSY spectrum (Figure 2) showed cross-peaks with signals at H-1 (δ_H 2.43, 2.56)/H-10 (δ_H 2.00); H-6 (δ_H 3.84)/H-7 (δ_H 1.61, 1.70)/H-8 (δ_H 1.76)/Me-17 (δ_H 0.90); H-14 (δ_H 7.09)/H-15 (δ_H 4.77). Moreover, the key HMBC correlations (Figure 2) of H-1 with C-2, H-3 with C-1, C-4, C-5, and C-18; Me-19 with C-4, C-5, C-6, and C-10, Me-17 with C-7, C-8, and C-9, Me-20 with C-9, C-10, and C-11, and methoxy proton with C-18 led to the construction of the decalin core of compound **1**, including a hydroxy group at C-6 and a methyl ester substituted at C-4. The linkage between C-12 and butenolide via C-13 was established by comparing the corresponding NMR data with those of similar analogues and confirmed by mass spectrometry analysis [22,24,27]. The planar structure of compound **1** is represented in Figure 2. The relative stereochemistry of compound **1** was deduced from nuclear overhauser effect spectroscopy (NOESY) correlations (Figure 2 and Figure S6) and by comparison of its spectroscopic data with those of clerodane analogues. The NOESY experiment showed correlations of H-6 (δ_H 3.84)/H-10 (δ_H 2.00)/H-8 (δ_H 1.76), which indicated protons located on the β face of the molecule. On the other hand, Me-20 presented NOESY correlations with Me-19 and Me-17, but neither Me-19 nor Me-20 correlated with H-10, suggesting that compound **1** is an *ent*-clerodane-type molecule with *trans*-decalin core [28]. The *trans* A/B ring junction was also evidenced by the carbon chemical shifts of C-19 (δ_C 14.0) and C-20 (δ_C 17.3) [29–31]. Thus, these correlations indicated that the hydroxy group at C-6 had an α -configuration, as confirmed by the coupling constants of H-6 with H-7 α ($J = 12.6\text{ Hz}$) and H-7 β ($J = 4.4\text{ Hz}$) [32,33]. All the spectral data appeared thus to be in agreement with the structure and stereochemistry of compound **1**.

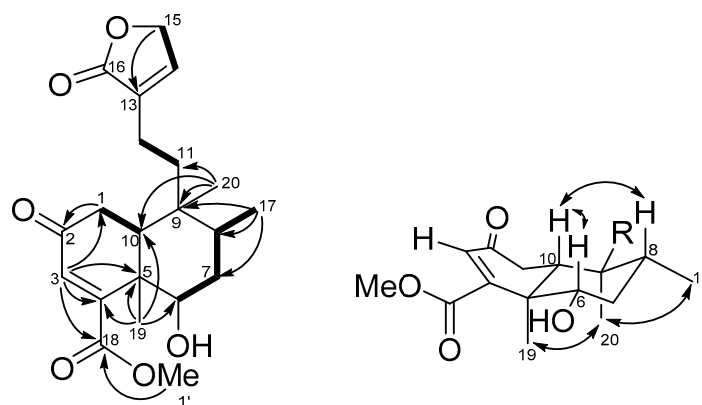


Figure 2. COSY (bold bond), selected HMBC (arrow), and NOESY (left-right arrow) correlations of compound **1**.

Callihypolin B (**2**) was isolated as a yellow oil. It possesses the molecular formula $C_{22}H_{32}O_5$, corresponding to seven indices of hydrogen deficiency, as determined by the HRESIMS ion at m/z 399.21419 $[M + Na]^+$ (calcd. 399.21420) (Figure S14) and ^{13}C NMR data. The IR spectrum revealed the presence of ester (1768 cm^{-1}) and conjugated carbonyl (1682 cm^{-1}) groups. The 1H NMR data of compound **2** (Table 1, Figure S7) demonstrated the presence of one ethoxy [δ_H 3.94 (m) and 3.74 (m); 1.27 (t, $J = 7.1\text{ Hz}$)], one secondary methyl [δ_H 0.81 (d, $J = 6.2\text{ Hz}$)], two tertiary methyls (δ_H 0.76 and 1.23), and two olefinic methines [δ_H 6.85 (m), and 6.76 (d, $J = 1.2$)], together with one hemiacetal methine [δ_H 5.79 (brd, $J = 1.2$)]. The ^{13}C NMR and DEPT spectra (Table 1, Figure S8) of compound **2** showed the presence of 22 carbon signals ascribable to 4 methyls, 7 methylenes (of which one was oxygenated), 2 olefinic methines, 3 aliphatic methines, 2 aliphatic quaternary carbons, 2 olefinic quaternary carbons, and 2 carbonyl carbons. Two carbonyls and two $C=C$ double bonds accounted for four indices of hydrogen deficiency, so the remaining three indices suggested that compound **2** was a tricyclic compound. In the 1H - 1H COSY spectrum (Figure S9), the correlations of H_2 -1/ H_2 -2/ H_2 -3, H_2 -6/ H_2 -7/ H -8/Me-17, H_2 -11/ H_2 -12, H -14/ H -15, and H_2 -1'/Me-2' were used to establish the presence of five fragments, as shown in Figure 3. In the HMBC spectrum (Figure 3, Figure S11), the cross-peaks of H-3 with C-4 and C-18; of Me-19 with C-4, C-5, C-6, and C-10; and of H-10 with C-1 and C-5 revealed the presence of a cyclohexene ring (ring A), in which a carboxyl group and Me-19 were attached to C-4 and C-5, respectively. The presence of a cyclohexane ring (ring B) with Me-20 attached at C-9 was elucidated by the HMBC correlations of Me-20 to C-8, C-9, and C-10, as well as of H-10 to C-9. Additionally, both H_3 -20 and H-10 showed correlations with C-11 and indicated the linkage between ring B and C-11 via C-9. The HMBC cross-peaks of H-14 to C-13 (δ_C 139.0) and C-16 (δ_C 171.5); H-15 (δ_H 5.79) to C-16 and C-1' (δ_C 66.0), as well as H_2 -12 to C-13 and C-16, revealed the presence of an α,β -unsaturated γ -lactone ring with an ethoxy group located at C-15. Thus, the planar structure of compound **2** could be established. The stereochemistry of compound **2** was determined by its NOESY spectrum, relative NMR data, and circular dichroism spectrum. The NOESY experiments (Figure 3 and Figure S12) carried out on compound **2** showed correlations of Me-19/Me-20/Me-17, and H-6 β (δ_H 2.44)/H-10/H-8, whereas no correlation was revealed between H-10 and Me-19. These data, as well as the carbon chemical shift of Me-19 at δ_C 20.5 [29], indicated that compound **1** is characterized by a type TC clerodane skeleton under a chair conformation of ring B [34], a *trans* relationship between rings A and B, α -orientations of Me-17, Me-19, and Me-20, and β -orientation of H-10. The ethoxy group attached at C-15 in the butenolide moiety was assigned to the α -face by comparison with the circular dichroism (CD) data of known butenolides and by applying the octant rule. The CD spectrum showed a negative Cotton effect near 243 nm (π - π^*) and supported the *S* configuration of C-15 [31,35,36]. Thus, the structure and stereochemistry of compound **2** were clearly determined.

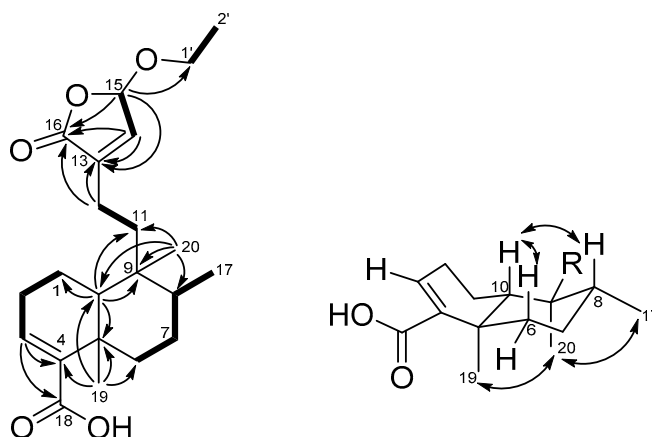


Figure 3. COSY (bold bond), selected HMBC (arrow), and NOESY (left-right arrow) correlations of compound **2**.

Table 1. ^1H and ^{13}C NMR Data of compounds **1** and **2** in CDCl_3 .

Position	1 ^a		2 ^b	
	δ_{H} Mult. (J in Hz)	δ_{C} , Type	δ_{H} Mult. (J in Hz)	δ_{C} , Type
1	2.56 (dd, 18.0, 14.2) 2.43 (dd, 18.0, 3.5)	34.4, CH_2	1.46 (m) 1.66 (m)	17.3, CH_2
2		199.0, C	2.27 (m)	27.4, CH_2
3	5.96 (s)	126.6, CH	6.85 (m)	140.3, CH
4		160.4, C		141.2, C
5		45.5, C		37.5, C
6	3.84 (dd, 12.6, 4.4)	72.5, CH	2.44 (m) 1.14 (m)	35.7, CH_2
7	1.70 (dt, 12.6, 4.4) 1.61 (m)	36.1, CH_2	1.46 (m) 1.42 (m)	27.2, CH_2
8	1.76 (m)	34.5, CH	1.50 (m)	36.2, CH
9		38.5, C		38.7, C
10	2.00 (dd, 14.2, 3.5)	44.9, CH	1.32 (d, 11.6)	46.6, CH
11	1.61 (m) 1.47 (m)	34.8, CH_2	1.50 (m) 1.66 (m)	35.7, CH_2
12	2.19 (m) 2.00 (tm, 13.0)	18.7, CH_2	2.20 (m) 2.03 (m)	18.9, CH_2
13		134.0, C		139.0, C
14	7.09 (quin, 1.7)	143.9, CH	6.76 (quin, 1.2)	141.4, CH
15	4.77 (dd, 3.9, 1.7)	70.2, CH_2	5.79 (brd, 1.2)	101.6, CH
16		174.0, C		171.5, C
17	0.90 (d, 6.8)	15.3, CH_3	0.81 (d, 6.2)	15.9, CH_3
18		169.8, C		172.3, C
19	1.33 (s)	14.0, CH_3	1.23 (s)	20.5, CH_3
20	0.84 (s)	17.3, CH_3	0.76 (s)	18.2, CH_3
1'	3.81 (s)	52.8, CH_3	3.94 (m) 3.74 (m)	66.0, CH_2
2'			1.27 (t, 7.1)	15.0, CH_3

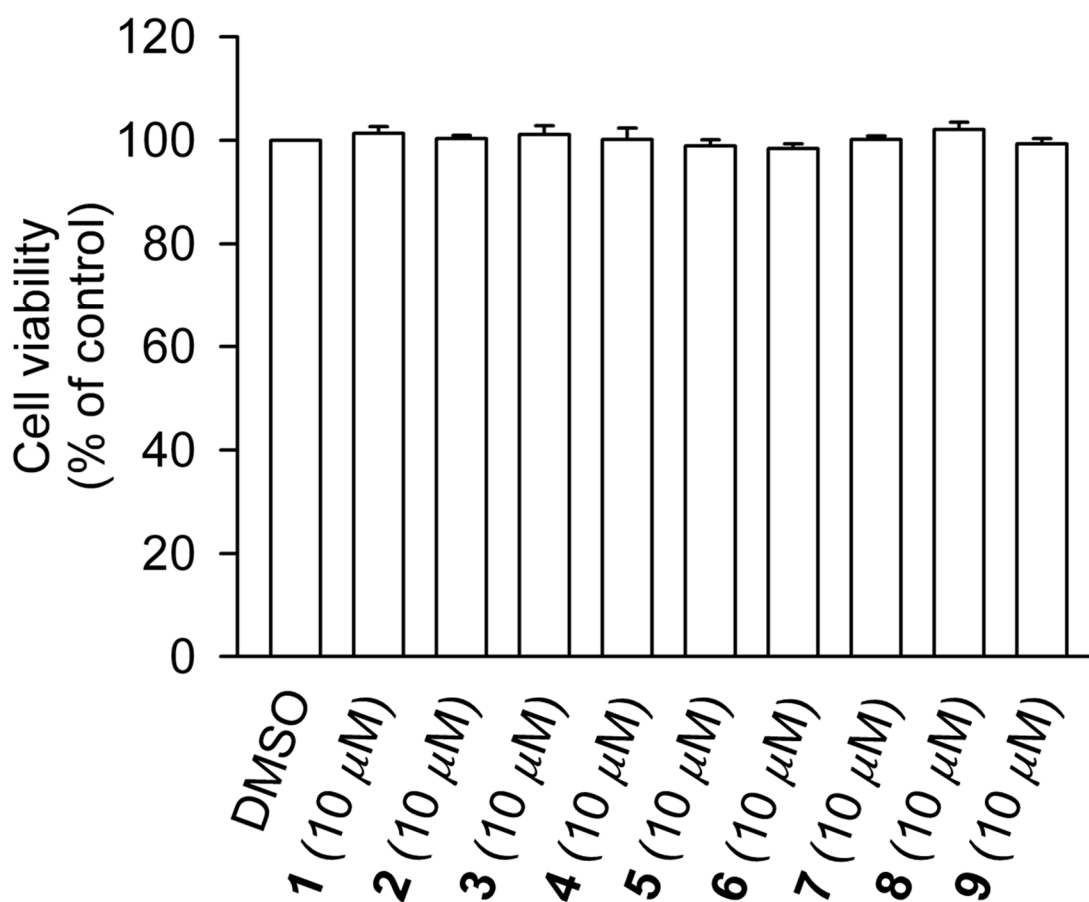
^a ^1H and ^{13}C -NMR were measured at 600 and 150 MHz. ^b ^1H and ^{13}C -NMR were measured at 400 and 100 MHz.

Compounds **1–9** were evaluated for their inhibitory activities on superoxide anion generation and elastase release in formyl-methionyl-leucyl-phenylalanine (fMLF)/cytochalasin (CB)-induced human neutrophils. The formyl peptide fMLF in combination with the priming agent CB serves as a stimulator that mimics the over-activation of neutrophils by a pathogen or an immune system reaction [37]. As shown in Table 2, compounds **2–4** exerted anti-inflammatory activity by suppressing superoxide anion generation and elastase release. The positive control genistein, which acts via inhibition of protein tyrosine kinases, showed a profound effect on the respiratory burst (89% inhibition of superoxide generation) and only a mild effect on degranulation (22.8% inhibition of elastase release). Among the tested samples, the new compound **2** showed the best activity, suppressing 32.2% of superoxide generation and 17.6% of elastase release. To exclude possible toxicity to the cells, the lactate dehydrogenase (LDH) release assay was employed, and none of the tested clerodane diterpenoids resulted toxic to human neutrophils (Figure 4). Clerodane diterpenes with an open lactone ring at C16 were previously reported to exert inhibitory effects on the function of neutrophils activated by fMLF/CB, including respiratory burst [38] and degranulation [39]. Thus, our results well correlate with the anti-inflammatory effects of previously isolated clerodane diterpenes and indicate the potential of the new compounds for the development of anti-inflammatory drugs targeting neutrophils.

Table 2. Inhibitory effects of compounds 1–9 on superoxide anion generation and elastase release in formyl-methionyl-leucyl-phenylalanine (fMLF)/ cytochalasin (CB)-induced human neutrophils.

Compound	Superoxide Anion Inh %		Elastase Release Inh %	
1	20.28 ± 5.98	*	8.26 ± 3.72	
2	32.19 ± 6.92	**	17.55 ± 2.64	***
3	31.19 ± 5.99	**	12.15 ± 2.38	***
4	32.88 ± 4.41	***	13.57 ± 1.48	***
5	23.65 ± 7.67	*	7.33 ± 1.56	**
6	8.44 ± 6.40		10.50 ± 3.23	*
7	7.93 ± 5.86		9.30 ± 2.91	*
8	15.23 ± 6.37		11.80 ± 3.55	*
9	18.80 ± 7.82		16.30 ± 3.74	**
Genistein ^a	89.00 ± 3.00	***	22.79 ± 2.25	***

Percentage of inhibition (Inh %) at 10 μ M concentration. Results are presented as mean \pm S.E.M. (n = 4–5); * p < 0.05, ** p < 0.01, *** p < 0.001 compared with the control (solvent). ^a Genistein served as a positive control.

**Figure 4.** Compounds 1–9 do not cause LDH release in human neutrophils. Human neutrophils were incubated with DMSO (as a control) or compounds 1–9 (10 μ M) for 15 min. Cytotoxicity was evaluated by LDH release. All data are presented as the means \pm S.E.M. (n = 3).

3. Experimental

3.1. General

Silica gel 60 (Merck) was used for open-column chromatography (CC). Luna C₁₈ (5 m, 250 \times 10 mm, Phenomenex), Luna CN (5 m, 250 \times 10 mm, Phenomenex), and Luna phenyl-hexyl (5 m, 250 \times 10 mm, Phenomenex) semi-preparative columns were used for high-performance liquid chromatography

(HPLC). HPLC used a Shimadzu LC-10AT pump with an SPD-20A UV-Vis detector. The UV spectra were obtained by using a Jasco UV-530 ultraviolet spectrophotometer (Jasco, Tokyo, Japan), whereas the IR spectra were obtained on a Jasco FT-IR-4600 spectrophotometer (Jasco, Tokyo, Japan). Optical rotations were measured with a Jasco P-1020 digital polarimeter (Jasco, Tokyo, Japan). NMR spectra were obtained using JEOL JNM ECS 400 MHz (JEOL, Tokyo, Japan) and Varian 600 MHz NMR spectrometers (Varian, Palo Alto, CA, USA). ESI-MS data were collected on a VG Biotech Quattro 5022 mass spectrometer (VG Biotech, Altrincham, UK). High-resolution ESI-MS data were obtained with a Bruker APEX II spectrometer (Bruker, Bremen, Germany). Circular dichroism spectra were recorded on a JASCO J-810 spectrophotometer (Jasco, Tokyo, Japan).

3.2. Plant Material

The plant samples of *C. hypoleucophylla* were collected in Kaohsiung city, Taiwan, in May 2018. The plant material was identified by one of the authors, Dr. Ming-Hong Yen. A voucher sample (specimen code: CH001) was deposited at the Graduate Institute of Natural Products, College of Pharmacy, Kaohsiung Medical University, Kaohsiung, Taiwan.

3.3. Extraction and Isolation

Air-dried leaves and twigs of *C. hypoleucophylla* (17.0 kg) were extracted three times with 95% ethanol at room temperature for 72 h each time. The extract was evaporated under reduced pressure to get a crude extract (3.6 kg). Next, the ethanol extract of *C. hypoleucophylla* was suspended and dissolved in H₂O and then partitioned with ethyl acetate to obtain an ethyl acetate layer (118.3 g). The ethyl acetate layer was further partitioned between hexanes and 75% MeOH to acquire hexanes and MeOH layers, respectively.

Due to the results of the cytotoxic assay, the MeOH layer (45.6 g) was selected for further isolation. At first, it was loaded on a normal-phase silica gel open column and was eluted by stepwise hexanes with ethyl acetate (1:0~0:1) followed by stepwise ethyl acetate with methanol (1:0~0:1) to obtain seven subfractions (CH1~7), according to TLC analysis. The third sub-fraction, CH3, was isolated on Sephadex LH-20 and eluted with MeOH to afford four subfractions (CH3-1~4). Then, repeated column chromatography isolation on CH3-3 yielded CH3-3-1~5 fractions. CH3-3-2 (500.3 mg) was separated by silica gel CC (dichloromethane/MeOH, 100:1→0:1) to afford more subfractions (CH3-3-2-1~6). Fr. CH3-3-2-6 was purified by normal-phase HPLC using a Phenomenex Luna-CN column (hexane/dichloromethane/methanol, 30:10:1, 1.5 mL/min) to give compounds **2** (33.1mg), **3** (7.2 mg), **4** (62.7 mg), and **5** (26.7 mg). Fr. CH3-3-2-4 was isolated by reverse-phase HPLC using a CN column and gave compounds **1** (1.9 mg) and **7** (0.7 mg). Fr. CH3-3-3 was subjected to silica gel CC (CH₂Cl₂/MeOH, 1:0→0:1) followed by NP-CN HPLC and elution with (hexane/dichloromethane/methanol, 40:10:1, 2.0 mL/min) to obtain compound **8** (9.8 mg). In addition, Fr. CH3-2 was separated by normal-phase silica gel CC with hexane/dichloromethane/methanol (100:40:1→0:0:1) to afford Frs. CH3-2-1~5. Fr. CH3-2-5 was purified by silica gel CC (CH₂Cl₂/MeOH, 1:0→0:1) followed by RP-phenyl-hexyl HPLC (methanol/H₂O, 65/35, 2.0 mL/min) to give compounds **6** (2.5 mg) and **9** (7.0 mg).

3.4. Spectroscopic Data

Callihypolin A (**1**) yellow oily, $[\alpha]_D^{26} -1.0^\circ$ (c 0.05, MeOH); IR (neat) ν_{\max} 3452, 2956, 1768, 1682, 1376, 1342, 1202, 1141, 1018 cm⁻¹; ¹H-NMR and ¹³C-NMR (CDCl₃, 600/150 MHz) see Table 1; HRESIMS *m/z* 399.17785 (calcd for C₂₁H₂₈O₆Na, 399.17781).

Callihypolin B (**2**) yellow oily, $[\alpha]_D^{26} -47.6^\circ$ (c 0.05, MeOH); IR (neat) ν_{\max} 3451, 2930, 1739, 1678, 1450, 1253, 1072 cm⁻¹; ¹H-NMR and ¹³C-NMR (CDCl₃, 400/100 MHz) see Table 1; HRESIMS *m/z* 399.21419 (calcd for C₂₂H₃₂O₅Na, 399.21420).

3.5. Superoxide Anion Generation and Elastase Release Assays by Human Neutrophils

Human neutrophils were obtained from the venous blood of healthy adult volunteers (20–30 years old), following a reported procedure [37]. Superoxide anion generation by fMLF (0.1 μ M)/CB (1 μ M)-activated neutrophils was evaluated based on the reduction of ferricytochrome c, as previously described [37,40]. Elastase release by the fMLF (0.1 μ M)/CB (0.5 μ M)-activated neutrophils was determined using N-methoxysuccinyl-Ala-Ala-Pro-Val-p-nitroanilide as the elastase substrate, according to a previous protocol [37,40]. The concentration was 10 μ M for compounds 1–9. Genistein was used as a positive control.

3.6. Cytotoxicity Test

A lactate dehydrogenase (LDH) assay kit (Promega, Madison, WI, USA) was utilized to evaluate the cytotoxicity of the samples in human neutrophils. Human neutrophils were treated with DMSO or compounds 1–9 for 15 min at 37 °C. Cell-free supernatants were collected, and the amount of LDH was evaluated [37].

4. Conclusions

The first phytochemical investigation of the leaves and twigs of the Taiwanese endemic plant *Callicarpa hypoleucophylla* has resulted in the isolation of nine clerodane-type diterpenoids, compounds 1–9, including two new compounds designated callihypolins A and B (compounds 1 and 2). All isolates from *C. hypoleucophylla* possess a TC *ent*-clerodane skeleton, which is different from that of the phyllocladane and labdane diterpenoids that were identified as major components of the other well-studied species *Callicarpa macrophylla* Vahl, which is recorded in the Pharmacopoeia of the People's Republic of China. These results reflect the unique properties of *C. hypoleucophylla* from the perspective of chemotaxonomy. Moreover, the anti-inflammatory activity of the isolated compounds highlights the potential of clerodane-type diterpenoids for further pharmaceutical development.

Supplementary Materials: The NMR spectra of compounds 1 and 2 are available online.

Author Contributions: Y.-B.C., C.-Y.C. and C.-H.W. conceived and designed the experiments; Y.-C.L. and J.-J.L. carried out the plant extraction and isolation of the compounds; T.-L.H., S.-Y.F., and M.K. conducted the biological studies; M.-H.Y. collected and identified the material; C.-Y.C., Y.-S.L., and T.-Y.W. assisted with the interpretation of various data; Y.-C.L., S.-R.C., Y.-B.C. contributed to the writing of the manuscript. All authors have read and agreed to the published version of the manuscript.

Funding: This work was funded by grants from the Ministry of Science and Technology of Taiwan (MOST-107-2628-B-037-001 and MOST-108-2320-B-037-013-MY3 awarded to Prof. Yuan-Bin Cheng; MOST 106-2320-B-255-003-MY3 and MOST 108-2320-B-255-003-MY3 awarded to Prof. Tsong-Long Hwang). This work was also supported by grants from Zuoying Branch of Kaohsiung Armed Forces General Hospital (KAFGH-ZY-A-109030).

Conflicts of Interest: The authors declare no conflict of interest.

References

1. Tu, Y.; Sun, L.; Guo, M.; Chen, W. The medicinal uses of *Callicarpa*, L. in traditional Chinese medicine: An ethnopharmacological, phytochemical and pharmacological review. *J. Ethnopharmacol.* **2013**, *146*, 465–481. [[CrossRef](#)] [[PubMed](#)]
2. Kawazu, K.; Inaba, M.; Mitsui, T. Studies on fish-killing components of *Callicarpa candicans*. *Agr. Biol. Chem.* **1967**, *31*, 494–497.
3. Cantrell, C.L.; Klun, J.A.; Bryson, C.T.; Kobaisy, M.; Duke, S.O. Isolation and identification of mosquito bite deterrent terpenoids from leaves of American (*Callicarpa americana*) and Japanese (*Callicarpa japonica*) beautyberry. *J. Agric. Food Chem.* **2005**, *53*, 5948–5953. [[CrossRef](#)] [[PubMed](#)]
4. Zhang, L.; Dong, L.; Huang, J.; Liu, M.; Li, G.; Zhang, C.; Zhang, K.; Wang, J. 3,4-*seco*-Labdane diterpenoids from the leaves of *Callicarpa nudiflora* and their inhibitory effects on nitric oxide production. *Fitoterapia* **2013**, *89*, 218–223. [[CrossRef](#)]

5. Dong, L.; Zhang, L.; Zhang, X.; Liu, M.; Wang, J.; Wang, Y. Two new 3,4-*seco*-labdane diterpenoids from *Callicarpa nudiflora* and their inhibitory activities against nitric oxide production. *Phytochem. Lett.* **2014**, *10*, 127–131. [\[CrossRef\]](#)
6. Cheng, H.H.; Cheng, Y.B.; Hwang, T.L.; Kuo, Y.H.; Chen, C.H.; Shen, Y.C. Randainins A–D, based on unique diterpenoid architectures, from *Callicarpa randaiensis*. *J. Nat. Prod.* **2015**, *78*, 1823–1828. [\[CrossRef\]](#)
7. Zhou, Z.; Wei, X.; Fu, H.; Luo, Y. Chemical constituents of *Callicarpa nudiflora* and their anti-platelet aggregation activity. *Fitoterapia* **2013**, *88*, 91–95. [\[CrossRef\]](#)
8. Wu, A.Z.; Zhai, Y.J.; Zhao, Z.X.; Zhang, C.X.; Lin, C.Z.; Zhu, C.C. Phenylethanoid glycosides from the stems of *Callicarpa peii* (hemostatic drug). *Fitoterapia* **2013**, *84*, 237–241. [\[CrossRef\]](#)
9. Luo, Y.H.; Zhou, Z.Q.; Ma, S.C.; Fu, H.Z. Three new antioxidant furofuran lignans from *Callicarpa nudiflora*. *Phytochem. Lett.* **2014**, *7*, 194–197. [\[CrossRef\]](#)
10. Cai, H.; Xie, Z.; Liu, G.; Sun, X.; Peng, G.; Lin, B.; Liao, Q. Isolation, identification and activities of natural antioxidants from *Callicarpa kwangtungensis* Chun. *PLoS ONE* **2014**, *9*, e93000. [\[CrossRef\]](#)
11. Jones, W.P.; Lobo-Echeverri, T.; Mi, Q.; Chai, H.B.; Soejarto, D.D.; Cordell, G.A.; Swanson, S.M.; Kinghorn, A.D. Cytotoxic constituents from the fruiting branches of *Callicarpa Americana* collected in southern Florida. *J. Nat. Prod.* **2007**, *70*, 372–377. [\[CrossRef\]](#) [\[PubMed\]](#)
12. Mei, W.L.; Han, Z.; Cui, H.B.; Zhao, Y.X.; Deng, Y.Y.; Dai, H.F. A new cytotoxic iridoid from *Callicarpa nudiflora*. *Nat. Prod. Res.* **2010**, *24*, 899–904. [\[CrossRef\]](#) [\[PubMed\]](#)
13. Xu, J.; Sun, Y.; Wang, M.; Ren, Q.; Li, S.; Wang, H.; Sun, X.; Jin, D.Q.; Sun, H.; Ohizumi, Y.; et al. Bioactive diterpenoids from the leaves of *Callicarpa macrophylla*. *J. Nat. Prod.* **2015**, *78*, 1563–1569. [\[CrossRef\]](#) [\[PubMed\]](#)
14. Chen, J.J.; Wu, H.M.; Peng, C.F.; Chen, I.S.; Chu, S.D. *seco*-Abietane diterpenoids, a phenylethanoid derivative, and antitubercular constituents from *Callicarpa pilosissima*. *J. Nat. Prod.* **2009**, *72*, 223–228. [\[CrossRef\]](#) [\[PubMed\]](#)
15. Huang, B.; Fu, H.Z.; Chen, W.K.; Luo, Y.H.; Ma, S.C. Hepatoprotective triterpenoid saponins from *Callicarpa nudiflora*. *Chem. Pharm. Bull.* **2014**, *62*, 695–699. [\[CrossRef\]](#) [\[PubMed\]](#)
16. Luo, Y.H.; Fu, H.Z.; Huang, B.; Chen, W.K.; Ma, S.C. Hepatoprotective iridoid glucosides from *Callicarpa nudiflora*. *J. Asian. Nat. Prod. Res.* **2016**, *18*, 274–279. [\[CrossRef\]](#)
17. Chung, P.Y.; Chung, L.Y.; Navaratnam, P. Potential targets by pentacyclic triterpenoids from *Callicarpa farinosa* against methicillin-resistant and sensitive. *Staphylococcus aureus*. *Fitoterapia* **2014**, *94*, 48–54. [\[CrossRef\]](#)
18. Gupta, S.K.; Gupta, A.; Gupta, A.K.; Pakash, D.V. *In vitro* anti-arthritis activity of ethanolic extract of *Callicarpa Macrophylla* flower. *Int. Res. J. Pharm.* **2013**, *4*, 160–162. [\[CrossRef\]](#)
19. Yadav, V.; Jayalakshmi, S.; Singla, R.K.; Patra, A.; Khan, S. Assessment of anti-inflammatory and analgesic activities of *Callicarpa macrophylla* Vahl. roots extracts. *Webmed Cent. Pharmacol.* **2012**, *3*, WMC003366.
20. Ahmad, V.U.; Farooq, U.; Abbaskhan, A.; Hussain, J.; Abbasi, M.A.; Nawaz, S.A.; Choudhary, M.I. Four new diterpenoids from *Ballota limbata*. *Helv. Chim. Acta.* **2004**, *87*, 682–689. [\[CrossRef\]](#)
21. Pinto, M.E.F.; Silva, M.S.D.; Schindler, E.; Filho, J.M.B.; El-Bachá, R.D.S.; Castello-Branco, M.V.S.; Agra, M.D.F.; Tavares, J.F. 3',8"-Biisokaempferide, a cytotoxic biflavonoid and other chemical constituents of *Nanuza plicata* (Velloziaceae). *J. Braz. Chem. Soc.* **2010**, *21*, 1819–1824. [\[CrossRef\]](#)
22. Farooq, U.; Khan, A.; Ahmad, V.U.; Kousar, F.; Iqbal, S. Limbatolide F and G: Two new *trans*-clerodane diterpenoids from *Otostegia limbata*. *Pol. J. Chem.* **2005**, *79*, 1757–1762. [\[CrossRef\]](#)
23. Ahmad, V.U.; Khan, A.; Farooq, U.; Kousar, F.; Khan, S.S.; Nawaz, S.A.; Abbasi, M.A.; Choudhary, M.I. Three new cholinesterase-inhibiting *cis*-clerodane diterpenoids from *Otostegia limbata*. *Chem. Pharm. Bull.* **2005**, *53*, 378–381. [\[CrossRef\]](#) [\[PubMed\]](#)
24. Iqbal Choudhary, M.; Mohammad, M.Y.; Musharraf, S.G.; Onajobi, I.; Mohammad, A.; Anis, I.; Shah, M.R.; Atta-Ur-Rahman. Biotransformation of clerodane diterpenoids by *Rhizopus stolonifer* and antibacterial activity of resulting metabolites. *Phytochemistry* **2013**, *90*, 56–61. [\[CrossRef\]](#) [\[PubMed\]](#)
25. Raha, P.; Das, A.K.; Adityachaudhuri, N.; Majumder, P.L. Cleroinermin, *aneo*-clerodane diterpenoid from *Clerodendron inermi*. *Phytochemistry* **1991**, *30*, 3812–3814. [\[CrossRef\]](#)
26. Huang, Z.; Jiang, M.Y.; Zhou, Z.Y.; Xu, D. Two new clerodane diterpenes from *Dodonaea viscosa*. *Z. Naturforsch.* **2010**, *65b*, 83–86. [\[CrossRef\]](#)
27. Song, B.; Ding, G.; Tian, X.H.; Li, L.; Zhou, C.; Zhang, Q.B.; Wang, M.H.; Zhang, T.; Zou, Z.M. Anti-HIV-1 integrase diterpenoids from *Dichrocephala benthamii*. *Phytochem. Lett.* **2015**, *14*, 249–253. [\[CrossRef\]](#)

28. Rustaiyan, A.; Simozar, E.; Ahmadi, A.; Grenz, M.; Bohlmann, F. A hardwickiic acid derivative from *Pulicaria gnaphalodes*. *Phytochemistry* **1981**, *20*, 2772–2773. [[CrossRef](#)]
29. Heymann, H.; Tezuka, Y.; Kikuchi, T.; Supriyatna, S. Constituents of *Sindora sumatrana* M₁Q. III. new *trans*-clerodane diterpenoids from the dried pods. *Chem. Pharm. Bull.* **1994**, *42*, 1202–1207. [[CrossRef](#)]
30. García, A.; Ramírez-Apan, T.; Cogordan, J.A.; Delgado, G. Absolute configuration assignments by experimental and theoretical approaches of *ent*-labdane- and *cis-ent*-clerodane-type diterpenes isolated from *Croton glabellus*. *Can. J. Chem.* **2006**, *84*, 1593–1602. [[CrossRef](#)]
31. Chang, F.R.; Huang, S.T.; Liaw, C.C.; Yen, M.H.; Hwang, T.L.; Chen, C.Y.; Hou, M.F.; Yuan, S.S.; Cheng, Y.B.; Wu, Y.C. Diterpenes from *Grangea maderaspatana*. *Phytochemistry* **2016**, *131*, 124–129. [[CrossRef](#)] [[PubMed](#)]
32. Calderón, C.; De Ford, C.; Castro, V.; Merfort, I.; Murillo, R. Cytotoxic clerodane diterpenes from *Zuelania guidonia*. *J. Nat. Prod.* **2014**, *77*, 455–463. [[CrossRef](#)] [[PubMed](#)]
33. Oberlies, N.H.; Burgess, J.P.; Navarro, H.A.; Pinos, R.E.; Fairchild, C.R.; Peterson, R.W.; Soejarto, D.D.; Farnsworth, N.R.; Kinghorn, A.D.; Wani, M.C.; et al. Novel bioactive clerodane diterpenoids from the leaves and twigs of *Casearia sylvestris*. *J. Nat. Prod.* **2002**, *65*, 95–99. [[CrossRef](#)] [[PubMed](#)]
34. Tokoroyama, T. Synthesis of clerodane diterpenoids and related compounds—stereoselective construction of the decalin skeleton with multiple contiguous stereogenic centers. *Synthesis* **2000**, *5*, 611–633. [[CrossRef](#)]
35. Wu, T.H.; Cheng, Y.Y.; Liou, J.R.; Way, T.D.; Chen, C.J.; Chen, Y.H.; Kuo, S.C.; El-Shazly, M.; Chang, F.R.; Wu, Y.C.; et al. Clerodane diterpenes from *Polyalthia longifolia* var. *pendula* protect SK-N-MC human neuroblastoma cells from β -amyloid insult. *RSC Adv.* **2014**, *4*, 23707–23712. [[CrossRef](#)]
36. Itokawa, H.; Morita, H.; Katou, I.; Takeya, K.; Cavalheiro, A.J.; de Oliveira, R.C.; Ishige, M.; Motidome, M. Cytotoxic diterpenes from the rhizomes of *Hedychium coronarium*. *Planta Med.* **1988**, *54*, 311–315. [[CrossRef](#)]
37. Liu, F.C.; Yu, H.P.; Chen, P.J.; Yang, H.W.; Chang, S.H.; Tzeng, C.C.; Cheng, W.J.; Chen, Y.R.; Chen, Y.L.; Hwang, T.L. A novel NOX2 inhibitor attenuates human neutrophil oxidative stress and ameliorates inflammatory arthritis in mice. *Redox Biol.* **2019**, *26*, 101273. [[CrossRef](#)]
38. Chang, F.R.; Hwang, T.L.; Yang, Y.L.; Li, C.E.; Wu, C.C.; Issa, H.H.; Hsieh, W.B.; Wu, Y.C. Anti-inflammatory and cytotoxic diterpenes from formosan *Polyalthia longifolia* var. *pendula*. *Planta Med.* **2006**, *72*, 1344–1347. [[CrossRef](#)]
39. Chang, H.L.; Chang, F.R.; Chen, J.S.; Wang, H.P.; Wu, Y.H.; Wang, C.C.; Wu, Y.C.; Hwang, T.L. Inhibitory effects of 16-hydroxycleroda-3,13(14)*E*-dien-15-oic acid on superoxide anion and elastase release in human neutrophils through multiple mechanisms. *Eur. J. Pharmacol.* **2008**, *31*, 332–339. [[CrossRef](#)]
40. Yang, S.C.; Chung, P.J.; Ho, C.M.; Kuo, C.Y.; Hung, M.F.; Huang, Y.T.; Chang, W.Y.; Chang, Y.W.; Chan, K.H.; Hwang, T.L. Propofol inhibits superoxide production, elastase release, and chemotaxis in formyl peptide-activated human neutrophils by blocking formyl peptide receptor 1. *J. Immunol.* **2013**, *190*, 6511–6519. [[CrossRef](#)]

Sample Availability: Samples of the compounds are available from the authors.



© 2020 by the authors. Licensee MDPI, Basel, Switzerland. This article is an open access article distributed under the terms and conditions of the Creative Commons Attribution (CC BY) license (<http://creativecommons.org/licenses/by/4.0/>).



Development of flavanone and its derivatives as topical agents against psoriasis: The prediction of therapeutic efficiency through skin permeation evaluation and cell-based assay



Ahmed Alalaiwe^a, Chwan-Fwu Lin^{b,c,d}, Chien-Yu Hsiao^{c,e,f}, En-Li Chen^g, Chien-Yu Lin^g, Wan-Chen Lien^g, Jia-You Fang^{c,d,g,h,*}

^a Department of Pharmaceutics, College of Pharmacy, Prince Sattam Bin Abdulaziz University, Al Kharj, Saudi Arabia

^b Department of Cosmetic Science, Chang Gung University of Science and Technology, Kweishan, Taoyuan, Taiwan

^c Research Center for Food and Cosmetic Safety and Research Center for Chinese Herbal Medicine, Chang Gung University of Science and Technology, Kweishan, Taoyuan, Taiwan

^d Department of Anesthesiology, Chang Gung Memorial Hospital, Kweishan, Taoyuan, Taiwan

^e Department of Nutrition and Health Sciences, Chang Gung University of Science and Technology, Kweishan, Taoyuan, Taiwan

^f Aesthetic Medical Center, Department of Dermatology, Chang Gung Memorial Hospital, Kweishan, Taoyuan, Taiwan

^g Pharmaceutics Laboratory, Graduate Institute of Natural Products, Chang Gung University, Kweishan, Taoyuan, Taiwan

^h Chinese Herbal Medicine Research Team, Healthy Aging Research Center, Chang Gung University, Kweishan, Taoyuan, Taiwan

ARTICLE INFO

Keywords:

Skin absorption

Psoriasis

Flavanone

Naringenin

Quantitative structure-permeation relationship

Keratinocyte

ABSTRACT

Flavonoids inhibit skin inflammation. Previous study suggests that the flavonoids with flavanone backbone were beneficial to penetrate into the skin. We aimed to investigate the possibility of psoriasis treatment by topically applied flavanone and its derivatives including naringenin, hesperetin, 6-hydroxyflavanone, flavanone, and 6-bromoflavone. The skin absorption of the compounds was determined by Franz cells. Molecular modeling was used to compute the physicochemical and molecular parameters of the penetrants in order to elucidate the correlation between structure and permeation. Among the compounds tested, flavanone showed the greatest skin absorption. The in vitro skin absorption predicted efficient skin targeting of 6-bromoflavone with minimal risk of circulation absorption. The permeation of naringenin was remarkably enhanced 13-fold in the barrier-defective skin mimicking inflamed skin. The penetrants with fewer hydrogen bond number, total polarity surface, and molecular volume were advantageous for facile skin absorption. In the cell-based study, IL-1 β inhibition in imiquimod (IMQ)-stimulated keratinocytes was increased following the increase in compound lipophilicity. Naringenin, a flavanone analog with three hydroxyl moieties, could suppress IL-6 overexpression to baseline control. We assessed the anti-inflammatory potency of the chemicals in comparison with tacrolimus as reference in a psoriasis-like mouse model. Flavanone was found to mitigate scaling and epidermal hyperplasia at a higher level than naringenin. Flavanone lessened IL-6 overexpression by 80% in the psoriasiform plaque. The skin barrier function recorded by transepidermal water loss (TEWL) was recovered by naringenin but not flavanone. The experimental data indicate that naringenin and flavanone are potential candidates for anti-psoriatic therapy.

1. Introduction

The largest group of phenolics in plants is flavonoids. The flavonoid structure contains two aromatic rings linked by a bridge with three carbons. The role of this structure is to suppress proinflammatory mediators for treating inflammatory disorders (Leyva-López et al., 2016). Because of the anti-inflammatory and antioxidant effects, flavonoids show evidence of their ability to resolve problems involving

skin such as wrinkles, acne, dermatitis, and cancer (Arct and Pytkowska, 2008; Działo et al., 2016). There are six subgroups of flavonoids: flavonols, flavones, isoflavones, flavanones, flava-3-ols, and anthocyanidins. Our previous study (Chuang et al., 2017) demonstrated that aglycone flavanones were the compounds with greater skin absorption than the other subclasses. This indicates the potential development of topically applied flavanones to treat inflammatory skin. Flavanones are abundant in tomatoes, mint, and citrus fruits. It is

* Corresponding author at: Pharmaceutics Laboratory, Graduate Institute of Natural Products, Chang Gung University, 259 Wen-Hwa 1st Road, Kweishan, Taoyuan 333, Taiwan.

E-mail address: fajy@mail.cgu.edu.tw (J.-Y. Fang).

<https://doi.org/10.1016/j.ijpharm.2020.119256>

Received 17 December 2019; Received in revised form 18 March 2020; Accepted 22 March 2020

Available online 24 March 2020

0378-5173/ © 2020 Elsevier B.V. All rights reserved.

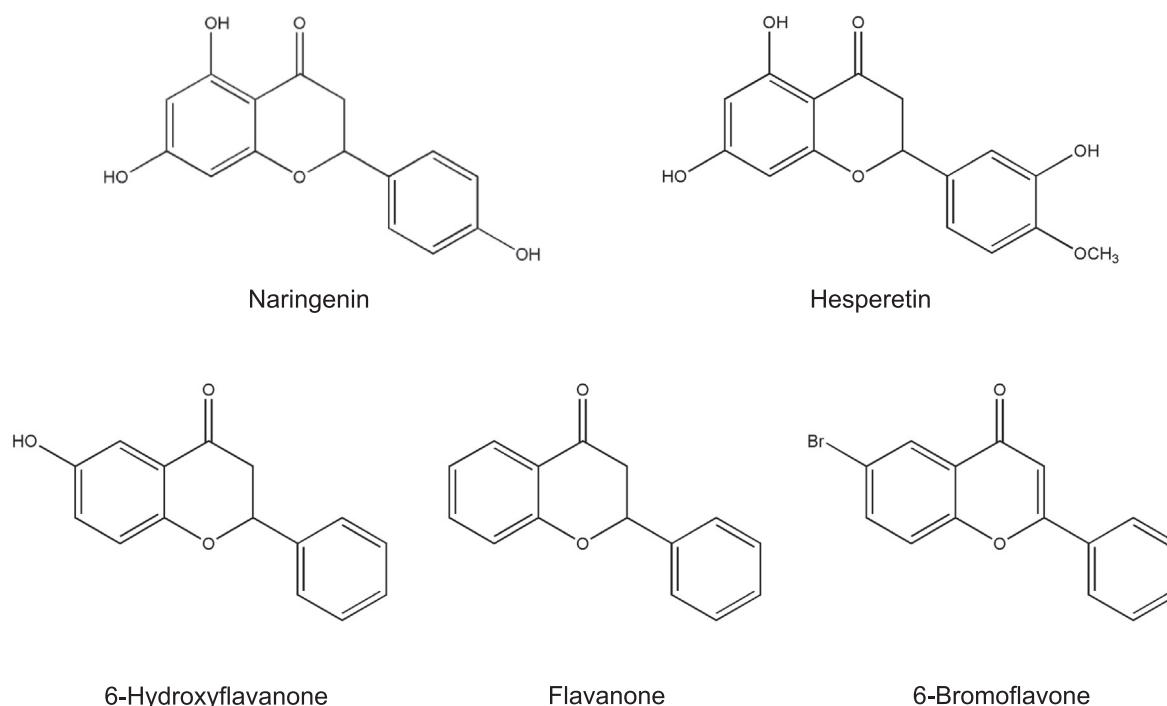


Fig. 1. The chemical structures of naringenin, hesperetin, 6-hydroxyflavanone, flavanone, and 6-bromoflavone.

reported that flavanones are effective in treating skin-related diseases such as psoriasis (Domínguez-Villegas et al., 2014; Parlapally et al., 2016), melanogenesis (Itoh et al., 2009; Santi et al., 2017), and photoaging (Shireen et al., 2017).

Psoriasis is a major autoimmune skin disorder described by abnormal keratinocyte proliferation in the epidermis and immune cell infiltration in the dermis due to innate and adaptive immune dysfunction. This inflammatory chronic disease affects 2–3% of the global population (Rendon and Schäkel, 2019). Topical therapy is the first-line management for patients with mild-to-moderate psoriasis. However, advances in topical treatment are limited due to irritation, phototoxicity, carcinogenic immunosuppression, and unsatisfied symptom relief (Kerdell and Zaiac, 2015). Finding novel candidates for topical delivery to achieve the purposes of fewer side effects and greater therapeutic efficiency is urgent. Discovering natural products for alternative psoriasis treatment is a strategy to achieve these goals. The objective of this study was to assess the potential of topically applied flavanones for treating psoriasis. The compounds tested here included: naringenin, hesperetin, 6-hydroxyflavanone, flavanone, and 6-bromoflavone (Fig. 1). Three lines of experiment were conducted. First, the in vitro skin delivery of these penetrants was determined. Second, we evaluated the anti-psoriatic activity of the compounds by cell-based assay using keratinocytes as the model cells. Finally, the therapeutic efficacy of the selected flavanones on psoriasis was examined in the imiquimod (IMQ)-stimulated psoriasiform mouse model. The skin absorption profiles of flavanone and the related derivatives were obtained via Franz diffusion assembly. It is crucial that the topically applied agents reach the specific action site with minimal distribution to circulation and non-targeted tissues. We detected the cutaneous targeting ability of the penetrants by calculating the *S* value (skin deposition/flux). Pig skin was treated to remove stratum corneum (SC), SC lipids, sebum, and protein for establishing barrier-defective skins, which were beneficial in mimicking the inflammatory skin condition for evaluating skin absorption. Flavanones reveal somewhat different physicochemical characteristics based on the different types and numbers of functional moieties. Skin delivery is largely influenced by the physicochemical properties of the penetrants (Seo et al., 2017). We explored the

relationship between chemical structure and skin delivery to understand the percutaneous mechanisms of flavanone and its analogs. The in vivo therapeutic efficiency of flavanones was checked by gross observation, histopathology, and cytokine concentration in psoriasis-like mouse skin. We found that skin penetration and cell-based study were applicable to predict the anti-psoriatic potential of flavanones.

2. Materials and methods

2.1. Materials

All flavanone analogs and IMQ used in this study were purchased from Sigma-Aldrich (St. Louis, MO, USA). The test compounds for skin permeation were used as the (±) racemic mixtures. Tacrolimus ointment (Protopic®, 0.1%) was obtained from Astellas Pharma (Tokyo, Japan). The cellulose membrane with a molecular weight (MW) cut-off of 6000–8000 g/mol was supplied by Membrane Filtration Products (Seguin, TX, USA). All ELISA kits were provided by BioLegend (San Diego, CA, USA).

2.2. HPLC setup and capacity factor ($\log K'$)

The $\log K'$ value was calculated from the retention time of the compounds in the HPLC chromatogram. The HPLC setup was an HPLC system (Hitachi) with a LiChrospher C18 column (Merck). The mobile phase was a mixture of methanol and double-distilled water adjusted by phosphoric acid to pH 2 (65:35). The flow rate and wavelength for detection were 1 ml/min and 287 nm, respectively. The validation of this method was conducted by calibration curves. The compound solution was prepared with concentrations ranging from 2 to 100 µg/ml (2, 10, 30, 50, and 100 µg/ml) from a stock solution. Each concentration was prepared with triplicate. The calibration curve was estimated after HPLC analysis of the standard solutions. The acceptance criterion for calibration was the achievement of correlation coefficient (r^2) of ≥ 0.999 . The $\log K'$ was measured as $\log [(t_r - t_0)/t_0]$, where t_r and t_0 were the retention time of the compound and solvent signal, respectively.

2.3. Partition coefficient ($\log P$)

The compounds were added into methanol to produce a concentration of 0.5 mg/ml. Methanol was evaporated by vacuum. *n*-Octanol and double-distilled water were pipetted into the test tube with compounds for 24-h shaking at 37 °C. Subsequently, the tube was centrifuged at 10,000g for 10 min. The compound concentration in both phases was quantified by HPLC. The $\log P$ was calculated as $\log(\text{concentration in } n\text{-octanol}/\text{concentration in water})$.

2.4. Saturated solubility in aqueous medium

The saturated solubility in 25% PEG400/pH 7.4 phosphate buffer was detected by loading the compounds (5 mM) and shaken at 37 °C for 24 h. The aqueous suspension was centrifuged at 10,000g for 10 min to collect the supernatant. HPLC was utilized to analyze compound solubility in supernatant.

2.5. Computational modeling

The compound structures were sketched by Discovery Studio 4.1 workstation (Accelrys) to obtain the hydrogen bond acceptor number, hydrogen bond donor number, total polarity surface, and molecular volume.

2.6. Animals

The specific-pathogen-free one-week-old pigs were purchased from the Animal Technology Institute Taiwan. Female Balb/c mice at 8 weeks were provided by the National Laboratory Animal Center (Taipei, Taiwan). The protocols for animal use were approved by the Institutional Animal Care and Use Committee of Chang Gung University.

2.7. In vitro skin absorption

The dorsal skin was excised from the pigs after sacrifice. The skin was mounted between the donor and receptor of Franz cell with SC facing the donor. Different barrier-defective skins, including SC stripping, lipid removal, sebum removal, and protein denaturation, were created by the procedures described previously (Campbell et al., 2012; Liu et al., 2016). The receptor medium (5 ml) was 30% ethanol in pH 7.4 buffer. The stirring rate and receptor temperature were maintained at 600 rpm and 37 °C, respectively. The penetrant at 5 mM or saturated solubility in 25% PEG400/pH 7.4 buffer were loaded in donor (0.5 ml). A 0.3-ml aliquot in receptor was withdrawn at the determined time after penetrant application, followed by replacement with fresh medium. The penetrant in receptor was quantified by HPLC. After 24 h, the skin was removed to determine skin deposition of the penetrant. The skin sample with an effective diffusion area (0.785 cm²) was weighed, cut, and homogenized by MagNA Lyser (Roche). The homogenate was centrifuged to collect the supernatant for HPLC quantification of the penetrant.

With respect to the data analysis of skin permeation, the penetrant amount in receptor was plotted as a function of time. The flux (nmol/cm²/h) was measured by the slope of the cumulative amount-time curve. The skin deposition was determined as the molar amount of penetrant in skin (nmol/mg). In the case of the skin penetration from saturated solution, the flux was divided by the saturated solubility of the penetrant to obtain permeability coefficient (PC, cm/h) for comparison of absorption between penetrants. The calibrated skin deposition (CSD) was estimated by the skin deposition divided by the saturated solubility. The *S* value was computed using an equation of skin deposition/flux or CSD/PC for equivalent penetrant dose or saturated solubility, respectively. The therapeutic index (TI) is an indicator of penetrant bioactivity after percutaneous absorption. TI was obtained by

multiplying skin deposition and cytokine/chemokine inhibition percentage of the compounds. The data of cytokine/chemokine inhibition percentage were achieved in the cell-based study.

2.8. Hair follicle uptake

The skin removed from Franz cell after penetrant application for 24 h was stripped by applying adhesive cellophane tape 20 times for ablating the SC layers. A drop of ethyl cyanoacrylate superglue was added onto a glass slide; the SC-stripped skin was then pressed onto the slide. After polymerization for 5 min, the slide was removed with a quick action. The superglue on the slide was scraped off and then extracted by methanol (2 ml) for 3-h shaking. After evaporation, the mobile phase was added to dilute the sample for HPLC analysis of penetrant uptake by hair follicles.

2.9. Cytotoxicity of keratinocytes

The keratinocytes (HaCaT) were cultured in DMEM supplemented with 10% fetal bovine serum and 1% penicillin-streptomycin. Flavanone and the derivatives at the concentrations of 1–1,000 μM were incubated in the cell medium with 1.25×10^5 cells/ml for 24 h. The cytotoxicity was evaluated by adding 5-mg/ml 3-(4,5-dimethylthiazol-yl)-2,5-diphenyltetrazolium bromide (MTT) into the wells at 37 °C for 4 h. The wells were read by spectrophotometer at 550 nm for estimating cell viability.

2.10. Keratinocyte activation by IMQ

The cells were activated by IMQ (10 $\mu\text{g}/\text{ml}$) to show an inflammation-like condition. Flavanone and the derivatives at 1 μM were added into the HaCaT medium (1.25×10^5 cells/ml) 1-h before IMQ stimulation. The culture supernatant for cytokine and chemokine assay was collected after 24 h.

2.11. Enzyme-linked immunosorbent assay (ELISA)

The levels of IL-1 β , IL-6, and CXCL1 in HaCaT were detected via the ELISA method. Commercial kits (BioLegend) were used according to the manufacturer's instruction.

2.12. Psoriatic plaque induction by IMQ

The anti-psoriatic effect of topical flavanones was assessed in an IMQ-induced psoriasiform lesion model. The Balb/c mouse back was exposed with IMQ cream (Aldara) at 62.5 mg each day for 6 d. The detailed process was described previously (Lin et al., 2018). The mice were divided into 5 groups with 6 animals per group: (i) Control: healthy mice without any treatment; (ii) IMQ: IMQ stimulation with topical application of vehicle (25% PEG400/pH 7.4 buffer); (iii) IMQ/tacrolimus: IMQ stimulation with topical application of Protopic (tacrolimus ointment at a dose of 0.1%) as the positive control; (iv) IMQ/naringenin: IMQ stimulation with topical application of naringenin; and (v) IMQ/flavanone: IMQ stimulation with topical application of flavanone. The skin surface was monitored by a digital magnifier (Mini Scope-V). Transdermal water loss (TEWL) was determined by Tewameter (TM300). After a 6-d application, the animals were sacrificed for further examination of cytokine expression and histopathology. Cytokine was quantified by ELISA. The extraction method of skin for ELISA was described earlier (Lin et al., 2018).

2.13. Histopathology

Skin species were sliced into a thickness of 5 μm for hematoxylin and eosin (H&E) staining. The Psoriasis Area and Severity Index (PASI) score as an objective scoring system was assigned from histological

observation on a scale of 0–4 (Jain et al., 2016). The epidermal thickness was measured based on the computation from H&E-stained histology. For immunohistochemical (IHC) staining, the skin was incubated with antibody for 1 h, and then incubated with biotinylated donkey anti-goat IgG for 20 min. All photomicrographs of histopathology were taken by Leica DMI8 microscopy.

2.14. Statistical analysis

The statistical difference in the data on different treatment groups was analyzed using the Kruskal-Wallis test. The post hoc test for checking individual differences was Dunn's test. The levels of probability including 0.05, 0.01, and 0.001 were taken as statistically significant.

3. Results

3.1. Physicochemical characterization of the penetrants

The experimental and predicted physicochemical properties of flavanone and the related analogs were determined to know the relationship with skin absorption. Table 1 summarizes the experimental physicochemical characteristics of these penetrants. The MW ranged between 224 (flavanone) and 302 (hesperetin) g/mol. The lipophilicity of the chemicals can be indicated by log K' and log P . The log K' is the lipophilicity index acquired from the retention time of chromatography, which is increased following the increase of lipophilicity. The tendency of log K' was naringenin < hesperetin < 6-hydroxyflavanone < flavanone < 6-bromoflavone. The tendency of log P was the same as that of log K' , except the lower log P of hesperetin compared to naringenin. The penetrants with lower lipophilicity showed higher solubility in aqueous medium. Naringenin was the compound with the greatest solubility, namely 760-fold more soluble than 6-bromoflavone with the least solubility. The physicochemical properties estimated by molecular modeling are depicted in Table 2. The hydrogen bond (H-bond) number and total polarity surface are indicators of molecular lipophilicity. The number of H-bond acceptors and donors increased following the increase of hydroxyl moieties in the structure. Greater H-bond number implied more polar interaction with aqueous medium to increase aqueous solubility. The trend of total polarity surface was inversely correlated with that of log K' . The largest molecular volume was detected for hesperetin, followed by naringenin, 6-bromoflavone, hesperetin, 6-hydroxyflavanone, and flavanone.

3.2. In vitro skin permeation evaluation

The facile skin absorption of topically applied agent is a prerequisite to achieve bioactivity in skin. In vitro skin permeation evaluation is an applicable platform for the screening and comparison of penetrants aimed at optimizing cutaneous delivery. The donor penetrant dose was set at equivalent concentration (5 mM) and saturated solubility to form the supersaturated suspension and saturated solution, respectively. The

Table 2

The hydrogen bond number, molecular volume, and total polarity surface of flavanone and its derivatives determined by molecular modeling.

Compound	Hydrogen bond acceptor number	Hydrogen bond donor number	Total polarity surface	Molecular volume
Naringenin	5	3	86.99	204.42
Hesperetin	6	3	96.22	227.06
6-Hydroxyflavanone	3	1	46.53	185.21
Flavanone	2	0	26.30	184.53
6-Bromoflavone	2	0	26.30	195.16

skin deposition which indicates penetrant reservoir within the skin after topical application at equivalent concentration is shown in Fig. 2A. A sequence of flavanone > 6-bromoflavone ≥ 6-hydroxyflavanone > hesperetin ≥ naringenin was noted. The skin deposition of flavanone was 18-fold that of naringenin. Flux shown in Fig. 2B is a parameter predicting the possibility of penetrant reaching systemic circulation after topical administration. The same as skin deposition, the flux of flavanone was much higher than that of the other candidates. The S value is employed to specify the selectivity between cutaneous targeting and the risk of circulation absorption. As shown in Fig. 2C, the highest S value for 6-bromoflavone suggests potent targeting to the skin with less systemic effect. The penetrants were also dosed with saturated solubility to reflect maximum thermodynamic activity. As observed in Fig. 2D, the tendency of CSD from saturated solution is quite different compared to the skin deposition from suspension. The CSD increased along with the increase of lipophilicity. The trend of PC is identical to that of CSD as presented in Fig. 2E. Both hesperetin and 6-bromoflavone demonstrated the greatest S value in the case of saturated solution, followed by flavanone, naringenin, and 6-hydroxyflavanone, sequentially.

We next appraised the skin penetration by using barrier-damaged pig skins. The barrier-defective skins were used to determine the transport nature of flavanones in inflammatory skin and elucidate the delivery pathways through the skin. The penetrants at the equimolar dose were chosen as the donor in this experiment. Fig. 3A summarizes the skin deposition of five penetrants in barrier-defective skins. The enhancement fold of barrier-defective skin absorption compared to intact skin absorption is shown above the columns in Fig. 3A. SC stripping increased skin deposition; the less-lipophilic penetrants revealed the greater deposition enhancement. SC removal compared to intact skin promoted naringenin deposition by 14-fold, which was the highest enhancement among the penetrants tested. The removal of SC lipids evoked skin deposition to the similar level with SC layer stripping. The sebum removal could only enhance skin deposition to less than 2-fold. The enhancement fold in the absence of sebum was comparable for all penetrants. Protein denaturation significantly increased the skin deposition of naringenin and hesperetin to 1.7- and 2.0-fold, respectively. No significant difference between the deposition of intact and protein-denatured skin was detected for the other penetrants. Fig. 3B exhibits

Table 1

Physicochemical properties of flavanone and its derivatives.

Compound	Molecular formula	MW ^a (Da)	log K' ^c	log P ^b	Solubility in 25% PEG400 (mM)
Naringenin	C ₁₅ H ₁₂ O ₆	272.26	0.11 ± 0.001	3.18 ± 0.24	3.58 ± 0.04
Hesperetin	C ₁₆ H ₁₄ O ₆	302.27	0.12 ± 0.002	2.74 ± 0.08	2.12 ± 0.07
6-Hydroxyflavanone	C ₁₅ H ₁₀ O ₃	240.25	0.27 ± 0.02	3.10 ± 0.29	0.31 ± 0.02
Flavanone	C ₁₅ H ₁₂ O ₂	224.25	0.37 ± 0.01	3.45 ± 0.27	0.14 ± 0.01
6-Bromoflavone	C ₁₅ H ₉ BrO ₂	301.13	0.52 ± 0.03	4.91 ± 0.31	0.0047 ± 0.0002

Each value represents the mean and S.E.M. ($n = 4$).

^a MW, molecular weight.

^b log P , partition coefficient measured by n -octanol/water partitioning.

^c log K' , logarithm of $t_r - t_0 / t_0$, t_r is the retention time of compound peak, t_0 is the retention time of solvent peak.

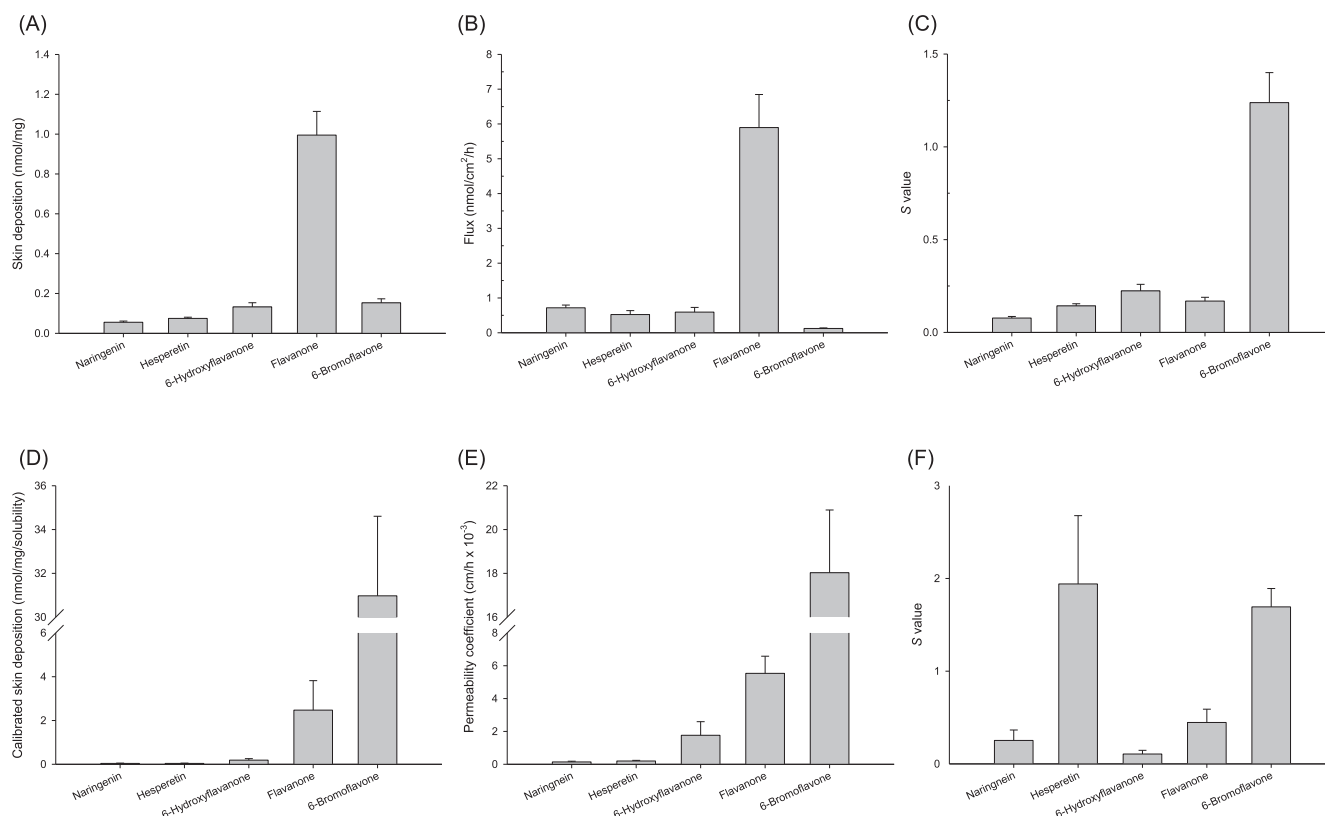


Fig. 2. In vitro skin permeation of flavanone and its derivatives: (A) skin deposition at a dose of 5 mM after topical treatment on pig skin, (B) flux at a dose of 5 mM after topical treatment on pig skin, (C) S value at a dose of 5 mM after topical treatment on pig skin, (D) calibrated skin deposition at a dose of saturated solubility after topical treatment on pig skin, (E) permeability coefficient at a dose of saturated solubility after topical treatment on pig skin, and (F) S value at a dose of saturated solubility after topical treatment on pig skin. All data are presented as the mean of four experiments \pm S.E.M.

the flux across different barrier-defective skins. The same as the results of skin deposition, SC stripping and lipid removal greatly enhanced naringenin flux. This phenomenon was also detectable in the case of hesperetin, although the flux enhancement by lipid removal was less than that of naringenin. The enhancement of flux in the absence of SC lipids was even higher than that of SC stripping in the cases of 6-hydroxyflavanone and 6-bromoflavone. Sebum removal and protein denaturation marginally reduced flavanone flux.

Hair follicles provide the appendageal pathways for skin delivery. Hesperetin, followed by 6-bromoflavone and naringenin, displays the largest follicular uptake as shown in Fig. 3C. The least follicular delivery was detected for topically applied flavanone. The release behavior of the penetrants from the vehicle was examined by using cellulose membrane as the barrier. A steady increase of penetrant release to receptor over time is observed in Fig. 3D. The release profile followed zero-order kinetics. It was apparent that the release rate was increased following the decrease of lipophilicity.

3.3. Cell-based assay

Besides the successful delivery to skin, it is important to recognize the antipsoriatic activity of flavanone and its derivatives. Keratinocytes play a potent role in the initiation of cutaneous inflammation during psoriasis development. The HaCaT cell line was used as a keratinocyte model to examine the effect of flavanones on inflammation suppression. At first, the cytotoxicity of the compounds against HaCaT was checked, as shown in Fig. 4A. None of the compounds exerted a significant cytotoxicity (cell viability < 80%) up to 10 μ M. The viability decreased as the dose increased. Flavanone treatment showed near complete cell death at the concentrations > 250 μ M. 6-Hydroxyflavanone could maintain the cell viability to 60% at 1000 μ M. The non-toxic dose of

1 μ M was chosen to evaluate the anti-inflammatory activity of the compounds. The cultured keratinocytes were activated by IMQ for detecting the expression of cytokines and chemokines. The left panel of Fig. 4B illustrates the IL-1 β expression after compound treatment with or without IMQ stimulation. No compounds altered the IL-1 β level in the inactivated keratinocytes (without IMQ treatment). IMQ significantly elevated IL-1 β by 2.5-fold compared to the control. IL-1 β inhibition effect was comparable for all compounds. TI is calculated to predict the possible IL-1 β inhibition after topical treatment, as shown in the right panel of Fig. 4B. Skin absorption via both intact and SC-stripped skins was utilized to calculate TI. The SC-stripped skin can be a model of diseased or inflamed skin. The highest TI for IL-1 β was detected for flavanone because of its superior absorption into intact and barrier-damaged skins. The index for IL-1 β of flavanone was about 10-fold that of the other compounds.

IL-6 expression in HaCaT is shown in the left panel of Fig. 4C. IMQ increased IL-6 level 18-fold that of the control. The compounds at 1 μ M restrained IMQ-induced IL-6 expression. Naringenin inhibited IL-6 to the baseline. The TI values observed in the right panel of Fig. 4C demonstrate the highest index for flavanone. Naringenin exhibit high TI in the SC-stripped skin. The facile SC-stripped skin deposition and superior IL-6 inhibition in HaCaT contributed to this high TI. CXCL1 is a chemokine derived from keratinocytes. As shown in the left panel of Fig. 4D, the IMQ-induced CXCL1 is not suppressed by the compounds, except for 6-bromoflavone. This chemical repressed CXCL1 level by 60% compared to the stimulated cells without compound treatment. Again, flavanone was the compound revealing the highest TI for CXCL1 inhibition. 6-Bromoflavone showed high TI secondary to flavanone in the intact skin. However, this predominance was unapparent in the case of SC-stripped skin because of the finite enhancement of cutaneous 6-bromoflavone deposition after stripping.

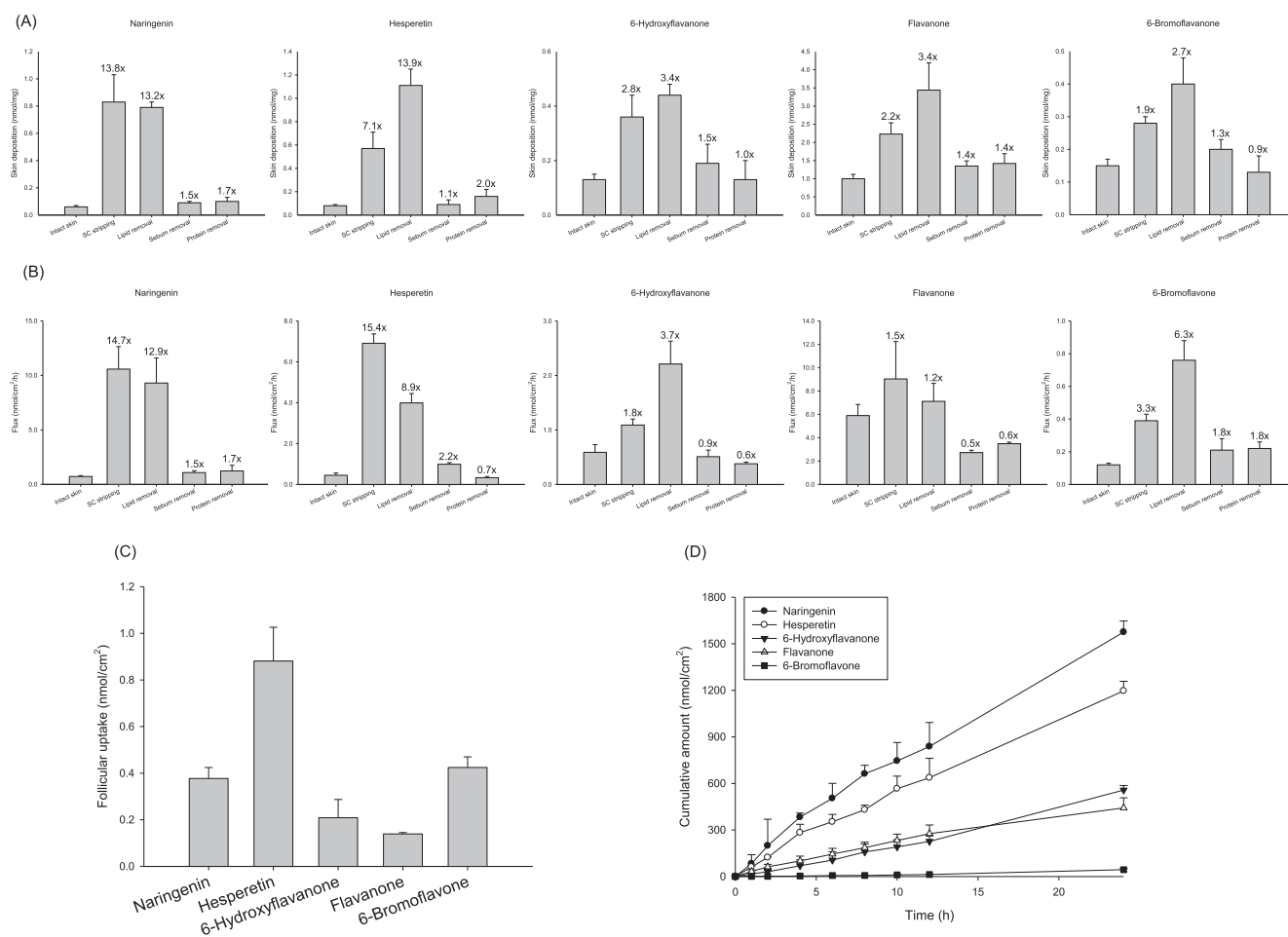


Fig. 3. The released percentage, skin deposition, and flux of flavanone and its derivatives (5 mM) via cellulose membrane, stratum corneum (SC)-stripped skin, delipid skin, de-sebum skin, and deprotein skin: (A) skin deposition in pig skin, (B) flux across pig skin, (C) follicular uptake in pig skin, and (D) release across cellulose membrane. All data are presented as the mean of four experiments \pm S.E.M.

3.4. In vivo anti-psoriatic activity

It is speculated that in vivo therapeutic efficiency is mainly dependent upon the cutaneous absorption of the actives and the availability at the action site. Naringenin and flavanone were selected to be administered topically to IMQ-treated animals for testing the anti-psoriatic efficacy. Both compounds and tacrolimus as the positive control were comparatively examined for psoriasisform lesion mitigation. The phenotypic and microscopic images of mouse skin surface are presented in Fig. 5A and 5B, respectively. IMQ stimulation for 6 d resulted in the development of red patches covered with silvery scales, which simulated psoriatic lesion in human. The flavanone compounds and reference tacrolimus reduced the symptoms of psoriasis. The scaling was less for tacrolimus and flavanone than for naringenin. Compared to the control, the histology of IMQ-treated skin shows increased epidermal thickness and inflammatory exudates in the dermis, as displayed in Fig. 5C. Topical delivery of flavanones and tacrolimus indicated reduced hyperplasia. The immune cell infiltration was decreased by flavanone and tacrolimus but not by naringenin. The PASI score is a summary of erythema, epidermal thickness, and scaling for assessing psoriatic severity. As depicted in Fig. 5D, topical tacrolimus exhibits the lowest score among the chemicals tested. The PASI reduction was comparable between naringenin and flavanone. Fig. 5E reveals the epidermal thickness calculated by histology. The thickness was increased from 16 to 93 μ m by IMQ. Tacrolimus exhibited maximum reduction in the thickness, followed by flavanone and naringenin. TEWL, as a sign of skin barrier property, is determined during

IMQ treatment, as shown in Fig. 5F. IMQ significantly elevated TEWL after 4-d application. Although naringenin showed less improvement of psoriasisform plaque compared to flavanone according to histology and epidermal thickness, TEWL was significantly decreased by topical naringenin. The administration of flavanone did not ameliorate the barrier function disrupted by IMQ.

IHC of Ly6G, as shown in Fig. 6A, displays neutrophil accumulation in dermis after 5-d IMQ treatment. Some neutrophils infiltrated to superficial skin, known as Munro's microabscesses. Tacrolimus almost cleared the neutrophil accumulation. Flavanones caused a significant inhibition in neutrophil migration, with flavanone showing better mitigation than naringenin. The location of IL-17 in the skin was detected by IHC, as visualized in Fig. 6B. IL-17 with a brownish color was observed in the basal cell layer of epidermis after IMQ stimulation. This overexpression was prohibited by tacrolimus and flavanones. Fig. 6C depicts the keratinocyte proliferation in the basal layer stained by Ki-67. A significant proliferation was found after IMQ stimulation. The greatest inhibition of IMQ-induced keratinocyte proliferation was detected after application of tacrolimus, followed by flavanone and naringenin sequentially. We employed ELISA to quantify psoriasis-related cytokines in the skin. These included IL-1 β , IL-6, and TNF- α (Fig. 6D-F). IMQ-treated mice exhibited a significant increase of these cytokines. Topical tacrolimus was able to decrease these cytokines to baseline control. The overexpressed IL-1 β produced by IMQ did not reveal any significant change in the groups of naringenin and flavanone. Both flavanones significantly inhibited IL-6 in IMQ-treated skin, with flavanone causing a lower cytokine level than naringenin. The overexpressed

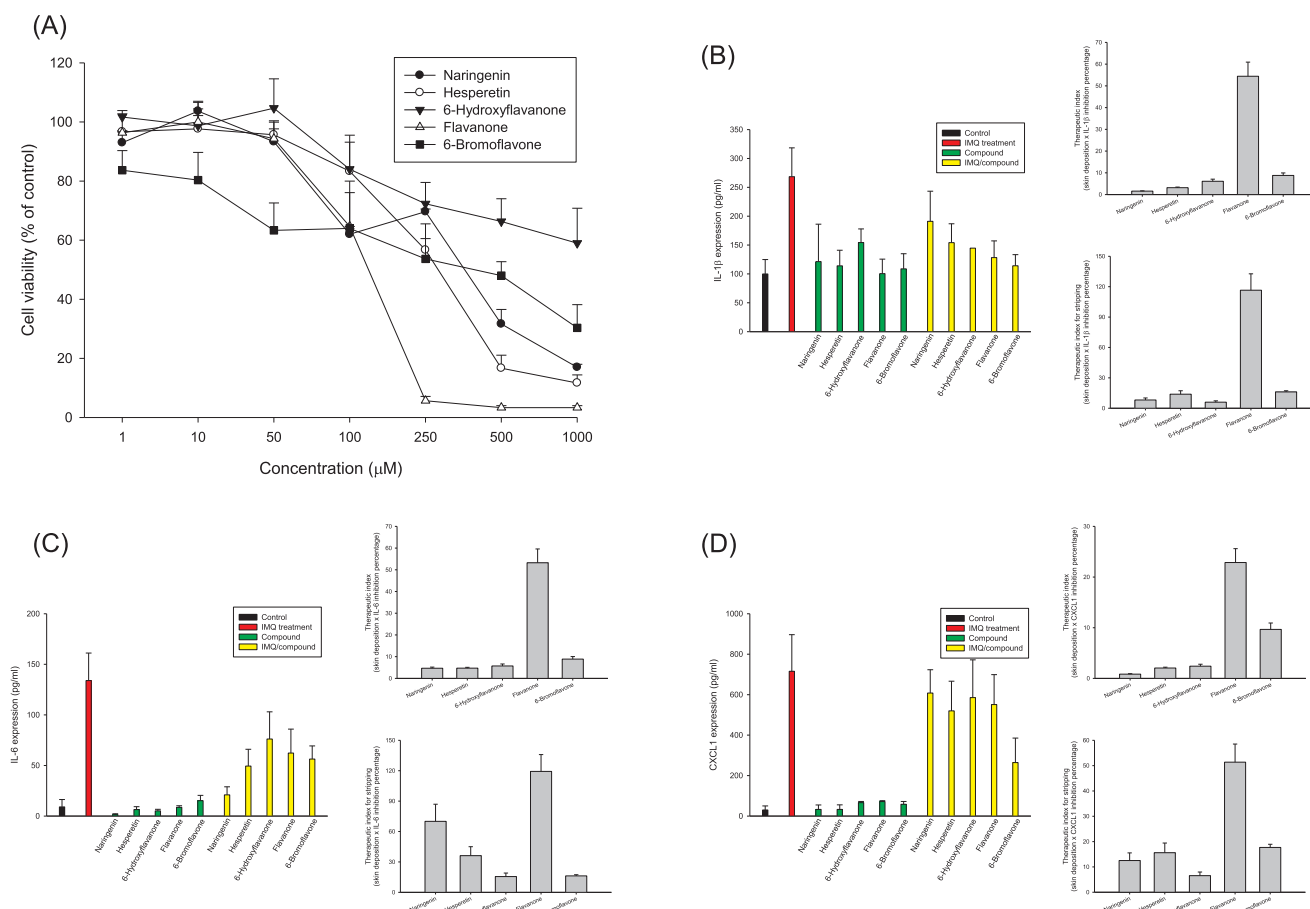


Fig. 4. Keratinocyte-based study for examining the anti-inflammatory activity of flavanone and its derivatives: (A) cell viability, (B) IL-1 β expression and the therapeutic index for IL-1 β , (C) IL-6 expression and the therapeutic index for IL-6, and (D) CXCL1 expression and the therapeutic index for CXCL1. All data are presented as the mean of four experiments \pm S.E.M.

TNF- α was significantly repressed by flavanone but not naringenin.

4. Discussion

Our previous study (Chuang et al., 2017) demonstrated the highest skin absorption of flavonoids with flavanone backbone among the flavonoids with different categories. Most of the compounds tested here are flavanones, except 6-bromoflavone. We included 6-bromoflavone in this study because of the structure backbone similarity to flavanone and the presence of bromine. We could explore the role of halogen on the skin permeation of flavanones. The penetrants selected in the present work show bioactivity on skin. For instance, naringenin inhibits cutaneous inflammation to treat atopic dermatitis and UV irradiation (Kim et al., 2013; Martinez et al., 2015). It also acts as a tyrosinase inhibitor to treat tanning (Bouzaïene et al., 2016). Recent studies report the usefulness of hesperetin for dermal function such as skin whitening, UV protection, anti-inflammation, and tumor suppression (Tsai et al., 2010; Man et al., 2019). 6-Hydroxyflavanone is a compound showing anti-tyrosinase and antioxidant effects for skin whitening (Chunhakant and Chaichareonpong, 2019). The decision of skin absorption is of importance for the anticipation of benefit for skin and the risk of circulation exposure (Fabian et al., 2017). The in vitro Franz cell as a gold standard of skin absorption assessment is a platform for using human or pig skin as the penetration barrier (Ashrafi et al., 2018). We employed pig skin in this study because of its resemblance to human skin regarding histology and biochemistry.

The significant barrier nature of SC contributes to the important step of skin delivery for the penetrants. The facility of passive transport

into the skin depends upon the ability to enter into SC. The increase of penetrant lipophilicity is favorable to increase SC affinity and skin permeation since SC can be regarded as a lipophilic environment. Our data attested to this hypothesis. Flavanone and 6-bromoflavone with the highest lipophilicity displayed the greatest skin deposition. However, a parabolic correlation was found between skin permeation and lipophilicity in the case of equimolar dose. The skin deposition and flux of 6-bromoflavone was greatly lower than those of flavanone. Although the penetrants with extremely high lipophilicity facilitate penetrate into the SC layer, it is difficult to diffuse into the viable skin with relatively low lipophilicity (Liu et al., 2011). The high lipophilicity of 6-bromoflavone can be a hindrance to skin transport. Aqueous solubility is also a driving force of skin absorption (Liu et al., 2017). The penetrant should be in the solubilized form for diffusion into the skin. The dramatically low solubility of 6-bromoflavone in vehicle was unfavorable for its absorption. Viable skin is a key diffusion layer controlling the flux into systemic circulation (Yamaguchi et al., 2008). The minimal 6-bromoflavone flux in the case of equimolar dose could be due to the low skin deposition and the difficulty of 6-bromoflavone partitioning into viable skin. The highest CSD and PC of 6-bromoflavone among the penetrants indicated the importance of solubility as a driving force for skin diffusion.

The absorption into/across barrier-damaged skins is informative to explore the penetration pathways and mechanisms of flavanone and its derivatives. The skin absorption enhancement by SC stripping was minimal for 6-bromoflavone among all the chemicals tested. SC functions as a major reservoir for penetrants. The penetrant concentration in SC can be a predictor of the total amount absorbed (Pople and Singh,

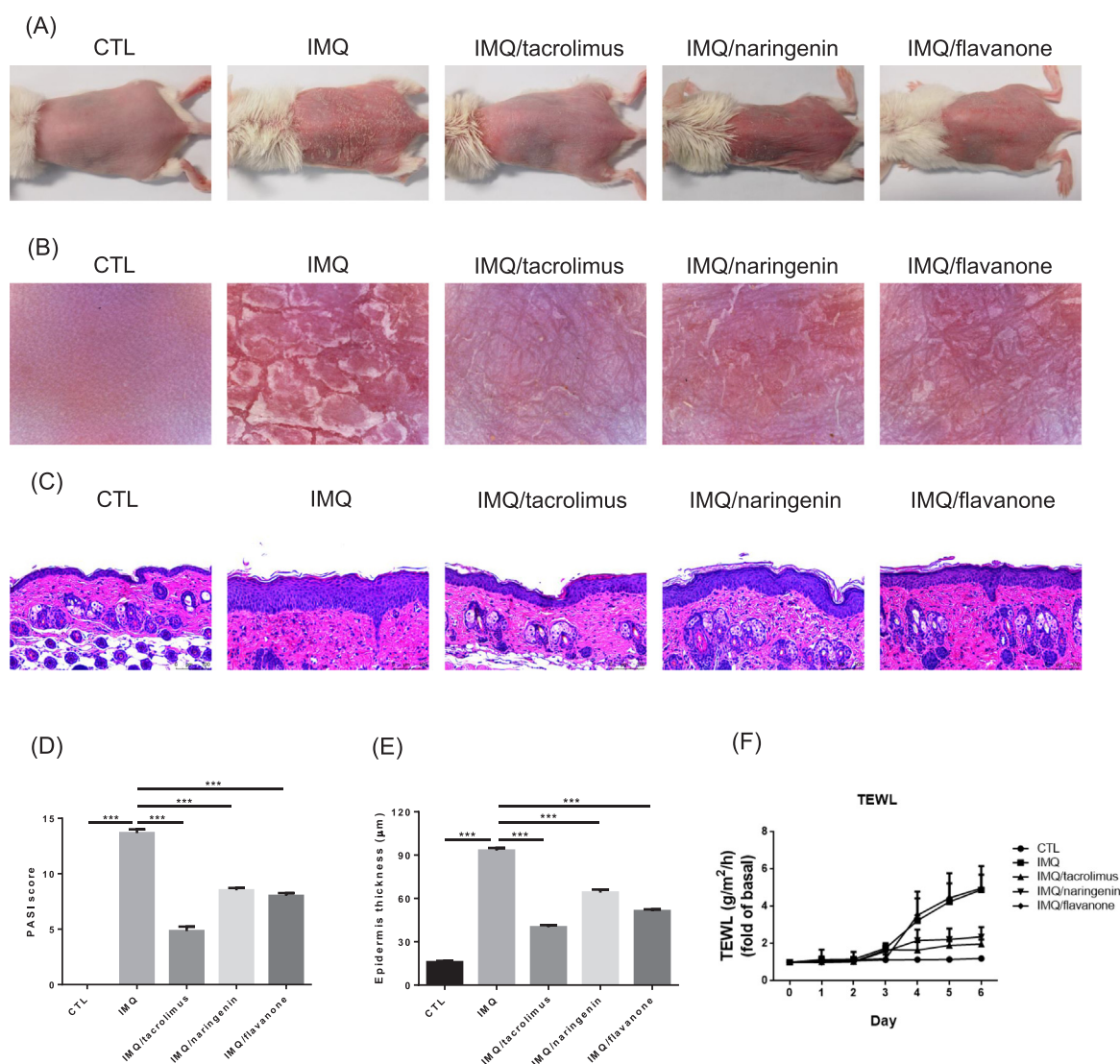


Fig. 5. IMQ-induced mouse psoriatic lesion evaluation after topical application of tacrolimus, naringenin, and flavanone: (A) the gross images of mouse back skin were represented on day 5 by digital camera, (B) the close-up imaging by handheld digital microscopy, (C) skin sections stained by H&E, (D) quantification of mouse skin histology examined using PASI score, (E) epidermal thickness quantified from H&E staining, and (F) TEWL measurement. All data are presented as the mean of six experiments \pm S.E.M.

2012). The minimal 6-bromoflavone absorption enhancement of SC stripping indicates that this molecule readily entered into the SC barrier. We found that the stripping-increased absorption was less for more-lipophilic penetrants, suggesting that the principal resistance for more-lipophilic molecules could be viable epidermis/dermis. The lipophilicity determined by $\log K'$ and $\log P$ is a net result of intermolecular forces. It is insufficient to model the penetration via skin. The *in vitro* skin absorption of the chemicals can be explained by structure-permeation relationship employing physicochemical properties based on molecular level for highly informative interpretation (Tsakovska et al., 2017). These include H-bond number, total polarity surface, and molecular volume. Total polarity surface can be a molecular view of lipophilicity defined as the sum of the surface area belonging to nitrogen, oxygen, and hydrogen atoms bound to electronegative atoms (Ertl et al., 2000). Our result demonstrated an inverse correlation between total polarity surface and skin absorption of flavanones.

H-bond number is another factor inversely correlated with skin diffusion. Ceramides in SC possess the headgroups to form lateral intermolecular H-bond. Alikhan et al. (2009) demonstrate that the increase of H-bond acceptor number retards SC permeation since SC itself is mainly the H-bond acceptor. Contrary to this concept, Geinoz et al.

(2004) suggests that H-bond donor number predominates over acceptor number to lower skin absorption. Anyway, it can be confirmed that the H-bond number is a detrimental factor for skin absorption. Magnusson et al. (2004) propose that the penetrants with the H-bond acceptor of < 3 are advantageous for facile transport across SC. In the case of flavanone and the relative derivatives, flavanone and 6-bromoflavone could achieve this criterion. Molecular size is a major determinant for skin absorption. MW is a direct parameter for deciding molecular size. The high MW of hesperetin could partially clarify the low absorption into intact skin. Nevertheless, 6-bromoflavone with MW similar to hesperetin manifested much greater absorption than hesperetin. More functional groups in the six-member rings might form steric hindrance for skin permeation. Although the MW of hesperetin and 6-bromoflavone are similar, the 3 hydroxyl groups and 1 methoxyl moiety in hesperetin structure produced an obstacle for SC diffusion. Molecular volume is thought to provide a better estimate for molecular size (Tsakovska et al., 2017). The data on molecular volume verified the smaller size of 6-bromoflavone (195) than hesperetin (227). The smallest molecular volume of flavanone (185) among the penetrants also led to its great absorption via intact skin.

Although the skin transport of naringenin and hesperetin was low

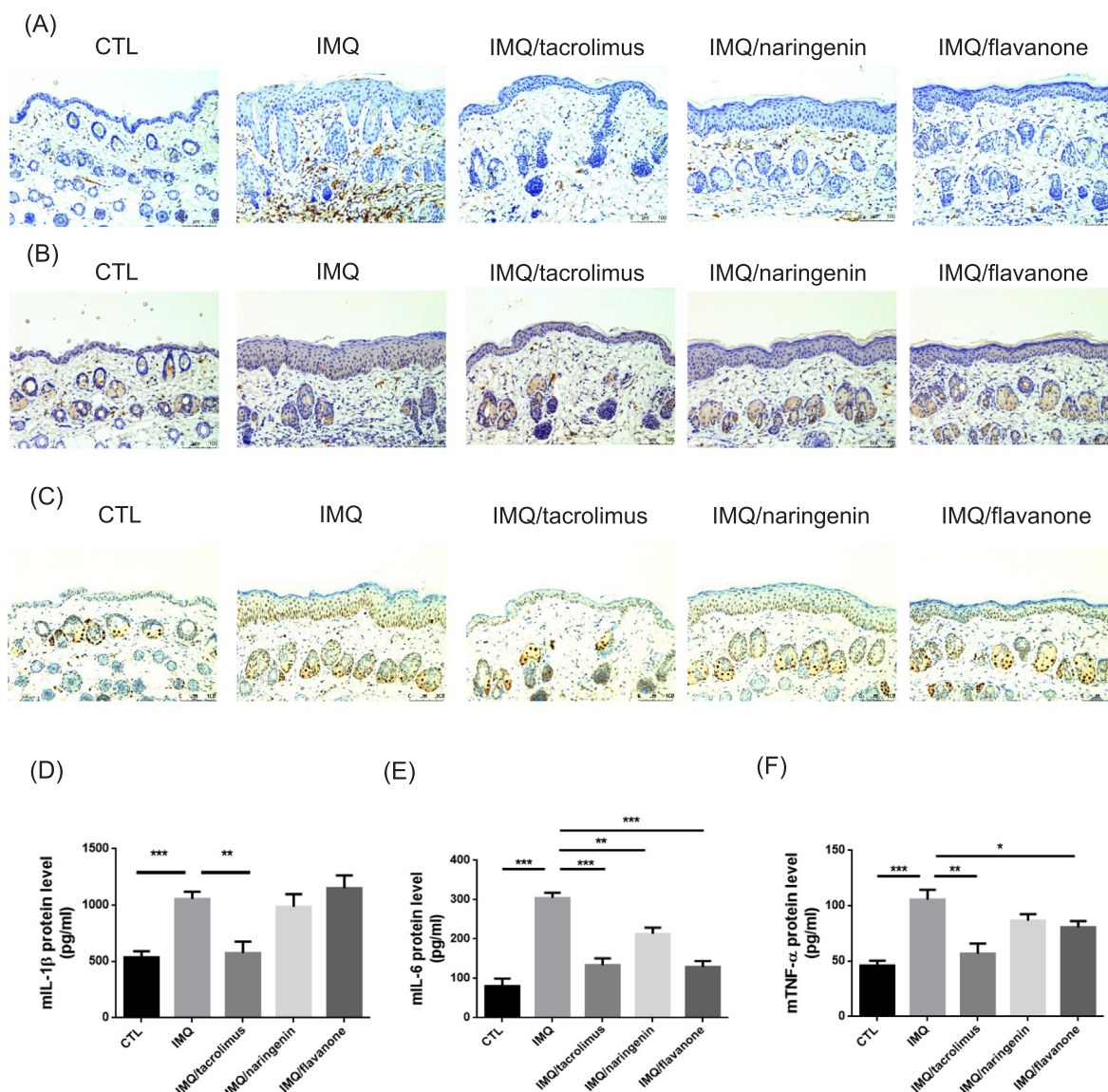


Fig. 6. Evaluation of IMQ-induced mouse psoriatic skin inflammation based on IHC and cytokine assay: (A) IHC stained by Ly-6G, (B) IHC stained by IL-17, (C) IHC stained by Ki-67, (D) ELISA assay for IL-1 β expression in mouse skin, (E) ELISA assay for IL-6 expression in mouse skin, and (F) ELISA assay for TNF- α expression in mouse skin. All data are presented as the mean of six experiments \pm S.E.M.

due to high hydrophilicity, the absorption was largely increased after the SC removal. The H-bond number mainly affects the diffusion across SC layer (Yamaguchi et al., 2008). The prediction of skin absorption by this number is generally of no use in the absence of SC. The favorable partition and diffusion of more-hydrophilic flavanones into the viable skin could be observed. The absorption into viable skin is controlled not only by simple partitioning to the epidermis/dermis, but also by tissue binding. The result suggested the abundant interaction of the molecules of hydrophilic flavanones with viable skin. Naringenin achieved a high skin deposition secondary to flavanone after SC stripping, indicating a large barrier function of the SC layer for naringenin delivery. The release rate was increased with the increase of hydrophilicity, with naringenin exhibiting the highest rate. Domínguez-Villegas et al. (2014) demonstrated that the flavanones with numerous hydroxyl groups are expected to have high aqueous solubility and H-bond with the receptor medium of Franz cell. Naringenin was able to show facile absorption into the skin in the absence of the interference of SC barrier because of the partitioning into viable skin and fast release rate.

The penetrant passage across SC can be divided into two pathways: intermolecular lipid-rich and intracellular protein-rich pathways. The

deposition in the skin with lipid removal approximated that in SC-stripped skin for all compounds tested. This signified that flavanones mainly partition into the lipid domain of the SC for permeation. The polar pathways were limited for the SC permeation of flavanones. The partitioning into the rate-limiting SC of the chemicals is usually the vital rate-controlling factor (Riviere et al., 2014). Sebum secretion from sebaceous glands would cover the SC surface to form a thin film. The first step of penetrant partitioning to SC in the real condition is that the penetrant should partition into sebum film. We also examined the skin delivery of flavanones in the absence of sebum. The result showed a negligible change of skin absorption after sebum removal, indicating that the partitioning to sebum was not the rate-controlling factor for topically applied flavanones. Hair follicles offer an alternative pathway for skin passage. The follicular route can provide an easy way for penetrant delivery into deeper skin strata since the follicular epithelium is more permeable compared to perifollicular SC (Zorn-Kruppa et al., 2018). We estimated follicular uptake of the penetrants in pig skin. The follicular structure of the pig mimics that of human (Godin and Touitou, 2007). We signified that the follicular route was the most important for hesperetin, followed by 6-bromoflavone and naringenin. Patzelt and

Lademann (2013) indicated the importance of the follicular pathway for macromolecule transport. The penetrants with higher MW are beneficial for entering follicles. Our data revealed the facile follicle delivery of the flavanones with larger size than smaller size. Further elucidation is needed to explain the detailed mechanisms of follicular uptake.

In addition to the investigation of transport routes for flavanones, the barrier-defective skin was applicable to understand the cutaneous delivery in diseased skin. The inflamed skin always exhibits a dysfunction of barrier property. SC stripping can act as a permeation model of dermatitis (Abdel-Mottaleb and Lamprecht, 2016). The delipid skin resembles the diseased condition of xerosis, ichthyosis, and psoriasis (Sahle et al., 2015). The penetrant absorption into the skin with SC protein denaturation mimics the model of photoaging and atopic dermatitis (Biniek et al., 2012). We found that flavanone showed high absorption in both intact and barrier-defective skins. The naringenin deposition in intact skin was low. However, the absorption of naringenin could accomplish a satisfactory level after SC stripping and lipid removal. This molecule can be a potential candidate for treating inflamed skin.

Epidermal keratinocytes play a crucial role in cutaneous inflammation. Keratinocytes are an integral part of resident immune system due to their capacity as antigen presenting cells to elicit innate immune mediators (Albanesi et al., 2018). These basal cells can be an important target for antipsoriatic therapy. Overproduction of proinflammatory mediators, such as cytokines and chemokines, leads to the occurrence of psoriasis. The critical action of flavonoids is the inhibition of these mediators to perform anti-inflammatory function (Tuñón et al., 2009). IL-1 β and IL-6 are major cytokines largely produced by IMQ-activated keratinocytes (Schön et al., 2006). IMQ produces the overexpression of IL-1 β and IL-6 through the elevation of mitogen-activated protein kinases and AP-1 phosphorylation in keratinocytes (Weng et al., 2019). Flavanone and the related analogs could inhibit the upregulation of IL-1 β and IL-6 by IMQ to different levels. Naringenin even suppressed IL-6 overexpression to a level near baseline control, implying efficient psoriasis management. A previous report (Leyva-López et al., 2016) suggests that the presence of hydroxyl groups at C¹ and C⁴ in the B ring is an important feature of flavonoids exerting anti-inflammatory activity. Naringenin fits this prototype. Topical application of naringenin for mitigating atopic dermatitis, photoaging, and psoriasis via the inhibition of cytokines and chemokines has been reported previously (Kim et al., 2013; Chlapanidas et al., 2014; Martinez et al., 2015; Karuppagounder et al., 2016).

CXCL1 is a chemokine showing an essential position in the evolution of psoriasis. Only 6-bromoflavone could significantly reduce IMQ-induced CXCL1 expression in keratinocytes. The other flavanones tested were invalid in seeking to reduce CXCL1. 6-Bromoflavone possesses a structure featuring flavones but not flavanone. It has been proposed by Lago et al. (2014) that the unsaturation in the C ring between C² and C³ positions is substantial for displaying anti-inflammatory action. The highest TI was detected for flavanone owing to its superior skin absorption compared to the other compounds. It may indicate the possible success of topically applied flavanone for treating psoriasis. Naringenin revealed an impressive TI of SC-stripped skin in IL-6 inhibition. Both naringenin and flavanone were selected for further in vivo experiments. The *S* value of 6-bromoflavone was higher than that of the other penetrants, demonstrating the efficient targeting to skin with restrained risk of systemic absorption. However, the absolute skin deposition of 6-bromoflavone was restricted. The minimal skin deposition enhancement of 6-bromoflavone by SC stripping and lipid removal indicated limited absorption in the inflamed skin. It also manifested that this flavone might strongly associate with the SC lipids with less entrance into the viable skin, the nidus of psoriatic inflammation; this was the reason we excluded 6-bromoflavone as a promising candidate for psoriasis treatment.

IMQ intervention on mouse skin stimulated the signs of psoriasiform

lesion approaching human psoriasis. Tacrolimus ointment was employed as the positive control. Tacrolimus (0.1%) has been proved to be useful for ameliorating the psoriasiform lesion induced by IMQ in mouse (Paschon et al., 2018). Topical tacrolimus is especially effective to treat inverse psoriasis in clinics (Malecic and Young et al., 2016). The in vivo data demonstrate the effectiveness of tacrolimus in suppressing the hyperplasia and inflammation induced by IMQ. The vital capacity to recover skin barrier function by tacrolimus ointment in this study coincided with the previous investigation (Boakye et al., 2017). Tacrolimus is an immunosuppressant drug for the treatment of immune-mediated inflammation, including psoriasis (Malecic and Young, 2016). Nevertheless, the immunosuppression by tacrolimus after long-term use causes increased risks of tumorigenesis, renal impairment, and tremor (Becker et al., 2006). Topical naringenin and flavanone were efficacious in mitigating psoriasis-like plaque, although this effect was minor compared to tacrolimus. IMQ application results in keratinocyte activation to increase cytokine generation. IL-1 β and TNF- α have been associated with psoriasis pathogenesis producing keratinocyte hyperproliferation (Herman and Herman, 2016). Our results revealed significant TNF- α reduction by flavanone, but not by naringenin. The H&E- and Ki-67-stained histology showed greater reduction of epidermal hyperplasia for flavanone than for naringenin. TNF- α is an important cytokine mediating immune response and for inflammation in psoriasis. The TNF- α blockade represents a major pathway in psoriasis treatment. The lower TNF- α suppression by flavanones than tacrolimus led to less amelioration of psoriasiform lesion as observed in the in vivo results. IL-1 β , IL-6, and TNF- α enhance the activation of infiltrated neutrophils in psoriasis-like plaque (Sun et al., 2013). Our data showed the capability of flavanone to inhibit IL-6 and TNF- α in IMQ-treated mice. Naringenin could suppress IL-6 at a lower inhibition level than flavanone. This result confirmed the greater suppression of neutrophil migration in psoriasiform skin by flavanone than by naringenin.

The psoriatic lesion improvement by naringenin and flavanone suggest the sufficiency of cutaneous absorption to trigger the anti-inflammatory activity in skin. The superior performance of flavanone over naringenin was due to the greater skin deposition for increased availability at the site of action. Naringenin still demonstrated the capability to mitigate psoriasiform lesion, especially in the recovery of the cutaneous barrier. Psoriatic skin is characterized by the barrier dysfunction with the enhanced permeability as compared to healthy skin (Mattozzi et al., 2016). Furthermore, mouse skin is much more permeable than human or pig skin. A prominent enhancement of naringenin absorption was gained in the defective skin, although this skin absorption did not achieve the level of flavanone. In the practical viewpoint, it is difficult to rate skin penetration and bioactivity directly by in vivo experiments. A strategy of utilizing an in vitro model to correlate with in vivo data can shorten and economize the procedure of drug development. The results obtained in our in vivo platform confirmed the in vitro data of skin delivery and cell-based study, indicating a feasible prediction of in vivo outcome by in vitro profiles. Structure-permeation relationship described in this study provided an insight to explain the permeation trend and mechanism of flavanone and the derivatives. A therapy of at least a 75% reduction of PASI is needed for successful psoriasis treatment (Abrouk et al., 2017). Topical naringenin and flavanone only achieved an intermediate decline of PASI between 50% and 75%. The epidermal thickness of psoriasiform skin was not restored to healthy control after administration. Further effort is required to raise the anti-psoriatic capability. The formulation design and increase of applied dose can be considered as possible viable approaches.

5. Conclusions

Psoriasis is a chronic autoimmune skin disorder constituting a major health threat worldwide. It is urgent to develop new drug candidates to increase therapeutic efficiency and minimize side effects. We aimed to

search for the optimized flavonoids for psoriasis management through the evaluation of topical delivery capability by Franz cell and inflammation inhibition by cell-based study. Among the penetrants tested, flavanone showed the highest skin absorption. Naringenin permeation achieved a remarkable enhancement in the barrier-defective skins, which simulated the inflamed condition. IL-6 overproduction in the activated keratinocytes was markedly inhibited by naringenin. The signs of psoriasiform lesion were attenuated by topically applied naringenin or flavanone superior to vehicle control. The in vivo tendency of the antipsoriatic effect coincided with the in vitro experimental and predicted data. The skin penetration of topical flavanones could be well described by accounting for the physicochemical and molecular properties of the penetrants. When considering that flavanone and naringenin displaying the best result in skin absorption test, as well as the vital anti-inflammatory activity, both compounds could be proposed as candidates for topical antipsoriatic agents. Clinical trial cannot be replaced by any animal study since the clinical outcome does not necessarily reflect the results of animal model. Both compounds may proceed to further steps in clinical studies in the future.

CRedit authorship contribution statement

Ahmed Alalaiwe: Conceptualization, Writing - review & editing. **Chwan-Fwu Lin:** Methodology, Validation. **Chien-Yu Hsiao:** Software, Validation. **En-Li Chen:** Investigation, Data curation. **Chien-Yu Lin:** Investigation, Data curation. **Wan-Chen Lien:** Investigation. **Jia-You Fang:** Supervision, Writing - original draft.

Declaration of Competing Interest

The authors declare that they have no known competing financial interests or personal relationships that could have appeared to influence the work reported in this paper.

Acknowledgements

The authors are grateful for the financial support from Ministry of Science and Technology of Taiwan (MOST-107-2320-B-182-016-MY3) and Chang Gung Memorial Hospital (CMRPF1J0041).

References

- Abdel-Mottaleb, M.M.A., Lamprecht, A., 2016. In vivo skin penetration of macromolecules in irritant contact dermatitis. *Int. J. Pharm.* 515, 384–389.
- Abrouk, M., Nakamura, M., Zhu, T.H., Farahnik, B., Koo, J., Bhutani, T., 2017. The impact of PASI 75 and PASI 90 on quality of life in moderate to severe psoriasis patients. *J. Dermatol. Treat.* 28, 488–491.
- Albanesi, C., Madonna, S., Gisoni, P., Girolomoni, G., 2018. The interplay between keratinocytes and immune cells in the pathogenesis of psoriasis. *Front. Immunol.* 9, 1549.
- Alikhan, A., Farahmand, S., Maibach, H.I., 2009. Correlating percutaneous absorption with physicochemical parameters in vivo in man: agricultural, steroid, and other organic compounds. *J. Appl. Toxicol.* 29, 590–596.
- Arct, J., Pytkowska, K., 2008. Flavonoids as components of biologically active cosmetics. *Clin. Dermatol.* 26, 347–357.
- Ashrafi, P., Sun, Y., Davey, N., Adams, R.G., Wilkinson, S.C., Moss, G.P., 2018. Model fitting for small skin permeability data sets: hyperparameter optimization in Gaussian process regression. *J. Pharm. Pharmacol.* 70, 361–373.
- Becker, J.C., Houben, R., Vetter, C.S., Bröcker, E.B., 2006. The carcinogenic potential of tacrolimus ointment beyond immune suppression: a hypothesis creating case report. *BMC Cancer* 6, 7.
- Biniek, K., Levi, K., Dauskardt, R.H., 2012. Solar UV radiation reduces the barrier function of human skin. *Proc. Natl. Acad. Sci. USA* 109, 17111–17116.
- Boakye, C.H.A., Patel, K., Doddapaneni, R., Bagde, A., Marepally, S., Singh, M., 2017. Novel amphiphilic augments the co-delivery of erlotinib and IL36 siRNA into the skin for psoriasis treatment. *J. Control. Release* 246, 120–132.
- Bouzaiane, N.N., Chaabane, F., Sassi, A., Chekir-Ghedira, L., Ghedira, K., 2016. Effect of apigenin-7-glucoside, genkwanin and naringenin on tyrosinase activity and melanin synthesis in B16F10 melanoma cells. *Life Sci.* 144, 80–85.
- Campbell, C.S.J., Contreras-Rojas, L.R., Delgado-Charro, M.B., Guy, R.H., 2012. Objective assessment of nanoparticle disposition in mammalian skin after topical exposure. *J. Control. Release* 162, 201–207.
- Chlapanidas, T., Perteghella, S., Leoni, F., Faragò, S., Marazzi, M., Rossi, D., Martino, E., Gaggeri, R., Collina, S., 2014. TNF- α blocker effect of naringenin-loaded sericin microparticles that are potentially useful in the treatment of psoriasis. *Int. J. Mol. Sci.* 15, 13624–13636.
- Chuang, S.Y., Lin, Y.K., Lin, C.F., Wang, P.W., Chen, E.L., Fang, J.Y., 2017. Elucidating the skin delivery of aglycone and glycoside flavonoids: how the structures affect cutaneous absorption. *Nutrients* 9, 1304.
- Chunhakant, S., Chaicharoenpong, C., 2019. Antityrosinase, antioxidant, and cytotoxic activities of phytochemical constituents from *Manilkara zapota* L. bark. *Molecules* 24, 2798.
- Domínguez-Villegas, V., Clares-Naveros, B., García-López, M.L., Calpena-Campmany, A.C., Bustos-Zagal, P., Garduño-Ramírez, M.L., 2014. Development and characterization of two nano-structured systems for topical application of flavanones isolated from *Eysenhardtia platycarpa*. *Colloids Surf. B Biointerf.* 116, 183–192.
- Działo, M., Mierziak, J., Korzun, U., Preisner, M., Szopa, J., Kulma, A., 2016. The potential of plant phenolics in prevention and therapy of skin disorders. *Int. J. Mol. Sci.* 17, 160.
- Ertl, P., Rohde, B., Selzer, P., 2000. Fast calculation of molecular polar surface area as a sum of fragment-based contributions and its application of drug transport properties. *J. Med. Chem.* 43, 3714–3717.
- Fabian, E., Oesch, F., Ott, K., Landsiedel, R., van Ravenzwaay, B., 2017. A protocol to determine dermal absorption of xenobiotics through human skin in vitro. *Arch. Toxicol.* 91, 1497–1511.
- Geinoz, S., Guy, R.H., Testa, B., Carrupt, P.A., 2004. Quantitative structure-permeation relationships (QSPerS) to predict skin permeation: a critical evaluation. *Pharm. Res.* 21, 83–92.
- Godin, B., Touitou, E., 2007. Transdermal skin delivery: predictions for humans from in vivo, ex vivo and animal models. *Adv. Drug Deliv. Rev.* 59, 1152–1161.
- Herman, A., Herman, A.P., 2016. Topically and herbal products for the treatment of psoriasis-Mechanism of action, drug delivery, clinical studies. *Planta Med.* 82, 1447–1455.
- Itoh, K., Hirata, N., Masuda, M., Naruto, S., Murata, K., Wakabayashi, K., Matsuda, H., 2009. Inhibitory effects of *Citrus hassaku* extract and its flavanone glycosides on melanogenesis. *Biol. Pharm. Bull.* 32, 410–415.
- Jain, A., Doppalapudi, S., Domb, A.J., Khan, W., 2016. Tacrolimus and curcumin co-loaded liposphere gel: synergistic combination towards management of psoriasis. *J. Control. Release* 243, 132–145.
- Karuppagounder, V., Arumugam, S., Thandararayan, R.A., Sreedhar, R., Giridharan, V.V., Pitchaimani, V., Afrin, R., Harima, M., Krishnamurthy, P., Suzuki, K., Nakamura, M., Ueno, K., Watanabe, K., 2016. Naringenin ameliorates skin inflammation and accelerates phenotypic reprogramming from M1 to M2 macrophage polarization in atopic dermatitis NC/Nga mouse model. *Exp. Dermatol.* 25, 386–412.
- Kerdell, F., Zaiac, M., 2015. An evolution in switching therapy for psoriasis patients who fail to meet treatment goals. *Dermatol. Ther.* 28, 390–403.
- Kim, T.H., Kim, G.D., Ahn, H.J., Cho, J.J., Park, Y.S., Park, C.S., 2013. The inhibitory effect of naringenin on atopic dermatitis induced by DNFB in NC/Nga mice. *Life Sci.* 93, 516–524.
- Lago, J.H.G., Toledo-Arruda, A.C., Mernak, M., Barrosa, K.H., Martins, M.A., Tibério, I.F.L.C., Prado, C.M., 2014. Structure-activity association of flavonoids in lung diseases. *Molecules* 19, 3570–3595.
- Leyva-López, N., Gutierrez-Grijalva, E.P., Ambriz-Perez, D.L., Heredia, J.B., 2016. Flavonoids as cytokine modulators: a possible therapy for inflammation-related diseases. *Int. J. Mol. Sci.* 17, 921.
- Lin, Z.C., Hsieh, P.W., Hwang, T.L., Chen, C.Y., Sung, C.T., Fang, J.Y., 2018. Topical application of anthranilate derivatives ameliorates psoriatic inflammation in a mouse model by inhibiting keratinocyte-derived chemokine expression and neutrophil infiltration. *FASEB J.* 32, 6783–6795.
- Liu, K.S., Chen, Y.W., Aljuffali, I.A., Chang, C.W., Wang, J.J., Fang, J.Y., 2016. Topically applied mesoridazine exhibits the strongest cutaneous analgesia and minimized skin disruption among tricyclic antidepressants: the skin absorption assessment. *Eur. J. Pharm. Biopharm.* 105, 59–68.
- Liu, K.S., Huang, T.H., Aljuffali, I.A., Chen, E.L., Wang, J.J., Fang, J.Y., 2017. Exploring the structure-permeation relationship of topical tricyclic antidepressants used for skin analgesia. *Int. J. Pharm.* 523, 386–397.
- Liu, X., Testa, B., Fahr, A., 2011. Lipophilicity and its relationship with passive drug permeation. *Pharm. Res.* 28, 962–977.
- Magnusson, B.M., Pugh, W.J., Roberts, M.S., 2004. Simple rules defining the potential of compounds for transdermal delivery or toxicity. *Pharm. Res.* 21, 1047–1054.
- Malecic, N., Young, H., 2016. Tacrolimus for the management of psoriasis: clinical utility and place in therapy. *Psoriasis* 6, 153–163.
- Man, M.Q., Yang, B., Elias, P.M., 2019. Benefits of hesperidin for cutaneous functions. *Evid.-based Complement. Altern. Med.* 2019, 2676307.
- Martinez, R.M., Pinho-Ribeiro, F.A., Steffen, V.S., Caviglione, C.V., Vignoli, J.A., Barbosa, D.S., Barakat, M.M., Georgetti, S.R., Verri, W.A., Casagrande, R., 2015. Naringenin inhibits UVB irradiation-induced inflammation and oxidative stress in the skin of hairless mice. *J. Nat. Prod.* 78, 1647–1655.
- Mattozzi, C., Paolino, G., Richetta, A.G., Calvieri, S., 2016. Psoriasis, vitamin D and the importance of the cutaneous barrier's integrity: an update. *J. Dermatol.* 43, 507–514.
- Parlapally, S., Cherukupalli, N., Bhumireddy, S.R., Sripathi, P., Aniseti, R., Giri, C.C., Khareedu, V.R., Vudem, D.R., 2016. Chemical profiling and anti-psoriatic activity of methanolic extract of *Andrographis nallamalayana* J.L.Ellis. *Nat. Prod. Res.* 30, 1256–1261.
- Patzelt, A., Lademann, J., 2013. Drug delivery to hair follicle. *Expert Opin. Drug Deliv.* 10, 787–797.
- Pischon, H., Radbruch, M., Ostrowski, A., Schumacher, F., Hönzke, S., Kleuser, B., Hedtrich, S., Fluhr, J.W., Gruber, A.D., Mundhenk, L., 2018. How effective is

- tacrolimus in the imiquimod-induced mouse model of psoriasis? *J. Dermatol. Sci.* 138, 455–458.
- Pople, P.V., Singh, K.K., 2012. Targeting tacrolimus to deeper layers of skin with improved safety for treatment of atopic dermatitis-Part II: in vivo assessment of dermatopharmacokinetics, biodistribution and efficacy. *Int. J. Pharm.* 434, 70–79.
- Rendon, A., Schäkel, K., 2019. Psoriasis pathogenesis and treatment. *Int. J. Mol. Sci.* 20, 1475.
- Riviere, J.E., Brooks, J.D., Collard, W.T., Deng, J., De Rose, G., Mahabir, S.P., Merritt, D.A., Marchiondo, A.A., 2014. Prediction of formulation effects on dermal absorption of topically applied ectoparasiticides dosed in vitro on canine and porcine skin using a mixture-adjusted quantitative structure permeability relationship. *J. Vet. Pharmacol. Ther.* 37, 435–444.
- Sahle, F.F., Gebre-Mariam, T., Dobner, B., Wohlrab, J., Neubert, R.H., 2015. Skin diseases associated with the depletion of stratum corneum lipids and stratum corneum lipid substitution therapy. *Skin Pharmacol. Physiol.* 28, 42–55.
- Santi, M.D., Peralta, M.A., Mendoza, C.S., Cabrera, J.L., Ortega, M.G., 2017. Chemical and bioactivity of flavanones obtained from roots of *Dalea pazensis* Rusby. *Bioorg. Med. Chem. Lett.* 27, 1789–1794.
- Schön, M.P., Schön, M., Klotz, K.N., 2006. The small antitumoral immune response modifier imiquimod interacts with adenosine receptor signaling in a TLR7- and TLR8-independent fashion. *J. Invest. Dermatol.* 126, 1338–1347.
- Seo, J.E., Kim, S., Kim, B.H., 2017. In vitro skin absorption tests of three types of parabens using a Franz diffusion cell. *J. Expo. Sci. Environ. Epidemiol.* 27, 320–325.
- Shireen, P.A., Mujeeb, V.M.A., Muraleedharan, K., 2017. Theoretical insights on flavanones as antioxidants and UV filters: a TDDFT and NLMO study. *J. Photochem. Photobiol. B Biol.* 170, 286–294.
- Sun, J., Zhao, Y., Hu, J., 2013. Curcumin inhibits imiquimod-induced psoriasis-like inflammation by inhibiting IL-1 β and IL-6 production in mice. *PLoS One* 8, e67078.
- Tsai, Y.H., Lee, K.F., Huang, Y.B., Huang, C.T., Wu, P.C., 2010. In vitro permeation and in vivo whitening effect of topical hesperetin microemulsion delivery system. *Int. J. Pharm.* 388, 257–262.
- Tsakovska, I., Pajeva, I., Al Sharif, M., Alov, P., Fioravanzo, E., Kovarich, S., Worth, A.P., Richarz, A.N., Yang, C., Mostrag-Szlichtyng, A., Cronin, M.T.D., 2017. Quantitative structure-skin permeability relationships. *Toxicology* 387, 27–42.
- Tuñón, M.J., García-Mediavilla, M.V., Sánchez-Campos, S., González-Gallego, J., 2009. Potential of flavonoids as anti-inflammatory agents: modulation of pro-inflammatory gene expression and signal transduction pathways. *Curr. Drug Metab.* 10, 256–271.
- Yamaguchi, K., Mitsui, T., Aso, Y., Sugibayashi, K., 2008. Structure-permeability relationship analysis of the permeation barrier properties of the stratum corneum and viable epidermis/dermis of rat skin. *J. Pharm. Sci.* 97, 4391–4403.
- Weng, J.R., Huang, T.H., Lin, Z.C., Alalaiwe, A., Fang, J.Y., 2019. Cutaneous delivery of [1-(4-chloro-3-nitrobenzenesulfonyl)-1H-indol-3-yl]-methanol, an indole-3-carbinol derivative, mitigates psoriasisiform lesion by blocking MAPK/NF- κ B/AP-1 activation. *Biomed. Pharmacother.* 119, 109398.
- Zorn-Kruppa, M., Vidal-y-Sy, S., Houdek, P., Wladykowski, E., Grzybowski, S., Gruber, R., Gorzelanny, C., Harcup, J., Schneider, S.W., Majumdar, A., Brandner, J.M., 2018. Tight junction barriers in human hair follicles-role of claudin-1. *Sci. Rep.* 8, 12800.



Cytotoxic and anti-inflammatory effects of lignans and diterpenes from *Cupressus macrocarpa*

Eman Al-Sayed^a, Tzu-Yi Ke^b, Tsong-Long Hwang^{c,d,e,f}, Shu-Rong Chen^b, Michal Korinek^{c,d,g}, Shu-Li Chen^b, Yuan-Bin Cheng^{b,h,i,*}

^a Department of Pharmacognosy, Faculty of Pharmacy, Ain-Shams University, Cairo 11566, Egypt

^b Graduate Institute of Natural Products, Center for Natural Product Research and Development, College of Pharmacy, Drug Development and Value Creation Research Center, Kaohsiung Medical University, Kaohsiung 80708, Taiwan

^c Graduate Institute of Natural Products, College of Medicine, Chang Gung University, Taoyuan 33302, Taiwan

^d Research Center for Chinese Herbal Medicine, Research Center for Food and Cosmetic Safety, and Graduate Institute of Health Industry Technology, College of Human Ecology, Chang Gung University of Science and Technology, Taoyuan 33302, Taiwan

^e Department of Anesthesiology, Chang Gung Memorial Hospital, Taoyuan 33302, Taiwan

^f Chinese Herbal Medicine Research Team, Healthy Aging Research Center, Chang Gung University, Taoyuan 33302, Taiwan

^g Department of Biotechnology, College of Life Science, Kaohsiung Medical University, Kaohsiung 80708, Taiwan

^h Department of Marine Biotechnology and Resources, National Sun Yat-sen University, Kaohsiung 80424, Taiwan

ⁱ Department of Medical Research, Kaohsiung Medical University Hospital, Kaohsiung 80708, Taiwan

ARTICLE INFO

Keywords:

Cupressus macrocarpa
Diterpenes
Lignans
Cytotoxicity
Anti-inflammatory
Superoxide anion
Elastase

ABSTRACT

Cupressus macrocarpa is a windbreak tree and is reported to have various cytotoxic effects. A natural product study on the leaves of *C. macrocarpa* has yielded ten secondary metabolites, including three new diterpenoids (1–3), four known diterpenoids (4–7), and three known lignans (8–10). The structures of all isolated compounds were elucidated via the interpretation of spectroscopic methods, especially 2D NMR and mass analyses. In the cytotoxic assays, compounds 1–3 and 7–10 showed inhibition effect against HepG2, MDA-MB-231, and A549 cells with IC₅₀ values ranging from 0.004 to 19.9 µg/mL. Moreover, the anti-inflammatory assays revealed that (–)-matairesinol (8) had significant inhibitory activities on superoxide anion generation (IC₅₀ = 2.7 ± 0.3 µM) and elastase release (IC₅₀ = 6.6 ± 0.7 µM).

Plants from the genus *Cupressus* are members of the Cupressaceae family which comprises coniferous plants. Different *Cupressus* species was used in traditional medicine for the treatment of various ailments, including inflammation and infection.¹ *Cupressus macrocarpa* Hartw. ex Gord is one of the most-known cultivated ornamental trees.² Several contributions have been reported on the composition of the essential oils of *C. macrocarpa*²; however, few studies have been reported on the non-volatile constituents of *C. macrocarpa*. The major chemotaxonomic secondary metabolites of *Cupressus* plants are lignans,³ biflavonoids,^{1,4} and diterpenes.⁵ Our previous work showed that cupressuflavone, a biflavonoid obtained from *C. macrocarpa* has a hepatoprotective activity against CCl₄-induced hepatotoxicity in rats.⁶ The extracts of different *Cupressus* plants, including *C. lusitanica* exhibited cytotoxic and apoptotic effects against a panel of cancer cell lines.⁷ Different labdane diterpenes demonstrated significant cytotoxic effects.⁸

Despite the diverse medicinal properties of different *Cupressus*

species, no study has so far been reported on the cytotoxicity and anti-inflammatory activity of the diterpenes and lignans of *C. macrocarpa*.⁹ The present study led to the isolation of three new diterpenes along with four known diterpenes and three lignans from the leaves of *C. macrocarpa*.¹⁰ All isolated compounds were identified based on their HRESIMS, optical activity, IR, ¹H NMR, ¹³C NMR, and 2D NMR spectroscopic data.¹¹ Several compounds showed potent anti-inflammatory and cytotoxic activities.

Air-dried powdered leaves of *C. macrocarpa* were extracted with MeOH, followed by solvent fractionation of the total extract by partitioning with hexane, CH₂Cl₂ and EtOAc successively. The CH₂Cl₂ fraction was separated on a flash silica gel column eluted with *n*-hexane: EtOAc mixtures, followed by purification using different chromatographic methods to give ten secondary metabolites, including three new diterpenes, named cupresins A–C (1–3). The isolated compounds were identified based on their ESIMS and NMR data, along with

* Corresponding author at: Graduate Institute of Natural Products, Center for Natural Product Research and Development, College of Pharmacy, Drug Development and Value Creation Research Center, Kaohsiung Medical University, Kaohsiung 80708, Taiwan.

E-mail address: jmb@kmu.edu.tw (Y.-B. Cheng).

<https://doi.org/10.1016/j.bmcl.2020.127127>

Received 3 January 2020; Received in revised form 17 March 2020; Accepted 19 March 2020

Available online 20 March 2020

0960-894X/ © 2020 Elsevier Ltd. All rights reserved.

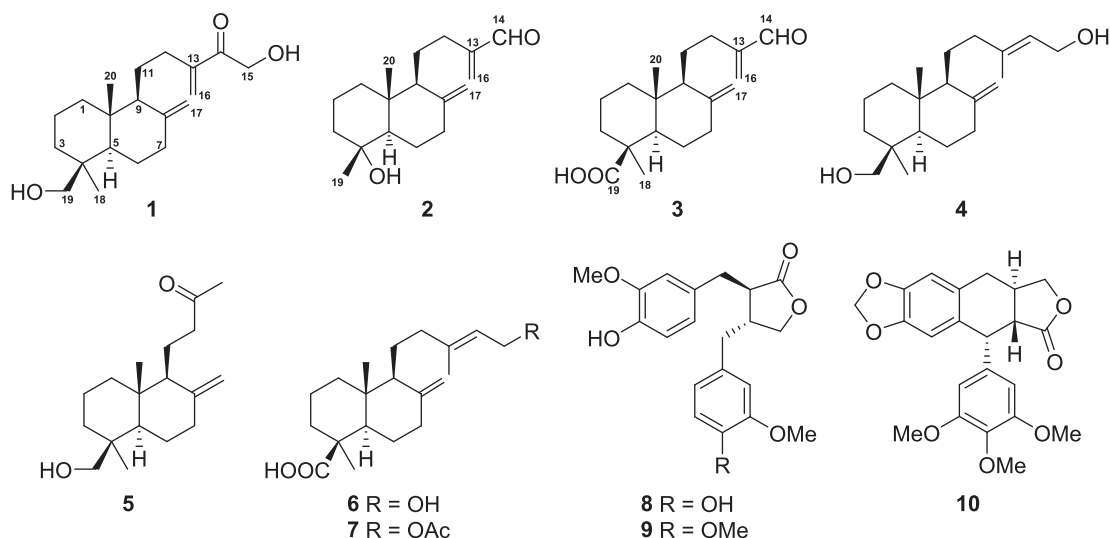


Fig. 1. Structures of compounds 1–10 isolated from the leaves of *C. macrocarpa*.

comparing these data with literature. The known compounds were identified as: agathadiol (4),⁸ 19-hydroxy-13-oxo-15,16-dinor-ent-labda-8(17)-ene (5),¹² isocupressic acid (6),¹³ acetyliscupressic acid (7),⁸ (–)-matairesinol (8),¹⁴ arctigenin (9),¹⁴ and (–)-deoxy-ypodophyllotoxin (10) (Fig. 1).¹³

Cupresin A (1)¹⁵ was obtained as an off white powder and identified based on its HR-ESIMS, IR, optical rotation and NMR data. The molecular formula of 1 was assigned to be $C_{20}H_{32}O_3$ based on HRESIMS spectrum which showed a parent ion peak at m/z 343.2245 $[M + Na]^+$ (calculated: 343.2249). The IR spectrum showed stretching absorption bands at 3441 cm^{-1} (a broad peak assigned to OH group), 3082 and 2930 cm^{-1} (stretching bands for sp^2 and sp^3 C–H stretching, respectively), 1685 cm^{-1} (unsaturated carbonyl group), and 1643 (exocyclic conjugated C=C). Also, bands pertaining to CH_2 and CH_3 bending vibrations were recognized at 1449 and at 1380 cm^{-1} , respectively.

The 1H NMR spectrum of 1 (Table 1) showed characteristic signals of a bicyclic labdane-type diterpene, as characterized by two pairs of geminal exocyclic olefinic proton signals. The first one H-16 appeared

at δ 5.82 and 5.93 ppm, while the second one H-17 was observed at δ 4.59 and 4.86 ppm. Furthermore, the DEPT and HMQC spectra also displayed two methylene exocyclic olefinic carbons δ_C 107.0 and 125.0 corresponding to C-17 and C-16, respectively, together with two quaternary olefinic carbons at δ_C 147.9 and 146.5 for C-8 and C-13, respectively. Also, the 1H NMR spectrum showed the presence of two singlet methyl groups at δ_H 0.98 and 0.64, which showed HMQC correlations with C-18 (δ_C 27.2) and C-20 (δ_C 15.1), respectively. Four geminal oxygenated methylene protons at δ_H 3.39, 3.75 corresponding to H-19 and δ_H 4.56, 4.57 corresponding to H-15, suggested the presence of two OH groups at C-19 and C-15. The ^{13}C NMR data of 1 (Table 1) exhibited a signal at δ_C 200.0 suggesting the presence of a CO functionality. The proton correlations between H-19 and CH-20 in the NOESY spectrum indicated the disposition of these groups at C-4 and C-10 are both axial (Fig. 2). Furthermore, the NOESY correlations between H-9, H-5 and CH-18 suggested the confirmation of these groups.

The HMBC correlations (Fig. 2) were observed between the olefinic protons H-17 and C-9, C-7 confirming the presence of an exocyclic

Table 1

1H (600 MHz) and ^{13}C (150 MHz) NMR data of 1–3 in $CDCl_3$.

NO.	1		2		3	
	δ_H mult. (J in Hz)	δ_C , type	δ_H mult. (J in Hz)	δ_C , type	δ_H mult. (J in Hz)	δ_C , type
1	1.74 m; 1.02 m	39.1, CH_2	1.69 m; 1.04 m	38.4, CH_2	1.80 m; 1.05 m	39.2, CH_2
2	1.49 m	19.1, CH_2	1.63 m; 1.44 m	20.6, CH_2	1.84 m; 1.51 m	20.0, CH_2
3	1.82 m; 0.96 m	35.5, CH_2	1.77 m; 1.35 m	43.1, CH_2	2.15 m; 1.05 m	38.2, CH_2
4		39.0, C		72.6, C		44.2, C
5	1.25 m	56.4, CH	1.38 m	57.1, CH	1.32 dd (12.4, 3.1)	56.4, CH
6	1.81 m; 1.32 m	24.6, CH_2	1.94 m; 1.33 m	23.5, CH_2	1.98 m; 1.87 m	26.2, CH_2
7	2.51 m; 2.09 m	38.7, CH_2	2.43 m; 1.99 m	38.0, CH_2	2.41 m; 1.88 m	38.8, CH_2
8		147.9, C		147.6, C		147.6, C
9	1.62 m	56.7, CH	1.68 m	56.3, CH	1.60 d (12.0)	55.9, CH
10		39.7, C		40.4, C		40.5, C
11	1.59 m; 1.46 m	22.8, CH_2	1.61 m; 1.51 m	22.4, CH_2	1.63 m; 1.48 m	22.3, CH_2
12	2.40 m; 1.93 m	30.3, CH_2	2.42 m; 2.03 m	27.5, CH_2	2.43 m; 2.04 m	27.5, CH_2
13		146.5, C		151.0, C		151.0, C
14		200.0, C	9.54 s	195.0, CH	9.53 s	195.0, CH
15	4.57 d (3.5)	64.9, CH_2				
16	4.56 d (3.5)					
17	5.93 s; 5.82 s	125.0, CH_2	6.24 s; 5.98 s	134.1, CH_2	6.24 s; 5.98 s	134.1, CH_2
18	4.86 s; 4.59 s	107.0, CH_2	4.90 s; 4.63 s	107.4, CH_2	4.89 s; 4.60 s	106.9, CH_2
19	0.98 s	27.2, CH_3			1.24 s	29.1, CH_3
20	3.75 d (10.8)	65.2, CH_2	1.11 s	23.3, CH_3		181.3, C
	3.39 d (10.8)					
	0.64 s	15.1, CH_3	0.64 s	14.1, CH_3	0.59 s	13.0, CH_3

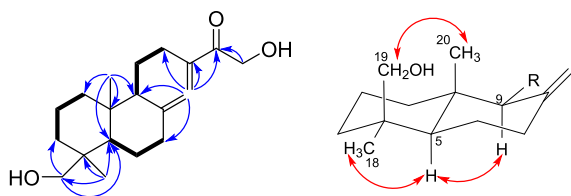


Fig. 2. COSY (bold bond), HMBC (arrow), and NOESY (left right arrow) correlations of **1**.

double bond. Moreover, the position of the other exocyclic double bond at C-8 was deduced on the basis of the HMBC correlations from H-16 to C-12, C-13 and the carbonyl group C-14. The HMBC correlations between the methylene protons H-15 and C-14 were also recognized confirming the structure. The HMBC correlations between CH₃-20 protons and C-1, C-5, C-9, and C-10 indicated the position of the methyl group at C-10. The position of the other oxygenated methylene protons was recognized from the HMBC correlations between the geminal protons H₂-19 and C-5 and C-3, along with the HMBC correlations between the protons H₃-18 with C-19, C-5 and C-4. All other protons were assigned based on the ¹H, DEPT, ¹³C, COSY, HMQC and HMBC NMR spectroscopic data. Based on these data, compound **1** was characterized as 15,19-dihydroxy-14-oxolabda-8(17),13(16)-diene.

Cupresin B (**2**)¹⁶ was obtained as an off white powder and its HRESIMS spectrum showed a peak at *m/z* 299.1982 [M + Na]⁺, suggesting a molecular formula of C₁₈H₂₈O₂Na (calculated: 299.1987). The IR spectrum of **2** displayed typical weak stretching vibration pairs of C–H of an aldehyde at 2856 and 2705 cm^{−1}. Similar to compound **1**, the IR spectrum of **2** displayed stretching absorption bands at 3424 cm^{−1} (a broad peak consistent with an OH group), 3081 and 2932 cm^{−1} (stretching bands for *sp*² and *sp*³ C–H), and a band for unsaturated carbonyl group of CHO at 1685 cm^{−1}. Also, an exocyclic conjugated C=C band at 1643 cm^{−1} was observed.

The ¹H NMR spectrum of **2** (Table 1) displayed characteristic signals of a bicyclic labdane-type diterpene similar to **1**. Furthermore, a typical CHO singlet at δ_H 9.54, along with HMQC correlation for its carbon at δ_C 195.0 suggested a conjugated CHO group. Similarly, two pairs of geminal exocyclic olefinic proton signals were also observed at δ_H 4.63, 4.90, 5.98, and 6.24. Unlike **1**, no oxygenated methylene or methine protons were observed; however, a hydroxylated quaternary carbon at δ 72.6 was observed corresponding to C-4. The position of the aldehyde group at C-13 was suggested by the HMBC correlations between the aldehyde proton H-14 and C-13. HMBC correlations were also detected between the olefinic protons H-16 and CHO carbon, which confirmed the position of CHO group. The HMBC correlations of CH₃-20/C-1, C-9, and C-10, and of CH₃-19/C-3, C-4, and C-5 demonstrated the position of the methyl group at C-10 and C-4, respectively. The relative stereochemistry of CH₃-19 and CH₃-20 was deduced to be in the β configuration (axial, axial) from the cross-peaks in the NOESY spectrum (Fig. 3). In addition, correlations between H-9 and H-5 in the NOESY spectrum suggested their axial orientation. The structure of compound **2** was thus deduced from ¹H, DEPT, ¹³C, and 2D NMR spectroscopic data as 15,18-bisnor-4-hydroxy-labda-8(17),13(16)-diene-14-al.

Cupresin C (**3**)¹⁷ was isolated as off white powder and exhibited a peak at *m/z* 327.1932 [M + Na]⁺ corresponding to a molecular formula

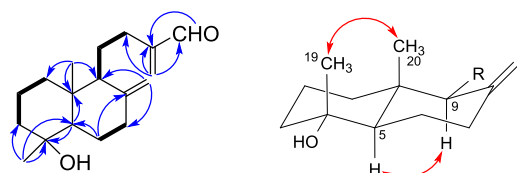


Fig. 3. COSY (bold bond), HMBC (arrow), and NOESY (left right arrow) correlations of **2**.

of C₁₉H₂₈O₃Na (calculated: 327.1936). A band at 1646 cm^{−1} was consistent with an exocyclic conjugated C=C functionality. A typical CHO singlet at δ_H 9.53 was consistent with a conjugated CHO (C-14) group as in **2**. The presence of two pairs of geminal exocyclic olefinic proton signals suggested a similar structure as **2**. HMBC correlations were observed between the signals of aldehyde proton H-14 and C-12, C-13 and C-16. In addition, a signal at δ_C 181.3 was observed indicating the presence of a COOH. Moreover, HMBC correlations with this COOH group and the CH₃ protons at C-4, along with HMBC correlations with H-3 and H-5 confirmed the position of COOH at C-4. The NOESY cross-peaks of H-5/H-1/H-9 suggested that these protons are α-oriented. The absence of NOESY correlation between CH₃-18 and CH₃-20 implied the equatorial and axial disposition of these two methyl groups, respectively. The structure of **3** was concluded to be 15-nor-4-carboxy-labda-8(17),13(16)-diene-14-al.

The isolated lignans: (−)-matairesinol (**8**), arctigenin (**9**), and (−)-deoxypodophyllotoxin (**10**) showed strong cytotoxic effects,^{18,19} especially (−)-deoxypodophyllotoxin (**10**) significantly inhibited the growth of breast cancer (MDA-MB-231) and lung cancer (A549) cell lines with IC₅₀ values of 0.07 and 0.004 μg/mL, respectively, which is far more potent than doxorubicin (Table 2). Moreover, **9** also displayed potent cytotoxicity against all tested cell lines, with IC₅₀ values of 2.8, 1.1, and 0.8 μg/mL for liver cancer cells HepG2, MDA-MB-231, and A549 cells, respectively. (−)-Matairesinol (**8**) demonstrated moderate cytotoxic effect on HepG2 cells only (IC₅₀ = 15.1 μg/mL). These results are in accordance with previous reports which demonstrated that **9** has cytotoxic effects against different cell lines like HL-60, K562, AGC, and Hepa 1c1c7 cell lines. Previous studies also showed that (−)-matairesinol (**8**) inhibited AGC and Hepa 1c1c7 cells.¹⁴ As for the isolated diterpenes, the present study showed that new compounds **1–3** displayed a moderate cytotoxicity against MDA-MB-231 cells, with IC₅₀ values of 19.9, 14.8 and 14.1 μg/mL, respectively. Compound **1** also displayed cytotoxicity on A549 cells (IC₅₀ = 19.8 μg/mL). It is worth noting that acetyliscupressic acid (**7**) exhibited cytotoxic effect on MDA-MB-231 (IC₅₀ = 14.8 μg/mL) and A549 (IC₅₀ = 8.9 μg/mL) cells, whereas, isocupressic acid (**6**) did not show any cytotoxic effect. Experimental evidence showed that labdane diterpenes have cytotoxic effects against different cell lines. Agathadiol (**4**), isocupressic acid (**6**) and acetyliscupressic acid (**7**) displayed significant cytotoxicity on NUGC and HONE-1 cells indicating that 13-ene and 15-OH functional groups are necessary for the cytotoxic activity.⁸ However, the current study has indicated that compounds **1–3** possessing the 13-ene functionality but lacking the 15-OH group, are cytotoxic. Previous reports have also suggested that the cytotoxicity depends on the functional groups at C-19. Substitution with a CHO group gives the most potent cytotoxicity, followed by CH₂OH and finally a COOH functionality.⁸ In contrast, the present study did not show any difference in the cytotoxicity of these compounds based on the aforementioned groups.

Because the limited amount of isolated compounds, compounds **4–6** and **8** were evaluated for their anti-inflammatory activity. Fortunately, these compounds displayed anti-inflammatory activities

Table 2
Cytotoxicity (IC₅₀, μg/mL) against HepG2, MDA-MB-231, and A549 Cells.^a

Compound	HepG2	MDA-MB-231	A549
1		19.9	19.8
2		14.8	
3		14.1	
7		14.8	8.9
8	15.1		
9	2.8	1.1	0.8
10	14.5	0.07	0.004
doxorubicin ^b	0.4	0.6	0.057

^a Inactive compounds are omitted.

^b Positive control.

Table 3

Inhibitory effects of active compounds on superoxide anion generation and elastase release in fMLF/CB-induced human neutrophils.

Cpd.	Superoxide anion		Elastase	
	IC ₅₀ (μM) ^a	Inh %	IC ₅₀ (μM) ^a	Inh %
4	9.6 ± 0.3	50.7 ± 0.4	***	22.3 ± 5.9
5		33.5 ± 4.1	**	15.7 ± 4.4
6	4.8 ± 0.2	78.0 ± 4.4	***	19.9 ± 4.2
8	2.7 ± 0.3	95.2 ± 2.2	***	61.9 ± 5.9
Pos.^b	1.5 ± 0.2	96.3 ± 3.2	***	73.4 ± 4.5

Percentage of inhibition (Inh %) was tested at 10 μM concentration.

^aConcentration necessary for 50% inhibition denotes IC₅₀. Results are presented as means ± SEM (n = 3 ~ 4). *P < 0.05, **P < 0.01, ***P < 0.001 compared with the control (DMSO). ^bPositive control is LY694002.

on elastase and superoxide anion release from human neutrophils.^{20–23} As illustrated in Table 3, (–)-matairesinol (**8**) markedly inhibited superoxide anion (IC₅₀ = 2.7 μM) and elastase release (IC₅₀ = 6.6 μM). While agathadiol (**4**) (IC₅₀ = 9.6 μM) and isocupressic acid (**6**) (IC₅₀ = 4.8 μM) only inhibited the superoxide anion release from neutrophils. In line with our results, (–)-matairesinol (**8**) has been recently reported to inhibit TNF-α secretion from LPS-activated neutrophils²⁴ and NO production²⁵ and iNOS and COX-2 expression via NF-κB and MAPK pathways²⁶ in macrophages. Such results indicated inhibitory effects of **8** on the function of immune cells. Furthermore, agathadiol (**4**) (IC₅₀ = 9.6 μM) and isocupressic acid (**6**) (IC₅₀ = 4.8 μM), a major isolated compound, inhibited solely the superoxide anion release from neutrophils indicating selectivity towards respiratory burst of neutrophils.

In our investigation of the leaves of *Cupressus macrocarpa*, ten compounds including three new diterpenes (**1–3**) were isolated and the cytotoxic and anti-inflammatory effect of the isolated compounds were evaluated. New compounds **2** and **3** can selectively inhibit the triple-negative breast cancer cell line (MDA-MB-231). The major compound [isocupressic acid (**6**), yield 0.012%] was found to have a profound anti-inflammatory effect on respiratory burst in human neutrophils, which is consistent with the traditional medicinal records of this plant. Lignan (–)-matairesinol (**8**) showed potent anti-inflammatory activity. Our findings prove that *C. macrocarpa* is a rich source of lignans and diterpenes with potential cytotoxic and anti-inflammatory properties.

Declaration of Competing Interest

The authors declare that they have no known competing financial interests or personal relationships that could have appeared to influence the work reported in this paper.

Acknowledgments

This work was funded by grants from the Ministry of Science and Technology of Taiwan (MOST-107-2628-B-037-001 and MOST-108-2320-B-037-013-MY3 awarded to Prof. Yuan-Bin Cheng; MOST 106-2320-B-255-003-MY3 and MOST 108-2320-B-255-003-MY3 awarded to Prof. Tsong-Long Hwang). We thank the Center for Research Resources and Development of Kaohsiung Medical University for providing the service of LC-MS and NMR.

Appendix A. Supplementary data

Supplementary data to this article can be found online at <https://doi.org/10.1016/j.bmcl.2020.127127>.

References

- Ibrahim NA, El-Seedi HR, Mohammed MM. Phytochemical investigation and hepatoprotective activity of *Cupressus sempervirens* L. leaves growing in Egypt. *Nat Prod Res.* 2007;21:857–866.
- El-Ghorab AH, El-Massry KF, Shaaban HA. Effect of drying on the chemical composition of the Egyptian *Cupressus macrocarpa* (Hartw. ex Gordon) essential oils and their biological characteristics. *J Essent Oil-Bear Plants.* 2007;10:399–411.
- Cowan S, Bartholomew B, Watson AA, et al. Lignans from *Cupressus lusitanica* (Cupressaceae). *Biochem Syst Ecol.* 2001;29:109–111.
- Kim HP, Park H, Son KH, Chang HW, Kang SS. Biochemical pharmacology of bi-flavonoids: implications for anti-inflammatory action. *Arch Pharmacol Res.* 2008;31:265–273.
- Rawat P, Khan MF, Kumar M, et al. Constituents from fruits of *Cupressus sempervirens*. *Fitoterapia.* 2010;81:162–166.
- Al-Sayed E, Abdel-Daim MM. Protective role of cupressuflavone from *Cupressus macrocarpa* against carbon tetrachloride-induced hepato- and nephrotoxicity in mice. *Planta Med.* 2014;80:1665–1671.
- López L, Villavicencio MA, Albores A, et al. *Cupressus lusitanica* (Cupressaceae) leaf extract induces apoptosis in cancer cells. *J Ethnopharmacol.* 2002;80:115–120.
- Chiang Y-M, Liu H-K, Lo J-M, et al. Cytotoxic constituents of the leaves of *Calocedrus formosana*. *J Chin Chem Soc.* 2003;50:161–166.
- The leaves of *C. macrocarpa* were collected in May 2017 from El-Maryland Botanical Garden, Cairo, Egypt. The plant was taxonomically identified by Eng. Anour Ezeldein, the taxonomy specialist at the herbarium of El-Maryland Botanical Garden, Cairo, Egypt. A voucher specimen of *C. macrocarpa* was deposited at the herbarium of the Department of Pharmacognosy, Faculty of Pharmacy, Ain Shams University, Cairo, Egypt (ASU CMC2017).
- Air-dried powdered leaves of *C. macrocarpa* (3 kg) were extracted three times with MeOH. The total extract was concentrated under vacuum to yield a residue (200 g), then dissolved in 70% MeOH and partitioned successively with n-hexane. The MeOH layer was then dried, re-dissolved in 50% MeOH and partitioned with CH₂Cl₂ to give the CH₂Cl₂ fraction (83 g). The remaining 50% MeOH fraction was concentrated and dried then dissolved in water and fractionated against EtOAc. Column fractionation of part of CH₂Cl₂ fraction (30 g) was achieved using flash silica gel 60 (5 × 50 cm), eluted with n-hexane followed by n-hexane: EtOAc mixtures of increasing polarities. Fractions are combined based on their analytical TLC profiles to afford 6 major fractions. The fraction eluted with n-hexane: EtOAc (4:6) was concentrated to obtain a gummy residue (10 g) rich in diterpenes. This fraction was then subjected to column fractionation on a silica gel 60 column (5 × 30 cm) with elution performed using CH₂Cl₂: EtOAc mixtures to yield 4 main sub-fractions (I–IV). Sub-fraction I (2 g) was applied on a Sephadex LH-20 column (2.5 × 20 cm) and eluted with CH₂Cl₂: MeOH, to obtain 10 sub-fractions. Sub-fraction I-6 was subjected to preparative HPLC (method 1) to obtain compound 10 (8.6 mg). Sub-fraction I-7 was subjected to repeated preparative HPLC (method 1) to give compounds 7 (0.5 mg) and 9 (6.2 mg). Sub-fraction II (64 mg) was first dissolved in MeOH, the MeOH-soluble part was subjected to preparative HPLC (method 2) to obtain compound 8 (9.3 mg). Fraction IV (3 g) was subjected to Sephadex LH-20 column (2.5 × 20 cm) eluted with CH₂Cl₂: MeOH, to obtain two main sub-fractions IV-1 and IV-2. Sub-fraction IV-1 (521 mg) was applied on a silica gel 60 column and eluted with CH₂Cl₂: acetone: MeOH (10:1:0:0:1) to yield 4 main sub-fractions. Fraction IV-1-2 (44.0 mg) was purified on preparative HPLC (method 3) to obtain compounds 1 (1.0 mg), 2 (0.8 mg), 3 (1.4 mg), and 5 (3.3 mg). Fraction IV-1-3 (129.0 mg) was purified on a silica gel 60 column and eluted with hexane: acetone: MeOH (5:1:0:0:1) followed by preparative HPLC (method 4) to obtain compound 4 (29.0 mg). Sub-fraction IV-2 (1.2 g) was applied to a silica gel 60 column and eluted with CH₂Cl₂: acetone: MeOH (60:1:0:0:1) to yield 6 sub-fractions. From sub-fraction IV-2-3, compound 6 (353.4 mg) was obtained. Method 1 of separation: The mobile phase consisted of acetonitrile (A) and 0.4 % formic acid (B). The elution profile was 0 min (40% A in B); 0–22 min, 40–100% A in B; 22–25 min, 100%–40% A in B; with constant flow rate of 2.0 mL/min, UV: 210 nm. Method 2 of separation: The mobile phase consisted of 43% MeOH and 0.1% TFA in water, flow rate of 3.0 mL/min, UV: 210 nm. Method 3 of separation: The mobile phase consisted of 67% MeOH and 0.1 % TFA in water, flow rate of 3.0 mL/min, UV: 210 nm. Method 4 of separation: The mobile phase consisted of 73% MeOH and 0.1 % TFA in water, flow rate of 2.0 mL/min, UV: 210 nm.
- The NMR spectra were measured by JEOL (Tokyo, Japan) JNM-ECZS series 400 MHz FT NMR spectrometer. CDCl₃ was used as a solvent. Proton and carbon spectra were referenced internally to the CDCl₃ signal using the values of 7.26 and 77.0 ppm, respectively. The UV spectra were obtained with a Jasco (Tokyo, Japan) V-530 UV/VIS spectrophotometer. The IR spectra were recorded by a Jasco FT-IR 4100 spectrometer. The optical rotations were measured on a Jasco P-2000 digital polarimeter. ESIMS was performed on a Waters (Milford, MA, USA) 2695 Separations Module with a cone voltage 20V. HRESIMS was performed on a Bruker (Bremen, Germany) APEX II 30e spectrometer. For compounds 7, 9, and 10: Preparative HPLC was performed using a Knauer (Berlin, Germany) system composed of preparative pump K-1001, connected to a UV detector with multiple wavelength K-2501, injector D-14163, and a dynamic mixing chamber. The column used was Kromasil (Bohus, Sweden) RP-C18, 5 μm, 250 mm × 10 mm. For compounds 1–6 and 8: Semi-preparative HPLC was performed using a Shimadzu (Kyoto, Japan) system composed of system controller CBM-20A, pump LC-20AT with dynamic mixing chamber, PDA detector SPD-M20A, fraction collector FRC-10A, and Rheodyne (Bensheim, Germany) injector 7725i. A Phenomenex (Torrance, CA, USA) Luna C18 column (5 μm, 250 mm × 10 mm) was selected. Sephadex LH-20 was purchased from Amersham Biosciences, Sweden. RP-C18 was obtained from Sigma-Aldrich GmbH, Germany and pre-coated silica gel TLC GF254 was purchased from Riedel-De Haën.

- AG, Seelze Germany.
12. Xin Z, Lu Y, Xing X, Long J, Li J, Xue X. Synthesis of (–)-agathic acid and (–)-copalic acid from andrographolide via a regioselective Barton-McCombie reaction. *Tetrahedron*. 2016;72:555–562.
 13. Carpenter CD, O'Neill T, Picot N, et al. Anti-mycobacterial natural products from the Canadian medicinal plant *Juniperus communis*. *J Ethnopharmacol*. 2012;43:695–700.
 14. Sun LX, Chen Y, Liu LX, Jia YR, Li YC, Ma EL. Cytotoxic constituents from *Wikstroemia indica*. *Chem Nat Compd*. 2012;48:493–497.
 15. Cupresin A (1): off white amorphous powder; $[\alpha]_D^{23} + 36$ (CH₂Cl₂, c 0.05); UV (MeOH) λ_{max} (log ϵ): 208 (2.39), 224 (2.21). IR (neat) ν_{max} : 3441, 3082, 2930, 2850, 1685, 1643, 1449, 1380, 1261, 1026, 891, 803, 738 cm^{–1}; ¹H NMR (600 MHz, CDCl₃) and ¹³C NMR (150 MHz, CDCl₃) see Table 1; HRESIMS: m/z 343.2245 [M + Na]⁺ (calcd for C₂₀H₃₂O₃Na, 343.2249).
 16. Cupresin B (2): off white amorphous powder; $[\alpha]_D^{23} + 28$ (CH₂Cl₂, c 0.05); UV (MeOH) λ_{max} (log ϵ): 207 (2.39), 219 (2.30); IR (neat) ν_{max} : 3424, 3081, 2960, 2932, 2856, 2705, 1685, 1643, 1448, 1382, 1261, 1094, 1034, 801 cm^{–1}; ¹H NMR (600 MHz, CDCl₃) and ¹³C NMR (150 MHz, CDCl₃) see Table 1; HRESIMS: m/z 299.1982 [M + Na]⁺ (calcd for C₁₈H₂₈O₂Na, 299.1987).
 17. Cupresin C (3): off white amorphous powder; $[\alpha]_D^{23} + 42$ (CH₂Cl₂, c 0.05); UV (MeOH) λ_{max} (log ϵ): 208 (2.33), 217 (2.31); IR (neat) ν_{max} : 3438, 2937, 2848, 1690, 1646, 1448, 1261, 1178, 1091, 1030, 801 cm^{–1}; ¹H NMR (600 MHz, CDCl₃) and ¹³C NMR (150 MHz, CDCl₃) see Table 1; HRESIMS: m/z 327.1932 [M + Na]⁺ (calcd for C₁₉H₂₈O₃Na, 327.1936).
 18. Cell culture: hepatocellular carcinoma (HepG2), lung adenocarcinoma (A549), and breast cancer (MDA-MB-231) human cancer cell lines were purchased from the Food Industry Research and Development Institute (Hsinchu, Taiwan). The cells were maintained in DMEM-F12, with 10% FBS, 100 U/mL penicillin and 100 µg/mL streptomycin. Cytotoxicity assay: The cytotoxic activity of all compounds were evaluated by the MTT assay.²³ The experiment was done in triplicate. Inhibition % of cell viability and IC₅₀ were estimated. Doxorubicin was chosen as the standard control. Absorbance at 550 nm was measured by an ELISA reader (Thermo electron cooperation, Waltham, MA, USA).
 19. van de Loosdrecht AA, Nennie E, Ossenkoppele GJ, Beelen RH, Langenhuijsen MM. Cell mediated cytotoxicity against U937 cells by human monocytes and macrophages in a modified colorimetric MTT assay: a methodological study. *J Immunol Methods*. 1991;141:15–22.
 20. Human neutrophils were obtained from healthy human volunteers (from Chang Gung Medical Foundation, IRB: 104-8612C; Date of the study approval: November 25, 2018), and were isolated by Ficoll centrifugation and dextran sedimentation. Purified neutrophils were re-suspended in calcium (Ca²⁺)-free HBSS buffer at pH 7.4, and were maintained at 4 °C before use.²⁴ The assays for respiratory burst (superoxide anion generation) and degranulation (elastase release) in human neutrophils were performed as described before with some modifications.^{25,26} For superoxide anion generation assay, neutrophils (6 × 10⁵ cell/mL) were equilibrated in ferricytochrome c (0.6 mg/mL) and Ca²⁺ (1 mM) at 37 °C for 5 min and incubated with DMSO (0.1%) or tested compounds for another 5 min. Cells were activated with formyl-methionyl-leucyl-phenylalanine (fMLF, 0.1 µM) for 10 min after the priming with cytochalasin B (CB, 1 µg/mL) for 3 min. The change in absorbance was monitored continuously at 550 nm with a spectrophotometer (U-3010; Hitachi). For elastase release assay, neutrophils (6 × 10⁵ cell/mL) were equilibrated in MeO-Suc-Ala-Ala-Pro-Val-p-nitroanilide (100 µM) and Ca²⁺ (1 mM) at 37 °C for 5 min and incubated with DMSO (0.1%) or test compounds for another 5 min. Cells were activated with fMLF (0.1 µM) for 10 min after the priming with CB (0.5 µg/mL) for 3 min. The change in absorbance was monitored continuously at 405 nm with a spectrophotometer. The results are recorded as the mean ± SEM of three measurements. The inhibition % were measured at 10 µM concentration of each compound and IC₅₀ values were estimated from dose-response curves. Statistical analysis using Student's t-tests with SigmaPlot (Systat Software, San Jose, CA, USA).
 21. Chung Y-M, Chang F-R, Tseng T-F, et al. A novel alkaloid, aristopyridinone A and anti-inflammatory phenanthrenes isolated from *Aristolochia manshuriensis*. *Bioorg Med Chem Lett*. 2011;21:1792–1794.
 22. Yang S-C, Chung P-J, Ho C-M, et al. Propofol inhibits superoxide production, elastase release, and chemotaxis in formyl peptide-activated human neutrophils by blocking formyl peptide receptor 1. *J Immunol*. 2013;190:6511–6519.
 23. Hwang T-L, Leu YL, Kao SH, Tang MC, Chang HL. Viscolin, a new chalcone from *Viscum coloratum*, inhibits human neutrophil superoxide anion and elastase release via a cAMP-dependent pathway. *Free Radic Biol Med*. 2006;41:1433–1441.
 24. Michalak B, Filipiek A, Chomicz P, et al. Lignans from *Forsythia x Intermedia* leaves and flowers attenuate the pro-inflammatory function of leukocytes and their interaction with endothelial cells. *Front Pharmacol*. 2018;9:401.
 25. Fan C-Q, Zhu X-Z, Zhan Z-J, Ji X-Q, Li H, Yue J-M. Lignans from *Saussurea conica* and their NO production suppressing activity. *Planta Med*. 2006;72:590–595.
 26. Lee JY, Cho BJ, Park TW, et al. Dibenzylbutyrolactone lignans from *Forsythia koreana* fruits attenuate lipopolysaccharide-induced inducible nitric oxide synthetase and cyclooxygenase-2 expressions through activation of nuclear factor- κ B and mitogen-activated protein kinase in RAW264.7 cells. *Biol Pharm Bull*. 2010;33:1847–1853.

Anti-inflammatory, Antiplatelet Aggregation, and Antiangiogenesis Polyketides from *Epicoccum sorghinum*: Toward an Understating of Its Biological Activities and Potential Applications

Chi-Ying Li,^{1,†} Ching-Chia Chang,^{1,†} Yi-Hong Tsai, Mohamed El-Shazly, Chin-Chung Wu, Shih-Wei Wang, Tsong-Long Hwang, Chien-Kei Wei, Judit Hohmann, Zih-Jie Yang, Yuan-Bin Cheng, Yang-Chang Wu, and Fang-Rong Chang*



Cite This: *ACS Omega* 2020, 5, 11092–11099



Read Online

ACCESS |



Metrics & More

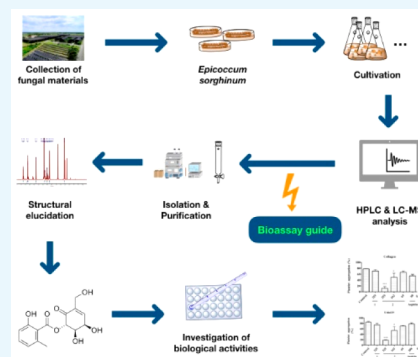


Article Recommendations



Supporting Information

ABSTRACT: The ethyl acetate extract of an endophyte *Epicoccum sorghinum* exhibited anti-inflammatory activity at a concentration of $<10 \mu\text{g/mL}$. By bioassay-guided fractionation, one new compound, named epicorepoxydon A (1), and one unusual bioactive compound, 6-(hydroxymethyl)benzene-1,2,4-triol (6), together with six known compounds, were isolated from *E. sorghinum*. The structures of all isolates were established by spectroscopic analyses. The relative configuration of 1 was deduced by the NOESY spectrum and its absolute configuration was determined by X-ray single-crystal analysis. The biological activities of all isolates were evaluated using four types of bioassays including cytotoxicity, anti-inflammatory, antiplatelet aggregation, and antiangiogenesis activities. Compounds 4 and 6 showed potent anti-inflammatory activity, compound 2 possessed potent antiplatelet aggregation and antiangiogenesis activities, and compound 6 demonstrated antiangiogenesis activity. This fungal species can cause a human hemorrhagic disorder known as onychia. In this study, we identified the active components with antiplatelet aggregation and antiangiogenesis activities, which may be related to the hemorrhagic disorder caused by this fungus. Moreover, we proposed a biosynthetic pathway of the isolated polyketide secondary metabolites and investigated their structure–activity relationship (SAR). Our results suggested that *E. sorghinum* is a potent source of biologically active compounds that can be developed as antiplatelet aggregation and anti-inflammatory agents.



INTRODUCTION

Natural products from terrestrial plants, microbial organisms, and marine organisms played a key role in drug discovery and development throughout the last two centuries. Many current therapeutic drugs have their origins from natural products or their derivatives.^{1,2} Mother Nature provided humanity with continuous sources of medicinal bioactive components that were active against numerous diseases.^{2–4} Among the major sources of biologically active compounds are fungi. They produce diverse groups of bioactive secondary metabolites, which have been utilized in food, agriculture, or pharmaceutical industries such as cyclosporine, lovastatin, and penicillin.^{1,2} Endophytic fungi, which reside in inter- and/or intracellular parts of plants, are known to enhance host growth and generate numerous prominent bioactive secondary metabolites.^{5–7} These fungi may improve plants' ability to stand for various types of living stresses and increase their resistance to insects and pests.^{6,7} Therefore, the chemical and biological exploration of endophytic fungi continued to be helpful for the discovery of bioactive natural products.

Continuing our effort in discovering the chemical diversity and biological activities of natural compounds,^{8–10} the fungal

strain *Epicoccum sorghinum*, isolated from the stem of *Arundo donax* Linn, was investigated due to the potent anti-inflammatory activity of its ethyl acetate (EtOAc) crude extract at a concentration of $<10 \mu\text{g/mL}$. Few phytochemical investigations have focused on this plant and its endophytic fungi. Indole derivatives were isolated from *A. donax*, which was collected from the Dr. Cecilia Koo Botanic Conservation Center (KBCC) after seasonal pruning.^{11,12} *E. sorghinum* is considered as a major component of the sorghum grain-mold disease complex and potent producer of tenuazonic acid (TeA).¹³ This mycotoxin is a tetrameric acid derivative and has the potential to inhibit protein biosynthesis.^{13,14} Sorghum is regarded as the fifth most important cereal crop around the world.¹⁵ Fungal contamination is deemed as one of the major problems associated with cereal crop production because some

Received: March 5, 2020

Accepted: April 24, 2020

Published: May 6, 2020



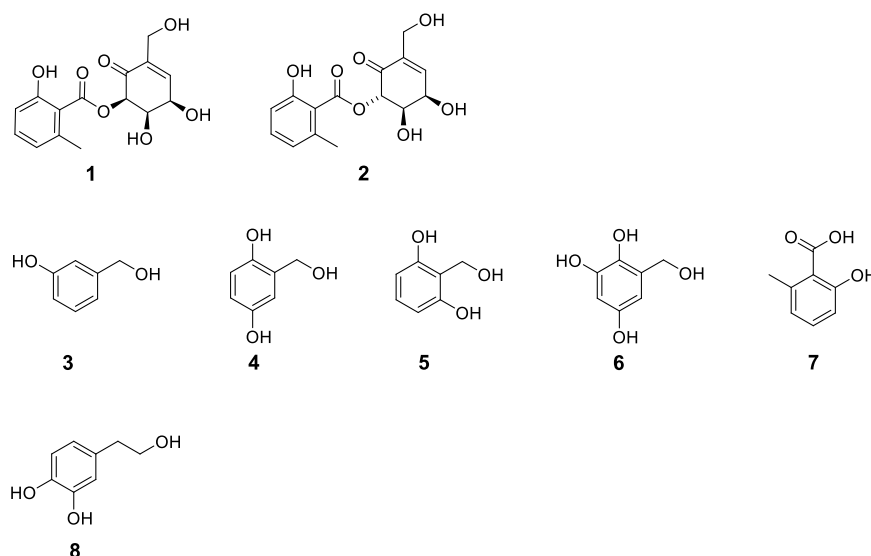


Figure 1. Structures of all isolates 1–8.

fungus species such as *Epicoccum* species can generate mycotoxins, which are harmful to humans and animals.^{13,15} Certain species of *Epicoccum* cause a human hemorrhagic disorder known as onyalai.¹³ *Epicoccum* species can contaminate various foods and beverages and cause leaf spot disease in different types of plants.^{13,15}

Onyalai is a hemorrhagic disorder that is characterized by the presence of blood blisters in the mouth and a form of thrombocytopenic purpura.^{13,16} This disease results from eating sorghum grains contaminated with *E. sorghinum*. However, no direct correlation was identified between onyalai and compounds isolated from *E. sorghinum*. Explaining the pathology of onyalai disease needs rigorous, comprehensive, and even long-term investigations. Advanced evidence needs to be explored in the future.

Several studies on *Epicoccum* species demonstrated a diversity of chemical components and a broad spectrum of biological activities.^{17–19} However, few studies focused on the secondary metabolites and their biological activities of *E. sorghinum*.^{20,21} Therefore, we performed an extensive chemical and biological investigation on this fungus and identified eight secondary metabolites, including one new compound, epicorepoxydon A (1), one unusual bioactive compound, 6-(hydroxymethyl)benzene-1,2,4-triol (6), one known ethyl phenyl-skeleton derivative, and five known benzyl-skeleton derivatives (Figure 1). The structure of 6 was illustrated in the PubChem database and no reference was reported.

Herein, we report the structural elucidation of a new compound (1) and its absolute configuration, which was deduced by X-ray single crystal analysis. We evaluated the cytotoxicity, anti-inflammatory, antiplatelet aggregation, and antiangiogenesis activities of all isolates to identify the secondary metabolites responsible for onyalai and all possible potential applications of this fungus. We also proposed a biosynthetic pathway of the isolated polyketide secondary metabolites and the structure–activity relationship (SAR) of the isolates.

RESULTS AND DISCUSSION

Compound 1 was obtained as brown acicular crystals. The molecular formula of $C_{15}H_{16}O_7$ was suggested for 1 based on a

deprotonated molecular ion at m/z 307.0822 $[M - H]^-$ in the negative mode HR-ESI-MS and ^{13}C NMR data indicating eight degrees of unsaturation. The IR spectrum absorption bands at 3448 and 1635 cm^{-1} implied hydroxyl and carbonyl functionalities, respectively. The 1H NMR spectrum (Table 1) showed the presence of one methyl group at δ_H 2.56 (s),

Table 1. 1H and ^{13}C NMR Data of 1 in CD_3OD^a

no	δ_H (mult, J in Hz)	δ_C , type
1		193.3, C
2		138.1, C
3	6.78, m	145.5, CH
4	4.80, d (5.7)	69.3, CH
5	4.50, dd (5.7, 2.4)	75.6, CH
6	5.80, d (2.4)	78.8, CH
7	4.27, s	59.3, CH_3
1'		116.2, C
2'		161.1, C
3'	6.75, m	115.7, CH
4'	7.26, t (7.6)	134.4, CH
5'	6.78, m	123.5, CH
6'		142.1, C
7'	2.56, s	22.8, CH_3
8'		170.2, C

^a 1H and ^{13}C NMR data (δ) were measured at 400 and 100 MHz, respectively; chemical shifts are in ppm; J values in Hz are in parentheses.

one methylene at δ_H 4.27 (s), three oxygenated methines at δ_H 4.50 (dd, J = 5.7, 2.4 Hz), δ_H 4.80 (d, J = 5.7 Hz), and δ_H 5.80 (d, J = 2.4 Hz), as well as four aromatic or olefinic methines at δ_H 6.75 (m), 6.78 (m, 2H), and 7.26 (t, J = 7.6 Hz). Fifteen signals were observed in the ^{13}C NMR (Table 1) and DEPT spectra of 1. These signals resulted from one methyl (δ_C 22.8), one methylene (δ_C 59.3), three oxygenated methines (δ_C 69.3, 75.6, and 78.8), four olefinic methines (δ_C 115.7, 123.5, 134.4, and 145.5), four quaternary carbons (δ_C 116.2, 138.1, 142.1, and 161.1), and two carbonyl carbons (δ_C 170.2 and 193.3).

Analyzing its 1H and ^{13}C NMR data, this compound showed high similarity to 2.²⁰ Thus, the structure of 1 was suggested as

one of the stereoisomers of the polyketide secondary metabolite **2**.

The COSY correlations of H-3' (δ_{H} 6.75)/H-4' (δ_{H} 7.26)/H-5' (δ_{H} 6.78) and the HMBC correlations of CH₃-7' (δ_{H} 2.56) with C-1' (δ_{C} 116.2), C-2' (δ_{C} 161.1), C-5' (δ_{C} 123.5), and C-6' (δ_{C} 142.1) as well as H-4' (δ_{H} 7.26) with C-2' (δ_{C} 161.1) and C-6' (δ_{C} 142.1) suggested hydroxy and methyl groups attached to a benzene ring moiety. This partial structure of **1** was deduced and showed similarity to **7**²² with an ester carbonyl moiety. The HMBC correlation of H-6 (δ_{H} 5.80) with C-8' (δ_{C} 170.2) suggested the connection of the ester carbonyl unit. Other parts of the COSY correlations, H-4 (δ_{H} 4.80)/H-5 (δ_{H} 4.50)/H-6 (δ_{H} 5.80), and HMBC correlations, H-6 (δ_{H} 5.80) with C-1 (δ_{C} 193.3) as well as H-7 (δ_{H} 4.27) with C-1 (δ_{C} 193.3), C-2 (δ_{C} 138.1), and C-3 (δ_{C} 145.5), established the linkage of a carbonyl functionality (Figure 2).

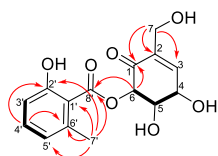


Figure 2. Key COSY (bold lines) and HMBC (red arrows) correlations of **1**.

The relative configuration of **1** was deduced by the analysis of NOESY correlations and comparison with the chemical shifts with the published compounds.²⁰ The NOESY correlations of H-4/H-5/H-6 suggested that these protons showed the same orientation (Figure 3).

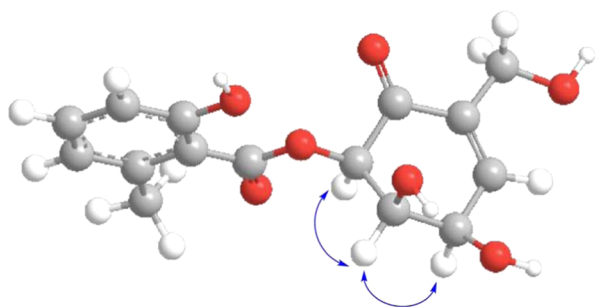


Figure 3. Key NOESY (blue double-headed arrows) correlations of **1**.

Compared with **2**, the missing correlation between H-5 and H-6 suggested that these two protons were pointed at different orientations. The proposed stereochemistry of **1** was further confirmed by X-ray single crystallographic analysis (Figure 4), and the name of the new compound, epicorepoxydon **A**, was given. Crystallographic data for **1** have been deposited at the Cambridge Crystallographic Data Centre with the deposition number of CCDC 1993524.

The structure of compound **6** was only displayed on the PubChem database with no reference nor spectroscopic data. The ¹H and ¹³C NMR data of **6** are summarized in Table S1. Interestingly, a series of unusual simple phenolic/polyphenolic benzyl/benzoic compounds with no common *para*-hydroxyl substitution, such as compounds **3–7**, were identified from this species for the first time (Table S4).

According to previous reports in the literature, *E. sorghinum* is regarded as the major component of the sorghum grain-mold

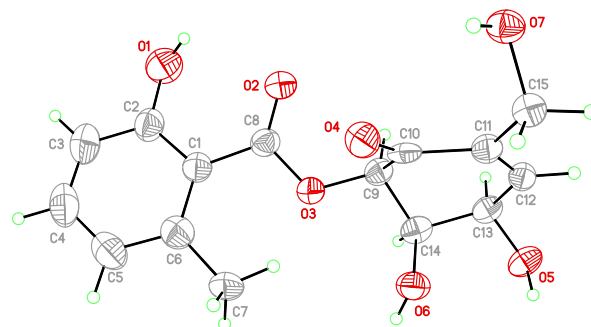


Figure 4. X-ray single crystallographic analysis of **1**.

disease complex and a producer of tenuazonic acid (TeA) that inhibits protein biosynthesis in sorghum.^{13–15} In the past, many researchers considered *Alternaria* sp. as the major producer of TeA causing food contamination. But in recent years, some researchers found that *E. sorghinum* (formerly identified as *Phoma sorghum*) produces TeA even more than *Alternaria* sp.^{13,23} These findings encouraged us to investigate if TeA was available in our *E. sorghinum* extract. After examining the extract by HPLC, TeA was observed under the standard separation condition (Figure S1). However, TeA was not separated because it was present in minute quantity. Such observation suggested that the isolated endophytic strain *E. sorghinum* did not produce large amounts of TeA under liquid PDB media cultivation, and the type of media significantly affected the metabolic profile of the fungal extract.

The structural similarities of the isolated compounds encouraged us to propose a plausible biosynthetic pathway of the isolated polyketide secondary metabolites based on the previously isolated analogs with similar partial structures (Figure 5).^{22,24} One acetyl-CoA and three malonyl-CoA combine to form a polyketide precursor that undergoes dehydration to afford **7**. Compound **7** undergoes decarboxylation followed by hydroxylation to produce **3** and **4**. Compound **4** undergoes dehydrogenation and hydroxylation to yield isoeopoxydon.²⁴ Isoeopoxydon undergoes hydrolysis to form (–)-gabosine C and (–)-gabosine E, respectively. (–)-Gabosine C reacts with **7** to obtain **1**. On the other hand, (–)-gabosine E reacts with **7** to furnish **2**. Theoretically, the hydrolysis that occurred on the epoxide at the C-5 and C-6 of isoeopoxydon would form four stereoisomers. The rule of acid-catalyzed hydroxylation of epoxides should result in a *trans* dihydroxy rather than a *cis* arrangement. However, biosynthesis has frequently shown that arrangements of chemical functions may not be transmitted according to chemical priority. Therefore, rare *cis* products may be available in the biosynthetic pathway.

Fungi generated many secondary metabolites that demonstrated a plethora of biological activities.^{1,25} The isolated compounds were subjected to a panel of biological assays. The crude extract was subjected to anti-inflammatory assay and by utilizing bioassay-guided fractionation, two potential candidates were purified and identified. Compound **6** exhibited promising inhibitory activity on both superoxide anion generation (IC₅₀ 0.25 ± 0.02 μM) and elastase release (IC₅₀ 1.60 ± 0.05 μM). Compound **4** also showed an anti-inflammatory effect by inhibiting superoxide anion generation with an IC₅₀ value of 4.54 ± 0.52 μM. The presence of **4** and **6** in large quantities in the extract suggested that these

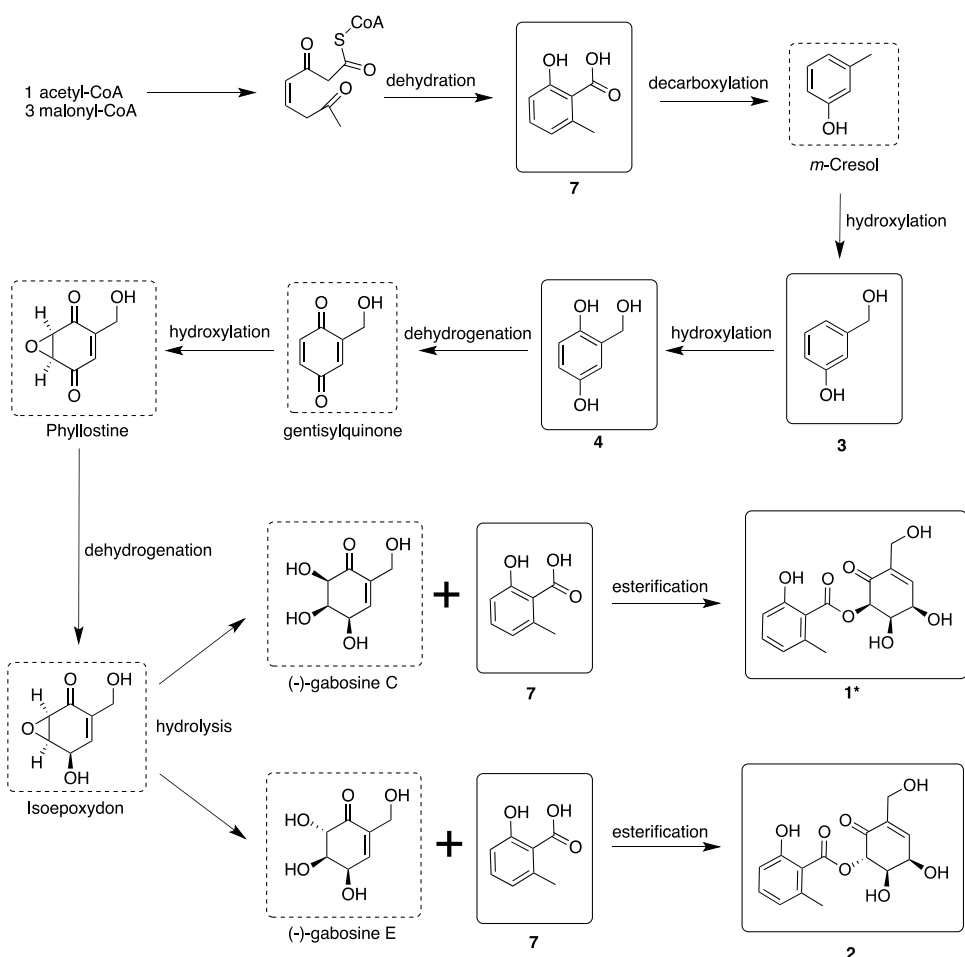


Figure 5. Plausible biosynthetic pathway of the five polyketide secondary metabolites from *E. sorghinum*.

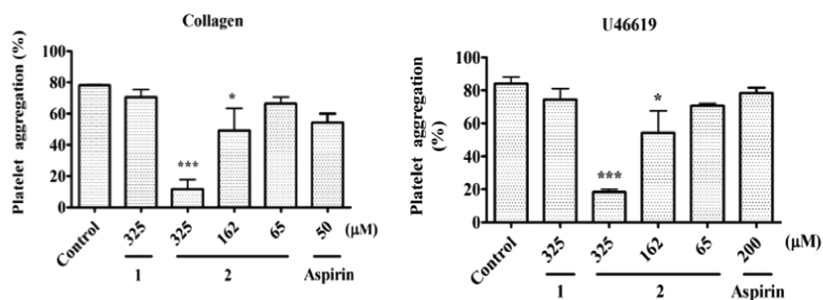


Figure 6. Antiplatelet aggregation activity of compounds 1 and 2. Aspirin was used as the positive control. Results are presented as mean \pm SEM ($n = 3$). * $P < 0.05$ as compared with the control. *** $P < 0.005$ as compared with the control.

components are responsible for the anti-inflammatory activity of the extract.

Certain secondary metabolites from endophytic fungi such as *Epicoccum nigrum* exhibited anti-inflammatory and inhibited the platelet-activating factor-induced release of β -glucuronidase from rat polymorphonuclear leukocytes *in vitro*.²⁶ Bisdethiobis-(methylthio)-gliotoxin from *Penicillium terlikowskii* was found to inhibit the platelet-activating factor (PAF)-induced rabbit platelet aggregation with IC_{50} 8.4 μ M.²⁷ Fungal toxins such as trichothecenes were found to induce hematological disorders including thrombopenia, neutropenia, and aplastic anemia in animals and humans.²⁸ *E. sorghinum* causes a human and animal hematological disease, which is known as onyala, after eating sorghum grains contaminated with the fungus.^{13,15}

Onyala is characterized by the presence of blood blisters in the mouth and a form of thrombocytopenic purpura.^{13,16} Platelets are the smallest blood cells that play an indispensable role in maintaining hemostasis. Dysfunction in the platelet activation process is manifested in hemorrhagic and thrombotic related diseases.²⁹ Collagen is a part of the primary hemostatic agonists, whereas thrombin, ADP, and TXA_2 are secondary stimulants.³⁰ Angiogenesis plays an important role in physiological conditions such as bone remodeling, embryonic development, reproduction, and tissue repair. The process of angiogenesis involves endothelial cell proliferation, migration, and tube formation to form new blood vessels.³¹ Until now, no one has investigated the relation between onyala and the natural components isolated from *E. sorghinum*. Among all

isolates, **2** displayed potent activity against two platelet aggregation factors, collagen and U46619. The IC_{50} values of **2** were 168.74 and 181.85 μM , respectively, while aspirin was the positive control. It also possessed significant antiangiogenic activity with an IC_{50} value of $11.0 \pm 0.50 \mu M$ (Figure 6). Although **1** is the C-6 position epimer of **2**, it was inactive in cytotoxicity, anti-inflammatory, antiplatelet aggregation, and antiangiogenesis assays. Compound **6** exhibited potent antiangiogenic activity with an IC_{50} $65.0 \pm 5.50 \mu M$. The cytotoxicity of all isolates was not significant against the tested cancer cells of A549, Hep-G2, and MDA-MB-231.

CONCLUSIONS

The chemical and biological investigation of the endophytic fungal strain *E. sorghinum* was carried out resulting in the isolation of one new and seven known compounds; the biosynthetic pathway of epicorepoxydon A (**1**) was proposed. The biological activities of **2**, **4**, and **6** in this study were reported for the first time. Interestingly, the different stereochemistry at the C-6 position between **1** and **2** resulted in a significant difference in their biological activities. Our findings suggested the first insights into the antiplatelet aggregation and antiangiogenesis activities of *E. sorghinum* components.

MATERIALS AND METHODS

Isolation of Compounds. In the current study, the culture broth of *E. sorghinum* was cultivated using 120 Erlenmeyer flasks (500 mL); each flask contained 300 mL of potato dextrose broth (PDB) media. The flasks were incubated for 7 days using a rotatory shaker (150 rpm and 25 °C). After incubation, 36 L of the whole culture broth was filtered to separate the filtrate from the mycelia. The filtrate was extracted with ethyl acetate (EtOAc) and concentrated under reduced pressure to obtain the EtOAc extract (9.3 g). The EtOAc extract was subjected to a series of column chromatography procedures to yield the new compound, epicorepoxydon A (**1**), along with seven known compounds including 4,5-dihydroxy-6-(6'-methylsalicyloxy)-2-hydroxymethyl-2-cyclohexen-1-one (**2**),²⁰ 3-hydroxybenzyl alcohol (**3**),³² gentisyl alcohol (**4**),³³ hydroxymethyl resorcinol (**5**),³⁴ 6-(hydroxymethyl)benzene-1,2,4-triol (**6**), 2-hydroxy-6-methyl benzoic acid (**7**),²² and hydroxytyrosol (**8**).³⁵ All isolates were deduced by analyzing and comparing their spectroscopic data with the literature values.

Fungal Material. The fungus *E. sorghinum* was isolated from the leaves of *A. donax* collected from the Dr. Cecilia Koo Botanic Conservation Center (KBCC), Pingtung, Taiwan, which deposits over 30 000 living plants. The leaves of *A. donax* were washed and air-dried. To clean the surface, the dried leaves were immersed in 0.01% Tween 20(aq), dd-H₂O, and 0.01% bleach(aq) for 1 min. The leaves were treated with 75% ethanol then the central parts (5 × 5 mm²) of the leaves were sliced by sterilized scissors and seeded on the potato dextrose agar. The fungal strains were maintained in potato dextrose agar media at 25 °C. After duplicated purification, the mycelia of the pure strain were deposited in 2 mL tubes containing 1.5 mL of potato dextrose broth media as well as 0.2 mL of sterilized glycerol and kept at −80 °C. The fungal strain was identified by Chi-Ying Li and Ching-Chia Chang. A voucher specimen (code number: K060107S-B) was deposited

at the Graduate Institute of Natural Products, College of Pharmacy, Kaohsiung Medical University, Kaohsiung, Taiwan.

Species Identification. The fungal sample was preserved in phosphate-buffered saline (PBS) at ambient temperature. The DNA extraction was accomplished by utilizing AxyPrep Multisource Genomic DNA Miniprep Kit (AxyPrep, #02815KC1) according to the manufacturing company's instructions. A pair of primers of the internal transcribed spacer, ITS 4 and ITS 5 (ITS 4: 5'-TCCTCCGCTTATTGATATGC3'/ITS 5: 5'-GGAAGTAAAGTCGTAACAAGG-3'), was selected for amplifying the 18S rRNA. Polymerase chain reaction (PCR) amplifications were carried out by FlexCycler² (Analytik, Jena, Germany) under the following conditions: 95 °C (5 min), 30 cycles of 95 °C (30 s), 55 °C (30 s), and 72 °C (40 s), with the last extension at 72 °C (7 min). The amplified PCR products were further delivered to the Mission Biotech Co., Ltd. (Taipei, Taiwan) for sequencing services and blasted with the National Center for Biotechnology Information (NCBI) database. The blasting results displayed that the sample shared 99.5% sequence identity with *E. sorghinum* (GenBank accession number: KX611667.1).

Fermentation, Extraction, and Isolation. The whole fermented broth (36 L) was filtered through filter paper to separate the supernatant from the mycelia. The filtrate was extracted by ethyl acetate (EtOAc) and concentrated by a rotary evaporator to obtain the EtOAc crude extract (9.3 g). This EtOAc crude extract (9.3 g) was subjected to Sephadex LH-20 column chromatography eluted via MeOH to yield five fractions (Fr. 1–Fr. 5). Fraction 3 (3020.3 mg) was separated using silica gel column chromatography and stepwise eluted by CH₂Cl₂/MeOH (29:1 to 9:1) to afford five subfractions (Fr. 3-1–Fr. 3-5). Fraction 3-2 (613.8 mg) was subjected to silica gel column and stepwise eluted with CH₂Cl₂/MeOH (49:1 to 9:1) to give eight subfractions (Fr. 3-2-1–Fr. 3-2-8). Fraction 3-2-1 (459.5 mg) was further isolated by silica gel open column and eluted stepwise with CH₂Cl₂/MeOH (17:1 to 9:1) to get **3** (386.8 mg). Fraction 3-2-2 (17.3 mg) was further purified by reversed-phase (RP) HPLC (Luna 5 μm Phenyl-Hexyl, 250 × 10 mm, Phenomenex, flow rate = 2.0 mL/min, UV detector) eluted with 45% MeOH(aq) to afford **5** (10.8 mg). Fraction 3-3 (1178.6 mg) was submitted to a silica gel open column chromatography with a gradient of CH₂Cl₂/MeOH (33:1 to 9:1) to furnish seven subfractions (Fr. 3-3-1–Fr. 3-3-7). Fraction 3-3-3 (448.2 mg) was chromatographed on a silica gel open column and eluted stepwise with CH₂Cl₂/MeOH (33:1 to 9:1) to obtain five subfractions (Fr. 3-3-3-1–3-3-3-5). Fraction 3-3-3-1 (67.1 mg) was further isolated by RP-HPLC (Luna 5 μm Phenyl-Hexyl, 250 × 10 mm, Phenomenex, flow rate = 2.0 mL/min, UV detector) using 30% MeOH(aq) as the eluent to yield **1** (7.6 mg) and **8** (2.1 mg). Fraction 3-3-3-2 (297.4 mg) was fractionated by silica gel column chromatography and eluted stepwise with CH₂Cl₂/MeOH (24:1 to 9:1) to afford eight subfractions (Fr. 3-3-3-2-1–3-3-3-2-8). Fraction 3-3-3-2-1 (149.4 mg) was further separated by RP-HPLC (Luna 5 μm Phenyl-Hexyl, 250 × 10 mm, Phenomenex, flow rate = 2.0 mL/min, UV detector) and eluted with 37% MeOH(aq) to obtain **2** (70.5 mg) and **6** (45.3 mg). Fraction 3-3-4 (263.2 mg) was subjected to silica gel column chromatography with a gradient elution of CH₂Cl₂/MeOH (29:1 to 9:1) to furnish eight subfractions (Fr. 3-3-4-1–3-3-4-7). Fraction 3-3-4-3 (18.3 mg) was further purified by RP-HPLC (Luna 5 μm Phenyl-Hexyl, 250 × 10 mm, Phenomenex, flow rate = 2.0 mL/min, UV detector) eluted

with 30% MeOH_(aq) to afford **4** (6.2 mg). Fraction 3-5 (500.3 mg) was separated using silica gel column chromatography eluted stepwise with CH₂Cl₂/MeOH (21:1 to 9:1) to give **7** (346.1 mg).

Epicorepoxydon A (1): Brown acicular crystals; [α]_D²⁵ –25 (c 0.05, MeOH); UV (MeOH) λ_{max} (log ϵ) 211 (3.79), 241 (3.42), 308 (2.91) nm; IR (neat) ν_{max} : 3448, 1635 cm^{–1}; ¹H NMR (CD₃OD, 400 MHz) and ¹³C NMR (CD₃OD, 100 MHz) data shown in Table 1; HR-ESI-MS m/z 307.0822 [M – H][–] (calcd for C₁₅H₁₆O₇, 307.0823).

TeA Examination. The EtOAc crude extract and TeA standard were monitored by RP-HPLC on a Cosmosil reversed-phase column (C-18, 250 × 4.6 mm², 5 μ m, 1.0 mL/min, Nacalai Tesque, Kyoto, Japan) with acetonitrile and water (0.1% H₃PO₄) as the mobile phase (0–5 min: 20:80, 5–20 min: from 20:80 to 0:100, 20–30 min: 0:100).

Anti-inflammatory Activity Assay. The method for anti-inflammatory activity assay was similar to the method previously described.³⁶ In brief, human neutrophils were collected from healthy volunteers through venipuncture and separated by Ficoll centrifugation. Dextran was employed for sedimentation. After resuspension in calcium (Ca²⁺)-free HBSS buffer at pH 7.4, the isolated neutrophils were incubated at 4 °C before use.

Measurement of Superoxide Generation. The measurement of superoxide generation has been previously described.³⁶ In brief, neutrophils (6 × 10⁵ cell/mL) were balanced in ferricytochrome *c* (0.5 mg/mL) and Ca²⁺ (1 mM) at 37 °C for 5 min and then incubated with 0.1% DMSO or the tested samples for another 5 min. Cells were activated by utilizing fMLP (0.1 μ M) for 10 min and treated with cytochalasin B (CB, 1 μ g/mL) for 3 min. The spectrophotometer (U-3010; Hitachi) was employed for continuous detection of the changes in absorbance at 550 nm.

Measurement of Elastase Release. The measurement of elastase release has been previously described.³⁶ In brief, neutrophils (6 × 10⁵ cell/mL) were balanced in MeO-Suc-Ala-Ala-Pro-Val-*p*-nitroanilide (100 μ M) and Ca²⁺ (1 mM) at 37 °C for 5 min and incubated with 0.1% DMSO or the tested samples for another 5 min. Cells were activated with fMLP (0.1 μ M) for 10 min and treated with CB (0.5 μ g/mL) for 3 min. The spectrophotometer (U-3010; Hitachi) was employed for continuous detection of the changes in absorbance at 550 nm.

Antiangiogenesis Activity Assay. Isolation and Cultivation of Human EPCs. Peripheral blood (80 mL) was collected from healthy volunteers with informed consent before collection. The peripheral blood mononuclear cells (PBMCs) were fractionated from other blood components by centrifugation on Ficoll-Paque Plus (Amersham Biosciences, Uppsala, Sweden) based on the manufacturer's instructions. Utilizing CD34 MicroBead kit and MACS Cell Separation System (Miltenyi Biotec, Bergisch Gladbach, Germany), the CD34-positive progenitor cells were obtained from the separated PBMCs. The isolation and maintenance of CD34-positive EPCs were carried out as previously described.³⁷

Tube Formation Assay. Matrigel (BD Biosciences, Bedford, MA) was utilized to facilitate the differentiation of EPCs into a capillary tube-like structure. For polymerization, Matrigel was loaded into 96-well plates and maintained at 37 °C for 30 min. After gel formation, EPCs (1.5 × 10⁴ cells) were seeded per well on the layer of polymerized Matrigel in MV2 medium (containing 2% FBS) with the presence of tested compounds

and incubated at 37 °C for 24 h. The methods were performed as previously described.³⁷

Cytotoxicity Assay. EPCs were incubated using 96-well plates in a density of 5 × 10³ cells in each well. Cells were primed with MV2 medium (containing 2% FBS) in the indicated concentration of the tested compounds for 24 h. The percentage of LDH release was measured by the ratio of LDH activity in the medium to LDH activity in the cell lysate.³⁷

Antiplatelet Activity Assay. Preparation of Washed Human Platelets. The platelet suspension was prepared on the basis of the previously described procedures.³⁸ Briefly, human blood anticoagulated with acid citrate dextrose was collected from healthy donors, who had not taken any medicines during the previous 2 weeks. Platelets were suspended in Tyrode's solution (2 mM Ca²⁺, 11.1 mM glucose, and 3.5 mg/mL bovine serum albumin) at a concentration of 3 × 10⁸ platelets/mL.

Measurement of Platelet Aggregation. Before adding the platelet activators, the platelet suspension was incubated with dimethyl sulfoxide (DMSO) as a vehicle or with the tested samples at different concentrations at 37 °C for 3 min under stirring (80.5 × g). After adding the indicated concentration of platelet inducers (U46619 1 μ M; collagen 5 μ g/mL), the level of platelet aggregation was estimated as the maximal increase of light transmission within 5 min. The light-transmission aggregometer (Chrono-Log Co., Havertown, PA) was employed for measuring platelet aggregation.³⁸

■ ASSOCIATED CONTENT

Supporting Information

The Supporting Information is available free of charge at <https://pubs.acs.org/doi/10.1021/acsomega.0c01000>.

HR-ESI-MS, ¹H, ¹³C, and DEPT and 2D NMR spectra of **1** as well as the ¹H and ¹³C data of **6** (Table S1); results of HPLC examination of fungal crude extract and TeA standard; bioassay results of anti-inflammatory and antiangiogenesis activities (PDF)

■ AUTHOR INFORMATION

Corresponding Author

Fang-Rong Chang – Graduate Institute of Natural Products, College of Pharmacy, Drug Development and Value Creation Research Center, and Department of Medical Research, Kaohsiung Medical University Hospital, Kaohsiung Medical University, Kaohsiung 807, Taiwan; Department of Marine Biotechnology and Resources, National Sun Yat-sen University, Kaohsiung 804, Taiwan; orcid.org/0000-0003-2549-4193; Phone: +886-7-312-1101; Email: aaronfrc@kmu.edu.tw

Authors

Chi-Ying Li – Graduate Institute of Natural Products, College of Pharmacy, Kaohsiung Medical University, Kaohsiung 807, Taiwan

Ching-Chia Chang – Graduate Institute of Natural Products, College of Pharmacy, Kaohsiung Medical University, Kaohsiung 807, Taiwan

Yi-Hong Tsai – Graduate Institute of Natural Products, College of Pharmacy, Kaohsiung Medical University, Kaohsiung 807, Taiwan

Mohamed El-Shazly – Department of Pharmacognosy, Faculty of Pharmacy, Ain-Shams University, Cairo 11566, Egypt; Department of Pharmaceutical Biology, Faculty of Pharmacy

and Biotechnology, German University in Cairo, Cairo 11835, Egypt; orcid.org/0000-0003-0050-8288

Chin-Chung Wu – Graduate Institute of Natural Products, College of Pharmacy, Kaohsiung Medical University, Kaohsiung 807, Taiwan

Shih-Wei Wang – Department of Medicine, Mackay Medical College, New Taipei City 252, Taiwan

Tsong-Long Hwang – Graduate Institute of Natural Products, College of Medicine, Chang Gung University, Taoyuan 333, Taiwan; Research Center for Chinese Herbal Medicine, Research Center for Food and Cosmetic Safety, and Graduate Institute of Health Industry Technology, College of Human Ecology, Chang Gung University of Science and Technology, Taoyuan 333, Taiwan; Department of Anesthesiology, Chang Gung Memorial Hospital, Taoyuan 333, Taiwan

Chien-Kei Wei – Graduate Institute of Natural Products, College of Pharmacy, Kaohsiung Medical University, Kaohsiung 807, Taiwan

Judit Hohmann – Department of Pharmacognosy, Interdisciplinary Excellence Center and Interdisciplinary Centre for Natural Products, University of Szeged, H-6720 Szeged, Hungary; orcid.org/0000-0002-2887-6392

Zih-Jie Yang – Graduate Institute of Natural Products, College of Pharmacy, Kaohsiung Medical University, Kaohsiung 807, Taiwan

Yuan-Bin Cheng – Graduate Institute of Natural Products, College of Pharmacy, Kaohsiung Medical University, Kaohsiung 807, Taiwan; orcid.org/0000-0001-6581-1320

Yang-Chang Wu – Graduate Institute of Integrated Medicine, China Medical University, Taichung 404, Taiwan; Chinese Medicine Research and Development Center, China Medical University Hospital, Taichung 404, Taiwan

Complete contact information is available at:

<https://pubs.acs.org/10.1021/acsomega.0c01000>

Author Contributions

^{††}C.-Y.L. and C.-C.C. contributed equally to this work.

Author Contributions

F.-R.C. and Y.-C.W. contributed to the manuscript preparation and revision. C.-Y.L. and C.-C.C. contributed equally to the manuscript by designing the experiment, analyzing, and discussing the data acquisition, and writing the manuscript. M.E.-S. contributed to the manuscript revision. Y.-H.T., C.-K.W., J.H., Z.-J.Y., and Y.-B.C. contributed to the data analysis. C.-C.W. contributed to the antiplatelet aggregation activity assay. S.-W.W. contributed to the antiangiogenesis activity evaluation. T.-L.H. contributed to the anti-inflammatory activity test. C.-Y.L. and C.-C.C. contributed to the design of the Table of Contents creation.

Notes

The authors declare no competing financial interest.

ACKNOWLEDGMENTS

This work was supported by grants from the Ministry of Science and Technology, Taiwan, awarded to F.-R.C. (Grant number: MOST 105-2628-B-037-001-MY3, MOST 106-2320-B-037-008-MY2, MOST 108-2320-B-037-022-MY3, 108-2811-B-037-511, and 109-2927-I-037-502). In addition, this research was funded by the Drug Development and Value Creation Research Center, Kaohsiung Medical University & Department of Medical Research, Kaohsiung Medical University Hospital, awarded to F.-R.C. (Grant number: KMU-TC108A03-11). We

appreciate the Center for Research Resources and Development for providing 400 MHz NMR as well as ESI-MS instrumentation support at the Kaohsiung Medical University; HR-ESI-MS was supported by the National Sun Yat-sen University.


REFERENCES

- (1) Cragg, G. M.; Newman, D. J. Natural products: a continuing source of novel drug leads. *Biochim. Biophys. Acta* **2013**, 1830, 3670–3695.
- (2) Newman, D. J.; Cragg, G. M. Natural products as sources of new drugs from 1981 to 2014. *J. Nat. Prod.* **2016**, 79, 629–661.
- (3) Lahlou, M. The success of natural products in drug discovery. *Pharmacol. Pharm.* **2013**, 4, 17–31.
- (4) Dias, D. A.; Urban, S.; Roessner, U. A historical overview of natural products in drug discovery. *Metabolites* **2012**, 2, 303–336.
- (5) Zhang, H. W.; Song, Y. C.; Tan, R. X. Biology and chemistry of endophytes. *Nat. Prod. Rep.* **2006**, 23, 753–771.
- (6) Aly, A. H.; Debbab, A.; Proksch, P. Fungal endophytes: unique plant inhabitants with great promises. *Appl. Microbiol. Biotechnol.* **2011**, 90, 1829–1845.
- (7) Gouda, S.; Das, G.; Sen, S. K.; Shin, H. S.; Patra, J. K. Endophytes: a treasure house of bioactive compounds of medicinal importance. *Front. Microbiol.* **2016**, 7, No. 1538.
- (8) Chiu, C. P.; Liu, S. C.; Tang, C. H.; Chan, Y.; El-Shazly, M.; Lee, C. L.; Du, Y. C.; Wu, T. Y.; Chang, F. R.; Wu, Y. C. Anti-inflammatory cerebrosides from cultivated *Cordyceps militaris*. *J. Agric. Food Chem.* **2016**, 64, 1540–1548.
- (9) Li, C. Y.; Lo, I. W.; Wang, S. W.; Hwang, T. L.; Chung, Y. M.; Cheng, Y. B.; Tseng, S. P.; Liu, Y. H.; Hsu, Y. M.; Chen, S. R.; et al. Novel 11-norbetaenone isolated from an entomopathogenic fungus *Lecanicillium antillanum*. *Bioorg. Med. Chem. Lett.* **2017**, 27, 1978–1982.
- (10) Korinek, M.; Tsai, Y. H.; El-Shazly, M.; Lai, K. H.; Backlund, A.; Wu, S. F.; Lai, W. C.; Wu, T. Y.; Chen, S. L.; Wu, Y. C.; et al. Anti-allergic hydroxy fatty acids from *Typhonium blumei* explored through ChemGPS-NP. *Front. Pharmacol.* **2017**, 8, 356.
- (11) Jia, A. L.; Ding, X. Q.; Chen, D. L.; Chao, Z. Z.; Liu, Z. Y.; Chao, R. B. A new indole alkaloid from *Arundo donax* L. *J. Asian Nat. Prod. Res.* **2008**, 10, 105–109.
- (12) Ghosal, S.; Dutta, S. K.; Sanyal, A. K.; Bhattacharya, S. K. *Arundo donax* L. (Graminae). Phytochemical and pharmacological evaluation. *J. Med. Chem.* **1969**, 12, 480–483.
- (13) Oliveira, R. C.; Carnielli-Queiroz, L.; Correa, B. *Epicoccum sorghinum* in food: occurrence, genetic aspects and tenuazonic acid production. *Curr. Opin. Food Sci.* **2018**, 23, 44–48.
- (14) Oliveira, R. C.; Nguyen, H. N.; Mallmann, C. A.; Freitas, R. S.; Correa, B.; Rodrigues, D. F. Influence of environmental factors on tenuazonic acid production by *Epicoccum sorghinum*: an integrative approach of field and laboratory conditions. *Sci. Total Environ.* **2018**, 640–641, 1132–1138.
- (15) Oliveira, R. C.; Goncalves, S. S.; Oliveira, M. S.; Dilkin, P.; Mallmann, C. A.; Freitas, R. S.; Bianchi, P.; Correa, B. Natural occurrence of tenuazonic acid and *Phoma sorghina* in Brazilian sorghum grains at different maturity stages. *Food Chem.* **2017**, 230, 491–496.
- (16) Lurie, A.; Kats, J.; Ludwin, S. K.; Seftel, H. C.; Mets, J. Platelet life-span and sites of platelet sequestration in onyalai. *Br. Med. J.* **1969**, 4, 146–148.
- (17) Braga, R. M.; Padilla, G.; Araujo, W. L. The biotechnological potential of *Epicoccum* spp.: diversity of secondary metabolites. *Crit. Rev. Microbiol.* **2018**, 44, 759–778.
- (18) Araújo, F. D. D.; Fávoro, L. C. D.; Araújo, W. L.; de Oliveira, F. L.; Aparicio, R.; Marsaioli, A. J. Epicolactone – natural product isolated from the sugarcane endophytic fungus *Epicoccum nigrum*. *Eur. J. Org. Chem.* **2012**, 2012, 5225–5230.

- (19) Zhang, Y.; Liu, S.; Che, Y.; Liu, X. Epicoccins A–D, epipolythiodioxopiperazines from a *Cordyceps*-colonizing isolate of *Epicoccum nigrum*. *J. Nat. Prod.* **2007**, *70*, 1522–1525.
- (20) Venkatasubbaiah, P.; Chilton, W. S. An epoxydon-derived ester from a *Phoma* sp. pathogenic to rhubarb. *J. Nat. Prod.* **1992**, *55*, 639–643.
- (21) Li, C.; Sarotti, A. M.; Yang, B.; Turkson, J.; Cao, S. A new *N*-methoxypyridone from the co-cultivation of Hawaiian endophytic fungi *Camporesia sambuci* FT1061 and *Epicoccum sorghinum* FT1062. *Molecules* **2017**, *22*, No. 1166.
- (22) Guo, C. J.; Sun, W. W.; Bruno, K. S.; Wang, C. C. C. Molecular genetic characterization of terreic acid pathway in *Aspergillus terreus*. *Org. Lett.* **2014**, *16*, 5250–5253.
- (23) Oliveira, R. C.; Davenport, K. W.; Hovde, B.; Silva, D.; Chain, P. S.; Correa, B.; Rodrigues, D. F. Draft genome sequence of sorghum grain mold fungus *Epicoccum sorghinum*, a producer of tenuazonic acid. *Genome Announc.* **2017**, *5*, No. e01495-16.
- (24) Bertrand, R. L.; Abdel-Hameed, M.; Sorensen, J. L. Lichen biosynthetic gene clusters part II: homology mapping suggests a functional diversity. *J. Nat. Prod.* **2018**, *81*, 732–748.
- (25) Schueffler, A.; Anke, T. Fungal natural products in research and development. *Nat. Prod. Rep.* **2014**, *31*, 1425–1448.
- (26) Wang, J. M.; Ding, G. Z.; Fang, L.; Dai, J. G.; Yu, S. S.; Wang, Y. H.; Chen, X. G.; Ma, S. G.; Qu, J.; Xu, S.; et al. Thiodiketopiperazines produced by the endophytic fungus *Epicoccum nigrum*. *J. Nat. Prod.* **2010**, *73*, 1240–1249.
- (27) Okamoto, M.; Yoshida, K.; Uchida, I.; Nishikawa, M.; Kohsaka, M.; Aoki, H. Studies of platelet activating factor (PAF) antagonists from microbial products. I.: bisdethiobis(methylthio)gliotoxin and its derivatives. *Chem. Pharm. Bull.* **1986**, *34*, 340–344.
- (28) Rio, B.; Lautraite, S.; Parent-Massin, D. *In vitro* toxicity of trichothecenes on human erythroblastic progenitors. *Hum. Exp. Toxicol.* **1997**, *16*, 673–679.
- (29) Tsai, J. Y.; Redei, D.; Forgo, P.; Li, Y.; Vasas, A.; Hohmann, J.; Wu, C. C. Isolation of phorbol esters from *Euphorbia grandicornis* and evaluation of protein kinase C- and human platelet-activating effects of euphorbiaceae diterpenes. *J. Nat. Prod.* **2016**, *79*, 2658–2666.
- (30) McNicol, A.; Israels, S. J. Platelets and anti-platelet therapy. *J. Pharmacol. Sci.* **2003**, *93*, 381–396.
- (31) Su, C. M.; Hsu, C. J.; Tsai, C. H.; Huang, C. Y.; Wang, S. W.; Tang, C. H. Resistin promotes angiogenesis in endothelial progenitor cells through inhibition of microRNA206: potential implications for rheumatoid arthritis. *Stem Cells* **2015**, *33*, 2243–2255.
- (32) Liu, C.; Bao, H.; Wang, D.; Wang, X.; Li, Y.; Hu, Y. Highly chemoselective hydrogenation of active benzaldehydes to benzyl alcohols catalyzed by bimetallic nanoparticles. *Tetrahedron Lett.* **2015**, *56*, 6460–6462.
- (33) Malak, L. G.; Ibrahim, M. A.; Bishay, D. W.; Abdel-baky, A. M.; Moharram, A. M.; Tekwani, B.; Cutler, S. J.; Ross, S. A. Antileishmanial metabolites from *Geosmithia langdonii*. *J. Nat. Prod.* **2014**, *77*, 1987–1991.
- (34) Chen, L.; Fang, Y.; Zhu, T.; Gu, Q.; Zhu, W. Gentisyl alcohol derivatives from the marine-derived fungus *Penicillium terrestre*. *J. Nat. Prod.* **2008**, *71*, 66–70.
- (35) Fernandez-Pastor, I.; Fernandez-Hernandez, A.; Rivas, F.; Martinez, A.; Garcia-Granados, A.; Parra, A. Synthesis and antioxidant activity of hydroxytyrosol alkyl-carbonate derivatives. *J. Nat. Prod.* **2016**, *79*, 1737–1745.
- (36) Yang, S. C.; Chung, P. J.; Ho, C. M.; Kuo, C. Y.; Hung, M. F.; Huang, Y. T.; Chang, W. Y.; Chang, Y. W.; Chan, K. H.; Hwang, T. L. Propofol inhibits superoxide production, elastase release, and chemotaxis in formyl peptide-activated human neutrophils by blocking formyl peptide receptor 1. *J. Immunol.* **2013**, *190*, 6511–6519.
- (37) Li, C. Y.; Lo, I. W.; Hsueh, Y. P.; Chung, Y. M.; Wang, S. W.; Korinek, M.; Tsai, Y. H.; Cheng, Y. B.; Hwang, T. L.; Wang, C. C. C.; et al. Epigenetic manipulation induces the production of coumarin-type secondary metabolite from *Arthrobotrys foliicola*. *Isr. J. Chem.* **2019**, *59*, 432–438.
- (38) Tsai, Y. C.; Chiang, S. Y.; El-Shazly, M.; Wu, C. C.; Beerhues, L.; Lai, W. C.; Wu, S. F.; Yen, M. H.; Wu, Y. C.; Chang, F. R. The oestrogenic and anti-platelet activities of dihydrobenzofuroisocoumarins and homoisoflavonoids from *Liriope platyphylla* roots. *Food Chem.* **2013**, *140*, 305–314.

Review

Cancer Stem Cell Functions in Hepatocellular Carcinoma and Comprehensive Therapeutic Strategies

Yu-Chin Liu ^{1,2}, Chau-Ting Yeh ³ and Kwang-Huei Lin ^{1,2,3,4,*} 

¹ Department of Biochemistry, College of Medicine, Chang-Gung University, Taoyuan 333, Taiwan; k1506820@gmail.com

² Department of Biomedical Sciences, College of Medicine, Chang-Gung University, Taoyuan 333, Taiwan

³ Liver Research Center, Chang Gung Memorial Hospital, Taoyuan 333, Taiwan; chauting@adm.cgmh.org.tw

⁴ Research Center for Chinese Herbal Medicine, College of Human Ecology, Chang Gung University of Science and Technology, Taoyuan 333, Taiwan

* Correspondence: khlin@mail.cgu.edu.tw; Tel./Fax: +886-3-211-8263

Received: 5 May 2020; Accepted: 22 May 2020; Published: 26 May 2020



Abstract: Hepatocellular carcinoma (HCC) is a significant cause of cancer-related mortality owing to resistance to traditional treatments and tumor recurrence after therapy, which leads to poor therapeutic outcomes. Cancer stem cells (CSC) are a small subset of tumor cells with the capability to influence self-renewal, differentiation, and tumorigenesis. A number of surface markers for liver cancer stem cell (LCSC) subpopulations (EpCAM, CD133, CD44, CD13, CD90, OV-6, CD47, and side populations) in HCC have been identified. LCSCs play critical roles in regulating HCC stemness, self-renewal, tumorigenicity, metastasis, recurrence, and therapeutic resistance via genetic mutations, epigenetic disruption, signaling pathway dysregulation, or alterations microenvironment. Accumulating studies have shown that biomarkers for LCSCs contribute to diagnosis and prognosis prediction of HCC, supporting their utility in clinical management and development of therapeutic strategies. Preclinical and clinical analyses of therapeutic approaches for HCC using small molecule inhibitors, oncolytic measles viruses, and anti-surface marker antibodies have demonstrated selective, efficient, and safe targeting of LCSC populations. The current review focuses on recent reports on the influence of LCSCs on HCC stemness, tumorigenesis, and multiple drug resistance (MDR), along with LCSC-targeted therapeutic strategies for HCC.

Keywords: hepatocellular carcinoma; liver cancer stem cells; stemness; self-renewal; tumorigenicity; therapeutic resistance

1. Introduction

Embryogenesis of both normal and tumor cells involves similar processes, including proliferation, motility, homing, dynamic morphologic changes, cellular heterogeneity, and interactions with the microenvironment. However, carcinogenesis is described as deregulation of malignant organogenesis regulated by abnormally proliferating and metastatic cancer and activated stromal cells that trigger angiogenesis, fibrosis, and inflammation [1]. One such case is liver cancer, which is classified as primary or secondary. Primary liver cancer refers to initiation of liver cell growth, and secondary liver cancer refers to spread of cancer cells to other organs from the liver. Primary liver cancer can be classified as growth of a single lump or growth in many places in the liver at the same time. Primary liver cancer types include hepatocellular carcinoma, cholangiocarcinoma, liver angiosarcoma, and hepatoblastoma. Hepatocellular carcinoma (HCC), also known as hepatoma, is the most common type worldwide, accounting for ~75% of all liver cancers. HCC is influenced by several important

risk factors, with two distinct mechanisms of molecular pathogenesis: hepatitis infection (HBV or HCV) or toxin/environmental (alcohol or aflatoxin B) or metabolic (insulin resistance, obesity, type II diabetes or dyslipidemia in nonalcoholic HCC) factors that trigger liver tissue damage, leading to cirrhosis associated with hepatic regeneration and subsequent HCC [2] and genetic/epigenetic changes that influence the expression patterns of oncogenes or tumor suppressor genes [3–7]. The above factors are correlated with multiple dysregulated signaling pathways, such as growth factor-mediated angiogenic signaling (vascular endothelial growth factor (VEGF), platelet-derived growth factor (PDGF), epidermal growth factor (EGF), insulin-like growth factor (IGF), hepatocyte growth factor (HGF)/c-MET), mitogen-activated protein kinase (MAPK), phosphatidylinositol-3 kinase (PI3K)/AKT/mammalian target of rapamycin (mTOR), and Wnt/ β -catenin pathways, which contribute to HCC development and tumorigenesis [8]. Elucidation of these signaling mechanisms is interesting from a therapeutic perspective, since targeting them may aid in reversing, delaying, or preventing the occurrence of HCC. Sorafenib is a first-line treatment approved by the United States Food and Drug Administration (USFDA) shown to benefit post-therapy survival rates in unresectable HCC cases. Subsequently identified target drugs, including regorafenib and lenvatinib, are currently used as second-line treatments for HCC. The above drugs can be effectively combined with radiation therapy and chemotherapy for clinical treatment of HCC. However, the therapeutic effects remain limited, which is ascribed to high recurrence and drug resistance of liver cancer stem cells (LCSCs), a subpopulation of liver cancer cells isolated via flow cytometry with self-renewal, differentiation, and tumorigenesis capabilities [9] that play critical roles in tumor progression and therapeutic resistance. In this review, the functions of LCSCs in HCC and targeted therapeutic strategies are comprehensively discussed.

2. Identification and Plasticity of LCSCs

2.1. Concept of Cancer Stem Cells (CSCs)

Cancer stem cells (CSCs) have similar characteristics to normal stem cells, including self-renewal and differentiation. CSCs are also called as tumor-initiating cells (T-ICs) or cancer stem-like cells, which were first evidenced by injecting the AML cells into SCID mice by xenotransplant; the experiments indicated that expression of specific CSCs marker ($CD34^+CD38^-$) could promote production of large numbers of colony-forming progenitors [10]. This discovery suggested a new CSCs concept, according to which heterogeneity and tumor hierarchy is organized by a subset of cells with CSCs. This avoids traditional thoughts that heterogeneity is the progressive accumulation of multiple genetic [11] or epigenetic changes [12]. Several CSCs have been isolated from malignancies including lung cancer, pancreatic cancer, breast cancer, prostate cancer, colon cancer, glioma, and liver carcinoma [13–16]. CSCs have been found to possess highly tumorigenic, metastatic, and chemotherapy- and radiation-resistant properties, possibly leading to tumor relapse after therapy. CSCs evade multiple drug actions (MDR) with the aid of various intrinsic and external mechanisms [17]. Intrinsic mechanisms of chemoresistance include DNA damage repair pathway activation, high-level expression of drug efflux-related proteins, the capability of reconstituting original tumors, and the influence of epithelial-to-mesenchymal transition (EMT) and self-renewal-related genes [18]. External mechanisms of chemoresistance include activation of signaling pathways involved in epithelial-mesenchymal transition (EMT), hypoxia stimulation, and abnormal angiogenesis [17]. Besides, CSCs enter a dormant state (arrest in the G0 phase) of reduction of cell proliferation activity and persist resistance to chemotherapy for a few years, eventually leading to relapse. The relationship between tumor microenvironment (TME) and CSCs play an important role in influencing resistance therapeutics and promoting trans-differentiation of non-CSCs into CSCs by providing anti-apoptosis, stemness-maintaining factors, and matrix components. Thus, to study how to improve therapeutic resistance of CSCs in cancer is a critical issue.

2.2. Correlation between Hepatocellular Carcinoma and Cancer Stem Cells

CSCs of hepatocellular carcinoma (HCC) are termed liver cancer stem cells (LCSCs). LCSCs display specific features, such as the ability to generate new tumors displaying the phenotypes of xenotransplanted tumors, chemoresistance, metastasis, and recurrence [19] (Figure 1 and Table 1). Both metastasis and recurrence are associated with drug resistance [20]. So far, several surface markers and side population cells (SP) of HCC have been isolated, including EpCAM, CD133, CD44, CD13, CD90, CD24, CD47, and OV6. Other surface markers, such as K19, c-kit, ABCG2, and ALDH, have additionally been identified, which individually affect resistance to radiotherapy or chemotherapy and tumorigenesis by influencing drug efflux-related gene expression [21–24], activation of growth signaling, and stem cell-related and anti-apoptosis pathways [25–27]. LCSCs possess the capability of circulation within the body that significantly promotes distant metastasis and homing ability, compared to other tumor cell types. In other words, LCSCs promote tumor growth of primary cancer cells and metastasis of transplanted secondary tumors, leading to recurrence of HCC [28]. LCSCs are therefore closely related to metastasis, recurrence, and MDR and serve as an important diagnostic marker for HCC. In recent years, accumulating research has focused on identifying different surface markers of HCC through fluorescence-activated and magnetically activated cell sorting approaches, which could be effectively developed for eliminating LCSCs to achieve inhibition of tumor recurrence [29].

Table 1. Surface markers influencing the signaling pathways, phenotypes, and resistance to clinical drugs in LCSCs.

LCSCs	Phenotypes of LCSCs (Source)	Signaling Involving LCSCs	Resistance to Clinical Drug	Ref.
EpCAM	cell–cell adhesion, metabolism, cell signaling, differentiation, metastasis, regeneration, organogenesis, tumorigenesis, chemoresistance and self-renewal (Hep3B, HepG2, Huh7, Huh1, and Dt81Hepa1-6 cells)	Activation of the Wnt signaling pathway	Sorafenib	[30–33]
CD133	tumorigenic, cell cycle progression, differentiation, chemoresistance, and self-renewal (Huh7, SMMC7721, PLC8024, PLC8024, HepG2, and HCCLM3 cells)	Activation of AKT/PKB,	Doxorubicin, Fluorouracil (5-FU) and Sorafenib	[27,34–36]
CD44	proliferation, survival, migration/invasion, and chemoresistance, and self-renewal (primary HCC, HepG2, Hep3B, Huh7, SUN-368, SUN-354, SMMC-7721, and MHCC97-H cells)	Activation of AKT/GSK-3 β / β -catenin, and ERK/Snai pathways	Doxorubicin	[21,37–42]
CD13	chemoresistance, tumorigenesis and self-renewal (Huh7, PLC, and HepG2 cells)	Activation of ERK1/2 signaling pathway	Sorafenib, Doxorubicin, and Fluorouracil (5-FU)	[43,44]
CD90	tumorigenesis, metastasis, self-renewal and chemoresistance (MHCC97L, PLC, HepG2, Hep3B, primary HCC, and JHH-6 cells)	Activation of mTOR signaling pathway	Doxorubicin	[45–48]
CD24	metastasis, differentiation, self-renewal and chemoresistance (MHCC97H, HCCLM3, PLC/PRF/5, Huh7, and Hep3B cells)	Autophagy activation, activation of AKT/mTOR signaling pathway, and Notch1 signaling pathway	Cisplatin, Sorafenib	[49–52]
OV-6	self-renewal, tumorigenicity, and chemoresistance (SMMC7721, and HuH7 cells)	Activation of Wnt/ β -catenin signaling	Cisplatin	[53,54]
Side population	differentiation, chemoresistance, and metastasis (Huh7, PLC/PRF/5, HCCLM3, MHCC97-H, MHCC97-L, and Hep3B cells)	Activation of AKT signaling pathway	Doxorubicin, Fluorouracil (5-FU), and Gemcitabine	[23,24,55]

Table 1. Cont.

LCSCs	Phenotypes of LCSCs (Source)	Signaling Involving LCSCs	Resistance to Clinical Drug	Ref.
CD47	self-renewal, tumor initiating, tumorigenicity, and chemoresistance (MHCC97L, PLC, and Huh7 cells)	Activation of IL-6/STAT3 signaling pathway, and NF- κ B	Doxorubicin, Sorafenib	[56–58]
SALL4	proliferation, differentiation, and chemoresistance (Huh7, PLC/PRF/5, and patients of HCC)	Interaction with NuRD, regulation of PTEN, and PI3K/AKT signaling pathway	Fluorouracil (5-FU)	[59,60]
CD13 ⁺ CD133 ⁺	tumor initiation, chemoresistance, and anti-apoptosis (Huh7 and PLC cells)	Reduction of ROS-induced DNA damage and inhibition of apoptosis	Doxorubicin, Fluorouracil (5-FU)	[43]
CD13 ⁺ CD90 ⁺	tumor initiation, chemoresistance, and anti-apoptosis (Huh7 and PLC cells)	Reduction of ROS-induced DNA damage and inhibition of apoptosis	Doxorubicin, Fluorouracil (5-FU)	[43]
EpCAM ⁺ CD90 ⁺	metastasis, tumorigenesis (patients of HCC and primary HCC)	activation of the TGF- β pathway		[61]
CD90 ⁺ CXCR4 ⁺ and CD133 ⁺ CD90 ⁺	tumor development, tumor spheres, and metastasis (primary HCC)			[62]

2.3. EpCAM

The epithelial cell adhesion molecule, EpCAM, belonging to the type I transmembrane protein family is glycosylated and expressed in various tissues, including human epithelial and tumor tissues as well as progenitor/stem cells [63]. The EpCAM structure comprises an extracellular domain with epidermal growth factor (EGF) and thyroglobulin repeat-like domains, a single transmembrane domain, and a short 26-amino acid intracellular domain designated EpICD [63]. Interestingly, EpCAM is not only detectable in normal adult hepatocytes also expressed in embryonic liver, bile duct epithelium, and proliferating bile ductulus in cirrhotic liver and is thus considered a progenitor/stem cell marker in adult liver [64]. Data from systematic analyses suggest that EpCAM expression is essential for all human adenocarcinomas, including specific types of squamous cell carcinoma, retinoblastoma, and hepatocellular carcinoma [65,66]. EpCAM is not only involved in cell–cell adhesion, as the name indicates, but also cell proliferation, migration, cell cycle metabolism, signaling, differentiation, metastasis, regeneration, organogenesis, and tumorigenesis of the liver. EpCAM has additionally been detected on the surface of LCSCs and pancreatic CSCs [32,67]. Transplantation of isolated EpCAM⁺CD45[−] cells from HCC patients into NOD/SCID mice initiated tumor formation, whereas EpCAM[−]CD45[−] cells failed to form tumors, suggesting that EpCAM⁺ confers the stem/progenitor cell trait of HCC and promotes tumor growth [68]. EpCAM is involved in two major signaling pathways, specifically, intramembrane proteolysis and shedding of the extracellular domain [69]. EpICD is found in the cytoplasm generated from EpCAM cleavage by two important proteins (tumor necrosis factor- α converting enzyme (ACE) and presenilin 2 (PS-2)) and subsequently interacts with β -catenin through four-and-a-half LIM domain protein 2 (FHL2) [63]. Simultaneously, accumulation of β -catenin in the cytoplasm is dependent on inhibition of phosphorylation through induction of the β -catenin degradation complex (AXIN, APC, GSK3) by the Wnt signaling pathway [31]. Accumulated β -catenin interacts with FHL2 and EpICD to form a large protein complex that is translocated to the nucleus. The nuclear protein complex regulates transcription of EpCAM target genes, including c-myc, cyclins, and TCF1 [30,63]. Gene expression and pathway analyses suggest that activation of Wnt/ β -catenin signaling enriches the EpCAM⁺ cell population. EpCAM⁺-rich cell subpopulations isolated from HCC present liver cancer stem cell features, which promote self-renewal, differentiation, and invasiveness [70]. Dt81 Hepa1-6, a new cell line derived from Hepa1-6 through in vivo passage in C57BL/6 mice, displays higher tumorigenicity, which is attributable to increased EpCAM and β -catenin expression [71]. In another study, EpCAM-positive circulating tumor cells were identified from HCC

patients undergoing curative resection, which displayed stem cell-like and EMT phenotypes that were likely to cause tumor recurrence after surgical resection [68]. Additionally, stemness genes, such as Nanog, Sox2, and Oct4, were expressed in EpCAM-positive HCC cells and TSC2-AKT signaling activated upon Sorafenib treatment, further exacerbating hepatocellular carcinoma progression [33]. In another study, gene and protein expression profiles were analyzed from 245 and 144 hepatocellular carcinoma patients, respectively. EpCAM⁺ cells abundantly expressed CDH4, a chromatin remodeling enzyme, and influenced PPAR and DNA double-stranded break repairs to enhance chemoresistance of HCC cells [72]. Clinical analyses showed higher EpCAM expression in HCC tumor than adjacent normal liver tissue and positive correlation with differentiation grade among the clinicopathological parameters examined. Kaplan–Meier analyses showed that at advanced clinical stages, high EpCAM expression and poor differentiation grade were associated with poor survival rates. These results collectively support the utility of EpCAM in HCC as a predictive biomarker for unfavorable prognosis [73].

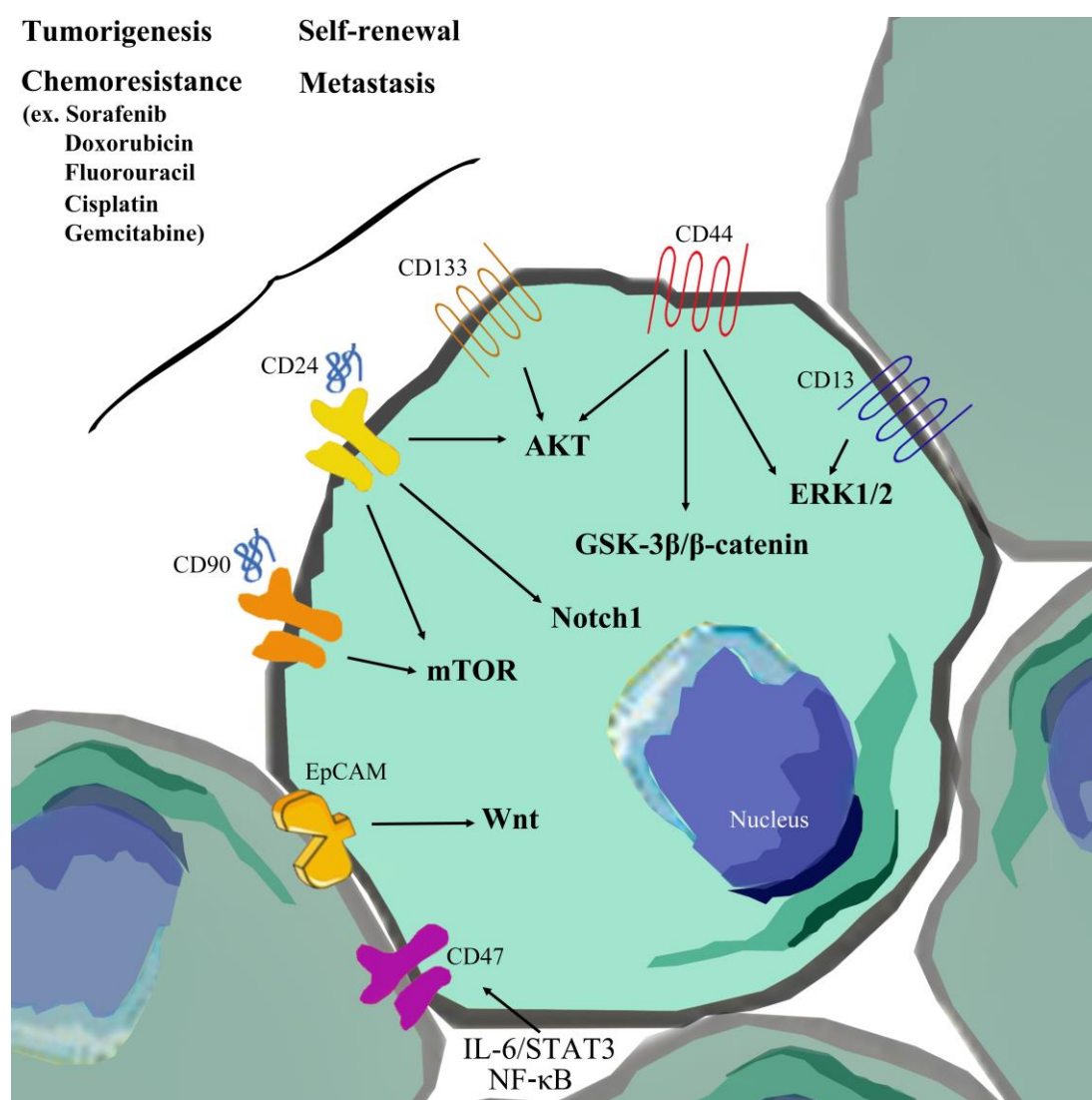


Figure 1. Activation of signaling pathways in liver cancer stem cells (LCSCs) influences hepatocellular carcinoma (HCC) development. Surface markers (including EpCAM, CD133, CD44, CD13, CD90, CD24, and CD47) influence the activation of signaling pathways, phenotypes, and resistance to clinical drugs in LCSCs

2.4. CD133

CD133 (human prominin-1, PROM1) is a glycoprotein with five transmembrane domains and two larger extracellular glycosylation chains that serves as an important surface marker, showing abundant expression in both cytoplasm and nucleus of various tumor tissues, including hepatocellular carcinoma (HCC), brain tumor, pancreatic cancer, prostate cancer, and colon cancer [74–78]. The CD133⁺ subpopulation was initially isolated from Huh7, one of the benign HCC cell lines, and was shown to play potential roles in proliferation and tumorigenesis [34] in both SMMC7721 and PLC8024 cells [35,79]. Additionally, 0–65% human HCC cells are CD133⁺. Knockout of CD133 in HCC cells is reported to reduce tumorigenicity and cell cycle progression [35]. Similar findings were obtained with clinical HCC patients, whereby high CD133 expression was correlated with poor prognosis. Simultaneously, increased CD133 levels in HCC patients were associated with shorter overall survival and higher recurrence rates, indicating that CD133 may be a suitable prognostic marker [80]. Recent studies suggest that CD133 induces differentiation into non-hepatocyte-like lineages and may act as a progenitor cell marker not only in damaged liver and HCC tissue but also cholangiocarcinoma, both in vitro and in vivo [81,82]. CD133 is involved in numerous molecular mechanisms, including self-renewal, multi-lineage differentiation, and tumorigenic and therapeutic resistance. Following EMT promotion of HBx-infected hepatoma cells, TGF- β expression of neighboring endothelial cells is increased, leading to significantly enhanced CD133 expression [36]. Aquaporin 3 (AQP3) is reported to maintain stemness and self-renewal capacity through inducing CD133 transcription activity via promoting stimulation and nuclear translocation of signal transducer and activator of transcription 3 (STAT3) and CD133 promoter-acetylated histone H3 [83]. In patients with hepatocellular carcinoma (HCC) recurrence, the majority of hepatic stem/progenitor cell (HSC/HPC) biomarkers are overexpressed, including cytokeratin 19, ABCG2, CD133, Nestin, and CD44, and angiogenesis agents CD34, VEGF, and PD-ECGF. Additionally, RFA-induced VEGF promotes tumor stemness and tumorigenesis via Nanog and activation of VEGFR2, which are positively correlated with CD133 expression in HCC tissues derived from patients with early recurrence. These results clearly suggest that VEGF and CD133⁺ stemness markers are positively correlated with early HCC recurrence [84]. Isolated CD133⁺ subpopulations of HCC cells and xenograft mouse models confer increased chemoresistance to doxorubicin (DOX) and fluorouracil (5-FU) through activation of Akt/PKB and Bcl-2 survival pathways [27]. Additionally, the epigenome cooperates with other regulatory factors, such as non-coding RNAs, allowing differentiation between short non-coding RNAs (miRNAs and sRNAs; <200 nucleotides) and long non-coding RNAs (lncRNAs; >200 nucleotides) [85]. MiR-130b overexpressed in CD133⁺ tumor-initiating cells (TIC) of HCC enhances chemoresistance, tumorigenicity, and self-renewal via suppression of its downstream target gene, TP53INP1 [86]. Dysregulation of lncRNAs in primary HCCs has additionally been shown to influence HCC tumorigenesis.

2.5. CD44

CD44 is a transmembrane glycoprotein encoded by a single gene expressed as several isoforms that acts as a receptor for hyaluronic acid (HA). CD44 has been identified in both normal and tumor cells. Tumor cell behaviors, including proliferation, survival, migration/invasion, and chemoresistance, are closely associated with upregulation of CD44 [37–40]. Tumor-associated macrophages (TAM) are a class of immune cells often found in the microenvironment of solid tumors. TAMs produce IL-6 with subsequent activation of signal transducer and activator of transcription 3 (STAT3) and promote expansion of CD44⁺ populations and tumorigenesis in cultures as well as growth of xenograft tumors in mice [87]. CD44s, one of the isoforms of CD44, plays a completely opposite role to CD44. Knockout of the CD44 gene in HCC expressing CD44s only resulted in decreased maintenance of CSCs and increased drug sensitivity [88]. CD44 overexpression in HCC patients and cell lines is regulated by TGF- β and confers a TGF- β -mediated mesenchymal phenotype through increased AKT/GSK-3 β / β -catenin activity [42], with a further major influence on EMT-related genes, such as positive correlation with vimentin expression, negative correlation with E-cadherin expression,

high percentage of phospho-Smad2-positive nuclei, and reduced disease-free and overall survival [89]. Simultaneous analysis of clinicopathological parameters of other patient groups revealed that CD44 is also involved in local aggressive HCC recurrence through regulation of EMT genes (including low E-cadherin, high vimentin, and high N-cadherin expression) after local ablation therapy (LAT) [90]. Data from a functional assay established that knockdown of CD44 significantly reduces migration and invasion via repression of the ERK/Snail pathway, subsequently leading to decreased metastasis upon tail vein injection of KD CD44 of HCC cells into a metastatic mouse model [41]. CD44 is often combined with other CSC markers to enrich hepatic CSC populations, including CD133 and EpCAM. Upon knockout of CD44 in HCC, both CD133 and EpCAM are significantly downregulated [88]. Additionally, overexpression of the CD133⁺ CD44⁺ population in HCC cells promotes stem/progenitor cell properties, including extensive proliferation, self-renewal, differentiation, and increased resistance to chemotherapeutic agents, via upregulation of ABC transporters (ABCB1, ABCC1, and ABCG2) [21]. CD44 influences differentiated cells that experience carcinogenic insult to become proliferative cancer progenitors via activating AKT signaling and promoting Mdm2 translocation into the nucleus, with subsequent termination of the p53 response. In other words, HCC cells undergo DNA damage to escape p53-induced death and senescence and respond to proliferative signals that promote mutation and transmission to daughter cells that go on to become HCC progenitors [91]. Interestingly, an earlier study showed no correlation of CD44 with clinicopathological parameters in tumor tissues, with no differences in disease-free survival rates relative to the control group. However, in non-tumor tissues, the disease-free survival rate in the CD44-low expression group was significantly longer, compared to the CD44-high expression group. These initial findings clearly suggest that CD44 in non-tumor tissues is potentially associated with risk of tumor recurrence after hepatic resection for HCC [92].

2.6. CD13

CD13 (Aminopeptidase N) is a membranous glycoprotein and an extracellular peptidase, the major function of which is cleavage of single neutral amino acid from the N terminus of small peptides. However, CD13 plays a different kind of function and substrate depending on where it is expressed. For example, CD13 in the brain cleaves opioid peptide and enkephalins to regulate neuronal signaling. In the intestine, CD13 plays a critical role in cleaving peptides in the final digestion and resorption [93]. CD13 also acts as a candidate liver cancer stem cell marker. Microarray analyses have identified CD13 as an important candidate surface marker of the side population (SP) fraction. The CD13⁺ population was mainly detected in the G0/G1 phase and comprised dormant or slow-growing cancer cell populations correlated with chemoresistance through ABC transporter expression and recurrence. Additionally, CD13 is localized predominantly in the G0/G1 phase of the cell cycle, suggesting a role as a marker of the dormant or semi-stationary status of LCSCs [43]. Similar to CD44, CD13 could combine with other surface markers, including CD133 or CD90, and effectively initiate tumor formation, leading to increased HCC tumorigenesis [43]. CD13⁺CD133⁺ and CD13⁺CD90⁺ cells are reported to enhance not only HCC tumor initiation but also genotoxic chemoresistance to doxorubicin (DXR) and fluorouracil (5'Fu). Treatment with both DXR and 5'FU increased the CD13 population and subsequently reduced ROS-induced DNA damage after genotoxic stress along with inhibition of HCC apoptosis. [43]. TGF- β -induced EMT phenotypes and tumorigenicity in HCC are associated with elevated CD13 expression. Flow cytometry analyses have shown that cells positive for N-cadherin, an EMT marker, are localized in CD13-positive cell fractions, suggesting that TGF- β elicits both N-cadherin and CD13 expression. Additionally, CD13 could metabolize TGF- β /EMT-induced ROS and facilitate cell survival through evasion apoptosis, contributing to drug resistance [94]. Interestingly, CD13 can be induced not only by genotoxic chemotherapeutic agents but also by sorafenib in human HCC cells. Mechanistically, CD13⁺ CSCs are dependent on Tyr metabolism, rather than glucose, as an energy source. Simultaneously, Tyr metabolism produces nuclear acetyl-CoA. Stabilization and acetylation of Foxd3 are regulated by increasing CBP acetyltransferase activity through activation of the ERK1/2 signaling pathway [44]. Clinical data suggest that CD13 expression is correlated with that

of EMT markers, such as E-cadherin and vimentin. Both disease-free and overall survival curves in high CD13 expression groups were significantly poorer than those of low CD13 expression groups. In view of the collective data on the association between CD13 and EMT markers, CD13 may serve as a prognostic marker of early recurrence after surgery [95].

2.7. CD90

CD90 (Thy-1) is a glycosphosphatidylinositol (GPI)-anchored protein that is expressed in a variety of cell types, including T-cells activation [96], thymocytes, neurons outgrowth modulation [97], endothelial cells, the vesicular release of neurotransmitter at the synapse [98], astrocyte adhesion [99] and fibroblasts. In addition, CD90 is also involved in cytoskeleton organization, cell migration, and inflammation. CD90 is not only implicated in the tumorigenic and metastatic capacities of various HCC cell lines but also serves as a marker of LCSCs [45]. CD90⁺ cell populations have been isolated from both HCC specimens and blood samples of liver cancer patients and could initiate tumor nodule formation following intrahepatic injection into SCID/beige mice and subsequent secondary and tertiary transplantation into immunodeficient mice. These findings support the utility of CD90 as a surface marker for diagnosis of HCC malignancy [100]. Gene expression analysis of sorted cells has disclosed different features of EpCAM and CD90 populations. EpCAM possesses characteristics of epithelial cells while CD90 contains vascular endothelial cell features. Moreover, these markers are correlated with different clinicopathological parameters. Upon transplantation into xenografts, EpCAM⁺ cells promoted tumor growth in subcutaneous lesions and CD90⁺ cells induced high metastatic capacity in lung cells. Furthermore, CD90 influenced EpCAM⁺ cell motility through activation of the TGF- β pathway [61]. Cyclin D1 overexpression promoted stemness properties and enhanced chemoresistance through increasing CD90⁺ and EpCAM⁺ populations. Mechanistically, cyclin D1 interacted with and activated Smad2/3 and Smad4 signaling pathways to regulate LCSC self-renewal [48]. Circulating tumor stem cell (CTSC) populations within circulating tumor cells (CTC) play critical roles in the formation of distal metastatic tumors [101]. CD90⁺CXCR4⁺ present a better surface marker of CTSCs than CD133⁺CD90⁺, promoting the formation of tumor spheres in vitro, tumor development in primary and subsequent secondary and tertiary transplantation experiments, and distal metastatic tumors following subcutaneous transplantation [62]. Analysis of clinical HCC patients confirmed that CD90 is an important surface marker that is positively correlated with a number of clinicopathological parameters, including histopathology grade and tumor size. Additionally, CD90 expression is significantly associated with early recurrence and short-term survival of HCC patients [102,103]. Experiments on human tissue samples and JHH-6 HCC cell lines indicate that CD90 is significantly overexpressed in tumors and positively associated with growth factors, including hepatocyte growth factor (HGF), fibroblast associated protein (FAP), and alpha smooth muscle actin 2 (ACTA2). Moreover, CD90 induces chemoresistance to doxorubicin through reducing ABCB1 and increasing the ABC transporter proteins ABCG2 and Oct4, [46,47]. CD90 expression has been detected in not only LCSCs but also tumor-associated fibroblasts (CAFs). CD90 is positively correlated with clinicopathologic characteristics, including pathological grade, satellite lesions, PVTT, and recurrence, suggesting a role as a predictor of poor prognosis in CAFs, and is consistently determined as a reliable biomarker for prognosis of HCC patients subjected to hepatic resection [104].

2.8. CD24

CD24 is a mucin-like cell surface glycoprotein expressed in stem/progenitor cells and a variety of human malignancies, including hepatocellular carcinoma, breast cancer, renal cell carcinoma, colon cancer, B-cell lymphoma, differentiating neuroblasts, small cell and non-small cell lung carcinoma, and nasopharyngeal carcinoma. In addition, CD24 plays an important role in regulating neural development by contributing to the downstream signaling network by glycosyl- phosphatidylinositol (GPI) link to the cell surface [105]. CD24 expression has been reported in undifferentiated bipotential mouse embryonic liver stem and 3,5-diethoxycarbonyl-1,4-dihydrocollidine-treated oval cells and can

help differentiate progenitor/stem cells from normal adult liver. Moreover, CD24 enhances expression of CK19, epithelial cell adhesion molecule, Sox 9, and FN14, which facilitate differentiation into hepatocytes [106]. These earlier studies suggest that CD24 is involved in metastasis, differentiation, self-renewal, and chemoresistance of HCC cells. Consistent with these findings, CD24 expression was shown to be positively correlated with metastasis in the HCC cell lines MHCC97H and HCCLM3, which display enhanced proliferation, migration, and invasive properties through increasing the CD24 population. Moreover, CD24 expression is associated with tumor number, tumor size, vascular invasion, encapsulation, differentiation, satellite lesions, and poor TNM stage in overall and relapse-free survival. CD24 is positively associated with PCNA and β -catenin, correlated with clinicopathologic features, including low AFP levels, and confers a greater propensity for multiple tumors and liver cirrhosis. Simultaneously, CD24 expression influences type II and III tumor recurrence. Taken together, the data clearly support the value of CD24 as a prognostic factor for HCC after surgery [49]. CD24 is proposed to play an important role in tumor-initiating cells (T-ICs) from chemoresistant (cisplatin) hepatocellular carcinoma (HCC) xenograft tumors orthotopically transplanted into SCID mice, promoting tumor-forming and self-renewal abilities through phosphorylation of STAT3 and induction of NANOG expression. mRNA microarray analyses further showed that the CD24 level is increased in chemoresistant groups despite no changes in other liver T-IC markers, including CD133, CD90, and EpCAM [50]. In an earlier investigation, CD24⁺ cells were isolated from two patient samples, followed by injection of 4000 CD24⁺ cells into NOD/SCID mice, which led to higher tumor development capability than CD24⁻ cells, supporting the tumorigenic property of CD24 [50]. In addition, CD24 induced resistance to both cisplatin and sorafenib. CD24 is more highly expressed in sorafenib-resistant relative to untreated wild-type cells, conferring greater resistance through activating autophagy and inhibiting the AKT/mTOR signaling pathway [51]. CD24⁺ LCSCs display enhanced levels of inducible nitric oxide synthase (iNOS), which triggers the Notch1 signaling pathway in a manner dependent on cGMP/PKG-mediated activation of TACE and upregulation of iRhom-2, further promoting self-renewal and tumor growth properties [52].

2.9. OV-6

OV-6 is a monoclonal antibody raised against cells isolated from carcinogen-treated BALB/c mouse liver [53,107]. The OV-6 population obtained from HCC cell lines and primary HCC tissues acts as a hepatic progenitor marker [108] and promotes self-renewal with endogenous activation of Wnt/ β -catenin signaling. In other words, OV-6 expression is enriched in tumor cells via Wnt activation while inhibition of β -catenin signaling decreases the OV-6⁺ population in HCC. Moreover, OV6⁺ HCC cells display enhanced resistance to chemotherapeutic drugs, such as cisplatin [53]. OV6 promotes HCC tumors and leads to increased self-renewal capacity, tumorigenicity, and invasive and metastatic properties through positive correlation with C-X-C chemokine receptor type 4 (CXCR4) and its specific ligand, CXCL12 (SDF-1) [109]. The same research group proposed that HBx influences HCC self-renewal, stem cell-associated gene expression, tumorigenicity, and chemoresistance through stem-like properties of the OV6⁺ population. In terms of the underlying mechanism, HBx directly interacts with MDM2 to form a protein complex and subsequently inhibits MDM2 ubiquitin-directed self-degradation. Translocation of the HBx-MDM2 complex into the nucleus enhances transcriptional activity and expression of CXC4 and CXC12 and subsequent activation of the Wnt/ β -catenin signaling pathway promotes the stem-like properties of OV6⁺ CSCs in liver [54].

2.10. Side Population Cells

Side population (SP) cells are originally shown to be enriched in stem cell compartments of various tissues and organs [110,111]. Subsequently, SP cells were detected in hepatocellular carcinoma cell lines, including Huh7 and PLC/PRF/5, using Hoechst 33342 dye staining in flow cytometry. The results suggested that SP cells may effectively serve as markers to distinguish between LCSCs and HCC cells and initiate tumorigenesis by upregulating stemness genes along with tumor formation in xenograft

transplant experiments [112]. Microarray analysis of HCC cell lines demonstrated that other genes are additionally influenced in SP, compared with non-SP cells, such as GATA6 which is associated with embryonic development and hepatocytic differentiation and some ABC transporter genes, including ABCG2, ABCB1, and CEACAM6, linked to chemoresistance to doxorubicin, 5-fluorouracil, and gemcitabine, in addition to epithelial and mesenchymal markers. SP cells are therefore potentially involved in differentiation, chemoresistance, and metastasis of HCC [24,55]. Among these, ABCG2 in HCC cell lines is particularly significant. Flow cytometry experiments to isolate the ABCG2⁺ subpopulations of HCC cell lines sub-cultured for 4 weeks revealed the presence of both ABCG2⁺ and ABCG2[−] progenies, supporting critical roles of ABCG2 in maintenance of the cancer cell hierarchy of HCC [113]. The researchers further showed intrinsic expression of ABCG2 in HCC tissues and cell lines. Furthermore, ABCG2 is reported to significantly influence drug efflux-related chemotherapy resistance in SP cells by altering subcellular localization through activation of the Akt signaling pathway [23].

2.11. CD47

CD47 is a transmembrane member of immunoglobulin, also as an integrin-associated protein (IAP), which is the expression in platelets, and binds to the signal-regulatory-protein- α (SIRP α) followed by inhibition of phagocytosis [57,114]. CD47 has been indicated to not only play an important role in immune evasion but to also regulate tumor apoptosis, angiogenesis, metastasis, tumor-initiating ability, chemoresistance, and proliferation in many cancers, including HCC. CD47 is overexpression in the HCC tumor cells and positively correlates with CD68⁺ (which is a macrophages marker) expression. Further, the results suggested that IL-6 derives from tumor-infiltrating macrophages that can induce CD47 expression in HCC by activation of the STAT3 signaling pathway. In addition, the same group also suggested that blocking of CD47 and combination with chemotherapeutic drugs enhance macrophage-mediated phagocytosis, which means lower expression of CD47 benefits the treatment with adjuvant transcatheter arterial chemoembolization (TACE) of HCC patients [58]. In addition, CD47 is one of the TICs markers, which shows the highest overexpression compared to other TICs markers in the sorafenib resistance cells. Both the clinical HCC sample and sorafenib resistance suggested positive correlations between NF- κ B and CD47. CD47 is regulated by NF- κ B, which can specifically bind to the CD47 promoter, and then up-regulation CD47 transcription activity follows [56]. CD47 in HCC is one of the LCSCs that has been developed of antibodies and widely studied. CD47 is blocked by an anti-CD47 monoclonal antibody, causing not only inhibition of self-renewal, tumorigenicity, migration, and invasion abilities but also synergizes in combination with chemotherapeutic drugs, including doxorubicin and cisplatin [115].

3. Interactions of LCSCs Influencing HCC and Therapeutic Strategies

3.1. The Wnt/ β -Catenin Pathway

Wnt/ β -catenin signaling is highly and evolutionarily conserved in normal cells and participates in tissue homeostasis [116]. The canonical Wnt/ β -catenin pathway is critical for HCC progression and tumorigenesis. β -catenin is a functional protein that plays a dual role in cell–cell adhesion and gene transcription and serves as an intracellular signal transducer in the Wnt signaling pathway [117–120]. Moreover, β -catenin is one of the subunits of cadherin that binds E-cadherin. However, mutation and overexpression of β -catenin promotes tumor progression in many cancer types, including hepatocellular carcinoma [121]. Under normal conditions, β -catenin in the cytosol is marked for ubiquitin-mediated proteolysis by specific phosphorylation of serine residues through an enzymatic complex including adenomatous polyposis coli (APC), Axin, and the kinases glycogen synthase kinase-3 β (GSK-3 β) and casein kinase I [122]. Wnt protein directly interacts with cell surface Frizzled receptors and LRP5/6 co-receptors upon activation of the Wnt/ β -catenin pathway. Immediately after this step, Dishevelled protein is activated and released, leading to formation of the destructive enzymatic APC/Axin/GSK-3 β complex and inhibition of GSK-3 β . Further accumulation and stabilization leads to

β -catenin translocation from the cytoplasm to nucleus and subsequent binding to TCF/LEF proteins, which activates downstream target genes, including MMP3, MMP7, ADAM10, Twist, Slug, Tiam1, c-Myc, cyclin D1, and fibronectin (Figure 2A) [123,124]. Frequent hyperactivation of the Wnt/ β -catenin pathway in HCC patients leads to accumulation of β -catenin in tissue and nucleus, which serves as a hallmark of Wnt signaling. Activation of Wnt/ β -catenin signaling has been shown to promote self-renewal, differentiation, and invasiveness in LCSCs [30,63,70,71]. Inhibition of Wnt/ β -catenin signaling via small-molecule inhibitors reduces expression of Wnt and β -catenin proteins in LCSCs and further suppresses HCC stemness. One identified small-molecule inhibitor of Wnt/ β -catenin signaling is CWP232228, an antagonist that competes with β -catenin for binding to TCF in the nucleus and suppresses transcriptional activity of downstream genes. This compound inhibits HCC self-renewal and tumor initiation through suppression of gene (Oct4, KLF4, Nanog, and SOX2) and surface marker (CD133⁺/ALDH1⁺) expression of LCSCs (Figure 2A.) [125]. FH535 is another antagonist that inhibits the Wnt/ β -catenin signaling pathway and peroxisome proliferator-activator receptor (PPAR γ and PPAR δ) signaling [126]. This compound suppresses proliferation and motility of HCC cells through significant downregulation of cyclin D1 and MMP9 mRNA [127]. Additionally, FH535 is a potent therapeutic inhibitor that, upon combination with Sorafenib, exerts synergistic inhibition of proliferation and induction of apoptosis via enhancing cleaved poly (ADP-ribose) polymerase (PARP), inhibiting cyclin D1, Bcl-2, survivin, and c-MYC levels and reducing both mitochondrial respiration and glycolytic rates to disrupt the bioenergetics of HCC/LCSC cells [128,129]. WM130, a derivative of matrine, a Sophora alkaloid, has been shown to exert better pharmacological activities and anticancer effects against HCC than its parent compound. Results to date suggest that WM130 suppresses proliferation and self-renewal capability in both HCC and doxorubicin-resistant hepatoma cells by decreasing phosphorylation of GSK3 β and subsequent degradation of β -catenin through downregulation of the CSC biomarker, EpCAM, and other stemness-related genes. Additionally, combined treatment with WM130 and doxorubicin synergistically inhibits tumor growth [130]. WM130 not only influences proliferation but also inhibits invasion and migration and induces apoptosis of HCC cells via suppression of EGFR/ERK/MMP-2 and PTEN/AKT signaling pathways [131]. Another inhibitor derived from matrine, (6aS, 10S, 11aR, 11bR, 11cS)-10- methylamino-dodecahydro- 3a,7a-diazabenzode (de) (MASM), inhibits the PI3K/AKT/mTOR and AKT/GSK3 β / β -catenin pathways, with subsequent reduction of Bcl-2 and cyclin D1 expression along with increased PARP cleavage and p27 expression, and markedly reduces the EpCAM⁺/CD133⁺ cell population. These combined effects achieve inhibition of cell proliferation, induction of apoptosis, and cell cycle arrest, in addition to suppression of xenograft tumor growth for HCC [132]. Two anti-FZD antibodies are currently in clinical trials. One is OMP-18R5, which can interact with 5 out of 10 FZD receptors and competitively block Wnt3A interactions with FZD receptors. This compound has been shown to suppress tumor growth in a mouse model and exerts a greater inhibitory effect on tumor growth and delay in tumor recurrence in combination with a chemotherapeutic agent. OMP-18R5 has recently been evaluated in phase 1 clinical trials in patients with lung, breast, and pancreatic cancer [133]. The other preclinical anti-FZD antibody is OMP-54F28, a truncated FZD8 receptor fused to the IgG1 Fc region that competes with Fzd8 receptor for ligand binding, leading to suppression of the Wnt/ β -catenin signaling pathway, inhibition of solid tumor growth, and decrease in CSC frequency, either alone or in combination with other chemotherapy drugs, such as gemcitabine [134]. Evaluation of the safety and pharmacokinetics/pharmacodynamics of OMP-54F28 combined with sorafenib in HCC patients has been completed in phase 1b clinical trials ([ClinicalTrials.gov](https://clinicaltrials.gov) identifier: NCT02069145) [133]. The results suggested that the success of providing completed the safety and pharmacokinetics/pharmacodynamics of FZD-targeted therapy in HCC patients in phase 1 trials as well as suggested potential combinations of FZD-targeted and FDA-approved targeted therapy in HCC patients.

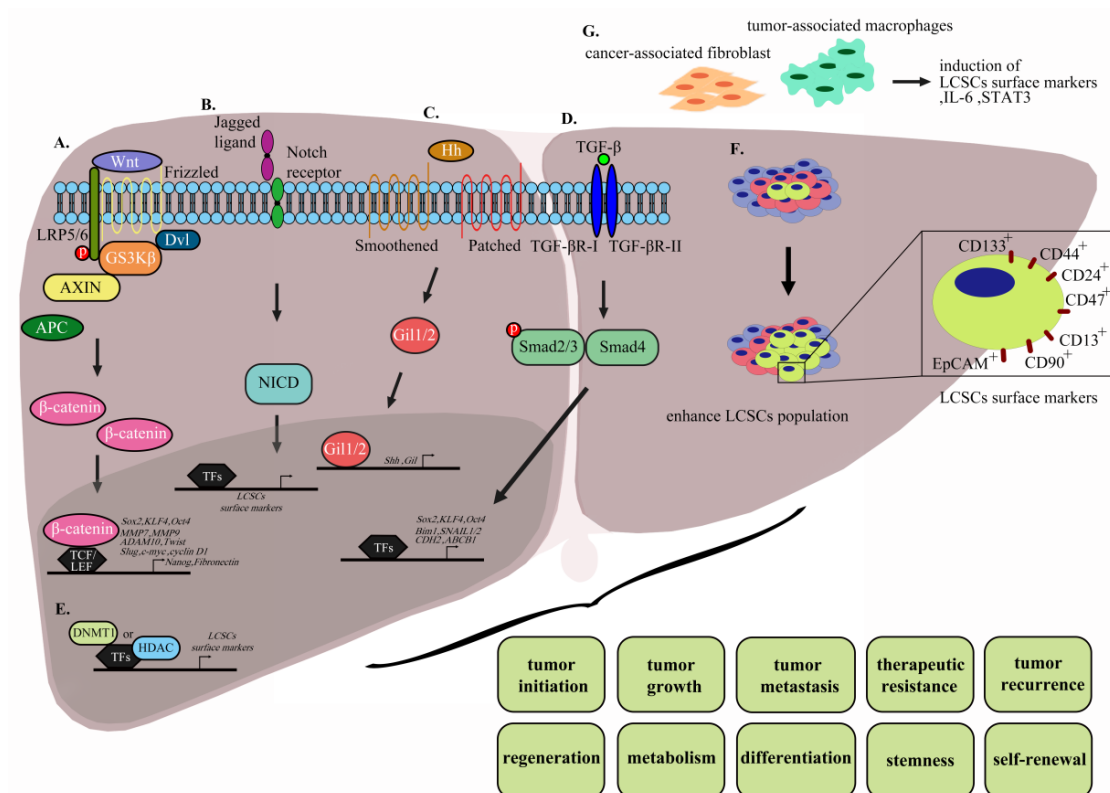


Figure 2. Interactions of LCSCs influencing HCC. (A) The Wnt protein directly interacts with cell surface receptor Frizzled and LRP5/6 co-receptors for activation of the Wnt/β-catenin pathway. Immediately after, Dishevelled protein is activated and released, leading to the generation of destructive enzymatic complex (APC/Axin/GSK-3β) and inhibition of GSK-3β. Following accumulation and stabilization, β-catenin translocates from the cytoplasm to the nucleus and subsequently binds TCF/LEF proteins to activate transcription of downstream target genes, including MMP3, MMP7, ADAM10, Twist, Slug, Tiam1, c-Myc, cyclin D1, and Fibronectin. (B) Ligand binding to NOTCH leads to cleavage and release of the Notch intracellular domain (NICD), promoting transcription factor complex (CBF1/RBPjk/Su(H)/Lag1 (CSL)) translocation from the cytoplasm to nucleus and activation of downstream target genes. (C) Desert hedgehog (DHH), Indian hedgehog (IHH), or Sonic hedgehog (SHH), the ligands binding PTCH1 or PTCH2, promote SMO localization to primary cilium on the cell membrane. Subsequently, glioma-associated oncogene homolog (GLI), a transcription factor, translocates to the nucleus and activates transcription of downstream genes. (D) Interactions with ligand stabilize TβRI and TβRII, following which TβRII phosphorylates the GS domain of TβRI, leading to further activation. Subsequent recruitment of intracellular SMAD proteins and translocation to the nucleus stimulate downstream gene transcription. (E) DNA methylation transferase (DNMT1) and histone deacetylases (HDAC) act as key epigenetic regulatory factors for downstream gene transcription. (F) Enhancement of surface markers of LCSC populations, including EpCAM, CD133, CD44, CD24, CD13, CD90, and CD47. (G) Cancer-associated fibroblast (CAFs) and tumor-associated macrophages (TAMs) promote LCSC surface marker populations (IL-6 and STAT3) within the microenvironment.

3.2. Notch Signaling

The Notch pathway is a highly conserved cell signaling mechanism in multicellular organisms that regulates proliferation, maintenance of stem cells, differentiation, neurogenesis, embryonic development, maintenance of adult tissue homeostasis, and angiogenesis. The Notch receptor is a single-pass transmembrane receptor protein composed of functional extracellular (NECD), transmembrane (TM), and intracellular (NICD) domains. The protein exists as four isoforms, designated NOTCH1, NOTCH2, NOTCH3, and NOTCH4 [135,136], which interact with transmembrane ligands, such as Delta and Serrate, on neighboring cells. Ligand binding to NOTCH triggers

cleavage and release of the Notch intracellular domain (NICD) and promotes translocation of the transcription factor complex (CBF1/RBPjk/Su(H)/Lag1 (CSL)) from the cytoplasm to nucleus, in turn, stimulating downstream target gene transcription (Figure 2B) [137]. Tumor progression, self-renewal, and CSC differentiation are influenced by Notch signaling, which is activated in most types of cancer. Accumulating research has focused on eliminating CSCs via targeting Notch signaling as a therapeutic strategy for cancer [137]. Several LCSC-related proteins, including CD90, Notch1, Nanog, and Sox2, which are overexpressed in parenchymal hepatic cells, have been identified via IHC. However, only CD90 was exclusively detected in HCC patient samples, supporting a correlation of this biomarker with poor prognosis. Isolated CD90⁺ populations from HCC cell lines were subsequently shown to exhibit increased tumorigenicity, chemoresistance, tumor invasion, and metastasis through Notch signaling activation. Moreover, the Notch signaling pathway promoted self-renewal, invasion, and migration of CD90⁺ cells. The collective data suggest that CD90 is an effective biomarker for LCSCs and specifically upregulates stem-associated genes Nanog, Oct4, and Sox2 through activated Notch signaling [138]. C8orf4 deletion promotes nuclear translocation of NICD and subsequently triggers Notch2 signaling, which enhances CD133⁺/CD13⁺ expression and sustains LCSC stemness [139]. Notch3 is overexpressed in HCC patients and positively correlated with clinicopathological parameters, including alpha-fetoprotein (AFP) levels, poor prognosis (shorter survival time), and cisplatin resistance. Moreover, high Notch3 is correlated with lower expression of β -catenin but higher aldehyde dehydrogenase (ALDH) activity, supporting the theory that Notch3 regulates tumor stemness through inactivation of Wnt/ β -catenin [140]. Notch and Wnt/ β -catenin signaling pathways are intercalated and play critical roles in stemness characteristics and metastasis of LCSCs. Notch1 is upregulated and activates Notch1 intracellular domain (NICD) expression in HCC through Wnt/ β -catenin signaling. Treatment with the Wnt/ β -catenin-specific tankyrase1/2 inhibitor (XAV939) and γ -secretase inhibitor (DAPT) that block the Wnt/ β -catenin and Notch signaling pathways, respectively, leading to suppression of tumor growth [141]. PF-03084014 is a γ -secretase inhibitor that blocks self-renewal and proliferation of cancer stem cells. The compound has been shown to reduce both hepatocellular carcinoma tumors growth and metastasis in sphere-derived orthotopic tumor model and one patient-derived xenograft (PDX) model. Additionally, low-dose PF-03084014 induces sphere differentiation of hepatocellular carcinoma and further reduces chemoresistance, supporting its value as a novel antitumor and antimetastatic therapeutic agent for HCC [142].

3.3. Hedgehog Signaling Pathway

The hedgehog signaling (Hh) pathway facilitates normal development of mammalian embryos and regulates cell proliferation, survival, and differentiation. Hh is limited to stem cell subsets that undergo rapid turnover and modulate tissue repair in adult tissue, such as nervous system, skin, and intestines [143–146]. The canonical Hh pathway is activated by three ligands, specifically, Desert hedgehog (DHH), Indian hedgehog (IHH), and Sonic hedgehog (SHH), which interact with the 12-pass transmembrane protein receptors Patched 1 (PTCH1) and Patched 2 (PTCH2). In the absence of ligand, Smoothened (SMO), a 7-pass transmembrane G-protein-coupled signal transduction molecule, is localized in vesicles. Ligand binding to PTCH1 or PTCH2 promotes SMO localization to primary cilium on the cell membrane. This step initiates translocation of glioma-associated oncogene homolog (GLI), a transcription factor, to the nucleus and subsequent activation of the downstream genes GLI1, PTCH1, cyclin D, VEGF, and c-myc (Figure 2C). However, upon overexpression of Hh ligands, loss of function of the receptor or abnormal transcription factor expression leads to dysregulation of the Hh pathway and further initiation and progression of multiple cancer types, including breast cancer, prostate cancer, hepatocellular carcinoma, pancreatic cancer, and brain cancers [147]. In clinical HCC cases with both HBV infection and HBx transgenic mice (HBxTg), correlations with Hh marker upregulation have been reported. Therefore, blocking the Hh signaling pathway may inhibit HBx-induced migration, anchorage-independent growth, and HBxTg tumor development [148]. A number of studies have shown that Hh markers are overexpressed in HCC patients and positively correlated with clinicopathological

parameters (tumor differentiation, encapsulation, vascular invasion, early recurrence, and intrahepatic metastasis) along with significantly poorer overall and disease-free survival [149,150]. Dysregulation of Hh signaling contributes to maintenance of stemness in CSCs and influences tumor growth, metastasis, drug resistance, and differentiation [151]. In a highly tumorigenic CD133⁺ population of HCC, Smoothened (SMO) is abundantly expressed in association with the Hh signaling pathway and influences liver cancer stemness maintenance [35]. Current development of therapeutic agents that target Hh signaling has primarily focused on natural and synthetic antagonists of SMO and GLI1, which have undergone clinical trials with varying degrees of success [152]. Cyclopamine, an isolate of *V. californicum*, was initially shown to inhibit the Hh pathway by direct binding to SMO [153]. Cyclopamine inhibits tumor proliferation and growth in multiple cancer types, including HCC. The compound is reported to suppress Hep3B hepatocarcinogenicity by inhibiting SMO and blocking overactivation of Hh signaling by 50%, along with decreasing c-myc transcription activity [154]. However, cyclopamine-induced reduction of tumor growth is associated with several adverse side effects, including weight loss, dehydration, and death, in a mouse model [155,156]. GDC-0449, a second-generation cyclopamine, also directly binds SMO to prevent GLI activation with subsequent inhibition of the Hh pathway [157]. The compound was approved by the FDA as the first Hh signaling inhibitor for treatment of primary or recurrent cancers. GDC-0449 induces a significant decrease in liver myofibroblasts, progenitors, and liver fibrosis through inhibitory effects on Hh signaling, leading to suppression of HCC metastasis with no adverse effects on mortality [158]. These results support the utility of GDC-0449 as a safe clinical therapeutic agent for cancer. Moreover, activation of Hh signaling enhances the liver macrophage-mediated proinflammatory response and critical progression of nonalcoholic fatty liver disease (NAFLD). The overall findings clearly indicate that GDC-0449 and LED225 effectively reduce macrophage activation and proinflammatory cytokine expression (TNF- α , IL-1 β , MCP1, and IL-6) as well as further NAFLD progression through direct binding to SMO and blocking of the Hh signaling pathway, supporting their potential utility as effective therapy for NAFLD-induced liver cancer [159]. LDE-225 is a second-line treatment agent for cancer approved by the FDA that exerts its effects by inhibiting the Hh signaling pathway. Data from Phase I/II clinical trials support the efficacy of LDE-225 as both monotherapy and combination therapy for numerous solid or hematological malignancies, including hepatocellular carcinoma (HCC) and Child-Pugh A cirrhosis (CPA). Phase I trial results indicate that the maximum safe dose of LDE-225 can be used to effectively treat advanced or metastatic HCC and CPA ([ClinicalTrials.gov](https://clinicaltrials.gov/ct2/show/study/NCT02151864) Identifier: NCT02151864). GANT-61 is a Gli transcription inhibitor that modulates genes involved in cell proliferation, self-renewal, and metastasis, resulting in suppression of pancreatic CSC characteristics and tumor growth. The compound is reported to show efficacy as a chemotherapeutic agent for human pancreatic cancer by regulatory activity on apoptosis markers [160]. The above studies have reported that the Hh signaling pathway is activated in HCC and effectively targeted by related small-molecule inhibitors for therapeutic purposes. Additionally, the group of Wang [161] showed that GANT61 induces autophagy that contributes to apoptosis and, further, suppression of HCC tumor growth. Clearly, autophagy plays an important role in determining the response to Hh-targeted therapies for HCC.

3.4. TGF- β Signaling Pathway

TGF- β family ligands not only play critical roles in cell proliferation, growth, homeostasis, and differentiation but also influence self-renewal of many stem cell types. TGF- β proteins initiate intracellular signaling by binding to the surface protein complexes of transmembrane kinases, which can distinguish between T β RI and T β RII. Interactions with ligand stabilize both T β RI and T β RII. Subsequently, T β RII phosphorylates the GS domain of T β RI, leading to its activation. Subsequent recruitment of the intracellular SMAD protein and translocation to the nucleus triggers downstream gene transcription (Figure 2D) [162]. TGF- β plays a dual role in liver cancer development, acting as a tumor suppressor at the early stages while promoting metastasis in the late stages of cancer

progression [163,164]. Tumor-associated macrophages (TAM), a critical component of immune cells in the tumor microenvironment are positively correlated with the EpCAM⁺ population and enhance cancer stem cell-like properties via upregulation of CSC transcription factors Bmi1 and Klf4. However, blockage of TGF- β expression using anti-TGF- β antibodies significantly inhibits stem cell-like behavior via downregulation of Bmi1 and Klf4 transcription [165]. In addition, TGF- β displays the capability to induce CD133 and further promotes tumor initiation upon subcutaneous inoculation into nude mice [166]. LY2157299, also known as galunisertib, specifically inhibits TGF- β receptor (T β R)-I activation and exerts anti-proliferative and anti-invasive effects against HCC. Treatment of IHC with LY2157299 reduced expression of the proliferation marker, Ki67, and induced that of caspase-3, an apoptosis marker. In patient samples, LY2157299 could effectively inhibit proliferation and induce apoptosis upon administration as both monotherapy and in combination with Sorafenib. LY2157299 has been shown to exert synergistic therapeutic effects with Sorafenib [167]. However, the utility of LY2157299 in LCSCs remains to be established. Furthermore, a number of small-molecule inhibitors of TGF- β signaling have been developed with a specific focus on Smad protein, which effects LCSCs expression in HCC. GP73 is reported to enhance Smad2/3 phosphorylation via activation of TGF- β 1 and promote EMT via upregulation of EMT marker expression while SB431542 specifically inhibits Smad2/3 phosphorylation and reverses EMT in HCC [168]. Cyclin D is dependent on activation of Smad2/3 and Smad4, leading to enhancement of single sphere formation, CD90⁺ and EpCAM⁺ populations, stemness gene expression, and chemoresistance (Figure 2D). Smad inhibitors impaired cyclin D-induced self-renewal, enhanced sensitivity to chemotherapy, and suppressed tumor growth in a cyclin D sphere-derived xenograft model [48].

3.5. Targeting of LCSC Surface Markers

Several therapeutic surface markers have been identified to date. CD133 is a surface marker isolated from tumor-initiating cells (TICs), which is significantly correlated with poor prognosis of HCC patients. Two types of oncolytic measles viruses (MV), MV-141.7 and MV-AC133, have been described that target CD133 and selectively destroy CD133⁺ tumor cells [169]. Moreover, enhanced oncolytic activities and prolonged survival of CD133-targeted viruses in clinical trials, compared with parental MV-Nse, support their close association with oncolytic agents. VB4-845, a recombinant fusion protein, is an anti-EpCAM single-chain antibody. In eight HCC cell lines, VB4-845 strongly suppressed sphere formation ability, compared to 5-FU. In addition, in high EpCAM⁺ expressing cell populations, VB4-845 suppressed cells expressing CD133 and CD13 while treatment with 5-FU induced CD133- and CD13-positive populations [170]. Evaluation of VB4-845 in clinical trials for various cancer types, including urothelial carcinoma, bladder cancer, squamous cell cancer, and head-and-neck cancer, support its therapeutic efficacy for HCC [171]. Isolated CD90⁺CD44⁺ cells from HCC displayed better tumorigenic capacity than CD90⁺CD44⁻ cells. Thus, a CD44-antibody could effectively target CD90⁺CD44⁺ cell population and induce apoptosis in HCC [45]. In another study, CD44 antibody-mediated liposomal nanoparticles in HCC promoted apoptosis and reduced tumor growth through specifically targeting CD44 [172]. A further potential therapeutic strategy is development of surface marker inhibitors, such as Ubenimex, which suppress CD13 and are widely used as an immunoenhancer for treating solid tumors and hematological neoplasms. Ubenimex is reported to reverse multidrug resistance (MDR) of HCC by suppressing Pim3, BCL-2, and BCL-XL expression, decreasing Bad phosphorylation and further enhancing tumor cell apoptosis [173].

3.6. Epigenetic Changes

Alterations in epigenetic control of gene expression play a substantial role in disease progression, including hepatocellular carcinoma (HCC) [174]. Epigenetic modification mechanisms include DNA methylation, histone modification, and chromatin remodeling. Notably, epigenetic changes can influence activation of certain genes but not the genetic code of DNA [175–177]. Recent studies have suggested that epigenetic changes are correlated with LCSC phenotypes. For instance, suppression

of DNA methylation via treatment with the DNMT1 inhibitor, zebularine (ZEB), induced highly tumorigenic cells within the side population (SP) fraction, leading to increased tumorigenicity of HCC [178]. Treatment of high-density cells with ZEB reduced expression of surface markers (such as CD133, CD44, EpCAM) and cancer stem cell properties as well as tumorigenesis, concomitant with upregulation of genes related to apoptosis and differentiation. Taken together, the results suggest that DNA methylation acts as a key epigenetic regulatory factor of LCSCs (Figure 2E) [179]. In clinical HCC patients, SALL4 was positively correlated with EpCAM and significant decrease in overall survival [60]. SALL4 is highly expressed in HCC and associated with elevated serum alpha-fetoprotein levels, high frequency of hepatitis B virus infection, and poor prognosis. In addition, SALL4 is reported to induce spheroid formation and upregulation of LCSC markers, including KRT19, EPCAM, and CD44, in HCC. HDAC activity was induced in SALL4-positive cells via SALL4 interactions with nucleosome remodeling and deacetylase (NuRD) complexes. The HDAC inhibitor, SBHA, may present an effective option to inhibit SALL4-positive cell proliferation [180].

3.7. MicroRNAs and Long Non-Coding RNAs

Evidence from a systematic review suggests that high-resolution microarray and deep sequencing techniques have encouraged studies on non-coding RNAs (ncRNAs) including short non-coding RNAs (miRNAs and sRNA) (<200 nucleotides) and long non-coding RNAs (lncRNAs) (>200 nucleotides). In human plasma and tumor tissues of HCC, several miRNAs and lncRNAs that regulate LCSCs show promise as biomarkers for diagnosis and prognosis as well as response to therapy. Both miRNAs and lncRNAs can act as critical regulators of self-renewal, differentiation, and tumorigenicity of CSCs. For example, microRNA-150 upregulated in a CD133⁺ subpopulation of HCC interacts with 3'UTR of c-myc mRNA, consequently inhibiting c-myc protein levels. Overexpression of microRNA-150 significantly reduced the CD133⁺ cell population and further inhibited cell growth and tumor sphere formation, inducing cell cycle arrest and apoptosis [181]. MicroRNA-449a is overexpressed in poorly differentiated HCC tissues, drug-resistant cell lines, and Nanog-positive liver cancer cells. Upregulation of microRNA-449a is proposed to increase stemness in HCC. Notably, knockdown of miR-449a via transcription factor 3 (TCF3) reduced Nanog transcription and influenced cellular stemness [182]. Oct4/miR-1246 in CD133⁺ HCC is correlated with a poor diagnosis which promotes cancer stemness through activation of the Wnt/ β -catenin pathway through miR-1246 targeting to degradation of β -catenin complexes suppressing AXIN2 and GSK3 β expression [183]. miR-125b is down-regulated in HCC by TGF- β 1-induced and negatively correlated with LCSCs expression. Besides, in vitro and in vivo studies suggested that EMT and EMT-associated traits of HCC are inhibited by targeting SMAD2 and SMAD4 by ectopic expression of miR-125b [184]. miR-216a/217 prompted migration and metastatic ability and increased the stem-like cells population and tumor recurrence in HCC by activation of PI3K/Akt and TGF- β pathways by induction of targeting PTEN and SMAD7 expression [185]. Recent findings by our group suggest that high BC200 expression in the CD133⁺ population of HCC promotes tumor growth and sphere formation, supporting its requirement in self-renewal and maintenance of LCSCs [186]. LncSox4 is highly expressed in HCC tissues and liver tumor-initiating cells (TICs) and required for liver TIC self-renewal and tumor initiation. LncSox4 regulates TIC self-renewal by recruiting STAT3 that binds the Sox4 gene promoter and induces Sox4 transcription activity. Simultaneously, Sox4 is positively correlated with expression of the surface markers EpCAM and CD133 that promote TIC self-renewal [187]. Both lncRNAs and Wnt/ β -catenin signaling pathways influence LCSCs of HCC. HCC tumors and LCSC-containing HCC cell lines (CD133⁺CD133⁺) highly express LncTCF7, a critical regulator of LCSC self-renewal and tumor propagation. LncTCF7 recruits SWI/SNF complex binding to the TCF7 promoter and triggers TCF7 transcription and further activation of Wnt signaling-induced tumorigenic activity in liver cancer stem cells [188]. The long non-coding RNA, MEG3, a tumor suppressor in HCC, is reported to promote β -catenin degradation through increasing PTEN, leading to inhibition of hepatocarcinogenesis [189]. Lnc- β -Catm is promoted β -catenin stabilization by methylation of β -catenin by methyltransferase EZH2, thereby regulation of

self-renewal of LCSCs [190]. LncDANCR in the stem-like cells of HCC is overexpression and further increases stemness features and promotes tumorigenesis of HCC via interacting with CTNNB1 mRNA and derepression of CTNNB1 [191]. Overexpression of LncDILC has dramatically decreased LCSCs expression by down-regulation of IL-6 transcription and abrogation of STAT3 activation then inhibition of IL-6/STAT3 signaling [192]. LncHDAC2 is highly expressed in CD13⁺CD133⁺ cells, which promotes LCSC self-renewal and tumor progression by recruiting NuRD complex binding to the promoter of PTCH1, leading to inhibition of transcriptional activity and subsequent activation of Hh signaling [193]. The collective findings support the potential utility of ncRNAs as therapeutic targets against LCSCs in liver cancer.

3.8. The LCSC Microenvironment

Accumulating studies have shown that in addition to genetic, epigenetic, and signaling pathways, the microenvironment (niche) is an important influencer of stem cell behavior and differentiation. For instance, embryonic stem cells can significantly suppress tumorigenicity of aggressive cancer cells induced by the microenvironment [194]. Similarly, the tumor microenvironment influences cancer stem cell characteristics, leading to malignant phenotypes. For example, adding conditioned medium of mouse Lewis lung carcinoma to Nanog miPS cells leads to acquisition of CSC features and subsequent formation of spheroids in suspension culture, along with induction of high tumorigenicity and angiogenesis ability in Balb/c nude mice [195]. Single-cell CSC clones from human liver cancer microvascular endothelial cells were isolated and further treated with different tumor cell-derived conditioned culture media mimicking the tumor microenvironment. The results showed differentiation into the corresponding tumor cells and expression of specific tumor cell markers [196]. The major component of tumor stromal cells is cancer-associated fibroblasts (CAFs), which positively express CD90 and CD44. Upon co-culture with the human HCC cell lines Huh7 and JHH-6, CAFs enhanced mRNA expression of TGFB1 and FAP, compared to non-tumoral fibroblasts (NTF) (Figure 2G). These findings suggest that CAFs and HCC interact with each other to function in the maintenance and progression of liver disease [197]. The α -SMA(+)CAF population is regulated with T-ICs via activation of FRA1, dependent on ERK signaling activation by HGF. Activated FRA1 binds to downstream genes, stimulating HEY1 promoter transcription activity, and further enhances HCC self-renewal and tumorigenesis. These findings suggest that T-ICs of HCC are regulated extrinsically within the tumor microenvironment [198]. Isolation of the CD44⁺ population from human HCC cells and incubation with TAM induced expansion of this cell population and tumor sphere formation. In addition, TAMs and co-culture with HCC cell lines promoted expression of the cytokine IL-6 and expansion of CD44⁺ cells. Knockdown of STAT3 or treatment with tocilizumab blocked IL-6 signaling and further inhibited TAM-stimulated activity of CD44⁺ cells (Figure 2G) [87]. In a hypoxic tumor microenvironment, rapid tumor growth further influences the proportion of LCSCs in HCC [199]. Artemis (ARTN), a hypoxia-responsive factor, is a necessary regulator promoting hypoxia-induced LCSC expansion of the CD133⁺ population in HCC, leading to enhanced tumor sphere formation and tumorigenesis [200]. Disulfiram (DS) is an anti-cancer drug that specifically inhibits the scavenger activity of reactive oxygen species (ROS) but has a very short half-life in the bloodstream. To solve this issue, a poly lactic-co-glycolic acid (PLGA)-encapsulated DS (DS-PLGA) was developed, which could inhibit the liver cancer stem cell population with a synergistic cell killing effect in combination with 5-FU or sorafenib. These findings suggest that the anti-HCC efficacy of DS is mediated through inhibition of LCSCs [201].

4. Conclusions

LCSCs can be identified based on a series of surface markers, including EpCAM, CD133, CD44, CD13, CD90, CD24, OV-6, CD47, and isolated SP cells. Functional studies suggest that LCSCs influence tumorigenesis, metastasis, and therapeutic resistance, as well as recurrence of HCC, and identification of this cell population should assist with diagnosis and prognosis predictions, patient

stratification for administration of individualized therapy, and development of novel LCSC-targeted therapeutic strategies for HCC. LCSCs regulate tumor progression and therapeutic resistance via several mechanisms, including gene mutations, distribution of epigenetics, dysregulation of signaling, and alterations in the microenvironment. Small-molecule inhibitors against dysregulation of signaling pathways, such as Wnt/ β -catenin, Notch, Hh, and TGF- β , may effectively suppress LCSC-mediated tumorigenesis, metastasis, and self-renewal. OMP-18R5 and OMP-54F28 (inhibitors of the Wnt/ β -catenin signaling pathway), LED225 (a Hh inhibitor), and LY2157299 (a TGF- β inhibitor) are progressing to clinical trials alone or in combination with other chemotherapeutic agents targeting LCSCs of HCC [133]. Oncolytic measles viruses specifically targeting CD133 (MV-141.7 and MV-AC133) and anti-surface marker antibodies have additionally been developed for clinical trials, including anti-EpCAM (VB4-845) and anti-CD44, which block surface markers of LCSCs alone or in conjunction with other chemotherapeutic agents for HCC. Epigenetic regulation plays a critical role in every step of tumorigenesis and progression. Some LCSC features are influenced by epigenetic control, and therefore, inhibitors of epigenetic regulation mechanisms (such as zebularine and SBHA) can achieve significant suppression of tumor-inducing characteristics of LCSCs. However, epigenetic modulation is not effective for targeting specific genes, which could become non-specific alterations. A number of other factors influence LCSCs, such as the tumor microenvironment and non-coding RNAs (miRNAs and lncRNAs). Currently, combinations of chemotherapy agents and small-molecule inhibitors are being developed to reduce LCSC populations for effective treatment of HCC. Since LCSCs share a number of similar characteristics with stem cells, distinguishing between the molecular signaling pathways or mechanisms of the two cell subpopulations remains a considerable challenge, and thus treatment approaches that target LCSCs are limited. Further research focus on the biological differences between normal stem cells and LCSCs is warranted. Elucidation of the unique biological or phenotypic properties of LCSCs should facilitate the development of effective therapeutic agents without the need for normal stem cells.

Author Contributions: The conceptualization, Y.-C.L. and K.-H.L.; investigation, Y.-C.L.; writing—original draft preparation, Y.-C.L.; writing—review and editing, Y.-C.L. and K.-H.L.; visualization, Y.-C.L.; supervision, K.-H.L.; funding acquisition, C.-T.Y. and K.-H.L. All authors have read and agreed to the published version of the manuscript.

Funding: This work was supported by grants from Chang Gung Memorial Hospital, Taoyuan, Taiwan (CMRPD1G0421, CMRPD1G0422, CMRPD1G0423, CMRPD1J0051, CMRPD1H0631, CMRPD1H0632, NMRPD1G0943, and NMRPD1G0953 to K. H. Lin) and from the Ministry of Science and Technology of the Republic of China (MOST 106-2320-B-182-031-MY3 and 106-2320-B-182-032-MY3 to K. H. Lin). We would like to thank the Taiwan Liver Cancer Network (TLCN) for providing the hepatoma tissue samples and related clinical data (all anonymous).

Conflicts of Interest: The authors declare no conflict of interest.

References

1. Yamashita, T.; Wang, X.W. Cancer stem cells in the development of liver cancer. *J. Clin. Investig.* **2013**, *123*, 1911–1918. [[CrossRef](#)] [[PubMed](#)]
2. Bugianesi, E. Review article: Steatosis, the metabolic syndrome and cancer. *Aliment Pharmacol. Ther.* **2005**, *22* (Suppl. 2), 40–43. [[CrossRef](#)] [[PubMed](#)]
3. Villanueva, A.; Newell, P.; Chiang, D.Y.; Friedman, S.L.; Llovet, J.M. Genomics and signaling pathways in hepatocellular carcinoma. *Semin. Liver Dis* **2007**, *27*, 55–76. [[CrossRef](#)]
4. Feitelson, M.A.; Pan, J.; Lian, Z. Early molecular and genetic determinants of primary liver malignancy. *Surg. Clin. North Am.* **2004**, *84*, 339–354. [[CrossRef](#)]
5. Wang, X.W.; Hussain, S.P.; Huo, T.I.; Wu, C.G.; Forgues, M.; Hofseth, L.J.; Brechot, C.; Harris, C.C. Molecular pathogenesis of human hepatocellular carcinoma. *Toxicology* **2002**, *181–182*, 43–47. [[CrossRef](#)]
6. Thorgeirsson, S.S.; Grisham, J.W. Molecular pathogenesis of human hepatocellular carcinoma. *Nat. Genet.* **2002**, *31*, 339–346. [[CrossRef](#)]

7. Liu, Y.C.; Lu, L.F.; Li, C.J.; Sun, N.K.; Guo, J.Y.; Huang, Y.H.; Yeh, C.T.; Chao, C.C. Hepatitis B Virus X Protein Induces RHAMM-Dependent Motility in Hepatocellular Carcinoma Cells via PI3K-Akt-Oct-1 Signaling. *Mol. Cancer Res.* **2020**, *18*, 375–389. [[CrossRef](#)]
8. Whittaker, S.; Marais, R.; Zhu, A.X. The role of signaling pathways in the development and treatment of hepatocellular carcinoma. *Oncogene* **2010**, *29*, 4989–5005. [[CrossRef](#)]
9. Vu, N.B.; Nguyen, T.T.; Tran, L.C.; Do, C.D.; Nguyen, B.H.; Phan, N.K.; Pham, P.V. Doxorubicin and 5-fluorouracil resistant hepatic cancer cells demonstrate stem-like properties. *Cytotechnology* **2013**, *65*, 491–503. [[CrossRef](#)]
10. Lapidot, T.; Sirard, C.; Vormoor, J.; Murdoch, B.; Hoang, T.; Cacerescortes, J.; Minden, M.; Paterson, B.; Caligiuri, M.A.; Dick, J.E. A Cell Initiating Human Acute Myeloid-Leukemia after Transplantation into Scid Mice. *Nature* **1994**, *367*, 645–648. [[CrossRef](#)]
11. Nowell, P.C. The clonal evolution of tumor cell populations. *Science* **1976**, *194*, 23–28. [[CrossRef](#)] [[PubMed](#)]
12. Baylin, S.B.; Jones, P.A. A decade of exploring the cancer epigenome - biological and translational implications. *Nat. Rev. Cancer* **2011**, *11*, 726–734. [[CrossRef](#)] [[PubMed](#)]
13. Kim, C.F.B.; Jackson, E.L.; Woolfenden, A.E.; Lawrence, S.; Babar, I.; Vogel, S.; Crowley, D.; Bronson, R.T.; Jacks, T. Identification of bronchioalveolar stem cells in normal lung and lung cancer. *Cell* **2005**, *121*, 823–835. [[CrossRef](#)] [[PubMed](#)]
14. Hermann, P.C.; Huber, S.L.; Herrler, T.; Aicher, A.; Ellwart, J.W.; Guba, M.; Bruns, C.J.; Heeschen, C. Distinct populations of cancer stem cells determine tumor growth and metastatic activity in human pancreatic cancer. *Cell Stem Cell* **2007**, *1*, 313–323. [[CrossRef](#)] [[PubMed](#)]
15. Li, C.W.; Heidt, D.G.; Dalerba, P.; Burant, C.F.; Zhang, L.J.; Adsay, V.; Wicha, M.; Clarke, M.F.; Simeone, D.M. Identification of pancreatic cancer stem cells. *Cancer Res.* **2007**, *67*, 1030–1037. [[CrossRef](#)]
16. O'Brien, C.A.; Pollett, A.; Gallinger, S.; Dick, J.E. A human colon cancer cell capable of initiating tumour growth in immunodeficient mice. *Nature* **2007**, *445*, 106–110. [[CrossRef](#)]
17. Maugeri-Sacca, M.; Vigneri, P.; De Maria, R. Cancer stem cells and chemosensitivity. *Clin. Cancer Res.* **2011**, *17*, 4942–4947. [[CrossRef](#)]
18. Calcagno, A.M.; Salcido, C.D.; Gillet, J.P.; Wu, C.P.; Fostel, J.M.; Mumau, M.D.; Gottesman, M.M.; Varticovski, L.; Ambudkar, S.V. Prolonged drug selection of breast cancer cells and enrichment of cancer stem cell characteristics. *J. Natl. Cancer Inst.* **2010**, *102*, 1637–1652. [[CrossRef](#)]
19. Ji, J.; Wang, X.W. Clinical implications of cancer stem cell biology in hepatocellular carcinoma. *Semin. Oncol.* **2012**, *39*, 461–472. [[CrossRef](#)]
20. Guo, W.; Lasky, J.L., 3rd; Wu, H. Cancer stem cells. *Pediatrics Res.* **2006**, *59*, 59R–64R. [[CrossRef](#)]
21. Zhu, Z.; Hao, X.; Yan, M.; Yao, M.; Ge, C.; Gu, J.; Li, J. Cancer stem/progenitor cells are highly enriched in CD133+CD44+ population in hepatocellular carcinoma. *Int. J. Cancer* **2010**, *126*, 2067–2078. [[CrossRef](#)] [[PubMed](#)]
22. Ma, S.; Chan, K.W.; Lee, T.K.; Tang, K.H.; Wo, J.Y.; Zheng, B.J.; Guan, X.Y. Aldehyde dehydrogenase discriminates the CD133 liver cancer stem cell populations. *Mol. Cancer Res.* **2008**, *6*, 1146–1153. [[CrossRef](#)] [[PubMed](#)]
23. Hu, C.; Li, H.; Li, J.; Zhu, Z.; Yin, S.; Hao, X.; Yao, M.; Zheng, S.; Gu, J. Analysis of ABCG2 expression and side population identifies intrinsic drug efflux in the HCC cell line MHCC-97L and its modulation by Akt signaling. *Carcinogenesis* **2008**, *29*, 2289–2297. [[CrossRef](#)] [[PubMed](#)]
24. Haraguchi, N.; Utsunomiya, T.; Inoue, H.; Tanaka, F.; Mimori, K.; Barnard, G.F.; Mori, M. Characterization of a side population of cancer cells from human gastrointestinal system. *Stem Cells* **2006**, *24*, 506–513. [[CrossRef](#)]
25. Xin, H.W.; Ambe, C.M.; Hari, D.M.; Wiegand, G.W.; Miller, T.C.; Chen, J.Q.; Anderson, A.J.; Ray, S.; Mullinax, J.E.; Koizumi, T.; et al. Label-retaining liver cancer cells are relatively resistant to sorafenib. *Gut* **2013**, *62*, 1777–1786. [[CrossRef](#)]
26. Piao, L.S.; Hur, W.; Kim, T.K.; Hong, S.W.; Kim, S.W.; Choi, J.E.; Sung, P.S.; Song, M.J.; Lee, B.C.; Hwang, D.; et al. CD133+ liver cancer stem cells modulate radioresistance in human hepatocellular carcinoma. *Cancer Lett.* **2012**, *315*, 129–137. [[CrossRef](#)]
27. Ma, S.; Lee, T.K.; Zheng, B.J.; Chan, K.W.; Guan, X.Y. CD133+ HCC cancer stem cells confer chemoresistance by preferential expression of the Akt/PKB survival pathway. *Oncogene* **2008**, *27*, 1749–1758. [[CrossRef](#)]

28. Fan, S.T.; Yang, Z.F.; Ho, D.W.; Ng, M.N.; Yu, W.C.; Wong, J. Prediction of posthepatectomy recurrence of hepatocellular carcinoma by circulating cancer stem cells: A prospective study. *Ann. Surg.* **2011**, *254*, 569–576. [\[CrossRef\]](#)
29. Philip, P.A.; Mooney, M.; Jaffe, D.; Eckhardt, G.; Moore, M.; Meropol, N.; Emens, L.; O'Reilly, E.; Korc, M.; Ellis, L.; et al. Consensus report of the national cancer institute clinical trials planning meeting on pancreas cancer treatment. *J. Clin. Oncol.* **2009**, *27*, 5660–5669. [\[CrossRef\]](#)
30. Yamashita, T.; Budhu, A.; Forgues, M.; Wang, X.W. Activation of hepatic stem cell marker EpCAM by Wnt-beta-catenin signaling in hepatocellular carcinoma. *Cancer Res.* **2007**, *67*, 10831–10839. [\[CrossRef\]](#)
31. Behari, J. The Wnt/beta-catenin signaling pathway in liver biology and disease. *Expert. Rev. Gastroenterol. Hepatol.* **2010**, *4*, 745–756. [\[CrossRef\]](#) [\[PubMed\]](#)
32. Cioffi, M.; Dorado, J.; Baeuerle, P.A.; Heeschen, C. EpCAM/CD3-Bispecific T-cell engaging antibody MT110 eliminates primary human pancreatic cancer stem cells. *Clin. Cancer Res.* **2012**, *18*, 465–474. [\[CrossRef\]](#) [\[PubMed\]](#)
33. Guan, D.X.; Shi, J.; Zhang, Y.; Zhao, J.S.; Long, L.Y.; Chen, T.W.; Zhang, E.B.; Feng, Y.Y.; Bao, W.D.; Deng, Y.Z.; et al. Sorafenib enriches epithelial cell adhesion molecule-positive tumor initiating cells and exacerbates a subtype of hepatocellular carcinoma through TSC2-AKT cascade. *Hepatology* **2015**, *62*, 1791–1803. [\[CrossRef\]](#) [\[PubMed\]](#)
34. Suetsugi, A.; Nagaki, M.; Aoki, H.; Motohashi, T.; Kunisada, T.; Moriwaki, H. Characterization of CD133(+) hepatocellular carcinoma cells as cancer stem/progenitor cells. *Biochem. Biophys. Res. Commun.* **2006**, *351*, 820–824. [\[CrossRef\]](#)
35. Ma, S.; Chan, K.W.; Hu, L.; Lee, T.K.; Wo, J.Y.; Ng, I.O.; Zheng, B.J.; Guan, X.Y. Identification and characterization of tumorigenic liver cancer stem/progenitor cells. *Gastroenterology* **2007**, *132*, 2542–2556. [\[CrossRef\]](#)
36. Rawal, P.; Siddiqui, H.; Hassan, M.; Choudhary, M.C.; Tripathi, D.M.; Nain, V.; Trehanpati, N.; Kaur, S. Endothelial Cell-Derived TGF-beta Promotes Epithelial-Mesenchymal Transition via CD133 in HBx-Infected Hepatoma Cells. *Front. Oncol.* **2019**, *9*, 308. [\[CrossRef\]](#)
37. Underhill, C. CD44: The hyaluronan receptor. *J. Cell Sci.* **1992**, *103 Pt 2*, 293–298.
38. Bourguignon, L.Y. CD44-mediated oncogenic signaling and cytoskeleton activation during mammary tumor progression. *J. Mammary Gland Biol. Neoplasia* **2001**, *6*, 287–297. [\[CrossRef\]](#)
39. Bourguignon, L.Y. Hyaluronan-mediated CD44 activation of RhoGTPase signaling and cytoskeleton function promotes tumor progression. *Semin Cancer Biol.* **2008**, *18*, 251–259. [\[CrossRef\]](#)
40. Bourguignon, L.Y.; Shiina, M.; Li, J.J. Hyaluronan-CD44 interaction promotes oncogenic signaling, microRNA functions, chemoresistance, and radiation resistance in cancer stem cells leading to tumor progression. *Adv. Cancer Res.* **2014**, *123*, 255–275. [\[CrossRef\]](#)
41. Gao, Y.; Ruan, B.; Liu, W.; Wang, J.; Yang, X.; Zhang, Z.; Li, X.; Duan, J.; Zhang, F.; Ding, R.; et al. Knockdown of CD44 inhibits the invasion and metastasis of hepatocellular carcinoma both in vitro and in vivo by reversing epithelial-mesenchymal transition. *Oncotarget* **2015**, *6*, 7828–7837. [\[CrossRef\]](#) [\[PubMed\]](#)
42. Park, N.R.; Cha, J.H.; Jang, J.W.; Bae, S.H.; Jang, B.; Kim, J.H.; Hur, W.; Choi, J.Y.; Yoon, S.K. Synergistic effects of CD44 and TGF-beta1 through AKT/GSK-3beta/beta-catenin signaling during epithelial-mesenchymal transition in liver cancer cells. *Biochem. Biophys. Res. Commun.* **2016**, *477*, 568–574. [\[CrossRef\]](#) [\[PubMed\]](#)
43. Haraguchi, N.; Ishii, H.; Mimori, K.; Tanaka, F.; Ohkuma, M.; Kim, H.M.; Akita, H.; Takiuchi, D.; Hatano, H.; Nagano, H.; et al. CD13 is a therapeutic target in human liver cancer stem cells. *J. Clin. Investig.* **2010**, *120*, 3326–3339. [\[CrossRef\]](#) [\[PubMed\]](#)
44. Sun, L.; Zhang, L.; Chen, J.; Li, C.; Sun, H.; Wang, J.; Xiao, H. Activation of Tyrosine Metabolism in CD133+ Cancer Stem Cells Drives Relapse in Hepatocellular Carcinoma. *Cancer Res. Treat.* **2019**. [\[CrossRef\]](#)
45. Yang, Z.F.; Ho, D.W.; Ng, M.N.; Lau, C.K.; Yu, W.C.; Ngai, P.; Chu, P.W.; Lam, C.T.; Poon, R.T.; Fan, S.T. Significance of CD90+ cancer stem cells in human liver cancer. *Cancer Cell* **2008**, *13*, 153–166. [\[CrossRef\]](#)
46. Jia, Q.; Zhang, X.; Deng, T.; Gao, J. Positive correlation of Oct4 and ABCG2 to chemotherapeutic resistance in CD90(+)CD133(+) liver cancer stem cells. *Cell Reprogram* **2013**, *15*, 143–150. [\[CrossRef\]](#)
47. Sukowati, C.H.; Anfuso, B.; Torre, G.; Francalanci, P.; Croce, L.S.; Tiribelli, C. The expression of CD90/Thy-1 in hepatocellular carcinoma: An in vivo and in vitro study. *PLoS ONE* **2013**, *8*, e76830. [\[CrossRef\]](#)

48. Xia, W.; Lo, C.M.; Poon, R.Y.C.; Cheung, T.T.; Chan, A.C.Y.; Chen, L.; Yang, S.; Tsao, G.S.W.; Wang, X.Q. Smad inhibitor induces CSC differentiation for effective chemosensitization in cyclin D1- and TGF-beta/Smad-regulated liver cancer stem cell-like cells. *Oncotarget* **2017**, *8*, 38811–38824. [[CrossRef](#)]
49. Yang, X.R.; Xu, Y.; Yu, B.; Zhou, J.; Li, J.C.; Qiu, S.J.; Shi, Y.H.; Wang, X.Y.; Dai, Z.; Shi, G.M.; et al. CD24 Is a Novel Predictor for Poor Prognosis of Hepatocellular Carcinoma after Surgery. *Clin. Cancer Res.* **2009**, *15*, 5518–5527. [[CrossRef](#)]
50. Lee, T.K.W.; Castilho, A.; Cheung, V.C.H.; Tang, K.H.; Ma, S.; Irene, O.L.N. CD24(+) Liver Tumor-Initiating Cells Drive Self-Renewal and Tumor Initiation through STAT3-Mediated NANOG Regulation. *Cell Stem Cell* **2011**, *9*, 50–63. [[CrossRef](#)]
51. Lu, S.; Yao, Y.; Xu, G.L.; Zhou, C.; Zhang, Y.; Sun, J.; Jiang, R.Q.; Shao, Q.; Chen, Y. CD24 regulates sorafenib resistance via activating autophagy in hepatocellular carcinoma. *Cell Death Dis.* **2018**, *9*. [[CrossRef](#)] [[PubMed](#)]
52. Wang, R.H.; Li, Y.W.; Tsung, A.; Huang, H.; Du, Q.; Yang, M.Q.; Deng, M.H.; Xiong, S.; Wang, X.J.; Zhang, L.Y.; et al. iNOS promotes CD24(+)CD133(+) liver cancer stem cell phenotype through a TACE/ADAM17-dependent Notch signaling pathway. *Proc. Natl. Acad. Sci. USA* **2018**, *115*, E10127–E10136. [[CrossRef](#)] [[PubMed](#)]
53. Yang, W.; Yan, H.X.; Chen, L.; Liu, Q.; He, Y.Q.; Yu, L.X.; Zhang, S.H.; Huang, D.D.; Tang, L.; Kong, X.N.; et al. Wnt/beta-catenin signaling contributes to activation of normal and tumorigenic liver progenitor cells. *Cancer Res.* **2008**, *68*, 4287–4295. [[CrossRef](#)] [[PubMed](#)]
54. Wang, C.; Wang, M.D.; Cheng, P.; Huang, H.; Dong, W.; Zhang, W.W.; Li, P.P.; Lin, C.; Pan, Z.Y.; Wu, M.C.; et al. Hepatitis B virus X protein promotes the stem-like properties of OV6(+) cancer cells in hepatocellular carcinoma. *Cell Death Dis.* **2017**, *8*, e2560. [[CrossRef](#)]
55. Shi, G.M.; Xu, Y.; Fan, J.; Zhou, J.; Yang, X.R.; Qiu, S.J.; Liao, Y.; Wu, W.Z.; Ji, Y.; Ke, A.W.; et al. Identification of side population cells in human hepatocellular carcinoma cell lines with stepwise metastatic potentials. *J. Cancer Res. Clin. Oncol.* **2008**, *134*, 1155–1163. [[CrossRef](#)]
56. Lo, J.; Lau, E.Y.; Ching, R.H.; Cheng, B.Y.; Ma, M.K.; Ng, I.O.; Lee, T.K. Nuclear factor kappa B-mediated CD47 up-regulation promotes sorafenib resistance and its blockade synergizes the effect of sorafenib in hepatocellular carcinoma in mice. *Hepatology* **2015**, *62*, 534–545. [[CrossRef](#)]
57. Roberts, D.D.; Kaur, S.; Soto-Pantoja, D.R. Therapeutic targeting of the thrombospondin-1 receptor CD47 to treat liver cancer. *J. Cell. Commun. Signal* **2015**, *9*, 101–102. [[CrossRef](#)]
58. Chen, J.; Zheng, D.X.; Yu, X.J.; Sun, H.W.; Xu, Y.T.; Zhang, Y.J.; Xu, J. Macrophages induce CD47 upregulation via IL-6 and correlate with poor survival in hepatocellular carcinoma patients. *Oncoimmunology* **2019**, *8*, e1652540. [[CrossRef](#)]
59. Oikawa, T.; Kamiya, A.; Zeniya, M.; Chikada, H.; Hyuck, A.D.; Yamazaki, Y.; Wauthier, E.; Tajiri, H.; Miller, L.D.; Wang, X.W.; et al. Sal-like protein 4 (SALL4), a stem cell biomarker in liver cancers. *Hepatology* **2013**, *57*, 1469–1483. [[CrossRef](#)]
60. Jiang, Y.L.; Li, W.; Shen, H.G.; Ren, R.; Xu, Z.H.; Wan, D.W.; Han, Y.; Kuang, Y.T.; Zhi, Q.M. SALL4 expression is associated with poor outcome in hepatocellular carcinoma. *Int. J. Clin. Exp. Med.* **2017**, *10*, 4267–4277.
61. Yamashita, T.; Honda, M.; Nakamoto, Y.; Baba, M.; Nio, K.; Hara, Y.; Zeng, S.S.; Hayashi, T.; Kondo, M.; Takatori, H.; et al. Discrete nature of EpCAM+ and CD90+ cancer stem cells in human hepatocellular carcinoma. *Hepatology* **2013**, *57*, 1484–1497. [[CrossRef](#)] [[PubMed](#)]
62. Zhu, L.; Zhang, W.; Wang, J.H.; Liu, R. Evidence of CD90+CXCR4+ cells as circulating tumor stem cells in hepatocellular carcinoma. *Tumor. Biol.* **2015**, *36*, 5353–5360. [[CrossRef](#)] [[PubMed](#)]
63. Munz, M.; Baeuerle, P.A.; Gires, O. The emerging role of EpCAM in cancer and stem cell signaling. *Cancer Res.* **2009**, *69*, 5627–5629. [[CrossRef](#)] [[PubMed](#)]
64. Schmelzer, E.; Reid, L.M. EpCAM expression in normal, non-pathological tissues. *Front Biosci.* **2008**, *13*, 3096–3100. [[CrossRef](#)] [[PubMed](#)]
65. Baeuerle, P.A.; Gires, O. EpCAM (CD326) finding its role in cancer. *Br. J. Cancer* **2007**, *96*, 417–423. [[CrossRef](#)] [[PubMed](#)]
66. Trzpis, M.; McLaughlin, P.M.; de Leij, L.M.; Harmsen, M.C. Epithelial cell adhesion molecule: More than a carcinoma marker and adhesion molecule. *Am. J. Pathol.* **2007**, *171*, 386–395. [[CrossRef](#)]
67. Alibolandi, M.; Ramezani, M.; Sadeghi, F.; Abnous, K.; Hadizadeh, F. Epithelial cell adhesion molecule aptamer conjugated PEG-PLGA nanoparticles for targeted delivery of doxorubicin to human breast adenocarcinoma cell line in vitro. *Int. J. Pharm.* **2015**, *479*, 241–251. [[CrossRef](#)]

68. Sun, Y.F.; Xu, Y.; Yang, X.R.; Guo, W.; Zhang, X.; Qiu, S.J.; Shi, R.Y.; Hu, B.; Zhou, J.; Fan, J. Circulating stem cell-like epithelial cell adhesion molecule-positive tumor cells indicate poor prognosis of hepatocellular carcinoma after curative resection. *Hepatology* **2013**, *57*, 1458–1468. [\[CrossRef\]](#)
69. Maetzel, D.; Denzel, S.; Mack, B.; Canis, M.; Went, P.; Benk, M.; Kieu, C.; Papior, P.; Baeuerle, P.A.; Munz, M.; et al. Nuclear signalling by tumour-associated antigen EpCAM. *Nat. Cell Biol.* **2009**, *11*, 162–171. [\[CrossRef\]](#)
70. Yamashita, T.; Ji, J.; Budhu, A.; Forgues, M.; Yang, W.; Wang, H.Y.; Jia, H.; Ye, Q.; Qin, L.X.; Wauthier, E.; et al. EpCAM-positive hepatocellular carcinoma cells are tumor-initiating cells with stem/progenitor cell features. *Gastroenterology* **2009**, *136*, 1012–1024. [\[CrossRef\]](#)
71. Lacoste, B.; Raymond, V.A.; Cassim, S.; Lapierre, P.; Bilodeau, M. Highly tumorigenic hepatocellular carcinoma cell line with cancer stem cell-like properties. *PLoS ONE* **2017**, *12*, e0171215. [\[CrossRef\]](#) [\[PubMed\]](#)
72. Nio, K.; Yamashita, T.; Okada, H.; Kondo, M.; Hayashi, T.; Hara, Y.; Nomura, Y.; Zeng, S.S.; Yoshida, M.; Hayashi, T.; et al. Defeating EpCAM(+) liver cancer stem cells by targeting chromatin remodeling enzyme CHD4 in human hepatocellular carcinoma. *J. Hepatol.* **2015**, *63*, 1164–1172. [\[CrossRef\]](#) [\[PubMed\]](#)
73. Ko, C.J.; Li, C.J.; Wu, M.Y.; Chu, P.Y. Overexpression of epithelial cell adhesion molecule as a predictor of poor outcome in patients with hepatocellular carcinoma. *Exp. Ther. Med.* **2018**, *16*, 4810–4816. [\[CrossRef\]](#) [\[PubMed\]](#)
74. Chen, Y.L.; Lin, P.Y.; Ming, Y.Z.; Huang, W.C.; Chen, R.F.; Chen, P.M.; Chu, P.Y. The effects of the location of cancer stem cell marker CD133 on the prognosis of hepatocellular carcinoma patients. *BMC Cancer* **2017**, *17*, 474. [\[CrossRef\]](#) [\[PubMed\]](#)
75. Glumac, P.M.; LeBeau, A.M. The role of CD133 in cancer: A concise review. *Clin. Transl. Med.* **2018**, *7*. [\[CrossRef\]](#) [\[PubMed\]](#)
76. Guler, G.; Guven, U.; Oktem, G. Characterization of CD133(+)/CD44(+) human prostate cancer stem cells with ATR-FTIR spectroscopy. *Analyst* **2019**, *144*, 2138–2149. [\[CrossRef\]](#)
77. Gzil, A.; Zarebska, I.; Bursiewicz, W.; Antosik, P.; Grzanka, D.; Szyberg, L. Markers of pancreatic cancer stem cells and their clinical and therapeutic implications. *Mol. Biol. Rep.* **2019**, *46*, 6629–6645. [\[CrossRef\]](#)
78. Peng, L.; Fu, J.; Wang, W.; Hofman, F.M.; Chen, T.C.; Chen, L. Distribution of cancer stem cells in two human brain gliomas. *Oncol. Lett.* **2019**, *17*, 2123–2130. [\[CrossRef\]](#)
79. Yin, S.; Li, J.; Hu, C.; Chen, X.; Yao, M.; Yan, M.; Jiang, G.; Ge, C.; Xie, H.; Wan, D.; et al. CD133 positive hepatocellular carcinoma cells possess high capacity for tumorigenicity. *Int. J. Cancer* **2007**, *120*, 1444–1450. [\[CrossRef\]](#)
80. Song, W.; Li, H.; Tao, K.; Li, R.; Song, Z.; Zhao, Q.; Zhang, F.; Dou, K. Expression and clinical significance of the stem cell marker CD133 in hepatocellular carcinoma. *Int. J. Clin. Pract.* **2008**, *62*, 1212–1218. [\[CrossRef\]](#)
81. Tsuchiya, A.; Kamimura, H.; Takamura, M.; Yamagiwa, S.; Matsuda, Y.; Sato, Y.; Nomoto, M.; Ichida, T.; Aoyagi, Y. Clinicopathological analysis of CD133 and NCAM human hepatic stem/progenitor cells in damaged livers and hepatocellular carcinomas. *Hepatol. Res.* **2009**, *39*, 1080–1090. [\[CrossRef\]](#) [\[PubMed\]](#)
82. Yoshikawa, S.; Zen, Y.; Fujii, T.; Sato, Y.; Ohta, T.; Aoyagi, Y.; Nakanuma, Y. Characterization of CD133+ parenchymal cells in the liver: Histology and culture. *World J. Gastroenterol.* **2009**, *15*, 4896–4906. [\[CrossRef\]](#) [\[PubMed\]](#)
83. Wang, Y.; Wu, G.; Fu, X.; Xu, S.; Wang, T.; Zhang, Q.; Yang, Y. Aquaporin 3 maintains the stemness of CD133+ hepatocellular carcinoma cells by activating STAT3. *Cell Death Dis.* **2019**, *10*, 465. [\[CrossRef\]](#) [\[PubMed\]](#)
84. Liu, K.; Hao, M.; Ouyang, Y.; Zheng, J.; Chen, D. CD133(+) cancer stem cells promoted by VEGF accelerate the recurrence of hepatocellular carcinoma. *Sci. Rep.* **2017**, *7*, 41499. [\[CrossRef\]](#)
85. Qiu, M.T.; Hu, J.W.; Yin, R.; Xu, L. Long noncoding RNA: An emerging paradigm of cancer research. *Tumour Biol.* **2013**, *34*, 613–620. [\[CrossRef\]](#)
86. Ma, S.; Tang, K.H.; Chan, Y.P.; Lee, T.K.; Kwan, P.S.; Castilho, A.; Ng, I.; Man, K.; Wong, N.; To, K.F.; et al. miR-130b Promotes CD133(+) liver tumor-initiating cell growth and self-renewal via tumor protein 53-induced nuclear protein 1. *Cell Stem Cell* **2010**, *7*, 694–707. [\[CrossRef\]](#)
87. Wan, S.; Zhao, E.; Kryczek, I.; Vatan, L.; Sadovskaya, A.; Ludema, G.; Simeone, D.M.; Zou, W.; Welling, T.H. Tumor-associated macrophages produce interleukin 6 and signal via STAT3 to promote expansion of human hepatocellular carcinoma stem cells. *Gastroenterology* **2014**, *147*, 1393–1404. [\[CrossRef\]](#)
88. Asai, R.; Tsuchiya, H.; Amisaki, M.; Makimoto, K.; Takenaga, A.; Sakabe, T.; Hoi, S.; Koyama, S.; Shiota, G. CD44 standard isoform is involved in maintenance of cancer stem cells of a hepatocellular carcinoma cell line. *Cancer Med.* **2019**, *8*, 773–782. [\[CrossRef\]](#)

89. Mima, K.; Okabe, H.; Ishimoto, T.; Hayashi, H.; Nakagawa, S.; Kuroki, H.; Watanabe, M.; Beppu, T.; Tamada, M.; Nagano, O.; et al. CD44s regulates the TGF-beta-mediated mesenchymal phenotype and is associated with poor prognosis in patients with hepatocellular carcinoma. *Cancer Res.* **2012**, *72*, 3414–3423. [[CrossRef](#)]
90. Mima, K.; Hayashi, H.; Imai, K.; Kuroki, H.; Nakagawa, S.; Okabe, H.; Chikamoto, A.; Watanabe, M.; Beppu, T.; Baba, H. High CD44s expression is associated with the EMT expression profile and intrahepatic dissemination of hepatocellular carcinoma after local ablation therapy. *J. Hepatobiliary Pancreat. Sci.* **2013**, *20*, 429–434. [[CrossRef](#)]
91. Dhar, D.; Antonucci, L.; Nakagawa, H.; Kim, J.Y.; Glitzner, E.; Caruso, S.; Shalapour, S.; Yang, L.; Valasek, M.A.; Lee, S.; et al. Liver Cancer Initiation Requires p53 Inhibition by CD44-Enhanced Growth Factor Signaling. *Cancer Cell* **2018**, *33*, 1061–1077.e1066. [[CrossRef](#)] [[PubMed](#)]
92. Tovuu, L.O.; Imura, S.; Utsunomiya, T.; Morine, Y.; Ikemoto, T.; Arakawa, Y.; Mori, H.; Hanaoka, J.; Kanamoto, M.; Sugimoto, K.; et al. Role of CD44 expression in non-tumor tissue on intrahepatic recurrence of hepatocellular carcinoma. *Int. J. Clin. Oncol.* **2013**, *18*, 651–656. [[CrossRef](#)] [[PubMed](#)]
93. Shipp, M.A.; Look, A.T. Hematopoietic Differentiation Antigens That Are Membrane-Associated Enzymes - Cutting Is the Key. *Blood* **1993**, *82*, 1052–1070. [[CrossRef](#)] [[PubMed](#)]
94. Kim, H.M.; Haraguchi, N.; Ishii, H.; Ohkuma, M.; Okano, M.; Mimori, K.; Eguchi, H.; Yamamoto, H.; Nagano, H.; Sekimoto, M.; et al. Increased CD13 expression reduces reactive oxygen species, promoting survival of liver cancer stem cells via an epithelial-mesenchymal transition-like phenomenon. *Ann. Surg. Oncol.* **2012**, *19* (Suppl. 3), S539–S548. [[CrossRef](#)]
95. Yamanaka, C.; Wada, H.; Eguchi, H.; Hatano, H.; Gotoh, K.; Noda, T.; Yamada, D.; Asaoka, T.; Kawamoto, K.; Nagano, H.; et al. Clinical significance of CD13 and epithelial mesenchymal transition (EMT) markers in hepatocellular carcinoma. *Jpn. J. Clin. Oncol.* **2018**, *48*, 52–60. [[CrossRef](#)] [[PubMed](#)]
96. Barboni, E.; Gormley, A.M.; Rivero, F.B.P.; Vidal, M.; Morris, R.J. Activation of Lymphocytes-T by Cross-Linking of Glycophospholipid-Anchored Thy-1 Mobilizes Separate Pools of Intracellular 2nd Messengers to Those Induced by the Antigen Receptor Cd3 Complex. *Immunology* **1991**, *72*, 457–463. [[PubMed](#)]
97. Morris, R.J.; Tiveron, M.C.; Xue, G.P. The Relation of the Expression and Function of the Neuronal Glycoprotein Thy-1 to Axonal Growth. *Biochem. Soc. T* **1992**, *20*, 401–405. [[CrossRef](#)]
98. Jeng, C.J.; McCarroll, S.A.; Martin, T.F.J.; Floor, E.; Adams, J.; Krantz, D.; Butz, S.; Edwards, R.; Schweitzer, E.S. Thy-1 is a component common to multiple populations of synaptic vesicles. *J. Cell Biol.* **1998**, *140*, 685–698. [[CrossRef](#)]
99. Leyton, L.; Schneider, P.; Labra, C.V.; Ruegg, C.; Hetz, C.A.; Quest, A.F.; Bron, C. Thy-1 binds to integrin beta(3) on astrocytes and triggers formation of focal contact sites. *Curr. Biol.* **2001**, *11*, 1028–1038. [[CrossRef](#)]
100. Yang, Z.F.; Ngai, P.; Ho, D.W.; Yu, W.C.; Ng, M.N.; Lau, C.K.; Li, M.L.; Tam, K.H.; Lam, C.T.; Poon, R.T.; et al. Identification of local and circulating cancer stem cells in human liver cancer. *Hepatology* **2008**, *47*, 919–928. [[CrossRef](#)]
101. Chiba, T.; Kanai, F.; Iwama, A.; Yokosuka, O. Circulating cancer stem cells: A novel prognostic predictor of hepatocellular carcinoma. *Hepatobiliary Surg. Nutr.* **2013**, *2*, 4–6. [[CrossRef](#)] [[PubMed](#)]
102. Guo, Z.; Li, L.Q.; Jiang, J.H.; Ou, C.; Zeng, L.X.; Xiang, B.D. Cancer stem cell markers correlate with early recurrence and survival in hepatocellular carcinoma. *World J. Gastroenterol.* **2014**, *20*, 2098–2106. [[CrossRef](#)] [[PubMed](#)]
103. Kim, B.H.; Park, J.W.; Kim, J.S.; Lee, S.K.; Hong, E.K. Stem Cell Markers Predict the Response to Sorafenib in Patients with Hepatocellular Carcinoma. *Gut Liver* **2019**, *13*, 342–348. [[CrossRef](#)] [[PubMed](#)]
104. Zhao, R.C.; Zhou, J.; Chen, K.F.; Gong, J.; Liu, J.; He, J.Y.; Guan, P.; Li, B.; Qin, Y. The prognostic value of combination of CD90 and OCT4 for hepatocellular carcinoma after curative resection. *Neoplasma* **2016**, *63*, 288–298. [[CrossRef](#)] [[PubMed](#)]
105. Gilliam, D.T.; Menon, V.; Bretz, N.P.; Pruszek, J. The CD24 surface antigen in neural development and disease. *Neurobiol. Dis.* **2017**, *99*, 133–144. [[CrossRef](#)] [[PubMed](#)]
106. Qiu, Q.; Hernandez, J.C.; Dean, A.M.; Rao, P.H.; Darlington, G.J. CD24-Positive Cells from Normal Adult Mouse Liver Are Hepatocyte Progenitor Cells. *Stem Cells Dev.* **2011**, *20*, 2177–2188. [[CrossRef](#)]
107. Dunsford, H.A.; Sell, S. Production of monoclonal antibodies to preneoplastic liver cell populations induced by chemical carcinogens in rats and to transplantable Morris hepatomas. *Cancer Res.* **1989**, *49*, 4887–4893.

108. Strain, A.J.; Crosby, H.A.; Nijjar, S.; Kelly, D.A.; Hubscher, S.G. Human liver-derived stem cells. *Semin. Liver Dis.* **2003**, *23*, 373–384. [[CrossRef](#)]
109. Yang, W.; Wang, C.; Lin, Y.; Liu, Q.; Yu, L.X.; Tang, L.; Yan, H.X.; Fu, J.; Chen, Y.; Zhang, H.L.; et al. OV6(+) tumor-initiating cells contribute to tumor progression and invasion in human hepatocellular carcinoma. *J. Hepatol.* **2012**, *57*, 613–620. [[CrossRef](#)]
110. Goodell, M.A.; Brose, K.; Paradis, G.; Conner, A.S.; Mulligan, R.C. Isolation and functional properties of murine hematopoietic stem cells that are replicating in vivo. *J. Exp. Med.* **1996**, *183*, 1797–1806. [[CrossRef](#)]
111. Falciatori, I.; Borsellino, G.; Haliassos, N.; Boitani, C.; Corallini, S.; Battistini, L.; Bernardi, G.; Stefanini, M.; Vicini, E. Identification and enrichment of spermatogonial stem cells displaying side-population phenotype in immature mouse testis. *Faseb. J.* **2003**, *17*, 376–378. [[CrossRef](#)] [[PubMed](#)]
112. Chiba, T.; Kita, K.; Zheng, Y.W.; Yokosuka, O.; Saisho, H.; Iwama, A.; Nakauchi, H.; Taniguchi, H. Side population purified from hepatocellular carcinoma cells harbors cancer stem cell-like properties. *Hepatology* **2006**, *44*, 240–251. [[CrossRef](#)] [[PubMed](#)]
113. Zen, Y.; Fujii, T.; Yoshikawa, S.; Takamura, H.; Tani, T.; Ohta, T.; Nakanuma, Y. Histological and culture studies with respect to ABCG2 expression support the existence of a cancer cell hierarchy in human hepatocellular carcinoma. *Am. J. Pathol.* **2007**, *170*, 1750–1762. [[CrossRef](#)] [[PubMed](#)]
114. Willingham, S.B.; Volkmer, J.P.; Gentles, A.J.; Sahoo, D.; Dalerba, P.; Mitra, S.S.; Wang, J.; Contreras-Trujillo, H.; Martin, R.; Cohen, J.D.; et al. The CD47-signal regulatory protein alpha (SIRPα) interaction is a therapeutic target for human solid tumors. *Proc. Natl. Acad. Sci. USA* **2012**, *109*, 6662–6667. [[CrossRef](#)]
115. Lo, J.; Lau, E.Y.; So, F.T.; Lu, P.; Chan, V.S.; Cheung, V.C.; Ching, R.H.; Cheng, B.Y.; Ma, M.K.; Ng, I.O.; et al. Anti-CD47 antibody suppresses tumour growth and augments the effect of chemotherapy treatment in hepatocellular carcinoma. *Liver Int.* **2016**, *36*, 737–745. [[CrossRef](#)]
116. Mohammed, M.K.; Shao, C.; Wang, J.; Wei, Q.; Wang, X.; Collier, Z.; Tang, S.; Liu, H.; Zhang, F.; Huang, J.; et al. Wnt/beta-catenin signaling plays an ever-expanding role in stem cell self-renewal, tumorigenesis and cancer chemoresistance. *Genes Dis.* **2016**, *3*, 11–40. [[CrossRef](#)]
117. Kraus, C.; Liehr, T.; Hulsken, J.; Behrens, J.; Birchmeier, W.; Grzeschik, K.H.; Ballhausen, W.G. Localization of the human beta-catenin gene (CTNNB1) to 3p21: A region implicated in tumor development. *Genomics* **1994**, *23*, 272–274. [[CrossRef](#)]
118. Noordermeer, J.; Klingensmith, J.; Perrimon, N.; Nusse, R. Dishevelled and Armadillo act in the wingless signalling pathway in Drosophila. *Nature* **1994**, *367*, 80–83. [[CrossRef](#)]
119. Peifer, M.; Berg, S.; Reynolds, A.B. A repeating amino acid motif shared by proteins with diverse cellular roles. *Cell* **1994**, *76*, 789–791. [[CrossRef](#)]
120. MacDonald, B.T.; Tamai, K.; He, X. Wnt/beta-catenin signaling: Components, mechanisms, and diseases. *Dev. Cell* **2009**, *17*, 9–26. [[CrossRef](#)]
121. Morin, P.J. beta-catenin signaling and cancer. *Bioessays* **1999**, *21*, 1021–1030. [[CrossRef](#)]
122. Gedaly, R.; Galuppo, R.; Daily, M.F.; Shah, M.; Maynard, E.; Chen, C.; Zhang, X.; Esser, K.A.; Cohen, D.A.; Evers, B.M.; et al. Targeting the Wnt/beta-catenin signaling pathway in liver cancer stem cells and hepatocellular carcinoma cell lines with FH535. *PLoS ONE* **2014**, *9*, e99272. [[CrossRef](#)] [[PubMed](#)]
123. Behrens, J.; von Kries, J.P.; Kuhl, M.; Bruhn, L.; Wedlich, D.; Grosschedl, R.; Birchmeier, W. Functional interaction of beta-catenin with the transcription factor LEF-1. *Nature* **1996**, *382*, 638–642. [[CrossRef](#)] [[PubMed](#)]
124. Takigawa, Y.; Brown, A.M. Wnt signaling in liver cancer. *Curr. Drug Targets* **2008**, *9*, 1013–1024. [[CrossRef](#)]
125. Kim, J.Y.; Lee, H.Y.; Park, K.K.; Choi, Y.K.; Nam, J.S.; Hong, I.S. CWP232228 targets liver cancer stem cells through Wnt/beta-catenin signaling: A novel therapeutic approach for liver cancer treatment. *Oncotarget* **2016**, *7*, 20395–20409. [[CrossRef](#)]
126. Handeli, S.; Simon, J.A. A small-molecule inhibitor of Tcf/beta-catenin signaling down-regulates PPARγ and PPARδ activities. *Mol. Cancer Ther.* **2008**, *7*, 521–529. [[CrossRef](#)]
127. Tomizawa, M.; Shinozaki, F.; Motoyoshi, Y.; Sugiyama, T.; Yamamoto, S.; Ishige, N. FH535 suppresses the proliferation and motility of hepatocellular carcinoma cells. *Int. J. Oncol.* **2016**, *48*, 110–114. [[CrossRef](#)]
128. Turcios, L.; Vilchez, V.; Acosta, L.F.; Poyil, P.; Butterfield, D.A.; Mitov, M.; Marti, F.; Gedaly, R. Sorafenib and FH535 in combination act synergistically on hepatocellular carcinoma by targeting cell bioenergetics and mitochondrial function. *Dig. Liver Dis.* **2017**, *49*, 697–704. [[CrossRef](#)]

129. Galuppo, R.; Maynard, E.; Shah, M.; Daily, M.F.; Chen, C.; Spear, B.T.; Gedaly, R. Synergistic inhibition of HCC and liver cancer stem cell proliferation by targeting RAS/RAF/MAPK and WNT/beta-catenin pathways. *Anticancer Res.* **2014**, *34*, 1709–1713.
130. Ni, C.X.; Qi, Y.; Zhang, J.; Liu, Y.; Xu, W.H.; Xu, J.; Hu, H.G.; Wu, Q.Y.; Wang, Y.; Zhang, J.P. WM130 preferentially inhibits hepatic cancer stem-like cells by suppressing AKT/GSK3beta/beta-catenin signaling pathway. *Oncotarget* **2016**, *7*, 79544–79556. [[CrossRef](#)]
131. Qian, L.; Liu, Y.; Xu, Y.; Ji, W.; Wu, Q.; Liu, Y.; Gao, Q.; Su, C. Matrine derivative WM130 inhibits hepatocellular carcinoma by suppressing EGFR/ERK/MMP-2 and PTEN/AKT signaling pathways. *Cancer Lett.* **2015**, *368*, 126–134. [[CrossRef](#)] [[PubMed](#)]
132. Liu, Y.; Qi, Y.; Bai, Z.H.; Ni, C.X.; Ren, Q.H.; Xu, W.H.; Xu, J.; Hu, H.G.; Qiu, L.; Li, J.Z.; et al. A novel matrine derivate inhibits differentiated human hepatoma cells and hepatic cancer stem-like cells by suppressing PI3K/AKT signaling pathways. *Acta Pharmacol. Sin.* **2017**, *38*, 120–132. [[CrossRef](#)] [[PubMed](#)]
133. Chan, K.K.; Lo, R.C. Deregulation of Frizzled Receptors in Hepatocellular Carcinoma. *Int. J. Mol. Sci.* **2018**, *19*, 313. [[CrossRef](#)] [[PubMed](#)]
134. Le, P.N.; McDermott, J.D.; Jimeno, A. Targeting the Wnt pathway in human cancers: Therapeutic targeting with a focus on OMP-54F28. *Pharmacol. Ther.* **2015**, *146*, 1–11. [[CrossRef](#)] [[PubMed](#)]
135. Artavanis-Tsakonas, S.; Rand, M.D.; Lake, R.J. Notch signaling: Cell fate control and signal integration in development. *Science* **1999**, *284*, 770–776. [[CrossRef](#)] [[PubMed](#)]
136. Kumar, R.; Juillerat-Jeanneret, L.; Golshayan, D. Notch Antagonists: Potential Modulators of Cancer and Inflammatory Diseases. *J. Med. Chem.* **2016**, *59*, 7719–7737. [[CrossRef](#)] [[PubMed](#)]
137. Kopan, R. Notch signaling. *Cold Spring Harb. Perspect. Biol.* **2012**, *4*. [[CrossRef](#)]
138. Luo, J.; Wang, P.; Wang, R.H.; Wang, J.L.; Liu, M.; Xiong, S.; Li, Y.W.; Cheng, B. The Notch pathway promotes the cancer stem cell characteristics of CD90(+) cells in hepatocellular carcinoma. *Oncotarget* **2016**, *7*, 9526–9538. [[CrossRef](#)]
139. Zhu, P.; Wang, Y.; Du, Y.; He, L.; Huang, G.; Zhang, G.; Yan, X.; Fan, Z. C8orf4 negatively regulates self-renewal of liver cancer stem cells via suppression of NOTCH2 signalling. *Nat. Commun.* **2015**, *6*, 7122. [[CrossRef](#)]
140. Zhang, Q.Y.; Lu, C.J.; Fang, T.; Wang, Y.C.; Hu, W.H.; Qiao, J.; Liu, B.; Liu, J.; Chen, N.P.; Li, M.Y.; et al. Notch3 functions as a regulator of cell self-renewal by interacting with the beta-catenin pathway in hepatocellular carcinoma. *Oncotarget* **2015**, *6*, 3669–3679. [[CrossRef](#)]
141. Wang, R.; Sun, Q.; Wang, P.; Liu, M.; Xiong, S.; Luo, J.; Huang, H.; Du, Q.; Geller, D.A.; Cheng, B. Notch and Wnt/beta-catenin signaling pathway play important roles in activating liver cancer stem cells. *Oncotarget* **2016**, *7*, 5754–5768. [[CrossRef](#)] [[PubMed](#)]
142. Wu, C.X.; Xu, A.; Zhang, C.C.; Olson, P.; Chen, L.; Lee, T.K.; Cheung, T.T.; Lo, C.M.; Wang, X.Q. Notch Inhibitor PF-03084014 Inhibits Hepatocellular Carcinoma Growth and Metastasis via Suppression of Cancer Stemness due to Reduced Activation of Notch1-Stat3. *Mol. Cancer Ther.* **2017**, *16*, 1531–1543. [[CrossRef](#)] [[PubMed](#)]
143. Ihrie, R.A.; Shah, J.K.; Harwell, C.C.; Levine, J.H.; Guinto, C.D.; Lezameta, M.; Kriegstein, A.R.; Alvarez-Buylla, A. Persistent sonic hedgehog signaling in adult brain determines neural stem cell positional identity. *Neuron* **2011**, *71*, 250–262. [[CrossRef](#)] [[PubMed](#)]
144. Buller, N.V.; Rosekrans, S.L.; Westerlund, J.; van den Brink, G.R. Hedgehog signaling and maintenance of homeostasis in the intestinal epithelium. *Physiol. (Bethesda)* **2012**, *27*, 148–155. [[CrossRef](#)] [[PubMed](#)]
145. Solanas, G.; Benitah, S.A. Regenerating the skin: A task for the heterogeneous stem cell pool and surrounding niche. *Nat. Rev. Mol. Cell Biol.* **2013**, *14*, 737–748. [[CrossRef](#)] [[PubMed](#)]
146. Petrova, R.; Joyner, A.L. Roles for Hedgehog signaling in adult organ homeostasis and repair. *Development* **2014**, *141*, 3445–3457. [[CrossRef](#)] [[PubMed](#)]
147. Hanna, A.; Shevde, L.A. Hedgehog signaling: Modulation of cancer properties and tumor microenvironment. *Mol. Cancer* **2016**, *15*, 24. [[CrossRef](#)]
148. Arzumanyan, A.; Sambandam, V.; Clayton, M.M.; Choi, S.S.; Xie, G.; Diehl, A.M.; Yu, D.Y.; Feitelson, M.A. Hedgehog signaling blockade delays hepatocarcinogenesis induced by hepatitis B virus X protein. *Cancer Res.* **2012**, *72*, 5912–5920. [[CrossRef](#)]

149. Zhang, D.; Cao, L.; Li, Y.; Lu, H.; Yang, X.; Xue, P. Expression of glioma-associated oncogene 2 (Gli 2) is correlated with poor prognosis in patients with hepatocellular carcinoma undergoing hepatectomy. *World J. Surg. Oncol.* **2013**, *11*, 25. [[CrossRef](#)]
150. Chun, H.W.; Hong, R. Significance of the hedgehog pathway-associated proteins Gli-1 and Gli-2 and the epithelial-mesenchymal transition-associated proteins Twist and E-cadherin in hepatocellular carcinoma. *Oncol. Lett.* **2016**, *12*, 1753–1762. [[CrossRef](#)]
151. Wang, F.; Ma, L.; Zhang, Z.; Liu, X.; Gao, H.; Zhuang, Y.; Yang, P.; Kornmann, M.; Tian, X.; Yang, Y. Hedgehog Signaling Regulates Epithelial-Mesenchymal Transition in Pancreatic Cancer Stem-Like Cells. *J. Cancer* **2016**, *7*, 408–417. [[CrossRef](#)] [[PubMed](#)]
152. Rimkus, T.K.; Carpenter, R.L.; Qasem, S.; Chan, M.; Lo, H.W. Targeting the Sonic Hedgehog Signaling Pathway: Review of Smoothed and GLI Inhibitors. *Cancers (Basel)* **2016**, *8*, 22. [[CrossRef](#)] [[PubMed](#)]
153. Incardona, J.P.; Gaffield, W.; Kapur, R.P.; Roelink, H. The teratogenic Veratrum alkaloid cyclopamine inhibits sonic hedgehog signal transduction. *Development* **1998**, *125*, 3553–3562. [[PubMed](#)]
154. Sicklick, J.K.; Li, Y.X.; Jayaraman, A.; Kannangai, R.; Qi, Y.; Vivekanandan, P.; Ludlow, J.W.; Owzar, K.; Chen, W.; Torbenson, M.S.; et al. Dysregulation of the Hedgehog pathway in human hepatocarcinogenesis. *Carcinogenesis* **2006**, *27*, 748–757. [[CrossRef](#)]
155. Hirotsu, M.; Setoguchi, T.; Sasaki, H.; Matsunoshita, Y.; Gao, H.; Nagao, H.; Kunigou, O.; Komiya, S. Smoothed as a new therapeutic target for human osteosarcoma. *Mol. Cancer* **2010**, *9*. [[CrossRef](#)]
156. Mimeault, M.; Johansson, S.L.; Henichart, J.P.; Depreux, P.; Batra, S.K. Cytotoxic Effects Induced by Docetaxel, Gefitinib, and Cyclopamine on Side Population and Nonside Population Cell Fractions from Human Invasive Prostate Cancer Cells. *Mol. Cancer Ther.* **2010**, *9*, 617–630. [[CrossRef](#)]
157. Robarge, K.D.; Brunton, S.A.; Castaneda, G.M.; Cui, Y.; Dina, M.S.; Goldsmith, R.; Gould, S.E.; Guichert, O.; Gunzner, J.L.; Halladay, J.; et al. GDC-0449-a potent inhibitor of the hedgehog pathway. *Bioorg Med. Chem. Lett.* **2009**, *19*, 5576–5581. [[CrossRef](#)]
158. Philips, G.M.; Chan, I.S.; Swiderska, M.; Schroder, V.T.; Guy, C.; Karaca, G.F.; Moylan, C.; Venkatraman, T.; Feuerlein, S.; Syn, W.K.; et al. Hedgehog Signaling Antagonist Promotes Regression of Both Liver Fibrosis and Hepatocellular Carcinoma in a Murine Model of Primary Liver Cancer. *PLoS ONE* **2011**, *6*. [[CrossRef](#)]
159. Kwon, H.; Song, K.; Han, C.; Chen, W.; Wang, Y.; Dash, S.; Lim, K.; Wu, T. Inhibition of hedgehog signaling ameliorates hepatic inflammation in mice with nonalcoholic fatty liver disease. *Hepatology* **2016**, *63*, 1155–1169. [[CrossRef](#)]
160. Fu, J.; Rodova, M.; Roy, S.K.; Sharma, J.; Singh, K.P.; Srivastava, R.K.; Shankar, S. GANT-61 inhibits pancreatic cancer stem cell growth in vitro and in NOD/SCID/IL2R gamma null mice xenograft. *Cancer Lett.* **2013**, *330*, 22–32. [[CrossRef](#)]
161. Wang, Y.; Han, C.; Lu, L.; Magliato, S.; Wu, T. Hedgehog signaling pathway regulates autophagy in human hepatocellular carcinoma cells. *Hepatology* **2013**, *58*, 995–1010. [[CrossRef](#)] [[PubMed](#)]
162. Xu, P.; Liu, J.; Derynck, R. Post-translational regulation of TGF-beta receptor and Smad signaling. *FEBS Lett.* **2012**, *586*, 1871–1884. [[CrossRef](#)] [[PubMed](#)]
163. Meindl-Beinker, N.M.; Matsuzaki, K.; Dooley, S. TGF-beta signaling in onset and progression of hepatocellular carcinoma. *Dig. Dis.* **2012**, *30*, 514–523. [[CrossRef](#)] [[PubMed](#)]
164. Sakaki-Yumoto, M.; Katsuno, Y.; Derynck, R. TGF-beta family signaling in stem cells. *Biochim. Biophys. Acta* **2013**, *1830*, 2280–2296. [[CrossRef](#)] [[PubMed](#)]
165. Fan, Q.M.; Jing, Y.Y.; Yu, G.F.; Kou, X.R.; Ye, F.; Gao, L.; Li, R.; Zhao, Q.D.; Yang, Y.; Lu, Z.H.; et al. Tumor-associated macrophages promote cancer stem cell-like properties via transforming growth factor-beta1-induced epithelial-mesenchymal transition in hepatocellular carcinoma. *Cancer Lett.* **2014**, *352*, 160–168. [[CrossRef](#)] [[PubMed](#)]
166. You, H.; Ding, W.; Rountree, C.B. Epigenetic regulation of cancer stem cell marker CD133 by transforming growth factor-beta. *Hepatology* **2010**, *51*, 1635–1644. [[CrossRef](#)] [[PubMed](#)]
167. Serova, M.; Tijeras-Raballand, A.; Dos Santos, C.; Albuquerque, M.; Paradis, V.; Neuzillet, C.; Benhadji, K.A.; Raymond, E.; Faivre, S.; de Gramont, A. Effects of TGF-beta signalling inhibition with galunisertib (LY2157299) in hepatocellular carcinoma models and in ex vivo whole tumor tissue samples from patients. *Oncotarget* **2015**, *6*, 21614–21627. [[CrossRef](#)]

168. Yang, Y.; Liu, Q.; Li, Z.; Zhang, R.; Jia, C.; Yang, Z.; Zhao, H.; Ya, S.; Mao, R.; Ailijiang, T.; et al. GP73 promotes epithelial-mesenchymal transition and invasion partly by activating TGF-beta1/Smad2 signaling in hepatocellular carcinoma. *Carcinogenesis* **2018**, *39*, 900–910. [\[CrossRef\]](#)
169. Bach, P.; Abel, T.; Hoffmann, C.; Gal, Z.; Braun, G.; Voelker, I.; Ball, C.R.; Johnston, I.C.; Lauer, U.M.; Herold-Mende, C.; et al. Specific elimination of CD133+ tumor cells with targeted oncolytic measles virus. *Cancer Res.* **2013**, *73*, 865–874. [\[CrossRef\]](#)
170. Ogawa, K.; Tanaka, S.; Matsumura, S.; Murakata, A.; Ban, D.; Ochiai, T.; Irie, T.; Kudo, A.; Nakamura, N.; Tanabe, M.; et al. EpCAM-targeted therapy for human hepatocellular carcinoma. *Ann. Surg. Oncol.* **2014**, *21*, 1314–1322. [\[CrossRef\]](#)
171. Biggers, K.; Scheinfeld, N. VB4-845, a conjugated recombinant antibody and immunotoxin for head and neck cancer and bladder cancer. *Curr. Opin. Mol.* **2008**, *10*, 176–186.
172. Wang, L.; Su, W.; Liu, Z.; Zhou, M.; Chen, S.; Chen, Y.; Lu, D.; Liu, Y.; Fan, Y.; Zheng, Y.; et al. CD44 antibody-targeted liposomal nanoparticles for molecular imaging and therapy of hepatocellular carcinoma. *Biomaterials* **2012**, *33*, 5107–5114. [\[CrossRef\]](#) [\[PubMed\]](#)
173. Guo, Q.; Sui, Z.G.; Xu, W.; Quan, X.H.; Sun, J.L.; Li, X.; Ji, H.Y.; Jing, F.B. Ubenimex suppresses Pim-3 kinase expression by targeting CD13 to reverse MDR in HCC cells. *Oncotarget* **2017**, *8*, 72652–72665. [\[CrossRef\]](#) [\[PubMed\]](#)
174. Dawson, M.A.; Kouzarides, T. Cancer epigenetics: From mechanism to therapy. *Cell* **2012**, *150*, 12–27. [\[CrossRef\]](#)
175. Rosner, M.; Hengstschlager, M. Targeting epigenetic readers in cancer. *N. Engl. J. Med.* **2012**, *367*, 1764–1765. [\[CrossRef\]](#)
176. Waldmann, T.; Schneider, R. Targeting histone modifications—epigenetics in cancer. *Curr. Opin. Cell Biol.* **2013**, *25*, 184–189. [\[CrossRef\]](#)
177. Zhang, H.; Tian, X.J.; Mukhopadhyay, A.; Kim, K.S.; Xing, J. Statistical mechanics model for the dynamics of collective epigenetic histone modification. *Phys. Rev. Lett.* **2014**, *112*, 068101. [\[CrossRef\]](#)
178. Marquardt, J.U.; Factor, V.M.; Thorgeirsson, S.S. Epigenetic regulation of cancer stem cells in liver cancer: Current concepts and clinical implications. *J. Hepatol.* **2010**, *53*, 568–577. [\[CrossRef\]](#)
179. Raggi, C.; Factor, V.M.; Seo, D.; Holczbauer, A.; Gillen, M.C.; Marquardt, J.U.; Andersen, J.B.; Durkin, M.; Thorgeirsson, S.S. Epigenetic reprogramming modulates malignant properties of human liver cancer. *Hepatology* **2014**, *59*, 2251–2262. [\[CrossRef\]](#)
180. Zeng, S.S.; Yamashita, T.; Kondo, M.; Nio, K.; Hayashi, T.; Hara, Y.; Nomura, Y.; Yoshida, M.; Hayashi, T.; Oishi, N.; et al. The transcription factor SALL4 regulates stemness of EpCAM-positive hepatocellular carcinoma. *J. Hepatol.* **2014**, *60*, 127–134. [\[CrossRef\]](#)
181. Zhang, J.; Luo, N.; Luo, Y.; Peng, Z.P.; Zhang, T.; Li, S.L. microRNA-150 inhibits human CD133-positive liver cancer stem cells through negative regulation of the transcription factor c-Myb. *Int. J. Oncol.* **2012**, *40*, 747–756. [\[CrossRef\]](#) [\[PubMed\]](#)
182. Zhang, Q.Z.; Yang, Z.; Shan, J.J.; Liu, L.M.; Liu, C.G.; Shen, J.J.; Chen, X.J.; Xu, Y.M.; Chen, J.; Ma, Q.H.; et al. MicroRNA-449a maintains self-renewal in liver cancer stem-like cells by targeting Tcf3. *Oncotarget* **2017**, *8*, 110187–110200. [\[CrossRef\]](#) [\[PubMed\]](#)
183. Chai, S.; Ng, K.Y.; Tong, M.; Lau, E.Y.; Lee, T.K.; Chan, K.W.; Yuan, Y.F.; Cheung, T.T.; Cheung, S.T.; Wang, X.Q.; et al. Octamer 4/microRNA-1246 signaling axis drives Wnt/beta-catenin activation in liver cancer stem cells. *Hepatology* **2016**, *64*, 2062–2076. [\[CrossRef\]](#) [\[PubMed\]](#)
184. Zhou, J.N.; Zeng, Q.; Wang, H.Y.; Zhang, B.; Li, S.T.; Nan, X.; Cao, N.; Fu, C.J.; Yan, X.L.; Jia, Y.L.; et al. MicroRNA-125b attenuates epithelial-mesenchymal transitions and targets stem-like liver cancer cells through small mothers against decapentaplegic 2 and 4. *Hepatology* **2015**, *62*, 801–815. [\[CrossRef\]](#)
185. Xia, H.P.; Ooi, L.L.P.J.; Hui, K.M. MicroRNA-216a/217-induced epithelial-mesenchymal transition targets PTEN and SMAD7 to promote drug resistance and recurrence of liver cancer. *Hepatology* **2013**, *58*, 629–641. [\[CrossRef\]](#)
186. Lin, Y.H.; Wu, M.H.; Huang, Y.H.; Yeh, C.T.; Chi, H.C.; Tsai, C.Y.; Chuang, W.Y.; Yu, C.J.; Chung, I.H.; Chen, C.Y.; et al. Thyroid hormone negatively regulates tumorigenesis through suppression of BC200. *Endocr.-Relat. Cancer* **2018**, *25*, 967–979. [\[CrossRef\]](#)
187. Chen, Z.Z.; Huang, L.; Wu, Y.H.; Zhai, W.J.; Zhu, P.P.; Gao, Y.F. LncSox4 promotes the self-renewal of liver tumour-initiating cells through Stat3-mediated Sox4 expression. *Nat. Commun.* **2016**, *7*. [\[CrossRef\]](#)

188. Wang, Y.; He, L.; Du, Y.; Zhu, P.; Huang, G.; Luo, J.; Yan, X.; Ye, B.; Li, C.; Xia, P.; et al. The long noncoding RNA lncTCF7 promotes self-renewal of human liver cancer stem cells through activation of Wnt signaling. *Cell Stem Cell* **2015**, *16*, 413–425. [\[CrossRef\]](#)
189. Zheng, Q.D.; Lin, Z.J.; Xu, J.; Lu, Y.N.; Meng, Q.Y.; Wang, C.; Yang, Y.X.; Xin, X.R.; Li, X.N.; Pu, H.; et al. Long noncoding RNA MEG3 suppresses liver cancer cells growth through inhibiting beta-catenin by activating PKM2 and inactivating PTEN. *Cell Death Dis.* **2018**, *9*. [\[CrossRef\]](#)
190. Zhu, P.; Wang, Y.; Huang, G.; Ye, B.; Liu, B.; Wu, J.; Du, Y.; He, L.; Fan, Z. lnc-beta-Catm elicits EZH2-dependent beta-catenin stabilization and sustains liver CSC self-renewal. *Nat. Struct. Mol. Biol.* **2016**, *23*, 631–639. [\[CrossRef\]](#)
191. Yuan, S.X.; Wang, J.; Yang, F.; Tao, Q.F.; Zhang, J.; Wang, L.L.; Yang, Y.; Liu, H.; Wang, Z.G.; Xu, Q.G.; et al. Long noncoding RNA DANCR increases stemness features of hepatocellular carcinoma by derepression of CTNNB1. *Hepatology* **2016**, *63*, 499–511. [\[CrossRef\]](#) [\[PubMed\]](#)
192. Wang, X.; Sun, W.; Shen, W.; Xia, M.; Chen, C.; Xiang, D.; Ning, B.; Cui, X.; Li, H.; Li, X.; et al. Long non-coding RNA DILC regulates liver cancer stem cells via IL-6/STAT3 axis. *J. Hepatol.* **2016**, *64*, 1283–1294. [\[CrossRef\]](#) [\[PubMed\]](#)
193. Wu, J.; Zhu, P.; Lu, T.; Du, Y.; Wang, Y.; He, L.; Ye, B.; Liu, B.; Yang, L.; Wang, J.; et al. The long non-coding RNA lncHDAC2 drives the self-renewal of liver cancer stem cells via activation of Hedgehog signaling. *J. Hepatol.* **2019**, *70*, 918–929. [\[CrossRef\]](#)
194. Postovit, L.M.; Margaryan, N.V.; Seftor, E.A.; Kirschmann, D.A.; Lipavsky, A.; Wheaton, W.W.; Abbott, D.E.; Seftor, R.E.; Hendrix, M.J. Human embryonic stem cell microenvironment suppresses the tumorigenic phenotype of aggressive cancer cells. *Proc. Natl. Acad. Sci. USA* **2008**, *105*, 4329–4334. [\[CrossRef\]](#) [\[PubMed\]](#)
195. Chen, L.; Kasai, T.; Li, Y.; Sugii, Y.; Jin, G.; Okada, M.; Vaidyanath, A.; Mizutani, A.; Satoh, A.; Kudoh, T.; et al. A model of cancer stem cells derived from mouse induced pluripotent stem cells. *PLoS ONE* **2012**, *7*, e33544. [\[CrossRef\]](#) [\[PubMed\]](#)
196. Liu, H.; Zhang, W.; Jia, Y.; Yu, Q.; Grau, G.E.; Peng, L.; Ran, Y.; Yang, Z.; Deng, H.; Lou, J. Single-cell clones of liver cancer stem cells have the potential of differentiating into different types of tumor cells. *Cell Death Dis.* **2013**, *4*, e857. [\[CrossRef\]](#) [\[PubMed\]](#)
197. Sukowati, C.H.; Anfuso, B.; Croce, L.S.; Tiribelli, C. The role of multipotent cancer associated fibroblasts in hepatocarcinogenesis. *BMC Cancer* **2015**, *15*, 188. [\[CrossRef\]](#)
198. Lau, E.Y.; Lo, J.; Cheng, B.Y.; Ma, M.K.; Lee, J.M.; Ng, J.K.; Chai, S.; Lin, C.H.; Tsang, S.Y.; Ma, S.; et al. Cancer-Associated Fibroblasts Regulate Tumor-Initiating Cell Plasticity in Hepatocellular Carcinoma through c-Met/FRA1/HEY1 Signaling. *Cell Rep.* **2016**, *15*, 1175–1189. [\[CrossRef\]](#)
199. Muramatsu, S.; Tanaka, S.; Mogushi, K.; Adikrisna, R.; Aihara, A.; Ban, D.; Ochiai, T.; Irie, T.; Kudo, A.; Nakamura, N.; et al. Visualization of stem cell features in human hepatocellular carcinoma reveals in vivo significance of tumor-host interaction and clinical course. *Hepatology* **2013**, *58*, 218–228. [\[CrossRef\]](#)
200. Zhang, M.; Zhang, W.; Wu, Z.; Liu, S.; Sun, L.; Zhong, Y.; Zhang, X.; Kong, X.; Qian, P.; Zhang, H.; et al. Artemin is hypoxia responsive and promotes oncogenicity and increased tumor initiating capacity in hepatocellular carcinoma. *Oncotarget* **2016**, *7*, 3267–3282. [\[CrossRef\]](#)
201. Wang, Z.; Tan, J.; McConville, C.; Kannappan, V.; Tawari, P.E.; Brown, J.; Ding, J.; Armesilla, A.L.; Irache, J.M.; Mei, Q.B.; et al. Poly lactic-co-glycolic acid controlled delivery of disulfiram to target liver cancer stem-like cells. *Nanomedicine* **2017**, *13*, 641–657. [\[CrossRef\]](#) [\[PubMed\]](#)



© 2020 by the authors. Licensee MDPI, Basel, Switzerland. This article is an open access article distributed under the terms and conditions of the Creative Commons Attribution (CC BY) license (<http://creativecommons.org/licenses/by/4.0/>).



Article

1,4-Disubstituted 1*H*-1,2,3-Triazoles for Renal Diseases: Studies of Viability, Anti-Inflammatory, and Antioxidant Activities

Ching-Yi Cheng ^{1,2,*} , Ashanul Haque ^{3,4,*} , Ming-Fa Hsieh ^{5,*} , Syed Imran Hassan ⁴ ,
Md. Serajul Haque Faizi ⁶ , Necmi Dege ⁷ and Muhammad S. Khan ⁴

- ¹ Graduate Institute of Health Industry Technology, Research Center for Chinese Herbal Medicine and Research Center for Food and Cosmetic Safety, Chang Gung University of Science and Technology, No. 261, Wenhua 1st Rd., Guishan Dist., Taoyuan City 333, Taiwan
 - ² Department of Pulmonary Infection and Immunology, Chang Gung Memorial Hospital at Linkou, No. 5, Fuxing St., Guishan Dist., Taoyuan City 333, Taiwan
 - ³ Department of Chemistry, College of Science, University of Hail, Ha'il 81451, Saudi Arabia
 - ⁴ Department of Chemistry, College of Science, Sultan Qaboos University, P.O. Box 36, Al-Khod 123, Sultanate of Oman; imranhassan2@gmail.com (S.I.H.); msk@squ.edu.om (M.S.K.)
 - ⁵ Department of Biomedical Engineering, Chung Yuan Christian University, No. 200 Zhongbei Rd., Zhongli Dist., Taoyuan City 320, Taiwan
 - ⁶ Department of Chemistry, Langat Singh College, B.R.A. Bihar University, Muzaffarpur, Bihar 842001, India; faizichemist@gmail.com
 - ⁷ Department of Physics, Faculty of Arts and Sciences, Ondokuz Mayıs University, 55139 Atakum, Turkey; necmid@omu.edu.tr
- * Correspondence: jennycheng@mail.cgu.edu.tw (C.-Y.C.); a.haque@uoh.edu.sa (A.H.); mfhhsieh@cycu.edu.tw (M.-F.H.)

Received: 29 March 2020; Accepted: 26 May 2020; Published: 28 May 2020



Abstract: Inflammation is a hallmark of many metabolic diseases. We previously showed that ferrocene-appended 1*H*-1,2,3-triazole hybrids inhibit nitric oxide (NO) production in in vitro models of lipopolysaccharide-induced inflammation in the BV-2 cell. In the present study, we explored the viability, anti-inflammatory, and antioxidant potential of ferrocene-1*H*-1,2,3-triazole hybrids using biochemical assays in rat mesangial cells (RMCs). We found that, among all the ferrocene-1*H*-1,2,3-triazole hybrids, **X2–X4** exhibited an antioxidant effect on mitochondrial free radicals. Among all the studied compounds, **X4** demonstrated the best anti-inflammatory effect on RMCs. These results were supplemented by in silico studies including molecular docking with human cytosolic phospholipase A₂ (cPLA₂) and cyclooxygenase 2 (COX-2) enzymes as well as absorption, distribution, metabolism, excretion, and toxicity (ADMET) profiling. Besides, two new crystal structures of the compounds have also been reported. In addition, combining the results from the inducible nitric oxide synthase (iNOS), cPLA₂, COX-2, and matrix metalloproteinase-9 (MMP-9) enzymatic activity analysis and NO production also confirmed this argument. Overall, the results of this study will be a valuable addition to the growing body of work on biological activities of triazole-based compounds.

Keywords: tumor necrosis factor- α (TNF- α); cytosolic phospholipase A₂ (cPLA₂); prostaglandin E₂ (PGE₂); matrix metalloproteinase-9 (MMP-9); inducible nitric oxide synthase (iNOS)

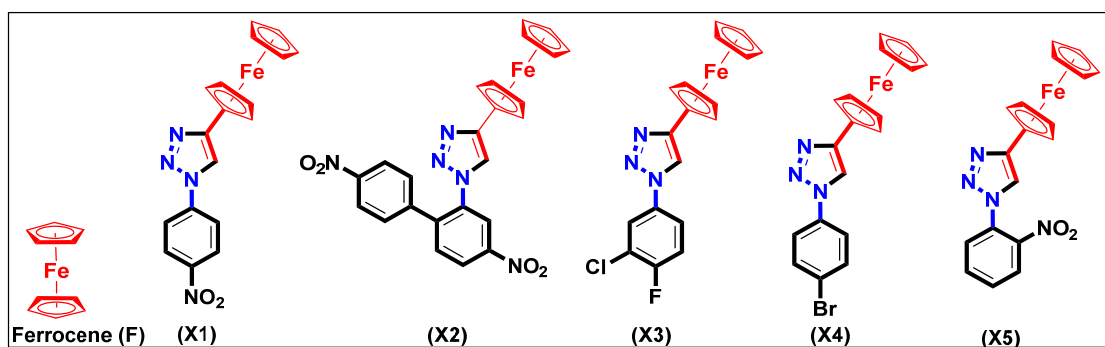
1. Introduction

Inflammation, the body's immune response to stimulus, is a complex biological process/defense mechanism that is triggered by external or internal stimuli. It is associated with minor infections/injuries

and with major disorders such as cancer, cystitis, arthritis, asthma, and psoriasis [1]. In renal disease, mesangial cells (MCs) play a vital role in the evolution of immune-mediated inflammation. It has been shown that tumor necrosis factor- α (TNF- α) levels are associated with the development of nephropathy [2]. Renal expression and circulating levels of bioactive TNF- α increase in lupus nephritis and correlate with disease activity [3]. TNF- α has been implicated in renal inflammation by its upregulation of inflammatory genes such as cyclooxygenase-2 (COX-2), cytosolic phospholipase A₂ (cPLA₂), prostaglandin E₂ (PGE₂), matrix metalloproteinase-9 (MMP-9), and inducible nitric oxide synthase (iNOS) [4,5]. Eicosanoids, which are involved in immune-mediated renal inflammatory diseases, are generated from arachidonic acid metabolism via cPLA₂ and COX-2. We previously identified some traditional Chinese medicines that were effective in treating TNF- α -induced MC inflammation via downregulation of cPLA₂ and COX-2 [6]. Several other studies also indicated the significance of MMPs and tissue inhibitors of metalloproteinases (TIMPs) in the progression of glomerulonephritis [7]. The production of nitric oxide (NO) is catalyzed by NO synthase (NOS), which degrades L-arginine to L-citrulline and NO. iNOS is one NOS isoform that is expressed by macrophages and other tissues in response to (pro) inflammatory mediators [8]. Therefore, the modulation of MC responses could offer a pathophysiology-based therapeutic approach to prevent glomerular injury.

To alleviate chronic inflammation and its related pain, the current drugs of choice are nonsteroidal anti-inflammatory drugs (NSAIDs) [8]. However, long-term use of classical NSAIDs has been associated with complications, including gastrointestinal ulcers, gastroduodenal erosions, renal dysfunction, and hepatotoxicity, mainly because of their variable selectivity towards COX enzymes [9]. These drawbacks led to the search for new synthetic anti-inflammatory agents, which has identified several new carbocyclic and heterocyclic small molecules that are in clinical use. For example, celecoxib, ramifenazone, and famprofazone are well-known examples of pyrazole-based anti-inflammatory drugs. However, serious side-effects, including bone marrow depression, water and salt retention, and carcinogenesis prompted researchers to continue the search for new anti-inflammatory drugs.

Among heterocyclic cores, 1,2,3-triazole enjoys a reputable position in the area of drug discovery. Easy synthesis/functionalization, ability to interact with bioreceptors, rigid, and stable structure are some of the leading reasons behind the popularity of this core. [10] Similarly, organometallic compounds such as ferrocene are known for their high metabolic stability, redox behavior, lipophilic and non-toxic features. Recently, Guo and co-workers demonstrated that ferrocene-based compounds could significantly reduce the LPS-induced NO secretion, IL-6, and TNF- α levels [11]. The structure activity relationship (SAR) studies indicated that the presence of planar spacers attached to the ferrocene fragment is beneficial for the inhibition of NO production in the in vitro model. It has been suggested that the new classes of anti-malarial, anti-tubercular, and anti-microbial agents could be achieved by merging these two cores, i.e., ferrocene-triazole hybrids [12]. Previously, we reported that 1,4-disubstituted 1*H*-1,2,3-triazoles (**F**, **X1–X5**, Scheme 1) inhibit NO production in in vitro models of lipopolysaccharide (LPS)-induced inflammation [9]. Prompted by these results, we decided to use rat mesangial cells (RMCs) as an in vitro cell culture model to examine the effects of ferrocene-1*H*-1,2,3-triazole hybrids on TNF- α -induced inflammation. First, the cell viability of these compounds on RMCs were evaluated. Next, we explored the effect of these compounds on TNF- α -induced inflammation in vitro. In addition, we report two new crystal structures.



Scheme 1. Structures of 1,4-disubstituted 1H-1,2,3-triazoles.

2. Results and Discussion

2.1. Synthesis and Characterization

We previously reported the detailed synthesis, structural and electrochemical characterization of **X1–X5** [9]. Briefly, these compounds were obtained in good yields and purity by azide-alkyne chemistry using ethynyl ferrocene and substituted amines. We were able to grow two new crystals (**X1** and **X5**) and the results are discussed below.

X-ray Crystal Structure

Single crystals of **X1** and **X5** were collected from dichloromethane solution after slow evaporation. The experimental details and the crystal data for **X1** and **X5** are given in Table 1, while their molecular structures are shown in Figure 1a,b. The structural parameters for both ferrocenyl substituents in compounds **X1** and **X5** were within the normal ranges, and the iron atom is sandwiched almost perfectly centrally between the two cyclopentadienyl rings in compound **X1** compared with **X5**. The distance of iron from the two cyclopentadienyl rings differs slightly in the two compounds. The iron was observed at 1.649 (5) and 1.652 (5) Å from the plane defined by the two cyclopentadienyl systems in **X1** but at 1.642 (5) and 1.652 (5) Å in compound **X5**. In both structures, the ferrocene has adopted an eclipsed conformation. The NO₂ group attached to the benzene ring formed dihedral angles of 5.160 (7)° in compound **X1** and 61.41 (7)° in compound **X5**. The variation in the dihedral angle may be associated with *ortho*- and *para*-substitution of the NO₂ group in compounds **X1** and **X5**, respectively. Single-crystal data indicate nitro N–O bond lengths of 1.216 (5) and 1.212 (5) Å in compound **X1** and 1.205 (5) and 1.216 (5) Å in compound **X5**, respectively. The crystal data indicate an N–O double bond and involvement of greater resonance in the *para*-containing nitro group in **X1** compared with the *ortho*-substitution in compound **X5**.

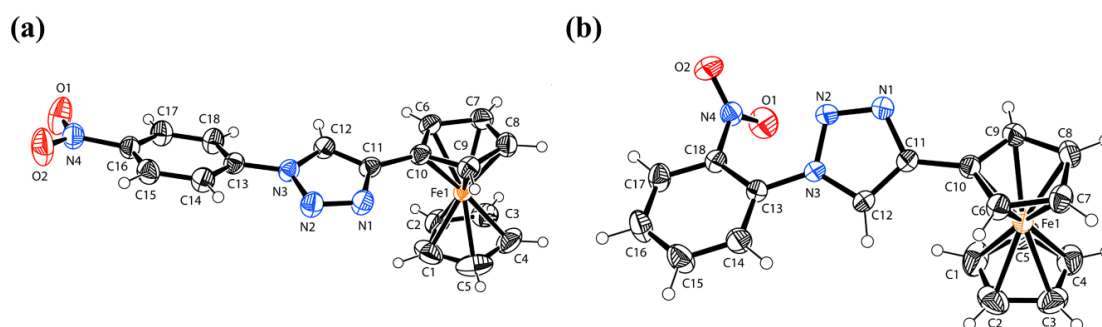


Figure 1. The molecular structure of compounds (a) **X1** and (b) **X5** with atom labeling. Displacement ellipsoids are drawn at the 40% probability level.

Table 1. Experimental details and crystal structure data for compounds **X1** and **X5**.

Experimental Details	Crystal Data of X1	Crystal Data of X5
CCDC	1537323	1537684
Chemical formula	C ₁₈ H ₁₄ FeN ₄ O ₂	C ₁₈ H ₁₄ FeN ₄ O ₂
Mr	374.18	374.18
Crystal system, space group	Monoclinic, P21/c	Monoclinic, P21/c
Temperature (K)	296	293
<i>a</i> , <i>b</i> , <i>c</i> (Å)	11.1502 (7), 5.7600 (2), 24.1625 (12)	10.1528 (7), 13.9830 (6), 11.2383 (7)
α , β , γ (°)	90.000 (4), 95.892 (4), 90.000 (4)	90.000 (4), 100.475 (5), 90.000 (4)
<i>V</i> (Å ³)	1543.64 (14)	1568.87 (16)
<i>Z</i>	4	4
Radiation type	Mo K α	Mo K α
μ (mm ^{−1})	1.00	0.98
Crystal size (mm)	0.50 × 0.25 × 0.11	0.72 × 0.37 × 0.13
Data collection Diffractometer	STOE IPDS 2	STOE IPDS 2
Absorption correction	Integration (X-RED32; Stoe & Cie, 2002)	Integration (X-RED32; Stoe & Cie, 2002)
<i>T</i> _{min} , <i>T</i> _{max}	0.755, 0.945	0.675, 0.900
No. of measured, independent and observed [<i>I</i> > 2 σ (<i>I</i>)] reflections	8127, 2976, 2356	7441, 3027, 2510
<i>R</i> _{int}	0.028	0.027
(sin θ/λ) max (Å ^{−1})	0.614	0.615
Refinement <i>R</i> [<i>F</i> ² > 2 σ (<i>F</i> ²)], <i>wR</i> (<i>F</i> ²), <i>S</i>	0.035, 0.094, 1.01	0.028, 0.073, 1.04
No. of reflections	2976	3027
No. of parameters	226	226
No. of restraints	12	0
H-atom treatment	H-atom parameters constrained	H-atom parameters constrained
$\Delta\rho_{\max}$, $\Delta\rho_{\min}$ (e Å ^{−3})	0.58, −0.36	0.21, −0.22

As is clear from the structure (Figure 1), the benzene ring (C13–C18) and cyclopentadienyl ring (C6–C10) form dihedral angles to the central triazole ring (N1–N3/C11–C12) at 17.09 (8)° and 12.58 (8)°, respectively, in compound **X1**. However, the benzene ring (C13–C18) and cyclopentadienyl ring (C6–C10) form dihedral angles to the central triazole ring (N1–N3/C11–C12) at 9.56 (7)° and 34.83 (7)°, respectively, in compound **X5**. This variation is due to the presence of substituted nitro groups at different positions in these compounds. The details of the intermolecular hydrogen bonds present in both compounds **X1** and **X5** are summarized in Table 2. Compound **X1** forms a dimer because of C—H···O interactions (Figure 2a) and is stabilized by packing because of $\pi\cdots\pi$ interactions (Figure 2b). Compound **X5** forms a one-dimensional polymeric structure because of C—H···N interactions (Figure 2c) and is also stabilized by packing due to $\pi\cdots\pi$ interactions (Figure 2d). The presence of such noncovalent interactions is very important in biological applications to allow understanding of many biological processes [13].

Table 2. Hydrogen-bond geometry (Å, °) of compounds **X1** and **X5**.

D—H···A	D—H	H···A	D···A	D—H···A
Compound X1				
C17—H17···O1 ⁱ	0.93	2.53	3.388 (3)	154.4
Compound X5				
C14—H14···N2 ⁱ	0.93	2.57	3.428 (2)	154.4

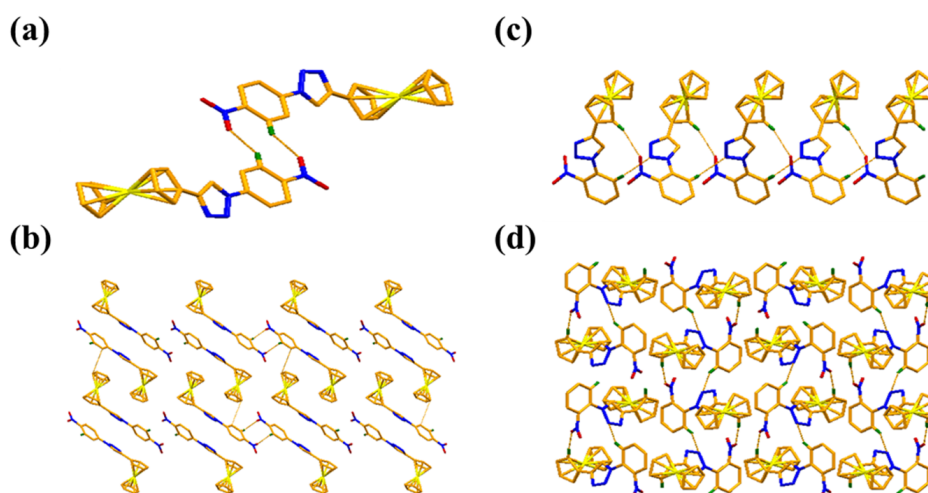


Figure 2. A view of the formation of dimer due to C—H···O interactions (a) and a packing diagram along the *b*-axis with $\pi\cdots\pi$ interactions (b), shown as pink dashed lines in **X1**. A view of the formation of a polymeric structure of **X5** due to C—H···N interactions (c) and packing diagram along the *a*-axis (d) are shown as pink dashed lines.

2.2. In Vitro Characterizations

2.2.1. Antioxidant Effect on RMCs

To identify a non-toxic dose, we first examined the cell viability on RMCs of various concentrations of ferrocene (**F**) and ferrocene-1*H*-1,2,3-triazole hybrids **X1–X5** using the 3-(4,5-dimethylthiazol-2-yl)-2,5-diphenyltetrazolium bromide (MTT) assay. As shown in Figure 3a, the compounds were noncytotoxic at concentrations up to 50 $\mu\text{g/mL}$. It is worthwhile to mention here that the incorporation of triazole fragment to the ferrocene did not affect the cell viability profile of the ferrocene. Since all the hybrid compounds exhibited similar cell viability effects on RMCs, it can be concluded that merging these two pharmaceutically active cores is a safe strategy. Accordingly, a concentration of 12.5 $\mu\text{g/mL}$ ferrocene-1*H*-1,2,3-triazole hybrids was used for all subsequent experiments.

Free radicals have the main role in inflammation and are divided into two categories, including reactive oxygen species (ROS) and reactive nitrogen species (RNS). ROS contains superoxide (O_2^-), hydroxy radical ($\bullet\text{OH}$), peroxy radical ($\text{ROO}\bullet$) and H_2O_2 . Superoxide (O_2^-) is mainly produced in the mitochondrial electron transfer chain. When the cell performs respiration to generate ATP, about 1%–3% of the electrons leak out in a series of transmission processes and combine with oxygen to produce superoxide [14]. In addition, cells will also produce superoxide through nicotine adenine dinucleotide phosphate (NAD(P)H) oxidase. Next, to quantitate the free radicals (ROS) in cells and in the mitochondria, we performed dihydroethidium (DHE) and MitoSOX staining (mitochondrial staining) followed by flow cytometric analysis and immunofluorescence, respectively. The results of this study indicated that, except hybrids **X1** and **X5** (Figure 3b), all other compounds showed antioxidant activities. Though there is no exact explanation behind the ineffectiveness of **X1** and **X5**, the antioxidant behavior of other hybrids (**X2**, **X3** & **X4**) and reference (**F**) compounds could be attributed to the following: Firstly, ferrocene-1*H*-1,2,3-triazole hybrid compounds are electroactive and can undergo facile redox changes. This means they have a propensity to scavenge free radicals (or at least alter their level). The electron-donating capability of the hybrid compounds is largely governed by the core attached to the ferrocene ring. For instance, electrochemical studies suggested that compound **X4** (E_{ox} (onset) = 0.32 V) has more tendency to get oxidized than **X3** (E_{ox} (onset) = 0.34 V) and **X1** (E_{ox} (onset) = 0.39 V) [9]. Interestingly, the same trend has been reflected in the antioxidant assay (antioxidant effect = **X4** > **X3** > **X1**). Secondly, it has been demonstrated that 1,2,3-triazole can

be readily oxidized at the N1 position of the triazole core [15], thus provide an additional site for radical scavenging by such hybrid compounds. Of the antioxidant compounds, X2–X4 exhibited a significant antioxidant effect on mitochondrial free radicals (Figure 3c). Absorption, distribution, metabolism excretion, and toxicity (ADMET) calculations (vide infra) supported this observation too, i.e., mitochondrial localization of the compounds. However, all the compounds cannot induce antioxidant enzymes, including HO-1 or SOD-2 (Supplementary Figure S1). Therefore, we suggest that the antioxidant mechanisms of these compounds were not via antioxidant enzyme expression. In the future, we can further explore the antioxidant mechanisms of these compounds.

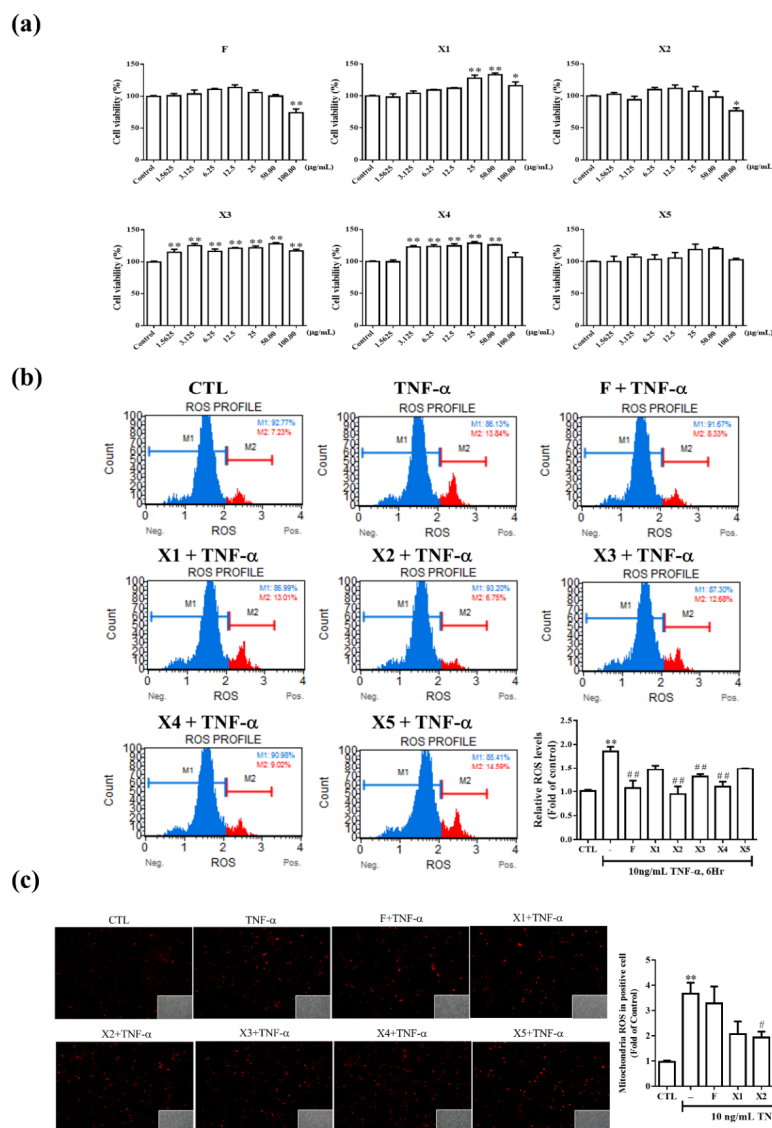


Figure 3. The antioxidant effect of ferrocene-1H-1,2,3-triazole hybrids in RMCs. Effect of ferrocene-1H-1,2,3-triazole hybrids on cell viability. (a) RMCs were treated with twofold serial dilutions of ferrocene-1H-1,2,3-triazole hybrids for 24 h, and cell viability was determined by the MTT assay. Data are expressed as % of control (1% dimethyl sulfoxide (DMSO)-treated group) and each column represented the mean \pm standard error of the mean (SEM) of four independent tests. (b,c) Interacellular ROS in RMCs treated with F, X1, X2, X3, X4, or X5 at 12.5 μ g/mL for 2 h at 6 h post-TNF- α (10 ng/mL) incubation were assessed using DHE fluorescence followed by flow cytometric analysis (b), and MitoSOX staining (mitochondrial staining) followed by immunofluorescence. Results are expressed as mean \pm SEM of at least three repeated and independent assays, * $p < 0.05$; ** $p < 0.01$ versus control; # $p < 0.01$; ## $p < 0.01$ versus TNF- α treatment alone.

2.2.2. Effect on iNOS Expression and NO Production in RMCs

RNS contains nitric oxide (NO^\bullet) and peroxynitroso (ONOO^-) anions. Nitric oxide is a gas with unpaired electrons produced by NOSs in tissues, which is widely distributed in the body and has many physiological functions, defense, signal transduction, etc. The peroxynitroso anion is produced by the reaction of NO^\bullet and superoxide. It is a kind of free radical with extremely active and super destructive power [16]. It has been shown that the progression of renal disease is associated with an increase in NO production and iNOS activity [17]. However, NO is a very polar molecule that is easily oxidized, whereas nitrite is a stable oxidative metabolite of NO. Therefore, NO production was represented by the accumulation of nitrite. In the present study, we measured nitrite levels and iNOS expression by Griess assay and real-time polymerase chain reaction (PCR), respectively. As shown in Figure 4a, a 24-h treatment with $\text{TNF-}\alpha$ (10 ng/mL) led to a 34.79-times higher expression of iNOS compared with control. Upon addition of ferrocene-1*H*-1,2,3-triazole hybrids (except X5) to the culture of RMCs, the iNOS level decreased remarkably compared with $\text{TNF-}\alpha$ -treated RMCs ($p < 0.01$). In a parallel experiment (Figure 4b), the production of NO was significantly increased in $\text{TNF-}\alpha$ -stimulated cells. Pretreatment with X1–X5 decreased this $\text{TNF-}\alpha$ -induced response. Inhibition of NO and iNOS indicated that ferrocene-1*H*-1,2,3-triazole hybrids could protect against inflammation in RMCs.

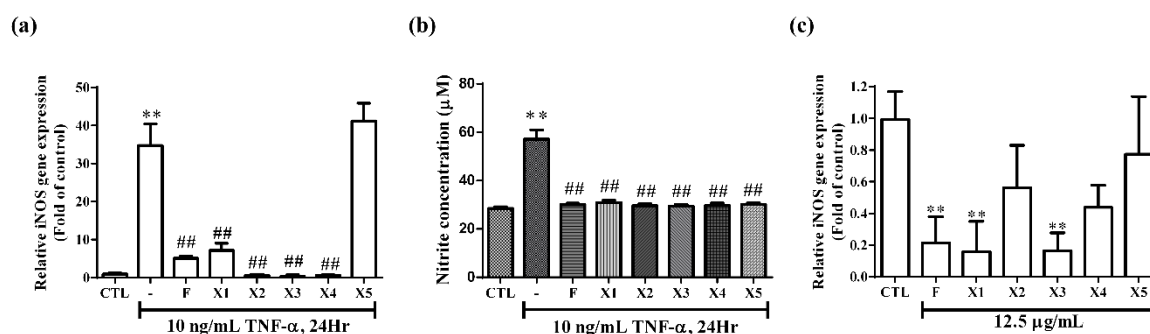


Figure 4. Effect of ferrocene-1*H*-1,2,3-triazole hybrids on iNOS expression and NO production in RMCs. Cells were pretreated with the compounds at 12.5 $\mu\text{g/mL}$ for 2 h and subsequently stimulated with $\text{TNF-}\alpha$ (10 ng/mL) for 24 h. The expression of iNOS and NO in RMCs were determined by (a) real-time PCR analysis and (b) nitric oxide assay, respectively. (c) Cells were incubated without or with F, X1, X2, X3, X4, or X5 at 12.5 $\mu\text{g/mL}$ for 24 h. The mRNA was extracted, reverse transcribed, and then analyzed the iNOS expression by real-time PCR. Data are expressed as fold of control (1% DMSO-treated group) and each column represents the mean \pm SEM of at least three repeated and independent assays. Asterisks indicate a significant difference compared with the control group, ** $p < 0.01$. Hashes indicate a significant difference compared with the $\text{TNF-}\alpha$ -treated group, ## $p < 0.01$.

To investigate whether ferrocene-1*H*-1,2,3-triazole hybrids could suppress iNOS gene expression in RMCs, the cells were treated with these compounds at a non-toxic dose of 12.5 $\mu\text{g/mL}$ for 24 h and analyzed by real-time PCR. As shown in Figure 4c, compounds F and X1–X5 did not spontaneously induce iNOS gene expression in RMCs. Among them, X2 and X4 attenuated endogenous iNOS expression, but only F, X1, and X3 significantly cause this inhibition (Figure 4c). Compared with other compounds, X5 was the weakest in inhibiting endogenous iNOS and did not reach statistical significance. The expression of endogenous iNOS in X5 alone treatment is close to that in the control group (Figure 4c). It may explain why it did not inhibit the expression of iNOS under the stimulation of $\text{TNF-}\alpha$ (Figure 4a). From the results obtained, it seems that the triazole core has an important role in the suppression of iNOS expression. In compounds X2 and X5, azole fragment is blocked by the substituents present at the *ortho* position of the ring attached to azole (see Figure 1b). In X1 and X3, the substituents are present on the *para* position and did not block azole fragments (see Figure 1a), thus causing inhibition. This steric effect fact is also supplemented by a comparative low inhibition profile of ferrocene alone, e.g., without steric effect. In addition, we speculate that the structure of

these compounds contains the iron in ferrocene to interact with NO induced by TNF- α , leading to decrease nitrite formation (Figure 4b). This may explain why X5 does not inhibit TNF- α -induced iNOS expression but inhibits nitrite production. The ability of F, X1, and X3 to suppress the NO concentration could be also ascribed to a number of factors, but we envision that the molecular weight (MW), hydrogen bonding capability, solubility profile, topology and planarity of the compounds played a major role here. Overall, these results implied that compounds F, X1, and X3 were better at preventing the elevation of NO concentrations.

2.2.3. Effect on the Expression of Inflammatory Proteins in RMCs

TNF- α is a pro-inflammatory cytokine that plays a vital role in human and experimental glomerulonephritis and lupus nephritis [3,4]. TNF- α has been reported to up-regulate inflammatory genes in various cells. Both of COX-2 and cPLA₂ can be considered as indicators of inflammation and play a vital role in several renal inflammatory diseases. In our previous study, we have established the relationship between COX-2 and cPLA₂ and suggested that TNF- α enhances PGE₂ generation via cPLA₂/COX-2 upregulation in RMCs [4]. In addition, increasing studies have reported the significance of MMPs and TIMPs in the progression of glomerulonephritis. MMP-9 produced by neutrophils participates in the progression of renal fibrosis [18]. Therefore, we investigate whether ferrocene-1*H*-1,2,3-triazole hybrids regulate the expression of inflammatory proteins in RMCs, the protein levels of COX-2, cPLA₂, and MMP-9 were examined. As demonstrated in Figures 5a and 6a, treatment with all ferrocene-1*H*-1,2,3-triazole hybrids significantly ($p < 0.05$) decreased the expression of all these proteins in RMCs in response to TNF- α treatment. The levels of transcription of COX-2 (Figure 5b) and MMP-9 (Figure 6b) were also examined. Among ferrocene-1*H*-1,2,3-triazole hybrids, X3 and X4 caused more significant inhibition of TNF- α -induced COX-2 mRNA level than F (Figure 5b), while X2, X4, and X5 significantly attenuated more TNF- α -induced MMP-9 mRNA level than F (Figure 6b). These results indicate that combining ferrocene and triazole motifs is an intriguing strategy to achieve an enhanced anti-inflammatory effect. In all the cases, we observed that the ferrocene-1*H*-1,2,3-triazole hybrids are more active than the ferrocene alone. However, the cells-treated with X3 spontaneously increased COX-2 protein expression (Figure 5c) and the cells treated with X5 spontaneously increased MMP-9 transcription (Figure 6c). In addition, RMCs treated with X2 do not decrease COX-2 mRNA level in response to TNF- α (Figure 5b). Taken together, among all the ferrocene-1*H*-1,2,3-triazole hybrids, X4 demonstrated the best anti-inflammatory effect on RMCs. From the results of Figure 5a,b, we can speculate that the main pharmacological mechanism of F, X1, and X2 may be to inhibit TNF- α -induced COX-2 protein synthesis rather than mRNA transcription inhibition. In contrast, the X3–X5 group may inhibit COX-2 mRNA transcription hence protein levels. We further analyze the effect of these compounds on the activity of COX-2 and cPLA₂. As shown in Figure 5d, treatment with all ferrocene-1*H*-1,2,3-triazole hybrids significantly decreased the activity of cPLA₂ as well as COX-2 in RMCs in response to TNF- α treatment. In this study, we also proved that cPLA₂ affects COX-2 activity by AACOCF₃ (a cPLA₂ inhibitor) pretreatment, which is consistent with our previous publication [4]. On the inhibitory mechanisms of ferrocene-1*H*-1,2,3-triazole hybrids in TNF- α -induced MMP-9 expression, X2 and X4 mainly inhibit transcription level, but the rest of the compounds may affect enzyme activity (Figure 6a,b). It is worth noting that the treatment of healthy cells with X3 and X5 under a safe dose will cause side effects, because these two compounds cause the expression of inflammatory proteins. It is not recommended to use it in healthy food or for preventing inflammation in the future.

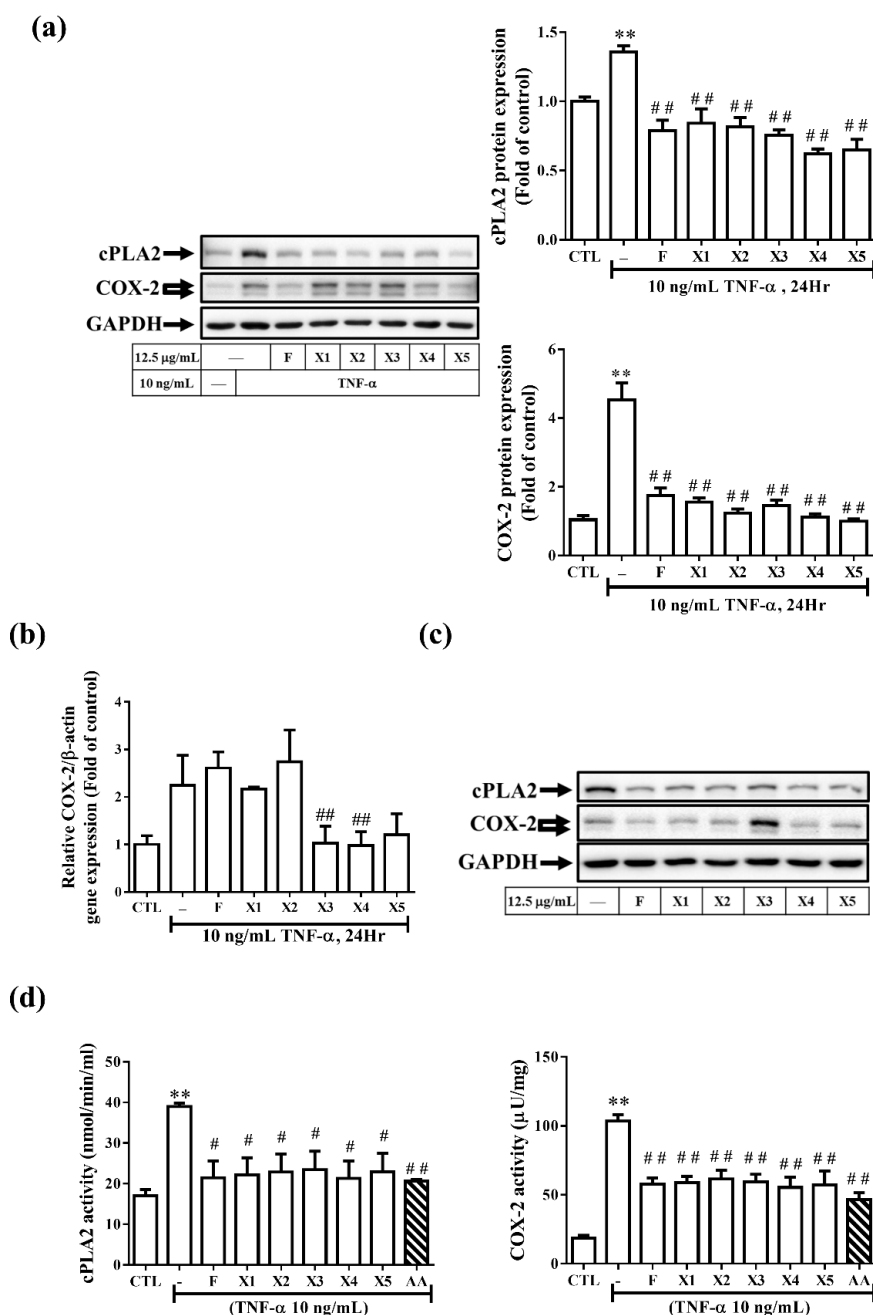


Figure 5. Effect of ferrocene-1*H*-1,2,3-triazole hybrids on the protein expression of cPLA₂ and COX-2 in RMCs. (a,c) Western blot assay to detect COX-2 and cPLA₂ expression in cell lysate. (b) The COX-2 mRNA level was determined by real-time PCR. The sequence of addition of TNF-α reagent and compounds was as follows. In panels (a,b), RMCs were treated with ferrocene-1*H*-1,2,3-triazole hybrids (12.5 µg/mL) for 2 h and then exposed to TNF-α for another 24 h. In panel (c), RMCs were treated without or with F, X1, X2, X3, X4, or X5 at 12.5 µg/mL for 24 h. COX-2 and cPLA₂ expression were measured by comparison with that of GAPDH (internal control). In panel (d), the enzyme activity assay kits to detect of endogenous cPLA₂ and COX-2 activity in RMC cell lysate (6 µg) stimulated without or with ferrocene-1*H*-1,2,3-triazole hybrids or AACOCF3 (AA) in the presence of 10 ng/mL TNF-α. Data were obtained from at least three independent experiments and are expressed as mean ± SEM. One-way analysis of variance (ANOVA) followed by Bonferroni's multiple-comparisons test was used to identify significant differences between multiple groups. Asterisks indicate a significant difference compared with the control group, ** $p < 0.01$. Hashes indicate a significant difference compared with the TNF-α-treated group, ## $p < 0.01$; # $p < 0.05$.

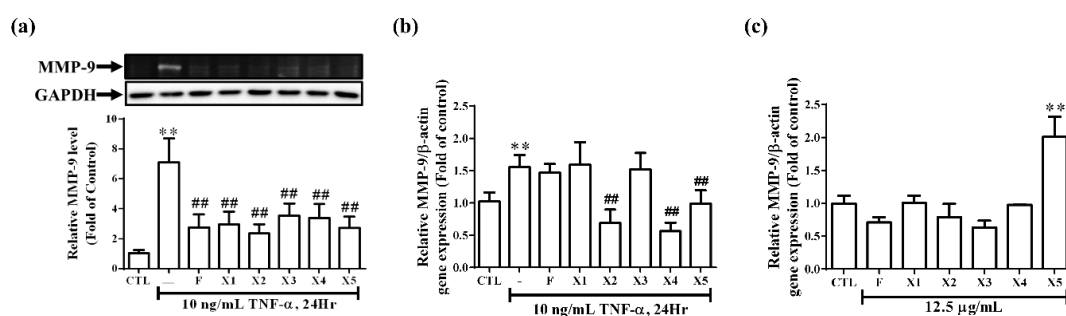


Figure 6. Effect of ferrocene-1H-1,2,3-triazole hybrids on MMP-9 expression in RMCs. RMCs were treated with ferrocene-1H-1,2,3-triazole hybrids (12.5 $\mu\text{g/mL}$) for 2 h and then exposed to TNF- α for an additional 24 h. (a) MMP-9 expression was examined by gelatin zymography of the culture media. GAPDH was used as an internal control and examined by Western blotting. Densitometric quantification of MMP-9 in culture media is presented. (b) The mRNA levels of MMP-9 and β -actin were determined by real-time PCR. Results are presented as the mean \pm SEM. Data are combined from three independent experiments with three replicate samples per group in each experiment. One-way ANOVA and Bonferroni's multiple-comparisons tests were used to identify significant differences between multiple groups. Asterisks indicate a significant difference compared with the control group, ** $p < 0.01$. Hashes indicate a significant difference compared with the TNF- α -treated group, ## $p < 0.01$. (c) Cells were treated without or with F, X1, X2, X3, X4, or X5 at 12.5 $\mu\text{g/mL}$ for 24 h. MMP-9 mRNA level was determined by real-time PCR.

2.3. In Silico Studies

2.3.1. ADMET Predictions

To obtain more information on the bioactivity and potential use of the reported molecules as drugs, we predicted their ADMET; the results of this analysis are presented in Table 3. From the data, it is clear that the compounds possess acceptable physicochemical, pharmacokinetic, and toxicity profiles. For example, all compounds returned positive results for blood–brain barrier (BBB) transition, gastrointestinal (GI) absorption, and oral bioavailability criteria, indicating their ability to pass through the BBB and be absorbed into tissues. Compounds X1, X2, and X5 exhibited similar GI absorption ($p = 0.8939$), while compound X3 ($p = 0.8706$) and compound X4 ($p = 0.8252$) had comparatively lower probability of absorption. The fact that all compounds showed category III acute oral toxicity indicates that they may be acceptable for oral delivery. Moreover, all compounds showed the probability of mitochondrial localization, which is well reflected in the results of the antioxidant assays (Figure 3c). It should be noted that all these values are calculated and therefore, in vivo studies are required to confirm these observations.

Table 3. Pharmaceutical prediction of in silico ADMET properties.

Code	Physicochemical Properties				Pharmacokinetics		Toxicity Parameters		
	MW ^a	HBA ^b	HBD ^c	RB ^d	log <i>P</i>	GIA ^e	OB ^f	Carcino genesis	Irritation
X1	374.18	5	0	3	3.96	+	+	–	+
X2	495.28	7	0	5	5.54	+	+	–	–
X3	381.62	3	0	2	4.85	+	+	–	–
X4	408.08	3	0	2	4.82	+	+	–	+
X5	374.18	5	0	3	3.96	+	+	–	+

a = Molecular weight, b = Hydrogen bond acceptor, c = Rotatable bonds, d = Hydrogen bond donor, e = Gastrointestinal absorption, f = Oral bioavailability.

2.3.2. Docking Results

Molecular docking studies have become a common technique to identify molecular targets for treating disease. Using this method, one can easily predict the biological potential of compound(s),

and active/catalytic sites within an enzyme. Biological results indicated that ferrocene-1*H*-1,2,3-triazole hybrids **X1–X5** exhibit neuroprotective effects via the inhibition of NO production in microglial cells (BV-2). To rationalize this observation at the supramolecular level, we carried out docking studies of the compounds with the enzymes established for participation in inflammatory processes. It is reported that compounds bearing 1,2,3-triazole core exhibit an anti-inflammatory effect via the inactivation of microglia localized COX isoenzymes [19]. Similarly, Chuang et al. [20] have shown that cPLA₂ plays a crucial role in ROS/NO signaling in LPS activated BV2 cells; thus, cPLA₂ can be considered as an intriguing therapeutic target for inflammation control.

In the present study, we carried out shape-based docking studies of compounds into the active sites of cPLA₂ (apo form, PDB code: 1CJY) [21] and COX-2 (PDB code: 6COX) [22] using Autodock vina tools [23]. Since the crystal structure of cPLA₂ had some missing regions, it was modelled using an online server, SWISS Model prior to the docking studies [24]. The results of the docking studies indicated that all hybrid compounds preferred to enter the active site of the enzyme and interact with the nearby residues (Figure 7). For instance, it has been reported that, in order to impart COX-2 inhibitory activity, a ligand should interact with conserved (His90), nonconserved (Arg513) and nearby residues (Arg120, Tyr355 and Glu524, Trp387, Phe518, Ser530, Arg120, Tyr355, Glu524 and Val523) of COX-2 via polar and nonpolar interactions [13]. Our docking result indicated that the ferrocene-1*H*-1,2,3-triazole hybrids prefer to enter the active site of the target and interact via multiple H-bonds (Table 4).

Table 4. Binding energy and interacting residues of **X1–X5** for COX-2 and cPLA₂.

PDB	Compound Code	H-bonding Site Residues	Binding Energy (kcal/mol)	Distance (Å)
6COX	X1	Arg120, Tyr355	−9.04	2.9, 3.1
6COX	X2	Gln203, Tyr409	−10.33	2.7, 3.0, 3.2
6COX	X3	Tyr115	−7.75	2.9
6COX	X4	Tyr115	−8.23	2.9, 3.0
6COX	X5	Arg513, Tyr355, Ser353, His90	−9.35	2.7, 2.8, 3.1, 3.4
1CJY	X1	Gly551, Leu552, Lys595	−6.97	3.5, 3.2, 2.6
1CJY	X2	Gly197, Gly198, Ser228, Asp549, Gly551	−11.51	2.5, 2.6, 2.8, 3.0
1CJY	X3	Asp345	−9.13	2.8
1CJY	X4	Asp345, Trp346, Pro559	−9.94	2.9, 3.2, 3.4
1CJY	X5	Asn262, Val407, Asn682, Gly684	−7.15	2.7, 2.8, 3.0, 3.1, 3.5

Docking studies with cPLA₂ (PDB code: 1CJY) indicated that, except **X2**, compounds **X1–X5** did not make any contact with the catalytic residue Ser228 or with the “oxyanion hole” (residues Gly197/Gly198) of the enzyme [25]. However, they interacted with the nearby residues of the catalytic site of cPLA₂ (Figure 8 and compiled in Table 4). The binding propensity of the ligand is significantly controlled by the functionalities present over the phenyl ring of triazole fragment. Unfortunately, we found that the docking energies do not match with the observed activity. However, in both cases, we observed that compound **X2** has the highest binding energies than the others, which is not very well reflected in in vitro studies. This can be ascribed to several factors, but we envisaged that high molecular weight (MW), hydrogen bonding propensity, solubility, and structural rigidity played important roles here.

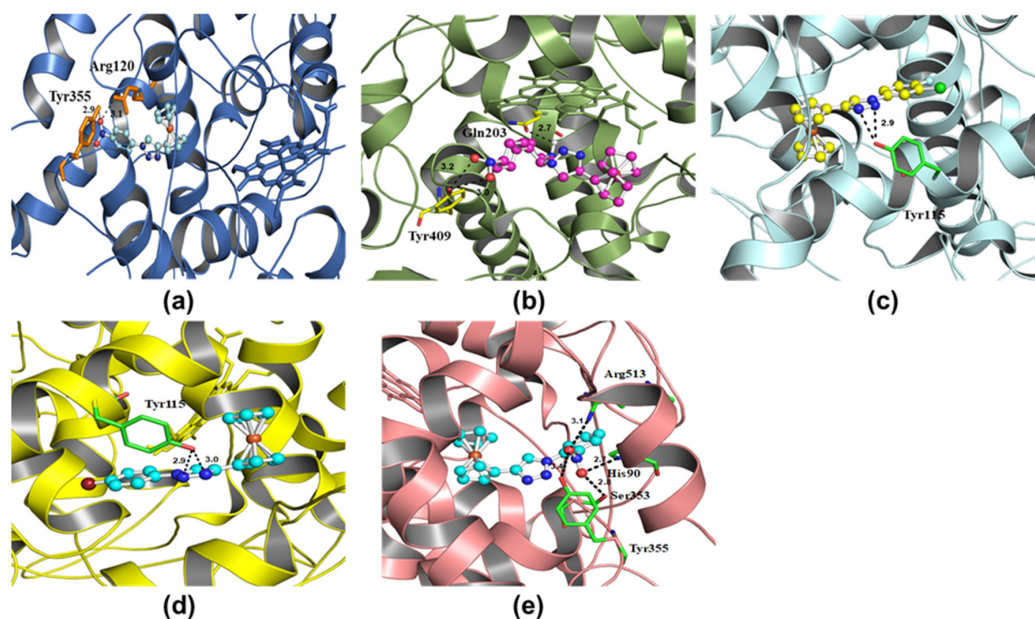


Figure 7. Molecular docking of hybrid compounds X1 (a), X2 (b), X3 (c), X4 (d), and X5 (e) with cyclooxygenase-2 (PDB code: 6COX).

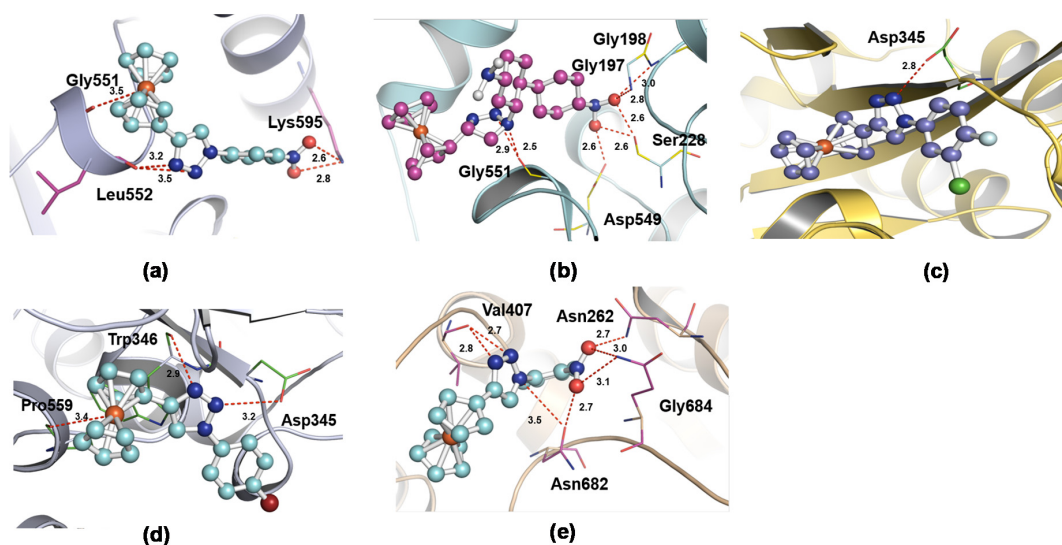


Figure 8. Molecular docking of hybrid compounds X1 (a), X2 (b), X3 (c), X4 (d), and X5 (e) with cPLA₂ (PDB code: 1CJY).

For instance, compound X2 has five HBA units (due to two nitro groups), which explains why it showed high affinity and binding energy with the enzymes in docking studies. At the same time, compound X2, due to its comparatively higher MW (Table 3), lower solubility ($\log P = 5.54$, Table 3), and less structural rigidity (due to the presence of rotatable biphenyl units) leads to lower in vitro activity. Similarly, compounds X3 and X4, bearing halogen atoms over the phenyl ring with moderate MW and lowest number of HBA units showed high activities.

3. Materials and Methods

3.1. Synthesis and Characterization

All chemicals, except where stated otherwise, were obtained from Merck (Darmstadt, Germany) and used as received. The detailed synthesis and characterization of compounds 1-(4-nitrophenyl)-4-ferrocenyl-1*H*-1,2,3-triazole (**X1**), 1-(4,4'-dinitro-2-biphenyl)-4-ferrocenyl-1*H*-1,2,3-triazole (**X2**), 1-(3-chloro-4-fluorophenyl)-4-ferrocenyl-1*H*-1,2,3-triazole (**X3**), 1-(4-bromophenyl)-4-ferrocenyl-1*H*-1,2,3-triazole (**X4**), and 1-(2-nitrophenyl)-4-ferrocenyl-1*H*-1,2,3-triazole (**X5**) can be found in our previous report [9]. Single-crystal X-ray diffraction for compounds **X1** and **X5** was carried out on a Stoe IPDS 2 diffractometer equipped with a graphite crystal monochromator situated in the incident beam for data collection at room temperature [26]. The determination of unit cell parameters and data collection were performed using Mo-K α radiation ($\lambda = 0.71073 \text{ \AA}$). [27] Unit cell dimensions were obtained with least-squares refinements, and all structures were solved by direct methods with SHELXT2015 [28,29]. All H atoms were located from difference-Fourier maps, but in the final cycles of refinement they were included in the calculated positions and treated as riding atoms: C-H = 0.93–0.98 \AA with Uiso (H) = 1.2 Ueq (C). Selected geometric parameters (\AA , $^\circ$) of the compounds are listed in Supplementary Tables S1 and S2.

3.2. In Vitro Characterizations of Synthesized Compounds

3.2.1. Cell Culture in the Presence of Ferrocene-1*H*-1,2,3-Triazole Hybrids

RMCs (from the American Type Culture Collection (ATCC; Rockville, MD, USA)) were cultured in Dulbecco's minimal essential medium containing 10% heat-inactivated fetal bovine serum (FBS) at 37 $^\circ\text{C}$ in a 5% CO $_2$ atmosphere. For the measurement of protein expression, enzymatic activity, and mRNA levels, 2×10^5 cells/well were seeded into 12-well plates. In anti-inflammation experiments, cells were starved in 0% FBS and cultured with or without **X1–X5** for 2 h prior to TNF- α (R&D Systems, Minneapolis, MN, USA) treatment for 24 h.

3.2.2. Viability Assay

Cells were seeded at a density of 3×10^5 cells per well into 96-well plates and treated with different concentrations of **X1–X5** (from 1.5625 to 100 $\mu\text{g/mL}$ in 1% DMSO) for 24 h, followed by the addition of 0.5 mg/mL MTT (Merck) for another 2 h. The MTT solution was then discarded and 100 μL of DMSO (Merck) was added to dissolve the formazan crystals. The level of colored formazan was analyzed on a microplate reader (SpectraMax 250, Molecular Devices, San Jose, CA, USA) at a wavelength of 540 nm. The values were determined by comparing the optical density of the **X1–X5**-treated group with that of the vehicle-treated group (1% DMSO).

3.2.3. Gelatin Zymography

MMP-9 expression was analyzed as previously described [30]. Briefly, after treatment, the culture medium was collected and centrifuged at $10,000 \times g$ for 5 min at 4 $^\circ\text{C}$ to remove cell debris. Next, the supernatants were mixed with 5 \times nonreducing sample buffer and electrophoresed on a 10% polyacrylamide gel containing 0.15% gelatin. After electrophoresis, the gel was washed twice in 2.5% Triton X-100 and then incubated in developing buffer at 37 $^\circ\text{C}$ overnight. After incubation, the gel was stained with staining buffer (30% methanol, 10% acetic acid, and 0.5% (wt/vol) Coomassie brilliant blue). Gelatinolytic activity was observed as white bands on a blue background.

3.2.4. Nitrite Production

After cell treatment, the conditioned medium was collected and analyzed for nitrite production by Griess assay [31]. Briefly, 50 μL of a solution containing 4% sulfanilic acid, 0.2% N-(1-naphthyl) ethylenediamine dihydrochloride, and 10% phosphoric acid was added to 50 μL of conditioned medium. Absorbance reading was taken at 550 nm after samples were incubated at 25 $^\circ\text{C}$ for 10 min

in the dark. The standard curve of various NaNO_2 concentrations was used to calculate the NO production in the sample.

3.2.5. Western Blotting for Inflammatory Proteins

Western blotting was conducted as previously described [4]. Briefly, after the cell culture, RMCs were washed, scraped, collected, and centrifuged at $45,000\times g$ for 1 h at 4°C to yield the whole-cell extract. The whole-cell extracts were quantitated, adjusted for concentration, denatured, resolved with 10% sodium dodecyl sulfate polyacrylamide gel electrophoresis, and transferred to polyvinylidene fluoride membranes (Millipore, Bedford, MA, USA). Membranes were incubated with primary anti-COX-2 (Cell Signaling Technology, Danvers, MA, USA), anti-cPLA₂ (Cell Signaling Technology) or anti-GAPDH antibody, which was used as a loading control (Santa Cruz Biotechnology, Santa Cruz, CA, USA) at 4°C overnight and secondary anti-rabbit or anti-mouse horseradish peroxidase antibody for 1 h at room temperature. The immunoreactive signals detected by enhanced chemiluminescence reagents were developed using a LumiFlash Ultima chemiluminescent substrate horseradish peroxidase system (Visual Protein Biotech Corporation, Taipei, Taiwan). The densitometry units of COX-2, cPLA₂ and GAPDH were quantified by ImageLab TM 5.0 Software (Bio-Rad Laboratories, Inc., Hercules, CA, USA).

3.2.6. Real-time PCR

Real-time PCR was performed using the CFX Connect Real-time PCR Detection System (Bio-Rad Laboratories) to determine the expression of inflammatory genes, as per the workflow steps described previously [4]. Briefly, total RNA was extracted and provided as a template for cDNA reverse transcription. The thermal conditions used were 3 min at 95°C , 40 cycles of 10 s at 95°C and 30 s at 58°C . Relative gene expression was determined by the $2^{-\Delta\Delta\text{Ct}}$ method. Gene expression was normalized relative to unstimulated cells and fold variation was normalized to levels of β -actin expression (an endogenous control). The primers used for real-time PCR were as follows: 5'-CGTGAAAAGATGACCCAGATCA-3' (forward) and 5'-CTCCGG AGTCCATCACAATG-3' (reverse) for β -actin; 5'-ACATTCAGGCAGCAGAGGA-3' (forward) and 5'-CCACCACAGGCACAT CAC-3' (reverse) for cPLA₂, and 5'-CAAGAATCAAATTACC GCTGAAG-3' (forward) and 5'-CGAAGGAAGGGAATGTTGTT-3' (reverse) for COX-2; 5'-CGCTTTCACCAAGACTGTGA-3' (forward) and 5'-GCATCCCAAGTACGAGTGGT-3' (reverse) for iNOS.

3.2.7. cPLA₂ and COX-2 Enzyme Activity

The experimental procedure of COX-2 activity detection is in accordance with the manufacturer's instructions (Abcam, Cambridge, UK). The following are simple instructions: First, we established a standard curve by a series of diluted resorufin standards. Resorufin is a redox fluorescent probe that can be used to visualize cell respiration directly. Next, for sample preparation, 5×10^6 cells treated without or with compounds in the presence of TNF- α were scraped off from the culture plate and washed with cold PBS. After centrifuging at $500\times g$ for 3 min, we discarded the supernatant and resuspended the cell pellet in 0.2 mL of lysis buffer with protease inhibitor cocktail on ice for 5 min. After centrifuging at $12,000\times g$ 4°C for 3 min, we collected the supernatant used as the sample. Sample and COX-2 positive control were separately loaded into each of the 96 wells at 20 μL and then 2 μL DMSO (for total COX activity detection) and 2 μL COX-2 inhibitor (Celecoxib, for COX-2 activity detection) were added in two groups. Reaction mix reagents (containing COX Probe, Diluted COX Cofactor and COX Assay Buffer) at 68 μL were loaded into each well and mixed enough, using a multichannel pipette to add 10 μL diluted arachidonic acid/NaOH solution into each well to initiate the reaction at the same time. After addition of the arachidonic acid, the fluorescence (Ex/Em = 535/587 nm) was measured immediately in a kinetic mode once every 15 sec for at least 30 min. One Unit COX activity = amount of COX which generates 1.0 μmol of resorufin per min.

The activity of COX-2 in the test samples is calculated as:

$$COX\ Activity = \left(\frac{B}{\Delta T \times M} \right) = \text{pmol/min/mg or uU/mg} \quad (1)$$

where

B = Amount of resorufin from Standard Curve (pmol).

ΔT = Reaction time (min).

M = Protein amount added into the reaction well (mg)

at pH 8.0, 25 °C.

Use the $\Delta RFU_{535/587nm}$ to obtain B pmol of resorufin generated by COX-2 during the reaction time ($\Delta T = T_2 - T_1$).

$$\Delta RFU_{535/587nm} = (RFU_{S2} - RFU_{S1}) - (RFU_{I2} - RFU_{I1}) \quad (2)$$

where

RFU_{S2} is the sample (DMSO) reading at time T2.

RFU_{S1} is the sample (DMSO) reading at time T1.

RFU_{I2} is the inhibitor sample (Celecoxib) at time T2.

RFU_{I1} is the inhibitor sample (Celecoxib) at time T1.

PLA₂ sample that can utilize arachidonoyl thio-PC as a substrate can be measured by colorimetric cPLA₂ assay kit (Abcam). Among them, any residual sPLA₂ can be removed from the samples by using a membrane filter with a molecular weight cut-off of 30,000. To avoid any measurement of iPLA₂ activity in the sample, use the iPLA₂-specific inhibitor Bromoenol Lactone. Briefly, we added 15 μ L of assay buffer (non-enzymatic control), positive control (bee venom PLA₂) and sample (including iPLA₂-specific inhibitor) to wells. We initiated the reactions for 1 h at room temperature by adding 200 μ L substrate solution. The addition of 10 μ L of DTNB/EGTA to each well stopped enzyme catalysis and developed the reaction for 5 min at room temperature. The absorbance was read at 414 nm using a microplate reader (SpectraMax 250). The activity of cPLA₂ in the test samples is calculated as:

$$cPLA_2\ Activity = \frac{\Delta A_{414}/\text{min}}{10.66\ \text{mM} - 1} \times \frac{0.225\ \text{mL}}{0.01\ \text{mL}} \times \text{Sample dilution} = \text{umol/min/mL} \quad (3)$$

where

$A_{414}/\text{min} = A_{414}(\text{sample}) - A_{414}(\text{blank}) / 60\ \text{min}$

$\Delta A_{414}/\text{min} = (A_{414}/\text{min}_{\text{Sample}} - A_{414}/\text{min}_{\text{Inhibitor}})$

3.3. In Silico Studies

The physicochemical properties and oral bioavailability of compounds **X1–X5** were predicted using admetSAR 2 webserver. [32,33]. SMILE formats (as input) of the molecules were generated using Marvin 16.11.28.0, 2016, ChemAxon (<http://www.chemaxon.com>). Shape-based molecular docking studies were performed on an Intel (R) Core (TM) i5 CPU (2.3 GHz) with a Windows 2010-based operating system. Cif files of the ligands were converted to PDB files which were further used for docking analysis. The ligands were docked into the active sites of human cPLA₂ (PDB code 1CJY) and COX-2 (PDB code: 6COX). The crystal structures were downloaded from the Brookhaven Protein Data Bank (<http://www.rcsb.org>). The pdbqt format of the compound and enzyme were obtained using AutoDock Tools (ADT) 1.5.4 [34]. Preparation of parameter files for grid and docking was done using the following parameters: grid box size of 108 \times 86 \times 78 Å with 0.375 Å spacing that included the whole enzyme. Autodock vina was used for the docking studies [35]. The docking results were analyzed using PyMol [36] for possible polar and hydrophobic interactions. Of the different conformations obtained, the least energetic and most stable conformation was selected.

4. Conclusions

A series of ferrocene-1*H*-1,2,3-triazole hybrids were investigated for their viability, anti-inflammatory, and antioxidant effects. X-ray single-crystal structure studies indicated that the position of the nitro group (*ortho* or *para*) controlled the structure of the compound (dimeric or polymeric) in the solid state. We found that, among all the ferrocene-1*H*-1,2,3-triazole hybrids, **X2–X4** exhibited antioxidant effect on mitochondrial free radicals, and among all, **X4** demonstrated the best anti-inflammatory effect on RMCs. In silico studies confirmed the safety of the compounds and their ability to bind to the active site of the pro-inflammatory factors. Overall, the results of the present study indicated that ferrocene-1*H*-1,2,3-triazole hybrid, **X4**, can be used as a lead to optimize and develop a new anti-inflammatory and antioxidant agent.

Supplementary Materials: Supplementary Materials can be found at <http://www.mdpi.com/1422-0067/21/11/3823/s1>.

Author Contributions: Conceived and designed the experiments, C.-Y.C., A.H., and M.-F.H.; performed the experiments, C.-Y.C., A.H., and M.-F.H.; analyzed the data, S.I.H., C.-Y.C., and M.-F.H.; collected and analyzed the structural data, M.S.H.F. and N.D.; contributed reagents/materials, M.S.K.; writing—original draft preparation, C.-Y.C., and A.H.; writing—review and editing, C.-Y.C., M.S.K., and M.-F.H.; funding acquisition, C.-Y.C., M.-F.H. All the authors reviewed the results and approved the final version of the manuscript. All authors have read and agreed to the published version of the manuscript.

Funding: This research was funded by Ministry of Science and Technology, Taiwan, grant number MOST 108-2119-M-033-002 and Chang Gung Medical Research Foundation, Taiwan under grant number CMRPF3G0013; CMRPF3K0041 and BMRPD16, Chang Gung University of Science and Technology, Taiwan under grant number ZRRPF3J0081.

Acknowledgments: A.H. acknowledges the Department of Chemistry, University of Hail, Kingdom of Saudi Arabia for providing infrastructure support during the preparation of this manuscript. S.I.H. and M.S.K. acknowledge Sultan Qaboos University, Oman for support.

Conflicts of Interest: The authors declare no conflict of interest.

Abbreviations

MMP-9	Matrix metalloproteinase-9
PGE ₂	Prostaglandin E ₂
cPLA ₂	Cytosolic phospholipase A ₂
TNF-α	Tumor necrosis factor-α
MCs	Mesangial cells
NSAIDs	Nonsteroidal anti-inflammatory drugs
NOS	NO synthase
TIMPs	Tissue inhibitors of metalloproteinases
iNOS	Inducible nitric oxide synthase

References

1. Garavito, R.M. The cyclooxygenase-2 structure: New drugs for an old target? *Nat. Struct. Biol.* **1996**, *3*, 897–901. [[CrossRef](#)] [[PubMed](#)]
2. Wang, H.; Li, J.; Gai, Z.; Kullak-Ublick, G.A.; Liu, Z. TNF-α deficiency prevents renal inflammation and oxidative stress in obese mice. *Kidney Blood Press. Res.* **2017**, *42*, 416–427. [[CrossRef](#)] [[PubMed](#)]
3. Yung, S.; Cheung, K.F.; Zhang, Q.; Chan, T.M. Mediators of inflammation and their effect on resident renal cells: Implications in lupus nephritis. *Clin. Dev. Immunol.* **2013**, *2013*, 1–10. [[CrossRef](#)] [[PubMed](#)]
4. Lee, I.-T.; Lin, C.-F.; Huang, Y.-L.; Chong, K.-Y.; Hsieh, M.-F.; Huang, T.-H.; Cheng, C.-Y. Protective mechanisms of resveratrol derivatives against TNF-α-induced inflammatory responses in rat mesangial cells. *Cytokine* **2019**, *113*, 380–392. [[CrossRef](#)]
5. Sato, T.; Van Dixhoorn, M.; Heemskerk, E.; Van Es, L.; Daha, M. C1q, a subunit of the first component of complement, enhances antibody-mediated apoptosis of cultured rat glomerular mesangial cells. *Clin. Exp. Immunol.* **1997**, *109*, 510–517. [[CrossRef](#)] [[PubMed](#)]

6. Narula, S.; Tandon, C.; Tandon, S. Role of matrix metalloproteinases in degenerative kidney disorders. *Curr. Med. Chem.* **2018**, *25*, 1805–1816. [[CrossRef](#)] [[PubMed](#)]
7. Luiking, Y.C.; Engelen, M.P.; Deutz, N.E. Regulation of nitric oxide production in health and disease. *Curr. Opin. Clin. Nutr. Metab. Care* **2010**, *13*, 97–104. [[CrossRef](#)]
8. Fiorucci, S.; Meli, R.; Bucci, M.; Cirino, G. Dual inhibitors of cyclooxygenase and 5-lipoxygenase. A new avenue in anti-inflammatory therapy? *Biochem. Pharmacol.* **2001**, *62*, 1433–1438. [[CrossRef](#)]
9. Haque, A.; Hsieh, M.-F.; Hassan, S.I.; Faizi, M.S.H.; Saha, A.; Dege, N.; Rather, J.A.; Khan, M.S. Synthesis, characterization, and pharmacological studies of ferrocene-1H-1, 2, 3-triazole hybrids. *J. Mol. Struct.* **2017**, *1146*, 536–545. [[CrossRef](#)]
10. Kolb, H.C.; Sharpless, K.B. The growing impact of click chemistry on drug discovery. *Drug Discov. Today* **2003**, *8*, 1128–1137. [[CrossRef](#)]
11. Guo, W.-Y.; Chen, L.-Z.; Shen, B.-N.; Liu, X.-H.; Tai, G.-P.; Li, Q.-S.; Gao, L.; Ruan, B.-F. Synthesis and in vitro and in vivo anti-inflammatory activity of novel 4-ferrocenylchroman-2-one derivatives. *J. Enzym. Inhib. Med. Chem.* **2019**, *34*, 1678–1689. [[CrossRef](#)] [[PubMed](#)]
12. Singh, A.; Lumb, I.; Mehra, V.; Kumar, V. Ferrocene-appended pharmacophores: An exciting approach for modulating the biological potential of organic scaffolds. *Dalton Trans.* **2019**, *48*, 2840–2860. [[CrossRef](#)]
13. Johnson, E.R.; Keinan, S.; Mori-Sánchez, P.; Contreras-García, J.; Cohen, A.J.; Yang, W. Revealing noncovalent interactions. *J. Am. Chem. Soc.* **2010**, *132*, 6498–6506. [[CrossRef](#)]
14. Kovacic, P.; Pozos, R.S.; Somanathan, R.; Shangari, N.; O'Brien, P.J. Mechanism of mitochondrial uncouplers, inhibitors, and toxins: Focus on electron transfer, free radicals, and structure-activity relationships. *Curr. Med. Chem.* **2005**, *12*, 2601–2623. [[CrossRef](#)] [[PubMed](#)]
15. González-Mojica, N.; Almazán-Sánchez, L.; García-Torres, J.G.; Santana-Martínez, I.; Martínez-Otero, D.; Sánchez-Carmona, M.A.; Cuevas-Yañez, E. Oxidation of 1, 4-disubstituted-1, 2, 3-triazoles with H₂O₂–CF₃CO₂H: Efficient synthesis of 1, 2, 3-triazole 3-oxides. *Synth. Commun.* **2019**, *49*, 679–687. [[CrossRef](#)]
16. Carr, A.C.; McCall, M.R.; Frei, B. Oxidation of LDL by myeloperoxidase and reactive nitrogen species: Reaction pathways and antioxidant protection. *Arterioscler. Thromb. Vasc. Biol.* **2000**, *20*, 1716–1723. [[CrossRef](#)] [[PubMed](#)]
17. Oates, J.C.; Shaftman, S.R.; Self, S.E.; Gilkeson, G.S. Association of serum nitrate and nitrite levels with longitudinal assessments of disease activity and damage in systemic lupus erythematosus and lupus nephritis. *Arthritis Rheum.* **2008**, *58*, 263–272. [[CrossRef](#)]
18. Wang, H.; Gao, M.; Li, J.; Sun, J.; Wu, R.; Han, D.; Tan, J.; Wang, J.; Wang, B.; Zhang, L. MMP-9-positive neutrophils are essential for establishing profibrotic microenvironment in the obstructed kidney of UUO mice. *Acta Physiol.* **2019**, *227*, e13317. [[CrossRef](#)]
19. Perrone, M.G.; Vitale, P.; Panella, A.; Fortuna, C.G.; Scilimati, A. General role of the amino and methylsulfamoyl groups in selective cyclooxygenase (COX)-1 inhibition by 1, 4-diaryl-1, 2, 3-triazoles and validation of a predictive pharmacometric PLS model. *Eur. J. Med. Chem.* **2015**, *94*, 252–264. [[CrossRef](#)]
20. Chuang, D.Y.; Simonyi, A.; Kotzbauer, P.T.; Gu, Z.; Sun, G.Y. Cytosolic phospholipase A₂ plays a crucial role in ROS/NO signaling during microglial activation through the lipoxygenase pathway. *J. Neuroinflammation* **2015**, *12*, 199. [[CrossRef](#)]
21. Ng, C.Y.; Kannan, S.; Chen, Y.J.; Tan, F.C.K.; Ong, W.Y.; Go, M.L.; Verma, C.S.; Low, C.-M.; Lam, Y. A new generation of arachidonic acid analogues as potential neurological agent targeting cytosolic phospholipase A₂. *Sci. Rep.* **2017**, *7*, 1–12. [[CrossRef](#)] [[PubMed](#)]
22. Hassan, G.S.; Abou-Seri, S.M.; Kamel, G.; Ali, M.M. Celecoxib analogs bearing benzofuran moiety as cyclooxygenase-2 inhibitors: Design, synthesis and evaluation as potential anti-inflammatory agents. *Eur. J. Med. Chem.* **2014**, *76*, 482–493. [[CrossRef](#)] [[PubMed](#)]
23. Kitchen, D.B.; Decornez, H.; Furr, J.R.; Bajorath, J. Docking and scoring in virtual screening for drug discovery: Methods and applications. *Nat. Rev. Drug Discov.* **2004**, *3*, 935–949. [[CrossRef](#)] [[PubMed](#)]
24. Schwede, T.; Kopp, J.; Guex, N.; Peitsch, M.C. SWISS-MODEL: An automated protein homology-modeling server. *Nucleic Acids Res.* **2003**, *31*, 3381–3385. [[CrossRef](#)]
25. Mouchlis, V.D.; Michopoulou, V.; Constantinou-Kokotou, V.; Mavromoustakos, T.; Dennis, E.A.; Kokotos, G. Binding conformation of 2-oxoamide inhibitors to group IVA cytosolic phospholipase A₂ determined by molecular docking combined with molecular dynamics. *J. Chem. Inf. Model.* **2012**, *52*, 243–254. [[CrossRef](#)]

26. Stoe, C. *X-Area (Version 1.18) and X-Red32 (Version 1.04)*; Stoe & Cie: Darmstadt, Germany, 2002.
27. Farrugia, L.J. WinGX and ORTEP for Windows: An update. *J. Appl. Crystallogr.* **2012**, *45*, 849–854. [[CrossRef](#)]
28. Sheldrick, G.M. A short history of SHELX. *Acta Crystallogr. Sect. A Found. Crystallogr.* **2008**, *64*, 112–122. [[CrossRef](#)]
29. Sheldrick, G.M. Crystal structure refinement with SHELXL. *Acta Crystallogr. Sect. C Struct. Chem.* **2015**, *71*, 3–8. [[CrossRef](#)]
30. Cheng, S.-C.; Wu, Y.-H.; Huang, W.-C.; Pang, J.-H.S.; Huang, T.-H.; Cheng, C.-Y. Anti-inflammatory property of quercetin through downregulation of ICAM-1 and MMP-9 in TNF- α -activated retinal pigment epithelial cells. *Cytokine* **2019**, *116*, 48–60. [[CrossRef](#)]
31. Shultz, P.J.; Raij, L. Endogenously synthesized nitric oxide prevents endotoxin-induced glomerular thrombosis. *J. Clin. Investig.* **1992**, *90*, 1718–1725. [[CrossRef](#)]
32. Cheng, F.; Li, W.; Zhou, Y.; Shen, J.; Wu, Z.; Liu, G.; Lee, P.W.; Tang, Y. admetSAR: A comprehensive source and free tool for assessment of chemical ADMET properties. *J. Chem. Inf. Model.* **2012**, *52*, 3099–3105. [[CrossRef](#)] [[PubMed](#)]
33. Yang, H.; Lou, C.; Sun, L.; Li, J.; Cai, Y.; Wang, Z.; Li, W.; Liu, G.; Tang, Y. admetSAR 2.0: Web-service for prediction and optimization of chemical ADMET properties. *Bioinformatics* **2019**, *35*, 1067–1069. [[CrossRef](#)]
34. Sanner, M.F. Python: A programming language for software integration and development. *J. Mol. Graph. Model.* **1999**, *17*, 57–61. [[PubMed](#)]
35. Trott, O.; Olson, A.J. AutoDock Vina: Improving the speed and accuracy of docking with a new scoring function, efficient optimization, and multithreading. *J. Comput. Chem.* **2010**, *31*, 455–461. [[CrossRef](#)] [[PubMed](#)]
36. DeLano, W.L. PyMOL. In *The PyMOL Molecular Graphics System*; DeLano, W.L., Ed.; DeLano Scientific: San Carlos, CA, USA, 2002.



© 2020 by the authors. Licensee MDPI, Basel, Switzerland. This article is an open access article distributed under the terms and conditions of the Creative Commons Attribution (CC BY) license (<http://creativecommons.org/licenses/by/4.0/>).

RESEARCH

Open Access



Rottlerin, a natural polyphenol compound, inhibits upregulation of matrix metalloproteinase-9 and brain astrocytic migration by reducing PKC- δ -dependent ROS signal

Tsong-Hai Lee^{1†}, Jiun-Liang Chen^{2†}, Pei-Shan Liu^{3†}, Ming-Ming Tsai^{4,5}, Su-Jane Wang⁶ and Hsi-Lung Hsieh^{4,7*} 

Abstract

Background: Upregulation of matrix metalloproteinase-9 (MMP-9) has been indicated as one of the inflammatory biomarkers. In the central nervous system (CNS), the MMP-9 is induced by several proinflammatory mediators and participates in the CNS disorders, including inflammation and neurodegeneration. In addition, protein kinase Cs (PKCs) has been shown to be involved in regulation of various inflammatory factors like MMP-9 by several stimuli in many cell types. Several phytochemicals are believed to reduce the risk of several inflammatory disorders including the CNS diseases. The rottlerin, a principal phenolic compound of the Kamala plant *Mallotus philippinensis*, has been shown to possess an array of medicinal properties, including anti-PKC- δ , antitumor, anti-oxidative, and anti-inflammatory activities.

Methods: Herein, we used rat brain astrocytes (RBA) to demonstrate the signaling mechanisms of phorbol 12-myristate 13-acetate (PMA)-induced MMP-9 expression by zymographic, RT-PCR, subcellular isolation, Western blot, ROS detection, and promoter reporter analyses. Then, we evaluate the effects of rottlerin on PMA-induced MMP-9 expression in RBA and its influencing mechanism.

Results: We first demonstrated that PMA stimulated activation of various types of PKC, including PKC- δ in RBA. Subsequently, PMA induced MMP-9 expression via PKC δ -mediated reactive oxygen species (ROS) generation, extracellular signal-regulated kinase 1/2 (ERK1/2) activation, and then induced c-Fos/AP-1 signaling pathway. Finally, upregulation of MMP-9 by PMA via the pathway may promote astrocytic migration, and the event could be attenuated by rottlerin.

(Continued on next page)

* Correspondence: hlhsieh@mail.cgu.edu.tw

[†]Tsong-Hai Lee, Jiun-Liang Chen and Pei-Shan Liu contributed equally to this work.

⁴Department of Nursing, Division of Basic Medical Sciences, Research Center for Chinese Herbal Medicine, and Graduate Institute of Health Industry Technology, Chang Gung University of Science and Technology, 261 Wenhua 1st Road, Guishan, Taoyuan, Taiwan

⁷Department of Neurology, Chang Gung Memorial Hospital, Taoyuan, Taiwan
Full list of author information is available at the end of the article



© The Author(s). 2020 **Open Access** This article is licensed under a Creative Commons Attribution 4.0 International License, which permits use, sharing, adaptation, distribution and reproduction in any medium or format, as long as you give appropriate credit to the original author(s) and the source, provide a link to the Creative Commons licence, and indicate if changes were made. The images or other third party material in this article are included in the article's Creative Commons licence, unless indicated otherwise in a credit line to the material. If material is not included in the article's Creative Commons licence and your intended use is not permitted by statutory regulation or exceeds the permitted use, you will need to obtain permission directly from the copyright holder. To view a copy of this licence, visit <http://creativecommons.org/licenses/by/4.0/>. The Creative Commons Public Domain Dedication waiver (<http://creativecommons.org/publicdomain/zero/1.0/>) applies to the data made available in this article, unless otherwise stated in a credit line to the data.

(Continued from previous page)

Conclusions: These data indicated that rottlerin may have anti-inflammatory activity by reducing these related pathways of PKC- δ -dependent ROS-mediated MMP-9 expression in brain astrocytes.

Keywords: Rottlerin, Matrix metalloproteinase-9, Protein kinase C- δ , Reactive oxygen species, Brain astrocytes, Neuroinflammation

Background

Natural medicinal plants are an important part of traditional medicine, an ancient complex therapy considered today as one of the most complete complementary medicine system. Recently, several natural products have been included into European Pharmacopoeia. The past decade has also witnessed an intense interest in natural herbal medicines in which phytochemical components can have long-term health promoting or medicinal qualities. Phytochemicals present in natural products such as herbs are believed to reduce the risk of several major diseases including cardiovascular diseases, cancers, and neurodegenerative disorders [1]. A likely mechanism of at least some of the activities is interacting with redox balance and prevention of oxidative stress. During the past two decades, hundreds of natural products, extracts, and isolated compounds have been screened for their antioxidant properties in vitro and in vivo. Consequently, some of natural products can be regarded as source of very efficient antioxidant compounds, and this activity could explain some of their therapeutic and preventive usefulness [2]. The rottlerin is a polyphenol natural product isolated from the Asian Kamala plant *Mallotus philippinensis* [3] and displays a complex spectrum of pharmacology and an array of medicinal properties. It has been used as a protein kinase C- δ (PKC- δ) inhibitor. Although there is extensive published documentation to support the use of rottlerin as a selective PKC- δ inhibitor, there has been some controversy in the literature over this claim [4]. It has been demonstrated to exhibit antitumor, autophagy, anti-proliferative, anti-metastasis, and anti-invasive properties [5–7]. In the central nervous system (CNS), previous report has indicated that several natural phenolic compounds like rottlerin may as potential neuroprotective agents to treat Parkinson's disease [5]. However, the mechanisms of rottlerin in the CNS neuroprotective action remain unclear.

The astrocytes are one type of glial cells in the CNS, which have been proposed to exert a wide range of functions including participating in the immune and repairing responses to brain injury and diseases [8, 9]. Following injury to the human CNS, astrocytes become reactive and respond in stereotypical manner termed astrogliosis [10] which is characterized by astrocyte proliferation and functional changes in inflammatory diseases [11]. In brain,

PKC and related kinases are activated during trauma, stroke, and neurogenic inflammation [12, 13], which may play a critical role in the initiation of the CNS inflammatory diseases. However, the effect of rottlerin on PKC-dependent MMP-9 expression is still unclear, although we have demonstrated that PKCs, PKC- δ especially, contribute to bradykinin-induced MMP-9 expression in brain astrocytes [14].

Matrix metalloproteinases (MMPs) are a large family of zinc-dependent endopeptidases which is a crucial molecule for the turnover of extracellular matrix (ECM) and pathophysiological processes [15]. In the CNS, MMPs, MMP-9 especially, has been demonstrated to participate in morphogenesis, wounding healing, and neurite outgrowth [16]. Several lines of evidence have showed that upregulation of MMP-9 may contribute to the pathogenic process of brain diseases by several brain injuries [17]. Moreover, several proinflammatory mediators such as cytokines and endotoxin have been shown to induce MMP-9 expression and activity in rat brain astrocytes [18, 19]. Our previous studies have showed that several proinflammatory mediators can induce MMP-9 expression and MMP-9-related functions in brain astrocytes [20]. These studies indicated that MMP-9 may play a critical role in brain inflammation and disorders, and this has aroused our interest to investigate the effects of natural products like rottlerin on MMP-9 expression in brain astrocytes. Here, we used the model of upregulation of MMP-9 by a PKC activator, phorbol 12-myristate 13-acetate (PMA), in brain astrocytes (RBA) to evaluate the effects of rottlerin on MMP-9 regulation and the relative events such as cell migration.

Reactive oxygen species (ROS) are produced by various enzymatic and chemical processes or directly inhaled, including $O_2^{\bullet-}$, $\bullet OH$, and hydrogen peroxide (H_2O_2). The ROS at low level have physiological roles as signaling molecules in various cellular and developmental processes [21, 22] and killing of invading microorganisms [23]. In contrast, recent report indicated that oxidative stress plays an important role in the progression of various diseases [23]. Moreover, ROS has been shown to interact with DNA, lipids, proteins, and carbohydrates that lead to cellular dysfunctions and inflammatory responses [22, 24]. Under pathological conditions, many proinflammatory mediators induce expression of several inflammatory genes during brain injury via increasing ROS production

[20, 22, 25]. Moreover, increasing evidence attributes the neurodegenerative diseases such as Alzheimer's disease (AD) to oxidative stress (generation of free radicals) that leads to brain inflammation during CNS pathogenesis [22, 25, 26]. Moreover, ROS also exert as a signaling factor mediated microglial activation induced by several proinflammatory mediators [27]. The effects of PKCs associated with ROS generation have been reported in several organ diseases [28, 29]. Our previous reports indicated that ROS is critical for upregulation of MMP-9 responses in rat brain astrocytes [30, 31].

Based on these backgrounds and our previous studies in the brain inflammatory responses by MMP-9 induction [20], the experiments were performed to evaluate the effects and molecular mechanisms of rottlerin on PMA-induced MMP-9 expression in brain astrocytes (RBA). In the study, we found that the rottlerin reduced PMA-induced MMP-9 expression and astrocytic migration. Moreover, PMA-stimulated phosphorylation of protein kinases (e.g., PKC- δ , ROS, and ERK1/2) also been inhibited by pretreatment of rottlerin. Furthermore, the rottlerin decreased PKC- δ -mediated Nox/ROS/ERK-dependent activation of c-Fos/AP-1 pathway in RBA cells. These results suggested that the rottlerin may be has neuroprotective effects by anti-oxidative and anti-inflammatory action in the CNS.

Methods

Materials

Dulbecco's modified Eagle's medium (DMEM)/F-12 medium, fetal bovine serum (FBS), and TRIzol were from Invitrogen (Carlsbad, CA). Hybond C membrane and enhanced chemiluminescence (ECL) Western blot detection system were from GE Healthcare Biosciences (Buckinghamshire, UK). PKC isotypes (PKC- α , PKC- β , PKC- γ , PKC- ϵ , PKC- δ) and PhosphoPlus ERK1/2 (Thr²⁰²/Tyr²⁰⁴) antibodies were from Cell Signaling (Danver, MA). Anti-glyceraldehyde-3-phosphate dehydrogenase (GAPDH) antibody was from Biogenesis (Bournemouth, UK). Rottlerin, apocynin, PD98059, tan-shinone IIA (TSIIA), and MMP2/9 inhibitor (2/9i) were from Biomol (Plymouth Meeting, PA). Bicinchoninic acid (BCA) protein assay reagent was from Pierce (Rockford, IL). Phorbol 12-myristate 13-acetate (PMA), N-acetyl-cysteine (NAC), enzymes, and other chemicals were from Sigma (St. Louis, MO).

Cell cultures and treatments

The rat brain astrocytic cell line (RBA, CTX TNA2) was purchased from BCRC (Hsinchu, Taiwan) and used throughout this study. Cells were plated onto 12-well culture plates and made quiescent at confluence by incubation in serum-free DMEM/F-12 for 24 h, and then incubated with PMA (0.01 ~ 10 μ M) at 37 °C for the

indicated time intervals. When the inhibitors were used, cells were pretreated with the inhibitor for 1 h before exposure to PMA (1 μ M). Treatment of RBA with these inhibitors alone had no significant effect on cell viability determined by an XTT assay (data not shown).

MMP gelatin zymography

Growth-arrested cells were incubated with PMA for the indicated time intervals. After treatment, the cultured media were collected and analyzed by gelatin zymography [32]. Gelatinolytic activity was manifested as horizontal white bands on a blue background. Because cleaved MMPs were not reliably detectable, only pro-form zymogens were quantified.

Total RNA extraction and reverse transcription-PCR analysis

Total RNA was extracted from RBA cells [33]. The cDNA obtained from 0.5 μ g total RNA was used as a template for PCR amplification. Oligonucleotide primers were designed on the basis of Genbank entries for rat MMP-9, c-Fos, and β -actin. The primers were:

MMP-9: 5'-AGTTTGGTGTTCGCGGAGCAC-3' (sense)

5'-TACATGAGCGCTTCCGGCAC-3' (antisense)

c-Fos: 5'-AGACGAAGGAAGACGTGTAAGCACTGCAGCT-3' (sense)

5'-AAGGAGAATCCGAAGGGAAAGGAATAAGATG-3' (antisense)

β -actin: 5'-GAACCCTAAGGCCAACCGTG-3' (sense)

5'-TGGCATAGAGGTCTTTACGG-3' (anti-sense)

The amplification was performed in 30 cycles at 55 °C, 30 s; 72 °C, 1 min; 94 °C, 30 s. PCR fragments were analyzed on 2% agarose 1X TAE gel containing ethidium bromide, and their size was compared with a molecular weight markers. Amplification of β -actin, a relatively invariant internal reference RNA, was performed in parallel, and cDNA amounts were standardized to equivalent β -actin mRNA levels. The image densitometry analysis was quantified by an UN-SCAN-IT gel 6.1 software (Orem, UT).

Preparation of subcellular fractions and detection of PKC isoforms translocation

RBA cells were seeded in a 10-cm dish. After reaching 90% confluence, the cells were starved for 24 h in serum-free medium and treated with PMA (1 μ M) for the indicated times. The cells were washed once with ice-cold phosphate-buffered saline (PBS). Two hundred microliter of homogenization buffer A (20 mM Tris-HCl, pH 8.0, 10 mM EGTA, 2 mM EDTA, 2 mM dithiothreitol, 1 mM phenylmethylsulfonyl fluoride, 25 mM aprotinin, 10 mM leupeptin) was added to each dish,

and the cells were scraped into a 1.5-mL tube with a rubber policeman. The cytosolic and membrane fractions were prepared by centrifugation as described previously [34].

Preparation of cell extracts and western blot analysis

Growth-arrested cells were incubated with PMA at 37 °C for the indicated time intervals. The cells were washed with ice-cold PBS, scraped, and collected by centrifugation at $45,000 \times g$ for 1 h at 4 °C to yield the whole cell extract, as previously described [14]. Samples were analyzed by Western blot, transferred to nitrocellulose membrane, and then incubated overnight using an anti-PKC isotypes (e.g., PKC- α , PKC- β , PKC- γ , PKC- ϵ , and PKC- δ), anti-phospho-ERK1/2, ERK2, or GAPDH antibody. Membranes were washed four times with TTBS for 5 min each, incubated with a 1:2000 dilution of anti-rabbit horseradish peroxidase antibody for 1 h. The immunoreactive bands were detected by ECL reagents and captured by a UVP BioSpectrum 500 Imaging System (Upland, CA). The image densitometry analysis was quantified by an UN-SCAN-IT gel 6.1 software (Orem, UT).

Measurement of intracellular ROS generation

The peroxide-sensitive fluorescent probe 2',7'-dichlorofluorescein diacetate (DCF-DA) was used to assess the generation of intracellular ROS [35] with minor modifications. RBA cells on monolayers were incubated with 5 μ M DCF-DA in RPMI-1640 at 37 °C for 45 min. The supernatant was removed and replaced with fresh RPMI-1640 medium before exposure to PMA (1 μ M). Relative fluorescence intensity was recorded at the indicated time by using a fluorescent plate reader (Thermo, Appliskan) at an excitation wavelength of 485 nm, and emission was measured at a wavelength of 530 nm. The fluorescent images were also obtained by using fluorescence microscopy (Axiovert 200 M; Zeiss).

MMP-9 promoter-luciferase reporter gene assay

The upstream region (– 1280 to + 19) of the rat MMP-9 promoter was cloned to the pGL3-basic vector containing the luciferase reporter system [14]. All plasmids were prepared by using QIAGEN plasmid DNA preparation kits. These constructs were transfected into RBA cells by using a Lipofectamine reagent according to the instructions of the manufacture. The transfection efficiency (~ 60%) was determined by transfection with enhanced GFP. After incubation with PMA, cells were collected and disrupted by sonication in lysis buffer (25 mM Tris, pH 7.8, 2 mM EDTA, 1% Triton X-100, and 10% glycerol). After centrifugation, aliquots of the supernatants were tested for promoter activity using a luciferase assay

system (Promega, Madison, WI). Firefly luciferase activities were standardized for β -galactosidase activity.

Cell migration assay

RBA cells were cultured to confluence in 6-well plates and starved with serum-free DMEM/F-12 medium for 24 h. The monolayer cells were scratched manually with a blade, and the detached cells were removed with PBS. Serum-free DMEM/F-12 medium with or without PMA (1 μ M) was added to each dish as indicated after pretreatment of inhibitors for 1 h, containing a DNA synthesis inhibitor hydroxyurea (10 μ M) during the period of experiment. Images were observed and taken at 0 and 24 h with a digital camera and a microscope (Olympus, Japan). These resulting four phase images for each point were averaged and then normalized based on the initial image at 0 h. The normalized values were averaged for each experimental condition. The data presented are generated from three separate assays.

Statistical analysis of data

All data were estimated using GraphPad Prism Program (GraphPad, San Diego, CA). Quantitative data were analyzed by one-way ANOVA followed by Tukey's honestly significant difference tests between individual groups. Data were expressed as mean \pm SEM. A value of $P < 0.05$ was considered significant.

Results

Phorbol 12-myristate 13-acetate (PMA) induces MMP-9 expression in brain astrocytes

The PKCs are crucial for regulation of MMP-9 in brain inflammatory diseases [14]. First, we investigate whether the PKC activator, phorbol 12-myristate 13-acetate (PMA), can upregulate MMP-9 expression in rat brain astrocytes (RBA), cells were treated with PMA (1 μ M) for the indicated time intervals, and then the conditioned media were collected and analyzed. As shown in Fig. 1a, treatment with PMA (1 μ M) significantly induced MMP-9 expression in a time-dependent manner determined by gelatin zymography. The expression of a housekeeping protein GAPDH, as an internal control, was not changed. There was a significant increase between 6 and 24 h. A maximal increase was achieved at 24 h during the period of observation. Moreover, the RBA cells were incubated with different concentrations of PMA (0.01, 0.1, 1, and 10 μ M) for 24 h. In addition, RBA cells were incubated with various concentrations of PMA (0.01, 0.1, 1, and 10 μ M) for 24 h, and the MMP-9 was determined by gelatin zymography (Fig. 1b). The induction response of PMA was in a concentration-dependent increase, and there was a significant increase from 100 nM of PMA. A maximal induction of PMA was obtained at the concentration of 10 μ M. To further

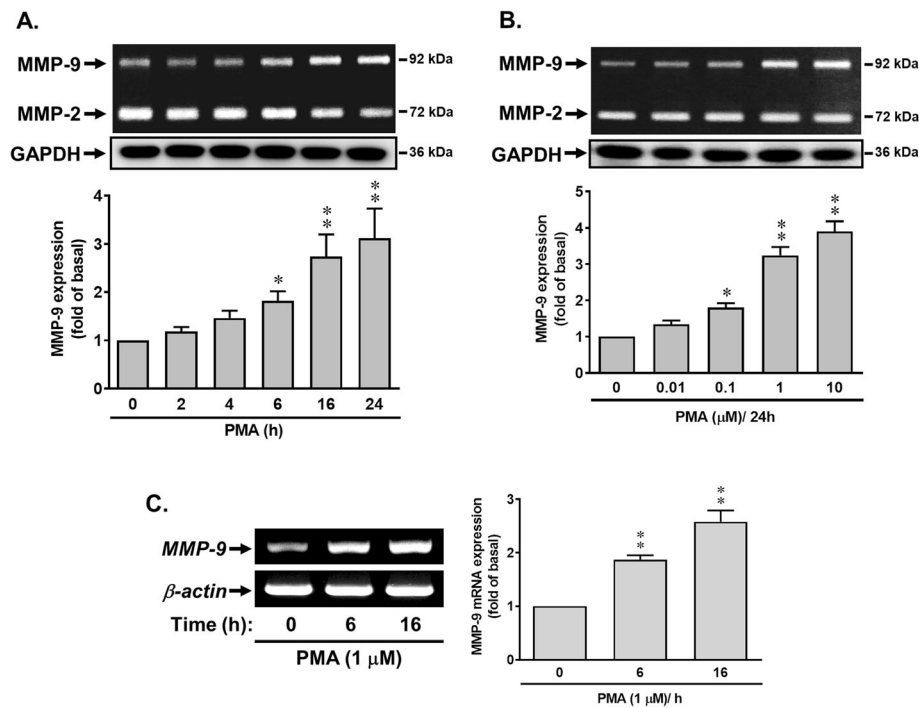


Fig. 1 Phorbol 12-myristate 13-acetate (PMA), a PKC activator, induces MMP-9 expression, but not MMP-2, in brain astrocytes (RBA). **a** Time dependence of PMA increase of MMP-9 expression. RBA cells were treated with 1 μ M PMA for the indicated time intervals. **b** Concentration dependence of PMA-induced MMP-9 expression. Cells were treated with various concentrations of PMA (0.01, 0.1, 1, and 10 μ M) for 24 h. **c** Time dependence of PMA-induced MMP-9 mRNA expression. Cells were treated with 1 μ M PMA for the indicated times. The conditioned media, cell lysates, and total RNA were collected and analyzed by gelatin zymography (MMP2/9), Western blot (GAPDH, as an internal control), and RT-PCR (MMP-9 and β -actin) as described under the “Methods” section. The intensity of zymographic (**a, b**) and PCR product (**c**) bands was quantitated by scanning densitometry and expressed as fold of untreated control. Data are expressed as the mean \pm SEM ($N = 3$). * $P < 0.05$; ** $P < 0.01$, as compared with the respective values of untreated control. The image represents one of three individual experiments

examine whether the increase in MMP-9 expression by PMA resulted from the increase of MMP-9 mRNA expression, the RT-PCR analysis was performed. As shown in Fig. 1c, the levels of mRNA for MMP-9 in RBA cells were determined by RT-PCR. PMA time dependently induced the mRNA expression of MMP-9 in the cells, whereas the expression of β -actin mRNA, a housekeeping gene product used as an internal control, was not changed. These data revealed that PMA induced the expression of MMP-9 by increasing mRNA level and suggested that PKCs might play an upregulatory role in PMA-induced MMP-9 expression in RBA cells.

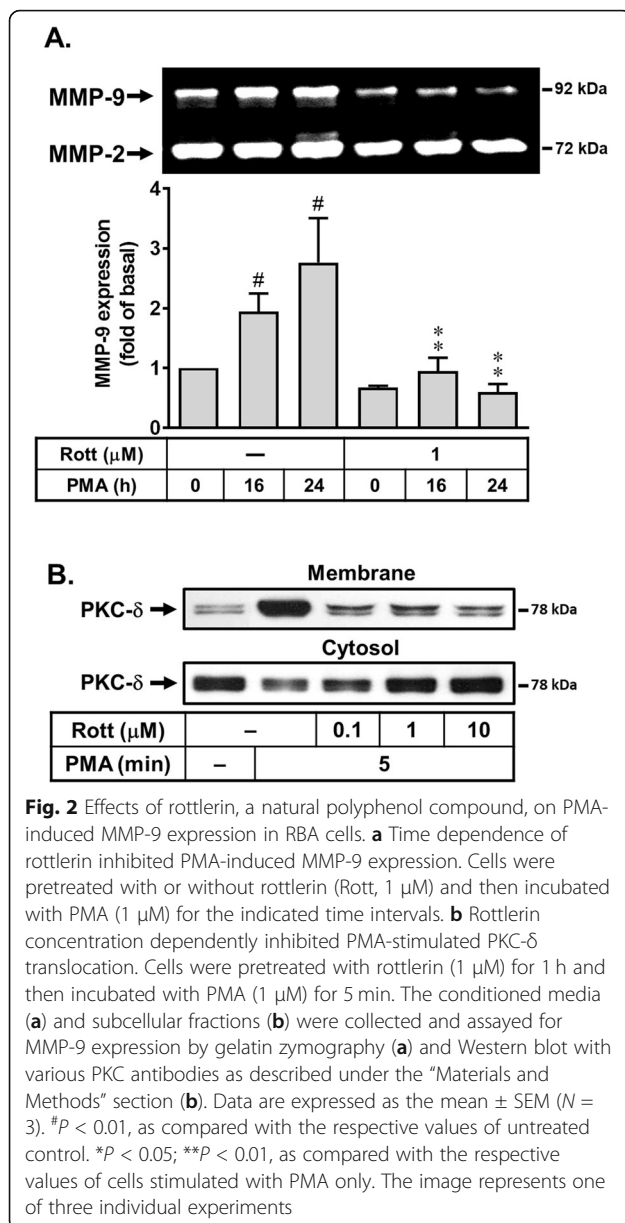
Effects of rottlerin, a natural polyphenol compound, on PMA-induced MMP-9 expression

Our previous data have shown that upregulation of MMP-9 requires PKC- δ -mediated manner [14]. To determine the role of PKC- δ in PMA-induced upregulation of MMP-9, a selective PKC- δ inhibitor rottlerin (a natural polyphenol compound) was used. The cells were pretreated with rottlerin (1 μ M) for 1 h and then incubated with PMA for the indicated times. As shown in Fig. 2a, pretreatment with rottlerin caused a significant

inhibition on PMA-induced MMP-9 expression revealed by gelatin zymography, suggesting that PKC (PKC- δ especially) may play a potential role in PMA-induced MMP-9 expression in RBA cells. Moreover, we also found that PMA stimulated several PKC isoform translocation, including PKC- α , PKC- β I, PKC- γ , PKC- ϵ , and PKC- δ (data not shown). Next, to determine the effect of rottlerin on PMA-stimulated PKC- δ translocation, the cells were pretreated with various concentration of rottlerin (0.1, 1, and 10 μ M), and then the PKC- δ translocation was analyzed. The results showed that rottlerin concentration dependently inhibited PMA-stimulated membrane translocation of PKC- δ analyzed by Western blot (Fig. 2b). These results suggested that rottlerin may block PMA-induced MMP-9 expression via blocking PKC- δ activation in RBA cells.

Role of rottlerin in PMA-induced MMP-9 expression via Nox-mediated ROS production

Recent report has indicated that ROS may contribute to MMP expression in various cell types [36]. The NADPH oxidase (Nox) is considered to be a major source of ROS in many physiological and pathological processes [23, 37].



Previous studies have demonstrated that Nox-derived ROS signaling cascade is involved in upregulation of MMP-9 by BK in astrocytes [30]. Thus, to determine whether rottlerin-reduced PMA-induced MMP-9 is due to decreasing Nox-dependent ROS production, the ROS scavenger *N*-acetylcysteine (NAC) and a Nox activity inhibitor apocynin were used. As shown in Fig. 3a, pretreatment with NAC (0.1, 0.5, or 5 mM) markedly inhibited PMA-induced MMP-9 expression in a concentration-dependent manner. Moreover, pretreatment with apocynin (Apo, 0.1, 1, or 10 μM) also blocked PMA-induced MMP-9 expression in a concentration-dependent manner (Fig. 3b). The data suggested that Nox-derived ROS generation may play a potential role in PMA-induced MMP-9 expression in RBA cells.

To explore whether PMA induces ROS generation, the cells were loaded with DCF-DA (a ROS probe) and then stimulated with PMA (1 μM) for the indicated time intervals. As shown in Fig. 3c, PMA stimulated a time dependently ROS production with a maximal response within 10 min and sustained over 30 min. The results were further supported by the data of fluorescence images obtained using a fluorescent microscopy (Fig. 3c, internal panel). The image data showed that PMA stimulated ROS generation in RBA cells. Pretreatment of cells with NAC (5 mM) and Apo (1 μM) markedly attenuated PMA-stimulated ROS generation (Fig. 3d). Additionally, to examine the effects of rottlerin on PMA-stimulated ROS generation, the cells were pretreated with rottlerin (Rott, 1 μM) for 1 h and then incubated with PMA for 10 min. As shown in Fig. 3d, PMA-stimulated ROS generation was markedly attenuated by pretreatment with Rott, suggesting that upregulation of MMP-9 by PMA is mediated through a PKC-δ-dependent Nox-derived ROS production in RBA cells. Herein, we also demonstrated that rottlerin may be possessed of anti-oxidative effect in the event.

Rottlerin attenuates upregulation of MMP-9 by PMA through blocking the Nox/ROS-mediated ERK1/2 activation in RBA cells

Activation of MAPKs by various stimuli could modulate cellular functions of brain cells [32, 38]. Moreover, previous reports have pointed out that ERK1/2 is critical for the regulation of MMP-9 expression in brain astrocytes [14]. Thus, to determine whether ERK1/2 also participated in PMA-induced MMP-9 expression, cells were pretreated with or without PD98059 (10 μM) for 1 h and then incubated with PMA for the indicated time intervals. As shown in Fig. 4a, pretreatment with PD98059 attenuated PMA-induced MMP-9 expression, suggesting that ERK1/2 may be involved in PMA-induced MMP-9 expression. We further demonstrated that PMA stimulated time dependently ERK1/2 phosphorylation with a maximal response within 5 min and sustained over 30 min by Western blot (Fig. 4b). These results suggested that PMA-induced MMP-9 expression is mediated through ERK1/2 pathway in RBA cells. Next, to determine whether PMA-stimulated ERK1/2 phosphorylation is mediated through Nox/ROS-dependent pathway, cells were pretreated with NAC, Apo, or PD98059 (PD) and then incubated with PMA (1 μM) for the indicated time intervals. The results showed that pretreatment with NAC (5 mM), Apo (1 μM), or PD (10 μM) significantly attenuated PMA-stimulated ERK1/2 phosphorylation during the period of observation (Fig. 4c), suggesting that PMA stimulated Nox/ROS-dependent phosphorylation of ERK1/2 in these cells. Moreover, we further evaluated the effect of rottlerin in phosphorylation of ERK1/2 by PMA. As shown in Fig. 4d, pretreatment with rottlerin (Rott, 1 μM) markedly

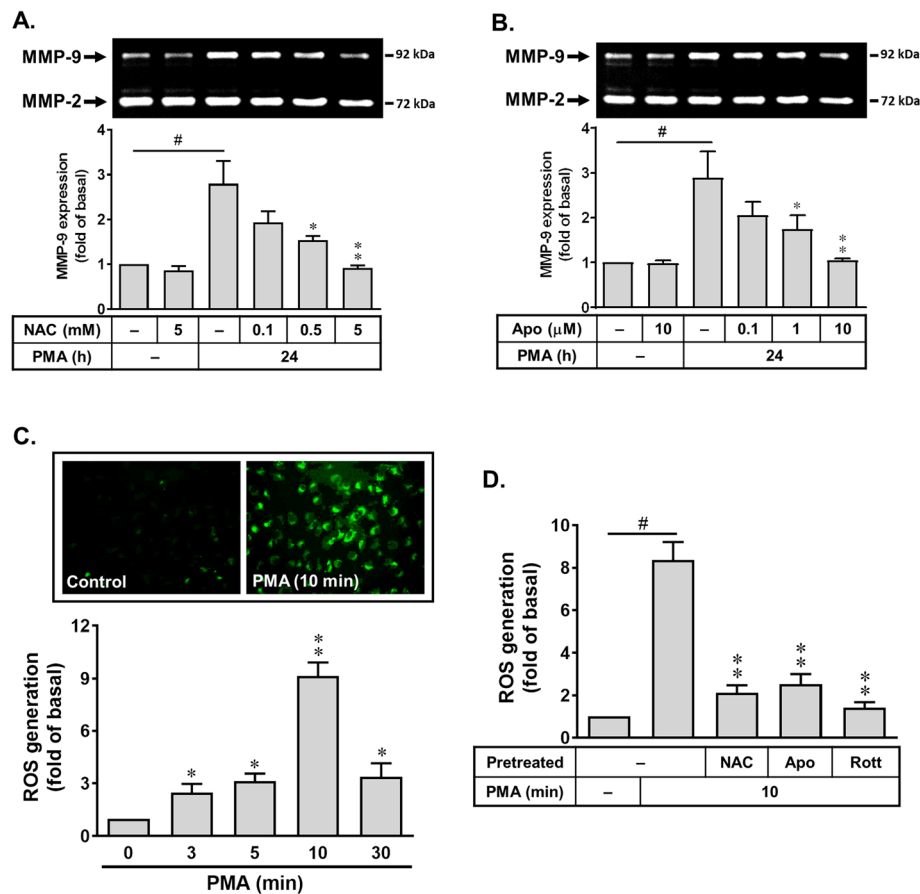


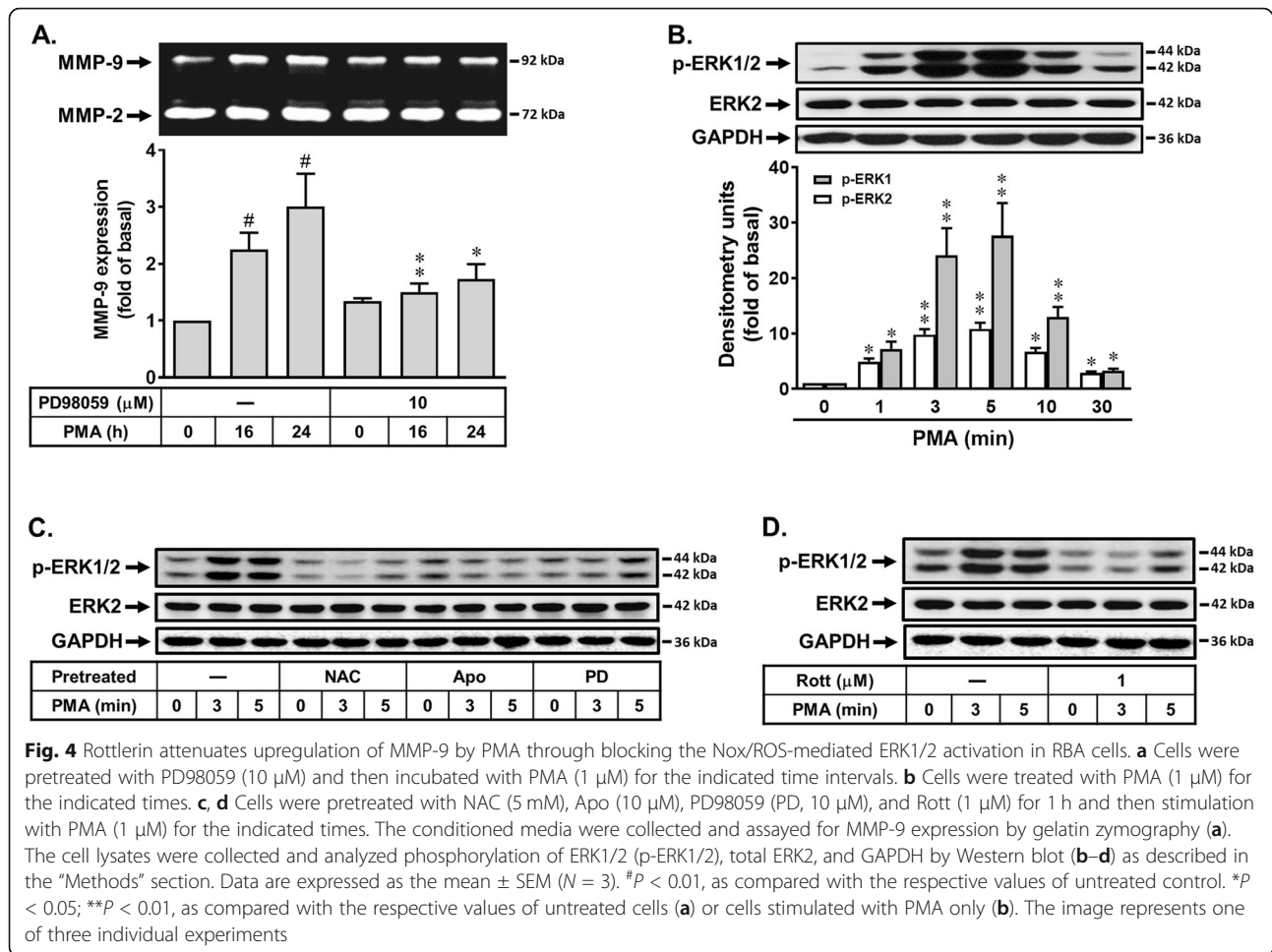
Fig. 3 Roles of rottlerin in PMA-induced MMP-9 expression via Nox-mediated ROS production. **a, b** The Nox/ROS system inhibitor concentration dependently blocked PMA-induced MMP-9 expression, and cells were pretreated with **a** NAC (0.1, 1, and 5 mM) or **b** apocynin (Apo, 0.1, 1, 10 μM) and then incubated with PMA (1 μM) for 24 h. **c, d** PMA stimulates ROS generation. Cells were incubated with the DCF-DA (5 μM) for 45 min, followed by stimulation with PMA (1 μM) for the indicated times (**c**), or pretreatment with NAC (5 mM), Apo (10 μM), and Rott (1 μM) for 1 h and then stimulation with PMA (1 μM) for 10 min (**d**). The conditioned media were collected and assayed for MMP-9 expression by gelatin zymography (**a, b**). The fluorescence intensity (ROS generation) and images of cells (**c, d**) were determined as described in the “Methods” section. Data are expressed as the mean ± SEM ($N = 3$). # $P < 0.01$, as compared with the respective values of untreated control. * $P < 0.05$; ** $P < 0.01$, as compared with the respective values of untreated cells (**c**) or cells stimulated with PMA only (**a, b, d**). The image represents one of three individual experiments

attenuated PMA-stimulated ERK1/2 phosphorylation, suggesting that activation of ERK1/2 may be involved in PMA-induced MMP-9 expression through PKC- δ -dependent manner. These results demonstrated that rottlerin blocked PMA-induced MMP-9 expression is mediated through inhibiting Nox/ROS-dependent ERK1/2 activation in RBA cells.

Effects of rottlerin in PMA-stimulated activation of transcription factors such as AP-1

The AP-1-dependent pathways have been demonstrated to involve in MMP-9 expression in various cell types [20]. We first determine whether PMA-induced MMP-9 expression is mediated through activation of AP-1 (e.g., c-Fos). As shown in Fig. 5a, pretreatment with an AP-1 inhibitor tanshinone IIA (TSIIA, 10 μM) significantly inhibited PMA-induced

MMP-9 expression, suggesting that the transcription factor AP-1 may be involved in PMA-induced MMP-9 expression. Furthermore, the results of RT-PCR analysis showed that PMA can induce c-Fos, a subunit of AP-1, mRNA expression (~ 6-fold), pretreatment with TSIIA (10 μM), NAC (5 mM), Apo (1 μM), or PD (10 μM) attenuated PMA-stimulated c-Fos/AP-1 mRNA expression (Fig. 5b). These results demonstrated that PMA induced MMP-9 expression via Nox/ROS/ERK1/2-mediated activation of c-Fos/AP-1 cascade in RBA cells. Next, to evaluate the effects of rottlerin on PMA-induced c-Fos/AP-1 gene expression, the results were obtained by RT-PCR analysis. The results showed that pretreatment of RBA with rottlerin (Rott, 1 μM) significantly reduced PMA-stimulated c-Fos/AP-1 gene expression (Fig. 5b). Moreover, previous studies indicated that MMP-9 promoter region contains AP-1 binding sites [39]. Hence, we



next examined whether rottlerin also affects PMA-induced MMP-9 promoter activity by blocking AP-1 activation, a rat MMP-9 promoter reporter constructs (pGL-MMP-9-Luc) was used [30, 39]. The data showed that pretreatment with TSIIA, NAC, Apo, PD, or rottlerin significantly attenuated PMA-increased MMP-9 promoter activity (Fig. 5c). We further demonstrated that PMA-induced MMP-9 mRNA expression was also mediated through this pathway determined by RT-PCR analysis (Fig. 5d). These results confirmed that PMA-induced MMP-9 mRNA expression is mediated through Nox/ROS/ERK-mediated upregulation of c-Fos/AP-1 linking to the MMP-9 promoter activity in RBA cells. In addition, rottlerin may play a suppressor in PMA-induced MMP-9 expression via reducing c-Fos/AP-1-mediated MMP-9 transcription activity in these cells.

Rottlerin affects the PMA-induced MMP-9-mediated astrocytic migration

The MMP-9 has been reported to be elevated in various brain injuries and participates in the pathogenesis of several CNS disorders. Moreover, upregulation of MMP-9 has been shown to involve in brain inflammation and

cell migration [14, 40]. Therefore, we further investigated the effects of rottlerin on PMA-induced MMP-9-mediated cell functional changes such as cell migration. First, the images of RBA cell migration were observed and taken at 24 h after treatment of PMA (1 μM). Pretreatment with MMP-9 inhibitor (9i, 1 μM) significantly blocked PMA-induced RBA cell migration (Fig. 6, upper panel), demonstrating that the PMA-induced MMP-9 expression led to RBA cell migration. Next, we evaluated the effects of rottlerin on the cell migration response, and cells were pretreated with rottlerin (Rott, 1 μM) and then incubated with PMA for 24 h. The data showed that PMA-induced RBA cell migration was inhibited by pretreatment of rottlerin (Rott). The number of migratory RBA cells was counted, and the statistical data are presented in Fig. 6 (lower panel). The results demonstrated that rottlerin repressed PMA-induced cell migration via reducing MMP-9 expression in brain astrocytes.

Discussion

MMPs contribute to a wide range of biological activities in different tissues, including several CNS diseases, such

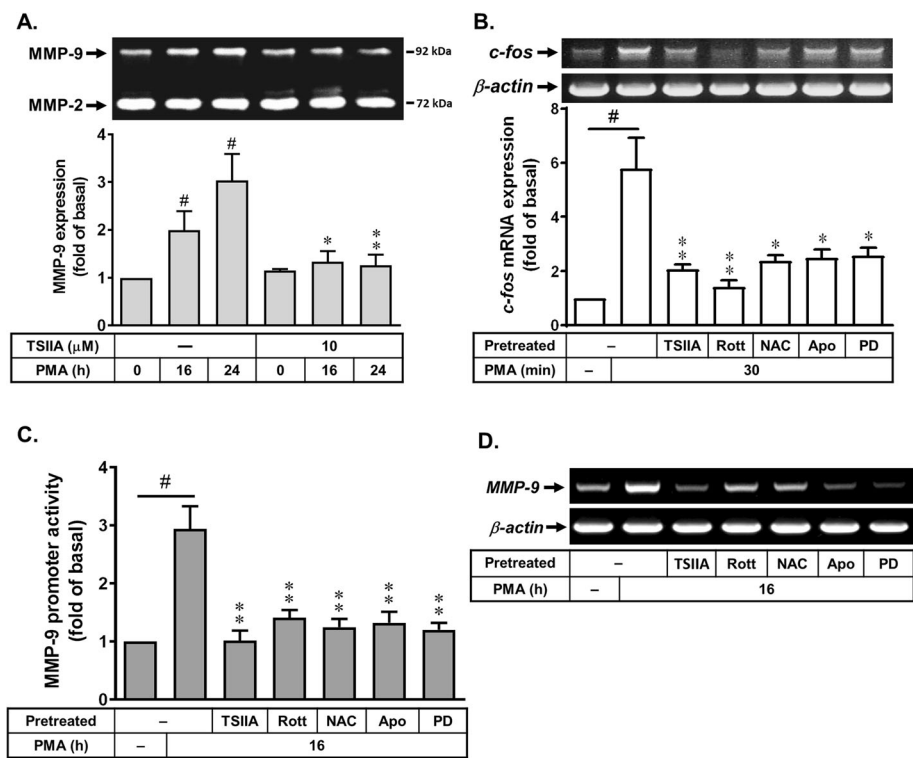
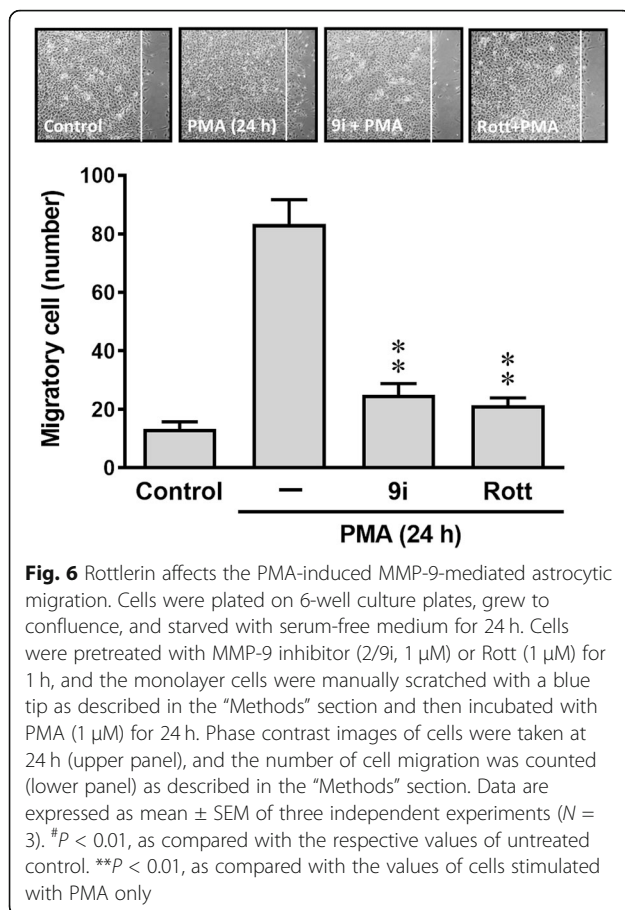


Fig. 5 Effects of rottlerin in PMA-stimulated activation of transcription factors such as AP-1. **a** Cells were pretreated with tanshinone IIA (TSIIA, 10 μM) and then incubated with PMA (1 μM) for the indicated time intervals. The conditioned media were collected and assayed for MMP-9 expression by gelatin zymography. **b, d** Cells were pretreated with TSIIA (10 μM), NAC (5 mM), Apo (10 μM), PD98059 (PD, 10 μM), and Rott (1 μM) for 1 h and then stimulation with PMA (1 μM) for 30 min (**b**) or 16 h (**d**). The total RNA was collected and analyzed *c-fos* mRNA (30 min) and *MMP-9* mRNA (16 h) expression by RT-PCR analysis as described in the “Methods” section. **c** Cells were transiently transfected with pGL-MMP9-Luc and pGal for 24 h, pretreated with TSIIA (10 μM), NAC (5 mM), Apo (10 μM), PD98059 (PD, 10 μM), and Rott (1 μM) for 1 h and then stimulation with PMA (1 μM) for 16 h. After stimulation, luciferase activity of MMP-9-promoter construct was measured as relative promoter activity to that of β-galactosidase. Data are expressed as the mean ± SEM (N = 3). #P < 0.01, as compared with the respective values of untreated control. *P < 0.05; **P < 0.01, as compared with the respective values of cells stimulated with PMA only. The image represents one of three individual experiments

as stroke, Alzheimer’s disease, and malignant glioma [17]. Among MMPs, MMP-9 expression and activation play a critical role in tissue remodeling in the pathogenesis of brain diseases [17]. Reduction of MMP activity by pharmacological inhibitors or gene knock-out strategies protects the brain from BBB disruption, cell death, and advanced neuroinflammation [41]. These studies suggest that upregulation of MMP-9 by pro-inflammatory factors may be a great effect upon brain injury, inflammation, and neurodegeneration. Therefore, the inhibition of MMP-9-mediated inflammatory pathways may provide therapeutic strategies to brain inflammation and neurodegenerative diseases. Moreover, BK and related peptides are simultaneously produced and released following brain injury [20]. Our previous data have demonstrated that PKCs, PKC-δ especially, contribute to up-regulation of MMP-9 in astrocytes which may change astrocytic functions such as cell motility and neuroinflammation [30, 39]. These findings of PKC-mediated MMP-9 expression in RBA imply that PKCs may play an

important role in brain injury, astrogloma, or CNS diseases. Pharmacological and knockout-mouse approaches suggest that targeting MMP-9 and their upstream signaling pathways should yield useful therapeutic targets for brain injury, tumor, and neuroinflammation. Herein, we evaluate whether the natural product rottlerin possess anti-oxidative and anti-inflammatory effects on PMA-induced MMP-9 expression in brain astrocytes and its inhibitory mechanism. The results suggest that in brain astrocytes, the rottlerin-reduced PMA-induced MMP-9-dependent astrocytic migration is mediated through inhibition of the PKC-δ-activated Nox/ROS/ERK signal leading to induction of c-Fos/AP-1 pathway. Here, we first found that a natural compound rottlerin can inhibit PMA-induced MMP-9 gene expression in RBA cells (Fig. 2). This result is the first finding that rottlerin can suppress MMP-9 upregulation by PMA in brain astrocytes. Next, many reports and our previous data have indicated that PKCs may contribute to various stimuli-induced MMP-9 expression in brain astrocytes



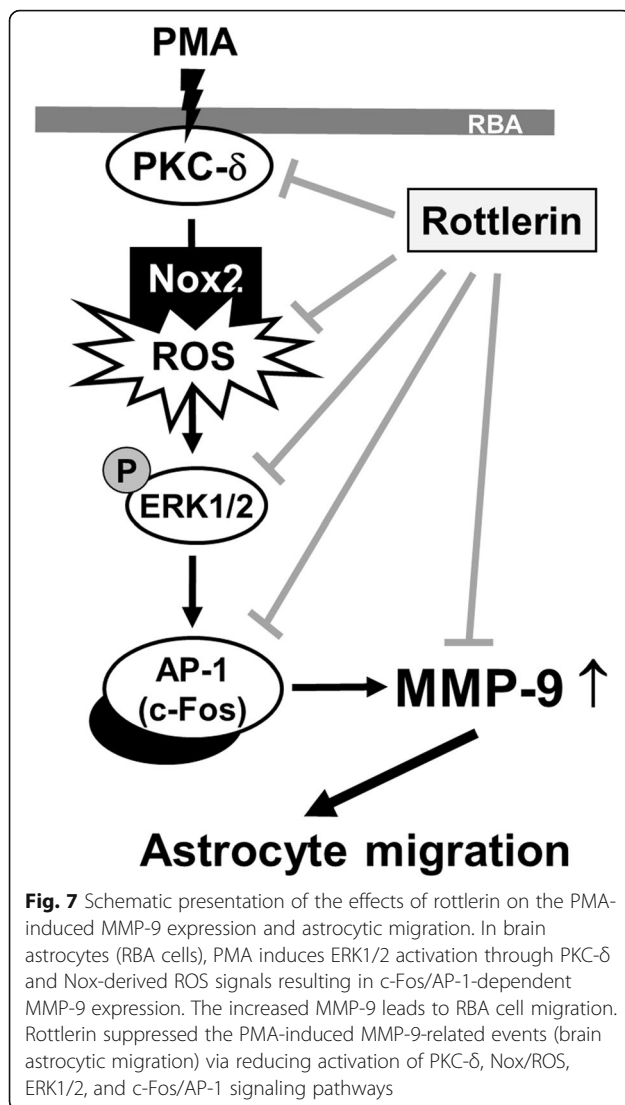
[14, 30]. Moreover, several reports also demonstrate that PKC- δ is crucial for MMP-9 expression [14]. Thus, we investigated whether the inhibition of rottlerin is mediated through blocking the activation of PKC signals, PKC- δ especially, by PMA in brain astrocytes. The results showed that PMA stimulated PKC activation (translocation), including PKC- δ , which were attenuated by pretreatment with rottlerin in RBA cells (Fig. 2). These data demonstrated that rottlerin may inhibit PMA-induced MMP-9 expression via reducing PKC (i.e., PKC- δ)-mediated pathways in RBA cells.

Redox imbalance plays a causative role in numerous pathologies of degenerative diseases [26]. ROS concentration dependently exerts a key role in the normal physiological functions and the inflammatory responses [24]. In the brain, ROS also extend to the control of vascular tone which is tightly modulated by metabolic activity within neurons [25]. Moreover, increasing ROS generation by diverse stimuli can regulate the expression of inflammatory genes in pathogenesis of brain disorders [42]. Recently, the cellular damage in neurodegenerative disorders such as Alzheimer’s disease (AD) is attributed to oxidative stress in brain inflammatory disorders [22, 26]. In

astrocytes, our recent data have demonstrated that in both in vitro and in vivo studies, the ROS-dependent pathways contribute to upregulation of MMP-9 in brain astrocytes. Moreover, we found that upregulation of MMP-9 by BK is mediated through Nox-mediated ROS generation [30]. In the study, we further demonstrated that rottlerin may have an anti-oxidative activity (Fig. 3). Herein, we are the first group to establish that rottlerin reduce Nox/ROS signal induced by PMA in brain astrocytes. The finding is consistent with previous study indicated that PKC- δ phosphorylation is an upstream event of GSK3 inactivation-mediated ROS generation in TGF- β 1-induced senescence [43]. It is consistent with previous report indicated that rottlerin induces cyclooxygenase-2 upregulation through reactive oxygen species-independent pathway in HEI-OC1 cells [44].

The MAPK regulation has been reported to act as an important inflammatory event through activation of MAPK cascades in different cell types [45, 46]. Abnormal MAPK regulation may occur in several models of CNS inflammation and injury [19]. Previously, we have demonstrated that MAPKs such as ERK1/2 were essentially required for upregulation of MMP-9 by BK [14, 30]. Here, our data showed that activation of ERK1/2 participated in PMA-induced MMP-9 expression in RBA cells (Fig. 4), which was activated via Nox/ROS-dependent pathway. Moreover, rottlerin reduced MMP-9 expression by inhibiting PMA-stimulated ERK1/2 MAPK activation in RBA cells (Fig. 4). These results suggest that rottlerin can block PMA-induced MMP-9 expression through reducing PKC- δ -mediated activation of Nox/ROS-ERK1/2 cascade in RBA cells. The findings are similar with the report showed that PMA induces MUC16 expression via PKC- δ and p38 MAPK, but not ERK1/2, in human airway epithelial cells [47]. Moreover, another study indicated that the activation of PKC- δ induced cell growth arrest in NPA cells, through an ERK-dependent pathway. PKC- δ may be an effective molecular target for novel therapy in thyroid cancer [48]. In contrast with the previous study showed that rottlerin enhances IL-1 β -induced COX-2 expression through sustained p38 MAPK activation in MDA-MB-231 human breast cancer cells [49], these differences suggest that the nature of its effects may vary in a stimuli-dependent or cell-type-specific manner.

The progressive increase of oxidative stress during injuries not only causes oxidative damage to cellular macromolecules, but also modulates the pattern of gene expression through functional alterations of transcription factors. The transcription factors such as AP-1 play a key role in the regulation of several gene expressions including MMP-9 during inflammation, cell proliferation, and



apoptosis associated with physiological and pathological events [50]. In addition, several reports also indicate that AP-1 is involved in the pathogenesis of brain inflammation [20]. In the CNS, various stimuli can induce expression of several inflammatory mediators such as MMP-9 through ROS-mediated activation of AP-1 manner in astrocytes [20]. Previously, we have demonstrated that AP-1 participates in upregulation of several genes including MMP-9 by proinflammatory factors through ROS-dependent manner [30, 51]. These results implicate that AP-1 may play a critical role in upregulating MMP-9 expression and lead to inflammatory gene expression in pathological events including the CNS inflammation [20]. Therefore, we focus on the effects of rottlerin on PMA-stimulated activation of the transcription factor AP-1 in RBA cells. The results showed that PMA-induced MMP-9 expression is mediated through up-regulation of AP-1 (Fig. 5). The Nox/ROS and ERK1/2 were involved in

PMA-stimulated c-Fos/AP-1 expression. Moreover, PMA-stimulated increase of AP-1 (c-Fos induction), MMP-9 promoter activity, and MMP-9 mRNA expression were significantly inhibited by rottlerin (Fig. 5b–d). These results suggested that rottlerin may alleviate upregulation of MMP-9 by PMA via inhibiting activation of the transcription factor AP-1 in brain astrocytes. Moreover, our data also showed that PMA directly induces MMP-9 expression via PKC-δ-mediated Nox/ROS and ERK1/2 signals, linking to activation of c-Fos/AP-1, which results in the brain astrocytic (RBA) migration (Fig. 6).

Conclusions

Based on the observations from literatures and our findings, Fig. 7 depicts a model for the inhibitory action of rottlerin on PMA-induced MMP-9-dependent events like RBA cell migration. Herein, the data showed that pretreatment with rottlerin can inhibit activation of several signaling molecules in PMA-induced MMP-9 expression, including PKC-δ, Nox/ROS, ERK1/2, and c-Fos/AP-1. These findings concerning the natural product rottlerin-reduced PMA-induced PKC-δ-mediated Nox/ROS signal, MAPKs (i.e., ERK1/2), and MMP-9 expression in brain astrocytes imply that rottlerin (as a PKC-δ inhibitor) may play a critical role in the anti-oxidative and anti-inflammatory properties. Rottlerin may be as a neuroprotective natural product in several brain inflammatory disorders.

Abbreviations

CNS: Central nervous system; AD: Alzheimer's disease; ECM: Extracellular matrix; PMA: Phorbol 12-myristate 13-acetate; MMP-9: Matrix metalloproteinase-9; PKC: Protein kinase C; ROS: Reactive oxygen species; RBA: Rat brain astrocytes; ERK: Extracellular signal-regulated kinase; GAPDH: Glyceraldehyde-3-phosphate dehydrogenase; DMEM/F-12: Dulbecco's modified Eagle's medium/Ham's nutrient mixture F-12; FBS: Fetal bovine serum; ECL: Enhanced chemiluminescence; BCA: Bicinchoninic acid; PBS: Phosphate-buffered saline; RT-PCR: Reverse transcription-polymerase chain reaction; DCF-DA: 2',7'-Dichlorofluorescein diacetate; NAC: N-acetyl-cysteine

Acknowledgements

The authors are grateful to Ms. Ssu-Yu Chen, Yin-Chen Chen, and Shu-Ching Hsu for their technical assistance for their excellent technical assistance. The authors thank Professor Ying-Tung Lau for his support.

Authors' contributions

All authors were involved in drafting the article or revising it critically for important intellectual content, and all authors approved the final version to be published. H.L.H. had full access to all of the data in the study and takes responsibility for the integrity of the data and the accuracy of the data analysis. Study conception and design: H.L.H., T.H.L., and J.L.C.; acquisition of data: H.L.H., P.S.L., S.J.W., and M.M.T.; analysis and interpretation of data: H.L.H., T.H.L., and J.L.C. The authors read and approved the final manuscript.

Funding

This work was supported by the Ministry of Science and Technology, Taiwan; grant number: MOST107-2320-B-255-003 and MOST108-2320-B-255-002-MY3; Chang Gung Medical Research Foundation, grant number: CMRPF1F0132, CMRPF1H0051, CMRPF1I0041, CMRPF1H0052, CMRPF1I0042; Chang Gung University of Science and Technology, Grant number: ZRRPF3H0131, ZRRPF3J0081.

Availability of data and materials

The datasets used and/or analyzed during the current study are available from the corresponding author on reasonable request.

Ethics approval and consent to participate

Not applicable.

Consent for publication

Not applicable.

Competing interests

The authors declare that they have no competing interests.

Author details

¹Stroke Center and Stroke Section, Department of Neurology, College of Medicine, Chang Gung Memorial Hospital, Linkou Medical Center and Chang Gung University, Taoyuan, Taiwan. ²Division of Chinese Internal Medicine, Center for Traditional Chinese Medicine, Chang Gung Memorial Hospital and School of Traditional Chinese Medicine, College of Medicine, Chang Gung University, Taoyuan, Taiwan. ³Department of Microbiology, Soochow University, Taipei, Taiwan. ⁴Department of Nursing, Division of Basic Medical Sciences, Research Center for Chinese Herbal Medicine, and Graduate Institute of Health Industry Technology, Chang Gung University of Science and Technology, 261 Wenhua 1st Road, Guishan, Taoyuan, Taiwan. ⁵Department of General Surgery, Chang Gung Memorial Hospital, Chiayi, Taiwan. ⁶School of Medicine, Fu Jen Catholic University, New Taipei City, Taiwan. ⁷Department of Neurology, Chang Gung Memorial Hospital, Taoyuan, Taiwan.

Received: 8 January 2020 Accepted: 29 May 2020

Published online: 06 June 2020

References

- Kumar GP, Khanum F. Neuroprotective potential of phytochemicals. *Pharmacogn Rev*. 2012;6:81–90.
- Matkowski A, Jamiolkowska-Kozłowska W, Nawrot I. Chinese medicinal herbs as source of antioxidant compounds where tradition meets the future. *Curr Med Chem*. 2013;20:984–1004.
- Gschwendt M, Müller HJ, Kielbassa K, Zang R, Kittstein W, Rincke G, Marks F. Rottlerin, a novel protein kinase inhibitor. *Biochem Biophys Res Commun*. 1994;199:93–8.
- Soltoff SP. Rottlerin: an inappropriate and ineffective inhibitor of PKCdelta. *Trends Pharmacol Sci*. 2007;28:453–8.
- Santos CM. New agents promote neuroprotection in Parkinson's disease models. *CNS Neurol Disord Drug Targets*. 2012;11:410–8.
- Maioli E, Torricelli C, Valacchi G. Rottlerin and cancer: novel evidence and mechanisms. *ScientificWorldJournal*. 2012;2012:350826.
- Ma J, Hou Y, Xia J, Zhu X, Wang ZP. Tumor suppressive role of rottlerin in cancer therapy. *Am J Transl Res*. 2018;10:3345–56.
- Levinson SW, Goldman JE. Astrocyte origins. In: Murphy S, editor. *Astrocytes: pharmacology and function*. San Diego: Academic; 1993. p. 1–22.
- Kimelberg HK. Receptors on astrocytes—what possible functions? *Neurochem Int*. 1995;26:27–40.
- Eng LF, Ghirnikar RS. GFAP and astrogliosis. *Brain Pathol*. 1994;4:229–37.
- Ridet JL, Malhotra SK, Privat A, Gage FH. Reactive astrocytes: cellular and molecular cues to biological function. *Trends Neurosci*. 1997;20:570–7.
- Richardson JD, Vasko MR. Cellular mechanisms of neurogenic inflammation. *J Pharmacol Exp Ther*. 2002;302:839–45.
- Yang CM, Yang SH, Lee TH, Fang JY, Lin CF, Jou MJ, Hsieh HL. Evaluation of anti-inflammatory effects of *Helminthostachys zeylanica* extracts via inhibiting bradykinin-induced MMP-9 expression in brain astrocytes. *Mol Neurobiol*. 2016;53:5995–6005.
- Hsieh HL, Wu CY, Yang CM. Bradykinin induces matrix metalloproteinase-9 expression and cell migration through a PKC-delta-dependent ERK/Elk-1 pathway in astrocytes. *Glia*. 2008;56:619–32.
- Dollery CM, McEwan JR, Henney AM. Matrix metalloproteinases and cardiovascular disease. *Circ Res*. 1995;77:863–8.
- Yong VW, Krekoski CA, Forsyth PA, Bell R, Edwards DR. Matrix metalloproteinases and diseases of the CNS. *Trends Neurosci*. 1998;21:75–80.
- Yong VW, Power C, Forsyth P, Edwards DR. Metalloproteinases in biology and pathology of the nervous system. *Nat Rev Neurosci*. 2001;2:502–11.
- Gottschall PE, Yu X. Cytokines regulate gelatinase a, B (matrix metalloproteinase 2 and 9) activity in cultured rat astrocytes. *J Neurochem*. 1995;64:1513–20.
- Lee WJ, Shin CY, Yoo BK, Ryu JR, Choi EY, Cheong JH, Ryu JH, Ko KH. Induction of matrix metalloproteinase-9 (MMP-9) in lipopolysaccharide-stimulated primary astrocytes is mediated by extracellular signal-regulated protein kinase 1/2 (Erk1/2). *Glia*. 2003;41:15–24.
- Hsieh HL, Yang CM. Role of redox signaling in neuroinflammation and neurodegenerative diseases. *Biomed Res Int*. 2013;2013:484613.
- Demchenko IT, Oury TD, Crapo JD, Piantadosi CA. Regulation of the brain's vascular responses to oxygen. *Circ Res*. 2002;91:1031–7.
- Halliwell B. Oxidative stress and neurodegeneration: where are we now? *J Neurochem*. 2006;97:1634–58.
- Chrissobolis S, Faraci FM. The role of oxidative stress and NADPH oxidase in cerebrovascular disease. *Trends Mol Med*. 2008;14:495–502.
- Kamata H, Hirata H. Redox regulation of cellular signalling. *Cell Signal*. 1999;11:1–14.
- Chan PH. Reactive oxygen radicals in signaling and damage in the ischemic brain. *J Cereb Blood Flow Metab*. 2001;21:2–14.
- Lewén A, Matz P, Chan PH. Free radical pathways in CNS injury. *J Neurotrauma*. 2000;17:871–90.
- Qin L, Liu Y, Wang T, Wei SJ, Block ML, Wilson B, Liu B, Hong JS. NADPH oxidase mediates lipopolysaccharide-induced neurotoxicity and proinflammatory gene expression in activated microglia. *J Biol Chem*. 2004;279:1415–21.
- Rastogi R, Geng X, Li F, Ding Y. NOX Activation by subunit interaction and underlying mechanisms in disease. *Front Cell Neurosci*. 2017;10:301.
- Volpe CMO, Villar-Delfino PH, Dos Anjos PMF, Nogueira-Machado JA. Cellular death, reactive oxygen species (ROS) and diabetic complications. *Cell Death Dis*. 2018;9:119.
- Lin CC, Hsieh HL, Shih RH, Chi PL, Cheng SE, Chen JC, Yang CM. NADPH oxidase 2-derived reactive oxygen species signal contributes to bradykinin-induced matrix metalloproteinase-9 expression and cell migration in brain astrocytes. *Cell Commun Signal*. 2012;10:35.
- Hsieh HL, Lin CC, Shih RH, Hsiao LD, Yang CM. NADPH oxidase-mediated redox signal contributes to lipoteichoic acid-induced MMP-9 upregulation in brain astrocytes. *J Neuroinflammation*. 2012;9:110.
- Hsieh HL, Yen MH, Jou MJ, Yang CM. Intracellular signaling underlying bradykinin-induced matrix metalloproteinase-9 expression in rat brain astrocyte-1. *Cell Signal*. 2004;16:1163–76.
- Wang HH, Hsieh HL, Wu CY, Sun CC, Yang CM. Oxidized low-density lipoprotein induces matrix metalloproteinase-9 expression via a p42/p44 and JNK-dependent AP-1 pathway in brain astrocytes. *Glia*. 2009;57:24–38.
- Hsieh HL, Wu CY, Hwang TL, Yen MH, Parker P, Yang CM. BK-induced cytosolic phospholipase A₂ expression via sequential PKC-δ, p42/p44 MAPK, and NF-κB activation in rat brain astrocytes. *J Cell Physiol*. 2006;206:246–54.
- LeBel CP, Ischiropoulos H, Bondy SC. Evaluation of the probe 2',7'-dichlorofluorescein as an indicator of reactive oxygen species formation and oxidative stress. *Chem Res Toxicol*. 1992;5:227–31.
- Nelson KK, Melendez JA. Mitochondrial redox control of matrix metalloproteinases. *Free Radic Biol Med*. 2004;37:768–84.
- Infanger DW, Sharma RV, Davisson RL. NADPH oxidases of the brain: distribution, regulation, and function. *Antioxid Redox Signal*. 2006;8:1583–96.
- Wang JQ, Mao L. The ERK pathway: molecular mechanisms and treatment of depression. *Mol Neurobiol*. 2019;56:6197–205.
- Sato H, Seiki M. Regulatory mechanism of 92 kDa type IV collagenase gene expression which is associated with invasiveness of tumor cells. *Oncogene*. 1993;8:395–405.
- Yang CM, Hsieh HL, Lin CC, Shih RH, Chi PL, Cheng SE, Hsiao LD. Multiple factors from bradykinin-challenged astrocytes contribute to the neuronal apoptosis: involvement of astroglial ROS, MMP-9, and HO-1/CO system. *Mol Neurobiol*. 2013;47:1020–33.
- Rosenberg GA. Matrix metalloproteinases in neuroinflammation. *Glia*. 2002;39:279–91.
- Floyd RA. Neuroinflammatory processes are important in neurodegenerative diseases: a hypothesis to explain the increased formation of reactive oxygen and nitrogen species as major factors involved in neurodegenerative disease development. *Free Radic Biol Med*. 1999;26:1346–55.
- Byun HO, Jung HJ, Kim MJ, Yoon G. PKCδ phosphorylation is an upstream event of GSK3 inactivation-mediated ROS generation in TGF-β1-induced senescence. *Free Radic Res*. 2014;48:1100–8.

44. Woo SM, Lee WK, Min KJ, Kim DE, Park SH, Nam SI, Kwon TK. Rottlerin induces cyclooxygenase-2 upregulation through an ATF4 and reactive oxygen species-independent pathway in HEI-OC1 cells. *Mol Med Rep.* 2016; 14:845.
45. Liebmann C. Bradykinin signalling to MAP kinase: Cell-specific connections versus principle mitogenic pathways. *Biol Chem.* 2001;382:49–55.
46. Schwaninger M, Sallmann S, Petersen N, Schneider A, Prinz S, Libermann TA, Spranger M. Bradykinin induces interleukin-6 expression in astrocytes through activation of nuclear factor- κ B. *J Neurochem.* 1999;73:1461–6.
47. Bae CH, Kim HS, Song SY, Kim YD. Phorbol 12-Myristate 13-Acetate Induces MUC16 Expression via PKC δ and p38 in Human Airway Epithelial Cells. *Clin Exp Otorhinolaryngol.* 2012;5:161–9.
48. Koike K, Fujii T, Nakamura AM, Yokoyama G, Yamana H, Kuwano M, Shirouzu K. Activation of protein kinase C delta induces growth arrest in NPA thyroid cancer cells through extracellular signal-regulated kinase mitogen-activated protein kinase. *Thyroid.* 2006;16:333–41.
49. Park EJ, Kwon TK. Rottlerin enhances IL-1 β -induced COX-2 expression through sustained p38 MAPK activation in MDA-MB-231 human breast cancer cells. *Exp Mol Med.* 2011;43:669–75.
50. Haddad JJ. Oxygen-sensitive pro-inflammatory cytokines, apoptosis signaling and redox-responsive transcription factors in development and pathophysiology. *Cytokines Cell Mol Ther.* 2002;7:1–14.
51. Hsieh HL, Chi PL, Lin CC, Yang CC, Yang CM. Up-regulation of ROS-dependent matrix metalloproteinase-9 from high-glucose-challenged astrocytes contributes to the neuronal apoptosis. *Mol Neurobiol.* 2014;50: 520–33.

Publisher's Note

Springer Nature remains neutral with regard to jurisdictional claims in published maps and institutional affiliations.

Ready to submit your research? Choose BMC and benefit from:

- fast, convenient online submission
- thorough peer review by experienced researchers in your field
- rapid publication on acceptance
- support for research data, including large and complex data types
- gold Open Access which fosters wider collaboration and increased citations
- maximum visibility for your research: over 100M website views per year

At BMC, research is always in progress.

Learn more biomedcentral.com/submissions

